PROCEEDINGS OF THE 1999 PARTICLE ACCELERATOR CONFERENCE

VOLUME 5 OF 5
PAGES 2963 - 3779

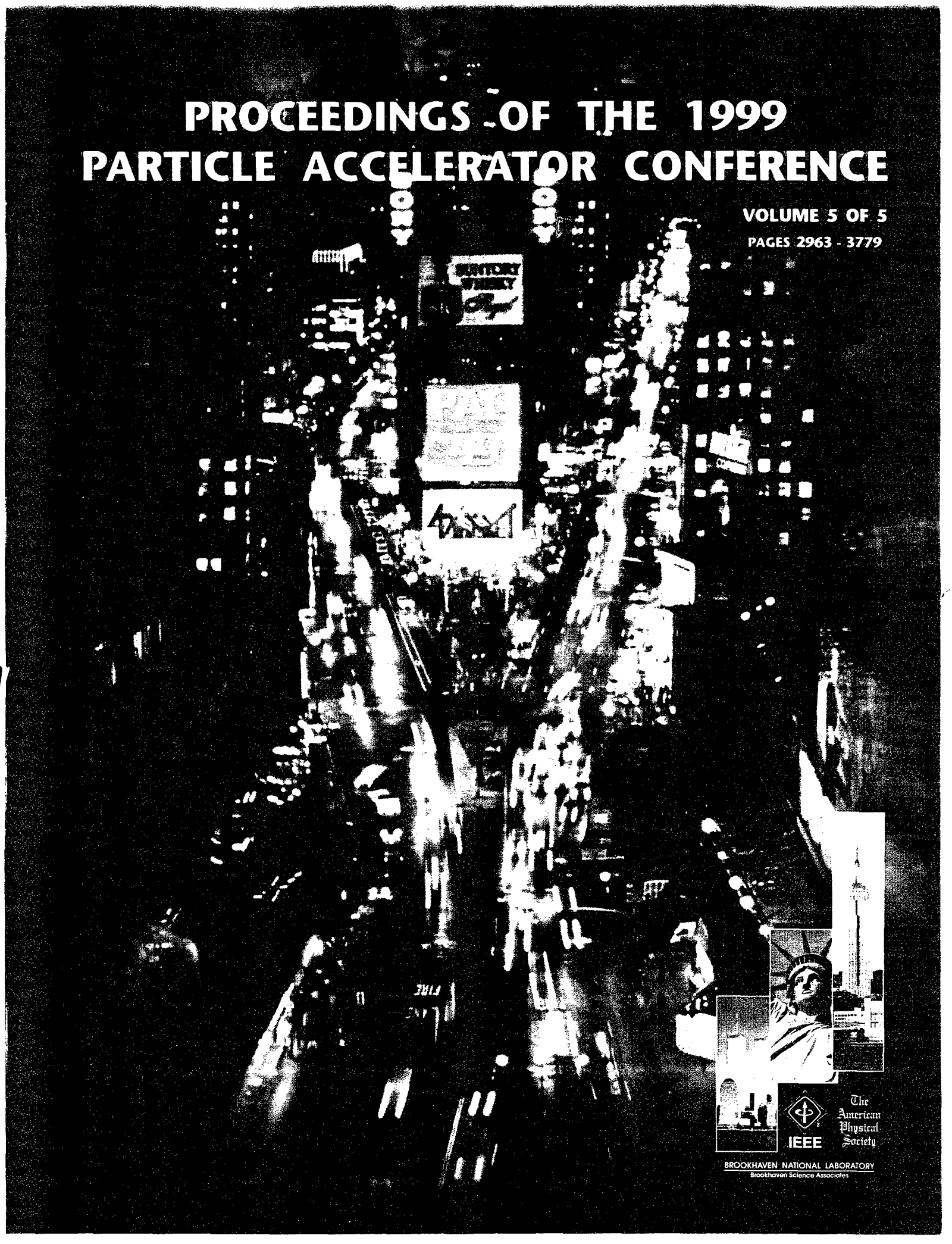

IEEE
The American Physical Society
BROOKHAVEN NATIONAL LABORATORY
Brookhaven Science Associates

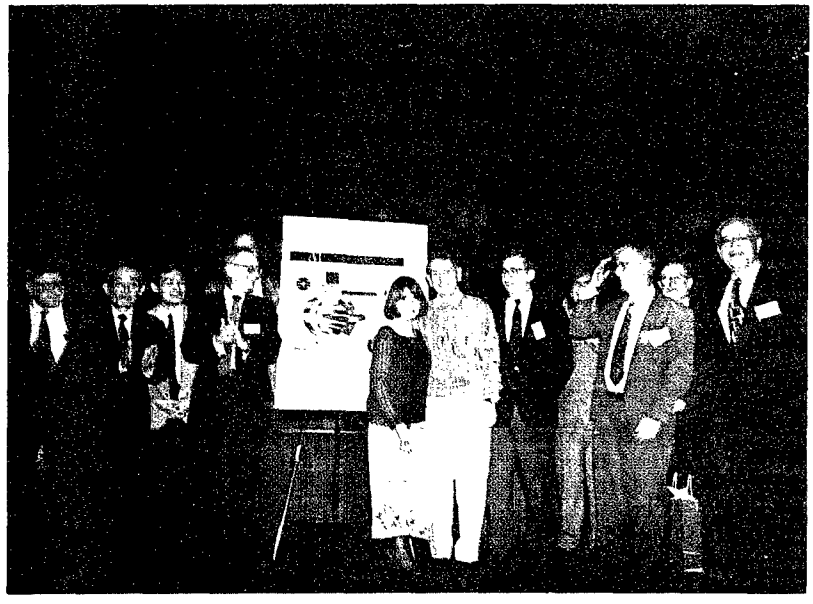

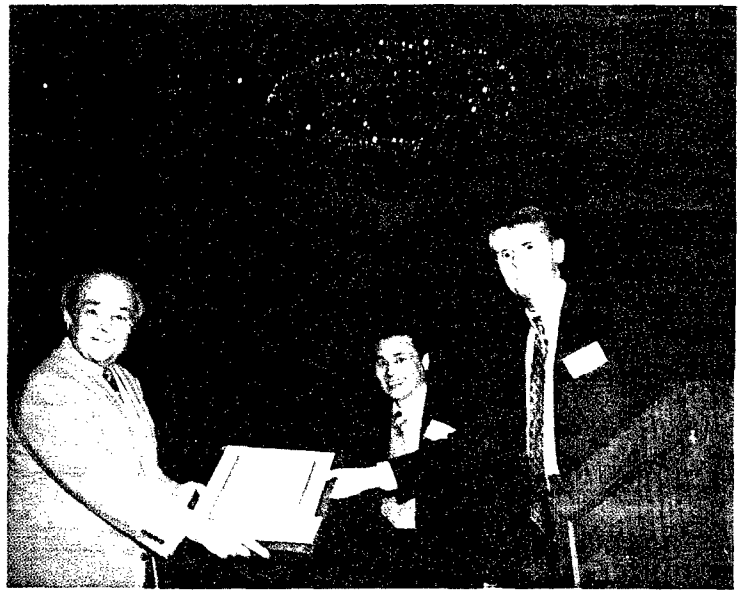

REPORT DOCUMENTATION PAGE

Form Approved
OMB No. 0704-0188

Public reporting burden for this collection of information is estimated to average 1 hour per response, including the time for reviewing instructions, searching existing data sources, gathering and maintaining the data needed, and completing and reviewing the collection of information. Send comments regarding this burden estimate or any other aspect of this collection of information, including suggestions for reducing this burden, to Washington Headquarters Services, Directorate for Information Operations and Reports, 1215 Jefferson Davis Highway, Suite 1204, Arlington, VA 22202-4302, and to the Office of Management and Budget, Paperwork Reduction Project (0704-0188), Washington, DC 20503.

1. AGENCY USE ONLY *(Leave Blank)*	2. REPORT DATE	3. REPORT TYPE AND DATES COVERED
	June 1999	**Final; March 27- April 2, 1999**

4. TITLE AND SUBTITLE
Proceedings of the 1999 Particle Accelerator Conference
Volumes 1 through 5

5. FUNDING NUMBERS
G

6. AUTHORS
A. Luccio, W. MacKay - editors

7. PERFORMING ORGANIZATION NAME(S) AND ADDRESS(ES)
Brookhaven National Lab
P.O. Box 500
Upton, NY 11973

8. PERFORMING ORGANIZATION REPORT NUMBER

9. SPONSORING / MONITORING AGENCY NAME(S) AND ADDRESS(ES)
U.S. DOE
National Science Foundation
Office of Naval Research

10. SPONSORING / MONITORING AGENCY REPORT NUMBER

11. SUPPLEMENTARY NOTES

12a. DISTRIBUTION / AVAILABILITY STATEMENT
Available to public

12b. DISTRIBUTION CODE

13. ABSTRACT *(Maximum 200 words)*
Papers for the eighteenth biennial Particle Accelerator conference, an international forum on acceleator science and tehnology held March 27-April 2, 1999 in New York City, organized by Brookhaven National Lab.

14. SUBJECT TERMS

15. NUMBER OF PAGES
3779

16. PRICE CODE

17. SECURITY CLASSIFICATION OF REPORT	18. SECURITY CLASSIFICATION OF THIS PAGE	19. SECURITY CLASSIFICATION OF ABSTRACT	20. LIMITATION OF ABSTRACT
Unclassified	**Unclassified**	**Unclassified**	**UL**

NSN 7540-01-280-5500

Standard Form 298 (Rev. 2-89)
Prescribed by ANSI Std. Z39-1
298-102

20000229016

BROOKHAVEN
NATIONAL LABORATORY

The
American
Physical
Society

Proceeding of the 1999 Particle Accelerator Conference

(Editors: A. Luccio, W. MacKay)

Volume 5 of 5

Pages 2963 – 3779

DISTRIBUTION STATEMENT A
Approved for Public Release
Distribution Unlimited

Papers from the eighteenth biennial Particle Accelerator Conference, an international forum on accelerator science and technology held March 27 – April 2, 1999 in New York City, organized by Brookhaven National Laboratory. Sponsored by the Institute of Electrical and Electronics Engineers Nuclear and Plasma Sciences Society and the American Physical Society Division of Physics of Beams, and with support from the U.S. Department of Energy, the National Science Foundation, the Office of Naval Research, and Brookhaven Science Associates (BSA).

DTIC QUALITY INSPECTED 3

20000229 016

Proceedings of the
1999 IEEE Particle Accelerator Conference

Abstracting is permitted with credit to the source. Libraries are permitted to photocopy, beyond the limits of U.S. Copyright law for private use of patrons, those articles in this volume that carry a code at the bottom of the first page, provided the per-copy fee indicated in the code is paid through the copyright Clearance Center, 222 Rosewood Drive, Danvers, MA 01923. For other copying, reprint, or republication permission, write to the IEEE Copyright Manager, IEEE Service Center, 445 Hoes Lane, P.O. Box 1331, Piscataway, NJ 08855-1331. All rights reserved. Copyright ©1999 by the Institute of Electrical and Electronics Engineers, Inc.

IEEE Catalog Number: 99CH36366
Library of Congress Number: 88-647453

ISBN Softbound: 0-7803-5573-3
Casebound: 0-7803-5574-1
Microfiche: 0-7803-5575-X
CD-Rom: 0-7803-5576-8

Additional copies of this publication are available from:

IEEE Service Center
445 Hoes Lane
Piscataway, NJ 08854-4150, USA

1-800-678-IEEE (1-800-678-4333)
1-732-981-1393
1-732-981-9667 (FAX)
e-mail: customer.service@ieee.org

VOLUME 5: CONTENTS

(A DETAILED TABLE CAN BE FOUND IN VOLUME 1)

Volume 5: POSTER, pp. 2963 - 3779

ELECTRON STORAGE RINGS AND CIRCULAR ACCELERATORS 2963

ACCELERATORS AND STORAGE RINGS, OTHER 3065

SUPERCONDUCTING MAGNETS 3158

PULSED POWER ACCELERATORS 3248

HIGH INTENSITY ACCELERATORS 3274

ROOM TEMPERATURE MAGNETS 3306

ELECTRON LINEAR 3384

LINEAR ACCELERATORS 3495

NEW ACCELERATION TECHNIQUES 3600

POWER SUPPLIES 3734

THE EXPERIMENT OF THE SINGLE INTERACTION POINT SCHEME IN BEPC

X. Luo, N. Huang, F. Zhou, IHEP, CHINA

Abstract

In order to increase the luminosity of Beijing Electron-Positron Collider (BEPC), the single interaction point (SIP) schemes were adopted. Then the electron and positron beams were separated at the north IP and collided at the south IP. Some experiments were done during these years. The results are given in the paper.

1 INTRODUCTION

There are two interaction points in the storage ring of BEPC. Only one detector BES (BEijing Spectrometer) has been used at the south IP since BEPC was built [1]. The higher luminosity is needed so that BES can acquire data efficiently. One of way to increase the luminosity is to adopt SIP collision scheme. As the beam current already reached the limit by the beam-beam interaction for the double IPs (DIP) scheme, reducing the number of the IP is one of the way to increase the beam current. Then the luminosity can be enhanced. Some experiments were done with several kinds of SIP schemes during these years. The current and luminosity were increased compared with DIP scheme in 1998.

2 SIP SCHEMES

Several SIP schemes were used according to the different hardware and the lattices of the BEPC storage ring. But we couldn't try each of them in detail as there was no enough time for the machine study of the SIP schemes. Two typical modes were used.

2.1 SIP scheme with the original lattice

The vertical phase advance between the two close separators (SP) is not π degree in the DIP lattice, and there is no space or independent power supplies of the quadrupoles to change them to π. This produces a small separation between electron and positron beams at the south IP after turning off the south SP. So the south SP must be given a little value in order to make electron and positron beams collide exactly at the south IP. The two auxiliary power supplies of SP were installed in the BEPC storage ring in 1993. Some experiments were done with adjusting the two auxiliary power supplies in the year. We got some good results [2]. But the luminosity was less than that of DIP. And the beam current was not increased compared with the DIP scheme.

During the beam collision, the coherent oscillation was observed from the synchrotron radiation monitor. This is because there was a large closed orbit distortion (COD) in the whole ring. The electron and positron beams passed different orbits in the ring. And there was a large COD in RF cavities and other magnets. The nonlinear effects gave rise some instabilities to the beams. So it is better to make the COD outside the north two SP eliminate.

2.2 Lattice modification

The BEPC storage ring is 4-fold symmetric. Normally one power supply should control four quadrupoles. It is impossible to change the vertical phase advance between the two SP to π. In the luminosity upgrade project of BEPC, four power supplies of the insertion qradrupoles were prepared in order to adopt mini-β scheme. We used these four power supplies to calculate the lattice again so that the vertical phase advance between the north two SP was π. Then after turning off the south SP, the COD outside the north SP is zero. So the beams should be stable. Figure 1 shows the COD in which the north SP was on and the south SP was off.

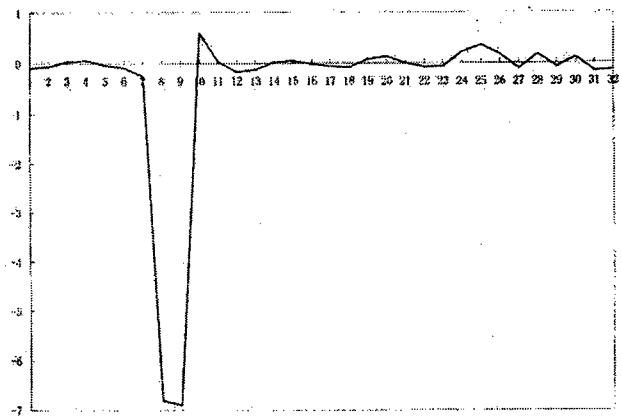

Figure 1: COD of the SIP scheme

Of course, the power supplies of the north SP can be used to adjust the colliding angle (Y'_s) between the electron and positron beams in order to realize head-on collision.

$$Y_s' = \frac{\theta_{spn\,1} - \theta_{spn\,2}}{2 \sin \pi\nu_y} \sqrt{\frac{\beta_{spn}}{\beta^*_{ys}}} \qquad (1)$$

θ_{spn1}, θ_{spn1} express the bending angle by the two north SP, β_{spn}, β^*_{ys} the β-function of the north SP and the south IP.

0-7803-5573-3/99/$10.00@1999 IEEE.

We calculated the two kinds of lattices with adding the four power supplies. The emittances were kept nearly unchanged:

1. We modified the DIP lattice so that the optics parameters outside the north SP were same as DIP. But the vertical phase advance between the north SP was π. So the tunes were changed lot which were just above integer and half integer for the horizontal and vertical ones respectively, $\nu_x/\nu_y = 6.12/6.60$;
2. The tunes were nearly same as that of DIP, $\nu_x/\nu_y = 5.58/6.70$. But the parameters in the whole ring were quite different from that of DIP. The coupling correction is not same either.

3 RESULTS OF THE EXPERIMENTS

We mainly studied the first SIP scheme that was easy to be operated as the most of part of the ring is same as DIP. Table 1 gives the parameters of the SIP and DIP schemes.

Table 1: Parameters of SIP (1) and DIP lattices

	SIP (1)	DIP
Energy	1.548 GeV	1.548 GeV
South β_y^*	0.05 m	0.05 m
North β_y^*	5 m	0.05 m
ν_x/ν_y	6.12/6.60	5.79/6.78
Phase advance of north SP	$\pm 0.250\times 2\pi$	$\pm 0.267\times 2\pi$

Some good results were gained in the first half of 1998. Figure 2 shows the luminosity comparison between the DIP and SIP.

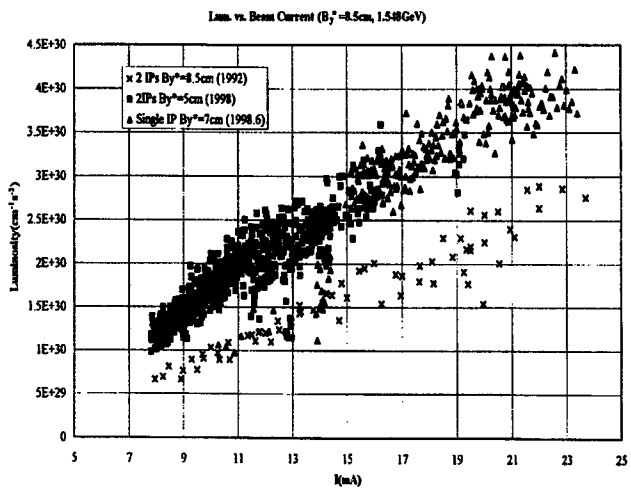

Figure 2: Luminosity comparison between the DIP and SIP schemes

The maximum current was 49.3 mA, and the peak luminosity was 4.4×10^{30} $cm^{-2}s^{-1}$. At that time, the maximum current and the peak luminosity of DIP scheme were 39.5 mA and 3.6×10^{30} $cm^{-2}s^{-1}$ respectively. So both the beam current and the luminosity were increased significantly with the SIP scheme. From the detector of BES, the hadron events were enhanced obviously. This will be benefit for the BES to take data efficiently.

4 BETA-FUNCTION AT IP

The nominated β-function at the south IP (β_y^*) of SIP scheme is 7 cm instead of 5 cm which was used in the DIP lattice. We measured the β_y^* of SIP with colliding beams. The value was less than 7 cm. According to the linear theory, the beta function should be changed as the equation 2:

$$\beta^*_{y0}\, sin\, \nu_{y0} = \beta^*_y\, sin(\, \nu_{y0} + \Delta\nu\,) \qquad (2)$$

Here β^*_{y0} is the undisturbed vertical beta function at the south IP, ν_y the vertical tune, $\Delta\nu$ the vertical tune shift.

We choose $\Delta\nu$=0.035, then the calculated beta function β_y^* = 5.4 cm. So the operation β_y^* was reduced because the tunes were just above the integer and half integer which were quite different from the DIP scheme.

We tried to reduce the β_y^* to 5 cm, but it's difficult to get high current. The maximum one was about 22 mA. We need time to enlarge it.

For the second kind of SIP scheme, the parameters are shown in the table 2.

Table 2: Parameters of SIP (2) and DIP lattices

	SIP (2)	DIP
Energy	1.548 GeV	1.548 GeV
South β_y^*	0.05 m	0.05 m
north β_y^*	4 m	0.05 m
ν_x/ν_y	5.57/6.70	5.79/6.78
Phase advance of north SP	$\pm 0.250\times 2\pi$	$\pm 0.267\times 2\pi$

The maximum current was about 33 mA at β_y^* = 5 cm. The disturbed beta function was about 5.4 cm with the equation 2. But the luminosity reduced lot. The reason is not clear now. We also need time to improve it.

5 COMPARISON OF BEAM-BEAM EFFECT VERSUS BEAM CURRENT

Figure 3 and figure 4 show the comparison of the luminosity and beam-beam effect (ξ_y) vs. beam currents at β_y^* =8.5 cm.

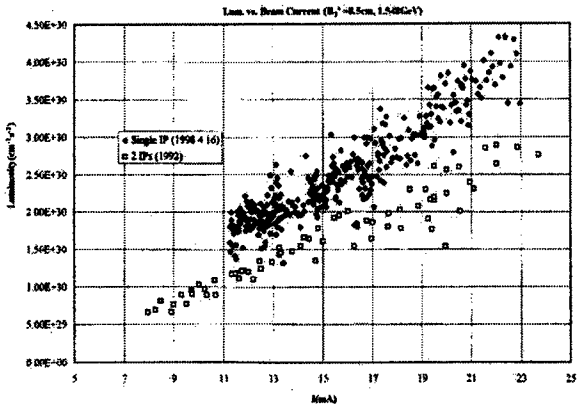

Figure 3: Comparison of the luminosity vs. beam currents at β_y^* =8.5 cm

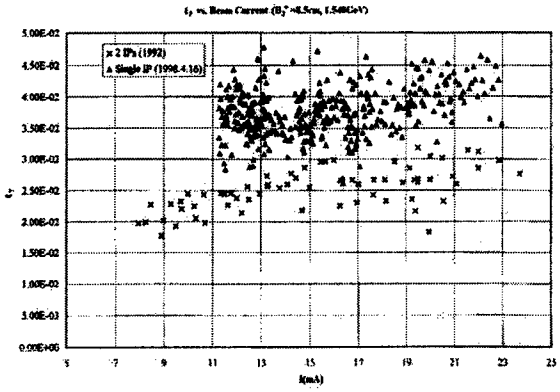

Figure 4: Comparison of the beam-beam effects (ξ_y) vs. beam currents at β_y^* =8.5 cm

From the figure 3 and figure 4, we can see the luminosity and ξ_y of SIP was increased about 50% compared with DIP at the same currents.

Figure 2 and figure 5 show the comparison of the luminosity and ξ_y vs. beam currents at β_y^* =7 cm for SIP scheme and DIP scheme at β_y^* =8.5 and 5 cm.

It is obviously that the luminosity and ξ_y were increased with the SIP scheme. This is reason why we try to use the SIP scheme in the BEPC storage ring. Of course, the background will be studied carefully.

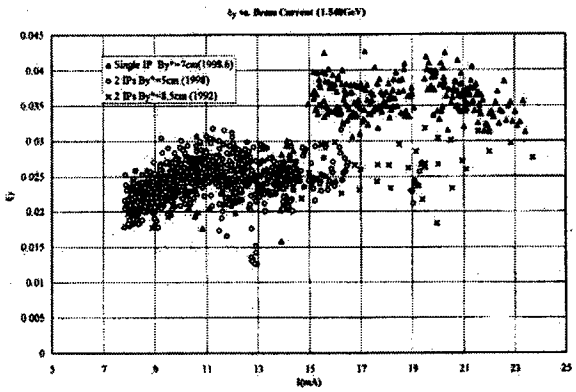

Figure 5: Comparison of the ξ_y vs. beam current

It took us about 15 days to adjust the SIP scheme in 1998. The time was too short to do more detail study as the most of beam time were used for BES and the synchrotron radiation facility.

There are still many problems for the SIP schemes. When the beam current was increased more, such as larger than 50 mA, the beam blow-up always happened. Sometimes changing the coupling or the chromaticity could eliminate the blow-up. But it is not always useful. For the next step, we shall spend more time to adjust the tunes, closed orbit and other parameters carefully in order to enhance the luminosity further.

We would like to thank all persons of the accelerator physics group. They gave many good suggestions and contributed lot during the commissioning of the SIP scheme. We also acknowledge the support by the hardware group.

5 REFERENCES

[1] N. Huang and X. Luo, Possibility Study of Single Interaction Point in BEPC, Workshop on BEPC Luminosity Upgrades, 1990, Beijing

[2] X. Luo, Z. Guo and N. Huang, Study on the Single Interaction Point Collision in BEPC, The 5th Japan-China Joint Symposium on Accelerators for Nuclear Science and Their Applications, 1993

[3] D.L. Rubin and L.A. Schick, Single Interaction Point Operation of CESR

[4] J. Urakawa et al., Performance of the Accumulation Ring e+/e- Collider With Beam Separation at North Interaction Region, Particle Accelerators, 1990, Vol 31, pp 165-170

DETECTION OF COUPLING ELEMENTS IN CESR*

D. Sagan
Wilson Laboratory, Cornell University, Ithaca NY, 14853, USA

Abstract

At the Cornell Electron/positron Storage Ring CESR, the measurement of the coupling between the horizontal and vertical beam motions has led to the ability to locate the position of a coupler and to calculate its strength. Once the identity of a coupler is known, steps can be taken to remove it or to nullify its effect. This coupling analysis can also be used to calibrate correction skew quadrupoles.

1 INTRODUCTION

In a storage ring, the presence of couplers, which couple the horizontal and vertical motions of a beam, can lead to an increase in the vertical beam size with an attendant loss in luminosity[1]. In order to be able to keep the coupling under control, a technique for measuring the coupling has been developed at the Cornell Electron/positron Storage Ring CESR[2]. This involves shaking the beam at the betatron resonant frequencies and measuring the response at the 100 or so detectors in the ring. In order to be able to find unwanted sources of coupling, an analysis program has been developed that can locate isolated coupling elements. This analysis is presented below[3] and is analogous to the technique of using orbit data to find isolated steering kicks. As an added benefit, the analysis can also be used to calibrate the strength of skew quadrupoles.

2 ANALYSIS

2.1 How the Coupling is Defined

Any longitudinal oscillations are ignored and, following Sagan and Rubin[4], the 4×4 1–turn transfer matrix $\mathbf{T}(s)$ is written in normal mode form

$$\mathbf{T} = \mathbf{V}\,\mathbf{U}\,\mathbf{V}^{-1}, \tag{1}$$

where the normal mode matrix $\mathbf{U}$ is of the form

$$\mathbf{U} = \begin{pmatrix} \mathbf{A} & \mathbf{0} \\ \mathbf{0} & \mathbf{B} \end{pmatrix}, \tag{2}$$

and $\mathbf{V}$ is of the form

$$\mathbf{V} = \begin{pmatrix} \gamma\mathbf{I} & \mathbf{C} \\ -\mathbf{C}^{+} & \gamma\mathbf{I} \end{pmatrix}, \tag{3}$$

with "+" denoting the symplectic conjugate. Since $\mathbf{V}$ is required to be symplectic, γ and $\mathbf{C}$ are related by

$$\gamma^2 + ||\mathbf{C}|| = 1. \tag{4}$$

$\mathbf{C}(s)$ is a measure of the coupling; if $\mathbf{C} = \mathbf{0}$ then $\mathbf{V} = \mathbf{1}$ and $\mathbf{T}$ is decoupled. Instead of working with $\mathbf{C}$, though, it is convenient to work with the normalized matrix $\overline{\mathbf{C}}$ given by

$$\overline{\mathbf{C}} = \mathbf{G}_a\,\mathbf{C}\,\mathbf{G}_b^{-1}, \tag{5}$$

where $\mathbf{G}_a$ and $\mathbf{G}_b$ are normalization matrices for the a and b normal modes respectively given by

$$\mathbf{G} = \begin{pmatrix} \frac{1}{\sqrt{\beta}} & 0 \\ \frac{\alpha}{\sqrt{\beta}} & \sqrt{\beta} \end{pmatrix}. \tag{6}$$

At CESR, $\overline{\mathbf{C}}$ is measured by observing the horizontal and vertical oscillation of the beam at the detectors in the ring while shaking the beam at a betatron resonance[2]. In order to be able to extract the strength and location of coupling elements from the data, it is necessary to know how $\overline{\mathbf{C}}$ changes across a coupler, and how $\overline{\mathbf{C}}$ propagates in a region where there are no coupling elements.

2.2 $\overline{\mathbf{C}}$ Variation

If there are no couplers in a local region then the variation of $\overline{\mathbf{C}}$ is given by[4]

$$\overline{\mathbf{C}}(s) = \lambda\,\mathbf{S}(\phi_0 - \phi_+(s)) + \kappa\,\mathbf{R}(\theta_0 + \phi_-(s)), \tag{7}$$

where λ, ϕ_0, κ, and θ_0 are constants, $\mathbf{R}$ and $\mathbf{S}$ are rotation and "anti-rotation" matrices of the form

$$\mathbf{R}(\theta) \equiv \begin{pmatrix} \cos\theta & \sin\theta \\ -\sin\theta & \cos\theta \end{pmatrix}, \tag{8}$$

and

$$\mathbf{S}(\phi) \equiv \begin{pmatrix} \cos\phi & \sin\phi \\ \sin\phi & -\cos\phi \end{pmatrix}, \tag{9}$$

with the sum and difference phase advances being

$$\begin{aligned} \phi_+ &\equiv \phi_a + \phi_b, \quad \text{and} \\ \phi_- &\equiv \phi_a - \phi_b. \end{aligned} \tag{10}$$

To compute the change in $\overline{\mathbf{C}}$ across a coupler, it is assumed that the coupling is small so that terms second order in $\mathbf{C}$ (or $\overline{\mathbf{C}}$) may be neglected. Thus, from Eq. (4), to first order in the coupling

$$\gamma = 1. \tag{11}$$

Using this, and Eqs. (1), (2), and (3), gives to first order

$$\mathbf{T} = \begin{pmatrix} \mathbf{A} & \mathbf{CB} - \mathbf{AC} \\ \mathbf{BC}^{+} - \mathbf{C}^{+}\mathbf{A} & \mathbf{B} \end{pmatrix}. \tag{12}$$

Eq. (12) shows that the on–diagonal 2×2 submatrices of $\mathbf{T}$ are unaffected by the coupling. Thus, to first order, the

* Work supported by the National Science Foundation

0-7803-5573-3/99/$10.00@1999 IEEE.

eigenmode betas, β_a and β_b and the eigenmode phases, ϕ_a and ϕ_b, are equal to what would be calculated if the coupling is absent.

Couplers are modeled as thin skew quadrupoles. The 4×4 transfer matrix $\mathbf{T}_{\mathrm{coup}}$ for a coupler is then

$$\mathbf{T}_{\mathrm{coup}} = \begin{pmatrix} \mathbf{1} & -\mathbf{q} \\ -\mathbf{q} & \mathbf{1} \end{pmatrix}, \tag{13}$$

where

$$\mathbf{q} = \begin{pmatrix} 0 & 0 \\ \delta q & 0 \end{pmatrix}, \tag{14}$$

with δq being the strength of the coupler. The 1–turn matrix $\mathbf{T}_{0+}$, located at a point just after a coupler, is related to the 1–turn matrix $\mathbf{T}_{0-}$, located at a point just before the coupler, via

$$\mathbf{T}_{0+} = \mathbf{T}_{\mathrm{coup}}\, \mathbf{T}_{0-}\, \mathbf{T}_{\mathrm{coup}}^{-1}. \tag{15}$$

Multiplying out Eq. (15), and comparing with Eq. (12), gives, to first order, and with the help of Eq. (5)

$$\overline{\mathbf{C}}_{0+} = \overline{\mathbf{C}}_{0-} - \overline{\mathbf{q}}, \tag{16}$$

where

$$\overline{\mathbf{q}} = \begin{pmatrix} 0 & 0 \\ \delta\bar{q} & 0 \end{pmatrix}, \tag{17}$$

with

$$\delta\bar{q} = \sqrt{\beta_a \beta_b}\, \delta q. \tag{18}$$

2.3 *Isolated Coupler Analysis*

Given a coupler of interest at some point s_0, it is assumed that the coupler is "isolated" so that it is the only coupler in some local region. Since we have linearized the problem, the general solution for $\overline{\mathbf{C}}$ is the sum of a homogeneous part $\overline{\mathbf{C}}_h$ plus an inhomogeneous part $\overline{\mathbf{C}}_i$

$$\overline{\mathbf{C}}(s) = \overline{\mathbf{C}}_h(s) + \overline{\mathbf{C}}_i(s). \tag{19}$$

The homogeneous part is the solution when there is no coupler and is given by Eq. (7). The inhomogeneous part is the solution with the coupler and with some boundary condition which we are free to choose. This boundary condition will be chosen to be $\overline{\mathbf{C}}(s) = \mathbf{0}$ for $s < s_0$. From Eqs. (7) and (16), the inhomogeneous solution is

$$\overline{\mathbf{C}}_i(s) = \begin{cases} \mathbf{0} & s < s_0 \\ \frac{\delta\bar{q}}{2}\left[\mathbf{R}\left(\frac{\pi}{2} + \phi_-(s) - \phi_-(s_0)\right) - \right. & \\ \quad \left. \mathbf{S}\left(\frac{\pi}{2} - \phi_+(s) + \phi_+(s_0)\right)\right] & s > s_0 \end{cases} \tag{20}$$

At CESR, the coupling measurement can measure the $\overline{C}_{11}$, $\overline{C}_{12}$, and $\overline{C}_{22}$ components of $\overline{\mathbf{C}}$. For various technical reasons, the errors in the $\overline{C}_{12}$ data are less than the errors present in the measurement of the other components. Therefore, the following analysis will consider only the $\overline{C}_{12}$ component. Extending the analysis to the other components is a trivial matter. From Eq. (7), the general solution for $\overline{C}_{12}$ can be written as

$$\overline{C}_{12}(s) = \begin{cases} \gamma_a \sin\phi_-(s) + \zeta_a \cos\phi_-(s) + & \\ \quad \lambda_a \sin\phi_+(s) + \rho_a \cos\phi_+(s) & s < s_0 \\ \gamma_b \sin\phi_-(s) + \zeta_b \cos\phi_-(s) + & \\ \quad \lambda_b \sin\phi_+(s) + \rho_b \cos\phi_+(s) & s > s_0 \end{cases} \tag{21}$$

The procedure for locating a coupler is as follows: Given a putative coupler location, two regions are chosen. One region, labeled "A", is chosen to be just before the coupler. The other region, labeled "B", is chosen to be just after the coupler (See the example at the end of the paper). Since the betatron phase is, to first order, independent of the coupling, the phase is taken to be equal to the phase in the design lattice. With this, the sine and cosine functions in Eq. (21) may be evaluated and then a least squares fit can be used to determine γ_a, ζ_a, λ_a, and ρ_a using the data from the A region. Similarly, γ_b, ζ_b, λ_b, and ρ_b are obtained from a least squares fit using the data from the B region. The inhomogeneous part of the solution is now obtained from Eq. (21) by subtracting out the homogeneous part to give

$$\overline{C}_{i,12} = \begin{cases} 0 & s < s_0 \\ \gamma_{ba} \sin\phi_-(s) + \zeta_{ba} \cos\phi_-(s) + & \\ \quad \lambda_{ba} \sin\phi_+(s) + \rho_{ba} \cos\phi_+(s) & s > s_0 \end{cases} \tag{22}$$

with

$$\begin{aligned} \gamma_{ba} &= \gamma_b - \gamma_a, \quad \zeta_{ba} = \zeta_b - \zeta_a, \\ \lambda_{ba} &= \lambda_b - \lambda_a, \quad \rho_{ba} = \rho_b - \rho_a. \end{aligned} \tag{23}$$

The phase at the coupler is found by comparing Eq. (20) with Eq. (22)

$$\begin{aligned} \tan\phi_+(s_0) &= \frac{\lambda_{ba}}{\rho_{ba}}, \quad \text{and} \\ \tan\phi_-(s_0) &= \frac{\gamma_{ba}}{\zeta_{ba}}. \end{aligned} \tag{24}$$

There are multiple solutions to Eqs. (24) spaced π apart. However, valid solutions must have the corresponding ϕ_a and ϕ_b (from Eq. (10)) corresponding to a location somewhere between the A and B regions.

The magnitude of the coupler is given by comparing Eq. (20) to (22)

$$\begin{aligned} \frac{\delta\bar{q}}{2} &= -\lambda_{ba} \sin\phi_+(s_0) - \rho_{ba} \cos\phi_+(s_0), \quad \text{or} \\ \frac{\delta\bar{q}}{2} &= \gamma_{ba} \sin\phi_-(s_0) + \zeta_{ba} \cos\phi_-(s_0). \end{aligned} \tag{25}$$

Changes in amplitudes for the $\mathbf{R}$ and $\mathbf{S}$ components of $\overline{C}_{12}$ may be defined by

$$A_{s,ba}^2 \equiv \lambda_{ba}^2 + \rho_{ba}^2, \quad A_{r,ba}^2 \equiv \gamma_{ba}^2 + \zeta_{ba}^2. \tag{26}$$

Using this, Eqs. (25) may be put in a more transparent form

$$|\delta\bar{q}| = 2A_{s,ba} = 2A_{r,ba}. \tag{27}$$

The disadvantage of Eqs. (27), as opposed to Eqs. (25), is that the sign of $\delta\bar{q}$ is lost.

2.4 *Error analysis*

Even with a good fit to the data, the analysis can be off if there is more than one coupler between the A and B regions. From Eqs. (27), if there is only one coupler, then $A_{s,ba} = A_{r,ba}$. A figure of merit χ_{BA} can thus be defined by

$$\chi_{BA} \equiv \frac{|A_{s,ba} - A_{r,ba}|}{A_{s,ba} + A_{r,ba}}. \tag{28}$$

The condition for a good fit with only one coupler is then

$$\chi_{BA} \ll 1. \tag{29}$$

3 EXAMPLE

The coupling analysis presented above can be used for finding unwanted sources of coupling, and for calibrating skew quadrupole magnets. Figure 1 shows how coupling data is analyzed. In CESR, there are approximately 100 detectors numbered from 0 to 99. The $\overline{C}_{12}$ data shown in figure 1a is the difference between two coupling measurements obtained while varying a skew quadrupole placed between detectors 48 and 49. The A region was chosen to be between detectors 20 and 48 and the B region was chosen to be between detectors 50 and 80. Figure 1b shows the $\overline{C}_{12}$ data with the fit to the A region subtracted off. There is a good fit to the data as evidenced by the fact that the plot is near zero within the A region. The general location of the coupler can be located by eye by noting where, just to the right of the A region, the data becomes significantly nonzero. Figure 1c shows the data with the B region fit subtracted off. Again, there is a good fit to the data. Table 1 shows the values of the fitted parameters. From these values, and Eqs. (10), (24) and (25), it is found that there is a single valid solution given by $\phi_a = 31.86$, $\phi_b = 29.70$, and $\delta\bar{q} = 0.14$ with $\chi_{BA} = 0.09$. This verifies the location of the coupler and gives the magnitude of the kick.

In the above example, the A and B regions could be chosen a priori since the location of the coupler was known before hand. When the location is not initially known, the regions can be chosen through trial and error just by looking at the plotted results until a good fit is obtained. If the space between the A and B regions is too wide, Eqs. (24) will have multiple solutions. However, since the solutions are spaced apart in phase (and hence are some distance apart), it is normally a simple matter to be able to select the correct solution.

Region	λ	ρ	γ	ζ
A	-0.008	0.114	-0.195	-0.186
B	0.057	0.093	-0.128	-0.231
$B-A$	0.065	-0.021	0.067	-0.045

Table 1: Fitted parameters λ, ρ, γ, and ζ.

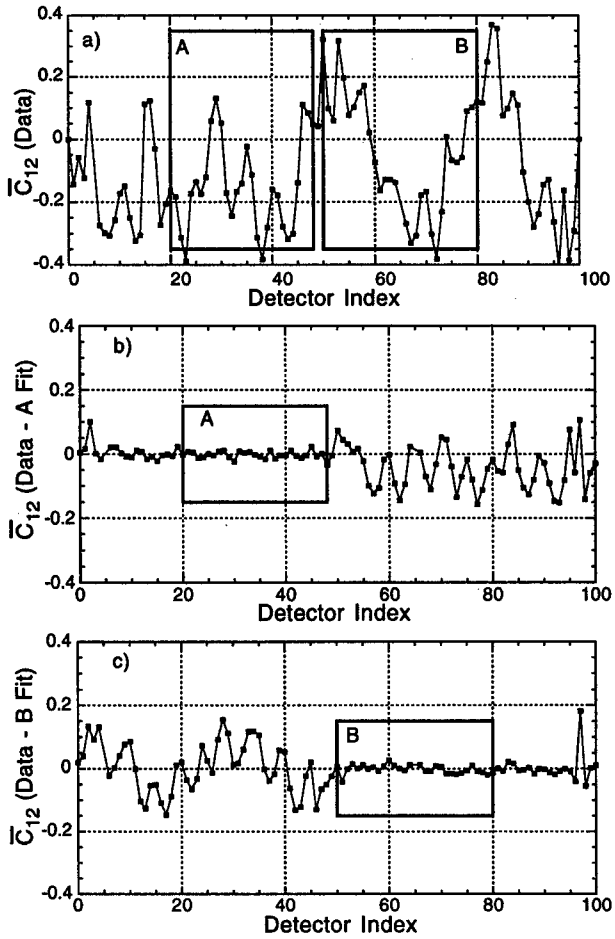

Figure 1: Coupling data. The A and B fit regions are indicated by the boxes. a) Data obtained by varying a skew quadrupole. b) The data with the A region fit subtracted off. c) The data with the B region fit subtracted off.

4 ACKNOWLEDGEMENTS

My thanks to Dave Rubin and for useful discussions and to the rest of the CESR operations group for their support.

5 REFERENCES

[1] D. Sagan, "The Effect of Coupling on Luminosity Performance," Proc. 1995 Part. Acc. Conf. (San Francisco) p. 3382, (1995).

[2] P. Bagley and D. Rubin, "Correction of Transverse Coupling in a Storage Ring," Proc. 1989 Part. Acc. Conf. (San Francisco) p. 874, (1989).

[3] An expanded version of this paper will be published in the PAC99 special Edition of the on–line journal Phys. Rev. Special Topics — Acc. and Beams (PRST–AB).

[4] D. Sagan and D. Rubin, "Propagation of Twiss and Coupling Parameters," Cornell CBN 96-20 (1996). Can be obtained from the web at: http://w4.lns.cornell.edu/public/CBN/

INCREASING THE LUMINOSITY WITH THE BEAM–BEAM INTERACTION LUMINOSITY MONITOR*

D. Sagan
Wilson Laboratory, Cornell University, Ithaca NY, 14853, USA

Abstract

At the Cornell Electron/positron Storage Ring CESR, a fast luminosity monitor has been implemented[1]. The monitor works by measuring the amplitude of oscillation of a given bunch while the corresponding opposing bunch is shaken. A disadvantage with the luminosity monitor is that the monitor signal, besides being a measure of the luminosity, is also dependent upon other factors such as the vertical tune and the vertical beta function at the IP. To overcome this deficiency, a software program has been developed to give a normalized signal that only depends upon the specific luminosity. In HEP conditions, this normalized signal is used as input to an "optimizer" program that automatically varies machine parameters to keep the luminosity at a maximum.

1 INTRODUCTION

In a colliding beam storage ring it is essential to be able to monitor the luminosity so as to be able to adjust machine elements (magnets, separators, etc.) to maximize the luminosity. Recently, a fast luminosity monitor has been developed at the Cornell Electron/positron Storage Ring CESR[1]. The monitor is shown schematically in Fig. 1. Selected bunches of one beam are shaken vertically at a given frequency. These "shaker" bunches shake the corresponding "detected" bunches at the interaction point (IP), and the amplitude of oscillation of the detected bunches are then monitored, via a BPM detector, by a lock–in amplifier. In standard practice at CESR, the amplitude of the shaker bunch is only a few percent of the vertical beam size. Thus, the operation of the monitor has no significant affect on operations. While the amplitude of oscillation of the detected bunches at the BPM is of order 1 μm, and the monitor signal level is of order 100 μV, the inherent noise rejection of the lock–in gives an excellent signal–to–noise ratio. Typically, for a 1 second time constant, the signal–to–noise ratio is 100 to 1 or better. A problem with the monitor, though, is that the monitor signal is not simply proportional to the luminosity, but is dependent upon other factors as well. For head–on collisions, the monitor signal S is proportional to[1]

$$S \propto \mathcal{L}\,\beta_y(\mathrm{ip})\sqrt{\beta_y(\mathrm{sh})\beta_y(\mathrm{det})}\,F_{sh}\,F_{det}/I, \qquad (1)$$

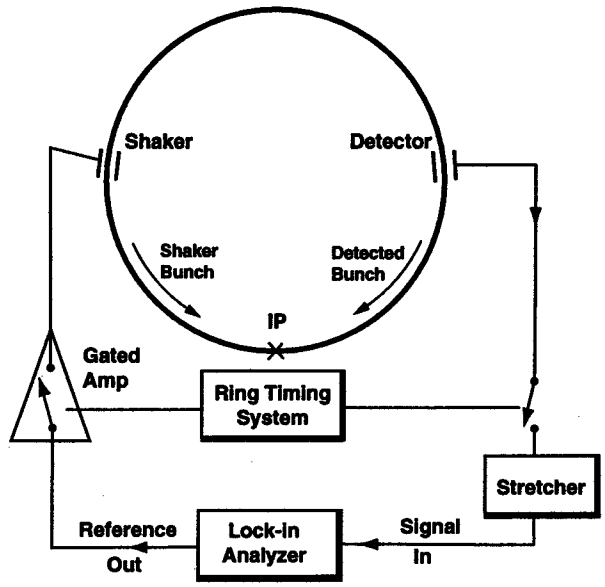

Figure 1: Schematic diagram of the BBI luminosity monitor configuration.

where $\mathcal{L}$ is the luminosity, I is the bunch current, and F_{sh} and F_{det} are defined by

$$F_{sh}(Q_y, Q_s, \phi_y(\mathrm{sh})) \equiv \frac{A_s(\mathrm{ip})}{A'_s(\mathrm{sh})\sqrt{\beta_y(\mathrm{sh})\,\beta_y(\mathrm{ip})}}, \qquad (2)$$

and

$$F_{det}(Q_y, Q_s, \phi_y(\mathrm{det})) \equiv \frac{A_d(\mathrm{det})}{A'_d(\mathrm{ip})\sqrt{\beta_y(\mathrm{ip})\beta_y(\mathrm{det})}}. \qquad (3)$$

Here $A'_s(\mathrm{sh})$ is the amplitude of the kick given the skaker bunch at the shaker, $A_s(\mathrm{ip})$ is the amplitude of the shaker bunch oscillations at the IP, $A'_d(\mathrm{ip})$ is the amplitude of the kick given the detected bunch at the IP, and $A_d(\mathrm{det})$ is the amplitude of the detected bunch oscillations at the detector.

$F_{sh}(Q_y, Q_s, \phi_y(\mathrm{sh}))$ depends upon the vertical tune Q_y, the frequency of shaking Q_s, and the phase advance between the shaker and the IP $\phi_y(\mathrm{sh})$ [2]. Similarly, $F_{det}(Q_y, Q_s, \phi_y(\mathrm{det}))$ is dependent upon Q_y, Q_s and $\phi_y(\mathrm{det})$ — the phase advance between the detector and the IP.

* Work supported by the National Science Foundation

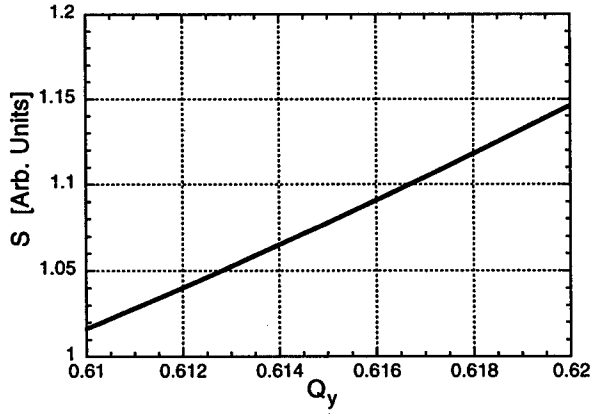

Figure 2: Variation of S as a function of vertical tune with the luminosity and horizontal tune held constant.

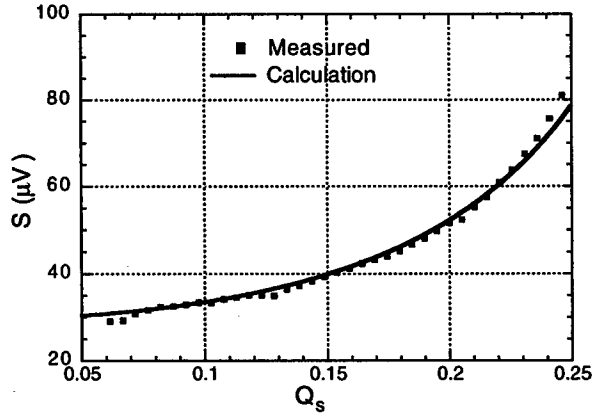

Figure 3: Calculated and measured monitor signal as a function of shaker frequency. With the calculated S there is one adjustable constant that gives the overall gain of the system. This constant was chosen to best match the measured results.

Parameter	Value	Parameter	Value
Q_s	0.26 (100 kHz)	Q_y	0.61
A'_s(sh)	0.5 μrad	ξ_y	0.03
β_y(ip)	0.019 m	σ_y(ip)	7 μm
β_y(sh)	21.5 m	β_y(det)	32.3 m
ϕ_y(sh)	$2\pi \cdot 0.86$	ϕ_y(det)	$2\pi \cdot 0.27$
F_{sh}	0.79	F_{det}	0.82

Table 1: CESR BBI luminosity monitor parameters.

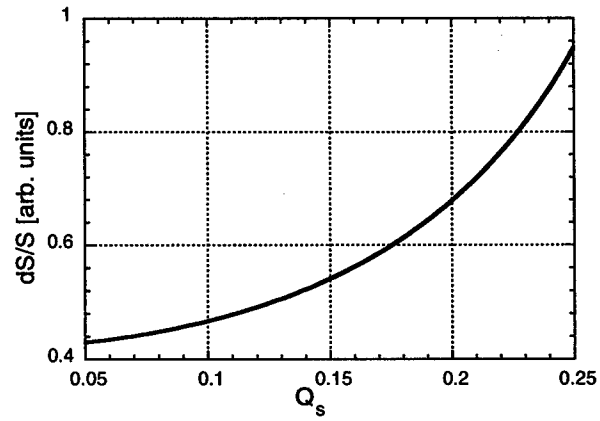

Figure 4: Relative Sensitivity of the monitor signal to changes in vertical tune as a function of shaker frequency. dS is the change in S, for a fixed change in Q_y, as computed from Eq. (1).

2 NORMALIZATION PROGRAM

An example of how the monitor signal is dependent upon things other than the luminosity is shown in Figure 2. Figure 2 shows S, as calculated from Eq. (1), as a function of vertical tune while holding the luminosity and the horizontal tune constant. Parameters used in the computation are typical of CESR high energy physics (HEP) conditions and are given in Table 1. The change in Q_y is simulated by varying the strengths of the quadrupoles in the arcs to give minimal change in the beta functions. Over the tune range of the graph, which is typical of the range over which the tune can be varied during an HEP run, S varies of order 10%. This variation can be larger than the actual variation of the luminosity. The trend of S in the figure can be simply understood as a resonance phenomena by noting that, as the tune is increased, the aliased tune, $1 - Q_y$, is moving nearer the shaking frequency at $Q_s = 0.26$.

In order to overcome the dependency of the monitor signal on the vertical betas and phases, a software program has been developed that normalizes the signal to give a quantity that, at least in theory, is directly a measure of the specific luminosity. The normalization program works by using Eq. (1) to compute the "predicted" signal S_p assuming constant $\mathcal{L}/I$. With this, the normalized signal S_n is given by

$$S_n = \frac{S}{S_p I}. \tag{4}$$

At the start of a HEP run, the values for the quadrupole strengths, quadrupole rotation angles, and sextupole strengths[3] are read in from the CESR data base. It is assumed that these initial settings correspond to the settings for the theoretical design lattice. That is, the initial Twiss parameters are assumed equal to the Twiss parameters of the design lattice. S_p is computed assuming a constant value for $\mathcal{L}/I$ with head–on collisions.

The program recomputes S_n approximately 8 times a second and puts this number in the CESR data base for general use. To save on computation time, the database is monitored, and only if any of the quadrupole or sextupole settings have changed are the Twiss parameters and S_p recomputed. This recomputation is based upon the change in

the settings and the known calibration constants.

The working of the normalization program rests on the assumption that Eq. (1) accurately reflects reality. A good indication that this is so is shown by the good agreement between measured and calculated monitor signal levels as a function of shaking frequency Q_s. This is shown in Figure 3. The greatest weakness in the above procedure is the assumption that the initial conditions correspond to the design lattice. This assumption is necessary since hysteresis in the magnets precludes an accurate enough absolute calibration. In practice, the assumption is generally close enough so that the normalized signal generally follows the luminosity. One way to desensitize the signal dependence on tune would be to lower Q_s as shown in Figure 4. Figure 4 shows, as a function of Q_s, the quantity dS/S — the change in S, for a fixed change in Q_y, normalized by S. Lowering Q_s, however, has the drawback of lowering S (cf. Figure 3) since, currently at CESR, the shaker driver amplifier is near maximum output and so $A_s'(\mathrm{sh})$ cannot be increased. Moreover, lowering Q_s does nothing to lessen the dependence on the betas.

3 OPTIMIZATION PROGRAM

At CESR, the normalized luminosity signal is used with an "optimizer" program to provide automatic adjustment of machine parameters to maximize the luminosity. The optimizer program is a general purpose program in that it can be used to maximize (or minimize) any quantity that is stored in the CESR data base using any control variables in the data base. Several optimizing strategies are available for use. However, for maximizing the luminosity, the favorite strategy used involves varying a variable back and forth over some range while recording the normalized signal. To reduce the noise, the signal vs. variable curve is smoothed using a sliding window and the maximum of the curve is found. The variable is then set to the value corresponding to the maximum and the cycle is started over with the next variable on the list of variables to use.

The use of the optimizer has lead to some puzzling behavior. It has been found that, at the start of a HEP run, the optimum conditions have a small but significant coupling component in the arcs. Why this should be so is so far unexplained, but one clue is that, as the run progresses, and the beam current decays, the optimizer steadily decreases the coupling by reducing the strength of skew quadrupoles under its control. This strongly suggests that the explanation involves the beam–beam interaction.

4 CONCLUSION

Without the normalization program, the beam–beam interaction luminosity monitor was useful for making sure that the beams collided head–on and for adjusting skew quadrupoles for minimum beam size — both of which did not depend upon variation of the Twiss parameters. With the normalization program, the range of usefulness has been extended to the ability to adjust quadrupole or sextupole settings. With this, the luminosity monitor, along with the optimizer program, is in standard use at CESR.

5 ACKNOWLEDGEMENTS

My thanks to Stu Henderson and John Sikora for helping with the beam-beam interaction luminosity monitor and to the rest of the CESR operations group for their support. Especial thanks to Flora Sagan for her editorial support.

6 REFERENCES

[1] D. Sagan, J. Sikora, and S. Henderson, "A Luminosity Monitor using the Coherent Beam–Beam Interaction," Proc. 1997 Part. Acc. Conf., pg. 1765 (1997).

[2] there is also a dependence upon the damping decrement but this dependence is small away from resonance and can be ignored.

[3] Since a pretzeled orbit is used to separate the beams (which share a common beam pipe), the sextupoles affect the Twiss parameters and thus need to be monitored.

CESR LUMINOSITY DEPENDENCE ON MAGNETIC ALIGNMENT*

R. Holtzapple+ and D. Rice
Laboratory of Nuclear Studies, Cornell University, Ithaca, NY 14853

Abstract

The Cornell electron-positron storage ring (CESR) luminosity has increased by a factor of >3 over the last 3 years with a peak luminosity of $8.0x10^{32}$ $cm^{-2}sec^{-1}$ and a record integrated luminosity of 750 pb^{-1} for one month. This increase in luminosity is in part due to improved alignment of magnetic elements. Operation with a pretzel [1] orbit in multiple bunch mode places particular importance on alignment because of the side effects of magnetic correctors. We report the improvements in alignment and estimate the effects on colliding beam performance.

1 CESR LUMINOSITY

While accurate alignment of magnetic elements is essential for good performance in all accelerators, the multi-bunch operation of CESR places additional demands on magnet alignment. Most of the two orders of magnitude increase in CESR luminosity since initial operation has been due to using many bunches in each beam [1].

The interaction between counter-rotating bunches, primarily through long range electromagnetic fields, must be limited at all parasitic (i.e., not intended for collisions) crossing points to avoid dilution of the beams' phase space density and resonance induced particle losses. Since only a single vacuum chamber is available in CESR the interaction is reduced by establishing separate closed orbits for the two counter rotating beams by means of electrostatic separators. These separate orbits follow large (~15 mm peak) pseudo-sinelike betatron trajectories around the complete circumference.

Since the beams are far from the centerline of the magnets (with opposite displacements) for most of the circumference, sensitivity to nonlinear fields is increased and corrections are more difficult since electrons and positrons are affected differently. Horizontal-vertical coupling created by skew-quadrupole fields cannot be simply corrected by two appropriately placed skew quads since not only the coupling vector phases but also vertical betatron phases must be matched. Because of the vertical correctors' poor fringe field quality their strength must be limited for reliable beam-beam performance.

Increased alignment demands extend to vacuum chambers also since synchrotron radiation power can increase to dangerous levels when chambers are misaligned.

For a given ring and optics, luminosity may be quantified by two parameters - total beam current and beam-beam parameter, proportional to luminosity divided by a geometric mean of the two beam currents. The beam-beam parameter, ξ, is most directly affected by magnet alignment. Unintentional coupling, dispersion, and beta function errors directly affect ξ, as do unnecessarily strong correction magnets (e.g., to correct vertical orbit errors).

Effects on beam current will be less direct if an unrelated phenomenon limits currents. Otherwise resonances and dynamic aperture may reduce beam current due to magnet alignment errors.

2 ALIGNMENT OF CESR

There are 84 dipole and 102 quadrupole magnets in CESR. The vertical height, radial position, and rotation of the CESR quadrupoles are routinely measured and aligned to eliminate any unwanted orbit distortion of the CESR beam. Recently the dipole magnets have also been aligned as well. By aligning the quadrupole and dipole magnets in CESR we have reduced the dependence on steering magnets needed for orbit correction. Measurement of the magnetic elements in CESR is done with conventional techniques and is described in detail elsewhere [2,3,4]. In this paper a brief description of the method will be described and the accuracy of the measurement will be quoted.

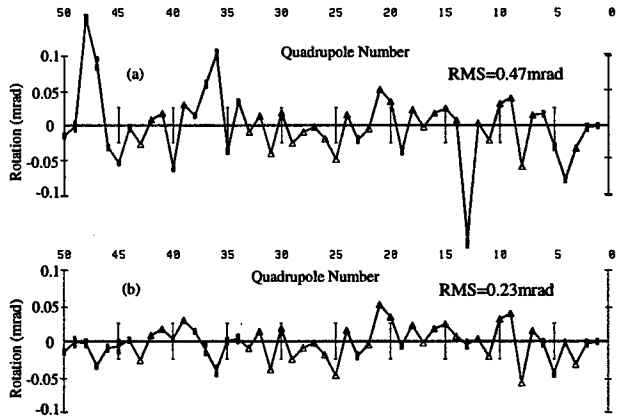

Figure 1. The rotation of the half of the quadrupole magnets in CESR (a) before alignment and (b) after alignment.

* Work supported by the National Science Foundation.
+Email:RLH@CESR10.LNS.Cornell.edu

The vertical height of magnetic elements is measured using an optical level. This technique has a quadrupole to quadrupole accuracy of ~5 mils. The rotation (or level) of magnetic elements is measured using an electronic bar level. The bar level has an accuracy of ~0.1 mrad. The radial measurement consists of wire measurements that relate each magnet to the magnets on either side. The radial positioning can be done to ~20 mils rms. The alignment data is analyzed using a series of computer programs that have been written specifically for CESR. Figure 1 is the rotation of the CESR quadrupole magnets before and after the magnets were aligned. It should be noted that when the CESR ring is aligned not all of the magnets are moved, only the ones that are outside of our prescribed tolerances.

3 ORBIT MEASUREMENTS

Several beam parameters have been measured to validate the usefulness of aligning the magnetic elements in CESR. They are (i) the zero corrector orbit, (ii) the coupling of CESR, and (iii) the corrector strengths during colliding beam physics. These quantities directly effect the performance of CESR by influencing the beam-beam tune parameter ξ. The following data were measured before and after quadrupole magnets were aligned in CESR and represent the type of improvement one would expect by aligning the quadrupole magnets.

The zero corrector orbit is the beam orbit with all steering correctors turned off. If all the magnetic elements were perfectly aligned with ideal fields then the zero corrector orbit would be zero and the beam would travel through the centers of the beam detectors and magnets. As an example, Figure 2 is the horizontal zero corrector orbits before and after the quadrupole magnets were aligned in CESR. The rms horizontal zero corrector orbit went from 5.30mm to 4.52mm by aligning the quadrupole magnets. We have not been as successful reducing the vertical zero corrector orbit. During the same quadrupole alignment period the rms vertical zero corrector orbit went from 5.56mm to 5.60mm.

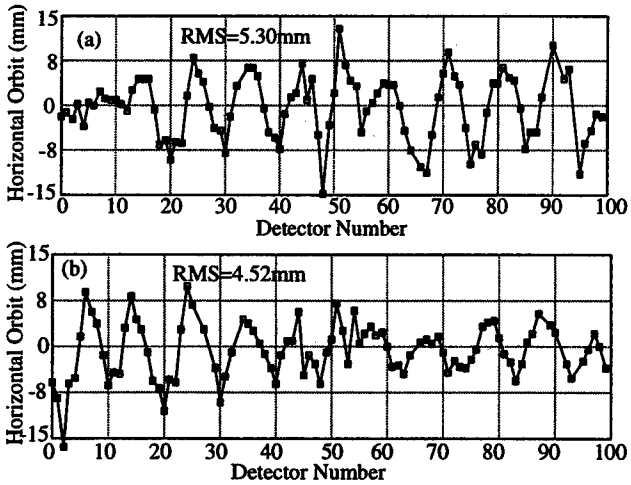

Figure 2. The CESR zero corrector horizontal orbit (a) before and (b) after aligning the quadrupole magnets.

Rotated quadrupoles introduce coupling between the horizontal and vertical planes which results in an increase in the vertical beam size and reduces the luminosity. A performance benefit that can be attributed to leveling the quadrupoles in CESR is the reduction of transverse coupling. To measure coupling in CESR a normal mode of the beam is coherently excited by a shaker and the relative phase and amplitude of the two normal transverse (vertical and horizontal) modes is measured [5]. From this measurement the coupling transfer matrix $\overline{C}$ can be determined. The $\overline{C}_{12}$ term of the 2x2 coupling matrix was measured before and after the quads were leveled and the results are shown in Figures 3.

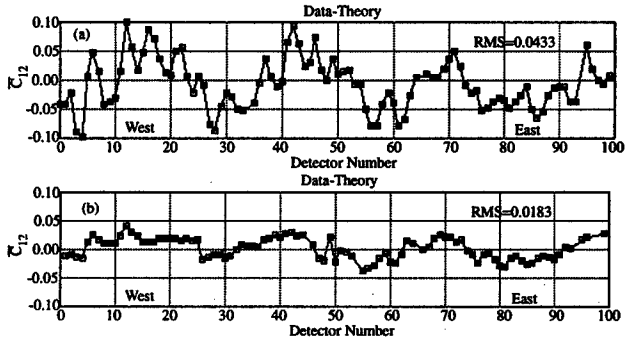

Figure 3. $\overline{C}_{12}$ at each detector around the ring measured (a) before and (b) after the quadrupoles were leveled. The rms. value is 4.3% before and 1.8% after the quadrupoles were aligned [6].

Several comments can be made about the coupling results. 1) The coupling measurements shown were made with the skew quadrupoles turned off so the two measurements are on equal footing as far as coupling goes. 2) During the down period the back-leg windings of some of the dipole steering were moved away from the beam-pipe and that might have reduced the coupling in addition to leveling the quadrupoles. 3) Both measurements have significant global coupling (long wavelength) but the localized coupling (short wavelength) is greatly reduced after the quadrupole magnets were leveled.

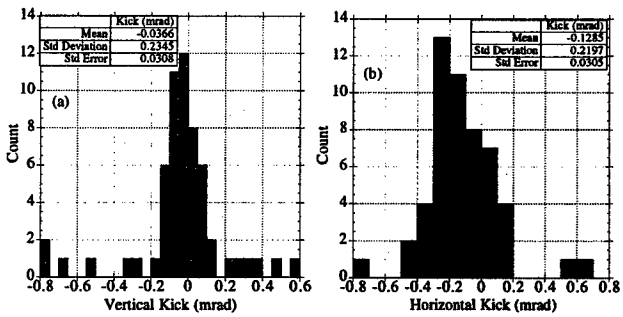

Figure 4. The (a) vertical and (b) horizontal corrector strength for during collisions before the magnetic elements were aligned in CESR.

Vertical and horizontal corrector magnets steer the beam to an ideal orbit tuned for luminosity. The pretzel orbit used in multiple bunch operation has the beam far

from centered in these steering magnets. For the steering coils, nonlinear fields increase with displacement and reduce the dynamic aperture of CESR. It is therefore imperative to rely on these corrector magnets as little as possible. Aligning magnetic elements in CESR reduces the dependence on corrector magnets. The corrector strengths during colliding beams were measured before and after the magnets were aligned (Figures 4 and 5).

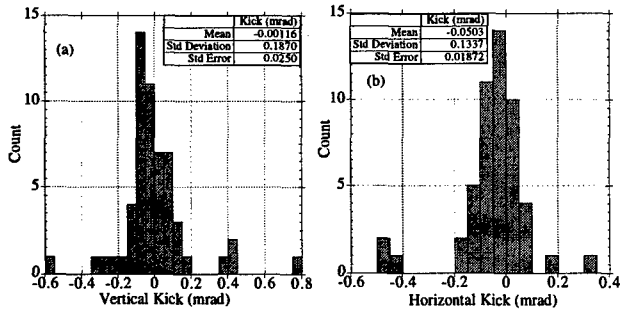

Figure 5. The (a) vertical and (b) horizontal corrector strength during high energy physics collisions after the magnetic elements were aligned in CESR.

The reduction in the standard deviation of the corrector strength was by 25% for vertical correctors and 64% for horizontal correctors.

These results prove the usefulness of aligning the magnetic elements in CESR.

4 LUMINOSITIES DEPENDENCE ON MAGNETIC ALIGNMENT

The luminosity of an electron-positron storage ring is

$$L \approx \frac{f_0 N \gamma \xi}{2 r_e \beta_V^*}$$

where N is the number of particles per bunch, f_0 is the revolution frequency, r_e is the classical electron radius, ξ is the beam-beam parameter, $\gamma = E/mc^2$, and β_V^* is the vertical beta function at the interaction point. The luminosity is directly proportional to the beam-beam parameter and we will try to correlate the increase in the beam-beam parameter, and hence luminosity, with magnetic alignment.

The beam-beam parameter is recorded during CESR beam collisions. Figure 6 is the average peak beam-beam for each running cycle from November of 1992 to February of 1999. The schedule for colliding beams at CESR consists of running periods usually 10 to 20 weeks in length followed by down periods for improvements and maintenance. Each data point is the average beam-beam parameter for that running period. The arrows denote the down periods when significant alignment of magnetic elements occurred with the expectation of an improvement to CESR performance. Several interesting features should be pointed out from Figure 6. 1) The beam-beam parameter on average goes up by $11 \pm 6\%$ when the magnetic elements are aligned during the down period. 2) The beam-beam parameter goes down on average by $4 \pm 5\%$ when the magnetic elements are not aligned during the down period. 3) If magnets are not aligned over several running periods the beam-beam parameter tends to suffer. It should be noted that during each downperiod other modifications of CESR are made. The gain in the beam-beam parameter is not solely due to magnetic alignment.

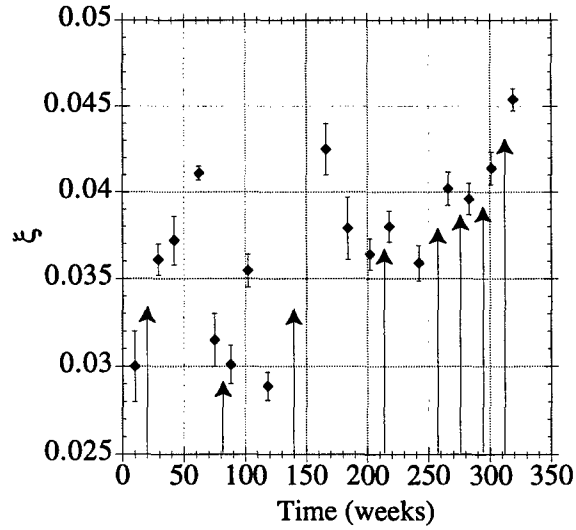

Figure 6. The mean peak beam-beam parameter from November 1992 to February 1999. The arrows indicate a downperiod when the CESR magnetic elements were aligned.

5 CONCLUSION

Aligning the magnetic elements in CESR reduces the dependence on steering correctors, reduces coupling, and increases the beam-beam parameter and, on average, increases the delivered luminosity of CESR. We have noted an increase in luminosity of ~11% due to magnetic alignment of CESR.

6 ACKNOWLEDGEMENTS

The authors would like to thank David Sagan for taking the coupling measurements and the survey and alignment group (SAG) for an excellent job of aligning the magnets. Gerry Rouse, who has lead the survey group for the past ten years, will be greatly missed.

7 REFERENCES

[1] Littauer R., "Multibunch Operation of CESR", IEEE NS-32, 1610 (1985).

[2] Holtzapple R., et. al., "Radial Alignment of the Quadrupole Magnets in the Cornell Electron-Positron Storage Ring", to be published

[3] Holtzapple R., et. al., "Alignment of the Dipole Magnets in the Cornell Electron-Positron Storage Ring", CBN-98-22

[4] Holtzapple R., et. al., "Leveling of the Quadrupole Magnets in the Cornell Electron-Positron Storage Ring", To be published.

[5] Bagley, P. and Rubin, D.,"Correction of Transverse Coupling in a Storage Ring", Proc. 1989 Part. Acc. Conf. (San Francisco) p. 874, 1989.

[6] The CESR coupling measurements are provided by David Sagan.

STREAK CAMERA MEASUREMENTS OF THE LONGITUDINAL DISTRIBUTION WITH MULTIPLE BUNCHES IN CESR*

R. Holtzapple+, M. Billing, and D. Hartill
Laboratory of Nuclear Studies, Cornell University, Ithaca, NY 14853

Abstract

The Cornell Electron-Positron Storage Ring (CESR) has a longitudinal dipole-coupled-bunch instability that limits the total amount of current that can be stored in the ring. As a result, it is one of the major limitations for higher luminosity [1]. This paper reports the results from a streak camera used to measure the dependence of the bunch's distribution on current and accelerating RF voltage for multiple bunches in CESR, as well as the effects of the longitudinal instability on the bunch distribution. Measurements of the bunch's longitudinal distribution at CESR, with multiple bunches present in the ring, help give an understanding of the nature of the longitudinal instability.

1 MULTIPLE BUNCH OPERATION AT CESR

Multiple bunches refers to more than one bunch of electrons or positrons being present in CESR at one time. Multiple bunches in CESR are necessary to achieve high luminosity. Under present high-energy physics colliding beam conditions, there are nine nearly evenly spaced bunch trains, with up to five bunches in each train, for a total of 45 electron and 45 positron bunches (Figure 1). The bunches are separated at crossing points other than the interaction region by vertical and horizontal electrostatic separators. The separators are used to make a "pretzel" orbit to insure separation between bunch crossings at locations other than the interaction region. Different distributions of bunches in the trains are observed to have different dipole-coupled bunch instability thresholds.

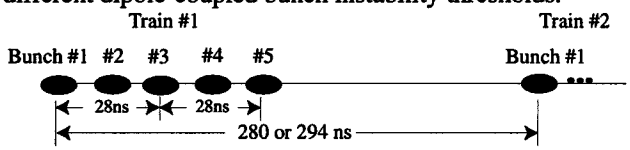

Figure 1. There are nine trains of bunches in CESR and each train can have up to five bunches present (five bunches per train are shown in this figure). Each train is separated by 280 or 294 ns and the bunch spacing in the train are in multiples of 14 ns.

2 DATA ANALYSIS

Measurements of the CESR longitudinal bunch distribution were made with a 500-femtosecond resolution Hamamatsu streak camera. A description of the camera and experimental set-up is described in detail elesewhere [2].

To determine the bunch length, the longitudinal profiles of the beam distribution are fit to an asymmetric Gaussian function with a constant background given by

$$I(z) = I_0 + I_1 \exp\left\{-\frac{1}{2}\left(\frac{(z-\bar{z})}{(1+\mathrm{sgn}(z-\bar{z})A)\sigma_z}\right)^2\right\}$$

where I_0 is the pedestal, and I_1 is the peak of the asymmetric Gaussian. The term $\mathrm{sgn}(z-\bar{z})A$ is the asymmetry factor that parameterizes the shape of this Gaussian. The mean rms width, σ_z, and asymmetry factor, A, from each experiment, are used to examine the pulse-to-pulse fluctuations in the beam distribution. Each distribution is fit to the mean rms width and asymmetry factor and the area and mean position of the distribution can vary. The difference, (or residuals) between the fit and the data will show variations between an average distribution and individual data acquisitions.

3 STABLE BUNCH MEASURMENTS

The electron bunch distribution, as a function of current, was measured with nine trains of two bunches per train. The separation between the two bunches, in a train, was 42 ns. The wiggler magnets were closed during this measurement. The mean and the root mean error for the bunch width and asymmetry factor, at each current setting, is plotted in Figures 2 (a) and (b).

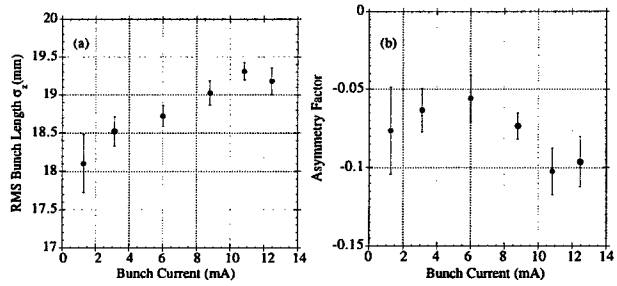

Figure 2. The electron (a) bunch length as a function of current with 18 bunches in the CESR ring, and the (b) asymmetry factor as a function of current.

Several observations can be made from the results: 1) between the currents from 1 to 13 mA per bunch, the electron bunch length increases by 6.0%. This steady bunch length increase is not accompanied by a steady increase in the Gaussian asymmetry factor. 2) The single electron bunch length at low current is expected to be

* Work supported by the National Science Foundation.
+ Email: RLH@CESR10.LNS.Cornell.edu

$\sigma_z = 17.30mm$ according to the CESR model. The measured single bunch length at low current was $\sigma_z = 17.89 \pm 0.35mm$, which is close to the multibunch measurement at low current of $\sigma_z = 18.10 \pm 0.38mm$ [2]. 3) With the bunch spacing of 42 ns between bunches, the longitudinal instability was not present. The threshold for the instability is ~240 mA for this bunch spacing. A single data acquisition of the longitudinal bunch distribution for each of two different current settings is plotted in Figures 3 (a) and (c).

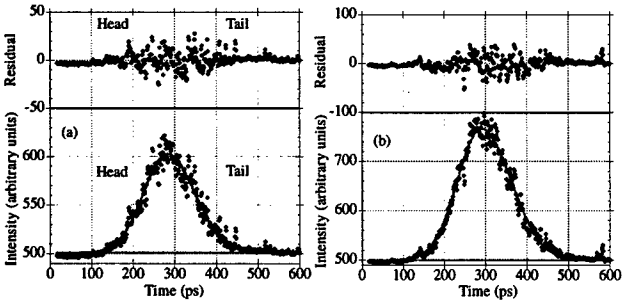

Figure 3. Single streak camera pictures of the CESR electron longitudinal bunch distribution and residuals at the current settings of: (a) 1.3 mA and (b) 12.5 mA per bunch.

The bunch length was measured as a function of the RF accelerating voltage. The measurements were made with electrons at each RF voltage, while keeping the bunch current constant. The measurement was made at a high current, and low current, with nine trains of two bunches separated by 42 ns. The mean bunch width and root mean error is plotted at each RF voltage in Figures 4 (a) through (b).

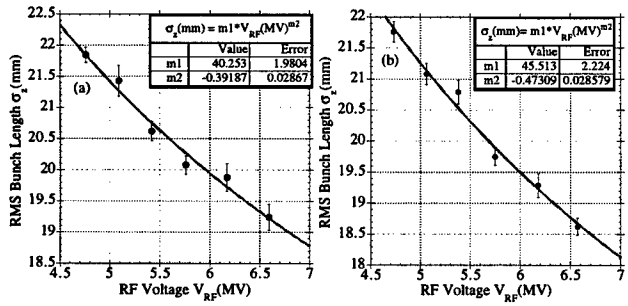

Figure 4. The electron bunch length as a function of RF accelerating voltage, with 18 bunches in the CESR Ring, at a current of (a) 9.0 mA per bunch and (b) 3.2 mA per bunch.

Fitting the data to the equation $\sigma(V_{rf}) = AV_{rf}^{m}$ the electron bunch lengths' dependence on the RF accelerating voltage was determined. In the low current case, $m = -0.47 \pm 0.03$, and in the high current case, $m = -0.39 \pm 0.03$. The expected value was $m = -0.50$. This is in good agreement with the measured value in the low current case. As the current increases, the bunch length dependence on RF voltage decreases, most likely due to beam loading in the RF cavities.

The bunch distribution was measured for both electrons and positrons, as a function of current, during high-energy collisions. The bunch spacing was 42 ns. Each streak camera picture of the bunch distribution was fit to an asymmetric Gaussian distribution, and the width and asymmetry factor were plotted as a function of the current in Figures 5 (a) and (b).

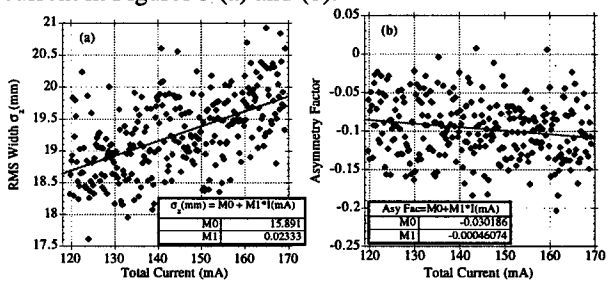

Figure 5. The electron (a) bunch length and (b) asymmetry factor, as a function of current, during high-energy collisions in CESR. The fit to the data is linear and points out the slow decrease in the bunch length and asymmetry factor as a function of current.

The bunch length, for both the electrons and positrons, decreases as a function of current. At the time of these measurements the total peak current during high-energy physics was 170 mA per beam. The runs lasted about 70 minutes, or until the single beam current was 120 mA. Then CESR was refilled. The asymmetry factor, for both electrons and positrons, decrease as a function of current. Overall the electrons and positrons exhibit the same behavior in CESR.

4 UNSTABLE BUNCH MOTION

The CESR longitudinal instability is a dipole-coupled bunch instability, and it is only observed with multiple bunches per train. The characteristics of the instability are described elsewhere [3]. The threshold of the instability depends upon the mode of operation. We observed that: 1) at the instability threshold current, a signal at $f_r \pm f_s$ appears in the beams spectra, which indicates a predominately dipole structure in phase space. 2) As the current is increased, well above the threshold, the signal at $f_r \pm 2f_s$ appears. 3) The threshold current for the instability is dependent on the bunch spacing in the train. 4) The instability degrades the CESR luminosity.

Measurements of the longitudinal instability were made at several different bunch spacings. They all have the same characteristics, except for different instability current thresholds. The one presented here is with nine trains of two bunches, with 14 ns spacing between bunches. The instability threshold with this bunch spacing was approximately 110 mA. Just above the instability threshold, measurements of the electron bunch distribution were taken with the streak camera; both with the feedback on (no instability present), and with the longitudinal feedback off (the inability is present). A spectrum analyzer was used, in conjunction with the streak camera, to measure of the longitudinal instabilities presence.

The features of the longitudinal instability from the measurement are the following: 1) The dipole mode is not

detectable by the streak camera (Figure 6). The bunch length and asymmetry factor, with and without the instability present, are in agreement (Table 1). 2) No structure is detected in the residuals of each of the data acquisitions.

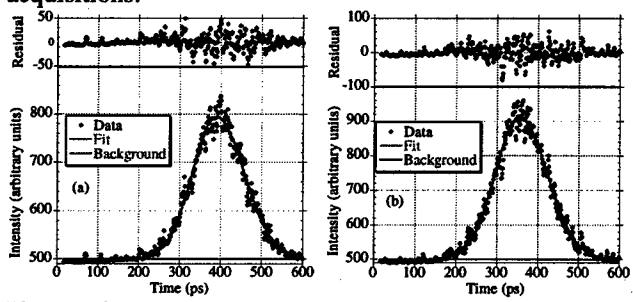

Figure 6. The CESR electron longitudinal bunch distribution measured by the streak camera when (a) the longitudinal instability is present and (b) the longitudinal instability is not present.

	Stable Beam	Unstable Beam
RMS Width $\sigma_z(mm)$	18.78 ± 0.13	18.73 ± 0.09
Asymmetry Factor	-0.07 ± 0.01	-0.07 ± 0.01

Table 1. The measured electron bunch length and asymmetry factor for a stable and unstable beam in CESR.

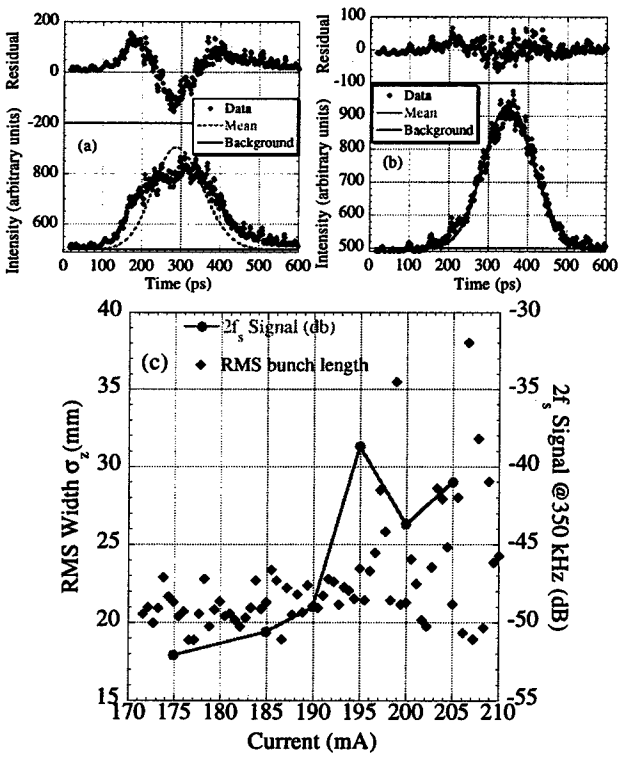

Figure 7. (a)-(b) The CESR bunch distribution fit to the mean stable bunch distribution when the beam is unstable (f_s and $2f_s$) with the current above 200 mA. The residuals are above the distribution. (c) The bunch length and $2f_s$ signal amplitude as a function of current.

Exploring the instability behavior further, the current was increased and several interesting features appeared: 1) there is a steady increase in the bunch length as a function of current. Bunch lengthening increases dramatically, and the beam oscillates in size (signature of the quadrupole mode). 2) As the current increases, the $f_r \pm 2f_s$ signal in the spectra appears, and it grows in strength as a function of current. The $2f_s$ signal is plotted in Figure 7 (c) as a function of current. There is a dramatic jump in the signal amplitude, and the bunch distribution changes dramatically. Above 195 mA the bunch distribution oscillates violently. Figures 7 (a) and (b) are bunch distributions above 200 mA. There is little evidence of the quadrupole mode in Figure 7 (b) and strong evidence in Figure 7 (a).

5 CONCLUSIONS

The measurements of CESR provided information about multibunch operations, as well as the behavior of the bunch, when the coupled-bunch longitudinal instability was present in CESR. The general conclusions from the measurements are that there is no difference between the positrons and electrons in CESR, in terms of longitudinal dynamics. The coupled-bunch longitudinal instability is a dipole mode instability, and a strong feedback system has allowed the instability to be damped, and increased the current thresholds [4]. The presence of the longitudinal instability was noticed in the beam spectra. It was also noted with the streak camera, but only when the quadrupole mode was present.

These studies of the longitudinal dynamics in CESR helped quantify some effects, such as: 1) the bunch length and asymmetry of the bunch increases as a function of current while colliding beams. 2) The bunch length increases as a function of current with multiple bunches in CESR. 3) The coupled bunch longitudinal instability is a dipole instability, but when the current is increased, it incites the quadrupole instability, and the bunch distribution changes drastically. Nonlinearites in the potential well and the large amplitude motion, in the dipole mode, give rise to the quadrupole mode. With the present feedback system, the coupled bunch instability is eliminated at currents above threshold for the quadrupole mode.

The streak camera has been invaluable as a diagnostic device for the measurement of the longitudinal parameters of CESR.

6 ACKNOWLEDGMENTS

The authors would like to thank the Stanford Linear Accelerator Center for the loan of the streak camera, especially Robert Siemann and Boris Podobedov.

7 REFERENCES

[1] Belomestnykh, S., Billing M., "Observation of a Longitudinal Coupled Bunch Instability in CESR", this proceeding.

[2] Holtzapple, R.L., et al, "Single Bunch Longitudinal Measurements at the Cornell Electron-Positron Storage Ring," CBN 98-23.

[3] Billing, M., "Observation of a Longitudinal Coupled Bunch Instability with Trains of Bunches in CESR," CLNS 98/1564.

[4] Sikora, J., et al, "Longitudinal Feedback at CESR", this proceeding.

STREAK CAMERA MEASUREMENTS OF THE LONGITUDINAL DISTRIBUTION OF A SINGLE BUNCH IN CESR

R. Holtzapple*#, M. Billing, D. Hartill, and M. Stedinger
Laboratory of Nuclear Studies, Cornell University, Ithaca, NY 14853
B. Podobedov+
Stanford Linear Accelerator Center, Stanford University, Stanford, CA 94309

Abstract

Measurements of the beam's bunch length in the Cornell Electron-Positron Storage Ring (CESR) were made using a streak camera. The experimental set up and the analysis techniques used are described in this paper. For a single bunch in CESR, the dependence of the longitudinal distribution on the bunch current and accelerating RF voltage, was measured and compared with a simple theoretical model of the CESR vacuum chamber impedance. Some basic parameters of this model were determined from the measured bunch distributions presented in this paper.

1 EXPERIMENTAL SET-UP AND ANALYSIS TECHNIQUE

The streak camera uses synchrotron radiation produced by the accelerator dipole magnets to determine the longitudinal bunch distribution. The synchrotron light pulse is transported from the source, out of the vacuum chamber, to a safe location shielded from radiation, where the streak camera measurements can be made.

The longitudinal profiles of the beam distribution are fit to an asymmetric Gaussian function with a constant background given by

$$I(z) = I_0 + I_1 \exp\left\{-\frac{1}{2}\left(\frac{(z-\bar{z})}{(1+\mathrm{sgn}(z-\bar{z})A)\sigma_z}\right)^2\right\}$$

where I_0 is the pedestal, and I_1 is the peak of the asymmetric Gaussian. The term $\mathrm{sgn}(z-\bar{z})A$ is the asymmetry factor that parameterized the shape of this Gaussian.

2 CESR SINGLE BUNCH DYNAMICS

The longitudinal phase space in the storage ring is determined from accelerator components as well as from collective effects. In CESR, the electromagnetic fields which affect the bunch distribution are from the more than four hundred magnets, which guide the bunches around the accelerator, two RF accelerating stations, to counteract the bunch energy loss due to synchrotron radiation, and two wiggler magnets used to create synchrotron radiation for the CHESS X-ray Facility. Ignoring collective effects, the standard deviation bunch length is given by [1]

$$\sigma_\tau = \langle\tau^2\rangle^{1/2} = \frac{\alpha}{\Omega_s}\sqrt{C_q E_0^2\left(\frac{I_3}{2I_2+I_4}\right)}$$

where I_2, I_3, and I_4 are the synchrotron integrals. The term α is the momentum compaction, E_0 is the nominal energy, and Ω_s is the synchrotron frequency. The synchrotron integrals that reflect CESR, when the streak camera experiments were performed, are denoted in Table 1.

	Wigglers Open	Wigglers Closed
I_1	$8.791m$	$8.791m$
I_2	$9.336x10^{-2}m^{-1}$	$1.047x10^{-1}m^{-1}$
I_3	$1.716x10^{-3}m^{-2}$	$2.372x10^{-3}m^{-2}$
I_4	$2.088x10^{-3}m^{-1}$	$2.744x10^{-3}m^{-1}$
I_5	$3.890x10^{-4}m^{-1}$	$5.386x10^{-4}m^{-1}$
U_0	$1.0290MeV$	$1.1541MeV$
$\frac{\sigma_E}{E}$	$6.115x10^{-4}$	$6.782x10^{-4}$
σ_Z	$1.565x10^{-2}m$	$1.739x10^{-2}m$

Table 1. The synchrotron integrals for CESR for the case when the wiggler magnets are open (CHESS is not collecting data) or closed.

Wigglers	RMS σ_z(mm)	Asymmetry Factor
Closed	17.89 ± 0.35	-0.020 ± 0.022
Open	15.91 ± 0.12	-0.0024 ± 0.029

Table 2. The CESR low current bunch length results with wiggler magnets open and closed.

The longitudinal distribution at low current is valuable to minimize collective effects and gives the opportunity to compare the CESR model with the time calibration of the streak camera. The results of the streak camera measurements at low current (Table 2) can be compared with the CESR model (Table 1). There is a systematic difference between the CESR model and the measured values. The theoretical bunch length is 3.3% smaller than the measured bunch length when the wiggler magnets are closed, and 2.1% smaller than the measured bunch length when the wiggler magnets are open. A

* Work supported by the National Science Foundation.
# Email:RLH@CESR10.LNS.Cornell.edu
+ Work supported by the Department of Energy contract DE-AC03-76SF00515.

single snap shot of the bunch distribution with the wiggler open and closed is shown in Figures 1 (a) and (b).

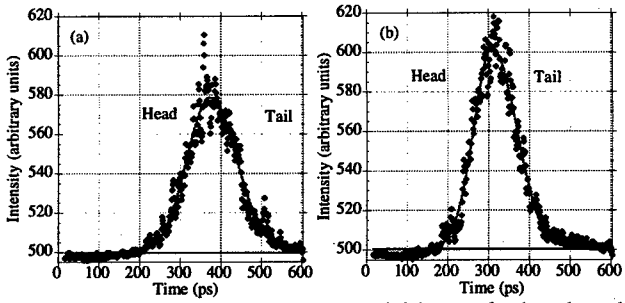

Figure 1. A single data acquisition of the bunch distribution in CESR with: (a) the wiggler magnets closed at a current of 1.4 mA. (b) The wiggler magnets open at a current 1.4 mA.

At low current, the collective effects for the bunch are small. As a result, the equilibrium bunch length in a storage ring is inversely proportional to the square root of the RF accelerating gap voltage. At low current the electron bunch length in CESR was measured as a function of RF accelerating voltage. The mean and root mean error were calculated at each RF setting and plotted in Figure 2(a). Fitting the data to the function $\sigma_z = A(V_{RF})^m$ gives a value of $m = -0.43 \pm 0.02$.

The measurement was also made at high current. The mean and root mean error were calculated at each RF setting and plotted in Figure 2(b). Fitting the data to the function $\sigma_z = A(V_{RF})^m$ gives a value of $m = -0.40 \pm 0.04$.

Comparing the low and high current results, it can be concluded that the dependence of the bunch length, on the RF accelerating voltage, does not change as the current changes in CESR and m<0.5.

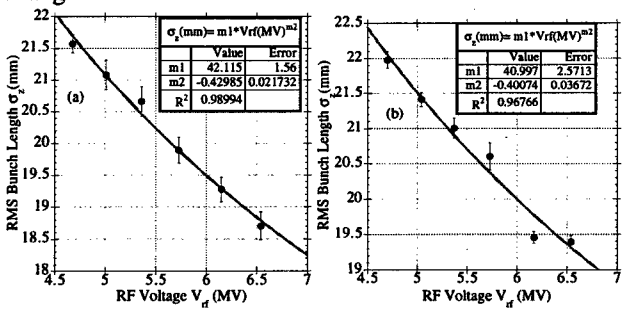

Figure 2. The bunch length as a function of RF accelerating voltage when the current in CESR is (a) 3.20 mA and (b) 15.00 mA.

3 CESR HIGH CURRENT MEASUREMENTS

The electron bunch distribution was measured for currents from 1 mA up to 35 mA with wigglers open and closed. A plot of the bunch length and asymmetry factor, as a function of current, with the wigglers open and closed is shown in Figures 3(a) and (b).

There are several noteworthy features of the experimental data: 1) There is a 12% growth in the bunch length between the currents from 1 to 30 mA. 2) The asymmetry factor (shown in Figures 4 (a) and (b)), which measures the departure from a Gaussian distribution, increases in both cases as a function of current. The asymmetry factor is linear with current, whether the wigglers are open or closed. 3) The tail of the distribution gets longer as the current increases, which is a signature of potential well distortion due to the resistive impedance of the vacuum chamber. Figures 5 (a) through (c) are single data acquisition, at three different currents, fit to an asymmetric Gaussian function. These distributions can be used to determine the vacuum chamber impedance of CESR.

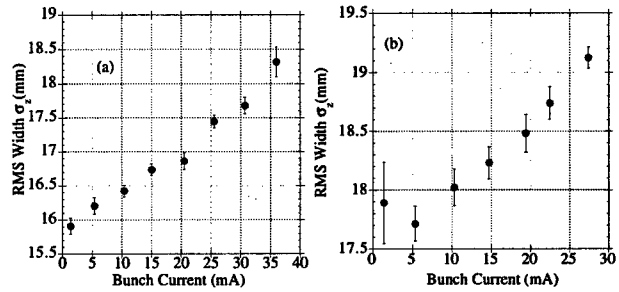

Figure 3. The bunch length in CESR as a function of current for wiggler magnets: (a) open and (b) closed.

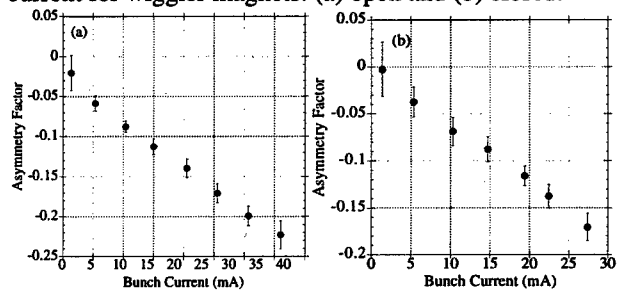

Figure 4. The asymmetry factor as a function of current in CESR for wiggler magnets: (a) open (b) closed.

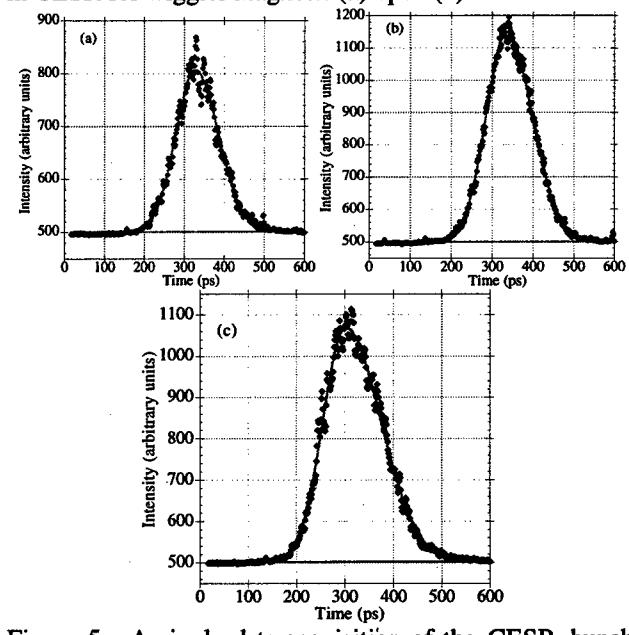

Figure 5. A single data acquisition of the CESR bunch distribution when the wiggler magnets are open, and a single bunch current is (a) 5.40 mA, (b) 15.0 mA, and (c) 30.5 mA.

4 CESR IMPEDANCE

In the same manner that the RF accelerating fields affect the bunch distribution, beam induced voltages from longitudinal wakefields also influence the shape of the bunch distribution [2,3]. With potential well distortion, the bunch distribution is static but distorted from a Gaussian distribution by the beam induced voltage. We observe in CESR a greater distortion for higher beam current. Assuming that the bunch's wakefield may be parameterized by

$$V_w(t) = RI_b(t) + L\frac{dI_b(t)}{dt},$$

the charge distribution can be determined numerically by integration [3]. Under the assumption that the resistance and inductance are constant over the measured range of bunch lengths, the resistive and inductive impedance components of the CESR storage ring vacuum chamber are determined from a χ^2 fit between the measured bunch distributions and the simulated bunch distributions. The χ^2 fit is given by

$$\chi^2 = \sum_{i=1}^{n} \frac{\left(S(t_i) - M(t_i)\right)^2}{S(t_i)}$$

where $S(t_i)$ and $M(t_i)$ are the simulated and measured bunch height at time t_i in the distribution. From the minimum χ^2 fit the resistance and inductance for each current setting are inferred to be

$$R_{open} = 1523 \pm 343\Omega \text{ and } R_{closed} = 1322 \pm 310\Omega$$

and

$$L_{open} = 65 \pm 12nH \text{ and } L_{closed} = 72 \pm 13nH.$$

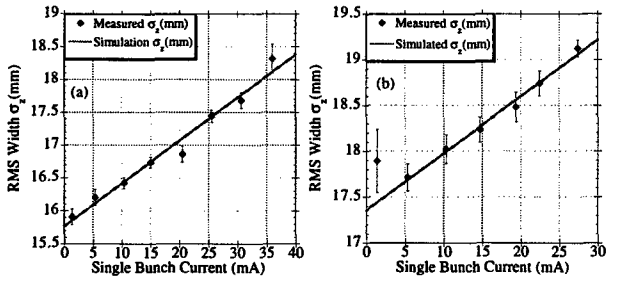

Figure 6. The measured and simulated bunch length as a function of current when the wiggler magnets are (a) open and (b) closed.

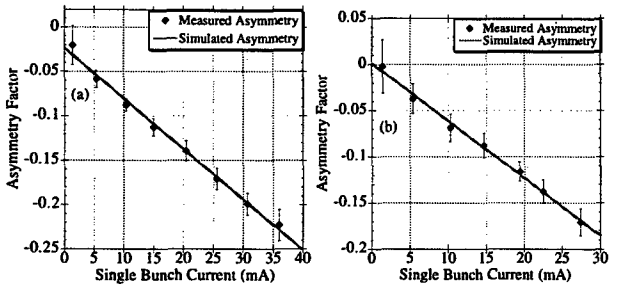

Figure 7. The measured and simulated bunch asymmetry as a function of current when the wiggler magnets are (a) open and (b) closed.

The uncertainties were determined by varying the simulation over the range of measurement errors on the asymmetry factor and rms width. Comparisons between the simulated bunch distributions using the above resistance and inductance and the streak camera measurements are shown in Figures 6 and 7.

5 CONCLUSION

In this paper, we have reported the results from the single bunch streak camera measurements that were done for the first time at CESR. These experiments allowed us to resolve the details of the beam distribution not available by other techniques. We have also established that the potential well distortion is the main single bunch collective effect in CESR. It leads to some asymmetry and lengthening of the beam distribution at high current. We have looked for single bunch coherent instabilities but have not registered any up to the highest value of current allowed by the CLEO detector background thresholds. Finally we have also established that the wiggler magnet changes the synchrotron integrals, as expected, resulting in a change in bunch length.

The low current single beam bunch length measurements are in close agreement with a simple theoretical model of CESR. The bunch length growth with current, when the wiggler magnets were closed and opened, was used to determine the impedance of CESR, in this model.

The assumption that the resistive and inductive impedance is constant, over the bunch lengths measured, is consistent with the results. The impedance was determined by comparing the measured bunch length dependence on the current and comparing it to simulations. With this method, the vacuum chamber impedance has a resistance of $1523 \pm 343\Omega$ and $1322 \pm 310\Omega$ and an inductance of 65 ± 12nH and 72 ± 13nH for the case of the wiggler magnets open and closed, respectively.

These measurements confirm our understanding of the theoretical model of the CESR and were valuable in exploring the possible future usage of streak cameras as a diagnostic tool in the CESR accelerator complex.

6 ACKNOWLEDGEMENTS

The authors would like to thank the Stanford Linear Accelerator Center for the loan of the streak camera, especially Robert Siemann and Marc Ross.

7 REFERENCES

[1] Helm, R., Lee M., Morton P., Sands M., "Evaluation of Synchrotron Integrals," SLAC-PUB-1193, March 1973.

[2] Haissinski, J., "Exact Longitudinal Equilibrium Distribution of Stored Electrons in the Presence of Self-Fields," Il Nuovo Cimento, Vol. 18B, N.1, 11 November 1973, p. 72.

[3] Billing, M.,"Bunch Lengthening via Vlasov Theory", CBN 80-2, 1980, 15pp. The updated software was written by M. Stedinger and M. Billing[1998].

LATTICE DIAGNOSTICS USING SINGLE KICK CLOSED ORBIT AT KEKB

Y. Ohnishi, K. Akai, N. Akasaka, A. Enomoto, J. Flanagan, H. Fukuma, Y. Funakoshi, K. Furukawa, S. Hiramatsu, K. Hosoyama, N. Huan, T. Ieiri, N. Iida, T. Kamitani, S. Kato, M. Kikuchi, E. Kikutani, H. Koiso, M. Masuzawa, S. Michizono, T. Mimashi, T. Nakamura, Y. Ogawa, K. Ohmi, S. Ohsawa, N. Ohuchi, K. Oide, D. Pestrikov, K. Satoh, M. Suetake, Y. Suetsugu, T. Suwada, M. Tawada, M. Tejima, M. Tobiyama, N. Yamamoto, M. Yoshida, and S. Yoshimoto
High Energy Accelerator Research Organization(KEK), Tsukuba, Ibaraki, Japan

Abstract

We have measured beta functions using single kick closed orbit at KEKB. The measured beta functions were compared with the model lattice and gradient errors were extracted from the result in a beta beat. The gradient errors were also obtained by changing strength of steering magnets and measuring beam positions as the second method. The methods of the error estimation and preliminary results will be reported.

KEKB[1] is an asymmetric-energy, double-ring, electron-positron collider. The beam energy is 3.5 GeV for positron(LER) and 8.0 GeV for electron(HER), respectively. The requirement of the peak luminosity is $10^{34}\mathrm{cm}^{-2}\mathrm{s}^{-1}$ for study of CP violation. In order to achieve such high luminosity operations, large beam current and small β_y^* which is the beta function at I.P. in the vertical plane are needed. The β_y^* = 1cm optics has been done successfully for both rings. The final focusing of two beams is provided by a pair of super conducting quadrupole magnets which are called QCS. The small β_y^* produces a large amount of chromaticity which makes the field of sextupole magnets strong. The nonlinear of sextupole magnets reduces the transverse dynamic aperture. It is, therefore, considered to use a pair of identical sextupole magnets which are connected with a -I' transformer in both the horizontal and vertical planes. The nonlinear effect due to the sextupole magnets should be compensated by the -I' transformer up to the third order in Hamiltonian.

Diagnostics of the lattice has been studied since the commissioning of KEKB started in December 1998. Measurements of the closed orbit distortion(COD) give us a large amount of information for a lattice.

The formula for the closed orbit distortion, Δx, induced by a single steering magnet is

$$\Delta x_i = R_{ij}\theta_j, \tag{1}$$

where θ_j is a kick angle of the j-th steering magnet. The response coefficient, R_{ij} of the j-th steering magnet to the i-th BPM is calculated by

$$R_{ij} = \frac{\sqrt{\beta_i\beta_j}}{2\sin\frac{\mu}{2}}\cos\left(\frac{\mu}{2} - |\,\psi_i - \psi_j\,|\right) - \frac{\eta_i\eta_j}{\alpha C}, \tag{2}$$

where $\mu = 2\pi\nu$ is the betatron tune, ψ is the betatron phase advance, β is the betatron function, η is the dispersion function between two locations, α is the momentum compaction factor, and C is the circumference of the ring. If the last term of eq.(2) can be ignored and the location at a pair of the steering magnet and the BPM is considered, the beta function is obtained from

$$\beta_j = 2\left(\frac{\Delta x_j}{\theta_j}\right)\cdot\tan\frac{\mu}{2} \tag{3}$$

When the beta functions have been measured and a significant discrepancy between the measurement and the model has been found, the sources of the discrepancy can be specified. If the error sources come from a gradient error in one or more of quadrupole magnets, the difference of measured from the model beta functions are described as follows:

$$\Delta\beta_j = \sum_m \frac{\beta_j\beta_m}{2\sin\mu}\cos(\mu - 2\,|\,\psi_j - \psi_m\,|)\cdot\Delta K_m, \tag{4}$$

where ΔK_m is the gradient error of the m-th quadrupole magnet(method-1).

On the other hand, assumed that the error is the gradient error of the quadrupole magnets, the measured COD induced by a single steering magnet is written by

$$\Delta x_i^{meas.} = \Delta x_i^{model} + \sum_m R_{im}\Delta K_m \Delta x_m^{model}, \tag{5}$$

where

$$\Delta x_i^{model} = R_{ij}\theta_j \tag{6}$$

$$\Delta x_m^{model} = R_{mj}\theta_j, \tag{7}$$

where R_{ij} and R_{mj} are the response coefficients from the j-th steering magnet to the i-th BPM or the m-th quadrupole

0-7803-5573-3/99/$10.00@1999 IEEE.

magnet, respectively. The last term of eq. (5) is the correction term due to the gradient errors of the quadrupole magnets against the model(method-2).

Another constraint to determine the errors of the lattice is

$$\Delta K_m = \pm\frac{2}{\beta_m}\{\cot\mu(\cos\Delta\mu - 1) + \sin\Delta\mu\}, \qquad (8)$$

where $\Delta\mu$ is defined by $\mu^{meas.} - \mu^{model}$, and the $\pm$ sign refers to the horizontal and vertical planes, respectively. If the tune changes small and not close to the half integer or integer resonances, eq. (8) can be simplified as follows:

$$\Delta\mu \simeq \pm\frac{1}{2}\sum_m \beta_m \Delta K_m \qquad (9)$$

with taking all gradient errors into account.

In order to extract the gradient errors of the lattice, there are two methods as described above. The beta function at I.P, $\beta_y^* = 1$ cm optics was utilized. The horizontal-vertical coupling has been neglected. Before the measurements of the COD, orbit corrections with the steering magnets were performed. There are 462 horizontal and 456 vertical steering magnets available in LER. In this analysis, 87 horizontal and 88 vertical steering magnets were chosen to measure the single kick closed orbit. The dispersion functions at those steering magnets are less than 0.1m in order to avoid the uncertainties of dispersion functions between the model and the real machine.

There are 449 BPMs available to measure the beam positions. The beam positions are determined by an average of 8 measurements and the resolutions of the BPMs are typically less than 5μm. The closed orbit has been measured at BPMs before and after changing every steering magnets along the ring to minimize effects of orbit drifting. The orbit drifting at large beta function was less than 200μm in horizontal and 1 mm in vertical plane during this measurement, respectively. Each steering magnet is set to the kick angle of 50μrad added to the original setting.

The beta functions were measured by the beam position and a single kick angle from eq. (3). Measured transverse tunes were used in eq. (3). Difference between the beta functions at the steering magnet and those of the nearby BPM is typically less than 10% which is estimated from the model calculation. We used SAD program[2] to calculate twiss parameters of the lattice model. Figure 1 shows the beta functions at BPMs nearby the steering magnet. A significant discrepancy between measured beta functions and those of the model without corrections can be found(fig. 1(a)). In most cases, the difference from the model beta function will be a beta beat which is an oscillation of the measured beta function around the design beta function at twice the betatron frequency. The gradient errors were estimated by eq. (4) using an iterative procedure(Micado[3]). In eq. (4) measured transverse tunes are utilized and betatron phase advances are also scaled by the ratio of measured to the model tunes. The error source is identified

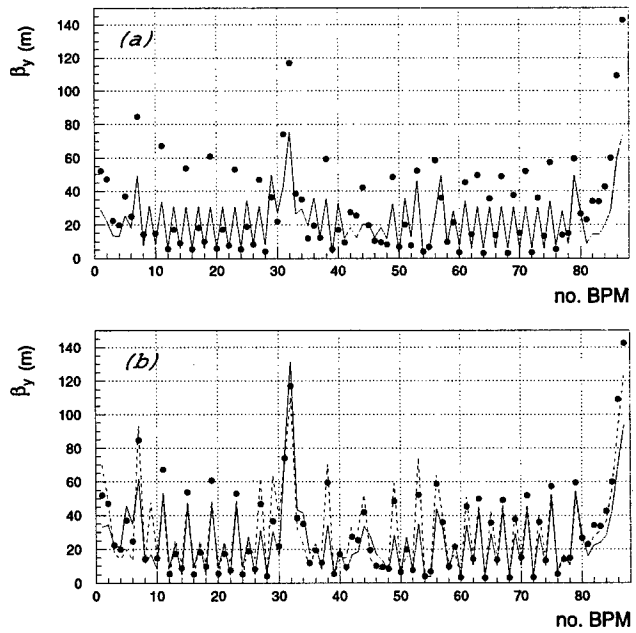

Figure 1: The β functions at BPMs nearby the steering magnet which induces a single kick closed orbit. The measured beta functions(plots) and the model calculations for (a) no correction and (b) after corrections in the vertical plane. The solid line in fig. (b) shows only correction of QCS magnet identified from method-1 and the dashed line shows correction of the QCS and other quadrupole magnets from method-2.

with QCS magnets which locate at vicinity of the interaction point. The strength of magnetic field was stronger than the expected value by 0.47%. Figure 1 (b) shows the corrected model for the QCS(solid line) and the beta functions from the model lattice can well reproduce the measured beta functions. After the correction of QCS, measured vertical tune is different from the model by 0.18, on the other hand, the difference before the correction was 0.25.

Figure 2 represents the typical single kick closed orbit in the vertical plane at LER. The model calculation after the correction of QCS agrees with the measured beam positions at BPMs.

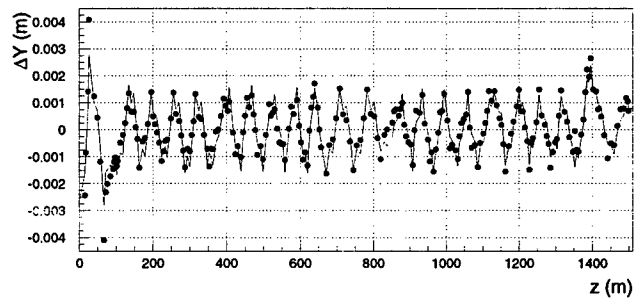

Figure 2: The single kick closed orbit in the vertical plane for a half of circumference at LER. The plots shows measured beam positions by BPMs and the solid line shows those of the lattice model with corrections of the gradient errors for the QCS magnet.

Figure 3 shows the gradient errors obtained from eq. (5) and eq. (9). The gradient error for all quadrupole magnets are estimated by one single kick closed orbit. In order to derive the gradient errors, the singular value decomposition(SVD)[4] is performed to solve equations described above. Because multiple error estimations for each quadrupole magnet are available, the average of errors and the standard deviations are plotted in fig. 3. Not only the gradient error of the QCS but also a series of defocusing quadrupole magnets(QD3P, QD5P) can be found. Those quadrupole magnets are connected to the same power supply. The beta functions(dashed line) calculated by the model after corrections of QCS and other quadrupole magnets are superimposed in fig. 1 (b) and also reproduce the measured beta functions well.

The error estimations between method-1 and method-2 are consistent with each other for the QCS. However, the gradient errors of quadrupole magnets besides the QCS were not clearly found by method-1 against method-2. The reason is that one BPM is used for one single kick in method-1, on the other hand, all BPMs are used for one single kick and more information can be obtained in method-2.

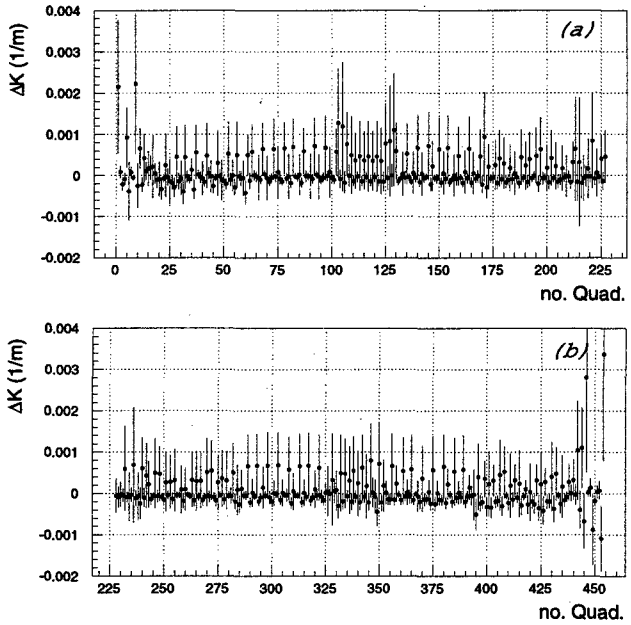

Figure 3: The gradient errors of quadrupole magnets predicted by method-2 at LER. Error bar shows the standard deviation estimated from the measurements using a single kick orbit induced by every steering magnets. The first and last number of quadrupole magnet corresponds to the QCS magnets in question. A series of quadrupole magnets which have small gradient errors are found systematically.

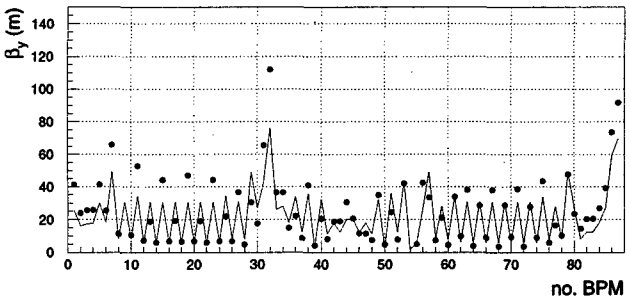

Figure 4: The β functions at BPMs nearby the steering magnet which induces a single kick closed orbit after adjustment of the real QCS. The solid line shows the beta functions calculated by the lattice model.

We have measured beta functions using the single kick closed orbit. The gradient errors of quadrupole magnets have been estimated using two methods. The gradient error of the QCS could be found by both methods. The corrected model calculations can well reproduce the measured beta functions and the measured closed orbit by BPMs. The error of the QCS was also verified from a magnetic-field measurement independent of this analysis and K value of the real QCS was corrected by 0.37%. Figure 4 shows the measured beta functions compared with the model after this correction. The errors of other quadrupole magnets were also found by method-2, however, those are still under investigation. The HER should be studied and in progress.

We would like to thank the KEKB Operations staff for their help with this experiment.

REFERENCES

[1] KEKB Design Report, KEK Report 95-7.

[2] SAD is the accelerator design tool program developed at KEK.

[3] H.G. Hereward, PS/Int. TH 59-5 (1959).
B. Autin and Y. Marti,CERN ISR-MA/73-13.

[4] W. Press, et al., "Numerical Recipes", Section 2.9, Cambridge University Press, Cambridge(1986).

COMMISSIONING STATUS OF THE KEKB LINAC

Y.Ogawa*, Linac Commissioning Group (LCG)#
KEK, 1–1 Oho, Tsukuba, Ibaraki 305-0801 Japan

Abstract

After entering into the full-commissioning phase of the KEKB linac in May, 1998, we have established two linac injection modes for the KEKB ring: an 8-GeV electron beam and a 3.5-GeV positron beam, as well as beam modes for the rings of the synchrotron light sources. All modes are easily switched for almost one minute without any trouble. The linac beam characteristics have been substantially improved by introducing several fine-tuning procedures, while key features concerning stable operation have been pursued by employing, for instance, energy-feedback loops. We report on the present status of the linac commissioning while especially emphasising the operational characteristics.

1 INTRODUCTION

The KEK electron-positron linac is the injector for two asymmetric rings (8-GeV electron and 3.5-GeV positron rings) of the KEK B-factory (the KEKB linac is named just after this), as well as for two different rings (2.5-GeV electron rings) of the Photon Factory (PF). It has been pointed out that since beam-mode switching among various kinds of beams should be quite frequent, perfect reproducibility of each beam could be one of the key issues for the successful operation of the KEKB ring [1], which requires frequent and speedy injection for high-luminosity collisions.

Full-commissioning of the KEKB linac [2] was started in May, 1998, while continuing ordinary injection into the PF ring. The principal goal of the full commissioning was to accomplish stable operation for injection to the KEKB rings as well as to assure efficient injection to two PF rings. The beam reproducibility has been pursued mainly regarding three aspects: the establishment of reliable beam-mode switching, various improvements of the beam quality, and beam-stability issues. In the following, the present status of the linac commissioning is reported while placing particular emphasis on these issues.

2 BEAM-MODE SWITCHING

2.1 Beam Modes

In Table I, two beam modes for KEKB and two modes for PF are listed, showing a wide variety of beam characteristics: a beam energy of 2.5 to 8 GeV and a beam charge of 0.3 to 10 nC. Beam-mode switching among these modes requires a change of at least several hundred parameters: the magnetic field strength for the beam optics and orbit, the accelerating rf phases and acceleration/standby modes of the klystrons for the energy and energy spread, the feedback parameters for beam stability, the beam-monitor settings for beam diagnosis and so on.

Table 1: Beam-mode specifications

Mode	Energy	Charge
KEKB e^-	8.0 GeV	1.2 nC, single bunch
KEKB e^+	3.5 GeV	10 nC for primary e^- 0.64 nC for e^+, single bunch
PF1	2.5 GeV	0.3 nC, multibunch
PF2	2.5 GeV	0.5 nC, multibunch

2.2 Switching Beam Modes

A beam-mode-switching panel (Fig. 1) has been prepared so that all of the parameters can be easily and quickly changed among the beam modes. For the present, we are using two electon guns for the KEKB and PF beams, respectively, which was inevitable because we had to continue injection to the PF rings even during construction of the KEKB linac [3]. This situation makes beam switching between the KEKB and PF beams quite complicated, though this situation will be improved in the future. Since the energy ranges from 2.5 to 8 GeV and the field strength of quadrupole magnets must be correspondingly changed, we have introduced a simple standardization of the magnets so as to avoid any hysteresis effects. This procedure mainly determines an overall time for switching of almost 1 minute. A reliability check has been carried out not only by examining the beam characteristics along the linac, but also by actually injecting each beam into the corresponding ring. It has turned out that beam switching, itself, in a short period is quite reliable, although a long-term drift of the beam characteristics has been observed (see section 4).

* Email: yujiro.ogawa@kek.jp
#N. Akasaka, A. Enomoto, J. Flanagan, H. Fukuma, Y. Funakoshi, K. Furukawa, T. Ieiri, N. Iida, T. Kamitani, T. Kawamoto, M. Kikuchi, H. Koiso, S. Michizono, T. T. Nakamura, Y. Ogawa, Y. Ohnishi, S. Ohsawa, K. Oide, K. Satoh, M. Suetake, T. Suwada

0-7803-5573-3/99/$10.00@1999 IEEE.

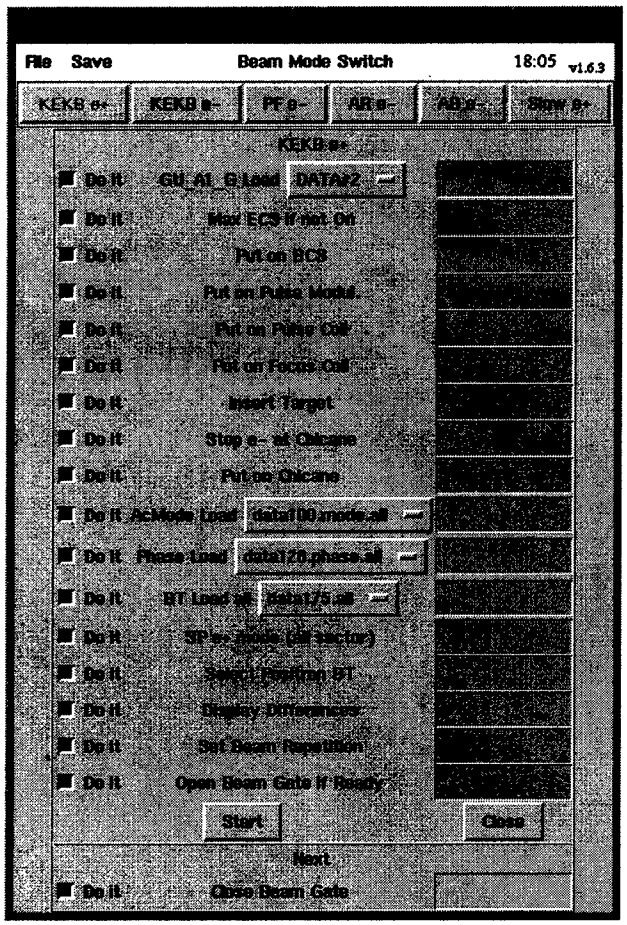

Figure 1: Beam-mode switching panel.

3 IMPROVEMENTS OF BEAM QUALITY

3.1 Software Feedback Loop

Some software feedback loops have been introduced in order to stabilise the gun energy, the powers of two sub-harmonic bunchers (SHB) and the beam energy and the orbits at the J-arc section (1.5 GeV) and at the end of the linac, while hardware feedback loops are implemented for the rf phase-lock system in the SHBs. Fig. 2 shows an example of the feedback panels [4]. The time constant of the software feedback is over several seconds. As a result, the medium-period drift during beam injection was greatly improved. A sudden large variation of the quantities, however, which is discussed in the next section, can not be cured by this feedback, simply because the dynamic range is limited by various boundary conditions.

3.2 Wire Scanners for Matching

There are several regions where optics matching is necessary: at the exit of the bunching section, before/after the J-arc section and at the end of the linac. In order to facilitate and automate this matching, sets of a wire scanner system comprising at least three monitors at appropriate intervals in each section were installed and hardware-tested to measure the beam size [5]. Recently, the software, which nearly automates the optics matching as well as the beam-size measurement, has been completed and beam-tested at the beam-transport line to the KEKB ring. The results so far obtained are quite satisfactory and will be applied to the above-mentioned section at the linac.

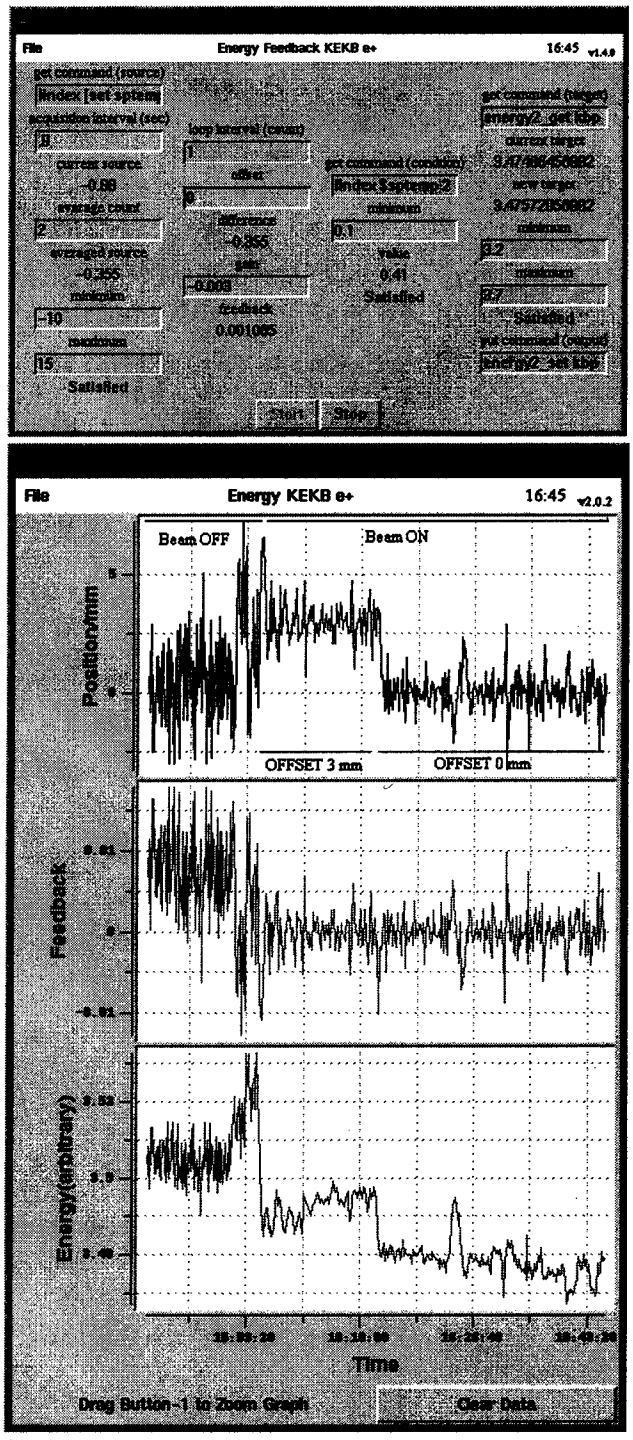

Figure 2: Example of the feedback panels. (upper: control panel, lower: status log)

4 STABILITY ISSUES

The beam-stability issues in our linac are somehow complicated in that we must accomplish stable operation of different kinds of beams repeating a frequent beam switching. A simple classification concerning the stability, such as long- or short-term variations, is not clear, since only one beam can not be continuously observed for monitoring. It may happen that the status of some equipment changes, even during beam switching. In this case, for instance, it is not easy to identify the sources of variations by observing just the status of different beams. In this connection, various efforts to search for the sources of variation have been pursued through deriving information from the status of not only the beams, but also all equipment.

4.1 Search for Sources of Orbit Variation by Singular Value Decomposition (SVD)

The technique of singular value decomposition (SVD) [6] was applied to search for the sources of the orbit variation from the exit of the bunching section to the two upstream sectors of the linac. The matrix comprises time sets of the row vectors consisting of the signals of many beam-position monitors (BPM) along the linac. Figure 3 shows an example of the orbit patterns corresponding to the largest singular value. It seems that the sources of orbit variation originate just at the beginning of the linac. We have tried to identify them by checking the corresponding equipment, but have not yet succeeded.

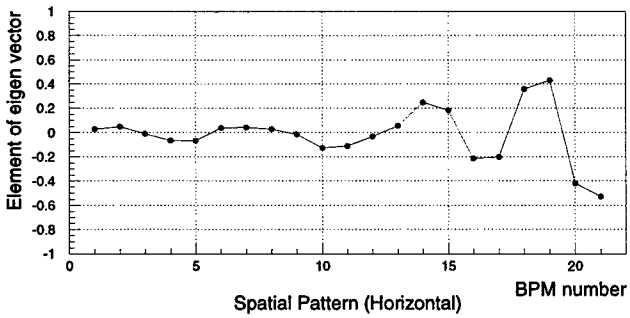

Figure 3: Example of the orbit patterns corresponding to the largest singular value by the SVD method.

4.2 Reinforcement of Stability-Monitoring System

In order to identify the sources of variation, a stability-monitoring system is being prepared. One of the most essential systems is an rf phase-monitoring system. For the moment, this system works only in three upstream sections, but has already been shown to be a quite powerful tool for stability monitoring. For instance, it has turned out that the phase of the first klystron for the bunching section sometimes varies by a few degrees (Fig. 4), possibly due to the environmental temperature.

Another example of a new monitoring system is a fast BPM detection system [7], in which data-taking at a beam repetition rate of 50 Hz can be realized. A FFT-analysis of the data taken at a point of large dispersion in the J-arc section suggests the existence of energy variations, rather than simple orbit fluctuations, in the upstream sections. A statistical treatment, such as a correlation analysis, for all data taken by the above-mentioned system is being applied in order to figure out what is happening in the linac.

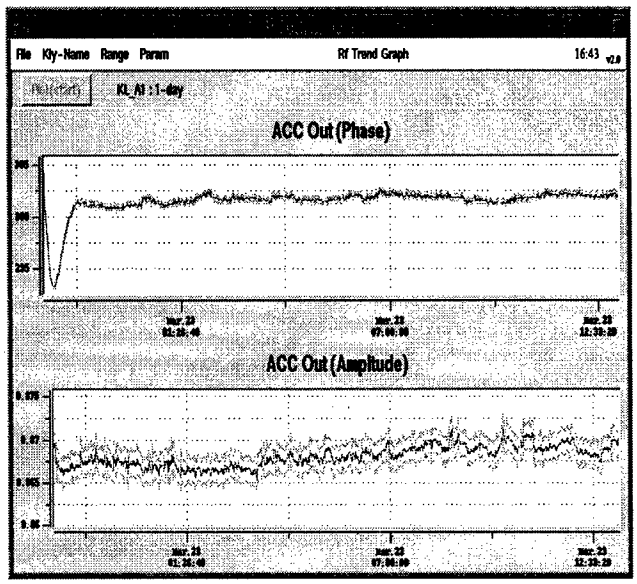

Figure 4: Observed phase variation of the first klystron for the bunching section (upper).

5 CONCLUSIONS

Two linac injection modes for the KEKB rings and those for the Photon Factory rings have been established. Beam-mode switching among four kinds of beams has been successfully verified by injecting a beam into each ring, employing various beam-tuning procedures, including feedback loops. The operation experience so far indicates that there are some stability issues to be figured out in order to maintain a high-quality beam. Many efforts are being made to identify the sources of variations.

6 REFERENCES

[1] K. Oide, in these proceedings.

[2] Y. Ogawa, "Commissioning of the KEKB Linac", to be published in Proc. of LINAC98, Chicago, August 23-28, 1998.

[3] A. Enomoto, "Commissioning of the KEKB 8-GeV e^- / 3.5-GeV e^+ Injector Linac", Proc. of EPAC98, Stockholm, June 22-26, 1998.

[4] K. Furukawa et al., in these proceedings.

[5] Y. Funakoshi et al., in these proceedings.

[6] Y. Ohnishi et al., private communication.

[7] T. Suwada, private communication.

THE SLAC LINAC DURING THE PEP-II ERA

F.-J. Decker, R.H. Iverson, H. Smith, M.S. Zelanzny, SLAC*

Abstract

The 3 km long linac of the Stanford Linear Accelerator Center (SLAC) has for many years provided low emittance beams for the SLC collider. With the beginning of the operation of the B-Factory, PEP-II, the linac will now serve primarily as an injector for the low (LER) and high energy rings (HER) of PEP-II. The different beams are stabilized by a new regional linac energy management (LEM) program, which keeps the magnet strengths and therefore the deflections constant at each of the four extraction points. They are at 3.1 GeV (positrons for LER), 9 GeV (electrons for HER), 25 GeV (electrons for the positron production), and 28.5 GeV (electrons for other purposes such as test beams, plasma experiments, and iris destruction tests). Since many components of the accelerator can be configured on each pulse, it is possible to run these beams with different intensities, bunch length, energies, rates, etc. Only the quadrupole magnet strengths are fixed, producing different lattices for different energy beams, which must be matched at extraction from the linac. Since PEP-II injection does not require all of the full 120 Hz rate, it is possible to run other experiments at the same time. That might include an extension of the SLC run or a high charge, fixed target experiment, which will require some additional pulsed magnets.

1 INTRODUCTION

For the SLC-collider, the SLAC linac ran at 120 Hz and co-accelerated three beams together: positrons, electrons and a scavenger bunch to the positron target at 2/3 of the linac length. For the PEP-II era the main purpose is to provide a stable fill rate for the low and high energy ring. The linac runs mainly at 30 Hz till 2/3 of the linac and 60 Hz in the first 3 sectors till the extraction of the positrons into the by-pass line. So there are the following rates available: 10 Hz for e^-, 10 Hz for e^-(scav) and an extra 10 Hz for an e^--beam for additional experiments (like plasma acceleration or plasma lens in final focus test beam area, FFTB). The positrons are in between this in a 60 Hz timeslot. On demand this can be changed to 30 Hz e^- to HER, or 30 Hz e^-(scav) and 30 Hz e^+ to LER for a three times faster fill rate.

Besides the scheduling issues, the linac has to provide stable and sometimes special beam properties for the different beams.

*Work supported by Department of Energy contract DE-AC03-76SF00515.

2 NEW LEM

The linac energy management program (LEM) keeps the magnet focussing lattice stable by accounting for the different klystrons which accelerate the beam. Since each klystron can be on for one beam and off for another, it is impossible to adjust the magnets to the same lattice on a pulse by pulse basis. Different strategies are possible.

2.1 "Anti-LEM"

During the SLC-run the PEP-positrons got decelerated in their last part in the linac and got after each quadrupole adjustment by LEM a big kick in the last quadrupole where they are off-axis. This needed corrector changes (anti-LEM) and re-matching in some degree.

2.2 Regional LEM

To avoid these frequent adjustments, a regional LEM was introduced, which keeps the end energy and magnet strengths for each of the four beams constant (e^+: 3.1 GeV, e^-: 9 GeV, e^-(scav): 25 GeV, e^-(FFTB): 28.5 GeV). This is only perfect when each beam has the same acceleration. But since this keeps the lowest energy beam constant, a higher energy, mismatched beam will see a weaker lattice, which is not too bad.

2.3 Additional Matching

In principle this mismatched beam could be re-matched after the lower energy beam got extracted from the linac. This was never tried and has the potential of disturbing other careful adjusted beam parameters like wakefield bumps which cancel unknown errors at a special betatron phases.

2.4 Identical Energy Profiles

This leaves only the solution of identical energy profiles. But since the FFTB beam needs a big initial energy spread for transverse stability, which is accomplished by a 20° phase offset (BNS-damping), the energy would be different again, but the following trick helps. By timing the klystrons (which use SLED) for the positrons pulse 240 ns late, so that the accelerator structure is not completely filled, the e^+-energy on the rf-crest is adjusted to be identical to the FFTB beam, which is 20° off crest (see Fig. 1).

0-7803-5573-3/99/$10.00@1999 IEEE.

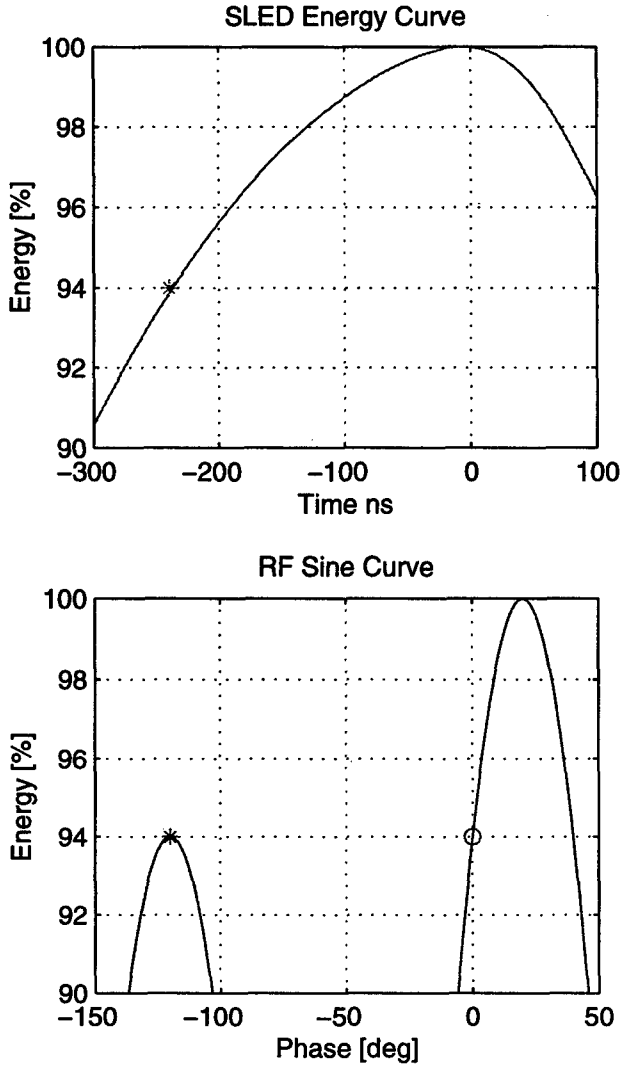

Fig. 1: Equal beam energies.
Injecting the positrons 240 ns early on crest (left) gives the same energy like being 20° off crest but on the peak of the (SLEDded) klystron fill curve (right).

3 SENSITIVITY TO BEAM CHANGES

Since the PEP-II rings are not very sensitive to changing beam emittances or offsets, the tuning is much relaxed, just the availability for filling counts. This might change when background issues get more important with the BaBar detector in place. On the other hand the FFTB beam for the plasma experiments has to be maintained to much better accuracy. For instance, when the linac steering feedbacks were keeping the e^-(scav) "stable", the emittance for the FFTB beam changed easily by a factor of three. By switching the feedback to the FFTB beam, this beam has stabilised, but also helped to keep the other beams in a smaller range of variations.

4 POSITRON ENERGY SPREAD

Since the positrons have with 3.1 GeV the smallest energy, their energy spread is still dominated by the energy spread introduced by the compression in the ring-to-linac section (RTL). With a damping ring bunch length of 6 mm and an energy spread of 0.07% at 1.19 GeV, the following energy spreads are possible (see Tab. 1). A total compression on a linear slope is assumed, and wakefields and the rf sine curvature in the linac are ignored.

Table 1: Possible Energy Spreads

Com-pressor	ΔE	σ_z	$\Delta E/E$ at 3.1 GeV
30 MeV	10.7 MeV	0.47 mm	0.34 %
25 MeV	8.9 MeV	0.56 mm	0.28 %
15 MeV	5.3 MeV	0.94 mm	0.17 %
12 MeV	4.3 MeV	1.18 mm	0.14 %
10 MeV	3.6 MeV	1.41 mm	0.11 %

This table seems to be in discrepancy with the data where at 27 MeV a 0.15% energy spread is achieved (see below).

4.1 Longitudinal Emittance

The longitudinal emittance is given by the damping ring rf. The maximum reduction is about 10 %, by raising the rf amplitude by 20 %.

4.2 Longitudinal Phase Space

The longitudinal phase space can be adjusted by lowering the bunch length and raising the energy spread, which is mainly done in the compression region. Three different corrections come to mind to change this adjustment.

- Pre-compression in the damping ring: This will lower the bunch length and therefore the non-linear part of the compression rf.
- Changing R_{56} in the compression region (which is the basic assumption of Table 1): This will require changes of up to a factor of three in magnet strength, which might be not easily feasible.
- Correlated energy spread cancellation: By under-compressing the beam, the bunch length will be longer and there will be an energy-length correlation. This correlation can be taken out later in the linac by accelerating the beam at the right amount off crest. This will reduce the energy spread, giving an explanation why at 27 MeV the energy spread can be as low as 0.15 % in the experiment.

4.3 Simulations

To compare the analytic result with reality, the longitudinal phase space changes were simulated taking into account the linac rf and wakefields. Fig. 2 shows the 1-, 2- and 3-sigma contour lines after the compression (RTL)

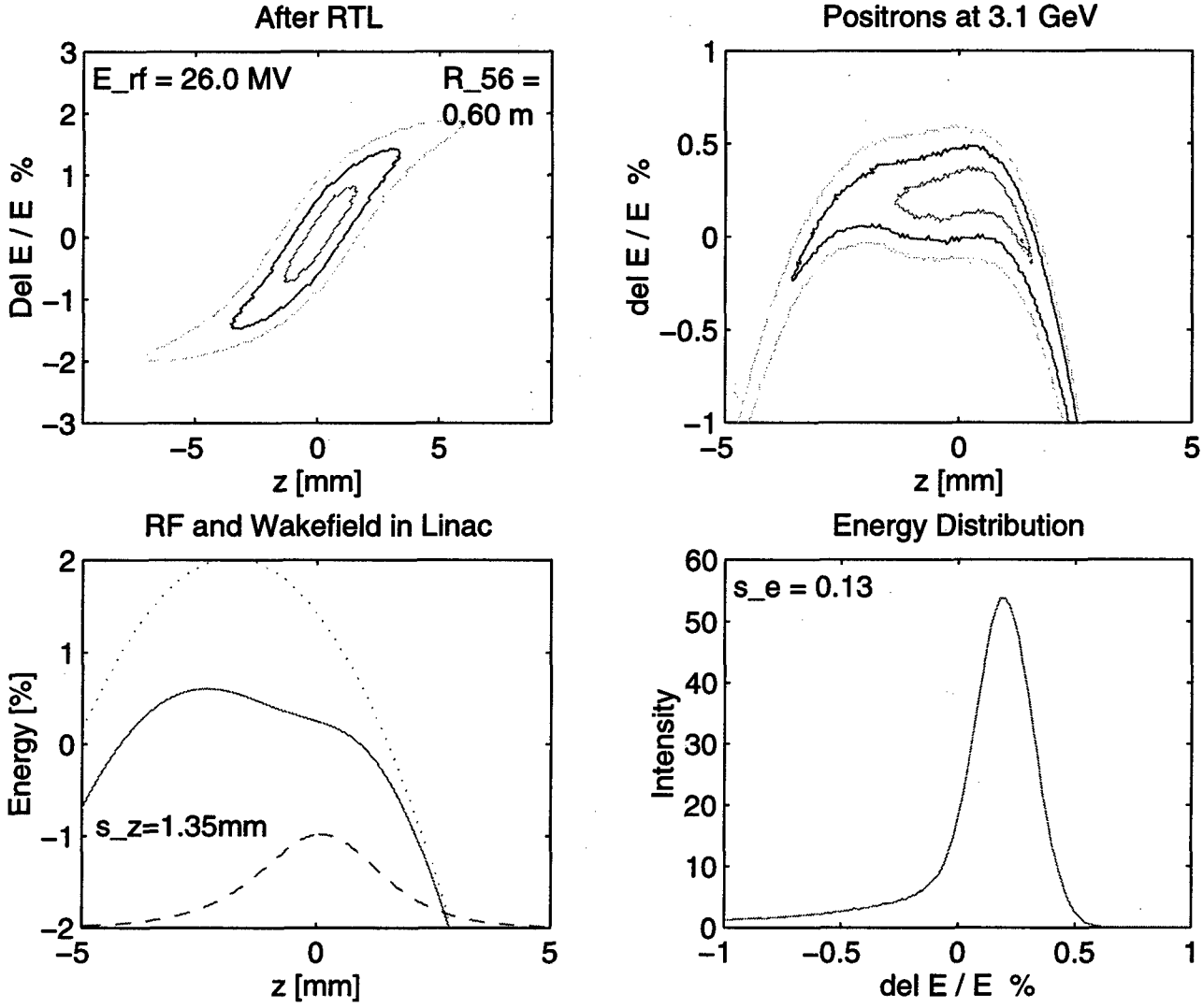

Fig. 2: Low positron energy spread.

By cancelling the correlated energy spread after compression in the RTL with the opposite correlation of the linac rf (including wakefields), a 0.13% energy spread can be achieved.

and at the 3.1 GeV energy point in the linac. By compensating the E-z-slope of the under-compressed beam with the slope created by the rf in the linac (and the wakefield for $2{\cdot}10^{10}$ particles), a fitted energy spread of 0.13% can be achieved (plus low energy tail). The longitudinal wakefields help to flatten the curve, which allows a longer bunch length, making a better correlation compensation possible.

5 DIFFERENT BEAM CHARGES

At $2{\cdot}10^{10}$ particles per bunch the beam loading within the bunch reduces the energy by nearly 2% (compare Fig. 2). This implies that a very low charge ($2{\cdot}10^{9}$) for topping of and equalising the PEP-II bunches in the ring, will require a different energy and phase in the linac. This is also true for $4{\cdot}10^{10}$ FFTB beams or a fixed target experiment, running together with PEP-II.

6 SUMMARY

PEP-II requires beams with different property, filling or topping of the rings and other experiments together with PEP-II. This can be solved mainly by pulsed devices or needs a compromise in the set-up. The positron energy spread is an example, where a careful cancellation can be used to reduce the energy spread by a factor of two.

7 REFERENCES

[1] V.E. Balakin, A.V. Novokhatski, V.P. Smirnov, VLEPP, *Transverse Beam Dynamics,* 12th Int. Conf. On High Energy Accel., FNAL (1983) 119.

[2] D. Farkas, H. Hoag, G. Loew, P. Wilson, *SLED: A Method of Doubling SLAC's Energy,* SLAC-PUB 1453, June 1974.

BACKGROUND MEASUREMENTS DURING PEP-II COMMISSIONING*

T. Mattison#, D. Aston, B. Byers, D. Coupal, H. Destaebler, T. Fieguth, L. Keller, W. Kozanecki, W.R. Nelson, M. Petree, S. Petrak, S. Shapiro, A. Snyder, M. Sullivan, S. Wagner, SLAC, A. Boucham, D. Boutigny, Y. Karyotakis, J-Y. Nief, P. Petitpas, V. Tisserand, K. Zachariadou, Annecy, C. Goodenough, T. Lanting, British Columbia, A. Hasan, A. McKemey, Brunel, S. Devmal, T. Geld, B. Meadows, M. Sokoloff, Cincinnati, T. Borak, R. Malchow, W. Toki, Colorado State, K. Benabed, N. Treps, Ecole Polytechique, F. Goozen, J. Kadyk, R. Kerth, N. Roe, M. Ronan, LBNL, R. Cizeron, R. Cousin, A. Durand, G. Fubiani, V. LePeltier, S. Sen, S. Trincaz-Duvoid, A. Valassi, G. Wormser, Orsay, F. LeDiberder, S. Versillé, Paris VI&VII, R. Aleksan, G. DeDomenico, S. Emery, J-C. Faivre, A. Gaidot, B. Mayer, Saclay, J. Beach, P. Burchat, Ch. Cheng, X. Huynh, D. Kirkby, T. Meyer, E. Nehrlich, C. Roat, A. Soha, H. Tanaka, Stanford, S. Berridge, W. Bugg, J. Hargis, A. Weidemann, Tennessee, C. Hast, E. Potter, V. Sharma, UCSD, H. Band, J. Johnson, Wisconsin

Abstract

A variety of background detectors were installed at the interaction point of PEP-II for measurements of machine backgrounds during commissioning. Results from these detectors, machine experiments, and simulations have been used to reduce the backgrounds at PEP-II before the installation of the BaBar physics detector.

1 INTRODUCTION

The PEP-II collider has a design luminosity of 3×10^{33} $cm^{-2}s^{-1}$, which requires beam currents of 1 and 2 amperes in the rings. The synchrotron radiation flux from the magnetic beam-separation scheme, and the particle loss rate from beam-gas scattering, are potential sources of high backgrounds for the BaBar detector. Many detectors were installed at the interaction point (IP) to measure the backgrounds, from the start of PEP-II commissioning. The background simulations used in the design of PEP-II were enhanced to help understand the measurements. Dedicated beam experiments were done to diagnose and reduce the backgrounds.

2 DETECTORS

An X-ray spectrometer measured the synchrotron radiation (SR) spectrum. A 3×3×2 mm cadmium-zinc-telluride crystal was enclosed in a copper collimator with 3° acceptance and remotely movable lead and steel filters. The collimator was mounted on a remotely steerable TV camera. The readout was through a local pre-amplifier, remote post-amplifier, PC-based pulse-height analyzer, and rate-to-voltage converter. Energy resolution was 4% at 6 keV to 1% at 100 keV, where the efficiency began to fall off. The early commissioning IP beam pipe had poor SR masking, and rates >1 kHz/mA were observed. Interestingly, the spectra had prominent Bragg-scattering features, rather than the expected material fluorescence peaks. The final beam pipe had much better masking, with X-ray rates difficult to distinguish from lost-particle (LP) backgrounds.

PIN diodes measured both SR and LP backgrounds on the IP beam pipe. Pairs of 1 cm^2, 300μ thick reverse-biased PIN diodes separated by 1 mm lead absorbers with a thermally coupled thermistor were mounted at 3 positions in Z and 8 in phi. Readout was 20-bit charge integrating ADCs with analog and digital filtering giving 15 pA resolution on currents up to 1μA at 7.5 Hz. An onboard microcontroller asynchronously passed data over a Controller Area Network bus to a VME single-board computer running vxWorks. The data was logged to disk by a Java server running on a SUN workstation. Real-time data for beam-tuning and background experiments was also available. In addition, the increase in leakage current over time measured the integrated radiation dose to the diodes, calibrated by the offline integrated dose.

A BaBar double-sided silicon strip detector with final radiation-hard electronics and full readout chain measured occupancies next to the beam pipe. Occupancies were initially very high but decreased to 0.5-1% per 100 mA of current for both beams by the end of commissioning. Large steps in the detector leakage current were observed over the running period. These were due to bursts of radiation causing bias voltage to punch through strip capacitors, inducing p-stop shorts. Bias voltage to the BaBar silicon vertex tracker will be turned off during injection to avoid this problem.

The Mini-TPC detector gave fine-grain 3D tracking information from 4.5 to 10 cm in radius (less a 110° wedge for the silicon strip) and 10 cm in Z. It had 6 sectors of 8 radius rows of 4 phi cathode pads (trapezoidal to maximize charge sharing), and operated with a drift field of 200 V/cm at a gas gain of 50000. The gate grid normally had ±220 V on alternate wires to reduce space-charge effects

*Work supported iby U.S. Department of Energy contrace DE-AC03-76SF00098, CEA, IN2P3, and PPARC.

0-7803-5573-3/99/$10.00@1999 IEEE.

and was opened for 20 μs at a few Hz for readout. The pad pre-amps were 5 m away, and 30 MHz FADCs digitized the data, which was recorded to disk on a microVax. Resolution from a test-beam at CERN was 25% for dE/dx, $70\mu \times \sqrt{L_{cm}} \oplus 170\mu$ in Z, 210μ in R-phi, and 9 and 4 mrad in polar and azimuthal angles. An event display and the hit and track counts were available in real time, and the chamber current was also available as a hardware signal. A detailed Monte Carlo simulation included a complete digitization in the miniTPC.

The Straw Chamber (originally built for the Crystal Ball) was 544 aluminum tubes, 4 mm in diameter, 34 cm long, in two double layers at 13 and 17 cm radius from the beam. The signal from both ends of each wire was amplified then recorded by analog storage, multiplexing, and a NIM ADC combined with a scanner-memory module in a CAMAC crate controlled by a PC. The chamber current also gave a real-time measurement of the radiation level.

The Crystal Ring measured the MeV photon background using 12 CsI(Na) crystals with photomultiplier tube (PMT) readout. The crystals were 6×6×15 cm, at radius 30 cm from the beam, on a trolley that scanned ±80 cm in Z. A RAID 8235 processor running EP/LX controlled a CAMAC crate with FERA ADCs that could be self-triggered for calibration with the 1.46 MeV photons from KCl salt-substitute. This system also measured background photon spectra at low beam current. The PMT current was used as the background measurement at higher beam current, since the spectrum was dominated by pileup and the PMT voltage was limited by anode heating. A fiber-optic and LED pulser system propagated the calibration from the source+ADC system to the PMT current system at lower voltage.

The mini-Stand-Off-Box (mSOB) background detector simulated the 6000 liter water tank with 10000 PMTs on one surface that is the external part of the BaBar Cherenkov particle identification system. The mSOB water tank was 1 ft^3 with a quartz window at one face, allowing 48 PMTs to view the Cherenkov light created in the water. A CAMAC ADC system with 100-500 ns gates was controlled by a small Unix workstation via GPIB. The backgrounds were primarily MeV photons which Compton scatter, making electrons just above Cherenkov threshold, typically producing a single photoelectron in a single tube. Since the rate was high, in later runs a single mSOB tube was fed into a frequency to voltage converter for real-time measurements. This system was also used with $(3\ in)^3$ lead-glass blocks glued to PMTs, with a sensitivity similar to the mSOB but easier to manipulate. The mSOB single-tube rate extrapolated to 1 MHz for the HER and 10 MHz for the LER at design currents, motivating the construction of shielding upstream of BaBar.

The BaBar Calorimeter Prototype detector measured the photon background from 20 MeV to a few GeV. It was four CsI crystals mounted near the future BaBar endcap calorimeter location, read out by PMTs via scalars and ADCs in a CAMAC crate controlled by a Macintosh. The single crystal rate was 140 Hz with a 100 MeV threshold for a LER current of 300 mA in February 1999. A drop in the light yield of about 30% has been found after an exposure estimated to be a few hundred rads.

The instrumented flux return (IFR) background detector simulated the outer layers of the BaBar IFR. Eight resistive plate chambers (RPCs) about $(1\ m)^2$ and operated at 8 kV alternated with 1.25 in steel plates, with the first and last layers covered with 0.25 inch of steel. Counting rates as a function of position were recorded using BaBar IFR electronics and a CAMAC crate controlled by a PC. Early data motivated the addition of shielding on the two exposed edges of the chambers, and the corresponding areas of BaBar, and shielding in the PEP-II tunnels.

An array of 8 RadFETs was positioned at the future inner radius of the BaBar CsI calorimeter to measure the integrated dose via threshold shifts. From November 1998 to February 1999, a dose of about 600 rads was accumulated in unshielded devices.

3 SIMULATIONS

The program SYNC_BKG traced the beam envelope through the magnets near the IP, calculated the number and spectrum of SR photons from each magnet, and projected them to apertures that modelled the beam pipe. This was input to MASKING, which used EGS4 to calculate the number, energy, and angle distribution of the photons that scatter from, for instance, a mask tip and penetrate the IP beam pipe to register as background in the SVT. MASKING could also generate an output file of photons to be used as input to detector simulations.

Lost-particle rates from bremsstrahlung and Coulomb scattering were calculated with the LP_TURTLE Monte Carlo, derived from Decay TURTLE. The optics and apertures of both rings were modeled for their entire circumferences. Information about the trajectory of particles striking apertures near the IP was stored to file in the form of ntuples. LP_TURTLE output was input for collimator placement studies, multi-turn and longitudinal beam-dynamics simulations, and detector simulations.

The BaBar detector simulation with GEANT3 (BBSIM) includes the PEP-II beam pipe, magnet material, and magnetic fields to 8 m from the IP. An equally complete simulation was done of the IP configuration used for early commissioning of the HER, and of the various background detectors. Rays which hit TURTLE apertures close to the IP were backed out to 8 m and tracked again in BBSIM since it has a more detailed 3D model of the apertures in the detector. BBSIM modelled electromagnetic showering and energy deposition in detectors.

4 EXPERIMENTS

Initially backgrounds were much higher than expected from simulations. Turning off distant vacuum pumps increased the background, indicating that distant beam-gas

scattering was important, which had not been included in the initial LP_TURTLE simulation. Reducing the RF voltage to the point where the quantum lifetime was short did not increase the backgrounds, indicating that distant bremsstrahlung was not dominant.

Backgrounds were sensitive to beam steering at the IP, particularly changes in IP angle, which corresponds to beam position in the high-beta quads. In the initial IP geometry with poor masking, extreme steering bumps varied the SR contribution differently from the LP contribution, which allowed them to be separated in some detectors. Backgrounds also decreased in some detectors when the IP beta function was increased, decreasing the beam size in the quads. Later in commissioning, single-sided fixed collimators were installed in the HER 350 m upstream of the IP, at points where the beam could be bumped close the aperture. This reduced backgrounds, and the sensitivity to steering and beta function.

Measuring the backgrounds as a function of beam current was very informative. Synchrotron radiation and beam-gas scattering on base pressure and give linear current dependence, and beam-gas scattering on dynamic pressure induced by the beam gives a quadratic contribution. The quadratic term was dominant at high current.

There were many non-evaporable getter (NEG) pumps in the IR, which expelled hydrogen when they were heated for regeneration. Heating a NEG pump produced a large localized pressure bump of known composition, with magnitude measured by the nearby ion pumps or by the change in beam lifetime. The increase in backgrounds from the pressure bump allowed a precision check of the simulation. The agreement was good.

5 CONCLUSIONS

Measured backgrounds from the January 1998 configuration of the HER were consistent with a factor of 7-10 more background at design current than estimated in the BaBar design report [1]. The measurements were consistent (within a factor of 1.5-2) with a simulation using measured pressure profiles rather than a uniform 1 nTorr, LP_TURTLE simulation of the full ring rather than just the IP and a short arc region, and BBSIM shower simulation including all the IP quads rather than just those inside the detector. See figure 1. Collimators reduced the HER arc contribution by a factor of 2-5 in the final HER configuration.

Measured backgrounds from the LER (without collimators) were comparable to the HER at the same current. The absolute LER background levels agreed with the extended simulation to within factors of 2-5; work is in progress to clarify the origin of these differences.

Extrapolating present measurements to design currents, LER background would dominate. A substantial reduction in LER background is expected from distant Coulomb collimators presently being installed. Some reduction is expected from the larger aperture of the final Q2 vacuum chamber. The LER vacuum will improve with further scrubbing, and a program of vacuum improvements in the LER is underway.

6 REFERENCES

[1] BaBar Technical Design Report, SLAC-R-95-457, March 1995

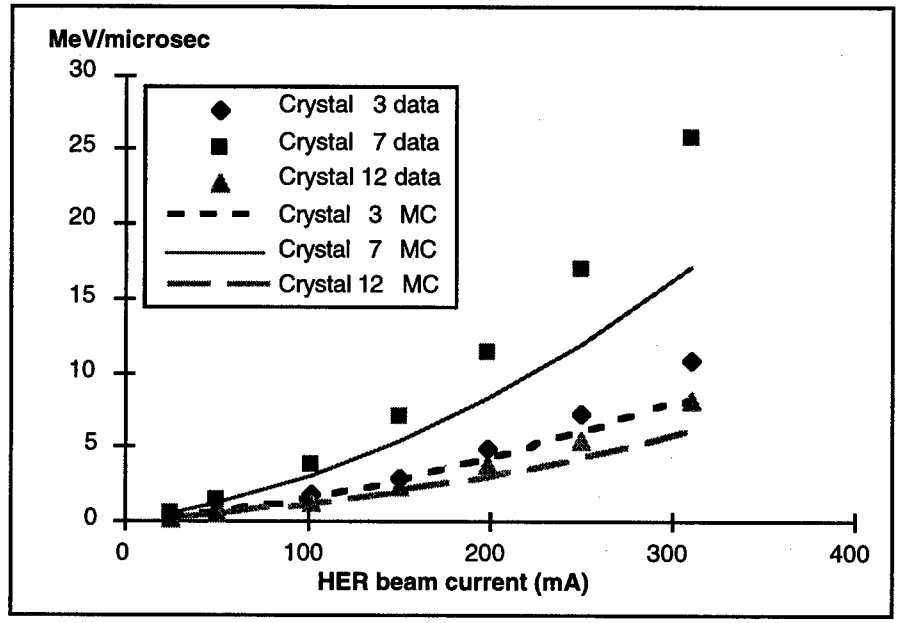

Figure 1: Comparison of measured and simulated backgrounds in the Crystal Ring detector as a function of beam current during HER commissioning in January 1998.

BEAM COMMISSIONING OF THE PEP-II HIGH ENERGY RING*

U. Wienands, S. Anderson, R. Assmann†, V. Bharadwaj, Y. Cai, J. Clendenin, P. Corredoura, F.J. Decker, M. Donald, S. Ecklund, P. Emma, R. Erickson, J. Fox, T. Fieguth, A. Fisher, S. Heifets, A. Hill, T. Himel, R. Iverson, R. Johnson, J. Judkins, P. Krejcik, A. Kulikov, M. Lee, T. Mattison, M. Minty, Y. Nosochkov, N. Phinney, M. Placidi‡, S.Prabhakar, I. Reichel, M. Ross, J. Safranek, S. Smith, V. Smith, H. Schwarz, J. Seeman, M. Stanek, M. Sullivan, D. Teytelman, R. Tighe, R. Traller, J. Turner, F. Zimmermann†; *Stanford Linear Accelerator Center, Stanford, CA*;
W. Barry, J. Byrd, S. Chattopadhyay, J. Corlett, W. Decking, M. Furman, D. Li, H. Nishimura, G. Portmann, R. Rimmer, A. Zholents, M. Zisman; *Lawrence Berkeley Laboratory, Berkeley, CA*;
W. Kozanecki; *DAPNIA-SPP, CEA/Saclay, France*;
A. Hofmann, B. Zotter; *CERN, Geneva, Switzerland*;
C. Steier; *Physikalisches Institut, U. Bonn, Germany*;
W. Bialowons, M. Lomperski; *DESY, Hamburg, Germany*;
A. Lumpkin; *Argonne National Laboratory*

Abstract

The PEP-II High Energy Ring (HER), a 9 GeV electron storage ring, has been in commissioning since spring 1997. Initial beam commissioning activities focused on systems checkout and commissioning and on determining the behaviour of the machine systems at high beam currents. This phase culminated with the accumulation of 0.75 A of stored beam—sufficient to achieve design luminosity—in January 1998 after 3.5 months of beam time. Collisions with the 3 GeV positron beam of the Low Energy Ring (LER) were achieved in Summer of 1998. At high beam currents, collective instabilities have been seen. Since then, commissioning activities for the HER have shifted in focus towards characterization of the machine and a rigorous program to understand the machine and the beam dynamics is presently underway.

1 HER COMMISSIONING

The PEP-II [1] High Energy Ring (HER) was completed at SLAC in Spring of 1997. It is located in the PEP tunnel at SLAC, where it is part of the *B*-Factory together with the Low Energy Ring (LER) and the BABAR detector. Beam commissioning of the HER began in earnest in June 1997, and the ring reached 0.75 A of stored beam current—sufficient to achieve the design luminosity of 3×10^{33}— in January of 1998, after 3.5 mo. of running time. Parameters of the Ring are given in Reference [1]. Since July of 1998, HER commissioning work has focused on understanding and tuning of the beam parameters, background measurement and reduction, tuning of the beam feedback systems and understanding of the multi-bunch instabilities and supporting collisions [2] with the completed LER.

Table 1 gives an overview of the commissioning results achieved up to date.

Beam commissioning has been helped significantly by fairly good hardware performance: for the last run, hardware availability was 79% for the PEP-II facility, this includes HER, LER and the Injector.

In this report, we will not cover the rf system [3, 4] or the beam feedbacks [5, 6] since they are described elsewhere.

1.1 Magnet System and Lattice Functions

Alignment of the ring magnets appears to have been within the stated accuracy of 250μm (rms), judged by the ease with which the first turn was achieved and the rms corrector strength needed to reduce orbit excursions to a reasonable level. As of this writing, rms orbit excursions of 0.75 mm rms are routinely achieved. Figure 1 shows a plot of the lattice functions in the vertical plane, together with the design values, measured on-line by phase-advance analysis. The agreement is rather good, but to reach this level of agreement the inner insertion quadrupole had to be tweaked by

Table 1: HER Commissioning results

Parameter	Unit	Design	Achieved
Energy	GeV	9	$9 \rightarrow 9.1 \rightarrow 9$ (ramped)
Current	A	0.99‡	0.75
Luminosity	$cm^{-2}s^{-1}$	3×10^{33}	5×10^{32}
β_x^*	cm	50	50
β_y^*	cm	2	1.5
Bunch length	cm	1.15	1.15
$\delta p/p$	%	0.061	0.066
ϵ, horiz.	πnmr	48	56
ϵ, vertic.	πnmr	1.9	4
Coupling		0.03	0.0007
Life time	h	12	20 @ 50 mA 2.5 @ 0.75 A

‡ for β_y^*=2 cm

* Supported by US DOE under contract DE-AC-76SF00515
† Now at CERN
‡ On leave from CERN, Geneva, CH

0-7803-5573-3/99/$10.00@1999 IEEE.

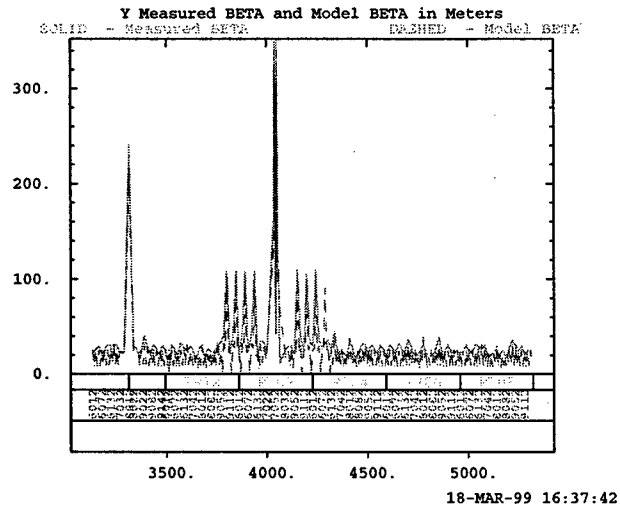

Figure 1: Measured vertical lattice functions

about 0.13%. The amount of correction needed has varied for different lattice configurations and is now thought to arise from a longitudinal position error rather than a calibration error. [7] There are still differences in the details of the lattice functions that remain to be understood.

1.2 *Vacuum System*

Until early 1998 the vacuum system of the HER has cleaned up according to the schedule outlined in the PEP-II CDR [8], see Fig. 2. With the installation of the final inter-

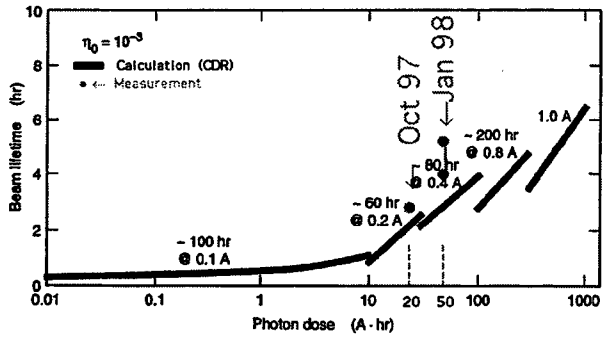

Figure 2: Beam life time *vs* photon dose

action region, beam life times have slid back somewhat due to the extensive vacuum work and the large number of new chambers installed. In the Fall of 1998, however, beam life time recovered and up to 24 h were measured at low beam current.

In general, the HER has not experienced significant dust trapping. However, in our last run we have seen occasional life-time reductions, mainly at beam currents below 200 mA, which sometimes could only be cured by aborting the beam and reinjecting. Without a systematic study it is not possible to give a cause for this behaviour.

On the other hand, at high residual pressures the beam has been clearly less stable than under good vacuum conditions. Also, the presence of a gap (usually 10%) in the fill is mandatory at high intensity to preserve beam stability. This strongly suggests the presence of ion trapping. The measurement of fill-pattern dependent ion-clearing currents further supports this assertion.

1.3 *Transverse Beam Dynamics*

Machine resonances have been measured by systematic scans of beam life time *vs* tune and by following an off-axis injected bunch over 1024 turns and Fourier-analysing the result. Identified lines are indicated in Fig. 3.

Transverse beam size has been measured by performing scraping experiments using beam scrapers installed in one of the straight sections. Horizontally, the beam size is within 10% of the prediction, but vertically the results indicate almost twice the beam size predicted. This is to be considered an upper limit, since the measurement of the small vertical extent of the beam by scraping is difficult. There also is evidence for vertical tails.

1.4 *Longitudinal Beam Dynamics*

Once the rf stations were phased w.r.t. each other, the synchrotron tune was measured at the design value (0.0446 at 14 MV). Beam life time was measured against rf voltage, the result indicates a momentum spread of 0.066% (rms), about 8% larger than the expected 0.0614%. Bunch length was measured using a streak camera and agrees with the predicted σ_l of 1.15 cm at 14 MV.

1.5 *Single-Bunch Intensity Related Effects*

Tune shift *vs* beam current relates to the broadband impedance in the ring (which is inductive) and was measured several times. The measured tune shifts have increased slightly over time, this is attributed to the changes in the vacuum system made during the various down

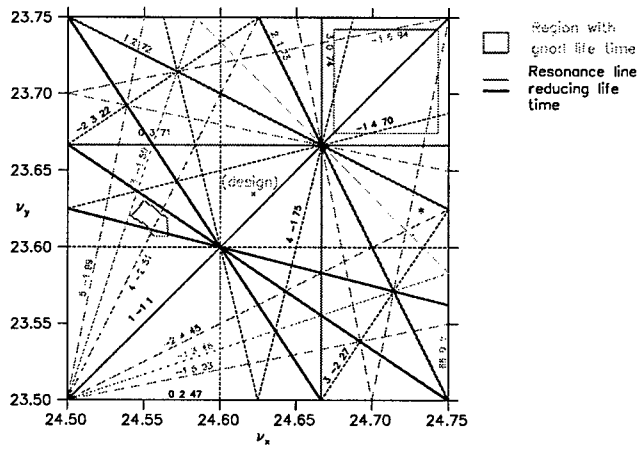

Figure 3: Working diagram of the HER; dark lines reduce beam life time

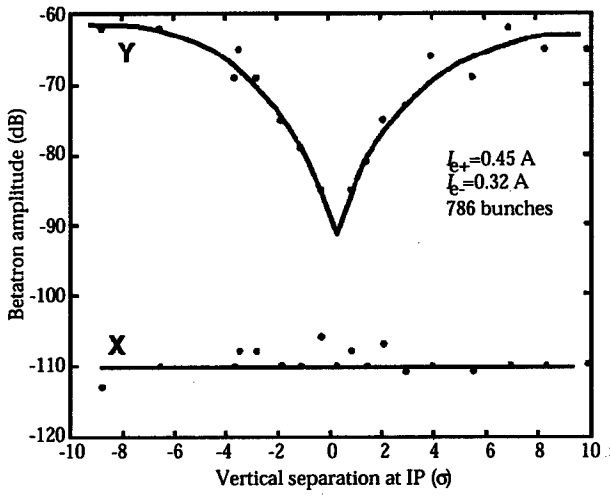

Figure 4: Betatron motion *vs* beam separation

times. In the present configuration the tune shifts are -0.56×10^{-3}/mA horizontally and 1×10^{-3}/mA vertically. The resulting impedance of $>$ 100 nH is larger than predicted by a factor of about 2. However, the max. single-bunch current is limited not by beam dynamics but by hardware considerations and so this is of no consequence. Bunch lengthening up to 2.5 mA bunch current was found to be consistent with potential-well distortion, with no indication for the onset of turbulence.

Excess heating of the shielded bellows close to the beam scrapers was seen and indicates excitation of a localized wakefield. This excitation arises from the step transitions that these experimental scrapers introduce in the vacuum system. These scrapers will be replaced with tapered collimators in the near future.

1.6 Multi-Bunch Effects

Longitudinal Plane Based on the measured HOM spectrum of the rf cavities (which are very well damped) the HER was expected to be stable up to 330 mA, with the longitudinal bunch-to-bunch feedback system designed to be able to stabilise the beam well beyond 1 A current. Grow-damp measurements were carried out demonstrating that the first modes going unstable were a cluster around mode 750...800, with a threshold around 550 mA. The modes agree in frequency with a measured cavity resonance[4]. The increased threshold is thought to arise from the Landau damping introduced by the sizeable synchrotron-tune shift along the fill (due to the 10% ion-clearing gap).

Transverse plane Instability thresholds have been unexpectedly low in both planes in the HER. Even at low beam current coherent bunch motion is detectable. The modal spectrum shows predominantly low-order modes, with indication of a shift from mode 0→1→2...with increasing beam intensity. The instability shows grossly non-linear growth rates, saturating before the beam is lost unless the beam intensity is several hundred mA. This behaviour is consistent with trapping of heavier ions like CO. However, in a recent run a strong dependence of the growth rate on a vertical orbit wave at a certain phase was observed, which would indicate the presence of a local high-Q impedance.

Bunch-train experiments have shown the instability to be dependent on chromaticity (above $\xi \approx +10$ the beam was markedly less unstable) and on coupling (a fully coupled "round" beam could have about 50% more intensity for the same level of beam motion). These observations were *not* confirmed for even fills with a small gap, indicating that the bunch-train behaves in a way qualitatively different from the even fills.

Improved beam stability was observed during collisions, most likely due to increased Landau damping. A quantitative measure of this effect is the reduction in height of the betatron peak when the HER beam is brought into collision with the LER beam; this is shown in Fig. 4. The damping due to this effect exceeds that obtained from the bunch-to-bunch feedback system.

2 SUMMARY

Beam commissioning of the HER has progressed well, with most of the important commissioning milestones met or exceeded. Multibunch beam operation, however, has uncovered a transverse instability the cause and exact nature of which still remains to be explained. While the excited modes and nonlinear behaviour are consistent with ion trapping, the orbit dependence is not. Preliminary indication from our collision runs is that the Landau damping due to the beam-beam effect will greatly increase the transverse instability threshold, however.

3 REFERENCES

[1] J.T. Seeman, "Commissioning Results of KEK-B and PEP-II *B* Factories," *these proceedings*.

[2] M. Sullivan *et al.*, "Beam-Beam Collisions at the PEP-II *B*–Factory," *these proceedings*

[3] P.L. Corredoura, "Architecture and Performance of the PEP-II Low-Level RF System," *these proceedings*.

[4] R.A. Rimmer *et al.*, "Commissioning of the PEP-II High-Power RF Systems,"Proc. European Part. Accel. Conf., Stockholm, Sweden, June 1998, pp 1805-7.

[5] W. Barry *et al.* "Operational Experience with the PEP-II Transverse Coupled-Bunch Feedback Systems," *these proceedings*.

[6] J.D. Fox, "Multi-Bunch Instability Diagnostics via a Digital Feedback System at PEP-II, DAFNE, ALS and SPEAR," *these proceedings*.

[7] J. Safranek *et al.* "Optics characterization and Correction for SLAC's PEP-II *B*-Factory," *these proceedings*.

[8] "PEP-II An Asymmetric *B*-Factory" Conceptual Design Report, SLAC-418, LBL-PUB-5379, CALT-68-1869, June 1993.

OVERVIEW OF LEP OPERATION IN 1998

G. Arduini, R. Assmann, R. Bailey, H. Burkhardt, A. Butterworth, P. Collier, K. Cornelis, A. Faugier, M. Jonker, M. Lamont, M. Meddahi, G. Morpurgo, P. Raimondi, G. Roy, J. Uythoven*, J. Wenninger
CERN, SL Division, Geneva, Switzerland

Abstract

After the installation of 32 additional RF cavities in the 1997-1998 shutdown LEP was operated at a beam energy of 94.5 GeV. The total integrated luminosity for the year 1998 clearly surpassed its target and reached 198 pb^{-1}. Vertical beam-beam tuneshifts of more than 0.07 were obtained. The performance did not seem to be beam-beam limited, but the total beam current was limited by power dissipation problems to around 6 mA.
A high phase advance optics (102°, 90°), with a smaller natural emittance, was used for regular operation in 1998. This contributed to the excellent performance of LEP, together with the further reduction of both the horizontal and vertical beta function at the interaction points. No dynamic aperture problems were encountered.

1 PERFORMANCE

The total integrated luminosity delivered by LEP to each of the experiment during 1998 was 198 pb^{-1}. This is significantly more than the performance of the previous years. Figure 1 gives a comparison of the LEP performance over the last six years with the corresponding beam energies. The beam energy increased over the years following 1995 because of the addition of superconducting cavities to the existing copper RF system. The operating beam energy for 1998 was 94.5 GeV, apart from 3.2 pb^{-1} at the Z^0 peak (45 GeV) used for detector calibration.

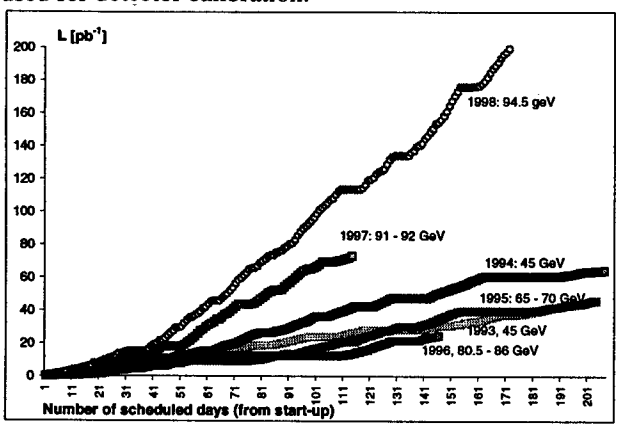

Figure 1: Comparison of the integrated luminosities for the years '93 to '98 with the corresponding beam energies.

The total beam current was limited to around 6.2 mA by the RF system (see section 2). Operation was with two beams of four bunches, except for the Z^0 running where two beams of eight bunches were used due to beam-beam limitations.

Vertical beam-beam tune shifts of more than 0.07 have been obtained on several occasions, with peak luminosities of about 10^{32} $cm^{-2}s^{-1}$. From figure 2 it is apparent that the beam-beam limit has not been reached. Beam size measurements do, however, show beam-beam blow-up when large beam currents are collided [1].

The improved performance, compared to 1997, can be attributed to the small beam size of the high phase advance optics, the further squeezing of the beta function at the interactions points, the larger beam currents (typically 6.0 mA in 1998 compared to 5.2 mA in 1997) and the good performance of the RF system.

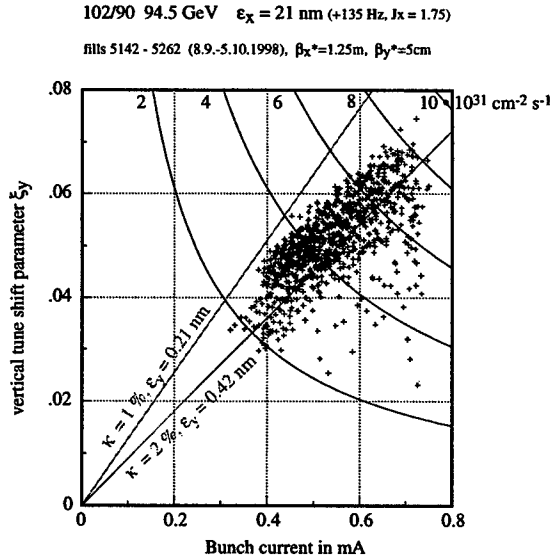

Figure 2: Vertical beam-beam tuneshift versus bunch current for the fills during the month of September.

2 THE RADIO FREQUENCY SYSTEM

The beam energy of 94.5 GeV could be obtained by the installation of 32 additional superconducting RF cavities. The RF system consisted of 272 superconducting cavities and 48 copper cavities. The maximum total voltage

* E-mail: jan.uythoven@cern.ch

0-7803-5573-3/99/$10.00@1999 IEEE.

obtained was 2870 MV, while the required operating voltage to have sufficient quantum lifetime was 2720 MV (this allows operation with $J_x = 1.75$). This safety margin was generally sufficient: only about 10 % of the fills that were put in physics were lost due to the RF system. The good performance can for a large part be attributed to the new control facilities which included automatic switch on of tripped cavities, automatic field reduction in case of field oscillations and an automatic tuner set-point control to reduce the ponderomotive oscillations.

The total beam current that could be accelerated in LEP during 1998 was limited by the heating of the main antenna cables to around 6.2 mA. The antenna cables couple out a fraction of the higher order modes above 3 GHz. At high enough power levels the cables can be irreversibly damaged (burnt). As the signal from the main antenna cables are also used for the tuning of the cavities, the cavity becomes unusable if both main antenna cables are damaged.

The higher order modes above 3 GHz depend strongly on the bunch length. For this reason the bunch length was kept as long as possible during the ramp and generally above 10 mm. This involved careful control of the wigglers, RF voltage, frequency offset (to lengthen the bunch) and betatron tunes to avoid dangerous resonances. The gymnastics which were necessary is illustrated in figure 3. It shows the measured bunch length and the power measured at the exit of an antenna cable during the energy ramp.

A study estimated the maximum power level which could be tolerated by the antenna cable to be 8.0 W. A beam dump interlock was established at 8.5 W. Attempts to push the power limit higher towards the end of the year lead to a rapid increase in the number of broken cables. The total number of broken cables at the end of the running period was 31, resulting in 8 cavities being out of function.

During the 1998-1999 shutdown all main antenna cables will be replaced so they will not limit the beam current in 1999.

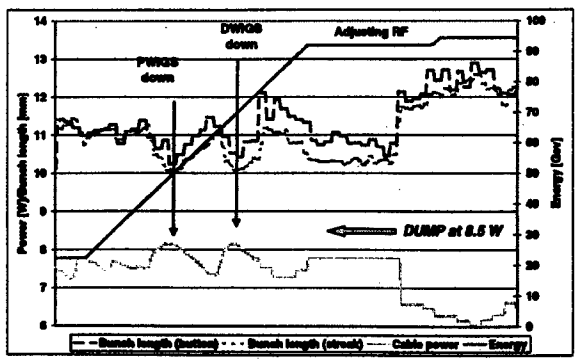

Figure 3: Bunch length and power measured at the exit of the RF antenna cable during the energy ramp.

3 OPTICS

Towards the end of the 1997 operational period a new high phase advance optics (102°, 90°) was commissioned [2, 3]. This optics was used for both the high energy running and the Z^0 calibration run in 1998. The main advantage of the (102°, 90°) optics relative to the previously used (90 °, 60 °) optics is the small natural emittance of 39.4 nm, at 94.5 GeV, compared with 50.8 nm for the (90°, 60°) optics. The high phase advance optics has a smaller momentum compaction factor which increases the energy that can be achieved for a given RF voltage.

No evidence of dynamic aperture problems were found, even not after further squeezing the horizontal and vertical beta functions at the interaction points during the year. Table 1 summarises the β^* values used over the year. The initial squeeze of the horizontal beta function had a clear positive effect on the luminosity. The following reductions of the beta functions probably contributed to the improved performance, but were hard to unravel from the other optimisations which took place continuously.

At injection and during the energy ramp the frequency offset was 115 Hz. This was necessary to lengthen the bunch during the ramp (see section 2). During physics the frequency shift was generally 135 Hz, resulting in a value of J_x of about 1.75. This reduced the horizontal emittance to 22.1 nm at 94.5 GeV. Assuming that the vertical emittance stays constant, this increased the luminosity by 33 %. The reduced beam size was also beneficial for the reduction of the background. However, the background was sensitive to small changes in especially the horizontal tune, resulting in background storms [4].

Table 1: The values of the horizontal and vertical beta functions at the interaction points during 1998.

Date	β_x^*	β_y^*
Startup: 6th May	2.0 m	5.0 cm
29th May	1.5 m	5.0 cm
8th September	1.25 m	5.0 cm
5th October	1.25 m	4.0 cm

4 PHASES OF OPERATION

4.1 Injection

Injection took place at the usual 22 GeV using synchrotron injection. The maximum bunch current was around 775 μA, resulting in a total beam current of 6.2 mA. The injection efficiency was often not very good and had a typical value of about 60 %. Almost all the RF cavities were kept on at injection, so the time lost waiting during the ramp for switching on cavities was minimised. The 520 MV demanded at the injection energy kept the RF cavities near the lower limit of their operational voltage.

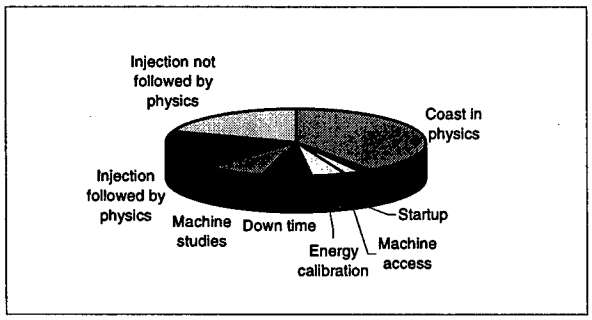

Figure 4: Distribution of the total time available for operation in 1998.

Figure 4 shows that 38 % of the total time available for operation was spent injecting particles. This was significantly larger than in other years.

4.2 Energy Ramp

Because of the limitation imposed on the bunch length and the working points at injection and full energy, the energy ramp was difficult and a lot of time was spent optimising the ramp, varying betatron and synchrotron tunes. This is reflected by figure 4, which shows that only about half of the total time which was spent injecting particles, was followed by a physics coast.

The development of the ramp was made a lot easier by the use of the Q-loop, a real time feedback of the measured betatron tunes to a pair of trim power supplies which act on the main quadrupoles. The fine control of the coherent betatron tunes would have been very difficult without it.

Once a good ramp was established excellent transmission rates (current at injection divided by the current in physics) were obtained, generally above 90 %.

Initially the squeeze of the beta functions took place near 45 GeV (the Z^0 energy). Small beam losses were observed in the ramp between 50 and 60 GeV, possibly caused by an insufficient momentum aperture of the squeezed (102°, 90°) optics. Squeezing the beta functions above 92 GeV proved to be a solution to get rid of these beam losses.

At 92 GeV a pause in the ramp was made to optimise the RF system if necessary. At this energy the RF was already ramped to the level needed at 94.5 GeV (2720 MV). Once the RF system was optimised, the continuation of the ramp to 94.5 GeV was generally without any problems.

4.3 Physics

As in the previous years a continuous optimisation of the horizontal and especially the vertical orbit took place to find the so-called 'golden orbit'. Even once this orbit was found it needed regular updating because of the continuously changing machine conditions. It is likely that the golden orbit is the result of an empirical search for the orbit with the lowest residual vertical dispersion for both beams. Typical values for the RMS vertical dispersion were around 3 cm. The coupling was well corrected. Dispersion free steering was also developed and will be available in 1999 [6].

4.4 Turn-around

The average turn-around, the time between dumping a fill which was in physics and restarting physics for the next fill, was 1 hour and 38 minutes, with a minimum of 42 minutes. Poor turn around was mostly related to poor injection or optimisation of the RF system.

The average time after which a physics coast was dumped was 3 hours and 42 minutes.

5 ENERGY CALIBRATION

Four percent of the operational machine time was used to measure the beam energy by resonant depolarisation. A dedicated (60°, 60°) optics was used for these measurements. For the first time polarisation was measured and the beam energy calibrated at an energy of 60 GeV. More details of the energy calibration results can be found in [7].

6 CONCLUSIONS

The year 1998 was a very successful year of LEP operation with a total integrated luminosity of 198 pb^{-1} at a beam energy of 94.5 GeV. The total beam current was limited to about 6 mA due to the heating of the RF antenna cables. The heating of the cables also imposed a limit on the bunch length during the energy ramp which resulted in a laborious development of different ramps.

The (102°, 90°) optics, developed in 1997, was used during the whole of 1998 for both the high energy run and the Z^0 run. The small emittance of this optics together with the additional squeeze of the beta functions at the interaction points and the operation with $J_x = 1.75$ largely contributed to the excellent machine performance.

REFERENCES

[1] D.Brandt, W.Herr, M.Meddahi, "Is LEP Beam-beam Limited at its Highest Energy ?", these proceedings.

[2] D.Brandt, W.Herr, J. Jowett, M.Lamont, M.Meddahi, A.Verdier, "A candidate low emittance optics for LEP". Proc. 6th Eur. Part. Acc. Conf., Stockholm 1998.

[3] D.Brandt, W.Herr, M.Lamont, M.Meddahi, A.Verdier, "Experience with a Low Emittance Optics in LEP", these proceedings.

[4] G. von Holtey, "Protection of LEP Experiments against Particle Background at Highest Beam Energies", these proceedings.

[6] R.Assmann, P.Raimondi, G.Roy, A.Verdier, J.Wenninger, "Dispersion free steering", Proceedings of the workshop on LEP-SPS performance - Chamonix IX, Chamonix 1999, CERN-SL-99-007 DI.

[7] R. Assmann, B. Dehning, M. Hildreth, J. Matheson, M. Placidi, F. Roncarolo, E. Torrence, F. Sonnemann, J. Uythoven, J. Wenninger, A. Blondel, "Observation of Radiative Spin-Polarization in LEP at 60 GeV", these proceedings.

OBSERVATION OF RADIATIVE SPIN-POLARIZATION AT 60.6 GeV

R. Assmann, B. Dehning, M. Hildreth, J. Matheson, G. Mugnai, M. Placidi, F. Roncarolo, E. Torrence, F. Sonnemann, J. Uythoven, J. Wenninger, CERN, SL Division, Geneva, Switzerland
A. Blondel, LPNHE Ecole Polytechnique Palaiseau, France

Abstract

Radiative spin-polarization has been used extensively at LEP to accurately measure the beam energy around the Z resonance. As the LEP physics has moved on to the W boson the calibration based on polarization must be extended towards higher beam energies. This is difficult as the depolarizing effects of spin resonances grow rapidly with beam energy. At LEP it has been possible for the first time to measure transverse beam polarization at 60.6 GeV. To allow a build-up of polarization the tunes and the energy were chosen accurately. A low phase advance optics was used and careful orbit correction was carried out using dynamic beam based alignment data. Harmonic spin matching was applied both in a deterministic and a novel semi-empirical way.

1 INTRODUCTION

Transverse spin polarization in LEP builds up spontaneously due to the Sokolov and Ternov effect [1]. Polarized beams are used in LEP since 1990 for the precise measurement of the beam energy [2]. Resonant depolarization of the initially polarized beams provides the by far most accurate method to measure the absolute energy scale. The method allowed determining the properties of the Z at $2E_{\text{beam}} = 91$ GeV with unsurpassed accuracy [3]. As LEP physics has moved on towards the W boson at around $2E_{\text{beam}} = 190$ GeV, energy calibration must be extended into this range. This is difficult as the depolarizing effects of spin resonances grow rapidly with beam energy.

The LEP strategy for determining the energy scale of the W is to calibrate the absolute beam energy at the highest possible energy, using the highly accurate method of resonant depolarization (a minimum level of 5% polarization is required). The scale is then extrapolated using other methods. The final error on the energy scale for the W depends on the range that must be extrapolated. In 1998 polarization was for the first time established in LEP at 60.6 GeV, allowing a more accurate energy calibration of LEP.

2 OVERVIEW ON POLARIZATION OPTIMIZATION IN LEP

The polarization build-up in a e^+e^- storage ring is characterized by a build-up time τ_p. The build-up time is inversely proportional to the fifth power of the beam energy; polarization build-up is therefore strongly enhanced with increasing beam energy. Concurrently unavoidable imperfections cause depolarizing effects. They are characterized by a depolarization time τ_d. The asymptotic polarization P_∞ describes the equilibrium between the two processes:

$$P_\infty = \frac{92.4\,\%}{1+\frac{\tau_p}{\tau_d}} = \frac{92.4\,\%}{1+\alpha^2 E_{\text{beam}}^2} \qquad (1)$$

The term τ_p/τ_d has been parameterized by an energy-independent imperfection term α and the beam energy E_{beam}. The given scaling law applies only for the most optimistic scenario, the so-called *linear regime* of polarization. LEP, for higher energies, operates in the so-called *higher-order regime* and the decrease in equilibrium polarization is much steeper with increasing energy. The theory of polarization for high energy e^+e^- storage rings is summarized in [4] and is evaluated for LEP in [5].

The process of polarization optimization in LEP trys to maximize the degree of spin-polarization in LEP. It is crucial to minimize the imperfection term α. The optimization process at LEP can be summarized as follows:

- **Problem**: *Imperfections* in beam position monitors (BPM's) and quadrupoles. **Solution**: Hardware alignment, dynamic beam-based alignment.
- **Problem**: *Orbit offsets and dispersion* due to residual imperfections. **Solution**: Orbit correction, knob tuning, dispersion-free steering, low phase advance optics.
- **Problem**: *Excitation of depolarizing resonances* due to residual orbit offsets and dispersion. **Solution**: Energy and tune scan to sit in between resonances, deterministic and semi-empirical harmonic spin matching.

A strong effort is invested at LEP in order to improve the chances for polarized beams at highest beam energies.

2.1 Accelerator alignment and optics

Vertical quadrupole misalignments are the main origin of depolarizing effects. They are minimized with a yearly realignment of all LEP quadrupoles. The vertical offsets of the BPM's with respect to the center of the quadrupoles is determined via a dynamic beam-based alignment technique [6]. The effects of the residual quadrupole misalignments on the beam orbit are minimized with a low phase advance optics.

2.2 Basic orbit and energy setup

The residual imperfections cause orbit offsets and dispersion. Standard MICADO orbit correction is used to minimize the vertical orbit especially in the arcs of the storage ring. Special attention must be put on eliminating any

0-7803-5573-3/99/$10.00@1999 IEEE.

π-bump in the accelerator. A coupling correction is performed via special coupling knobs. A dispersion-free orbit correction reduces dispersion and allows to find additional π-bumps. This method has been tested in 1998 and will be used routinely starting from 1999.

Depolarization is a resonant process. Therefore special care must be taken to avoid depolarizing resonances. The beam energy must be adjusted such that the working point has a maximum distance to all important spin resonances. The required accuracy in the setting of the beam energy is on the order of ± 10 MeV for high energies. Nuclear magnetic resonance devices are used to extrapolate the beam energy from a measurement at about 45 GeV.

2.3 *Harmonic Spin-Matching*

Depolarization for high energy storage rings is mainly driven by the residual vertical orbit deviations y_i ($i = 1, N$) in the N quadrupoles. The Fourier components of the orbit deviations are important:

$$a_k = \frac{1}{\pi} \sum_{i=1}^{N} y_i \cos[k\alpha_i] \, \delta\alpha_i \quad (2)$$

$$b_k = \frac{1}{\pi} \sum_{i=1}^{N} y_i \sin[k\alpha_i] \, \delta\alpha_i \quad (3)$$

Here, k is the harmonic number, α_i is the integrated bending angle up to quadrupole i (running from 0 to 2π) and $\delta\alpha_i$ is the change in bending angle for quadrupole i. a_k is the "cosine" strength and b_k the "sine" strength of harmonic k. τ_p/τ_d can then be written as:

$$\frac{\tau_p}{\tau_d} = \kappa' \nu^2 \sum_k \frac{a_k^2 + b_k^2}{(\nu - k)^4} \quad (4)$$

Here, ν is the spin tune ($\nu = E_{\text{beam}}/440.65$ MeV) and κ' is some constant. It is seen that only the two closest harmonics $k_0 = \text{Int}(\nu)$, $k_1 = \text{Int}(\nu)+1$ are important. ν is put close to an half-integer for LEP. The polarization is then:

$$P_\infty \approx \frac{92.4}{1 + \frac{\tau_p}{\tau_d}_0 + \kappa \left(a_{k_0}^2 + b_{k_0}^2 + a_{k_1}^2 + b_{k_1}^2\right)} \quad (5)$$

Note that for a given energy the spin tune and κ' terms have been put into the constant κ. The term $(\tau_p/\tau_d)_0$ takes into account depolarizing effects from less important sources.

Harmonic Spin Matching (HSM) is performed by introducing perturbations $\hat{a}_{k_0}$, $\hat{b}_{k_0}$, $\hat{a}_{k_1}$ and $\hat{b}_{k_1}$ such that the harmonics due to vertical orbit offsets are cancelled [7]. Special orbit bumps are used in LEP to generate the harmonics [8]. The bumps are chosen such that changes in dispersion, coupling etc. are minimized and additional depolarization is not introduced. The bumps were re-optimized in 1998. The HSM consists in minimizing the following system:

$$\frac{92.4\%}{P_\infty} \approx 1 + \frac{\tau_p}{\tau_d}_0 + \kappa[(a_{k_0} - \hat{a}_{k_0})^2 + (b_{k_0} - \hat{b}_{k_0})^2 + (a_{k_1} - \hat{a}_{k_1})^2 + (b_{k_1} - \hat{b}_{k_1})^2] \quad (6)$$

Two different approaches have successfully been applied.

A) A fully empirical approach, where each of the four harmonics is scanned in turn while polarisation is measured. For each bump the setting where polarisation is maximum is kept. This is the method applied at PETRA [9] and HERA [10], with several (typically 5) settings for each harmonic. The most important difficulties in applying this empirical method to LEP are: *1) The long polarization time (τ_p = 300 minutes at 45 GeV, 80 minutes at 60 GeV). 2) The low degree of polarization. 3) The limited accuracy in the polarisation measurement* ($\approx 0.8\%$*/minute.* At high energies the initial LEP polarisation is 1-2%. A polarization of 1% corresponds to $\tau_p/\tau_d \approx 100$. Halving τ_p/τ_d increases the polarization to about 2%. This is difficult to measure.

B) The deterministic spin-matching, where the orbit data are used to determine the Fourier harmonics directly. This method is ideal if precision is sufficient, and has proven very successfull at the Z peak [11]. However, as energy increases the strength of depolarizing resonances increases and the precision required is very high. The quality of the orbit measurement has been improved recently with the dynamic beam-based alignment [6]. The deterministic method does give a good starting point and an estimate of the location of the overall optimum, but is often insufficient by itself at high energies to provide optimal results.

The two established methods of HSM are not sufficient for LEP at high energies. A semi-empirical method has therefore been applied in 1998. It can be noticed that Eq. 6 depends on only five parameters: Four optimal settings $\hat{a}_{k_0}$, $\hat{b}_{k_0}$, $\hat{a}_{k_1}$, $\hat{b}_{k_1}$ and the residual depolarization $(\frac{\tau_p}{\tau_d})_0$. The semi-empirical HSM procedure consists in measuring the polarization for five different settings of the HSM bumps and then performing a fit of the observed polarization levels to Eq. 6. We now take as an example the case where the starting polarization level is around 2%. This means that the total depolarization term $\frac{\tau_p}{\tau_d} \simeq 50$. If one hopes to reach a polarization level of 6%, this means that $\frac{\tau_p}{\tau_d}_0$ is around 15. The harmonics to be corrected contribute 35, i.e. typically 9 per harmonic; the harmonics are typically off by 3 units. This sets the scale for the changes to make to the bumps in order to scan them efficiently. When all four considered HSM bumps have been scanned, a total of five points is available. A fit to the polarization data gives a new optimum. One can then set oneself to the predicted optimum, and repeat the procedure.

3 MEASUREMENT AT 60.6 GeV

In September 1998 sufficient polarization for energy calibration was established for the first time at 60.6 GeV. A careful application of the optimization procedures provided a polarization of 2-3% after deterministic but before semi-empirical HSM. At this time the process of semi-empirical harmonic spin matching was applied. Table 3 summarizes the settings $\hat{a}_{k_0}$ (cos), $\hat{b}_{k_0}$ (sin), $\hat{a}_{k_1}$ (cos), $\hat{b}_{k_1}$ (sin) for harmonics $k_0 = 137$ and $k_1 = 138$. Figure 1 shows the observed response in polarization and the fits of the asymptotic polarization level. The fit results are tabulated in Ta-

ble 3. Data were taken with the 60/60 degree optics, no low beta and experimental solenoids off.

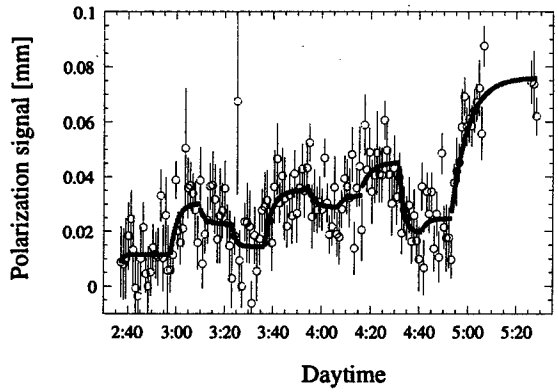

Figure 1: Polarization data from 21 September 1998. Shown is the measured polarization signal. Superimposed is the result of the polarization fits. The horizontal axis is the daytime.

Table 1: Results of polarization fits for different harmonic components. The last line shows the result of the global fit over all measurements.

	HSM bumps settings				Fit results
Time hr:min	137 (cos)	137 (sin)	138 (cos)	138 (sin)	P_∞ (%)
02:35	0.0	0.0	0.0	0.0	1.15 ± 0.23
02:58	2.0	0.0	0.0	0.0	3.03 ± 0.37
03:10	2.0	0.0	2.0	0.0	2.28 ± 0.30
03:23	2.0	0.0	2.0	2.0	1.45 ± 0.27
03:36	2.0	2.0	2.0	0.0	3.51 ± 0.28
03:54	2.0	2.0	2.0	-2.0	2.88 ± 0.25
04:06	2.0	2.0	2.0	0.0	3.33 ± 0.40
04:16	4.0	2.0	2.0	0.0	4.53 ± 0.34
04:33	6.0	2.0	2.0	0.0	1.86 ± 0.27
04:41	3.0	4.0	2.0	0.0	2.66 ± 0.35
04:53	3.0	2.0	0.6	-0.6	7.69 ± 0.36

The last line of Table 3 shows the result from the global fit of the optimal harmonic components. The fitted harmonics were applied and polarization rose to $(7.7 \pm 0.4)\%$. This level of polarization was comfortably above the 5% as required for energy calibration by resonant depolarization. The process of semi-empirical HSM required about 1.5 hours, being significantly faster than empirical HSM.

The maximum measured polarization levels in LEP are shown in Figure 2 as a function of beam energy. The measurement at 60.6 GeV is higher than the polarization observed at 55 GeV, demonstrating the excellent setup at 60.6 GeV. The observed decrease in polarization from 45 GeV to 60.6 GeV can be fully explained from the higher-order polarization theory [5].

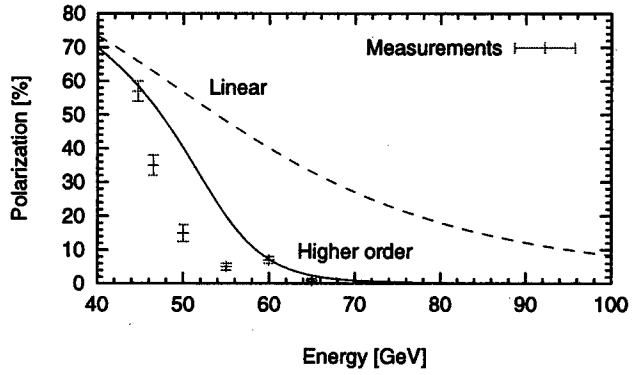

Figure 2: Measured maximum polarization in LEP for different energies. The data is compared to the higher-order (solid curve) and the linear (dashed curve) prediction, assuming equal residual imperfections after correction.

4 CONCLUSION

Highly accurate energy calibration at LEP requires transverse spin-polarization of at least 5% up to the highest beam energies. Polarization drops sharply with increasing beam energy. Therefore extensive optimizations of the storage ring are required in order to extend polarization to the highest beam energies. The quadrupoles are aligned and a special optics is being used; the tunes and the beam energy are chosen accurately to avoid spin resonances; a careful orbit correction is carried out using dynamic beam based alignment data; harmonic spin matching is applied both in a deterministic and a novel semi-empirical way. The optimization allowed for the first time to establish a clear polarization signal at 60.6 GeV. After optimization a polarization degree of $(7.7 \pm 0.4)\%$ was measured. This is, in terms of residual machine imperfections, equivalent to the polarization record of 57% at 44.7 GeV. In 1999 it will be tried to extend polarization and energy calibration to 70 GeV or even higher [5].

5 REFERENCES

[1] A.A. Sokolov and I.M. Ternov, Sov. Phys. Dokl. 8(1964)1203.

[2] L. Arnaudon et al, Z. Phys. C66(1995)45.

[3] R. Assmann et al, Eur. Phys. J. C6(1999)187-223.

[4] Ya.S. Derbenev, A.M. Kontratenko and A.N. Skrinsky, Part. Acc. 1979, Vol. 9, pp. 247-266.

[5] R. Assmann, these proceedings.

[6] B. Dehning et al., CERN SL/98-38-BI.

[7] R. Rossmanith and R. Schmidt, Nucl. Instr. Meth. A236(1985)231.

[8] R. Assmann et al., CERN SL/94-08(AP).

[9] H.D. Bremer et al, DESY-M 82-026(1982).

[10] D.P. Barber et al, DESY 93-038.

[11] R. Assmann, et al., CERN SL/94-62.

THE REGIMES OF POLARIZATION IN A HIGH ENERGY e^+e^- STORAGE RING

R.W. Assmann, CERN, SL Division, Geneva, Switzerland

Abstract

Several regimes of polarization must be considered for high-energy e^+e^- storage rings. Based on a theoretical paper by Derbenev, Kontratenko and Skrinsky from 1979 we describe the different cases. Particularly, it is shown that from a certain high energy onwards the polarization degree is expected to increase with energy. This is in sharp contrast to the usually considered regime where the expected polarization level decreases for higher beam energies. The theory of Derbenev, Kontratenko and Skrinsky is applied to the LEP storage ring with its energy range from the Z at 91 GeV to the W at 200 GeV. Though the theoretical expectations for beam polarization at the highest beam energy remain low, it is shown that the depolarization can move into a new regime for LEP above 60 GeV. The high energy LEP is the first storage ring that operates in this new and experimentally unknown regime of beam spin dynamics.

1 INTRODUCTION

Radiative polarization of the particle beams provides the most accurate tool to measure the beam energy in LEP [1,2]. In order to determine the W mass with the required accuracy it is important to establish polarized beams for the highest possible energies. Sufficient radiative spin-polarization in LEP was measured up to 60.6 GeV [3]. In order to examine the possibilities for establishing polarization at even higher energies, the theory of radiative spin polarization in e^+e^- storage rings must be analyzed carefully. This paper reviews the relevant theory and applies it to LEP parameters.

2 THEORY OF POLARIZATION AT ULTRA-HIGH ENERGIES

The particle beams in LEP spontaneously polarize due to the Sokolov-Ternov effect [4]. A polarization build-up time τ_p and an ideal final polarization degree of 92.4% characterize the process. The polarization rate λ is the inverse of the build-up time τ_p and is here used in units of the LEP revolution frequency. It is a steep function of the spin tune ν. The spin tune is the precession frequency of the spin vectors and can be expressed via the beam energy E: $\nu = a\gamma = E / 440.6486$ MeV. Unavoidable imperfections in the vertical orbit cause depolarization. It turns out that synchrotron radiation drives both polarizing and depolarizing processes. The depolarization is characterized by a depolarization time τ_d and the asymptotic degree of polarization is reduced to:

$$P = \frac{92.4\%}{1+\tau_p/\tau_d} \qquad (1)$$

Polarization theories aim at estimating the depolarization term τ_d. Here, we follow the basic theory by Derbenev, Kondratenko and Skrinsky from their summary paper in 1979 [5].

2.1. Basic Quantities

A few basic beam and machine parameters determine the behavior of polarization:
1) The *spin tune* ν describes the energy dependence of polarization. 2) The *polarizing rate* λ determines the speed of polarization buildup. 3) The *synchrotron tune* Q_s gives the distance between synchrotron sidebands of spin resonances. 4) The *spin tune spread* σ_ν causes a smearing out of spin precession frequencies so that they eventually overlap Q_s sideband resonances.
The particles in LEP traverse the ring about 11000 times per second. Let's assume the average spin tune ν_0 is not on any resonance. However, particles perform synchrotron oscillations around the average spin tune: $\nu = \nu_0 + \delta\nu$. Depending on the spin tune spread some particles might be on a spin resonance, for example $\nu = k \pm n \cdot Q_s$. During a large number of subsequent turns the particles will periodically cross the spin resonance. In order to evaluate the depolarizing effect on the ensemble polarization, it must be determined whether subsequent passings of a spin resonance are correlated or not. As shown by Derbenev, Kondratenko and Skrinsky, the criterion for correlated passings is:

$$\alpha = \frac{\nu^2\lambda}{Q_s^3} < 1 \qquad (2)$$

If subsequent passings are correlated then spin rotations can average out to some extent and their effect is less severe.

2.2. Correlated Spin Resonance Passings

The following theory applies if the correlation criterion in Equation 2 is true. Polarization can be described by:

$$\frac{\tau_p}{\tau_d} = \frac{11}{18}\nu^2 \sum_{k,m} \frac{|w_k|^2 \langle T_m^2(\Delta/Q_s)\rangle}{\left[(k-\nu-mQ_s)^2 - Q_s^2\right]^2} \qquad (3)$$

0-7803-5573-3/99/$10.00@1999 IEEE.

Here, w_k is the complex strength of the spin resonance at integer k, ν is the spin tune averaged over the ensemble and m an integer giving the order of the synchrotron sideband resonance. The equation contains a Bessel function term T_m. Assuming a Gaussian distribution over squared amplitudes Δ of synchrotron oscillations one obtains:

$$\left\langle T_m^2 \right\rangle = I_m\left(\frac{\sigma_\nu^2}{2Q_s^2}\right)\cdot\exp\left(-\frac{\sigma_\nu^2}{2Q_s^2}\right) \qquad (4)$$

The I_m are the modified Bessel functions. The spin tune spread is of central importance for the strength of the T_m term. The above equations are valid in the approximation of high energy. Note that betatron spin resonances with the transverse tunes Q_x and Q_y do not appear. For high energy lepton storage rings they are much weaker than synchrotron resonances and are therefore neglected here.
Two regimes are distinguished in the regime of correlated spin resonance passings. If the spin tune spread is much smaller than the synchrotron tune then higher order synchrotron sidebands are not important and only the linear spin resonances ($k \pm Q_s$) affect the achievable polarization degree. In the following this is called the "linear" theory. If the spin tune spread becomes larger than the synchrotron tune then the higher order synchrotron sidebands limit the achievable polarization degree. This is referred to as "higher-order theory".

2.2. Uncorrelated Spin Resonance Passings

A different situation is encountered if subsequent passings of spin resonances are uncorrelated. They are uncorrelated if the criterion from Equation 2 is not true and in addition $\sigma_\nu >> \nu_\gamma$. In this case passings of synchrotron resonances are completely uncorrelated. For LEP uncorrelated passings are always completely uncorrelated. With $\sigma_\nu << 1$ the polarization can be calculated from:

$$\frac{\tau_p}{\tau_d} = \frac{11\pi^4}{54}\cdot\nu^2\cdot\left|w_{[\nu]}\right|^2\cdot\left[1+\frac{108\exp(-2\sigma_\nu)^{-2}}{11\pi^3\sqrt{\pi}\,\nu^2\lambda}\right] \qquad (5)$$

In the case of $\sigma_\nu >> 1$ Derbenev, Kondratenko and Skrinsky have obtained a very simple result for the expected depolarization:

$$\frac{\tau_p}{\tau_d} = \frac{\pi\left|w_k\right|^2}{\lambda} \qquad (6)$$

Polarization does not show any resonant dependence on beam energy in this regime, but exhibits an increase with energy, as the polarizing rate λ becomes very large for highest energies. In this regime the spin tune spread σ_ν is very large and particles constantly sweep over spin resonances. As the polarization rate increases, depolarization does not increase as rapidly any more.

The theory by Derbenev, Kondratenko and Skrinsky does not include the LEP energy sawtooth that causes rapid energy changes of ± 500 MeV with 100 GeV average beam energy. The single particles constantly cross the integer and linear spin resonances. The crossings are very fast, about 40 times faster than the synchrotron oscillation. Therefore the associated crossings of spin resonances might be fully correlated and cause little harm. However, the consequences of the sawtooth on the spin motion in LEP are not clear and require further study.

3 LEP PARAMETERS

The polarizing rate λ (in units of the revolution frequency) for LEP is:

$$\lambda = \frac{1}{\tau_p} = 3.9\times10^{-19}\cdot\left(\frac{E}{0.44065\ \mathrm{GeV}}\right)^5 \qquad (7)$$

The resonance strength w_k is calculated from 57% polarization at 44.7 GeV [6][1]:

$$\left|w_k\right|^2 = 1.94\times10^{-10}\cdot\left(\frac{E}{0.44065\ \mathrm{GeV}}\right)^2 \qquad (8)$$

The spin tune spread σ_ν is proportional to the square of the beam energy E:

$$\sigma_\nu = 6.76\times10^{-6}\cdot\left(\frac{E}{0.44065\,\mathrm{GeV}}\right)^2 \qquad (9)$$

4 PREDICTIONS FOR LEP

The numerical evaluation of the correlation criterion is shown in Figure 1. It is seen that the LEP1 working point is clearly in the correlated regime as is the working point at 60.6 GeV with Q_s = 1/11. With high energy and small Q_s LEP moves into the uncorrelated regime of spin polarization.

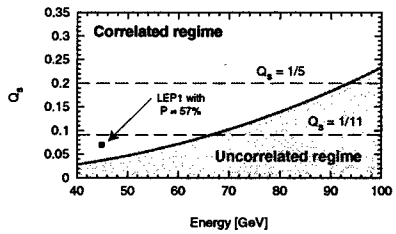

Figure 1: Evaluation of correlation criteria as a function of beam energy and Q_s. LEP can stay in the correlated regime by increasing the value of the synchrotron tune Q_s.

The polarization optics (60°/60°) allows a high Q_s of above 0.25 until its aperture limit at around 75 GeV (see Figure 2). With that Q_s LEP remains in the correlated

[1] The linear polarization then decreases with the fourth power of energy. This result by Derbenev, Kontratenko and Skrinsky is not in agreement with other predictions. Their result might be overly pessimistic.

regime of spin resonance passings and the higher-order polarization theory can be used to predict the achievable polarization degree (Equations 3 and 4). Note that this theory correctly predicts the decrease of polarization with energy that is observed in LEP (see Figure 3). The predicted polarization degree has been evaluated as a function of beam energy and for different values of the synchrotron tune Q_s. In order to achieve the maximum distance to all spin resonances, Q_s is chosen to be equal to one over an odd integer. For illustration we consider Q_s values of 1/13 (LEP1 value), 1/5 and 1/3. The predicted dependence of polarization on energy is shown in Figure 4. High Q_s values significantly improve the chances of spin polarization for higher beam energies.

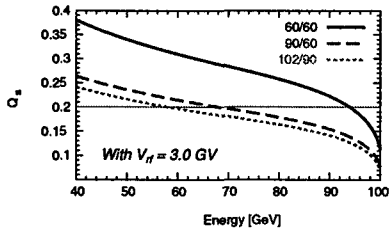

Figure 2: Maximum achievable Q_s as a function of energy and for different optics (with 3 GV RF voltage).

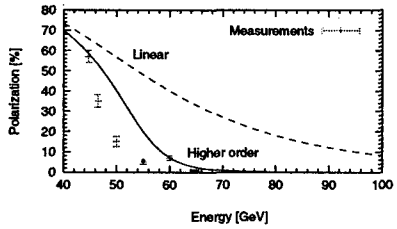

Figure 3: Measured maximum polarization degrees in LEP compared with higher-order correlated polarization theory (solid) and linear theory (dashed).

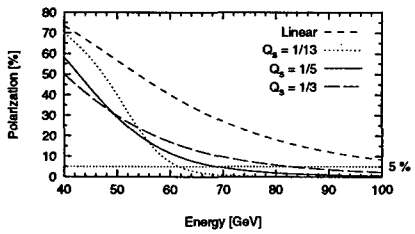

Figure 4: Predicted transverse spin polarization in LEP as a function of beam energy for different values of Q_s.

The expected polarization is shown in Figure 5 for both the correlated and uncorrelated regime. For the highest LEP energies at 90-100 GeV the uncorrelated regime must be considered. We evaluate this regime under the assumption of a large spin tune spread ($\sigma_\nu >> 1$). Including the energy sawtooth LEP will just enter into this regime at the highest beam energies. It is seen that the polarization prediction in this regime increases with the beam energy. At about 100 GeV a polarization degree of roughly 1% is expected. This is not sufficient for energy calibration. However, in view of the uncertainties in this energy regime, an experimental test is clearly warranted. At the end of the 1998 run it was tried to measure polarization at 90 GeV. This attempt was unsuccessful due to problems in the detector shielding at high energies.

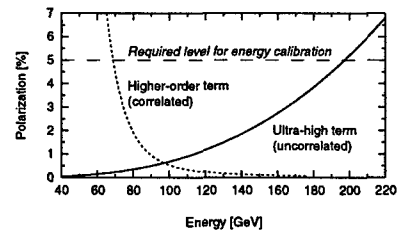

Figure 5: Expected polarization in LEP for ultra-high energies. The higher-order theory in the correlated regime (Q_s = 1/5) and the "ultra-high term" (Equation 6) in the uncorrelated regime are shown. LEP is expected to enter the uncorrelated regime at around 80 GeV.

5 CONCLUSIONS

Transverse beam polarization and accurate energy calibration has been extended to 60.6 GeV in 1998. The additional range in energy calibration helps to reduce the extrapolation error for physics energies and the W mass.

The application of the polarization theory to LEP parameters shows that a 5% polarization degree can be expected up to about 70 GeV with the polarization optics and high Q_s. This extension of polarization range will be studied at the end of regular energy calibrations in 1999. If polarization is found at up to 70 GeV, it can be used for energy calibration.

The prospects for polarization in LEP at around 100 GeV are very uncertain. However, it cannot be excluded that polarization of a few percent is possible in the so-called uncorrelated regime. A dedicated experiment in 1999 will try a to explore this regime of beam polarization.

6 REFERENCES

[1] L. Arnaudon et al, "Accurate Determination of the LEP Beam Energy by Resonant Spin Depolarization", Z. Phys. C66(1995)45.

[2] R. Assmann et al, "Calibration of Centre-of-Mass Energies at LEP1 for Precise Measurements of Z Properties", CERN-SL/98-12.

[3] R. Assmann et al, "Observation of Radiative Spin-Polarization in LEP at 60 GeV", these proceedings.

[4] A.A. Sokolov and I.M. Ternov, "On Polarization and Spin Effects in the Theory of Synchrotron Radiation", Sov. Phys. Dokl. 8(1964)1203.

[5] Ya.S. Derbenev, A.M. Kondratenko and A.N. Skrinsky, "Radiative Polarization at Ultra-High Energies". Part. Acc. 1979, Vol. 9, pp. 247-266.

[6] R. Assmann et al, "Polarization Studies at LEP in 1993", CERN-SL/94-08 (AP).

IS LEP BEAM-BEAM LIMITED AT ITS HIGHEST ENERGY ?

D. Brandt, W. Herr*, M. Meddahi and A. Verdier, CERN, Geneva, Switzerland

1 ABSTRACT

The operation of LEP at 45.6 GeV was limited by beam-beam effects and the vertical beam-beam parameter ξ_y never exceeded 0.045. At the highest energy of 94.5 GeV, the increased damping allows higher beam-beam parameters ξ_y. Values above 0.07 in the vertical plane averaged over four experiments have been obtained frequently with peak values up to 0.075 in a single experiment. Although the maximum intensity in LEP is presently limited by technical considerations, some observations indicate that the beam-beam limit is close and the question of the maximum possible values can be raised. These observations are shown in this paper and possible consequences are presented. The optimum operation of LEP in the neighbourhood of the beam-beam limit is discussed.

2 TUNE SHIFT AND BEAM-BEAM LIMITS

2.1 *Beam-beam tune shift*

For stable motion, the relation between the tune shift ΔQ and the beam-beam parameter ξ is [1]:

$$\cos(2\pi Q + 2\pi\Delta Q) = \cos(2\pi Q) - 2\pi\xi\sin(2\pi Q) \quad (1)$$

and

$$\beta^* = \frac{\beta\sin(2\pi Q)}{\sin(2\pi Q + 2\pi\Delta Q)} \quad (2)$$

where Q is the tune of the machine and β and β^* are the unperturbed and perturbed β-functions at the collision point. The unperturbed beam-beam parameter ξ is written as:

$$\xi_{x,y} = \frac{N r_e \beta_{x,y}}{2\pi\gamma\sigma_{x,y}(\sigma_x + \sigma_y)} \quad (3)$$

For small tune shifts, it can be shown that $\Delta Q \approx \xi$, but is different for large values. The perturbed β^* can be written as [1]:

$$\beta^* = \frac{\beta}{\sqrt{1 + 4\pi\xi(\cot(2\pi Q^i)) - 4\pi^2\xi^2}} \quad (4)$$

where $2\pi Q^i$ is the phase advance between two interaction points. The tune shift is therefore a function of the tune which can be chosen to keep the actual beam-beam tune shift small, i.e. a working point close to the integer is preferable unless this is prohibited for other considerations. Since the tune shift is amplitude dependent, it will also create a tune spread which cannot be corrected. While for small ξ the tune shift and β^* hardly change over a large range of the phase advance, for larger ξ this variation is strong and therefore for the high values of beam-beam parameters now observed at LEP, one can expect significant effects on the optics and beam dynamics. For LEP, the vertical tune is 96.19 and Fig.1 shows the vertical tune shift ΔQ_y as a function of the unperturbed beam-beam parameter ξ_y for this tune value. For the maximum beam-beam parameter observed in LEP, i.e. 0.070, the tune shift is around 0.05 and β_y^* is reduced from 5 cm to 2.8 cm at the collision points for small amplitude particles. It is this actual tune shift ΔQ_y which is important for the evaluation of resonances excited by the beam-beam force while the beam-beam parameter ξ merely measures the strength of the beam-beam effect and could be used to compare operational performance. The LEP2 values can easily compete

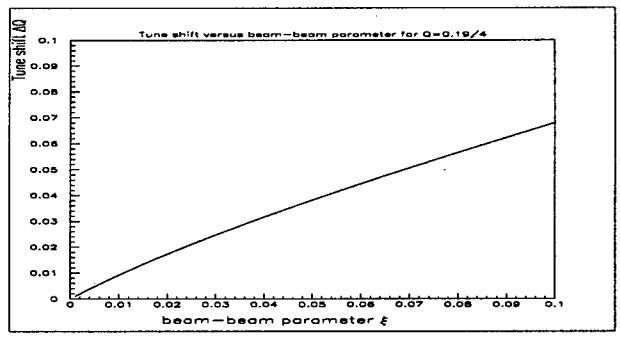

Figure 1: Beam-beam tune shift as function of beam-beam parameter for typical LEP tune

with previously achieved records: at ADONE the beam-beam parameter was as high as 0.08, but the tune shift ΔQ_y was around 0.03 [2], i.e. significantly lower than for LEP2. During a dedicated experiment with round beams [3] at CESR, a beam-beam parameter up to 0.09 was measured, however with rather large β_y^*, therefore low luminosity and only a single experiment. The LEP2 values are the highest observed in high luminosity operation.

2.2 *"Strong" beam-beam limit*

What is generally recognized as a signature of the beam-beam limit is a linear rather than a quadratic increase of the

*Email: Werner.Herr@cern.ch

0-7803-5573-3/99/$10.00@1999 IEEE.

luminosity with intensity. This is interpreted as a saturation of ξ with the bunch intensity and an emittance increase with increasing intensity. It is desirable to operate LEP at or near this "first beam-beam limit" since the luminosity would reduce only linearly with decreasing bunch intensity and give a larger integrated luminosity. Various tools such as e.g. artificial emittance increase with wigglers, damping partition change, coupling and optics are used to control this limit. However, this limit is not very sharp and already well below other effects may be observed. Particles at large amplitudes exhibit an unstable behaviour, leading to the formation of tails and a decreased life time. This can usually be understood by resonances exciting particles at large amplitude. Together with a reduced dynamic aperture this "second beam-beam limit" may be found early and the region of constant ξ cannot be reached. Therefore care must be taken to provide sufficient dynamic aperture when the machine is operated close to the beam-beam limit. In LEP both effects were clearly observed.

2.3 *"Weak" beam-beam limit*

Apart from the classical beam-beam limits discussed above, a strong beam-beam interaction can cause effects on the beam dynamics which manifest themselves in other types of limitations or operational difficulties, eventually leading to a limited performance. Signs of such weak limits are clearly observed in LEP. The coherent beam-beam effect can limit the available space in the working diagram significantly and beam-beam induced orbit distortions lead to collision offsets or parameter splitting between the two beams. Such effects eventually limited the performance of LEP running with bunch trains [4]. The excitation of coherent modes is usually damped with a finite chromaticity, however significant chromaticity splits between the two beams caused by strong beam-beam effects can severely limit this possibility. As it was already mentioned, the beam-beam interaction perturbs the beam optics in a predictable way. Combined with possible imperfections such as e.g. phase errors or collision offsets this can lead to significant distortions and limit the overall performance. This will be treated in more detail in a later section.

3 EXPERIENCE AT 45.6 GEV

LEP was run for 7 years at 45.6 GeV, corresponding to the Z^0 resonance. Since beam-beam effects are stronger at lower energies, they were the main intensity limitation. Details about running LEP at lower energy and the operational procedures can be found in [5] and are not discussed here. Only the main observations are summarized.

Already at rather low intensities LEP showed the typical behaviour of operation at the beam-beam limit, i.e. saturation of the beam-beam parameter ξ. Using wigglers to control the horizontal beam size allowed to run at the limit for several hours and the ultimate limit for the bunch intensity was due to the significant amount of non-Gaussian tails. For most of the time an optics with phase advance of $90^0/60^0$ in the horizontal and vertical planes was used which had a sufficient dynamic aperture and the region of constant ξ was reached at bunch intensities around 400 μA, corresponding to $\xi_y^{max} \approx 0.045$.

4 OBSERVATIONS AT HIGH ENERGY

With increasing energy the effects of synchrotron radiation increase rapidly. For a given optics, the horizontal emittance increases with E^2 and therefore the horizontal beam-beam parameter decreases with E^{-3}. Special low emittance optics have been developped for high energies [7] to compensate for the emittance increase. The damping times also decrease with E^{-3} and one can expect that larger values for ξ can be obtained before the beam-beam limit is reached because the effects of resonances are suppressed.

4.1 *Luminosity and tune shift*

The vertical beam-beam parameter ξ_y is computed from the luminosity measured by the experiments, using the measured bunch intensity, the unperturbed β_y and the theoretical horizontal emittance. All values quoted are averaged over the 4 experiments and 2 minutes. With this procedure maximum values of 0.07 for ξ_y and around 0.05 for ξ_x have been obtained at 94.5 GeV. The highest value was 0.075, however only in a single experiment and for less than one minute. The Fig.2 shows the evolution of the vertical beam-

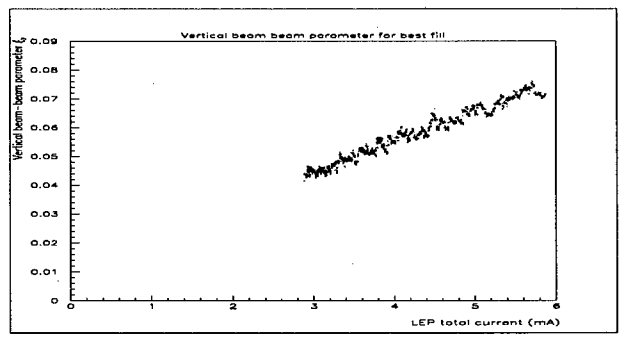

Figure 2: Vertical beam-beam parameter ξ_y as function of intensity for one fill

beam parameter during one of the best fills as a function of the decreasing bunch intensity. No sign of saturation can be seen up to the maximum of $\xi_y = 0.07$ and ξ seems to linearly decrease with the intensity. At this energy LEP is operated with four bunches per beam and the current per bunch at the start of a fill was approximately 750 μA. From Fig.1 it can be derived that the tune shift per interaction point is around 0.05, i.e. a very significant part of the tune space is occupied by the beam-beam tune spread. For both planes it is increasingly difficult to find a working point to avoid resonances. It was demonstrated [6] that in particular the background generated from tails or coherent motion is extremely sensitive to the choice of the horizontal working

point. This requires a continuous monitoring and adjustment of the tune while it changes with decreasing current.

4.2 *Optics dependence of beam-beam effects*

The effects of the beam-beam interaction depend on the optics used. In particular they depend on the phase advance between the interaction points, the lattice non-linearities and imperfections. In the course of the search for an appropriate low emittance lattice it was found that the beam-beam interaction can create or enhance beam tails which can limit the performance of the machine when the dynamic aperture is not sufficiently large. This effect and its dependence on the optics parameters is treated in another paper [7].

4.3 *Optical functions at interaction point*

The beam-beam forces at the interaction points act as non-linear lenses and therefore distort the optics. The most obvious manifestation of these distortions is the tune shift ΔQ and the amplitude dependent beating of the optics functions. Such effects are non-negligible and must be taken into account for beam measurements, such as e.g. emittance measurements[8, 9]. The change of the β-functions at the interaction points can be calculated as shown above for small amplitude particles: without any further imperfections, the effect of four symmetric beam-beam collisions is a decrease of the horizontal and vertical β. This effect is equal for all collision points when the phase advance between them is equal (eq. (4)). Phase advance errors between the collision points can break this symmetry. A "phase bump", i.e. a small phase advance error between two interaction points and compensated in the following arc usually introduces a global beating and reduces the β symmetrically everywhere. In the presence of beam-beam interactions however, this symmetry is broken and β is drastically decreased in one single interaction point, possibly leading to different luminosities. Such imbalanced luminosities have been observed during a large part of LEP running in 1998 [10] and beam-beam induced optics distortions remain a possible explanation. A similar effect is reproduced by small collision offsets. While for head on collisions the modification of the optics function is fully symmetric, with small collision offsets of the order of the beam size a strong beating is introduced, similar to that due to phase advance errors. The correction of a collision offset in one collision point will therefore also improve the performance in the others. These effects are summarized for one example in Fig.3. The value of β_y is shown for the four interaction points under different conditions. The unperturbed values are indicated as (•) and the effect of a pure phase advance error before and after IP4 as (○). The phase error introduced to produce this effect was around 10°. Further we show the effect of a symmetric beam-beam interaction without imperfections (△), phase advance error with beam-beam (×) and beam-beam with a small offset in IP2 (◇). It is clear that running LEP in the strong beam-beam regime requires a careful setting of the machine parameters, in particular phase advance errors or collision offsets must be avoided.

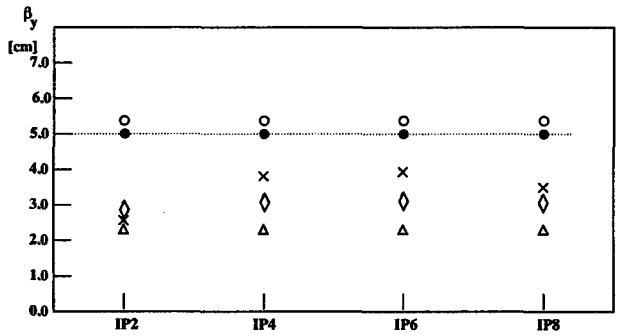

Figure 3: Optical functions at interaction point modified by beam-beam interactions

5 CONCLUSION

The beam-beam effect in LEP was analysed as a function of the bunch intensity and no sign of saturation of the luminosity or the beam-beam parameter was found. Although LEP is therefore not beam-beam limited in the classical sense, the very strong beam-beam effect with beam-beam parameters above 0.07 is the origin of other effects which indirectly limit the performance and constitute therefore a "beam-beam induced" limit, or a "weak" beam-beam limit.

6 REFERENCES

[1] A. Chao; *Beam-beam instability*; in Phys. of High Energy Part. Acc., AIP Conf. Proc. **127**, (1983).

[2] M. Basetti; *Numerical Computation of space charge effects in a positron and electron storage ring*; in Proc. 5th Int. Conf. on High Energy Particle Accelerators, Frascati, (1965).

[3] E. Young *et al.*; *Collisions of resonantly coupled round beams at the Cornell electron-positron storage ring (CESR)*;

[4] B. Goddard *et al.*; *Bunch trains for LEP*; Part. Accelerators Vol.**57**, Number 4, p. 237, (1998). in Proc. PAC 1997, Vancouver 1997, (1997).

[5] H. Burkhardt; *Energy dependence of beam-beam interactions in LEP*; in Proc. PAC 1997, Vancouver 1997, (1997).

[6] G. v.Holtey; *Protection of LEP experiments against particle backgrounds at highest beam energies*; these proceedings.

[7] D. Brandt *et al.*; *Experience with a low emittance optics in LEP*; these proceedings.

[8] E. Keil; *Optics imperfections*; Proc. 3th workshop on LEP performance, Chamonix 1993.

[9] P. Castro; *How does β-beating affect the luminosity ?*; Proc. 4th workshop on LEP performance, Chamonix 1994.

[10] G. Morpurgo; *Do we understand the luminosities imbalance in LEP*; Proc. 9th workshop on LEP performance, Chamonix 1999.

PROTECTION OF LEP EXPERIMENTS AGAINST PARTICLE BACKGROUND AT HIGHEST BEAM ENERGIES

G. von Holtey, M. Lamont, CERN, Geneva, Switzerland

Abstract

The protection system used to shield LEP experiments against particle backgrounds has been upgraded in view of the much higher photon background rates expected at LEP2 energies. General experience with background rates in the LEP experiments at highest beam energies is reported and special features are highlighted.

1 INTRODUCTION

The main particle backgrounds at LEP are off-energy electrons and positrons produced by beam-gas bremsstrahlung and synchrotron radiation (SR) photons produced in the closest bending magnets and in quadrupoles in the straight sections on either side of the experimental detectors. While off-energy electron rates under normal vacuum conditions are acceptable and are not expected to increase with energy, the low energy SR photon background is many orders of magnitude larger than can be tolerated and increases rapidly with beam energy. The LEP collimator protection system, designed for 45 GeV, therefore had to be extended in order to cope with the much increased photon rates to be expected at twice the beam energy. The most important limit on photon background comes from aging of gas tracking detectors. They are designed to be sensitive to energy depositions of ≤1keV for minimum-ionizing charged particles and are therefore sensitive to keV photons, which interact in the gas or other local material [1].

After a description of the LEP2 background protection system, experience with detector backgrounds at high beam energies are reported.

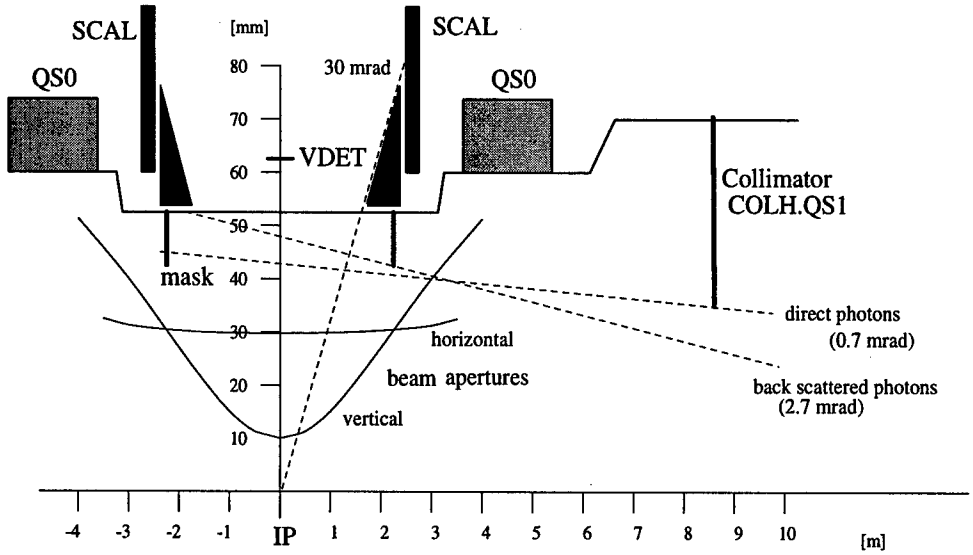

Figure 1: Schematic layout of SR-mask around a LEP IP, indicating the boundary conditions for a mask solution.

2 LEP BACKGROUND PROTECTION

The LEP detectors are protected against beam induced background particles by a system of movable two-jaw collimators placed at strategical locations in the experimental insertions. The LEP1 system is composed of 16 horizontal or vertical collimators for each experiment, plus six aperture limiting collimators located in a non-experimental insertion [2]. Simulations of SR-photon background at 90 GeV indicated a large increase of the photon rate, mainly due to back-scattering of photons from the first 50 m of vacuum chambers around the IP [3]. The solution proposed was to enlarge where ever possible vacuum chambers, to install eight more collimators per experiment, and as the main defense to incorporate cylindrical tungsten

0-7803-5573-3/99/$10.00@1999 IEEE.

absorbers into the experimental vacuum chambers [4]. The functionality of these SR-masks and the MC predictions were verified with a test SR-mask installed in DELPHI during 1994 and 1995 using 45 GeV and 65 GeV beams [5]. A schematic layout of a SR-mask is shown in Figure 1, a comparison of measured background rates with different simulations is given in Figure 2.

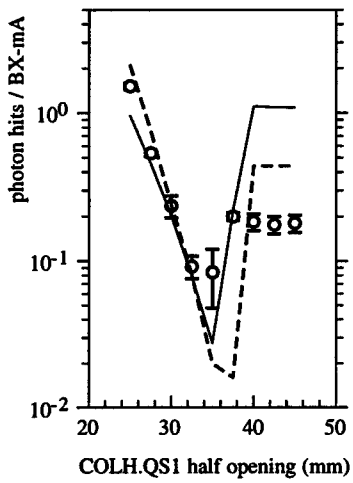

Figure 2: Monte Carlo predictions and measurements in the DELPHI TPC. Data points (photons per bunch crossing BX) are from the TPC, solid line MC [3], broken line MC [6]. E_{beam} = 65 GeV.

Following the positive test results, the upgraded LEP2 protection system, including SR-masks, was installed for the 1997 run in all four experiments and has proven since to protect the detectors well at increasing beam energies up to the 94.5 GeV run during 1998. As an example SR-photon and off-energy background rates for different energies and LEP optics measured by OPAL are shown in Figure 3. Rates increase linearly with current. The large fluctuation of the SR-photon rate reflects the strong dependence of this background on several machine parameters.

3 LIMITATIONS OF THE MASK SOLUTION

On the other hand, as the SR-masks are protruding into the vacuum chamber only 2.5 m away from the IP, they become very effective sources for low energy photons to be scattered into the detectors. The absorber rings are therefore shaped in such a way as to suppress all forward scattering. Back-scattering however from the downstream mask can not be avoided. The only solution is therefore to shield the downstream mask against direct photon hits.

This is achieved by a pair of additional horizontal collimators (COLH.QS3 or 4), placed close to a horizontal beam waist, some 50 m from the IP's. However, as LEP beam optics are considerably different in insertions IP4 and IP8 compared to the two other insertions, the horizontal beta-functions at the collimator location in IP4 and IP8 are two times larger and the mask protection is consequently not as good.

Sufficient protection can, however, still be achieved for both types of insertions as long as the density distribution of the horizontal beam tails stay close to Gaussian. An example is shown in Figure 4. Closing the protection collimators to 14 σ_x, the minimum allowed setting before scraping into the beam, good protection is obtained in OPAL (IP6) and DELPHI (IP8). The measurement also demonstrates the limited margin left for the collimator opening in DELPHI, at which point the SR-mask is no longer protected and the photon rate starts to increase exponentially.

According to simulations for IP8 the downstream SR-masks are hit by about 3.10^3 photons per bunch crossing (BX) with Gaussian beams of 3 mA, against about 7.10^6 photons/BX with exponential beam distributions. These photons are radiated by electrons on •6 sigma orbits in straight section quadrupoles 50 to 150 m upstream of the IP. The scattering probability from the tungsten mask into the detector for photons in the several 100 keV energy range is of order 5.10^{-5}, which amounts to several 100 photon hits/BX in the case of exponential beams. As the trip level for the central detectors is in the region of •10 photons/BX, such high rates could not be tolerated.

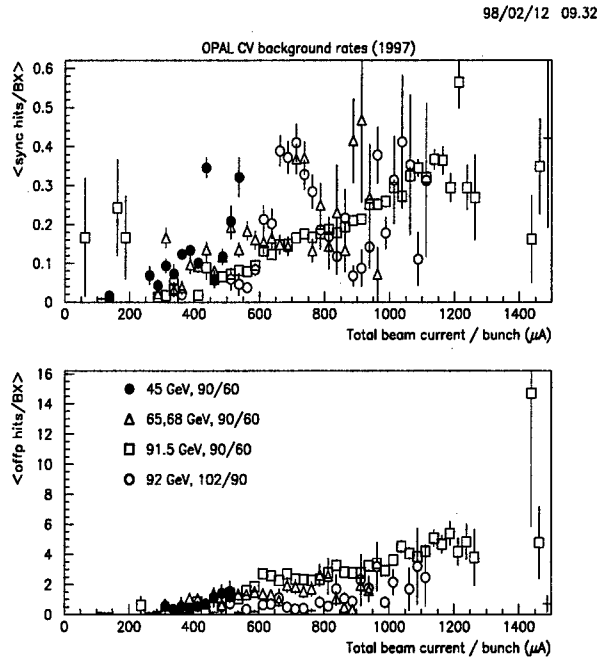

Figure 3: Hit rates per bunch crossing of synchrotron radiation photons and off-energy electrons measured in the OPAL Vertex Drift Chamber (CV) are shown as function of the total current in the two crossing bunches. The different symbols belong to different beam energies and LEP optics. One unit of

'figure-of-merit' corresponds to a photon hit rate of about 0.6/BX and an electron hit rate of about 0.9/BX [7].

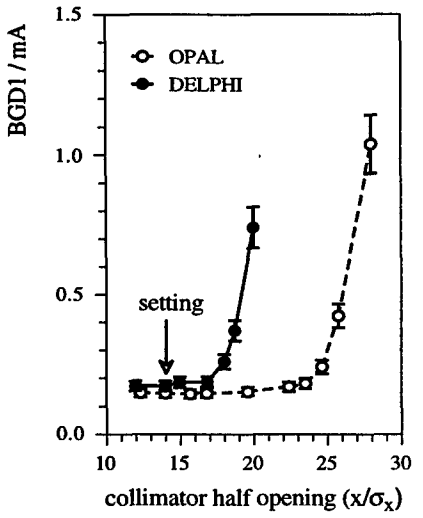

Figure 4: "Figure-of-merit" for SR-photons (BGD1) measured in DELPHI and OPAL as function of the opening of horizontal collimators COLH.QS3 and COLH.QS4, respectively. (92 GeV, ε_x= 30 nm).

While off-energy and SR-photon background rates stayed acceptably small under normal beam conditions during 1998 running at 94.5 GeV with currents up to 3 mA/beam, occasionally large spikes and short periods of high photon background were observed, which led in many cases to detector trips, particularly in ALEPH (IP4) and DELPHI (IP8) [8].

These "photon storms" are believed to be due to resonance build-up of non-Gaussian beam tails in the horizontal plane. In the two insertions, where limited mask protection exists, SR-photons radiated by electrons in the far tails can reach the inner tip of the downstream mask and back-scatter into the detectors. Photon storms can occur several times during a fill, apparently uncorrelated to beam current. The slow exponential rise of the photon rate over several minutes can be stopped and restored by a very small increase of the horizontal tune of order 0.005 (see Figure 5).

In a MD experiment [9] photon storms could be triggered by reducing the horizontal tune to reach the 3Qx+Qy=1 resonance. No reduction of the beam lifetimes was observed, however, tail scans unveiled a strong increase of the particle density in the horizontal and vertical tails of one of the beams.

Further beam studies are needed to better understand the underlying effects during data taking conditions and to isolate the resonance's in question. Better collimator protection can be achieved if the horizontal aperture limit can be reduced below the present $12\sigma_x$. Increasing the horizontal beta-value at the interaction points will reduce the beam size at the low-beta quadrupoles and allow for closer collimator settings.

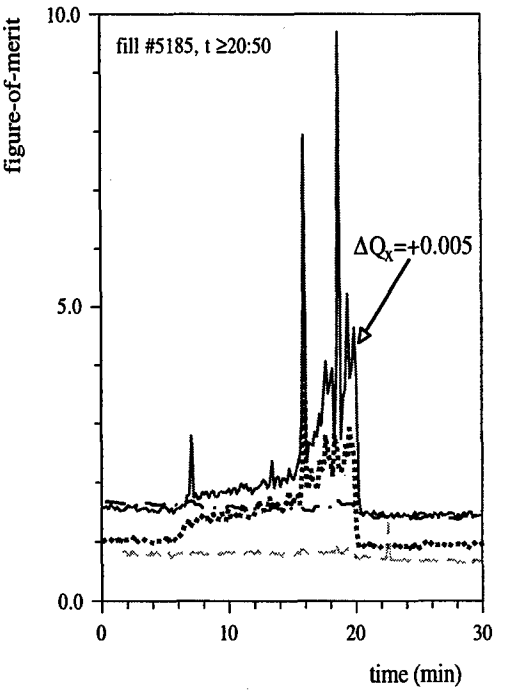

Figure 5: Background rates in ALEPH (dotted line), DELPHI (full line), OPAL (dash-dotted line) and L3 (dashed line) during a "photon storm" with data taking at 94.5 GeV. The exponential rise was stopped and the rates restored by a Q_x trim of +0.005.

REFERENCES

[1] J. Rothberg, Limitations due to background at LEP1, Proc. 5th Workshop on LEP Performance, Chamonix, 1995

[2] G. von Holtey and K.M. Potter, Estimation of synchrotron radiation background in LEP experiments, IEEE Particle Accelerator Conference, Washington. DC, 1987

[3] G. von Holtey, Simulations of photon backgrounds to LEP detectors at 90 GeV beam energy, CERN SL/92-54, 1992

[4] G. von Holtey et al., Nucl. Instr. and Meth. in Phys. Res. A 403 (1998) 205

[5] The LEPC Working Group on LEP2 Backgrounds, CERN/LEPC93-10, 1993

[6] P. Roudeau, unpublished.

[7] P. Estabrookes, OPAL, private communication, 1998

[8] G. von Holtey, Particle backgrounds at the LEP detectors at 94.5 GeV, Proc. 9th Workshop on LEP Performance, Chamonix, 1999

[9] K. Affholderbach et al., "Beam tails and background storms with colliding beams at 94.5 GeV", SL-Note-98-073 MD (1998)

ENERGY LOSS MEASUREMENTS AT LEP2

H. Burkhardt, A.-S. Müller*, J. Wenninger, CERN, Geneva, Switzerland

Abstract

The accurate measurement of the W Boson mass at LEP requires to determine the beam energy to the highest possible precision. Present schemes rely on accurate energy determinations in the range from 40 to 60 GeV using resonant depolarization and on precise extrapolations to high energy. Several methods based on measurements of the energy loss due to synchrotron radiation have been studied. Different approaches such as the study of the damping time of transverse oscillations, the radio frequency sawtooth and the dependence of the synchrotron tune on the total accelerating voltage are described and results are discussed.

1 MOTIVATION

LEP2 provides a rather unique opportunity to study energy loss and synchrotron frequency in an environment with major energy losses and high Q_s. The main motivation for the studies presented below however is the development of a reliable energy determination at the highest energies with an accuracy of 20 MeV or better. The presently used extrapolation methods using magnetic measurements cross-calibrated with resonant depolarization in the range from 40 to 60 GeV show systematic effects of the order of 20 MeV at highest energies [1]. The methods mentioned below are alternatives, based mainly on determinations of the energy loss and using existing LEP equipment.

2 MEASUREMENTS

2.1 Damping of Coherent Oscillations

A coherent horizontal oscillation is excited by a single kick and the center-of-charge position of the bunch is observed over 1024 consecutive turns. A fit to the data by a damped oscillation with amplitude dependent frequency yields the coherent damping time τ as described in [2]. The coherent damping at LEP is composed of radiation and head-tail damping:

$$1/\tau_{\text{coh}} = 1/\tau_0 + 1/\tau_{\text{head-tail}} \quad \text{with} \quad 1/\tau_{\text{head-tail}} \sim \frac{Q'}{E_0} I_b$$

where Q' is the chromaticity, I_b the bunch current and E_0 the beam energy. An extrapolation to $I_b = 0$ yields the damping rate due to synchrotron radiation τ_0^{-1} from which the energy loss or energy can be extracted. Table 1 gives the results for measurements at 60 and 45.625 GeV. Although the measurements are in good agreement with the MAD [3] predictions, the resulting relative energy uncertainty is of the order of $\mathcal{O}(1\%)$.

energy [GeV]	energy loss [MeV]	
	MAD	measured
45.625	127	126 ± 9
60.000	380	382 ± 4

Table 1: *Results and* MAD *predictions of the energy loss due to synchrotron radiation at 45.6 and 60 GeV beam energy.*

2.2 The Energy Sawtooth

The horizontal beam position is a function of the local momentum. The continuous energy loss in the arc sections leads to sawtooth-like horizontal orbits in the LEP ring. The difference between the positron and electron orbits can be used to determine the energy loss with the help of the horizontal dispersion. Results of fits to the sawtooth are shown in figure 1 where the energy loss is plotted as a function of the day in the year. Details on the fit method can be found in [4]. The fit results seem to scatter around a central value but there are clear "jumps" some of which correspond to BPM calibrations (dashed lines). The other jumps could not yet be accounted for. The RMS of the energy loss distribution before day 275 is relatively small and corresponds to a relative uncertainty of the energy of around $\mathcal{O}(5 \cdot 10^{-4})$. This method however is strongly limited by systematic effects. The fit results differ between the octants, depend on the selection of rejected (faulty) BPMs and exhibit "jumps"

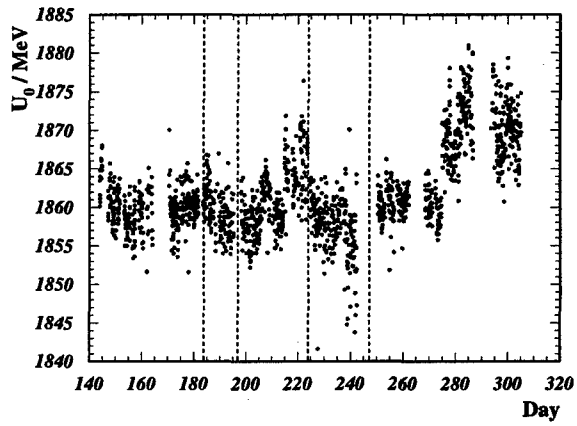

Figure 1: *Energy loss from the sawtooth fits in MeV as function of day in year. The dashed lines denote BPM calibrations.*

* CERN and University of Mainz, Germany,
Email: Anke-Susanne.Muller@cern.ch

0-7803-5573-3/99/$10.00@1999 IEEE.

sometimes correlated to BPM calibrations. The good intrinsic accuracy and the parasitic measurement favor this method but the systematics are not yet under control.

2.3 Q_s and total RF Voltage

As the synchrotron tune depends on the beam energy as well as on energy loss U_0 and total RF voltage V_{RF}, measurements of these dependencies can be used to determine the beam energy. The upper plot of fig. 2 shows a measurement of the synchrotron tune as function of total RF voltage at 50.005 GeV. The curve is a best fit according to

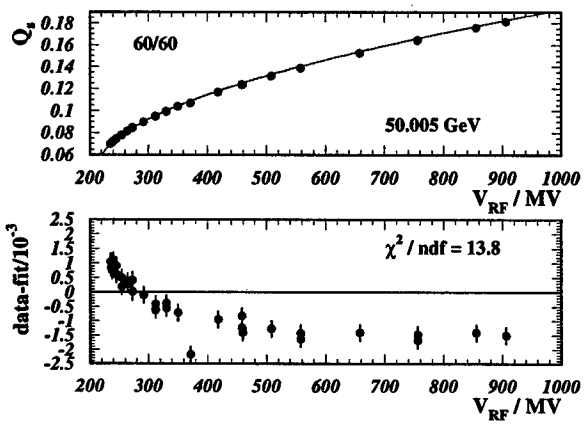

Figure 2: *Upper plot: Synchrotron tune as function of total RF voltage measured at 50.005 GeV. The curve is a best fit according to eq.(1). Lower plot: Difference between data and fit for the same range.*

$$Q_s^2 = \left(\frac{\alpha_c h}{2\pi E}\right)\sqrt{V_{RF}^2 - U_0^2} \qquad (1)$$

with $U_0 = C_\gamma/\rho\, E^4$, α_c being the momentum compaction factor, h the harmonic number and ρ the average magnetic radius. This analytical model is only valid when the RF voltage is homogenously distributed along the ring and for slow synchrotron oscillations. It has to be refined to take into account the large energy loss of $U_0/E \sim 2\%$ at highest energies. The bottom plot of fig. 2 shows the difference between data and fit. Residuals and χ^2 show the sensitivity of the data to additional corrections which can be determined in the fit or included as constraints from separate measurements and calculations. A first step is the correction of the energy for differences between the central frequency and the actual RF frequency

$$E_c = E\left(1 - \frac{1}{\alpha_c}\,\frac{(f_{RF} - f_{RF}^c)}{f_{RF}}\right) \qquad (2)$$

and the introduction of a "voltage correction factor" $V_{RF} \rightarrow g\, V_{RF}$ to take care of RF voltage calibration and phasing errors. In addition to the synchrotron radiation loss in dipoles other energy losses have to be taken into account: energy loss from quadrupoles due to sawtooth and closed orbit distortions, energy loss from correctors, parasitic mode losses, corrections due to finite beam size and to the momentum offset due to central frequency and tides. The finite beam size adds a contribution equivalent to a shift of the beam by one RMS beam size. The sum of these losses is $K = 2.57$ MeV at 50.005 GeV and $K = 2.65$ MeV at 60.589 GeV with an overall uncertainty of $\Delta K = \pm\ 0.50$ MeV. The total energy loss U_0 used in eq.(1) is finally

$$\tilde{U}_0 = \frac{C_\gamma}{\rho} E^4 + K \qquad (3)$$

To study the fit quality and to find a correction for the unequally distributed RF voltage, the model was tested with the MAD simulation program. Figure 3 shows Q_s generated for a beam energy of 50.005 GeV with different RF configurations: a realistic case with the normal LEP RF distribution, a case where the same total voltage is concentrated in one point and the limit of a homogenous distribution where the voltage is distributed over the whole ring. To account

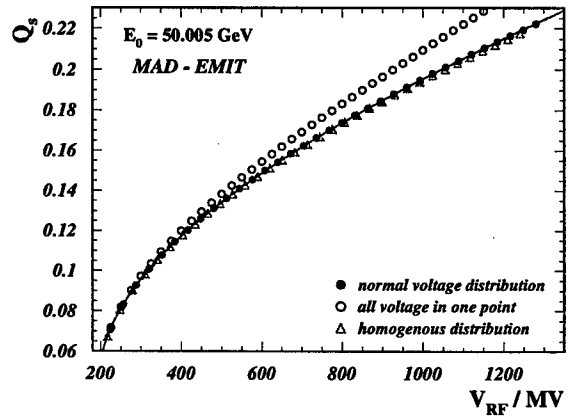

Figure 3: *Synchrotron tune as function of total RF voltage as calculated with* MAD *for different RF configurations. The curve is a fit to the "realistic" RF distribution using the fit model eq.(4) with appropriate input parameters.*

for the RF distribution, a term proportional to V_{RF}^4 has to be added to eq.(1). The weight factor M is taken from the fit to the MAD dataset. The final model reads as follows:

$$Q_s^4 = \left(\frac{\alpha_c h}{2\pi}\right)^2 \left\{\frac{g^2 V_{RF}^2}{E_c^2} + M g^4 V_{RF}^4 - \frac{1}{E_c^2}\,\tilde{U}_0^2\right\} \qquad (4)$$

with the relations from equations (2,3). The energy extracted from a fit to simulation data is in good agreement with the input energy. A systematic uncertainty of $\pm$ 10 MeV is assigned to the fit results. Figure 4 shows the measurements at 50.005 and 60.589 GeV. The curves are best fits using the "final" model of eq.(4). The momentum compaction factor α_c and the voltage nonlinearity factor M are taken from MAD. All other parameters were allowed to vary in the fit. Figure 5 shows the residuals of the fit to the 50.005 GeV data. It is clearly visible that the model is able to reproduce the measurements quite accurately. External knowledge was incorporated in the fit by introducing constraints of the type $(a - a_{\rm nom})^2/\sigma_a^2$ where a stands for a

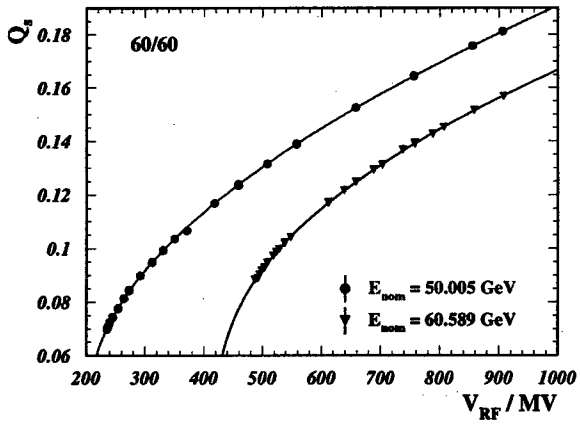

Figure 4: *Measurements of Q_s as function of total RF voltage. The curves are the results of the fits according to eq.(4).*

fit parameter and σ_a for its estimated uncertainty to the χ^2-function. a_{nom} is the value the parameter is constrained to. The beam energy was constrained to the nominal energy, σ_E was set to $\pm$ 50 MeV. The central value of K was set to the given values with an error of $\pm$ 0.5 MeV. The voltage correction factor g was constrained to the average value obtained from the measurements. σ_g was estimated from the spread of the results. The value of $g = 0.95415 \pm 0.0005$ implies that the effective voltage is about 5% less than the nominal voltage. In table 2 fit results are compared to the

E_{nom}	E_{fit}	$\Delta E/E$	E_{pol}
50.005	50.013 ± 0.026	$5.2 \cdot 10^{-4}$	50.020
60.589	60.576 ± 0.021	$3.5 \cdot 10^{-4}$	60.597

Table 2: *Results of the fits using the model of eq.(4). All energies are given in GeV. The systematic uncertainty assigned to the results from studies with* MAD *is $\pm$ 10 MeV.*

nominal machine energy (obtained from the magnet calibration curves) and to the energies measured with resonant depolarization in the following fill. The impact of the energy constraint on the final errors is small. For both measurements the fitted energies are lower than the polarization energies but still agree within their errors. The error is of the required magnitude. Preliminary measurements at high energy indicate that the absolute error is essentially energy independent, $\Delta E \approx 25 MeV$. This value can be improved

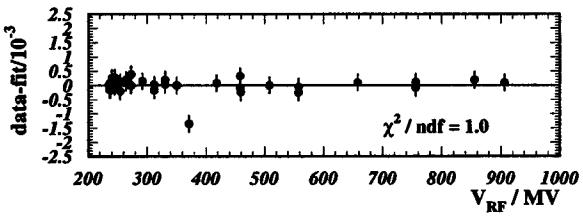

Figure 5: *Difference between data and fit for the final fit model.*

if tighter bounds can be set on K and g. If the energy is known from other measurements (resonant depolarization) the same fits can be used to extract the momentum compaction factor. The relative uncertainty resulting from this method is $\Delta\alpha_c/\alpha_c \approx 1 \cdot 10^{-3}$ whereas conventional measurements have relative uncertainties of 1 - 2%. All measurements of the momentum compaction factor are in good agreement with the MAD value.

3 SUMMARY

Several methods to measure the energy from the energy loss using existing LEP equipment have been studied. To be useful, the relative calibration uncertainty should not exceed a few times 10^{-4}. The determination of the energy loss from the damping of coherent oscillations gives a relative error of $\mathcal{O}(1\%)$. The measurement of the energy loss using the energy sawtooth has a good intrinsic accuracy ($\mathcal{O}(5 \cdot 10^{-4})$) and does not require dedicated beam time. However the systematics are not yet under control. The most promising method is the measurement of the synchrotron tune as function of the total RF voltage. External information is introduced into the fit in a controlled way which also allows to assess sensitivities to input parameters and simulation biases. A relative energy error of $\Delta E/E = 2.8 \cdot 10^{-4}$ has been reached and further improvements are possible.

4 ACKNOWLEDGEMENTS

Sincere thanks to all who have contributed to the results presented above in helpful and instructive discussions. Many thanks as well to A. Butterworth and E. Peschardt for their help with the RF in MD and analysis and in particular to A. Hofmann, A. Verdier and J.M. Jowett.

5 REFERENCES

[1] A. Blondel et al. Evaluation of the LEP Centre-of-Mass Energy Above the W-Pair Production Threshold. CERN–EP–98–191, CERN, 1998.

[2] J. Wenninger and A.-S. Müller. Measurements of Coherent Damping and Tune Shifts with Amplitude at LEP. In *Proceedings of the 6th European Particle Accelerator Conference*, pages 1377–1379, 1998.

[3] H. Grote and F. C. Iselin. The MAD Program, User's Reference Manual. SL Note 90-13 (AP) (Rev. 4), CERN, March 1995.

[4] A.-S. Müller. Energy Calibration for the Prize of a Fig. In J. Poole, editor, *Proceedings of the 9th Workshop on LEP-SPS Performance*, CERN–SL–99–007 DI, pages 237–240, 1999.

Observation of Radial Ring Deformations using Closed Orbits at LEP

J. Wenninger*, CERN, Geneva, Switzerland

Abstract

With a circumference of 26.7 km the LEP ring is subject to long range geological deformations which must be monitored accurately to guarantee a sufficient precision on the beam energy for the LEP experiments. Changes of the LEP circumference can be extracted from the radial position of the closed orbits with an accuracy better than 0.1 mm. The observed tidal deformations with amplitudes of up to 1 mm were found to be in good agreement with geological models. Besides such periodic effects seasonal circumference variations of 2 mm are also observed. A summary of measurements collected between 1993 and 1998 is presented.

1 INTRODUCTION

The influence of terrestrial tides on the LEP beam energy was discovered in 1991 when calibrations were performed for the first time by resonant depolarization [1, 2]. In 1992 and 1993 further studies demonstrated that the beam energy variations were in good agreement with the predictions of tide models [3]. But it also became clear that in addition to tidal deformations the ring was subject to long term circumference oscillations with an annual periodicity. Energy calibrations by resonant depolarization have an accuracy of 10 ppm but can only be performed when the beam are not colliding. For very precise measurements of the Z boson mass and width this calibration must be extrapolated in time to the periods where the beams collide and the LEP experiments take data without spoiling the excellent accuracy [4]. Information extracted from closed orbits has been used to track and understand circumference changes which alter the LEP beam energy [5, 6]. This paper reviews the present knowledge on radial deformation at LEP.

2 RADIAL DEFORMATIONS

Since in LEP the particles are ultra-relativistic, their orbit length is determined by the frequency of the RF system which is normally kept constant. As a consequence of a circumference change ΔC, the beam is forced to adapt its radial position in the quadrupoles. The additional bending field leads to a change in energy ΔE :

$$\frac{\Delta E}{E} = -\frac{1}{\alpha}\frac{\Delta C}{C} = -\frac{\epsilon}{\alpha} \qquad (1)$$

where α is the momentum compaction factor. ϵ is the horizontal strain. For the LEP optics used between 1993 and 1998 α varied between $1.43 \cdot 10^{-4}$ and $1.86 \cdot 10^{-4}$.

The horizontal movement of the beam relative to the quadrupoles can be observed either through the energy change or directly with the beam orbit measurement system. To enhance the sensitivity and reduce the systematic errors, the horizontal beam position is averaged over all BPMs (Beam Position Monitors) located in the regular arc FODO cells at the vertically focussing quadrupoles [5, 6]. Up to 240 BPMs can be used to compute this average beam position which will be denoted X_{ARC}. The horizontal dispersion D_x is ideally identical at all the selected BPMs. X_{ARC} is related to ΔC by

$$\Delta X_{ARC} = D_x \frac{\Delta E}{E} = -\frac{D_x}{\alpha}\frac{\Delta C}{C} \qquad (2)$$

The factor D_x/α can be measured using a controlled change of the RF frequency f_{RF} since this leads to a position shift of

$$\Delta X_{ARC} = -\frac{D_x}{\alpha}\frac{\Delta f_{RF}}{f_{RF}} \qquad (3)$$

The ratio $D_x/\alpha \approx 2.5 - 2.9 \cdot 10^3$ (m) depends slightly on the beam optics. The measurements agree with MAD [7] calculations within 2%.

3 EARTH TIDES

Tides are caused by the $1/r^2$ dependence of the gravitational attraction of the sun and the moon. The presence of a celestial body leads to a quadrupolar deformation of the Earth surface. The radius change ΔR is

$$\Delta R \sim \frac{M}{a^3} P_2(cos\theta) = \frac{M}{2a^3}(3cos^2\theta - 1) \qquad (4)$$

where θ is the angle between the vertical and the celestial body and a is the distance to the body of mass M. P_2 is the 2^{nd} order Legendre polynomial. Figure 1 shows a sketch of the lunar tide bulge. Sun tides are about 50% weaker than Moon tides. Under the influence of the tidal forces the earth surface moves vertically by about $\pm$ 12 cm in the area around Geneva. The associated horizontal strain ϵ induces peak-to-peak circumference changes of up to 1 mm.

The influence of the tides on LEP can be described by a CTE (Cartwright-Taylor-Edden) model which includes the 505 main tide harmonics [8]. A program based on such a

*Email: Jorg.Wenninger@cern.ch

0-7803-5573-3/99/$10.00@1999 IEEE.

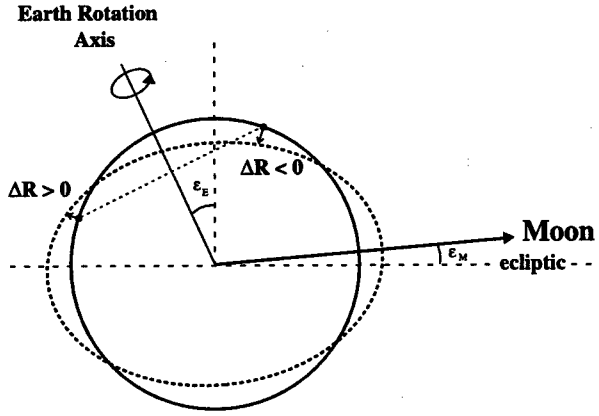

Figure 1: Tidal deformation of the Earth surface due to the presence of the Moon. The inclination ε_E of the Earth rotational axis with respect to the plane of the ecliptic is 23.5°. The inclination ε_M of the lunar orbital plane is 5.1°.

tide model, where some parameters are adjusted with actual gravity measurements, is available to estimate the tidal change in gravitational acceleration Δg which must then be related to the strain ϵ. Figure 2 shows an example of tide predictions for LEP. At high tides $|\Delta g|$ reaches 1.5 $\mu m/s^2$ around LEP for an average acceleration of gravity $g = 9.805\ m/s^2$.

The fraction of gravity change that couples into a horizontal strain ϵ can be described by a coupling parameter λ_T :

$$\epsilon = \frac{\Delta C}{C} = \lambda_T \frac{\Delta g}{g} \qquad (5)$$

where $\lambda_T \approx -0.16$ from geological observations [8]. The maximum strain ϵ reaches a tiny $\approx \pm 2.2 \cdot 10^{-8}$.

The beam position measurement X_{ARC} can now be related to Δg :

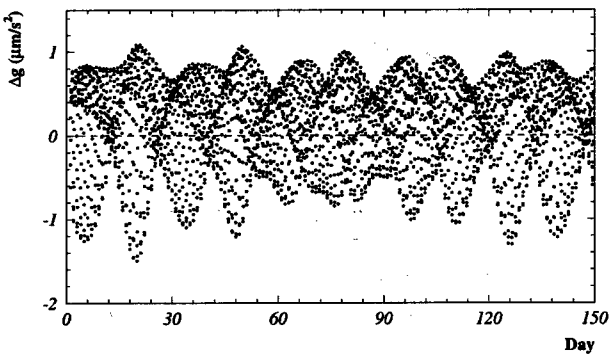

Figure 2: Local gravity change Δg predicted for LEP. The time scale starts on January 1^{st} 1996. The largest amplitudes occur every 14 days at full and new Moon. The first high tide on January 5^{th} corresponds to full Moon. The amplitudes are modulated by the eccentricity of the lunar orbit and the seasonal variation of the Sun position.

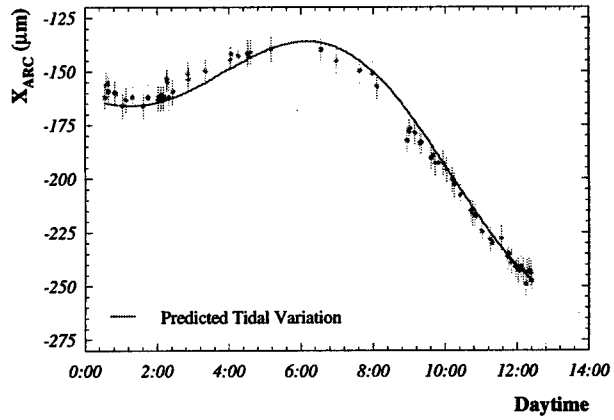

Figure 3: Example of the evolution of X_{ARC} during a LEP fill. The data points follow the variation expected from the CTE tide model.

$$\Delta X_{ARC} = -\frac{D_x}{\alpha}\frac{\Delta C}{C} = -\frac{D_x \lambda_T}{\alpha}\frac{\Delta g}{g} \qquad (6)$$

Figure 3 shows an example of a tidal distortion of the ring observed with the BOM system over a LEP fill.

A sample closed orbits acquired in stable beam conditions in 1994 and 1995 has been used for the analysis of tide effects. The sample of ARC BPMs is scanned for channel which show frequent problems or a suspicious behaviour. Such BPMs (about 40 out of the 240) are completely removed from the analysis. To avoid biases due to slow changes of the circumference that are not related to tides, only the changes of X_{ARC} with respect to its fill average (maximum 12 hours) are fitted to Δg. The residuals of the individual measurements after the fit are typically 5 to 7 μm. Figure 4 shows the spread of X_{ARC} around its

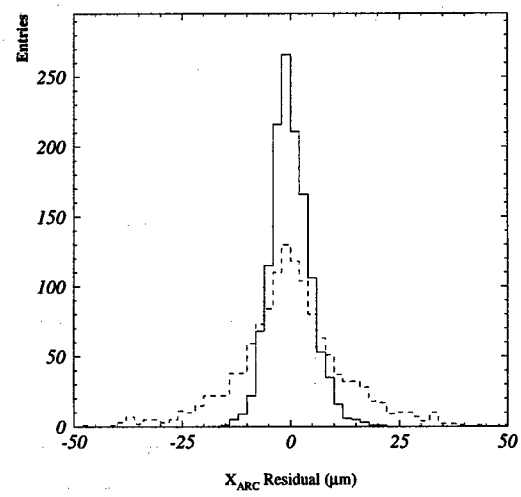

Figure 4: Distribution of the residuals of X_{ARC} with respect to the fill average before (dashed histogram) and after tide correction (solid histogram). The RMS is reduced from 14 to 5 μm.

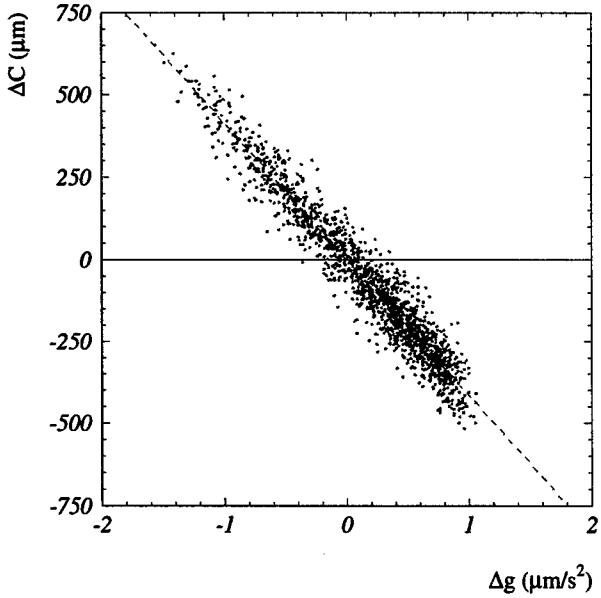

Figure 5: Correlation between the change in circumference ΔC measured with the BOM system and the predicted tidal gravity correction Δg. The slope is $-410 \pm 20\ s^2$.

average value over a fill before and after correction for the tides.

The correlation between Δg and ΔC is shown in Figure 5. The slope $\lambda_T C/g$ (Equation 6) is measured to be $-410 \pm 20\,s^2$, yielding $\lambda_T = -0.15 \pm 0.01$, in good agreement with independent geological measurements. The error is dominated by systematic effects due to tails in the distribution of the fit residuals (Figure 4).

The measurements obtained from this analysis agree well with the results from energy calibration by resonant depolarization [3, 5].

4 LONG TERM RING DEFORMATION

Besides the periodic tidal movements LEP is also subject to much slower long term circumference changes. Figure 6 displays the circumference changes ΔC of LEP between 1993 and 1998. ΔC has been calculated from X_{ARC} after correction for tidal effects. Data from different runs or years can be related by measuring the RF frequency for which the beam is on average centred in the quadrupoles. Between May and November the LEP ring experiences circumference changes of up to 2 mm, the general trend being reproducible from one year to the next. The circumference usually increases during the Summer months. Some of the changes are clearly correlated to rainfall and to fluctuations in the underground water table height. It was not possible to develop a model able to predict ΔC with good accuracy because the geological problem is complex and too many variables are unknown.

Those seasonal variations of the circumference are very important to understand the LEP beam energy. The circumference changes shown in Figure 6 are an important

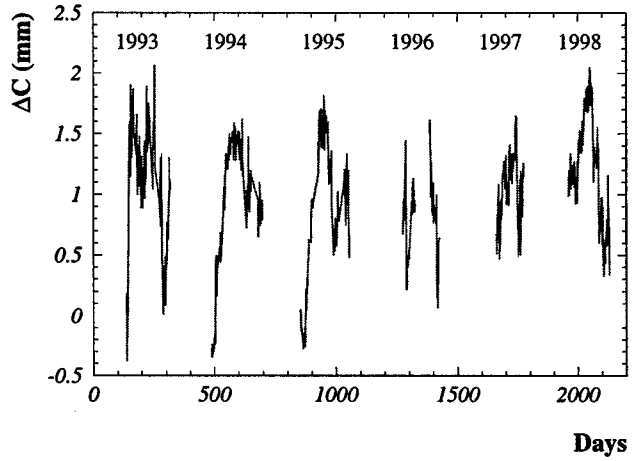

Figure 6: Relative change of the LEP circumference ΔC between 1993 and 1998.

ingredient to model the LEP beam energy. The associated energy variation is $\Delta E/E \approx 4 - 5 \cdot 10^{-4}$, which is more than one order of magnitude larger than the desired accuracy on E.

5 CONCLUSION

Closed orbits have been used for a quantitative determination of the deformation of LEP due to terrestrial tides. The measured decrease of the LEP circumference of 4.1 ± 0.2 μm for a relative increase in the local gravity of 10^{-9} is in good agreement with previous measurements by resonant depolarization and with geological observations.

Besides those periodic tide effects even larger seasonal circumference variations of about 2 mm peak-to-peak have been observed from the beam position relative to the quadrupoles.

The information gained from the closed orbit data has been successfully used to track beam energy changes and to guarantee a precise measurement of the Z boson mass and width.

6 REFERENCES

[1] L. Arnaudon et al., Phys. Lett. B 307 (1993) 187.

[2] L. Arnaudon et al., Phys. Lett. B 284 (1992) 431;
L. Arnaudon et al., Z. Phys. C 66 (1995) 45.

[3] L. Arnaudon et al., Nucl. Instr. Meth. A 357 (1995) 249.

[4] R. Assmann et al., Z. Phys. C 66 (1995);
R. Assmann et al., Eur. Phys. J. C 6 (1999) 2, 187.

[5] J. Wenninger, "Study of the LEP Beam Energy with Beam Orbits and Tunes", CERN SL/94-14 (BI).

[6] J. Wenninger, "Radial Deformations of the LEP Ring", CERN SL/Note 95-21 (OP).

[7] H. Grote, C. Iselin, The MAD program V8.10, CERN-SL/90-13 Rev. 3 (AP).

[8] P. Melchior, The Tides of the Planet Earth, 2nd Edition, Pergamon Press (1983).

THE INTRINSIC UPPER LIMIT TO THE BEAM ENERGY OF AN ELECTRON-POSITRON CIRCULAR COLLIDER

J. Gao, LAL, B.P. 34, F-91898 Orsay cedex, France

Abstract

In this paper we predict that there exists an intrinsic upper limit to the beam energy of an e^+e^- circular collider due to the beam-beam effects. The maximum beam energy is given by $E_{0,max} = 85.17\sqrt{N_{IP}}$(GeV), where N_{IP} is the number of the interaction points in the ring. It is concluded that LEP is the only machine on this planet which has the potential to test the validity of this theoretical prediction by reducing its interaction points to one.

1 INTRODUCTION

Since the first report on the interactions of 200MeV+200MeV e^+e^- beams in the single storage ring device, named AdA, was appeared in 1964 [1], the energy of the interacting electron and positron beams has increased by a factor of 300 in about 30 years. Due to synchrotron radiation the cost of an e^+e^- circular collider is increasing with energy squared [2]. It is taken for granted that e^+e^- collisions at energies beyond LEP II [3] can only be realized by using a linear collider. The questions one may ask, however, are that disregarding the problem of cost whether there exists an intrinsic upper limit for the beam energy of an e^+e^- circular collider, and if it exists, which value it takes. In this paper we try to answer these questions.

2 THEORY

Let's consider a storage ring of single beam (without interaction points and the beam-beam effects of course). Apparently, in this case we could not see any physical reason which limits the possible beam energy. As far as an e^+e^- storage ring collider is concerned the situation is quite different, and obviously, the difference is due to the additional interaction points and the beam-beam effects. To answer our questions it is worthwhile to start with the discussion on the beam-beam effects and the maximum beam-beam tune shift. The luminosity of a circular collider can be expressed as

$$\mathcal{L} = \frac{I_{beam}\gamma\xi_y}{2er_e\beta_y^*}\left(1+\frac{\sigma_y^*}{\sigma_x^*}\right) \tag{1}$$

where r_e is the electron radius, β_y^* is the beta function value at the interaction point, γ is the normalized particle energy, σ_x^* and σ_y^* are the bunch transverse dimensions after the pinch effect, respectively, I_{beam} is the circulating current of one beam, and

$$\xi_y = \frac{N_e r_e \beta_y^*}{2\pi\gamma\sigma_y^*(\sigma_x^*+\sigma_y^*)} \tag{2}$$

is the vertical beam-beam tune shift. At each interaction point particles in a bunch will be deflected transversely by the counter-rotating bunch. According to the linear theory of beam-beam dynamics [4], one knows that for two equal charge Gaussian bunches after each collision, the average beam-beam kicks of each particle in the horizontal and the vertical planes are expressed as follows

$$\delta x' = -\frac{2N_e r_e x}{\gamma\sigma_{x,+}^*(\sigma_{x,+}^*+\sigma_{y,+}^*)} \tag{3}$$

$$\delta y' = -\frac{2N_e r_e y}{\gamma\sigma_{y,+}^*(\sigma_{x,+}^*+\sigma_{y,+}^*)} \tag{4}$$

where $\sigma_{x,+}^*$ and $\sigma_{y,+}^*$ are the bunch transverse dimensions just before the interaction point. In fact, these kicks are *random* and they will move the zero-current equilibrium transverse beam sizes to the new values which depend on the bunch current [5]. Assuming that there are N_{IP} interaction points in the machine, and taking into account of these additional independent random kicks, one gets the new equilibrium horizontal and vertical emittances expressed as [5]:

$$\epsilon_x = \epsilon_{x0}\left(1-\frac{(e^2N_e\mathcal{K}_{IP,BB,x})^2N_{IP}\tau_x}{4T_0E_0^2}\right)^{-1} \tag{5}$$

and

$$\epsilon_y = \epsilon_{y0}\left(1-\frac{(e^2N_e\mathcal{K}_{IP,BB,y})^2N_{IP}\tau_y}{4T_0E_0^2}\right)^{-1} \tag{6}$$

where T_0 is the revolution period, E_0 is the beam energy, τ_x, τ_y are the horizontal and vertical damping time, respectively, ϵ_{x0}, ϵ_{y0} are the horizontal and vertical natural emittance, respectively, and

$$\mathcal{K}_{IP,BB,x} = \frac{\beta_x^*}{2\pi\epsilon_0\sigma_{x,+}^*(\sigma_{x+}^*+\sigma_{y,+}^*)} \tag{7}$$

$$\mathcal{K}_{IP,BB,y} = \frac{\beta_y^*}{2\pi\epsilon_0\sigma_{y,+}^*(\sigma_{x,+}^*+\sigma_{y,+}^*)} \tag{8}$$

where ϵ_0 is the permittivity of vacuum. For an isomagnetic ring, one gets

$$\epsilon_x = \epsilon_{x0}\left(1-\frac{3\epsilon_0R(eN_e\mathcal{K}_{IP,BB,x})^2N_{IP}}{2m_0c^2\gamma^5J_x}\right)^{-1} \tag{9}$$

and

$$\epsilon_y = \epsilon_{y0}\left(1-\frac{3\epsilon_0R(eN_e\mathcal{K}_{IP,BB,y})^2N_{IP}}{2m_0c^2\gamma^5}\right)^{-1} \tag{10}$$

0-7803-5573-3/99/$10.00@1999 IEEE.

where R is the local bending radius. For a flat bunch ($\sigma^*_{y,+} << \sigma^*_{x,+}$, in the following we restrict ourselves to this case), from eq. 10 one knows that

$$\sigma^*_{x,+}\sigma^*_{y,+} > \left(\frac{3RN_{IP}(eN_e\beta^*_y)^2}{8\pi^2\epsilon_0 m_0 c^2\gamma^5}\right)^{1/2} \quad (11)$$

Defining

$$H = \frac{\sigma^*_{x,+}\sigma^*_{y,+}}{\sigma^*_x\sigma^*_y} \quad (12)$$

where H is a measure of the *pinch* effect, and keeping in mind the physics of beam-beam effect at the interaction point, one can write

$$H = \frac{H_0\sqrt{N_{IP}}}{\gamma} \quad (13)$$

where H_0 is a constant and its value will be determined later. H is an important quantity and we will go back to it later. Combining eqs. 2, 11 and 13 one gets finally [5] (isomagnetic case)

$$\xi_y \leq \xi_{y,max} = H_0\sqrt{\frac{\gamma r_e}{6\pi R}} \quad (14)$$

or, for general cases

$$\xi_y \leq \xi_{y,max} = \frac{H_0}{2\pi\gamma}\sqrt{\frac{T_0}{\tau_y}} \quad (15)$$

We have therefore found the analytical expression for $\xi_{y,max}$ and explained the well-known phenomenon in circular colliders that $\xi_y \leq \xi_{y,max}$. The experimentally reached maximum H_0 is found to be about $\frac{1}{6} \times 10^6$. The validity of eqs. 14 and 15 has been demonstrated in ref. 5. On the road to arrive at eqs. 14 and 15 one has defined, expressed and used the pinch effect factor, H (see eq. 13). Now we go back to it and bear in mind that this quantity is one of the base stones of the analytical expressions for the maximum beam-beam tune shift which agree well with the experimental results. The reason why we call H a measure of the *pinch* effect lies in the fact that one has always (for the existing operational e^+e^- circular colliders) $H > 1$. The beam-beam effects not only increase the beam transverse emittances, as shown in eqs. 9 and 10, hence the transverse beam sizes, but also contribute to the maintenance of the beam transverse stabilities. One can imagine that one interaction point acts as a locally fastened belt on the beam "waist". At this point it is natural for one to raise his hand and ask the following question: *what happens if* $H \leq 1$? It is clear that by definition when $H = 1$ the pinch effect disappears, and the colliding beams in the collider act as a single beam in a storage ring (but with larger transverse equilibrium emittances due to the random beam-beam excitations). As for the case when $H < 1$ the physical intuition suggests us that this situation be unstable

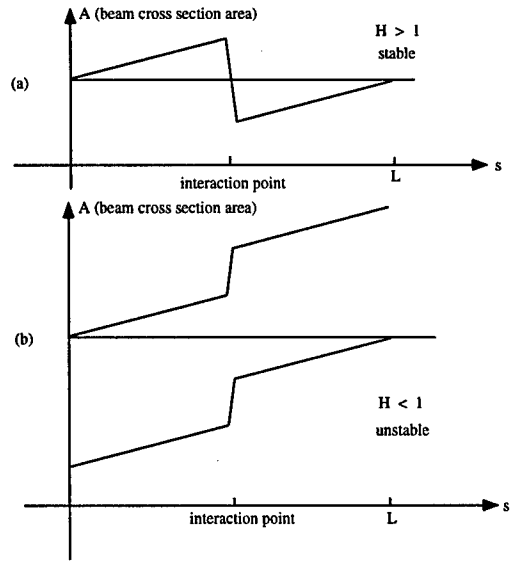

Figure 1: Schematical showing the difference between $H > 1$ and $H < 1$, where there is only one ineraction point in the ring for simplicity, and L is the perimeter of the ring.

since the interaction point explodes the beam as shown in Fig. 1. As bold as one can be we predict that

$$\gamma_{max} = H_0\sqrt{N_{IP}} \quad (16)$$

which corresponds to $H = 1$, as the intrinsic upper limit to the beam energy of an e^+e^- circular collider. For $N_{IP} = 1$ one gets from eq. 16 that $\gamma_{max} = H_0 = \frac{1}{6} \times 10^6$ or $E_0 = 85.17$GeV. Apparently, LEP has not met the limit due to its multi-interaction points ($E_{0,max}$(GeV)$= 85.17\sqrt{N_{IP}}$). It is interesting to predict that LEP II [6] (90GeV+90GeV) can not be realized if there is only one interaction point. In this planet LEP is the largest e^+e^- circular collider and the only machine having the potential to test this theoretical prediction by reducing the number of its interaction points to one.

From the point of view of the author the choice of an e^+e^- linear collider as the replacement to the circular one at energies beyond LEP II has its physical reason behind.

3 CONCLUSION

In this paper we predict an intrinsic upper limit to the beam energy in an e^+e^- circular collider due to beam-beam instabilities. The maximum energy is expressed as $E_{0,max} = 85.17\sqrt{N_{IP}}$(GeV). It is obvious that LEP is the only machine on this planet to have the potential to test this theoretical prediction by reducing the number of its interaction points to one.

4 REFERENCES

[1] C. Bernardini, "Bruno Touschek and AdA", in "ADONE a milestone in the particle way", edited by V. Valente, Frascati Physics Series Vol. VIII (1997), p. 1.

[2] B.H. Wiik, "e^+e^- at the TeV Scale", *ibid.*, p. 171.

[3] L. Foà, "Physics at LEP", *ibid.*, p. 151.

[4] E. Keil, "Beam-beam dynamics", CERN 95-06, p. 539.

[5] J. Gao, "Analytical expression for the maximum beam-beam tune shift in electron storage rings", *Nucl. Instr. and Methods* **A413** (1998), p. 431.

[6] S. Myers, "LEP status and plans", Proceedings of PAC95, Washington, USA (1995), p. 476.

ICOOL: A SIMULATION CODE FOR IONIZATION COOLING OF MUON BEAMS

R.C. Fernow*
Bldg. 901A, Brookhaven National Laboratory, Upton, NY 11973

Abstract

Current ideas [1,2] for designing a high luminosity muon collider require significant cooling of the phase space of the muon beams. The only known method that can cool the beams in a time comparable to the muon lifetime is ionization cooling [3,4]. This method requires directing the particles in the beam at a large angle through a low Z absorber material in a strong focusing magnetic channel and then restoring the longitudinal momentum with an *rf* cavity. We have developed a new 3-D tracking code ICOOL for examining possible configurations for muon cooling. A cooling system is described in terms of a series of longitudinal regions with associated material and field properties. The tracking takes place in a coordinate system that follows a reference orbit through the system. The code takes into account decays and interactions of ~50-500 MeV/c muons in matter. Material geometry regions include cylinders and wedges. A number of analytic models are provided for describing the field configurations. Simple diagnostics are built into the code, including calculation of emittances and correlations, longitudinal traces, histograms and scatter plots. A number of auxiliary files can be generated for post-processing analysis by the user.

1. PROGRAM OVERVIEW

A major part of the cooling simulation effort for the Muon Collider Collaboration has been directed toward the development of two programs. The first, ICOOL, provides the flexibility to quickly examine widely different ideas for implementing ionization cooling. For example, setting up desired field configurations is accomplished in ICOOL using predefined, analytic field models. This simplifies the adjustment of parameters for the field to obtain some desired result. The second program, DPGeant [5], is based on the GEANT code system [6]. It is possible to describe very complicated 3-D problem geometries using DPGeant and to calculate quantities to greater accuracy than with ICOOL. DPGeant typically gets its field distributions from maps generated by other, more accurate field computation codes. In our experience the two codes have been quite complementary. One code is frequently used to check results from the other.

ICOOL uses a command input file consisting of five parts: simulation control variables, beam definition, control of physics interactions, diagnostics, and region definition. Current ideas for ionization cooling make extensive use of solenoidal channels. For this reason we define a region to encompass a cylindrical volume which has a fixed length along the reference orbit. A region can be subdivided radially in up to 5 subregions. Each subregion has a field type, material type, and material geometry associated with it. Particles are allowed to pass back and forth between radial subregions. Wedge shaped material geometries are provided for reducing the momentum spread in dispersive regions. There is no practical limit on the number of regions in a problem. After validity checking, the region data are stored in a direct access disk file.

The program tracks the particles to the end of a given region and generates any desired diagnostics. It then moves on to track the surviving particles to the end of the next region. This program structure was adopted to make it possible to eventually add space charge interactions. At present the code only has a very crude space charge model applicable in pillbox cavity regions.

The region description language has two looping structures to aid in describing complicated, repetitive systems. A group of regions, such as *rf* cavity cells, may be repeated as often as desired using a REPEAT structure. Groups of REPEAT structures and isolated regions may be combined into a CELL structure, which may also be repeated as often as desired. In addition a CELL has its own field type associated with it. This allows applying a background solenoid field, for example, over a sequence of regions, each of which has its own local field.

In addition to the physical regions described above, the user can insert "pseudoregions" into the command file at various locations to accomplish tasks, such as forcing diagnostic output, collimating the beam, transforming the beam with a TRANSPORT element, redefining the reference particle, etc.

The program can initialize the phases of long strings of *rf* cavities by using an on-axis reference particle. The most commonly used algorithm tracks the reference particle through absorbers and other non-cavity regions, taking into account the mean energy lost there. The energy of the reference particle is increased in *rf* cavity regions by assuming the particle gains a constant energy per unit length. It is then possible to calculate the time the

* Email: fernow@bnl.gov

0-7803-5573-3/99/$10.00@1999 IEEE.

reference particle passes the center of each cavity and to adjust the cavity electric fields to be at zero crossing at these times. After the relative cavity phases have been determined, the user can control the beam's interaction with the *rf* fields by adjusting the mean launch time of the particles in the beam or by applying additional phase shifts to individual cavities.

For maximum compatibility across the Muon Collider collaboration it was decided to write the code in Fortran 77 and to restrict graphics inside the program to simple character based "printer plots". The current version of the program has ~11,000 lines of source code. The program has been run successfully on UNIX, PC, and Macintosh platforms.

A simulation of transverse cooling using the alternating solenoid configuration [7,8] takes 8.2 min on a 450 MHz Pentium PC. This simulation involved tracking 1000 muons through 24 m. There were 578 regions consisting of liquid hydrogen absorbers with aluminum windows and pillbox *rf* cavities with beryllium windows, all immersed in a 15 T periodic solenoidal field lattice.

2. PARTICLE GENERATION

The user can choose to generate gaussian or uniform initial particle distributions inside the program. Available particles are electrons, muons, pions, kaons and protons of either sign.

It is possible to generate a number of important correlations in the initial beam distribution. (1) The beam can be given an initial angular momentum that is appropriate for starting the simulation inside a solenoidal field. (2) The beam can have a correlation between its forward velocity and its transverse position and/or divergence. This is necessary to counteract the bunch lengthening from path length differences encountered in a long solenoid. (3) The longitudinal phase space can be prepared in an *rf* bucket that matches the requirements of a subsequent *rf* cavity. (4) The transverse phase space can be initialized with an arbitrary set of Twiss parameters $\{\alpha, \beta, \varepsilon\}$ for matching into the subsequent lattice.

The initial beam specification is quite flexible, allowing a mixture of particle types, each with its own phase space distributions and correlations. The input beam information may also be read in from an existing set of particle data on an external file. There is no practical limit on the number of particles. Currently the first 50,000 are stored in memory and particles in excess of this are stored on a direct access disk file. The program can save the particle state after any region in the same format required for input, so problems can be run in stages

3. ELECTROMAGNETIC FIELDS

Typically the user chooses one of the predefined field types in Table 1 as the region field. There are usually several models for each type of field configuration representing different approximations or symmetry assumptions. Usually one of these models, e.g. a constant B_z solenoid region, is simple enough so that the particle's interaction with the field may be readily understood. Other more complicated models that satisfies Maxwell's equations can be used for more accurate modeling, e.g. the solenoidal field from a cylindrical current sheet.

Table 1 Electromagnetic field models

Type	Models
rf accelerator	4
Bent solenoid	2
Current loop	3
Deflection cavity	2
Sector dipole	2
Alternating solenoid lattice	2
Quadrupole	2
Current carrying rod	4
Sextupole	2
Annular current sheet	3
Solenoid	4
Tapered current rod	1
Tapered solenoid	1

If the superposition of a region and a cell field is not sufficient, a background field can be defined on a 3-D grid. This field can be built up from any combination of the fields in Table 1.

Sometimes the fringe field of a region has not fallen to 0 at the defined end of the region. For this reason, an option exists to include in the field of a given region contributions from the fields in neighboring regions.

Simulations of longitudinal emittance cooling have used bent solenoids to generate the required dispersion together with wedge shaped absorbers for removing the momentum spread. ICOOL uses an analytic model [9] of the bent solenoid fields. Linear and polynomial shaped wedge regions are provided in the program.

The following function is widely used in the code to give a continuous expression for a magnetic field or vector potential component on the axis.

$$f(s)=\frac{1}{2}\left[\tanh\left(\frac{s-E}{\lambda}\right)-\tanh\left(\frac{s-C-E}{\lambda}\right)\right]$$

where E is the distance of the leading edge of the field pattern from the start of the region, C is the width of the central "high field" part of the distribution, and λ gives the rate of fall off at the ends. Other field components on and off the axis are calculated from Maxwell's equations. One nice feature of the function f(s) is that the derivatives can also be calculated analytically to any order. Derivatives up to seventh order are used in the code.

4. INTERACTIONS AND DECAYS

Muon and pion decays can be simulated. An option exists to continue tracking the charged daughter product from a decay. Energy loss, straggling and scattering in matter are simulated as continuous processes. The code currently uses a set of 12 internally defined elements and compounds that are of greatest interest for ionization cooling. The mean value of the energy loss is computed using the Bethe-Bloch formalism including the density effect. Fluctuations in the energy loss may be sampled from Gaussian, Landau or Vavilov distributions [6]. Sampling from the Vavilov distribution is switched to a Gaussian or Landau distribution if the local values of the stepsize and velocity require it. Multiple Coulomb scattering may be sampled from Rossi-Greisen, Highland or Lynch-Dahl Gaussians, Rutherford single scattering or the Moliere distribution [6,10]. Some additional user control is provided for the parameters used in the Moliere theory, since the amount of scattering is very important in ionization cooling and there is some uncertainty in the application of Moliere theory to low Z materials. Sampling from the Moliere distribution is switched to plural Rutherford scattering if the stepsize is so small that the effective number of scatters is less than 20. Delta ray events with correlated angle-energy loss variables may also be simulated. Nuclear interactions, pair production and bremsstrahlung are not simulated.

5. TRACKING

Since the system is defined in terms of regions along the reference trajectory (s), the independent variable in the equations of motion is ds. The dependent variables are the transverse positions, momentum, and the polarization. The position and momentum equations are defined up to third order in the deviations from the reference orbit [11]. The radius of curvature is always assumed to lie in the x-s plane. When vertical bending is desired, the user must first specify a coordinate rotation by 90° around s. Particle stepping can be done using fixed steps or by using an adaptive stepsize algorithm. The adaptive algorithm takes into account constraints due to the validity of the multiple scattering and straggling models and due to the local gradient of the field. Particle stepping is done using fourth-order Runge-Kutta integration [12].

6. DIAGNOSTICS

ICOOL has a number of built-in diagnostics, which can be used to check if the simulation is working properly. Kinematic variables and field values can be plotted for individual particles as a function of distance (Z-history). The mean, standard deviation, minimum and maximum values for the ensemble of particles can be plotted for any variable at the end of each region (R-history). In addition the program has a number of statistical analyses. Any defined variable can be histogramed at the end of any region. Scatter plots may be made of any variable at one region with any variable at the same or any other region. Moments are computed for each of the histogram and scatter plot variables. Emittances, polarization values and/or covariance matrices may be computed after any region.

Besides the built-in diagnostics, the program can write out files of particle and field information. These files can be generated (1) after specified regions, (2) automatically at the end of every region, or (3) repeatedly after a specified number of steps inside a region. This information can be used for more sophisticated analysis or plotting in a separate post-processing program. Other diagnostic files can be written giving the magnetic field grids or the *rf* phases generated by the program.

ACKNOWLEDGEMENTS

I would particularly like to thank R.B. Palmer, J.C. Gallardo, H.G. Kirk, Y. Fukui, P. Lebrun, and D. Neuffer for their helpful suggestions. This research was supported by the U.S. Department of Energy under Contract No. DE-AC02-98CH10886.

REFERENCES

[1] Muon Collider Collaboration, Status of muon collider research and development and future plans, BNL-65-623; Fermilab-PUB-98/179; LBNL-41935; http://www.cap.bnl.gov/mumu/status_report.html, submitted to Phys. Rev. Special Topics.

[2] Muon Collider Collaboration, Muon-muon collider: feasibility study, BNL-52503; Fermilab-Cnf-96/092; LBNL-38946; Proc. New Directions for High Energy Physics, Snowmass 96.

[3] A.N. Skrinsky & V.V. Parkhomchuk, Methods of cooling beams of charged particles, Sov. J. Part. Nucl. 12:223-247, 1981.

[4] D. Neuffer, Principles and applications of muon cooling, Part. Acc. 14:75-90, 1983.

[5] Most of the DPGeant development was done by P. Lebrun at FNAL.

[6] CERN Program Library, GEANT 3.2.1 Detector description and simulation tool, 1993.

[7] R.C. Fernow et al, Transverse cooling in the muon collider, BNL-65698, 1998; submitted to Proc. 8th Workshop on Advanced Accelerator Concepts.

[8] J.C. Gallardo et al, Description and performance calculations of an ionization cooling channel for muon beams based on alternating solenoids, these proceedings.

[9] J.C. Gallardo et al, Muon dynamics in a toroidal sector magnet, in D. Cline (ed), Physics Potential and Development of μμ Colliders, AIP Conf. Proc. 441, 1998, p.282-288.

[10] Particle Data Group, Review of particle properties, Eur. Phys. J. C 3:144-151, 1998.

[11] M.F. Tautz, Third order aberrations for ion orbits in static magnetic fields with mid-plane symmetry, Nuc. Instr. Meth. 84:29-36, 1970.

[12] W.H. Press et al, Numerical Recipes in Fortran, 2nd ed., Cambridge University Press, 1992, p. 704-716.

A Solenoidal Capture System For Neutrino Production*

M. Diwan, S. Kahn, R. B. Palmer, BNL, Upton, NY

Abstract

This paper describes the use of a high field solenoidal magnet to capture secondary pions from the production target. The captured pions subsequentially decay to produce the neutrino beam. A pion capture system using a high field solenoid magnet has been proposed for the muon collider[1]. This technology would also be available for neutrino beam production. It will be shown that a high field solenoid would produce a larger flux of neutrinos with energy, $E_\nu < 1.3\,GeV$, than a neutrino beam produced with a horn system. The $\nu_e, \bar{\nu}_e$ flux contamination in the solenoid neutrino beam is only 0.15%.

1 INTRODUCTION

The recent paper from the Super Kamiokande Collaboration[2] [3] indicating evidence for oscillations of atmospheric neutrinos has created interest in verifying the results with an accelerator based neutrino experiment. The probability of oscillation of one species of neutrino into another is proportional to $sin^2[\frac{1.27\Delta m^2 L}{E_\nu}]$. For oscillations in the small Δm^2 region it is advantageous to have either or both a long distance or small E_ν. A high field solenoid can capture all pions produced from proton interactions on a target up to a transverse momentum, P_T, determined by the field, B_s, and the solenoidal radius, R_s. The pion capture solenoid (currently) proposed for the muon collider has $B_o = tesla$ and $R_s = cm$ These parameters would limit the capture to pions with $P_T < 0.225\ GeV/c$ which would keep only 33% of the pions. Since muons from low P_T pions can be more efficiently cooled, these parameters are reasonable for a muon collider. For neutrino production a larger solenoid aperture is preferred.

The solenoid field is 20 tesla in the vicinity of the target. The gradient of field, as it falls off moving away from the target, provides focussing by increasing the longitudinal momentum while decreasing the transverse momentum. The form of the field along the longitudinal axis is

$$B_s(z) = \frac{B_o}{1. + az} \qquad (1)$$

where B_o is the nominal field at the target and a is a parameter that determines $\nabla\vec{B}$ and consequently the focussing. A solenoid tends to focus low momentum pions better than high momentum pions. The ν flux from solenoidally captured pions will dominate the ν flux from a horn beam at low neutrino energy. There is an additional contribution of $\bar{\nu}$ from a solenoid since the solenoid does not sign select as a horn does.

* Work performed under Contract No. DE-AC02-76CH00016 with the U.S. Department of Energy.

2 SIMULATION

A simulation study of solenoid focussed pion beam for ν production was made using GEANT[4]. The GEANT model used in the (now defunct) BNL long baseline experiment[5] was used as a basis. The two horn system in the GEANT model was replaced by the high field solenoid. The solenoid is 20 meters long with the radius varying as

$$R(z) = R_o\sqrt{1 + az} \qquad (2)$$

where R_o is the radius of the solenoid in the vicinity of the target. $R_o = cm$ is chosen so that all πs with $P_T < 0.45\ GeV/c$ are kept. This aperture will capture 75% of the πs produced. a is chosen to give the proper focussing. Choosing $a = 0.05\ cm^{-1}$ will give a radius of 160 cm at the far end of the solenoid.

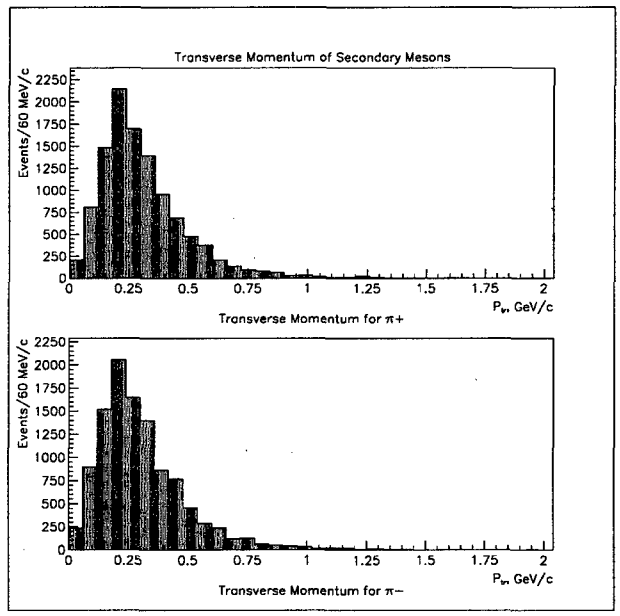

Figure 1: Transverse momentum distribution of secondary pions from the target using the FLUKA option in GEANT. P_T is in GeV/c.

The solenoid for computational purposes is described by a sequence of 100 current rings with radius given by Eq 2 and spacing between the rings as approximately inversely proportional to the field strength. The current in the rings is varied so as to obtain the desired field on the axis. The magnetic field is obtained by summing the contribution from each ring where the field from each ring is calculated from an analytic expression[6]. This procedure for field computation is accurate and manifestly satisfies Maxwell's equation. It does not suffer from the descretation errors that would be present in using a field map for a 20 meter long

expanding radius solenoid. It is however a very time consuming calculation.

In this study we use a 28.3 GeV proton beam with a circular transverse profile with $\sigma_r = 0.8\ mm$ and $\sigma_{r'} = 0$. The beam is incident on a copper target with 1 cm radius and 22.5 cm length (1.5 interaction lengths). Table1 indicates the number of produced secondaries of each species per incident proton on target. The rates quoted are the same whether the secondaries are captured by a solenoid or a horn system. Table1 shows the secondary meson production rates for both the FLUKA[7] and GHEISHA[8] hadronic shower packages in GEANT. The rates using the FLUKA and GHEISHA are not consistent with each other. The FLUKA secondary πs show less of a correlation between $P_\perp$ and $P_\parallel$. The FLUKA results are used for the analysis.

Table 1: Rates for secondary meson production at the target. Rates are for mesons produced per incident proton on target.

Particle	Fluka	Gheisha
π^+	2.83	3.73
π^-	2.49	3.39
K^+	0.13	0.09
K^-	0.06	0.03
K_L	0.10	0.07
K_S	0.10	0.06

After the secondary mesons are produced they are transported through the field which captures and focuses them. The produced πs can either decay in the field or in the decay tunnel following the solenoid or interact it the walls of the solenoid or tunnel. Fig 2 shows the momentum spectrum of the decaying and interacting πs. The decay length for lower momentum πs is shorter, we expect the decaying πs to have lower momentum. Fig 2 also shows the decay (interaction) position of the πs. This figure shows that the πs that interact will preferentially do that in the solenoid (axial position less than 20 meters) by hitting the wall of the solenoid. For computational efficiency, each decaying meson is allowed to decay 10 times producing neutrinos in different parts of phase space. The neutrinos produced are appropriately weighted to preserve the normalization.

3 SPECTRUM

Fig 3 shows the neutrino spectrum at 1 kilometer from the target along the incident beam direction. The spectrum is given in units of $\nu s/(GeV \cdot m^2 \cdot POT)$, where POT refers to *protons on target*. Fig 3 shows three spectral curves. The dashed curve corresponds to the solenoidal focussed beam described above. It shows the ν flux is largest below 1.2 GeV falling off sharply above that. The dotted curve shows the ν spectrum of the two horn focus beam that was designed to be used for the BNL Long Baseline experiment. This beam peaks with $E_\nu \approx 1.5\ GeV$ and

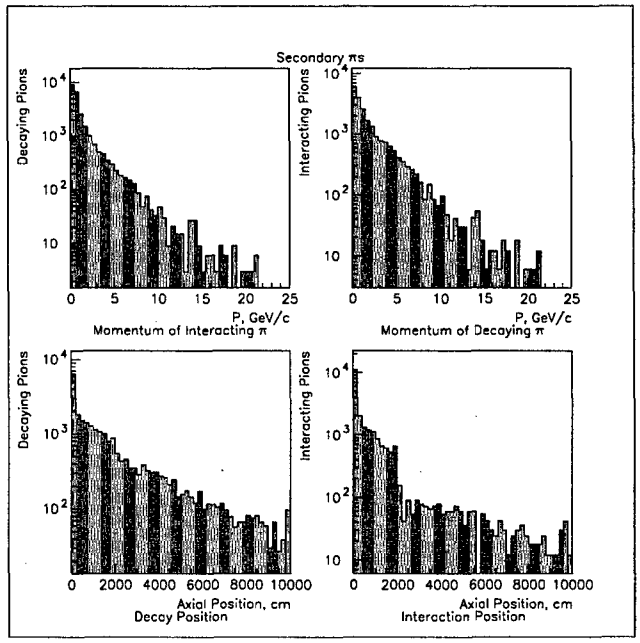

Figure 2: Momentum and decay(interaction) point of decaying (interacting) pions.

extending to about 4 GeV. The solid curve represents the spectrum of the so-called *perfect focussed* neutrino beam. For the *perfect focussed* beam it is assumed that each secondary meson exiting the target has its direction parallel to the incident proton beam. The perfect beam would have the largest ν spectrum imaginable, but it is not physically achievable. The ν_μ flux from the solenoidal focussed beam

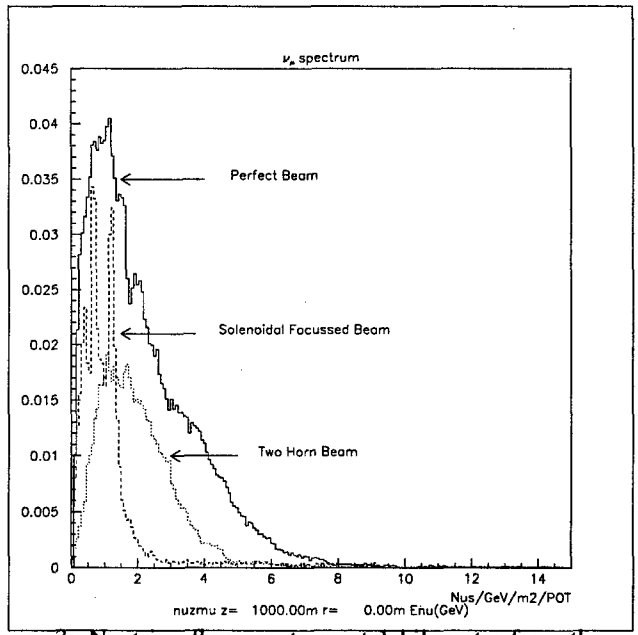

Figure 3: Neutrino flux spectrum at 1 kilometer from the target along the beamline. The three curves indicate the solenoidal focussed beam (dashed), two horn beam (dotted) and *perfect focussed* beam (solid).

dominates the flux from the two horn beam below 1.3 GeV.

Table 2 compares the integrated ν_μ flux per proton on target at a detector situated 1 kilometer from the target. ν_μs with $E_\nu < 0.45\ GeV$ are not interesting since the cross section to produce a charge current event is very small and consequentially the normalization for neutrino oscillations would be difficult. Table 2 separates the integrated flux into energy ranges $0.45 < E_\nu < 1.28\ GeV$ where the solenoidal focussed beam is larger than the horn beam and the region $E_\nu > 1.28\ GeV$ where the horn beam beam is effective. In the region $0.45 < E_\nu < 1.28\ GeV$, the solenoidal ν beam will produce 67% more ν_μ than the two horn system.

Table 2: Integrated ν_μ flux at a detector 1 kilometer from the target. The units are number of 10^{-3} νs per m^2 per proton on target.

Range, GeV	Solenoid	2 Horn	Perfect
All	0.453	0.597	1.454
$0.45 < E_\nu < 1.28$	0.250	0.150	0.409
$E_\nu > 1.28$	0.146	0.433	0.954

A solenoid will focus both π^+ and π^- whereas a horn focussed beam will select the sign of the πs. A neutrino experiment could use both the ν_μ and $\bar{\nu}_\mu$ events. Fig 4.a shows

$$1 \times [\nu\ spectrum] + \frac{1}{3} \times [\bar{\nu}\ spectrum] \qquad (3)$$

The $\frac{1}{3}$ corrects for the fact that the $\bar{\nu}$ cross section is (approximately in this energy range) one third of the ν cross section. Table 3 shows the integrated flux for the total neutrino flux.

Table 3: Integrated $\nu_\mu + \frac{1}{3}\bar{\nu}_\mu$ flux at a detector 1 kilometer from the target. The units are number of 10^{-3} νs per m^2 per proton on target.

Range, GeV	Solenoid	2 Horn	Perfect
All	0.571	0.605	1.824
$0.45 < E_\nu < 1.28$	0.317	0.152	0.523
$E_\nu > 1.28$	0.179	0.439	1.184

This *effective total flux* for the solenoidal focussed beam is twice that of the two horn focussed beam in the energy range from 0.45 to 1.28 GeV. The ν_e and $\bar{\nu}_e$ contamination for the solenoidal focussed beam is expected to be small since K production is small at low E_ν. The ratio of $\nu_e, \bar{\nu}_e$ flux to $\nu_\mu, \bar{\nu}_\mu$ flux is 0.15% for the solenoid beam and 0.78% for the two horn beam. Fig 4.b shows the ν_e spectrum of the solenoid and horn beams.

4 CONCLUSIONS

A solenoidal focussed neutrino beam would produce a larger ν flux in the interesting energy range where one would like to look for $\nu_\mu \rightarrow \nu_e$ oscillations. In the energy range $0.45 < E_\nu < 1.28$ the *solenoid* would produce 60% of the neutrino flux of the *perfect* beam. The solenoidal focussed beam would produce almost twice the number of

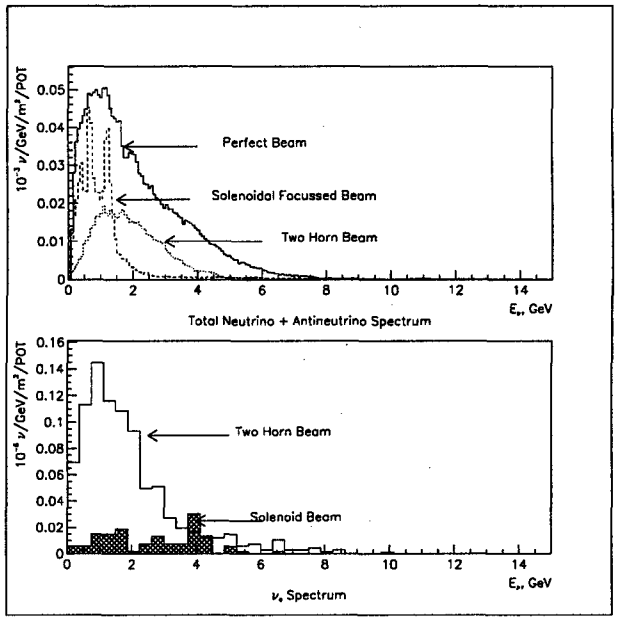

Figure 4: Part a: Sum of the effective spectra from ν and $\bar{\nu}$ at 1 kilometer from the target along the beamline. The figure sums the neutrino spectrum with weight 1 and the antineutrino spectrum with weight $\frac{1}{3}$. The three curves indicate the solenoidal focussed beam (dashed), two horn beam (dotted) and *perfect focussed* beam (solid). Part b: ν_e flux for the solenoidal focussed beam and horn focussed beam

$\nu + \bar{\nu}$ events as a horn focussed beam. The solenoidal focussed beam would have a much smaller ν_e contamination than the horn focussed beam. However, a 20 meter solenoidal capture and focussing magnet with a 20 tesla peak field would not be as cost effective as a standard two horn focus system. If however such a magnet were to be built for another application, such as a muon collider, it could also be used to produce high intensity low energy neutrino beam that would be ideal for $\nu_\mu \rightarrow \nu_e$ oscillations.

5 REFERENCES

[1] Muon Collider Status Report, to be submitted to Phys Rev. BNL-65623, FNAL-PUB-98/179, LBNL-41935

[2] Y. Fukuda, et al., *Evidence of Oscillations of Atmospheric Neutrinos*, Phys. Rev. Lett. **81**, 1562 (1998)

[3] S. Hatakeyama et al., *Measurement of the Flux and Zenith-Angle Distribution of Upward Through-Going Muons in Kamiokande II + III*, Phys. Rev. Lett. **81**, 2016 (1998)

[4] *GEANT Detector Description and Simulation Tool*, CERN Program Writeup W5013

[5] Long Baseline Neutrino Oscillation Experiment, E889 Physics Design Report, BNL No. 52459, (1995)

[6] W.R. Smythe, Static and Dynamic Electricity, 2nd Edition (1950), p271

[7] P.A.Aarnio et al., FLUKA User Manual, Technical Report TIS-RP-190, CERN, (1987,1990)

[8] H.C.Fesefeldt, *Simulation of Hadronic Showers, Physics and Applications*, Technical Report PITHA 85-02, (1985)

The Instrumentation Channel for the MUCOOL Experiment*

S. A. Kahn, BNL, Upton, NY 11973
H. Guler, C. Lu, K. T. McDonald, E. J. Prebys, S. E. Vahsen, Princeton University, Princeton, NJ 08544

Abstract

The MUCOOL facility is proposed to examine cooling techniques that could be used in a muon collider. The solenoidal beam channel before and after the cooling test section are instrumented to measure the beam emittance. This instrumentation channel includes a bent solenoid to provide dispersion and time projection chambers to measure the beam variables before and after the bend. The momentum of the muons is obtained from a measurement of the drift of the muon trajectory in the bent solenoid. The timing measurement is made by determining the phase from the momentum of the muon before and after it traverses RF cavities or by the use of a fast Cherenkov chamber. A computer simulation of the muon solenoidal channel is performed using GEANT. This study evaluates the resolution of the beam emittance measurement for MUCOOL.

1 INTRODUCTION

The MUCOOL facility has been proposed as an experimental program for testing techniques that can be used for muon cooling in a muon collider[1]. The facility would include a target area in the FNAL meson area, followed by a quadrupole focussed decay channel, a bending magnet for muon momentum selection, an instrumented muon solenoid channel before and after the experimental region to measure the beam emittance[2]. This paper will discuss the measurement of the emittance in the instrumentation channels. Fig. 1 illustrates the instrumentation channel. It is a bent solenoidal channel. The solenoidal bend causes a drift vertical to the plane that is proportional to the particle momentum. This drift will be used to measure the muon momentum. Time projection chambers (TPC) are positioned before and after the solenoidal bend. These TPCs are filled with a low pressure methane gas that has a long mean free path. The TPCs can measure the transverse beam variables : x, y, x' and y'. By comparing TPC beam measurements before and after the bend one can measure the beam momentum. Fig. 1 shows two bent solenoid regions with RF cavities in between. This arrangement is chosen to be able to measure the muon momentum before and after the RF cavities. The comparison of the momenta can be used to extract the time information from the RF phase. Using RF for the time information is one of two approaches under consideration. The other is to use a fast Cherenkov device for the time information. The scope of this paper is to examine how well one can measure the beam momentum using the bent solenoid. Table 1 lists the important parameters describing the instrumentation channel.

* Work supported under Contract No. DE-AC02-76CH00016 with the U.S. Department of Energy.

The experiment has set as a goal the ability to measure the emittance with a relative error of 3%[3]. To achieve this goal the desired relative uncertainty in the measurement of each of the six phase space variables should be $\approx 1\%$. Table 2 shows the required detector resolution to achieve 1 % accuracy in the measurement of the phase space parameter.

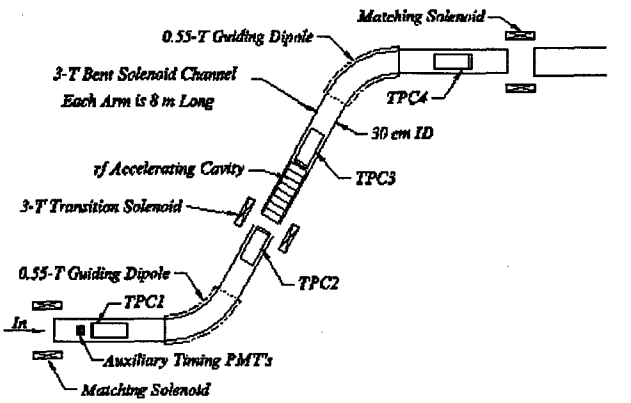

Figure 1: Schematic of the measurement channel

Table 1: Parameters used for the MUCOOL Instrumentation Channel.

Parameter	Value
RF frequency	805 MHz
Momentum	171 MeV/c
$B_{solenoid}$	3 tesla
$B_{guiding}$	0.56 tesla
θ_{bend}	1 radian
R_{bend}	100 cm
$R_{aperture}$	15 cm
β^*	36.7 cm
TPC length	45 cm
$\sigma_x = \sigma_y$	12 mm
$\sigma_{x'} = \sigma_{y'}$	60 mrad
Total length	9.2 m

2 SIMULATION

The MUCOOL instrumentation channel was modelled in GEANT[4]. The channel is designed to transport muons with a mean momentum of 171 MeV/c. The solenoidal magnet field of the instrumentation channel is described with current rings. The field for a single ring can be expressed by an analytic expression[5]. The field at any point in the solenoidal channel is obtained by summing the con-

Table 2: Required detector resolution to achieve 1 % accuracy of the phase space parameter.

Parameter	Resolution
$\delta\sigma_x = \delta\sigma_y$	200 μm
$\delta\sigma_{x'} = \delta\sigma_{y'}$	5 mrad
$\frac{\delta P}{P}$	0.14%
$\delta\sigma_z$	2 mm
$\delta\sigma_t$	8 ps

tributions of the single rings. This procedure accurately describes the field in the transition region between the straight and curved solenoids. A dipole magnet field is superimposed on the bent region of the solenoid. This dipole field is set to cancel the drift of a muon with the mean momentum. Fig 2 shows the local magnetic field components along the center of the channel. The axial field is 3 tesla at the center and varies radially from the center of curvature in the bent region. The vertical field in the bent region has a central value of 0.56 tesla and has a *hyperbolic tangent* form as an approximation for the ends. The dipole field falls off with an attenuation length equal to the solenoid aperture radius. The shape of the local B_x (in-plane transverse field) component depends on how abrupt the transition is between the straight and curved regions of the channel.

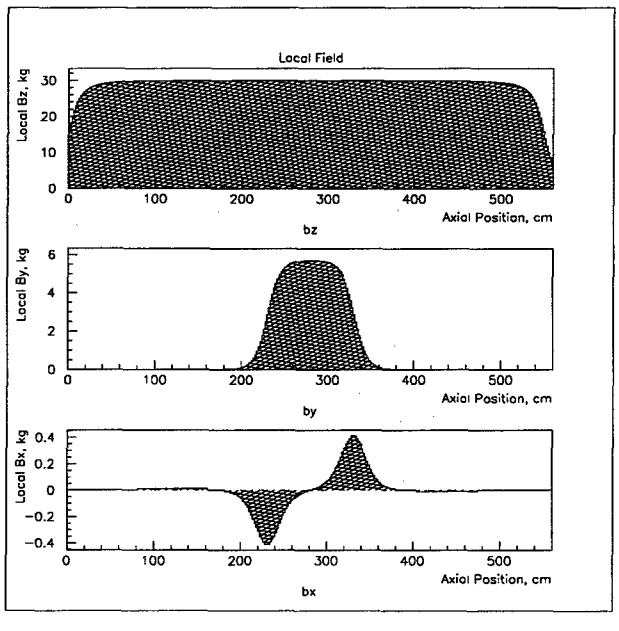

Figure 2: Components of the field as seen in the local coordinate system along the center of the solenoid channel. The field is in *kilogauss.*

The GEANT simulation will produce hit digitization in the TPCs. These hits include uncertainties for the measurement and for drift in the TPC low pressure methane gas. The measurement uncertainties for the hit position are 200 μm in transverse directions and 2 mm in the axial direction. The uncertainties from diffusion in the TPC gas is $0.0025\sqrt{z}\ cm$ in the transverse direction and $0.135\sqrt{z}\ cm$ in the longitudinal direction. The longitudinal drift error can be 1 cm for a point that is on the opposite side of the chamber from the readout.

3 ANALYSIS

Events are generated in GEANT corresponding to a normalized transverse emittance of $1300\,\pi\ mm\ mrad$ in each direction. 184 MeV/c muons initially have a spread of $\frac{\Delta P}{P} = 3\%$ and loose energy traversing the auxiliary timing scintillator. The TPCs before and after the bent solenoid will typically produce about 12 hits on a track. The TPC hits are fitted to a helix in a reconstruction program[6]. The beam variables can be determined from the fitted helix parameters and compared to the beam variables known in GEANT. Fig 3 shows the deviation of the reconstructed beam variables x, x', y, y' from the known variables. Table 3 gives the RMS errors for the beam variables determined from Fig 3.

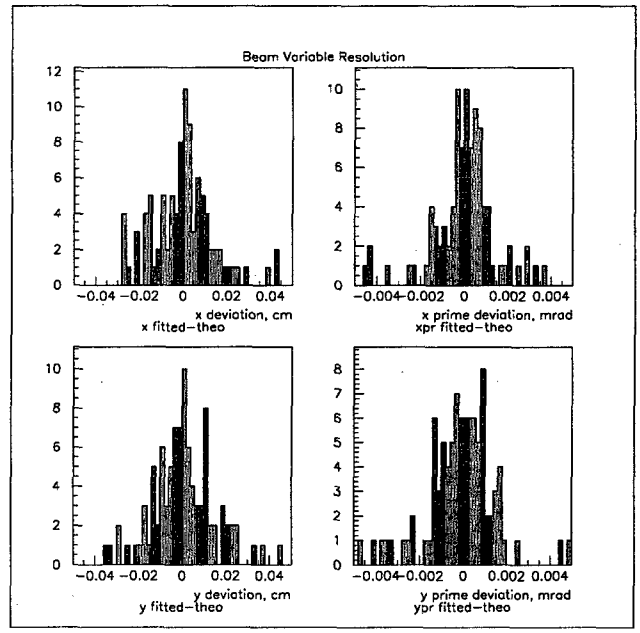

Figure 3: Deviation of reconstructed beam variables, x, x', y, y', from known values in GEANT. x and y are in cm and x' and y' are in radians.

The muon will traverse the solenoidal channel with a helical path. One wishes to measure the drift of the centroid of the helix, not the position of the muon at some specific phase. The center of the helix is known from the path reconstruction. The errors in the measurement of the helix center (x_{ctr}, y_{ctr}) at the TPC is given in Table 3. The error in determining the helix center will contribute to the ultimate error in the determination of the momentum.

Fig 4.a shows a scatter plot of P_μ known from GEANT verses the vertical drift traversing the bent solenoid. There is a strong correlation between P_μ and Δy as expected.

Table 3: Resolution of the beam variables achieved in the simulation.

Parameter	Resolution
$\delta x = \delta y$	127 μm
$\delta x' = \delta y'$	1.0 mrad
$\delta x_{ctr} = \delta y_{ctr}$	150 μm
$\frac{\delta P}{P}$ from ΔY	1.3%
$\frac{\delta P}{P}$ from Pitch	1.8%

Fig 4.b shows the deviation in momentum of the points from the best fit straight line through the data. This figure establishes the error in momentum from the vertical drift to be 2.3 MeV/c or $\frac{\delta P}{P} = 1.3\%$. Fig 4.c shows the deviation in momentum obtained from measuring the helix pitch in the TPC alone. This independent measurement sets the momentum error at 3.0 MeV/c or $\frac{\delta P}{P} = 1.8\%$. These determinations of momentum are not adequate for the emittance measurement, particularly if time is measured from the RF phase since a difference in momentum before and after the RF cavities would be necessary for that.

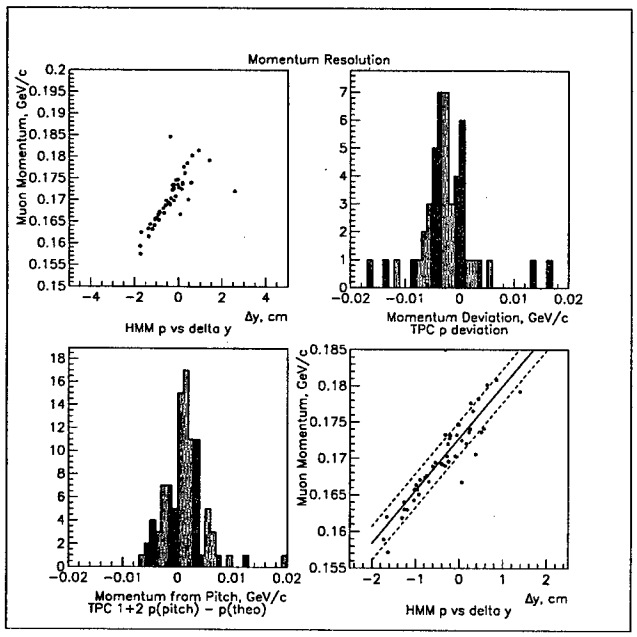

Figure 4: *a*: Scatter plot of P_μ vs Δy; *b*: Deviation of P_μ from best line fit to data. *c*: Deviation of momentum determined from pitch measurement in the TPCs.

4 DISCUSSION

The ΔP_μ spread in P_μ determined from the vertical drift shown in Fig 4 is likely to come from different paths that the different muons take through different parts of the field. Fig 5 shows a histogram of the path lengths that the individual muons traverse from the center of TPC1 to the center of TPC2. An individual muon will sample a different B_x as it enters the bent part of the solenoid than when it leaves the bent solenoid. The non cancelation of the B_x component can affect the vertical displacement of a particle. Fig 5 shows the path length and integrated fields seen by each muon in its local frame. The variation in $\int B_x\, ds$ could account for the ΔP_μ.

A possible procedure to improve the precision of the muon momentum measurement is the following: Using the vertical drift as a first estimate of the muon momentum, track a particle from TPC1 through the solenoid channel magnetic field to TPC2 using several values of the momentum in the vicinity of the first estimate. A χ^2 comparing x, x', y, y' can be assigned to each momentum *guess*. One can use an iterative process find the best momentum. An evaluation of this procedure has not been completed at this moment.

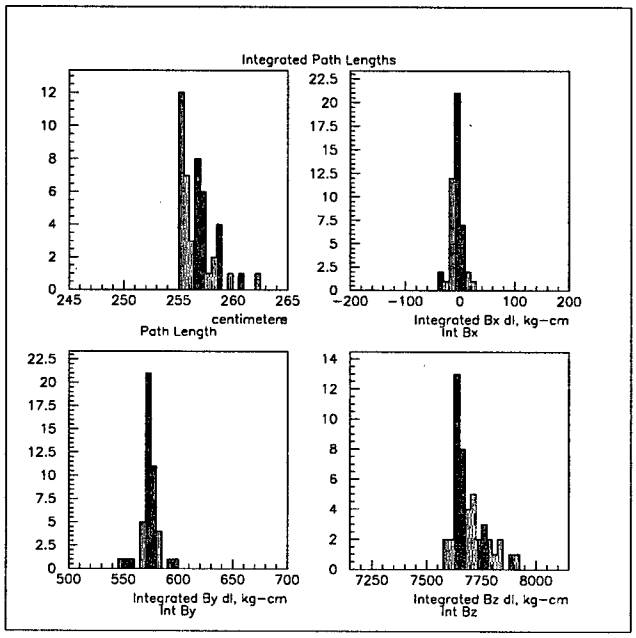

Figure 5: *a*: Total path length from TPC1 to TPC2; *b*: $\int B_x\, dx$ *c*: $\int B_y\, dy$, *d*: $\int B_y\, dz$

5 REFERENCES

[1] MUCOOL Proposal: Ionization Cooling R & D Program for a High Luminosity Muon Collider, Fermilab proposal 904

[2] A Detector Scenario for the Muon Cooling Experiment, C. Lu, K.T. McDonald and E.J. Prebys, Princeton/$\mu\mu$/97-8.

[3] Accuracy of Measurements in the Muon-Collider Cooling Experiment, K.T. McDonald and E.J. Prebys, Princeton/$\mu\mu$/97-4.

[4] GEANT Detector Description and Simulation Tool, CERN Program Writeup W5013.

[5] W.R. Smythe, Static and Dynamic Electricity, 2nd. Edition (1950), p271.

[6] The program uses TpcTrack fitting algorithms written by Xihong Yang for use in the BNL E910 experiment

TARGETRY FOR A $\mu^+\mu^-$ COLLIDER *

H.G. Kirk†,Brookhaven National Laboratory, Upton, NY 11973-5000
for the Muon Collider Collaboration

Abstract

The requirement for high luminosity in a $\mu^+\mu^-$ collider leads one to conclude that a prodigious source of pions is needed followed by an efficient capture/decay channel. Significant targetry issues are raised by these demands. Among these are i) the best target configuration to tolerate a high-rep rate, high-power proton beam ($\sim 10^{14}$ ppp at 15 Hz), ii) the pion spectra of the produced pions and iii) the best configuration for maximizing the quantity of captured pions. In this paper, the current thinking of the $\mu^+\mu^-$ collider collaboration for solutions to these issues is discussed. In addition, we give a description of the R&D program designed to provide a proof-of- principle for a muon capture system capable of meeting the demands of a future high-luminosity machine.

1 INTRODUCTION

Since leptons are point-like particles, in contrast to hadrons which are a composite of quarks and gluons, leptons fully participate in high-energy interactions. For hadrons, such as protons or mesons, kinetic energy is shared with their constituents thus diluting the energy reach of the collision. This lepton energy advantage is on the order of a factor of 10, i.e. a lepton-lepton collision of 1 TeV has the same physics reach as a $\sim$ 10 TeV proton-proton collision. The muon shares this lepton energy advantage with the electron.

The muon, on the other hand, has a mass of 105.6 MeV and is therefore a factor of 207 times more massive than the electron. This provides one with the important capability of reducing synchrotron radiation by this mass ratio to the 4th power. Consequently, with muons, one can contemplate the possibility of circular high-energy lepton machines. This capability means that high-energies can be achieved with the possibility of recirculating the particle beams thus providing more efficient use of accelerating systems while allowing for a smaller footprint for the entire machine complex. Once the goal energy has been reached, we can now consider circulating colliders which have a luminosity which is proportional to the number of circulating turns within the collider rings. Finally, because of the suppressed synchrotron radiation, the energy spread of the colliding beams can be much reduced over that of electron colliders. Some machine scenarios contemplate energy spreads as low as 0.003%. This can be an important advantage when studying narrow resonances.

Muons, however, do possess a significant attribute which mitigates their usefulness, namely they decay with a lifetime of $\sim$ 2 μsec when at rest. To overcome this problem, the muon collider collaboration adopts the strategy of producing prodigious amounts of muons via a chain of; 1) pion production from a robust proton beam impinging on a high-Z target, 2) conducting these pions down a solenoid based decay channel allowing the muons to appear as pion decay products and 3) conducting the resulting muons through an ionization cooling channel[1] in order to reduced their phase space to dimensions suitable for subsequent acceleration and to achieve a high luminosity at the subsequent collider (as an example, 7 10^{34} cm^{-2}s^{-1} for a 1.5 TeV center-of-mass (CoM) machine[2]).

2 PION PRODUCTION

In order to achieve the design luminosity, 2 10^{12} muons per pulse (for the 1.5 TeV CoM machine) must be introduced into the recirculating collider (for each sign). We assume 1/4 survival rate due to aperture and decay losses in the ionization cooling and acceleration stages and a 50 % efficiency for the decay/phase rotation channel. This leads to the requirement that we produce $\sim$ 2 10^{13} pions within the collection energy band (KE= 50-650 MeV) at the target.

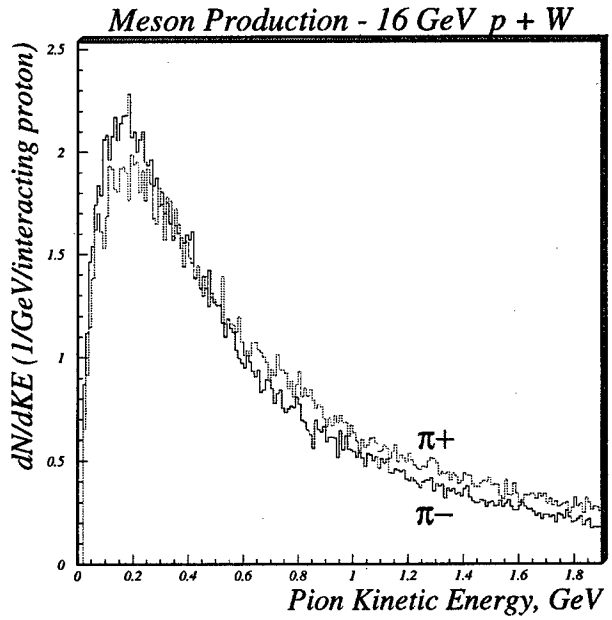

Figure 1: Meson production using the MARS code. Note that the most prolific portion of the pion energy spectrum lies below 600 MeV

Extensive modeling using three different Monte Carlo computer codes have been performed[3][4][5] resulting in the conclusion that we require a 4 MW proton beam (15

* Work supported in part by DOE Contract no. DE-AC02-98CH10886.
† Email: hkirk@bnl.gov

Hz operation) impinging on a high-Z material target. In order to benchmark these codes in the important low-energy portion of the pion production spectrum, the muon collaboration has participated in an AGS experiment, E-910[6], where good efficiencies for detecting forward low-energy pions within a time projection chamber is realized. Data from this experiment is currently being analyzed.

3 TARGETS

Maintaining target integrity with beam powers at the level of 4 MW is difficult. Since about 10% of the proton beam energy is ultimately deposited into the target, this leads us to infer that the target must absorb 400 kW of sustained power and also withstand an instantaneous energy deposition of 30 kJ.

Water cooling via a thermal bath is not considered viable as it would lead to unacceptable losses due to the absorption of the produced pions. Radiative cooling is inadequate for these power levels in a compact target. We therefore consider moving targets as the best solution and choose as our baseline approach moving free-liquid targets where disruption due to shock damage from the single pulse energy deposition can be more easily contained.

Liquid targets have the additional advantage of being relatively easy to move and cool. Contained liquids are not preferred as they will expose the containment vessel to possible high-shock thresholds. Jets of liquid mercury have already been demonstrated[7] but without exposure to a high-power beam.

4 TARGETRY SYSTEM

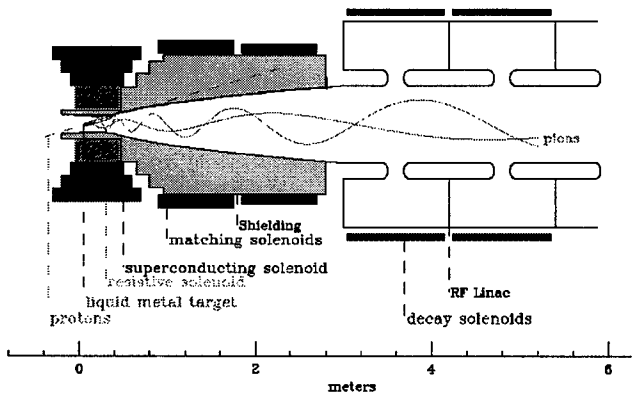

Figure 2: Schematic view of the muon collider targetry system. The proton beam is incident on a skewed target inside a solenoidal magnetic field which tapers from 20 T at the target to 1.25 T at the beginning of the rf linac.

We show in Figure 2, a schematic of our baseline targetry/capture system. The capture solenoid is a hybrid magnet consisting of a inner 6-T, water-cooled hollow-conductor magnet with an inner diameter of 24 cm and an outer diameter of 60 cm. There is space for additional shielding between this coil and the beam pipe. The outer coil is a superconducting magnet extending to an outer diameter of 80 cm. It will generate an additional 14-T field at the target.

The product of solenoid field (B) and the beam pipe radius (R) determines the maximum transverse momentum which the produced pions can possess and still be captured. On the other hand, the transverse emittance of the resulting captured beam is proportional to BR^2, hence we benefit by selecting a high-magnetic field coupled with a small bore radius. Our baseline parameters call for a solenoidal field of 20 T and a bore radius of 7.5 cm thus yielding a maximum transverse-momentum of p_t = 225 MeV/c for those pions which are conducted into the decay channel.

In order to realize maximum pion production efficiencies, we favor using high-density target material embedded within the high-field capture solenoid. Optimum target geometry calls for a small target diameter in order to reduce the effect of pion reabsorption after production. We find that it is advantageous to tilt the target slightly (100-150 mrad) to avoid having the pions spiral back onto the target and be lost through absorption.

The rf linac depicted in Figure 2 represents the beginning of the phase rotation channel. The phase rotation system is designed to contain and shape the longitudinal emittance parameters of the captured muon beam. The initial frequency is determined mainly by the longitudinal spread of the proton driver bunch ($\tau \sim$ 1 to 2 ns) and the drift space from the target to the initial cavity. Based on a capture kinetic energy band of 50 to 650 MeV and a drift distance of 3 m, the initial frequency needs to be on the order of 100 MHz. Modeling of this system[8] has yielded typical phase rotation exit parameters of dE/E = 15% and an rms $c\tau$ of 1.5 m.

The 20-T capture magnetic field is tapered adiabatically down to a lower field in the phase rotation channel. We keep the total magnetic flux constant but reduce the axial magnetic field by a factor of 16 to a more manageable 1.25 T while increasing the beam bore radius by a factor of 4 to 30 cm.

Although we are exploring methods of separating the pions by charge state, our current baseline calls for producing pions of each sign with separate proton pulses. The solenoid channel will transport each sign with equal facility and the phase rotation can work equally well with each charge state provided the rf frequencies are configured to be odd multiples of a fundamental harmonic and the proton drive beam is delivered with a phase separation of $n\pi$ within the fundamental harmonic.

5 R&D PROGRAM

We have identified several critical issues which need to be addressed in order to insure the success of our program.

- Identification of the appropriate material for a liquid jet target.

- Performance of a liquid jet in a 20-T solenoidal field.
- Performance of a liquid jet in a 4 MW proton beam.
- Operation of a 20-T hybrid solenoid in a high-power proton beam environment.
- Operation of a rf cavity in a high-radiation environment.

Not so technically demanding but important to the eventual success of a muon collider is the optimization of the target parameters in order to maximize the pion capture efficiency.

We have embarked on an R&D program to address these and other important issues. Included in this program are:

- Study of liquid/proton beam interactions.
- Build prototype liquid jets.
- Study the effects of eddy currents on the liquid jet propagation through a 20-T field at the National High Magnetic Field Laboratory.
- Study the effects of a high-power proton beam on the liquid jets at Brookhaven's AGS.
- Conduct an experimental test of the proposed targetry system at Brookhaven's AGS.
- Build a 70 MHz rf cavity and operate it in a high-radiation environment.

The cornerstone of this R&D effort is found in our BNL proposal[9] in which we detail our plans to build and test the key components of our targetry scheme in a high-power proton beam environment. We show in Figure 3 the layout of our proposed experiment.

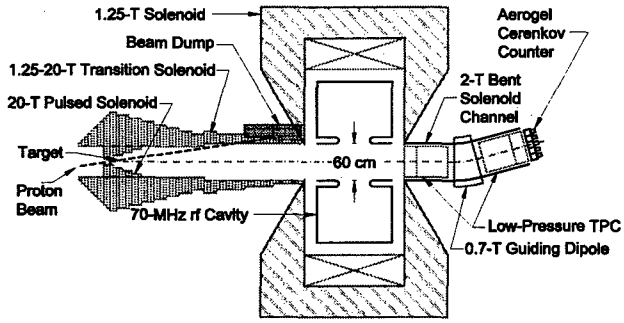

Figure 3: Schematic view of the proposed targetry experiment at the Brookhaven AGS.

In order to minimize cost while retaining the essential functionality of a 20-T solenoidal field at the target, we have chosen to build a pulsed resistive based solenoid in which we will sacrifice repetition rate for cost savings. Additional cost savings may be realized by using an iron-dominated resistive solenoid to surround the rf cavity.

The bent solenoid channel at the end of the experimental setup will serve as a spectrometer to measure the pions/muons spectra and evaluate the pion/muon yield achieved by the chosen target configuration.

6 REFERENCES

[1] Juan C. Gallardo, Richard C. Fernow, Harold G. Kirk, Robert P. Palmer, Paul Lebrun, Alfred Moretti, Alvin Tollestrup, Dan Kaplan, and Yasuo Fukui, *An Ionization Cooling Channel for Muon Beams Based on Alternating Solenoids*, Submitted to this conference.

[2] Charles M. Ankenbrandt, et al., *Status of Muon Collider Research and Development and Future Plans*, BNL Report 6523, Fermilab-Pub-98/179, LBNL Report 41935.

[3] N.V. Mokhov and A. Van Ginneken, *Pion Production and Targetry at $\mu^+\mu^-$ Colliders*, Fermilab-Conf-98/041 (Jan. 1998)

[4] S.H. Kahana, Y. Pang and T.J. Schlagel, Proceedings Heavy Ion Physics at the AGS -HIPAGS '93, ed. by G.S.F. Stephans et al.

[5] J. Ranft, DPMJET version II.3 and II.4, INFN-AE-97-45 (1997)

[6] Experiment E-910 at the BNL AGS
http://www.nevis.columbia.edu/heavyion/e910/

[7] C. Johnson, *Solid and Liquid Targets Overview*, Presented at the Muon Collider Workshop, Oxford, MS, Jan. 17-18 (1998)

[8] R.B. Palmer, *Progress on $\mu^+\mu^-$ Colliders*, Proceedings PAC'97, Vancouver, Canada, May 12-16, page 286, (1997)

[9] James Alessi, et al., *An R&D Program for Targetry and Capture at a Muon-Collider Source*, Proposal submitted to the Brookhaven National Laboratory AGS, (Sept. 28, 1998)

AN IONIZATION COOLING CHANNEL FOR MUON BEAMS BASED ON ALTERNATING SOLENOIDS*

Juan C. Gallardo, Richard C. Fernow, Harold G. Kirk, Robert B. Palmer, BNL, Upton NY
Paul Lebrun†, Alfred Moretti, Alvin V. Tollestrup, FNAL, Batavia, IL.
Daniel M. Kaplan, IIT, Chicago, IL.
Yasuo Fukui, KEK, Tsukuba, Japan

Abstract

The muon collider requires intense, cooled muon bunches to reach the required luminosity. Due to the limited lifetime of the muon, the cooling process must take place very rapidly. Ionization cooling seems to be our only option, given the large emittances of the muon beam from pion decay. However, this ionization cooling method has been found quite difficult to implement in practice. We describe a scheme based on the use of liquid hydrogen absorbers followed by r.f. cavities ("pillbox" or "open iris" type), embedded in a transport lattice based on high field solenoids. These solenoidal fields are reversed periodically in order to suppress the growth of the canonical angular momentum. This channel has been simulated in detail with independent codes, featuring conventional tracking in e.m. fields and detailed simulation of multiple scattering and straggling in the the absorbers and windows. These calculations show that the 15 Tesla lattice cools in 6-D phase space by a factor ≈ 2 over a distance of 20 m.

1 INTRODUCTION

Ionization cooling of intense muon beams ($\approx 2.10^{12}$ particles per bunch) has been recognized as one of the most challenging aspects of the design of a high energy, high intensity Muon Collider[1]. The principle of ionization cooling via deceleration in an absorber followed by re-acceleration in a LINAC, proposed more than 20 years ago[2], is relatively straightforward[1]. However, due to the relatively short muon lifetime, such cooling channels must be very efficient. This entails reaching low values for the $\beta_\perp$ function rapidly, and therefore high focusing magnetic fields. The performance of such lattices needs to be verified with accurate simulations, with complete field maps and detailed simulation of the straggling and multiple scattering in the absorbers and foils. Three distinct computer codes were used to study the performance of this channel: (i) a special version of PARMELA[3] in which multiple scattering was simulated using the Gaussian approximation; (ii) ICOOL[4]; (iii) an extended version of the GEANT3 package[5], DPGeant, featuring higher numerical accuracy in tracking particles over large distances and full e.m. field simulation in the r.f. cavities. Although results presented in this paper have been obtained with DPGeant, these various simulation agree within the expected code accuracy.

* Work supported by the U.S. Department of Energy.
† Email: lebrun@fnal.gov

2 DESCRIPTION OF THE 15 TESLA ALTERNATING SOLENOID COOLING CHANNEL

We here consider one component of a single cooling stage, consisting of the transverse cooling channel. This muon cooler, sketched in figure 1 is based on the use of the lowest Z material, liquid hydrogen (LH_2), embedded in a strong (15 T) solenoidal magnetic field. Linacs are inserted between these absorbers, to compensate for the energy loss. This channel has been designed for a nominal momentum of 187 MeV/c ($\beta = 0.87$) and accepts a transverse normalized emittance of $\approx$ 1600. mm mRad, a momentum spread of $\approx$ 3% and a bunch length of $\approx$ 1.5 cm. The linac r.f. frequency is 805 MHz.

To provide the longitudinal focusing required to keep this single bunch together these linacs must be separated by short distances (less than 50 to 75 cm). Thus one section (defined as one deceleration in the absorber followed by one LINAC) is approximately 2 m long, where the muons will lose and gain $\approx$ 20 MeV, leaving the momentum unchanged after one section. Without the absorbers and linacs, the beam would have a constant (0) value for the canonical angular momentum, despite the large fluctuation of the $\beta_\perp$ function. However, the presence of the absorbers causes the canonical angular momentum to grow and would lead to severe transverse emittance growth at the end of a channel made of multiple sections. This growth is stopped by reversing the direction of the solenoidal field each time the beam goes though the high $\beta_\perp$ points in the lattice, which are located in the middle of the linacs.

The transport in such a channel is far from isochronous: particles at large transverse amplitude have longer path lengths, causing a longitudinal growth as they reach the linac slightly out of phase. It is therefore necessary to start with a bunch where particles at large amplitude have higher momentum, by up to $\approx 20\ MeV/c$ for a particle at $\approx 3\sigma$.

For a fixed maximum field (15 T), the transverse cooling rate decreases as the beam goes though these sections, because this rate is proportional to the transverse emittance.

0-7803-5573-3/99/$10.00@1999 IEEE.

The longitudinal emittance grows because of the stochastic processes in the absorbers (energy loss and multiple scattering). In addition, there are higher order effects in the beam optics and the longitudinal/transverse coupling induce longitudinal motions that are are difficult to compensate for. Thus, the length of such a channel has to be limited to approximately 20 m, after which one must go though an emittance exchange section.

The performance of such a channel has been studied for two different lengths of a section: the 2 m (1.5 m) section has a 64 cm (42. cm) liquid hydrogen absorber and 1.3 m (0.98 m) r.f. cavity, respectively. For the short section case, two different configurations of the linac have been simulated:

1. A "pillbox" type cell, $\pi/2$, with a peak field on axis of 36 MV/m. and 12 identical cells. The beams goes though the walls of each cell, traversing 13 125. μm beryllium foil

2. A more conventional open cell cavity runs in π mode, where the iris aperture matches the transverse size of the beam (radius $\approx$ 4.5 cm at the entrance and exit points of the cavity, and 8 cm at $\beta_\perp$ max). The peak field on axis is 60 MV/m, implying maximum field of $\approx 90\ MV/m$ on the iris wall.

The lengths of these cavities as well as the phase for the synchronous, on axis particle were kept identical. This synchronous phase[6] was set to $\approx$ 30 degrees, so only approximately one half of the voltage is used for acceleration, the linac acts as much as a buncher as an accelerator. Finally, the liquid hydrogen must be contained in a vessel thermally insulated from the linac, this is achieved using thin ($\approx$ 1.5 mil) stainless steel window(s).

3 PERFORMANCE AND ISSUES

The transverse and longitudinal emittances as function of the distance along the channel are shown in figure 2, for the 1.5 m long section and for the open-iris cavity. Over a distance of 25. meters, the channel achieves a cooling of about a factor 2.3 in transverse emittance and a significant longitudinal reheating of about 2.1. Therefore, the overall 6-D emittance is reduced from 2.2 10^9 $(\pi\ mm\ mRad)^3$ down to 0.86 $(\pi\ mm\ mRad)^3$. Correspondingly, the r.m.s. beam size (radius) in the channel decreases from 1.09 cm down to 0.7 cm.

Over 20 m, the non-decay loss is found to be less than 1 %. For longer channels, this beam loss increases rapidly as the bunch length grows; at the end of the channel, the bucket develops an "alpha" shape, signaling the need to stop cooling transversely and recover control of the longitudinal emittance. Very similar results were obtained with the pillbox cavity. Provided the average net acceleration across the cavity is matched to the energy loss in the absorber and sufficient voltage is applied to ensure re-bunching, the net cooling merit factor of such a channel does not depend on

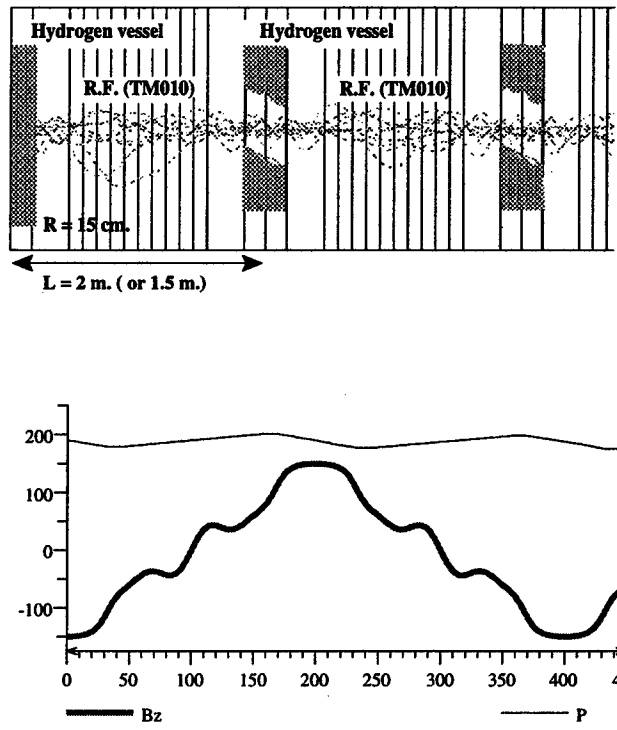

Figure 1: The Alternate Solenoidal muon cooling channel (top). The hashed lines are actual traces of muons obtained via the DPGeant package. Also shown (bottom), with approximately the same horizontal scale, are the longitudinal component of the magnetic field in KG., and the momentum for the synchronous particle (MeV/c).

the details of the acceleration system. However, the multiple scattering occurring at relatively high $\beta_\perp$ in the lattice must remain small, i.e., thin ($\leq$ 125. μm) beryllium windows must be used. The tolerance on the phase ($\pm$3 degrees is not particularly stringent. The difference in peak field is simply due to the different transit time factors for the two modes (π vs $\pi/2$.).

The 2 m long section was found to be slightly worse than the 1.5 m one. The ratio of 6D emittances initial over final is about 10% smaller than for the 1.5 m long section. In principle, a longer cell period could give us faster transverse cooling time because less longitudinal space is wasted in providing access cooling/shielding equipment between the absorber and the r.f. Longer section section also minimizes multiple scattering in the windows of the LH_2 vessels. However, the non-relativistic bucket would drift for a longer time in the absorber, resulting in a faster increase of the longitudinal emittance.

At injection, and during the cooling process, there is a strong coupling between the longitudinal and transverse motion in this channel. Particles at a large transverse amplitude tend to have large synchrotron motions because pathlengths depend on the betatron motion or the transverse amplitude. The synchrotron oscillation tune in such channel is ill-defined: as the stochastic processes (energy loss straggling while loosing energy in the absorber and, more importantly, scattering in the absorber or the foils) move the particles suddenly in a slightly different location in phase space. As a result, one can only quote a broad range for the synchrotron wave length, of about 5 to 15 m This is also the scale at which the correlation between the transverse amplitude and the momentum fades away, concurrent with the longitudinal emittance growth. The loss of this correlation itself implies a emittance growth, which has not been taken into account quoting the emittance at injection.

The result presented in figure 1 has been obtained for 50 μm thick stainless steel LH_2 windows. This is a rather conservative design. We have studied the cooling performance of the channel varying the thickness and material for these window, and observed a degradation of 5 to 10 % in the ratio the initial/final 6D emittance per additional 25 μm of stainless steel. Titanium or Aluminium could also be used, but does not provide significantly better performance, because such window must be slightly thicker. Note that these windows can be made hemispherical, which gives enhanced mechanical strength without compromising the beam dynamics.

Another uncertainty in this calculation is due to the imperfect simulation of multiple scattering in Geant, (or similar packages), via the Moliere formalism [7]. The Moliere theory has been verified in numerous situation. However, for light materials, the uncertainty in the effective atomic screening angle could lead to uncertainties of a few %. But, more relevant to our application, the Moliere formalism no longer holds for very thin absorbers where the "effective number of collisions" is small [8]. The LH_2 vessel must be divided into such thin layers while tracking, because of the betatron motion of the particles. The average scattering angle in small steps becomes comparable to the angle due to the Larmor precession in the high magnetic field. In LH_2, such steps are of the order of a few microns, with angle of tens of μrad. A detailed simulation, (few μm steps !) indicates that the Moliere approximation overestimates the radial displacement of the muon track in the absorber, leading to an over estimate of the beam reheating process. Based on a preliminary result, the ratio on the initial to final 2-D emittance could be 30% to 50% larger than estimated via the Moliere formalism.

Finally, if this channel remains a single-pass device (i.e., not embedded in a cooling ring), one could consider slightly increasing (few % per section) the magnetic field in order to keep the cooling rate optimal.

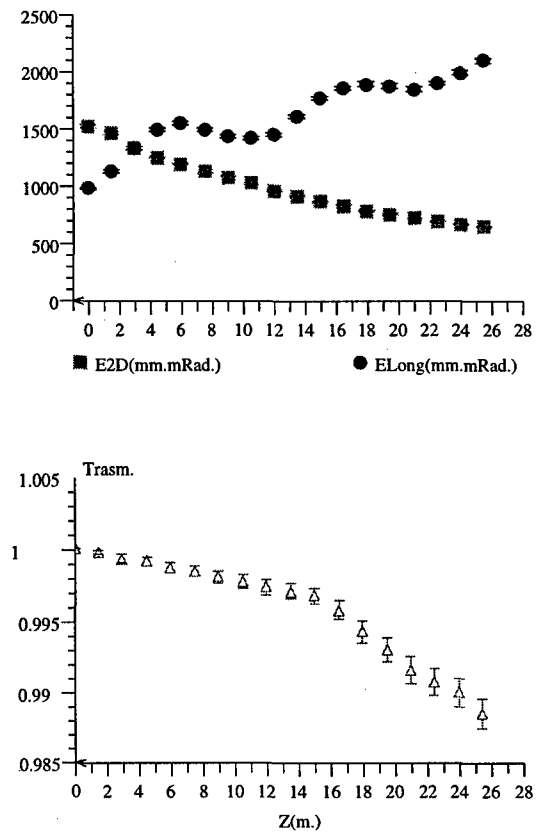

Figure 2: Top: the 2-dim. transverse emittance (squares) and the longitudinal emittance (dots) versus the distance along the channel, showing a net 6-dim. cooling. Also shown (bottom) is the transmission, (The decay loss of about 2. % is not included).

4 REFERENCES

[1] *Status of the Muon Collider Research and Development and Future Plans* submitted to Phys. Rev., BNL-65-623, Fermilab -PUB-98/179, LBNL-41935.

[2] G. I. Budker and A. N. Skrinsky, *Electron cooling and new possibilities in elementary particle physics*, Sov. Phys. Usp. **21** 277 (1978)

[3] H. Kirk, *Parmela Modeling of Alternate Solenoids*, presented at the mini-workshop on Ionization Cooling (BNL, 1998).

[4] R. C. Fernow, *ICOOL: A Simulation Code for Ionization Cooling of Muon Beams* , these proceedings, THP31.

[5] Geant Manual, V3.2.2.1, CERN Program Library W5013 (cern 1994). http://wwwinfo.cern.ch/asdoc/geant_html3/geantall.html

[6] Convention taken from *An introduction to the physics of high energy accelerators*, John Wiley & Sons, 1993, by D.A. Edwards and M.J. Syphers, p. 33.

[7] See for instance C. Caso *et al* Eur. Phys. J. C 3 1-794 (1998), page 146.

[8] H. A. Bethe Phys. Rev. **89** 1256 (1953)

MUON COLLIDERS: THE ULTIMATE NEUTRINO BEAMLINES

Bruce J. King, Brookhaven National Laboratory [1]

Abstract

It is shown that muon decays in straight sections of muon collider rings will naturally produce highly collimated neutrino beams that can be several orders of magnitude stronger than the beams at existing accelerators. We discuss possible experimental setups and give a very brief overview of the physics potential from such beamlines. Formulae are given for the neutrino event rates at both short and long baseline neutrino experiments in these beams.

1 INTRODUCTION

Recent feasibility studies and design work for muon colliders [1] has begun to focus attention on the exciting physics possibilities from the uniquely intense neutrino beams at proposed muon storage rings (muSR) that will use muon collider technology to produce and store large muon currents. Such muSR include both storage rings dedicated to neutrino physics and the parasitic use of the accelerator and collider rings of muon colliders themselves.

2 POTENTIAL FOR NEUTRINO PHYSICS

The neutrino beamlines can be used for two sorts of neutrino experiments:

1. short baseline (SB) experiments, where the detector is placed close to the neutrino source to obtain the most intense beam possible and hence gather very high event statistics of neutrino interactions.

2. long baseline (LB) experiments, where a very massive neutrino detector is placed far away from the neutrino source, deliberately sacrificing event rate in order to study baseline-dependent properties of the neutrinos and, in particular, whether there are "flavor oscillations" in the types of neutrinos composing the beam.

The large muon currents and tight collimation of the neutrinos results in extremely intense beams – intense enough even to constitute a potential off-site radiation hazard [2]. This gives several advantages over the neutrino beams produced today from pion decay at accelerator beamlines:

1. event statistics for short-baseline (SB) experiments that might be three or more orders-of-magnitude larger than in today's high-rate neutrino experiments

2. both higher statistics and longer baselines for long baseline (LB) experiments

3. extremely well understood and pure two-component beams with accurately predictable energy spectra, angular divergences and intensities

4. the first high flux electron-neutrino and electron-antineutrino beams at high energies

5. the possibility of tuning the flavor composition of the beam by varying the polarization direction of the muons.

Recent evidence of neutrino oscillations from several different experiments has resulted in much recent interest in LB neutrino oscillation experiments. LB experiments at muSR have the potential [3,4,5] to either convincingly refute or precisely characterize much of today's evidence for neutrino oscillations.

SB experiment have a different physics motivation, involving several precision measurements that can contribute mainly to our understanding of the interactions between elementary particles. In this respect, they have the potential [3,4,5] to make important measurements have comparable value to (and are complementary to) some of the best precision measurements at today's colliders: LEP, SLC, CLEO, Tevatron, HERA and the B factories that are now coming on-line.

The huge increase in beam intensity allows the use of novel high-performance SB neutrino detectors that are capable of much better reconstructing neutrino events than today's huge high-rate neutrino detector targets. An example of such a detector [3] is shown in figure 1.

3 NEUTRINO PRODUCTION AND EVENT RATES

Neutrinos are emitted from the decay of muons in the collider ring:

$$\begin{aligned} \mu^- &\rightarrow \nu_\mu + \overline{\nu_e} + e^-, \\ \mu^+ &\rightarrow \overline{\nu_\mu} + \nu_e + e^+. \end{aligned} \quad (1)$$

The thin pencil beams of neutrinos for experiments will be produced from long straight sections in either the collider ring or a ring dedicated to neutrino physics. From relativistic kinematics, the forward hemisphere in the muon rest frame will be boosted, in the lab frame, into a narrow cone with a characteristic opening half-angle, θ_ν, given in obvious notation by

$$\theta_\nu \simeq \sin\theta_\nu = 1/\gamma = \frac{m_\mu}{E_\mu} \simeq \frac{10^{-4}}{E_\mu(\mathrm{TeV})}. \quad (2)$$

[1] web page: http://pubweb.bnl.gov/people/bking/, email: bking@bnl.gov. This work was performed under the auspices of the U.S. Department of Energy under contract no. DE-AC02-98CH10886.

0-7803-5573-3/99/$10.00@1999 IEEE.

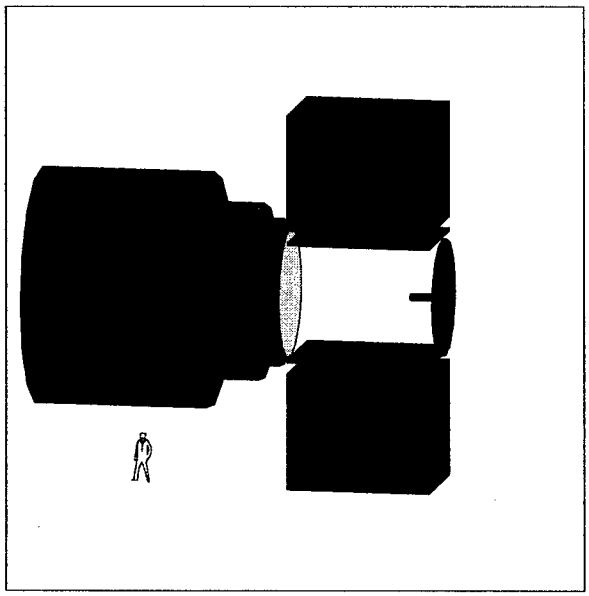

Figure 1: Example of a general purpose SB neutrino detector. A human figure in the lower left corner illustrates its size. The neutrino target is the small horizontal cylinder at mid-height on the right hand side of the detector. Its radial extent corresponds roughly to the radial spread of the neutrino pencil beam, which is incident from the right hand side. Further details are given in reference [3].

The decays of muons into neutrinos are very well understood and it is possible [6] to derive simple, approximate quantitative expressions for the neutrino fluences at experiments and the corresponding experimental event rates in a given target.

The neutrino targets at SB experiments might reasonably cover the boosted forward hemisphere of the neutrino beam. Besides the beam properties, the event rate depends on the depth of the neutrino target, l, in units of gm.cm^{-2} and on the number of years of data-taking, Y. Thus, a convenient benchmark for the size of neutrino event samples the beam can produce is N^{sb}, defined as

$$\text{no. of } \nu \text{ events} = N^{sb}[\text{events/yr/(gm.cm}^{-2}]) \times l[\text{gm.cm}^{-2}] \times Y, \quad (3)$$

Ref [6] derives the following numerical expression for N^{sb} in SB detectors satisfying a couple of reasonable assumptions:

$$N^{sb}[\text{events/yr/(gm.cm}^{-2}]) \simeq 2 \times 10^{-15} \times E_\mu[GeV] \times N_\mu^{ss}[yr^{-1}], \quad (4)$$

where the parameter N_μ^{ss} is the number of forward-going muons decaying in the production straight section per year.

Similarly, the number of LB events depends on the neutrino beam, the baseline distance, L, from neutrino source to detector and the detector mass (L) through:

$$\text{no. of } \nu \text{ events} = N^{lb}[\text{events/yr/(kg.km}^{-2})] \times \frac{M[kg]}{(L[km])^2} \times Y, \quad (5)$$

with

$$N^{lb}[\text{events/yr/(kg.km}^{-2})] \simeq \frac{1.6 \times 10^{-20} \times N_\mu^{ss}[yr^{-1}] \times \times (E_\mu[GeV])^3}{(\gamma \cdot \delta\theta)^2}. \quad (6)$$

(The parameter, $\gamma \cdot \delta\theta$ has value 1 except for neutrino beams from muon beams with large angular divergences.)

Reference [6] also tabulates the expected event rates for plausible muon collider scenarios. These predictions are reproduced as table 1. Extraordinary event samples of 10^{10} interactions appear plausible for SB experiments at muSR with muon energies of order 100 GeV or above.

4 CONCLUSIONS

In conclusion, the essentially *free* neutrino beamlines at muon colliders and the beams from other muSR using muon collider technology could provide happy prospects for the future of neutrino physics.

5 REFERENCES

[1] The Muon Collider Collaboration, "Status of Muon Collider Research and Development and Future Plans", to be submitted to Phys. Rev. E.

[2] B.J. King, "Potential Hazards from Neutrino Radiation at Muon Colliders", these proceedings.

[3] B.J. King, "Neutrino Physics at a Muon Collider", Proc. Workshop on Physics at the First Muon Collider and Front End of a Muon Collider, Fermilab, November 6-9, 1997. Available at http://pubweb.bnl.gov/people/bking/.

[4] B.J. King, "Neutrino Physics at Muon Colliders", Proc. 4th Int. Conf. on Workshop on the Physics Potential and Development of Muon Colliders, San Francisco, December 1997, ed. David B. Cline. Available at http://pubweb.bnl.gov/people/bking/.

[5] B.J. King, "Muon Colliders: New Prospects for Precision Physics and the High Energy Frontier", BNL CAP-224-MUON-98C, Proc. Latin Am. Symp. on HEP, April 8-11,1998, San Juan, Puerto Rico, Ed. J.F. Nieves. Available at http://pubweb.bnl.gov/people/bking/.

[6] I. Bigi *et al.* "An Overview of the Potential for Neutrino Physics at Future Muon Collider Complexes". Work in progress. Contact B.J. King, email: bking@bnl.gov .

Table 1: Predicted neutrino fluxes and event rates for muSR's or muon colliders at several energies.

muon energy, E_μ	2 GeV	20 GeV	50 GeV	175 GeV	500 GeV	5 TeV
(μ^- or) μ^+/year,$N_\mu[10^{20}]$	3.0	3.0	6.0	6.0	3.2	3.6
fract. str. sect. length, f_{ss}	0.40	0.30	0.12	0.12	0.12	0.03
ν ang. diverg., $\gamma \cdot \delta\theta_\nu$	1	1	1	1	10	1
time to beam dump, $t_D[\gamma\tau_\mu]$	no dump	no dump	no dump	no dump	0.5	no dump
N^{sb}[evt/yr/(g.cm^{-2})]	5.1×10^5	3.8×10^6	6.5×10^6	2.7×10^7	2.3×10^7	1.0×10^8
$l \times Y$[gm/cm^2] for 10^{10} events	2.0×10^4	2600	1500	370	430	100
N^{lb}[evt/yr/(kg.km^{-2}]	16	1.2×10^4	1.4×10^5	6.2×10^6	5.0×10^5	2.2×10^{10}

STUDIES FOR MUON COLLIDER PARAMETERS AT CENTER-OF-MASS ENERGIES OF 10 TEV AND 100 TEV

Bruce J. King, Brookhaven National Laboratory [1]

Abstract

Parameter lists are presented for speculative muon colliders at center-of-mass energies of 10 TeV and 100 TeV. The technological advances required to achieve the given parameters are itemized and discussed, and a discussion is given of the design goals and constraints. An important constraint for multi-TeV muon colliders is the need to minimize neutrino radiation from the collider ring.

1 INTRODUCTION

The main motivation for research and development efforts on muon collider technology is the assertion that affordably priced muon colliders might provide lepton-lepton collisions at much higher center of mass (CoM) energies than is feasible for electron colliders, and perhaps eventually explore the spectrum of elementary particles at mass scales inaccessible even to hadron colliders.

This paper attempts a first look at these assertions through discussion and evaluation of the self-consistent muon collider parameter sets given in table 1, at CoM energies of 10 TeV and 100 TeV. These parameter sets have the purpose of pin-pointing the challenges of very high energy muon colliders and they have not been studied or discussed in detail within the Muon Collider Collaboration (MCC) or elsewhere.

The 10 TeV parameter set was presented previously [1] and the parameter values appear to be internally consistent. In contrast, the 100 TeV parameter set represents work in progress to improve in luminosity and other parameters over the self-consistent 100 TeV parameter set given in reference [1] and it's parameters are not yet fully consistent, as discussed below.

2 GENERATION OF PARAMETER SETS

As described previously [1], the parameter sets in table 1 were generated through iterative runs of a stand-alone FORTRAN program, LUMCALC. The parameter sets are calculated from the input values for several input parameters – namely, the CoM energy (E_{CoM}), the collider ring circumference (C) and depth below the Earth's surface (D), the beam momentum spread (δ) and 6-dimensional invariant emittance (ϵ_{6N}), the reference pole-tip magnetic field for the final focus quadrupoles ($B_{4\sigma}$), and the time until the beams are dumped (t_D) – and from the input of maximum allowable values for several other parameters – namely, the bunch repetition frequency (f_b), the initial number of muons per bunch (N_0), the beam-beam tune disruption parameter ($\Delta\nu$), the beam divergence at the interaction point (σ_θ), the maximum aperture for the final focus quadrupoles ($A_{\pm 4\sigma}$), and maximum allowable neutrino radiation where the plane of the collider ring cuts the Earth's surface.

As a preliminary stage of calculation, LUMCALC makes any parameter adjustments that may be required to satisfy the input constraints. These are, in order: 1) reducing σ_θ to the limit imposed by $A_{\pm 4\sigma}$ (based on scaling to existing final focus designs at 0.1 TeV and 4 TeV[1]), 2) reducing N_0 to attain an acceptable $\Delta\nu$, and 3) reducing f_b until the neutrino radiation is acceptable.

3 DISCUSSION

The physics motivation for each of the parameter sets in table 1 is discussed in [2]. Briefly, the number of $\mu\mu \rightarrow$ ee events gives a benchmark estimate of the discovery potential for elementary particles at the full CoM energy of the collider, while the production of hypothesized 100 GeV Higgs particles indicates roughly how the colliders would perform in studying physics at this fixed energy scale.

Both parameter sets give exciting luminosities with good potential to explore the physics processes at and below their respective CoM energy scales.

The output luminosity may be derived in terms of the input parameters as:

$$\begin{aligned}\mathcal{L}[\mathrm{cm}^{-2}.\mathrm{s}^{-1}] &= 2.11\times 10^{33}\times H_B\times(1-e^{-2t_D[\gamma\tau_\mu]}) \\ &\times\frac{f_b[\mathrm{s}^{-1}](N_0[10^{12}])^2(E_{CoM}[\mathrm{TeV}])^3}{C[\mathrm{km}]} \\ &\times\left(\frac{\sigma_\theta[\mathrm{mr}].\delta[10^{-3}]}{\epsilon_{6N}[10^{-12}]}\right)^{2/3}. \qquad (1)\end{aligned}$$

This formula uses the standard MCC assumption[1] that the ratio of transverse to longitudinal emittances can be chosen in the muon cooling channel to maximize the luminosity for a given ϵ_{6N}. The pinch enhancement factor, H_B, is very close to unity (see table 1), and the numerical coefficient in equation 1 includes a geometric correction factor of 0.76 for the non-zero bunch length, $\sigma_z = \beta^*$ (the "hourglass effect").

In practice, the muon beam power and current are limited so the optimization of parameters actually involves the "specific luminosity"

$$l \equiv \frac{\mathcal{L}}{f_b \times N_0}. \qquad (2)$$

Further, the parameter sets at these high energies are always limited by $\Delta\nu$ and it is useful and easy to rewrite

[1] web page: http://pubweb.bnl.gov/people/bking/, email: bking@bnl.gov. This work was performed under the auspices of the U.S. Department of Energy under contract no. DE-AC02-98CH10886.

0-7803-5573-3/99/$10.00@1999 IEEE.

equations 1 and 2 in the form

$$l \propto \frac{\Delta\nu}{\beta*}, \qquad (3)$$

with no explicit dependence on emittance for a given energy. This is misleading, however, since smaller emittances mean smaller magnet apertures and hence allow the design of lattices with smaller $\beta*$'s and, in practice, one can almost always gain in specific luminosity by reoptimizing parameter sets with smaller emittances.

The assumed 6-dimensional emittances are factors of 3.5 (10 TeV) and 50 (100 TeV) smaller than the value 170×10^{-12} m^3 that is normally used in MCC scenarios for first generation muon colliders, in anticipation that the muon cooling channel may eventually be improved through further design optimization, stronger magnets, higher gradient rf cavities and other technological advancements and innovations.

The final focus region presumably presents the most difficult design challenge that is relatively specific to high energy muon colliders. (The muon cooling channel is, of course, a formidable challenge for all muon colliders.) Progressively stronger focusing is required at higher energies to generate the smaller spot sizes necessary to increase the luminosity. The strength of the focusing can be gauged from the overall beam demagnification, defined as $M \equiv \sqrt{\beta_{\max}/\beta^*}$. This is a dimensionless parameter that should be closely correlated with fractional tolerances in magnet uniformity, residual chromaticity etc. Hence, it might be prudent to decrease the fractional momentum spread of the beams, δ, to compensate for an increasing M. In the absence of final focus designs for these parameter sets the difficulty of the chromatic correction for the final focus has simplistically been assessed by the value of a single parameter: the "chromaticity quality factor" $q \equiv M\delta$ [3].

In the absence of "proof by example" lattice designs, the next generation of proposed linear e+e- colliders (LC's) may well provide the best benchmarks for heuristically assessing the difficulty of the final focus parameters. For the 10 TeV parameter set, each of $\beta*$, M and q are roughly comparable to those proposed for these LC's. The 100 TeV parameter set necessarily has a much larger $\beta*$ and M but the value of δ was forced down to $\delta = 8 \times 10^{-5}$ to nearly hold steady the value of q. Unfortunately, this is clearly inconsistent with the rising energy loss due to beamstrahlung at the ip. Following the lead of the LC's, the next iteration of the 100 TeV parameter set will use colliding *flat beams* to make the parameter sets fully consistent. The spot size – clearly indicative of vibration and alignment tolerances – also falls with energy, but even at 100 TeV it remains an order of magnitude above the spot size in the y coordinate for future LC design parameters.

Neutrino radiation is an extremely serious problem for many-TeV muon colliders and further information and discussion on this can be found in these proceedings [4]. The radiation levels are predicted to rise rapidly with the collider energy [4] and beyond CoM energies of a few TeV it may well be necessary to build the colliders at isolated sites where the public would not be exposed to the neutrino radiation disk.

4 CONCLUSIONS

Muon colliders from 10 to 100 TeV CoM energies may offer an exciting long-term future to experimental HEP and are not obviously infeasible to this author. However, they clearly introduce some daunting new challenges beyond those common to all muon colliders and the parameter sets in table 1 will require some technological extrapolations.

5 REFERENCES

[1] The Muon Collider Collaboration, "Status of Muon Collider Research and Development and Future Plans", to be submitted to Phys. Rev. E.

[2] B.J. King, "Discussion on Muon Collider Parameters at Center of Mass Energies from 0.1 TeV to 100 TeV", 19 June, 1998, Submitted to Proc. Sixth European Particle Accelerator Conference (EPAC'98), Stockholm, Sweden, 22-26 June, 1998. Available at http://pubweb.bnl.gov/people/bking/.

[3] The idea to use this parameter emerged through discussions with Frank Zimmermann and Carol Johnstone .

[4] B.J. King, "Potential Hazards from Neutrino Radiation at Muon Colliders", these proceedings.

Table 1: Example parameter sets for 10 TeV and 100 TeV muon colliders. The generation of these parameter sets is discussed in the text. These parameters represent speculation by the author on how muon colliders might evolve with energy. The beam parameters at the interaction point are defined to be equal in the horizontal (x) and vertical (y) transverse coordinates.

center of mass energy, E_{CoM}	10 TeV	100 TeV
collider physics parameters:		
luminosity, $\mathcal{L}$ [$cm^{-2}.s^{-1}$]	1.0×10^{36}	3.1×10^{37}
$\int \mathcal{L}dt$ [fb^{-1}/det/year]	10 000	310 000
No. of $\mu\mu \rightarrow$ ee events/det/year	8700	2700
No. of 100 GeV SM Higgs/det/year	1.4×10^{7}	6.5×10^{8}
fract. CoM energy spread, σ_E/E [10^{-3}]	1.0	0.08
collider ring parameters:		
circumference, C [km]	15	100
ave. bending B field [T]	7.0	10.5
beam parameters:		
(μ^- or) μ^+/bunch,N_0[10^{12}]	2.4	2.0
(μ^- or) μ^+ bunch rep. rate, f_b [Hz]	15	10
6-dim. norm. emittance, ϵ_{6N}[$10^{-12}m^3$]	50	3.5
x,y emit. (unnorm.) [$\pi.\mu$m.mrad]	0.55	0.0046
x,y normalized emit. [π.mm.mrad]	26	22
fract. mom. spread, δ [10^{-3}]	1.4	0.084
relativistic γ factor, E_μ/m_μ	47 322	473 220
ave. current [mA]	24	7.9
beam power [MW]	58	320
decay power into magnet liner [kW/m]	1.4	2.4
time to beam dump, $t_D[\gamma\tau_\mu]$	no dump	0.5
effective turns/bunch	1039	985
interaction point parameters:		
spot size, $\sigma_x = \sigma_y$[nm]	780	93
bunch length, σ_z [mm]	1.1	0.185
β^* [mm]	1.1	0.185
ang. divergence, σ_θ [mrad]	0.71	0.5
beam-beam tune disruption parameter, $\Delta\nu$	0.100	0.100
pinch enhancement factor, H_B	1.108	1.130
beamstrahlung fract. E loss/collision	2.3×10^{-7}	6.5×10^{-4}
final focus lattice parameters:		
max. poletip field of quads., $B_{4\sigma}$ [T]	15	20
max. full aperture of quad., $A_{\pm 4\sigma}$[cm]	20	88
β_{max}[km]	1100	260 000
final focus demagnification, $M \equiv \sqrt{\beta_{max}/\beta^*}$	31 000	1.2×10^{6}
chrom. quality factor, $Q \equiv M\delta$	43	100
synchrotron radiation parameters:		
syn. E loss/turn [MeV]	17	25 000
syn. rad. power [MW]	0.4	200
syn. critical E [keV]	12	1700
neutrino radiation parameters:		
collider reference depth, D[m]	300	300
ν beam distance to surface [km]	62	62
ν beam radius at surface [m]	1.3	0.13
str. sect. length for 10x ave. rad., L_{x10}[m]	1.0	2.4
ave. rad. dose in plane [mSv/yr]	0.66	12.6

A CUPRONICKEL ROTATING BAND PION PRODUCTION TARGET FOR MUON COLLIDERS[1]

B. J. King[2], S.S. Moser[3], R.J. Weggel, BNL[4]; N.V. Mokhov, Fermilab[5]

Abstract

A conceptual design is presented for a high power cupronickel pion production target. It forms a circular band in a horizontal plane with approximate dimensions of: 2.5 meters radius, 6 cm high and 0.6 cm thick. The target is continuously rotated at 3 m/s to carry heat away from the production region to a water cooling channel. Bunches of 16 GeV protons with total energies of 270 kJ and repetition rates of 15 Hz are incident tangentially to arc of the target along the symmetry axis of a 20 Tesla solenoidal magnetic capture channel. The mechanical layout and cooling setup are described. Results are presented from realistic MARS Monte Carlo computer simulations of the pion yield and energy deposition in the target. ANSYS finite element calculations are beginning to give predictions for the resultant shock heating stresses.

1 INTRODUCTION

High power pion production targets are required in current scenarios [1] for muon colliders. The pion secondaries from protons on the target are captured in a solenoidal magnetic channel and decay into the muon bunches needed for cooling, acceleration and injection into the collider ring. Bunched proton beams of several megawatts will be needed for the currently specified muon currents [1]: approximately 6×10^{20} muons of each sign at repetition rates of 15 Hertz and in bunches of up to 4×10^{12} muons per bunch. This is an extrapolation from today's high power targets in rate of target heating, shock stresses and integrated radiation damage to the target.

Because of the high beam power, liquid metal jet targets have been the subject of much recent study and form the bulk of a proposed experimental R & D program of targetry studies that has recently been submitted [2] to the BNL AGS Division. More conventional solid targets have several challenges. Along with concerns about shock heating stresses and radiation damage, it is challenging to design a cooling scenario consistent with both the large beam power and the small target cross sections that are needed for high pion yields.

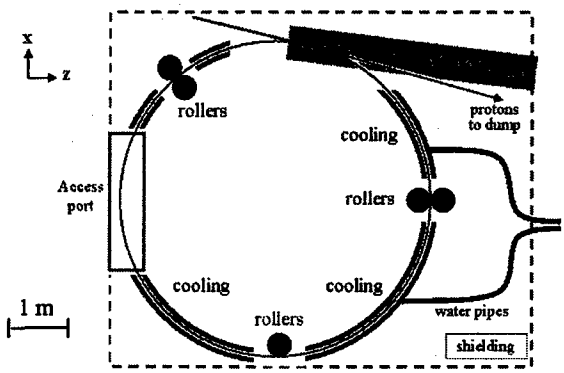

Figure 1: A conceptual illustration of the targetry setup.

This paper introduces the idea of a solid target in the form of a band that addresses this cooling issue by rotating the band to carry heat away from the targetry region and through a cooling channel.

Figures 1 and 2 give *schematic* views of the targetry setup we are considering and figure 3 shows the trajectory of the proton beam into the target band. It must be emphasized that details such as the rollers and cooling setup are only shown schematically and no effort has been put into their design.

The target band is enclosed in a 20 Tesla solenoidal magnetic pion capture magnet whose general design has previously been studied [1] by the Muon Collider Collaboration (MCC). The major design modification specific to this particular geometry concerns the provision of entry and exit ports for the target band.

The high-power bunched proton beam strikes the target band at a glancing angle and travels along inside the target material for two nuclear interaction lengths before the curvature of the band brings it again to an exit point at the outer edge of the band. The beam is tilted at 150 milliradians to the longitudinal axis of the solenoidal magnet; MARS simulations described below show that this gives a larger pion yield than a beam parallel to the solenoid.

2 MARS SIMULATIONS OF TARGET HEATING AND PION YIELD

Full MARS [3] tracking and showering Monte Carlo simulations were conducted for a 16 GeV proton beam of

[1]This work was performed under the auspices of the U.S. Department of Energy under contract no. DE-AC02-98CH10886.

[2]Submitting author, email: bking@bnl.gov .

[3]on academic leave from Saint Joseph's College, Indiana.

[4]Brookhaven National Laboratory, P.O. Box 5000, Upton, NY 11973-5000

[5]Fermi National Accelerator Laboratory, P.O. Box 500, Batavia, IL 60510-0500

0-7803-5573-3/99/$10.00@1999 IEEE.

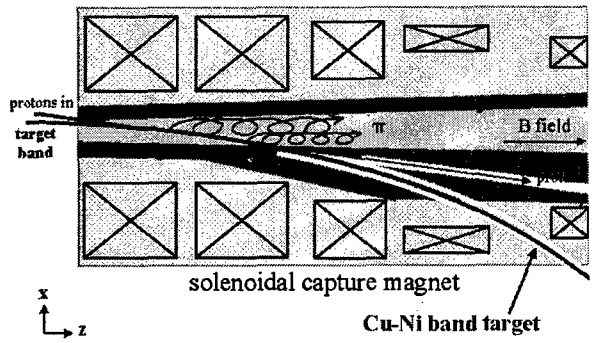

Figure 2: A conceptual illustration of the target layout around the pion production region.

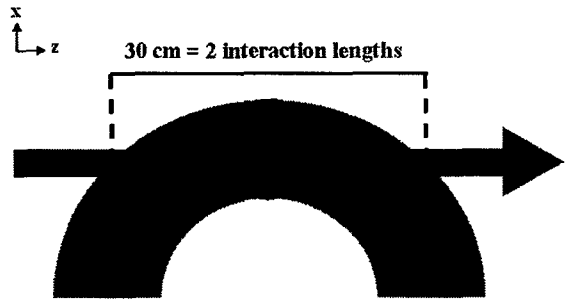

Figure 3: The trajectory of the proton beam into the target band.

1×10^{14} ppp with a repetition rate of 15 Hz on Ni band (R=250 cm, 6 cm height, 0.6 cm thickness) in a 20 T solenoid of R_a=7.5 cm half-aperture. Both untilted targets and targets tilted by α=150 mrad were studied and detailed 3-dimensional maps of energy deposition densities were generated for input to the ANSYS stress analyses.

The yield per proton at 90 cm downstream from the central intersection of the beam with the target was determined for pions plus muons in the momentum range 0.05<p<0.8 GeV/c. The yields of positive and negative pions were, respectively, Y_+ = 0.491 and Y_- = 0.498 at α=0 and Y_+ = 0.622 and Y_- = 0.612 at α=150 mrad. Figure 5 shows the momentum spectra for all hadrons and figure 6 gives more detailed information for the pions. Figure 7 shows the time distribution for when these pions are formed and figure 8 shows several scatter plots to illustrate their distribution in phase space. These pion yields and densities in phase space are comparably good to the predictions for the best of the liquid jet targets under consideration.

The peak energy deposition density was found to be 68.6 J/g per pulse, corresponding to a temperature rise of ΔT=150.5°C. This corresponded to a total power dissipation in the target of 0.324 MW at α=150 mrad. Contributions to the deposited energy come from dE/dx from hadrons and muons (44%), electromagnetic showering (46%) and from absorbtion of sub-threshold particles (10%). Power dissipation in inner layer of tungsten shielding (7.5<r<15 cm) was also determined, and was found to be 0.624 MW at α=0 and 0.766 MW at α=150 mrad.

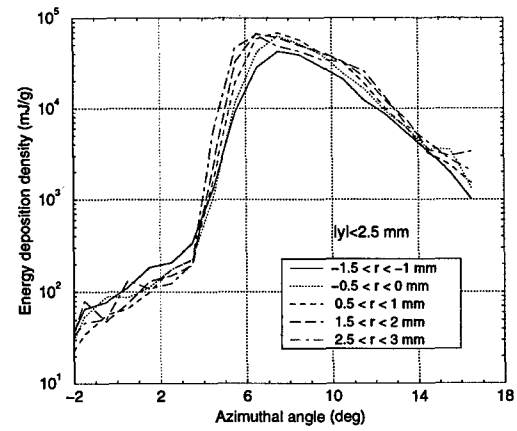

Figure 4: Energy deposition density in the band target *versus* azimuthal angle for a tilt angle α=150 mrad.

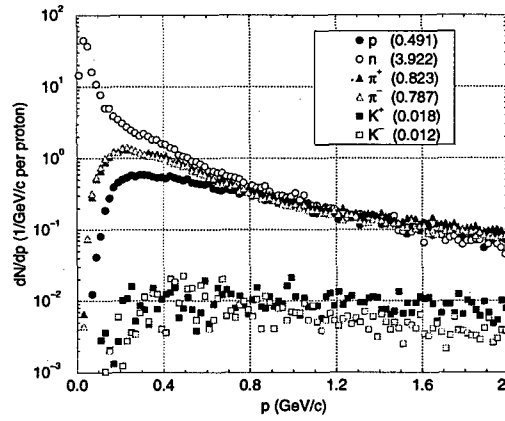

Figure 5: Momentum spectra of hadrons at L=90 cm and R<7.5 cm for a tilt angle α=150 mrad. Integrated yield is shown in parentheses.

3 ANSYS STRESS SIMULATIONS

The survivability of solid targets in the face of repeated shock heating is probably the most challenging problem faced in these scenarios for pion production for muon colliders.

To investigate this, we are beginning to conduct finite element computer simulations of the shock heating stresses

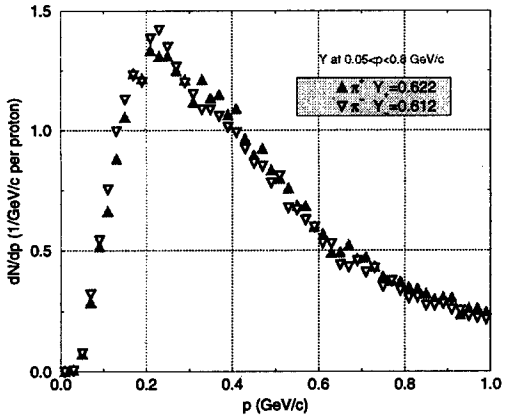

Figure 6: Pion momentum spectra at L=90 cm and R<7.5 cm for a tilt angle α=150 mrad.

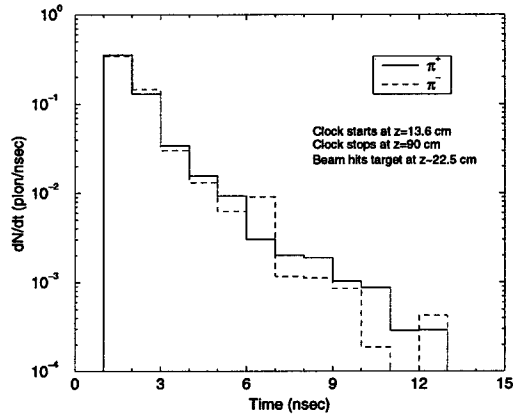

Figure 7: Pion time spectra at L=90 cm and R<7.5 cm for 0.05<p<0.8 GeV/c and a tilt angle α=150 mrad.

using ANSYS, a commercial package that is very widely used for stress and thermal calculations. These studies are still at an early stage.

It is encouraging that the instantaneous temperature rise predicted by MARS of approximately 70 degrees per proton pulse is much less than the 500-600 degree temperature rise in microsecond timescales that the Fermilab pbar source nickel target routinely operates at. Further, if the predicted stresses turn out to be higher than, say, 50% of the target's tensile strength then possibilities exist for redimensioning the target and the proton spot size to reduce the stress.

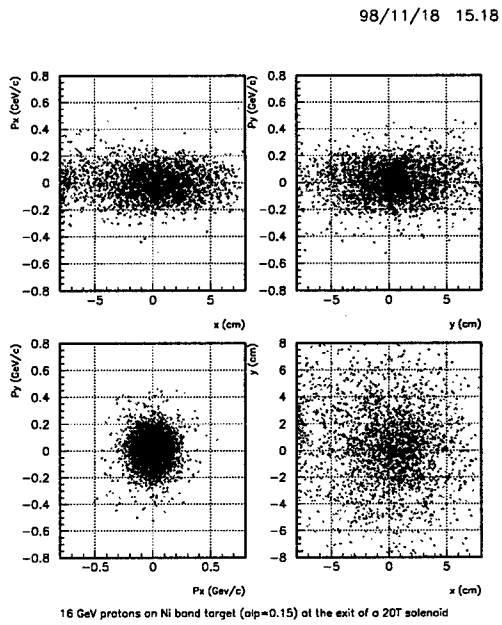

Figure 8: π^+ (red) and $\pi-$ (green) scatter plots at L=90 cm and R<7.5 cm for a tilt angle α=150 mrad.

4 CONCLUSIONS

In conclusion, initial studies indicate that cupronickel rotating band targets may well be a viable and attractive option to satisfy the difficult high power targetry requirements of muon colliders.

5 REFERENCES

[1] The Muon Collider Collaboration, "Status of Muon Collider Research and Development and Future Plans", to be submitted to Phys. Rev. E.

[2] Alessi *et al.*, "An R & D Program for Targetry and Capture at a Muon-Collider Source - A Proposal to the BNL AGS Division". Spokesperson Kirk T. McDonald, email: mcdonald@puphep.princeton.edu .

[3] N.V Mokhov, "The MARS Code System User's Guide, Version 13 (98)", FERMILAB-FN-628 (Feb. 1998).

Muon Colliders - Ionization Cooling and Solenoids*

Z. Parsa, Brookhaven National Laboratory, 901A, Upton, NY 11973, USA

Abstract

For a muon collider, to obtain the needed luminosity, the phase space volume must be greatly reduced within the muon life time. The ionization cooling is the preferred method used to compress the phase space and reduce the emittance to obtain high luminosity muon beams. Alternating solenoid lattices has been proposed for muon colliders, where the emittance are large. We present an overview, discuss formalism, transfer maps for solenoid magnets and beam dynamics.

1 INTRODUCTION

Alternating solenoid lattices has been proposed as desirable for use in the earlier cooling stages of Muon Colliders, where the emittances are large. Since the minimum $\beta_\perp$'s must decrease in order to obtain smaller transverse emittances as the muon beam travels down the cooling channel. This can be done by increasing the focusing fields and/or decreasing the muon momenta, where the current carrying lithium lenses may be used (to get a stronger radial focusing and to minimize the final emittance) for the last few cooling stages. The use of 'bent solenoids' may provide the required dispersion for the momentum measurement. Where the off-momentum muons are displaced vertically by an amount:

$$\Delta y \approx \frac{P}{eB_s}\frac{\Delta P}{P}\theta_{\rm bend}, \qquad (1)$$

where B_s is the field of the bent solenoid and $\theta_{\rm bend}$ is the bend angle. In Fig.1, the bending of the solenoid produce the dispersion required for the longitudinal to transverse emittane exchange. Where after one bend and one set of wedges the beam cross-section is asymmetric then the symmetry is restored by going through the second bend and wedge system (which is rotated by 90 degrees w.r.t. the first) [1].

2 FORMULATION AND MAPS FOR SOLENOIDS

The canonical equations in 2n-Dimensional phase space (e.g. 6 Dim., in our calculation) can be expressed as $\frac{d\psi_i}{dt} = [\psi_i, H]$, $i = 1, 2, \ldots 2n$, and in terms of the Lie transformations as

$$\frac{d\psi_i}{dt} = -:H:\psi_i, \qquad i = 1, 2, \ldots 2n \qquad (2)$$

Where the Lie operator (: H :) is generated by the Hamiltonian, (H), and Lie transformation, $M = e^{-t:H:}$, could

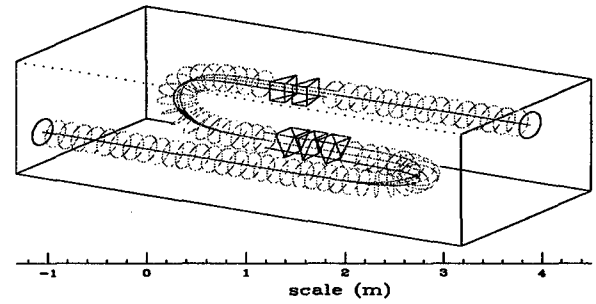

Figure 1: Example of bent solenoids and Wedges - for emittance exchange. May be used for muon collider longitudinal cooling see e.g., Refs. in [1].

generate the solution to Eq. (2) as $\psi_i = M\psi_i(0)$, where ψ_i is the value of $\psi_i(t)$ at $t > 0$ and $\psi_i(0)$ is the initial trajectory. The interest is to find solutions to equations of motion which differ slightly from the reference orbit Thus, one can choose the canonical variables, from the values for the reference trajectory (for small deviations) and Taylor expand the Hamiltonian (H) about the design trajectory $H = H_2 + H_3 + \ldots$. Where H_n is a homogeneous polynomial of degree n in the canonical variables. After transformations to the normalized dimensionless variables, one can obtain the effective Hamiltonian $H^{\rm New}$, expressed as

$$H^{\rm New} = F_2 + F_3 + F_4 \ldots . \qquad (3)$$

Thus the particle trajectory $\vec{\psi} = (X, P_X, Y, P_Y, \tau, P_\tau)$ through a beamline element of length L can be described by $\dot{\psi}_i = -:H^{\rm New}:\psi_i, i = 1, 2, \ldots 2n$. The exact symplectic map that generates the particle trajectory through that element is $M = e^{-L:H^{\rm New}:}$, where M describes the particle behavior through the element of length L. Using the factorization and expanding $H^{\rm New}$ as in Eq. (3), results in

$$M = e^{-L:H^{\rm New}:} = e^{:f_2:}e^{:f_3:}e^{:f_4:}\ldots , \qquad (4)$$

(e.g., for a map through 3rd order we need to include terms of f_2, f_3, and f_4).

To illustrate the above formalism, consider the evolution of the motion of particles in an external electromagnetic field described by the Hamiltonian $H = \sqrt{m^2c^4 + c^2[(p_x - qA_x)^2 + (p_y - qA_y)^2 + (p_z - qA_z)^2]} + e\phi(x, y, z; t)$, where m and q are the rest mass and charge of the particle, A and ϕ are the vector and scalar potentials such that $\vec{B} = \nabla \times \vec{A}, \vec{E} = -\nabla\phi - \nabla\vec{A}/\partial t$.

Making a canonical transformation from H to H_1 and changing the independent variable from time t to z (for convenience) for a particle in magnetic field (e.g. of solenoid) results in $p_z = [(p_z - qA_x)^2 + (p_y - qA_y)^2 + p_t^2/c^2 - m^2c^2]^{1/2}$. Where $H = -p_t$, $H_1 = -p_z$ and $t = (z/v_{0z})$ the time as a function of z. We next make a

* Supported by U.S. Department of Energy Contract Number DE-AC02-98CH10886.

†E-mail: parsa@bnl.gov

canonical transformation from H_1 to $H^{\rm New}$, with a dimensionless deviation variables (for convenience), $X = x/l$, $Y = y/l$, $\tau = c/l(t - z/v_{0z})$, $P_x = p_x/p_0$, $P_y = p_y/p_0$, $P_\tau = (p_t - p_0 t)/p_0 c$, where l is a length scale (taken as 1 m in our analysis), with $\mathbf{P} = \vec{P}_x + \vec{P}_y$ and $\mathbf{Q} = \vec{X} + \vec{Y}$ defined as two dimensional vectors [5], p_0 and $p_0 c$ are momentum and energy scales. Where p_0 is the design momentum, v_{0z} is the velocity on the design orbit and $p_0 t$ is a value of p_t on the design orbit ($p_{0t} = \sqrt{m^2c^4 + p_0^2 c^2}$) (reminding that design orbit for the solenoid is along the z-axis). Thus, expanding the new Hamiltonian Eq. (3) leads to:

$$F_2 = \frac{P_\tau^2}{(2\beta^2\gamma^2)} - \frac{1}{2}B_0(\vec{Q}\times\vec{P})\cdot\hat{+}\frac{1}{8}B_0^2Q^2 + \frac{P^2}{2} \quad (5)$$

$$F_3 = \frac{P_\tau^3}{(2\beta^3\gamma^2)} - \frac{P_\tau}{2\beta}B_0(\vec{Q}\times\vec{P})\cdot\hat{z} + \frac{P_\tau}{8\beta}(B_0^2Q^2 + 4P^2) \quad (6)$$

$$F_4 = \frac{P_\tau^4(5-\beta^2)}{8\beta^4\gamma^2} + \frac{P_\tau^2Q^2B_0^2(3-\beta^2)}{16\beta^2} - \frac{P_\tau^2}{2}(\vec{Q}\times\vec{P})\cdot\hat{z}\frac{B_0(3-\beta^2)}{2\beta^2} + \frac{P_\tau^2}{2}\frac{P^2(3-\beta^2)}{2\beta^2} + \frac{Q^4}{16}(B_0^4 - 4B_0B_2)/8 + \frac{Q^2}{4}\frac{P^2 3B_0^2}{4} + \frac{Q^2}{4}(\vec{Q}\times\vec{P})\cdot\hat{z}(B_2 - B_0^3)/4 - \frac{1}{8}(\vec{P}\cdot\vec{Q})^2B_0 - \frac{P^2}{4}(\vec{Q}\times\vec{P})\cdot\hat{z}B_0 + \frac{P^4}{8} \quad (7)$$

Following the Hamiltonian flow generated by:

$H^{\rm New} = F_2 + F_3 \ldots$

from some initial ψ_0 to a final ψ_f coordinates we can calculate the transfer map M (Eq. (4)) for the solenoid. Where F_2, F_3, and F_4 would lead to the 1st, 2nd, and 3rd order maps. The effects of which can be seen from Eqs. (5–7). For example, the 2nd order effects due to solenoid transfer maps are purely chromatic aberrations Eq. (6). In addition, we note the third order geometric aberrations Eq. (7). As shown by Eqs. (5–7), the coupling between X, Y planes produced by a solenoid is rotation about the z-axis which is a consequence of rotational invariance of the Hamiltonian $H^{\rm New}$, due to axial symmetry of the solenoid field. For beam simulations, M can be calculated to any order using numerical integration techniques such as Runge-Kutta method depending on the computer memory and space available [5].

3 HIGHER ORDER KINEMATIC INVARIANTS AND CORRELATIONS:

Let $\rho(\psi)$ be the distribution of particles in phase space at any instant e.g. $d^6N = \rho(\psi)d^6\psi$, where d^6N and $d^6\psi$ are the number of particles, and small volume in the 6-dimensional phase space ($\psi = [\vec{q}, \vec{p}], q_i, p_i = 1, 2, 3$), respectively. Let $\rho(M^{-1}\psi)$ be the final distribution at the end of the system such that a set of initial moments are ($j \doteq$ index), defined as $k_j^0 \equiv \int \rho(\psi)F_j(\psi)d^6\psi$. Where the final moments become $k_j^f = \int \rho(\psi')F_j(M\psi')d^6\psi'$ with $F_j(M\psi) = \sum D_{j\ell}(M)F_\ell(\psi)$, ($D_{j\ell}$ is a matrix and $F_j(\psi)$ are a complete set of homogeneous polynomials.) Thus, the moment transport can be expressed in a simple form as $k_j^f = \sum_\ell F(M)_{j\ell}k_\ell^0$. $D_{j\ell}(M)$ are quadratic functions of matrix elements M_{ij}.

In 6-Dim. phase space, there are 3 functionally independent kinematic invariants made up of quadratic moments, e.g. ϵ_x^2, ϵ_y^2, ϵ_τ^2, such that $I_2(k) = \epsilon_x^2 + \epsilon_y^2 + \epsilon_\tau^2$, $I_4(k) = \epsilon_x^4 + \epsilon_y^4 + \epsilon_\tau^4$, and $I_6(k) = \epsilon_x^6 + \epsilon_y^6 + \epsilon_\tau^6$, or in general $I_n(k) = \frac{1}{2}(-1)^{n/2}t_{\rm v}(\psi J)^2$, where $\psi = 6\times 6$ matrix, whose entries are moments, $\psi_{jk} = \langle\psi_j\psi_k\rangle$, with $I = 3\times 3$ identity matrix and $J = -\begin{bmatrix} 0 & I \\ -I & 0 \end{bmatrix}$. E.g., $I_2(k) = \langle x^2\rangle\langle p_x^2\rangle - \langle xp_x^2\rangle + \langle y^2\rangle\langle p_y^2\rangle - \langle yp_y\rangle^2 + \langle\tau^2\rangle\langle p_\tau^2\rangle - \langle\tau p_\tau\rangle^2 + 2\langle xy\rangle\langle p_x p_y\rangle - 2\langle xp_y\rangle\langle yp_x\rangle + \ldots$. This is a generalization of 2-Dim. mean square emittance (e.g. see Refs. [2, 5]). Thus, higher order kinematic invariants (e.g. cubic and quartic moments); and correlations between various degrees of freedom may be constructed, and used as a tool, in nonlinear dynamic studies. E.G., for a beam transport system one may use an invariant: $I \equiv \langle x^2\rangle\langle p_x\rangle^2 + \langle p_x^2\rangle\langle x\rangle^2 - 2\langle xp_x\rangle\langle x\rangle\langle p_x\rangle$ constructed from a linear and quadratic moments. Noting that, the inclusion of correlations between the variables may be detrimental in (the accuracy of) beam dynamic studies.

4 MUON COOLING

Muon colliders have the potential, to provide a probe for fundamental particle physics. To obtain the needed collider luminosity, the phase-space volume must be greatly reduced within the muon life time. The Ionization cooling is the preferred method used to compress the phase space and reduce the emittance to obtain high luminosity muon beams. We note that, the ionization losses results not only in damping, but also heating: transverse heating appears due to multiple Coulomb scattering and longitudinal one is due to so named "straggling" of the ionization losses (we note that, this straggling is produced by fast "knock-on" ionization electrons), e.g. see [4]. The longitudinal muon momentum is then restored by coherent re-acceleration, leaving a net loss of transverse momentum (transverse cooling).To achieve a large cooling factor the process is repeated many times. The transverse cooling can be expressed (neglecting correlations) as

$$\frac{d\epsilon_n}{ds} = \frac{1}{\beta^2}\frac{dE_\mu}{ds}\frac{\epsilon_n}{E_\mu} + \frac{1}{\beta^3}\frac{\beta_\perp(0.014GeV)^2}{2\,E_\mu m_\mu\,L_R} + \ldots, \quad (8)$$

where β = v/c, ϵ_n is the normalized emittance, $\beta_\perp$ is the betatron function at the absorber, dE_μ/ds is the energy loss, and L_R is the radiation length of the material. The first term in this equation is the cooling term, and the second is the heating term due to multiple scattering. To minimize the heating term, a strong-focusing (small $\beta_\perp$) and a low-Z absorber (large L_R) is needed.

In obtaining Eq. 8, the correlations were neglected (as e.g. in the Status Report see [1]), e.g. $\langle xP_x\rangle = 0$), and the relation $\langle x^2\rangle = \epsilon\beta_\perp = \frac{\epsilon_n\beta_\perp}{\gamma\beta}$ was used, which can not be

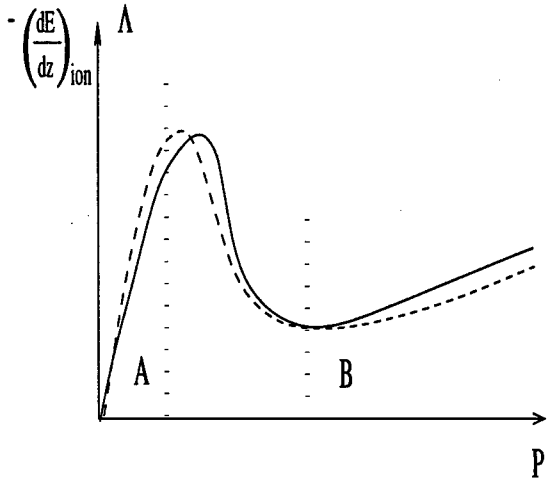

Figure 2: Schematic of the dependence of ionization losses on momenta.

assumed if the correlations are properly taken into account. Thus, if $\langle xP_x \rangle \neq 0$ then transverse cooling to be expressed as

$$\frac{d\epsilon_n}{ds} = \frac{1}{\beta^2}\frac{dE_\mu}{ds}\frac{\epsilon_n}{E_\mu} + \frac{1}{\beta^3}\frac{\langle x^2\rangle (0.014GeV)^2}{2\epsilon_n E_\mu m_\mu L_R} + ..., \quad (9)$$

As in Fig. 1, by introducing a transverse variation in the wedge (absorber) density or thickness, where there is dispersion (i.e. the transverse position is energy dependent), the energy spread, and the longitudinal emittance can be reduced. As we noted earlier, from theoretical point of view, a situation with ionization cooling completely corresponds to a situation with radiation cooling whose theory is well developed. For some standard "hierarchy" of methods for analyzing such systems see e.g. Ref. [4].

In ionization method, muons passing through a material medium lose momentum and energy through ionization interactions in transverse and longitudinal directions. The normalized emittance is reduced due to transvers energy losses. The curve in Fig. (2) shows the dependence of ionization losses on momenta. Damping rates (decrements) of individual particles in the absence of wedges (natural damping rate) are defined by the following formula:

$$\lambda_\perp = -\frac{dE}{dz}_{ion}\frac{1}{2\beta^2\gamma mc^2}$$

$$\lambda_\parallel = -\frac{1}{z}\frac{d}{dp}\left[\left(\frac{dE}{dz}\right)_{\rm ion}\frac{1}{v}\right] \quad (10)$$

Where $\lambda_\perp$ and $\lambda_\parallel$ are natural transverse and longitudinal damping respectively. Here $\left(\frac{dE}{dz}\right)_{\rm ion}$ is the ionization losses of energy, m is the muon mass, β, γ are relativistic parameters, p, v are momentum and longitudinal velocity of muons being cooled. It was established, that the sum of all increments is invariant of the cooling system: $\Lambda = 2\lambda_\perp + \lambda_\parallel$. This curve is also plotted in Fig. (2) (as the dotted line). In Fig. (2) we see that there are two natural regions for cooling: region A ("frictional cooling") and region B ("ionization cooling" for intermediate and high energies). Frictional Cooling is convenient only for cold (low energy) muons (e.g. Kinetic energy 10 to 150 KeV), and therfore it is difficult to use for high energy muon source, (in addition to big noises due to coulomb scattering etc.). Classical Ionization Cooling is useable for kinetic energy range of 30 to 100 MeV. Which due to abscence of "natural" longitudinal cooling it is necessary to use "wedges" for which R & D is needed. A propsal for such studies is being considered [1].

5 MUON COOLING "MERIT FACTOR"

Luminosity of collider L is defined by the following expression:

$$L \sim \frac{N^2 f}{g_x g_y} = \frac{N^2 f}{\epsilon_\perp^f \cdot \beta_\perp^f} \quad (11)$$

Where N = a number of muons per bunch, f = mean repetition frequency of collisions, $\epsilon_\perp^f$ = emittance at collision point and $\beta_\perp^f$ = β-function at collision point. Usually $\beta_\perp^f$ is limited by condition: $\beta_\perp^f \geq \sigma_z^f$ where σ_z^f is a longitudinal bunch size. Let us assume, that: 1) $\frac{\Delta p_f}{p}$ is known (monochromatic experiments); 2) we can redistribute emittances inside a given six-dimensional phase volume. Then, taking into account losses in the cooling system, we can rewrite Eq. (11) in the following form:

$$L \sim \frac{N_0^2 \exp\left(-\frac{2}{cT_0}\int_0^z \frac{dz}{\gamma(z)}\right) D^2}{\sqrt{V_6^N \cdot \epsilon_\parallel^f}} \cdot \left(\frac{\Delta p}{p}\right)_\parallel^f \quad (12)$$

Here "N_0" is a number of particles at an entrance of the cooling system, "exp" describes muon decay, "D" describes muon losses in cooling section, and "V_6^N" is an invariant six-dimensional phase volume of muon beam.

Thus we can introduce "merit factor" which describes a quality of muon cooling system. We obtain

$$R = \frac{D^2 \exp\left[-\frac{2}{cT_0}\int_0^z \frac{d_z}{\gamma(z)}\right]}{\sqrt{V_6^N}} \quad (13)$$

Note that, the dependence on V_6^N may be stronger. With account of all the circumstances, we can write

$$R \sim (V_6^N)^\alpha \quad (14)$$

with α in interval (0.5; 2/3). For more info. see Refs. [1-5].

6 REFERENCES

[1] Status of Muon Collider Research and Development and Future, BNL Report BNL-65623; MUCOOL Collab (S. Geer) proposal (April 15, 1998). *Future High Energy Colliders* Z. Parsa, ed., AIP CP **397**, 1997.

[2] Z. Parsa, ed., *Beam Stability and Nonlinear Dynamics*, AIP-Press CP **405**, 1997.

[3] K. McDonald TN/98-17 (98). b) J. Norem, Private Comm.

[4] Z. Parsa, Ionization Cooling and Muon Dynamics, in *Physics Potential & Development of Muon-Muon Colliders*, AIP CP 441, pp 289-294 (1998).

[5] E.g., used in L. Gluckstern, F. Neri, G. Raingarajan, & A. Dragt, Univ. of Maryland Note (1988) and MARYLIE; W. Lysenko, M. Overley, AIP CP 177, (1988). Z. Parsa, Proc. of IEEE 0-7803-1203,p. 509 (1993).

PION YIELD VS. GEOMETRY OF TARGET AND ~20 T PULSE SOLENOID FOR A MUON COLLIDER EXPERIMENT

R. J. Weggel[♠], BNL[♥], Upton, NY and N.V. Mokhov[♦], FNAL[♣], Batavia, IL

Abstract

The Muon Collider Collaboration is proposing a pion-capture experiment that employs BNL's Alternating Gradient Synchrotron, a liquid metal target, and a pulse solenoid precooled by liquid nitrogen. This paper compares the yield with various target diameters, orientations and magnetic field profiles. To equalize costs, all magnets have the same mass, 12 metric tons. The magnet has two nested shells, energized sequentially. The outer set of coils, energized at 4 MVA, generates ~1/3 of the field in the target, most of the field downstream from it, and stores ~21 MJ, from which to energize the inner coil.

The computer code MARS predicts that the meson yield 5 meters from the target can be ~0.35 per 16-GeV proton. This is with a mercury target of 20 mm diameter and 0.3 m length, tilted 100 mr from the field axis. The magnet field is 20 T, averaged over the target, ramping downward as $(1+5z)^{-1}$ over a 3 m length, while the bore increases inversely with the square root of the field.

1 NEED TO MODEL PION CAPTURE

To supply the particles for a muon collider [1] one needs three components. One is a source of nanosecond bunches of protons of multi-GeV energy. Another is a target in which the protons generate mesons (~95% pions and ~5% kaons), which decay into muons. The third component is a solenoid of large field and bore, to capture the mesons by bending their trajectories into helices spiralling around field lines. One seeks to maximize the yield of muons per unit proton energy, and to minimize the volume of their phase space, for the sake of high collider luminosity.

2 TARGET & PION-CAPTURE MAGNET

The energy deposition from the proton beam is nearly instantaneous and may be of so high a density as to produce a violent shock wave in the target. A liquid jet is immune from permanent damage but, if electrically conducting, will decelerate and deform from Lorentz interactions with the field. To observe the behavior of the jet in the magnetic field, and thereby to assess its suitability as a target, is one goal of the pion-capture experiment.

♠Email: weggel@bnl.gov

♥Supported by U.S. Dept. of Energy, contract #DE-AC02-98CH10886

♦Email: weggel@bnl.gov

♣Work supported by the Universities Research Association, Inc., under contract DE-AC02-76CH00300 with the U.S. Department of Energy

To capture most of the forward-directed mesons generated in the target requires a large volume of intense field. Capture to a transverse momentum of 225 MeV/c needs 3 T-m—e.g., 20 T in a bore of 0.15 m. A continuous-field magnet of this performance is too expensive, either for the superconducting magnet or for the power supply. The constraint on power dictates a system pulsed from liquid nitrogen temperature, which improves the initial electrical conductivity by a factor of about seven. A crucial additional innovation is to employ two nested sets of coils, as in Fig. 1, energized sequentially. The modest power supply available to BNL, 16 kA at 250 V, energizes only the massive outer set of coils, which inductively stores ~21 MJ. Insertion of a 125 mΩ resistor across its terminals then provides a voltage—initially 2 kV—to energize the inner coil quickly to high field.

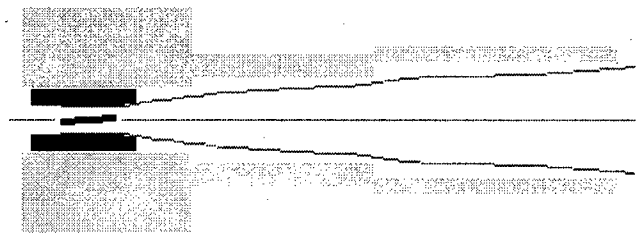

Figure 1: Pion-capture magnet, with average field B_0 in target, $-0.3<z<0$ meters. Magnet mass = 12 metric tons. 4 MW, 21 MJ outer set of coils energizes inner coil. Bore is ~0.15 m near target, ~0.6 m at mouth, z=L. For $0<z<L$, the field profile ramps downward as $B_0/(1+z/L)$. The cone is the envelope of captured mesons.

2.1 Design of LN_2-Precooled Pulse Magnet

The prediction of magnet performance is complicated by the increase in resistance of each coil as it heats up during the pulse. Another complication is the inductive crosstalk between coils. This complexity precludes an analytical solution. Instead, one partitions the pulse into dozens of brief time intervals, in each of which one approximates the current, temperature and resistance of each coil as a power series of order 2 or more.

In a typical system, energizing the outer coil set takes about 20 seconds. Its peak field reaches ~10 teslas. Energizing the inner coil to its peak field of ~13 T takes only ~0.3 s. Meanwhile, the field from the outer set of coils has decayed to ~7 T, for a total of ~20 T. The total field is within 10% of its peak for ~0.8 s. When the inner coil has approximately doubled in resistance, insertion across its terminals of a resistor of ~0.2 Ω dumps its current, dissipating most of its stored energy at room temperature and

0-7803-5573-3/99/$10.00@1999 IEEE.

limiting its peak temperature rise to ~40 K. The total energy dissipated in the coils themselves is ~32 MJ—enough to boil off 200 liters of liquid nitrogen. Figure 2 graphs these parameters for the L=3 m magnet of Fig. 1.

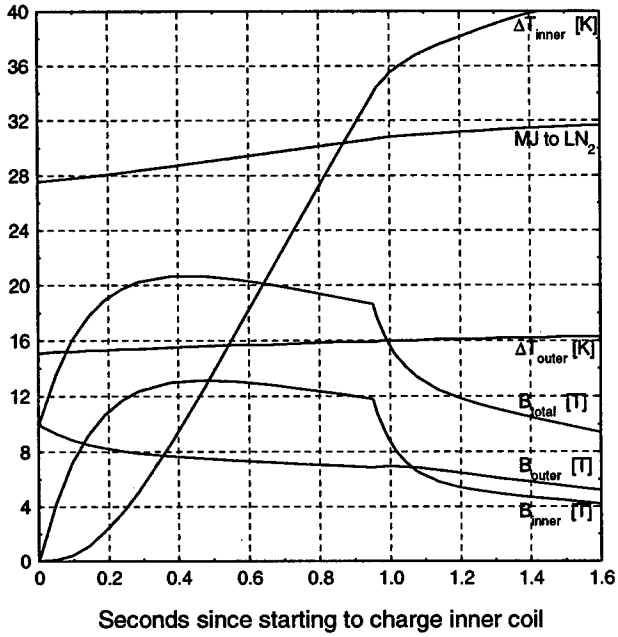

Figure 2: Field, temperature rise and cumulative heat dissipation vs. time in pulse magnet of Fig. 1, in which a 4 MW outer set of coils energizes the inner coil. The fields are at z=–0.15 m, halfway down the target.

2.2 *Peak Field vs. Field Profile of Magnet*

For the magnets of Fig. 1, with their fixed mass and peak power, the field within the target depends on the field profile further downstream—the more gradual the downramp (the greater the length L), the lower the peak field. Figure 3 shows that if the ramp length L=2 m, then B_0, the average field in the target, is 20.9 T; if L=3 m, B_0 is 20.0 T; and if L=5 m, B_0 is only 17.3 T.

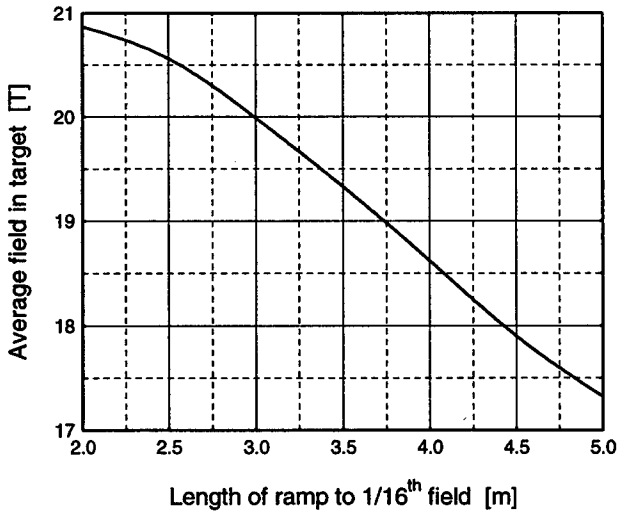

Figure 3: Field, averaged over the target, of the magnet of Fig. 1, vs. the length L that defines the field profile, $B(z)=B_0/(1+15z/L)$, for $0<z<L$.

3 PION YIELD AT Z=L & Z=5 METERS

The full Monte Carlo with the latest version of the computer program MARS(13)99 [2] predicts with unprecedented accuracy the production and trajectories of particles. The MARS simulation implements fully the target and magnetic field geometry as described above. Within the target the field is uniform, B_0; downstream, over a length L, it decays sixteenfold as $B(z) = B_0/(1+k\ z) \equiv B_0/\zeta$. For z>L, $B = B_0/16$. The aperture radius $r(z) = 0.075\ \zeta^{1/2}$. Maxwellian expansion, to 2nd order, of the on-axis field gives the field components off axis as:

$$B_z(r,z) = (B_0/\zeta)\ [1 - 0.5\ (k\ r/\zeta)^2]$$

$$B_r(r,z) = 0.5\ B_0\ [k\ r/\zeta^2]\ [1 - 0.75\ (k\ r/\zeta)^2]\ .$$

The program predicts the power dissipation in the target and in the first 50 mm radial depth of the solenoid windings, and predicts the residual dose rate in the target and solenoid. It also provides complete information on the particles at the solenoid mouth z=L, and at z=5 meters. The target is tilted about its center, z=–0.15 m, by up to 150 milliradians. The particle momenta ranges are $0.05<p_\pi<0.8$GeV/c and $0.1<p_\mu<0.6$GeV/c. Results are rather close to those with a simple $p_t<0.225$ GeV/c cut.

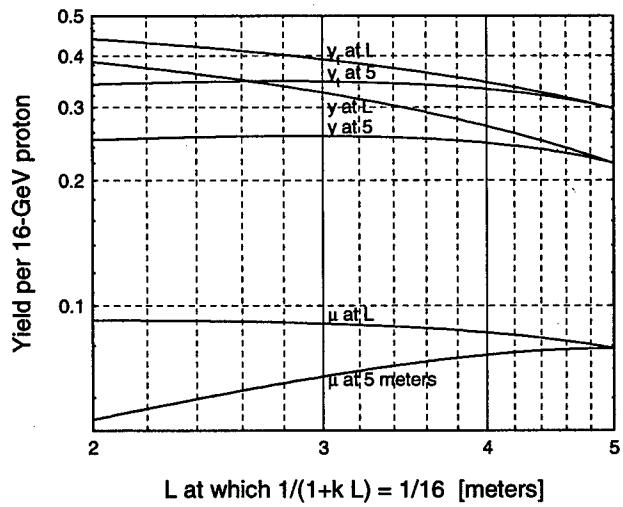

Figure 4: Meson yield per 16-GeV proton. Beam: $\sigma_x=\sigma_y=$ 4mm. Target: Hg, 20 mm dia. by 0.3 m long, tilted 50 mr. $y\equiv\pi+K$; $y_t=y+\mu$.

Pion momentum spectra at z=5 m (Fig. 5) are peaked at p_m=200 MeV/c. One can see about 20% more negative than positive pions when $p_\pi<p_m$, and 20% fewer when $p_\pi>p_m$. Most of the pions have rather low transverse momenta, with the distribution having two pronounced slopes: steep at $p_t<100$ MeV/c and shallow at higher momenta (Fig. 6). Radial distribution of pion flux at z=5 m is shown in Fig. 7. One sees that the entire system focuses generated pions rather well. It is true for produced muons and other particles, too. Good focusing properties of the

proposed configuration are confirmed by a compact phase space—and emittance appropriately—as shown in Fig. 8 for pions at the exit from the matching solenoid.

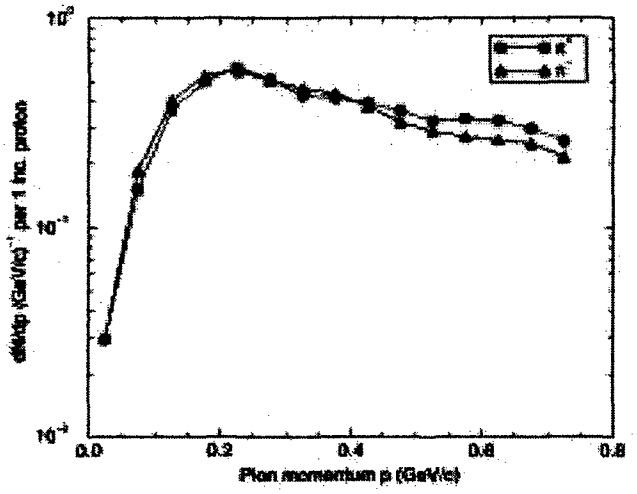

Figure 5: Pion momentum spectra at z=5 m.

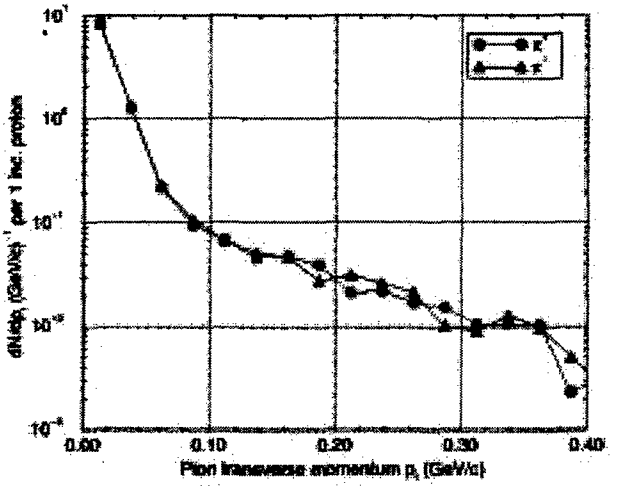

Figure 6: Pion transverse momentum distribution at z=5 m

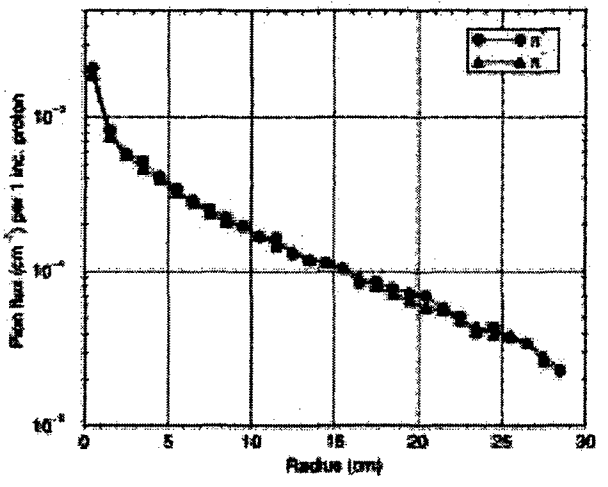

Figure 7: Lateral distribution of pion flux at z=5 m.

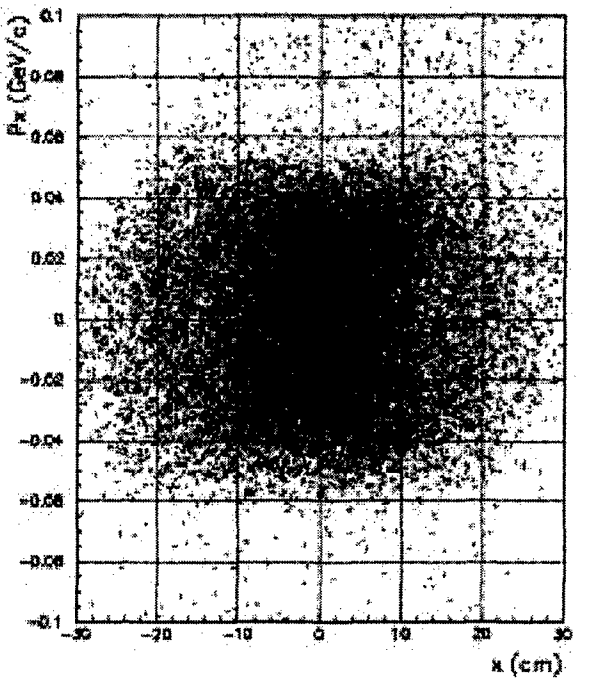

Figure 8: Horizontal phase space scatter plot for π^+ at z=5m.

5 REFERENCES

[1] C. M. Ankenbrandt et al., "Status of Muon Collider Research and Development and Future Plans," Fermilab-Pub-98/179 (1998)

[2] N. V. Mokhov, "The MARS Code System User Guide, Version~13 (95)," LANL Report LA-UR-98-5716 (1998); nucl-th/9812038 v2 16 Dec 1998; http://www-ap.fnal.gov/MARS/

50×50 GeV $\mu^+\mu^-$ COLLIDER BEAM COLLIMATION *

A. I. Drozhdin†, C. J Johnstone, N. V. Mokhov, FNAL, Batavia, IL
A. A. Garren, LBNL, Berkeley, CA
V. M. Biryukov, Institute for High Energy Physics, Protvino, Russia

Abstract

A summary of different techniques and systems to scrape beam halo in a 50×50 GeV $\mu^+\mu^-$collider is presented. Such systems are installed in a special utility section with optics specifically designed to meet both the requirements of the scraping system and of injection. Results from a realistic Monte Carlo simulation (STRUCT-MARS) show that a system consisting of steel absorbers several meters in length suppresses halo-induced backgrounds in the collider detector by more than three orders of magnitude. The heat load in superconducting magnets near the scraper system can be reduced to tolerable levels by appropriate collimator design and location. This reduction applies to both injection and collider mode of operation. Also discussed is extraction of halo particles using electrostatic deflectors and bent crystals, although neither appears to be effective for a muon collider at this energy.

1 INTRODUCTION

The halo-originated background in a $\mu^+\mu^-$collider detector arises from muons which strike and subsequently interact in the physical apertures of the machine[1, 2]. Muons lost anywhere along the lattice contribute to the source term, because they can penetrate through tens and hundreds meters of lattice components. Only with a dedicated beam cleaning system far from the interaction point (IP) can one mitigate this problem[1, 3]. Three beam halo scraping schemes are investigated here for a 50×50 GeV $\mu^+\mu^-$collider:

- collimation using a solid absorber,
- halo extraction using electrostatic deflectors,
- halo extraction using a bent crystal.

Previously, our studies[1, 3] showed that no absorber—ordinary or magnetized—will suffice for beam cleaning at high energies (2 TeV); in fact the disturbed muons are often lost in the IP vicinity. At 50 GeV, on the other hand, scraping muon halo with a steel absorber is exceptionally effective. The second scheme is attractive because halo muons which spill into the deflector gap are completely extracted from the machine and can be directed into a beam dump. Only those muons interacting with the septum wires appear to be lost on the limiting apertures in the machine. The third scheme with a Si bent crystal is inexpensive and compact, and, therefore, its efficiency is also studied in this paper.

A 50 GeV beam of 4.2×10^{12} muons with a normalized emittance of 90π $mm \cdot mrad$ is assumed in the simulations. A utility section of about 100 m long was incorporated into the collider lattice on the side of the ring opposite to the IP[4] (Fig. 1). It consists of two identical cells with phase advance of about π between cells and two matching regions. A large β-function of 100 m in horizontal and vertical planes was designed into the lattice in order to scrape efficiently. A high dispersion is also required to intercept and scrape the tails of the energy distribution. Monte-Carlo simulations of the beam halo collimation are done in three steps. Primary muon interactions with a collimator and electrostatic deflector wires are simulated with the MARS code[5]. Multi-turn muon tracking in the collider lattice with scattering in collimators and bent crystals and the analysis of particle losses on physical apertures are performed using the STRUCT code[6] supplemented with CATCH[7]. Following this, full-scale hadronic and electromagnetic shower simulations in the collider and detector components are tracked in MARS.

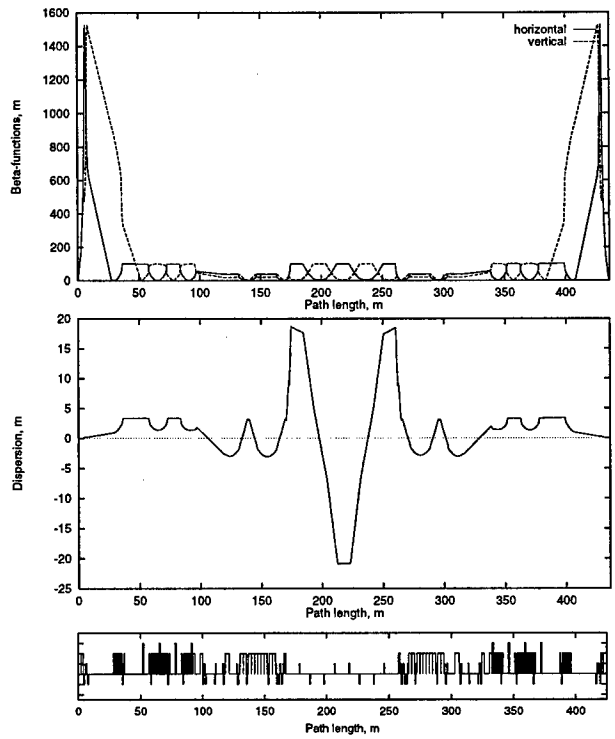

Figure 1: Muon collider β-functions and dispersion.

* Work supported by the U. S. Department of Energy under contract No. DE-AC02-76CH03000
† Email: drozhdin@fnal.gov

2 SOLID ABSORBER

Horizontal collimators are placed in the high-β and high-dispersion region with a π-phase advance between them (Fig. 2). Vertical collimators are installed in a high vertical β region with a $\pi/2$ phase advance downstream of the horizontal ones. On average, 50 GeV muons loose 8% of their energy and receive a significant angular deflection (Fig. 3) after interacting with a 4 m long steel absorber. As a consequence, almost all of the scraped muons are lost in the utility section (where in this scheme conventional magnets can be used) or in the first 50 m downstream (in a superconducting part of lattice, Fig. 4).

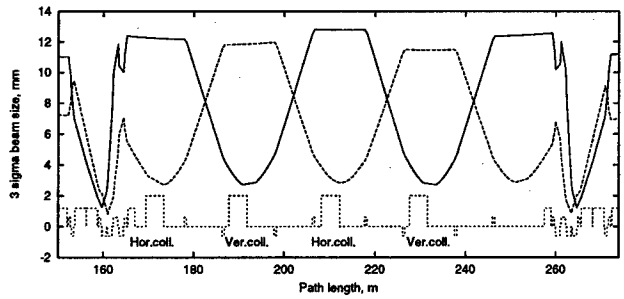

Figure 2: A 3σ horizontal (solid) and vertical (dashed line) beam envelopes in the scraping region with an absorber.

The power density distribution in the SC coils is strongly nonuniform azimuthally, peaking—contrary to the decay-induced process—on the inner side of the magnet aperture relative to the ring center. As shown in[1], the heat load to the SC can be reduced to an acceptable level with a tungsten liner. Assuming 1% of the beam is scraped, about 4×10^6 muons are lost at the IP over the first few turns after injection. Later—during collisions—muons hit the absorber with a very small impact parameter ($\sim$ μm) undergoing smaller orbit distortions than at the beginning of the store. Assuming 5% of the beam is scraped over the duration of the store, 6×10^7 muons in total are lost at the IP.

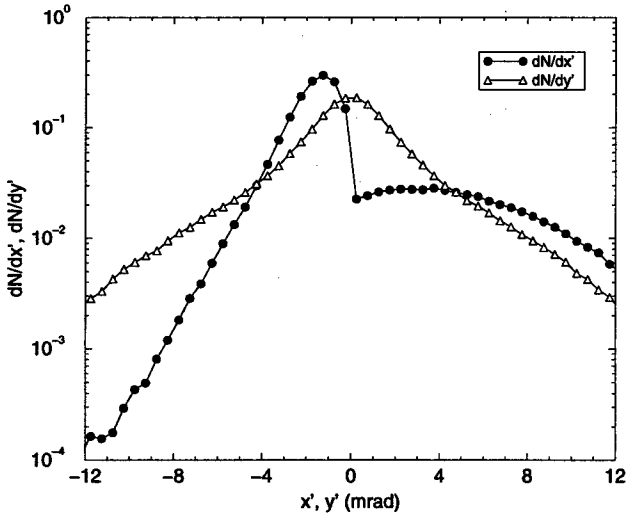

Figure 3: Muon angular distribution after a 4-m steel half-absorber (x>0) at 50 GeV.

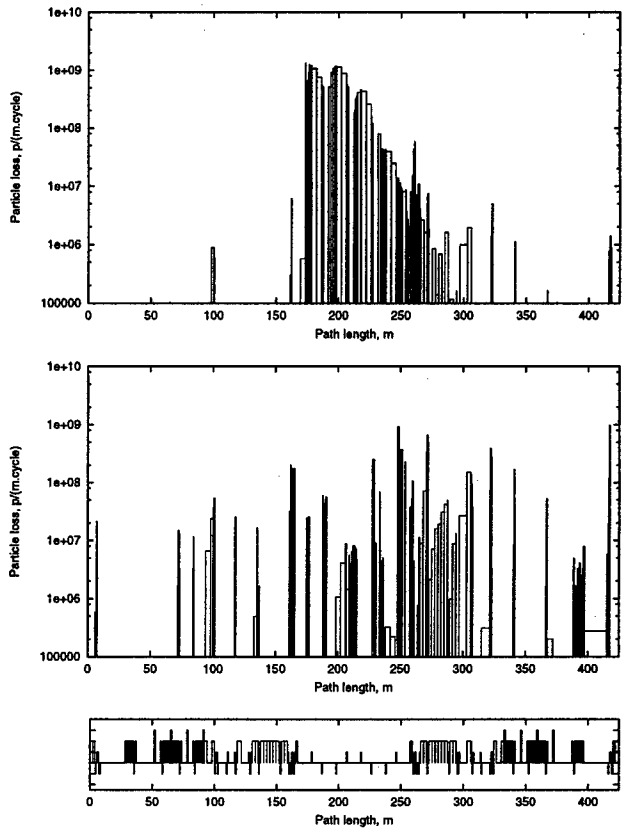

Figure 4: Beam loss at injection with scraping using a 4 m steel absorber (top) and with halo extraction (bottom).

3 HALO EXTRACTION

In this scheme, a horizontal scraping section consists of an electrostatic deflector $ES(h)$ positioned at 3σ off-axis to clean the μ^+ and μ^- beams simultaneously, and two Lambertson magnets $LAMB(h)$ positioned symmetrically at approximately a phase advance of π away from $ES(h)$ (Fig. 5). Such a scheme extracts muons with Δp of both signs. Vertical halo extraction is done by a separate electrostatic deflector $ES(v)$ and a septum-magnet $SM(v)$ for each beam. The beam halo is separated from the circulating beam at the entrance to $LAMB(h)$ and $SM(v)$ (Fig. 6) which allows magnetic septa to be placed between the beams. Large amplitude and halo muons scatter from the ES wires are extracted by $LAMB(h)$.

In this scheme, about 86% of beam halo is extracted from the collider. Muons interacting with the ES wires, loose on average 0.2% of their energy and are mostly lost in the first 50 m downstream of the utility section (Fig. 4). Unfortunately, a significant fraction of them reaches the low-β region upstream of IP and are lost there at the rate significantly higher than in the first scheme. With 1% of the beam scraped at injection and 5% over the store, one obtains 3.5×10^8 and 5×10^9 muons, respectively, lost in the IP region. It has been shown in[1, 3] that in the high-energy 2×2 TeV $\mu^+\mu^-$collider, this extraction-based scraping has a very high efficiency.

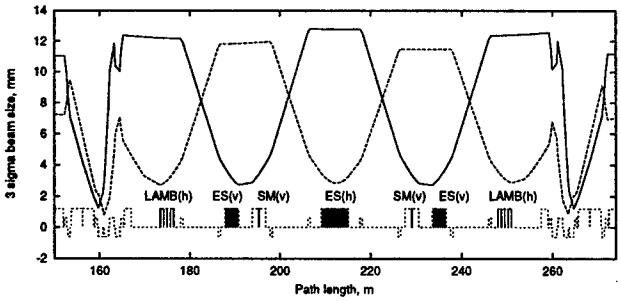

Figure 5: A 3σ horizontal (solid line) and vertical (dashed line) beam envelope for the halo extraction section.

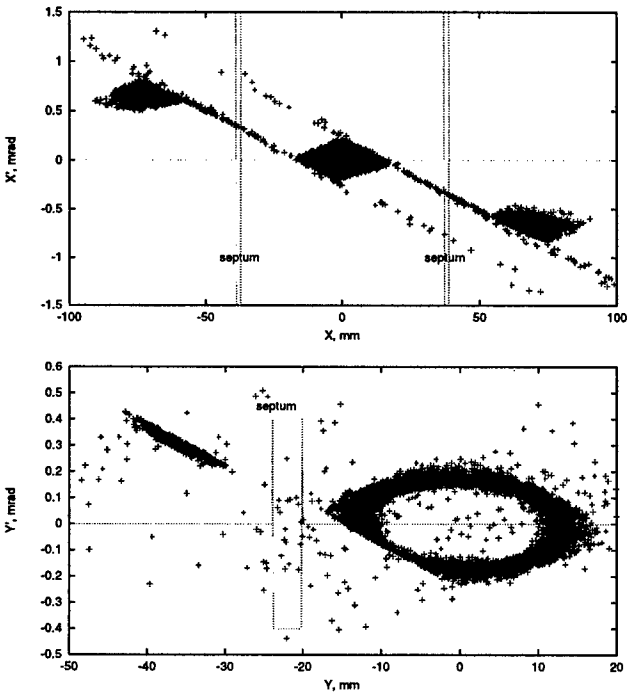

Figure 6: Halo phase space at the entrance to $LAMB(h)$ (top) and $SM(v)$ (bottom).

4 BENT CRYSTAL EXTRACTION

The Si crystal length needed to bend a 50 GeV muon beam by 3 mrad is equal to 5 mm. The natural divergence of the beam in the high-β regions is ± 0.15 mrad and the critical angle in a Si bent crystal is $\pm 20\mu$rad. Therefore one can expect an extraction efficiency of only 13%, which is unacceptably low. In addition a narrow angular acceptance requires the bent crystal to be aligned to $\pm 5\mu$rad with respect to the beam. Simulations performed show that only a few percent of the beam halo is extracted from the collider at 50 GeV. The rest is scattered by the crystal as by an amorphous target, and is lost at collider apertures. The calculated background in the detector is tremendously larger compared to the first two schemes.

5 CONCLUSIONS

The studies of halo scraping performed for a 50×50 GeV $\mu^+\mu^-$collider show that a simple and compact absorber-based beam cleaning system provides excellent suppression of the beam loss rate and backgrounds in the collider detector vicinity. That is about hundred times better than with a system based on the halo extraction. In addition, the heat load to the superconducting magnets downstream of the non-superconducting scraping section is higher for the halo extraction scheme compared to the absorber-based system. In any case, a tungsten liner (or other methods) is needed there to protect a group of the superconducting magnets. The use of a bent crystal for halo extraction at the given muon beam parameters was found to be very inefficient.

6 REFERENCES

[1] A. Drozhdin, N. Mokhov, C. Johnstone, W. Wan and A. Garren, "Scraping Beam Halo in $\mu^+\mu^-$Colliders", Fermilab-Conf-98/042 (1998) and Proceedings of the 4th International Conference on Physics Potential and development of $\mu^+\mu^-$Colliders, p. 242, San Francisco, CA (1997).

[2] C. M. Ankenbrandt et al., "Status of Muon Collider Research and Development and Future Plans", Fermilab-Pub-98/179 (1998).

[3] A. Drozhdin, C. Johnstone and N. Mokhov, "2×2 TeV $\mu^+\mu^-$Collider Beam Collimation System", Workshop on Muon Collider, Orcas Island, WA (1997).

[4] C. Johnstone, A. Drozhdin, N. Mokhov, W. Wan and A. Garren, "An Isohronous Lattice Design for 50 on 50 GeV Muon Collider", Proceedings of the 4th International Conference on Physics Potential and Development of $\mu^+\mu^-$ Colliders, p. 209, San Francisco, CA (1997).

[5] N. V. Mokhov, "The MARS Code System User Guide, Version 13(95)", Fermilab-FN-628 (1995); N. V. Mokhov et al., Fermilab-Conf-98/379 (1998); LANL Report LA-UR-98-5716 (1998); *nucl-th/9812038 v2 16 Dec 1998*; http://www-ap.fnal.gov/MARS/.

[6] I. S. Baishev, A. I. Drozhdin and N. V. Mokhov. "STRUCT Program User's Reference Manuel", SSC-MAN-0034 (1994).

[7] V. M. Biryukov, Yu. A. Chesnokov and V. I. Kotov, "Crystal Channeling and its Application at High Energy Accelerators", Berlin, Springer (1997)

LONGITUDINAL INSTABILITY IN A 50GEV×50GEV MUON COLLIDER RING *

Eun-San Kim[1], Andrew M. Sessler[2], Jonathan S. Wurtele[1,2]
[1]Department of Physics, University of California, Berkeley, CA 94720
[2]Lawrence Berkeley Laboratory, Berkeley, CA 94720

Abstract

Simulations of the longitudinal dynamics in a 50GeV×50GeV muon collider ring have been performed. Operation of the ring close to the slippage factor $\eta_1 \simeq 10^{-6}$, such that synchrotron motion is frozen, minimizes the need for rf to maintain the bunch length. Without appropriate rf compensation, however, the bunch wake induces an intolerable head-to-tail energy spread. This paper demonstrates that the bunch wake may be compensated by two rf cavities with low rf voltages. With this rf setup the small energy spread of the beam ($\delta E/E$=3×10^{-5}) in the 50GeV×50GeV muon collider ring can be maintained during the 1000 turn lifetime of the muons. These studies were made at the nominal design point, and sensitivities to errors were explored. The simulation also demonstrates that the computation of the wake field using bins of variable width (each with a constant number of macroparticles) accurately reproduces the wake and yields reduced computing time compared to the evaluation of the wake as the direct sum over the wakes of all preceding macroparticles.

1 INTRODUCTION

This paper presents investigations of the longitudinal dynamics in a 50GeV×50GeV muon collider ring. The critical design parameters of a 50GeV×50GeV muon collider ring, from the viewpoint of collective effects, are: The bunch has a large charge (N=4×10^{12}), the bunch length is long (σ_z=13cm) compared to the pipe radius(b), the beam energy spread is very small (σ_δ=3×10^{-5}), as is the slippage factor, ($\eta_1 \simeq -10^{-6}$). The muon has a life time, $\tau_\mu \simeq 1.1ms$ at 50 GeV, corresponding to 1000 turns in the ring with a circumference(C) of 300 meters. The need to minimize rf voltage leads to $\eta_1 = -10^{-6}$ and a synchrotron oscillation period much longer than the storage time. The small slippage over the storage time leads to dynamics similar to that in a linac. The large bunch charge induces, through the wakefield, an undesirable head-to-tail energy spread. Maintaining an intense beam with a low energy spread provides a challenge to the ring design.

We show a means of controlling the longitudinal dynamics in the 50GeV muon collider ring. That is, to limit rf, one operates the ring close to the transition (η_1=−10^{-6}) such that the synchrotron motion is frozen in the storage time, and uses two rf cavities to compensate for the ring impedance arising from beam and ring structures. Since the beam intensity decreases, due to the muon decay, rf voltages must also vary in time.

The utility of the simulation depends on the ability to calculate a sufficiently accurate wake without excessive computation. In the present code, the wake is calculated by summing the wakes from bins of variable bin width in front of the particle and δ-wakes from preceding particles in the same bin. We tested this method of calculating wakes, and found that it gives the desired accuracy and a substantial reduction in computing time when compared to wake calculations using unbinned macroparticles [1]. A more complete description of this work may be found in Ref.2 [2].

2 THE COMPUTATION OF THE WAKEFIELD AND MACROPARTICLE EQUATIONS

The wake generated by a beam interacting with discontinuities of components in the ring is approximated by a broad-band impedance. The longitudinal wake function $W_0'(z)$ for a broad-band impedance is given by [3]

$$W_0'(z) = \begin{cases} 0 & \text{if } z > 0 \\ \alpha R_s & \text{if } z = 0 \\ 2\alpha R_s e^{\alpha z/c}(cos\frac{\bar{\omega} z}{c} + \frac{\alpha}{\bar{\omega}} sin\frac{\bar{\omega} z}{c}) & \text{if } z < 0, \end{cases} \quad (1)$$

where $\alpha = \omega_R/2Q$ and $\bar{\omega} = \sqrt{w_R^2 - \alpha^2}$, Q=$R_s\sqrt{C/L}$ is the quality factor, $w_R = 1/\sqrt{LC}$ is the resonant frequency and R_s is the shunt impedance. For the broadband model, $Q = 1$ and $\omega_R = c/b$. The more common impedance $Z_{||}/n_h$=$(2\pi b/C)R_s$. Here, n_h is the harmonic number.

The variable bin size technique mentioned above works as follows. Firstly, the bunch is sliced into longitudinal bins with a constant number of particles, N_B, in each bin. This results in bins of variable bin width. The wake is then expressed, for the i^{th} particle, assumed to be in bin I, as

$$W(z_i(n)) = -\frac{N_p r_o}{N_m \gamma}[\sum_J^{I<J} N_B W_o'(z_I(n) - z_J(n)) - \sum_j^{i<j} W_o'(z_i(n) - z_j(n)) - W_o'(0)], \quad (2)$$

where N_p is number of particles in the bunch and N_m is the number of macroparticles. The lower case indices refer to particles in the same bin, while the upper case indices refer to different bins. The wake from macroparticles in preceding bins ($J > I$) is calculated (the first term on the RHS

* Work supported by the U.S. Department of Energy under contract No. EDDEFG-03-95ER-40936 and DE-AC03-76SF00098

of Eq.(2)) as arising from a *single* macroparticle located at z_J, the center of bin J. The interaction between macroparticles in the same bin is included as δ-function wakes (the second term on the RHS of Eq.(2)), and finally $-W_o'(0)$ is the wake generated by the macroparticle itself.

We used of order 2000 bins for 44000 macroparticles in the simulation. The wake field that was in good agreement with analytical results. The numbers of bins and macroparticles must be properly chosen, as they depend on ring parameters such as the bunch length and the radius of the beam pipe.

Macroparticles, with an initially Gaussian distribution, are tracked in phase space with equations of motion which include kicks by two rf cavities, a longitudinal wake kick and a drift that depends on the momentum compaction. Each macroparticle i has position and energy coordinates (z_i, δ_i) and is tracked for 1000 turns. The longitudinal difference equations for the i'th macroparticle at revolution number n is derived from its coordinates on turn $n-1$ by:

$$\delta_i(n) = \delta_i(n-1) + K_{rf}(n-1) + W(z_i(n)), \quad (3)$$

$$z_i(n) = z_i(n-1) + (\eta_1\delta + \eta_2\delta^2 + \eta_3\delta^3)C. \quad (4)$$

Here, z is the longitudinal coordinate with respect to the bunch center, $\delta = \delta P/P$ is the relative momentum error of the particle, η_1, η_2, η_3 are the linear and higher order momentum compaction parameters. The rf impulse $K_{rf}(n-1)$ due to the two rf voltages is given by

$$K_{rf}(n-1) = \frac{eV_{rf1}e^{-\frac{T_o(n-1)}{\gamma\tau_\mu}}}{E_o} sin(\frac{w_{rf1}}{c}z_i + \phi_1) + \frac{eV_{rf2}e^{-\frac{T_o(n-1)}{\gamma\tau_\mu}}}{E_o} sin(\frac{w_{rf2}}{c}z_i + \phi_2). \quad (5)$$

An example of rf parameters that compensate the wake are shown in Table 1. The factor $e^{-\frac{T_0(n-1)}{\gamma\tau_\mu}}$ in the rf voltages is introduced to compensate for the decreasing beam intensity due to muon decay. Here, T_0 is the revolution period.

Table 1: Rf parameters used in the simulation.

	One cavity	Two cavities
rf frequency f_{rf} (MHz)	570	823 and 399
harmonic number(n_h)	570	823 and 399
rf voltage V_{rf} (KV)	14.1	4.26 and 12.12
phase offset ϕ(radian)	3.55	3.755 and 3.415

2.1 *Numerical example of the compensation of the bunch wake*

Figs.1(a) and (b) show the beam phase space after 1 turn and 1000 turns in the case that one cavity in Table 1 has been choosen to minimize the induced energy spread, respectively. One cavity compensates for the wake in the center of the bunch. After 1000 turns, the tail particles gain or lose energy from the large rf kick at the longitudinal positions where the bunch wake becomes small, as seen in Fig.1(b).

Fig.2(a) show the beam phase space after 1000 turns when two cavities in Table 2 are applied. The beam distribution after 1000 turns is not distorted by the sum of the rf voltages and the bunch wake and the beam distribution remains intact. This can be understood from examination of Fig.2(b), where the rf voltage (curve (1)), bunch wake voltage (curve (2)), and the resulting total voltage (curve (3)) are plotted after 1000 turns. Fig.2(b) shows the cancellation of the wake by the rf voltages. We note that the bunch wake in the 50GeV×50GeV muon collider ring can be compensated by very low rf voltages.

3 SENSITIVITY STUDIES OF LONGITUDINAL DYNAMICS

3.1 *Sensitivity to beam current and $Z_{||}/n_h$*

We investigated the beam phase space with beam current varying from its design value by -10%,-5%,+5% and +10%. The rf parameters are fixed. The energy spread has increased roughly 8% for variation of ±10%, and 2% for ±5 % after 1000 turns.

We also investigated the beam phase space for variations of the impedance: $Z_{||}/n_h$ = 0.1Ω, 0.5Ω, 0.7Ω and 1Ω. Voltages in the rf cavities are varied proportionally to the magnitude of $Z_{||}/n_h$. The potential well distortion due to the bunch wake increases with $Z_{||}/n_h$ and becomes quite noticeable at 1Ω.

3.2 *Dependence of longitudinal dynamics on σ_δ and η_1, η_2, η_3*

Fig.3(a) shows the beam phase space with σ_δ=10^{-3} and η_1= -10^{-2}. When $\delta'(s)$ integrated over 10^3 turns is small compared to σ_δ, the motion of a particle is determined by the magnitude of η_1. The large slippage dominates the motion and leads to streaming in z motion, as is seen in Fig.3(a). Fig.3(b) shows the beam phase space in the case of σ_δ= 3×10^{-5} and η_1= -10^{-2}. In the case of large η_1, and small energy spread, the dynamics is significantly more complicated, showing energy spread and streaming in z, as shown in Fig.3(b). In the calculations for Figs.3, we have had η_2=η_3=0 and the equation of motion is $z' = \eta_1\delta(s)$, where $z' = \frac{dz}{ds}$ and s is distance traveled in the ring. The resultant phase space after 10^3 turns is summarized as a function of (η_1, σ_δ) in Fig.4. Regions (a) and (b) in Fig.4 were covered in Figs.(1).

On the other hand, the two rf voltages compensation reduces the phase space distortions of the beam for the (a), (b) and (d) regions of Fig.4. The motion in region (c) of Fig.4 is dominated by slippage, and the rf does not affect the dynamics. In summary, two rf cavities can be used to remove the beam tail of region (b) of Fig.4 and the energy spread of region (d) of Fig.4.

Longitudinal dynamics for varying η_2 and fixed η_1=-10^{-6} and η_2=0 has been examined. The z' equation includes a nonlinear term, z'=$(\eta_1 + \eta_2\delta(s))\delta(s)$. With two rf cavities used to compensate the bunch wake, the energy does not show significant change after 1000 turns, and the motion is a nonlinear streaming with the energies taken as their initial values. We see this in Fig.5(a) with η_2=100, where the energy spread of the macroparticles is basically unchanged. The nonlinearity of the streaming is noticeable for particles with $\eta_2 > \eta_1/\delta(s)$. The behavior of the phase space parameterized by η_2 and σ_δ is summarized in Fig.5(b).

Longitudinal dynamics for varying η_3 and fixed η_1=-10^{-6} and η_2=0 have also been examined. The energy evolution is small due to good compensation, and the position evolves according to $z' = (\eta_1 + \eta_3\delta^2(s))\delta(s)$, where the energy can be taken roughly to be fixed at its initial value. The nonlinear coefficient η_3 becomes important when $\eta_3 > \eta_1/\delta^2(s)$. One case with η_3=100 is shown in Fig.6(a). The parameter space for varying η_3 and σ_δ is summarized in Fig.6(b).

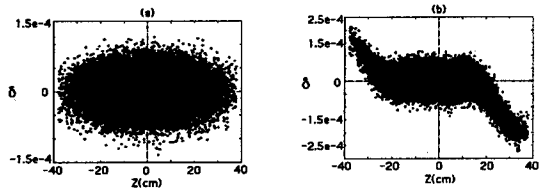

Figure 1: Longitudinal beam phase space at (a) turn 1 and (b) turn 1000 when one rf cavity in Table 1 is applied. The tails of the bunch are distorted by the partly compensated rf voltage. σ_δ=3×10^{-5}, η_1= -1×10^{-6} and $\left|\frac{Z_{||}}{n_h}\right|$=0.1Ω.

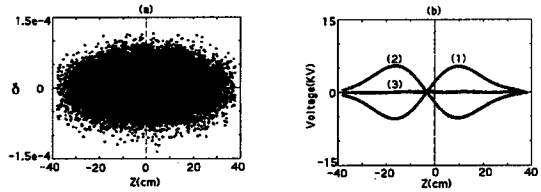

Figure 2: (a) longitudinal beam phase space after 1000 turns when two rf voltages in Table 1 are applied. (b) shows voltages due to the two rf cavities (curve(1)), the bunch wake (curve(2)), and the net voltage (curve(3)) after 1000 turns. The bunch wake is well-compensated by the two rf cavities. σ_δ=3×10^{-5}, η_1= -1×10^{-6} and $|Z_{||}/n_h|$=0.1Ω.

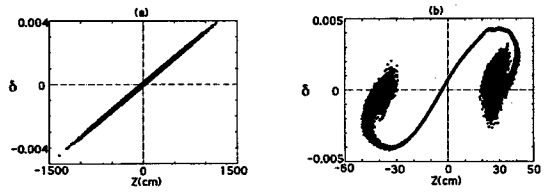

Figure 3: The longitudinal phase space after 1000 turns for different values of σ_δ and η_1. One rf voltage in Table 1 is used to compensate for the bunch wake. σ_δ=10^{-3} and η_1= -0.01 in (a); σ_δ=3×10^{-5} and η_1= -0.01 in (b).

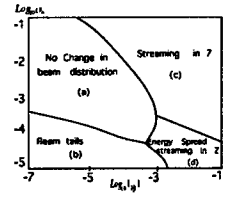

Figure 4: A summary of the beam dynamics in σ_δ and η_1 parameter space. One rf voltage in Table 1 is used to compensate for bunch wake. $|Z_{||}/n_h|$=0.1Ω.

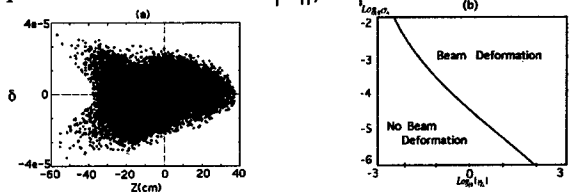

Figure 5: (a) the longitudinal phase space after 1000 turns for η_2=100. Two cavities are used to compensate for bunch wake. η_1= -10^{-6}, η_3=0, σ_δ=3×10^{-5} and $|Z_{||}n_h/|$=0.1Ω. (b) shows beam dynamics in the σ_δ and η_2 parameter space. Right upper parameter space shows the beam streaming.

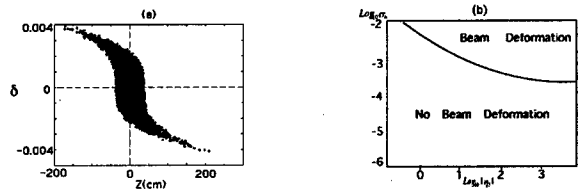

Figure 6: (a) the longitudinal phase space after 1000 turns with η_3=100. η_1=-10^{-6}, η_2=0, σ_δ=10^{-3} and $\left|\frac{Z_{||}}{n_h}\right|$=0.1Ω. (b) shows beam dynamics in the σ_δ and η_3 parameter space. Right upper parameter space shows the beam streaming.

4 CONCLUSION

Longitudinal motion in the 50GeV×50GeV muon collider ring is investigated with a multi-particle tracking code. A binning scheme is used to enhance the computational efficiency of the simulation and muon decay is included. The operation of a ring with small η_1, so that the synchrotron oscillation is frozen during the storage time, and with the bunch wake compensated by two low rf cavities, is studied.

The longitudinal dynamics is seen to be controllable with proper choice of rf parameters. One cavity can be used to control the motion of the core of the bunch, while a second controls the tails. We studied the role played by important ring parameters in the longitudinal dynamics. Longitudinal motion with compensation of the wake was studied with various slippage factors (η_1, η_2 and η_3). The sensitivity of the compensation scheme to variations in ring parameters was examined.

5 REFERENCES

[1] W.-H.Cheng, A.M. Sessler and J.S. Wurtele, LBL-40224.1997.

[2] E.S.Kim, A.M. Sessler and J.S. Wurtele, submitted to Phys.Rev. Special Topics:Acceleratrs and Beams,Jan.1999.

[3] A.W. Chao, Physics of Collective Instabilities in High Energy Accelerators, (John Wiley & Sons, New York, 1993).

TRANSVERSE INSTABILITY IN A 50GEV×50GEV MUON COLLIDER RING *

Eun-San Kim[1], Andrew M. Sessler[2], Jonathan S. Wurtele[1,2]
[1]Department of Physics, University of California, Berkeley, CA 94720
[2]Lawrence Berkeley Laboratory, Berkeley, CA 94720

Abstract

The intense bunch which is called for in the muon collider design will be subject to transverse instability. It has been suggested that tune spread due to BNS damping be used to control the instability. The transverse dynamics in a 50GeV×50GeV muon collider ring is examined numerically using a broad-band impedance. In addition to the BNS damping, tune spreads due to chromaticity, amplitude dependent tune shift and the beam-beam interaction are taken into account. It is shown that each of these tune spreads adequately stabilize the transverse dynamics.

1 INTRODUCTION

The design of a 50 GeV muon collider ring, from the view of collective effects, has some features which need to be examined. The bunch has a large charge: N=4×10^{12}. The bunch length is long: σ_z=13cm. The momentum compaction η_1 is very small: $\eta_1 \sim -10^{-6}$: a muon would undergo 1 synchrotron oscillation in 20000 turns. Muons have a very short lifetime: $\tau_\mu \simeq 1.1$ ms at 50 GeV, corresponding to 1000 turns in a ring with the circumference of 300 meters. These parameters lead us to careful analysis in the ring operation: the intense bunch may cause instabilities and the very small η_1 gives dynamics similar to a linac.

This paper presents investigations on the collective transverse beam dynamics in a 50GeV×50GeV muon collider ring. To limit rf, it has been proposed to operate the ring close to the transition (η_1=-10^{-6}), such that the synchrotron motion is almost frozen over the storage time. This will require the use of two rf cavities to compensate for the energy spread induced through the longitudinal wakefield[1]. Furthermore, because only a small rf voltage is required to compensate the longitudinal wake, the impedances of the two rf cavities are negligible compared to the ring impedance. In this paper, the transverse force on the muons was modeled by a broadband impedance, corresponding to an averaged wakefield that does not include the rf cavities. The wakefield in the simulation is calculated by using a technique, described in Ref. [1], where bins of variable width increase the accuracy and reduce computing time.

Since synchrotron radiation damping and Landau damping are negligible, they do not help in stabilizing against collective instabilities. It was previously shown that a BNS tune spread damps the transverse instability [2]. In this paper, it is shown through a numerical simulation, that the transverse instability is also damped by tune spreads due to chromaticity, amplitude dependent tune shifts, and the beam-beam interaction.

* Work supported by the U.S. Department of Energy under contract No. EDDEFG-03-95ER-40936 and DE-AC03-76SF00098

2 THE COMPUTATION OF THE WAKEFIELD AND MACROPARTICLE EQUATIONS

The transverse wake generated by a beam interacting with discontinuities of components in the ring is approximated by a broad-band impedance with quality factor of the order of unity. The transverse wake function is simply related to the longitudinal impedance [3],

$$Z_1^\perp \sim \frac{2c}{b^2 w} Z_0^{||}, \tag{1}$$

$$W_1(z) = \frac{-i}{2\pi} \int_{-\infty}^{\infty} Z_1(w) e^{iwz/c} dw, \tag{2}$$

With this definition and a broadband resonator model for the longitudinal impedance, the transverse wake function $W_1(z)$ for the broad-band impedance is given by

$$W_1(z<0) = \frac{2cR_s\omega_R}{b^2 Q\bar{\omega}} e^{\alpha z/c} \sin\frac{\bar{\omega} z}{c}, \tag{3}$$

where $\alpha = \omega_R/2Q$ and $\bar{\omega} = \sqrt{w_R^2 - \alpha^2}$, Q=$R_s\sqrt{C/L}$ is the quality factor, $w_R = 1/\sqrt{LC}$ is the resonant frequency and $R_s = C/(2\pi b)Z_{||}/n_h$ is the shunt impedance. For the broad-band model, $Q = 1$ and $\omega_R = c/b$, where b is the vacuum pipe radius. Here C is the ring circumference and n_h is the harmonic number.

The transverse equation of motion is

$$y''(z,s) + (\omega_\beta^2/c^2)\, y(z,s) = -(r_0/\gamma C) \int_z^\infty dz' \rho(z') W_1(z-z') y(z',s), \tag{4}$$

where w_β is the betatron frequency, r_o=$e^2/m_\mu c^2$, $\gamma = E/m_\mu c^2$ and $\rho(z)$ is the particle distribution function.

Macroparticles are tracked in phase space with equations of motion which include a transverse wake due to a broad-band impedance and betatron oscillation. Each macroparticle i has transverse coordinates (y_i, y_i') and is tracked for 1000 turns. $' = d/ds$, where s measures distance around the ring. The transverse dynamics from the betatron motion for the i^{th} macroparticle on any turn n are derived from its coordinates on turn $n-1$ by:

$$\begin{pmatrix} y_i(n) \\ y_i'(n) \end{pmatrix} = \begin{pmatrix} \cos(\frac{\omega_\beta C}{c}) & \sin(\frac{\omega_\beta C}{c}) \\ -\sin(\frac{\omega_\beta C}{c}) & \cos(\frac{\omega_\beta C}{c}) \end{pmatrix} \begin{pmatrix} y_i(n-1) \\ y_i'(n-1) \end{pmatrix} \quad (5)$$

$$\omega_\beta = \omega_{\beta o}(1 + a(y_i^2 + y_i'^2) + \xi\delta + \Delta\nu_{BNS}/\nu_\beta), \quad (6)$$

where $a(y_i^2(n) + y_i'^2(n))$ is the amplitude dependent tune shift, $\xi\delta$ is the tune spread due to chromaticity and $\Delta\nu_{BNS}/\nu_{\beta o}$ is the tune spread due to BNS damping. Here a is the nonlinearity parameter, ξ is the chromaticity and $\delta = \delta P/P$ is the relative momentum error of the particle,

The wakefield force is included by a kick:

$$\Delta y_i'(n) = -\frac{c}{\omega_\beta}\frac{N_p r_o}{N_m \gamma}\sum_J^{I<J} Y(J) W_1(z_I(n) - z_J(n)), \quad (7)$$

where $Y(J)$ is the sum of the transverse displacements of the macroparticles in the J bin, and $z_I(n) - z_J(n)$ is the longitudinal separation of the bins ($z(I)$ is the average longitudinal position of the particles in the bin I). The i^{th} particle is in bin I. Also, N_p is the number of particles in the bunch and N_m is the number of macroparticles.

We used 1000 bins for 20000 macroparticles in the simulation. The numbers of bins and macroparticles must be properly chosen, as they depend on ring parameters such as the bunch length and the radius of the beam pipe. The initial coordinates of macroparticles are chosen to have a Gaussian distribution. Since the beam intensity decreases due to the muon decay, rf voltage is also varied in time. Rf parameters used in the simulation is shown in Table-1.

Table 1: Parameters of a 50GeV collider ring and rf parameters used in the simulation.

Beam energy (E)	GeV	50
Muons per bunch (N)	10^{12}	2
Circumference (C)	m	300
Bunch length (σ_z)	cm	13
Bunch energy spread (σ_δ)	%	0.003
Slippage factor (η_1)	10^{-6}	-1
Beam pipe radius (b)	cm	3
Beam-beam parameter(ζ)	10^{-2}	1.5
RF energy (V_{rf})	MV	0.34 and 0.99
RF frequency (f_{rf})	MHz	823 and 399
RF phase-offset (ϕ_{rf})	radian	3.755 and 3.415

3 BEAM BREAKUP

Due to the very small slippage factor(η_1=-10^{-6}), the synchrotron motion is frozen in the storage time and transverse dynamics is similar to that in a linac. In the case that a beam is not centered in the beam pipe, the transverse wake field driven by the head of the bunch perturbs the tail, causing beam breakup(BBU)-like instability. A dimensionless growth parameter that characterizes the BBU strength is

$$\Upsilon(z) = N r_0 W_1(z)/2k_\beta\gamma, \quad (8)$$

where k_β is the betatron wave number, and $W_1(z) = \int_z^\infty dz' W_1(z-z')\rho(z')$ is the transverse wake function [3].

Fig.1 shows the BBU-like instability using a broad-band resonator model in the absence of betatron tune spread. The initial displacement of the beam (Δ_y) is 0.2cm. The transverse motion shows unstable although there is not much growth. The growth can be damped due to betatron tune spreads, as discussed below.

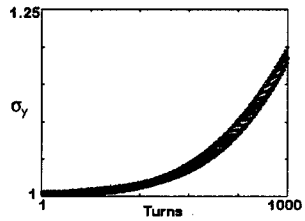

Figure 1: Blowup of the rms beam size, due to a BBU-like instability. In Figs.1-3 and 5-6, R_s=13000Ω, Δ_y=0.2cm and ν_β=28.816.

4 DAMPING OF BEAM BREAKUP BY BETATRON TUNE SPREADS

4.1 *BNS damping*

The BNS damping can be obtained by introducing a slightly stronger betatron focusing of bunch tail than bunch head [3]. A slightly different focusing strength for the bunch tail can eliminate the beam breakup. This happens because the additional focusing force compensate for the defocusing dipole deflection due to the wake field left behind by the bunch head. The tune spread is defined by

$$\omega_\beta = \omega_{\beta o}(1 + \frac{\Delta\nu_{BNS}}{\nu_\beta}), \quad (9)$$

$$\frac{\delta\nu_{BNS}}{\nu_\beta} = -\frac{N r_o}{2k_\beta^2\gamma\, C}\int_z^\infty W_1(z-z')\rho(z')dz', \quad (10)$$

where k_β is the betatron wave number. Fig.(2) shows that the BBU-like instability is stabilized by BNS damping. The simulation (in runs not shown) indicates that BNS damping more effective when bunch length is small compared to beam pipe radius. Fig.(3) shows the BNS tune spread which is applied in the longitudinal positions of the beam to satisfy Eq.(10). Fig.(4) separates parameter regions of beam pipe radius and shunt impedance(R_s) according to the appearance of a BBU-like instability.

4.2 *Tune spread due to chromaticity*

The betatron oscillation frequency of a particle in ring depends on the energy error δ of the particle. If we denote

betatron frequency of an on-momentum particle as $\omega_{\beta o}$, the betatron frequency for an off-momentum particle can be written as $\omega_\beta(\delta) = \omega_{\beta o}(1 + \xi\delta)$. Fig.(5) shows that tune spread from chromaticity stabilizes the motion.

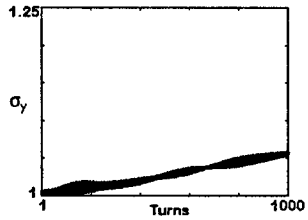

Figure 2: Rms beam size when there is a BNS tune spread.

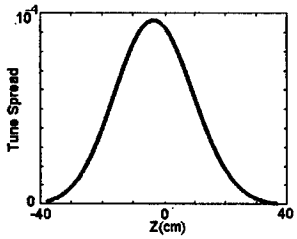

Figure 3: Maginitudes of the BNS tune variation with longitudinal position.

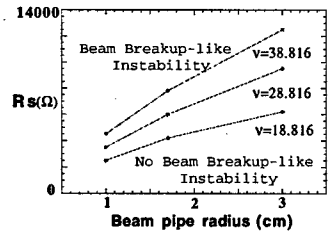

Figure 4: Parameter regions for various tunes, ν, as a function of pipe radius and shunt impedance(R_s).

4.3 *Amplitude dependent tune shift*

We consider the case when the tune spread is associated with the lattice nonlinearity. The amplitude dependent tune shift is defined by $\omega_\beta = \omega_{\beta o}(1 + aJ)$, where $\omega_{\beta o}$ is the betatron frequency at zero betatron amplitude, $J = y^2 + y'^2$ is the amplitude of the betatron oscillation of a particle. The tune spread in a beam may be caused by the amplitude dependent tune shift since the beam has a distribution in amplitude. Fig.(6) shows the stabilized motion when there is an amplitude dependent tune shift.

4.4 *Beam-beam interaction*

We use a round beam model to study beam-beam effects. The beam-beam kick is calculated by using a weak-strong model. A macroparticle is kicked at interaction point(IP) as

$$\Delta y = 0, \quad \Delta y' = \frac{8\pi\zeta\epsilon_N}{\gamma}\frac{1}{\sqrt{2}y}(1 - e^{-y^2/\sigma_y^2}), \qquad (11)$$

where $\zeta = \frac{r_o N}{4\pi\epsilon_N}$ is the beam-beam parameter and ϵ_N is the normalized emittance. A beam-beam parameter greater than ζ=0.035 damps the transverse instability.

Since a 50 GeV muon beam has very small energy spread and long bunch length, in addition to the transverse kick, the model of the beam-beam interaction should include energy change caused by the opposing bunch at the IP [4, 5]. Our simulation predicts a factor of 4.6 increase in the energy spread after 1000 turns. This is easily compensated for by rf, as will be presented in a later publication.

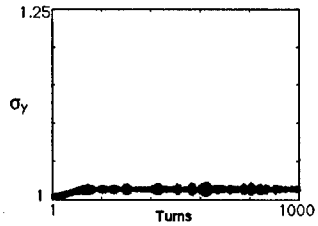

Figure 5: Rms beam size when there is tune spread due to the chromaticity, ξ=-2.

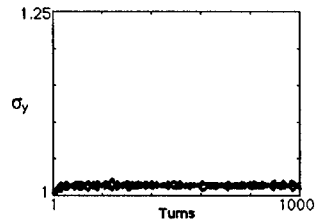

Figure 6: Rms beam size when there is the amplitude dependent tune shift, a=10^{-4}.

5 CONCLUSIONS

The transverse instability of a bunch with a small η_1 and strong wake fields is seen to be BBU-like and can be stabilized by betatron tune spreads. BNS damping, chromaticity, amplitude dependent tune shift and beam-beam parameter greater than ζ=0.035 all cause betatron tune spreads and each provide adequate Landau damping against the transverse instability for parameters of the 50GeV×50GeV muon collider ring.

6 REFERENCES

[1] E.S. Kim, A. M. Sessler and J.S. Wurtele, *submitted to Phys. Rev. Special Topics: Accelerators and Beams*, Jan. 1999.

[2] W.H. Cheng, A.M. Sessler and J.S. Wurtele,*EPAC96 (1996)*

[3] A. W. Chao, *Physics of Collective Beam Instabilities in High Energy Accelerators*, (John Wiley & Sons, 1993).

[4] A. Zholents, private communication

[5] K.Hirata, et. al., Particle Accelerators 40, (1993) 205.

AN ANALYSIS OF BNS DAMPING TECHNIQUES IN STORAGE RINGS AND COLLIDERS*

G. Penn, J.S. Wurtele, UC Berkeley / LBNL CBP, Berkeley, CA

Abstract

Transverse instabilities in linacs can be controlled by BNS damping, in which the transverse oscillation frequency is chirped from the head to the tail of the bunch. It has been suggested that this technique could be applied to quasi-isochronous rings, such as are proposed for a muon collider. We adopt a reduced phase space model, taking averages over transverse coordinates and with proscribed longitudinal synchrotron motion, to study the growth of transverse displacements of a bunch in the presence of synchrotron oscillations.

1 MOTIVATION

Proposed parameters for muon collider require transverse emittances to be very small. Muons do not have significant cooling from synchrotron radiation; in addition, very low momentum compaction factors will be used to limit the RF requirements. For these reasons, coherent ring instabilities need to be investigated in parameter regimes different from present-day accelerators and may require new techniques to control them. The beam dynamics resembles linac physics; however, total storage time in a 2Tev × 2Tev muon collider will be comparable to the synchrotron period so the longitudinal motion of the particles cannot be neglected. In addition, collider designs may require beams to be very precisely targeted, a condition which will be increasingly difficult to achieve as the emittance of the beam is made smaller.

2 FORMALISM

This work considers a simplified formalism for the analysis of transverse instabilities. Key features of this formalism are the use of a reduced phase space, with only longitudinal coordinates, and suppression of time scales shorter than the synchrotron period and instability growth time. The transverse displacement of the beam is described in terms of a complex amplitude which isolates the dipole moment, although this can be generalized to higher order modes.

The dynamic variables for individual particles are z,δ, y, and p_y. Instead of time, the variable s is used, representing distance travelled in the ring. The quantity $\delta = \Delta P/P$ is the normalized momentum deviation, and p_y is the transverse angle dy/ds. The equations of motion can be summarized as

$$z' = -\eta\delta, \qquad \delta' = z\omega_s^2/\eta c^2$$
$$y' = p_y, \qquad p_y' = -Ky + F_W \qquad (1)$$

The synchrotron frequency ω_s is taken to be constant, whereas $K = \omega_\beta^2/c^2$ is allowed to vary. The forcing term F_W is from the wakefield generated collectively by the particle bunch. Here, the symbol $'$ refers to differentiation with respect to s. We assume $\omega_s \ll \omega_\beta$.

We now define the complex transverse amplitude of a single particle. When there is no wakefield forcing term, the particle dynamics are given by

$$y = \Re\mathrm{e}\,\frac{A}{\sqrt{\beta}}e^{i\Phi}, \qquad p_y = \Re\mathrm{e}\,\frac{1}{\sqrt{\beta}}\left(i + \frac{1}{2}\beta'\right)Ae^{i\Phi} \qquad (2)$$

Here, A is a constant, complex amplitude, Φ is a phase which satisfies $\Phi' = 1/\beta$, and the beta function satisfies the standard equation

$$2\beta\beta'' - (\beta')^2 + 4\beta^2 K = 4. \qquad (3)$$

When $F_W \neq 0$, Eqs. 1 and 2 can still be used to describe A and its evolution:

$$A\sqrt{\beta}\,\mathrm{e}^{i\Phi} = y - i(\beta y' - \beta' y/2) \qquad (4)$$

$$\frac{i}{\sqrt{\beta}}A'e^{i\Phi} = y'' + Ky = F_W. \qquad (5)$$

Note that the wake must be expressed in terms of A.

Collective dynamics are described by the Vlasov equation, $f' = Df/Ds = 0$, where $f(y, p_y, z, \delta, s)$ is the phase space density and D/Ds is the convective derivative. Taking $K = K(s, z, \delta)$ to be independent of the transverse coordinates, we form moments of the Vlasov equation by integrating over the coordinates y and p_y. This yields equations in a reduced phase space, with reduced density

$$F(z, \delta, s) \equiv \int dy\, dp_y\, f,$$

so $0 = F' = [\partial/\partial s - \eta\delta\partial/\partial z + (z\omega_s^2/\eta c^2)\partial/\partial\delta]F$.

The "average" transverse displacement Y is defined by

$$Y(z, \delta, s) \equiv \frac{1}{F}\int dy\, dp_y\, yf$$

Note the linear number density is $\rho(z) = \int d\delta\, F$. The equation Y satisfies is

$$Y'' + KY = F_W,$$

where F_W is now the wakefield force from the dipole moment of the beam. We next define a collective oscillation amplitude A in terms of Y and Y', in exactly the same way as for a single particle, and average over betatron oscillations.

* Supported by the U.S. DoE under grant No. DEFG-03-95ER-40936.

3 SUPPRESSION OF FAST TIME SCALES

The complex amplitude satisfies

$$A' = i\frac{r_0}{2\gamma L}\int d\tilde{z}\, W(z-\tilde{z})\int d\tilde{\delta}\,\sqrt{\beta\tilde{\beta}}\,\tilde{F} \left[\tilde{A}\, e^{i(\tilde{\Phi}-\Phi)} + \tilde{A}^*\, e^{-i(\tilde{\Phi}+\Phi)}\right] \quad (6)$$

where the $m = 1$ wakefield forcing term has been expressed as

$$F_W(z) = -\frac{r_0}{\gamma L}\int d\tilde{z}\, W(z-\tilde{z})\int d\tilde{\delta}\,\tilde{Y}\tilde{F}. \quad (7)$$

Here $\tilde{}$ refers to quantities evaluated at $\tilde{z}$, $\tilde{\delta}$, and W refers to the wakefield function integrated along the ring. The A and A^* terms arise from the real part of $A\exp(i\Phi)$. Note that $\tilde{\Phi}-\Phi$ is a slowly varying quantity, because the difference in phase only arises from effects like chromaticity. However, the term proportional to A^* is rapidly oscillating and will not contribute to the long-term evolution of the bunch.

An average over one turn results in

$$A' \simeq i\frac{r_0 c}{2\gamma L\omega_{\beta 0}}\int d\tilde{z}\, W(z-\tilde{z})\int d\tilde{\delta}\,\tilde{F}\tilde{A}\, e^{i(\tilde{\Psi}-\Psi)} \quad (8)$$

where $\omega_{\beta 0}$ is a normalization related to an "average" beta function, and the head-tail phase averaged over a turn is

$$\Psi(z,\delta) \equiv \frac{1}{L}\oint ds\ [\Phi(s,z,\delta) - \Phi(s,0,0)]$$

Equivalently,

$$\Psi'(z,\delta) = \frac{\omega_{\beta 0}}{c}\frac{\Delta Q}{Q}$$

where Q is the total tune of the ring for the reference orbit, and we defined $\omega_{\beta 0} \equiv 2\pi Qc/L$.

In going from Eq. 6 to Eq. 8, we integrated the product of the wakefield function and the beta function around the ring. Thus, it is clear that the "total" wakefield function is actually weighted by the beta function; the local value of $\beta W(z-\tilde{z})$ is replaced by $(c/\omega_{\beta 0})W(z-\tilde{z})$ to smooth out the driving term over a single turn. Finally, we are left with quantities that only vary with the synchrotron period and the growth time.

4 HEAD-TAIL PHASE

We consider tune shifts ΔQ from chromaticities ξ, and BNS-like terms κ z, (e.g., induced by RF quadrupoles)[1], that can vary across the bunch. Explicitly,

$$\frac{\Delta Q}{Q} \simeq \xi_0\delta + \xi_1\frac{z}{\sigma_z}\delta + \kappa z.$$

The head-tail phase is then given by

$$\Psi = -\chi_0\frac{z}{\sigma_z} - \frac{1}{2}\chi_1\frac{z^2}{\sigma_z^2} + \chi_{BNS}\frac{\delta}{\sigma_\delta}$$

where σ_z and σ_δ are the characteristic longitudinal dimensions of the bunch. Here, $\chi_{0,1} \equiv \omega_{\beta 0}\xi_{0,1}\sigma_z/\eta c$ and $\chi_{BNS} \equiv \omega_{\beta 0}\eta c\kappa\sigma_\delta/\omega_s^2$.

4.1 *Unified treatment of detuning*

Incorporating the effect of tune shifts into an overall head-tail phase allows for a unified treatment of ring dynamics, including chromaticity, variable focussing, and more general longitudinal dynamics. Aspects of the beam which cannot be directly modelled in this way are transverse amplitude dependent tune shifts, and coupling between longitudinal and transverse motion.

If we consider the weak beam limit where the synchrotron motion is the dominant effect, it is useful to use the longitudinal coordinates r_z, ϕ_z, where $z = r_z\cos\phi_z$, $\delta = (\omega_s r_z/\eta c)\sin\phi_z$. The longitudinal amplitude r_z is a constant of the motion, and the convective time derivative can be expressed as $D/Ds = \partial/\partial s + (\omega_s/c)\partial/\partial\phi_z$. In the weak beam limit, modes having the form $A = A_n(r_z)e^{in\phi_z}$ are only weakly coupled. For an "air-bag" beam model, where all of the particles have the same longitudinal amplitude, the mode frequency satisfies the equation

$$\omega_\ell - \ell\omega_s = -\frac{r_0 c^2 N}{8\pi^2\gamma L\omega_{\beta 0}}\oint d\phi_z\oint d\tilde{\phi}_z\, W(z-\tilde{z})e^{i(\tilde{\Psi}-\Psi)} \quad (9)$$

Without the head-tail phase, the wakefield only generates a frequency shift, and there is no instability until the modes strongly couple. This corresponds to the strong head-tail instability. However, when there is a head-tail phase, for example from chromaticity ($\xi_0 \neq 0$), we recover the weak head-tail instability[2].

4.2 *Parity of the head-tail phase*

In general, the effect of the head-tail phase depends strongly on the parity of the phase with respect to the energy deviation δ. Because the unperturbed beam is symmetric in δ, a perturbation which is odd in energy will give no net contribution to the wakefield. To lowest order in beam intensity, a head-tail phase which is odd in δ will only couple with odd modes and so will not lead to instability. We can see this explicity by dividing the head-tail phase into even and odd parts, $\Psi \equiv \Psi_e + \Psi_o$. Then as an example, Eq. 9 can be rewritten as

$$\omega_\ell - \ell\omega_s = -\frac{r_0 c^2 N}{8\pi^2\gamma L\omega_{\beta 0}}\oint d\phi_z\oint d\tilde{\phi}_z\, W(z-\tilde{z}) \times \cos\Psi_o\cos\tilde{\Psi}_o\exp(i\tilde{\Psi}_e - i\Psi_e) \quad (10)$$

The growth rate depends on $\sin(\tilde{\Psi}_e - \Psi_e)$, and there is only a weak beam instability if the head-tail phase has a term which is even in δ. Thus, chromaticity can lead to instability whereas variable focussing across the bunch is not by itself destabilizing. This suggests that bunch stabilization through varying chromaticity, as considered in Ref. [3], requires a larger tune shift across the bunch than through BNS damping. On the other hand, a time-varying chromaticity $\xi_0(s)$ would introduce an odd component into the head-tail phase and should have a different effect on the beam.

5 NUMERICAL RESULTS

Here, we evaluate linear growth rates for a weak beam. A broadband impedance model is used for the wakefield:

$$W(z<0) = W_0 \exp\left(\frac{\omega_R z}{c}\sin\theta\right)\sin\left(\frac{\omega_R z}{c}\cos\theta\right) \tag{11}$$

where $\omega_R = c/b$. The simplest model might use b equal to the pipe radius, $\theta = \pi/6$, and $W_0 = 16\pi R_0/\mu_0 c b^2$, where R_0 is related to the shunt impedance.

Growth rates normalized to $W_0 r_0 c^2 N/8\pi^2\gamma L\omega_{\beta 0}$ are shown in Fig. 1 as a function of $\sigma_z c/\omega_R$, for the case where $\xi_0 = 0.1$. The lowest harmonics are shown. When $\sigma_z < c/\omega_R$, the broadband impedance model is qualitatively similar to the approximation of a constant wakefield[2] where the sign of the growth rate for the $n = 0$ mode is opposite to that of all other modes.

We now fix $\sigma_z/b = 13/3$. In Fig. 2, we consider a linear dependence in tune as a simple form of BNS damping, and compare it to a varying chromaticity. Both effects are taken to induce comparable tune shifts $\Delta\omega_\beta \simeq \omega_s$.

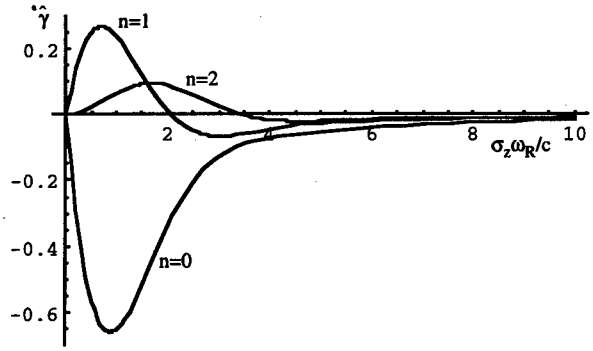

Figure 1: Normalized growth rates for $\chi_0 = 0.1$ as a function of σ_z/b. The lowest harmonics are shown.

6 LINAC MODEL

When the slip factor η is small, then the transverse dynamics become similar to the case of a linac. As a basic example, when Ψ is independent of energy (e.g., chromaticity effects), then we can define a local amplitude $\mathcal{A} = \int d\delta\, FA$ which satisfies

$$\frac{\partial\mathcal{A}(z,s)}{\partial s} \simeq i\frac{r_0 c\rho(z)}{2\gamma L\omega_{\beta 0}}\int d\tilde{z}\, W(z-\tilde{z})\mathcal{A}(\tilde{z},s)e^{i\Psi(\tilde{z})-i\Psi(z)} \tag{12}$$

This can be solved recursively to find the evolution of the beam, yielding the solution found in Ref. [2] when $\Psi \equiv 0$. When expressed in terms of the impedance Z, the time evolution operator has different contributions from the real and imaginary parts. While the real part leads to instability,

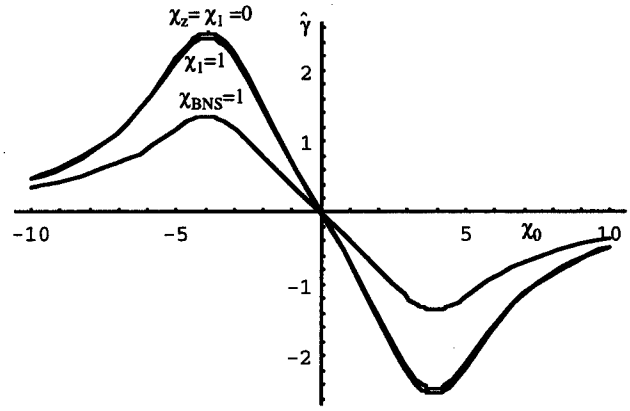

Figure 2: Normalized growth rates as a function of χ_0 for the lowest harmonic. Chromaticity alone, variable chromaticity with $\chi_1 = 1$, and BNS-like chirping with $\chi_{BNS} = 1$ are shown.

in the strong beam limit adding to $\Im m\, Z$ causes mixing of modes and can actually lower instability. For accelerators with intense beams, modifying the form of the impedance can be another way to stabilize the beam.

7 CONCLUSIONS

A formalism for treating transverse instabilities has been used to unify a wide range of physical effects on a beam, including variable chromaticity and BNS damping. The phase space has been reduced from four to two dimensions. The weak beam case reduces to the standard head-tail instability in a circular accelerator, while a strong beam with low slip factor is similar in form to beam dynamics in a linac.

Future work will focus on regimes where linac and ring physics have similarities, such as muon colliders. This analysis can be compared with existing numerical studies[4] for instabilities in a muon ring. In addition, the maximum displacement of the beam from wakefield forces can be calculated more efficiently in a reduced phase space, and adaptations of BNS damping evaluated on this basis.

8 REFERENCES

[1] V.V. Danilov, "Increasing the transverse mode coupling instability threshold by RF quadropole", Phys. Rev. STAB **1**, 041301 (1998).

[2] A. Chao, *Physics of Collective Beam Instabilities in High Energy Accelerators*, John Wiley & Sons, NY, 1993.

[3] W.-H. Cheng, A.M. Sessler, J.S. Wurtele, "Varying chromaticity: A damping mechanism for the transverse head-tail instability", Phys. Rev. E **45** 4695 (1997).

[4] E.-S. Kim, A.M. Sessler, J.S. Wurtele, "Transverse instability in 50GeV × 50GeV Muon collider ring", poster THP45, PAC99.

THE DESIGN OF A LIQUID LITHIUM LENS FOR A MUON COLLIDER*

A. Hassanein, J. Norem*, C. Reed, ANL; R. Palmer, BNL;
G. Silvestrov, T. A. Vsevolozhskaya, BINP; V. Balbekov, S. Geer, N. Holtkamp,
D. Neuffer, A. Tollestrup, P. Spentzouris, P. Lebrun, FNAL

Abstract

The last stage of ionization cooling for the muon collider requires a multistage liquid lithium lens. This system uses a large (~0.5 MA) pulsed current through liquid lithium to focus the beam while energy loss in the lithium removes momentum which will be replaced by linacs. The beam optics are designed to maximize the 6 dimensional transmission from one lens to the next while minimizing emittance growth. The mechanical design of the lithium vessel is constrained by a pressure pulse due to sudden ohmic heating, and the resulting stress on the Be window. We describe beam optics, the liquid lithium pressure vessel, pump options, power supplies, as well as the overall optimization of the system.

1 INTRODUCTION

The muon collider is being studied as a way of looking at particle interactions at the energy frontier[1]. The event rate in such a machine is goes like ε^{-1}, so the muon emittance, ε, must be minimized.

An attractive configuration for final stages of μ cooling is obtained by passing the beam though a conducting light metal rod which acts simultaneously as a focusing element and as an energy loss absorber. The magnetic field produced is given by $B_\Theta(r) = \mu_0 ir/2$, where i is the current density, r the radius and μ_0 the permeability constant. This azimuthal magnetic field combined with the longitudinal velocity produces a radial focusing force with the equation of motion, $d^2r/ds^2 + B'r/B\rho = 0$. The beta function for a Li lens is then $\beta_\perp = (B\rho/B')^{1/2} \propto (p/i)^{1/2}$, where the field gradient, B', can be very large. For a lens with r_{max} = 2 mm and the muon momentum in the lens, p = 300 MeV/c, one can achieve $\beta_\perp$ = 1 cm, which is difficult to achieve with solenoidal focusing systems.

Multiple scattering sets a lower limit to the emittance that can be obtained using this method. This limit is the equilibrium emittance, $\varepsilon_{equil,N}$, where ionization cooling is balanced by multiple scattering,

$$\varepsilon_{eq,N} = \frac{0.014^2 \beta_\perp}{2\beta mc^2 L_R dE/dx} = \beta_\perp C/\beta \propto (p/i)^{1/2} C/\beta,$$

where L_R is the radiation length, dE/dx is the energy loss, β, and m are the relativistic, velocity and muon mass, and constant C depends on the material. For Hydrogen, Lithium and Beryllium this constant is 42, 79 and 103 mm-mr/cm respectively. Thus the lowest emittances are obtained with low momenta. high current densities, and low Z materials. The lower momentum limit is determined by the muon velocity spread and the slope of dE/dx at low momentum, both of which increase the emittance.

For muon cooling, relatively long lengths are needed to obtain large energy losses (total loss should be a few hundred MeV, at dE/dx ~ 87.5 MeV/m), and the high ohmic power deposition assiciated with higher frequency operation would melt the Li.

A complete Lithium lens system would consist of a number of lithium lenses, matching optics required to transmit the beam from one lens to another and linacs used to replace the momentum lost by ionization. Since the performance of the muon collider is related to the current density in the lithium lens, one must look at the structural and mechanical limits of the design of the lens.

The present plan is to produce a conceptual design of lenses with r = 0.5 cm, B_{max} = 15 & 20 T, L = 1 m for testing as part of the MUCOOL experiment[2]

2 THE PRESSURE PULSE

The lithium lens is powered by a capacitor bank which produces a voltage proportional to a half cosine wave which produces a half sine wave current pulse. The length of the current pulse, τ, must be sufficient to allow the current to penetrate the lens uniformly. The skin depth δ is proportional to $(\rho_{Li}\tau)^{1/2}$, for resistivity, ρ_{Li}, of Lithium, (which melts at 180 °C).

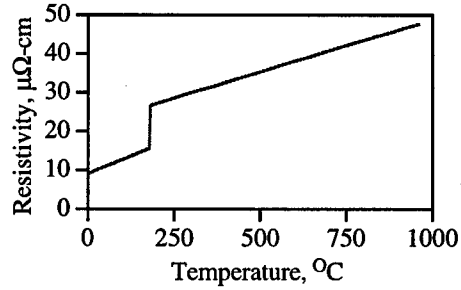

Figure 1, Resistivity of Lithium.

The ohmic power produces heating, thermal expansion, and subsequently pressure pulses which will ultimately limit the performance of the lens. Power deposited in the

*Work supported in part US-DOE.
* Email: norem@hep.anl.gov

lithium must be removed by circulating it, and we assume this would be done at the beam repetition rate.

The lithium lens can be modeled as a cylindrical tube of internal radius 4.5 mm contained in a thin steel shell 0.5 mm thick. In this example, 0.5 MA is drawn through the lens by a voltage pulse which is a half sine wave 50 μs long. The hydrodynamic equations, as well as the response of the envelope are considered in the HEIGHTS package [3]. Lithium is heated by Joule heating as well as energy loss from the muon beam, which is introduced 25 μs into the 50 μs pulse, producing a discontinuity in the temperature. The temperature pulse is shown in Figure 3.

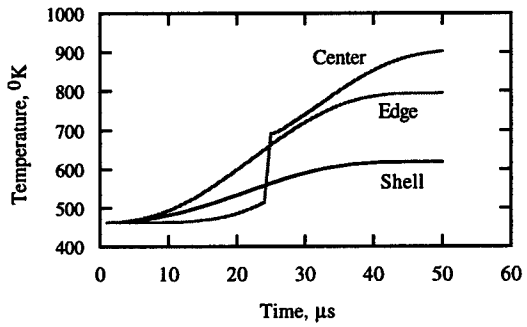

Figure 3. The temperature profile of the center and edge of the lens, showing the contribution from the muon beam at the center. The edge heats first, and the shell stays cooler due to the higher specific heat

The stress and strain generated by the pressure pulse, and the expansion of the Li is shown in Figure 4 for a current of 0.5 MA. The initial compression due to the magnetic field pressure is followed by the expansion due to the heating of the Li.

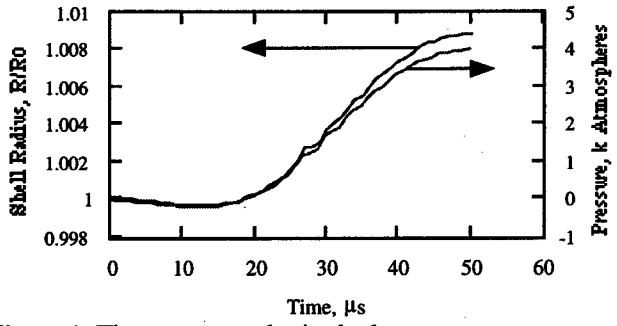

Figure 4. The pressure pulse in the lens.

3 THE PRESSURE VESSEL

There are a number of severe requirements on the pressure vessel holding the liquid Lithium. The pressure vessel must confine the liquid lithium flowing through it while requiring the pulsed current to pass longitudinally down the Lithium. The large pressure pulses must be supported without exceeding fatigue limits, and the insulators, which confine the electrical current, must survive the large mechanical shocks. The emittance of the muon beams must be increasedas little as possible by the structure and the windows, which must be thin Beryllium.

Two options are under consideration for the pressure vessel itself, one which would absorb as much of the pressure pulse as possible radially, the other would provide a solid surface which would direct the pressure pulse down the length, and utilize a buffer volume at the ends of the lens to absorb the increased volume of Lithium [4],[5].

Pumping the liquid Lithium has been studied using two techniques: electromagnetic pumps, which have been used with great success at BINP, and centrifugal pumps, which have been used for years atANL after modification. Either designs might be modified to be more compatible with the large pressure pulses from the lens.

4 BEAM OPTICS BETWEEN LENSES

Because the energy loss required for cooling muons is greaterthan that providedby a single lens, a number of Li Lenses are required. The beam must be reacceleratedand transportedbetween lenses with minimum loss [6][7]. In addition, periodic $\varepsilon_L \rightarrow \varepsilon_T$ emittance exchangesections are required to confine and cool the beam longitudinally. Modulation of the beam envelope is unavoidablein such a section because the Li lens provides a stronger focusing force than any other component. This modulation leads to significant chromatic effects which increase ε_T. It is not possible to use dispersion and sextupoles to control this modulation because of attendant nonlinear effects.

The chromatic effects can be attenuated to tolerable levels by varying the energy deviation, ΔE, along the length of the beamline. This is done by requiring a synchrotron phase advanceof at least π. When this phase advanceis used, each particle traverses approximately half the beamline below the median energy and half above it, thus averaging the chromatic contributions to zero. This requires at about 5 m of linac, with a frequency f = 805 MHz, and 30 MV/m gradients. At high momenta, approximately p = 300 MeV/c, this works comparatively well because $\Delta E \propto \Delta p$, but at lower momenta nonlinearities are more significant.

Emittance exchange is another problem, since the energy spreadof the beam is large. Lower energy particles tend to lose more energy due to ionization, and straggling widens the energy distribution of the beam, both effects increase the longitudinal emittance. The emittance exchange systems consist of an element which produces dispersion, combined with wedge absorbers which reduce the energy spreadof the beam. We are primarily looking at bent solenoids to provide the momentum dispersion. The emittance exchange should be done at the end of the transport section to avoid complicating the chromatic matching[7].

The proposed system which accomplishes these goals consists of a strong solenoid to match the strongly divergent beam coming out of the Li lens, followed by a

weaker solenoid containing a linac section. If the solenoid is bent, the dispersion is sufficient to do the emittance exchange with wedges. At the end of the section is another strong solenoid which focuses the beam on the input of the next Li lens. The long solenoid has a field of 3.1 T, and the short solenoids, used to match to the Lithium lens, have a field of about 12-20 T. The total length of the section is about 10 - 12 m. The optics of this system and more detailed information about its components are described elsewhere [6][7][8].

Studies are being made to determine the optimum cooling energy [8]. Although lower momentum seems desirable, this seems to involve shorter Li absorbers and more tightly constrained beam optics.

5 CONTAINMENT AND SAFETY

Although liquid Lithium freezes at fairly high temperatures, it is reactive and should be confined. The lens under construction at BINP for Fermilab uses an outer vacuum system filled with Argon to isolate the Li system from the environment.

7 CONCLUSIONS

The design of the liquid lithium lens involves both mechanical and electrical issues associated with the pressure vessel as well as beam optics considerations related to the transport lines between lenses. The mechanical problems are dominated by the requirements of coping with the very large pressure pulse produced by Joule and beam heating of the liquid lithium. The design of the beam optics is concerned with the efficient transport of large six dimensional emittance beams between the small lenses. A liquid Lithium lens is being constructed and the problems are going to be the subject of an experimental program.

REFERENCES

[1] C. Ankenbrandt, et. al., Phys Rev Spec Topics/ Accel. and Beams, to be published (1999)

[2] The MUCOOL Collaboration, *A Proposal for Ionization Cooling R & D for a High Luminosity Muon Collider*, Fermilab, (1999)

[3] A .Hassanein Private Communication, Argonne (1999)

[4] B. Bayanof, V. Belov, A Cherniakin, G. I. Silvestrov, Liquid Lithium Lens for High Magnetic Field, This conference,

[5] G. Silvestrov, A. Skrinsky, T. Vsevolozskaya, Final Stage of Muon Beam Cooling, This conference,

[6] V. Balbekov *Ionization cooling of muon beam by multistage system of lithium lenses with matching sections* This conference

[7] P. Spentzouris and D. Neuffer, *Design and Simulation studies of an Ionization cooling channel using Lithium Lenses and solenoidal transport channels*, This conference

[8] J. Norem, *Bent Solenoids for Spectrometers and Emittance Exchange Sections*, This conference

[9] R. Palmer, *The Muon Collider, a set of lectures given at the accelerator school at Vanderbilt University*, Jan 1999

LATTICE DESIGN FOR A 50 ON 50 GeV MUON COLLIDER*

C Johnstone, † and W. Wan, FNAL, Batavia, IL 60510
A. Garren, UCLA, Los Angeles, CA 90024

Abstract

Two modes are being considered for a 50 on 50-GeV muon collider: one being a high-luminosity ring with broad momentum acceptance (dp/p of $\sim$ 0.12%, rms) and the other lower luminosity with narrow momentum acceptance (dp/p of $\sim$ 0.003%, rms). To reach the design luminosities, the value of beta at collision in the two rings must be 4 cm and 13 cm, respectively. In addition, the bunch length must be held comparable to the value of the collision beta to avoid luminosity dilution due to the hour-glass effect. To assist the rf system in preventing the bunch from spreading in time, the constraint of isochronicity is also imposed on the lattice. Finally, the circumference must be kept as small as possible to minimize luminosity degradation due to muon decay. Two lattice designs will be presented which meet all of these conditions. Furthermore, the lattice designs have been successfully merged into one physical ring with mutual components; the only difference being a short chicane required to match dispersion and floor coordinates from one lattice into the other.

1 INTRODUCTION

After one μ^+ bunch and one μ^- bunch have been accelerated to collision energy, the two bunches are injected into the collider ring, which is a fixed-field storage ring. Collider ring lattices have been developed for two of the collision energies in this table: 100 GeV[1] and 3 TeV[2] in the center of mass. In addition, a preliminary interaction region for a 500 GeV lattice has been designed.

Three operational modes are proposed in the above table for the 100-GeV collider, each requiring a different machine optics. The following sections discuss a 100-GeV collider lattice for two of the modes, the broad momentum (dp/p of 0.12%, rms) application and the monochromatic mode (dp/p of 0.003%, as well as comparison with a 3-TeV collider lattice.

2 COLLIDER LATTICES

Design criteria Stringent criteria have been imposed on the collider lattice designs in order to attain the specified luminosities. The first and most difficult criterion to satisfy is provision of an Interaction Region (IR) with extremely low β^* values at the collision point consistant with acceptable dynamic aperture. The required β^* values for the 100-GeV collider are 4 cm for the broad momentum-width case and 14 cm for the narrow-width case. For the 3 TeV machine, β^* is only 3 mm. These β^* values were tailored to match the longitudinal bunch lengths in order to avoid luminosity dilution from the hour-glass effect. Achieving this requirement in the 3 TeV lattice is complicated by the high peak beta-function values in the final-focus quadrupoles requiring 8-10 cm radial apertures. The correspondingly weakened gradients combined with the ultra-high energy make for a long final-focus structure. (In contrast, the lower energy and larger β^* values in the 100 GeV collider lead to an efficient, compact final-focus telescope.) Compounding the problem, particularly for the 3-TeV design, is the need to protect superconductoring coils from the decay products of the muons. Placing a tungsten shield between the vacuum chamber and the coils can increase the radial aperture in the 3-TeV quadrupole by as much as 6 cm, lowering still further available gradients. Final-focus designs must also include collimators and background sweep dipoles, and other provisions for protecting the magnets and detectors from muon-decay electrons. Effective schemes have been incorporated into the current lattices.

Another difficult constraint imposed on the lattice is that of isochronicity. A high degree of isochronicity is required in order to maintain the short bunch structure without excessive rf voltage. In the lattices presented here, control over the momentum compaction is achieved through appropriate design of the arcs.

A final criterion especially important in the lower-energy colliders, is that the ring circumference be as small as feasible in order to minimize luminosity degradation through decay of the muons. To achieve small circumference requires high fields in the bending magnets as well as a compact, high dipole packing-fraction design. To meet the small circumference demand, 8 T poletip fields have been assumed for all superconducting magnets, with the exception of the 3-TeV final-focus quadrupoles, whose poletips are assumed to be as high as 12 T. In addition, design studies for still higher field dipoles are in progress.

rf system The rf requirements depend on the momentum compaction of the lattice and on the parameters of the muon bunch. For the case of very low momentum spread, synchrotron motion is negligible and the rf system is used solely to correct an energy spread generated through the impedance of the machine. For the cases of higher momentum spreads, there are two approaches. One is to make the momentum compaction zero to high order through lattice design. Then the synchrotron motion can be eliminated, and the rf is again only needed to compensate the induced energy spread correction. Alternatively, if some momentum compaction is retained, then a more powerful rf system

* Work supported by the U.S. Department of Energy under contract No. DE-AC02-76HO3000
† email: cjj@fnal.gov

0-7803-5573-3/99/$10.00@1999 IEEE.

is needed to maintain the specified short bunches. In either case, rf quadrupoles will be required to generate BNS [3, 4] damping of the transverse head-tail instability.

3-TeV lattice The 3-TeV ring has a roughly racetrack design with two circular arcs separated by an experimental insertion on one side, and a utility insertion for injection, extraction, and beam scraping on the other. The experimental insertion includes the interaction region (IR) followed by a local chromatic correction section (CCS) and a matching section. The chromatic correction section is optimized to correct the ring's linear chromaticity, which is almost completely generated by the low beta quadurupoles in the IR. In designs of e^+e^- colliders, it has been found that local chromatic correction of the final focus is essential, as was found to be the case here. The 3-TeV IR and CCS are displayed in Fig. 2.

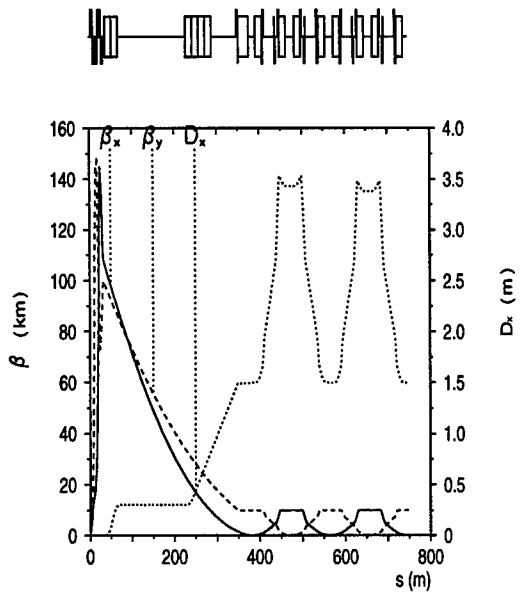

Figure 1: 3-TeV IR and Chromatic Correction

100-GeV lattices In contrast, the 100-GeV ring geometry is highly compact and more complicated than a racetrack, but the lattice has regions with the same functions as those of the 3-TeV ring.

The need for different collision modes in the 100-GeV machine led to an Interaction Region design with two optics modes: one with broad momentum acceptance (dp/p of 0.12%, rms) and a collision β of 4 cm, and the other basically monochromatic (dp/p of 0.003%, rms) and a larger collision β of 14 cm. This lattice design, shown in Fig. 2 and Fig. 3, has a total circumference of about 350 m with arc modules accounting for only about a quarter of the ring circumference.

The low beta function values at the IP are mainly produced by three strong superconducting quadrupoles in the Final Focus Telescope (FFT) with pole-tip fields of 8 T. Because of significant, large-angle backgrounds from muon decay, a background-sweep dipole is included in the final-focus telescope and placed near the IP to protect the detector and the low-β quadrupoles [5]. It was found that this sweep dipole, 2.5 m long with an 8 T field, provides sufficient background suppression. The first quadrupole is located 5 m away from the interaction point, and the beta functions reach a maximum value of 1.5 km in the final focus telescope, when the maxima of the beta functions in both planes are equalized. For this maximum beta value, the quadrupole apertures must be at least 11 cm in radius to accommodate 5 σ of a 90 π mm mrad, 50-GeV muon beam (normalized rms emittance) plus a 2 to 3 cm thick tungsten liner [6]. The natural chromaticity of this interaction region is about -60.

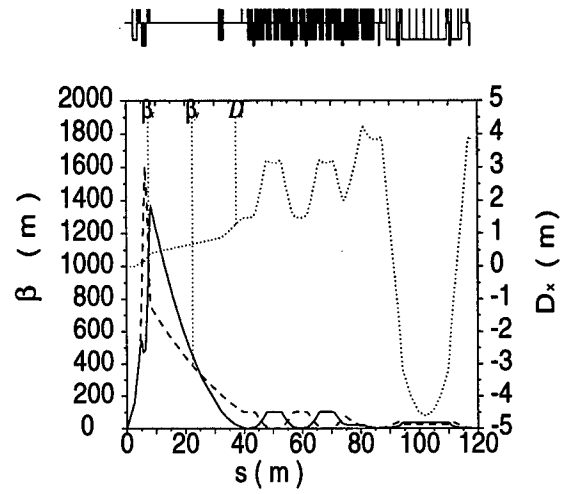

Figure 2: 4 cm β^* Mode showing half of the IR, local chromatic correction, and one of three arc modules.

Local chromatic correction of the muon collider interaction region is required to achieve broad momentum acceptance. The CC contains two pairs of sextupoles, one pair for each transverse plane, all located at locations with high dispersion. The sextupoles of each pair are located at positions of equal, high beta value in the plane (horizontal or vertical) whose chromaticity is to be corrected, and very low beta waist in the other plane. Moreover, the two sextupoles of each pair are separated by a betatron phase advance of near π, and each sextupole has a phase separation of $(2n+1)\frac{\pi}{2}$ from the IP, where n is an integer. The result of this arrangement is that the geometric aberrations of each sextupole is canceled by its companion while the chromaticity corrections add.

The sextupoles of each pair are centered about a minimum in the opposite plane ($\beta_{min} < 1$), which provides chromatic correction with minimal cross correlation between the planes. A further advantage to locating the opposite plane's minimum at the center of the sextupole, is that this point is $\frac{\pi}{2}$ away from, or "out of phase" with, the source of chromatic effects in the final focus quadrupoles; i.e. the plane not being chromatically corrected is treated like the IP in terms of phase to eliminate a second order chromatic aberration generated by an "opposite-plane" sextupole.

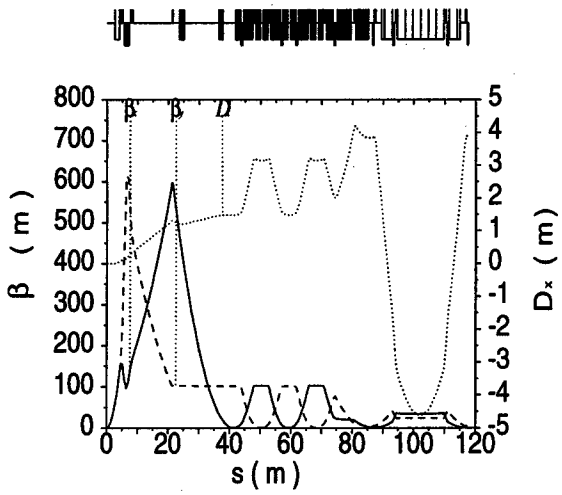

Figure3: 14 cm β^* Mode showing half of the IR, local chromatic correction, and one of three arc modules.

In this lattice example, the CC was optimized to be as short as possible. The $\beta_{\max}$ is only 100 m and the $\beta_{\min}$ = 0.7 m, giving a β_{ratio} between planes of about 150, so the dynamic aperture is not compromised by a large amplitude-dependent tuneshift.

This large beta ratio, combined with the opposite-plane phasing, allows the sextupoles for the opposite planes to be interleaved, without significantly increasing the nonlinearity of the lattice. In fact, interleaving improved lattice performance compared to that of a non-interleaved correction scheme, due to a shortening of the chromatic correction section, which lowers its chromaticity contribution. The use of somewhat shallower beta-minima with less variation in beta through the sextupoles were also applied to soften the chromatic aberrations, although this caused a slight violation of the exact π phase advance separation between sextupole partners. The retention of an exact π phase advance difference between sextupoles was found to be less important to the dynamic aperture than elimination of minima with $\beta_{\min} < 0.5$ m.

The total momentum compaction contributions of the IR, CC, and matching sections is about 0.04. The total length of these parts is 173 m, while that of the the momentum-compaction-correcting arc is 93 m. From these numbers, it follows that this arc must and does have a negative momentum compaction of about -0.09 in order to offset the positive contributions from the rest of the ring.

The arc module is shown as a part of Fig. 2. It has the small beta functions characteristic of FODO cells, yet a large, almost separate, variability in the momentum compaction of the module which is a characteristic associated with the flexible momentum compaction module [7].

A very preliminary calculation of the dynamic aperture without optimization of the lattice nor inclusion of errors and end effects is given in Fig. 4. One would expect that simply turning off the chromatic correction sextupoles in the 4 cm β^* mode would result in a linear lattice with a large transverse aperture. With only linear elements, the 4 cm β^* optics showed to be strongly nonlinear with limited on-momentum dynamic acceptance.

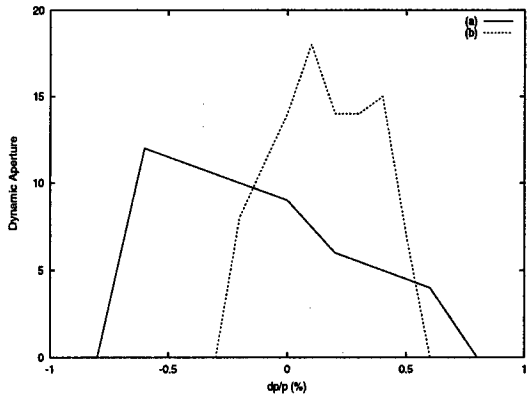

Figure 4: A preliminary dynamic aperture for the 4 cm β^* mode where σ (rms) = 82μm (solid line) and the 14 cm β^* mode where σ (rms) = 281μm (dashed line).

A normal form analysis using COSY INFINITY showed that the tune-shift-with-amplitude was large, which was the source of the strong nonlinearity in the seemingly linear lattice. Numerical studies showed that a similar dynamic aperture and tune-shift-with-amplitude terms. This ruled out the possibility that the dynamic aperture was limited by the low beta points in the local chromatic correction section and points to the IR as the source of the nonlinearity. Further analytical study using perturbation theory showed that the first-order contribution to the tune shift with amplitude is proportional to $\gamma_{x,y}^2$ and $\gamma_x \gamma_y$, which are large in this IR. These terms come from the nonlinear terms of p_x/p_0 and p_y/p_0, which, to the first order, equal the angular divergence of a particle. It was therefore concluded and later shown that the dynamic aperture of the more relaxed β^* of 14 cm would not have the same strong nonlinearities due to the reduced angular terms. In fact, the tune shift with amplitude was less by an order of magnitude; hence the large transverse acceptance shown in Fig. 4 (dashed line).

Thanks to S. Ohnuma his contributions to this work.

3 REFERENCES

[1] C. Johnstone et al, AIP Conf. Proc. **441**, p.209 (1998).

[2] C. Johnstone and A. Garren, PAC Conf. Proc. **1**, p. 411 (1997).

[3] K. Brown, SLAC-PUB-4811 (Dec., 1988).

[4] K. Brown, et al, SLAC-PUB-4219, (Feb., 1987).

[5] C. Johnstone and N. Mokhov, FERMILAB-Conf-96-366 (1996).

[6] A. Drozhdin, et al, AIP Conf. Proc. **441**, p. 242 (1998).

[7] K. Ng, S. Lee, and D. Trbojevic, FNAL-FN595 (Fermilab, 1992).

FIXED FIELD CIRCULAR ACCELERATOR DESIGNS *

C. Johnstone, † and W. Wan, FNAL, Batavia, IL 60510
A. Garren, UCLA, Los Angeles, CA 90024

Abstract

The rapid rate and cycle time required to efficiently accelerate muons precludes conventional circular accelerators. Recirculating linacs provide one option, but the separate return arcs per acceleration pass may prove costly. Recent work on muon acceleration schemes has concentrated on designing fixed-field circular accelerators whose strong superconducting fields can sustain a factor of 4 increase in energy from injection to extraction. A 4 to 16 GeV fixed-field circular accelerator has been designed which allows large orbit excursions and the tune to vary as a function of momentum. Acceleration is .6 GeV per turn so the entire cycle consists of only 20 turns. In addition a 16 to 64 GeV fixed-field circular accelerator has been designed which is more in keeping with the traditional Fixed Field Alternating Gradient machines[2]. In this work all three machine designs are described.

1 INTRODUCTION

Rapid acceleration in a multi-stage system is needed for a muon collider to limit intensity loss from muon decay. For the lower-energy acceleration stages, this consideration dominates the design. Ultra-rapid cycling synchrotrons and recirculating linacs with multiple return arcs have been considered for muon accelerators[1]. Given the technical complexity or expense of these proposed schemes, the idea of using fixed-field, single-path accelerators has been revisited in recent work. The arcs of such machines, composed of large-aperture, single-bore superconducting magnets, can be designed to accomodate the large energy range from acceleration. Lattices have been developed which can contain an energy change of a factor of four from injection to extraction. The multistage acceleration scheme considered here employs a linac as the first stage followed by two fixed-field machines, one accelerating from 4 GeV to 16 GeV and the next from 16 GeV to 64 GeV.

The 4-16 GeV stage is a FODO-based cell structure with the goal to maximize bend per cell and minimize overall circumference and intensity loss from decay. The 16-64 GeV stage is similar to an FFAG design developed at MURA[2] whose magnets have a magnetic field characterized by constant radial field indices. The lower energy lattice was optimized for minimum circumference, in consideration of muon lifetime. The higher energy lattice design minimizes aperture (cost), which may be the more important consideration for that energy range. The design approaches varied accordingly. The following sections will describe the two lattice designs and venture a few comparisons and conclusions.

2 FIXED-FIELD LATTICE DESIGN

A circular accelerator system can be designed using magnets with alternating gradient focusing, but with fields that remain constant for the duration of the acceleration cycle. The closed orbits move during the cycle but remain within the (single) aperture of each magnet. Such FFAG rings were first designed and studied at MURA[2], and are distinct from other possible accelerators, such as linacs, pulsed synchrotrons, or recirculating linacs with multiple-path return arcs. The following examples made are intended for use in a low-energy muon collider in a center-of-mass range of about 100 GeV (called a Higgs factory), but the ideas are applicable to higher energy colliders as well.

We will discuss two specific FFAG accelerator designs for the Higgs factory, one accelerates muons from 4 GeV to 16 GeV, the other from 16 GeV to 64 GeV. The rf systems are assumed to deliver on the order of 0.5-2 GeV per turn. In order to explore different possibilities, these two rings use different design approaches, though both are FFAG in the sense mentioned above. The lower and higher energy rings use non-scaling and scaling FFAG lattices respectively. In a non-scaling lattice the orbit properties of the closed orbits are a function of energy, while in a scaling lattice they are independent of energy.

The cells of the low energy, non-scaling ring contain a horizontally focusing quadrupole and a vertically focusing combined-function bending bending magnet. This magnet configuration was chosen to maximize the net bend per cell for a given magnet aperture, implying the fewest arc cells and minimal ring circumference.

The cells of the high energy, scaling ring contain one F magnet, one D magnet and short drift spaces. Each of the magnets has a magnetic field profile $B(\rho) \sim \rho^n$, where n is negative and positive in the F and D magnets respectively, which gives the AG focusing. In order to decrease the radial aperture, the magnetic field directions also alternate, causing the orbits to curve successively towards and away from the ring center in the F and D magnets, and the closed orbits to describe a scalloped set of parallel curves. To close the ring, the F magnets are made longer than the D magnets.

The non-scaling aproach yields the smallest design circumference, but a radial aperture which is generally larger than in the scaling approach. In the scaling aproach, lattice parameters do not vary with energy and radial excursions and magnet apertures can be reduced, but at the price of a

* Work supported by the U.S. Department of Energy under contract No. DE-AC02-76HO3000

† email: cjj@fnal.gov

0-7803-5573-3/99/$10.00@1999 IEEE.

larger circumference.

3 NONSCALING FFAG LATTICE

A nonscaling FFAG lattice relies on a strong-focussing FODO cell composed of large-bore superconducting magnets to contain the large range in momenta. The cell presented here consists of a horizontally-focussing (F) quadrupole followed by a vertically-focussing, combined-function (D) magnet. The cell could also be comprised of separated-function magnets, but the magnetic field layout chosen here produces the largest bend per cell for a given maximum excursion of the closed-orbit during acceleration. (The peak of the closed orbit excursion always occurs at the center of the F quadrupole.)

The optimal lengths of the magnets can be analytically obtained assuming thin lense kicks and imposing closure on both the orbit and lattice functions over a half cell. To solve the equations, the maximum off-axis orbit excursion in the F quadrupole must be chosen along with the F quadrupole's aperture and poletip field. To insure stability in both planes, the D quadrupole strength is taken to be equal to the F quadrupole strength. In the work presented here a maximum closed-orbit excursion of 7 cm has been chosen for the F quadrupole (implying a physical half-aperture of about 10-13 cm horizontally), and a gradient of 70 T-m. The spacing between magnets is taken to be 0.25 m. The aperture required in the combined function magnet will be close to half that of the F quadrupole. In practice, the bend and corresponding length of the combined function magnet must be rescaled to the desired maximum off-axis excursion due to the approximations inherent in the thin lense kick model, keeping the vertical focussing strength of the combined function magnet equal to the F quadrupole strength during the rescaling.

The lattice components and functions of the resulting cell are plotted in Figure1. Orbit excursions at 4 GeV are plotted in Figure2. The corresponding orbit excursion at 16 GeV is almost an inversion of the curve in Figure2. Tunes per cell vary from $\mu_{x,y} \sim 0.4$ at 4 GeV to $\mu_{x,y} \sim 0.075$ at 16 GeV. The arc contains about 100 cells, 1.6 m long, giving a total length of 160 m. If one assumes 100 m for rf, then the total circumference of this ring is less than 300 m. Adding an additional 100 m of rf and keeping the same choice of parameters, but scaling the ring to 16 to 64 GeV energy range, increases the circumference to 772 m. The circumference can be compared to the 1.36 km circumference of the 16 to 64 GeV scaling FFAG lattice described below.

The main drawback to this approach are the large pathlength changes as a function of energy. The pathlength shape is parabolic and changes by 70 cm from a minimum at 10 GeV to injection at 4 GeV and extraction at 16 GeV. We are presently studying the needed rf frequency and phasing requirements for different applications to see what is feasible. In subsequent calculations, a fixed-field sextupole component was added to the quadrupole fields to change the parabolic shape of the pathlength variation to one which increases almost monotonically with energy. Chicanes could be incorporated into this version of the lattice to eliminate pathlength changes at the expense of circumference.

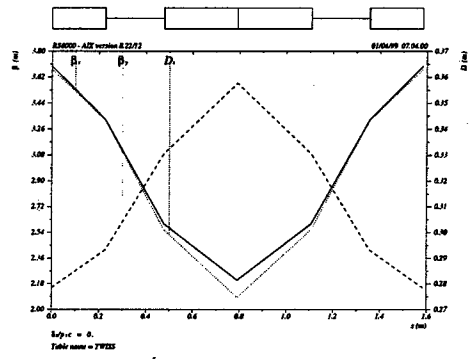

Figure 1: Lattice functions of nonscaling FFAG cell.

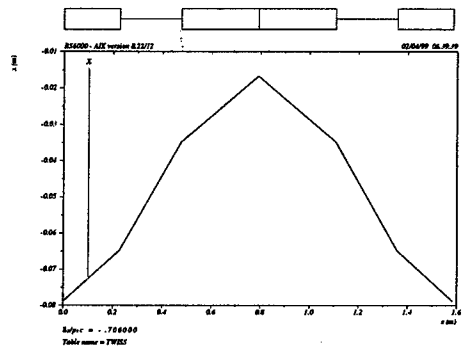

Figure 2: 4 GeV orrbit excursion of nonscaling FFAG cell

4 SCALING FFAG ACCELERATOR LATTICE

This design is based on FFAG concepts developed at MURA in the 1950s. All of the orbits accelerated traverse a single vacuum tube in one set of magnets, and the radial extent of these orbits is small compared to the radius of the ring.

A cell of this lattice contains one F magnet, one D magnet and short drift spaces. Each of the magnets has a magnetic field $B(\rho) \sim \rho^n$, where ρ is the distance from the local center of curvature of each magnet to the orbit. Hence the field index $n = -(\rho/B)(dB/d\rho)$ is independent of ρ. The F and D magnets have opposite signs of both B and n, the same magnitudes,and different lengths, so the orbits curve successively towards and away from the ring center

in the F and D magnets. In both magnets the magnitude of the field increases outward from the center of the ring. The closed orbits are a scalloped set of parallel curves, the magnet edges lie on radii from the ring center, and the closed orbits are normal to them.

To make the ring close, the F magnets are made longer than the D magnets, in a ratio of about 3/2, which gives a circumference factor $R/\rho \sim 5$.[1] The cells have constant tune values with energy because the transverse focusing equations, when expressed with $\theta = s/R$ as the independent variable (R = circumference/2π), only depend on $n(\theta)$, which is independent of energy. Typical cell tunes are $\mu_x = 5\pi/6, \mu_y = \pi/6$. For given tunes and field strength, the magnet lengths and radial extent of the closed orbits decrease with increasing values of n. Arc cell parameters are given in Table 1 and lattice functions plotted in Figure3.

There are three main advantages of this design: the betatron tunes are independent of energy, the radial width of the orbits can be made very small for a large accelerated energy range, and the variation of orbit lengths is also small. The disadvantages are the large circumference factor and the difficulty of designing superconducting magnets with large n.

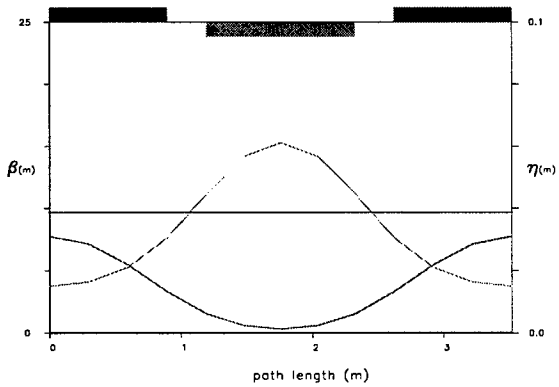

Figure 3: Arc cell with constant field-index magnets

Long straight sections can be included in a scaling radial sector FFAG. One can design matched insertions by using focusing magnets identical to the cell F and D magnets, but with different lengths and spacings. Long straight drift spaces can be placed between triplets, and the dispersion can be reduced to zero in the long drift space by placing pairs of 0-gradient dipoles at each end of the drift. As a result the radial spread of the orbits in the long drifts is reduced from that in the arc cells by a factor of about five. Figure4 shows a sector of the ring which includes this insertion with a drift straight section.

[1]The magnet lengths and $|n|$ determine the cell tunes. If the magnet length ratio is too large, the cell is vertically unstable.

Table 1: Arc cell parameters

Lattice: $C = F/2\ O\ D\ O\ F/2$			
Rigidity at 40 GeV	T-m	$B\rho$	133.4
Magnetic field at 40 GeV	T	B	4.86
Gradient at 40 GeV	T/m	B'	125
Magnetic field index $(-B'/B\rho)$		n	707
Magnetic radius	m	ρ	27.5
Cell length	m	L_C	3.51
F-magnet length	m	L_F	1.79
D-magnet length	m	L_D	1.13
Drift space length	m	L_O	0.8
Cell tune - horizontal		μ_x	0.416
Cell tune - vertical		μ_y	0.084
Horizontal beta maximum	m	$\hat{\beta}_x$	7.8
Vertical beta maximum	m	$\hat{\beta}_y$	15.3
Dispersion (constant in cells)	cm	D	3.87

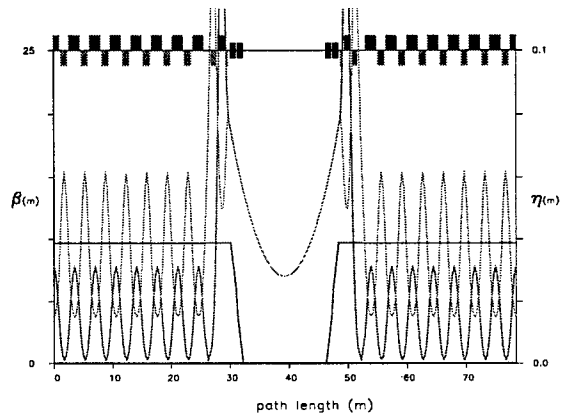

Figure 4: Insertion with 14 m drift space.

As an example of a scaling radial sector FFAG accelerator, we consider a ring that might function as the final acceleration stage for a Higgs factory muon collider. It would accelerate muons over an energy factor of about four, say from 16 GeV to 64 GeV.

The ring lattice is made up of 16 sectors; each sector consists of 14 FODO cells and one insertion containing a 14 meter straight section. A one-period wiggler is installed in every fourth long straight section. The wigglers reduce the variations of circumference with energy. Thus the ring has four superperiods, each containing three sectors with drift straight section insertions and one sector with a wiggler insertion. Four of the drift straight sections are used to inject or extract one of the two muon beams and the other eight drift straight sections contain rf cavities. The total circumference of this ring is 1356 km.

5 REFERENCES

[1] "Muon Collider Status Report", http://www.cap.bnl.gov /mumu/status-report.html

[2] K Simon, MURA-KRS-6, (MURA-43) (1954); K. Simon, et al, Phys. ReV. **103** p. 1837, (1956).

LARGE ACCEPTANCE MUON STORAGE RINGS FOR NEUTRINO PRODUCTION: LATTICE DESIGN*

C. Johnstone, †, FNAL, Batavia, IL 60510, B. Autin,CERN, Geneva, Switzerland

Abstract

The possibility of achieving the high muon fluxes suggested in recent work on muon colliders has revived interest in the idea of using muon storage rings for neutrino production. Through proper design of the lattice, a significant fraction of the stored muons can be converted into an intense, low-divergence beam of neutrinos. This work examines the incorporation of a long, high-beta straight section for production of neutrino beams into a lattice which is otherwise optimized for transverse and longitudinal admittance. (The ring must be able to accept a very large emittance and large momentum spread muon beam.)

1 INTRODUCTION

A muon storage ring is also a source of neutrinos from muon decay. By recirculating the intense muon source beam, a muon storage ring is capable of efficient and intense neutrino production when the muons decay in long field-free regions (or straight sections). This paper discusses two 10-GeV muon storage rings designed to optimize neutrino-beam production.

2 DESIGN CONSIDERATIONS

There are three principal considerations when optimizing a muon storage ring for neutrino beam production. The overriding consideration is to design a ring with an exceptionally large acceptance, both transversely and longitudinally, thereby reducing as much as possible the beam cooling required. This condition also presumes large-emitance muon beams can be effectively accelerated. The next two are specific to neutrino production. One is the conversion of a significant fraction of the stored muons into a directed beam of neutrinos; that is, the production straight must occupy a substantial portion of the ring circumference. Another is that the properties of the secondary neutrinos include the dynamics of the muons in the production straight. This implies that the neutrino beam will be colinear (at least to within the limits set by the decay kinematics) if the divergence of the parent muon beam is less than or comparable to the muon decay angle (which is 10 mr at 10 GeV). Since the muon beam divergence in the decay straight can be controlled with a straightforward high-beta insert, the lattice parameters are not overly constrained. This allows the base lattice to be designed consistent with unusually large transverse and momentum admittances. (The intent here is that the greater the acceptance achieved in the storage ring, the fewer muon cooling stages will be required upstream with a considerable savings in complexity and expense.) The challenge, then, in the design of the storage ring is to extend the exceptionally large transverse and longitudinal emittances characteristic of the arc design to include the high-beta insertion. For reference, the muon beam entering the initial cooling stage has a normalized transverse emittance of 15,000 π mm-mr and a momentum spread of about $\pm$ 5%.

3 BASIC LATTICE DESIGN

With long opposing straights, the natural layout of the storage ring is racetrack. Strong-focussing FODO cells are the best choice for the arcs because of their potential for large momentum acceptance (larger than $\pm$5%) as compared with more complicated focussing structures. At 10-GeV, large-bore superconducting quadrupoles are recommended in order to maintain a strong gradient over the large aperture required to accomodate both the large transverse admittance and the large displacement of off-momentum orbits. The high-beta insert, on the other hand, is a weaker-focussing structure and must be carefully designed and matched to the arc to transmit the large range in momenta in addition to creating a parallel beam for neutrino production.

Table 1: Parameters of the large-momentum acceptance arc cells for a 10-GeV muon storage ring

	Initial	Later
intermagnet spacing (m)	0.1451	0.2
dipole length (m)	3.422	0.645
dipole bend (rad)	$\pi/18$	0.174
dipole field (T)	1.7	9
quadrupole length (m)	0.4	0.387
arc quadrupole strength (m^{-2})	0.75	1.8
arc quadrupole poletip field (T)	> 5	7.8
arc quadrupole radius (cm)	20	13
cell phase advance (deg)	≈ 74	≈ 90
horiz. sextupole strength (T)	0	2.3
vert. sextupole strength (T)	0	3.5

The initial design is simply constructed using two identical high-beta straights matched directly to the connecting arcs. Each arc is composed of six full FODO cells plus an extra half cell with cell properties given as the first example in Table 1. Two cells at each end of the arcs have reduced deflections to suppress dispersion in the two long straights. The arcs and dispersion suppression modules account for 44% of the ring which is 394 m in circumference. The high-beta straight for neutrino production was

* Work supported by the U.S. Department of Energy under contract No. DE-AC02-76HO3000

† email: cjj@fnal.gov

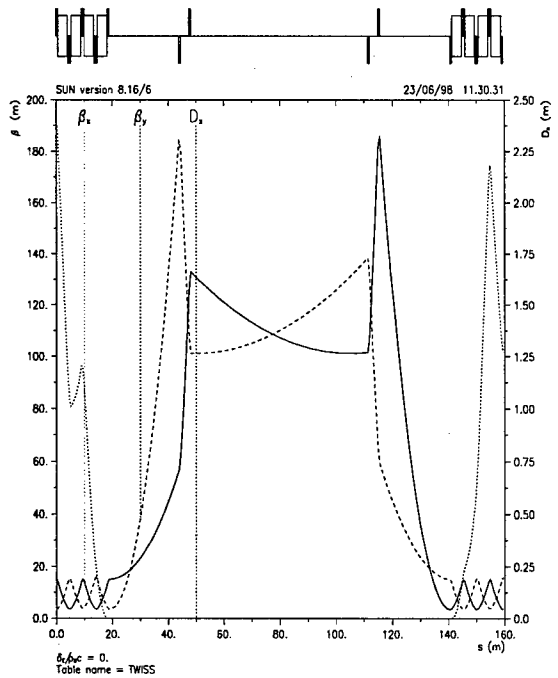

Figure 1: Initial design: The neutrino production region flanked by matching sections and dispersion-suppression cells

formed using an antisymmetric doublet quadrupole structure and represents about 16% of the total ring circumference. The matching section between the arc and and the high-beta straight accounts for 12% of the total circumference and its increased divergence contributes to the backgrounds associated with neutrino detection. Fig. 1 shows the beta and dispersion functions for the high-beta region, flanking matching sections, and dispersion suppression cells. The rest of the circumference is occupied by a second long straight which is opposite to and presently identical to the production straight. This region will eventually be redesigned as a utility section to include injection. The periodicity of this ring is one.

The admittance of the initial ring design was calculated using a β_{max} in the high-beta quadrupoles of 200 m (from Fig. 1), a quadrupole radial aperture of 20 cm, and assuming a $\pm 3\ \sigma$ rms beam size. These parameters give a normalized rms emittance of 2111 mm-mr; given that the upstream acceleration is not the limiting aperture. Errors have not been included in calculating this ideal aperture.

The momentum dependence of the initial lattice was studied and tracked using MAD[2]. The tune of the ring is $\nu_x = 5.46$ and $\nu_y = 5.65$. Tracking studies indicate that this fractional tune is near optimal and also that the momentum aperture is best when the x and y plane fractional tunes are close. (Although symmetric inserts were studied, it was more difficult to make the fractional tunes between the two planes close–at least in the present lattice version–and the dynamic aperture was smaller when tracked.) Although a closed orbit exists for a dp/p of -6.7% to 5.8%, the orbit excursions were large at the low momenta and the betas too high at the high momenta. If an orbit cutoff of ± 15 cm and a β_{max} of 200 m is enforced, then the acceptable momentum range of the initial lattice design appears to be -5.3% to 5%.

4 LATTICE IMPROVEMENTS

Noting that the neutrino production straight is only 16% of the ring circumference, one of the first modifications to the design was to match the short FODO cells of the arc into much longer FODO cells to build up the high-beta production region. Use of a periodic unit allows almost complete flexibility in the length of the region. Additionally, peak beta values were reduced by a factor of two. The insertion was kept antisymmetric so that the periodicity of the ring remained one. The improvements in this later lattice allows for a production straight which can be easily varied from $\approx$ 22% of the total circumference for a 428 m ring to $\approx$ 40% for a 717 m circumference ring. In the initial design the matching sections are almost equivalent in length to the production straight (75% of), but in the later work, they fall to 30% the length of the production straight in the 428 m ring and 10% in the 717 m ring.

A significant problem with the initial design is that the tune changes by $\nu_x = 5.82, \nu_y = 6.01$ to $\nu_x = 5.11, \nu_y = 5.28$ over the accepted momentum range. Such a large tune spread unavoidably covers an integer or half-integer resonance; consequently substantial beam loss is expected. Therefore, another improvement in the later design was to insert sextupole correctors at the center of each quadrupole in the arcs and cancel most of the linear chromaticity. (In the calculation, the quadrupoles were divided in two and short, 0.2 m sextupole magnets inserted; hence their large poletip fields. It should be possible instead to insert sextupole correction coils along the length of the quadrupole at a reduced field.)

Not only were sextupoles correctors added, the arc cell was also redesigned to keep the off-momentum excursions under ± 8 cm and arc quadrupole apertures modest. Reducing off-momentum orbit excursions means shorter cells with stronger quadrupoles and shorter, stronger dipoles. The amount of bend per arc cell was left virtually unchanged so the number of cells per arc remains the same (7.5). Additionally, at the central momentum of 10 GeV, the arc quadrupole strengths were tuned to give to a near $\pi/2$ phase advance per cell (keeping the focussing and defocussing quadrupoles equal strength). The new parameters of the arc FODO cells are included in Table 1 for comparison. It should be noted that the 9 T fields in the dipoles can be reduced to 6–7 T without compromising the basic lattice design or its properties; this requires adding 2 to 4 cells per arc.

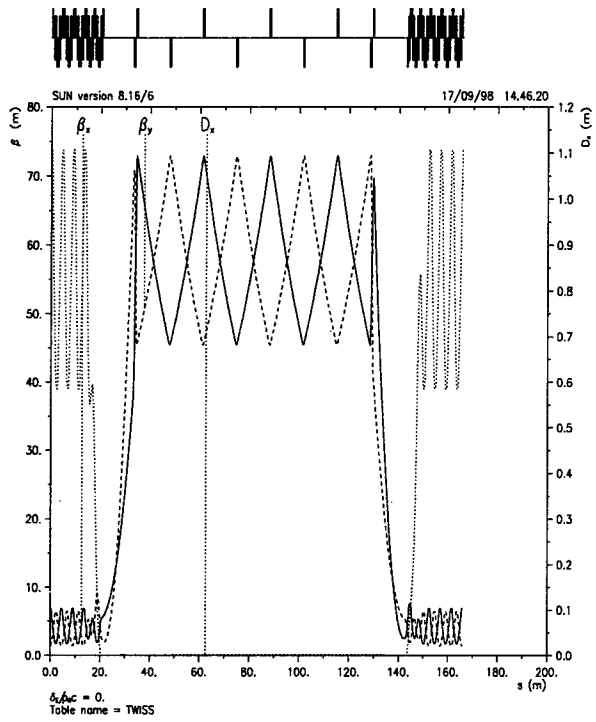

Figure 2: Later design: Lattice functions of the high-beta FODO cells for neutrino production flanked by matching sections, dispersion supression cells, and three arc modules.

5 LATTICE PERFORMANCE

The optimal dynamic aperture for both transverse and longitudinal was found to be near a fractional tune of $(2n + 1)\pi/2$. In the latest lattice shown Fig. 2, the fractional tune of the horizontal plane was set near 0.25 and the vertical plane near 0.75.) This choice keeps off-momentum particles from approaching either integer or half-integer resonances using the weakest sextupole strengths. It also minimizes second-order chromatic effects. With this fractional tune, the normalized rms emittance accepted by the high-beta quadrupoles–assuming a 20 cm quadrupole radius, a β_{max} of 100 m and a 3σ distribution–is about 4200 mm-mr. The transverse acceptance is limited by the high-beta quadrupole aperture and, fortunately, not by the nonlinear tuneshifts generated by the chromatic correction sextupoles.

With the sextupoles cancelling most of the linear chromaticity, the total tune swing is reduced from $\delta\nu_x = 0.71, \delta\nu_y = 0.73$ to $\delta\nu_x = 0.12, \delta\nu_y = 0.16$. Further reduction of this tune swing is possible, but does not appear necessary and stronger sextupoles decrease the currently large on-momentum aperture.

6 RESULTS

At the rms emittance quoted (2111 mm-mr), the rms angle of the muon beam in the 63.3 m-long production region (between the quadrupole doublets) is less than 1 mr, or less than 1/10 the natural opening angle of the neutrinos. It is therefore an insignificant contribution to the final divergence of the neutrino beam. However, the matching sections outside of the doublet contribute between 1 and 3 mr over 33.2 m, rising to 2-5 m over the 14 meters occupied by the high-beta quadrupole doublet.

In the later lattice, the rms angle of divergence, on average, in the production straight (assuming 4200 mm-mr) is about 1.3 mr both horizontally and vertically, despite the increase in the transverse acceptance. There is a short burst of highly divergent beam, 14-17 mr, over the short distance ($\approx$1 m) comprising the high-beta quadrupole doublet. However, the resulting background neutrinos should dissipate rapidly before the intended target. The divergence in the remaining 12–13 m in each matching section (representing over 90% of the length of this section), drops to 3-5 mr, which is similar to the previous design. Overall, the contribution of the matching sections to the neutrino beam is reduced by a factor of 2.5–7 from the initial design.

7 DISCUSSION AND SUMMARY

In the initial design, all quadrupoles must have large, 20-25 cm radial apertures to accomodate the large displacements ($\pm$15 cm) of off-momentum orbits in the arcs and the 200 m high-beta peaks in the insert. This includes both arc and high-beta quadrupoles. In the arcs of the second design, the quadrupole apertures are smaller by about a factor of two due to the reduced orbit swing of off-momentum orbits. If needed, the strength and cell length can be adjusted to lower the poletip fields in both quadrupole and dipole components. Since the high-beta peak in the insert is lower by a factor of two, the transverse dynamic aperture of the second lattice is correspondingly larger.

To summarize, ideal lattices have been designed which successfully include a long, low-divergence, straight section for neutrino production without compromising an exceptional dynamic aperture in both transverse and momentum space. The production straights nominally occupy 20–40% of the ring circumference indicating a large conversion of stored muons into useable neutrinos. Although a large dynamic aperture has been obtained, clearly, a realistic set of errors must be introduced into the tracking to determine to what extent this ideal aperture deteriorates.

Thanks to S. Ohnuma for useful suggestions on sextupoles

8 REFERENCES

[1] S. Geer, Fermilab-PUB-97/389 (hep-ph/9712290)

[2] H. Grote and F. Iselin, CERN publication CERN/SL-90-13(AP), version 8.17.

NEUTRINO INDUCED RADIATION AT MUON COLLIDERS *

N. V. Mokhov†, and A. Van Ginneken, FNAL, Batavia, IL

Abstract

Intense highly collimated neutrino beams are created from muon decays at high-energy muon colliders causing significant radiation problems even at very large distances from the collider ring. A newly developed weighted neutrino interaction generator permits detailed Monte Carlo simulations of the interactions of neutrinos (and of their progeny) to be performed using the MARS code. Dose distributions in a human tissue-equivalent phantom (TEP) are calculated when irradiated with neutrino beams (100 MeV–10 TeV). Results are obtained for a bare TEP, one embedded in several shielding materials and for a TEP located at various distances behind a shield. The distance from the collider ring (up to 60 km) at which recommended annual dose limits can be met is calculated for 0.5, 1, 2, 3 and 4 TeV muon colliders. The possibility to mitigate the problem via beam wobbling is investigated.

1 INTRODUCTION

As pointed out by King [1] neutrinos from muon decay may cause significant radiation problems at large distances from the collider ring. Dose at a given location grows with muon energy roughly as E^3 due to the increase with energy of the neutrino cross section, of total energy deposited, and of the collimation of the decay neutrinos—each responsible for a factor of E. From simple geometry, dose is expected to decline with radial distance as R^{-2} and it is estimated that for a 2+2 TeV collider the Fermilab off-site annual dose limit of 10 mrem is reached only after some 34 km [2]. Detailed Monte Carlo calculations [3] confirm the great importance of this problem for high-energy muon colliders. In these studies a weighted neutrino interaction generator is developed and incorporated in the MARS [4] code. Ref. [1] uses the 'equilibrium assumption' which deals with a human TEP embedded in an essentially infinite tissue-equivalent medium. By contrast ref. [5] assumes the TEP is surrounded everywhere by a vacuum. These rather sweeping assumptions bear greatly on the maximum dose encountered within the TEP. In a more realistic situation the TEP may be embedded in, e.g., soil, concrete, steel, lead—or placed in an evacuated region and then embedded into a material medium. Each of these geometries affects neutrino interaction probabilities and subsequent shower development in different ways. This is investigated here for mono-energetic neutrinos as well as for those produced by a muon collider.

* Work supported by the Universities Research Association, Inc., under contract DE-AC02-76CH00300 with the U. S. Department of Energy.

† Email: mokhov@fnal.gov

2 NEUTRINO INTERACTION MODEL

The model represents energy and angle of the particles—$e^{\pm}$, $\mu^{\pm}$, and hadrons—emanating from a simulated interaction. These particles, and the showers initiated by them, are then further processed by the MARS transport algorithms in the usual way. The four types of neutrinos are distinguished throughout: $\nu_\mu, \overline{\nu}_\mu, \nu_e, \overline{\nu}_e$. The model identifies the following types of neutrino interactions for ν_μ ($\overline{\nu}_\mu$) and similarly for ν_e, ($\overline{\nu}_e$): $\nu_\mu N \to \mu^+ X, \nu_\mu N \to \nu_\mu X, \nu_\mu p \to \mu^+ n, \nu_\mu p \to \nu_\mu p, \nu_\mu n \to \nu_\mu n, \nu_\mu e^- \to \nu_\mu e^-, \nu_\mu e^- \to \nu_e \mu^-, \nu_\mu A \to \nu_\mu A$. Total and differential cross sections for all these processes are taken from the literature. The corresponding sampling algorithms are developed and implemented into the MARS [4] code. For example, for the first reaction—corresponding to charged current deep inelastic neutrino interactions—total cross sections are assumed to be [6] $6.7\times10^{-39} E_\nu$ cm^2 per nucleon (E_ν in GeV) for neutrinos and half of that for antineutrinos. The differential cross section is taken from [7] as

$$\frac{d\sigma}{dx\,dy} = \frac{G^2 x s}{2\pi}\left(Q(x) + (1-y)^2\,\overline{Q}(x)\right) \qquad (1)$$

where $x = -q^2/2M\nu$ with q the momentum transfer, M the nucleon mass, and ν the energy loss of the neutrino in the lab, $y = \nu/E_\nu$, G is the Fermi coupling constant, s is the total energy in the center of mass, and $Q(x), \overline{Q}(x)$ represent the quark, antiquark momentum distributions inside the nucleon. Both $xQ(x)$ and $x\overline{Q}(x)$ are taken from experiment in numerical form. For antineutrinos the roles of $Q(x), \overline{Q}(x)$ in Eq. 1 are interchanged. Once the direction and momentum of the lepton is decided in the Monte Carlo, its center-of-mass momentum is balanced by a single pion which is then forced to undergo a deep inelastic interaction in the target nucleus. The latter approximates particle production associated with deep inelastic neutrino events.

3 NEUTRINOS ON PHANTOM

A neutrino induced dose delivered to a person—represented in this study by a 30 cm thick TEP—depends strongly on whether any material is present upstream of the TEP and on the composition and location of that material. The minimal dose results from cascades developed by particles produced in ν-interactions within the TEP itself. Any material immediately upstream the TEP would only amplify the maximum dose which in all cases occurs at the TEP exit plane. Dose reduction due to removal of the ν by interactions or scattering is completely negligible—even after hundreds of kilometers of soil. Fig. 1 shows maximum dose in a TEP for a

0-7803-5573-3/99/$10.00@1999 IEEE.

ν_μ broad beam as a function of energy for for a bare TEP suspended in vacuum and for the equilibrium case in comparison with [5]. Instead providing shielding, the presence of soil upstream enhances the dose by a factor of ~1000 in the TeV region compared to the bare TEP.

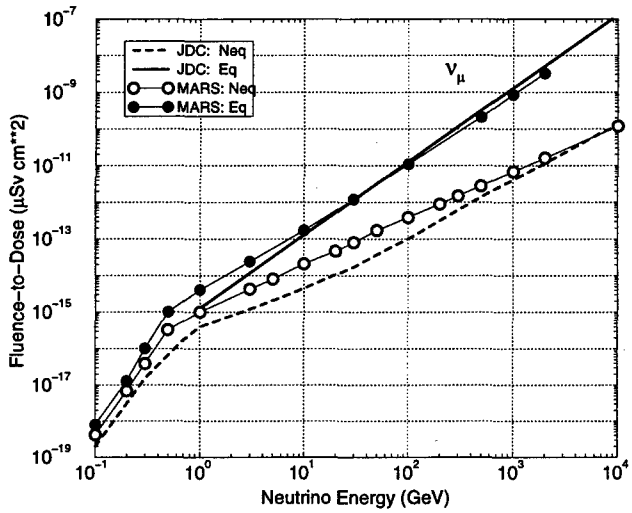

Figure 1: Dose equivalent in a bare (Neq) TEP and in one embedded in infinite soil (Eq) per unit neutrino fluence as calculated with MARS and from [5].

Calculations show that in a bare TEP, dose for ν_e is very close to that for ν_μ and is about a factor of two lower for the $\overline{\nu}_\mu$ and $\overline{\nu}_e$ beams. Equilibrium dose is practically achieved after some 5 m of soil at all energies of interest here. Maximum dose in a TEP downstream of a thick wall grows with Z: in pSv per incident neutrino it is 0.12 for water or tissue, 0.19 for soil, 0.25 for steel and 0.48 after a lead wall.

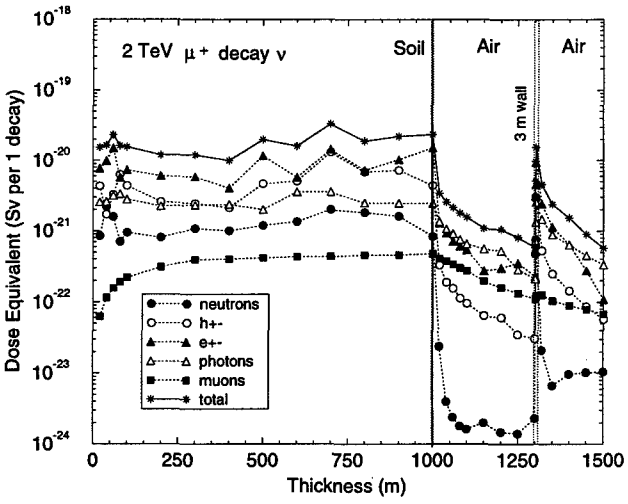

Figure 2: Total and partial maximum dose equivalent in a TEP at different locations in soil, air downstream, a 3 m concrete wall, and air downstream of the wall, for a 2 TeV μ^+ decay neutrino beam.

4 STRAIGHT MUON BEAM

Using a 2 TeV μ^+ decay neutrino beam as a source term—a typical situation downstream of a straight section or spent muon beam—a series of calculations is performed on dose in a TEP for various shielding configurations. Fig. 2 shows that the dose remains roughly constant through the soil shielding, then drops quickly in the air downstream. Any object thick enough (e. g., a 3 m concrete wall) restores the dose back to its original level in soil after which dose decays again in air or vacuum. For a TEP embedded into soil ('equilibrium case'), the dose is mainly due $e^\pm$, with photons and charged hadrons contributing noticeably. In the air downstream, the dose is first determined by $e^\pm$, then by photons and—after several hundred meters—by muons.

5 RADIATION AROUND RING

The magnet and beam parameters [2] for both low– and high-energy muon colliders, assumed embedded into Fermilab type soil, are implemented into MARS [3]. For a strictly planar orbit ν-spreading is exclusively due to the transverse momentum acquired at decay. For 2 TeV muons, the fraction of ν-energy—or dose—contained within 10 μrad spreads only over 1 cm after traversing 1 km and dose decreases rather slowly with the radial distance in the orbit plane (Figs. 3-4). The DOE off-site annual dose limit of 100 mrem (=1 mSv) and the Fermilab recommended limit of 10 mrem are reached at radial distances shown in Table 1. Assuming a spherical earth, this radial distance tells us how deep below ground the collider must be placed by equating dose limit(s) with surface dose—apart from legal considerations pertaining to dose delivered deep underground. Note that several meters of soil everywhere around the tunnel are needed in all cases to protect against hadrons and muons.

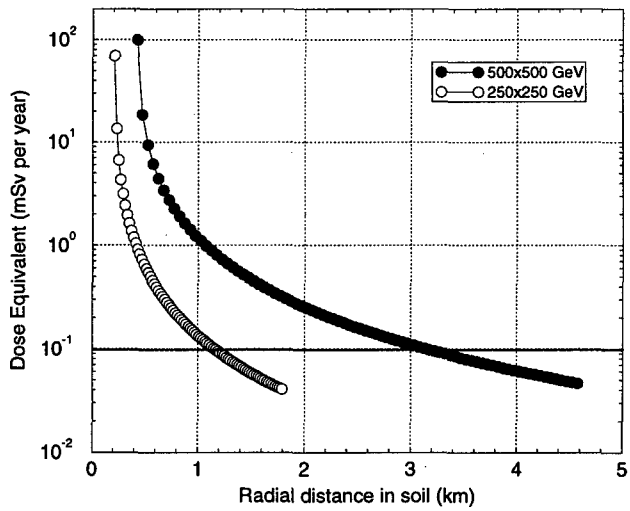

Figure 3: Maximum dose equivalent in TEP embedded in soil in low-energy muon collider orbit plane with 2×10^{20} decays per year *vs* distance from ring center.

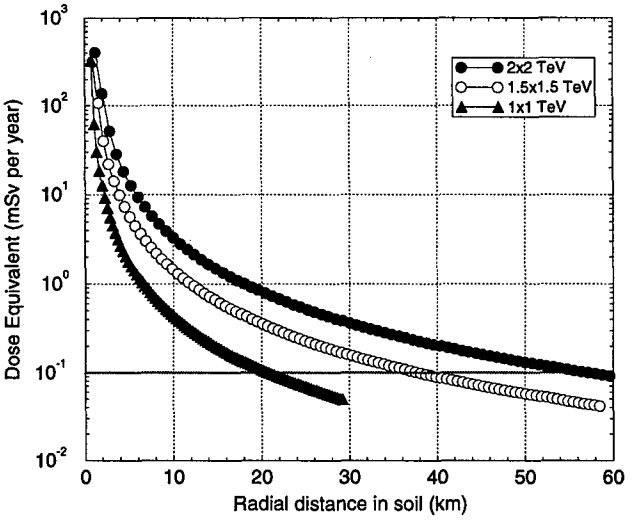

Figure 4: Maximum dose equivalent in TEP embedded in soil in high-energy muon collider orbit plane with 1.2×10^{21} decays per year *vs* distance from ring center.

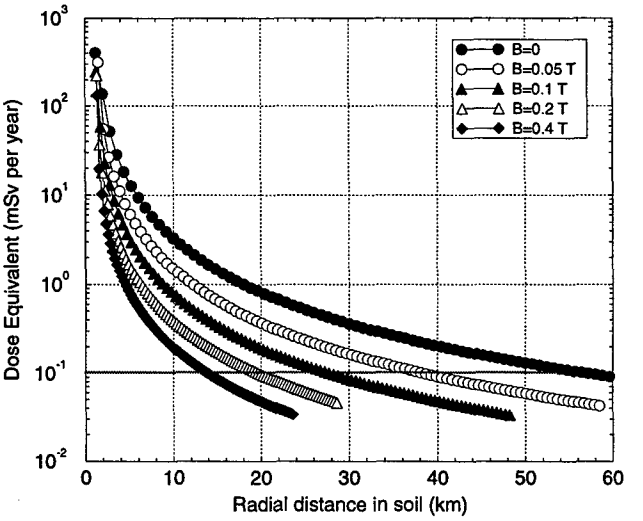

Figure 5: Average dose in TEP located in orbit plane *vs* distance from ring center in soil around a 2+2 TeV muon collider with 1.2×10^{21} decays per year for five values of vertical wave field.

6 MITIGATION

Since the ν-beam is highly collimated and directional—the intrinsic divergence is only 50μrad from 2 TeV muon decay—it was proposed to vary the direction in which the secondary ν-beam is produced [3, 8]. The beam is already spread in a horizontal disc by the collider dipoles. A vertical wave can be introduced to distribute the radiation over a larger area with lower average dose. This vertical wave should vary in strength and phase over time so as to best dilute the dose. MARS calculations indicate that such a floating vertical wave installed in the arcs can reduce the ν-flux by more than an order of magnitude (Fig. 5). The ~8 m arc dipoles can be rolled by 20 mrad to achieve the desired 200 μrad kick (B~0.2 T in Fig. 5). To avoid the complication of skewed quadrupoles, net rolls or horizontal magnetic fields are canceled before entering quadrupoles. That is, the first dipole in a set of three is rolled 10 mrad horizontally, the next double that in the opposite direction, and the last by the same amount in the original direction to almost exactly cancel coupling, vertical dispersion, and amplitude effects. Reverse rolls and other changes can be executed from time to time to reduce dose levels in all directions.

Table 1: Radial distance, R, from the ring center with center-of-mass energy, $\sqrt{s}$, and depth, d, needed to reduce neutrino-induced dose at surface to DOE (100 mrem) and Fermilab (10 mrem) annual off-site limits at N_D decays/yr.

	$\sqrt{s}$ (TeV)	0.5	1	2	3	4
	$N_D\times10^{21}$	0.2	0.2	2	2	2
100 mrem	R (km)	0.4	1.1	6.5	12	18
	d (m)	≤1	≤1	3.3	11	25
10 mrem	R (km)	1.2	3.2	21	37	57
	d (m)	≤1	≤1	34	107	254

7 CONCLUSIONS

Neutrino induced radiation is one of the main challenges to the design and civil engineering aspects of a high-energy muon collider. The newly updated MARS provides a valuable tool to calculate the extent of the problem and address proposed mitigations. Preliminary results presented here show how dose depends strongly on muon collider energy and on the geometry between source and TEP. Beam wobbling holds promise to significantly alleviate the problem.

8 REFERENCES

[1] B. J. King, private communication (1996).

[2] C. M. Ankenbrandt et al., "Status of Muon Collider Research and Development and Future Plans", Fermilab-Pub-98/179 (1998).

[3] N. V. Mokhov and A. Van Ginneken, "Muon Collider Neutrino Radiation", Muon Collider Collaboration Meeting Book, Orcas Island, WA, May 1997.

[4] N. V. Mokhov, S. I. Striganov, A. Van Ginneken, S. G. Mashnik, A. J. Sierk, and J. Ranft, "MARS Code Developments", Fermilab-Conf-98/379 (1998); LANL Report LA-UR-98-5716 (1998); *nucl-th/9812038 v2 16 Dec 1998*; http://www-ap.fnal.gov/MARS/.

[5] J. D. Cossairt, N. L. Grossman, and E. T. Marshall, "Assessment of Dose Equivalent Due to Neutrinos", Health Physics, **73**, pp. 894-898, 1997.

[6] Particle Data Group, Phys. Lett. B204, 1 (1988).

[7] F. Halzen and A. D. Martin, *Quarks and Leptons*, Wiley, New York (1984).

[8] C. J. Johnstone and N. V. Mokhov, "Shielding the Muon Collider Interaction Region", *Proceedings of the 1997 IEEE Particle Accelerator Conference*, Vancouver, May 1997.

COLLECTIVE INSTABILITIES OF THE 50-50 GeV MUON COLLIDER

K.Y. Ng, FNAL*, Batavia, IL 60510

Abstract

Single bunch instabilities for the 50-50 GeV muon collider are discussed. An impedance budget for the collider is estimated. An $|\eta| = 1 \times 10^{-6}$ is desired to avoid excessive rf systems. Potential-well distortion can be compensated by rf cavities. Longitudinal microwave growth can be reduced by smoothing the bunch distribution before injection. Transverse microwave instability can be damped by chromaticities and octupoles. Beam breakup can be cured by BNS damping in principle, but is nontrivial in practice. More detailed discussions are given in Ref. 1.

1 IMPEDANCE BUDGET

Each of the bunches in the 50-50 GeV muon collider will have an intensity of $N = 4 \times 10^{12}$ muons, rms bunch length $\sigma_\ell = 4$ cm, and rms momentum spread $\sigma_\delta = 1.2 \times 10^{-3}$. There is another mode of operation for precision determination of the Higgs mass, when the rms momentum spread is only $\sigma_\delta = 3.0 \times 10^{-5}$ and rms bunch length $\sigma_\ell = 13$ cm. With such a high intensity and small momentum spread, the study of bunch instabilities becomes an important task.

Because there is about 3.5 cm of tungsten shielding in the superconducting magnets, the physical aperture of the colliding ring will not be large. As a result, careful bunch monitoring becomes essential. Assuming strip-line beam-position monitors like those of the Tevatron, the low-frequency longitudinal and transverse impedances for M pairs of strip lines are [2, 3]

$$\frac{Z_\parallel}{n} = j2MZ_c\left[\frac{\phi_0}{2\pi}\right]^2\frac{\ell}{R}, \quad Z_\perp = \left[\frac{4}{\phi_0}\right]^2\frac{R}{2b^2}\sin^2\frac{\phi_0}{2}\left[\frac{Z_\parallel}{n}\right]. \quad (1)$$

Here, each strip-line has a length $\ell \sim 10$ cm subtending a full angle of $\phi_0 \sim 75°$ at the axis of the cylindrically symmetric beam pipe of radius b, and forms a transmission line of characteristic impedance $Z_c = 50\ \Omega$ with the vacuum chamber. Note that these impedances are roughly independent of the circumference $C = 2\pi R = 350$ m of the collider ring, because more BPM's will be needed for a larger ring. Assuming $M = 56$ pairs of strip lines, 28 for the horizontal and 28 for the vertical, we obtain $Z_\parallel/n = j0.44\ \Omega$ and $Z_\perp = j0.066$ MΩ/m (half of the ring with $b = 2$ cm and half with 4 cm). It is worthwhile to point out that the longitudinal impedance is independent of the beam pipe radius.

The impedances of the bellows are roughly proportional to the ring circumference. For the Tevatron, which has a circumference of 6.28 km, the contributions at low frequencies are [3] $Z_\parallel/n \sim j0.4\ \Omega$ and $Z_\perp \sim j0.4$ MΩ/m. However, there are many more elements per unit length for the muon colliders. We scale them by a factor of 10 to get $Z_\parallel/n \sim j0.04\ \Omega$ and $Z_\perp \sim j0.04$ MΩ/m. The Tevatron bellows are unshielded. Thus, these impedances will be much smaller if the bellows in the muon collider are shielded.

For the resistive walls of the vacuum chamber, the contributions to the impedances are

$$\frac{Z_\parallel}{n} = \frac{\mathrm{sgn}(n) + j}{2b}\left[\frac{Z_0\rho C}{\pi|n|}\right]^{1/2}, \quad Z_\perp = \frac{C}{\pi b^2}\left[\frac{Z_\parallel}{n}\right]. \quad (2)$$

where $Z_\perp$ is to be evaluated at $n + \nu_\beta$ and ν_β is the betatron tune. For an aluminum beam pipe with resistivity $\rho = 0.0265\ \mu\Omega$-m, we obtain $Z_\parallel/n = [\mathrm{sgn}(n) + j]0.62|n|^{-1/2}\ \Omega$ and $Z_\perp = [\mathrm{sgn}(n) + j]0.13|n + \nu_\beta|^{-1/2}$ MΩ/m, using $b = 2$ and 4 cm for each half of the ring. Thus, at the beam-pipe cutoff frequency, $f_c = 2.405c/(2\pi b) = 5.74$ GHz, c being the light velocity, the resistive-wall contributions become negligible compared with those from the BPM's.

The lattice of the collider ring entails large variations of the betatron functions, ∼1500 m in the final focusing quadrupoles, ∼ 100 m in the local chromaticity-correction region, and $\lesssim 25$ m in the arcs. For this reason, there will be plenty of transitions in beam-pipe cross section, leading to significant contributions to the coupling impedances. If a broad-band impedance model with quality factor $Q = 1$ is assumed, it will be difficult to have $\mathcal{I}mZ_\parallel/n \lesssim 0.5\ \Omega$, $\mathcal{I}mZ_\perp \lesssim 0.1$ MΩ/m at low frequencies. The resonant angular frequency is chosen as $\omega_r = 50$ GHz, ∼ 38% above cutoff, because $|Z_\parallel/n|$ does not roll off up to $\omega = 60$ GHz in both the CERN LEP and the SLAC damping rings.

2 CHOICE OF SLIPPAGE FACTOR

Longitudinally, the worst fast collective growth is the microwave instability, which has a stability limit of [4]

$$\left|\frac{Z_\parallel}{n}\right| \le \frac{2\pi|\eta|E\sigma_\delta^2}{eI_{\mathrm{pk}}}, \quad (3)$$

where I_{pk} is the peak current, E the muon energy, and e its charge. Taking the $\sigma_\ell = 4$ cm bunch, stability can be assured only if the slippage factor $|\eta| > 0.0021$. Neglecting the influence of coupling impedance, to keep such a bunch in an rf bucket, the synchrotron tune will be $\nu_s = |\eta|R\sigma_\delta/(2\pi\sigma_\ell) = 3.54 \times 10^{-3}$, and the rf voltage will be $V_{\mathrm{rf}} = 2\pi E\nu_s^2/|\eta| = 1.86$ GV, which is very large. Another choice is to make $|\eta|$ as small as possible. Although we have to give up Landau damping, hopefully, the growth rate, which is proportional to $\sqrt{|\eta|}$, will be slow enough and cause insignificant harm. Here, we are talking about the total spread in η, since the latter is a function of momentum spread. Because η is related to the momentum-compaction factor, to reduce η and its spread, we need to reduce the contribution of the higher-order momentum compaction also. Roughly speaking, sextupoles can be used to reduce η_1, octupoles reduce η_2, etc. The experience with the 2-2 TeV muon collider lattice [5] tells us that it will be hard to reduce the spread of $|\eta|$ to below 1×10^{-6}, and this value will be used in our discussion below. A particle at an energy spread of $3\sigma_\delta$ will drift by 4.2 ps (0.13 cm) only in 1000 turns. For this reason, it appears that a bunching rf will not be necessary. However, this is not true in the presence of the coupling impedance.

* Operated by the Universities Research Association, under contract with the US Department of Energy

0-7803-5573-3/99/$10.00@1999 IEEE.

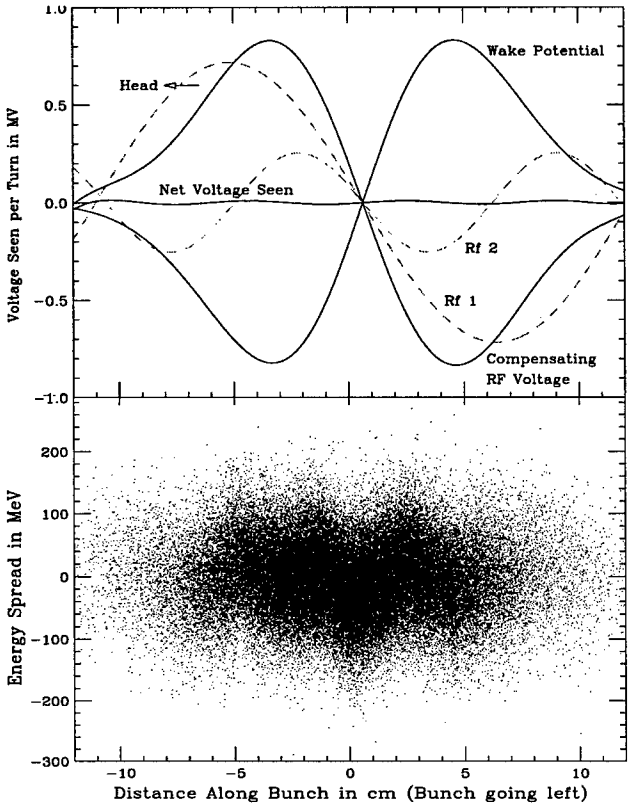

Figure 1: Top: Wake potential, compensating rf voltages, and net voltage seen by particles in the 4-cm bunch at injection. Bottom: Bunch distribution after 1000 turns.

3 POTENTIAL-WELL DISTORTION AND MICROWAVE INSTABILITY

Particles in the high-intensity bunch will be affected by the wake from the particles ahead. Assume a linear Gaussian distribution and a broad-band with $Q = 1$ and $\mathcal{R}e\, Z_\parallel/n = 0.5\ \Omega$ at the angular resonance frequency $\omega_r = 50$ GHz. At such a high resonant frequency, the wake potential seen by a bunch particle is roughly equal to the derivative of the Gaussian with a maximum and minimum of $\sim \pm 0.83$ MV, as shown in the top plot of Fig. 1. Therefore, in 1000 turns some particles will gain and some will lose as much as $\sim$ 499 MeV, taking into consideration the reduction in intensity due to muon decay, while the designed rms energy spread is only 60 MeV. With such a large energy spread, there will be some drift in time, especially if $|\eta|$ is not too small. Thus, there may be bunch lengthening as well as particle loss due to the limited physical aperture of the vacuum chamber. If the linear distribution is parabolic, a sinusoidal rf of wavelength longer than the bunch length will compensate for this bunch distortion due to wake potential. If the linear distribution is cosine-square, a sinusoidal rf with wavelength exactly equal to the bunch length will do the job. For a Gaussian distribution, one needs a combination of sinusoids [6]. For example, to compensate up to $\pm 3\sigma_\ell$, we need at injection two sinusoidal rf's of frequencies 1.290 and 2.673 GHz, of voltages 717.4 and 253.4 kV, and of phases 170.55° and 159.33°, as shown in the top plot of Fig. 1, with the voltages decreasing turn by turn according to the decay of the muons. Tracking was done for 1000 turns using 2×10^6 macro-particles with bin size 15 ps (0.45 cm). The result is shown in lower plot of Fig. 1. We see that the compensation rf's do a good job by keeping the muons bunched without any increase in bunch length. However, there are some wigglings along the bunch. They are not due to inexact compensation, because the top plot of Fig. 1 shows that the net voltage seen has a wiggling with wavelength about 210 ps and $\sim \pm 0.008$ MV at injection or $\sim \pm 4.8$ MV for 1000 turns. On the other hand, the lower plot in Fig. 1 shows a wiggling of $\sim \pm 40$ MeV with wavelength of $\sim$ 125 ps corresponding to the resonant frequency of the coupling impedance. These are signs of microwave instability. Figure 2 shows the 1000-turn tracking simulation of a rms 13-cm bunch using the same number of macro-particles with the same bin width and subject to the same broad-band impedance. The best fitted compensation rf's used at injection are at 0.3854 and 0.7964 GHz, 65.40 and 24.74 kV, and 177.20° and 174.28°. Note that the rf's can only compensate for potential-well distortion and *cannot* cure microwave instability.

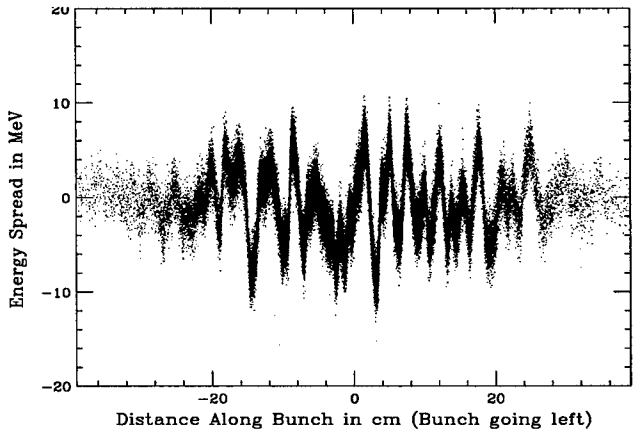

Figure 2: Distribution of 13-cm bunch after encountering the wake potential and the compensating rf's for 1000 turns

The Keil-Schnell criterion can be rewritten in the form

$$n_r \omega_0 \sqrt{\frac{|\eta| I_{\rm peak} |Z_\parallel/n|}{2\pi e E}} \le 2\omega_0 |\eta| \sqrt{\frac{n_r \ln 2}{\pi}}\,, \qquad (4)$$

$\omega_0/(2\pi)$ being the revolution frequency and n_r the resonant harmonic, where the left side is the raw microwave growth rate without damping and the right side the Landau damping rate, which is a few orders of magnitude smaller than the left side for both bunches and can be neglected. We therefore obtain the growth rates as $4.91{\times}10^4$ and $2.72{\times}10^4\ \mathrm{s}^{-1}$, respectively, for the 4-cm and 13-cm bunches. The 4-cm bunch should have a larger growth rate because the peak current is larger and momentum spread plays no role since the Landau damping rate is too small. However, Fig. 1 actually shows a less violent growth than Fig. 2. One reason is that the same number of macro-particles and same bin widths have been used in the two situations. The 4-cm distribution will have more macro-particles per bin than the 13-cm bunch and therefore smaller fluctuations, thus providing smaller seeds for the growth. The other reason is

that the impedance wavelength is comparable to the rms bunch length of the 4-cm bunch, over which the local current drops to $\sim e^{-1/2} = 0.6$ of its peak value, thus reducing the growth rate. It is important to point out that Figs. 1 and 2 *do not* indicate the actual particle distributions after 1000 turns. The actual growth depends on the initial linear bunch shape. If the initial bunch shape is extremely smooth, the total growth in 1000 turns may be very minimal. On the other hand, if the initial bunch distribution is very rugged, it will provide a large seed and the final distribution after 1000 turn can be much more violent than those depicted in Figs. 1 and 2. Therefore, to prevent excessive microwave instability, methods must be devised to smooth the bunch distribution after ionization cooling and linac acceleration. Further reduction in impedance and $|\eta|$ will lower the growth. Since the growth rate is proportional to frequency, one must try to smooth the vacuum chamber so that the impedance contribution at high frequencies will be reduced to a minimum.

4 TRANSVERSE MICROWAVE INSTABILITY

The Keil-Schnell-like stability criterion for transverse microwave instability can be written at chromaticity ξ as [7]

$$\frac{eI_{\rm pk}|Z_\perp|c}{4\pi E\nu_\beta} \le \frac{4\sqrt{2}\omega_0}{\pi}|(n_r-\nu_\beta)\eta+\xi|\sigma_\delta\,, \qquad (5)$$

where the left side is the raw growth rate without damping and the right side the damping rate. With $\nu_\beta \approx 8$, the raw growth rates are 11.4×10^3 and $3.51\times10^3\ {\rm s}^{-1}$, respectively, for the 4-cm bunch and 13-cm bunch. For stabilization, one requires $|(n_r-\nu_\beta)\eta+\xi| > 1.7$ and 21, respectively, for the two bunches. Although our choice of η is small, stability can still be maintained if the chromaticities are less than 1.7 and 21, if octupoles are installed to provide additional amplitude-dependent tune spread. Also, the presence of a small growth may not be serious for only 1000 turns.

5 TRANSVERSE BEAM BREAKUP

Since bunch particles do not move much longitudinally with respect to the bunch center during their lifetime, any off-axis particle will affect its followers constantly leading to beam breakup. Take the simple two-particle model, by which the bunch is represented by two macro-particles of charge $\frac{1}{2}eN$ separated by a distance $\hat{z} \sim \sigma_\ell$. The transverse displacements of the head, y_1, and the tail, y_2, satisfy

$$y_1'' + \frac{\nu_\beta^2}{R^2}y_1 = 0\,,\ \ y_2'' + \frac{\nu_\beta^2}{R^2}y_2 = \frac{e^2NW_1(\hat{z})}{2CE}y_1\,. \qquad (6)$$

In a length L, the displacement of the tail will grow $\Upsilon = e^2NW_1(\hat{z})L/(8\pi E\nu_\beta)$ times [8]. For a broad-band impedance with $Z_\perp = 0.1$ MΩ/m at $\omega_r = 50$ GHz and $Q = 1$, the wake function has a maximum of $W_1 = 2\omega_r Z_\perp \cot\phi \sin\phi\, e^{-\phi\cot\phi}$ at $z = c\phi/(\omega_r \sin\phi) < \hat{z}$, where $\cos\phi = 1/(2Q)$, indicating that the two-particle model is not suitable for long bunches and high resonant frequencies. As an estimate, with this maximum value of W_1, the displacements of some particles along the bunch will be doubled in ~ 27 turns.

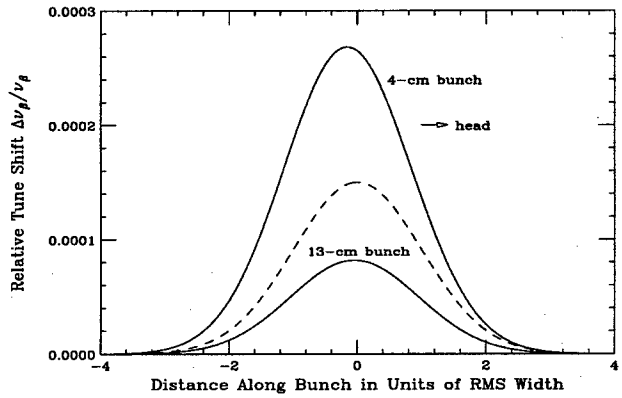

Figure 3: Relative tune shift compensation as functions of distance along the bunch to cure beam breakup. The bunch profile is plotted in dashes as a reference.

This beam breakup can be cured by varying the betatron tune of the beam particles along the bunch, so that resonant growth can be avoided. The is known as BNS damping [9]. In order that all particles in the bunch will perform betatron oscillation with the same frequency and same phase, special focusing force is required to compensate for the variation of betatron tune along the bunch according to [8]

$$\frac{\Delta\nu_\beta(z)}{\nu_\beta} = \frac{e^2NR}{4\pi\nu_\beta^2E}\int_z^\infty dz'\rho(z')W_1(z'-z)\,, \qquad (7)$$

If the linear bunch distribution ρ is a Gaussian interacting with a broad-band impedance, the integration simplifies to

$$\frac{\Delta\nu_\beta(z)}{\nu_\beta} \approx \frac{e^2N\omega_rZ_\perp R}{2(2\pi)^{3/2}\nu_\beta^2QvE}\left[1-\frac{z}{vQ\sigma_\ell}\right]e^{-z^2/(2\sigma_\ell^2)}\,, \qquad (8)$$

where use has been made of $v = \omega_r\sigma_\ell/c \gg Q$, which is certainly satisfied for both bunches. The relative tune shifts required for the two bunches, shown in Fig. 3, are small. To cure beam breakup, however, an rf quadrupole must be installed and pulsed according to the compensation curve for each bunch as the bunch is passing through it. Note that the compensations are only slightly shifted backward instead of linearly increasing towards the tail. These are the results of long bunches and high resonant frequencies, as was indicated in the two-particle model discussion. The shift will be more towards the tail as v decreases. In practice, compensations matching these tune-shift curves are nontrivial.

6 REFERENCES

[1] K.Y. Ng, "Beam Instability Issues of the 50GeV-50GeV Muon Collider", Fermilab Report FN-678, 1999.
[2] K.Y. Ng, Part. Accel. **23**, 93 (1988).
[3] K.Y. Ng, "Impedances and collective instabilities of the Tevatron at Run II", Fermilab Report FN-536, 1990.
[4] E. Keil and W. Schnell, CERN/ISR-TH/69-48, 1969.
[5] K.Y. Ng, Nucl. Inst. Meth. **A404**, 199 (1998).
[6] E.-S. Kim, A,M, Sessler, and J.S. Wurtele, "Analysis of the Longitudinal Collective Behavior in a 50GeVx50GeV Muon Collider Ring", LBL Report, 1999.
[7] B. Zotter, Proc. First Course Int. School Part. Accel., Erice, Nov. 10-22, 1976, p. 176.
[8] A.W. Chao, "Physics of Collective Beam Instabilities in High Energy Accelerators", John Wiley & Sons, Inc., 1993, p. 70.
[9] V. Balakin, A. Novokhatsky, and V. Smirnov, Proc. 12th Int. Conf. High Energy Accel., Fermilab 1983, p 119.

MUON COLLECTION CHANNEL SIMULATIONS*

D. Neuffer# and A. Van Ginneken, FNAL, Batavia, IL

Abstract

Results of Monte Carlo simulations of the processes in a collection channel for a muon collider are presented. In the simulations, pions are produced in a target, captured and then transported within solenoid focusing systems where they decay into muons. Muon yield and phase space characteristics at the end of the channel can be improved by placing rf cavities and absorbers along the channel as well as by providing a supplemental toroidal field along with the absorbers. Results for a sample of such scenarios are presented.

1 INTRODUCTION

A key requirement for a μ^+-μ^- collider is to capture and collect a maximal number of muons from the proton source. For this, the proton beam from the source must be optimally focused onto a production target and the beam optics must be arranged to capture the maximal number of π's and confine them within a transport channel for $\pi \rightarrow \mu$ decay. A number of options for the target, the π-capture optics, and the $\pi \rightarrow \mu$ decay transports have been studied.[1,2] From these studies it appears that an optimum scenario for producing forward π's for μ-collection is to use a high power 10—30 GeV proton beam which is focused onto a relatively high-Z, high-density target. The target is immersed in a high-field solenoid (20T in these studies) designed to capture π's with transverse momentum up to 250 MeV/c. The captured π's continue downstream from the target in a high-acceptance transport, which is based on solenoidal focusing with a low-frequency rf-bunching system, designed to capture the μ's from π-decay. Fig. 1 shows an overview of the target and initial portion of the collection and capture section, including the production target within a high-field capture solenoid and the transition into a lower-field solenoidal transport with a low-frequency rf system for capture and rotation.

In this transport the π's decay into muons ($\pi \rightarrow \mu\nu$) and the design problem is to optimize this transport to accept the maximum number of μ's, to capture them within a minimal phase-space volume, and transport them into an ionization cooling section. In this paper we explore several variations on designs for this capture section, including the possibility of providing some initial cooling in this section. (Much of this material is presented in more detail in ref. 4.)

Figure 1: Overview of the targetry + initial capture section of the $\pi \rightarrow \mu$ collection channel.

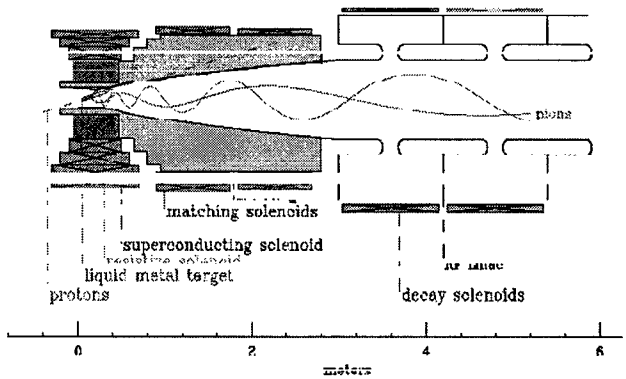

2 CAPTURE AND COLLECTION SCENARIOS

The key parameters of the capture and cooling section (in the baseline design of solenoidal focusing plus rf capture) are the focusing field, the apertures, and rf parameters including rf voltage, frequencies, and phases.

In the simulations, π production is generated using the MARS code.[4] The 16 GeV proton beam (σ_x, σ_y=0.4cm) and bunch length of 0.3m (rms) is incident on a 36cm long, 1cm radius Ga target, situated in a 20T, 7.5cm radius, solenoid, and the simulations track the secondary particles from that source. The π trajectories initiate as helices in the 20T field. This field is adiabatically reduced in a transition solenoid to a smaller value which is sustained throughout the remaining transport/rf section. Final values of 5T and 1.25T are considered in the present simulations, some of which are presented in more detail in ref. [4]. In the adiabatic field decrease the radius of the transport channel is increased, keeping Br^2 constant, to 15 cm with 5T and 30 cm with 1.25 T.

These studies of the capture and rf rotation process are based on previous studies by H. Kirk, R. Palmer and others, presented in ref. 1. Simulations by Palmer and Gallardo[5], by Y. Fukui[6], and the present studies, obtain ~0.2 μ/p from the rf capture section with 16 GeV protons. Table 1 shows parameters of such a system. Our simulations show that at the end of the 42m rf rotation system ~0.22 μ/p are captured within the r=15cm B=5T transport, within an acceptance window of p=275±125 MeV/c. The rms normalized emittance is 0.018 mrad, and $\sigma_p \cong 50$ MeV/c, σ_{ct}= 1.9m.

*Research supported by DOE contractDE-AC02-76CH03000.

Email: neuffer@fnal.gov

Table 1: parameters of an rf rotation/capture system for capture of μ's from π→μν decay

Section	Length (m)	Rf frequency (MHz)	V'(rf) MV/m
1	6	90	5.2
2	18	50	3.15
3	18	30	2.1

This beam, however, has a large size (x, y, and z), and a large momentum spread at a relatively small momentum, and it is difficult to match into a following cooling and capture transport system.

Based on these earlier studies and with some reoptimization a somewhat different capture scenario is developed, with parameters displayed in Table 2. This section is designed to capture the maximum number of muons from a target within a compressed bunch, using the large-aperture solenoid for transverse focusing, and an rf system for capturing and compressing the beam. The beam is significantly accelerated in preparation for subsequent cooling and capture transports. The bunch length/energy spread criterion used is an acceptance aperture of ±3m in longitudinal position and ±150 MeV in energy.

As shown in Table 2, the initial bunching is at higher rf frequencies, and the rf frequency decreases as the bunch travels downstream, matching the increase in bunch length. rf voltages also decrease, since high-gradient is more difficult at lower frequencies. A double-frequency rf system is used throughout; the initial 90MHz rf voltage is supplemented by a double harmonic (180MHz) at 1/3 voltage. The double harmonic rf format improved capture from that obtained with single harmonic systems. The rf waveform is designed to decelerate the high energy end of the beam while accelerating the low energy end, reducing the energy spread with some increase in bunch length. In Fig. 2, the evolution of the bunch along the channel is displayed. The rf waveform in each section is also displayed, illustrating the bunch-rotation rf. The rf capture system is designed to accelerate the average beam energy to ~450 MeV/c, in order to prepare the beam for subsequent cooling.

Table 2: Parameters of an rf capture system and initial acceleration system. The rf system is double-harmonic, with an additional component at 2× the fundamental frequency and 1/3 the voltage, phase shifted by 2.2 radians.

Section	Length (m)	Fundamental rf frequency (MHz)	V'(rf) MV/m (fundamental)
1	7.2	90 → 60	13.5→11.7
2	7.2	54 → 44	10.8→9.0
3	19.2	42 → 34	8.55→5.85
4	24	33.5 → 26	5.4
5	24	25	5.4

Figure 2: Simulations of rf rotation in a 80m long, 5T solenoid channel, with the rf bunching systems of Table 1. The bunching wave form is shown as a line in each graph, which display the beam at regular intervals along the 80.4m transport, distance in cm is shown in each graph.

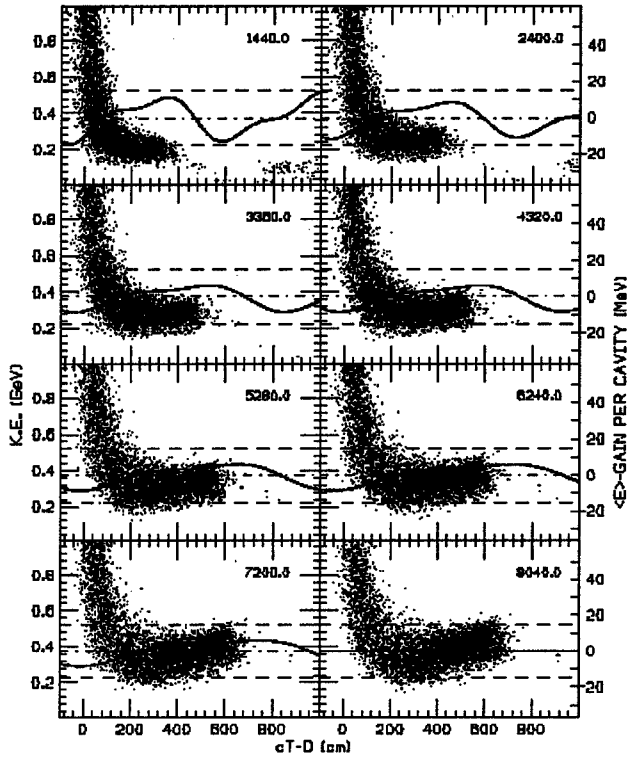

3 COOLING IN CAPTURE SCENARIOS

To explore the initiation of cooling within the μ-collection system, an ionization cooling channel is added to the end of the rf rotation section, within the same transport. For ionization cooling, 0.1m long sections of LiH absorbers (ρ=0.82 gm/cm^3, dE/dx = 1.56 MeV/cm) are placed every 1.2m in a 72m long additional section. The rf acceleration is increased by ~15MV/m to compensate for the beam energy losses in the absorbers. Simulations show that the system cooled transverse emittances by ~2× and 6D emittance by ~4× for the 5T case. (see Table 3) However the system heats the beam in the 1.25T case, causing large beam loss. The heating is caused by multiple scattering heating, which is 4× larger for that case, because of the weaker focusing. Adding toroidal magnets for additional focusing reduces the heating effect.

While these simulations show significant cooling, the system needs further development to be realized in practice. The rf gradients required are large for this frequency. The focusing system, even with an added toroidal field, is weaker than desired to suppress multiple scattering. Also some energy cooling is needed. Other systems, such as the alternating solenoid system presented in ref. [2], with emittance exchange cooling, should be developed and compared with this system.

The simulations do show that, from an initial production system, as many as 0.35 μ/p can be captured from a 16 GeV proton beam, which initially produces ~1.1 π/p at the target. An initial transverse cooling system within the solenoid channel can reduce beam sizes by a factor of two, which could make transfer from the rf rotation solenoid to a further cooling system much easier. Somewhat better capture is obtained using the stronger-focusing 5T lattice than the larger-aperture 1.25T case, and the more compact beam size is better suited for matching into downstream cooling sections.

Further modifications could make the system more practical and/or affordable. The many continuously-changing double-harmonic systems could probably be reduced to a few (i. e., 90, 60, 30) with little loss in performance. The initial cooling system could be modified to decelerate the beam with cooling, which may be more efficient, and alternating-solenoid focusing could replace the toroids in focusing the beam. Deceleration would reduce rf requirements; our initial scenario actually accelerates the beam. However, more reacceleration in cooling segments would be needed. A sparser absorber configuration (possibly using H_2 absorbers as in ref. 2) would reduce gradient requirements, while lengthening the system. Some energy cooling in this initial stage is desirable.

4 DISCUSSION: FUTURE STUDIES

The chief difficulty which needs further study is the problem of matching the very large beam from the rf rotation channel into a following cooling channel. At that point the beam has an rms δp/p of ~15%, a bunch length of ~1.4m rms (6m full width), and transverse beam sizes of ~7cm radius (15 cm full radius) with an angular width of 100 mrad. The general technique of inserting some initial cooling within the rf rotation channel will probably be used, and both transverse cooling and emittance-exchange components are needed. An important challenge which needs a specific solution is the design of a first energy-cooling (emittance-exchange) system which can accommodate the very large emittances and momentum spreads at the end of the rf rotation channel, with minimal dilution and losses.

5 REFERENCES

[1] μ^+-μ *Collider: A Feasibility Study*, BNL-52503, FNAL-Conf-96/692, LBNL-38946, presented at Snowmass 1996.

[2] C. M. Ankenbrandt et al., *Status of Muon Collider Research and Development and Future Plans*, BNL-65623, Fermilab-PUB-98/179,LBNL-41935, to be published in Phys. Rev. Spec. Topics AB (1999)

[3] A. Van Ginneken and D. Neuffer, Fermilab-Pub-98/296(1998), to be published in Nucl. Inst. and Meth. A (1999)

[4] N.V.Mokhov, *The MARS Code System Users Guide*, FNAL-FN-628 (1995), MARS files provided by N.V. Mokhov.

[5] R. Palmer and J. Gallardo, MCMuon simulation results, unpublished (1998).

[6] Y. Fukui, unpublished (1998).

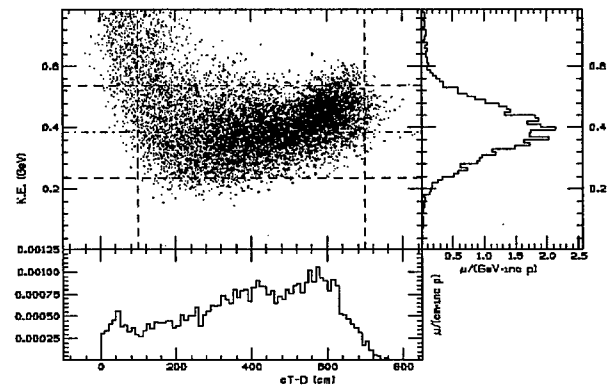

Figure 3: Longitudinal profiles of the beam at the end of the rf capture sequence, but before any cooling.

Table 3: Results of simulations of rf rotation scenarios for 5T and 1.25T focusing systems. In the second column cooling absorbers are added, and an additional focusing field is added in the third column.

	no absorbers		*absorbers*		*+toroidal field*	
$R_{sol}, cm/B_{sol}, T$	15/5	30/1.25	15/5	30/1.25	15/5	30/1.25
N_μ	0.349	0.287	0.302	0.130	0.324	0.258
ϵ_6, cm^3	225	257	63	271	63	153
$\langle \epsilon_T^2 \rangle^{1/2}, cm$	1.63	1.73	0.91	1.81	0.86	1.36
ϵ_z, cm	2.18	2.08	0.92	2.11	0.89	1.37
$\langle x^2 \rangle^{1/2}, cm$	4.85	10.12	4.45	11.17	3.06	5.02
σ_E, MeV	72	78	68	62	72	61
$\langle E_{kin} \rangle, MeV$	350	307	407	475	480	484
$N_\mu^2/\sqrt{\epsilon_6}, cm^{-3/2}$	0.0081	0.0051	0.0115	0.0010	0.0132	0.0054

Design and Simulation studies of an Ionization Cooling channel using lithium lenses and solenoid transport channels.*

P. Spentzouris†, D. Neuffer, FNAL, Batavia, IL

Abstract

The successful design of a high luminosity muon collider requires that the six dimensional phase-space of the muon beam generated by pion decay be reduced by a factor of $\sim (10^5 - 10^6)$ before it enters the collider. This "beam cooling" has to take effect in a time scale comparable to the lifetime of the muon. Because of this time limitation, Ionization Cooling is the preferred option for the muon collider. In this paper we discuss the design issues for an Ionization Cooling channel based on lithium lenses and solenoid transport channels and we present simulation results obtained using a detailed tracking code with a complete model of muon-atom interactions. Cooling results for a minimal configuration of two lithium lenses and one matching section are presented, for beams with a normalized transverse emittance of 0.0067 m-rad. The cooling factor obtained is ~ 1.5.

1 INTRODUCTION

In the current muon collider scenarios [1] the 6-D phase-space reduction required to obtain a high luminosity collider is on the order of $10^5 - 10^6$. This "beam cooling" must be obtained in time scales on the order of the muon lifetime ($\sim 2\ \mu s$). The technique which in principle could accomplish this task, within the required time window, is ionization cooling [2, 3]. In ionization cooling the beam, while passing through material, loses both transverse and longitudinal momentum by ionization loss (dE/dx). The longitudinal momentum is then restored by passing the beam through acceleration cavities. Since Multiple Coulomb Scattering in the material constitutes a heating term, the absorbers have to be placed in strong focusing field to minimize this contribution. Note that this method in its simple form cools only in the transverse dimensions of the 6-D phase space. A complete discussion for 6-D designs is presented in reference [1].

Cooling by large factors requires many successive stages of energy loss and acceleration. In this paper we discuss specific implementations of ionization cooling using lithium lenses as the cooling elements, and solenoids as the transport and matching elements. The performance of such channels depends critically on the accurate modeling of ionization and multiple scattering, and the beam emittance involved is so large that the par-axial approximation is inadequate. In order to obtain realistic modeling, we base the simulations of our design on the GEANT3 package [4], a detailed tracking code, with a complete implementation of muon interactions in matter. In addition, the field maps required correspond to the actual geometry of the elements of the beamline, including fringe fields. Finally, in order to maintain high accuracy in computing traces over large distances, the precision of this package has been upgraded to double precision, DPGeant package [5].

2 DESIGN PARAMETERS AND CONSTRAINS

The use of an active lens absorber (such as a Li lens) in ionization cooling seems to be very advantageous. The azimuthal magnetic field, $B_\theta = \frac{\mu I r}{2\pi R^2}$ in a cylindrical conductor of radius R provides linear radial focusing, with an equilibrium betatron function of $\beta = (B\rho/B')^{1/2}$, where B' is the field gradient. For a nominal beam momentum of 300 MeV/c and $B' = 1000T/m$, β of $\sim 0.03m$ is obtained. This β, together with the radiation length and dE/dx values for lithium makes Li lenses very efficient ionization cooling devices (see reference [1] for a discussion on various ionization cooling options). The main issue for constructing a cooling channel based on Li lenses is optics, since following each active lens the muons have to be accelerated, and the matching section between the lens and the accelerating section has to be short, in order to avoid decay losses. In addition, energy straggling in the absorber dilutes the longitudinal phase space. In our design we use 1/4 Larmor wavelength (λ_L) long solenoid lenses to match in and out of the accelerating section, which consists of $805MHz$ open cell RF cavities embedded in a weak solenoidal field. The $\lambda_L/4$ length requirement is imposed to provide minimum beam divergence into the acceleration channel. For particles with the design momentum the transverse focusing is essentially point to parallel, $\alpha = 0$, entering the acceleration channel, and parallel to point exiting it (entering the next Li lens). No chromatic fitting has been performed at this stage of the simulation ($\frac{\partial \beta}{\partial \frac{\delta p}{p}} = 0$, $\frac{\partial \alpha}{\partial \frac{\delta p}{p}} = 0$). The length of the solenoid in the acceleration section is constrained to be an integral number of Larmor wavelengths. The apertures and the field strengths are selected to match (or at least accept) the incoming beam parameters, so they vary accordingly depending on the particular configuration. The maximum field strengths used are limited to values that could be obtained either with currently available technology or with the completion of ongoing R&D efforts [6]. The RF frequency is constrained by the high gradient requirements ($30MV/m$) of the channel. In principle, lower frequency RF provides more flexibility in the design of such channels, but high gradients are not currently feasible at low RF frequencies. In order to control the longitudinal phase space growth, the choice of RF frequency constrains the beam en-

* Work supported by the U.S. Department of Energy.

† Email: spentz@fnal.gov

0-7803-5573-3/99/$10.00@1999 IEEE.

ergy to be higher than the optimal for transverse cooling [7].

3 SIMULATION RESULTS

The first implementation of our design was for a beam with a transverse normalized emittance of 6.7 mm-rad. This example corresponds to an "upstream" cooling stage of the baseline muon collider design [1]. The design parameters of this channel were first obtained using a matrix representation of the focusing elements [8]. These values were then used to generate the realistic fields and geometric description used in the detailed DPGeant simulation. They were optimized by using the optimization package Minuit [9] which iterated the passage of 500 muons selected to cover the beam phase space through the fully simulated channel. The channel parameters are tabulated in table 1. The section simulated consisted of 2 lithium lenses (1 and 2 in the table), a matching section with 2 strong solenoid lenses (front and back), and a solenoid transport section where the RF cavities were placed. These RF cavities were divided into 3 groups, the first and last used for longitudinal focusing, and the second for acceleration. The RF characteristics are shown in table 2 and the accelerating field is 30MV/m. The beam injected into this channel has momentum of 473 MeV/c, with transverse momentum r.m.s size of 32 MeV/c, beam radius r.m.s of 2.2 cm, r.m.s bunch length of 1.5 cm and a r.m.s energy spread of 16 MeV. The results of the simulation are shown in figures 1- 4. In figure 1 the normalized transverse emittance and transmission of the channel are plotted as a function of position along the beamline. The emittance is reduced in the first Li lens from 0.0067 m-rad to 0.0052 m-rad, stays constant in the matching section and acceleration channel, and then is reduced again in the second lens to 0.0047 m-rad. The losses are only non-decay (muon decays were turned off during this simulation) and they are about 1% inside the first Li lens (due to large angle scatters from particles on the tail of the beam distributions), and on the order of 5% in the second Li lens because of the development of additional tails in the matching and accelerating sections. The beam envelope is shown in figure 2, together with the average $\beta\gamma$ of the beam. The second order correlation coefficients are shown in figure 3. As expected, the (P_x, y) and (P_y, x) correlations are maximal and opposite in sign inside the solenoid, while the (P_x, x) and (P_y, y) are equal and show the transverse motion properties of the beam in the matching section. All other correlations are zero, except the (P_z, ct) correlation which shows the effects of the focusing and acceleration RF sections on the beam.

For the all of the above plots, the points on the horizontal axis correspond to the entrance and exit of the first Li lens, the entrance and exit of the first matching solenoid, the middle of each RF cell, the entrance and exit of the second matching solenoid, and the entrance and exit of the second lithium lens. The beam phase space is described using the transverse variables x, P_x, y, P_y, and the longitudinal variables ct and P_z. The emittance is calculated according to the statistical (rms) definition [10]. Since in the presence of an axial magnetic field there are correlations between (x, P_y) and (y, P_x) in the lab frame, the normalized transverse emittance is calculated using the determinant of the 4x4 covariance matrix of the transverse coordinates. The values shown in figure 1 are calculated from the square root of the above determinant: $\epsilon_x \times \epsilon_y = (det)^{1/2}/m_0^2$. Since the beam is symmetric, the correlations mentioned above exactly cancel (figure 3), and $\epsilon_x = \epsilon_y$. The longitudinal phase space of the beam at the entrance of the first Li lens and at the exit of the second Li lens is shown in figure 4. There is some tail development, but overall the longitudi-

Table 1: Channel Specifications

	Field (T)	Length (m)	Diameter (m)
LiLens1	1.3	1.8	0.176
Sol Front	2.5	1.24	0.39
Sol Transport	0.78	10	0.51
Sol Back	3.3	1.45	0.39
LiLens 2	1.62	1.8	0.142

Table 2: RF Specifications

	Length (m)	Stable Phase (degrees)
Focus1	2.84	6
Acceleration	4.8	90
Focus2	2.4	4.4

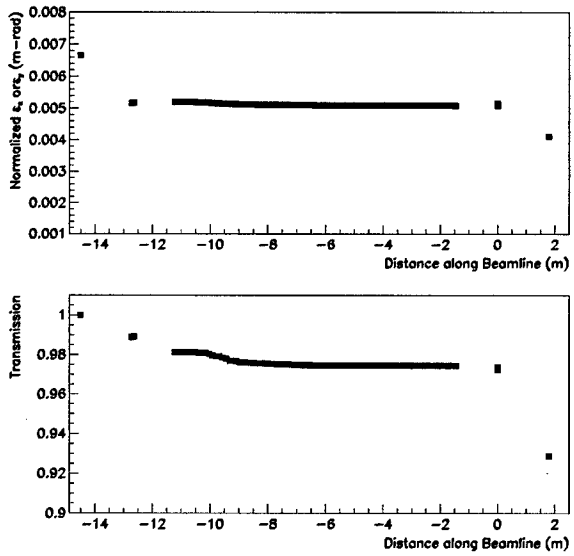

Figure 1: Transverse normalized emittance (top) and transmission (bottom) as a function of the longitudinal position along the channel.

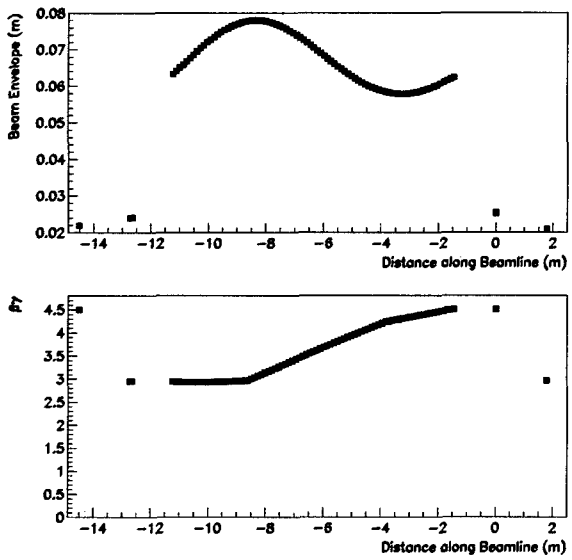

Figure 2: Beam envelope (top) and $\beta\gamma$ (bottom) as a function of the longitudinal position along the channel.

nal phase space is kept under control. The same calcula-

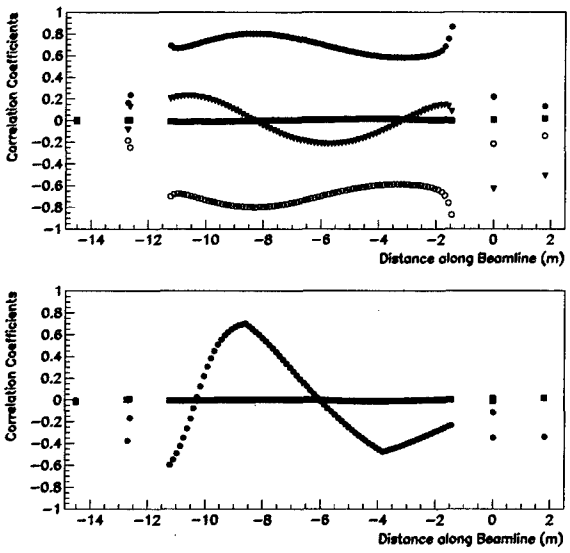

Figure 3: Correlation coefficients for P_x and P_y (top) and P_z (bottom) as a function of the longitudinal position along the channel. The only non zero correlations are for P_x y (bullets), P_y x (open symbol), P_x x and P_y y (filled triangles), and P_z ct (bullets).

tion was repeated for a smaller beam (normalized transverse emittance $\sim$0.00061 m-rad), after scaling the strengths and radii of the lenses and the phase of the focusing and accelerating sections. The cooling results were similar, but the losses were much larger ($\sim$ 25%), mostly due to amplified chromatic effects.

In summary, we have designed and simulated in full detail an ionization cooling channel which consists of two lithium lenses a solenoidal matching section, and an RF section at 805 MHz. The transverse cooling factor obtained for 473 MeV/c muons with a normalized transverse emittance of 0.0067 m-rad is $\sim$ 1.5, while the longitudinal emittance remains under control, and the losses are at the 7% level.

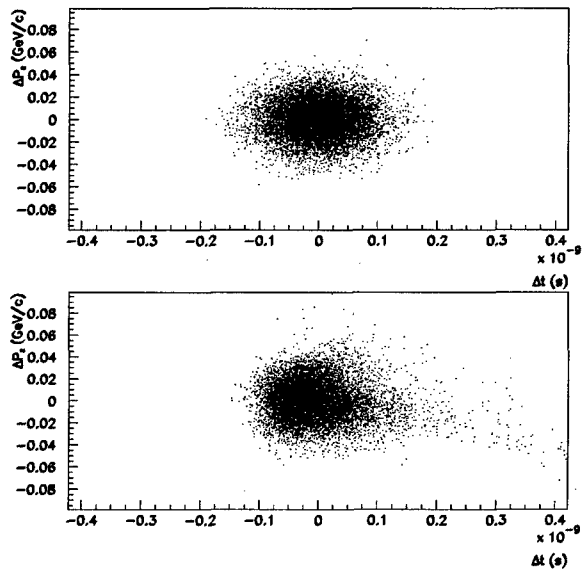

Figure 4: The Beam longitudinal phase space (P_z vs t) at the entrance of the channel (top) and at the exit (bottom).

4 REFERENCES

[1] *Status of the muon Collider Research and Development and Future Plans* BNL-65-623, Fermilab -PUB-98/179, LBNL-41935, *submitted to Phys. Rev. ST Accel. Beams.*

[2] G.I.Budker and A.N.Skrinsky, *Electron cooling and new possibilities in elementary particle physics*, SoV. Phys. Usp. **21** 277 (1978).

[3] D.Neuffer, Particle Accelerators **14** 75 (1983).

[4] Geant Manual V3.2.2.1, CERN Program Library W5013.

[5] See P.Lebrun's contribution in these proceedings.

[6] G.Silvestrov, in *Proceedings of the 9th Advanced ICFA Beam Dynamics Workshop,* editor J.C.Gallardo (AIP Press, Woodbury, New York, 1996), Vol. 372.

[7] B.Palmer and R.Fernow, *Cooling notes, USPAS, January 1999,* http://pubweb.bnl.gov/people/palmer/course/

[8] V. Balbekov, *805MHz, 30 MV/m, Li-lenses based cooling channel,* internal Muon Collider report, unpublished.

[9] Minuit Reference Manual, V94.1, CERN Program Library Writeup D506.

[10] P.M.Lapostolle, IEEE Trans. Nucl. Sci NS-18, No 3, 1101 (1971)

LIQUID LITHIUM LENS WITH HIGH MAGNETIC FIELDS

B. Bayanov, V. Belov, A. Chernyakin, V. Eschenko, V. Karasuk, M. Petrichenkov, G. Silvestrov#, T. Vsevolozhskaya, BINP, Novosibirsk, Russia

Abstract

The analysis of mechanical stresses in different lenses constructions with solid and liquid lithium is performed. It's shown that in lenses with solid lithium both in design with rigidly supported and in design with the thin wall elastic titanium shell the field value can not exceed 10 T substantially. The only possibility to obtain 15-20 T fields is creation of lenses constructions with liquid lithium and big buffer volumes.

Lithium lens is a lithium cylinder through which the electric current with uniform distribution is conducted. It provides the linear axially-symmetrical focussing of particle beam passing along the axis of cylinder. Lithium cylinder is placed into the thin-wall cylindrical titanium shell and expands at the ends in radial direction where the axially-symmetrical current input is realized. The cylinder is limited at the ends by beryllium windows for the beam input and output. Such optical systems were developed for the first time in 1974 and applied for powerful collection of positrons from the target in the electron-positron conversion system of accelerator complex VEPP-2 BINP [1]. In 1979-1984 years the longer lenses for protons focussing to the target [2] and for antiprotons collection in the FNAL antiproton source [3] were created. Later in 1989 the lens for applying in antiproton complex ACOL CERN [4] was created, also. The value of magnetic field at the surface of lithium cylinder didn't exceed 10 T in these lenses. Last time owing to development of muon colliders projects the problem of creation of long, in the order of 1 m and more, lithium lenses has appeared. Such lenses are proposed to be used as current degraders in the systems of ionization muon cooling. In this case the question of getting 15-20 T magnetic field at the surface of the lithium cylinder is appeared.

The value of magnetic field in such systems is limited by mechanical strength of elements of the lens structure, taking up forces caused by passing of pulsed current through the lithium cylinder and thin wall titanium shell. There are two sources of mechanical stresses in the system. One of them is the pressure of magnetic field compressing the lithium current-carrying conductor and transmitting to the beryllium windows of the lens. The maximum value of this pressure corresponds to the maximum of sine current pulse passing through the lithium rod and depends quadratically on the value of magnetic field. At 10 T magnetic field the magnetic pressure is $P_M = 400$ atm. The second source of mechanical stresses is the pressure caused by thermal expansion of lithium during the fast pulse heating. This pressure reaches it's maximum at the end of current pulse and transmits both to the ends of the lens and to the thin wall titanium shell around lithium rod. The value of this pressure is strongly dependent on the real lens construction and is defined by equation:

$$P = \frac{\alpha \cdot T}{\chi \cdot \left(1 + \frac{V_b}{V_0}\right) + \frac{R}{\Delta} \cdot \frac{2}{E_{Ti}}} \qquad (1)$$

where $\alpha = 1.8 \cdot 10^{-4}$ deg^{-1} – the coefficient of volume thermal expansion of lithium, $\chi_{sol} = 9 \cdot 10^{-6}$ cm^2/kG – the compressibility of lithium, $E_{Ti} = 1.13 \cdot 10^6$ kG/cm^2 – the elasticity modulus of titanium, R –radius of lithium cylinder, Δ – the thickness of thin wall titanium shell, V_0 – volume of heated part of lithium, V_b – volume of non-heated part of lithium at the region of current inputs.

Mechanical stresses in the wall of titanium shell are defined by the expression:

$$\sigma = \frac{\alpha \cdot T}{\chi \cdot \frac{\Delta}{R} \cdot \left(1 + \frac{V_b}{V_0}\right) + \frac{2}{E_{Ti}}} \qquad (2)$$

There are two designs of the lens.

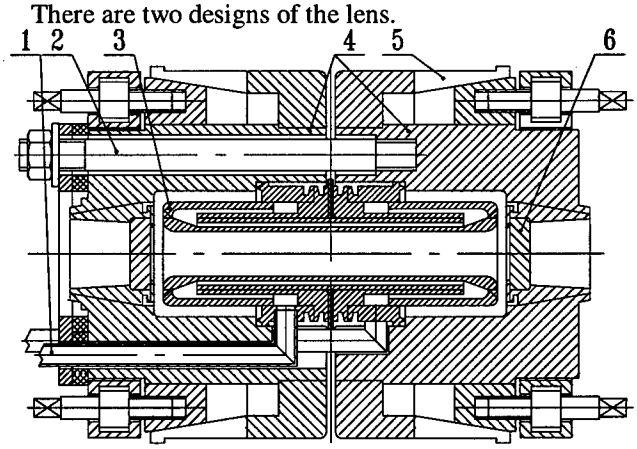

Fig. 1. BINP solid lithium lens with elastic shell.

1 – water supply; 2 – retaining bolts; 3 – titanium body of the lens; 4 – steel body of the lens; 5 – collecting contact; 6 – beryllium windows.

G.I. Silvestrov@inp.nsk.su

0-7803-5573-3/99/$10.00@1999 IEEE.

The lens in Fig. 1 has a free external surface of titanium shell, flown by cooling water. The shell in this case is the basic elastic element of the construction, taking up thermal expansion of lithium and reducing the pulse pressure in the system.

The lens in Fig. 2 has a rigidly supported external surface of titanium shell and the role of single elastic element of the construction plays the compressibility of lithium – χ_{sol}.

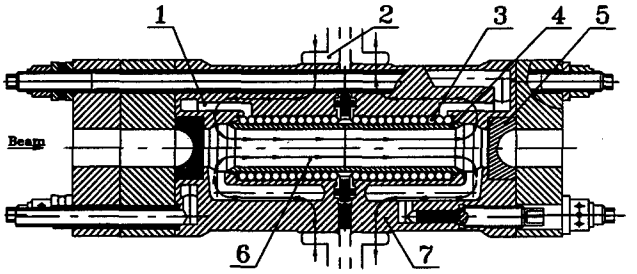

Fig. 2. CERN solid lithium lens with rigidly supported shell.

1– cooling inlet channels; 2 –current contacts; 3 – silicon nitride spheres; 4 –stainless steel container; 5 – titanium window; 6 –lithium rod, 7 –steel housing.

The non-heated buffer volumes play important role in mechanical behavior of the lens. The compressibility of this volumes takes up the thermal expansion of lithium at the pulsed heating of cylindrical operational part of lens V_0 and reduces the pressure in the system. However, it's impossible to use buffer volumes effectively in lenses with solid lithium because owing to high viscosity of solid lithium after it's compression in buffer volumes the system returns to the stationary pressure distribution slowly and the relaxation time is several tens of seconds [5]. The use of buffer volumes in this case is even dangerous because it can results in unrestored to the next cycle breaking-off of operational part of lithium from titanium shell. So, in lenses with solid lithium it's necessary to consider $V_b/V_0 \to 0$ and then in a "rigid" construction the pressure value will be $P = \dfrac{\alpha \cdot T}{\chi_{sol}}$

The uniform current density in the lens cross-section is reached at pulse duration corresponding to $\delta/R \approx 0.7$, where δ – is a thickness of flat skin-layer in lithium. In this case the average temperature in the cross-section of lithium rod per pulse will be $T = 60°$ at $H = 10$ T and the pressure in a "rigid" construction will reach $P_r = 1200$ atm.

In the elastic structure with free surface of thin titanium shell the pressure value will be significantly less $P_{el} = \dfrac{\alpha \cdot T}{\chi + \dfrac{R}{\Delta} \cdot \dfrac{2}{E_{Ti}}} \cong 370$ atm., but mechanical stresses in the wall equal in this case to $\sigma = P \cdot R/\Delta$ will be $\sigma = 3700$ kG/cm^2 – close to the strength limit of titanium at multiple cyclic loads. Therefore in lenses with solid lithium the field value 10 T is apparently ultimate.

The only possibility to create lenses with 15÷20 T field is transition to the lens constructions with liquid lithium. The advantages of liquid lithium are defined mainly by two factors. The first one is possibility to use buffer volumes effectively. The pressure relaxation times in lenses with liquid lithium are comparable with sound propagation time in the system, so the value of buffer volumes working effectively can be chosen $V_b/V_0 = 5 \div 6$. Moreover, liquid lithium has a significantly bigger compressibility $\chi_{liq} = 50 \cdot 10^{-6}$ atm^{-1}. Thus, we'll obtain factor ~30 in expression (1) reducing the pressure in the system caused by thermal expansion of lithium to several tens of atmospheres. So, this pressure can be neglected.

One variant of the lens design with liquid lithium is performed in Fig. 3. Since there is no water cooling in the system, realized in case of solid lithium through the thin titanium shell (2) it [shell] is rigidly supported through the ceramics insulation on the thick wall pipe (3), limiting buffer volumes(4). Input and output (5) of liquid lithium is realized through the hydrodynamical dampers (6), preventing the compression wave expansion from buffer volumes into the pumping and cooling system.

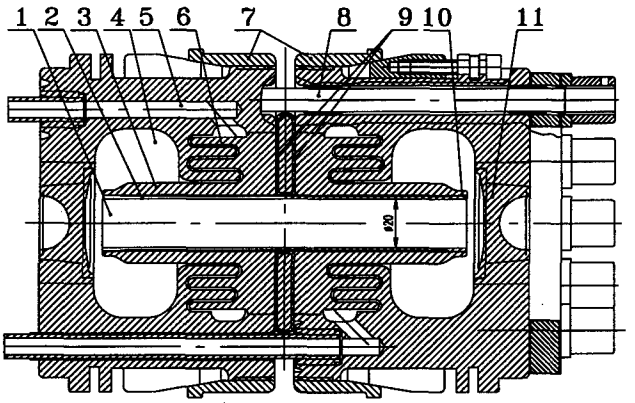

Fig. 3. Lens with liquid lithium.

1 – lithium rod; 2 – thin wall titanium shell; 3 – thick wall pipe; 4 – buffer volume; 5 – liquid lithium input; 6 – hydrodynamical dampers; 7 – current input; 8 – retaining bolts; 9 – insulation gap; 10 – weld; 11 – beryllium windows.

The important source of mechanical stresses in the lens is pulse pressure of magnetic field in current inputs (7). It is applied in the insulating gap (9) to two halves of the

lens body and transmits to retaining bolts (8). Full magnetic field force passing to the bolt is expressed as $F_M = 2\pi \cdot \ln r_1/r_0$, where P_M – pressure of magnetic field at the surface of lithium cylinder with radius r_0, r_1 – outer diameter of the lens body, where the current contact is performed. In given geometry at 10 T field $F_M = 5000$ kG The retaining bolts must provide the preliminary longitudinal compression of the construction with the force $F_C > F_M$ to avoid opening of joint into insulation gap (9). If $F_C < F_M$ the magnetic field force will be transmitted to the weld (10) between the thick wall support cylinder (3) and thin wall titanium shell (2). This shell is the most responsible element of the construction, defining the reliability of the lens operation.

If one can provide an absolutely rigid longitudinal compression of the lens bodies , the only source of stresses in the weld end joints of the thin wall titanium shell of the lithium cylinder would be its longitudinal thermal expansion at the lens pulse heating. These stresses are the basic limit of the shell long term operation. With the shell heating up to temperature ΔT at the points of its rigid welding the compression stresses $\sigma = E_{Ti} \cdot K \cdot \Delta T$ will occur where $K=8 \cdot 10^{-6}$ is the coefficient of its thermal expansion of titanium. The shell heating occurs in two stages. When passing through lens a fraction of the current pulse goes along titanium causing the fast pulse heating of the shell up to temperature $T_{Ti} = T_{Li} \cdot \frac{\rho_{Li} \cdot c_{Li} \cdot \gamma_{Li}}{\rho_{Ti} \cdot c_{Ti} \cdot \gamma_{Ti}}$. In order to reduce the fraction of current branched to titanium and pulse heating value to their minima the shell is made of the VT6 titanium alloy with the specific resistance $\rho_{Ti} = 140 \cdot 10^{-6}$ Ohm·cm. At the specific resistance of liquid lithium $\rho_{Li} = 30 \cdot 10^{-6}$ Ohm·cm the titanium heating is $T_{Ti} \approx 0.15 T_{Li}$

At the lens surface field of 10 T, the lithium pulse heating is $\Delta T \approx 60^\circ$ and it grows quadratically with an increase in a field. In this case, the titanium pulse heating is $\Delta T \approx 10^\circ$ and mechanical stress occurred in a shell does not exceed $\sigma \approx 150$ kG/cm^2 However, after the fast pulse heating similar to thermal shock the titanium temperature will grow due to thermal conductivity up to the lithium temperature. This heating will result in the stress raise up to $\sigma \approx 400$ kg/cm^2. With an increase in the field even up to 20 T these stresses can not reach those ultimately admissible for titanium fatigue stresses during the tens million cycles of the lens operation.

So, in lenses with liquid lithium the only fundamental limitation of magnetic field value is the pressure caused by magnetic field compression of current-carrying lithium cylinder transmitting to the face windows with beryllium inserts (11). At 20 T field this pressure reaches $P_M = 1600$ atm. thus the close consideration of strength properties of beryllium inserts is required.

The disadvantage of construction of the lens with liquid lithium is the necessity to create a high static pressure in lithium contour (~300 atm.) It's connected with the increased compressibility of liquid lithium. This static pressure must compensate partially the compression of lithium rod by magnetic field which can result in separation of lithium rod surface from titanium shell. It is not evident that this effect is destructive and it must be a subject for the experimental investigation.

The use of liquid lithium, pumped through the lens allows us to solve problem of removal of power releasing in lithium rod and provide the lens operation at higher frequency of cycles up to 15 Hz, discussed in projects of muon colliders.

Lenses with liquid lithium were developed and tested at BINP in 1987 [6] for the first time.

Now the liquid lithium lens for the FNAL antiproton source (Fig. 3) has been created and the investigations of behavior of elements of liquid lithium contour in regimes of cyclic loads at field values up to 13 T are being carried out at this lens.

REFERENCES

1. B.F. Bayanov et al. "Powerful Optics with Large Magnetic Fields for Effective Production of the Secondary Particles Beams"10 th Int. Conf. of High Energy Accelerators, Protvino, (1977) vol. 2, p. 103

2. B.F. Bayanov et al. "A Lithium Lens for Axially Symmetrical Focussing of High Energy Particle Beams" NIM 190 (1981) 9–14

3. G. Dugan "P-bar Production and collection at the FNAL Antiproton Source" Proc of the 13 th Int. Conf. of High Energy Accelerators, Novosibirsk, 1986, vol. 2, pp. 264-271.

4. R. Bellone et al. "The Result of Prototype Test and Field Computations of the CERN Lithium Lens" Proc of the 13 th Int. Conf. of High Energy Accelerators, Novosibirsk, 1986, vol. 2, pp. 272-275.

5. B.F. Bayanov et al. "Study of the Stresses in and Design Development of Cylindrical Lithium Lens" Preprint BINP 84-168

6. B.F. Bayanov et al. "Large Cylindrical Lenses with Solid and Liquid Lithium" EPAC, Rome, June 7-11, 1988, vol.1, pp. 263-265.

FINAL STAGE OF MUON BEAM COOLING

G. I. Silvestrov, A. N. Skrinsky, T. A. Vsevolozhskaya,BINP, Novosibirsk, Russia

Abstract

We consider the final stage of ionization cooling of muons, realized with the use of bent current-carrying lithium-beryllium rods, providing an optimum correlation between the cooling rates in all tree directions and minimum value of 6-dimensional emittance. The matching of lattice functions in a rod with those in accelerator structure is considered.

1 INTRODUCTION

The final stage of ionization cooling is characterized with reasonably low 6-emittance of muon bunches, achievable by very small magnitudes of betatron functions of the beam in slowing medium. Meanwhile the relative energy spread in a beam is not small, being equal to several percents even by optimum distribution of summary decrement between transverse and longitudinal degrees of freedom. This creates a problem of minimization of chromatic aberration effect by matching the low-beta focus in slowing medium with focusing structure of rather long-wave accelerator units.

2 TRANSFER OF COOLING RATE TO LONGITUDINAL DIRECTION

Bent current-carrying lithium-beryllium rods join in itself the functions of efficient focus and of degrader, necessary for transverse ionization cooling, and create a dispersion function, providing the longitudinal cooling – when correlated with transverse gradient of electron density in slowing matter – on account of redistribution of cooling decrement between transverse and longitudinal directions. The portion of decrement, transferred to longitudinal direction, is defined as $\Delta\delta = \delta_0\psi\left(\eta + \frac{1}{R}\right)$. Here δ_0 is transverse decrement, equal to ratio ξ/pv, with ξ standing for mean rate of ionization loss of energy, $\xi = -\overline{\frac{dE}{dz}}$; ψ denotes dispersion function, $\eta = \frac{1}{n_e}\frac{dn_e}{dr}$ - relative value of electron density gradient, and R is the bend radius. Full expression for longitudinal decrement reads:

$$\delta_{\parallel} = \xi' + \delta_0\psi\left(\eta + \frac{1}{R}\right),$$

where ξ' is a derivative of mean rate of ionization loss with respect to particle energy. It represents the natural longitudinal decrement. In energy region of logarithmic grow of loss rate the value of ξ' hardly achieves 7% of transverse decrement, while below $pc \sim 400$ Mev, where it is negative , its absolute value $|\xi'| \cong 2\left(\frac{1}{\gamma^2} - \frac{1}{L_i}\right)$ ($L_i \sim 25 \div 30$ is the logarithmic factor in expression for mean rate of ionization loss of energy) is growing fast with energy decrease and becomes equal to $\sim 0.9\delta_0$ at momentum $\sim$100 MeV/c. Thus, the energy of cooling is defined by a magnitude of product $\psi\eta$ we can create.

We consider two ways of creation of electron density gradient in current- carrying rods. In first (see fig. 1 a) the rod is composed of wedge-shape parts of two different metals [1]. One is the lithium, and another - the beryllium alloy with the same electrical conductivity as lithium. The relative gradient of electron density in such rod is found as: $\eta \cong \frac{1}{r_0}\frac{n_{e,Be} - n_{e,Li}}{n_{e,Be} + n_{e,Li}}$, where r_0 is a rod radius. Dispersion function in bent rod is equal to $\psi = r_0\frac{H_0}{H_m}$, where H_0 is bending field and H_m - the focusing one, defined as $H_m = r_0\frac{dH}{dr}$. By equal each other magnitudes of above fields the value of ψ is simply equal to r_0, and product $\eta\psi$ – to $\eta\psi = \frac{n_{e,Be} - n_{e,Li}}{n_{e,Be} + n_{e,Li}}$, that is to ~ 0.56. The ratio

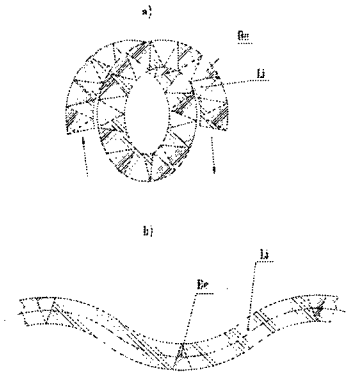

Figure 1: Two geometries of bent lithium-beryllium current-carrying rod.

$\psi/R = r_0/R$ adds to this a value of the order of 0.1, so the longitudinal decrement is equal to $\delta_{\parallel} \cong \xi' + 0.66\delta_0$. This provides the positive value of longitudinal decrement by beam momentum above 140 Mev/c.

Another way of creation of electron density gradient consists in insertion of thin beryllium wedges between sections of lithium carrent-carrying rods (see fig. 1 b). Wedge length Δl (by the bottom) can not exceed ~ 0.2 of lithium section length l without sufficient violation of focusing structure, which restricts an effective η by a value: $\eta_{\text{eff}} \cong \frac{1}{r_0}\frac{n_{e,Be}\Delta l}{2n_{e,Li}l + n_{e,Be}\Delta l} \leq 0.26$. This is sufficiently less the value got in first case, however this reduction can be compensated by means of enlarging of dispersion function magnitude at wedges. This is achieved by a special configuration of bent rod, providing the parallel shift of a beam between the wedges. With phase advance of free particle

0-7803-5573-3/99/$10.00@1999 IEEE.

oscillations between two subsequent wedges equal to 220° -240°, the absolute value of ψ at wedges is increased by 3 -3.5 times. This permits to get the product $\psi\eta$ equal to $\sim 0.8 \div 0.9$.

3 ULTIMATE VALUE OF NORMALIZED 6-EMITTANCE

An optimum relation between the transverse and longitudinal decrements by cooling in current-carrying rods with restricted value of maximum field at the rod surface, defines the longitudinal decrement as equal to one fourth of the sum decrement of ionization cooling $\delta_\Sigma = 2\delta_0 + \xi'$, i.e. $\delta_\parallel^{(\mathrm{opt})} = \delta_0/2 + \xi'/4$.

In the wedge-rod scheme the optimum value of $\delta_\parallel$ is achieved with $\Delta l/l \cong 0.13$ by cooling at 200 MeV/c momentum.

Dependence of an ultimate value of normalized 6-dimensional emittance on energy is defined by a factor $\sim \frac{(\gamma^2+1)\sqrt{\gamma}}{\beta^2}$ [2]. It is minimum at $pc \cong 100\mathrm{MeV}/c$, where the value of $\epsilon^{(6)}_{\mathrm{eq,N}}$ is estimated as:

$$\epsilon^{(6)}_{\mathrm{ult,N}} \sim \cdot 10^{-4} \frac{1}{H_m^2} \sqrt{\frac{\lambda}{2\pi e\varepsilon}}\ \mathrm{cm}^3$$

in dependence on maximum focusing field H_m, acceleration rate $e\varepsilon$, and wave length of accelerating voltage λ. With $H_m = 10$T, $\lambda = 10$ cm, and $e\varepsilon_{\mathrm{eff}} \cong 1.2$ MeV/cm one gets: $\epsilon^{(6)}_{\mathrm{ult,N}} \sim 1.2 \cdot 10^{-6}$ cm^3 .

At particle momentum $200\mathrm{MeV}/c$ and with more moderate accelerator parameters – $\lambda \cong 30$cm and $e\varepsilon_{\mathrm{eff}} \cong 0.5\mathrm{MeV}/\mathrm{cm}$ – this value is: $\epsilon^{(6)}_{\mathrm{ult,N}} \sim 4.0 \cdot 10^{-6}$ cm^3 .

Cooling of $\sim$ 200 MeV/c momentum muons in a system, composed of bent lithium rods and beryllium wedges of 0.13 relative length, is illustrated in figure 2.

Curves 1 and 2 show, accordingly, the radial and axial normalized emittances in MeV/c cm and 3 – the longitudinal emittance in MeV cm versus the number of degrader-accelerator cells. Thin lines present the numerical solution with the use of kinetic equation, thick ones – the result of simulation with Moliere formulae, used for the Coulomb scattering angle distribution, and Vavilov formulae – for straggling of energy loss.

Dashed line shows the ratio R_t of rod radius to maximum r.m.s. particle coordinate, got by the numerical solution, while dashed squares at figure bottom show the particles (from 100 initial), found lost by simulation. Both dipole and maximum focusing fields are taken equal to 10T, acceleration rate – to 0.5 MeV/cm, and λ – to 30 cm. The initial r.m.s. momentum spread is $\pm 4.5\%$ and longitudinal coordinate – $\pm$1cm.

The rod radius is gradually reduced with beam cooling from $\sim$ 8 mm down to $\sim$ 3.5 mm, which provides with almost constant value of R_t, equal to $\sim 2.5(r_0 \cong 3.5\sigma_\perp)$. The rod length is also decreased in proportionality with $\sqrt{r_0}$ to keep constant value $\nu\varphi_0 = \frac{2}{3}\pi$. The energy loss

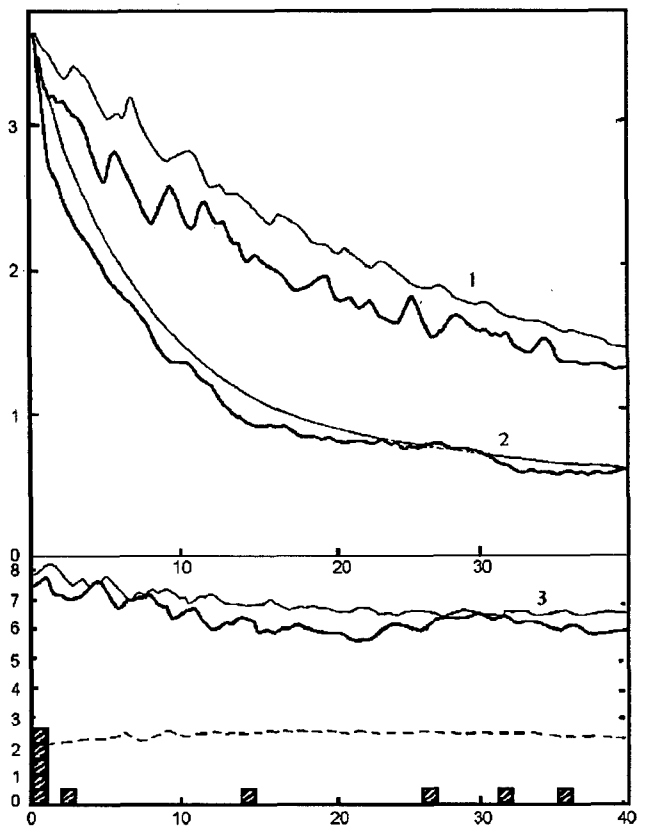

Figure 2: Cooling of 200 MeV/c muons.

per cell is about 30 MeV in the beginning and about 20 MeV in the end.

The final radial emittance is more than two times larger than the axial one, which proves, that more than half of radial decrement is transferred to the longitudinal direction. The initial longitudinal emittance is taken close to the equilibrium value and thus only slightly decreases with cooling.

The magnitude of normalized 6-dimensional equilibrium emittance, got in the end of 40-cell cooling, is equal to $\sim 4.5 \cdot 10^{-6}\mathrm{cm}^3$ in good accordance with analytic estimation.

4 COMPENSATION OF LINEAR CHROMATICITY BY ACCELERATION

To get the defined above ultimately small normalized 6-emittance of muon beam there has to be solved a problem of minimization of chromaticity of focusing by acceleration between the degrading sections being the necessary part of ionization cooling scenario.

Such minimization is achieved by compensation of linear component of chromaticity, as it is considered below.

The transverse mean square beam characteristics by acceleration are defined with equations:

$$\frac{\partial\langle r^2\rangle}{\partial y} - 2\frac{p\langle r\theta\rangle}{e\varepsilon_0} = 0$$
$$\frac{\partial p\langle r\theta\rangle}{\partial y} - \frac{p^2\langle\theta^2\rangle}{e\varepsilon_0} + \frac{k_{\mathrm{eff}}p^2\langle r^2\rangle}{e\varepsilon_0} = 0 \qquad (1)$$

$$\frac{\partial p^2\langle\theta^2\rangle}{\partial y} + 2\frac{k_{\text{eff}}p^3\langle r\theta\rangle}{e\varepsilon_0} = 0.$$

Here r and θ are 2-vectors of transverse coordinate and angle, accordingly, y stands for particle rapidity $y = ln\frac{E+p}{M}$, E and p are energy and momentum, and velocity of light is put equal to 1; $e\varepsilon_0$ denotes the acceleration rate, and k_{eff} – the focusing strength, defined by means of derivative of angle with respect to longitudinal coordinate as $k_{\text{eff}}r = -\frac{d\theta}{dz}$.

Let us consider the focusing strength to be of quadratic dependence on particle momentum, $k_{\text{eff}} \propto 1/p^2$, and about uniformly distributed through the length of acceleration. Such a focusing can be really created with the use of continuous train of short quadrupoles[1] with accelerator, placed in their aperture (see fig. 3). The focal distance of short FD pair f is about equal to $\frac{1}{k^2l^3}$ with $k = e\frac{dH}{dr}/pc$ and l being a length of quadrupole unit. The effective value of $\frac{d\theta}{dz}$ is thus equal to $\sim \frac{r}{2lf}$, and $k_{\text{eff}} \cong k^2l^2/2$.

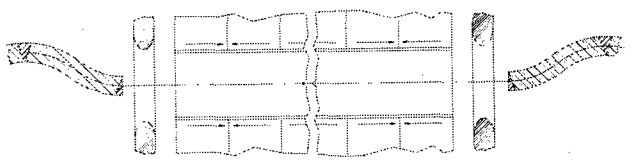

1,3–short solenoidal lenses with field up to 25T;
2–quadrupole (helic) tract.

Figure 3: Scheme of beam focus between degraders.

Solution of system (1) reads:

$$\begin{aligned}
\langle r^2\rangle &= \langle r_0^2\rangle\cos^2\omega(y-y_0) + \frac{\langle\theta_0^2\rangle p_0^2}{\kappa}\sin^2\omega(y-y_0)\\
\langle r\theta\rangle p &= \frac{\langle\theta_0^2\rangle p_0^2 - \kappa\langle r_0^2\rangle}{2\sqrt{\kappa}}\sin 2\omega(y-y_0) \qquad (2)\\
\langle\theta^2\rangle p^2 &= \langle\theta_0^2\rangle p_0^2\cos^2\omega(y-y_0) + \kappa\langle r_0^2\rangle\sin^2\omega(y-y_0)
\end{aligned}$$

with $\kappa = k_{\text{eff}}p^2$, and $\omega = \frac{\sqrt{\kappa}}{e\varepsilon_0}$. Here we neglected the value of $\langle r_0\theta_0\rangle$, which is small in current-carrying rod.

To get a small betatron function at entrance to next lithium rod the phase advance $\omega(y-y_0)$ is to be chosen equal to π (or 2π and so on), which defines the necessary value of κ by fixed acceleration rate. On acceleration from ~170 up to 200 MeV/c ($y - y_0 \cong 0.14$) with phase advance equal π and acceleration rate $e\varepsilon_0$ to ~ 0.5 MeV/cm, the value of κ is ~ 126 MeV^2/c^2 cm^2.

The magnitudes $\langle r^2\rangle$ and $\langle\theta^2\rangle$ at accelerator exit in linear approach do not depend on particle energy deviation. Aberrational effect manifests itself only through $\langle r\theta\rangle$. It is proportional to a difference $\langle\theta_0^2\rangle p_0^2 - \kappa\langle r_0^2\rangle$, which is not small as far as κ is much less than corresponding magnitude in a rod: $\kappa << p_0^2/\beta_0^2$. In result, the value of $\delta\langle r\theta\rangle$ at accelerator exit is rather large. In following lithium rod it gives rise to oscillating addition to betatron function:

$$\delta\beta_0 \cong -\frac{\delta E}{e\varepsilon_0}\frac{p_0}{p}\left(1-\frac{p_0}{p}\right)\sin 2\sqrt{k_0}z$$

with amplitude, being of the order of or even exceeding the value of β_0 by $\delta p/p$ equal to several percents.

This makes evident the necessity of matching lens to be inserted between the lithium rod and accelerator. Such a lens, making the $\pi/2$ transformation with focal distance $f_0 \cong \sqrt{\frac{\beta_0 p_0}{\sqrt{\kappa}}}$, will provide zero value of $\langle r\theta\rangle$ by acceleration. Simultaneously a lens with focal distance $f \cong \sqrt{\beta_0 p\sqrt{\frac{p}{p_0\kappa}}}$, put after accelerator, will match the beam with focus in next rod.

Thus the linear chromaticity of focusing by acceleration is compensated. This, however, does not mean the compensation of chromatic aberration, but the trajectory of aberrational displacement of particle coincides in lenear approach with transverse phase trajectory.

The matching lenses also make contribution to the aberrational effect. With account for this made, the necessary value of f_0 is defined as:

$$f_0 \cong \sqrt{\frac{p_0}{p}}\left\{\frac{\beta_0^2 p_0(p-p_0)}{\nu e\varepsilon_0 E}\Big/\left[\frac{E_0}{E}+\left(\frac{p_0}{p}\right)^{7/4}\right]\right\}^{1/3},$$

where ν stands for a power of matching lens focal distance dependence on particle momentum: $f_0 \propto p^\nu$. The value of f is found as $f = f_0\left(\frac{p}{p_0}\right)^{3/4}$.

By $p_0 = 170$ MeV/c and $p = 200$ MeV/c, $e\varepsilon_0 = 0.5$ MeV/cm, $\beta_0 = 2$ cm and $\nu = 2$ the magnitudes of f_0 and f are equal to 4.3 and 5.4 cm, accordingly.

The lens with such a focal distance for particles of ~ 200 MeV/c momentum is a problem. It can not be the lithium one because with beta-function of beam, exceeding 10 cm, the multiple scattering in lithium will result in beam emittance increase by $\sim 10\%$ of equilibrium value in each lens.

The only solution seems to be a short solenoidal lens with very high – up to 25 T – pulsed magnetic field.

The use of "linear" systems ($k_{eff} \propto 1/p$) for beam focusing by acceleration would evidently give an advantage in aberrational effect as compared to the "quadratic" ones. As such a "linear"systems the plasma lenses can be considered. Having the focal distance linearly dependent on particle momentum, such lenses by rather moderate parameters would provide an efficient focusing with minimum chromatic aberration.

5 REFERENCES

[1] . Skrinsky, AIP Conference Proceedings 441, p. 249, (1997).

[2] . A. Vsevolozhskaya, Proc. of EPAC'98
NIM A, being published.

[1] Technologically preferable looks the helical quadrupole tract

DAMPING SPURIOUS HARMONIC RESONANCES IN THE APS STORAGE RING BEAM CHAMBER*

Y. Kang, G. Decker, and J. Song, ANL, Argonne, IL

Abstract

The APS storage ring beam chamber has been storing the beam up to 100 mA successfully. However, in some beam chambers, spurious signals corrupted the BPM outputs. The cause of the unwanted signals was investigated, and it was found that transverse electric (TE) longitudinal harmonic resonances of the beam chamber were responsible. The beam chambers have small height in the area between the oval beam chamber and the antechamber. The structure behaves like a ridge waveguide so that the cut-off frequency of the waveguide mode becomes lower. The pass-band then includes the frequency around 350 MHz that is important to the beam position monitors (BPMs). The spurious harmonic resonances are damped with two types of dampers to restore the useful signals of the BPMs; coaxial loop dampers and lossy ceramic slab loading are used.

1 INTRODUCTION

Since the commissioning of the Advanced Photon Source in 1995, significant progress has been made in the area of beam stabilization [1,2]. A mystery that has only recently been solved was connected with the observation that systematic errors in beam position monitor (BPM) readbacks have historically been an order of magnitude greater for vertical readbacks than for horizontal. Considering that the BPM monopulse rf receiver electronics multiplexes between horizontal and vertical readings on alternate turns, and that the horizontal and vertical difference signals are computed in real time by rf hybrids in the tunnel, it was difficult to attribute the observations to an electronics malfunction.

After a substantial effort to exonerate the electronics as the culprit, including various combinations of cable swapping, other causes were investigated. Among these was a suspected mechanical instability in the storage ring vacuum chamber (Figure 1). Certain misbehaving units demonstrated step-like behavior at the 150-micron scale. A dial indicator with remote camera display was used in several arrangements to show that the sudden step change in vertical BPM readback was not correlated with vertical vacuum chamber motion. At wit's end, a network analyzer was used to measure the transmission of rf power in the frequency band near the ring rf frequency of 351.93 MHz, from one end of the suspect chamber to the other using the BPM pickup electrodes mounted at

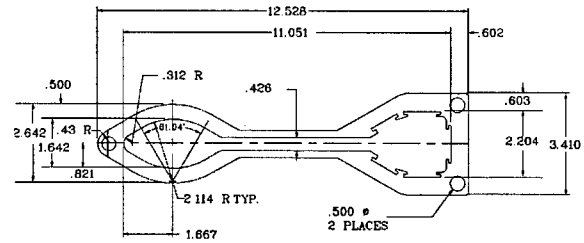

Figure 1: Storage ring vacuum chamber cross section (dimensions shown are inches)

opposite ends of the vacuum chamber. It has been known that the cut-off frequency for the storage ring vacuum chamber was above 1 GHz for TM modes, well outside the 20-MHz band centered on 352 MHz where the rf BPMs are sensitive. The result of the measurement, however, was that several resonance lines with Qs of the order of 1000 were discovered near 352 MHz. Simulations indicated that these "rogue" microwave modes were similar to TE01 waveguide modes. The electric field for these modes is oriented vertically with magnetic field lines circulating parallel to the beam in the beam chamber (the left-hand portion of Figure 1) and returning back on the right hand portion of the chamber (the antechamber), where nonevaporable getter (NeG) vacuum pumping strips are mounted. The vertical electric field orientation explained why only vertical BPM readbacks were affected.

The chamber design and rf analysis for beam-induced transverse magnetic (TM) modes appeared in Refs. [3][4]. Because the beam chamber and antechamber are connected through a narrow channel with a small height, the vacuum chamber resembles a ridged waveguide. The area with a small height introduces a large capacitive loading that lowers the cut-off frequency for TE01-like modes of the chamber in comparison to a rectangular waveguide having the same width.

Investigations of damping systems to suppress the unwanted resonances in the chambers without major mechanical modification were conducted. Computer simulations and bench measurements were made to find an optimal solution. The use of matched load terminated coaxial loop antennas, lossy ceramic tiles, and the introduction of shorting bars inside chambers were considered. Because shorting bars would intercept synchrotron radiation and require cooling, only the coaxial dampers and lossy ceramics were tested. Measurements with beam were conducted using the coaxial damper option.

*Work supported by U. S. Department of Energy, Office of Basic Energy Sciences under Contract No. W-31-109-ENG-38.

0-7803-5573-3/99/$10.00@1999 IEEE.

2 SIMULATION

The wavelength in a hollow waveguide satisfies the relationship:

$$f = c\,[1 + (\lambda_g / \lambda_c)^2\,]^{1/2} / \lambda_g$$

where c is the speed of light in free space, λ_c is the cut-off wavelength, and λ_g is waveguide wavelength. Using chamber length L = 4.81 m and λ_g = 2L/N (N=1,2,3....), the resonance frequencies can be estimated. The chambers showing the largest effect are slightly curved, and are installed in the gap of the storage ring dipole magnets. The first resonance is the one closest to the cut-off frequency of the waveguide. The waveguide wavelengths for these lower-order modes are much longer than free space wavelengths.

A MAFIA code simulation was used for the chamber model to check the harmonic resonances and ensure the damping schemes worked properly. Table 1 lists the first ten excited resonances in the chamber. The structure was approximated as a straight chamber since the curvature is small compared to the chamber's bending radius. The NeG strips were not included in the simulations. The results show that the frequency spacing increases as predicted above. Three matched-load coaxial probes mounted in the antechamber (right-hand side of Figure 1) using loop antennae mounted in existing vacuum ports were simulated with results also shown in Table 1.

Table 1: Calculated resonance frequencies and Q-factors of the chamber modes without and with the coaxial dampers

	Bare Chamber		With Three Coaxial Dampers	
#	Freq (MHz)	Q	Freq (MHz)	Q
1	324.0	3846	310.4	351
2	328.3	3931	313.9	249
3	335.3	4019	323.3	718
4	345.0	4193	332.6	390
5	356.9	4339	343.2	186
6	371.1	4544	357.7	202
7	387.1	4743	373.6	221
8	404.8	4909	390.7	120
9	424.0	5117	407.7	65
10	444.5	5320	426.5	108

The simulation showed that damping with coaxial probes can be a factor of ~10 at around 350 MHz. This was considered helpful but not sufficient to eliminate the problem. Therefore, slabs of rf absorbing material were used in the chamber slot area for further damping. Simulations were made with the ceramic material to see the damping performance and to optimize the position of the slabs inside the chamber.

Table 2 gives calculated resonance frequencies and Q factors for chamber modes in the presence of a 5 cm × 5 mm × 25 cm slab of lossy dielectric material placed in the "slot" region of a vacuum chamber at a distance d from the upstream end. This portion of the vacuum chamber is "shadowed" from synchrotron radiation. Note that the calculated Q-factors become very low and do not depend strongly on the dimension d. Since the ceramic damping dominates, the addition of coaxial dampers makes very little difference. Also note that the lower mode frequencies become even lower with the ceramic slab loading.

Table 2: Calculated chamber resonance frequencies and Q factors in the presence of lossy dielectric slabs

	Ceramic Damper, d=0.25m		Ceramic Damper d=0.5m	
#	Freq (MHz)	Q	Freq (MHz)	Q
1	132.6	2.7	131.7	2.8
2	226.8	2.8	225.2	3.0
3	327.5	144.5	327.6	54.0
4	331.8	13.2	331.2	5.86
5	335.9	5.3	335.3	9.3
6	342.7	18.5	344.3	36.0
7	353.9	51.8	357.0	74.7
8	368.1	86.7	372.7	103.3
9	384.6	102.5	391.0	95.7
10	403.2	81.5	410.7	37.8

The rf absorbing material was chosen to be vacuum compatible, stable, and efficient for damping. Good thermal conductivity was also desired. A few different types of lossy dielectric material were considered. Aluminum nitrite (AlN) with a high content of silicone carbide (SiC) was chosen for its properties that satisfy the above requirements. The most important material properties for our application are summarized in Table 3.

Table 3: Mechanical and electrical properties of the ceramic, AlN with 40% SiC

Thermal Conductivity (W/m°K)	120
Expansion Coefficient (10^{-6}/°C)	~ 4
Dielectric Constant (ε_r)	~ 30
Loss Tangent (tan δ)	~ 0.4

3 MEASUREMENT

Resonance frequencies and Q factors in a spare beam chamber were measured and compared with the simulation values shown in Table 1. The measurement was repeated with the addition of coaxial dampers on the 1.4" antechamber ports of the spare chamber. A vector network analyzer was used to measure transmission between BPM pickup electrodes mounted at opposite ends of the chamber. A four-channel rf 180-degree rat-race hybrid was used at one end of the chamber to drive the top two button pickups out of phase from the bottom

two, coupling to the vertical electric field. The transmission coefficient S_{21} from the hybrid "vertical" port to a single button at the opposite chamber end is shown in Figures 2 and 3. The peaks of the coupled modes are not constant since the coupling of the different modes to the BPM buttons is not uniform.

Note that the calculated Q factors are much higher than the measured values shown in Figure 2. A possible explanation is that the NeG strips were not included in the model. The NeG strips are located in the antechamber where the magnetic field dominates so that the surface loss becomes greater, damping the resonances significantly. Figure 3 shows the same measurement with two coaxial dampers mounted in the antechamber.

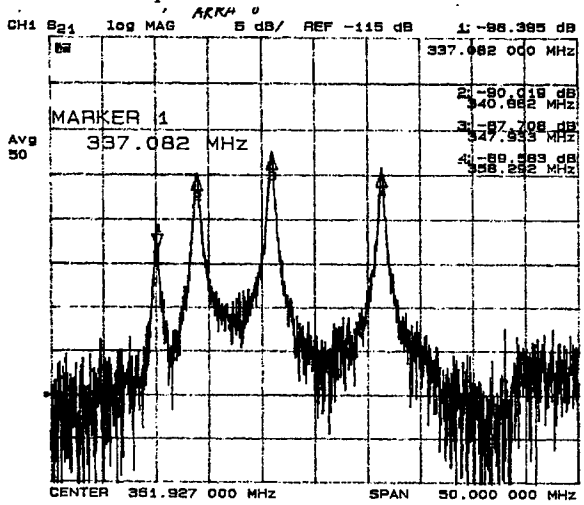

Figure 2: Resonances in a chamber with NeG strips

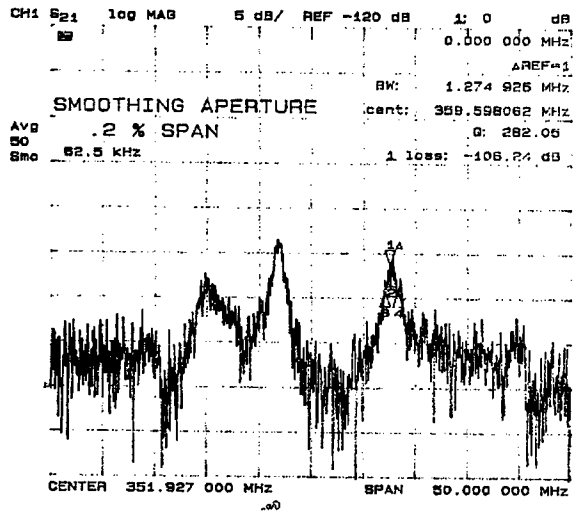

Figure 3: Resonances in a chamber with two coaxial dampers and NeG strips

Shown in Figure 4 is a single-bunch beam spectrum taken from the vertical difference output of a four-channel rf hybrid connected at a BPM pickup location where this mode was causing severe problems.

A single bunch was used because of its extremely simple spectrum, namely a series of uniformly spaced spectral lines of equal amplitude, with 271-kHz spacing (the APS revolution frequency). The two data sets shown in Figure 4 were collected five months apart, the control set (top) employing a broad-band hybrid, while the "after" data set (bottom) used the standard BPM hybrid that includes a 20-MHz bandwidth bandpass filter on the output. The degree to which the spectral lines in the broad-band data differ in amplitude is a measure of the impact of the chamber resonance. The feature centered near the 352-MHz rf frequency was responsible for pathological BPM behavior and was substantially suppressed by the single probe installed (the other available vacuum ports on that chamber were being used for vacuum diagnostics).

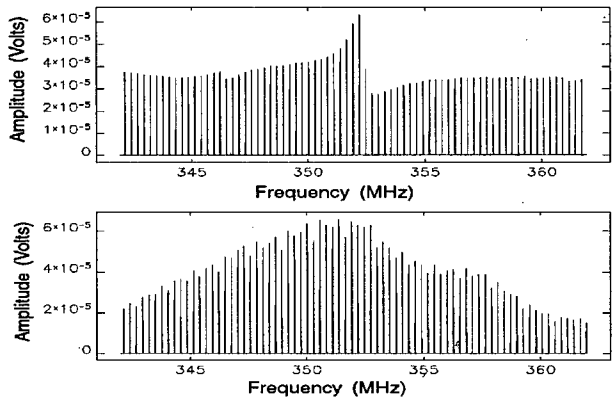

Figure 4: BPM signal without dampers (top), and with one coaxial damper (bottom, 20 MHz band limited)

4 CONCLUSIONS

A set of microwave modes that are present in APS vacuum chambers and have significant impact on vertical BPM performance have been discovered. Solutions to damp these modes include coaxial dampers and the introduction of lossy dielectric material. The coaxial damper solution has been successfully employed with beam; however, the lossy dielectric approach promises better damping of more modes. Research into viable installation configurations is ongoing.

5 ACKNOWLEDGEMENT

Authors are thankful to J. Galayda, Accelerator Systems Division Director of the APS, for his direction and encouragement on the investigation of the problem.

6 REFERENCES

[1] G. Decker et al., "Fundamental Limits on Beam Stability at the APS," BIW'98, AIP 451, pp. 237-244 (1998).

[2] J. Carwardine and F. R. Lenkszus, "Real-Time Orbit Feedback at the APS," BIW'98, AIP 451, pp. 125-144 (1998).

[3] R. Wehrle et al., "Vacuum System for the Synchrotron X-ray Source at Argonne," Proc. 1987 IEEE PAC, Washington D.C., pp. 1669-1671 (1987).

[4] R. Kustom et al., "Analysis of rf Modes in the ANL APS Vacuum Chamber Using Computer Simulation, Electron Beam Excitation, and Perturbation Techniques," Proc. 1989 IEEE PAC, pp. 1755-1757 (1989).

APS SR FLEXIBLE BELLOWS SHIELD PERFORMANCE*

J. Jones#, S. Sharma, D. Bromberek
Argonne National Laboratory, 9700 South Cass Avenue, Argonne, IL 60439 U.S.A.
J. Howell, Fermi National Laboratory, Batavia, IL 60510 U.S.A.

Abstract

The Advanced Photon Source (APS) storage ring (SR) consists of long rigid vacuum chambers connected by flexible formed bellows components. These SR bellows and additional diagnostic chambers are designed with leaf spring beryllium-copper (Be-Cu) alloy contact fingers that insert into mating rigid sleeves to function as electromagnetic shields. The shields protect the bellows convolutions from particle beam image currents and rf energy and reduce beam-induced rf resonances in the diagnostics chambers. The beam aperture of the shields is approximately the same as that of the beam chambers so that the beam impedance of the SR is minimized.

The bellows shields systems' thermal performance has been tested and is monitored during APS SR beam operations. Testing included infrared radiometer camera imaging and thermocouple instrumentation of the rigid sleeve. Direct results indicate that the liners perform well under all stored beam fill loadings through and including 100-mA, 8-bunch operations. Maximum temperatures of the bellows liner systems are typically 35-50° Celsius during standard 100 mAmp stored beam fills and 50-70° Celsius during fills, producing both maximum peak and total current simultaneously. The indirect observations of ring vacuum levels support the temperature data.

1 INTRODUCTION

The APS SR interchamber bellows and diagnostic components are protected from particle beam image currents with Be-Cu alloy contact fingers. These fingers function as leaf spring contacts where the contact force is generated from the deflection of the fingers as a flexible liner is inserted into a mating rigid sleeve. The contact fingers typically span the bellows convolutions, and during bake-out the fingers flex and slide within mating rigid sleeve liner components to accommodate the temporary chamber expansions. The contact fingers are of various lengths, widths, and thicknesses. The rigid sleeve components' outer surfaces are either exposed to atmosphere and convection cooled (see Figure 1) or contained completely within the ring vacuum (see Figure 2). This paper discusses the bellows shield systems' design, testing, monitoring, and performance during APS SR beam operations.

2 BELLOWS SHIELD DESIGN

In selecting the contact finger material, both operational performance and process temperature compatibility were considered. For the APS, the Be-Cu spring alloy UNS number C17200 was chosen for its relatively high electrical and thermal conductivities and for its very high yield strength that is not affected by the APS bakeout temperature of 150° Celsius.

The flexible bellows shields are fabricated from quarter-hard Be-Cu sheet that is easily worked in the pre-hardened condition. The Be-Cu sheet is partially slit into contact fingers by either wire electrical discharge machining of the 0.036-inch-thick material or chemical etching of material up to 0.020 inch thick. The cut finger

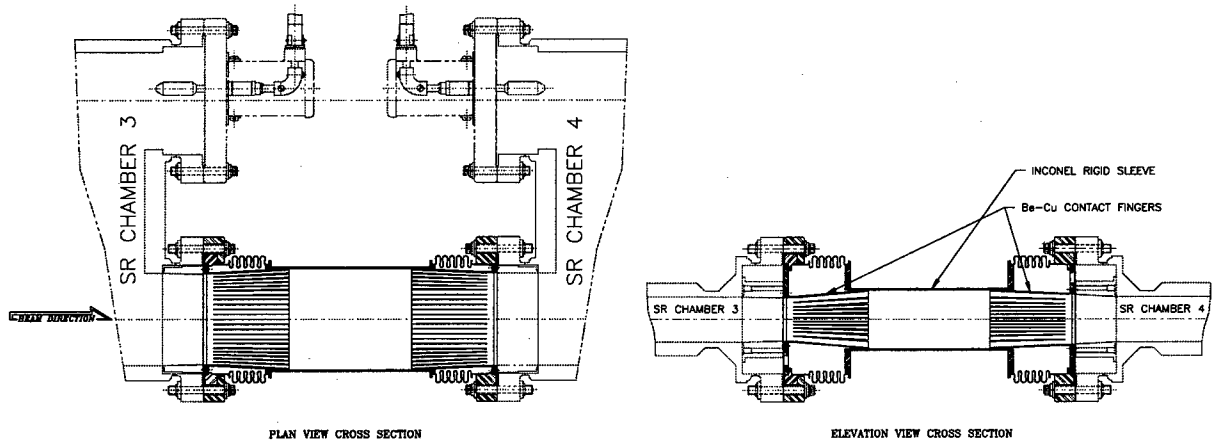

Figure 1: APS SR convection-cooled shield and bellows assembly

* Work supported by the U.S. Department of Energy, Office of Basic Energy Sciences, under Contract No. W-31-109-ENG-38.
# Email: jones@aps.anl.gov

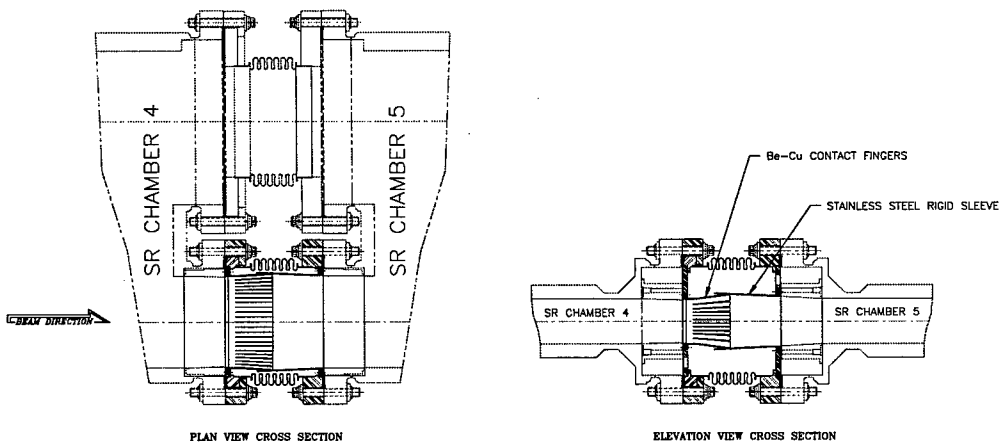

Figure 2: APS SR in-vacuum shield and bellows assembly

stock is then formed to the shape of the APS SR beam tube aperture. A similar aperture is machined into a copper disk that is used both to support the contact fingers and to capture a Be-Cu coil-spring gasket that ensures contact between the bellows shield assembly and the adjacent ring vacuum chamber component within the vacuum chamber flange enclosure. The two items are vacuum furnace brazed to form the typical flexible bellows shield assembly. After brazing, the Be-Cu contact fingers are fully solution hardened by heating at a temperature of 315° Celsius for two hours.

Specialized flexible shield assemblies employ 304 stainless steel mounting disks with the flexible shields attached by welding or screw fasteners. The mating rigid sleeve components are fabricated from Inconel® 625 or 316 stainless steel. The Inconel® rigid sleeves are an integral part of the ring bellows vacuum enclosure assemblies. As such, the exterior of the Inconel® rigid sleeves is in direct contact with air and is convection cooled. The stainless steel rigid sleeves are enclosed completely within the vacuum of the APS SR, and are primarily employed in the shortest bellows applications.

3 TEST AND MONITORING

The performance of both of the bellows shield designs has been monitored during SR beam operations. However, due to limited cooling, the vacuum-enclosed liner systems have been extensively tested and are continuously monitored during APS SR beam operations.

Testing included infrared radiometer camera imaging and thermocouple instrumentation of the rigid sleeve. The test set-up is shown in Figure 3. The infrared radiometer, an Inframetrics PM200, is capable of both thermal imaging of the contact fingers and rigid sleeve, and collecting and storing actual temperatures of the items in the image. A calcium fluoride, (CaF_2), infrared-transparent window is used to allow the imaging of the in-vacuum bellows shield components. The view into the window is shown in the inset of Figure 3. The Be-Cu fingers are coated with graphite to increase the emissivity of the metal surface to approximately 0.8. The radiometer is protected from radiation damage by a lead brick enclosure.

The optics include two front-silvered mirrors in a periscope arrangement in addition to the CaF_2 viewport. The thermocouples are type K, consisting of Chromel® and Alumel® wires. The thermocouple junctions are welded to the exterior of the rigid sleeve. Ten thermocouple junctions are evenly distributed across the lower perimeter of the rigid sleeve at the approximate location of the spring finger contacts. The individual thermocouple wires are insulated with binder-free fiberglass insulation. Two five-pair type-K thermocouple feedthroughs are employed to extract the thermocouple voltage, and an ion gauge is employed to measure local vacuum levels. The infrared radiometer set-up was used during one maximum peak current operation studies period, while the thermocouple instrumentation is a permanent installation.

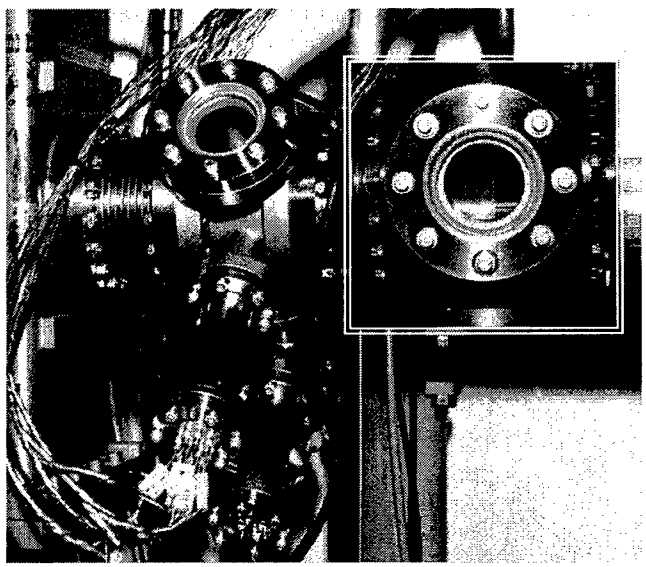

Figure 3: APS bellows shield test assembly

4 RESULTS

Results indicate that the liners perform well under all stored beam fill loadings through and including 100-mA, 8-bunch, 7-GeV operations. During the maximum peak current studies period, the operating mode was primarily high currents singlets fills. The highest observed temperatures were observed on the rigid sleeve components between the spring finger contacts location and the base of the sleeve. This was observed in the infrared imaging of the bellows shield assembly through the CaF_2 viewport. Also observed is the expected result that the peak heating occurs at the minor axis of the "elliptical" bellows shield assembly where the beam image currents are the largest.

Maximum temperatures of the vacuum-enclosed bellows shield systems are typically 35-50° Celsius during standard 100-mA stored beam fills, and 50-70° Celsius during fills producing both maximum peak and total current simultaneously. Plots of the bellows shield thermocouple data for the typical APS SR singlets 100-mA fill operations are shown in Figures 4 and 5; the reference beam-off cold temperature for this data is 28° Celsius. This data shows that the thicker 0.036-inch-thick Type I contact fingers run approximately 15° Celsius cooler than the 0.020-inch-thick Type II contact fingers under the same operating conditions. The difference is a function of both the finger contact force and the finger heat conduction area. Previous thermocouple measurements of the temperature of the convection cooled Inconel® rigid sleeve showed no significant heating. Ion pump ring vacuum monitoring supports the temperature data.

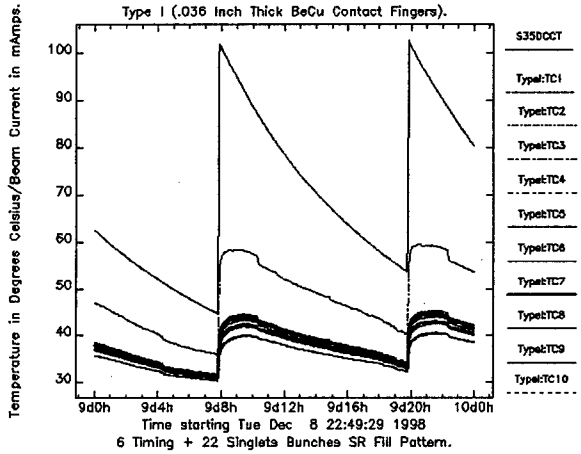

Figure 4: APS Type I bellows shield performance

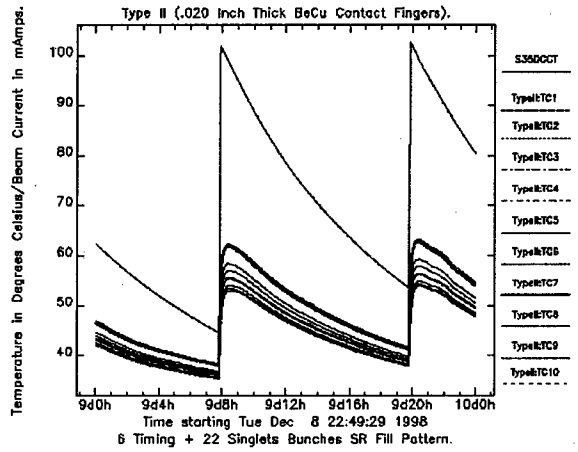

Figure 5: APS Type II bellows shield performance

5 CONCLUSIONS

First and foremost we conclude that the bellows shields are working very well under the present APS SR 100-mA current operations. The maximum operating temperature of 70° Celsius is well below the minimum annealing temperature of 176° Celsius of the Be-Cu alloy. At this temperature the contact fingers can be expected to provide positive contact force for an indefinite period of time. The indirect vacuum level monitoring and beam lifetime projections support this conclusion.

The future operating goals of the APS SR include continuous stored beam top-up and higher stored beam currents of up to 300 mA. As such, some improvements in the bellows shield design are being considered. The proposed rigid sleeve modification is to copper plate the stainless steel surface to reduce the electrical resistance. The thickness of the copper plating will be 0.0003-0.0005 inch, which is more than two times thicker than the 0.00014-inch copper skin depth of rf electrical currents generated by the fundamental frequency of the 352-MHz APS SR rf power system. All beam image current and rf resonant current resistive heating energy is expected to be deposited well within this skin depth.

The proposed modification to the flexible shield is to fabricate the spring contact fingers from Glidcop, which is alumina dispersion strengthened copper. Glidcop has nearly twice the electrical and thermal conductivity of Be-Cu and is much less susceptible to thermal aging and annealing. These improvements are being implemented in an ongoing machine development effort.

Finally, it must be stated that the convection-cooled bellows shield design is the preferred system but, due to SR real estate consraints, it is not always an option.

6 ACKNOWLEDGEMENTS

The authors would like to acknowledge Cathy Eyberger for her assistance in preparing and editing this paper. We would like to acknowledge Michael Borland and Jim Stevens for their help in data collection and instrumentation, and Kathy Harkay and Louis Emery for their machine operations during the APS SR bellows shield performance studies. We would also like to recognize Jean_Marie Lefebvre of ESRF for the collaborative testing of APS bellows shields at the ESRF.

Crossing Intrinsic Depolarizing Resonances in ELSA with Pulsed Betatron Tune Jump Quadrupoles

C. Steier, W. v. Drachenfels, F. Frommberger, M. Hoffmann, D. Husmann, J. Keil,
Bonn University, Germany;
S. Nakamura, T. Nakanishi, Nagoya University, Japan; H. Sato, T. Toyama, KEK, Japan

Abstract

At the electron stretcher accelerator ELSA of Bonn University an external fixed target experiment using a polarized electron beam has been started. To provide a polarized beam with sufficient intensity a dedicated source for polarized electrons is used (with a GaAs-AlGaAs superlattice photocathode). To prevent depolarization during acceleration in the circular accelerators several depolarizing resonances have to be corrected for. One type of resonances (the intrinsic ones) is compensated using two pulsed betatron tune jump quadrupoles. This method is applied because adiabatic crossing techniques that became popular in proton accelerators in the last years cannot be used in an electron accelerator due to synchrotron radiation effects at higher energies.

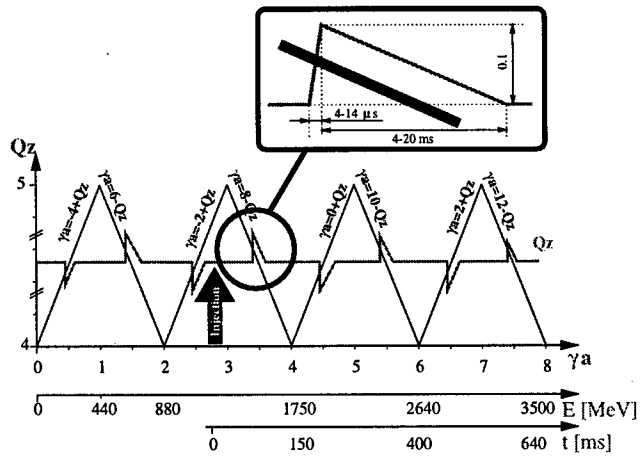

Figure 2: Fast tune jumping of all resonances in ELSA.

1 INTRODUCTION

At ELSA [1] external fixed target experiments with longitudinally polarized electrons or circularly polarized photons (produced by Bremsstrahlung) are carried out. For this purpose a polarized electron source is used. With a GaAs superlattice crystal a polarization level of about 66% at the source has been achieved [2]. The polarized electron beam is preaccelerated in a LINAC and a fast cycling booster (50 Hz). After injection into the main ring further acceleration up to 3.5 GeV is possible. The polarization of the extracted beam can be determined with a Møller polarimeter.

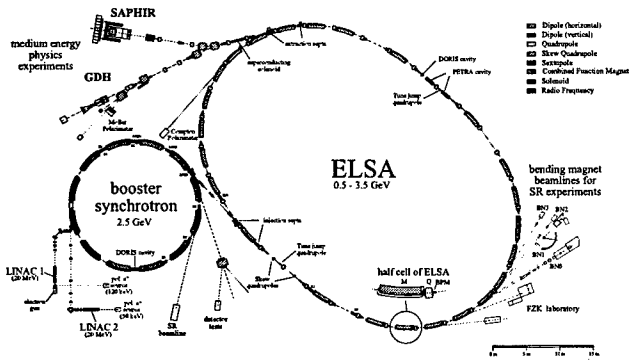

Figure 1: The ELSA facility at Bonn University.

In ELSA depolarization is caused mainly by intrinsic and imperfection resonances [3][4]. The spin originally oriented nearly perpendicular to the accelerator plane precesses around the direction of the magnetic field in the bending magnets. During circulation of the particles in the synchrotron only the polarization component parallel to the guiding field is conserved while the other components are lost. So, horizontal magnetic fields may cause polarization loss in the case of a resonance with the spin precession frequency.

Intrinsic resonances are driven by the vertical betatron motion of the electrons, characterized by the vertical betatron tune Q_z.

Depolarization caused by the linear crossing of an isolated resonance is quantified by the Froissart-Stora-Formula [5]

$$\frac{P_f}{P_i} = 2e^{-\frac{\pi|\epsilon|^2}{2\alpha}} - 1 \quad . \qquad (1)$$

In this formula the influence of synchrotron radiation is neglected, so it cannot be used for resonances at high energies in electron accelerators. Spin tracking studies show especially that a total spin flip ($\frac{P_f}{P_i} = -1$) is impossible there.

Small polarization losses can be obtained for a small resonance strength ϵ or a high crossing speed $\alpha = \frac{\dot{\gamma}a \mp \dot{Q}_z}{\omega_0}$ which can be achieved by fast shifting the vertical betatron tune Q_z for intrinsic resonances using pulsed quadrupoles.

For the resonances in ELSA an absolute tune shift of $\Delta Q_z \approx 0.1$ is needed with a rise time of about 10 μs. This tune jumping is illustrated in Fig. 2. Before crossing the resonance, the vertical betatron tune is shifted very fast by the tune jump quadrupoles.

0-7803-5573-3/99/$10.00@1999 IEEE.

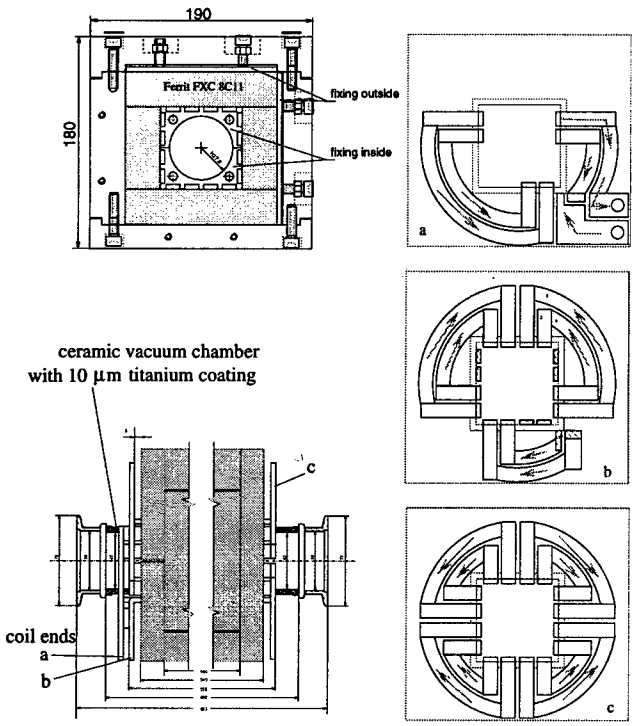

Figure 3: Design of the tune jump quadrupoles: the end cap design consisting of three layers (right), sectional and side view of the magnets (left).

2 TUNE JUMP MAGNETS

For ELSA a fast tune jump system was designed. It consists of two quadrupoles which can be pulsed up to 500 A in 4-14 μs. These quadrupoles are of Panofsky type with square shaped ferrite yokes (see Fig. 3) [6]. Calculations for optimization of the design to achieve a low inductance have been applied [7]. Therefore a special end cap design (a,b and c) was carried out. The vacuum chamber is made of Al_2O_3 ceramics with a 10 μm thin titanium coating on the inner surface. This coating shields the electromagnetic fields of the beam but does not distort the pulsed magnetic field.

The main parameters of the quadrupoles are:

resistance:	(4.298 ± 0.001) mΩ (=)
inductance:	(9.0 ± 0.1) μH (=)
max. pulse current:	500 A
max. field gradient:	(1.1241 ± 0.005) T/m.

Because of the high resistance of the ferrites there are no significant eddy currents inside the yoke. Frequency dependencies of the impedance lead to a slight dispersion of the pulse shape which has to be compensated by the power supply.

The Power Supplies

The pulsed power supplies (one for each magnet) were constructed by PPT[1]. A schematic drawing is shown in Fig. 4.

The design concept is similar to the pulsed power supplies used for COSY in Jülich [8].

Each supply consists of three main components, which could be realized in semiconductor technology. First a 1 kV high voltage power supply charges a capacitor bank. The charging is controlled by a PLC (programmable logic controller). An insulated gate bipolar transistor (IGBT) connects the capacitor bank with the load. The IGBT is controlled by the PLC to generate a linear rising edge, which can be varied from 4 to 14 μs.

The second part consists of a 50 V power supply and generates the falling edge. It is connected by a MOSFET switch to the load. The falling edge can be varied between 4 and 20 ms.

The third part is a H-bridge, necessary for polarity changes.

The PLC is connected by a VME computer to the control system of the accelerator.

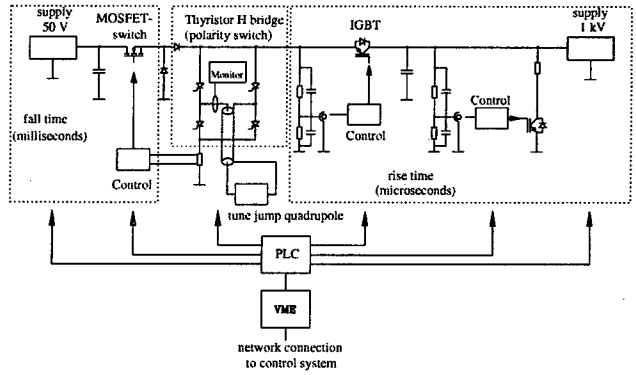

Figure 4: Schematic drawing of the pulsed power supplies.

3 CALIBRATION AND MEASUREMENTS

Using a stored beam in ELSA the pulse amplitude of the tune jump magnets was calibrated by jumping onto a half integer betatron resonance ($Q_z = 4.5$) from various distances with various pulse heights. The betatron tune was measured by analyzing the spectrum of the vertical beam oscillations. When jumping onto the resonance significant beam loss was observed, reducing the lifetime of the beam from 4 h to less than 10 min.

The measured value of $\frac{\Delta Q_z}{\Delta I} = (1.77 \pm 0.08) \cdot 10^{-4}\,\mathrm{A}^{-1}$ at 2.3 GeV is in good agreement with the calculations.

Calculations and measurements concerning closed orbit distortions and emittance growth due to the change of the optical functions were carried out [9].

[1] Puls Plasma Technik, Dortmund, Germany

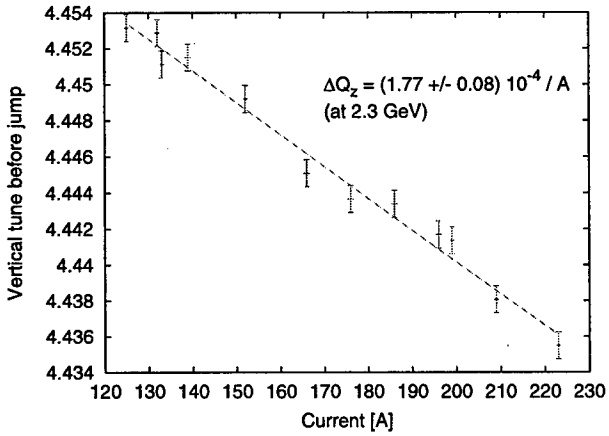

Figure 5: Calibration of the pulsed quadrupoles using a jump onto a half integer betatron resonance.

Fig. 6 shows the maximum distortion of the closed orbit caused by a tune jump of $\Delta Q_z = 0.1$ at 1.5 GeV during the energy ramp. The rise time of the pulse was 10 μs and the fall time 20 ms.

The distortions are all smaller than 1 mm and can therefore be neglected.

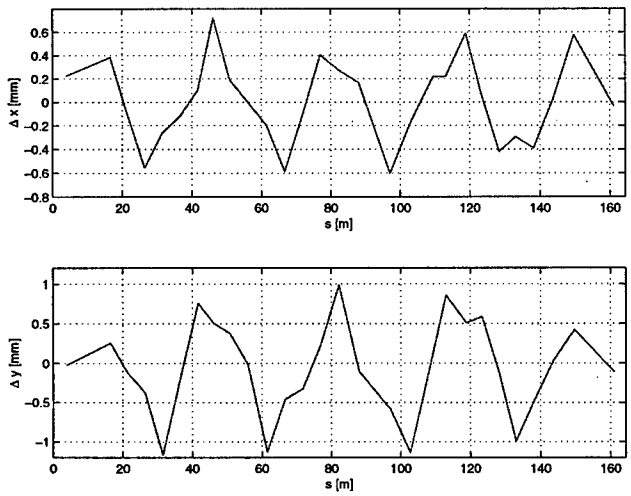

Figure 6: Change of the horizontal and vertical closed orbit during a tune jump for the uncorrected closed orbit.

The successful operation of the tune jump magnets was tested first on the intrinsic resonance at 2.0 GeV [9]. Without tune jump the resonance causes a depolarization of 25%. Using the pulsed quadrupoles the depolarization could be minimized to less than 2%. Variation of the trigger time of the tune jump magnets leads to the curve shown in Fig. 7. If the jump is triggered too early stronger depolarization could be observed, which is expected because the resonance crossing speed is lower on the falling edge of the pulse than without any pulse. The width of the optimal time window changes with the pulse amplitude. A higher pulse amplitude broadens the window and therefore minimizes sensitivity to time shifts. However, too large amplitudes, may cause beam loss, because of jumping onto a neighbouring betatron resonance.

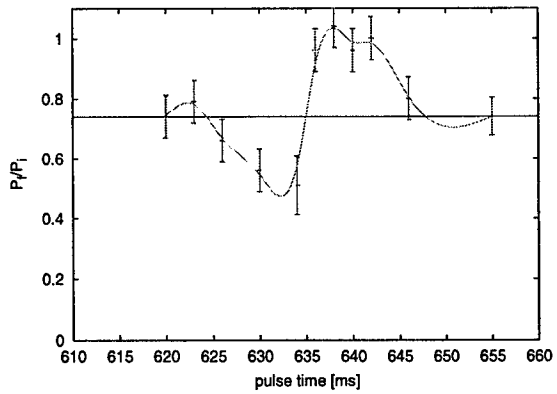

Figure 7: Jumping over the $(0 + Q_z)$-resonance: Polarization dependency of the jump time. The pulse amplitude was -110 A with each magnet, corresponding to a $\Delta Q_z = -0.047$.

4 SUMMARY

Polarized electrons have been accelerated at ELSA without significant losses in polarization degree. In the case of crossing intrinsic resonances a fast betatron tune jump magnet system has provided the conservation of polarization. First measurements have shown that the depolarization due to the strong intrinsic resonance at 2.0 GeV can be reduced to less than 2% with the tune jump magnets.

Further investigations will follow soon to adjust the amplitudes and trigger times to minimize the influence of the remaining intrinsic resonances. Together with a harmonic correction of the imperfection resonances in ELSA a polarized beam will be provided up to the maximum energy in near future.

5 REFERENCES

[1] K.H. Althoff et al., Part. Acc. 27 (1990) 101

[2] S. Nakamura et al., AIP Conf. Proc. 421, Urbana (1997) 497

[3] C. Steier, D. Husmann, Proc. 1997 Part. Accel. Conf., Vancouver

[4] S. Nakamura et al., Nucl. Instr. & Meth. A 441 (1998) 93

[5] M. Froissart and R. Stora, Nucl. Instr. & Meth. 7 (1960) 297

[6] M. Hoffmann, diploma thesis, BONN-IB-98-10

[7] T. Toyama, C. Steier et al., BONN-ME-97-01

[8] A. Lehrach, PhD thesis, Jülich, IKP-98-12-034 (1997)

[9] C. Steier, PhD thesis, BONN-IR-99-07 (1999)

LINEAR OPTICS CALIBRATION AT THE MIT-BATES SOUTH HALL RING*

F. Wang, K. Jacobs, A. Carter, D. Cheever, B. McAllister, C. Sibley,
MIT-Bates Linear Accelerator Center, Middleton, MA
J. Safranek,
Stanford Linear Accelerator Center,Stanford University, Stanford,CA

Abstract

The MIT-Bates South Hall Ring has been successfully commissioned for internal target experiments. More than 150 mA of stored beam has been circulated through a 40 cm long 1.5 cm diameter internal target cell. The ring has also been tuned for the first experiment on an external target using a resonantly extracted high duty factor beam. Beam-based measurements of the ring optics by means of analyzing the beam orbit response matrix, and comparing the results with models, have produced much needed information to set up the ring optics. Efforts have been made to improve the measurement precision, and to put the entire process on-line for use during machine operation.

1 INTRODUCTION

The MIT-Bates South Hall Ring (SHR) is designed to serve medium energy nuclear physics experiments. The ring is composed of four achromatic bending sections which form a pair of symmetry corrected second order achromatic 180° bends. There are two long straight sections, one for injection and the internal target, the other for extraction and the installation of a new spin rotator to maintain beam polarization[1]. Adjusting ring chromaticity does not disturb the symmetry corrected second order centroid shifting aberrations at the extraction and internal target locations. The design does require a relatively large number of independent quadrupole families. There are 81 quadrupoles, of 19 different gradient values, organized into 34 groups by power supply.

A discrepancy between the design optics and that achieved by setting the quadrupoles to their calculated values has been noticed for some time. Initially, correction was made by increasing all quadrupole strengths about one percent, and using the extraction straight section quadrupoles for fine adjustments. This method could bring the betatron tunes to design values, but distortions in the β amplitude functions were significant. This was particularly a problem in the two long straight sections, where specific Twiss parameters are required.

Beam based determination of the ring linear optics was considered a realistic and precise way to correct the optics. The idea of beam based measurements of the optics by means of analyzing the beam orbit response matrix is illustrated in [2], and the computer code LOCO (Linear Optics from Closed Orbits) has been used for modeling. The beam orbit response matrix is defined as

$$\begin{pmatrix} x \\ y \end{pmatrix} = \mathbf{M} \begin{pmatrix} \theta_x \\ \theta_y \end{pmatrix} \quad (1)$$

where θ_x and θ_y are the angles imparted to the beam by steering magnets, and x and y are the resulting orbit perturbations at the ring beam position monitors (BPMs). **M** is an $l \times m$ matrix, where l is the number of BPMs, and m is the number of steering correctors. The LOCO code adjusts the parameters (quadrupole gradients, etc.) of an optics model to fit the model response matrix to the measured response matrix. Assuming the deviations between the model and measured matrices are linear functions of a set of the n varied parameters $\vec{X}_n$, then the minimization of the deviations is to solve the linear matrix equation

$$\mathbf{A}\Delta\vec{X}_n = -\vec{V}. \quad (2)$$

where $A_{i,n} = (\partial V_i/\partial X_n)$. **A** is an $(l \cdot m) \times n$ matrix, and $\vec{V}$ is an $l \cdot m$ vector which represents the element deviations between the model and measured response matrices. The LOCO analysis involves solving an over-constrained problem, fitting many self-consistent constraints. In addition to the quadrupole gradients, BPM and steering corrector gains are treated as fit parameters. Also the beam energy shift associated with the deflection by a horizontal steering magnet is included.

In the SHR model, there are 187 independent variables: 34 quadrupole groups, 60 BPM gains, 62 steering magnet gains, and 31 energy shifts caused by horizontal steering magnets. **A** is then a 3720 × 187 matrix. Without x-y coupling, half of the elements of **A** will be null.

2 CALIBRATION PRECISION

The precision of the quadrupole gradient determination can be estimated by comparing the LOCO analysis results from repeated beam response matrix measurements. The factors that appear to determine the precision are the BPM resolutions, the sensitivity of the ring optics to the parameters being varied, and beam conditions. The accuracy of the modeling is verified by independent measurements of the optical parameters, such as betatron tunes, β amplitude functions, dispersion, and so on.

2.1 BPM Resolution

The original ring BPM system[3] was aimed at fast turn-by-turn beam position measurement. The system used 8

* Work supported by U.S. Department of Energy.

0-7803-5573-3/99/$10.00@1999 IEEE.

bit flash ADCs and had a position measurement resolution of 0.1 mm. The measured RMS BPM noise level was about 40 μm, consistent with the 78 μm / bit ADC digital resolution. It was concluded after early beam response matrix measurements and optics modeling, that the ADC resolution was the main obstacle to achieving a more precise linear optics measurement[4]. To alleviate this, a parallel signal processing system was added. Now the 60 BPM signals are multiplexed to eight ADC channels via an existing video switch board. The signals are integrated over 62 μs (95 turns), held, and then digitized by an 8 channel, 12 bit VMIC 4514 ADC card. Data aquisition is under the newly installed EPICS system, with an update rate up to 60 Hz. Under this new BPM system, the measured BPM noise level without beam is down to about 5-10 μm. This is closer to, but does not reach, the desired $\pm 2.4\,\mu$m ADC digital resolution. The measured BPM noise level with beam was about 5-10 μm in the horizontal plane, but 2-3 times larger in the vertical plane.

2.2 *Optics sensitivity*

The precision of the quadrupole gradient measurement by LOCO depends on how the quadrupoles are grouped, the quadrupole gradients, and the ring optics.

A simulation was done to examine the details of these effects. The extent the optics change for a change in an individual parameter is related to the overall RMS BPM response, which is the RMS average of the change in all the BPM readings, for beam deflections by all the steering correctors. Table 1 lists the RMS BPM response for a 0.5 % gradient change in eight of the thirty-four quadrupole groups. The steering magnet deflection is chosen to produce $\sim$ 0.8 mm RMS closed orbit perturbations.

Table 1: RMS change in orbit response matrix (μm) for quad $\Delta k/k = 0.005$

	Storage mode			Extraction mode		
Q group	k ($1/m^2$)	δx	δ y	k ($1/m^2$)	δx	δy
QSW3	2.0011	22.3	11.8	2.0011	21.8	7.8
QSW8	-1.1281	12.7	37.4	-1.281	13.4	24.4
QS2F	3.1284	41.3	17.8	3.1284	47.1	11.3
Q26	4.3156	1.7	0.9	4.3156	1.5	0.6
Q40	2.5521	17.3	7.3	2.8189	21.7	5.2
Q41	-1.8327	5.2	8.9	-2.4326	6.4	8.3
Q44	1.6950	10.3	2.8	0.9177	9.6	4.8
Q45	-1.8807	3.1	11.7	0.2342	3.1	0.2

From Table 1, if the BPM resolution is in the 2-4 μm range, it is possible to determine the quadrupole gradient of groups such as QSW8 or QS2F to better than 5 parts in 10,000. However, for a "weak" quadrupole group, such as Q26, the gradient prediction precision will be in the 5×10^{-3} range, or even a few percent.

There are other effects which may limit the precision of the measurement. The model averages over all gradients of each quadrupole group, and does not include possible errors in the ring dipole gradients (expected field index $n = 0.539$).

Because of how some quadrupoles are grouped, it is possible for a change in one quadrupole to be compensated by changes in others, leaving the ring optics almost the same. An example of this is the extraction straight section, when operated in pulse stretcher mode. For the same response matrix measurements, but slightly different dispersion measurements, different optical solutions were obtained which had Q45 gradient variations of up to 6 %. These variations were compensated by changes in other quadrupoles. The resulting lattices had identical tunes and almost the same betatron amplitudes. The overall horizontal RMS β amplitude differences were less than 0.05 m. The maximum β_x difference of 0.5 m occurred at a high β_x (50 m) location. The vertical RMS difference was three times smaller. We have tried using piecewise fitting to limit these "optical uncertainties". The procedure is to determine the settings for the quadrupoles which have better measurement precision, fix these settings (do not vary them in later fitting), and then do a second fit to find the values for the less well determined quadrupoles. This technique met with some success in storage mode when working with the 8 bit BPM ADCs. In a future run, it will be tested for the poorly determined extraction section quadrupoles in pulse stretcher mode, after setting up the better known quadrupoles in the rest of the ring.

2.3 *Beam condition effects*

The quality of the linear response matrix measurement is closely related to beam conditions. The dominant beam instability observed for some time has been a persistent vertical betatron oscillation with large amplitude (several millimeters in some locations) and varying amplitude modulation frequency. The measured BPM noise in the vertical plane is always 2 to 3 times larger than in the horizontal. The oscillation was eventually eliminated by changing the vertical tune, based on a proposal[5] which suggested the oscillation may be excited by ions, and could be suppressed by setting the vertical tune to a proper value. Whether the vertical BPM noise level will be reduced now that this persistent betatron oscillation has been eliminated, will be carefully tested in the next ring run.

The beam current and lifetime also affect the measurement. The better measurements have been conducted at low stored current levels (5-40 mA). At higher currents, the measured BPM responses contain larger, possibly systematic, errors. Some measured BPM positions drifted during the noise measurement period (a few minutes). We suspect current related phenomenon such as synchrotron radiation effects on some BPM horizontal pickups. In storage mode, at low currents and very long lifetimes, the measurement results were reproducible. However in extraction mode, where the horizontal tune is closer to half integer resonance, minimal effort has been made to improve the closed orbit so as to achieve a long lifetime. There, with a beam lifetime of $\sim$ 200 s, the position "drift" on a number of BPMs was observed even at low current. Beam scraping may be contributing to the problem.

3 ON-LINE APPLICATION

It is important for commissioning to make this calibration process an on-line, real-time operational application.

For the SHR, the beam response matrix measurement typically takes about 10 minutes, being mainly limited by the steering magnet setting time, plus the analog signal switching control rate (4 Hz). Computation time for the LOCO analysis depends on the details of the parameters being optimized. A workstation with a 450 MHz Pentium II processor is dedicated to the LOCO analysis. It takes less than 3 minutes to make one LOCO analysis iteration, for the 34 quadrupole groups in the model, and about 10 minutes for the entire calculation. The most difficult and time consuming process during commissioning is determining the quality of raw measurement data.

For the entire measurement and analysis process, a semi-interactive application has been created on a local web site. This has proven efficient for data analysis, and flexible for development. The application consists of measurement set-up and model initialization, the actual measurement, raw data display and analysis, LOCO analysis and display of those results, and generation of a script with new quadrupole settings to achieve the model optics. Most of the data transfer, analysis, and display are done on-line. A Java applet has been developed to handle graphical display. To avoid security issues, some of the actual ring hardware operation commands are required to be made locally under a machine operations account. The site also provides additional data analysis tools.

The raw beam response measurement data analysis and display are extremely helpful. Ordinary mistakes like control system misconnections to BPMs and steering coils can be detected immediately. It has also been useful to help solve more complicated problems, such as video switch hardware and software troubles. Under normal operations, the entire LOCO process can be done in half an hour. Usually several measurements are made and analyzed before a solution is adopted to correct the optics. The analysis and measurement can be done in parallel.

4 RESULTS AND PLAN

The beam-based linear optics calibration has been applied on-line, during the last ring commissioning run, for setting up both the storage and extraction optics. Independent optics measurements and ring performance proved the optics corrected by LOCO were close to the design model. In storage mode, the RMS errors of quadrupole gradient predictions were in the 5×10^{-4} and 5×10^{-3} ranges (for different quadrupole groups). In extraction mode, the errors were typically 2 to 3 times larger than in storage mode, and even worse for some quadrupole groups. Further improvement of the BPM resolution and beam conditions are needed. Figure 1 shows β_x before and after one iteration of correction, in extraction mode. The LOCO determinations of β_x are very close to those obtained by quadrupole gradient (k) modulation techniques. Deviations in β_y after correction were much less. Although the measurement precision in extraction mode was limited, the solution of the first LOCO iteration was sufficiently close to the model optics to give us good resonant extraction. This allowed us to measure our first coincidence spectra with high duty factor beam, on an external target[6].

An advantage of having the response matrix measurement and analysis running as an on-line application, is that it is also an effective tool to help diagnose BPM system performance, and expose beam related problems.

Future ring plans call for installation of superconducting solenoids, plus associated skew and normal quadrupoles, for spin control. This will necessitate changing the LOCO model to include x-y coupling. To improve the measurement precision, we will reduce the noise on the BPM electronics, and operate at a tune with no persistent β_y oscillations. As part of the conversion of the ring controls and instrumentation, the response matrix measurement programs will be moved to EPICS. More work will be done with the piecewise fitting approach. Finally, shunts will be added to many of the quadrupoles which are powered in groups, to allow us to verify the β functions at more locations.

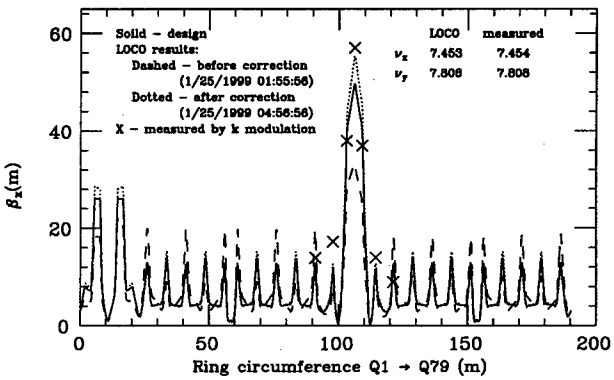

Figure 1: β_x before and after LOCO correction.

5 REFERENCES

[1] P. M. Ivanov, Yu. M. Shatunov, G. T. Zwart, "A Universal Superconducting Spin Rotator for the MIT Bates South Hall Ring", Bates Int. Rep. B/SHR 93-10 (1993); F. Wang, K. Jacobs, "SHR East Straight Changes for Spin Rotator Installation", Bates Int. Rep. B/SHR 98-04 (1998).

[2] J. Safranek, Nucl. Inst. and Meth. A338 (1997) 27.

[3] O. Calvo, T. Russ, J. Flanz, Proc. 1991 IEEE Part. Accel. Conf., 1467.

[4] F. Wang, K. Jacobs, "Beam Response Matrix Measurements and Linear Optics Calibration: Results from the Nov.6-Dec. 1997 South Hall Ring Run", Bates Int. Rep. B/SHR 98-03 (1998).

[5] C. Tschalaer, "Electron Beam Oscillation Excited by Trapped Ions", Bates Int. Rep. B/SHR 99-01 (1999).

[6] J. Shaw and the OOPS Collaboration, "First Coincidence Measurement using SHR Extracted Beam", http://mitbates.mit.edu/coinc.stm

MEASUREMENTS AND SIMULATIONS OF LONGITUDINAL RELAXATION OSCILLATIONS INDUCED BY HOMs*

C.Limborg, J.Sebek, SSRL/SLAC, Stanford, CA

Abstract

Although the linear theory of stable and unstable synchrotron oscillations has long been understood, there is no such satisfactory description of the large amplitude highly non-linear synchrotron motion. With an appropriate tuning of RF cavity impedance, large amplitude, low frequency, self-sustained relaxation oscillations of this synchrotron motion can be observed. This paper presents experimental data and computer simulations that give insights into the details of the mechanism involved.

1 INTRODUCTION

The voltage induced by the beam on the cavity impedance, at the upper synchrotron sideband of the revolution harmonics has a destabilizing effect on the beam. The instability commonly known as the coupled bunch instability occurs when this force exceeds the net damping force. On the SPEAR electron storage ring, such an instability can be produced from a multi-traversal effect acting on a single bunch. Linear theory predicts that above instability threshold the amplitude of the bunch synchrotron oscillation would grow to infinity. However, it has been long observed [1] [2] that the amplitude of oscillation can also saturate. In particular, at the onset of instability, there exists a regime in which the bunch performs relaxation oscillations. Extensive measurements were performed to give the details which constitute the basis of the theoretical model explaining the physics of the mechanism [3].

2 EXPERIMENTAL RESULTS

2.1 Motivations

While characterizing the RF cavities in order to improve the stability of SPEAR and focusing our attention on the growth of the HOM induced instabilities, a regular modulation about the saturation level was observed (figure (1a)) [4]. Its period was always longer than a radiation damping time. This modulation is often small, but certain machine parameters can make it very large, regular, and quite striking (figure (1b)). The possibility of adjusting the HOM frequency, by positioning a moveable RF cavity tuner in the passive RF cavity, made such observations very repeatable and convenient to study on the SPEAR ring.

2.2 Experimental parameters

The experimental parameters are presented in table 1. The

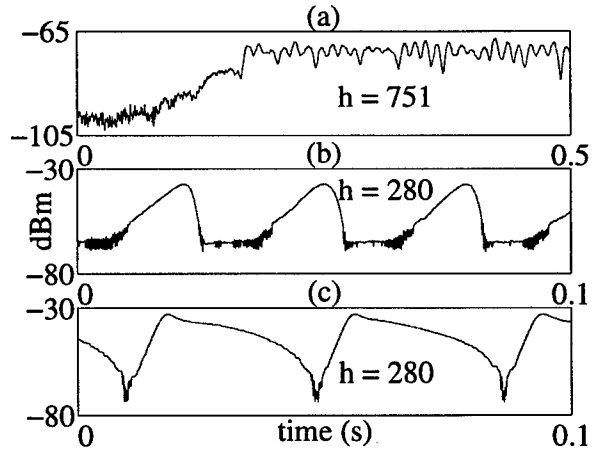

Figure 1: Output from the cavity signal at $hf_0 + f_s$. Note the different growth and damping rates in (b) and (c).

Energy	U_0	V_{RF}	τ_{damp}	R_S
2.3 GeV	193 keV	1.68 MV	10 ms	10 MΩ

Table 1: Machine parameters

resonance studied is the fundamental resonance, $f_{HOM} = f_{RF}$. The large variety of time scales involved in the relaxation mechanism is presented in table 2.

2.3 Description of measurements

Since the effect of interest depends on the HOM strength, the largest available impedance was chosen for the study. SPEAR has two RF cavities, but only one is powered for normal operation. Therefore, the largest available impedance is the fundamental mode of the idle RF cavity; this mode was chosen for our study. The strength of this impedance means that the HOM produces a strong long-range wakefield at currents for which the short-range effects of the wakefield are not very important. (In this paper, liberty has been taken with the term HOM, since here

	Frequency	Period	N_{turns}
$f_{sawtooth}$	< 100 Hz	> 10 ms	> 12800
f_{so}	28.4 kHz	35 μs	45
α_R	56 kHz	17.8 μs	23
f_o	1.28 MHz	0.78 μs	1
$f_{RF} = f_{HOM}$	358.5 MHz	2.8 ns	1/280
$(1/\sigma_\tau)$	10 GHz	100 ps	1/7840

Table 2: System time scales

* Work supported by the Department of Energy, contract DE-AC03-76SF00515.

it also refers to the fundamental mode in the idle cavity.)

Spectrum analyzer Data were first taken on an RF spectrum analyzer from an RF signal coming from an RF cavity probe (figure 1). The spectrum analyzer was used as a narrowband receiver, in zero-span mode, tuned on the upper synchrotron sideband of the fundamental RF harmonic. Its resolution bandwidth, 10 kHz, allowed reasonable rejection of the RF harmonic while preserving the ability to see fast dynamic changes in the amplitude of the sideband over the variation of the synchrotron frequency during the relaxation oscillation.

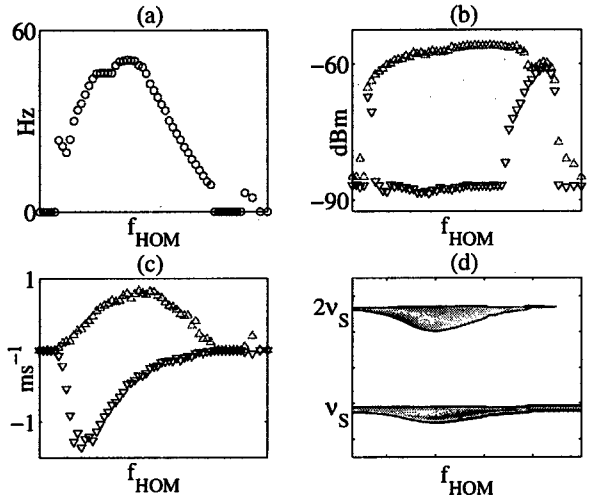

Figure 2: Relaxation oscillation parameters vs f_{HOM}: (a) relaxation oscillation frequency, (b) maximum ($\triangle$) and minimum (∇) power of oscillation, (c) growth times ($\triangle$) and damping times (∇), (d) ν_s, showing $\sim$ 15% deviation over the range of f_{HOM}.

The evolution of crucial parameters of the relaxation oscillation as a function of the resonator frequency is summarized in figure 2. From the amplitude information, (2b), one sees that the amplitude of oscillation is large along most of the resonance. The growth rate, as a function of frequency, is symmetric with respect to the center frequency, (2c). It correlates with the resistive part of the resonator impedance. The damping rate is not nearly as symmetric (2c). It is very small over the second half of the resonance curve (2b). Because of this asymmetry, the frequency of this relaxation oscillation (2a) as a function of the HOM frequency is also asymmetric.

Digital spectrum analyzer The variation and/or spread of the synchrotron tune during these oscillations was also measured. This data was obtained by observing the demodulation of a signal coming from a ring pickup on a digital spectrum analyzer. Since the analyzer averaged over many relaxation periods, this measurement could not resolve the difference between a tune variation and a spread over the oscillation. The frequency deviation showed a decrease of 15% from the nominal synchrotron frequency, corresponding to the shift for large amplitude pendulum oscillations (figure (2d)).

Streak camera The spectrum analyzer data only gives information about the dipole moment of the beam. With a streak camera, details about the internal structure of the beam could be observed. Data were taken both at a slow scan rate, i.e. slow enough to see the entire relaxation oscillation cycle, and at a fast rate, at which one could see the single bunch every third revolution period.

On the slow scan range, the entire relaxation oscillation cycle was captured. While growing, the envelope visible in the slow scan shows the bunch to be concentrated near the extremes of the oscillation. But its charge density decreases with time (figure 3a). The maximum amplitude of oscillation reached is about $\pi/2$ radians. In the damping phase, this macroparticle still exists and damps, but it has a much reduced intensity compared to its initial value. At the end of this phase, particles have accumulated around the center. In the particular case of f_{HOM} slightly above $pf_0 + f_{so}$, when the damping is very slow, a second accumulation point clearly forms near the origin (figure 3b). The charge at this point grows in both amplitude and intensity as the original macroparticle continues its decay. The second accumulation point, when seen, is phase-locked to the initial macroparticle, but approximately π out of phase with it (figure (3c)(3d)).

As a summary, the oscillation starts when one center grows exponentially, then saturates and loses particles, and finally begins to damp. These lost particles accumulate at a second center which grows, accumulating more particles, as the first center migrates to the origin while still losing its charge. The two centers have now exchanged roles in this oscillation, giving the system its bistable character.

3 SIMULATIONS

3.1 Simulation program

The multiparticle simulation code gives the evolution of the phase space distribution of a single bunch, turn after turn, in the presence of a perturbing long range wakefield. As the streak camera images showed a loss and an asymmetric variation of charge density, it was essential to examine the evolution of the internal distribution of the bunch.

The equation of motion of individual particles obeys a second order difference equation. This turn by turn difference equation of the code includes the synchrotron radiation emission through losses, radiation damping, and quantum fluctuations. The long memory of the high Q cavity is retained by the use of propagators. Propagators enable the accurate retention of the phase information of the rapidly oscillating wake over the comparatively long time scale of one revolution period. To get more than an entire relaxation cycle, 10^5 turns were commonly computed for a pop-

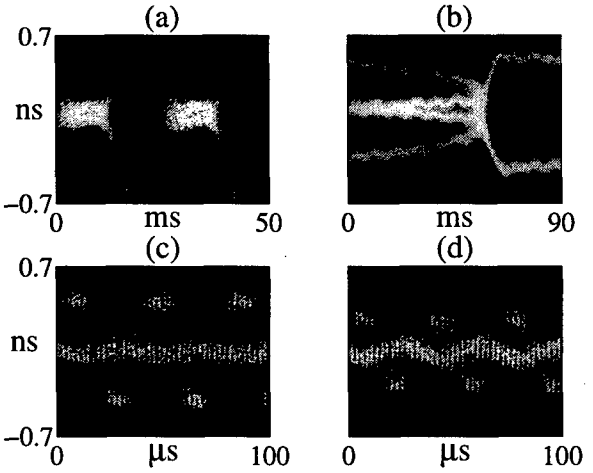

Figure 3: Relaxation cycles for two different values of f_{HOM}: (a) $f_z \sim f_s$. (b) $f_z > f_s$, showing appearance of second center. Note that (b) has much slower damping than (a). (c) Individual streaks are now visible. The second center has more charge than the original main body, yet its oscillation amplitude is still small. (d) The second center now has most of the charge. Its amplitude continues to grow while that of the original main body continues to damp. Oscillations are about π out of phase.

ulation of 20000 particles, distributed over a binning of 300 cells covering the 2π size of the RF bucket.

The wake from the earlier particles is computed by propagating the fields from the previous bin over the time Δt. With $\Phi_t = \omega'_R \Delta t$, the propagator can be represented

$$\begin{pmatrix} W_{t+\Delta t} \\ W'_{t+\Delta t} \end{pmatrix} = e^{-\alpha \Delta t} \begin{pmatrix} \cos\Phi_t & \frac{1}{\omega'_R}\sin\Phi_t \\ -\omega'_R \sin\Phi_t & \cos\Phi_t \end{pmatrix} \times \begin{pmatrix} W_t \\ W'_t \end{pmatrix} + \begin{pmatrix} 2\alpha R_s n_{t+\Delta t} \\ -4\alpha^2 R_s n_{t+\Delta t} \end{pmatrix}$$

3.2 *Simulation results*

The code is in good agreement with the data. It reproduces the very low frequency of the relaxation oscillation (always below 100 Hz in our case). It confirms qualitatively the evolution of frequency and amplitude as a function of the induced voltage. The code reproduces the $\pi/2$ limit cycle amplitude observed with the streak camera. Finally, the code corroborates the streak camera data, discussed above, that shows the bunch grow as a macroparticle which loses charge density to an attractor at the center (figure 4).

Based on these agreements, the predictions of the code can be viewed with confidence. They were used to gain further insight into the details of the oscillation too sensitive to be seen with our experimental setup. The tracking code phase space distribution shows that the filamentation starts from the head of the bunch. Particles spiral from the head of the bunch towards the center of phase space (figure (4b)). One can observe that those particles perform synchrotron oscillations at a higher frequency than those still attached to the main body. These results gave important clues for the theoretical model.

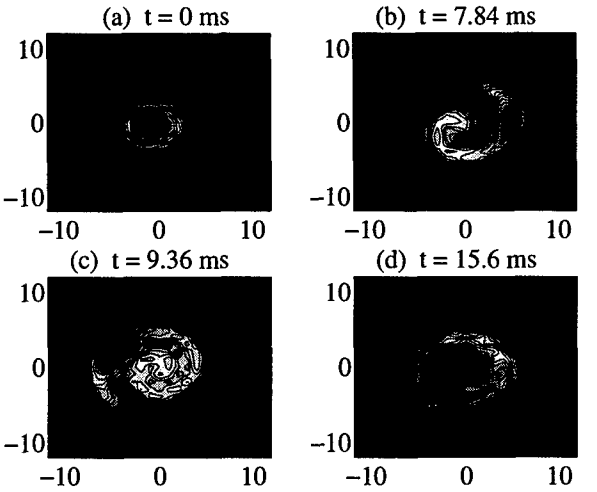

Figure 4: Simulations of bunch in four stages of relaxation oscillation. Intensity scale is logarithmic.

4 CONCLUSION

An extensive campaign of measurements was performed on SPEAR to characterize the low frequency relaxation oscillations produced by long range wakefields. The main features of the relaxation oscillation were: growth of the amplitude of oscillation of the bunch, saturation of the oscillation amplitude, breakup of the bunch, and subsequent damping of the system back to the beginning of the next cycle. The period of this relaxation oscillation is always longer than a radiation damping time. An analytical model was developed to explain these characteristics [3].

5 ACKNOWLEDGEMENTS

We thank H. Wiedemann and M. Cornacchia for their support and encouragement, and we would like to thank our colleagues J. Hinkson and J. Byrd (LBNL), A. Fischer (SLAC) and A. Lumpkin (APS) for their assistance in obtaining the beautiful pictures with the streak camera.

6 REFERENCES

[1] A. Wrulich *et al.*, "Observation of multibunch instabilities in ELETTRA," in *Proc. of EPAC96*, 1996.

[2] G. Rakowsky, "Coherent synchrotron relaxation oscillation in an electron storage ring," in *Proc. of PAC85*, 1985.

[3] J. Sebek and C. Limborg, "Theoretical model of longitudinal relaxation oscillations induced by HOMs," in *Proc. of PAC99*.

[4] J. Sebek and C. Limborg, "Characterization of RF cavity HOMs with beam," in *Proc. of 1997 ICFA Conference*, (Frascati), 1997.

Theoretical model of longitudinal relaxation oscillations induced by HOMs*

J.Sebek, C.Limborg
SSRL/SLAC Stanford, CA, USA

Abstract

Taking advantage of the vastly different time scales of the problem, a simple analytical model of the relaxation oscillations has been developed. First a continuous approximation of the impulsive discrete forces is made. Then only the synchronous components of the force are retained to describe the slowly varying amplitude and frequency of the relaxation oscillation. A two particle version of this model reproduces the main characteristics of the system. A more complete paper is in preparation [1].

1 ANALYTICAL MODEL

1.1 Continuous Approximation

A particle in a storage ring generates a electromagnetic field, a wakefield, that acts back on itself. The wakefield of a cavity can be represented as the impulse response of a narrow-band resonator of resistance, R_S, frequency, ω_R, and damping factor α_R.

$$W(t-\tau) \cong U(\tau)\, 2\alpha_R R_S e^{-\alpha_R(t-u)} \cos\omega_R(t-\tau)$$

The wake seen by any particle is the sum of all wakes generated by it and all other particles in all previous turns. For a single bunch, the decelerating wake potential seen at time, t, is then

$$W(t) = 2\alpha_R R_S \sum_{u=-\infty}^{t} e^{-\alpha_R(t-u)} \cos\omega_R(t-u),$$

The arrival times of the source particle generating the wakefield, u, and the particle experiencing the wakefield, t, are expressed by $t = nT_0 + \tau_n$ and $u = kT_0 + \tau_k$, where $\tau_n, \tau_k \ll T_0$. Representing $\omega_R = p\omega_0 + \omega_z$ as an integral multiple and a fractional part of the revolution harmonic, the sum becomes

$$W(t) \cong 2\alpha_R R_S \frac{1}{T_0} \int_{(k-1)T_0}^{kT_0} \sum_{k=-\infty}^{n} e^{-\alpha_R(n-k)T_0} \times \cos\left(\omega_z(n-k)T_0 + \omega_R(\tau_n - \tau_k)\right) du$$

When the bunch has N particles of charge, e, giving a machine current, I, the electrical potential $V(t)$ generated by the wake is

$$V(t) = 2\alpha_R R_S I \int_{-\infty}^{t} e^{-\alpha_R(t-u)} \times \cos\left(\omega_z(t-u) + \omega_R(\tau(t) - \tau(u))\right) du$$

* Work supported by the Department of Energy, contract DE-AC03-76SF00515.

1.2 Evaluation of the Integral

The continuous approximation of the synchrotron motion is that of common pendulum motion, for which oscillations as large as $\pi/2$ are still very sinusoidal. Therefore $\tau(t)$ and $\tau(u)$ can be represented as

$$\tau_t = \widehat{\tau}_t \cos(\omega_{st}t + \phi_t); \quad \tau_u = \widehat{\tau}_u \cos(\omega_{su}t + \phi_u)$$

with $\widehat{\tau}_t$, $\widehat{\tau}_u$, ω_{st}, ω_{su}, ϕ_t, and ϕ_u all slowly varying compared to the synchrotron period. The exponential damping in the integral means that only important contributions come from times no further back than a few damping times, during which the these quantities can be treated as constant. With the notation $r_t = \widehat{\tau}_t\omega_R$, $r_u = \widehat{\tau}_u\omega_R$, the integral in the driving term can be expressed as the real part of

$$\sum_{p,k=-\infty}^{\infty} \frac{j^{p-k} J_p(r_t) J_k(r_u)}{\alpha_r + j\left(k\omega_{su} - \omega_z\right)} e^{j(k(\omega_{su}+\phi_u)+p(\omega_{st}+\phi_t))t}$$

1.3 Application of KBM Method

The averaging method of Krylov, Bogoliubov, and Mitropolskii [2] [3] is well suited to such an oscillatory problem with slowly varying parameters [4]. To solve a driven harmonic oscillator, $\ddot{x} + \omega_{so}^2 x = f_x(x, \dot{x})$, new variables, $(r(t), \phi(t))$, are defined in terms of $(x(t), \dot{x}(t))$ by

$$x = r\cos(\omega_{so}t + \phi); \quad \dot{x} = -\omega_{s_0} r \sin(\omega_{so}t + \phi)$$

The averaged evolution equations of the oscillation amplitude and phase become

$$\dot{\bar{r}} = -\frac{1}{2\omega_{so}} F_{S1}(\bar{r}, \bar{\phi}); \quad \dot{\bar{\phi}} = -\frac{1}{2\omega_{so}\bar{r}} F_{C1}(\bar{r}, \bar{\phi})$$

F_{S1} and F_{C1} are the Fourier coefficients of the frequency ω_{su} in the wakefield generated by the particle at (r_u, ϕ_u).on the particle at (r_t, ϕ_t)

$$F_{S1} = -2A\alpha_R R_S I \sum_{k=1}^{\infty} J_k(r_u)\left[J_{k-1}(r_t) + J_{k+1}(r_t)\right] \times \left[\left(a_k^- - a_k^+\right)\cos(k\Delta\phi) - \left(b_k^- - b_k^+\right)\sin(k\Delta\phi)\right] \quad (1)$$

$$F_{C1} = 2A\alpha_R R_S I \left\{2b_0^+ J_0(r_u) J_1(r_t) + \sum_{k=1}^{\infty} J_k(r_u)\left[J_{k-1}(r_t) - J_{k+1}(r_t)\right] \times \left[\left(b_k^- - b_k^+\right)\cos(k\Delta\phi) + \left(a_k^- - a_k^+\right)\sin(k\Delta\phi)\right]\right\} \quad (2)$$

where $A = \frac{\omega_{s0}^2}{V_{RF}|\cos\phi_s|}$, $\Delta\phi = \phi_t - \phi_u$ and

$$a_k^{\pm} = \frac{\alpha_R}{\alpha_R^2 + (k\omega_{su} \pm \omega_z)^2}; \quad b_k^{\pm} = \frac{(k\omega_{su} \pm \omega_z)}{\alpha_R^2 + (k\omega_{su} \pm \omega_z)^2}$$

This paper discusses only the case when $\omega_R = \omega_{RF}$. Extensions to other values of ω_R are straightforward.

The wakefield is not the only perturbation to the harmonic equation. A radiation damping term, $-\alpha_{rad.}\bar{r}_t$, contributes to the $\dot{\bar{r}}_t$ equation. The amplitude dependent decrease in pendulum frequency can be approximated by a term quadratic in $\bar{r}_t$ [3]. The KBM method is applied by treating the three terms as independent contributions to the equations of motion of $\bar{r}$ and $\bar{\phi}$, giving the final, averaged equations of motion for a test particle at (r_t, ϕ_t) due to a macroparticle at (r_u, ϕ_u)

$$\dot{\bar{r}} = -\frac{1}{2\omega_{st}} F_{S1}\left(\bar{r}_t, \bar{\phi}_t, \bar{r}_u, \bar{\phi}_u\right) - \alpha_{rad.}\bar{r}_t \quad (3)$$

$$\dot{\bar{\phi}} = -\frac{1}{2\omega_{st}\bar{r}_t} F_{C1}\left(\bar{r}_t, \bar{\phi}_t, \bar{r}_u, \bar{\phi}_u\right) - \frac{1}{16}\bar{r}_t^2\omega_{so} \quad (4)$$

2 ANALYSIS OF RELAXATION OSCILLATIONS:

2.1 *Properties of Wakefield Terms*

The convenient reference frame for these equations is one rotating in phase with τ_u, and in which τ_u moves radially along the $\phi = 0$ axis. The angular position of τ_t is the difference in phase, $\Delta\phi$, between it and the source. As τ_t rotates in this frame, the forces from τ_u change character, from damping to anti-damping, and from frequency increase to frequency decrease. For narrow band resonators tuned with $\omega_z = \omega_{su}$, the line of maximal growth and zero frequency shift both lie close to $\Delta\phi = 0$.

2.2 *Linear regime*

For the case of a single macroparticle model, $r_t = r_u$, and $\Delta\phi = 0$. In most cases, the $m = 0$ and $m = 1$ terms of the series give a good approximation to the total force. Using the narrowband resonator impedance approximation, for small r, after defining $Z_k^p = Z(p\omega_0 + k\omega_z)$, one recovers the formulae for growth and frequency shifts given in references[5][6].

$$\dot{\bar{r}} = \frac{\omega_{s0}}{2V_{RF}|\cos\phi_s|} I\,\mathrm{Re}\left\{Z_1^h - Z_{-1}^h\right\}\bar{r} - \alpha_{rad}\bar{r}$$

$$\dot{\bar{\phi}} = \frac{\omega_{s0}}{2V_{RF}|\cos\phi_s|} I\,\mathrm{Im}\left\{2Z_0^h - Z_1^h - Z_{-1}^h\right\}$$

2.3 *Growth as a Macroparticle*

Equations 1 and 2 give the driving force acting on a test particle $(r_t, \Delta\phi)$ produced by the main body $(r_u, \Delta\phi = 0)$. In expansions around the main body, Δr is defined as $\Delta r \triangleq r_t - r_u$.

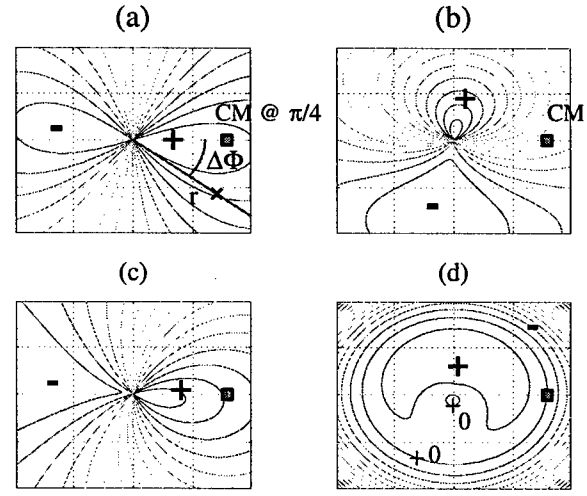

Figure 1: $\dot{\bar{r}}$, $\dot{\bar{\phi}}$ terms in (r_t, ϕ_t) plane. (a) F_{S1}; (b) F_{C1}; (c) F_{S1} and $\alpha_{rad}\bar{r}$; (d) $\dot{F}_{C1}$ and pendulum shift

Figure 1 shows the effect of the growth and frequency shift due to the macroparticle wake in the rotating frame:

- particles ahead of (behind) the main body $(r_u = 0, \Delta\phi > 0\,(\Delta\phi < 0))$ experience a lesser (greater) $\dot{\bar{\phi}}$ than the main body and will fall back (catch up) to it.(figure 1(b))
- particles at $(\Delta r < 0\,(\Delta r > 0), \Delta\phi = 0)$ feel more (less) growth than the main particle and will grow (fall) toward it (figure 1(a),(c))

This justifies why the bunch keeps its cohesion during its growth [7]; the main body is an attractor for all the particles of the bunch. As the oscillation increases to moderate amplitudes, two nonlinear effects become important: the Bessel terms decrease the growth rate; the pendulum frequency shift starts to dominate the frequency term.

2.4 *Filamentation*

The pendulum frequency shift now causes a strong enough asymmetry in Δr that the test particles start to escape from the front of the bunch.

- Particles with $\Delta r = 0$ experience the same growth as the main body, and will tend to group back towards it as during the growth.
- Particles with $(\Delta r > 0, \Delta\phi = 0)$ slow down more than the main body and acquire a $\Delta\phi < 0$. This leads them to an area of smaller radial growth, decreasing Δr, and hence increasing frequency. This sequence leads back to the main body.
- But particles with $(\Delta r < 0, \Delta\phi = 0)$ speed up more than the main body and acquire a $\Delta\phi > 0$. Once they cross the angle of maximal growth, the particles

at positive $\Delta\phi$ experience a smaller driving force and move to even more negative Δr. The particles escape from the front of the bunch.

The experimental data shows the decrease in strength of the growth term, only part of which comes from the weaker Bessel terms. The bunch saturates at lower amplitudes than this effect predicts. Streak camera images reveal the loss of particles [7]. The relaxation of the oscillation comes from the loss of growth due to the leakage of particles away from the main body and the formation of a second attractor close to the center of phase space.

2.5 *Damping of system*

As the escaping particles spiral away from the main body towards the center, they alternately experience positive and negative forces from the main body. Over a rotation of $\Delta\phi = 2\pi$, the net growth due to the main body nearly vanishes, so the particles damp at about the radiation damping rate. The only growth they see is due to other particles synchronous to them.

The finite main body amplitude, $\tau_u \neq 0$, implies equations 1 and 2 are non-zero at the origin; therefore all values of $\dot{\bar{\phi}}$ exist near there (equation 4). On the locus of points in phase with the main body, the particles will again feel the main body's wake. On the locus exists a point at which the radial growth vanishes; very close by is an attractor for particles leaving the main body. To experience no growth from the wake, $\Delta\phi \sim \pi/2$ when $\omega_z = \omega_{so}$ (figure 1). As charge accumulates at this point, its self-generated wake increases in strength and $\Delta\phi$ of the stable point increases to acquire damping from the main body. The second attractor is actually not fixed, but grows slowly in amplitude, attracting more and more particles until it becomes the new main body in the next relaxation cycle.

2.6 *Visualization of second attractor*

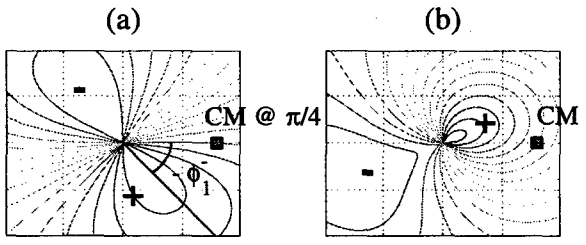

Figure 2: $\dot{\bar{r}}$, $\dot{\bar{\phi}}$ terms for $\omega_z > \omega_{su}$. (a) F_{S1}; (b) F_{C1};

An interesting case is observed when the lower edge of the resonance coincides with the synchrotron sideband ($\omega_z > \omega_{so}$) [7]. The second attractor forms away from the center nearly π out of phase with the main initial body and the system damps much more slowly than when $\omega_z = \omega_{so}$. Defining $\phi_k^{\pm} \triangleq \arctan\left[(k\omega_{su} \pm \omega_z)/\alpha_R\right]$, the line of maximal growth is now approximately $\left|\phi_1^-\right|$ ahead of the main body (figure 2). Test particles now trying to escape from the front have a more difficult time than for the case $\omega_z = \omega_{so}$ for two reasons:

- as $\Delta\phi$ of the particles increase, the particles move closer to the line of maximal growth, grow radially and slow down;
- they need to precess $\Delta\phi = 2\left|\phi_1^-\right|$ before their radial growth is less than that of the macroparticle.

Longer escape times mean longer damping times of the relaxation oscillation for $\omega_z > \omega_{so}$.

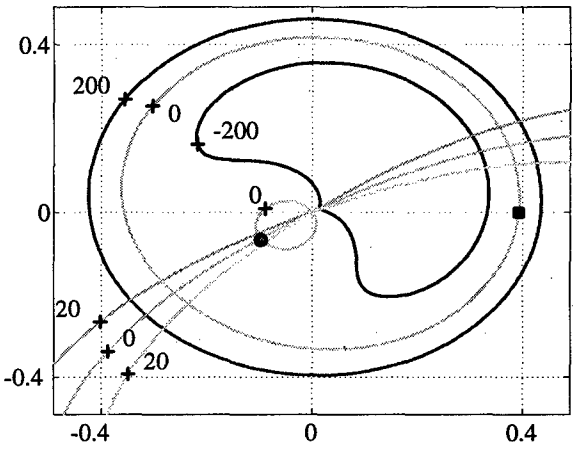

Figure 3: Attractor location for $\omega_z > \omega_{su}$. Initial main body at $(0, .4)$. Second attractor around $(-.1, -.06)$

In this case the second attractor starts at $\phi \sim \pi/2 + \left|\phi_1^-\right|$ and increases in phase towards π as it gains particles and grows in amplitude (figure 3).

3 REFERENCES

[1] C. Limborg and J. Sebek, "Relaxation oscillations of the synchrotron motion due to narrow band impedances," *submitted to Physical Review E*, 1999.

[2] N. M. Krylov and N. N. Bogoliubov, *Introduction to nonlinear mechanics.* Annals of mathematical studies, Princeton: Princeton University Press, 1947.

[3] E. A. Jackson, *Perspectives of nonlinear dynamics*, vol. 1. Cambridge: Cambridge University Press, 1989.

[4] S. Krinsky, "Saturation of a longitudinal instability due to nonlinearity of the wake field," in *Proc. of PAC85*, PAC, (Vancouver), pp. 2320–2322, IEEE-APS, 1985.

[5] A. W. Chao, *Physics of collective beam instabilities in high energy accelerators.* New York: John Wiley, 1993.

[6] A. Hofmann, "Beam instabilities," in *Proc. of CAS 1993* (S. Turner, ed.), vol. 1 of *CAS*, (Geneva), pp. 307–330, CERN, September 1995.

[7] C. Limborg and J. Sebek, "Measurements and simulations of longitudinal relaxation oscillations induced by HOMs," in *Proc. of PAC99.* in these proceedings.

First Beam Circulation Test of an Electron Storage/Stretcher Ring, KSR

T.Shirai, T.Sugimura, Y.Iwashita, H.Fujita, H.Tonguu, A.Noda, M.Inoue
NSRF, Institute for Chemical Research, Kyoto University
Gokasho, Uji, Kyoto 611-0011, Japan

Abstract

In Kyoto University, we are constructing a compact electron storage/stretcher ring (KSR). The circumference is 25.7 m and the maximum beam energy is 300 MeV. The electron beam is injected from a 100 MeV linac through the doubly achromatic transport line. The beam test of the injection line was finished and the beam size and the dispersion were measured. The results are consistent with the design calculation. The beam current is 100 mA and the energy spread is +/-0.5 % (FWHM). KSR uses the 1-turn injection scheme. The bump orbit is created by the perturbation magnet for the injection. The test of the bump magnet was carried out.

1 INTRODUCTION

A compact electron ring (Kaken Storage Ring, KSR) is now under construction at the Institute for Chemical Research, Kyoto University [1]. The main parameters are shown in table 1 and the view of the ring is shown in Fig.1. KSR has a triple bend doubly achromatic lattice (TBDA). It has two operation modes. One is a stretcher mode. The 100 MeV electron beam is injected from an S-band electron linac [2] and extracted slowly using the 3rd order resonance and an RF-knockout method [3]. Experiments of the coherent X-ray radiation are planned using the extracted beam. The another one is a storage mode. The injection energy is 100 MeV and it is accelerated up to 300 MeV. The design beam current is 100 mA and the critical wavelength is 17 nm. In the storage mode, some experiments are prepared using the insertion devices in the long straight section.

The injector linac consists of a thermal electron gun, a buncher and three accelerator tubes. The output beam energy is 100 MeV. The maximum beam pulse width is 1 μsec and the repetition is 20 Hz. For the injection to KSR, the pulse width is 0.1 μsec, which correspond to the revolution time of KSR.

2. INJECTION LINE

2.1 Design

The injection and the extraction line for KSR are shown in Fig. 2 (a). There are two bending magnets, two doublets of the quadrupole magnets and the inflector septum magnet in the injection line. The design goal of the injection line is to satisfy the following three conditions at the injection point,

I : $D_x = D_{px} = 0$ (doubly achromatic condition),
II : $\beta_y = 6.3$, $\alpha_y = -2.3$ (matching condition in Y-Y'),
III : $\beta_x < 7$ (aperture limit of the septum).

But it is difficult to satisfy all conditions because the degree of freedom of the magnet arrangement is limited due to the small area around the linac and KSR. We adopt the large edge of 40° on the exit pole face of BM1 to satisfy the doubly achromatic condition.

Table 1 Main parameters of KSR

Circumference	25.689 m
Lattice	TBDA
Curvature	0.835 m
Length of straight section	5.619 m
Tune	(2.36,1.43)
RF frequency	116.7 MHz
Stretcher mode	
Beam energy	100 MeV
Extracted beam (design)	5×10^{10} e⁻/sec
Repetition	1 Hz
Storage mode	
Maximum energy	300 MeV
Stored current (design)	100 mA
Critical wavelength	17 nm

Figure 1 View of KSR. The injection line exists in the right side.

0-7803-5573-3/99/$10.00@1999 IEEE.

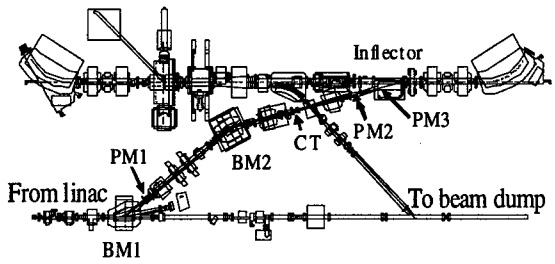

Figure 2 (a) Injection line from the linac to KSR.

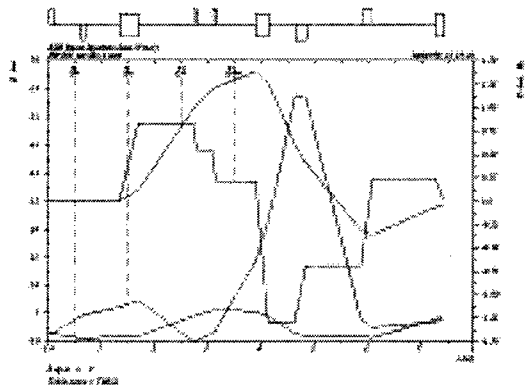

Figure 2 (b) Twiss parameters in the injection line. The beta function (β_x, β_y), the dispersion function (D_x) and its derivative (D_{px}) are shown.

Table 2 Twiss parameters at the injection point of KSR.

	Simulation results	KSR acceptance
β_x (m)	6.5	6.4
α_x	-2.5	-0.43
β_y (m)	5.4	6.23
α_y	-2.6	-2.3
D_x (m)	0	0
D_{px}	0	0

Figure 2 (b) shows the beta and the dispersion function in the injection line. It is calculated by the program code, MAD [4]. The initial point of the simulation is at the entrance of the quadrupole magnet behind the accelerator tube No.3, where β_x = 3.0 m, α_x = 2.0, β_y = 3.0 m, α_y = 2.0. The Twiss parameters at the injection point are shown in table 2. The dispersion and its derivative are zero. There is a mismatching in Y-Y' plane. Figure 3 shows a ring acceptance and the beam emittance at the injection point. The beam emittance is assumed to be 0.4 π·mm·mrad and 1.3 π·mm·mrad in X-X' and Y-Y' phase space, respectively [5]. The acceptances are 161 π·mm·mrad and 11.7 π·mm·mrad in the X-X' and Y-Y' planes. The beam ellipse is located inside the acceptance but the emittance becomes 2.1 times larger due to the mismatching in Y-Y' phase space.

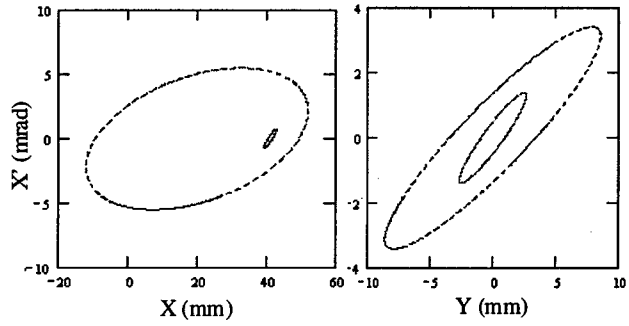

Figure 3 Beam emittance (solid line) and the ring acceptance (dotted line) at the injection point. The beam emittance is 0.4 π·mm·mrad and 1.3 π·mm·mrad in the X-X' and Y-Y' planes, respectively. The acceptances are 161 π·mm·mrad and 11.7 π·mm·mrad in the X-X' and Y-Y' planes.

2.2 Measurements

In the injection line, there are 3 beam profile monitors (PM1, PM2 and PM3) and one current transformer (CT). The beam sizes are measured by the profile monitors. The results are almost consistent with the MAD calculation and the beam size at PM3 is 6 mm, which is smaller than the septum aperture (8mm). The dispersion is also measured by the profile monitors. The beam energy is changed by the RF phase adjustment of the accelerator tube No.3 and the beam position shift were measured. The measured dispersion at PM2 is 17 cm, where the design value is 28 cm. The energy spread was measured by PM1. It is +/- 0.5 % (FWHM) and +/-1.2 % (total) with the beam current of 100 mA and the pulse width of 100 nsec. It is acceptable value for the chromaticity correction by sextupole magnets [6].

3 INJECTION SCHEME IN KSR

The layout of KSR and the Twiss parameters are shown in figure 3 (a) and (b). The characteristic point of the optics is long dispersion free sections. The injection also uses this section. The injected beam is bent 15 degree by the septum magnet and merged into the ring orbit. The injection point is 41 mm apart from the centre orbit.

3.1 Stretcher Mode

In the stretcher mode, one turn injection is used. The beam pulse width is 100 nsec and the beam current is 100 mA. The repetition is 1 Hz. To inject the beam, the bump orbit is created by a beam perturbation magnet (BPM). Figure 4 shows the waveform of the excitation current for the BPM. The maximum magnetic field of BPM is 360 Gauss and the time constant is 300 nsec. Figure 5 shows the beam distribution at the injection point in X-X' phase space when the kick angle of the BPM is 6 mrad. The index in the figure shows a circulation number of the

beam. The shaded area is a septum. To improve the emittance of the stored beam, the more precise control of the close orbit by the correction magnets is needed.

3.2 Storage Mode

In the storage mode, the same injection scheme is used. The differences are the repetition and a beam window. The beam repetition is 0.2 Hz because the damping time is 9.6 sec in the horizontal direction. The thin foil is attached in the inflector septum as a beam window to isolate the vacuum system between the beam line and the ring because the design vacuum pressure is 10^{-9} Torr in the ring, while it is 10^{-7} Torr in the beam line. The foil is Kapton with the thickness of 25 μm. The emittance growth is induced by the multiple scattering in the foil. The angular distribution f(θ) of the scattered electron becomes the gaussian function and the width can be estimated by the Moliere's formula [7],

$$f(\theta) = A\exp\left(-\frac{\theta^2}{\sigma^2}\right) = A\exp\left(-\frac{\theta^2}{B\chi^2}\right),$$

$$\chi = \sqrt{4\pi N(Z^2+Z)}\frac{e^2}{pc},$$

where p is a momentum of the electron. The width σ is 0.85 mrad in this case. The emittance becomes 2.0 times larger. This effect leads to the beam loss of 30 %. So the multiple injection after the damping is needed in the storage mode.

ACKNOWLEDGEMENTS

The authors would like to present our thanks to the support of the HIMAC group in NIRS and the accelerator group in JAERI. Special thanks to Mr. Kazama for his technical help.

REFERENCES

[1] A.Noda, et al., "Electron Storage and Stretcher Ring, KSR", Proc. of the 5th European Particle Accelerator Conference, Sitges (Barcelona), Spain, 451-453 (1996)

[2] T.Shirai, et al., "A 100 MeV Injector for the Electron Storage Ring at Kyoto University", Proc. of the Particle Accelerator Conference, Dallas, USA, 1079 (1995).

[3] A.Noda, et al., "Slow Beam Extraction at KSR with Combination of Third Order Resonance and RFKO", contribution paper in this conference.

[4] H. Grote, F. Chistoph Iselein. The MAD Program. (Methodical Accelerator Design) Version 8.10 User's Reference Manual. CERN, 1993

[5] T. Sugimura, et al., "Present Status of the Electron Linac as the Injector for KSR", Proc. of the Particle Accelerator Conference, Vancouver, Canada, 1206 (1997)

[6] A.Noda, et al., "KSR as a pulse stretcher", Proc. of the Particle Accelerator Conference, Vancouver, Canada, 339 (1997)

[7] A.O.Hanson, et al., "Measurement of Multiple Scattering of 15.7 MeV Electrons", Physical Review **84**, 634 (1951)

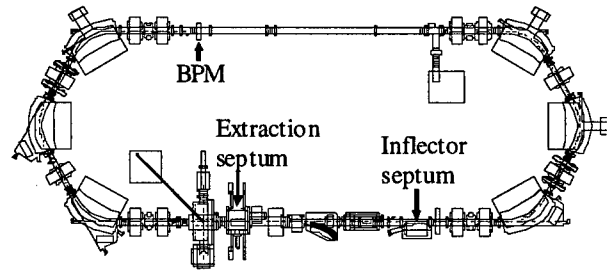

Figure 3 (a) Layout of KSR

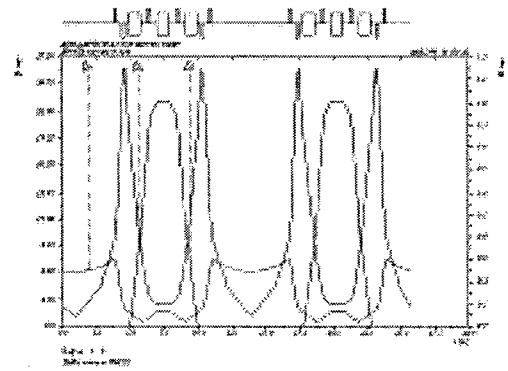

Figure 3 (b) Twiss parameters in KSR.

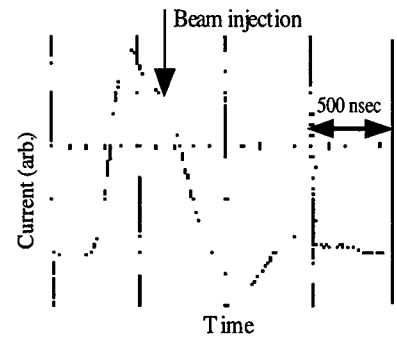

Figure 4 Waveform of the excitation current of the BPM.

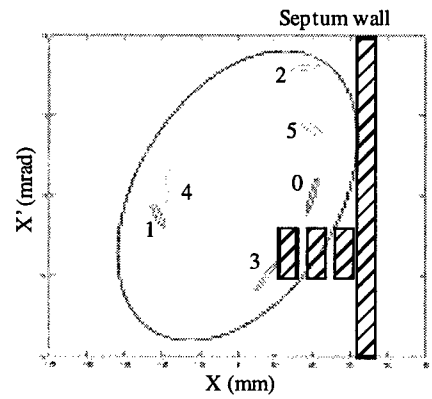

Figure 5 Beam distribution at the injection point in X-X' phase space when the kick angle by the BPM is 6 mrad. The index in the figure shows a circulation number of the beam. The shaded area is a septum.

LANDAU DAMPING OF THE VERTICAL COHERENT MOTIONS DUE TO LATTICE NONLINEARITIES IN STORAGE RINGS

Yukinori Kobayashi and Kazuhito Ohmi
Photon Factory, High Energy Accelerator Research Organization
Oho 1-1, Tsukuba, Ibaraki 305-0801, Japan

Abstract

The systematic measurements of the vertical coherent motion were made with various chromaticities, octupole magnetic currents, beam currents and betatron tunes to study its damping mechanism at the Photon Factory storage ring (PF-ring). The polarity of the octupole magnetic currents corresponding to the sign of the amplitude dependent tune shift played an important roll in the damping of the vertical coherent motions. This is the same as the horizontal coherent motions.

1 INTRODUCTION

Recently we showed that the sign of the amplitude dependent tune shift produced by lattice nonlinearities played an important roll with the wake force in the damping of the horizontal coherent motions [1]. The Landau damping is suppressed for the positive amplitude dependent tune shift due to head-tail effects at higher beam current, while it is amplified for the negative tune shift. The phenomenon is well understood through both of two particle model and multi-particle tracking simulation compared with the experimental results [2]. Next we will try to understand the damping mechanism of the vertical coherent motion. In this conference we will demonstrate the experimental results on the damping of the vertical coherent motions with various chromaticities, octupole magnetic currents, beam currents, and betatron tunes.

2 EXPERIMENTAL CONDITIONS

The experiment was performed in the single bunch operation mode at the PF-ring, which is a 2.5 GeV dedicated synchrotron light source. The principal parameters of the PF-ring are shown in Table I. The experimental method was quite simple. The stored beam was deflected with a vertical fast kicker magnet, which can give a just single kick to the beam. The kicked beam begins to circulate in the ring with a large amplitude coherent betatron oscillation. The amplitude can be controlled by the voltage supplied to the kicker magnet. During the measurements the voltage was fixed to keep that the initial vertical amplitude becomes about 5 mm at a place of βy=5 m. Then the beam position of the coherent betatron motion was detected with the turn-by-turn monitor system at a place of the ring [3]. The data were taken till 16384 turn (about 10 msec), which is longer than the radiation damping time. The vertical chromaticities was controlled by the defocus sextupole magnets (SD). The amplitude dependent tune shift was arranged with eight octupole magnetic currents and the value is given by the following equation,

$$\Delta\nu_y = 3.3\times10^{-4}\cdot I_{oct}(A)\cdot y(mm)^2$$

where y indicates the vertical amplitude. The sign of the tune shift can be changed by the polarity of the octupole magnetic currents. Though the magnets can be excited independently, the same currents were set during these measurements.

Table 1: The principal parameters of the PF-ring

Beam Energy	E (GeV)	2.5
Circumference	C (m)	187
Harmonic number	h	312
RF frequency	f_{RF} (MHz)	500.1
Revolution period	τ_{rev} (nsec)	624
Betatron tune	ν_x, ν_y	8.45, 3.30
Synchrotron tune	ν_s	0.023
Emittance	ε_x, ε_y (nmrad)	125, 2.5
Beam size at β=5m	σ_x, σ_y (mm)	0.8, 0.1
Radiation damping time	τ_x, τ_y, τ_s (msec)	7.8, 7.8, 3.9
Energy spread	σ_ε	0.00078

3 EXPERIMENTAL RESULTS

3.1 Dependence of the octupole magnetic currents

First, we measured the dependence of the octupole magnetic currents. The vertical chromaticity and betatron tune are fixed at ξ_y=-0.11 and ν_x=3.30, respectively. Except for octupole magnetic currents and beam currents, other parameters are fixed. The measurements were made at seven different octupole magnetic currents (I_{oct}= +1.0, +0.5, +0.2, 0.0, -0.2, -0.5 and –1.0 A) to three beam currents (I_{beam}=3.0 , 5.0 and 10 mA). Figure 1 shows the measured results at a beam current of 5.0 mA.

0-7803-5573-3/99/$10.00@1999 IEEE.

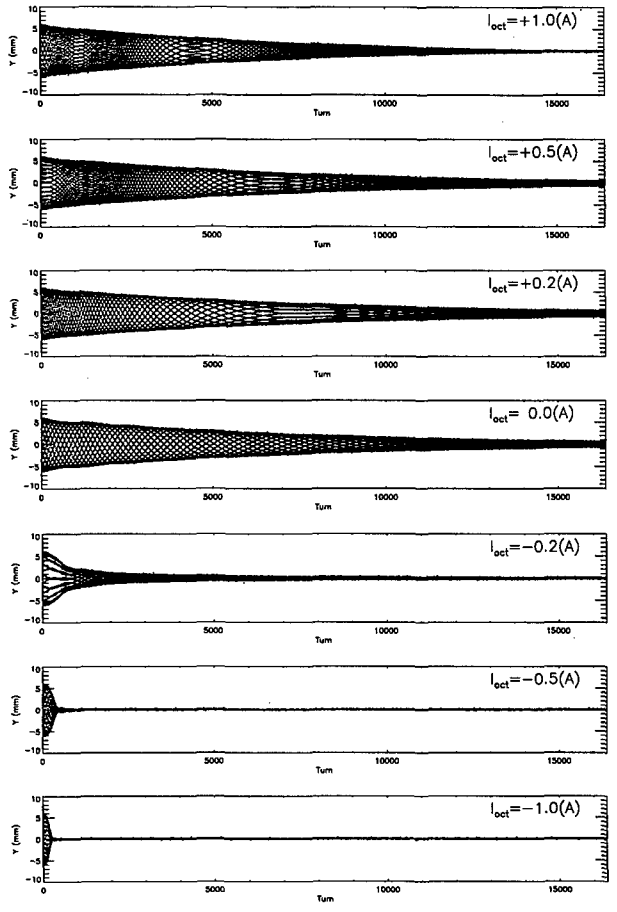

Figure 1: The dependence of the octupole magnetic currents in the damping behavior of the vertical coherent motions is shown. Data were taken at a beam current of 5 mA and the vertical chromaticity, betatron tune and other parameters are fixed.

The damping behavior of the vertical coherent motion was rapidly changed when the magnetic currents became a negative value, which is corresponding to the negative sign of the amplitude dependent tune shift. When the magnetic currents are positive value, the coherent motions damp exponentially. This phenomenon is the head-tail damping. On the other hand, the coherent motions damp very rapidly within 100 turn when the magnetic currents are negative. This is interpreted as Landau damping (nonlinear smear). So it is seemed that the Landau damping of the vertical coherent motion is suppressed for the positive polarity of the octupole magnetic currents in beam currents of 3-10 mA. This is the same situation as the horizontal coherent motions [2].

3.2 Dependence of the vertical chromaticities

Next, we measured the dependence of the vertical chromaticities. The beam current and betatron tune are fixed at Ibeam=5.0 mA and νx=3.30, respectively. Except for octupole magnetic currents and beam currents, other parameters are fixed. The measurements were made at

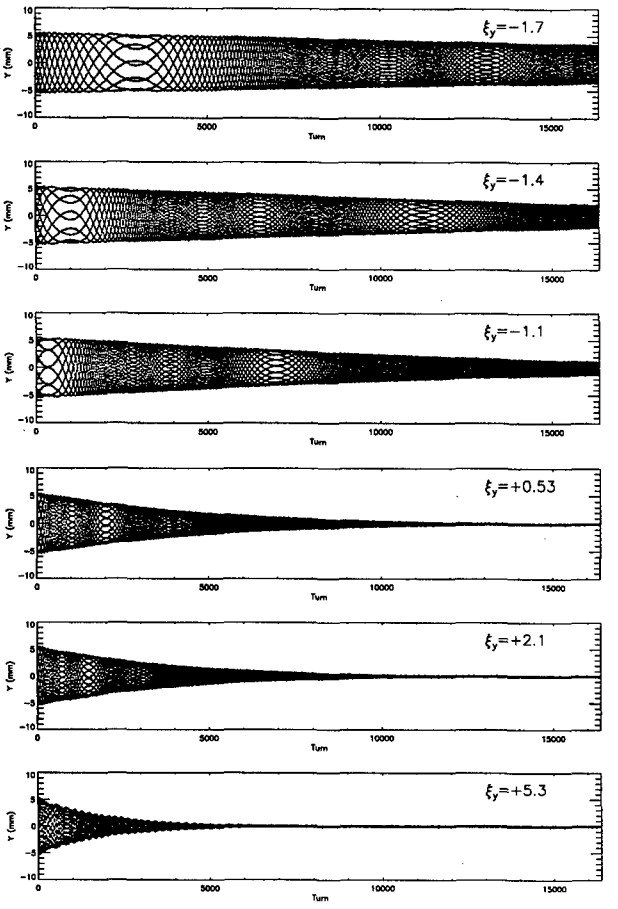

Figure 2: The dependence of the vertical chromaticities in the damping behavior of the vertical coherent motions is shown. Data were taken at an octupole magnetic current of +1.0 A and the beam current of 5.0 mA, betatron tune and other parameters are fixed.

six different vertical chromaticities (ξy= -1.7, -1.4, -1.1, +0.53, +2.1, and +5.3) to three octupole magnetic currents (Ioct= +1.0, 0.0 and -1.0 A), which were selected as the positive, zero and negative polarity of the currents. Figures 2 and 3 show the measured results at the currents of +1.0 and -1.0 A, respectively. Only head-tail damping of the coherent motions was observed at the current of +1.0 A although the damping time depended on the chromaticities. The situation of 0.0 A was almost same as of +1.0 A. On the other hand, only Landau damping was observed at the current of -1.0 A, and then the damping time never depended on the chromaticities.

3.3 Measurements at lower beam current or other vertical betatron tune

We measured the dependence of the octupole magnetic currents and vertical chromaticity at the lower beam

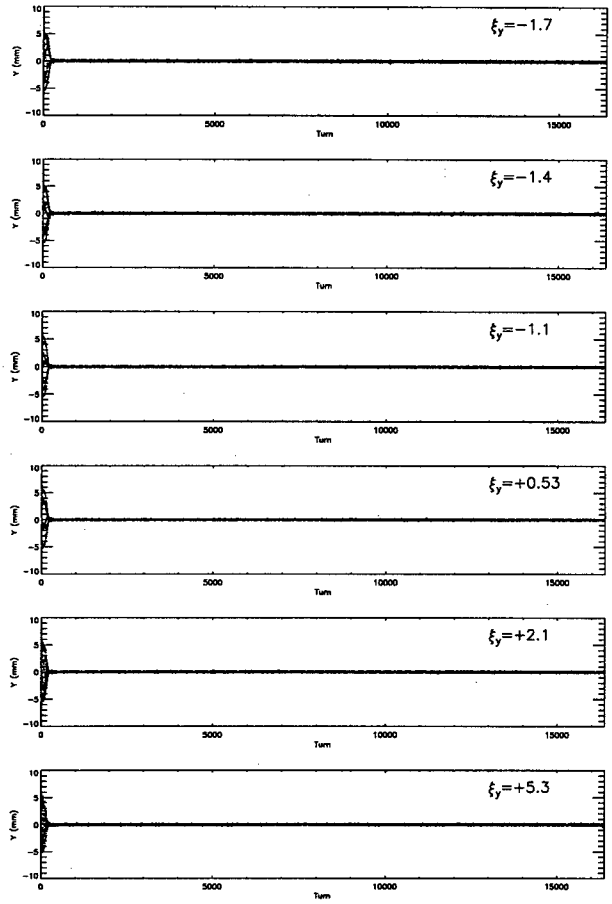

Figure 3: Same as figure 2, but data were taken at a n octupole magnetic current of -1.0 A.

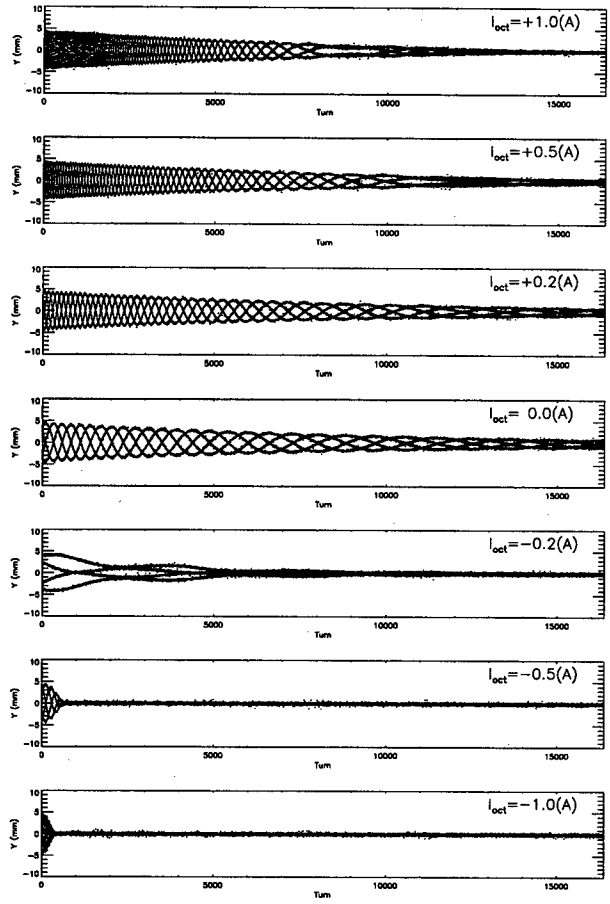

Figure 4: Same as fig.2, but data were taken at a beam current of 1.0 mA and vertical betatron tune was changed from 3.30 to 3.25.

current of 1.0 mA and another vertical betatron tune (νy =3.25). The results are shown in fig. 4 . However, the damping behaviors were not different from those of higher beam currents and νy=3.30. So we may need much lower beam current or more different betatron tune to meet the different behavior.

4 SUMMARY

We measured the systematic damping behaviors of the vertical coherent motions to various chromaticities, octupole magnetic currents, beam currents and betatron tunes. In the beam currents between 0.5 and 10 mA, only head-tail damping was observed for the positive polarity of the octupole magnetic currents and the damping time depended on the vertical chromaticities. On the other hand, only Landau damping was observed for the negative polarity, but the damping time never depended on the chromaticities. Now we are going to make a multi-particle tracking simulation to compare the experimental results quantitatively.

5 REFERENCES

[1] K. Ohmi and Y. Kobayashi, 'Head-tail effect due to lattice nonlinearities in storage ring', Phys. Rev. E59, 1167 (1999)

[2] Y. Kobayashi and K. Ohmi, 'Measurement of the beam decoherence due to the octupole magnetic fields at the Photon Factory storage ring', Proc. of EPAC 98

[3] Y. Kobayashi et al., ' Phase space monitor system at the Photon Factory storage ring', Proc. of EPAC 96

SINGLE-PARTICLE BEAM DYNAMICS STUDIES FOR THE UNIVERSITY OF MARYLAND ELECTRON RING

L.G. Vorobiev, X. Wu and R.C. York

NSCL, Michigan State University, East Lansing, MI 48824

Abstract

A single particle analysis without space charge of the University of Maryland Electron Ring was performed. Higher order multipole terms of the dipole magnets and quadrupole lenses were included. The influence of the Earth's magnetic field was balanced by Helmholtz-like wires and the misalignments effects were corrected by short dipoles (correctors) together with adjustment of the lattice dipoles. Mispowering studies showed that the closed orbit distortions and lattice functions variations were within acceptable limits.

1 INTRODUCTION

The goal of the Electron-Ring project is the construction of a compact, low-energy electron ring operating with very high current electron beams. Experiments with this facility should help improve our understanding of space charge dominated beam [1], and thus, support practical designs for projects such as Heavy Ion Driven Inertial Fusion and other advanced accelerator applications.

A necessary (but by no means sufficient) condition for the E-Ring is reliable operation at zero current. The present work is concentrated on single particle analysis in the absence of space charge. The lattice working point, the influence of magnet multipoles on beam dynamics, compensation of the Earth's magnetic field, as well as correction of effects due to mechanical misalignment were evaluated. The effects of magnet mispowering and overall influence of imperfections were also considered. The computational tool used was the DIMAD code [2].

A general layout of the E-Ring is shown in Figure 1. It has a circumference of 11.52 m and an injected beam rigidity of 3.39 gauss·m. There are 36 dipoles (each bending 10°) and 72 quadrupole lenses. The one cell structure is FODO with the E-Ring consisting of 36 cells (=18 segments).

2 LATTICE WORKING POINT

According to preliminary estimates of the E-Ring design parameters, the focusing structure should have a phase advance of about 76° per cell for a zero current beam. The working point (ν_x= 7.78 and ν_y= 7.70) was chosen to avoid all resonances up to 4th order. Since the estimated space charge tune shift for full current will be about $\Delta\nu \approx 6.0$ (see [3]), the working point will drift through many resonances and will be a topic of further studies.

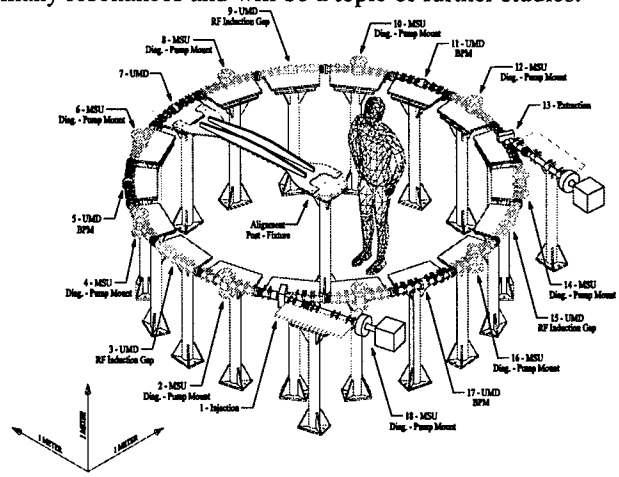

Figure 1. E-Ring layout.

Machine functions for a cell. Given the chosen $\nu_{x,y}$, machine functions of the E-Ring from DIMAD are shown in Figure 2 where the Twiss functions and dispersion are plotted for one segment (two cells). The matched machine functions are: β_x =0.261 m, α_x =-1.31, β_y=0.264 m, α_y= +1.32, η_x = 0.0358 m, η'_x = 0.1447. The phase advances for one cell are ν_x=0.2161, ν_y=0.2139.

Smear. To check the choice of the working point, a quantitative criterion "the smear factor" was used to estimate the phase volume dilution after multi-turn tracking.

Single particle tracking (typically 1000 turns) produced a data array of phase coordinates (x, x′, y, y′) after every turn. The Courant-Snyder invariants for each turn was then calculated from the machine functions and the phase coordinates at that point. The array of these invariants was then processed and the maximum ($A^{max}_{x,y}$), minimum ($A^{min}_{x,y}$), and mean ($A^{mean}_{x,y}$) invariant values were found [4]. The smear factors for the horizontal and vertical planes were calculated as: $S_{x,y}=(A^{max}_{x,y} - A^{min}_{x,y})/A^{mean}_{x,y}$.

For purely linear motion, the smear value is equal zero. In the presence of non-linear terms and/or mechanical misalignments, mispowering etc. the smear increases. From DIMAD tracking to 2nd order, the total smear increase in both planes for the unperturbed lattice was found to be <1.5% for an emittance of 10 π mm-mrad.

0-7803-5573-3/99/$10.00@1999 IEEE.

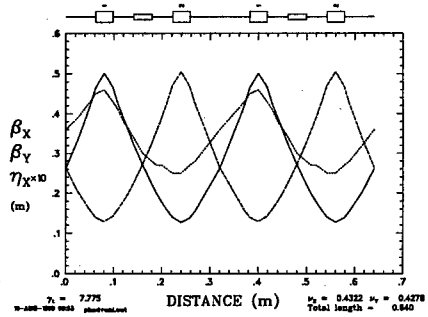

Figure 2. Machine functions (βx – solid, βy - dashed, ηx - dots) for one segment (2 cells).

3 MAGNET MULTIPOLES

All the ring magnetic elements will be fabricated using "printed-circuit" technology. Magnetic measurement data for the dipoles and quadrupoles, obtained from the University of Maryland and included in the optics analysis. In the tracking, we assumed that all allowed multipoles were systematic (errors due to elements fabrication), whereas all errors corresponding to non-allowed multipoles (errors due to focusing structure assembling) were random.

Dipole multipole analysis. The magnetic field in the dipoles may be represented by $B^D = B\rho \sum_{n=0}^{n=4} K_n^D x^n$ where $B\rho$=3.39 gauss·m is the beam magnetic rigidity and K_n^D are the expansion coefficients. The value $K_0^D = B_0^D/B\rho$=4.64 [1/m] (with B_0^D=15.73 gauss and an effective length of 37.6 mm providing a 10° bend). For n>1 one obtains $K_n^D = K_0^D B_n^D /(B_0^D R)$ and B_n^D /B_0^D are listed in Table 1.

Table 1. Dipole multipole measurements.

N	Amplitude B_n^D/B_0^D	K_n^D	Type
1	0.076%	1.481e+00	Random
2	2.00%	1.637e+02	Systematic
3	0.00%	0	Random
4	0.49%	7.074e+04	Systematic

Quadrupole multipole analysis. For the magnetic field of a quadrupole, we use a similar representation: $B^Q = B\rho \sum_{n=1}^{n=5} K_n^Q x^n$ .The value K_1^Q =227 [1/m^2] was found from lattice fitting, and since $B_1^Q = B\rho K_1^Q R$ and $B_n^Q = B\rho K_n^Q R^n$ and for $n > 1$ are given by $K_n = K_1^Q B_n^Q /(R^{n-1} B_1)$. The quadrupole multipole values are listed in Table 2.

Smear from Magnet Multipoles. The smear factor was used to estimate the influence of the higher-order multipoles on the beam dynamics of the E-Ring. All random errors were assumed to have a Gaussian distribution with 1σ corresponding to the value of the coefficients K_n^Q for the random terms. The values for the systematic terms were fixed at the values given since their contribution to smear was found negligible even for several times the measured values. (See Tables 1 and 2).

Table 2. Quadrupole multipole analysis.

N	Amplitude B_n^Q/B_1^Q	K_n^Q	Type
2	1.00%	1.737e+00	Random
3	0.30%	2.188e+02	Random
4	0.56%	1.715e+00	Random
5	0.112%	7.940e+05	Systematic

The smear $S_{x,y}$ was evaluated as a function of the multipole strength by taking the σ value for the Gaussian distribution to be 1, 2, 3, or 4 times the values given in Table 1 and Table 2. Even for random errors three times that measured, the smear is still below 5% after 1000-turn tracking for a beam of emittance 10 π mm-mrad [3]. Hence, the measured dipole and quadrupole multipoles are adequate for the ring operation.

We found that random errors (non-allowed poles) are the major contributors to smear growth with the systematic errors providing minor contributions to the smear. The largest contributions were due to K_1^B (the quadrupole component in the dipoles) and to K_1^Q (the sextupole component in the quadrupoles).

4 EARTH'S MAGNETIC FIELD

Consistent with measurements by the University of Maryland group of the Earth's magnetic field in the vicinity of the ring, for the tracking analysis, the Earth's magnetic field was represented as:

B_r=0.225sin θ [gauss] (the radial field) and

B_z=-0.55 [gauss] (the vertical field)

Where θ is the azimuthal position around the ring.

The effect of the Earth's magnetic field was represented by 13 kicks per segment or 234 kicks around the ring. The vertical field was balanced by adjustment of the 36 ring dipole magnets. The radial field was compensated by 18 segments of Helmholtz-like conductors with the current of 4.6 A. Under these conditions (the multipole values of Table 1 and Table 2 are included), the analysis of the closed orbit distortion after compensation resulted in:

x_{rms}=0.508 mm, y_{rms}=0.167 mm

x_{max}=0.868 mm, y_{max}=0.453 mm

5 MISALIGNMENTS AND CORRECTIONS

Misalignments of the ring magnetic elements were evaluated. The estimated probable misalignment values

are given in Table 3 where Δx, Δy, Δz denote shifts in the horizontal, vertical and longitudinal directions, respectively, and Δz′ is the rotation around the z-axis. The mechanical misalignments were then represented by a Gaussian distribution with the σ values of Table 3.

Table 3. Mechanical misalignment values.

Misalignment	1σ – value
Δx	0.1 mm
Δy	0.1 mm
Δz	1.0 mm
Δz'	4.0 mrad

The mechanical misalignments result in closed orbit distortions (CODs). The correction of these CODs requires beam position monitors (BPMs) combined with active correctors in both planes. The simulated correction scheme used the readjustment of the 36 ring dipole magnets for horizontal compensation and 36 vertical correctors placed between the dipoles and quadrupoles for the vertical correction. (The vertical corrector magnetic field strengths required were <1 gauss at the injection energy assuming an effective length of 1.7 cm).

Under these conditions (multipole values of Tables 1-2 included, but without the effects of the Earth's magnetic field), the CODs were evaluated.

Table 4. CODs as a function of BPM number for the misalignment values of Table 3. *No BPMs.

BPM #	Xmax (mm)	Ymax (mm)	Xrms (mm)	Yrms (mm)
0*	1.81	1.86	0.61	0.77
15	1.14	1.34	0.34	0.44
18	1.14	1.07	0.30	0.38

We have explored three cases: CODs before correction, CODs after correction with 18 (one per segment) and 15 (one missing per segment) BPMs. In Table 4 for 15 BPMs, the CODs were evaluated as a function of the misalignment values. The sigma of the Gaussian distribution was taken to be 1, 2, and 3 times the values of Table 3. The results are given in Table 5.

Table 5. CODs values after correction with 15 BPMs as a function of the scaled misalignment values of Table 3.

σ scale factors	**Xmax** (mm)	**Ymax** (mm)	**Xrms** (mm)	**Yrms** (mm)
1	1.14	1.34	0.34	0.44
2	2.28	2.62	0.70	0.88
3	3.43	3.84	1.08	1.32

6 MAGNET MISPOWERING

The beam dynamics will also be affected by mispowering of the ring magnetic elements. Mispowering of the dipole magnets will result in COD, whereas quadrupole mispowering will primarily cause variation of lattice functions and tune. The analysis was performed to determine the appropriate power supply specifications with the multipoles of Tables 1-2 (no other perturbations were included). The mispowering perturbations were considered systematic and the effect of mispowering was simulated by DIMAD assuming a systematic error in the momentum spread. The CODs as a function of the dipole mispowering and the βx,y functions variance as a function of quadrupole mispowering showed that dipole and quadrupole power supplies with ripple specifications of 10^{-4} and 10^{-3} respectively, ensures acceptable performance.

7 DISCUSSION AND CONCLUSIONS

Finally, under the conditions:

- Magnet Multipoles (values of Tables 1-2.)
- Earth's Magnetic Fields and Corrections
- Mechanical Misalignments (the values of Table 3) and corrections with 15 BPMs
- Magnet Mispowering (set at 10^{-4} and 10^{-3} for the dipoles and quadrupoles respectively)

The overall CODs with all errors included simultaneously were:

x_{rms}=1.0 mm, y_{rms}=0.47 mm
x_{max}=2.3 mm, y_{max}=1.30 mm.

We conclude that the choice of the focusing structure will provide adequate ring performance in the absence of space charge. An unusual feature of the E-Ring is the significant influence of the Earth's magnetic field. The Helmholz-like wires were found to be an efficient mechanism for compensation of the radial component of this field. Though not investigated, it might be possible to utilize the corrector dipole magnets (used to correct for the mechanical misalignments) in lieu of the Helmholz coils.

REFERENCES

[1] M.Reiser et al. Fusion Eng. Des. **32-33**, 293 (1996). See also: http://www.ipr.umd.edu/ebte/ring/
[2] Users Guide to the Program DIMAD, SLAC Report 285 UC-28 (1985).
[3] L.G.Vorobiev, X.Wu and R.C.York, MSUCL-1114 Report, MSU/NSCL, East Lansing, September (1998).
[4] Physica Reference Manual, TRIUMF, Canada (1994).

CORRECTION OF LINEAR COUPLING ON THE BASIS OF RESPONSE MATRIX MODELLING AND X-RAY PINHOLE MEASUREMENT

R. Nagaoka, P. Elleaume, L. Farvacque, J.M. Filhol, ESRF, Grenoble, France

Abstract

A new attempt is made to model a linearly coupled machine using the measured coupled-orbit response. Rather than seeking for the skew errors of the existing magnets, the aim is to obtain an effective skew error distribution that consistently describes the measured coupling characteristics. Such a solution is actually found, which is assured by the simulation that the measured orbit cross-talk provides sufficiently accurate information on the locally integrated skew errors in the ESRF configuration. To pursue the limit of correction, an optimisation of the skew corrector position is then made with respect to the obtained error distribution, with which a large reduction by nearly an order of magnitude is achieved on the model as compared to the standard correction. The actual steps in realising the lowest coupling values on the real machine with additional correctors are described. In the regime where the magnitude of the orbit cross-talk is already too small to be measured, the X-ray pinholes are utilised, which are capable of measuring the vertical emittance down to several picometres.

1 INTRODUCTION

The correction of linear coupling is of great importance at the ESRF [1], as the coupling is inversely proportional to the brilliance, the principal machine performance. The coupling at the ESRF is corrected to better than 1% for daily operation from the initial value of larger than 10% with 16 skew correctors. Focusing upon the fact that a non-zero off-diagonal orbit response matrix, otherwise called the orbit cross-talk, results from the linear coupling, the correction starts from minimising the orbit cross-talk to a certain degree, which provides a good base for the subsequent resonance compensations. This motivated us to develop an improved minimisation of the orbit cross-talk to further reduce the coupling.

In the meanwhile, an accurate calibration of quadrupoles was carried out using the diagonal part of the response matrix [2], which triggered our second motivation to solve for the skew errors from the off-diagonal matrix, as a natural extension of the work on the diagonal matrix. In the coupled equations of the orbit response due to a steerer excitation, the skew strengths appear linearly in the dipolar terms for the orthogonal orbit. A vertical orbit shift Δz_{CO} due to jth horizontal steerer by $\Delta\theta_{Hj}$, can be represented for example in the matrix notation as

$$\frac{\Delta z_{CO}}{\Delta \theta_{Hj}} = \mathbf{R}^{(V)}_{ik} \bullet \mathbf{R}^{(H)}_{kj} \bullet \mathbf{a}, \qquad (1)$$

where **a** represents an array of skew errors, the positions of which are defined by the model. $R^{(H)}{}_{kj}$ and $R^{(V)}{}_{ik}$ are respectively, the horizontal response matrix from steerer j to skew quadrupole k, and the vertical from skew quadrupole k to BPM i. It is assumed that they are known accurately from the diagonal matrix analysis. The skew errors can thus be solved via the matrix inversion (e.g. SVD method).

2 MODELLING OF A LINEARLY COUPLED MACHINE [3]

2.1 Simulation

Minimisation of the orbit cross-talk is found to be made effectively with a general least square method, readily bringing the rms of the cross-talk orbit down to several microns. A noteworthy finding resulted, however, that the reduced orbit cross-talks do not necessarily produce smaller couplings. The relation turns out to depend sensitively on the steerer-BPM-skew corrector configuration. In the case of ESRF, the best solutions for the coupling even increase the orbit cross-talk.

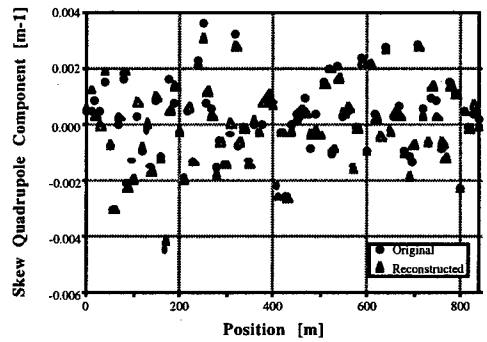

Figure 1: Locally integrated skew strengths (every 10 meters) between the original and reconstructed machines.

Although the orbit cross-talks and the betatron motions satisfy the same coupled equations, the fact that the former are special periodic solutions is suspected to be the underlying reason for this non-trivial correlation. With respect to the solution of Eq. 1 for the specific ESRF configuration, we find that there is not a good enough resolution to identify the individual tilt errors of the quadrupoles. However, locally integrated strengths can be well reproduced (Fig. 1), which describe the coupling of

0-7803-5573-3/99/$10.00@1999 IEEE.

the original machine locally and globally in a satisfactory manner. In contrast to the work made on the same principle [4], the importance of building an *effective skew distribution* may therefore be stressed, which also conforms with the fact that the skews errors due to vertical orbit offsets in the sextupoles are comparable to the quadrupole tilts for the ESRF machine.

2.2 *Application to the Real Machine*

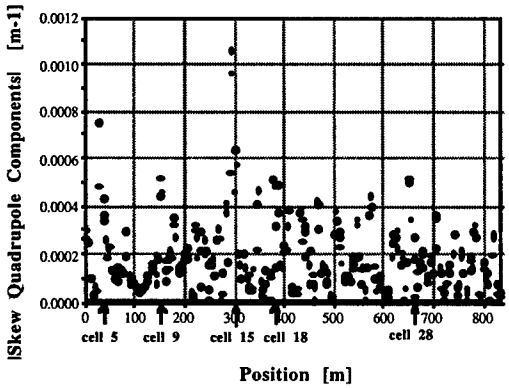

Figure 2: Obtained skew distribution of the uncorrected coupling.

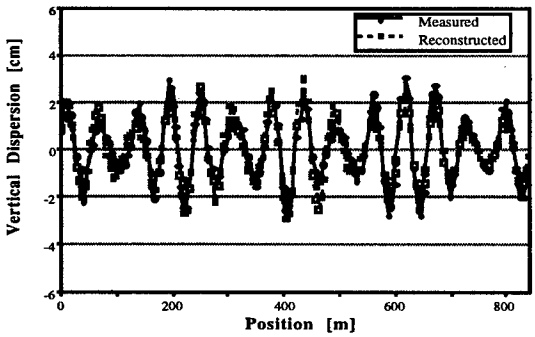

Figure 3: Predicted vertical dispersion of the uncorrected coupling, in comparison with the measured one.

With the measured matrices, the effect of averaging turns out to be particularly important in removing the involved imperfections. Equation 1 is solved with the SVD method for a pair of steerers belonging to the same family, optics wise, whose skew distribution is averaged over the entire pairs. Searching the best number of eigenvectors is found to be equally important. The measured coupled orbits are reproduced typically to few microns rms. The resultant skew distribution of the machine without coupling correction exhibits several localised peaks (Fig. 2). It reproduces well the measured vertical dispersion (Fig. 3), as well as the tune separation around the coupling resonance (Fig. 4), i.e. the two major coupling observables. Most computations were made with 10 skew flags per cell. Although valid solutions can be obtained with a smaller number of flags, it results in increasing the magnitude of the individual skew strengths.

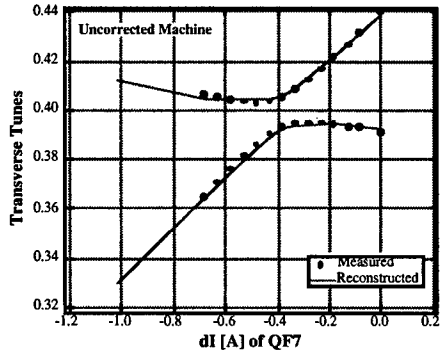

Figure 4: Predicted tune separation of the uncorrected coupling, in comparison with the measured one.

3 COUPLING CORRECTION

Having obtained the effective error skew distribution of the ESRF machine, one can attempt to correct the coupling on the model. The resulting skew corrector strengths agree well with those actually obtained from the standard corrections on the field.

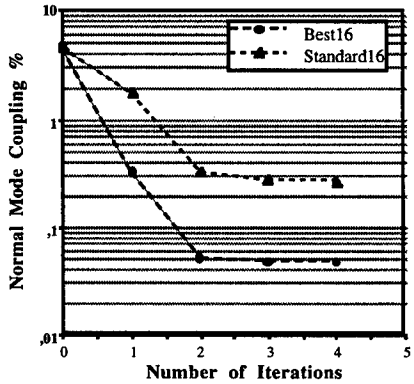

Figure 5: Correction efficiency of the most effective correctors, in comparison with the standard ones.

As an useful application of the model, a search was made for the most effective corrector positions with respect to the skew errors. Placing 96 skew correctors around the model machine at allowed locations, minimisation of the normal mode coupling was made with the best corrector method, taking account of the correlation among the selected correctors. A large reduction to ~0.05% was obtained on the model coupling with 16 selected correctors, as compared to ~0.3% reached with the standard correctors (Fig. 5). Interestingly, the orbit cross talk is simultaneously suppressed in the optimised correction. Figure 6 summarises the relation between the coupling and the orbit cross-talk for the three characteristic coupling states: 1) Uncorrected. Best corrected with 2) the existing correctors, and with 3) the most effective correctors.

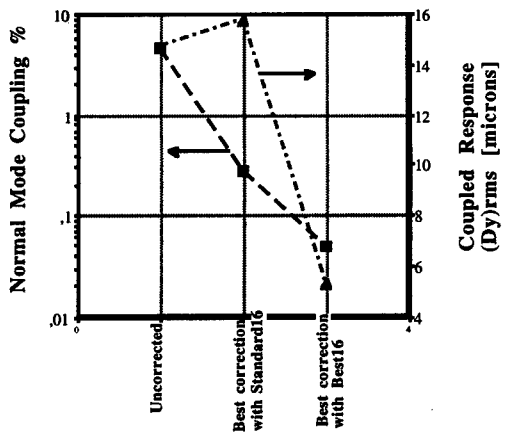

Figure 6: Relation between the coupling and the orbit cross-talk for three different correction states described in the text.

16 additional skew correctors were installed accordingly in the ring. Anticipating unavoidable discrepancies between the model and the real machine as well as the reduction of the orbit cross-talk which would prevent from iterating the response matrix analysis, an alternative correction method was prepared. The developed scheme minimises the vertical beam sizes measured with the X-ray pinhole cameras at two different locations in the ring. Utilising the bending magnet radiation, the pinhole set-ups are capable of measuring the vertical emittances down to 5 pm·rad. Details are found in Ref. 5. Simulations show that with the vertical dispersion included with a proper weighting, the minimisation of the vertical beam sizes at the two pinhole locations manages to reduce the coupling.

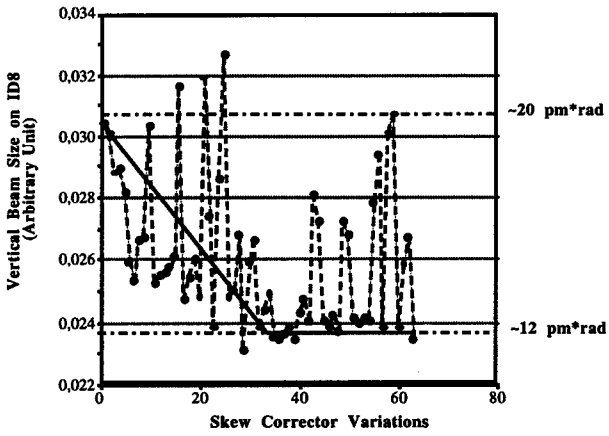

Figure 7: Reduction of the measured vertical beam size with the number of steps in the empirical correction.

Applying the model solutions to the machine, the coupling expectedly reached a level lower than the standard value. The empirical minimisation of the measured vertical beam sizes further reduced successfully the vertical emittances down to 12 pm·rad (0.3% coupling). In accordance with the prediction, the measured orbit cross talk was significantly suppressed (the rms is 5 μm against 4 μm of predicted). Together with the vertical dispersion which is reduced to ~0.3 cm rms (instead of 0.15 cm predicted), the reached setting is expected to be in the vicinity of the best point.

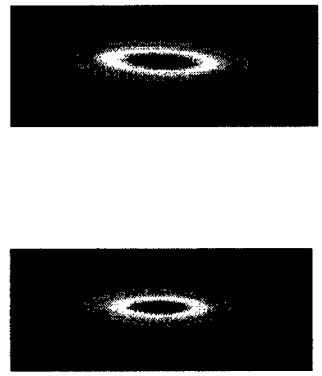

Figure 8: The two beam images of the X-ray pinholes at the lowest coupling achieved (ε_V ~12 pm·rad). Note that the beta values at the source points are approximately 2.7 m horizontally and 35 m vertically.

4 CONCLUSION

It was demonstrated that from the coupled-response matrix (orbit cross-talk), sufficiently accurate information can be extracted on the source of the linear coupling, namely the effective error skew distribution. The present approach therefore has the great advantage of understanding quantitatively the local details of the coupling of the machine, which is of particular importance for synchrotron light sources. The derived model was successfully utilised to perform the most effective correction by optimising the corrector locations. Starting from the model solution, minimisation of two vertical beam sizes measured with X-ray pinholes managed to lower the coupling to ~0.3% from the standard value of ~0.8%. The reason for the remaining discrepancy to the predicted coupling is to be investigated.

5 ACKNOWLEDGEMENT

The authors would like to express their thanks to all those who supported this work from different groups at the ESRF.

6 REFERENCES

[1] J.M. Filhol, L. Hardy and U. Weinrich, ESRF Status Report, this conference.

[2] L. Farvacque and R. Nagaoka, "Calibration of Quadrupole Magnets via Response Matrix Modelling", EPAC98, Stockholm, June 1998.

[3] R. Nagaoka, "Modelling of a Linearly Coupled Machine Using the Coupled-Response Matrix", EPAC98, Stockholm, June 1998.

[4] J. Safranek, "Experimental Determination of Storage Ring Optics Using Orbit Response Measurements", Nucl. Instr. And Meth., A388 (1997) 27.

[5] P. Elleaume, C. Fortgang, C. Penel and E. Tarazona, "Measuring Beam Sizes and Ultra-Small Electron Emittances Using an X-ray Pinhole Camera", J. Synchrotron Rad., 2 (1995) 209.

A COMPACT X-RAY SOURCE BASED ON COMPTON SCATTERING

E. Bulyak, A. Dovbnya, P. Gladkikh, Yu. Grigor'ev, I. Karnaukhov, A. Khodyachikh,
S. Kononenko, V. Lapshin, V. Molodkin, A. Mytsykov, V. Nemoshkalenko, A. Shcherbakov,
A. Shpak, Yu. Telegin, A., Zelinsky
NSC KIPT, 310108, Kharkov, Ukraine

Abstract

The paper discusses the use of Compton backscattering of an intense laser light on a relativistic electron beam to produce high-intensity γ beams, and also the practicability of the concept. Requirements on the parameters of electron and photon beams are described, and the lattice of the electron storage ring with a beam energy up to 150 *MeV* is proposed, wherein experiments on intense photon beam generation and laser cooling of the electron beam can be conducted. Electron beam parameters in the storage ring are calculated with due regard for the intrabeam scattering, photon beam parameters are also estimated. The scheme of experiment that enables the production of a photon beam with an intensity of $\sim 10^{13} s^{-1}$ is proposed.

1 INTRODUCTION

Telnov [1] has proposed the method of cooling the electron beam with a laser light, that makes it possible to reduce the transverse beam emittance by 1 to 3 orders of magnitude.

Huang and Ruth [2] have put forward a proposal to create a laser-electron storage ring (LESR) with an electron energy ranging from a few *MeV* to several hundred *MeV*, wherein the laser cooling is used for compensating the intrabeam scattering effects; this permits one to minimize transverse beam emittances and to produce intense beams of photons.

The electron beam is injected to the storage ring, and simultaneously, an intense laser pulse is introduced in a high - Q-factor optical resonator. The laser pulse path length is chosen in such a way as to exactly correspond to the revolution period of electron beam. Then, with each revolution, electrons collide with a light pulse in the resonator focus. The laser pulse in the LESR acts on the beam much like a very strong undulator or a wiggler, therefore a rapid laser cooling leads to very low beam emittances even at moderate (about 100 *MeV*) energies.

2 CHOICE OF THE LESR LATTICE

In deciding on a particular lattice of the LESR intended for performing experiments on laser cooling of the stored beam and on γ generation with the use of Compton backscattering, it is necessary to solve the following problems:

- to provide the maximum density of the electron beam in the region of its interaction with the photon beam (interaction point - IP) stored in the optical resonator;
- an increase in the electron beam density leads to an increase in the nonlinear Coulomb tune shift and in the enhancement of intrabeam scattering effects; therefore, the beam dimensions around the whole circumference of the ring must be much greater than at the IP. In other words, the lattice must comprise only one low-β insertion;
- the strong focusing of the beam in the low-β insertion determines a high natural chromaticity of the ring. The presence of only one low-β insertion reduces the degree of storage ring symmetry down to $N=1$ and this drastically extends the spectrum of azimuthal harmonics of nonlinear perturbations and restricts the dynamic aperture (DA).

In view of these considerations, we have suggested a version for reconstruction of the operative storage ring N-100 [3] in order to carry out Compton backscattering experiments. The layout of the focusing structure elements are shown schematically in fig. 1.

The arc lattice and phase advances of betatron oscillations are chosen proceeding from the requirements of providing optimum conditions for correction of natural chromaticity of the ring. The matching of arcs and long straight sections is accomplished by quadrupole lens triplets. The existing bending magnets of the ring N-100 with a bending angle $\varphi = 90°$ will be used.

The momentum compaction factor under operating conditions with two dispersion-free long straight sections will be high. The equilibrium energy spread during Compton photon generation makes up several percent [2] and holding such a beam in the facility with a high momentum compaction factor calls for great voltages of *RF* power supply. The placement of a sufficient number of accelerating structures in the compact facility appears impossible.

The abandonment of the dispersion-free injection section makes the solution of this problem possible. In this case, the mode of operation of the storage ring can be easily varied to control the value of the momentum compaction factor. At these operating conditions, the long straight section with the IP remains dispersion-free, while at the injection section the dispersion function is non-zero.

0-7803-5573-3/99/$10.00@1999 IEEE.

Retuning is realized by all quadrupole lenses of the ring, while the tunes remain unchanged and the optical functions of the ring vary insignificantly (naturally, exclusive of the dispersion function). Among the advantages of this mode of operation is the fact that the existence of an additional dispersion section makes it possible to optimize the task of correcting the natural chromaticity of the ring, this being a currently central problem for compact rings with great beam energy spreads. With the additional high-dispersion section it appears possible to weaken the intrabeam scattering effects and to diminish the electron beam dimensions that have set in. Since retuning is carried out at fixed tunes, the beam can be stored at operating conditions with a dispersion-free injection section, and thereafter the operating conditions with a low momentum compaction factor can be adjusted. Incidentally, the DA of the storage ring permits beam injection at conditions with a lower value of momentum compaction factor, too.

The main parameters of the storage ring for the stored beam energy E = 100 *MeV* are given in table 1 (values given in brackets correspond to a low momentum compaction factor). The beam parameters with due regard for the intrabeam scattering effects were calculated using the results of [4]. In the calculations, the coupling coefficient of vertical and radial betatron oscillations was put to be 0.1. The stored current in the bunch was assumed to be 10 *mA* (~ $2.5 \cdot 10^9$ particles).

Table 1.

Main parameters of the storage ring

Parameter	Value
Operating energy range *[MeV]*	40-160
Injection energy *[MeV]*	70
Circumference *[m]*	12.004
Tunes:	
horizontal, Q_x	3.162
vertical, Q_z	1.220
Amplitude functions at IP *[cm]*:	
horizontal, β_x	3
vertical, β_z	6
RF voltage amplitude *[MV]*	0.4
RF frequency *[MHz]*	699.28
Harmonic number, h	28
Momentum compaction factor, α	0.098 (0.0061)
Synchrotron oscillation tune, Q_s	0.041 (0.010)
Energy acceptance, *[%]*	±3 (±12)
Natural emittance ε_x, *[nm]*	14.7(14.0)
Horizontal beam size at *IP* with *IBS*, *[μm]*	120(160)
Natural chromaticity:	
in horizontal plane, ξ_x	-3.89 (-4.22)
in vertical plane, ξ_z	-10.9 (-10.9)

Fig. 2 shows the amplitude and dispersion functions of focusing for the operating conditions with low momentum compaction factor $\alpha = 0.0061$.

The DA dimensions calculated for peak values of amplitude functions are found to be about ±22 *mm* and ±30 *mm* in horizontal and vertical planes, respectively (energy spread δ=±0.5%). The DA dimensions in the horizontal plane are approximately coincident with the physical aperture size, while in the vertical plane they are far in excess of the latter, and are quite sufficient for realizing injection, beam storage and conducting physical experiments. The problems of correcting natural chromaticity of the ring for high values of the steady energy spread need further consideration.

3 OPTICAL EQUIPMENT OF THE LESR

The straight section of the storage ring and the half-axis of the optical resonator are aligned. The resonator is formed by two high-quality mirrors and with the reflection coefficients close to unity. The doubled spacing between the resonator mirrors is equal to the electron orbit length in the storage ring. The single-mode laser generates light pulses of 50 *ns* length (light bunch length σ_f = 15 *mm*), with a pulse-repetition frequency $f \sim 10^4$ and an average power P = 100 *W* (flash energy being about 10 *mJ*). The laser active element is manufactured from an yttrium-aluminum garnet crystal activated with neodymium (*Nd: YAG*). The wavelength of the main harmonic is λ = 1.06 *μm*. The photon beam is focused so that its minimum transverse size is achieved in the middle of the interaction region.

4 PARAMETERS OF ELECTRON AND PHOTON BEAMS

Proceeding from the parameters of storage ring and optical equipment as given in the previous sections, as well as from the consideration presented in [2], we can estimate the parameters of the electron beam and the photon beam in the LESR N-100 for the electron beam energy E = 100 *MeV*, the photon energy in the beam $\varepsilon_{\gamma 0}$ = 1.17 *eV* (this corresponding to the laser wavelength of 1.06 *μm* - *Nd: YAG* laser).

For the given laser flash energy E_L =10 *mJ*, the number of photons in the flash will be $n_\gamma = 5.33 \cdot 10^{16}$. The average energy loss by the electron on its interaction with the laser flash photon is $\varepsilon_\gamma \sim$ 100 *KeV*, and the average energy losses by the electron beam per turn are given by

$$(\Delta E)_e = \varepsilon_\gamma \frac{n_\gamma \sigma_c}{s} = \varepsilon_\gamma \frac{n_\gamma \sigma_c}{\pi \sigma_x^2} \approx 5\, eV,$$

where σ_c – Compton scattering cross-section,
σ_x – horizontal size of electron beam.

At a stored beam energy E = 100 *MeV*, the synchrotron radiation losses make up 17.7 *eV*. In principle, this will permit experimental verification of laser cooling effects.

The balance between the damping rate and the growth rate of transverse emittance gives the values of minimum normalized transverse emittances:

$$(\varepsilon_x^n)_{\min} = \frac{3}{10}\frac{\lambda_C}{\lambda_L}\beta_x^* \approx 1.8\cdot10^{-8}$$

where β_x^* - amplitude function in *IP*.

At Compton scattering the energy spread in the beam increases because of energy fluctuations of scattered electrons. The energy spread that set in is given by:

$$(\sigma_\delta)_{\min} \equiv \left(\frac{\sigma_E}{E}\right)_{\min} = \sqrt{\frac{7}{5}\frac{\lambda_C}{\lambda_L}\gamma} \approx 2.6\ \%$$

For the RF acceptance σ_{RF} = 12% the quantum lifetime will be τ_q ~ 450 *s*, this being quite sufficient for conducting experiments.

At a particle number in the bunch $N_e \sim 2.5\cdot10^9$, a mirror reflectivity of 0.9999, the beam size at the IP $\sigma_x \sim 150\ \mu m$ and the laser pulse frequency $f = 10^4$, the total number of Compton photons will make up $N_\gamma \sim 2.5\cdot10^{12}\ s^{-1}$. An increase in the energy spread of the electron beam as it interacts with the laser photon beam will depress the intrabeam scattering effects, and this must cause the Compton photon yield to increase.

5 CONCLUSION

A scheme of re-designing the electron storage ring N-100 to generate backward Compton gamma-quanta with an intensity of ~ $10^{13}\ s^{-1}$ is proposed. The facility can provide high-intensity γ beams over a wide energy range due to both the variation in the wavelength of laser light and energy readjustment of the electron storage ring. The facility will permit research into the process of laser cooling of the electron beam in the storage ring.

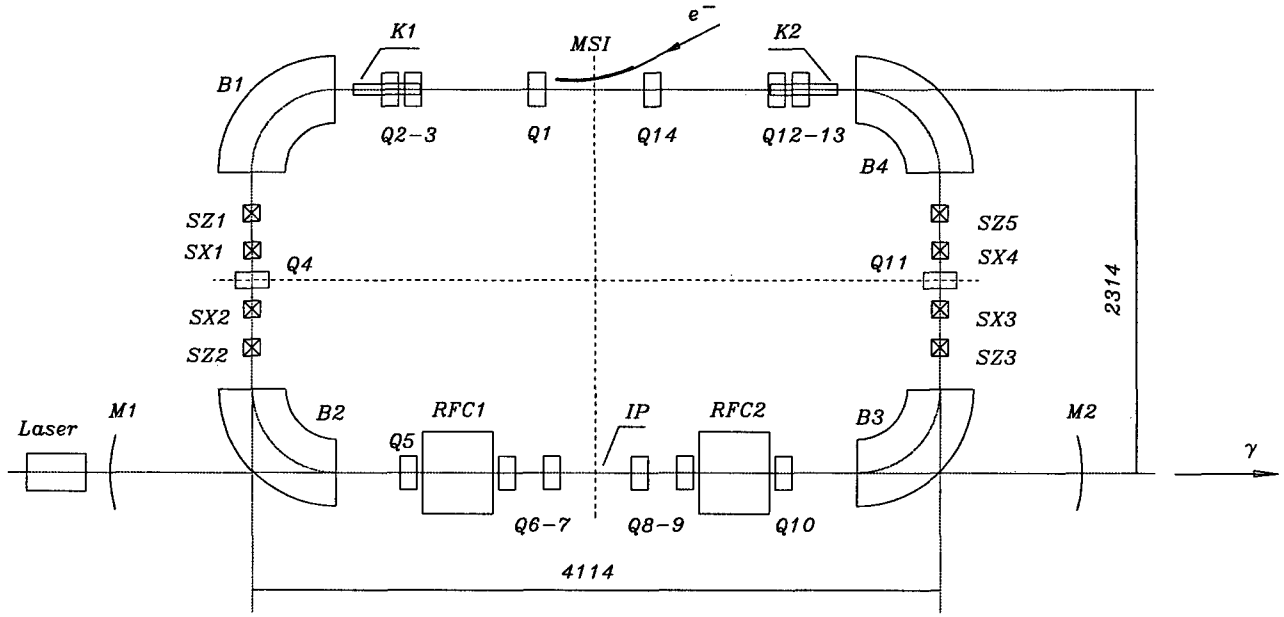

Fig. 1. Layout of the storage ring.

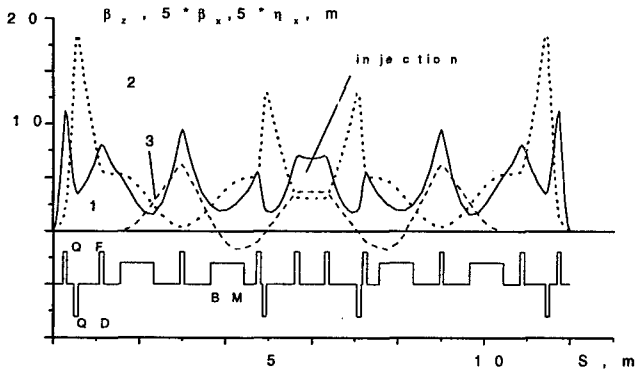

Figure 2. Amplitude functions (horizontal (1), vertical (2) and dispersion(3)) of focusing for the mode of operation with a momentum compaction factor (α = 0.0061). *BM* - bending magnets, *QF* and *QD* - quadrupole lenses focusing and defocusing in the horizontal plane.

6 REFERENCES

[1] V. Telnov, Phys. Rev. Letters, 78, 1997, p.4757
[2] Z. Huang, R. Ruth, SLAC-PUB-7556, September 1997, p.11.
[3] Yu.N. Grigoriev et al., At. Ehnerg. 23(6), 1967, p.531
[4] J.D.Bjorken and S.K.Mtingwa, Intra-beam scattering, Part.Accel. 13, 1983, p.115.

STATUS OF THE LNLS BOOSTER PROJECT

Liu Lin, A.C. Lira, P.F. Tavares* and G. Tosin, LNLS, Campinas, Brazil

Abstract

We present the status of prototype work on the main components of the LNLS 500 MeV booster synchrotron project. We present results of the characterization of the booster magnets and power supplies.

1 INTRODUCTION

The Brazilian National Synchrotron Light Laboratory, LNLS, is currently building a 500 MeV booster synchrotron to increase the injection energy into the UVX 1.37 GeV electron storage ring, which has been running routinely for synchrotron radiation research since July 1997. The decision to upgrade the injection energy arose from the need to install small gap insertion devices and also to further increase the stored beam current by improving the injection efficiency. Figure 1 shows the layout of the booster, which will be installed inside the storage ring. Table I shows the main machine parameters. A detailed account of the machine conceptual design and the rationale for the choice of the main parameters was given in previous work [1]. In this report, we concentrate on the first results from the booster magnet and power supply prototypes.

2 BOOSTER MAGNETS

The booster magnets are laminated and laser cut from 1.5 mm thick low carbon steel sheets and assembled without welding by using tie rods. This technique already proved to produce good quality magnets and provides very high flexibility in changing the lamination profile during the prototyping phase. The faces of the laminations were oxidized to minimize eddy current effects in the magnetic field. The Poisson 2D [2] code has been used to optimize the pole and coil shapes.

Prototypes of the dipoles, quadrupoles, sextupoles and corrector magnets have been built and characterized.

Table I: Injector ring main parameters.

Maximum energy	500	MeV
Injection energy	120	MeV
Circumference	34.0	m
RF frequency	476.0	MHz
Horizontal tune	2.27	
Vertical tune	1.16	
Horizontal natural chromaticity	-2.1	
Vertical natural chromaticity	-2.5	
Repetition rate	0.2	Hz
Current (@ 500 MeV)	70	mA
Storage ring filling time (300 mA)	2	min

2.1 Dipoles

Table II shows the main parameters of the dipole magnets, including some results of the first prototype. The basic constraints guiding the design were the maximum field, the small space available for magnet

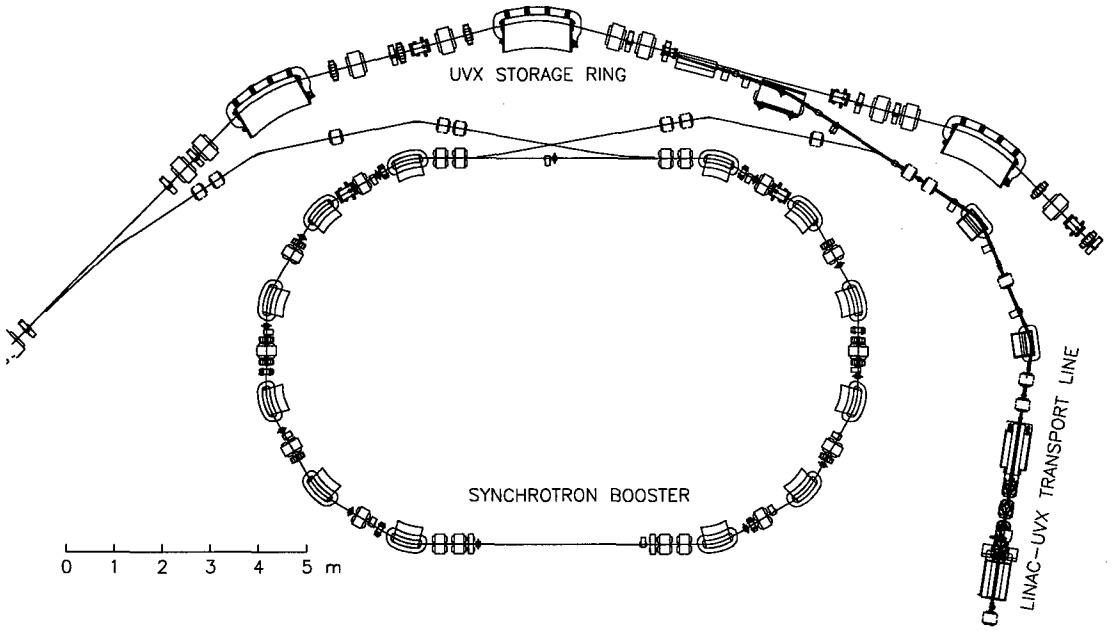

Fig. 1: Layout of the new injector for the LNLS UVX storage ring.

*E-mail: pedro@lnls.br

0-7803-5573-3/99/$10.00@1999 IEEE.

installation, the working load limit of the crane available in the machine hall and a maximum time constant (inductance/resistance) of one second. These considerations led us to choose a water cooled rectangular C-shaped staggered magnet.

The field map on the symmetry plane of the magnet has been measured with a Hall probe and the results have been used to optimize the pole profile with shims. Figure 2 shows the resulting integrated field transverse profile.

Dynamic measurements (figure 3) have shown that the influence of eddy currents in the integrated field are less than 0.1% as could be anticipated from the rather low booster repetition rate (0.2 Hz) and correspondingly long ramping time (3 s).

Table II: Main parameters of the booster dipole magnets (* indicates maximum *measured* values).

Deflection	30	deg
Bending radius	1.026	m
Gap	36	mm
Required good field region:	$1\ 10^{-4}$	±10 mm
	$1\ 10^{-3}$	±25 mm
Current*	300	A
Current density*	4.55	A/mm^2
Voltage*	9.8	V
Power*	8940	W
Magnetic Field*	16770	Gauss
Inductance*	0.11	H

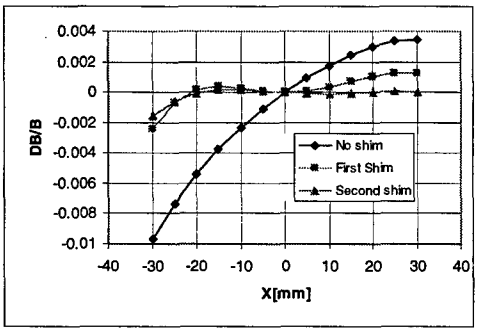

Fig. 2: Dipole magnet integrated field profile before and after shims were added (current = 180 A).

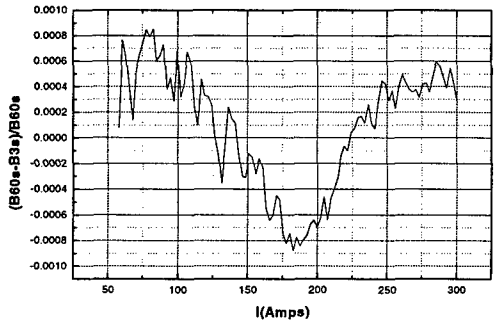

Fig. 3: Relative variation of the field in the centre of the dipole magnet as a function of ramping time. Two ramping times are compared (60 seconds and 3 seconds).

2.2 *Quadrupoles*

The main constraint to be observed in the quadrupole design was to achieve the required field gradient without water cooling the coils. Table III shows the main parameters.

The rotating coil method has been used to make the harmonic analysis and figure 4 illustrates the results obtained with this technique. The harmonic composition of the integrated field is not critically dependent on the excitation current. The field perturbation produced by eddy currents measured in the middle of the magnet and 10 mm far from its center, is about 1.5 Gauss.

Table III: Booster quadrupole magnet parameters.

Bore radius	27	mm
Core length	180	mm
Total length	270	mm
Current*	10	A
Current density*	1.06	A/mm^2
Voltage*	10.39	V
Power*	103.9	W
Gradient*	7.35	T/m
Inductance*	0.26	H
Coil temperature*	46	°C

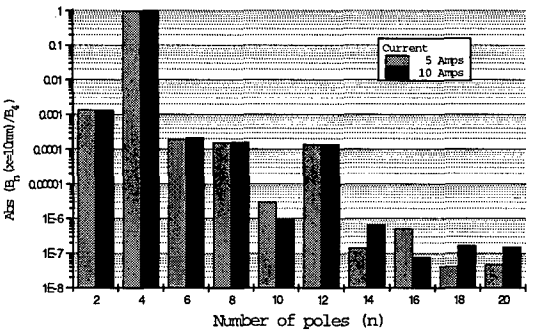

Fig. 4: Harmonic analysis of the integrated quadrupole field.

2.3 *Sextupoles*

The sextupole was divided into just two parts to guarantee radial symmetry of the poles (Table IV). For this design, the main difficulty comes from the small space available for the coils.

Table IV: Booster sextupole magnet parameters.

Bore radius	27	mm
Core length	100	mm
Total length	150	mm
Current*	10	A
Current density*	2.14	A/mm^2
Voltage*	5.30	V
Power*	53	W
Gradient*	224	T/m^2
Inductance*	0.023	H
Coil temperature*	42	°C

3 BOOSTER MAGNET POWER SUPPLIES

Table V shows the main parameters of the booster power supplies. Prototypes of all booster magnet power supplies have been built and tested. Except for the dipole power supply, all others have been tested under full load operation.

The dipole power supply is a combination of a 6-pulse thyristor power supply in series with Switch Mode Power Supply (SMPS) which works an active filter [3] to provide low ripple and tracking of the current reference during ramping (figure 5). The SPMS deals only with a fraction of the total power and provides for the fast response.

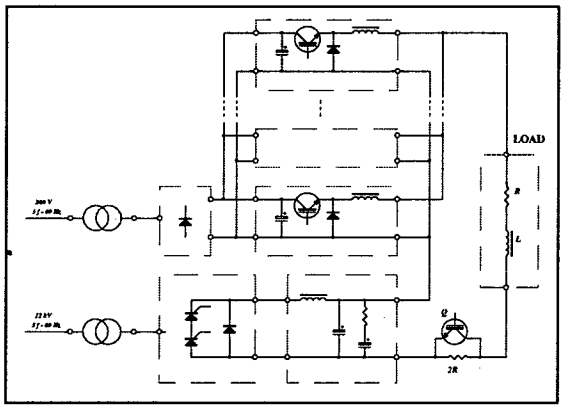

Fig. 5: Booster magnet power supply topology.

Up until now, this power supply has been tested with the first booster dipole prototype (time constant = 1 sec). In order to achieve the design repetition rate for the booster, we use a solid state switch in parallel with a resistor equivalent to twice the dipole resistance, so that when the current reference is reduced (nearly instantly) from the maximum value to the minimum at the end of each ramping cycle, the additional resistor is switched in, thus reducing the circuit time constant. Figure 6 shows a typical operation cycle for this power supply.

The power supplies for the quadrupoles and sextupoles consist of an off-line AC/DC converter followed by a chopper stage. Current regulation is accomplished by current limit modulation, which provides a fast and simple mode of operation.

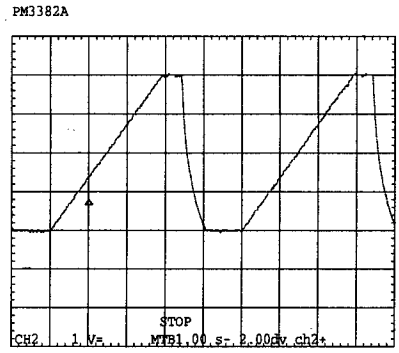

Fig. 6: Typical dipole current waveform in a cycle of operation (60 A/div, 1 sec/div).

4 OTHER COMPONENTS

Design and prototype work is also under way for various other booster components. The pulsed magnets (injection and ejection septa) have been designed and most components (ferrite blocks, high voltage power supplies, thyratrons, etc.) have been ordered from industry. These are all ferrite core magnets with thyristor or thyratron switched pulsers. The most challenging one is the ejection kicker, which must provide a very fast rise time (shorter than 20 ns) in order to guarantee a large transfer efficiency to the storage ring. The control system is basically the same as developed for the storage ring, with special care taken to guarantee the fast response needed to implement the energy ramp. The RF power requirements are sufficiently low (below 1 kW) that a solid state amplifier is being considered.

REFERENCES

[1] A.R.D.Rodrigues et at, *Design of a Booster for The Brazilian Synchrotron Light Source*, EPAC 98, Stockholm, Sweden.

[2] *Reference Manual for The Poisson/Superfish group of codes, Los Alamos* LA-UR-87-126.

[3] J. A. Pomílio, D. Wisnivesky and A. C. Lira, *A Novel Topology for the Bending Magnets Power Supply at LNLS*. IEEE–TNS vol.39 no. 5, oct/92. p. 1506-1511.

Table V: Booster magnet power supplies.

Magnet	# Mags. per supply	# Power supplies	Current Range (A)	Ripple ($\Delta I/I_{max}$)	Stability	L (H)	R (Ω)
Dipoles	12	01	58 – 300	10^{-4}	10^{-5}	1.44	1.2
Quads	02	09	0 - 10	10^{-4}	10^{-5}	0.12	0.25
Sext.	04	02	0 - 10	10^{-4}	10^{-5}	0.05	2.2

A DESIGN STUDY OF THE PROTON STORAGE RING FOR THE NEUTRON SCIENCE PROJECT AT JAERI

M. Kinsho, F. Noda, J. Kusano, M. Mizumoto, and H. Yokomizo
Japan Atomic Energy Research Institute
Tokai-mura, Naka-gun, Ibaraki-ken 319-1195, Japan
email : kinsho@linac.tokai.jaeri.go.jp

Abstract

The goal of the proposed Neutron Science Project (NSP) at JAERI is to provide a short pulsed proton beam of less than 1μs with an average beam power of 5MW. To achieve such purpose, a proton storage ring operated at 50Hz with 4.17×10^{14} protons per pulse at 1.5GeV is required. Two kinds of a lattice are examined as a lattice of the proton storage ring for neutron science project. One is FODO lattice and the other is Triple Bend Achromatic (TBA) lattice. This paper describes preliminary results of the lattice design for the proton storage ring.

1 INTRODUCTION

Japan Atomic Energy Research Institute, JAERI, has been proposing the Neutron Science Project (NSP) which is composed of research facilities based on a proton linac and a proton storage ring with an energy of 1.5GeV[1]. In the proton storage ring, the pulsed beam from the linac is accumulated, and high intensity pulsed beam is produced for the neutron scattering experiment. The goal of the proton storage ring is to provide a short pulsed proton beam of less than 1ms with an average beam power of 5MW with two rings. The study of the proton storage ring whose beam power is 2.5MW has been performed. To achieve a beam power of 2.5MW with an energy of 1.5GeV, it is necessary to accumulate 2.08×10^{14} protons. When the beam injection is completed, accumulated protons are extracted from the ring during 1 turn. The basic parameters of the proton storage ring are shown in Table 1.

Lattice design for high intensity proton storage ring has been performed. Two kinds of a lattice are examined as a lattice of the proton storage ring for neutron science project. One is FODO lattice and the other is Triple Bend Achromatic (TBA) lattice. Each lattice has zero dispersion regions and long straight sections. The betatron variation around the ring of the FODO lattice is smooth[2]. Such a property will minimize the possible envelope oscillation for beams with large space charge tune shift. There are long straight sections in the TBA lattice. Such a property will give enough space for injection, rf cavity, and extraction. The consideration of beam dynamics , instabilities, injection scheme, and extraction scheme for each lattice is important to decide which is better lattice for the proton storage ring. This is the main subject for our study of the ring. This paper describes preliminary results of the lattice design for the proton storage ring.

Table 1 Basic parameters of the proton storage ring

Beam Average Power	2.5 MW / ring
Kinetic Energy	1.5 GeV
Average Current	1.67 mA / ring
Repetition Frequency	50 Hz
Linac Peak Current	30 mA
Linac Pulse Length	3.72 ms
Number of Turns Injected	2777 turns/ ring
Injected Pulse Length	400 ns
Injected Beam Gap	270 ns
Harmonic Number	1
Revolution Frequency	1.49 MHz
Circumference	185.4 m
Magnetic Rigidity	7.51 Tm
Circulating Current	49.75 A / ring
No. of Circulating Protons	2.08×10^{14} protons / ring
Injection Beam	2πmm.mrad
Emittance	(100% unnormalized)
Momentum Spread	±0.4%

2 LATTICE

Two kinds of the magnet lattice are studied for the proton storage ring. One is 20 cell FODO lattice and the other is Triple Bend Achromatic (TBA) lattice. A large transverse beam emittance is required in the ring to restrict the transverse space charge tune shift. The chosen values for an un-normalized 100% transverse emittance of an injected H^- beam, a ring acceptance and a collimator acceptance are 2πmm-mrad, 530πmm-mrad, and 200πmm-mrad, respectively. This transverse emittance restricts the space charge tune shift to less than 0.1. The parameters of the 20 cell FODO lattice and the TBA lattice are shown in Table 2.

The betatron variation around the ring of the FODO lattice is smooth. Such a property will minimize the possible envelope oscillation for beams with large space charge tune shift. There are long straight sections in the TBA lattice. Such a property will give enough space for injection, rf cavity, and extraction. The consideration of beam dynamics for each lattice is important to decide which is better lattice for the proton storage ring. This is the main

0-7803-5573-3/99/$10.00@1999 IEEE.

subject for our study of the ring. Parameters of the FODO lattice and TBA lattice are shown in Table2. It is possible to get a dynamic aperture of 4000πmm.mrad and wide tune variations for horizontal tune and vertical tune for each lattice. For the tune variations, there is a strong dependence between horizontal tune and vertical tune for TBA lattice. Therefore the tunability of TBA lattice is not so good, however this is not a serious problem for the lattice.

Table 2 Parameters of the FODO lattice and the TBA lattice

	FODO	TBA
Super Periodicity	4	4
Operating Tune	(4.84, 4.78)	(3.75, 2.8)
Chromaticity	(-4.70, -5.28)	(-3.52, -6.01)
Transition Energy	4.51	5.59
Slippage Factor	-0.099	-0.11
Space Charge Tune Shift	<-0.1	<-0.1
Momentum Spread	±0.365%	±0.34%
Physical Acceptance	200πmm.mrad	200πmm.mrad
Dynamic Acceptance	4000π mm.mrad	4000π mm.mrad
Tune Variation	$4.1<\nu_x<5.9$ $4.1<\nu_y<5.9$	$2.1<\nu_x<3.9$ $2.1<\nu_y<3.9$
Magnets		
Bending	1.0T	1.0T
QD	-2.4 ~ -4.1T/m	-4.0 ~ -7.3T/m
QF	2.5 ~ 3.3T/m	6.0 ~ 8.4T/m
RF Cavity		
Fundamental Frequency	1.49MHz.	1.49MHz
Harmonic Number	1st+2nd+3rd	1st+2nd+3rd
Voltage	30+30+12kV	30+30+12kV
Extraction Kicker Magnet		
Reflection Angle	9mrad	12mrad
Magnetic Field Strength	0.02T	0.03T
Total Magnetic Length	3.4m	3.0m

3 BEAM INJECTION SCHEME

There is a main source of beam loss in an injection area and hence the most critical item for the ring because the main loss is due to H^- or H^+ beam intersection with a stripper foil during and after injection. H^- injection method in which H^- beam is converted to H^+ beam with the stripping foil located in the injection magnet is adopted for the storage ring. In this method H^0 atoms emerging from the stripper foil are in a distribution of excited states resulting from the stripping reaction $H^- \rightarrow H^{0*}(n) + e^-$ where n is the principal quantum number. The lifetime of H^0 atoms depends on the Stark state in the magnet [3]. The lifetime of 1.5GeV H^0 atoms was calculated[2]. It was obvious from this calculation data that the H^0 atoms with $n \leq 4$ remain as H^0 and may be removed from the ring, and atoms with $n>5$ rapidly become H^+ and are accepted in the ring with the injection magnet whose strength of the magnetic field is 0.15T. The injection scheme which should be adopted to reduce the beam loss in the ring has been studied.

A large transverse beam emittance is required not only to restrict the transverse space charge tune shift but also to reduce the circulating proton beam intersection with a stripping foil. To obtain the large transverse emittance the phase-space painting is also considered [4]. Injection schemes of the FODO lattice and TBA lattice are shown in Fig.1. For the TBA lattice a set of 4 pulsing and 2 fixed field dipole and a set of 4 pulsing and 1 fixed field dipole for FODO lattice will be used to create an orbit bump to paint the injection proton population into the optimum phase space. The optimum distribution will be determined by computer simulation. The H^- ions which missed the stripping foil and H^0 atoms emerging from the foil should be disposed in proper beam dump. A thick stripping foil which is placed in the path of the H^0 atoms converts entire beam to protons. The H^- ions bent by the downstream low magnetic field bending magnet for TBA lattice and by the downstream quadrupole for FODO lattice will travel to the high magnetic field bending magnet, and because of the high magnetic field, they will be stripped to H^0 atoms in the field. A thick stripping foil which is placed upstream the bending magnet strips H^0 atom to protons.

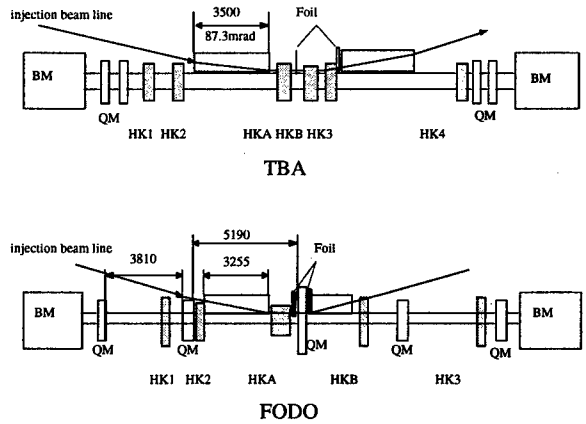

Fig.1 Injection scheme of the TBA and the FODO lattice

4 BEAM EXTRACTION

The fast extraction method is used from the request of the neutron scattering experiment. In this extraction method, when injection of all bunches is completed, accumulated beam is extracted from the ring during 1 turn. An interval

between bunches is 270ns from the injection beam pulse structure which is chopped to 670ns bunch width with 60% duty cycle. It is necessary that the magnetic field of a kicker magnet is enough to extract the beam from the ring to less than 270ns and is kept with the strength to more than 400ns. In fact, the required field rise time of kicker magnet is less than 150ns considering the increase of the beam bunch due to synchrotron oscillation and divergence by the space charge effect during multi-turn ring injection. When the un-normalized 100% emittance and beta function are 200πmm-mrad and 15m, respectively, the reflection angle becomes about 8.7 mrad. A kicker magnet of 0.02T and 3.4m is required in order to realize this extraction process.

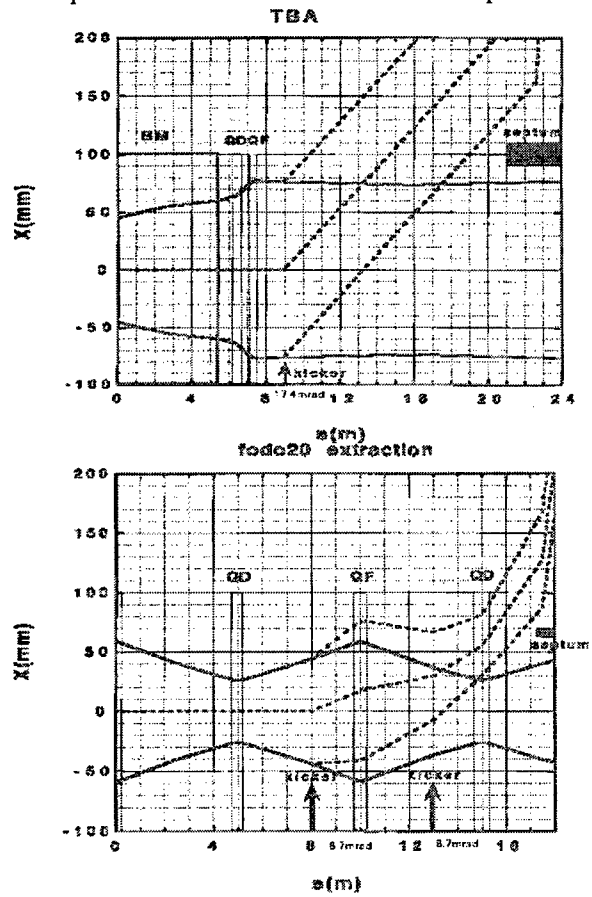

Fig.2 Beam extraction orbits

Figure 2 shows the extraction beam orbit for TBA lattice and FODO lattice. Because there is a long straight section with zero dispersion in TBA lattice, it is easy to install kicker magnets to extract the proton beam from the ring.

5 SUMMARY

Two kinds of a lattice are examined as a lattice of the proton storage ring for neutron science project. One is FODO lattice and the other is Triple Bend Achromatic (TBA) lattice. In order to decide which is better lattice for the proton storage ring, we considered of beam dynamics , injection scheme, and extraction scheme for each lattice. From these considerations, it was not decided better lattice for our proton storage ring. This study will be continued based on these two kinds of lattice.

6 REFERENCES

[1] M.Mizumoto et al. : 'High Intensity Proton Accelerator for the Neutron Science Project at JAERI', Proc. of the 1st Asia Particle Accelerator Conference, KEK March 1998, to be published

[2] M. Kinsho et al. : 'A Study of the Proton Storage Ring for the Neutron Science Project at JAERI', Proc. of the 6st European Particle Accelerator Conference, Stockholm, Sweden, June 1998, to be published

[3] R. Damburg and V. V. Kolosov : Theoretical studies of hydrogen Rydberg atoms in electric fields, eds. R. F. Stebbings and F. B. Dunning, "Rydberg states of atoms and molecules", Cambridge University Press, 1983, p31-71

[4] F. Noda et al, : 'A Beam Simulation of the Proton Storage Ring for the Neutron Science Project', Proc. of the 11th Symposium on Accelerator Science and Technology, Spring-8 21-23 October 1997, p350-352

THE RF SYSTEM FOR THE 3RD HARMONIC CAVITY OF ALS*

C.C. Lo**, J. Byrd, R. Rimmer, K. Baptiste and J. Julian
Advanced Light Source Division
Lawrence Berkeley National Laboratory
1 Cyclotron Road,
Berkeley, CA 94720

Abstract

A higher harmonic cavity system is under construction in the ALS to extend beam lifetime. The implementation will be carried out in stages. The plan is to operate the system in the passive mode as a start and, depending on various factors, the plan may evolve into an active system eventually to attain the optimum beam lifetime at all beam current levels. The RF system must be designed accordingly to support the various stages of implementation. This report will describe the various RF systems along the path leading to the fully implemented system.

Introduction

To a user of synchrotron radiation, the beam lifetime is one of the most important aspects of a synchrotron light source. In low to medium energy storage ring light sources, the lifetime is usually dominated by large-angle intrabeam (Touschek) scattering in which elastic collisions of electrons within the bunch have a finite probability of transferring enough longitudinal momentum to each electron such that they no longer are within the momentum acceptance of the storage ring and are lost. This process is particularly important for storage rings such as the Advanced Light Source (ALS) because of the high density of electrons resulting from the small transverse beam size. One proven method for increasing the lifetime from Touschek effect without compromising the transverse beam brightness is to reduce the peak charge density of an electron bunch. This requirement can be met by adding a second voltage to the 500MHz main RF voltage with an amplitude and phase such that the slope at the bunch center is zero. The energy distribution is unaffected but the bunch lengthens and the peak charge density decreases and the lifetime improves. This voltage must be a higher harmonic of the main RF voltage.

We have chosen to add five third harmonic (1.5GHz) cavities to the storage ring to achieve the goal. Furthermore we are going to start with a passive system using the beam to induce the required voltage in the cavities. This mode of operation will enhance the beam lifetime at higher beam current. A complete discussion on this subject are given in reference 1 and 2.

Cavity

The ALS third harmonic cavity is a single cell re-entrant type resonator much like the two main 500MHz cavities. The cavity shape and size were modeled with Urmel and Mafia extensively before cutting metal. Figure 1 shows a picture of the final shape of the cavity design.

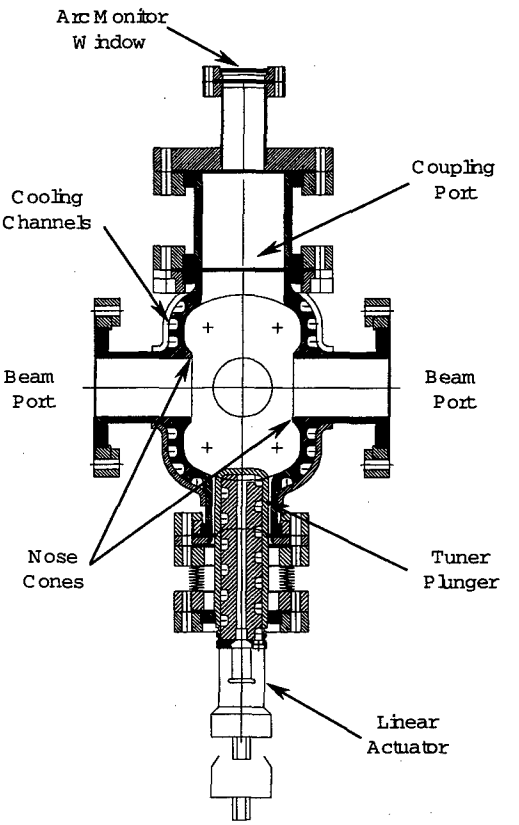

Fig. 1 The ALS Third Harmonic Cavity

There are a total of six ports on the cavity body, two beam ports, two tuner ports, one coupling port and one other port for signal probe. The shunt impedence of the cavity with all the ports is about 1.5Mohm and the loaded Q is about 12000. Detail design, modeling and construction technique are given in separate reports[3,4].

0-7803-5573-3/99/$10.00@1999 IEEE.

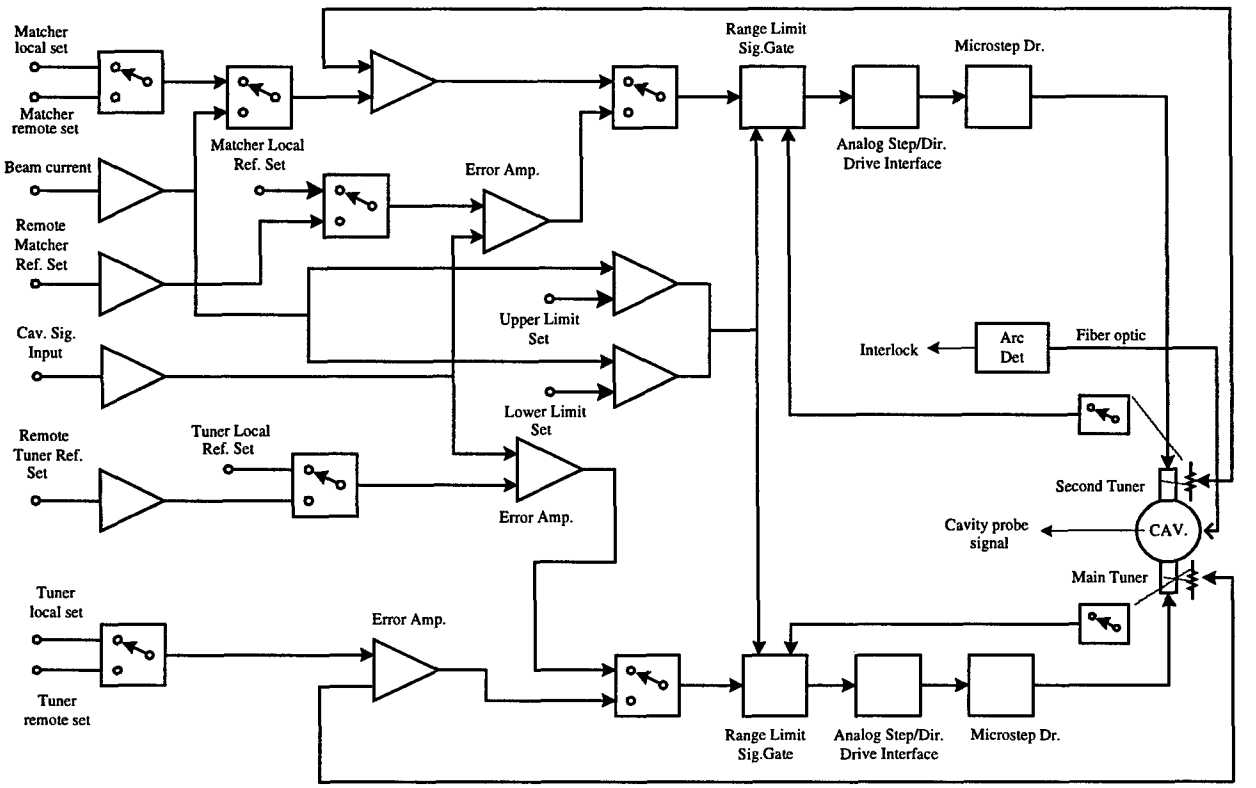

Fig. 2 ALS Third Harmonic Passive RF System Block Diagram

The Passive RF System

Figure 2 shows the block diagram of the passive RF system. Since we are not using the coupling port in this phase of operation, an arc detector will be mounted on this port to monitor cavity arcing. This detector will shut off the main RF system and hence the beam when an arc is detected. The main tuner can be controlled either manually or with the amplitude loop. Each cavity has its own amplitude loop that can be tuned off resonance individually and parked at some frequency that would not affect the main RF signal. A second tuner is installed in a side port. This tuner is manually settable via remote control and could possibly be used for tuning HOMs to safe frequencies. With the passive system, the power of the cavities comes from the main 500MHz RF system via the beam. Each cavity will require 5kW of power, therefore, 25kW of additional power will be taken from the main RF system. The total maximum voltage produced by these five cavities is 500kV, one third of that of the main RF voltage at the optimum level.

The operation of this phase one system can be summarized as the following:

At maximum beam current level, the cavities will be tuned right at resonance and then de-tuned to a higher frequency to set the voltage operating point at a level lower than the resonant peak. As the beam current decays, the tuner will tune the cavity back towards resonance to keep the voltage amplitude constant. It is obvious that this tuning scheme would only work through a limited beam current range, and also this amplitude can only be set to one optimum operating point[1].

The phase-two version of the passive system or an active system, as the case may be, will include a tunable wave guide coupler (not shown) that will be mounted on top of the input port of the cavity where an arc detector is located at this time. The adjustable coupler could be used to set the coupling factor to a to an optimum value according to the beam current or a predefined value in a feed forward scheme. This will maintain an optimum voltage in the cavity for maximum beam lifetime operation across most of the spectrum of the beam current. The detail of such scheme and specifics of future RF system will be formulated as we gain more experience in the performance of this phase one passive system.

The Amplitude Loop Control Module

There are two separate loops in this module as mentioned in the last paragraph. See fig. 2. In this phase one system, one loop is used by the tuner to hold the cavity voltage amplitude constant at a predetermined value, the other loop is used to set the second tuner position in the 'loop open' mode. This second loop was intended for a tunable matching coupler for the phase two passive system or an active system. In this phase one operation this is used for controlling a second tuner. When operating in the closed loop mode the main tuner is actively engaged to hold the cavity voltage amplitude constant. Caution must be exercised to make sure that the loop is active only in a well defined range of beam current. Outside of this range the loop must be deactivated and the tuner plunger will hold its position until such time the beam current would fall back to within the operational range of the system again. This window is extremely important to prevent run away tuners causing de-tuning of all the cavities. The amplitude loop control module has been designed to have maximum flexibility to accommodate various operational requirements. The same module can be used to control klystron output power should an active system be implemented in the future.

The Active RF System

In the active RF system only 4 cavities will be needed to generate the 500kV of voltage required. We intend to power each cavity with a separate klystron. Each klystron will be capable of providing at least 5kW of RF power. In the active system there will also be a phase loop that keeps the RF phase constant by using the cavity main tuner. The amplitude loop, in this case, will be using either the klystron's modulation anode or the klystron's drive power as the amplitude control element. At the input coupling port of each cavity there will be an adjustable coupler to set the coupling factor to the desirable value. The setting of this coupling factor may be done according to the beam current or some other parameters. The fiber optic of the arc detector will be moved to either the second tuner port or could be installed side by side with the cavity signal pick up probe. The active system will require RF windows. We will mostly likely locate the windows away from the cavity input port to reduce undesirable effects of RF heating and breakdown due to high cavity electric field. The signal source in the active RF system will be derived from the main storage ring cavity probe signals to keep the third harmonic RF voltage phase locked to that of the main cavities.

Conclusions

All sections of this project are progressing well. We expect to commission the phase-one passive system in June 1999. Results from operation will determine which direction the next step would be. Most components in this phase-one passive system have been designed with the possibility of upgrading to either the phase-two passive system or an active system.

Acknowledgement

The authors thank Tom Henderson, Dave Plate of LBNL and their mechanical group for the complex mechanical design of the system and Mark Franks of LLNL and his group's diligence and expertise of manufacturing the cavities.

References

1. John Byrd et.al., "Design of a higher harmonic cavity for Advanced Light Source", In preparation.
2. A. Hofmann and S. Myers, "Beam dyanmics in a double RF system", Proc. Of the 11th Int. Conf. On High Energy Acc. ISR-TH-RF/80-26 (1980)
3. Robert Rimmer et.al., PEP-II EE note 97.07.
4. R.M. Franks, et.al., "Fabrication Process for the PEP-II Cavities", Proc. of the 1997 Part. Acc. Cong., Vancouver, B.C.

*Work supported by the Director, Office of Energy Research, Office of Basic Energy Science, Materials Science Division, of the U.S. Department of Energy under Contract No. DE-AC03-76F00098

** cclo@lbl.gov

CHARGED PARTICLE STORAGE DEVICE

Frank Krienen, Boston University

Abstract

This paper deals with the motion of charged particles in a magnetic bottle.

The realization entails an assembly of current loops, which in the present treatment is simplified to three components: a solenoid and two dipoles. For a given configuration of the magnetic field and the initial position and momentum of the particles, it has been found that the particles can be stored in a racetrack-like fashion, looping around at near constant radius, somewhat toe-ing in upon reflection from the repeller at the end of the bottle.

1 EQUATION OF MOTION

The disposition of the magnetic components is shown in Figure 1. We identify 4 parameters which determine the magnetic field, namely the distance a of the dipoles to the median plane, the field B of the solenoid and the moments of the upper dipole b' and the lower dipole b".

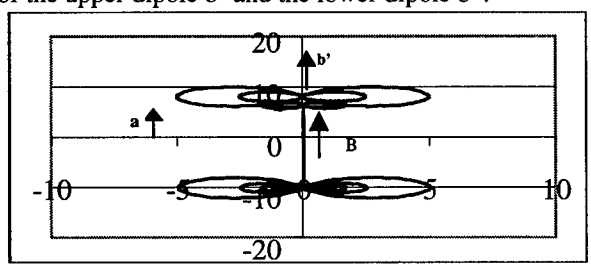

Figure 1: Magnetic Components

A relativistic Hamiltonian which is θ-independent contains only one tangential component A of the magnetic potential.

$$H=[P_r^2*c^2+\{P_\theta/r-e*A\}^2*c^2+P_z^2*c^2+m^2*c^4]^{1/2} \quad (1)$$

The contribution to A of a dipole in the origin will be

$$\mathbf{A}_{dipole}=(\mu/(4*\pi))*\mathbf{m}\times\nabla(1/r)_{spherical} \quad (2)$$

where **m** is located on the z-axis. We obtain in cylindrical co-ordinates:

$$A_{dipole}=(\mu*|\mathbf{m}|/(4*\pi))*r/(r^2+z^2)^{3/2}=b*r/(r^2+z^2)^{3/2} \quad (3)$$

$$b=\mu*|\mathbf{m}|/(4*\pi) \quad (4)$$

The contribution to A of a solenoid is $A_{sol}=B*r/2$ (5)

The contribution to A of the system shown in Fig.1:

$$A=B*r/2+b'*r/[r^2+(z-a)^2]^{3/2}+b''*r/[r^2+(z+a)^2]^{3/2} \quad (6)$$

$$B_r=-\delta A/\delta z=3*b'*r*(z-a)/[r^2+(z-a)^2]^{5/2}+$$
$$+3*b''*r*(z+a)/[r^2+(z+a)^2]^{5/2} \quad (7)$$

$$\delta A/\delta r=B/2+b'*[(z-a)^2-2*r^2]/[r^2+(z-a)^2]^{5/2}$$
$$+b''*[(z+a)^2-2*r^2]/[r^2+(z+a)^2]^{5/2} \quad (8)$$

$$B_z=A/r+\delta A/\delta r=B+b'*[2*(z-a)^2-r^2]/[r^2+(z-a)^2]^{5/2}$$
$$+b''*[2*(z+a)^2-r^2]/[r^2+(z+a)^2]^{5/2} \quad (9)$$

$$dr/dt=\delta H/\delta P_r=P_r*c^2/H \quad (10)$$

$$d\theta/dt=\delta dH/\delta P_\theta=\{P_\theta/r-e*A\}*c^2*r^{-1}/H \quad (11)$$

$$dz/dt=\delta H/\delta z=Pz*c^2/H \quad (12)$$

$$dP_r/dt=\delta H/\delta r=\{P_\theta/r-*A\}*\{P_\theta/r+e*r*(\delta A/\delta r)\}*c^2*r^{-1}/H \quad (13)$$

$$dP_\theta/dt=-\delta H/\delta\theta=0 \quad (14)$$

$$dP_z/dt=-\delta H/\delta z=\{P_\theta/r-e*A\}*\{e*r*(\delta A/\delta z)\}*c^2*r^{-1}/H \quad (15)$$

substituting (11) in (13) and (15):

$$dP_r/dt=(d\theta/dt)*\{P_\theta/r+e*r*(\delta A/\delta r)\} \quad (13a)$$

$$dP_z/dt=(d\theta/dt)*\{e*r*(\delta A/\delta z)\} \quad (15a)$$

2 MEDIAN PLANE

2.1 Parallel Dipoles (b'=b")

In the median plane, z=0, B_r=0, so that the symmetry is:

$$B_r(r,z)=-B_r(r,-z) \text{ and } B_z(r,z)=B_z(r,-z) \quad (16)$$

We will track charged particles which start off the median plane, perpendicular to it and at a given momentum and look for conditions so that the particle is reflected and crosses the median plane again perpendicular to it. In this case the crossing occurs at the same initial radius and momentum but not necessarily at the same θ. This particle continues to be reflected and upon every reflection there will be a constant phase advance Δθ, so that the particle seems to meander in space.

If the phase advance per half cycle can be written like Δθ=k*π/n, k and n integer and k/n irreducible, the particle track closes upon itself, provided k=odd, after 2*n half-cycles. If k=even, the track collides upon itself after n half-cycles. Thus for a given configuration (a,b',b",B), we may be able to establish the relation $(r,\Delta\theta,p_t)$, where p_t is the total momentum.

The method of calculating the system of first order differential equations, eq.(10) through (15) is that of *Runge-Kutta*, or its variants. We resort to this method because it is highly unlikely that an analytical solution can be found for the above magnetic field profile -and- if found, highly unlikely that such field can be realized. In fact, we look for an existence proof by trial and error, and consider a successful outcome for p_t a resonance.

2.2 Anti-parallel dipoles (b'=-b")

For B=0: $B_r(r,z)=B_r(r,-z)$ and $B_z(r,z)=-B_z(r,-z)$ (17)

Applying the method of *3.1*, a resonance shows that the phase advance of the second half cycle changes sign, so

that the particle follows a closed loop, having the shape of a race track in elongated structures, (r<<a).

3 SCALING ALGORITHMS

The solution of a system of first order differential equations, resulting from the expression for H, eq.(1), via the Runge-Kutta method is quite laborious. The following *scaling algorithms* may alleviate the work.

3.1 Mass-less Particles In the absence of an electric potential, the momentum of the particle determines its path: the mass is irrelevant. Thus one might as well calculate trajectories of *mass-less* particles having an electronic charge. Such fictitious particles travel with the speed of light, facilitating comparison.

3.2.Momentum Particles with different momentum would have identical trajectories if one scales b',b" and B, but not a, proportionally to the momentum ratio.

3.3 Linear scaling λ of the device would scale a given trajectory to the extent that at each corresponding point the radius of curvature is increased by a factor λ. The solenoid does not scale, λ^0. The dipole field scales as λ^{-3}, hence we need to scale b' and b" by λ^3 to assure the same magnetic field in corresponding points. It follows that one must scale the momentum by a factor λ^1 to agree with the larger radius of curvature.

3.4 Multiple charged particles would follow the same trajectory if b',b" and B are reduced in the same ratio.

3.5 Phase Advance. All of the above does not affect the phase advance nor any spatial angle in comparable points of either trajectory.

3.6 Scenario Clearly, the above mentioned *scenarios* may be applied one after the other, ad infinitum.

4 SOME CONSIDERATIONS

A solenoidal magnetic field may modulate the phase advance considerably, but, since the effect is predominantly in the region where the particle approaches its apogee, an assembly of circular current loops will have the same outcome. In fact, a concentration of current loops , situated near z=±a may simulate the above mentioned dipoles, but, computationally, the magnetic potential equation (6) is easier to use.

The apogee of a trajectory is characterized by P_z=0, but a resonance requires in addition P_r=0.

With respect to this turning point, the co-ordinates r and z are symmetric and the co-ordinates P_r, P_z and θ are anti-symmetric, as will be shown in subsequent Figures.

For a given set of parameters (a,b',b",B), resonances turn out to be multi-valued. The simplest pattern seems to be related to the highest momentum and highest penetration into the mirror and may be most useful.

The total momentum vs. the radius follows more or less an inverse square power of r; corrections thereto seem to agree with: $p_{total} \propto (r^{-2}+a^{-2})$, (r<a) (18)

For each iteration , the co-ordinates are fed back into (1), resulting in a chart dH/H vs. time. The area above and below the abscissa seems to cancel out fairly well upon crossing the median plane. Fig.2c shows an example.

A *Variable Iteration Step* is applied, based on the radius of curvature R and the slope α of each of the co-ordinates: See Fig.2b.The *Iteration Step* $\propto 1/\Sigma(1/(R*\cos\alpha))$ (19)

A race track may have adjacent branches moving in opposite direction. This would suggest to fill the bottle with one or more monochromatic particle beams until all branches are filled. If the moving charges remain trapped for measurable and useful time spans, a sudden electro – magnetic disturbance could merge adjacent branches, opening a new way to measure cross sections or reaction rates, either nuclear or chemical.

In this respect collisions occur with equal and opposing momentum in the laboratory frame, independent of the mass of the participating species.

The self-magnetic field of multi-prong beams evenly distributed in a circular shell tend to be less than distributions concentrated in only a few branches.

A small value of B of the solenoid does modulate the kinematics at the apogee appreciable, but the main function of B is to reduce the spatial divergence of the multi-prong particle beams.

5 NUMERICAL RESULTS

The parameters for a trajectory may be written in two arrays: *i) the system parameters* (a,b',b",B,e,m,c,H) and *ii) the initial values* $(t,r,\theta,z,P_r,P\sim_\theta P_z)_{initial}$

We note that $P\sim=(P_\theta/r-e*A)$= *the tangential momentum* .

In view of the *scaling algorithms*, it is sufficient to treat only cases where m=0 and e is a single electronic charge. Table 1. Shows the dimension of the system parameters:

Table 1: System Parameters

Distance from Dipoles to Median Plane (m)	a
Upper Dipole Strength (Tesla*meter^3)	b'
Lower Dipole Strength (Tesla*meter^3)	b"
Solenoid Strength (Tesla)	B
Light Velocity (m/s)	c
Total Energy (eV)	H

The calculation is best done with dimensionless values. In this respect, the initial array transforms as

$(t,r,\theta,z,P_r,P\sim_\theta P_z)_{initial}=(T,u,v,w,U,V\sim,W)_{initial}$

The relation between corresponding values is shown in Table 2.

Table 2: Conversion Ratio

T=t*c/a	u=r/a	v=θ/(2*π)	w=z/a
U=c*P_θ/H	V~=c*P~/H	W=c*P_z/H	V=c*P_θ/(a*H)

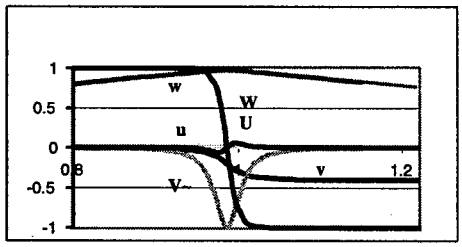

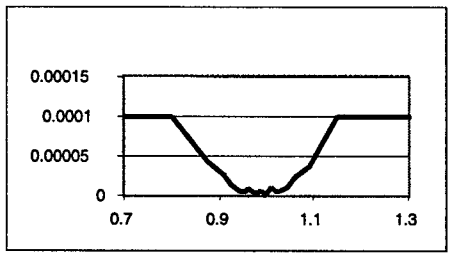

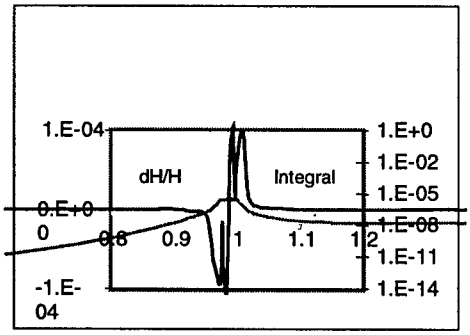

Figure 2 is a 2-Prong Race Track. (b =-b), u(0)=0.02
Figure 2a: Co-ordinates vs. Time.
Figure 2b: Shows (dT) vs. Time.
Fig.2c: Shows (dH/H) vs. T, and ∫(dH/H)dT vs.T
(a,b,b ,BH)=(5,5E-6,-b ,0,43720).

This case is scaleable for electron cooling of, say, 9 GeV/c antiprotons that may have a cooling length of 2*a=30 m and $H_{electron}$=4.92 MeV

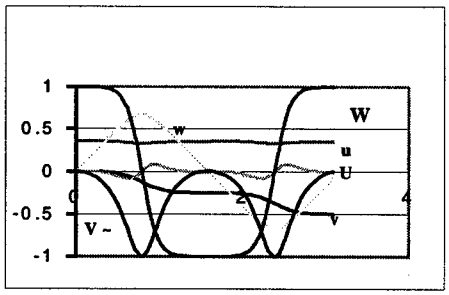

Figure 3a Coordinates vs. Time

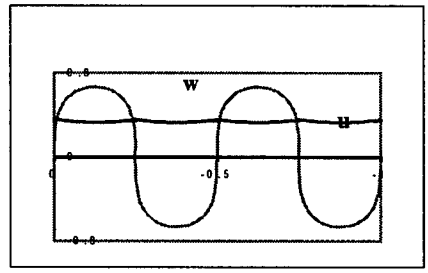

Figure 3 is a Closed 4-Prong Loop u(0)=0.0355
Fig.3a shows (u,v,w,U,$V_\perp$,W) vs. T. Fig.3b shows (u,w) vs. v, (a,b,b ,BH)=(0.2,5E-6,b,0,98000).

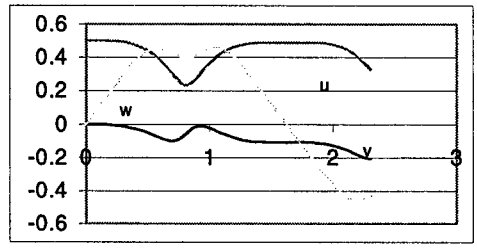

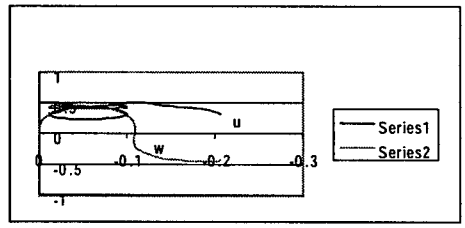

Figure 4 is a Multi-Valued Resonance.

Fig.4a shows (u,v,w) vs. T and Fig.4b shows (u,w) vs. v
u(0) = 0.5. (a,b.b ,BH) = (0.2,5.2E-5,b,1E-3,254558)

6 DISCUSSION

No attempt has been made in this paper to devise means to focus stored particle beams. The author conjectures that for short enough time spans, some sort of confinement is possible. For instance the study of cross sections and reaction rates of nuclear or chemical species are head-on, of equal momentum in the laboratory frame, do not need real time and feature independence of the mass of either species.

But in cases of production, such as fuel or chemistry or electron cooling, focusing the beams is of importance. The possibility of organizing the storage in circular shells and/or in several concentric shells, where adjacent beams move in opposition, may alleviate the issue of magnetic pressure or the issue of efficiency or both.

The injection of charged particle beams seems quite feasible: the beams will be bunched in any case and the switching on or off is current practice.

Charge neutrality is again a big issue: the pulsed nature of the device may help to cope with this feature.

NEW DESIGN AND DEVELOPMENT OF 13 MeV PET CYCLOTRON IN KOREA*

J.S.Chai†, J.H. Ha, H. Y. Lee, Y. S. Kim, KCCH, Korea
S. Oh, M. Yoon, Dept. of Physics, POSTECH, Korea

Abstract

Since 1997 design studies have been in progress in a joint collaboration between the Korea Cancer Center Hospital (KCCH) and the Pohang University of Science and Technology (POSTECH) for a 13 MeV PET (Positron Emission Tomography) cyclotron. It will accelerate H^- (negatively charged hydrogen) ions, which, after acceleration, will be stripped of its electrons by a stripping foil and then, on entering the target chamber, interact with the target material to produce positron emitters such as ^{18}F, ^{15}O, ^{13}N and ^{11}C. In this paper we describe the main features of the cyclotron.

1 INTRODUCTION

The era of nuclear medicine started in Korea in the 1960s when the research reactor TRIGA Mark-2 (which was installed at the site of the former Korea Atomic Energy Research Institute in Seoul) began to supply radio-isotopes to KCCH. By the early 1980s however, it was recognized that the species of radio-isotopes that were available from the nuclear reactor were rather restricted and therefore it was felt that an isotope production cyclotron was needed. In 1986 the KCCH's 50 MeV cyclotron, which was built and supplied by Scanditronix, started operation to produce radio-isotopes on site. In the mid-1990s, the benefits of the PET began to be recognized by some of the major hospitals in Korea and, by 1996, two hospitals in Seoul, Korea had installed in-house PET cyclotrons. At KCCH, increasing desire for an uninterrupted, reliable and timely supply of the radio-isotopes to customers and patients has prompted obtaining a dedicated 5-13 MeV cyclotron for PET applications (this energy range contains one of the optimum yield peak for ^{18}F production) and, at the same time, pursuing the purchase of another 30 MeV medical cyclotron for isotope production in the very near future. A decision has been made to obtain an in-house built PET cyclotron this time. This will not only ease the problems associated with maintenance during operation but will also keep the door open for continuous upgrading of the machine in the future. The project is supported by the Ministry of Science and Technology of the government, as a part of the 2nd phase of the mid- and long-term nuclear energy research plan. The cyclotron design study project was approved in 1997, but a formal approval for construction is expected to be given in April 1999. The cyclotron consists of a cyclotron magnet, rf dees and resonators, the vacuum chamber, an ion source, power supplies, an H-beam stripping foil and its holders, internal targets and chambers, and control systems. In the following sections, the design features of the cyclotron magnet, dees and resonators and the ion source will be described.

Table I : Main parameters of the 13 MeV PET cyclotron

Parameter	Unit	Value
Maximum energy	MeV	13
Beam species		Negative hydrogen
Number of sectors		4
Ion source		Internal negative PIG
Hill angle	degrees	46.0
Valley angle	degrees	44.0
Maximum average magnetic field	T	1.2
Harmonic number		4
Radio-frequency	MHz	72
Maximum average radius of a beam	cm	43
Maximum orbit distance from the cyclotron center	cm	45
Maximum magnetic field at the hill center	T	1.85
Maximum magnetic field at the valley center	T	0.48
Beam current	μA	$\sim$20

2 CYCLOTRON MAGNET AND CYCLOTRON DESIGN PARAMETERS

The cyclotron magnet consists of poles, pole-tips, return yokes, top and bottom return plates and excitation coils. The magnet has a four-sector radial ridge geometry with a rather large valley-gap to hill-gap ratio. This choice, together with the choice of the fourth harmonic mode of operation for particle acceleration, will provide relatively strong axial focusing while at the same time leaving ample space for placing dees. Table I shows the main design parameters for this 13 MeV PET cyclotron. The hill is constructed from eight pieces of wedge-shaped high quality, low carbon content (0.003 %) steel plates with a wedge angle of 46 degrees. The angular width measured from the center of the cyclotron will, however, be a varying angle from close to zero near the center of the cyclotron to close to 46 degrees near the outer edge of the cyclotron. The side edges of these plates are stepped to provide bolt holes to attach the plates to the poles. The inner surface of these plates are also stepped progressively with radius to provide an appro-

* This work is supported by Ministry of Science and Technology of Korean government
† Email: jschai@kcchsun.kcch.re.kr

0-7803-5573-3/99/$10.00@1999 IEEE.

priate isochronism throughout the radius. The step heights needed are calculated using TOSCA [1], a commercially available three dimensional magnetic field program. The accuracy of the magnetic field predicted by the program is expected to be in the range of 2%. Fig. 1 is a schematic diagram of the cross sectional view seen from a side. A 16 cm diameter hole in each valley is provided to serve for pumping and rf power connection to the dees. A more detailed description for the magnetic field is presented separately in these conference proceedings and elsewhere [2, 3].

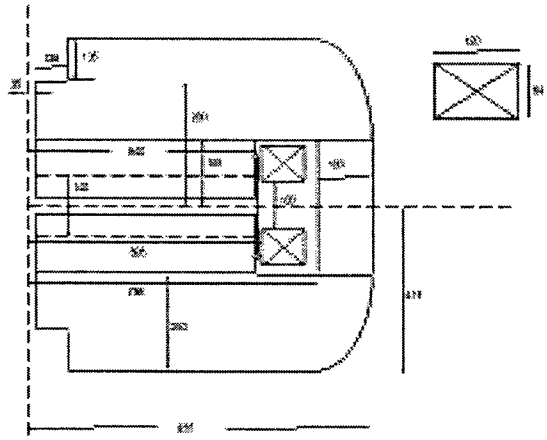

Figure 1: Cross-sectional side view of the cyclotron.

3 DEES AND RESONATORS

The dees we aim to design are supposed to provide an energy gain of 160 keV per H^- ion revolution in the magnetic field of the cyclotron. We decided to accelerate the ions in the fourth harmonic mode of particle revolution frequency, corresponding to 72 MHz. Accordingly a pair of dees with azimuthal width of 43.6°, radial length of 48 cm, vertical height of 3 cm with a vertical gap of 1.25 cm between the dee and the liner, was design studied. The power will be fed to the dee-resonator system by an inductive coupling. For the design studies we used SOPRANO, a commercial software supplied by the Vector Field Company. With the use of this software the rf electric field in the region between the dee electrode and the ground shield liners are investigated. The result showed that, to obtain 40 kV peak-to-ground rf voltage we need 10 kW in rf power. The appropriate dimensions of the rf dee and cavity can be obtained from the effective $\frac{\lambda}{4}$ wave method with zero-impedance at 72 MHz and it turns out to be 124 cm. In the design of the above resonator, due consideration was given for the dee-dee liner distance and the co-axial cavity length. The zero crossing result is shown in Fig. 2.

The adequacy of the chosen dimensions for the dee-resonator system was comfirmed from the voltage-current relation as a function of cavity length. As shown in Fig. 3., the cavity resonates at 72 MHz and maintains almost constant voltage distribution over the entire dee length. A test bench cavity was constructed for further study in the very near future.

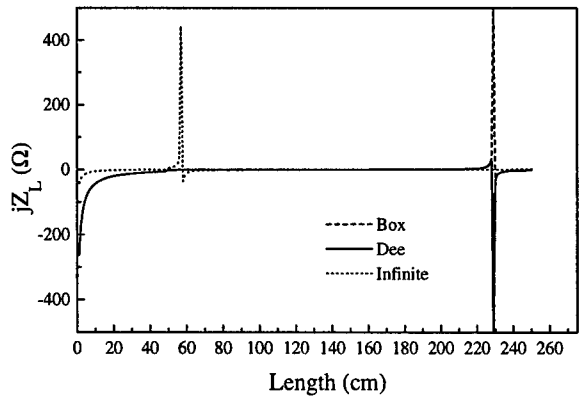

Figure 2: Calculated impedance as a function of cavity length.

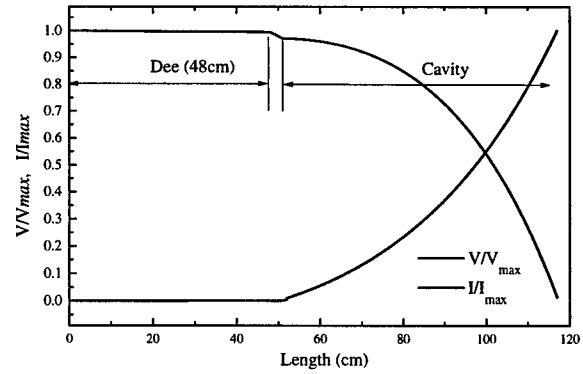

Figure 3: Current and voltage distribution as a function of cavity length.

4 INTERNAL PIG SOURCE

An internal PIG source is located near the center of the cyclotron magnetic field and produces H^- ions. The H^- PIG source is known to release a large amount of hydrogen gas (both atomic and molecular) out into the cyclotron central region. To minimize the gas stripping losses of the accelerated H^- ions, we plan to install two diffusion pumps with 20 cm diameter. A pair of 16 cm vertical holes are provided in each valley of the cyclotron magnet. Fig. 4 shows the schematic diagram of the PIG ion source.

The cathode is envisaged to be made of LaB_6 with tantalum coating. A prototype PIG source was constructed and is now placed in a circular magnet with a field strength of 0.4 Tesla. The source is being tested and studied for further improvements. Computer studies of the beam dynamics from the ion source through several turns will be carried

out. At the same time, we are constructing a model of the 13 MeV cyclotron central region to carry out experimental beam dynamics studies for up to 1 MeV acceleration. The model cyclotron has a uniform magnetic field of 1.2 Tesla, a figure which is identical to the field strength at the center of the 13 MeV cyclotron. A pair of dee-tips will be installed inside and 40 kV of rf at 72 MHz will be fed to it. The purpose is to investigate the optimum central region geometry experimentally as well as theoretically.

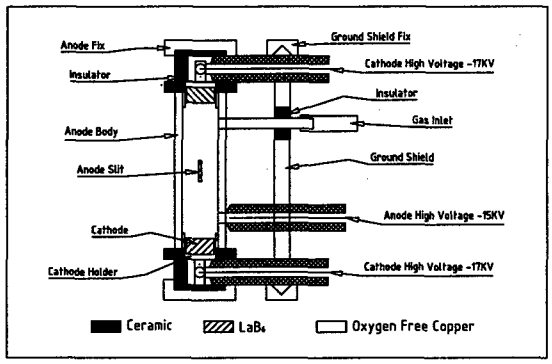

Figure 4: Schematic drawing of the PIG ion source

5 CONCLUSION

Design studies for a 13 MeV PET cyclotron are underway in KCCH and POSTECH. It is aimed at operation in 2002.

6 REFERENCES

[1] Commercial package by Vector Fields Co.

[2] M. Yoon, J.S.Chai, J.W.Kim, W.Y.Yang and S.Oh, Proceedings of the International Cyclotron Conference, Caen, France,1998

[3] S. Oh, W.Y. Yang, M. Yoon, J.S.Chai, J.H. Ha, J.W. Kim, Proceedings of the European Particle Accelerator Conference, Stockholm, Sweden, 1998

SNS INJECTION SIMULATIONS WITH SPACE CHARGE*

J. Galambos, S. Danilov, D. Jeon, J. Holmes, D. Olsen, ORNL, Oak Ridge, TN

Abstract

Injection scenarios are investigated for the Spallation Neutron Source (SNS) accumulator ring using a new computer model that includes transverse space charge effects. Transverse halo growth is compared for a variety of painting schemes, lattice tunes, and lattice types. Of these, the lattice tune has the strongest impact on the halo growth.

1 INTRODUCTION

The SNS accumulator ring will have a high intensity (~ 10^{14}) low energy (1 GeV) beam and required uncontrolled particle loss rates of ~ one part in 10^4. For these beam parameters, space charge effects could drive beam halo growth, which would lead to violation of the stringent loss criterion. In this paper we investigate the transverse halo growth due to space charge using a newly developed simulation tool, ORBIT [1]. We examine a variety of injection schemes, the effect of the lattice tune, and also the impact of using a FODO or doublet lattice. Painting schemes are examined for (1) directly correlated horizontal (X) - vertical (Y) closed orbit bumps, (2) anti-correlated horizontal - vertical bumps, and (3) horizontal closed orbit bump (fixed vertical smoke ring). Next we examine a wide range of lattice tunes for a fixed injection scheme. The tune is found to have a strong impact on halo growth. Finally we compare halo growth in FODO and doublet lattices with the same tunes and the same injection scenario. Neither lattice type is consistently superior regarding halo production.

The space charge model in ORBIT uses a PIC calculation with an FFT method to calculate the force [2]. For cases shown here we use 480 transverse space-charge kicks/turn (or about 60 per betatron oscillation), 50,000 macro-particles, and a 64x64 PIC grid. We inject particles with emittance < 120 π-mm-mrad, and we define halo as particles with emittance > 180 π-mm-mrad, the acceptance of the SNS primary collimators. All cases are for injection of 2×10^{14} particles. These results do not include lattice errors or wall impedance effects.

2 PAINTING SCHEMES

The SNS ring design allows both horizontal and vertical closed orbit bumps at the foil, providing flexibility in the possible painting schemes. Three primary painting strategies are: (1) inject correlated horizontal and vertical distributions; (2) inject anti-correlated horizontal and vertical distributions; and (3) inject a painted horizontal or vertical smoke-ring distribution. The first scheme has the advantage of pulling the painted distribution away from the foil in both directions, resulting in the fewest foil traversals. At completion, the anti-correlated painting scheme yields a distribution roughly similar to a K-V distribution. However, in this scheme one direction is pulled toward the foil during injection, resulting in higher foil traversals, and a larger aperture is required than in the other two cases. The smoke-ring scheme is the simplest, as only one bump direction is employed.

Table 1. Results of different painting scenarios.

<Foil Hits>	ε_{RMS} (π-mm-mrad	Beam % with $\varepsilon_{(X/Y)} > 180$ (π-mm-mrad)	Max. tune spread (X / Y)
Correlated painting			
2.7	26 / 27	0.004	0.20 / 0.21
Anti-correlated painting			
5.8	24 / 16	0.25	0.20 / 0.30
Vertical smoke ring painting			
3.7	30 / 21	0.038	0.16 / 0.23

Table 1 shows results of the three painting options. In each of these cases the closed orbit trajectory was optimized during injection painting to minimize the amount of halo produced and the tune shift. All cases use the nominal SNS FODO cell lattice with tunes of ν_x= 5.82 and ν_y = 5.90, which result in little beam halo. In the anti-correlated painting scheme particles are injected initially with a large emittance in one direction and a small emittance in the other direction. We chose to inject a large vertical and small horizontal emittance at the outset. This means that particles with large vertical emittance spend more time in the beam during injection, compared to the correlated case in which painting proceeds from smallest to largest emittance in both directions. In the correlated case, any emittance growth in the existing beam is continually painted over during the injection. This is one reason why the correlated painting case develops little halo. Both the smoke-ring and anti-correlated injection schemes have been optimized to reduce halo production by injecting most

* SNS research is sponsored by the Division of Materials Science, U.S. DOE, under contract number DE-AC05-96OR22464 with LMER Corp. for ORNL.

0-7803-5573-3/99/$10.00@1999 IEEE.

particles a smaller emittance than the final target value. However, this results in small RMS emittances and large tune spreads, which may be troublesome in the presence of magnet errors.

Figure 1 shows the real space distributions for the final correlated and anti-correlated painting schemes. The rectangular shape for the correlated painting scheme occurs because the particles with the largest horizontal actions J_x also have the largest vertical actions J_y, and the elliptical shape for the anti-correlated scheme is that expected for a K-V distribution. Figure 2 shows the vertical phase at the end of injection, with and without transverse space charge effects, for the vertical smoke ring case. Space charge forces spread and fill the distribution dramatically, This behavior has been observed experimentally [3].

Figure 1. Real space profiles for correlated painting,:

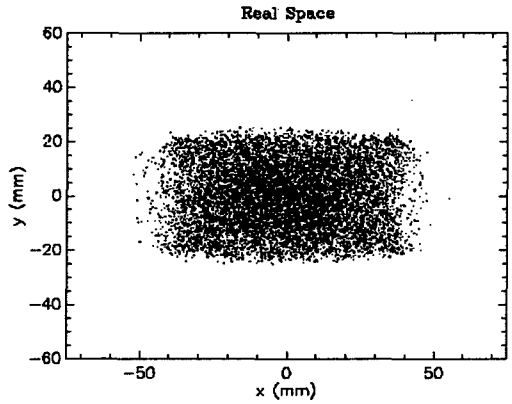

and for anti-correlated painting:

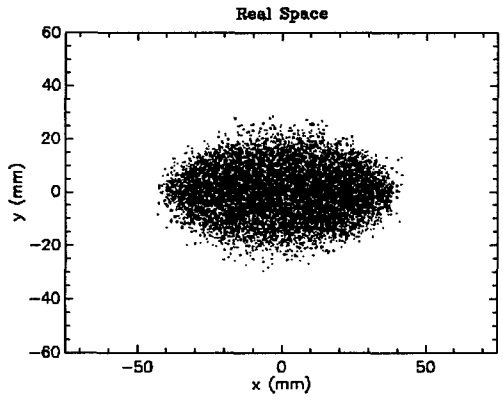

3 OPERATIONAL TUNE

Space-charge-driven resonances have been shown to result in rms beam mismatch that leads to halo growth [4]. In this section we survey the impact of varying the bare tune in the SNS lattice for a fixed injection painting scheme. We use a correlated X-Y painting scheme parameterized to minimize halo production for the nominal tunes of ν_x= 5.82 and ν_y = 5.80. Figure 3 plots the resulting fraction of the beam with emittance > 180 π-mm-mrad (in either X or Y) vs. the bare vertical tune. For each of these cases, the horizontal tune is held fixed, and the dispersion in the ring straight sections is maintained at a level comparable to the baseline (< 0.4 m). As seen in Fig. 3, the amount of generated halo depends strongly on the operating tune. There are large amounts of halo at tunes flanking integer values, and there are also regions of very little halo generation, for example just below the integer tunes at ν_y = 5.9 and ν_y = 4.85. The peaks and minima in this figure have not been investigated in detail, but is apparent that the choice of tune is important.

Figure 2. Vertical phase space distribution for smoke ring injection, calculated with transverse space charge:

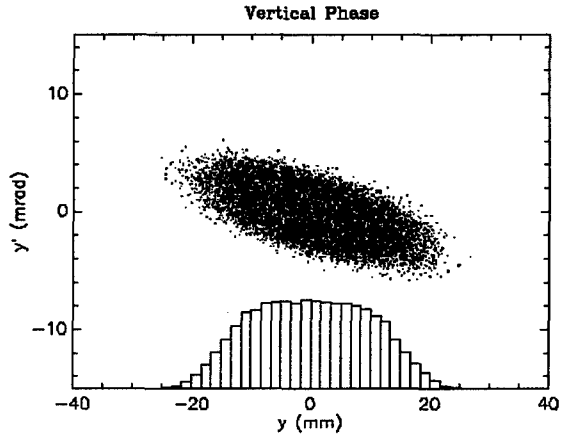

and without transverse space charge.

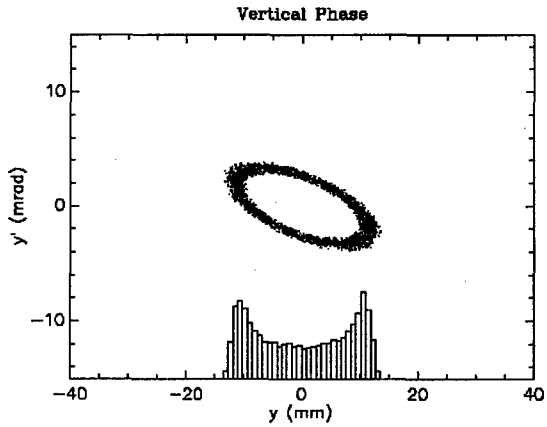

The vertical beam profiles at the end of injection for three of the cases shown in Fig. 3 are plotted in Figure 4. Even though the painting scheme is the same for all three cases, the final profile shape is affected by the lattice tune through the influence of space charge.

Figure 3. Halo generation as a function of the lattice bare vertical tune.

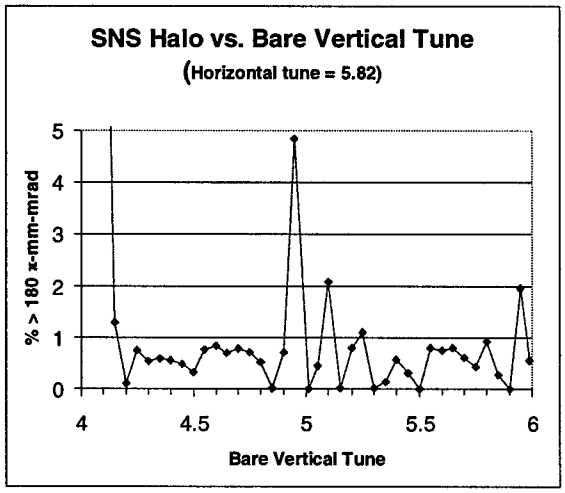

Figure 4: Final vertical beam profiles for three of the tunes shown in Figure 3.

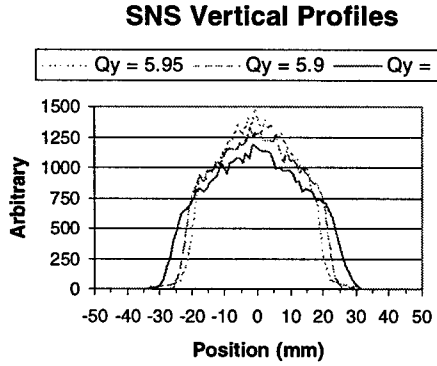

3 LATTICE TYPE

The baseline SNS lattice is a FODO lattice having four super-periods. We use a doublet with similar parameters (see Table 2) to test the sensitivity of the halo generation to the lattice type. The doublet lattice used here does not include the fixed injection chicane that is in the nominal SNS lattice. Figure 4 shows the fraction of the beam with emittance > 180 π-mm-mrad at the end of injection for (1) the nominal SNS FODO lattice, (2) the SNS FODO lattice without the injection chicane, and (3) the doublet lattice. There is little difference between the SNS FODO lattice with and without the injection chicane. Both the doublet and FODO lattices show a similar trend of halo vs. tune, with minimum halo generation for a tune of 5.90. The doublet case has more halo for $\nu_x = 5.85$, and less halo for $\nu_x = 5.95$.

4 SUMMARY

Injection scenarios have been investigated for the SNS, with particular emphasis on minimizing the space-charge-induced halo growth. Halo levels for correlated X-Y painting are smaller than anti-correlated X-Y, or vertical smoke ring painting, The correlated painting scheme also results in the fewest foil traversals, and the smallest tune spread. A broad survey of the effect lattice operational tune shows a strong impact on beam halo production. Finally, we see no systematic difference in halo production between comparable doublet and FODO lattices with similar tunes and injection scenarios.

Table 2: Parameters of lattices used in halo calculation comparison.

	FODO	*Doublet*
Length (m)	220.7	220.7
Super-periods	4	4
$\beta_{x/y}$ max (m)	19.1 / 19.5	16.2 / 16.9
Dispersion – max(m)	4.14	3.80
# quads	48	48
# dipoles	32	32
Max. straight (m)	5.29	10.1
Quad lengths (m)	0.5	0.5
Quad separation (m)	5.29	1.0

Figure 5: Halo generation for similar injection in a FODO and a Doublet lattice.

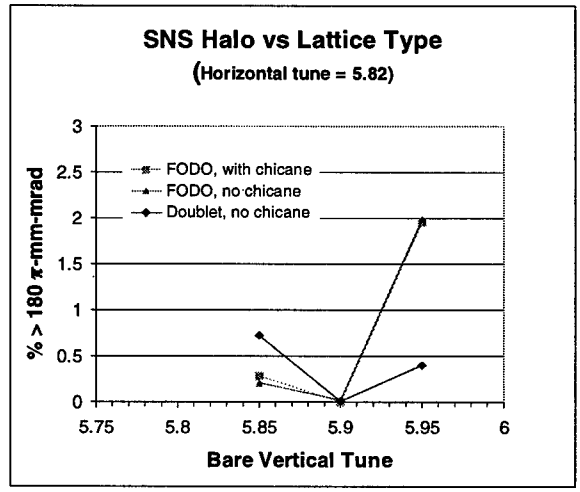

5 REFERENCES

1. J. Galambos, V. Danilov, D. Jeon, J. Holmes, D. Olsen, J. Beebe-Wang, A. Luccio "ORBIT – A Ring Injection Code with Space Charge, these proceedings.
2. J.A. Holmes, J.D. Galambos, D-O Jeon, D.K. Olsen, M. Blaskiewicz, A.U. Luccio, and J.J. Beebe-Wang, "Dynamic Space Charge Calculations for High Intensity Beams in Rings", presented at the International Computational Accelerator Physics Conference, Monterey, CA, September 1998.
3. J. Galambos, S. Danilov, D. Jeon. J.A. Holmes, D.K. Olsen, F. Neri, M. Plum, SNS/ORNL/AP Tech. Note 009.
4. D. Jeon, J. A. Holmes, S. Danilov, J. Galambos, and D.K. Olsen, submitted to Phys. Rev. Lett. (1999).

ORBIT – A RING INJECTION CODE WITH SPACE CHARGE*

J. Galambos, S. Danilov, D. Jeon, J. Holmes, D. Olsen, ORNL, Oak Ridge, TN
J. Beebe-Wang, A. Luccio, BNL, Upton, NY

Abstract

ORBIT (Objective Ring Beam Injection and Tracking) is a new particle tracking code for rings. Modelling capabilities include H^- foil injection mechanisms, longitudinal and transverse space charge effects, and second order matrix transport. Additional code features include a programmable interactive driver shell, and interactive plotting.

1 INTRODUCTION

ORBIT, Objective Ring Beam Injection and Tracking, is a new C++ code developed for the Spallation Neutron Source (SNS) project to build the most intense pulsed neutron source. The code includes H^- foil injection modelling features needed to simulate realistic injection scenarios. Because the SNS project will produce intense pulses, 1-2x10^{14}, of low energy protons, 1 GeV, and is concerned with keeping uncontrolled beam losses to less than 1 part in 10^4, space charge models are provided to calculate beam halo, allowing minimisation of losses. The general code features are described, and some example calculations are shown. A more detailed description of using the code is given in a ORBIT User Manual [1].

2 FEATURES

2.1 Driver Shell

ORBIT is written in C++, and uses an interactive programmable driver shell [2], which can access variables and routines in the compiled accelerator modules. Additionally the driver shell allows the introduction of interpreted code for specific applications. Input files are scripts (in C++ syntax) which set-up the problem by appropriate variable initialisation, and routine calls and contain a combination of interpreted code and calls to compiled code. Because the driver shell is programmable, the tools provided in the compiled accelerator modules can be used together in a generalised fashion, and there are few predetermined execution flow paths. Input files are actually small programs. A portion of a typical input script is show in Table 1, illustrating some driver features such as mixing interpreted and compiled code.

2.2 Accelerator Classes

The accelerator modelling is structured in an object-oriented manner, based on two fundamental classes. First there is a MacroPart class which contains information about a "herd" of macro-particles being tracked. Also there is a Node class, which includes information about different actions that macro-particles may experience as they traverse about the ring. Examples of Node sub-classes are shown in Table 2. The Node class objects are related to the MacroPart classes in that they accept a MacroPart reference as an argument. This arrangement facilitates easy implementation of tracking multiple herds simultaneously. This is useful, for example, in some of the diagnostic procedures which are provided. The class structure is described in more detail in the ORBIT User Manual [1]. In setting up a ring for a particular run, the nodes may be put together in a general fashion.

Table 1: A portion of an input script for an ORBIT run.

```
////////////////////////////////////
// Add a non-accelerating  RF Cavity //
////////////////////////////////////
  Real tFactor;
  Integer nRFHarms = 1;
  RealVector volts(nRFHarms),
    harmNum(nRFHarms), RFPhase(nRFHarms);
  harmNum(1) = 1; RFPhase(1) = 0.;

// make a new interpreted routine:
  Void PSRVolts()
  {
   tFactor = time/0.825;
   if(tFactor > 1.) tFactor = 1.;
   volts(1) = 8. + 9. * tFactor;
  }
//   call a compiled routine:
  addRampedRFCavity("RF 1", 75, nRFHarms,
      volts, harmNum, RFPhase, PSRVolts);

// change a "compiled" variable:
     nLongBins = 64;
```

2.3 Modules and Other Features

Each of the accelerator classes in Table 2 represents an abstraction of an accelerator simulation action and is included in a separate module. Each module has an interface and an implementation. The interface describes how the module appears to a user, i.e. which variables and routines can be manipulated from the shell. The implementation contains the actual algorithms. The ability for the driver shell to communicate with specific module variables and routines is achieved by pre-processing the interface during the code build.

The code also includes features for flexible output and interactive plotting, either X-window or postscript. No proprietary software is used, but several freely available

* SNS research is sponsored by the Division of Materials Science, U.S. DOE, under contract number DE-AC05-96OR22464 with LMER Corp. for ORNL.

packages are incorporated. ORBIT has run on LINUX (Pentium PCs and DEC alpha's), Digital UNIX, IBM and SUN workstations. Typical run times for full space charge treatments are about 16 hours to simulate 1200 turn injection of the SNS accumulator ring using 100,000 macro-particles and 480 azimuthal steps per turn.

Table 2: Node classes in the ORBIT code. Indented entries represent sub-classes.

Node Class	Description
Transfer Matrix	Fundamental transport mechanism, using externally generated matrices from MAD.
1st order	Used for linear tracking.
2nd order*	Used for tracking at 2nd order.
Acceleration	Provides energy kicks due to an RF cavity.
RFCavity	Used for non-accelerating RF structures.
	Used for accelerating RF structures.
RampedBAccel*	For synchronous particle acceleration, with a prescribed B and Voltage ramp.
Longitudinal Space Charge	Gives a longitudinal space charge kick.
FFTLSpaceCharge	Use an FFT method, and optionally includes wall impedance effects.
Transverse Space Charge	Gives a transverse momentum kick from space charge.
PWSum	Calculate the space charge force using pairwise sum over macro-particles.
BrueForcePIC	Calculate the space charge force using a brute-force PIC.
FFT-PIC	Calculate the space charge force using an FFT PIC implementation.
Bump	Moves the closed orbit up (or down) as a function of time.
Foil	H^- source, and scattering element. Also calculates foil traversals.
Aperture	Either counts hits at a prescribed position, or removes macro-particles.
RectAperture	For a rectangular shaped aperture.
Thin Lens	Provides macro-particles with a thin lens kick.
ThinMPole*	Generalised multipole kick..
Diagnostic	Calculates diagnostic properties for a macro-particle herd.
MomentNode	Calculate moments of a herd.
StatLatNode	Calculate the statistical lattice parameters.
PMTNode	Poincare-Moment-Tracking – dumps the particle coordinates of a test herd, every "core oscillation" of the main herd.
LongMountainNode	Dumps the longitudinal histogram for a herd.

* These capabilities have been installed and are undergoing testing.

3 EXAMPLE CALCULATIONS

This section illustrates some examples of calculations that can be performed with ORBIT. By no means is it an exhaustive set of examples.

3.1 Injection Painting

Figure 1 shows an example of transverse and longitudinal phase space distributions resulting at the end of a programmed closed orbit bump painting, with no transverse space charge. These plots illustrate the built-in plotting capabilities. The hollow horizontal phase space profile was produced by a programmed closed orbit bump that spent more time injecting at the outer regions of x than for the inner regions of x.

3.2 Space Charge

Figure. 2 shows an example of a tune spread "necktie" diagram calculated by ORBIT with space charge at the end of injection. The tunes were calculated by the tune diagnostic and subsequently dumped to a file. Then this tune plot was created by an auxiliary plotting application, gnuplot. There are many built-in methods for dumping information to files, and it is also possible to perform customised data dumps from input script files by creating new output streams on the fly. Another example of a space charge diagnostic is a beam quadrupole moment shown in Fig. 3. This diagnostic shows the beam quadrupole moment for two different beam intensities during three turns at the end of injection. This is an example of a "high frequency" diagnostic. These moment diagnostics, as well as other diagnostics can also provide information at lower frequency, such as, once a turn. As indicated in Table 2, there are many diagnostic tools provided to understand the behaviour of the transverse space charge effects.

Finally in Fig. 4 we show an example of a benchmark comparison of simulated and experimentally observed beam profiles. This is a simulation of a Proton Storage Ring case, and is described in detail in Ref. [3]. Figure 4 shows the experimentally observed vertical beam profile, the simulated beam profile, and the simulated profile neglecting space charge effects. The simulated profile

agrees fairly well with the experimentally observed profile, but the agreement is not good if space charge effects are neglected. The ORBIT code is available at http://www.ornl.gov/~jdg/APGroup/Codes/Codes.html .

4 REFERENCES

1. J. Galambos, J. Holmes, D. Olsen, "ORBIT User Manual, V.1.0", SNS-ORNL-AP Tech. Note 11, March 1999.
2. S. W. Haney, "Using and Programming the SuperCode", UCRL-ID-118982, Oct. 1994.
3. J. Galambos, S. Danilov, D. Jeon. J. Holmes, D. Olsen, F. Neri, M. Plum, SNS/ORNL/AP Tech. Note 009.

Figure 1. Example ORBIT plots for transverse, upper, and longitudinal, lower, phase space distributions, calculated at the end of a programmed injection bump.

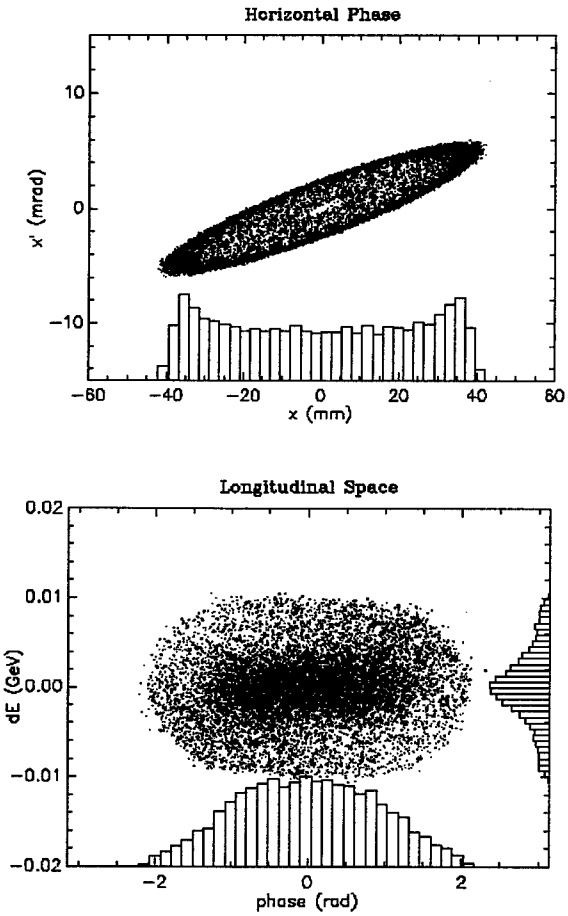

Figure 2. Transverse tune spread "necktie" information calculated by ORBIT at the end of injection.

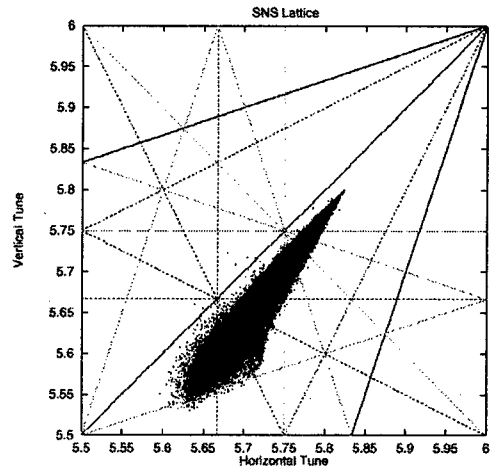

Figure 3. Example of the beam quadrupole moment verses position for three turns around the PSR ring near the end of injection, for two different intensities.

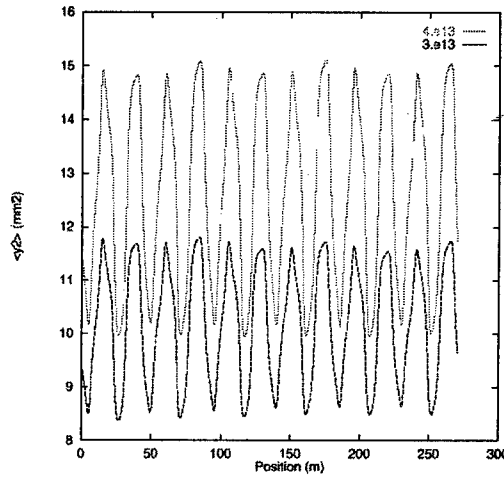

Figure 4. Comparison of calculated and measured PSR beam profiles. Inclusion of space charge is crucial to matching the observed profiles

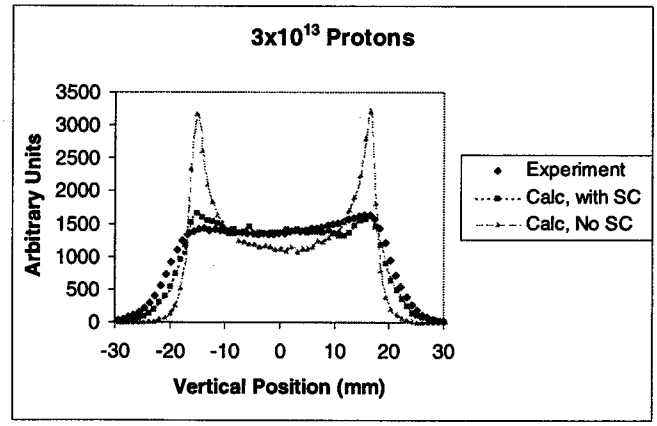

IONIZATION COOLING OF MUON BEAM BY MULTISTAGE SYSTEM OF LITHIUM LENSES WITH MATCHING SECTIONS*

V.I.Balbekov, FNAL, Batavia, IL

Abstract

System of lithium lenses with matching sections as the last stage of ionization cooling for muon collider is considered. The matching section including accelerating cavities, straight and bent solenoids, and wedge absorbers provide both acceleration and focusing of the beam as well as transverse-longitudinal emittance exchange. Results of analytical calculations and Monte Carlo simulations with scattering and straggling are presented. Suppression of nonlinear and chromatic effects is discussed.

1 INTRODUCTION

The latest stage of ionization cooling for muon collider requires a multistage lithium lens which can provide a long-distance β - function about 1 cm really unachievable with any other device[1, 2]. Average β - function of matching sections between Li lenses is much more and has more or less significant modulation. Chromatic aberrations are strong in such conditions laying obstacles to focusing of the beam on the next Li lens. Usual way of suppression by sextupole correctors is unusable in this case because of attendant nonlinear effects. But it can be attenuated by taking opposite energy offset ΔE of any particle on the beginning and the end of the matching section what achieved at synchrotron phase advance π per section. It requires rather high momentum of particles ($P \simeq 300$ MeV/c) because chromatic effects are proportional not ΔE but $\Delta p/p$ (another reason is nonlinearity of longitudinal motion, which discussed later).

The 805 MHz, 30 MeV/m accelerating system is considered now as the most perspective[3]. About 5 m of such a linac is required for the phase rotation and approximately the same for 'pure' acceleration to get more or less satisfactory efficiency of the accelerating system. It means that energy gain in the section should be about 150 MeV, and rather long Li lenses (1.5 - 1.8 m) are required.

Emittance exchange is another big problem. Typical energy spread of cooled muon beam is about ± 50 MeV on 3σ level which should be decreased approximately on 20% by wedge absorber to compensate straggling in Li lens. It means that energy loss in the center of the absorber is about 10 MeV requiring 7 - 8 cm of LiH. It gives a scale of average β - function in the absorber and means that scattering in it may be comparable with scattering in Li lens of 1 cm β - function. Therefore a using of wedge absorbers in very end of the cooling channel is at least undesirable.

Another important effect is violation of balance of chromaticity by wedge absorber which changes energy distribution. Therefore it can be placed only at the end of matching section to avoid accumulation of chromatic distortions. It means also that only 1 wedge per section may be used providing exchange of longitudinal emittance with one transverse direction. The exchange with other direction is available in practice only in the following matching section.

* Work supported by the U.S. Department of Energy under contract No DE-AC02-76CH0300

2 SCHEMATIC AND PARAMETERS OF THE COOLER

A system of 5 Li lenses with 4 matching sections is considered to meet these conditions (Fig.1). It includes 2 sections with and 2 ones without wedge absorbers. Main parameters of the cooler are listed in Table 1.

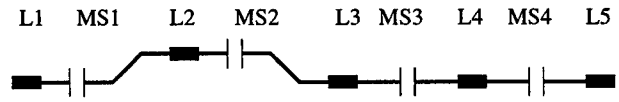

Figure 1: Schematic of the cooler.

Table 1: Parameters of the cooler

Muon momentum, MeV/c	298.9 - 463.6
Total length, m	49.69
Length of Li lens	1.686 and 1.807
Length of matching section, m	9.875 - 10.667
Accelerating frequency, MHz	805
Accelerating gradient, MV/m	30

Scheme of a matching section is shown on Fig.2. 1st short solenoid matches strongly divergent beam going out the Li lens with a long central solenoid. By this, there is no beam envelop modulation in the central solenoid what weaken chromatic effects. Short solenoids in the end of the section focus the beam on the center of next Li lens. Sections 3 - 4 without emittance exchange include 1 straight solenoid whereas 1st and 2nd sections include additionally 2 bent solenoids to excite and suppress dispersion. Bent solenoids placed inside of combine function magnets with field index 0.5 to prevent vertical drift. Such a system has almost the same transfer matrix as usual solenoid and creates easy controlled dispersion function. All front and back

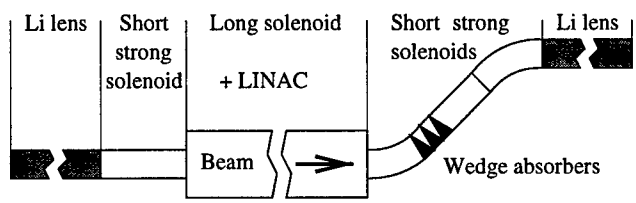

Figure 2: Matching section with emittance exchange.

solenoids have a length $\lambda_{Larmor}/2$, and central solenoid – $4\lambda_{Larmor}$. Parameters of the matching sections are listed in Table 2.

Table 2: Parameters of matching section

No of MS	1	2	3	4
Length, m: Total	10.657	10.544	9.933	9.875
Front solenoid	.255	.228	.197	.171
Central solenoid	9.500	9.500	9.500	9.500
Any back solenoid	.304	.272	.236	.204
Field, T: Front s.	12.29	13.74	15.86	18.32
Central solenoid	3.157	3.154	3.145	3.142
Any back solenoid	15.97	17,86	20.62	23.81

Traveling wave linacs are placed inside central solenoids. Each of them is divided on 3 subsections with different stable phases to get synchrotron phase advance π and avoid an inadmissible adiabatic increase of energy spread of the beam.

Table 3: Length (m)/Stable phase (deg) of subsections

MS	1	2	3	4
SS1	3.776/11.6	3.821/13.7	3.944/12.0	3.968/12.0
SS2	2.498/90	2.391/90	2.048/90	1.966/90
SS3	3.225/38.9	3.288/40.0	3.508/43.5	3.567/44.4

3 NONLINEAR AND CHROMATIC DISTORTIONS

Fig.3 shows nonlinear distortion of longitudinal motion. Nonlinearity of accelerating field as well as nonlinear dependence of flying time on energy are responsible for this. The latest effect become very stronger at lower energy which is another (besides chromaticity) reason to take high energy muons for the cooling.

Fig.4 demonstrates chromatic effects in 4th matching section. It is assumed that phase ellipse in the beginning is canonical corresponding to the beam boundary on the level 3σ. It is seen that chromatic effects is suppressed almost totally at $-\sigma_E < \Delta E < 3\sigma_E$ and not very strong at $-3\sigma_E < \Delta E < -2\sigma_E$. Effect depends both on particles energy and *distribution of synchronous phases* which probably can be optimized more. 1st and 2nd sections give more chromaticity because of wedge absorbers.

Fig.5 demonstrates transverse nonlinear effects in 4th section for equilibrium particles. Initial phase ellipses are canonical corresponding to transverse emittance on the levels 1,2,3 σ. These distortions are tolerable, but it is necessary to remember that effect substantially enhanced for non-equilibrium particles.

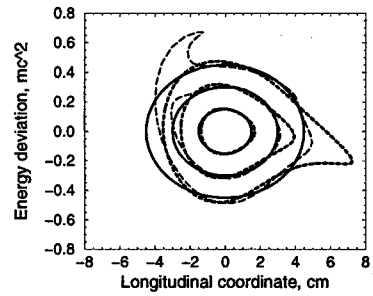

Figure 3: Effect of longitudinal nonlinearity. Solid lines – initial phase ellipses (levels 1,2 3 σ), dashed lines – after 1 cell, long dashed – after 2 cells.

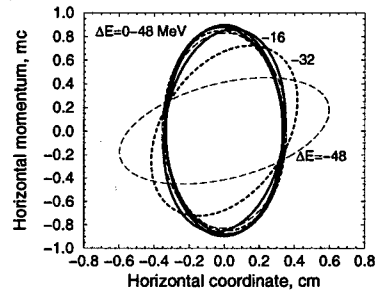

Figure 4: Phase ellipse after 4th section at different energy deviations. Initial phase ellipse is canonical, $\sigma_E = 16$ MeV.

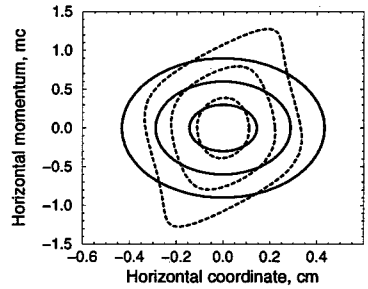

Figure 5: Nonlinear distortion in 4th section. Solid lines – phase ellipses before the section (1,2,3 σ - levels), dashed lines – phase ellipses after the section.

4 LITHIUM LENSES

Any section provides cooling of transverse emittance by factor $\lambda = \varepsilon_{out}/\varepsilon_{in}$,

$$\lambda = \frac{p_{min}}{p_{max}}\left(1 + \frac{\beta_{max}}{2\epsilon_{in}}\int\sqrt{\frac{p}{p_{max}}}\frac{d\langle\theta^2\rangle}{ds}ds\right), \quad (1)$$

where p is momentum, ϵ – geometrical emittance, β_{max} – β - function in the beginning of Li lens, $d\langle\theta^2\rangle/ds$ – r.m.s. angle of multiple scattering per unit of length. Calculation of the integral gives 0.0015 at given energy.

The cooling goes down when emittance decreases. To avoid this, it is necessary to decrease β - functions of Li lenses in the series to keep constant angle spread of the beam x'[4]; then $\epsilon_{in} = \beta_{max}x'^2$. At $x' = 1/15$ scatter-

ing increases the cooling factor on 20% and gives $\lambda = 0.75$ in good agreement with simulation. Therefore transverse momentum spread decreases by factor 0.77 what should be compensated in matching sections to have constant spread in any Li lens (it achieved by appropriate ratio of fields of front and back solenoids). As a result, beam radius decreases from lens to lens by factor 0.75 but it grows up to 0.8 in 1st and 2nd sections because of emittance exchange.

Choosing initial transverse emittance of the beam as 1π mm, it is possible to pre-estimate r.m.s. beam radius in any Li lens. The lens radius should be 3.5 times more to avoid excessive particle loss (see below). It allows to calculate all the lenses parameters which are listed in Table 4. The first lenses are shorter because wedge absorbers additionally decrease the energy on 10.6 MeV. Current of all the lenses is 440 kA.

Table 4: Parameters of Li lenses

Lens No	1	2	3	4	5
Length, m	1.686	1.686	1.686	1.807	1.807
Radius, cm	1.166	0.932	0.700	0.524	0.393
Grad, T/cm	6.476	10.12	17.99	31.98	56.86
Max field, T	7.551	9.432	12.59	16.76	22.35

5 SIMULATION

Gaussian distribution with parameters: $\sigma_x = \sigma_y = 3.33$ mm, $\sigma_{p_x} = \sigma_{p_y} = 32$ MeV/c, $\sigma_z = 1.5$ cm, $\sigma_E = 16$ MeV was taken for simulation. The distribution was cut on the level 3σ according to radius of 1st Li lens.

Fig.6 gives distributions of injected (left) and cooled beams on transverse phase plane. Very similar picture is obtained in linear approximation. It means that nonlinear and chromatic transverse distortions are suppressed rather good. Longitudinal distortions are more significant as shown on Fig.7. Both straggling and nonlinearity cause a beam halo and large additional loss of particles. The distributions have different slops because reside in different ends of the lenses and have canonical form in centers.

Fig.7 shows dependence of normalized r.m.s. emittance on distance along the cooler. Filled and unfilled symbols are related to nonlinear and linear consideration of the matching sections. Lower lines give a behavior of transverse emittance and confirm that distortions are rather small in this direction. Upper lines concerning to longitudinal motion are less regular because longitudinal perturbations in any section partially compensated by nonlinearity of the next one (see Fig.3). Because of aperture restriction, final 6-dimensional emittance is almost the same in both considerations (0.20 and 0.23 mm^3) but loss of particles is very different: 8% and 32%. Distribution of the losses ate: decay about 3%, scattering/straggling in Li lens and wedge absorber 5%, imperfection of the matching sections 24%.

6 CONCLUSION

Li lenses with surface field 20-25 T can provide 6-dimension emittance required for muon collider but particle loss in matching sections is large still and an improvement of the system is necessary. A good result gives decrease of accelerating frequency. Emittance exchange is unsolved problem for a beam with ultimate small transverse emittance, too. Interesting idea is the exchange inside Li lens[5] but it is very very difficult technical problem.

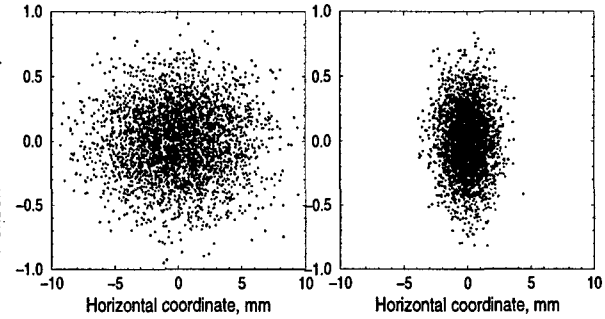

Figure 6: Initial and final transverse distributions.

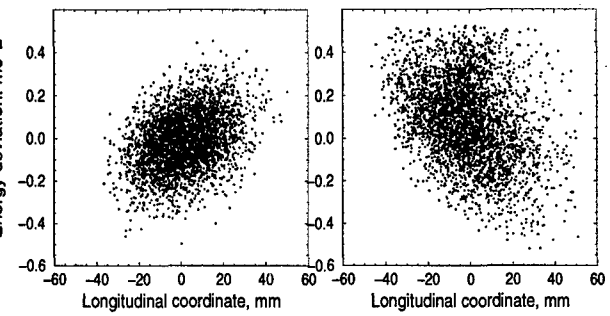

Figure 7: Initial and final longitudinal distributions.

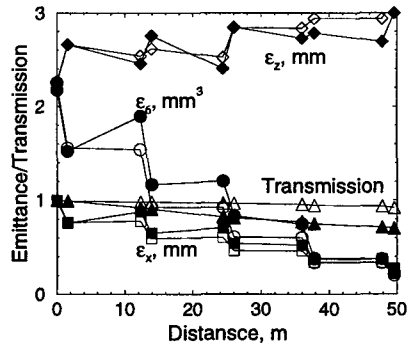

Figure 8: Dependence of emittance and transmission on distance. Unfilled symbols – linear approximation

7 REFERENCES

[1] B.F.Bayanov et al., Antiproton Target Station on Base of Lithium Lenses. XI Int. Conf. on High Energy Acc., Geneva, CERN, 1980, p.362.

[2] G.Silvestrov, Lithium Lenses for Muon Collider, AIP Conf. Proc. **372**, 168 (1996).

[3] R.B.Palmer, Progress on $\mu^+\mu^-$ Colliders, Proc. PAC 97 (Vancouver, Canada , 1997), p.286.

[4] V.I.Balbekov, Achievable Transverse Emittance of Beam in Muon Collider, AIP Conf. Proc. **372**, 140 (1996).

[5] T.A.Vsevolozhskaya, Kinetics of 3-D Ionization Cooling of Muons, Budker INP 98-48, Novosibirsk (1998).

RF ACCELERATING STRUCTURES FOR THE MUON COOLING EXPERIMENT*

J.N. Corlett#, D. Li, R.A. MacGill, M. Green, W.C. Turner, N. Hartman, LBNL, Berkeley, CA
N. Holtkamp, A. Moretti, FNAL, Batavia, IL
H. Kirk, R.B. Palmer, Y. Zhao, BNL, Brookhaven, NY
D. Summers, Univ. of Mississippi, MS

Abstract

The ionization cooling of muons requires longitudinal acceleration of the muons after scattering in a hydrogen target. In order to maximize the accelerating voltage, we propose using linear accelerating structures with cells bounded by thin beryllium metal foils. This produces an on-axis field equivalent to the maximum surface field, whereas with beam-pipes the accelerating field is approximately half that of the peak surface field in the cavity. The muons interact only weakly with the thin foils. A $\pi/2$ interleaved cavity structure has been chosen, with alternate cells coupled together externally, and the two groups of cells fed in quadrature. At present we are considering an operating temperature of 77K to gain a factor of at least two in Q-value over room temperature. We will describe the design of the $\pi/2$ interleaved cavity structure, design of an alternative π-mode open structure, preliminary experimental results from a low-power test cavity, and plans for high-power testing.

1 INTRODUCTION

Feasibility studies of muon colliders for high energy physics experiments have been underway for some years, and critical issues and experiments have been identified [1, 2]. One of the more important issues is that of cooling the overall 6-dimensional phase space of the collected muons by a factor of approximately 10^6 in a time dictated by the short muon decay time.

An ionization cooling scheme has been developed, in which the muons lose momentum in a low-Z material, after which they regain their longitudinal momentum in an RF accelerating section. Sections of absorber and RF accelerator alternate inside a solenoidal magnetic focussing field, and bent solenoid emittance exchange sections provide 6-dimensional cooling. The entire cooling channel may consist of about 20 modules, with a factor 2 cooling per module.

The large transverse emittance of the muon beam requires large apertures, and the RF cavities must accommodate up to a 16 cm beam diameter. Such a large bore leads to a low shunt impedance in conventional open beam-pipe structures, however we propose to study cavities with up to 16 cm diameter thin (127 μm) beryllium windows through which the muon beams pass with low scattering rate [3,4]. This allows the shunt impedance of the device to be increased, the maximum surface field to equal the on-axis accelerating field, and the phase advance per cell to be arbitrarily chosen.

In addition to the pillbox design, we are studying a standing wave multicell cavity with open apertures, scaled to match the beam profile through the structure.

2 RF SYSTEM REQUIREMENTS

The purpose of the RF accelerating system is to replenish longitudinal momentum lost by the muons in scattering in the liquid hydrogen target. Each section must restore the longitudinal energy lost in the preceding target, resulting in an average gradient requirement of 34 MVm^{-1} experienced by the muon beam.

Beryllium window thickness is limited by the additional emittance increase resulting from Coulomb scattering within the metal. Although the tolerance to Be is greater at the input to the cooling channel, where the emittance is largest, we choose to use the thinner (127 μm) windows demanded at the low-emittance end of the cooling channel.

An alternating solenoidal magnetic field will be applied throughout the cooling channel to focus the beam. Peak fields of 15 T or greater are produced by superconducting solenoids, and the RF structures must sit inside the bore of the solenoids. The length of the RF accelerating structure is 1.3 m.

Table 1: Cooling section RF system specifications

Frequency (MHz)	805
Muon momentum (MeV/c)	180
Relativistic ß	0.87
Average accelerating gradient (MVm^{-1})	34
Beryllium window thickness (μm)	< 127

3 $\pi/2$ INTERLEAVED CAVITY

The $\pi/2$ interleaved cavity consists of two chains of side-coupled cavities with Be windows, interleaved, with a difference of $\pi/2$ in the phase of the drive power to each chain. Figure 1 shows a section of the structure. Each cell is a modified pillbox, with beryllium windows defining

* *Work supported by the U.S. Department of Energy under Contract Nos. DE-AC0376SF00098 (LBNL), DE-AC02-76CH00016 (FNAL), DE-AC02-98CH10886 (BNL), DE-FG02-91ER40622 (University of Mississippi)
# email: jncorlett@lbl.gov

0-7803-5573-3/99/$10.00@1999 IEEE.

the end plates, through which the muon beam passes. The peak surface field is thus equal to the peak accelerating field on axis. Coupling between cells is through a side-coupled cell, and the phase advance between cells is determined to be $\pi/2$ by appropriate choice of cell length for the given muon velocity, and phase of drive to each chain of cells. Each chain is powered from a waveguide coupled into one of the accelerating cells. Coupling cells are coaxial structures, resonant at the frequency of the accelerating cells. The design has a high shunt impedance and is tolerant to dimensional errors.

To further increase the shunt impedance, we propose to investigate the possibility of cooling the structure to liquid nitrogen temperatures. The resulting increase in conductivity of copper is about a factor of two over room temperature, and a greater increase may be expected for the beryllium windows. The physical properties of beryllium at low temperatures, however, are not well determined and are the subject of several channels of investigation, including the manufacture of a low-power test cavity with interchangeable windows. We expect an improvement in Q-value, and hence shunt impedance, of a factor of two at 77K.

2.1 Beryllium windows

The inclusion of beryllium windows, allowing the accelerating field to equal the peak surface field, and isolation of cells in the interleaved structure, increase the shunt impedance of the structure over conventional designs. The trade-offs are with difficulties in mechanical construction and stability of the structure, power and voltage handling capabilities, and dark current generation. Wakefield effects of the thin beryllium foils may be advantageous.

As the cavity cools to liquid nitrogen temperatures, differential contraction between the beryllium window and the copper body of the cavity results in compressive stresses on the beryllium, causing it to distort. The resulting frequency change is unacceptable, and we are studying window frame designs of composite materials and pre-stressing the foil to overcome the compressive forces on the foils. Heating by RF currents in the foil causes expansion and additional distortions, complicated by the sensitivity of beryllium materials properties to temperature [5]. It is clear that the stresses induced by RF heating are beyond yield strength if operated at room temperature, we are investigating solutions at 77K.

Voltage handling capability is being studied in tests at the A0 facility at FNAL. Here, small (16mm diameter) samples of beryllium foils of thickness varying from 125 μm to 50 μm are being tested at high field in a 1.5 GHz RF gun structure. To date, no damage to foils has been observed up to the maximum achievable gradient of 35 MVm^{-1}. Tests will continue at higher gradients in an effort to determine the damage level for the foils. Dark current may also be investigated in this apparatus. Additional tests are planned for a pillbox cavity with beryllium surfaces on the end plates, operated at high power and in a magnetic field to study surface breakdown. Wakefield effects of a subrelativistic beam in a pillbox structure are under investigation.

We will also test a low-power cavity to investigate several of these aspects, as described in section 5.

Properties of the $\pi/2$ interleaved structure at room temperature are listed in table 2.

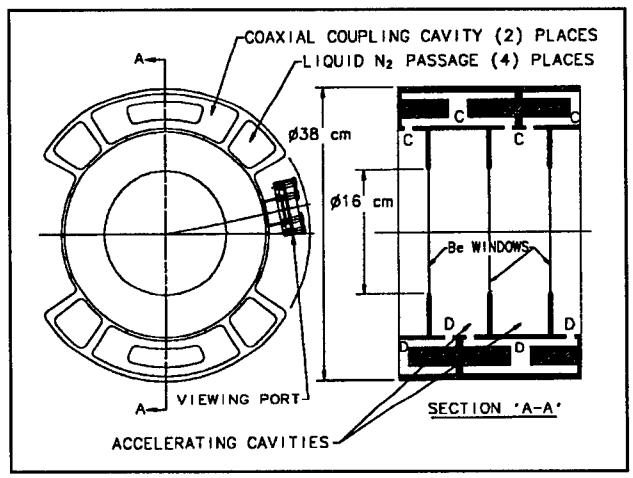

Figure 1: Layout of $\pi/2$ interleaved cavity structure

Table 2: $\pi/2$ interleaved cavity specifications (room temperature)

Transit time corrected shunt impedance ($M\Omega m^{-1}$)	37.8
Q_0	19600
Transit time T	0.9
Filling time τ (μs)	3.9
Cell length (cm)	8.1
Power for 34 MVm^{-1} ($MW\ m^{-1}$)	31

4 OPEN IRIS STRUCTURE

An alternative to the $\pi/2$ interleaved structure is the conventional multi-cell cavity with open irises through which the beam passes. This design avoids the complications of mounting and controlling distortions in thin metal foils, but involves the use of more power (the structure has a lower shunt impedance), and operating at higher peak surface fields. Table 3 lists the RF characteristics of the open-iris structure shown in figure 2, a π-mode eight cell linac (a half-structure is modeled here). We plan to build three-cell structures to high power test in strong magnetic fields to determine the viability of operating cavities under conditions required in the muon cooling experiment. Lacking the more complex engineering challenges of the $\pi/2$ interleaved structure, the open-iris design may allow the most rapid development of a structure for the initial cooling tests.

Table 3: Open iris cavity specifications

Transit time corrected shunt impedance ($M\Omega m^{-1}$)	17
Q_o	29500
Transit time T	0.6
Filling time τ (μs)	12
Cell length (cm)	16.2
Power for 34 MVm^{-1} ($MW\ m^{-1}$)	68

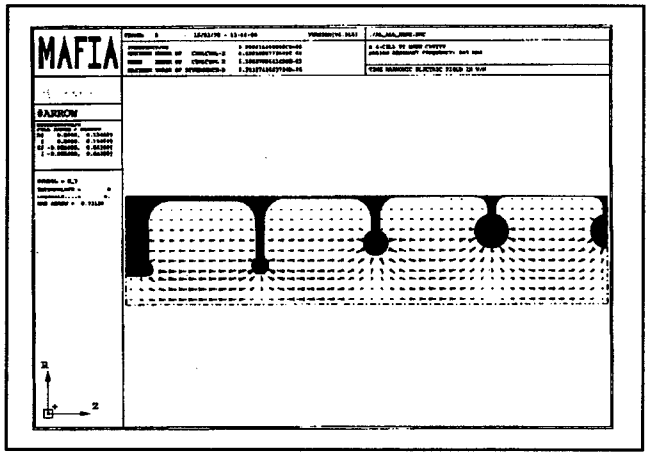

Figure 2: Open-iris cavity design, showing electric field in an 8-cell structure

5 EXPERIMENTAL STATUS

An experimental low-power test cavity consisting of two coupled half-cells and one full cell of the $\pi/2$ interleaved cavity structure has been built to test mechanical stability, Q, and thermal effects to LN2 temperatures. Figure 3 shows the two halves of the $\pi/2$ interleaved cavity low-power test structure. The irises are open in this view. The beryllium foils are diffusion bonded into in a sturdy beryllium ring, which is then clamped into the copper cavity with RF contact established by circumferential springs mounted inside the iris and clamp ring. Center conductors are mounted in the coupling cell, and the two halves and also end plates are bolted together. Springs mounted in recesses provide RF contact at joints, and tuning screws are provided for each cell along with coupling loops and probes for RF power input and measurements.

Cooling channels will be wrapped around the outside (grooves shown in figure 3), and the structure will be inserted into a vacuum tank with liquid nitrogen flowing through the cooling tubes to reduce it's operating temperature. Low-power measurements of the frequency and Q of modes will be made as a function of temperature.

To test the effects of heating in the structure, a high-power feed will be provided also. An average power of up to 450 W is required to simulate the average power dissipation under long-pulse operation in the cooling channel RF systems.

The low-power cavity is being measured at LBNL, currently at room temperature, and measurements at low temperatures are scheduled to begin soon.

Beryllium properties are also being investigated in experimental apparatus at BNL, and at the University of Mississippi. Measurements of beryllium strips in a structure resonant at 805 MHz have been made as a function of ambient temperature, to determine the resistivity of beryllium in commercial grade foils. D.C. measurements are also being made, and initial results show a discrepancy between the low-temperature measurements at d.c. and at 805 MHz, with the RF measurements indicating substantially higher resistivity.

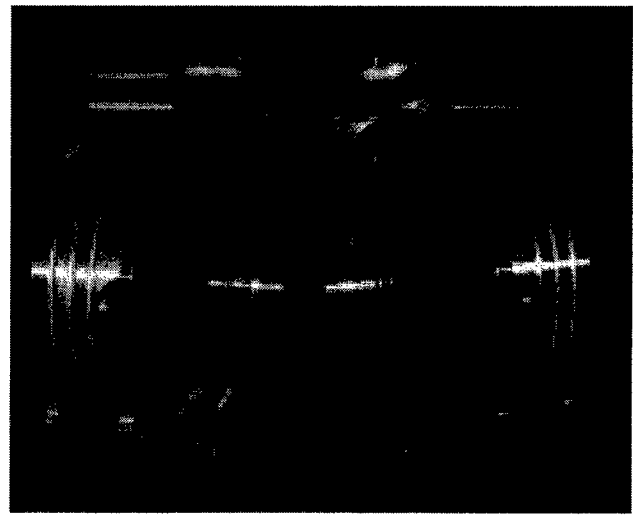

Figure 3: $\pi/2$ interleaved cavity low-power test structure, copper cavity halves

High-power testing of cavities will take place at FNAL, within a 5T solenoidal magnetic field, and using an existing 805 MHz klystron operating at up to 15 MW. Plans are well advanced, and high-power testing is scheduled to begin in September 1999.

6 REFERENCES

[1] R. Palmer, A. Tollestrup and A. Sessler, Proc. Of 1996 DPF, DPB Summer Study "New Directions for High Energy Physics", Snowmass, CO, (1996)

[2] "Status of Muon Collider Research and Development and Future Plans", Fermilab-PUB-98/179

[3] "RF System Concepts for a Muon Cooling Experiment", A. Moretti, J.N. Corlett, D. Li, W.C. Turner, H.G. Kirk, R.B. Palmer, Y. Zhao, European Particle Accelerator Conference, Stockholm, 1998.

[4] "$\pi/2$ Interleaved Cavity Developments for the Muon Collider Cooling Experiment", A. Moretti, J.N. Corlett, D. Li, W.C. Turner, H.G. Kirk, R.B. Palmer, Y. Zhao, Linear Accelerator Conference, Chicago 1998.

[5] "Temperature Distribution Calculations on Beryllium Windows in RF cavities for a Muon Collider", D. Li, J. Corlett, W. Turner, Linear Accelerator Conference, Chicago 1998.

ACCELERATION STAGES FOR A MUON COLLIDER

J. S. Berg, Indiana U.; A. A. Garren, LBNL;
J. E. Griffin, C. Johnstone, F. E. Mills, A. Moretti, D. V. Neuffer, W. Wan, FNAL;
R. B. Palmer, BNL; D. Summers, U. Mississippi

Abstract

Using muons in high energy colliders has an advantage in that the muons emit negligible synchrotron radiation, but has the disadvantage that the lifetime of the muons is very short. The latter requires that the muons be accelerated as rapidly as possible to prevent particle loss. The former allows one to loop back and pass through the same linac multiple times, thereby achieving potentially significant cost advantages. Some of the acceleration systems will use recirculating linacs to achieve the reuse of the accelerating structures. However, the large longitudinal beam emittances make it difficult to simultaneously achieve large gradients by using high frequency RF and design an arc with a sufficient energy acceptance. The current state of the design for the acceleration stages for a muon collider will be presented, with emphasis on systems accelerating to 70 GeV per beam. Known difficulties will be described as will their possible solutions. In particular, the use of an FFAG-like lattice for the arcs of a recirculating linac will be described which accepts a beam with a very large energy spread over a wide range of energies, allowing a single arc to be used instead of multiple arcs.

1 INTRODUCTION

This paper will describe the design issues and the current status of the acceleration stages for a first muon collider. In particular, it will focus on the design of systems to accelerate up to 70 GeV. While future machines will need to go to much higher energies, the lower energy acceleration systems will be necessary. One of the design criteria the acceleration systems for a 70 GeV muon collider is that they could be reused with minimal modifications in a higher energy collider. Table 1 gives some of the parameters needed for the design of the acceleration stages.

1.1 Overall Scheme

We could conceivably get to 70 GeV with a single linac. However, this fails to take advantage of the fact that the muons have negligible synchrotron radiation and can therefore follow a curved trajectory. Because of this, an acceleration system can be created where the muons loop back around and pass through the same linac several times, potentially achieving significant cost savings. In doing this, one must take into account the additional decay losses when the muons are not being accelerated. This essentially eliminates the possibility of using ramped magnets in a synchrotron-like configuration at the lower energies (the magnets would need to be ramped too quickly, or too much circumference of the ring would be wasted in arc).

Table 1: Relevant parameters. Numbers are given for a low energy spread "Higgs factory" scenario and for a high energy machine. N is the number of particles per bunch (after acceleration), N_{bunch} is the number of bunches of each charge, ϵ_{6n} is the 6-D normalized emittance (after acceleration), ϵ_n is the transverse normalized emittance (after acceleration), and p_{in} is the momentum of the muons entering the acceleration systems.

	Higgs	High E
N	4×10^{12}	2×10^{12}
N_{bunch}	2	4
ϵ_{6n}, $(\pi\text{m})^3$	170×10^{-12}	
ϵ_n, πm	290×10^{-6}	50×10^{-6}
p_{in}, MeV/c	186	

The acceleration systems will be divided into several stages. As the beam energy increases, the (unnormalized) emittance decreases, allowing the use of higher frequency (and therefore higher gradient) RF and allowing the arcs to have a smaller energy acceptance. However, the required bending radius for the arcs increases with increasing energy. Thus, different types of acceleration systems will be used for different energy ranges, and different stages of a given type of acceleration system may be used in sequence (for instance, increasing the arc bending radius and increasing the RF frequency from one energy range to the next).

1.2 Expected RF parameters

We're assuming the following relationships for the parameters of the r.f. cavities:
$r_s = 25\ \text{M}\Omega/\text{m}\sqrt{f/800\ \text{MHz}}$, $Q = 30000\sqrt{800\ \text{MHz}/f}$, and $v_{\text{max}} = 30\ \text{MV/m}\sqrt{f/800\ \text{MHz}}$; here r_s is the shunt impedance per unit length, v_{max} is the maximum peak gradient, and f is the frequency. These are parameters which we expect to be reasonably achievable before the time that a muon collider is built.

2 TYPES OF STAGES

Various types of systems have advantages and disadvantages which make them more or less suitable for various

0-7803-5573-3/99/$10.00@1999 IEEE.

energy ranges.

2.1 *Pure Linac*

A linac has the advantage that it has no arcs, and therefore does not have the energy acceptance issues associated with arcs. There is still an energy acceptance associated with the height of the bucket, however. One disadvantage is that the particles make only one pass through such a system.

A linac is probably optimal for the lowest energies (up to 1 GeV, for example): it does not need to be particularly long, and the larger longitudinal emittance at the lowest energies is more readily accommodated by a linac.

In reality, several linacs would be required, since the requirements that the beam be matched longitudinally and fit inside the RF bucket require different frequencies at different energy ranges to achieve the optimal acceleration gradients (which is very important at these low energies due to the shorter muon lifetime). The following would be close to the optimal scheme to accelerate to 1 GeV:

Energy range	Frequency	Length
186–300 MeV/c	50 MHz	20 m
300–600 MeV/c	100 MHz	40 m
600–1000 MeV/c	200 MHz	45 m

The matching requirement requires that one runs rather far off crest (over 50°), reducing the gradient, and it should therefore be considered whether that is necessary or useful. Further study is required to determine whether the lowest frequencies above are realistic.

2.2 *Multiple Arc Recirculating Linac*

This design (used in CEBAF) has the advantage that several passes are made through the linacs, thereby getting a larger amount of acceleration from a given length of linac and amount of RF power. The primary difficulty with such a system is related to the larger longitudinal emittance of the beam. Since the RF frequency needs to be as high as possible to maximize the acceleration gradient, this leads to a relatively large energy spread in the beam. This energy spread, at least at lower energies, is often so large that $\pm 3\sigma$ of the beam will not pass through a traditionally designed arc. In addition, the energy spread in the beam is too large to have passive switching into the appropriate arc, and so very fast kickers are required, which additionally must have larger strengths and transverse apertures.

One solution to avoid the cost of individual magnets for each arc is to have a single magnet with multiple bores that the beam can pass through, depending on the energy. The disadvantage of this is that one may lose turn-by-turn control of the path length and other parameters. Superconducting magnets with as many as 18 apertures with fields varying over the range of 0.7 to 7.0 T have been designed [1].

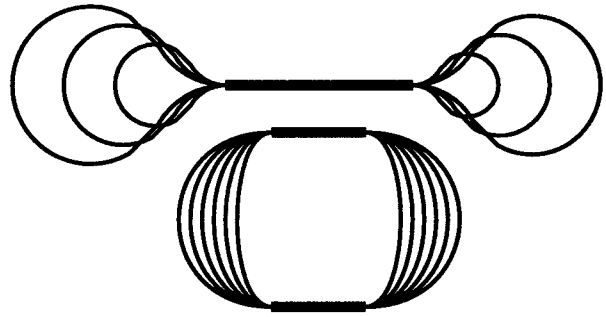

Figure 1: Comparable dogbone (above) and recirculating (below) geometries. Arcs are disproportionately long.

2.3 *FFAG Recirculating Linac*

This is an attempt to address the issue of the energy acceptance of the arcs by making a single arc with an enormous energy acceptance; we have looked at designs for the 4–16 GeV range and the 16–70 GeV range. This additionally can avoid the need for kickers to switch between arcs, as well as allowing multiple beamlines and therefore multiple sets of magnets. There are several difficulties with such a system, however: when using only a single arc for all energies, one loses the ability to control parameters such as path length on a turn-by-turn basis, as well as the local momentum compaction; the arc design becomes much more complex; matching into straight sections becomes more difficult and can be done perfectly only for one energy; and the magnets are large and require high fields.

Two types of FFAG designs are being considered: a "scaling FFAG," where the orbits have the same geometric shape for all energies [2]; and a non-scaling variety which is generally more compact than the scaling FFAG.

One compromise solution may be to use a FFAG-like lattice to increase the energy acceptance of a multiple-arc recirculator.

2.4 *Dogbone*

As far as muon decays are concerned, any time in an arc is bad. In an racetrack recirculating linac design, the distance between the two linacs is determined by the radius of curvature required for the maximum energy. The minimum radius of curvature for lower energies is significantly smaller than the minimum radius at the maximum energy, and so if the linacs were closer, one could have a smaller distance traveled in the arcs. One solution to this problem is a "dogbone" scheme: the two linacs are placed in line with each other (instead of parallel), the beam goes through the two linacs, turns around, and enters the same linac that it just exited (see comparison in figure 1). The radius of curvature for the arcs can be as small as possible for the energy of each particular. Thus, there is a substantial reduction in the amount of time spent in arcs at the lower energies. Not only will this reduce the muon decays, but it can potentially

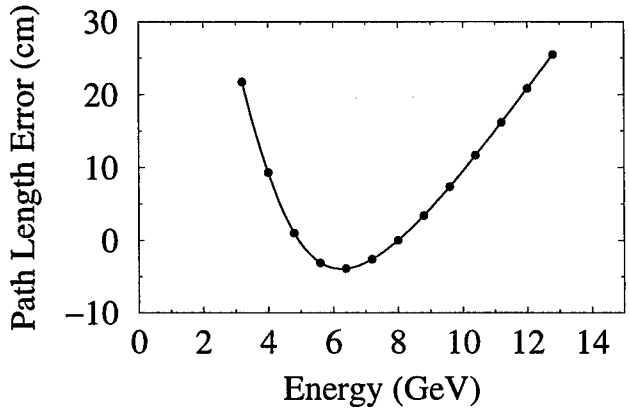

Figure 2: Path length as a function of energy for an FFAG arc. This is the error for a single turn, not a cumulative error; changing the RF frequency only changes where zero lies in this graph.

reduce the droop in RF voltage due to wall losses, giving slightly higher effective gradients. At higher energies, the path length is actually slightly longer than it would be with an racetrack design, but it is the low energies which are critical for muon decays since the muon lifetime is shorter for lower energies. There could potentially be higher costs, however, since each arc would most likely require its own tunnel, and there would be no opportunity to use multiple-bore magnets.

One promising use for the dogbone scheme is in an early stage of the acceleration scheme, where the energies are still relatively low. The dogbone could be designed so that the sequence that the beam sees is linac-arc-linac-arc-linac, eliminating the requirement for multiple arcs at each end (and the associated kickers), and yet using the same linac for three passes. This is currently our preferred solution for the 1-4 GeV range; it would require a single 1 GeV linac to accelerate from 1 to 4 GeV. Using 200 MHz RF, we could hope to keep such a linac under 100 m long.

3 SPECIFIC ISSUES

3.1 *Dynamic RF Control*

With a recirculating system, there are difficulties in synchronizing the beam with the RF from one turn to the next. This is especially important for the FFAG arcs, since the path length cannot be controlled on individual turns, and the path length varies substantially with energy (see figure 2). In addition, there will be a variation in the beam loading (and therefore the output energy of the acceleration stages) with the bunch current, which will not be known a priori to high accuracy. To correct for this, some kind of dynamic control of the RF systems is necessary, which may require that at least the phase of the RF can be changed (maybe substantially) from one turn to the next.

There are three potential ways to do this: one can pump in power, one can use ferrites which have their permittivity changed dynamically (changing the RF frequency), or one can create a path length variation using fast magnets. Pumping in power to correct phase errors like those in figure 2 could potentially double the peak power requirements, and thus is an undesirable solution (but may be possible for correcting variations from beam current fluctuations). Ramping magnets sufficiently quickly to achieve substantial path length variations in the smaller rings (such as a 300 m long 4–16 GeV FFAG) is probably impossible. Thus, using ferrites or some other mechanism to dynamically change the RF frequency is an attractive solution. Whether it is possible to do this with these types of RF systems is being studied.

3.2 *Kickers*

For injection and extraction, as well as for switching between arcs in any of the multiple-arc recirculation schemes, we require kickers which are both fast and have a large transverse acceptance.

The case giving the most stringent requirements for a kicker will probably be a recirculating linac or FFAG in the 4-16 GeV range: the circumference is the smallest of all the recirculating-type machines (around 300–400 m), and the beam emittance will be at its largest (amongst the recirculating machines). Taking a β-function of 50 m, and a ring circumference of 300 m, the requirements for such a kicker at 4 GeV would be approximately

Aperture (full width)	12 cm
Kick strength	43 mT/m
Rise time (full)	500 ns
Repetition time	60 ms

From table 1 in [3], these appear to be reasonably achievable requirements (that table gives significantly longer repetition times, but there is no reason to believe that those designs could not be run at higher repetition rates). Up to a point, the β-function can be reduced to reduce the required aperture at the cost of increasing the required kick strength. The required rise time increases to 1000 ns if the kickers are only required for injection and extraction.

3.3 *Other Effects*

There are other effects which have not been discussed here; amongst them are HOM wakefield effects, the effect of having two beams, and magnet technology necessary for the arcs (particularly the FFAG's).

4 REFERENCES

[1] S. Khan, G. Morgan, and E. Willen, "Recirculating arc dipole for the 2+2 TeV μ^+-μ^- Collider," unpublished (1996).

[2] K. R. Symon *et al.*, "Fixed-Field Alternating-Gradient Particle Accelerators," Phys. Rev. **103**, 1837–1859 (1956).

[3] G. H. Schröder, "Fast Pulsed Magnet Systems," CERN-SL-98-017, to appear in *Handbook of Accelerator Physics and Engineering*, edited by A. Chao and M. Tigner, World Scientific (1999).

Measurements of Intrabeam Scattering Rates below Transition in the Fermilab Antiproton Accumulator*

C. Bhat, L. K. Spentzouris and P. L. Colestock
Fermi National Accelerator Laboratory
P. O. Box 500, Batavia, IL 60510, USA

Abstract

An important factor in the successful operation of the Antiproton Recycler Project at Fermilab is the rate at which intrabeam scattering heats the stored beam in each plane. This machine will operate below transition energy. An application of classical intrabeam scattering theory for such a machine indicates that transverse or longitudinal cooling might occur, rather than heating, under certain conditions. However, this effect has not been studied experimentally. Hence, we have undertaken a study of the heating/cooling rates below transition in a coasting antiproton beam in the Fermilab Accumulator Ring, in an attempt to verify the theoretical models in this regime. This storage ring employs a variety of stochastic cooling systems which can be used to alter the ratio of emittances in each plane as the initial conditions for our experiment. We have used both a conventional free-expansion technique as well as a longitudinal-echo-decay-rates technique to determine the scattering rates. In this paper, we present a preliminary analysis of our data and its comparison with various intrabeam scattering models below transition.

1 INTRODUCTION

It is a well-known theoretical result that inter-particle collisions cause an exchange of energy from the directed motion of relativistic beam above transition into thermal energy in all three planes of motion. [1], [2] A body of experimental results [3] has confirmed the general character of this model. It is also expected that below the transition energy, the behavior of the beam particles approaches that of a normal gas. Namely each degree of freedom exchanges energy with another according to its relative temperature. In particular, it is possible to expect cooling of the horizontal plane below transition, as the longitudinal plane in typical situations is initially colder than either of the transverse planes. This behavior has not yet been observed in a high-energy storage ring.

In the Fermilab Recycler, a stored beam of antiprotons will exist below the transition energy of that device, and it is important to understand the effects that intrabeam scattering will have on emittance growth, as this fixes the requirement for cooling of the stored beam. To elucidate this issue, we have carried out a series of experiments in the Fermilab Antiproton Accumulator below transition, and compared the results with the existing models. In this paper we discuss both the experimental results and the comparison with theory.

2 EXPERIMENTAL RESULTS

The approach taken in this work was to study the free expansion of the stored beam beginning from a variety of initial conditions, facilitated by the flexible stochastic cooling system on the Accumulator. In addition, longitudinal echoes [4] were used to provide a second measurement of the longitudinal diffusion. Both methods are expected to be valid over a range of scattering times, but the echo method is in principle valid to much longer decay times than where free expansion measurements can readily yield useful results. For these experiments, a suitable lattice for below-transition operation was prepared, along with procedures for decelerating the stored beam. The lattice used had a transition gamma of 5.42, and the beam was successfully decelerated to a gamma of 4.86. Beam losses during deceleration prevented operation at lower energies. While this energy is not sufficiently far below transition to clearly demonstrate transverse cooling, it extends into a new regime of the scattering models that has not received detailed study, and will help confirm the applicability of the scattering models below transition.

The measurement technique consisted of observing the free expansion of the beam with all cooling systems turned off, starting from a variety of initial conditions which spanned the achievable transverse and longitudinal emittance spaces. Emittances were monitored continuously by measuring the spectral width of the longitudinal Schottky noise or by a similar measurement of the transverse fluctuations. Since the translation of this data into emittance values requires detailed knowledge of the twiss parameters, some systematic error is expected to be introduced in this step, as these parameters were not directly measured in these experiments. Longitudinal echoes were also used as a second check of the longitudinal diffusion rates, especially because the accuracy of the echo measurement extended to the ultra-weak diffusion regime ($< 0.1 hrs^{-1}$) where free expansion measurements are limited by measurement error. Echo measurements were carried out at the beginning and end of each free expansion measurement to aid in corroboration of the two methods. Typical expansion data is shown in Fig. 1. Typical echo decay data is shown in Fig. 2.

* Operated by the Universities Research Association,Inc, under contract with the U.S. Department of Energy

0-7803-5573-3/99/$10.00@1999 IEEE.

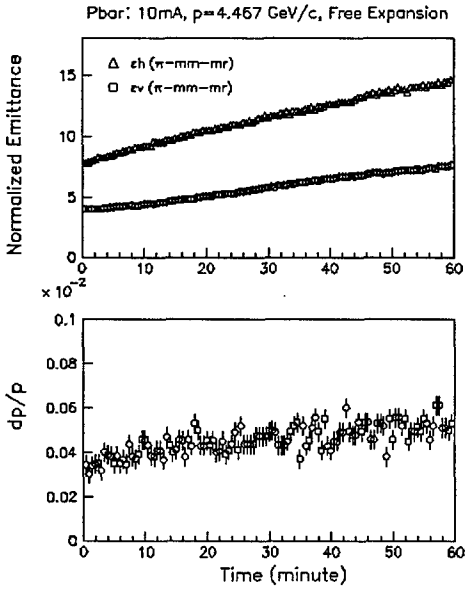

Figure 1: Free expansion measurements. All cooling systems are switched off for these measurements. The growth time is found by fitting a low-order polynomial to the emittance evolution with time.

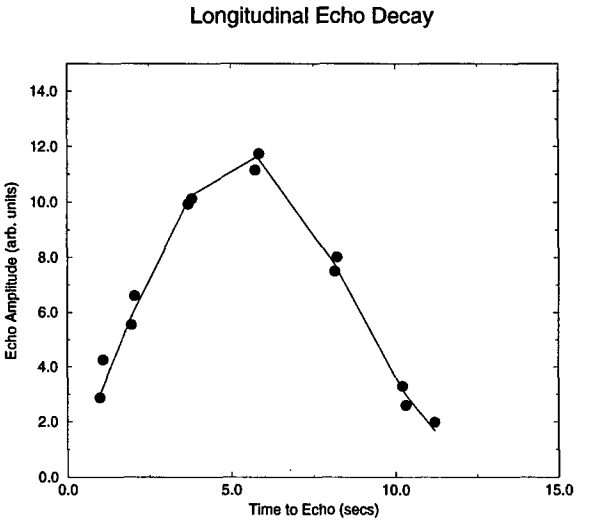

Figure 2: Longitudinal echo decay measurements. All cooling systems are switched off for these measurements. The growth time is found by fitting a two-parameter model (solid line) to the measured decay envelope (points) which yields both the amplitude and the inverse scattering time.

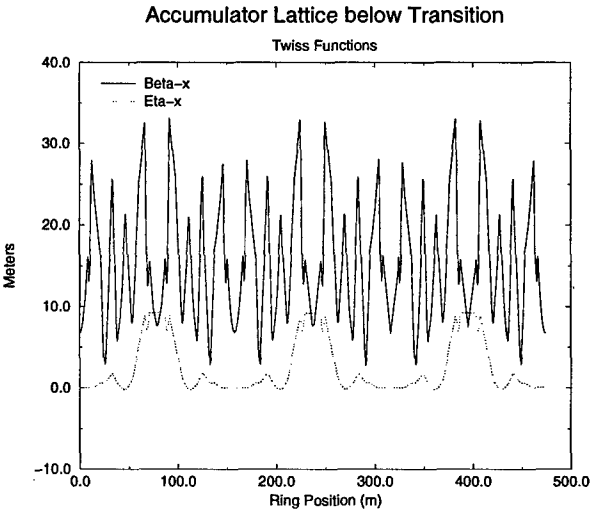

Figure 3: Below transition lattice as calculated by MAD. Similar functions are found for the vertical plane.

2.1 *Comparison with Theory*

The theoretical predictions are based on the complete intrabeam scattering theory [2] as applied to the full lattice model of the Accumulator below transition. The calculation of the growth times depends on detailed knowledge of the twiss parameters of the machine, which were not directly measured for these experiments, but were calculated using the MAD code. The results of this calculation for these experiments are shown in Fig. 3, and are subject to an estimated 30% systematic error. This corresponds to a similar error in the calculated growth times. In addition, measurements of the beam emittances were subject to a systematic error estimated at 20%. While this leaves considerable lattitude in comparing the theory with the experiment, the systematic character of the error does permit a comparison of the scaling of the scattering rates.

For the lattice shown in Fig. 3 , the growth rates evaluated locally for an uncoupled lattice are shown in Fig. 4. The comparison of the experimental data with the theory for growth in the longitudinal plane is shown in Fig. 5. We find an overall favorable agreement in the scaling over a factor of one hundred in the growth rate, although adjustments in both the transverse and longtiudinal emittances did have to be made to achieve this agreement, as noted. Since the vertical growth for an uncoupled machine is negligibly small, the observed equal growth rates in each plane suggest strong coupling. [5] While the source of coupling in the machine was not measured, and hence could not be calculated, the observed equal growth rates in the vertical and horizontal planes suggests 100% coupling existed. As such, a useful approach is then to average the emittances in the two planes for calculating the growth rates. Hence, the transverse emittances were assumed to be equal, and re-

duced from the calculated values by 30%. The longitudinal emattance was reduced by 25%. Both of these assumptions are considered consistent with the expected accuracy of the calculated twiss functions. We note that there is excellent agreement between the free expansion data and the echoes where the data overlaps. Moreover, the echo data extends far into the weak diffusion regime ($< 0.1 hrs^{-1}$).

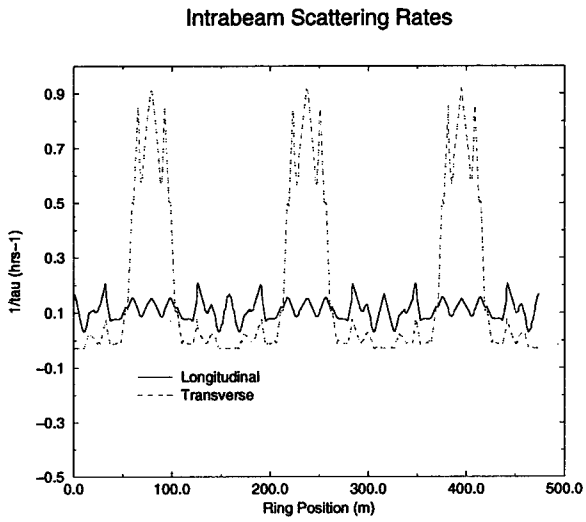

Figure 4: Intrabeam scattering rates evaluated locally around the ring for a specific set of measured emittances.

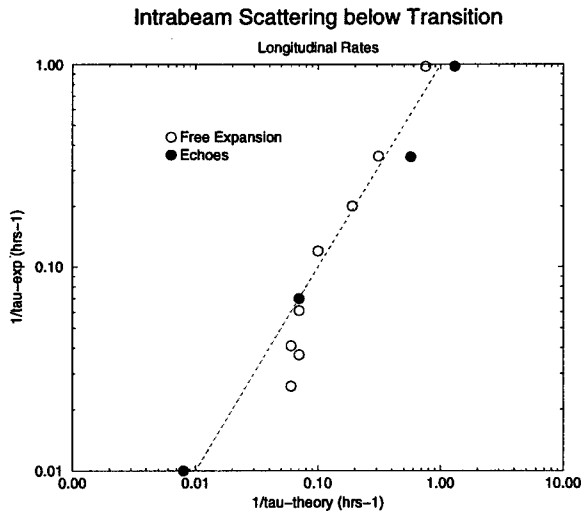

Figure 5: Comparison of the theory to experiment for longitudinal scattering rates. The dashed lines represents agreement.

The corresponding transverse data is shown in Fig. 6 as derived from free expansion data. Here the correspondence to the theory is less satisfactory, however there are expected uncertainties of the twiss functions and transverse emittances, in addition to measurement errors at long growth times. As such, the overall scaling can be viewed as roughly consistent with the theoretical model.

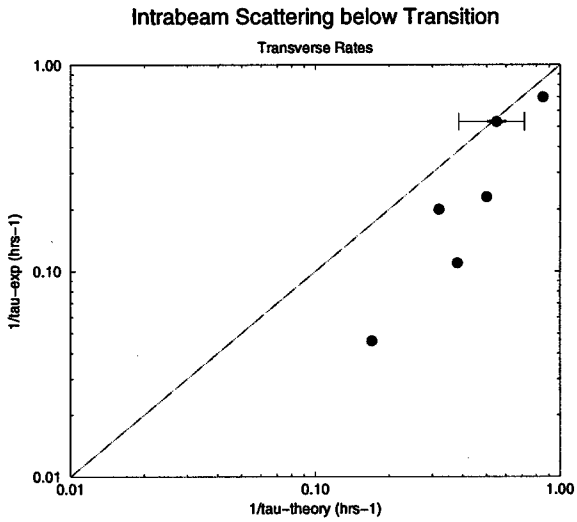

Figure 6: Comparison of the theory to experiment for transverse scattering rates.

2.2 *Discussion*

We find very good agreement between the experimental intrabeam scattering data and the models provided the following adjustments are made. First, the transverse emittances are reduced by 30% to accomodate a systematic uncertainty in the emittance measurements. Second, coupling was invoked to explain the observed heating of the vertical plane, as noted above. Finally, a 20% reduction of the longitudinal emittance was assumed. Since, neither coupling nor emittance measurements were verified by an alternative method, we have no way of directly corroborating these assumptions. However, once correction factors are determined and applied to the data, the observed agreement of the scaling between theory and experiment suggests that the model is likely correct. We conclude that the existing scattering models are at least consistent with the experimental data in the regime around and below transition.

3 REFERENCES

[1] A. Piwinski, Proc. 9th Int. Conf. on High Energy Accelerators, Stanford, p. 406, (1974)

[2] J. D. Bjorken and S. K. Mtingwa, Particle Accelerators, Vol. 13, p. 115 (1983)

[3] M. Martini, CERN PS/84-9 (1984)

[4] L. K. Spentzouris, *et al.*, *Phys. Rev. Lett.* **76**, 4 (1996)

[5] A. Piwinski, DESY 90-113, Sept. (1990)

POWER SUPPLY SYSTEM FOR SUPERCONDUCTING MAGNETS AT KEKB-IR

T.Ozaki#, A.Akiyama, Ta.Kubo, T.Nakamura, T.Ogitsu, N.Ohuchi, K.Tsuchiya, M.Yoshida,
KEK, Tsukuba, Japan.

Abstract

At KEKB, a pair of superconducting magnets is installed symmetrically with respect to the Tsukuba Interaction Region (IR) in order to focus and steer the beams. Two quadrupole magnets (QCS) are being prepared to focus the beams, two solenoid coils are to shield the magnetic field of the solenoid coil of the detector, and 6 correction coils are to steer the beams. These magnets are to be energized by high-stability power supplies (P.S.s) to maintain a long-term magnetic field. This paper discusses the details concerning the P.S.s and their control.

1 MAIN P.S. FOR QCS MAGNETS

In the TRISTAN main ring, 4 pairs of superconducting quadrupoles (QCS) were used at each 4 colliding sections. The 4 P.S. were fabricated [1]. At KEKB, one of them was improved to excite new QCS magnets. The KEKB QCS magnets are compact compared to the TRISTAN QCS magnets. The 2 QCS magnets are powered in series.

The QCS P.S. consists of a main P.S. and an auxiliary P.S. as shown in Fig.1. The main P.S. has a capability of 3500 A and 15 V. This P.S. consists of a converter and a quench-protection circuit. The converter consists of 12-pulse phase-controlled rectifies, a passive filter and an active filter. A thyristor switch has prepared to intercept the dc current in the case of any quench trouble.

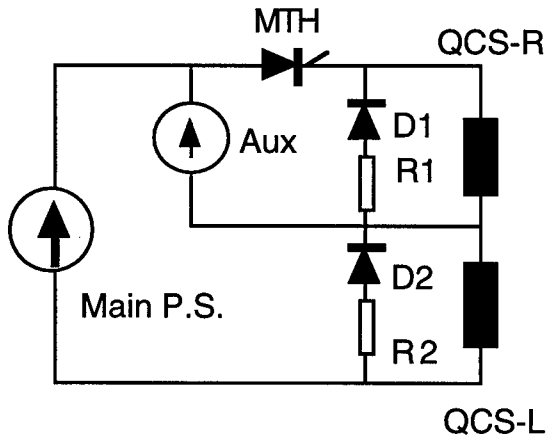

Figure 1: The circuit of QCS main and auxiliary P.S..

1.1 Effect for New Load

The inductance of the load becomes 36.4 mH instead of 120 mH. The resistance of the cable remains at 1.5 $m\Omega$.

In the KEKB operation, the QCS magnets is excited to generate the field gradient of 21.3 T/m at a current of 2830A. We can therefore use the TRISTAN QCS P.S. with a few improvements.

The transfer-function block diagram of the closed-loop control in the P.S. is given in Fig. 2. The system has two closed control loops. The minor auto-voltage regulation (AVR) loop is inside the auto-current regulation (ACR) loop. The simulations show that the responses become slow. However, it is not serious because KEKB is a storage ring without acceleration.

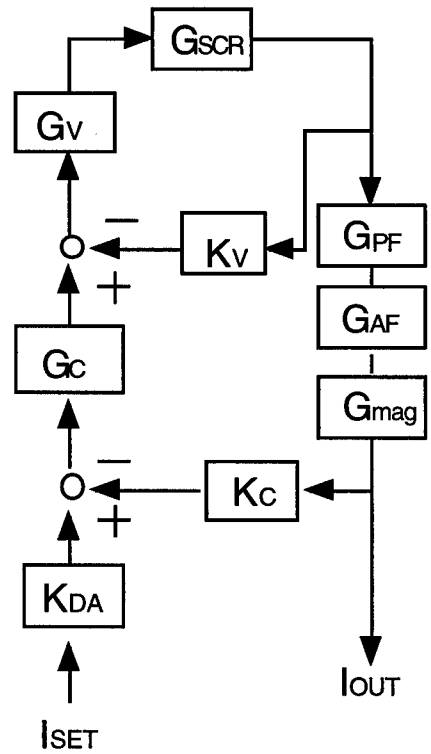

Figure 2: The transfer function block diagram of QCS main power supply is shown. The elements are given as follows:

$$G_{SCR} = 20 \cdot 1.35 \cdot \frac{1}{8.25}$$

$$G_{PF} = \frac{63000}{s^2 + 980s + 63000}, \; G_{AF} = \frac{1}{0.2s+1},$$

$$G_{mag} = \frac{1}{8s+1}, \; G_V = \frac{1000}{s}, \; G_C = \frac{54.5}{s} + 94,$$

$$K_C = \frac{10}{4000}, \; K_{DA} = \frac{9.5}{3500} \cdot \frac{35}{40} \cdot \frac{10}{9.5}.$$

Email: ozaki@post.kek.jp

1.2 Fast-Stop and Slow-Stop

The fast stop of the QCS P.S. is triggered from one of 3 quench detectors. The thyristor switch (MTH) intercepts the dc current within 1 ms, and the energy stored in the magnets dissipates in stainless-steel resistors (R_1 and R_2) through the diodes as shown Fig.1.

In KEKB, the inductance (L_1) of QCS of the right side is 16.2 mH, and L_2 of the left side is 20.2 mH. In order to reduce the current in the neutral line, we changed resistor R_1 based on the condition $L_1 / R_1 = L_2 / R_2$. The resistors are 0.1 Ω and 0.125 Ω, respectively.

In the slow-stop mode, a counter IC (which connected to the DAC) counts down by 1 bit per clock pulse. The current decreases at a rate of about 10 A/s.

2 AUXILIARY P.S. FOR QCS-R

A bipolar 40 A auxiliary P.S. is connected to the QCS-R magnet. Such a connection produces an unbalance between two QCS magnets to zero with the required accuracy. On the contrary, it has the possibility to produce an imbalance of the field integrals between two magnets.

The circuit of the auxiliary P.S. is shown in Fig.1. The output terminals of the auxiliary P.S. are connected to a magnet through contactors. The relay contactors are used to change the polarity on the magnet. In minus polarity, the plus voltage of the main P.S. imposes the output of the auxiliary P.S.. To avoid this situation, a series of diodes is installed in line, which produces an offset voltage of 7 V.

3 P.S. FOR SOLENOID COIL

The detector BELLE at IR has a solenoid field with 1.5T to distinguish the particle track. The solenoid field couples the horizontal and vertical betatron oscillations of the beam. This makes a ring less dynamically stable and lowers the peak luminosity. The simplest compensation is to place two half-solenoids at each side of the IR. The solenoids produce an axial magnetic (B_Z) field opposite to the detector solenoid.

Superconducting solenoid coils are installed before the first quadrupole QCS. The inductance of the right-side solenoid is 1.44 H and that of the left side is 0.9 H. Since the resistances of the cabling from the P.S. to the magnet are 8.3 $m\Omega$ and 11 $m\Omega$, the time constants are 173 s and 82 s, respectively.

3.1 Switching Power Supply

In KEKB, many switching P.S.s are installed. We adopted the switching type for the superconducting coils. The ratings of the solenoid P.S. are 650 A and 30 V. In the P.S., the three-phase input (AC 420V) is rectified and filtered to provide an unregulated dc voltage (DC 600V). The unregulated dc is converted into high-frequency square waves by the IGBTs. The square waves through the high-frequency transformers are rectified. The output voltage of the converter is controlled by the PWM (pulse width modulator) circuit. Power FETs so as to control the output current precisely is used. The current regulator obtains its feedback signal from a high-precision DCCT (DANFYSIK 864I DCCT). This type DCCT is compact and cheap compared to the 4-core-type DCCT used in TRISTAN [2]. The output current must be compared with a current reference. The reference source is a 16-bit DAC on its 9.5 V dc scale. The error signal is sent to the FET bank.

3.2 Fast-Stop

DCCBs (Direct Current Circuit Breaker) are adopted to intercepts the dc current. The response speed is about 30 ms, which is much slower than the thyristor switch because of opening the mechanical contactors. The operation is limited to 500 times. However, the cost is very cheap compared to that of the thyristor switch. A damping resistor of 0.71 Ω is connected to the terminals through a diode.

At the initial cool-down testing of solenoid coils, the current was limited by quenching at about 210 A. Fig.3 shows the output voltage and current of the ESR P.S.. The current ramps from 200 A at the speed of 1 A/s. Around 210 A, the voltage suddenly increases. DCCB intercepts the dc current, the minus voltage of 150V is produced, and the current decays at the time constant of 2 sec.. Afterward, the quench origin was revealed, and expeditious remedial measures were taken. At the second cool-down test, no quenching occurred for currents up to 110 % of the design values.

Interference effects between these solenoids and the detector solenoid were measured by the pseudo-quench tests. The peak voltages on the output terminals of the each P.S. when the quench of the detector solenoid occurred were 7V and 4.5V, respectively.

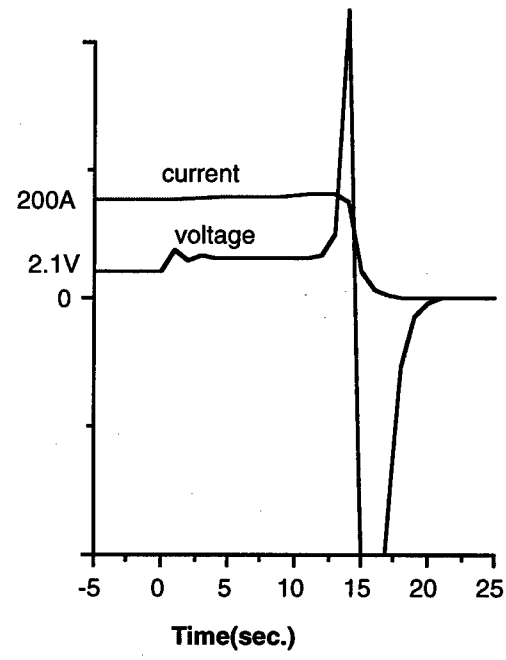

Figure 3: The fast-stop operation of solenoid ESR power supply is shown .

3.3 Slow-Stop

In the slow stop, the gate pulses to fire IGBTs are blocked and the source voltage of the converter is vanished. The current through the magnet naturally decays. The current decreases of the ESR P.S. and ESL P.S. are shown in Fig.4, respectively. The decreases are faster than the exponential decays of the time constant of the load by the nonlinear resistances such as FETs and diodes in the P.S..

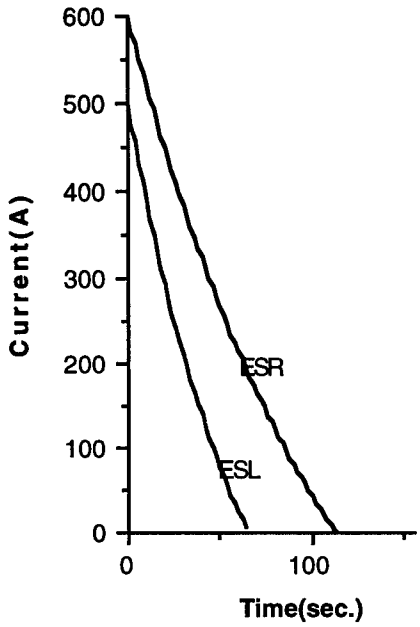

Figure 4: The slow-stop operations of solenoid power supplies are shown.

4 P.S. FOR CORRECTION COIL

Correction coils (a skew quadrupole, an H-dipole and a V-dipole) are housed in each of the QCS cryostats. These 6 coils are excited by 6 bipolar P.S.s. The inductance of the skew is 23 mH, and that of the steering is 45 mH. The rating of the P.S. is ± 50 A and ± 20 V. The field strength of the steering coil is about 0.05 T and the gradient of the skew quadrupole is about 0.4 T/m.

The terminals of the DC output of a P.S. are connected to the magnet though relay contactors. The relay contactors are used to change the polarity. An energy-damping circuit and DCCB is installed between the relay contactors and the magnet.

The current is monitored using two DCCTs. One is for current stabilization control and the other for the monitor of the damping current.

5 CONTROL SYSTEM

These P.S.s are operated by computers via VME-ARCNET. They are also operating under a safety system. Each P.S. has a fast-stop mode and a slow-stop mode.

5.1 Current Setting

The exciting current is remotely set by computers through the VME-ARCNET. The VME-ARCNET is adopted in stead of the CAMAC in TRISTAN. The interface board in each P.S. receives current setting signals from an Input/Output Controller (IOC) in a VME crate and send fault-signals to the IOC. The communication between IOC and interface board employs ARCNET. The VME is connected to the KEKB computer system. The system has utilized EPICS (Experimental Physics and Industrial Control System).

The interface board sends 16-bit digital signals to a DAC (Digital to Analog converter) in the P.S.. The output of the DAC is used as a current reference.

5.2 Fast-Stop Interlock

When a quench in a magnet occurs, the exciting current must be quickly decayed. The quench detection is based on measurements of the voltage among the ends and center tap of the coil. If a quench occurs, a differential voltage appears, and the quench is detected. As soon as the detector sends a trigger signal to the P.S., it must be quickly stopped. The typical quench threshold is set at 1V for 10 ms or more.

5.3 Slow-Stop Interlock

In some cases, the current must be decreased slowly based on the judgment of the cryogenic computer or the operators. The EX1000 computer which controls the cryogenic system can command the P.S.s to stop either quickly or slowly. In a different way, the P.S.s can be stopped slowly by pressing stop-buttons for rotary warning lights .

6 CONCLUSIONS

The power supply system for superconducting magnets at KEKB were designed and fabricated [3]. Since the KEKB commissioning of December of 1998, the superconducting magnet power supply system is under operation.

7 REFERENCES

[1] T. OZAKI, K.EGAWA, K. ENDO, N. OHUCHI, Y. OHSAWA, A. KABE, Ta. KUBO, S. KURODA, R. SUGAWARA, K. TSUCHIYA, H. FUKUMA, Y. MORITA and S. OGAWA, " Power Supply System for Superconducting Quadrupole Magnets of the TRISTAN main ring", Proceeding of the 8th Symposium on Accelerator Science and Technology (1991) pp232-233.

[2] Toshiyuki OZAKI, "DCCTs for Magnet Power Supplies", Proceeding of the 10th Symposium on Accelerator Science and Technology (1995) pp106-108.

[3] T. OZAKI, A. AKIYAMA, T. OGITSU, N. OHUCHI, Ta. KUBO, K. TSUCHIYA and M. YOSHIDA, "Power Supplies for Superconducting Magnets at KEKB-IR", Proceeding of the 11th Symposium on Accelerator Science and Technology (1997) pp383-385.

CONSTRUCTION OF HELICAL MAGNETS FOR RHIC*

E. Willen#, E. Kelly, M. Anerella, J. Escallier, G. Ganetis, A. Ghosh, R. Gupta+, A. Jain, A. Marone, G. Morgan, J. Muratore, A. Prodell, and P. Wanderer, BNL, Upton, NY
M. Okamura, RIKEN, Japan

Abstract

Helical magnets are required in RHIC to control proton spin in a program for polarized proton colliding beam experiments. The basic construction unit is a superconducting magnet producing a four tesla dipole field that rotates through 360 degrees in a length of 2.4 meters. These magnets are assembled in groups of four to build four Snakes to control spin in the lattice and eight Rotators to orient spin at two collision points. A collaboration with the Japanese institute RIKEN is providing financial support to carry out the program. After a successful R&D program to validate the design, the magnets are in the construction phase. The design of the magnets will be reviewed, the construction approach will be described, and test results from the first completed units will be presented.

1 INTRODUCTION

Previous papers [1-5] have described the parameters needed to control the spin of protons in RHIC. Specifications for the magnets include a large aperture (100 mm), a dipole field (4 T) that rotates through 360° in a distance of 2.4 m, and operation at modest current (<500A). By the standards of superconducting accelerator magnets, the field quality requirements are modest (harmonics $<10^{-3}$ of main field). The error allowed on the rotation angle is two degrees. The complete program in RHIC requires 48 of these magnets. A half-length prototype tested in 1997 validated the current design [1,4] and led to the construction program now underway.

2 DESIGN

A cross section drawing of the helical magnet is shown in Fig. 1. The coil structure consists of aluminum tubes with slots that are filled with Kapton-insulated superconducting cable (called windings). The tubes are surrounded by a yoke made of single piece, low-carbon steel laminations. Holes near the outer perimeter of the yoke allow for tie rods, warm-up heaters, passage of helium coolant, and bus work for magnet interconnections. The slots rotate along the magnet length but the holes in the yoke do not; these were therefore designed with rotational symmetry in mind. Azimuthal Lorentz forces are contained in the individual slots and, in contrast to the case of cos θ dipole magnets made with keystoned cable, do not build up on the midplane turns. Along the length of the magnet, the outward Lorentz forces are ultimately contained by the single piece yoke. In the ends [6], the difficult Lorentz force problem is again solved by containing the forces in the individual slots, as shown in Fig. 2. This figure also shows the reliefs machined into the tubes for the leads.

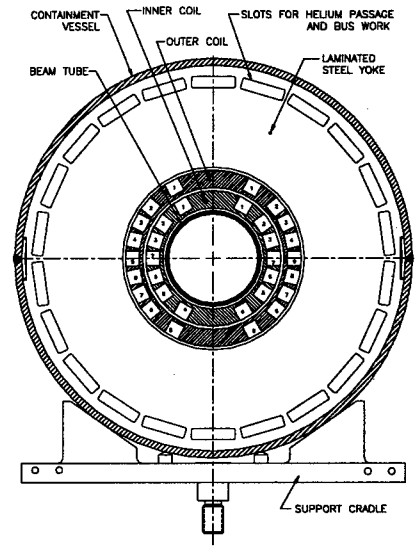

Fig. 1: Cross section of the helical magnet. The yoke OD is 14". The innermost conductor is at an ID of 100 mm. The coil tube outer diameters are 4.945", 6.425".

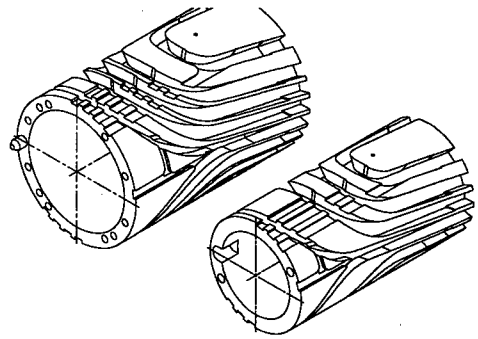

Fig. 2: Drawing of the coil tube ends. End Lorentz forces are contained in the slots.

3 COILS

3.1 Coil Mechanics

The aluminum tubes are purchased as blanks ready for the machining of the slots. Steps in their manufacture include extrusion, annealing, gun-drilling, honing (ID), and machining (OD). The most critical dimension is the inner surface of the outer tube, where the diameter is specified

*Work supported by RIKEN and by the US Department of Energy
email: willen@bnl.gov
+Now at LBNL, Berkeley, CA

±2 mils. Straightness over the full length is specified ±10 mils. Slots are machined into the tubes at BNL using an IGES file generated by AutoCad design software. The machining operation is done on a milling machine using a 0.5" end mill to cut the 0.560" wide slot in successive passes, each pass removing a depth of 0.25" material. A finishing end mill is used to finish the sides and bottom of the slot. All dimensions are measured relative to a keyway or pin at the end of the tube. Errors in slot position are approximately ±10 mils or less along the length of the slot. The slot length can be off by up to 20 mils, due primarily to temperature variations and compressive forces during the machining operation.

Before winding, the slots are lined with Kapton for additional electrical insulation of the conductor. Preformed three mil strips secured with two mil 3M Corp. 465 adhesive film are applied along the length of the slot. Fig. 3 is a drawing of the slot showing this insulation. In the ends, the slots are insulated with short 3/8" wide, one mil thick, 50% overlapped strips of Kapton backed with silicone adhesive. This is labor intensive but no less

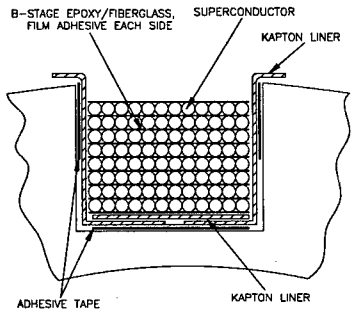

Fig. 3: Cross section of a slot. It is 0.560" wide and 0.512" deep. Each slot has 108 turns except the pole slots, which contain 96 turns. All slots have the same dimensions, which aids the construction.

costly way has been found to apply insulation free of wrinkles and voids in that region. The integrity of the insulation is checked to 4 kV by passing a conductive piece of foam along the full length of each slot. Thin Nomex barriers are used as necessary to prevent damage to the conductor or to the Kapton insulation.

The superconducting cable is placed, either by machine or by hand, without tension into the slots in an ordered array. The width of the slot is such that 12 turns of the cable (each 0.045" diameter including 0.039" cable, 0.004" Kapton insulation and 0.002" adhesive coating) have on average about one mil space between turns. A layer of B-stage fiberglass/epoxy (either Fiber-Resin Corp. 8600 or Fravillig Materials Corp. epoxy phenolic) with adhesive film (3M 465) on each side is placed between each layer (Fig. 3). This material contains ~40% by weight of epoxy.

After winding, press plates of 0.125" thick G10 fiberglass are applied to each slot and secured with ring clamps. These plates are preformed to a helical shape or to the end shape by heating and forcing into an appropriate shallow slot. A wrap of Kevlar 29 (Denier 1000, 20 lb tension or 720, 10 lb tension) is applied to the tube in a prescribed pattern. The Kevlar stretches and applies pressure on the press plates. In the subsequent curing operation, the stretch in the Kevlar allows the press plates to move radially inward without losing all tension, thereby compressing the windings and removing voids in the slots as the epoxy softens and fills the remaining spaces. Thus, after curing, the cable is held in a strong matrix of fiberglass and resin that can later withstand the Lorentz forces that would cause motion and quenching. Helium is still able to penetrate this package and fill the ~10% free space inside the Kapton wrap and around the wires of the cable.

As the cable is pressed radially inward during curing, it expands axially because of the helix and, in the ends, because of the curvature of the cylinder. To accommodate this growth, additional axial space (0.030") is allowed in the slot ends. The windings are observed to sometimes fill this space but not to do so consistently. If they do not, the growth is absorbed along the length of the winding. In all cases, any spaces left in the ends after the curing operation are filled with Emerson & Cummings Corp. Stycast 2850FT epoxy while the structure is being gently vibrated to ensure that all voids are filled. Cut-outs in the press plates provide access to the windings for this filling operation.

After curing to the prescribed recipe, the Kevlar is removed to allow access for the aforementioned filling and the dressing and securing of leads (using Stycast 2850MT epoxy). The tube is then wrapped with a layer of fiberglass cloth to cushion sharp edges that might damage the final Kevlar wrap. A new wrap of Kevlar 29 Denier 1000 is applied with 10 lb tension and a pitch of 0.036". A layer of Tedlar is wrapped over the Kevlar to prevent epoxy of the final wet-wrap of fiberglass and epoxy from penetrating into the Kevlar. This is done to prevent cracking of epoxy bonds due to stress from differential thermal coefficients upon cooldown to cryogenic temperature. Multiple layers of fiberglass cloth and Shell 815V40 epoxy are applied to build a radial thickness sufficient to avoid hollows when the tube is subsequently machined to its finished diameter. The tube is continuously rotated while this epoxy cures.

3.2 Slot Wiring

A machine has been built to place the insulated cable into the slots under computer control. The computer follows the same slot description used by the milling machine that cut the slots. The stylus of the machine guides the cable into its proper position and, using ultrasonic energy, melts the adhesive coating on the cable sufficiently to fasten it to the substrate. After each layer is wound, the machine pauses while the operator places the next layer of substrate. The machine has been used to wind a number of slots but, because of materials problems and error

accumulation in slot position, is not yet ready for routine production. In the meantime, the slots are being wound manually. The wiring is checked by applying high voltage (1 kV) and by measuring resistance.

4 MAGNET ASSEMBLY

The two coils are first assembled together, then aligned and pinned in a fixture using machined features on the tube ends. This assembly is then oriented vertically and bolted to a plate that also serves as the primary alignment reference in the magnet. Still in a vertical orientation, stacks of yoke laminations several inches high are lowered around the coils with tooling designed to hold the laminations level so as to avoid binding. Typical clearances between tubes and between tube and yoke are several mils. The straightness of the tubes is critical for this assembly, and the use of aluminum tubes ensures freedom from stresses that might distort the tubes when slots are machined into their walls. After the pre-weighed number of laminations is installed, stainless steel tie bars are inserted through four of the yoke holes and secured with bolts that hold the lamination stack. The yoke length is thus controlled by the machined length of the tie bars. The tie bars and the coils are held on a plate at only the lead end of the coils. The coils, controlled by the aluminum tubes, are therefore free to contract axially inside the yoke upon cooldown. A photograph of a completed magnet (the first production unit) is shown in Figure 4.

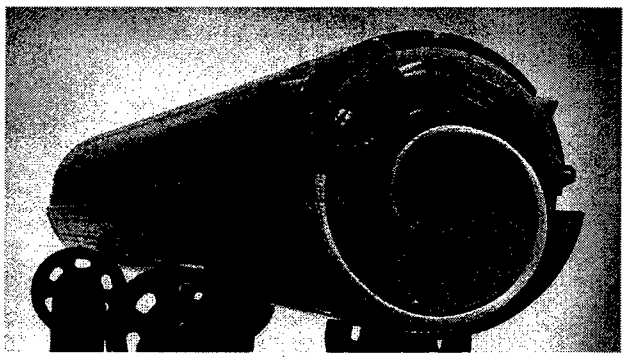

Fig. 4: Photograph of a completed production magnet. It is 2.4 m long. Electrical connections are under the G10 boards seen at the end of the magnet.

5 ELECTRICAL CONNECTIONS

Yoke warmup heaters are installed through four of the yoke slots, then circuit boards are fastened to the lead end of the magnet. Each of the individual windings is connected in a series connection on the circuit boards. A 50 mΩ resistor is connected across each of the windings to avoid damage that might occur from energy dissipation in a winding when the magnet quenches. These resistors are made of five folded 12.6" lengths of 16 gauge nichrome wire brazed in parallel into a copper block. Warm field measurements are made before the resistors are installed.

The room temperature resistance of a winding is typically 20 Ω. The average inductance of a winding is 0.3 H. The large inductance of the windings and the 50 mΩ parallel resistance leads to an indeterminate field in the magnet when it is ramped. This is acceptable because the magnet is designed to be operated only in a DC mode or with very slow (<1 A/s) ramp rates. Diodes could be used in series with the resistors if faster ramp rates were needed.

6 TEST RESULTS

The first full-length magnet was recently completed and tested at BNL. Quench results at 4.35K are shown in Fig. 5. Although some training was necessary, the magnet eventually reached a level well above the

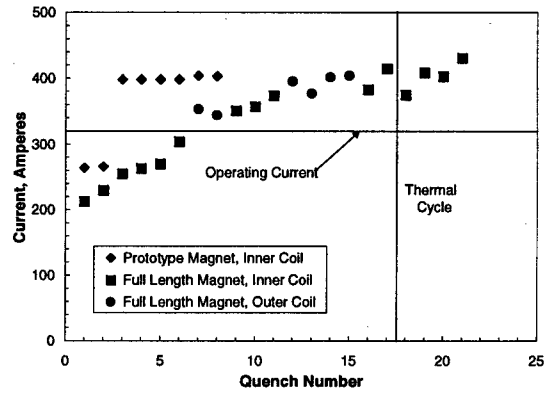

Fig. 5: Quench results for the first full length production magnet, and the earlier prototype magnet.

maximum required operating current. The training may indicate that the windings are not sufficiently filled with epoxy in this first production unit. The test results for the half-length prototype magnet tested in 1997, where no training was observed after several early lead-related quenches, are shown for comparison.

7 REFERENCES

[1] E. Willen et al., A Helical Magnet Design for RHIC, Proc. PAC97, Vancouver, BC, May, 1997, p. 3362.

[2] M. Syphers et al., Helical Dipole Magnets for Polarized Protons in RHIC, ibid, p. 3359.

[3] Design Manual: Polarized Proton Collider at RHIC, M. Syphers, Editor, BNL, July, 1998.

[4] M. Okamura et al., Field Calculations and Measurements of a Helical Snake Magnet for RHIC, MT15, Beijing, October, 1997, p. 250.

[5] T. Katayama et al., Field Calculation and Measurement of a Full Length Snake Magnet for RHIC, EPAC, Stockholm, June, 1998, p. 2005.

[6] G. Morgan, End Design of a Helically-Wound Magnet for RHIC, ICEC17, Bournemouth, England, July, 1998, p. 431.

ROTATION ANGLE OF A HELICAL DIPOLE

T. Tominaka#, and M. Okamura, RIKEN, Japan
T. Katayama, University of Tokyo & RIKEN, Japan

Abstract

With the collaboration between Brookhaven National Lab. (BNL) and RIKEN, the helical dipole magnets is under construction for RHIC spin project.[1] It is required that the deflection of beam is negligible in the helical dipoles.[2] The relation between the rotation angle in the helical dipole and the cancellation of the integral of transverse field along the beam axis is investigated.[3-5] Then, with the derived optimization method, the optimal length of the full-length helical dipoles is obtained from the measured field of the half-length prototype.

1 A DEFINITION OF THE EFFECTIVE ROTATION ANGLE FOR HELICAL DIPOLES

As a natural extension of the effective magnetic length with the replacement of the axial coordinate z by the phase angle φ of dipole, the effective magnetic rotation angle Δφ can be defined as follows,

$$\Delta\varphi = \frac{1}{B_{10}}\int B_1(\varphi)d\varphi = \frac{1}{B_{10}}\int B_1(\varphi(z))\frac{d\varphi}{dz}dz = \overline{\frac{d\varphi}{dz}}L \quad , \quad (1)$$

where $B_1(\varphi)$ is the amplitude of the dipole field at the angle $\varphi(z)$ with the definition of $\varphi(z=0) = 0$, and $B_{10} = B_1(\varphi=0) = B_1(z=0)$ is the amplitude of dipole field at the center, and L is the effective magnetic length.
According to this definition, it means that the magnetic field of the region where $d\varphi/dz = 0$ does not contribute to the effective magnetic rotation angle.

2 RELATION BETWEEN THE ROTATION ANGLE AND THE CANCELLATION OF THE TRANSVERSE INTEGRATED FIELD

In general, the cancellation of the integral of the field component B_a for the arbitrary direction with the angle φ_0 for the y axis, can be expressed as follows,

$$\int B_a(z)dz = \int B_1(\varphi(z))\cos(\varphi(z)-\varphi_0)dz = 0 \quad . \quad (2)$$

Then, it can be verified that the cancellation of the integral of B_a for the arbitrary direction is equivalent to those for two transverse directions, x and y directions,

$$\begin{cases} \int B_1(\varphi(z))\cos\varphi(z)dz = \int B_y(z)dz = 0 \\ \int B_1(\varphi(z))\sin\varphi(z)dz = -\int B_x(z)dz = 0 \end{cases} \quad (3)$$

In addition, $B_x(z)$ can be defined as an odd function from the symmetry for the magnet center, z=0, where the dipole field is in the y-direction with $B_y(z=0) = B_{10}$ and $B_x(z=0) = 0$. Therefore, the integral of the x-directional field B_x can be always chosen to be zero for every symmetric helical dipole. Then, it results that the cancellation of the integral of the y-directional field B_y is essential for that of the integrated field for the arbitrary direction.

2.1 Optimization of Rotation Angle

The optimal length or rotation angle of helical dipoles can be calculated for the following general field distribution,

$$\begin{cases} B_1(z) = B_1(z=0) = B_{10}, \quad \dfrac{d\varphi}{dz} = k, \quad 0 \le z \le z_e \\ B_1(z-z_e) = B_{10}\cdot b(z-z_e), \quad \varphi = \varphi(z-z_e), \quad z_e \le z \le z_f \end{cases} \quad , \quad (4)$$

where the function of $z\text{-}z_e$, $b(z\text{-}z_e)$ describes the z dependence of the normalized dipole field, and $\varphi(z\text{-}z_e)$ also describes the phase angle of dipole in the end regions.
The following equation is required to meet the condition of the zero integrated transverse field,

$$B_{10}\int_0^{z_e}\cos(kz)dz + \int_0^{z_f-z_e} B_1(z-z_e)\cos[\varphi(z-z_e)+kz_e]dz = 0 \quad . \quad (5)$$

Then, the optimal half length z_e of the helical body portion can be calculated numerically from the following equation,

$$\int_0^{z_f-z_e} b(z-z_e)\cos[\varphi(z-z_e)+kz_e]dz = -\frac{\sin(kz_e)}{k} \quad . \quad (6)$$

For the various cases, the optimal rotation angles for the cancellation of the transverse integrated field can be calculated with the deviation from 2π for the general cases, as listed in Table 1.[5]

Email: tominaka@postman.riken.go.jp

Table 1: Optimal rotation angles for the cancellation of the transverse integrated field for various cases. [ref.5]

Case	Helical body*	End**	Rotation angle
#a	k	(no end)	2π
#b	k	k_e = const. = k	2π
#c	k	k_e = const. $\neq$ k	$\neq 2\pi$
#d	k	$k_e \neq$ const.	$\neq 2\pi$

*) k : constant phase rotating rate of dipole in the body
**) k_e : phase rotating rate of dipole in the ends

3 MEASURED RESULTS OF THE HALF-LENGTH PROTOTYPE

For the half-length prototype, the z dependence of the amplitude $B_1(z)$ and the phase angle $\varphi(z)$ of the dipole field was obtained from the magnetic field measurement with the Hall probe at I=105 A and 220 A, as shown in Fig.1.[6-8] In these figures, the central position z = 0 of the magnet is defined as the middle point for the magnetic length. The difference of the magnetic structures in both of non-lead (the left side in Fig.1) and lead ends is not so large.

The rotation angles calculated from Eq.(1) for the helical body and end potions are listed in Table 2. In Table 2, $\Delta\varphi$ [body], $\Delta\varphi$ [non-l], and $\Delta\varphi$ [lead] mean the calculated rotation angles for the helical body, and the non-lead, and lead end portion.

In addition, due to the thermal contraction of helical dipole, the phase rotating rate of the dipole field of the helical body portion (- 0.4 m < z < + 0.4 m), k = $d\varphi/dz$ deviated from the design value at room temperature of 150 deg/m, as shown in #1 and #2 of Table 2. The measured results are almost consistent to k = $2\pi/\{2.4 \times (1 - 0.00415)\}$ = 150.6 (deg/m), expected from the thermal contraction of Al coil bobbin of 0.415 % from the room temperature to 4.2 K.

4 CALCULATION FOR A HELICAL MAGNET WITH FULL LENGTH

On the assumption of the symmetric magnetic structure with identical coil ends that both ends have the same measured field distribution of the lead end at I = 220 A, the length of the half body z_e was numerically optimized from Eq.(6) with the calculational error of about 2×10^{-6} Tm for the integral of B_y, obtaining z_e = 1.000 m. This means that the helical body portion of the prototype magnet from z = - 0.4 m to + 0.4 m, should be elongated by (1.000 - 0.4) × 2 = 1.200 m for that of the optimal full-length magnet. This result was almost equivalent to other optimization calculations.[3,4]

Furthermore, the non-symmetric full-size helical dipole can be composed from this optimal helical body and the different ends, as #4 in Table 1. The field distribution for B_{10} = 4.0 T of this non-symmetric full-length helical dipole are shown in Figs.2-5.

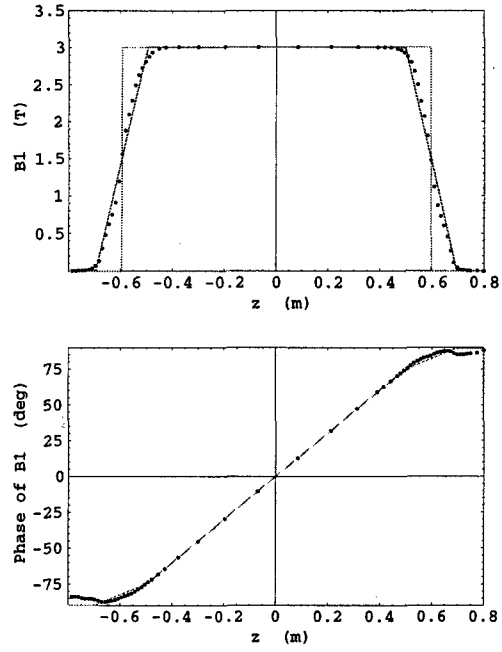

Fig. 1: The amplitude $B_1(z)$ and the phase $\varphi(z)$ of dipole along the beam axis at I=220 A for the half-length prototype.

Table 2: Comparison between the calculated rotation angles of the half-length prototype (#1 & #2) and the optimized full-length helical dipole (#3 & #4)

Half or Full	k (deg/m)	$\Delta\varphi$ [body] (deg)	$\Delta\varphi$ [non-l] (deg)	$\Delta\varphi$ [lead] (deg)	$\Delta\varphi$ [total] (deg)
#1) H (105 A)	150.7	120.3	22.7	23.6	166.6
#2) H (220 A)	150.4	120.4	23.0	23.4	166.8
#3) F (Sym.)	150.6	301.2	23.4	23.4	348.0
#4) F (non-S)	150.6	301.2	23.0	23.4	347.6

In these figures, black dots are shown at every 5.0 mm along the beam axis for the indication of the relation between the same z positions in each plot. The comparison between the integrals of the magnetic field between two cases, the symmetric ends (#3) and the non-symmetric ends (#4) in Table 2, is compiled in Table 3. Especially, the integrated value of B_a for the direction with the angle, φ_0 = + 30 degree is listed, together with those of B_x, and B_y, in Table 3. It results that the deviation from zero of the transverse integrated field become larger for the non-symmetric dipole. It will be also possible to seek the better optimal length for the non-symmetric case with the modification of Eqs.(4)-(6).

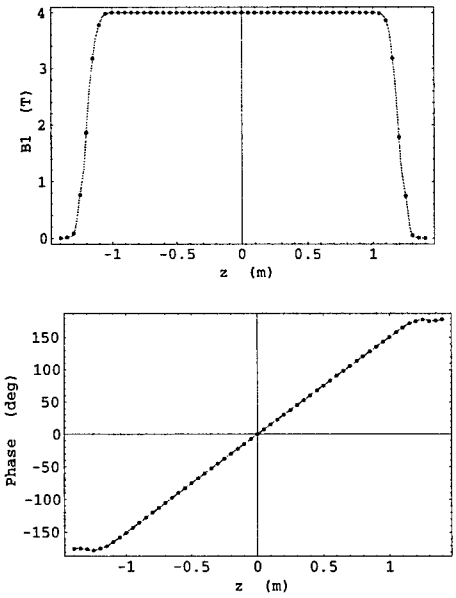

Fig. 2: The amplitude B_1 (z) and the phase angle $\varphi(z)$ of the dipole field along the beam axis of optimal full-length helical dipole with different ends.

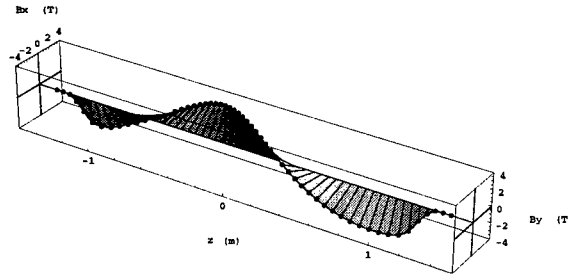

Fig. 3: 3D plot of the dipole field along the beam.

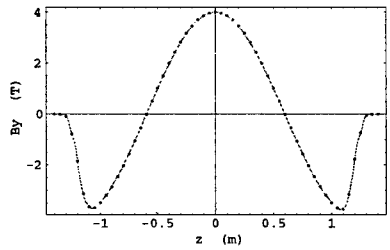

Fig. 4: B_y along the beam axis.

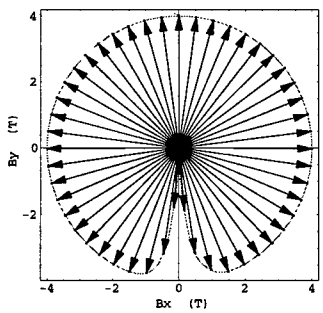

Fig. 5: Plot of (B_x, B_y) along the beam axis.

Table 3: The integrated values of the transverse field along the beam axis.

Case	Int. of B_x (Tm)	Int.of B_y (Tm)	Int. of B_a [$\varphi_0 = 30°$] (Tm)
#3) Symmetric	0	≈ 0	≈ 0
#4) Non-symmetric	$+1.5\times10^{-3}$	$+5.8\times10^{-4}$	-2.5×10^{-4}

5 CONCLUSION

The definition of the effective rotation angle for helical dipoles is proposed, similarly with the effective magnetic length. From the relation between the effective rotation angle and the cancellation of the transverse integrated field, it results that the rotation angle of helical dipoles, which meets the condition of the cancellation of the transverse integrated field, generally deviates from 2π.

In general, the rotation of the dipole field is specified only by the rotation of the coil in the helical body region. On the other hand, the field rotation in the end region is not specified only by the rotation of the coil, but also depends on the end structure of the iron yoke, etc.

It is shown that the length of the helical dipoles can be optimized for the measured (or known) ends with the derived optimization method. In addition, it is revealed that the integrated transverse fields for helical dipoles with the non-symmetric ends become larger than that with the symmetric ends.

6 ACKNOWLEDGMENTS

The authors are indebted for providing the experimental data to A. Jain and R. Thomas, and for helpful discussions and comments to E. Willen, M. Syphers (now Fermilab), and T. Roser in BNL.

7 REFERENCES

[1] E. Willen et al., "Construction of Helical Magnets for RHIC", in these proceedings.

[2] M. J. Syphers, "Total Pitch Specification for RHIC Helical Dipole Magnets", AGS/RHIC/SN No.58, August 4, (1997).

[3] M. Okamura, "Optimization of Rotation Angle of the Helical Dipole Magnets", AGS/RHIC/SN No.61, August 28, (1997).

[4] A. Jain, "Estimation of "Rotation Angle" in the Full Length Helical Dipole Based on Data in the Half- Length Prototype HRC001", AGS/RHIC/SN No.62, September 22, (1997).

[5] T. Tominaka, "Rotation Angle of a Helical", AGS/RHIC/SN No.64, September 22, (1997).

[6] A. Jain, Private Communications.

[7] R. Thomas, "Recalibration of Vertical Positions of Hall Probe Vertical Transporter", BNL Memorandum (1997).

[8] M. Okamura et al., "Field Calculations and Measurements of a Helical Snake Magnet for RHIC", MT15, Beijing, October, (1997), p.250.

MAGNETIC FIELD SHIMMING, MEASUREMENT AND CONTROL FOR THE BNL MUON (G–2) EXPERIMENT

S. I. Redin*, Yale University, New Haven, CT
for the (g-2) collaboration

Abstract

An ultraprecise superferric magnet, 14 m in diameter, was built for the muon (g–2) experiment currently in progress at Brookhaven National Laboratory. The principal quantities to measure in the experiment are the frequency of (g–2) oscillations and the average magnetic field, which imply stringent requirements on the homogeneity of the magnetic field as well as on the precision of its measurement and control system. This paper describes (g–2) magnet, shimming technics used to improve it and advanced NMR and Hall probes systems to measure and monitor magnetic field.

1 INTRODUCTION

Precision measurement of muon $a_\mu = \frac{1}{2}$ (g–2) value probes short–distance structure of the theory and hence provides stringent test of the Standard Model or, alternatively, search for New Physics beyond. Previous measurement of a_μ [1] confirms theoretically predicted contributions from QED and strong interactions with experimental precision of 7.2 ppm (parts per million). The goal of current BNL muon (g–2) experiment [2] is to lower experimental error to 0.35 ppm, which would allow us to see also week interactions contribution at the level of 3–4 sigma.

In the muon (g–2) experiment we measure ω_a, the spin precession frequency relative to the momentum vector cyclotron precession for a muon in a uniform magnetic field. Muon a_μ value is evaluated from relation $\omega_a = a_\mu \frac{eB}{mc}$ and hence two quantities, muon (g–2) precession frequency ω_a and magnetic field B, must be measured in this experiment precisely.

Frequency ω_a is measured from time distribution of decay electrons registrated by detector stations [3] and its knowledge is principally limited by statistical error of the fit. Magnetic field is measured and controlled by the system of NMR probes. It is designed to provide accuracy and stability of the field (averaged over muon distribution) at the 0.1 ppm level. To achieved this goal, magnetic field across the muon storage region should be shimmed to ~ 1 ppm level of homogeneity.

Magnetic field shimming, measurement and control with advanced NMR system is the main part of this presentation. A number of measurements of the magnetic field were also done with Hall probes. These include measurement of the radial component of the field in the storage ring and measurement of highly nonuniform magnetic fields near the beam injection point and in the region of straw chambers used for decay electron tracking.

* Email: redin@bnl.gov

2 SHIMMING OF THE MAGNET

The BNL (g–2) magnet provides a magnetic field of about 1.45 Tesla over the muon storage region, which is of toroidal shape with the radius of the central orbit being 711.2 cm (280 inches) and cross sectional diameter being 9 cm. The cross section of the muon storage ring is shown in Fig. 1. The magnet has a C-shape to allow decay electrons to be observed inside the ring. The field in the storage region is determined dominantly by the iron, i.e. its geometry, construction tolerances, temperature control, etc. The air gap between the pole pieces and the yoke serves to decouple the magnetic field in the storage region from that in the yoke.

The magnet is excited by four ring-shaped superconducting coils. That provides thermal stability, low power consumption, low resistance R and hence use of a low voltage well regulated (to 0.3%) power supply, high L/R and hence low ripple currents, thermal independence of the coils and the iron.

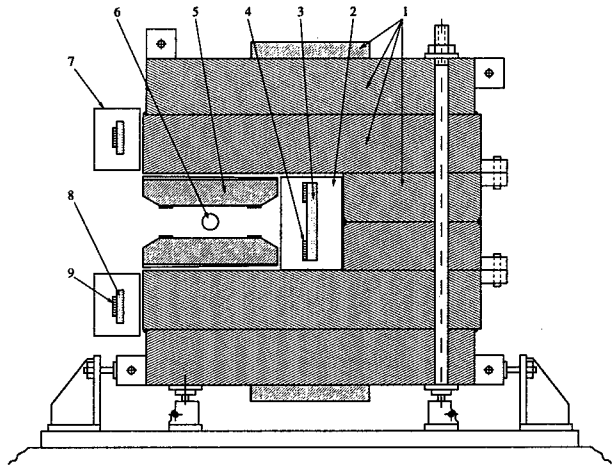

Figure 1: Muon storage ring. 1 – yoke plates, 2 – outer cryostat, 3 – outer mandrel, 4 – outer lower coil, 5 – pole, 6 – muon storage region, 7 – inner upper cryostat, 8 – inner lower mandrel, 9 – inner lower coil.

Magnetic field measured at the first powering of the mag-

0-7803-5573-3/99/$10.00@1999 IEEE.

net in 1996 varied peak-to-peak by up to 1400 ppm (0.14%) in different azimuthal locations in the ring and up to 300 ppm across the muon storage region. Several techniques, shown in Fig. 2, were used to shim the magnet to acceptable level of homogeneity of magnetic field.

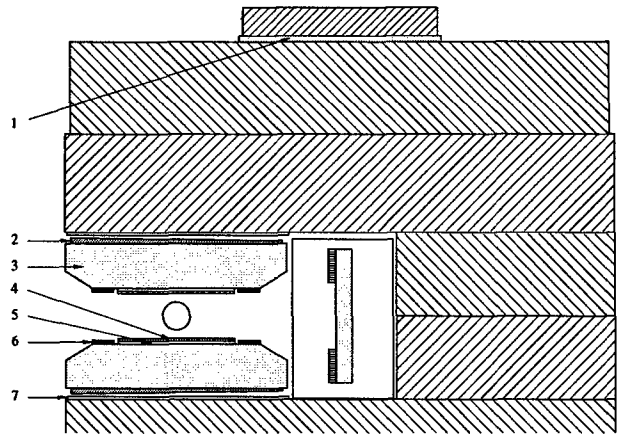

Figure 2: Shimming techniques: 1 – aluminum or iron shims between top and/or bottom iron plate and the rest of the yoke; 2 – iron wedges; 3 – tilting of poles; 4 – aluminum/iron sandwiches; 5 – surface correction coils; 6 – Rose (edge) shims; 7 – dipole correction coils

We started shimming by leveling the pole pieces to eliminate steps between adjacent poles to 0.0005 inch or less. We also adjusted the poles at certain small angle to the horizontal plane such that both top and bottom poles would be horizontal in the powered state.

Aluminum or iron shims between top plate and the rest of the yoke were used to reduce broad azimuthal variations of the field from 1400 ppm to $\sim$ 300 ppm. For relatively short variation, the iron wedges between poles and yoke were moved radially in– or outward.

For correction of the field distribution across the muon storage region, it was extremely fruitful to use Rose (or edge) shims. These are iron strips 5 cm wide on the edges of the poles surfaces. They are 10° long in azimuth, their thickness can be machined to correct the field. Because the Rose shims are so close to the muon storage region, they are a very powerful tool for both wide and local corrections. Shimming with the Rose shims was done in several steps. First, we measured shimming effect of all four shims by taking one 10° section of them out or machine off $\sim$ 1 mm of their thickness between two field measurements. Then we calculated the optimal thicknesses and machine Rose shims for one half of the ring (with some margin). Necessary corrections were applied and all of the Rose shims were machined to the optimal value, uniformly all over the ring. This allowed us to lower pole-by-pole variations of the field across the muon storage region (averaged azimuthally over the ring) to $\sim$ 25 ppm level, see Fig. 3a.

Number of further improvements were made after the

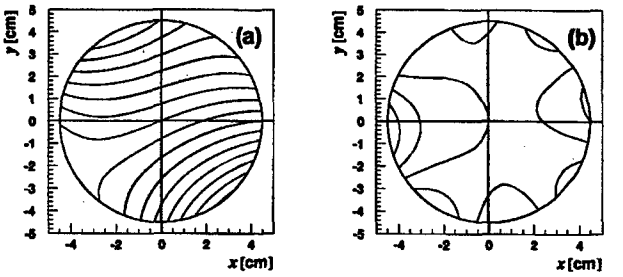

Figure 3: Magnetic field distribution across the muon storage region for 1997 (a) and 1998 (b) runs. The interval between the contours of equal field strength is 2 ppm.

1997 run. The iron yoke was thermally insulated (wrapped) for better temperature stability of the magnetic field. Rose shims were machined individually to reduce large pole-by-pole variations. Other shimming techniques applied before 1998 run were aluminum/iron strips sandwiches to correct local field variations, mostly at boundaries of adjacent pole pieces, and current in the surface correction coils, which are the strips on the printed circuit boards connected together to form loops azimuthally all over the ring. Surface correction coils can be used to correct virtually any set of multipoles. Fig. 3b shows contour plot distribution of magnetic field during the 1998 run, when all techniques, including the surface correction coils, were applied. The peak-to-peak variations were lowered to 5 ppm level.

3 MAGNETIC FIELD MEASUREMENT AND CONTROL WITH NMR PROBES

To measure and control the magnetic field with 0.1 ppm relative accuracy, a pulsed NMR system has been developed [4]. 25 NMR probes were mounted on a movable platform (shimming trolley) and used for the magnet shimming. 17 NMR probes were mounted on a beam tube trolley [5] and used for the mapping the magnetic field during the data taking runs.

The beam tube trolley is a vacuum–tight vessel with cylindrical shape and a length of 0.5 m, curved with the same radius as the storage ring. The trolley drive mechanism pulls the trolley along the ring with an electrical cable. The same cable is used for communication between the trolley and computer in the control room. The trolley rides on rails which help to form the desired electrical quadrupole field. During data taking the trolley is parked in its garage, located radially inward from the muon storage region. The trolley garage mechanism can move a complete 50 cm section of the rails with trolley on it radially outward (inward) at the beginning (end) of magnetic field measurements. Both trolley drive and trolley garage are parts of the muon vacuum chamber, so field measurement with the beam tube trolley can be done without breaking the vacuum.

During the run the measurements with the beam tube trolley were taken every 24 to 72 hours. Each field map

consists of about 6000 readings for each of the 17 NMR probes. Between these measurements the drift of magnetic field was monitored by the 366 fixed NMR probes embedded in the walls of the vacuum chamber in 72 azimuthal locations.

Fixed probes are calibrated by beam tube trolley probes during each field mapping. At the end of the run the 17 trolley NMR probes were calibrated against a single calibration probe [4]. It was, in turn, calibrated with a standard NMR probe [6], which was constructed to measure the NMR frequency of protons in a spherical sample of pure water with a systematic uncertainty of 0.034 ppm.

4 MAGNETIC FIELD MEASUREMENT WITH HALL PROBES

A number of field measurements [7] were done with Hall probes in regions with inhomogeneous magnetic field or for determination of the direction of the field, i.e. when NMR probes can not be used. The most important was measurement of the radial component of magnetic field, which in this experiment must be kept below 50 ppm (averaged over the ring). Our measurement achieved an accuracy of 10 ppm, which was adequate for shimming and control of the radial field.

The Hall probes device, built for this purpose, contains two Hall probes BH–206 installed on the $Z-\Theta$ plane and the electrolytic tilt sensor RG33A along the R axis, on the aluminum support as shown in Fig. 4. The support itself is mounted on the system of platforms in such a way, that it can be tilted (adjusted) within $\pm 0.5°$ from horizontal in $Z-R$ plane and rotated around the vertical Z axis by 180°.

To measure angle between magnetic field and the R axis, we first set the tilt of the aluminum support at some small arbitrary angle δ (readout of the tilt sensor) and record the output voltage from the Hall probe V. Then we make 180° rotation, adjust the angle of the support to the same angle δ and take another Hall probe voltage, V'. The angle α between the magnetic field and the vertical axis is given by

$$\alpha = \frac{1}{2}\,\frac{V - V'}{V(1.45\,T)}\,,$$

where $V(1.45\,T)$ is a Hall probes output for magnetic field of 1.45 T.

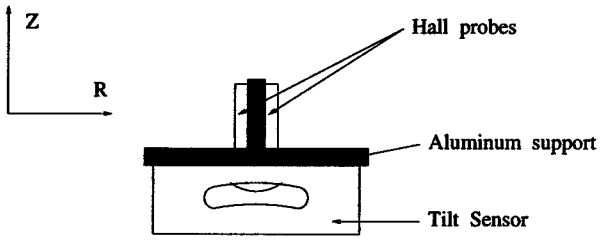

Figure 4: Hall probe device for the radial magnetic field measurements

The formula above is insensitive to the following sources of systematic errors: (1) the axis of the 180° rotation is not exactly vertical in $Z-R$ plane, (2) the Hall probes output has offset, (3) the electrolytic tilt sensor output has offset, (4) the axis of the electrolytic tilt sensor is not exactly orthogonal to the plane of the Hall probes, (5) temperature change over time larger than one measurement cycle (before and after flip), which is about 5 minutes. Also note that the systematic error due to not exactly 180° rotation is of second order.

A potentially important systematic error is the planar Hall effect [8]. To eliminate this error, we use two Hall probes with parallel planes, but with orthogonal directions of the Hall currents, in the vertical and horizontal (azimuthal) direction, respectively. After averaging these two Hall probes measurements, the net result will not be affected by this source of systematic errors.

Another important measurement done with Hall probes was the measurement of magnetic field in the region of the traceback system which occupies the radial region from $R = 680$ cm to 705 cm and the vertical region from $Z = -10$ cm to +10 cm, where the magnetic field varies from 1.45 T to $\sim$ 0.2 T. Both vertical and radial components of the field are needed for reconstruction of electron tracks. The azimuthal component of the field is assumed to be zero from symmetry.

The apparatus used for magnetic field measurements in the traceback region consists of two Hall probes mounted on a system of two translation stages which in turn are mounted on the rigid aluminum support and the whole assembly is bolted to the top and bottom poles. The Hall probes were oriented so that one of them measured the vertical component of the field and the other measured the radial component. The translation stages provided radial and vertical motion of the probes. Measurements and calculations are in agreement at the 10^{-3} level, which is sufficient accuracy for the electron track reconstruction.

Magnetic field maps taken by the NMR beam tube trolley have missing points near the beam injection point, where field is highly inhomogeneous. Measurement of radial and azimuthal components of the field with Hall probes improved significantly the model used to describe field distribution in this region.

5 REFERENCES

[1] J. Bailey et al., Nucl. Phys. B150, 1 (1979)

[2] Design Report of BNL experiment E821, 1995

[3] S. Sedykh et al., Proc. of 7th Int. Conf. on Calorimetry in High-Energy Physucs (CALOR 97), Tucson, AZ, 1997

[4] P. Prigl et al., Nucl. Instr. Meth. A374, 118 (1996)

[5] A. Grossmann, Ph.D. thesis, University of Heidelberg, 1998

[6] X. Fei et al., Nucl. Instr. Meth. A394, 349 (1997)

[7] S. I. Redin, Ph.D. thesis, Yale University, 1999

[8] B. Turk, Nucl. Instr. Meth. 95, 205 (1971)

QUENCH PERFORMANCE AND FIELD QUALITY OF DX DIPOLES FOR RHIC*,

A. Jain#, J. Muratore, M. Anerella, G. Ganetis, A. Marone, G. Morgan, A. Prodell, J. Schmalzle, R. Thomas, P. Wanderer, BNL, Upton, NY 11973-5000

Abstract

DX dipoles, with an aperture of 18 cm, are located on each side of the six intersection regions of RHIC. All DX dipoles were tested at 4.35 K for quench performance, and trained successfully to at least a 10% margin above the operating field (4.3 T at 6.6 kA). Field quality in these dipoles was measured at room temperature and at 4.35 K using a rotating coil system. The measured harmonics were corrected for offsets of the measuring coil from the magnetic axis, determined by a variety of techniques. All harmonics were found to be within acceptable limits.

1 INTRODUCTION

The Relativistic Heavy Ion Collider (RHIC) at BNL has six intersection regions. Immediately on each side of these regions is a dipole, named the DX dipole, through which both beams pass. These magnets require a large aperture of 18 cm, operate at 4.3 T, and the magnetic length is 3.75 m. There are 12 of these magnets installed in the accelerator and one more production magnet was built as a spare. The magnet coils have 71 turns in six blocks. A detailed description of magnet features and construction experience can be found in reference [1]. This paper summarizes results of quench and field quality tests.

2 QUENCH TESTS

All 13 production DX dipoles were trained to 7.26 kA, 10% above the 6.6 kA operating current. The magnets were tested in liquid helium at 4.35 K (nom.) and ramped at 100 A/sec. A summary of the training data for the 12 magnets installed in RHIC is shown in Fig. 1. The filled diamond symbols indicate quench currents, while the open diamonds indicate a ramp to 7.5 kA (the limit of the leads in RHIC) without quenching. Two magnets were not ramped to 7.5 kA due to limitations on test time. The lower final quench for magnet 102 followed an instrumentation-induced quench at high field after reaching 7.5 kA.

Constraints on test time permitted thermal cycles only of the spare magnet, number 114. During its initial cooldown, the magnet trained to the operating current in four quenches and to 7.5 kA in twelve quenches. After one cycle to room temperature, four quenches were needed to reach operating current; after a second cycle, three quenches were needed.

Quench location information was available only from the three standard voltage taps. The data indicate that the quenches originated at different locations in both coil halves. Spikes in these signals also indicated significant superconductor motion during most quenches.

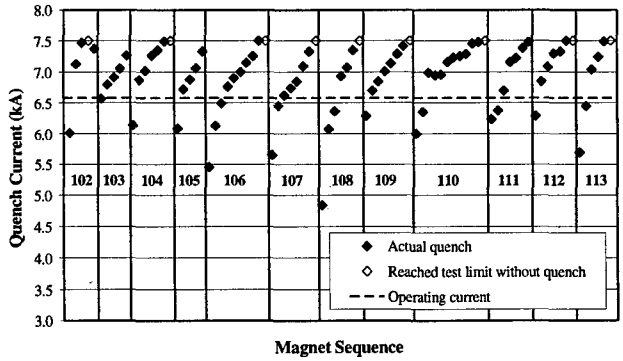

Fig. 1: Quench history of DX dipoles installed in RHIC

3 FIELD QUALITY MEASUREMENTS

The field quality is characterized by a set of harmonics, b_n and a_n, defined (in "units") by the relation

$$B_y + iB_x = 10^{-4} \times B_0 \sum_{0}^{\infty} (b_n + ia_n)\left(\frac{x+iy}{R_{ref}}\right)^n \qquad (1)$$

where B_0 is the strength of the dipole field and R_{ref} is a suitable reference radius, chosen to be 60 mm for the DX magnets. The field quality in all the DX magnets was measured using a rotating coil system comprising of five tangential coils [2] at a radius of 74.1 mm for warm measurements and 68.5 mm for measurements at 4.35 K. The length of coils used for both warm and cold measurements was 0.921 m. Harmonics were measured at five axial positions, spaced by one coil length, to obtain the integral harmonics.

3.1 Warm measurements

The warm measurements were carried out at three different currents (10 A, 20 A and 30 A) with the magnet placed horizontally on a level granite table. The "true" harmonics were determined from the slope of a linear fit between the measured normal or skew terms and current, thus subtracting out any remnant fields. The measuring coil was equipped with a gravity sensor, which enabled determination of the dipole field angle with respect to gravity. Several fiducials on the magnet cold mass were optically surveyed during the same set up to correlate the field direction with the fiducials. This information was used to install the magnets into the cryostats in the ring.

3.1.1 Centering of Data

Any radial offset of the measuring coil axis with respect to the magnetic axis is a source of error in the

* Work supported by the US Department of Energy under contract no. DE-AC02-98CH10886.

jain@bnl.gov

determination of harmonics. For all the other types of dipoles in RHIC, the Quadrupole Configured Dipole (QCD) method [3] was used for data centering. This method requires a separate measurement with the two magnet coil halves powered with opposite currents. This could not be done for the warm measurements in the DX magnets due to presence of a separate quench protection diode across each coil half.

A variant of the QCD method was devised for centering of data in the warm DX magnets. Measurements were made in the regular dipole mode, and in a "half dipole mode" where only one coil of the magnet was powered. The usual QCD mode data was then synthesized by subtracting the "half-dipole" data weighted by a factor of 2 from the dipole mode data. This technique was tested on the 10 cm aperture RHIC D0 dipoles and good agreement with the regular QCD method was found.

3.1.2 Harmonics from warm measurements

The harmonics measured at the three central positions were used to obtain the average harmonics in the straight section of the magnet. The normal and skew terms from all the five positions were added to obtain the integral harmonics. The results are summarized in Figs. 2(a) and 2(b). The straight section values for individual magnets are shown by crosses and the integral values by open circles. The average values of straight section and integral harmonics are shown by the solid and the dashed lines respectively.

It is seen from Fig. 2 that on an average, the terms unallowed by the dipole symmetry, viz. the odd numbered normal terms (b_1, b_3, etc.) and all the skew terms, are quite small in the straight section of the magnet. The only exception is the skew quadrupole, which arises primarily from a size mismatch between the two magnet coils.

A comparison between the straight section and the integral harmonics indicates the contribution from the ends. This is generally seen to be negligible, except for the allowed normal terms and the skew sextupole (a_2). Most of these contributions were found to be from the lead end of the magnet.

3.1.3 The integral transfer function

Due to small errors in the axial positioning of the measuring coil, the integral transfer function obtained by summing the five measurements has a typical accuracy of only ~0.1%. A very long (10 m) non-rotating coil of 24.3 mm radius was therefore used for this purpose. The magnet was ramped from 0 A to 30 A and the signals from two orthogonal dipole windings were analyzed to obtain the integral transfer function. Fig. 3 gives a trend plot. The mean value is 2.5053 T.m/kA with a standard deviation of 0.03%. The reproducibility of measurements in a given magnet was better than 0.01%.

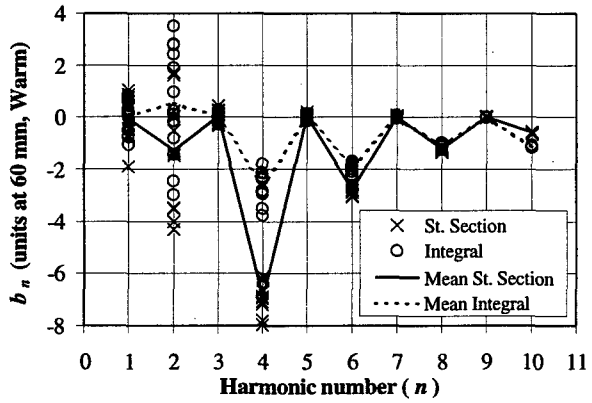

Fig. 2(a): Normal harmonics in DX magnets (warm)

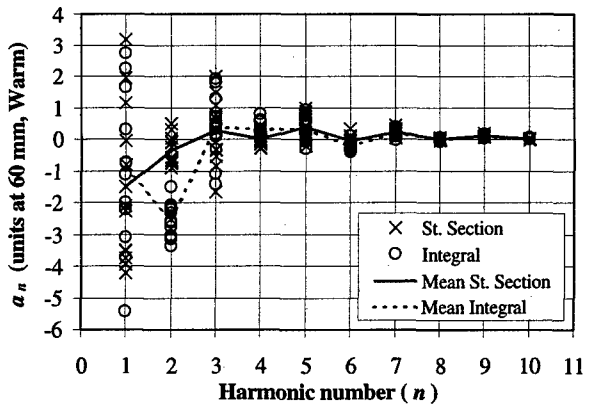

Fig. 2(b): Skew harmonics in DX magnets (warm)

3.2 *Measurements at 4.35 K*

Field quality was measured at liquid helium temperature, following quench tests in a vertical dewar. The measuring coil built for these measurements was not available during tests of several of these magnets. In such cases, measurements were made with a smaller radius (34.1 mm) rotating coil. The higher order harmonics were not reliably measured in this case.

At each of the five axial locations of the probe, the harmonics were measured at several currents between 50 A and 7000 A during both the upward and the downward sweep of the current. The current was ramped from one value to the next, and then held fixed during the measurements (DC loop). Space limitations above the vertical test facility precluded use of the long coil for cold integral transfer function measurements.

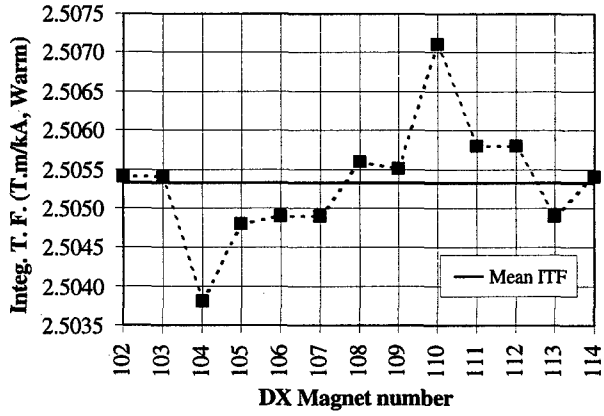

Fig. 3: Integral transfer function (warm) in DX dipoles.

3.2.1 Centering of Data

The regular QCD measurements were used to determine the offsets of the measuring coil. Since there is practically no voltage across the magnet in the superconducting state, the presence of separate diodes across the magnet coils did not prevent the use of this method. These measurements were carried out at 125A and 250A using two trim power supplies, either immediately before or after each DC loop. The offsets were then used to "center" the measured harmonics.

In some magnets, a pronounced current dependence was seen in the skew terms a_1, a_3, a_5, etc. above ~6500 A. As an example, Fig. 4 compares the current dependence of a_7 and a_9 in magnets DRX110 (filled symbols) and DRX112 (open symbols). DRX112 shows little current dependence in these harmonics, as expected, but this is not the case with DRX110. Magnet to magnet variation in the behavior of such higher order skew terms is very unusual. A closer look at the magnitudes of changes in various harmonics suggested that these could be explained by a

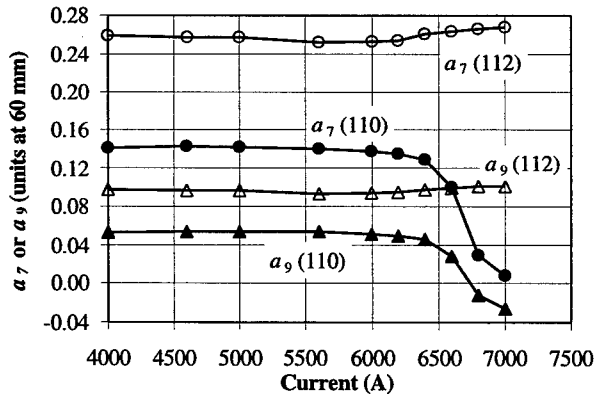

Fig. 4: Current dependence of a_7 and a_9 in a straight section region. The dependence in DRX110 at high fields is believed to be an artifact due to a small transverse motion of the magnet.

small (~0.5 mm) motion of the magnet at high fields relative to the measuring coil. In order to account for such a motion in the analysis, harmonics were first obtained at low fields using centers from the QCD measurements. A second pass was then made with centers determined such that the current dependence in very high order harmonics (a_9 and a_{11}) was eliminated. This procedure eliminated current dependence in other lower order skew terms as well, except the skew quadrupole, which could have a real current dependence due to local top-bottom asymmetries in the iron yoke weights.

A typical excitation curve is shown in Fig. 5. The standard deviation of the straight section transfer functions measured in 6 magnets is ~0.03%. The normal and skew harmonics at 6600 A (4.33 T) in these six magnets are shown in Figs. 6(a) and 6(b). Changes in harmonics due to quench and thermal cycle were studied in one magnet and were generally ~0.1 unit or smaller.

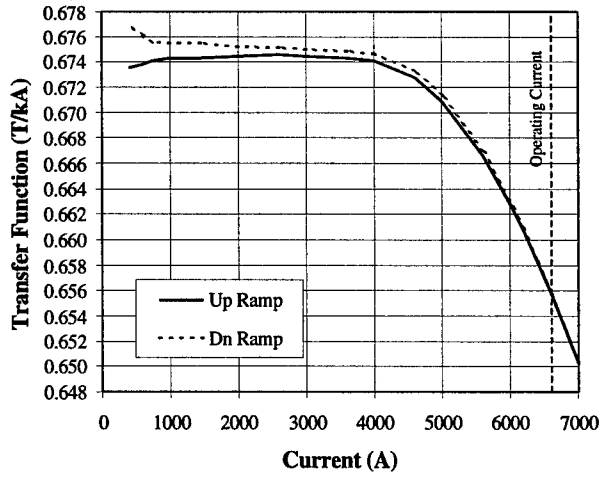

Fig. 5: Excitation curves in a typical magnet, DRX113.

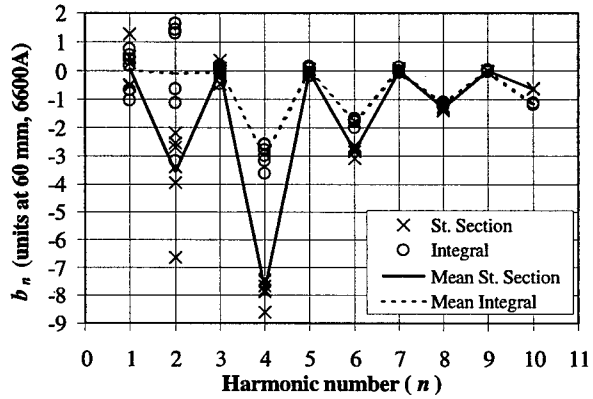

Fig. 6(a): Normal harmonics in DX magnets (6600A)

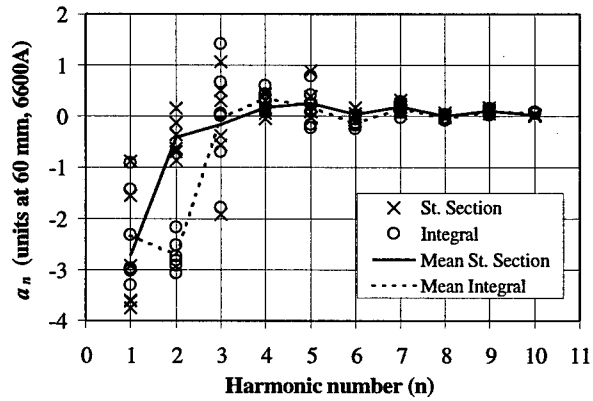

Fig. 6(b): Skew harmonics in DX magnets (6600A)

REFERENCES

[1] J. Schmalzle, "DX Magnet R&D, Prototype Construction and Magnet Production", BNL Note RHIC-MD-279, October 27, 1998.

[2] J. Herrera et al., "Measurement of the Magnetic Field Coefficients of Particle Accelerator Magnets", Proc. of 1989 Particle Accel. Conf., IEEE Catalog No. 89CH2669-0, pp. 1774-6.

[3] C.R. Gibson et al., "Locating the Magnetic Center of the SSC CDM Using a Temporary Quadrupole Field", Proc. 1992 Applied Superconductivity Conf., Chicago, Aug.23-28, 1992 in IEEE Trans. on Applied Superconductivity, 3, No.1, p.646-9 (March, 1993).

FIELD QUALITY IN THE TWIN APERTURE D2 DIPOLES FOR LHC UNDER ASYMMETRIC EXCITATION*,

A. Jain#, P. Wanderer and E. Willen, BNL, Upton, NY 11973-5000

Abstract

Twin aperture D2 magnets are one of the several types of dipoles to be built by BNL for the interaction regions of LHC. To minimize the number of dipole correctors required in the interaction regions, D2 will also be used as part of the steering system. Consequently, the operating fields in the two apertures may differ by up to ~10% at 7 TeV operation and ~33% at injection in order to compensate for the strengths of the correctors that would otherwise be required. Such asymmetric excitation of the two apertures may induce undesirable field harmonics. The saturation behavior of various harmonics is studied using POISSON and OPERA-2D. It is shown that the changes in harmonics resulting from the anticipated asymmetry are within tolerable limits.

1 INTRODUCTION

As part of the US-CERN collaboration for the Large Hadron Collider (LHC), Brookhaven National Laboratory (BNL) will build a number of superconducting insertion magnets. There are six different styles of dipoles, all with a magnetic length of 9.45 m. Also, all dipoles will use the same 80 mm aperture coil design that was used for the RHIC arc dipoles. In the twin aperture D2 and D4 magnets, the dipole field points in the same direction in the two apertures. This presents design challenges, particularly for the D2/D4B magnets where the separation between the two apertures is only 194 mm. Preliminary magnetic designs of all the dipoles to be built by BNL can be found in reference [1].

In order to minimize the number of dipole correctors required in the interaction regions, it was decided to use D2 as part of the steering system also. Consequently, the operating fields in the two apertures may differ by up to ~10% at 7 TeV operation and ~33% at injection in order to compensate for the strengths of the correctors that would otherwise be required. Such asymmetric excitation of the two apertures may induce undesirable field harmonics. The saturation behavior of various harmonics under asymmetric excitation is studied in this paper.

2 MAGNETIC DESIGN OF D2 DIPOLES

A preliminary design [1] of D2 dipoles minimized saturation induced harmonics, but was based on tentative locations and sizes of bus slots and other cut outs needed in the iron yoke. It was assumed in this optimization that the two apertures will be operated at the same dipole field. Subsequently, the locations of bus slots and various cut outs were changed significantly from the original design due to engineering reasons. This required a new optimization of the yoke for the twin aperture magnets. The current design for the D2/D4B magnets is shown schematically in Fig. 1. In particular, the saturation control holes near the center of the yoke had to be enlarged to compensate for the proximity of the bus slots. Instead of rectangular holes of the original design, holes with semicircular ends were used in order to maintain sufficient distance from the collars. This design was obtained by minimizing current dependence of various harmonics, calculated using POISSON. Only one fourth of the magnet was modeled to obtain maximum precision. This implied equal currents for the coils in the two apertures.

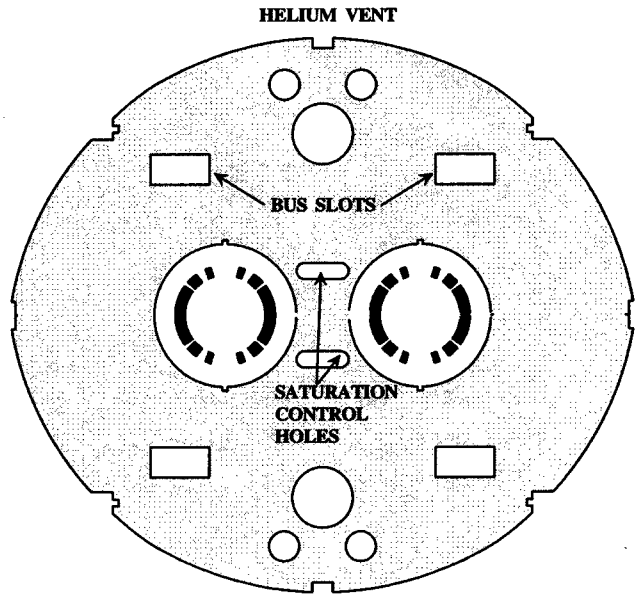

Fig. 1: Design of the D2 cold mass with the relocated bus slots and other cut outs.

3 ASYMMETRIC EXCITATION OF D2

As mentioned before, it is planned to use D2 as part of the steering system in order to minimize the number of dipole correctors required in the interaction regions. The required correction strength is 0.55 T.m at injection and 2.5 T.m at 7 TeV operation. Assuming a magnetic length of 9.45 m, these strengths correspond to 0.0582 T in the D2 magnet at injection and 0.265 T at 7 TeV. The lowest operating fields for D2 (at regions IR1 and IR5) are 0.176 T at injection and 2.74 T at 7 TeV. Thus, the correction strength amounts to ~33% of the field at injection and ~10% of the field at 7 TeV.

Since the iron in the yoke is far from saturation at the very low fields at injection, even an asymmetry of 33%

* Work supported by the US Department of Energy under contract no. DE-AC02-98CH10886.

jain@bnl.gov

in the excitation of the two apertures is not expected to produce any undesired harmonics. However, at high fields, the iron is saturated and an asymmetric powering is likely to produce a different current dependence in various harmonics.

In order to study the effect of asymmetric excitation, it is necessary to model at least one half of both the apertures, thus doubling the problem size. This made it difficult to obtain precise results at all values of excitation with the currently implemented problem size limits in the BNL version of POISSON. Consequently, the problem was also analyzed using the program OPERA-2D, which permitted a finer mesh. Good agreement was found between the results of OPERA-2D and POISSON for the cases where the POISSON solution converged.

In order to obtain a conservative estimate, a current asymmetry of 15% was studied. This is 50% over the maximum asymmetry expected at 7 TeV operation. Three cases were studied – (a) equal currents in both the apertures, (b) current in the left aperture higher than that in the right aperture by 15% and (c) current in the left aperture lower than that in the right aperture by 15%. Fig. 2 shows a sample output from OPERA-2D.

4 RESULTS

For each of the three cases studied, the harmonics were calculated with the center of the right aperture as the origin. The harmonics, in "units", are defined according to the expansion

$$B_y + iB_x = 10^{-4} \times B_0 \sum_{1}^{\infty} (b_n + ia_n)\left(\frac{x+iy}{R_{ref}}\right)^{n-1} \qquad (1)$$

where B_0 is the strength of the dipole field, R_{ref} is a suitable reference radius, chosen to be 17 mm [2], and x and y are the horizontal and the vertical displacements from the chosen origin (center of the right aperture). In practice, the normal and skew coefficients, b_n and a_n, were obtained by a Fourier analysis of the B_θ component at a radius of 35 mm, and then scaled to 17 mm. Due to a top-bottom symmetry in the model, the skew coefficients were zero.

The low field transfer function is 0.6345 T/kA for all the three cases. Fig. 3 shows the change in transfer function (from the low field value) in the right aperture as a function of the dipole field in this aperture. For a given

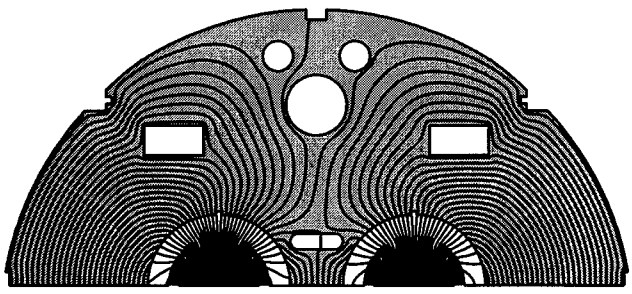

Fig. 2: Field lines calculated using OPERA-2D at 3.77 T (6kA) in the right aperture, with 15% more current in the left aperture

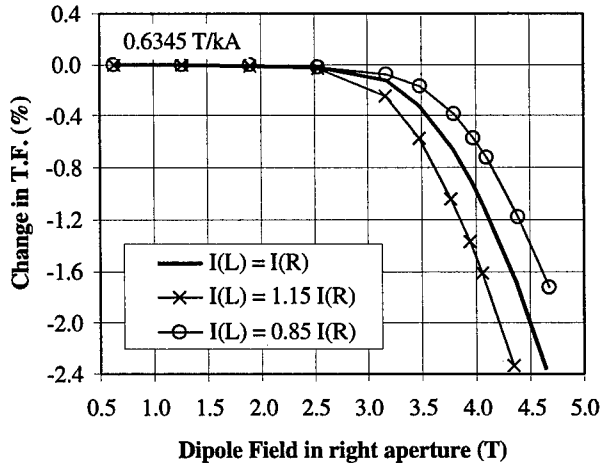

Fig. 3: Changes in transfer function from the low field value as a function of dipole field for various asymmetries in excitation of the two apertures.

dipole field, there is a bigger drop in transfer function when the other aperture is powered with a higher current, as compared to the case of a symmetric powering. A ±15% asymmetry in excitation gives rise to a ±0.4% change in transfer function at ~6 kA. This implies that the current required to achieve the same field in a given aperture may vary by up to ±23 A at 3.8 T depending on the excitation level of the other aperture.

The saturation behaviors of various harmonics ranging from quadrupole to 14-pole are shown in Figs. 4 through 9. For each harmonic, any systematic value at low fields is subtracted out to obtain the contribution from iron saturation alone. As can be seen from these figures, the saturation induced harmonics are well below 1 unit in the case of symmetric excitation (solid lines) up to the maximum operating field of 3.83 T for these dipoles (7 TeV operation). In the case of asymmetric excitation, the lowest order quadrupole and sextupole harmonics are the most affected. Even for these harmonics, it is seen from Figs. 4 and 5 that the saturation induced harmonics

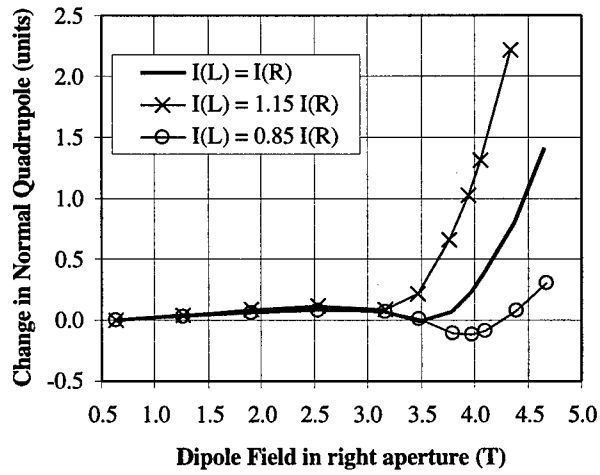

Fig. 4: Saturation behavior of the quadrupole term

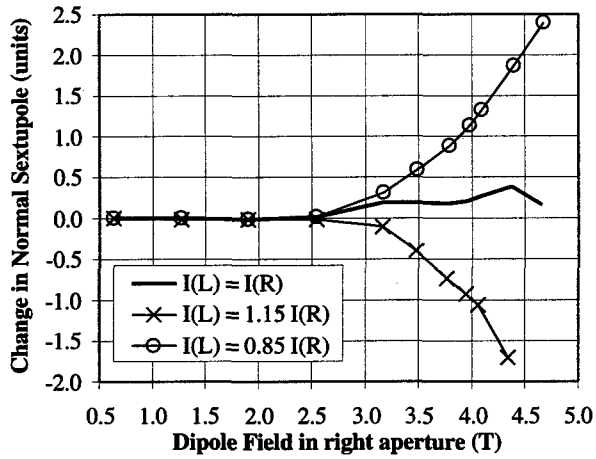

Fig. 5: Saturation behavior of the sextupole term

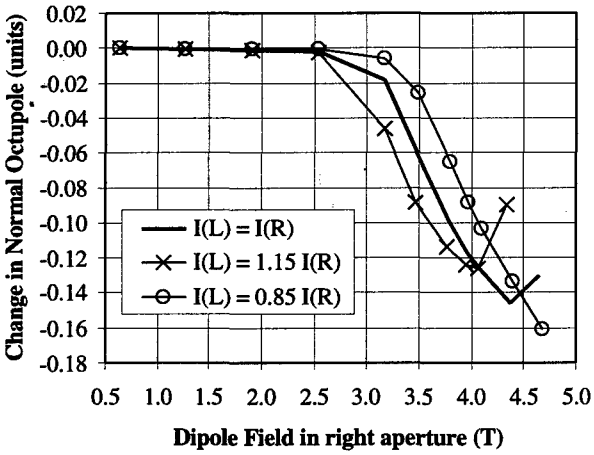

Fig. 6: Saturation behavior of the octupole term

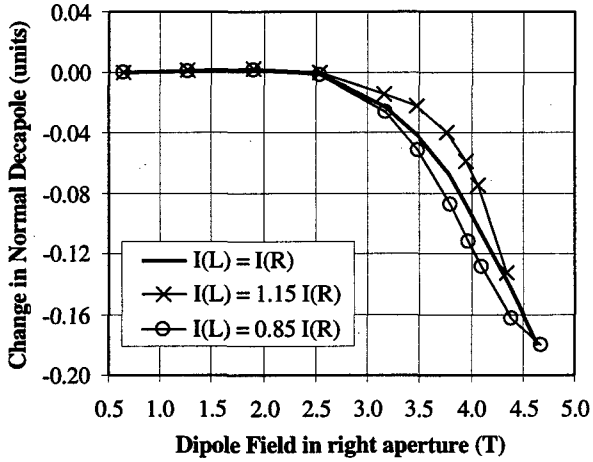

Fig. 7: Saturation behavior of the decapole term

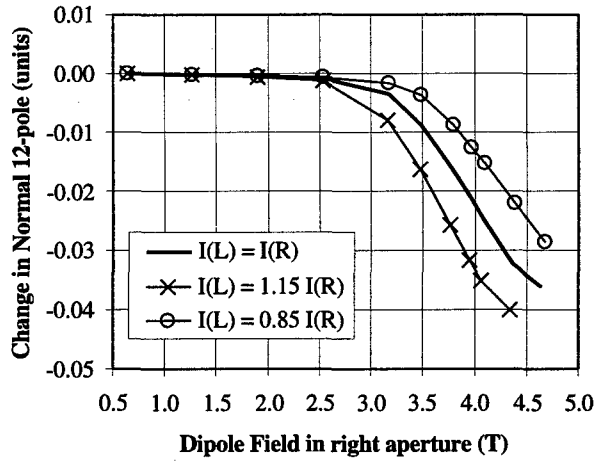

Fig. 8: Saturation behavior of the 12-pole term

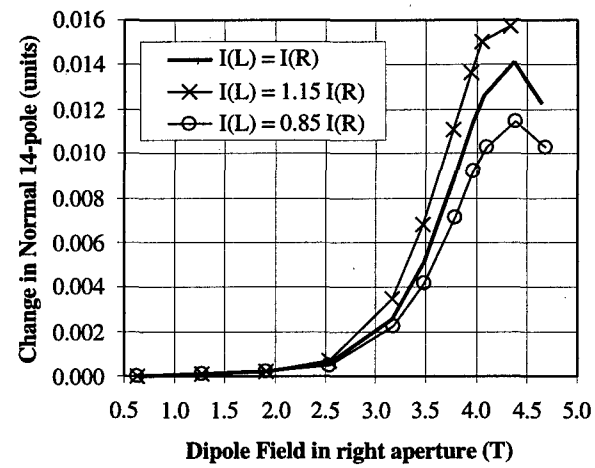

Fig. 9: Saturation behavior of the 14-pole term

are still below 1 unit at the highest operating point. Since the actual asymmetry needed in operation is expected to be less than 10%, and that too at a lower field, the small deterioration in the saturation behaviour should be quite acceptable. For the higher order terms, octupole through the 14-pole, the changes are at the level of 0.02 unit or less. These changes also are not expected to limit the performance of the D2 dipoles.

ACKNOWLEDGEMENTS

We thank S. Kahn and B. Parker for their help with the OPERA-2D calculations.

REFERENCES

[1] A. Jain, et al., "Magnetic Design of Dipoles for LHC Insertion Regions", Proc. EPAC98, pp. 1993-5.

[2] R. Wolf, "Field Error Naming Conventions for LHC Magnets", CERN report LHC-MMS/ES/01

REAL-WORLD SORTING OF RHIC SUPERCONDUCTING MAGNETS*

J. Wei†, R. Gupta, M. Harrison, A. Jain, S. Peggs, P. Thompson, D. Trbojevic, P. Wanderer
Brookhaven National Laboratory, Upton, NY 11973, USA

Abstract

During the seven-year construction of the Relativistic Heavy Ion Collider (RHIC), more than 1700 superconducting dipoles, quadrupoles, sextupoles, and multi-layer correctors have been constructed and installed. These magnets have been sorted at several production stages to optimize their performance and reliability. For arc magnets, priorities have been put first on quench performance and operational risk minimization, second on field transfer function and other first-order quantities, and finally on nonlinear field errors which were painstakingly optimized at design. For Interaction-Region (IR) magnets, sorting is applied to select the best possible combination of magnets for the low-β^* interaction points (IP). This paper summarizes the history of this real-world sorting process.

1 INTRODUCTION

The RHIC magnet system consists primarily of superconducting dipole, quadrupole, sextupole and corrector magnets for guiding, focusing, and correcting the counter-circulating ion beams into the design orbits in the regular arcs of the machine lattice. A large complement of special superconducting magnets is also required for steering the beams into collisions at the six interaction regions (IR) where the ion beams interact. During the seven-year construction cycle, more than 1700 superconducting magnets have been constructed, measured, installed and tested. In order to optimize the performance of these magnets, sorting has been applied whenever possible.

For a majority of the arc magnets, priorities have been put first on quench performance and operational risk minimization and second on field transfer function and other first-order quantities. Since nonlinear field errors were painstakingly optimized at design, and their sorting priority was low. For IR magnets, sorting was applied to select the best possible combination of magnets for 2 out of 6 IRs where β^* will be lowered to 1 meter for high luminosity experiments. In order to minimize the relative misalignment between magnets in a common cryostat, sorting was also applied both before and after cryostat assembly. In contrast to an idealized magnet sorting, sorting in a real world is often constrained by the assembly and installation schedule, available storage space, etc. This paper summarizes the history of this real-world sorting process. In Section 2, we review the overall procedure of magnet analysis, acceptance, and sorting. In Sections 3 and 4, we summarize the actual sorting experience for arc and IR magnets.

* Work performed under the auspices of the US Department of Energy.
† Email: wei1@bnl.gov

2 MEASUREMENT DATA ANALYSIS

Besides reaching fields with substantial margins above the required range, all of the RHIC magnets must meet stringent requirements for field quality, reproducibility, and long-term reliability. In order to fulfill this goal, a committee of magnet division and RHIC accelerator physics personnel jointly reviewed the field quality, quench test performance, survey and other engineering aspects of the magnets. After individual magnet elements (coldmasses) are measured and tested, the magnetic field quality data, including transfer function, field angle, multipole harmonics, magnetic center offsets, etc. at all the test currents, [1] are recorded along with the warm mechanical survey measurements of the fiducial positions, sagitta, mechanical length and field angle. The data are transferred from the magnet division into the RHIC SYBASE database, and then analyzed by studying trends, comparing with the expected values, and evaluating the deviation from the mean using the computer program MAGSTAT [2]. As shown in Fig. 1, after their review and acceptance, magnets contained in their own cryostats (e.g. arc dipoles) are sorted for their candidate installation locations. Magnets belonging to a common cryostat assembly go through a second stage of

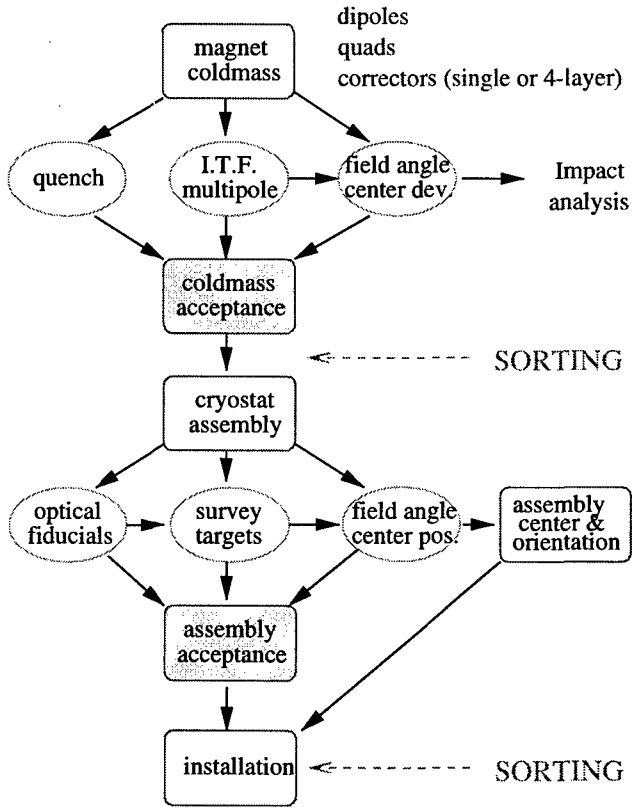

Figure 1: Magnet acceptance and sorting procedure.

0-7803-5573-3/99/$10.00@1999 IEEE.

review, acceptance and sorting. At this stage, the assembly is surveyed with either colloidal-cell optical or stationary-coil pick-up (antenna) techniques to locate the magnetic centers of the components relative to the cold mass fiducials and the externally accessible cryostat fiducials. This survey data is transferred into the database and analyzed using the computer program SURVSTAT [3]. Based on a second-round review and balance of both coldmass and assembly data, the assemblies are sorted for final installation.

3 ARC REGION MAGNET SORTING

RHIC arc dipoles, quadrupoles and sextupoles are industry-built magnets. Despite close communication and detailed quality assurance procedures, unexpected changes in the manufacturing process still occurred. Magnet acceptance review and the subsequent sorting played an essential role in optimizing the final performance.

3.1 Arc Dipoles

During the acceptance, a drop in the integral transfer function (ITF) of about 0.1% was noticed and traced to the narrower width of the phenolic insulator used between the coil and the iron. Although the problem was corrected, about 20 magnets were affected. These magnets were sorted along with all subsequent dipole magnets. The sorting procedure was based on the strength minimization of dipole correctors required to compensate for the variation in the integral transfer function. With sorting, the maximum current required for such compensation was decreased from 12 A to about 3 A.

The dominant multipoles of the dipole magnets are b_2 (normal sextupole) and b_4 (normal decapole) resulting from the dipole symmetry of the magnets, and a_1 (skew quadrupole) resulting from the asymmetric vertical placement of the magnet cold mass in the cryostat. Due to the relatively high injection energy and the small diameter of the coil filaments, the persistent current effects are small. Magnet design has minimized b_2 and b_4 for both injection and storage currents by optimizing the cross-sections of the coil and the yoke taking into account the persistent current and saturation effects. The minimization of a_1 is achieved by sorting the yoke weight during the assembly process so that the lower half yoke is heavier than the upper half.

Among the eight dipoles allocated as spare magnets, five of them have off-normal skew quadrupole component (a_1 up to -5.9 units [4]), some caused by a known coil size mismatch; one has an excessive twist (2.5 mr standard deviation in body field angle) along the magnet body, and one has low transfer function at high fields.

3.2 Arc Quadrupoles

At the early stage of industrial manufacture, midplane shims were incorrectly changed on 5 quadrupoles, resulting in a b_3 of about -6 units. These magnets were sorted and distributed among the two rings to minimize their effects.

The dominant multipoles of the quadrupoles are b_5 and a_5 resulting from the quadrupole symmetry of the coil and the end configuration, and b_3 resulting from the asymmetry between the horizontal and vertical planes. b_3 was compensated in the design by making the coil to midplane gap appropriately asymmetric, while b_5 was reduced by compensating the body with the ends of the magnet.

Among the eight quadrupoles allocated as spare magnets, four of them are of concern with off-normal coil size or low collaring pressure, some resulting in large a_2; two have excessive b_2 (-5 units); one has an engineering repair.

3.3 Arc Sextupoles

In general, the performance of the sextupole magnets exceeded the design goal. However, the epoxy contained in about 42 magnet coils is significantly weaker than normal. Consequently, the average quench currents (about 170 A) of these magnets, although exceeding the design operating current (100 A), are lower than the average of the regular magnets (above 200 A). To minimize possible long-term effects, these magnets have been sorted and allocated to the focusing locations around the two rings where the required strength of the sextupoles for chromaticity correction is about 50% of that at the defocusing locations.

3.4 Arc Trim Quadrupoles

Trim quadrupoles all have minimum quench currents above 200 A, well exceeding the design operating current of 100 A. One trim quadrupole coldmass was designated as a spare due to rust on the yoke caused by rain damage.

3.5 Arc Correctors

All of the correctors, either single-layer or four-layer, were built in-house and cold tested. After initial training, all the magnets quench above the design operating current of 50 A. Since the dipole corrector layers are all powered individually, the variation in the integral transfer function (typically 1% rms) is of little concern. Correctors with layers of excessive field angle deviation (up to $\sim$20 mr) or erratic quench training were selected as spare magnets.

3.6 Arc CQS Assembly

Arc corrector, quadrupole, and sextupole magnets were welded into a single "CQS" assembly. The CQS assembly also includes a beam position monitor and (for some) a recooler. The CQS components need to be aligned with each other so that their magnetic centers are on a straight line. It was found in the early stage of installation that "Springs" (made of G-10 plastic) needed to be installed or refitted in the support posts, confining the coldmass transversely while allowing free longitudinal motion. Special welding stripes were applied to the CQS shell to align the magnetic centers of the individual coldmasses for assemblies that exceeded a tolerance of 0.25 mm. Subsequently, the welding sequence is carefully choreographed to balance "curling" distortions against each other.

Correctors with large misalignments can generate serious feed-down harmonics. Two early CQSs with corrector offsets larger than 2 mm have been removed from the tunnel, and were later corrected.

4 IR MAGNET SORTING

The IR triplet cryostat contains two dipoles, six quadrupoles, and six four-layer corrector packages of the two rings. Field imperfection of the IR magnets limits the machine performance at collision when β^* is squeezed. Among the 6 interaction points, 2 of them are planned to run at a low β^* of 1 m. Most sorting efforts have been to select the best IR magnets for these 2 "golden" IPs.

4.1 IR Dipoles

In general, two IR dipoles, one on each side of the IP, are powered by the same shunt power supply. Sorting has been performed to pair dipoles of similar transfer function to the same IP. Two dipoles with off-normal transfer function are assigned to special locations where individual shunt supplies exist. Early magnets with imperfect field quality (large b_2) were assigned to non-golden region. Since the outstanding random error is a_1, magnets of similar a_1 are sorted to the opposite side of the same IP to minimize their action kicks [5]. One dipole is designated as a spare due to erratic quench performance.

4.2 IR Quadrupoles

The manufacturing sequence of IR quadrupoles follows the level of required performance, starting with the less-critical Q1. Several iterations were made on the magnet cross section to optimize the field quality. Application of tuning shims is also practiced at this stage.

In one Q2 quadrupole, an excessive amount of axial variation in multipole errors was found (change of 15 units of a_2) and suspected to be due to cracked insulators. The quench performance, though adequate, was lower than average. Efforts were made at the last stage of installation to replace this "golden candidate" with a "spare candidate".

Due to lack of time for cryogenic testing, 11 out of 72 IR quadrupoles were measured only at room temperature. Because of imperfect correlation between the warm and cold measurements, the field quality of these magnets is less well known than the field quality of magnets which have been cold tested. Since this information is the critical base for IR correction, these magnets were sorted to "non-golden" IRs. Spare magnets were mostly selected based on off-normal multipole errors. One quadrupole with a partially inserted shim was first allocated as a spare but later installed to meet schedule requirements for the first sextant test.

4.3 IR Correctors

Sorting on IR correctors was performed along with the quadrupoles before their attachment to minimize the relative magnetic center offset and field angle. After sorting, for CQ combinations with excessive relative offset and roll, shimming adjustment were made before welding of the assembly.

4.4 IR CQ Assembly

IR correctors were welded to IR quadrupoles to form CQ assemblies. At a later stage of IR CQ assembly, electric shorts were found at the octupole leads of IR correctors precipitated by a routing misdesign. Rework was done on all the correctors which were still in coldmass state. For correctors designated as "golden" and yet with their end plates already welded on, their end plates were removed to allow a complete rework. About 8% of the CQ assemblies fully installed in the machine were not reworked, and their chance of octupole layer malfunction is less than 10%.

Table 1: Summary of RHIC magnet sorting ($n = 1$ is quadrupole).

Magnet	Number (used+spare)	Sorted quantity
Arc dipole	288+8	ITF, yoke weight (a_1) twist, b_2
Arc quad.	372+8	coil size, midplane shim size collaring pressure coil saddle crack repair, b_2
Arc sext.	288+12	epoxy level (quench)
Arc corr.	420+10	quench, field angle
D5I	12+1	vacuum vessel straightness
D5O	12+1	vacuum vessel straightness
D96	48+1	
Trim quad.	72+6	rust on yoke
CQS	282+8	corrector offset
CQT	72+6	
CQ	60+2	
Interaction region magnets:		
IR dipole	24+2	quench, ITF, b_2, a_1
IR quad.	72+6	data availability (schedule) axial variation of a_2 partial shim, multipoles
IR corr.	72+6	center offset, roll
DX dipole	12+1	
IR CQ	72+6	potential corrector shorts
Total	1692+65	

4.5 Separating Dipoles DX

After a design iteration based on the prototype magnet, the field errors (b_2, b_4) of these large-bore (18 cm coil diameter) dipoles were greatly reduced and are well within the capability of IR correction [6].

We thank members of the Magnet Acceptance Committee for their contribution.

5 REFERENCES

[1] P. Wanderer, CERN 98-05 (1998) p. 273.

[2] J. Wei, G. Ganetis, R. Gupta, M. Harrison, M. Hemmer, A. Jain, F. Karl, S. Peggs, S. Tepikian, P.A. Thompson, D. Trbojevic, and P. Wanderer, EPAC96 (1996) p. 2222.

[3] J. Wei, R. C. Gupta, A. Jain, S. G. Peggs, C. G. Trahern, D. Trbojevic, and P. Wanderer, PAC95 (1995) p. 461.

[4] Multipole errors are normalized to 10^{-4} of their integral strength at a reference radius of about 2/3 coil radius. $n = 1$ is quadrupole.

[5] J. Wei, W. Fischer, V.Ptitsin, R. Ostojic, J.Strait, PAC99 (1999).

[6] A. Jain, PAC99 (1999).

US-LHC MAGNET DATABASE AND CONVENTIONS*

J. Wei†, D. McChesney, A. Jain, S. Peggs, F. Pilat, BNL, Upton, NY 11973, USA
L. Bottura, CERN, 1211 Geneva 23, Switzerland
G. Sabbi, Fermi Lab, P. O. Box 500, Batavia, IL 60134, USA

Abstract

The US-LHC Magnet Database is designed for production-magnet quality assurance, field and alignment error impact analysis, cryostat assembly assistance, and ring installation assistance. The database consists of tables designed to store magnet field and alignment measurements data and quench data. This information will also be essential for future machine operations including local IR corrections.

1 INTRODUCTION

The US part of the Large Hadron Collider (US-LHC) accelerator program is responsible for manufacturing superconducting magnets for the Insertion Region (IR) inner triplet and RF Region dipoles. Dipoles built at Brookhaven National Laboratory, quadrupoles built at Fermi Lab and Japan's KEK, and correctors built in Europe will be measured and assembled in cryostats in the US and then shipped to CERN for installation. In a multi-laboratory collaboration like this, it is necessary to unify the measurement and application conventions, and to establish a database structure commonly accepted by CERN and other collaborating laboratories. The US-LHC Magnet Database [1] is designed for production-magnet quality assurance, field and alignment error impact analysis, cryostat assembly assistance, ring installation assistance. The database consists of tables designed to store magnet field and alignment measurements data and quench data. This information will also be essential for future machine operations including local IR corrections.

The design of US-LHC Magnet Database is based on the existing structure used for the Relativistic Heavy Ion Collider (RHIC). Analysis and monitoring software for field quality [2] and alignment quality [3] have also been adapted for US-LHC magnet use.

2 DATABASE FUNCTIONS AND DATAFLOW

Fig. 1 shows the function of Magnet Database during the production stage, at installation, and after operation. After individual magnet elements (coldmasses) are constructed and measured, quench data, field quality data (integral transfer function, center offset and field angle relative to mechanical fiducials, field harmonics, etc.) and alignment data (fiducial positions, magnetic center, etc.) are collected. After processing (analyzing measurement conditions and statistics, correcting calibration and other systematic errors, etc.), a minimum set of representative data is transfered to the US-LHC Magnet Database. Based on these stored data, computer tracking and simulation is performed to assess the impact of errors; statistical and trend analysis is performed to monitor field quality and to assist in magnet coldmass acceptance; information of magnetic center and field angle can be used for alignment sorting [4] before cryostat assembly; and multipoles with signs defined according to the convention are used for future machine operation including IR correction [5].

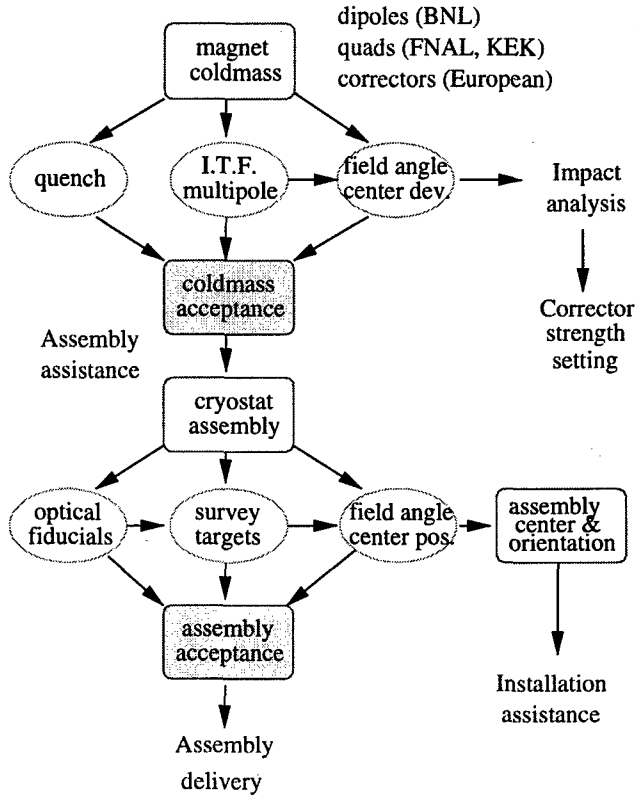

Figure 1: Dataflow for US-LHC magnet field and alignment quality analysis.

During cryostat assembly, survey and alignment data are extracted and stored in the database. Sufficient information is contained to provide the center and field angle of the assembly relative to the cryostat fiducials. Along with the completed assembly, this information will be delivered to CERN to assist in ring installation.

3 MEASUREMENT AND ANALYSIS CONVENTIONS

3.1 Measurement Convention

Conventions are established among BNL, CERN and FNAL defining the reference measurement coordinates. Magnetic multipoles are defined in the reference system [6, 7] illustrated in Fig. 2. The description is 2-dimensional

* Work performed under the auspices of the US Department of Energy.
† Email: wei1@bnl.gov

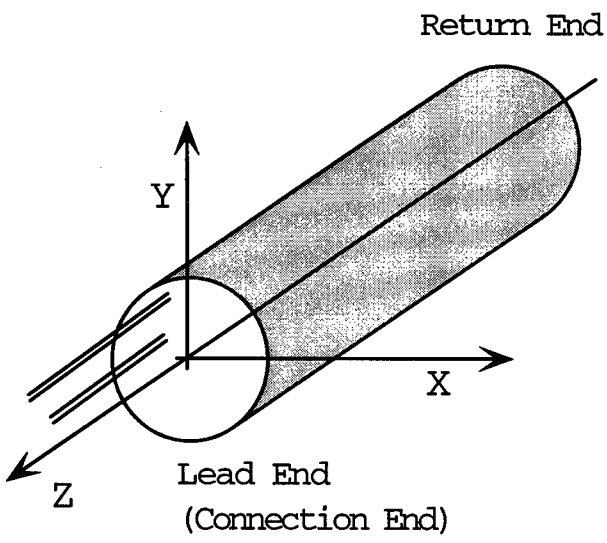

Figure 2: Reference frame for the measurement of magnetic multipoles.

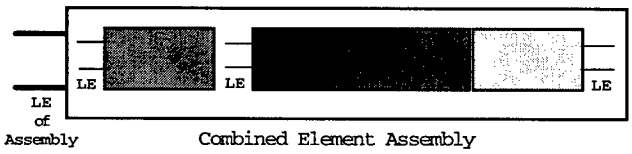

Figure 3: Lead end of a combined element assembly.

with $x-y$ axes chosen such that the skew (or normal) component in the main field of a normal (or skew) magnet is zero.

If the measurement is performed on a single magnet element (coldmass), the reference frame is defined with respect to the lead end of the element. If the measurement is performed on a magnet element contained in a combined element assembly, the reference frame is defined with respect to the lead end of the assembly (which may be opposite to that of the individual element), as shown in Fig. 3

3.2 *Multipole Sign Convention*

Both the magnitude and sign of measured multipole errors are important for error analysis and for IR local correction [5]. For example, the systematic a_2 from the lead ends of the triplet quadrupole is significant. Since IR magnets at opposite side of the interaction point (IP) are oriented symmetrically towards the IP, the actual sign of a_2 seen by the beam changes accordingly.

Fig. 4 shows the change of magnet multipole sign from their measured value for a beam circulating counterclockwise. In general, rules for multipole transformation under 180° rotation around vertical (y) axis (orientation flip), longitudinal (z) axis (upside-down change) and radial (x) axis are summarized in Tab. 1.

4 DATABASE STRUCTURE

Presently, the database contains 17 tables as listed in Tab. 2. The first 13 tables are intended for quench and field quality

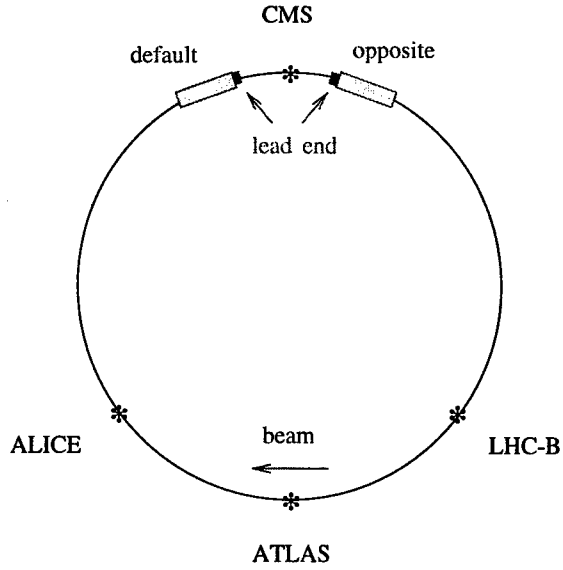

Multipole transformation for "opposite" orientation magnets:

quadrupole: $b_n \Rightarrow (-)^n b_n$; $a_n \Rightarrow (-)^{n+1} a_n$

dipole: $b_n \Rightarrow (-)^{n+1} b_n$; $a_n \Rightarrow (-)^n a_n$

Figure 4: Change of the sign of magnet multipoles from their reference measurement value for a beam circulating counterclockwise.

of individual magnet coldmass, while the last 4 tables are intended for survey and alignment data.

The Integral table contains the integral harmonics and transfer function information. In the case of short magnets, this information may be obtained from a single measurement with a suitably long measuring coil. For long magnets, e.g. the RF dipoles, the integral harmonics will be obtained from a sum of several measurements (a Z-Scan). In the case of a Z-Scan, one can also extract the harmonics averaged over the straight section as well as the integrated contributions from the two ends. If available, these results will be stored in the BodyHarmAvg and EndsHarm tables

Table 1: Transformation rule for magnet multipoles. It is assumed that the magnet polarity is adjusted, if necessary, so that the fundamental term remains positive. $N = 2$ is for quadrupole magnet, while $n = 2$ is for quadrupole order.

Item	Normal magnet of order N	Skew magnet of order N
Orientation:		
b_n	$(-)^{n+N} b_n$	$(-)^{n+N+1} b_n$
a_n	$(-)^{n+N+1} a_n$	$(-)^{n+N} a_n$
Upside-down:		
b_n	$(-)^{n+N} b_n$	$(-)^{n+N} b_n$
a_n	$(-)^{n+N} a_n$	$(-)^{n+N} a_n$
180° about x:		
b_n	b_n	$-b_n$
a_n	$-a_n$	a_n

Table 2: Summary of US-LHC Magnet Database tables.

Name	Content
Magnets	magnet name, ID, summary info.
Assembly	combined element assembly info.
Quench	quench performance
Integral	int. geometric multipole
LocalHarm	multipoles measured at one position
BodyHarmAvg	average body multipole
EndsHarm	lead and return end multipole
IntField	integral field strength
Magz	magnetization multipole
Eddy	Eddy current multipole
TDecay	time decay multipole
Centers	magnetic centering offsets
WarmCold	ITF & multipole warm/cold conversion
FidMagInfo	survey information summary
FidOpt	fiducial position from optical survey
CentMag	mag. center wrt external reference
Angle	mag. field angle wrt external reference

respectively. In addition, each individual measurement in a Z-Scan will be recorded in the table LocalHarm. The entries for various positions in the LocalHarm table can be used to identify any location which may be unusual from the field quality point of view. Such spots of concern are generally difficult to identify from the integral or the average body harmonics, and the information can be essential in establishing models for study of, e.g. magnet fringe field.

Tables Integral, BodyHarmAvg, EndsHarm contain transfer function, multipoles and field angle data of individual magnet coldmass. Both normal and skew Multipoles up to order 15 are recorded in accordance with the convention. Both the body and the ends harmonics are normalized to the value of the main field component in the straight section, whereas the integral harmonics are normalized to the integrated main field component. Thus both the body and integral harmonics are expressed in units. Since the ends harmonics are integrated values over a certain length of the magnet, these are expressed in unit·m rather than units.

The integral transfer function obtained by summing several measurements in a Z-Scan may not be very accurate due to small errors in positioning of the measuring coil. If this be the case, an independent measurement of integral transfer function is needed, for example with a long non-rotating coil, as was done for RHIC. With this in mind, a separate table (IntField) is created to store the most accurate measurements of integral transfer function.

For measurements in the superconducting state, measurements during the upward and the downward sweeps of current reveal contribution to harmonics due to superconductor magnetization. The difference between the up ramp measurements and the average of up and down ramp measurements will be stored in the table Magz. Similarly, if harmonic measurements are made while the magnet current is still ramping, then such harmonics will include any contributions from eddy currents generated in the superconductor. These harmonics will be stored in the Eddy table. Another superconductor related table is Tdecay, which will contain the time dependence of various harmonics at a fixed current (most important is the injection current) soon after a ramp.

Table Centers will contain the centering offsets and field angles from the magnetic measurements. These values are meaningful only when the measuring coil is well centered in the magnet yoke. In such cases, one can use this information, for example, to better align various elements in a combined element magnet.

Table WarmCold will contain the systematic values of warm to cold offsets based on data from all the magnets of a particular type for which both types of data exist. This table is only of academic interest if all magnets are measured cold. However, the table can be used to obtain the best estimates of cold harmonics if some magnets are only measured warm.

Tables CentMag and Angle contain information of assembly center offset and orientation relative to the external fiducials. This, together with Tables FidMagInfo and FidOpt containing information of fiducial positions, provides guidance to final ring installation of the magnet assembly.

5 SUMMARY

Along with the magnet assembly delivered for installation at CERN, magnet measurement data containing tables of quench performance, field quality, alignment and survey data will be transferred to CERN. This information is essential both for ring installation and for future machine operation including IR corrections. US-LHC Magnet Database has been designed to fulfill such tasks, and it will also benefit production stage quality assurance, error impact analysis, and assembly assistance including sorting.

We thank participants of the 1998 US-LHC Magnet Database Workshop for contributing to the establishment of the database structure.

6 REFERENCES

[1] J. Wei, D. McChesney, et al. *Summary on US-LHC Magnet Database Workshop*, RHIC/AP Note 160 (1998).

[2] J. Wei, R. C. Gupta, A. Jain, S. G. Peggs, C. G. Trahern, D. Trbojevic, P. Wanderer, *Field Quality Evaluation of the Superconducting Magnets for the Relativistic Heavy Ion Collider* PAC95, (1995) 461.

[3] J. Wei, G. Ganetis, R. Gupta, M. Harrison, M. Hemmer, A. Jain, F. Karl, S. Peggs, S. Tepikian, P.A. Thompson, D. Trbojevic, P. Wanderer, *Misalignment Evaluation of Superconducting Magnets in the Relativistic Heavy Ion Collider* EPAC96, Sitges (1996) 2222.

[4] J. Wei, et al., *Real-World Sorting of RHIC Superconducting Magnets*, PAC99 (1999).

[5] J. Wei, W. Fischer, V. Ptitsin, R. Ostojic, J. Strait, *IR Local Correction for the LHC*, these proceedings.

[6] A. Jain, et al., *RHIC Magnetic Measurements: Definitions and Conventions*, RHIC/AP/95 (1996).

[7] R. Wolf, *Field Error Naming Conventions for LHC Magnets*, LHC-MMS/ES/01 (1998).

AN ALTERNATIVE LATTICE FOR THE SPALLATION NEUTRON SOURCE ACCUMULATOR RING*

C. J. Gardner†, Y. Y. Lee, N. Tsoupas, J. Wei, BNL, Upton, NY 11973, USA

Abstract

As a key component of the Spallation Neutron Source (SNS) Project, the Accumulator Ring will collect the proton beam from the SNS LINAC at an intensity of 2×10^{14} per pulse at 60 Hz for a total power of 2 MW, exceeding present performance value of existing facilities. Requirements of minimum beam loss for hands-on maintenance and flexibility for future upgrade are essential for the lattice design. In this paper, we study an alternative lattice emphasizing various injection schemes and flexibility for future upgrade. Working points, sextupole families for chromaticity control, and alternate extraction schemes are also considered.

1 THE NOMINAL LATTICE

The nominal lattice [1, 2] for the SNS Accumulator Ring consists of four superperiods, each containing a 90° arc and a long straight section. The arc consists of four identical 8-meter-long FODO cells, each cell containing two 11.25° bends and having a horizontal betatron phase advance of $\pi/2$. The arc therefore has unit transfer matrix in the horizontal plane, ensuring zero dispersion in the long straights. Two identical 11.586-meter-long FODO cells form each of the four long straights which house injection, collimation, rf cavities, and extraction systems, respectively. The horizontal and vertical tunes of the nominal lattice were originally taken to be $Q_H = 5.82$ and $Q_V = 5.80$ with a vertical phase advance of 2π in each arc. However, in order to minimize transverse coupling, a "split-tune" option with $Q_H = 5.82$ and $Q_V = 4.80$ has been considered. Here the vertical tune is lowered one unit by reducing the vertical phase advance in each arc to $3\pi/2$ (67.5° per cell). This option has the added advantage that it reduces the β_{max}/β_{min} ratio (from 13.6 to 7.3). The lattice functions for the split-tune case are shown in Fig. 1 where the plot runs from the center of one arc to the center of the next. The drift regions of the long straights in the nominal lattice are 5.293 m long (with 0.5 m quadrupoles). These can accommodate the necessary injection, collimation, rf, and extraction elements. Fig. 2 shows the nominal charge-exchange injection scheme [3, 2]. Here the three bends produce a fixed injection bump which allows the chopped H^- beam from the Linac to be injected through a stripping foil in the central 3 kG bend. The 8 fast kickers (shown in green) allow for horizontal and vertical transverse painting as some 1225 turns are accumulated.

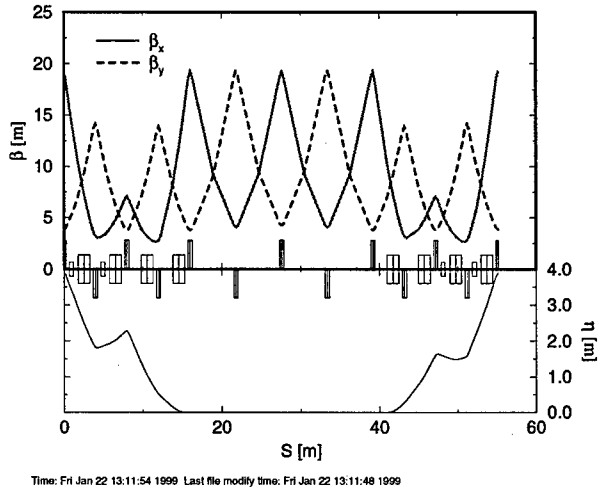

Figure 1: Split-tune FODO lattice.

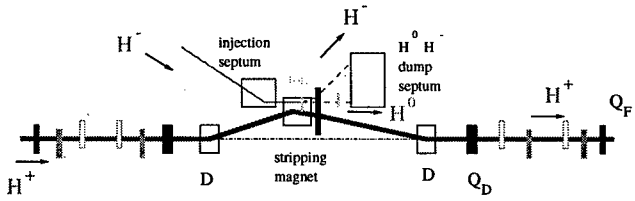

Figure 2: Foil injection in nominal FODO lattice.

2 DOUBLET/FODO HYBRID LATTICE

One of the key issues of the ring design is flexibility for future upgrade. Of particular interest is the ability to accommodate H^- injection with laser-undulator stripping [4, 5] should this become a viable option in the future. With this in mind, we have been studying the benefit of an alternative lattice, the so-called hybrid lattice, which has the same FODO arcs as the nominal lattice but has a doublet structure in the straights. The beta functions and dispersion for such a lattice are plotted in Fig. 3. Here the tunes are split ($Q_H = 5.82, Q_V = 4.80$) and the vertical phase advance in the arcs has been reduced to 55.8° per cell to minimize the beta function mismatch between the Doublet and FODO cells; the circumference is the same as that of the nominal lattice. The strength of the doublet quadrupoles is approximately three times that of the FODO quadrupoles in the nominal lattice straights. Comparing with Fig. 1 we see that the maximum beta is only slightly larger (21 versus 19.4 m). The doublet structure opens up 9.086 m drifts on either side of the central triplet. (The quadrupoles are 0.5 m long and the spacing within the doublets and triplet is 0.5 m.) If need be, these can be made longer while keep-

* Work performed under the auspices of the US Department of Energy.
† Email: cgardner@bnl.gov

ing the length of the arcs fixed. Fig. 4 shows the effect of adding length ΔL to the drifts. An important figure-of-merit here is the β_{max}/β_{min} ratio, which shows only small variation over the range of ± 4 m. We are currently studying the relative sensitivity of the hybrid lattice to random and systematic magnetic errors and are developing a correction scheme similar to that of the nominal lattice [6].

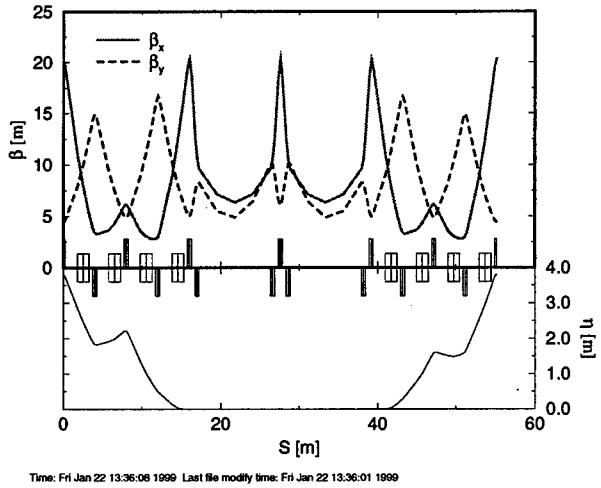

Figure 3: Doublet/FODO hybrid lattice.

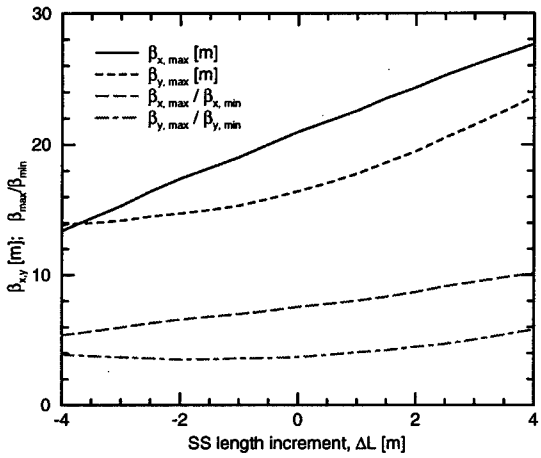

Figure 4: Variation of hybrid lattice parameters with ΔL.

3 ALTERNATIVE INJECTION SCHEMES

The long drifts of the hybrid lattice provide the necessary space for a future laser-undulator charge-exchange injection scheme [4, 5] such as the one depicted in Fig. 5. Possible foil injection schemes that would fit in the same space are shown in Figures 6 and 7. The scheme of Fig. 6 is the same as that of the nominal lattice except that the beams emerging from the foil must pass through a triplet instead of a single horizontally focusing quadrupole. Here one must be careful that any excited H^0 beam emerging from the foil does not pass through fields greater than 2.5 kG in the triplet. (Keeping the field below 2.5 kG ensures that H^0 atoms with principle quantum numbers of $n = 4$ or less will survive the field [3].) In both the nominal scheme and that of Fig. 6, the 8 fast kickers (shown in green) produce a closed orbit bump (used for transverse painting) that is off-center in the central quadrupoles of the injection straight. This couples the injection setup with the tune of the lattice, which, although not a problem in principle, makes tuning more complicated in practice. Complete decoupling can be achieved by housing the entire injection scheme in one drift space as shown in Fig. 7. The magnitude of the kicks required in this case is 12 milliradians, twice that of the nominal scheme.

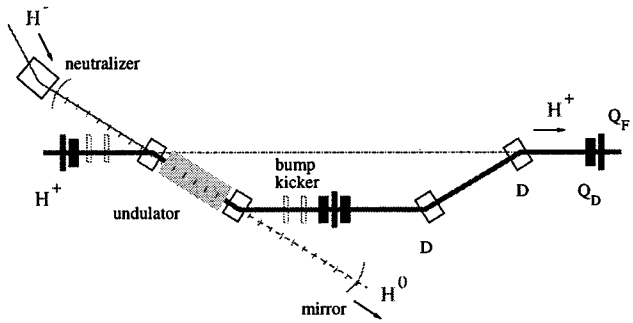

Figure 5: Doublet straight with laser-undulator injection.

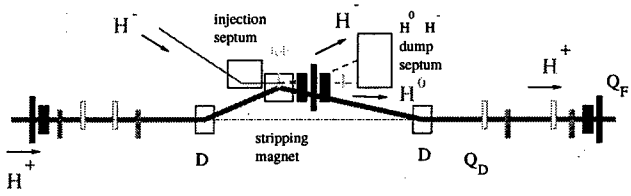

Figure 6: Doublet straight with foil injection.

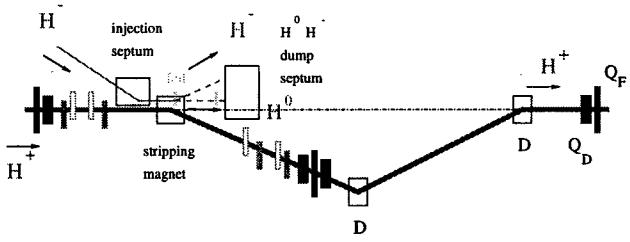

Figure 7: Doublet straight with decoupled injection.

In all of the injection schemes considered, the bending magnets break the four-fold symmetry of the ring. In the nominal scheme, where the bend angles are small (less than 2.4°), a small amount of dispersion (0.3 m) is introduced in the long straights and there is a small perturbation (0.5 m) of the beta functions. The same is true of the scheme in Fig. 6. However, for the laser-undulator scheme, where the bends may be as large as 8.5°, and for the decoupled

scheme, where the central bend is 4.9°, the perturbation of the symmetry is more severe. (For the decoupled scheme, a dispersion of 0.7 m is introduced in the long straights.)

4 EXTRACTION

The extraction scheme of the nominal lattice [2] is shown in Fig. 8. Here the fast kickers provide a vertical kick that allows the beam to clear a Lambertson magnetic septum. The Lambertson magnet deflects the beam by 15.5° with a field of about 5 kG, bringing the beam into the Ring-to-Beam-Target transport line. A possible extraction scheme for the hybrid lattice is shown in Fig. 9. Here the kickers are located close to the central triplet so that the effect of the lattice tune on the extraction setup is minimal.

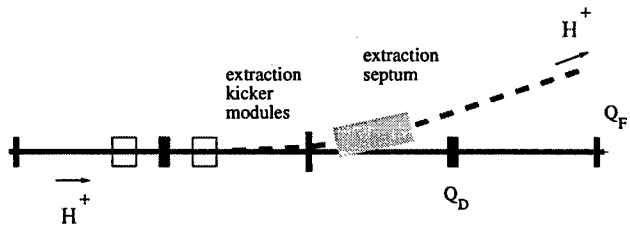

Figure 8: Extraction scheme for the nominal lattice.

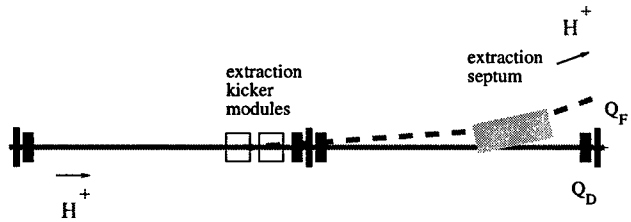

Figure 9: Extraction scheme for the hybrid lattice.

5 SEXTUPOLE OFF-MOMENTUM OPTICS MATCHING

In recent months, we have been studying the potential benefit of arc sextupoles in minimizing off-momentum optics mismatch and improving off-momentum dynamic acceptance [7]. Using 16 sextupoles of moderate strength (3 kG at 10 cm) grouped in 4 families, the amplitude of the off-momentum beta wave can be reduced from ±12% to less than ±3%; this is shown in Fig. 10. Consequently, the off-momentum dynamic aperture can be increased by as much as 30%. The chromatic tune variation can be adjusted as desired across the entire range of beam momentum. Without enhancing the nonlinear chromaticity, the linear chromaticity can be either reduced or enhanced for tune spread optimization and possible instability damping.

6 CONCLUSIONS

Although the nominal lattice has a simple FODO structure that allows for considerable flexiblity in tuning, it does not have the long drift spaces required for the laser-undulator charge-exchange injection schemes which may become a reality in the future. The hybrid lattice considered here employs doublets to open up the necessary dirft spaces in the long straights. Both the laser-undulator and foil injection schemes can then be accommodated. The long drifts can also possibly accommodate the entire dynamic injection bump so that injection painting and lattice tuning are decoupled. Furthermore, the long drifts maximize the flexibility of the collimation device arrangement [7]. The acceptance of the hybrid lattice is comparable to that of the nominal lattice, but sensitivity to magnet errors remains to be examined.

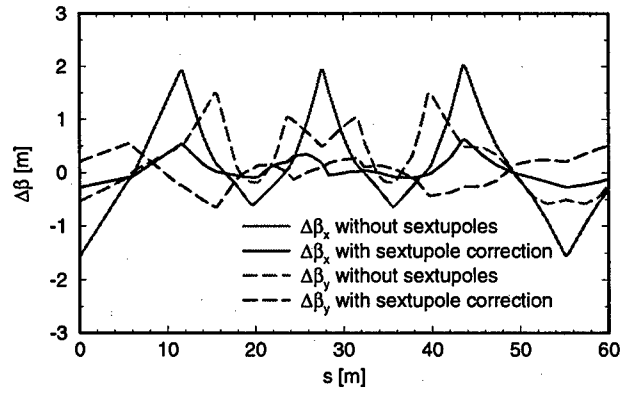

Figure 10: Beta-wave correction.

7 ACKNOWLEDGEMENTS

The authors would like to thank W. T. Weng for his guidance and support, and G. H. Rees for several useful discussions.

8 REFERENCES

[1] C. Gardner, Y. Y. Lee, A. Luccio, "Accumulator Ring Lattice for the National Spallation Neutron Source", Proceedings of the 1997 PAC, Vancouver, B. C., Canada, May 12–16, 1997.

[2] Spallation Neutron Source Design Manual, June 1998.

[3] Y. Y. Lee, "The Spallation Neutron Source Accumulator Ring", Application of Acceleration Technology, Gatlinberg, Tn., Sept. 20–23, 1998.

[4] Y. Suzuki, ICFA Mini-Workshop on Injection and Extraction, (1999).

[5] I. Yamane, ICFA Mini-Workshop on Injection and Extraction, (1999).

[6] C. J. Gardner, Y. Y. Lee, W. T. Weng, "Random and Systematic Field Errors in the SNS Ring: A Study of Their Effects and Compensation", EPAC-98, Stockholm, Sweden, June 22–26, 1998.

[7] J. Wei, et. al.,"Beam-Loss Driven Design Optimization for Spallation Neutron Source Ring", PAC99 (1999).

BEAM-LOSS DRIVEN DESIGN OPTIMIZATION FOR THE SPALLATION NEUTRON SOURCE (SNS) RING*

J. Wei†, J. Beebe-Wang, M. Blaskiewicz, P. Cameron, G. Danby, C.J. Gardner, J. Jackson, Y.Y. Lee
H. Ludewig, N. Malitsky, D. Raparia, N. Tsoupas, W.T. Weng, S.Y. Zhang, BNL, USA

Abstract

This paper summarizes three-stage design optimization for the Spallation Neutron Source (SNS) ring: linear machine design (lattice, aperture, injection, magnet field errors and misalignment), beam core manipulation (painting, space charge, instabilities, RF requirements), and beam halo consideration (collimation, envelope variation, e-p issues etc).

1 INTRODUCTION

The SNS ring compresses 2×10^{14} protons at 1 GeV into a 1 μs pulse at a repetition rate of 60 Hz providing a beam power of 2 MW [1]. At such intensity and power, beam loss is a critical issue. Four levels of loss control are implemented: to guarantee hands-on maintenance (average 1 W/m [2]), the total uncontrolled beam loss in the ring needs to be limited well below 10^{-3}; the collimators are designed to collect beam halo at a level of 10^{-3}; hardware and shielding are designed to withstand 10^{-2} for engineering reliability; and the machine can withstand a couple of full beam pulses for emergency handling and commissioning.

Presently, concern of beam loss is incorporated in the design of the ring and transfer lines (HEBT, RTBT) at three stages: linear machine design (lattice, aperture, injection and extraction, magnet field errors and misalignment, etc.), beam core manipulation (space charge, painting, instabilities, RF requirements, etc.), and beam halo consideration (collimation, beam envelope variation, e-p issues, etc.).

2 LINEAR MACHINE OPTIMIZATION

2.1 Lattice and Acceptance Optimization

The SNS ring lattice is four-fold symmetric with FODO structures in the arc which are flexible for tuning. By lowering the vertical tune [3], the transverse tunes can be separated by 1 unit to minimize the transverse coupling. Reducing the phase advance in the arcs also makes focusing smoother and, consequently, reduces beam envelope variation (by a factor of 2 in β_{max}/β_{min}). Recent space charge simulation using SIMPSONS [4] indicates that emittance growth and tail development is noticeably reduced.

In order to minimize off-momentum optics mismatch and to improve dynamic acceptance (DA), we proposed a correction scheme using 4 families of arc sextupoles. By reducing the off-momentum beta wave from $\pm12\%$ to less than $\pm3\%$, the off-momentum DA is increased by as much as 30% (Fig. 1). The momentum aperture is also increased by about 30% (Tab. 1).

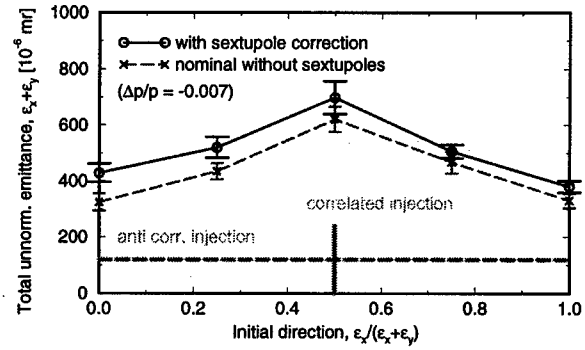

Figure 1: Improvement in the DA due to off-momentum optics optimization using arc sextupoles. The 6 dimensional tracking is done with TEAPOT incorporating expected magnetic errors, misalignments, and physical aperture of the machine with 10 random seeds at 5 transverse initial directions.

Table 1: Momentum aperture and sextupole improvement.

Item	Value
Beam momentum spread (99%)	$\pm$ 0.007
RF acceptance at 40 kV	$\pm$ 0.010
Ring acceptance at nominal emittance	$\pm$ 0.015
Ring acceptance with sextupole correction	$\pm$ 0.020

In order to decouple injection ramping from lattice tuning, and to accommodate possible future laser-undulator charge exchange injection schemes [5], we designed an alternative hybrid lattice [3] with FODO arcs but doublet straight sections. The long uninterrupted straight section can possibly accommodate the entire injection assembly. Since locations of peak $\beta_{x,y}$ are only at places of large aperture quadrupoles, the horizontal DA is increased by about

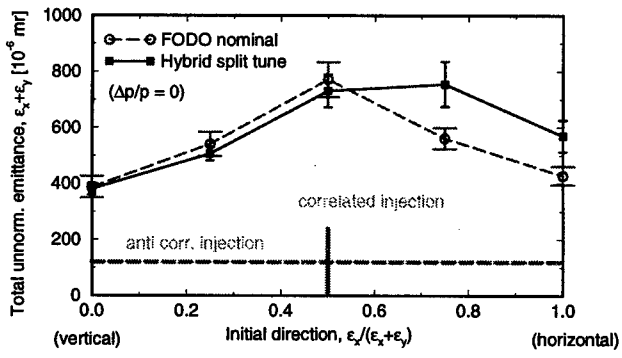

Figure 2: Improvement in the DA with the hybrid lattice.

* Work performed under the auspices of the US Department of Energy.
† Email: wei1@bnl.gov

0-7803-5573-3/99/$10.00@1999 IEEE.

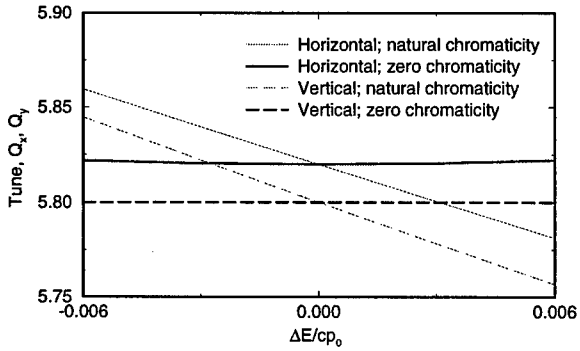

Figure 3: Chromatic tunability with 4-family sextupoles.

30% (Fig. 2).

2.2 *Chromatic Tunability*

With four families of sextupoles, desired chromatic tune variation can be achieved across the entire range of beam momenta. Without enhancing the nonlinear chromaticity, the linear chromaticity can be either reduced or enhanced for tune spread and DA optimization and for possible instability damping (Fig. 3).

2.3 *Magnetic Errors and Misalignments*

Field errors in both dipoles and quadrupoles (Tab. 2) are designed to be at 10^{-4} level within a 92% (7.6 cm) of radius to iron pole tip. Dipole ends are optimized to provide sector magnet function to 10^{-4} accuracy. Quadrupole ends are optimized to reduce the integrated b_6 error. With such field quality, the magnet error impact is small. Magnet misalignment (Tab. 3) can cause significant closed orbit offset and coupling requiring designed corrections [6].

Tab. 4 indicates that the leading sources of loss are expected to be incoming LINAC halo, LINAC gap residual, injection loss, and foil scattering. Foil loss is doubled in the anti-correlated painting scheme. At an off-normal condition of doubled LINAC emittance, the loss will again be doubled due to increasing foil hits.

Table 2: Expected magnetic errors of ring quadrupoles based on AGS Booster magnet measurement data and end optimization. Normalized to 10^{-4} of the main field at the reference radius (R_{ref}) of 7.6 cm. ($n = 2$ is quadrupole).

n	Normal		Skew	
	$\langle b_n \rangle$	$\sigma(b_n)$	$\langle a_n \rangle$	$\sigma(a_n)$
Body	[unit]			
3	–	-2.46	–	-2.5
4	–	-0.76	–	-2.0
5	–	-0.63	–	1.29
6	0.20	0.0	–	1.45
7	–	0.02	–	0.25
8	–	-0.63	–	0.31
9	–	0.17	–	-0.11
10	0.70	0.0	–	1.04
14	-1.41	0.0	–	0.26
End	[unit·m]		(Length=0.15 m)	
6	0.25	–	–	–

Table 3: Expected alignment errors of ring magnets.

Item	Value
Integral Transfer Function variation (rms)	10^{-4}
Ring dipole sagitta deviation	3 cm
Magnetic center position (rms)	0.1 mm
Magnet longitudinal position (rms)	0.5 mm
Mean field roll angle (rms)	0.2 mr

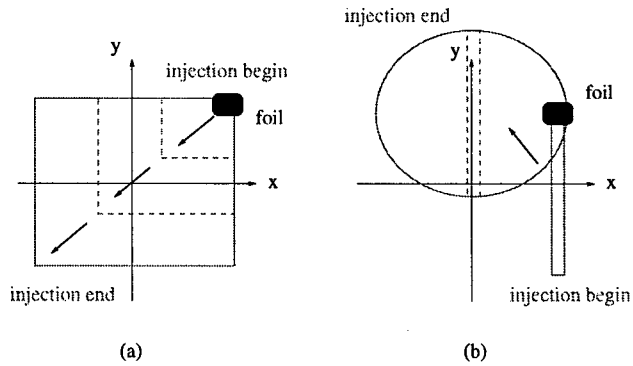

Figure 4: Correlated and anti-correlated painting of the transverse phase space (physical space shown).

3 BEAM CORE MANIPULATION

3.1 *Injection Painting and RF Gymnastics*

The beam phase space distribution is manipulated [7] during H^- injection both to achieve desired beam distribution at the target and to maintain the space charge tune shift at a moderate level (~0.2). The beam is injected at a location of near-zero dispersion to avoid complications caused by transverse-longitudinal coupling. In the longitudinal direction, the frequency of the pre-injection transfer line RF system is modulated to broaden the beam momentum spread without enhancing the momentum tail. In the transverse direction, both correlated and anti-correlated painting schemes (Fig. 4) can be accommodated to optimize operation. The anti-correlated scheme minimizes the impact of transverse coupling produced by misalignment and space charge forces, while the correlated scheme reduces halo development by gradually painting to larger action.

Table 4: SNS ring loss budget at 2 MW power assuming 400μg/cm^2 foil density with the anti-correlated painting.

Mechanism	Controlled loss	Uncontrol. loss
LINAC incoming halo		10^{-4}
LINAC gap residual		10^{-5}
Injection loss:		
missing foil	0.12	–
foil elastic scattering	–	$5.2\times^{-5}$
foil inelastic scattering	–	3.7×10^{-5}
H^0 production	0.02~0.11	$2\sim11\times10^{-8}$
ionization energy loss	–	5×10^{-6}
beam hitting septum	$< 10^{-3}$	
Ring collimator	$\sim 10^{-3}$	
Fault condition:		
1 kicker missing	< 0.1	–
LINAC off-normal:		
doubled emittance	0.03~0.11	2.1×10^{-4}

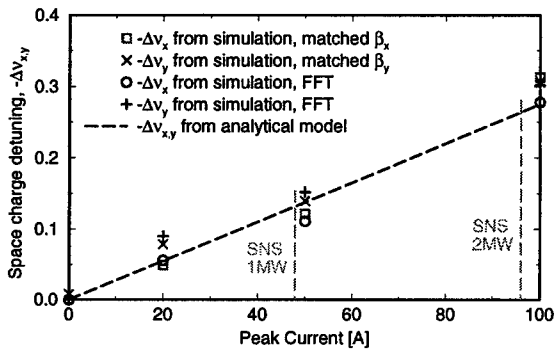

Figure 5: Benchmarking of SIMPSONS simulation.

3.2 *Space Charge Simulation*

Files prepared by TEAPOT [8, 9] containing magnetic field errors, misalignments, and corrections are used for SIMPSONS [4] space charge simulation (Fig. 5).

4 BEAM HALO CONSIDERATION

Incoming beam halo from the LINAC is collimated transversely at the first two FODO cells of the transfer line (HEBT) using movable foil stripping and collimator/dump combination, and longitudinally at the maximum dispersion location of the 90° achromat bend in the HEBT.

4.1 *Two-Stage Ring Collimation*

Ring collimation employs two-stage system located in a shielded non-dispersive straight section. The movable primary collimator (Fig. 6) can be used both to intercept incoming halo and for beam diagnosis. Three secondary collimators located around 220 πmm·mr acceptance at phases (ϕ_1, ϕ_2, ϕ_3) determined from efficiency optimization and lattice constraints, are designed to catch scattered particles.

4.2 *Surface Grazing*

The Collimators consists of layers of steel, borated water, etc to contain charged and uncharged secondary particles [10, 11]. Coated, saw-toothed surface is studied to minimize secondary electron emission, as confirmed in a recent experiment at the Tandem [12]. Surface preparation together with two-stage collimation also minimizes beam loss caused by grazing scattering (Tab. 5).

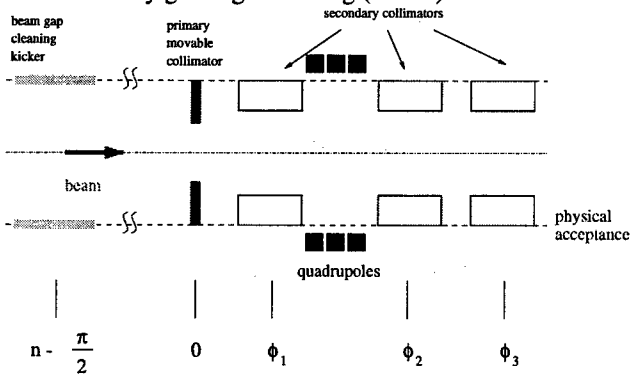

Figure 6: Schematic layout of SNS ring beam gap cleaning and collimation devices. The collimators are housed and shielded in a single straight section.

Table 5: Monte-Carlo simulation of proton grazing showing probability of escape, median escape angle, median energy loss, and correlation coefficient of scattered proton as functions of incident angle.

Angle [mr]	Prob. of escape	Med. esc. angle [mr]	Med. energy loss [MeV]	Corr. coeff.
0.1	0.96	0.3	0.05	0.9
1	0.84	3.2	4.4	0.9
5	0.67	12	60	0.8
10	0.54	20	153	0.8
15	0.45	28	239	0.7
20	0.37	35	314	0.7
25	0.30	41	369	0.7

4.3 *Beam Gap Cleaning*

Chopper inefficiency, foil ionization, etc. can produce residual beam between subsequent micro bunches resulting in uncontrolled loss at extraction. A gap cleaning kicker is designed to be located at a straight section with a vertical betatron phase 90° (modulus integer) from that of the primary collimator, where beam loss is measured with a fast gated loss monitor [13]. The hardware is similar to that of the RHIC Damper/Tune Monitor System, which uses commercially available MOSFET banks to supply 5 kV, 120 A, 10 ns rise and fall time pulses to a transmission line kicker. Burst mode frequency is greater than 1 MHz, permitting turn-by-turn kicking. With 5 meters of kicker length, the gap can be cleaned in about 25 turns.

4.4 *Impedance, Instability, e-p Issues*

We have compiled an impedance budget and started measurement to benchmark impedance model. Based on the budget, instability growth rate is monitored to guide the design. Experimentally, we are studying a newly observed e-p like instability in AGS Booster to understand the mechanism [14, 15].

We thank G. Rees for many enlightening discussions, S. Machida, R. Talman for codes assistance, and many others including J. Alessi, J. Galambos, A. Jason, A. Luccio, R. Macek, T. Satogata, T. Sen, A. Soukas, S. Tepikian, P. Thieberger, J. Tuozzolo, J.G. Wang, C. Warsop, R. Witkover.

5 REFERENCES

[1] Spallation Neutron Source Design Manual, June 1998.
[2] T. Wangler, *RF Linear Accelerators*, Wiley & Sons, p. 285.
[3] C.J. Gardner, Y.Y. Lee, N. Tsoupas, J. Wei, PAC99 (1999).
[4] S. Machida, Nucl. Instrum. Methods, **A309** (1991) 43.
[5] Y. Suzuki; I. Yamane, ICFA Inj./Ext. Workshop (1999).
[6] C.J. Gardner, Y.Y. Lee, W.T. Weng, EPAC98 (1998).
[7] J. Beebe-Wang, et al, PAC99 (1999).
[8] L. Schachinger, R. Talman, Part. Accel. **22**, 35 (1987).
[9] N. Malitsky, J. Smith, J. Wei, PAC99 (1999).
[10] H. Ludewig, et al, PAC99 (1999).
[11] S.Y. Zhang, PAC99 (1999).
[12] P. Thieberger, et al. BNL/SNS 57 (1999).
[13] R. Witkover, et al, BNL/SNS 49 (1998); PAC99 (1999).
[14] J. Wei, et al, ICFA Newsletter No.19 (1999).
[15] M. Blaskiewicz, PAC99 (1999).

TESTING AND EVALUATION OF SUPERCONDUCTING CABLES FOR THE LHC*

R. Thomas#, A. Ghosh, D. McChesney, and A. Jain, BNL, Upton, NY

Abstract

As one of the activities of the US-LHC Accelerator Project, BNL is testing short samples of superconducting cables that will be used in the main LHC dipoles and quadrupoles. The purpose of these tests is to verify that the reels of superconducting cables as supplied by the vendors meet the required critical current specifications. The short-sample testing facility and the computer-assisted testing techniques for acquiring the data will be described. We also describe the data analysis, data storage, and data transmission methods.

1 APPROACH

Electrical tests of cable samples must be done during cable production so that cable manufacturing problems may be detected as early as possible. During the period that CERN is procuring superconductor cable for the LHC project, BNL is providing resources to verify the superconducting properties of the cables. The BNL short-sample test facility is used to measure the critical current, I_{ct}, of short (≤1 meter) samples of LHC dipole and quadrupole cables.

The number of tests that must be performed is set by the cable production schedule and reaches a peak rate of about 20 samples per week. The total number of tests that will be performed over the six-years of the collaborative effort will exceed 3000.

A large quantity of information needs to be acquired, analyzed, and stored. Also, reports on individual runs, summary sample reports, and compatible raw data files must be regularly transferred to CERN. Because the data handling tasks themselves present the largest challenges, the database is the key organizing structure for all other operations.

This approach is possible as a result of recent advances in networked databases and distributed object-oriented software programming. These allow software programs located anywhere on a network (either a local intranet or the world-wide Internet) to interact with a database using the client/server model.

As samples are received, information about each sample is entered into a table (CableTrack) in the database. When an assembly of four samples is placed in a sample holder for testing, information about the assembly is entered into the CableAssembly table.

When the actual testing takes place, the data acquisition program interacts directly with the same database to give the user a drop-down list of assemblies from which he selects the assembly being tested. From that selection alone, the data acquisition program can obtain information from the remote database regarding the physical characteristics of the samples being tested and their instrumentation wiring. Fig. 1 shows the data flow and database interactions.

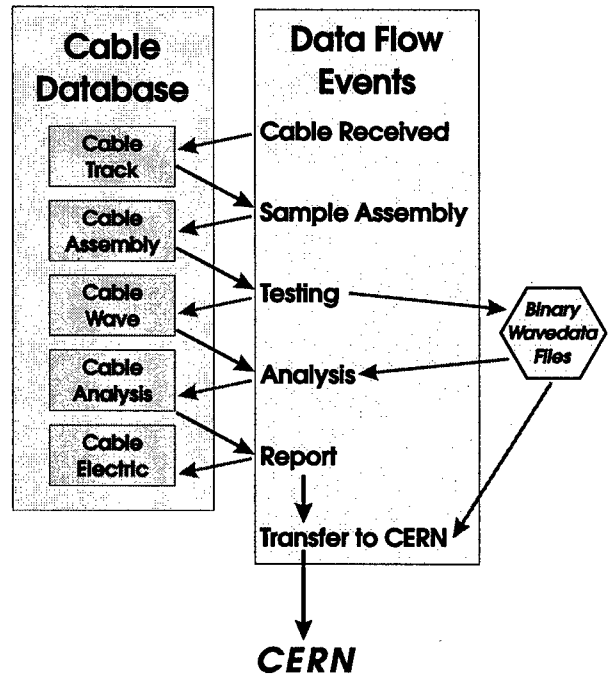

Figure 1. Selected tables of the Cable Database and interactions with the data flow events.

When data are acquired, values are written into the CableWave table of the database describing the experimental conditions and, the name of the raw binary data file (a copy of which is automatically placed on the network file server).

Once this information has been obtained, data analysis can be carried out on any machine connected to the network. (Software has been produced that loads data into workbooks, fits the data to a model, and writes results back into the CableAnalysis table of the database.) Other programs allow the user to select records from the CableAnalysis table which the program then uses to produce summary reports.

*Work supported by the U. S. Department of Energy, Contract No. DE AC02-98CH10886.

#Email: thomas1@bnl.gov

0-7803-5573-3/99/$10.00@1999 IEEE.

Finally, result files, plain-text raw data files, summary reports are shipped to CERN using ftp (file transfer protocol). Although there is a program to assist in this step, it has not yet been fully automated. Also, the construction of a web page that allows those at CERN to follow the status of any sample is still under development.

2 SHORT SAMPLE TEST FACILITY

The standard tests are performed at 4.2 K. Approximately 10% of the cable samples are being tested in superfluid helium at 1.9 K to determine the consistency of the ΔH shift of the I_{ct} vs. H curve from 4.2 K to 1.9 K. Four samples can be tested in one cool-down of a single test station (cryostat), so two additional test stations are being built to meet the LHC production schedule.

The layout of the four samples in the sample holder is shown in Fig. 2. The sample holder is placed in a cryostat which also holds a superconducting dipole magnet which can produce fields as high as ~9 T at 1.9 K [1]. The magnet is energized by a 8.5 kA power supply; a superconducting switch allows it to operate in the persistent mode.

Figure 2. Sample arrangement in the sample holder.

As the critical current of the cable will generally be in the range of 10–20 kA, two 15 kA supplies are operated in parallel to supply the cable test current.

In addition to the power supplies and their controls and safety devices (quench detectors and fault detection circuits), the facility includes the instrumentation necessary for controlling the cryogenic environment and for measuring the critical current of the samples under test.

Two computer systems are used: 1) a cryogenic system that monitors liquid helium levels, temperatures, and pressures and both sets and monitors the flow of helium through the gas-cooled leads, and 2) an experimental system for controlling the sample power supply, taking data, and storing data in the SQL database.

3 TEST

The goal of the short-sample cable tests is to determine the transport critical current of the samples. This critical current is a function of temperature and the magnetic field. In order to obtain standardized results for a specified reference temperature and reference field, raw data must be obtained for several applied fields with the samples at the temperature of the helium bath; that is, one acquires a set of critical currents, I_c, at bath temperatures, T_b, and applied fields, B_a, for each sample.

By pairing samples which are believed to have similar properties, it is possible to acquire data on two samples simultaneously. Also, as there are three gas-cooled leads connecting the two sample pairs to the sample power supplies (see Fig. 2), four samples can be tested in a single cool-down, with the pairs being tested sequentially.

To acquire the I_c data, the operator first sets the current in the dipole magnet for the desired applied field, then connects the sample power supply to the first sample pair to be tested. He then enters the required information into the data acquisition program regarding the ramp rate and maximum current for the ramp on the form shown in Fig. 3.

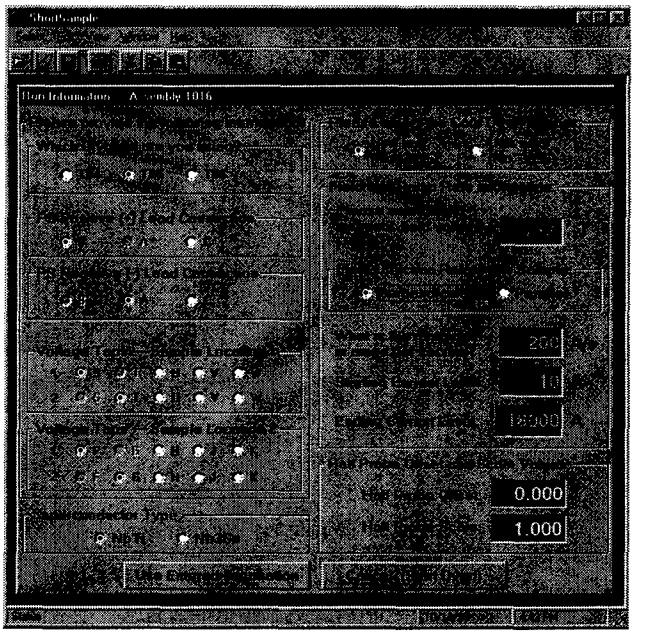

Figure 3. User form for entering run information .

Three high-resolution volt meters are triggered simultaneously as the current is ramped to obtain the voltage drops across the two samples and the current level as a function of time, as shown in Fig. 4.

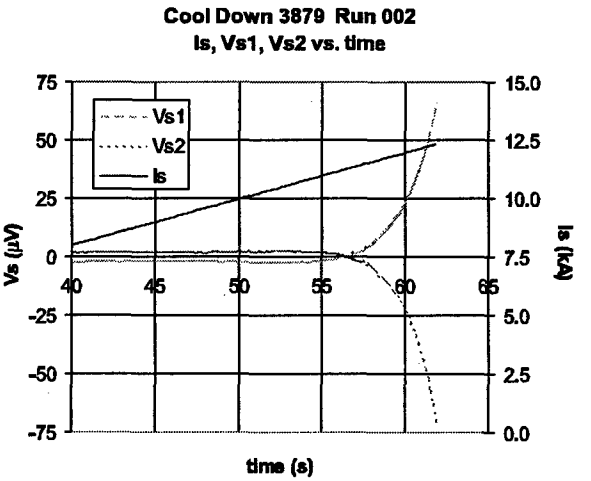

Figure 4. Actual signals for low-noise conditions.

Several sets of data are obtained at different dipole field levels for each sample pair.

4 ANALYSIS AND REPORTING

Once the raw data have been collected, analysis can begin on any workstation connected to the network, since all the required information for each run can be extracted from the database. On many occasions there is considerable electrical noise visible on the signals, primarily as a result of phase and voltage flicker that is produced by the synchrotron accelerators located nearby. When this is the case, the use of a model and a fitting procedure allow the value of I_c to be extracted. (See Fig. 5.)

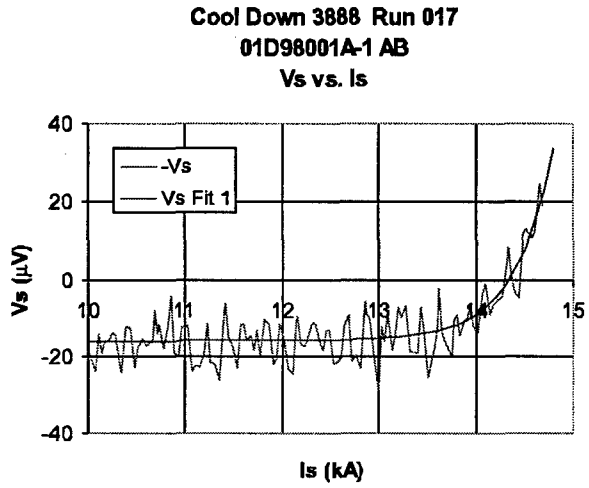

Figure 5. Noisy data and model fit results.

The results of the analyses are automatically stored in the database. The reporting application then extracts this information, converts the I_c values to I_{ct}'s (the critical current at the specified reference temperature, T_{ref}), and computes the peak field, H, experienced by the sample (the sum of the applied field and the self-field [2]). Then the program performs a linear fit to the $I_{ct}(H)$ values to calculate I_{ct} at the reference field. See Fig. 6.

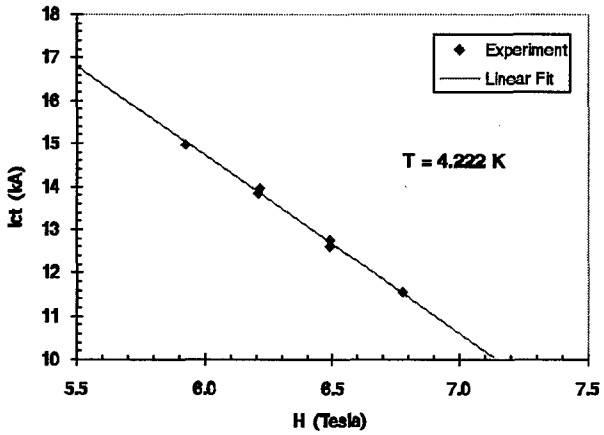

Figure 6. Linear fit to experimental I_{ct} results.

Other programs access the database to create plain-text files of results and reports and then transfer these to CERN. A web-based status page is under development which will always be current, since it uses Active Server Page technology to obtain information directly from the database whenever the page is accessed.

5 SUMMARY AND CONCLUSIONS

Our experience to date indicates that a database-centered approach to this data intensive cooperative program is both practical and feasible. The state of development of commercial operating system components for distributed applications, software development language tools, data analysis applications, and database servers is sufficiently mature that users can develop and maintain sophisticated client/server applications.

Using the database as the organizing structure around which software is developed for carrying out the many tasks of the collaborative effort unifies all the elements of the process and makes it possible for the users to have a comprehensive understanding of the state of the project.

The principal disadvantage is that this approach requires a rather complete understanding of what kinds of information are to be collected. If there has already been considerable experience with the procedures that need to be carried out and the difficulties that can possibly arise in acquiring and entering the data, then this approach is especially appropriate. If, on the other hand, there are many unknowns regarding what data it is necessary to collect and what difficulties may occur in collecting the data, a database-centered architecture may be less useful. As all the applications depend on the database tables, if it is necessary to frequently change the structures of these tables during the initial stages of the project to satisfy the requirements of one or another of the applications, these changes have a cascading effect and may require that other applications be updated.

However, this is not a fault of the database-centered approach itself, but merely an indication of the interrelatedness of the various tasks.

In general this data-driven method is unsuited for new exploratory investigations of an open-ended nature, but is well suited for organizing repetitive experimental and reporting procedures of a known complexity.

6 ACKNOWLEDGMENTS

The authors wish to thank A. Verweij and L. Obeli (CERN) for useful discussions.

7 REFERENCES

[1] R. McClusky, K. E. Robins, and W. B. Sampson, "A Nb_3Sn High Field Dipole," *IEEE Trans. On Magnetics*, Vol. 27, p. 1993 (1991).

[2] M. Garber, *et. al.*, "The Effect of Self-Field on the Critical Current Determination of Multifilamentary Superconductors," *IEEE Trans.on Magnetics*, Vol. 25, p. 1940 (1989).

A DIGITAL QUENCH DETECTION SYSTEM FOR SUPERCONDUCTING MAGNETS*

D.F. Orris+, S. Feher, M.J. Lamm, J. Nogiec, S. Sharonov, M. Tartaglia, J. Tompkins, FNAL, Batavia, IL

Abstract

A system has been developed for digitally detecting superconducting magnet quenches in real time. This system has been fully tested and is completely integrated into a Vertical Magnet Test Facility (VMTF)[1] at FNAL. The digital technique used for this system relies on the application of digital signal processing (DSP) algorithms running on a native Motorola PowerPC VME processor. The performance of this digital system has been shown to be superior to the analog technology typically used for quench detection; *i.e.*, it detects resistive voltages reliably at low thresholds with minimum delay and is a more flexible system.

1 INTRODUCTION

The quench management system for VMTF has two primary components: The quench logic hardware, and the quench detection system. The quench logic hardware controls the power supplies, the dump, and the heater power supplies, while the quench detection system provides the quench trigger event for initiating the magnet protection and data logging sequences.

A digital quench detection system was developed for this purpose. Multiple quench threshold values can be set for special purpose triggers, the channel configuration is programmable, it can perform digital balancing, and is controlled through a GUI. The system design will be discussed, followed by the methods of filter design, system optimization, and software operation.

2 DIGITAL QUENCH DETECTION SYSTEM DESIGN

A number of analog voltage tap signals from the magnet are converted to digital signals by passing them through an anti-aliasing filter before conversion by an ADC, which are then are digitally processed by the CPU. These modules reside together along with the other quench management hardware in the same VME crate for fast communication.

The important parameters for the real time digital quench detection (DQD) system design include the CPU load, the ADC performance specifications, the anti-aliasing filter response, and the digital filter specifications.

2.1 The ADC Specifications

The ADC used for this system is a 16-Bit, 8-channel (expandable to 256 channels), successive approximation device with built-in sample-and-hold. Each channel has a differential input with a range of +-10V. The input amplifiers are instrumentation quality with four programmable gains for each channel. The maximum aggregate conversion rate is 409.6 kHz.

A VxWorks driver was written for this ADC in order to provide a means for streaming the data to the processor. The method of streaming the data to the VME processor was optimized in order to reduce the CPU load associated with filtering. Flexible control over sampling, decimating, and filtering was provided.

2.2 Anti-Aliasing Filter Parameters

Since the ADC chosen for this system is a sample-and-hold device, an anti-aliasing input filter was necessary. An 8-Channel, 5th-order, zero-error, Bessel filter was built for this purpose. The chosen cut-off frequency was 1KHz, and the noise rejection in the stop band was measured at 60dB, though the critical folding frequency actually occurs at ~9KHz (see Fig. 1).

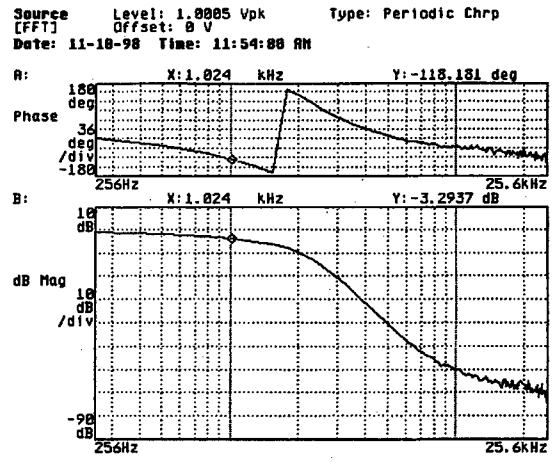

Figure 1: Bessel Filter Test Results

A primary concern in the design of this system was to minimize the total group delay of the signals used for

* Work supported by the United States Department of Energy

+ orris@fnal.gov

making the digital quench decision. A larger group delay will result in a longer delay of the event that causes the power supply to ramp down after a quench. The net effect of this delay will be to increase the probability of damaging the magnet under test due to high voltage to ground, or from excess ohmic heating.

Since eight separate Bessel filters were implemented, one for each ADC input channel, the cut-off frequency was chosen high enough so that filter matching was not an issue and the group delay is kept to a minimum. The group delay of these filters was measured at 0.23msec.

2.3 FIR Filter Design Requirements

The dominant source of noise across the magnet coil is generated by the power supply. It can be seen from Fig. 2 that 720Hz is the primary noise component measured in the VMTF system, though there are several other nontrivial components as well.

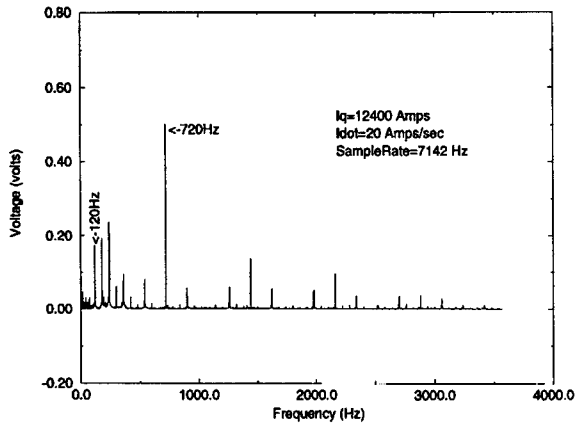

Figure 2: FFT of the Unfiltered Whole Coil Signal

There are two particular concerns with 720Hz noise: One, this frequency is not attenuated much by the Bessel filter; and two, residual bucked noise can occur due to small phase differences between two bucked channels.

Since 720Hz should be the only noise component produced by the power supply, action should be taken to attenuate it. The presence of any other noise should be removed at the source.

A digital filter with a cut-off frequency low enough to provide adequate 720Hz attenuation was implemented. Since the same digital filter would process all eight ADC signals, all group delays would be exactly matched.

A FIR filter was implemented for this reason. An IIR filter was considered because the group delay can be very small. However, the inherent stability of the FIR filter made it more attractive -- a spike produced on a coil due to the discharge of a strip heater could produce a false quench trigger if the filter was to become unstable.

The requirements of the FIR filter include the following: One, attenuate 720Hz as much as possible; two, keep the number of taps to a minimum; and three, minimize gain error and overshoot.

2.4 FIR Filter Performance Characteristics

The FIR filter taps were determined using the Parks-McClellan algorithm. The desired sample rate was from 12KHz to 18KHz, so in order to keep the total group delay down to ~ 1ms, forty taps or less was required.

Optimal design parameters were determined after successive tests on the filter using a step response. The design band edges used were from 0.0 to 0.0082189 and from 0.049565 to 0.5. The Band Gains were, Band 1 = 1.0 and Band 2 = 0.0, and the Weighting was, Pass band = 1.0 and Stop Band = 18.0. This optimisation resulted in a 40-tap FIR filter with no overshoot and a 0.0003% gain error. The attenuation in the Stop-Band region is 50dB (see Fig. 3).

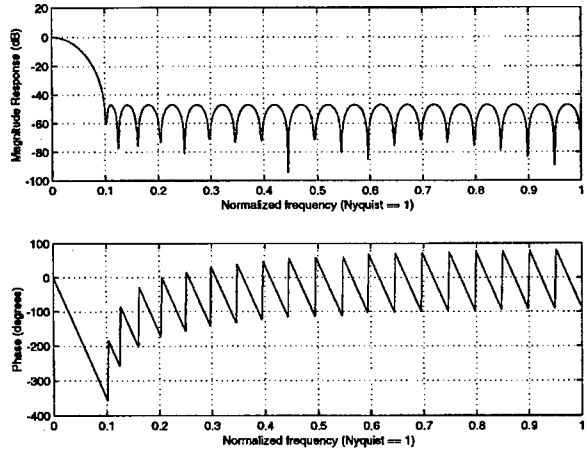

Figure 3: 40-Tap FIR Filter Response

2.5 Digital Quench Detection Processor

The processor used for this system is a Motorola PowerPC VME processor (MVME-1604-022). It is a 133MHz processor with 16Mbyte memory, and 256Kbytes of L2 cache.

This processor communicates with all the quench modules in the quench management system as well as with several other modules in our distributed processing environment. It performs the digital signal processing functions to the streamed ADC data, and it provides the quench management system with the required quench triggers. It performs filtering, digital bucking, threshold checking, trigger event generation, and balancing.

2.6 The Digital Quench Detection Program

The quench detection software was written in 'C' and runs under the VxWorks (real time) operating system. Since considerable care must be taken to guard against quench

decision delays, separate cyclic processes are run in parallel with very high priority. For example, the data is streamed from the ADC to the CPU in arrays sized to match the FIR filter tap size. The data contained in these arrays are sampled at some frequency >10KHz, but the arrays of data are sent to the CPU at some decimated frequency, which is set by the user.

The quench process also runs in parallel with a very high priority. This tight cyclic process waits for filtered data to arrive and then sends the hardware a heartbeat, which is required every 8.2msec. The quench process then performs the necessary functions leading up to a threshold decision and then returns to wait for more data from the ADC.

2.7 Digital Quench Detection Design Optimisation

Since the minimum sample rate of the ADC is dictated by the Nyquist criterion, a choice must be made for the attenuation magnitude of the alias-free dynamic range. For example, if the desired attenuation magnitude were 60dB, then its corresponding frequency of 9KHz would dictate a minimum ADC sample rate of 18KHz. A reasonable attenuation goal for this system was thought to be somewhere between 50dB to 60dB. This would dictate an ADC sample rate between 12KHZ and 18KHz.

The final choice for the sample rate was 11,520Hz. Since the stop band response of the FIR filter is 50dB, there is little to be gained, with respect to the Bessel filter, from higher sample rates. Another good reason for this choice is that for this sampling rate, the second attenuation peak in the FIR filter response occurs at 720Hz (see Fig. 3), resulting in 78dB attenuation of this frequency (see Fig. 4).

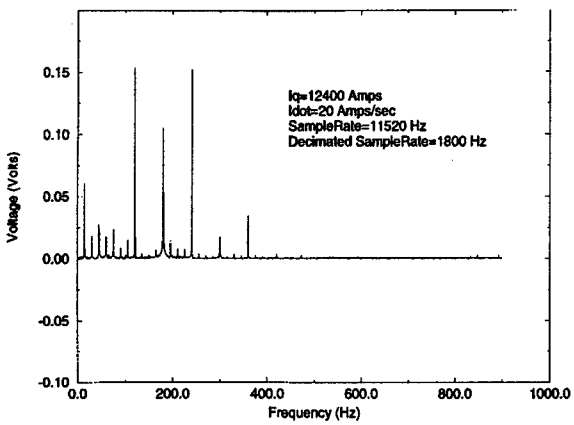

Figure 4: FFT of the Filtered Whole Coil Signal

In addition, 11,520Hz is a common multiple of 15Hz, which happens to be present in the power bus due to an external source -- the Booster Ring. Therefore, off-line filtering of 15Hz, and many of its harmonics, is made more efficient for off-line analysis.

The resulting group delay of the FIR filter associated with this sample rate is 1.6ms. Including the Bessel filter, the total group delay of the system is 1.83ms.

A decimated sample rate of 1800Hz was chosen based on the CPU load. Since the quench decision is based on this data rate, the time resolution is 0.56ms.

A typical plot of a real-time digitally detected quench is shown in Fig. 5. The peak noise spikes are ~15mV at a current of 12400Amps. This is good in comparison to the threshold setting of 300mV.

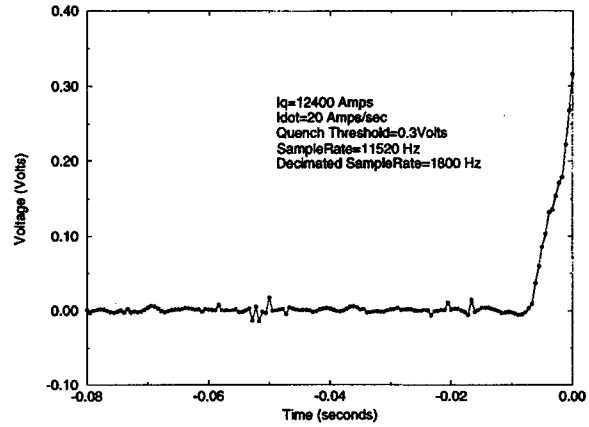

Figure 5: Real Time Quench Detect -- Bucked Half Coils

3 CONCLUSIONS

A Digital Quench Detection system was implemented using mostly commercially available components. By optimising this system to reject noise while minimising group delay, a successful method of digitally detecting quenches was accomplished.

The primary advantage to a digital quench system is its flexibility. For example, this system was easily coupled with a Software Quench Detection[2] system used to test High Temperature Superconducting Leads[3]. Also, since it is capable of generating multiple trigger events, other DAQ systems can be triggered at very low trigger thresholds for special magnet studies. This system has been in operation for two years and has an excellent performance history.

4 REFERENCES

[1] M.J. Lamm *et al.*, "A New Facility to test Superconducting Accelerator Magnets", PAC'97, Vancouver, Canada, 1997

[2] J.M. Nogiec *et al.*, "Architecture of HTS Leads Software Protection System", PAC'99, New York, USA, 1999

[3] G. Citver *et al.*, "HTS Power Lead Test Results", PAC'99, New York, USA, 1999

FIELD QUALITY OF QUADRUPOLE R&D MODELS FOR THE LHC IR*

N. Andreev, T. Arkan, P. Bauer, R. Bossert, J. Brandt, D. Chichili, J. DiMarco, S. Feher, J. Kerby, M. Lamm, P. Limon, F. Nobrega, I. Novitski, T. Ogitsu, D. Orris, J. Ozelis, T. Peterson, G. Sabbi, P. Schlabach, J. Strait, C. Sylvester, M. Tartaglia, J. Tompkins, S. Yadav, A. Zlobin, Fermilab, IL
S. Caspi, R. Scanlan, Lawrence Berkeley National Laboratory, Berkeley, CA

Abstract

Superconducting quadrupole magnets operating in superfluid helium at 1.9 K, with 70 mm bore and nominal field gradient of 205 T/m at collision optics, are being developed by the US LHC Accelerator Project for the Interaction Regions of the Large Hadron Collider (LHC). A magnet model program to validate and optimize the design is underway. This paper reports results of field quality measurements of four model magnets.

1 INTRODUCTION

In order to achieve a luminosity of 10^{34} $cm^{-2}s^{-1}$ at the LHC, special quadrupole magnets are required for the final focusing triplets [1]. These magnets must provide a field gradient of 205 T/m over a 70 mm bore with sufficient cooling capacity to withstand the heavy heat load deposited by secondary particles from beam-beam collisions. At the same time, high field quality is required due to large and rapidly varying values of the β-function. A design based on two-layer coil geometry has been developed by a Fermilab-LBNL collaboration for inner triplet quadrupoles (MQXB). Five short models (HGQ01-HGQ05) have been fabricated. Four have been tested in superfluid helium at the Fermilab Vertical Magnet Test Facility. In this paper, field harmonics measured in the magnet straight section and in the end regions are presented and compared with calculations based on as-built magnet geometry and with preliminary field quality specifications.

2 MAGNET DESIGN

Figure 1 shows the magnet cross-section. The design is based on four two-layer coils connected in series, surrounded by collar and yoke laminations. No modifications to the design cross-section were made during the magnet model program, but different coil shimming schemes have been implemented in each model in order to obtain the desired coil modulus and prestress.

The end regions underwent several design changes during the model program. The five models built have a four-block end configuration. With respect to the design of HGQ01, the second-wound group of the outer coil was shifted by 2 cm in the positive z direction starting with HGQ02 to reduce the peak field in the coil. A more compact design for the coil to coil joint in the lead end was introduced in HGQ03 and HGQ05. A new five-block configuration will be implemented in future models which will improve the mechanical stability of inner layer conductors during winding. The new design also reduces the peak field in the coil and significantly improves end field quality.

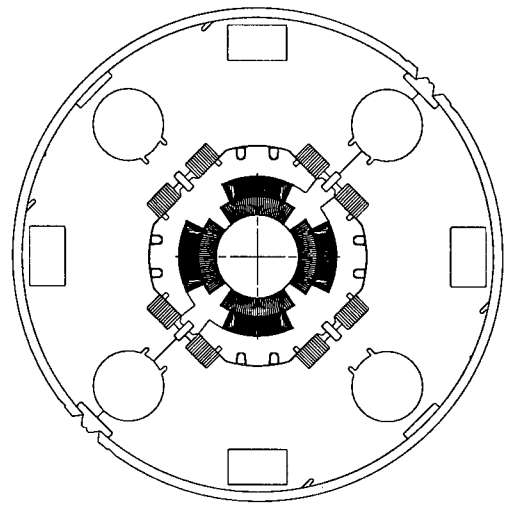

Figure 1: Magnet cross-section.

3 MEASUREMENT SYSTEM

Magnetic measurements presented in this paper were performed using a vertical drive, rotating coil system. Probes used have a main tangential winding for measurement of higher order harmonics as well as specific dipole and quadrupole windings for measurement of the lowest order components of the field. These windings also allow for bucking the large dipole and quadrupole components in the main coil signal. Most measurements presented in this paper were made with a coil of 40.6 mm nominal diameter and length 82 cm.

Coil winding voltages are read using HP3458 DVMs. An additional DVM is used to monitor magnet current. DVMs are triggered simultaneously by an angular encoder on the probe shaft, synchronizing measurements of field and current. Feed down of the quadrupole signal to the dipole is used to center the probe in the magnet.

* Work supported by the U.S. Department of Energy.

0-7803-5573-3/99/$10.00@1999 IEEE.

Table 1: Reference collision harmonics for MQXB

n	$<b_n>$	$d(b_n)$	$\sigma(b_n)$	$<a_n>$	$d(a_n)$	$\sigma(a_n)$
Straight section (magnetic length 4.76/5.56 m)						
3	.0	.3	.8	.0	.3	.8
4	.0	.2	.8	.0	.2	.8
5	.0	.2	.3	.0	.2	.3
6	.0	.6	.6	.0	.05	.1
7	.0	.05	.06	.0	.04	.06
8	.0	.03	.05	.0	.03	.04
9	.0	.02	.03	.0	.02	.02
10	.0	.02	.03	.0	.02	.03
Lead end (magnetic length 0.41 m)						
2	-	-	-	40.	-	-
6	2.	2.	.8	.0	.5	.2
10	-.2	.2	.1	.0	.1	.1
Return end (magnetic length 0.33 m)						
6	.0	1.2	1.	-	-	-
10	-.25	.25	.1	-	-	-

4 FIELD QUALITY ANALYSIS

In the straight section of the magnet, the field is represented in terms of harmonic coefficients defined by the power series expansion

$$B_y + iB_x = B_2 10^{-4} \sum_{n=1}^{\infty} (b_n + ia_n) \left(\frac{x+iy}{r_0} \right)^{n-1} \quad (1)$$

where B_x and B_y are the transverse field components, B_2 is the quadrupole field, b_n and a_n are the $2n$-pole coefficients (b_2=10^4). The reference radius r_o is 17 mm.

Table 1 shows the reference harmonics at collision for MQXB magnets (version 2.0). For each harmonic component, values of the mean, uncertainty in mean and standard deviation are listed. This table provides a common reference for the discussion of field quality issues from the viewpoint of magnet development, machine performance and IR systems layout. The goal of the R&D phase is to converge on a set of numbers satisfacting these requirements that can be adopted as a field quality specification for magnet production. Preliminary results of beam tracking studies aimed at evaluating the impact of magnet field errors on LHC dynamic aperture indicate that the values listed in Table 1 are acceptable from the machine performance standpoint [2].

Due to the thick coil shims (up to 450 μm) needed to obtain the required pre-stress, allowed harmonics b_6 and b_{10} were large in HGQ01. Also, due to 80 μm differences in size between inner coils used in quadrant 1 and 3 and those used in quadrant 2 and 4 and the corresponding adjustments of shim thickness, non-zero systematic values appeared for harmonic components a_4 and a_8. Since then, significant improvements have been made in the coil fabrication procedure. Adjusments have been made to curing cavity size, curing pressure, cable insulation scheme and bare cable size. The coil shim thickness was reduced by about a factor of 2 from each magnet to the next, and better uniformity in size and modulus from coil to coil has been achieved with field quality improving correspondingly as the conductor positions approach design values.

Table 2: Comparison of measured straight section harmonics (6 kA) with calculations based on as-built parameters.

n	HGQ01	HGQ02	HGQ03	HGQ05
b_6, calc.	-4.24	-2.86	-1.39	-0.08
b_6, meas.	-3.91	-1.54	-1.02	-0.30
b_{10}, calc.	-0.14	-0.09	-0.04	0.01
b_{10}, meas.	-0.10	-0.10	-0.04	0.01
a_4, calc.	1.27	0.94	0.00	0.00
a_4, meas.	2.00	0.53	0.32	0.19
a_8, calc.	0.02	0.00	0.00	0.00
a_8, meas.	0.02	0.02	0.03	0.00

Table 2 shows a comparison between measured harmonics and calculations based on as-built parameters for the harmonic components b_6, b_{10}, a_4 and a_8. The measurements are made at a current of 6 kA where all non-geometric components (conductor magnetization, iron saturation, conductor displacement under Lorentz forces) are small. Calculations and measurements are generally in good agreement. A reduction of the errors of about one order of magnitude is observed from magnet HGQ01 to magnet HGQ05. In magnet HGQ05, all four harmonics are within the uncertainties specified by the reference table. Table 3 shows the measured straight section harmonics up to the 20-pole for all four models. In magnet HGQ05, all central harmonics are within one standard deviation of the random error specified in Table 1. From the values in Table 3, averages and standard deviations over the four models have been obtained for each component (Table 4). In the attempt to eliminate the effect of systematic errors due to coil shims, the values for b_6, b_{10}, a_4 and a_8 in Table 4 have been obtained after taking the difference between measured values and those calculated based on as-built parameters (Table 2). All average values and standard deviations in

Table 3: Measured harmonics in straight section (6 kA).

n	HGQ01	HGQ02	HGQ03	HGQ05
b_3	0.36	-0.70	1.04	0.72
b_4	0.26	0.18	0.14	0.00
b_5	-0.29	0.09	-0.34	-0.04
b_6	-3.91	-1.54	-1.02	-0.30
b_7	-0.08	-0.01	-0.06	0.01
b_8	0.06	0.01	0.00	0.00
b_9	0.04	0.00	0.00	0.00
b_{10}	-0.10	-0.10	-0.04	0.01
a_3	0.27	0.55	-0.30	0.12
a_4	2.00	0.53	0.32	0.19
a_5	0.02	-0.17	0.26	0.05
a_6	-0.08	0.03	0.07	-0.03
a_7	-0.05	0.00	-0.03	0.01
a_8	0.02	0.02	0.03	0.00
a_9	0.01	-0.01	0.01	0.00
a_{10}	0.02	0.00	-0.01	0.00

Table 4: Average and standard deviation of harmonics

n	$<b_n>$	$\sigma(b_n)$	$<a_n>$	$\sigma(a_n)$
3	0.36	0.76	0.16	0.35
4	0.15	0.11	0.21	0.47
5	-0.15	0.20	0.04	0.18
6	0.46	0.63	0.00	0.07
7	-0.04	0.04	-0.02	0.03
8	0.02	0.03	0.01	0.02
9	0.01	0.02	0.00	0.01
10	0.01	0.02	0.00	0.01

Table 4 are within the limits specified in Table 1. Note the b_6 result is strongly influenced by the relatively large difference between calculation and measurements in a single magnet (HGQ02). Moreover, one can expect smaller variations in a magnet production series than those observed in the first few models of a new design.

Figure 2 shows the measured dodecapole in model HGQ05 along with calculations of geometric and dynamic effects. The magnet design provides good compensation of the saturation and Lorentz force effect, and the total change of the mean dodecapole between injection and operating current is very small. This is actually the case for all harmonics. In particular, the 6 kA measurements (Table 3) do not differ significantly from those taken at higher currents. A simulation of the conductor magnetization effect on the normal dodecapole agrees very well with HGQ05 measurements, assuming a systematic (geometric) shift of -0.3 units. The magnetization effect is similar for all magnets, as expected from the uniformity of conductor properties. One exception is a specific pattern which appeared in magnet HGQ02 and HGQ03 which show a larger effect on the first cycle after quench than during subsequent cycles.

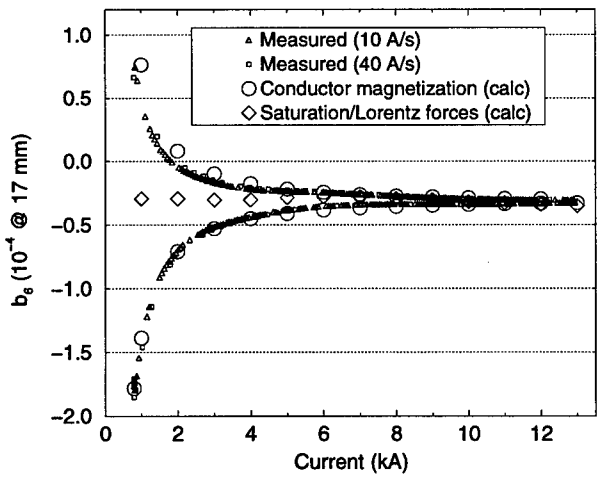

Figure 2: Normal dodecapole vs current (HGQ05).

The ramp-rate dependent distortions of the multipoles are weak (Figure 2), indicating a high average cross-contact resistance. Estimations of the cross-contact resistance based on AC-loss measurements of HGQ02 and HGQ03 yielded an average value of approximately 100 $\mu\Omega$. No systematic ramp-rate dependent patterns on the multipoles were observed. The lack of systematics in the ramp-rate effects indicates the large spread of the electrical cross-contact resistance typical of cables made of uncoated copper strands.

In the magnet end regions, additional terms (pseudo-multipoles) are required in the harmonic expansion for the local field. A simple expansion based on Equation 1 can however be applied to the total integral of the transverse field across the end region. The reference integration interval for harmonic coefficients in the magnet ends is defined to be [-0.57, 0.25] m for the return end and [1.31, 2.03] m for the lead end. This matches the length of the measurement probe. A comparison of measured and calculated harmonics in the magnet lead end is given in Table 5. Except for HGQ01, [1] the end harmonics quoted in Table 5 are computed for the design geometry without considering the effect of coil shims, using program ROXIE [3]. For magnet HGQ02 and HGQ03, which used soft ULTEM end parts, thick mid-plane shims were applied to reach the desired pre-stress, resulting in a negative contribution to the dodecapole. In HGQ05, which uses G10 end parts, the thickness of the end shims was substantially reduced. This change in end shims, together with the reduction of the negative contribution from the straight section b_6, contributes to the positive jump in the measured dodecapole of HGQ05 with respect to HGQ03. Although the present lead end b_6 is larger than specified in the table of reference harmonics, a reduction by about 30% of its systematic value is expected after implementation of the new 5-block end design.

Table 5: Calculated/measured harmonics in lead end.

n	HGQ01	HGQ02	HGQ03	HGQ05
b_6	3.1/2.9	5.5/4.2	5.4/3.8	5.4/8.0
b_{10}	-0.3/-0.3	-0.3/-0.2	-0.4/-0.4	-0.4/-0.2
a_6	0.5/0.1	0.4/0.2	-0.1/-0.3	-0.1/-0.6
a_{10}	-0.1/-0.1	0.0/0.0	0.0/0.0	0.0/0.0

5 CONCLUSIONS

Magnetic measurements of MQXB short models confirm design calculations for geometric harmonics, magnetization and Lorentz force effects. Refinements in magnet fabrication have significantly improved the field quality from each model to the next. Observed current-dependent effects are small. The systematic and random straight section harmonics are within specifications. The systematic normal dodecapole in the lead end is presently larger than the value listed in Table 1, but a significant improvement is expected after implementation of the new 5-block design.

6 REFERENCES

[1] "LHC Conceptual Design", CERN AC/95-05 (LHC).

[2] J. Wei, et al., this conference. N. Gelfand, this conference.

[3] S. Russenschuck, Proc. ACES Symposium, Monterey, 1995.

[1] A correction of -2 units was applied to the calculated b_6 integral for HGQ01 to include the contribution of mid-plane shims.

Quench Performance of Fermilab High Gradient Quadrupole Short Models for the LHC Interaction Regions

N. Andreev, T. Arkan, R. Bossert, J. Brandt, D. Chichili, J. DiMarco, S. Feher, J. Kerby, M.J. Lamm, P.J. Limon, F. Nobrega, D. Orris, I. Novitski, J.P. Ozelis, T. Peterson, G. Sabbi, P.Schlabach, J.Strait, M.Tartaglia, J.C.Tompkins, S.Yadav, A.V.Zlobin*, FNAL, Batavia, IL
S. Caspi, A.D. McInturff, R.M. Scanlan, LBNL, Berkeley, CA
A. Ghosh, BNL, Upton, NY

Abstract

Fermilab and LBNL are in the midst of a superconducting magnet R&D program to test and optimize the design of quadrupoles to be used in the LHC Interaction Region inner triplets. The magnets are required to deliver a 215 T/m gradient across a 70mm aperture. Five quadrupole short models have been fabricated and four of them have been tested. This paper describes the last model design details and reports the results of the magnet quench performance study.

1 INTRODUCTION

Quadrupole magnets for the LHC inner triplets have to provide a nominal field gradient of 205 and 215 T/m (high and low luminosity IRs) in a 70 mm bore, and to operate in superfluid helium at 1.9 K. The design of these magnets has been developed by the collaboration of Fermilab, BNL and LBNL [1-3].

A series of 2 m long model magnets (HGQ) is being built now at Fermilab to test and optimize the design and assembly method before proceeding to the construction of a full scale prototype magnet. Three models HGQ01-03 have each been tested in two thermal cycles. Model HGQ05 is currently being tested in a second thermal cycle. This paper reports the design optimization and summarizes quench performance of the HGQ short model magnets.

2 DESIGN OPTIMIZATION

Magnet cross-section is shown in Figure 1. It consists of a two-layer cos(2θ) coil made of Rutherford-type cables, stainless steel collar laminations and a cold iron yoke. The details of base-line design have been described elsewhere [2,3].

The training histories for the first three models HGQ01-03 were summarized in [3]. These models demonstrated long and slow training at 4.5 K and 1.9 K. Short sample limit at 1.9 K has not been reached.

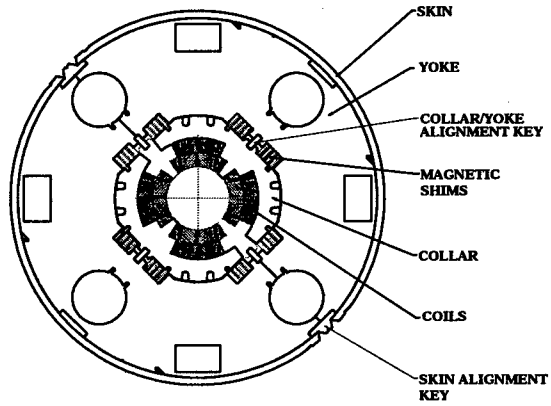

Figure 1: High Gradient Quadrupole cross-section.

Maximum achieved field gradient of ~215 T/m is close to the nominal field gradient but it is much lower than the magnet design gradient of 250 T/m. Significant retraining effect was observed on HGQ03.

Analysis of HGQ01-03 results showed that the observed quench performance was associated with several manufacturing and design details, such as insufficient and non-uniform coil end and end-body transition prestress, low coil end rigidity, a significant difference of thermal contraction for the Ultem spacers and conductor in the coil, longitudinal instability of the collar structure.

Model HGQ05 included a set of changes which addressed the issues raised by previous models. The most important of the changes from the base-line design included on HGQ05 are:

- Use of G10 as end part material
- Re-cure of inner coil at higher pressure, resulting in a higher inner layer elasticity modulus and more uniform inner/outer coil mechanical properties
- A continuous body/end transition, including elimination of key extension
- Welded 75mm collar packs with pole filler pieces
- Aluminum end can assemblies over both ends
- Attachment of the end cans to the end plate, which ensures contact between the coil ends and end plates as well as stretches the coil straight section after cool-down

Work supported by the U.S. Department of Energy.
* E-mail: zlobin@fnal.gov

3 TEST RESULTS AND DISCUSSION

All models have been tested at the Fermilab Vertical Magnet Test Facility (VMTF) [4] in normal and super-fluid liquid Helium in the temperature range of 1.8K-4.5K. During the quench performance study about 70% of the stored energy were extracted and dissipated into external dump resistor. Each model was instrumented with 96 voltage taps installed on the inner and outer coils. Pole turns and turns around wedges were instrumented with four voltage taps each to distinguish between the coil end and straight section quenches.

Coil azimuthal stress and longitudinal end force measurements were made at room temperature during fabrication and during cold test in each excitation cycle. The results for HGQ05 and other models are summarized in Table 1.

Table 1: Mechanical measurement summary

Model number	HGQ 01	HGQ 02	HGQ 03	HGQ 05
Azimuthal prestress 300K				
inner layer, MPa	67	73	187	99
outer layer, MPa	72	94	97	55
Azimuthal prestress 1.9K				
inner layer, MPa	38	76	173	N/A
outer layer, MPa	58	84	102	49
Azimuthal Lorentz force				
inner layer, MPa/kA^2	-0.28	-0.31	-0.29	-0.2
outer layer, MPa/kA^2	-0.13	-0.15	-0.13	-0.13

According to the strain gauge data no unloading of the coil was observed up to reached highest operating currents. Coil deformation by Lorentz force was elastic in operation current range.

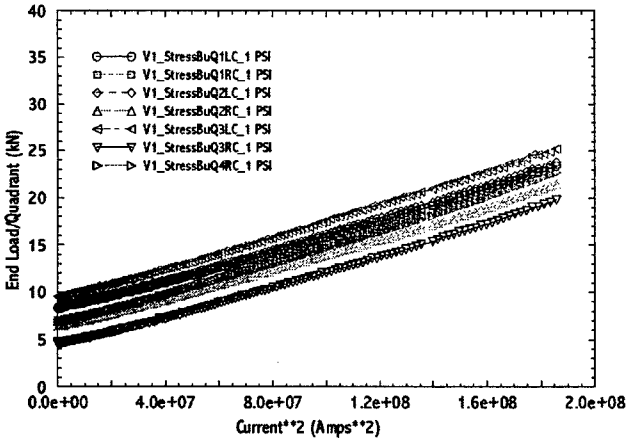

Figure 2: HGQ05 longitudinal Lorentz force.

Figure 2 shows a typical longitudinal coil force measurement for magnet HGQ05. End longitudinal prestress remained on both ends after cooling down. The slope of end force with current represents was about 25% of the calculated Lorentz force.

Training results for this magnet at 4.5 K and 1.9 K in first thermal cycle are presented in Figure 3.

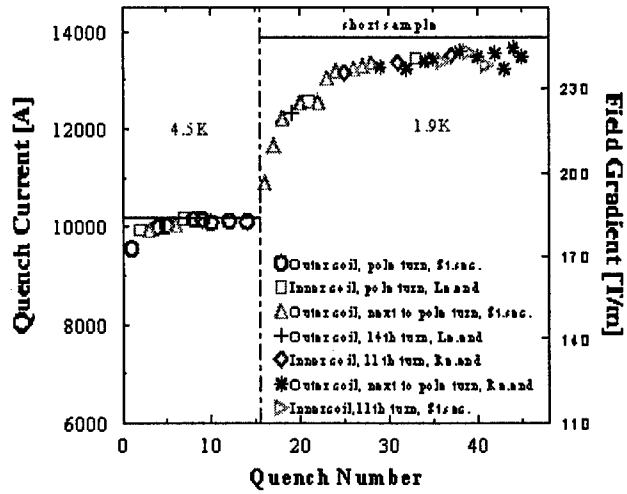

Figure 3: HGQ05 training results at 4.5 K and 1.9 K.

At 4.5 K after short training the estimated short sample limit has been achieved. At 1.9 K only two quenches were required to reach a field gradient of 215 T/m. When the quench current reached 95% of the short sample limit the training rate slowed and the erratic quenches occurred in the inner coil turn adjacent to the wedge and in the outer coil return end next to pole turns.

Quench performance in first thermal cycle for the HGQ short models is summarized in Table 2. First quench currents at 4.5 K and 1.9 K as well as number of quenches required to reach 11.5 kA are presented.

Table 2: Quench performance summary

Model number	Iq1(4.5K), A	Iq1(1.9K), A	N(11.5kA)
HGQ01	8776	10327	8
HGQ02	7365	9191	23
HGQ03	7057	10019	7
HGQ05	9553	10896	2

As it can be seen a dramatic improvement of the magnet training in HGQ05 at both temperatures 4.5 K and 1.9 K was observed. The maximum gradient achieved was ~240 T/m which is well above the nominal field gradient. The magnet training memory will be studied in the second thermal cycle.

The dependence of quench current with. current ramp rate for HGQ05 at 1.9 K is shown in Figure 4. One can see two regions on this curve: flat, ramp rate independent region at low current ramp rates and region with monotonic decrease of quench current with the increase of current ramp rate. It was found high ramp rate quenches were determined by AC losses in the cable near inter layer splices.

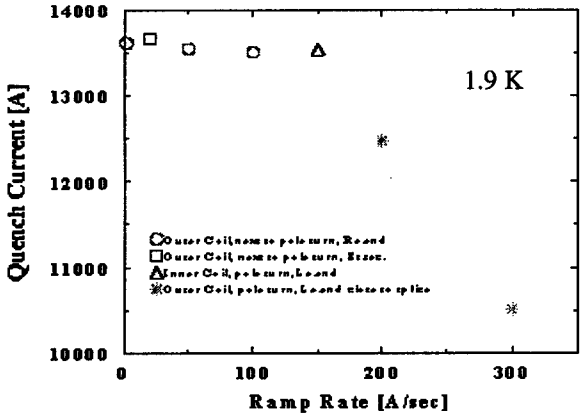

Figure 4: HGQ05 quench current ramp rate dependance.

Summary of magnet ramp rate sensitivity and coil curing temperature is reported in Table 3.

Table 3: Ramp rate sensitivity

Model number	Coil curing temperature	Ic(150 A/s), A	Ic(300 A/s), A
HGQ01	135°C	11752	10965
HGQ02	190°C	-	11335
HGQ03	195°C	11756	11298
HGQ05	130°C	13531	10519

For all magnets the quench current ramp rate sensitivity was low for current ramp rates up to 300 A/s. This ramp rate is an order of magnitude higher than the nominal LHC current ramp rate. Quench current did not depend on the coil curing temperature (interstrand resistance in the cable was still quite high). Since the high ramp rate quenches are observed near the inter layer splices, the probable explanation for this ramp rate dependence is the combination of AC losses and cooling conditions in the solder-filled splice cable.

The dependance of quench current vs. temperature for HGQ05 is presented in Figure 5. This dependence was measured after the completion of magnet test at 1.9 K.

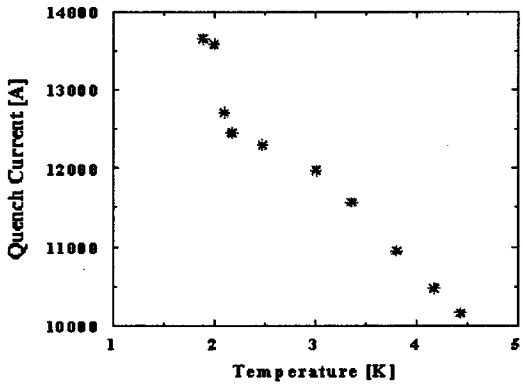

Figure 5: HGQ05 quench current temperature dependance.

The monotonic decrease of quench current with temperature increase was observed at temperatures above 1.9 K. Quenches in the temperature interval 2.2-3.0 K originated in the outer layer coil near one of the inter-layer splices. High resistive heating and restricted cable cooling conditions in splice area can cause a significant reduction of magnet quench current with respect to its short sample limit [5]. Inter-layer splice cooling conditions will be optimized in the next models.

The measured and calculated quench currents at 4.5 K and 1.9 K are reported in Table 4.

Table 4: Quench current @ 1.9 K and 4.5 K

Model number	Ic(1.9K), A		Ic(4.5K), A	
	Measured	Calculated	Measured	Calculated
HGQ01	12.6	14.02	10.5	10.32
HGQ02	11.5	14.39	10.7	10.49
HGQ03	12.2	14.38	10.6	10.48
HGQ05	13.7	14.03	10.1	10.23

After training at 1.9 K all magnets reached their short sample limit at 4.5 K. With nominal superconductor parameters the temperature margin at nominal operation current for this design is about 2.3 K.

4 CONCLUSIONS

Four High Gradient Quadrupole short models have been fabricated and tested at Fermilab. Significant improvement in magnet training at 4.5 K and 1.9 K was achieved in last model (HGQ05) as a result of the optimization of design details of magnet support structure. Test of HGQ05 in a second thermal cycle continues. Although the results obtained demonstrate that the magnet design can provide the required quench performance some further optimization is desirable. The short model R&D program is being re-evaluated based on the program goals and results achieved. Three additional short models are included in the program to complete design optimization.

5 ACKNOWLEDGMENTS

Authors would like to thank engineers and technicians of Fermilab Technical Division for the contribution to this work.

REFERENCES

[1]. R. Bossert et al., "Development of a High Gradient Quadrupole for the LHC Interaction Regions", IEEE Trans. on Applied Superconductivity, Vol. 7, No 2, June 1997, p. 751.

[2]. R. Bossert et al., "Fabrication of the First Short Model of High Gradient Quadrupole for the LHC Interaction Regions", MT-15, Beijing, October 1997.

[3]. R. Bossert et al., "Design, Development and Test of 2m Quadrupole Model Magnets for the LHC Inner Triplet", presented at Applied Superconductivity Conference (ASC'98), Palm Desert (CA), September 1998.

[4]. M. J. Lamm et al., "A New Facility to Test Superconducting Accelerator Magnets", PAC'97, Vancouver, Canada, 1997.

[5]. S. Feher et al., "Study of Low-β Quadrupole Magnet with Inter-Layer Quench Protection Heaters", MT-15, Beijing, October 1997.

THE PROTECTION SYSTEM FOR THE SUPERCONDUCTING ELEMENTS OF THE LARGE HADRON COLLIDER AT CERN

K. Dahlerup-Petersen, R. Denz, J. L. Gomez-Costa, D. Hagedorn, P. Proudlock,
F. Rodriguez-Mateos[+], R. Schmidt, CERN, Geneva, Switzerland
F. Sonnemann, RWTH Aachen, Germany

Abstract

The protection system for the superconducting elements of the Large Hadron Collider (LHC) [1] at the European Laboratory for Particle Physics (CERN), and its associated equipment are presented: quench detectors, cold diodes, quench heaters and related power supplies, extraction resistors and associated current breakers. Features such as radiation resistance, redundancy and required reliability are discussed.

1 INTRODUCTION

The LHC enters into a phase where construction started and components are being produced [2]. Injection of beam into the first sector (1/8 of the LHC) is expected for 2003, and the start-up of the completed machine is foreseen for 2005. The very flexible LHC optics requires a large number of superconducting magnet circuits, their connections with superconducting bus bars, and current leads as part of the electrical circuits. In total, about 8000 magnets connected in 1800 electrical circuits will be installed [3]. All superconducting elements require protection in case of a quench or other failures which may perturb accelerator operation or even damage equipment. Some elements require a complex system, and for others the protection can be fairly simple depending on the design of the elements and their powering.

In this paper we describe the elements of the protection system and the specific protection procedures, as well as the elements performing the monitoring of the integrity of the system, and the data acquisition of a large number of signals for analysis.

Due to the large stored energies in many of the circuits, and because of the difficulty accessing elements working at cryogenic temperatures for repair, the protection systems need to be very reliable. Equipment will be simple and robust to minimise maintenance of a large number of components. Most of the electronics will be installed in the LHC tunnel and need to be radiation tolerant at a level of some ten Gy.

The following solutions for the protection are envisaged:

- The main dipole and quadrupole magnets operate at a nominal current of about 12 kA and require protection with quench heater strips on the magnet coils, cold by-pass diodes and extraction of energy.
- The quadrupole magnets in insertions and matching sections (nominal current in the range of 6kA to 12kA) will be protected with quench heaters.
- 544 circuits with corrector magnets with a nominal current of 600A require extraction of the energy.
- If an individually powered orbit corrector magnet quenches, its power converter must be switched off.

2 ELEMENTS OF THE SYSTEM

2.1 Quench detectors

Each main quadrupole and dipole magnet will have its own protection system that is fully redundant and independent of other magnets (see Figure 1). When a quench is detected, the protection will activate the powering of the quench heater strips, shut down all power converters in the sector and open the switches across the dump resistors. For a quench in a bus bar, the system will shut down the power converter of the circuit and open the dump switches without firing heaters.

The quench detection for the dipole magnets is based on floating bridge detectors. The voltages across the two apertures are compared. A quench is detected if the absolute voltage difference exceeds a pre-set threshold. For the main quadrupole magnets, the comparison will be made between two sets of two poles, since the two apertures of the quadrupole magnets are powered separately.

Quenches in bus bars for main dipole and quadrupole magnets are very unlikely, as they are installed in regions of low field, protected from direct radiation and highly stabilised with copper. It is sufficient to detect any resistive growth on long stretches, using differential signals. Where possible, redundant detection will be performed with voltage taps at the cold side of the current leads feeding the circuit.

For most of the circuits with corrector and insertion magnets, the voltage at the bottom of the current leads will be measured to detect a quench.

[+] E-mail:Felix.Rodriguezmateos@cern.ch

0-7803-5573-3/99/$10.00@1999 IEEE.

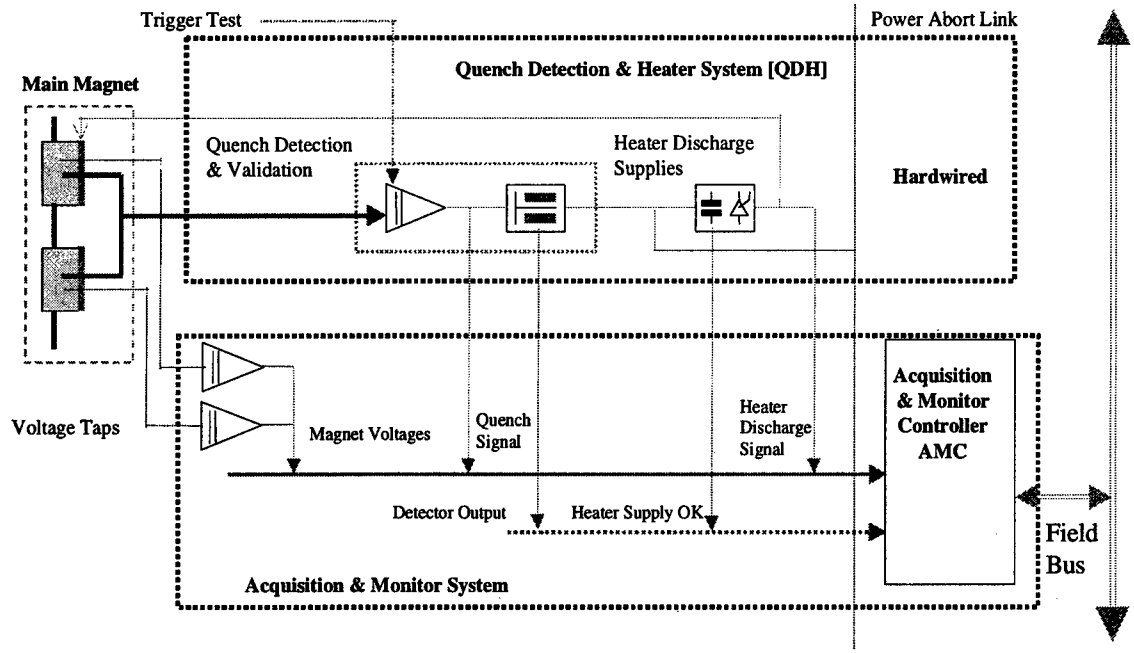

Figure 1: Block diagram for the protection system of the LHC main magnets.

The protection of current leads (800 pairs) using high temperature superconductors depends on the quench propagation velocity. At a later stage it will be decided if they can be included into the global protection schemes

2.2 Quench heaters and their discharge supplies

The quench heater strips are sandwiched composites made of two layers of polymide-epoxy glue embedding stainless steel strips. In order to limit the discharge voltage the strips are copper plated (a few micrometer copper thickness) to heat only a part of a strip [4].

Powering of quench heaters will be performed discharging capacitor banks by triggering thyristors in series with the strips. The heater discharge units will contain two banks of 3 capacitors connected in parallel. The capacitors will be operated at 75%±5% of their rated voltage leading to an increased lifetime and a lower leakage current. The thyristors (SCR) foreseen for the power supplies are intentionally overrated in order to cope with irradiation induced changes of the device parameters.

Besides the power part, the heater power supply units require an interface to the Acquisition and Monitoring Controllers (see below) in order to monitor their status [5].

2.3. Cold Diodes

The high-current silicon diodes of the diffusion type connected in parallel to the superconducting magnets will operate inside the magnet cryostat at a temperature of 1.9K. The quadrupole diodes have to withstand safely an estimated dose of about 400Gy and neutron fluence of about 2.4 10^{12}n/cm^2 during 20 years of operation. For the dipole diodes a dose of about 60Gy and a neutron fluence of about 3.0 10^{11} n/cm^2 has been estimated [6]. In case of a resistive transition in the superconducting magnet, the turn-on voltage of the diode is exceeded and the current commutates from the quenched magnet to the diode during the de-excitation of all magnets in the circuit.

One by-pass diode will be installed across each twin-aperture dipole magnet. As focusing and de-focusing quadrupoles will be powered separately, each single quadrupole aperture requires a diode. The two diodes assembled in one pack are galvanically separated. Each diode package must be able to conduct an ultimate current pulse of 13kA peak with a nominal decay time constant of about 100s for the dipole circuit, and about 40s for the quadrupole circuit respectively. The heat sinks have to absorb an energy of about 1.5MJ for a dipole diode; and 0.7MJ for a quadrupole diode. The diodes have to operate within a temperature range of 1.8K–450K, withstand the associated thermal stresses, and continue to operate reliably after several cold-warm cycles.

Before installation, all diode packages will be tested at liquid helium temperature. As the differences of the electrical characteristics between 1.9K and 4.2K are rather small, most tests will be carried out at 4.2K. Only a few of the series diode assemblies will be tested at 1.8K to verify their turn-on characteristics.

2.4 Data acquisition and monitoring

The controllers for data acquisition and monitoring (AMC) will monitor the status of the protection system, allow for powering, and acquire data for both on-line and post-mortem analysis (magnet voltages, quench detector signals, signals from the heater power supplies).

The AMC units are continuously acquiring the signals and storing them in a circular buffer. When a quench is detected, the acquisition continues during a defined short period of time and then stops. On request the data is sent to the operators allowing the analysis of the event.

The integrity of the protection system is monitored, for example if heater discharge units are not correctly charged, heater discharge units are not fired, or failures of quench detectors. If an error is detected, the operators will be informed.

In terms of monitoring and data acquisition, each machine sector will be sub-divided into 5 zones, each having about 60 AMC systems and connected via a field bus to an intermediate controller (WAN-PLC). This controller acts as a bridge between the AMC units and the Control Room (see Figure 1). In order to minimise cost and development, it has been decided to use a PLC-like structure. This allows to have an Off-The-Shelf system, with only the program to be developed at CERN. Each unit will have a Data Memory exceeding 48Kbytes, an acquisition cycle less than 10ms, and analogue inputs with an accuracy of 10 bits. For the communication protocol PROFIBUS will be used.

Since the electronics will be installed in the tunnel, tests will be performed to qualify components for radiation tolerance before final selection.

3 ENERGY EXTRACTION

For a fast de-excitation in the case of a quench, many of the magnet chains will be equipped with external energy extraction systems with mechanical circuit breakers and energy-absorbing dump resistors.

The 1.33 GJ of stored energy in the dipole magnets of each sector will be extracted into two, symmetrically placed energy dump facilities, inserted in series with the two half-chains. This configuration limits the maximum voltage to ground to 500V; it halves the energy deposit in each resistor unit and allows symmetrical grounding of the power circuit (the mid-point of the mid-arc dump resistor). Transfer function analysis of the chains has shown that this grounding concept provides important advantages for ripple, ramping and transient phenomena. The resistance value (75mΩ each unit) limits the maximum current decay rate to -125A/s. Four 4.5kA D.C. circuit breakers will carry the current, fed from a current-equalising bus-way. Each cluster of breakers consists of eight individual units, with two breakers in series for redundancy. Each breaker has two independent release mechanisms (no-volt coil for slow opening and current impulse for fast release). The low-inductance dump resistors incorporate a forced air-to-water heat exchanger, as heat dissipation into the tunnel air is inadmissible. Their cooling time is approximately one hour.

A single extraction system is foreseen for each of the quadrupole chains. The dump resistance values are 7.7mΩ and 6.6mΩ, which give a maximum decay rate of –325A/s. The same breakers as for the dipole magnets are used.

4 RADIATION TOLERANT EQUIPMENT

The equipment installed in the tunnel includes capacitor discharge power supplies for firing the quench heaters, quench detectors, breaker control electronics, data acquisition systems, programmable logic controllers (PLC) and interfaces to field buses. Due to beam losses and interactions with the residual gas in the beam tube this equipment will be exposed to radiation (order of magnitude: 1 to 10Gy per year) during LHC operation. The test of all these devices under conditions similar to those expected in LHC are performed in the newly created irradiation test zone in the northern fixed target area of the CERN SPS accelerator [7]. The dose rate in this area is about 10Gy per week corresponding to a fast neutron fluence of some 10^{11} n/cm^2. The zone is equipped with cable connections to a local control allowing for dynamic, on-line measurements of components and radiation levels.

In a first step the main components of the heater discharge power supplies, namely capacitors and thyristors, shall be qualified with respect to radiation tolerance, ageing and environmental influences.

5 ACKNOWLEDGEMENT

The authors would like to express their gratitude to colleagues at CERN and other National Laboratories who have contributed with many discussions to this work. Special thanks go to R. Saban for his collaboration and support, mainly in the development of AMC.

6 REFERENCES

[1] The LHC Study Group, The Large Hadron Collider Conceptual Design, CERN/AC/95-05 (1995)

[2] L.Evans, Ph.Lebrun, Progress in Construction of the LHC, HEACC'98, September 98, Dubna, Russia

[3] P.Proudlock, "Update on the Powering Strategy of LHC", this conference

[4] B.Szeless et al., LHC Project Report 48, ICEC'96, Japan, 20-24 May, 1996

[5] F.Rodriguez-Mateos, "Heater Power Supplies: Technical Description", Revision December 1998, private communication

[6] G.Stevenson, private communication

[7] R.Rausch, M.Tavlet, CERN-TIS-TE/IR/98-11

THE LHC MAGNET STRING PROGRAMME : STATUS AND FUTURE PLANS

F.Bordry, J.Casas-Cubillos, P.Cruikshank, K.Dahlerup-Petersen, F.Rodriguez-Mateos, P.Proudlock, G.Riddone, R.Saban, R.Schmidt, L.Serio, C.Wyss, CERN, Geneva, Switzerland.

Abstract

String 1, with one twin aperture quadrupole and three twin aperture 10-m dipoles (MB1, MB2 and MB3) powered in series and operating at 1.9 K, has recently been dismantled after four years of operation interrupted by technical stops and shutdowns for upgrading or exchanging equipment. Following the validation of the main LHC systems (cryogenics, magnet protection, vacuum, powering and energy extraction) the experimental programme was oriented towards the optimisation of the design and the observation of artificially induced fatigue effects.

The design study for String 2 has been completed. This facility, which will be commissioned in December 2000, is composed of two LHC half-cells each consisting of one twin aperture quadrupole and three 15-m twin aperture dipoles. A cryogenic distribution line housing the supply and recovery headers runs parallel to the string of magnets. An electrical feedbox is used to power, with high temperature superconductor current leads, the circuits as in the regular part of an LHC arc.

This paper reviews the experiments carried-out with String 1 and summarises the results obtained after more than 12800 hours of operation below 1.9 K and 172 quenches. It also describes the layout and the components of String 2 and explains the objectives pursued by its designers.

1 STRING OPERATION

The facility was operated between December 1994 [1] and December 1998. During this time, the magnets experienced 172 quenches. 144 were provoked by firing quench heaters. 70 quenches were above nominal current (12.4 kA). The magnets remained excited at nominal current for 314 hours [2].

Each *cool-down* lasted 3 to 5 days depending on the limitations imposed on temperature gradients across individual magnets. Following a quench, automatic procedures took 6 to 12 hours to cool-down the magnets from approximately 30 K [3,4]. The temperature of the magnets was controlled by a Joule-Thomson valve with very stringent operational constraints (0.025 K control band) imposed by the superconducting magnets characteristics, the capacity of the cryogenic system, the variability of heat loads and the accuracy of instrumentation (± 0.01 K).

Model-based predictive control (MBPC) algorithms were investigated in order to obtain a narrower control band compared to standard PID control loops [5,6]. Preliminary results were encouraging but the temperature operational range was limited because only linear approximations of the process were used. Future developments are the implementation of non-linear models into the MBPC controller. Before being able to power the magnets an in-situ calibration of the temperature sensors was necessary. The observed reproducibility between sensors was better than 0.01 K and no degradation was measurable during the 4 years of operation.

The String was controlled and monitored [7] from a dedicated control room but could be controlled from any remote terminal with appropriate privileges. Over 600 process variables were archived during the lifetime of the String every second and, transients on voltage taps, quench detectors, pressure, etc. were recorded with a resolution of up to one millisecond. The data, over 500 million values, is available for analysis via the Web.

A few incidents occurred during the lifetime of String 1. The epoxy-glass fiber rod connecting the actuator to the closing inset of a valve disconnected: the valve was replaced without completely warming-up the magnets. All the voltage taps of one aperture of the quadrupole disconnected during a quench. Reconfiguration of the quench detection system allowed the continuation of the operation. Several quench heater power supplies (one per year) failed and were replaced. A mains power cut occurred during unattended operation. The emergency procedures which had been put in place were executed thus preventing any damage.

2 EXPERIMENTS

Six *experimental runs* were conducted [8,9]. Operating modes of the superfluid helium cooling loop in co-current and counter-current flow were explored. The counter-current mode was abandoned because of flow capacity limitations. The intensive testing on the superfluid helium cooling loop permitted to validate the performance and sizing rules of the bayonet heat exchanger for transporting linear heat loads in the W m^{-1} range over the distance of several tens of metres.

Experiments on thermohydraulics of quenches [10,11] permitted to establish and validate a model representing the physical process of heat deposition from the magnet

0-7803-5573-3/99/$10.00@1999 IEEE.

coil to the superfluid helium bath and subsequent pressure rise. Experiments were performed to understand the propagation of a quench [11,12]. The first experiments were performed by firing the quench heaters for the quadrupole magnet. In this case the mechanism for quench propagation after 40-70 s is thermal conduction through the main bus-bar. Since the energy stored in a dipole magnet exceeds the energy in a quadrupole magnet by about one order of magnitude, the experiments were repeated by quenching the third dipole. These experiments have shown that the mechanism of heat propagation through the helium dominates over the quench propagation by solid conduction via the bus-bars. During the series of experiments the magnet current and the opening pressure of the valves were varied. The thermohydraulic propagation through the helium can be slowed down by increasing the opening pressure of the quench relief valves. The number of magnets to which a quench can propagate has been found to be limited to a few units, thus having no significant impact on the cryogenic recovery time, the helium inventory and exergy recovery.

Experiments on the insulation vacuum have shown that the intermittent operation of cold cathode gauges during thermal transients can significantly extend their lifetime, and the use of turbomolecular pumps minimises natural warming of magnet cold masses during cryoplant stoppages. In addition, experiments have been made on the beam vacuum system to quantify the very slow propagation speed of a helium leak along in the 1.9 K tubes.

3 THE SHUTDOWNS

A number of shutdowns took place to modify the configuration of String 1 and add or repair equipment or instrumentation [13]. During the first shutdown (June 1995) a third dipole and a vacuum barrier in the insulation vacuum were added. During the second shutdown (June 96), a total of 22 modifications or interventions were carried out: they ranged from the repair or installation of instrumentation for cryogenics and vacuum, the installation of a cold diode and to the replacement of a dipole. The main reason for the third shutdown (December 97) was the installation of a tube containing a prototype auxiliary bus-bar cable. This tube ran in one of the apertures of the String from the front of MB1 to the rear of MB3 and was hydraulically connected to the cold mass of MB3. A ceramic leak tight feedthrough was installed, for the first time in operational conditions, to route the signal wires for the temperature sensors and the voltage taps out of the 1.9 K bath.

Leaks in the beam-screen capillary had prevented the connection of the beam screens to the cooling circuit during the previous shutdown. The opportunity of this shutdown was taken to install a cryogenically cooled beam-screen in the other aperture of MB3. The leaks, resulting from the use of brazing fluxes for low temperature brazing on thin wall stainless steel, occurred at two other locations in the insulation vacuum on similar components. Future use of brazing flux on LHC components will be prohibited.

The initial installation, together with the three shutdowns, permitted the development of detailed leak test procedures for the beam and insulation vacuum systems.

4 THE ELECTRICAL AND THERMAL CYCLING

Part of the experimental program was devoted to artificially inducing fatigue to components of String 1 and their interconnects. This was achieved by electrically cycling the String between injection (800 A) and nominal current (12.4 kA) and, thermally cycling the magnets either between room temperature and 1.9 K or between room temperature and 100 K.

During the first electrical cycling campaign, the ramp rates (10 A/s) were similar to those which will be experienced by the magnets during the acceleration phase. Assuming 200 days of operation per year and one injection per day, the experiment simulated 10 years of operation of the collider. During a second campaign a year later, faster ramp rates (25 and -50A/s) as well as longer cycles leaving the magnets at nominal current for 6 hours were executed. In total the magnets experienced the 3275 cycles.

After the first electrical cycling campaign, one of the dipoles exhibited an erratic quench behaviour when pushed to natural quench well above nominal current [14]. In order to avoid compromising the experimental program, it was decided to exchange the dipole and measure it on the magnet test bench. These measurements confirmed the erratic quench behaviour but failed to highlight the reason [15]. In an attempt to understand its behaviour, the magnet is currently being disassembled.

In addition to the 6 thermal cycles due to shutdowns and technical stops, 9 further thermal cycles were carried out. During the last cool-down the constraint of 70 K on the temperature gradients across individual magnets was removed and the cool-down from room temperature started with a forced flow of gaseous helium at 90 K.

Following the cycling experiments, no other damage to the magnets or their interconnects was observed.

5 STRING 2

String 2 has the same layout as a LHC cell in the regular part of an arc and follows the curvature of the tunnel [15]. The first half-cell starts with a Short Straight Section (SSS), which is connected to the cryogenic line

and is followed by three 15-m dipoles. Following the simplified cryogenic scheme, the second half-cell is not connected to the cryogenic line.

An electrical feed box which supplies current to 17 of the 21 electrical circuits of String 2 precedes the first half-cell. The four remaining circuits are locally supplied from current leads installed on the SSSs.

Each SSS contains a 3.10 m. twin aperture quadrupole, the twin-aperture nested sextupole-dipole magnet and two single aperture octupole lattice corrector magnets. The technical service module of both SSSs contains the beam position monitors, the protection diodes for the quadrupole magnets and the cold mass instrumentation capillaries. In the first SSS, the technical service module includes a vacuum barrier, the jumper connection to the separate cryogenic line and the helium phase separator for the full cell.

The performance of the cryogenic system with the separate line and its connection every cell to the collider will be measured for the first time with real loads, with the new cylindrical bayonet heat exchanger and in a portion of the machine which is installed in a horizontal plane. The thermohydraulics of quenches with the new configuration and pressure-settings of the quench relief valves (two per cell) will be observed.

The presence of several independently powered electrical circuits will allow the investigation of their mutual influence during normal operation and in case of quench. Furthermore, techniques for tracking the main dipole magnets as well as their correctors during transients will be studied. The final design of the tube external to the magnet cold mass routing the auxiliary bus-bars will be tested in real operating conditions and installation aspects of the cables inside the tube will be verified. Operational experience will be gained with a prototype of the d.c. breaker facility which is foreseen for the LHC machine.

The design of the magnet protection system with individual magnet quench detection and heater control systems will be validated.

Results of dipole-to-dipole quench propagation experiments performed with String 1 will be verified with the different and final dipole-to-dipole mechanical and hydraulic interface, as well as with the larger inductance of the final coils. Quench propagation from main magnet to corrector, dipole to quadrupole, central dipole to neighbouring dipoles and half-cell to half-cell will be studied.

The beam vacuum will be fully equipped with beam screens, intermagnet RF junctions and beam position monitors (BPM). It will be assembled according to UHV procedures. In order to simulate proton beam heating effects, heaters will be attached to beam screens and BPMs. Experiments with vacuum barriers present within the separate cryogenic line, in the magnet string and between the string and the cryogenic line will be conducted. The cooling of the beam screens installed in each half-cell and independently controlled will be studied and validated.

Last but not least, String 2 will offer a unique occasion to rehearse the assembly and exchange sequences and to verify the assembly procedures foreseen for each step of the interconnection of magnets as well as the exchange of a diode or instrumentation.

In addition to these studies which will be conducted for the first time, a number of experiments, measurements or exercises which already took place with String 1 will be repeated either to confirm the results obtained or to test newly developed versions of an already verified/tested component.

String 2 will provide the operations crews with valuable experience in view of running the superconducting collider.

6 REFERENCES

[1] P.Faugeras for the String Team, Assembly and Commissioning of the LHC Test String, PAC '95, Dallas, Texas, May 1995

[2] F.Rodriguez-Mateos et al., Electrical Performance of a String of Magnets Representing a Half-Cell of the LHC Machine, MT14, Tampere, Finland, June 1995.

[3] A.Bézaguet et al., The Superfluid Helium Cryogenics System for the LHC Test String: Design, Construction and First Operation, Cryogenics Engineering Conference, Columbus, Ohio, July 1995.

[4] A.Bézaguet et al., Cryogenic Operation and Testing of the Extended Prototype Magnet String, ICEC16, Kitakyushu, Japan, May 1996.

[5] B. Flemsaeter et al., Applying Advanced Control Techniques for Temperature Regulation of the LHC Superconducting Magnets, ICEC 17 July 1998, p. 631, IOP 1998

[6] E. Blanco et al., Predictive Temperature Control of the LHC Superconducting Magnets, to be presented in: European Control Conference (ECC 99), Karlsruhe

[7] R.Saban et al., The Control and Data Acquisition of the LHC Test String, ICALEPCS'95, Chicago, Illinois, November 1995.

[8] R.Saban et al., The LHC Test String: First Operational Experience, EPAC '96, Sitges, Spain, June 1996.

[9] J.Casas-Cubillos et al., Operation, Testing and Long-term Behaviour of the LHC Test String Cryogenic System, ICEC 17, Bournemouth, June 1998

[10] M.Chorowski et al., Thermohydraulics of resistive transitions on the LHC prototype magnet string: theoretical modelling and experimental results, CEC/ICMC 97, Portland, USA,July 1997.

[11] F.Rodriguez-Mateos et al., Thermohydraulic Quench Propagation at the LHC Superconducting Magnet String, ICEC 17, Bournemouth, June 1998

[12] L.Coull et al., Quench Propagation Tests on the LHC Superconducting Magnet String, EPAC '96, Sitges, Spain, June 1996.

[13] R. Saban et al, Shutdown Report, LHC Project Notes 107 and 148, CERN Internal Note.

[14] R. Saban et al, Experiments and Cycling at the LHC Prototype Half-Cell, Pac'97, Vancouver BC, Canada, May 1997.

[15] A.Siemko et al., Quench Test Results of the MTP1A2 Twin Aperture Superconducting Dipole Model Magnet for LHC, MT15, Beijing, China, October 1997

[16] R.Saban et al., The LHC prototype Full-cell : Design Study, LHC Project Report 170, CERN Internal Note.

A METHOD TO EVALUATE THE FIELD-SHAPE MULTIPOLES INDUCED BY COIL DEFORMATIONS

P. Ferracin, W. Scandale*, E. Todesco, P. Tropea, CERN - LHC Division, Geneva, Switzerland

Abstract

A semi-analytical method to evaluate the effect of coil deformations on the field-shape imperfections of the LHC dipole is presented. The deformation induced by the collaring procedure and by the thermal stresses is evaluated numerically with a finite element code. The vector field of mechanical displacements is approximated with truncated Taylor and Fourier series. The fitting function agrees with the numerical data to within less that 10 μm. The decomposition in modes of the truncated series permits identification of displacements which are dangerous for the multipolar content and how they could be cured. An application to compare two designs of the LHC dipole is given.

1 THE LHC DIPOLE MODEL

In this paper we deal with the field quality evaluation in the LHC main superconducting dipoles [1]. The magnet cross section should optimize field quality to obtain a sufficiently constant magnetic field to provide a wide dynamic aperture for the beam [2]. Indeed, the nominal design may be difficult to reach under realistic conditions, and coils can be deformed by either manufacturing forces or tolerances in the mechanical parts (see for instance [3]). In this paper we analyse the effect of deformations due to manufacturing and we develop a formalism to work out the dependence of the multipolar coefficients of the field expansion on the deformations.

Mechanical models have been already used to evaluate the displacement of the LHC dipole coils induced by manufacturing and thermal effects. The present model considers one quarter of the two-in-one dipole, i.e. half aperture, with an up-down symmetry that allows only normal multipoles, and a left-right symmetry that imposes the same multipoles on both apertures. Computations are carried out at 1.9 K, and at the injection energy where the problem of the field quality is more relevant. The coil prestress in the midplane, at 1.9 K is fixed at 40 MPa.

The finite element code ANSYS [4] provides the field of deformations induced in the superconducting coil. A Fortran code (ANSIA [5]) produces displaced coordinates for each conductor in a format compatible with ROXIE [6]. The latter evaluates the magnetic field as a multipolar expansion. The model used to carry out the magnetic computations only considers the effect of deformations on the nominal geometry; the contribution due to iron deformations can be assumed to be negligible.

The mechanical model includes the nonlinear elasticity of the coil [7, 8] as obtained from experimental data [9]. Particular care was taken in preparing the representation of the elastic modulus of the copper wedges and insulation, that are considered a unique material in the model. Our computations show that the multipoles exhibit a strong dependence on mechanical deformations. Experiments to verify our results are in preparation.

* Email: walter.scandale@cern.ch

2 TOOLS FOR THE DEPENDENCE OF MULTIPOLES ON DEFORMATIONS

The deformation is a field of 2D vectors that is evaluated through the finite element code ANSYS on a finite set of nodes in a 2D space (the magnet cross section). Since this vector field is rather smooth, we propose to parametrize the deformations by interpolating them with low-order Taylor and Fourier series. In this way all the information relative to the deformations can be reduced to a few coefficients, thus simplifying the analysis of the relation between deformations and multipoles. We numerically estimate the influence of single deformation modes on the multipoles, thus identifying the most dangerous.

Since deformations are implemented in ROXIE as shifts in the position of the inner part and of the outer part of the conductor, we consider a field of deformation defined over four radii (r_1, r_2, r_3, r_4)=(28, 43.4, 43.9, 59.3) mm that surround the inner and the outer layers of the coils; the field then depends on the discrete variable r_i and on the continuous angular variable ϕ. Deformations are then decomposed into a radial $dr(r_i, \phi)$ and a tangential $dp(r_i, \phi)$ component.

Radial deformations are well interpolated by the sum of the first orders of an even Fourier series in the azimuthal variable ϕ

$$dr(r_i, \phi) = \sum_{k=0}^{K} a_{k,i} cos(k\phi) \qquad i = 1, 4.$$

Here the index i runs over the four concentric circles that surround inner and outer coils, and k runs over the modes. The mode zero $a_{0,i}$ gives rise to a contraction or to a dilatation of the coil; the mode one $a_{1,i}$ produces an horizontal shift in the coil, whilst higer order modes correspond to radial waves of deformations with decreasing period. The up-down symmetry is responsible of the absence of sine terms in the Fourier series.

Tangential deformations are well interpolated by low order odd Taylor series in each half of the aperture

$$d\phi(r_i, \phi) = \sum_{j=0}^{J} b_{j,i} \phi^{2j+1} \quad i = 1, 4 \quad \phi \in [-\pi/2, \pi/2]$$

0-7803-5573-3/99/$10.00@1999 IEEE.

$$d\phi(r_i,\phi) = \sum_{j=0}^{J} c_{j,i}\phi^{2j+1} \quad i = 1,4 \quad \phi \in [\pi/2, 3\pi/2]$$

The mode zero $b_{0,i}$ and $c_{0,i}$ corresponds to tangential compression or dilatation, uniform along the azimuth. Higher order modes correspond to tangential waves of compressions and dilatations. Also in this case, the up-down symmetry implies the presence of odd terms only.

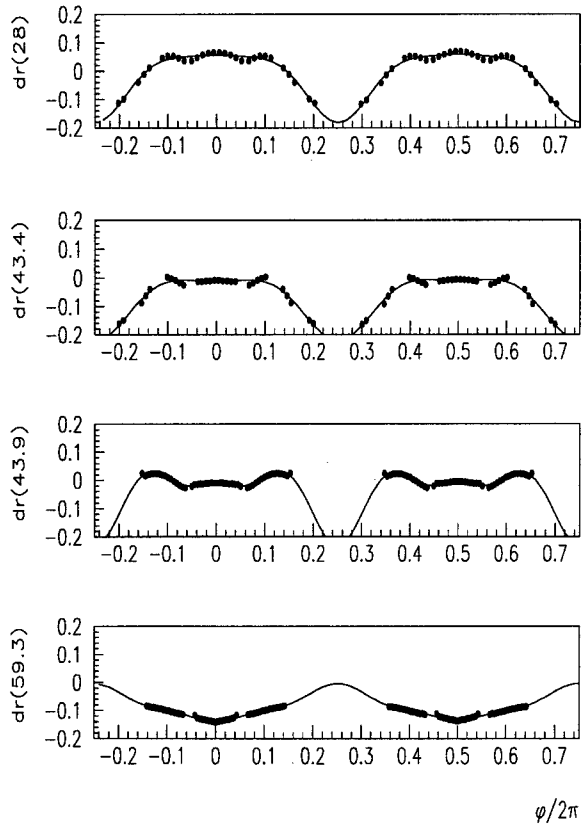

Figure 1: Plot of radial deformations for each of the four coil contours, stainless steel collars. Dots: ANSYS values. Lines: interpolation.

In Figs. 1 and 2 we show the radial and tangential deformations evaluated through ANSYS (dots) and the interpolation (solid line) with seven radial modes and two tangential modes (K=6 and J=1). If the displacements evaluated through ANSYS are replaced by the interpolating field, the resulting multipoles agree with the ANSYS results (see Table 1, last two rows). This means that low order Taylor and Fourier series can take into account the part of the deformations that are relevant to evaluate the multipoles.

The contribution of each mode to the multipoles is given in Table 1. For symmetry reasons, even radial modes only contribute to odd multipoles, and odd radial modes to even multipoles. One can distinguish two main effects.

- Radial deformation of order 2 (i.e., circles are de-

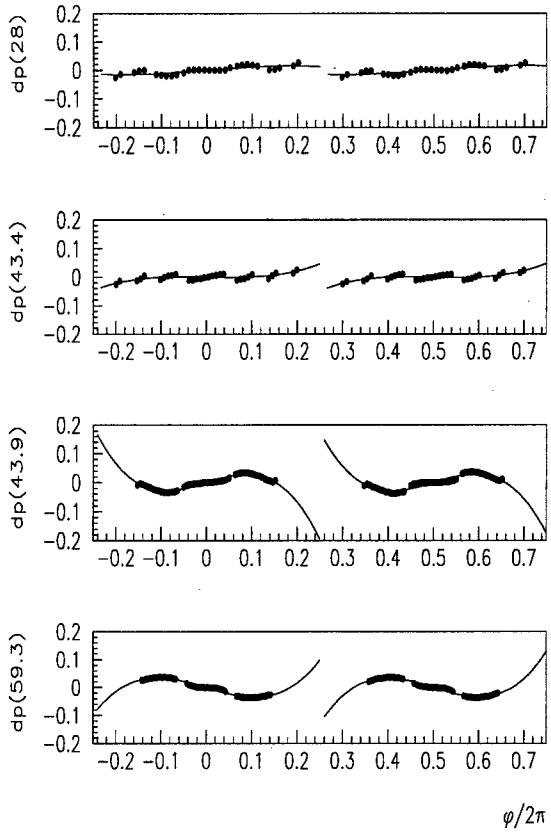

Figure 2: Plot of tangent deformations for each of the four coil contours, stainless steel collars. Dots: ANSYS values. Lines: interpolation.

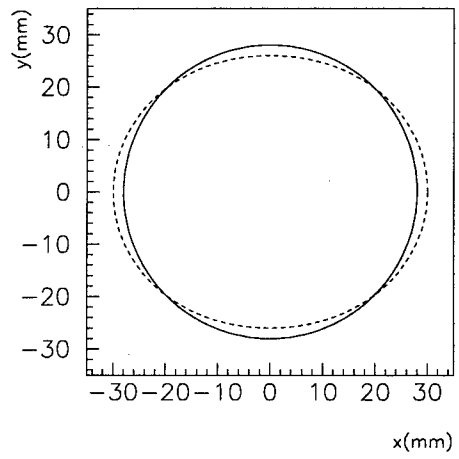

Figure 3: Plot of radial deformations, mode 2, in cartesian coordinates. Undeformed circle (solid line) versus deformed circle (dotted line).

Table 1: Contribution of radial and tangential modes to the multipoles shift induced by deformation, total effect of 7 radial and 2 tangential modes, and comparison with ANSYS results. Multipole shifts are given in units of 10^{-4} at R_{ref}=17 mm.

	b_2	b_3	b_5	b_7
radial				
k=0	0.00	0.11	-0.06	0.01
k=1	0.05	0.00	0.00	0.00
k=2	0.00	-2.98	0.18	-0.04
k=3	0.08	0.00	0.00	0.00
k=4	0.00	0.53	0.69	0.01
k=5	0.00	0.00	0.00	0.00
k=6	0.00	0.02	-0.05	-0.07
tang.				
j=0	0.04	0.17	-0.05	0.02
j=1	-0.01	0.03	-0.01	0.00
total	0.16	-2.12	0.70	-0.07
ANSYS	0.16	-2.19	0.59	-0.08

formed into ellipses, see fig. 3) have a strong effect on the sextupole (≈ -3 units) and on the decapole (≈ 0.2 units).

- Radial deformation of order 4 gives rise to 0.5 units of b_3 and 0.7 units of b_5.

Simulations have also shown that the radial deformations are rather well decoupled with the tangential one. In Table 1 the effect of the tangential modes seems to be very limited (only some contribution to b_3): in our computations we fixed the coil length to an optimal value that allows to recover the nominal length under deformations, at 1.9 K. Indeed, a non optimized coil length produces tangential deformations that strongly affects the field multipoles.

- Tangent deformations due to a coil length different from the nominal one have a large influence on b_3, b_5 and b_7. Simulations show that a 0.1 mm longer coil gives rise to around -3 units of sextupole, and 0.5 of decapole.

Therefore, the determination of the exact coil length under manufacturing forces and at cold is crucial to obtain a correct estimate of the absolute value of the multipoles. Other contributions of the deformations are not very relevant, giving rise to multipole shifts of less than 0.1 units. In particular, the following effects are negligible:

- The effect of the first order (see Table 1, mode j=1) tangential mode (tangetial waves fo compression and dilatation) is negligible.

- The radial mode of order zero (see Table 1, mode k=0), i.e. the radial shrinkage due to low temperature, is negligible.

- Odd radial modes (see Table 1, mode k=1,3,5), i.e. modes related to left-right asymmetries, are very low. Therefore, deformations have negligible effect on even multipoles.

3 CONCLUSIONS

We have analysed the variation of the field quality in the superconducting LHC dipoles due to deformations of the coils with respect to the nominal design.

We propose a method, based on interpolation, to reduce the deformation field to a few coefficients of radial and tangential modes. This leads to a reduction in the complexity of the problem and to relate modes to multipoles. We are able to identify which modes are more dangerous and which are negligible. We showed that the effect of deformation on multipoles is relevant, and that the main contributions come from radial deformations of order two and four (see for instance fig. 3). Moreover, a systematic difference in the coil length between the nominal and the real one (i.e., at 1.8 K and under deformations) leads to additional multipole shifts. These effects are uncoupled.

We wish to acknowledge A. Desirelli, P. Fessia, D. Leroy, M. Modena, D. Perini, Prof. Rebora, G. Spigo and R. Vuillermet for their help in the definition and in the understanding of the mechanical model. We also thank S. Russenschuck for providing the ROXIE code and the files of the magnetic model.

4 REFERENCES

[1] The LHC study group, *CERN* **95-05** (1995).

[2] C. Wyss et al., *CERN LHC-MMS 98-198* **IT 2325** (1998).

[3] R. Bartolini, P. Ferracin, P. Fessia, W. Scandale, E. Todesco, ', in *Sixth European Accelerator Conference*, edited by C. Petit-Jean Genaz (IoP, New York, 1998) pp. in press.

[4] ANSYS 5.4, licensed by and trademark of Swanson Analysis Inc., Houston, PA, USA.

[5] E. Todesco, private communication.

[6] S. Russenschuck, *LHC Project Report* **159** (1997).

[7] W. Scandale, E. Todesco, P. Tropea, in preparation.

[8] P. Tropea, A. Rebora, E. Todesco, *CERN LHC-MMS Internal Note* **99-04** (1999).

[9] D. Tommasini, S. Russenschuck, L. Bottura, in: *Proceedings of the first international conference of Roxie users*, CERN Yellow Report, in press.

FIELD-SHAPE VARIATION INDUCED BY THERMAL CYCLING AND EXCITATION IN THE LHC DIPOLE

O. Pagano, W. Scandale*, E. Todesco, CERN, LHC Division, Geneva, Switzerland

Abstract

The field-shape imperfections measured at room temperature before and after thermal cycling and excitation up to maximum field in three 10 m-long models of the LHC dipole are presented. A systematic variation is observed in the normal sextupole and decapole components. The variation of the other components turns out to be negligible or to randomly vary (as for normal and skew quadrupoles). We show how the systematic variation can be justified by assuming outward radial shift in four blocks of the inner coil. Qualitative tests using Fuji paper confirm this conjecture.

1 INTRODUCTION

The field quality in the LHC dipoles will depend on several effects, such as the nominal coil geometry, persistent currents, deformations induced by manufacturing and variation of the nominal geometry related to mechanical tolerances. When the magnet is powered at maximum current or when a quench occurs, coil movements may take place, and this may modify the field quality. In order to evaluate the relevance of this effect we present and analyse the experimental data relative to three dipoles models that have been measured before and after the first training cycle. Magnetic measurements were taken at room temperature and with low current ($\approx 20A$): this assures that only the geometry of the coils affects the field quality. Therefore, variations of the field components are only induced by coil displacements. The aim of this work is the following: a) To evaluate which multipoles are affected by the first training cycle and how much; b) Separate the multipole variation that appears to be systematic in all magnets and apertures from the variations that are dependent on the magnet, on the aperture, and even on the position along the magnet axis; c) Evaluate what kind of coil displacement can produce these multipole variations. A similar analysis has been carried out in Ref. [1] for the IR quadrupoles of RHIC.

2 EXPERIMENTAL DATA

Three 10 m long dipoles models [2], named MBL1J2, MBL1N1 and MBL1N2 respectively, have been considered in our analysis. All of them have 5-block coils. The magnetic field inside both apertures were measured at room temperature using a 300 mm-long 18 mm-wide rotating coil and the standard multipolar expansion of the field was worked out. Normal and skew components was computed at a reference radius R_{ref} of 17 mm, along 11 longitudinal positions. We analysed the variation of the multipoles before and after the first training and power test (at $1.9K$ and $12kA$) for both apertures of the three models. Data for the dipole MB1LN1 are given in Fig. 1. Data for the dipoles MBL1N2 and MLB1J2 can be found in Ref. [3]. Variations averaged along the magnet axis that may be significant for the dynamics are summarised in Table 1. One can distinguish three groups of multipole variations:

- Systematic variations in all magnets and apertures (b_3 and b_5), with a non-negligible longitudinal average.
- Random variations changing from magnet to magnet and from aperture to aperture (a_2 and b_2), with a non-negligible longitudinal average.
- Random variations that become small when averaged along the magnet axis: (a_4, b_4 and b_9).

Table 1: Multipole variation induced by training cycle, averaged along the magnet axis, reference radius at 17 mm, units of 10^{-4}.

	J2 left	J2 right	N1 left	N1 right	N2 left	N2 right
b_3	+1.29	+1.36	+1.63	+1.65	+1.07	+0.68
b_5	−0.32	−0.39	−0.40	−0.38	−0.38	−0.26
b_2	+0.25	−0.64	−0.13	+0.06	+0.35	−0.47
a_2	+0.05	−0.16	−0.14	+0.08	−0.41	−0.19
b_4	−0.02	−0.02	+0.02	−0.05	−0.05	+0.02
a_4	−0.05	+0.12	+0.10	−0.02	+0.11	+0.08
b_9	−0.08	−0.04	−0.04	+0.03	+0.10	+0.12

One can argue that only the multipole variations of the first and second type have an influence on particle motion in the LHC, since the longitudinal average along the magnet is large. Instead, the data of the third type are irrelevant for beam dynamics. Anyway, all the previous data are relevant for mechanics and will be used to analyse and predict the mechanical stability of the dipoles.

3 ANALYSIS OF SYSTEMATIC EFFECT

The data relative to the variation of b_3 and b_5, that appear to be systematic in all magnets and apertures, show that the ratio $\Delta b_3/\Delta b_5$ ranges from -2.7 to -4.5

Starting from the nominal geometry of the coil we computed the effect of simple movements of the blocks in order to work out a possible explanation for the systematic shift in b_3 and b_5. To this extent, we somehow arbitrarely only selected simple coil displacements, that preserve up-down and left-right symmetry:

- Displacement of a single block (and its corresponding symmetrical blocks) either by a radial shift or by a tangential shift or by a tilt, i.e. a rotation of the block around one

* Email: walter.scandale@cern.ch

0-7803-5573-3/99/$10.00@1999 IEEE.

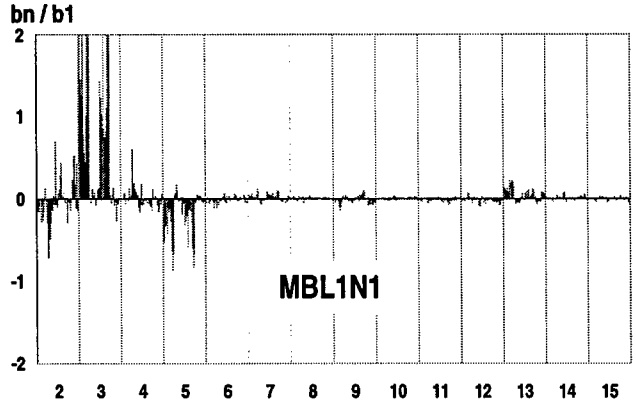

Figure 1: Multipole variation induced by training cycle in dipole MBL1N1; normal (black/blue) and skew (grey/red) components are measured in the two apertures and in 11 positions along the magnet axis. Above order 11, the amplitude of the harmonics is increased by a factor of 10. Reference radius at 17 mm, units 10^{-4}.

vertex.

• Displacement of the inner layer or of the outer layer, either radial or tangential.

Amongst all these movements, the only one that features a ratio b_3/b_5 that falls into the measured range is a radial shift of block 5, 10, 15 and 20, as shown in Fig. 2. The amplitude of these shifts for each magnet and each aperture are given in Table 2.

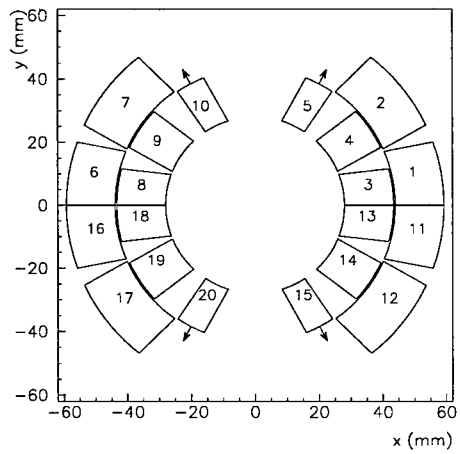

Figure 2: Nominal geometry of the 5-block coil; the arrows are the displacements (magnified by 100) needed to induce the observed b_3 and b_5 shifts

As it is pointed out in Ref. [4], the inverse problem is in general undetermined, i.e. the number of degrees of freedom relative to block displacements is larger than the number of experimental data to fit. Therefore, in general there exist n-parameter families of solutions that can fit experimental data, where n is the difference between the number of degrees of freedom of the blocks and the numbers of multipole to fit. In our approach we arbitrarily reduce the complexity of the problem as follows: a) we reduce the number of multipole to fit by considering only b_3 and b_5 that produce the only systematic effect on all magnets and apertures; b) we reduce the number of degrees of freedom by considering only some simple movements of the blocks and by imposing a 4-fold symmetry.

Indeed, the validity of our solution is confirmed by additional experimental data provided by the Fuji papers, that provide a qualitative indication of the pressure existing between the collar and the coils in the different parts of the collar cavity. The analysis of Fuji papers inserted in a 5-block 10 m-long model shows that between the collars and the inner coils there is a reduced pressure during manufacturing, in all the four symmetric positions corresponding to blocks 5, 10, 15 and 20 [5]. This means that a gap is likely to occur between the collar and the coil during and after manufacturing, and that the effect of the Lorenz forces during the powering cycle is to push these blocks against the collar. The symmetry of the movements is caused by the symmetry of the electromagnetic forces and of the collar cavity.

Table 2: Amplitude (in μm) of outward radial movements of blocks 5, 10, 15 and 20 that produce observed shift in b_3 and b_5.

Magnet	Left aperture	Right aperture
MBL1J2	44	51
MBL1N1	57	56
MBL1N2	44	28

4 ANALYSIS OF THE RANDOM EFFECT

For the analysis of the non-allowed harmonics we considered variation of multipoles in excess of 10^{-7} units, and the dependence along the magnet axis (no average is carried out over data). The most relevant components are a_2 and b_2. They can be generated by displacements that break the up-down symmetry and the left-right symmetry respectively. An asymmetric movement such as a positive radial displacement for blocks 5 and 10, and a negative one for blocks 15 and 20, would produce relevant multipole shifts in a_2, a_4, and a_6 only, and perfectly correlated. Indeed, such a correlation between even skew multipoles is not observed [3]. The same happens for even normal multipoles. The total loss of correlation between even multipoles implies that they are due to random displacements of the coils. These small displacements should also strongly depend on the position along the magnet axis, since as it is shown in Fig. 1 these multipoles have a very wide variation along the magnet axis.

In Ref. [3] we have shown through numerical simulations that a random displacement of blocks or of conduc-

tors gives rise to very simple scaling laws for the multipoles: the σ_n, i.e. the standard devation of the distributions of normal or skew multipoles of order n are approximately the same, and moreover they scale linearly with the amplitude of the random displacement d and according to a power law in n:

$$\sigma_n(d) = d\ A\ B^n\ C^{n^2} \qquad (1)$$

with A, B and C independent of d. In Fig. 3 we compare the measurements of the multipoles along the magnet axis to the obtained scaling laws, with random displacements of the blocks, for the magnet MBL1N1. For each multipolar harmonics and for each aperture we have 11 values: we compute the sigma of these values of each harmonics measured in a dipole and we compare it with the corresponding sigma of the above equation.

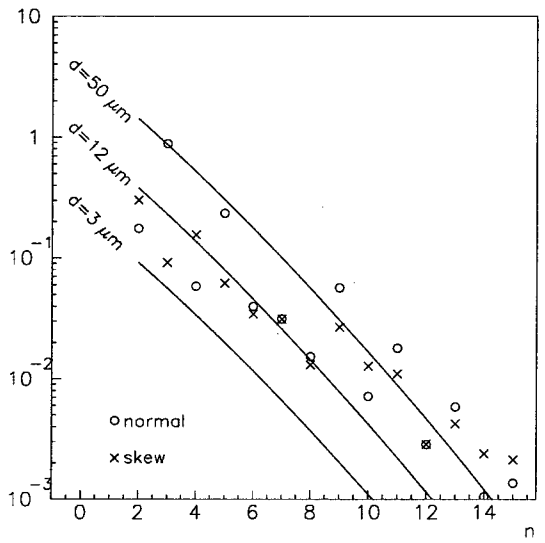

Figure 3: Multipoles of dipole MBL1N1 versus harmonic order n. Circles and crosses: r.m.s. of the multipoles computed for 22 values measured along the axis in both apertures, versus multipole order n. Solid lines: r.m.s multipoles obtained from scaling laws based on random displacements of blocks. Harmonics are given in 10^{-4} units at $17mm$ reference radius.

Disregarding the peaks of the b_3 and b_5, related to the systematic effect described in section 3, the other measured multipoles up to b_8 are consistent with random displacements of blocks with a sigma of around 12 μm (see Fig. 3), or equivalently of random displacements of superconducting wire conductors whose sigma is around 25 μm [3]. High order multipoles (from b_9 onward) seem in both cases to be larger compared to the scaling law. Anyway, these high order multipoles are rather low in absolute value and therefore should not endanger the particle dynamics. Similar results hold for the other magnets MBL1N2 and MBL1J2. One can observe that since the error patterns are very similar, the three models feature the same behaviour, both from a qualitative and from a quantitative view point. Contrary to the effect on normal sextupoles and decapole discussed in the previous section, that should be easily corrected, the multipole shifts discussed in this section are very hard to cure, since they are induced by the displacement of several blocks, and since different displacements are observed in different transversal sections of the magnet.

5 CONCLUSIONS

The variation in the multipolar content of three 10 m-long model LHC dipoles before and after training cycle is analysed. The systematic change of normal sextupole and decapole is explained in term of an outward radial shift of around 50 μm of the four blocks 5, 10, 15, 20, symmetrically located in Fig. 2. The contact between these blocks and the collar is eventually too weak during manufacturing as confirmed by the analysis of the Fuji paper inserted in one of the long models. This effect could be cured by guaranteeing a complete contact between collars and inner coil during collaring. We have already indications that 6-block coil design and an improved collaring procedure at an advanced state of specification are sufficient to fulfil this requirement.

The changes of the other multipoles are interpreted in terms of a random displacement of all blocks. Experimental data are compatible with simulations where the random displacement of the block has an r.m.s. value of 12 μm. This provides an useful order of magnitude of the coil movements that can be expected during the first powering cycle.

Finally, we remark that all the three models show very similar features, both for the systematic and for the random effects. In fact, in terms of field quality it seems that the three analysed magnets are equivalent.

We would like to thank A. Devred, D. Giloteaux, R. Gupta, D. Leroy, M. Modena. D. Perini, S. Russenschuck, G. Spigo, D. Tommasini, J. Vlogaert, and C. Wyss.

6 REFERENCES

[1] R.Gupta et al. These Proceedings.

[2] J. Billan et al., *EPAC* **99**, (1999) 2041–3.

[3] O. Pagano, W. Scandale,E. Todesco, *LHC Project Note* **180** (1999).

[4] S. Russenschuck, *LHC Project Report* **159** (1997).

[5] M. Modena, private communication (1999).

SEXTUPOLE CORRECTION MAGNETS FOR THE LARGE HADRON COLLIDER

R. B. Meinke#, W. M. Hinson, M. Senti, Advanced Magnet Lab, Inc. Palm Bay, FL
W.J. Op de Beeck, C. De Ryck, SMCE NV, Heist-op-den Berg, Belgium

Abstract

About 2,500 superconducting sextupole corrector magnets (MCS) are needed for the Large Hadron Collider (LHC) at CERN to compensate persistent current sextupole fields of the main dipoles. The MCS is a cold bore magnet with iron yoke. The coils are made from a NbTi conductor, which is cooled to 1.9 K. In the original CERN design 6 individual sub-coils, made from a monolithic composite conductor, are assembled and spliced together to form the sextupole. The coils are individually wound around precision-machined central islands and stabilized with matching saddle pieces at both ends. The Advanced Magnet Lab, Inc. (AML) has produced an alternative design, which gives improved performance and reliability at reduced manufacturing cost. In the AML design, the magnet consists of three splice-free sub-coils, which are placed with an automated winding process into pockets of prefabricated G-11 support cylinders. Any assembly process of sub-coils with potential misalignment is eliminated. The AML magnet uses a Kapton-wrapped mini-cable, which allows helium penetration into the vicinity of the conductor, increasing its cryogenic stability. Eliminating all internal splices from the magnet significantly reduces heat loads and the risk of magnet failure during operation. A tested prototype reached the critical current limit of the conductor in the first quench.

1 INTRODUCTION

In the LHC, currently under construction at CERN, each bore of the main bending dipole is equipped with a superconducting sextupole (MCS) corrector magnet to enable compensation of systematic sextupole errors in the dipole field. About 2500 sextupole magnets of this type are needed for the accelerator.

In the original CERN design [1] the MCS magnet consists of six coils, which are individually wound and then assembled and spliced to form the required sextupole. Twelve MCS prototypes of this kind have been manufactured and tested. All magnets showed significant training behavior at 1.9 K and unacceptable heat loads from the conductor splices [2].

This paper describes an alternative design of the MCS sextupole developed by the AML under contract of CERN. The sextupole has significantly improved quench performance, uses stronger insulation to avoid electrical shorts in the coil, eliminates all internal splices in the magnet, and uses an automated coil winding process to guarantee reliable mass production at a minimum manufacturing cost. Key features of the new design and results form the first tests are presented in this paper.

Email: rmeinke@magnetlab.com

2 SEXTUPOLE DESIGN

2.1 Original CERN Design

The key parameters of the MCS sextupole are summarized in Table 1 [1].

Table 1: Main parameters of MCS sextupole

Item	Unit	Value
Field gradient	T/m^2	1657
Integrated field at 10 mm	T m	0.0187
Nominal current	A	550
Effective length	mm	113
Overall Length	mm	160
Bore of magnet	mm	60
Operating temperature	K	1.9

The sextupole consists of six sub-coils, each occupying an exact 60° cylindrical sector. The individual coils are wound as double pancake coils around a precisely machined central G-11 island (see Figure 1). At the two ends of the coils, G-11 saddle pieces are placed to impart rigidity and to serve as a support for the lead end connections.

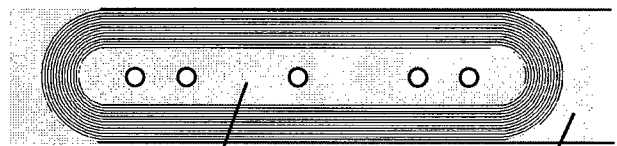

Figure 1: Sketch of individual sextupole coil of original CERN design.

A rectangular NbTi conductor with a Cu/SC ratio of 1.6 and bare dimensions of 1.13×0.61 mm^2 is used for the coils. The conductor is insulated with thin layer (0.06 ±0.01 mm) of Polyester-imide. The coils are wet wound and then cured at a slightly elevated temperature.

0-7803-5573-3/99/$10.00@1999 IEEE.

Six coils are aligned on a mounting fixture and glued together at their mating faces to form the sextupole. A premachined tube of insulating material is glued over this assembly. The conductors from the individual coils are spliced together to achieve a series connection of the six coils. The whole assembly is surrounded by a laminated soft iron yoke and inserted in an aluminum shrink cylinder.

2.2 AML Sextupole Design

Under contract of CERN the Advanced Magnet Lab, Inc. in Palm Bay Florida has developed an alternative design of the MCS sextupole and produced two prototype magnets.

The coils are wound from a NbTi round mini-cable with 6-around-1 strands. Important parameters of the used conductor are summarized in Table 2.

Table 2: Superconducting cable parameters

Item	Unit	Value
Number of wires		7
Wire diameter	mm	0.33
Filament diameter	μm	10
# filaments / wire		310
Cu/SC ratio		2.5 ± 0.1
Twist pitch	Twist/cm	1.06
Diameter bare	mm	0.99
Diameter insulated	mm	1.07
Icrit at 5 T, 4.2 K	A	476

In contrast to a conductor with rectangular cross section, the round cable can be easily bent in any direction. This feature significantly simplifies the winding process, and in particular facilitates the manufacturing of coil ends. A rectangular conductor requires complex, constant-perimeter conductor arrangements, which require significant design and manufacturing effort.

The mini-cable is wrapped with Kapton foil (50% overlap), which forms an insulating sleeve around the conductor. The Kapton is mechanically stronger than varnish insulation and the probability of an electrical short in the coil is significantly reduced. Experience with Kapton has shown that slight movements of the conductor inside the insulation do not trigger a quench of the superconductor. Furthermore, helium can penetrate into the Kapton sleeve and make direct contact with the superconductor. It therefore takes a significantly higher energy deposition to trigger a quench in such a coil.

2.3 Coil Design

The conductor layout of the AML coil with the sub-coil interconnections is shown in Figure 2. Each sub-coil has two layers; the inner layer is wound from the outside towards the inside of the coil and the outer layer from the inside back to the outside.

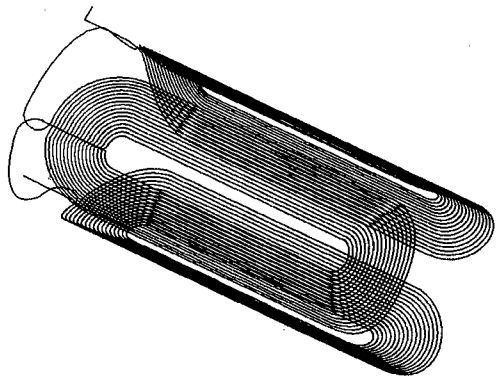

Figure 2: Coil cross section of AML designed MCS coil. For reasons of clarity only one conductor layer is shown.

A fiber-reinforced tube with the required inner magnet diameter is used as a coil support. Pockets are machined or molded into this tube to accommodate 3 sub-coils that form the sextupole magnet. The outer diameter of the support tube is chosen to be flush with the conductor of the inserted coils. The bottom of the pockets have a wall thickness of about 0.5 mm to guarantee good mechanical stability of the coil assembly (see Figure 3).

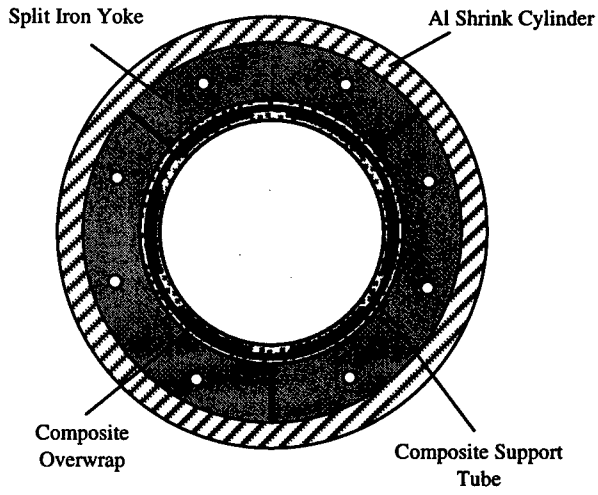

Figure 3: Cross section of MCS designed by AML.

The coils are directly wound into the machined pockets of the support tube, using AML's "Direct Adhesive" coil winding technology. In this winding process the conductor

is precisely placed with the help of a multi-axis robot and instantaneously bonded to the support structure. Adhesive for conductor bonding inside of the coil is automatically added during the winding process. The coils are wound with a continuous conductor; the leads from one sub-coil to the next are placed and stabilized in grooves of the support tube.

The common support tube for the three sub-coils and the continuous winding process, automatically yield a precise alignment of the individual sub-coils relative to each other.

Remaining gaps between the coils and the walls of the support tube pockets are filled with epoxy putty to avoid any movement of the conductor during current excitation. The support tube with the inserted coils is over-wrapped with epoxy impregnated fiberglass and cured at an elevated temperature. The result is a precise, very stable coil assembly, which contains all required interconnections. AML used its own adhesive systems for coil winding. Standard cryogenic tests [3] of the CERN proposed epoxy-resin system, AW 106 and HV 953 U Hardener from CIBA, showed severe cracking in the first shock cycle, while 25 cycles without cracking are recommended.

The outer surface of the overwrap is machined to precisely fit the laminations of the surrounding soft iron yoke (see Figure 3).

The laminations are divided into 120° sections, which leave small gaps between them. These gaps close when the magnet is cooled down and the outer aluminum shrink cylinder puts the coil assembly under radial pressure.

3 TEST RESULTS

The first test coil without iron yoke, but equipped with an aluminum shrink cylinder underwent quench tests at CERN. Three test series at different temperatures were performed with warm-up cycles of the coil between tests. The test results are shown in Figure 4.

The coil reached the critical current of the conductor in the first quench and shows no significant variation in quench current thereafter. The current ramp rate was 10 A/sec throughout the tests.

The second magnet, which was equipped with an iron yoke, showed unexplained ramp rate dependence in a preliminary test and will be retested.

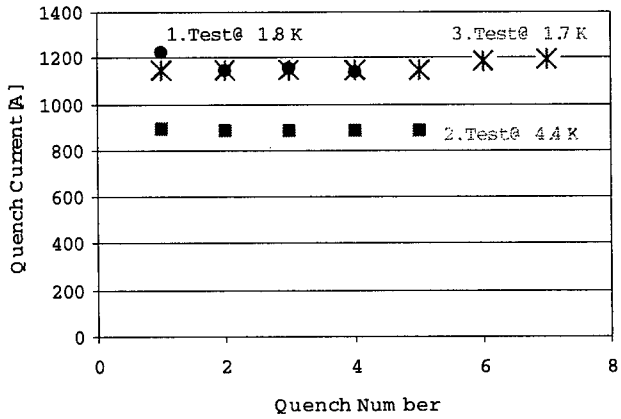

Figure 4: Quench test results of 1 test coil.

4 SUMMARY

The MCS sextupole magnet, designed by AML for the LHC project, offers the following improvements over the original CERN design. The used mini-cable offers better quench performance since each conductor strand is surrounded by helium, which penetrates into the Kapton insulation surrounding the cable. The round, flexible cable simplifies the coil ends, can be used in an automatic winding process, and the redundancy of conductors in the cable improves the reliability of the magnets.

The proposed design eliminates more than 12,500 splices in LHC for the sextupoles alone and solves the heat load problem of the previous CERN design. The applied coil manufacturing technology significantly simplifies the magnet assembly process by eliminating any sub-coil alignment and assembly process.

The new AML design offers magnets with improved quench performance, reduced heat loads, and better operational reliability. The simplified manufacturing process and the automated coil winding reduce the overall cost of these magnets. The proposed design and manufacturing technology is directly applicable to the more than 2,500 decapoles needed for LHC.

5 REFERENCES

[1] Technical Specification of the Sextupole Corrector Magnet", CERN/LHC-ICP/JS/98-001.

[2] J. Salminen et al. "Experience with the Fabrication and Testing of the Sextupole Superconducting Corrector Magnets for the LHC", MT-15 Proceedings, Oct. 1997.

[3] A.B. Brennan et al, "Epoxy Materials for Improved Performance at 4 K", Proceedings of the International Workshop "High Magnetic Fields: Applications, Generation, Materials, 1996.

CONCEPTUAL DESIGN OF SUPERCONDUCTING QUADRUPOLE ARRAYS FOR HEAVY-ION FUSION *

R. B. Meinke#, Advanced Magnet Lab, Inc. Palm Bay, FL
A. Faltens, R. O. Bangerter, Lawrence Berkeley National Lab, Berkeley, CA

Abstract

Extensive studies have been performed to optimize the design of superconducting quadrupole arrays for beam transport in future heavy-ion fusion accelerators. In these arrays 20 or more quadrupole coils are densely packed with their axes aligned in parallel. Field strengths between 3 and 5 tesla at the inner coil diameters have been investigated. The aperture of the individual quadrupoles has been varied between 60 and 240 mm. The coils have a typical length of 1 m, and special effort has been made to minimize the length of the interconnect region between the array and adjacent accelerator components. The relative orientation of quadrupoles in the array is chosen to optimize field sharing between neighboring cells. Field uniformity in the boundary cells is maintained by placing concentric correction coils onto these cells. A conceptual cryostat design, which minimizes heat loads on the cryogenic system, has been analyzed. Since Inertial Fusion Energy has to compete with other long-term energy sources, cost and reliability of these magnets are major issues. The presented design uses a round NbTi mini-cable, which allows for a cost-effective, highly automated manufacturing of the required superconducting coils.

1 INTRODUCTION

Conventional accelerator technology meets the requirements of drivers for inertial fusion energy production. Existing accelerators operate reliably 24 hours/day with lifetimes of more than 40 years in densely populated areas and yield high pulse repetition rates with high efficiency. Beams in accelerators are transported in high vacuum, using magnetic dipoles for beam steering and quadrupoles for focusing. For fusion, the beam current for a given aperture and quadrupole strength is limited more by space charge effects than by emittance. The necessary beam currents for fusion drivers can only be achieved by using 20 or more beams in parallel [1]. Beam transport in such an accelerator with many parallel beams requires arrays of quadrupoles, which furnish the necessary number of parallel focusing channels.

The work presented in this paper addresses these issues for the superconducting quadrupole arrays. An array has been designed that meets the technical specifications of a fusion driver. The individual quadrupole cell is value-engineered by considering all costs from materials to manufacturing technology. The developed design is scalable over an inner coil diameter (ID) from 60 to 240 mm and in field strength at the coil ID from 3 to 5 tesla. A cost model developed for this design can be used in a global accelerator optimization to find the most cost-effective parameters of the quadrupoles.

Using the value-engineered quadrupole, an array has been designed that optimizes flux sharing between the individual cells. Required field quality in the boundary cells of the array is achieved with the help of small correction coils that are directly wound onto these outer cells. A conceptual design of the cryostat has been produced, which guarantees good relative alignment of the quadrupoles and has low heat loads at 4.2 K.

2 INDIVIDUAL QUADRUPOLE CELL

2.1 Superconductor

The coils are wound from a NbTi round mini-cable with 6 around 1 strands. A round cable is less expensive than a Rutherford type cable, shows no significant degradation in critical current density due to the cabling process, and is easier to handle in coil winding since it can be bent easily in any direction. The parameters related to the cable are listed in Table 1.

Table 1: Cable Parameters

Item	Value	Unit
Number of Strands	7	
Strand Diameter	0.65	mm
Cable Diameter	~2	mm
Cu/SC ratio	2.5/1	
Critical Current @ 4.2 K, 5 tesla	3,100	A/mm^2
Insulation	Kapton wrap	

In the accelerator the quadrupole arrays will not be adjacent to each other, and the magnet current has to be routed through an external transfer line to the next magnet. It is therefore advantageous to operate the magnets at

* This work was supported in part by U.S. Department of Energy under contract No. DE-AC03-76SF00098.
# Email: rmeinke@magnetlab.com

a relatively low current. The round mini-cable has the additional advantage that the splices between the individual coils of the array are easier to make and require less space than would be needed for a Rutherford type cable. This is of particular importance for the quad arrays since only about 250 mm are available at both ends of the magnet for the connection to adjacent accelerator components.

The operational parameters of the magnet are summarized in Table 2.

Table 2: Operational Parameters

Item	Value	Unit
Nominal Current	2,366	A
Safety Margin	20	%
Operational Temp.	4.35	K
Critical Temp.	4.78	K
Current Density in Cu	1,200	A/mm^2

With a strand diameter of 0.65mm, the cable diameter is about 2 mm. It is assumed that the critical current of the conductor is 3,100 A at 4.2 K and 5 tesla, which is the best conductor currently available. The nominal current is 2,366 A.

2.2 Coil Design

A cross section that is typical for all considered quadrupoles is shown in Figure 1. All coils consist of 5 to 9 layers of conductor, depending on their diameter and field strength.

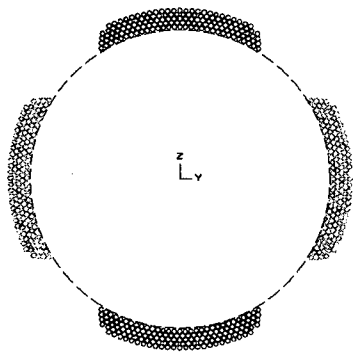

Figure 1: Coil cross section of 4-tesla, 120-mm diameter quadrupole.

The coil is wound onto a fiber-reinforced composite structure (see Figure 2), which rests on a stainless steel (SS) support tube. The coil is totally embedded into a fiber-reinforced composite and then surrounded by an aluminum (Al) shrink cylinder. This structure has sufficient stability to counteract the Lorentz forces during coil excitation in radial and axial direction of the coil.

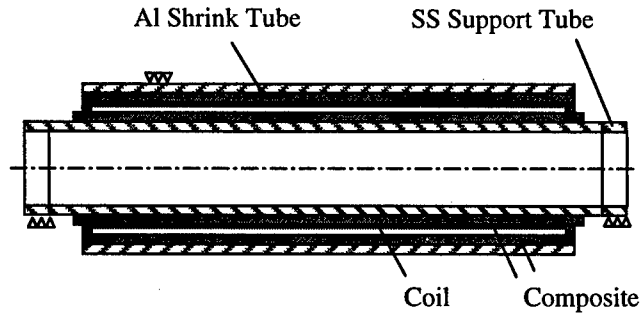

Figure 2: Layout of individual quadrupole coil

The ends of the SS tube are machined to be concentric to each other, and the outer surface of the Al cylinder is machined to be concentric with these ends. These machined surfaces guarantee a precise alignment of the coils in the array.

The coils are wound with an automatic winding machine, which allows placing the round mini-cable into machined pockets in the composite structure. Adhesive for conductor bonding inside of the coil is automatically added during the winding process. The computer-controlled winding process does not only guarantee precise conductor placement, but also yields a very inexpensive manufacturing process of coils with excellent performance [2].

3 ARRAY LAYOUT

The individual coils are assembled to form an array of quadrupoles. A section of such an array with the individual cell orientation is shown in Figure 3.

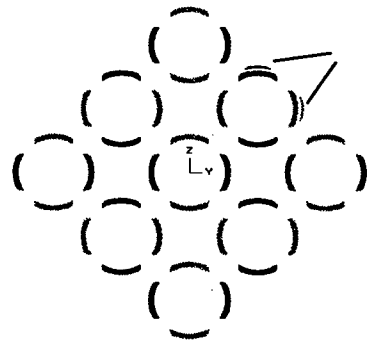

Figure 3: Arrangement of cells in the array. One boundary cell equipped with correction coils.

3.1 Flux Sharing

Since the coils are in close proximity to each other flux penetrates into neighboring cells. The relative orientation, indicated in Figure 3, enhances the flux in neighboring cells, and about 30% of the fields in any cell are due to flux from its neighbors. The cells in this arrangement

yield both, horizontal and vertical focusing, which can be accommodated in the accelerator lattice. Because the channels are dependent on each other, a completely separate lower-field iron core array consisting of correction coils is required for independent beam steering.

3.2 Edge Termination

Cells at the array boundaries have no neighbors on one side and a strong dipole field component results. This could be corrected with dummy cells at the edge of the array. A more cost-effective edge termination scheme is indicated for one of the boundary cells in Figure 3. A small correction coil wound with the same conductor and in series with the main coil totally corrects the field in this cell.

A superconducting shield, which surrounds the whole array at a certain distance, is under consideration. Persistent currents induced into this passive shield would automatically arrange themselves in such a way that the flux at the outside of the shield is zero. This shield would eliminate any magnetic effect on neighboring accelerator components.

4 CRYOSTAT

4.1 Cell Support

The individual quadrupole coils are held in place by large aluminum carrier plates. As indicated in Figure 4 the individual coils fit into precisely machined holes in the carrier plates. The 10-mm thick plates are spaced with gaps of 75 mm width along the axes of the coils. The plates hold and align the individual coils, and strengthen the Al shrink cylinders. SS alignment keys position the carrier plates relative to each other.

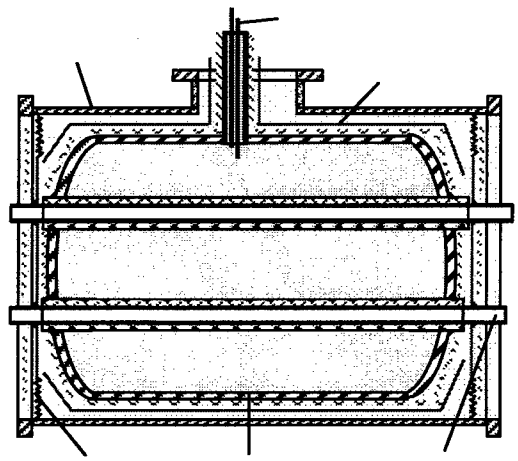

Figure 4: Schematic layout of cryostat. For reasons of clarity, only two beam tubes are shown.

Al is chosen as a material for the shrink cylinders and the carrier plates because of its thermal contraction, which is larger than SS. During cool down of the coils the Al shrinks more than the SS support tubes and puts the superconducting coils under compression.

An SS cylinder around the carrier plates forms the helium containment vessel. This cylinder is closed at both ends with SS end plates, which are welded helium-tight to the SS support tubes. Due to the strengthening by the SS tubes, thin straight end plates are sufficient for this pressure vessel, which has to take the overpressure with sufficient safety margin from gaseous helium during a quench. The straight plates help to reduce the total length of the array.

A radiation shield and blankets of superinsulation surround the helium containment vessel. Struts are used as a support inside of the outer vacuum vessel, which is evacuated to achieve thermal insulation.

4.2 Beam Tube

Beam tubes are inserted into the SS coil support tubes to maintain low residual gas pressure for beam transport. The beam tubes have to be operated at 77 K, the temperature of the thermal shield, to reduce their heat load into the superconducting coil to an acceptable level. With a beam tube polished on the outside and the SS support tube on the inside no superinsulation is required, and the heat load due to thermal radiation from up to 50 beam tubes is less than 1 watt.

5 SUMMARY

Superconducting quadrupole arrays for a future heavy ion fusion accelerator have been designed. The scalable coil design allows variations of aperture from 60 to 240 mm and fields at the coil ID from 3 to 5 tesla. The novel coil design significantly reduces cost in comparison to conventional collared coils made from Rutherford type cable. A cost model has been developed that allows one to identify the most cost effective parameters for the quadrupole array. A preliminary design of the array cryostat has been developed that minimizes space requirements along the array axis and has heat loads comparable to existing high-energy physics accelerators.

6 REFERENCES

[1] Proceedings of 12th International Symposium on Heavy Ion Inertial Fusion, Heidelberg, Germany, September 1997, Nuclear Instruments & Methods in Physics Research (Section A) – VoL. 415 (1998) Nos. 1,2, pp. 1-508.

[2] R.B. Meinke et al., "Sextupole Correction Magnets for the Large Hadron Collider", submitted to this conference.

SOME FEATURES OF SUPERCONDUCTING DUAL BORE LENS*

A. A. Mikhailichenko
Wilson Laboratory, Cornell University, Ithaca, NY 14850†

Abstract

Design of dual bore superconducting quadrupole for CESR upgrade is represented. The lens has a gradient about 1 kG/cm, dual aperture of 54 mm each, length about 800 mm, The axes spacing about 80 mm allows a good separation of counter rotating beams. Harmonics content measured below 0.05%. Some concepts used in this dual bore lens could be used for design of any multi aperture lens, where the high field quality required.

1 INTRODUCTION

Cornell storage ring CESR finished Stage II upgrade, achieved highest luminosity what exceeds now $L \cong 7 \cdot 10^{32}$ $cm^{-2}s^{-1}$. After the Stage III is finished, the luminosity will increase up to $3 \cdot 10^{33}$ $cm^{-2}s^{-1}$. More drastic increase is expecting after Stage IV is finished [1-3], Fig. 1. This Stage when completed will allow to have at least 180 counter rotating bunches $3x3A^2$ total in individual vacuum chambers. The beams having equal energies will deliver a 25 $fb^{-1}month^{-1}$ with $L \cong 3 \cdot 10^{34}$ $cm^{-2}s^{-1}$. The vacuum chambers will share wide aperture room temperature dipole magnets and will have dual bore superconducting magnets. These superconducting magnets include dual bore quadrupole, dual bore sextupole, and dual bore dipole correctors. Also some dual bore octupoles or skew quadrupoles will be used instead of dipole correctors. All three types of these magnets will share the same cryostat and considered as one unit. About 88 such units together with 156 regular arc dipoles will be installed on the top of existing synchrotron, Fig.1. These new rings will be feed directly from this synchrotron, allowing CESR as a dedicated synchrotron source.

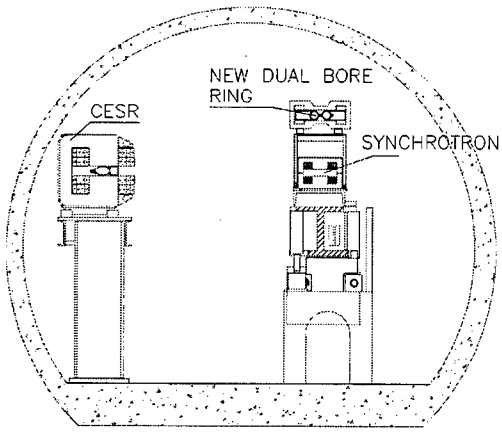

Figure 1: The tunnel cross-section.

Utilization of CESR as a *booster* between synchrotron and this new dual bore machine could bring the luminosity further up to $L \geq 10^{35}$ $cm^{-2}s^{-1}$ level.

Extreme beam parameters yield extreme requirements to the magnet and vacuum system design. These requirements are the field quality, ability to work under extreme expose to SR and closest position of the beams axes. The last required for minimal dipole magnet cross-section.

In this publication we describe a dual bore quadrupole lens design and results of its test. This quadrupole magnet itself was tested in a Dewar up to 200 A feeding current [2,5]. The test showed that the field accuracy required has been achieved [5]. Now mostly attention was paid to a *cryostat*, holding the cold mass with dual bore magnets. The vacuum chamber of superconducting magnet must hold about 2 kW/m of SR power in normal operation. This fact strongly complicated the design.

For normal operation the number of current leads from room temperature to the cold mass is twelve per magnet unit. Utilization of High Temperature Superconductor (HTS) leads is crucial here. We are planning to compare the HTS leads manufactured by Hoechst Company and American Superconductor.

Results obtained in the test described will be used for a final magnet design.

2 QUADRUPOLE CONCEPT

Each of quadrupoles is a combination of two quadrupole magnets that share the same iron yoke. Axes separation needs to be as small as possible. Technical limitations make this distance about 80 mm. The field quality required for the quadrupole is about $[B_y(x) - G \cdot x]/G \cdot x \leq 5 \cdot 10^{-4}$, where $B_y(x)$ is the field across the aperture, G is a gradient. When dual bore lenses shared the same yoke and placed close one to another, some magnetic lines travel around both centers, Fig.2. So in the presence of neighboring lens, magnetic lines *lose its quadrupole symmetry in the yoke*, and, hence in all lens. Now *not* only quadrupole-associated harmonics allowed. Dipole and sextupole components are the strongest among allowed now. The same happens, sequentially, for the whole lens. Proper modeling includes the lowest symmetry piece taking into account this effect [5]. So one needs to have ability for effective compensation of this effect. This mechanism needs to be simple and effective. The lenses, where the poles *and* the coils acting *together* for the field generation were chosen finally for the next

* Work supported by National Science Foundation
† Phone: (607) 255-3785, Fax: (607) 255-8062, e-mail: mikhail@lns62.lns.cornell.edu

0-7803-5573-3/99/$10.00@1999 IEEE.

stage of CESR upgrade. This type of lens was suggested in [4]. The superconducting coils used there are a racetrack type of single layer windings.

For the requirements of the beam optics the gradients in both neighboring lenses have the same sign and about the same value. So the neighboring currents on the sides of the septum have the same value. The last yields that vertical component of magnetic induction in the iron septum is absent practically.

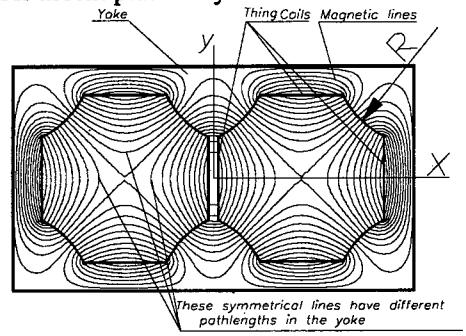

Figure 2: Magnetic lines in dual bore lens. Windings are single layer racetrack coils, which cross-sections are thin in the drawing's scale. They occupy the whole straight sides. The gradients in both lenses have the same sign. The distance between quadrupole axes is 79 mm. Yoke septum is 4 mm. Printout from MERMAID [6]

Similar behavior has any dual bore symmetrical lens. One can also see from Fig.2, that the lines spaced at the same distance from the center of each quad have different path lengths in the material of yoke. The shortest ways have the lines that travel around currents in the center of the lens. So the region marked as x-y quadrant is minimal for proper modeling.

To compensate this effect, some appropriate non-symmetrical deformation of the poles required. Calculations show, that the accuracy of *fabrication* must be $\delta \approx 8.5 \cdot 10^{-3}$ mm. One can see that the profile is rather complicated. In simplest case, however, when an arc of constant radius approximates hyperbola, the arc radius of the left and right poles could be made slightly *different*, keeping the vertex of the arcs in the same place. We keep the radiuses of all poles *the same*, but different from one, obtained, when one lens is far apart from neighboring one. Below we represent the graphs of *absolute* deviation of the field for different pole radius. Absolute value of gradient is also slightly different in each case. The smallest deviation from linear law indicates the lens with the pole radius of 37.45 mm. Maximum deviation of 0.15 Gauss occurs at distance 2.25 cm. Magnetic field value, associated with pure quadrupole having gradient $G = 1.075$ kG/cm (for this particular radius and for 6 kA/coil) is 2.4187 kG. So, relative deviation in this point is $0.15/2418.7 = 6.2 \cdot 10^{-5}$. Namely this radius was chosen for manufacturing.

At the end of the lens some soft iron shields made. They prevent the field interference from neighboring lenses.

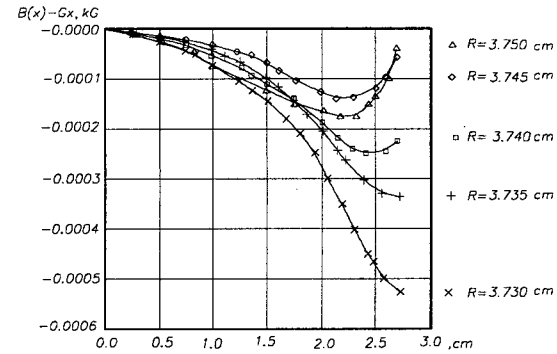

Figure 3: Calculated field deviation (in *kG*) from linear behavior for different pole radius (R in Fig.2).

The lens was fabricated and tested. Results of measurements are represented in Fig. 4.

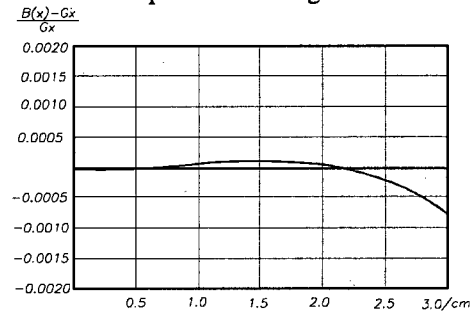

Figure 4: Measured relative field deviation in one of the dual bore aperture. *G=1.075kG/cm.*

The graph plotted is a reconstruction of a vector sum of different harmonics measured in assembled dual bore magnet. These measurements were carried out in a Dewar. Warm long coil was rotated inside the space arranged with two coaxial stainless steel tubes going through the magnet, see [2].

3 CRYOSTAT

Cryostat serves as a vessel for liquid Helium with cold mass in it. Supposed that the Helium/Nitrogen duct running along the ring will have the branches to each magnet. The cryostat concept is shown in Fig. 5. Mostly crowded place here is inner region. SR is accepted by the inner chamber made on two coaxial copper tubes having the gap about 1.5mm for the water flow in between. The thickness of the copper tubes is about 1.5mm also. The inner chamber is made removable. This inner chamber wrapped by superinsulation. The next 1.5 mm thick tube is a part of a Nitrogen shield and also wrapped by superinsulation. Cooling of these last tubes is going through the ends. The vacuum chamber of the ring and the vacuum volume inside the cryostat are independent. The next tube is a part of Helium vessel. All tubes are polished to a mirror shine. Design of supports (hatched in Fig.5) allows shrinkage of the length keeping the central part of quadrupole in fixed position. It allows positioning of cold mass and Nitrogen shield in the cabinet also. HTS leads at cold end bolted to feeds- through into liquid

Helium vessel and at the other side bolted to the Nitrogen shield with thing layer of mica for electrical insulation.

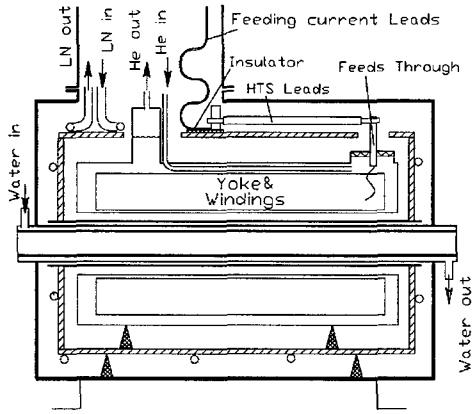

Figure 5: Basic principles of cryostat design.

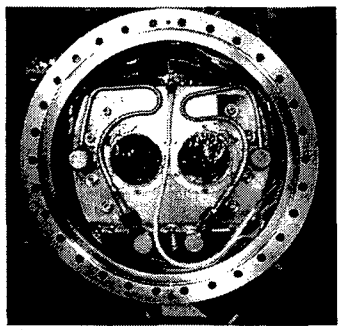

Figure 6: Inside view to the cryostat. Here one can see a Nitrogen temperature shield with tubing. End flange and superinsulation removed. Inner diameter is $\cong$ 10 inches. One can see here two independent apertures.

The cryogenic test proved the principles. The magnet was attached to the existing system for Superconducting RF cavity feed. This system includes both liquid Helium and Nitrogen tubing. The necessary cooling was achieved. Vacuum inside the cryostat goes to 2.8 10^{-8} Torr as a result of cryocooling. In this test the HTS leads made by American Superconductor were used. These leads are 16" long and must have a critical current of 150 A. The feeding of the lens with current showed however, that the current of 25 A yields a loss of HTS ability to carry the current. This was explained by inadequate cooling of HTS leads. The latest modification done includes the increase of cooling of HTS leads. Also done some improvements in pressure relief system, in monitoring the pressure inside the cold mass, in measuring the temperature of cold mass and Nitrogen cooled shield. In nearest future we will continue the test of the cryostat. Modeling of SR deposition will be done with a special heater located inside the vacuum chamber.

4 CONCLUSION

The nonlinarities arisen from broken quadrupole symmetry into iron can be taken into account by proper choice of problem for modeling. The set of tests done proved the principles of design made. More attention to the proper cooling of HTS leads was stressed.

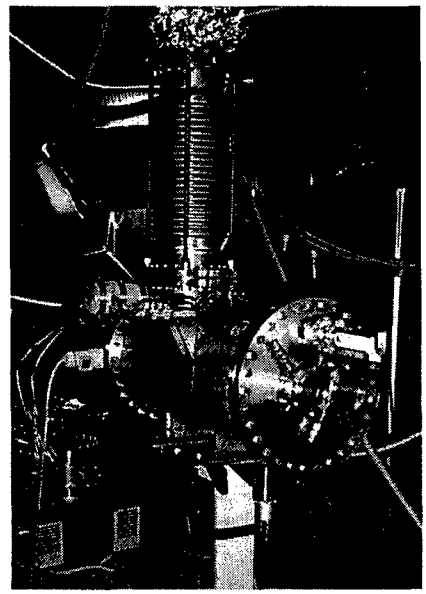

Figure 7: Dual bore magnet installed in a cryostat for cryogenic test. In a vertical bellow there are joints to existing cryogenic system. The joints to a duct line running along the ring will be located there in a future.

The same ideas of cancellation interference were applied to other dual bore multipole elements (such as sextupole, skew quadrupole, octupole and dipole corrector) of the ring. Serially installed quads and sextupoles in each module also may give the way for adjustment the resulting field quality for whole unit.

Mostly strong interference occurs at the magnet dual edge. Solution of this problem in application to the dual bore magnet was found and proved experimentally in this design.

5 REFERENCES

[1] D. Rubin, M. Tigner, *Shared bends and Independent Quadrupoles*, Cornell CON 94-28, 1994.

[2] A. Mikhailichenko, D. Rubin, *Concentric Ring Colliding Beam Machine with Dual Aperture Quadrupoles*, Cornell CLNS 96-1420, 1996.

[3] G. Dugan, A.A.Mikhailichenko, J. Rojers, D. Rubin, *Dual Aperture High Luminosity Collider at Cornell*, Talk on Particle Accelerator Conference PAC 97, Vancouver, B.C. Canada, 12-17 May 1997, 6B10. Proceedings, p. 318.

[4] A. Mikhailichenko, *3D Electromagnetic Field. Representation and measurement*, CBN 95-16, Cornell, 1995.

[5] A. A. Mikhailichenko, *Some peculiarities of Magnetic Field Behavior in Dual Bore Magnets*, CBN 97-32, October17, 1997, Cornell.

[6] MERMAID --MEsh oriented Routine for MAgnet Interactive Design, SIM Limited, Novosibirsk, P.O. Box 402, Russia.

CESR Phase III Interaction Region *

S. Henderson, J. J. Welch †, M. Billing, G. Cherwinka, G. Codner, G. Dugan, S. Greenwald, Z. Greenwald, Y. Li, W. Lou‡, N. Mistry, E. Nordberg, D. Rice, S. Roberts, D. Rubin, A. Temnykh, Cornell University, Ithaca NY
D. Cinabro, L. Perera, Wayne State University, Detroit MI

The goal of the third phase of the CESR/CLEO upgrade is to take the CESR luminosity as far as one can go with a single-ring collider [1]. We expect CESR's luminosity to more than double from the present 8×10^{32} cm^{-2}s^{-1} to 1.7×10^{33} cm^{-2}s^{-1} as a result of the Phase III upgrade.

In the present configuration of CESR (Phase II) trains of closely spaced bunches collide at a small horizontal crossing angle ($\theta_c \simeq \pm 2$ mrad). The Phase III upgrade program relies on increasing the colliding beam current from the present 0.5A to 1A by exploiting bunch-train collisions to the fullest extent possible. The Phase III design calls for colliding 9 trains of bunches, each of which consists of 5 bunches spaced by 14 ns.

The closely spaced bunches in a train generate crossing points close to the interaction point (IP) where bunches from opposing beams pass by one another and interact. To ameliorate the destructive effects of these long range beam-beam interactions new interaction region (IR) optics are required. A combination of short focal length and large physical aperture are optimum in this respect, and best implemented with insertion optics consisting of two pairs of high-gradient superconducting (SC) quadrupoles and a pair of short permanent magnets. The IR quadrupoles will be positioned with a precision beam-based alignment system to ensure stable closed orbits and reduce commissioning time. The SC magnet package also includes skew quadrupole magnets for detector solenoid compensation and dipole magnets to provide precise alignment of the magnetic centers within the physical aperture of the vacuum chamber.

In order to handle the increased heat loads and detector backgrounds new detector shielding and IR vacuum chambers are being constructed. The design of the machine-detector interface was based on our experience with the CESR Phase II IR [2]. In order to facilitate installation and maintainence a remotely actuated vacuum seal called the "magic flange" has been developed and built. We plan to install the Phase III IR hardware in mid-2000.

The new interaction region is ideal for various possible future upgrade paths which could take CESR into the 10^{34} cm^{-2}s^{-1} luminosity range. For example, a two-ring upgrade [3] would use the large aperture for a crossing angle. An upgrade involving smaller β^* would benefit from the short focal length since the peak beta function and chromaticity are thereby reduced. Finally, space for an additional magnet for a round beam insertion optics has been provided as well.

1 OPTICS

The Phase III IR optics, shown in Figure 1, accomodate the various constraints that arise from the required beam separation in the IR, injection considerations and beam-generated detector background requirements.

As mentioned, the challenge for operating with 14 ns spacing between bunches in a train is providing adequate separation at the nearby parasitic crossing points in the IR (spaced at 2.1 m intervals). In order to minimize the long-range beam-beam tuneshifts suffered at these crossings the beam separation to horizontal width ratio must be maximized, and the β-functions at the crossing points must be minimized. The latter feature is accomplished by placing the final-focus quadrupoles as close to the IP as possible so that the $\hat{\beta}$ points are reduced and lie between the IP and the first parasitic crossing point. This solution, made possible only with high-gradient SC quadrupoles, maintains the β-functions at the IR crossing points below 40 m, a value which is comparable to that at crossing points in the CESR

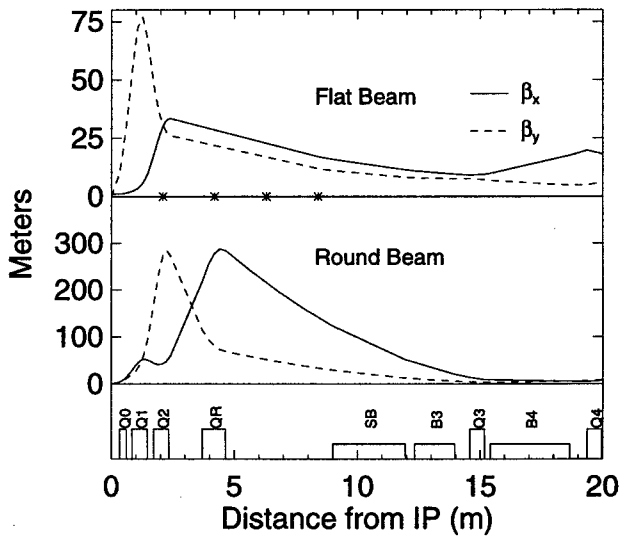

Figure 1: CESR Phase III IR optics with $\beta_y^* = 10$ mm (upper) and round-beam optics (lower). Parasitic crossing point locations are marked with a star. The trim quadrupole (QR) is powered only in the round beam optics.

* Supported by the National Science Foundation
† welch@lns.cornell.edu
‡ presently at ADC Telecommunications, CT

0-7803-5573-3/99/$10.00@1999 IEEE.

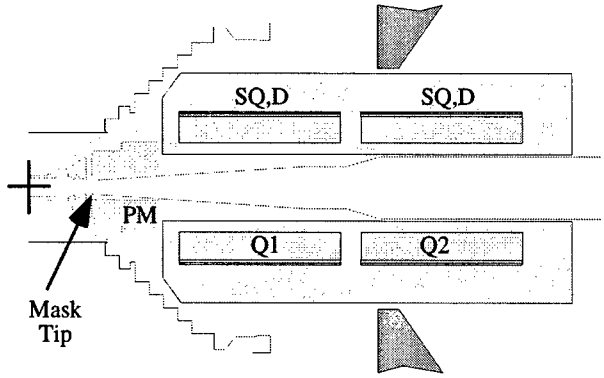

Figure 2: IR layout showing 7 magnetic elements.

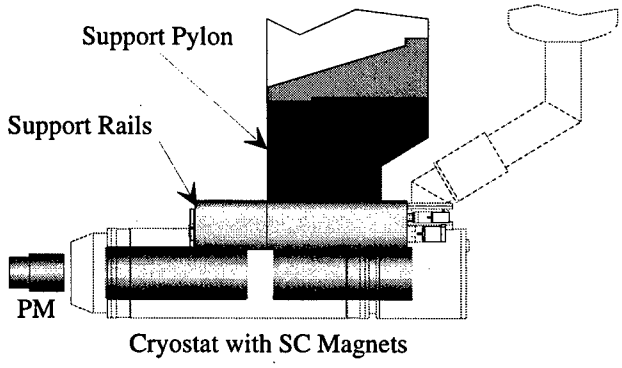

Figure 3: A representation of a cryostat containing two superconducting magnets.

arcs.

Constraints on the machine aperture in the IR arise from injection and detector background considerations. During injection the beams are separated horizontally at the IP with a symmetric electrostatic displacement bump. As a result, increased aperture at Q2 is required. In a crossing-angle orbit, the beam is displaced in the nearby horizontally focusing IR quadrupole (Q2). This off-axis beam generates large synchrotron radiation (SR) fluxes which give rise to detector backgrounds. To minimize backgrounds, a horizontal IP displacement bump is applied, reducing the displacement in Q2 at the expense of increased aperture requirements.

The high-gradient quadrupoles provide considerable flexibility in lattice design. For example, considerable latitude is allowed in choosing $\beta_v^\star$ for optimizing luminosity. Figure 1 shows IR optics for $\beta_v^\star = 10$ mm but optics with $\beta_v^\star$ as small as 7 mm are possible. Further increases in luminosity may be possible with round colliding beams [4]. With the addition of a trim quadrupole, round-beam optics with $\beta_v^\star = \beta_h^\star = 3$ cm, shown in Figure 1, may be realized.

2 INTERACTION REGION MAGNETS

In total there are 14 different magnets arranged symmetrically around the IP that form the insertion optics (see Figure 2). Starting only 337 mm from the IP, vertical focussing (VF) is provided by a short set of permanent magnets (PM). Most focussing, however, is provided by two pairs of strong superconducting main quadrupoles (MQ) which are arranged in doublets called Q1,Q2. Skew quadrupoles (SQ) concentrically wound on top of each of the MQ effectively rotate the main quadrupole field as part of the coupling compensation for the detector solenoid. Dipoles (D) concentrically wound on top of the SQ's generate a horizontal field for vertical adjustment of the quadrupole field axes. The entire insertion optics focussing is contained within ± 2.55 m from the IP.

The PM's are made from Neodymium Iron Boron with intrinsic coercivity H_{ci} of 21 kOe and remnant field B_r of 12 kG [5]. The ID is a constant $\phi 67$ mm but the OD is stepped to take advantage of slightly more radial space available further from the IP. The poles are temperature and magnetically stabilized and then individually selected for uniformity. Despite a temperature coefficient for B_r of -0.1 % $^\circ C^{-1}$, adequate temperature control can be provided with a simple closed circuit cooling loop and bands around the outside of the magnet since the PM only provides about 23% of the total vertical focussing power.

One cryostat is installed on each side of the IP and contains two multifunctional SC magnets [6]. The cryostats are supported and aligned by eccentrically driven cam bearings held by support rails, which are in turn mounted on a heavy steel pylon attached to the CLEO detector steel. (See Figure 3). The cryostat has a warm bore with an ID of $\phi 145$ mm and a maximum OD of $\phi 495$ mm.

All four SC magnets are identical and consist of three independent sets of coils with effective lengths of 0.65 m. The MQ's are capable of gradients of up to 48.4 T/m at 1225 A. The SQ field is about 10% that of the MQ and superimposed on the MQ field. The dipole coils produces a horizontal dipole field with a maximum strength of 0.13 T.

The design of the MQ coils was highly influenced by the recently built LEP 200 Interaction Region quadrupoles [7, 8], especially in choice of bore and conductor. The other SC coils are loosely modeled after corrector magnets under development for the LHC. To improve training and reliability the design current of all magnets is no more than 70% of the theoretical quench current under worst case conditions (multiple coils energized and the presence of the 1.5 T CLEO solenoid field).

Because of the relatively short length compared to diameter, end effects are proportionally more important. Several independent checks were made to be sure the 3D fields from the ends were calculated correctly and the coil design optimized for field quality [9]. The basic specification is that all non-quadrupole and non-dipole field harmonics shall be less than 5×10^{-4} of the quadrupole field measured at a radius of 50 mm.

The SC magnets will interact strongly with the detector solenoid magnetic field. Q1 will be totally within the 1.5 T soleonoid field. The solenoid field and the current in the dipole will generate a very large moment of 12,000 Nm

on Q1. Q2 will have one end in the solenoid fringe field while the other end is essentially field free, resulting in a net horizontal force on Q2 of up to 14,000 N. These forces and moments must be borne by the cryostats and supports, consequently these constructions are made very robust.

3 DETECTOR BACKGROUNDS

Beam-generated detector backgrounds [2] arise from scattered synchrotron radiation (SR) emitted in nearby quadrupoles and bends and from the interaction of beam particles with residual gas in the vacuum chamber ("beam-gas" interactions). Shielding of the detector from scattered SR is accomplished by careful placement of mask tips to shield the detector beampipe from direct SR and to minimize the scattered photons which strike the detector. The principal component is a stepped copper mask whose profile is designed such that SR illuminates only those surfaces which are not directly visible by the detector beampipe. Thus, the only remaining detector backgrounds arise from SR which forward scatters through the mask tips ("tipscattering") or which backscatters from the mask surface just downstream of the beampipe. To further reduce the SR flux entering the detector, the inner surface of the beryllium beampipe is coated with a thin layer of gold. The placement of mask tips and choice of materials was optimized with a detailed simulation of SR backgrounds.

Beam-gas backgrounds arise from Coulomb scattering and Bremstrahlung interactions with residual gas. Only those interactions within ~40 m from the IP contribute to detector backgrounds. Detector shielding for beam-gas backgrounds is provided by the PM quads themselves. Additionally, beam-gas backgrounds are reduced with increased pumping in the IR straight.

The detector background simulations provide an estimate of the detector occupancy in the inner layer of the CLEO-III silicon vertex detector. The detector occupancy predictions from the various sources at full 1 A beam current and $\theta_c = 2.5$ mrad are as follows (in units of $\%/\mu s$): SR - Tipscattering, 0.027 ; SR - Backscattering, 0.012 ; beam-gas Bremsstrahlung, 0.23 ; beam-gas Coulomb, 0.04. The total estimated occupancy is $0.31\%/\mu s$, which is well below the design goal of $1\%/\mu s$.

4 VACUUM SYSTEM

The central detector beampipe (manufactured by Brush Wellman - Electrofusion Products) is a double-walled actively cooled beryllium beampipe which is based on one presently in use at CESR [10]. The beampipe consists of two Be sleeves of thickness 0.013 in and 0.009 in with a 0.017 in coolant gap. The sleeves are sealed with a manifold at each end. The inner sleeve is joined to a copper vacuum pipe through a stainless steel transition. The beampipe, cooled with PF-200, is capable of dissipating 400 W with 5°C temperature rise.

An important component of the SR shielding is a gold coating on the inside of the beryllium beampipe. A 5 μm average thickness coating was applied with a cylindrical magnetron sputtering technique [11]. The total average beampipe thickness is 0.4% radiation length.

The IR vacuum system utilizes several existing components and new components within ±6 m from the IP. IR Pumping [12] is accomplished in large plenums which incorporate massive titanium sublimation pumps. Pumping plenums are located at ±3 m, ±5 m, ±7 m, ±10 m and ±13 m from the IP. The pressure in the IR will be maintained below 3.5 nTorr at full 1 A beam current.

The inclusion of a pair of remotely operable ultra-high vacuum joints about ±30 cm from the IP greatly facilitates the installation and assembly of the IR components. Without this joint, two very difficult field-welds would need to be performed to join UHV flanges to the beryllium beampipe subassembly. The magic flange uses a shaft seal with differentially pumped o-rings (including one which provides the RF seal) in order to eliminate the bulk of the gas load which would arise from permeation. The o-rings have been extensively tested for radiation damage and RF sealing capability. A compact gear-and-nut assembly provides the closing and opening forces in the very small space allowed.

5 REFERENCES

[1] D.L. Rubin, Proc. EPAC 1998, http://www.cern.ch/EPAC

[2] S. Henderson, Proc. Second Workshop on Backgrounds at the Machine Detector Interface, World Scientific, p.6 (1998); also S. Henderson, Proc. Part. Acc. Conf. 1997, Vancouver

[3] A. Mikhailichenko and D. Rubin, CLNS-96-1420, http://www.lns.cornell.edu/public/CLNS

[4] E. Young et. al., Proc. Part. Acc. Conf. 1997, 1542.

[5] W. Lou, et. al., Proc. Part. Acc. Conf. 1997,3236, http://www.lns.cornell.edu/public/CBN/1997

[6] J.J.Welch, et. al., Proc. Part. Acc. Conf. 1997, 3383, http://www.lns.cornell.edu/public/CBN/1997

[7] M. Begg, A. Ijspeert, T.M. Taylor, CERN AT/94-27 (MA), LEP2note 94-14, presented at EPAC 94, (1994)

[8] T.M. Taylor, G. Trinquat, L.R. Williams, IEEE Trans on Magn., vol 28 No 1, pp 382-385, January 1992

[9] G. Dugan, CBN 96-5, http://www.lns.cornell.edu/public/CBN/1996

[10] S. Henderson, Proc. 8th Mtg. of DPF (Albuquerque NM), World Scientific, (1994) 1480.

[11] S. Henderson and S. Roberts, these proceedings.

[12] N. Mistry, Proc. Part. Acc. Conf., 1997, 3559.

QUENCH PROTECTION FOR SUPERCONDUCTING IR MAGNETS IN CESR*

G. Codner+, G. Dugan, W. Lou#, J. Welch
Laboratory of Nuclear Studies, Cornell University, Ithaca, NY 14853

Abstract

Analysis and design details are provided on quench protection for the Cornell Electron Storage Ring (CESR) Phase III interaction region (IR) superconducting magnets. The proposed scheme extracts much of the stored energy thereby reducing thermal stress on the magnets and mitigating liquid helium loss. Protection is somewhat complicated by the fact that each cold mass consists of quadrupole, skew quadrupole and dipole windings, and that each cryostat contains two magnet units.

1 INTRODUCTION

The CESR (Cornell Electron Storage Ring) Phase III Upgrade includes a low beta interaction region that includes several superconducting (SC) magnets [1]. There are two (2) magnet assemblies comprised of two (2) magnet units per assembly. Each unit includes a main quadrupole, a skew quadrupole and a dipole magnet. The three magnets in each unit are integrally wound into as small a space as possible. This paper describes quench detection and protection for these magnets.

2 APPROACH

The CESR SC IR magnets are designed to survive quenches without damage, even without active protection. However, it is prudent to minimize stress on the magnets by detecting quenches and dumping as much of the energy as is practical into an external load. Furthermore, diverting this energy reduces the amount of liquid helium that would be boiled off in the event of a quench, thereby saving time and money. Since it is not necessary to divert all of the stored energy, the simple approach of using a fast, electro-mechanical D.C. switch is used.

CESR quench detection uses the coil voltage comparison method. Since the voltage across a winding that is quenching is relatively low (the voltage across the quench resistance is mostly canceled by $L\ dI/dt$ of the coil), the rate of change of current must be detected, assuming the current regulation loop is slow. The simplest way to do this is to sense the voltage across another coil in the same magnet. Assuming both windings do not quench simultaneously, the changing current due to the quench induces a voltage across the non-quenching coil.

*Work supported by the National Science Foundation

+email gcodner@lns.cornell.edu

#Now with ADC Telecommunications, Shelton, CT

2.1 Calculations

Fundamental calculations were performed [2] to determine the quench resistance as a function of time, the relationship between deposited energy and coil temperature and to find the optimal value of the dump resistor R_d for each magnet. A trade-off must be made between extracted energy and magnet lead voltage. R_d was chosen such that the maximum internal and external voltages during a quench are equal.

For the CESR SC IR magnets, a normal zone bounded in two dimensions after a time t_a is applicable. The magnet's time-dependent resistance during the early part of a quench may be roughly approximated by [3]:

$$R_Q(t) = \begin{cases} \dfrac{3Lt^5}{t_Q^6} & for\ 0 \le t < t_a \\ \dfrac{L\left(15t_a^2t^3 - 15t_a^3t^2 + 3t_a^5\right)}{t_Q^6} & for\ t \ge t_a \end{cases} \quad (1)$$

where t_a and L are parameters determined by the physical characteristics of each magnet coil whereas t_Q depends on the physical magnet parameters and the initial stored energy. Table 1 lists currently predicted or measured values of these parameters for the three types of magnets.

Table 1: Calculated CESR SC IR Magnet Parameters

Magnet Type	t_a [sec]	t_Q [sec]	L♣ [henry]	I_0 [amps]
Main Quad	0.067	0.45	0.244	1225
Skew Quad	0.024	0.12	0.115	325
Dipole	0.047	0.18	0.024	200

♣measured

2.2 Spice Modeling

A circuit model was used to explore the behavior of the detection method and to perform the calculations done in [2] based on the latest information available including measured magnet data, the actual detection circuitry and time delay of the quench switch. These parameters were used in a PSpice model that simulates the growth in quench resistance with time and the action of the detection circuitry and quench switch. The model may also include power supply behavior, for example, fast current regulation.

0-7803-5573-3/99/$10.00@1999 IEEE.

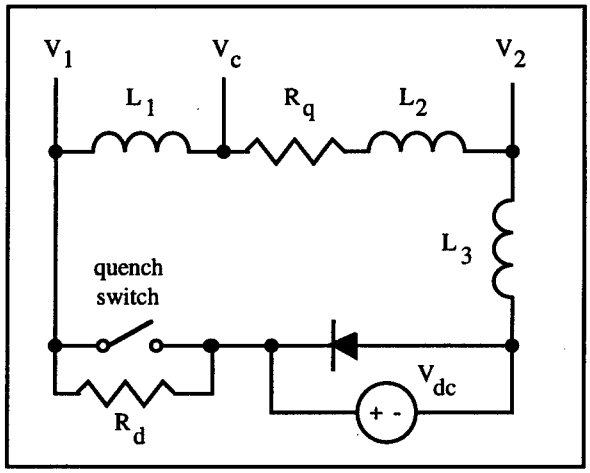

Figure 1: Equivalent circuit of CESR SC IR magnet and quench protection for a quench in coil L_2 (the quench switch is shown in its protection state).

The PSpice model includes the effects of coupling between windings as opposed to a simpler model that considers the total inductance to be split into equal parts for each winding. It was found that coupling was not very important in its effect on quench detection and that the simple model is adequate for these calculations.

Figure 1 shows an equivalent circuit of a magnet during a quench. L_1 and L_2 are coils that are sensed for comparison. A quench in L_2 is represented by time-dependent resistor R_q. The quench switch opens after a quench is detected placing R_d in series with the magnet. In the simple model L_3 represents any other coils in series with the magnet, for example, the other two coils in a quadrupole magnet. The model with coupling uses each coil explicitly.

The standard method of sensing coil voltages uses a common point between two coils. However, a quench that starts at this common point would propagate in both directions away from that point so in that case this method of detection would fail or produce a long delay. Therefore, we will compare voltages of opposite facing coils of the quads. The dipole is still susceptible to some quenches that would not be detected in a timely manner, however, the stored energy is low and the consequences of delayed quench detection in that case are minimal.

2.3 Calculation Results

Table 2 lists dump resistor values and quench protection delay times. Figure 2 shows the current waveform for the main quad with a total delay time of 0.19 second due to the chosen detection threshold, quench propagation time and quench switch actuation time of 100 ms. Table 3 lists calculated results for the three types of magnets.

Table 2: Dump resistor values and protection times

Magnet Type	Dump Resistor [ohm]	Protection Delay [seconds]
Main Quad	0.24	0.19
Skew Quad	0.70	0.13
Dipole	0.11	0.16

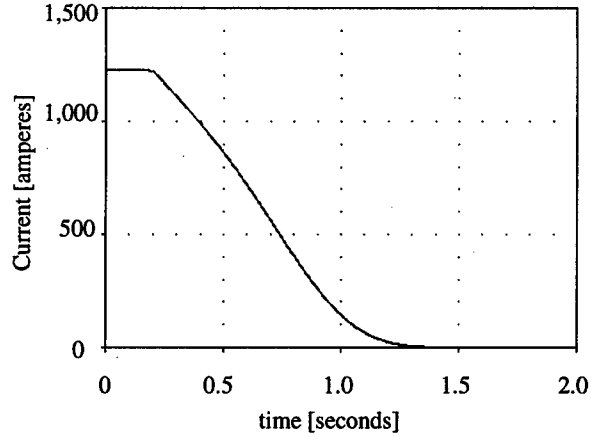

Figure 2: CESR SC IR main quad predicted current.

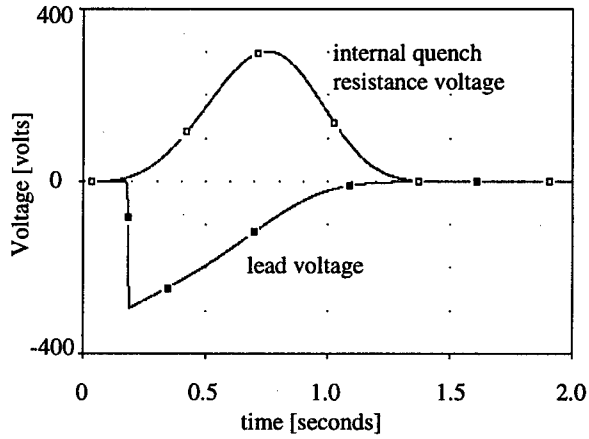

Figure 3: CESR SC IR main quad predicted voltages

Table 3: Calculated energy and voltage

Magnet Type	Stored Energy [kJ]	Extracted Energy [kJ]	Peak Voltage [volts]
Main Quad	183	107	300
Skew Quad	6.1	1.9	198
Dipole	0.48	0.15	19

3 DESIGN

Figure 4 is a block diagram of the quench detection and protection system. There are two magnet assemblies in CESR, one in the East IR and one in the West IR. Each magnet assembly contains two units, each unit comprising a main quad, a skew quad and a dipole magnet. Each magnet has leads brought out from superconducting regions for sensing magnet coil voltages. With the sense leads attached to superconducting regions and with little current flow in these leads, the desired 0.5 volt detection threshold is reasonably high. For the main quad, this threshold gives a detection delay time approximately equal to the quench switch delay time.

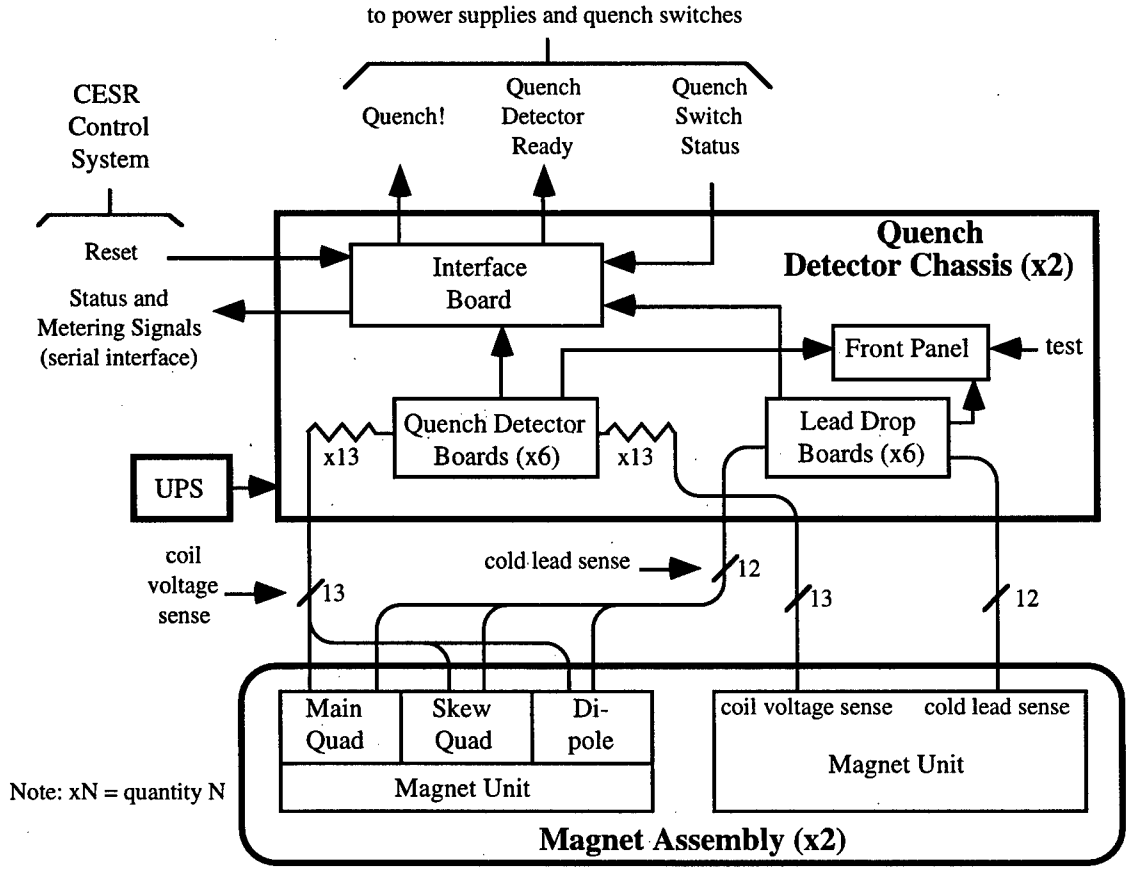

Figure 4: CESR Superconducting Interaction Region Magnet Quench Detection System.

The coil sense leads enter the quench detection chassis through connectors rated at 600 volts. Current limiting resistors are placed in series with each lead which then connect to isolation amplifiers on the detector boards. The AD202 isolation amplifier has a common mode range of ±1000 volts, but a maximum differential voltage of only ±5 volts so the input must be clamped.

Appropriate coil voltages are subtracted and applied to window comparators with ±0.5 volt thresholds. The comparator outputs are latched until reset by the CESR control system. A quench detected in one magnet of a unit opens the quench switches for all three magnets in that unit and also turns off the power supplies for all six magnets associated with that side of the IR.

Electrically actuated D.C. contactors are used as quench protection switches and stamped, stainless steel resistors are used for dump resistors. There is one quench switch and one dump resistor per magnet.

To reduce the number of nuisance quench detections, the quench detector chassis are powered from a common Uninterruptible Power Supply (UPS) allowing the system to operate through line transients and power outages.

Each quench detection chassis also houses monitoring electronics for the vapor-cooled magnet leads. Excess voltage drop in a lead activates the quench switches to protect the magnet leads from over dissipation.

4 CONCLUSION

An approach for quench detection and protection of CESR superconducting interaction region magnets has been described. A design has been presented based on the predicted behavior of these magnets. When the magnets are fully tested, actual coil voltages and currents during quenches will be measured to test the calculations presented here.

5 ACKNOWLEDGEMENTS

Thanks to Mike Comfort, Ted Vandermark and Ron Yaeger at Wilson Lab for their expertise and to the National Superconducting Cyclotron Laboratory at Michigan State University.

6 REFERENCES

[1] J.J. Welch, G. Dugan, E. Nordberg, D. Rice, "The Superconducting Interaction Region Magnet System for the CESR Phase III Upgrade", Cornell University, PAC97

[2] G. Dugan, "Quench Protection Considerations for CESR Superconducting IR Quadrupoles," CBN 97-27, http://www.lns.cornell.edu/public/CBN/1997/.

[3] M.N. Wilson, Superconducting Magnets, p. 214, Oxford:1983.

Bent Superconducting Solenoids for the Muon Cooling Experiment*

Y. Eyssa**, M. A. Green*+, S. Kenney**, J. R. Miller**, S. Prestemon**, S. T. Wang***
*Lawrence Berkeley National Laboratory, University of California, Berkeley CA 94720
**National High Magnetic Field Laboratory, Florida State University, Tallahassee FL 32310
**Wang NMR Inc., Livermore CA 94550

Abstract

This report describes some solenoid design work done for the cooling experiment for the muon collider collaboration. This report describes an analysis section of superconducting solenoids that have a center line induction of 3.0 T. The section is bent in the shape of an S. Each bend in the S bends the muon beam one radian (57.3 degrees). The warm bore diameter of the solenoid bent solenoid is 300 to 320 mm. The radius of the bend at the solenoid center line is 1000 mm. This report shows the results of three dimensional field calculations and presents a solenoid design that will include four TPC detectors that are 240 mm in diameter and 550 mm long as well as a 1300 mm long section of 1300 MHz RF cavities. The TPC sections need a solenoid warm bore diameter of about 300 320 mm while RF cavities require a warm bore diameter of 440 mm. The superconducting solenoid design must take into account the varying warm bore diameter requirements for the magnet string yet meet the stringent solenoidal field uniformity requirements within the active volume of the four TPCs.

1 BACKGROUND

The proposed muon cooling experiment[1,2] consists of a pair of S shaped solenoid bends each of which has two bent solenoids, and straight solenoids for four TPC detectors and an 805 MHz RF cavity[3]. Between the two S shaped bend sections is a straight muon cooling section. The energy and momentum of the muon beam are analyzed by the S shaped bent solenoid systems before and after the straight solenoidal muon cooling section.

After the beam first analysis, the muon beam enters a muon cooling section that is about 15 meter long. The cooling section consists of ten alternating solenoids with a peak induction of 15 T. The muons are cooled by a liquid hydrogen section that is about 400 mm long and 70 mm in diameter. After the muon momentum has been reduced by about 25 MeV/c, the muon are re accelerated by a 900 mm long 805 MHz RF cavity section back to their original energy of about 200 MeV. The second S shaped solenoid section analyzes the energy and momentum of the muons after they have gone through cooling.

The bent solenoid separates muons by momentum spatially across the bore of the solenoid following the bent solenoid. A coil that generates a pure dipole field in the bent solenoid moves the momentum separated muons so that their momentum separation is distributed around the center of the solenoid following the bent solenoid.

* This work was supported by the Office of High Energy and Nuclear Physics United States Department of Energy under contract number DE-AC03-76SF00098.
+ email: magreen.lbl.gov

2 THE BENT SOLENOID DESIGN

The following design assumptions were used for the preliminary design of the superconducting bent solenoid system: 1) Magnetic flux is conserved in the solenoids. Magnetic flux conservation means that all of the solenoid coils have the same average current radius. 2) The warm bore diameter for the for the two TPC solenoids and the bent solenoid is 320 mm. The solenoid around the RF cavity has a warm bore diameter of 440 mm. 3) The bend angle for the bent solenoid is 57.3 degrees (1 radian). The bend radius for the bent solenoid axis is 1000 mm. 4) The bent solenoid induction on axis is 3.0 T. The bent solenoid dipole is set at 0.51 T on the axis. The dipole windings are assumed to be separately powered from the solenoid windings in the bent solenoid. The value of the bent solenoid dipole induction can be increased to 0.75 T, if needed. 5) Standard MRI superconductor is assumed for the solenoid windings. The solenoids are hooked together electrically in series. 6) In the TPC, the integral of the r component of field over the integral of the z component of field is less than 0.0002 within the TPC active volume. The TPC active volume is assumed to be 160 mm in diameter by 500 mm long near the center of the TPC solenoid. 7) The TPC cables are fed out of the solenoid through room temperature slots between coils that are located at the ends of the TPCs away from the bent solenoid. 8) The two TPC solenoids, the bent solenoid and the RF solenoid share a common cryostat vacuum vessel. The two straight solenoids and the bent solenoid are assumed to have separate cold mass support systems. The cryostat ends at the center of the RF cavity so that the RF wave guide can enter the cavity between the solenoids. 9) Conduction cooling to a system of pipes carrying two-phase helium is assumed.

The superconducting magnet system from the first TPC solenoid to the solenoid that covers half of the RF cavity is shown in Figure 1. The average coil diameter for the magnets shown in Figure 1 is 480 mm. The smallest coil diameter in the TPC magnet section is about 450 mm. The coils around the RF coil clear the warm bore of the cryostat by about 10 mm. The coils around the RF cavities are located inside of an aluminum support structure that has the helium cooling tube attached to it. The extra dipole coils for the bent solenoid ate not shown in Fig. 1. The solenoidal coils parameters are shown in Table 1. All of the solenoidal coil shown in Fig. 1 and described in Table 1 are designed to be powered by a single power supply. The total stored energy in the string shown in Fig. 1 is 3.44 MJ. The high current density magnet coils (163.3 A per square mm) would require that the coils be subdivided so that they can be protected by cold diodes and resistors.

0-7803-5573-3/99/$10.00@1999 IEEE.

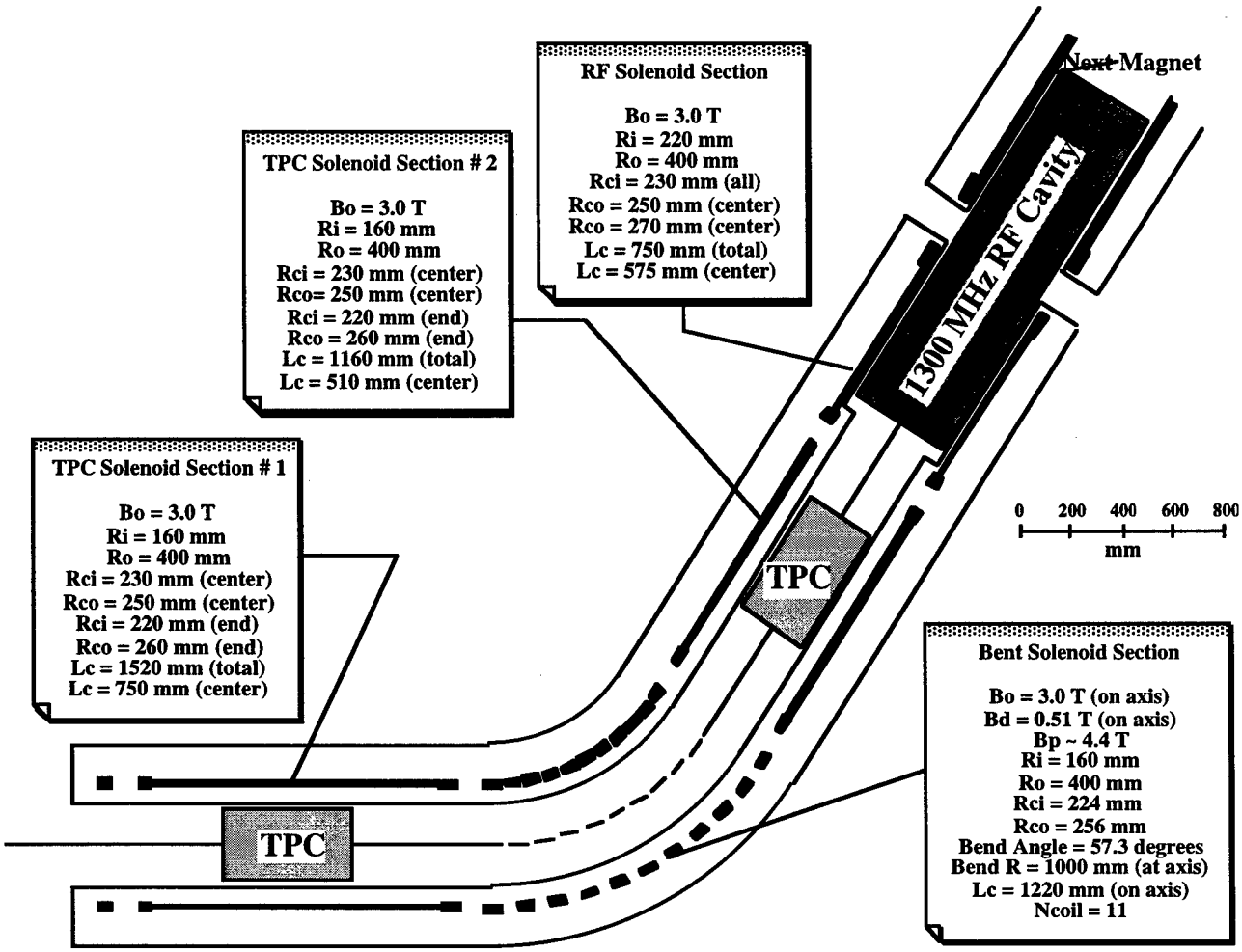

Figure 2: A Cross-section of a 57.3 degree Bent Solenoid section with Straight Solenoid Sections for Half of an RF Cavity and two TPC Detectors

Table 1: Magnet Parameters for the Bent Solenoid System

	TPC # 1	Bent Sol.	TPC #2	RF Sol.
Warm Bore Diameter (mm)	320	320	320	440
Cryostat Outer Diameter (mm)	800	800	800	800
Cryostat Section Length on axis (m)	1.7	1.2	1.6	0.8
Coil Average Diameter (mm)	480	480	480	480
Coil Thickness (center) (mm)	17.9	25.7	17.9	17.9
Coil Thickness (ends) (mm)	34.8	NA	34.8	34.8
Number of layers (center)	16	23	16	16
Number of Layers (ends)	32	NA	32	32
Central Induction on axis (T)	3.0	3.0	3.0	3.0
Coil Design Current (A)	257.3	257.3	257.3	257.3
Coil Section Stored Energy (MJ)	1.10	0.78	1.04	0.52
Coil Section Inductance (H)	33.2	23.7	31.4	15.7
Conductor Current Density (A mm^{-2})	163.3	163.3	163.3	163.3
EJ (J A^2 m^{-4})*	2.9 x 10^{22}	2.1 x 10^{22}	2.8 x 10^{22}	1.4 x 10^{22}

* Quench protection must be supplied to each magnet. Cold diode and resistor quench protection is attractive for these magnets. A separate power supply can be used for each string of magnets. HTS current leads could be used.

3 THE BENT DIPOLE

Figure 1 does not show the dipole coils needed to move the momentum separated muon back to the center of the solenoid. When the muon momentum is 180 MeV/c and the bent solenoid induction on axis is 3.0 T, a pure dipole of 0.51 T will center the muon momentum spread about the physical center of the dipole. The dipole must be a pure dipole to do this. At first blush, it appears that mounting a cosine theta current distribution on the outside of the bent solenoid (or just inside the bent solenoid coils) would produce a pure dipole. Unfortunately, it produces a gradient dipole (a pure dipole plus a quadrupole) that is stronger on the inside than on the outside. Redistributing the cosine theta coils so that the current density as a function of angle is the same on the inside of the bend and the outside of the bend will get rid of the gradient. This means that the pole for the dipole is displaced outward away from the axis of the major bend. The displacement angle with respect to a bent plane that passes through the bent axis of the solenoid is only a few degrees. The amount of this angle is dependent on the radius of the dipole with respect to the minor axis.

The ends of the dipole pose a problem in that they introduce local field errors. The integrated dipole field along the minor axis of the bent solenoid due to the ends of the dipole can be made quite good. This is an acceptable solution provided the longitudinal gyration period of the muons in the solenoid is long compared to the radius of the dipole coils.

The dipole coils should be separately powered from the solenoid coils. This will allow the dipole to be adjusted for the average momentum of the muons in the cooling channel. The muon cooling experiment is expected to be done over a range of muon momenta from 160 MeV/c to 250 MeV/c. An adjustment of the dipole field that is separate from the solenoid field will permit a range of muon momenta to be analyzed. The design peak induction (on the center of the bent solenoid) for the dipole in the bent solenoid could be as high as 0.8 T, whereas the nominal dipole induction is 0.51 T.

4 SOLENOID FIELD UNIFORMITY

The field uniformity specification for the straight solenoids is nominally 1 part in 1000 at a 75 mm radius. The studies that were done were done for solenoids with coils that have a 200 mm current radius. The field uniformity possible appears to be about 1 part in 2000 within this region. The studies also indicate that a field uniformity of better than 1 part in 1000 is achievable even when there is a 100 mm gap between coils, provided the ends of the coils are built up to make up for the missing current in the gap.

The field times the radius from the major axis within the curved section is for the most part good to 1 part in 500. The computer model used ten straight coils with an average current radius of 200 mm to calculate the field uniformity within the bent solenoid. The uniformity of the field times the distance from the major axis improves as the number of coils in the bent solenoid increases, The greatest field non uniformity occurs at the transition from the straight section to the curved section. The pure dipole field can be made uniform to 1 part 1000 except where the ends cross over the solenoidal coils. Moving the current sheet out to a radius of 240 mm should improve the field uniformity by more than a factor of two.

5 CONCLUDING COMMENTS

It appears that a superconducting bent solenoid system can be built for the muon cooling experiment using existing MRI superconductor. The dipole coils can also using MRI superconductor. Conduction cooling of the superconducting coils using two-phase helium in tubes appears to be a good way of cooling these coils.

The field uniformity required for the TPC detectors appears to be achievable in a superconducting solenoid magnet with an average coil radius of 240 mm. The bent solenoid field uniformity (defined as the field uniformity times the distance from the major axis) within a bore that is 75 mm in radius is also acceptable for a ten coil bent solenoid with an average current radius of 240 mm.

A winding configuration of a pure dipole coil mounted onto the bent solenoid also appears to be possible to fabricate. The major problem with this dipole is the effect of end windings on the field uniformity within both the straight and bent solenoids. For the dipole solution to be acceptable, the integrated dipole field must be uniform and the gyration length for the muons in the solenoid must be long compared to the dipole radius.

ACKNOWLEDGMENTS

The authors acknowledge discussions with Robert Palmer, Kirk McDonald and others concerning the bent solenoid system for the muon cooling experiment. This work was supported by the Office of High Energy and Nuclear Physics, United States Department of Energy under contract number DE-AC03-76SF00098.

REFERENCES

[1] The Muon Collider Collaboration, "Status of Muon Collider Research, Development and Future Plans," BNL-65-623, Fermeilab-PUB-98/179 and LBNL-41935 (1998)

[2] K. T. McDonald, "Muon Colliders: Status of R&D and Future Plans," (This Proceedings) the Proceedings of the 1999 Particle Accelerator Conference, New York, NY 29 March to 2 April 1999, IEEE Publications (1999)

[3] S. A. Kahn, H. Guler, C. Lu, K. T. McDonald, E. Prebys and S. E. Vahsen, "The Instrumentation Channel for the MUCOOL Experiment," (This Proceedings) the Proceedings of the 1999 Particle Accelerator Conference, New York, NY 29 March to 2 April 1999, IEEE Publications (1999)

A Common Coil Magnet for Testing High Field Superconductors*

A.K. Ghosh#, J.P. Cozzolino, M.A. Harrison, W.B. Sampson, P.J. Wanderer
Brookhaven National Laboratory, Upton, NY 11973, USA

Abstract

A one-meter long magnet has been fabricated to provide background field for testing racetrack shaped coils made from high field materials such as Nb_3Sn, Nb_3Al and the new high temperature superconductors, BSCCO and YBCO. The magnet is of the double aperture common coil type and uses high current Nb-Ti main coils to produce an applied field of approximately 7T on inner coils fabricated from pre-reacted tape conductors. The performance of the magnet is summarized along with test results from insert coils wound from N_3Sn ribbon conductor.

1 INTRODUCTION

Superconducting magnets for accelerator applications have been made almost exclusively from the ductile alloy NbTi. In the LHC machine at CERN the superconducting coils will be operated in superfluid helium to extract the highest possible performance from this versatile material. Future accelerators designed to operate at even higher fields and temperatures will have to utilise superconductors with less desirable mechanical properties. The A15 compounds N_3Sn and Nb_3Al have much higher upper critical fields than NbTi but are brittle and can only be subjected to limited mechanical strain. This is also true for the new high temperature superconductors such as BSCCO and YBCO so that magnets made from these materials must be formed by either reacting the conductor after winding or developing a design in which the conductor is subjected to limited stress during fabrication. Gupta [1] has proposed a magnet with flat racetrack shaped coils readily wound from high aspect ratio conductor. In this geometry the magnet has two apertures with magnetic fields of opposite polarity, ideal for colliding beam machines. This configuration also allows the minimum bending radius of the conductor to be determined by the separation of the apertures. A magnet of this type is illustrated in Fig. 1. It can be viewed as two classical "window frame" magnets in a single yoke. Both the windings shown on the right side of the diagram are part of the same racetrack coil with

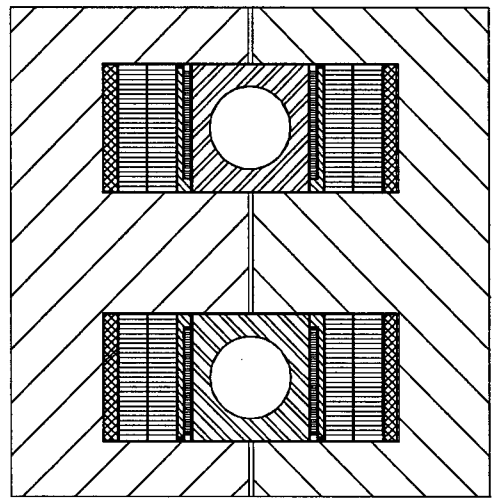

Figure 1 Cross section of the windings in the common coil magnet. The turns on the right form one half of the upper and lower dipoles, but are part of the same racetrack coil. Similarly, the turns on the left side form the other half of each dipole. The test windings are positioned inside the high current cable coils in a region of relatively uniform field.

the upper block of conductors forming one half of the windings of the top magnet and the lower block of conductors forming half of the lower magnet, thus the name "common coil". The magnetic force distribution in this device is quite different than in a Cosθ coil so that most of the force is across the width of the conductor rather than across its thickness. This is because the coils are connected in opposition to force the flux up or down thru the apertures as illustrated in Fig. 2. Because the coils are flat and the minimum bending radius can be quite large they are ideally suited to fabrication from relatively brittle conductors.

2 MAGNET DESIGN

Since the present high cost and limited performance of high temperature superconductors (HTS) makes it impractical to design a double dipole using only HTS material, we have

*Work supported in by the U.S. Department of Energy under Contract No. DE-AC02-98CH10886 (BNL).

Email: Ghosh1@bnl.gov

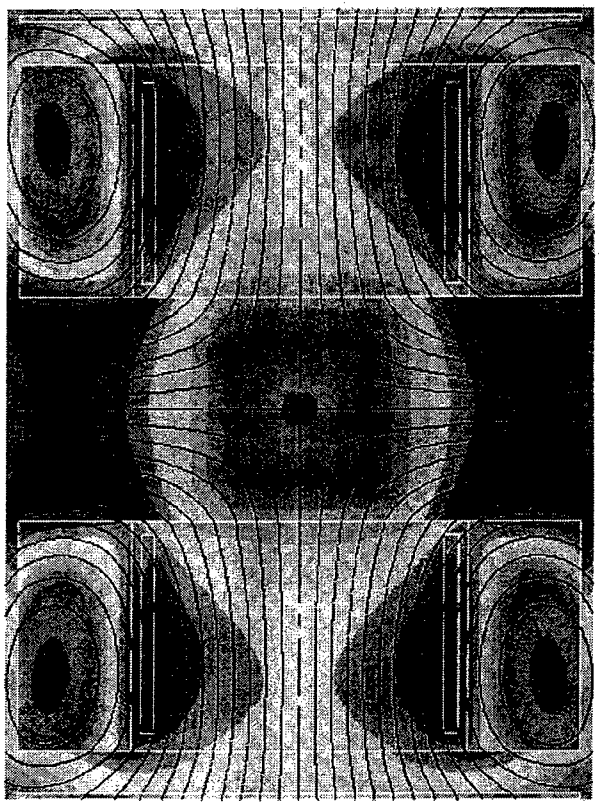

Figure 2. The field distribution in the straight portion of the common coil magnet. Field strength is indicated by the shading.

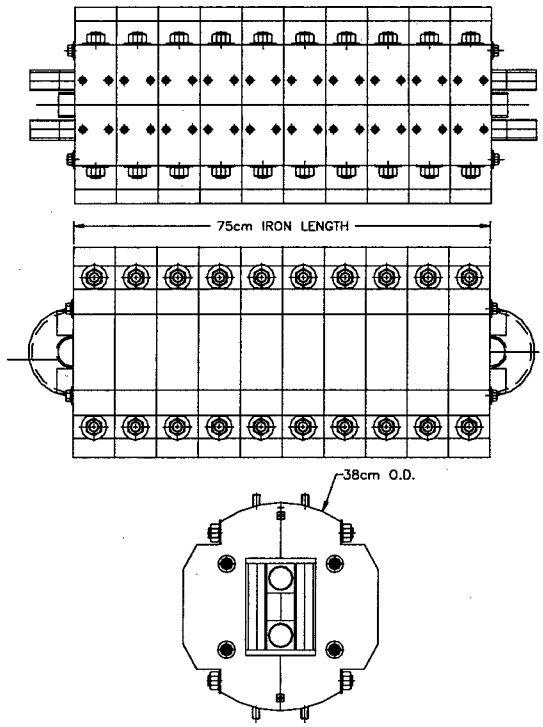

Figure 3. The mechanical details of the common coil magnet. The iron core is split vertically to facilitate changing the insert coils.

chosen a hybrid design where the main coils are made from NbTi cable (surplus from the SSC Project) and auxiliary or insert coils are made from developmental conductors (see Fig. 1). The NbTi coils are wound using techniques and insulation perfected by the SSC and RHIC Projects. Each coil is formed as a double pancake from a single length of conductor. The iron yoke halves are made of blocks cut from 3" thick plate and epoxyed together. Figure 3 shows the mechanical details. This yoke is split vertically so that the magnet can be separated easily to replace the insert coils.

Rectangular aperture pieces fit between the coils to simulate beam tubes and provide access for magnetic measurements. Mechanical loading of the coils is provided face on by the large bolts holding the yoke together and from the side by a series of set screws as shown in Fig. 3. The tape insert coils are wound on G-10 formers using Kapton insulation and then coated with epoxy. The magnet is assembled in halves and then bolted together. Only one connection is required between each set of coils so that changing inserts is relatively straightforward. The main coils provide a reasonably uniform field over the volume occupied by the insert coils.

When the current density and economic aspects of HTS conductors improve, the NbTi coils will be replaced.

3 MAGNET PERFORMANCE

The magnet exhibited considerable "training" when powered as shown in Fig. 4. A peak field of 5.8T was achieved before the first quench and 6.6T after five quenches. The maximum field expected based on measurements of the conductor used is 7.3T at 9kA. When the magnet is energized the coils are forced apart and the resulting motion is thought to be the source of the disturbances that initiate premature quenches. In principle a large part of this training could be eliminated by preloading the coils using the large bolts which hold the yoke halves together. In practice, it was found that turn to turn short circuits in the coil appeared at quite low pressure (~5mPa) so that it was not possible to put a significant preload on the coil and maintain electrical integrity. Despite this limitation the magnet was able to produce over 90% of the expected background field for testing insert coils. The shorting problem is confined to the transition region between the two halves of the double pancake winding. It is expected that improved insulation will allow higher preloading and reduced training in subsequent tests.

4 INSERT COIL PERFORMANCE

The first set of insert coils were wound from Nb_3Sn tape 3mm wide and 0.3 mm thick. These dimensions are typical of HTS conductors and this coil was intended as a benchmark for comparing the performance of these new materials with more conventional low temperature superconductors. The test consisted of setting the applied field at a predetermined level with the main winding and then increasing the current in the insert coils until a quench occurs. The results are shown in Fig. 5. The field on the test coil increases slightly with current due its self field. The conductor used in this coil appears to be inherently unstable since the quench currents are well below the critical current at all field levels and independent of applied field. The coils do not train but quench randomly at values between 200 and 300 amps. The conductor used in these coils is made by diffusing tin into a thin niobium sheet to form a Nb_3Sn layer on each side and then laminating with copper stabilizer. Since the superconducting material is in a continuous film large magnetization currents can develop during ramping possibly leading to premature quenching. Additional tests at very low ramp rates are scheduled for the next experimental run to examine the dynamic properties of these coils.

5 CONCLUSIONS

The training behaviour observed in the main coils indicate improvements are needed in the mechanical structure of the magnet. Improving the insulation so that higher prestress can be applied during assembly should reduce or eliminate this problem. While the performance of the insert coils is considerably below expected levels, they do provide a useful reference point for gauging the performance of similar windings made from HTS conductor.

6 ACKNOWLEDGEMENTS

Among the many members of the RHIC Magnet Division who contributed to the development of this magnet, three deserve special mention. Lon Werner was responsible for winding the main coils and assembling the magnet, Larry Welcome fabricated the insert coils and Andy Sauerwald performed the testing.

7 REFERENCES

[1] R. Gupta, "Coil Design for High Field 2 in 1 Accelerator Magnets", Proc. of the Part. Acc. Conf., Vancouver, Canada., p 3344 (1998).

[2] W.B. Sampson and A.K. Ghosh, "The Performance of BSCCO Racetrack Coils at 4.2K", Proc. App. Superconductivity Conf., Palm Desert, California, 1998 in press.

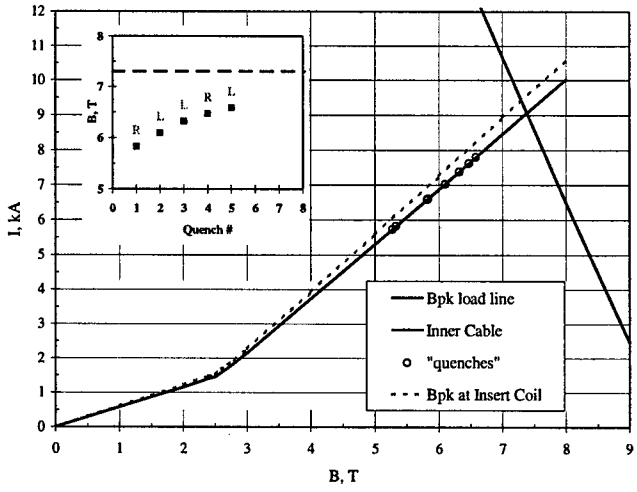

Figure 4. The training behaviour of the main winding of the common coil magnet.

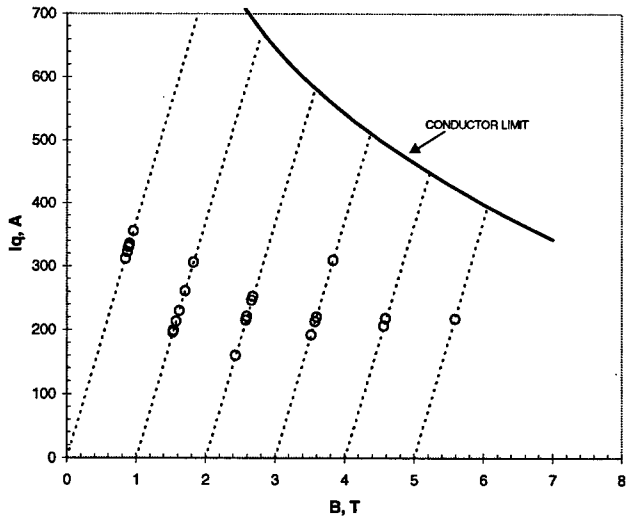

Figure 5. Nb_3Sn insert coil quench currents plotted against the applied field for ramp rates greater than 1A/s

OPERATIONAL CHARACTERISTICS, PARAMETERS, AND HISTORY OF A (13T) Nb3Sn DIPOLE*

R.Benjegerdes, P. Bish, S. Caspi, K.Chow, D. Dietderich, R. Hannaford, W. Harnden, H. Higley, A. Lietzke, A. McInturff†, L. Morrison, M. Morrison, R. Scanlan, J. Smithwick, and C. Taylor
Lawrence Berkeley National Laboratory, Berkeley, California 94720

Abstract

The early design and test results have been previously reported. [1] During the subsequent operation of "D20" the accelerator prototype dipole has provided both additional and more detailed data as to its characteristics and performance. D20's use as a test facility for high field critical current measurements [2] has provided operational experience and history pertaining to accelerator required characteristics. There has been recently obtained data related to field quality, operational reproducibility and reliability, which will be presented. This prototype "D20" has attained the highest magnetic field of any accelerator prototype dipole constructed and tested to date. The magnet has continued to operate routinely.

1 INTRODUCTION

D20 was designed as a "proof of principle" demonstration that a high field >10T accelerator type dipole could be constructed from brittle superconductor (A-15, hi-T_c, etc) and operate in the range above ten tesla. The magnet design parameters [3] and its early test data have been reported.[1] There was a concern at that time that a serious performance limit had arisen from possible conductor degradation. There were a number of erratic quenches occurring in the Nb_3Sn conductor near a Nb_3Sn /NbTi splice box. These events were occurring at lower and lower fields (~11T(4.4K)). It had been previously decided to use D20 as a facility to provide high fields for long straight cable critical current "I_c" measurements. In the course of obtaining the Nb_3Al "I_c" data, the magnet was cycled to fields ~12.5T(4.5K) without incident. There has been a re-examination of the early data. These checks have discovered some data filtering problems as well as a few calibrations that needed to be updated. The subsequent analysis results and those corrected data are reported at this time as well.

2 DESIGN & OPERATIONAL PARAMETERS

†Email: admcinturff@lbl.gov

*The work is supported under contract # DE-AD03-76SF00098 by Director, Office of Energy Research, Office of High Energy Physics, US Dept. of Energy.

D20 is a four layer graded cable cosine Θ winding distribution 50mm bore 1meter long dipole. The inner two layers (1&2) used one size and the outer two layers (3&4) another. The coils are double layers of Nb_3Sn/Cu "Rutherford" cable wound, reacted, fiberglass insulated and fully epoxy impregnated. In Table 1 the inner cable design current densities and currents are compared to the measured cable and strand value.[4] The magnet's operational and peak performance current densities achieved at 4.4K are given as well. These data are compared at the position where the critical current at the local stress level are reached as either measured by the cable I_c(strain, H) or the strand extrapolated by using the percentage reduction seen by cables made from it. There were strands of two different geometries used and their sensitivity to transverse strain was different by a factor

Table 1: Currents/turn, Current Densities, and Fields

	Amp/turn (kilo-amp)	A/mm²(overall)	Central Field (T)
Design (140MPa) [measured]	6400	276	13 [12.96]
IGC cable meas.[4] (~95MPa*) I_c	6320	273	12.82
TWA cable meas.[4](~95MPa) I_c	6618	285	13.44
IGC strand meas. (~95MPa) I_c	6820	294	13.7
TWA strand meas. (~95MPa) I_c	6904	298	13.84
D20 operating at 4.4K	6303	272	12.78
D20 normal operation at 4.4K	6109	263	12.44

*This is the critical peak field/strain point value

of six at 100MPa (3.7% vrs. 23%). These results lead to the conclusion that the mechanism operating here is extrinsic and can be designed for a minimum impact. The two manufacturers of the two types of strand were Intermagnetics General Corporation (IGC) and Teledyne Wah Chang (TWCA). The magnet has not spontaneously quenched in the critical peak field/strain location as of yet. The coil's end, pole, azimuthial, and axial spacers were made from Al-bronze. The bronze was reasonably matched the windings thermo-mechanical properties. The double layered coils were assembled with the appropriate shimming and placed in a bronze sleeve. The assembly was then placed inside the iron yoke pieces on the straight sections and stainless steel(ss) on either end. The coil assembly with bronze sleeve and longitudinally bolted yokes was covered by a split thin ss bobbin and 18 layers of tensioned rectangular ss wire was wound in it to

0-7803-5573-3/99/$10.00@1999 IEEE.

preload the coils to ~100 and ~65 MPa, inner and outer layer respectively. Next, a set of iron end plates were bolted on and an outer ss skin was welded to them. The end bullets were then torqued in stages to axially compress the coil up to 820 kN. The assembly of D20 is shown in Figure 1 with the location of instrumentation. The windings were actively protected by 25μm thick ss

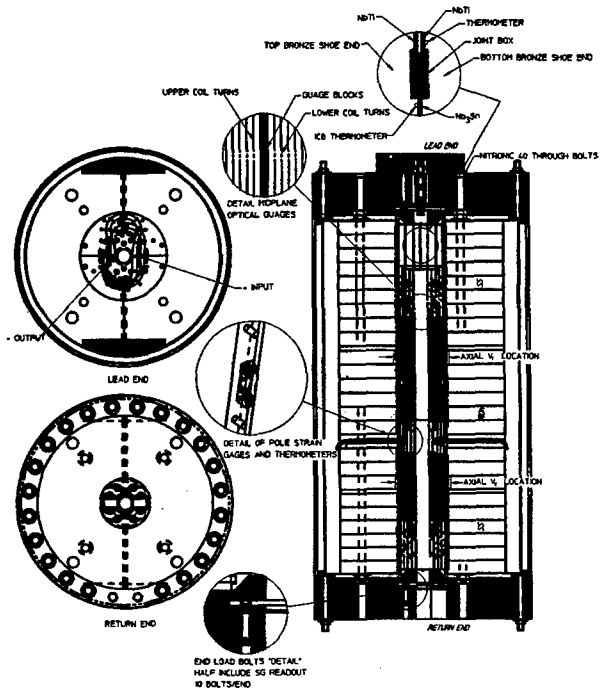

Figure 1: D20 Assembly

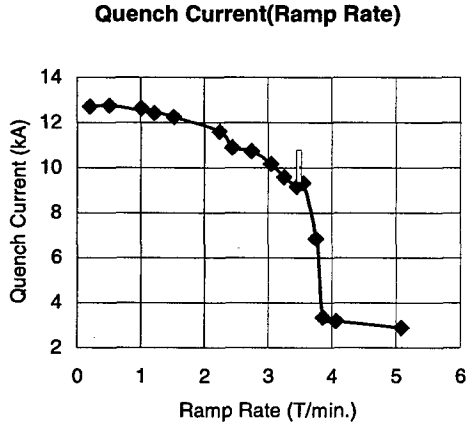

Figure 2: Quench current at 4.4K versus ramp rate

heaters which covered >80% of the turns, and were located next to each layer in a ss/Kapton laminate with the voltage tap traces. The protection heaters routinely operated at a surface power density of 75 and 27 w/cm^2 for inner and outer layers respectively. The highest average winding temperatures after quench were in the outer layers (between 165K-185K). When the quench originated in an outer turn, the highest hot spot estimate was 234K. By comparison, the inner two layers averaged 80K - 120K and if it originated there the highest temperature estimate was 152K. The maximum number of Miits(Million-ampere^2-seconds) absorbed during a quench during the test was 4.3. The Miits of the 4.4K quenches increase almost linearly from 3 to 4 from fields of 10 to 12.8T. In super fluid helium Miits vary from 3.8 to 4.3 from 12 to 13.1 and dropped back to 4.1 by 13.5T. The quench history as a function of ramp rate with an open bore filled with LHe at 4.4K is given in Figure 2. During the Nb_3Al "I_c" test, it was found that the knee of the curve had moved from 1T/min to about half that value. This was attributed to the restriction of LHe in the magnet aperture. The magnet tolerated the modest heat input from the Nb_3Al cable sample being driven normal in the aperture conducting a few kiloamperes at magnetic fields up to ~12.5T.

3 HISTORY

There have been three full cool down cycles from room to LHe temperature of D20 to date. Each of these cycles was to change the aperture configuration therefore requiring the cryostat to be partially disassembled and reassembled. In order to measure the harmonic content of the aperture field; there had to be an anti-cryostat installed and aligned in the bore of D20. Once this was accomplished a high speed "Morgan Coil" was inserted and harmonic data obtained. The time constant for the sextupole decay from ramped values to dc at fields >1T was ~1.5min. Table 2 gives dc values of the Fourier Coefficients normalized at 1cm at 2.5T as measured by the rotating "Morgan Coil". The dc harmonics measured

Table 2: D20 Harmonics at 2.5T(I=1086A)

NΘ	Desig n	Meas.	Units
2Θ	-0.0	-1.5$^+$ ±0.8	x10^{-4}cm^{-1}
3Θ	-0.8	-3.8 ±1.6	x10^{-4} cm^{-2}
4Θ	0.0	< | 1.2 | ±1.2	x10^{-4} cm^{-3}
5Θ	0.0	-0.8 ±0.5	x10^{-4} cm^{-4}

$^+$ out of phase.

are on the order of the design values with the exception of the quadrupole term. The quadrupole term however was expected due to the size difference of the double layer inner coils, top compared to the bottom. The width of the sextupole dc hysteresis curve at 1.5T is 6.5units and at 9T <1unit. At a ramp rate of 1T/min, the width of the sextupole hysteresis curve at 9T is 5units as analyzed by the tangential/bucked coil system. [5] The transfer function varies from 23.5 g/amp at 2T to 21.7 g/amp at 10T. The third full thermal cycle occurred in order to

install the 1m long "short cable" sample mount and the Nb_3Al cable in order to measure the critical currents from 10T to 12.5T at 4.4K. The sample joints were made to the copper return leg in the low field regions between the magnet winding ends and the iron end plates. (Figure 1) D20 was quenched a few times until the increased sensitivity to ramp rate was appreciated when the bore is not full of liquid helium. This sensitivity had been present on the second cool down but had not been recognized. There were problems with the co-axial power leads quenching the current joints of the sample. This situation resulted in quite a bit of heat being generated in the aperture during the measurements. However unlike the second full thermal cycle where quench performance had been at best erratic; D20 returned to fields of ~12.5T without quenching other than the ramp rate driven type early in the test. (Figure 3) The problematic area of the magnet (i.e. the outer layer coil lead between the magnet and just before the Nb_3Sn/NbTi splice and splice box) appears to be stable at this time. There are several unique features about this particular area in this particular coil as was noted earlier [1] and the presence of a thick Kapton shim (254μm) additionally locally reduces the modulus.

4 CONCLUSIONS & DISCUSSION

It appears that D20 has not been degraded (or at least appears not to be presently limited in quench current by conductor damage) by the 60+ spontaneous quenches and the 60+ experimentally initiated quenches. In Table 3 the 4K maximum current densities and design values are given. The outer cable has been quenched with a copper stabilizer current density "J" of 1535 amps/mm^2 in Super Fluid helium. D20 has routinely operated at currents that in the advent of a quench; the "J(Cu)" would be 1400 amps/mm^2. To date, the maximum temperature during 4.4K operation measured in the windings after a quench have been in the 100K to 200K range, which appears moderate. During the experiments using the inner protection heaters to measure the wattage margin of the inner windings,[1] it became apparent that the magnet was protected by the outer winding protection heater sets(4) alone with less than a 50K increase. It is not clear at this time that this is true for the inner layer sets(4) as well. It has been decided to mount "D20" in a vertical dewar in order to decrease the turn-around-time for its use as a short sample facility.

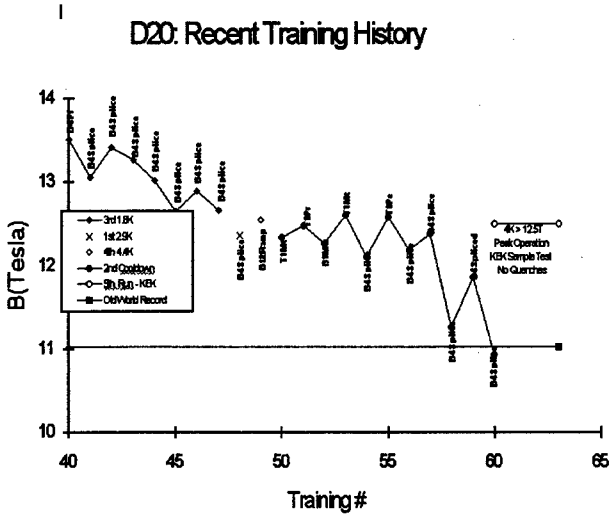

Figure 3: Recent Training History at 4.4K

Table 3: Current Densities

D20 @ 13T 6420A @4.2K	Inner Cable IGC @ 4.4K		Outer Cable TWCA @ 4.4K	
	Design	Reached	Design	Reached
J_{cu} (A/mm^2)	1302	1282	1462	1440
$J_{non\,cu}$ (A/mm^2)	559	551	1550	1527

REFERENCES

[1] A. McInturff, et. al. "Test Results for a high field (13 T) Nb_3Sn Dipole", 1997 PAC Proceedings, Vancouver, B.C., pp. 3212-3214.

[2] M. Wake, et. al., "Insertion Nb3Sn coils for Magnet Development", to be published in proceedings of Magnet Technology conference MT-15 Beijing, China.

[3] D. Dell'Orco, et. al., "Design of the Nb_3Sn Dipole D20", IEEE Trans. On Appl. Superconductivity, 3 #1 March 1993, pp. 82-86.

[4] D. Dietderich, et. al., "Critical Current of Superconducting Rutherford cable in High Magnetic Fields with Transverse Pressure", to be published in the proceedings ASC'98, Palm Desert, CA, 14-18 Sept. 1998.

[5] S. Caspi, et. al., "Development of High Field Dipole Magnets for Future Accelerators", to be published in the proceedings of Magnet Technology Conference, MT15, Beijing, China, Oct. 20-24, 1997.

MECHANICAL DESIGN OF A HIGH FIELD COMMON COIL MAGNET*

S. Caspi, K. Chow†, D. Dietderich, S. Gourlay, R. Gupta, A. McInturff, G. Millos, R. Scanlan,
Lawrence Berkeley National Laboratory, Berkeley, CA

Abstract

A common coil design for high field 2-in-1 accelerator magnets has been previously presented as a "conductor-friendly" option for high field magnets applicable for a Very Large Hadron Collider [1,2]. This paper presents the mechanical design for a 14 tesla 2-in-1 dipole based on the common coil design approach. The magnet will use a high current density Nb_3Sn conductor. The design addresses mechanical issues particular to the common coil geometry: horizontal support against coil edges, vertical preload on coil faces, end loading and support, and coil stresses and strains. The magnet is the second in a series of racetrack coil magnets that will provide experimental verification of the common coil design approach.

1 INTRODUCTION

The superconducting magnet program at Lawrence Berkeley National Laboratory (LBNL) is focused on development of high field accelerator magnets using brittle superconductors. The current designs follow a "common coil" approach wherein a pair of racetrack coils is shared between two apertures to produce opposing fields in each aperture [1]. A 6 tesla magnet using Nb_3Sn conductor has been built and tested as a first step towards the ultimate goal of attaining 15 T accelerator quality dipoles [3,4]. This paper describes the mechanical design of a second magnet in the common coil series: a 14 T Nb_3Sn magnet of limited field quality (field quality will be addressed in the next magnet).

A preliminary design has been previously described elsewhere [2]. The design has since been refined to allow a modular and flexible R&D program for systematic testing of different issues related to high field magnets that use brittle superconductor. The design also addresses several mechanical issues particular to a high field common coil geometry: horizontal support on coil edges, vertical preload on coil faces, end support, and coil stresses and strains. Figure 1 shows the basic components in a cross section of the magnet straight section.

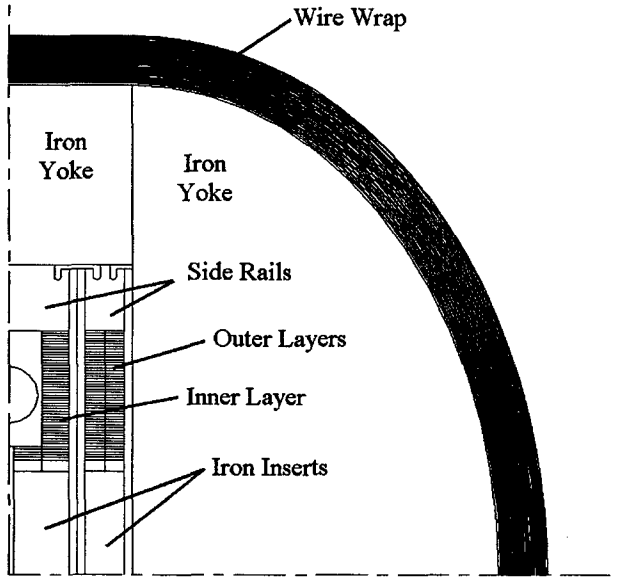

Figure 1: Basic components in magnet cross section (only one quadrant shown).

2 MAGNETIC DESIGN

The primary purpose of this magnet is to demonstrate the viability of high field dipoles based on the common coil geometry in a mechanical structure suitable for high field accelerator magnets. As such, field quality issues will not be addressed in this magnet but will be fully addressed in subsequent common coil magnets [5]. Table 1 lists the major parameters of the present design.

Table 1: Major parameters of the present design.

Bore diameter	35 mm
Main coil spacing (aperture)	40 mm
Computed quench field at 4.2 K	14.3 T
Peak field, inner layer	15.1 T
Peak field, outer layer	10.3 T
Quench current	12.3 kA
Wire Non-Cu J_c {4.2 K, 12 T}	2000 A/mm^2
Cu/Non-Cu ratio, inner & outer	0.7, 1.7
Strand diameter	0.8 mm
Number of strands, inner & outer	40, 26
Cable width, inner & outer	17.2, 11.3 mm
Number of main coil layers	1 + 3
Straight section length, inner&outer	500, 600 mm
Number of turns (half magnet)	5+48+48+48
Height of each main coil layer	80 mm
Minimum coil bend radius	70 mm
Bore spacing	220 mm
Yoke outer height and width	300 mm
Total wire wind thickness	30 mm

†Email: kpchow@lbl.gov

*Work supported by the U.S. Department of Energy under contract No. DE-AD03-76SF00098.

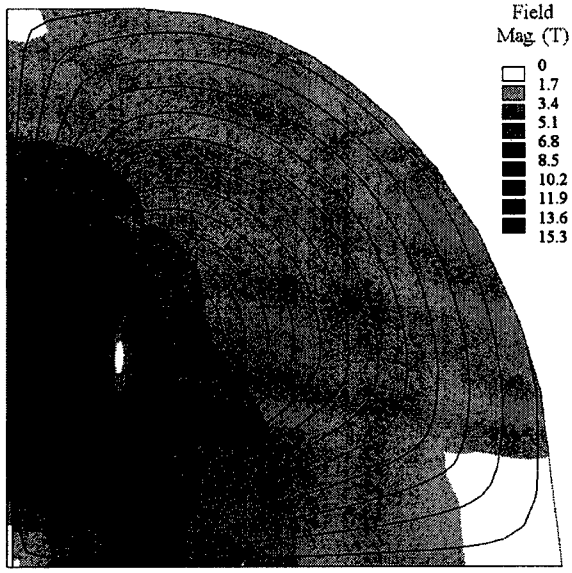

Figure 2: Field magnitude contours and flux lines in a quadrant of magnet cold mass (wire wind not shown).

This design uses a total of six main coil layers and two auxiliary coil layers (Fig. 1). Computed short sample (quench field) in the magnet bore is 14.3 tesla at 4.2 K (this field value uses the strand short sample and does not include any cable strain degradation). Figure 2 shows the field lines and field magnitude in a cross section of the current design.

3 MECHANICAL DESIGN

The mechanical design is governed by the need to support high Lorentz forces and manage coil stresses. The integrated horizontal Lorentz forces total 18.9 MN for the magnet, acting to push the windings apart. A rigid support structure is required to minimize coil displacements and maintain magnet integrity. Within the coil winding, Lorentz forces compress the winding and result in accumulated stresses approaching 150 MPa (principal compressive stress). One method of reducing coil stresses being developed in a high field magnet design at Texas A&M University is incorporation of rigid structural elements within the winding [6,7]. For the current 14 T design, no stress management is considered. The high coil stresses are not in areas of highest field and a previous high field magnet (D20) behaved well with similar levels of stress [8,9]. In addition to structural concerns, thermal conductance is an issue because adequate heat transfer is required for magnet thermal stability.

The current magnet design is based on design criteria for a flexible R&D program. In contrast to accelerator quality production magnets, the magnet is designed to be modular; the magnet is separated into three types of components and each serves a dedicated function. The first component is the magnet core and is comprised of coil modules. The second component is the iron yoke, which serves as a flux return. The third component is an external wire wrap applied around the yoke to provide preload and support. Due to the modular nature of this design, the magnet can be reassembled with different coil modules for a flexible magnet system appropriate for conducting systematic R&D parametric studies.

3.1 Inner and Outer Coil Modules

Vertical preload and support of magnet coil windings is provided completely by the coil module structure. The magnet core has three modules: one inner module sandwiched between two outer modules. Each outer module contains one double pancake winding, islands, end shoes, side rails, faceplates, and an iron insert. The inner module contains two pancake windings (each pancake has 48 turns for the main layer and 5 turns for the auxiliary layer), islands, end shoes, side rails, face plates, bore spacers, and iron inserts.

After epoxy impregnation of the Nb_3Sn windings the outer coils are assembled into the coil module structure. The windings are preloaded in the direction normal to the cable faces and the module faceplates are welded to the side rails to maintain preload. For the outer coil modules, application of 150 MPa of pressure on the cable faces yields 37 MPa of preload after the faceplates are welded and the complete structure is cooled to 4 K (Fig. 3a, 3b). This preload prevents the coil inner turn from separating from the island when the magnet is energized. Magnet training is expected to be reduced by preventing energy release due to coil movement. Each outer module supports 450 kN per meter of straight section length. The inner module is preloaded in a similar manner to the outer modules. For the inner module coil windings, 40 MPa of vertical preload is required to prevent coil separation at the islands. The inner module supports 245 kN per meter of straight section length.

Magnet ends are also supported within each coil module. Preload and support is provided through the module end shoes and reacted against the faceplates and side rails. The coil has a higher thermal contraction than iron inserts at the racetrack centers and the iron inserts exert an axial force against the winding ends when the magnet is cooled to 4 K. In addition to this internal preload from the iron inserts, an external preload is also applied against the end shoes. A gap is designed into the iron inserts to balance the internal and external preload.

3.2 External Support Structure

The external support structure provides all of the horizontal preload and support for the magnet. The coil modules are assembled between a set of yokes comprised of two rectangular sections and two half-elliptical sections (Fig. 1). Thirty layers of 1 mm thick stainless steel wire will be wound on a bobbin around the yoke perimeter with a tension of 220 MPa to preload the

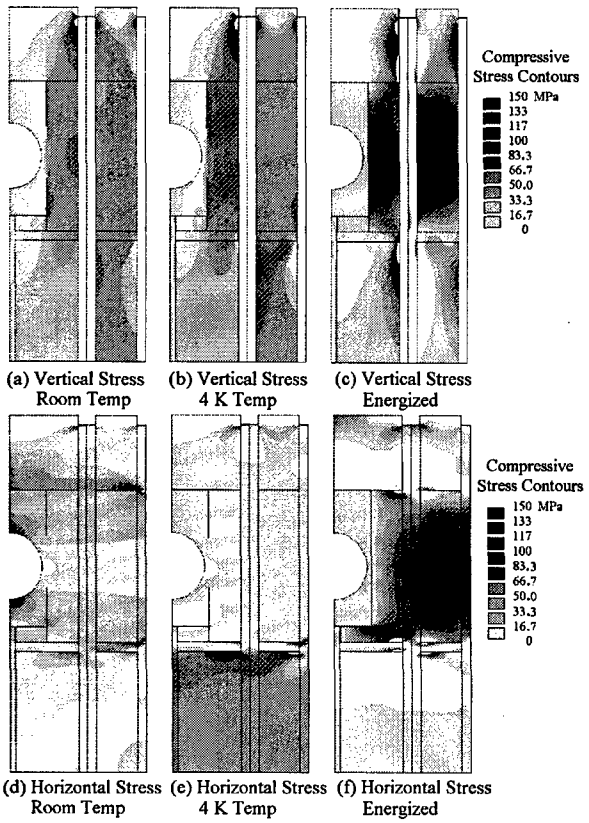

Figure 3: Vertical and horizontal stresses in one quadrant of the coil module straight section (yokes not shown).

yokes and provide rigid support for horizontal Lorentz forces. After the last wire layer is applied, tension in the innermost wire layer decreases to 125 MPa. When the magnet is cooled to 4 K the wire tension increases to 300 MPa in the first layer and 400 MPa in the last layer. This wire tension preloads the iron yokes in compression to minimize coil horizontal displacements when the magnet is energized. The total horizontal force of 18.9 MN is supported by the preloaded yokes and wire winding.

The coil modules are designed to stack 0.05 mm wider than the rectangular yoke components. During the wire winding at room temperature, the coil modules are compressed horizontally to a maximum stress of about 30 MPa (Fig. 3d). When cooled down to cryogenic temperatures, the coil modules contract more than the iron yoke components and the horizontal compressive stress on the coils decreases to less than 10 MPa (Fig. 3e). (Correspondingly, the horizontal compression on the yokes increases as the magnet is cooled.) With less than 10 MPa of horizontal preload, the coil surfaces on either side of the magnet bores separate from the bore spacer at low field and are essentially free at high fields.

When the magnet is energized, the stresses within the coil windings approach 150 MPa in both the horizontal and vertical directions (Fig. 3c, 3f). However, the region of highest coil stress is not near the region of highest field. The region of highest horizontal stress coincides with the region of lowest magnetic field. The highest vertical stress exists in a region with a magnetic field magnitude of 9 T. A previous epoxy impregnated Nb_3Sn magnet behaved well with similar coil stress levels [8,9] and we do not expect the high coil stresses to be a limiting factor. The epoxy impregnation increases the mean stiffness of the composite coil and provides support for the brittle superconductor. At field levels beyond 14 or 15 T the coil strength (epoxy impregnated) may become a critical issue and stress management may be necessary to prevent significant cable degradation.

4 CONCLUSIONS

The design of a high field 2-in-1 dipole based on a common coil design has been presented. The magnet is designed to provide a modular platform for flexible R&D parametric studies of high field magnets using brittle superconductor. Coil modules may be replaced, added, or substituted to achieve new magnet configurations and improved field quality. An external wire winding structure that was successfully used in the past provides preload and supports the substantial horizontal Lorentz forces. The structure is also easily scaled for higher field magnets. Stresses within the coil winding when the magnet is energized approach critical levels; however, stress management has not yet proven necessary at ~14 T field levels. Lastly, the common coil design uses flat racetrack coils with a large bend radius in the ends, enabling the future introduction of coils made with high temperature superconductors (HTS).

5 REFERENCES

[1] R. Gupta, "A Common Coil Design for High Field 2-in-1 Accelerator Magnets," Proceedings of the 1997 Particle Accelerator Conference, Vol. 3, pp. 3344-3346, May 1997.

[2] R. Gupta, et al., "A High Field Magnet Design for A Future Hadron Collider," Applied Superconductivity Conference, Palm Desert, CA, September 1998.

[3] K. Chow, et al., "Fabrication and Test Results of a Prototype, Nb_3Sn Superconducting Racetrack Magnet," Applied Superconductivity Conference, Palm Desert, CA, September 1998.

[4] S.A. Gourlay, et al., "Fabrication and Test Results of a Prototype, Nb_3Sn Superconducting Racetrack Dipole Magnet," 1999 Particle Accelerator Conference, New York, NY, March 1999.

[5] R. Gupta, "Common Coil Magnet System for VLHC," 1999 Particle Accelerator Conference, New York, NY, March 1999.

[6] N. Diaczenko, et al., "Stress Management in High Field Dipoles," Proceedings of the 1997 Particle Accelerator Conference, Vol. 3, pp. 3443-3445, May 1997.

[7] T. Elliot, et al., "16 Tesla Nb_3Sn Dipole Development at Texas A&M University," IEEE Transactions on Applied Superconductivity, Vol. 7, #2, pp. 555-557, June 1997.

[8] A.D. McInturff, et al., "Test Results for a High Field (13 T) Nb_3Sn Dipole," Proceedings of the 1997 Particle Accelerator Conference, Vol. 3, pp. 3212-3214, May 1997.

[9] S. Caspi, et al., "Development of High Field Dipole Magnets for Future Accelerators," Fifteenth International Conference on Magnet Technology, Beijing, China, October 1997.

COMMON COIL MAGNET SYSTEM FOR VLHC*

Ramesh Gupta#, Lawrence Berkeley National Laboratory, Berkeley, CA 94720 USA

Abstract

This paper introduces the common coil magnet system for the proposed very large hadron collider (VLHC) [1]. In this system, the high energy booster (HEB), the injector to VLHC, is integrated as the iron dominated low field aperture within the coldmass of the common coil magnet design introduced earlier [2]. This 4-in-1 magnet concept for a 2-in-1 machine should provide a major cost reduction in building and operating VLHC. Moreover, the proposed design reduces the field quality problems associated with the large persistent currents in Nb_3Sn magnets. The paper also shows that the geometric field harmonics can be made small. In this preliminary magnetic design, the current dependence in harmonics is significant but not unmanageable.

1 INTRODUCTION

The efforts are underway to prepare a proposal for VLHC to be built after the completion of the Large Hadron Collider (LHC) at CERN. The main challenge is to develop approaches that would significantly reduce the cost [3]. The superconducting magnets [4] are the single most expensive and perhaps technically most challenging component of the high field option. In addition to the cosine theta designs [5], the other design approaches can be broadly divided in two categories. The low field design based on the low cost transmission line iron dominated magnet that is being pursued at FNAL [6] and the high field design based on a common coil geometry that is being pursued at LBNL [7,8] and BNL [9].

The common coil design [2] offers the possibility of a simple, high field, low cost magnet construction based on the racetrack coil geometry. This design, developed independently, has some features similar to the design presented earlier by Danby [10]. The block coil geometry is also favored for containing the large Lorentz forces generated by high fields. Moreover, the bend radius in the ends of common coil magnets is large as it is determined by the spacing between the two apertures rather than the size of aperture. This is an important consideration in high field magnets that must use brittle superconductors (Nb_3Sn or HTS) and may also use the "React and Wind" technology. The modular nature of the design also offers a unique facility to embark on a systematic and innovative magnet R&D.

*Work supported by the U.S. Department of Energy under contract No. DE-AD03-76SF00098.

#Email: RGupta@lbl.gov

2 COMMON COIL MAGNET SYSTEM

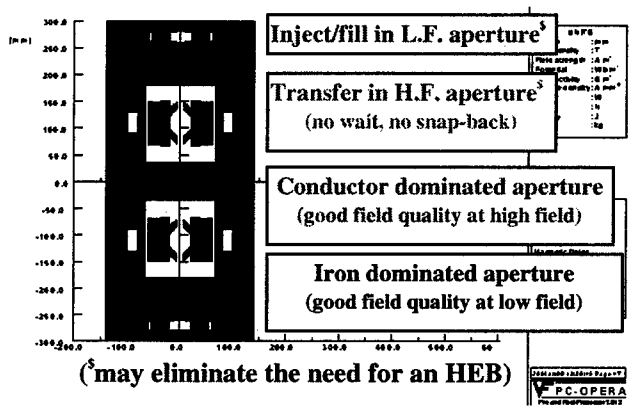

Figure 1: The common coil magnet system concept.

The proposed common coil magnet system concept is shown in Fig. 1. This has a total of four apertures: two iron dominated low field apertures (upper most and lower most) and two conductor dominated high field apertures (in the middle). The windings of one of the two pole blocks of the high field aperture (the one that is away from the center of coldmass) returns in the low field aperture and generates a part of the field. In the high field aperture, all racetrack coils are placed vertically with large bend radius and none cross the aperture horizontally. The later would have necessitated a small bend radius and eliminated various possibilities that exist now. The outer coil of the low field aperture may be independently powered for flexibility and/or de-linking the field between the low field and the high field aperture. In that case, the current in the outer coil of the low field aperture can also be used for controlling the saturation-induced harmonics in the high field aperture.

3 INJECTION AND BEAM TRANSFER

The beam is injected in the iron dominated window frame aperture at a field of 0.1 T (or perhaps even less if acceptable from beam dynamics considerations). Since the field quality at low field is determined by iron, the problem associated with the large persistent currents in a Nb_3Sn magnet is suppressed. The low field aperture in fact makes the high energy booster (HEB) based on the low field magnet design. Once the HEB is filled by several injection cycles of the machine before that (the medium energy booster), the beam is accelerated by ramping the magnets to 1.5-2.5 T. The field in the high field conductor dominated aperture (whose one coil block is shared with the low field aperture) goes up at a different rate particularly at fields over 2 T.

0-7803-5573-3/99/$10.00@1999 IEEE.

The entire beam is transferred in a single turn from the low field aperture to the high field aperture when the field in the two apertures is identical and is somewhere in the range of 1.5-2.5 T. The field in the high field aperture continues to ramp up as the beam is continuously accelerated and the problem of "snap back" is avoided. The term "snap back" refers to the sudden change in field harmonics at the beginning of a conventional acceleration cycle when the field starts to rise from a steady state value of beam injection/fill. In addition to the large persistent current induced harmonics, the "snap back" could be a major problem in a VLHC based on conventional Nb_3Sn magnets. This is because of the fact that (a) at present, the persistent current induced harmonics in Nb_3Sn magnets based on cosine theta designs are an order of magnitude more than that in Nb-Ti magnets and (b) the VLHC will be an order of magnitude bigger machine than any hadron collider built so far. It may be explicitly mentioned that the beam in the conductor dominated aperture is not injected here in the conventional multi-turn injection; it is transferred on the fly in a single turn while the magnets are ramping up. This means that the beam does not stay at a lower field for a long time. Moreover, the minimum field for the beam in the conductor dominated aperture is 1.5-2.5 tesla rather than conventional 0.3-0.7 T. Since the size of the aperture is primarily determined by the injection conditions, the above two reasons should help reduce the high field aperture.

4 MAGNETIC DESIGN

The viability of the common coil design has been demonstrated in a Nb_3Sn 6 T magnet that was tested recently at LBNL and reached the cable short sample field without any training quenches [7]. The mechanical design work is now underway to develop a structure for a 14-15 T dipole [8]. Following the program outlined earlier [11], the next steps for developing an accelerator quality magnet are (a) first demonstrate through computer codes that a dipole based on the common coil design can produce the required field shape and (b) then measure and verify that the required field quality is obtained in a magnet of this design.

This paper presents an initial magnetic design developed with a goal of optimizing the field quality while minimizing the amount of conductor and the size of the coldmass. The preliminary design presented here is based on the similar cable that is used in the 14-15 T magnet now under engineering development [8]. The major parameters of this field quality design are given in Table 1. There are three full layers that go from midplane to pole with each containing 24 turns on the average and one partial layer that is at the pole (see Fig. 1) containing 8 turns only. A preliminary analysis shows that the amount of conductor required in this design is comparable to that in a similar field cosine theta design.

At low currents, the magnitude of the field in the low field and high field apertures is about the same. However, as the current is increased, the field in the high field aperture reaches the computed quench field of ~14.8 T (at 4 K, assuming no degradation in cable), the field in the low field aperture remains under 4.6 T due to iron saturation. This paper does not address the iron saturation and other field quality issues in the low field aperture. They will be addressed in the subsequent papers. The low field aperture can also be a combined function magnet.

In the high field aperture, the field harmonics at low to medium field (geometric harmonics) are optimized by using the following parameters: (a) spacers within the coil, (b) block heights of various layers, (c) slant angle of the pole blocks while keeping the inner and outer surfaces parallel (vertical) to other coils. In this hand optimized design, the harmonics are reduced to less than 0.2 unit (see Table 2). The skew (a_n) and normal (b_n) components of field harmonics are defined (in units) as:

$$B_y + iB_x = 10^{-4} B_o \sum_{n=0}^{\infty} [b_n + ia_n] \left[\frac{x+iy}{R}\right]^n,$$

where B_x and B_y are the components of the field at (x,y) and B_o is the magnitude of the field at a reference radius R which is 10 mm here.

Table 1: Major parameters of the design.

Coil aperture	40 mm
Number of layers	3 + 1
Computed quench field at 4.2 K	14.8 T
Peak Fields, inner & outer layers	15.0 T & 10.5 T
Quench current	12.1 kA
Wire Non-Cu J_{sc} (4.2 K , 12 T)	2000 A/mm^2
Strand diameter	0.8 mm
No. of strands, inner & outer layers	40, 26
Cable width, inner & outer layer (insulated)	16.9 mm, 11.1 mm
Cu/Non-Cu ratio, inner & outer	0.7, 1.7
No. of turns per quadrant per aperture	80
Max. height of each layer from midplane	40 mm
Bore spacing	220 mm
Minimum coil bend radius (in ends)	70 mm
Yoke size (full width X full height)	280 mm X 600 mm

The computed field harmonics in the high field aperture remain practically constant till about 2 T (see Fig. 2). The odd normal and even skew harmonics are not allowed by the symmetry. Odd skew harmonics are the manifestation of the inherent up-down symmetry in an over-under design. The variation in harmonics (due to iron saturation) in this preliminary design is significant

but manageable. The harmonics higher than decapole (n=4), show a variation of less than 0.1 unit. The variation in octupole and decapole is under 0.4 unit and in skew quadrupole is about 1 unit.

Table 2: Optimized harmonics at 1.8 T in an initial magnetic design of a common coil dipole at 10 mm.

N	SKEW(a_n)	NORMAL(b_n)
1	-0.01	--
2	--	0.00
3	0.01	--
4	--	0.04
5	0.02	--
6	--	0.05
7	0.01	--
8	--	-0.17
9	0.00	--
10	--	-0.03
11	0.00	--
12	--	0.00

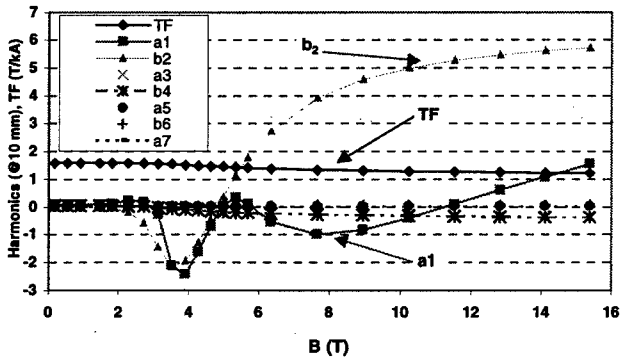

Figure 2: Current dependence of the field harmonics and Transfer Function (TF) as a function of the bore field in the high field aperture (preliminary design).

The maximum computed saturation is in normal sextupole harmonic (b_2). It is still, however, under 6 units till 15 T. This value is comparable to that in a conventional cosine theta design for a 12 T dipole [12]. It may be pointed out that the magnetic design of the common coil magnet is in early stages with the required tools (codes) still under development. The situation is expected to improve, as the computer codes get developed and the design matures. The computer code ROXIE [13] will be used to further optimize the 2-d coil geometry. ROXIE will also be used to design the ends of this magnet which do not have an up-down symmetry. The integrated up-down asymmetry, as seen by the beam along the axis, will be minimized. Conceptually, the up-down asymmetry in the magnet ends may be compensated by (a) an asymmetry in the axial length of conductor blocks relative to the midplane and (b) an asymmetry in the straight section (body) of the magnet.

5 DISCUSSION AND CONCLUSIONS

The common coil magnet system presented here has the potential of significantly reducing the cost of VLHC while improving the technical performance. The need for an HEB is eliminated, reducing the cost of building and operating a major sub-system. The design also mitigates the problem associated with the large persistent currents in conventional Nb_3Sn magnets. The conductor dominated high field aperture may be made smaller as the injection conditions (beam transfer, in this case) are significantly changed and the minimum field increased.

Strategies and tools are being developed for optimizing the field quality while minimizing the conductor and the size of coldmass in a common coil dipole. In the preliminary design presented here, the field harmonics are minimized using the first principles. As compared to this four aperture, 14.8 T common coil dipole, the single aperture, 13.5 T, D20 dipole [14] was 2.4 times bigger and the dual aperture ~9 T, 2-in-1, LHC dipole [15] is 1.4 times bigger. The common coil design should reduce the magnet cost due to its simplicity in construction and compactness in size.

ACKNOWLEDGEMENTS

Discussions with W. Barletta, A. McInturff, R. Scanlan and others (within and outside the Berkeley Lab) are appreciated.

REFERENCES

[1] Electronic proceedings of workshops on VLHC at http://vlhc.org/; Annual meeting to be held at Monterey, CA, June 28-30, 1999.

[2] R. Gupta, "A Common Coil Design for High Field 2-in-1 Accelerator Magnets", Proceedings of the 1997 Particle Accelerator Conference.

[3] HEPAP Subpanel on "Planning for the Future of U.S. High Energy Physics", February, 1998 (Gilman Panel).

[4] R. Scanlan, "High Field Superconducting Magnets", these proceedings.

[5] A.V. Zlobin, et al., "Conceptual Design of the Fermilab Nb_3Sn High Field Dipole Magnet", these proceedings.

[6] "Turquois" Book. W. Foster, et al., Fermilab Report (1998).

[7] S. Gourlay, et al., "Febrication and Test Results of a Prototype Nb_3Sn Superconducting Racetrack Dipole Magnet", these proceedings.

[8] K. Chow, et al., "Mechanical Design of a High Field Common Coil Magnet", these proceedings.

[9] W. Sampson, et al., "A Common Coil Magnet for Testing High Field Superconductors", these proceedings.

[10] G. Danby, et al., "Proceedings of the 12th International Conference on High Energy Accelerators", Fermilab, Aug. 1983.

[11] R. Gupta, et al., "A High Field Magnet Design for a Future Hadron Collider", Palm Desert, CA, Sept. 1998.

[12] S, Caspi, "A 12 T Dipole for the VLHC", LBL Note No. SC-MAG-651, Dec. 16, 1999, unpublished.

[13] S. Russenschuck, "ROXIE -- A Computer Code for the Integrated Design of Accelerator Magnets," Sixth European Particle Accelerator Conference, Stockholm, Sweden, June 1998.

[14] A. McInturff, et al., "Operational Characteristics, Parameters, and History of A (13T) Nb_3Sn Dipole", these proceedings.

[15] C. Wyss, "LHC Arc Dipole Status Report", these proceedings.

NIOBIUM-TIN MAGNET TECHNOLOGY DEVELOPMENT AT FERMILAB *

D.R. Chichili†, T.T. Arkan, I. Terechkine, Fermilab, Batavia, IL, USA
J.A. Rice, Composite Technology Development Inc., Lafayette, CO, USA

Abstract

As a part of the Fermilab high field Nb_3Sn dipole development program, various issues of magnet technology are being investigated. In cable insulation development, S-2 fiber glass sleeve and a new ceramic insulation developed by Composite Technology Development Inc. (CTD) were studied as a possible candidates. For each type of insulation, Nb_3Sn ten-stack samples were reacted and then vacuum impregnated with epoxy. Measurements of modulus of elasticity and Poisson's ratio under compression were made at room temperature and at 4.2 K. For comparison, an epoxy impregnated NbTi composite was also tested.

1 INTRODUCTION

Fermilab, in collaboration with LBNL and KEK, is developing a high field Nb_3Sn dipole for use in the next generation Hadron Collider. The conceptual design for the first magnet, detailed in [1], is based on a 2-layer cosθ coil structure and cold iron yoke. As a part of this program, various issues of the magnet technology such as cable insulation, heat-treatment, epoxy impregnation and thermo-mechanical properties of the composite are being investigated. Due to limited space, this paper presents results only in the azimuthal direction. Readers are referred to [2] for more results.

2 SAMPLE PREPARATION

2.1 Cable Parameters

A summary of Nb_3Sn and NbTi cable parameters used in the present study are given on Table 1. The variation of Nb_3Sn cable mid-thickness with pressure before and after reaction is shown in Fig. 1. The cable mid-thickness increases with reaction and decreases with pressure [3]. On the other hand, the cable length contracted by about 4.5 μm/mm and the cable width increased from 14.232 mm to 14.669 mm due to reaction. Note that these measurements are taken at zero pressure.

2.2 Cable Insulation

The most common insulation material used for Nb_3Sn cables is S-2 fiber glass either in tape form or sleeve [4,5]. In the present work, we investigated S-2 fiber glass sleeve and a new ceramic insulation.

Table 1: Cable Parameters

	Nb_3Sn	NbTi
Number of Strands	28	38
Strand diameter	1.012 mm	0.808 mm
Cable Thickness	1.7852 mm	1.4573 mm
Cable Width	14.232 mm	15.3943 mm
Keystone angle	0.91 deg.	1.038 deg.

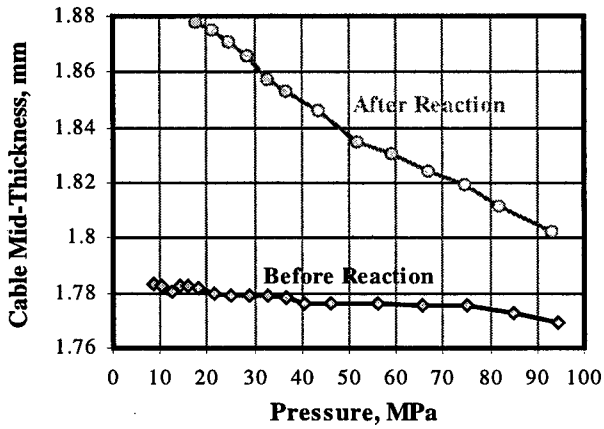

Figure 1: Variation of cable thickness with pressure.

The organic binder used on the S-2 fiber glass sleeve which provides protection/lubrication for the glass strands during processing left a carbon residue during reaction under argon atmosphere. This could create turn to turn shorts in the coil. So the sleeve was first heat-treated at 450 °C in air to remove the binder and a different binder was applied that would not leave much carbon residue during reaction [5,6].

Ceramic tape on the other hand does not have any organic sizing. The binder (CTD-1002x) which is applied to the tape is also inorganic and can be used to preform the coils in shape before reaction by curing at 120°C for 30 min. Hence with the binder we can have a insulated and cured coil before reaction which helps to define the coil shape. This also makes the coils easier to handle. After reaction the ten-stack samples remain bonded together, however the binder became porous and formed crystals due to shrinkage. This is useful as it allows the epoxy to penetrate during impregnation.

* Work supported by the U.S. Department of Energy
† Email: chichili@fnal.gov

2.3 Epoxy Impregnation

Insulated ten-stack samples were first reacted and then vacuum impregnated with CTD-101K. Note that the samples were compressed with a pusher block during impregnation and the effect of this impregnation pressure on the mechanical behavior was also investigated. Fig. 2 shows an epoxy impregnated composite with direction convention used in this paper.

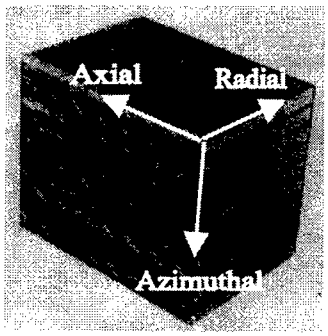

Figure 2: Epoxy impregnated composite.

3 MECHANICAL PROPERTIES

Strain gauges were mounted to measure strains both in the direction of load and transverse to the direction of the load. A calibrated load cell was used to record the force applied on the sample. Both monotonic and load-unload-reload tests were performed at 300 K and at 4.2 K and the test results are discussed below.

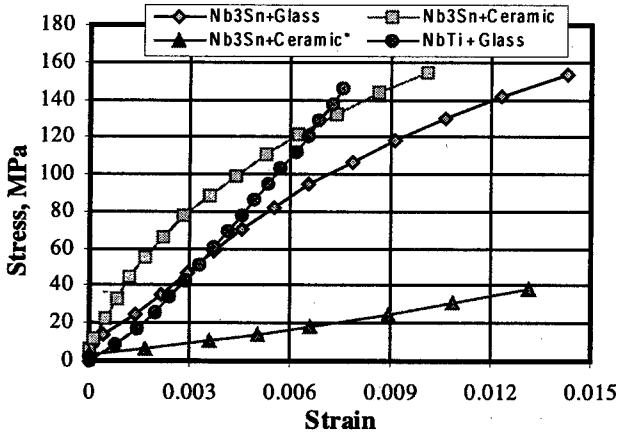

Figure 3: Mechanical behavior at room temperature. (*Nb_3Sn stack with ceramic insulation cured and reacted; but not impregnated).

3.1 Azimuthal Direction: Monotonic Loading

Fig. 3 shows the test results at room temperature. Note that the Nb_3Sn composite exhibits non-linear behavior in contrast to the linear behavior observed for NbTi composite. This behavior of Nb_3Sn composite was first thought to be due to low impregnation pressure (10 MPa) compared to NbTi composite (45 MPa). To test this hypothesis, another Nb_3Sn composite was fabricated at higher impregnation pressure (45 MPa) and tested. The results shown in Fig. 4 show that the mechanical response in azimuthal direction does not depend on impregnation pressure.

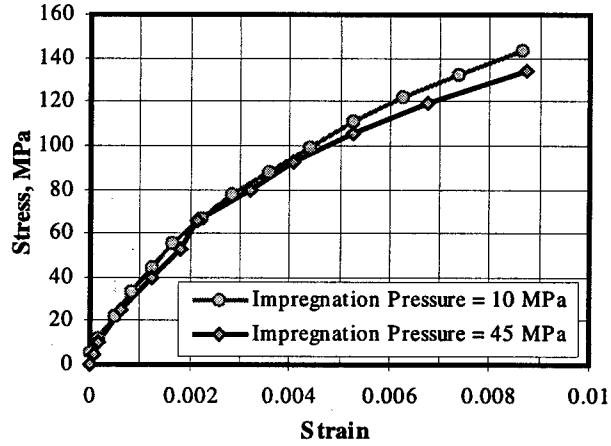

Figure 4: Effect of impregnation pressure.

The effect of temperature on the mechanical response of Nb_3Sn composite is shown in Fig. 5. There is significant increase in the modulus for Nb_3Sn composite with S-2 glass. However with ceramic insulation, the modulus did not change with temperature except that the composite behavior is more linear at 4.2K than at 300K. This behavior was very repeatable and even the load-unload-reload tests (see next section) show this behavior.

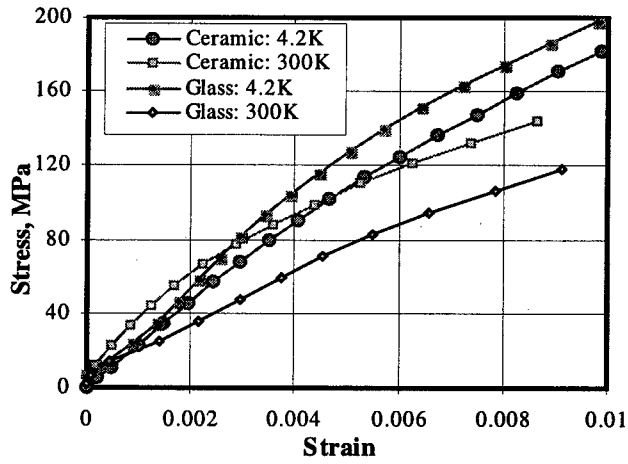

Figure 5: Effect of temperature.

3.2 Azimuthal Direction: Load-Unload-Reload

The coils in a magnet are subjected to loading, unloading and reloading repeatedly during assembly, cool-down and excitation. Hence it is very important to understand the mechanical behavior of the composite under these loading conditions. Fig. 6 shows load-unload-reload test results for Nb_3Sn composite with ceramic insulation both at 300K and at 4.2K. The following observations can be inferred from these results (i) the overall behavior of the composite under loading is similar to that under

monotonic loading, (ii) there is no apparent change in modulus by decreasing temperature. Fig. 7 shows the behavior of the Nb_3Sn composite under cyclic loading after initial "massaging" to 100 MPa. The results show that we could massage the coils up to a peak stress before assembly, which would then result in a composite with higher modulus and a linear mechanical behavior. This massaging also results in a plastic deformation of 0.3% in the composite which should be taken into account while designing the magnet cros-section.

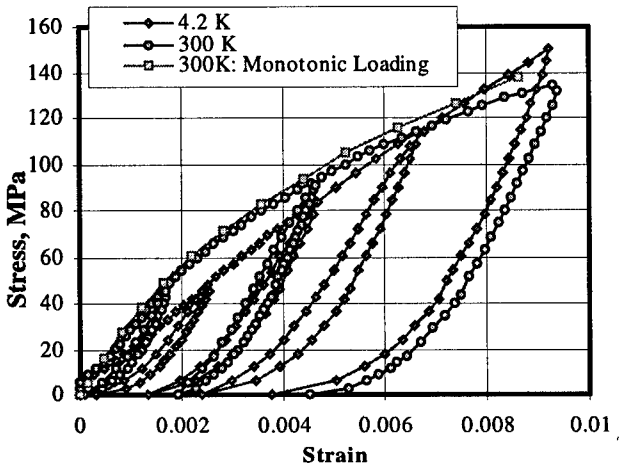

Figure 6: Load-Unload-Reload Tests.

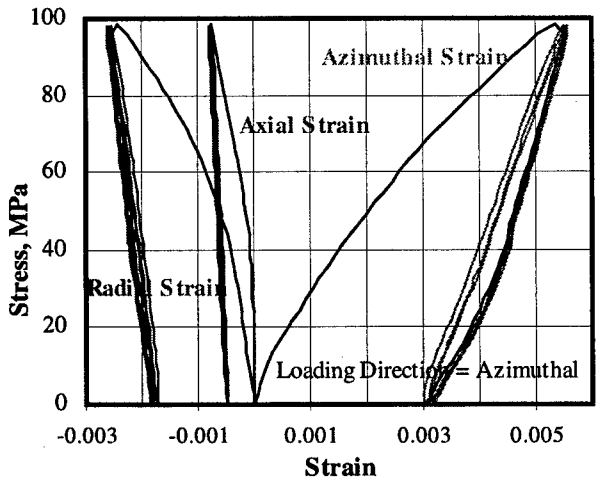

Figure 7: Cyclic loading tests up to a certain stress.

Fig. 7 also shows the Poisson's ratio measurements for the load-unload-reload tests. Note that the Poisson's ratio in the axial direction is higher than in radial direction. Also it remained constant in the axial direction from the first cycle to the second cycle at 0.14, however in the radial direction it decreased from 0.45 to 0.33.

Similar load-unload-reload experiments were conducted for the Nb_3Sn composite with S-2 glass insulation. The mechanical behavior was found to be similar to that with ceramic insulation.

4 SUMMARY

Table 2 summarizes the mechanical properties under monotonic loading for different composites tested. At room temperature, the behavior is nonlinear and hence two moduli are specified, one at low pressures and the other at higher pressures. Included in the table also are the data reported by LBNL[5,7] and University of Twente [4]. The moduli of the composite tested here are much lower than that reported by LBNL and higher than that measured at [4]. These differences in the data quoted here and else where in the literature are not understood yet.

Table 3 provides the data for Nb_3Sn composite after massaging to 100 MPa. The idea for the first short model dipole to be built at Fermilab, is to massage the coils to about 100MPa before assembly which would then increase the modulus to 38 GPa both at 300K and at 4.2K with linear mechanical behavior.

Table 2: Data under monotonic loading.

Composite	E, GPa		Poisson's Ratio
	300K	4.2K	
Nb_3Sn + S-2	17.5 6.5	26.0 14.0	$\nu_{21} = 0.16$ $\nu_{23} = 0.46$
Nb_3Sn + ceramic	27.0 10.0	22.0 14.0	$\nu_{21} = 0.14$ $\nu_{23} = 0.45$
NbTi + S-2	20.0	32.0	$\nu_{23} = 0.29$
Nb_3Sn + S-2 [5]	35.0		
Nb_3Sn + S-2 [7]	44.0		
Nb_3Sn + S-2 [4]	2 to 5		

Table 3: Mechanical properties of the Nb_3Sn composite after massaging to 100 MPa.

Composite	E, GPa		Poisson's Ratio
	300 K	4.2K	
Nb_3Sn + S-2	39.0	40.0	$\nu_{21}= 0.15$; $\nu_{23}= 0.34$
Nb_3Sn+ ceramic	38.0	38.0	$\nu_{21}= 0.14$; $\nu_{23}= 0.33$

REFERENCES

[1] T. Arkan et al., "Conceptual Design of the Fermilab Nb_3Sn High Field Dipole Model", PAC, NY (1999).

[2] D.Chichili et al., "Measurements of Thermo-Mechanical Properties of Nb_3Sn Composite", Fermilab pre-print, FERMILAB-Conf-99/ 052 (1999).

[3] I. Bogdanov et al., "Study of the Nb_3Sn Cable Characteristics for SC - Quadrupole with High Gradient", MT-15, Beijing, (1997).

[4] A. den Ouden et al., "An Experimental 11.5 T Nb_3Sn LHC Type of Dipole Magnet", IEEE Transactions of Magnetics, Vol. 30 (1994).

[5] D.Del'Orco et al., "Fabrication and Component Testing Results for a Nb_3Sn Dipole Magnet", IEEE Trans. of Applied Superconductivity, Vol. 5 (1995).

[6] T.Arkan, et al., "Studies on S-2 Fiber Glass Insulation", Fermilab Technical Note, TD-98-063 (1998).

[7] K.Chow et. al., "Measurements of Modulus of Elasticity and Thermal Contraction of Epoxy Impregnated Niobium-Tin and Nb-Ti Composites", presented at ASC, Palm Desert CA (1998).

INTERACTIVE PROCEDURE FOR RAPID PERFORMANCE ESTIMATES OF MAGNET DESIGNS*

Carl L. Goodzeit#, M. J. (Penny) Ball, M J B Plus Inc., DeSoto, TX,
Rainer B. Meinke, Advanced Magnet Lab Inc., Palm Bay, FL

Abstract

This paper illustrates the use of a simple interactive magnetic field calculator (IMC) program to estimate field strength and allowed harmonics for cosine theta dipole or quadrupole magnets. Niobium-tin coil designs from Saclay and the University of Twente are used as examples, and the IMC results are compared with the values from the magnet designers.

1 MAGNETIC FIELD CALCULATOR

One of the features included in a CD-ROM tutorial on superconducting accelerator magnets [1] is an interactive procedure for calculating magnetic field strength and allowed field harmonics in single layer cosine theta dipole or quadrupole magnets. This procedure uses a simplified geometry for the coil, which can contain a single wedge and an optional iron yoke. The yoke is defined by its inner radius and is assumed to be iron with infinite μ.

However, this interactive magnetic field calculator (IMC) can be applied to more complicated magnet structures, consisting of multiple layers with several wedges, by use of superposition, i.e., decomposing the structure into several simple ones and adding the results. Using this technique, the results from the IMC are in good agreement with precise calculations for the central field, the peak field, and the x and y components of the Lorentz force. The allowed multipoles are in good agreement only when the conductor blocks and wedges are radially disposed (i.e. without any tilt). The details of using the interactive magnetic field calculator (IMC) have been previously described [2]. Input values define the coil geometry and the total current flow. Output includes the field strength and normalized multipole coefficients, a color-coded graph of the field strength in the conductor region, and the Lorentz forces on the coil.

The calculation procedure uses an ideal approximation of the coil geometry in which the conductor block and wedge edges are assumed to be radial. The input data consists of the inner and outer radius of the coil (R1 and R2), the start and stop angles of the coil (A1 and A2), the inner radius of the optional yoke (Ryoke), the start and stop angles of the optional wedge (A3 and A4), the average current density in the conductor area (J), and the radius and angle at which field values are calculated (Rref and Aref). The data are entered into a graphical user interface which then displays the defined cross section.

*Work supported in part by U.S. Dept. of Energy SBIR grant # DE-FG03-94ER-81813

#Email: carl@mjb-plus.com

2 SACLAY QUADRUPOLE EXAMPLE

Saclay developed a protoype design for a quadrupole magnet with the LHC quadrupole dimensions but using a Nb_3Sn conductor. This magnet coil has two layers with tilted current blocks [3]; the inner and outer layer coil cross sections are shown in Figure 1.

In order to use the IMC, this cross section is idealized into a radially disposed configuration; the angles for the idealized coil were selected to provide an average fit with the tilted coil blocks. The parameters for the LHC quadrupole magnet and those used for the idealized coils are summarized in Table 1. The average current density for the idealized coils was obtained by dividing the product of the number of turns (10 for the inner and 14 for the outer coil) and the operating current (11870 A) by the area of the idealized current blocks.

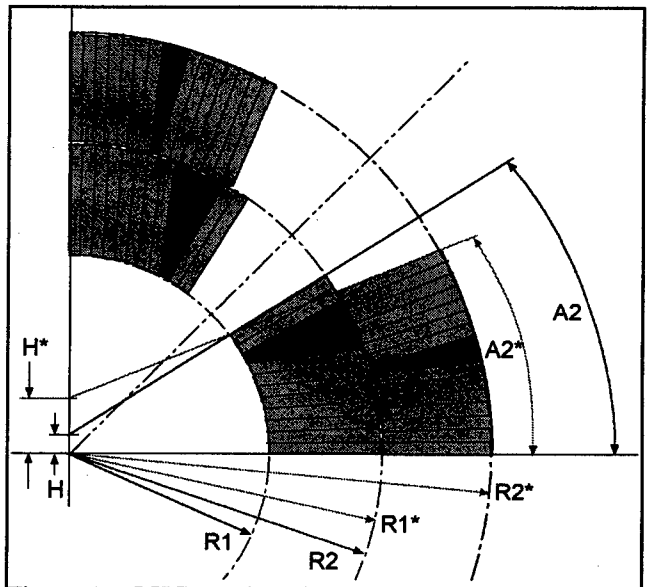

Figure 1. LHC quadrupole coil geometry. (Outer coil parameters are indicated by *)

Table 1. Parameters for LHC quad (actual and idealized coils)

Parameter	Inner coil	Outer coil	Idealized inner coil	Idealized outer coil
A1	0°	0°	0°	0°
A2	31.1°	22.42°	36°	30.4°
H, mm	2.53	6.65	0	0
A3	Tilted wedge	Tilted wedge	23.4°	14.6°
A4			29.7°	17°
R1, mm	28.00	43.88	28	43.88
R2, mm	43.15	59.00	43.15	59
R_{yoke}, mm	90, μ=∞		90, μ=∞	
R_{ref}, mm	10		10	
A_{ref}	0°		0°	
J, A/mm^2	410	410	425	437

The fields produced by the inner and outer coils are calculated separately and then the harmonic contributions are summed to give the total harmonic for the magnet. Table 2 shows these results and the values from Saclay calculations [4] using an iron yoke with $\mu=\infty$. (Note that the negative sign for the field components is an arbitrary sign convention.) Since the current blocks have been made radial, the allowed multipoles appear higher that those obtained by calculations that consider the tilt of the current blocks.

Table 2. Results for LHC quad field calculation.

	Inner coil	Outer coil	Total	Saclay value
B1, T	-1.231	-0.9149	-2.15	2.23
B5/B1 x 10^4	-6.50	3.67	-2.83	0.47
B9/B1 x 10^4	-2.30	2.71	0.41	0.05
Gradient, T/m			-215	223
Fx (octant), kN/m*			496	540
Fy (octant), kN/m*			780	730

* For multilayer examples, forces can be approximated, but not rigorously computed, by superposition. In this case the force on each coil is calculated individually at the field produced by the single layer. Then this force is scaled linearly for each layer by the ratio of the total field produced by both coils to the field produced by the individual coil. The forces for the two layers are then summed to give the total force.

The operating margin can be computed from the ratio of the current density in the superconductor to its critical current density at operating temperature and the maximum field on the conductor, Bmax.

The IMC output includes color-coded graphs of the field strength in the conductor region. (These neglect the field enhancement in the coil ends.) These show that the maximum field on the conductor occurs at the pole turn of the inner coil at its inner radius. However, for a multilayer coil, Bmax must be computed from the contributions of all coil layers. Figure 2 shows the computation of the x and y field components due to the outer coil at the inner coil location; note that the input screen has Rref = 28 and Aref = 36°. The x and y field components due to the inner coil must also be computed at this same reference point. For the inner coil, Bx=-1.954 and By=-2.822; for the outer coil, Bx=-1.529 and By=-2.058. The magnitude of Bmax is thus 5.995.

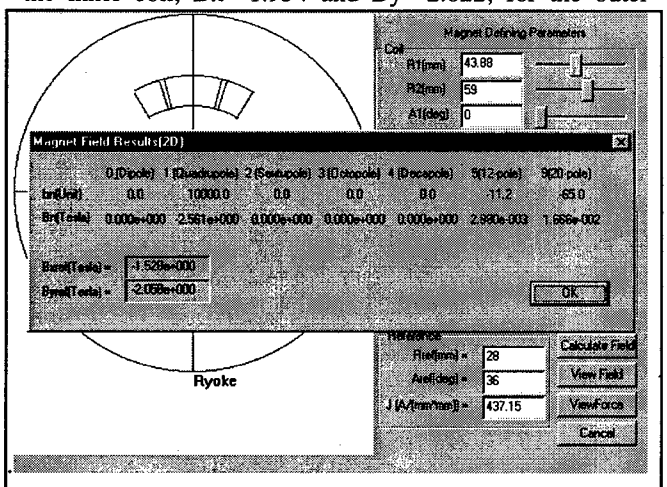

Figure 2. Field component calculation for LHC quad at location of peak field.

Table 3. LHC quad operating margin calculation

Nb3Sn Strand diameter	0.78 mm
Cu/non-Cu	1.7
Strands/cable	36
Operating current	11870 A
Operating temperature	1.9 K
C_0	12,000 $AT^{1/2}/mm^2$
Area of cable conductor	17.20 mm^2
SC area in cable	6.37 mm^2
Current density in conductor	1863.09 A /mm^2
Peak field on conductor, B_{max}	6.00 T
J_c @B_{max} and T_{op}*	2796 A/ mm^2
Margin	33.37%

* J_c @B_{max} and T_{op} is obtained from the Material Properties Library in the Superconducting Magnet Tutorial. This interactive procedure computes the critical current density as a function of applied field and temperature using the Summer's formula.

The cable and operating parameters are shown in Table 3. C_0 is the coefficient used in the Summer's formula [5] for computing the critical surface of Nb_3Sn.; the value of C_0 listed is that set by the VAMAS (Versailles Agreement Meeting on Applied Science) and is used in the magnet tutorial to compute J_c for Nb_3Sn. For comparison, the Saclay calculation indicated an operating margin of 19.7% with a peak field on the conductor of 6.85 T.

3 U. TWENTE DIPOLE EXAMPLE

A two-layer dipole design developed by the University of Twente [6], and designated MSUT, was proposed as an LHC dipole prototype. This magnet used powder-in-tube Nb_3Sn conductor. The cross section of the coils is shown in Figure 3. In this case there are two wedges in the inner coil and both coils have tilted current blocks.

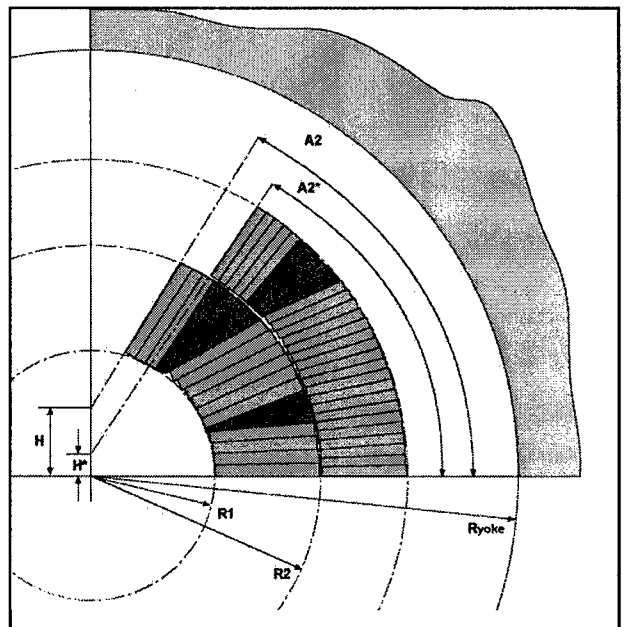

Figure 3. MSUT dipole coil geometry, constructed from data supplied by U. Twente. (Outer coil parameters are indicated by *)

To use the interactive magnetic field calculator (IMC), the inner coil needs to be broken into two separate coils in order to conform to the single wedge limitation. Thus, three separate calculations need to be performed and summed in order to compute the total field in this magnet.

The values of the IMC input parameters for the three idealized coil sections with radial current blocks are listed in Table 4; the angles were determined by visual adjustment to achieve an average position of the radial line. The current density in each coil section was computed using the same method as that described for the LHC quadrupole example.

Table 4. Input parameters for MSUT magnet model using three coil sections.

Parameter	Inner coil-1	Inner coil-2	Outer coil
A1	0°	21.95°	0°
A2	18.8°	74.56°	58.01°
A3		52.32°	42.07°
A4		56.68°	48.11°
R1, mm	24.95	24.95	47.16
R2, mm	46.75	46.75	64.56
Ryoke, mm	105	105	105
Rref, mm	12.5	12.5	12.5
Aref	0°	0°	0°
Operating current, A	19100		
J, A/mm^2	297.93	294.24	519.95

The IMC results for the field and Lorentz forces and a comparison with those obtained from U. Twente are shown in Table 5 for the case of iron with infinite or high μ; the B0 results of the calculation for the case of no iron are shown also. These IMC calculations show reasonably good agreement with the U. Twente results, except for the sextupole; as usual, the sextupole from the IMC is much higher than values calculated from the actual design with tilted current blocks. The actual field attained in this magnet should be lower that the values shown because of iron saturation effects; during tests, this magnet attained a field of 11.3 T at 19.1 kA.

Table 5. MSUT Magnet Calculation for Iron without saturation.

	Interactive calculation μ=∞			Total	U. Twente μ=999
	Inner-1	Inner-2	Outer		
B0, T	-1.852	-3.098	-7.147	-12.097	12.230
B2, T	-0.194	0.318	-0.0414	0.08277	-8.0E-04
B4, T	-0.0211	0.0154	0.00226	-0.003466	n/a
Fx /quadrant, kN/m*	299	1110	2480	3890	3650
Fy /quadrant, kN/m*	-479	-253	-1420	-2160	-1770

MSUT Magnet Calculation without Iron.

	Interactive calculation μ=1			Total	U. Twente
B0, T	-1.89E+00	-2.80E+00	-5.60E+00	-10.29	10.13

The maximum field on the conductor (Bmax) occurs at the inner radius of the pole turn of the inner coil (neglecting the field enhancement in the coil ends). The IMC can be used to compute the field components at that location due to each of the three coil segments, and the results summed. For the case of μ=∞, Bx = 0.122 (= –0.197 +0.438 –0.119) and By = -12.584 (= -1.338 – 4.258 –6.988); thus Bmax = 12.585. Since iron saturation takes place in this magnet, the peak field on the conductor is not as high as this. We cannot compute a reasonable estimate of the operating margin for this magnet without a precise value of Bmax. Also, the powder-in-tube conductor for this magnet has a higher Jc than that represented by the Summer's formula with C_0= 12,000.

4 CONCLUSION

We have illustrated how the interactive magnetic field calculator (IMC) which is included in the Superconducting Accelerator Magnets CD-ROM tutorial can be used to estimate the magnetic fields and Lorentz forces in multiple layer magnets with more than two wedges per coil.

Two examples of magnets with Nb3Sn conductor were considered. In both cases, the central field values calculated by the IMC were in close agreement with the designers' calculation results. However, these magnets used tilted current blocks, and thus the IMC approximation to the allowed multipole fields was not very close to the designers' calculation results. For the LHC quadrupole, the operating margin could also be estimated by using the tutorial's interactive calculation of Jc from the Summer's formula.

Although this simple IMC procedure does not give precise results for field harmonics, it can be very helpful in making preliminary comparisons of cosine theta magnet designs.

5 REFERENCES

[1] "Superconducting Accelerator Magnets" CD-ROM tutorial information at www.mjb-plus.com

[2] Meinke, R. B, Goodzeit, C. L. and Ball, M. J., Interactive Procedure for Estimating Performance of Magnet Designs, Poster Paper LFB-06 Presented at the 1998 Applied Superconductivity Conference, September 13-18, Palm Desert CA USA. A PDF copy is available at the web site given in the previous reference.

[3] Dimensional data from LHC Project Magnet Parameters, CERN 01/28/99 and communicated by Arnaud Devred, CEA Saclay, 01/08/97.

[4] Communicated by Arnaud Devred, CEA Saclay, calculation of 02/08/97.

[5] L.T. Summers, J.C. McKinnell, S.L. Bray and J.W. Ekin, "Characterization of Multifilamentary Nb_3Sn Superconducting Wires for Use in the 45-T Hybrid Magnet", IEEE Trans. Appl. Superconductivity, vol. 5, no. 2, 1764, June 1995

[6] Data for this magnet was communicated by Andries den Ouden, University of Twente, Faculty of Applied Physics, Feb. 1999.

CURRENT STATUS OF THE RECIRCULATOR PROJECT AT LLNL*

L. Ahle#, T. C. Sangster, D. Autrey, J. Barnard, G. Craig, A. Friedman, D. P. Grote, E. Halaxa, B. G. Logan, S. M. Lund, G. Mant, A. W. Molvik, W. M. Sharp, LLNL, Livermore, CA
S. Eylon, LBNL, Berkeley, CA
A. Debeling, W. Fritz, Becthel Nevada Corporation, Las Vegas, NV

Abstract

The Heavy Ion Fusion Group at Lawrence Livermore National Laboratory has for several years been developing the world's first circular ion induction accelerator designed to transport space charge dominated beams. Currently, the machine extends to 90 degrees, or 10 half-lattice periods(HLP) with induction cores for acceleration placed on every other HLP. Full current transport with acceptable emittance growth without acceleration has been achieved [1]. Recently, a time stability measurement revealed a 2% energy change with time due to a source heating effect. Correcting for this and conducting steering experiments has ascertained the energy to an accuracy of 0.2%. In addition, the charge centroid is maintained to within 0.6-mm throughout the bend section. Initial studies of matches dependencies on beam quality indicate significant effects.

1 WHY THE RECIRCULATOR

Currently, heavy ion beams are being pursued as a candidate for a driver of an Inertial Fusion(IFE) power plant. In such a power plant, ion beams would provide the input energy necessary to ignite small D-T capsules [2]. The accelerator for such a driver would need to accelerate space charge dominated ion beams to a total kinetic energy of a few GeV while providing pulse compression and be able to operate at a rate of ~5-Hz [3,4]. Usually the conceptual design of such a machine is linear, but an alternative concept, which may provide significant cost savings [5], is a circular machine, or recirculator. However, a space charge dominated, ion induction, circular machine has never been built before. Thus, the HIF Group at LLNL has been developing a small recirculator in order to investigate the validity of such a concept.

2 THE RECIRCULATOR

In order to validate the recirculator for an IFE power plant driver, coordinating bending and acceleration of the beam while maintaining transverse and longitudinal control and beam brightness must be demonstrated [6]. Table 1 lists some important characteristics of the recirculator. In designing this machine, all of the important dimensionless beam parameters, such as perveance, were kept the same as a full scale driver machine. Each half-lattice period(HLP) of the recirculator consists of a permanent magnetic quadrupole for focusing, an electrostatic dipole for bending, an induction core, for acceleration and longitudinal compression, and a capacitive beam probe, or C-probe, for position monitoring. The dipole plates are designed to bend the beam by 9 degrees while the modulators are designed to accelerate the beam by 500-eV. The C-probes provide position measurements to within 100-μm.

Table 1: Recirculator Specifications

Circumference	14.4m	
Beam Species	K^+	
# of laps	15	
Max. Beam Radius	1.5 cm	
Beam Statistic	Lap 1	Lap 15
Beam Energy	80 keV	320 keV
Pulse Duration	4 μs	1 μs
Beam Current	2 mA	8 mA
Undepressed Phase Advance	78°	45°
Depressed Phase Advance	16°	12°

Figure 1 shows the current layout of the machine. Initially, a 4-μs beam pulse is injected by a source diode with an energy of 80-keV through a 1-cm diameter aperture which provides an initial beam current of 2-mA. Upon injection the beam enters an electrostatic matching section used to convert the uniformly expanding beam to an AG focused beam. A short magnetic transport section follows which then leads to the 90 degree bend section. Following the bend section is the End Tank which houses several diagnostics (a Faraday cup, parallel slit scanner, and a gated beam imager) to measure beam quality. Also magnetic induction cores exist on 5 of the 10 HLP's as shown.

As reported earlier [1], full current transport through the 90° bend section was achieved with no acceleration and DC voltages (+/- 6.575-kV) on the bending dipole plates. The RMS normalized emittance,

$$\varepsilon_{rms}^2 = 4\gamma\beta\left(\langle x^2\rangle\langle x'^2\rangle - \langle xx'\rangle^2\right)$$

for 90% of the full beam current after 90° was found to be below the acceptable limit for emittance growth. In the bend plane (x), the measured value is 0.045π-mm-mR while the out-of-plane (y) emittance is 0.068π-mm-mR. This compares to 0.021π-mm-mR measured directly after the source aperture.

* This work has been performed under the auspices of the US DOE by LLNL under contract W-7405-ENG-48.

ahle1@llnl.gov

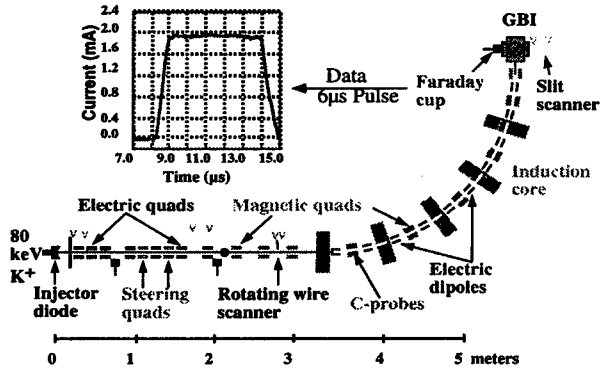

Figure 1: Current Recirculator Layout and Faraday cup data at 90 degrees.

3 TIME STABILITY

A time stability check of the C-probe signals was conducted. The accelerator was turned on and data taken at regularly time intervals. The measured y positions were stable to within the accuracy of the C-probes, but the x positions varied extensively, as much as 5 mm, before stabilizing after 6-7 hours of operation. This behavior was eventually determined to be caused by the heating of the alumino-silicate source, which operates at a temperature of 1000°C. Even though the source is heat shielded, the temperature of capacitors around the source diode were found to increase by 40°C, which lowers their capacitance. The lowering of this capacitance actually raises the voltage on the source diode, increasing the energy of the emerging beam. Thus, the x positions of the beam through the bend section change.

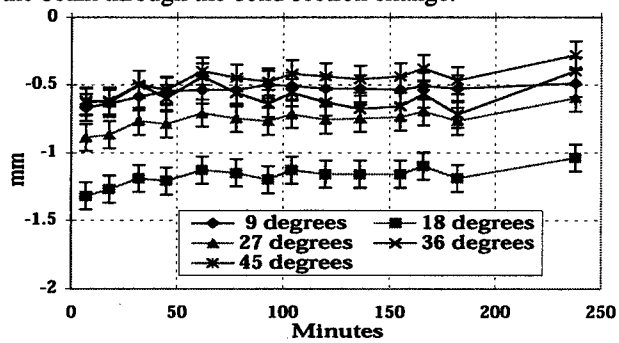

Figure 2: X Positions vs Time for different locations along the bend section (degrees of bend) after the temperature compensation amplifier was installed.

To solve this problem, a new control circuit was introduced for the source pulser power supply. A thermistor was added to the source tank to monitor the rise in temperature and put into the feedback loop of an approximately gain 1 amplifier. The amplifier modifies the DC control voltage for the power supply. As the temperature rises, the control voltage lowers, which lowers the output voltage of the power supply and compensates for the lower capacitance. Figure 2 shows the resulting x positions. With the compensation circuit, the x positions, as well as the y positions are constant in time to the accuracy of the C-probes.

4 STEERING

With the time dependence problem solved, the C-probe data clearly showed betatron motion in both x and y (see figure 3). This motion could be caused by misalignments of the source, matching section quads, straight section, or the bend section, or some combination of all four. To help ascertain the cause, steering experiments were performed using the steerers in the matching section. These steerers have the same mechanical structure as the quadrupoles, but the configuration of voltages provide dipole fields in x and y.

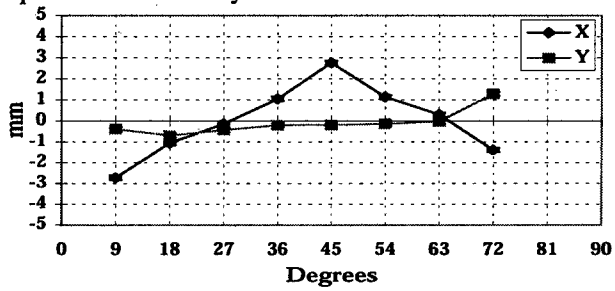

Figure 3: X and Y positions vs Bend Angle without steering.

In these experiments, it is assumed that most of the betatron amplitude arises from misalignments of the source and the quads before the first steerer, S1. First, the voltages on S1 were varied until the amplitude of the x betatron motion was minimized. This condition corresponds to the beam leaving S1 parallel to the beamline center. The amplitude of the betatron motion is the offset of the beam at S1. Then, by monitoring the C-probe approximately one betatron period, ~10 HLP's, away from the second steerer, S2, the field in S1 was increased until the beam centroid at S2 was near zero. Voltage were then applied to S2 and the strength varied until the betatron motion was minimized, which will occurs when the beam leaves S2 along the beamline center. This minimum occurs with the S1 field ~80V/cm and the S2 field ~60V/cm.

Figure 4 shows the measured x positions through the bend section with the above steering fields applied. The betatron motion is greatly reduced by applying steering voltages, which supports the assumption that most of the betatron motion is caused by misalignments of the source and of the first few quads. The betatron motion, however, does seem to grow as the beam passes through the bend section indicating the energy of the beam and the bending dipole fields are not exactly matched. The voltages on the dipole plates are know to an accuracy of 0.2% but the energy is less well known. Therefore, the energy of the beam was lowered by 0.5%, and the steering experiment was redone, with the steering fields becoming ~130V/cm in S1 and ~120V/cm in S2. The result is also plotted in figure 4. The x position of the beam now remains within 0.6-mm of the center all the way through the entire bend section.

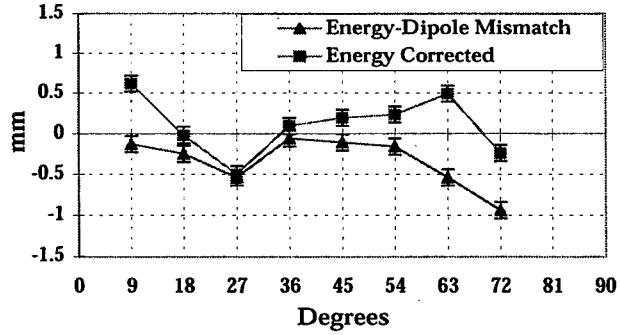

Figure 4: X positions vs Bend Angle with steering before and after energy-dipole mismatch correction.

5 MATCH SENSITIVITY

One important goal of the recirculator project is to study causes of emittance growth. One such possible cause is the matching section, which converts the uniformly diverging beam emitted from the source to the alternating focused-defocused beam needed for beam transport in the bend section. The requirement of a matched envelope in the bend section, puts four constraints on the quadrupoles strengths in the matching section. But there are seven quads in the matching section, or seven degrees of freedom. Thus, the problem of determining the matching section quadrupole strengths is an under constrained problem, with many possible solutions. But do all these solutions produce the same beam quality?

In order to answer that question, four different matches, or configurations of quadrupole strengths, were determined from solving the envelope equation numerically. The four matches are called the Unique, Best, Good, and Bad match. The Unique match, has the last three quads set to the same strength as the magnetic quadrupoles of the bend section. The Best and Good provide well matched envelopes in the bend section, but the behavior of the envelopes in the matching section is more erratic for the Good match. The Bad match does not provide a well matched envelope in the bend section and the behavior in the matching section is even more erratic than the Good match.

Table 2: Emittances (π-mm-mr) for Various Matches

Match	Q1Y defocus ε_y at matchbox	Q1Y focus ε_y at matchbox	Q1Y focus ε_x at 90°
Unique	0.026	0.035	0.076
Best	0.025	0.039	0.065
Good	0.030	0.045	0.073
Bad	0.116	0.039	0.099

Table 2 lists the emittance for the four matches as measured by a slit scanner at the end of the matching section, right before the seventh quad. The measured emittance is in the out-of-bend plane dimension, y, and is measured for the two different polarity settings. Also shown is the in-bend plane emittance measured after the 90° bend section. The plot shows that only the Bad match has a significantly different emittance at the end of the matching section. However, there is some difference between the matches after the bend section. At this point the Best match has the lowest emittance value, being slightly less than the Unique and Good matches. The Bad match is still the match with the highest emittance value.

Even though the Good match has similar emittance values at the end of the matching section as the other matches, the phase space plot for the Q1Y negative polarity setting showed a unique behavior. The plot is shown in figure 5. One can clearly see a second spiral arm present in the phase space plot. As to the exact cause of this feature and why it only appears with the Good match is unclear at this time.

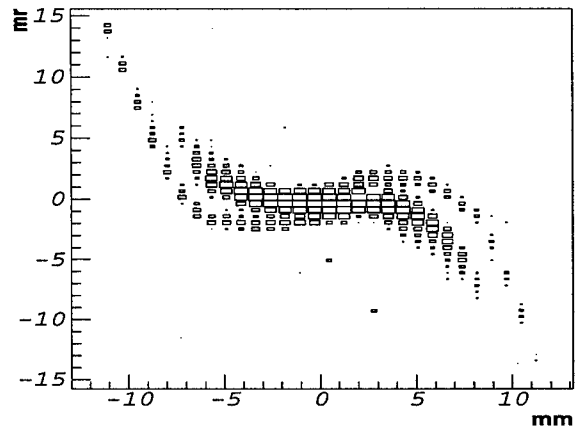

Figure 5: Phase space plot measure at end of matchbox with Q1Y defocusing and for the Good match.

6 SUMMARY

Experiments on the 90° bend section of the Recirculator are continuing. The beam position measurements are stable with time to the accuracy of the C-probes, beam steering experiments have made it possible to maintain the centroid position to within 0.6-mm throughout the bend section, and initial sensitivities studies of beam quality on the match has yielded significant differences. These results are all positive indications in the feasibility of recirculating space charge dominated heavy ion beams.

7 REFERENCES

[1]L. Ahle, et al., "Recent Progress in the Development of a Circular Ion Induction Accelerator for Space Charge Dominated Beams at LLNL", Proc. of LINAC98, Chicago, IL, Aug. 23-28, 1998, to be published.

[2]R. O. Bangerter, *Nuovo Cimento* **106A** (11), 1445-1456 (1993).

[3]M. Tabak et al., *Nuclear Fusion* **38** (4), 509 (1998).

[4]R. Moir, "Inertial Fusion Energy Power Plants Based on Laser or Ion Beams," Proc. of ICENES 98, Tel-Aviv, Israel, June 28 -July 2, 1998, to be published.

[5]W. R. Meier et al., "An Integrated Systems Model for Heavy Ion Drivers," Proc. of Inter. Symp. on Heavy Ion Inertial Fusion, Heidelberg, Germany, Sept. 24-27, 1997, to be published in *Nucl. Inst. and Meth. A.*

[6]A. Friedman et al., *Fusion Engineering and Design* **32-33**, 235-246 (1996).

THE MECHANICAL DESIGN FOR THE SECOND AXIS BEAM TRANSPORT LINE FOR THE DARHT FACILITY*

O.J. Alford, L.R. Bertolini#, A.C. Paul, C.C. Shang, G.A. Westenskow
Lawrence Livermore National Laboratory, Livermore, CA 94550 USA

Abstract

This paper describes the mechanical design of the downstream beam transport line for the second axis of the Dual Axis Radiographic Hydrodynamic Test (DARHT II) Facility. The DARHT II project is a collaboration between LANL, LBNL and LLNL. DARHT II is a 20-MeV, 2000-Amperes, 2-μsec linear induction accelerator designed to generate short bursts of x-rays for the purpose of radiographing dense objects. The downstream beam transport line is an 18-meter long region extending from the end of the accelerator to the bremsstrahlung target. Within this proposed transport line there are 17 conventional solenoid, quadrupole and dipole magnets; as well as several specialty magnets, which transport and focus the beam to the target and beam dumps. There is a high power beam dump, which is designed to absorb 80-kJ per pulse during accelerator start-up and operation. The beamline vacuum chamber has an 8-cm diameter aperture and operates at an average pressure of 10^{-7} Torr.

1 INTRODUCTION

We are starting the engineering design for the downstream components of the DARHT II Accelerator [1]. Beam transport studies for this design are described elsewhere in these proceedings [2]. Figure 1 shows the proposed layout for the elements in the system. The beamline from the exit of the accelerator to the target is about 18 meters long. Only four short (16 to 100 nsec) pulses separated by about 600 nsec are desired at the bremsstrahlung target.

The function of the kicker system is to "kick" four pulses out from the main 2-μsec pulse leaving the accelerator. The kicker includes a bias dipole operated so that the non-kicked parts are deflected off the main line into the main beam dump, while the kicked parts are sent straight ahead. Focusing elements between the kicker and the septum would complicate operation. Therefore, to achieve a narrow beam waist at the septum, solenoid S3 must "throw" a waist to the septum. The first 3 meters of beamline allow the beam to expand from its 5-mm matched radius in the accelerator to 2.25-cm at solenoid S3. The system is designed to have a 20% energy acceptance to transport to the main beam most of the leading and falling edge of the pulse exiting the accelerator. The proposed system using a quadrupole septum magnet [2] allows for a larger beam pipe radius than the more conventional dipole septum magnet studied earlier. This increases the energy acceptance of the transport line to the main beam dump. Although desirable, we do not expect to include the "Enge-magnet" system described in the transport studies in the beamline for the initial commissioning of the accelerator.

The kicker system is described elsewhere in these proceedings [3]. After the kicker system, there are 3 quadrupole magnets to restore the beam to a round profile and to compensate for edge focusing from the bend elements (BM1, BM2, BM3, BM4 as shown in Figure 1.) in the Chicane. Also, we have included beamline elements in this region to allow energy and emittance measurements of the "kicked" pulses. Experience has shown ejecta material from the target can travel the length of the accelerator. To keep this material from reaching the injector and accelerator cells we have included a Chicane system that does not allow direct line-of-sight between the target and the upstream elements.

Finally the beam will be pinched to a tight focus at the target to provide an intense spot of x-rays for radiographic purposes. Work on the target is also presented in these proceedings [4].

2 MAGNETS

The magnets within the DARHT II transport line are all water-cooled conventional dc electromagnets with the exception of the final focus solenoid magnet, which is pulsed. The magnets are listed in Table 1 along with their design parameters.

The transport solenoids have external iron shrouds with water-cooled copper coils. Solenoid coils are wound into individual two-layer "pancake" coils. Each magnet has an even number of these pancake coils. The pancakes are installed in an A-B-A-B orientation to minimize axial field errors. The inside diameters of the solenoid coils are sized large enough to fit over the outside diameter of the beam tube flanges.

The transport quadrupole and dipole magnets have solid iron cores with water-cooled copper coils. The quadrupole magnets are two-piece, solid-core construction. The dipole magnets are two-piece, solid-core, "H" style construction.

The alignment requirements for the transport magnets are ±0.4-mm positional tolerance and ±3-mrad angular tolerance. All transport magnets have fiducials mounted on the outside of the iron. The magnets are magnetically

*This work was performed under the auspices of the U.S. Department of Energy by LLNL, contract W-7405-ENG-48.

Email: bertolini1@llnl.gov

mapped and aligned on the transport line with respect to the fiducials.

Table 1: Magnet specifications

Magnet Name	Length (m)	Field (kG)	Bore (cm)	Bend (deg)
Solenoid S3	0.25	3.0	22	-
Quad Septum	0.15	15.0	16	-
Dipole Septum	0.40	1.2	16	-35
Quadrupole QV	0.15	1.0	16	-
Quadrupole QH	0.15	1.0	16	-
Quadrupole QS	0.15	1.0	16	-
Dipole EAM	0.40	1.5	16	-45, +90
Solenoid S5	0.25	3.0	22	-
Dipole BM1	0.15	1.0	8	+6.6
Dipole BM2	0.15	1.0	8	-6.6
Dipole BM3	0.15	1.0	8	-6.6
Dipole BM4	0.15	1.0	8	+6.6
Solenoid S6	0.25	3.0	22	-
Solenoid SFF	0.05	20.0	8	-

3 VACUUM SYSTEM

The vacuum chambers for the DARHT II Transport Line are circular beam pipes constructed from 304L stainless steel. The region from the end of the accelerator through the septum has a 16-cm bore diameter. From the septum to the target, the bore diameter is reduced to 8 cm. The vacuum seals are made with conflat style knife-edge flanges with annealed copper gaskets. RF seals between flanges are made with copper "gap rings" which are compressed between the conflat flanges and fill the gap at the inside bore of the beamline between the flanges. The use of all-metal seals is driven by the potential requirement to *in situ* bake the transport vacuum system. *In situ* bake-out may be required to minimize adsorbed gas on the beam tube walls, which may be desorbed by beam halo scraping the walls.

The vacuum design requirement for the transport line is 10^{-7} Torr average pressure. Above this pressure, predictions indicate that there will be detrimental effects to the beam. In addition, the vacuum pressure at the target is desired to be in the 10^{-8} Torr range. To meet these requirements, a combination of cryopumps, and turbomolecular pumps are employed along the length of the beamline. The pump sizes and spacing was determined by calculating the vacuum pressure profile along the beamline utilizing a one-dimensional pipeline pressure code [5]. For this analysis, the beamline is characterized as a series of discrete segments. Length, axial conductance, gasload, and pumping speed define each segment. The pump speeds and locations of the pumps were varied to determine the most economical approach to vacuum pumping the transport line. The pressure profile for the transport line is shown in Figure 1. The average beamline pressure is 8.5×10^{-8} Torr (85 nTorr).

The pump located at the end of the accelerator is a 20-cm diameter cryopump. A cryopump was selected for this location to pump the relatively high gas loads from the last accelerator segment. The remaining pumps in the transport line are 250 liters per second turbomolecular pumps because the gas loads in the transport line are lower and the axial conductance of the beamline is significantly less than in the accelerator. All vacuum pumps must pump the beamline through pumping crosses equipped with RF screens to minimize perturbations on the beam.

Throughout the beamline there are beam position monitors (BPMs) to measure the location and angle of trajectory of the beam. The BPMs mount between the flanges of adjacent transport beam tubes. The accurate transverse location of the BPMs is critical to the operation of the transport line and it is their positional requirements, which set the alignment tolerances for the beam line vacuum system. To satisfy the BPM requirements, the transport line beam tubes must be aligned to within 0.2 mm offset. Each beam tube will be manufactured with fiducials, which allow the survey crew to measure and position external to the centerline.

4 BEAM DUMPS

There are three beam dumps included in the DARHT II downstream transport system; a main beam dump, an energy analyzer dump, and an emittance diagnostic dump. The main beam dump absorbs the portion of the beam that is not deflected by the kicker magnet. The beam is initially deflected by the bias dipole, it then passes through the septum quadrupole to the septum dipole and into the main dump. The normal horizontal beam size at the main beam collector is 8 cm. However, the startup parameters for the beam will not be well known. We must therefore provide some safety margin. First consideration is to keep the instantaneous temperature (temperature at the end of the 2-μsec pulse) of the impact area below the damage point for the material. At a 5 pulse per minute repetition rate we can manage the average temperature increase. The beam's energy is 80-kJ per pulse and the average thermal power is 6.67-kW. We also desire to keep the neutron yield low to minimize activation of components and simplify radiation shielding. The construction of the beam dump must be compatible with high vacuum as explained in the previous section. Studies are looking at using graphite material to decelerate the beam electrons.

The energy analyzer dump and the emittance diagnostic dump are similar in design. These two dumps are designed to absorb the kicked portion of the beam, which is deflected to either diagnostic for evaluation. This beam's energy is 4.0-kJ per pulse and the average thermal power is 0.33-kW at 5 pulses per minute.

In addition to the beam dumps, there is a beam stop, which is a safety feature in the transport line. The purpose

of the beam stop is to allow accelerator operations to continue while personnel are working in the target area outside the accelerator hall. The beam stop is located at the end of the accelerator hall, within the penetration in the 5-foot thick concrete wall. The beam stop is a composite absorber, made up of a 3-inch thick graphite block, backed by 12-inches of tungsten. There is additional shielding surrounding the beam stop to absorb radiation. A permanent magnet dipole will be installed administratively before the beam stop to deflect any beam accidentally transported beyond the diagnostic dumps.

5 INSTRUMENTATION AND DIAGNOSTICS

Beam diagnostics for the DARHT II transport line include BPMs which feed back to corrector magnets for steering, a spectrometer for measuring beam energy, and a "pepper-pot" for measuring beam emittance.

Vacuum diagnostics include convectron and ion gages located at each pumping cross. There are convectron gages located on either side of the beam line isolation valves to prevent opening the valve when one side is "up to air".

6 REFERENCES

[1] M.J. Burns, et al., "DARHT Accelerator Update and Plans for Initial Operation," to be published in the proceedings of this conference.

[2] A.C. Paul, et al., "The Beamline for the Second Axis of the Dual-Axis Radiographic Hydrodynamic Test Facility," to be published in the proceedings of this conference.

[3] Y.J. Chen, et al., "Precision Fast Kickers for Kilo-ampere Electron Beams," to be published in the proceedings of this conference.

[4] S.E. Sampayan, et al., "Beam-Target Interaction Experiments for Bremsstrahlung Converter Application," to be published in the proceedings of this conference.

[5] "A Method for Calculating Pressure Profiles in Vacuum Pipes," PEP-II AP Note 6-94, March 1994.

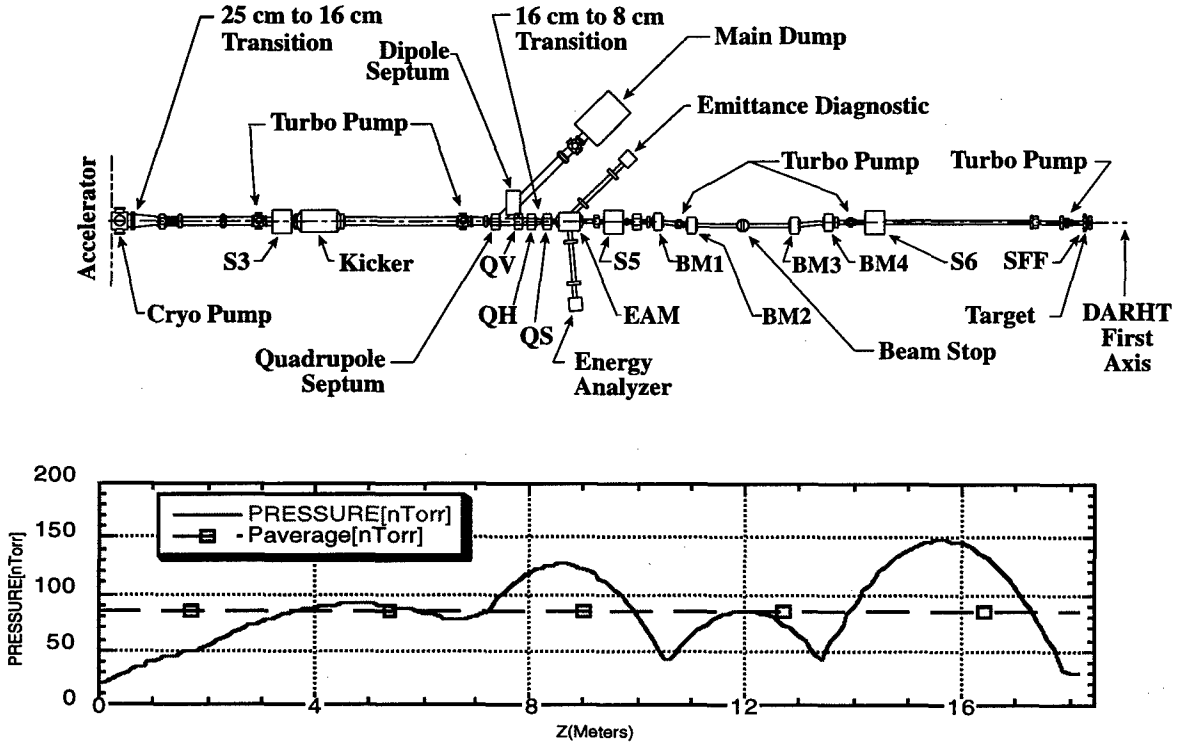

Figure 1. Proposed DARHT II Downstream Beam Transport Layout and Vacuum Pressure Profile

THE BEAMLINE FOR THE SECOND AXIS OF THE DUAL AXIS RADIOGRAPHIC HYDRODYNAMIC TEST FACILITY+

Arthur C. Paul†, George J. Caporaso, Yu-Jiuan Chen, Yu Ju (Judy) Chen, Glen Westenskow
Lawrence Livermore National Laboratory, Livermore, CA. 94550, USA

William M. Fawley, Edward P. Lee
Earnest Orlando Lawrence Berkeley National Laboratory, Berkeley, CA. 94720, USA

Abstract

During normal DARHT II[1] operation, the beam exiting the accelerator will be well characterized by its nominal design parameters of 20-MeV, 2000-Amperes, 2-μsec-pulse length, and 3 cm-mr unnormalized emittance. Normal operation will have the beam delivered to a beam dump via several DC magnets. A 2-way kicker magnet is used to deflect portions of the beam into the straight ahead beamline leading to either a diagnostic beamline or to the converter target beamline. During start up and or beam development periods, the beam exiting the accelerator may have parameters outside the acceptable range of values for normal operation. The Enge beamline must accommodate this range of unacceptable beam parameters, delivering the entire 80 KiloJoule of beam to the dump even though the energy, emittance, and/or match is outside the nominal design range.

1. THE BEAMLINE

The beamline system consists of four operationally distinct beamlines: 1) the Enge beamline, 2) the main dump beamline, 3) the diagnostic beamline, and 4) the target beamline. These lines share some components and floor space within the DARHT building. The beamline considered here extends from the exit of the accelerator, some 12 meters before the beginning of the shielding wall. Depending on the magnet settings, the beam from the accelerator is transported to the "Enge dump," a "tuning dump," kicked into a "diagnostic line," or kicked into the "transport line" with eventual delivery to the x-ray converter target outside the shielding wall. The two dump beamlines and diagnostic beamline are constrained to lie within the DARHT shielding wall. The beamline to the converter target penetrates the shielding wall and extends some 5.9 meters from the exit of that wall to the converter target. When ready to produce a radiograph we use the 2-way kicker to cancel the DC field of the kicker bias dipole allowing a section of the beam to pass undeflected into the target beamline. We repeat this up to four times during the 2-μsec-beam duration, producing up to four beam pulses separated by 600 ns. The x-rays are produced when the electrons are tightly focused by the final focusing lens to the correct position on a Bremsstrahlung target.

2. THE BEAM

The beam delivered by the DARHT accelerator consists of a 2-μsec-beam body of 20-MeV electrons. This is preceded by the "beam head," a 0.4-μsec dribble of electrons 8-20 MeV with current increasing from .1 to 2 kA. If a beam head cleanup section is used after the first 8 cells, this head is reduced to a 0.05-μsec dribble of particles in the energy range of 15-20 MeV, current 0 to 2 kA

3. THE ENGE BEAMLINE

The Enge beamline must be capable of handling the entire 80 KiloJoule of thermal energy over a wide range of beam energy, emittance, or other parameters. This beamline is capable of handling and characterizing the beam from the accelerator "no matter" what its energy, emittance, or other parameters are. This beamline consists of a series of solenoid lens leading to an Enge magnet [1] that bends the beam about 90 degree independent of beam energy. The bent beam is then strongly overfocused by a lens and deposited into a beam dump. After the beam energy and emittance is determined, the Enge magnet is turned off and the beamline magnets are set to pass the beam into the tuning dump.

4. THE TUNING DUMP BEAMLINE

The tuning dump beamline also handles the entire 80 KiloJoule of thermal beam energy. A pair of 8 cm diameters beam scrapers separated by 2.0 meters provides a degree of phase space limitation of the beam that can be passed through the kicker. The kicker DC bias dipole deflects the beam by 0.59 degrees (kicker off). This beam enters a quadrupole septum 2.78 meters downstream 3.33 cm off axis. The quadrupole gradient is -13.44 kG/m vertically focusing. The beam offset contributes a 447 Gauss dipole field component that increases the beam

+ This work was performed under the auspices of the US Department of Energy by LLNL, contract W-7405-ENG-48 and by LBNL under contract AC03-76SF00098
† acpaul@llnl.gov
[1] Second axis of the Dual Axis Radiographic Hydrodynamic Test facility.

0-7803-5573-3/99/$10.00@1999 IEEE.

deflection angle to 9.5 degrees. 0.2 meters further downstream the beam enters a 1.06 kG dipole septum magnet. The fringe focusing of this magnet combined with the focusing of the quadrupole septum is sufficient to reduce the energy density of the 20-MeV 2-μsec beam to less than 600 Joule/cm^2 at the beam dump. The 20 MeV beam is bent by 45 degrees, the beam head is spread between 45 and 85 degrees.

5. THE DIAGNOSTIC BEAMLINE

The diagnostic beamline handles up to 4 KiloJoule of thermal energy. This beamline consists of a magnetic spectrometer with better than a 1/4 percent momentum resolution, and an emittance measuring diagnostic. After accurate determination of the beam parameters, the target beamline magnets are set and the diagnostic beamline turned off. The beam can then be kicked into the line for delivery to the x-ray target.

6. THE TARGET BEAMLINE

Beam sections are kicked into the straight-ahead beamline through the center of the quadrupole septum. Three additional quadrupoles re-establish a round beam matched to solenoid transport. This beam passes through a 4 dipole chicane with maximum offset of 7 cm to prevent target ejecta from coming back into the accelerator. The final focus lens is an 18 kG pulsed solenoid with a 10 μsec flat top to reduce power consumption. The beam final focus on the target is 0.1 meters beyond the exit of that lens. The beam must be focused to smaller than 1.3 mm FWHM time integrated.

7. TARGET IMAGE SIZE SENSITIVITY

We have investigated the sensitivity of the final spot to variations in initial beam parameters. Figure 1 shows the final target beam radius vs. beam momentum, accelerator exit radius, accelerator exit match, and beam emittance. The nominal design operating points is at 20.505 MeV/C, 0.5 cm, and 3.0 cm-mr.

8. OPERATING GOAL

The high power 80 KiloJoule beam from DARHT cannot be allowed to hit the wall. This is why we have developed several beamlines allowing the successively more accurate characterization of the beam all the while, delivering that beam to the high power beam dumps. If you are going to transport an 80 kJ beam through some transport space, you better know its parameters, for if you don't and that beam hits something, the vacuum becomes atmosphere and you have a problem. The beamline sections following the kicker-septum only handle beam pulses of 4 or less KiloJoule of thermal energy.

In this spirit, we attempt to accommodate beams with emittance an order of magnitude above the design value, with energy that is "unknown." This is necessary so that during tune-up and debugging periods of operation, the machine can be adjusted without having the beam blasting holes through the vacuum wall. Figures 2, 3, and 4 show the beamline layout and beam profile for the tuning dump and target beamlines [2].

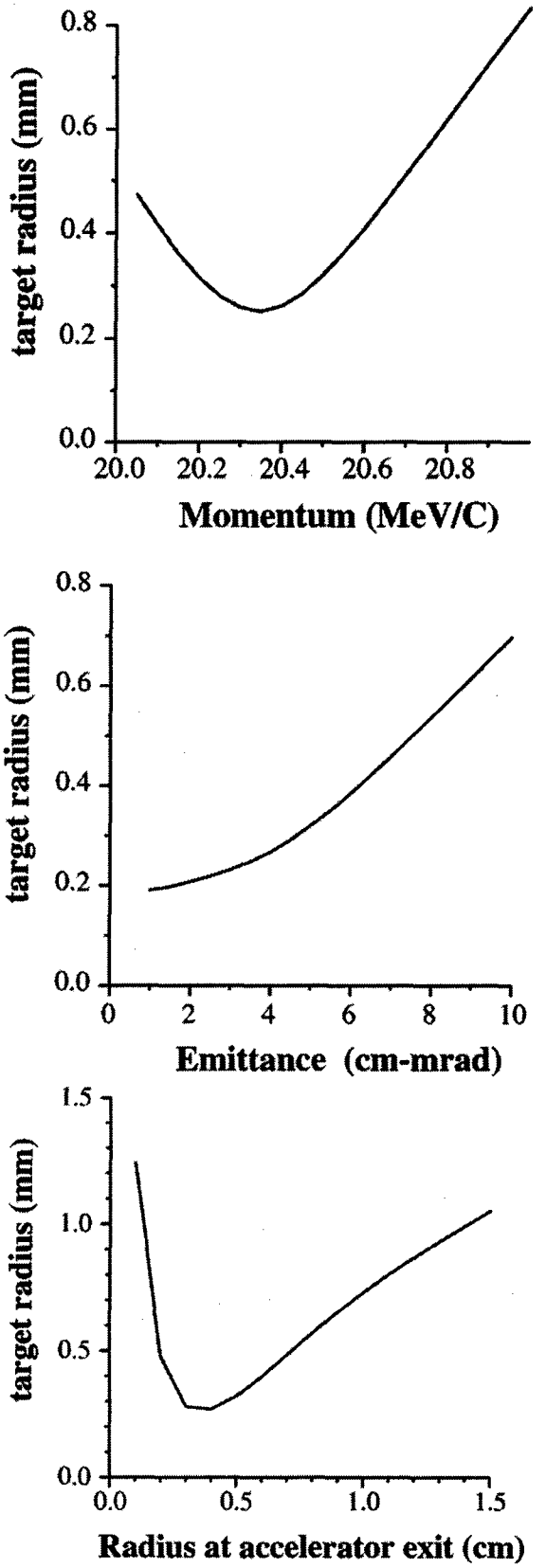

Figure 1.

References
[1] "Achromatic Magnetic Mirror for Ion Beams," Harold A. Enge, Review of Scientific Instruments, April 1963, page 385-389.
[2] "Transport – An Ion Optic Program LBL Version," Arthur C. Paul, Feb. 1975, LBL-2697. Modified at LLNL for X11 Graphics and DARHT application.
[3] "The Mechanical Design for the Second Axis Beam Transport Line for the DARHT Facility," L. R. Bertolini, et al, to be published in the proceedings of this conference

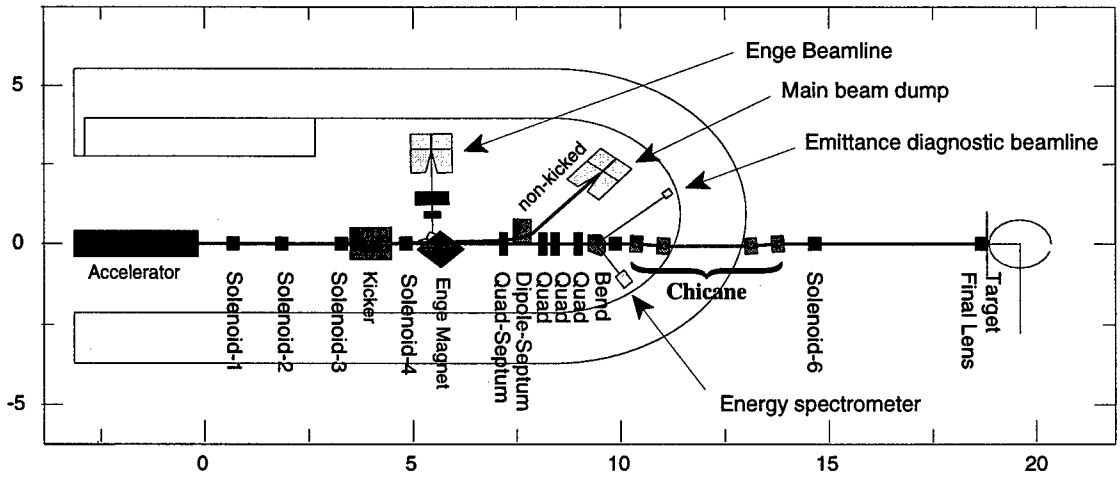

Figure 2. Layout of the proposed transport elements in the DARHT-II hall.

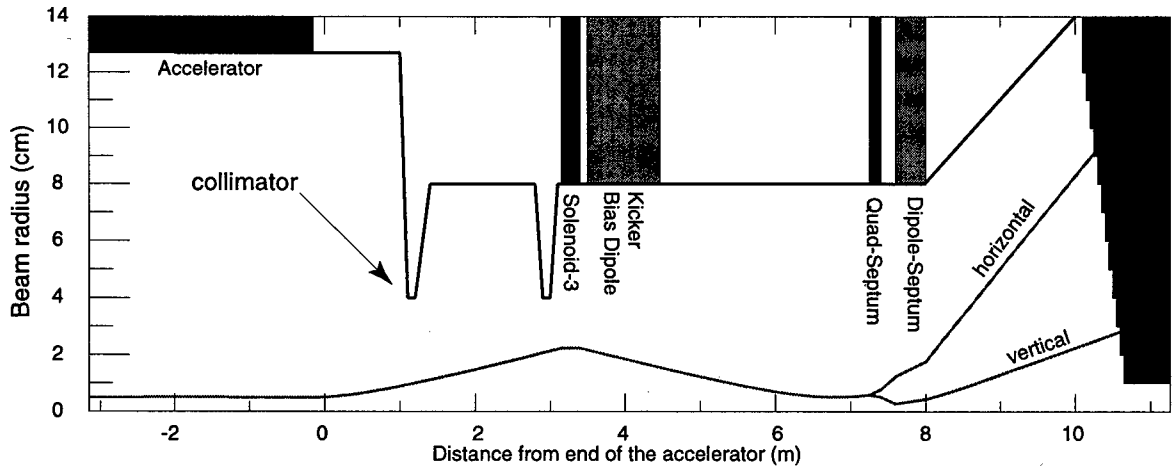

Figure 3. Transport for the non-kicked portion of the beam from the end of the accelerator to the beam dump.

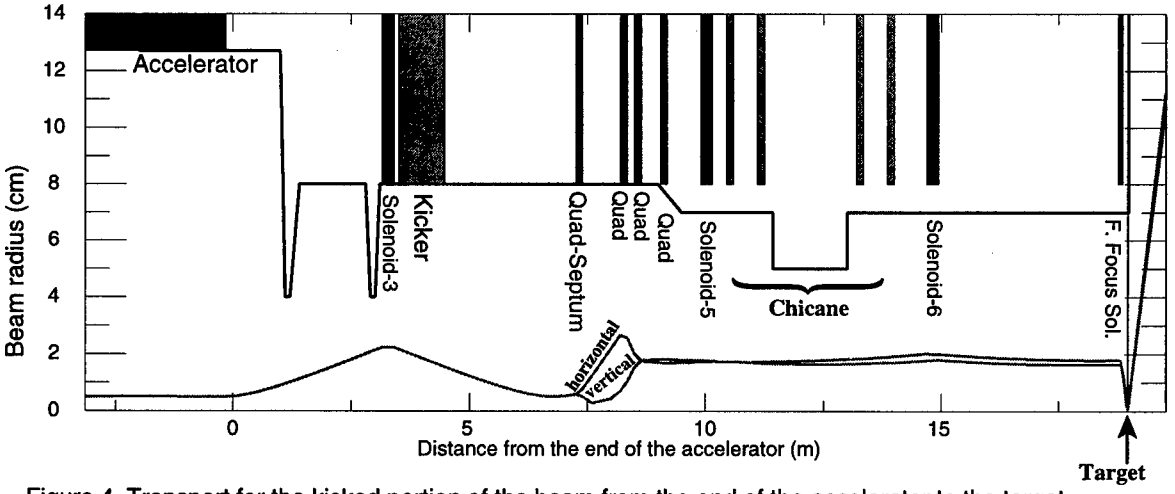

Figure 4. Transport for the kicked portion of the beam from the end of the accelerator to the target.

A LONG PULSE LINAC FOR THE SECOND PHASE OF DARHT*#

E.L. Burgess, J.D. Comins, W.M. Fawley, D.V. Munson, M. Nyman, L.T. Jackson, C. Peters,
L. Reginato, H.L. Rutkowski+, M.C. Vella, W. Waldron, S.S. Yu,
Lawrence Berkeley National Laboratory, One Cyclotron Road, Berkeley, CA

Yu-Jiuan Chen, T. Houck, Lawrence Livermore National Laboratory,
7000 East Ave., Livermore, CA 94550

R. Briggs, Science Application International Corporation, 7041 Koll Center Pkwy, Pleasanton, CA
D. Birx, Science Research Laboratory, 3300 Crismore Lane, Oakley, CA

ABSTRACT

We present the design for an induction linac that is fed by a long pulse injector that will generate a 20 MeV, 2 kA, 2μs electron beam pulse for the DARHT second axis at Los Alamos National Laboratory. The accelerator cells are shielded gap cavities with Mycalex insulators and Metglas cores. A large bore (14") block of eight cells follow the injector while the remaining 80 cells have a 10" bore. Blocks of eight cells are interspersed with intercells that provide pumping, diagnostics and space for cell removal. RF properties of the cells have been calculated and measured. Response to BBU modes and corkscrew have been calculated. Design details of the cells, solenoids, corrector coils, intercells and pulsers will be presented along with prototype data.

1 INTRODUCTION

The induction linear accelerator section of the DARHT second axis accelerator consists of 88 induction cells arranged axially into 11 cell blocks of 8 cells each. The entire accelerator inside the building is shown in fig.1.

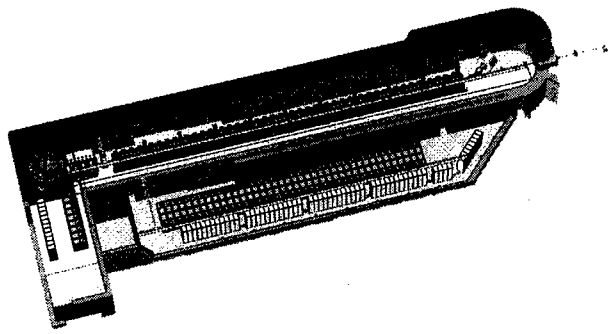

Fig. 1 DARHT Second Axis Accelerator System

The injector is at the left. It is a 3.2 MV diode which provides the induction linac with a 2kA electron beam. The subject of this paper is the induction linac itself which adds 16.8 MeV to the beam energy. An intercell is placed between each pair of cell blocks to provide vacuum pumping and a removable section to allow removal of cells for repair. As can be seen from fig.1, a large gap exists between the first and second cell block. This is to provide space for a beam-pulse-head-dump which will be designed and built by Los Alamos National Laboratory. The purpose of this dump is to lose the risetime portion of the beam pulse (approx. 400ns) in a non destructive way. The flat portion of the beam pulse is just longer than 2μs. Fig.1 shows the pulsers and the electrical racks for the linac cells at a level below the accelerator. The pulsers and racks for the first eight cells are shown above the injector Marx generator tank. Downstream of the accelerator is a beam chopper system being developed by Lawrence Livermore National Laboratory to chop four short pulses out of the 2μs macropulse and to dump the rest of the beam. The cells and pulsers are being designed to allow an upgrade in
current to 4kA, if needed, without serious modification.

2 PHYSICS DESIGN ISSUES

The issues most important to the physics design of the linac are generation of ions by spilled beam, beam breakup (BBU) instability, corkscrew motion of the beam centroid, and emittance growth. Spilled beam or halo may generate ions that could disrupt the transport of the beam or backstream into the injector cathode. Ions generated by beam loss can also create breakdown in the gap-insulator zone. BBU is a result of resonant coupling between transverse beam motion and TM cavity modes in the cells. It can be reduced by increasing pipe diameter decreasing

*Dual Axis Hydrodynamics Test

#This work was supported by the U.S. Department of Energy under Contract No. DE-ACO3-76F00098.

+Email: HLRutkowski@lbl.gov

0-7803-5573-3/99/$10.00@1999 IEEE.

the accelerating gap, reducing insulator dielectric constant, or increasing the solenoid transport field. Corkscrew motion comes from a combination of solenoid field misalignment and varying beam energy. Emittance growth can come from large beam envelope oscillations, non-linear focusing fields and non-uniform radial beam density. In the sections below we discuss how the cells are designed to avoid these problems.

3 ACCELERATOR CELLS

Injector Cells

There are two types of induction cells in the linac. The first block of 8 are called "injector cells" while the remaining 80 are called "standard cells". The part of the linac immediately after the injector is most susceptible to ion generation from beam spill and BBU generation because the beam is large and transport field must be low. The injector cell is shown in fig.2a.

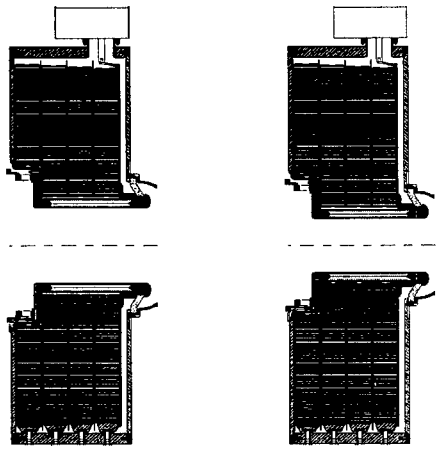

a) b)

Fig. 2 Injector Cell a), Standard Cell b)

The main distinctive feature of the cell is a 14 inch beam pipe diameter compared to the 10 inch pipe in the standard cell. The reasons for the larger pipe are: less generation of ions from spilled beam, smaller probability of gap breakdown from spilled beam, and reduction of transverse mode impedances that contribute to BBU. The solenoid transport field cannot be raised too rapidly at low beam energies because of possible emittance growth. The scaling of the transverse mode impedance for a pillbox cavity goes as W/b^2 where W is the accelerating gap length and b is the pipe radius. AMOS calculations of the dominant mode impedances for these cells give values ~ 180Ω/m. The beam pipe is stainless steel and the body of the cell is aluminium. A prototype of the cell using an insulator different from the final design geometry is being tested for beam spill effects at the THOR machine at Los Alamos. The insulator is Mycalex (a glass-mica mixture) the cross section of which is a section of a cone that has a 30° angle between the electric field lines and the insulator surface to drive electrons away from the surface. The original injector cell prototype used a backward curved insulator geometry in an effort to create space for a diagnostic station in each cell and to provide some frequency shifting of the TM modes with respect to the standard cells. However, high voltage testing showed that this cell required repeated conditioning after being turned off and that voltage retreat was required after a breakdown to recondition. It was determined that diagnostics were not needed in each cell. Therefore it was abandoned.

The ferromagnetic material is Allied Signal 2605 SC Metglas. The cores are 4 inches wide and tape wound with 2.5-4μ thick Mylar insulation. The injector cells have fewer volt-sec of core material then the standard cells and operate at 173kV. There are four cores in each cell each of which is radially continuous and immersed in dielectric oil. Damping ferrites to reduce the Q's of TM modes are placed on the oil side of the insulator interface. There are four current feeds to the cores to prevent quadrupole moments from being induced that could perturb the beam.

The maximum enhanced electric field stress on the negative electrode is 78 kv/cm and the surface gradient on the insulator is 43 kv/cm. The insulator is epoxied to the metal components to ensure that oil-vacuum leaks will not occur.

Standard Cells

Eighty of the eighty eight cells are of the design in fig. 2b). There are three major differences with the other cell design. The beam pipe is 10" diameter. The Metglas cores have smaller ID but the same OD. Finally, the solenoid has twice as many layers because higher transport fields are needed at higher energies. The insulator and gap geometries are the same. The solenoids are water cooled and capable of 0.22T maximum.

The design current has been reduced to 2 kA from 4 kA but the design has been left unchanged to allow the possibility of upgrading in the future to 4 kA. The standard cells operate at 193 kV and the maximum enhanced field stress on the negative electrode in the gap is 85 kV/cm.

Intercells

The intercells are metal boxes, that allow pumping to achieve the 10^{-7} Torr required beamline vacuum, and to create a section that can be removed transversely from the beamline making space to slide the interlocking induction cells out for repair. The intercell is 17" long and contains a 6 " long, 0.25T solenoid to reduce ripple in the magnetic transport line. Between the intercell and the first induction cell of the next block is a diagnostic ring containing beam position monitors and B-dot diagnostics. Current return rods are built into the intercells to allow for pumping and yet shield the beam from the cavity.

4 PULSERS

Each cell is driven by a pulser that is a four stage Marx generator each stage of which is a seven capacitor pulse forming network (PFN). The pulser is capable of driving a 2.4μs pulse into a 20 Ω matched load at 200 kV and 10 kA. The PFN impedance is tapered to handle the non linear core magnetizing current. The PFN inductance is tuned by insertion of a copper tube to maximize the voltage flatness up to ±0.5% when the pulser is attached to the cell. The cell cores will be individually tested and selected so that individual tuning for each pulser/cell combination is not required. Components in the pulser are being rated conservatively to achieve long life and high reliability.

5 MOUNTING AND ALIGNMENT

The exterior of the cells is shown in fig. 3.

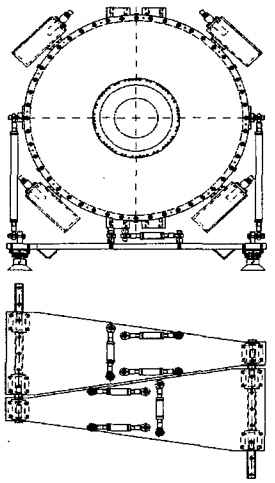

Fig. 3 Cell Exterior and Mounting

Each cell weighs approximately 5 Tonnes and is mounted with a six degree of freedom set of differential screw struts to a base plate. These struts, used at the LBNL Advanced Light Source, allow precision positioning of heavy components. Also shown are the four cans for each cable feed that contain the core compensation circuits. A view of two base plates nested together is also shown with three of the six struts visible. Each cell is individually aligned to the ideal beam line using the struts. Cell to cell and cell to intercell vacuum sealing is done by inflatable bladder units which squeeze face seal O-rings against the cell housing.

6 ACCELERATOR SYSTEM PERFORMANCE

The destructive effects of ion production from spilled beam or halo are being minimized by using large beam pipe diameters and possibly scrapers if necessary. Tests on the THOR facility at LANL will be carried out soon to understand the tolerable limits for beam spill on the accelerator cell gaps. Beam tuning will be optimized to stay within those limits. The insulator has been well shielded and conservatively designed to avoid breakdowns.

BBU is being minimized by keeping the pipe size large and using ferrite dampers in the cells to lower the Q's of TM modes. AMOS was used to optimize the cell design for transverse mode impedance and to properly place damping. Mycalex with a dielectric constant of 6.9 makes it more difficult to keep $Z_\perp$ low compared to Rexolite (2.5). Mycalex has been chosen because of its robustness under electrical breakdown both mechanically and in electrical recovery. Tests at LBNL indicated that Rexolite did not recover well from long pulse breakdowns (~2μs). The AMOS modelling indicates a minimum practically achievable $Z_\perp$ of about 350Ωm for the standard cells. The injector cells would be lower primarily because of pipe size scaling. Measurements have been carried out on a cavity mock up without Metglas cores and on a full prototype standard cell with cores and oil. The latter used a two wire exciter-loop pickup technique developed by Briggs.[1] The measurements showed a $Z_\perp$ at 230 MHz of 350-450Ω/m with ferrite damping on the oil side and Q's of 4-5. Measurements using a standard two wire technique[2] will be performed soon to confirm these results.

The total transverse beam motion at the end of the accelerator due to both BBU and corkscrew motion must be less that 10% of the beam radius. The corkscrew is being minimized by making the accelerating voltage as flat as possible (±0.5%) and aligning the solenoids as well as possible using the Stretched Wire Alignment Technique.[3] Accuracies of ± 0.1mm on solenoid axis location and ±0.3 mrad on tilt should be achievable

A calculation of the beam motion at the end of the machine assuming the configuration discussed above but without intercells has been performed. The calculation assumes a 200 MHz, 100μ injector transverse noise seed and a beam-pulse-head-dump which creates a small precursor pulse ahead of the equilibrium pulse. Cell transverse mode impedances of 180 Ω/m and 340 Ω/m for the injector and standard cells were used at 200 MHz. Q's were 2 and 1.9 respectively. This somewhat pessimistic calculation gave 125μ of BBU motion superimposed on 350μ of corkscrew motion. The beam radius was 8 mm so the transverse motion was well within the 800μ budget.

7 REFERENCES

(1) D. Birx, R. Briggs, L. Reginato, BBU Impedance Measurements on the DARHT-2 Cell, LBNL-42876, February 2, 1999

(2) L.S. Walling, D. E. McMurray, D. V. Neuffer, H. A. Thiessen, Nuc. Inst. Meth., A281, 1989, p.433

(3) L.V. Griffith, F. J. Deadrick, Proc. 1990 Lin. Accel. Conf., Albuquerque, Sept. 1990, p. 423

STATUS OF THE AIRIX ACCELERATOR

E. Merle, R. Boivinet, M. Mouillet, J.C. Picon, O. Pierret
CEA / DIF / PEM 51490 PONTFAVERGER-MORONVILLIERS - FRANCE

Ph. Anthouard, J. Bardy, C. Bonnafond, A. Devin, P. Eyl
CEA / CESTA BP n°2 33114 LE BARP - France

Abstract

AIRIX is a linear induction accelerator that will be used for flash X-ray radiography. It will deliver a 20 MeV, 3.5 kA, 60 ns electron beam. This accelerator is now under installation at PEM. The injector, that produces a 3.5 kA, 4 MeV, 60 ns electron beam and 16 induction cells powered by 8 high voltage generators (250 kV per cell) are already operational. At this point, the AIRIX LIA has the same dimension than the PIVAIR prototype installed at CESTA [1]. This paper relates the electron beam characterization that we have made to compare the two accelerators. Those experiments consist first, on beam imaging to validate beam transport code at three points on the beam line. In a second time we measure the energy of the beam with the time-resolved spectrometer to control the acceleration of the beam and to precisely tune the chronometry of the machine. Finally, we measure the emittance of the beam with the Pepper-pot method to compare the value before and after acceleration. We will present also the accelerator update and the experiments we plan to do when the 64 induction cells and the 32 H.V. generators will be installed.

1 INTRODUCTION

The installation of the AIRIX induction accelerator is going on at Moronvilliers. An experimental break has been realized during two months (december 98, january 99) and consisted to work with the injector and 16 induction cells. Different aims were expected:

- the validation of the technical choices for the machine
- the complete electron beam characterization after the nominal acceleration.
- the validation of the beam transport calculations
- the extrapollation to the AIRIX performances

This campaign is still under analysis, but we present here the first results. In a first part, we expose the beam initial characteristics measurements. The high voltage performances of the induction cells are related in the second point, and we expose also the associated energy spectrums. In the two following paragraphs, we present respectively, the beam emittance, and the beam radius measurement for different transport calculations.

2 INJECTOR CHARACTERISTICS

The complete electron beam characterization has been made for two running points of the injector : (4.0 MeV; 3.5 kA) and (3.6 MeV; 3.0 kA) [2]. The time-resolved energy spectrum [3] shows that, for a ± 1% energy spread, the flat top duration is 60 ns (fig. 1).

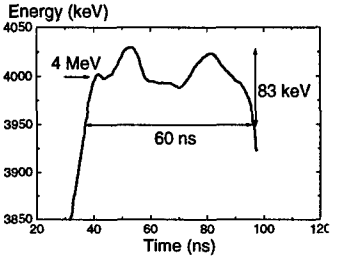

Figure 1: injector time-resolved energy spectrum

The emittance (ε) measurement has been made with the Pepper-pot method [4].

ε (π mm mrad)	X axis	Y axis
4.0 MeV	1150	1181
3.6 MeV	977	1001

Table 1 : Emittance values measured with the pepper-pot method

We have choosen to use the normalized geometrical emittance. The 'global' emittance value, published until now, is higher because the emittance diagram is distorted by the pepper-pot focalization effect [4].

The determination of the beam initial parameters (radius R_0 and envelope slope R'_0) is made with the classical three gradients method. The electron beam visualization is made by an intensified and gated camera observing Cerenkov radiation obtained by the beam interaction with a 5 μm thin aluminized mylar foil.

Energy	3.6 MeV		4.0 MeV	
Axis	X	Y	X	Y
R_0 (mm)	32.4	33.4	29.7	30.04
R'_0 (mrad)	75.7	77.5	70.21	70.03
ε (p mm mrad)	1013	826	1190	1025
f.o.m. (%)	2.1	2.1	1.94	1.45

Table 2 : Beam initial parameters

The factor of merit (f.o.m.) evaluates the good adequation between the calculated values of the beam diameter and the measured values. In a perfect case, (measured and calculated values are identical) the f.o.m. is zero.

0-7803-5573-3/99/$10.00@1999 IEEE.

We can notice, that the emittance values obtained with the two different methods are very closed. More, in the two directions, X and Y axis, R_0 and R'_0 are very closed too. The beam seems to be symetrical along the electron beam propagation axis (z).

3 INDUCTION CELLS

The induction cells installed on the AIRIX machine are vacuum technology cells [5]. They are powered by high voltage generators (250 kV per cell, 2 cells per generator). The ferrite section has been increased by 9 %, in comparison with the PIVAIR cells, in order to delay ferrite saturation and decrease overvoltage stresses.

A high accuracy energy measurement of the accelerated beam, has been made with the time-resolved energy spectrometer. On the figure 2 we can observe a typical H.V. signal measured on the cells, and on the figure 3 the associated spectrum.

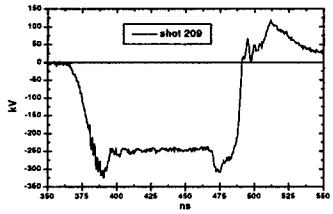

Figure 2: induction cell high voltage signal

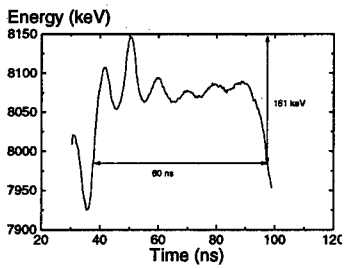

Figure 3: accelerated beam energy spectrum

The two peaks on the cells high voltage signal are caused by the presence of the beam that has a smaller duration, and that procures a different impedance of the cell. We can see also those picks because the ferrite material is not yet saturated.

The first peak that we can see on the spectrum (8020 keV) corresponds to the rise time of the beam pulse. At this time, the beam current is smaller than the 3.5 kA nominal value and the H.V. seen by those electrons is higher than the 250kV nominal value (peaks on the high voltage signal).

The presence of the two peaks (figure 2), facilitates the synchronisation of the machine. More, it can absorb the 5 ns of the high voltage power units jitter.

The figure 3 shows that the energy nominal value is 8 MeV, and the ± 1% energy spread is preserved although the shape has been singularly modified, compared to the injector energy spectrum one (figure 1).

We can act on this shape by tuning the delay between the beam and the high voltage accelerating pulse. In the two cases presented here (figure 4 and 5) with the spectrum and the associated cells H.V. signals, the difference between the delays is 10 ns. We observe that the first rise-time peak can disappear completely (shot 282), but the two following ones have too high level. In opposite, the rise-time peak can be integrated to the spectrum and makes it wider.

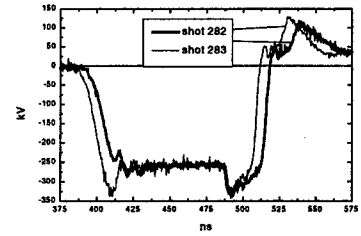

Figure 4: Cells H.V. signal for two shots with 10 ns different delays between the injector and accelerator

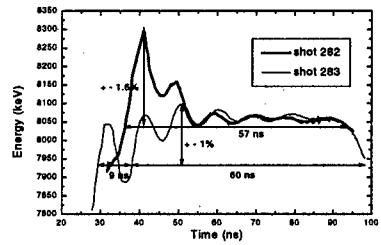

Figure 5: Spectrum associated to the shots 282 and 283

In routine, we will work with a symetrical H.V. signal, to preserve the minimum energy spread, during the 60 ns pulse width (figure 2,3).

4 BEAM EMITTANCE

The normalized beam emittance has been measured with the Pepper-pot method.

ε (π mm mrad)	X axis	Y axis
8.0 MeV	1376	1273
7.6 MeV	1330	1266

Table 3 : emittance measurement after 4MeV acceleration

The emittance increase is around 200 π mm mrad, and is the same as the one measured on the PIVAIR machine.

5 ELECTRON BEAM TRANSPORT

To calculate the electron beam transport, we use the classical envelop equation:

$$R'' + k^2 R - \frac{K}{R} - \frac{\varepsilon^2}{\beta^2\gamma^2 R^3} = 0$$

$$K = \frac{2I}{17.045\beta^3\gamma^3} \text{ (I in kAmps); } k = \frac{e\,c\,B_z}{2\beta\gamma mc^2}$$

The ENV code [6] takes into account the effect of the ferrite cores in the calculation of the axial magnetic field. We have improved several beam transport configurations, and each time, we have measured the beam diameter at the exit of the 16th cell.

In a first case (figure 6), we have transported the 7.6 MeV (3.6MeV+16*250keV) electron beam on a 40 mm diameter (400 Gauss axial magnetic field). In the second case (figure 7), the beam has a 20 mm diameter along the

accelerator (700 Gauss axial magnetic field), and final energy is 8 MeV.

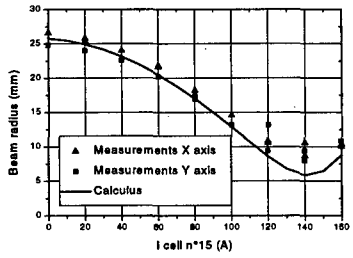

figure 6: variation of beam diameter with magnetic field on the 15th cell

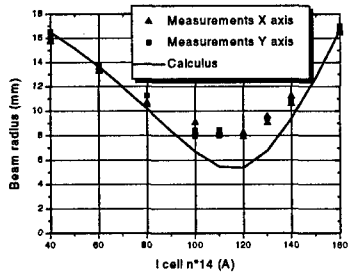

figure 7: variation of beam diameter with magnetic field on the 14th cell

We can distinguish two parts on those curves. In a first part (I<100A), the electron beam is homogeneous, and has a classical square profile. The correlation between measurements and calculus is good. With those currents, the beam has not been focalised (small beam-waist) before the target. We will be generally in that case to transport the beam throughout the machine.

In the second part of the curves, the beam has been focalized before the target, and then the difference between the measured and calculated radius grows up to 3 mm. Perhaps in that case the envelop equation used is not complete, or there are 2D effects. The beam profile is not square for those points. Different numerical and analytical investigations have been initialized to understand those differences.

Nevertheless, those results prove that the electron beam transport on the AIRIX machine can be calculated with the ENV code that is well predictive in most of cases.

We have improved also the centering procedure to have a centered beam all along the machine. One BPM (Beam Position Monitor) is installed on each four cells block. To optimize the entrance of the beam in the accelerator, we have installed another BPM, 50 cm before the one placed on the first cell. With those two measurements, we can obtain a centered beam with a minimum centroïd slope. If the centering procedure at the entrance of the accelerator is made rigorously, the beam is centered in a 2 mm diameter circle all along the machine.

On the figure 8, we have reported the first 7 BPM measurements. Each point per BPM corresponds to one shot, and represents the mean value of the beam centroïde motion calculated during 40 ns on the flat top of the current pulse. Day after day, the third and the last shot of the day are identical (same parameters for the machine). With this method, we can evaluate the machine stability, as shown on the next figure where 9 shots, corresponding to 4 days, are plotted.

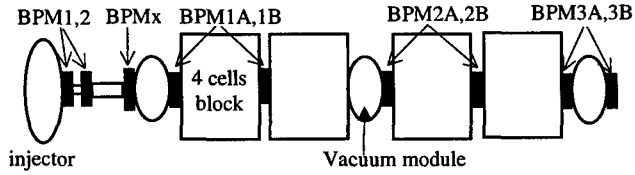

Schema of the 'AIRIX 16 cells' experiment

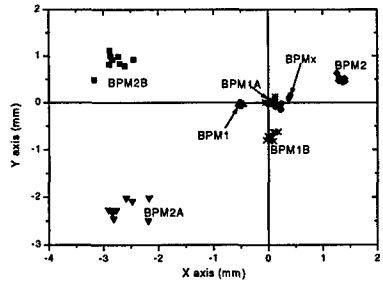

figure 8: centroïd beam measurement

The space occupied by the centroïd is larger at the end of the machine. This is due to the reliability of the power supplies that delivers current to the steering magnet. Modifications are under realization to correct this defect.

6 CONCLUSION

The "AIRIX 16 cells experiment", has been complete and comprises also BBU measurements. Several parametric variations in the magnetic field configuration have been tested. The results are now under analysis and will be published subsequently.

At this time, the 32 H.V. units are already installed on the machine, and 36 induction cells too. The machine will be complete next summer. The acceptance test will consist essentially in the time-resolved energy measurement, and a reproducibility of the electron beam characteristics test.

We plan to make the first hydrotest with radiographic diagnostic in december 99.

REFERENCES

1 Ph. Anthouard et al., "AIRIX prototype technological results at CESTA", Proc.. of PAC 97.

2 E. Merle et al., "Installation of the AIRIX induction accelerator", Proc. of LINAC 97.

3 D. Villate et al., "AIRIX alignment and high current electron beam diagnostics", Proc of PAC 95.

4 C. Bonnafond et al. "Optical and time-resolved diagnostics for the AIRIX high current electron beam.", Proc. of DIPAC 97

5 Ph. Anthouard et al., "AIRIX and PIVAIR accelerator status" Proc. of Beams 98.

6 J. Bardy - ENV "Envelop electron bem transport code", Private communication

CELL DESIGN AND TEST FOR AN INDUCTION LINAC

Huacen Wang, Zhi Zhang Kai, Long Wen, Yong Zou,
Lai Qinggu, Wenwei Zhang , Jianjun Deng , Bonan Ding,
Institute of Fluid Physics, P.O.Box 523, Chengdu, 610003, P.R.China

Abstract

The prototype cell design and test for an induction linac are presented. The two prototype cells, which are expected to operate at 250kV, are composed of a ferrite core immersed in oil (MODI) or in vacuum(MODII), an gap with curved stainless steel electrodes, a solenoid magnet with two dipole coils, and finally a insulator in MODI. The test results of the cells are introduced.

1 INTRODUCTION

An induction linac consists of an injector and a series of induction cells. Therefore, the final performance of the accelerator strongly depends on the cell feature. The Beam Break-up(BBU) instability due to the interaction between beam and cells and the corkscrew motion caused by misalignment and chromatic aberration of optical elements can also adversely effect the beam quality. The crucial issues considered in the cell design with emphasis on the measures taken for minimizing the transverse impedance and beam instability while optimizing the cell high-voltage stand-off are introduced briefly in this paper. The test results of the prototype cells are given.

Two prototype cells have been developed and are referred to as MODI and MODII shown in Fig. 1.

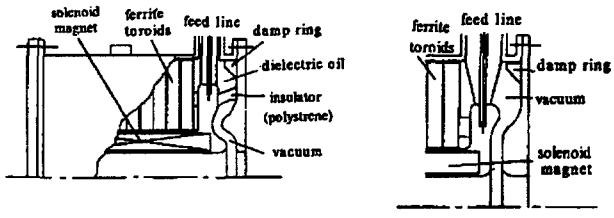

(a) MODI (b) gap region of MOD II

Figure 1: Schematic of the prototype cells

2 HIGH-VOLTAGE DESIGN AND TEST

The cross sectional area, A, of the induction cores is determined by the required voltage , U, pule duration, τ, and the magnetic flux swing, ΔB

$$U \cdot \tau = \Delta B \cdot A \qquad (1)$$

11 home-made ferrite toroids with 237mm ID, 508mm OD, 25.4mm thick were used in MODI while 10 corner- radiused toroids with 254mm ID, 508mm OD, 25.4mm thick used in MODII to provide the accelerating pulse. The 148mm cell bore is a engineering compromise between the large bore needed to lower the transverse impedance and the small bore required to reduce the costs and to provide enough space for the solenoid magnet.

The designed maximum electric field stress was limited to 190kV/cm for Ocr18Ni9 stainless steel electrodes that form the accelerating gap. The electrodes were laser welded and grit blasted to ensure that 300kV voltage pulse can be sustained by the gap. The breakdown electric field of the insulator separating the oil-filled ferrite core from the vacuum portion of the cell in MODI was maximized by holding 42° angle between the insulator and the calculated electric potential line and carefully treating the "triple points "(vacuum, metal, and insulator interfaces). The insulator was also completely shielded from direct line-of-sight with the beam to prevent it charging and UV-induced breakdown in a way that reduces the MODI transverse impedance. The maximum electrical fields on the electrodes surface calculated by LWE2D and ELECAF2D are 185kV/cm (MODI) and 189kV/cm (MODII) and 70kV/cm in the insulator. Each cell is assembled as a ferrite loaded transmission line in favor of the pulse flattop, the impedance, R_f, and electrical length, T, of which are characterized by

0-7803-5573-3/99/$10.00@1999 IEEE.

$$R_f = \left[(\mu_r\mu_0/\varepsilon_r\varepsilon_0)^{1/2}/2\pi\right]\ln(R_0/R_i) \quad (2)$$

$$T = l(\mu_r\varepsilon_r)^{1/2}/c \quad (3)$$

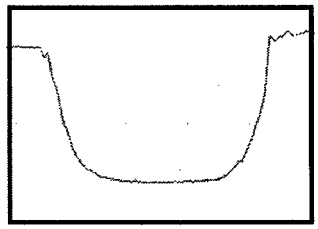

(a) 252kV with flattop74ns,144kV/div,25ns/div

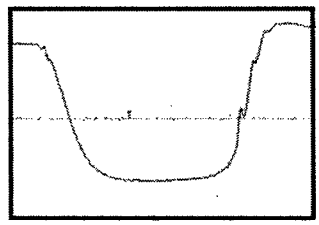

(b) 300kV with flattop70ns,160kV/div,25ns/div

Figure 2: MODI accelerating voltage pulses

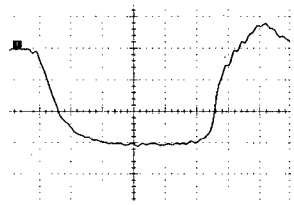

(a) 250kV with flattop 62ns,84kv/div,20ns/div

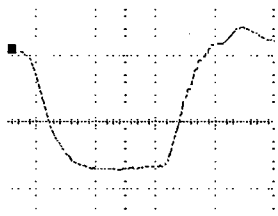

(b) 300kV with flattop 58ns, 85kV/div, 20ns/div

Figure3: MOD II accelerating voltage pulses

where l is the length of the ferrite core. ε_r , μ_r and ε_0 , μ_0 are the permittivity and permeability of the ferrite core and free space respectively. c is the speed of light in vacuum. R_0 , R_i are the outer and inner radii of the ferrite toroids. The auto-reset circuit of the core and the conducting ceramic resistors provide adequate and stabilized reset current for the core and compensate the fluctuations in accelerating pulse caused by the variations of cell impedance and beam current[1]. The accelerating pulses measured are shown in Fig.2,3.

3 CELL TRANSVERSE IMPEDANCE

The beam instability arising from the high-frequency transverse oscillations degrades the beam brightness and time-integrated beam spot size at the final focus of the accelerator. Theoretic analysis have shown that the transverse impedance of the cells can be reduced by using insulator material, the dielectric constant of which is near to that of oil used in MODI, placing the insulator close to the cell bore, slanting the insulator at approximately the Brewster angle to enhance the *rf* waves to the ferrite, exposing the ferrite to the cell to absorb the *rf* waves , putting a piece of ferrite at the cell corner to damp the cell modes. The curved gap in MODI was designed to form a section of coaxial transmission line inserted between the cell structure and the accelerating region to cut off the cell TM110 mode[2], thereforeto reduce the transverse impedance of this mode. To further lower the transverse impedance , a conducting ceramic ring is being fabricated to replace the nylon insulator.

The cell transverse impedance measured by biwire method[3] are shown in Fig. 4. It shows that the transverse impedance corresponding to TM110 in MODI is lower than that in MODII. The value shown in Fig. 4. will be reduced by about 20% at operation, because of the core bias.

4 ALIGNMENT

The chromatic aberration of the focusing elements and misalignmentof the accelerator may result in transverse oscillation of the beam centroid referred to as corkscrew motion. Special care was taken in the cell

design and fabrication to control the mechanical

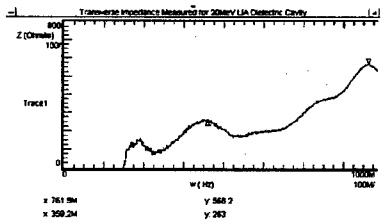

(a) MOD I

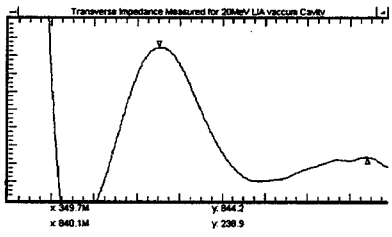

(b) MOD II

Figure 4: The cell transverse impedance

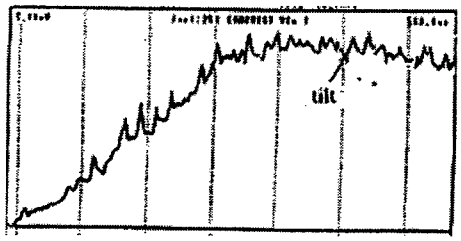

(a) tilt

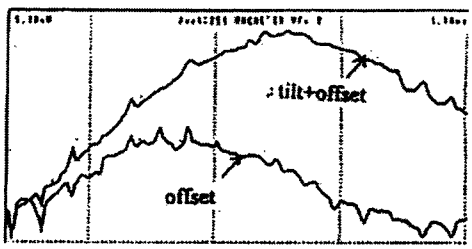

(b) tilt and offset

Figure 5: Signals of magnetic tilt and offset

tolerance. The magnet are positioned with respect to the bore to ensure that the magnetic alignment is as good as mechanical. The quadrufilar windings, the iron field-smoothing ring, and the corrective coils are used to improve the magnetic alignment.

The pulsed taut-wire[4] measurements show the offset and tilt of the magnetic axis from the mechanical axis are 0.2mm and 1.0mrad respectively(Fig. 5).

5 CONCLUSION

Both of the two prototype cells exhibited good properties for constructing electron-beam induction linac. Compared to MODII, the MODI is even better.

6 ACKNOWLEDGEMENTS

The authors would like to thank Prof. Li Xianwen , Cheng Nianan, Dr. Zhang Linwen and Prof Yuan Jiansheng , Wang Guangwei from Qinghua University for their help and fruitful discussion.

7 REFERENCES

[1]Wang Huacen, et al. Physical design study on linear induction accelerator cell. High power laser and particle beams, 1996, 8(3): 313.

[2] Miller R.B, et al . The effect of accelerating gap geometry on the beam break up instability in linear induction accelerators. J. Appl. Phys. 1998, 63(4):997.

[3] Walling L, et al. Transverse impedance measurements of prototype cavities for a dual-axis radiographic hydrotest (DARHT)facility. Part. Accel. Conf. San Franciso, CA, USA, 1991. 2961

[4] Melton JG, et al. Pulsed taut-wire measurement of the magnetic alignment of the ITS induction cells. Part. Accel. Conf. washington DC, USA, 1993. 2944

PRODUCTION OF ULTRA-SHORT, HIGH CHARGE, LOW EMITTANCE ELECTRON BUNCHES USING A 1 GV/M DC GUN.

M.J. de Loos, S.B. van der Geer, Pulsar Physics
J.I.M. Botman, O.J. Luiten, M.J. van der Wiel, TU-Eindhoven

Abstract

Advanced acceleration schemes, for example those based on wake fields of laser pulses traveling through plasma, require the injection of very high quality relativistic femtosecond electron bunches. Such bunches can be produced by a photoexcited RF gun followed by longitudinal bunch compression. Currently we are investigating a different pre-acceleration scheme, which avoids the necessity of magnetic compression and the associated potential emittance growth due to coherent synchrotron radiation.

Instead of an RF cavity, we propose 1 GV/m DC acceleration of laser excited electrons across a 2 mm gap, following recent developments at Brookhaven Nat. Lab. [1]. The gun is powered by a 2 MV, 1 ns pulse. Simulation results using the General Particle Tracer (GPT) code show that with the DC gun scheme a 100 pC bunch can be accelerated to 2 MeV with a final bunch length of 70 fs and an emittance well below 1 π mm mrad.

1 INTRODUCTION

At the Eindhoven University of Technology a new project has been started with the goal to do experiments with coherent transition radiation and plasma acceleration. For these experiments a new electron gun with very strict requirements is being designed. The design goals are a bunch charge of 100 pC with a bunch length of 100 fs. Furthermore an emittance below 1 π mm mrad and an energy of 10 MeV is required.

To meet these requirements two possible routes can be followed. The first is to use an RF photoinjector and perform bunch compression. The problem with this method is that bunch compression systems based on for example chicanes cause the emission of coherent synchrotron radiation and this has undesirable effects on the bunch length and energy spread. At this point it is not clear whether the listed requirements can be met using this method.

An alternative method is to eliminate the bunch compressor by generating a short bunch and keeping it short. Initial simulations show that for this method an acceleration field of at least 500 MV/m is required until the beam is relativistic. Lower acceleration gradients produce longer bunches. Such fields can be achieved by means of a pulsed power supply, producing a DC voltage of 2 MV during 1 ns. A power supply of these specifications is presently being developed for this project at the Efremov Institute, St. Petersburg. When this pulse is applied across a diode with a gap of 2 mm a 1 GV/m field is achieved. Fields of this magnitude can be maintained without breakdown for the duration of 1 ns [1]. The drawback of this method is that a second acceleration stage is needed to increase the beam energy from 2 MeV to 10 MeV.

From the simulation results the method based on the diode followed by an RF booster looks very promising. Therefore we have chosen to follow this path. In this paper we will present the simulation results for the diode and give a brief description of the used simulation package.

2 THE DIODE SET-UP

The diode set-up consists of a hollow spherical copper cathode and a flat anode with a circular aperture, schematically shown in Figure 1. The field in the diode is produced by a power supply generating a pulse of 2-2.5 MV during 1 ns. When this negative pulse is applied across the gap, acceleration fields of 1 GV/m are attainable. Because of the extremely high gradient and because no additional focusing is needed, this device could be much better suited for ultra-short bunch generation than a conventional photo-cathode.

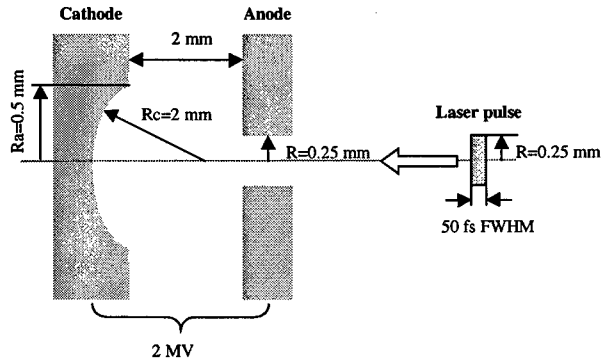

Figure 1: Schematic of the diode (not to scale).

The cathode is curved to produce a transverse focusing field, thus eliminating the need for external focusing. The opening in the anode is kept as small as possible to prevent the field from leaking out of the gun and thereby lowering the acceleration gradient. The set-up parameters are listed in Table A.

The laser used to photoexcite electrons on the cathode surface is injected on-axis and limited in radial size by the

0-7803-5573-3/99/$10.00@1999 IEEE.

anode aperture. The very high electric field in the diode results in a considerable lowering of the surface work function due to the Schottky effect. This means that the pulses from the Ti:Sapphire laser, operating at 810 nm, will only need to be frequency-doubled to extract electrons from the copper surface by single photon emission. The minimum pulse length of the laser we plan to use for the experiments is 50 fs FWHM for a gaussian temporal profile.

Table A: Set-up parameters.

Parameter	Value
Input voltage	2 MV
Electric field	1 GV/m
Cathode curvature radius	2.0 mm
Cathode aperture radius	0.5 mm
Gap length	2.0 mm
Anode length	1.5 mm
Anode aperture radius	0.25 mm
Laser radius	0.25 mm
Initial emittance	0.12 π mm mrad
Bunch charge	100 pC
Laser pulse length	50 fs FWHM

3 THE GENERAL PARTICLE TRACER

The simulations for the design of the diode were performed using the General Particle Tracer (GPT) simulation package [2,3]. GPT is a 3D particle tracking code developed for the design of accelerators and beam lines. The differential equations for the particle trajectories are solved using a fifth order embedded Runge-Kutta method. GPT includes many standard elements representing beam line components and custom elements can easily be added by the user. It also incorporates a number of different space-charge models. Furthermore it includes a Windows 95/NT user interface complete with data analysis and graphics. The code is written in C/C++ and UNIX versions are also available. For the simulations presented in this paper, GPT was used in combination with the POISSON [4] set of codes to import the electric field-map of the diode.

3.1 2D space-charge model

For the diode simulations GPT's 2D space-charge model was used, instead of the standard 3D point-to-point model. The 2D space-charge model can be used to calculate the effect of self-fields in axially symmetric beams by representing every particle as a homogeneously charged circle. Because every particle represents a complete ring, the amount of particles needed to obtain correct statistics is less than in 3D point-to-point calculations.

The equations for a homogeneously charged circle with radius R and charge Q in its rest frame are given by [5]:

$$E'_r = \frac{Q}{4\pi^2\varepsilon_0 r\sqrt{d^2+4Rr}}\left(K(\alpha)-\frac{R^2-r^2+z^2}{d^2}E(\alpha)\right)$$

$$E'_z = \frac{QzE(\alpha)}{2\pi^2\varepsilon_0 r\sqrt{d^2+4Rr}}$$

where $d^2=(R-r)^2+z^2$, $\alpha=4Rr/(d^2+4Rr)$ and K and E are elliptic integrals. Transforming this field back to the lab frame and adding the contributions of all particles j yields:

$$E_x=\sum_{j\neq i}\gamma_j E'_{x,j} \qquad B_x=\sum_{j\neq i}-\gamma_j\beta_{z,j}E'_{y,j}/c$$

$$E_y=\sum_{j\neq i}\gamma_j E'_{y,j} \qquad B_y=\sum_{j\neq i}+\gamma_j\beta_{z,j}E'_{x,j}/c$$

$$E_z=\sum_{j\neq i}E'_{z,j} \qquad B_z=0$$

This cylindrical symmetric space-charge model is fully relativistic and has a fast convergence. However there is a small error in the transverse electric field near the axis due to the finite number of rings included in the simulation. This is due to the neglect of the self-field within a ring.

4 SIMULATION RESULTS

The diode is modeled using an electrostatic 2D field-map imported into GPT to calculate the particle trajectories. The particles are emitted from the cathode with a radius of 0.25 mm and an initial emittance of 0.12 π mm mrad. In the simulation the particles are emitted in time: Particles are added as they emerge from the cathode. The simulations were carried out to determine the beam characteristics using the pulsed diode and to optimize the geometry.

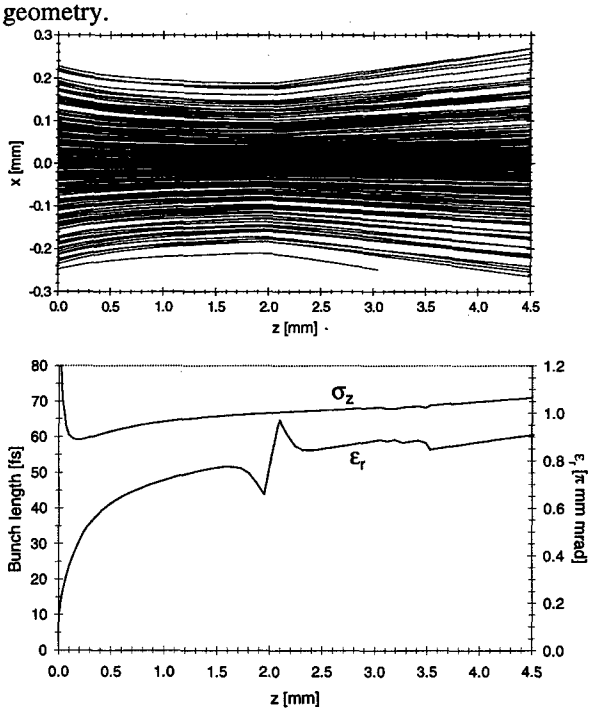

Figure 2: Particle trajectories in the diode and the evolution of the bunch-length and emittance. The beam is clipped slightly by the anode.

Figure 2 shows the beam behavior in the diode. It can be seen that the flow is laminar, but 6% of the bunch is clipped at the anode. Emittance growth mainly occurs in the first 500 μm, when the beam energy is less than 0.5 MeV. The exit emittance is determined by the space-charge forces and the normalized transverse emittance at the anode is 0.85 π mm mrad with a RMS bunch length of 70 fs. These values meet the set criteria, but they have to be maintained in the second accelerator.

The curved cathode produces a waist in the beam, thereby eliminating the need for external focusing. The radius of the curvature has been optimized. A small curvature radius increases the bunch-length and the emittance, while a large radius causes clipping of the beam at the anode. We have chosen to use a cathode curvature radius of 2 mm because this greatly improves the beam qualities for a beam loss of only 6%.

The initial beam radius has a significant effect on the bunch length and emittance. A small radius causes beam loss in the anode because the beam blows up due to space-charge, while a large initial radius increases the bunch length and emittance.

4.1 Radial laser profile

The previous GPT simulations are performed with a uniform radial laser intensity function. According to Serafini [6] the best emittance results are obtained by clipping a laser beam with a gaussian radial intensity distribution at a radius specified by:

$$R = \sqrt{\tfrac{2}{3}}\,\sigma_r \approx 0.8\,\sigma_r$$

where σ_r is the RMS radius of the gaussian distribution. To investigate the effect of a different radial laser profile, we varied the cut-off distance, relative to sigma, of a gaussian intensity profile while keeping the initial beam radius constant at R=0.25 mm. The transverse emittance has an optimum when the laser is truncated at σ_r=R, as shown in Figure 3. The emittance is improved by 10%.

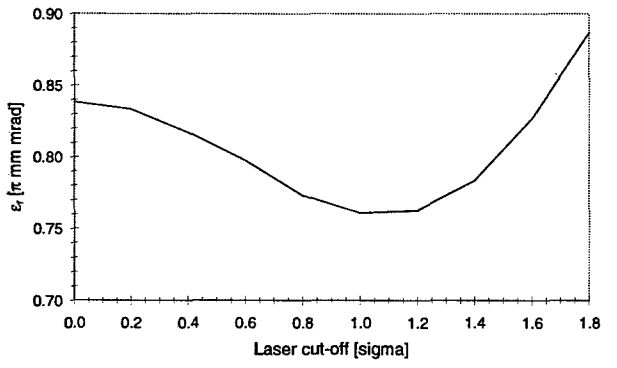

Figure 3: Transverse emittance as function of cut-off distance of a truncated gaussian radial laser intensity profile. The beam profile is varied from uniform (left) to almost a full gaussian (right).

4.2 Bunch charge

To better understand the beam dynamics in the diode, the effect of the charge in the bunch has been investigated. As shown in Figure 4, the bunch length grows linearly with the initial charge, with an offset of the laser pulse length. A high initial charge in the bunch increases the beam loss due to clipping at the anode aperture. The emittance at the exit of the diode grows with the bunch charge exiting the anode.

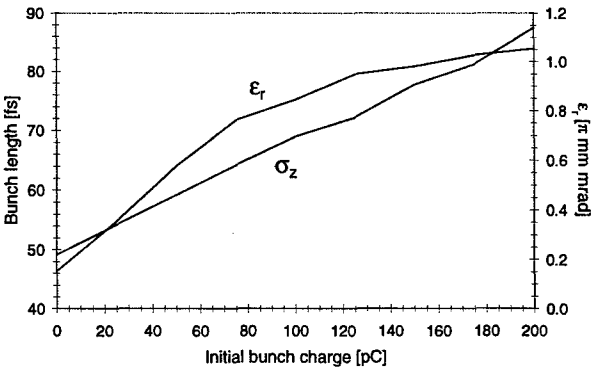

Figure 4: Effect of the initial bunch charge on the bunch length and emittance at the anode exit.

5 CONCLUSION

The beam parameters at the exit of the diode are very promising. We have obtained, in simulations, a bunch of 94 pC with a bunch length of 70 fs. The transverse emittance is 0.85 π mm mrad for a beam of 2 MeV. Currently we are designing an RF booster capable of maintaining these characteristics.

6 ACKNOWLEDGEMENTS

The authors gratefully thank Luca Serafini for his interest in this project and his stimulating comments.

7 REFERENCES

[1] K. Batchelor et al., Proc. 1998 Particle Accelerator Conf., Stockholm, Sweden (1998) pp. 791.
[2] S.B. van der Geer, M.J. de Loos, Proc. 1998 Particle Accel. Conf., Stockholm, Sweden (1998) pp. 1245.
[3] GPT User Manual, Pulsar Physics, De Bongerd 23, 3762 XA Soest, The Netherlands, http://www.pulsar.nl/gpt.
[4] J.H. Billen, L.M. Young, POISSON SUPERFISH, Los Alamos National Lab. Report LA-UR-96-1834.
[5] T.P. Wangler, Principles of RF Linear Accelerators, John Wiley, New York (1998), pp. 271.
[6] L. Serafini, Proc. Advanced Accelerator Concepts Workshop, Port Jefferson (NY) 1992, AIP Conf. Proc. 279 (1993) 645.

LIMITS OF PLASMA FOCUSING OF HIGH CURRENT ELECTRON BEAMS

S. Adamenko, E. Bulyak *, V. Stratienko, N. Tolmachev Ukraine

Abstract

Limits of the electron beam density in the focus are evaluated. As it shown, the maximal beam density is achievable in the relativistic vacuum diode with the needle anode. In such a device, the initial emittance of a beam is rather small. The electron beam gains emittance while being focused with positive ions into the anode due to collisions with the ions. Based on the paraxial beam model, the beam density in the focus is estimated. As is shown, the lowest limit of focus length is proportional to square root from ratio of the beam particle energy to the initial beam density. The maximal coefficient of the beam initial density multiplication in the focus is proportional to the initial transverse dimension of the beam and square root from the beam current.

1 INTRODUCTION

The report is aimed at estimation of the limiting parameters for the beams undergo plasma focusing on the needle–like anode.

We study the beam dynamics in the inter–electrode gap where there is no acceleration voltage. Therefore, the beam particle motion is considered as uniform, without acceleration.

2 MODEL SET–UP

Let us consider the laminar cylindrical beam of electrons with relativistic factor γ and longitudinal density N_b entering a system filled with plasma of the density sufficient to neutralize the beam space charge. The beam is focused with the space charge of plasma ions. For the ideal case, the focus spot is of the zero size. Accounting for the pair electron–ion collisions leads to heating of the beam. As a result, the beam phase space is increased yielding increasing the spot size in the focus. Our goal is to estimate the maximal beam density which can be reached in the system under consideration.

Kinetics of the axially symmetrical beam with the transverse distributing function $f(r, p_r; p_\varphi, t)$ can be described as

$$\frac{\partial f}{\partial t} + \frac{p_r}{m}\frac{\partial f}{\partial r} + \frac{p_\phi}{mr^2}\frac{\partial f}{\partial \phi} + \left(\frac{p_\phi^2}{mr^3} - \frac{\partial U}{\partial r}\right)\frac{\partial f}{\partial r} = 0. \tag{1}$$

* Email: bulyak@kipt.kharkov.ua

Here U is a potential for the radial force acting on the beam electrons; $p_\varphi = \dot{\varphi}\gamma r^2$ is the canonical momentum conjugated to the coordinate φ.

2.1 *Focusing of a laminar collisionless beam*

Let $p_\varphi = 0$ in (1) and consider the trajectory of a particle at the beam bound.

Potential for the radial force of the completely neutralized beam with the initial radius a based on the fact that the repulsive force $\sim (1-\beta)$ whereas the attractive ~ -1, is [1]:

$$U(r) = -\frac{e^2 N_b \beta^2}{2\pi\epsilon_0}\log\frac{r}{a} = -\frac{2\nu mc^2(\gamma^2-1)}{\gamma^2}\log\frac{r}{a}, \tag{2}$$

where $\nu \equiv N_b r_0$ is the Budker parameter equal to production of the longitudinal density N_b by the electron classical radius r_0. It is worth to emphasize that at $\nu = \gamma$ the beam current is equal to the Alfven limit current.

As is seen from (2), the transverse potential is independent on time, hence the corresponding hamiltonian is an invariant of motion:

$$H = \frac{p_r^2}{2\gamma m} + U(r) = \text{const}\,. \tag{3}$$

Here we take the transverse motion being nonrelativistic, and the longitudinal velocity being constant. After the simple derivations we arrive at the implicit expression for the beam envelope:

$$s = \frac{1}{2}\sqrt{\frac{\gamma}{n_b r_0}}\,\mathrm{Erf}\left[\sqrt{-2\log\frac{r}{a}}\right]. \tag{4}$$

Here s is the longitudinal coordinate (along the z–axis); n_b is the initial beam density (at the system front end); Erf is the error function. The focus length can be derived from (5):

$$S_f = \frac{a}{2}\sqrt{\frac{\pi\gamma}{\nu}} = \frac{1}{2}\sqrt{\frac{\gamma}{r_0 n_b}}, \tag{5}$$

We should emphasize the fundamental feature of the expression for the shortest possible focus length — this length is proportional to the initial beam radius and square root from the ration of the particle energy to the Budker parameter of the beam.

0-7803-5573-3/99/$10.00@1999 IEEE.

3 BEAM HEATING BY THE SHORT–RANGE COLLISIONS

As is yielded from the previous section, the fully neutralized beam shrinks into a point (its density is risen to infinity).

Effect, preventing the beam density reach infinity at full neutralization, is the multiple scattering of electrons on the focusing ions. As a result, the initially cold beam possesses definite transverse temperature that yields a finite beam density in the focus spot.

As the radial velocity of particles near the spot is much exceeded that due to the radial temperature, we neglect this impartment and limit our consideration just to the tangential (spinning) partial temperature. This temperature causes the centrifugal repulsive force, $F_r = \gamma m v^2/r$ acting against the focusing force.

For a collision with an ion, electron's squared transverse momentum is increased by:

$$\left\langle \Delta p_i^2 + \Delta p_j^2 \right\rangle = \frac{8(r_0 m_0 c)^2)}{a^2} \ln \frac{a}{r_m} = \frac{8(r_0 m_0 c)^2)}{a^2} \Lambda \,. \tag{6}$$

The speed of the momentum growth is

$$\dot{\Delta p^2} = N_b \beta c \left\langle \Delta p^2 \right\rangle = \frac{8\nu r_0 (mc^2)^2 \beta \Lambda}{a^2 c} \,. \tag{7}$$

As the both transverse degrees of freedom are independent each other, then

$$\dot{\Delta p_\phi^2} = \frac{1}{2} \dot{\Delta p^2}$$

Dependence of the tangential momentum on time is

$$p_\phi^2(t) = \frac{4\nu r_0 (mc^2)^2 \beta}{c} \int_0^t \frac{\Lambda(a) dt'}{a^2(t')} \,. \tag{8}$$

Equation for the RMS beam envelope expressed in dimensionless variables could be written as:

$$\frac{\mathrm{d}^2 \rho}{\mathrm{d}\zeta^2} + \frac{2\nu}{\rho\gamma} \left[1 - \frac{2 r_0 \Lambda \gamma}{(\gamma^2 - 1) r_a} \int_0^\zeta \frac{\mathrm{d}\zeta}{\rho^2(\zeta)} \right] = 0 \,, \tag{9}$$

where the space variables: the beam radius ρ and longitudinal coordinate ζ are related to the initial beam radius r_a:

$$\rho \equiv \frac{r}{r_a} \,; \quad \zeta \equiv \frac{z}{r_a} \,.$$

Analysis of the integro–differential equation (9) is rather complicated, nevertheless a few general results are obtainable. As far as the equation contains the only longitudinal beam density ν, energy of particles γ, and initial beam radius r_a as parameters, all the features of focusing are only dependent on them. Then, a term at the integral in (9) comprises a small parameter — ratio of the classical radius of electron r_0 to the initial beam radius r_a ($r_0/r_a \ll 1$) which manifests smallness of the repulsive force.

Estimation for the maximal beam density could be derived under assumption that the limit of focusing is reached if the focusing force is neutralized with the centrifugal one:

$$1 = \frac{2 r_0 \Lambda \gamma}{(\gamma^2 - 1) r_a} \int_0^\zeta \frac{\mathrm{d}\zeta'}{\rho^2(\zeta')} \,. \tag{10}$$

Putting roughly $\rho(\zeta) \approx \rho_m$, we get the estimated minimal squared beam radius (the reversed magnitude, ρ^{-2} produces the multiplication factor for the initial beam density):

$$\rho_m^2 = \frac{r_0 \Lambda \gamma}{(\gamma^2 - 1) r_a} \sqrt{\frac{\pi\gamma}{\nu}} \,. \tag{11}$$

As it is yielded, the obtained estimated beam radius is in good excess of the classical electron radius.

4 RESULTS AND SUMMARY

Estimation of the limit focusing for the initially parallel probe beam with current $I = 10\,\mathrm{kA}$, energy $E = 1\,\mathrm{MeV}$ ($\gamma \approx 3$), and initial radius $r_a = 50\,\mathrm{mkm}$ yields: the focusing length is $S_f = 95\,\mathrm{mkm}$
the maximal possible beam density is

$$j_m = \frac{I^{3/2}(\gamma^2 - 1)^{1/4}}{r_a} 1.36 \times 10^{11} = 3.57 \times 10^{21}\,\mathrm{A/m^2}$$

(the minimal radius is $8.4 \times 10^{-15}\,\mathrm{m} \approx 30\, r_0$).

Thus, the results of study the idealized model are physically reasonable. The esteems have to be considered as the ideal, ever achievable parameters. Any deviation from the ideal conditions, such as under neutralization of the beam space charge, or extra density of ions (then capturing electrons), etc., gives rise to the focus spot area.

5 REFERENCES

[1] E. Bulyak, *Storage of Ions by the Intense Pulsed Electron Beams.* Ph.D. Thesis, Kharkov, 1988

[2] S. Heifets, Y.T. Yan, *Quantum Effects in Tracking,* SLAC–PUB–773, 1998

EFFECT OF AUTO–FOCUSING OF THE ELECTRON BEAM IN THE RELATIVISTIC VACUUM DIODE

S. Adamenko, E. Bulyak *, V. Stratienko, N. Tolmachev, Ukraine

Abstract

A hypothesis of the beam auto–focusing in the relativistic vacuum diode with a needle anode is proposed. A physical model of the effect is elaborated. As is shown, auto –focusing of high current beam can be caused by ions emitting from the anode. Initial (pre focusing) stage of focusing is provided with ionization of the gas molecules absorbed in the anode surface. Then (at quasi–steady stage), the focusing is driven by the metal ions being evaporated from the anode heated by the beam. Simulation of the process shown the duration of initial pre focusing stage would be within 0.1–0.2 nsec.

1 INTRODUCTION

Experiments on electrical discharge in the relativistic vacuum diode with a needle anode yielded strong focusing of the electron beam in the anode. Such a device has some micrometers radius of the anode and a few millimeters the cathode–anode gap. After applying 1 MV pulse of nanosecond duration, a tiny hole along the anode axis was appeared [1]. It is obvious that beam focusing into a small fraction of the anode surface for a relatively long time could be possible if a feedback presents. The paper aimed at physical ground of the phenomenon called the beam self–focusing.

2 MODEL

It is physically reasonable that focusing of the moderately relativistic beam into a small crossover requires a short–focus lens to be placed at the anode. This lens might be provided with axially symmetrical cloud of positively charged ions.

Presence the ions themselves is not sufficient for the entire current pulse to be focused. The matter is that the time interval for which an electron crossed the cathode–anode gap sufficiently (by 3–4 orders of magnitude) shorter than the pulse duration.

Therefore, during a pulse the beam parameters such as current, energy of electrons, density of ions undergo variations. Due to these variations the focus spot is deviated. Thus, explanation of the self–focusing is required presence of the feed–back — the ion density must be bounded to the spot size.

* Email: bulyak@kipt.kharkov.ua

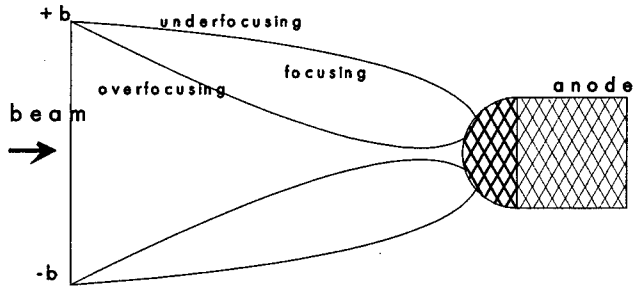

Figure 1: Anode half of the relativistic diode

Let us consider the anode surface being covered with a thin layer of neutral atoms (molecules). Also, suppose the density of the layer dependent on the density of the beam hitting upon this layer. The equation of the neutrals balance can be read as

$$\frac{\mathrm{d}\nu_0}{\mathrm{d}t} = -\lambda\nu_0 + \kappa\dot{\nu}_b(t), \tag{1}$$

where ν_0 is the surface density of the 'vapor'; $\dot{\nu}_b = n_b(t)\beta c$ is the density of electron flux onto the anode; βc is the velocity of electrons; λ is the coefficient of 'condensation'; κ is 'the conversion factor' (number of neutrals produced by an electron hitting the anode).

A solution to (1) with the initial condition $\nu_0 = \nu(0)$ at $t = 0$ has the form:

$$\nu_0(t) = \exp(-\lambda t)\left[\nu^{(0)} + \beta c\frac{\kappa}{\lambda} \times \int_0^{t\lambda} n_b(\tau/\lambda)\exp(\tau)\mathrm{d}\tau\right], \tag{2}$$

$$\lim_{t\to\infty}\nu_0(t) = n_b\beta c\frac{\kappa}{\lambda}. \tag{3}$$

The ions produced from ionization of the neutrals in the layer are accelerated in the near–to–anode space up to velocity V_i. Density of the ions beyond the accelerating space is satisfied to the discontinuity equation:

$$\frac{\partial n_i}{\partial t} + \mathrm{div}\left(\vec{V}_i n_i\right) = 0. \tag{4}$$

For the case of spherical geometry we have:

$$n_i(r,t) = \left(\frac{r_a}{r}\right)^2 n_i(r_a,t'), \tag{5}$$

$$t' \equiv t - \frac{r - r_a}{V_i}.$$

0-7803-5573-3/99/$10.00@1999 IEEE.

where

$$n_i(r_a,t) = \frac{n_b(t)\beta c\sigma_i}{V_i} n_b \beta c \frac{\kappa}{\lambda}\,, \qquad (6)$$

σ_i is the ionization cross section.

The ion cloud around the anode produces the electrostatic potential

$$\begin{aligned}\Phi(r,t) &= \Phi_a + \frac{r_c(r-r_a)}{r(r_c-r_a)} \\ &\quad [\Phi_c - \Phi_a + \Psi(r_c,t)] - \Psi(r,t)\,; \qquad (7)\\ &\quad \Psi(r,t) \equiv \frac{er_a^2}{\epsilon_0}\int_{ra}^{r}\frac{\mathrm{d}r'}{r'^2} \\ &\quad \times \int_{ra}^{r'} n_i\left(r_a, t - \frac{r''-r_a}{V_i}\right)\mathrm{d}r''\,.\end{aligned}$$

Here e is the electron charge. $\Phi_{a,c}$ is the voltage of the anode and cathode, respectively.

For the time–independent ion cloud density in the near–to–anode layer, $n_i(r_a,t) = \mathrm{const} = n_i(r_a)$,

$$\Psi(r) = \frac{en_i(r_a)r_a^2}{\epsilon_0}\left[\ln\frac{r}{r_a} - \frac{r-r_a}{r}\right] \qquad (8)$$

Let consider the cylindrical parallel electron with the radius b and density $n_b(\rho)$ enters the system at the velocity βc. Being focused by the positive ions that left the spherical cathode with the velocity V_i, the η fraction of the beam hits the anode and produces new ions from the near–to–anode neutrals (density of neutrals is ν_0). Also consider the steady–state and neglect the self–beam space charge that can change the only quantitative (not qualitative) features of the process [2], we come to the potential of the form:

$$\begin{aligned}&\Phi(r) = \mathrm{const} + \Psi(r) = \\ &\quad \mathrm{const} + \frac{en_i(r_a)r_a^2}{\epsilon_0}\left(\ln\frac{r}{r_a} - \frac{r-r_a}{r}\right) \approx \\ &\qquad \mathrm{const} + \frac{en_i(r_a)r_a^2}{\epsilon_0}\ln\frac{r}{r_a}\,, \qquad (9)\end{aligned}$$

where r_0 is the classical electron radius.

In the cylindrical geometry ($r^2 = \rho^2 + (z-z_s)^2$), an equation describing the beam envelope reads as:

$$\begin{aligned}y'' + k\frac{y}{x^2} &= 0; \qquad (10)\\ k &\equiv r_0\frac{4\pi n_i(r_a)r_a^2}{\gamma\beta^2}\,;\end{aligned}$$

$$y \equiv \rho/r_a\,; \quad x \equiv z/r_a\,.$$

A solution to this equation depends on the density of ions n_i^l

$$n_i^* = \frac{\gamma^2+1}{16\pi r_0 r_a \gamma}$$

If $n_i(r_a) \gg n_i^*$, then we have

$$\begin{aligned}\rho(z) &= \rho_0\sqrt{\frac{z_s-z}{z_s}}\cos\left(s\ln\frac{z_s-z}{z_s}\right); \qquad (11)\\ s^2 &= \frac{4\pi r_0 r_a^2\gamma n_i(r_a)}{\gamma^2-1} = \mu I_a\end{aligned}$$

As it yields from (11), at the specific density of ions n_i^{f} for the given system geometry, the whole beam is focused into the anode ($\eta = 1$):

$$n_i^{\mathrm{f}} = \frac{\pi z_s^2(\gamma^2+1)}{16 r_a^4\gamma r_0}\,. \qquad (12)$$

The beam current providing the spot not exceeding the anode transverse dimension, spans the interval:

$$I_\pm = \left[\frac{z_s}{\mu r_a}\left(\frac{\pi}{2} \mp \frac{r_a}{b}\left(1+\frac{r_a}{2z_s}\right)\right)\right]^2\,. \qquad (13)$$

the magnitude of current is proportional to $(z_s/r_a)^2$, while the relative width

$$\frac{\Delta I}{I} = \frac{4r_a}{\pi b}\,.$$

In other words, for bigger demultiplication (ratio of the initial beam radius to that at the anode) the focusing takes place within the narrower interval of the beam current.

3 SIMULATION OF THE TRANSITING STAGE

The consideration presented above indicates that under the certain conditions (presence of neutral atoms in the anode surface) the steady beam focusing into the anode can be achieved. Another necessary condition is 'attraction' of the beam to the focused state: the system shall transit itself into the stable focused state.

The computer code has been written to simulate evolution in time of the envelope of initially parallel beam. The code inherits the potential (7) and the source of neutrals (2). The species of neutral atoms can cover either all the anode semisphere or a near–to–axis circle. Variations in time in the ion density are self–consistent, according to (6).

Results of simulation of the transition regime show out that capturing the beam into the focused state requires the neutral atoms of constant (in time) density or the 'evaporation–condensation' eqiullibrium to be presented in the anode surface. Latter produces capturing in less time, besides the focal area being smaller. In any case for the transition into focused state, it is necessary the neutrals to cover the anode surface. 'Condensing' means that these neutrals decrease in number due to ionization.

The sample of the beam radius evolution is presented in Fig 2. Also it was found duration of the transition depends on the density of absorbed neutrals.

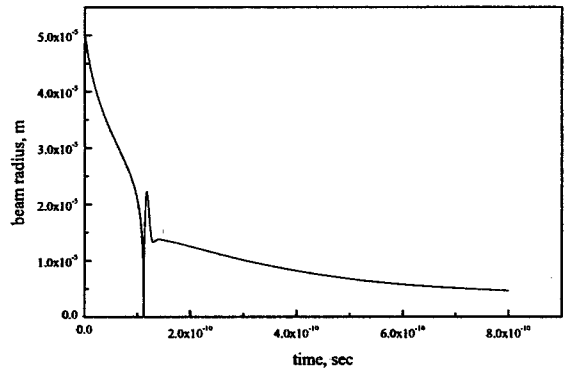

Figure 2: The beam radius evolution

4 SUMMARY

The study proves the hypothesis of the beam self–focusing with ions produced from the anode 'vapor'. At first warming–up stage, the neutrals absorbed in the anode are involved. After, the self–stabilizing mechanism of focusing due to evaporation of the neutrals from the anode is driven.

The width of the interval of current where the entire beam comes into the anode head surface, is proportional to ratio of the anode radius to the initial radius of the beam. The beam space charge will shift the focused beam current to larger values. Also it was shown that the only overfocused state can be equillibrium. The time required to reach the steady state can be less than a nanosecond. The results of the numerical simulation are in qualitative agreement with the experimental data: the self–focusing of the beam with energy of particles 0.5–1 MeV and current of a few kA can be produced at the distance of a few millimeters for less than a nanosecond.

5 REFERENCES

[1] V.A. Stratienko, S.V. Adamenko, A.N. Dovbnya, et al. "Generation and Application of the Dense Secodary Emitting Beams," in: VANT, ser. YaFI, (1997), No 2,3 (29,30), p 296

[2] E. Bulyak, "Ion clearing methods for the electron storage rings," in *Proc of EPAC–96 (Barcelon, Spain)*, 1996, p. 1048

THE PROBLEM OF DISPERSION MATCHING IN SPACE CHARGE DOMINATED BEAMS*

M. Venturini†, R.A. Kishek, and M. Reiser
University of Maryland, College Park, Maryland 20742

Abstract

We recently proposed a new analytical model that incorporates the dispersion function into the framework of the rms envelope equations. Here we show how it can be used to achieve proper matching of space charge dominated beams. Comparison is done against a PIC code (WARP) simulations.

1 INTRODUCTION

Understanding the combined effect of space charge and an energy spread in a circular lattice and more specifically, inclusion of space charge forces in the calculation of the dispersion function has been the subject of a number of papers over the last few years [1 – 6] The surge of interest has been motivated by the need of high intensity and quality beams in applications like the Spallation Neutron Source, the drivers for Heavy Ion Fusion or in studies of beam physics as in the Maryland Electron Ring [7]. In all these cases meeting optimal matching conditions (including the dispersion function) will be critical for a proper machine operation. In the presence of very high beam currents the calculation of the dispersion function is complicated in two regards: On the one hand space charge forces have to be taken into account to compute the dispersion function properly; on the other dispersion itself has a role in determining the space charge forces by affecting the beam shape. In [4] we developed an analytical model that describes both aspects of the interplay between space charge and dispersion for the case of continuous beams. The model is an extension of the standard rms evelope equations that are routinely used to solve the matching problem in straight channels. It consists of a set of three coupled differential equations for the horizontal and vertical envelopes and dispersion function. A distinctive feature is the dependence on a generalized rms emittance, which unlike the usual rms emittance is a linear invariant in the presence of an energy spread and bending magnets. A preliminary positive test on the validity of our generalized rms envelope equations was already discussed in [4]. The test was carried out against earlier calculations [5] involving a fully self-consistent analysis of beam distributions in smooth dispersive channels. Later [6] we compared the solutions of the new equations with simulations performed with a PIC code (WARP, [8]) for a periodic circular lattice consisting of FODO cells and bends. At that stage no effort was done to match the dispersion function at injection, while the envelopes were matched using the standard rms envelope equations. Comparison showed good agreement over the scale of the first (depressed) betatron oscillation period. However, after the first betatron oscillation period one could observe relaxation phenomena driven by the space charge nonlinearities in the form of a damping in the oscillations of the horizontal rms emittance and an increase in the vertical rms emittance (see also [2]). These features are not captured by the generalized rms envelope equations (if used in conjunction with the assumption that the vertical rms emittance and the generalized rms emittance are invariant of the motion). Nevertheless we speculated that for the purpose of determining the matching conditions those equations should be adequate – as long as the matching is done over a length shorter than the betatron oscillation period. In this paper we finally test that guess and apply the generalized rms envelope equations to the problem of determining the matching conditions at both injection and extraction for the Maryland E-Ring. The results are reported in Section 3. First, in Section 2 we briefly review the form of the generalized rms envelope equations.

2 THE MODEL

The theory described in this paper applies to the dynamics of a continuous beam of charged particles confined in a dispersive channel and described by the Hamiltonian

$$H=\frac{1}{2}(p_x^2+p_y^2)+\frac{1}{2}(\kappa_x x^2+\kappa_y y^2)+\frac{\psi}{mv_z^2\gamma^3}-\frac{\delta}{\rho}+\frac{m^2c^4}{E_0^2}\delta^2, \tag{1}$$

where v_z is the longitudinal velocity, γ the relativistic factor, m and q the mass and charge of the beam particles. The self-force is described by the potential ψ. Each particle has a momentum $p=p_0(1+\delta)$, with a relative derivation δ from the design momentum p_0; E_0 is the corresponding energy. The external focussing forces, described by the κ_x and κ_y, are assumed to be linear. In this model we also neglect chromatic effects (i.e. terms like $x^2\delta$ in the Hamiltonian). Finally, ρ is the local radius of curvature. Also, notice that the model (1) does not entail beam acceleration. The derivation of the generalized rms envelope equations from the Hamiltonian (1) can be carried out following steps similar to those needed to derive the usual rms envelope equations. The major differences are that i) there are two additional equations involving the moments $\langle x\delta\rangle$ and $\langle p_x\delta\rangle$; ii) the usual rms emittance is more conveniently replaced by a quantity [see below Eq. (3)] that is a linear invariant in the presence of an energy spread. Under the assumption that the beam density maintains an elliptical symmetry it can be shown [4] that the beam envelopes

* Work supported by the U.S. Department of Energy.
† venturin@physics.umd.edu

0-7803-5573-3/99/$10.00@1999 IEEE.

$\sigma_x = \sqrt{\langle x^2 \rangle}$, $\sigma_y = \sqrt{\langle y^2 \rangle}$ and the dispersion function D obey the system of equations:

$$\sigma_x'' = \frac{\epsilon_{dx}^2 + (\sigma_x \sigma_x' - DD'\langle\delta^2\rangle)^2}{\sigma_x(\sigma_x^2 - D^2\langle\delta^2\rangle)} - \frac{(\sigma_x')^2}{\sigma_x} + \kappa_x \sigma_x + \frac{K}{2(\sigma_x + \sigma_y)} + \frac{\langle\delta^2\rangle}{\sigma_x}\left(\frac{D}{\rho} + D'^2\right),$$
$$\sigma_y'' = \frac{\epsilon_y^2}{\sigma_y^3} - \kappa_y \sigma_y + \frac{K}{2(\sigma_x + \sigma_y)}, \qquad (2)$$
$$D'' = -\left[\kappa_x - \frac{K}{2\sigma_x(\sigma_x + \sigma_y)}\right] D + \frac{1}{\rho},$$

where the generalized perveance is $K = 2I/(I_0\beta^2\gamma^3)$ with $I_0 = 4\pi\epsilon_0 mc^3/q$ (in MKS units), and $\sqrt{\langle\delta^2\rangle}$ is the relative rms momentum spread. In this model the dispersion function D and its derivative are identified by $D(z) = \langle x\delta\rangle/\langle\delta^2\rangle$ and $D'(z) = \langle p_x\delta\rangle/\langle\delta^2\rangle$. Physically this identification is legittimate if before injection $\langle x\delta\rangle = \langle p_x\delta\rangle = 0$ (i.e. the pairs (x,δ) and (p_x,δ) are uncorrelated). We found this to be a natural way to extend the concept of dispersion function to include beams of self-interacting particles. The generalized rms emittance ϵ_{dx} appearing in the first equation in (2) is defined by

$$\epsilon_{dx}^2 = \epsilon_x^2 - \langle\delta^2\rangle\langle[p_x D(z) - xD'(z)]^2\rangle, \qquad (3)$$

where ϵ_x is the usual rms emittance. For matching purposes Eqs. (2) are of practical use if ϵ_{dx} does not change significantly as a result of the nonlinearities associated with space charge. One of our goals in checking Eqs. (2) against a PIC code is to establish the extent to which such an assumption is verified in practice.

3 MATCHING DISPERSION

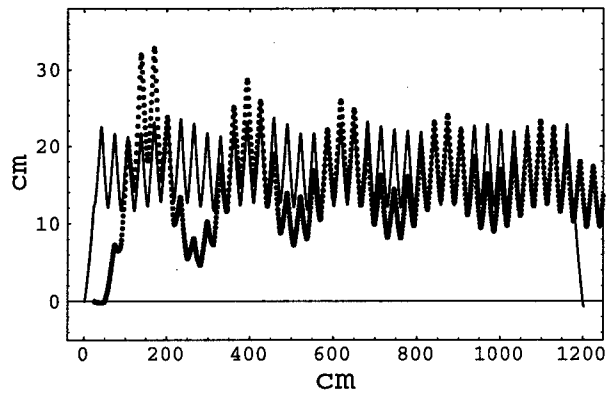

Figure 1: Dispersion function (in cm) with (solid line) and without (dots) dispersion matching; I=50 mA.

In this section we report the simulations done with the PIC code WARP to test various matching schemes worked out using the generalized rms envelope equations (2). The calculations presented here refer to a hard edge model of the Maryland E-Ring [7]. The E-Ring is designed for circulation of a 10 KeV electron beam with a current in the proximity of 100 mA. It consists of 36 identical FODO cells, each one including a 10° dipole bend, for a circumference length of 11.52 m. In the calculations reported here injection into the Ring is accomplished by a dispersion matching module consisting of two dipoles and one quadrupole. Matching of the envelopes σ_x and σ_y can be carried out separately in the transport line between the electron source and the dispersion matching module using the standard rms envelope equations.

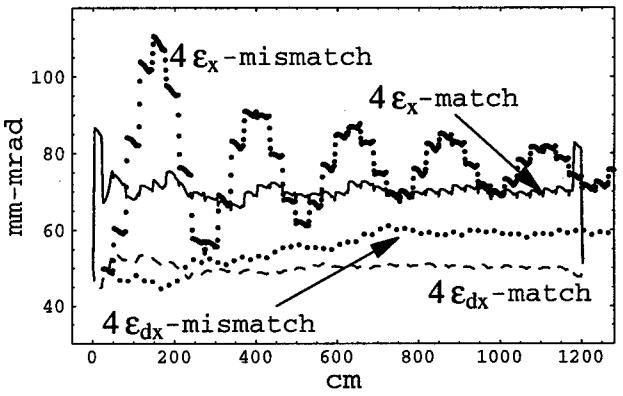

Figure 2: Horizontal effective emittances (in units of mm-mrad) and invariant (2) for the matched and mismatched cases; I= 50 mA.

The first set of pictures shows results from simulations obtained with the PIC code for a beam of $I = 50$ mA, corresponding to a tune depression of $\nu/\nu_0 = 0.29$ [the initial rms emittances are $\epsilon_x = \epsilon_y = 12.5$ mm-mrad and the energy spread is 300 eV (i.e. $\sqrt{\langle\delta^2\rangle} = 0.015$); such an unrealistically large value has been chosen to emphasize the effect of dispersion in this study]. The beam evolution is followed from the beginning of the dispersion matching module through one turn of the E-Ring and through a dispersion matching module at extraction. The purpose of the extraction module is to bring the dispersion function and its derivative back to zero. Specifically, Fig. 1 shows the profile of the dispersion function for the matched case as calculated by WARP. For comparison we also report the dispersion function that one would get if no dispersion matching is done at injection (dots). In this case the dispersion function undergoes large oscillations that are rapidly damped by the space charge nonlinearities. In Fig. 2 the horizontal effective emittance is plotted for the matched and mismatched cases together with the rms invariant ϵ_{dx} defined in Eq. (3). One can observe that the damping in the oscillations displayed by the disperson function in the mismatched case (see Fig. 1) is reproduced here. As a result, the final value for the emittance that one can extrapolate for the mismatched case is larger (although not dramatically) than the corresponding value of the emittance in the case with dispersion matching (before extraction is done). Notice however that after extraction ϵ_x is brought back to a

value very close to the one it had initially. In other words, if maching is done the ϵ_x emittance growth appears to be almost completely reversible (at least over one turn). This is consistent with ϵ_{dx} remaining basically constant. On the other hand ϵ_{dx} increases noticeably in the mismatched case.

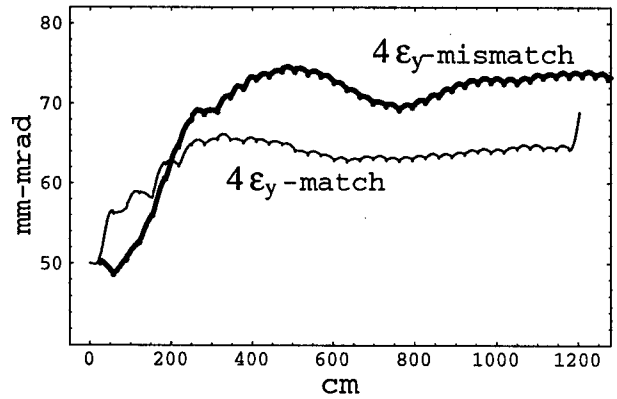

Figure 3: Vertical effective emittances (in units of mm-mrad) for the matched and mismatched case; I=50 mA.

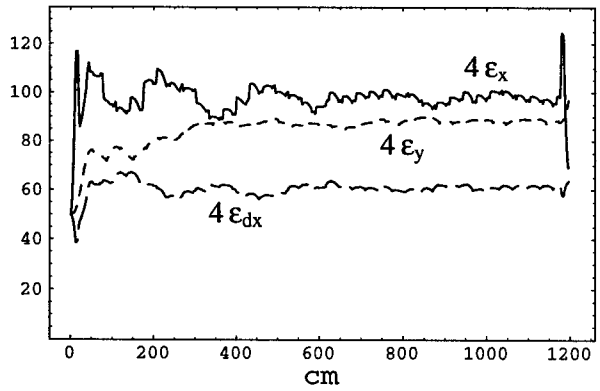

Figure 4: Horizontal and vertical effective emittances and invariant of Eq. (2) (in units of mm-mrad) for the matched and mismatched case; I= 100 mA.

Next, in Fig. 3 the evolution of the vertical emittances are reported. The rms ϵ_y emittance increases because of the nonlinear coupling with the horizontal motion induced by space charge. This effect is not captured by Eqs. (2). However, notice how a matching based on Eq. (2) nevertheless succeeds in reducing the amount of the y-emittance growth. The sharp growth that we can observe at extraction is due in part to the fact that at extraction the matching was done under the assumption that ϵ_y was the same as at injection. In Fig. 4 we show the evolution of the emittances for a case with larger current $I = 100$ mA (corresponding to a detuning $\nu/\nu_0 = 0.15$). In this case the matching is less efficient although still significant. In the last picture (Fig. 5) we report the case in which the matching is done using the equations proposed by A. Garren [1]. One can see that under the regime we are considering that model would lead to an even more pronounced mismatch (A. Garren's equations coincide with Eqs. (2) in the zero energy spread limit).

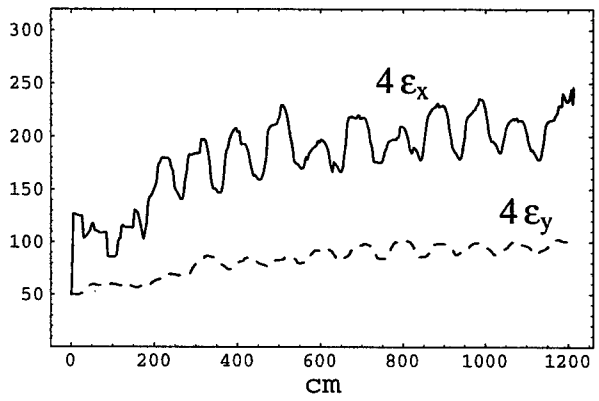

Figure 5: Horizontal and vertical effective emittances (in units of mm-mrad) for a matching done using a less accurate model; I= 50 mA.

4 CONCLUSIONS

The results reported in this paper show that use of the generalized rms envelope equations appears to be effective in achieving acceptable matching conditions for space charge dominated beams in the presence of an energy spread. Moreover, if the tune depression is not extreme the rms emittance growth in the horizontal plane due to dispersion seems to be to a large extent reversible. A measure of the non reversibility is given by the growth of the generalized emittance defined in Eq. (3).

5 AKNOWLEDGEMENTS

We are grateful to A. Friedman and D. Grote for permission to use and assistance with the code WARP.

6 REFERENCES

[1] A. Garren, Proc. Heavy Ion Fusion Workshop 1979, Reports LBL-10301/SLAC-PUB 2575, UC-28, p. 297.

[2] J.J. Barnard et al., 1992 Linear Accelerator Conference Prof. AECL-10728 Vol. 1, p. 229; J.J. Barnard et al., AIP Conf. Proceedings, 448 (1998), p. 221.

[3] S.Y. Lee and H. Okamoto, Phys. Rev. Lett. 80, 23 (1998) p. 5133; J.A. Holmes et al., AIP Conf. Proceedings, 448 (1998) p. 254.

[4] M. Venturini and M. Reiser, Phys. Rev. Lett. 81, 1 (1998), p. 96.

[5] M. Venturini and M. Reiser, Phys. Rev. E, 57, 5 (1998), p. 4725.

[6] M. Venturini, R.A. Kishek, and M. Reiser, AIP Conf. Proceedings, 448 (1998), p. 278.

[7] M. Reiser et al., The Maryland Electron Ring for Investigating Space-Charge Dominated Beams in a Circular FODO System, These Proceedings.

[8] A. Friedman, AIP Conf. Proceedings, 448 (1998), p. 329.

INTRABEAM SCATTERING ON HALO FORMATION

N. Pichoff*, CEA/DSM/DAPNIA/SEA, France

Abstract

The effect of the coulombian collision between particles of a beam (intra-beam scattering) is investigated. Starting from the basic two-bodies cross section formula in the centre of mass referential, the maximum energy gain that can be catched by a particle along one direction is calculated as a function of the equipartition factor. Then, assuming that particle trajectories are ellipses in (x, x') phase-space (linear force ~ no space charge forces), the intra-beam scattering halo magnitude is calculated and shown to be very small. These calculations are done with different beam distribution functions and equipartition factor. The effect of space-charge is then investigated.

1 INTRODUCTION

Numerical studies have shown that transporting a beam in equipartition conditions could be less halo-producing than in non equipartition ones [1]. The intrabeam scattering, even if badly simulated by space-charge routines, could be suspected to be responsible of this halo production. We have undertaken to specifically study the magnitude of this effect on halo formation in proton linac.

2 ASSUMPTIONS AND DEFINITIONS

Let f(x,y,z,x',y',z') be the distribution function of a beam in 6D phase-space. The projections of this function in 2D phase or real spaces are assumed to be elliptical.

Let $\mathbf{x_0}$, $\mathbf{y_0}$, $\mathbf{z_0}$, $\mathbf{x'_0}$, $\mathbf{y'_0}$ and $\mathbf{z'_0}$ be the maximum values of respectively x, y, z, x', y' and z' which can be reached by a beam-particle. We have :

$$\left(\frac{x}{x_0}\right)^2+\left(\frac{x'}{x'_0}\right)^2+\left(\frac{y}{y_0}\right)^2+\left(\frac{y'}{y'_0}\right)^2+\left(\frac{z}{z_0}\right)^2+\left(\frac{z'}{z'_0}\right)^2 \le 1. \quad (1)$$

We assume that $x'_0 = y'_0 = r'_0$, (same temperature in both transverse directions).

We define the equipartition factor χ as :

$$\chi = \frac{z'_0}{r'_0}, \quad (2)$$

which equals 1 if the beam is equipartitionned.

For each particle, we define its "x-emittance" along x-direction ε_x :

$$\varepsilon_x = \left(\frac{x}{x_0}\right)^2+\left(\frac{x'}{x'_0}\right)^2, \quad (3)$$

in the beam, $\varepsilon_x \le 1$.

We will assume that ε_x is a constant of motion in the particle transport. This is the case in a linear confinement force (with no space-charge force). We will discuss later about this assumption in presence of high space-charge forces.

We will calculate the probability, per unit time, for a particle to scatter to an x-emittance ε_x such that $\varepsilon_x \in [\varepsilon, \varepsilon+\Delta\varepsilon]$.

3 HALO CALCULATION - NO SPACE CHARGE

2.1 Extent

Watching a binary collision in the centre of mass frame $\Re_c$, it can be shown [2] that the maximum energy (or slope) along x direction that can be reached by a particle is given by the collision of two particles (#1 and #2) such that:

$$y'_1 = y'_2 = 0, \text{ (not necessary if } \chi = 1),$$

$$x'_1 = x'_2 = \frac{1}{\sqrt{1+\chi^2}} \cdot x'_0,$$

$$z'_1 = -z'_2 = \frac{\chi^2}{\sqrt{1+\chi^2}} \cdot x'_0,$$

with a maximum energy transfer to one particle along x direction.

Then, this particle could reach a maximum slope $\mathbf{x'_{max}}$ given by :

$$x'_{max} = \sqrt{1+\chi^2} \cdot x'_0. \quad (4)$$

The extent of the halo of an equipartitionned beam is smaller than this of a non equipartitionned one. This is true for the halo extending in the direction with the smallest temperature, but not for the other one.

2.2 Magnitude

• The number of beam particle scattering, per unit time, to an emittance between ε and $\varepsilon+d\varepsilon$ is:

$$\frac{dN_\varepsilon}{d\varepsilon} \cdot d\varepsilon = \iiint_{x,y,z} \iiint_{x'_i,y'_i,z'_i} \left(\frac{dP'_\varepsilon}{d\varepsilon} \cdot d\varepsilon\right) \cdot f(\,)\, dz'_i\, dy'_i\, dx'_i\, dz\, dy\, dx \,. \quad (5)$$

$f(\,) = f(x,y,z,x'_1,y'_1,z'_1)$ is the distribution function of the beam..

* Email: npichoff@cea.fr

• $\frac{dP'_\varepsilon}{d\varepsilon}\cdot d\varepsilon$ is the probability, per unit time, for one particle at position (x,y,z,x'_1,y'_1,z'_1) in phase-space to scatter to a x-emittance between ε and $\varepsilon+d\varepsilon$, it is given by:

$$\frac{dP'_\varepsilon}{d\varepsilon}\cdot d\varepsilon = \int_{x'_2}\int_{y'_2}\int_{z'_2} \frac{dP_\varepsilon}{d\varepsilon}\cdot d\varepsilon \cdot dx'_2\, dy'_2\, dz'_2 \,. \quad (6)$$

• $\frac{dP_\varepsilon}{d\varepsilon}\cdot d\varepsilon$ is the probability, per unit time, for one particle at (x,y,z,x'_1,y'_1,z'_1) to scatter 1) on a particle with slopes between x'_2 and $x'_2+dx'_2$, y'_2 and $y'_2+dy'_2$ and z'_2 and $z'_2+dz'_2$, 2) to a x-emittance between ε and $\varepsilon+d\varepsilon$:

$$\frac{dP_\varepsilon}{d\varepsilon}\cdot d\varepsilon = \frac{dP_{\Delta X'}}{d\Delta X'}\left(\Delta X' = x'_0\sqrt{\varepsilon-(x/x_0)^2} - x'_1\right)\frac{x'^2_0}{2(x'_1+\Delta X')}\cdot d\varepsilon \quad (7)$$

• $\frac{dP_{\Delta X'}}{d\Delta X'}\cdot d\Delta X'$ is the probability, per unit time, for one particle at position (x,y,z,x'_1,y'_1,z'_1) in the phase-space to scatter 1) on a particle with slopes between x'_2 and $x'_2+dx'_2$, y'_2 and $y'_2+dy'_2$ and z'_2 and $z'_2+dz'_2$, 2) with a x-angle $\Delta X'$ between $\Delta X'$ and $\Delta X'+d\Delta X'$:

$$\frac{dP_{\Delta X'}}{d\Delta X'}\cdot d\Delta X' = \frac{-d\Delta X'}{2\pi W'_1}\cdot\int_{\theta_{min}}^{\theta_{max}}\frac{dP_\theta}{d\theta}\cdot\frac{d\theta}{\sin\theta\cdot\sin\left(\text{acos}\left(\frac{\Delta X'-X'_1\cdot(\cos\theta-1)}{W'_1\cdot\sin\theta}\right)\right)} \quad (8)$$

with:

$$\theta_{min} = \text{asin}\left(\frac{X'_1+\Delta X'}{V}\right)-\theta_0\,,\ \theta_{max} = \pi-2\cdot\theta_0-\theta_{min}\,,$$

$$V=\sqrt{X'^2_1+Y'^2_1+Z'^2_1}\,,\ W'_1=\sqrt{Y'^2_1+Z'^2_1}\,,$$

$$X'_1=\frac{x'_1-x'_2}{2},\ Y'_1=\frac{y'_1-y'_2}{2},\ Z'_1=\frac{z'_1-z'_2}{2},$$

and $\tan\theta_0=\frac{X'_1}{W'_1}$.

• $\frac{dP_\theta}{d\theta}\cdot d\theta$ is the probability, per unit time, for one particle at (x,y,z,x'_1,y'_1,z'_1) to scatter 1) on a particle with slopes between x'_2 and $x'_2+dx'_2$, y'_2 and $y'_2+dy'_2$ and z'_2 and $z'_2+dz'_2$, 2) to a collision angle between θ and $\theta+d\theta$, :

$$\frac{dP_\theta}{d\theta}\cdot d\theta = \frac{d\sigma}{d\theta}(\theta,V)\cdot v_1\cdot\beta c\cdot f(x,y,z,x'_2,y'_2,z'_2)\,dx'_2\,dy'_2\,dz'_2\,d\theta \quad (9)$$

with $v_1=\sqrt{x'^2_1+y'^2_1+z'^2_1}$.

• $\frac{d\sigma}{d\theta}(\theta,V)$ is the cross section, differential to the scattering angle θ, of a coulombian collision in $\Re_c$ [2, Annexe 1] :

$$\frac{d\sigma}{d\theta}(\theta,V) = -\frac{2\pi\cdot r_0^2}{(2V\cdot\beta)^4}\cdot\frac{\cos\theta/2}{\sin^3\theta/2}\,, \quad (10)$$

$r_0=\frac{q^2}{4\pi\varepsilon_0 mc^2}$ is the classical radius of proton,

ε_0 is the vacuum permitivity,

q and m are the charge and the mass of particle,

βc is the beam velocity in the lab frame,

V is the half relative slope of the 2 particles (slope of one particle in $\Re_c$).

4 RESULTS

A program making the numerical integration needed to solve equation (5) with Gauss quadrature method has been written. Calculations have been done with a water-bag beam :

$$f(x,y,z,x',y',z')=\begin{cases} f_0 & \text{if } \left(\frac{x}{x_0}\right)^2+\left(\frac{x'}{x'_0}\right)^2+\left(\frac{y}{y_0}\right)^2+\left(\frac{y'}{y'_0}\right)^2+\left(\frac{z}{z_0}\right)^2+\left(\frac{z'}{z'_0}\right)^2\le 1 \\ 0 & \text{otherwise}\end{cases} \quad (11)$$

If N is the number of particles in the bunch, we have :

$$f_0=\frac{6\cdot N}{\pi^3\cdot x_0\cdot y_0\cdot z_0\cdot x'_0\cdot y'_0\cdot z'_0}\,. \quad (12)$$

On figure 1 have been represented the intrabeam scattering tails created per meter in different equipartition conditions at 2 beam energies (6.7 and 100 MeV). The beam is a typical APT beam. Vertical lines represent the theoretical halo extent obtained from equation (4).

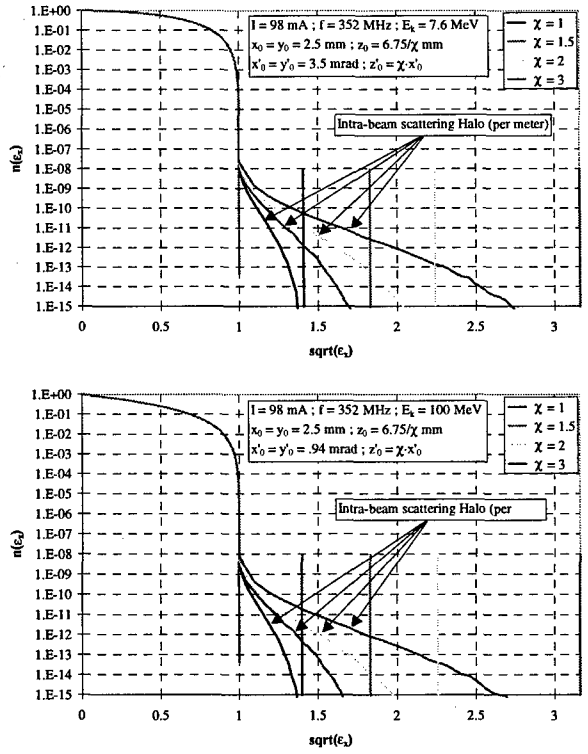

Figure 1 : Intrabeam scattering halo (per meter) of the typical APT beam at 6.7 MeV (up.) and 100 MeV (down) in $(x/x_0,\ x'/x'_0)$.

Calculations with other beam distributions have been done. They give nearly the same results (see figure 2).

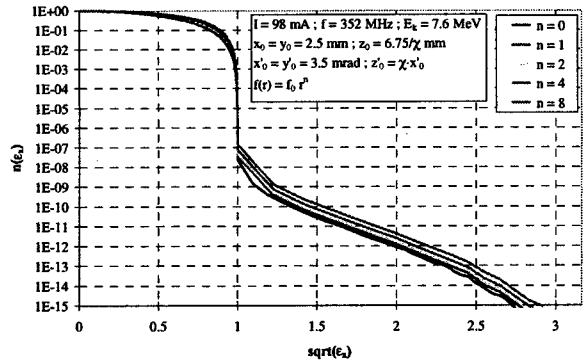

Figure 2 : Intrabeam scattering halo (per meter) of the typical APT beam at 6.7 MeV for different particle distribution functions.

5 INFLUENCE OF SPACE-CHARGE

Let's η be the depress tune factor in the beam. We have developed a model describing the trajectories of particles around a space-charge driven beam [3]. Using this model, the particle amplitude distribution around a space-charge driven beam can be deduced from the one obtained without space-charge. The particle amplitude distribution then obtained for different tune depressions is presented on figure3. The equipartition factor is χ=3.

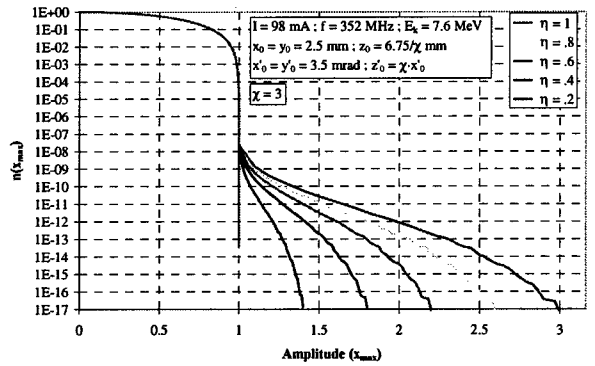

Figure 3 : Influence of space-charge on particle amplitude distribution.

This model gives a maximum amplitude :

$$x_{max}/x_0 = 1+\eta\left(\sqrt{1+\chi^2}-1\right). \qquad (13)$$

This shows that, with constant beam dimensions (x_0 and x'_0), the more space-charge dominated the beam is, the lower the extent and the magnitude of the halo are. This can be easily understood : In order to keep a beam with given dimensions (x_0, x'_0), the confinement potential should be deeper when η is small. This means that, in order to reach a given amplitude, a particle needs a higher transverse energy with a small η than with a bigger one. For a given energy (or maximum slope), the corresponding amplitude is then smaller. An equivalent result has been independently obtained by R. Glückstern and A. Fedotov in ref. [4].

6 CONCLUSION

The influence of the intrabeam scattering on halo formation seems to be negligible as well in extension as in density. Moreover, the space-charge reduces it a lot. R. Glückstern and A. Fedotov got the same conclusion, using an other model, in their paper presented in ref. [4]. The equipartition conditions are not made necessary by the intrabeam scattering phenomenon. The largest emittance growth and halo formation of non-equipartitionned beam observed in simulations can not be justified by intrabeam scattering. Are other physical effects (coupling resonance ?...) or spurious space-charge model effects [5] explaining these observations ?

7 ACKNOWLEDGMENT

I wish to thank Jean-Michel Lagniel and Subrata Nath for suggestions that led to this work. Exchanges with Alexei Fodotov and Robert Glückstern have been a big source of motivation for this work.

8 REFERENCES

[1] T.P. Wangler et al., "Dynamics of Beam Halo in Mismatched Beams", Proc. of Linac96, Geneva, August 26-30, 1996.

[2] N. Pichoff, "Intrabeam Scattering on Halo Formation", Note DAPNIA/SEA 98/46. Submitted to PAC.

[3] N. Pichoff, "Stationary distribution of space-charge driven continuous beam", Note DAPNIA/SEA 98/43.

[4] R.L. Gluckstern and A.V. Fedotov, "Coulomb Scattering Within a Spherical Beam Bunch in a High Current Linear Accelerator", these Proceedings; also Univ. of Maryland Physics Preprint 99-056 (1998).

[5] N. Pichoff et al., *Simulation Results with an Alternate 3D Space Charge Routine, PICNIC*, Proc. of Linac98, Chicago, August 23-28, 1998.

QUANTUM MECHANICAL ASPECTS OF THE HALO PUZZLE

Sameen A. Khan*, Modesto Pusterla† Dipartimento di Fisica Galileo Galilei, Università di Padova,
Istituto Nazionale di Fisica Nucleare (INFN), Sezione di Padova,
Via Marzolo 8, Padova 35131, ITALY

Abstract

An interpretation of the the "halo puzzle" in accelerators based on quantum-like diffraction is given. Comparison between this approach and the others based on classical mechanics equations is exhibited.

1 INTRODUCTION AND FORMALISM

The use of a formalism that closely resembles quantum mechanics (quantum-like theory) in the description of a collective motion of dense particles, has been proposed some time ago [1]. Applications of the Schroödinger-type equations were made to many physical systems, such as plasmas, and beams in linear and circular accelerators, with a suitable definition of the the characteristic parameters.

In this note we point out that, after linearizing the Schrödinger-like equation, for beams in an accelerator one can use the whole apparatus of quantum mechanics, with a new interpretation of the basic parameters (for instance the Planck's constant $\hbar \longrightarrow \epsilon$ where ϵ is the normalized beam emittance) and introduce the propagator $K(x_f, t_f | x_i, t_i)$ of the Feynman theory for both longitudinal and transversal motion. A procedure of this sort seems particularly effective for a global description of several phenomena such as intrabeam scattering, space-charge, particle focusing, that cannot be treated easily in detail by "classical mechanics" and are considered to be the main cause of the creation of the "Halo" around the beam line with consequent losses of particles.

Let us indeed consider the Schrödinger like equation for the beam wave function

$$\mathrm{i}\epsilon\partial_t\psi = -\frac{\epsilon^2}{2m}\partial_x^2\psi + U(x,t)\,\psi \tag{1}$$

in the linearized case $U(x,t)$ does not depend on the density $|\psi|^2$. ϵ here is the normalized transversal beam emittance defined as follows:

$$\epsilon = m_0 c\gamma\beta\tilde{\epsilon}\,, \tag{2}$$

$\tilde{\epsilon}$ being the emittance usually considered, where as we may introduce the analog of the De Broglie wavelength as $\lambda = \epsilon/p$. We now focus our attention on the one dimensional transversal motion along the x-axis of the beam particles belonging to a single bunch and assume a Gaussian transversal profile for a particles injected in to a circular machine. We describe all the interactions mentioned above, that cannot be treated in detail, as diffraction effects by a phenomenological boundary defined by a slit, in each segment of the particle trajectory. This condition should be applied to both beam wave function and its corresponding beam propagator K. The result of such a procedure is a multiple integral that determines the actual propagator between the initial and final states in terms of the space-time intervals due to the intermediate segments.

$$\begin{aligned}
&K(x+x_0, T+\tau|x',0)\\
&= \int_{-b}^{+b} K(x+x_0,\tau|x_0+y_n, T+(n-1)\tau')\\
&\quad\times K(x+y_n, T+(n-1)\tau'|\\
&\qquad\qquad x_0+y_{n-1}, T+(n-2)\tau')\\
&\quad\vdots\\
&\quad\times K(x+y_1, T|x',0)\,dy_1 dy_2\cdots dy_n
\end{aligned} \tag{3}$$

where $\tau = n\tau'$ is the total time of revolutions T is the time necessary to insert the bunch (practically the time between two successive bunches) and $(-b,+b)$ the space interval defining the boundary conditions. Obviously b and T are phenomenological parameters which vary from a machine to another and must also be correlated with the geometry of the vacuum tube where the particles circulate.

At this point we may consider two possible approximations for $K(n|n-1) \equiv K(x_0+y_n, T+(n-1)\tau'|x_0+y_{n-1}+(n-2)\tau')$:

1. We substitute it with the free particle K_0 assuming that in the τ' interval ($\tau' \ll \tau$) the motion is practically a free particle motion between the boundaries $(-b,+b)$.

2. We substitute it with the harmonic oscillator $K_\omega(n|n-1)$ considering the harmonic motion of the betatronic oscillations with frequency $\omega/2\pi$

We may notice that the convolution property (3) of the Feynman propagator allows us to substitute the multiple integral (that becomes a functional integral for $n \longrightarrow \infty$ and $\tau' \longrightarrow 0$) with the single integral

$$\begin{aligned}
&K(x+x_0, T+\tau|x',0)\\
&= \int_{-b}^{+b} dy K(x+x_0, T+\tau|x_0+y, T)\\
&\quad\times K(x_0+y, T|x',0)\,dy
\end{aligned} \tag{4}$$

In this note we mainly discuss the case 1. and obtain from equation (4) after introducing the Gaussian slit $\exp\left[-\frac{y^2}{2b^2}\right]$ instead of the segment $(-b,+b)$ we obtain from

$$K(x+x_0, T+\tau|x',0)$$

* Email: khan@pd.infn.it
† Email: pusterla@pd.infn.it

0-7803-5573-3/99/$10.00@1999 IEEE.

$$
\begin{aligned}
&= \int_{-\infty}^{+\infty} dy \exp\left[-\frac{y^2}{2b^2}\right] \\
&\quad \times \left\{\frac{2\pi i\hbar\tau}{m}\right\}^{-\frac{1}{2}} \exp\left[\frac{im}{2\hbar\tau}(x-y)^2\right] \\
&\quad \times \left\{\frac{2\pi i\hbar T}{m}\right\}^{-\frac{1}{2}} \exp\left[\frac{im}{2\hbar T}(x_0+y-x')^2\right] \\
&= \sqrt{\frac{m}{2\pi i\hbar}}\left(T+\tau+T\tau\frac{i\hbar}{mb^2}\right)^{-\frac{1}{2}} \\
&\quad \times \exp\left[\frac{im}{2\hbar}\left(v_0^2 T+\frac{x^2}{\tau}\right)\right. \\
&\qquad \left. +\frac{\left(m^2/2\hbar^2\tau^2\right)\left(x-v_0\tau\right)^2}{\frac{im}{\hbar}\left(\frac{1}{T}+\frac{1}{\tau}\right)-\frac{1}{b^2}}\right] \qquad (5)
\end{aligned}
$$

where $v_0 = \frac{x_0 - x'}{T}$ and $x_0$is the initial central point of the beam at injection and can be chosen as the origin ($x_0 = 0$) of the transverse motion of the reference trajectory in the test particle reference frame. Where as $\hbar$ must be interpreted as the normalized beam emittance in the quantum-like approach.

With an initial Gaussian profile (at $t = 0$), the beam wave function (normalized to 1) is

$$f(x) = \left\{\frac{\alpha}{\pi}\right\}^{\frac{1}{4}} \exp\left[-\frac{\alpha}{2}x'^2\right] \qquad (6)$$

r.m.s of the transverse beam and the final beam wave function is:

$$
\begin{aligned}
\phi(x) &= \int_{-\infty}^{+\infty} dx' \left(\frac{\alpha}{\pi}\right)^{\frac{1}{4}} e^{\left[-\frac{\alpha}{2}x'^2\right]} K\left(x, T+\tau; x', 0\right) \\
&= B\exp\left[Cx^2\right] \qquad (7)
\end{aligned}
$$

with

$$
\begin{aligned}
B &= \sqrt{\frac{m}{2\pi i\hbar}}\left\{T+\tau+t\tau\frac{i\hbar}{mb^2}\right\}^{-\frac{1}{2}}\left\{\frac{\alpha}{\pi}\right\}^{\frac{1}{4}} \\
&\quad \times \sqrt{\frac{\pi}{\left(\frac{\alpha}{2}-\frac{im}{2\hbar T}-\frac{m^2/2\hbar^2T^2}{\frac{im}{\hbar}\left(\frac{1}{T}+\frac{1}{\tau}\right)-\frac{1}{b^2}}\right)}} \\
C &= \frac{im}{2\hbar\tau}+\frac{m^2/2\hbar^2T^2}{\frac{im}{\hbar}\left(\frac{1}{T}+\frac{1}{\tau}\right)-\frac{1}{b^2}} \\
&\quad + \frac{\frac{\tau^2}{T^2}\left\{\frac{m^2/2\hbar^2T^2}{\frac{im}{\hbar}\left(\frac{1}{T}+\frac{1}{\tau}\right)-\frac{1}{b^2}}\right\}^2}{\left(\frac{\alpha}{2}-\frac{im}{2\hbar T}-\frac{m^2/2\hbar^2T^2}{\frac{im}{\hbar}\left(\frac{1}{T}+\frac{1}{\tau}\right)-\frac{1}{b^2}}\right)} \qquad (8)
\end{aligned}
$$

The final local distribution of the beam that undergoes the diffraction is therefore

$$\rho(x) = |\phi(x)|^2 = BB^*\exp\left[-\tilde{\alpha}x^2\right] \qquad (9)$$

where $\tilde{\alpha} = -(C+C^*)$ and the total probability per particle is given by

$$
\begin{aligned}
P &= \int_{-\infty}^{+\infty} dx\rho(x) = BB^*\sqrt{\frac{\pi}{\tilde{\alpha}}} \\
&\approx \frac{1}{\sqrt{\alpha}}\frac{mb}{\hbar T} \qquad (10)
\end{aligned}
$$

One may notice that the probability P has the same order of magnitude of the one computed in [2] if $\frac{1}{\sqrt{\alpha}}$ is of the order of b.

Similarly we may consider the harmonic oscillator case (betatronic oscillations) compute the diffraction probability of the single particle from the beam wave function and evaluate the probability of beam losses per particle.

2 PRELIMINARY ESTIMATES

Preliminary numerical estimates based on the above formulae for the two different cases of LHC [3] and HIDIF [4] designs give the following encouraging results:

LHC

Transverse Emittance, ϵ	=	3.75 mm mrad
Total Energy E	=	450 GeV
T	=	25 nano sec.
b	=	1.2 mm
P	=	3.39×10^{-5}

HIDIF

Transverse Emittance, ϵ	=	13.5 mm mrad
Kinetic Energy E	=	5 GeV
T	=	100 nano sec.
b	=	1.0 mm
P	=	2.37×10^{-3}

3 CONCLUSION

These preliminary numerical results are encouraging because they predict halo losses which seem under control. Indeed the HIDIF scenario gives a total loss of beam power per meter which is about a thousand higher than the LHC. However in both cases the estimated losses appear much smaller than the 1 Watt/m.

4 REFERENCES

[1] See R. Fedele and G. Miele, *Il Nuovo Cimento* D **13**, 1527 (1991); R. Fedele, F. Gallucio, V. I. Man'ko and G. Miele, *Phys. Lett.* A **209**, 263 (1995); Ed. R. Fedele and P.K. Shukla *Quantum-Like Models and Coherent Effects*, Proc. of the 27th Workshop of the INFN Eloisatron Project Erice, Italy 13-20 June 1994 (World Scientific, 1995); R. Fedele, "Quantum-like aspects of particle beam dynamics", *in*: *Proceedings of the 15th Advanced ICFA Beam Dynamics Workshop on Quantum Aspects of beam Physics*, *Ed.* P. Chen, (World Scientific, Singapore, 1999).

[2] Formulae (3-33) *in* R. P. Feynman and A. R. Hibbs, Quantum Mechanics and Path Integrals, (McGraw-Hill, New York).

[3] *Ed.* P. Lefèvre and T. Pettersson, Large Hadron Collider (LHC) Conceptual Design CERN/AC/95-05(LHC) (October 1995).

[4] *Ed.* I. Hofmann and G. Plass, Heavy Ion Driven Inertial Fusion (HIDIF) Study GSI-98-06 Report (August 1998).

UPGRADE STUDY OF INR PROTON LINAC FOR PRODUCTION OF 3 MW BEAM

L. V. Kravchuk# and P. N. Ostroumov
Institute for Nuclear Research RAS, 117312, Moscow

Abstract

There are many proposals for the construction of proton linacs with beam power up to 200 MW for various applications (energy production, nuclear waste transmutation, etc...). In Russia there is a discussion of the necessity for the construction of the proton linac, which must exceed the beam power by one order of magnitude with respect to the existing linacs. Such linac must produce 1 GeV energy beam with a 3 mA average current. The existing facility in the Institute for Nuclear Research allows an upgrade of the linac for the acceleration of higher intensity beam. The facility consists of a high intensity proton linac and an experimental area. The latter has been constructed for the transportation of several high intensity beams inside a 200 mm aperture beamline. Therefore it can be safely used for the transportation of very high power beam to target. For the production of a 3 mA beam it is proposed to extend the duty factor of the linac up to 6%. The accelerating structure above 200 MeV must be replaced by a superconducting structure operating at 594.6 MHz. The surface field of 17 MV/m in the superconducting structure provides acceleration of protons up to 1 GeV over the length of the existing linac.

1 INTRODUCTION

The nuclear waste transmutation concept based on the high power linear accelerator system is firmly supported by the Russian government and is considered as a high priority task for the next decade. The full-power linac requires about 100 mA CW current at 1 GeV beam energy. Successful operation of superconducting RF (SRF) structures for the last two decades motivates the use of SRF cavities for such linac in the energy range above ~200 MeV. There are two linacs in the world operating with high intensity beams. The most powerful linac at LANL can produce 0.8 MW beam. The linear accelerator of the Moscow Meson Factory (MMF) produces 100 μA beam at 500 MeV (the specified energy is 600 MeV). The next generation of high-intensity linacs is designed for much higher beam power. From the practical point of view the construction of the demonstration linac with intermediate beam power of ~5 MW is necessary. This paper deals with the study of the MMF linac upgrade in order to produce 3 MW beam. Its purpose is to confirm beam performance parameters, demonstrate an operation of SRF cavities and identify component failure modes.

The main task for the 3 MW linac is the development of transmutation technologies. After this problem will be successfully solved, the linac can be switched to the acceleration of H^- beam and can be transformed to a powerful spallation neutron source based on a compressor ring. For this purpose the linac will require the modification of its front end for the installation of an adequate chopper. However the laser stripping technology of the H^- beam is under good progress, therefore even chopper will not be required in order to operate as a neutron source.

2 SHORT OVERVIEW OF THE MMF LINAC

The MMF linac consists of three main parts: injector system, DTL up to 100 MeV and DAW cavities up to 600 MeV [1]. The general layout is shown in fig.1. The injector system includes H^+ and H^- ion sources with high voltage transformers, two transport channels with

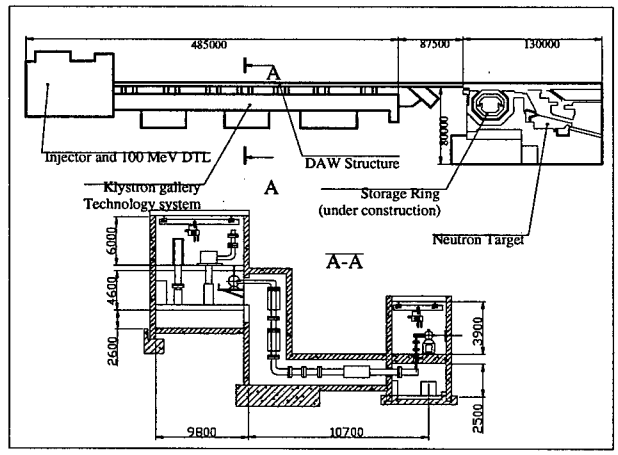

Figure 1: General layout of the MMF accelerator facility. The buildings of the auxiliary systems are not shown.

funneling magnet at 400 keV and booster RFQ in the energy range from 400 keV to 750 keV. The DTL operates at 198.2 MHz and accelerates the beam from 0.75 to 100 MeV. The DAW structure operates at 991 MHz and accelerates the beam up to 600 MeV.

Email: kravchuk@al20.inr.troitsk.ru

0-7803-5573-3/99/$10.00@1999 IEEE.

Originally the high voltage pulsed transformer has been used for acceleration up to 750 keV. The beam pulse length has been limited to ~80 μs due to the transformer saturation. In order to increase the duty cycle of the beam from 0.8% to 1.5% as well as to allow the simultaneous acceleration of two beams, H^+ and H^-, the booster RFQ in the energy range from 400 keV to 750 keV has been installed and commissioned recently.

The MMF linac operates typically with 70-100 μA average current for the proton beam at repetition rate of 50 Hz. However, the linac can operate at 100 Hz with a corresponding increase of the average current, if necessary. A further increase of the average beam current can be achieved by the acceleration of the beam with peak current of 20 mA. The latter is restricted by the DTL rf power system. We consider the MMF linac as the best candidate for the cheapest realization of a 3 MW demonstration linac for the following reasons:

- No capital investment is required for the construction of new buildings for the linac and auxiliary systems.
- The DTL part will remain the old one. The water cooling system is able to operate with an 8% duty factor of the DTL and 198.2 MHz rf system.
- The experimental area of the MMF has been designed for the simultaneous transport of seven separate beams in the same aperture. It will allow a safe transport of 3 MW beam to the target position.
- The target can be placed inside of the existing neutron source. A light modification of the shield will be required.

3 THE PROPOSED MODIFICATIONS

The general layout of the upgrade linac is shown in Fig. 2. The main beam parameters of the 3 MW linac listed in Table 1 are achieved with the following modifications of the MMF linac:

- An RFQ with the proton ion source installed directly upstream of the 100 MeV DTL;
- The main part of the linac from 100 MeV to 1 GeV contains room temperature Coupled Cavity Linac (CCL) up to 205 MeV and Superconducting Linac (SCL) for acceleration to the final energy. The operating frequency both for CCL and SCL is 594.6 MHz. The new klystrons, high voltage transformers and waveguides can be located in the existing buildings (see Fig. 1).

Table 1: Basic parameters of the 3 MW linac

Beam energy	1 GeV
Average current	3 mA
Pulsed current	50 mA
Beam pulse duration	600 μs
Repetition rate	100 Hz
Number of RF stations at 198.2 MHz	5
Number of RF stations at 594.6 MHz	49
Number of cryostats with $\beta_G = 0.6$	28
Number of cryostats with $\beta_G = 0.8$	60
Total length of the linac	464 m
Number of SRF cells	880

The existing 198.2 MHz triodes GI-54 allow the generation of 3.5 MW pulsed power with a duty factor of 8%. However these triodes are no longer available. The DTL tanks are supplied by two rf windows, therefore the power can be generated in two rf stations and added in the cavity. For this purpose the commercially available triodes from "Svetlana" can be used.

The most important modifications are on the high energy part of the linac above 100 MeV. Due to the lack of proven technology of the superconducting rf (SRF) structures in the energy range between 100 to 200 MeV we consider the use one of two types of accelerating

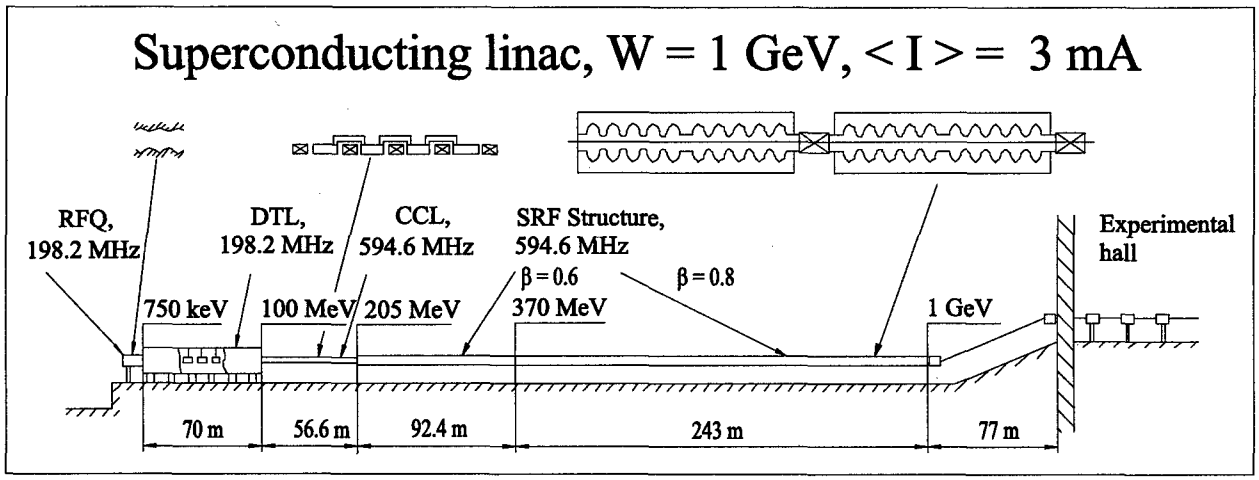

Figure 2: General layout of the 3 MW linac to be located in the MMF.

structures: the Disk and Washer Structure (DAW) [2] and the Cut Disk Structure CDS [3]. The CDS structure is very similar to the DAW structure as it concerned the electrodynamics parameters and vacuum conductivity. However the CDS is much compact and the cell diameter is only ~360 mm at 594.6 MHz. The CDS is simpler for the manufacture but requires more R&D for the operation with a high duty factor. The final decision for the CCL structure can be made later.

For the feeding both the CCL and SCL a 1.8 MW klystron operating at 594.6 MHz with anode modulation is considered.

The 198.2 MHz RFQ and transition energy of 750 keV is the reasonable choice for the matching of a 50 mA peak current beam. The first 44 periods of the DTL are made with a 15 mm aperture diameter which restricts the normalized acceptance of the first DTL to 8 π·mm·mrad. This allows scrapping of the beam halo at low energies and preserving total emittance low along the whole linac. The MMF linac originally has been designed for the acceleration of a 50 mA beam. The length of the focusing period of $2\beta\lambda_0$ (λ_0 is the rf wavelength of the fundamental frequency) and zero current phase advance σ_{0t}=45° are quite reasonable for the focusing of a 50 mA beam. At the beginning of the SCL the focusing period length is ~$4\beta\lambda_0$. Therefore the CCL will be designed for adiabatic matching of the transverse focusing properties. It will require the variation along the CCL the phase advance over the focusing period and focusing length counted in $\beta\lambda_0$. Both the DAW and the CDS are the best options for the high current acceleration due to the high coupling which is more than 30%. For the 6% duty factor the accelerating gradient ~3.5 MV/m of the CDS is restricted by the heat removal from the copper. The CCL will serve as an adiabatic matching in the longitudinal phase space. Therefore the use of the klystron power in the CCL cavities will be somewhat not optimal.

The SCL consists of two types of the SRF cavities with fixed geometrical beta: β_G = 0.6 and β_G = 0.8. The 5-cell cavities are best for the energy range from 200 MeV to 1 GeV. The sketch of the SRF cavities is shown in Fig. 3. Table 2 shows the basic parameters of the SCL.

Table 2: Basic parameters of the SCL

Geometrical β_G	0.6	0.8
Operating frequency, MHz	594.6	594.6
Number of cells in SRF cavity	5	5
Number of cavities in cryostat	2	2
Maximum electric field on the surface, MV/m	16.8	16.8
Accelerating field (over the length of $5\beta_G\lambda/2$ MV/m)	6.0	7.3
TTF	≥ 0.7	≥ 0.76
Synchronous phase	- 32°	- 32°

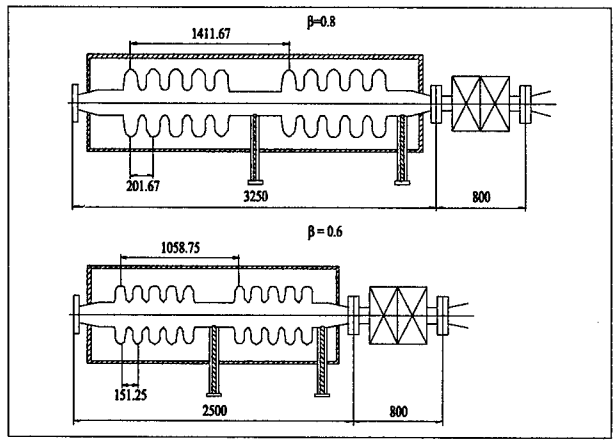

Figure 3: Two types of cryostats for a 1 GeV linac.

The accelerating gradient along the whole linac averaged over the focusing period is shown in Fig. 4.

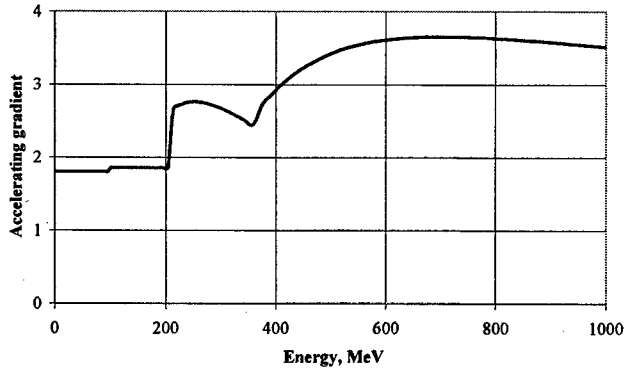

Figure 4: Average accelerating gradient along the linac.

4 ACKNOWLEDGEMENT

The authors thank their colleagues V.N. Leont'ev, A.I. Kvasha and V.V. Paramonov for helpful discussions.

5 REFERENCES

[1] S. K. Esin, L. V. Kravchuk, P. N. Ostroumov et. al. Commissioning/ Operation of the Moscow Meson Factory Linac. Proc. of the 1994 Linac Conf. August 21-26, Tsukuba, Japan, pp.31-35.

[2] V. G. Andreev et al. Study of High-Energy Proton Linac Structures. Proc. of the 1972 proton Linear Accel. Conf., p.114, LA5115, 1972.

[3] L. V. Kravchuk, V. V. Paramonov, V. A. Puntus. The Cold Model of the Cut Disk Structure. Proc. of the 1998 Linac Conf. To be published.

STATUS OF THE PROTON DRIVER STUDY AT FERMILAB

W. Chou*, Fermilab†, P.O. Box 500, Batavia, IL 60510, USA

Abstract

In order to enhance Fermilab hadron research program and to provide a proton source to a future muon storage ring or a muon collider, the study of a new high intensity proton machine called the Proton Driver is being pursued at Fermilab. It would replace the present linac and 8 GeV Booster and produce 20 times the proton intensity as the Booster. This paper gives a status report on a number of design issues of this machine.

1 INTRODUCTION

In the summer of 1997, a group of people at Fermilab led by S. Holmes launched a study for designing a new proton source that would replace the present booster. The goal was to increase the proton intensity by a factor of 20. The results are documented in Ref.[1], which describes the basic features of such a machine. Since November 1998, a design team has been formed. Its task is to complete a Technical Design Report (TDR) by the end of FY2000. This paper reports the status of the TDR work.

This is a dual-purpose machine. On the one hand, it could serve as an intense proton source of a future muon collider or a muon storage ring. On the other hand, it would also enhance Fermilab hadron research program. This machine shares a number of common features with other high intensity proton machines (SNS, ESS and JHF), such as large number of protons per cycle, rapid cycling and high beam power. However, the proton driver has a unique feature. Namely, it must keep the longitudinal emittance small so that at exit the bunch is short.

The proton driver consists of three new machines: a 1 GeV linac, a 3 GeV pre-booster and a 16 GeV booster. The design goals are: 1×10^{14} protons per cycle, 15 Hz rep rate, an rms bunch length 1-2 ns at exit. The construction of these new machines would be staged. In Phase I, a new 16 GeV booster would be built in a new tunnel. The present 400 MeV linac will be used as its injector. In this Phase, the proton intensity could reach 1/4 of the design goal, *i.e.*, 2.5×10^{13} per cycle. Then, in Phase II, a new linac and a pre-booster would be built to reach the design intensity. There are several reasons for taking this approach. (1) Phase I is a logical step in proton intensity upgrade. The present booster can only deliver 5×10^{12} protons per cycle, which is limited by the machine acceptance and radiation shielding. The present 400 MeV linac, on the other hand, can deliver 2.5×10^{13} H^- particles. The newly constructed Main Injector (MI), with certain upgrades, is also believed to be able to take 2.5×10^{13} protons from a booster batch. Thus, a new booster will remove the bottleneck and keep the linac-booster-MI operation in balance. (2) This approach gives the least disruption to the HEP experiments. (3) It also has immediate benefits to the existing program (NUMI, KAMI, MiniBooNE and long term collider experiments).

Table 1: Parameters

Stage	Phase I	Phase II
Machine	New booster	New linac & pre-booster
N (per cycle)	2.5×10^{13}	1×10^{14}
Rep rate (Hz)	15	15
E_{inj} (GeV)	0.4	1 (pre-boo), 3 (booster)
E_{max} (GeV)	16	16
P (MW)	1	4
f_{rf} (MHz)	53	7.5

2 BEAM PHYSICS

2.1 *Longitudinal dynamics*

One of the most demanding design parameters is the particle density in the longitudinal phase space. At 7.5 MHz, each bunch contains 2.5×10^{13} particles with an emittance $\epsilon_L = 2$ eV-s. This density is several times higher than that in most existing synchrotrons (except the ISIS, which operates at 2.1×10^{13} per eV-s). Therefore, longitudinal emittance preservation is essential, and the conventional "trick" of intentional ϵ_L blow-up for suppressing instabilities would not be applicable.

When such a high density proton beam is injected into the MI, it would create additional problems. The MI uses a 53 MHz rf system. The frequency is 7 times higher than the proton driver (7.5 MHz). This implies that only one out of every 7 buckets in the MI will contain particles. The number of protons in each bucket would be 2×10^{12}, which is 35 times higher than its present value (6×10^{10}). Thus the transition crossing could be a severe problem. Indeed, simulations show large particle losses at such a high bunch intensity. Fortunately, there are two methods that can effectively solve this problem: (1) A γ_t-jump system has been designed for the MI. It can provide a $\Delta\gamma_t$ from +1 to −1 within 0.5 ms. (2) An inductive insert can compensate the space charge impedance. When these measures are added in the simulations, the particle loss is reduced to zero and the emittance growth becomes moderate (20%).

*Email: chou@fnal.gov

† Operated by Universities Research Association Inc. under Contract No. DE-AC02-76CH03000 with the U.S. Department of Energy.

2.2 *Beam instability and space charge*

There are several open questions on this subject. (1) Is there any microwave instability below transition? The Keil-Schnell criterion shows no discrimination against cases either above or below transition. But in the real world, while numerous machines have reported microwave and negative mass instabilities above transition, none of them (to the author's knowledge) has seen these below transition. The capacitive space charge impedance certainly helps keep beam stable below transition. But whether a big resistive impedance could drive beam unstable remains to be seen. (2) Is there any fast head-tail instability in a proton machine? This type of instability is clearly observed in electron machines but has never been seen in any proton machine. A recent paper[2] claims the space charge would make the mode coupling more difficult, thus suppress this instability. This topic deserves more investigation.

To keep the incoherent space charge tune shift under control, the normal measures (higher injection energy, larger transverse emittance, painting, 2nd harmonic rf) will be taken. A large dispersion ($\pm$15 m) lattice in the pre-booster is also under consideration, which could lower the Laslett tune shift by enlarging the horizontal beam size. There is a speculation that it is the coherent tune shift caused by the space charge, not the incoherent one, that actually hurts the beam. If this is true, then a quadrupole damper could help. This is a research topic at several labs (*e.g.*, KEK and GSI),

2.3 *Lattice design*

The new booster size will be the same as the present booster (474 m). A primary reason for this choice is that it matches the size of the $\bar{p}$ Accumulator. The pre-booster is a third of the booster size (158 m). Two lattices are under study – FODO and FMC (flexible momentum compaction). Both must give a γ_t larger than the extraction energy to avoid transition crossing. The FODO is possible for the pre-booster but difficult for the booster because of the scaling $\gamma_t \sim \sqrt{R}$. The FMC is more flexible but generates large β-function swing, which could be a source of halo formation. A difficulty experienced in the lattice design is the needed utility region for rf, injection and extraction. It is hard to place all these in dispersion free sections due to the compact machine size. A compromise is to put rf in the short free space, where the dispersion could be large ($\sim$2 m). Then, one needs to understand the synchro-betatron coupling problem. Existing literatures (*e.g.*, Ref.[3]) has studied integer resonances ($k\nu_\beta \pm m\nu_s = n$ with $k = 1$) and provided a solution. Work is needed for general cases ($k = 2, 3, ..$). The H^- injection region has low β in both planes. The x-plane painting is achieved by using 4 slow bump magnets (for orbit bump) and 2 fast bump magnets (for painting), the y-plane painting by a steering magnet (varying y'). The dependence of temperature rise and emittance growth on the foil thickness is being calculated.

2.4 *Beam losses*

There is a widely quoted number, 1 W/m, for tolerable beam losses in the "quiet area." But this number needs to be checked. Using the preliminary lattice and magnet design of the proton driver, MARS calculation shows that 13 W/m can be tolerated for hands-on maintenance. (After 30-day irradiation and 1-day cooling, the residual dose at contact is less than 10 mrem/hr.) This means the tolerable beam loss can be an order of magnitude higher than what was previously believed. The ground water activation problem gives a somewhat lower limit but can be treated separately. Even if 13 W/m is adopted as the design criterion, beam loss is still a primary concern. A collimation system is necessary.

3 TECHNICAL SYSTEMS

3.1 *RF system*

There are two rf systems that are under design. In Phase I, the new booster will use a 53 MHz system; in Phase II, both the booster and pre-booster will use 7.5 MHz. The 53 MHz system is a modification of the present booster rf. The 7.5 MHz system is a new one. It uses the Finemet as the magnetic core. There are two advantages of this material: (1) It can stand high B-field ($>$ 5 kG). This means for the same accelerating voltage, the physical length of the rf cavity will be shorter (by 50%). This is important for small machines requiring high rf voltage. (2) It is broadband. So there is no need of tuning. Furthermore, one cavity can provide multiple harmonics (A 50% 2nd harmonic rf is needed for reducing the injection loss). There are also several concerns regarding the Finemet – high power consumption due to low shunt impedance R, and low gap capacitance due to high permeability μ. A radial cut in the core can help raise the Q value and lower R/Q and the effective μ. A prototype 200 kW cavity using five large size cut cores is being built. It will provide 20 kV at 7.5 MHz. This work is in collaboration with the KEK and is part of the US-Japan accord.

The challenges to the beamloading compensation system are: (1) high beam intensity (16 μC); (2) short beam pulse at exit (a few ns); (3) low Q of the rf cavity (which means the beamloading voltage has a rich Fourier spectrum). Several compensation methods are under study: feedforward, direct rf feedback and cathode follower. It is planned to set up an rf test station for high power rf test and for bench test of the beamloading compensation.

3.2 *Magnet and power supply*

The magnet has large aperture (5" $\times$ 10") and will use thin silicon steel laminations. The peak field is chosen to be 1.3 T to avoid saturation. The requirements on the end design are: (1) minimizing eddy current heating; (2) making uniform effective length in the end region; (3) minimizing harmonics. The ac loss data from the vendor's catalog are not directly applicable, because they are not measured at 15 Hz and have no dc bias. An ac loss measurement fa-

cility is being set up. A study was done to compare programmable with resonant power supply systems. Although the former has advantages, it is ruled out for two reasons: (1) Its cost is several times higher than the latter; (2) There is no existing solution for storage of large reactive power (about 400 MVA) at 15 Hz. Three different resonant systems are being studied: (a) A single resonance system at 15 Hz; (b) A dual-resonance system: 15 Hz plus a 12.5% 30 Hz component; (c) A dual-frequency system with a switch: up-ramp at 10 Hz, down-ramp at 30 Hz. The cost difference among the three systems is within 20%. The main advantage of (b) and (c) is the potential saving in rf power (about 25-33%). Simulation models for each circuit have been established. It seems there is no show stopper in either (a) or (b). The concern about (c) is the ripple effects at injection when the switch is turned off. An accurate estimate of the stray inductance and capacitance in a real system is crucial in this analysis. When a resonant power supply drives separate functioned magnets, tracking between dipoles and quads is a problem. One solution is to put the main dipoles and quads on the same bus, while using trim quads for tuning.

3.3 *Vacuum pipe*

There are two options for the beam pipe. One is a ceramic pipe with an rf shield inside, as used at the ISIS. This design works well. The shortcoming is the additional aperture it would take (about 1.5 - 2 inches), which makes the magnet more costly. The other option is a thin Inconel pipe. Because of its high strength and electrical resistivity, the eddy current heating of Inconel is about 1/4 of that of stainless steel. But still, the heating would reach about 3 kW/m, which must be removed by a cooling system. A prototype large aperture (5" × 8") thin (0.05") Inconel pipe with water cooling is being designed and fabricated. The eddy current induced field error is a few tenths of a percent, which may require correction elements.

3.4 *Collimation system*

A collimation system is crucial for localizing beam losses. This system is integrated in the early stage of the lattice design so that its location can be optimized. A preliminary collimator system has been designed and STRUCT tracking shows that more than 99% of the lost particles can be captured. It is a 2-stage system, consisting of a 3-mm thick primary collimator (graphite) and four 1.5-m thick secondaries (iron). Assuming 10% particle losses at 3 GeV, it gives 72 kW. This system can capture most of the lost particles and leave only about 480 W outside the collimator region. Thus, in the "quiet area", the loss will be below 10 W/m.

3.5 *H^- source and linac*

The present H^- source can deliver 50 mA, 90 μs pulses through the linac. This is adequate in Phase I, which requires 4000 mA-μs H^- beams. Phase II will call for the development of a new H^- source. The linac will be used in Phase I. At this moment, it is not clear if this linac can also be used in Phase II. To get the answer, two experiments are under way: (1) peak current test, (2) klystron pulse length test. The first experiment has been done by replacing the H^- source by a H^+ source. It shows that about 90 mA can go through the linac with good transmission (70% in the DTL and 95% in the CCL) and reasonable emittance (2.6 π mm-mrad, 90%). The second experiment will use a Boeing modulator and pulse transformer to generate 300 μs pulses to test the klystron. A 6-cell rf cavity will also be tested for its sparking rate at long pulses. An open issue in Phase I is how to chop the beam. Several schemes (ion source chopping, laser chopping, rf chopping, *etc.*) are under investigation. The design work of a new 1 GeV linac will start soon.

4 MACHINE EXPERIMENTS

4.1 *Short bunch experiments*

Three machine experiments have been performed. One was done at the AGS near the transition; another at the Fermilab booster by rf rotation near the exit. Both used low intensity beams and obtained short bunches. The third one was also done at the AGS but with a high intensity beam (9×10^{12} in one bunch) and at the top porch. The bunch length after the rf rotation is about 1/3 of that before. No adverse effects were observed other than a beamloading problem.

4.2 *Inductive compensation experiments*

By inserting an inductive component (such as ferrite rings) in the machine, it is expected that certain space charge effects (potential well distortion, negative mass instability above transition) could be reduced. An experiment was done at the PSR. There were evidences that the *e-p* instability threshold is improved due to a cleaner gap. This experiment will be repeated after the PSR upgrade.

5 ACKNOWLEDGEMENTS

This paper is a brief report of the work done by the following people: L. Allen, T. Anderson, C. Ankenbrandt, A. Drozhdin, S. Fang, J. Griffin, N. Holtkamp, C. Jach, D. Johnson, C. Johnstone, J. Johnstone, I. Kourbanis, O. Krivosheev, J. Lackey, E. McCrory, D. McGinnis, F. Mills, N. Mokhov, A. Moretti, K-Y. Ng, J. Norem, F. Ostiguy, H. Pfeffer, M. Popovic, Z. Qian, D. Ritson, C. Schmidt, J. Steimel, W. Wan, D. Wildman and D. Wolff. Supports from S. Holmes and R. Noble are greatly acknowledged.

6 REFERENCES

[1] S. D. Holmes, editor, FERMILAB-TM-2021 (1997).

[2] M. Blaskiewicz, *Phys. Rev. Special Topics - Accel. and Beams*, Vol. 1, 044201 (1998).

[3] T. Suzuki, *Particle Accel.*, Vol. 18, p. 115 (1985).

HIGH INTENSITY PROTON BEAMS FROM CYCLOTRONS FOR H_2^+

L. Calabretta , D. Rifuggiato, V. Shchepounov
I.N.F.N., Laboratorio Nazionale del Sud, Catania, Italy

Abstract

To deliver high intensity proton beams it is proposed to accelerate H_2^+ by cyclotrons and to use the stripping method to extract the beam. The high binding energy of the H_2^+ molecule allows to use very high magnetic fields produced by superconducting magnets even at energies as high as 1 GeV/n. High beam currents are achievable with these cyclotrons as extrapolated from the experimental results obtained by H^- cyclotrons. The main advantages, i.e. easy operation, high reliability and high conversion efficiency from electrical to beam power are presented.

1 INTRODUCTION

The interest for Accelerators Driven Systems (ADS), to be used for energy amplification or waste transmutation, has stimulated the study of cyclotrons able to deliver proton beams with current higher than 10 mAmp and energy as high as 1 GeV[1,2]. The main constraints required to ADS are: minimum beam losses, high reliability and high conversion efficiency from electrical to beam power. The cyclotron projects proposed as ADS are able to achieve low beam losses during the acceleration and extraction process by using large extraction radii ($\geq$ 6 m) and high accelerating voltages (8 MV/turn). In this paper superconducting cyclotrons, able to accelerate H_2^+, and the related advantages are described. The extraction of the H_2^+ beam is accomplished by a stripper which produces two free protons breaking the molecule. Extraction by stripping does not require well separated turns at the extraction radius and allows to use a low energy gain per turn during the acceleration process, with a significant reduction of thermal power losses for the RF cavities. Extraction by stripping is a very powerful tool to increase the reliability and simplify the operation mode as demonstrated by the success of commercial cyclotrons. The magnetic rigidity of H_2^+ is twice that for protons with the same velocity, neverthless using superconducting magnets it is possible to maintain the size of cyclotrons for H_2^+ at reasonable values. Another important advantage of accelerating H_2^+ is the reduced space charge effect due to the lower q/A ratio as compared with protons, which is expecially advantageous during the early stages of acceleration.
Thereunder the feasibility of extraction by stripping of H_2^+ is demonstrated simulating the extracted trajectories in the measured magnetic field of our K800 compact superconducting cyclotrons (CSC). Moreover a preliminary study on the possible use CSC and/or ring superconducting cyclotron (RSC) to accelerate high beam currents at high energies is presented.

2 EXTRACTION BY STRIPPING

The stripping process has largely been used to extract H^- ions at energies as high as 520 MeV (200 kW) and in many commercial cyclotrons to extract H^- or D^- beams with a beam power up to 40 kW. The small binding energy (0.7 eV) of H^- ions forbids the use of high magnetic fields, which would cause high losses produced by electromagnetic stripping, while the 16.3 eV binding energy of the H_2^+ molecule allows to use a magnetic field as high as 10 T even at energies as high as 1 GeV per nucleon. There are also other differences between the stripping process for H^- and H_2^+. In the first case two electrons have to be removed to extract one proton and the foil has to be thick enough to guarantee stripping efficiency of 100%. If the H_2^+ is not stripped at first cross it turns inside the cyclotron and hits once again the stripper until it is stripped. Then for H_2^+ it is possible to use a stripper with thickness smaller than for H^- and then a longer mean life is expected. Strippers made of pyrolitic graphite are used at TRIUMF to extract the 520 MeV H^- beam. These strippers have a mean life of 3-5 mAh [3]. For a beam current of 5 mA of H_2^+ a mean life of 0.5-1 hour is expected, which is a conservative limit if we consider that thinner foils can be used and that just one electron has to be removed to produce 2 protons. Moreover stripping of H_2^+ produces electrons but while for H^- the electrons are bent towards the centre of the machine and hit the stripper foil after spiraling in the magnetic field, for H_2^+ the electrons are bent towards the outer radius, so an electron catcher can be installed to remove the electrons emerging from the stripper and strongly reduce the stripper damage and increase its life. For RSC at energies of 1 GeV/n, a group of 4 or more thin stripper foils in cascade could be used to further increase more the mean life time. Anyway experimental data in this field are necessary in order to propose a final design.

3 ACCELERATION OF H_2^+

3.1 Compact superconducting cyclotron

To check the feasibility of stripping extraction in compact superconducting Cyclotrons the trajectories of H_2^+ inside our K800 Cyclotron were studied. The simulations show that for an enough large angular range of the stripper position inside the hill the particles escape from the trajectories of H_2^+ inside cyclotron magnetic field in one turn. According to our simulations small variations of the extraction radius have negligible effects on the extraction

0-7803-5573-3/99/$10.00@1999 IEEE.

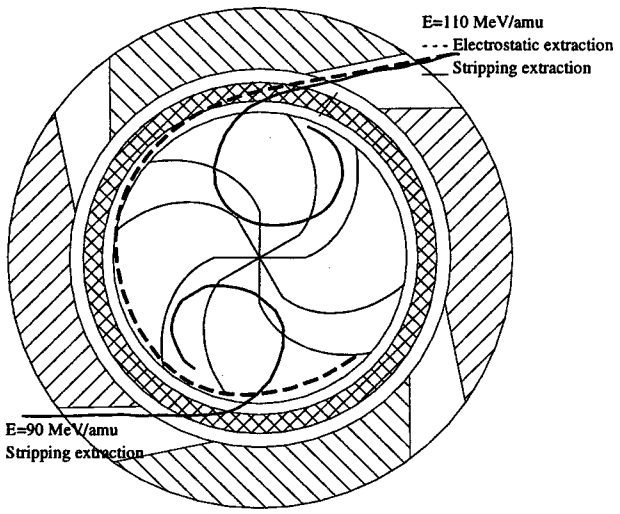

Figure 1: Layout of the 4 sectors CSC. The extraction trajectories for H_2^+ by stripping together with the trajectory for fully stripped ions q/A=0.5 extracted by electrostatic deflectors are shown

trajectory while the azimuth position has a strong effect on the size of the beam envelope. However a position which minimises the beam envelope in both the radial and axial plane along the whole trajectory was found too[4].
According to this evaluation and the positive experience of other laboratories [5] a design for a new CSC based on the design of our existing K800 cyclotron but with a lot of simplifications and some upgrading was started.
This cyclotron has been proposed as primary accelerator to produce radioactive ions beams at LNS[6]. In the framework of our upgrading program the new cyclotron have to accelerate a single kind of particle with q/A=0.5 at a fixed energy. The main simplifications are: single frequency, few trim coils with small size and power, fixed operation mode of the power supplies of the main coil, low liquid helium consumption, larger gap in the median plane and across the cryostat, more accessibility at the median plane.
Recently a design for a 4 sectors 110 MeV/amu CSC has been proposed by Mandrillon [7]. It presents some further advantages, i.e. a higher energy gain per turn and more space for RF cavities and vacuum pumps. This CSC can be used as a first acceleration step of an ADS [2]. In fig. 1 the simulated stripped trajectories for H_2^+ at 110 and 90 MeV/amu are shown. This CSC is also able to accelerate deuterons and fully stripped light ions (q/A=0.5, A≤32) up to the maximum energy. These beams could be extracted, obviously with a reduced power, by two electrostatic deflectors placed inside the valley.
The maximum current delivered by a CSC equipped with extraction by stripper is limited by the central region, due to space charge effects. According to the evaluation accomplished in [8], the TR30 compact cyclotron for H^- is able to accelerate a maximum of 3.3 mA. This experimental intensity limit is due both to the vertical space charge tune shift and to the longitudinal space charge effect. According to these considerations the TR30 compact cyclotron for H^- with a central region scaled up of a factor 1.44 should increase the current upper limit to 10 mAmp.
The beam dynamics features of H_2^+ in a CSC are similar to the case of H^- if the magnetic field, the accelerating voltage, injection energy are properly scaled. So we could extrapolate the space charge effect for the H_2^+ beam from corresponding figures for H^- Cyclotrons.
The intensity limit should be twice higher than the H^- case, as a consequence of the reduced charge to mass ratio q/A=0.5 of the H_2^+ ion. The selected values for the proposed CSC, of 60 keV for injection energy, 500 keV for the energy gain per turn and the 2 T magnetic field at the centre, allow to scale quite well the central region of the TR30. The expected maximum current, extrapolated according to [8] is then of 9 mA of accelerated H_2^+ and of 18 mA of extracted protons. A further significant advantage for injection of H_2^+ could be the higher injection energy and the better emittance and higher currents of H_2^+ sources as compared to the H^- sources.

3.2 A ring superconducting cyclotron

The spiral angle for a compact cyclotron has to be very large to produce enough axial focusing for energies higher than 200 MeV/amu. High energies as 1 GeV are achievable only by Ring Cyclotrons (RSC) which could produce large flutter values and enough axial focusing. A ring cyclotron similar to the PSI proposed cyclotron of 1 GeV [2], the so called "dream machine", but with magnetic field of 4.3 T instead of 2.1 T, has been investigated to accelerate H_2^+ to 1 GeV/amu. The PSI cyclotron proposal is based on 12 sectors layout and allows for the installation of 8 accelerating cavities, two flattopping cavities, and of the injection and extraction systems. The cyclotron for H_2^+ ions does not need the flattopping cavities, so the number of sectors could be reduced to 10, and it becomes possible to increase the size of the valleys and have enough room to install straight cavities similar to the existing cavities of the PSI Ring.
Preliminary study of this RSC shows that it is very difficult to achieve the required isochronous field using superconducting coils wrapped around the iron pole. More easy, advantageous and elegant is the use of the so called S-coils [9]. These are a pair of superconducting coils wrapped, out of the extraction radius, around the pole/yoke and perpendicularly to the median plane. This solution allows to have free space among the sectors, and the cryostat is now completely in the outer region, without any interference with the cavities and the accelerated beam. Preliminary and approximate evaluations by Poisson were done, while simulations with a 3D code have to be developed to optimise the magnetic design. The installation of a stripper foil system in a valley allows for the beam extraction without electrostatic deflector and with an efficiency of 100%, see fig.2.
A very important parameter for ADS is the conversion efficiency from electrical to beam power. For the so called "dream machine", the expected conversion efficiency is 44% [2].

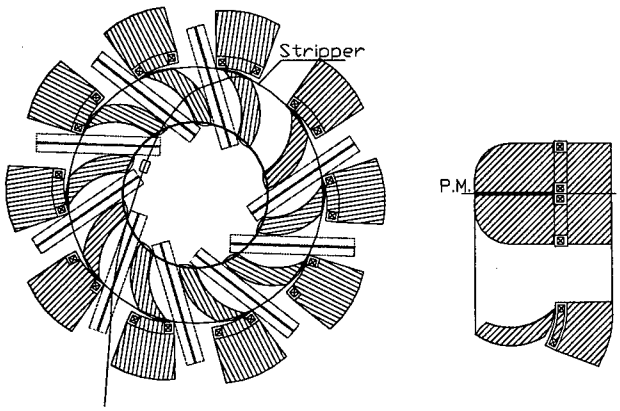

Figure 2: Layout of the 10 sectors RSC for 2 GeV H_2^+

According to the following formula:

$$\varepsilon_{tot} = P_{bt} / [(P_b + P_{loss})/\varepsilon_{ac} + P_{other}]$$

where:

ε_{ac}=75% is the AC/RF optimised conversion efficiency

P_{bt}=10 MW is the total beam power

P_b=9 MW beam power transferred by the Cyclotron

P_{other}= 3.5 MW for injector, pre-injector, magnets etc...

According to the data of PSI the thermal losses for each copper cavity at 750 kV should be 280 kW which gives a P_{loss}= 0.280*8 MW and an overall efficiency for ADS based on the proposed RSC of ε_{tot}=53%.

Table 1: Main parameter of the RSC shown in figure 2

E_f (MeV/n)	1000	$R_{ext.}$	5.5 m	$<B_{hill}>$	4.3 T
E_i (MeV/n)	130	$R_{inj.}$	3 m	$<B_{val}>$	0.9 T
N. Sectors	10	θ_{hill}	13°	ξ_{spiral}	56°
N. Cavities	8	V_{peack}	750 kV	$f_{cyc.}$	7.7 MHz

4 VACUUM REQUIREMENTS

As well known, due to the interactions with the residual gas, ions could lose the orbital electron along the acceleration path. The fraction of particles which survives is [10]:

$$T = N/N_0 = \exp(-3.35\ 10^{16} \int \sigma_l(E)\ P\ dl)$$

$$\sigma_l(E) \approx 4\pi a_0^2\ (v_o/v)^2 (Z_t^2 + Z_t)/Z_i$$

Where: P is the pressure (torr), L is the path length in cm. $\sigma_l(E)$ is the cross section of electron loss, v_0 and a_0 are the velocity and the radius of the orbit of Bohr respectively, and Z_t and Z_i are the atomic number of the residual gas and of the incident ion respectively. This formula gives a result in quite good agreement with experimental data. Anyway it is very important to have some measured values of the cross section for electron stripping of H_2^+ across residual gas. We plan to measure these cross sections next fall when at our laboratory an H_2^+ beam of 70 MeV/amu will be available. As shown in table 3, to maintain the amount of loss during the acceleration at the same level as the TRIUMF Cyclotron, the vacuum has to be 10^{-8} torr, twice better than the vacuum of TRIUMF Cyclotron. The proposed high energy cyclotrons here discussed are more compact and smaller than the TRIUMF one, so to achieve a better vacuum seems feasible. Moreover to reach good values of vacuum is useful to increase the reliability of the RF cavities too.

Table 2: Beam losses due to interactions with residual gas for TRIUMF and for the cyclotrons here considered

	E_{max} MeV	$\Delta E/\Delta n$ MeV	R_{ex} m	I_{lmax} mA	Vac. torr	T %	I_{loss} μA
TRIUMF	520	0.34	7.8	0.4	$2\ 10^{-8}$	1.66	6.6
CSC(H_2^+)	220	1	1.3	10	10^{-8}	0.02	2.
RSC(H_2^+)	2000	6	5.5	10	10^{-8}	0.08	8.

5 CONCLUSION

A lot of work has to be done to evaluate the difficulties related to the construction of H_2^+ Cyclotrons to achieve energies as high as 1 GeV, in particular the design of sector magnets able to produce magnetic fields of 4.5 T. However as here presented, now it is possible to construct superconducting cyclotron able to deliver high intensity proton beams with energy of 100-150 MeV. Cyclotrons used as ADS have to guarantee a high level of reliability and easy operation mode independent of the skilness of the operators, as well as high conversion efficiency from electrical to beam power. We believe that all these requirements are achievable by cyclotrons when designed to accelerate H_2^+ ions to be extracted by stripping.

6 REFERENCES

[1] C. Rubbia et al., proc. of E.P.A.C. '94, London (1994) 270
[2] Th. Stambach et al., Nucl. Instr. & Meth. in Phys. Res. B113(1996)1
[3] T. Kuo, TRIUMF, private communication
[4] L. Calabretta and D. Rifuggiato, proc. XV I.C.C.A, Caen (1998) to be published
[5] G. Gulbekian et al., proc. XIII I.C.C.A, Vancouver (1992)11
[6] G. Ciavola et al., Nucl. Phys. A (1997) 69
[7] P. Mandrillon and N. Fetier, proc. XV I.C.C.A, Caen (1998) to be published
[8] T. Kuo et al., proc. XV I.C.C.A., Caen (1998) to be published
[9] H. N. Jungwirth and J. G. de Villiers, proc. XIII I.C.C.A., Vancouver (1992) 709
[10]Betz, Rev. of Mod. Phys. Vol.44,N° 3(1972) 465

AGS RESONANT EXTRACTION WITH HIGH INTENSITY BEAMS*

L. Ahrens, K. Brown†, J. W. Glenn, T. Roser, N. Tsoupas, W. VanAsselt,
AGS Dept., BNL, Upton, NY

Abstract

The Brookhaven AGS third integer resonant extraction system allows the AGS to provide high quality, high intensity 25.5 GeV/c proton beams simultaneously to four target stations and as many as 8 experiments. With the increasing intensities (over $7x10^{13}$ protons/pulse) and associated longer spill periods (2.4 to 3 seconds long), we continue to run with low losses and high quality low modulation continuous current beams.[1] Learning to extract and transport these higher intensity beams has required a process of careful modeling and experimentation. We have had to learn how to correct for various instabilities and how to better match extraction and the transport lines to the higher emittance beams being accelerated in the AGS. Techniques employed include "RF" methods to smooth out momentum distributions and fine structure. We will present results of detailed multi-particle tracking modeling studies which enabled us to develop a clear understanding of beam loss mechanisms in the transport and extraction process. We will report on our status, experiences, and the present understanding of the intensity limitations imposed by resonant extraction and transport to fixed target stations.

1 INTRODUCTION

The Brookhaven AGS Resonant extraction system and the beam transport and switchyard systems were designed in the pre-AGS Booster era,[2, 3, 4] when the kinetic energy of the injected beam was 200 MeV. In the post-Booster era, this energy is now approximately 1.6 GeV. For these two energies the ratio of $\beta\gamma$ is approximately 3.5. Therefore the maximum possible beam emittance is over 3.5 times larger for post-Booster high intensity beams. In order to obtain high intensity beam, the transverse emittance is increased, even though the Booster acceptance is the same as the AGS acceptance.[1] Recent emittance measurements in the AGS Switchyard show that indeed, the beam is larger. The horizontal emittance is about 2 times larger and the vertical emittance is about 1.5 times larger, than they were in the pre-Booster era. [5]

In addition to the larger beams, other factors have changed significantly since the design of the AGS SEB systems. The AGS now uses fast quadrupole magnets to jump the gamma transition point during acceleration. For minimal beam losses to occur during the γ_{tr} jump the momentum spread of the beam has to be minimized. This puts constraints on how large the longitudinal emittance can be. This is due to the highly distorted dispersion function created by the fast quadrupoles, which defines the momentum aperture.[6] Among other changes, we have moved the locations of the drive sextupoles used to create the 26/3 resonance for SEB extraction. This changed the orientation of the separatrix at the electrostatic and the magnetic septums in the AGS, but only slightly. The reason for moving the locations of these sextupoles was to increase the available chromaticity correction. There are now 12 horizontal chromaticity sextupoles, plus the 4 drive sextupoles.

Another fundamental change is the harmonic number used for the AGS. Although this has no obvious impact on the SEB operation, when the system was designed the AGS only worked on an harmonic of 12. We have now operated SEB at high intensity with the AGS on harmonics of 8 and 6. When we ran at very high intensities on a harmonic of 8 it was observed that there were significant coupled bunch oscillations occurring after transition. These have the effect of increasing the longitudinal emittance and diluting the phase space. When we ran on a harmonic of 6 the coupled bunch oscillations were still there, but did not increase the emittance or dilute the phase space as well as before.

Finally, in order to further our understanding of the SEB process, and to try to understand beam loss mechanisms, we have improved and developed models of these systems. In particular is work we have done to track particles through actual field maps of the AGS magnets, to understand the dynamics of what is occurring when the beam is passing through the changing gradient of the combined function magnets. These modeling studies confirmed suspicions we had that significant tails were developing on the beams, which could not be contained in the aperture of the transport lines. The models also confirmed the location of beam losses in the beam line. This allowed us to come up with strategies for reducing and controlling these tails, allowing us to reduce the beam losses resulting from them.

2 SEB HIGH INTENSITY PERFORMANCE

Basic performance parameters are summarized in table 1.

* Work supported by the U.S. Department of Energy.
† Email: kbrown@bnl.gov

0-7803-5573-3/99/$10.00@1999 IEEE.

Table 1: AGS SEB Performance Parameters

Parameter	Value	Units
Momentum	25.5	GeV/c
Peak Intensity	71.5	10^{12} proton/pulse
Extract. Eff.	96-98	%
Transport Eff.	90-95	%
Rep. Period	5	second
Flattop Length	3	second
Spill Length	2.8	second
Working Point	8.67/8.76	Tune (ν_x, ν_y)
Chromaticity	-2.3/0.2	Chrom. (ξ_x, ξ_y)

2.1 *Beam Loss Issues*

The primary beam loss issues have not been in the extraction process itself, but in the transport of the extracted beam to target stations. There were two primary beam loss areas. First, and what was our most pressing problem, was beam losses in the region where the two highest intensity beam lines split off from each other. External "chipmunk" monitors (tissue equivalent ionization detectors, originally developed at FNAL) located outside the beam line shielding, limited the beam intensity that we could put into this region of the beam transport, thus limiting the amount of beam we could deliver to two major experiments. The main cause of the problem was not completely clear. We had made emittance measurements, including measurements of the initial twiss parameters, which showed the beam at the entrance to the switchyard had changed from the canonical set of parameters we had used in our models. Using the new twiss parameters and emittances we developed a new set of optics, which did help significantly (we were able to meet the experimenters requirements). But there were still unexplained losses in the transport.

Explaining the new twiss parameters and emittances gets us back to the extraction process. The beam certainly is larger, as we explained above, but why would the twiss parameters change ? Interestingly enough, the vertical twiss parameters did not change significantly, and could be argued to agree with pre-Booster era measurements. The horizontal twiss parameters were significantly different, although on careful inspection we realized that the ratio of α to β was the same for both the pre- and post-Booster era measurements. In other words, the angular orientation of the beam in phase space was the same, it was just much longer and fatter. Tables 2 and 3 summarize these emittance measurements (note: β and α are referred to switchyard S_0, after AGS magnet F13).

The second beam loss area, which was not fixed by having a new optics solution, was in the region of the transport between the thick septum ejector magnet from the AGS, located at F10, and the first matching quadrupole in the switchyard, located next to the F14 AGS magnet. This beam loss did not cause any chipmunks to limit the intensity but it was nevertheless significant. To understand this beam loss we developed models of the transport and orbit of the beam in the AGS during extraction. We did single particle tracking studies using field maps of the AGS combined function magnets. These studies showed, given the large internal emittance beam, that the extracted beam could easily develop a tail, which could not be confined in the acceptance of the switchyard.

Table 2: Horizontal emittance measurements

	$\epsilon_x^{95\%,N}$	β_x (m)	α_x
Pre-Booster	31.9	57.61	-6.636
Post-Booster	64.37± 9.60	8.77 ± 1.4	−0.92± 0.2

Table 3: Vertical emittance measurements

	$\epsilon_y^{95\%,N}$	β_y (m)	α_y
Pre-Booster	38.8	3.249	0.8708
Post-Booster	54.71± 5.0	4.18 ± 0.4	1.01 ± 0.09

Figure 1 shows the phase space of the beam at the entrance to the thin septum extraction magnet and the phase space at F13, just before entering the matching quadrupoles at the entrance of the switchyard. In this case the beam entering the switchyard has a large tail. Figure 2 shows particles from the edges of the phase space ray traced down the C line. As can be seen the tail cannot stay contained in the aperture in the matching section (at the beginning of the line) and again hits apertures in the middle of the line. Interesting enough, the latter location is where the beams split off between the B and C lines, the area of problems noted above. We can reduce, and even eliminate, the tail by moving the two septum magnets 2/10 inch further inside. This was done and it significantly reduced beam losses in both the two problem sections.

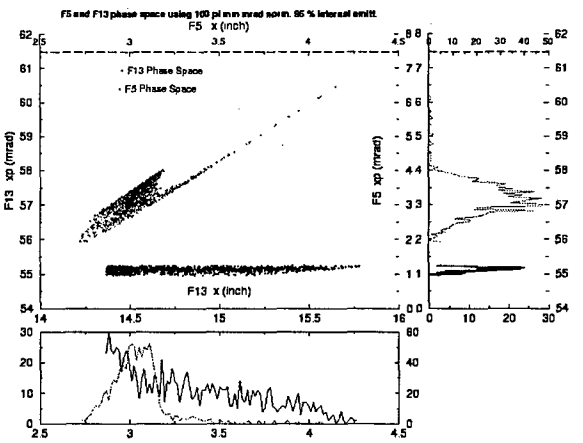

Figure 1: Tracking Simulation of extracted beam passing through AGS Main Magnets

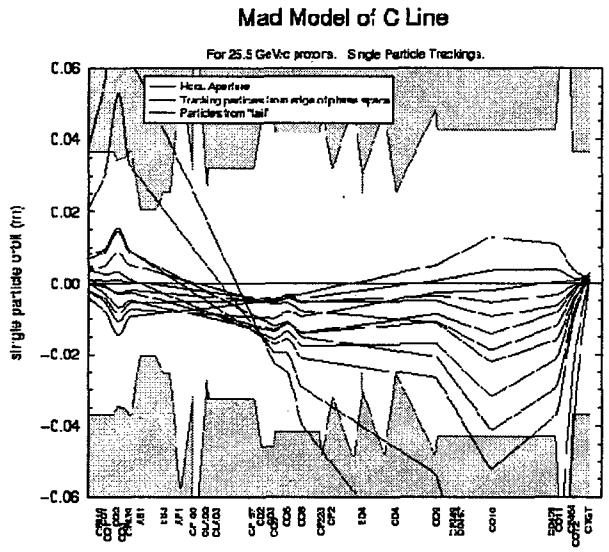

Figure 2: Single particle tracking for transport down C-Line

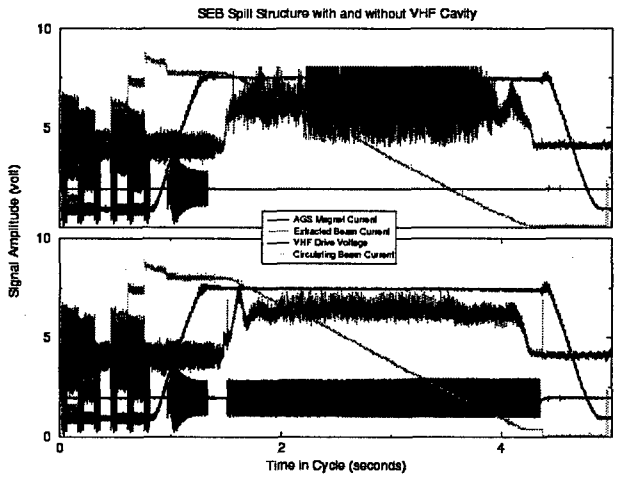

Figure 3: Extracted beam spill with and without VHF on

2.2 *Spill Structure*

In the FY98/99 SEB run we ran into a new problem; significant spill structure not associated with power supply ripple. This spill structure was analyzed and found to be random kilohertz oscillations. We found no correlations between these oscillations and power supply ripples. The power supply ripple only accounted for about 20 % of the spill structure. At high intensity the spill was 100 % modulated (intensity dependent). Recall that the spill structure is a consequence of variations in velocities in tune space:

$$S(t) = \frac{dN}{dQ} \cdot \dot{Q}_0(1 + \frac{\dot{Q}_v}{\dot{Q}_0}) \qquad (1)$$

When there is very little power supply ripple, the remaining structure is a consequence of the rate at which the beam is moved into resonance and the distribution of the particles in tune space. The random kilohertz structure appears to be a direct reflection of the distribution of particles in tune, or more properly, momentum space. Our solution to this problem was to use the VHF cavity during extraction, placing the 93 MHz buckets between the beam and the resonance, such that the particles were forced between the RF buckets before going into non-linear resonant growth. Since we have a slight negative $\dot{B}$ during extraction the RF buckets would have only a small space between which the beam could pass, breaking up any structure that existed in the beam. This potentially puts 93 MHz structure on the spill, which was not a problem for the experimenters using the beam. Figure 1 shows the beam spill with and without the VHF cavity on during extraction.

3 CONCLUSIONS

The AGS SEB system is able to supply high quality, high intensity proton beams for multiple simultaneous experiments. We are able to contend with instabilities that arise from the high current accelerated beams, as well as unexpected effects, such as spill structure uncorrelated with power supply ripple. For the AGS the VHF cavity has proven to be invaluable for diluting longitudinal phase space and now for smoothing spill structure.

4 REFERENCES

[1] L.A.Ahrens et al, "High Intensity Performance of the Brookhaven AGS", these proceedings.

[2] J.W.Glenn et al, "AGS Slow Extraction Improvements", IEEE NS26,No.3, 3167(1979)

[3] H. Weisberg and J.W. Glenn, "Exploitation of Nonlinear Growth of Betatron Oscillations to Obtain Efficient Slow Extraction at the AGS", Nucl. Inst. & Methos 169, 319(1980).

[4] L. Blumberg et al, "The AGS Slow External Beam Switchyard", BNL 24508R (1979)

[5] K.Brown et al, "FY96 SEB Emittance Measurements", AGS/AD Technical Note No. 445, 1996.

[6] L.A.Ahrens et al, "High Intensity Proton Acceleration at the Brookhaven AGS - An Update", Proceedings of the 1997 Particle Accelerator Conference, p.89, http://www.triumf.ca/pac97.html

[7] AGS 2000 Workshop Proceedings, BNL 52512, 1996

[8] J.W. Glenn et al, "MICRO-BUNCHING THE AGS SLOW EXTERNAL BEAM", Proceedings of the 1997 Particle Accelerator Conference, p.967, http://www.triumf.ca/pac97.html

[9] Cappi & Steinbach "Improvement of the Low Frequency ..." CERN/PS/OP 80-10 & IEEE NS-28, No 3, June 1981, pp 2806

GOLD BEAM LOSSES AT THE AGS BOOSTER INJECTION*

S.Y. Zhang and L.A. Ahrens
AGS Department, Brookhaven National Laboratory, Upton, NY, USA

Abstract

Gold beam injection efficiency decreases in proportional to the beam loss in the AGS Booster. A close look shows that large number of electrons, ions, and neutral particles are created when the gold beam scrapes wall. To investigate the neutral particle production due to the beam loss, local vacuum measurement was made during the 1998 run. It shows that the pressure created by the Booster Au^{31+} beam loss at injection has a 35 ms decay time constant. The beam loss created pressure bump in the ring is about 20 meters long. When 3×10^9 Gold ions scrapes wall, a pressure higher than 10^{-7} Torr was created. The beam lifetime calculated using these parameters is in agreement with the observed one.

1 INTRODUCTION

In [1], it is reported that the Gold beam Booster injection efficiency decreases in proportional to the beam loss in the ring. It is also observed that the beam life time decreases after a beam scraping in the ring. These results suggest that the gold ion lost in the ring has negative impact on the beam survival.

A close look at the effects of lost gold ions shows that there are large numbers of electrons, neutral particles, and ions (mostly positive) created when the gold beam scrapes wall [2,3]. It was found that the secondary electrons and ions are not the major culprit of the beam loss.

To investigate the neutral particle production due to the beam loss, vacuum measurement was performed during the 1998 run. The findings are as follows.

1. Vacuum pressure created by the Booster Au^{31+} beam loss at injection has a 35 ms decay time constant.
2. Crashing 3×10^9 gold ions into the wall, a pressure higher than 10^{-7} Torr was observed, up from the normal 5×10^{-11} Torr.
3. The beam loss created vacuum bump in the ring is about 20 meters long.
4. The beam lifetime calculated using these results is in agreement with the observed one, i.e. about 20 ms for high intensity injection.
5. A rough estimate shows that at Booster injection, a scraping Au^{31+} ion could produce as much as 10^5 molecules.

2 VACUUM PRESSURE DUE TO BEAM LOSS

The usual vacuum measurement, through the ion gauge controller, reports mean values over several seconds. This is because that the signal obtained from ion gauge is in pA level for a vacuum pressure at a few units of 10^{-11} Torr, whereas the noise can easily reach a nA level. To investigate the beam loss created vacuum pressure structure, therefore, the ion gauge controller has to be bypassed.

Using an electrometer, Keithley 480 Picoammeter, ion gauges at different locations in the Booster ring were directly measured for the vacuum pressure due to the lost gold beam.

The time constant of Keithley 480 has a dependence on the source capacitance. For example, at the nA range, a source capacitance 230 pf implies a time constant of 250 ms. It is found that this time constant applies to most ion gauges we used in the measurement. The dynamic model of the electrometer was obtained by the calibration.

2.1 Time structure of the pressure

The time structure of the vacuum pressure created by the beam loss was studied as follows.

1. The beam was crashed in the ring, and the response of the electrometer for the ion gauge was obtained.
2. Set up a vacuum pressure with a peak value and a decay time constant. The response of electrometer is obtained by a simulation using the calibrated first order delay model of electrometer.
3. Match the simulated vacuum pressure time structure to the observed response of the electrometer, by adjusting the peak value and the time constant.

One example of the observed response of the electrometer is shown in Fig.1A. The location is C3B, immediate down stream of the injection septum. The injected beam scraping on the septum wall was controlled by the horizontal steering magnet immediate up stream the septum. Two Booster injections occurred in 200 ms,

* Work performed under the auspices of the US Dept. of Energy.

and 5×10^{8} ions were estimated lost. The vacuum pressure reported through the ion gauge controller was 5×10^{-10} Torr.

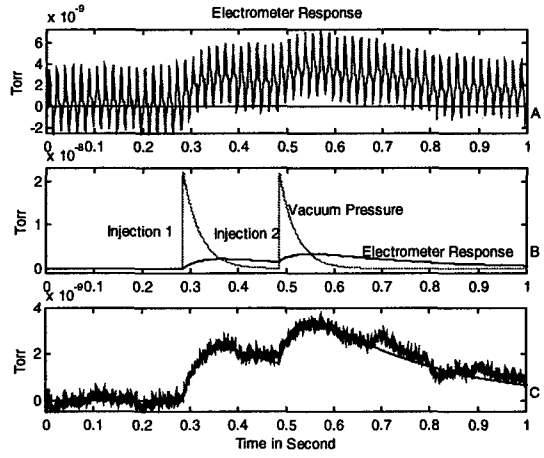

Figure 1

In Fig.1B, vacuum pressure with peak of 2.2×10^{-8} Torr and a decay time constant of 35 ms is shown, together with the simulated response of electrometer.

In Fig.1C, the measured response of electrometer, smoothed by a 60 Hz notch filter, and the simulated one are shown to be matched. It is found, therefore, that the beam loss created pressure has a decay time constant of

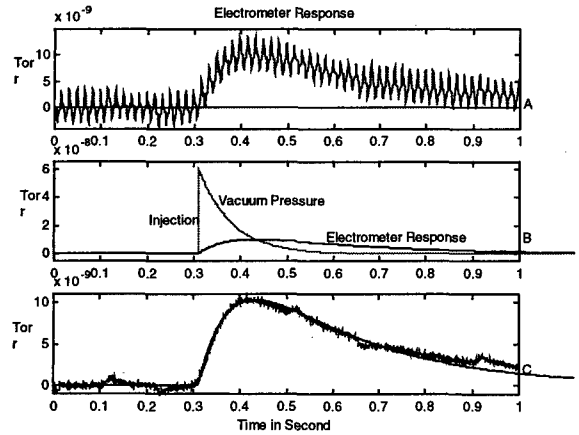

Figure 2

35 ms.

Six experiments performed in different locations in the ring, with different intensities, have showed consistent results of a 35 ms decay time constant. The losses were from 3×10^{8} ions to 10^{9} ions in these cases.

With larger beam losses, and higher vacuum pressure, the observed vacuum decay time was a little longer. The example shown in Fig.2 represents about 1.5×10^{9} beam loss. The vacuum pressure reported through the ion gauge controller was 1.5×10^{-9} Torr.

Under the condition of very high pressure, the functioning of the ion pumps is likely to be different, also the nonlinearity of the ion gauge may be involved.

2.2 Peak pressure

The Booster vacuum pressure reported through the ion gauge controller is the average value over the whole cycle, 3 seconds. Taking the vacuum pressure decay time of 35 ms, this pressure accounts for only about 1% of the real pressure created by the beam loss.

By crashing about 3×10^{9} ions into the Booster injection inflector, a pressure higher than 2×10^{-9} Torr was observed through the ion gauge controller. This implies that the real vacuum pressure is higher than 10^{-7} Torr.

2.3 Pressure bump in the ring

To observe the vacuum pressure bump in the ring, the gold beam was crashed into several locations. The vacuum pressure recorded is simply the one observed in the control room, through the ion gauge controller. One example is shown in Table 1.

Ion Gauge	C6	C7	C8	D1	D2	D3	Unit
Distance	0	4.2	8.4	12.6	16.8	21	m
Normal	0.3	0.2	0.1	0.0	0.2	0.2	10^{-10} Torr
Scraping	0.8	1.4	2.0	4.5	1.0	0.6	10^{-10} Torr

Table 1

In average, the vacuum bump created by the beam scraping is about 15 to 25 meters long.

3 BEAM LOSS MECHANISM

Electron impact capture and ionization cross sections reported in [4] for gold ions are shown in Fig.3.

At the Booster injection energy, with $\beta=0.044$, the ionization would not occur, whereas the electron impact capture cross section is about 10^{-17} cm^2 for Au^{31+} ions.

The sputtering can create neutral particles, in forms of particles, molecules, or clusters. Also, the high energy secondary electrons could stimulate gas desorption, which also generate neutral particle. For convenience, we simply consider the product of the lost ions as molecules.

Taking the molecules created by the lost gold beam as N_2 equivalent, the capture cross section can be taken as $\sigma_C \approx 10^{-16} cm^2$ for Au^{31+} ions.

Assuming that at high intensity run, the vacuum bump created by the beam loss is 20 meters long, with the pressure of $P_p = 10^{-7}$ Torr, the molecule density can be calculated by,

$$n_m = 3.3\times10^{16} P_p$$

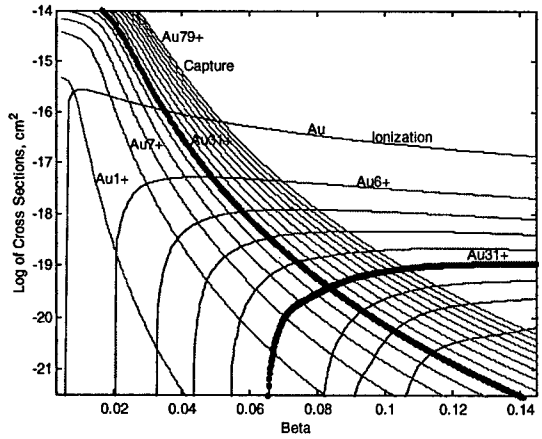

Figure 3 *Electron impact cross sections. Bold lines are for* Au^{31+}

The beam life time is estimated by,

$$\tau_{beam} = \frac{1}{\sigma_C n_m \beta c} \times \frac{201}{20}$$

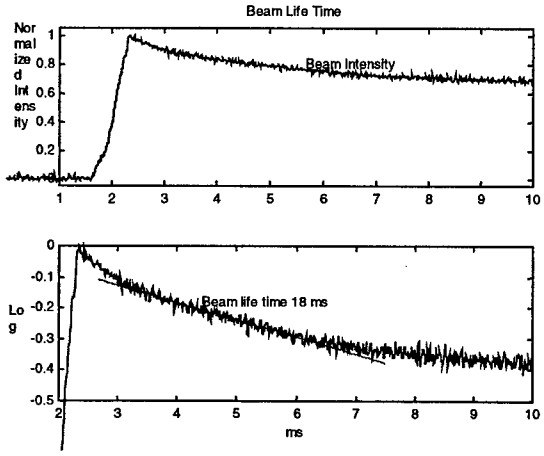

Figure 4

where c is the speed of light, and 201 meter is the Booster circumference. We get $\tau_{beam} \approx 23ms$.

The beam lifetime calculated using these parameters is in agreement with the observed one. In Fig.4, The gold beam current in about 10 ms starting from the injection of a typical high intensity run is shown. The Booster injection intensity was 5.2×10^9 ions, whereas 2 ms after the stacking, the beam intensity was 2.4×10^9 ions. About 2.8×10^9 gold ions were lost in less than 3 ms. The beam life time was about 18 ms, from 1 ms to 5 ms after the stacking.

4 MOLECULES CREATED BY THE LOST IONS

The molecules created by one lost gold ion can be calculated by,

$$N_{molec.} = 3.3\times10^{16} P_p V_\lambda / N_{loss}$$

The resulted molecules per lost ion is in the order of 10^5.

5 ACKNOWLEDGMENT

We like to thank H.C. Hseuh, M. Mapes, T. Roser and P. Thieberger for valuable discussions, we also like to thank V. Usack and D. Warburton for technical assistant in the study.

6 REFERENCE

[1] S.Y. Zhang and L.A. Ahrens, EPAC98, p.2149, 1998.

[2] *Sputtering by Particle Bombardment III*, Edited by R. Behrisch and K. Wittmaack, Springer-Verlag, N.Y., 1991.

[3] S.Y. Zhang, AGS Tech Note, No.477, May, 1998.

[4] S.Y. Zhang, AGS Tech Note, No.482, Dec., 1998.

SECONDARY ELECTRON PRODUCTION AT THE SNS STORAGE RING COLLIMATOR*

S.Y. Zhang
AGS Department, Brookhaven National Laboratory, Upton, NY, USA

Abstract

Secondary electron (SE) production is briefly reviewed. If the collimator of the SNS storage ring allows proton beam scraping to take place, the electron yield might be quite large.

At the AGS Booster, by steering the Au^{31+} ion beam into the electrostatic inflector, beam scraping effect on SE production is studied.

The results of this experiment can be translated into the situation of proton beam scraping at the SNS collimator. It seems sufficient to support a new look of the SNS ring collimator design.

1 SECONDARY ELECTRON PRODUCTION

In secondary electron emission, the electronic stopping (Coulomb collision) is dominant if the projectile velocity is larger than the Bohr velocity $2.18\times10^8 cm/s(\beta=0.0073)$. If the primary ion, proton, or electron have the same velocity, the kinetics of the collision is very similar [1,2]. The Seiler model shows that the peak SE production energy of projectile is around $E_k \approx 0.9 MeV/u(\beta=0.044)$. Also according to this model, the SE production rate at the SNS beam energy, $E_k \approx 1.0 GeV/u(\beta=0.875)$, is about 10% of the peak yield.

Since the electronic stopping power of the target is approximately proportional to q^2, where q is the charge state of the projectile, it was believed that the SE yield Y also has a q^2 dependence [5,6]. However, experimental results have shown that it is more likely a $q^{1.7}$ dependence [7].

Probably the most profound factor in SE emission is the projectile scraping effect. Only the excited electrons near the surface have a chance to escape, and a major part of stopping power of a grazing projectile is deposited on the surface. In [3], this dependence is estimated as a factor $(\cos\theta)^{-n}$, where a perpendicular incident has an angle $\theta=0$, and a range of the index $0.8\le n\le 1.5$ is indicated. The complication of this mechanism, both theoretically and experimentally, in fact prohibits any accurate account on this factor.

Following an experimental observation, in [8], it was calculated that $Y\approx 200$ for a grazing proton at the PSR of LANL, $\beta=0.841$. The electron collection there seems in agreement with this yield.

If the collimator of the SNS storage ring allows proton beam scraping to take place, the electron yield will probably be around 200. Note that this yield is about 1,000 times higher than the yield that has been theoretically and experimentally confirmed, without the functioning of the scraping effect.

To be more confident with the necessity to eliminate proton beam scraping on the surface of the collimator, an experiment was performed at the AGS Booster to study the beam scraping effect on the SE production.

2 EXPERIMENT AT THE AGS BOOSTER

By horizontally steering the Au^{31+} ion beam into the electrostatic inflector, which guides the ion beam from the Tandem transfer line into the Booster orbit, a situation of beam scraping on the inflector surface at different angles is created. Since the projectile energy and charge state effects on the SE production are known, this scraping study could be a useful reference for the SNS collimator electron production.

The inflector has a horizontal aperture $17mm$, and is normally charged at $24KV$. The capacitance at the inflector is about $300pf$, and the charging resistance is $1M\Omega$. The anode of the inflector is grounded, therefore, the cathode carries a voltage of $-24KV$. By steering the ion beam into the cathode, the electrons there may escape from the surface, then these electrons are expelled by the cathode. By observing the cathode voltage, therefore, the secondary electron emission can be estimated.

The gold ions from the Tandem to Booster transfer line (TtB) carry a positive charge of 31. The kinetic energy is $E_k \approx 0.9 MeV/u(\beta=0.044)$, which happens to be the peak production energy of SE.

* Work performed under the auspices of the US Dept. of Energy

In a normal running condition, the Tandem to Booster transfer line horizontal dipole 29T DH2 upstream the inflector was set at $-0.55A$. The beam full width half magnitude (FWHM) size was $4mm$. It is believed that during $670\mu s$ multiturn injection period, beam scraping at either the anode or the cathode causes a voltage drop at the inflector. This voltage decline is almost invisible at low intensity, and it is about $300V$ at the high intensity injection. After the stacking, the inflector voltage is recovered by the charging current of the power supply. The high intensity of gold beam injection usually implies more than 3×10^9 ions per pulse.

By setting the DH2 current at $-3.76A$, $-3.96A$, and $-4.16A$, the detected inflector voltage variation is shown in Fig.1. For convenience, the voltage has been offset by $-24KV$. We observe that at the end of injection period, the inflector cathode voltage is raised by $2KV$, $8.6KV$, and $7KV$, respectively. In other words, the cathode voltage becomes $-22KV$, $-15.4KV$, and $-17KV$ at the end of stacking, respectively.

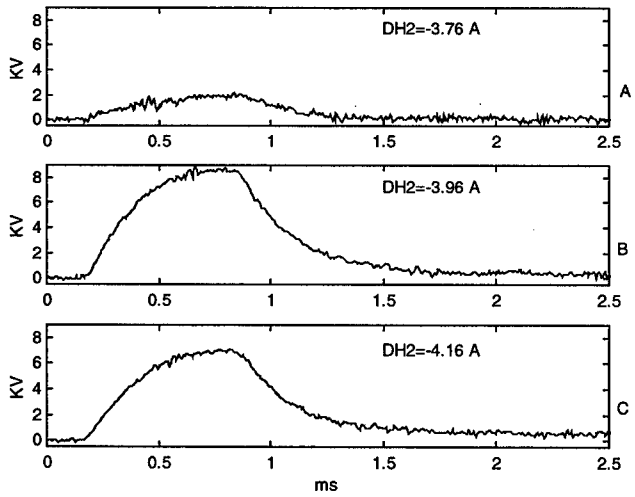

Fig.1. Beam Scraping Induced Voltage on the Inflector

A simple model is used to explain the results. A constant voltage source, at $V_1=-24KV$, charges the inflector through $R=1M\Omega$. The inflector itself is represented by a capacitance of $C=300pf$, and its voltage is V_2. The ion beam generated SE production is modeled as a current source I. At the beginning of stacking, we have $V_1=V_2=-24KV$ and $I=0$. Once the ion beam is steered into the cathode, $I\neq0$. The inflector cathode voltage rises, which in turn induces the charging current through R. At the end of the stacking, once again $I=0$. The inflector cathode voltage is recovered by the charging current. The following equation can be used to describe this model.

$$V_2=V_{2,0}+\frac{1}{C}\int\left(\frac{V_1-V_2}{R}-I\right)dt \tag{1}$$

where $V_{2,0}=-24KV$ is the static cathode voltage. Using the detected V_2, we find I, which is then used to get the SE yield. This is,

$$I(t)=\frac{V_1-V_2}{R}-C\frac{dV_2}{dt} \tag{2}$$

By fitting to V_2, we find that both the rising and falling of this voltage are exponential. The time constant of the rising is $\tau_{rise}=2\times10^{-4}$ sec., and the falling time constant is $\tau_{fall}=3\times10^{-4}$ sec. This is shown in Fig.2, where the amplitude of V_2 is normalized to unity. The falling time constant confirms that $R=1M\Omega$ and $C=300pf$,

$$\tau_{fall}=RC=3\times10^{-4}\text{ sec.} \tag{3}$$

On the other hand, the fit of the rising voltage, during the stacking period, requires I to be time dependent.

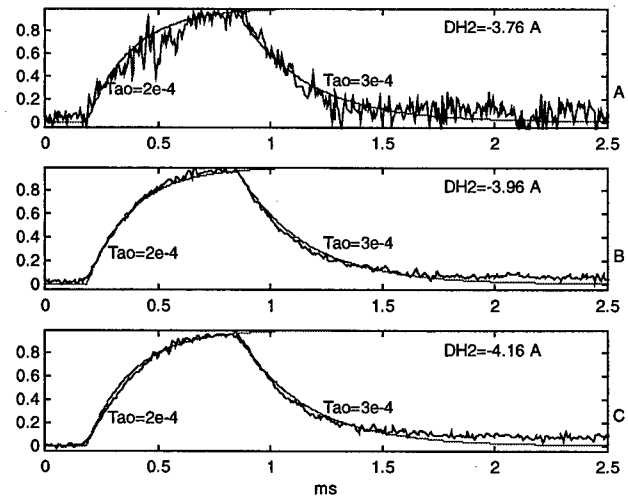

Fig.2. Time Constants of the Rising and Falling Voltage on the Inflector Cathode

Take the case that the DH2 current of $-3.96A$ as an example. The current I is calculated using (2) and the measured V_2. The result is shown in Fig.3. At the beginning of stacking, this current is $13.3mA$ and at the end of stacking, it is reduced to $9mA$. This variation is not a surprise. However, a convincing explanation of this is difficult to reach. Among possible reasons, the most noticeable ones are:

1. Electrostatic potential that deflects the projectile. In our case, the inflector voltage has been dropped significantly during stacking. In fact, shortly after the beginning of stacking, most ions in the beam have been completely deflected and hit the anode.
2. Electron-depletion effect. At $13.3mA$, the electrons escape the surface at a rate of 8.3×10^{16} per second. Depending on the thickness of the electron exciting layer, depletion might take place.

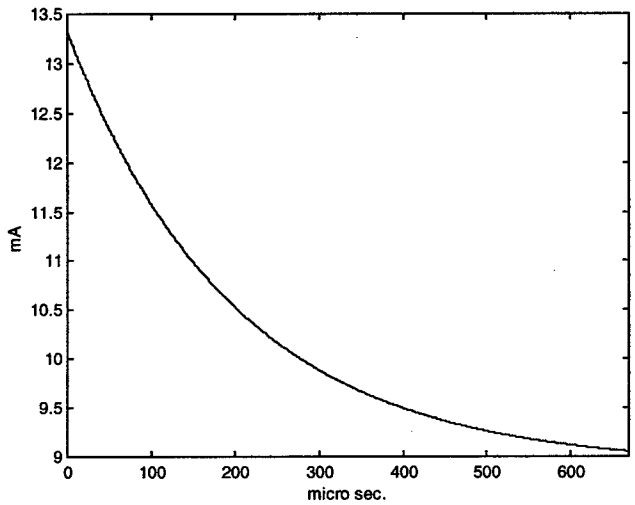

Fig.3. Equivalent Current due to the Beam Scraping

To estimate the SE yield due to beam scraping, therefore, the peak current of $13.3mA$ can be used.

A nontrivial question is how much scraping ions are responsible for these secondary electrons. Let us assume that the DH2 current $-0.55A$ places the beam in the center of the inflector aperture, and the current $-4A$ steers the beam center into the cathode. Therefore, the current of $3.45A$ steers the beam horizontally by half the inflector aperture, $8.5mm$. It is shown in Fig.1 that at the DH2 current of $-3.76A$, the cathode voltage is raised by $2KV$ at the end of stacking. Decreasing the current by $0.2A$, the cathode voltage is raised by $8.6KV$, and another $0.2A$, it is $7KV$. DH2 current of $0.2A$ implies a $0.5mm$ beam horizontal position shift. In comparison, we note that the beam FWHM size was $4mm$, and $\sigma = 1.7mm$.

3 SECONDARY ELECTRON YIELD

Let us take 20% of the beam per pulse to be responsible for the scraping effect in producing SE. This is 6×10^8 ions. Thus, we have the SE yield per lost gold ion,

$$Y_1 = 9.3\times10^4 \tag{4}$$

To translate this yield into the SNS situation, we take the SE production rate at 1 GeV as 10% of that in the experiment. Also we assume the projectile charge state dependence as $q^{1.7} = 31^{1.7} = 343$. Then, the SE yield shown in (4) is,

$$Y_2 = \frac{Y_1}{10\times343} = 27 \tag{5}$$

This yield is smaller than the one estimated in [8], however, it is much larger than the one observed in experiments without scrapping effect. For instance, see [9]. Note also that the early estimate of the SNS collimator SE yield was 0.25 to 2, depending on the collimator edge angle [10].

4 CONCLUSION

The experiment performed at the AGS Booster, using Au^{31+} ion beam to scrape on the electrostatic inflector, has shown the significance of the scraping effect on the secondary electron production. The result of this experiment seems sufficient to support a new look at the SNS ring collimator design [11].

Recent study performed at the BNL Tandem has confirmed the glancing effect of SE production. Using the serrated plate with a sawtooth surface, the SE production reduced dramatically [12].

5 ACKNOWLEDGMENT

The author would like to thank L.A. Ahrens, C.J. Gardner, and A.V. Soukas for valuable discussions and help in the experiment.

6 REFERENCES

[1] A.B. Laponsky, J. Appl. Phys. 34, 1568 (1963).
[2] J.E. Borovsky, D.J. McComas and B.L. Barraclough, Nucl. Instrum. Methods, B30, 191 (1988).
[3] H. Seiler, J. Appl. Phys. 54, R1 (1983).
[4] S.Y. Zhang, AGS Tech. Note, No. 477, BNL, May, (1998).
[5] H.A. Bethe and J. Ashkin, Experimental Nuclear Physics, Vol. I, Edited by E. Segre (Wiley, New York, 1953).
[6] J. Lindhard, Nucl. Instrum. Methods, 132, 1 (1976).
[7] J.E. Borovsky and D.M. Suszcynsky, Phys. Rev. A43, 1416 (1991).
[8] M. Plum, PSR-95-001, LANL, Feb. (1995).
[9] O. Grobner, LHC Project Report, 127 (1997).
[10] L.N. Blumberg, Jan. 1998, unpublished.
[11] H. Ludewig, private communication.
[12] P. Thieberger et. al, private communication.

CALCULATION OF THE MAXIMUM TEMPERATURE ON THE CARBON STRIPPING FOIL OF THE SPALLATION NEUTRON SOURCE

C.J. Liaw, Y.Y. Lee, J. Alessi, J. Tuozzolo, BNL, Upton, NY 11973

Abstract

The maximum temperatures expected on both 220 μg/cm^2 and 400 μg/cm^2 carbon foils, used to strip the 1 GeV H$^-$ beam at injection into the accumulator ring of the Spallation Neutron Source (SNS), were determined by finite-element analysis. This beam will have a pulse length of 1 ms with a repetition rate of 60 Hz and an average current over a single beam pulse of 18.2 mA. The foil size will be 10 mm x 30 mm and will be mounted in a 20 cm diameter stainless steel beam pipe in the injection area of SNS. In the model, the heat generated in the foil was radiated to the wall of the beam pipe, which was exposed to ambient temperatures. The results showed that the maximum temperatures were 1728 K for the 400 μg/cm^2 case and 1574 K for the 220 μg/cm^2 case. A 225 μg/cm^2 thick commercial carbon foil was tested to verify the analysis. The experiment used the 750 keV H$^-$ beam at the AGS Linac, which has a pulse length of 0.5 ms and a repetition rate of 7.5 Hz. By using the same mathematical model as described above, the maximum temperatures on the foil corresponding to various energy depositions were calculated and were compared against the carbon melting temperature (3973 K). The results showed that: 1. When the predicted maximum temperature was above the carbon melting temperature, the foil failed within 1 minute of running time. 2. When the predicted maximum temperature was below the carbon melting temperature, the performance of the foil was not affected up to the end of our 10 minutes tests.

1 INTRODUCTION

Injection into the accumulator ring of the Spallation Neutron Source (SNS) will be done by stripping H$^-$ beam provided by the Linac. A carbon foil [1,2] will be used to fully strip the electrons at one location. The foil will be located in the gap of a dipole magnet which is part of the injection orbit bump. The 1 GeV H$^-$ beam from Linac has a pulse length of 1 ms with repetition rate of 60 Hz and an average current over a single beam pulse of 18.2 mA. The energy lost on the carbon foil will heat the foil and could destroy it. The lifetime of the stripping foil will depend on the maximum temperature of the carbon foil, the repetition rate of the beam, and the fabrication method of the carbon foil. The performance of the foils fabricated by various methods has been reported previously [3,4,5]. This paper focuses on determining the maximum temperatures that the carbon stripping foil can operate at before failure. Analysis was done for 220 μg/cm^2 and 400 μg/cm^2 foils. A 225 μg/cm^2 thick carbon foil was tested to verify the analysis result. More testing to determine foil lifetime is planned.

2 THERMAL ANALYSIS OF THE CARBON STRIPPING FOIL

The carbon foil (10 mm x 30 mm) will be mounted in a 20 cm diameter stainless steel beam pipe in the injection area of SNS. Fig. 1 shows the layout of SNS injection foil and the model that was used for the thermal analysis.

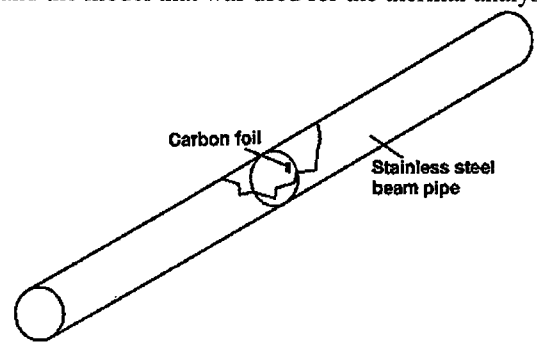

Fig.1: A carbon foil inside a stainless steel beam pipe

2.1 Assumptions

The assumptions for the analysis are as follows:

1. SNS injected beam properties [1,2]:

Kinetic energy	1 GeV
Beam pulse length	1 ms
Repetition rate	60 Hz
Ave. beam current (1 MW)	18.2 mA
RMS emittance (x &y dir.)	0.14 π mm-mr
Beta function	17.4 m (x dir.) 4.56 m (y dir.)
Beam current density distribution on the foil	2-D Gaussian distribution
Beam size @ 1- σ	3.1 mm (x.dir.) 1.6 mm (y.dir.)

2. The power density, P, on the carbon foil could be derived using the following equation [6]: (for the case of stripping a 1 GeV H$^-$ beam)

$$P = 6837551 \times t \times I \quad (W/m^2) \qquad (1)$$

where t is the foil thickness in g/cm^2 and I is the current density in A/m^2.

0-7803-5573-3/99/$10.00@1999 IEEE.

3. Material properties [7,8]:

	Carbon	S. Steel
Density, ρ, kg/m^3	1900	8044
Thermal cond., k, W/m-K	(See Fig. 2)	16.2
Heat Capacity, c, J/kg- K	(See Fig. 2)	502
Rad. View factor, f	1	1
Rad. Emissivity, ε	0.8	0.05

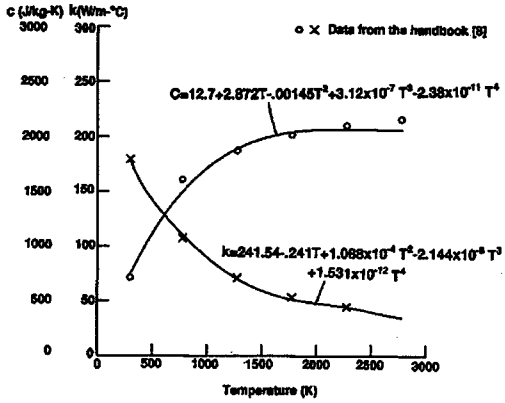

Fig. 2: Variation of carbon properties with temperatures

4. The convection coefficient at the outer surface of the pipe, h =8.17 W/m^2- K
5. Stefan-Boltzmann constant, σ = 5.67 x 10^{-8} W/m^2- K^4
6. Neglect the heat conduction from the foil to the foil holder.
7. Ambient temperature, T_o=297 K.
8. Initial condition: all components @ 297 K.

2.2 Mathematical models

1. The ANSYS model

The governing equations for the heat transfer analysis can be expressed as follows [9]:

On the carbon foil:

$$\nabla^2 T_c + 1/(k_c t_c)[P - 2\sigma f \varepsilon_c (T_c^4 - T_b^4)] = 1/\alpha_c \partial T_c/\partial \tau \qquad (2)$$

and on the beam pipe:

$$\nabla^2 T_b + 1/(k_b t_b)[2\sigma f \varepsilon_b (T_c^4 - T_b^4) - h(T_b - T_c)] = 1/\alpha_b \partial T_b/\partial \tau \qquad (3)$$

where $\nabla^2 = \partial^2/x^2 + \partial^2/y^2 + \partial^2/z^2$, $\alpha_c = k_c/\rho_c c_c$, T_c = temperature on the foil, $\alpha_b = k_b/\rho_b c_b$, T_b = temperature on the beam pipe, t_c = thickness of the foil, τ = time, and all other parameters are defined in Section 2.1. Subscript, b and c, are for the beam pipe and for the carbon foil respectively.

An ANSYS model of the system was developed to solve Eq. (2) and Eq. (3) simultaneously. The beam properties, material properties, heat loads and the other assumptions are shown in Section 2.1. Due to the significant property changes of the carbon material over a wide temperature range [8], the heat capacity (c) and the heat conduction coefficient (k) of the carbon foil were modeled as functions of the temperature. For the convenience of the calculations, the best fitted polynomials were used. (See Fig. 2.) This model included the radiation heat transfer between the carbon foil and the stainless steel beam pipe, heat conduction through the foil to its base, a natural convection condition on the outer surface of the beam pipe, and a Gaussian distribution for the power density from the beam (in the x and y directions) on the foil. Two thicknesses, 220 μg/cm^2 and 400 μg/cm^2, were analyzed. After a few lengthy transient and non-linear numerical analyses, the maximum temperatures on the foil verse time are plotted in Fig. 3 and Fig. 4 (the continuous lines). The plots show the initial four cycles when beam first starts hitting the foil.

2.The simplified model

For comparison, a simplified model was developed to verify the correctness of the finite element analysis. This model neglected the heat conduction across the carbon foil and assumed a constant temperature for the inner wall of the beam pipe. Therefore, Eq.(2) (for the carbon foil) could be decoupled from Eq. (3), which resulted in the following ordinary differential equation:

$$\rho_c V_c c_c \, dT_c/d\tau = -2\sigma f \varepsilon_c A_c (T_c^4 - T_0^4) + PA_c \qquad (4)$$

where V_c = volume of the carbon foil, T_c = temperature on the carbon foil, τ = time, A_c = area on the foil surface, and all other parameters are given in Section 2.1. The integrated results of Eq. (4) for the initial four cycles are also shown in Fig. 3 and Fig. 4. (See the phantom lines.)

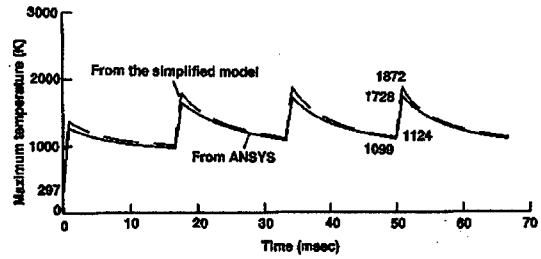

Fig. 3: The maximum temperatures on the carbon foil verse time in SNS (area density: 400 μg/cm^2)

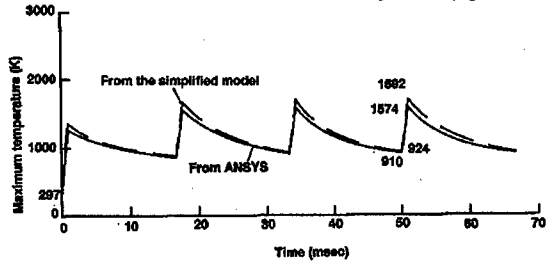

Fig. 4: The maximum temperatures on the foils verse time (area density: 220 μg/cm^2)

2.3 Results

The analysis results are as follows: (1) The temperature cycles on both 400 μg/cm^2 and 220 μg/cm^2 thick foils

become stable after the third heating cycle. (2) During the operation, the maximum temperature on the foil would fluctuate from 1099 K to 1728 K for the 400 μg/cm^2 case and from 910 K to 1574 K for the 220 μg/cm^2 case. (3) The maximum temperatures on the foil, which were calculated by the simplified model were slightly higher than those computed by the ANSYS model. This is because that the simplified model does not include the heat conduction effect on the foil.

3 CARBON FOIL TEST

Since there is no pyrometer fast enough to detect the maximum temperature on the carbon foil while stripping the H$^-$ beam with a pulse length being shorter than 1 ms, the following test was used as an alternative method to verify the analysis results. This test was based on the assumption that the carbon foil would fail within a short period of time only if the temperature on the carbon foil is equal or higher than the melting point of the material. Using the equations from Section 2, the maximum temperatures on the foil verse energy depositions were calculated analytically. The melting point of carbon (3973 K) was obtained from a handbook [7]. By measuring the critical energy deposition above which the foils would fail immediately the analysis results could be verified.

3.1 Test setup

The test setup included a viewing box, an upstream collimator (a carbon rod with 1 mm dia. center hole), a 225 μg/cm^2 carbon foil (17 mm x 62 mm) mounted on an aluminum frame. The frame was mounted on a linear drive mechanism positioned by a stepping motor so multiple shots at various energies could be taken on the same foil. A Faraday cup downstream of the foil detected the beam current. The carbon foil was made by Arizona Carbon Foil Company. It was glued onto the mounting frame along one edge to prevent any restriction when the foil deforms. The foil was positioned 1.83 cm away from the collimator so that the beam size is very close to the aperture of the collimator. The 750 keV H$^-$ ion beam, generated in Linac of BNL, was used in the test. The pulse length was 0.5 ms and the repetition rate was 7.5 Hz. Different energy depositions on the foil were achieved by varying the beam current. The test was performed with the foil under the vacuum. The beam size and current density at the foil location were carefully measured before the test, using the emittance heads.

3.2 Comparison between the analytical and the test results

The power densities deposited on the carbon foil were calculated based on the beam size given by the emittance measurements, the beam current, and the energy of the beam. The maximum temperatures on the foil verse the applied power densities were derived by integrating Eq. (4) with the material properties, given Section 2.1.

Eight tests were conducted at increasing current levels. (See Fig. 5.) The results showed that (1) The beam current densities that predicated a temperature above the carbon melting temperature (3973 K)[7] caused the foil to fail after < 1 minute of running time. (2) The beam current densities that predicted a temperature below the carbon melting temperature did not affect the performance of the foil after 10 minutes of testing. (3) Even at operating temperatures below the foil melting point there was permanent deformation of the foil. From the current readings this deformation did not affect the performance of the foil.

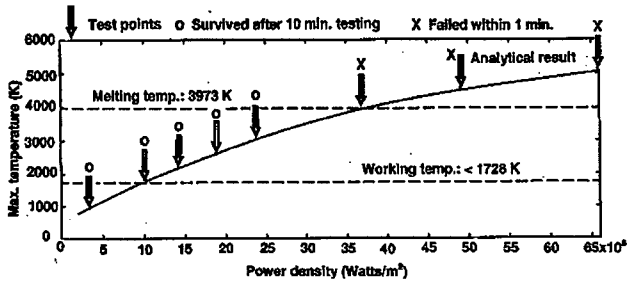

Fig. 5: Comparison of the test results with the analytical calculations

4 REFERENCES

[1] SNS Project Design Manual, 1998, Brookhaven National Laboratory.

[2] SNS Conceptual Design Report, 1997, Brookhaven National Laboratory.

[3] I Sugai, et al, "Development of thick, long-lived carbon stripper foils for PSR of LANL", Nucl. Instr. and Meth. A 362 (1995)70.

[4] M.J. Borden, "Long-life Carbon-fiber-supported carbon stripper foils", Nucl. Instr. and Meth. A 303 (1991)63.

[5] I Sugai, et al, " A new method for making long-lived carbon foils for heavy Ion beam strippers", Nucl. Instr. and Meth. A 236 (1985)576.

[6] Herbert L. Anderson " A Physicist's Desk Reference", 2nd Ed.of Physics Vade Mecum, AIP, New York.

[7] Brady, Clauser, & Vaccari, " Materials Handbook" 14th Ed., McGraw Hill Book Company.

[8] "Handbook of Materials Science", CRC Press, 2nd ed., Vol III.

[9] J.P. Holman, " Heat Transfer" 5th Ed., McGraw Hill Book Company.

IN-BEAM SNS RING COLLIMATION OPTIMISATION*

D. Jeon, V.V. Danilov, J.D. Galambos, J.A. Holmes, D.K. Olsen, ORNL, Oak Ridge, TN 37831

Abstract

Hands-on maintenance of the Spallation Neutron Source (SNS) Accumulator Ring requires an uncontrolled beam loss of less than 1nA/m. A collimator system will be used to obtain this low uncontrolled beam loss. Some beam dynamics questions related to the collimators have been studied. Various factors are optimised with the given SNS ring lattice such as collimating tube length, location, number of collimators, aperture size of primary collimators and secondary collimators, and collimator material. The beam dynamics studies indicate that movable shielding may be necessary for a few hot places downstream of the primary collimators and also that secondary collimators could be designed according to their significantly less activation. These simulations indicate that with proper collimation the uncontrolled beam loss requirements of the SNS accumulator ring may be achievable.

1 INTRODUCTION

The Spallation Neutron Source (SNS) is the most powerful pulsed neutron source under construction [1]. With a repetition rate of 60 Hz, the SNS accelerates a proton beam up to 1 GeV with 1 MW initial beam power that is to be upgraded to 2 MW. SNS operation requires acceleration of intense beam for which space charge effects may play an appreciable role. It is understood that a certain level of beam loss is unavoidable during operation of the accumulator ring that comes from various sources such as halo generation due to the space charge force, magnet non-linearity, errors and harmonic modulations etc. Hands-on maintenance requires that uncontrolled beam loss should be less than 1 nA/m, which corresponds to 1 ppm of 1 MW beam power per meter. In order to meet the beam loss requirement, a special betatron collimator system is needed which can absorb halo protons and contain activation due to secondary particles.

Betatron and momentum collimation in circular accelerators has been studied [2-4]. Collimation in a linear collider was also studied [5]. A very effective collimator was designed at BNL [6] by using the LAHET Code System [7]. However, there remain a few questions that need to be answered with beam dynamics. These questions are as follows:

- What is the optimal length of the inner collimating tube of the collimators?
- What are the number and location of collimators?
- What should the aperture size of secondary collimators be with respect to that of the primary collimators to minimise the activation of downstream beam line components?
- On what components and what level of activation should be expected downstream from the collimators?
- What material should be used for the inner collimating tube?
- How much residual halo is anticipated from the collimators?

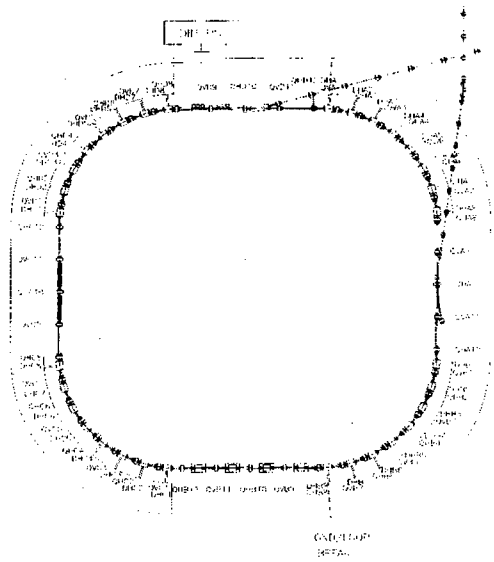

Figure 1: Layout of the SNS accumulator ring.

2 RESULTS

To answer these questions numerical simulation were performed with the ACCSIM H- injection code [8]. The x (y) bare tunes of the SNS accumulator ring lattice were set at 5.82 (5.80). With these tunes the numerical simulation of injection with space charge indicates that about 0.5% of the beam is generated as halo protons with emittance greater than 180 π mm mad. The maximum number of particles that can be tracked is about 400,000, which is much too small to get statistically meaningful data to one part in a million. Consequently, from the 0.5% halo particles obtained from the numerical simulation with space charge, we constructed 100,000 halo particles and tracked them without space charge for the collimator simulation. However, due to other errors, we assume that about 1% of beam will appear as halo protons. The collimators are rectangular.

*Work supported by DOE under contract No. DE-AC05-96OR22464.

- *Length of inner collimating tube*

When halo protons hit a collimator face, some of them are not absorbed and scattered back into the collimating tube with large transverse momentum. These protons are either removed at the later part of the collimating tube or scattered into the collimating tube again as shown in Fig. 2. Consequently, there are always scattered protons spewed out from the downstream end of a collimator. The vertical line and dots in Fig. 2 at 3.5 m represent these particles where a downstream quadrupole is located, and those protons that have larger transverse displacement than 100 mm at that point may activate the quadrupole. It is most effective to have a long inner collimating tube as possible in order to reduce the activation of the downstream quadrupole and beam pipe. Of course, a longer collimator is more expensive to build and space is limited. The simulations indicate that at least a 2-m or longer collimating tube is required.

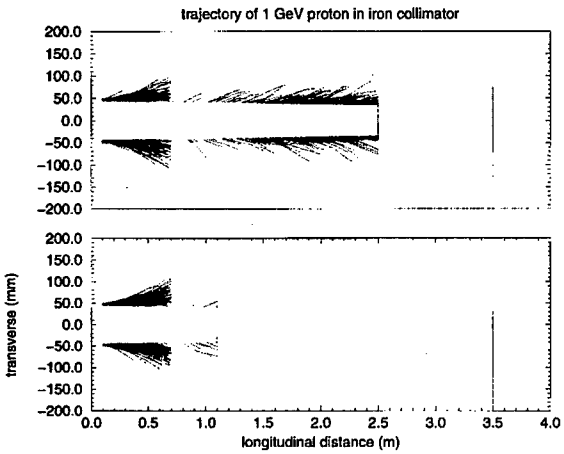

Figure 2: The trajectory of protons in the collimators. The length of the collimator is 2.4 m (upper plot) and 1.0 m (lower plot). The line at 3.5 m represents the scattered protons where a downstream quadrupole is located.

- *Number and location of collimators*

Due to the difference in phase advance between the x and y planes, and also due to the scattered protons from the downstream end of a collimator, it is necessary to place a collimator in every drift space. Consequently, four collimators are required to minimise the activation of downstream components. The Collimator-4 loss fractions are listed in Tables 1 and 2 and these fractions justify the need for a fourth collimator. Figure 2 shows that the scattered protons out of a collimator usually have large transverse momenta and reach the beam pipe aperture quickly. To minimise the activation of downstream quadrupoles from these scattered protons, the distance between a collimator and the following quadrupole should be minimised. The minimum distance is set at 1.0 m to reserve space for maintenance and installation.

- *Aperture size of secondary collimators*

The aperture of the primary collimators is set to 180π mm mrad. The aperture of secondary collimators should be set large enough to avoid direct interception of halo protons and yet be small enough to intercept the scattered protons from the upstream primary collimators. Numerical simulations with space charge indicate that the aperture of the secondary collimators, as shown in Fig.3, should be about 210π mm mrad for the 2 MW SNS ring.

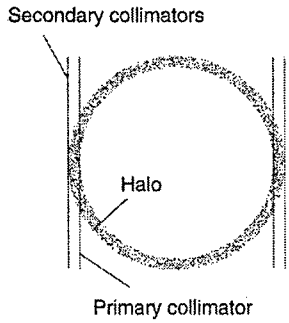

Figure 3: Schematic drawing of the aperture of primary and secondary collimators.

Table 1: Loss fractions verse collimator configurations.

	Case 1	Case 2
Collimator 1	57.94 %	88.30 %
QD	0.30 %	0.46 %
Pipe 2	1.40 %	2.61 %
Collimator 2	35.24 %	6.60 %
QF	0.19 %	0.03 %
Pipe 3	1.40 %	0.08 %
Collimator 3	2.71 %	1.03 %
QD	0.01 %	0.01 %
Pipe 4	0.04 %	0.01 %
Collimator 4	0.47 %	0.20 %
QF	0. %	0. %
Pipe 5	0.01 %	0.01 %
Pipe 6	0.02 %	0.01 %
Pipe 7	0.02 %	0.02 %
Pipe 8	0.05 %	0.04 %
Pipe 9	0.01 %	0. %
Pipe 10	0. %	0. %
Pipe 11	0.05 %	0.02 %
Pipe 12	0.10 %	0.06 %
Pipe 13	0.01 %	0.01 %
Pipe 14	0. %	0. %
Sum of Pipes 5 to 14	0.27 %	0.17 %

Clearly Collimator 1 should be primary and Collimators 3 and 4 secondary. Table 1 lists loss fractions at each component if Collimator 2 is primary (Case 1) or if Collimator 2 is secondary (Case 2). When Collimator 2 is an additional primary collimator (Case 1), the scraping of

halo particles is faster and the load of Collimator 1 is reduced. However, the summed activation level of downstream components is less if Collimator 2 is secondary (Case 2).

- *Downstream activation and collimator material*

Table 2 lists loss fractions for both iron and tungsten collimating tubes. The collimator configuration of Case 2 is used where Collimator 1 is the only primary collimator with aperture size 180π mm mrad and Collimators 2, 3

Table 2: Loss fractions verses collimator material.

	Fe (ρ =7.87)	W (ρ =19.3)
Collimator 1	88.30 %	95.41 %
QD	0.46 %	0.31 %
Pipe 2	2.61 %	1.18 %
Collimator 2	6.60 %	2.18 %
QF	0.03 %	0.01 %
Pipe 3	0.08 %	0.04 %
Collimator 3	1.03 %	0.28 %
QD	0.01 %	0. %
Pipe 4	0.01 %	0. %
Collimator 4	0.20 %	0.04 %
QF	0. %	0. %
Pipe 5	0.01 %	0. %
Pipe 6	0.01 %	0. %
Pipe 7	0.02 %	0.01 %
Pipe 8	0.04 %	0.02 %
Pipe 9	0. %	0. %
Pipe 10	0. %	0. %
Pipe 11	0.02 %	0.01 %
Pipe 12	0.06 %	0.02 %
Pipe 13	0.01 %	0. %
Pipe 14	0. %	0. %
Sum of Pipes 5 to 14	0.17 %	0.06 %

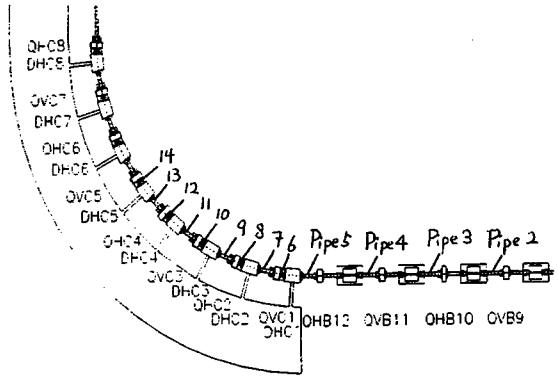

Figure 4: Beam line element labels used in Tables 1and 2 where the beam circulates in clockwise direction.

and 4 are secondary collimators with aperture size 210π mm mrad. Clearly dense material is more effective in removing halo particles and subsequently reducing downstream activation levels. However tungsten is very expensive. Calculations indicate that lead is very effective for scattering; however lead produces a lot of secondary neutrons.

3 CONCLUSION

The main problem in obtaining statistically accurate loss fractions is the limitations on computing power. In order to get a statistically meaningful accuracy down to 0.01%, at least 0.1 billion halo particles are necessary. From the 2D PIC code simulations, it is shown that about 0.5% of the beam appears as halo with emittance greater than 180π mm mrad. Therefore at least 20 billion macro particles would need to be injected and tracked in the SNS ring to do the simulations properly, which greatly surpasses current computing capability.

Nevertheless, these simplified initial numerical simulations indicate that the required uncontrolled beam loss of 1nA/m may be achievable with a properly designed collimation system. The simulations indicate that long collimating tubes made from heavy metal would be most effective. The collimators need to be located as close as possible to the next downstream quadrupole. Four collimators should be used, but the halo load on the last two collimators could be significantly less than on the first two. Movable shielding may be necessary for a few hot places downstream of the primary collimator. More detailed numerical simulations, including turn by turn halo growth from the space charge effect, need to be carried out.

4 REFERENCES

[1] National Spallation Neutron Source Conceptual Design Report, Volumes 1 and 2, NSNS/CDR-2/V1, 2, (May, 1997); at http://www.ornl.gov/~nsns/CDRDocuments/CDR.html

[2] T. Trenkler and J.B. Jeanneret, Part. Accel. **50**, 287 (1995).

[3] P.J. Bryant, CERN Accelerator School CERN 94-01 Vol. 1, p.159.

[4] J.B. Jeanneret, Phys. Rev. Special Topics – Accelerators and Beams, **1**, 081001 (1998).

[5] N. Merminga, J. Irwin, R. Helm, and R.D. Ruth, Part. Accel. **48**, 85 (1994).

[6] H. Ludewig, A. Aronson, R. Blumberg, J. Walker, J. Brodowsi, D. Raparia, M. Todosow, BNL/SNS Technical Note No. 044 1998.

[7] R.E. Prael and H. Lichtenstein, 'User Guide to LCS: The LAHET Code System', Los Alamos National Laboratory, Los Alamos, NM, LA-UR-89-3014 (1989).

[8] J.A. Holmes *et al*, Proc. of International Computational Accelerator Physics Conference, (Monterey, CA, September 98); F. Jones, Users' Guide to ACCSIM, TRIUMF Design Note TRI-DN-90-17 (1990).

MAKING DIPOLES TO SPECTROMETER QUALITY USING ADJUSTMENTS DURING MEASUREMENT*

G. Biallas#, D. Bullard, D. Douglas, A. Guerra, L. Harwood, T. Hiatt, J. Karn, T. Menefee, K. Sullivan, K. Tremblay, R. Wolfley, JLab, Newport News, VA and V. Christina, T. Schultheiss, F. Tepes, Advanced Energy Systems Inc., Medford, NY

Abstract

Twenty-seven window frame dipole magnets requiring spectrometer-like fields were made for the IR-FEL at the Thomas Jefferson National Accelerator Facility. These magnets incorporate Purcell gaps, mu metal pole faces and adjustable field clamps. After outlining their specifications, this paper describes the processes used in magnet manufacturing, the program of magnetic mapping used, as well as the adjustments made to meet tight optics-driven requirements. Described are the measurements made to quantify fringe fields, verify field homogeneity, map core and integrated field as a function of current, and characterize the horizontal and vertical focusing terms designed into the dipoles. Also described are the techniques that were successfully used to tune individual magnets to meet the tight tolerancing of all these parameters.

1 INTRODUCTION

Twenty-seven dipoles in six families were required for the injection, extraction and recirculation beam paths (Table 1) of the 1 kW IR Demonstration Free-Electron Laser at the Thomas Jefferson National Accelerator Facility (Jefferson Lab). The FEL [1] achieves higher efficiency by recycling the spent electron beam's energy. The injector for the accelerator produces a 10 MeV, 5 mA CW electron beam. The injected beam is accelerated to 42 MeV using a single CEBAF-style cryomodule. A wiggler and optical cavity produce light in the 3 to 6.6 μm range. A set of transport arcs recirculate the beam exiting the wiggler back through the cryomodule for energy recovery.

Table 1: Dipole Family Characteristics

Family and Use	Qty.	Effective Length	Core Field
		m	kG
DU - Injection/ Extraction	7	0.21	0.45 - 0.67
DV - Injection/ Extraction	2	0.43	0.45 - 0.67
DW - Optical Chicane	8	0.41	1.04 - 2.48
DX - Recirculation Jog	4	0.51	1.10 - 2.64
DQ- Recirculation Reverse Jog	4	0.51	1.10 - 2.64
DY- Recirculation Pi (180°) Bend	2	3.14	1.10 - 2.64

*Work supported by the U.S. DOE under Contract #DE-AC05-84ER40150
Email: biallas@jlab.org

All magnets met their tight specifications only after being extensively measured, adjusted and re-measured at the Magnet Measurement Facility at Jefferson Lab. The recirculation magnets were designed for use up to 79 MeV, and were characterized between their 37 and 79 MeV operating currents. Table 1 lists family characteristics.

2 SPECIFICATIONS

Specifications for the dipoles derived from a beam performance driven error budget [2]. This error budget evolved to ensure that stringent beam handling requirements would be met during commissioning and operation of the FEL, which demands both production of a properly configured phase space at the wiggler and the management and energy recovery of a very low energy (40 MeV), high current (5 mA CW) electron beam.

The transport system relies on the dipoles to both bend and focus the beam. Consequently, both field integral and absolute field magnitude must fall within specified tolerances. Stringent requirements on beam performance also demand that an accurate representation of all dipole focusing effects be included in the machine description. Dipole end field roll-off (K_1) profiles must therefore be known and included in machine modeling [3].

These constraints must be fulfilled to high precision at relatively low field (~1 kG), a limitation imposed by the low electron beam energy and a design philosophy that attempted to avoid excessively strong bending and focusing (with attendant sensitivities to chromatic effects and field inhomogeneities). The constraints must, in addition, hold over a relatively large working aperture to accommodate a high current beam that will, in some instances, exceed horizontal dimensions of 10 cm or more. The resulting specification suite is summarized in Table 2.

Table 2: Dipole Field Quality Specifications

Characteristic	Tolerance
Excitation - absolute core field error	$\Delta B/B < 10^{-3}$ (1 G at 1 kG)
Field quality - variation of core field and field integral over full working aperture	$\Delta B/B < 10^{-4}$ $\Delta BL/BL < 10^{-4}$ (0.1 G at 1 kG)
End-field roll-off integral K_1=0.27	±0.05 family to family, ±0.005 within family
Transverse aperture - focal length error tolerance	$\sigma_{\beta'\gamma} / \beta\rho < 6.25 \times 10^{-4}$/m

3 DESIGN

The lessons learned in the prototype effort [4] were included in the production designs. The Purcell gap [5] and

0-7803-5573-3/99/$10.00@1999 IEEE.

mu metal pole tip were the greatest aid to transverse uniformity. Saddle coils and field clamps also contributed uniformity while reducing fringe fields and stabilizing the end field roll-off. Adjustability of field clamps along the beam axis provided first and second order adjustment of the field integral. The prototype effort also taught us to take extra care to evenly distribute conductors in the window frame gap to avoid nonuniformity.

Two prudent improvements were added. We widened the magnets to expand the expected zone of good field and we placed the coil terminations away from the yokes to avoid any unbalanced induction in the yokes [6].

Brass was chosen to form the Purcell (non-magnetic) gap because it is an acceptable match to the thermal expansion of iron and mu metal. Even with small differences in thermal expansion of bonded materials, a shear stress develops at the edges. We specified a 3 mm wide bullet shaped taper to all edges of the brass. Finite element analysis [7] showed this reduces peak shear stress in the bond at the edge from 7.5 MPa to 5.1 MPa with a 17 C temperature excursion.

We attached the Purcell gap and mu metal material to the pole tip with epoxy because this method attained simple and reliable placement of these materials against one another to the required accuracy. We selected an epoxy with average bond strength but low viscosity because it squeezed out of the bond area under 5 atmospheres of pressure to a predictable and reproducible minimum thickness of about 25 μm.

The most difficult specification to achieve was the field integral uniformity of $\Delta BL/BL < 10^{-4}$. This tolerance implies that the entire good field region of the 5 cm gap has a tolerance budget of 5 to 10 μm. In our designs many parts share this tolerance budget in series. The critical dimensions were (1) the height of the return leg pieces; (2) the flatness of the two pole faces and the thicknesses of (3) the two Purcell gap sheets, (4) the two mu metal sheets and (5) their four epoxy bonds.

4 MANUFACTURING

4.1 Material Considerations

To promote uniform high permeability, all dipole yoke parts were given a hydrogen anneal [8] before their final machining cut. We made the parts for the field clamps out of 1018, cold rolled steel because tests showed no performance difference. The cost advantage was that only sawing and drilling holes were necessary. The remaining surfaces were used as received.

4.2 Fabrication

These magnets required individual custom fabrication in order to achieve the tolerances required of the pole gaps. Uniformity of the height of the return legs at 1/10th the budget level was achieved by our contractors subcontracting the work to specialty grinding vendors while the pole slabs were machined flat within 1/2 the budget by the vendors themselves.

No supplier of brass or mu metal sheet would consider supplying those materials to the micron level tolerances we required. Instead, in cooperation with our vendors, we custom selected these parts from stock material. The brass sheet was uniform within 10 microns over the central 80% of a four foot wide sheet and consistent along its length. Jefferson Lab personnel inspected the mu metal at the vendor's supplier. The mu metal was found to be similarly uniform over 80% of its 3 foot wide sheet while it varied stepwise along its length. Consequently, we used material only out of these zones of high tolerance.

If all four sheets were randomly superposed, the thickness variation was beyond tolerance. Instead, we cut and oriented the pieces so that the deviations would cancel. For example, a piece of mu metal with a taper in thickness was paired opposite a piece with the reverse of the taper. For the magnet families that shared the same power supply, the gaps had to correlate at the 25 μm level. Since we knew the stackup of the actual thicknesses of the sheet materials, we revised the specification for the height of the return legs (which hadn't been final machined) so that the gaps of all the related magnets fell within their assigned tolerance.

4.3 Assembly

As one of the four successful bidders, (a single coil fabricator and three yoke manufacturers) Everson Electric received the fixed price contract to assemble the magnets on a "best effort" basis. Trial gluings of sheet materials to sample yoke slabs were funded as development items in the contract. These first trial gluings, using a press, gave Everson the confidence to proceed with most of the magnets. Additional trial gluings were necessary for the two Pi (180°) Bends because of their size and because the magnets had the complication of staggered seams in the sheet materials. In the Pi Bend's case, the 5 atmosphere pressure during gluing was achieved with its own bolts.

We specified taper pins as the mechanism to reestablish the relative position of the yoke pole pieces upon reassembly. However, if care was not taken during assembly, the weight of the slabs interfered with the taper pin's ability to jog the upper and lower pieces to their proper position. Instead, the soft annealed iron would "mushroom" under the high compressive pressure caused by the pin as it was being forced in. The mushroomed volume would distend into the joint with the return leg piece and consequently drive the height of the pole gap out of specification. We experienced this problem with magnets received from the assembly vendor and with magnets reassembled by in-house personnel. As a result, only trained personnel are allowed to reassemble these magnets. Hardened tooling pins and bushings installed in the yoke parts at the machining stage may be a cost effective solution for future designs.

5. MAGNET MEASUREMENT & ADJUSTMENT

5.1 Measurement Philosophy

Our philosophy was to measure, adjust and measure until the specifications were met. First we would run a suite of absolute magnetic measurements on the first article of each

family. (The Pi Bends were treated somewhat differently [9].) Through a series of iterations, the field clamps were adjusted and magnetic measurements taken to set the effective length and verify uniformity of the integral gradient. With the positions of the clamps established for the first article, the field clamps of the family were adjusted to the identical positions and were given the suite of absolute measurements and the test for integral gradient uniformity. After passing these tests, each member of the family was measured against a member designated as the "standard" in very accurate, bucked probe coil configuration. This test gave relative field integral variation versus transverse position within the family.

5.2 Inspection

Magnets were inspected first, concentrating on the gap and the field clamp position and the centering of the coils in the yoke. (After many magnets were received and measurement started, we found that the saddle coils required better constraint and consistency along the Z axis.)

5.3 Absolute Measurements

All measurements started with 2 1/2 cycles to highest current and back to zero followed by bringing the current down from high current to the desired setting. This established the magnet at a reproducible point on its hysteresis loop. Using the Stepper Stand's (see below) Group 3 Hall Effect Probe and Metrolab NMR Tesla meter [4], we completely characterized the field in the aperture and fringe zones for the several levels of excitation of interest. This data revealed absolute core field plus absolute field integral to the 10^{-3} level (yielding effective length) as well as K_1 and core field transverse flatness.

Very adaptable for short runs, the Stepper Stand uses the probes mounted to an arm with a height adjustment for "y" on a cart that rolls on a granite surface plate. Readings are taken along lines as the cart is moved by hand to centimeter scale marks for "z" along a rail that is repositionable in "x". A PC-based data acquisition system records the probe values at each scale position.

5.2 Field Clamp Adjustments

The initially measured effective length was never the design value. Adjusting the Z position of the field clamps (to ±25 μm accuracy) corrected this error. At a later stage, by adjusting the yaw of the field clamps, we lowered the residual error in the gradient integral to the 10^{-4} level. (In retrospect, a micrometric adjustment for this feature would have been cost effective.) After acceptance, the field clamps were pinned in these adjusted positions. Note that K_1 was dependent on field clamp position but deviations were always in tolerance.

5.3 Integrating Coil Stand

The instrument that measures uniformity of the gradient integral and relative properties of the family members is the Integrating Coil Stand. It is an extension of the motion and resolver mechanisms of the device that measures CEBAF dipoles. It consists of two coil support sets, each with a stationary portion and a moving portion that is driven identically with the moving portion of the other set. Each support set is accurately mounted in the bore of one of the two magnets to be compared. The standard magnet uses the set with two 50 turn Litz wire coils. Unique to this set and mounted to its movable portion, a constant area coil measures integral gradient uniformity. A second coil changes area, with one coil segment mounted to the movable portion of the support while the remaining coil segment is mounted to the stationary portion. This coil is duplicated in the support set mounted in the second magnet. The signal from this pair of changing area coils is bucked as the moving portions of the supports trace out identical motions. The bucked signal resolves the field integral variation between the standard magnet and family members compared to it at the 10^{-5} level.

5.4 Additional Interventions

Three families required additional or further adjustment. The core field in the dipoles at the center of the injection/ extraction chicanes (DVs) was stronger than the core field in the matching wedge magnets (DUs). Soft iron shims added to the return legs of the DUs increased gap and lowered core field to provide the match. The DQ magnets didn't meet the transverse field integral gradient tolerance. A set of four pole tip windings, run at constant current, corrected the problem. A local field ripple in the second 180° dipole was caused by a combination of out-sized bullet nose tapers on the brass sheets at one joint and a coincident local thinning in the mu metal [9]

6 CONCLUSION

By a combination of exacting manufacturing, patient magnet measurement and adjustment by skilled technicians, twenty seven dipoles in six families met their spectrometer like field specifications. The quality journey by all involved is born out with the attainment of 3.8 mA recirculated beam achieving 710 W (5 mA & 1000 W goal) at an early stage of commissioning of the FEL [1].

7 REFERENCES

[1] Bohn, C. L. et al., "Performance of the Accelerator Driver of Jefferson Laboratory's Free-Electron Laser", Proc. 1999 IEEE Part. Acc. Conf., New York, (1999).
[2] D. Douglas, "Lattice Design for a High-Power Infrared FEL", Proc. 1997 IEEE Part. Acc. Conf., Vancouver, (1997).
[3] K. Brown "A 1st and 2nd Order Matrix Theory for the Design of Beam Transport Systems and Charged Particle Spectrometers", SLAC Report 75, (June 1982).
[4] J. Karn et al., "Magnetic Measurements of the Prototype Dipole for the IR-FEL at the TJNAF", Proc. 1997 IEEE Part. Acc. Conf., Vancouver, (1997).
[5] Suggested by L. Harwood.
[6] Our thanks to the management, engineers and designers of Advanced Energy Systems Group of Northrop Grumman Corp. for their help in designing these magnets.
[7] T. Schultheiss, Northrop Grumman Corp., private communication.
[8] 930 to 1000 C for 3.5 hrs. in H_2 or N2 w/5% H_2, cool at 27 C/hr. to 400 C.
[9] K. Tremblay et al., "Magnetic Measurement for the Pi Bend Dipole Magnets for the IR-FEL at TJNAF", Proc. 1999 IEEE Part. Acc. Conf., New York, (1999)

MODIFICATION OF THE CEBAF TRANSPORT DIPOLES FOR ENERGY UPGRADE CONSIDERATIONS

D. Bullard, L. Harwood, T. Hiatt, J. Karn*, E. Martin, W. Oren, C. Rode, K. Sullivan, R. Wines, M. Wiseman, Thomas Jefferson National Accelerator Facility, Newport News, VA

Abstract

The CEBAF accelerator at the Thomas Jefferson National Accelerator Facility contains 415 resistive dipoles in the recirculation arcs and transport lines. These dipoles were originally designed and magnetically mapped to support the operation of the accelerator at 6 GeV. Recent interests in upgrading the CEBAF energy beyond 6 GeV prompted a study into operating the dipoles beyond their design limits. Finite element modeling was performed to quantify saturation effects at higher currents and to test simple modifications to improve magnetic performance. For confirmation, various setups were prototyped and magnetically measured. Measurement results agreed with finite element models and showed that saturation could be reduced to manageable levels. It was found that the most populous dipole families could be modified to reach twice their design field with minimal cost and effort. At these higher fields, the magnets operate at a reasonable thermal state with minimal saturation losses and little degradation in field quality. Work continues on studying the smaller populations of dipoles to determine their performance at higher fields.

1 INTRODUCTION

CEBAF is a 4 GeV electron accelerator producing CW beams for nuclear physics research. The accelerator consists of a 45 MeV injector and two parallel 400 MeV superconductor linacs. The beam is recirculated through both linacs four additional times to achieve 4 GeV of total acceleration. Multiple beams can be extracted after selected orbits and delivered to any, or each, of the three experimental halls.

The 2,200 magnets in the accelerator were designed and magnetically measured to support an eventual upgrade to 6 GeV. Refinements in SRF cavity performance [1][2] have succesfully increased the linac energies and produced beams for physics as high as 5.5 GeV. A run up to 6 GeV is scheduled for next year.

A proposal is being formulated to increase the energy of the existing five-pass machine to 11 GeV with delivery to the three existing halls. An additional 6th pass through one linac would increase the energy to 12 GeV. The 12 GeV beam would only be delivered to a new, and fourth, experimental hall.

* Work supported in part by the U.S. DOE under contract #DE-AC05-84ER40150.

Email: karn@jlab.org

A study is underway to determine the feasibility of operating the existing magnets at nearly double their design fields. Quadrupoles, sextupoles, and trim correctors, which make up the bulk of the magnet population, have adequate range in most instances. Only a small number of these magnets would need to be replaced. The largest magnet expense, and the most difficult to characterize, are the main bending dipoles. This paper describes simple modifications to a typical CEBAF dipole that significantly improves the magnet's performance at the higher fields.

2 BASELINE DIPOLE

The majority of the bending dipoles (390 out of 415) share a common design. They consist of a solid C-shaped core of modified 1006 steel and pancake coils wound from hollow copper conductor and potted in epoxy. The "*common arc dipole*" typifies these magnets and was chosen as the subject for modeling and prototyping. A cross section of this magnet is shown in Figure 1.

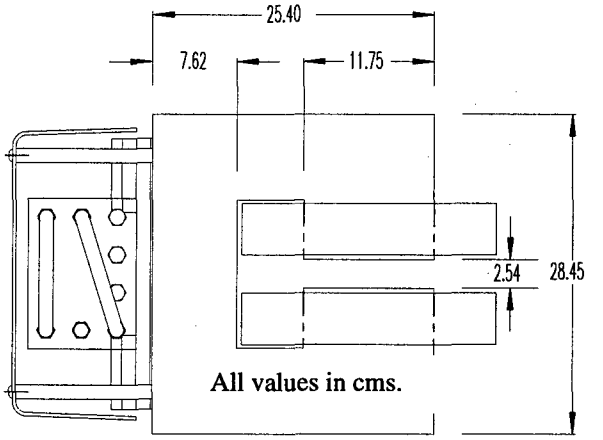

Figure 1: Arc Dipole Cross Section

The dipoles were magnetically mapped up to 300 amps to meet the original 6 GeV design goal. The upgraded dipole would need to run close to 600 amps. Rather than compromising one of the existing spare arc dipoles, a new magnet was fabricated. Care was chosen to use steel from the same heat as the production magnets and follow identical annealing conditions. The fabricated magnet was a "BB" style of magnet which has the cross section shown in Figure 1 and a steel pole length of 2 meters.

The BB prototype was powered up to 600 amps and measurements were made of its magnetic and thermal properties.[3] A point-by-point mapping was made inside the pole gap using Hall and NMR probes. Results from

measurements showed the field began saturation at 400 amps and was reduced by 18% (from linearity) at 600 amps.

To better understand the saturation effects, the BB cross section was modeled using the PC-OPERA 2D finite element package [4]. A plot of the percent saturation is shown in Figure 2 for the measured and PC-OPERA data. As expected, the main area of saturation was the *return leg* of the dipole. A PC-OPERA contour plot of the B field amplitude is shown in Figure 3.

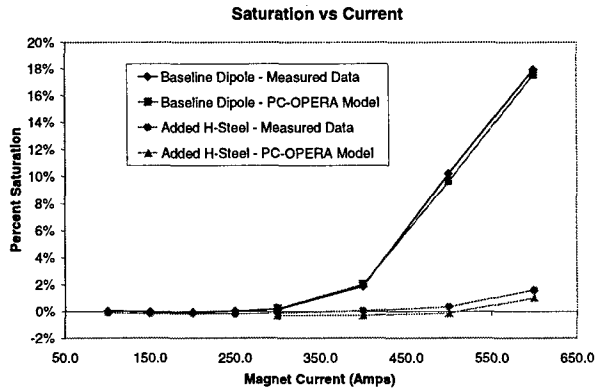

Figure 2: Saturation Plot

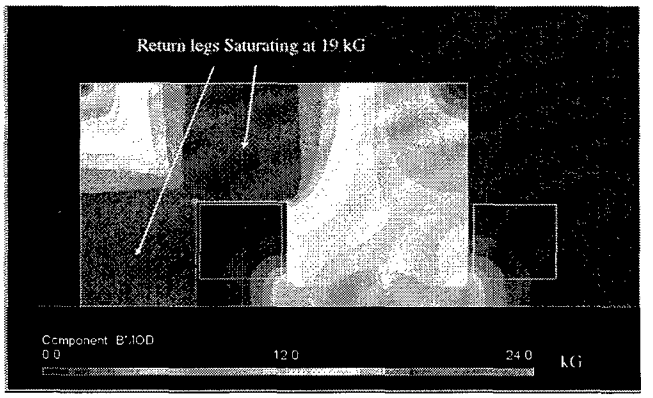

Figure 3: PC-OPERA Model of Baseline BB

3 MODIFIED DIPOLE

The excessive saturation needed to be eliminated in order to reduce power supply requirements. Adding steel to the return leg could reduce saturation effects in the magnet. However, this is the side of the magnet containing the coil terminations and the side that faces the support stands in the accelerator enclosure. A more simplistic fix would involve adding a second return leg to the *outside* of the magnet. That is, convert the C-shaped core to a modified H-shaped core. This solution has several rewarding mechanical features. It faces the aisle of the accelerator enclosure that permits installing the extra steel without having to remove the magnets from their mounts. Further, the existing coil supports can be removed and the same bolt pattern used to hold the added steel, and in turn, support the coils.

Modeling was made in PC-OPERA of the BB cross section with the added *H-Steel*. The design goal is to find the minimal amount of steel required that brings the saturation to an acceptable level. Figure 4 shows that in the optimized model a 3.8 cm. thick side leg and 5.1 cm. thick top/bottom legs would reduce saturation to the one percent level. The required H-steel pieces were prototyped from commercial 1006 steel, annealed, and mounted to the magnet. The steel pieces were deliberately mounted over the existing paint on the magnet to test the effect of the small paint gap. Having to not scrape paint from the mating surfaces would significantly ease future installation efforts. A photograph of the BB with H-steel is shown in Figure 5.

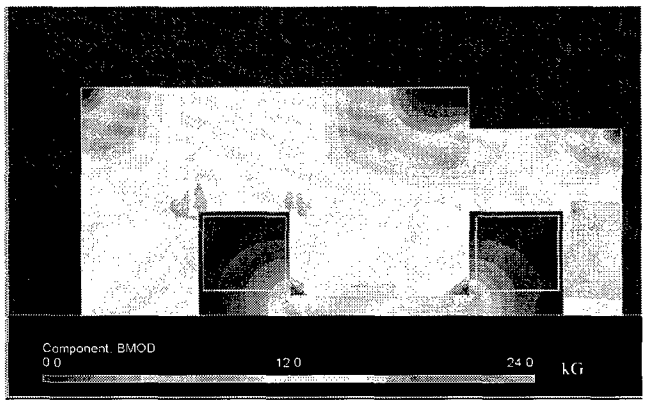

Figure 4: PC-OPERA Model of BB with Added H-Steel

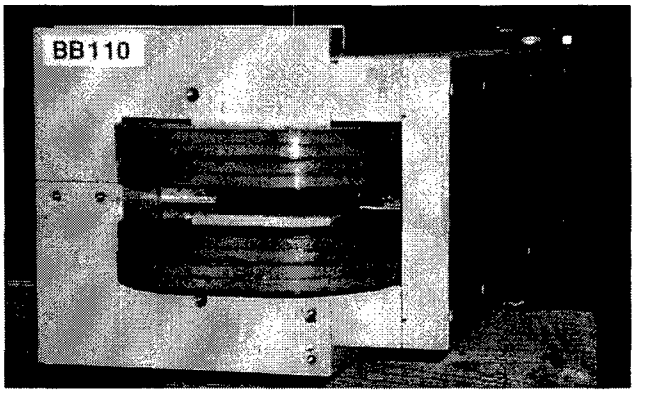

Figure 5: BB with Added H-Steel

Magnetic measurements were performed on the BB with the added H-Steel. The measured data agreed with PC-OPERA modeling to within 0.6% and showed that the saturation was reduced to below one percent (Figure 2.)

4 FIELD PROFILE

Also of concern was that the transverse good field was not compromised from pole tip saturation. Transverse profile measurements were made inside the core using a hall probe at 300 and 600 amps. Figure 6 shows a decrease in the 0.1% good field region from 7.0 to 6.5 cms. This measurement was repeated when the H-steel was added to

the core and a minimal change in the profiles was observed.

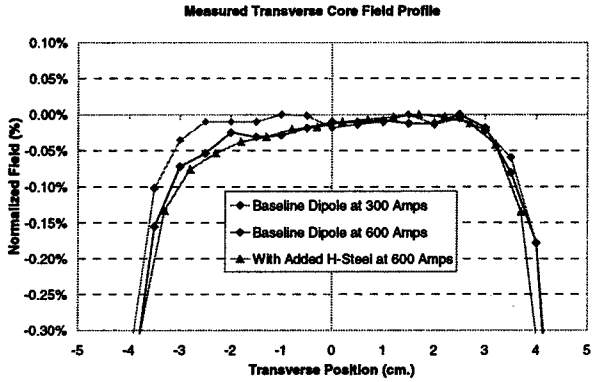

Figure 6: Core Profile

The core field measurements show a small loss in good field, but the accelerator specification is based on the longitudinal field integral. Existing magnet measurement probes capable of this measurement were based on the open C-shaped cores and integrated along a straight line. The closed off cores created by the added H-steel and the request for integrals along a beam-following curved trajectory have complicated measurement efforts. Until measurement data is available, OPERA-3D [4] can be used to model these profiles. Figure 7 shows an OPERA-3D profile of the gradient integral at 300 and 600 amps. Even at the high currents, these magnets still meet the accelerator specification.

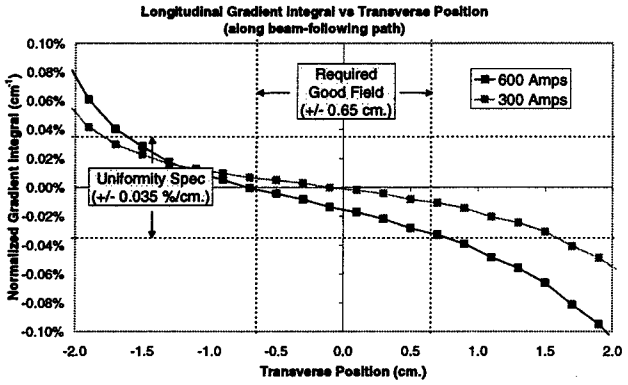

Figure 7: Gradient Integral Profile

5 THERMAL MEASUREMENTS

In addition to magnetic measurements, the thermal properties at the higher current were studied. The magnet was outfitted with thermocouples to measure the steel core and cooling water temperatures. To represent the *highest power* magnet in the accelerator, the water flow was set to 2.12 GPM and the dipole powered to 550 amps. The cooling water temperature increased from 29.4°C to 66.6°C and the steel core reached an equilibrium temperature of 39.1°C. The total input power to the magnet was 16.9 kW and the output power matched within two percent. These are acceptable operating temperatures and calculations are underway to determine the need for additional plant cooling.

6 OTHER DIPOLES

As mentioned earlier, the BB was chosen to be prototyped since its cross section represents the largest population of bending dipoles. The remaining dipoles consist of twenty families differing in cross section and coil turns. Design efforts for these magnets will rely heavily on finite element analysis routines and less prototyping. This is justified from the excellent agreement between finite element models and measured data. To characterize the limitations of these magnets, a considerable amount of PC-OPERA and OPERA-3D modeling is underway. Those families that experience the return leg saturation can be improved by the addition of H-steel. In some cases, coil turns can be added into the pole gap to reduce pole tip saturation and maximize the transverse good field.

7 CONCLUSIONS

An effort is underway to study the feasibility of pushing the existing CEBAF magnets beyond their design capabilities. Simple and cost effective modifications can be made to the majority of the bending dipoles to achieve the required field strengths. Finite element modeling and magnetic measurements were performed to support this study. Measurements also verified the thermal integrity of the magnets and that field quality was not compromised. Work continues on characterizing the smaller populations of bending dipole families.

8 REFERENCES

[1] J. Preble, *Cryomodule Development for the CEBAF Upgrade*, these proceedings.

[2] J. Delayen, *Upgrade of the CEBAF Acceleration System*, these proceedings.

[3] J. Karn, A. Guerra, L. Harwood, and E. Martin, *Magnetic Measurement of a Common Arc Dipole for Energy Upgrade Considerations*, Jefferson Lab Tech Note 98-032, 1998.

[4] PC-OPERA and OPERA-3D are products of Vector Fields Inc., 1700 N. Farnsworth Ave., Aurora, IL 60505

MAGNETIC MEASUREMENT OF THE PI BEND DIPOLE MAGNETS FOR THE IR-FEL AT THE THOMAS JEFFERSON NATIONAL ACCELERATOR FACILITY*

G. Biallas, D. Douglas, J. Karn, K. Tremblay#
Thomas Jefferson National Accelerator Facility, Newport News, VA

Abstract

A family of large bending dipoles has been successfully magnetically measured, installed and is operational in the high power IR-FEL. These magnets are unique in that they bend the beam 180 degrees on a 1 meter radius. The optics requirements for the magnets include low fields, large horizontal apertures, tight field homogeneity, high repeatability of core field & integrated field, and control of the horizontal & vertical focusing terms that are designed into the magnets. Quantifying the optics requirements proved to be a difficult task, due to the magnet's mechanical construction and sharp bending radius. The process involved in measuring and achieving the results are discussed.

1 INTRODUCTION

The free-electron laser at the Thomas Jefferson National Accelerator Facility has delivered its 1st light and in the process, broken the record for power developed by a free-electron laser by seventy times (710 watts)[1]. In order to increase the power to the desired 1 kW level, the beam is re-circulated through the elements to the CEBAF-style SRF cryomodule. At the return legs of the transport system are the pi-bend dipole magnets. The pi-dipoles have a design bend radius of 1 meter and a bend angle of 180°. In conjunction with these physical constraints were very tight tolerances for the magnetic field measurements. The physical design of the magnets required that a new test stand for the magnetic measurements be developed.

2 MAGNET MEASUREMENT REQUIREMENTS

The lattice design of the IR-FEL was tightly constrained due to the low energy, high current, and the 5% relative momentum spread of the re-circulated beam [2]. The pi-bending dipoles are one of 6 families that are used for beam transport in the IR-FEL. The total number of dipoles is 27. Table 1 summarizes the operating range requirements for the pi-bends. Table 2 displays the specifications for the mechanical design values. The optical and design values are listed in Table 3[3].

Parameter	Minimal	Nominal	Maximum
Energy (MeV)	33	42	79
Field (kG)	1.1008	1.4010	2.6352
Current (amps)	87.49	111.35	209.45

Table 1: Dipole Operating Range

Parameter (Unit)	Value
Distance between Coils (cm)	16.51
Length of Iron (cm)	309.02
Gap (cm)	5.08

Table 2: Mechanical Design Values

Parameter (Unit)	Value
Hysteresis Loop Current (amps)	$0 \rightarrow 220 \rightarrow 0$
Maximum Voltage (volts)	57.8
Effective Length (cm)	314.16
Good Field Width (cm)	11.00
End-Field roll-off integral (unitless)	0.27
Longitudinal field uniformity	$2x10^{-3}$/10cm

Table 3: Optical and Design Values

Measurement of the absolute core and integrated fields of the pi-bends was important since they were to be powered in series with several of the other dipole families. Precise control of excitation errors to avoid poor steering and focusing was necessary[4]. The tolerances for the magnetic field are listed in Table 4[3].

Constraint	Tolerance
Reproducibility of integrated field	$1x10^{-4}$
Accuracy of core field	$1x10^{-3}$
Accuracy of integrated field	$1x10^{-3}$
Tracking within dipole family	$1x10^{-3}$

Table 4: Dipole excitation error tolerances (rms.)

3 TEST STAND / PROBE CART

3.1 Hardware Setup

The pi-bend magnet presented many challenges when it came time to magnetically map the field. Typically, bend magnets at Jefferson Lab have been either an open face 'C' magnet design or one of a linear nature where a probe

*Work supported by the U.S. DOE under contract #DE-AC05-84ER40150

Email: tremblay@jlab.org

0-7803-5573-3/99/$10.00@1999 IEEE.

could be translated through the entire region. The 1 meter bend radius of the pi-bend magnets did not allow this. A probe mounted to a straight rod could only be inserted a few centimeters into the magnet.

A precisely manufactured wheel and cart which held two Group 3 Hall Effect Probes and two Metrolab NMR Teslameters was devised. The measurement wheel was manufactured in 4 sections allowing the magnet to be leveled and positioned precisely to a granite table without having to split the magnet. A sheet of 25mm aluminum plate was placed upon the granite table to facilitate the positioning of the wheel relative to the magnet. Figure 1 shows the magnet aligned to the table and the wheel. The long rod that hangs over the table was used to move the wheel through the dipole.

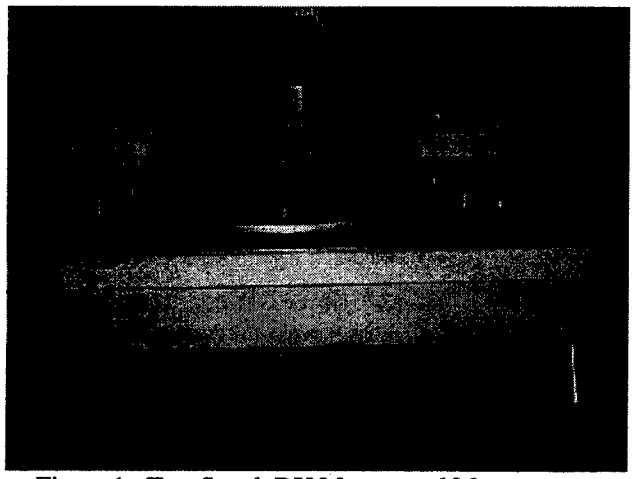

Figure 1: Test Stand, DY Magnet and Measurement Wheel

Once the magnet was positioned relative to the table, the wheel was threaded through the core, piece by piece. The bottom of the wheel was covered with a Teflon base which allowed easy movement of the wheel. Precision tooling balls had been placed onto the magnet during manufacture using a CNC machine to a tolerance of ± 0.08 millimeters. To ensure that the wheel was properly centered about the magnet, a theodolite alignment check was carried out. This verified the precision of the wheel and how well it had been centered about the pole face (approximately $\pm$ 0.15 millimetres).

To ensure that all areas of the good field would be mapped, the four probes were attached to a 1mm thick G10 panel, parallel to each other and separated by 22.2mm. The two Hall Probes were mounted on the outside of the panel, with the two NMR probes in the middle positions. This panel was then mounted to the cart, and moved to seven different transverse positions on the cart, one for each longitudinal measurement sequence. The seven positions (separated by 11.1mm) covered the good field region by collecting data at radii ranging from 93.3 cm to 106.7 cm. This in turn provided a method for verifying the Hall Probe calibration by overlapping a NMR probe path and a Hall Probe path along the same radial path.

3.2 Measurement Sequence

Figure 2 shows the beginning of the path that the longitudinal measurements take. The 1st measurement begins 30 centimeters perpendicular to the entrance point of the magnet. At this position the wheel is not moved, but rather the cart travels along a slot notched in the measurement wheel. The cart continues in a straight line until the entrance point is reached.

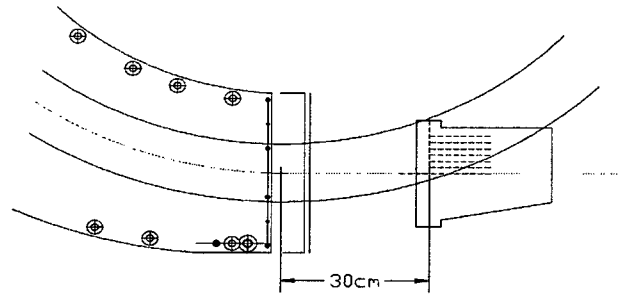

Figure 2: Plan View Cart and Pi-Bend Entrance

At the entrance point, the cart was locked to the wheel and then rotated through the magnet until the exit point was reached. At the exit, the cart was unlocked from the wheel and measurements were taken along a 30 centimetre line perpendicular to the exit. Figure 3 shows the cart entering the magnet. Seven runs were taken, moving the G10 sheet holding the probes to a new radial position on the cart. Probe readings were taken at each of the 361 positions along the path. Distances between measurements varied from 1 centimetre outside the magnets field, to 2 millimetres at the exit and entrances to the magnet, and 5 centimetres in the body of the magnet where the field was consistent.

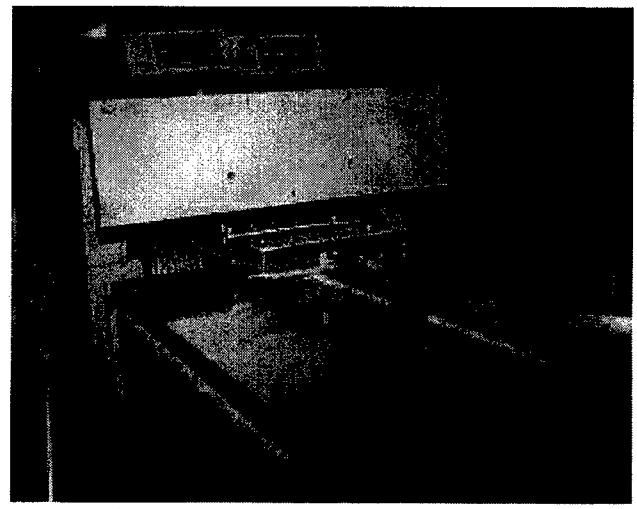

Figure 3: Cart Entering Pi-Bend Magnet

4 ANALYSIS

4.1 Probe Position Calibration

The longitudinal positions consisted of 2 straight line portions combined with a unique radial component for each of the seven positions. The wheel was checked dimensionally using a precise survey and then aligned to the magnet using tooling balls. A scale taped to the outside edge of the wheel and a pointer attached to the aluminium plate, determined wheel position along its path. Based on each of these positions, the precise location of the probes could be determined anywhere in the core.

4.2 Probe Calibration

Hall probes accuracy is dependant on the probe's perpendicularity to the field. To correct for this the hall probes were calibrated relative to the NMR probes. This was achieved by positioning the cart at the approximate magnet center and recording hall and NMR values at currents from 220 amps to 80 amps in 10 amp steps. This calibration was taken with the hall probes at the extreme outer positions and once when they straddled the center of the core.

4.3 Magnetic Data Calculation

Four measurement probes were read using the Jefferson Lab Stepper Stand Data Acquisition code developed using National Instruments Lab-Windows© software. The output files were then analyzed using Microsoft Excel©.

4.4 Results

Data for the 1st of the two pi-magnets was acquired and analyzed with little difficulty. There was some concern about the final effective length values (average deviation – 0.125%) and the end-field roll-off integral (K_1 deviation

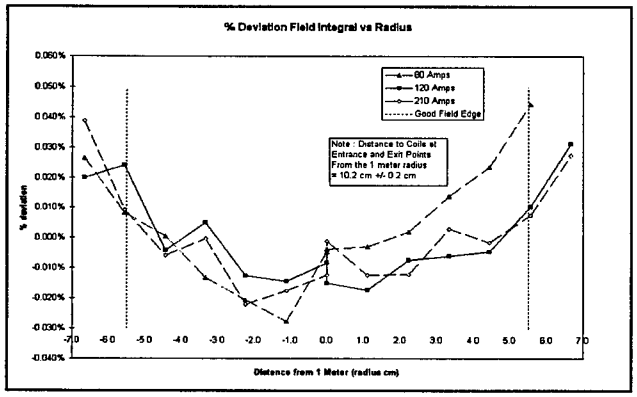

Figure 4: Deviation Field Integral vs Radius DY001

13.80%), but proper accelerator setup rendered these values acceptable. Figure 4 displays the deviation of the field integral as a function of the radius of the core, while Figure 5 shows the longitudinal field uniformity for the 1st dipole.

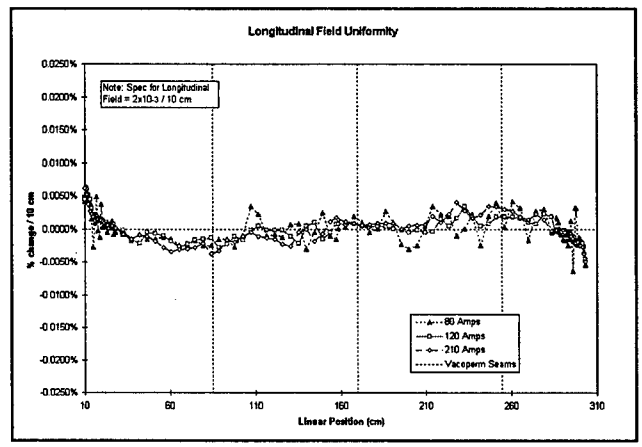

Figure 5: Longitudinal Field Uniformity DY001

The 2nd pi-magnet proved to be more cantankerous. As the data was being gathered and analyzed, problems became obvious. The calibration of the hall probes in the magnet center gave values that were similar to the first dipole, but once the longitudinal values were used as a check on this calibration, it appeared that there were large swings in the field strength, dependant upon location. As there were only 2 magnets in the sample, concerns arose as to the validity of the measurement method.

The magnet was disassembled to check for the source of the inconsistencies. The problem was traced to the installation of a brass layer between the poles and top layer of mumetal. The mumetal and brass layers had been added to the poles to improve field flatness[4]. These layers were reworked and the magnet reassembled. Measurements then continued and results similar to the first dipole were obtained.

5 CONCLUSIONS

The test stand design proved to be an efficient method to accurately map the pi-bend magnets. Results obtained by the mapping were used in conjunction with the optical steering of the beam to assist in the successful delivery of light at the IR-FEL facility.

REFERENCES

[1] F. Dylla and G. Neil, IR Demo Project Weekly Report for March 8-12,1999, Thomas Jefferson Accelerator Facility News Release, March 1999.

[2] D. R. Douglas, Lattice Design for a High-Power Infrared FEL, Proceeding of IEEE Particle Accelerator Conference, Vancouver, British Columbia, Canada, 1997.

[3] D. R. Douglas, Error Estimates for the IR FEL Transport System, Jefferson Lab Tech Note # 96-035, 1996.

[4] J. Karn, et al., Magnetic Measurement of the Prototype Dipole for the IR-FEL at the Thomas Jefferson National Accelerator Facility, Proceeding of IEEE Particle Accelerator Conference, Vancouver, British Columbia, Canada, 1997.

HYSTERESIS STUDY TECHNIQUES AND RESULTS FOR ACCELERATOR MAGNETS WITH UNIPOLAR CURRENT EXCITATION

B. C. BROWN,* Fermi National Accelerator Laboratory † P.O. Box 500, Batavia, IL 60510

Abstract

Using an automated magnet measurement system employing a variety of current excitation ramps, extensive studies of the hysteretic behavior of magnet strength have been carried out. An analytic description which is accurate at better than 0.1% has been achieved. Prescriptions for setting field strength using these formulas will be adequate for multi-energy operation of the Fermilab Main Injector, for deceleration in the Main Injector and Accumulator and for multi-energy operation of various beamline magnets. An overview of this work is provided. Important regularities of the magnet behavior are identified.

1 INTRODUCTION

Accelerator and Beam Line systems at Fermilab have a variety of operating modes which require knowledge of the hysteretic behavior of magnet systems. Measurement strategies have been developed[1] to achieve the needed knowledge of the behavior of a variety of magnet systems. To prescribe the current *vs.* time profile which matches a required field strength *vs.* time requires further development. Interpolation schemes are made complex by the strong dependence of the field on current history in addition to the dependence on magnet current. A strategy of restricting operation to use only excitation histories which match measured histories would permit a simple interpolation but is considered unnecessarily restrictive. A scheme which attempts to properly interpolate in both preparation history and magnet current is assumed to be of sufficient complexity as to compromise algorithmic reliability. We choose to develop an analytic description of sufficient complexity and precision. Using this description, software which controls the magnet power supplies can calculate the field strength produced at all times along any prescribed magnet current history. The goal of this work was to achieve a relative strength error of a few parts in 10,000 at all strengths for a variety of ramping options which match all known requirements. The measurements were designed with the hope of characterizing any simplifying regularities over a range beyond any expected operational requirements.

2 RAMP PROFILES FOR MEASUREMENTS

Based on experience in characterizing various magnet systems, we have assumed that, for the magnets under study which have copper coils, iron-dominated field shapes and yokes comprised of thin laminations (1.5 mm typical thickness), the field is essentially static when the current is constant. Measurements are performed at constant current using a rotating full length cylindrical coil. Coil rotation times are characteristically about 1 second and the rotation begins many milliseconds after the completion of current changes. Eddy current and flux flow effects are largely complete following each current change before measurements begin.

We use the term *ramp* to characterize a portion of a larger ramp cycle[2] in which the sign of dI/dt is constant. The reset current for a ramp occurs at the beginning of the ramp where the sign of dI/dt has just changed. For this analysis we describe a preset current which is the reset current of the immediately preceding ramp. We believe that reversals of the sign of dI/dt prior to the preset current have small effects.

The current control has proven to be very precise, permitting repeated measurements at the same current setting to achieve the same value to $\approx 3 \times 10^{-5}$. However the current measurement involves additional electronics and has shown, for some of the studies, changes of more than 1 A. Some of the analysis will employ a recalibration of the requested current rather than using the measured current.

3 TYPICAL HYSTERESIS STUDY DATA

In Figure 1 we show the non-linear portion of the measured strength of a Main Injector dipole as measured on a pattern of current histories. We note a pattern which we describe by an upramp or downramp state. These states are approached approximately exponentially following a reversal of dI/dt. We identify these as upramp or downramp *hysteresis* curves. They may depend at most weakly on the reset and preset current. We identify the strength curve which connects from the down ramp *hysteresis* curve at reset and approaches the upramp curve as the *interjacent* curve.

Figures 2 and 3 explore limits to the algorithms we are developing. We see that the field remaining after a ramp depends weakly on the peak current to which it was driven (downramp reset current). After a reset, the magnetic state approaches the upramp or the downramp state closely but small differences remain.

This small effect becomes even smaller after the field is reversed again. We explored this with a different study in which the upramp response was examined after preset currents of 9500 A and 7100 A. The measurement was repeated six times for each preset current. The results in Figure 4 confirm that there is an effect. Ramping from 0 A to 500 A has greatly decreased the magnitude of this preset current dependence. We conclude that the difference in strength between 7100 A (120 GeV) preset currents and

*Email: bcbrown@fnal.gov

† Work supported by the U.S. Department of Energy under contract No. DE-AC02-76CHO3000.

0-7803-5573-3/99/$10.00@1999 IEEE.

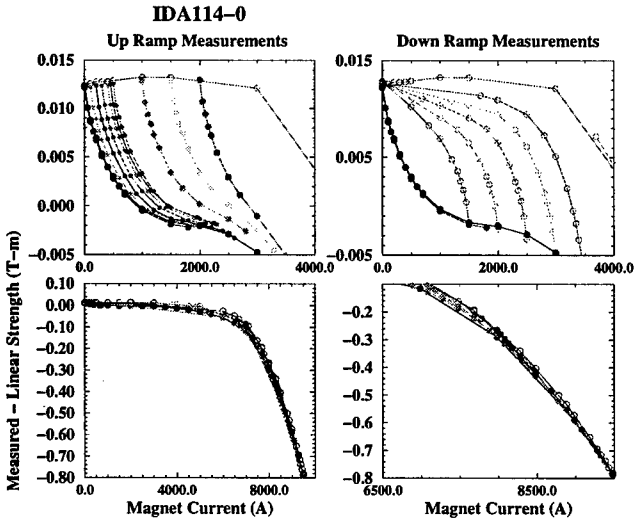

Figure 1: Measured non-linear strength for IDA114-0 with a variety of histories. The linear response is characterized by fitting the strength for currents below 2000 A (about 0.8 T) after excitation to about 9500 A. Each plot shows data at many currents on an upramp to 9500 A then on a down ramp to 0 A. Upramp data is shown using filled circles while downramp data uses open circles. On the upper right is also data on down ramps following a variety of peak currents. On the upper left data on up ramps following a variety of reset currents is shown. The lower left plot shows the complete data set. The lower right plot expands the data near the peak of the saturation.

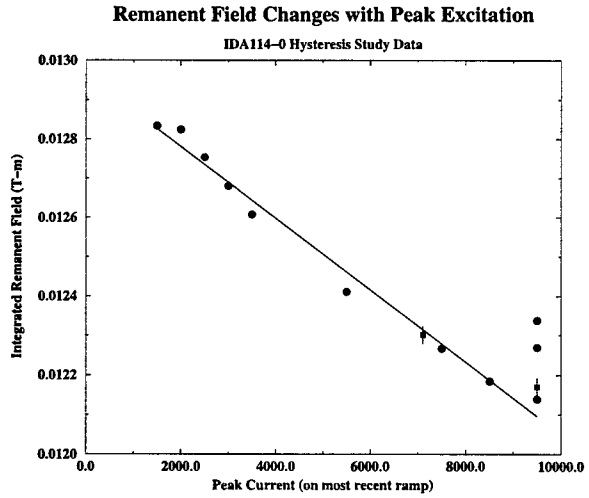

Figure 2: Remanent changes for IDA114-0.

9500 A (150 GeV) is 4.4 ± 2.4 × 10^{-5} T-m. Measurements at nearby currents determine the change in strength for a change in the preset current. At 500 A, we observe a change of 1.75 × 10^{-5} T-m/A. This predicts that a change of less than 3 A in the reset current would compensate differences between 120 GeV and 150 GeV ramp preset currents. Since the nature of these effects is not known, we are not surprised that measurements of related effects using the

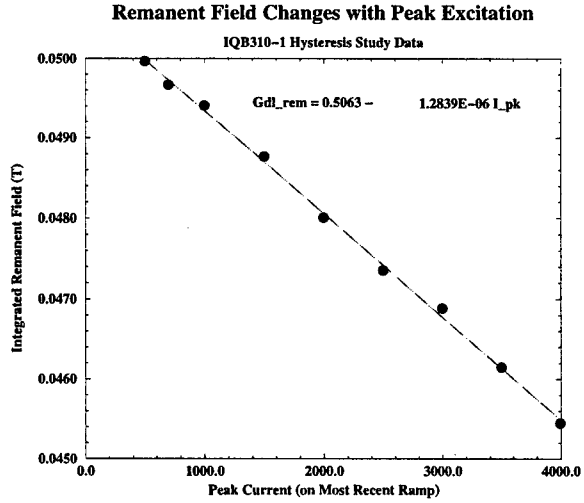

Figure 3: Remanent changes for IQB310-1.

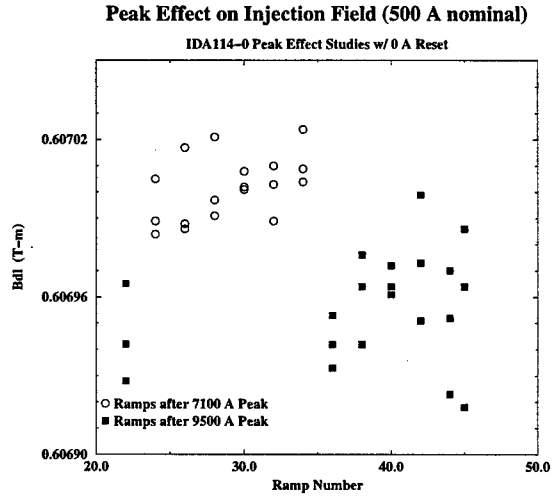

Figure 4: Studies of changes in Main Injector dipole injection field after 120 GeV and 150 GeV ramps.

beam momentum to sense the field showed that nearly 20 A was needed in a preliminary measurement[3].

4 ANALYTIC DESCRIPTION

To describe the data shown in Figure 1 above, we consider the magnet strength M ($\int B_1 dl$, $\int B_2 dl$ or $\int B_3 dl$) to be comprised of four terms, L (linear), R (remanent), H (hysteretic) and J (interjacent) . We continue to explore suitable expressions for these contributions but find that the goals stated above are met with the following functional relations:

$$M(I, I_r, I_p, D) = L(I) + R(I_p, D) + H(I, D) + J(I, I_r, I_p, D)$$

where I is the magnet current during the measurement, I_r is the reset current, I_p is the preset current, and D is the ramp direction with +1 for upramps and -1 for downramps. We express the relations with normalized variables to provide

consistency of representation among magnets. Use I_{scale} as a maximum current of interest (rounded) and I_S as a characteristic current for saturation.

$$x = \frac{I - I_S}{I_{scale}} \quad x_0 = \frac{-I_S}{I_{scale}} \quad L(I) = Slope * I$$

$$R(I_p, D) = RemStr_D + RemSlp_D * (I_p - I_{scale})$$

$$H(I, D) = C_1 * I/I_{scale} - \sqrt[4]{h_4}x - \sqrt[4]{h_4x^4 + h_3x^3 + h_2x^2 + h_1x + h_0} + \sqrt[4]{h_4}x_0 + \sqrt[4]{h_4x_0^4 + h_3x_0^3 + h_2x_0^2 + h_1x_0 + h_0}.$$

Note that H is defined to have the value 0 at $I = 0$. Each parameter is distinct for the upramp or downramp curve and could be expressed as h_{iD} or C_{1D} . Two forms have been used for fitting J:

$$J(I, I_r, I_p, D) = A(I_r, I_p, D)(se^{-\frac{I-I_r}{I_{C1,D}}} + (1-s)e^{-\frac{I-I_r}{I_{C2,D}}})$$

$$J(I, I_r, I_p, D) = A(I_r, I_p, D)e^{-(\frac{I-I_r}{I_{C,D}})^N}$$

where N is a real number, typically less than 1. The amplitude function A is the difference in hysteresis curves at the reset current.

$$A(I_r, I_p, D) = H(I_r, -D) - H(I_r, D) + R(I_p, -D) - R(I_p, D).$$

A software system to extract data from the Sybase measurement database and fit the results using MINUIT[4] has been developed with Perl and FORTRAN. If all parameters are released for fitting, the system is usually not stable so a manual interaction is interposed to permit separate fitting of various subsets of the parameters.

Data from IDA114-0 and IQB310-1 have been fitted successfully. Residuals reveal a pattern (not random) suggesting that the structure of the data is yet to be fully accounted for with these fitting functions. However, the pattern remaining confirms that the parameters which control the shape of the interjacent curves are the same over a wide range of magnet excitation levels. The relative magnitude of the residuals is less than 3×10^{-4} at all currents for both of these data sets when compared to the full magnet strength at the same current. This is sufficient for existing accelerator control needs. Figure 5 shows portions of the fits at low fields to the non-linear portion of the strength along with the resisuals for all the data. We plan to characterize the full set of measurements for Main Injector dipoles and quadrupoles by fitting the available production measurements to determine the linear, hysteretic, and remanent terms, constraining the remanent slope and the interjactent terms from the special study data. Parameters used for the commissioning of the Main Injector[3] were determined from these two magnet measurements but with cruder fits to a simpler function, achieving residuals of about 0.1%.

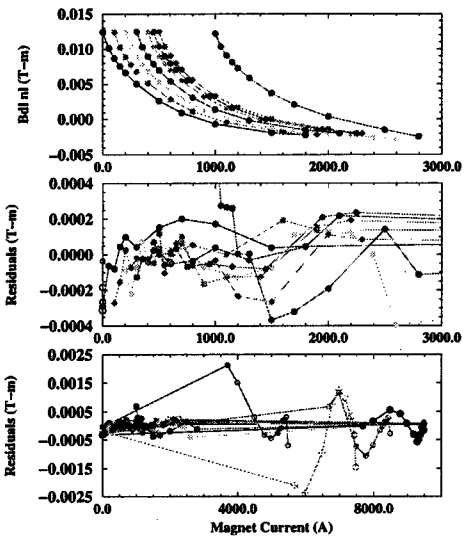

Figure 5: Selected data from the IDA114-0 hysteresis study were fit with the interjacent curve described by 2 exponentials. Top plot shows fits to the selected upramp data. Center and lower plots show residuals (measured - fitted) on scales which emphasize the low field and high field results.

5 SUMMARY

Measurement plans and analysis tools have been developed for studying the hysteretic magnetic strength of accelerator and beamline dipole, quadrupole and sextupole magnets which experience excitation currents of only one polarity. Guidance for changing currents during tuning or for multi-energy operation of beamline is obtained directly from plots of the non-linear strengths. For a more detailed understanding, we have developed a model, expressed in analytic fitting functions which describes the strength of electromagnets in terms of distinct hysteretic states for upramp and downramp operation, with transitions between these states which are described by interjactent curves. We suspect that an adequate description might become more complex for symmetric or asymmetic bipolar operation. However, sextupoles which have been measured with modest excitations with reversed current still show similar behavior.

6 REFERENCES

[1] B. C. Brown *et al.* Results on Fermilab Main Injector Dipole Measurements. *IEEE Trans. on Magnetics*, 32:2186, 1996.

[2] Bruce Brown, Dave Harding, and James W. Sim. Design of the **currents** Virtual Database. Technical Report MTF-92-0011 1.3, Fermilab, July 1992.

[3] G. WU *et al.* Tune Control in the Fermilab Main Injector. This Conference (PAC99).

[4] F. James. Minuit function minimization and error analysis. CERN Program Library Long Writeup D506, CERN, Geneva, Switzerland.

STRENGTH AND SHAPE OF THE MAGNETIC FIELD OF THE FERMILAB MAIN INJECTOR DIPOLES*

D.J. Harding#, B.C. Brown, J. Dimarco, H.D. Glass, P.S. Martin, P.O. Mazur, C.S. Mishra, D.F. Orris, J.W. Sim, J.C. Tompkins, K. Trombley-Freytag, D.G.C. Walbridge, Fermi National Accelerator Laboratory, P.O. Box 500, Batavia, IL 60510 USA

Abstract

Measurements of 230 6-meter and 136 4-meter dipoles constructed for the Fermilab Main Injector were carried out as part of the magnet production effort. An automated measurement system provided data on magnetic field strength and shape using several partially redundant systems. Results of these measurements are available for each individual magnet for use in accelerator modelling. In this report we will summarise the results on all of the magnets to characterise the properties which will govern accelerator operation.

1 INTRODUCTION

Over the last decade the Fermilab Main Injector and its magnets have been planned [1,2], designed [3,4,5,6] prototyped [7,8,9,10], produced [11,12], measured [13,14,15,16,17,18], installed [19], and commissioned [20,21]. Every dipole has been measured thoroughly, providing a rich set of data that is used for magnet assignments and beam modeling. Here we present an overview to give a flavor of the Main Injector dipoles.

In all, 230 6-meter and 136 4-meter dipoles were built and measured, including spares. These may be divided into several groups whose behavior differs for well-understood reasons: 1) Six 6-m R&D dipoles, 2) Six 4-m R&D dipoles, 3) the first 46 6-m dipoles, 4) the balance of the 6-m dipoles, and 5) the balance of the 4-m dipoles. Groups 1 and 2 were built with steel from Vendor A. Group 2 was built too long by 2.5-mm. Group 3 was built all or in part from steel from Vendor B's first production run. Groups 4 and 5 were built entirely with steel from Vendor B's later runs.

The integrated strength and the harmonic composition of the magnetic field was measured at multiple currents using a rotating tangential probe that extended through the magnet following the path of the beam. Field strength and shape were also measured using an integrating coil that could be held on center as the current ramped or moved transversely at a fixed current. A sample of magnets was further measured with an NMR and Hall probe package that scanned the magnet longitudinally.

* Work supported by the United States Department of Energy under contract No. DE-AC02-76CH03000.

Email: harding@fnal.gov

2 MAGNET STRENGTH

Groups 4 and 5 define our nominal magnet strength at each current. The mean strength, including the 4-m magnets weighted at 2/3 of the 6-m magnets, was calculated for each current. Deviations from that strength (for the 6-m magnets) or from 2/3 of that strength (for the 4-m magnets) are normalized to the nominal strength of the 6-m magnets. These deviations are quoted here in "units" of parts in 10^4.

Figure 1 shows the distribution of deviations of magnet strength from nominal for all magnets as a function of magnetic field. The profile is dominated by a narrow peak around the nominal strength composed primarily of Groups 4 and 5. The standard deviation of the distribution, due to variations in magnet length, magnet gap, steel properties, and random measurement errors, is in the range of 2 to 4 units.

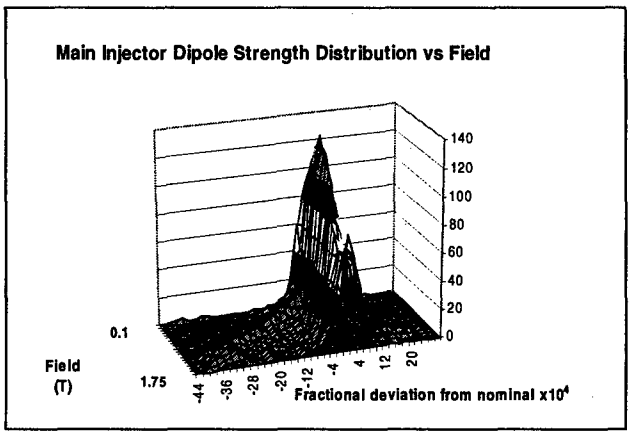

Figure 1: Main Injector dipole magnet strength distribution as a function of field. The field ranges from the injection value of 0.1 T to its peak of 1.75 T.

A second, lower ridge branches from the main stem at about 0.3 T and diverges to lower strength roughly linearly. These are Group 3 magnets with early steel from vendor B. [22] A handful of magnets appear below the nominal peak at 0.1 T, and the same magnets appear above the peak around 1.5 to 1.6 T. These are Groups 1 and 2 showing first a lower remanent field and then slower saturation. A modification to the back leg has allowed us to match the nominal field at 1.4 T and at 1.7 T, though it runs high in between.[23] The identity of

0-7803-5573-3/99/$10.00@1999 IEEE.

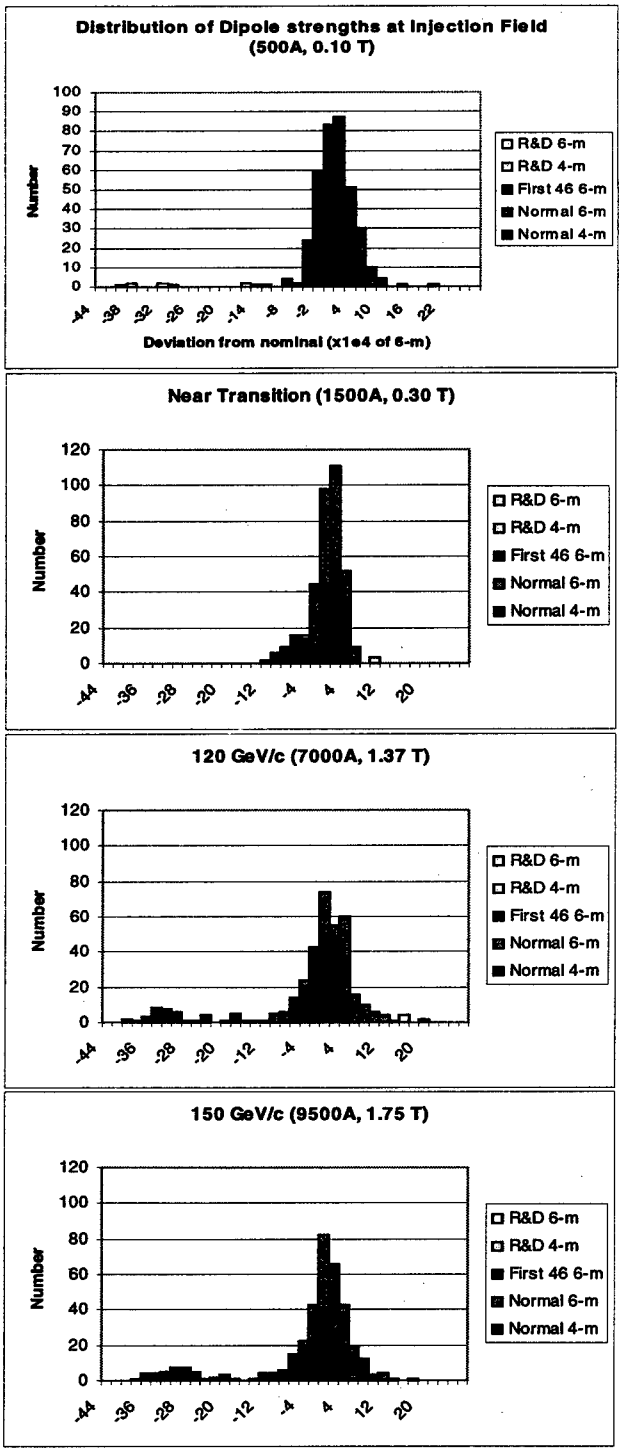

Figure 2: Distribution of magnet strength at four key excitations.

these groups of magnets is clear in the histograms of Figure 2 which represent slices though the Figure 1 mountain range.

The hysteresis in the dipoles has also been studied. The variety of operational modes requires that it be included in control systems calculations.[24,25]

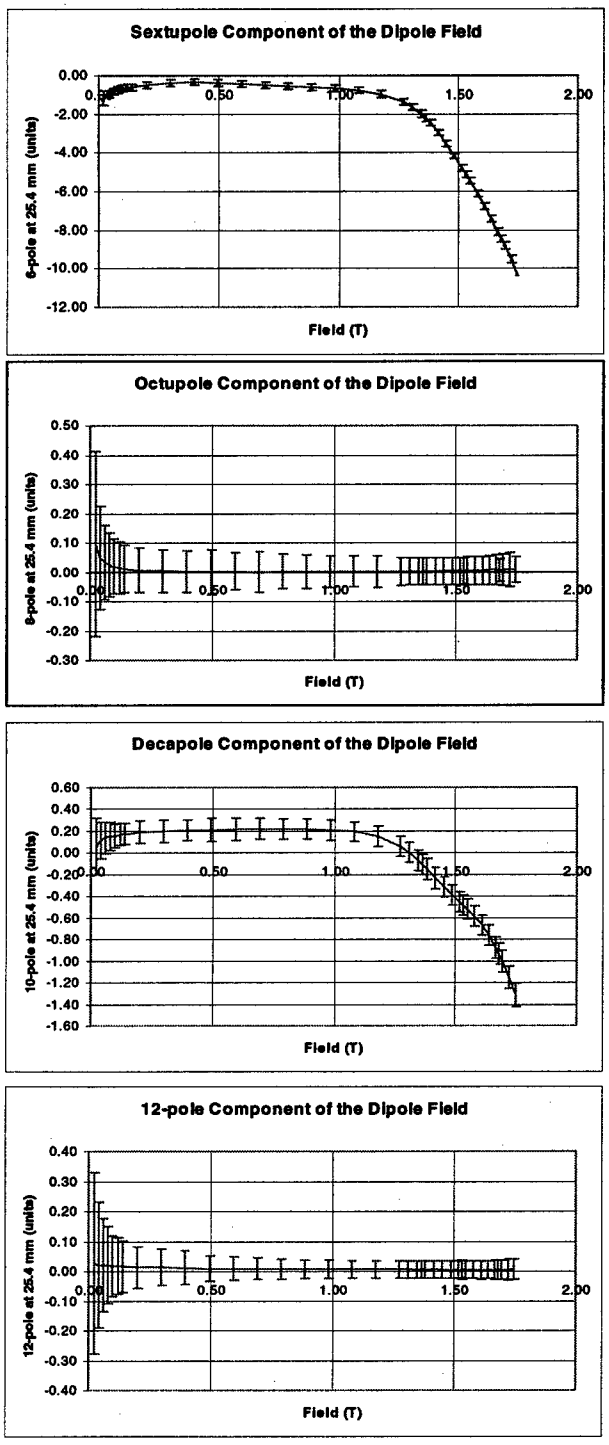

Figure 3: Multipole components of the dipole magnets as a function of magnetic field. The ordinate scales vary.

3 HARMONICS

We characterize the variation of the magnet field across the aperture by the coefficients of its harmonic decomposition. The coefficient we quote is the fraction of the field due to the component in question at 25.4 mm (typical of the maximum beam size) relative to the dipole component in "units" or parts in 10^4.

Figure 3 shows the distribution of the normal sextupole, octupole, decapole, and 12-pole as a function of magnetic field. The error bars represent one standard deviation. Note that the plots extend below the injection field of 0.10 T. As expected, we see some contribution of even terms as the steel saturates, reflecting the symmetry of the magnet, but the design and fabrication process minimizes the antisymmetric terms.

In operation, a significant sextupole field is also generated by eddy currents in the beam tube.[26,27]

4 CONCLUSION

Although the variation in steel properties prevented the overall Main Injector dipole strength variation from meeting expectations, within a steel run the uniformity was excellent. The field shapes meet the project requirements.[28] The non-standard magnets have been assigned locations in the ring where they produce small, local two-bumps, minimizing their impact on the closed orbit.[29]. Care has been taken to reserve a suitable collection of spare magnets to allow replacement of any magnet with a like magnet.

Purchasing all the steel before the project was funded would have alleviated the strength variation by increasing the uniformity of the steel and permitting homogenization of the magnet cores. In the end, the cost and schedule savings enabled by the phased steel purchases justify the extra effort required.

5 REFERENCES

[1] S.D. Holmes *et al.*, "The Fermilab Upgrade", In *Proceedings of the 1989 Particle Accelerator Conference*, Chicago, (1989).

[2] S.D. Holmes, "Tevatron Performance Goals for the Coming Decade", In Proceedings this Conference, (1999).

[3] *The Fermilab Main Injector Technical Design Handbook*, (Fermilab, Batavia, 1997).

[4] D.J. Harding *et al.*, "Design Considerations and Prototype Performance of the Fermilab Main Injector Dipole", In *Proceedings of the 1991 Particle Accelerator Conference*, San Francisco, (1991).

[5] M. Bleadon *et al.*, "The Fermilab Main Injector Dipole Construction Techniques and Prototype Magnet Measurements", Presented at the 12th International Conference on Magnet Technology, Leningrad, (1991).

[6] B.C. Brown *et al.*, "The Design and Manufacture of the Fermilab Main Injector Dipole Magnet", Presented at the EPAC Conference, Berlin, (1992).

[7] J. Ostiguy, "Magnet End Design: The Main Injector Dipoles", In *Proceedings of the 1991 Particle Accelerator Conference*, San Francisco, (1991).

[8] J. Ostiguy, "Longitudinal Profile and Effective Length of a Conventional Dipole Magnet", In *Proceedings of the 1993 Particle Accelerator Conference*, Washington, (1993).

[9] H. D. Glass, "Techniques for Measurement of Dipole Endfields with a Rigid Integrating Coil", In *Proceedings of the 1993 Particle Accelerator Conference*, Washington, (1993).

[10] D.J. Harding *et al.*, "Design and Measurements of Prototype Fermilab Main Injector Dipole Endpacks", In *Proceedings of the 1993 Particle Accelerator Conference*, Washington, (1993).

[11] D.J. Harding *et al.*, "Experience with the Source Evaluation Board Method of Procuring Technical Components for the Fermilab Main Injector", In *Proceedings of the 1993 Particle Accelerator Conference*, Washington, (1993).

[12] A.D. Russell *et al.*, "Selecting Magnet Laminations Recipes Using the Method of Simulated Annealing", In *Proceedings of the 1997 Particle Accelerator Conference*, Vancouver, (1997).

[13] H. D. Glass *et al.*, "Flatcoil Systems for Measurements of Fermilab Magnets", Presented at the Fourteenth International Conference on Magnet Technology, Tampere, Finland, (1995).

[14] B.C. Brown *et al.*, "Software Design for a Database Driven System for Accelerator Magnet Systems", In *Proceedings of the 1991 Particle Accelerator Conference*, San Francisco, (1991).

[15] J.W. Sim *et al.*, "A Relational Database for Magnets and Measurement Systems at the Fermilab Magnet Test Facility", In *Proceedings of the 1995 Particle Accelerator Conference*, Dallas, (1995).

[16] J.W. Sim *et al.*, "Software for a Database-Controlled Measurement System at the Fermilab Magnet Test Facility", In *Proceedings of the 1995 Particle Accelerator Conference*, Dallas, (1995).

[17] D.J. Harding *et al.*, "Magnetic Field Measurements of the Initial Fermilab Main Injector Production Dipoles", In *Proceedings of the 1995 Particle Accelerator Conference*, Dallas, (1995).

[18] B.C. Brown *et al.*, "Results on Fermilab Main Injector Dipole Measurements", Presented at the Fourteenth International Conference on Magnet Technology, Tampere, (1995).

[19] J.A. Satti, "The Fermilab Main Injector Dipole and Quadrupole Cooling Design and Bus Connections", In *Proceedings of the 1995 Particle Accelerator Conference*, Dallas, (1995)

[20] P.S. Martin *et al.*, "Fermilab Main Injector Commissioning Status", In Proceedings this Conference, (1999).

[21] C.S. Mishra, "Simulation and Measurements of the Fermilab Main Injector Dynamic Aperture", In Proceedings this Conference, *(1999)*.

[22] P.S. Martin *et al.*, "Variations in the Steel Properties and the Excitation Characteristics of Fermilab Main Injector Dipoles", In *Proceedings of the 1997 Particle Accelerator Conference*, Vancouver, (1997).

[23] P.S. Martin *et al.*, "Modifications to the Excitation Characteristics of Fermilab Main Injector Dipoles by Machining", *Proceedings of the 1997 Particle Accelerator Conference*, Vancouver, (1997).

[24] B.C. Brown *et al.*, "Design for Fermilab Main Injector Magnet Ramps which Account for Hysteresis", In *Proceedings of the 1997 Particle Accelerator Conference*, Vancouver, (1997).

[25] B.C. Brown *et al.*, "Analytic Fits to Hysteretic Fields in Main Injector Dipoles, Quadrupoles and Sextupoles", In Proceedings this Conference, (1999).

[26] D.G.C. Walbridge *et al.*, "Measurements of Beam Pipe Eddy Current Effects in Main Injector Dipole Magnets", Presented at the XVth International Conference on High Energy Accelerators, Hamburg, (1992).

[27] D.G.C. Walbridge *et al.*, "Field Errors Introduced by Eddy Currents in Fermilab Main Injector Magnets", In *Proceedings of the 15th International Conference on Magnet Technology*, Beijing, (1997).

[28] F.A. Harfoush *et al.*, "Defining the Systematic and Random Multipoles Errors for Main Injector Tracking," In *Proceedings of the 1993 Particle Accelerator Conference*, Washington, (1993).

[29] P.S. Martin *et al.*, "Excitation Characteristics of Fermilab Main Injector Dipoles and Magnet Assignment to Reduce Closed Orbit Errors", In *Proceedings of the 1997 Particle Accelerator Conference*, Vancouver, (1997).

Magnetic Field Alignment in the Beam-Beam Compensation Device

C. Crawford, A. Sery, V. Shiltsev, FNAL , Batavia, IL
A. Aleksandrov, B. Skarbo, B. Sukhina, BINP, Novosibirsk, Russia

Abstract

Guiding solenoidal magnetic field of the Tevatron beam-beam compensation device has to be carefully aligned with respect to a straight trajectory of the antiproton beam. We present in this paper an optical method which allows to measure the direction of the magnetic field, results of magnetic measurements, and results of the field quality improvement with dipole correctors.

1 INTRODUCTION

Beam-beam interactions in the planned Tevatron upgrades Run II and TEV33 will cause betatron tune spread within bunch as well as bunch-to-bunch tune spread which will be high enough to enhance diffusion of particles due to high order resonances and to limit beam lifetime and luminosity.

Some of these beam-beam effects can be compensated by use of a counter-traveling electron beam ("electron lens") with appropriate charge distribution, which will apply additional linear or nonlinear defocusing for the antiproton beam, while it will pass through the electron beam [1]. Compensation of the beam-beam effects only for the antiprotons is sufficient since the proton bunch population is significantly higher than the antiproton bunch population.

Parameters of the electron beam for the beam-beam compensation are: beam current $J_e = 2$ A, beam radius $a = 1$ mm, beam length $L_e = 2$ m, energy $U_e = 10$ kV. The electron beam should be born in a weak magnetic field, and then, in order to provide sufficient "rigidness" of the electrons and also to increase the electron current density by means of the adiabatic magnetic compression of the beam, injected and transported in a strong longitudinal magnetic field. Considerations of electron beam distortions by the antiproton bunch and of a possible electron beam driven head tail instability in the antiproton beam suggested that the magnitude of the longitudinal magnetic field in the region where the antiprotons pass through the electron beam should be about 4–5 Tesla, while the field at the cathode of the electron gun should be about 0.1–0.2 Tesla [1].

2 FIELD QUALITY REQUIREMENTS

The electrons are highly magnetized in a guiding magnetic field of the beam-beam compensation device and thus follow the direction of the field, while the trajectory of the antiprotons, due to their high energy, is almost straight in the beam-beam compensation device. The straightness of magnetic field is therefore essential for the beam-beam compensation to work properly. Deviation of the electron trajectory from the straight line should be $\Delta x_e \lesssim 0.1a$ that is about 0.1 mm. The electron beam deviation is equal to:

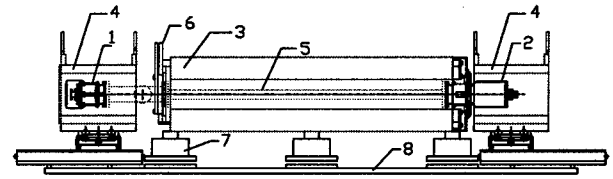

Figure 1: Prototype of the beam-beam compensation device. 1– electron gun, 2– collector, 3– 4kG solenoid with 16 pairs of dipole corrector coils, 4– gun and collector solenoids, 5– vacuum pipe, 6– current input/output for main solenoid, 7– adjustable supports, 8– assembly table.

$$x_e(z) = \int^z (B_\perp / B_\parallel)\, dz'. \qquad (1)$$

The requirement on the transverse field then depends on the wavelength λ of the field imperfection:

$$B_\perp(\lambda)/B_\parallel \lesssim \Delta x_e\, 2\pi/\lambda.$$

For the longest relevant wavelength ($\lambda \approx 2L_e$) we get $B_\perp/B_\parallel \lesssim 1.5 \cdot 10^{-4}$ that is comparable with what is typically required in electron cooling devices. However, in our case the requirement becomes less stringent for shorter wavelength λ, in contrast with electron cooling magnetic systems. The problem of the field straightness measurement and its correction is nevertheless an important issue, which inspired development of a suitable technique that has been tested at a prototype of the beam-beam compensation device recently commissioned at Fermilab [2].

The goals of the prototype (see Figure 1) were to obtain a low energy ($\lesssim 10$ kV) 2-meter long electron beam with total current up to 2A propagating in a precise solenoid magnet, to test the current modulation in a few MHz bandwidth, and to study the electron beam dynamics. Parameters of the experimental installation are about the same as for the full scale device to be used in the Tevatron, except for a lower magnetic field and thus lower electron current density in the central solenoid.

The "electron-lens" prototype magnetic system consists of the main solenoid (2 meter long, 4 kG maximum field) and two additional solenoids (0.5 meter long, maximum field about 4 kG) where the gun and collector are installed. The solenoids of the prototype are warm while the full scale device will require the main solenoid to be superconductive. The field in all solenoids can be changed independently, which provides a possibility to compress adiabatically the electron beam in the main solenoid and also to optimize the collector efficiency (see Figure 2). The field straightness tolerance is applicable only to the field in the main solenoid.

0-7803-5573-3/99/$10.00@1999 IEEE.

The main solenoid consists of two 0.96 meter long sections. The sections have been designed and built for an electron cooling set-up MOSOL [3]. The sections are placed on adjustable supports which provides their relative alignment. The coil of the main solenoid is a precisely fabricated single layer copper spiral with 32 turns per section and with internal diameter 20 cm. The spiral cross-section is 26×34 mm, the current corresponded to 4 kG field is about 10 kA. In order to provide reliable electrical connection between two sections with such a high current density, precisely matched flat surfaces of the corresponding spiral edges of two sections were connected with high stress provided by four titanium wedge bolts. Total force applied to the contact is about several tons. A thin indium foil is placed between surfaces to increase the effective area of the contact. The current is returned to the commutation end by 8 straight copper bars which have been aligned in parallel with the solenoid axis. Special measures have been taken to distribute the return current evenly amongst the bars in order to ensure that the field direction coincide with the geometrical axis of the main solenoid.

Fine alignment of the magnetic field is provided by 4 pairs of 50 cm long and 12 pairs of 12 cm long dipole corrector coils installed atop the main solenoid in both planes. The short coils are placed at the ends of sections and the long coils in the center. Each pair of coils is fed by separate ±2 A power supply and can produce up to ±20 G at the solenoid axis. One additional dipole coil is installed in the gap between collector solenoid and the main solenoid. This coil compensates field distortion produced by current commutation of the main solenoid.

3 FIELD MEASUREMENTS AND ALIGNMENT

The probe that allows to measure the direction of magnetic field is a flat mirror with attached magnetic arrow (see Figure 3). The mirror has 2 degrees of freedom so that it is oriented along magnetic field lines allowing optical measurements of the field imperfection. The diameter of the reflective surface is 21 mm, diameter and length of the arrow are

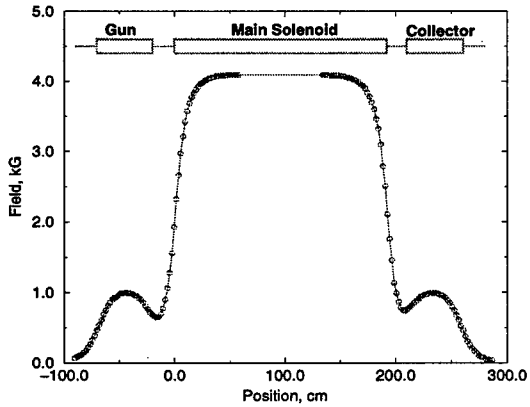

Figure 2: Longitudinal magnetic field in the "electron lens" prototype.

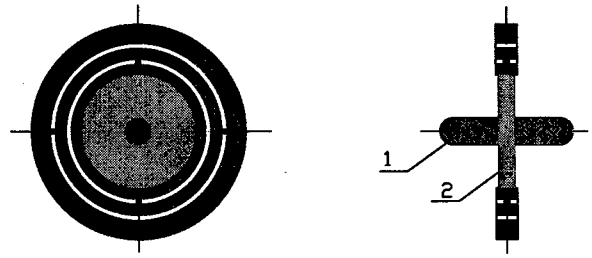

Figure 3: Mirror with magnetic arrow. 1– arrow, 2– reflective surface.

$2r_a = 5$ mm and $l_a = 25$ mm. The mirror is installed on a special nonmagnetic wheeled cart. The mirror with the magnetic arrow is the most delicate part of this measurement scheme. The mirror has to be sufficiently flat, it must be well balanced and the friction in axis should be small. We use a mirror previously used for similar measurements at the IUCF electron cooler [4].

Autocollimators are widely used for similar measurements in electron cooling devices. Since our field quality requirements are less stringent, we have chosen less expensive technique based on a use of a laser beam and two-dimensional Position Sensitive Device (PSD). Signal of a PSD is proportional to the laser spot displacement with respect to the PSD center.

The scheme of measurements is shown in the Figure 4. Diode laser delivers a red light beam with $\lambda = 670$ nm, initial beam size 3 mm and total beam divergence 0.35 mrad, which provides acceptably small beam spot at the mirror. The PSD (produced by Hamamatsu) has a 13 × 13 mm^2 working area, sensitivity of about 1 V/mm, and resolution of about 5 μm. An optical filter in front of the PSD is necessary to separate only the laser wavelength in order to decrease background of the PSD. The laser, a beam splitter, the filter and the PSD were assembled all together and placed at about 1 m from the collector solenoid. The assembly was placed on a mover which allowed position and angular correction in two transverse planes in order to align the system with respect to the axis of the main solenoid.

An aluminum tube (380 cm long, 10 cm diameter) was placed inside the solenoid on axis to provide a guide for the mirror cart. The cart can move along the tube by means of a plastic belt and a stepping motor placed in the field free region near one end of the tube. Standard Hall probes with longitudinal and transverse sensors can be optionally installed on the cart. The PSD signals are preamplified and

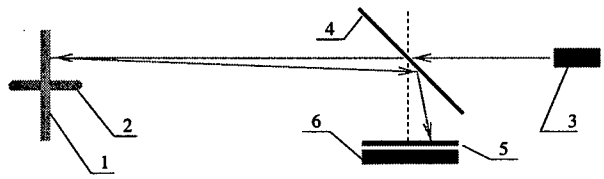

Figure 4: Scheme of measurements. 1 and 2 – mirror with magnetic arrow, 3– diode laser, 4– beam splitter, 5– optical filter, 6– PSD.

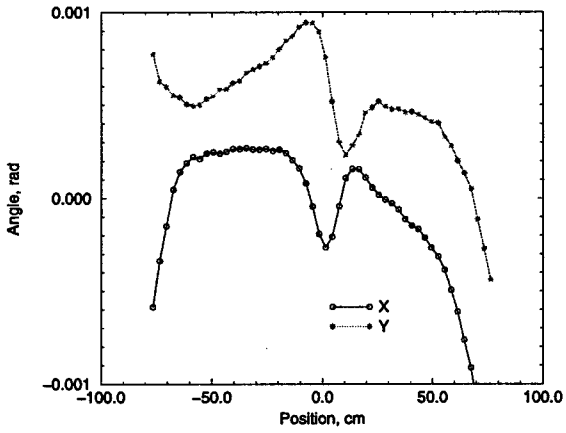

Figure 5: Angular deviation of the main solenoid field. Zero position corresponds to the middle of the main solenoid.

measured by an ADC. The entire system is controlled by LabView (TM) based data acquisition system.

Precision of the method depends on several factors. If the magnetic field is weak, then the precision is determined by friction in the mirror axises. The measured angular precision (repeatability) of the mirror is $\alpha_{\rm rms} \approx 1.5 \times 10^{-4}\,(1{\rm kG}/B)^2$. The dependence $\alpha_{\rm rms} \propto 1/B^2$ is valid for $B \lesssim 1.5$ kG, then the arrow is saturated and the dependence becomes $\alpha_{\rm rms} \propto 1/B$. The precision of measurements in a higher field, at about 4 kG, is also determined by other factors such as vibrations, electrical noises, etc., and was of the order of 10–20 μrad.

The region of linearity of the system is determined by the size of the PSD working area and by the laser spot size at the PSD. The linearity range in terms of the spot displacement on the PSD face is found to be about ± 6 mm, that corresponds to ± 1 mrad for the mirror located 3 m away from the PSD. The field deviation at the ends of the main solenoid is larger than this value. However, this limitation is not significant for the procedure of the field alignment by dipole corrector coils, since the field deviation will decrease in the iterative procedure of alignment.

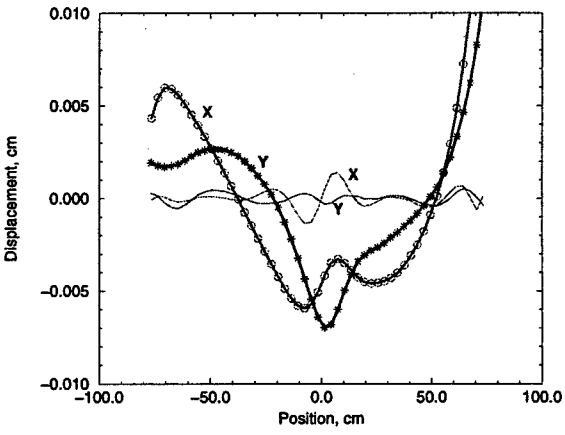

Figure 6: Electron beam displacement without (stars and circles) and with correction by dipole coils (simulation).

Angular deviation of the magnetic field $B_\perp/B_\parallel$ in the main solenoid is shown in Figure 5. One can see that the initial field quality is mostly determined by the edge effects. Exposure to the support table on which the solenoid is installed and current commutators at the ends of the main solenoid are thought to be major disturbances. Deviations of the field in the middle are caused by the force that provides electrical contact between sections and which also deforms the spiral of the solenoid at the place of connection, resulting in the field perturbation.

Electron beam trajectory in the measured magnetic field can be calculated using Eq.1 (see Figure 6). The rms trajectory displacement over 80% of the length of the main solenoid was found to be $\sigma_x = 0.05$ mm and $\sigma_y = 0.04$ mm, which satisfies the requirements for the "electron lens". Use of corrector coils allows further field quality improvement. The beam trajectory corresponded to simulated alignment of the magnetic field by use of dipole coils is shown in the Figure 6. The rms orbit displacement in this case is $\sigma_x = 0.005$ mm and $\sigma_y = 0.003$ mm that is 10 times less than required. These results suggest that the same field quality in the *full scale* beam-beam compensation device can be achieved with few dipole correctors at the ends of the main 5 T solenoid.

4 CONCLUSION

The guiding solenoidal magnetic field of the prototype of the beam-beam compensation device has been measured using a simple optical method based on a use of a mirror with a magnetic arrow, a diode laser and a position sensitive device. The field quality in the test facility was found to be good enough in the central part of the main solenoid while a modest correction by dipole coils is required at the ends of the solenoid. The results will help to determine a proper field alignment technique for the full scale beam-beam compensation device.

5 ACKNOWLEDGEMENT

We acknowledge useful discussions with S. Nagaitsev and A. Shemiakin and valuable technical assistance came from L. Arapov, A. Chupira, G. Kuznetsov, J. Santucci and A. Warner.

6 REFERENCES

[1] V.Shiltsev, D.Finley, A.Sery, V.Danilov, "Compensation of Beam-Beam Effects in the Tevatron Collider with Use of Electron Beams", these Proceedings; see also FNAL-Pub-98/260 (1998).

[2] C.Crawford, *et. al*, "Prototype "Electron Lens" Set-Up for the Tevatron Beam-Beam Compensation", these Proceedings.

[3] L. Arapov, *et. al*, "Precision Solenoid for Electron Cooling", in *Proc. Int. Conf. Charged Particle Accelerators*, Novosibirsk, vol.1, (1986), p.341.

[4] The mirror was kindly provided to us by S. Nagaitsev.

COMPUTER GENERATED END SHIMS FOR RECYCLER RING MAGNETS

C.N. Brown, G.W. Foster[+], G. P. Jackson, J. T. Volk, FNAL*, Batavia, IL

Abstract

The procedure for automatically producing customized end shims for the Recycler Antiproton Storage Ring gradient magnets is described. Magnets were first measured with a harmonics probe. The observed field defects were then fed into a computer program (initially a spreadsheet) which generated the toolpath code for a numerically controlled milling machine which produced individually customized end shims that eliminated the measured defect. Field defects through decapole were corrected to an accuracy (limited by the reproducibility of the measurement apparatus) to a few x 10^{-5}.

1 INTRODUCTION

The Fermilab Recycler Antiproton Storage Ring [1] requires approximately 400 permanent magnets with field defects of order 10^{-4} or better for the low multipoles. Under these circumstances the circulating aperture is expected to be limited by the physical aperture of the magnets (5cm magnet gap with ~4.5cm x 8cm clear aperture inside beam pipe) rather than the dynamic aperture due to magnetic field defects [2].

Most of the Recycler magnets are gradient dipoles with gap fields of approximately 1.5kGauss. Their "hybrid" design uses temperature-compensated permanent magnet material [3] to drive the magnet and steel pole tips to shape the field. The steel is very well behaved at this field level (high permeability and low hysteretic effects) and the magnetic field errors are almost exclusively due to geometric effects in the steel shape and magnet assembly.

Experience with the early prototypes indicated that the observed multipoles in the as-built magnets were near or at the tolerable limit: a few x10^{-4} gradient error, sextupole through decapole errors of order 10^{-4}, and smaller amplitudes for higher multipoles. (Multipoles were measured a probe radius of 2cm and expressed at a reference radius equal to the magnet half-gap of 2.54cm). Therefore to ensure that the field quality specifications were met, a procedure of applying an individual end shim to each magnet was initiated. This procedure was capable of trimming normal multipoles through decapole and allowed the field quality specifications for both systematic and random multipole errors to be exceeded.

+ email: GWF@FNAL.GOV

* Operated by Universities Research Association Inc., under contract with the U.S. Department of Energy.

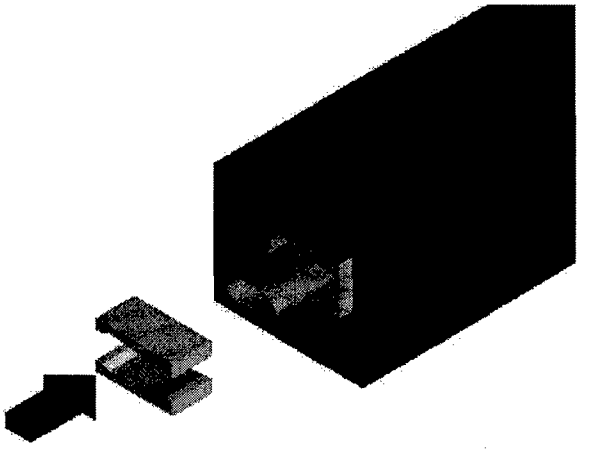

Fig. 1 – Recycler Permanent Magnets showing installation locations of shims on the ends of the gradient pole tips. The magnet ends were protected by steel cover plates (not shown).

2 SHIMMING PROCEDURE

The shimming procedure which evolved over the production of the magnets worked as follows:

1) Each assembled magnet was tested with a harmonics probe (a Morgan coil) which measured the low harmonics with an RMS accuracy of 1-2x10^{-5}.
2) The measurements were used to determine the shape of a custom piece of steel (a "Z-shim") which was applied to the ends of the pole tip. These were pieces of pole tip steel with the standard transverse cross section but cut to a variety of shapes as viewed from the top (see fig. 2).
3) The calculated shape was used to generate the toolpath programming for a numerically controlled (NC) vertical mill which machined the required piece from blank pole tip stock. Initially the toolpath code [4] was written out directly from a spreadsheet program, and later generated automatically by a subroutine called from the magnet analysis code. The steel shims were typically produced in batches at the FNAL machine shop.
4) The custom shim was applied to the magnet. This five-minute procedure required a wrench and a little bit of experience in wrestling any previously mounted end-shim off of the end of the energized permanent magnet.
5) The magnet was re-measured, and in occasional cases where the field quality still did not meet specifications, steps 2-5 were iterated.

0-7803-5573-3/99/$10.00@1999 IEEE.

For many of the later series of magnets an inventory of "semi-custom" end shims was maintained which allowed the most common field defects to be cured with a pre-fabricated end shim. When it was possible to use one of the pre-built shims on a magnet it represented a considerable time savings since the magnet did not have to be dismounted and remounted on the magnet test stand while a custom shim was being machined.

It was decided to place an individualized shim on only one end of each magnet. The shim on the other end was a "standard" shim (identical for all magnets of a given type) which was chosen to correct for one-half of the average systematic defect as measured in the first ~20 magnets of the production run. Having a standard shim on one end of the magnet leaves open the possibility of retrofitting a new standard shim on all magnets of a given type if modifications to the field shape of the magnets are desired after machine commissioning.

3 END SHIM DESIGN

The basic mechanism by which a z-shim works is that the integrated field of a magnet is proportional to the length of the pole tip. Thus if the end of pole is sliced diagonally, the magnet is stronger on side of the aperture than the other. This introduces an effective gradient in the integrated field ("edge focussing"). Similarly, if the pole tip is cut with a parabolic shape a sextupole field is generated. A cubic profile introduces an octupole and so on. See fig. 2. Thus it is possible to compensate small defects in the body field of a magnet by making changes to the end shape of the pole tip.

A number of issues complicate this simple picture. Firstly, the simple polynomial shaping of the pole tips does not generate a simple result: for example, a cubic Z-shim profile will generate not only an octupole term but also a gradient shift. Secondly, there are a variety of feed-down effects present in gradient magnets. For example, if a gradient magnet is cut diagonally it generates not only a gradient but also a sextupole term ("edge sextupole") since the amount of quadrupole seen by the beam depends on the position across the aperture. Analogous effects exist for higher multipoles. Finally, the Z-shim is inherently a 3-dimensional field shaping technique and effects such as the interaction of the pole tip ends with the flux return box cannot be neglected.

In practice we had magnets to build, so that the approach taken was to build a set of trial shims with the elementary monomial defects (linear, quadratic, cubic, etc.). The multipole shifts induced by each of these shims was measured, then a matrix was inverted to determine which linear combinations of polynomial defects will produce e.g. one unit of pure decapole change. This orthogonalization procedure was iterated by producing a second set of shims designed to produce a pure shift in each of the low multipoles. Linear combinations of these shapes can be superimposed to cancel arbitrary sets of errors in the low multipoles.

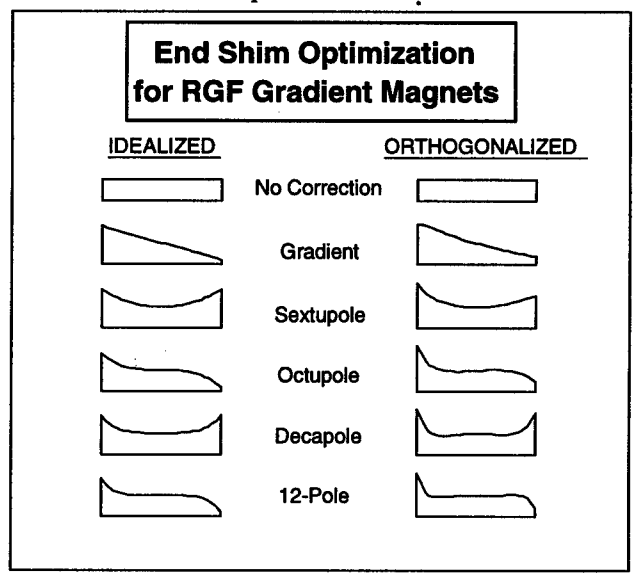

Fig. 2 – Elementary monomial Z-shim designs used as a starting point, and shim designs which were found to produce pure multipole shifts after re-orthogonalizing the multipole contributions from the elementary shims.

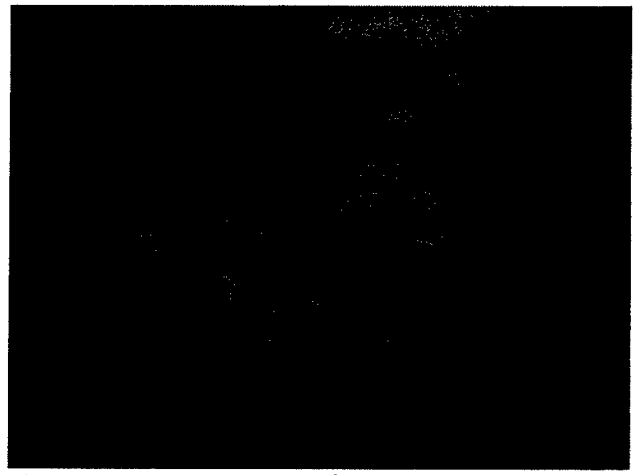

Figure 3: Customized end shims produced on a NC mill to null out error multipoles on Recycler magnets.

There is no guarantee that this process should be extremely linear. If a single correction term becomes large enough, it will produce a shim design that will extend the pole tip out near the flux return shield and behave very nonlinearly. Also, shim design which contains both quadrupole and decapole corrections may induce cross terms including, say, octupole. However in practice for the small (few $x10^{-4}$) defects being cancelled with the shims, they were adequately linear to achieve a 5-fold reduction in the error harmonics in a single iteration.

To get a feeling for the size of the end shimming needed, a gradient error of 10^{-4}/cm in the body field of a 4 meter magnet can be compensated for by a z-shim slope of $(400cm)*10^{-4}/cm = 4\%$. This corresponds to a slope of

6mm across the width of a 15cm pole tip. Shim corrections for higher multipoles get large fast, but errors in higher multipoles tend to fall off with multipole number just as fast. There was also a tendency for large corrections to be of opposite sign: for example a large positive sextupole might be accompanied by a large negative decapole error. This behavior is not accidental. The fractional gap width of the magnet is controlled to a mechanical tolerance which in our case was ~±100μ out of a 50mm gap or ~0.2%. The fluctuations in gap width allowed by this tolerance could be compensated by a Z-shim which varied the magnet length by roughly the same ~0.2% or 8mm out of a 4m magnet. In no case did we find a magnet with a field defect so extreme that it was impossible to define a set of shims which would bring it to zero. Within the constraints of custom shimming only one end of the magnet and a maximum +/-1" shim length, we occasionally left one or more multipoles only partially corrected.

Skew multipoles can also be trimmed with this procedure, although less effectively. Early in the Recycler R&D program we performed experiments to verify that skew multipoles could be trimmed as well. However it appeared from particle tracking studies that the skew multipoles observed in the magnets had no impact on the beam and were therefore ignored. The skew quadrupole was trimmed in these magnets by another technique, namely varying the relative strengths of the permanent magnet material behind the top and bottom pole tips.

A minor annoyance was the interaction between the strengths of the permanent magnets and the end shims. Magnets with strengths that had been previously trimmed to a few parts in 10^{-4} would find that changing a field quality shim would bring the magnet strength out of specifications. The strength trimming would then have to be repeated. The mechanism for this strength change can be understood by considering a sextupole shim, which redistributes flux towards or away from the center of the bore of the magnet and out towards the edges of the pole tips. The total flux available to the pole tip is determined by the magnetic material available. Thus a positive sextupole shim (longer at the edges of the aperture than at the center) will reduce the amount of flux seen by a probe (or the beam) located at the center of the aperture. In practice this was easily dealt with since the strength change was detected while the magnet was already mounted on the test stand and the amount of ferrite could be easily adjusted *in situ*.

5 RESULTS

A typical field error distribution before and after the full custom shims were applied is given in Fig. 4. In this case the RMS values of the octupole error were reduced by a factor of 4, and the systematic (average) value of the octupole was reduced by a factor of 5. This was typical in cases where a full-custom shim was applied to each magnet. As mentioned previously, not all magnets required full custom shims in order to meet specifications. Thus the overall production distributions which included magnets with "semi-custom" shims was somewhat wider.

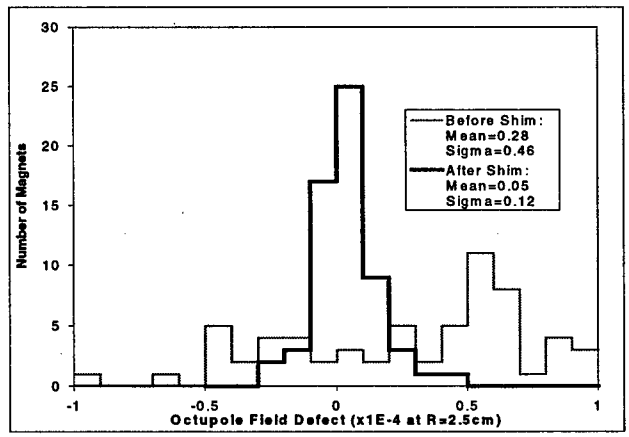

Fig. 4 - Effect of end shimming on the octupole error distribution for Recycler gradient magnets. The two curves show the octupole errors before and after full-custom shims were applied. After shimming, random and systematic defects are at the 10^{-5} level (R=2.5cm)

4 CONCLUSIONS

The technique of computer generated and machined custom end shims to cancel observed multipole errors proved a convenient and cost-effective method of improving the field quality of Recycler magnets. The technique described is generally applicable to warm-iron magnets and can be used to reduce at least the low multipoles errors to the limit of measurement accuracy or $dB/B \sim 10^{-5}$.

5 REFERENCES

[1] "Storage Ring for Increased Antiproton Production at Fermilab", G.W. Foster and G. P. Jackson, PAC '95. "Recycler Design Report", FNAL-TM-1991, G. P. Jackson, ed.

[2] "Simulation of the Recycler Ring Dynamic Aperture", D. Johnson and S. Mishra, PAC '99.

[3] "Temperature Considerations in the Design of a Permanent Magnet Storage Ring", K. Bertsche, G.W.Foster, and J-F. Ostiguy, PAC '95.

[4] Most machine tools accept an ASCII code commonly referred to as "G-code" which is supposedly standardized but in practice differs significantly on different NC machines. My suggestion to anyone attempting this is to have your machinist make you a sample part, then ask him for a floppy disk file and code up something which produces modified versions of the code for the sample part.

MEASUREMENTS OF A CRENELATED IRON POLE TIP FOR THE VLHC TRANSMISSION LINE MAGNET

J.DiMarco, G.W.Foster, V.Kashikhin[+], A. Makarov, P.Schlabach
Fermi National Accelerator Laboratory*, Batavia, IL

Abstract

The Very Large Hadron Collider (VLHC) is under conceptual design in Fermilab. One option under development is a 2-Tesla warm iron 2-in-1 single turn superferric magnet built around an 80kA superconducting transmission line. A normal-conducting test stand was built to optimize the iron lamination shape for this magnet. It uses a water-cooled copper winding to provide the 100 kA-turns needed to generate 2 Tesla fields in both 20mm air gaps of the magnet. A magnetic measurement facility has been set up for magnetic field mapping, which includes a flat measurement coil, precision stage for coil motion and integrator. Results from a first test of the "crenelation" technique to mitigate the saturation sextupole in iron magnets are described and future plans are discussed.

1 INTRODUCTION

Parameters of the VLHC Transmission Line Magnet [1] are given in Table 1.

Magnet Type	Warm Iron Superferric
Number of turns	1
Beam gaps	2-in-1
Drive Conductor	80-100kA Supercond. Transmission Line
Maximum field	2 Tesla
Injection field	0.1 Tesla
Gradient	+/- 3 %/cm
Quadrupoles	None required
Air gap height	20 mm
Good field (< 0.01%) diameter: Injection 2 Tesla	 20 mm 10 mm
Superconductor	NbTi or Nb3Al
Magnetic field energy	12 kJ/m @100kA

An important issue with this magnet design is the preservation of field quality as the iron approaches saturation at B=1.7~2.2T. In this superferric magnet the cost of providing the additional ampere-turns is low, in contrast to copper-driven magnets. However this advantage can only be realized if the field quality is preserved at high excitation, at least to the extent sufficient to preserve dynamic aperture for the small beam sizes at flat top. A number of techniques are available to control saturation effects in iron magnets. These include holes in the laminations in the regions above the pole tip and "crenelation" techniques [1,2]. Roughly speaking, all these methods work by reducing the average density of the iron near the middle of the pole tip so that the magnet saturates uniformly and field quality is preserved. Understanding and controlling these techniques will likely take many design iterations and a convenient test facility.

2 TEST STAND

The cryogenic and superconductor development program underway for this magnet is described in [3]. To optimize the warm iron lamination design it is expedient to use a normal conducting test stand on which variants of the iron shape can be tested without the complexities of a cryogenic system.

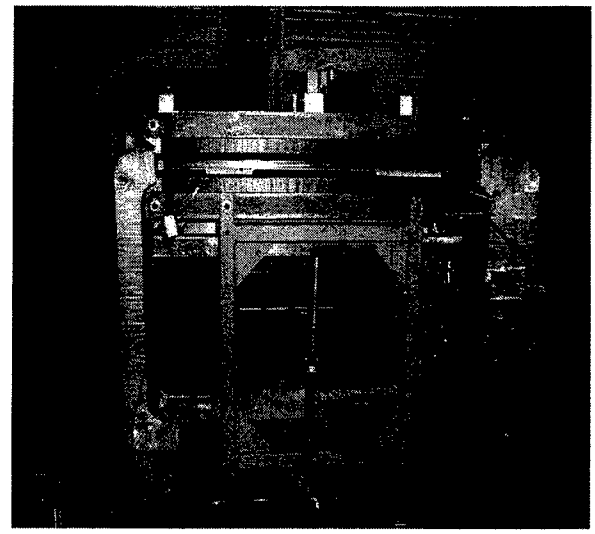

Fig. 1 – Transmission line magnet test stand including 1 meter long laminated steel cores and 100kA-turn copper coil with ten individual water circuits.

The test stand constructed at Fermilab to investigate various forms and designs of magnetic core for transmission line magnets is shown in fig. 1. The test requires 80-100kA-turns to pass through the 8cm hole in the center of the magnet that would normally be occupied by the superconducting transmission line. It is

*Operated by the URA, under contract with the U.S. DOE
[+] email:Kash@fnal.gov

0-7803-5573-3/99/$10.00@1999 IEEE.

calculated that only small field shape differences will occur between the superconducting and normal conductors arising from the difference in their radial extents. This current density is an engineering challenge with water-cooled copper coils and required ten separate water circuits for each of the 10 turns of 10kA each. The coil was powered by the filtered and regulated 10kA supply originally used to test dipoles for the Fermilab Main Injector. The coil, magnet core, and probe station are mounted on an aluminum frame.

3 MAGNET CORES

The magnet cores were manufactured from 1.5 mm thick low carbon steel laser cut laminations. See fig. 2. Each core has two holes (not shown) for alignment pins which run the full length of the magnet. Two aluminum bars installed between cores fix the air gaps on both sides of the magnet. Four threaded rods on both sides of magnet clamp the upper and lower cores into one mechanical structure. This arrangement allows simple and quick assembly/disassembly of the magnet. Both magnet air gaps are open for field measurements.

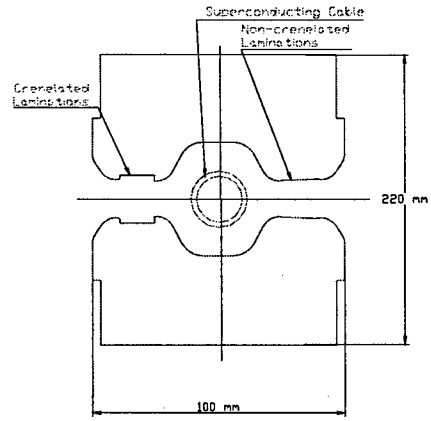

Fig. 2 – Lamination drawing of the steel cores showing position of the superconducting transmission line (or copper drive coil) and the two air gaps for the beams. In the crenelation technique every ~10th lamination has a cutout (shown in left gap on figure) which reduces the average iron density in the center of the pole tip to reduce the saturation sextupole.

4 MAGNET MEASUREMENTS

Field shape measurements were made with a flat coil glued to a G-10 plate. The coil had 3 turns, 2mm width, and 800mm length. The coil could be moved in horizontal and vertical directions by high precision (accuracy 1um) computer controlled stage. Field shape measurements were made using the integrated signal from the coil as it was moved into the aperture. The power supply was turned off at the start and end of each measurement in order to measure the zero point of the flux and cancel the effects of integrator drift.

A reference probe placed in the second magnet gap was used to normalize out the effects of power supply noise (mostly 720 Hz). At low field levels (0.1-0.5T) power supply noise was still significant and a MathCad filtering technique was used to smooth the data.

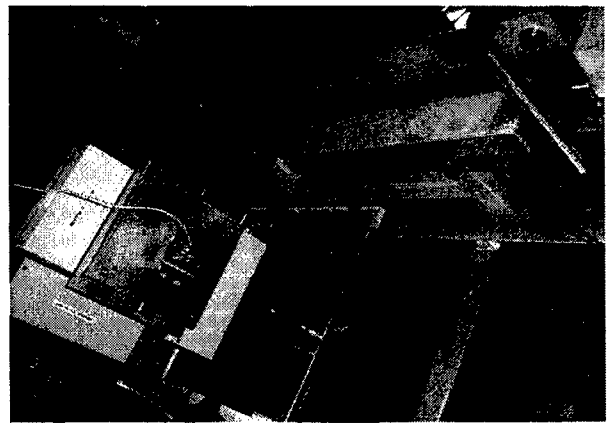

Fig.3 - Stage and Measuring Coil

5 POLE TIP DESIGN ISSUES

The main design problem in this type of magnet is to retain high magnetic field quality at the top end of the 0.1T – 2T operating range. The saturation of the flux return regions of the iron cores can be controlled by increasing their thickness. However the pole tips are unavoidably highly saturated when the fields reach 2 Tesla. The magnetic permeability changes by about a factor of 1000 from injection to maximum field, and the saturation is most pronounced at the corners of the pole profiles which carry maximum flux. This reduces the gap flux disproportionately at the edges of the aperture at high excitation, leading to the "saturation sextupole" at high fields. In addition, gradient shifts can occur in combined-function or asymmetric designs.

A number of technical approaches have been tried reduce these effects. Most of them use active field correction by placing an additional winding into the air gap. It is possible also to split the main winding in window frame magnet and change the current ratio between the parts to reduce the sextupole component during acceleration cycle. This technique was used in the TAC design of a superferric magnet for the SSC.

The "Crenelation" technique was proposed in [1]. The main idea is to reduce the iron density in the pole center by machining small indentations ("crenelations") in each N-th lamination. See fig. 2. The height and the width of this slot should be optimized using computer codes. Such an attempt was made using 2-dimensional codes and described in [4,5]. However it should be noted that the flux redistribution around "crenelations" is a three-dimensional problem which is only approximated by the reduced average

density ("stacking factor") of 2-dimensional codes. A direct solution to the 3D-magnetostatic problem is prohibitively difficult. Our goal in these measurements is to obtain an effective 2-D model for the crenelation which can be used for overall pole tip optimization.

6. RESULTS

For this investigation we used the simplified lamination configuration shown on Fig.2. Because the laminations were laser cut to an accuracy of only ~0.003", the field defect on the midplane was of order 0.1% at the design aperture. This was acceptable for this study since the field shape ***change*** could still be studied as a function of excitation and crenelation structure. Several variants of the pole "crenelations" were measured at currents up to 100kA and stacking factors Kc ranging between 0 and 17.7%.

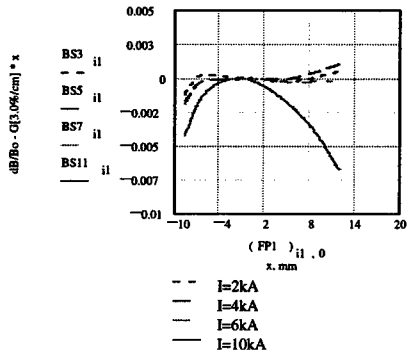

Fig.4 Field shape without crenelations.

In the pole tip without crenelations (fig.4) the field shape was stable between 0.1 and 1.7T as expected. Above 1.7T the field developed a significant sextupole as well as a gradient shift arising from the asymmetry of the double-C magnet design.

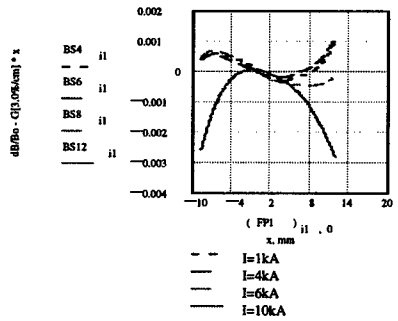

Fig.5 Field shape with crenelations, Kc=10%.

With every 10th lamination crenelated (fig. 5) two effects were observed. Firstly the saturation sextupole at high field was reduced as expected. Secondly (and unexpectedly) the low field shape changed by several parts in 10^{-4}. This effect is not predicted by the 2-D models of the crenelation, which indicate that the field shape should be independent of the crenelations for B<1 Tesla. Presumably this is due to 3-D flux redistribution effects and/or the early onset of saturation in the exposed, sharp corners near the crenelations.

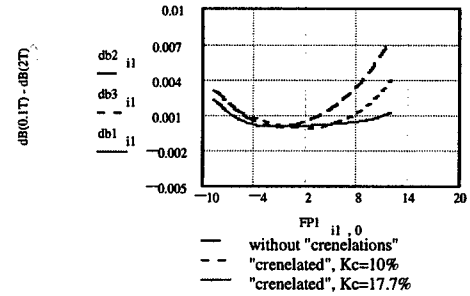

Fig.6 - Field shape change between 0.1T and 2T for no crenelations, 10% crenelation, and 17.7% crenelation. Positive curvature indicates negative sextupole at 2T.

The results are summarized in fig. 6, which shows the shape change between 0.1T and 2T for different crenelation stacking factors. The curves that even this simple crenelations causes significant reduction in field shape change due to saturation.

7. CONCLUSIONS

The field measurements confirmed the positive influence of crenelations on the field quality for highly saturated magnets. It seems plausible that an optimized crenelation will be able to substantially eliminate the saturation defect at 2 Tesla. An unexpected result is that crenelations also influence (at the level of level of a few parts in 10^{-4}) the shape of the magnetic field at low excitation. This makes the crenelation technique less attractive to use since the low field pole tip shape and the design of the crenelation become coupled. The field correction by "holes in the poles" remains a promising approach which should avoid these difficulties.

REFERENCES

[1] R.R.Wilson Procceedings of Snowmass 1982.

[2] S. Snowdon, "Magnetic Considerations in a Superferric Dipole" FNAL-TM-1210 March 1983.

[3] G.W. Foster et al, these proceedings.

[4] G.W.Foster "Magnetic Calculations for the Transmission Line Magnet". Proceedings of Snowmass '96, January 1997.

[5] V.Kashikhin-Jr., G.W.Foster, V.Kashikhin, EPAC '98, Stockholm, 1998,p.1934 – 1936.

Nb_3Al PROTOTYPE CONDUCTOR FOR THE TRANSMISSION LINE MAGNET

E. Barzi, G. W. Foster, E. Malamud#, P. O. Mazur, H. Piekarz, Fermilab*, Batavia, IL
M. Wake, KEK, Tsukuba, Japan
K. Hayashi and M. Koganeya, Sumitomo Electric Industries, Ltd., Osaka, Japan

Abstract

The Very Large Hadron Collider (VLHC), under consideration for construction at Fermilab in the next 1-2 decades, is a 100 TeV cm pp collider [1]. A major cost driver is the magnet. R&D is underway on several possible magnet designs. A low-field (2T) superferric magnet, sometimes called a transmission line magnet [2], may be the most cost-effective route to the VLHC. Although NbTi is now the cheapest superconductor measured in cost/kA-meter, Nb_3Al has the potential advantage that it remains superconducting at higher temperature. It may be particularly suited to the single "turn" and long straight lengths of the transmission line design. The combination of the simple magnet design and the higher strain tolerance than e.g. Nb_3Sn allows a simple process of cable fabrication, reaction, and magnet assembly. This higher strain tolerance is an advantage for splicing in the field. Sumitomo Electric Industries is producing Nb_3Al conductor for the Fermilab low-field magnet program [3].

1 COMPARISON OF Nb_3Al AND NbTi

The graph compares the critical current density of the two materials at 1T, the field at the conductor in the transmission line magnet. We plan to operate the low field vlhc magnets at ~6K. One can see the increased current carrying capacity of Nb_3Al at this temperature.

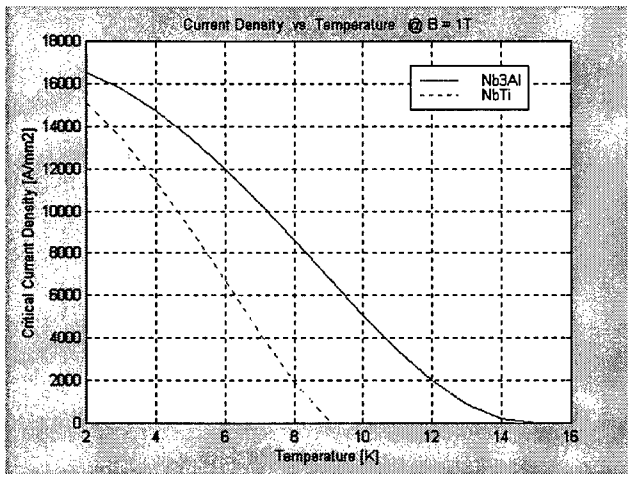

* Operated by Universities Research Association under contract to the U.S. Department of Energy

Email: malamud@fnal.gov

A higher operating temperature reduces the power required for the cryogenics system. The higher operating temperature also substantially reduces the size and complexity of the cryogenic distribution system. If one chooses to not increase T_{op}, Nb_3Al provides a higher enthalpy margin for beam-induced quenches.

2 CONDUCTOR SPECIFICATIONS

Sumitomo's wire is a Nb/Al composite assembled using a modified jellyroll process [4]. A thin Nb sheet, slit with controlled interconnection distances, is rolled up with an Al sheet, inserted in a copper container, and cold worked into a wire.

Diameter (one strand)	0.809 mm
Cu/non-Cu ratio	1.4
"Geometry"	"Jelly-roll"
Number of filaments	96
Filament Diameter	53 microns
Twist pitch	30 mm
Heat treatment (react)	750 ± 5 °C, 50 hours
Critical current (1 μV/cm)	133 A @ 12T, 4.2 K

3 CABLE SPECIFICATIONS

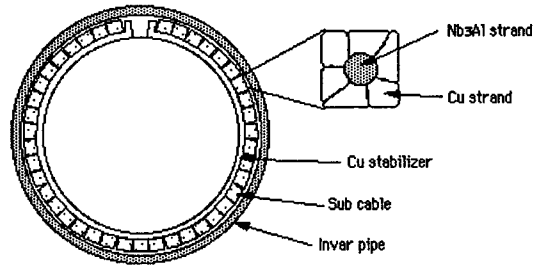

Number of sub-cables	41
Sub-cable dimensions	1.85 x 1.92 mm^2
Sub-cable topology	1 Nb_3Al, 6 Cu
Cabling pitch	~ 4 mm
OD of assembly (Invar ID)	35.7 mm
OD of Invar pipe	38.1 mm (1.5 in)
Thickness of invar	1.2 mm (0.047")
Copper (OHFC) RRR	>100
Copper stabilizer width	85 mm
Copper stabilizer ID	29 mm
Copper stabilizer thickness	1 mm
Specified performance @ 1T, 6.5K	>75 kA

0-7803-5573-3/99/$10.00@1999 IEEE.

The figure shows how the Nb_3Al strand is enclosed with 6 copper strands to form one sub-cable. This configuration is to prevent contact between the Nb3Al and the Invar during reaction.

4 COPPER INVAR COMPATIBILITY TEST

A test was performed in order to observe the behavior of Invar in contact with copper during the high temperature reaction cycle for Nb_3Al conductor. As a control, a similar test was performed using 300-series stainless steel in place of the Invar.

Samples of stainless steel pipe 32-mm (1.25-inch) in diameter and Invar pipe 38-mm (1.5-inch) in diameter were cleaned. The pipes were wrapped in a spiral pattern with clean 0.25-mm thick copper foil. The typical thickness was 2-3 layers of foil. The copper foil was covered with stainless foil and stainless steel hose clamps in ~ six locations and the hose clamps tightened. The foil was held in close contact with the pipe in the areas under the clamps.

The prepared pipe/foil samples were placed in a furnace evacuated to 2×10^{-3} Torr and backfilled with argon. The furnace was heated to 800°C and held there for 15 hours. It was let cool to room temperature. An argon purge continued for the duration of the thermal cycle.

4.1 Results

The stainless steel foil was bonded to the copper foil, and the copper foil was bonded to itself. A slit was made along the length of the pipe, cutting through the foil to the underlying pipe. The foil was peeled back from the pipe.

The **stainless steel** pipe had discolored to a much darker gray than the original color. The copper foil was bonded to the pipe at only a few spots of area ~ one square mm. The copper peeled away from the pipe had a light discoloration where it had been held most tightly in contact with the pipe. The stainless was darkened in most areas although where the copper was most tightly clamped, the darkening was reduced. It seemed as if there was a fixed amount of darkening material and some was removed with the copper foil in the pattern of the hose clamps.

Unlike the stainless case the **Invar** pipe was not discolored. The copper foil was bonded much more solidly than in the stainless case. Areas of several square cm under the hose clamps were bonded between the Invar and the copper. No discoloration of the Invar or of the copper foil was seen in the areas where we peeled the copper away from the Invar.

4.2 Conclusion

Invar pipe does not contaminate the copper during the reaction process.

5 J_c MEASUREMENTS

A strand sample from Sumitomo was wound on a grooved cylindrical barrel made of a Ti-6Al-4V alloy, and fixed on two removable Ti-alloy end rings. This assembly was heat treated for 50 hours at 750°C in argon to form a wire having 96 filaments 53 μm in diameter, and a copper to non-copper ratio of 1.4.

I_c measurements were carried out at the Fermilab Short Sample Test Facility (SSTF) [5] [6]. The I_c dependence on field and temperature was measured with the 10^{-14} Ω·m resistivity criterion from 4T to 15T and temperatures of 3.5K, 4.2K and 4.5K. The measurements are shown in the table

B field [T]	I_c @ 4.5K [A]	I_c @ 4.2K [A]	I_c @3.5K [A]
4	1044		
5	793	830	923
6	602		
8	357		
10	210		
12	117	126	153
15	37	41	

Sumitomo's specification gives an I_c of 133A at 4.2K and 12T. This is defined at a critical field of 1 μV/cm. Our measurement with the more commonly used 10^{-14} Ω·m resistivity criterion gives an I_c of 126A at the same temperature and field.

5.1 Derivation of J_c at Higher Temperatures

The low-field vlhc magnets will operate at higher strand currents than can be measured at the SSTF. To infer J_c outside the field and temperature data ranges where measurements were done, data were fitted with parameterization by Summers et al [7] and Lubell [8].

$$J_c(B,T)=\frac{C_0}{\sqrt{B}}\left[1-\frac{B}{B_{c20}\left[1-\left(\frac{T}{T_{c0}}\right)^2\right]}\right]^2\left[1-\left(\frac{T}{T_{c0}}\right)^2\right]^2 \quad (1)$$

$$\begin{cases} B_{c2}(T) = B_{c20}\left[1-\left(\dfrac{T}{T_{c0}}\right)^{1.7}\right] & (2) \\ T_c(B) = T_{c0}\left[1-\dfrac{B}{B_{c20}}\right]^{0.59} & (3) \end{cases}$$

Strain degradation was assumed to be zero. There are three parameters: B_{c20}, the upper critical field at zero temperature, T_{c0}, the critical temperature at zero field, and C_0, a normalization parameter expressed in $AT^{1/2}mm^{-2}$.

The best fit gives B_{c20} = 20T, T_{c0} = 15K, and C_0 =19003 $AT^{1/2}mm^{-2}$. The difference between parameterization and data is < 5% at 8T, and < 2% at 4T.

The parameterized J_c can now be used to obtain values at other temperatures.

J_c's inferred at 1T using these formulas are:

- 14,055 A/mm^2 at 4.5K (I_c = 3,010 A)
- 11,040 A/mm^2, at 6.5K (I_c = 2,364 A)
- 7,516 A/mm^2 at 8.5K (I_c = 1,610 A)

5.2 Conclusion

We therefore predict that the 41 sub-cable assembly will quench at 97 kA at 1T and 6.5 K. This exceeds the Sumitomo specification.

6 TEST PROGRAM

A test facility is being assembled in the MW9 building at Fermilab. A BM-105 analysis magnet and normal conducting primary excite a superconducting secondary turn.

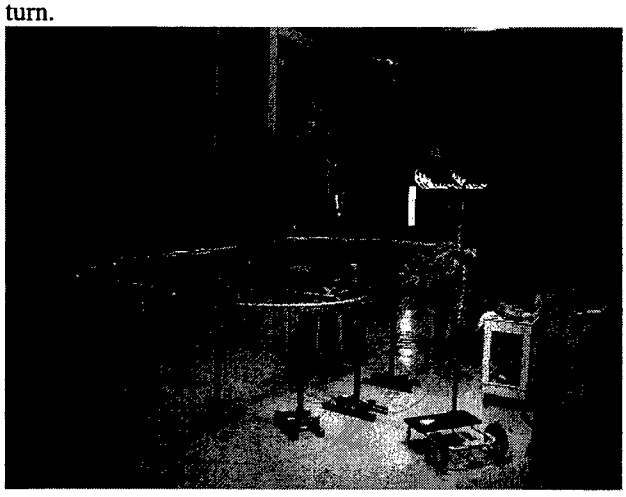

Pressurized helium flow is established through the pumped loop. Pressure, temperature, and flow rate of helium can be controlled. The loop is appropriately instrumented with temperature sensors and voltage taps. Current is measured by an external Hall probe array.

A 4-m section of the loop can be removed and replaced with a test piece. This is where the Nb_3Al sections will be tested.

We will test the performance of the Nb_3Al transmission line at different currents and temperatures. By dividing the flow in the test region of the conductor and heating the helium in contact with the conductor under test, an elevated temperature region can be created [9]. Thus we will be able to test the middle of the Nb_3Al section at higher temperatures than either the rest of the loop which is made of NbTi or the NbTi-Nb_3Al splices.

7 REFERENCES

[1] E. Malamud, "The Very Large Hadron Collider," presented at HEACC'98, September 1998.
http://fnalpubs.fnal.gov/archive/1998/conf/Conf-98-274.pdf

[2] G. W. Foster, "Status Report On The Transmission Line Magnet," September 1997.
http://www-ap.fnal.gov/VLHC/vlhcpubs/pubs1-100/5/mag_stat.html

[3] E. Malamud, E. Barzi, G. William Foster, P. O. Mazur, H. Piekarz, M. Wake, K. Hayashi, M. Koganeya "Nb3Al Prototype Conductor for the Transmission Line Magnet, " Presented at the "Magnets for a Very Large Hadron Collider" Workshop, Port Jefferson, L.I., N.Y., Nov. 16-18, 1998 (available at http://vlhc.org)

[4] T. Ando, Y. Nunoya, N. Koizumi, M. Sugimoto, H. Tsuji, K. Sato, Y.Yamada, "Dependence of Critical Current Density on Temperature and Magnetic Field in Multifilamentary Nb3Al Strands made by the Jelly Roll Process," IEEE Transactions on Applied Superconductivity,7, no. 2, June 1997.

[5] E. Barzi, C. Boffo, J. Ozelis, *Short sample J_c measurements at the Short Sample Test Facility*, TD-98-057.

[6] Emanuela Barzi, "Sumitomo's Nb_3Al J_c Measurements at the Short Sample Test Facility," Fermilab Technical Division report, TD-99-004. January 25, 1999.

[7] L.T. Summers, M.W. Guinan, J.R. Miller, P.A. Hahn, *A model for the prediction of Nb_3Sn critical current as a function of field, temperature, strain and radiation damage,* IEEE Trans. Magn., **27** (2): 2041-2044, 1991.

[8] M.S. Lubell, *Empirical scaling formulas for critical current and critical fields for commercial NbTi*, IEEE Trans. Magn., **MAG-19** (3): 754-757, 1983.

[9] P. O. Mazur, "Transmission Line Manufacture, Test, Reliability Issues,"
Magnets for A Very Large Hadron Collider Workshop, Port Jefferson, November 1998.

PRECISION MAGNETIC ELEMENTS FOR THE SNS STORAGE RING*

G. Danby, J. Jackson, C. Spataro, BNL, Upton, NY

Introduction

Magnetic elements for an accumulator storage ring for a 1 GeV Spallation Neutron Source (SNS) have been under design. The accumulation of very high intensity protons in a storage ring requires beam optical elements of very high purity to minimize higher order resonances in the presence of space charge. The parameters of the elements required by the accumulator lattice design[1] have been reported. The dipoles have a 17cm gap and are 124cm long. The quadrupoles have a physical length to aperture diameter ratio of 40cm/21cm and of 45cm/31cm. Since the elements have a large aperture and short length, optimizing the optical effects of magnet ends is the major design challenge. Two dimensional (2D) computer computations [2] can, at least on paper, produce the desired accuracy internal to magnets, i.e. constant dipole fields and linear quadrupole gradients over the desired aperture to $1x10^{-4}$. To minimize undesirable end effects three dimensional (3D) computations can be used to design magnet ends.[3] However, limitations on computations can occur, such as necessary finite boundary conditions, actual properties of the iron employed, hystersis effects, etc., which are slightly at variance with the assumed properties. Experimental refinement is employed to obtain the desired precision.

1 SNS DIPOLE MAGNETIC DESIGN

Edge shims are employed inside the dipole in order to give a uniform field over the desired aperture (Fig. 1). The computed (2D) field is everywhere more uniform than $\Delta B/B=1x10^{-4}$ inside the "isofield" of $1x10^{-4}$. The computed field in terms of the multipoles expressed at a design radius of r=7cm are all small compared to $1x10^{-4}$.

An actual magnet design must minimize construction errors. For reference, the dipoles constructed for the high intensity Booster [4] upgrade of the Brookhaven AGS proton synchrotron were assembled from one piece lamination stampings. By left-right, up-down inversion in assembly, the small residual errors due to die dimensions, steel rolling direction, etc were rendered symmetric. As a result actual measurements showed essentially agreement with predictions. The SNS dipole cross-section is too large for a one piece stamping. Joining of two nominally identical pieces at a mid-plane is required. Careful control must be designed in for precision relative alignment of the two pole surfaces.

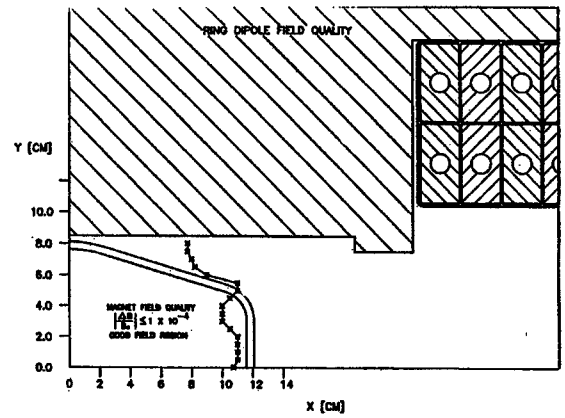

Fig. 1
Dipole Pole Profile and Isofield

For the SNS accumulator, a design option is to make the magnet a mechanical assembly out of solid steel plate. A prototype is under construction. The yoke is composed of 4 pieces. Precision machining of the two mid-plane pieces simultaneously should ensure parallel top and bottom yoke surfaces, to which each pole piece is attached. If required, a thin shim placed on either side could eliminate gradient fields to high order of accuracy. The magnetic field is iron dominated. The coil is located sufficiently remote from the pole surface so that even with the inevitably much cruder tolerances on location in coil construction, the influence on the field can be expected to be at the $1x10^{-4}$ level, interior to the magnet.

2 DIPOLE END EFFECTS

The SNS dipoles are straight. The ends are wedge shaped, where the angle of each wedge end equals half the total beam angle of deflection. The proton beam central axis enters and exits the magnet normal to the plane of the pole ends. In the simplest, first order form, the pole cross-section ends abruptly with each end a plane vertical surface. This geometry has been computed. The integral of the magnetic field through the magnet was calculated. Because of the wedge ends,

*Work performed under the auspices of the U. S. Dept. of Energy

0-7803-5573-3/99/$10.00@1999 IEEE.

the magnetic length varies linearly across the HMP, as required optically.

Because of the finite width of the poles and of the coil ends, the field end effects also show a relatively large nonlinearity. Fig. 2 shows the residual integral of field through the magnet on the HMP, normalized to the central field integral, after the wedge induced gradient is subtracted out. This calculation was done with pole edge shims running the entire length of the poles as shown in Fig. 1. As a result the Fig. 2 field aberration computed is entirely located in the magnet ends.

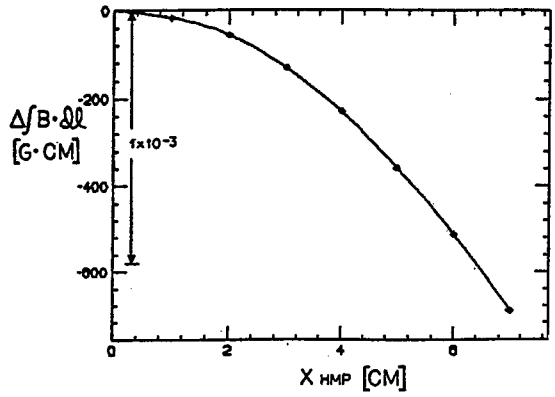

Fig. 2
Residual Nonlinear Field Integral

Detailed shaping of the end regions will be employed. Field and orbitral calculations are being used to minimize optical aberrations. This will be refined on the soon to be available prototype dipole. The magnet pole ends contain removable short sections which will facilitate shaping in 3 dimensions. Integral and point by point precision measurements will be made, using techniques and apparatus largely available from the development of the AGS Booster dipole.

3 SNS QUADRUPOLE MAGNETIC DESIGN

The SNS quadrupoles are particularly sensitive to end effects because of the very small ratio of length to aperture diameter. Fortunately, precision 16.5cm quadrupoles were developed for the AGS Booster which were also relatively short with a ratio of length to aperture diameter of 3/1. The SNS quadrupoles can be directly scaled from the precision Booster design. However, the ends will have to be modified to compensate for the even smaller ratio of length to diameter.

A model quadrupole of 21 cm diameter has been designed. This will be studied and ends optimized. Fig. 3 shows the computed cross-section.

Eq. 1 presents in cylindrical coordinates the axially symmetric 3D radial field for quadrupole symmetry. This is for the case where symmetry breaking imperfections are zero. In the case of the AGS Booster 4 piece laminations were mounted on 4 corner precision located pins. In fact, this did maintain 4-fold symmetry

$$\begin{aligned} B_r = &\sin 2\theta\,[\{(2r\,f_{2,2}(z)\}+4r^3(-1/12)f_{2,2}^{ii}(z)+\ldots] \\ &+\sin 6\theta\,[\{6r^5f_{6,6}(z)\}+8r^7(-1/28)f_{6,6}^{ii}(z)+\ldots] \\ &+\sin 10\theta[\{10r^9f_{10,10}(z)\}+12r^{11}(-1/44)f_{10,10}^{ii}(z)+\ldots] \\ &+\ldots \end{aligned} \quad (1)$$

to a high degree. Azimuthal and longitudinal field equations are also listed in a reference.[5]

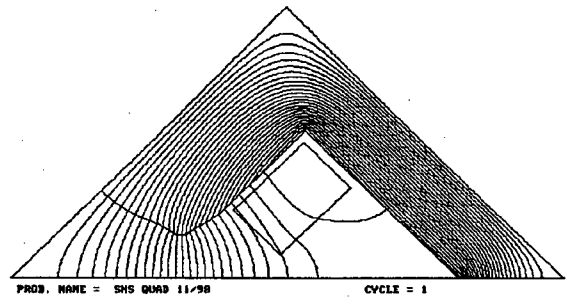

Fig. 3
Quadrupole Flux pattern

Shaping of the pole ends is used so that the 6θ, 10θ, 14θ, etc., allowed aberration terms in Eq.1 are very small both internal to the magnet and integrated through the ends. The shaping is used so that the even derivatives of these multipoles, plus the even derivatives of the quadrupole term f 2,2 (z) also present in Br and Bθ integrate to small values over each quadrupole end. Because the Booster 16.5 cm quadrupoles [4] were highly developed, the SNS quadrupoles are directly scaled to the larger diameter required. The shaped ends will be approximately the same as for the Booster, but because both the 21cm and 31cm diameter SNS quadrupoles are very short, some further interpolation will be required. This is because there is essentially no "internal" 2D region (magnets are essentially mostly ends) and also because the excitation coil is quite different in shape, and coil ends make a significant contribution to end fields. For the Booster quadrupoles, the integral allowed multipoles were at the $1x10^{-4}$ level at 92% of radius to the pole tip.[6]

The purpose of end shaping of the quadrupole is to arrange that positive and negative lobes are of equal magnitude. Fig. 4 shows the experimental result for the Booster quadrupole of shaping the dominant 12-pole, 6θ term in the vicinity of the pole end. The second

derivative of the 6θ term (see Eq. 1) is very small, normalized to ∫f 2,2 (z) dz, ie., to the quadrupole strength. The integral, ∫f 6,6 (z) dz of 6θ though the ends is very small $<1x10^{-4}$. The same technique is used to minimize the effect of the much smaller 20 pole (10θ) symmetric aberration. These techniques will be directly applied to the SNS quadrupole designs. Prototypes are in the process of being ordered.

The same measurement techniques, and in fact much of the same apparatus that was used in the Booster development will be directly applied to the SNS prototypes. Note that there can be an extremely small optical error not present in the integral magnetic measurement, which corresponds to a proton having the same transverse coordinates as it traverses each lobe in Fig. 4. In practice, the proton will vary very slightly in radius passing through each lobe. For a 10 milliradian angle at r=5cm, the error is ~ $2x10^{-4}$.

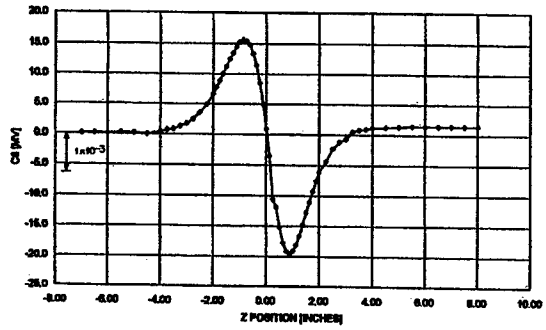

Fig. 4
Booster Quadrupole 6θ Term After End Shaping

4 CORRECTION ELEMENTS

Because of the high intensity, low loss proton beam requirements, corrections elements are required to compensate for small residual errors and also to deliberately introduce small controlled nonlinearities.

Correction elements used in the high intensity AGS and AGS Booster can be directly scaled to the somewhat larger aperture. These have not been developed yet in detail for the SNS accumulator ring, other than the rectangular box magnet which can provide various normal and skew terms.[7] Such a multifunction box magnet was previously designed and installed in the Booster, providing the necessary corrections and although very short azimuthally, with the necessary optical precision.[8]

5 REFERENCES

[1] SNS Design Manual (1998).
[2] POISSON Users Guide, LA-UR-87-115.
[3] OPERA-3D Reference Manual, VF-03-98-04.
[4] G. Danby, et al. PAC87 (1987).
[5] G. Danby, S. Lin, J. Jackson, PAC67 (1967).
[6] G. Danby, J. Jackson, PAC 91 (1991).
[7] N. Tsoupas, private communication.
[8] G. Danby, J. Jackson, MT-13 (1993).

DESIGN OF AN AC–DIPOLE FOR USE IN RHIC*

B. Parker#, M. Bai, A. Jain, G. McIntyre, M. Meth, S. Peggs,
T. Roser, R. Sanders and D. Trbojevic, BNL, Upton, NY

Abstract

We present two options for implementing a pair of AC-dipoles in RHIC for spin flipping, measuring linear optical functions and nonlinear diagnostics. AC-dipoles are magnets that can be adiabatically excited and de-excited with a continuous sine-wave in order to coherently move circulating beam out to large betatron amplitudes without incurring emittance blow up[1]. The AGS already uses a similar device for getting polarized proton beams through depolarizing resonances[2]. By placing the magnets in the IP4 common beam region, two AC-dipoles are sufficient to excite both horizontal and vertical motion in both RHIC rings. While we initially investigated an iron-dominated magnet design, using available steel tape cores; we now favor a new air coil plus ferrite design featuring mechanical frequency tuning, in order to best match available resources to demanding frequency sweeping requirements. Both magnet designs are presented here along with model magnet test results. The challenge is to make AC-dipoles available for year 2000 RHIC running.

1 AC-DIPOLE REQUIREMENTS

AC-dipole operating frequency is application dependent. When used with polarized protons as a spin flipper, the frequency is swept in the vicinity of the spin tune, i.e. $\approx 0.5 \times f_{rev}$, or specifically 37±2 kHz for RHIC. Linear optics measurements can use a constant frequency excitation at either 15 or 63 kHz but sweeping is needed for nonlinear optics measurements. An integrated field strength of ≈300 gauss·m is needed but ±3% field inhomogeneity is tolerable. Since the RHIC injection kicker ceramic beam pipe assembly (length ≈1.3 m) fits twice in the available IP4 space and has sufficient (42 mm) inner aperture, it will also be used for the AC-dipoles to save on spares.

Since high frequency currents flow mostly on conductor outer surfaces due to the skin effect, we intend to use Litz wire. Litz wire has many fine strands twisted and braided together so as to link the same magnetic flux. This arrangement yields a uniform current distribution across the conductor cross section. Therefore, the Litz AC-resistance is ≈DC value for dramatically lower power dissipation as compared to a solid conductor. Round Litz cable, made from #38 gauge (0.1 mm diameter) copper wire is sufficiently fine for our application and the cable is easily bent in any plane (helpful for forming coil ends).

*Work supported by U.S. Department of Energy under Contract No. DE-AC02-98CH10886.

#Email: parker@bnl.gov

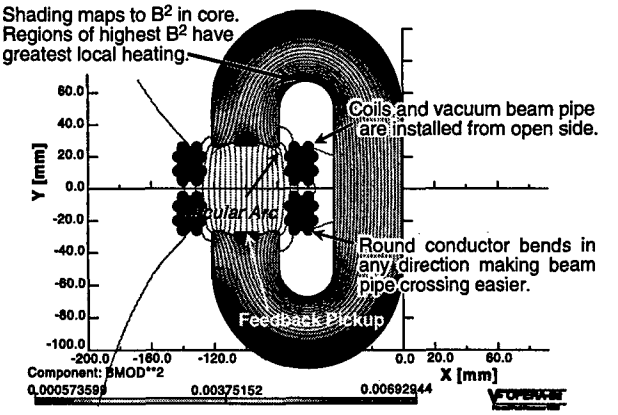

Figure 1. C-magnet made from Litz wire and tape-wound steel C-core. Each half coil has 12 turns of #6 Litz wire. Field uniformity is better than 0.5% at 10 mm radius.

Initially we focused on using #6 Litz wire coils in an iron-dominated C-magnet due to the availability of unused tape wound cores (left over since 1981 after construction of the Fermilab Main Ring Abort Kickers). These cores consist of 3% silicon steel tape, 0.05 mm thick, wound in a racetrack configuration. The small lamination thickness reduces eddy current effects in these cores and makes them suitable for short period pulses.

2 C-CORE MAGNET DESIGN

The proposed C-core magnet cross section is shown in Opera-2d[3] output plot in Figure 1. The C-geometry returns magnetic flux along a low reluctance path and thereby reduces the amp·turns needed for a given field strength, compared to an air coil magnet. It also permits easy installation of the vacuum beam pipe and coils through the gap. In an iron-dominated magnet, the field shape is largely determined by the pole configuration. For the ≈300 gauss field strength, saturation is not an issue; therefore, the pole face is recessed to achieve desired field quality. This pole shape has been produced via an initial straight cut followed by fine milling along a circular arc on a numerically controlled milling machine.

From the average core B^2 calculated in Opera-2d, we can estimate the core eddy current losses. Since higher B^2 areas contribute more to losses, the coil configuration and pole gap were optimized to reduce average B^2. Experience with similar laminated materials shows that core losses should scale as $f^{1.6}$ (i.e. between hysteresis linear with f and f^2 from eddy currents). In practice even the estimated 63 kHz loss of ≈2.4 kW is much smaller than anticipated external circuit losses in frequency sweeping components. At 15 kHz the 200 W estimated core loss is ≈1/3 the resistive losses of an equivalent air coil due to the C-magnet's more efficient use of excitation current.

0-7803-5573-3/99/$10.00@1999 IEEE.

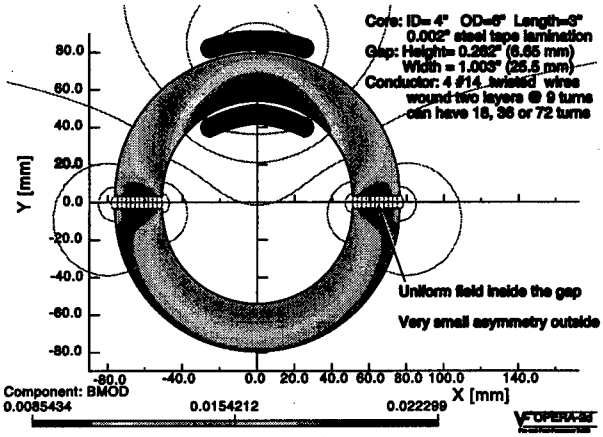

Figure 2. AC-dipole test magnet cross section.

3 TEST MAGNET MEASUREMENTS

Since 15 and 63 kHz are nearly equivalent for beam dynamics, the originally specified ±5 kHz frequency tuning seemed easier to achieve as a ±8% spread at 63 kHz than as a much larger ±33% spread at 15 kHz; however, would eddy currents reduce or distort the field in the gap more at the higher frequency? In order to address this concern we constructed a small test magnet using a pair of 0.05 mm lamination semicircular tape cores as indicated in the Opera-2d output shown in Figure 2. The test magnet has a dual 6.7 mm gap and a tight fitting fixture was made for positioning a small 6-turn probe coil inside the magnet. Because the 30 mm probe coil length is much less than the 76 mm core length, magnet end effects are small. The 6.7 to 26 mm gap to pole width ratio yields a uniform central field which can be reasonably mapped with the 3 mm wide probe coil.

The impedance of the test magnet was matched to 50Ω by a capacitor network and verified via network analyzer. Reproducible probe coil placement was possible via scribe lines at 19 measurement positions. Since probe response is proportional to frequency, the probe signal was divided by frequency in comparing scans (yielding a frequency normalized transfer function). The excitation current was measured by two methods which agreed to better than 0.3%. Repeat field maps are practically indistinguishable. Test magnet field maps were measured 9 times at 66.26, 15.(×2), 10.(×2), 5.(×2), 0.97 and 0.5 kHz.

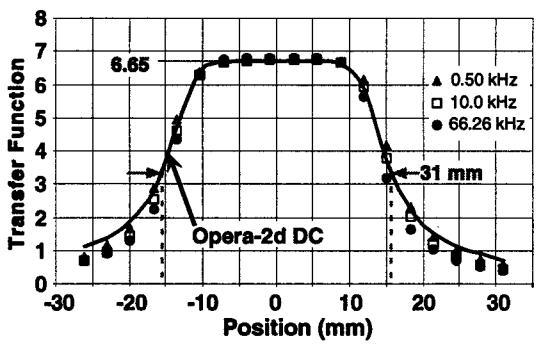

Figure 3. Comparison of measured transfer function for DC (Opera-2d prediction) and f = 0.5, 10 and 66.26 kHz.

The central transfer function was found to be constant to 0.8% and agreed with an Opera-2d static prediction to ≈2% using uncalibrated geometric areas.

A comparison for three frequencies is shown in Figure 3. The fringe field drops relative to the central field with increasing frequency. When all measurements for a given frequency are summed to yield an integrated transfer function (ITF), a 7% average ITF drop with frequency is observed between 500 Hz and 66.26 kHz. This drop is consistent with the ≈15% magnet inductance change measured separately.

4 FREQUENCY TUNING SCHEMES

One difficult AC-dipole design challenge is to sweep the oscillation frequency quickly during nonlinear measurements and spin flipping. The originally requested ±33% tuning (15±5 kHz) was deemed too difficult; however, we did analyze power supply schemes capable of yielding 39±5 kHz (spread equiv. to 63±8 kHz). A simple but very brute force approach is to add sufficient circuit dissipation (dummy loads) to reduce system Q to 4 for broad band frequency response. Then a pickup coil inside the magnet gap can be used for amplitude feedback. While the circuitry for this scheme is quite simple, a 100 kW vacuum tube based power supply is needed.

Instead of spoiling Q, a variable series inductance could be included in the circuit. Here we could borrow existing water-cooled ferrite cores (50 cm OD, 4L2 grade) and wind 9 pairs, first with alternate bias turns, and then common magnet excitation turns. Frequency response is then proportional to bias current; unfortunately, significant energy dissipation in the ferrite cores still requires a 20 kW vacuum tube for ±5 kHz and these relatively expensive cores would some day have to be purchased or returned.

An alternate tuning approach is to vary the AC-dipole inductance directly. The C-cores, in which the AC-field is rapidly cycling back and forth, could have a large perpendicular DC bias field applied to them. The bias field would partially saturate the C-cores and thereby modify the inductance of the magnet. Varying the bias field alters the resonant frequency. The system frequency thus follows the bias field as long as the Q is not too high compared to the rate of change (i.e. analogous to cavity filling time). Unfortunately, steel is not an optimum material for this scheme since very large bias fields are then needed. Configurations with ferrite yokes were also investigated; however, it was not found possible to make large inductance changes and simultaneously maintain adequate field quality and low AC-losses with reasonable ferrite geometry.

5 AIR COIL PLUS FERRITE OPTION

While investigating ferrite plus air coil inductance biasing schemes we realized that the magnet stored energy was much more sensitive to ferrite position than to ferrite

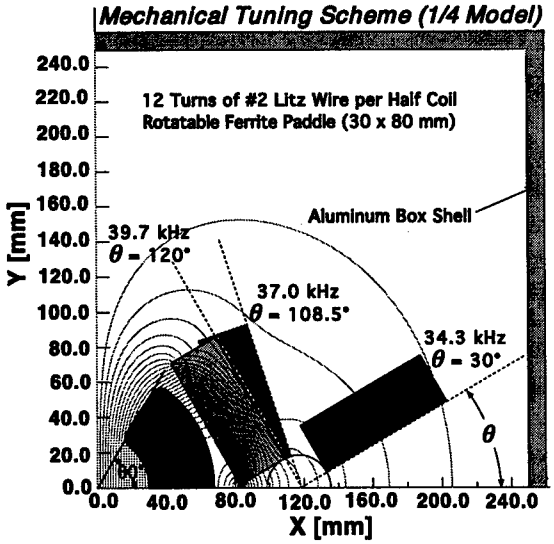

Figure 4. Magnet with variable reluctance frequency tuning. Scheme uses air coil plus movable ferrite insert. Magnet inductance changes as ferrite angle is varied.

permeability. Even pulling the ferrite's relative permeability down to $\mu=4$, which would require a large bias current, is not as effective as moving the ferrite away from the coil (i.e. getting $\mu=1$). Our latest scheme, shown in Figure 4, starts from an approximate cos-theta current distribution (i.e. $\approx 60°$ half angle) for each 3-layer half coil using 12 turns of Litz wire. To partially offset the increase in excitation current needed to achieve the same central field with the air coil's poor transfer function, #2 (6mm OD) Litz wire is needed.

Introduction of the ferrite tile close to the coil decreases the stored energy (or inductance) by more than 30%, so there is potential for ±7% tuning about a central resonant frequency. For mechanical simplicity the ferrite tile is rotatable about a pivot point (note that only 1/4 of the model is shown in Figure 4, so there are actually four ferrite tiles which must be moved symmetrically). The relationship between the ferrite angle and system resonant frequency is shown in Figure 5. We find that most of the tuning range is covered by 90° motion from 120° to 30°.

The few parts per mil field quality achievable with this system, shown in Figure 6, is much better than needed and it is clear that final field quality will be dominated by

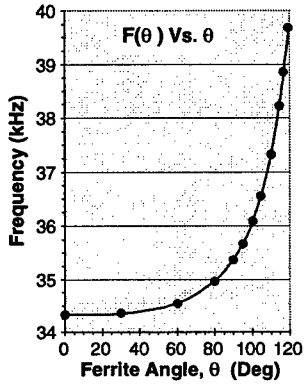

Figure 5. Relationship between ferrite angle and system frequency for mechanical tuning scheme described above.

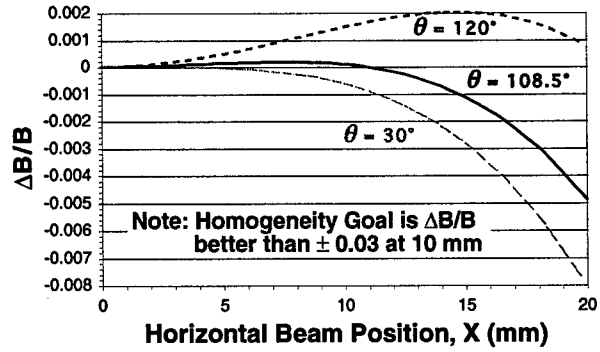

Figure 6. Field quality achievable with mechanical tuning. The curves shown span the intended tuning range.

the coil end effects and construction errors. A simple servomotor plus computer interface system already exists which could be adapted to move the ferrite tiles either under direct computer control or via a programmable logic system. The servomotor and belt drive system can be mounted on the outside of an aluminum box. The box serves to shield the magnet from external influences and to contain otherwise annoying AC fringe fields. Estimates indicate that eddy current losses in the ferrite tiles and box walls are small compared to dissipation in the coil and matching capacitor network.

We hope to run the system frequency control almost open loop and use pickup coils above and below the beam pipe for amplitude feedback. We anticipate that a medium conductance path should also be provided, close to the beam pipe, for passing the two beam image currents in order to avoid wake field trapping.

6 CONCLUSIONS

Although tests indicate that the tape wound core design would be suitable for meeting AC-dipole requirements, when evaluating a complete system, cost and schedule considerations favor using the variable magnetic reluctance path mechanical frequency tuning scheme described above. Implementation of this scheme, denoted here as air coil plus ferrite in a box, should be possible for use during RHIC year 2000 running; however, there are still many details which must be worked out.

7 ACKNOWLEDGMENTS

We thank Gerry Morgan, Pat Thompson, Daniel Sullivan, Richard Spitz, John Escallier, Mike Harrison, Ray Zaharatos and many others for numerous discussions and technical support. In addition, we appreciate Fermilab making available tape wound cores for this work.

8 REFERENCES

[1] S. Peggs, "Nonlinear Diagnostics Using AC Dipoles," these proceedings (1999).

[2] M. Bai *et. al.*, PRE 56 (1997) 6002; M. Bai, Ph.D. Thesis, U. Indiana (1999); M. Bai *et. al.*, "Beam Manipulation with an RF Dipole," these proceedings (1999).

[3] Vector Fields Inc., 1700 N. Farnsworth Ave., Aurora, IL 60505.

A PULSED ELLIPTICAL QUADRUPOLE ARRAY FOR TRANSPORT OF MULTIPLE HIGH CURRENT BEAMS

A. Faltens, N.Y. Li, G. Ritchie, D. Shuman*, LBNL, Berkeley,CA

Abstract

We present the design of a pulsed quadrupole magnet array for side by side transport of multiple high current particle beams in induction linear accelerators. The design is directly applicable to low field superconducting quadrupole arrays and can be modified for high fields. The magnetic design minimizes current requirements by placing a modified cosine 2θ current distribution inside an elliptical iron boundary. The resulting magnet aperture more closely matches the beam's elliptical cross-section, and only the space the beam occupies is magnetized to the required field quality. By eliminating unneeded high field area in the magnet aperture, energy requirements are halved, as compared to an equivalent circular design. The magnet serves double duty as a UHV vacuum chamber/beam tube, and reduced radial thickness results from lower current requirements. Each interior magnet's neighbors serve as the return flux paths and the poles are placed as close as possible to each other to facilitate this. All the above features serve to reduce the beam-to-beam spacing, leading to significant reductions in the size and cost of the induction cores which surround the array, as well as the pulsed power supplies which drive them. The design shown here is for a 21 beam array, yet it is suitable for larger or smaller numbers of beams, as required.

1. DESIGN OVERVIEW

The pulsed quadrupole magnet is a high voltage, low inductance, current dominated design, with conductors arranged around an elliptical iron boundary. Figure 1 shows the complete array, and figure 2 shows a cross section view of one quadrupole magnet cell. The magnet's main coil package consists of four 2-layer coils, of 10 turns per coil, 5 turns per layer, epoxy potted onto a thin stainless steel beam tube/end flange assembly, for eddy current minimization. Large, 3.8mm diameter insulated copper conductors are used to reduce electrical stress concentrations. Fiberglass cloth and flexible printed circuit correction coils are incorporated into the coil casting for strength and beam steering, respectively. The magnet coil casting carries all magnetic and vacuum loads, both radial and axial.

*Work supported by the Director, Office of Fusion Energy, U.S. DOE, under Contract No. DE-AC03-76SF00098

• email: DBShuman@lbl.gov

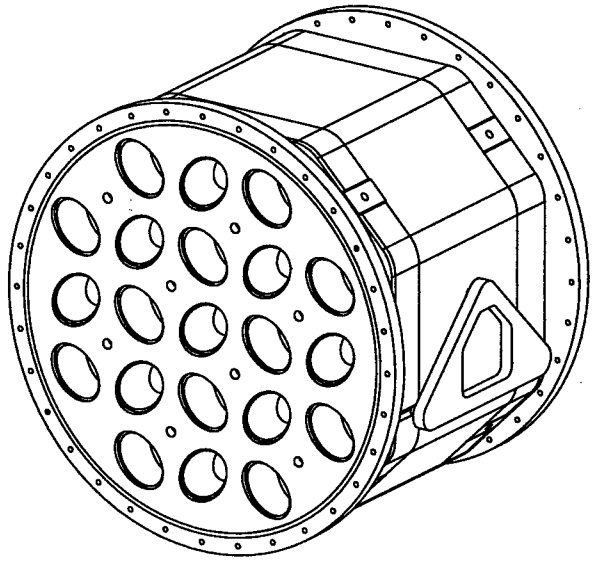

Fig. 1 Complete Quadrupole Array

The laminated iron core serves to position and support the magnets, to provide further reduction in energy requirements by providing a high permeability flux path to the neighboring magnets, to provide a flux return path for the magnets at the edge of the array, and to provide channel isolation for steering coil fluxes.

2. MAGNETIC DESIGN

To minimize stored energy, the magnetic field and vacuum volume is confined to an elliptical cross-section,

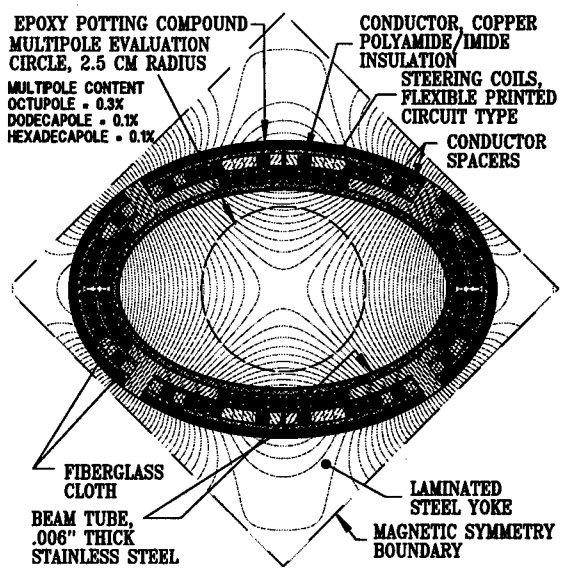

Fig. 2 Quadrupole Cross Section with flux plot

0-7803-5573-3/99/$10.00@1999 IEEE.

which corresponds to the beam cross section, with clearance for halo, misalignment, and mis-steering. Conductors are arranged inside an elliptical iron boundary cross section instead of the usual circular one.

Surface current density, K, on the boundary follows an analytic function per Faltens, and is proportional to the tangential field component at the iron boundary:

$$K = K_0 \frac{a^2 y^2 - b^2 x^2}{\sqrt{(a^2 y) + (b^2 x)}}$$

Where: a, b = major, minor diameters of elliptical boundary, respectively.

The number of turns is minimized to reduce magnet voltages. The acceptable multipole level at the beam edge determines the minimum number of turns. The conductor size is optimized between reducing eddy currents within the conductor and minimizing field energy outside the beam envelope vs. minimizing i^2R losses and field stresses. Lower losses are possible with finer conductor strands and a larger total conductor volume, but this choice tends to increase the initial stored energy and capacitor cost, and requires higher voltages which compromise magnet longevity. Coil resistive losses are limited to ~10% of the total energy.

A subsidiary goal is to approximate the conductor current densities (40 kA/cm^2) to those that would eventually be used in a superconducting array (30-100 kA/cm^2).

Table 1. Magnet Parameters

Beam Aperture Radius	5x3	cm (maj. x min.)
Magnet Transverse Pitch	11.8	cm (horiz., vert.)
Magnetic, Total Length	31, 47	cm
Field Gradient, B'	38	T/m
Maximum Field, B	1.9	T
Number of turns	10	Turns/coil
Conductor diameter	3.8	mm
Magnet Current, I	4400	A
Magnet Resistance, R	.012	Ohms
Magnet Inductance, L	.375	milliHenries
Magnet Voltage, max.	3	kV (1mS pulse)
Pulse energy/magnet	3	kJ
Energy loss/magnet	300	J
Pulse rate (w/cooling)	0.5	Sec^{-1} (25°C ΔT)

To reduce magnet transverse pitch spacing, return flux is routed through adjacent magnets, which allows coils to be placed essentially in contact with each other, as much as practical. Iron is used only to provide the elliptical boundary, to connect the poles in an efficient manner, and to provide for isolation of steering coil flux (skew quadrupole for rotation errors, plus crossed dipoles for positional errors). Higher order multipole corrections are not needed on every lattice period, if needed at all. If so, a separate multipole corrector magnet array will be located after a given number of lattice periods. The magnetic analysis program POISSON/PANDIRA was used, and conductor currents were scaled to account for differing lengths.

3. COIL DESIGN

The magnet's short pulse length of 1.0mS FMFW, requires a high voltage design, with 3kV between the high voltage lead and ground. As such, electrical stress reduction and good insulation is critical to insure longevity. 7 gauge (3.8mm dia.) copper wire was purchased with a high grade polyamide/imide insulation coating 0.05mm thick which tests to 10-15 kV for crossed conductors in a hi-pot test, even after significant bending.

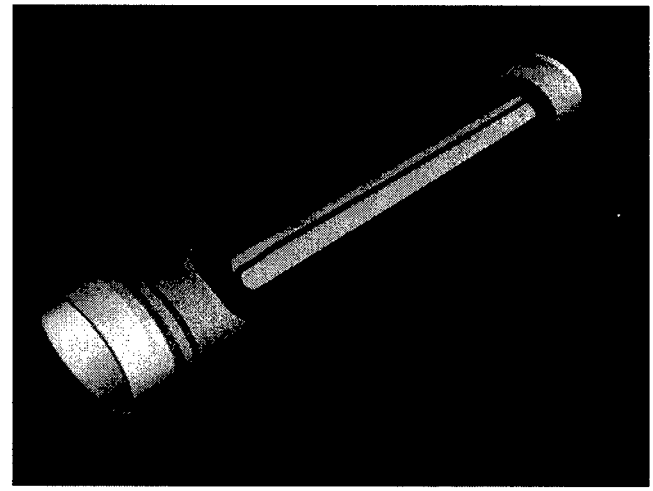

Fig. 3 Coil Casting with Beam Tube and End Flanges

Cooling is by conduction to the iron core, which can be fitted with water cooling channels if necessary. The beam tube/end flange assembly serves as the ground layer on the inner diameter, and a .001" stainless steel foil as the ground layer on the outer diameter (to shield steering coil edges).

4. VACUUM CHAMBER DESIGN

To minimize eddy current losses, a stainless steel thin wall tube 0.006" thick is utilized for a beam tube. The beam tube is brazed to end flanges which are flared outwards to allow the beam to expand towards a circular cross-section without beam scraping. To keep the tube from collapsing under vacuum load, it is both restrained by, and bonded to the epoxy potted magnet. The coil casting then carries the vacuum loads, and fiberglass cloth is incorporated in the casting for strength and rigidity. Finite element analysis predicts a maximum vacuum load deflection of 0.04 mm inward for a potted coil with 0.5mm fiberglass layers, both under and over the coils. Maximum stress in the stainless steel beam tube is 5 ksi.

5. CORE DESIGN

The core is laminated M36 magnetic steel, .025" thick, with C5 insulation. Each magnet bore extends past the (effective) end of the coil by the average magnet radius of 4cm to minimize stray fields. The core will be assembled and held together with insulated stainless steel bolts located between the minor diameters of the magnet bores. The holes between the major diameters are reserved for cooling channels, as heat generation is concentrated in this area. Field is low at the bolt locations, less than 1000G. After coil installation, the entire assembly will be potted in a high melting point wax, which will stabilize the magnets from impulse forces, and allow removal and repair of individual magnets. Magnet bakeout for vacuum purposes is not foreseen to be necessary. The magnet bore edges will be radiused to reduce electrical stress on the leads. Keyways on each magnet bore end align the coils to the core.

6. ACCELERATOR INTERFACE DESIGN

Each magnet's end flange features an elliptical cylinder exterior surface for vacuum sealing. The flange inserts into a corresponding aperture in the end manifold plate until the plate rests against the potted end of the magnet. Sealing is accomplished by compressing an O-ring around it using an elliptical O-ring compressor flange, installed from the drift region. This allows easy removal of the manifold plate and magnet repair or replacement, if necessary. Edge clamps or bolts, and perimeter seals are then used to connect the manifold plates to the insulator column edge bellows (not shown). Tie rods running through the core bolts connect the end manifold plates to carry vacuum loads. There is ½" clearance between the manifold plate and the end of the core. Magnet leads exit radially from the coil casting ¼" from the end of the coil casting, and exit through this clearance.

7. PULSER DESIGN

Two magnets are connected in series to each pulser, which produces +/-3kV, bipolar. The pulser is an SCR switched capacitive discharge circuit with a recirculator that

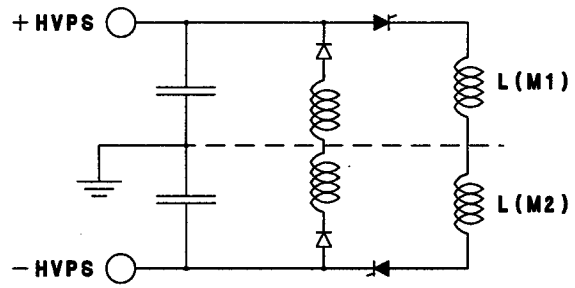

Fig. 4 Pulser Circuit

recovers energy not lost in resistance. For a given rep rate and pulse energy, this lowers the cost of the pulser as well as saves energy. The circuit is shown in fig 4. The components are commercially available except for the choke used in the recirculator, which was fabricated from the same 7 gauge wire as the magnet coils and cast in epoxy.

8. FABRICATION

Coils are wound "flat" on a single axis winder, one layer at a time. The individual turns of each layer are wound in an ascending spiral fashion between two plastic dies, one of which is fixed, and the other connected to a movable hydraulic ram. Thus, each wire turn is wound into its own groove, instead of on top of the previous turn, as is normally done. After winding under low tension, the wire ends are clamped off and the coil layer is stretched axially to the point of yield. This removes initial wire curvature and kinks, with negligible reduction in wire diameter or damage to insulation. This operation requires approx. 500lbf for each conductor run.

After winding and stretching, the coil collapses under its own weight into a flat, planar coil layer. Each coil layer is then placed between two plastic dies and pressed to form the elliptical curvature on the ends.

The beam tube/end flange assembly is formed by slipping a round, thin wall stainless steel tube over a three-piece expanding mandrel to form the correct elliptical shape. The end flanges are then low temperature brazed onto each end of the tube.

Magnet potting is done in two steps. First, the mandrel/beam tube/end flange assembly is wrapped with fiberglass cloth, then placed in the potting mold along with four mold inserts. These inserts cast in the central spacers for the bottom coil layers and provide the foundation for coil assembly. The coils and spacers are assembled onto this subassembly. The coils are connected, then wrapped with fiberglass cloth to hold them in place. The foil ground sheet and steering coils, interleaved with fiberglass veil cloth are then wrapped around this subassembly before final potting.

9. MAGNET PROTOTYPE

Two single channel quadrupoles were constructed and tested to measure electrical properties of the combined pulser and magnet system, and to verify voltage holding capability. These magnets were connected in series and pulsed (0.8mS) at +/-3.2kV each (4000A), at a rate of one pulse every three seconds for 5 hours. After fixing an initial breakdown in one of the leads, the magnets operated successfully with no breakdown or signs of corona. Return voltage available to the recirculator is 82% of input, or 67% energy recovery possible. A 20°C temperature rise was measured at the end of the test; there was no water or forced air cooling, only thermal conduction to the core, with free convection air cooling.

DESIGN AND CONSTRUCTION OF SEPTUM MAGNETS AT THE 7-GeV APS*

A. Gorski,# R. Wright, C. Pitts, S. Sharma
Advanced Photon Source, Argonne National Laboratory, 9700 S. Cass Avenue, Argonne, IL 60439

Abstract

The mechanical design, construction, and assembly procedure of six different septum magnet designs used in the Advanced Photon Source (APS) facility will be described. This will include a positron accumulator ring (PAR) AC septum magnet, a synchrotron thin injection septum, AC thin and thick extraction septa, and storage ring AC thick and thin injection septum magnets.

Design parameters, material selection, assembly procedures, and operational results will be presented.

1 INTRODUCTION

The development of septum magnet fabrication at the APS facility has been a challenging endeavor. Pulsed septum magnet design and construction offers the magnet engineer several challenges in material selection, magnet assembly, and construction tolerances. Nonsteady-state forces can lead to material flexture and resultant metal fatigue. High radiation environments limit material selection for coil electrical insulating materials. In some situations, designs require that the laminated core of the magnet be in the vacuum environment. Outgassing of trapped interlamination air can be a major concern when one is required to maintain an ultrahigh vacuum. With core-in-vacuum designs special care must be taken with water connections. No water to vacuum joints are allowed in the septum magnet design. The electrical constraints are no less trivial. Pulsed septum magnets naturally imply high currents of the order of 500 to 12000 amps.

The most important feature of septum magnets is to have a homogeneous field in the magnet gap and a low to zero leakage field outside the gap such that the circulating beam is not affected. A single septum conductor is used to separate the gap field from the zero field external region. To facilitate merging of the injected and stored beams, the septum conductor is designed to be as thin as possible without compromising its mechanical, thermal, electrical, or magnetic shielding performance. In some designs, septum conductors can be 2.5 mm thick or less.

*Work supported by the U.S. Department of Energy, Office of Basic Energy Sciences, under Contract No. W-31-109-ENG-38.
Email: gorski@aps.anl.gov

2 MECHANICAL AND OPERATIONAL PARAMETERS

The APS facility uses six different septum magnets that are described below.

2.1 PAR AC Injection and Extraction Septum

The PAR AC septum magnet is mechanically the most complex of all the APS septa. Designed to operate with a peak current of 12.057 kA and a repetition rate of 60 Hz, its thermal design required considerable development. The complete magnet is contained in a vacuum enclosure 61 cm long by 25.4 cm wide by 17.8 cm high. The core, septum plate, and backleg conductor are all water cooled. The septum plate thickness is 2 mm. The core is stacked laminations of M22 silicon steel with C5 coating on both sides; each lamination thickness is 0.36 mm. The core end-pack is fabricated from laminations that are modified with tapered bevels designed to reduce heating at the ends. Additional cooling plates are provided on the end packs for water cooling. All power and cooling water feedthroughs are electrically insulated from the vacuum enclosure. The magnet is shown schematically in Fig. 1 with operational parameters listed in Table 1.

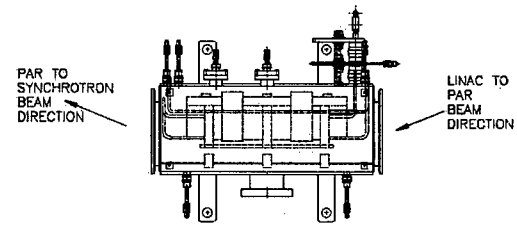

Figure 1. PAR AC septum magnet

Table 1: PAR AC septum magnet parameters

Number	1
Physical Length	0.48 m
Effective Length	0.4 m
Field Strength	0.75 T
Maximum Septum Thickness	2 mm (+)
Magnetic Field Aperture	7.0 x 2.0 cm
Bending Angle	199.6 mrad
Peak Current	12.057 kA
Peak Power	29 kW
Rep Rate	60 pps
Pulse Length (half sine wave)	275 μs
Average Power	0.574 kW

0-7803-5573-3/99/$10.00@1999 IEEE.

2.2 Synchrotron Injection Thin Septum

The synchrotron injection thin septum magnet is of the core-in-vacuum design. The core is stacked to a radius of curvature of 3.18 m. The laminations are 0.36-mm-thick M22 silicon steel coated with a C5 type insulation on both sides. The laminations are oven baked before use to insure cleanliness. As is usual in the stacking process, the laminations are stacked in approximately 25.4 mm packs, alternating the witness notches from one side to another. The ends of the stack have solid end packs 1.19 cm thick, composed of CRS-1018 steel. As can be seen in Fig. 2, all the magnet components are put into a vacuum-tight box-like structure. The septum plate itself is 2 mm thick and machined from explosion-bonded copper and steel material. It is not direct-driven but rather acts as an eddy-current shield preventing field from leaking into the field free region. The single-turn primary coil is fabricated from OFHC copper of dimensions 1.59 cm by 0.635 cm. The synchrotron injection thin septum is shown schematically in Fig. 2 with operational parameters given in Table 2.

At the present time, another synchrotron injection thin septum magnet of an out-of-vacuum core design is being assembled. With core laminations outside the vacuum envelope, this design will allow quick pump down in case of a vacuum leak.

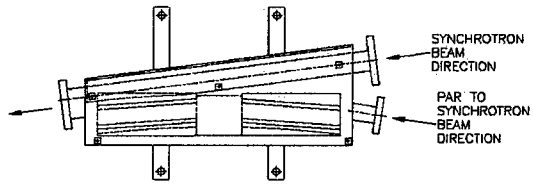

Figure 2: Synchrotron injection thin septum

Table 2: Synchrotron injection thin septum parameters

Number	1
Maximum Allowable Septum Thickness	4 mm
Physical Length	0.9 m
Effective Length	0.85 m
Bending Angle	0.2771 rad
Peak Field at 450 MeV	0.49 T
Gap Height	30 mm
Gap Width	40 mm
Peak Current	11.8 kA
Peak Power	30 kA
Pulse Width	333 μs
Average Power	0.02 kW

2.3 Synchrotron AC Thin Extraction Septum

This septum magnet is of the core-in-vacuum type with a total septum plate thickness of 4 mm. The core itself is composed of a stack of approximately 2680 laminations (0.36 mm thick) stacked to a core length of 1.03 m. The laminations are a low carbon silicon steel coated with C5 insulation on each side. The ends of the core have solid end packs of CRS-1018 steel, 1.19 cm thick. The core was stacked and welded in the same fixture alternating 2.54-cm packs of laminations along the length of the core.

The septum plate itself is fabricated from explosion-bonded copper and steel plate. The total septum plate thickness is 3.76 mm and again acts as an eddy-current shield. The septum magnet is shown schematically in Fig. 3. Some operational parameters are given in Table 3.

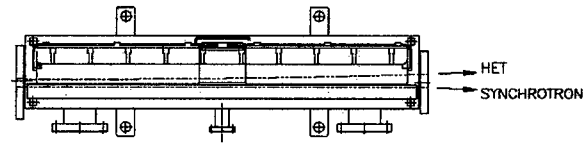

Figure 3: Top view synchrotron extraction AC thin septum

Table 3: Synchrotron AC thin extraction septum parameters

Number	1
Maximum Effective Septum Thickness	4 mm
Physical Length	1.06 m
Effective Length	1.05 m
Bending Angle	33 mrad
Peak Field at 7 GeV	0.73 T
Gap Height	20 mm
Gap Width	34 mm
Peak Current	11.74 kA
Peak Power	62 kW
Pulse Width (1.5 kHz 1/2 sine wave)	333 μs
Average Power	0.042 kW

2.4 Synchrotron AC Thick Extraction Septum

This septum magnet is of the core-out-of-vacuum design, stacked to a radius of curvature of 30.5 m, yielding a bending angle of 73.53 mrad. The core is composed of stacked laminations (4712) with laminated end packs that are chamfered at 45°. The core length is 1.7 m.

The coils used in this magnet are fabricated from 4.19-mm square conductor with a 2.41-mm diameter hole for water cooling. The material is oxygen-free copper with CDA alloy no. 102. The coil configuration itself is a 6 × 6 matrix with dimensions of 2.86 cm × 2.86 cm with a 4.19-cm gap. The coil is a saddle type, 1.76 m long, and weighs 15 kg. This magnet is shown schematically in Fig. 4 with operational parameters given in Table 4.

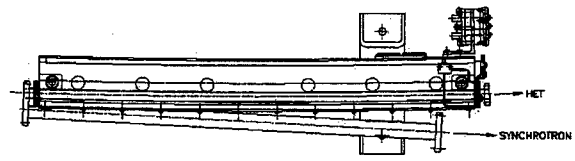

Figure 4: Top view synchrotron AC thick extraction septum

Table 4: Synchrotron AC thick extraction septum and storage ring thick injection septum parameters

Number	1
Minimum Septum Thickness	30 mm
Physical Length	1.79 m
Effective Length	1.75 m
Bending Angle	73.53 mrad
Peak Field at 7 GeV	0.98 T
Gap Height	30 mm
Gap Width	40 mm
Peak Current	0.66 kA
Peak Power	80 kW
Pulse Width	10 ms
Average Power	0.797 kW

2.5 Storage Ring AC Thick Injection Septum

The core and coils used for this magnet are identical to those used in the synchrotron AC thick extraction septum. The vacuum chamber used in this magnet is a curved rectangular chamber 1.535 inches high made from an Inconel® channel. The coils are the same as in the synchrotron AC thick extraction septum.

This magnet is shown schematically in Fig. 5 with operational parameters given in Table 4.

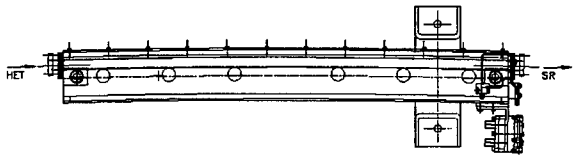

Figure 5: Storage ring AC thick injection septum

2.6 Storage Ring AC Thin Injection Septum

The core of the storage ring AC thin injection septum is comprised of 0.356-mm thick laminations (M22 silicon steel with C5 coating) stacked to a length of 1.04 m. On each end of the core are 2.52-cm-thick laminated end packs. The core, which is stacked straight, is held together with side and bottom tie bars. Inside the gap is a formed beam vacuum tube. This tube is made from Inconcel 625 metal and is 127.8 cm long with a 0.347-mm wall thickness. It is positioned in the core by means of five tube supports fabricated from MYKROX/MYCALEX GRADE machinable ceramic. The copper septum conductor is 1.1 mm thick. Following assembly of the core, Inconel vacuum chamber, and ceramic stand-offs, the remaining open volume of the magnet gap is filled with a concrete type material thereby yielding a solid, one-piece unit suitable for high radiation environments. The magnet is then completed with the addition of the field-free tube vacuum chamber which doubles as a magnetic shield, tie bars, flanges, etc. The gap between the inside wall of the embedded vacuum chamber and the inside wall of the stored beam vacuum chamber is specified to be 2.4 mm; however, in actuality it is 3.5 mm. Special care is necessary in welding the vacuum chambers to prevent weld bead from enlarging this area. The septum magnet is shown in Fig. 6. Some operational parameters are given in Table 5.

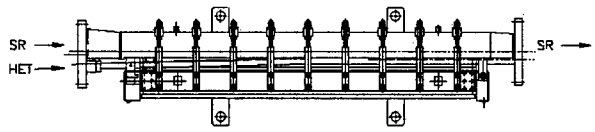

Figure 6: Top view of the storage ring AC thin injection septum

Table 5: Storage ring AC thin injection septum parameters

Number	1
Maximum Effective Septum Thickness	3.5 mm
Physical Length	1.06 m
Effective Length	1.05 m
Gap Height	20 mm
Gap Width	34 mm
Bending Angle	33 mrad
Peak Field	0.73 T
Peak Supply Current	11.74 kA
Peak Power	62 kW
Power	0.042 kW
Pulse Width (1.5 kHz 1/2 sine)	530 μs
Average Power	0.042 kW

3 CONCLUSION

The primary septum effort at the APS is complete, and spare magnets have been assembled and tested. Existing magnets in the facility are being monitored for their performance, and maintence and upgrades are made as rquired. A new out-of-vacuum core direct-drive design for the synchrotron injection septum will soon be complete.

4 ACKNOWLEDGMENTS

The septum magnet program at APS has occupied the talents of many physicists, engineers, designers, and technicians. The author (AG) is at the end of a long effort that was a collaboration of many very capable people, listed below.

Physicists: Kenneth Thompson, Klaus Halbach, Fred Mills, Stephen Milton, John Galayda; Engineers: Stan Reeves, Sam Sheynin, James Humbert, Jack Jagger; Designers: Glen Cherry, Frank McConologue, Mike Harkins, Thomas Crain, Steven Hanuska, Ron Kmak; Technician: John Pace.

HARMONIC MEASUREMENT FOR KEK B-FACTORY STEERING MAGNETS

Y.Han, Z.Q.Feng, W.Chen, B.G.Yin,G.Y.Zhao
Institute of High Energy Physics, Chinese Academy of Sciences, Beijing

Abstract

Total of 920 steering magnets for KEK B-Factory have been measured by the microcomputer controlled measurement system at IHEP. It took more than two years. During this period, two reference magnets were measured many times. The reproducibility for the reference magnets is better than 8×10^{-4}.This system was used to measure magnets for BEPC (Beijing Electron Positron Collider) ten years ago. But it has been improved and updated to meet the new requirements. This paper will cover the details of the measurement system devices, method as well as results.

1 INTRODUCTION

The measurement system has been improved to measure the steering magnets for KEK B-Factory at IHEP. According to the field measurement requirement for KEK B-Factory steering magnets, we measured 920 KEK B-Factory steering magnets. We started this work in February 1996 and finished it in July 1998. These magnets are divided into four types according to their different field strength. We use the same measurement system but different magnet power supplies. The requirements of measurement specification are as follows:

- Multiple contents at the reference radius of 50 mm
- The integral field distribution along the vertical direction
- Excitation curve of the integral field

2 HARMONIC MEASUREMENT SYSTEM

The measurement system is based on the harmonic coil method. The block diagram of rotating long coil measurement system is shown in Fig.1. It consists of rotating long coil, AC motor and data acquisition system.

- Rotating long coil: It was used to measure magnets for BEPC ten years ago. The measurement system was updated for KEKB magnets.
- Switch box: It was used to improve the bucking ratio by precise potentiometer. For these measurements, we used the unbucked method.
- Amplifier and 14 bit Analog and Digital Converter.
- Angular encoder: 5VN271DZ, 1024 cycles per turn with index signal.
- AC Motor: 11turns per second by decelerator.
- Computer: The computer controls the measurement procedures and performs the data process. The software is written in Quick BASIC language.
- Magnet power supply: It is controlled by the computer. The current stability is better than 1×10^{-4}.

The resolution of the measurement coil and data acquisition system is the order of 10^{-5} .The relative precision of the rotating measurement system is better than 2×10^{-4}. The absolute precision is better than 5×10^{-4}.

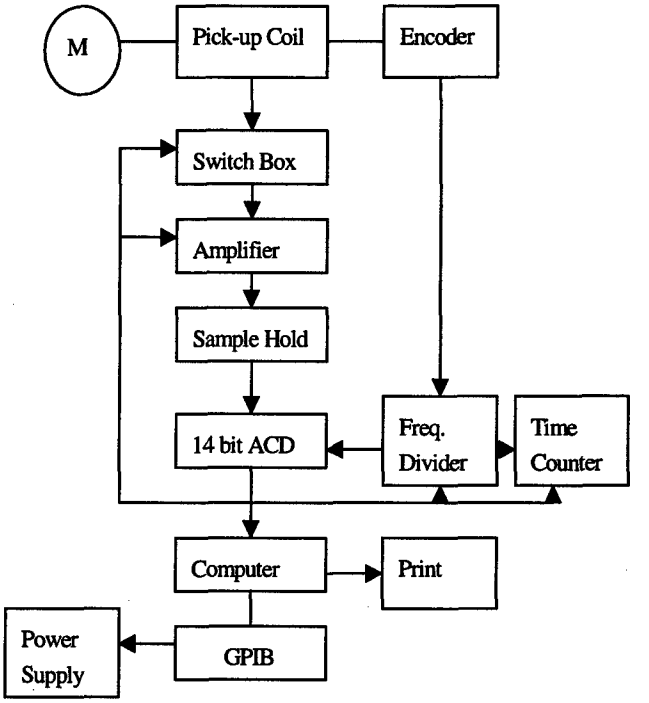

Fig.1 Block Diagram of the measurement system

3 FIELD MEASUREMENT RESULTS

- Quality of magnetic field

The field measurements include multiple contents, integral field distribution and excitation cure of the integral field. The excitation curve of KEK-HER-400 is shown in Fig.2. The average values of integral field for 400 KEKB-HER-STV magnets and 420 KEKB-LER-STV magnets are 22317.5 Gs-cm and 14174.05 Gs-cm respectively. The integral field dispersion of 400 KEKB-HER-STV magnets at 3A is shown in Fig.3 and 420 KEKB-LER-STV magnets in Fig.4. Their Standard Deviations are 8.36×10^{-4} and 1.54×10^{-3}.

Y.Han Email hanyi@bepc3.ihep.ac.cn

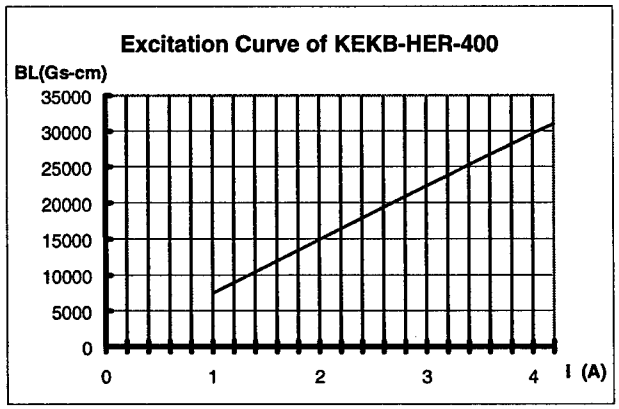

Fig.2 Excitation Curve of KEK-HER-400

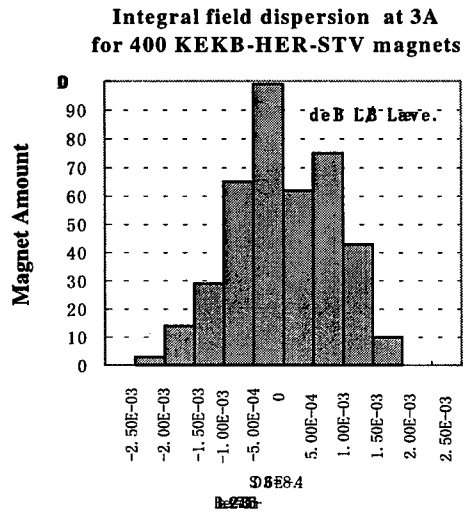

Fig.3 Integral field dispersion at 3A for 400 KEKB-HER-STV magnets

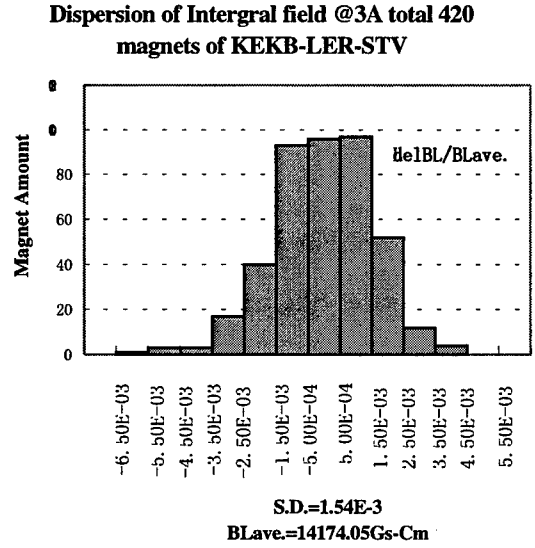

Fig.4 Integral field dispersion at 3A for 420 KEKB-LER-STV magnets

Position	S.D. (HER)	S.D. (LER)
-5	8.06E-04	9.24E-04
-4.5	6.84E-04	7.76E-04
-4	5.92E-04	6.68E-04
-3.5	5.08E-04	5.71E-04
-3	4.29E-04	4.80E-04
-2.5	3.53E-04	3.94E-04
-2	2.80E-04	3.11E-04
-1.5	2.09E-04	2.30E-04
-1	1.39E-04	1.52E-04
-0.5	6.91E-05	7.54E-05
0	0	0
0.5	6.91E-05	7.44E-05
1	1.38E-04	1.48E-04
1.5	2.08E-04	2.22E-04
2	2.79E-04	2.95E-04
2.5	3.51E-04	3.69E-04
3	4.24E-04	4.44E-04
3.5	4.99E-04	5.21E-04
4	5.77E-04	6.01E-04
4.5	6.61E-04	6.90E-04
5	7.66E-04	8.19E-04

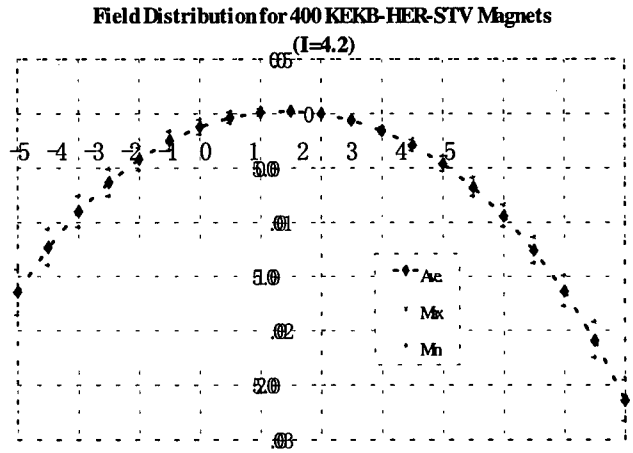

Fig.5 Field distribution for 400 KEK-HER-STV magnets

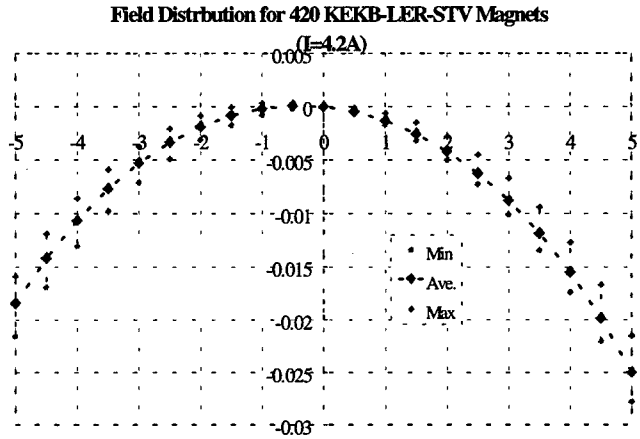

Fig.6 Field distribution for 420 KEK-LER-STV magnets

The field distribution for 400 KEKB-HER-STV magnets is shown in Fig.5, 420 KEKB-LER-STV magnets in Fig.6. These magnets are C type, their left sides are opened.

- Reproducibility of measurement

We regarded KEKB-LER-400 and KEKB-HER-400 as reference magnets. We monitored the stability of measurement system by measuring the reference magnets. We measured two reference magnets 29 times during this period. The reproducibility of the integral dipole field is better than 8×10^{4}. The integral field dispersion $\Delta \int$ Bdl/($\int$ Bdl)ave. of KEKB-LER-400 magnet at 2A is shown in Fig.7, and that of KEKB-HER-400 magnet is shown in Fig.8

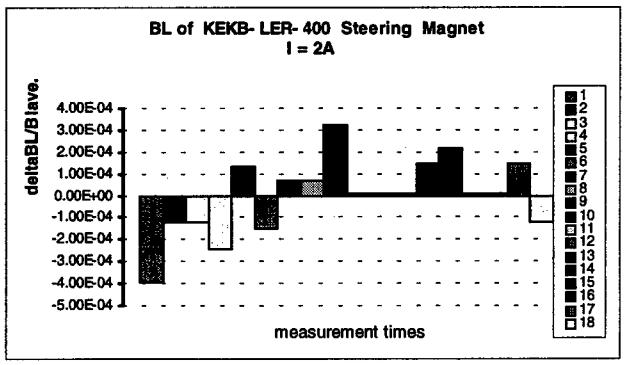

Fig.7 The integral field dispersion of KEKB-LER-400 at different measurement times

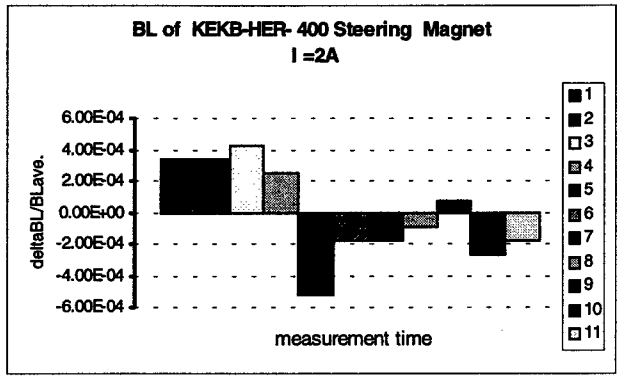

Fig.8 The integral field dispersion of KEKB-HER-400 at different times

4 CONCLUSION

The field performance of the magnets satisfies the KEK B-Factory specification requirements. From the measurement results, it is concluded that the harmonic measurement system has the performance with high resolution and repeatability.

5 ACKNOWLEDGEMENT

The authors would like to thank Prof. Z.S.YIN, R.HOU and Z.CAO for giving us a lot of help. Thanks should also be given to colleagues in IHEP for their help.

6 REFERENCES

[1]R.HOU, F.L.REN " The Field Measurement System for PEP-II LER Quadrapoles" MT-15,Oct. 1997

EDDY FIELD MEASUREMENT BY USING SEARCH COILS FOR BENDING MAGNET

Y. Kanai* and M. Fujioka, Tohoku University, Sendai 980-8578, JAPAN
Y.Mori, M.Muto, E.Yanaoka, KEK-Tanashi, 3-2-1 Midori-cho, Tanashi 188-8501, JAPAN
H.Someya, F.Q. Zhang, T.Adachi, KEK, 1-1 Oho, Tsukuba 305-0801, JAPAN

Abstract

In order to estimate a field disturbance of a guiding field of a synchrotron due to an eddy current, magnetic fields in a bending magnet have been measured. The magnet was excited by a sinusoidal current with a repetition of 30 Hz. Two search coils were used in the measurements. One is a reference coil and the other is a measurement coil. An imaginary part of an eddy field was derived from phase difference between two coil signals. The results were compared with a simple two-dimensional model.

1 INTRODUCTION

The JHF(Japan Hadron Facility) plan is being progressed. The JHF accelerator complex comprises the 200 MeV linac, the 3 GeV synchrotron and the 50 GeV synchrotron.

The 3 GeV booster synchrotron is a rapid-cycling synchrotron with a repetition of 25 Hz. In such a rapid-cycling synchrotron, it is expected that an eddy field disturbs a guiding field. There are some eddy current sources: metal wall of a vacuum chamber installed in a pulsed magnet and magnet components(e.g. magnet core, a end plate made of stainless steel and coil conductor).

Since a ceramic chamber is usually used in a rapid-cycling synchrotron, the eddy current induced in magnet components mainly contributes to the field disturbance.

Therefore, it is important to estimate an effect of the eddy field due to magnet components. It has been known that the eddy field became larger as closer to the magnet edge [1].It implies that a contribution of the end plate to the eddy field is rather large than magnet core and conductor material. Taking into account this consideration, we constructed a simple two-dimensional model.

This paper describes the results of the field measurement and our simple model.

2 FIELD MEASUREMENT

2.1 Measurement

A test magnet for the JHF 50 GeV ring was used for the eddy-field measurement. Fig. 1 shows the test magnet. The test magnet was excited with a repetition of 30Hz by an ac power supply using IGBT [2]. Fig 2 shows cross sections of the magnet: the left is cut by x-y plane and the right cut by y-z plane. The coordinate system defined here is used through this paper.

*Email: ianak@tanashi.kek.jp

The field measurement was performed on the median plan($y = 0$).

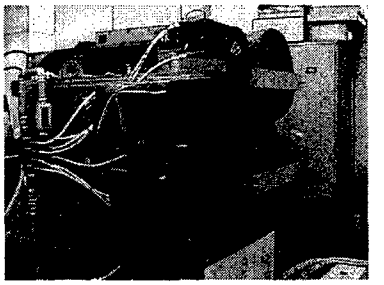

Figure 1: Test magnet for the JHF 50 GeV ring

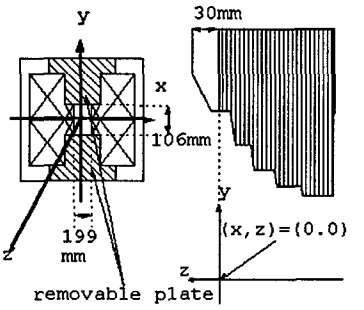

Figure 2: Cross section of the test magnet

In this measurement, two search coils were used: one is a reference coil and the other is a measurement coil. The reference coil was fixed at the center of the magnet, since the eddy current effect was expected to be negligible at this position. On the other hand, the measurement coil was moved on the median plan. Since the magnet is excited by a sinusoidal current with the repetition of 30 Hz, magnetic flux density at the reference point(B_{ref}) is given by,

$$B_{ref} = B_0 e^{i\omega t} \tag{1}$$

The flux density at measuring point (B_{meas}) is given by,

$$B_{meas} = (b_1 + b_2 e^{i\delta}) e^{i\omega t} = B_1 e^{i(\omega t + \theta)} \tag{2}$$

where b_1 is the amplitude of a main field and $b_2 \exp(i\delta)$ is it the amplitude of the eddy field. θ and B_1 are given by,

$$\theta = \tan^{-1}\left(\frac{b_2 \sin\delta}{b_1 + b_2 \cos\delta}\right) \tag{3}$$

and

$$\begin{aligned} B_1 &= (b_1{}^2 + b_2{}^2 + 2b_1 b_2 \cos\delta)^{\frac{1}{2}} \\ &\approx b_1 + b_2 \cos\delta, \end{aligned} \tag{4}$$

0-7803-5573-3/99/$10.00@1999 IEEE.

respectively. Here, we assumed that the eddy field is sufficiently small compared with the main field, i.e. $b_1 \gg b_2$

In terms of eqs (3) and (4), an imaginary part of the eddy field is obtained as follows:

$$b_2 \sin\delta = B_1 \tan\theta. \tag{5}$$

In order to measure a contribution of the end plate definitely, we made a part of the end plate removable, as shown in figure 2.

Signals of two search coils were sent to a fft servo analyzer, and phase difference θ and B_1 was measured.

2.2 *Experimental Results*

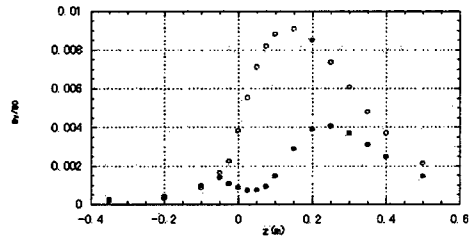

Figure 3: Longitudinal dependence of the eddy field.

The longitudinal dependence of the imaginary part of the eddy field is shown in figure 3. Here, open-circles denote the results in the normal case and solid-circles denote the results in the case that the removable plate is changed by a Bakelite plate. The eddy field is normalized by a component of the main field(B_0) at the magnet center.

The results show that the contribution of the end plate is rather large. It is consistent with the former results[1].

The contribution of the removable plate to the eddy field can be estimated by subtracting the latter results from the former. It will be compared with a simple two-dimensional model.

3 TWO-DIMENSIONAL MODEL

3.1 *Formulation*

The fundamental equations describing eddy currents are as follows:

$$\begin{aligned} rot\vec{E} &= -\frac{\partial \vec{B}}{\partial t} \\ rot\vec{H} &= \vec{j} \\ \vec{j} &= \sigma\vec{E}, \end{aligned} \tag{6}$$

where $\vec{H}$ and $\vec{E}$ are the magnetic and electric field strength, respectively. $\vec{B}$ is the magnetic flux density and $\vec{j}$ is the current density, μ and σ are magnetic permeability and electric conductivity, respectively.

It is assumed that all material parameters are constant both in time and space. Eliminating $\vec{E}$ and $\vec{j}$ from the fundamental equations, one can obtain the following equation.

$$\nabla^2\vec{H} - \sigma\mu\frac{\partial\vec{H}}{\partial t} = 0. \tag{7}$$

In a vacuum, assuming that $\sigma = 0$,

$$\nabla^2\vec{H} = 0. \tag{8}$$

Here, the magnetic field $\vec{H}$ is superposition of the external field $\vec{H}_{ext}$ and the eddy field $\vec{v}$.

$$\vec{H} = \vec{H}_{ext} + \vec{v}. \tag{9}$$

In addition, setting $\vec{H} = \hat{\vec{H}}e^{i\omega t}$, we obtain the following equation:

$$\nabla^2\hat{\vec{v}} - i\omega\sigma\mu(\hat{\vec{H}}_{ext} + \hat{\vec{v}}) = 0. \tag{10}$$

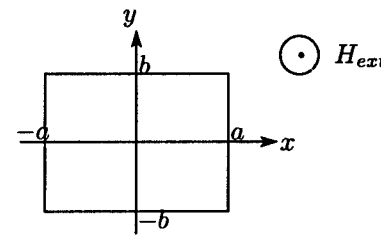

Figure 4: two-dimensional problem

In order to solve the above equation, we make a problem to be restricted to two-dimensional case, where the eddy current is bounded in a conducting plane, which is rectangular plane with size of $2a \times 2b$, and the external field is perpendicular to the plane, as shown figure 4.

The solution is obtained by giving a boundary condition that $\hat{v} = 0$ along the circumference. The result is as follows:

$$\hat{v} = -k\hat{H}_{ext}\frac{16}{\pi^2}\sum_{m,n=1}^{\infty} \frac{(-1)^{m+n}\cos\frac{2m-1}{2a}\pi x\cos\frac{2n-1}{2b}\pi y}{\{(\frac{2m-1}{2a}\pi)^2 + (\frac{2n-1}{2b}\pi)^2 + k\}(2m-1)(2n-1)}, \tag{11}$$

where $k = i\omega\sigma\mu$ and we assumed that $\hat{H}_{ext} = constant$. The eddy current can be obtained by $\vec{j} = rot\vec{v}$, therefore j_x and j_y is given by,

$$\frac{j_x}{\hat{H}_{ext}} = k\frac{16}{\pi^2}\sum_{m,n=1}^{\infty} \frac{(-1)^{m+n}\frac{2n-1}{2b}\pi\cos\frac{2m-1}{2a}\pi x\sin\frac{2n-1}{2b}\pi y}{\{(\frac{2m-1}{2a}\pi)^2 + (\frac{2n-1}{2b}\pi)^2 + k\}(2m-1)(2n-1)} \tag{12}$$

and

$$\frac{j_y}{H_{ext}} = -k\frac{16}{\pi^2}\sum_{m,n=1}^{\infty} \frac{(-1)^{m+n}\frac{2m-1}{2a}\pi \sin\frac{2m-1}{2a}\pi x \cos\frac{2n-1}{2b}\pi y}{\{(\frac{2m-1}{2a}\pi)^2+(\frac{2n-1}{2b}\pi)^2+k\}(2m-1)(2n-1)}. \quad (13)$$

A fraction of the eddy current of the conducting plane contributes the eddy field at the field point, P, by $d\vec{H}_{eddy}$, as shown in figure 5.

$$d\vec{H}_{eddy} = \frac{I}{4\pi}\frac{d\vec{s}}{|\vec{r}_1|^2} \times \frac{\vec{r}_1}{|\vec{r}_1|}. \quad (14)$$

We must also take into account magnetic charge, τ, induced on the surface of the magnet core. τ is approximately given by

$$\tau \approx \mu_0(\vec{H}_{eddy})_\perp, \quad (15)$$

where $(\vec{H}_{eddy})_\perp$ is the component of the eddy field perpendicular to the core surface. Hence, the contribution of the magnetic charge at P , $d\vec{H}_m$ is obtained as

$$d\vec{H}_m = \frac{\tau dx'dy'}{4\pi\mu_0|\vec{r}_2|^2}\frac{\vec{r}_2}{|\vec{r}_2|}. \quad (16)$$

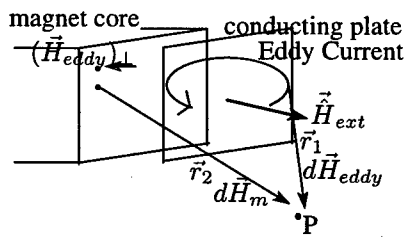

Figure 5: Model of the field calculation

Consequently, the magnetic field at P is given by,

$$\vec{H} = \int_{coresurface} dH_m + \int_{conductorplane} dH_{eddy}. \quad (17)$$

3.2 *Comparison with Measurements*

The figure 6 and 7 show longitudinal and transverse distribution of the eddy field, respectively. Open circles and dots denote experimental results and calculations, respectively.

Unfortunately, the values of the experimental results are larger than the calculation by a factor of 1.7.

In order to compare a shape of distribution, each result is normalized by peak value of figure 7. As shown in the figures, the shape of the field distribution is well explained by our model.

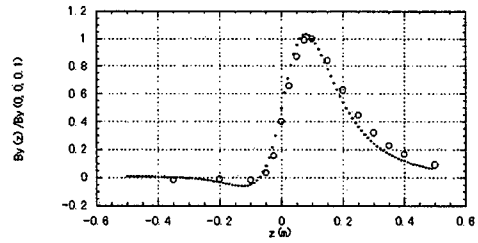

Figure 6: Longitudinal distribution of the eddy field

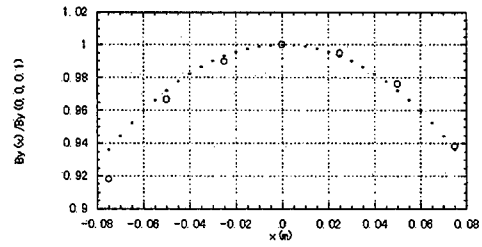

Figure 7: Transverse distribution of the eddy field

4 CONCLUSION

The field disturbance due to the eddy current induced in a magnet end plate was measured. The results are compared with a simple analytical model. The model can explain the shape of distribution, while the values are less than the experimental results. Such a discrepancy may be caused by an assumption of a constant external field($\vec{H}_{ext}$), since $\vec{H}_{ext}$ is not constant actually on the end plate.

Another possibility is that the contribution of the magnetic charge induced by the eddy field is not sufficiently estimated. This problem is now being considered.

An eddy field due to a vacuum chamber in a pulsed magnet can be also calculated using our model. Therefore the eddy field due to the vacuum chamber will be measured soon.

5 ACKNOWLEDGMENTS

The authors would like to say thanks Dr. A. Takagi for his advice during this work. We also would like to thank KEK members for their fruitful help.

6 REFERENCES

[1] Y.Kanai, T.Adachi, M.Fujioka and Y.Mori, "Eddy field Measurement Using a Peaking-Strip" ,11th Symposium on Accelerator Science and Technology, Japan,(1997).

[2] M.Muto, Y.Kanai, T.Kubo, Y,Mori, T.Morimoto, K.Niki, Y.Nishiyama, H,Sato, K.Shino and E.Yanaoka, "Magnets and Power Supply System of JHF 50-GeV Main Ring",APAC'98,Japan,(1998).

FIELD MEASUREMENT RESULTS OF THE KEK B-FACTORY QUADRUPOLE AND SEXTUPOLE MAGNETS

K.Egawa, M.Masuzawa#, KEK, Tsukuba, Japan

Abstract

The magnetic properties of the quadrupole and sextupole magnets for the KEK B-factory rings (LER and HER)[1] are measured by two sets of harmonic coil systems, one for the LER magnets and the other for the HER magnets, at KEK over an 18 month period[2]. The main field strength, offsets between the mechanical and magnetic centers, higher order multipole components and effective lengths of the magnets are measured.

1 INTRODUCTION

The design parameters of the quadrupole and sextupole magnets are given in Table 1[1]. QA(HER) and QB(HER) are recycled TRISTAN magnets[3]. QA(LER), Qs(HER), Qx(HER), QA(HER) and QB(HER) are the quadrupole magnets in the arc sections. Qrf(LER) and Qrf(HER) are the quadrupole magnets for the straight sections where the RF stations are located[1]. The skew quadrupole magnets are Qsk(LER), Qsk1(HER), and Qsk2(HER). The remaining magnets in the table are the sextupole magnets. The field gradient in the table is calculated at the maximum current of the power supplies used. The maximum current values are 200A for the skew quadrupoles, 500A for the other quadrupoles and 425A for the sextupoles. All of the magnets are fabricated from 0.5 mm-thick lamination plates. The specified tolerance for the core assembly is 0.35mm[3].

Table 1: Magnet parameters

Magnet	r (mm)	L (mm)	B'(T/m) or B''(T/m^2)	# of mag
QA(LER)	55	400	10.2	414
Qrf(LER)	83	500	6.3	36
Qsk(LER)	105	200	0.7	8
Sx(LER)	56	300	340	104
SxC(LER)	85	300	77.5	4
Qs(HER)	50	500	12.7	80
Qx(HER)	50	760	12.7	4
Qrf(HER)	83	1000	6.3	43
Qsk1(HER)	105	500	0.7	7
Qsk2(HER)	80	300	1.3	5
QA(HER)	50	762	8.5	199
QB(HER)	50	960	8.5	110
SxF(HER)	56	300	340	56
SxD(HER)	56	1000	350	48

Note: r and L denote the bore radius and the lamination length, respectively.

2 HARMONIC COIL MEASUREMENTS

2.1 Quadrupole Magnets

The integrated quadrupole field along the beam line (Z-axis) is measured by a harmonic coil, 1.5m in length for the LER system and 1.8m for the HER system. The dipole components measured by 0.2m short coils are used to calculate the transverse offset between the mechanical and magnetic centers. Figs. 1(a)-(c) show the field strength distributions at various currents for QA(LER). Fig. 1(d) gives the distribution of the ratio of the central field measured by the central short coil to the integrated field measured by the long coil. This is proportional to the effective length of the magnet. Figs. 1(a)-(e) present the corresponding distributions for different currents. The standard deviation has a slight dependence on the field strength. This is due to the iron permeability characteristics at different field strengths. Fig. 2 shows the normalized higher order multipole components for QA(LER). A pole-end shim correction is made in order to reduce the n6 component. The offsets between the mechanical and magnetic centers are shown in Fig. 3 for QA(LER). X, y and z correspond to the horizontal, vertical and beam directions, respectively. The measurement results are summarized in Table 2 for the quadrupole magnets.

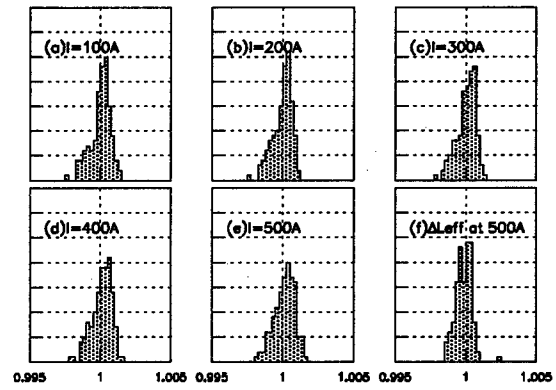

Figure 1: QA(LER) quadrupole field strength distribution at (a)100A (σ=7.1e-04), (b)200A (σ=6.7e-04), (c)300A (σ=6.7e-04), (d)400A (σ=7.2e-04) and (e)500A (σ=7.2e-04). The integrated quadrupole field is normalized by the average value. Fig. 1(f) represents the distribution of the effective length at I=500A (σ=5.7e-04).

Email: mika@post.kek.jp

0-7803-5573-3/99/$10.00@1999 IEEE.

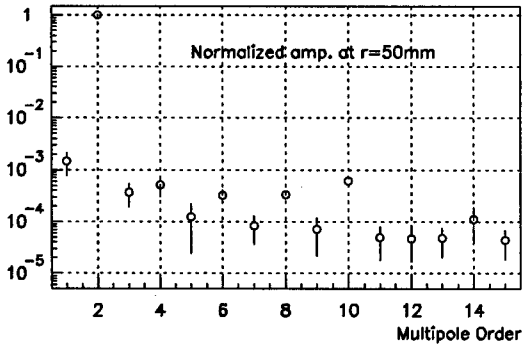

Figure 2: Normalized amplitude is plotted against harmonic numbers for QA(LER). Error bars correspond to one standard deviation.

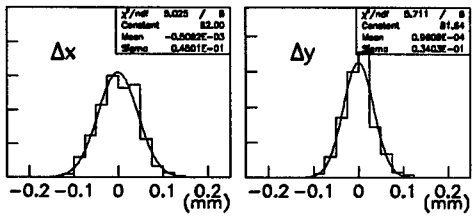

Figure 3: The horizontal and vertical offsets between the mechanical and magnetic centers for QA(LER).

Table 2: Measurement Results for the Quadrupoles

Magnet	ΔB'L	Δx	Δy	ΔL_{eff}
QA(LER)	7.2e-04	50	30	4.5e-04
Qrf(LER)	6.8e-04	30	30	3.5e-04
Qsk(LER)	7.1e-04	50	70	7.0e-04
Qs(HER)	4.9e-04	60	50	6.0e-04
Qx(HER)	7.5e-04	60	10	2.0e-04
Qrf(HER)	5.5e-04	50	40	3.8e-04
Qsk1(HER)	3.1e-04	30	30	4.2e-04
Qsk2(HER)	2.1e-04	40	10	2.7e-04
QA(HER)	6.0e-04	40	70	4.4e-04
QB(HER)	5.0e-04	50	60	4.2e-04

ΔB'L is the RMS of the normalized quadrupole field distribution at the field strength given in Table 1. Δx and Δy are the horizontal and vertical offsets in μm between mechanical and magnetic centers. ΔL_{eff} is the RMS of the effective length.

2.2 *Sextupole Magnets*

The sextupole magnets are measured with the same system as the quadrupole magnets. The normalized integrated sextupole field is plotted against the magnet production number in Fig. 4. The lamination punching dye was modified after the first ~40 magnets. There is a noticeable effect as is shown in the plot. According to the field strength, all of the sextupole magnets are paired so as to keep the difference between the pair below 5.e-04. The sextupole field strength errors are shown in Figs. 5(a)-(d) for SxD. Fig. 5(d) presents the remnant field distribution, which reflects the variation of the coercive force of the iron. The higher order multipole components normalized to the sextupole strength at I=425A is plotted in Fig. 6(a) for SxD(HER) and (b) for SxC(LER). The other measurement results for the sextupole magnets are given in Table 3.

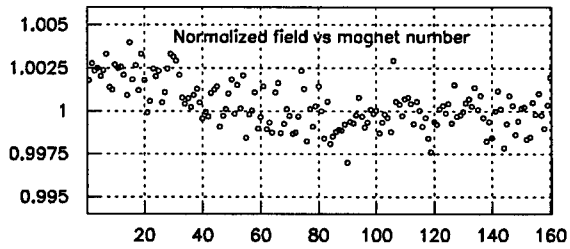

Figure 4: Normalized (by the average) integrated sextupole field plotted against the production number of the magnets.

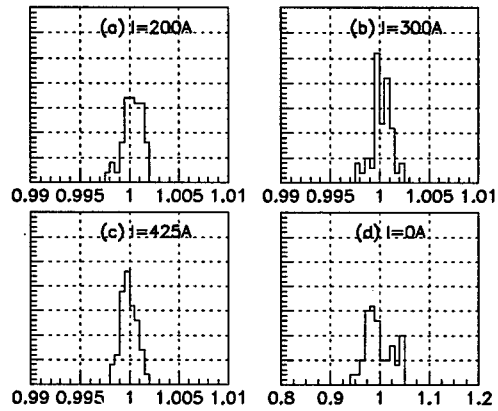

Figure 5: The sextupole field strength distribution at (a)I=200A, (b)I=300A, (c)I=425A and (d)I=0A for SxD. The field is normalized by the average for each current. The RMSs are (a)9.7e-04, (b)1.0e-03, (c)8.0e-04 and (d)2.7e-02.

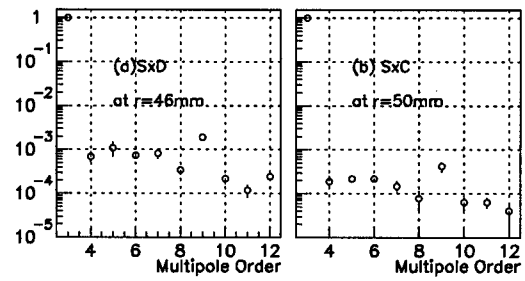

Figure 6: Higher order multipole components at I=425A for (a) SxD(HER) and (b)SxC(LER). A larger bore radius results in the better field quality of SxC(LER).

Table 3: Measurement Results for the Sextupoles

Magnet	ΔB''L	Δx(μm)	Δy(μm)
Sx(LER),SxF(HER)	1.3e-03	30	40
SxC(LER)	3.3e-04	20	20
SxD(HER)	8.1e-04	40	40

3 MAPPING

A mapping is performed for one magnet in each group. The system consists of a twin-flip coil[4]. The coil moves along the Z-direction and the field is measured every 10mm. Fig. 7 and Fig. 8 are the field distribution along the Z-direction for Qrf(LER) and QB(HER). Table 4 summarizes the effective lengths of the quadrupole and sextupole magnets at the maximum field strengths. The L_{eff} dependence on the current (field strength) is plotted for various types of LER and HER quadrupole magnets in Figs. 9(a) and (b).

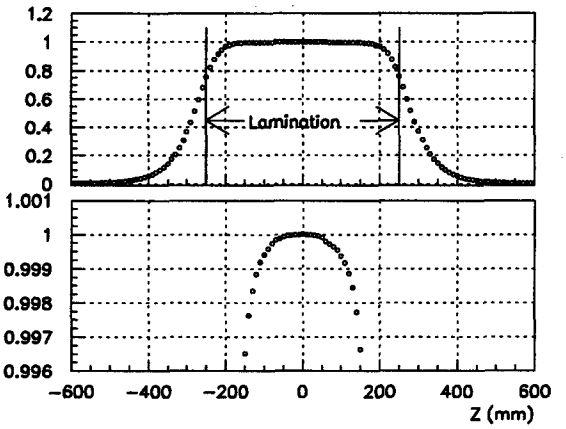

Figure 7: Qrf(LER) mapping results. The top plot shows the entire mapping region while the bottom one shows the central region only (fine scale). The magnet center corresponds to Z=0.

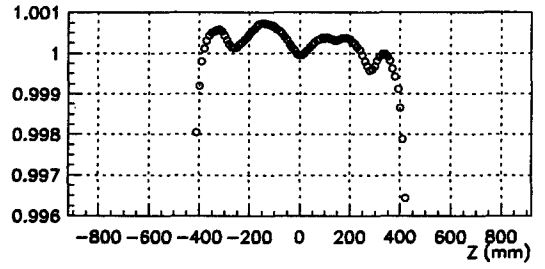

Figure 8: QB(HER) fine scale mapping results. The distribution indicates an uneven lamination stacking or/and a distortion from welding.

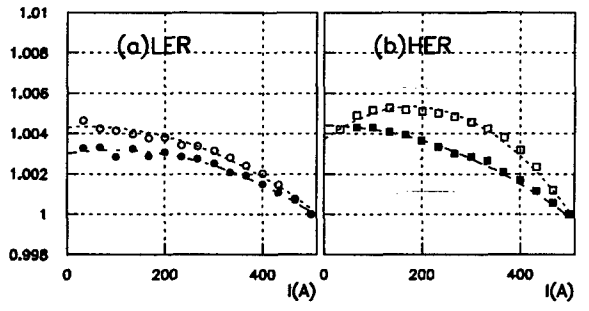

Figure 9: Normalized L_{eff} as a function of I. L_{eff} is normalized by the values in Table 4. Solid circle, open circle, solid square and open square correspond to QA(LER), Qrf(LER), QS(HER) and Qrf(HER), respectively.

Table 4: Effective Lengths calculated from Mapping

Magnet	L_{eff}(mm)	Magnet	L_{eff}(mm)
QA(LER)	458.987	Qrf(HER)	1079.31
Qrf(LER)	582.129	Qsk1(HER)	593.12
Qsk(LER)	297.802	Qsk2(HER)	379.86
Sx(LER)	355.795	QA(HER)	825.42
SxC(LER)	552.767	QB(HER)	1015.51
Qs(HER)	554.102	SxF(HER)	355.80
Qx(HER)	812.589	SxD(HER)	1019.13

4 CALIBRATION

The harmonic coil system is calibrated with a dipole magnet of known integrated dipole field strength, BL. BL is translated into the radius of the harmonic coil and thus the calibration constant is obtained. The calibration constants obtained from this method, however, are still preliminary. Calibration with other methods is needed in order to determine the quadrupole and sextupole field strengths to within 1.e-03 accuracy.

5 SUMMARY

Series measurements of the KEK B-factory LER and HER quadrupole and sextupole magnets are completed. The quality of the newly fabricated magnets and the recycled TRISTAN magnets have been checked. The RMSs of the offsets between the mechanical and magnetic centers are smaller than the beam optics requirements of 0.1 mm in both x and y directions. The RMS of the field strength distributions, the magnitude of the higher order multipole components and the strength of the main field also satisfy the optics requirements.

6 ACKNOWLEDGMENTS

The authors would like to thank the measurement crew for their hard work, the KEK magnet group for many useful discussions.

7 REFERENCES

[1] KEKB B-Factory Design Report 95-7.
[2] K. Egawa and M. Masuzawa, "Preliminary Results of the KEKB Quadrupole Magnet Measurements", EPAC'98, Stockholm (1998).
[3] "TRISTAN electron-positron colliding beam project", KEK Report 6-24 March 1987.
[4] K.Egawa and M.Masuzawa, "Field Measurements of the KEK B-Factory Dipole and Wiggler Magnets", Contribution to PAC99.

STUDY OF THE MAGNETIC COUPLING BETWEEN QUADRUPOLE AND DIPOLE CORRECTOR MAGNETS FOR THE KEK B-FACTORY

K.Egawa, M.Masuzawa, KEK, Tsukuba, Japan

Abstract

Most of the quadrupole magnets in the KEK B-factory are accompanied by a set of vertical and horizontal dipole corrector magnets in both the LER and HER rings[1]. The typical separation between a quadrupole and a dipole corrector magnet is 202 mm, as measured from the laminated ends. This corresponds to ~3.7 (2.4) times of the bore radius of a quadrupole magnet in the arc (straight) sections. Since the series measurements of quadrupole magnets were performed without any magnetic material nearby[2], the effect of the magnetic coupling from the corrector dipole magnet in the actual beam line needs to be measured. Measurements of the coupling between quadrupole and dipole corrector magnets are presented.

1 INTRODUCTION

Magnetic coupling between a quadrupole and a dipole corrector magnet is measured with two systems, a harmonic coil system and a mapping system[3]. The harmonic coil system is used to measure each of the field components with and without a magnet nearby at various separations between the two magnets. The mapping system is used to measure the field distribution along the beam line to obtain the effective length. Table 1 shows the parameters of the magnets discussed in the following sections.

Table 1: LER Magnet parameters

Magnet name	Magnet type	Lamination length(mm)	r(mm) or g/2
QA	quadrupole	400	55
Qrf	quadrupole	500	83
StV(arc)	dipole corrector	200	76.5
StH(arc)	dipole corrector	200	58
StV(wide)	dipole corrector	200	100
StH(wide)	dipole corrector	200	86

Note: QA and Qrf represent quadrupole magnets in the LER arc sections and straight(RF) sections, respectively. StV(arc) and StH(arc) are the vertical and horizontal dipole corrector magnets in the arc sections. StV(wide) and StH(wide) are the vertical and horizontal dipole corrector magnets for the straight sections, respectively.

2 EFFECT ON THE QUADRUPOLE FIELD

2.1 Effect on the main quadrupole field

A 2.5m harmonic coil is used to measure the magnetic coupling between the quadrupole and dipole corrector magnets as shown in Fig. 1. The quadrupole field is measured without a dipole corrector magnet first. A dipole corrector magnet is placed at various distances and the field of the quadrupole magnet is measured at each distance. No current is applied to the dipole corrector magnet during the measurement.

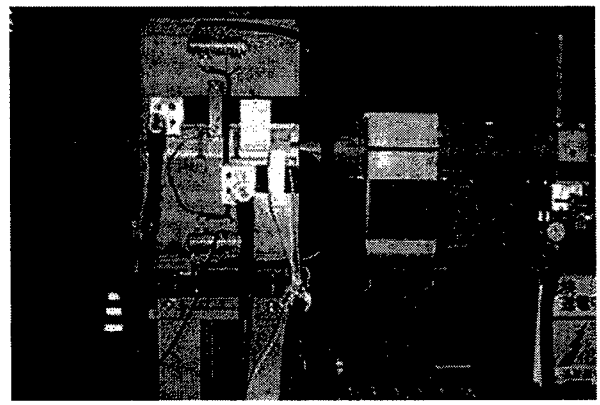

Figure 1: The magnetic coupling measurement between QA (on the left) and StV(arc) by a harmonic coil.

Fig. 2 shows the magnetic coupling effect on the QA integrated quadrupole field when there is an StV(arc) or an StH(arc) nearby. The field is normalized to the case where there is no dipole corrector magnet nearby and plotted against the separation. At a separation of 202 mm (the standard position in the KEKB rings) the integrated main quadrupole field (B'L) is reduced by 0.1% and 0.09% for the combinations of [QA, StH(arc)] and [QA, StV(arc)], respectively. The other combination, [Qrf, StV(wide)] shows a larger coupling effect of 0.2% at the same separation. This is due to the larger Qrf bore radius.

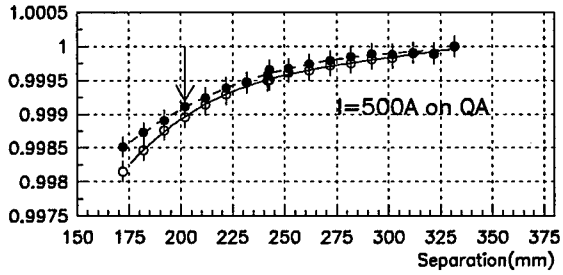

Figure 2: B'L/(B'L with no dipole corrector magnet nearby) is plotted as a function of the separation. The open and solid circles correspond to the combinations of [QA, StH(arc)] and [QA, StV(arc)], respectively. The arrow indicates the standard position of StV(arc) and StH(arc) with respect to QA in the KEKB tunnel.

The magnetic coupling dependence on the QA field strength (i.e., QA current) is measured. Figs. 3(a) and (b)

0-7803-5573-3/99/$10.00@1999 IEEE.

show the coupling effect as a function of QA current. As seen, the current dependence is not significant.

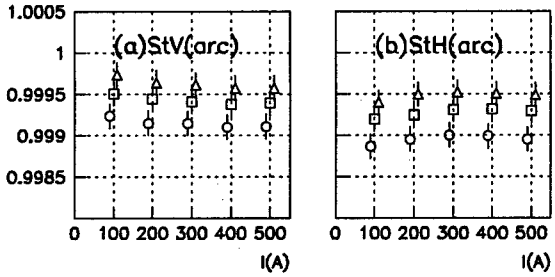

Figure 3: Magnetic Coupling dependence plotted against various QA currents (100A, 200A, 300A, 400A and 500A) for the combinations of [QA, StV(arc)] (a) and [QA, StH(arc)] (b). The open circles, squares and triangles correspond to a separation of 202mm, 222mm and 242mm, respectively.

2.2 *Effect on the higher order multipole components*

In Fig. 4, the effect on the multipole components is shown for the [Qrf, StV(wide)] combination. As mentioned, this combination shows a larger coupling effect than the [QA, StV(arc)] combination. However, no significant effect from the magnetic coupling is observed in the higher order multipole components.

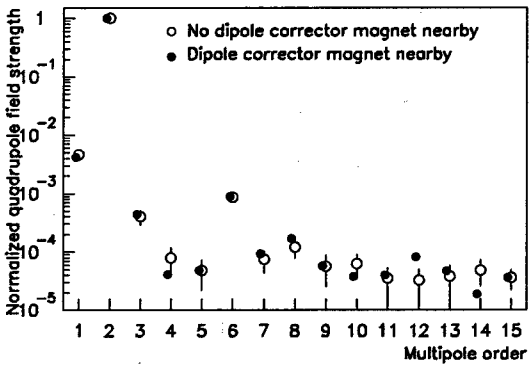

Figure 4: Normalized multipole components of Qrf are plotted. Open circles show the case when there is no dipole corrector nearby. Error bars indicate one standard deviation. Solid circles correspond to the case when a StV(wide) is placed at its standard location.

2.3 *Effect on the effective length*

Fig. 5 shows the mapping system used to obtain the field distribution along the beam line. The effective length, L_{eff}, of QA is calculated from the field distribution shown in Fig. 6(a). L_{eff} changes from 458.99 mm to 458.60 if StV(arc) is placed at the standard position. The reduction in L_{eff} is 0.085%, which agrees with the $\Delta B'L$ measurement made with the harmonic coil discussed in section 2.1. The right side of the field distribution is distorted as shown in Fig. 6(b), which indicates that the field is partially absorbed by StV(arc). Fig. 6(c) shows the difference between the distorted and the original distributions. The absorbed field peaks at z=202 mm, where the StV(arc) lamination begins. The normalized absorbed field is plotted in Fig. 6(d). Almost 100% of the quadrupole field is absorbed by StV(arc) at z=300 mm, which corresponds to the center of the dipole corrector magnet. Table 2 summarizes the coupling effects on QA.

Table 2: Magnetic coupling effect on **QA**

corrector dipole	$\Delta B'L$	Δcenter(mm)
StV(arc)	0.09%	0.236
StH(arc)	0.10%	0.275

Note : The magnetic center moves away from the nearby dipole corrector magnet.

Figure : 5 Mapping system

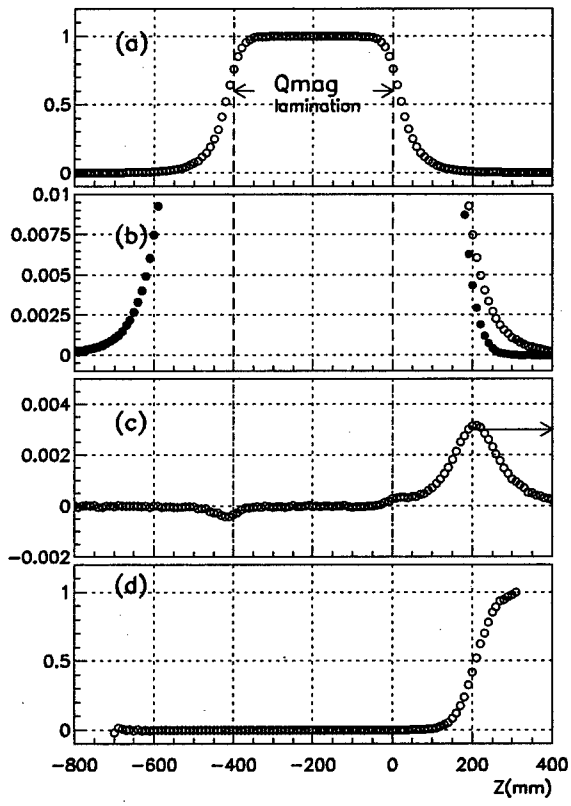

Figure 6: (a) The field distribution along the beam line. z=0 corresponds to the position where QA lamination begins. (b) Two cases with StV(arc) (solid circle) and without StV(arc) (open circle). (c)Difference between the two distributions in (b). Difference distribution (c) is normalized by distribution (a) and plotted in (d).

3 EFFECT ON THE DIPOLE CORRECTOR FIELD

The dipole corrector field also becomes smaller due to the presence of a quadrupole magnet nearby. Fig. 7(a) shows the field distribution of StV(wide) along the beam line with and without a quadrupole magnet in the standard position. A distortion of the field is observed near the quadrupole magnet. The difference between the two distributions is plotted in Fig. 7(b). L_{eff} is reduced from 390.27 mm to 358.29 mm, which corresponds to a 8.9% decrease in BL (kick angle). The dipole magnetic field is absorbed mainly at z=300 mm, where the quadrupole lamination begins, as is shown Fig. 7(c). The effect on the integrated dipole field is also measured by the harmonic coil system. The field reduction is measured to be 8.5%. This indicates that the magnetic coupling effect takes place locally and does not effect the field in the center of the magnet.

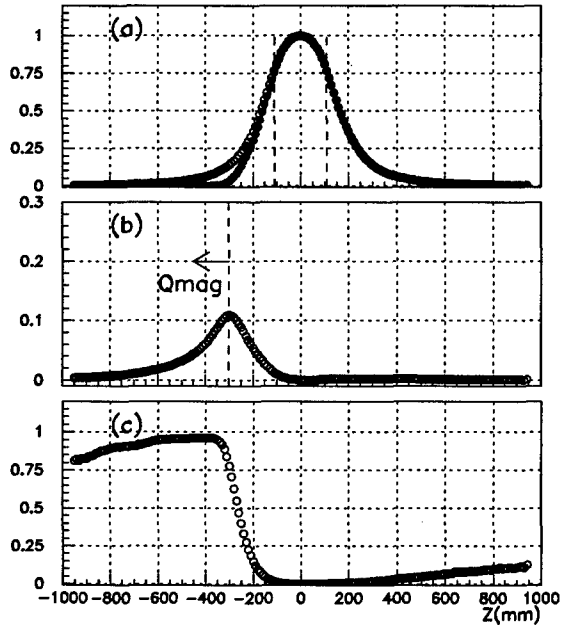

Figure 7: (a) StV(wide) field distribution along the beam line with (solid circle) and without (open circle) a quadrupole magnet. The field is distorted by the presence of a quadrupole magnet. (b) The difference between the two distributions in (a). (c)Absorbed field normalized by the original field.

The partial integrated dipole field strength, i.e., ΣB(z)(sum from z=-950 mm to z), is plotted as a function of z in Fig. 8(a). The central area of Fig. 8(a) is magnified and plotted in Fig. 8(b). Points (1) and (2) in Fig. 8(b) correspond to the centers of gravity of the dipole corrector magnet without and with a quadrupole magnet nearby. A shift in the magnetic center is observed. The 8.9% reduction in L_{eff} results in a 15 mm shift for the combination of [QA, StV(wide)]. This reduction of the dipole corrector field and shift in the magnetic center are summarized in Table 3, for various types of dipole correctors used in the KEKB LER.

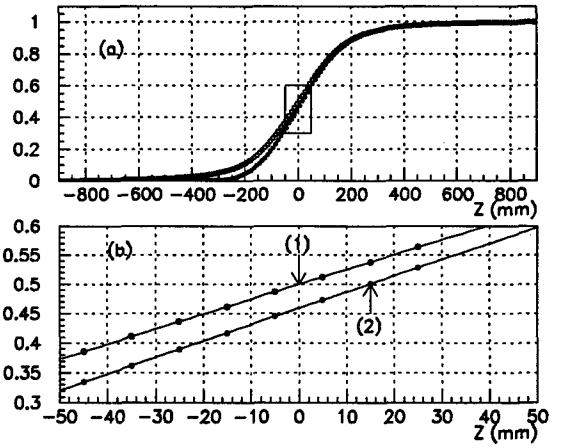

Figure 8: (a)A partial sum of the dipole field strength as a function z. (b) The difference in the magnetic centers. Point (1) and (2) are the centers of gravity of StV(wide) without and with a nearby quadrupole magnet. A shift is observed.

Table 3: Magnetic coupling effect on the LER dipole corrector magnets from a nearby quadrupole magnet

corrector	L_{eff}(mm)	ΔBL	Δcenter(mm)
StV(arc)	359.00	6.5%	10.3
StH(arc)	319.29	4.2%	3.6
StV(wide)	390.27	8.5%	14.7
StH(wide)	372.88	8.2%	11.6

Note :The dipole field is compared at a level corresponding to ~1 mrad of kick angle. L_{eff} in the table is the effective length, when there is no magnetic material nearby.

4 SUMMARY

The magnetic coupling between quadrupole and dipole corrector magnets has been measured. Reduction in the integrated main field is observed to be 0.1~0.2% for the quadrupole magnets and 4.0~9.0 % for the dipole corrector magnets. The effects on the integrated field strength agree quantitatively with the mapping results where ΔL_{eff} is measured. Magnetic coupling causes a distortion of the field distribution and thus shift in magnetic center. No significant effects on the higher multipole components are observed for the quadrupole magnets.

5 ACKNOWLEDGMENTS

The authors would like to thank the measurement crew for their hard work and the KEK magnet group for many useful discussions.

6 REFERENCES

[1] KEKB B-Factory Design Report 95-7
[2] K. Egawa and M. Masuzawa, "Preliminary Results of the KEKB Quadrupole Magnet Measurements", EPAC'98, Stockholm (1998)
[3] K. Egawa and M.Masuzawa "Field Measurements of the KEK B-Factory Dipole and Wiggler Magnets", Contribution to PAC99

FIELD MEASUREMENTS OF THE KEK B-FACTORY DIPOLE AND WIGGLER MAGNETS

K. Egawa #, M. Masuzawa, KEK, Tsukuba, Japan

Abstract

The KEK B-Factory (KEKB) [1] consists of 3.5 GeV positron (LER) and 8.0 GeV electron (HER) rings and has more than 290 dipole and 150 wiggler magnets. Both the LER and the HER use four types of dipole magnets. Wiggler magnets are used for the LER. Three long flip-flop coil systems were used to measure the transverse distribution of the integrated magnetic field along the beam direction. Each dipole magnet was measured using one of these system according to its size. The wiggler magnets were measured using a rotating coil which contains one long coil and two half coils. The long coil measured the net residual integrated magnetic field and each half coil measured the magnetic flux of each pole. Field mapping has also been performed for at least one of each type of magnet. Effective length and field distribution along the beam direction were measured by using a flip-flop mapping coil system. The absolute magnetic field strength at dipole center was calibrated by NMR. These measurement results are summarized.

1 MAGNET SYSTEM

Many kinds of magnets more than 1600 magnets are used for the KEKB besides correctors. Quarter of the main magnets are recycled from the TRISTAN electron-positron collider (TR) [2]. All the magnets were newly fabricated for the LER. All the dipoles except one are recycled for the HER. The main parameters of the dipole and wiggler magnets are summarized in Table 1. All the cores except B_V and B_S are made by using laminated construction technique. The required magnetic properties of the steel are shown in Table 2. The main coil is made of O_2 free Cu hollow conductor. Each magnet has correction coil with about 1 % ampere-turns compared to the main coil and also has 1 turn coil per pole for magnetic flux monitor. The brief summary of the KEKB magnet system is given in the contribution of EPAC98 [3].

Table 2 : Magnetic Properties of the silicon steel

$B_{50} > 1.6$ T	$\Delta B_{50} / B_{50} < \pm 1$ %
$Hc^{1.5} < 70$ A/m	$\Delta Hc^{1.5} / Hc^{1.5} < \pm 5$ %

2 MEASUREMENTS

The tolerances of higher multipole errors required for the dipole magnets are given in Table 3. Three flip coils and one rotating coil were used for the measurement of the dipole and the wiggler magnets respectively. The effective length and field distribution along the beam direction were measured by using a flip-flop mapping coil.

Table 3 : Tolerances of systematic multipole errors

	Tolerance at 50 mm radius
Dipole magnets	B3 / B1 < 0.12 %
	B5 / B1 < 0.45 %

2.1 Series Measurement

All the dipoles except B_V were measured by the flip coil systems. The LER B_{arc} were measured by a newly constructed 2 m flip coil. The LER B_{lc} for chromaticity correction and the HER B_{arc} were measured by 3.6 m and 6.6 m flip coils recycled from TR respectively. Each probe has a few turns coil wound on glass epoxy cylinder. At each system, a pair of test and reference dipoles are facing each other and the probe moves horizontally between two dipoles. The integrated magnetic field BL (integrated along beam direction) was obtained to measure the induced voltage by flipping the probe in the dipole field. MetroLab high precision integrators (PDI5025) were used to digitize the induced voltage. The BL's were measured along transverse direction at several different currents. After measuring a test magnet, the probe came back to the reference magnet and measured it to eliminate

Table 1: LER and HER Dipole Magnet Parameters

	g/2 (mm)	L.lam (m)	B(T).dsgn	No.of.mag	ampere/pole	L.eff [m]	B[T].meas
LER / Barc	57	0.76	0.848	134	1250A × 32	0.8876	0.83616
Blc	57	2.1	0.52	26	1000A × 24	2.2273	0.52697
Bv	55	1.2	0.2	4	500A × 18	1.3561	0.20523
Bs	57	0.3	0.21	3	500A × 20	0.4085	0.21994
wigg	55	0.75	0.77	192	944.4A × 36	0.6939	0.77056
HER / Barc	35	5.804	0.3	117	840A × 10	5.9006	0.29974
Bw	35	2.8	0.048	6	10A × 150		
BsFL	35	1.14	0.214	1	500A × 12	1.2393	0.21473
BsFR	57	0.76	0.339	1	500A × 32	0.8935	0.35205

Email : kazumi.egawa@kek.jp

0-7803-5573-3/99/$10.00@1999 IEEE.

system errors. The typical measurement results of LER B_{arc}, HER B_{arc} and LER B_{Ic} are shown in Fig.1, 2 and 3 respectively. The BL's of the LER B_{arc}'s were adjusted by the end shim considering the fabrication error of the core length which was thought to be worse than the longer dipoles due to its short length. The result is shown in Fig. 1 lower left. The measurement accuracy of relative BL is about a few $\times 10^{-5}$ as shown in Fig. 1 lower right.

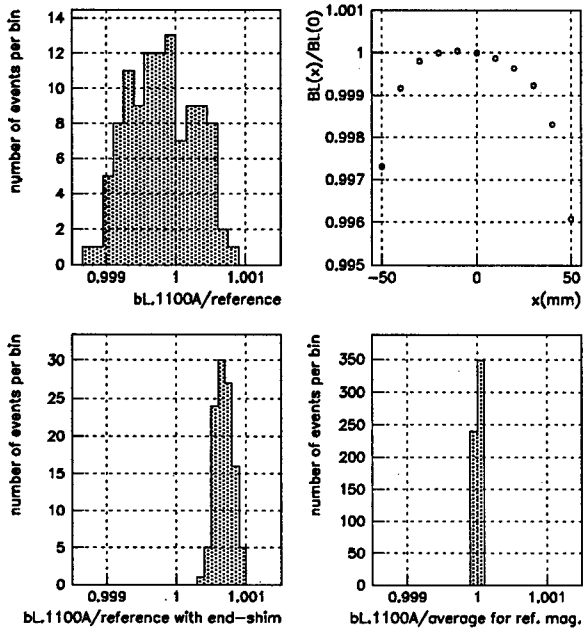

Figure 1 : The normalized integrated field histogram and an example of its transverse distribution for LER B_{arc}. The BL's after end shim correction and the reproducibility of the LER flip coil system are also shown below.

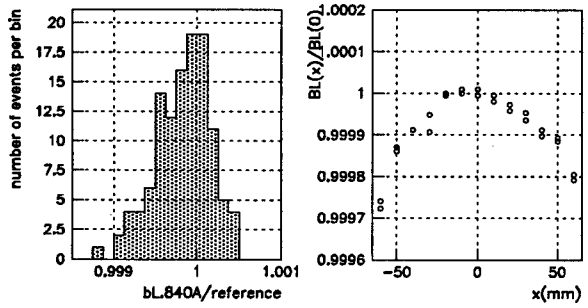

Figure 2 : The normalized integrated field histogram and an example of its transverse distribution for HER B_{arc}

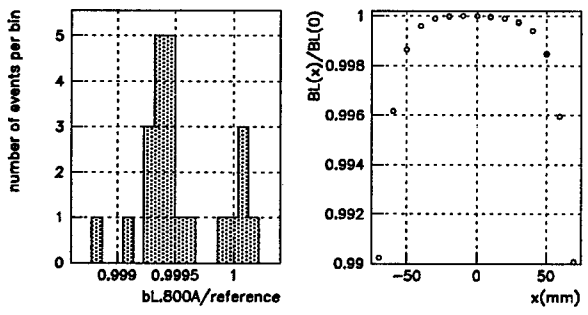

Figure 3 : The normalized integrated field histogram and an example of its transverse distribution for LER B_{Ic}

The LER wigglers have alternate magnetic field in their front and back poles. They were measured by the rotating coil mounted in aluminum cylinder having one long coil and two half coils. The residual integrated field Δ[BL] was measured by the long coil and the BL for each pole was obtained by each half coil. The induced voltage of the probe was measured by using a spectrum signal analyzer HP3562A. The results are shown in Fig. 4. The little non-zero offset of Δ[BL] is thought to be due to the configuration of the current leads.

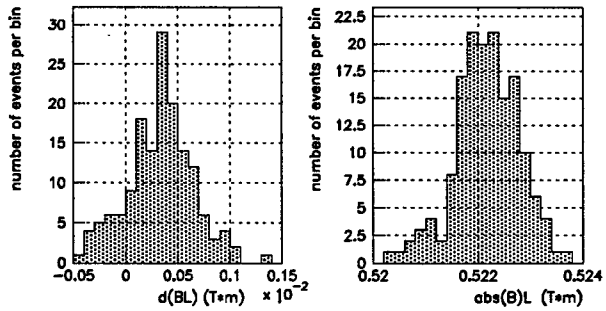

Figure 4 : The Δ[BL] and |B|L histograms of the wigglers at I = 950 A

All the dipoles except Bw have correction coils. Once the correction coil is excited, the magnet changes the field from its initial value even if the correction current is set to be 0A again. These hysteresis effects were measured on the every dipoles and some results are shown in Fig. 5.

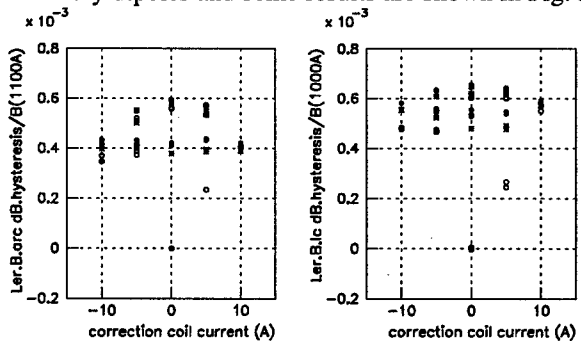

Figure 5 : The hysteresis caused by the correction coil excitation for LER B_{arc} and LER B_{Ic} at I = 1100A and 1000A respectively. The dB is defined as dB[Ic]= B[Ic] - k*Ic -B[Ic=0A], where Ic is the correction current and k is a linear fit coefficient of B[Ic] as a function of Ic. The white circles show dB's in the first ±10A loop, the asterisks and the black circles are in the second and the third loops respectively.

2.2 *Field Mapping and Absolute Value*

The field mappings have been performed by using a flip-flop mapping coil, which consists of twin small coils apart from 10mm each other. Each coil has 2090 turns windings with 8 mm in diameter and 12 mm height. Dipole field was measured by using one coil. On the other hand, quadrupole field was obtained by measuring the difference of the induced voltages of two coils (twin mode). Each coil gain was calibrated in the dipole field which absolute strength was determined by NMR. The distance between each coil was determined by searching

zero-cross of the induced voltage of each coil in quadrupole field. The field mappings were carried out at several currents for each type of dipole and wiggler. The effective lengths were determined by these field mappings. The absolute field strength of each type of dipole was measured at its center by NMR. The effective length of each type quadrupole was measured by the twin mode field mapping. The absolute field gradient of the quadrupoles were calculated from the gain and the distance of the twin coils. Some results of the field distributions along the beam direction are shown in Fig. 6, 7, 9 and 10. The effective lengths are shown as functions of the currents for LER B_{arc} and LER B_{lc} in Fig. 8. This flip-flop mapping coil were also used to measure the magnetic couplings between adjacent quadrupole and corrector. The quadrupole mapping results [4] and the coupling effects [5] are mentioned in the other contributions of this conference.

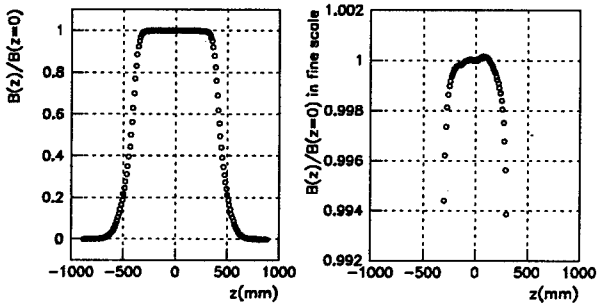

Figure 6 : The normalized magnetic field along the beam direction b[z] for LER B_{arc}.

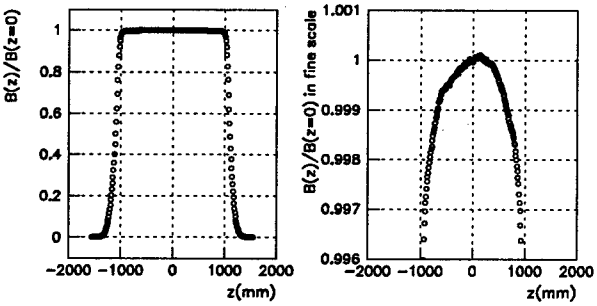

Figure 7 : The b[z] for LER B_{lc}.

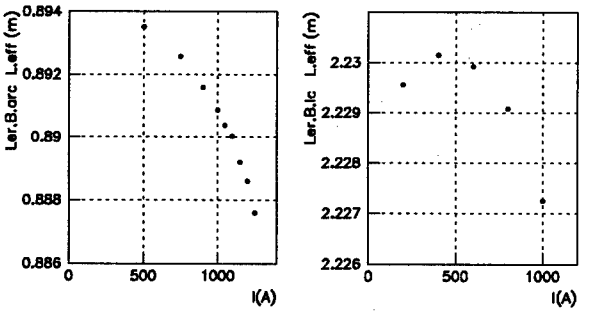

Figure 8 : The effective lengths as a function of current for LER B_{arc} and LER B_{lc}.

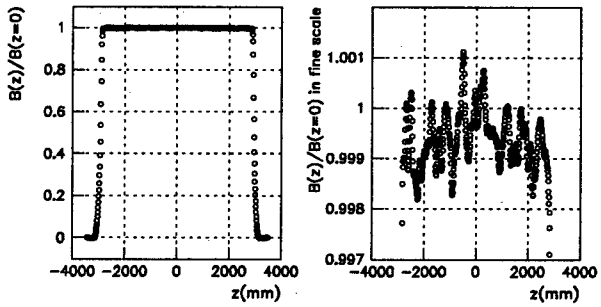

Figure 9 : The b[z] for HER B_{arc}.

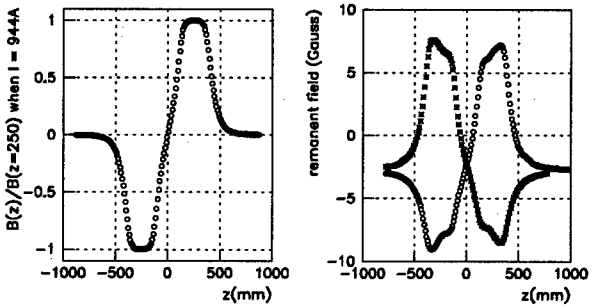

Figure 10 : The b[z] at I = 944A (left) and the remanent field along the beam direction (right) for LER Wiggler. In the right figure, the white circle shows the remanent field after +944A excitation and the asterisk shows the remanent after -944A excitation. The negative offset is thought to be due to the terrestrial magnetic effect.

3 SUMMARY

The series measurements and the field mappings of the KEKB magnet system were completed. The performances of the magnets are almost acceptable. The measured parameters such as the BL, B'L, effective lengths and magnetic coupling effects are utilized in the operation of the KEKB. Further measurements of environmental effects (air temperature, cooling water flow and its temperature, etc.) on magnetic field are under way.

4 ACKNOWLEDGMENTS

The authors would like to thank the measurement crew for their hard work and continuous efforts and also thank the KEK magnet group for many useful discussions and their help.

5 REFERENCES

[1] KEKB B-Factory Design Report 95-7

[2] TRISTAN electron-positron colliding beam project", KEK Report 86-24 March 1987

[3] K. Egawa and M. Masuzawa, "Magnet field measurement for KEK B-Factory", EPAC'98, Stockholm (1998)

[4] M. Masuzawa and K. Egawa, "Field Measurement Results of The KEK B-Factory Quadrupole and Sextupole Magnets", Contribution to PAC99

[5] M. Masuzawa and K. Egawa, "Study of The Magnetic Coupling between Quadrupole and Corrector Magnets for The KEK B-Factory", Contribution to PAC99

TECHNIQUES FOR MAGNETIC FIELD MONITOR OF THE LOW FREQUENCY TRAPEZOIDAL PULSE MAGNET WITH THE NMR

Hikaru Sato, Katsumi Marutsuka, Katsuhiko Mikawa, Takeshi Sueno, Masashi Shirakata
High Energy Accelerator Research Organization (KEK),Tsukuba, 305-0801, Japan

Tsukasa Nakajima
Echo Electronics co., LTD., Saitama, 353-0007, Japan

Abstract

Measurement of magnetic field of the lattice bending magnet is important to control the beam orbit, tune control and the timing of the fixed magnetic field. Hole probe and search coil are used conventionally and NMR has been considered to know the only DC magnetic field. Authors have developed the technique for the magnetic field monitor of the pulsed magnet such as the main ring magnet of the 12GeV KEK-PS. During the injection (550 ms) and flat top (1-2 s) periods, magnetic field is measured by NMR probes with the frequency scanning. If we want the timing pulse at any magnetic field during acceleration, NMR probe can measure it with a fixed frequency mode. It depends on the principle of the NMR, which occur the nuclear magnetic resonance in the relation between the quantum axis magnetic field and the frequency of the rotational magnetic field in the perpendicular plane. The performance of the technique for the magnetic field monitor by NMR and some unique results of the magnetic field in the lattice bending magnet will be presented.

1 INTRODUCTION

Magnetic-field measurement by nuclear magnetic resonance (NMR) has been very well described. This is known as the Larmor frequency, is directly proportional to the magnetic field, H, and it's angular velocity is given by

$$\omega_0 = \gamma H ,$$

where γ is the gyromagnetic ratio. The field is measured by exciting the resonance with an rf oscillator and measuring the frequency at which energy is either absorbed by the sample (resonance absorption).

1) As a case of the low frequency trapezoidal pulse magnetic field, such as a hadron synchrotron, NMR method can be applied during a beam injection and a flat top period.

2) NMR occurs when an oscillating field equal to the frequency of the Larmor frequency. Then, even if during accelerating period, when the bending field become to the fixed rf frequency NMR will occur.

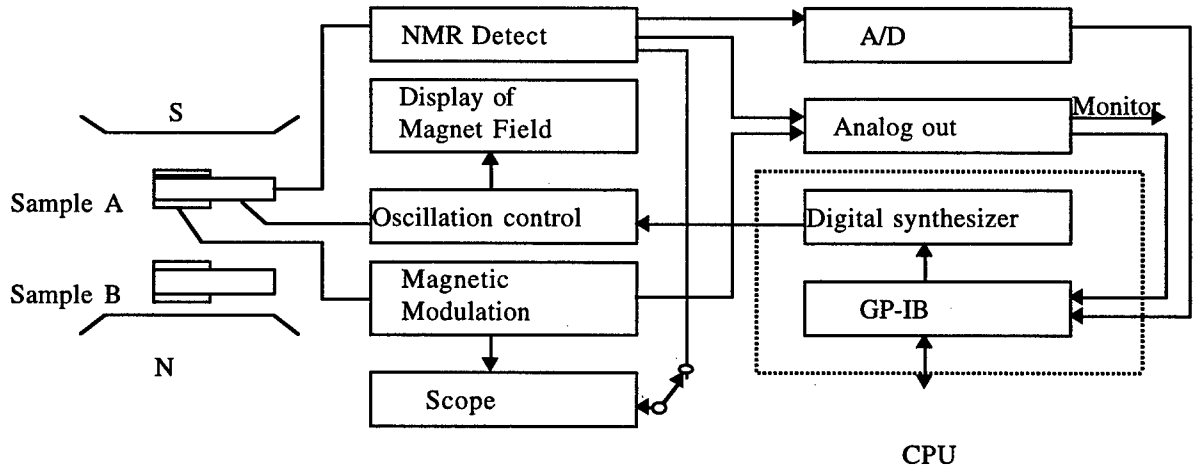

Figure 1 : Block diagram of the NMR measurement system.

0-7803-5573-3/99/$10.00@1999 IEEE.

Resonance absorption sample is a solid proton, then the resonance frequency is 42.567 MHz/T.

Specification of this system is as follows [1];

- Measurement Field Range: 0.14 T - 1.7 T
- Resolution: 2×10^{-5}
- Sample: Solid Proton
- Frequency Stability: 1×10^{-5}/min.
- SCOPE-Y: 1V (p-p)
- SCOPE-X: 5V (p-p)
- Dimension of Probe: 15 × 20 × 30 min.
- Uniformity: 1×10^{-4}/cc

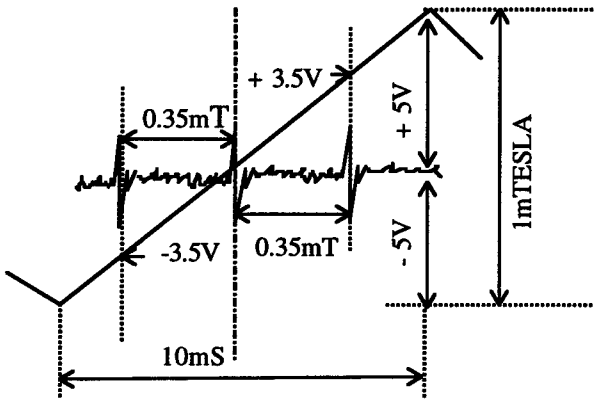

Figure 2 : Conception of the NMR measurement system.

2 CONCEPTION OF THE MEASUREMENT SYSTEM

2.1 Measurement of the Injection and the Flat Top Period

Figure 1 shows a block diagram of the NMR measurement system. The resonance frequency is divided two at a fixed magnetic field of an injection and a flat top period. Then, two absorption samples (A and B in Figure 1) are set in the magnet gap. According to the strength of the magnetic field, the frequency which can be obtained the NMR absorption signal should be set. The magnetic field can be measured with a range of ± 5G around the set frequency. Frequency is scanning by the time of 10 ms and following 10ms is the initializing time, then the measurement can be done in every 20 ms. Out-put signal level is 1G/V, that is full scale is 10 V. Two resonance absorption samples were set for the injection field and the flat top field, respectively. For the flat top measurement, the scanning frequency is provided to four range, a : 0.11 - 0.25 T, b : 0.25 - 0.5 T, c : 0.5 - 1.06 T and d : 1.06 - 1.8 T, to meet the variable flat top energy.

Conception of the measurement principle is shown in Figure 2.

2.2 Measurement of the Gradient Field (in Time)

Slow rise time magnetic field such as a synchrotron magnet can be measured by NMR. As more detail, one can recognize when the magnetic field comes to the value of resonance absorption at a fixed frequency oscillation field. This phenomena likes that which is well known as the spin depolarizing resonance during acceleration [2]. As a case of KEK 12 GeV-PS, the main bending magnetic field rises about 2T/s. We can know the time from an acceleration start to when NMR occurs. Range of the magnetic field is too wide, 0.14 T - 1.7 T for this case, to measure by one absorption sample, then four samples cover each four ranges, A: 0.15 - 0.25 T, B: 0.25 - 0.5 T, C: 0.5 - 0.98 T and D: 0.98 - 1.7 T. Figure 3 shows a measurement results of the 12 GeV operation. Horizontal axis is a time from acceleration start and vertical axis is the magnetic field. Fig. 4 shows a time fluctuation for ten minuets at a set of RF frequency for 1 tesla. Fluctuation is about 400 μs full width. It is considered that this fluctuation caused from the line fluctuation of the main ring power supply.

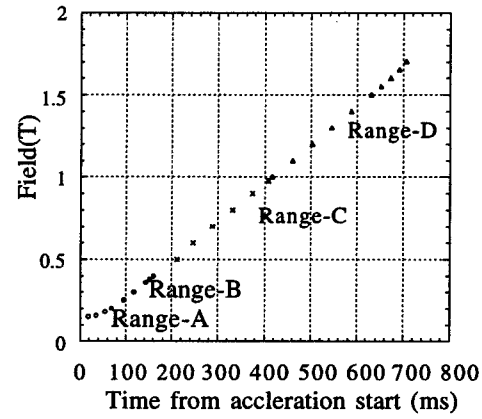

Figure 3 : Magnetic field measurement using NMR during acceleration.

3 CONCLUSION

At this present, several tools are set of measure the main bending magnetic field in the gap, a hall prove to measure the injection field and the gauss meter to monitor the magnetic pattern[3] and the NMR measuring system described above. As a result of using the NMR measuring system, we become to know the new information, that is, the dynamic phenomena of the magnetic field such as time delay of magnetizing depends on the time-length of the flat top and/or the current of the flat top. For example, a delay of the magnetic field at the beginning of the flat top field is shown in Figure 5. From the fitting functions, there are two component of the time constant, 70 ms and 660

ms. When the magnetic field of the flat top is low, there is one time constant of 70 ms. This phenomena is still in investigation, but it is considered the magnetic viscosity. As a measurement of the time from an acceleration start to the fixed magnetic field, this can be applied to the timing pulse in stead of the conventional gauss clock when we need the timing during acceleration, such as a transition crossing.

4 ACKNOWLEDGMENTS

The authors would like to express their sincere thanks to M. Kihara, the director general of accelerator department and I. Yamane, the director of PS division, for there encouragement. They are much indebted to PS staff and operation staff for their help and collaboration.

5 REFERENCES

[1] Echo Electronics Co. Ltd. Series EFM-309 and EFM-409 Operation Manual

[2] H. Sato et al., Nucl. Instrum. & Methods A 272 (1988) 617
S. Y. Lee, Spin Dynamics and Snakes in Synchrotron, World Scientific

[3] F.W. Bell Series 9900 Gaussmeter Operation Manual

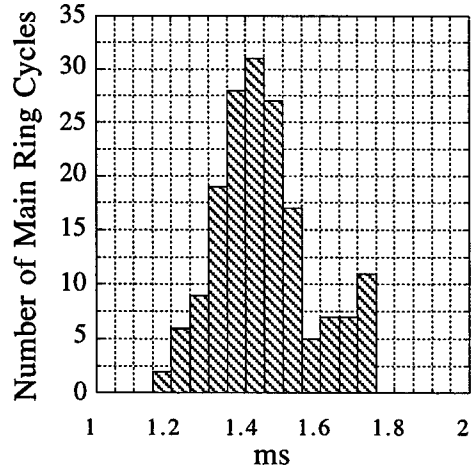

Figure 4 : Fluctuation of the time from acceleration start to 1 tesla for about ten minutes.

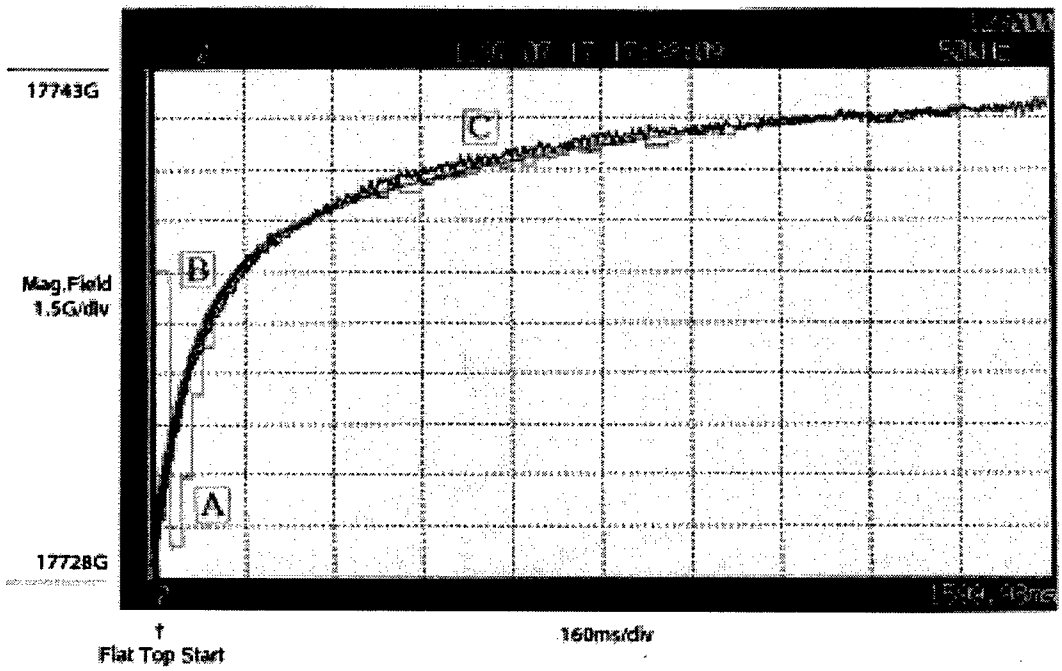

Figure 5 : Example of the time delay of the magnetization. Flat top start means the end of acceleration, 2T/sec, and the field comes to constant of 1.77 T.
A : NMR measurement. B : Fitting function. $f = 17742.4 - 7 \times e^{-t/0.07} - 5.5 \times e^{-t/0.66}$
C : Backleg winding measurement to check the systematic error.

FIELD MEASUREMENT OF THE MAGNET PROTOTYPES FOR THE VSX PROJECT

T. Koseki[1], Y. Kamiya, H. Kudo, N. Nakamura, T. Shibuya,
K. Shinoe, H. Takaki and Y. Takiyama, The Institute for Solid State Physics (ISSP),
The University of Tokyo, Tokyo, Japan
Y. Kobayashi, Photon Factory, High Energy Research Organization (KEK), Ibaraki, Japan
K. Kuno, Energy & Industrial Research Center, Mitsubishi Electric Corporation, Kobe, Japan

Abstract

Prototypes of the dipole and the fast steering magnet for the VSX project have been fabricated and measured. The field mapping and the end-shim correction were carried out for the dipole, and the frequency response was tested up to 2 kHz for the fast steering. The design of the magnets and measured results are presented.

1 INTRODUCTION

The University of Tokyo has been promoting a project to construct a VUV and Soft X-ray (SX) synchrotron radiation facility in a new campus of the university, Kashiwa campus. The project, which is called "VSX project", is composed of two phases. The first is to construct a 1.0 GeV racetrack ring which has an emittance of 0.7 nm·rad, a circumference of about 230 m and two 30 m long straight sections for insertion devices [1]. It can reach an emittance of diffraction limit and can provide extremely high-brilliance radiation more than 10^{20} [photons/sec/mm^2/mrad^2/0.1%b.w.] in the region between 100 eV and 1 keV. The second is to construct a 2.0 GeV ring, which has a circumference of 388 m, an emittance of 5 nm·rad and 16 long straight sections [2]. High-brilliance synchrotron radiation over a wide range from VUV and SX can be generated by various kinds of insertion devices.

We have been carrying out the design study and R&D's of the magnet system for both the 1.0 GeV and 2.0 GeV rings. Detailed design of main and corrector magnets for these rings has been almost completed. For the 1.0 GeV ring, prototypes of the dipole, quadrupole and fast steering are being fabricated now. The quadrupole will be delivered to ISSP in this May and the dipole and steering in October. For the 2.0 GeV ring, the dipole, quadrupole, sextupole and fast steering prototypes have been already fabricated by Mitsubishi Electric Corporation, and their field measurements are well under way at ISSP. Some results of the dipole, quadrupole and sextupole measurement have been reported in elsewhere [3,4].

In this paper, we present recent progress of the magnetic measurement of the dipole and the fast steering prototypes for the 2.0 GeV ring. The measurement is being carried out using a computer-controlled 3D mapping system with a Hall probe unit (SERIES-9900 gaussmeter, F. W. BELL). For the dipole measurement, an NMR system (PT2025, METROLAB) is also used to obtain the absolute field strength and to calibrate the Hall probe unit.

2 DIPOLE MAGNET

Figure 1 shows the end view of the dipole prototype. The magnet core has C-type rectangular configuration and is made of forged low-carbon solid-steel. The shape of pole profile has been optimized using the 2D program LINDA to obtain a field uniformity better than 5 $\times 10^{-4}$ over a horizontal region of ±40 mm. The main parameters of the dipole are listed in Table 1.

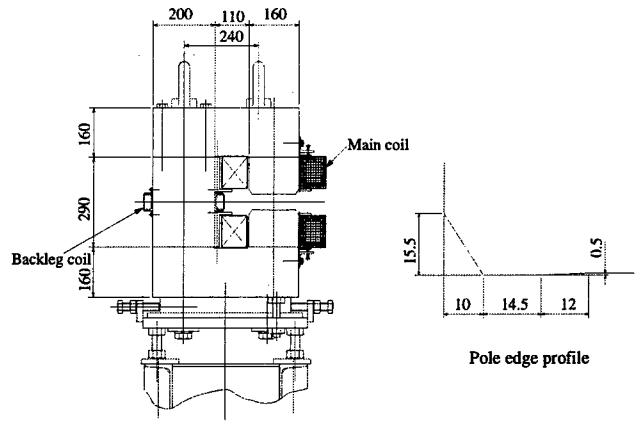

Figure 1: End view of the dipole prototype

Figure 2 shows the measured longitudinal field distribution along the design orbit. The excited field strength at the center of the magnet is 1.006 T. The effective length, defined as the field integral along the design orbit divided by the field at the magnet center, was calculated to be 1364.0 mm.

[1] # Email: koseki@issp.u-tokyo.ac.jp

0-7803-5573-3/99/$10.00@1999 IEEE.

Table 1: The parameters of the dipole prototype

Bending angle	11.25°
Bending radius	6.626 m
Gap height	50 mm
Core length	1.299 m
Maximum field strength	1.26 T
Turns / pole	30
Maximum current	960 A
Conductor size	16×15-ϕ9 mm
Resistance	21 mΩ
Water flow	37.8 l/min

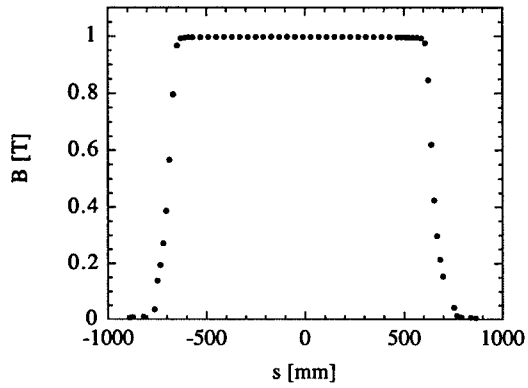

Figure 2: Longitudinal field distribution along the design orbit

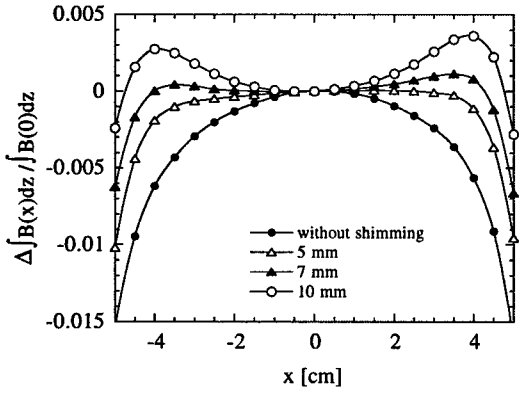

Figure 3: Integrated field profile

Near the magnet end, the sextupole component becomes relatively larger and it makes worse the horizontal field uniformity. In order to reduce the sextupole component, the end correction was carried out by shimming the magnet pole ends. The pieces of the end-shim are pure-iron plates of 25 mm × 139 mm, and 2 mm or 5 mm thick. Figure 3 shows the integrated field uniformity for various thickness of end-shimming. Each integrated field is calculated from mapping data along the longitudinal (z-axis) direction between z = 450 mm and z = 700 mm (z = 650 mm is the position of the magnet end). This figure implies the most proper thickness is about 6 mm, by which the integrated field uniformity better than 5×10^{-4} is obtained.

3 FAST STEERING MAGNET

The prototype of fast steering magnet is shown in Fig. 4. The steering has an aperture of 151 mm (width)× 46 mm (height) and provides both horizontal and vertical fields. The magnet core is composed of four glued stacks of 0.5 mm-thick silicon-steel lamination. The main parameters of the fast steering are listed in Table 2.

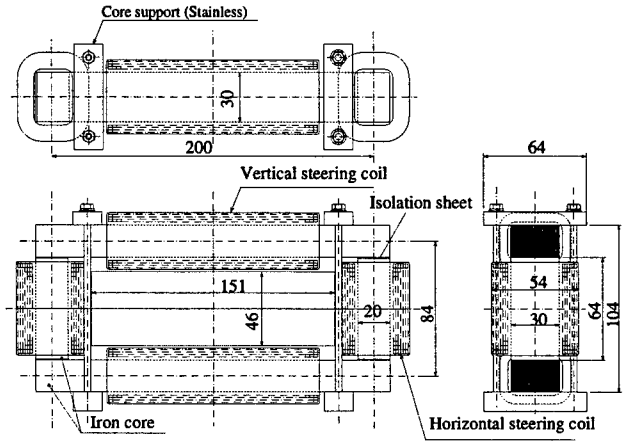

Figure 4: Fast steering prototype

Table 2: The parameters of the fast steering magnet

	(Vertical steering)	(Horizontal steering)
Deflection angle	0.09 mrad	0.1 mrad
Magnet gap	180 mm	64 mm
Turns / coil	140	120
Maximum current	5 A	5 A
Coil resistance	0.25 mΩ	0.24 mΩ
Coil inductance	7 mH	8 mH
Frequency range	DC ~ 100 Hz	DC ~ 100 Hz

The fast steering is expected to operate in a frequency range up to 100 Hz. We measured the frequency response of the steering using a dynamic signal analyzer (HP35670A). A swept sine signal from the analyzer was fed into a bipolar AC power supply (IPM-BP series, IDX). The frequency response of the output current of the power supply or the signal of the Hall probe was measured.

Figures 5 and 6 show the Bode diagram of the horizontal and vertical steerings, respectively. The data were measured with the output signal of the Hall probe

put on the position of steering center. The output current of the power supply was set to be 800 mA peak-to-peak, that is a maximum current required for the fast orbit feedback system. A 1 m long vacuum chamber made of aluminum was inserted into the aperture of the steering magnet to examine the effect of eddy current induced on the chamber. The chamber has the same cross section as the beam duct of straight section of the VSX 2.0 GeV ring [5]. As shown in these figures, the steering magnet itself has a good frequency response up to 1 kHz for both the horizontal and vertical directions. Field attenuation due to the effect of eddy current on the vacuum chamber is not very serious in the frequency range up to 100 Hz.

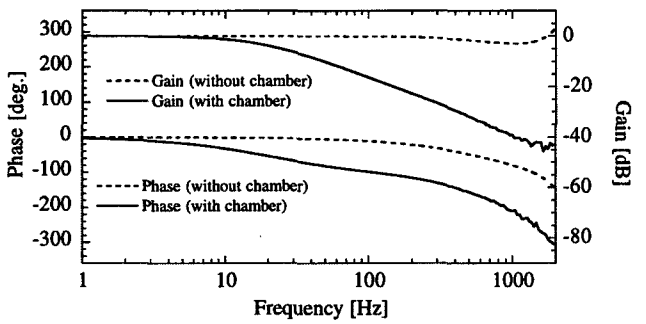

Figure 5: Frequency response of the horizontal steering field

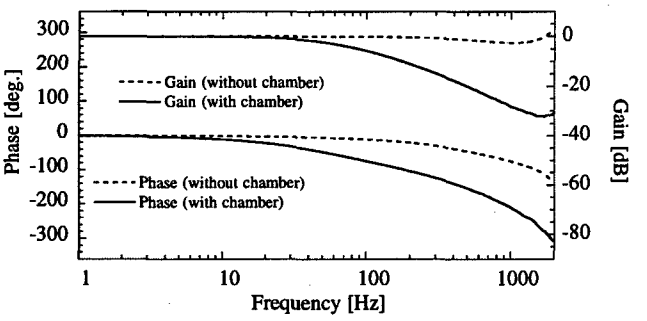

Figure 6: Frequency response of the vertical steering field

In the measurement of Figs. 5 and 6, the data of the vertical steering was taken when the horizontal excitation switched off and vice versa. If both the steerings are excited in the same time, that is the actual situation of feedback operation, the interference between the two steerings may occur due to mutual inductance of the coils. Thus the frequency response should be measured with both of them are switched on. Two AC bipolar power supplies were used in the measurement and driven by the identical signal from the signal analyzer. Figure 7 shows the measured Bode diagram of the power supply output current for vertical steering when the horizontal steering switched on. The driving current was 800 mA peak-to-peak. The data without horizontal steering is also shown in this figure. There is no significant difference between them. It indicates that the magnetic field is given by a linear combination of the horizontal and vertical steering fields. In fact, even when both the steerings are switched on, the frequency response measured with the Hall probe well agrees with the data in Figs. 5 and 6. It means that independent feedback operation in the horizontal and vertical directions is possible using these steering magnets.

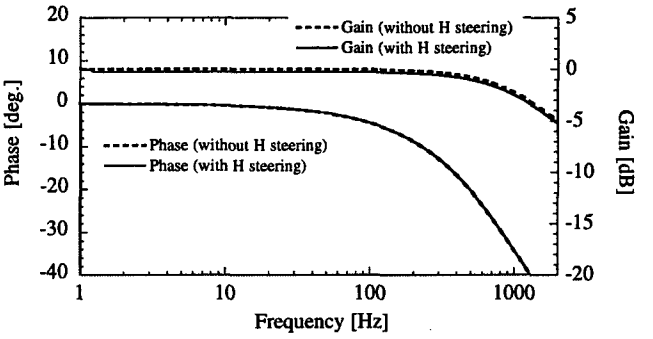

Figure 7: Frequency response of the output current monitor of the vertical steering

4 REFERENCES

[1] H. Takaki, K. Harada, T. Koseki, N. Nakamura, Y. Kamiya and Y. Kobayashi, "The Lattice of 1.0 GeV VSX Storage Ring", in these proceedings.

[2] H. Takaki, T. Koseki, N. Nakamura, Y. Kamiya, Y. Kobayashi and T. Nagatsuka, "A Lattice for the Future Project of VUV and Soft X-ray High-Brilliant Light Source", 1997 PAC, Vancouver, (1997).

[3] T. Koseki, Y. Kobayashi, H. Takaki, N. Nakamura, Y. Kamiya and K. Kuno, "The Magnet of the VSX Light Source", APAC98, Tsukuba, (1998).

[4] T. Koseki, Y. Kamiya, H. Kudo, N. Nakamura, K. Shinoe, H. Takaki, Y. Takiyama, Y. Kobayashi and K. Kuno, "Magnetic Measurement of the VSX Prototype Magnets", EPAC98, Stockholm, (1998).

[5] N. Nakamura and T. Koseki, "Influence of Resistive Wall Impedance on the VSX Light Source", 1997 PAC, Vancouver, (1997).

MAGNETIC FIELD MEASUREMENT OF THE AIR SLOT DIPOLE MAGNET

M. Umezawa*, K. Hiramoto, Power & Industrial Systems R & D Laboratory, Hitachi Ltd.,
7-2-1, Omika-cho, Hitachi-shi, Ibaraki-ken, 319-1221, Japan,
M. Tadokoro, J. Hirota, Hitachi Works, Hitachi Ltd.,
3-1-1, Saiwai-cho, Hitachi-shi, Ibaraki-ken, 317-8511, Japan

Abstract

Field measurement results of the air slot type dipole magnet are presented. The vacant portion, called the air slot, located in the iron core controls the flow of the magnetic flux and improves uniformity of the magnetic field. This magnet realizes a better magnetic field distribution over a wide range of field strengths. The prototype of the magnet had been fabricated and tested to verify the design principle. The results of measurements by the Hall-probe showed good agreement with the numerical calculations for magnetic field strengths ranging from 0.27T to 1.83T. The field uniformity $\Delta B/B$ was below 0.04% in the good field region.

1 INTRODUCTION

We have proposed a new design concept for bending magnets which can improve magnetic field distribution[1]. The design concept is based on control of the flow of the magnetic flux in the magnet pole by introducing vacant portions into the magnet iron core. This new concept was proposed originally to develop a combined function bending magnet[2]. Effectiveness had been confirmed by numerical study[3] and the results of further study will be presented[4].

In the conventional dipole bending magnet, application of shims to the magnet pole face has been considered an effective way of improving magnetic field uniformity. However, the shape of the shims for very high fields often had a bad influence on the field distribution at low magnetic field, and their shape for low field is not suitable for high magnetic field. In order to obtain a good field distribution over a wide range of magnetic field strengths, it is necessary to overcome this problem. Therefore, we applied the present design concept to dipole bending magnets and confirmed by numerical study that the vacant portion in the iron core can improve the magnetic field distribution at various excitation levels. Additionally, the air slot type pole width can be narrower than that of the conventional type and the yoke size and weight of the magnet can be smaller. Because of these advantages, the air slot type magnet is widely applicable as a synchrotron magnet and for beam transport, rotating gantry, and so on.

* Email: umezawa@erl.hitachi.co.jp

The dipole magnet for a compact proton synchrotron[5], which has two air slots in its magnet pole, has been investigated by two- and three- dimensional numerical calculations[1]. In order to verify this new design principle, that is the effect of the air slots, the prototype of this magnet was constructed and magnetic field measurements were made with the Hall-probe for magnetic field strengths from 0.27T to 1.82T. The measurement results showed that the air slots had their designed effect.

2 DESIGN OF THE MAGNET

2.1 Design Principle

The scheme for improving the magnetic field distribution by introducing air slots in the magnet pole is outlined below. The magnetic susceptibility of the air slots is much lower than that of the iron core. At high magnetic field, the perimeter of the iron pole saturates earlier than the central area as excitation goes up. On the other hand, introducing air slots in the central area leads to an increase of the magnetic flux density in the iron region around the air slots. If the position and shape of the air slots are adjusted to equalize the magnetic flux density in the whole pole iron at high field, the magnetic field distribution can be flattened. At low magnetic field where the magnetic flux does not saturate, the effect of air slots is very small and the magnetic field distribution is controlled only by the shape of the pole surface. This new concept is useful for improving the dynamic range of the magnetic field and extending the good field region size, if both slotting and shimming would be used together.

2.2 Design Requirements

We designed the air slot type bending magnet for a compact proton synchrotron[5]. In this synchrotron, the beam can be accelerated from 7MeV up to 270MeV at a repetition cycle of 0.5Hz for proton radiography as well as cancer treatment. The magnet yoke is made of stamped laminated steel of 0.5mm thickness to reduce the eddy current effect. The mean radius and the circumference of the synchrotron are about 3.5m and 23m, respectively, so the curvature radius of the bending magnet is 1.4m. In order to shorten the straight section for the extraction deflector, the deflection by the 22° defocusing edge angle

0-7803-5573-3/99/$10.00@1999 IEEE.

of the bending magnet is needed. The minimum magnetic field strength is 0.273T for beam injection and the maximum is 1.808T for extraction. The good field region is determined based on our analysis of the beam size in the synchrotron. The specifications of the magnet are listed in Table 1.

Table 1: Specifications of the dipole magnet

Minimum Magnetic Field (T)	0.273
Maximum Magnetic Field (T)	1.808
Curvature Radius (m)	1.4
Bending Angle (degree)	60
Field Length (m)	1.466
Edge Angle (degree)	22
Gap Height (mm)	56
Good Field Region (mm)	±50
Required Magnetic Field Uniformity (%)	0.04

2.2 *Calculation Results*

Based on these specifications, the magnet shape is determined using the computer code PANDIRA. The air slot type magnet design is shown in Fig. 1. The pole width is 300mm and quarter circles are used to prevent the local edge effect at both ends of the pole. This pole width can be narrower than that of the shimmed type magnet[1] due to the effect of the air slot. Air slots have an oval shape with 70mm length and 10mm width. Figure 2 shows two-dimensional magnetic field distribution. The horizontal and vertical axes show, the radial distance from the design orbit and the deviation of the magnetic field strength from the value on the design orbit (r=0), respectively. The packing factor is assumed to be 0.98.

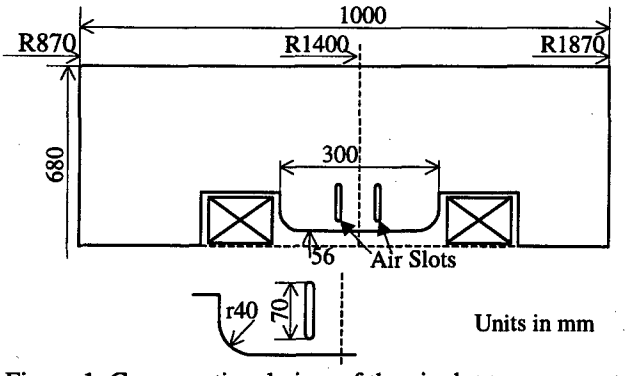

Figure 1: Cross-sectional view of the air slot type magnet

As shown in Fig. 2, the good field region is wider than ±60mm, and the magnetic field distribution does not change very much from 0.27T to 1.81T. The position, length and width of the air slot are adjusted to flatten the magnetic field distribution at various field strengths.

In order to decide the magnet end shape and estimate the effective edge angle and multipole components of the magnetic field, three-dimensional field calculations were performed using the computer code TOSCA. Both ends of the magnet are designed to approximate Rogowski's curve to avoid the saturation at the sharp edge of iron core by 4 step cuts in a 60mm long region along the orbit.

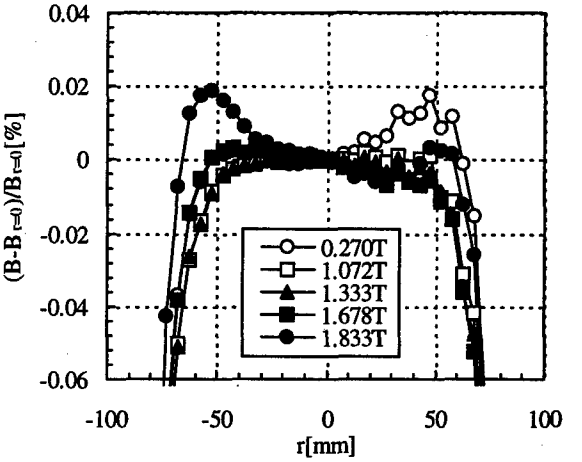

Figure 2: Two-dimensional magnetic field distributions of the air slot type magnet

3 FIELD MEASUREMENT AND ANALYSIS

Figure 3 shows the prototype dipole magnet which was fabricated to verify the design as mentioned above. The magnetic field measurements were made using the Hall-probe mounted on the arm of a computer-controlled positioning x-y-z table. The absolute calibration of the system was established by comparison with NMR probe measurements. The interval of the mesh point for the midplane measurements was less than or equal to 10mm inside the gap and 500mm outside it in beam direction. Analyses of measurement results at various excitations were performed in the same way as for the calculation results.

Figure 3: The prototype dipole magnet

Results of the excitation are compared with the results calculated by PANDIRA in Fig. 4. The vertical axis shows the magnetic field strength at the center of the magnet. The excitation current measured at 1.83T is 10%

larger than that of the linear case because of saturation of the iron core.

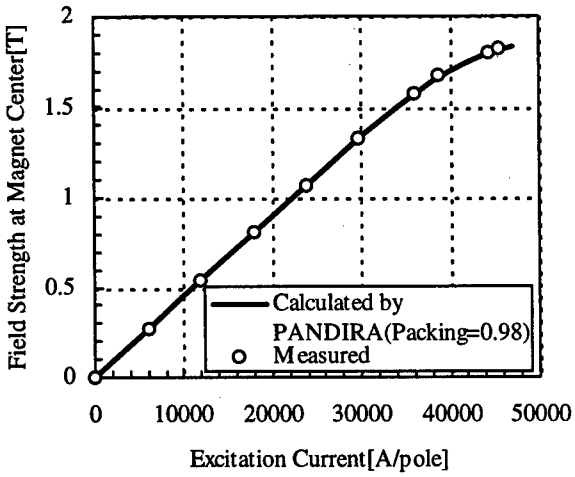

Figure 4: Magnetic field strength as a function of excitation current

Figure 5 shows the measured uniformity of the magnetic field at various excitations. Deviations of the field strength are less than 0.04% in the good field region at all excitation levels. Comparing results of the calculation (Fig. 2) and measurements (Fig. 5) shows some deviations, about 0.01% order, which can be expected from uncertainties in the manufacturing process. These results show that the effect of the air slots performs as designed.

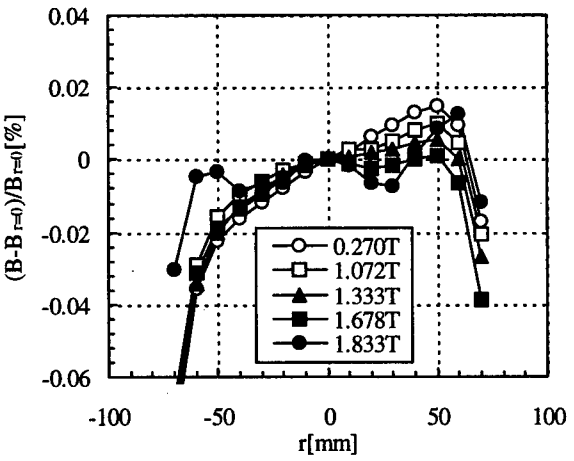

Figure 5: Measured uniformity of magnetic field strength

To estimate the effect of the non-linear components, the field strength as a function of distance in the radial direction is fitted by a Taylor expansion and the components are integrated along the beam reference orbit. The sextupole component normalized by magnetic rigidity is -0.03 m^{-2} at injection and over -0.2 m^{-2} at field strength 1.83T because of the saturation effect at magnet end. These values can be expected based on three-dimensional calculations. We confirmed by particle tracking calculations that the operation of the synchrotron from injection to extraction can be done on the assumption that the multipole components mentioned above are included in the magnetic field at fringing region.

4 CONCLUSION

We carried out magnetic field measurements of the air slot type magnet to verify our design principle. The air slots in the magnet pole improve the magnetic field distribution by controlling the flow of magnetic flux. Using the air slot type design, we can obtain the magnet which has a good field distribution at several excitation levels. The size and weight can be reduced because of the narrower pole width achieved by the effect of the air slots. Because of these advantages, this magnet design can be applied widely to synchrotron, beam transport, rotating gantry, and so on.

The prototype of the magnet was constructed for the main dipole of a compact proton synchrotron. Measurements using the Hall-probe were consistent with two- and three- dimensional calculation results. The results verified that the design principle which we proposed was valid and the air slots in the iron core performed as desired. Detailed analysis of the measurement results showed that the model magnet will achieve the specifications of the compact synchrotron we designed.

5 REFERENCES

[1] M. Umezawa et al., "A New Dipole Bending Magnet with Improved Magnetic Field Distribution", Proc. of the 11th Symposium on Accelerator Science and Technology, Spring-8, Japan(1997)380-382.

[2] M. Tadokoro et al., "A Combined Function Magnet for a Compact Synchrotron", Proc.of 1996 Part. Accel. Conf., Vancouver, Canada (1996) 3294-3296.

[3] A. Noda et al., "Development of Compact Proton Synchrotron with Combined Function Dedicated for Cancer Therapy", Proc. of the 11th Symposium on Accelerator Science and Technology, Spring-8, Japan (1997)314-316.

[4] A. Noda et al., "A Compact Proton Synchrotron with Combined-Function Lattice dedicated for Cancer Therapy", Proc. of this conference.

[5] K. Hiramoto et al., "A Compact Synchrotron for Cancer Treatment", Proc. of 1996 Part. Accel. Conf., Vancouver, Canada(1996)3813-3815

DESIGN, SIMULATION AND TEST OF PULSED PANOFSKY QUADRUPOLES*

Y. Li#, P.Chin, R. Kishek, M.Reiser, M. Venturini, J.G. Wang[a] and Y. Zou,
University of Maryland, College Park, MD 20742
T.F. Godlove, FM Technologies, Inc. Fairfax, VA 22032

Abstract

Two Panofsky quadrupoles with rectangular aperture and fast rise time are proposed for the injection area in the University of Maryland electron ring project (UMER) [1,2,3]. The theoretical current distribution needed on the surface of a rectangular aperture to produce a quadrupole field is derived [4]. The conductor location is determined mostly by the theoretical current distribution, with some free factors to optimise the field. The design is based on the linearity of longitudinal integrated field. Each quadrant of the Panofsky quadrupole consists of 10 loops of conductors to minimize inductance while retaining the field quality. A 2:1 scaled model has been made and the magnetic field was measured. Two 1:1 models have been made to measure inductance, mutual inductance and the rise time. Simulations of beam propagation with Panofsky quadrupoles demonstrated the linearity of the design.

1 INTRODUCTION

An electron ring, UMER, is under development at the University of Maryland for the purpose of studying space charge dominated beams in a circular FODO lattice [1,2]. Two pulsed Panofsky quadrupoles shown in Figure 1 with rectangular aperture and fast rise time are proposed in the injection area [3]. Q1 is centered on the ring, replacing one of the regular ring quadrupoles. It must be turned on after the injection beam passes by. Q2 is centered on the injection line and is on only during injection. The dimensions of Q1 and Q2 are slightly different so that they can be overlapped physically.

In the design, due to the small aspect ratio, the integral of the field along the z-direction, rather than the field itself is used. The magnetic field is calculated with a computer code MAG-PC from certain conductor locations. The goal of our design is:

- To have good enough field linearity. Inside 0.7R (R is the pipe radius), the linearity should be better than 1%. The integral gradient is 28 Gauss.
- To have fast enough time constant. The field construction time should be less than 100~150ns for 50 ns bunch. Small inductance is preferred.
- To have as small as possible voltage and power requirement to the pulse generator.

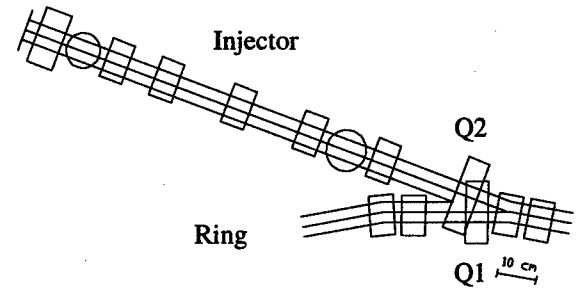

Figure 1: Schematic injector layout of UMER.

2 DESIGN

The conductors are located on the four surfaces of a rectangular box. At first two designs, a parallel structure and a loop structure, were explored. In the parallel structure design, the active conductors with same length are all parallel with the z-axis. In the loop structure design, the conductors form loops in each of the quadrants. After carefully designing and comparing, the loop structure was chosen because it needs less current and voltage while both the designs satisfy the field linearity and rise time requirement. Only the loop structure is discussed in the later sections of this paper.

2.1 Theoretical Formulas

The surface current distribution for a quadrupole with a rectangular aperture is derived [4]. The current distribution is such that all the integrated (along the z-axis) multipole components of the field vanish, except for the quadrupole term. The surface current density along the z-axis on the top and bottom surface, $\rho_z(x)$, and that on the left and right surface, $\rho_z(y)$ are:

$$\rho_z(x)=\sum_{l=0}^{l_{max}}\rho_l\left(1+\frac{x^2}{a^2}\right)^{-1/2}\left(\left(1+i\frac{x}{a}\right)^l+\left(1-i\frac{x}{a}\right)^l\right)$$
$$\rho_z(y)=\sum_{l=0}^{l_{max}}\rho_k\left(1+\frac{y^2}{b^2}\right)^{-1/2}\left(\left(1+i\frac{y}{b}\right)^k+\left(1-i\frac{y}{b}\right)^k\right) \quad (1),$$

where x, y are the horizontal and vertical axis and a, b are the half length of the rectangular aperture in the x and y direction. The current density is then approximated by the first two terms: $\rho_z(x)=\alpha\cdot\rho_0(x)+(1-\alpha)\cdot\rho_1(x)$, with

*Work supported by the US Department of Energy.
#Email: liyun@glue.umd.edu
a: Present Address: ORNL and Visiting at BNL.

α the weight of the first term. Similar in y with the weight β.

In the loop structure with a continuous current model, the active currents (currents that go along the z-axis) do not have the same length because of the return current which goes in the x or y direction. Let the effective active current (adjusted by the current length) to be the current needed to produce a quadrupole field. Then making use of the continuity of the current [5], the curve of the loop corner must satisfy:

$$\begin{aligned}(\frac{f(x)}{L})^2 &= 1-\alpha(\frac{x}{a})-(\frac{1-\alpha}{k})Arc\sinh(\frac{x}{a}),\\ (\frac{g(y)}{L})^2 &= 1-\beta(\frac{y}{b})-(\frac{1-\beta}{k})Arc\sinh(\frac{y}{b})\end{aligned} \quad (2),$$

where $k = Arc\sinh(1)$ is a constant; L is half length of the quadrupole.

2.2 Conductor Location

The return current, which is perpendicular to the z-axis, is located with equal intervals at $Z[n]$. The active conductors are then located according to the curve of the loop corners. Their location, $X[n]$ and $Y[n]$, must satisfy:

$$\begin{aligned}(\frac{Z[n]}{L})^2 &= 1-\alpha(\frac{X[n]}{a})-(\frac{1-\alpha}{k})Arc\sinh(\frac{X[n]}{a}),\\ (\frac{Z[n]}{L})^2 &= 1-\beta(\frac{Y[n]}{b})-(\frac{1-\beta}{k})Arc\sinh(\frac{Y[n]}{b})\end{aligned} \quad (3).$$

The factors α and β are adjusted carefully to optimise the field and keep the distance between the conductors not too small. The number of loops N is a trade-off between the field quality and the inductance of the circuit.

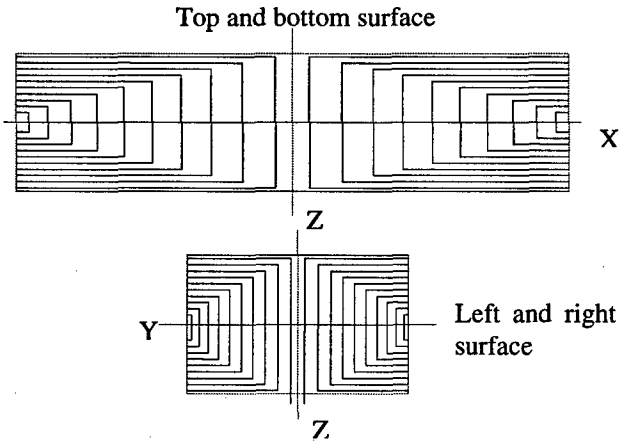

Figure 2: Conductor location of Panofsky quadrupole.

The size of the Panofsky quadrupole used in the ring is 4.4cm long, 13.4cm wide, and 5.6cm high. The design with a 10-loop structure, given in Figure 2, uses α=-2.14, β=-2.0. This design retains good field quality, shown in Table 1, and small inductance, as we will see later.

2.3 External Connections

For the final Panofsky quadrupole to be used in UMER, each of the 4 quadrants will be in series with an external 50Ω resistor and driven by a separate pulse generator. A common dc power supply will be used to power the 4 pulse generators and ensure equal pulse voltage.

For the 10 loop design in section 2.2, a current of 28.2A in each conductor is needed to produce an integrated gradient of 28 Gauss. The required generator voltage is 1.4kV. The quadrupole is on for 20μs, which corresponds to 100 revolutions in the ring. If the ring operates in 60 Hz, the duty factor is as small as 1.2×10^{-3}. This gives a total average power of 156w, or 47w per resistor. The inductance of each quadrant is about 3μH (see section 3.2 for detail), and gives a time constant of 30ns.

The mechanical part of the design is not finalized yet. Both the wire method and a printed circuit are being explored.

Table 1: The deviation of integral gradient at different radius and angle. The pipe radius is R=2.5cm.

	0°	30°	60°	90°
0.2R	-0.02%	-0.02%	0.0%	0.03%
0.4R	-0.03%	-0.11%	0.0%	0.19%
0.7R	0.50%	-0.63%	-0.58%	-0.59%

3 TEST AND SIMULATION

3.1 Prototype Field Measurement

A 2:1 scaled prototype of 16 loops (Figure 3) has been built to measure the magnetic field. (The 10-loop design was done after this measurement). A 1.67MHz, 30V sinusoidal signal is used to drive the prototype quadrupole, and a small coil of 20 turns is put into the quadrupole to get the induced voltage. The magnetic field is then calculated from the induced voltage. The magnetic field measurement agrees very well with the MAG-PC calculation, which is shown in Figure 4.

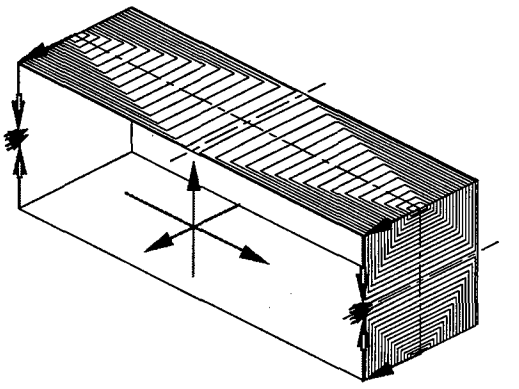

Figure 3: The prototype of Panofsky quadrupole.

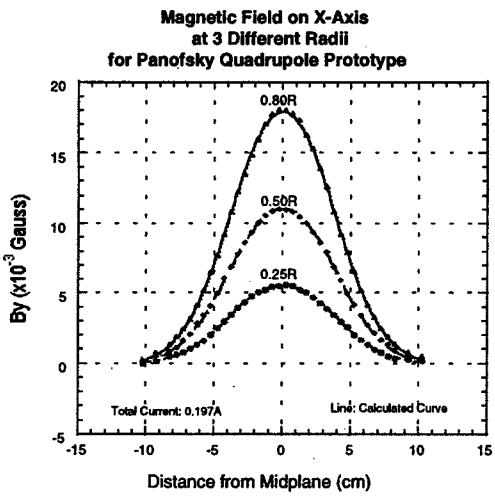

Figure 4: Magnetic field measurement (markers) and calculation (curve).

3.2 *Inductance Measurement*

Two 1:1 models of the 10-loop design have been built to measure the inductance and check the interaction between them. One is a little bit larger than the other in the size. The inductance of each quadrant is 2.5 μH and 3.3 μH respectively for the two models.

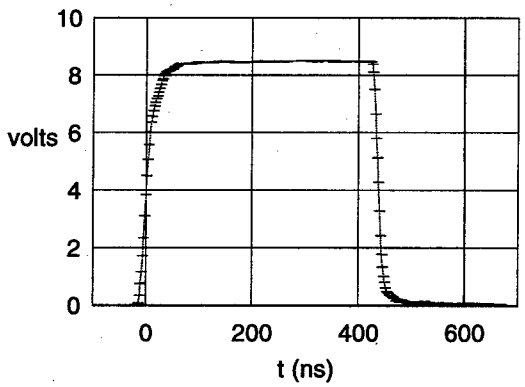

Figure 5: Circuit response of the Panofsky quadrupole model.

In the circuit response measurement, each quadrant is in series with a nominal 22Ω resistor to guarantee equal current in each quadrant. The 4 quadrants are then in parallel. This arrangement is then in series with a 46Ω resistor and driven by a rectangular pulse with a time constant about 10ns. Figure 5 is the signal picked up from the 46Ω resistor. This signal exhibits fast enough rise time and also fall time.

In order to check the interaction between the quadrupoles, two relative locations have been tested: one is when the two models are far away, the other is when the small model is overlapped with the large one a little bit, according to their relative position in Figure 1. The large one is driven by an 80ns rectangular pulse while the small one is driven by the same pulse but with 100ns delay. The output waveform has no detectable difference between the two cases. This shows that the mutual inductance is not a serious problem. However, these measurements will be repeated in the final arrangement.

In the future, maybe after the Panofsky quadrupole are built, the rotating coil system is to be used in the measurement of the harmonic components of the DC magnetic field; and the taut wire method is being employed to measure the pulsed magnetic field [7].

3.3 *Effect to beam, by Simulation*

The Panofsky quadrupole has a different field profile than the regular cylindrical quadrupoles designed for UMER. Beam simulation by a particle in cell code, WARP [8], has been done to check this effect on the beam. In Figure 6, the lower curve is the emittance growth in the x direction with only regular quadrupoles, while the upper curve is after changing 2 regular quadrupoles into Panofsky quadrupoles. The result shows that there is no large difference in emittance growth, and therefore verifies the field linearity of the design. [6]

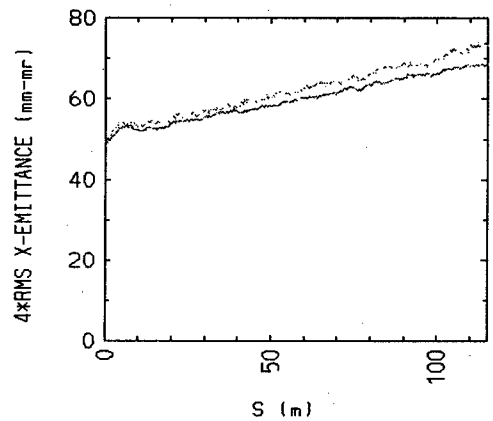

Figure 6. WARP simulation of Panofsky Quadrupole.

4 SUMMARY

A pulse Panofsky quadrupole with rectangular aperture is designed. Prototype field measurement and inductance measurement have been done. Simulation has been done to check the linearity. The mechanical construction and pulse generator is under development.

5 REFERENCE

[1] M. Reiser, et al., "The Maryland Electron Ring for Investigating Space-Charge Dominated Beams in a Circular FODO System," in these proceedings.
[2] J.G. Wang, et al., Nucl. Instrum. Methods Phys. Res. A. (1998), vol. 415, no. 1-2, P.422-7.
[3] D. Kehne, et al., "The 10 keV Injector for the University of Maryland Electron Ring Project," in these proceedings.
[4] M. Venturini, Electron Ring Project Technical Notes, Nov, 1996.
[5] M. Venturini, Electron Ring Project Technical Notes, July, 1995.
[6] R. Kishek, et al., "Simulations of Collective Effects in the Space-Charge-Dominated Beam of the University of Maryland Electron Ring," in these proceedings.
[7] W.W. Zhang, et al., "Magnetic Field Measurement of Printed-Circuit Quadrupoles and Dipoles," in these proceedings.
[8] D. P. Grote, et. al., Fus. Eng. & Des. 32-33, 193-200 (1996).

MAGNETIC FIELD MEASUREMENTS OF PRINTED-CIRCUIT QUADRUPOLES AND DIPOLES*

W.W. Zhang#, S. Bernal, P. Chin, R. Kishek, M. Reiser, M.Venturini, J.G. Wang, V. Yun
University of Maryland, College Park, MD 20742

Abstract

Printed-Circuit (PC) quadrupoles and dipoles have been designed and developed for focusing and bending a space-charge dominated electron beam in the University of Maryland Electron Ring (UMER) [1], currently under development. Due to the rather small aspect ratio (length/diameter < 1) of the magnets, the field quality, especially the nonlinear fringe field, has been a concern for the success of the UMER project. Extensive theoretical and experimental studies of the field structure of the magnets have been performed. Simple and precise methods for the magnetic field measurements of the PC magnets have been developed. In this paper, we present the various techniques and results of the measurements. The magnetic multipole components of quadrupoles and dipoles are determined from measurements with a long rotating coil. In addition, the integrated field of quadrupoles is obtained with the pulsed, taut-wire method. A comparison between the experimental results, theoretical analysis and calculation with a magnetics code, MAG-PC, is presented.

1 INTRODUCTION

A compact Electron Ring is being developed at the University of Maryland to study space charge effects and collective behavior of beams in a circular lattice [2]. The UMER has been designed to transport an electron beam of 10 keV, 100 mA, and 50 ns in a circular lattice of 11.5 m in circumference. The key components of the electron ring lattice are Printed Circuit (PC) quadrupoles and dipoles. The electron beam is focused by 72 PC quadrupoles and deflected by 36 PC dipoles. Table 1. lists the physical parameters of the PC quadrupoles and dipoles. These very short, air core magnets are made of current loops on flexible printed circuits [3]. This approach can meet not only the demand for beam transport in the electron ring, but also a significant reduction in cost. Nevertheless, the challenging problem is that the magnets have a rather small aspect ratio, resulting in highly nonlinear fringe fields. This concern has been addressed by extensive study of the field structure of the magnets in both theory and experiments.

Table 1: Physical parameters of PC magnets

	Quadrupole	dipole
Radius R	2.79 cm	2.872 cm
Length L	4.65 cm	4.437 cm
L/2R	0.833	0.772
Grad (B Field)	4.14 G/cm-A	5.22 G/A

2 SPATIAL HARMONICS MEASUREMENT

An accurate, widely used method of measurement of harmonics content in magnetic quadrupoles is the rotating coil [4]. A rectangular coil with dimensions 2.54 cm by 12.7 cm has been built [5]. It is used in such a way that one side of the coil is always positioned along the axis of the magnets, so the only relevant component of the magnetic field is B_ϕ. The voltage waveform induced in the rotating coil, spinning at 6±0.001 Hz, is digitized and fast-Fourier transformed in a scope. The oscilloscope is triggered by a synchronous signal related to the angular position of the rotating coil. Figure 1 is a photo of the basic setup.

Figure 1: Rotating coil setup (without μ-metal shield). The PC quadrupole is the block labeled "Q4" in the photo.

* Research supported by the U. S. Department of Energy
# Email: wwz@glue.umd.edu

The Earth's field and environmental noise are carefully compensated, since otherwise they produce a dipole term and other harmonic terms that affect the accuracy of measurement. To shield the effect of the Earth's field, a μ-metal box is employed; the residual field is about 5 mG. The effect of random noise is reduced by averaging more than ten measurements. The first step is to adjust the PC magnet relative to the rotating coil to minimize the dipole component (for the quad), or the quadrupole component (for the dipole); a 3-axis support fitted with non-magnetic micrometer screws is used for this purpose, which makes quadrupole magnetic axis corresponding to the mechanical axis of the coil. In this way, the rotating coil allows us to determine the magnetic axis of each quadrupole relative to its mechanical axis to within 0.025 mm. Figure 2 shows a typical spectrum from one quadrupole (with μ -metal shield).

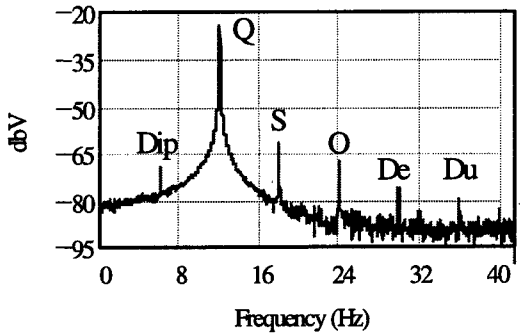

Figure 2: Harmonic spectrum of PC quadrupole: Dip(ole), Q(uadrupole), S(extupole), O(ctupole), De(capole) and Du(odecapole).

Both theoretical analysis [6] and MAG-PC calculations show that the only high order harmonic term allowed in the UMER PC quadrupole is the duodecapole; for the PC dipole, the sextupole and decapole terms occur. The unexpected measured high order harmonic terms in both PC magnets can be traced to machining errors in the metal mandrels, small errors in assembly, and possible distortions of the printed circuit. The dipole term in the quad spectrum is due mostly to the residual Earth's field. Table 2 lists the measured harmonic multipole terms relative to the main component in both PC quadrupoles and dipoles. Each number is the average of thirty-two measurements.

Theoretical analysis [6] yields a duodecapole term for the PC quadrupole equal to 0.098 %, while MAG-PC calculations give 0.12 %, both in agreement with the measured value, within experimental error. The measured multipole terms have been used in single-particle studies and error analysis of the University of Maryland Electron Ring [7]. They also provide important information for the mechanical alignment of the UMER.

Table 2: Measurement results

Magnet / Harmonic	Dipole(%)	Quadrupole (%)
Dipole	100	0.3
Quadrupole	0.37	100
Sextupole	0.51	0.3
Octupole	0.14	0.2
Decapole	0.11	0.19
Duodecapole	------	0.15

3 MAGNETIC FIELD MEASUREMENT

Because of the small size of the PC magnets, direct measurements with, for example, a Hall-probe gaussmeter is impractical. An alternative is to derive the field from integrated-field measurements using the pulsed taut-wire method [8,9]. Figure 3 shows the experiment setup.

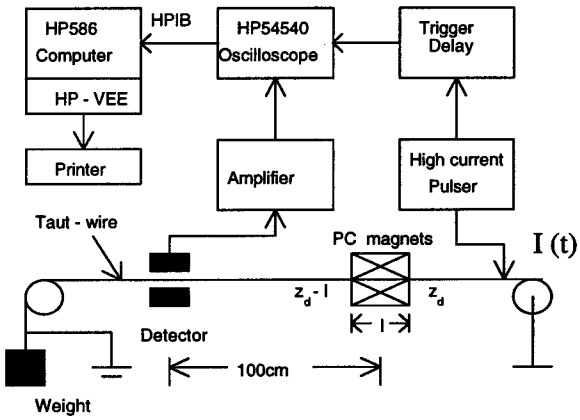

Figure 3: Setup for integrated magnetic field measurement with a pulsed taut-wire.

A current pulse (about 4 A, 300 μs at 0.2 Hz) is applied to a long straight wire parallel to and some distance from the PC magnet axis. The Lorentz force on the wire produces a mechanical vibration that a photogate sensor turns into a voltage. The amplitude of the voltage waveform is proportional to the integral of the transverse magnetic field. In order to reduce the effects of room vibration and noise, the waveforms are averaged over at least 100 pulses. Since the Earth's magnetic field affects the motion of the wire, the waveform produced by the Earth's field alone is first obtained and then subtracted from the measurements. Figure 4 shows the result of a typical waveform after subtracting the Earth's field signal.

To obtain an accurate value of the integrated magnetic field, a calibration is required. The simplest calibration method uses a set of small Helmholtz coils: the integrated magnetic field of the coils is carefully determined from measurements with both a gaussmeter and the taut-wire; thus the correspondence between amplitude of measured waveform and integrated field (i.e. number of volts per Gxcm) is established. Since the optical sensor has a limited linear area, the calibration is performed with care taken to avoid changing the sensor and taut-wire relative positioning used during the magnet measurements.

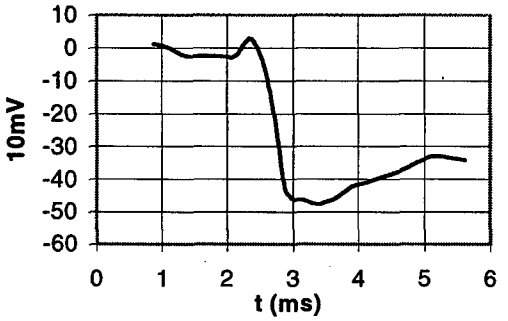

Figure 4: Typical signal from photogate sensor in the taut-wire method.

After differentiation and normalization of a waveform similar to Figure 4, the normalized field profile of Figure 5 is obtained. The difference between experimental results and calculations is more pronounced in the tails, where the sensitivity of the taut-wire apparatus becomes a problem.

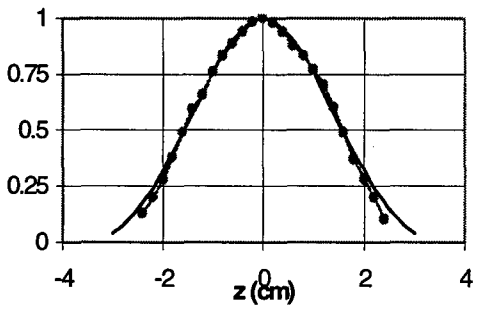

Figure 5: Normalized field profile of a PC quadrupole at r=0.45×quad radius and θ=45°. The solid line is the result of MAG-PC calculations.

An obvious improvement is to increase the peak current (without changing the pulse width) applied to the wire or the DC current applied to the magnet. This latter option, however, results in quadrupole heating.

The taut-wire method is also suitable for measuring the integrated magnetic field of pulsed magnets like the Panofsky quadrupole and the injector/extractor dipole intended for the Maryland Electron Ring [10].

4 SUMMARY

A rotating coil and a pulsed taut-wire apparatus have been used to measure the harmonic content and integrated magnetic field, respectively, of the PC magnets for the University of Maryland Electron Ring. These complementary measurements provide detailed information on the field quality of the small aspect ratio lenses, important for simulations of the beam dynamics as well as a realistic design of the mechanical lattice. The measurements are also significant on their own right, since the magnets are possibly the shortest (relative to their aperture), in existence.

The results of both the rotating coil and the pulsed-taut wire measurements are consistent with calculations with the iron-free magnetics code MAG-PC. The rotating coil results are also in fair agreement with theoretical predictions.

Studies similar to the ones reported here for DC magnets are planned for the pulsed elements of the UMER.

5 REFERENCES

[1] M. Reiser et al., these Proceedings

[2] M. Reiser et al, Fusion Engineering and Design, 32-33,293 (1996); J. G. Wang et al., Particle Accelerator Conf., 1997, p. ????.

[3] T.F. Godlove, S. Bernal and M. Reiser, Particle Accelerator Conf., 1995, p. 2117.

[4] W.G. Davies, Nucl. Instr. and Meth. Phys. Res. A311, 399-436 (1992).

[5] Rawson-Lush Instruments Co., Inc. Acton, Massachusetts.

[6] M. Venturini, Ph.D. dissertation, University of Maryland, July, 1998.

[7] L.G. Vorobiev, X. Wu and R.C. York, Michigan State University unpublished Report, October, 1998.

[8] O. Shahal et al., Nucl. Instr. and Meth. Phys. Res. A259, 299-302 (1989).

[9] H.Nishihara and M.Terada, Journal of Appl. Phys. 41, 8, 3322-3324, (1970).

[10] Y. Li et al., these Proceedings.

MAGNETIC MEASUREMENTS OF THE ANKA STORAGE RING MAGNETS

D.Einfeld, A.Krüssel, M.Pont[1,2] Forschungszentrum Karlsruhe GmbH,
Projektgruppe Errichtung ANKA, Postfach 3640, D-76201 Karlsruhe, Germany

Abstract

ANKA is a 2.5 GeV storage ring under construction. The storage ring consists of 16 bending magnets with a maximum field of 1.5 T, 40 quadrupoles divided in five families with a maximum gradient of 20 T/m, 24 sextupoles with a maximum second order differential of 550 T/m^2, and 44 correctors with a maximum kick capability of 0.8 mrad. The production of all the magnets is now finished and the magnets have been mechanically and magnetically characterized to ascertain their excitation curves and field uniformity. For the dipoles a Hall probe has been used to map the magnetic field while for the quadrupoles and sextupoles a rotating coil system has been used to determine the magnitude of the high order multipoles. In this paper the analysis of these data is discussed and results for measured magnets are presented.

1 INTRODUCTION

The magnetic system of the ANKA storage ring [1] is summarised in table I. It consists of 16 bending magnets, 40 quadrupoles, divided in 5 magnetically different families and two families of sextupoles.

Table I

Magnet type	Name	Number	Max. magn
Bending	BEN	16	1.5 T
Quadrupole	Q320	8	18.1 T/m
Quadrupole	Q320	8	18.1 T/m
Quadrupole	Q320	8	18.1 T/m
Quadrupole	Q320	8	18.1 T/m
Quadrupole	Q390	8	17.9 T/m
Sextupole	SH	8	551 T/m^2
Sextupole	SV	16	482 T/m^2

There are 32 magnets of the Q320 type. They have been organised in families according to the magnetic measurements.

For each type of magnet a prototype was produced to test the expected magnetic performance. The results [2,3,4,5] indicated a performance comparable to what had been expected, therefore the magnets were produced with only minor modification from the prototypes.

2 THE MAGNETIC MEASUREMENTS

The magnetic measurements on the bending magnets have been performed using a Hall probe mounted on a bench that allows movement in three directions [6]. The resolution of the read-out is 1 μm in each axes, while the precision is smaller than 5 μm for the three axes. The Hall probe is calibrated against an NMR system to better than ± 1 G.

To characterise the quadrupoles and the sextupoles a rotating coil system has been used [7]. The system has a relative accuracy better than $\pm 2.10^{-4}$ for the main harmonic, and has a reproducibility better than $\pm 2.10^{-4}$ for the ratio of the high order components to the main component.

3 PRELIMINARY RESULTS FOR THE MAGNETIC MEASUREMENTS

3.1 Bending Magnets

Figure 1 shows the dependence of the normalised magnetic field with respect to the current for a typical magnet. At the nominal current (approx. 650 A) there is a saturation of 7 %.

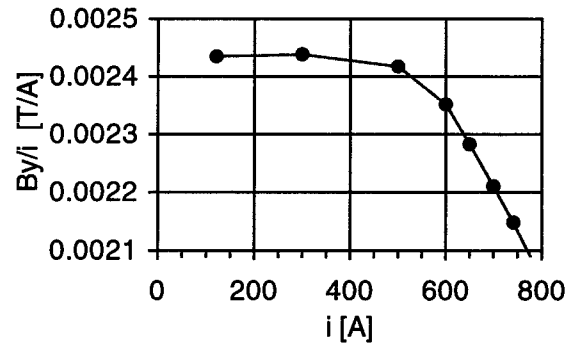

Figure 1 Normalised magnetic field versus current for a typical bending magnet

Figure 2 shows a typical field quality in the transversal direction at different currents. At the

[1] On leave of absence from IFAE-LLS, Barcelona , Spain
[2] Email: pont@anka.fzk.de

0-7803-5573-3/99/$10.00@1999 IEEE.

nominal current, one can clearly see a quadrupole component due to the magnetic forces in the pole gap. This quadrupole component is $1.34.10^{-2}$ T/m and the sextupole component is -0.8 T/m^2 according to a fit of the measured data in the centre of the magnet.

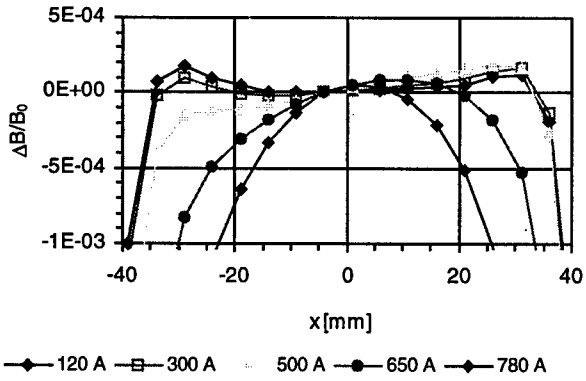

Figure 2 Transversal field quality for a bending magnet

Magnetic field maps have been measured in the midplane of the bending magnet at three different currents; injection (0.5 GeV; 125 A), at mid-energy (1.6 GeV; 400 A) and at nominal energy (2.5 GeV; 650 A). The electron trajectory has been calculated from the field maps and the field integral has been determined from the trajectory.

Figure 3 shows the relative difference from the mean integrated field for the magnets that have been measured up till now at nominal current. The relative difference is below $\pm$ 2.10^{-3}, which corresponds to a kick of $\pm$ 0.8 mrad, representing a deterioration of the close orbit deviation, that can be easily suppress using the corrector magnets distributed around the ring and an appropriate sorting procedure.

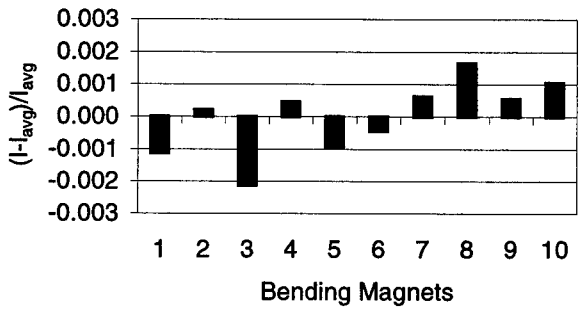

Figure 3 Relative deviation from the mean field integral for the up-to-now measured bending magnets at 650 A

3.2 Quadrupole Magnets

Quadrupoles Q320 will work at an approximate current of 350 A at nominal energy, while for the same energy quadrupoles Q390 will work at a current of 300 A. The difference between the measured gradient and the ideal gradient is below 5 % for both magnets.

Figure 4 (see next page) shows the relative difference between the measured integrated gradient and the mean integrated gradient. For the 32 Q320-quadrupoles, $\Delta g/g$ stays below $\pm$ 5.10^{-3}. These 32 quadrupoles are further divided in 4 groups of 8 magnets. Once this is done the relative difference to the mean is below 1.10^{-3} for three groups and only for one set of magnets it goes up to $\pm$ 3.10^{-3}, which is within specifications. The tune shifts induced are below $\pm$ 10^{-4} and the beta beat is below 2% in both planes, once the magnets are properly sorted as has been shown by calculations done with MAD.

The main high order multipoles present are the allowed n=6 and n=10 components and the non-allowed components n=3 (normal and skew) and n=4. The non-allowed components are due to mechanical errors. Typically the systematic components are the same for all the quadrupoles, while the non-allowed components vary from quadrupole to quadrupole. Nevertheless the largest high order component is still below $\pm$ 5.10^{-4} (ratio of the high order component to the main component), which has been shown not to have any detrimental effect on the dynamic aperture of the machine.

In order to understand the presence of the non-allowed multipoles we have performed extensive mechanical measurements. The aperture diameter is for all the magnets 70$\pm$0.04 mm. In the interpole distances there is a larger variation, 22.78$\pm$0.06 mm. However, there is no clear correlation between the interpole distances and the presence of the non-allowed sextupole and/or octupole components.

For the quadrupoles Q390 the same measurements have been performed. Figure 5 shows that the relative deviation of the measured integrated gradient is below $\pm$ 4.10^{-3}. Again the high order multipoles are characterised by the allowed n=6 and 10 and the non-allowed sextupolar and octupolar components.

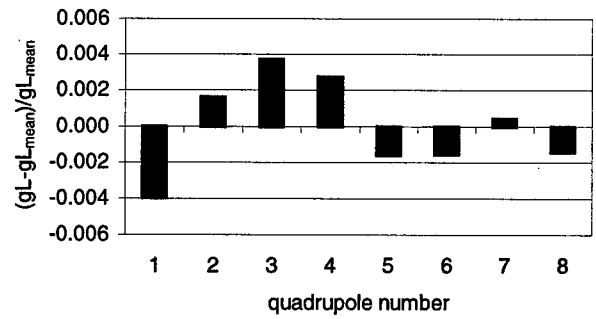

Figure 5 Relative deviation from the mean integrated gradient for the Q390 quadrupoles at 300 A, nominal current

3.3 Sextupole Magnets

Measurements on the vertical acting sextupoles SV have not yet started and those on SH are now under way, therefore only preliminary results will be here presented.

The sextupoles SH and SV will work at a nominal current of approx. 200 A with a saturation smaller than 2 %. The main high order harmonics present are the allowed n=9 and n=15. For all magnets the contribution of these high order harmonics to the main component is smaller than 5.10^{-3}.

Figure 6 presents the relative deviation from the mean integrated sextupolar component for the sextupoles SH at 200 A.

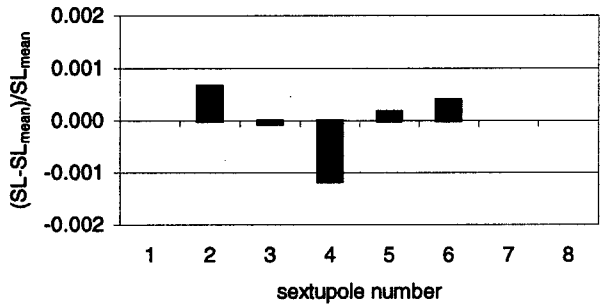

Figure 6 Relative deviation from the mean integrated sextupolar component for the SH sextupoles at 200 A

4 SUMMARY

The measurements of the ANKA magnets are well advanced. The 40 quadrupoles measured are within specifications. The relative spread in integrated quadrupole strength amongst the different families is below $\pm 3.10^{-3}$. The high order multipoles do not have any detrimental effect on the behaviour of the machine. The measurements performed up to now on the dipoles and sextupoles indicate also magnets within the magnetic specifications.

5 REFERENCES

[1] D.Einfeld et al. Status of the accelerator for the 2.5 GeV light source ANKA in Karlsruhe, this Conference
[2] M.Pont, A.Krüssel, Technical Report, MAG-98/02
[3] M.Pont, A.Krüssel, Technical Report MAG-98/03
[4] M.Pont, A.Krüssel, Technical Report MAG-98/07
[5] M.Pont et al. EPAC'98
[6] LLS measuring bench, private communication
[7] Danfysik Model 692 User Manual, Danfysik A/S, (DK)

Acknowledgements

The authors want to thank BESSY-II, specially D.Krämer, for lending us the rotating coil on which the measurements of the quadrupoles and sextupoles have been performed, also we would like to thank the LLS team for performing the measurements on the bending magnets.

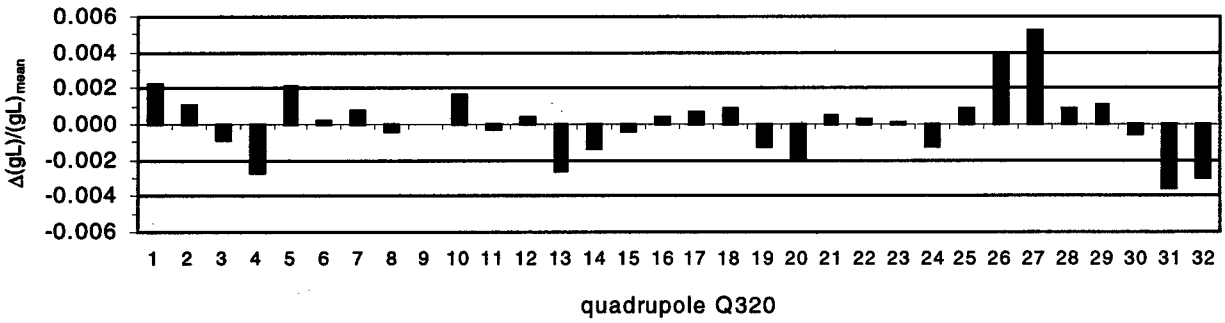

Figure 4 Relative deviation from the mean integrated gradient for the quadrupoles Q320 at 350 A, approximately nominal current

3 DIMENSIONAL FIELD CALCULATIONS COMPARED TO MAGNETIC MEASUREMENTS FOR CERN PSB-CPS TRANSFER LINE MAGNETS

M. J. Barnes, G. S. Clark, TRIUMF, M. Sassowsky, CERN

Abstract

The transfer line PSB-CPS recombines the four beams from the CERN PS Booster (PSB) into one beam, which is injected into the CERN 26 GeV Proton Synchrotron (CPS). As part of the "PS conversion for LHC" project [1], some of the magnets in this transfer line have been replaced by new magnets with laminated yokes and higher maximum current. The magnets were built and magnetically measured by TRIUMF as part of a Canadian contribution to the CERN LHC project. Detailed three dimensional mathematical models have been developed for two types of bending magnets. The models are compared to magnetic measurements and it is shown that the integrated homogeneity curves can be calculated from the 3D model with a precision significantly better than one per mill. The mathematical model is then used to predict the influence of shims on the magnetic field.

1 INTRODUCTION

The magnetic field inside an accelerator magnet and sufficiently far from the extremities, can be calculated using a two dimensional field calculation. This assumes that the magnetic vector potential only has a z-component. To predict the end field correctly, a full three dimensional field calculation is necessary.

The BV1 and BV2 magnets, to be used in the PSB-CPS transfer line, are window frame magnets described in [2] and the references therein. The end fields contribute significantly to $\int B\,dl$. The magnetic measurements [2] were carried out with a 1D Hall probe, which measured only the main component of the field. For the BV1 magnets a characteristic asymmetry caused by the single bedstead coil was found, which could be sufficiently well compensated by adding a shim to the yoke extension block.

A 3D code has been used to simulate BV1 and BV2, and the predictions have been compared with the measurements. The software used for the calculations is Opera-3D [6], which solves the field equations with boundary conditions by finite element discretisation. The non-linear properties of the magnet steel are taken into account by an iterative solution using a Newton-Raphson method.

2 MODELLING CONSIDERATIONS

2.1 Yoke

The yoke is built from 1.5 mm thick laminations of low carbon steel [5] stacked between two 10 mm thick massive endplates. The effect of the laminations is modelled by introducing effective permeabilities normal (μ_n) and tangential (μ_t) to the plane of the laminations [3]:

$$\mu_t = s\mu_{steel} + (1-s) \approx s\mu_{steel} \quad (1)$$

$$\mu_n = \left(\frac{s}{\mu_{steel}} + (1-s)\right)^{-1} \quad (2)$$

For common values of the stacking factor s (typically 0.96 to 0.99) and the steel permeabilitiy μ_{steel} (several thousand), the term $(1-s)$ in Eq. 2 dominates. Thus μ_n is only weakly dependant upon the steel permeability, and is small compared to μ_t and μ_{steel}. The physical meaning is that the B field lines are essentially parallel to the laminations. In Opera-3D, μ_n and μ_t are calculated from the BH curve, the stacking factor and the orientation of the lamination [7].

The longitudinal fringe field originates from the end plates with the field direction essentially normal to the lamination plane. It is therefore essential to include in the model the non-laminated endplate with an isotropic permeability equal to the steel permeability.

2.2 Coils

The coils of the BV1 and BV2 magnets are bedstead coils made of 8 circuits with 14 windings each. The coil heads are not identical, as one coil head contains the layer-to-layer transitions and the 16 coil tails for hydraulic and electrical connections. The model uses the GBED coil macro with the shape of the coil heads identical to the actual shape on the non-connection side of the coil. The absolute value of the current density was fine-tuned so that the local B field in the magnet centre is equal to the measured value.

2.3 Meshing and potential types

The model was built using hexahedral meshes. The results using a mesh generated with the new automatic tetrahedral mesh generator introduced in version 7 of Opera-3D were found to be not accurate enough. In the x-y-plane the finest meshing was generated in the centre of the aperture. Several triangular regions (containing degenerate tetrahedral meshes) create transitions to the outside regions with a coarser mesh. An air layer outside the dimensions of the magnet yoke was included to minimise the influence of the outer boundary conditions on the results. In the z-direction (longitudinal) the models consist of seven layers with the finest mesh size in the layers around the endplate. All regions containing the coil, and the region between the pole faces, are reduced potential regions [8]; the yoke and part of the outer air regions are total potential regions. The total potential regions and the reduced potential regions are topographically singly connected [8]. Fig. 1 shows perspective views of both models.

0-7803-5573-3/99/$10.00@1999 IEEE.

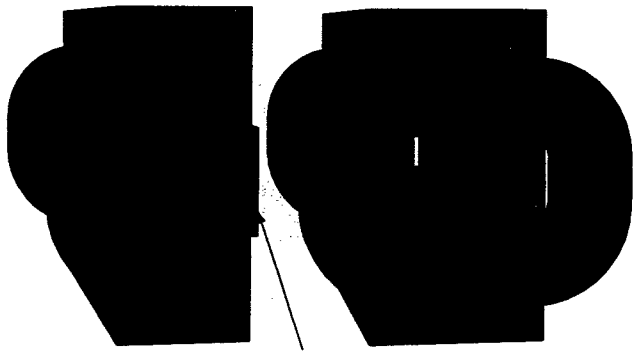

Figure 1: BV1 (left) and BV2 (right)

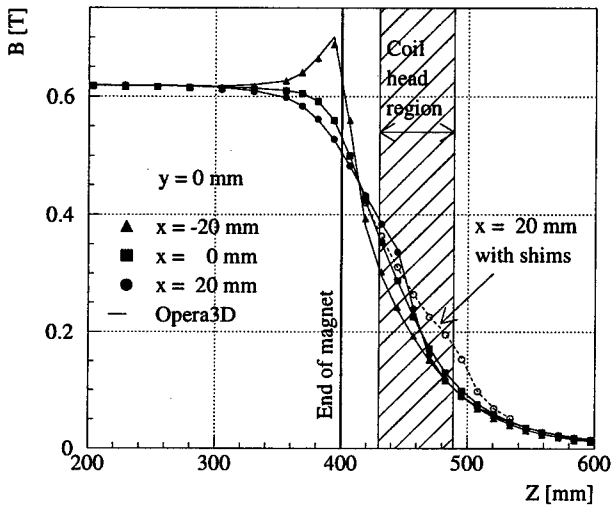

Figure 2: Measured and calculated B_x for BV1 #1

3 RESULTS

3.1 BV1

Fig. 2 shows the main field component B_x for BV1 as a function of the longitudinal position in the magnet; points represent the measurements and lines represent the calculations. A pronounced asymmetry caused by the single coil head can be seen. On the side of the coil head ($x < 0$) a maximum of the local field inside the yoke (at $z \approx 390$ mm) can be seen. The effect of the yoke extension block manifests itself by an increase of the local field for positive x up to $z \approx 450$ mm, which corresponds to the actual length of the block in the z-direction. In general the calculated values correspond well to the measured ones. With shims attached to the yoke extension block, the increase of the local field extends up to $z \approx 500$ mm.

Fig. 3 shows the difference between measured and calculated values, the largest systematic differences can be seen for negative x close to the end of the magnet. The RMS spread between the measured and calculated field is $1.47 \cdot 10^{-3}$ T (without shims) and $1.43 \cdot 10^{-3}$ T (with shims) [3] which corresponds to 2.3 ‰ of the central field. Comparing the measurements of BV1 #1 and #2 yields an RMS

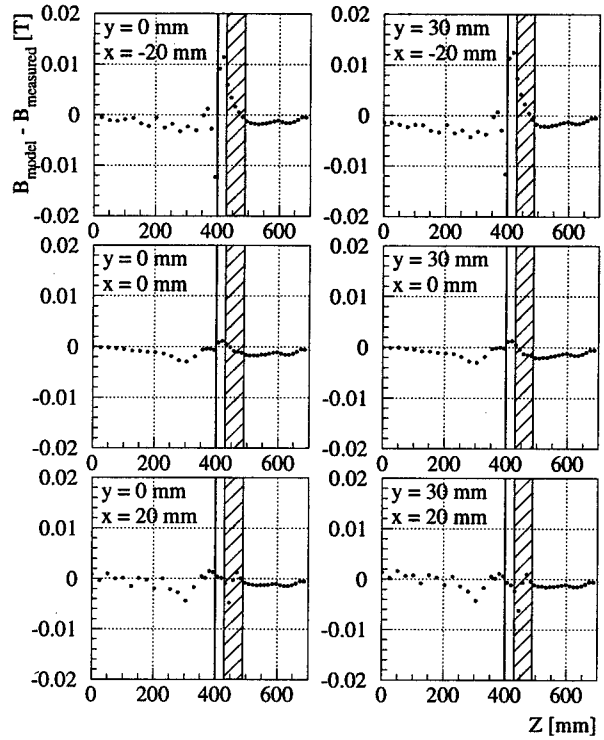

Figure 3: Predicted B_x - measured B_x for BV1

difference of $1.34 \cdot 10^{-3}$ T [3], corresponding to 2.1 ‰ of the central field. This means that the difference between model and measurements is not significantly larger than the difference between the two magnets.

Fig. 4 compares the measured and calculated homogeneity curves of BV1 #1 without shims and of BV1 #1 and #2 with shims. The predicted and measured values agree to better than one per mill. Again, the difference between measurement and model is not significantly larger than the difference between the measurements of the two magnets. Part of the systematic deviation can be attributed to a slope of the measured curves which is most probably due to a slight non-parallelism (0.1 mm) of the pole faces. On the other hand the model underestimates the curvature of the curve (i.e. sextupolar component) for x = -20 mm.

3.2 BV2

The agreement between measurements and calculations for BV2 is comparable to that reported above for BV1 [3]. The BV2 model is then used to predict the effect of wedge-shaped shims added to the end plate, as proposed in [4], to include a gradient component in the dipolar field.

Fig. 5 shows the end region of the BV2 model with the shims included, seen from the inside of the aperture. Fig. 6 shows the calculated homogeneity curves for three cases, with no shims (top row), with shims of an angle of 50 mrad (middle row) and with shims of an angle of 150 mrad (lower row). The left and right columns show the homogeneity as a function of y and x, respectively. The vertical gradient produced by the 50 mrad shim at $x = 0$ mm is

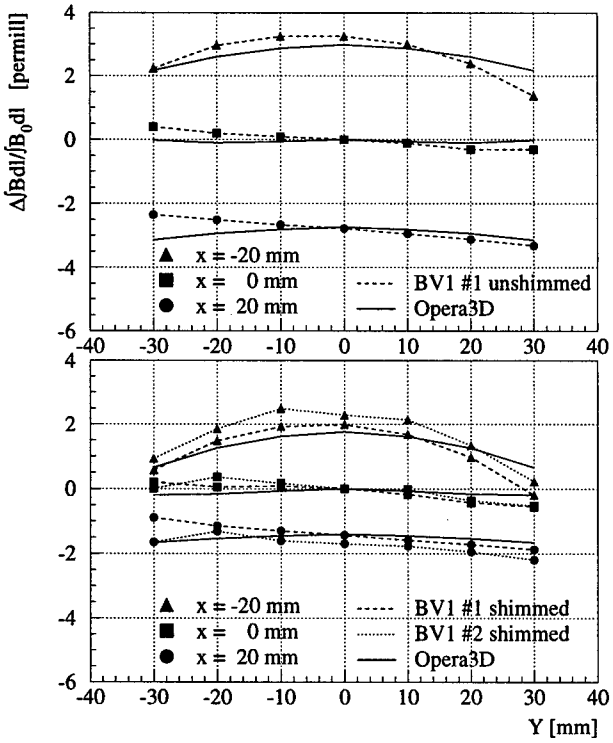

Figure 4: Measured and calculated homogeneity curves

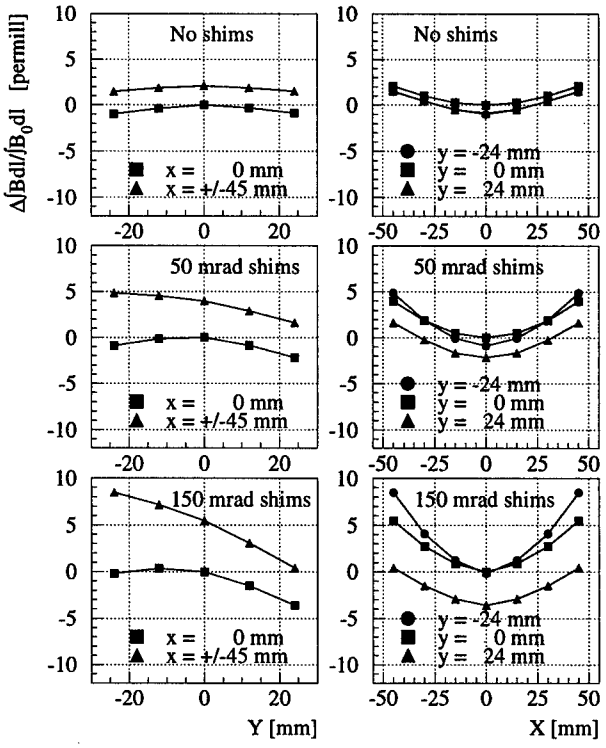

Figure 6: Calculated BV2 homogeneity curves

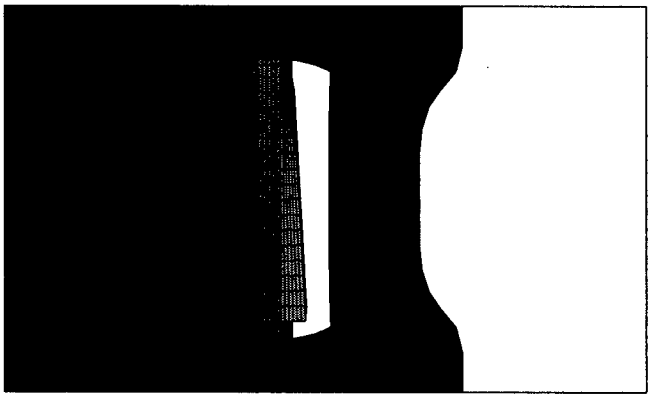

Figure 5: BV2 model with wedge shaped shims

only one third than what would be naively expected. Increasing the shim to an angle of 150 mrad can produce the desired vertical gradient, but creates a much stronger sextupolar component in the horizontal (x) direction.

4 CONCLUSIONS

The magnetic field of the BV1 and BV2 transfer line magnets has been calculated using the Opera-3D program. The integrated homogeneity curves can be calculated from the 3D model with a precision significantly better than one per mill. The influence of the BV1 shims is well described by the model. Wedge shaped shims with an angle of 150 mrad added to the BV2 model produce a vertical gradient component proposed in [4], but at the same time a significantly higher sextupolar component in the horizontal direction.

5 ACKNOWLEDGEMENT

The authors wish to thank D. Evans (TRIUMF) for carrying out the magnetic measurements on the BV1 and BV2 magnets.

6 REFERENCES

[1] F. Blas et al., Conversion of the PS complex as LHC proton pre-injector, PAC97, Vancouver, Canada, 12-16 May 1997

[2] M. J. Barnes et al., New magnets for the transfer line PSB-CPS, CERN SL-Note-98-052 MS

[3] M. J. Barnes, G. S. Clark, M. Sassowsky, Three dimensional field calculations compared to magnetic measurements for BV1 and BV2 transfer line magnets, CERN SL-Note-98-063 MS

[4] A. Jansson et al., Study of the emittance blow-up sources between the PS Booster and the 26 GeV PS, 1998 European Particle Accelerator Conference (EPAC 98), Stockholm, Sweden, 22-26 June 1998

[5] Magnetil BC steel, Cockerill Sambre, Seraing, Belgium

[6] Opera-3D version 7.005, Vector Fields Limited, 24 Bankside, Kidlington, Oxford OX5 1JE, England

[7] Opera-3D applications notes, VF-01-98-X6

[8] Opera-3D user guide, VF-01-98-D2, Chapter 2

A PROTOTYPE DIPOLE SEPTUM MAGNET FOR FAST HIGH CURRENT KICKER SYSTEMS*

L. Wang[1], S. M. Lund, G. J. Caporaso, Y. J. (Judy) Chen, B. R. Poole, LLNL, Livermore, CA
T. F. Brown, Bechtel Nevada Corporation, Las Vegas, NV

Abstract

A dipole "septum" magnet without a material septum has been designed and tested as part of a fast beam kicker system for use in intense, electron-beam induction accelerators. This septum magnet is a simple, iron-based electromagnet with two static, oppositely oriented dipole field regions used to provide further separation of beam centroids given a small angle kick by a fast beam kicker. The magnet geometry includes removable pole pieces to allow experimental flexibility. Field errors experienced by the beam depend crucially on the magnitude of the initial kick that provides displacement of the beam centroids from the transition region between the two dipole field regions. Results of simulations are reported.

1 INTRODUCTION

Intense electron-beam induction accelerators are presently under consideration at Lawrence Livermore National Laboratory (LLNL) for use in advanced flash x-ray diagnostics of implosions [1]. A key component of these radiography machines is a fast, high current stripline kicker used to rapidly switch an intense electron beam micro-pulse on the order of 50 ns in duration into separate beam transport lines to achieve multiple lines of sight on target [2]. This fast kicker system is composed of two elements in series as diagrammed in Fig. 1. The first is a fast dipole kicker that is only capable of imparting a small angle bend ($\theta_i \approx 1°$) to the centroid. This is followed by a short drift distance to allow the kicked beam centroids to radially separate (but not so long as to allow significant expansion due to the lack of transverse focusing), and then a static field dipole septum magnet that increases the angular separation of the centroids ($\theta_f \approx 15°$) and steers them into separate transport lines. In this study, we describe the design and construction of a prototype septum magnet with two oppositely oriented dipole field regions. This "septum" magnet is not a true septum since no material is allowed in the region between the two dipole field apertures across which intense electrons will spray during the beam switching process. Any material present in this region would be hit by intense electrons and resulting plasmas close to the beam reference orbits could interfere with subsequent micro-pulses. Unfortunately, this lack of a material septum makes achieving high field quality problematic. A simple, flexible iron-dominated dipole electromagnet has been designed for use in proof-of-principle experiments on the ETA-II accelerator at LLNL. This design scales to full radiographic parameters, and allows a wide range of experimental tuneability.

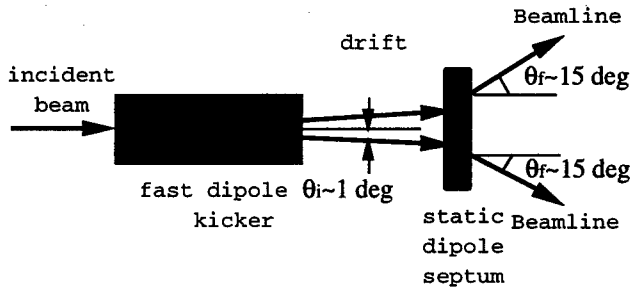

Fig. 1: Fast kicker system consisting of a pulsed, fast dipole kicker, a drift, and a static dipole septum magnet.

The ideal "box" geometry of the septum magnet is shown in Figure 2. There are two regions with oppositely oriented uniform, dipole magnetic fields of the same magnitude, radially separated by a thin field transition region. The two beams emerging from the kicker are incident in the uniform field region a radial distance d from the centerline and are further separated from each other by the dipole fields as the beams traverse the axial length l of the magnet.

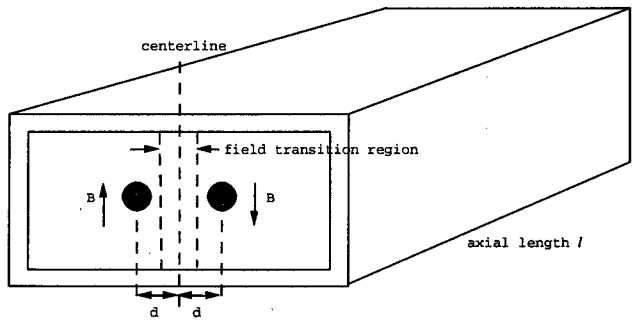

Fig. 2: Ideal box geometry of the dipole septum magnet.

The required dipole magnetic field B is related to the beam energy E_b and the incident and exiting beam angles θ_i and θ_f by

$$Bl = \frac{mc}{e}\sqrt{\left(\frac{E_b}{mc^2}\right)^2 + 2\left(\frac{E_b}{mc^2}\right)}\left[\sin\theta_f - \sin\theta_i\right]. \qquad (1)$$

*The work was performed under the auspices of the U. S. Department of Energy under contract W-7405-ENG-48.

[1] Email: wang22@llnl.gov

Here, m and e are the mass and charge of an electron, and c is the speed of light in vacuo. On traversing the magnet, the beam centroids will move radially a distance

$$\Delta = 1\frac{\left[\cos\theta_i - \cos\theta_f\right]}{\left[\sin\theta_f - \sin\theta_i\right]} . \quad (2)$$

2 SEPTUM MAGNET DESIGN

An iron electromagnet has been designed using iron poles with shims to enhance field quality. The magnet geometry is illustrated in Fig. 3 and is essentially two "C" type dipole magnets brought into close radial proximity. The poles consist of insertable plates allowing easy pole replacement enabling experimental evaluation of a range of aperture gaps, and field smoothing shims using the same basic assembly. The rapidity of the transition between the two dipole field regions depends critically on h/d, the ratio of magnet half-gap h relative to the incident centroid displacement d. The ratio d/r_b, where r_b is the beam radius, must also be sufficiently large such that the incident beam does not enter the field transition region. Achievable d is limited by the fast kicker technology and the maximum fast-kicker to septum magnet drift distance. Thus h was chosen as small as possible consistent with the transverse size of the nearly round beam incident on the septum magnet. The dipole fields bend the beam centroid into the good field region as the beam traverses the box magnet geometry. Due to this desire to increase the centroid motion Δ [Eq. (2)] and the desire to minimize 3D fringe field effects, weak bending fields were employed with long axial magnet length relative to the magnet half-gap h. Coils were stacked thin transversely and long vertically to allow a more rapid transition between the dipole field regions. Permanent magnets and/or additional coils could be used to enhance the rapidity of the field transition, but this was avoided for simplicity and to have the unsaturated field scale linearly with coil excitation. The upper and lower half coils were wound separately to allow the upper and lower magnet assemblies to be unbolted for easy removal of the magnet assembly and independent excitation of each dipole region. This allows easy access to the poles and the vacuum beam pipe as well as flexible experimental operation. Shims were employed near the field transition region to enhance field linearity. The vertical height of these shims was limited to prevent further restriction of a thin walled rectangular vacuum pipe that threads the magnet aperture, thereby limiting the degree of field smoothing these shims can produce. No shims were employed on the far radial extent of the poles since the poles can easily be made wide enough to achieve high field quality in that region.

The parameters chosen for the design are an axial length $1 = 20\,\text{cm}$, incident and exiting beam angles of $\theta_i = 1\,\text{deg}$ and $\theta_f = 15\,\text{deg}$, resulting in a bending field of $B \approx 250\,\text{Gauss}$ for the beam energy of $E_b \approx 6\,\text{MeV}$. The incident beam radius (r_b) and centroid separation ($2d$) at the septum magnet are about 1.5 cm and 6 cm, respectively. The beam centroid will exit the magnet a horizontal distance of $\Delta \sim 3\text{cm}$.

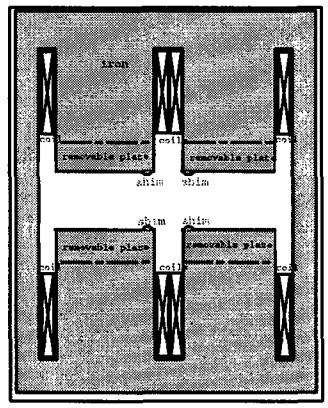

Fig. 3: Schematic of dipole septum magnet geometry (not to scale).

Figure 3 shows the 2D geometry of the septum magnet designed. The beams go through the aperture ($2h$) which is about 7 cm high. The coils on the left side and right side of the magnet have different polarities such that there are two field regions with oppositely oriented dipole magnetic fields. The amp-turns of each coil can be estimated as $NI \approx Bh/\mu_0 \sim 800$ Amp-turns. Here, h is the height of the half gap, μ_0 is the free space permittivity, and N is the number of turns of the coil. A total of $N = 300$ turns was chosen and the total power dissipation was small enough where no water cooling was needed. A part of each iron pole is made into a removable plate. Therefore, if the beam radius is larger than expected or if the field quality is insufficient, the gap structure can be easily modified without reconstructing the whole magnet assembly. Shims of trapezoidal shape were designed to make the fields more uniform in the transition region. A picture of the septum magnet built for use in proof-of-principle experiments on the ETA-II accelerator at LLNL is displayed in Fig. 4a. Figure 4b shows the septum magnet in the beamline. Because of the small aperture in the septum magnet, the round beam pipe from the kicker is tapered to a rectangular shape in the septum magnet region before reaching the diverging beamline.

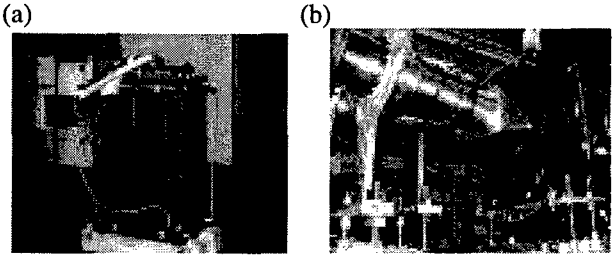

Fig. 4: (a) Septum magnet for the ETA-II experiment
(b) Septum magnet in the beamline

3 MAGNETIC FIELD SIMULATION

The magnetic field was simulated using the 2D magnetostatic code Poisson. Only a quarter of the symmetric structure was simulated. Due to the low fields, no iron saturation occurred for the full possible coil excitation. Figures 5a and 5b show the field contours near the transition region without and with the shims. The curved field lines indicate non-uniform fields, with a perfect dipole corresponding to straight lines.

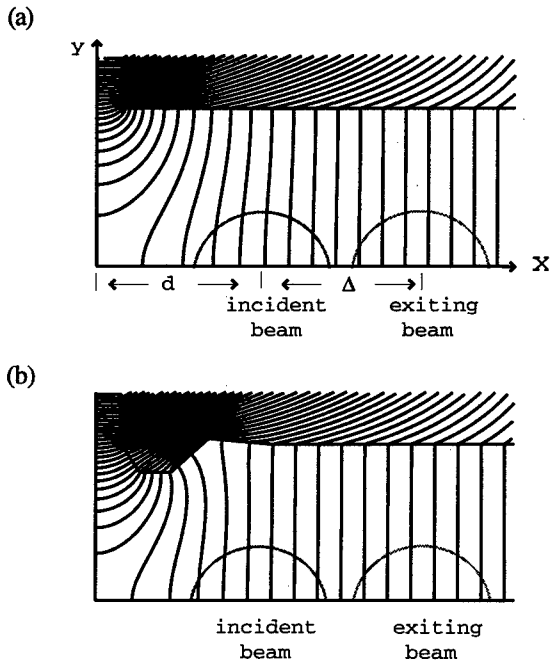

Figure 5: Simulated field lines in the half aperture of the septum magnet. (a) without shims. (b) with shims.

Note that with shims, the fields in the transition region are more uniform. Also the significant centroid motion of the beam from incident to exiting limits the effect of the larger incident field errors since the beam bends into the high field quality region. Note also that the shim includes a small tapered cut from the iron pole. The effect of the shim is further illustrated in Fig. 6, where the vertical magnetic field on the midplane ($y = 0$) of the septum magnet is plotted. Note that the shim reduces the undesirable variation in field at the beam edge and centroid for the incident beam.

A harmonic analysis of the multipole content of the field in the gap of was performed at x=3, 4, 5, and 6 cm and $y = 0$. Table 1 summarizes the multipole field contributions compared to the dipole field at that value of x when evaluated on a circle of radius 2.5 cm for harmonic numbers $N = 2$ (quadrupole), 3 (sextupole), and 4 (octupole).

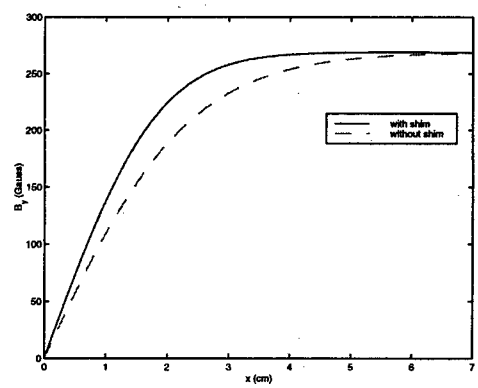

Figure 6: Vertical magnetic field on the midplane of the septum magnet verses radial distance from magnet center.

Table 1: Harmonic analysis of the field inside the aperture

N	x= 3cm	x=4cm	x=5cm	x=6cm
2	6.5%	1.4%	0.3%	0.04%
3	4.5%	1.1%	0.2%	0.1%
4	1.8%	0.6%	0.1%	0.00%

4 EMITTANCE CALCULATION

To estimate emittance growth in the magnet due to the field non-uniformity, a 3D PIC simulation was used to transport a uniform beam slice consisting of several thousand particles through the magnet [3]. The trajectories were calculated either by using an analytic approximation for the fields or by importing the 2D field map from Poisson simulations. Preliminary estimates show emittance growth on the order of 4% for the magnet, which is acceptable in the experiment.

5 CONCLUSION

An electromagnet septum magnet was designed and fabricated for experiments on the ETA-II accelerator. This design avoided the use of a material septum and was based on a simple scaleable geometry which allows a high degree of experimental flexibility. The device is in use in experiments. Results of more detailed measurements and experimental field map comparisons will be reported in future work.

6 REFERENCES

[1] G. J. Caporaso, in the Proc. of the Joint US-CERN-Japan International School, Maui, Hawaii, USA, November 3-9, 1994, edited by S. I. Kurokawa, M. Month, S. Turner, pp 594-615, (1996).

[2] Y. J. (Judy) Chen, G. J. Caporaso, J. T. Weir, "Precision Fast Kickers for Kiloampere Electron Beams", 1999 Particle Accelerator Conference, New York, New York, USA, March 29 - April 2, (1999).

[3] B. R. Poole, G. J. Caporaso, Y. J. (Judy) Chen, L.-F. Wang, "Analysis and Modeling of a Stripline Beam Kicker and Septum", XIX International Linac Conference, Chicago, IL, USA, August 23-28, (1998), LLNL UCRL-JC-130414.

LUMINOSITY UPGRADES FOR THE SLC*

P. Raimondi+, M. Breidenbach, J. E. Clendenin, F.J. Decker, M. Minty, N. Phinney#,
K. Skarpass VIII, T. Usher, M.D. Woodley, SLAC, Stanford, CA

Abstract

Recent performance improvements at the SLAC Linear Collider (SLC) have led to a proposal to further increase the luminosity up to a factor of four through a series of modest hardware upgrades. New final focus optics introduced in 1997 combined with permanent magnet octupoles have reduced the contribution to the final beam size due to higher order aberrations. The minimum betas achievable at the IP are presently limited by the increase in detector backgrounds as the beam is focused more strongly. By moving the final quadrupoles closer to the interaction point (IP), one can reduce the synchrotron radiation background while decreasing the IP betas. Other upgrades include increasing the bending radius in the final focus to minimize emittance dilutions due to synchrotron radiation, a fast feedforward from the linac to the final focus to cancel trajectory jitter, and a change in the horizontal damping ring partition number to reduce the emittance of the extracted beam. With these upgrades, the expected disruption enhancement should be 2.4.

1 INTRODUCTION

In the 1997/98 run, the luminosity of the SLC was increased by a factor of four [1]. This improvement was almost entirely due to changes in operating procedures and to reconfiguration of existing hardware, as opposed to costly upgrades. The luminosity increased steadily throughout the run reaching a peak of $3*10^{30}/cm^2/sec$ or a rate of 300 Z^0/hour. This demonstrates that the SLC remains on a steep learning curve and can continue to provide valuable experience on the physics and operation of linear colliders. Based on the knowledge gained in the last run, SLC/SLD have proposed another factor of three to four increase in the luminosity with modest hardware changes [2]. These include moving the final triplets closer to the interaction point (IP) in order to reduce backgrounds and allow higher angular divergence, a feedforward system from the linac to the IP to correct transverse jitter, and a number of smaller improvements to further reduce the beam emittance. Current research on higher polarization photocathodes could also potentially provide polarization in excess of 85%. The higher polarization together with an average luminosity of 25-50,000 Z^0s per week would support a significant physics program for SLD. These improvements would also allow the SLC to finally reach or surpass design luminosity.

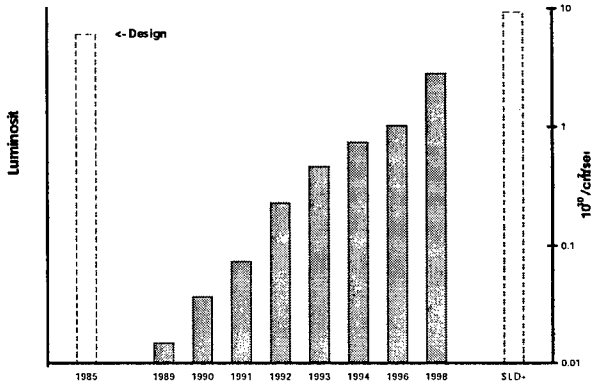

Figure 1: History of SLC luminosity from 1989 through 1998. Bar at left shows design luminosity. Bar at right shows expected luminosity with upgrades.

2 FINAL FOCUS MODIFICATIONS

With the installation of octupoles in the final focus in early 1998, the minimum beam size achievable at the IP is no longer limited by higher order aberrations. The operational performance is determined by the maximum angular divergence that can be sustained without causing excessive backgrounds in the detector. The primary source of background is synchrotron radiation emitted by the beam in the final triplet of superconducting quadrupoles which scatters into the detector. This can be greatly reduced by moving these magnets closer to the IP and increasing the field of the first quadrupole of each triplet. In this configuration, the clearance across the triplet would be increased by 20-30% in both planes. In addition, the synchrotron radiation swath would have a much shorter lever arm and exit more cleanly. This would allow operation with more optimal angular divergences of 600 by 280 microradians, an increase of 25% in the horizontal and 20% in the vertical. With the resulting smaller beam sizes and additional disruption enhancement, the expected increase in luminosity from this modification alone is about 70%.

The mechanical modifications required to move the triplets 71 cm closer to the IP are straightforward. One radiation shielding mask and the beam position monitor between the triplet and the IP would be removed, and the monitor reinstalled upstream. Turtle ray traces indicate

*Work supported by the U.S. Dept. of Energy under contract DE-AC03-76SF00515

Email: nan@slac.stanford.edu

+Present address: SL Division, CERN, CH1211 Geneva 23, Switzerland

that in the new configuration, the mask to be removed is no longer critical and, if desireable, additional masking could be installed inside the triplets. The choice of 71 cm allows the SLD luminosity monitors to remain without modification although their electronics would need to be relocated.

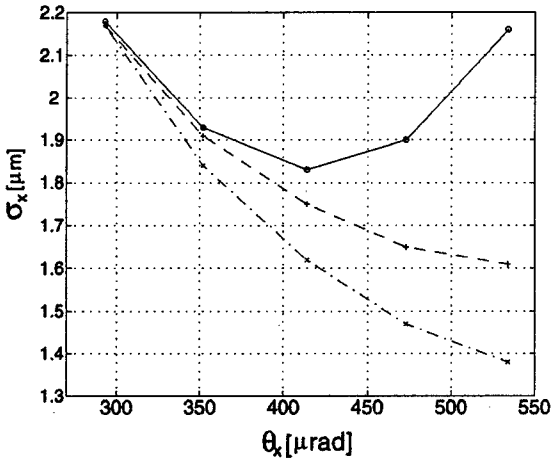

Figure 2: Horizontal beam size vs angular divergence at the SLC IP showing the reduction in beam size with increased divergence. The upper curves are for the 1996 optics, calculated using the RMS beam size (solid) and correct luminosity-weighted effective beam size (dashed). The lower curve (dot-dashed) is for the 1998 optics.

To take full advantage of the increased angular divergence and produce the smallest possible beams at the IP, it would also be desirable to reduce the residual aberrations due to synchrotron radiation from the bends in the chromatic correction section (CCS) of the final focus. A softened bend configuration was partially implemented at the end of 1997 using offset quadrupoles and steering dipoles. The radius of curvature can be further increased by adding more bend magnets in the CCS using existing magnets which are available and spare power supply channels. The expected luminosity increase from both final focus upgrades is 120%, including disruption.

3 LINAC-IP FEEDFORWARD

During present operation, transverse beam jitter is typically 20-40% of the beam size in the linac which causes a significant increase in the effective emittance. This can be reduced by a system to measure the beam trajectory at the end of the linac and correct it with fast kickers near the IP. It is possible to make a correction on the same pulse by taking advantage of the shorter communication path directly to the collider hall rather than the longer path followed by the beams around the arcs. Such a system was considered for the SLC several years ago and a similar system is under study for the NLC. Either a simple microwave or optical link would be used to send a fast signal to the collider hall. A digital signal processor would calculate the necessary corrections from position monitor data in the linac. Since the deflecting field needed is small, existing position monitors can be used as simple stripline kickers, driven by solid-state electronic pulsers.

An added benefit of reducing the sensitivity to jitter is the possibility of using a better linac lattice. The present lattice is a compromise between jitter control and chromatic emittance dilution. Reduced transverse jitter would also improve the resolution of the final optimization of the beams at the IP. The proposed feedforward system should increase the luminosity by about 30%, assuming a 60-80% reduction in the present jitter.

4 EMITTANCE REDUCTION

Several smaller upgrades would reduce the emittance of the beams at the end of the linac by 15-20% in X and Y for both electrons and positrons. These include an RF frequency shift to reduce the emittance from the damping rings, bellows shields in the ring to linac transfer lines (RTL) and additional independent supplies for a few RTL magnets. Improved feedback and steering methods would allow better optimization and stabilization of the linac orbits. Together these should increase the luminosity by 50-75% taking into account the additional disruption enhancement.

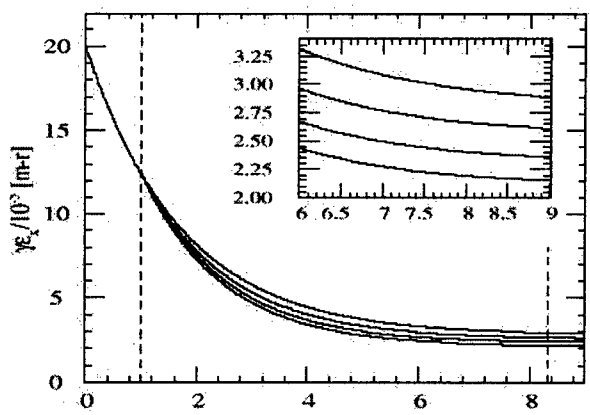

Figure 3: By changing the frequency in mid store the emittance extracted from the damping ring can be reduced by up to 25%. The normalized beam emittance is plotted as a function of store time in ms for different frequency shifts (25,50,100,150 kHz).

In the damping rings, the horizontal damping time and equilibrium emittance can be reduced by increasing the horizontal partition number [3]. This can be accomplished by modifying the closed orbit to go off-axis through the quadrupoles in dispersive regions. To shift the orbit, one can either physically displace the magnets or change the accelerating frequency. A mid-store frequency shift allows full aperture for injection while reducing the emittance. This has been tested in the both damping rings

Table 1: Parameters and Luminosity

		1998 parameters	Final Focus improvements only	Emittance improvements only	2000 parameters (All upgrades)
I	(particles/pulse)	$4.0*10^{10}$	$4.0*10^{10}$	$4.0*10^{10}$	$4.0*10^{10}$
ε_x^{FF}	(10^{-5} m-rad)	5.5	5.5	4.5	4.5
ε_y^{FF}	(10^{-5} m-rad)	0.9	0.9	0.7	0.7
θ^*_x	(μrad)	470	600	470	560
θ^*_y	(μrad)	240	280	240	260
σ_x^{IP}	(μm)	1.5	1.1	1.3	1.0
σ_y^{IP}	(μm)	0.65	0.50	0.55	0.40
Z_n	(Z/hr)	10	18	15	26
H_d		1.9	2.2	2.3	2.4
Luminosity	(Z/hr)	300	630	550	1000
	($cm^{-2}sec^{-1}$)	$2.8*10^{30}$	$5.8*10^{30}$	$5.1*10^{30}$	$9.3*10^{30}$

Table 1: Comparison of 1998 parameters and luminosity with those projected from the different upgrades. Column 1 lists recent operating parameters from the 1997-98 run. Column 2 shows the improvement from moving the final triplets closer to the IP and softening the FF bend radius. Column 3 shows the impact of emittance reduction in the damping rings and linac without the FF upgrades. Column 4 contains projected parameters with all upgrades.

and a 15% decrease in the horizontal emittance was measured for e^+ and a 10% decrease for e^-.

Two modifications are planned for the transfer lines (RTLs). A new optics was installed in 1997 to reduce the beam size in tight apertures where there were losses. Independent power supplies for a few quadrupoles near the end of the RTL would be added to allow the flexibility to further improve the optics. Wakefields from the bellows were identified as a source of emittance growth and some of the RTL bellows were shielded during the 1997-8 run. This reduced the positron vertical emittance by almost 50%. Shields should be installed for the rest of the RTL bellows. With these improvements one can expect a 10% decrease in the horizontal emittance of both beams, a 20% decrease in the electron vertical emittance, and about a 5% increase in throughput.

5 HIGHER POLARIZATION

The strained-layer GaAs/GaAsP photocathodes used in the SLC electron source until 1998 resulted in polarizations in the range of 76-80% while maintaining full SLC intensity. In principle such cathodes should produce polarizations >90% [4]. SLAC has an active photocathode research program with the short-term goal of raising the polarization to a value of over 85%. The two most promising directions are the further optimization of the strained-layer structure and the development of the superlattice structure. Thinner epilayers and gradient doping (lower dopant density in the bulk, higher in the final few nanometers at the surface) should help in the former case. Rapid advances in understanding the properties of superlattice structures combined with the larger number of adjustable parameters point to the strained superlattice as the strongest candidate for the future although the total effort to optimize is expected to be greater [5]. Both directions are being investigated.

6 SUMMARY

A series of modest hardware upgrades have been proposed which would increase the luminosity of the SLC by up to a factor of 4 to nearly $10^{31}/cm^2/sec$. This is significantly above the original design luminosity of $6*10^{30}/cm^2/sec$. In this parameter regime, the disruption enhancement should be 2.4, implying that nearly 60% of the total luminosity is due to disruption.

7 REFERENCES

[1] P. Raimondi, et.al., "Recent Luminosity Improvements at the SLC", EPAC, Stockholm, Sweden (1998).

[2] M. Breidenbach, et.al.,"SLC-2000: A Luminosity upgrade for the SLC," Linac 96, Geneva, Switzerland, (1996).

[3] M.G. Minty, et.al.,"Emittance reduction via dynamic RF frequency shift at the SLC damping ring", HEACC 98, Dubna, Russia, (1998).

[4] A.V. Subashiev et al., "Spin Polarized Electrons: Generation and Applications", Phys. Low-Dim. Struct. 1/2 (1999) 1, also issued as SLAC-PUB-8035 (1998).

[5] J.E. Clendenin, et.al., "Superlattice Photocathodes for Accelerator-Based Polarized Electron Source Applications", PAC99, New York, USA (1999).

RESULTS ON THE INTERACTION OF AN INTENSE BUNCHED ELECTRON BEAM WITH RESONANT CAVITIES AT 35 GHZ

J. Gardelle, T. Lefevre, J.L. Rullier, C. Vermare
CEA/Centre d'Etudes Scientifiques et Techniques d'Aquitaine, B.P. 2, 33114 Le Barp, France
W. Wuensch
Laboratoire Européen pour la Physique des Particules (CERN), CH-1211 Genève 23, Suisse
S. Lidia*
E.O. Lawrence Berkeley National Laboratory, Berkeley, California 94720, USA
G.A. Westenskow*
Lawrence Livermore National Laboratory, Livermore, California 94551, USA
J.T. Donohue
Centre d'Etudes Nucléaires de Bordeaux-Gradignan, B.P. 120, 33175 Gradignan, France
Y. Meurdesoif
Laboratoire de Physique Théorique (LPT), Université de Bordeaux I, 33400 Talence, France
J.M. Lekston
CEA Centre d'Etudes d'Ile de France (CIF), DPTA/SPPE, BP 12, 91680 Bruyères-le-Châtel, France

Abstract

The Two-Beam Accelerator (TBA) concept is currently being investigated both at Lawrence Berkeley National Laboratory (LBNL) and at CERN. As part of this program, a 7 MeV, 1-kA electron beam produced by the PIVAIR accelerator at CESTA has been used to power a free electron laser (FEL) amplifier at 35 GHz. At the FEL exit, the bunched electron beam is transported and focused into a resonant cavity built by the CLIC group at CERN. The power and frequency of the microwave output generated when the bunched beam traverses two different cavities are measured.

1 INTRODUCTION

In order to attain linear collider energies of order 1 TeV, it is desirable to develop efficient high-power microwave sources operating in the frequency range of 10-30 GHz, or even higher. In this context, the TBA [1] is being studied both at LBNL with the 11.4-GHz prototype RTA [2] and at CERN with the Compact Linear Collider (CLIC) project at 30 GHz [3]. In the TBA, the intense low-energy electron drive beam is bunched at the desired operating frequency and, upon passing through resonant cavities, it generates RF power to drive the high gradient accelerating structures of the main beam. An important issue of the TBA concerns the production of the bunched drive beam. At CESTA we have been studying the use of a FEL as a possible source of an intense bunched beam. We have observed and characterized the bunching which occurs in an induction linac-driven FEL both in amplifier [4] and in Self Amplified Spontaneous Emission (SASE) modes [5]. We report here on the recent results of an experiment which used the PIVAIR induction linac. Two resonant cavities designed by LBNL and built by CERN have been tested with the bunched beam exiting the wiggler of a 35 GHz amplifier. We describe here the results of this experiment.

*Work in the U.S. was performed under the auspices of the U.S. Department of Energy under contracts AC03-76SF00098 (LBNL) and W-7405-ENG-48 (LLNL).

2 EXPERIMENTAL SET UP

2.1 The PIVAIR induction linac

PIVAIR is the prototype of the AIRIX accelerator which is under construction in France for flash X-ray radiography [6]. The injector, developed by Pulse Sciences Inc. (PSI), delivers a single-shot, 3.6 MeV, 3 kA, 60 ns FWHM electron beam. The beam is subsequently accelerated to 7 MeV by 16 induction cells. The first 8 cells use rexolite gap insulators and are fed by 180 kV pulses coming from 4 external high voltage generators. The last 8 cells, working under vacuum with no gap insulators, are less sensitive to breakdown problems and are driven by 240 kV pulses. Inside each cell-block there are a solenoid and two steerers which are used to transport the beam to the accelerator exit. Beam

0-7803-5573-3/99/$10.00@1999 IEEE.

Position Monitors are installed every 4 induction blocks in order to monitor beam current and centroid position. PIVAIR has an excellent shot-to-shot reproducibility. The normalized edge emittance at the injector exit is 1000 π.mm.mrad and the energy spread is less than 1% over 60 ns.

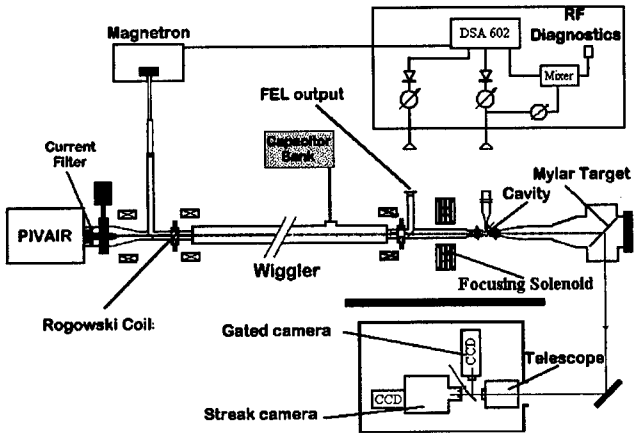

Figure 1: Layout of the experiment.

2.2 *The FEL experiment*

In figure 1, we show the overall experiment and Table 1 gives the main FEL parameters, PIVAIR is schematized at left. Immediately after the accelerator exit a current filter is used to reduce the beam current to 1 kA. Then, two solenoids match the beam into the pulsed helical wiggler of the FEL. A 35 GHz electromagnetic signal, produced by a magnetron, is injected into the wiggler and is amplified in the wiggler by the electron beam. As a consequence of the FEL mechanism, the beam bunches during its passage through the wiggler. A suitable magnetic profile at the wiggler entrance is necessary to obtain an adiabatic injection giving rise to the correct trajectories in the wiggler. Similarly, an adiabatic exit is needed to extract the beam from the wiggler on the axis. Upon leaving the FEL, the bunched beam is focused by a set of 4 thick coils which generate a magnetic field up to 2700 G in order to produce a narrow beam waist at the position of the RF cavity. The coils can be moved along the longitudinal axis to optimize the waist size. The latter is measured by the Cerenkov diagnostic and it must be as small as possible. Alignment is very critical and can be changed by moving the coils transversely or by tilting them. First, we use a dummy which simulates the cavity longitudinal dimensions. It permits us to adjust beam alignment by measuring the transmitted current. The FEL signal is deflected out of beam line by a wire mesh. FEL power and frequency measurements are performed using standard Ka-band waveguides, horns, attenuators and calibrated Shottky diodes. Rogowski coils are used to measure the beam current at different axial positions. Beam size and position are obtained by a gated camera which collects a small part of the Cerenkov emission produced when the beam passes trough a aluminized-mylar target. A fast streak camera is used to measure beam bunching.

Table 1: Main FEL parameters

Beam energy	7 MeV
Beam current	1 kA
Wiggler period	20 cm
Wiggler length	640 cm
Wiggler resonant field	1650 G
Beam pipe radius	19 mm
Frequency	35.04 GHz
Input power	5 kW

2.3 *The cavities*

Two pill-box cavities of length 1 mm, were designed by LBNL and built by CERN (figure 2). The internal diameter of the 11 mm-long pipe where the beam propagates in is 4 mm. In order to match to the main 38 mm internal diameter beam pipe, a smooth tapering in radius was necessary.

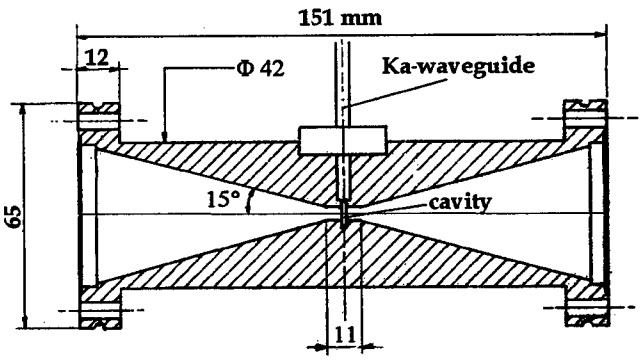

Figure 2: Drawing of the 35 GHz pill-box cavity support

The two cavities differ mainly by the size of their output ports. The port is attached to a connecting waveguide which is expanded to mate with standard WR28 rectangular guide. Their resonant frequencies and Q values are different in order to obtain two couplings [7]. The low-Q cavity has a radius of 3.92 mm whereas the medium-Q cavity has a radius of 3.8 mm. The latter is slightly detuned from 35 GHz in order to study the effects of the detuning on the output power as well as on the beam bunching.

3 EXPERIMENTAL RESULTS

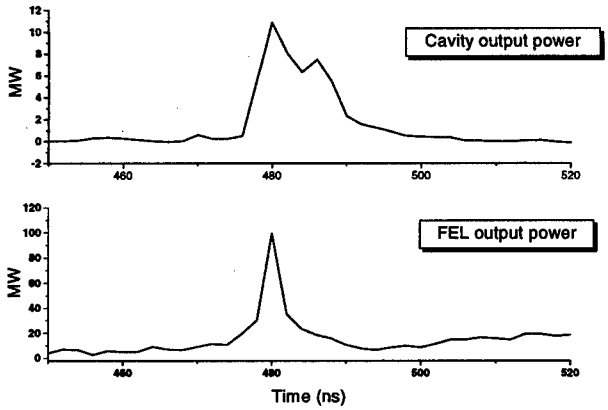

Figure 3: Example of the output signal from the low-Q tuned cavity and the coresponding FEL power

The injected RF signal coming from the magnetron was amplified by the FEL up to 100 MW at a measured frequency of 35.04 GHz. An important beam loss occurred in the wiggler. The Rogowski coil at the wiggler exit gives a value of about 300 A when 800 A are measured at the wiggler entrance. Nevertheless, the bunched beam was extracted from the adiabatic exit and focused to a 8-mm diameter waist by the four-coil module running at its maximum current of 200 A. Since the aperture of the cavities is only 4 mm, an additional loss of beam current occured when introducing the beam.
In figure 3, we display the output power from the low-Q cavity as well as the corresponding FEL signal. A microwave signal with a peak power of 12 MW was obtained in the output port of the cavity, whose frequency coincides, within errors, with that of the magnetron. With the medium-Q cavity, slightly detuned in frequency, the measured power is of order 700 kW at 35.6 GHz as shown in figure 4. In general the current value 10-cm upstream from the cavity is 250 ± 30 A, while at the exit the current is 120 ± 20 A.
The output power in the detuned cavity is less than what we obtained with the tuned cavity, as predicted by by the simulations [7]. The measurements of the frequency of the signals exiting the cavities are in very good agreement with the measurements of their "cold" resonances (35.2 GHz for the low-Q and 35.7 GHz for the medium-Q) which were obtained without the presence of the electron beam by using a network analyzer.

4 CONCLUSION

We have described here the results of an experiment which constitutes a first proof of principle of microwave power extraction from a bunched electron beam in simple a high frequency RF-cavity working at 35 GHz. At this

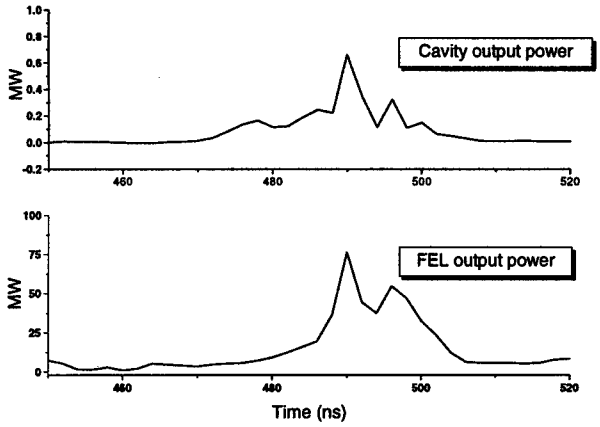

Figure 4: Example of the output signal from the medium-Q detuned cavity and the coresponding FEL power

time, we have not finished analyzing all the data but we
believe that an improved version of our experiment would be able to achieve a net increase of the output power from the cavity.

5 REFERENCES

[1] A.M. Sessler, The Laser Accel. of Part., AIP Conf. Proc. N°91 (American Institute of Physics, New York, 1982), p. 151.

[2] G.A. Westenskow, et. al., Proc. of LINAC'98, Chicago, (1998).

[3] J.P. Delahaye, et. al.., Proc. of VII International Workshop on Linear Colliders, Zvenigorod, Russia, (1997).

[4]] J. Gardelle, J. Labrouche, J.L. Rullier, Phys. Rev. Lett. 76, 4532 (1996). J. Gardelle, et. al.., Phys. Rev. Lett. 79, 3905 (1997).

[5] T. Lefevre, et. al., Phys. Rev. Lett. 82, 323 (1999).

[6] P. Anthouard, et. al., Proc. of the Part. Acc. Conf., Vancouver, Canada, (1997).

[7] S. Lidia , et. al., these proceedings.

INITIAL COMMISSIONING RESULTS OF THE RTA INJECTOR

S. Eylon, E. Henestroza, S.M. Lidia, D.L. Vanecek, S.S. Yu, LBNL, Berkeley, CA;
T.L. Houck, G.A. Westenskow, LLNL, Livermore, CA;
D.E. Anderson, LANL, Los Alamos, NM

Abstract

The creation of the drive beam remains one of the most challenging technical endeavours in constructing two-beam accelerators. We have begun testing the 1.2-kA, 1.0-MeV electron induction injector for the RTA experiment. The electron source is a 3.5-inch diameter, thermionic, flat-surface cathode with a maximum shroud field stress of approximately 165 kV/cm. The pulse length of the injector is approximately 250 ns, with a 120-ns flattop region. We report here measurements of the pulsed power system performance, beam voltage and current. Plans to measure the emittance and current density profile are discussed.

1 INTRODUCTION

Induction accelerators are a unique source for high current, high-brightness, electron beams. A collaboration between the Lawrence Livermore National Laboratory (LLNL) and Lawrence Berkeley National Laboratory (LBNL) has been studying rf power sources based on the Relativistic Klystron Two-Beam Accelerator (RK-TBA) concept for several years [1], [2]. A major technical challenge to the successful operation of a full scale RK-TBA is the transport of the electron beam through several hundred meters of narrow aperture microwave extraction structures and induction accelerator cells. Demanding beam parameters are required of the electron source, an induction injector, to achieve the transport goals. A test facility, called the RTA, has been established at LBNL [3] to verify the analysis used in the design study. The primary effort of the facility is the construction of a prototype RK–TBA subunit that will permit the study of technical issues, system efficiencies, and costing. In this paper, we will discuss the development of the RTA electron source and it's pulsed power system, which has recently been constructed and is now undergoing testing. For this paper, the RTA injector refers only to the 1-MV gun and does not include the planned 1.8-MV accelerator section.

2 RTA INJECTOR

A major part of our effort during the past year has been towards the design and construction of an electron source with much lower emittance than typical induction injectors. The electron source will be a 3.5"-diameter, thermionic, flat-surface W-type cathode with a maximum shroud field stress of approximately 165 kV/cm. An emission density of 20 A/cm^2 is required from the cathode to produce 1.2 kA beam. The RTA injector, depicted in Fig. 1, has 72 induction cores, each driven at 14 kV. The voltage across the A-K gap is 1 MV. The cores are segmented radially to reduce the individual aspect ($\Delta r/\Delta z$) ratio. The lower aspect ratio reduces the variation in core impedance during the voltage pulse simplifying the pulse forming network (PFN) design. Fig. 2 is a photograph of the injector, shielded hall and electrical racks.

High-voltage tests (no beam) to full operational parameters have been successfully completed on the injector. In operation, a 500 kV potential is developed across the two 30-cm-ID PYREX [4] insulators producing a 5.1 kV/cm average gradient along the insulator. The maximum field at the triple points, the intersection of insulator, vacuum, and metal, is designed to be less than 3.5 kV/cm. Maximum surface field in the cathode half of the injector electrode is about 85 kV/cm. The maximum field is about 116 kV/cm on the anode stalk.

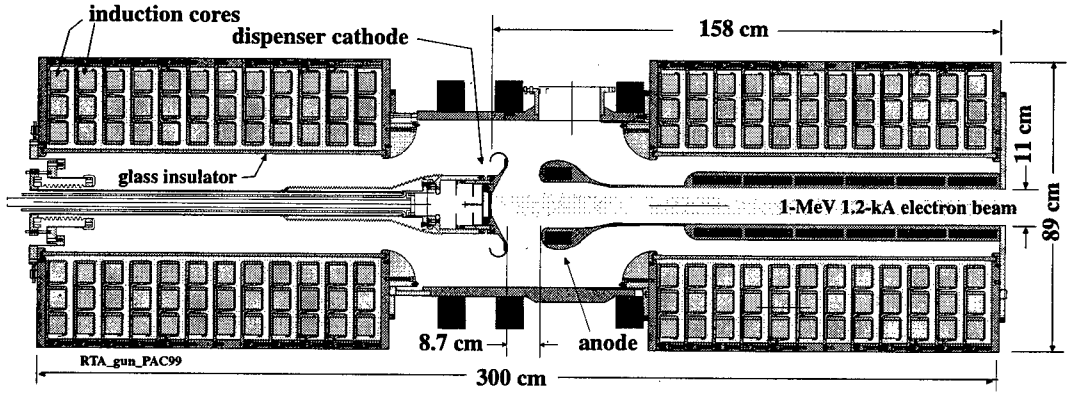

Figure 1. Schematic of the RTA injector depicting the 24 3-core cells, electrodes, glass insulators, and solenoids.

0-7803-5573-3/99/$10.00@1999 IEEE.

Beam tests have recently commenced. The maximum A-K gap voltage has been kept below 400 kV producing almost 200 A beam current while radiation surveys, subsystem checkouts, and cathode studies are performed. No electrical breakdowns have been observed at these lower voltages. Vacuum can be maintained in the high 10^{-8} Torr range with a cold cathode increasing into the low 10^{-7} Torr range during operations. Theoretical perveance for the installed A-K gap width is 1.0 μpervs. Measured perveance is • 0.84 μpervs with the uncertainty in the upper bound due to the present voltage calibration.

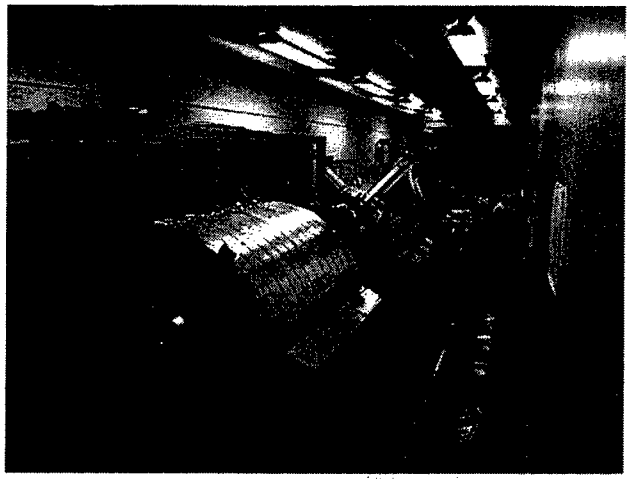

Figure 2. Photograph of the RTA injector looking from the cathode end of the injector down the beamline.

Initial beam focusing in the injector is accomplished by three large-bore air-core solenoids installed on the central pumping spool. The first solenoid is operated to null the magnetic field from the other solenoids at the cathode front surface. There are seven smaller solenoids located within the anode stalk to provide additional focusing to transport the beam to the end of the injector.

3 PULSED POWER SYSTEM

The injector's pulsed power system consists of a 20-kV High-Voltage Power Supply, 6-kJ Energy Storage Bank, two Command Resonant Charging (CRC) Chassis, 24 Switched Pulse Forming Networks, and four Induction Core Reset Pulsers. Each PFN drives a single 3-core induction cell of the injector.

Segmenting the core in the induction cell and driving the individual core segments avoids a high-voltage step-up transformer. This reduces the developmental effort needed to achieve a "good" flattop pulse (minimal energy variation) with fast risetime and improves the efficiency of the overall pulsed power system. Our system of low-voltage PFNs driving multiple core induction cells is similar to the system envisioned for the extraction section in the full-scale RK-TBA design. For the injector core material, we choose 20-μm-thick 2605SC METGLAS [5]. For the RTA extraction section we will use a lower loss 2714AS METGLAS for the induction cores.

Design of the switched PFNs follows easily from published METGLAS core loss data [6]. A flux swing of 2.6 T in 400 ns (FWHM) results in a magnetization rate of 6.5 T/μs for the injector cores. This rate generates a loss density of 1800 J/m^3, or a 30 J lost in a 3-core cell with 16.7x10^3 cm^3 of 2605SC METGLAS. For an input voltage of 14 kV applied for 400 ns, these losses require that 5900 A be supplied to the cell. An additional 3600 A is required to supply beam current (1200 A x 3 cores/cell), resulting in a total current of 9 kA. The required drive impedance for a cell is then 1.5 Ω.

Achieving the fast risetime necessary to minimise the volt-seconds required for the injector cores presented a challenge. Budget constraints coupled with the large availability of EEV CX1538 thyratrons from the ATA program at LLNL made these tubes an attractive option. However, their poor time rate of current change (4 kA/μs rating) made them questionable for this application, which requires about 40 kA/μs. A variety of techniques were tried to decrease the risetime. Each thyratron is located between two current sheets connecting the PFN output to the output cables to reduce the stray circuit inductance. In addition, the thyratron ionization time is substantially reduced by applying a 1-2 A pre-pulse to the keep-alive grid 300-400 ns prior to the arrival of the main control-grid pulse. We presently have risetimes less than 150 ns for all 24 cells. Since the thyratron turn-on time is voltage dependent, we are adjusting the trigger time of each individual tube. Faster risetimes were achieved with Triton F-130 ceramic thyratrons. An upgrade of the current thyratrons in the injector pulsed power system should allow us to achieve the design 100-ns risetime.

At the 1-MV, 1.2-kA operating conditions we hope to produce a ±1% injector voltage flat waveform for 120 ns. We will need to adjust the number of turns in appropriate sections of individual PFNs to achieve this goal. Insertion of ferrite material in the center of the inductors coils will allow additional small corrections to the waveform. There are 24 EEV CX1538 thyratrons used in the pulsed power system for the injector.

4 RTA INJECTOR DIAGNOSTICS

A variety of diagnostics will be used to determine the performance of the injector, both permanently installed monitors for general operations and temporary diagnostics specific to injector commissioning and troubleshooting.

4.1 Current Measurements

An accurate measurement of the emitted current from the cathode is required both for determining the performance of the injector and benchmarking codes. We have

electrically isolated the cathode from the stalk, forcing the current to flow through several parallel, 0.25 inch wide, strips of 25–μm thick stainless steel foil that act as current-viewing resistors (CVRs). The potential drop across the foil is measured and the current inferred. To improve the time response a parallel-strip shunt geometry is used where the foil is folded on itself to increase the resistance while lowering the series inductance. The beam dump is also electrically isolated similar to the cathode to allow the measurement of the total current deposited in the dump. Four CVRs, equally spaced azimuthally around the dump, are summed.

A resistive wall current monitor is located immediately following the injector. This monitor measures the potential drop of the return wall current across a known resistance generating a signal proportional to the current. The potential drop is measured at eight locations around the circumference of the beam tube permitting the measurement of total current and centroid position.

Magnetic pickup (B-dot) loops are available to be inserted in the transport section after the injector to determine the time derivative of the current pulse. The voltage induced on the loop can then be integrated to recover the current and centroid position. The advantage of the B-dot loops over the other current diagnostics is a higher frequency bandwidth.

4.2 A-K Voltage and Beam Energy

We are using two methods to determine the A-K voltage and infer the beam energy. The first method involves using resistive voltage dividers to measure the applied voltage to the induction cores at the power feed connections. Capacitive dV/dt pickup probes [7] are used for a more direct measurement of the A-K gap voltage and also to provide greater bandwidth with respect to the resistive dividers. We also hope to employ a conventional energy spectrometer comprised of an on-axis collimator, dipole magnet, scintillator, and viewing port to directly measure the beam energy.

4.3 Current Density Profile

The current density profile will be measured using Cherenkov radiation from intercepting foils. A primary concern with using foils is possible damage from beam energy deposition. Adjusting the repetition rate of the injector can control average heating of the foil. The difficulty is single shot heating where material can be melted and ejected before the heat is conducted away. To avoid damage to a thin quartz foil, we anticipate that the beam diameter must be greater than 2 cm for a 1-kA, 300-ns, relativistic electron beam.

The light generated at the beam/foil interaction will be recorded using both gated and streak cameras. The streak camera will be used principally to determine if the properties of the foil and/or beam change during the pulse. The significant levels of energy deposited in the foil could affect the dielectric constant or generate a surface plasma that could be confused as a variation in beam parameters.

4.4 Emittance Measurement

Measuring the beam emittance is expected to be very difficult as the beam is highly space charged dominated. A pepperpot emittance diagnostic has been constructed. The size of the apertures is the only variable for adjusting the relative contribution of emittance to space charge. For the designed RTA injector beam parameters, 1.2 kA, 1 MeV and 100 π-mm-mr, and using a 250-μm aperture, the emittance term for the beamlets passing through the aperture plate is approximately an order of magnitude larger than the space charge term. Our aperture plate will consist of a rectangular pattern of 121 (11x11) 250-μm apertures with 7 mm spacing on a 500-μm thick tungsten plate. The tungsten plate represents about two range thickness for 1-MeV electrons. The beamlets will strike a phosphor coated foil located about 80 cm after the aperture and imaged with a gated camera.

5 SUMMARY

Initial beam tests have commenced on the RTA injector generating a 400-KeV, 200-A, 400-ns (FWHM) electron pulse. Full operations (1-MV, 1-kA) will commence after the completion of radiation surveys and ancillary system checkouts. Upcoming tests will stress characterization of the beam parameters particularly the emittance and current density profile.

6 ACKNOWLEDGMENTS

The work was performed under the auspices of the U.S. Department of Energy by LLNL under contract W-7405-ENG-48, and by LBNL under contract AC03-76SF00098. We thank Andy Sessler and Swapan Chattopadhyay for their support and guidance and thank Wayne Greenway, Don Lester, William Strelo, and Bob Candelario for their outstanding technical support.

7 REFERENCES

1. Sessler, A.M. and Yu, S.S., "Relativistic Klystron Two-Beam Accelerator," *Phys. Rev. Lett.* **54**, 889 (1987).
2. Westenskow, G.A., and Houck, T.L., "Relativistic Klystron Two-Beam Accelerator," *IEEE Trans. on Plasma Sci.*, **22**, 750 (1994).
3. Houck, T.L., and Westenskow, G.A., "Prototype Microwave Source for a Relativistic Klystron Two-Beam Accelerator" *IEEE Trans. on Plasma Sci.*, **24**, 938 (1996).
4. Registered name of Corning Glass Works.
5. Registered name of AlliedSignal Corporation.
6. Smith, C., and Barberi, L., "Dynamic Magnetization of Metallic Glasses," in Proc. of the 5th. IEEE Int'l Pulsed Power Conf., 1985.
7. Houck, T.L., et al., "Diagnostics for a 1.2-kA, 1-MV Electron Induction Injector," Proc. of the 8th Beam Instrumentation Workshop, SLAC, 1998.

STUDY OF MODIFIED TBA DRIVER SCHEME*

A.V. Elzhov, A.A. Kaminsky, A.K. Kaminsky, V.I. Kazacha, E.M. Laziev, E.A.Perelstein, S.N. Sedykh, A.P. Sergeev, Joint Institute for Nuclear Research, 141980, Dubna, Russia

Abstract

A modified scheme of two beam accelerator (TBA) [1] driver based on a linear induction accelerator is studied in this paper. In the proposed scheme the electron beam bunching occurs at a rather low initial energy ~ 1 MeV. The bunched beam is accelerated in the accompanying enhanced synchronous microwave that provides the steady longitudinal beam bunching along the whole driver. There is no total microwave power extraction anywhere in the driver. A waveguide (initially corrugated and regular further) is used along the driver [2]. The simulation showed that a steady state is achieved when electron bunches accompanied after a TWT by an amplified microwave are simultaneously accelerated in an external electric field both for continuously distributed system parameters and for discrete parameters of accelerating sections. In the steady state the whole power, which is inserted into the beam by the accelerating field, transforms into the microwave power. Such kind of systems can serve effectively as a rather long (hundreds of meters) driver for the TBA concept. The experimental setup based on the JINR LIA-3000 facility to test the new scheme is under construction at present. It consists of the 800 keV, 200 A injector and two reaccelerating sections. The first experimental results of the beam bunching study have been presented.

1 INTRODUCTION

Some schemes of the TBA driver based on a linear induction accelerator (LIA) were discussed in [1-5]. In these schemes the driver electron beam moves through an alternating discrete row of microwave generators (free electron lasers (FEL), relativistic klystrons, etc.) and reaccelerating sections. The microwave power is totally extracted from the driver after every generation section. Such kind of driver was experimentally investigated in [6], where the reacceleration of a modulated with the chopper help electron beam through two induction accelerator cells was demonstrated. The continuous extraction along the whole driver length of the microwave power was designed in CLIC [7] and a corresponding beam dynamics was studied also in [8].

A new scheme of two beam accelerator (TBA) driver based on a linear induction accelerator is suggested in this work. The scheme is quite uniform and has the following characteristic properties: a) the electron beam bunching occurs at a rather low ~1 MeV initial energy; b) the bunched beam further acceleration occurs in the accompanying enhanced microwave that provides the steady longitudinal beam bunching along the whole driver; c) there is no total microwave power extraction anywhere in the driver; d) a waveguide is used along the driver.

The driver consists of an injector, buncher and long (a few hundreds of meters) row of separate LIA sections producing the external accelerating electric field and partitioned by transition chambers. The injector produces the initial electron beam with energy 1 through 2 MeV and current 0.5 through 1 kA. This beam is injected into the buncher. It may be a travelling wave tube (TWT) working in the amplification mode. It was shown in [8] that a high degree of bunching can be rather easily achieved in the TWT at the distance of ~ 1 m. Then the electron bunches continue moving in the LIA in accompaniment of the enhanced in the TWT microwave and simultaneously are accelerated in the LIA electric field. The microwave power extraction from the driver occurs only in the transition chambers. The system attains the steady state at first few tens of meters where the bunch energy increases up to the level of ~ 10 MeV. Then the section of quasi-stationary microwave generation begins where the total power, that the accelerating field inserts into the beam, transforms into the microwave power. The scheme has the following merits: 1. The possibility of providing the microwave phase and amplitude stability. The phase stability can be obtained at the expense of quasi-continuity of the system. It means that only mechanical tolerances will be of consequence; 2. Due to the bunched beam acceleration it is not necessary to have a high (~ 10 MeV) energy of the initial electron beam bunching.

2 SIMULATION RESULTS

We have three characteristic regions of the driver: 1) the bunching region with using of TWT and without acceleration, 2) transition region with a beam acceleration and 3) quasi-stationary beam propagation region. As it was shown in [9], one can obtain the electron beam bunching in a TWT at a rather short length ~ 50 cm for the following electron beam and E_{01} type wave parameters:

*Work is supported by the Russian Foundation for Basic Research, grants 97-02-16643 and 98-02-17685.

0-7803-5573-3/99/$10.00@1999 IEEE.

electron beam energy	~ 2.2 MeV ($\gamma_0 \sim 5.31$)
electron current inside TWT	I_b ~ 500 A
electron beam radius	~ 0.5 cm
microwave frequency	$f_0 = 17 \cdot 10^9$ Hz (λ ~1.76 cm)
initial microwave power in TWT	10 kW
output microwave power in TWT at the acceleration region entrance	13 MW.

Without accompanying microwave, the debunching process will immediately occur at the distance of about few tens of centimeters. The simulation showed that the electron bunches can be transported at the distance ~ 10 m if the bunch movement is accompanied by the microwave amplified in the TWT. The most encouraging situation is when the moving after the TWT output bunches are accompanied simultaneously by the amplified microwave and are accelerated in the external electric field. inside a corrugated waveguide. The waveguide must be transparent for a pulse accelerating field and a good screen for the microwave.

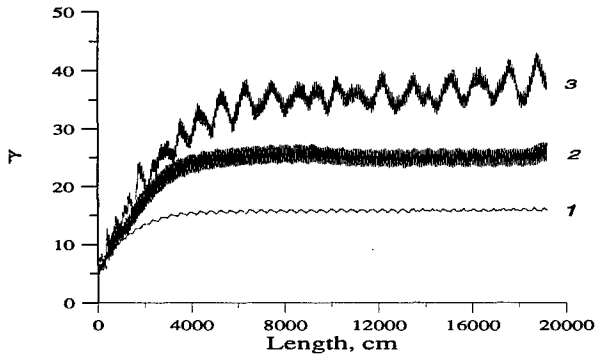

Figure: 1 The electron mean energy versus the distance for: 1 - continuously distributed driver parameters; 2 - discrete periodic cells, 3 - discrete cells with narrow accelerating gaps.

Our calculations showed that the bunching process in the TWT must be interrupted some earlier the moment when the bunching parameter B attains its maximum value. Then we have no particle losses in our further calculations in the driver. Fig. 1 shows the calculated dependence of the bunch mean energy $\bar{\gamma}$ on the distance ($z = 0$ corresponds to the TWT output). The dependencies of the microwave power and the bunching parameter B on the distance are depicted in the Fig. 2 and Fig. 3. As one can see from these figures, the steady state of the system is achieved at the distance ~ 40 m. The extracted microwave power in the steady state is equal to ~ 330 MW. The mean steady state bunch energy ~ 7.5 MeV. And at last we have rather high bunching parameter $B \cong 0.9$ in the steady state. The electron phase picture (see Fig. 4) shows that an initial bunch breaks down on two main bunches being at $\Delta\psi \cong 2\pi$ one from another.

The power put into the electron beam by external electric field is equal to ~ 500 MW/m. And it trans-

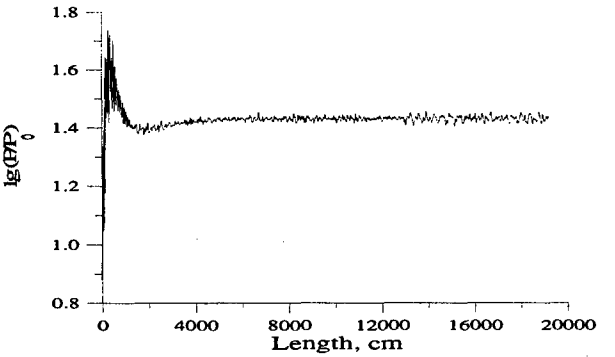

Figure: 2 The microwave power versus the distance for continuously distributed driver parameters.

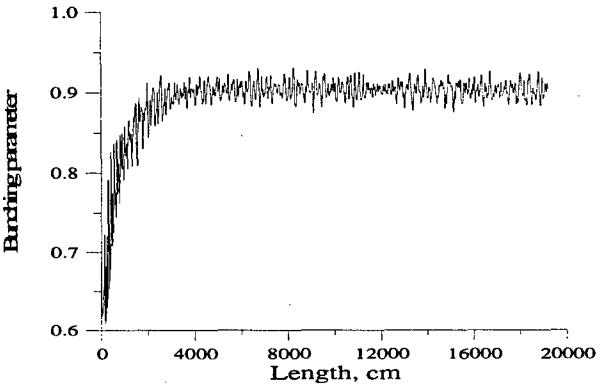

Figure: 3 The bunching parameter versus the distance for continuously distributed driver parameters.

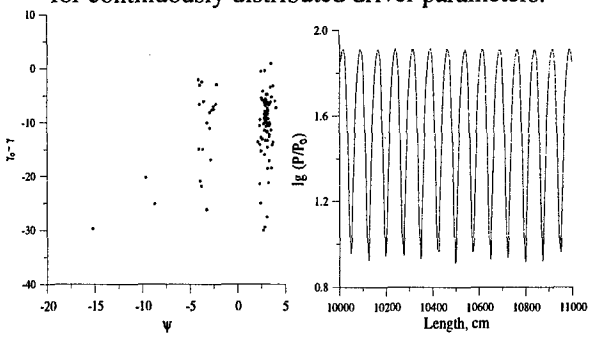

Figures: 4 and 5 The typical electron phase space picture at the distance of 100 m for continuously distributed driver parameters and the microwave power versus the distance from 100 m through 110 m for discrete periodic cells.

forms into the microwave power in the steady state.

The stability of the steady state solution with respect to the possible error in the electron beam current I_b was also investigated. The calculations showed that we still obtained the steady state solution up to error values $\delta I / I \approx \pm 10\%$.

A real LIA always consists of separate induction sections partitioned by transition chambers, so that it has a discrete structure. The second set of our calculations was performed for the realistic induction section parameters. As a result, the optimal lengths of

the induction sections ($l_s = 50$ cm) and transition chambers ($l_t = 25$ cm) were found. The microwave extraction was switched on only in the transition chambers. And the electric field E_a was equal to 1.5 MV/m inside the accelerating sections.

The dependence of the bunch mean energy on the distance is depicted in the Fig. 1 (curve 2). One can see a short range of dependence of the microwave power along the distance of 10 m (from $z = 100$ m through $z = 110$ m) in Fig. 5.

In the third set of calculations for the same lengths of the accelerating sections and the transition chambers the only difference was the following: accelerating potential of every section (750 kV) was concentrated only on the gap 7.5 cm long located at the beginning of every section to make more simple waveguide in this case. The dependence of the bunch mean energy on the distance is depicted in the Fig. 1 (curve 3). The steady state occurs also when the system has the discrete structure. The bunching parameter B stays also high along the driver ($B \cong 0.9$). The microwave power amplitude stays rather stable.

3 TEST FACILITY

Series of test experiments are prepared at JINR to study the scheme mentioned above. The scheme of the experimental setup based on the existing LIA-3000 facility is shown in Fig. 6. It consists of the injector and two reaccelerating sections. At the injector output the electron beam energy is about 800 keV and the current is equal to 200 A. The input microwave power is about of 10 kW with the wave length of 8 mm. Each reaccelerating section is 130 cm long and gives the energy gain of 360 keV. The microwave extraction and reacceleration voltage in this scheme are both located in the narrow gaps between accelerating sections each few centimetres long.

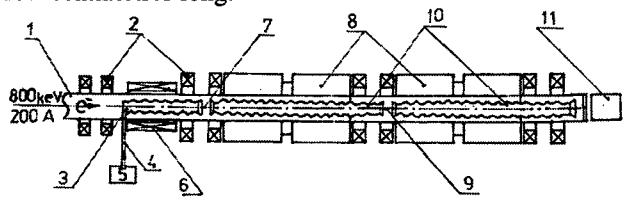

Figure 6: The experimental setup scheme on the base of LIA-3000: 1) injector exit; 2) magnetic field coils; 3) travelling wave tube; 4) waveguide; 5) magnetron; 6) magnetic solenoid; 7) first accelerating gap; 8) linear induction accelerating sections; 9) second accelerating gap;10) corrugated waveguide; 11) diagnostic chamber.

The fulfilled simulation of the beam propagation, acceleration and microwave extraction for the real LIA-3000 parameters gives that the extracted microwave power should amount by approximately 10-15 MW per gap. The obtained spatial evolution of the mean bunch energy is presented in Fig. 7. Two rapid increases in the energy exactly correspond to the accelerating gaps. From the figures one can see that the travelling electron beam maintain rather high bunching parameter, while the beam energy rises from 0.8 to 1.3 MeV.

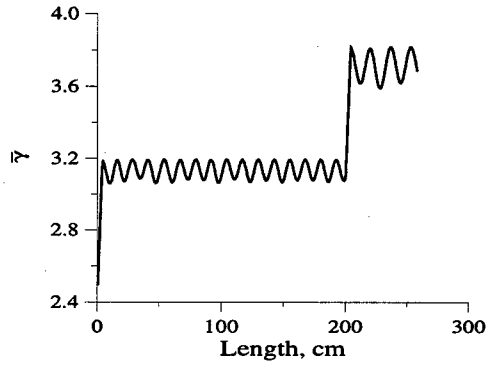

Figure 7: The electron mean energy versus the distance for LIA-3000 parameters. Point $z = 0$ corresponds to the beginning of the first accelerating gap in Fig. 6.

The development of the electron bunch diagnostics was carried out in the beginning of our designed experiments on the first facility base. The electron bunch dimensions were measured at the output of the FEL oscillator [9] with the help of the streak camera (Fig. 8). Sweep duration is equal to 700 ps (50 ps/mm).

Figure 8: Temporal profile of the bunched electron beam.

4 REFERENCES

[1] A.M. Sessler, Proc. Workshop on the Laser Acceleration of Particles, eds. C. Yoshi and T. Katsouleas, AIP Conf. Proc. 91 (1982), p. 154.

[2] A.V. Elzhov, V.I. Kazacha, E. A. Perelstein, Proceedings of XV International Seninar on Charged Particle Linear Accelerators, Kharkov (the Ukraine), v. II (1997), p. 129.

[3] A.M. Sessler et al., Nucl. Instr. Meth., A306, (1991), p. 592.

[4] T. Houck et al., IEEE Trans. on Plasma Science, vol.24, 3 (1996), p. 938.

[5] G.G. Denisov et al., Nucl. Instr. Meth., A358 (1995), p. 528.

[6] T.L. Houck and G.A. Westenskow, Preprint UCRL-JC-119021, LNLL, Livermore, California, USA, 1994.

[7] W. Schnell, CERN-LEP-RF/86-27 (1986); CERN-LEP-RF/88-59 (1988).

[8] N.S.Ginzburg et al., in: Relativistic High-Frequency Electronics, v. 5 (IAP AS USSR, Gorky, 1988), p. 37.

[9] E.A. Perelstein et al, JINR Preprint E9-97-5, Dubna, 1997.

THE DRIVE BEAM PULSE COMPRESSION SYSTEM FOR THE CLIC RF POWER SOURCE

R. Corsini, CERN, CH-1211 Geneva 23, Switzerland

Abstract

The Compact LInear Collider (CLIC) [1] is a high energy (0.5 to 5 TeV) $e^{\pm}$ linear collider that uses a high-current electron beam (the drive beam) for 30 GHz RF power production by the Two-Beam Acceleration (TBA) method. Recently, a new cost-effective and efficient generation scheme for the drive beam has been developed [2,3]. A fully-loaded normal-conducting linac operating at lower frequency (937 MHz) generates and accelerates the drive beam bunches, and a compression system composed of a delay-line and two combiner rings produces the proper drive beam time structure for RF power generation in the drive beam decelerator. In this paper, a preliminary design of the whole compression system is presented. In particular, the fundamental issue of preserving the bunch quality along the complex is studied and its impact on the beam parameters and on the various system components is assessed. A first design of the rings and delay-line lattice, including path length tuning chicanes, injection and extraction regions is also presented together with the simulation results of the beam longitudinal dynamics.

1 DESCRIPTION OF THE SYSTEM

A general layout of the bunch train compression system is shown in Figure 1. Its purpose is to split segments of the electron pulse delivered by the drive beam accelerator and later combine them in several stages in order to obtain 20 high-current pulses, each with 32 times the initial bunch repetition frequency and current. The system acts therefore both as a splitter and compressor as well as a frequency multiplier.

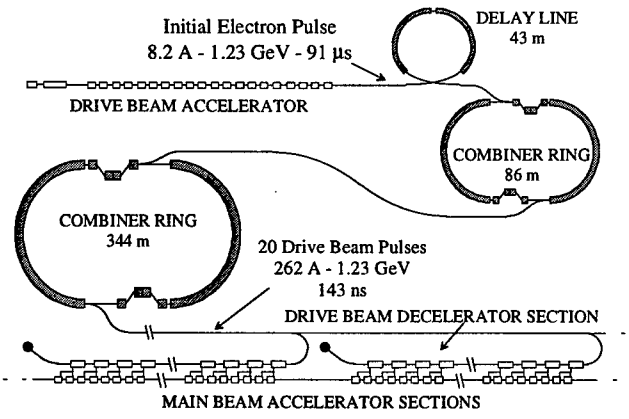

Figure 1: Layout of the drive beam compression system

The drive beam accelerator delivers 91 μs long electron pulses with a mean current of 8.2 A at 1.23 GeV. Each pulse is obtained by the combination at low energy of 640 bunch trains, 143 ns long, whose flat-top bunch charge is 17.6 nC. In each train the bunches occupy alternatively even and odd buckets of the drive beam accelerator fundamental frequency (937 MHz). At first, the individual trains are separated by a transverse RF deflector at the frequency of 468.5 MHz, and each "even" bunch train is delayed with respect to the following "odd" one by 143 ns, in order to recombine them using a second RF deflector at the same frequency. The whole device is called the "times-two delay combiner" (see Figure 1). After recombination, the pulse is composed of 320 trains whose spacing is equal to twice the train length (286 ns, or 86 m). The bunches fill all the buckets of the fundamental frequency (320 mm spacing). The same principle of electron bunch train combination is then used to combine the trains four by four in the first combiner ring, 86 m long. Two 937 MHz RF deflectors create a time-dependent local deformation of the equilibrium orbit in the ring. This bump is used for injection of a first train in the ring (all its bunches being deflected by the second RF deflector onto the equilibrium orbit). The ring length is equal to the spacing between trains plus $\lambda/4$, where λ is the spacing between bunches, equal to the wavelength of the RF deflectors. Thus for each revolution period the RF phase seen by the bunches circulating in the ring increases by 90°, and when the second train is injected, the first train does not see any deflection and its bunches are interleaved with the ones being injected (at a $\lambda/4$ distance). This is repeated twice, then the four interleaved trains are extracted from the ring by an ejection kicker half a turn later, and the same cycle starts again. After the first combiner ring the whole pulse is composed of 80 trains. The train spacing is equal to eight times the train length (1144 ns or 344 m), while the bunch spacing is 80 mm.

The trains are combined again, using the same mechanism, in the second combiner ring, 344 m long, yielding another factor four in frequency multiplication, and obtaining the final 20 trains, with a bunch spacing of 20 mm. The distance between trains is now 4.576 μs or 1375 m, corresponding to twice the length of a drive beam decelerator section. This spacing is now correct to obtain proper phasing with the main beam pulse, distributing the drive beam trains along the decelerator in the opposite direction to the main beam.

0-7803-5573-3/99/$10.00@1999 IEEE.

2 DESIGN ISSUES

The main problem to be solved in the system is to preserve the bunch quality during the compression. In particular, bunch length and longitudinal phase-space distribution must be preserved and train to train, bunch to bunch fluctuations in phase and transverse position minimised. The rings and the delay line must then be isochronous.

The final bunch length must be short in order to maximise the 30 GHz RF power production efficiency in the drive beam decelerator. At present the aim is a rms bunch length of σ = 0.4 mm (94% efficiency). Such high-charge (17.6 nC), short bunches can radiate coherently a considerable amount of synchrotron radiation, leading both to an average energy loss of the whole bunch and to an energy spread within the bunch itself [4]. The emission is concentrated at low frequencies ($\nu \leq 1/(2\,\sigma)$), and can be partly suppressed if at least part of the emitted spectrum is below cutoff in the beam pipe (shielding effect), but a limit is imposed by the necessary beam clearance. Since bunches belonging to different trains make a different number of turns in the rings (from 1/2 to 7/2), they will develop different energy distributions. This will cause relative phase errors between bunches, bunch lengthening and phase-space distortion through non-perfect isochronicity of the delay line and the combiner rings. Short, high-charge bunches will also interact with any small discontinuity of the beam chamber (e.g., bellows and septa), possibly being subject to longitudinal and transverse wake-fields. It is therefore highly desirable to manipulate relatively long bunches in the compression system and compress them just before injection into the drive beam decelerator sections. However, too long bunches experience a non-uniform kick in the RF deflectors, due to their phase extension, and the single-bunch emittance can grow. Therefore the bunch length at the exit of the accelerator is limited to 2 mm rms. The maximum emittance growth in this case is ~ 2% (for an initial rms normalized emittance of 2 $\times 10^{-4}$ π m rad), in the second combiner ring deflectors (3.75 GHz). A correlated energy spread (~ 1% rms), suitable for the final bunch compression, is obtained in the accelerator by the combined effect of RF curvature and longitudinal wake-fields. The need to preserve the correlation all along the compression system means that all the distortions of the longitudinal phase space must be kept small. In particular, attention must be given to the higher orders of the path length dependence on energy spread. A numerical analysis has shown that second order effects will hamper the final bunch compression and must be corrected by using sextupoles [3].

Another concern is the beam loading in the RF deflectors, especially just before extraction in the second combiner ring, where the average current along the train is very high and the frequency of the deflectors (3.75 GHz) is the highest in the compression system. In order to overcome this problem, a travelling-wave iris-loaded structures with a short filling time with respect to the train duration has been chosen. A steady state condition is then reached with minimum transient effects, although at the expenses of a loss in deflection efficiency. The extraction system for both rings is also a critical item, the issues being the high repetition rate (particularly in the first ring - 250 kHz) and the interaction with the high-current beam (particularly in the second ring – 262 A). The solution adopted for both rings is based on the use of travelling TEM wave transmission line pairs [5].

3 SUB-SYSTEMS AND COMPONENTS

In Table 1 and Table 2 the parameters of the sub-systems are presented. The lengths of the rings are fixed by the overall timing; the delay combiner geometry has been chosen to minimise both coherent synchrotron radiation emission and overall dimensions. One 3-bend magnetic chicane is located in the delay line and one in each ring arc. They are used for path length tuning (± 0.5 mm tuning range), in order to adjust the bunch relative phase and to compensate for orbit variations. Each chicane is 3.5 m long and works around an average bending angle θ_0 ~ 150 mrad. The tuning range is obtained with a bending angle variation $\Delta\theta$ = 1.5 mrad; such a small value of $\Delta\theta/\theta_0$ does not perturb the optics. Each chicane has a linear transfer matrix element R_{56} = 0.065.

Table 1: Delay combiner parameters

Length (line 1 / 2)	25/68	m
Bending radius (line 2)	3	m
# Dipoles (line 2)	16	
Dipole length	2	m
Dipole Field	1.25	T

Table 2: Rings parameters

	Ring 1	**Ring 2**	
Circumference	86	344	m
Bending radius	3.6	17.8	m
# Cells	4	20	
Cell length	13.6	13.6	m
# Dipoles	16	80	
Dipole length	1.4	1.4	m
Dipole field	1.1	0.22	T
# Quadrupoles	52	184	
Quadrupole length	0.3	0.3	m
Max quad gradient	14	14	T/m
# Sextupoles	20	84	
Sextupole length	0.3	0.3	m
Max sext gradient	26	120	T/m^2
Max β-function (h,v)	10.3 , 10.9	32.6 , 16.8	m

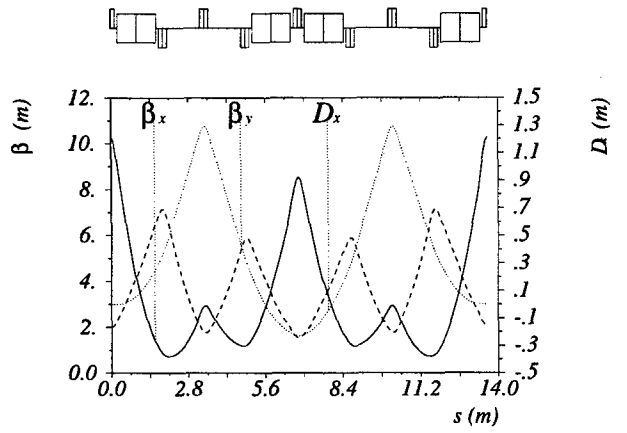

Figure 2: Basic isochronous cell lattice

Both the delay line and the ring arcs are based on the same type of isochronous lattice cell (see Figure 2), a modified four-cell FODO structure with "missing magnets" [6]. If other elements in the lattice (i.e., the chicanes) have a small nonzero R_{56}, the cell can be tuned to be quasi-isochronous, its residual R_{56} being such that the sum of the individual contributions is zero.

In order to avoid distortions in the longitudinal phase space, all the arcs are made isochronous up to second order by the use of sextupoles placed in the high-dispersion regions in correspondence with the missing magnets. By using different families of sextupoles it is possible to correct the third order as well. In principle, it should also be possible to tune the path length dependence from the energy spread (the isochronicity curve), in such a way as to compensate distortions in the longitudinal phase space of the electron bunches due to other non-linear effects. The ring injection is similar to a conventional fast injection scheme based on a septum and a fast kicker, where the kicker's role is taken by a RF deflector. Another deflector is placed upstream of the septum (at $-\pi$ phase advance), and provides the pre-compensation of the kick given by the injection deflector to the circulating bunches. A $\pi/2$ phase advance FODO lattice is used in the injection straight section, with the septum and deflectors close to the focusing quadrupoles, such that the angular kick from the deflector corresponds to a maximum displacement in the septum. All RF deflectors are short travelling wave iris-loaded structures, whose fundamental mode is a deflecting hybrid mode with a $2\pi/3$ phase advance per cell and negative group velocity [7]. The design is basically the same for all deflectors, with the dimensions of the cells scaled linearly with frequency. They are made up of 4 cells at 937 MHz and of 10 cells at 3.75 GHz and provide the needed 2 mrad deflection, equal in both rings, with 50 MW and 15 MW power consumption, respectively. The extraction kickers consist of travelling TEM wave transmission line pairs [5], powered in anti-phase, with the wave moving against the beam; the kicker length is chosen to be 2 m with a half-aperture of 1.5 cm. A deflection of 3 mrad requires a voltage of 11.3 kV, corresponding to 2.6 MW into each 50 Ω line. The kicker filling time of 6 ns remains small compared with the 143 ns available rise time. Due to the length of the extraction kicker, a different solution is used for the extraction region lattice, based on matching quadrupole doublets plus a triplet placed between the kicker and the extraction septum. The phase advance between the kicker and the septum is still ~ $\pi/2$, and the use of a central triplet allows a rather constant β-function along the kicker to be obtained.

4 BEAM DYNAMICS

As mentioned earlier, the preservation of the longitudinal phase-space of the bunches is important in order to be able to compress them before injection in the drive beam decelerator. The main sources of phase-space distortion in the compressor system chain are the coherent synchrotron radiation (CSR) emission and the higher-order non-isochronicity in the arcs. The bunch longitudinal dynamics in the both rings has been evaluated taking into account the CSR effect with shielding and the isochronicity curves for the arcs after sextupole correction up to second order [3]. The results are promising; the final bunch length after compression is smaller than the target one, with small bunch to bunch variation in final length (from 340 to 360 μm rms, depending on the number of turns in the rings). The contribution of the delay combiner arcs, as well as the non-linear contributions from the return arcs and the final compressor, have been neglected for the moment. Nevertheless, these contributions are smaller, and further improvement can be obtained, e.g., either by using different sextupole families in order to compensate nonlinearities, or by adding pulse stretchers and compressors in front of each ring and optimizing the bunch length in each component.

5 REFERENCES

[1] J.P.Delahaye and 30 co-authors, "CLIC, a 0.5 to 5 TeV e± Compact Linear Collider", Proc. EPAC'98, June 22-26 1998, Stockholm, Sweden, CERN/PS 98-09, and CLIC Note 360 (1998).

[2] H.H. Braun and 14 co-authors, "A New Method of RF Power Generation for Two-Beam Linear Colliders", Proc. EPAC'98, June 22-26 1998, Stockholm, Sweden, CERN/PS/98-14 (LP) and CLIC Note 367 (1999).

[3] H.H. Braun and 14 co-authors, "The CLIC RF Power Source, a Novel Scheme of Two Beam Acceleration for e± Linear Colliders", to be published as a CERN yellow report.

[4] J.B. Murphy, S. Krinsky and R.L. Gluckstern, "Longitudinal Wakefield for an Electron Moving on a Circular Orbit", Part. Acc. 57 (1997) 9.

[5] L. Thorndahl, CERN, Private Communication.

[6] R.C. York and D.R. Douglas, "Optics of the CEBAF CW Superconducting Accelerator", Proceedings of the 12th Particle Accelerator Conference, March 6-19, 1987, Washington, DC.

[7] Ph. Bernard, H. Lengeler and V. Vaghin, "New Disk-Loaded Waveguides for the CERN RF Separator", CERN 70-26 (1970).

Multi-Step Lining-up Correction of the CLIC Trajectory

E. T. d'Amico, G. Guignard, CERN, 1211 Geneva 23, Switzerland

Abstract

In the CLIC main linac it is very important to minimise the trajectory excursion and consequently the emittance dilution in order to obtain the required luminosity. Several algorithms have been proposed and lately the ballistic method has proved to be very effective. The trajectory correction method described hereafter retains the main advantages of the latter while adding some interesting features. It is based on the separation of the unknown variables like the quadrupole misalignments, the offset and slope of the injection straight line and the misalignments of the beam position monitors (BPM). This is achieved by referring the trajectory relatively to the injection line and not to the average pre-alignment line and by using two trajectories each corresponding to slightly different quadrupole strengths. A reference straight line is then derived onto which the beam is bent by a kick obtained by moving the first quadrupole. The other quadrupoles are then aligned on that line. The quality of the correction depends mainly on the BPM's and micro-movers' resolution and on the stability of the quadrupole strengths. Simulation statistics show that the beam offset from the center of the quadrupoles is typically 1.5 μm r.m.s.

1 INTRODUCTION

Two studies of trajectory correction are underway for CLIC, the ballistic alignment method [1] [2] and the Multi-step Lining-up (ML) described in this paper [3].

The latter has in common with the NLC correction and the ballistic method the idea to align as well as possible the main components of the linac on a straight line defined by the beam. The development of ML is also based on the observation that to align the quadrupoles on a reference line is more important that the real choice and straightness of this line, provided it is not too far away from the average-alignment line fixed by the positions of the components resulting from the pre-alignment. Instead of switching-off the quadrupoles, the ML method relies on a small change of their strengths in a linac section and on measurements of trajectory differences as in the dispersion-free correction [4] although used otherwise. This has the advantages of minimizing the heat-load variations, making the remanent-field and hysteresis effects negligible, keeping the beam focused and not too distant from the center of the elements (reducing wakefield effects) and eventually allowing on-line corrections by matching the detuned section to the rest of the linac. Trajectories are referred to the section injection line in order to make their differences independent of the injection parameters. As a first step, these differences are used in ML to estimate the off-sets of the quadrupoles relative to the same line. In the second step, a least square fit of the BPM measurements allows a good estimation of the injection parameters and the definition of a reference line onto which the quadrupoles are actually moved. The beam is bent towards this line by moving the first quadrupole of the section. As a last step in the correction, the BPMs sitting at the head of each girder are also displaced toward the reference line (by nullifying their measurements). This also aligns all the girders, reducing the cavity misalignments to their scattering with respect to each girder. Because the optics model is perturbed by the wakefields and other imperfections, the correction is an iterative process that rapidly converges [5]. Investigations show that with acceptable tolerances on the measurement- and micromover-resolution, acquisition noise and precision of the quadrupole power supplies, the ML trajectory correction allows a very good control of the beam offsets with respect to the center of the quadrupoles. Numerical investigations of the emittance blow-up after the ML correction will be done as soon as the algorithm is entirely implemented in a tracking program.

2 DESCRIPTION OF THE METHOD

The magnetic quadrupoles and the beam position monitors (BPM) of the CLIC main linac are assumed to be pre-aligned around an ideal line referred to as the average pre-alignment line. The optics is a FODO with a focal length f and a distance between quadrupoles L. The BPM is placed at a distance l in front of the quadrupole. Considering a section of N quadrupoles, let $\delta_{q,i}$ and $\delta_{p,i}$ be the offsets of the i-th quadrupole and i-th BPM from the average pre-alignment line respectively. The beam entering the first quadrupole follows the straight line defined by the injection offset x_{inj} and slope s_{inj} (see Fig.1). The beam trajectory

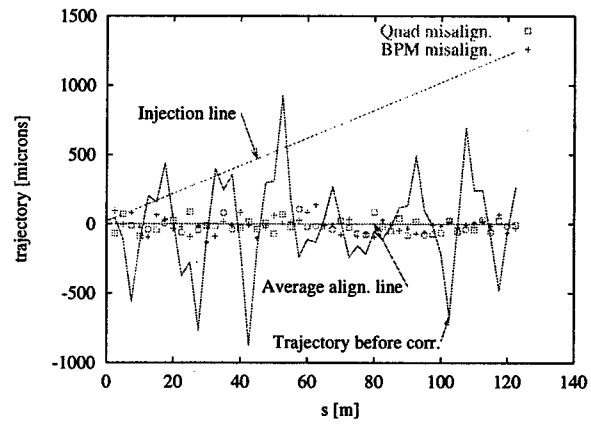

Figure 1: Beam trajectory and injection line with quadrupole and BPM offsets

0-7803-5573-3/99/$10.00@1999 IEEE.

offset from the i-th BPM center is given by the following expression [3] :

$$t_i = x_{inj}\left(1 - \sum_{k=1}^{i-1} u_{i,k}\right) + s_{inj}\left(iL - l - L\sum_{k=1}^{i-1} u_{i,k}k\right) + \sum_{k=1}^{i-1} u_{i,k}\delta_{q,k} - \delta_{p,i} \quad (1)$$

where $u_{i,k} = L\sum_{j=k}^{i-1} p_{j,k} - lp_{i-1,k}$ the $p_{j,k}$ being obtained iteratively [3]. The coefficients $u_{i,k}$ describe the beam transport in the FODO channel at each BPM and only depend on the lattice parameters L, l, f. The BPM unknown misalignments can be canceled out by making the differences of two trajectories at two different quadrupole strengths as in the dispersion-free correction [4]. The determinant of the resulting underdetermined linear system is null because the coefficients of x_{inj} and s_{inj} become linear combinations of the coefficients of the $\delta_{q,k}$. This fact suggests that it is possible to make the coefficients of the unknown variables x_{inj} and s_{inj} of the expression (1) independent of the quadrupole strengths by changing the reference system of the quadrupole offsets. The obvious choice is the injection line itself. The result obtained from (1) is:

$$\boxed{t_i = x_{inj} + s_{inj}(iL - l) + \sum_{k=1}^{i-1} u_{i,k}d_{q,k} - \delta_{p,i}} \quad (2)$$

where $d_{q,k} = \delta_{q,k} - x_{inj} - s_{inj}kL$. To get rid of both the BPM offsets $\delta_{p,i}$ and the injection parameters another beam trajectory is generated by slightly increasing the quadrupole focal length (typically 5 %). The difference between the two trajectories inside each BPM, one at the nominal focal length f_1 and one at the focal length f_2, is

$$t_i(f_1) - t_i(f_2) = \sum_{k=1}^{i-1} [u_{i,k}(f_1) - u_{i,k}(f_2)]\, d_{q,k} \quad (3)$$

from which the estimated quadrupole offsets $\hat{d}_{q,k}$ relative to the injection line are deduced. The estimation errors $\varepsilon_{d,k} = \hat{d}_{q,k} - d_{q,k}$ depend on the BPM resolutions and on the precision of the quadrupole strengths. Subtracting the estimated contribution of the quadrupole offsets from expression (2) a virtual trajectory around the injection line can be introduced :

$$t_{v,i}(f_1) = t_i(f_1) - \sum_{k=1}^{i-1} u_{i,k}(f_1)\hat{d}_{q,k} \quad (4)$$

$$= x_{inj} + s_{inj}(iL - l) - \delta_{p,i} - \sum_{k=1}^{i-1} u_{i,k}(f_1)\varepsilon_{d,k}.$$

Observing that the BPM offsets and the estimation errors $\varepsilon_{d,k}$ are randomly distributed, the injection parameters can be estimated by the Least Squares Method. The reference straight line on which the beam should be directed is the straight line which passes inside the first quadrupole at the estimated offset $\hat{x}_{inj} + \hat{s}_{inj}L$ from the average pre-alignment line and intersects this one inside the last quadrupole of the section. The beam is bent in the direction of the reference line by moving the first quadrupole of the section by $\Delta_{q,1} = -\hat{d}_{q,1} + f\Delta s$ where Δs is the difference between the reference and estimated injection slope. The other quadrupoles should be aligned onto the reference line by displacing them by the quantities $\Delta_{q,i} = -\hat{d}_{q,i} + \Delta s(i-1)L$. The broken line followed by the beam after these movements is different from the reference line as it is shown in Fig.2. However it has been established [3] that the offset $\delta_{t,i}$ of the beam relative to the i-th quadrupole center is given by

$$\boxed{\delta_{t,i} = \varepsilon_{d,i} - \sum_{k=1}^{i-1} u'_{i,k}\varepsilon_{d,k}} \quad (5)$$

where the $u'_{i,k}$ describe the beam transport at each quadrupole and are equal to the $u_{i,k}$ for $l = 0$. It is noteworthy that the above-mentioned offsets do not depend on the reference line parameters.

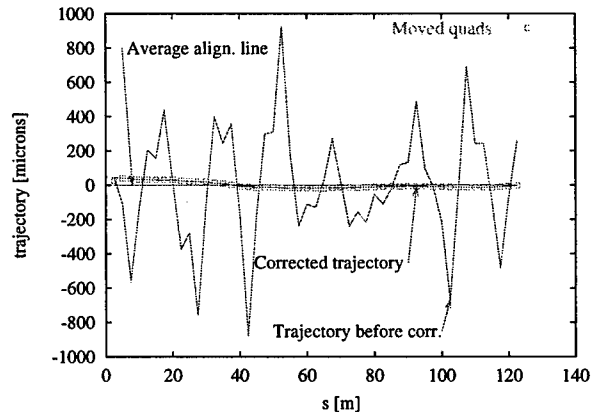

Figure 2: Beam trajectory before and after ML correction

3 CORRECTION STRATEGY

In this section, a correction procedure based on the Multi-step Lining-up method is proposed. As the result of the survey all the components of the linac are assumed to be randomly scattered around the so-called averaged-prealignment line. Acceptable r.m.s. offset amplitudes are of the order of 50 μm r.m.s. for both the quadrupoles and BPM. For the accelerating structures (cavities) placed on a single girder, the relevant quantity is their pre-alignment offset with respect to the BPM sitting on the same girder. This has to be within 2 and 10 μm r.m.s. . The relative misalignments between girders are given by those of the BPMs. For the first correction a single bunch is injected. Sections of N quadrupoles are successively dealt with in the linac. N is optimized for an accurate definition of the reference line and a good least squares fit of the measure-

ments over the BPMs used to estimate the injection parameters. Preliminary modeling shows that N can be as large as 50 or more, which opens the way to a correction section which could in principle be as long as a linac sector, defined by the FODO lattice being constant. The beam is injected into the nominal lattice and the beam positions are measured at each BPM. To gain a factor 10 on the resolution and acquisition errors, measurements should be averaged over typically 100 pulses (about 1 s). The beam is then injected into a lattice only detuned in the section considered and betatron-matched to the rest of the linac. The focal distance increment by ~ 5 % has been found to be sufficient because the difference between the two trajectories is enhanced by the phase advance shift. The beam positions are again measured and averaged over 100 pulses.
The ML algorithm is now applied following these steps:

1. Isolate the contribution of the quadrupole misalignments by building up the differences between the two trajectories. Solve the obtained triangular system of $N-1$ equations and $N-1$ unknowns which are the quadrupole displacements $d_{q,k}$ with respect to the injection line. Actually the results will be estimations $\hat{d}_{q,k}$. Restore the nominal lattice and suppress the betatron-matching.

2. Subtract the estimated contribution of the quadrupole misalignments from the nominal trajectory BPM readings. Assuming that the BPM misalignments are randomly distributed, these measurements scatter around the injection straight line. Estimates of its offset and slope are obtained by a least squares fit.

3. Compute the change of the slope (kick) that would steer the beam towards the average-prealignment line by using the estimated injection parameters. The obtained straight line is the reference line on which the quadrupoles should be aligned. To achieve this, the first quadrupole of the bin should be displaced in order to apply the computed kick . All the other quadrupoles should then be moved in order to align them onto the reference line.

4. Move all the BPMs sitting at the head of each girder to the reference line, by nullifying their reading within their resolution. This is a kind of "calibration" of the measurement system.

Moving the BPMs will also realign the girders. The cavity position scattering is consequently reduced to their starting pre-alignment imperfections on a single girder. The wake-field effects are accordingly decreased limiting the emittance growth. At least one iteration of this process is necessary because the lattice model used in the algorithm does not include the wake-fields. The procedure described here must be repeated section after section over the whole linac, before the full-intensity beam can be injected.
Simulations assume a BPM resolution of 0.1 μm, an acquisition noise of 0.1 μm, a micro-mover resolution of 0.5 μm and a precision of the quadrupole strength of $\Delta f/f = 5 \times 10^{-4}$. Results indicate that the reference line deviation with respect to the average prealignment line is of the order of 30 μm r.m.s. at the end of a section of 125 m. The most important result is that, although the actual line followed by the beam does not exactly coincide with the reference line, the remaining offsets between the beam and the quadrupole-centers (independent of the initial pre-alignment and of the line parameters) is of the order of $\sim$ 1.5 μm r.m.s. (see Fig.2).
Turning to time-dependent drifts of the components after the first correction has been completed, the BPMs may begin to measure non-zero deviations if the beam does not follow the change of the geometry. An on-line, one-to-one feedback can be applied in the case of smooth displacements as in an ATL-model. When BPM measurements indicate short-range position variations or the beam moving away from the linac component centers, the ML correction has to be repeated.
Considering now the first linac-section, the reference line obtained by ML can be used to correct for the injection jitter while maintaining the same trajectory over the rest of the linac. For this, it is necessary to apply two correction kicks, near the first quadrupole and for instance near one in the middle of the section, in order to maintain the beam on a constant trajectory through the BPMs following the second quadrupole (by keeping their reading equal to zero). To use this correction as a feedback may require two fast kickers near the two quadrupoles mentioned while static corrections of the injection can be done by actually moving the two quadrupoles.
Effects of jitter during BPM acquisitions and of the terrestrial magnetic field remain to be taken into account [6]. Full simulations with tracking programs [7] should be carried out to check the robustness of the method. The hope is to apply the ML correction on-line with only small focal changes and sector-matching, without interrupting the beam acceleration.

4 REFERENCES

[1] T. O. Raubenheimer, D. Schulte,"The ballistic alignment method", this conference.

[2] D. Schulte,"The CLIC Main Linac Lattice at 1 TeV", CLIC Note 356, 1998.

[3] E. T. d'Amico and G. Guignard,"A trajectory correction based on Multi-step Lining-up for the CLIC main Linac", CLIC Note 388, 1999.

[4] T. O. Raubenheimer,"The Generation and Acceleration of Low Emittance Flat Beams for Future Linear Colliders", SLAC Report 387, 1991.

[5] The NLC Design Group,"Zeroth-Order Design Report for the Next Linear Collider", SLAC report 474, 1996.

[6] S. Fartoukh, D. Schulte, Private communications.

[7] G. Guignard and J. Hagel,"MUSTAFA- A Tool for Numerical Simulations of the Beam Behaviour in a Linac", Proc. of the LINAC98 conf., Chicago, 1998.

TWO-FREQUENCY BEAM-LOADING COMPENSATION in the DRIVE-BEAM ACCELERATOR of the CLIC TEST FACILITY

H.H. Braun, M. Valentini#, CERN, 1211 Geneve 23, CH

Abstract

The CLIC Test Facility (CTF) is a prototype two-beam accelerator, in which a high-current "drive beam" is used to generate the RF power for the main-beam accelerator. The drive-beam accelerator consists of two S-band structures which accelerate a bunch train with a total charge of 500 nC. The substantial beam loading is compensated by operating the two accelerating structures at 7.81 MHz above and below the bunch repetition frequency, respectively. This introduces a change of RF phase from bunch to bunch, which leads, together with off-crest injection into the accelerator, to an approximate compensation of the beam loading. Due to the sinusoidal time-dependency of the RF field, an energy spread of about 7% remains in the bunch train. A set of idler cavities has been installed to reduce this residual energy spread further. In this paper, the considerations that motivated the choice of the parameters of the beam-loading compensation system, together with the experimental results, are presented.

1 THE CLIC TEST FACILITY II

CTF II [1] is an experimental facility of the Compact LInear Collider (CLIC) study dedicated to demonstrate the feasibility of the CLIC two-beam accelerator scheme and its associated 30 GHz technology [2]. A high-current drive-beam generates the 30 GHz power, while the main beam probes the accelerating field in the 30 GHz accelerator. Some operational parameters of the drive-beam injector are presented in Table 1.

The drive beam is generated by an S-band RF-photo-injector whose photo-cathode is illuminated by a short pulse (8 ps FWHM), UV laser. Two S-band, disk-loaded accelerating structures are used to provide acceleration to about 35 MeV. Since efficient 30 GHz power production requires short bunches, a magnetic chicane, together with optimised phasing in the accelerating structures, is used to compress the bunches to 5 ps FWHM. After bunch compression, the beam is injected into the 30 GHz decelerator where a part of its energy is converted into 30 GHz power.

Table 1: Operational Parameters of the Drive-Beam Injector during 1998

Number of bunches	48
Bunch spacing	10 cm
Bunch train charge	500 nC
Energy	35 MeV
Accelerating Field	36 MV/m
Total loss factor	13.7 V/pC
Beam line energy acceptance	14%
Residual train energy spread	~ 7%
Correlated single bunch energy spread	~ 7%
Bunch length after compression(FWHM)	5 ps

2 BEAM-LOADING COMPENSATION

The CTF drive-beam train of 500 nC during 16 ns extracts 1 GW of power from the 3 GHz accelerating structures. The related energy has to be provided by the energy stored in the structures and the heavy beam-loading has to be compensated. In the case of more moderate beam-loading, its compensation is provided by dedicated structures tuned at a frequency higher and lower than the bunch repetition frequency, while normal accelerating structures are used for acceleration [3]. In the CTF case, the drive beam accelerator has to provide both acceleration and beam-loading compensation.

Beam-loading compensation can be obtained with a single accelerating structure operated at a frequency slightly higher than the bunch repetition frequency and by injecting the first bunch of the train before the crest. This produces a phase advance along the train, i.e. the successive bunches arrive closer to the crest than the previous ones, experiencing a higher accelerating field which approximately compensates the beam-loading.

In the CTF II, simultaneously to acceleration and beam-loading compensation, the drive beam injector has to provide a way to establish the proper single-bunch energy-phase correlation required for magnetic bunch compression.

The single-bunch energy-phase correlation can be controlled by using two accelerating structures, one operated at a frequency higher and the other at a frequency lower than the bunch repetition frequency. By running the two accelerators at the same field amplitude and injecting the train at opposite phase, the single-bunch energy spread introduced in the first structure is compensated by the second one. However, by using the correct phasing and a reduction of the field amplitude in the second structure, it is possible to introduce the same energy-phase correlation in all bunches.

Email: marco.valentini@cern.ch

0-7803-5573-3/99/$10.00@1999 IEEE.

2.1 Theory

The energy gain of the *i-th* bunch (ΔT_i) of a bunch train in an accelerating structure operated at a frequency ν_l, is:

$$\Delta T_i = E_l L \cos\left(2\pi\frac{\nu_l}{\nu_b}(i-1)+\phi_l\right) - 2k_o q_b\left(\frac{1}{2}+\sum_{j=1}^{i-1}\cos\left(2\pi\frac{\nu_l}{\nu_b}j\right)\right) \quad (1)$$

where E_l is the structure mean field, L is the structure length, ν_b is the bunch repetition frequency, ϕ_l is the launching phase of the first bunch of the train into the accelerator, k_o is the beam loss factor ($k_o=\omega r'L/4Q$) and q_b is the bunch charge. Eq. 1 can be written as a function of the accelerator off-frequency ($\Delta\nu = \nu_l - \nu_b$), and the sum can be written in a closed form:

$$\Delta T_i = E_l L\cos(2\psi(i-1)+\phi_l) - k_o q_b\frac{\sin(2\psi(i-1/2))}{2\sin(\psi)} \quad (2)$$

where $\psi = \pi\,\Delta\nu/\nu_b$. In Eq. 2 the bunch number index i can be treated as a continuous variable. By introducing a continuous variable t to represent the time relative to the bunch centre, Eq. 2 can be modified to represent also the energy of bunch slices at time t. The energy-phase correlation of the *i-th* bunch is then given by: $\omega^{-1}d/dt\,\Delta T_i$.

The two accelerating structures of the CTF drive beam injector allow four free parameters, i.e. fields and phases (E_l, E_2, ϕ_l and ϕ_2), which allow the fulfilment of four conditions: minimum energy spread and equal energy-phase correlation along the train, maximum energy gain and achievement of the desired amount of correlation. The requirement of minimum energy spread and of equal correlation can be expressed mathematically by requiring both bunch energy and correlation to be independent of the bunch number in the middle of the train:

$$\left|\frac{d}{di}\Delta T_i\right|_{i=\frac{N+1}{2}} = 0 \quad \text{and} \quad \left|\frac{d}{di}\left|\left(\frac{d}{dt}\Delta T_i\right)\right|_{t=0}\right|_{i=\frac{N+1}{2}} = 0 \quad (3)$$

where the derivative is taken with respect to the bunch number index i, and N is the number of bunches in the train. As a result, the phase and the field of the second accelerator (ϕ_2 and E_2, respectively) are expressed as a function of the phase and the field of the first accelerator (ϕ_l and E_l, respectively), and of the off-frequency $\Delta\nu$:

$$\phi_2 = \alpha + \mathrm{atg}\left[\mathrm{tg}(\alpha+\phi_1)+\frac{2k_o q_b}{E_1 L}\frac{\cos(\beta)}{\sin(\beta)\cos(\alpha+\phi_1)}\right]$$

$$E_2 = E_1\frac{\cos(\alpha+\phi_1)}{\cos(\alpha-\phi_2)}$$

where $\alpha = \pi\,(\Delta\nu/\nu_b)(N\text{-}1)$ and $\beta = \pi\,(\Delta\nu/\nu_b)\,N$.

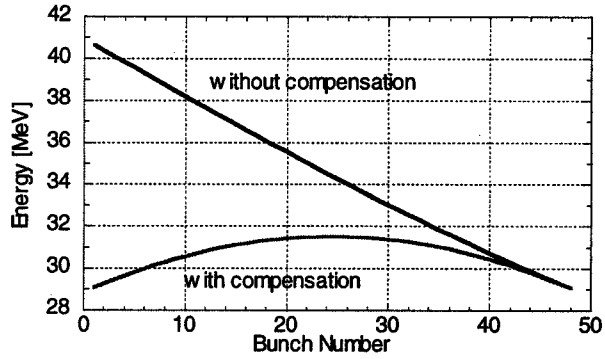

Fig. 1: Bunch energy gain along the train.

To maximise the energy gain, E_l is set to the maximum value that can be achieved. Then the choice of ϕ_1 sets the amount of energy-phase correlation. In the case of the CTF II, for E_l = 36 MV/m and a required correlation of 1% per degree of bunch phase extension, ϕ_1 is -60°, ϕ_2 is +25°, E_2 is 29 MV/m, and the train energy gain is about 30 MeV. The residual energy spread is about 7%.

The train energy profile after acceleration is shown in Fig. 1 as a function of the bunch number. Also shown is the energy gain without beam-loading compensation. The beam-loading compensation scheme reduces the energy gain of the train head so that the total energy spread is reduced to about 7%.

The ratio between the residual energy spread and the energy gain in the accelerating structures depends only on the accelerator off-frequency and on the train length. In the case of the CTF II, $\Delta\nu$ = 7.81 MHz, and N = 48, the relative energy spread is about 7% of the energy gain in the two accelerators.

2.2 The choice of the accelerator off-frequency

Together with the bunch train length, the choice of the frequency difference between the accelerating structures and the gun ($\Delta\nu$) determines the bunch train residual energy spread, the energy gain after beam-loading compensation and the versatility of the beam-loading compensation scheme. The frequency difference is then chosen to minimise the residual train energy spread and to maximise the bunch energy gain in the structures.

The train residual energy spread and the maximum energy gain as a function of $\Delta\nu$ in the case of the design parameters of the CTF injector are shown in Fig. 2. The maximum energy gain increases with $\Delta\nu$ and reaches a plateau at about 6 MHz, a larger $\Delta\nu$ does not lead to an appreciable additional energy gain. On the contrary, the residual energy spread increases more than linearly with $\Delta\nu$. However, for a given final energy and for a given bunch charge, the accelerator field required by the beam-loading compensation scheme scales inversely with $\Delta\nu$. In other words, a higher $\Delta\nu$ allows beam-loading compensation with a lower accelerating field, at the expenses of a higher residual train energy spread.

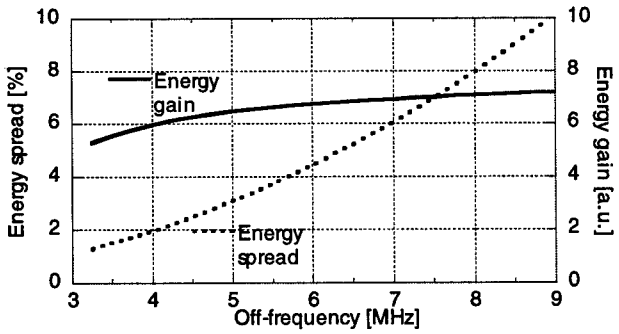

Fig. 2: Fractional energy spread [%] and maximum energy gain [a.u.].

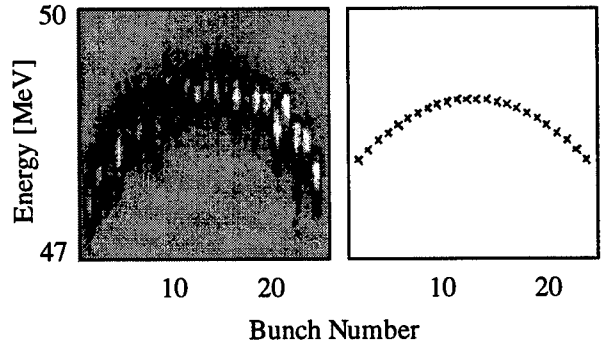

Fig. 3: Longitudinal phase space with beam-loading compensation. Left side: measured; right side: predicted.

2.3 *Hardware*

In CTF II, the possible choice of the accelerator off-frequency was limited to either 5 or 7.81 MHz by engineering constraints related to the timing system. The higher off-frequency has been chosen to obtain a more flexible beam-loading compensation system, effective for several combinations of bunch charges and accelerator fields.

Two special accelerating structures optimised for high-charge acceleration have been constructed at LAL, Orsay [4]. They are tuned at ± 7.81 MHz with respect to the bunch repetition frequency, they have a large iris aperture and they have been optimised for a low r'/Q (2200 Ω/m) to maximise the stored energy.

2.4 *Operation*

The installation of the beam-loading compensation system has been completed at the beginning of 1998. Despite the fact that the accelerating structures have been conditioned to only 36 MV/m instead of the design value of 60 MV/m, the beam-loading compensation system worked as predicted by the theory. Its flexibility allowed operation at high current levels, which enabled demonstration of the two-beam accelerator scheme [1].

Fig. 3 shows a longitudinal phase-space image of a 24 bunch train with a total charge of 120 nC. The measurement has been taken with a streak camera from a transition radiation screen in a spectrometer behind the accelerators. Only 24 bunches are shown because of the limited acceptance of the streak-camera.

Due to the gradients available to date in the accelerating structures, the single-bunch energy-phase correlation has been controlled by varying the injection phase of the train in the two accelerators, without lowering the field of the second one. This contradicts the prescription of the beam-loading compensation scheme (see Eq. 3) but produces the two-fold advantage of increasing the bunch train energy gain and of introducing a higher correlation in bunches in the bunch train tail. The latter contributes to obtaining equal bunch lengths along the bunch train, as late bunches are longer due to the beam-loading in the RF gun.

3 IDLER CAVITIES

To further reduce the train residual energy spread, a pair of 3-cell idler cavities has been constructed at the Alfvén Laboratory, KTH, Stockholm [5]. The cavities are tuned at frequencies 31.2 MHz higher and lower than the bunch repetition frequency. Due to this frequency difference, the beam-loading is maximum in the middle of the train and vanishes for the first and last bunch. This way, the energy of the central part of the train is lowered and the residual energy spread is further decreased. The idler cavity geometry has been optimised to reduce the train energy spread to less than 3% at the nominal charge. This is of the same order of the energy spread expected from high order modes. First tests of the idler cavities with beam are foreseen for spring 1999.

4 CONCLUSION

The high transient beam-loading of the CTF drive beam ($\langle I \rangle$ = 30 A during 16 ns) has been compensated by adopting a two-frequency beam-loading compensation system. In addition to providing acceleration, the system reduced the total energy spread to 7% and allowed the establishment of single-bunch energy-phase correlation of the order of 1% per degree of bunch phase extension.

5 REFERENCES

[1] H.H.Braun and 15 co-authors, "Demonstration of Two-Beam Aceleration in CTF II," Proc. Linac '98, Chicago, US and CERN/PS/98-038, 1998.

[2] J.P.Delahaye and 27 co-authors, "The CLIC Study of a multi-TeV Linear Collider," this conference and CERN/PS/99-05,1999

[3] "ATF Design and Study Report," KEK 1995.

[4] G. Bienvenu, J. Gao, "A Double High Current, High Gradient Electrons Accelerating Structure," Proc. EPAC '96, Sitges, 1996.

[5] H. Braun and S. Rosander, Resumé of disussion at Alfvén Laboratory, CTF Note, 1997.

TRAPPED MODES IN TESLA CAVITIES*

F. Marhauser‡, P. Hülsmann, H. Klein
Institut für Angewandte Physik der Johann Wolfgang Goethe-Universität Frankfurt
Robert Mayer-Straße 2-4, 60325 Frankfurt am Main, Germany

Abstract

In the TESLA linear collider scheme [1] the existence of trapped modes [2] within a TESLA cavity could be a severe problem to be overcome. Damping of trapped modes seems impossible due to their localization within the cavity, which prevents a coupling to the HOM dampers mounted to both ends of the beam pipes. As a consequence the energy of a trapped mode can achieve considerable values after several bunch passings, even in the case of a low shuntimpedance of such a mode. This effect gives additional heat load for the cooling system that has to be taken into account. In this paper we propose a method to prove the existence of these modes in a 9-cell copper TESLA cavity. RF-measurements with beam pipes and numerical simulations with MAFIA have been done. Longitudinal and transversal shuntimpedances of the trapped modes within a frequency range up to 10 GHz were calculated.

1 INTRODUCTION

In the proposed TESLA linear collider scheme longitudinal and transversal emittance growth in the linac is required to be kept small. Furthermore the heating of the cavity walls due to wakefields in the low and high frequency regime has to be limited. One source of wall heating in the low frequency regime seems to be trapped modes.

Trapped modes are caused by variations of the cell geometry of the TESLA cavity. The usual TESLA cavity has almost equally shaped cells except the end cells. Due to the presence of the beam pipes these end cells differ slightly from the middle cells to ensure a flat field distribution for the accelerating mode. Thus trapped modes within the TESLA cavity and within the beam pipes, beyond and above the related cutoff frequency of the beam pipe, are expected. Two HOM dampers are foreseen for each single TESLA cavity, mounted to the beam pipes (length = 3/2 λ_{fund}) on both ends nearby the end cells of the cavity. Consequently trapped modes within the beam pipes seem to be harmless because of their coupling to the HOM dampers.

* Work supported by the Graduiertenkolleg "Physik und Technik von Beschleunigern" der Deutschen Forschungsgemeinschaft DFG and by BMBF under contract 06OF841

‡ Email: frankmar@sunkist.physik.uni-frankfurt.de

But trapped modes within the cavity have vanishing field amplitudes in the end cells of the cavity and therefore only low or even no coupling to the HOM dampers is expected. Usually trapped modes have only a small characteristic impedance (R/Q per cavity) of several ohms up to several ten ohms for the highest R/Q-values. From the viewpoint of particle dynamics those modes seem to be harmless, but from the viewpoint of stored energy a power of several ten up to several hundred watts is radiated into those modes and the time between two macropulses is too short to damp the stored modes energy significantly. This accumulation of wakefield energy could lead to a quench in the worst possible case.

To prove the existence of these trapped modes RF-measurements were performed. Also numerical calculations have been done, with different boundary conditions, and have been compared with measurement results. Hence artifical trapped modes caused by the presence of the measurement antennas or other wall perturbations are out of question.

2 MEASUREMENT AND SIMULATION

2.1 The RF-Test-Setup

As mentioned above trapped HOMs within the cavity should be less affected than propagating HOMs by variing the peripheral boundary conditions within the waveguide pipe due to their vanishing field amplitudes in the end cells of the cavity. Changed peripheral boundary conditions are realized experimentally by movable shorts within beam pipes driven by stepper motors. Information about the field distribution of the trapped modes was delivered by an on axis bead pull measurement device. Therefore a nylon thread, driven by a stepper motor, was fed through the structure carrying a spherical dielectric bead in order to perturbate transversal and longitudinal electric field in like manner. The dielectric sphere measures the square of the value of the electric field strength at the position of the sphere. The nylon thread could be fed only through a small on axis hole without obstructing the movability of the shorts. The bead-pull measurements were suited to get the on axis electric field distribution. Therefore off axis measurements which are necessary to get the shuntimpedances of dipole modes were not possible but they were calculated by MAFIA for dipole modes as well as for monopole-TM modes. The trapped modes were excited by very small loops (to

0-7803-5573-3/99/$10.00@1999 IEEE.

minimize their own influence on the field distribution), which dived into the cells where we expected the strongest field amplitudes of the trapped mode under investigation. All RF-measurements were performed using a HP 8720A Network Analyzer (130 MHz-20 GHz). Figure 1 illustrates a schematical drawing of the RF-Test-Setup with a 9-cell copper TESLA cavity with beam pipes.

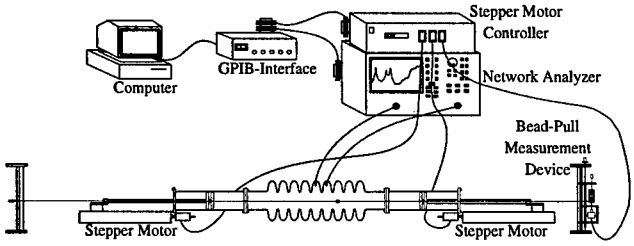

Figure 1: Drawing of the measurement setup with the TESLA 9-cell structure, the movable shorts in the beam pipes and the on axis bead-pull measurement device.

2.2 *Measurement Method*

We measured the transmission signal (S_{21}) between two coupling loops. A trapped mode can only be localized in frequency regions, where the transmission signal remains unaffected or shows only small changes for different positions of the movable shorts, which indicates clearly low coupling to the beam pipes and thus also low coupling to any kind of HOM dampers. At those frequency regions bead-pull measurements were performed in order to verify the existence of a localized electric field distribution. This method was proposed earlier [3] but a main problem arises since the passbands tend to overlap even for high frequencies. As a consequence we would not be able to find all possible trapped modes with this method. We therefore started to make numerical calculations as described below using the MAFIA code [4], whereby the problem of overlapping passbands vanishes. Using the numerical results we were able to verify trapped modes faster and more precisely with bead-pull measurements since we have additional information about the frequency, the field distribution and the azimuthal type of the trapped modes (i.e. monopole modes, dipole modes etc.). With automized measurements we could examine a frequency range up to 10 GHz, for which we got reliable results given by MAFIA allowing for the performance limit of our computer system.

2.3 *Numerical Calculations*

The method to find trapped modes with MAFIA is very similar to the method proposed for the measurements. We looked for the frequency differences of comparable modes found with the MAFIA eigenmode solver in two separate runs using two different boundary conditions at the end of the beam pipes. A large dependence of the calculated two frequencies of one mode indicates a strong field amplitude, whereas a small frequency shift of a given mode indicates low or even no field amplitudes within the beam pipes (comp. Fig. 2 and Fig. 4). For the first run we assumed ideal electric and in a second run ideal magnetic boundary conditions at the end of the beam pipes. We chosed a beam pipe length of 3/4 λ_{fund} on both sides of the cavity. This will not strongly perturbate the field of modes below cutoff with evanescent field amplitudes nearby the end cells within the beginning part of the beam pipes, like the fundamental accelerating mode at 1.3 GHz.

3 RESULTS

3.1 *Monopole-TM Modes*

Figure 2 shows the amount of frequency shift Δf depending on the boundary conditions versus mode number in order as they appear in the calculation. For trapped modes we have to look at local minima. The sudden step of Δf at mode no. 28 expresses the presence of the first beam pipe cutoff for monopole-TM modes (f_{TM01} = 2.95 GHz for a pipe radius of 39 mm). We find a very small "hill" just before the sudden step in the third passband (mode no. 19-27), which is located completely below the beam pipe cutoff, demonstrating the sensibility of this method to evanescent fields.

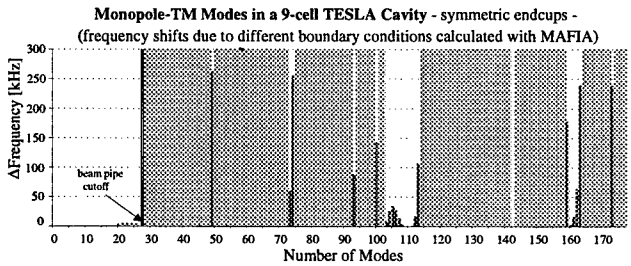

Figure 2: The Monopole-TM Modes in a 9-cell TESLA cavity calculated in two runs with different boundary conditions (see text!). Shown is the frequency shift Δf in [kHz] in dependence on the continuous number of calculated modes.

The first local minimum appears at mode no. 49, of which the calculated field distribution and the measured electrical field profile are presented in Fig. 3 as an example. At the top we see the electric field amplitude versus the position of the bead in arbitrary units. At the bottom the calculated field distribution is shown, which enables the reader to compare the position of the bead with the position in the cavity. The reason for the asymmetric field profile (comp. also Fig. 5) is due to small deviations from the perfect cell geometry caused for example by small fabrication errors or mechanical tensions. Relevant parameters of trapped Monopole-TM modes with the highest longitudinal shuntimpedances

above the beam pipe cutoff are given in Table 1 (mode numbers related to Fig. 2).

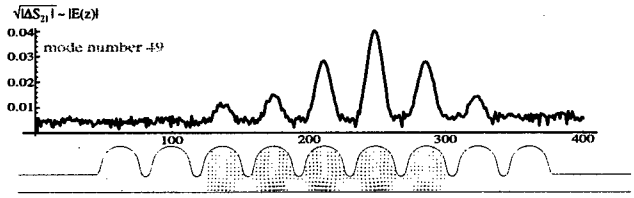

Figure 3: Electric field profile of trapped Monopole-TM mode no. 49 calculatad at f = 3.855 GHz (bottom) and measured at f = 3.854 GHz (top).

Table 1: Cavity parameters calculated by MAFIA

Mode Number	Frequency f [GHz]	Quality Factor Q	Longitudinal Shunt-impedance $R^{\parallel}_s$ [kΩ]	Characteristic Impedance $R^{\parallel}_s/Q$ [Ω]
49	3.855	35704	1226.3	34.35
93	5.461	62639	599.2	9.57
105	5.902	36396	73.7	2.03
106	5.912	37982	330.6	8.70
107	5.922	40022	124.5	3.11
142	6.687	44049	210.3	4.78

3.2 Dipole Modes

Analogous simulations had been made for dipole modes. The most trapped dipole modes can be found, where low frequency shifts occur in Fig. 4. In Table 2 we summarize relevant parameters for trapped dipole modes with the highest transversal shuntimpedances above the cutoff of the beam pipe.

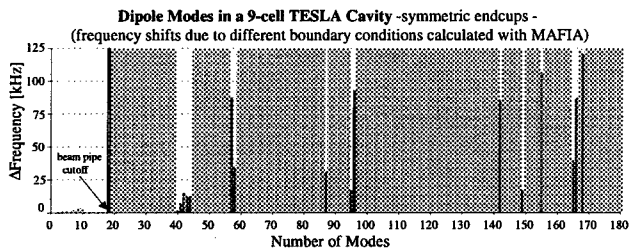

Figure 4: Results for dipole modes. Compare caption of Fig. 2 for details.

Table 2: Cavity parameters calculated by MAFIA

Mode Number	Frequency f [GHz]	Quality Factor Q	Transversal Shunt-impedance $R^{\perp}_s$ [kΩ]	Characteristic Impedance $R^{\perp}_s/Q$ [Ω]
43	3.088	74926	54.1	0.72
44	3.091	75539	196.7	2.60
60	3.359	39427	2.4	0.06
87	4.323	62268	6.9	0.11
149	5.651	92669	5.7	0.06
165	5.768	102813	3.7	0.04

The first two passbands (mode no. 1-18) are located below the cutoff (f_{TE11}=2.25 GHz), thus evanescent field amplitudes in the beam pipes cause only small frequency shifts. The first trapped mode above cutoff (mode no. 40) is the first mode of a whole passband showing only small amount of field strength in the beam pipes. Some examples of trapped modes are shown in Fig. 5 (mode no. 40, 87 and 95 from top to bottom).

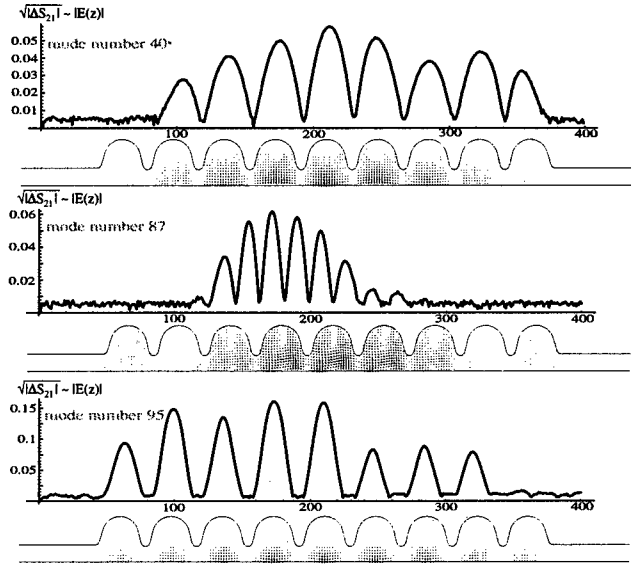

Figure 5: Trapped dipole mode (comp. Figure 4) no. 40 (f = 3.084 GHz MAFIA; 3.078 GHz meas.), mode no. 87 (f = 4.323 GHz MAFIA; 4.314 GHz meas.) and mode no. 95 (f = 4.426 GHz MAFIA; 4.421 GHz meas.).

4 CONCLUSION AND OUTLOOK

We proposed a method to measure trapped modes in TESLA cavities by using the information of numerical calculations. The numerical method avoids the in reality existing problem of overlapping passbands and delivers the field distributions of trapped modes and the frequencies for more accurate RF-(bead-pull)-measurements. The measurement results given are in good conformity with the numerical simulations. Field profile comparisions of several trapped modes within a frequency range of 10 GHz had been verified and their beam dynamic related parameters like quality factors and shuntimpedances were calculated. Numerical calculations for the current TESLA cavity design with asymmetric endcups [1], which helps to reduce the unwanted trapped modes, have been carried out and have to be proved with a copper model which will be delivered from DESY in the near future.

5 REFERENCES

[1] TESLA and SBLC Collaboration: "Conceptual Design Report for a 500 GeV Linear Collider with Integrated X-Ray Laser Facility", DESY Print, December 1996

[2] T. Weiland, U. van Rienen, P. Hülsmann, W.F.O. Müller, H. Klein "Investigations of higher order modes using a 36-Cell test structure", Physical Review Special Topics - Accelerator and Beams, March 1999

[3] F. Marhauser, H.-W. Glock, P. Hülsmann, M. Kurz, H. Klein: "Search for Trapped Modes in TESLA Cavities", 1997 Particle Accelerator Conference, Vancouver , B.C., Canada, May 1997

[4] T. Weiland et al.: "Solutions of Maxwells's Equations using the Finite Integration Algorithm"; Version 3.2; Darmstadt 1993

THE WAKEFIELDS AND LOSS FACTORS IN SUPERCONDUCTING ACCELERATING CAVITIES FOR TESLA COLLIDER

E. Plawski
The Andrzej Soltan Institute for Nuclear Studies, Swierk, P-10
05-400 Otwock-Swierk, Poland

Abstract

The first stage of TTF superconducting electron linac is a in its final state of assembling. Many of superconducting accelerating cavities attained already the planned for collider accelerating fields of 25 MV/m. However the problem of cost reduction of TESLA accelerating system is still actual. The propositions concerning modifications in accelerating cavities were signalled at several TESLA Meetings and reported also at the PAC97 Conference [1]. The cavities are the main source of wakefields, leading to beam instabilities in a linear collider. In the frame of scientific international cooperation the part of the work concerning the wakefield generation in new structures proposed by DESY was done in our Institute. The room temperature copper models of new type cavities were also produced in Swierk and will undergo the tests at DESY.

In this report the calculated longitudinal and transverse loss factors in enlarged iris cavity proposed in [1] and in superstructure composed of four 7-cell cavities [2] are compared with the corresponding values [3] in cavities currently used in TTF.

1 INTRODUCTION

The experience already gained during the development of 1.3 GHz superconducting RF accelerating cavities for TESLA collider indicates that some design parameters should be reconsidered having in mind the cost reduction of the future collider. This problem was reported on PAC'97 Conference [1] and on several TESLA Meetings [2] where the new shapes of accelerating cavity and cavities' arrangements were proposed. The points considered were the shape of the cavity and fill factor (the ratio of active acceleration length to total length) of the collider. The present design of TTF superconducting accelerating cavity consists of 9 weakly coupled cells-resonators operated in π mode at frequency 1.3 GHz. The string of 8 cavities each equipped with FM power coupler and 2 HOM couplers is encapsulated in a single unit-module and cooled down to 2 K. The shapes of RF accelerating cavity elaborated some years ago [4,5] were optimized to have possibly high coupling impedance (R/Q) for fundamental mode, to keep the safe values of the peak surface electric and magnetic fields and to keep small values of HOM impedances. The small iris aperture which is a compromise between the above criteria reduces the coupling factor k_{cc} between cells of the cavity. As the error of field amplitude in a standing wave cavity made of N cells is proportional to N^2/k_{cc}, the small value of k_{cc} makes the actual cavities very sensitive to technological processing during cavity preparation. This has impact on cavity production costs. To avoid the fundamental mode RF phase interference between neighbouring cavities the $3\lambda/2$ lengths beam tubes were chosen. This reduces the effective accelerating field by the ratio of cavity active length to total cavity length.

Two ways to solve this problem were proposed in last two years. In [1] it is proposed to enlarge the iris aperture and to enlarge also the end tube diameters of the cavity in order to facilitate the HOM damping.

The second approach [2] preserves the shape of TTF cavity inner cells but limits to 7 the number of cells in one cavity. The diameter of interconnecting beam tubes is increased and their length limited to $\lambda/2$ allowing the transmission of RF power from cavity to cavity. The set of 4 cavities (superstructure) is fed by 1 RF input power coupler.

The accelerating cavities are the main source of wakefields and related losses in a linac. The proposed changes influence significantly the wakes induced in cavities. The wake-potentials and loss factors were calculated for both proposed schemes and are reported in this paper.

2 WAKE-POTENTIALS

The wakes induced in a cavity by the gaussian bunch of standard deviation σ = 1mm or 0.5mm were evaluated by the procedure ABCI [6] used earlier for the actual TTF cavity wakefield calculations. For the case of large iris cavity this enables the direct comparison with TTF RF cavity regardless of possible systematic inaccuracy due to finite size of mesh dimensions used or possible imperfections inherent to the computation code used .

2.1 The large iris cavity

The changes of shapes proposed in [1] for a new cavity are illustrated in Fig. 1 and listed in Table 1.Each cell of the new cavity has elliptical shape in the equator region and circular with the 17 mm curvature radius at the iris aperture. End cells have slightly smaller equator radius to compensate the influence of the beam tube opening. The detailed data on optimized shapes of inner and outer cells were taken from [1].

0-7803-5573-3/99/$10.00@1999 IEEE.

Table1.

	TTF 9-cell cavity	Large iris 9-
R_{iris} of inner	35 mm	51 mm
$R_{equator}$ of inner	103.3 mm	108.08 mm
$R_{equator}$ of outer	103.30 mm	106.6 mm
R_{tube} of end	39 mm	55 mm

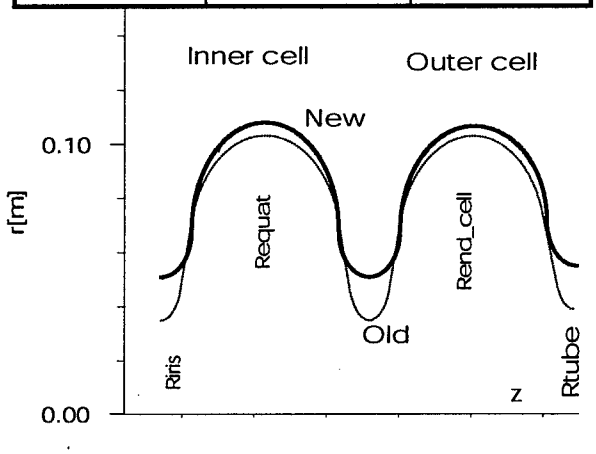

Fig. 1 Proposed modification of shape of 9-cell cavity.

The longitudinal (monopole) wakes induced in 9-cell cavity by σ =1 mm bunch are illustrated in Fig.2. The comparison is made between two cavities. Curve 1 shows the wake induced in the new cavity and curve 2 the wake in the old one at present in use in TTF.

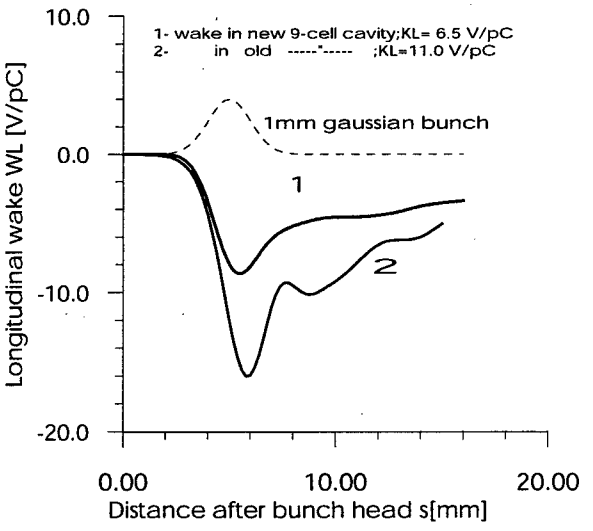

Fig. 2 $W_{\parallel}$ wake induced in 9-cell cavities.

The resulting loss factors for both cavities are summarised in Table 2. The listed monopole loss factors $k_{\parallel}$ include also the loss to fundamental mode passband.
For the σ =1mm bunch, the plot of longitudinal loss factor integrated up to 100 GHz is shown in Fig.3. The clean steps on this plot correspond to the increase of loss factor due to successive resonant modes. The fundamental mode loss factor read from this plot is equal

Table 2. The loss factors of 9-cell TESLA cavities

σ_{bunch} [mm]	TTF cavity $k_{\parallel}$ [V/pC]	TTF cavity $k_{\perp}$[V/pC/m]	New 9 cell cavity $k_{\parallel}$ [V/pC]	New 9 cell cavity $k_{\perp}$[V/pC/m]
1.0	11.05	20.6	6.53	6.21
0.5	15.58	12.96	10.20	4.74

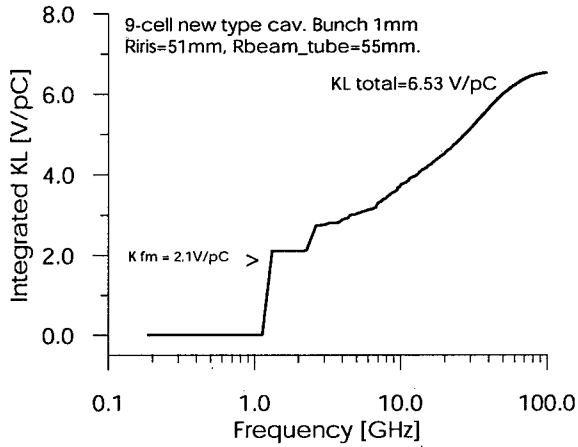

Fig. 3 Integrated longitudinal loss factor in the new type 9-cell accelerating cavity. σ = 1mm, gaussian

to 2.11 V/pC. The HOM loss factor of monopole modes is then: $k_{\parallel HOM} = k_{\parallel total} - k_{\parallel fm} = 4.4$ V/pC
for a new type 9-cell cavity.

2.1.1 Consequences

The opening of iris and beam tube apertures of 9-cell TESLA cavity as proposed in [1] has clear advantage as far as the loss factors are concerned. The $k_{\parallel}$ is reduced by the factor of 1.7 and $k_{\perp}$ by the factor of 3.3 when the new and old cavities are compared taking a bunch of σ =1mm The value of longitudinal loss factor of HOM is 4.4 V/pC in the new cavity; that parameter calculated in [3] for old cavity is 8.97V/pC. The transverse loss factor is reduced from 20.6 V/pC/m in old cavity to 6.21 V/pC/m in the new one. The values allowed in TESLA collider design project [7] are as follow: $k_{\parallel HOM} \leq 8$V/pC and $k_{\perp HOM} \leq 18$ V/pC/m for a bunch of σ =1 mm.

2.2 Superconducting Superstructure

The superstructure preserves the shape of TTF single cell but reduces to 7 the number of cells in one cavity. The input and output cell and interconnecting beam tubes are modified to allow the coupling of fundamental passband to the successive cavities. The string of 4 weakly coupled and separately tuned cavities form a basic unit (superstructure) with 28 supermodes. The number of RF power input couplers is thus reduced substantially (by a factor more then 3 in the case of 4 cavity superstructure).

The total length of 200GeV linac becomes shorter by ~ 20%. Those factors directly scale on investment cost reduction . The limited number of cells in cavity provide very important safety margin on field amplitude stability in individual cells.

Since the cavities in superstructure are no longer uncoupled the superstructure must be treated as one unit in wake fields evaluation. The calculations were made for single 7 cell cavity, two cavities and four cavities in superstructure. The wakes induced by 1mm and 0.5mm gaussian beam are illustrated in Fig. 4.

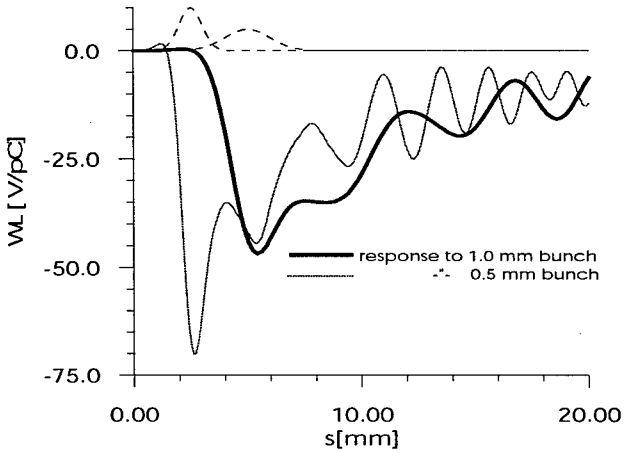

Fig.4 $W_{\parallel}$ wakes in 4 cavities superstructure due to σ =1mm and 0.5 mm gaussian bunch.

Table 3 lists the corresponding loss factors and Fig. 5 show the summed up longitudinal loss factor of 4 cavity superstructure.

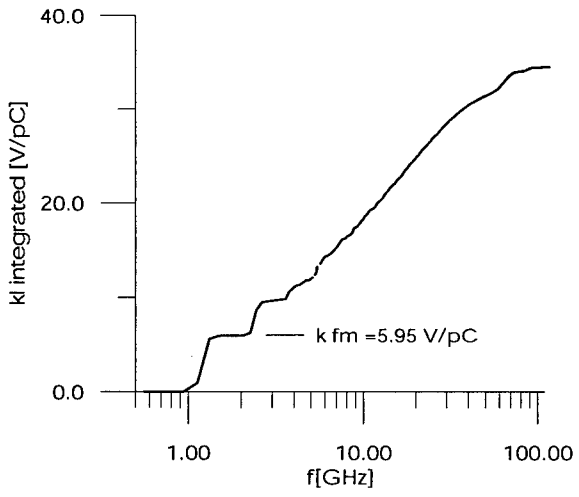

Fig. 5 Integrated $k_{\parallel}$ of superstructure composed of 4 cavities. σ =1mm gaussian; $k_{\parallel\ total}$=34.56V/pC.

To compare the TTF 9-cell cavity and superstructure the ratios of loss factor per 1cell is taken. No obvious difference is found in energy loss factors. The difference in $k_{\parallel}$/cell is within 2%. The gain is in $k_{\perp}$/cell where this parameter is by ~18% lower in superstructure.

Table 3. Longitudinal and transverse loss factors in superstructure

σ bunch	No of cavities	$k_{\parallel}$ [V/pC]	$k_{\perp}$ [V/pC/m]	$k_{\parallel dipole}$ [V/pC/m2]
1 mm	1x7-cell	-10.65	15.29	-10350
1 mm	2x7-cell	-18.64	27.4	-19680
1 mm	4x7cell	-34.73	52.54	-39040
0.5m	7-cell	-18.29	11.7	-16370
0.5m	2x7-cell	-29.17	21.01	-30600
05.mm	4x7cell	-51.17	38.05	-57960

3 SUMMARY AND CONCLUSIONS

The wakepotentials excited in proposed new schemes of accelerating cavities were evaluated and compared. The most favourable is ***large iris 9-cell cavity*** where the losses due to bunch current are lowest. The ***superstructure*** is favorised by arguments of high R/Q, safe margins on electron emission and quench level and by substantial reduction of investment costs in Tesla collider realisation. The room temperature models of 7-cell cavities were built in our Institute and sent to DESY/Hamburg where the working parameters of superstructure will be checked experimentally.

4 ACKNOWLEDGEMENTS

The author wish to thank J. Sekutowicz for the discussions and supplying all necessary data on the new cavities, and Y.H. Chin for advises concerning the use of ABCI code. Author is also indebted to D. Proch and S. Kulinski for their constant interest and support in this work.

5 REFERENCES

[1] J. Sekutowicz, D. Proch, C. Tang, „ Note on the SC Linear Collider TESLA Cavity Design", Reports at the PAC 97, May12-16,1997,Vancouver,Canada.

[2] J.Sekutowicz, C.Tang, M.Ferrario, „Superconducting Superstructure for the TESLA Collider", DESY, TESLA 98-07

[3] E. Plawski, „Wake-fields Induced by the Electron Beam Passing through the TESLA Accelerating System", DESY, June1997, TESLA 97-12

[4] E.Haebel, A.Mosnier. „Large or Small Iris Aperture in SC Multicell Cavities" Proc. of The 5th Workshop on RF Superconductivity, Hamburg 1991

[5] E. Haebel, A. Mosnier, J. Sekutowicz, „Cavity Shape Optimisation for a Superconducting Linear Collider", Proc. of XV International Conf. on HEACC, Hamburg,1992, p.957.

[6] Y.H. Chin, CERN-LEP/TH88-3 Report

[7] D.A. Edwards ed., "TESLA Test Facility Linac-Design Report", DESY TESLA Rep. 95-1

THE FIRST WAKEFIELD TEST ON THE C-BAND CHOKE-MODE ACCELERATING STRUCTURE

T. Shintake, H. Matsumoto, N. Akasaka, M. Yoshida, KEK, Tsukuba, Japan
C. Adolphsen, K. Jobe, D. McCormick, M. Ross, T. Slaton, SLAC, Stanford, CA

Abstract

A full-scale prototype C-band structure for the e+e- linear collider has been built in which the dipole powers are damped to suppress the long-range transverse wakefield. To verify that the damping works as expected, the C-band structure was tested in the Accelerator Structure SETup (ASSET) at SLAC. This paper presents results of the wakefield measurement with ASSET.

1 INTRODUCTION

The C-band scheme being considered at KEK for the 500 GeV to 1 TeV scale linear collider employs multi-bunch beam operation in a high accelerating gradient C-band linac [1]. If no any cares were taken in the accelerating structure, the high-Q transverse dipole mode, mainly TM110 mode, would produce an enormous blow up the transverse motion of the bunch train, resulting in loosing luminosity. In order to damp all the dipole modes in accelerator cavities, the author proposed the choke-mode cavity in 1992 [2]. In this scheme, the beam excited power is eliminated by a microwave absorbing material in the accelerator, thus the dipole modes are damped in each cell for a wide frequency-range. The choke is used as a notch-filter, which traps the rf power within a cavity at the operating frequency, thus a high accelerating field can be generated.

The basic principle of the choke-mode cavity was proved using an S-band model in 1994, where an electron beam was accelerated at the field-gradient as high as 50 MV/m driven by S-band power of 100 MW peak.

From 1996, we started design of C-band RF system, and developed a full-scale prototype for the C-band linear collider. The structure was installed in ASSET at SLAC, and its electrical performance was tested with electron/positron bunches in December 1998.

2 C-BAND STRUCTURE

Figure 1 shows the developed C-band structure, which is composed of the regular section (89 choke-mode cells), input/output couplers attached at each end, and two RF-BPMs for beam position alignment at both end. A wakefield monitor is prepared on the center cell in order to observe the beam induced HOM spectrum, and determine the beam position. To avoid unwanted transverse kick due to asymmetric field, the double-feed coupler using J-shaped waveguide is employed in the input/output couplers [3]. The whole structure is enclosed in a cooling-water jacket made by stainless steel.

2.1 Choke-Mode Cell Design

Figure 2 shows the cut-view of the C-band structure, including the wakefield monitor at the center cell. The beam-induced wakefield-power is damped in the microwave absorbers made by SiC-ceramic, which is mechanically attached in the copper cell with a metal-spring-insert. The design detail is reported in ref. [3].

In order to maximise the damping performance for the lowest dipole mode, the volume of the SiC ring was optimised using computer simulation [4]. Three different sizes of the SiC ring were used in the current design. The wakefield of the whole accelerating structure was approximately estimated by averaging the wakefield calculated at equally spaced 12 points. It was expected that the wakefield would be damped below 0.5 V/pC/m/mm at the second bunch at 2.8 nsec (0.84 m), which is lower than the limit of 0.7 V/pC/m/mm defined by the multi-bunch emittance dilution of 25% in the main linac.

2.2 RF-BPM

In the C-band linear collider, it is necessary to align the accelerating structure with respect to the beam in rather tight tolerances, a high-precision BPM will be attached at the both end of the structure and the transverse positions will be adjusted by fine movers. To limit the emittance dilution below 25% in the main linac, the structure should be aligned with accuracy better than 30 μm and fabricated with straightness within 50 μm.

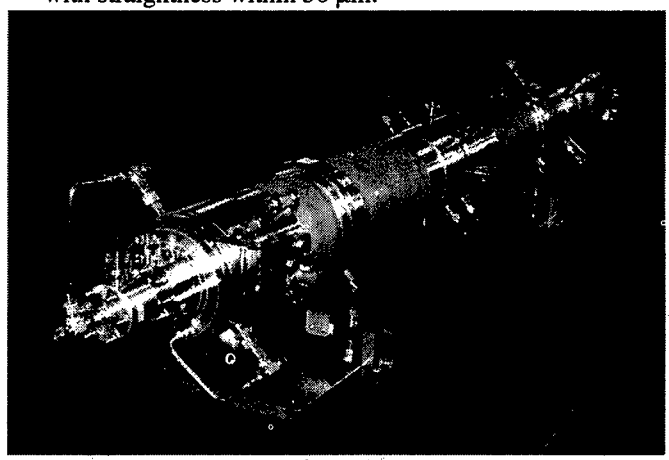

Figure 1: C-band accelerating structure. 2 m long, 91 cell.

0-7803-5573-3/99/$10.00@1999 IEEE.

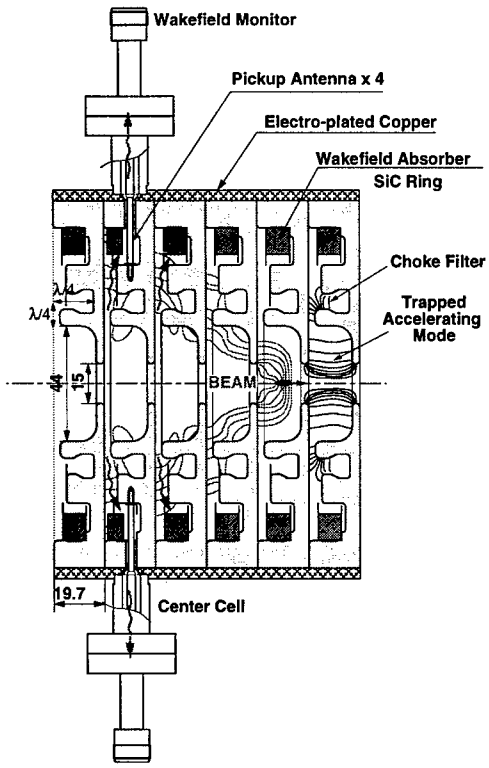

Figure 2: A cut view of the C-band choke-mode structure with a wakefield monitor.

For the C-band accelerator alignment, a new type RF-BPM was developed as shown in Fig. 3, which uses longitudinal slots to cut the common-mode signal from the beam-position signal. To achieve highly accurate BPM, especially to avoid unwanted shift of the electrical center (zero point), elimination of the common-mode power is the most important key [5]. In this new design, reduction of common mode by –40 dB or better can be made.

3 ASSET BEAM TEST

3.1 Wakefield Signal Spectrum

In order to monitor the microwave signal generated by the beam, four pick-up antennas were prepared on the center cell as shown in Fig. 2. The antenna is the straight metal rod, which forms a closed loop together with the ground plane, and couples with the magnetic field behind the SiC absorber. Figure 4 shows the measured spectrum for the

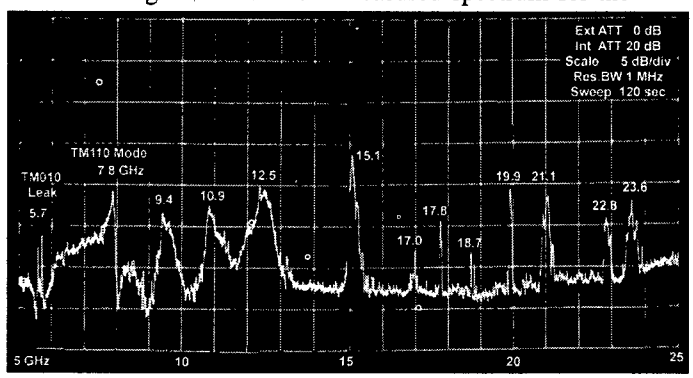

Fig. 4 Measured wakefield spectrum with a horizontal antenna.

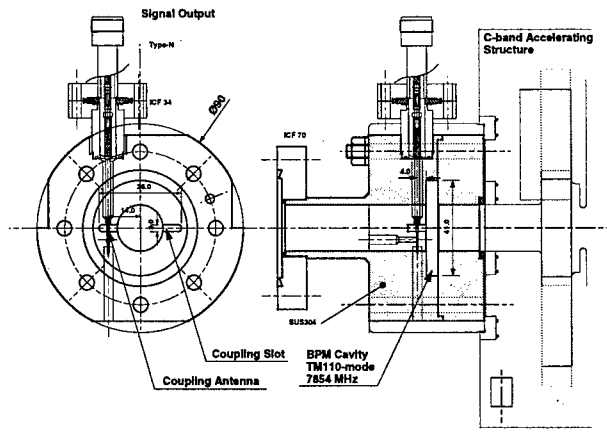

Figure 3: RF-BPM with common-mode less design.

frequency range between 5 to 25 GHz. The sharp peaks at 5.7 GHz are the leakage power from the beam excited dominant accelerating mode. The next peak at 7.8 GHz is the lowest dipole mode (TM110 mode). The measured Q-factor was 36, which is slightly higher than the expected value of 30 estimated with the computer simulation. As shown in Fig. 2, the microwave absorber in the monitor cell has smaller dimension, thus the Q-factor takes higher value than the regular cells. According to the computer simulation, the effective Q for the averaged wakefield is expected as low as 12.

Most of all peaks at higher frequency bands were identified with the simulated spectrum. Exception was a few sharp peaks around 20 - 24 GHz, which were not predicted at design time. The same peaks appeared as a long tail in the measured wakefield as discussed later.

In Fig. 4, the peak at 15 GHz seems to be the highest one, but its power is much lower than the dominant dipole mode at 7.8 GHz. This is due to the characteristic of the pick-up. Since the loop-coupler picks up the time-variation of the magnetic flux:

$$V \propto d\Phi / dt = \omega BS ,$$

A higher frequency component generates a higher output signal for the same intensity of magnetic field.

3.2 RF-BPM Test

Figure 5 shows the circuit diagram of the RF-BPM. The rf signal from two RF-BPMs, the wakefield monitor and the reference cavity are processed with the band-pass filters (7854 MHz, 3% BW), and down converted to 310 MHz signal, finally sampled with 4-ch digital scope (Tektronix TDS684B, 5Gs, 1GBW). The reference signal is used to find the beam timing and the beam phase. The wakefield signal from two pick-up antennas at the center BPM are combined in a 180-deg. hybrid to eliminate the common mode power.

Figure 6 is the correlation plot for three BPMs. The zero-cross point gives the vertical offset of the center BPM with respect to the mean center of the upstream and downstream BPMs. It was +63 μm. By taking account the calibration data, the straightness becomes

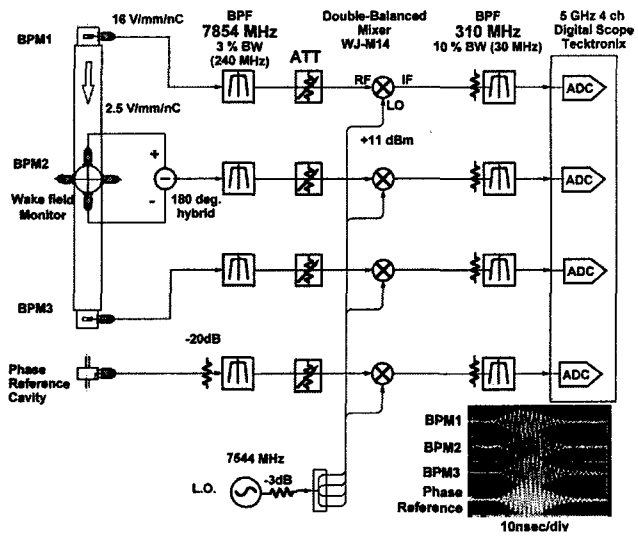

Fig. 5 RF-BPM detector circuit.

49 μm. This is just border of design tolerance. On the other hand, the straightness mechanically measured from outside was 90 μm. We need further study before concluding these test results, such as measurement of the straightness using laser-beam from inside of the structure. The observed spatial resolution was about 8 μm, which was limited by high digital noise in the sampling-scope.

3.3 Wakefield Measurement

We measured the wakefield generated in the C-band structure with the same method as done in the X-band structure R&D. The layout of the ASSET and detailed procedure are found in elsewhere [6].

We injected the positron beam first as a drive bunch, which extracted from the South Damping Ring. The bunch passed through the C-band structure and was then steered into a dump. Right after the positron, the electron bunch was injected from the North Damping Ring and the deflection angle due to the wakefield was measured with the BPMs in the linac. The measured data is shown in Fig. 7. The measured wakefield damps according to the expected waveform (solid line) up to 1.6 nsec (0.5 m) from about 15 to 1 V/pC/m/mm. However, after this

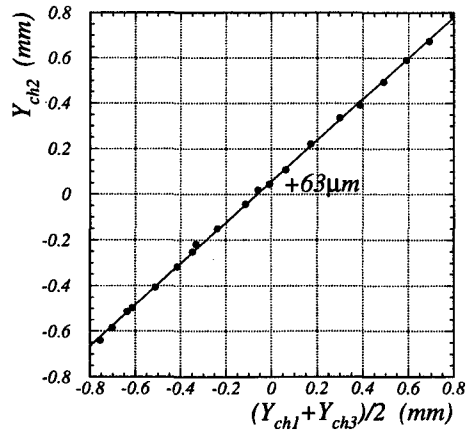

Fig. 6 Correlation plot on three BPM readout.

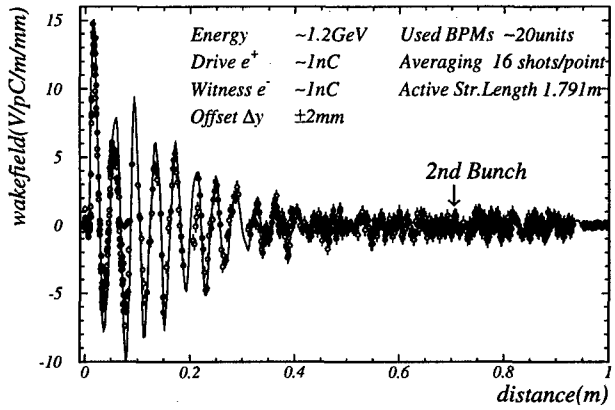

Fig. 7 Measured (circle) and expected (solid line) wakefield.

point, the measured wakefield showed a high frequency oscillation with an amplitude of 0.8~1.0 V/pC/m/mm. This is just the border-line of the 25% emittance dilution. Applying FFT, we found that the oscillation corresponds to the spectrum peak at 20, 23 GHz. With computer simulations, it was found that in some condition the mode can be trapped in the cavity at very high-frequency, whose field pattern has a node-point at the slot location, thus no power can leak out to the damper. This was caused by our design change. To improve the shunt-impedance by about 10%, we changed the disk thickness from 4 to 3 mm. However, the mode pattern in the cavity moved in z-direction, and occasionally created a node at the coupling slot. To solve this, we will shift z-location of the damping slot by 2 mm. With careful simulations, it was shown that the trapped mode could be eliminated. The new model is under design.

4 ACKNOWLEDGEMENT

We would like to thank Prof. David Burke for his encouragement, and Charles Yoneda, Leo Giannini, Leif Eriksson, Tony R. King, M. W. Perry, J. R. McDougal for their help in structure installation.

5 REFERENCES

[1] T. Shintake et al. ,"C-band RF Main Linac System for e+e- Linear Collider at 500 GeV to 1 TeV C.M. Energy", EPAC96, KEK Preprint 96-68, and K. Yokoya et al., "C-band Linear Collider with C.M. Energy 500 GeV to 1 TeV"

[2] T. Shintake, "The Choke Mode Cavity", Jpn. J. Appl. Phys. Vol.31, pp. L1567-L1570, Part2, No.11A, 1992

[3] H. Matsumoto, T. Shintake and N. Akasaka, "Fabrication of the C-band (5712 MHz) Choke-Mode Type Damped Accelerator Structure, LINAC98, KEK Pre-print 98-143.

[4] N. Akasaka T. Shintake and H. Matsumoto, "Optimisation on Wakefield Damping in C-band Accelerating Structure", LINAC98, August 23-28, Chicago, IL, KEK Pre-print 98-142

[5] T. Shintake, "Development of Nanometer Resolution RF-BPMs", HEACC98, Sept 1998, Dubna, Russia, KEK Pre-print 98-188.

[6] C. Adolphsen, et al., "Measurement of Wakefield Suppression in a Detuned X-band Accelerator Structure", LINAC94 Proc., p481

DEVELOPMENT OF THE X-BAND RF POWER SOURCE FOR JLC

Y. H. Chin[1], M. Akemoto, S. Fukuda, S. Matsumoto, S. Michizono, H. Mizuno, K.Takata, N. Toge, S. Tokumoto, H. Tsutsui, S. Yamaguchi, and J. Wang, KEK, Tsukuba, Japan
S. Kazakov, BINP, Protvino, Russia

Abstract

In this paper, we summarize our activities on X-band RF power source development for the Japan Linear Collider (JLC) project. First, we have designed and tested a solenoid-focused klystron at 11.424 GHz with a pulse length of 1.5 μs and with an efficiency of 47%. A periodic permanent magnet (PPM) klystron, the first in that kind at KEK, is also under development. In parallel to this activity, another PPM klystron has been developed and remodeled in collaboration with BINP. Second, a new RF window with 100-MW power-handling capability has been designed and tested. It utilizes the TW mixed mode (TE11 and TM11 modes) to reduce the surface field at the brazing edge of the ceramic. The cold model test shows a low electric field at the brazing point as predicted by HFSS calculations. The high power model is now in manufacturing and the testing will start soon. Third, the Blumlein modulator was upgraded to produce a pulse with 2 μs flat top and 200 ns rise time at 550 kV output voltage. Fourth, the multi-mode 2x2 DLDS (Delay Line Distribution System) pulse compression system has been designed, and its basic unit was manufactured and tested for proof of the principle. The measurement results show that the system works well with a high power distribution efficiency. The so-called mode stability experiment is also under preparation in the ATF linac tunnel in collaboration with SLAC. This experiment is aimed for examination of the stability of linearly polarized TE12 mode in a 55m long waveguide, a key issue in the present configuration of multi-mode DLDS. Details of these developments and measurement results are presented.

1 KLYSTRON

The 1-TeV JLC (Japan e^+e^- Linear Collider) project[1] requires about 3200 (/linac) klystrons operating at 75 MW output power with 1.5 μs pulse length. The main parameters of solenoid-focused klystron are tabulated in the second column of Table 1. The 120 MW-class X-band klystron program at KEK[2], originally designed for 80 MW peak power at 800 ns pulse length, has already produced 9 klystrons with solenoidal focusing system. To reduce the maximum surface field in the output cavity, the traveling-wave (TW) multi-cell structure has been adopted since the XB72K No.6. Four TW klystrons have been built and tested. All of them share the same gun (1.2 microperveance and the beam area convergence of 110:1) and the buncher (one input, two gain and one bunching cavities).Only the output structures have been redesigned each time. XB72K No.8 (5 cell TW) attained a power of 55 MW at 500 ns, but the efficiency is only 22%. XB72K No. 9 (4 cell TW) produced 72 MW at 520 kV for a short pulse of 200 ns so far. The efficiency is increased to 31%. The limitation in the pulse length attributes a poor conditioning of the klystron.

Table 1: Specifications of X-band solenoid-focused and PPM-focused klystrons for JLC.

	XB72K	PPM
Operating frequency (GHz)	11.424	11.424
RF pulse length (μs)	≥ 1.5	≥ 1.5
Peak output power (MW)	75	75
Repetition rate (pps)	120	120
RF efficiency (%)	47	60
Band-width (MHz)	100	120
Beam voltage (kV)	550	480
Perveance ($x10^{-6}$)	1.2	0.8
Maximum focusing field (kG)	6.5	
Gain (dB)	53-56	53-56

The latest tube, XB72K No.10, was designed at KEK, and has been build in Toshiba. The testing started from January 1999. It produces 29MW power at 379kV at 1.5 μs pulse length, 16% larger than the prediction. The output RF signal is shown in Fig. 1.

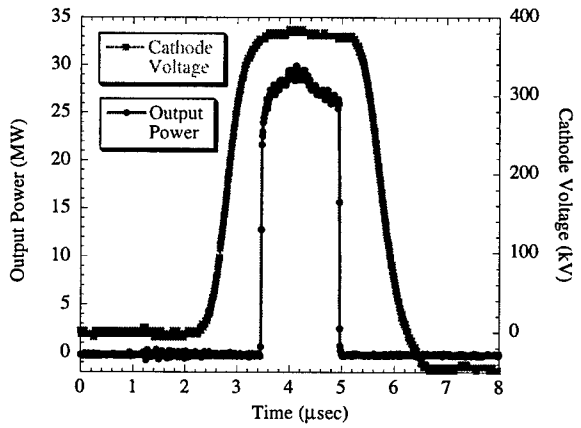

Figure 1: Output power and cathode voltage signals from XB72K No.10.

[1] E-mail: yongho.chin@kek.jp

0-7803-5573-3/99/$10.00@1999 IEEE.

At the beam voltage over 380kV and without input power, the oscillation signal is observed at 20.7 GHz in the spectra of the output RF signal and the signal reflected from the input. When the input power is increased, the oscillation signal disappears up to the cathode voltage of 390kV. The slight increase of the magnetic field down the drift space changes the signal frequency to 20.7 GHz. The measured perveance was found to be 20% larger (about 1.4μ) than the design value. It turned out that the manufactured gun has a wrong dimension, with no effects of the thermal expansion taken into account. The cathode and the wehnelt are closer to the anode by 1-2mm than the design, and their radial sizes are larger by 0.5-1 mm. As the result, the emitted beam has a 15% larger beam size than the design value, and has a large scalloping due to the mismatch with the focusing field. The fatter beam increases the coupling with the cavities: the measured gain is about 8 times larger than the design value. The analysis shows that the large scalloping pronounces the driving power to the parasitic modes in the range of 21 GHz. Further analysis and measurements are in progress.

Apart from the solenoid-focused XB72K series, KEK has also started a PPM (periodic permanent magnet) klystron development program. The design parameters are shown in the last column of Table 1. Its goal is to produce a 75MW PPM klystron with an efficiency of 60 % at 1.5 μs or longer pulse. The first PPM klystron was designed and built by BINP in the collaboration with KEK. It achieved 77 MW at 100 ns, but there is a clear sign of RF instability at higher frequencies (17GHz, 19.5GHz, and 21.2GHz). The DC current monitor in the collector shows about 30 % loss of particle when RF is on. The remodeling of the BINP PPM klystron has been made: the new buncher produces the RF current of 1.62. The inner walls of the output cavity and every tube between the cavities are brazed to stain-less steel to dampen trapped oscillations. The small solenoid magnet to control the focusing field to stop the particle interception replaces the periodic permanent magnet at the output cavity. The testing of the rebuild PPM klystron will start from fall of 1999.

2. RF WINDOW

All the windows with traveling waves (TW) in the dielectric use only one-mode. Namely, RF energy is carried by only one mode - either TE11, or TE01. The idea exploited in the development of a new window is to arrange the combination of space harmonics on the dielectric surface so that the electric field strength value almost vanishes at the brazing area. At the same time, the mode propagation regime in the dielectric is maintained to be close to that of pure traveling waves. Based on this idea, the windows for 11424 MHz have been developed with the dielectric 53 and 64 mm in diameter [3]. The permittivity was assumed to be equal to 9.8, i.e. that of Al_2O_3 ceramics. The dielectric thickness was chosen to be close to 1/4-wavelength to ensure the maximum bandwidth and the maximum tuning away of the operating frequency from the "ghost" modes. With the diameter 53 mm, the dielectric thickness becomes 2 mm, whereas it is 2.15 mm for 64 mm. All the computations were done using HFSS 4.0 code. The shapes of the window with 53 mm diameter is illustrated in Fig. 2.

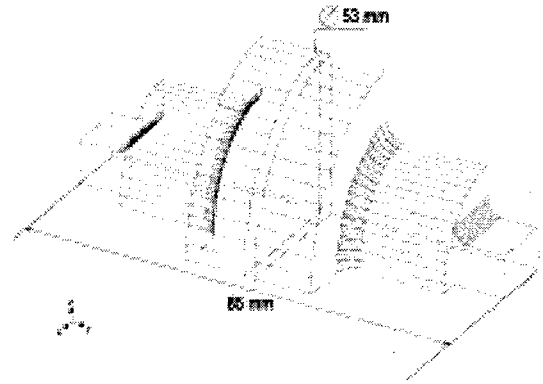

Figure 2: Shape of the TE11+TM11 mixed-mode type window with 53mm diameter.

Figure 3 shows the measurement results of ratio of electric field at the brazing point to that at the ceramic center for TE11+TM11 mixed-mode type window. The electric field decreases toward the ceramic surface as designed. The closest distance was limited by the finite size of the used bead. The high power model is now in manufacturing and the testing will start in summer 1999.

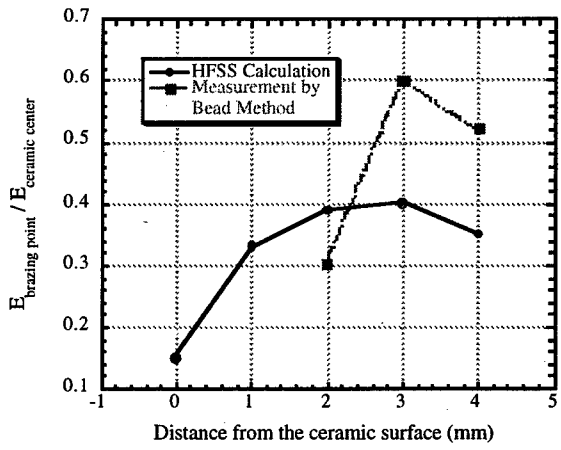

Figure 3: Measurement results of ratio of electric field at the brazing point to that at the ceramic center for TE11+TM11 mixed-mode type window with 53mm diameter.

3 DLDS PULSE COMPRESSION

The Delay Line Distribution System (DLDS) was invented by KEK for the compression and distribution of the RF power from klystrons to RF structures. In DLDS, the long pulse of combined klystron output is subdivided into a train of shorter pulses and each subpulse is delivered to accelerating structures through a delay line distribution system. This system utilises the delay of the electron beam in the accelerator structure of the linear collider to reduce the length of the waveguide assembly. A conceptual improvement is proposed by SLAC to further reduce the length of waveguide system by multiplexing several low-loss RF modes in a same waveguide. Thus, the subpulse in the distribution waveguide is carried by different waveguide modes so that they can be extracted at designated locations according to their mode patterns. Based on the SLAC multi-mode DLDS, a 2×2 DLDS [4] is proposed at KEK for JLC. The advantage of 2×2 DLDS is that it's simple and easy to be expended to accommodate combinations of more klystrons, and also it has good transmission efficiency.

A test unit is proposed and studied to verify the principle of multi-mode 2×2 DLDS[5]. It includes the TE01-TE11 mode launcher, the TE01 extractor and the TE11 to TE01 converter. Fig. 5 is the schematic layout of the unit.

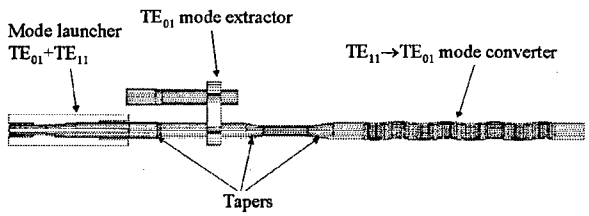

Figure 4: Schematic layout of the basic 2×2 DLDS unit.

Fig. 4 shows the electric filed pattern propagating in the system. The power of TE01 mode is extracted to a parallel waveguide with efficiency better than 96% as shown in Fig. 4(a), while the power of TE01 mode goes through the extractor directly and then is converted to again to TE01 as shown in Fig. 4(b). The transmission efficiency is better than 95%. All the above components have been manufactured. The low power test has been conducted. Figure 6 shows the measurement of azimuthal angle (along the circular waveguide) dependence of TE11 mode from the mode launcher. It has an almost pure sinusoidal shape of TE11 mode as designed.

In order to reduce the resistive loss in long distance transmission, the low loss TE12 mode is considered in the circular waveguide. The experiment to test the stability of TE12 mode propagating for long distance i.e. its sensitivity to all kinds of perturbations is being planed at the ATF tunnel as the joint activity between KEK and SLAC. The main purpose is to measure the purity of linearly polarized TE12 mode (largeness of rotation and conversion to other modes) in a 55m long waveguide whose diameter is 4.75 inches. To detect the change in the phase advances due to thermal expansion of waveguide, a special phase reference system has been designed and is being manufactured. The experiment is scheduled to be conducted in summer 1999

(a) TE_{01} mode input from left.

(b) TE_{11} mode input from left.

Figure 5: Electrical field patterns in the test unit.

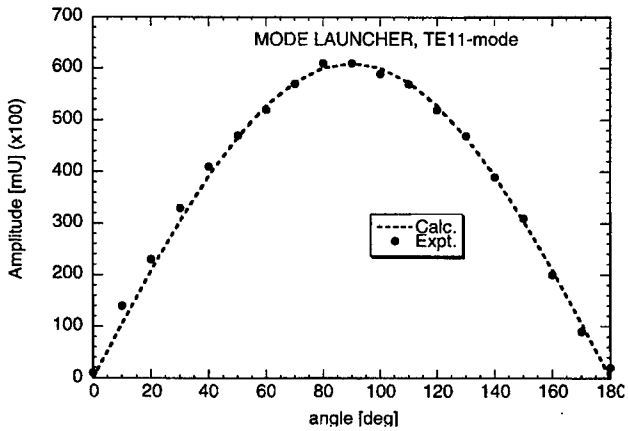

Figure 6: Measured azimuthal angle dependence of TE11 mode from the mode launcher.

4 REFERENCES

[1] "JLC Design Study", KEK Report 97-1, 1997.
[2] Y. H. Chin, et al., "Modeling and Design of Klystrons", in Proc. of LINAC98, 1998.
[3] S. Y. Kazakov, KEK Report 98-120, 1998.
[4] Y.H.Chin.et.al.,LCC-005, http:/lcdev.kek.jp/JLC/ISG/ISG2.html
[5] J. Q. Wang et al., "Design of 2x2 DLDS RF Components for JLC", ICAP98, Monterey, 1998.

CHALLENGE TO A STRAIGHT STRUCTURE FOR X-BAND LINEAR COLLIDER

K. Asano* , Y. Funahashi, Y. Higashi, T. Higo# , N. Hitomi, T. Suzuki, K. Takata,
T. Takatomi, N. Toge, Y. Watanabe
KEK, High Energy Accelerator Research Organization, Oho 1-1, Tsukuba, Ibaraki, 305-0081, Japan

Abstract

The structure of the X-band main linac for the linear collider requires a stringent straightness of the order of several microns. Especially the misalignment from cell-to-cell to over twenty cells should be minimized. An one-shot diffusion bonding technology has been developed at KEK aiming at this requirement. Two 1.3m-long detuned structures have been made with a gentle bow of 20 microns. Recently the technology was applied to the main body bonding of an 1.8m-long damped-detuned structure, DDS3. It resulted in a much larger bow but the cell misalignment showed very smooth behavior and can later be corrected mechanically. The technique is being refined to obtain a better performance of the main body of the round DDS structure, RDDS1. In the present paper are described the studies on the basic techniques applied for DDS3.

1 INTRODUCTION

For preserving a very low emittance through a linac for linear collider in a multi-bunch operation, it is essential to reduce the emittance dilution due to the long-range transverse wake field. For this aim, the frequencies of the transverse modes in an accelerating structure should be well distributed as designed and also the position of those modes should be located transversely within several microns level.

Several detuned structures were fabricated up to now to study the feasibility of realizing these requirements in X-band disk-loaded structures[1]. From these experiences, it was found that the one-shot diffusion bonding technology for joining the precisely machined cells to form a solid structure of one-meter size was very promising to meet the above requirements[1,2]. These structures were 80 mm in diameter and 1.3m in length. Frequency change due to bonding was small enough and the straightness were 10 to 20 μm, also satisfying the above requirements.

However, we decided to change the design of the structure to decrease the single-bunch wake field and to reduce the number of structures for a linac by enlarging the beam hole aperture and making the structure long. This decision was made in a collaborative work with SLAC[3]. The structure length became 1.8m. We also accepted the cell diameter of 61 mm as a working assumption.

Though it seems reasonable to choose the above mechanical parameters, the thin body makes the structure stiffness much lower than before. The geometrical moment of inertia of its cross section became small by a factor of 3. In addition, the long body makes its bow larger. If the structure is supported at both ends in a horizontal position, the sag due to self-weight becomes larger than before by a factor of 8. Considering this dependence into account, it was estimated that the structure of the present design may suffer from a difficulty in obtaining a good straightness than before.

On the other hand, we have supplied the cells for two 1.8m-long DDS structures for SLAC with 61 mm in diameter. In the first step, each 38-cell stack is bonded followed by the second step, where several stacks are brazed into a structure. It suffered from kinks between 38-cell stacks. In making the third structure, DDS3, we agreed to apply the same one-shot bonding method for its main body formation to realize a smoother variation of cell misalignment. This time LLNL made the cells where such a key characteristics as cell flatness of 0.5 μm, necessary for diffusion bonding, was surely realized [4].

In the present paper, we describe the studies and measurements done for stacking and bonding cells focusing on the cell misalignment.

2 STUDY PROCEDURES

One of the relevant issues of DDS3 is the straightness of the cells along the structure. A tolerance estimation[5] for the cell random misalignment along the structure shows about 5 μm rms misalignment tolerance in a regime from cell-to-cell to over than 10 cells. The tolerance for a longer wave length in misalignment relaxes as the wave length increases. Moreover, the global bow with a long wave length can easily be corrected through a mechanical measurement and forced bending before installation. Considering these in mind, we set targets for cell rms alignment of DDS3 as (1) cell-to-cell alignment to a few μm and (2) global one to 10 μm.

A dummy structure, DDS3D1, was firstly fabricated in order to confirm the method for DDS3. It was made directly following our previous technique, i.e. stacked on V-block, axially compressed at about 24 kg, then rotated to vertical position to be one-shot diffusion bonded (DB) at a high temperature. Unfortunately a bad design of jigging caused a big failure. Then, we tried to find the

* Present address: Electrical Engineering Department, Akita National College of Technology, 1-1 Iijima-bunkyo-cho, Akita-shi 011-8511, Japan.
# e-mail address: higo@mail.kek.jp

0-7803-5573-3/99/$10.00@1999 IEEE.

method for obtaining a smooth structure with least possibility to have fatal errors again.

It was known already then through a pilot study of pre-bonding process (PB) that it could make a fairly smooth 1.8m-long structure with 61 mm in diameter[6]. In the method the cells are bonded with axially pressed by 600 kg force and kept in a furnace at 180 °C for a day. This makes the bonding between cells which prevents further mutual movement in the following process such as a final diffusion bonding.

We decided to take the advantage of this technique for DDS3. For investigating relevant parameters and getting experiences, we made another dummy structure, DDS3D2, before making DDS3. Following table shows the processes for those structures and some of results on misalignment of cells.

Table 1 List of processes for three structures.

Structure	DDS3D1	DDS3D2	DDS3
Cell	Cylindrical	3D	3D
V block	Granite	Cr / Fe	Cr / Fe
1st Bonding	DB	PB	PB
2nd Bonding	None	DB	DB
Inclination	<0.2 mrad	~0.5mrad	~1 mrad
Bow(P-V)	~10 mm	0.5 mm	0.23 mm
cell-to-cell(rms.)	-	-	< 1 μm

DB=diffusion bonding at 890 °C, PB=pre-bonding at 180 °C for two days.

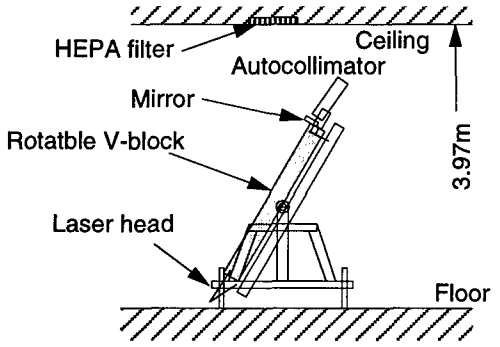

Fig. 1 Stacking set up in a clean room.

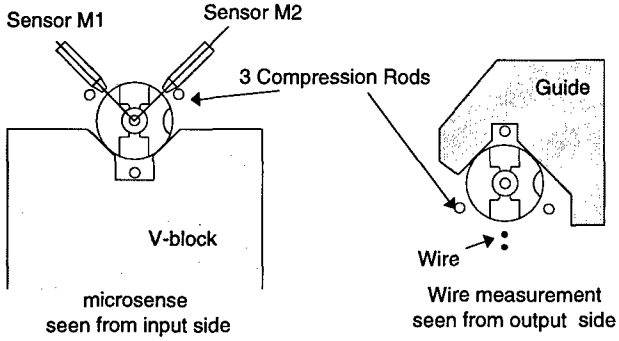

Fig. 2 Alignment measurement setup. Left: Capacitive sensors running along the V-block. Right: Vertically standing situation to measure the gap to a stretched wire.

A schematic drawing of the set up for stacking and measurement is shown in Fig. 1. The cells are stacked on a slanted V-block, typically at 60 degrees from horizontal, where the cell misalignment is also measured by running two capacitive gap sensors along the V-block as shown in Fig. 2(Left). The stacked cells and bonded ones are also measured in a vertical position by measuring the gap between the cells and a vertically stretched wire. These configurations are shown in Fig. 2(Right).

3 RESULTS

The quality of cells in three structures were similar; i.e. flatness of cells were mostly less than 0.5 μm as shown in Fig. 3.

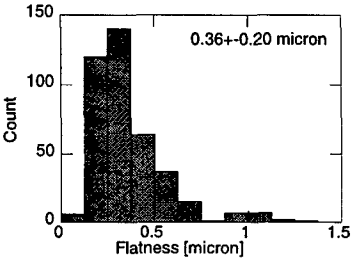

Fig. 3 Flatness of DDS3 cells. Average value and standard deviation are 0.36 and 0.20 μm, respectively.

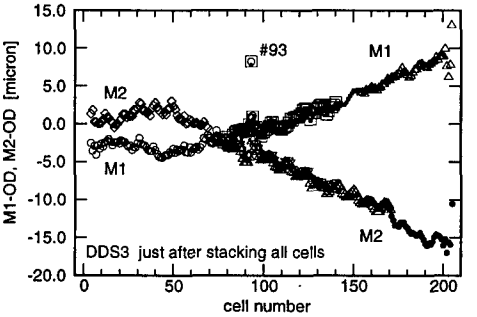

Fig. 4 Typical alignment of cells of DDS3 after stacking. Transverse constraint was applied during measurement.

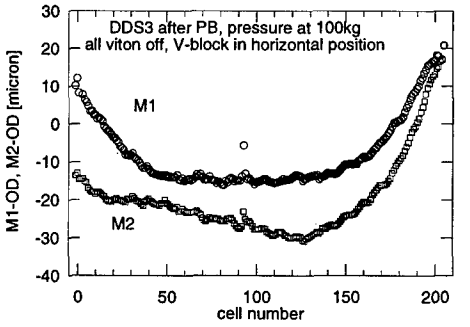

Fig. 5 Misalignment of cells after pre-bondingof DDS3.

Fig. 4 shows a typical example of the cell alignment of DDS3 just after stacking on a slanted V-block. A constraint against the transverse motion of cells was applied by Viton plates backedby stainless plates. In this case, the stacked-cellpillar was stable even if axial force of 100 kg was applied.

However, after pre-bonding process, the alignment of the structure became as shown in Fig. 5, where the alignment pattern changes by a few tens of microns. This measurement was performed by reducing the axial force to 100 kg. After diffusion bonding, the alignment became as shown in Fig. 6, where the structure was supported at two Bessel points without any axial force. Much larger global bow of about 230 μm was found to be in a plane, almost horizontal direction w.r.t. V-block.

The bow is huge but the random cell-to-cell alignment is less than 1 micron (rms) as shown in Fig. 7, where the slowly varying part from Fig. 6 was subtracted through a third-order polynomial fitting.

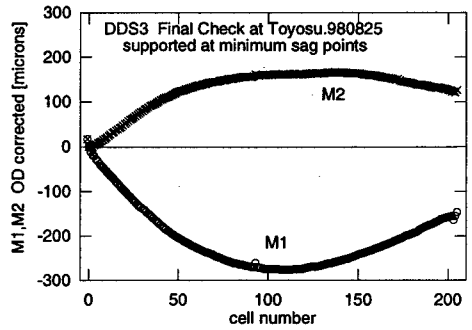

Fig. 6 Misalignment of cells after diffusion bonding of DDS3.

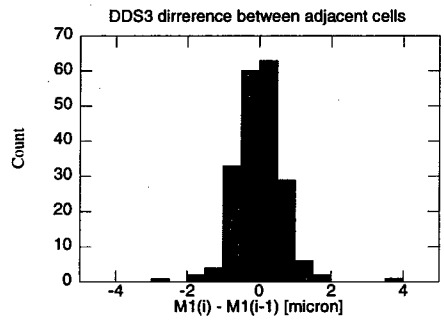

Fig. 7 Distribution of random cell-to-cell misalignment of DDS3 cells in a direction of one of the sensors.

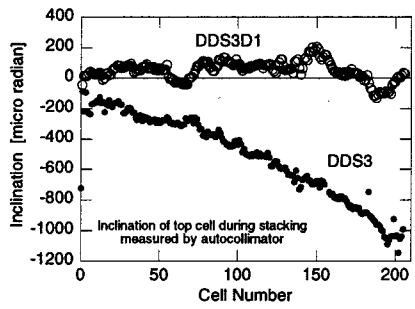

Fig. 8 Inclination of the lastly-stacked cell on top. Negative values mean falling down towards V-block.

An important issue was discussed after SLAC's measurement of a big bookshelf of the order of 500 μrad in DDS3[7]. The observed bookshelf seems consistent within a factor of two to the measured inclination of the top cell while stacking shown in Fig. 8. It is to be noted that the inclination in the case of DDS3D1 did not show the similar pattern, while it did in the DDS3D2 case, indicating the cause from the different processes before bonding. The relevant differences between the two cases are such as material of V-block and cylindrically symmetry of the cells, which should be studied in future.

4 SUMMARY AND DISCUSSION

Much experience was obtained through the three structure fabrications and these are feedback to the studies towards an on-going program, RDDS1.

The DDS3 main body bonding was successfully done with applying the pre-bonding process followed by a high-temperature diffusion bonding. The structure became smoothly bent with a maximum of 230 μm in a plane but the random cell-to-cell slippage was less than 1 μm (rms). These features satisfy the required cell alignment tolerance because mechanical straightening can be performed. However such a straightening by a factor more than 10 is probably too much so that we should develop a method to make a structure with a bow at most several tens of microns.

The bookshelving became as large as 1mrad in DDS3. Mechanism and cures should be studied to suppress it down to a tolerable level of 50 μrad.

Now we are preparing the RDDS1 following basically the same technology. So it may refrain the same bad features but the fabrication is planned to proceed more carefully such as by (1) checking the inclination in both directions, (2) checking bookshelf not only at the top cell but also at the already stacked cells, (3) stacking cells on a more stable base, (4) pressing axially with less transverse component and (5) making a better transverse constraint.

5 ACKNOWLEDGMENTS

This program was proceeded in a collaboration among three laboratories, Stanford Linear Accelerator Center (SLAC), Lawrence Livermore National Laboratory (LLNL) and High Energy Accelerator Research Organization (KEK). The authors greatly acknowledge those who support this collaboration.

All processes were done at Ishikawajima-Harima Heavy Industries (IHI) directed by KEK. It was proceeded as one of the contracts, but the authors want to express much thank to those staffs of the company for making great efforts to successfully complete this series of jobs.

6 REFERENCES

[1] T. Higo et al., Proceedings of The First Asian Particle Accelerator Conference, APAC98, Tsukuba, Japan.
[2] JLC Design Study, KEK Report 97-1, 1997.
[3] T. Raubenheimer and K. Yokoya, LCC-0003, SLAC, 1998.
[4] J. Klingmann et al., in this conference, MOP51, PAC99, 1999.
[5] G. Stupakov, presentation at ISG3, SLAC, Jan. 1999.
[6] N. Hitomi, presented at ISG1, SLAC, Jan. 1998, LCC-0002.
[7] C. Pearson, presented at ISG3, SLAC, Jan. 1999.

SLAC HIGH GRADIENT TESTING OF A KEK X-BAND ACCELERATOR STRUCTURE*

R.J. Loewen#, A. Menegat, A.E. Vlieks, J.W. Wang, SLAC, Stanford, CA
T. Higo, KEK, Tsukuba, Ibaraki, Japan

Abstract

The high accelerating gradients required for future linear colliders demands a better study of field emission and RF breakdown in accelerator structures. Changes in structure geometry, vacuum pumping, fabrication methods, and surface finish can all potentially impact the conditioning process, dark current emission, and peak RF power handling capability. Recent tests at SLAC of KEK's "M2" travelling wave x-band accelerator section provides an opportunity to investigate some of these effects by comparing its performance to previously high power tested structures at SLAC [1,2]. In addition to studying ultimate power limitations, this test also demonstrates the use of computer automated conditioning to reach practical, achievable gradients.

1 ACCELERATOR STRUCTURE

The design parameters of the M2 accelerating section are outlined in Table 1. The structure cells were manufactured by diamond turn machining, assembled in a clean room, and diffusion bonded. Complete details of the fabrication process are described in the KEK JLC Design Report [3]. For comparison, an earlier tested 1.8m SLAC x-band section (DS1) was built with conventional machining, assembled with little control over cleanliness, and brazed using standard techniques.

Table 1: M2 Design Parameters.

Structure Type	Detuned
Length	1.31m
Cell Number	150
Phase Advance/Cell	$2\pi/3$
Iris Aperture Diameter	5.35–3.67 mm
Cavity Diameter	22.5–21.3 mm
Disk Thickness	0.966–2.39 mm
Group Velocity	$1.03c$–$0.020c$
Filling Time (measured)	113 ns
Attenuation Parameter	0.609
Shunt Impedance R0	79 MΩ/m
Average Q	6300
Peak Power for 73 MV/m	130 MW
E_{surf}/E_{acc}	2.15

Just prior to high power testing, the structure was baked at 250°C for 2 days. It had been stored under vacuum of 10^{-9} torr for approximately 24 months after a wakefield ASSET [4] test conducted at SLAC in Aug. 1996.

2 TEST FACILITY

Two 50 MW x-band klystrons operating at 11.424 GHz and 1 μs pulse width combine in a magic tee to feed a SLED-II pulse compression system. The output 150 ns rf pulse then feeds the accelerator structure test area (ASTA). All system components before the accelerator structure were previously tested to more than 300 MW at this pulse width at a repetition rate of 60 Hz [5]. At this power, the average accelerating field in the M2 structure would be well over 100 MV/m.

Pairs of vacuum pumps located near the input and output couplers monitor gas activity. Since there is no pumping in the structure cells, these pumps, along with the beam line pump, supply the limited pumping speed for the bulk of the structure.

SLED and structure input powers are measured with a HP peak power meter. A crystal detector measuring reflected power is interlocked to remove triggers to the low-level drive of the klystrons for reflected peak power exceeding 5 MW. This interlock is meant to protect the klystron windows but it also prevents large gas bursts in the accelerator structure caused by multiple arcing.

One downstream faraday cup measures dark current and another off-axis faraday cup measures the dark current energy spectrum using a spectrometer. Radiation levels are monitored with 3 scintillators along the structure and a calibrated radiation meter measures contact levels at the input or output ends.

3 EXPERIMENTAL RESULTS

3.1 Conditioning Summary

Over the several week test, the high voltage running time meter logged more than 560 hours of which an estimated 440 hours can be considered as actively processing. At the 60 Hz repetition rate, this time gives approximately $1\text{x}10^8$ total pulses—a factor of 4–5 greater number of pulses than in previous structure tests at SLAC.

*Work supported by the Department of Energy, contract DE-AC03-76SF00515.
#Email: loewen@slac.stanford.edu

A PC system running LabVIEW handled the majority of processing by adjusting power levels based on structure vacuum and reflected arc interlock trips. Details of the algorithm are beyond the scope of this paper but the overall strategy for conditioning remained consistent between operator and computer control. The first 100 hours were mainly processed by hand to the 60 MV/m level. During this time, as indicated in Fig. 1, the SLED compression was not phased for maximal gain in order to allow average power heating to help outgas the structure.

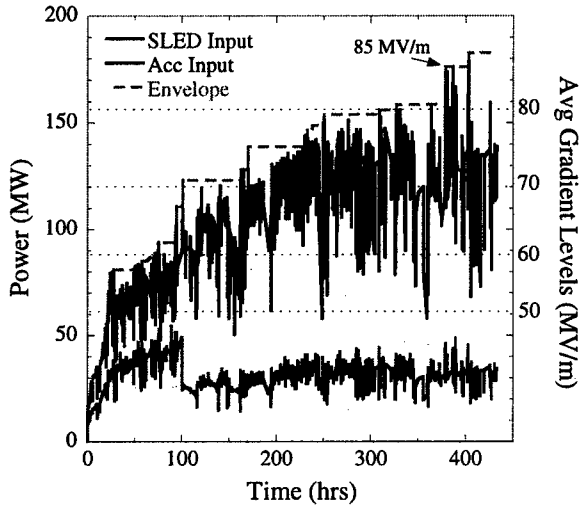

Figure 1: M2 active processing history.

Even at a conservative pace, only 20 hours were required to reach 50 MV/m average gradient and the structure suffered only a handful of reflected power trips due to rf breakdown. At higher powers, once arcing started, gas bursts and vacuum recovery limited progress. After the first 150–200 hours, gas activity associated with breakdown became quite negligible and only reflected trips prevented advancement. Although progress slowed dramatically, continued processing still seemed to increase achievable peak power. Reversing the axes of the previous plot reveals an exponential behaviour.

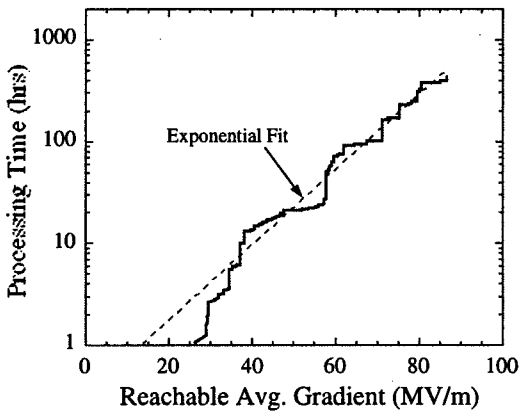

Figure 2: Time required to reach desired gradient using monotonic envelope from Fig. 1.

3.2 *High Gradient Performance*

At the end of testing, average gradients reached 85 MV/m and was sustainable for ~10 seconds before arcing. At 75 MV/m, however, the structure ran for one hour without any arc trips. Previous tests of SLAC's 1.8m DS1 structure reached gradients of only 68 MV/m and were limited by available power. Both structures showed similar patterns in processing difficulty, dark current emission, and dark current energy spectrum. Figure 3 compares the two structure's peak dark current readings from the downstream faraday cup. To evaluate the real difference between the two curves, corrections must be made for structure length, iris size, and cut-off hole size. Estimating these corrections, the structures may be within a factor of 2, with the leftover difference most likely attributable to cleanliness.

The dark current measured at a particular gradient did not steadily improve during processing as was witnessed in the DS1 tests. The M2, however, was constantly being pushed to reach higher power. Also note that the M2 dark current appears to deviate from expected values at very high gradients.

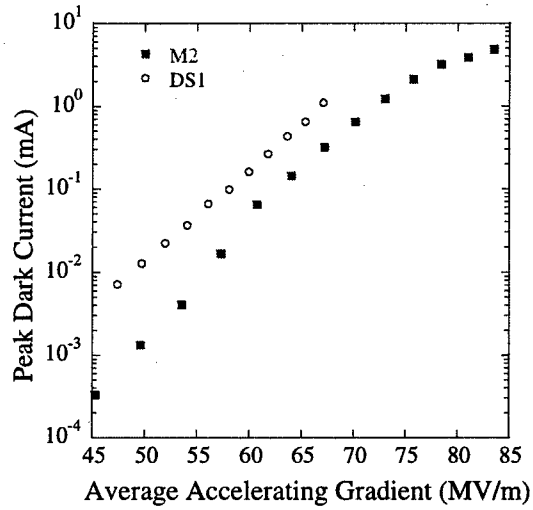

Figure 3: M2 and DS1 dark current comparison.

3.3 *Visual Inspection*

A conservative estimate of 3000 arcs occurred at average gradients over 50 MV/m. Once the high power test finished, the structure was visually inspected with a boroscope to evaluate the extent of damage to the cells.

Figure 4 compares sections of input and output cell irises. The output end showed no discernible damage to the cells; the copper still had a polished surface with grain boundaries easily identified. In marked contrast, the input cells were heavily damaged (but only the first 30 cells could be viewed); the cell irises were completely pitted with no signs of the original machined surface finish remaining. Both ends of the structure reached equivalent

average gradients, but the dynamics of rf breakdown seem to protect the downstream cells from arcing at the expense of cells upstream.

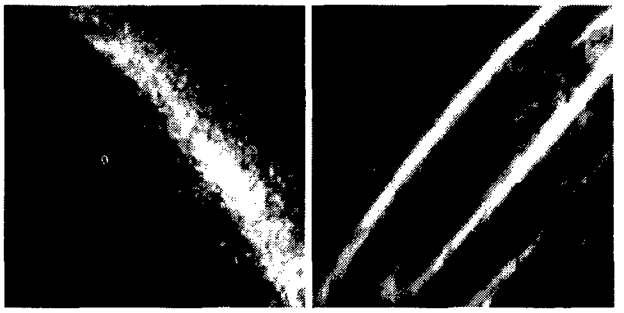

Figure 4: Typical cell irises near input (left) and output (right) of structure.

3.4 RF Evaluation

Degradation in rf performance was evaluated by bead-pull measurements [6] before and after high power testing. Figure 5 plots the integrated phase error of the accelerating mode as a function of position along the structure. The most dramatic changes occurred at the beginning cells in agreement with the visual evidence.

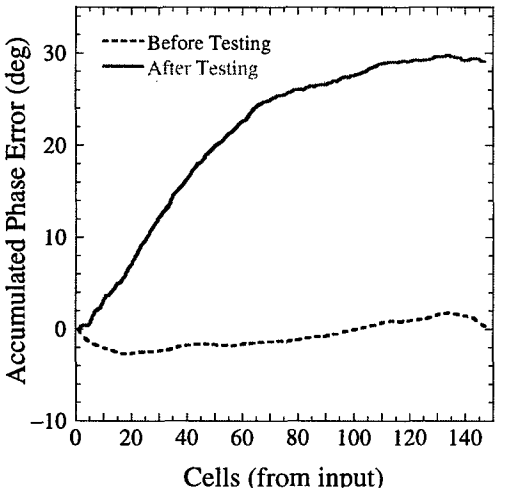

Figure 5: Accumulated phase advance error measured as a function of distance along structure.

Figure 6 uses the group velocity along the structure to plot the associated change of frequency in each cell. Cell to cell variation is due to uncertainties in measurement but an average of 1 MHz shift over the entire structure results in the observed 30° total phase shift. The change in frequency is equivalent to a copper layer of several microns being removed from the iris surface. The exact nature of the frequency shift is still being investigated.

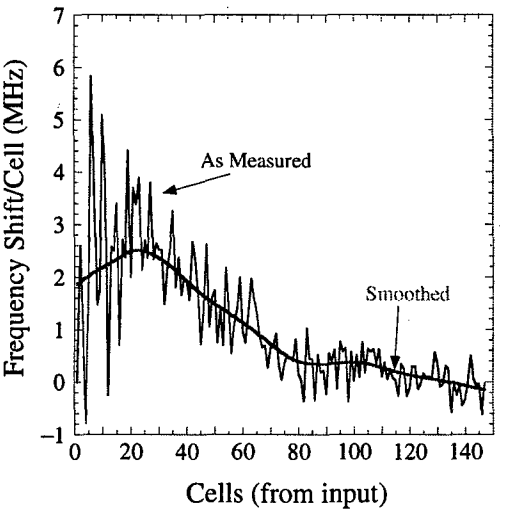

Figure 6: Frequency shift per cell as a function of position along structure.

4 SUMMARY

The M2 structure test achieved several milestones: with the aid of computer assisted processing, the total number of integrated pulses in conditioning approached $1x10^8$; stable and achievable gradients of 75 MV/m were demonstrated in a usable accelerator structure; and the effects of intensive conditioning were easily seen and quantified. As a result, tests at SLAC are underway to better understand arc formation and the mechanism of rf breakdown, particularly in long structures.

5 REFERENCES

[1] J. Wang et al, "High Gradient Experiments on NLCTA Accelerator Structures," SLAC-PUB-7243, 1996.

[2] C. Adolphsen et al, "RF Processing of X-Band Accelerator Structures in the NLCTA," this conference, 1999.

[3] JLC Design Report, KEK Report 97-1, pp 231-293, 1997.

[4] C. Adolphsen et al, "Measurement of Wakefield Suppression in a Detuned X-Band Accelerator Structure," Phys. Rev. Lett. 27, pg 2475, 1995.

[5] A.E. Vlieks et al, "High Power RF Component Testing for the NLC," Linac98, Chicago, IL, 1998.

[6] S.M. Hanna et al, "A Semi-Automated System for the Characterisation of NLC Accelerating Structures," SLAC-PUB-95-6811, 1995.

ACCELERATOR STRUCTURE R&D FOR LINEAR COLLIDERS*

J.W. Wang#, C. Adolphsen, K.L.Bane, G.B. Bowden, D.L. Burke, H. Deruyter, J. Cornuelle, Z.D. Farkas, W.B. Fowkes, S. Hanna H.A. Hoag, J. Irwin, R.M. Jones, K.Ko, N.Kroll, Z.Li, G.A. Loew, R.J. Loewen, R.H. Miller, C.K. Ng, J.M. Paterson, C.Pearson, T.O. Raubenhemer, J. Rifkin, R.D. Ruth, S.G. Tantawi, K.A. Thompson, K.W. Vaillancourt, A.E. Vlieks, P.B. Wilson, SLAC, Stanford, CA
K. Asano, Y. Funahashi, Y. Higashi, T. Higo, N. Hitomi, T. Suzuki, K. Takata, T. Takatomi, N. Toge, Y. Watanabe, KEK, Tsukuba, JAPAN
J. Elmer, J. Klingmann, M. Mugge, K. Van Bibber, LLNL, Livermore, CA

Abstract

For more than ten years, we have been working on R&D for X-band accelerator structures for the JLC/NLC linear collider. Several types of Detuned (DS) and Damped Detuned Structures (DDS) have been successfully designed and fabricated. They have been experimentally tested at both low power and high power to characterize their mechanical and electrical properties. Recently we started developing a new type of damped detuned structure with optimized round-shaped cavities (RDDS). This paper discusses the special specifications, design methods, fabrication procedures, measurement technologies, and anticipated future improvements for all these structures.

1 REQUIREMENTS OF STRUCTURES FOR LINEAR COLLIDERS

The critical requirements for the next generation of linear colliders are high luminosity and high RF efficiency.[1] We need to design the accelerator structures to control short and long range transverse wakefields to ensure the preservation of low emittance for multi-bunch beams. The suppression of the deflecting modes is achieved through precision alignment of cells and by detuning and damping higher order modes. We have to design and fabricate the accelerator structures for reliable high-gradient operation in order to optimize the linac length and cost. The increase in RF breakdown threshold and suppression of field emission current is achieved through optimized cell design, advanced machining, processing and handling techniques.

2 STRUCTURE TYPES – A BRIEF HISTORY

Starting in 1988, we studied various damped structures, which can heavily damp (external Q_e<10) higher dipole modes. We made computer simulations, microwave tests and theoretical analyses on the disk-loaded waveguide structures with radial slots in the disks and/or radial rectangular waveguides in the cavity walls, azimuthal waveguide structures.[2] Due to the fabrication complexity of those heavily damped structures (HDS), in 1990 we began to explore the detuned structure (DS) in which the frequencies of HOMs differ sufficiently from cell to cell that the wakefields decohere rapidly. The experimental measurements of beam-excited wakefields in a 50-cavity detuned structure in 1991[3] encouraged us to design the first 1.8m full length detuned section (DS1). Its cell radii, iris radii and disk thicknesses were varied smoothly (in a Gaussian distribution). This section was constructed and an accurate wakefield measurement (ASSET) was done in 1994.[4] The wake recohered after a few meters because the mode distribution was discrete. The suppression of the wake reappearance can be obtained by providing a moderate damping via vacuum manifolds. As a joint effort, the first damped detuned section (DDS1) was completed in 1996.[5] Figure 1 shows the calculated wakefields for the above two types of structures. After DDS1, two more DDS sections were built by an improved fabrication method with better pumping and HOM matching. In order to increase the RF efficiency, we are developing a new type of damped detuned structure with optimized round-shaped cavities (RDDS), which will lead to the final design for the JLC/NLC main linac structure. In summary, the accelerator parameters and test data for all major sections are listed in Table 1.

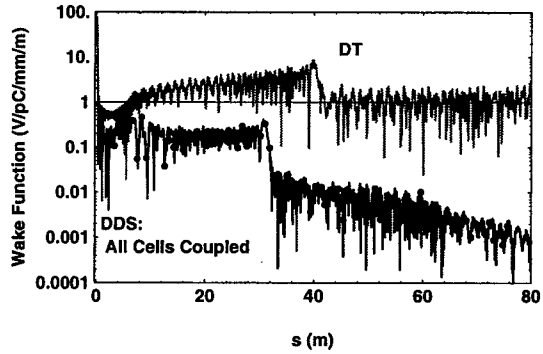

Figure 1: Wakefield Profiles for Detuned Structure and Damped Detuned Structure

*Work supported by U.S. Department of Energy, contract DE-AC03-76F00515, W-7405-ENG-48 and part of Japan-US Collaboration Program In High Energy Physics Research.
#Email: jywap@slac.stanford.edu

Table 1. Characteristics of Structures

Structures Name	75 cm	DS1	DS2	INJE1&2	DDS1	DDS2	DDS3	RDDS1
Old Names		MARK-1 DT1	MARK-2 DT2		DDT1			DDS5
Structure Type	Constant Impedance	Detuned	Detuned	Detuned	Damped Detuned	Damped Detuned	Damped Detuned	Damped Detuned
Length (m)	0.75	1.8	1.8	0.93	1.8	1.8	1.8	1.8
Number of Cells	86	206	206	106	206	206	206	206
Cell Shape	DLWG	DLWG	DLWG	DLWG	DLWG	DLWG	DLWG	Optimized
Phase Advance Per Cell	$2\pi/3$	$2\pi/3$	$2\pi/3$	$2\pi/3$	$2\pi/3$	$2\pi/3$	$2\pi/3$	$2\pi/3$
HOM Manifold Shape/ Size(mm)	N/A	N/A	N/A	N/A	Rect. / 5x11.0 - 5x9.8	Rect. / 5x11.0 - 5x10.0	Rect. / 5x11.0 - 5x10.0	Circular / Diameter 9.6 – 7.3
Iris Diameter, 2a (mm)	8.56	11.43 - 7.86	11.43 - 7.86	11.43 - 7.86	11.43 - 7.86	11.43 - 7.86	11.43 - 7.86	11.21 – 7.77
Cell Diameter, 2b (mm)	21.58	22.87 - 21.39	22.87 - 21.39	22.87 - 21.39	22.87 - 21.39	22.87 - 21.39	22.87 - 21.39	24.04 – 22.16
$\langle a \rangle / \lambda$	0.163	0.180	0.180	0.180	0.180	0.180	0.183	0.179
Disk Thickness, Web/Tip (mm)	1.46	1.0 – 2.0	1.0 – 2.0	1.0 – 2.0	1.0 – 2.0	1.0 – 2.0	1.0 – 2.0	0.8/1.2 – 1.4/2.2
Filling time, T_f (ns)	52	100	100	52	100	100	95	104
Shunt Impedance r (MΩ/m)	88.0	67.5 – 88.0	67.5 – 88.0	67.5 – 88.0	65.7 – 84.2	65.7 – 84.2	65.7 – 84.2	77.1 – 101.8
Group Velocity, v_g / c	0.048	0.118 – 0.03	0.118 – 0.03	0.118 – 0.03	0.118 – 0.03	0.118 – 0.03	0.118 – 0.03	0.111 – 0.029
<Q>, Fundamental Mode	~7000	~7030	~7030	~7030	~6780	~6780	~6800	~7810
<Q>, Lowest Dipole Band	~6500	~6500	~6500	~6500	~1000	~1000	~1000	~1000
Lowest Dipole Band Detuning, $\Delta f_{1,tot} / \langle f_1 \rangle$	N/A	10.1%, dn/df_1 (4σ)	10.1%, dn/df_1 (4σ)	10.1%, dn/df_1 (4σ)	10.1%, dn/df_1 (4σ)	10.1%, dn/df_1 (4σ)	10.159% kdn/df (4.78σ)	11.25% kdn/df (4.75σ)
Detuning Standard Deviation, $\sigma_{f1} / \langle f_1 \rangle$	N/A	2.5 %	2.5 %	2.5 %	2.5 %	2.5 %	2.125%	2.368%
Attenuation, τ	0.267	0.505	0.505	0.255	0.533	0.533	0.508	0.483
Ep / E_a	2.3	3.06 – 2.10	3.06 – 2.10	3.06 – 2.10	3.06 – 2.10	3.06 – 2.10	3.06 – 2.10	3.00 – 2.10
Machining Method	Single Diamond	Regular	Single Diamond	Regular	Single Diamond	Single Diamond	Single Diamond	Single Diamond
Cell Joint Method	Nested Brazing	Stacks, Nested Brazing	Stacks, Nested Brazing	Stacks, Nested Brazing	Stacks, Diffusion Bonding	Stacks, Diffusion Bonding	Section, Diffusion Bonding	Section, Diffusion Bonding
Completion Time	6/1993	1/1994	11/1996	4/1996	7/1996	4/1997	10/1998	Autumn, 1999
Wakefield Measurement		ASSET 3/1994			ASSET 8/1996		ASSET 11/1998	
Power Needed for $\langle E_a \rangle$=50 MV/m	52.2	88.8	88.8	69.7	89.8	89.8	94.5	82
Operated E-field $\langle E_a \rangle_{max}$ (MV/m)	79	68	50	70	68	50	N/A	N/A

3 DESIGN METHOD

Through a decade of working on various structures we have developed successful design procedures to:[6][7][8]

- Choose the basic accelerator parameters such as length, filling time and attenuation factor based on the rf source and system.
- Choose iris size and dipole detuning distribution based on beam emittance and wakefield suppression requirements.
- Optimize cavity shape for best shunt impedance, *r/Q* and low peak surface field.
- Calculate wakefield from a equivalent circuit and spectral function analysis using optimised HOM coupling slots and manifold size.
- Create cell dimension tables using high accuracy 3D modelling for typical cells.
- Design and simulate special portions of the structure like the input and output fundamental couplers and HOM couplers.
- Fabricate, mechanical QC and microwave QC typical cells and special coupler parts for final corrections of their essential geometries.
- Perform mechanical design to ensure electrical properties and manufacturability.

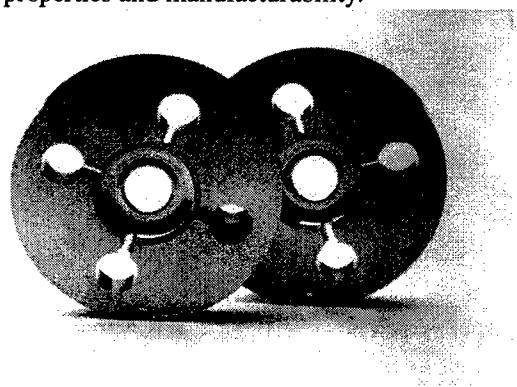

Figure 2: Disks for RDDS1 Structure

4 FABRICATION METHOD

A typical sequence follows. Disks and cells are rough-machined using regular lathes and milling machines with more than 50 μm of extra copper left on all surfaces except coupling slots and manifolds. Final machining is done using single crystal diamond turning with sub-micron accuracies and 50 nm surface finishs. After careful cleaning with ozonized pure water rinsing, the cells are stacked in a V-block of a special stacking fixture. The whole stack is pre-bonded at 180° C and final diffusion bonded at 890° C.[9] Final assembly including WR90 waveguides for fundamental mode and WR62 waveguides for HOM, flanges, and vacuum ports are brazed in a hydrogen furnace at 1020° C. The brazed section is installed in a strongback for final mechanical measurement and straightening in CMM machine.

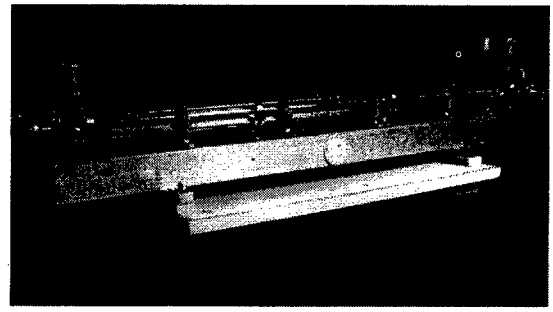

Figure 2: DDS3 Structure

5 CHARACTERIZATION TECHNIQUES

We have built several set-ups and facilities to evaluate the microwave properties and check the performance of various accelerator parts and sections.

- During fabrication we use two single cell microwave QC set-ups (one for the accelerating mode and one for the dipole modes) and a stack microwave QC set-up.
- At final assembly, a semi-automated bead pulling system gives a measurement of the field phase and amplitude along the accelerator sections.
- ASSET is used for wakefield and beam-based alignment experiments.
- NLC Test Accelerator and ASTA are used for high power tests and beam acceleration experiments. [10]

6 FUTURE R&D PLANS

We are making a schedule to design and fabricate more sections in order to finalize the JLC/NLC accelerator structure design and to study the manufacturability for low cost mass production of about ten thousand accelerator sections. The following are our main tasks:

- Design of more compact fundamental couplers with reduced and symmetric fields.
- Damping of all dipole modes in the output end.
- Wakefield simulation and analysis for high order deflecting modes.
- More detailed tolerance studies and application of the feedforward/feedback technique for large acceptance of mass production parts.
- Surface cleanliness techniques and high gradient considerations.
- More diffusion bonding studies to understand dimensional stability during high temperature processing.
- Automation for cell stacking and assembly lines.

7 REFERENCES

[1] Zeroth-order Design Report for the NLC, 1996, SLAC-PUB-5214.
[2] H. Deruyter et al., Proc. EPAC90, June 1990, SLAC-PUB-5263.
[3] J.W. Wang et al., PAC91, SLAC-PUB-5498.
[4] C. Adolphsen et al., Proc. LINAC94, SLAC-PUB-6629.
[5] R.H. Miller, Proc. LINAC96, SLAC-PUB-7288
[6] Z. Li et al., FRA41, this conference.
[7] R. Jones et al,. FRA37, this conference.
[8] G. Bowden et al., FRA19, this conference.
[9] T. Higo et al., FRA16, this conference.
[10] J. W. Wang et al., Proc. LINAC94, SLAC-PUB-6617.

A COMPACT RF POWER COUPLER FOR THE NLC LINAC *

G. Bowden†, W. B. Fowkes, R. J. Loewen, R. H. Miller, C. Ng,
C. Pearson, J.W.Wang, SLAC, Stanford, CA

Abstract

A high power RF coupler connecting WR90 rectangular waveguide to the disc loaded waveguide accelerating structure of NLC is described. The coupler design is symmetric and free of beam deflecting field components. It makes an efficient electrical match between the rectangular waveguide power feed and the accelerator structure while keeping electrical surface field enhancement low. Electrical and mechanical design of the coupler are presented as well as quantitative comparisons between numerical simulation and low power cold test models.

1 DESIGN REQUIREMENTS AND EVOLUTION

One important component of any accelerating structure is the fundamental mode input coupler. It must provide a perfect match at the correct frequency between rectangular waveguide and the accelerating structure. To preserve low emittance in multi-bunch beams, rf field and phase must be made symmetric across the coupling cavity to avoid transverse deflections. To reduce manufacturing cost and improve mechanical stability, the design should be compact. Our previous coupler designs for NLC drove the coupling cavity through separate waveguides which were costly to manufacture and difficult to tune for perfect symmetric matching after assembly. The starting point for our present design was the DESY input coupler [1]. A set of initial dimensions for the coupling cavity and iris were based on previous NLC coupler designs. These were then adjusted during numerical simulations and later during cold test of prototype couplers.

2 MECHANICAL LAYOUT

Fig. 1 shows the coupler geometry with rf dimensions in mm for 11.424 GHz. The rf design was separated into an upper T branched WR90 rectangular waveguide and a lower symmetric side coupled accelerating cavity. The coupler is machined from a single block of copper (ASTM F-68 MET Class 2). A 10 mm thick cover plate is then hydrogen furnace brazed over the coupler front. To accommodate machining tolerances, the cavities' final rf impedance match will be adjusted by local deformation of cylindrical walls in the coupler and the following two cavities. Thin easily deformable regions in these walls will be created by drilling blind radial holes (not shown). Small stud screws will be brazed to the ends of these holes for pulling and pushing so cavity resonant frequency can be both lowered as well as raised.

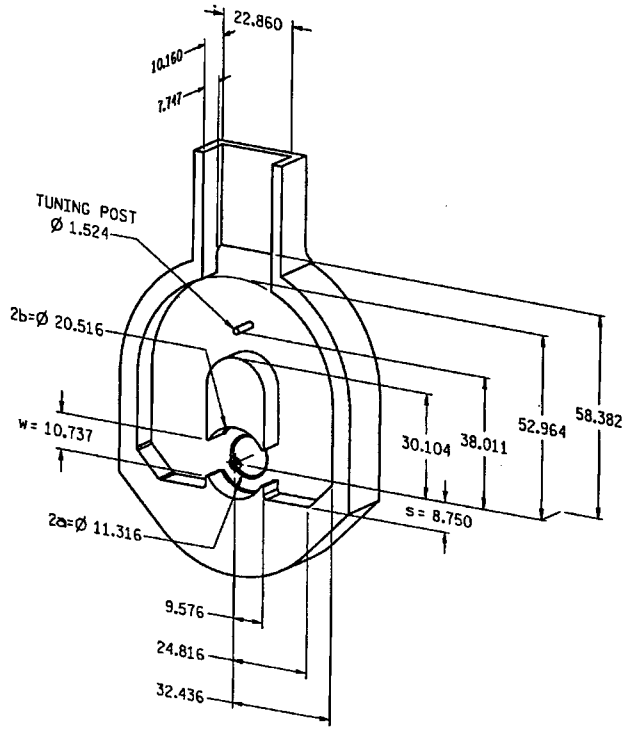

Figure 1: Input coupler geometry.

3 NUMERICAL SIMULATION

The matching and tuning of the compact RDDS[1] coupler structure is divided into two parts, namely, matching of the coupler cavity, and matching of the T-junction used for splitting the input power into two arms which feed the coupler cavity. The separation between the coupler cavity and T-junction is chosen long enough that effects of evanescent modes in connecting waveguides can be ignored. Thus overall matching can be achieved by matching each part individually.

3.1 Matching and Tuning of the Coupler Cavity

The matching and tuning of the RDDS coupler is achieved by adjusting the coupler cell diameter $2b$, the matching iris aperture w, and the terminated position of the waveguides s. (See Fig. 1.) The numerical procedure for achieving this has been studied previously [2]. Here, a new time-domain

* Work supported by the Department of Energy, contract DE-AC0376SF00515.

† Email: gbb@SLAC.Stanford.EDU

[1] RDDS stands for Round Damped Detuned Structure. The accelerating structure is a sequence of toroidal rounded cavities with dimensions chosen to detune higher order modes and damping slots to attenuate them.

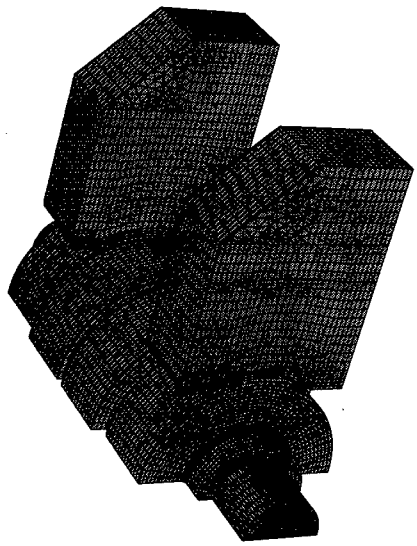

Figure 2: A 4-cell geometry for the coupler structure.

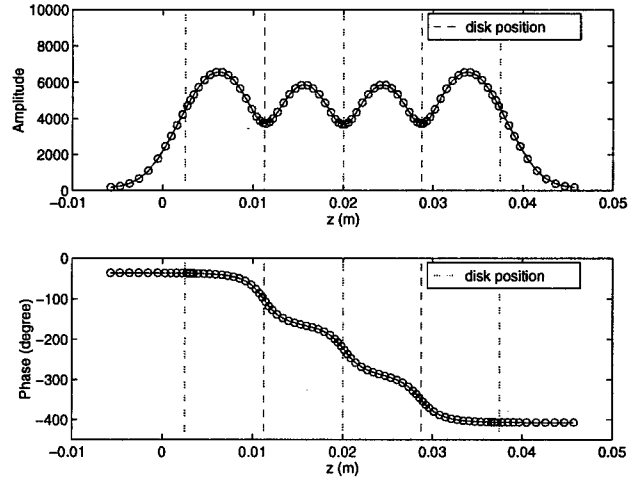

Figure 3: Longitudinal electric field along the axis

electromagnetic code, Tau3 [3], is employed for the numerical simulation. Tau3 uses an unstructured grid to model the exact curvatures of the structure. Fig. 2 shows the 3-dimensional model of the coupler structure using such an unstructured grid. The model consists of two coupler cells attached to identical input and output rectangular waveguides and two regular accelerator structure cells. Taking advantage of symmetry, only one half of the structure needs to be simulated. The transmission properties of the structure are determined by driving the TE_{10} mode at the input rectangular waveguide. The reflection coefficient at the input waveguide and the transmission coefficient at the output waveguide are computed once steady state is reached.

The reflection coefficient for the matched coupler is found to be 0.005 at 11.424 GHz. The amplitude and phase of the longitudinal electric field along the axis for the matched coupler are shown in Fig. 3. Field gradient is about 15% higher in the coupler cell than in the structure cells. The phase changes in the coupler and regular cells are 60° and 120° respectively, indicating a traveling wave with the correct phase advance of 120° per cell from coupler to coupler.

3.2 *Matching of T-junction*

Figure 4 shows the 3-dimensional model of the T-junction used for Tau3 simulations. Again because of symmetry, only one half of the structure is simulated. The T-junction requires a post to improve the impedance match and a tran-

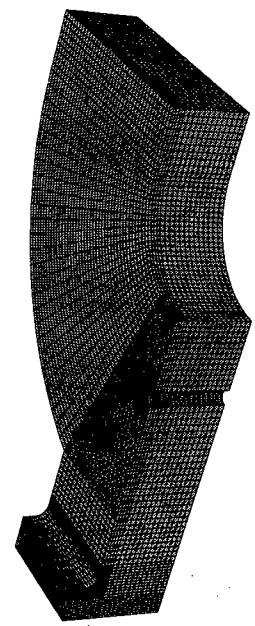

Figure 4: Geometry of the T-junction.

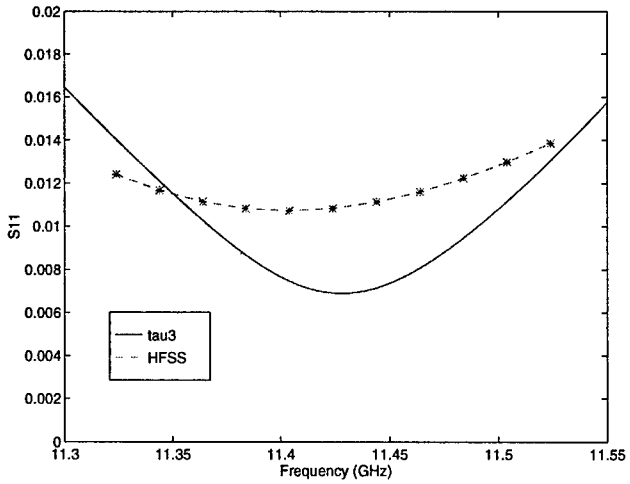

Figure 5: S_{11} spectrum of the T-junction.

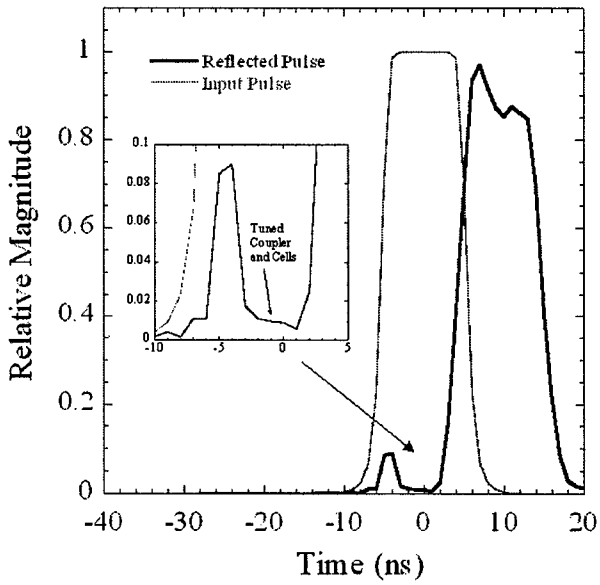

Figure 6: Coupler VSWR in the time domain.

sition step from the WR90 waveguide to the coupler thickness. The matching requirement of 0.01 reflection over a 200 MHz bandwidth centered at 11.424 GHz was met by adjusting the radii and locations of the post and step in the Tau3 simulation. Fig 5 shows that the reflection coefficient S_{11} at the WR90 input reaches a minimum of 0.007 at 11.424 GHz. Also plotted are the results of simulation using the HFSS code.

4 COUPLER COLD-TEST MEASUREMENTS

Final dimensions for the coupling iris w and cavity diameter $2b$ are determined by cold-testing. We start with a coupler assembly with excess metal (150 - 200 μm) in both w and $2b$. A stack of 15 traveling-wave cavities is clamped to the back of the coupler to provide a matching structure. A shorting plunger selectively detunes particular cells while a network analyzer measures the reflection coefficient. By iteratively machining, tuning the cell stack and remeasuring, an optimum set of dimensions is determined.

Kyhl's method [4] is used to evaluate coupling vs. tuning based on reflected phase at three frequencies calculated for the $\pi/2$ mode and the desired $2\pi/3$ modes. This method works reasonably well but an arbitrary reference of the coupler's shorting position and unknown calculational errors in the $\pi/2$ mode frequency lead to some uncertainty. For this reason a time-domain measurement was also done as a cross check. A broadband display in the frequency domain provides the ability to analyze the effects of a short pulse of rf as it reflects off the coupler before interfering with the large mismatch at the end of the cell stack. Although this method cannot distinguish cell tunning mismatches from coupling mismatches, it provides a clear unambiguous measurement.

An important caveat to the time-domain procedure is the requirement that the cell stack is uniformly tuned. Inadvertent stagger tuning of the stack could cancel a coupler mismatch. The RDDS structure has allowance for tuning only the first two cavities behind the coupler. Therefore as a final check, we randomly shuffled the cells in a tuned stack and verified the optimum coupler match by slight adjustment of the first two cavities. Fig. 6 illustrates the final time-domain measurement. After an initial reflection of high frequency components in the rise-time of the pulse, the coupler settles down to a VSWR of 1.02 before the end of the pulse is reached 8 ns later.

5 REFERENCES

[1] V. E. Kaljuzhny et. al., 'Design and Performance of a Symmetric High Power Coupler for a 6 Meter S-Band Linear Collider Accelerating Structure', DESY Internal Report DESY M-94-11, Oct. 1994, 32pp.

[2] C.-K. Ng and K. Ko, Numerical simulation of input and output couplers for linear accelerator structures, Proc. CAP93, p243 (1993).

[3] C.-K. Ng et. al., Simulation of RF structures in the time domain with unstructured grids, these proceedings.

[4] E.P. Westbrook, 'Microwave Impedance Matching of Feed Waveguides to the Disk Loaded Accelerator Structure Operating in the 2Pi/3 Mode', SLAC-TN-63-103, Dec 1963. 18pp.

THE NEXT LINEAR COLLIDER DAMPING RING COMPLEX*

J.N. Corlett, S. Marks , R. Rimmer, R. Schlueter
Ernest Orlando Lawrence Berkeley National Laboratory, Berkeley, CA, 94720
P. Bellomo, V. Bharadwaj, R. Cassel, P. Corredoura, P. Emma, R.K. Jobe, P. Krejcik, S. Mao, B. McKee, K. Millage, M. Munro, C. Pappas, T.O. Raubenheimer, S. Rokni, M.C. Ross#, H. Schwarz, J. Sheppard, C.M. Spencer, R.C. Tighe, M. Woodley
Stanford Linear Accelerator Center, Stanford, CA, 94309.

Abstract

We report progress on the design of the Next Linear Collider (NLC) Damping Rings complex (DRC) [1]. The purpose of the DRC is to provide 120 Hz, low emittance electron and positron bunch trains to the NLC linacs [2]. It consists of two 1.98 GeV main damping rings, one positron pre-damping ring, two pairs of bunch length and energy compressor systems and interconnecting transport lines. The 2 main damping rings store up to 0.8 amp in 3 trains of 95 bunches each and have normalized extracted beam emittances $\gamma\varepsilon_x$ = 3 μm-rad and $\gamma\varepsilon_y$ = 0.03 μm-rad. The preliminary optical design, performance specifications and tolerances are given in [1]. Key subsystems include 1) the 714 MHz RF system [3], 2) the 60 ns risetime injection / extraction pulsed kicker magnets [4], 3) the 44 m wiggler magnet system, 4) the arc and wiggler vacuum system, 5) the radiation management system, 6) the beam diagnostic instrumentation, 7) special systems used for downstream machine protection and 8) feedback-based stabilization systems. Experience at the SLAC Linear Collider has shown that the NLC damping rings will have a pivotal role in the operation of the high power linacs. The ring dynamics and instabilities will in part determine the design choices made for the NLC machine protection system. This paper includes a summary overview of the main ring design and key subsystem components.

Table 1: Main Damping Ring and Pre-Damping Ring parameters.

	Main Rings	Pre- Ring
Energy GeV	1.98	1.98
Circ. meter	297	214
Rotation frequency MHz ($1/T_0$)	1.01	1.401
RF (MHz)	714	714
h	708	510
τ_b (bunch spacing)	2.80 ns	2.80 ns
Fill pattern (# trains N_T, /# bunches)	N_T=3/ 95 3 gaps 68 ns	N_T =2/ 95 2 gaps 100 ns
$\tau_{x,y}$ (ms)	< 5.21	< 5.21
N_{max} /bunch	1.6×10^{10}	1.9×10^{10}
I_{max} (Amp)	0.75	0.80
Normalized extracted emittance $\gamma\varepsilon_x$ / $\gamma\varepsilon_y$	< 3/.03 μm-rad	<100 μm-rad
ε_x / ε_y	<800/8 pm-rad	<25 nm-rad
Gap voltage V_g (MV)	1.5 (3 cells)	2 (4 cells)
Loss/turn U_0	750 KeV	400 KeV
Momentum compaction α_p	6.6×10^{-4}	0.0051
Injected emittance $\gamma\varepsilon_{x0,y0}$	150 μm-rad	> 0.06 m-rad (Acceptance)
Bunch length σ_z	4.0 mm	8.4 mm
Energy acceptance	+/- 1.9%	+/- 1.3%

1 INTRODUCTION

The DRC provides damped e^+/e^- beams to the bunch length compressors at either end of the NLC. A pre-damping ring is required for e^+ because of the large source emittance. Except for the pre-damping ring and its associated transport lines, the e^+/e^- systems are identical. Figure 1 shows the layout of the e^+ rings.

In this paper we first review the optics design of the main damping ring and then describe progress on some critical subsystems. The pre-damping ring will be the topic of a future report.

2 DESIGN

The main damping ring design was substantially redone in order to accommodate a 2x larger inter-bunch spacing (τ_b). The equilibrium emittance (ε_{ye}) in the updated design was allowed to be relatively large, 0.02 μm-rad, so that component placement tolerances are not extreme. The optimum number of vertical damping times (N_τ) was then set by the emittance at injection such that ε_y is $1.5\varepsilon_{ye}$; resulting in N_τ=4.8. The vertical damping time (τ_y) is then

$$\tau_y \le \frac{N_T}{N_\tau f} = \frac{3}{4.8\cdot(120Hz)} \approx 5.2msec \ge \frac{(2.9\times10^{12}kG)T_0}{B_0\gamma^2}$$

* Work supported by the U.S. Department of Energy under Contract Nos. DE-AC03-76SF00515 (SLAC) and DE-AC0376SF00098 (LBNL)
# Email: mcrec@slac.stanford.edu

determined and the arc bend field ($B0$) is given above. A wiggler is needed to keep $B0$ reasonable at 1.98 GeV. The wiggler length (L_w) required is given by:

$$L_w \geq 6C\frac{(B\rho)^2}{r_e c\tau_y \gamma^3 B_w^2}\cdot\frac{F_w}{1+F_w} \geq 33m(B_w = 2.15T)$$

where B_w is the peak field of the wiggler. We have chosen a racetrack shape with the wiggler on one side and injection/extraction, RF, abort and feedback systems on the other.

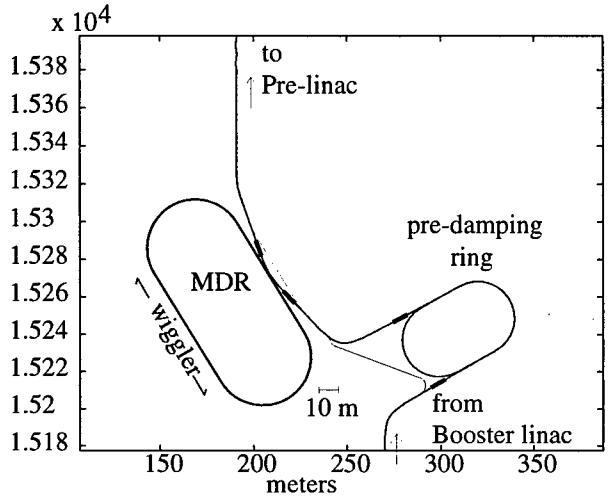

Figure 1: NLC e^+ damping ring complex shown with its associated transport lines and the first bunch length compressor (BC) stage (the BC wiggler is barely visible at the top of the figure). Two short bypass lines, to be used during construction and for possible future e^-/e^- operation can also be seen. The scale is in meters, referenced to the center of the NLC complex.

Table 2: Lattice parameters for the main damping ring.

ν_x / ν_y	23.85 / 11.23
#TME cells / length per cell	30 / 6.01 m
Phase adv. per TME ½ cell (x/y)	108 / 45 degrees
Straight length	58 m
Wiggler (length L_w / period λ / peak field B_w)	44 m / 0.27 m / 2.15 T
$U_{wiggler} / U_{arc} = F_w$ (ratio of wiggler loss/arc loss)	2.3

Detuned theoretical minimum emittance (TME) optics [5] are used in the arcs. The detuning factor (r) is set by 3 considerations: 1) to keep α_p as large as possible in order to stabilize the ring extraction energy and keep the transient longitudinal bunch length instability threshold as high as possible[6], 2) to reduce typical sextupole strength and 3) to minimize the number of cells. We have chosen r= 1.6. The ratio of damping done by the wiggler to that done in the arc (F_w) was also chosen to keep α_p large.

The ring extraction energy stability tolerance, $\Delta\delta$, is about 10% of the natural energy spread, $\sigma\delta \sim 10^{-3}$. The stability requirement for the ring size (C), is:

$$\Delta C \leq \alpha_p \Delta_\delta C \approx 20\mu m\left(\alpha_p = 6.6\times10^{-4}\right)$$

Relatively slow changes [7], (< 1 Hz), in C can be compensated by a magnetic chicane[8]. Faster changes, coming perhaps from ground vibration, may a concern. RF frequency correction, used in storage rings to compensate for ring size drifts, is cumbersome in the damping ring because the extracted train is subsequently injected into a linac whose frequency cannot be varied.

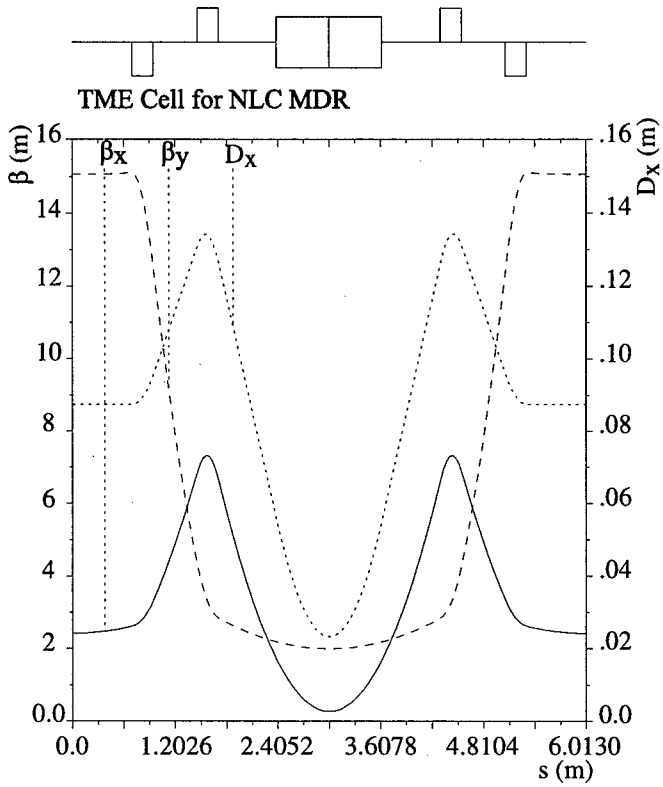

Figure 2: Optical functions of the 6 m DFBFD detuned TME arc cell. The top of the figure shows the QD, QF and bend magnets; the 4 sextupoles are not shown.

3 TECHNOLOGY

In many ways, the damping ring is similar to a 3rd generation light source with its high current, small coupling, low vacuum pressure (<1nTorr) and large synchrotron radiation power loading. In addition, the damping ring complex includes several challenges associated with fast damping, high throughput injection from a powerful injector, and clean extraction.

High current transient operation, where the rings can be filled and emptied in a few injector linac pulses, is peculiar to damping rings. The RF system is most affected by this. We are developing a heavily higher-order-mode damped cavity design, adapted from the PEP-II work, with a high level of control, feedback and feedforward

applied. The flexible low-level controls and feedback loops to control beam phase and energy under a variety of beam conditions are described in [9].

Our kicker design is modeled after the low beam impedance stripline kicker developed at DELTA [10]. Because of the difficulty of achieving proper performance with the SLC damping ring injection and extraction kickers[11],[12], development work on this system is important even though the requirements for the NLC rings are substantially reduced. In the prototype, a pair of shorted striplines is differentially driven from a 330 amp low voltage solid state pulser [13].

The 44 m wiggler section is a concern because of its high field strength and large size. Several technologies are under consideration for the wiggler; 1) electromagnet, 2) NdFe:B permanent magnet, and 3) superconducting magnet. Injected beam radiation damage effects are a serious concern, especially for 2) and 3). Some components close to the beam pipe in the SLC damping rings were exposed to 10^{14} rad [14] over a 5 year period. This level could result in partial demagnetization of permanent magnets and may be a heat load problem for a superconducting magnet. Since the NLC injector linac is 6 times more powerful than the SLC injector, the potential exists for higher radiation exposure rates. A collimation system will be needed for protection of the wiggler.

The vacuum chamber through the wiggler must be capable of dissipating about 60 W/cm. While this is ~3x less than a similar system in the PEPII LER [15], the specified pressure ceiling is 10x lower and work is underway to develop a symmetric antechamber design. Even though the typical trajectory distortion caused by the wiggler field is small, about 1 mm, the wiggler is so long that 90% of the radiation is dissipated within the straight section itself.

Since the primary purpose of the damping rings is to produce very low emittance beams, there are several sets of transverse and longitudinal beam size monitors. Typical transverse beam sizes are σ_x=100 x σ_y=10 μm, sizes too small for conventional wire scanner or video imaging techniques at the nominal full train intensity of $1.4\text{x}10^{12}$ e^+/e^- per pulse. Downstream of the ring, in BC1, a sequence of laser-based profile monitors [16] is used to measure emittance and energy spread.

Several special purpose subsystems in the damping ring will be used to integrate its operation with the operation of the collider as a whole. The most important of these is the machine protection system [17]. An emittance spoiler will, in the duration of a few pulses, increase the emittance to safe levels for injection of a single pulse into the main linac and the pulsed abort magnet that will be used to quickly dump the beam in the event of a downstream fault.

4 REFERENCES

[1] T.O. Raubenheimer *et al*, "A Damping Ring Design for the SLAC Next Linear Collider", Proc. *PAC95*, 701 (1995). Updated parameters can be found on the NLC Accelerator Physics Web pages found at http://www-project.slac.stanford.edu/lc/nlc-tech.html.

[2] V. Bharadwaj *et al*, "The NLC Injector System", *presented at PAC99*, (1999) (FRA27).

[3] R.A.Rimmer, *et al*, "The Next Linear Collider Damping Ring RF System", *presented at PAC 99*, (MOP60).

[4] C. Pappas and R. Cassel, "Damping Ring Kickers for the Next Linear Collider", *presented at PAC 99*, (TUP11).

[5] J.P. Potier and L. Rivkin, "A Low Emittance Lattice for the CLIC Damping Ring", Proc. *PAC97*, 476 (1997). Other references include: L.C. Teng, LS-17 1985, ANL-FNAL. and J.P. Delahaye and J.P. Potier, "Reverse Bending Magnets in a Combined-function Lattice for the CLIC Damping Ring", Proc. *PAC89* , 1611 (1989).

[6] K. Bane, *et al*, "High Intensity Single Bunch Instability Behaviour in the New SLC Damping Ring Vacuum Chamber", Proc. *PAC95*, 3109 (1995).

[7] Katsura, *et al*, "Horizontal Movement of the Storage Ring Floor at the Photon Factory", Proc. *PAC93*, 2260 (1993).

[8] P. Emma and T.O. Raubenheimer, "Circumference Control in Damping Rings Using Chicanes", *presented at PAC99*, (1999) (FRA23).

[9] P. L. Corredoura, "Architecture and Performance of the PEP-II Low-Level RF System", *presented at PAC99*, (THBL1) and L. HENDRICKSON *et al*, "Feedback Systems for Linear Colliders", *presented at PAC99*, (WECL2).

[10] G. Blokesch, *et al*, "A Slotted Pipe Kicker for High Current Storage Rings", Nucl.Instrum.Meth. A338:151-155,1994.

[11] T.S. Mattison *et al*, "Fast and Reliable Kicker Magnets for the SLC Damping Rings", Proc. *PAC95*, 1915 (1995).

[12] F. Zimmermann *et al*, "Ion effects in the SLC electron damping ring under exceptionally poor vacuum conditions", SLAC-PUB-7665 (1997).

[13] R.L.Cassel, "A Solid State Induction Modulator for SLAC NLC", *presented at PAC99*, (TUP9).

[14] M. Ross, *Proceedings of the Workshop on the SLAC Damping Rings in the 21st Century*, (1998), SLAC-WP-10.

15 J. Heim, *et al*, "Wiggler Insertion of the PEP-II B Factory LER", Proc. *PAC95*, 527 (1995).

[16] M. C. Ross *et al*, "A High Performance Spot Size Monitor", *Proceedings of the 18th Linac Conference*, (1996).

[17] C. Adolphsen *et al*, "The Next Linear Collider Machine Protection System", *presented at PAC99*, (TUDR4).

OPTICS DIAGNOSTICS AND TUNING FOR LOW EMITTANCE BEAM IN KEK-ATF DAMPING RING

H.Hayano, S.Kamada, K.Kubo, T.Naito, K.Oide, N.Terunuma, N.Toge, J.Urakawa, KEK; S.Kashiwagi, Graduate U. for Advanced Studies; T.Okugi, Tokyo Metropolitan U.; M.Takano, Toho U.; K.Bane, T.Kotseroglou, M.Minty, M.Ross, J.Turner, M Woodley and F.Zimmermann, SLAC

Abstract

The target of KEK-ATF is producing electron beam with vertical emittance of 0.01 nm-rad (1×10^{-11} m-rad). Corrections of the dispersions are essential to achieve the low emittance. Because the actual optics of the beam line should be known for these corrections, beam based optics diagnostics has been performed. Simulations showed the validity and the accuracy of the method. Effects of skew quadrupoles have also been studied.

1 OPTICS DIAGNOSTICS

In the early stage of the operation of the ATF Damping Ring, there were big discrepancies between observations of beam behavior and calculations based on our optics model. In order to make the model more accurate, optics diagnostics was performed. The method were reported with results of its test before[1].

Errors of quadrupole strengths of the quadrupole magnets and the combined bending magnets have been estimated using beams, by steering beam and measuring the orbit in down stream. There are about 100 steering magnets and 100 BPMs in the ring and the measured response coefficients (R_{12} and R_{34}) at the BPMs from the steering magnets are fit by errors of strength of quads, BPMs and steerings. Magnets are divided into 10 types and we assumed that each type of the magnets has a common error ratio because they have the same design. (See Table 1.) In order to correct the original model, which is based on magnetic field measurements, 'fudge factor' has been introduced for each type as relative error of the quadrupole field strength.

The diagnostics have been performed several times, especially when the optics setting was changed or beam position monitor (BPM) system was modified.

Results from the most recent measurement are shown in Fig.1 and Table 1 which was taken in November 1998 after improvement of the BPM electronics [3]. To avoid non-linear effects, sextupole magnets were turned off. Because a part of beam was lost far downstream for some settings, BPMs only in 30m downstream changed steering magnets were used for the analysis. 10 BPMs in the wiggler sections, which had big non-linear response were not used. Fig. 1(a) shows response coefficients from the steering magnets to the BPMs calculated using the original model without 'fudge' factors vs. measured coefficients. Fig. 1(b) shows the model with new 'fudge' factors vs. measured coefficients. The new fudge factors are listed in Table 1. The new model has different strength of quadrupole fields from the original model up to a few percent.

Table 1: Magnet types and fudge factors

Type	Number of Magnets	Fudge factors	
BH1R-N	6	-2.07E-3	Combined bend*
BH1R-Ma	16	2.87E-2	
BH1R-Mb	14	1.58E-2	
QF2R (thick)	26	1.11E-3	Main Quad in Arc Section
H2 (thin)	8	2.20E-2	Matching Quad in Arc Section
H3 (thick)	8	-8.94E-3	
H4 (thick)	16	-1.04E-2	Matching Quad in Straight Section
T1 (thin)	4	-1.95E-2	
T42L (thick)	4	5.47E-3	
T42S(thin)	6	1.01E-2	

*BH1R-N, -Ma, -Mb have the same spec. but made by different companies or from different lots.

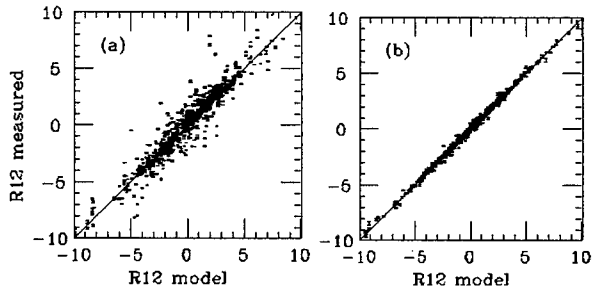

Fig. 1: Response coefficients from the steering magnets to the BPMs. (a):The original model vs. measurement and (b) corrected model vs. measurement. Both horizontal and vertical coefficients are plotted.

After the diagnostics, model calculations for orbit corrections and dispersion corrections have become useful in our beam tuning.

Simulations were done to estimate the accuracy of the method. The measurement of orbit change at BPMs changing steerings was simulated using the computer code SAD [2]. In the simulation, errors were set as in Table 2.

Table 2: Random errors in optics diagnostics simulation.

BPM resolution (pulse to pulse)	gaussian r.m.s. 10 μm
BPM position sensitivity factor	gaussian r.m.s 10 %
Steering's kick angle / current	gaussian r.m.s 10%
Quadrupole field(thick magnets)	Uniform +-1%
Quadrupole field(thin magnets)	Uniform +-2%

0-7803-5573-3/99/$10.00@1999 IEEE.

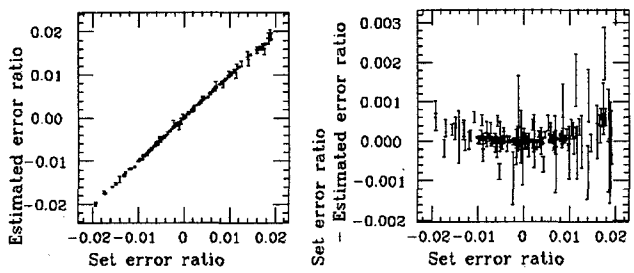

Fig 2 : Set error ratio vs. (left) estimated error ratio of the strength of quadrupole field and (right) difference between the estimated error ratio and the set error ratio. Results of all types from 22 different random seeds are plotted. The error bars are the estimated resolution.

The errors of position sensitivity factors and the kick angles seem over estimated but further simulation studies show that the fitting results of quadrupole field errors are not sensitive to these errors. Lengths of the quadrupole magnets are 18 cm (thick) or 6 cm (thin). We assumed the thick magnets have less error because their effective lengths are expected to be better known. The combined bending magnets were treated as thick magnets and BH1R-Ma and BH1R-Mb are regarded as the same type in this simulation.

BPM data were simulated from calculated beam positions considering the BPM resolution. 5 different currents, I=-1, -0.5, 0, 0.5, 1 A, were set for every steering magnets where 1 A corresponds to the kick angle of about 0.3 mrad. Optics was set as a design which is the base of the present operation optics.

The errors of quadrupole fields, the sensitivity factors of the BPM and the current-to- angle factors of the steering magnets were estimated using the same analysis program for the real data. Simulations were done with 22 random seeds.

The left of Fig. 2 shows set error ratio vs. estimated error ratio of the quadrupole field strengths of all types. Results from all 22 random seeds are plotted together. The right shows the difference of estimated error ratio and the set error ratio. The error bars are the estimated resolution propagated from the resolution of BPMs, 10 micron. Most of the estimations are consistent with the set values within the resolutions indicating the validity of this analysis. Fig. 3 shows the resolution for each type of magnets averaged over the 22 random seeds.

The result shows that the common error for the same type of magnets is expected to be estimated in good resolution.

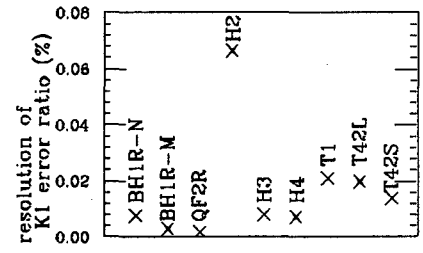

Fig. 3 : Estimated resolution of strength ratio for each type of magnets (%) averaged over the 22 random seeds.

2 TUNING FOR LOW EMITTANCE

2.1 Dispersion Correction

It is essential to make the vertical dispersion small in the arc sections for producing low vertical emittance beams. Relation between the dispersion and emittance was simulated using SAD [2]. In the simulation, all magnets were misaligned randomly with r.m.s. 20 micron. The vertical dispersions at the BPMs were tried to be zero using the steering magnets. Simulation was done for 2000 different random seeds. Fig. 4 shows square of the vertical dispersion averaged over the BPMs in the arc section vs. the vertical emittance calculated by SAD. Other effects such as the intrabeam scattering were not considered. One point corresponds to one random misalignment. The emittance has linear dependence on the square of the vertical dispersion at BPMs as

$$\varepsilon_y(\text{nm}-\text{rad}) \approx 0.0006 \left\langle \eta^2_{y,BPM}(\text{mm}^2) \right\rangle_{arc} \qquad (1)$$

where $\langle\ \rangle_{arc}$ means the average in the arc sections.

Though we assumed the random misalignment of 20 micron, results of further simulations with other realistic misalignment assumptions give almost the same dependence as the equation (1).

The result shows that the vertical dispersion at BPMs should be about 4 mm @to achieve our goal, 0.01 nm-rad.

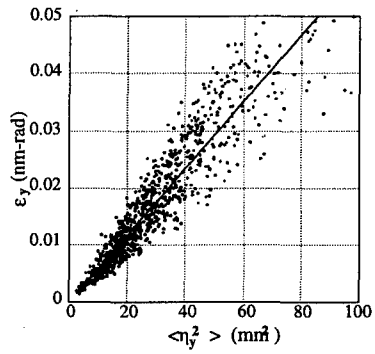

Fig. 4 : Square of the vertical dispersion averaged over BPMs in the arc section vs. the vertical emittance from simulation.

Dispersion function at BPMs in the ring are measured as the orbit difference for different RF frequencies.

A dispersion correction routine has been developed. Set of vertical steerings is calculated to reproduce the measured dispersion in the perfect model and opposite of the steerings are set. An typical example is shown in Fig. 5, the vertical dispersion before and after the correction. In this example, r.m.s. of the vertical dispersion in the arc sections are 13 mm before the correction and 4.3 mm after the correction, from the equation (1), corresponding to the vertical emittances of 0.10 and 0.011 nm-rad. On the other hand, apparent emittances, roughly monitored using SR-

interferometer [4], were about 0.08 and 0.05 nm-rad before and after the correction, respectively. The reason of the big difference in the case of after the correction has not been known yet. Both the emittance measurement and the dispersion measurement should be studied more.

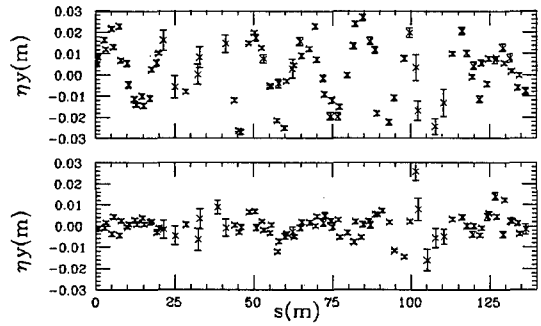

Fig. 5 : Measured vertical dispersion before (top) and after the correction (bottom).

2.2 *Local Orbit Bump*

Vertical orbit bumps have been applied in the ring to reduce the vertical emittance in try-and-error monitoring the vertical beam size using the SR-interferometer [4]. Because the dispersion correction program assumes no strength errors and no misalignment of magnets, the calculation can not be perfect and this empirical method is sometimes effective.

2.3 *Effect of Skew Quadrupole Fields*

Trim coils of 4 sextupole magnets are connected to produce skew quadrupole fields though there are not skew quadrupole magnets. The maximum strength of the field (SK_1) is estimated to be about 0.033 m^{-1} for each magnet. We have tried to see the effects of the skews to the vertical emittance but no clear effect has been observed so far.

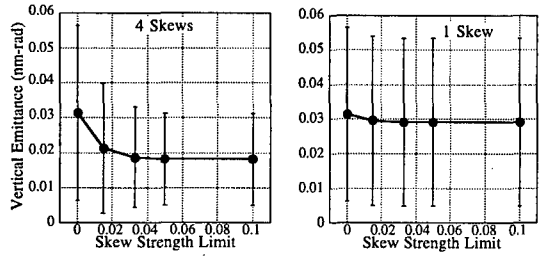

Fig 6 : Average of emittance vs. the limit of the strength. From simulation with 100 random seeds, the error bars represent r.m.s. fluctuation.

Fig. 6 shows result of simulation of effects of the skews. All magnets had random alignment errors of r.m.s. 30 micron and rotation error r.m.s. 0.5 mrad. Orbit and dispersion corrections were applied and strength of skew fields were searched for the minimum vertical emittance assuming the emittance was precisely monitored. The figure shows the average and the r.m.s. fluctuation of 100 random seeds vs. the limit of the strength of the skews. The left figure shows the case using all 4 skews and the right shows the case using only 1 skew. The results show that the present limit, 0.033 m^{-1}, is large enough, the effect of 1 skew will not be seen but proper set of 4 skews can reduce the emittance. As shown in Fig. 7, the emittance can be reduced more using more number of skews. The trim coils of the all sextupole magnets will be connected for skew quadrupole fields and the effects will be tested soon. However to find a good setting of the skews is not straight forward and we need good emittance monitors in order to try many settings.

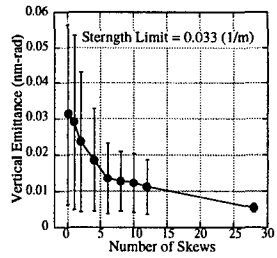

Fig. 7: Emittance vs. number of skews. From simulation with 100 random seeds, the error bars represent r.m.s. fluctuation.

3 SUMMARY

First order optics diagnostics was performed and the model calculations have been improved. The validity of the diagnostics method was demonstrated and the accuracy was estimated by simulations. Methods for tuning for the low vertical emittance, dispersion correction, local bumps and skew quadrupole fields, were discussed. The dispersion correction worked well and the apparent vertical dispersion seemed to be close to the goal for the vertical emittance, 0.01 nm-rad. But the apparent vertical emittance was still large [5,6] and more study of both the dispersion and the emittance measurement will be necessary. Effects of skew quadrupole fields have not been observed yet. The simulation showed that the effects will not be seen easily but it is possible to use the set of skews for the low emittance tuning with good emittance monitors.

4 ACKNOWLEDGMENT

The authors would like to thank professors Sugawara, Kihara and Takata for continuous support and encouragement.

5 REFERENCES

[1] K. Kubo et. al., "Test of Optics Diagnostics in ATF", PAC'97, Vancouver, May 1997.
[2] http://www-acc-theory.kek.jp/SAD/sad.html
[3] M. Takano et. al., "BPM electronics upgrade for ATF DR", EPAC98, Stockholm, June, 1998.
[4] T. Mitsuhashi et. al., "Beam size measurement at ATF DR by the use of SR interferometer", EPAC98.
[5] T.Naito et. al., "Emittance Measurement at ATF Damping Ring", this conference.
[6] T.Okugi et. al., "Vertical Emittance in the KEK Accelerator Test Facility", this conference.

TOLERANCES IN X-BAND MAIN LINACS OF FUTURE LINEAR COLLIDERS

T. Higo, K. Kubo and K. Yokoya, KEK, Tsukuba, Japan

Abstract

Tracking simulations have been performed for a realistic design of main linacs of X-band linear collider. We discuss about choice of the phase of the accelerating field relative to the bunches. The tolerances of the phase and the amplitude errors are studied.

1 INTRODUCTION

In order to preserve the low emittance through the main linacs of future linear colliders, various effects should be considered, errors of injection conditions, RF accelerating field, strength of magnets, misalignment and mechanical vibrations of magnets and accelerating structures and so on. Tracking simulations have been performed for a realistic design of main linacs of X-band linear collider with these errors [1]. Some of the estimated tolerances based on the simulations have been reported before [2,3]. Here we discuss about the choice of the phases of the accelerating field relative to the bunches and the tolerances of the phase and the amplitude errors. Because the vertical emittance will be much smaller than the horizontal emittance and tolerances will be much tighter, simulation results were shown only in the vertical plane.

2 PARAMETERS OF THE LINAC

One possible parameter set of the main linac of future linear colliders with CMS energy of 1 TeV was used in the simulations. Important parameters are listed in Table 1. The optics is a series of FODO cells, and the phase advance per length is proportional to the inverse of the square root of the beam energy [2,4].

Table 1: Parameters of the linac.

Initial beam energy	10 GeV
Final beam energy	500 GeV
Bunch charge	1.01x1010
Bunch length	125 mm
Nominal normalized vertical emittance	3x10-8 m-rad
Frequency of RF	11.424 GHz
Acc. gradient with loading	56.7 MV/m
Number of acc. structures	4788/linac
Acc. structure length	1.8 m
Averaged structure iris	0.18 λ
Length of a FODO cell	8.6 m at 10GeV
Phase advance/ FODO cell	90o at 10GeV

3 CHOICE OF RF PHASE

Energy distribution in a bunch is important in considering emittance preservation, e.g. as known as 'BNS damping' [5], and it can be controlled by the choice of the phases of the RF field along the linac. In addition to the relative energy spread (σ_E / E), let us define another parameter 'energy-z correlation' as follows,

$$\delta E / E \equiv \frac{1}{E\sigma_z q}\int E(z)z\rho(z)dz \qquad (1)$$

where σ_z is the bunch length, q the total charge, z the longitudinal coordinate, $\rho(z)$ the charge density and $E(z)$ the average energy at z.

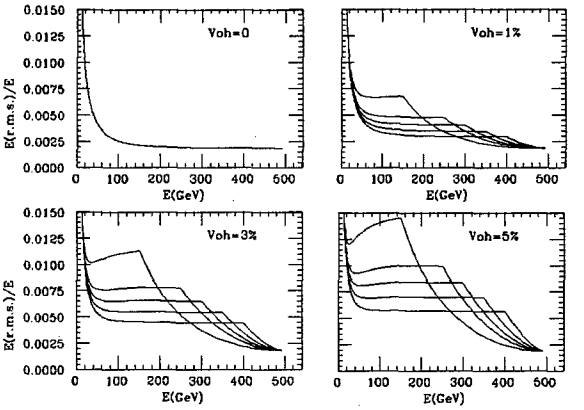

Figure 1: Relative energy spread along the linac.

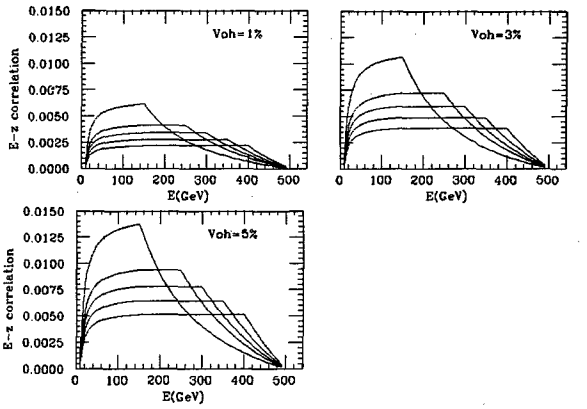

Figure 2: 'Energy-z correlation' along the linac.

We simulated six cases : (a) Constant phase, (b) Change phases at 150 GeV, (c) Change phases at 150 GeV and 250 GeV, (d) at 150 GeV and 300 GeV, (e) at 150 GeV and 350 GeV, (f) at 150 GeV and 400 GeV. In all cases, phases are chosen to make δE at the end of linac zero, and σ_E minimum. The phase in the case (a) is decided by this constraint as 15.4o (off crest angle of the bunch center). In the case of (c)~(f), the phases are chosen to make δE constant in the center energy region. 'Over head

0-7803-5573-3/99/$10.00@1999 IEEE.

voltage', V_{oh}, was a parameter which decide the phases in the cases (b)~(e).

$$V_{oh} \equiv V / V_{(a)} - 1 \quad (2)$$

where V is total of the RF voltage and $V_{(a)}$ that in the case (a). Making δE the bigger, δE becomes bigger and more voltage is needed for the same beam energy.

Cases of V_{oh}=0, 1, 3 and 5 % were simulated ($V_{oh}=0$ means the case (a)). σ_E / E is shown in Fig. 1 for the all cases and $\delta E / E$ is shown in Fig. 2 for the all cases except (a) which has almost zero $\delta E / E$. $\delta E / E$=0 and σ_E / E=0.02 were assumed at the beginning.

$\delta E / E$ for the auto phasing condition is approximately constant along the linac and a rough estimation gives

$$\delta E / E(\text{auto phasing}) \approx eq\beta^2 W_T(2\sigma_z)/8E \approx 0.022 \quad (3)$$

This is bigger than that even in the V_{oh}=5% cases. To make such big energy slope, a big over head voltage is needed and probably will not be realistic.

Emittance dilutions were simulated for injection errors, vibration of quadrupole magnets and misalignment of quadrupole magnets with a simple orbit corrections.

We take 'effective emittance'(ε_{eff}) as a measure of the beam quality for discussion of the jitters or fast errors which will not be corrected and emittance(ε) for the fixed or slowly changing errors which will be corrected.

$$\varepsilon_{eff} \equiv \sqrt{\langle y^2 \rangle \langle y'^2 \rangle - \langle yy' \rangle^2} \quad (4)$$

$$\varepsilon \equiv \sqrt{\langle (y-\langle y \rangle)^2 \rangle \langle (y'-\langle y' \rangle)^2 \rangle - (\langle yy' \rangle - \langle y \rangle \langle y' \rangle)^2} \quad (5)$$

where $\langle\ \rangle$ means the average of all particles.

Fig.3(a) shows ε_{eff} dilution due to injection jitters. The offset and the angle of the injected beam were randomly set as gaussian with sigma of 0.5 of the beam size. Except for the injection error, the linac was assumed to be perfect. Fig.3(b) shows ε_{eff} dilution due to transverse vibrations of quadrupole magnets. The transverse offset of quads were randomly set as gaussian with sigma of 10 nm. Except for the injection error, the linac was assumed to be perfect. The averages over 200 random seeds are shown.

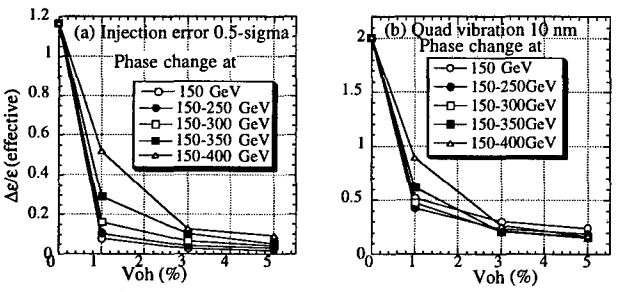

Fig. 3: Effective emittance dilution vs. V_{oh} with (a) injection jitters and (b) vibration of quadrupole magnets.

Fig.4 shows ε dilution due to transverse misalignment of quadrupole magnets with orbit corrections. A simple one-to-one orbit correction was assumed. There were steering magnets and BPMs at all quadrupoles. Only BPMs at focusing quads were used and the beam is steered to make the BPM readings zero. Transverse offset of the quads were randomly set as gaussian with sigma of 2 micron. The BPMs also have random transverse offset with sigma of 2 micron with respect to the quads' center. Resolution of the BPMs was 1 micron. Accelerating structures were aligned perfectly w.r.t. the beam. The averages over 100 random seeds are shown.

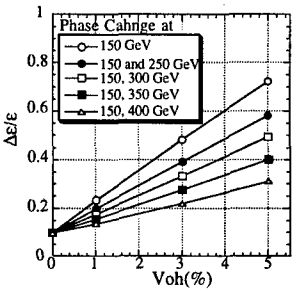

Fig. 4 : Average emittance dilution due to misalignment of quadrupole magnets with orbit correction.

It is obvious that $\delta E / E$ should be large, which means large over head voltage, to suppress the emittance dilution caused by the injection error and the quads' vibrations. On the other hand, a large energy spread makes the dispersive effects large which is shown in Fig.4. Of cause, considering the efficiency, a too large over head voltage should be avoided. As conclusion, the phases should be decided as a result of some compromise and the optimum V_{oh} will be 3~5 %.

For further simulations we pick up the four cases V_{oh}=0, V_{oh}=1% phase changes at 150 GeV and 250 GeV, V_{oh}=3% phase changes at 150 GeV and 300 GeV and V_{oh}=5% phase changes at 150 GeV and 350 GeV.

4. RF JITTER TOLERANCE

Simulations with jitter of the RF amplitude and phase have been done for the four cases of the phase choice. In the simulations, considering DLDS scheme [6], one RF unit consists of 12 accelerating structures and each unit has the same error of amplitude and phase with Gaussian distributions. All RF units have the same r.m.s. of the errors and no correlation was considered between different units.

4.1 Beam Energy

Here, we looked at final beam energy and energy spread with the error of the RF.

Amplitude jitter causes pulse to pulse fluctuations of the beam energy (average of the particles in one pulse). Assuming independent errors, the r.m.s. of the relative error of the beam energy can be estimated simply as

$$\sigma_{\langle E\rangle}/E = \sigma_{amp}/\sqrt{N_{RF}} = \sigma_{amp}/\sqrt{399} \qquad (1)$$

where σ_{amp} is the r.m.s. of the relative amplitude jitter of each unit and N_{RF} = 399 the number of RF units. Simulations confirmed the equation (1) and showed that the pulse to pulse fluctuation of the energy spread will be less than 1×10^{-6} up to σ_{amp}=8%.

The phase jitter causes the pulse to pulse fluctuations of the beam energy and also reduces the mean beam energy. Results of simulations with 200 random seeds are shown in Fig.5, the average of the relative beam energy and the fluctuations of the beam energy vs. r.m.s. of the phase jitter.

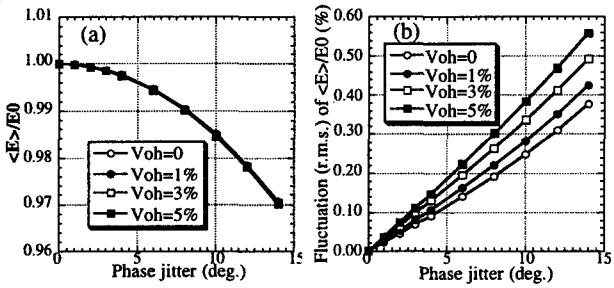

Figure 5: (a) Average of the relative beam energy and (b) fluctuations of the beam energy vs. RF phase jitter.

Assuming that the tolerance of the final energy error due to the RF error is 0.1%, the tolerances for the RF amplitude and phase jitters will be about 2% and 3o, respectively.

4.2 Transverse motion

Energy error along the linac may affect the transverse motion of the beam. The pulse to pule energy difference will cause a pulse to pule orbit difference due to the dispersive effect.

As the initial condition, we set random misalignment of the quads and calculated strength of the steering magnets for orbit corrections without RF errors. The misalignment and the setting of the magnets were saved and used in simulations with RF errors. Effective emittances were calculated with the position and the angle without jitters as the reference.

Fig. 6 shows ε_{eff} dilution vs. r.m.s. of the amplitude jitter and the phase jitter for the four cases of the phase choice. Each point represents average of 200 random seeds for jitters in one initial condition (1 linac). The same initial condition was used in the same case of the phase choice. Because the results are statistically poor, simulations were done for 50 different initial conditions and 50 different RF errors for each initial condition (50 linacs, 50 pulses for each linac) only in the case of V_{oh}=3%. Fig. 7 shows ε_{eff} increase vs. r.m.s. of the amplitude and phase jitter. In this figure, the average and the r.m.s. fluctuation of the additional increase of ε_{eff} due to the jitters are shown.

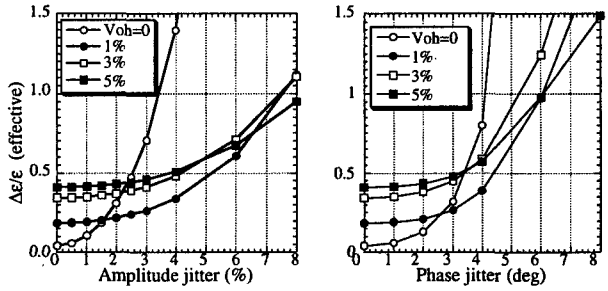

Fig.6: Effective emittance vs. r.m.s. of (a) amplitude jitter and (b) phase jitter. Each point represents average of 200 random seeds for jitters in one initial condition.

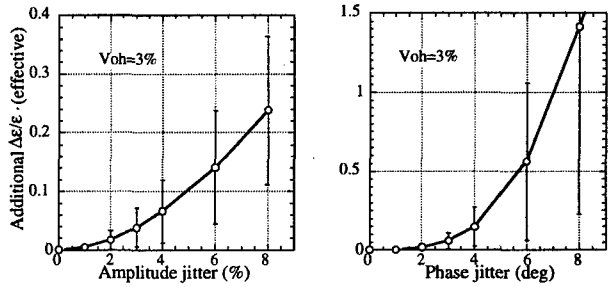

Fig. 7: Increase of effective emittance vs. r.m.s. of (a) amplitude jitter and (b) phase jitter of RF. Average and r.m.s. fluctuation from 50 different misalignments and 50 different jitters are shown.

Compared with the effect to the final energy, the effect of the RF jitter to the emittance will be not significant.

5 SUMMARY

The choice of the phases and the tolerances of the jitters of the phase and the amplitude of the RF accelerating fields have been studied for future X-band linear colliders. The phase choice can be represented by the 'over head voltage' (V_{oh}) and its optimum will be 3~5%. The tolerances of the jitters will be decided by the effects to the final energy error not to the emittances. Requiring the error of the final energy of less than 0.1 %, the jitter tolerances will be about 2% for the amplitude and about 3o for the phase.

6 ACKNOWLEDGMENT

The authors would like to thank Dr. T.O.Raubenheimer of SLAC for valuable suggestions and discussions.

7 REFERENCES

[1] K.Kubo et. al., NLCNote-13 (1995).
[2] JLC Design Study Group, KEK-Report, 97-1, (1997).
[3] e.g., K.Kubo et.al., Proc. of PAC95, p3112, (1995).
[4]"http://www.slac.stanford.edu/xorg/ilc-trc/Table3_2/table3_2.html".
[5] V.Balakin, A.Novokhatsky and V.Smirnov, Proc. of HEACC83, p119 (1983)
[6] H.Mizuno and Y.Otake, Proc. of LINAC94, p463, (1994)

CIRCUMFERENCE CORRECTION CHICANES FOR DAMPING RINGS*

P. Emma and T.O. Raubenheimer
Stanford Linear Accelerator Center, Stanford University, Stanford, CA 94309, USA

1 INTRODUCTION

Several low-emittance damping rings are presently being designed to meet the requirements of future linear colliders. These rings tend to have relatively large circumferences ~300 m so that they can damp many trains of bunches at the same time. With the large circumference, the ring path length may become quite sensitive to thermal and ground motion effects. In addition, most of the rings include damping wigglers whose path length varies with their strength.

In e^-/e^+ storage rings, the beam revolution time is determined by the rf frequency. Thus, to restore the proper revolution time, a change in the nominal path length will cause a change in both the beam energy and the closed orbit. The change in energy is given by:

$$\frac{dE}{E_0} = -\frac{1}{\alpha_p}\frac{\Delta C}{C_0}, \qquad (1)$$

where α_p is the momentum compaction and C_0 is the nominal ring circumference. The change in the closed orbit is simply given by the energy change and the dispersion function. This change in orbit and energy can decrease the dynamic acceptance of the ring and make it difficult to preserve the ultra-small damped emittances. Because damping rings need strong focusing to attain the small beam emittances and thus tend to have very small values of momentum compaction, they can be very sensitive to changes in their circumference. For example, to limit the energy fluctuations in the NLC damping rings to 10% of the beam equilibrium energy spread, the path length must be controlled to about 20 μm.

Circumference variations have been seen at most storage rings including LEP, the APS at Argonne, the SLAC damping rings, and the ATF damping ring test facility [1] at KEK. At the APS, typical path length variations are ~0.2 mm [2] and are correlated with seasonal, tidal, and diurnal fluctuations. The SLAC damping rings change by millimeters during approach to thermal equilibrium when the rings are started, but little variation is seen after equilibrium is reached. At the ATF, variations of up to ±3 mm over months have been observed [3]. The precise mechanisms responsible for these changes are not, at present, well understood.

Another path length variation arises when the strength of the damping wigglers is changed. Assuming a sinusoidal wiggler field, the circumference change is

$$\Delta C \approx \frac{1}{4}\frac{L_w}{\rho_w^2 \kappa_w^2}, \qquad (2)$$

where L_w is the wiggler length, ρ_w is the peak wiggler bend radius, and κ_w is its wavenumber ($\equiv 2\pi/\lambda$). At the ATF (and similarly for the NLC ring), the wigglers increase the circumference by ~2 mm at full strength.

Although some of the variation in path length can probably be reduced by design, the inclusion of a circumference correction method in the design of future damping rings seems prudent. There are a few possible approaches: 1) physical displacement of the arc magnetic elements; 2) control of the orbit using steering correctors or, equivalently, variation of the arc bending magnets and quadrupoles (the later is necessary to keep tunes constant); and 3) additional elements dedicated to path length control. In this note, we describe the correction available by adding a simple 4-dipole chicane to a straight-section in a damping ring. A chicane has the advantage of being varied without significantly affecting ring optics or trajectory outside of the chicane. Thus, the path length can be varied during operation and the chicane can be used in a feedback system to stabilize the circumference. In the following, we describe the effects of the chicane on critical ring parameters, including the equilibrium emittance and momentum compaction.

2 CHICANE IMPACT ON DAMPING RING PERFORMANCE

A standard 4-dipole chicane is shown in Figure 1 where the symbol definitions are indicated.

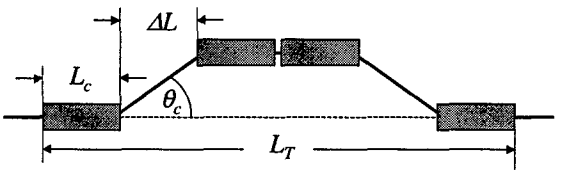

Figure 1: Four dipole chicane with symbol definitions indicated.

2.1 Path Length

For an 'on-energy' particle through this chicane, the change in path length (*i.e.* circumference), with respect to the path length with no chicane, and for $\theta_c << 1$, is

$$\Delta s \approx \theta_c^2\left(\frac{2}{3}L_c + \Delta L\right). \qquad (3)$$

Note that Δs is always positive so that providing a bipolar circumference correction requires a chicane with a

* Work supported by Department of Energy, contract DE-AC03-76SF00515.

0-7803-5573-3/99/$10.00@1999 IEEE.

nominal bias at nominal circumference (*i.e.* $\theta_c = \theta_{c0} \neq 0$). The path length is then increased (decreased) by an increase (decrease) of the dipole bend angles.

$$\Delta s_b \approx \left(\theta_c^2 - \theta_{c_0}^2\right)\left(\frac{2}{3}L_c + \Delta L\right) \qquad (4)$$

The subscript b is added to identify a bipolar correction from the unipolar one in Eq. (3), ($\Delta s_b = \Delta s - \Delta s_{max}/2$).

2.2 Emittance

The addition of the chicane dipoles will, of course, have some impact on the damped horizontal emittance. The normalized equilibrium emittance for a damping ring, with chicane included, can be written as [4]

$$\gamma\varepsilon = \cdot\frac{C_q\gamma^3 I_5}{I_2 - I_4} = \frac{C_q\gamma^3}{J_x I_2}\cdot\frac{I_5 + \Delta I_5}{1 + \Delta I_2/J_x I_2 - \Delta I_4/J_x I_2}, \qquad (5)$$

where I_j (j = 2,4,5) are the usual j^{th} synchrotron integrals, ΔI_j are their chicane induced changes, γ is the beam energy factor, J_x is the nominal horizontal partition, and $C_q \approx 3.8\times10^{-13}$ m. For an isomagnetic, uncoupled ring with the chicane of Figure 1, the first correction term ($\Delta I_2/J_x I_2$) at the right-side of Eq. (5) can be expressed as

$$\frac{\Delta I_2}{J_x I_2} = \frac{4}{N_B}\cdot\frac{\tau_x}{\tau_y}\cdot\frac{L_B}{L_c}\cdot\frac{\theta_c^2}{\theta_B^2}\cdot\frac{1}{1+F_w} << 1, \qquad (6)$$

where F_w (≥ 0) is the ratio of the energy loss per turn in the wiggler to that in the arcs (typically ~1), τ_x/τ_y (= $1/J_x$) is the ratio of horizontal to vertical damping times (typically ~1), L_B and θ_B are length and bend angle of an arc dipole, and N_B is the number of arc dipoles in the ring (typically >>1). As will be demonstrated, Eq. (6) is ~0.01 for a chicane with Δs_{max} = 5 mm placed in the 1.54 GeV ATF damping ring with wigglers switched on (see Table 1). Thus, this ΔI_2 term in the denominator of Eq. (5) can typically be ignored. Similarly, the ΔI_4 term in the denominator is related to Eq. (6) by

$$\frac{\Delta I_4}{J_x I_2} \approx \left(\frac{L_c + \Delta L}{2L_c}\right)\cdot\frac{\Delta I_2}{J_x I_2}\cdot\theta_c^2 << 1, \qquad (7)$$

which is smaller yet. For the ATF case above, Eq. (7) is ~6×10^{-5}, so this term is completely insignificant. These synchrotron integrals are not significantly changed by a reasonable chicane and, therefore, damping times, losses per turn, and partition numbers are also nearly unaffected. With these results, Eq. (5) becomes

$$\gamma\varepsilon \approx \frac{C_q\gamma^3}{J_x I_2}(I_5 + \Delta I_5), \qquad (8)$$

where J_x and I_2 are the nominal horizontal partition and 2nd synchrotron integral of the pre-chicane ring, including wigglers, and the ΔI_5-term is the change in the nominal equilibrium emittance due to the chicane.

The change in the 5th synchrotron integral is

$$\Delta I_5 = \frac{L_c}{|\rho_c|^3}\sum_i\left\langle\eta_i^2\gamma_i + 2\alpha_i\eta_i\eta_i' + \eta_i'^2\beta_i\right\rangle, \qquad (9)$$

where ρ_c ($\equiv L_c/\theta_c$) is the bend radius of the chicane dipoles, η_i and η_i' are the spatial and angular dispersion functions through each dipole, γ_i, β_i, and α_i are the Twiss parameters through each dipole, and the brackets denote the mean value over the length of each dipole. It can be shown that for a small initial α-function (at 1st dipole entrance), $|\alpha_1(0)| < 1$, and a initial β-function which satisfies $\beta_1(0) > L_c + \Delta L$, Eq. (9) reduces approximately to

$$\Delta I_5 \approx \frac{4L_c}{|\rho_c|^3}\bar{\beta}\left\langle\eta'^2\right\rangle = \frac{4|\theta_c|^3}{L_c^2}\bar{\beta}\left\langle\eta'^2\right\rangle, \qquad (10)$$

where β-*bar* is the mean beta function over all dipoles. (For small $|\alpha|$, the β-function is nearly constant.) In a symmetric chicane, the angular dispersion, $\eta'(s) = s/\rho_c$, is equal in all dipoles and its mean-squared value over L_c is $\langle\eta'^2\rangle = \theta_c^2/3$. Eq. (3) is now used to substitute for θ_c, and relations for the nominal 2nd synchrotron integral and horizontal partition are introduced.

$$I_2 = \frac{3C_0}{r_e c\gamma^3\tau_y}, \quad J_x = \frac{\tau_y}{\tau_x} \qquad (11)$$

Here, r_e is the classical electron radius and c is the speed of light. The length of the chicane is defined as $L_T \equiv 4L_c + 2\Delta L$. (This definition does not include a potential small drift between center bends which has no effect on these results.) With these relations added, the change in the nominal emittance from Eq. (8) becomes

$$\Delta\gamma\varepsilon \approx \frac{4}{9}C_q r_e c\cdot\frac{\tau_x\bar{\beta}\gamma^6}{C_0}\cdot\frac{\Delta s^{5/2}}{L_c^2(L_T/2 - 4L_c/3)^{5/2}}. \qquad (12)$$

The 6th power scaling in γ holds only for a constant τ_x. The emittance increase is minimum at $L_c = \Delta L = L_T/6$ and

$$\Delta\gamma\varepsilon \approx 393\cdot C_q r_e c\cdot\frac{\tau_x\bar{\beta}\gamma^6}{C}\cdot\frac{\Delta s^{5/2}}{L_T^{9/2}}, \qquad (13)$$

where the chicane must satisfy

$$|\theta_c| \approx 3\sqrt{\frac{2\Delta s}{5L_T}}, \quad L_c = L_T/6 = \Delta L. \qquad (14)$$

Eq. (13) is the equilibrium emittance increase produced by adding, to a damping ring, a chicane with additional path length Δs. Numerical results are described below.

2.3 Momentum Compaction

The effect on momentum compaction of the ring is

$$\alpha_p = \alpha_{p_0} - 2\frac{\Delta s}{C_0}, \qquad (15)$$

with α_{p0} the nominal momentum compaction. This is typically a very small change in α_p and also indicates that

the chicane's effect on the extracted bunch length ($\propto \alpha_p^{1/2}$) is insignificant.

2.4 Energy Spread

Finally, the relative change in the 3rd synchrotron integral is given by

$$\frac{\Delta I_3}{I_3} = \frac{4}{N_B}\cdot\frac{L_B^2}{L_c^2}\cdot\left|\frac{\theta_c}{\theta_B}\right|^3 << 1. \qquad (16)$$

For the ATF chicane described above, Eq. (16) is 0.074. In consideration of the small impact on I_2 and insignificant change in I_4 shown in Eqs. (6-7), the chicane's impact on the ring's energy spread can be approximated by

$$\sigma_\delta \approx \sigma_{\delta_0}\sqrt{1+\frac{4}{N_B}\cdot\frac{L_B^2}{L_c^2}\cdot\left|\frac{\theta_c}{\theta_B}\right|^3\left[1-\frac{2}{J_\varepsilon(1+F_w)}\cdot\frac{\theta_B}{\theta_c}\frac{L_c}{L_B}\right]}, \qquad (17)$$

where $J_\varepsilon = 3 - \tau_y/\tau_x$. Eq. (17) shows that the energy spread can increase or decrease, depending on parameters.

3 ATF DAMPING RING

Parameters of the ATF and NLC damping rings, with wigglers switched on, are listed in Table 1.

Table 1: ATF and NLC damping ring parameters with wigglers on and no chicane.

Parameter	sym.	unit	ATF	NLC
Beam energy	E	GeV	1.54	1.98
Arc-dipole magnet length	L_B	m	1.0	1.07
Arc-dipole bend angle	θ_B	deg	10.0	10.6
Total no. of arc-dipoles	N_B	—	36	34
Equilibrium X emit. (rms)	$\gamma\varepsilon_0$	μm	4.3	2.4
Horizontal damping time	τ_x	msec	6.8	5.2
Vertical damping time	τ_y	msec	9.1	5.2
Mean beta at chicane	$\langle\beta\rangle$	m	~10	~6
Ring circumference	C_0	m	139	282
Ratio wiggler to arc E-loss	F_w	—	1.6	2
Rel. energy spread (rms)	σ_δ	0.1 %	0.72	0.91
Momentum compaction	α_{p0}	—	1.9	0.58

In order to fit such a chicane into the existing ATF lattice requires a free beamline section of length $\geq L_T$. In the ATF, a 2.1-meter space can be made available by removing one of eight wiggler sections. In this case, (L_T = 2 m) the range of $\Delta s_b = \pm 1$ mm correction is possible with a maximum emittance increase (at $\Delta s_b = +1$ mm) of ~8% at 1.54 GeV. This is a fairly small circumference correction in light of the ±3 mm variations observed. It may, however, be possible to add two 2-meter chicanes which will double both the Δs_b range and the emittance increase. This should be compared with doubling the Δs_b range using a single, stronger chicane. The latter method multiplies the emittance increase by $2^{5/2} \approx 5.7$. The double chicane, however, requires the elimination of 25% of the ATF wiggler which will increase the vertical damping time by ~20%. A simple solution which provides a ±3-mm correction does not appear to be viable.

4 NLC MAIN DAMPING RING

Parameters of the 3-bunch train NLC main damping ring used here are listed in Table 1. These parameters represent a recent proposal which includes 40-meters of wiggler in order to increase the net momentum compaction to $>5\times10^{-4}$.

In order to provide a ±1 mm circumference correction range for the NLC ring requires a single chicane of L_T = 2.6 m, $\theta_{c_{max}} = 3°$, with $\Delta\varepsilon/\varepsilon_0 \approx 6\%$ at $\Delta s_b = +1$ mm. Two such chicanes can provide a ±2 mm range with a 12% maximum growth, or a ±1.5 mm range at a 6% maximum growth. Figure 2 shows the relative emittance increase for the NLC main damping ring, using Eq. (13), for chicane lengths of 1, 2, 3, 4, and 5 meters versus unipolar circumference correction, Δs.

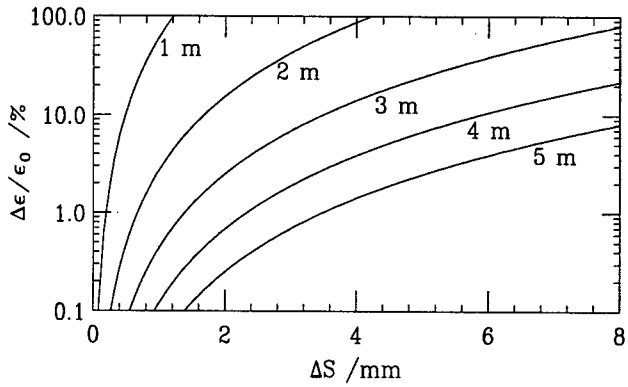

Figure 2: Relative equilibrium emittance increase vs. circumference change for NLC main damping ring with chicane lengths, L_T, of 1, 2, 3, 4, and 5 meters at 1.98 GeV, $\langle\beta\rangle$ = 6 m, $\gamma\varepsilon_0$ = 2.4 μm, τ_x = 5.2 msec.

The effect of a double chicane for the NLC can be estimated if both horizontal and vertical scales of Figure 2 are multiplied by 2. In this case Δs is the total path length change and $\Delta\varepsilon/\varepsilon_0$ is the total emittance increase. Providing more than ±2 mm correction range for the NLC using only chicanes may be problematic. Larger corrections, although not clearly necessary, can be generated by either displacing ring components or by changing arc magnet excitation levels.

5 REFERENCES

[1] J. Urakawa, "KEK/ATF Damping Ring", PAC97, Vancouver, B.C., Canada, (1997).

[2] M. Ross, M. Borland, private communication (1998).

[3] Report on 4th International Collaboration Meeting, July 17, 1998, J. Urakawa editor, internal note.

[4] R.H. Helm, et. al., "Evaluation of Synchrotron Radiation Integrals", SLAC-PUB-1193 (A), March 1973.

THE BALLISTIC ALIGNMENT METHOD*

T.O. Raubenheimer and D. Schulte†
SLAC, PO Box 4349, Stanford, CA 94309 and CERN, CH-1211, Geneva 23, Switzerland

Abstract

In order to preserve the very small beam emittance in the main linacs of future high-energy linear colliders a new alignment method, the so-called ballistic alignment method, has been developed. A description of the method is given and it is applied to the Compact Linear Collider (CLIC) [1]. In this scheme the quadrupoles are divided into bins which are corrected one after the other. In the first step, the quadrupoles in a bin are switched off to use a ballistic beam to align the beam position monitors (BPMs). Next, a simple one-to-one correction is used to align the quadrupoles. The dependence of the emittance growth on different error sources is investigated.

1 INTRODUCTION

In the main linac of CLIC, the beams are accelerated in 30 GHz structures. The high rf frequency allows for high acceleration gradients and therefore a high centre-of-mass energy, but also leads to strong transverse wakefield effects.

Descriptions of the CLIC main linac lattices are given in [2]. Here, the focus is on the machine with $E_{cm} = 1$ TeV, for which the lattice consists of 8 sectors of FODO cells of constant length and phase advance; the most important parameters are listed in Table 1. The ballistic alignment is followed by tuning the emittance with bumps to achieve an emittance growth of $\Delta\epsilon_y/\epsilon_{y,0} \leq 40\,\%$ however using the technique alone would not compromise the luminosity much, in contrast to the situation at higher energies.

In the CLIC lattice, a BPM is placed in front of each quadrupole; this is a significant difference to the NLC where the BPMs are positioned in the centres of the quadrupoles which allows very good relative alignment of the BPM and quadrupole using a shunt method [3]. On the other hand, placing the BPMs outside the magnets allows the CLIC design the use of very precise rf BPMs which have large outer diameters [4]. The alignment technique has been tailored to this difference; other possibilities are also being investigated [5].

2 DESCRIPTION OF THE METHOD

The linac is divided into bins which are corrected one after the other. Each bin starts with a quadrupole and ends with a BPM. The next bin starts with the quadrupole immediately following this BPM. The quadrupoles in the bin are switched off except for the first one. Its field strength is halved in order to minimise the beam size at the end of the bin. With correction coil of the first quadrupole, the beam is centred in the BPM at the end of the bin. Then, the positions of the other BPMs are redefined such that they are centred on the beam. This can be done either by moving them or by adding an offset to the measured position values. The quadrupoles are switched on again and their positions are adjusted so that again all BPMs show no offset.

In practice, the quadrupoles can not be switched off in a single step, since the beam can reach rather large offsets and might hit the beam pipe. By reducing the magnet strengths gradually and adjusting the correction coil in parallel this can be avoided. Furthermore, because the beam jitters transversely, it is not possible to steer it exactly to the centre of the last BPM. It is therefore necessary to use the position information once it is close to the centre and correct the measured values assuming a linear trajectory. The positions of the BPMs are moved using this corrected signal. When the quadrupoles are switched on again one has to use the same precautions as when switching them off.

Table 1: Parameters of the CLIC main linac and beam at $E_{cm} = 1$ TeV. The ϵ_x has not yet been fixed, its final value is taken overestimating the effects of coupling slightly.

Part. per bunch	N	$4 \cdot 10^9$
Initial horizontal emittance	ϵ_x	$1.48\,\mu$m
Initial vertical emittance	ϵ_y	$0.05\,\mu$m
Bunch length	σ_z	$50\,\mu$m
Linac active length		5500 m
Fill factor		74 %
Gradient	G	100 MV/m

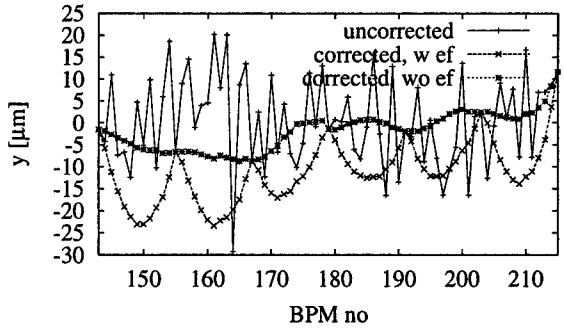

Figure 1: BPM positions before and after the ballistic correction step. The earth field was taken to be completely uncompensated (w ef) and fully compensated (wo ef).

* Work partially supported by the Department of Energy, contract DE-AC03-76SF00515.

† Email: Daniel.Schulte@cern.ch

A simple one-to-one correction is performed correcting the quadrupoles to again centre the beam in all BPMs.

It is also possible to achieve a ballistic beam by moving the centres of the quadrupoles in the bin onto the beam trajectory. This can be achieved by slightly varying their strength and finding a position where they do not change the trajectory. This implementation also works in simulations giving very promising results. It will not be considered in the following, since an error analysis remains to be done.

3 ERROR SOURCES

Even if the quadrupoles are switched off, the beam does not follow a straight trajectory. The transverse wakefields of the structures deflect the beam. If the bin is relatively long this deviation can become large. In order to prevent this from leading to an instability in the correction scheme, one has to either calculate the trajectory including the effect of the structures or to iterate the ballistic step.

The magnetic field of the earth also bends the trajectory. This effect can be reduced by shielding the beam line or by adding small dipoles to compensate the measured earth field. Even if this is not done, it is possible to take the effect into account in the correction algorithm as long as the field is measured. Other field sources may exist, for example, the remanent field in the quadrupoles when they are switched off. They can disturb the trajectory if the quadrupole centres are far from the beam trajectory. The alignment procedure can be repeated to yield convergence. While, in the first step, the quadrupoles can have large offsets with respect to the beams, these will be reduced after the first iteration due to the "few-to-few" correction with the quadrupoles switched on. This reduces the effect of the remanent fields on the beam trajectory, resulting in a beam that is closer to being really ballistic. Finally, the magnetic centres of the quadrupoles may shift as the magnets are switched on or off. In this case, some residual effect can be found.

4 ASSUMED TOLERANCES

All elements are assumed to be initially scattered around a straight line that defines the ideal beam line. These position errors are assumed to follow a normal distribution with a sigma of $\sigma_{BPM} = \sigma_{struct} = 10\,\mu$m for the BPMs and structures and $\sigma_{quad} = 50\,\mu$m if not otherwise mentioned. The resolution of the BPMs is $\sigma_{res} = 0.1\,\mu$m, the vertical and horizontal jitter of the beam at the linac entry are $\sigma_{jitt,y} = 0.1\sigma_y$ and $\sigma_{jitt,x} = 0.1\sigma_x$, respectively. The beam also has a constant offset of $\sigma_{off,x} = \sigma_{off,y} = 10\,\mu$m in the two planes. The remanent field of the quadrupoles is assumed to have a uniform distribution in the range $0 - 2\,\%$ of the full gradient. The centres are shifted between the two states by a Gaussian with $\sigma_{centre} = 10\,\mu$m, these shifts are constant from one iteration to the next.

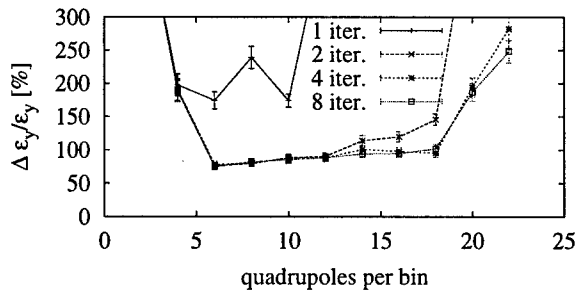

Figure 2: The normalised emittance growth for different number of quadrupoles per correction bin.

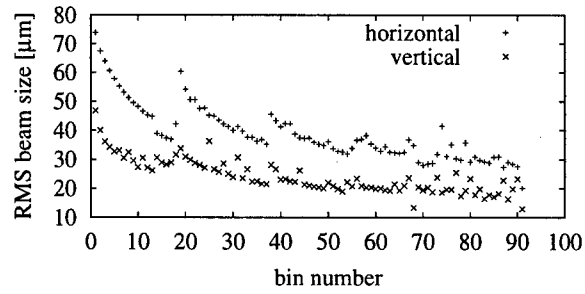

Figure 3: The maximum beam size along the linac during the ballistic correction step.

Only single bunch effects will be considered in the following. All simulations were performed using the code PLACET [6] for 100 different machines. The random number generator was set to the same initial state for each simulation.

5 CONVERGENCE

The length of the correction bin is important: if it is too short, the contribution from the kinks between bins becomes important; if it is too long, the transverse size of the ballistic beam becomes large and the beam starts to deviate significantly from a straight line due the different imperfections. In Fig. 2, the normalised emittance growth is shown for different numbers of quadrupoles per bin. The response coefficients are calculated without taking the wakefields into account. With a bin length of 6 quadrupoles, the method leads to good results, and, with two steps, the method converges. For long sectors, it starts to become bad again. This could be avoided by doing the ballistic step in several iterations with a small gain.

In the following, a bin length of 12 quadrupoles is taken. For this case, the horizontal and vertical beam sizes during the ballistic correction step are shown in Fig. 3.

The effect of the earth's magnetic field on the correction is displayed in Fig. 4. It is significant but not enormous for the assumed values of 40 μT vertically and 20 μT horizontally. The latter value certainly depends on the direction of the linac. Already a small suppression of the field almost completely eliminates the effect. In the following, the

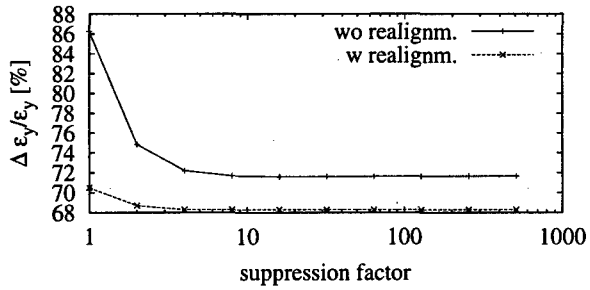

Figure 4: The dependence of the vertical emittance growth on the suppression of the magnetic field of the earth.

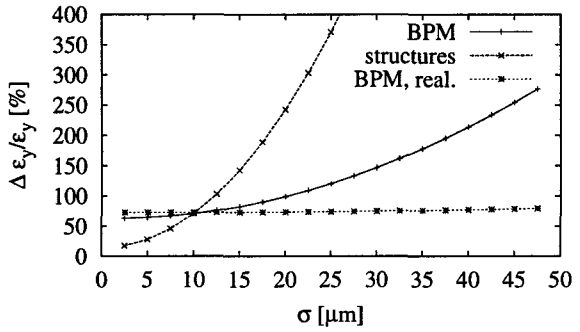

Figure 5: The dependence of the emittance growth on the size of σ_{struct} and σ_{BPM}.

earth's magnetic field will be disregarded.

6 INITIAL MISALIGNMENT

As can be seen in Fig. 5, the emittance growth depends strongly on the misalignment of the structures. The contribution from the initial misalignment of the BPMs is significantly smaller. It is possible to align the acceleration structures with respect to the beam after the ballistic correction using either the dipole signal from the structures or BPMs on the structure girders. Here, it is assumed that each structure can be aligned separately with a precision of $\sigma_{struct} = 10\ \mu$m which corresponds to the initial misalignment. The resulting emittance growth for different BPM offsets can also be found in Fig. 5. The emittance does not increase significantly with the initial BPM misalignments. Aligning the structures with the beam thus significantly relaxes the initial alignment tolerances not only for the structures themselves but also for the BPMs. Also, the effect of the earth's magnetic field is reduced, see Fig 4.

The emittance increase does not depend very much on the vertical beam jitter during correction. A jitter of $\Delta_y = 0.5\sigma_y$ leads to an additional emittance increase of only 2 %. But a beam with large jitter requires a significantly larger aperture to avoid losses and not to be sensitive to quadrupolar wakefields. This is more likely to limit the allowed jitter, especially since the resolution can in principle be refined by averaging over many pulses.

The resolution assumed for the BPMs is very good. It affects the precision of their alignement to the beam in the first step of the correction and the precision of the one-to-one correction performed in the second step. It is assumed that the signal used to align the BPMs and that used later to align the beam have the same error size. Figure 6 shows the dependence of emittance growth on the resolution.

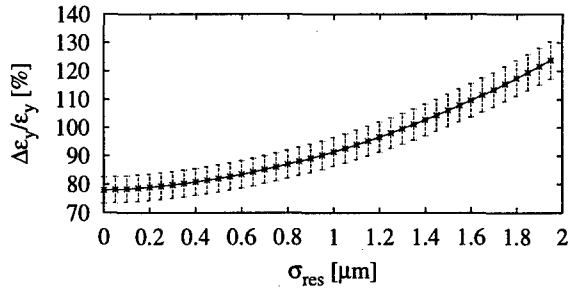

Figure 6: The emittance growth in the main linac versus the resolution of the BPMs.

7 CONCLUSION

In this paper, the properties of the ballistic alignment method have been presented in some detail. This simple method is able to achieve a small emittance growth in a linac where the BPMs are not inside the quadrupoles. The effect of earth's magnetic field, remanent fields in the quadrupoles, and beam jitter can be kept under control. It has been shown that aligning the structures with the help of the beam can significantly relax the alignment tolerances on all elements.

8 REFERENCES

[1] J.-P. Delahaye and 30 co-authors, "CLIC a 0.5 to 5 TeV Compact Linear Collider." *EPAC 1998* and *CERN-PS-98-009-LP*.

[2] D. Schulte. "Emittance preservation in the main linac of CLIC". *EPAC 1998* and *CERN-PS-98-018-LP*.

[3] The NLC Design Group. "Zeroth-Order Design Report for the Next Linear Collider". *SLAC-Report 474 (1996)*.

[4] J. P. H. Sladen, I. Wilson, and W. Wünsch. "CLIC beam position monitor tests". *CERN/PS-96-029-LP*.

[5] T. E. d'Amico and G. Guignard. "Multi-step lining-up correction of the CLIC trajectory". This conference.

[6] D. Schulte To be published.

RANDOM WALK MODEL FOR CELL-TO-CELL MISALIGNMENTS IN ACCELERATOR STRUCTURES*

G. V. Stupakov† and T. O. Raubenheimer
Stanford Linear Accelerator Center, Stanford University, Stanford, CA 94309

Abstract

Due to manufacturing and construction errors, cells in accelerator structures can be misaligned relative to each other. As a consequence, the beam generates a transverse wakefield even when it passes through the structure on axis. The most important effect is the long-range transverse wakefield that deflects the bunches and causes growth of the bunch train projected emittance. In this paper, the effect of the cell-to-cell misalignments is evaluated using a random walk model that assumes that each cell is shifted by a random step relative to the previous one. The model is compared with measurements of a few accelerator structures.

1 INTRODUCTION

The Next Linear Collider (NLC) is a proposed e^+e^- facility capable of achieving a luminosity in excess of $10^{34}\text{cm}^{-2}\text{sec}^{-1}$ at a center-of-mass energy of 1 TeV [1]. To achieve the desired luminosity with good rf-to-beam efficiency, a train of roughly 100 bunches is accelerated on each rf pulse in the X-Band (11.424 GHz) linacs. With the long bunch trains, the long-range transverse wakefield must be carefully controlled to prevent beam-breakup (BBU) and/or dilution of the projected transverse phase space.

To prevent BBU, the transverse wakefield is detuned, causing a rapid decoherence of the wakefunction, and then weakly damped to prevent re-coherence at a later time [2]. Because of the detuning, the projected emittance of the bunch train is relatively insensitive to rigid offsets or long wavelength misalignments of the accelerator structures, however, the internal misalignments of the accelerator structures break the detuning scheme causing multibunch emittance dilution.

The sensitivity to misalignments is usually calculated as a function of the misalignment wavelength as illustrated in Fig. 1. However, without knowledge of the typical misalignment wavelengths, such a description does not provide an easy method of quantifying the tolerances. This is particularly true for the manufacturing and construction tolerances which are short wavelength and thus cause multibunch dilution. In this paper, we describe a random walk model for the structure misalignments which yields simple tolerances that are straightforward to apply and reasonably models measurements.

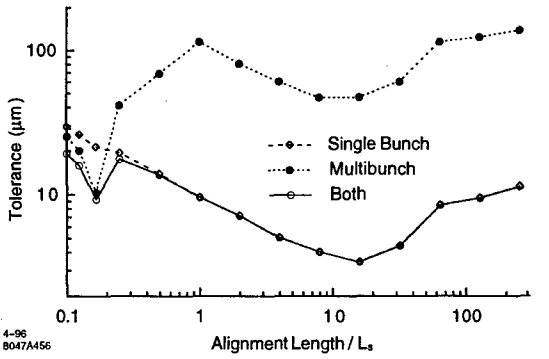

Figure 1: Example of tolerance vs. misalignment wavelength in units of the structure length from Ref. [1]; note that at long wavelength the tolerances are dominated by the short-range wakefield and single bunch dilutions while, at short wavelengths, the long-range wakefield and multibunch dilutions are most important.

Based on the matrix wakefield calculated for the NLC accelerator structure [2], and using analytical estimation for the emittance growth in the train [3], we find the emittance growth as a function of the step size in the random walk. This allows us to estimate the tolerances for the misalignment.

2 EMITTANCE GROWTH DUE TO LONG RANGE WAKEFIELD

In order to estimate the growth of the projected emittance $\Delta\epsilon$ of a train of bunches caused by randomly misaligned structure in the linac we will use the following formula for the expectation value of $\Delta\epsilon$ [3]

$$\langle\Delta\epsilon\rangle = r_e^2 N^2 \bar{\beta}_0 N_s L_s^2 \langle\Delta S_k^2\rangle \frac{1-(\gamma_0/\gamma_f)^{1/2}}{\gamma_0^{1/2}\gamma_f^{3/2}}, \quad (1)$$

where r_e is the classical electron radius, N is the number of particles in the bunch, $\bar{\beta}_0$ is the average value of the beta function at the beginning of the linac, N_s is the number of structures in the linac, L_s is the length of the structure, γ_0 and γ_f are the initial and final relativistic factors of the beam, and S_k is the sum wake. The quantity S_k is defined as a sum of the transverse wakes w_i generated by all bunches preceding the bunch number k (with

* Work supported by the Department of Energy, contract DE-AC03-76SF00515.
† Email:stupakov@slac.stanford.edu

$S_1 = w_1 = 0$),

$$S_k = \sum_{i=1}^{k} w_i \,, \tag{2}$$

and ΔS_k is the difference between S_k and the average value $\langle S \rangle$, $\Delta S_k = S_k - \langle S \rangle$, with

$$\langle S \rangle = \frac{1}{N_b} \sum_{k=1}^{N_b} S_k \,, \tag{3}$$

where N_b is the number of bunches. Eq. (1) is derived assuming a lattice with the beta function smoothly increasing along the linac as $\bar{\beta} \sim E^{1/2}$.

Usually, when the transverse wake is excited by an off axis beam passing through the structure, it is divided by the beam offset, and has dimension V/pC/m/mm. In our problem, however, the beam travels along the axis, and the wakefield arises due to the internal misalignment of the cells within the structure. Hence w_i has dimension V/pC/m. It is convenient, however, to introduce a quantity $\Sigma = \sqrt{\langle \Delta S_k^2 \rangle}/\Delta$, where Δ is the rms offset of cells in the structure

$$\Delta^2 = \frac{1}{N_c} \sum_{k=1}^{N_c} x_k^2 \,, \tag{4}$$

where x_k is the offset of kth cell ($\langle x \rangle = 0$), and N_c is the number of cells in the structure. With these definitions, Eq. (1) takes the form

$$\langle \Delta\epsilon \rangle = r_e^2 N^2 \bar{\beta}_0 N_s L_s^2 \Delta^2 \Sigma^2 \frac{1 - (\gamma_0/\gamma_f)^{1/2}}{\gamma_0^{1/2} \gamma_f^{3/2}} \,. \tag{5}$$

Now, specifying an allowable fraction of the emittance growth in the linac f, for a given pattern of cell misalignment, we can find a tolerance on the allowable Δ from the equation $\langle \Delta\epsilon \rangle = f\epsilon$, where ϵ is the normalized vertical beam emittance:

$$\Delta_{\rm tol} = \frac{1}{r_e N L_s \Sigma} \left[\frac{f\epsilon \gamma_0^{1/2} \gamma_f^{3/2}}{\bar{\beta}_0 N_s \left(1 - (\gamma_0/\gamma_f)^{1/2}\right)} \right]^{1/2} \,. \tag{6}$$

3 TOLERANCE

From Eqs. (2) and (3) and definition of ΔS_k one can express $\langle \Delta S_k^2 \rangle$ in terms of the wake w_i

$$\langle \Delta S_k^2 \rangle = \frac{1}{N_b^2} \sum_{i,k=1}^{N_b} D_{ik} w_i w_k \,, \tag{7}$$

where, in the limit $N_b \gg 1$,

$$D_{ik} = N_b(N_b - \max(i,k)) - (N_b - i)(N_b - k) \,. \tag{8}$$

For small misalignments, w_i is a linear function of cell offsets,

$$w_i = \sum_{k=1}^{N_c} W_{is} x_s \,, \tag{9}$$

which can be found from the solution of Maxwell's equations for the structure. The matrix W_{is} for the NLC structure RDDS1 with 206 cells has been calculated in Ref. [4]. It has a dimension of $N_b \times 206$. In our calculation we used $N_b = 90$ for bunch spacing 2.8 ns.

We assume that the quantities x_s are random numbers that vary from one structure to another subject to a statistical distribution that will be specified below. One can then average $\langle \Delta S_k^2 \rangle$ over random variation of x_s, and from Eqs. (7) and (9) find

$$\Sigma^2 = \frac{1}{N_b^2} \sum_{i,k=1}^{N_b} \sum_{s,l=1}^{N_c} D_{ik} W_{is} W_{kl} \overline{x_s x_l} \,, \tag{10}$$

where the bar indicates the statistical averaging.

We considered two cases of the linac with different final energies. For NLC-I we used: $E = 250$ GeV, $f = 10\%$, $N = 0.9 \cdot 10^{10}$, $L_s = 1.8$ m, $N_s = 2240$, $\bar{\beta}_0 = 7$ m, $E_0 = 10$ GeV, $E_f = 250$ GeV, $\epsilon = 4 \cdot 10^{-8}$ m. For NLC-II we assumed the same parameters except $E = 500$ GeV, $N_s = 4720$, $E_f = 500$ GeV, and $N = 1.1 \cdot 10^{10}$. Then Eq. (6) gives the tolerance in terms of the quantity Σ,

$$\Delta_{\rm tol}\,[\text{micron}] = \frac{35}{\Sigma\,[\text{V/pC/m/mm}]} \,, \qquad \text{NLC} - \text{I} \,, \tag{11}$$

and

$$\Delta_{\rm tol}\,[\text{micron}] = \frac{22}{\Sigma\,[\text{V/pC/m/mm}]} \,, \qquad \text{NLC} - \text{II} \,. \tag{12}$$

4 UNCORRELATED RANDOM CELL MISALIGNMENTS

As a simplest conceivable model for cell misalignments, we consider uncorrelated random cell offsets with an equal rms value Δ,

$$\overline{x_s x_l} = \Delta^2 \delta_{sl} \,. \tag{13}$$

Calculation of Σ in this case gives $\Sigma = 2.87$V/pC/m/mm with the tolerance equal to $\Delta_{\rm tol}$ =12.2 microns for NLC-1, and $\Delta_{\rm tol}$ =8.1 microns for NLC-2. However, this tolerance is unrealistic in that it does not model measured structure misalignments.

5 RANDOM WALK MODEL

A more reasonable model, the random walk model, assumes that each cell is randomly offset *relative to the previous one* (beginning from $x_1 = 0$) so that

$$x_i = \sum_{s=1}^{i-1} \xi_s \,, \qquad (i > 1) \,, \tag{14}$$

where ξ_i are uncorrelated random steps,

$$\overline{\xi_s \xi_k} = h^2 \delta_{sk} \,. \tag{15}$$

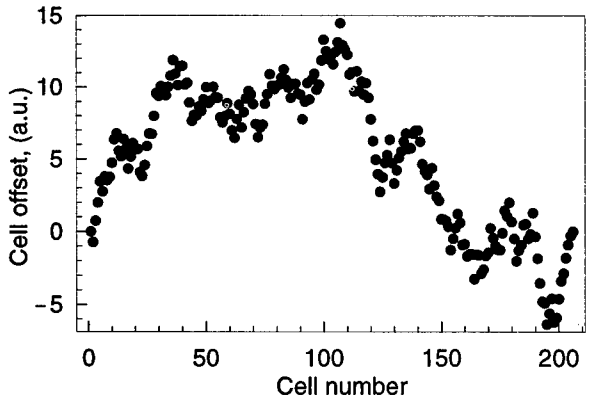

Figure 2: Example of random walk misalignment with fixed structure ends.

with zero average and rms value equal to h. In this model, the far end of the structure will be offset from the axis by the amount equal to the sum of all steps, and on the average, the structure will be tilted. In reality, this tilt can be easily corrected by rotating the structure by some angle. To take this correction into account, we add a linear slope to the offsets given by Eq. (14) such that the last cell has a zero offset, $x_{N_c} = 0$,

$$x_i = \sum_{s=1}^{i-1} \xi_s - \frac{i}{N_c} \sum_{s=1}^{N_c-1} \xi_s \,. \tag{16}$$

Using Eqs. (15) and (16), one can find the correlation function (in the limit $N_c \gg 1$)

$$\overline{x_i x_k} = h^2(\min(i,k) - \frac{ik}{N_c}) \,, \tag{17}$$

and the rms offset for kth cell

$$\sqrt{\overline{x_k^2}} = h\left[\frac{k(N_c-k)}{N_c}\right]^{1/2} \,, \tag{18}$$

and the rms offset for the whole structure

$$\Delta^2 = \frac{1}{N_c}\sum_{k=1}^{N_c} x_k^2 = \frac{h^2}{6} N_c \,. \tag{19}$$

For 90 bunches we have

$$\Sigma = 1.1 \text{ V/pC/m/mm} \tag{20}$$

which gives the tolerance $\Delta_{\rm tol} = 32$ microns for 250 GeV, and $\Delta_{\rm tol} = 20$ microns for 500 GeV. Using Eq. (19) we can convert these values into a tolerable step h, $h = 5.5\,\mu$m for NLC-1, and $h = 3.4\,\mu$m for NLC-2, respectively.

6 STRUCTURE MEASUREMENTS

Cell misalignments for NLC structures DDS1 and DDS3 measured, as described in in Refs. [5, 6], are shown in Figs. 3 and 4 respectively. Using the measurement data for DDS3 and theoretical wakefields from [4], we calculated the quantity (10) (without averaging indicated by the bar) and found the emittance growth using Eq. (5). Such a calculation assumes that the misalignment errors in different structures in the linac have the same statistical value of Σ as the measured one. Our result for the emittance growth expectation corresponding to the misalignments shown in Fig. 4 is $\langle \Delta\epsilon \rangle = 1.7 \times 10^{-9}$ m, or about 4% of the nominal vertical emittance of the beam.

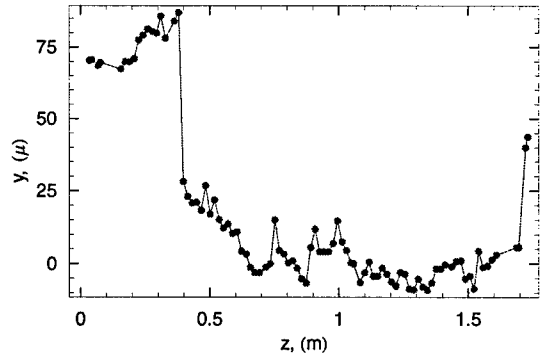

Figure 3: Measurements of the DDS1 structure alignment from Ref. [5]; note the large kink at roughly 35 cm arose when constructing the structure in segments and then bonding the segements together.

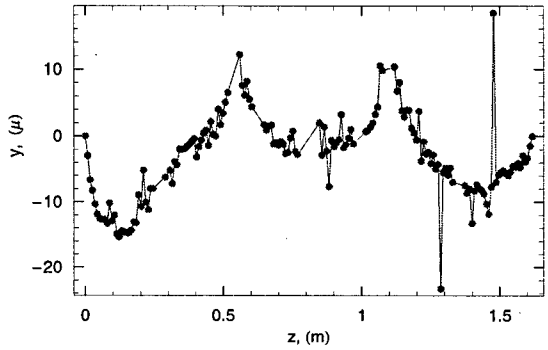

Figure 4: Measurements of the DDS3 structure alignment from Ref. [6].

7 REFERENCES

[1] NLC ZDR Design Group, "Zeroth-Order Design Report for the Next Linear Collider," SLAC Report 474 (1996).

[2] J.W.Wang et al. Paper LINCOL-00018, these proceedings.

[3] K.L.F. Bane *et al.*, "Issues in Multi-Bunch Emittance Preservation in the NLC," SLAC-PUB-6581, 1994.

[4] R. M. Jones et al. Paper LINCOL-00037, these proceedings.

[5] R. M. Jones et al. SLAC-PUB-7539 (1997).

[6] C. Adolphsen et al. Paper LINCOL-00051, these proceedings.

THE NLC INJECTOR SYSTEM*

V. Bharadwaj, J. E. Clendenin, P. Emma, J. Frisch, R. K. Jobe, T. Kotseroglou, P. Krejcik, A. V. Kulikov, Z. Li, T. Maruyama, K. K. Millage, B. McKee, G. Mulhollan, M. H. Munro, C. E. Rago, T. O. Raubenheimer, M. C. Ross, N. Phinney, D. C. Schultz, J. C. Sheppard#, C. M. Spencer, A. E. Vlieks, M. D. Woodley, *SLAC* K. van Bibber, *LLNL* S. Takeda, *KEK*

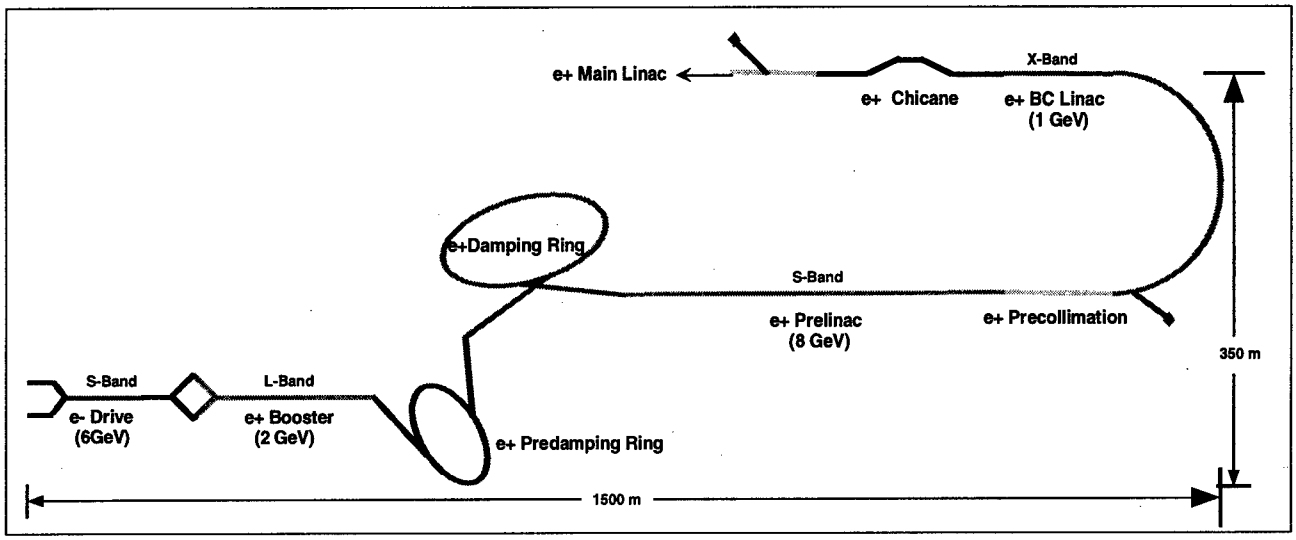

Figure 1: Layout of the NLC Positron Injector System.

Abstract

The Next Linear Collider (NLC) Injector System is designed to produce low emittance, 10 GeV electron and positron beams at 120 hertz for injection into the NLC main linacs. Each beam consists of a train of 95 bunches spaced by 2.8 ns; each bunch has a population of 1.15×10^{10} particles. At injection into the main linacs, the horizontal and vertical emittances are specified to be $\gamma\varepsilon_x = 3 \times 10^{-6}$ m-rad and $\gamma\varepsilon_y = 3 \times 10^{-8}$ m-rad and the bunch length is 100 μm. Electron polarization of greater than 80% is required. Electron and positron beams are generated in separate accelerator complexes each of which contain the source, damping ring systems, L-band, S-band, and X-band linacs, bunch length compressors, and collimation regions. The need for low technical risk, reliable injector subsystems is a major consideration in the design effort. This paper presents an overview of the NLC injector systems.

1 INTRODUCTION

In the NLC [1] Injector System, the electron and positron beams are generated in separate accelerator complexes located at the entrances to the two main linacs, separated by about 32 km. Each injector complex consists of a source system, a damping ring complex, and a prelinac and bunch length compression system. A schematic layout of the positron injector systems is shown in Figure 1. In the electron injector (not shown), redundant electron sources feed the e- Booster which is coupled directly to the e-Damping Ring (there is no e- Predamping Ring). Table 1 lists the beam parameters at injection to the main linacs.

Table 1: NLC Injector System Beam Parameters

Energy	E	10 GeV
Energy Spread	ΔE/E	1%
Single Bunch σ_E	σ_E/E	1.5%
Horizontal Emittance	$\gamma\varepsilon_x$	3×10^{-6} m-rad
Vertical Emittance	$\gamma\varepsilon_y$	3×10^{-8} m-rad
Bunch Length	σ_z	100 μm
Electron Polarization	P_e	>80%
Positron Polarization	P_p	No
Particles/Bunch	n_b	1.15×10^{10}
Number of Bunches	N_b	95 bunches
Bunch Spacing	T_b	2.8 ns
Repetition Rate	f	120 Hz

In the electron injector, polarized electrons are produced using a III-V semiconductor photocathode, accelerated to 1.98 GeV in an S-band linac and injected into a damping ring. Upon extraction from the damping ring, the bunch length is compressed and the beams are accelerated to 10 GeV in an S-band linac. Initial transverse collimation is

*Work supported by the U.S. Department of Energy under Contract Nos. DE-AC03-76SF00515, SLAC and W-7405-ENG-48, LLNL.
#Email: jcs@slac.stanford.edu

0-7803-5573-3/99/$10.00@1999 IEEE.

done prior to transport through a 180^0 turn-around. Second stage bunch length compression is accomplished using a 1 GeV X-band linac followed by a dipole chicane. An optical matching section and diagnostic region follow the compressor chicane. Tune-up dumps permit full beam preparation prior to injection into the 180^0 turn-around and into the main linac.

On the positron side, electrons are produced using a thermionic cathode and accelerated to an energy of 6.22 GeV in an S-band linac before impacting a target to produce positrons. Initial capture and acceleration of positrons to the damping ring energy of 1.98 GeV is done in an L-band linac system. Redundant e- and e+ sources are incorporated into the design to enhance availability. The large positron emittances are initially damped in a predamping ring prior to injection into the damping ring. The positron damping ring and subsequent accelerator systems are identical to those on the electron side with the notable exception that polarization spin manipulation solenoids and polarimeter are omitted. The positron beamlines allow for installation of spin preserving solenoids should the NLC be configured for electron-electron collisions.

The NLC emittance budget allows for dilution of the beam emittances by 20% in the horizontal and 50% in the vertical between extraction from the damping rings and injection into the main linacs. This budget is used to calculate tolerances. The values of $\gamma\varepsilon_x = 3\text{x}10^{-6}$ m-rad and $\gamma\varepsilon_y = 3\text{x}10^{-8}$ m-rad are the undiluted design emittances at extraction from the damping rings.

2 ELECTRON PRODUCTION

Polarized electrons are produced using a conventional dc gun and III-V semiconductor photocathode. Electron polarization of greater than 80% is required. The design has a 714 MHz, 2 cavity subharmonic bunching system to allow for a luminosity upgrade to 1.4 ns bunch spacing. The population of individual bunches is a relatively modest $2\text{x}10^{10}$ e-/bunch from the gun. This single bunch intensity target has been achieved in routine SLC operations with 80% polarization. The requirement of 95 successive bunches per beam pulse presents a significant challenge for initial electron production from the cathode due to the charge limit phenomenon [2]. R&D directed towards an NLC cathode capable of producing the requisite charge and polarization is ongoing at SLAC and Nagoya University. Care is also taken in the design of the bunching and linac systems to compensate for the long range longitudinal wakefield effects on the 95 bunch train.

3 POSITRON PRODUCTION

Positrons are produced by targeting a 6.22 GeV electron beam into an SLC style positron production system consisting of a water-cooled, 4 r.l. W-Re target followed by a 5.8 T magnetic flux concentrator, a 1.2 T tapered field solenoid, and a 0.5 T uniform field solenoid. L-band accelerator sections are used in the initial capture region to accelerate the beams to 250 MeV. After separation and removal of the electrons, the positrons are accelerated to the predamping ring energy of 1.98 GeV in an L-band linac. A yield of 2 positrons per electron into a phase space edge acceptance of 0.06 m-rad is expected. This yield normalized by the incident electron energy is a factor of 4 improvement over the SLC [3]. L-band (1428 MHz) has been chosen because of the large transverse aperture and longitudinal acceptance which are fully utilized in defining the acceptance and subsequent yield calculations. Energy loading in the initial capture regions is compensated using a ΔF correction scheme. ΔT compensation is employed in the rest of the L-band linac [4].

The 1998 failure of the SLC target has caused significant concern regarding the viability of the NLC positron system design which is based on the SLC system. The concern is whether the SLC system failed in an acute manner from exceeding the target damage threshold or from accumulated stress on the target. The former requires a significant redesign of the NLC positron systems whereas the latter means that the design is viable albeit the targets will age and require preemptive replacement. Analysis of the SLC target failure is being undertaken in collaboration with LLNL and LANL. This analysis is expected to be completed during the summer of 1999.

4 DAMPING RINGS

The vertical emittance of the beams is reduced by a factor of 3000 in the damping rings. The rings operate at 1.98 GeV and the design output emittances are $\gamma\varepsilon_x = 3\text{x}10^{-6}$ m-rad and $\gamma\varepsilon_y = 3\text{x}10^{-8}$ m-rad. The transverse damping time is 5.2 ms. Damping occurs dominantly from radiation produced in a 50 m wiggler section. Beams are damped in the rings for 25 ms (three inter-pulse periods); at any one time there are three pulse trains in each ring; the circumference of the rings is 300 m. A 1 MW, 714 MHz rf system generates gap voltages of 1.5 MV utilizing 3 PEP-II style damped, rf cavities [5]; the bunch length at extraction is $\sigma_z = 4$ mm. The rings are designed to operate at a maximum intensity of $1.6\text{x}10^{10}$ particles per bunch whereas the nominal operating intensity is about $1.2\text{x}10^{10}$.

A predamping ring reduces the initial positron rms emittances from $\gamma\varepsilon_{x/y} = 0.04$ m-rad down to $\gamma\varepsilon_{x/y} = 100\text{x}10^{-6}$ m-rad for injection into the positron main damping ring. Beams are predamped for 16.6 ms; there are two pulse trains in the system at any time; the circumference of the predamping ring is 210 m [6].

5 INJECTOR LINACS

Seven rf linacs, six capture regions, and four compressor sections are required in the NLC Injector System. These linacs are based on L-band, S-band, and X-band rf systems. S-band linacs are used for the initial

acceleration of electrons on both the electron and positron side, for energy compression of electrons prior to injection into the damping ring, and for acceleration from 1.98 GeV to 10 GeV after the damping rings on both sides. L-band linacs are used for the initial positron capture and acceleration to 1.98 GeV. L-band rf sections are also employed for energy compression of positrons prior to injection into the predamping ring and for the first stage of bunch length compression of both electrons and positrons. The linacs used for the second stage bunch length compression are based on the X-band technology being developed for the NLC main linacs. The beam loaded gradients in the L-band and S-band linacs have been chosen to be 13 MV/m (15 MV/m) and 17 MV/m (21 MV/m unloaded), respectively [7]. The operating gradient at X-band is 46 MV/m loaded (66 MV/m unloaded).

The standard L-band rf module consists of a single klystron feeding a single SLED system which in turn powers three 5 m long accelerator sections. A standard S-band rf module has a single klystron powering a single SLED system with the outputs of two SLEDs combined to power six 4 m long accelerator sections (each klystron effectively feeds 3 accelerator sections). A standard NLC X-band klystron 8-pack powers twelve 1.8 m accelerator structures.

Both the L-band and S-band systems use double iris, side-wall coupled KEK style SLED-I rf compression systems [8]. The L-band SLED systems are scaled versions of the S-band SLEDs with modification to the coupling β for performance optimization. A single klystron feeds a SLED system. The outputs of the S-band SLEDs are combined and distributed to the accelerator sections. The combination of the SLEDs permits vernier control of the rf waveform for beam loading compensation while allowing for constant power delivery to the structures in the event that beam pulses are suppressed or shortened during a machine protection system fault and recovery. At X-band, a modified DLDS is used for rf pulse compression. Modification is required because the distance between the triplets of sections is reduced in the Injector System design with respect to the layout in the NLC main linacs. The DLDS is doubled in length and folded back upon itself.

The output of the S-band klystron is 65 MW for 5 μs. It is essentially an improved version of the SLAC 5045 tube. L-band klystrons of 75 MW, 6 μs should be achievable with existing technology. The X-band tubes are standard NLC 75 MW, 1.5 μs devices.

In total, the NLC Injector System design has 441 accelerator sections powered by 157 klystrons and 136 SLEDs at S-band, 44 accelerator sections powered by 23 klystrons and 14 SLEDs at L-band, and 24 accelerator sections powered by 16 klystrons and 2 DLDSs. All of this hardware needs to be developed.

6 BUNCH LENGTH COMPRESSION

The bunch length of the extracted damping ring beam is reduced in 2 stages. An 80 MeV section of L-band linac and a 10-dipole wiggler reduces σ_z from 4 mm to 500 μm prior to injection into the prelinac. After acceleration to 10 GeV and precollimation, transport through a 314 m long 180^0 turn-around, a 1 GeV X-band linac, and a 32-magnet dipole chicane reduces σ_z from 500 μm to 100 μm for injection into the main linacs. Three bunch length diagnostic stations provide tune-up and monitoring capability. Each σ_z station contains an optical port for streak camera measurements and an rf cavity for parasitic monitoring. For σ_z = 100 μm, streak camera resolution may not adequate in which case fourier spectroscopy techniques will be used. As a backup, the first diagnostic station in the main linac can be used as a bunch length monitor using a standard cross-phasing technique.

7 SPIN SYSTEM AND PRECOLLIMATION

Superconducting solenoids are used in conjunction with the bending in the damping ring transport lines to rotate the electron spin into the vertical for damping and then into arbitrary orientation for injection into the prelinac system. After the damping ring, the asymmetry in beam emittances dictates that the solenoids be split and separated by an optical transformation of +I in X and –I in Y to prevent vertical emittance dilution due to coupling. A Compton polarimeter located at injection to the main linac utilizes a laser wire IP, polarized laser light, and the second tune-up dumpline. Polarization measurements require dedicated beam time.

Initial collimation of transverse beam halo and tails occurs prior to transport through the 180^0 turn-around of the second bunch length compressor. Collimation is done using a set of 8 horizontal and 4 vertical, adjustable jaw pairs. Additional cleanup of the debris generated by the collimation takes place downstream in the high dispersion regions of the 180^0 turn-around.

8 REFERENCES

[1]NLC Zeroth-Order Design Report, SLAC Report 474, also http://www-project.slac.stanford.edu/lc/ZDR/nlc_zeroth.htm

[2] H. Tang, *et al.*, "Experimental Studies of the Charge Limit Phenomenon in NEA GaAs Photocathodes", Proc. *EPAC94*, 46 (1994).

[3] H. Tang, *et al.*, "Design of the NLC Positron Source", Proc. *Linac96*, CERN 96-07, 647 (1996).

[4] Z. Li, *et al.*, "Beam Loading Compensation for the Low Frequency RF Linacs and Compressors in the NLC", *presented at PAC99*, (FRA43).

[5] J. Corlett, *et al.*, "The NLC Damping Ring Complex", *presented at PAC99*, (FRA20).

[6] J. Corlett, *et al.*, "The NLC Damping Ring RF Systemex", *presented at PAC99*, (MOP60).

[7] Z. Li, *et al.*, "Parameter Optimization for the Low Frequency RF Linacs of the NLC", *presented at PAC99*, (FRA44).

[8] H. Matsumoto, *et al.*, "High Power test of a SLED system with dual side-wall coupled irises for linear colliders", NIM A330 (1993) 1.

RECENT DEVELOPMENTS IN THE DESIGN OF THE NLC POSITRON SOURCE*

T. Kotseroglou# , V. Bharadwaj, J. E. Clendenin, S. Ecklund, J. Frisch, P. Krejcik, A. V. Kulikov, J. Liu, T. Maruyama, K.K. Millage, G. Mulhollan, W. R. Nelson, D. C. Schultz, J. C. Sheppard, J. Turner, SLAC; K. Van Bibber, LLNL; K. Flottmann, DESY; Y. Namito, KEK.

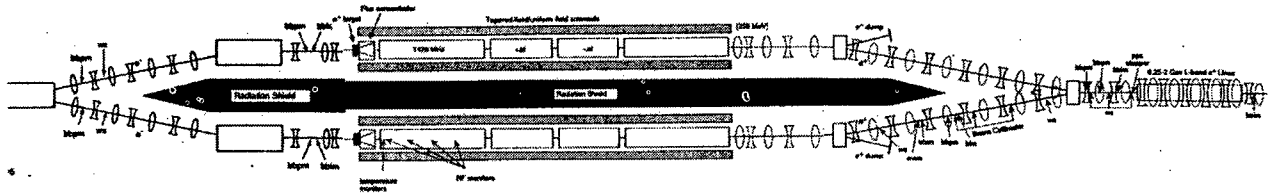

Figure 1. Schematic layout of the positron source. The S-Band electron injector at 6.22 GeV is at the left of the figure (not to scale). There are two positron targets for reliability purposes. The capture and acceleration system is chosen to be to L-Band (at the right of the figure, not to scale)

Abstract

Recent developments in the design of the Next Linear Collider (NLC) positron source based on updated beam parameters are described. The unpolarized NLC positron source [1,2] consists of a dedicated 6.2 GeV S-band electron accelerator, a high-Z positron production target, a capture system and an L-band positron linac. The 1998 failure of the SLC target, which is currently under investigation, may lead to a variation of the target design. Progress towards a polarized positron source is also presented. A moderately polarized positron beam colliding with a highly polarized electron beam results in an effective polarization large enough to explore new physics at NLC. One of the schemes towards a polarized positron source incorporates a polarized electron source, a 50 MeV electron accelerator, a thin target for positron production and a new capture system optimized for high-energy, small angular-divergence positrons. The yield for such a process, checked using the EGS4 code, is of the order of 10^{-3}. The EGS4 code has being enhanced to include the effect of polarization in bremsstrahlung and pair-production process.

1 INTRODUCTION

In the NLC electrons and positrons are generated in separate accelerator complexes. A schematic layout of the positron injector systems is shown in Figure 1. Table 1 lists the parameters of the drive electron beam that creates the positrons and of the positron target and Table 2 lists the positron beam parameters.

Table 1: NLC Injector Positron System Drive Electron Beam and Positron Target Parameters

Parameter	Value
Energy, E (GeV)	6.2
Energy Spread, dE/E (%)	± 1.0
Single Bunch, dEs/E (%)	<0.5
Linac Frequency (MHz)	2856
Emittance (10^{-6} m-rad)	100
Particles/Bunch, N_b (10^{10})	2
Pop. Uniformity dN_b/N_b (%)	<0.5
Number of Bunches N_b	95
Beam radius (mm rms)	1.6
Bunch-length , dt (ps, FWHM)	17.5
Total Beam power/area GeV/mm^2 (10^{12})	1.5
Bunch spacing (ns)	2.8
Repetition rate (Hz)	120
Average Beam Power (kW)	226
Target thickness W-Re (RL)	4
Target power (kW)	23

On the positron side, electrons are produced using a thermionic cathode and accelerated to an energy of 6.22 GeV in an S-band linac before impacting a target to produce positrons. Initial capture and acceleration of positrons to the damping ring energy of 1.98 GeV is done in an L-band (1428 MHz) linac system. The beam-loaded gradients in the L-band and S-band linacs have been chosen to be 13 MV/m and 17 MV/m, respectively (17 MV/m and 21 MV/m unloaded). For a detailed description please see ref. [3]

*Work supported by the U.S. Department of Energy under Contract Nos. DE-AC03-76SF00515, SLAC and W-7405-ENG-48, LLNL.

Email: theo@slac.stanford.edu

Table 2: NLC Injector System Positron Beam Parameters

Parameter	Value
Linac Frequency (MHz)	1428
Energy, E (GeV)	1.98
Energy Spread, dE/E (%)	<1
Single Bunch, dEs/E (%)	<1.2
Emittance, norm.(m-rad)	0.06 (edge)
Bunch-length, dz (mm, sigma)	3.7
Particles/Bunch, nb (10^{10})	1.6
Pop. Uniformity dnb/nb (%)	<1
Number of Bunches Nb	95
Bunch spacing (ns)	2.8
Repetition rate (Hz)	120
Pre-DR acceptance (m-rad)	0.09
Pre-DR Energy acceptance (%)	+- 1.5

Redundant e- and e+ sources are incorporated into the design to enhance availability (fig. 1). In the baseline design the positron damping ring and subsequent accelerator systems do not include polarization spin manipulation solenoids or polarimeters. The positron beamlines allow for a later installation of spin preserving solenoids should the NLC be configured for electron-electron collisions or address the issue of polarized positrons. The NLC emittance budget allows for dilution of the beam emittances by 20% in the horizontal and 50% in the vertical between extraction from the damping rings and injection into the main linacs. This budget is used to calculate tolerances. The initial positron rms emittances after the target are $\gamma\varepsilon_{x/y}$ = 0.04 m-rad and reduced to $\gamma\varepsilon_{x/y}$ = $100\text{x}10^{-6}$ m-rad for injection into the positron main damping ring [3].

2 BASELINE DESIGN FOR NLC POSITRON PRODUCTION

Positrons are produced by targeting a 6.22 GeV electron beam into an SLC style positron production system (fig. 1). The target module consists of a water-cooled, 4 r.l. W-Re target followed by a 5.8 T magnetic flux concentrator, a 1.2 T tapered field solenoid, and a 0.5 T uniform field solenoid as seen in fig.2 [1].

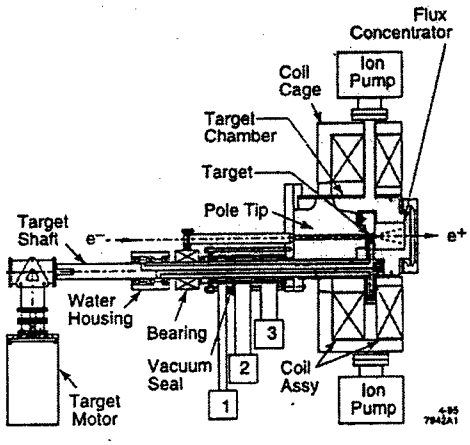

Figure 2. The target module

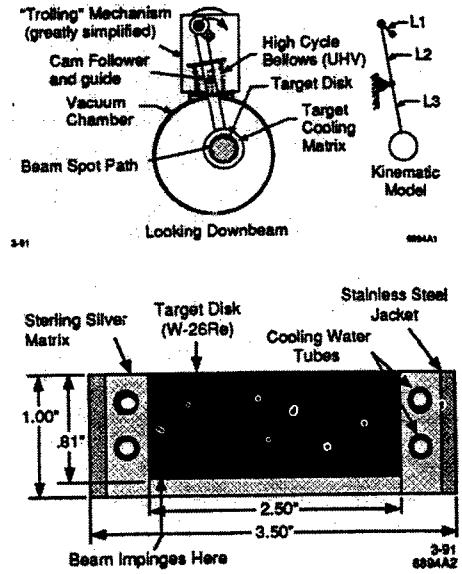

Figure 3. Cross section and detail of the cooling scheme of the SLC and proposed NLC target.

L-band accelerator sections are used in the initial capture region to accelerate the beams to 250 MeV. After separation and removal of the electrons, the positrons are accelerated to the pre-damping ring energy of 1.98 GeV in an L-band linac

A yield of 2 positrons per electron into a phase space edge acceptance of 0.06 m-rad is expected. This yield normalized by the incident electron energy is a factor of 4 improvement over the SLC. L-band has been chosen because of the large transverse aperture and longitudinal acceptance, which are fully utilized in defining the acceptance and subsequent yield calculations. Energy loading in the initial capture regions will be compensated using a ΔF correction scheme but ΔT will be used for the L-band Linac.

3 RECENT DEVELOPMENTS WITH THE SLC TARGET

During the 1998 SLC run the positron target (fig.3) failed, after many years of use, showing a water-to-vacuum leak. When the target system was removed from the beamline, some damage on the downstream side of the target was observed and target material was seen in the flux concentrator immediately downstream of the target.

This has caused significant concern regarding the viability of the NLC positron system design since the NLC design is based on the SLC system. The concern is whether the SLC system failed in an acute manner from exceeding the target damage threshold or from chronic degradation of the target. The former would require a significant redesign of the NLC positron systems whereas the latter would mean that the NLC design is viable albeit the targets will age and require preemptive replacement [3].

Analysis of the SLC target failure is being undertaken as a program that consists of calculations on target cooling and on shock waves from drive beam impact, and of analysis of the damaged SLC target. The calculations are performed in collaboration with LLNL. Material analysis of the target is done with collaboration with LANL. This work is currently concentrating on producing pictures of target details, x-ray and SEM pictures, performing material hardness tests and isotope analysis. This analysis is expected to be completed during the summer of 1999.

4 POLARIZED POSITRONS FOR NLC

There are some advantages for NLC if polarized electrons collide with polarized positrons [4,5]. Although the baseline design of NLC does not include polarized positrons we have started an effort of studying various new methods of polarized positron production. Currently the most promising is the helical undulator approach [6], although new experiments using CO_2 lasers on electron beams may also prove to provide an adequate source of polarized positrons [7]. We have been recently looking into a new idea of using a polarized electron beam on a thin target [8] and efficiently collecting the polarized positrons produced at the peak of the output energy distribution. Here we present a preliminary study of this scheme. We used a modified version of the EGS code that includes polarization for bremsstrahlung, Compton and pair production, with input electron drive beams [5]. The spin flip for input γ's is small for thin targets and can be calculated efficiently using a numerical code [7]. Using a 50 MeV electron drive beam and 0.2 radiation lengths of W-Re target, the yield of polarized positrons with energy higher than 25 MeV is approximately 0.06% with average polarization 85% of the input electron polarization (fig.4). The electron energy has not been optimized yet, but was chosen as a benchmark for the numerical calculations presented in [8]. The low yield suggests that a long pulse drive beam is needed in order to create the number of positrons needed at the IP, which complicates both the drive accelerator and the positron accelerator. Using the above-mentioned parameters, the electron beam power required to produce an NLC type positron beam is approximately 2.4 MW, if the capture system is 100% efficient. A sizable dump should be constructed to collect the electrons after the target, while the radiation issues due to gammas generated on the target create an extra problem. The energy loss in the target is approximately 4% and the power dissipated is 96 kW, which is 4 times that of the baseline NLC design. Assuming an input electron beam with σ =2 mm the energy density of the impinging electron beam is close to the upper experimental limit [2]. Furthermore, in order to recreate the pulsetrain of positron pulses needed at the IP an appropriate accumulator ring has to be designed. The high polarization positrons are concentrated in the forward direction so the capture system will vary from the baseline design (fig.5). We are currently studying the viability of the above-mentioned polarized positron scheme.

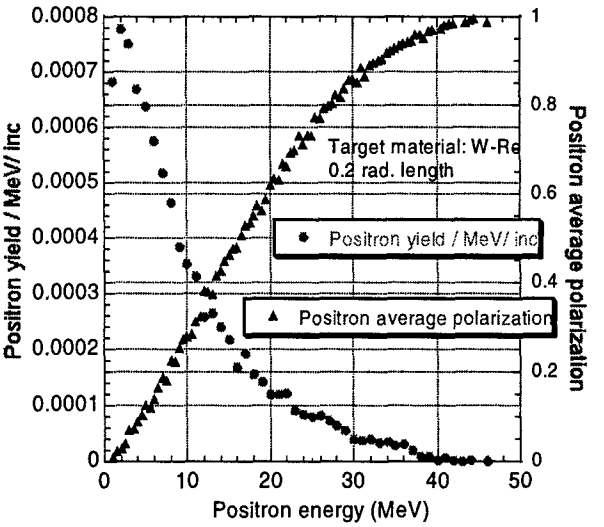

Figure 4. Positron yield and polarization for 50 MeV electron drive beam and 0.2 radiation lengths of W-Re.

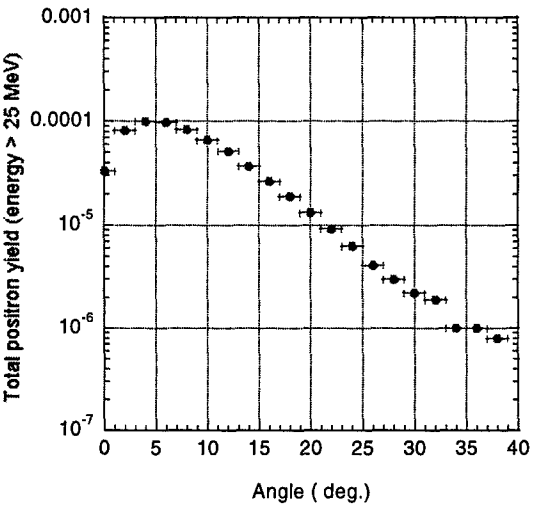

Figure 5. Positron yield vs polar angle of momentum vector.

5 REFERENCES

[1] H. Tang et al., Proc. of the 1995 Particle Accelerator Conference, Dallas, TX (1996) and SLAC-PUB-6852; and H. Tang et. al, Proc. LINAC '96, Geneva, Switzerland (1996) and SLAC-PUB-7270.
[2] Zeroth-Order Design Report for the Next Linear Collider, SLAC-Report 474, May 1996.
[3] J. C. Sheppard, The NLC Injector System (these Proceedings).
[4] T. Omori, Proc. Workshop on New Kinds of Positron Sources, Stanford, March 1997, SLAC-R-502, p. 285.
[5] K. Flottmann,PhD thesis, DESY-93-161A, Nov. 1993, also K. Flottmann, DESY-95-064, Nov. 1995.
[6] A.Mikhailichenko, Proc. Workshop on New Kinds of Positron Sources, Stanford, March 1997, SLAC-R-502.
[7] T. Okugi et al., Jpn. J. Appl. Phys. Vol. 35 (1996) pp. 3677-3680.
[8] A.P. Potylitsin, Nucl. Instrum. and Meth. A. 398 (1997) p.395-398. See also E.G. Bessonov et al., Proc. 5th European Particle Accelerator Conference, June 1996, Stignes, Spain, p.1516.

AN APPARATUS FOR THE DIRECT MEASUREMENT OF COLLIMATOR TRANSVERSE WAKEFIELDS *

P. Tenenbaum†, K. Bane, J. Irwin, R.K. Jobe, D. McCormick, T.O. Raubenheimer, M.C. Ross, G. Stupakov, D. Walz
Stanford Linear Accelerator Center, Stanford, CA

Abstract

The design of the NLC Beam Delivery System requires a firmer understanding of the effects of collimators on short, intense bunches than is presently available. We describe an experiment to directly measure these effects through use of a dedicated apparatus located at the 1.19 GeV point in the SLAC Linac. The apparatus consists of an outer vacuum vessel and an interchangeable insertion containing up to 5 distinct collimator apertures. The insertion is capable of remote-controlled translation, allowing the collimator apertures to be misaligned relative to the electron beam without changing the incoming beam orbit; the wakefield deflection is then measured by observing the change in the outgoing orbit on 32 beam position monitors. The parameters of the apertures have been selected to allow confirmation of the scaling laws for collimator wakefields, and to strongly enhance either the geometric or resistive wall contribution of each aperture. Details of the apparatus design, the aperture parameters, and the experimental program are discussed.

1 INTRODUCTION

The Next Linear Collider (NLC) post-linac collimation section is a 2.5 km long section of beamline the purpose of which is to prevent particles at large amplitudes from entering the final focus, where they would cause unacceptable detector backgrounds. The design of the NLC collimation section is substantially based upon experience at the Stanford Linear Collider (SLC) with a similar collimation system interleaved with accelerator structures in the last 300 meters of the linac.

One of the central design specifications of the NLC collimation system is the contribution to luminosity degradation from collimator short-range dipole wakefields. A beam which passes off-center through a collimator experiences a deflection due to wakefields; therefore a collimation system will amplify incoming jitter. The NLC collimation system has been limited to a 25% increase in beam jitter due to collimator wakefields.

The present understanding of collimator wakefields is not adequate to confidently predict the jitter amplification of a given collimator design. The NLC collimators are expected to utilize a smooth taper to match between a rectangular aperture and a cylindrical beampipe. The analytic expression for the deflection of an electron bunch due to the geometric wakefield of such a collimator is [1]:

$$\Delta y' = 2\frac{Nr_e}{\gamma}\frac{\pi h}{2\sqrt{\pi}}\frac{(r_0 - r_1)(r_0^2 - r_1^2)}{\sigma_z L_T r_0^2 r_1^2} y_0, \qquad (1)$$

where y_0 is the beam offset in the collimator, N is the bunch population, r_e is the classical electron radius, γ is the relativistic factor, σ_z is the RMS bunch length, L_T is the taper length, r_0 and r_1 are the radius of the beampipe and half-aperture of the gap, respectively, and h is the transverse width of the gap (e.g., the horizontal width of a vertical collimator). As expected, the deflection in Equation 1 vanishes when $r_1 \to r_0$; however, the deflection is also proportional to h, implying that the deflection from an infinitely-wide collimator diverges.

The resistive contribution to the wakefield deflection is expected to be [2]:

$$\Delta y' = 2\frac{\alpha_R}{\pi^{3/2}}\frac{e^2 N c L_T}{E\sqrt{\sigma_z}}\sqrt{\frac{Z_0}{\sigma}}\frac{r_0 + r_1}{r_0^2 r_1^2}\langle f\rangle y_0, \qquad (2)$$

where Z_0 is the impedance of free space, σ is the conductivity of the collimator, e is the electron charge, E is the beam energy, $\langle f\rangle$ is a constant arising from integration of the kick over the (presumed) Gaussian distribution in z ($\langle f\rangle \approx 0.724$), and α_R is a form factor equal to 1 for a cylindrical collimator and equal to $\pi^2/8$ for a rectangular collimator. Note that Equation 2 does not contain nonphysical divergences and predicts a deflection even from a perfectly regular vacuum pipe ($r_0 = r_1$). However, measurements of the deflection due to the wakefields from the SLC collimators have exceeded those predicted by Equations 1 and 2 by up to a factor of 4 [3].

Collimator wakefield measurements [3, 4, 5] have historically been difficult to interpret because they have been made on existing collimator installations, which are designed to minimize wakefield contributions rather than to amplify certain features of the wakefields over others. For example, the SLC collimator study discussed in [3] attempted to separate the resistive and geometric wakes by measuring the deflection as a function of bunch length: since Equation 1 predicts that $\Delta y' \propto 1/\sigma_z$, while Equation 2 predicts that $\Delta y' \propto 1/\sqrt{\sigma_z}$, the contributions from the two components could be inferred by such a measurement. However interpretation of such a measurement is far from straightforward due to uncertainty in the actual bunch length, response of beam monitors in the SLC under conditions of changing bunch length, and the impact of bunch length on the wakefields from the RF structures which fill the linac and complicate any trajectory measurement. A

* Work supported by the Department of Energy, contract DE-AC03-76SF00515.

† Email:quarkpt@slac.stanford.edu

0-7803-5573-3/99/$10.00@1999 IEEE.

more optimal measurement could be made at a dedicated facility, in which collimators of any design could be tested. As part of the NLC research project at SLAC, we have designed such a facility.

2 OVERALL DESIGN

The collimator wakefield apparatus is a vacuum vessel with approximate dimensions 1.7 meters × 0.6 meters × 0.3 meters, as shown in Figure 1. The vessel is designed with a lid which can easily be removed and replaced to allow access to the interior. The vessel contains an insertion, which is a long block of aluminum containing 5 apertures; each aperture can be fitted with a collimator of any geometry desired.

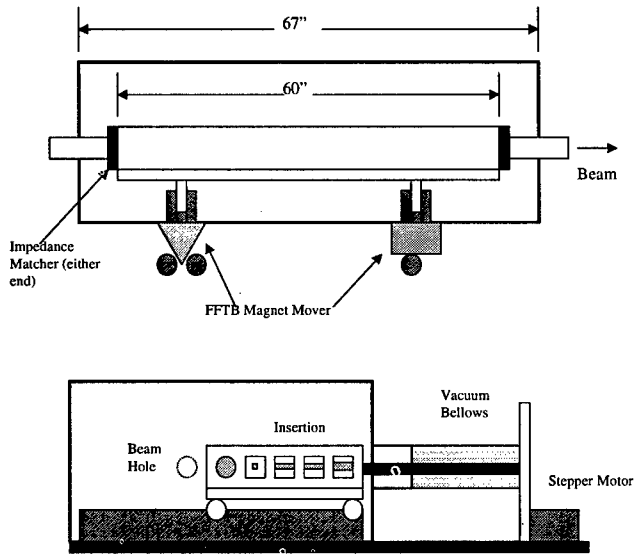

Figure 1: Diagram of collimator wakefield test apparatus, side view (top) and end view (bottom). The long, coarse translation stage and stepper motor move the insertion in x to engage a test aperture; the FFTB magnet mover then moves the entire vacuum vessel in y to produce a beam-aperture displacement, which results in a measurable deflection.

The cartridge rides on a platform which is connected to an external horizontal translation stage; the stage engages whichever of the apertures is to be used for experimentation. In this way a series of related collimators can be tested in sequence without entering the accelerator housing or disturbing the vacuum vessel. When the translation stage moves to its full-out position, the insertion is removed completely from the path of the beam.

The vacuum vessel is mounted on a vertical translation stage which has a range of ±1.5 millimeters and a step size of 1 μm. Once one of the test apertures is engaged, the vertical stage is used to make a precise translation of the apparatus. The wakefields due to the collimator in the aperture will produce a deflection, which can be observed on beam position monitors downstream of the apparatus.

Wakefield deflections are inversely proportional to beam energy, and therefore the apparatus should be installed at a location where the beam energy is relatively low. The location selected is the SLAC linac spin rotator location immediately downstream of the point where the damped 1.19 GeV beams re-enter the linac. This location is just upstream of the ASSET location, which allows a similar experiment on RF structures using a drive beam from the positron damping ring and a witness beam from the electron damping ring[6]. The collimator wakefield experiment will require only one beam. The deflection will be measured by recording the beam position on each of 32 beam position monitors downstream of the apparatus location, as well as several monitors upstream of the apparatus. The deflection will be reconstructed after pulse-to-pulse jitter is subtracted using the upstream BPMs. Because the downstream BPMs are largely interleaved with accelerator structures, it is desirable to use a low bunch charge so that the wakefields from the structures can be neglected. Our test apertures are designed to produce a measurable deflection for a bunch charge of 1×10^{10}. This is sufficiently below the threshold of instability in the linac that, if additional resolution is called for, the bunch charge can be increased moderately for some measurements.

3 INSERTION DESIGN

The bulk of the insertion should be constructed from a material with a high conductivity in order to avoid producing unwanted resistive-wall wakefields; it should be as light as possible to facilitate installation and removal in the cramped experimental area; and it should be made from a material which is easy to machine. On the basis of these criteria, aluminum was chosen for the material.

The insertion contains 1 circular beam channel and 4 square ones, each with a full bore of 4 cm. The total length of the insertion is 1.5 meters, in order to accomodate the longest collimators foreseen for measurement. In order to simplify installing and removing collimator apertures from the channels, it was constructed in a split configuration with a top half and a bottom half which can be disassembled and reassembled easily.

The clearance between the insertion and the impedance-matching flanges at either end of the vacuum vessel is 1 mm. This produces a small discontinuity wakefield, but the clearance was deemed necessary to ensure that the insertion could move easily on its horizontal stage. The deflection resulting from the discontinuity is believed too small to measure, but this will be checked by engaging the cylindrical channel without any collimator aperture and measuring the deflection as a function of the vertical stage position. This will allow us to subtract the deflection due to the vacuum vessel, discontinuities, and other construction features.

4 APERTURE DESIGN

In order to separately measure the contributions of geometric, resistive, surface finish, etc. wakefields, it is necessary to carefully construct each test aperture to enhance one particular source of deflections and reduce the rest. The first set of apertures are intended to maximize geometric wakefields. Therefore they are all constructed from copper, with a good finish, and all the apertures are short in z.

Table 1 shows the parameters of the first set of test apertures to be measured. Note that the predicted deflections are calculated for a round pipe tapering down to either a round or a rectangular aperture; we approximate these with a square pipe tapering down to a square aperture in the former case, and a square pipe tapering down to a rectangular aperture in the latter. Computation of the wakefields for our precise geometry is difficult and uncertain, but the expected deviation from the cylindrical approximation is on the order of 20%. The expected resolution of the technique, based on ASSET measurements, is 1 microradian, and all of the expected deflections are large relative to this.

Table 1: Parameters and predicted deflections for geometric wakefield test apertures, given a beam charge of 1×10^{10}, an energy of 1.19 GeV, and a 1 mm apparatus vertical offset.

Channel Number	Aperture (cm)	Taper Length (cm)	Kick (μrad)
1	4.0, round	None	≈ 0
2	0.4, square	5.0	1.9
3	0.4, rect.	5.0	51.3
4	0.4, rect.	10.0	33.9
5	0.8, rect.	5.0	25.6

The second set of test apertures will measure resistive-wall wakefields. This requires as axisymmetric a geometry as possible, in order to minimize geometric-wake contributions. The resistive wakefield can be further enhanced by using a material with a poor conductivity and including a long untapered section with a small gap in between the two tapers, which should enhance resistive deflections but leave geometric deflections unaffected. Ideally these measurements would use a second insertion in which all channels are cylindrical; machining considerations may mandate use of a square aperture once again. Table 2 shows the desired parameters for a resistive-wall wakefield test insertion. While we have used stainless steel as our resistive material in Table 2, we are presently leaning towards use of a pure element for this purpose, in order to achieve a uniform conductivity which does not depend upon relative densities of various alloyed materials in the surface.

Future insertions will test the effects of a subset of geometric features, namely surface finish and surface features, and also probe the behavior when geometric collimators of varying width are used. Ultimately an NLC-design collimator will be directly tested in this apparatus.

Table 2: Parameters and predicted deflections for resistive wakefield test apertures, given a beam charge of 1×10^{10}, an energy of 1.19 GeV, and a 1 mm apparatus vertical offset. Test apertures 1 and 2 are copper, while 3 through 5 are steel.

Coll. #	Aperture (cm)	Taper Length (cm)	Untapered Length (cm)	Kick (μrad)
1	0.4	5.0	0	1.9
2	0.4	5.0	100	2.6
3	0.4	5.0	100	7.1
4	0.4	5.0	50	4.5
5	0.8	20.0	100	3.2

5 EXPERIMENTAL PROGRAM

The vacuum vessel and insertion with the first set of test apertures is presently under construction, with installation in the SLAC linac scheduled for late April. Once the translation stages are fully commissioned, experimental measurements will be made parasitically during PEP-II collisions, as it is expected that the PEP-II program can be interleaved with collimator studies with minimal disruption of either program. Measurements are expected to continue on a periodic basis for the next several years.

6 ACKNOWLEDGEMENTS

The authors wish to thank G. Bowden and D. Burke for their ideas and encouragement, and B. Brugnoletti for designing the test apparatus.

7 REFERENCES

[1] G. Stupakov, "Geometrical Wake of a Smooth Flat Collimator," SLAC-PUB-7167 (1996).

[2] NLC ZDR Design Group, "Zeroth-Order Design Report for the Next Linear Collider," SLAC Report 474, 589 (1996).

[3] F. Zimmermann *et al*, "Measurements of Wakefields Generated by the Newly Coated Collimators in the SLAC Linac," SLAC-CN-415 (1997).

[4] F.J. Decker *et al*, "Design and Wake Field Performance of the New SLC Collimators," Proc. *Linac 96*, 137 (1996).

[5] K.L.F. Bane *et al*, "Measurement of the Effect of Collimator Generated Wake Fields on the Beams in the SLC," Proc. *PAC 95*, 3031 (1995).

[6] C. Adolphsen *et al*, "Measurement of Wake Field Suppression in a Detuned X Band Accelerator Structure," *Phys Rev Lett* 74:2475 (1995).

USE OF SIMULATION PROGRAMS FOR THE MODELLING OF THE NEXT LINEAR COLLIDER*

P. Tenenbaum†, P. Emma, L. Hendrickson, N. Phinney,
T.O. Raubenheimer, M. Woodley
Stanford Linear Accelerator Center, Stanford, CA

Abstract

The Next Linear Collider is an electron-positron accelerator unprecedented in its size, energy, and tight tolerances. We describe the suite of simulation tools which are widely used in designing and modelling the performance of the NLC. In order to achieve a uniform beamline description and permit simulation of all facets of the collider, an extended version of the Standard Input Format (xSIF) has been developed and implemented in MAD and DIMAD. We discuss several enhancements to the MAD and DIMAD calculation engines necessary to properly simulate the most challenging regions of the facility. We also describe enhancements to LIAR which allow it to be used as the tracking engine for a tuning/feedback simulation written in MATLAB. Finally, we discuss the additional software needed to model the beam stabilization and tuning processes.

1 INTRODUCTION

The Next Linear Collider (NLC) is a proposed e^+e^- facility capable of achieving a luminosity of up to $10^{34}\text{cm}^{-2}\text{sec}^{-1}$ at a center-of-mass energy of 1 TeV [1]. The facility includes 2 X-Band (11.424 GHz) linacs, each in excess of 10 km in length; 2 beam delivery systems, each in excess of 5 km in length; and several kilometers of injection linac and damping ring.

In order to reliably achieve such a high luminosity at the NLC, a wide variety of physical phenomena and tuning strategies need to be investigated in considerable detail during the design phase. These include:

- Control of long-range and short-range wakefield effects
- Feedback system architecture for control of instabilities
- Misalignment and error tolerances
- Tuning and capture ranges
- Geometric and chromatic aberrations
- Background sources and transport
- Transport of highly disrupted beams.

In general, we perform modelling and simulation studies of the NLC beamlines with tools which are in wide use throughout the accelerator physics community. However, these tools have been substantially modified to fit our particular needs. The modifications performed are described below. Finally, we should note that all codes are written in ANSI Fortran 77 or Fortran 90. We have adopted this standard for ease of transport and ease of modification. Further documentation on the modeling codes and standards can be found in Ref. [2].

2 EXTENDED STANDARD INPUT FORMAT

The base language for the description of all NLC beamlines is the Standard Input Format [3]. This is the input language used by MAD and DIMAD, as well as other programs. In order to appropriately handle the NLC beamlines, a number of modifications have been made to this language:

- The keywords, parameters, and syntax of the present-day MAD and DIMAD input parsers have been made consistent, generally by adopting the present MAD syntax where conflicts existed
- Apertures have been added to most elements (APERTURE parameter) for use in tracking
- The DIMAD element LCAV, which describes a linear accelerator structure, has been added to MAD; the original LCAV syntax has been extended to allow filenames for wakefield data to be included in the element description
- A number of instrument types (BLMO, SLMO, PROFILE, WIRE, IMONITOR) have been added
- All elements can take a 16 character alphanumeric engineering class (TYPE parameter) and a 24 character alphanumeric database name (LABEL parameter) as parameters
- The DIMAD parameter FINTX (exit-face fringe-field integral) has been added to MAD to improve description of bend magnets which are split into 2 elements in the deck.

The resulting beamline description language is known as the Extended Standard Input Format (XSIF). The NLC versions of MAD and DIMAD will read without errors a beamline description written in XSIF. In addition, a standalone library version of the DIMAD XSIF parser has been

*Work supported by the Department of Energy, contract DE-AC03-76SF00515.

† Email:quarkpt@slac.stanford.edu

0-7803-5573-3/99/$10.00@1999 IEEE.

created (for AIX, Solaris, NT, and VMS platforms) which can be linked to any new or existing application. The present version of LIAR[4] has been so linked. At this time, all NLC accelerator simulation programs in wide use can accept a common set of beamline descriptions in XSIF.

In addition to the XSIF standard, a fully-instantiated sequential ASCII beamline description was desired. The MAD tape format[5] was enhanced to include new beamline features (beam energy, engineering and database names, new instrument classes, and linac RF structures), resulting in the Extended Tape File Format (XTFF). The SURVEY XTFF provides a compact lattice description that can be used by the engineering teams for component layout while the TWISS XTFF is used to transfer the lattice information into an Oracle database which will become the backbone of the control system and provides a straightforward method of tracking components.

3 DIMAD

The program DIMAD[6] is the primary program for design and simulation of the beam delivery regions of the NLC, and is also used for some studies of the main linac. NLC-DIMAD has been converted to Fortran 90, and all shared data structures have been moved to MODULEs for ease of maintenance. The data space available for beamline and parameter data has been expanded to accomodate beamlines as large as the main linac (15,000 entries in the appropriate LINE).

The NLC main linac contains 4,968 RF structures. It was desired that the main linac deck describe the beamline efficiently, but that the flexibility of individually phasing the structures be preserved. This is accomplished by having a separate array of structure phases, which is set using a new command, PHASE. During calculations the phases in the new array are used rather than the phases in the deck. This permits the user to have a single LCAV in the deck, which can then be used an arbitrary number of times to describe independently-phased structures. NLC-DIMAD also included beam loading in its phasing operations, and can convolve the beam with a longitudinal wakefield description during tracking.

To improve the accuracy of tracking results in the beam delivery region, NLC-DIMAD allows the user to specify a twin-horned energy distribution (similar to that expected at the end of the main linac). The particle analysis code computes a luminosity-weighted RMS beam size, which de-weights the contributions of the beam tails in determining the effective beam size. This size is computed at the end of the beamline, and the luminosity-weighted size at the nearest waist is also estimated; thus if the waists are slightly mistuned the user still gets an estimate of the focused beam size. Several tracking-related variables (including RMS emittances at the end of the line and luminosity-weighted beam sizes) are available as conditions for the least-squares fitter, allowing higly nonlinear problems (such as "Brinkmann-sextupole" tuning) to be automated. For convenience, a syntax for specification of normalized emittances has been added to the BEAM command. In order to accurately track the low-energy tails of the disrupted post-IP beam, an extended chromatic precision option has been added: when this option is selected, quad and sextupole matrices are dynamically calculated for each particle, scaled to match that particle's energy. In the future, we will add to NLC-DIMAD routines for simulation of thermal-photon and residual-gas scattering of the electron beam [7], and use these and the extended chromatic precision option to model backgrounds and track low-energy tails through the system.

4 MAD

The most significant modification to the NLC version of MAD is the addition of linear acceleration and the resulting variation of the beam energy. The additions were made to MAD version 8.23/0 which is written in standard Fortran 77. The code now allows the beam energy to be specified at the entrance to a beamline and this energy will be modified by LCAVITY elements which model traveling wave accelerator cavities; note the LCAVITY elements are treated differently from the standard MAD RFCAVITY elements which do not modify the beam energy. This allows the code to be used for both storage rings and linacs.

The LCAVITY elements are specified in terms of a length, rf frequency, voltage, rf phase, and the loss parameter. All of these parameters are treated like all other MAD element parameters and can be specified in terms of expression, varied during matching, etc. In addition, the beam energy can be used as a matching constraint and is now included in the BETA0 structures. The LCAVITY elements also include approximate representation of the focusing that arises at the entrance and exit of the accelerator structures which can be significant in the low energy ($\sim$ 100 MeV) regions of the collider. Finally, one can also specify files containing the transverse and longitudinal wakefields for the structures which are used when tracking.

The calculation of the lattice functions has been modified to incorporate the variation in the beam energy. There are a couple of different methods of including the energy variation in the lattice functions. We could have maintained the original definition utilized in MAD where the lattice parameters simply depend on the transfer matrix [8]:

$$\beta_2 = \frac{1}{\beta_1}((R_{11}\beta_1 - R_{12}\alpha_1)^2 + R_{12}^2) \qquad (1)$$

etc., but this leads to lattice functions that, for a given periodic cell structure, decrease with acceleration as $1/E(s)$. For this reason, we normalize the individual transfer elements by the determinant of the transfer matrix. This leads to the more common definition which is consistant with that used in DIMAD.

Finally, three other changes have been implemented. First, different fringing fields can be specified for the upstream and downstream ends of bending magnets using a

FINTX parameter in the element definition. This provides greater flexibility when splitting components into multiple segments and can be used to prevent the error that arises when FINT$\neq$ 0 in split bending magnets. Second, an approximation for the effect of coherent synchrotron radition in the bending magnets can be used when tracking by setting a CSR parameter for bending magnets. Finally, the beamline length has also been added as a matching constraint since it is frequently desirable to minimize to overall length of the system.

5 LIAR

LIAR is a program for the simulation of linear accelerators with high gradients and strong wakefields. Like DIMAD, LIAR has been entirely converted to Fortran 90. This allowed LIAR's data structures to be cast into a standard form, which in turn permitted LIAR to be ported to several platforms with essentially no changes in its code (AIX, Solaris, VMS, NT). LIAR was also linked to the standalone XSIF parser, allowing it to read decks in the standard format and eliminating the need for conversion of the XSIF decks to TRANSPORT format[9].

The beam-based alignment command, QALIGN, has been supplanted by QALIGN_NEW, which allows greater flexibility in specifying the order in which various algorithms are applied to the beamline. A more consise "figure of merit" for multibunch position distortions (non-straight trains) has been added to the program.

LIAR's tracking engine includes longitudinal and transverse short-range wakefields. Because of this it was decided that the LIAR tracking engine would be used for simulations of the NLC trajectory feedback system. The state-space design for the feedback algorithms was written in MATLAB: the MATLAB system, using macros and control toolbox routines, enables easier prototyping than Fortran software, and provides powerful graphics capabilities. Different feedback formulations can be evaluated from this basic platform. LIAR's structure was revised to allow MATLAB to call LIAR routines from within a single MATLAB process, and to pass data between MATLAB and LIAR.

The feedback simulation is driven by MATLAB macros, which call LIAR functions to transport and perturm the beam and return beam position monitor readings. MATLAB routines perform calculations to simulate the feedback system and determine new corrector settings, which are communicated back to LIAR with an interface routine.

6 FUTURE DEVELOPMENTS

The most pressing modelling task facing the Next Linear Collider is simulation of the tuning process, and the related simulation of normal operation (for example, with all feedbacks operating/interacting, including bandwidth limitations). A "cradle-to-grave" simulation of the tuning procedure for the Final Focus Test Beam[10] was performed in SAD[11], and the NLC will require a similarly detailed exploration of its commissioning in order to determine the range and granularity of all tuning devices and the required performance of all instrumentation. Of particular interest is the interaction between the main linac steering feedbacks and the many feedbacks of various kinds in the beam delivery system.

One possible tool for this simulation is the Final Focus Flight Simulator (FFFS), which is an interactive GUI developed at SLAC for Third Order Transport [12]. However, the FFFS has many limitations which make it a non-optimal candidate for this simulation.

A more promising option is to develop a MATLAB interface to MAD or DIMAD, similar to the one presently available for LIAR. This would allow the existing calculational kernels of these two programs to be used without adding large amounts of special-purpose code to the compiled codebase. This is particularly attractive in that it would permit a simulation in which a beam is transported through the linac in LIAR, extracted into MATLAB, translated to a group of particles for MAD/DIMAD, and then transported in that form through beam delivery. This would permit studies of the entire accelerator, despite the fact that different areas are best served by different simulation programs.

7 ACKNOWLEDGEMENTS

The authors wish to acknowledge the contributions of P. Raimondi, G. Roy, I. Reichel, R. Helm, and K. Bane.

8 REFERENCES

[1] NLC ZDR Design Group, "Zeroth-Order Design Report for the Next Linear Collider," SLAC Report 474 (1996).

[2] NLC Accelerator Physics Web pages found at http://www-project.slac.stanford.edu/lc/nlc-tech.html.

[3] D.C. Carey and F.C. Iselin, "A Standard Input Language for Particle Beam and Accelerator Computer Programs," Proceedings *Snowmass 84* (1984).

[4] R. Assmann *et al*, "LIAR: A New Program for the Modeling and Simulation of Linear Accelerators with High Gradients and Small Emittances," Proc. *LINAC 96*, 464 (1996).

[5] H. Grote and F.C. Iselin, "The MAD Program Version 8.19 User's Reference Manual," CERN/SL/90-13(AP)Rev.5, 125 (1996).

[6] R.V. Servranckx *et al*, "Users' Guide to the Program DIMAD," SLAC-Report-285 (1985).

[7] I. Reichel *et al*, "Therman Photon and Residual Gas Scattering in the NLC Beam Delivery," Proc. *ICAP 98* (1998).

[8] K.L. Brown, SLAC Report 75, Rev. 3 (1972).

[9] K.L. Brown *et al*, "TRANSPORT: A Computer Program for Designing Charged Particle Beam Transport Systems," SLAC-Report-91 (1970).

[10] K. Oide, "Design of Optics for the Final Focus Test Beam at SLAC," Proc. *PAC 89*, 1319 (1989).

[11] http://www-acc-theory.kek.jp/SAD/sad.html.

[12] M. Woodley, private communication.

SIMULATION STUDIES OF MAIN LINAC STEERING IN THE NEXT LINEAR COLLIDER *

P. Tenenbaum†
Stanford Linear Accelerator Center, Stanford, CA

Abstract

In order to achieve the design luminosity of the Next Linear Collider, the main linac must accelerate trains of bunches from 10 GeV to 500 GeV while preserving vertical normalized emittances on the order of 0.05 mm.mrad. We describe a set of simulation studies, performed using the program LIAR, comparing several algorithms for steering the main linac; the algorithms are compared on the basis of emittance preservation, convergence speed, and sensitivity to BNS phase profile. The effects of an ATL mechanism during the steering procedure are also studied.

1 INTRODUCTION

The Next Linear Collider (NLC) is a single-pass electron-positron collider capable of achieving a luminosity of $10^{34}\text{cm}^{-2}\text{sec}^{-1}$ at a center-of-mass energy of 1 TeV [1]. The NLC uses a pair of X-Band ($f = 11.424$ GHz) linear accelerators, with approximately 5,000 RF structures and 750 quadrupoles in each linac, to accelerate the beams from 10 to 500 GeV. The total length of each linac is over 10 kilometers.

In order to achieve the desired luminosity, each linac must accelerate a 270 nanosecond train of 95 bunches on each 120 Hz machine cycle, and must preserve an incoming normalized emittance which can be as small as 0.03 mm.mrad. Novel structure designs can mitigate the emittance dilution due to long-range wakefields [2]; this leaves dispersion and short-range wakefields from the structures as the primary causes of emittance dilution. In both wakefields and dispersion, the emittance dilution can be controlled through proper alignment of the accelerator. The NLC design calls for an unprecedented emphasis on measurement and correction of misalignments:

- Each quad is supported on a remote-controlled translation stage capable of ± 2 mm motions in x and y, with submicron step sizes
- Each RF structure girder (3 structures) is supported on a remote-controlled translation stage capable of ± 2 mm motions in x and y at each end of each girder, with micron step sizes
- Each quad contains a beam position monitor with a resolution of 1 micron in x and y for a single bunch with a charge of 10^{10}
- Each structure contains a beam position monitor at each end with a resolution of 5 microns in x and y for a single bunch with a charge of 10^{10}.

We consider three algorithms for converting beam position information in the quad and structure BPMs into changes in translation stage positions.

2 DESCRIPTION OF THE ALGORITHMS

2.1 *"Canonical" Algorithm*

The algorithm used to study beam-based alignment in the 1996 NLC study divides the linac into N segments containing equal numbers of quads (in practice, 14 segments with approximately 50 quads per segment) and uses the quadrupole BPMs to compute a set of magnet moves which minimizes (in a least-square sense) the RMS BPM orbit. In order to prevent the magnet movers "ranging out," the algorithm simultaneously seeks to minimize the RMS magnet motion, resulting in an overconstrained fit. Once the quads have been moved, each structure girder in the segment is then moved to zero the average of the 6 structure BPMs on the girder.

In this algorithm the least-squares engine uses the wakefree optics model to predict the response to quad moves, and assumes that girder moves only change the readings of BPMs on the girder. Because the wakefield contribution is not included in the calculation, it is necessary in real life to iterate the algorithm on each segment several times before moving on to the next segment, and to pick segments which are short relative to the characteristic growth distance of wakefield instabilities.

In order to match the alignment from one segment into another, the magnets at the endpoints of a segment are held fixed in position: a steering magnet at the first quad is used to steer the beam into the last quad, and its value is determined as part of the least-squares fit. Thus the algorithm results in a piecewise-straight alignment, with kinks at the endpoints of segments.

2.2 *"Canonical" Algorithm with MICADO*

Under some circumstances the "Canonical" algorithm will leave an RMS orbit which is larger than the BPM resolution. Errors in positioning of the many quads will sometimes conspire to produce a betatron component to the orbit. In order to further reduce this, the "Canonical" algorithm can be followed by a MICADO algorithm [3], which attempts to identify the minimum number of magnet moves which produce the greatest improvement in the

* Work supported by the Department of Energy, contract DE-AC03-76SF00515.

† Email:quarkpt@slac.stanford.edu

orbit. For the purposes of this simulation, the MICADO algorithm was constrained to use no more than 7 magnets, and to seek an RMS orbit tolerance of 1 micron. In execution several iterations of the "canonical" algorithm would be performed on an alignment segment, followed by several MICADO algorithms.

2.3 *"French Curve" Algorithm*

The "canonical" algorithm inconveniently requires corrector magnets at the endpoints of each segment. An algorithm was sought which would not require such magnets, but still permitted the segment-to-segment alignment matching provided by the correctors. The "French Curve" algorithm is very similar to the "canonical" algorithm; however, no correctors are used, and instead after a segment is aligned the next segment is selected starting in the middle of the most recent one. Thus the alignment is performed on full segments but advances down the linac in half-segments, resulting in a smooth alignment without correctors.

3 SIMULATION STUDIES

Each of the 3 algorithms was studied with LIAR [4], a linear accelerator simulation program which performs tracking with transverse and longitudinal wakefields from RF structures. The general conditions of the simulation are described in the section above and in Table 1.

Table 1: General parameters used in the simulations.

Parameter	Value
Bunch Charge	1.1×10^{10}
Quad-BPM Offset	2 microns
Struct.-BPM Offset	0 microns
Incoming $\gamma\epsilon_y$	0.04 mm.mrad

3.1 *Mover Step Size*

Figure 1 shows the emittance dilution of each algorithm as a function of the magnet mover step size. In each case the algorithm was permitted to iterate to convergence (see next section). While MICADO can improve the performance of the "canonical" algorithm at large step sizes, it cannot reduce the residual emittance growth which occurs for small step sizes. The "french curve" algorithm has a smaller emittance growth for perfect movers than the "canonical;" its emittance dilution is also a weaker function of mover step size.

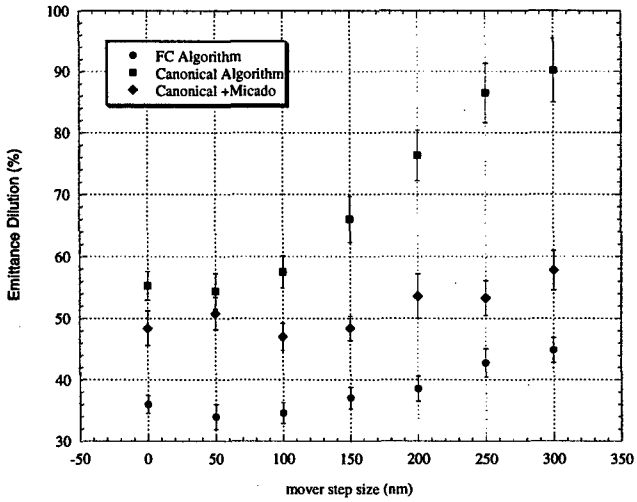

Figure 1: Emittance dilution as a function of magnet mover step size for 3 main linac steering algorithms.

3.2 *Convergence Speed*

Figure 3.2 shows the number of iterations required to reach convergence for "canonical" and "french curve" algorithms. While the latter algorithm required fewer iterations per segment, it also requires twice as many segments as the "canonical" algorithm, and is thus somewhat slower in terms of time.

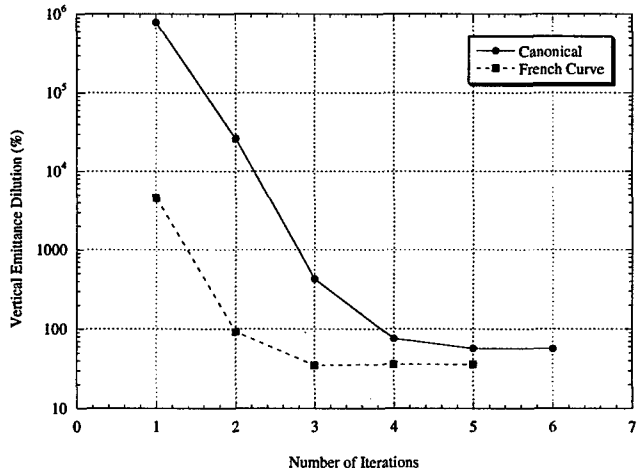

Figure 2: Emittance dilution as a function of number of iterations per segment for "canonical" and "french curve" algorithms.

3.3 *Energy Overhead*

In order to reduce the impact of incoming beam jitter on emittance, the NLC linacs will be operated with a substantial head-tail energy difference [5], which is parameterized here as linac energy overhead (linac voltage in excess of that needed to achieve the desired energy at extraction). Figure 3.3 shows that the emittance dilution increases linearly for both "canonical" and "french curve" algorithms

with energy overhead (note that this is contrary to the jitter behavior: more energy overhead results in less emittance dilution for a bunch executing a betatron oscillation down the full length of the linac). However the "french curve" performance is better for all values of energy overhead considered.

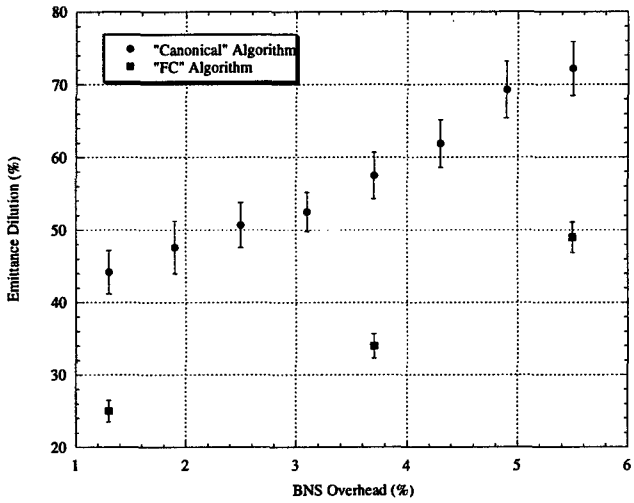

Figure 3: Emittance dilution as a function of energy overhead for "canonical" and "french curve" algorithms.

4 DIFFUSIVE GROUND MOTION

In recent years, Shiltsev [6] has offered evidence that accelerator alignment degrades according to a diffusive process. The so-called "ATL Law" states that components which are *ab initio* perfectly aligned will be misaligned by an RMS distance σ which is related to the distance between the components L and the elapsed time T by:

$$\sigma^2 = A \cdot T \cdot L. \qquad (1)$$

The coefficient A is a complex function of site geology, cultural noise, and construction techniques. Furthermore A is not precisely constant in time, but is subject to change over the course of many years. However on the scale of seconds, days, or months, Equation 1 may represent a lower bound on achievable alignment performance.

In order to simulate ATL misalignments in the context of accelerator steering it is necessary to assume a value for A and a time T over which alignment occurs. For this study we assume that the NLC will have a value of A of $5 \times 10^{-7} \mu^2/\text{meter/second}$, which is low but not unachievable. We assume that the initial steering of the accelerator from a coarse state of alignment (50 μ RMS misalignments) to convergence requires 1 minute per operation of quad or girder alignment (thus approximately 3 hours for the full linac), while subsequent steering operations require only 1 iteration per segment and only 30 seconds per operation. We assume that steering is performed constantly.

Figure 4 shows the performance of the "french curve" algorithm when ATL misalignments occur during steering. Pass 1 in Figure 4 is the 3 hour, multi-iteration pass: the emittance dilution is increased from 34% to 65% by ATL misalignments. The subsequent, fast passes achieve an equilibrium emittance dilution of 50%.

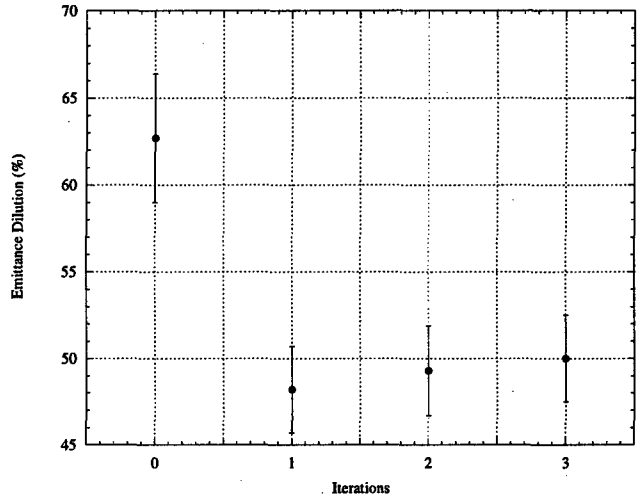

Figure 4: Performance of "french curve" algorithm with diffusive ground motion included.

5 CONCLUSIONS

We have evaluated several algorithms for steering the NLC main linac to reduce emittance dilution due to short-range wakefields and dispersion. We find that a relatively robust algorithm exists which produces acceptably small emittance dilution. Further studies of the algorithm are required. These include multibunch effects, improved modelling of the structure BPMs, interaction with steering feedbacks, and additional dilutions from other sources.

6 ACKNOWLEDGEMENTS

The authors wish to acknowledge the contributions of R. Assmann, T. Raubenheimer, and G. Stupakov.

7 REFERENCES

[1] NLC ZDR Design Group, "Zeroth-Order Design Report for the Next Linear Collider," SLAC Report 474 (1996).

[2] R.M. Jones *et al*, "Advanced Damped Detuned Structure (DDS) Development at SLAC." Proc. *PAC 97* (1997).

[3] B. Autin and Y. Marti, "Closed Orbit Correction of A.G. Machines Using a Small Number of Magnets," CERN ISR-MA/73-17 (1973).

[4] R. Assmann *et al*, "LIAR: A New Program for the Modeling and Simulation of Linear Accelerators with High Gradients and Small Emittances," Proc. *LINAC 96*, 464 (1996).

[5] V.E. Balakin, A.V. Novokhatsky, V.P. Smirnov, "VLEPP: Transverse Beam Dynamics," Proc. *HEACC 83*, 119 (1983).

[6] V. Shiltsev, "Space-Time Ground Diffusion: The ATL Law for Accelerators," Proc. *IWAA 95*, 352 (1996).

NEW DEVELOPMENTS IN THE NEXT LINEAR COLLIDER BEAM DELIVERY SYSTEM DESIGN *

P. Tenenbaum†, L. Eriksson, T. Markiewicz, T.O. Raubenheimer, A. Ringwall
Stanford Linear Accelerator Center, Stanford, CA

Abstract

We review many developments in the design of the Beam Delivery System for the Next Linear Colllider. The collimation system has been redesigned to reduce nonlinearities and ease tolerances, and the IP Switch line has been adjusted to permit a 300 meter longitudinal separation between the two detectors. Magnet designs have been changed to reduce the number of distinct magnet classes, produce a smoother vacuum chamber, and improve pumping. A revised set of interaction-region quadrupoles achieves the optical requirements of the system with improved beam stay-clears, and performance of the final focus at various energies has been simulated and found acceptable. Studies have begun on the set of feedbacks required to maintain the stability of the system and the changes in tolerances thus implied.

1 INTRODUCTION

The Beam Delivery System of the Next Linear Collider (NLC) encompasses all of the beamlines downstream of the main linac. These beamlines include a collimation section which removes particles which would otherwise intersect downstream apertures; an "IP Switch" which deflects the beam towards one of the two interaction points; a 10 milliradian arc for IP separation and muon protection; a section for measurement and correction of xy coupling; a chromatically corrected final focus; and the interaction point and detector. Figure 1 shows a schematic layout of the beam delivery system. Table 1 shows some of the critical system parameters.

Table 1: Parameters of NLC Beam Delivery System as a function of center-of-mass energy. Operation at 120 Hz and 95 bunches per train is assumed.

Parameter	500 GeV	1000 GeV
Bunch Charge	0.75×10^{10}	0.75×10^{10}
$\beta_{x,y}$, mm	10×0.1	10×0.125
$\gamma\epsilon_{x,y}$, mm.mrad	4×0.06	4×0.06
σ_z, μm	90	90
Luminosity, $\mathrm{cm}^{-2}\mathrm{sec}^{-1}$	7.3×10^{33}	13.5×10^{33}

* Work supported by the Department of Energy, contract DE-AC03-76SF00515.

† Email:quarkpt@slac.stanford.edu

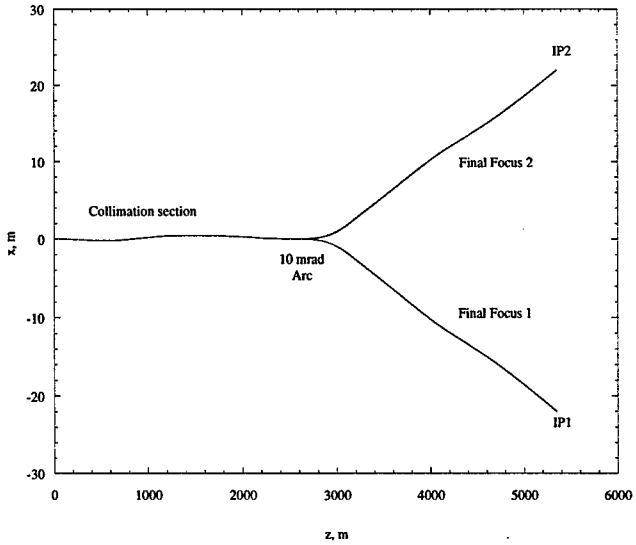

Figure 1: Schematic of NLC Beam Delivery System.

The Beam Delivery System was initially designed during the 1996 NLC study[1], and in the intervening time a number of aspects of the design have been further optimized and revisited. We review these developments below.

2 MAGNET DESIGNS

the original BDS design used a large number of different magnet designs, and incorporated arbitrary changes in the magnet apertures. The designs have been regularized to ease buildability. At the present time the BDS uses 5 standard quad geometries, 3 standard bend core geometries, and 3 standard sextupole geometries. All magnets upstream of the final focus have a full aperture of 1.2 cm, while all magnets in the final focus have a full aperture of 3.0 cm in order to maintain the desired beam stay-clears (14 σ_x, 60 σ_y) for the worst-quality beam at the lowest energy (175 GeV per beam, $\gamma\epsilon_{x,y} = 5.0 \times 0.14$ mm.mrad). Reduction in the number of distinct magnet families is expected to improve maintenance and reduce construction costs.

Increasing the vacuum chamber to 1.2 cm O.D. or larger from the original design (which used 1.0 cm O.D. in many locations) has other positive implications. With full apertures of 1.2 cm or larger, and assuming a 1 mm thick vacuum chamber, a base pressure on the order of 5×10^{-8} torr can be achieved without taking extraordinary measures in the areas of vacuum chamber processing or vacuum pump spacing. By eliminating most of the aperture transitions in the system, a smoother vacuum system without transition-induced wakefields can be used. One negative implication

0-7803-5573-3/99/$10.00@1999 IEEE.

is that about 10% of magnets have pole-fields in excess of 7 kG at 1 TeV C.M., and would need to be replaced in order to run NLC with a center-of-mass energy of 1.5 TeV.

3 COLLIMATION SYSTEM

The three design constraints which dictated the design of the collimation system were:

- Jitter amplification due to collimator wakefields should be less than 25%
- Collimation system should be capable of removing 1% of the beam power per degree of freedom (x, x', y, y', δ) indefinitely without damage
- Collimation system should be capable of surviving direct impact of a single bunch train (10^{12} electrons or positrons at 500 GeV) without damage.

Of the three, it is the third constraint which had the greatest impact on the system design: surviving the impact of a damped bunch train containing so many kilojoules required that the betatron functions at the collimators be enormous, which in turn required a very long (> 2 km) system. Collimating both phases at high-beta points ($\beta_y > 41$ km) had other unpleasant implications: sextupoles were required to correct the induced chromaticity; the R_{34} from the IP-phase collimators to the Final Doublet (FD) phase collimators was so large that submicron quad drifts could direct the beam into a collimator; the system length limited the number of iterations of collimation possible; large amplitude particles experienced unacceptable phase migration (from the loosely-collimated IP phase into the tight-apertured FD phase). Furthermore, the design was not yet long enough to survive an impact of a buch train at 750 GeV beam energy. An upgrade to 1.5 TeV C.M. would require lengthening the collimation system into the main linac, which would in turn amplify all the difficulties listed above.

Because the existing design is marginal in so many respects, we have begun to consider a design in which the single-train survival requirement is eliminated. In order to implement such a design, all sources of large oscillations coming from upstream must be sufficiently slow that the machine protection system (MPS) can detect them before they generate a bunch orbit which impacts a collimator. Since the energy of the linac cannot be assured on a pulse-to-pulse basis, the new design must extract off-energy particles or bunches before performing betatron collimation, rather than combining δ and x collimation as the present system does. In the new design, the betatron functions at the collimators can be reduced by over an order of magnitude, with a similar increase in magnet tolerances. The beam is now small enough that DC collimation of the halo can cause collimator damage. To eliminate this risk, the thick halo absorbers are eliminated entirely from the system; instead, a large number of spoilers, each approximately 1/4 radiation length in thickness, causes particles at large amplitudes to be far off energy, and the particles are removed by a dispersive section at the end of the collimation section. The changes in the system permit the collimation to be performed at 45° intervals in betatron phase, resulting in better collimation (and equal collimation depth for all phases). The new design also has a sufficient bandpass that sextupoles and other high-order multipoles are not needed.

4 IP SWITCH DESIGN

The beam delivery system contains an arc which deflects the beam by 10 mrad before entering the final focus system. This provides a separation between the two interaction regions of 40 meters, which is insufficient. The IP Switch module now incorporates an additional module 287 meters in length on the path to one of the two IR's. This provides a separation between IR's which is acceptable.

5 FINAL FOCUS

The apertures of the final doublet magnets of the final focus were found to be too small to accomodate beams at lower energy. In addition, the required pole-tip field in the permanent magnet Q1 was unacceptably high, especially since this magnet partially overlaps the detector solenoid's field. A compromise solution was arrived at, in which the lower energies (350-750 GeV CM) use a pair of permanent magnets with a larger aperture and smaller gradient, and the higher energies (750-1000 GeV CM) use a single permanent magnet with a higher gradient and smaller aperture but more acceptable pole-tip fields. Table 2 shows the parameters of the final doublet magnets.

Table 2: Parameters of NLC Final Doublet magnets. Q1B and Q1A are used at lower energies, and are replaced by Q1 at higher energies. "SC" represents a superconducting magnet, "PM" indicates permanent magnets.

Name/ Polarity	L_{eff} (m)	Full Bore (cm)	B_0 (kG)	Type
Q2A (F)	2.0	2.0	10.0	Fe elec.
Q2B (F)	2.0	2.0	10.0	Fe elec.
Q1SC (D)	1.5	2.0	30.0	SC
Q1B (D)	0.5	2.1	11.6	PM
Q1A (D)	1.0	1.8	12.5	PM
Q1 (D)	2.0	1.3	12.5	PM

Decreasing the gradient of the final lenses increases their total length, which in turn increases the severity of chromatic aberrations. Thus the bandwidth of the final focus can be degraded by selecting longer, weaker final doublet magnets. The bandwidth was improved by adding a fourth quadrupole to the matching region between the end of the chromatic correction section and the final doublet, thus allowing the phase advance of the matching region to be optimized in each plane for bandpass[2], and tuning 3 sex-

tupoles at IP images in the chromatic correction sections and final dispersion suppressor. The bandwidth as a function of center-of-mass energy is shown in Figure 2. The bandpass of the system is judged to be sufficient at all energies. The previous design called for using a larger bend angle in the CCX and CCY to reduce the necessary sextupole strength, which in turn would improve the bandpass; this is not considered necessary, given the bandpass as shown in Figure 2. The geometric luminosity (luminosity without disruption enhancement) as a function of energy is shown in Figure 3. Figure 3 includes effects of geometric and chromatic aberrations as well as synchrotron radiation in quads and bends.

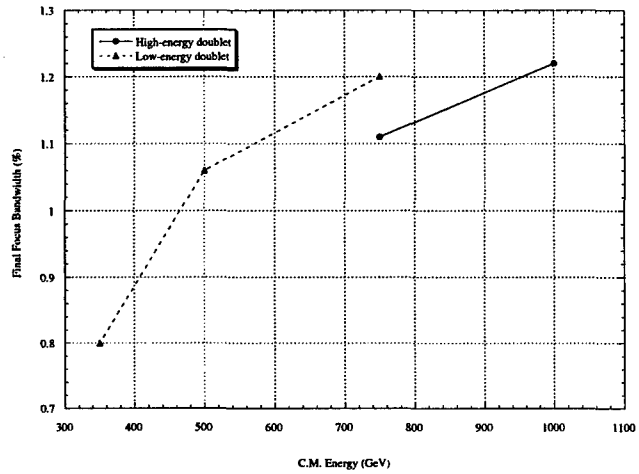

Figure 2: Luminosity bandwidth of NLC Final Focus as a function of center-of-mass energy.

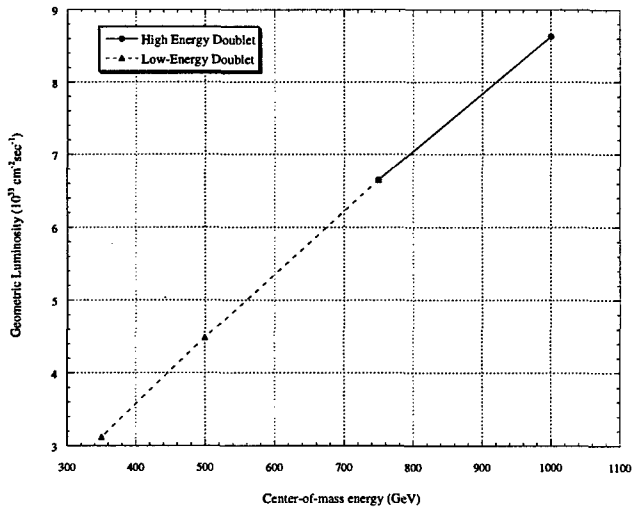

Figure 3: Luminosity of NLC Final focus as a function of center-of-mass energy.

6 IR LAYOUT

The NLC beams enter the detector with a 10 mrad horizontal angle with respect to the detector solenoid axis. The nonzero horizontal momentum in the solenoid causes a vertical displacement of the beams at the collision point. In addition, the beams have a very flat aspect ratio at the collision point, which can be severely impacted by coupling from the solenoid.

Previous studies of the interaction region have relied upon a "flux excluder", a solenoid around the last few quads which cancels the detector solenoid's effects. However, more complete modelling of the solenoid indicates that the effects of a real solenoid are much less severe than for a hard-edged field model: the fringe fields tend to cancel the effects of the main field. Thus the optical effects of the solenoid can be cancelled with very small skew quad fields and displacements of the last quad and the chromatic correction sextupoles at the level of a few microns. In addition, the solenoidal field falls off quickly with distance from the IP, and thus the permanent magnet quads (2 meters from the IP) are in no danger of demagnetizing due to the effect of the external solenoid field.

We conclude that the flux excluder can be removed from the IR design with only a miniscule impact on luminosity, and that no corrective elements are needed inboard of the last quadrupole magnet.

7 FEEDBACKS AND TUNING SIMULATIONS

Fast beam-based feedbacks were an essential component of the Stanford Linear Collider, and have been used extensively at synchrotron light sources to control instabilities and relax tolerances. Work has begun on identifying and defining the feedbacks needed in the beam delivery region of the NLC. These include several conventional feedbacks, which apply a correction to future bunch trains based on the measured performance of past train; dither feedbacks, which slowly vary a parameter (for example, IP dispersion) and measure a state (for example, luminosity) seeking an optimum value [3]; and a superfast IP feedback, which measures the beam-beam deflection of the first bunches of a train and applies a correction to subsequent bunches of the same train to achieve head-on collision.

8 ACKNOWLEDGEMENTS

The authors wish to thank R. Helm, L. Hendrickson, J. Irwin, and M. Woodley.

9 REFERENCES

[1] NLC ZDR Design Group, "Zeroth-Order Design Report for the Next Linear Collider," SLAC Report 474 (1996).

[2] N.J. Walker *et al*, "Third-Order Corrections to the SLC Final Focus," Proc. *PAC 93* 92 (1993).

[3] L. Hendrickson *et al*, "Luminosity Optimization Feedback in the SLC," SLAC-PUB-8027 (1999).

THE NEXT LINEAR COLLIDER EXTRACTION LINE DESIGN*

Y. Nosochkov†, T. O. Raubenheimer, K. Thompson and M. Woods
Stanford Linear Accelerator Center, Stanford University, Stanford, CA 94309

Abstract

The two main functions of the NLC extraction line include: 1) transmission of the outgoing disrupted beam and secondary particles to the dump with minimal losses; and 2) beam diagnostics and control. In this report, we describe the extraction line optics, present the results of tracking studies, and discuss the extraction line instrumentation.

1 INTRODUCTION

The power of the Next Linear Collider (NLC) [1] beams at 1 TeV (cms energy) can be as high as 10 MW and has to be safely disposed after the interaction point (IP). For the NLC beam parameters at the IP, a significant disruption [2] of the beam distribution occurs due to the beam-beam interaction, notably an increase in the beam angular divergence and energy spread. In addition, the beam collisions generate a significant amount of beamstrahlung photons, low energy e^+e^- pairs and other secondary particles; the number of the beamstrahlung photons from the IP is comparable to that of the primary beam particles. The need to transport the photon power to the dump places constraints on the extraction line design. Following earlier studies [3], the current design is based on a shared dump for the primary leptons and photons. To minimize beam losses due to large energy spread in the disrupted beam, it is critical to design optics with large chromatic bandwidth. Additional constraints are imposed by planned diagnostics after IP.

Several scenarios are currently under study for NLC beam parameters [1]. In this paper, we present the results for one scenario which gives the largest energy spread and beam loss for the disrupted beam. This set of beam parameters includes: 1046 GeV cms energy, 120 Hz repetition rate, 95 bunches per RF pulse and $0.75 \cdot 10^{10}$ bunch charge (see also Table 1). Since the colliding beam parameters are identical at IP, the extraction line design described below is applicable to both beams.

2 LATTICE

The primary requirement for the NLC extraction line is to transport the outgoing beams to the dump with minimal losses and provide conditions for beam diagnostics. The main optics includes: 1) a set of quadrupoles after IP to focus the outgoing lepton beam; 2) a horizontal chicane and secondary IP in the middle of chicane for beam measurements; and 3) a second quadrupole set at the end of the line to make a parallel beam at the dump. The strength of

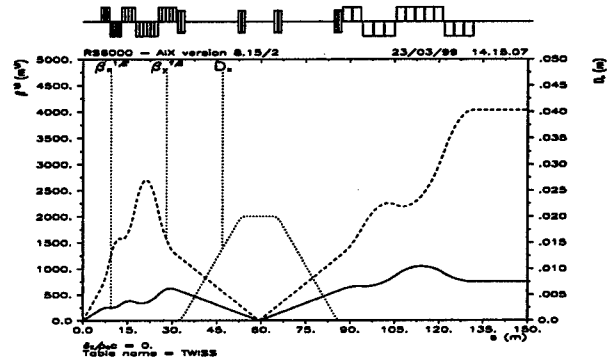

Figure 1: Lattice functions in the extraction line.

the first quadrupole system is defined by the point-to-point transformation from IP to secondary IP (R_{12}=R_{34}=0), and the second set of quadrupoles provides a point-to-parallel transformation to the dump (R_{22}=R_{44}=0). The optics calculations were made using MAD code [4].

The lattice functions of the extraction line are shown in Fig. 1. Since the beam size at IP is much smaller in the vertical plane, the first quadrupole after IP focuses the beam horizontally. This minimizes the overall beam size in the extraction line. For realistic magnet design, we use the quadrupole pole tip field $\leq$12 kG at 1 TeV (cms energy) and 8.2 kG field in the bends. The total length of the beam line is about 150 m.

The beam line optics is constrained by the following parameters and requirements:

- Crossing angle and positions of the final focus quads,
- Disrupted beam parameters at IP,
- Angular divergence of the beamstrahlung photons,
- Shared dump for a primary beam and photons,
- Secondary IP and chicane for beam diagnostics.

2.1 IP Constraints

The NLC beams cross at 20 mrad horizontal angle, and the nearest final focus quadrupoles are placed 2 m before the IP. To minimize geometric interference between the final focus and extraction line magnets, the latter should be placed as far as possible from the IP. However, a long free space after IP increases the beam size, apertures and length of the extraction line quadrupoles. In this design, we place the first extraction line quadrupole 6 m after IP. This clears the first three final focus quadrupoles.

2.2 Disrupted Beam Parameters

The strong beam-beam interactions change the beam parameters at IP. Notably, a significant increase occurs in the beam energy spread and horizontal angular divergence. The horizontal phase space for the disrupted primary beam

* Work supported by the Department of Energy Contract DE-AC03-76SF00515.

† E-mail: yuri@slac.stanford.edu.

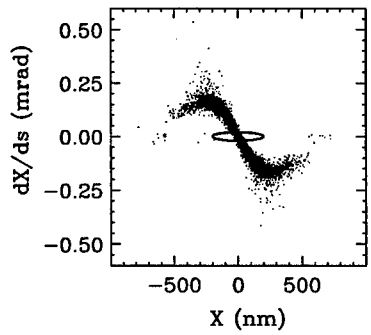

Figure 2: Horizontal phase space at IP: dots - disrupted beam, ellipse - 1σ undisrupted beam.

Table 1: Beam parameters at IP.

Beam parameter	Undisrupted x/y	Disrupted x/y
Emit. (m·rad) [10^{-13}]	39 / 0.59	120 / 1.02
rms size (nm)	198 / 2.7	198 / 3.2
rms divergence (μrad)	20 / 22	125 / 33
β^* (mm)	10.0 / 0.125	3.259 / 0.103
α^*	0 / 0	1.805 / 0.306

at IP is shown in Fig. 2. The beam distribution was calculated using GUINEA PIG beam-beam simulation code [5]. The undisrupted 1σ phase ellipse is shown for comparison in Fig. 2. The nominal and disrupted beam parameters are given in Table 1.

The energy distribution for the disrupted beam is shown in Fig. 3. The low energy tail extends to $\delta \sim -90\%$ (δ=$\Delta p/p$), and up to 1% of the beam power (~100 kW) is carried by the particles with δ<-50%. To minimize losses in this energy range, the optics requires a huge chromatic bandwidth and large magnet apertures. The methods used to improve the chromatic transmission are discussed below.

2.3 *Chromatic Bandwidth*

To satisfy optics conditions for the nominal energy, the use of quadrupole doublets in the beginning and end of the extraction line is sufficient. However, the strong doublets significantly overfocus the particles in the low energy range and lead to beam losses. To reduce the overfocusing, we replaced the doublets by 5 alternating gradient quadrupoles in the beginning and 4 quadrupoles at the end of the beam line (see Fig. 1). Since the net focusing for the nominal energy has to remain the same, the strengths of individual quadrupoles are reduced. As a result, the low energy particles experience less focusing in each quadrupole and oscillate through the alternating gradient system with less overfocusing. The strengths of individual quads were optimized by minimizing the low energy betatron amplitudes. The limitations of the described multi-quad system are the increased length of the focusing system and the large beam size and magnet apertures.

A simplified explanation of the multi-quad bandwidth can be made using analogy with a FODO system of n identical cells with fixed total phase advance μ. In such a system, the range of low energies satisfying stability conditions increases with n proportional to 1-sin($\mu/2n$).

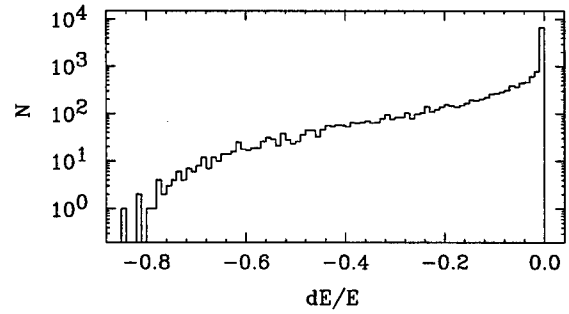

Figure 3: Energy distribution for disrupted beam.

2.4 *Beamstrahlung Photons*

Bending of the particle orbits due to beam-beam forces at IP results in radiation and significant flux of beamstrahlung photons from IP. The GUINEA PIG simulation shows that the rms angular spread of the photons is on the order of ± 100 μrad in the horizontal plane and a factor of 2 smaller in the vertical plane. In this design, the primary beam and the photons are transported to one shared dump. For beam diagnostics in the extraction line, it is desirable to avoid any material in the path of the beamstrahlung photons. Therefore, large apertures of the magnets and beam pipe have to be used to include the photon flux. For this design, we assumed the maximum photon beam divergence of ± 1 mrad and ± 0.5 mrad in the horizontal and vertical planes, respectively.

2.5 *Chicane*

The horizontal chicane allows to separate the outgoing electron and photon beams for measurements. In this design, the chicane is made of 4 pairs of bends which produce a closed bump with 2 cm of horizontal displacement and dispersion. This dispersion is sufficient to measure the energy spread of the undisrupted beam at the secondary IP. Since there are no quadrupoles between bends, the orbit bump is closed for all energies. The maximum displacement for the low energy particles increases with $1/E$.

2.6 *Magnet Apertures*

Large physical aperture is required for maximum transmission of the beam to the dump. We determined the extraction line aperture by: 1) 10σ beam size; 2) low energy horizontal excursions in the chicane; and 3) the maximum photon flux size. Schematically, this is shown in Fig. 4. Outside the chicane region the aperture is dominated by the ± 1 mrad horizontal angle of the photon flux. The quadrupole apertures vary from ± 1 cm for the first quadrupole after IP to ± 13 cm near the dump.

To minimize beam losses in the chicane region, we increased apertures to include low energy orbits up to $\delta = -90\%$. With the beam size included, the maximum horizontal aperture in the chicane is ± 20 cm. Since the orbit excursions in the chicane occur in the horizontal plane,

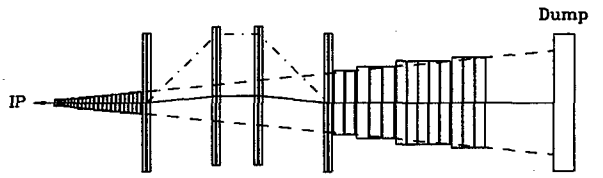

Figure 4: Aperture constraints: solid line - nominal beam; dash: ±1 mrad photon x-angle; dash-dot: δ=-90% x-orbit.

a smaller vertical aperture can be used in the bends. The tracking simulations showed that ±50 mm vertical gap in the bends is sufficient to minimize beam losses and include the ±0.5 mrad vertical photon angle.

3 DIAGNOSTICS

Beam line diagnostics fall into three categories: 1) standard diagnostics (BPMs, toroids and ion chambers) to facilitate cleanly transporting the beam to the beam dump; 2) luminosity diagnostics to measure and optimize the luminosity; and 3) physics diagnostics to measure the beam polarization, energy, and energy spread.

The luminosity diagnostics will include BPMs with 1 μm resolution for measurements of deflection angles, as well as detectors to monitor low energy particles produced at the IP from radiative Bhabha and pair production processes. The physics diagnostics will include a Compton polarimeter, an energy spectrometer, and a wire scanner to measure energy spread. The Compton polarimeter will collide a laser beam with the electron beam in the middle of the chicane, and its detector will analyze Compton-scattered electrons below 50 GeV after the chicane. A conventional wire scanner in the chicane can be used for the energy spread measurements. An SLC-style energy spectrometer is planned between the chicane and the beam dump to measure the separation of synchrotron light due to a precisely calibrated spectrometer magnet.

4 BEAM LOSS

The methods used to improve the beam transmission included: 1) the use of multi-quad focusing systems for large chromatic bandwidth; and 2) sufficiently large magnet apertures. To assure accuracy of the beam transport with low energy tail, we used a modified version of the DIMAD code [6] which can handle chromatic terms to all orders.

With up to 10 MW of the NLC beam power, even the loss of just 0.3% would be equivalent of losing the whole SLC beam (30 kW). Therefore, our goal was to reduce to a minimum the overall beam losses. In addition, an excessive beam loss would interfere with the planned diagnostics and experiments in the extraction line.

In tracking simulations, we used a disrupted distribution of 15,000 primary beam particles calculated with GUINEA PIG code. This distribution was tracked from IP to the dump and the beam losses were monitored along the beam

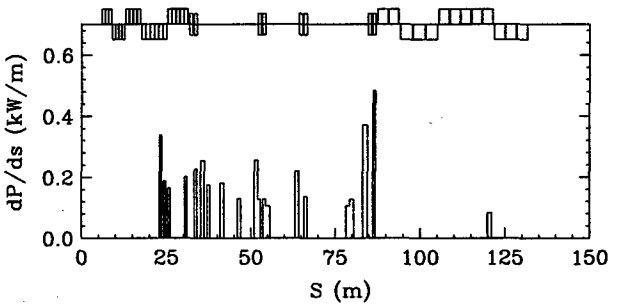

Figure 5: Distribution of the beam power loss.

line. We used round apertures for the quadrupoles and drifts, and rectangular aperture for the bends.

The most losses occur for the very low energy particles which experience strong overfocusing in quadrupoles and large horizontal deflections in the bends. The calculated beam power loss along the beam line is shown in Fig. 5. In this case, all particles with δ>-50% and most with the lower energies are transported to the dump. The total loss is 4.7 kW (0.25% particles) and the distributed power loss is below 0.5 kW/m. At the dump, the rms (x/y) beam size is 7.7/4.7 mm with the tails extending to ±100/40 mm.

The simulations included the 6 T detector solenoid (12 Tm after IP). Due to the crossing angle, the solenoid induces vertical orbit distortions. The study showed that with corrected vertical orbit after IP, the solenoid effect on the beam loss is negligible.

5 FUTURE STUDIES

In future studies, we need to increase statistics of GUINEA PIG simulations to obtain more accurately the distributions of electrons in the low energy tail and beamstrahlung photons at large angles. Tracking of these particles is needed to calculate signal to background ratios in the diagnostic detectors.

More details have to be included in the design of the beam line diagnostics, in particular the magnets for the energy spectrometer.

Methods of directing the main beam and photons to separate dumps and possibly reducing the backgrounds and neutron back-shine from the dump need to be investigated.

6 REFERENCES

[1] NLC ZDR Design Group, "Zeroth-Order Design Report for the Next Linear Collider," SLAC Report 474 (1996); with updated parameters at: http://www-project.slac.stanford.edu/lc/nlc-tech.html.

[2] R. Hollebeek, "Disruption Limits for Linear Colliders," *NIM*, **184**, p. 333 (1981).

[3] J. Spencer, *et al.*, "The SLAC NLC Extraction & Diagnostic Line," Proceedings of the 1995 IEEE Part. Acc. Conf., Dallas, p. 713 (1995).

[4] H. Grote, F. C. Iselin, CERN/SL/90-13 (AP) Rev.4 (1994).

[5] D. Schulte, Ph.D. thesis (1996).

[6] P. Tenenbaum, *et al.*, "Use of Simulation Programs for the Modelling of the NLC," these proceedings (1999).

THE TRANSVERSE LONG-RANGE WAKEFIELD IN RDDS1 FOR THE JLC/NLC X-BAND LINACS

R.M. Jones†, N.M. Kroll†‡, R.H. Miller†, T. Higo¥, Z. Li†, R.D. Ruth†and J. W. Wang†
†Stanford Linear Accelerator Center, M/S 26, P.O Box 4349, Stanford, CA 94309, USA
‡University of California, San Diego, La Jolla, CA 92093-0319.
¥KEK, Natl. Lab. for High Energy Physics, 1-1 Oho, Tsukuba-shi,
Ibaragi-ken 305, Japan

Abstract

The re-designed RDDS (Rounded Damped Detuned Structure) consists of 206 cells with a rounded cell profile formed by a number of circular arcs and a straight section. In the previous analyses [1] of the present structure all cells have been assumed to be coupled to the manifold via slots cut into the cells and, a perfect match to the HOM (Higher Order Mode) couplers has been used. In the structure being fabricated, four cells on either end of the structure are decoupled to accommodate the HOM couplers and, the HOM couplers have finite, frequency dependent, reflection coefficients. The wakefield is calculated incorporating both effects.

1 INTRODUCTION

In order to achieve high luminosity beams at the collision point in a linear collider scheme it is required to accelerate multiple bunches of low emittance particles. However, the first bunch in a train, will excite a transverse

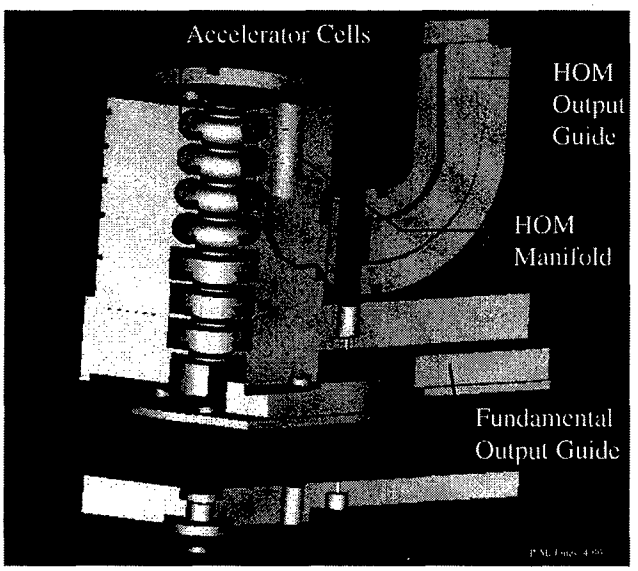

Figure 1: CAD exploded view of RDDS. The curvature of the cells and the HOM couplers are illustrated.

wakefield, which arises either by a slight transverse misalignment in the structure, or some jitter induced beam offset. This wakefield will kick successive bunches off axis and they will also generate wakefields themselves. If this effect is not reduced then the emittance of the beam will be diluted and a BBU (Beam Break Up) instabilty will develop. The main component of the modes is dipole in character. In the KEK/SLAC collaboration we have developed a scheme to damp these modes, which relies on Gaussian detuning the modes excited by the beam such that they do not add up in a coherent fashion, together with moderate damping of the long range wakes. The RDDS is illustrated in Fig. 1. Damping is required in addition to detuning because eventually the finite number of modes will partially recohere and lead to an unacceptably high wakefield. The long-range wakefield is carefully coupled out at each cell to four manifolds which lie parallel to the axis of the accelerator.

There have been three DDS, two of which, DDS 1 and 3 have been measured in the SLC using the ASSET facility [2]. The present design, RDDS1, has a 11.25% frequency bandwidth or about 4.75 in units of σ. This design has been carefully optimized to maximize the shunt impedance and to minimize the long range transverse wakefields. In the process of designing the structure it was necessary to decouple cells and it was found that, there will not in practice be a perfect match of the HOM load. The next section discusses the design of the load and in section 3, the influence of decoupling cells on thec wakefield is described.

2 MANIFOLD TERMINATIONS

The HOM terminations for the DDS are surprisingly critical: a VSWR as small as 1.05 on the loads at the downbeam end of the structure causes a noticeable increase in the wakefield amplitudes. However, our equivalent circuit model shows that the power flow in the manifold is predominantly in the direction of the beam, so that reflections at the upbeam end are of little consequence. In order to avoid the possibility of stray electrons charging the lossy ceramic in the loads and also the possibility of ceramic fragments falling into the accelerator structure, we have chosen to have the loads external to the accelerator structure. The power is brought out in rectangular double-mitered bends which have an excellent match over the 11% bandwidth of interest. The match from the round manifolds which are periodically loaded by coupling apertures into each cell (except the final 4) into the smooth rectangular guide in a short distance (order of 10mm) proved to be more difficult. For both the numerical modeling and the experimental cold test and optimization measurement the same approach

0-7803-5573-3/99/$10.00@1999 IEEE.

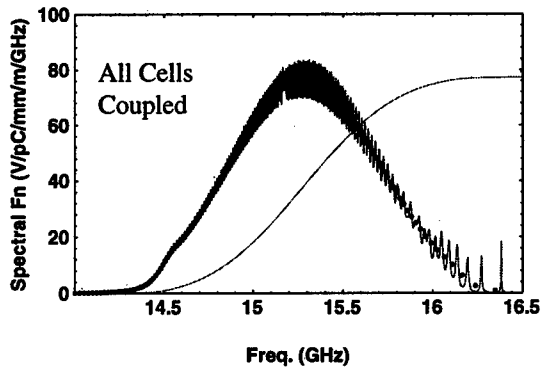

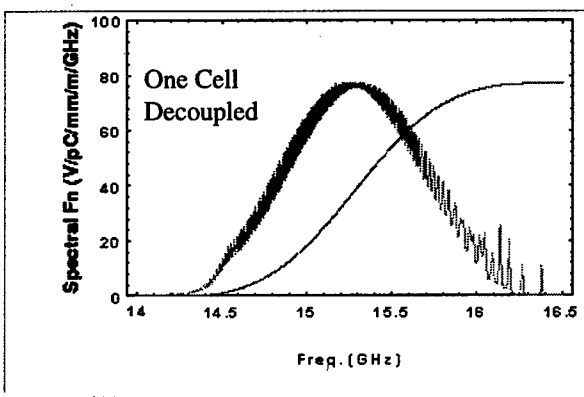

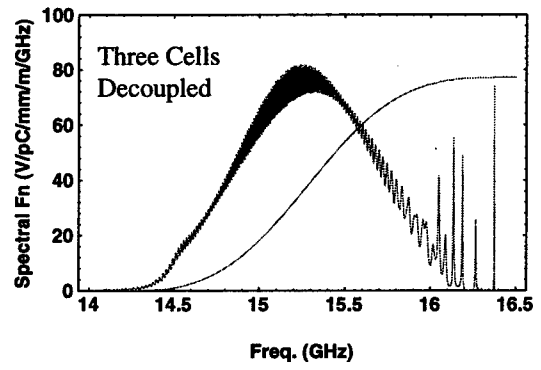

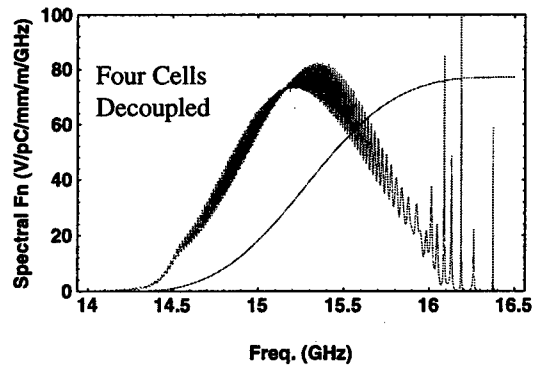

Figure 2: Uppermost is the spectral function for all cells coupled (where the dots indicate the smoothed undamped spectral function). The subsequent curves are computed for 1 cell decoupled, followed by three, and four cells (lowermost) decoupled from both the upstream and downstream end of the RDDS

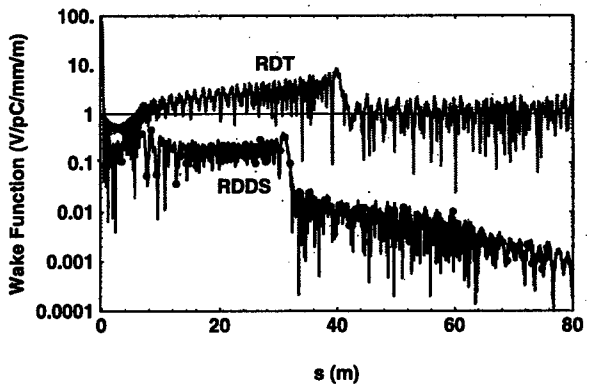

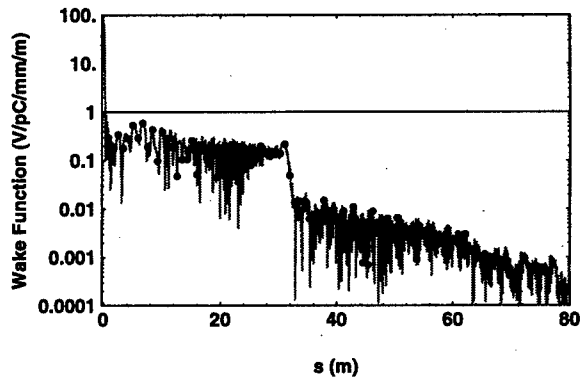

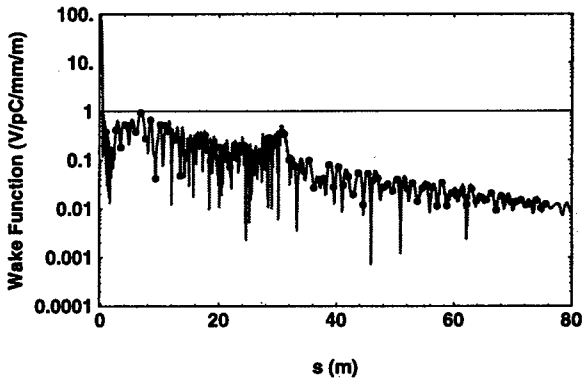

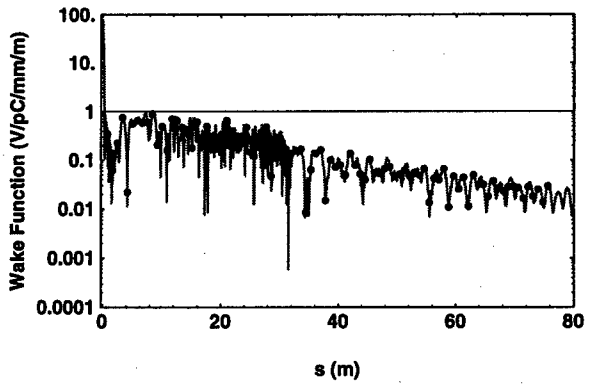

Figure 3: Uppermost is shown a comparison of the RDDS versus the RDT (Rounded Detuned, see main text) wake function for all cells coupled. The subsequent curves are computed for 1 cell decoupled, three, and finally 4 cells (lowermost) decoupled from both the upstream and downstream end of the RDDS.

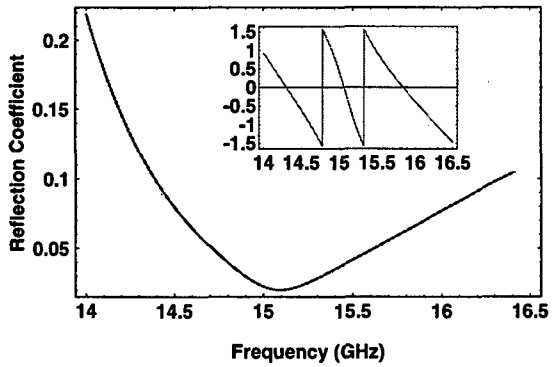

Figure 4: Magnitude of the reflection coefficient of the HOM couplers (shown inset is the corresponding phase)

was taken: two higher order mode couplers are put back and the distance between them was varied by integer numbers times the periodic length of the structure. So the rf power traveled from a source through a single mode rectangular waveguide, through the double mitered bend, through the transition from rectangular guide to the round TE_{11} manifold periodically loaded by slots into the accelerator cells every 8.75mm, up to about 5 periods, through another transition back to a smooth rectangular guide, and finally through the second double mitered bend to an output single mode rectangular guide to a matched load. If the system is lossless, as the number of periods between the input transition and the output transition is varied, the input impedance always lies on a circle in the complex plane. If the input and output transitions are identical, the circle passes through the origin so, in principle, two measurements determine the circle. For both the numerical simulation and the cold tests 3 or 4 different lengths are used, and for each length the impedance is measured as a function of frequency over the band from 14.0 to16.5GHz. The design was optimized using MAFIA in time domain driving the system with a pulse short enough to contain the required bandwidth. The forward and reflected waves were Fourier analyzed and the reflection coefficient calculated as a function of frequency. The reflection coefficient for a single HOM coupler calculated from the numerical simulation is shown in Fig 4. A bolt-together cold test model which permits changing the length between the transitions in period steps has been built and cold testing has begun.

3 DECOUPLED CELLS

The reason we are required to minimize the wakefield is that a cumulative BBU instability may develop if the wakefield couples resonantly to multiple bunches and kicks them off axis. Provided the wakefield is sufficiently small the BBU instability will not develop. In Fig 1, uppermost, the spectral function is computed for all cells coupled to the manifold and including the effect of the mismatch of the frequency dependent HOM coupler (shown in Fig 3). The oscillation imposed on the spectral function results from the imperfect match of the HOM coupler. The resulting wakefield is shown uppermost in Fig. 3. There is some degradation in the reduction in wakefield in the range 5 to 30m or so. Also indicated in Fig. 2 is the wakefield that would result if none of the cells were coupled to the manifold, i.e., if a purely DT (detuned structure) The wakefield resulting from the DT recoheres and for this reason additional damping is required.

The wakefield when all cells are coupled to the manifold, at the design value of the bunch spacing is sufficiently small to prevent BBU occurring. However, it has been found that the sum wake even for all cells coupled is quite sensitive to bunch spacing and this situation may give rise to a significant growth in the emittance. Including a perfect match to the HOM improves the wakefield and alleviates BBU. However, in practice mechanical design considerations require that a number of cells be decoupled. The resulting spectral function is shown in Fig. 1 (third from the top). Inspection of the spectral function in the high frequency region reveals a number of high Q modes have resulted from the decoupling. These high Q modes lead to an increase in the wakefield (shown by the third curve in Fig 2) in the region 4-8 meters and in the region immediately after the recoherence peak (situated at approximately 30m).

Decoupling cells enhances the wakefield to the extent that a single mode, or small number of modes, drives the bunches off axis and this results in BBU at the designed bunch spacing. Further, the difference between the wakefield achieved with 3 and 4 cells decoupled (lower-most in Fig 2) is seen to be quite small. And hence, to further ease the constraints on the method of minimizing the reflection coefficient of the transition between circular manifold and rectangular manifold (and on mechanical constraints imposed on the geometry) we finally decided upon a RDDS with 4 cells decoupled from the manifold.

4 RDDS EXPERIMENTS ENVISAGED

In the forthcoming ASSET experiment planned to measure the wakefield in RDDS 1 we will carefully design the horizontal manifold, such that only one cell is decoupled. This will allow us to compare the wakefields as a function of cell decoupling. Additionally, it may be possible to utilize the NLCTA to investigate BBU.

5 ACKNOWLEDGMENTS

This work is supported by Dept. of Energy grant numbers DE-AC03-76SF00515[†] and DE-FG03-93ER40759[‡].

6 REFERENCES

[1] R.M.Jones et al, Linac98 Conf., (SLAC-PUB 7934)
[2] C. Adolphsen et al, this Conf., FRA40

INCLUDING INTERNAL LOSSES IN THE EQUIVALENT CIRCUIT MODEL OF THE SLAC DAMPED DETUNED STRUCTURE (DDS)*

R.M. Jones†, N.M. Kroll†‡ and R.H. Miller†
†Stanford Linear Accelerator Center, M/S 26, P.O Box 4349, Stanford, CA 94309
‡University of California, San Diego, La Jolla, CA 92093-0319.

Abstract

In the equivalent circuit model for the DDS originally presented no losses were explicitly included in the cell circuits or the manifold circuits. Damping via the manifolds was effected by imposing matching conditions (including the possibility of reflection) on the ends of the manifolds. In this paper we extend the circuit theory to include lossy circuit elements. We discuss and compare shunt conductance and series resistance models for the cells. Manifold damping is modeled by introducing a shunt conductance per unit length in the transmission line elements of the manifolds. We apply the theory to the mitigation of performance degradation associated with fabricationally desireable decoupling of several cells at the ends of the structure from the manifolds.

1 INTRODUCTION

The SLAC DDS acronym refers to detuned accelerator structures in which the transverse wake field is controlled by detuning for proximate bunches and weak damping for remote bunches [1]. The damping is provided by four damping manifolds, waveguide like structures aligned symmetrically along the length of the structure, which drain dipole mode energy into external loads at both ends of the manifolds. In the original equivalent circuit studies, the manifolds were coupled to every structure cell and the manifold loads were matched. Furthermore, the equivalent circuit model [2] included no losses other than those resulting from the external manifold loads. Performance assessments have, however, always taken copper losses into account phenomenologically by multiplying computed wake functions by a decaying exponential with an appropriate damping time characteristic for each structure type, corresponding roughly to a Q of 6500 at 15 GHz (181 ns).

Subsequently the effect of manifold mismatch and the effect of decoupling a few cells from the manifolds have received a great deal of attention. Even quite small manifold mismatch leads to significant degradation of the transverse wake function [3,4]. Decoupling a few cells from the manifolds at the downstream end of the structure gives rise to a few modes with relatively high Q and large kick factors [5], which also leads to significant degradation. It is expected that both of these effects can be ameliorated by the addition of resistive damping to the equivalent circuit model. Adding resistive attenuation to the manifolds is likely to reduce the effect of termination mismatch, while individually damping the downstream cells not connected to the manifold is expected to reduce the Q of the modes discussed in [5]. In the following sections we first discuss equivalent circuit models which include cell damping and obtain the modified equivalent circuit expressions for the wake impedance defined in [6]. The wake function itself is then obtained by Fourier transforming the wake impedance without employing any direct appeal to contour modification or to analytic properties. This is followed by applications of the theory to uniform cell damping, intended to replace the phenominological model of copper losses mentioned above, and to the effect of damping the downstream cells not connected to the manifold. The effect of manifold attenuation will be discussed in a future publication.

2 CIRCUIT MODELS OF DAMPING

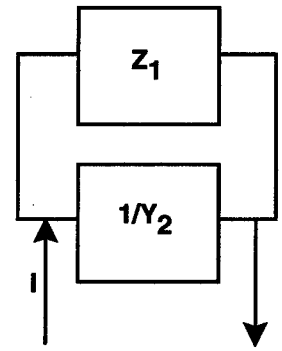

Figure 1: Circuit diagram indicating shunt loading

We describe and compare two circuit models of cell damping which we refer to as the series resistance model and the shunt conductance model. In the former, resistances of arbitrary magnitude are inserted in series with the cell loop inductances (see [2], especially Fig. 1), while in the latter, conductances are shunted across the cell loop capacitances. The impedance and inductance in Fig. 1 are given by:

$$Z_1 = j\omega(L+M)+R+Z_m$$
$$Y_2 = j\omega C+G \qquad (2.1)$$

where L, R, G, and C are diagonal 2Nx2N matrices (N

being the number of accelerator cells), M is the mutual coupling matrix and it has no diagonal elements, Z_m is the manifold impedance matrix. Furthermore, all the matrices are symmetric. In the series resistance model G = 0 and for the shunt conductance model R =0.

The impedance presented to the terminals may be written:

$$Z_1 = Z_1(1+Y_2Z_1)^{-1} = \frac{1}{\sqrt{Y_2}}\frac{\sqrt{Y_2}Z_1\sqrt{Y_2}}{1+\sqrt{Y_2}Z_1\sqrt{Y_2}}\frac{1}{\sqrt{Y_2}} \quad (2.2)$$

We write Z_1 because the circuit shown in Fig 1 represents the longitudinal impedance. Because Y_2 and Z_1 do not commute the order of factors in the above eqn. is significant. The second form, with the dimension-less quantity $\sqrt{Y_2}Z_1\sqrt{Y_2}$ is well-suited to expression in terms of our standard scaled variables. The transverse impedance, obtained from the above by application of the Panofsky Wentzel theorem in the usual way leads to an expression analogous to eqn. 5 of [6] with the expression $\overline{H}(1-f^2\overline{H})^{-1}$ which appears there replaced in the series resistance case by:

$$\overline{H}_Q(1-f^2\overline{H}_Q)^{-1} \quad (2.3)$$

with

$$\overline{H}_Q = \overline{H} - j(f_0fQ)^{-1}, Q = Q_R = \omega_0 L/R = 2\pi f_0 L/R \quad (2.4)$$

in the shunt resistance case by:

$$\overline{H}_G = U^{-1}\frac{U\overline{H}U}{1-f^2U\overline{H}U}U^{-1} \quad (2.5)$$

where:

$$U = \sqrt{1-jf_0/(fQ_G)}, Q_G = \omega_0 C/G \quad (2.6)$$

with the approximation

$$H_G \approx \tfrac{1}{2}\left(\overline{H}(1-f^2\overline{H}_Q)^{-1} + (1-f^2\overline{H}_Q)^{-1}\overline{H}\right), Q = Q_G \quad (2.7)$$

Comparing the series resistance and shunt conductance expressions with equal Q matrices, we see that the denominator matrix is the same in the two cases. For the series case, however, the numerator matrix contains a term $j/(ff_0Q)$ which has a pole at f = 0 and gives a non vanishing (and non physical) contribution to the wake function at infinite s. In the applications carried out so far this effect of this term has been suppressed be restricting the domain of integration, but in future work the shunt conductance model will be used. We propose to add manifold attenuation to the equivalent circuit model by adding attenuation to the manifold waveguide sections.

3 EVALUATING THE WAKE FUNCTION

In reference [6] we computed the (causal) wake function from:

$$W_c(s) = \theta(s)\int_0^\infty S(f)\sin[(2\pi s/c)f]\,df \quad (3.1)$$

where $S(f) = -4\mathrm{Im}\{Z(f-j\varepsilon)\}$. We recall some well known relations to argue that the same expression is appropriate here.

Because W is real, $\mathrm{Re}\{Z(f-j\varepsilon)\}=\mathrm{Re}\{Z(-f-j\varepsilon)\}$, and $\mathrm{Im}\{Z(f-j\varepsilon)\}= -\mathrm{Im}\{Z(-f-j\varepsilon)\}$ and thus:

$$W(s) = 2\int_0^\infty df\left\{Z_r\cos[2\pi s(f-j\varepsilon)] - Z_i\sin[2\pi s(f-j\varepsilon)]\right\} \quad (3.2)$$

Define:

$$W_c(s) = -4\theta(s)\int_0^\infty df Z_i\sin[2\pi s(f-j\varepsilon)] \quad (3.3)$$

where $Z=\mathrm{Im}\{Z\}$ and $Z_r=\mathrm{Re}\{Z\}$. If W vanished for negative s as it is physically required to do, we would have $W = W_c$. For then the cos integral must equal minus the sin integral. As has been noted before the equivalent circuit model has a non physical precursor so that the equality of the two terms is only approximate at small s. Physically, however, W must vanish both for negative s and at s = 0, so we consider W_c to be a better representation of the wake function than W. While this argument might lead one to conclude that it would be equally justified to use the cos integral, the sin integral is superior both because it vanishes at s = 0 and because it is easier to evaluate numerically. Practically speaking infinite integration ranges must always be replaced by finite ones, and generally speaking $\mathrm{Im}\{Z\}$ (in contrast to $\mathrm{Re}\{Z\}$) can be neglected outside the structure pass bands. If one ignores the fact that this argument fails near f = 0 for the series resistance case and confines the integration to the structure pass bands, the two models should give very similar results.

4 APPLICATIONS

The primary impetus of this work was to determine whether the deleterious effect of decoupling the last few downstream cells could be countered by damping these cells and to obtain quantitative information on how much damping would be required. In our previous analysis there were no losses in the circuit model, and we included Ohmic cell losses by including a decay constant after the taking the Fourier transform of the spectral function.

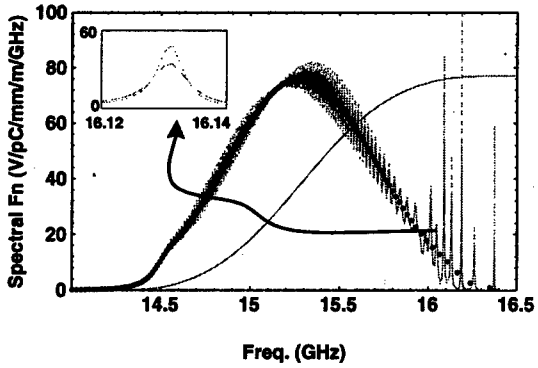

Figure 2: Spectral function for four cells decoupled from the manifold of RDDS1 and all loaded with a cell Q of 6500. Also shown is the smoothed undamped spectral function (indicated by dots).

However, in Fig. 2 the spectral function is calculated including Ohmic cell losses for both the TE and TM mode in all 206 cells. For our previous phenomenological model to have been a faithful representation of damping, the wake computed by both models should be quite similar and, the resulting wake shown in Fig. 3 reveals that the only noticeable difference in the wake is due to a slightly different sampling used in the the two Fourier transforms in the two methods. This gives us confidence in the reliablility of the method and, we calculate the effect of damping the last four and first four cells of the structure with a Q of 1000 (corresponding to the original design of an manifold-cell Q of 1000), and all other cells have purely copper losses.

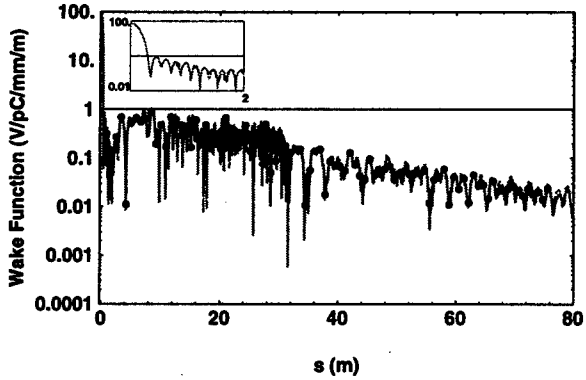

Figure 3: Wake function for four cells decoupled from the manifold of RDDS and all loaded with a cell Q of 6500, corresponding to all cells being loaded down with copper losses at room temperature. The bunches are spaced at 2.8ns and they are indicated by dots.

The spectral function for this situation, shown in Fig 4., has oscillations in the upper frequency end with considerably reduced amplitude compared with those in Fig. 2. Indeed, on computing the modal Q we find that the Q for the last 5 resonances ranges from approximately 1200 to 1500, as compared with a Q range of 3,000 to 12,800 for the situation in Fig 2. Thus the wakefield, illustrated in Fig. 5, is considerably improved in the region greater than 5m or so, in the the neighbourhood of the recoherance peak (about 30m or so), and thereafter.

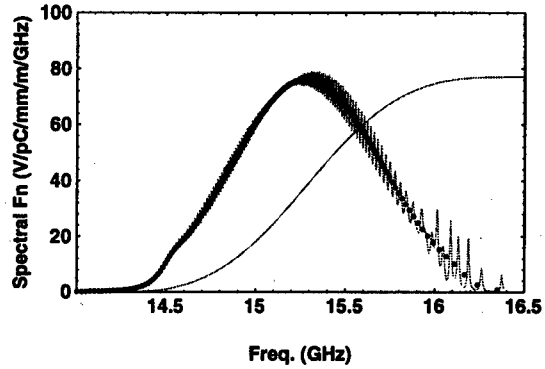

Figure 4: Spectral function for four cells decoupled from the manifold of RDDS and all are loaded with a cell Q of 6500, apart from the last four and the first four cells which are given Q of 1000.

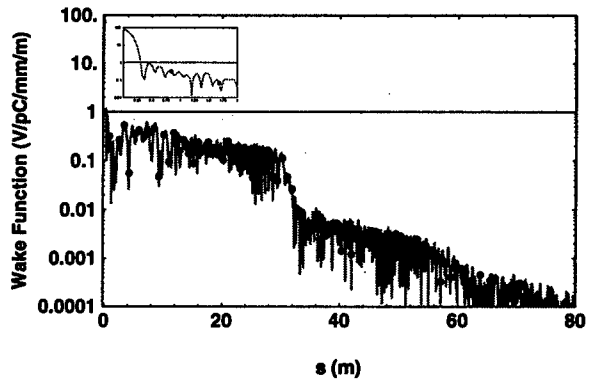

Figure 5: Wake function for four cells decoupled from the manifold of RDDS and all are loaded with a cell Q of 6500, apart from the last four and the first four cells which are given Q of 1000 Shown inset is the wakefield for the first 2m.

5 ACKNOWLEDGMENTS

This work is supported by Department of Energy grants DE-FG03-93ER40759[‡] and DE-AC03-76SF00515[†].

6 REFERENCES

[1] N.M.Kroll, The SLAC Damped Detuned Structure: Concept and Design, 1997 Particle Accelerator Conf. (also SLAC-Pub 7541)
[2] R.M. Jones, K. Ko, N.M. Kroll, R.H, Miller and K.A. Thompson, Equivalent Circuit Analysis of the SLAC Damped Detuned Structure, EPAC96(also SLAC-Pub 7187)
[3] R.H. Miller, et all, A Damped Detuned Structure for the Next Linear Collider, Linac96, (also SLAC-Pub 7288)
[4] R.M. Jones, N.M. Kroll, R.H. Miller, R.D. Miller, and J.W. Wang, Advanced Detuned Development (DDS) at SLAC, Proc. 1997 Particle Accelerator Conf. (also, SLAC-Pub 7537)
[5] R.M. Jones et al, The Transverse Long-Range Wakefield in RDDS1 for the JLC/NLC X-Band Linacs,this conf. FRA37
[6] R.M. Jones., N.M. Kroll and R.H. Miller, A Spectral Function Method Applied To The Calculation Of The SLAC Damped Detuned Structure. Intl. Linac Conf..1996 (SLAC-PUB 7287).

EMITTANCE DILUTION AND BEAM BREAK UP IN THE JLC/NLC

R.M. Jones†, K.L.F. Bane†, N.M. Kroll†‡, R.H. Miller†, T.O. Raubenheimer †and G.V. Stupakov†
†Stanford Linear Accelerator Center, M/S 26, P.O Box 4349, Stanford, CA 94309
‡University of California, San Diego, La Jolla, CA 92093

Abstract

The passage of a multi-bunch beam through an X-band accelerator with cells and structures misaligned gives rise to wakefields which disrupt succeeding bunches. As a consequence, there is growth in the overall emittance of the final colliding bunches. Here we study this process in the context of a JLC-NLC which employs the recently developed RDDS (Rounded Damped Detuned Structures) accelerators with 120 s fill time and drives a 90 bunch, 250 ns bunch train. We investigate cumulative beam break-up (BBU) under various parameter regimes appropriate to the structure which is in the process of being fabricated by KEK and SLAC. We compute the resultant emittance growth by means of analytical expressions and find good agreement with the results we obtain from a particle tracking code. We set misalignment tolerences by specifying allowable emittance growth.

1 INTRODUCTION

The primary consideration in a linear collider is the luminosity of the final colliding beams. The luminosity is given by: $L = fn_1n_2\left(4\pi\sigma_x\sigma_y\right)^{-1}$, where f is the collision frequency, n_1 and n_2 are the number of the particles in each of the colliding bunches and the beam dimension in the horizontal (vertical) plane is given by: $\sigma_{x(y)} = \left(\beta_{x(y)}\varepsilon_{x(y)}\right)^{1/2}$ Here, $\varepsilon_{x(y)}$ is the horizontal (vertical) emittance and $\beta_{x(y)}$ is the horizontal (vertical) focussing function. Thus, in order to maximize L it is required to minimize the emittance and maximize the population of each bunch. Also, to increase f, whilst using the RF energy more efficiently, in our design we accelerate a train of 90 bunches, each separated from its neighbor by 2.8 ns. As the highly charged bunches traverse the linac any misalignment in the structure, focussing magnets, or initial offset in the leading bunch, gives rise to wakefields [1] which dilute the emittance and the beam may break up down linac. This BBU can result from short range wakes over the bunch itself, in which the head drives the tail, or from a long range wake, in which trailing bunches are driven by leading ones and a cumulative BBU occurs due to the coupled motion of the bunches. The subject of this paper is stucture tolerance and cumulative BBU and means to avoid it.

2. BBU DUE TO LONG RANGE WAKES

To reduce the effect of modes adding together coherently and driving the bunches resonantly off-axis, we utilise 4,720 X-band RDDS structures [1]. The accelerating mode is that of an almost constant gradient structure, but the resulting transverse mode (predominantly dipole in character) is forced to decohere and the wakefield falls off in with a Gaussian profile. As there are a finite number of cells then the wake field eventually recoheres and for this reason, weak damping is provided via four manifolds [1] running along the axis of the accelerator If these wakes can be kept small enough the emittance dilution can be kept to acceptable levels, and this sets a limit on the structure alignment tolerances.

However, we have found that BBU occurs when the wakefield is relatively well-damped and it occurs due to a *single mode* or *small number of modes* which constitute the wakefield. One indication as to whether or BBU will occur is provided by S_σ, the RMS deviation of the sum wake from the mean wake (discussed in section 3) and we have conducted extensive investigations into S_σ as a function of the variation of a small error in the bunch spacing.

For the excellent damping provided by an idealized version of RRDS, the wakefield is insufficient for BBU to occur. The value of S_σ, at the nominal bunch spacing is approximately 0.3 V/pC/mm/m and this is not expected to give any serious instabilities. However, at 0.2% increase in the bunch spacing there is a peak in S_σ (almost double the value at the nominal bunch spacing) and for this worst case, we track [2] the beam down 10 km of accelerator structures. We perform a similar tracking of particles for a more realistic structure with HOM couplers terminated with VSWR $\neq 1$ and with the last and first cell of the structure decoupled from the manifold. In this case S_σ at the designed bunch spacing is 0.45 V/pC/mm/m and there is a maximum at approximately -0.7 % away from the nominal bunch spacing, where S_σ reaches 0.88 V/pC/mm/mm.

For both of these cases we record the emittance growth as the particles progress down the linac, and the vertical space at the end of the linac. The phase space is bounded by the unit circle and all points that lie within this circle are stable. In Fig 1 the idealised RDDS for both the vertical and horizontal planes (the latter being a factor of approximately 100 times larger than the former). In this case little emittance growth is seen to result from the long range wakefields. Similarly, the vertical displacement of the bunches at the end of the linac is small (the maximum displacement is approximately 0.125 μm). Furthermore, a glance at the lowermost curve indicates that all bunches are well contained within the unit circle. Decoupling a

0-7803-5573-3/99/$10.00@1999 IEEE.

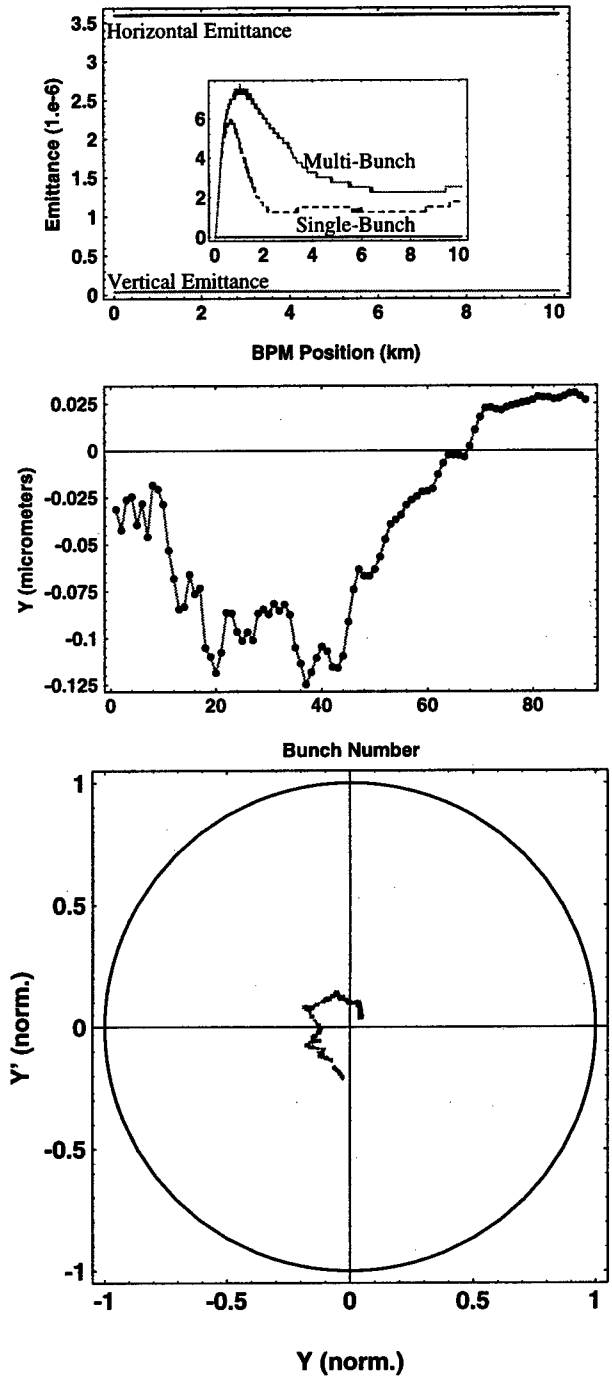

Figure 1: The above shows the result of tracking through 10 km of accelerator a beam with an initial bunch offset of 1 μm or approximately one quarter of σ_y (= 3.9μm) in the vertical plane and 1μm in the horizontal plane (σ_y = 35.9μm). Uppermost is shown the normalised vertical and horizontal emittance in units of μrad.m (and inset is indicated the emittance growth as a percentage of the initial emittance at injection to the Xband linacs, for both the single bunch and the multi-bunch cases). In phase space we normalise, Y, the vertical dispacement, with respect to $\left(\beta_y \varepsilon_y\right)^{1/2}$ and Y' with respect to $\left(\varepsilon_y / \beta_y\right)^{1/2}$

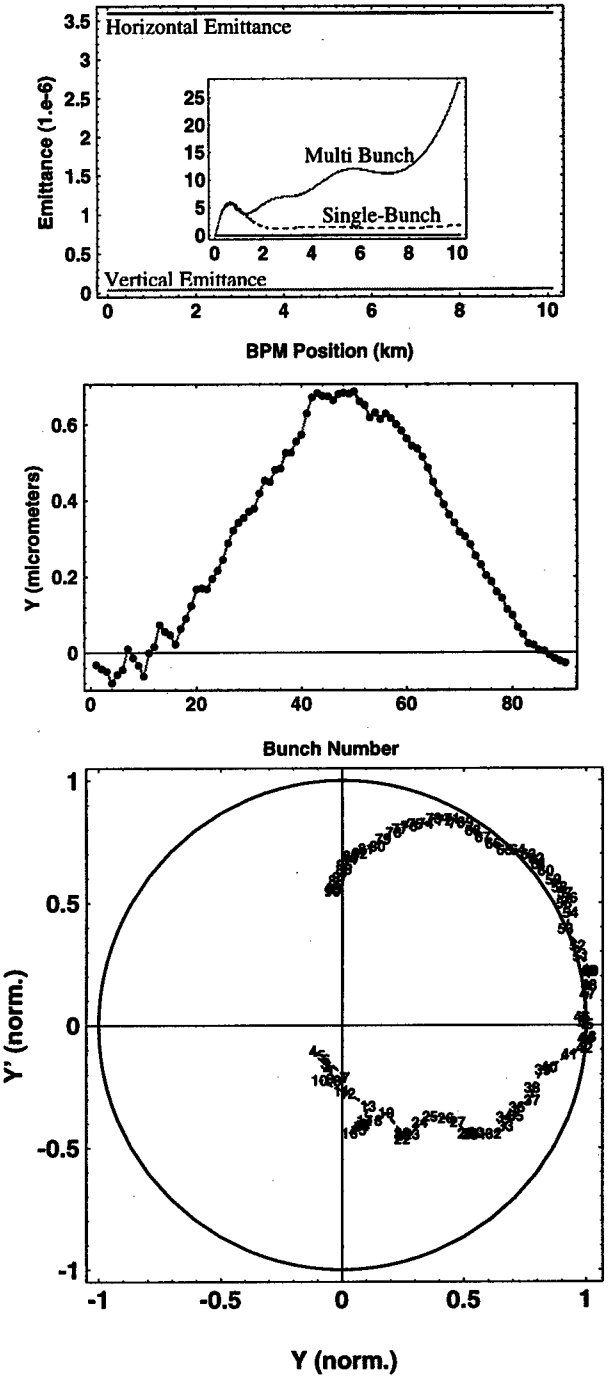

Figure 2: The simulation is similar to that of Fig. 4 except that all of the structures have one cell decoupled and the HOM couplers have realistic terminations, i.e. frequency dependent reflection coefficients corresponding to the transition between circular and rectangular manifold have been included. In both cases, the short range (transverse and longitudinal) wake has been included in the simulations, together with the long range tranverse wakefield. BNS damping of the short range wakefield has been included in the simulations by including a variation in the phase of the R.F. over the linac.

single cell leads to a quite different situation and, this is shown in Fig 2. Here the emittance grows significantly, to about 28% larger than the injected value and, as it continues to grow in an exponential fashion, any additional length added to the linac can be expected to lead to further emittance growth. The bunches rapidly are lost from the unit circle boundary in phase space as a cumulative mode of BBU develops within the linac (lower-most curve of Fig 2).

3. TOLERANCE ON ALIGMENT DUE TO LONG RANGE WAKEFIELDS

In order to estimate the growth of the projected emittance $\Delta\varepsilon$ of a train of bunches caused by misaligned structure cells we uses the following formula for the expectation value of $\Delta\varepsilon$ [3]

$$\langle\Delta\varepsilon\rangle = r_e^2 N^2 \bar{\beta}_0 L_s^2 \langle\Delta S_k^2\rangle \frac{1-(\gamma_0/\gamma_f)^{1/2}}{\gamma_0^{1/2}\gamma_f^{3/2}} \qquad (3.1)$$

where r_e is the classical electron radius, N is the number of is the number of particles in the bunch, $\bar{\beta}_0$ is the average value of the beta function at the beginning of the linac, N_s is the number of structures in the linac, L_s is the length of the structure, γ_0 and γ_f are the initial and final relativistic factors of the beam, and S_k is the sum wake. The quantity S_k is defined as a sum of the transverse wakes w_i generated by all bunches preceding the bunch number k, $S_k = \sum_{i=1}^{k} w_k$ and ΔS_k is the the difference between S_k and the average value $\langle S\rangle$, with $\langle S\rangle = N_b^{-1}\sum_{k=1}^{N_b} S_k$, where N_b is the number of bunches. Also, $S_\sigma = \langle\Delta S_k^2\rangle^{1/2}$. Eq. 3.1 is derived assuming a lattice with the beta function smoothly increasing along the linac as $\bar{\beta} \propto E^{1/2}$.

For small misalignments, w_i is a linear function of cell offsets, $w_i = \sum_{k=1}^{N_c} W_{is} y_s$ which can be found from the solution of Maxwell's equations for the structure. The matrix W_{is} for the NLC structure RDDS1 with 206 cells is based on the method [4]. It has a dimension of N_b x 206. In our calculation we used N_b=90 for bunch spacing 2.8 ns.

By splitting the structure into k pieces of length $l = L_s/k$ and randomly misaligning each piece with an rms value of Δ so that misalignments of different pieces are uncorrelated, we calculated the wake and found the emittance growth of the train of bunches as a function of parameter Δ. Requirement of the emittance growth to be less then 10% of the nominal vertical emittance of the NLC beam gives a tolerance for the amplitude of the misalignments. This tolerance is shown in Fig. 1 with the following linac parameters: beam final energy - E_f=500 GeV, number of structures in the linac – N_s = 4720, and number of particles in the bunch – N =1.1 x10^{10}.

To verify the accuracy of the analytical formula (3.1) we also calculated the tolerances using the computer simulation program LIAR . The results of the simulations are also shown in Fig. 3. It is seen that the analytical formula generally agrees rather well with the simulation.

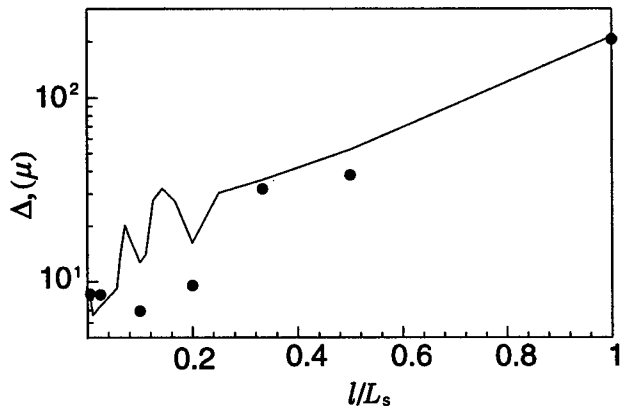

Figure 3: Tolerance Δ vs. misalignment length l in units of the structure length L_s. The solid curve shows the result of the analytical calculation based on Eq. (3.1); dots are the tolerances calculated using LIAR

Also, we found the tolerance for the structure bow which can be caused by either structure sagging between the support points under the influence of the structure weight, or thermal expansion of the structure. In this calculation, we assume that shape of a bowed structure is given by $y_s = y_0 \sin(\pi s/N_s)$, and that the amplitude y_0 is a random number for different structures in the linac. The tolerance for this kind of misalignment is Δ = 160 μm

4. DISCUSSION

In both scenarios envisaged in Fig. 1 and 2 the worst case of S_σ is used. In practice the structure will average over these errors and BBU will not necessarily occur in the case of one cell decoupled. However, additional tracking for the case of 4 cells decoupled (as in the present design for RDDS 1 which is in the process of being fabricated [5]) BBU will occur at the nominal bunch spacing. This may be alleviated by direct loading [6] of the final few cells with, for example, SiC slotted into the last 4 cells.

5. ACKNOWLEDGMENTS

This work is supported by Department of Energy grants DE-FG03-93ER40759[‡] and DE-AC03-76SF00515[†].

6. REFERENCES

[1] R.M. Jones *et al*, this conference, FRA37
[2] R. Assman *et al*, 1997, SLAC-PUB AP-103
[3] K.L.F. Bane *et al*, EPAC94 (also SLAC-PUB 6581)
[4] R.M. Jones *et al*, PAC97 (also SLAC-PUB 7538)
[5] J.W. Wang *et al*, this conference, FRA18
[6] R.M. Jones *et al*, this conference, FRA38

WAKEFIELD AND BEAM CENTERING MEASUREMENTS OF A DAMPED AND DETUNED X-BAND ACCELERATOR STRUCTURE *

C. Adolphsen#, K. Bane, R. Jones, N. Kroll, D. McCormick, R. Miller, M. Ross, T. Slaton, J.W. Wang, SLAC, Stanford, CA, and T. Higo, KEK, Tsukuba, Japan

Abstract

We present wakefield measurements of a prototype Next Linear Collider (NLC) accelerator structure that was built with dipole mode damping and detuning to suppress the long-range transverse wakefield induced by a beam. In addition, we describe beam centering tests that use as a guide the dipole power coupled out of the structure for damping purposes.

1 INTRODUCTION

Nearly all designs being considered for future linear colliders employ multibunch operation to improve efficiency. A major concern in these designs is the potentially strong coupling of the bunch motions from the long-range transverse wakefields generated as the beams traverse the linac accelerator structures. For the NLC X-band (11.4 GHz) structures, two methods have been developed to reduce the wakefields to a manageable level. One method is mode detuning whereby the frequencies of the lowest band of dipole modes (near 15 GHz) are systematically varied along the structure to produce a Gaussian distribution in the mode density [1]. This detuning results in the destructive interference of the mode contributions, yielding an approximately Gaussian falloff in the net wakefield generated after each bunch. The structure design parameters are chosen to produce about a two orders of magnitude reduction by 1.4 ns, the minimum bunch spacing being considered for the NLC.

This detuning works well to suppress the wakefield for about the first 30 ns, after which its amplitude increases due to a partial recoherence of the mode excitations. This has led to the introduction of weak mode damping to offset this rise [2]. The damping is achieved through the addition of four single-moded waveguides (manifolds) that run parallel to the structure and couple to the cells through slots (see Fig. 1). When terminated into matched loads, the manifolds reduce the mode Q's from about 6000 to 1000, enough to keep the wakefield from significantly increasing.

To date, three of these Damped and Detuned Structures (DDS) have been fabricated [3]. The cells for the most recent version, DDS3, were manufactured at LLNL [4] using single-diamond turning and then assembled in Japan using diffusion bonding [5]. This structure is 1.8 m long and contains 206 cells. Relative to its predecessors, the rf match through the output ports of the manifolds is better. The improvement came in part from using vacuum waveguide couplers on the downstream ports instead of windows. Also, the dipole frequency profile was changed slightly to enhance the effect of the detuning. Instead of a Gaussian profile in the mode density, it was made in the product of the mode density and the mode coupling strengths to the beam. In addition, the sigma of the frequency distribution was decreased (2.5% to 2.13% of 15.1 GHz), while the number of sigma was increased (4.0 to 4.78) to keep the frequency spread of the cells nearly the same.

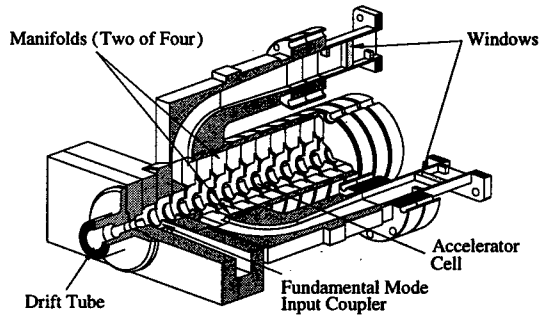

Fig. 1: Cutaway view of the upstream end of DDS3.

2 WAKEFIELD MEASUREMENTS

To measure the effect of the DDS3 changes on the wakefield, the structure was installed in the Accelerator Structure SETup (ASSET) facility which is located in the upstream end of the main SLAC Linac. Here a positron beam was used to induce wakefields in the structure that were then 'witnessed' by an electron beam. Just downstream of the structure, a chicane of magnets steered the positrons (drive beam) to a dump and the electrons (witness beam) into the linac where their trajectory was measured. During the test, the eight manifold ports were connected via Heliax cables to processing electronics in the Klystron Gallery above the linac tunnel. The signals were either measured with a spectrum analyzer or downmixed to 310 MHz and digitized to determine their amplitude and phase. A signal from a nearby stripline BPM served as the beam phase reference. Details of the wakefield and signal measurements are given in references [6] and [7].

In brief, each measurement of the wakefield amplitude began by setting the relative beam timing to some multiple of the linac rf period (350 ps). The relative timing was then stepped in 3 ps increments to map the wakefield over a few oscillation periods (≈ 200 ps). At

* Work Supported by DOE Contract DE-AC03-76F00515.
# Email: star@slac.stanford.edu

0-7803-5573-3/99/$10.00@1999 IEEE.

each step, the drive beam position was moved parallel to the structure over a +/– 2 mm range and the resulting deflections of the witness beam recorded. The deflection angle per unit drive offset was then computed and converted to a wakefield strength. Finally, the wakefield amplitude was obtained by fitting the wakefield strengths to a sine wave with a 15.1 GHz frequency, which is the mean frequency of the lowest dipole band.

The results from 35 such measurements over a 200 ns range are shown in Fig. 2. They are plotted versus the square-root of the relative beam time so values at short times are more discernible. Although the initial falloff of the wakefield is large, it was expected to stay below about 0.5 V/pC/m/mm out to 20 ns, instead of rising to values near 4 V/pC/m/mm as was observed. This difference is likely the result of the cell fabrication errors being larger than the design tolerances. The effect of such errors are included in the predictions in Fig. 1, which were obtained from an equivalent circuit model of the structure [8]. In the top plot, the errors are based on limited cell QC measurements made prior to the structure assembly. They are essentially equivalent to random cell-to-cell, 5 MHz rms, Gaussian frequency errors, and are larger than the ≈ 2 MHz rms design tolerance. In the bottom plot, the errors were increased to best match the wakefield measurements, which required 12 MHz rms values. Thus, the actual cell errors may be larger than the QC results indicated or more

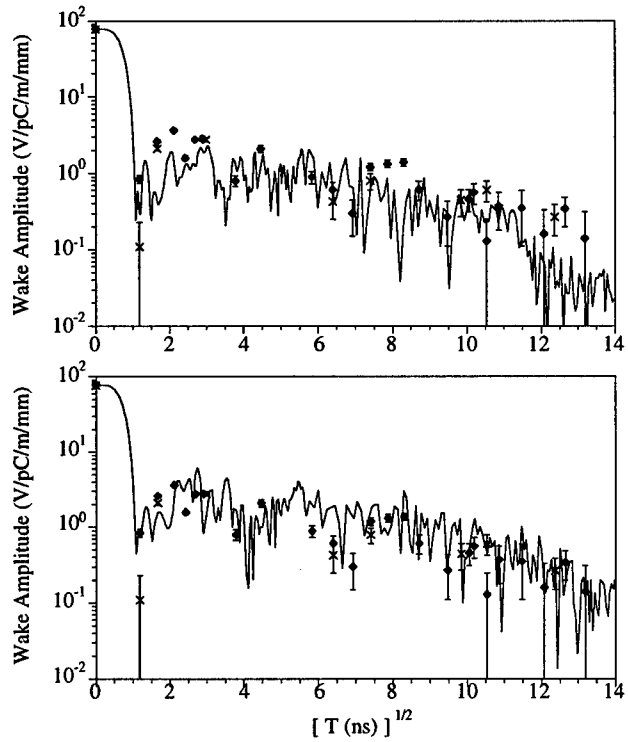

Fig. 2: Horizontal (crosses) and vertical (diamonds) wakefield measurements and predictions (solid lines) including 5 MHz rms cell frequency errors (top) and 12 MHz rms cell frequency errors (bottom).

systematic in nature, which can enhance their effect. The theory itself has worked well previously, yielding predictions in good agreement with the DDS1 measurements without added frequency errors [6].

The decrease in the wakefield that occurs at longer times is due to the mode damping. In contrast, the wakefield measured in a similar detuned-only structure slowly increases in time [9]. Another comparison of note is the similarity of the DDS3 horizontal and vertical results even though the upstream manifold ports for the horizontal modes were shorted for this test. This was done to assess the effect of removing the upstream ports in the future. However, the lack of a significant difference is not too surprising since the dipole mode power was expected, and measured, to go mainly (99%) to the downstream ports. Finally, we note that the short-range (< 50 ps) DDS3 wakefield measurements agree well with a prediction that includes contributions from higher band modes [10].

3 BEAM CENTERING

Although the manifolds were nominally added to damp the dipole modes, they are also a source of signals that can be used to measure the beam's transverse position in the structure. Moreover, the beam coupling to the modes is fairly localized (2 to 10 cells) so filtering the signals by frequency yields the beam offset at a particular location along the structure. The NLC goal is to use this signal information to keep the beams centered in the structures to about +/– 20 μm.

As a test, data were taken in which the beam was stepped transversely across the structure while the signal from a 15 MHz slice of the 14-16 GHz dipole spectrum was processed. Figure 3 shows data taken at 15.0 GHz. As expected, a 180 degree phase transition occurs when the signal power goes through a minimum. The solid lines in the plots are fits to the data: a parabola to the power and an arctan function to the phase. In each case, a fit parameter was included to account for the addition of an out-of-phase signal component. The size of this component is conveniently expressed in terms of an equivalent beam offset, that is, the beam displacement relative to its position at minimum power that increases the dipole power by an amount equal to the out-of-phase power. The phase data yields the best measure of this offset, 5 +/– 2 μm. However, values as large as 100 μm were initially observed. After some study, it was realized that an X-Z correlation along the bunch (σ_z = 0.7 mm) was the likely source. This correlation was reduced by tuning the dispersive properties of the beamline to decrease the horizontal bunch width. Thereafter, the measured offsets were generally smaller than the NLC beam centering tolerance, which is desirable since it will simplify signal processing in the NLC.

Another parameter obtained from the fits to the dipole signal data is the beam position at the minimum

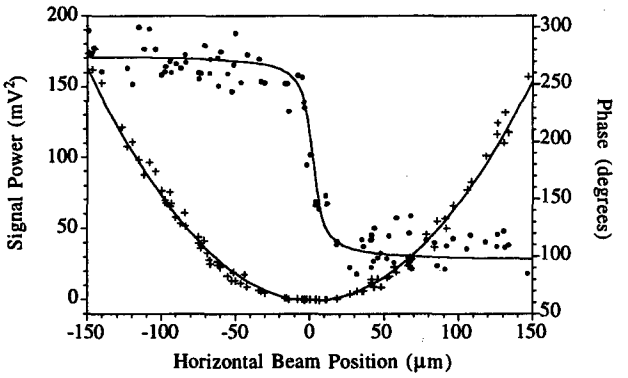

Fig. 3: 15 GHz dipole signal power (pluses) and phase (circles) versus beam position. The fits to the data (solid lines) are described in the text.

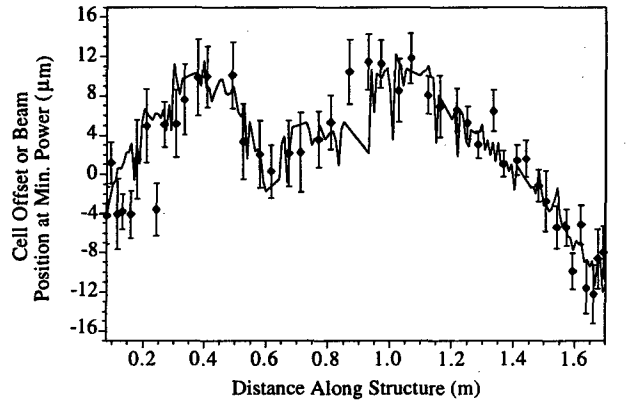

Fig. 4: Horizontal structure straightness measured with a beam (diamonds) and a CMM (solid line).

signal power. These values provide a measure of the structure straightness when plotted versus the corresponding points of origin of the signals (on average) along the structure. Figure 4 shows the horizontal straightness results that where derived using the frequency-to-cell mapping obtained from the equivalent circuit model of the structure [8]. Also shown are straightness results from a pre-installation survey of the outer surfaces of the cells (30 mm radii) that was done with a Coordinate Measuring Machine (CMM). The good agreement between these measurements, and micron-level local straightness of the structure, attest to the high precision with which the cells were fabricated and assembled. The vertical CMM and beam-based results agree less well, although a post-run survey of the structure indicates that it had vertically distorted by about 30 μm since the initial survey.

From the straightness results, a beam orbit can be derived that should zero the integrated short-range transverse wakefield through the structure. To test how well this can be achieved in practice, the ASSET drive beam was steered to an orbit based on the minimum dipole power results, and then the short-range wakefield (T < 200 ps) was measured with the witness bunch. In this case, an absolute wakefield was derived instead of one differential in the drive beam offset. For convenience, it was normalized to the differential short-range wakefield amplitude (i.e., the T = 0 point in Fig. 2). Hence, if the drive beam was offset by 20 μm, for example, the absolute wakefield should essentially be a sine wave with a 20 μm amplitude. In reality, additional components of wakefield were observed that were independent of the drive beam position. Figure 5 shows two measurements in which these contributions are apparent. In the top plot, the T < 50 ps values are shifted negative for data that otherwise appear consistent with a beam offset of about 40 μm. The shape of the added wakefield is better seen in the bottom plot where the beam was likely centered to < 10 μm. At this level, a sine-like 21 GHz component also becomes apparent. The T < 50 ps component is thought to originate from wakefields generated upstream of ASSET since it was also observed in measurements of a C-Band structure [11]. The origin of the 21 GHz component is not known, but it would have little impact on NLC operation. Despite these complications, the attempts to center the drive beam generally yielded offsets < 20 μm based on the size of the 15.1 GHz component. Thus, these techniques appear promising for meeting the NLC beam centering requirements.

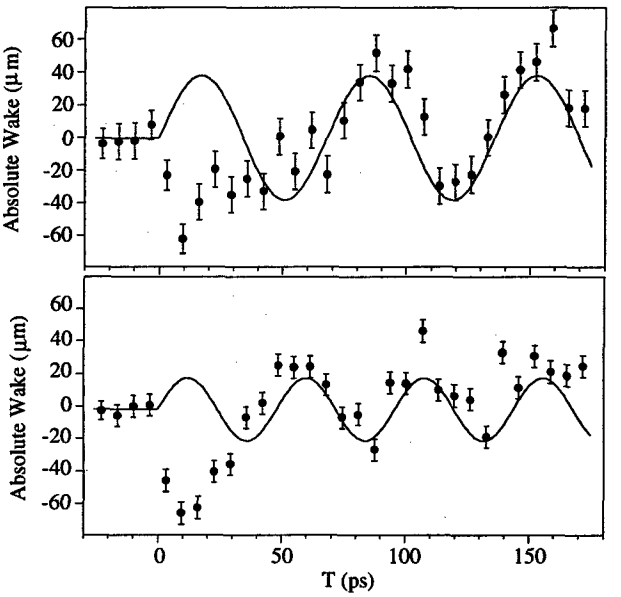

Fig. 5: Vertical absolute wakefield measurements made as part of the beam centering tests. The solid lines are 15.1 GHz (top) and 21 GHz (bottom) sine wave fits to the T > 50 ps data.

4 REFERENCES

[1] K. A. Thompson et al., SLAC-PUB-6032 (Nov. 1993).
[2] N. M. Kroll, SLAC-PUB-7541 (May 1997).
[3] J.W. Wang et al., FRA18, these proceedings.
[4] J. Klingmann et al., MOP51, these proceedings.
[5] T. Higo et al., FRA16, these proceedings.
[6] C. Adolphsen et al., SLAC-PUB-7519 (May 1997).
[7] M. Seidel, SLAC-PUB-7557 (June 1997).
[8] R. Jones, private communication.
[9] C. Adolphsen et al., SLAC-PUB-6629 (Aug. 1994).
[10] K. Bane, private communication.
[11] T. Shintake, FRA14, these proceedings.

RDDS CELL DESIGN AND OPTIMIZATION FOR THE LINEAR COLLIDER LINACS *

Z. Li, J. Irwin, K. Ko, R. J. Loewen, E. W. Lundahl, B. McCandless,
R. H. Miller, R. D. Ruth, Y. Sun, K. W. Vaillancourt, J. W. Wang,
Stanford Linear Accelerator Center, Stanford University, Stanford, CA 94039

Abstract

Each of the JLC/NLC main linacs will consist of ~1 million complex 3D accelerating cells that make up the 1.8-meter Rounded Damped Detuned Structures (RDDS) along its eight kilometer length. The RDDS is designed to provide maximum accelerating gradient to the beam while being able to suppress the long-range transverse wakefields to a satisfactory level. Using the 2D finite element code, Omega2, a 15% improvement in shunt impedance is found by changing the basic cell shape from a straight cylinder to a round outer wall contour that connects to slightly bulging circular disk noses. The HOM damping manifold is then designed around this optimal cell shape to improve the cell-to-manifold coupling for the dipole mode and the vacuum conductance under the frequency and minimal Q-reduction constraints for the fundamental mode. We use both MAFIA and the 3D finite element Omega3 code for this step to obtain a manifold geometry that consists of a round waveguide with additional narrow coupling slots that cut into the cell disks. As a time and cost saving measure for the JLC/NLC, the RDDS cell dimensions are being determined through computer modeling to within fabrication precision so that no tuning may be needed once the structures are assembled. At the X-band operating frequency, this corresponds to an error of a few microns in the cell radius. Such a level of resolution requires highly accurate field solvers and vast amount of computer resources. We will present calculations with the parallel code Omega3P that utilizes massively parallel computers such as the Cray T3E at NERSC. The numerical results will be compared with coldtest measurements performed on RDDS prototypes that are diamond-turned with dimensions based on Omega3P simulations.

1 INTRODUCTION

The Next Linear Collider (JLC/NLC) [1, 2] is a e^+, e^- machine to provide a luminosity of $10^{34}\text{cm}^{-2}\text{sec}^{-1}$ or higher at a center of mass of about 1 TeV. The main linacs of the NLC use normal-conducting traveling-wave copper structures operating at X-band (11.424 GHz) frequency. The accelerator structure will be 1.8 meter in length and will be powered by 75 MW klystrons with pulse compression using Delay-Line Distribution Systems (DLDS)[3]. About 10,000 accelerator structures operating at a gradient of about 70 MV/m are needed to obtain the 1 TeV center of mass energy. The linacs need to accelerate long bunch trains of 266 ns to obtain the required luminosity. The efficiency of the accelerator structure is a major factor that drives the cost of the the rf systems and thus the linac. The issues related to the long bunch train acceleration are the short- and long-range dipole wakefields associated emittance dilution and multi-beam breakup. Thus, the design requirements for the collider linac structures are to maximize the rf efficiency and to be able to suppress the dipole wakefields. There have been continuous efforts for the JLC/NLC R&D to build the high gradient X-band structures. A number of X-band structures based on a right-straight cylinder cell profile (DLWG as shown in Fig. 1) have been built and tested [4]. With modern numerically controlled machining, linac cells which are spheroid of revolution are negligible more expensive than right straight cylinders. On the other hand, significant cost saving can be achieved by optimizing the structure rf efficiency. With this motivation, the cell geometry were optimized to improve the shunt impedance. Round Damped Detuned Structure (RDDS) was designed based on the optimized cell profile to minimize the long-range dipole wakefields by using detuning and damping.

The structure was first optimized on a single cell level using finite-element code Omega2 [5]. Then the dimensions of the 206 cell of the 1.8-m structure were tailored to detune the important dipole modes. And thirdly, the damping manifold was designed using MAFIA [6] and Omega3 [7] around the detuned structure to improve the vacuum conductance and to suppress the long-range dipole wakefields. Finally, the cell dimensions of the 3D RDDS was calculated using parallel code Omega3P [7].

2 CELL PROFILE OPTIMIZATION

The traveling-wave structure was designed with a phase advance of 120^0 per cell. A number of modifications on the cell profile were made to improve the shunt impedance. Firstly, the rectangular cylinder cell was replaced by a revolution of a round contour, which improves the Q for the fundamental mode by about 10%. Then, the tip of the iris was reshaped to include a slight bulging to improve the R/Q. The cell profile of such a design is shown in Fig. 1. The top arc of the cell is a full half circle. The arc connecting the iris and the straight section in the disk has the same radius as the top arc. The peak surface E field appears on the surface of the round iris and is controlled by the bulging radius. The disk thickness t can be thinner than in a standard DLWG cell to improve the R/Q without en-

* Work supported by the Department of Energy, contract DE-AC03-76SF00515.

0-7803-5573-3/99/$10.00@1999 IEEE.

hancing the peak surface field. With the optimized profile, the average shunt impedance of the structure is about 15% higher than that of the DLWG structure. A comparison of the rf parameters of three representative cells in the detuned structure is shown in Table 2.

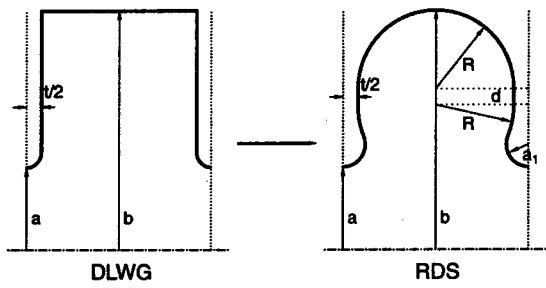

Figure 1: Disk loaded waveguide cell shapes.

Table 1: Comparison of DLWG and RDS RF parameters

Cell	Type	R($\frac{M\Omega}{m}$)	Q	R/Q	$\frac{E_s}{E_{acc}}$
001	RDS	76.9	8300	9260	3.01
	DLWG	66.7	7344	9219	3.11
103	RDS	90.7	7847	11556	2.41
	DLWG	79.7	7001	11386	2.43
206	RDS	103.5	7463	13866	2.19
	DLWG	88.8	6621	13413	2.09

3 CELL DIMENSIONS OF DETUNED STRUCTURE

To suppress the long-range dipole wakefield, the dimensions of the 206 cells in the structure are tailored to detune the dipole modes while maintaining the fundamental mode frequency at 11.424 GHz. The modes that have large contributions to the transverse wakefields are in the first, the third and the sixth dipole bands. The detuning of the dipole modes were realized by detuning the iris opening a for the first band, the disk thickness t for the third band, and the iris bulging radius a_1 for the six band. While varying a, t, and a_1 along the structure to detune the dipole modes, the cell radius b is adjusted accordingly to obtain 11.424 GHz for the fundamental mode. The average iris radius is determined by the short-range wakefield related structure-structure tolerance requirements as $a_{ave} = 0.18\lambda$, where λ is the rf wave length. The minimum disk thickness t is limited to 0.75 mm due to mechanical considerations. Among the three dipole bands, the modes in the first dipole band dominate the transverse wakefields. The transverse kick factors kdn/df of this band is detuned in a Gaussian manner as shown in Fig. 2, so that the dipole wakefields drop, following a Gaussian profile, by a factor of 100 within a distance of 0.42 meters due to de-cohere cancellations. The total detuning of the spectrum is 11.25%, in 4.75 σs, of the center frequency 15.2 GHz. Each of the dipole frequencies in the spectrum corresponds to one cell of the detuned structure. The third and sixth dipole bands are detuned with a similar detuned range. The cell and rf parameter distributions along the round detuned structure (RDS) are shown in Fig. 3.

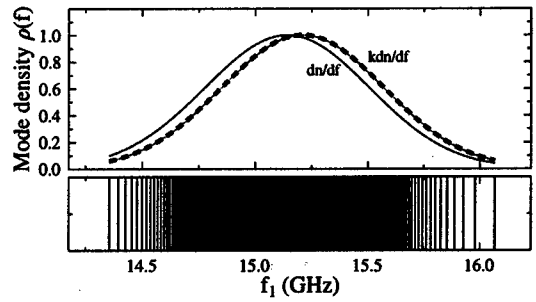

Figure 2: RDS structure dipole spectrum. kdn/df is the density of the transverse kick factor and dn/df is the modal density.

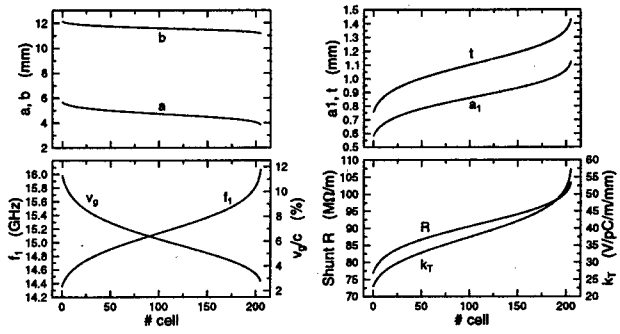

Figure 3: RDS structure cell dimensions and rf parameters.

4 ROUND DAMPED DETUNED STRUCTURE (RDDS)

The damping manifolds were designed on top of the optimized round detuned structure. The goals for the RDDS design were to improve the longitudinal vacuum conductance, to minimize the Q reduction for the fundamental mode, and to obtain adequate coupling for the dipole modes. As compared with the DDS1 [8], a number of new features were incorporated into the RDDS as shown in Fig. 4: firstly the rectangular manifold is replaced by a round manifold to maximize vacuum conductance, secondly narrow slots cutting into the disk are added to enhance the dipole mode coupling, and finally wide slots were added to raise the cutoff of the manifold mode (eliminating the ridged waveguide effect due to only a narrow slot), which allows a large round manifold and further improves the vacuum. The manifold dimensions were designed to cutoff frequencies bellow 12 GHz to avoid coupling to the fundamental mode. The narrow slot width is chosen to be 1.5 mm to minimize the effect on the fundamental mode. The longitudinal dimension of the wide slot is 6 mm. The width of the wide slot is optimized to minimize the Q_0

reduction of the fundamental mode due to the slot openings. Fig. 5 shows the rf parameters as functions of the wide slot width. A 3 mm wide slot was adopted for the current RDDS. The Q_0 reduction with such a design is less than 1%. The vacuum conductance of the RDDS structure is over 4 times better than a pure detuned structure. An appreciable dipole coupling was obtained with a 3 mm narrow slot depth, however the final narrow slot depth will be determined by the damping requirements for the long-range wakefields [9].

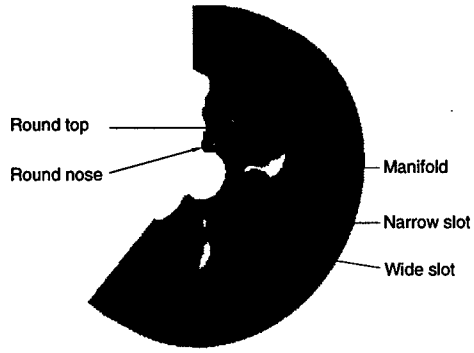

Figure 4: Damped RDDS structure cell.

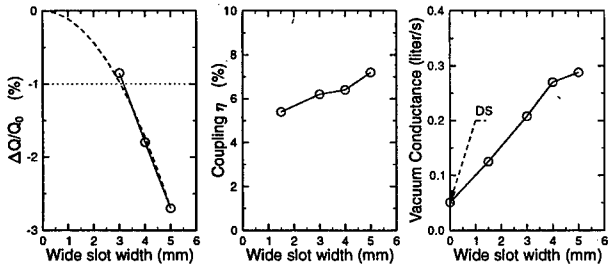

Figure 5: Optimization of wide-slot width for the RDDS. The length of the wide-slot is 6 mm and the depth of the narrow-slot is 3 mm in the simulations. The vacuum is estimated for one meter uniform RDDS with cell-206 parameters.

5 RDDS DIMENSION CALCULATION

A time and cost saving approach to determine the 3D RDDS dimensions is through computer modeling. The frequency tolerance on the fundamental mode of the X-band structure is about 1 MHz in order to maintain a better than 98% acceleration efficiency in the structure. At the 11.424 GHz, this tolerance corresponds to a few microns in the cell dimensions. To model the RDDS with such an accuracy, vast computer resources and accurate field solvers are required. This paper is the first attempt to use the newly devolved finite-element parallel code Omega3P to design the RDDS to an accuracy comparable to the hardware machining tolerance. The finite-element mesh to model the RDDS cell is as shown in Fig. 6, which has about one million degrees of freedom. The typical run time on such a grid using 48 processors on the NERSC T3E parallel supercomputer is less than half an hour. Fig. 7 shows the Omega3P results for the frequency shift due to the damping manifolds. The cell dimensions were adjusted based on these frequency shifts. The cell dimensions obtained by using Omega3P is within a couple of microns accuracy as compared with the coldtest results. The accuracy and turnaround time for modeling such a complicated geometry are unprecedented. Further improvement in accuracy can be achieved by reducing the element size in the model.

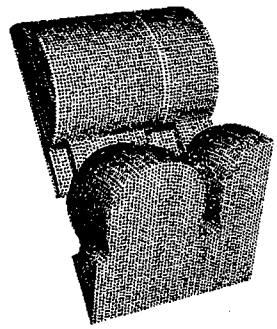

Figure 6: Finite element mesh for modeling RDDS using Omega3p.

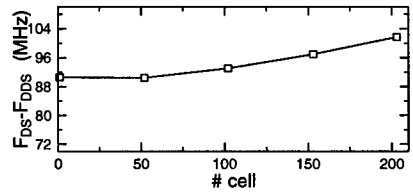

Figure 7: Frequency shift due to the damping slots.

6 REFERENCES

[1] JLC Design Study, KEK Report 97-001, 1997.

[2] Zeroth-order design report for the Next Linear Collider, LBNL-PUB-5424, SLAC Report 474, UCRL-ID-124161, 1996.

[3] S.G. Tantawi and *et al*, " A Multi-moded RF Delay Line Distribution System for the Next Linear Collider," Proceedings of EPAC98, Stockholm, June 1998.

[4] J.W. Wang and *et al*, "Accelerator Structure R&D for the Linear Colliders," this conference.

[5] X. Zhan, Parallel Electromagnetic Field Solvers Using Finite-element Method with Adaptive Refinement and Their Application to Wakefield Computation of Axisymetric Accelerator Structure, Ph.D. thesis, Stanford University, 1997.

[6] MAFIA User's Guide, CST GmbH, Darmstadt, Germany.

[7] Z. Li and *et al*, "OMEGA3P: A Parallel Eigensolver for the DOE Grand Challenge," this conference.

[8] R.H. Miller, Proc. LINAC96, SLAC-PUB-7288.

[9] R.M. Jones and *et al*, "The Transverse Long-range Wakefield in RDDS1 for the JLC/NLC X-band Linacs," this conference

BEAM LOADING COMPENSATION FOR THE LOW FREQUENCY LINACS AND COMPRESSORS IN THE NLC *

Zenghai Li†, T.O. Raubenheimer and Roger Miller
Stanford Linear Accelerator Center, Stanford University, Stanford, CA 94309

Abstract

The low frequency rf linacs and bunch compressors in the NLC are heavily loaded by beam currents up to 0.9 A. Beam loading generates bunch-to-bunch energy deviations, which need to be compensated to operate with long bunch trains in the linear collider. There are two basic compensation techniques, namely ΔT and ΔF schemes. The ΔF scheme is operationally straightforward but requires additional rf systems which are powered at slightly different frequencies. In contrast, the ΔT scheme does not require any additional rf and is thus expected to be less expensive. Here, the loading compensation is realized by early injection combined with rf phase and amplitude modulation. The phase/amplitude modulation is performed with fast phase shifters at low rf power before amplification by the klystrons. With combined phase and amplitude modulation, the ΔT scheme can be applied to both the accelerator and compressor linacs. In this paper, we present simulations of the ΔT compensation scheme for the NLC low rf accelerator and compressor linacs. We discuss different rf configurations using the ΔT scheme as well as some issues related to phase/amplitude modulations in such layouts.

1 INTRODUCTION

The Next Linear Collider (NLC) is an e^+e^- collider based on "high-frequency" X-band (11.4 GHz) rf power. The collider will be capable of achieving a luminosity in excess of $10^{34}\text{cm}^{-2}\text{sec}^{-1}$ at a center-of-mass energy of 1 TeV [1, 2] and will have the capability to be expanded to 1.5 TeV.

The e^+ and e^- injector complex for the NLC produces the low emittance bunch trains to be accelerated in the X-band linacs. The complex includes six L-band (1.428 GHz) and four S-band (2.856 GHz) linacs and compressors, listed in Table 1, which accelerate the beams to 10 GeV and operate heavily beam-loaded. All these "low-frequency" linacs will be powered with klystrons using SLED-I rf pulse compression systems [3]. In a SLED-I pulse compression system, the SLED cavities are charged by a long klystron pulse. The stored energy is then extracted by reversing the klystron phase and, for typical parameters, power gains of roughly 3-4 can be attained.

A typical SLED-I output is shown in Fig. 1*a*. The power of the pulse has a maximum immediately after the klystron phase reversal and then decays exponentially. The acceleration voltage generated by such a pulse in a traveling wave structure is shown in Fig. 1*b*. The acceleration reaches maximum after a structure fill-time, and then decreases due to the drooping rf power input. The loaded voltage seen by the bunch train is the sum of the rf voltage and the beam loading voltage and is generally not constant along the bunch train; it depends on the structure, klystron, and beam parameters. The energy deviation along the train will have a direct impact on beam transport and luminosity of the collider and thus compensating the energy deviation is a critical requirement in the linear collider design.

Table 1: NLC Low rf frequency linacs

Linac	Freq*	E (GeV)	Q_b (10^{10})	I (A)	BLC
e^+ capture	L(1)	0.250	7.9	4.5	ΔF
e^+ booster	L(1)	1.75	1.6	0.91	ΔT
e^+ drive	S(1)	6.0	1.45	0.83	ΔT
e^- booster	S(1)	1.98	1.45	0.83	ΔT
e^-, e^+ pre	S(2)	8.0	1.15	0.66	ΔT
EC,BC1	L(2×2)	~ 0.1	1.45	0.83	ΔT

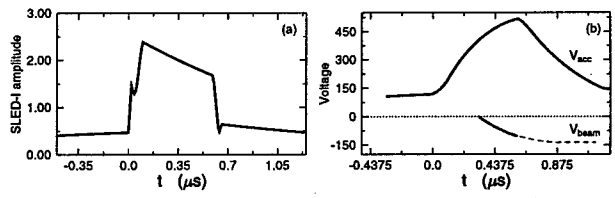

Figure 1: The pulse profile of a SLED-I system and the acceleration and beam voltages generated by a traveling wave structure. a) SLED-I amplitude; b) generator and beam induced voltages.

2 BEAM LOADING COMPENSATION

In the SLED-I driven systems, both the acceleration and beam loading voltages are transient. The goal of compensation is to obtain a uniform loaded voltage. In the following sections we will describe the ΔT and ΔF compensation schemes.

2.1 ΔF scheme

The beam voltage is compensated using additional rf structures operating at slightly different frequencies. The bunches in a bunch train are accelerated on different rf phases in these structures and the compensation that can be attained is proportional to the frequency difference ΔF. However, to maintain a roughly linear compensation along

* Work supported by the DOE, contract DE-AC03-76SF00515.
† Email:lizh@slac.stanford.edu

the train, the frequency difference ΔF is limited by the bunch train length. For the NLC bunch train, ΔF should not be more than a couple of MHz.

The advantage of the ΔF scheme is that it is quite flexible. The input power to the compensation structures can be scaled to compensate different beam loading conditions. However, the disadvantages of the ΔF scheme are the extra off-frequency rf systems required and the non-local correction since the compensation sections are distributed along the linac. Finally, the residual energy spread in this scheme is proportional to ΔF^2, and it adds in phase throughout the linac regardless of the sign of ΔF.

2.2 ΔT scheme

The ΔT compensation scheme uses the "natural" rising slope of the acceleration voltage as the structure fills to cancel the beam loading voltage. Complete cancellation requires, during the beam time,

$$\frac{dV_{acc}}{dt} = -\frac{dV_b}{dt} \quad (1)$$

The profile of the acceleration voltage, Fig. 1, shows that the rising slope of the acceleration voltage decreases with time. This indicates that for a given beam loading current, there is an optimal fill-time for the structure such that condition Eq. (1) is satisfied. For the ΔT scheme to operate efficiently, the optimal fill-time of the structure should be much longer than the bunch train length. At very high beam currents, the efficiency of the ΔT scheme can be poor due to short optimal fill-times—in such cases, the ΔF scheme should be considered.

There are number of advantages of the ΔT scheme. First, the scheme does not require additional rf systems. Second, the compensation is local and the energy deviation is minimized at the end of every structure. Finally, the residual error of the compensation is uncorrelated and does not accumulate. However, the structure design for optimal compensation is tightly coupled to the beam and rf parameters. Once the structure is optimized for a given current, the compensation at other loading conditions will not be perfect. To compensate at different loading conditions, amplitude modulation of the SLED-I pulse is needed to reshape the acceleration profile. Similarly, in the compressor linacs where the beam loading voltage is 90° out-of-phase with the acceleration voltage, phase modulation is needed to produce a component in phase with the loading voltage. Amplitude modulation is also required to obtain a flat compression voltage.

3 BEAM LOADING COMPENSATION IN THE S-BAND ACCELERATORS

All the S-band linacs will use the same structure design [4]. The parameters of the structure are optimized for the maximum pre-linac beam current since the 8 GeV pre-linacs constitute more than 60% of total S-band acceleration. The S-band klystrons are assumed to produce 66 MW of power in a 5 μs pulse, similar to the SLAC 5045 klystrons. The SLED-I cavity is assumed have an external $Q_{ext} = 2 \times 10^4$ with a coupling constant $\beta = 5$ yielding a compression factor of approximately four.

3.1 ΔT scheme for the e^+ drive and prelinacs

A power station consists of a pair of klystrons, each feeding a SLED-I system [5]. The SLEDed rf power from the klystron pair is combined and powers six 4-meter accelerator structures. With the pre-linac beam parameters, the optimal fill-time is 625 ns. The SLED-I pulse profile and the energy profile of the beam for the pre-linac compensation are shown in Fig. 2(a) yielding a loaded gradient of 17 MV/m. The best energy deviation using the SLED pulse alone is 4×10^{-3}. This can be further minimized with a slight amplitude modulation yielding better than 1.3×10^{-3}.

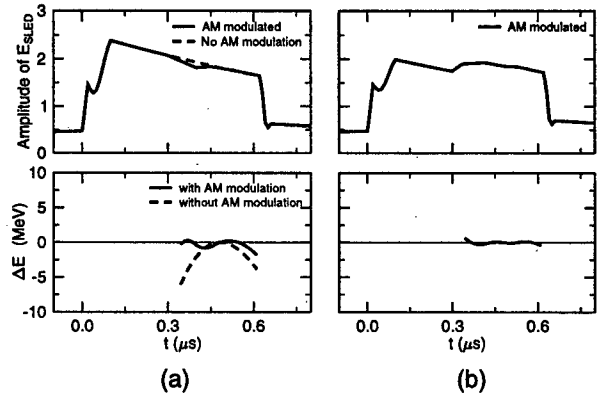

Figure 2: a) Compensation for the S-band pre-linacs. The SLED-I amplitude can be modulated to further reduce energy spread. b) Compensation for the e^- booster linac. Amplitude modulation is needed to enhance the slope of the acceleration.

3.2 ΔT scheme for the e^- booster

The beam current in the e^- booster linac is 25% higher than in the pre-linacs. Since the structure is optimized for the pre-linacs, amplitude modulation is necessary to compensate the loading in the booster. Fig. 2(b) shows the SLED-I pulse and the compensated energy deviation in the e^- booster. The loaded gradient in the e^- booster is 15.3 MV/m and the residual energy deviation is about 0.5×10^{-3}.

4 BEAM LOADING COMPENSATION IN THE L-BAND ACCELERATORS

The four L-band linacs will use a 5-meter structure optimized for the e^+ booster linac [4]. The L-band klystrons are assumed to produce a peak power of 75 MW at a pulse length of 5.5 μs. The SLED-I cavities are simply scaled from the the S-band SLED systems.

4.1 ΔT scheme for the e^+ booster

An accelerator module for the e^+ booster linac consists of six structures powered by a pair of SLEDed klystrons. The optimal fill-time obtained for ΔT compensation is 1010 ns yielding a loaded gradient of 13 MV/m. Without additional amplitude modulation, the minimum energy deviation is 1×10^{-3}. Figure 3(a) illustrates the energy profiles for the e^+ booster.

4.2 ΔF scheme for the e^+ capture

In the e^+ capture section, the beam loading is too large to be compensated with the ΔT method alone. Additional compensation is performed using the ΔF scheme. The capture linac consists of four 5-meter accelerator structures and two ΔF structures operating at 1428±1.14 MHz. Each ΔF structure is driven by a single klystron at 50 MW of peak power with SLED-I pulse compression and the loaded gradient in the capture is about 12.7 MV/m. The residual energy deviation is about 1×10^{-2} as shown in Fig. 3(b).

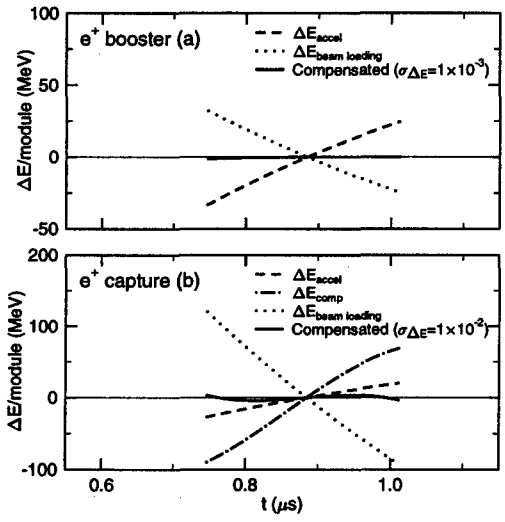

Figure 3: Compensation in the L-band e^+ booster and capture linacs. The fill-time is optimized for the booster linac with ΔT compensation. Extra beam loading in the capture linac due to higher current is compensated by using the ΔF scheme. Loaded gradients for both linacs are about 13 MV/m. No amplitude modulation on SLED-I.

4.3 ΔT scheme for the compressors

A module of two (or three) 5-meter structures would be sufficient to generate the voltage ($\sim$ 100 MV) in the compressors. In these systems, both the amplitude and phase are modulated to obtain a uniform compression (amplitude) and loading compensation (phase). The SLED amplitude and phase profiles required for the compressor are shown in Fig. 4 and the energy deviation obtained is $0.11/E_0$, where E_0 is the energy of the beam in the compressor. The compression voltage is within 1% deviation. One of the issues with the ΔT compensation for the compressor linac is the

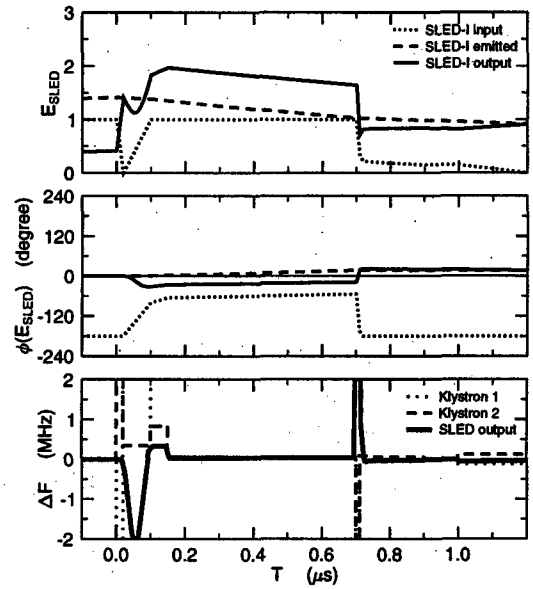

Figure 4: Compensation for the L-band compressor linacs: loaded gradient: 13 MV/m; energy deviation: $0.11/E_0$. Both amplitude and phase are modulated to compensate the beam loading and compression voltages.

frequency offset induced by the phase modulation. Simulation shows that the ΔF induced by the phase modulation is small in the SLED-I output, thus the effect of this frequency offset is expected to be small.

5 SUMMARY

The ΔT scheme has been shown to be effective in the NLC low rf frequency linacs, except for the e^+ capture linac where ΔF scheme is required. Once optimized for the nominal beam current, the ΔT scheme can be used to compensate at different beam loading regimes, such as the beam loading in the e^- booster, with proper amplitude modulations on the SLED-I pulse. Similarly, the scheme is applicable to these linacs when operating at "zero" beam current. In the future, we need to calculate the tuning tolerances and verify that the dispersive effects are minimal.

6 REFERENCES

[1] NLC ZDR Design Group, "Zeroth-Order Design Report for the Next Linear Collider," SLAC Report 474 (1996).

[2] NLC Accelerator Physics Web pages from http://www-project.slac.stanford.edu/lc/nlc-tech.html.

[3] Z. D. Farkas and *et al*, "SLED: A Method of Doubling SLAC's Energy," SLAC-PUB-1453, March 1974.

[4] Z. Li and *et al*, "Parameter Optimization for the Low RF Linacs of the NLC," this conference.

[5] J. C. Sheppard and *et al*, "The NLC Injector System," this conference.

PARAMETER OPTIMIZATION FOR THE LOW FREQUENCY LINACS IN THE NLC *

Z. Li†, T.O. Raubenheimer, K. Bane, J.C. Sheppard, R.H. Miller
Stanford Linear Accelerator Center, Stanford University, Stanford, CA 94309

Abstract

In the present Next Linear Collider (NLC) design, S and L-band linacs are used to accelerate the beams to 10 GeV, where they are injected into the main X-band linacs. As injectors for the main accelerator, these linacs are required to deliver clean beams while being reliable and cost effective. These requirements set stringent tolerances on the design of the accelerators. There are two types of misalignment tolerances that are of great concern: cell-to-cell and structure-to-structure tolerances, which are dominated by long- and short-range wakefield effects, respectively. For a given lattice design, the structure-to-structure tolerance (which has strong impacts on girder configurations) is mainly determined by the global parameters such as the average iris size, the length and the type of the structure. This paper will discuss the optimization of the structure parameters to allow looser structure-to-structure tolerances; the cell-to-cell tolerance is related to the details of the single structure design and will not be addressed here. The optimization described here was based on a cost model for NLC and a wakefield scaling law for the tolerance estimations.

1 INTRODUCTION

The Next Linear Collider (NLC) is a $e^+ - e^-$ linear collider that will be used to probe the physics phenomena at a center of mass around 1 TeV [1, 2]. The main linacs of this collider are based on X-band rf (11.424 GHz) technology. In the injector which accelerates the e^+ and e^- beams to 10 GeV, the beams are accelerated in lower frequency linacs operating at the L-band (1.428 GHz) and S-band (2.856 GHz). There are a total of ten low frequency linacs in the injector system which are listed in Table 1; a detailed discussion of the NLC injector systems is presented in Ref. [3].

Table 1: NLC low frequency linacs

Linacs	rf	N	E (GeV)	Q($\times 10^{10}e$)	I (A)
e^+ capture	L	1	0.25	7.8	4.5
e^+ booster	L	1	1.75	1.6	0.91
e^+ drive	S	1	6	1.45	0.83
e^- booster	S	1	1.9	1.45	0.83
pre-linacs	S	2	8	1.15	0.66
EC	L	2	0.1	1.45	0.83
BC1	L	2	0.1	1.45	0.83

* Work supported by the DOE, contract DE-AC03-76SF00515.
† email: lizh@slac.stanford.edu

Because of differences in the beam parameters in these linacs, the issues concerning the accelerator design are also quite different. In the L-band e^+ capture and booster linacs, the beam has a large emittance and energy spread and the primary issue is the aperture. A larger aperture in the structure allows larger beta functions, easing the strength and the tolerance requirements on the quadrupole magnets.

In the S-band pre-linacs, the beam emittance is small and the bunch length is short. The primary issues here are the emittance degradation and multi-bunch BBU associated with the long- and short-range wakefields in the structure. The tight emittance dilution and BBU requirements set stringent limits on the structure tolerances. The short-range wakefields, which are related to the average parameters of a structure, dominate the structure-to-structure tolerances, while the long-range wakefields, which are related to the details of the structure design, control the cell-to-cell tolerance of a structure. This paper will focus on the structure-to-structure tolerance associated with the short-range wakefields.

The beam loading voltage in these linacs will be compensated by using the ΔT scheme [4], except in the e^+ capture where the beam current is extremely high and the ΔF scheme is used. With the ΔT scheme, the structure design is tightly coupled to the beam loading conditions. Both the L- and S-band linacs will have a single structure design for all the corresponding linacs. We have optimized the L-band structure for the e^+ booster parameters while the S-band structure was optimized for the pre-linac parameters.

2 S-BAND LINACS

Both the structure tolerance requirements and the cost of the S-band linacs are dominated by the pre-linacs and thus the structure optimization is based on the pre-linac parameters. The cost and tolerance models we used are similar to the ones used for the ZDR [1] cost and tolerance calculations.

2.1 Cost estimation

A simple cost model, Eq. (1), is used to estimate the cost of the pre-linacs.

$$\begin{aligned} Cost = \quad & N_s(S_s + S_{bpm}) \\ + \quad & N_s M_s(Q_q + Q_{ps} + Q_{bpm}) \\ + \quad & N_M N_k(K_k + k_{rf}) \\ + \quad & N_M(P_{SLED} + P_{wg} + P_{phase} + P_{modul}) \end{aligned} \tag{1}$$

0-7803-5573-3/99/$10.00@1999 IEEE.

$$+ \quad \frac{N_s L}{S_f}(F_{tunnel} + F_{alcove})$$
$$+ \quad \frac{N_s L}{S_f}(V_{pipe} + V_{rf})$$

where the cost of the parts are

S_s, S_{bpm}	structure, structure BPM
Q_q, Q_{ps}, Q_{bpm}	quad, quad power supply, quad BPM
K_k, K_{rf}	klystron, klystron rf drive
$P_{SLED}, P_{wg},$	SLED-I system, waveguide,
P_{phase}, P_{modul}	phase control, modulator
F_{tunnel}, F_{alcove}	tunnel and alcove
V_{pipe}, V_{rf}	vacuum pipe and rf

N_s, N_M are the total number of structures and modules respectively. A 10% overhead is assumed in the number of modules for the linacs. N_k is the number of klystrons per module ($N_k = 2$ for ΔT compensation scheme) and M_s is the number of quads per structure; the focusing in the pre-linacs is provided with the FODO lattices. Finally, S_f is the filling factor of the accelerator structures in the linac which is assumed to be 80%.

In the calculation, we assumed that the structure cost is dominated by the assembly and coupler costs and thus the cost of the linacs scales with the number of structures and not the structure length. All cost estimations were scaled to a linac design based on a 3-meter SLAC-type accelerator structure.

2.2 *Structure-to-structure tolerance*

The structure-to-structure tolerance is associated with the short-range wakefield effects of the structure which depends mainly on the average parameters of the structure, e.g. the average aperture and length. To the lowest order, the short-range wakefield scales as the 4th power of the average iris radius. Assuming the β functions are scaled with the structure length, the structure-to-structure tolerance is proportional to

$$y_{tol} \propto \frac{a^4}{L_{acc}} \tag{2}$$

where a is the average iris radius and L_{acc} is the total net accelerator length.

2.3 *Length vs structure-structure tolerance*

In a constant gradient traveling wave structure, the unloaded acceleration voltage of a accelerator section is

$$V = \sqrt{P_{in} RL(1 - e^{-2\tau})} \tag{3}$$

and the transient beam loading voltage ($0 < t < t_f$) is

$$V_{beam} = -\frac{RI_0 L}{2(1 - e^{-2\tau})}\left(1 - e^{-\frac{\omega t}{Q}} - \frac{\omega e^{-2\tau}}{Q} t\right) \tag{4}$$

where L is the structure length, R is the shunt impedance per unit length, t_f is the filling time, and $\tau = \omega t_f / 2Q$ is the attenuation constant. With the same τ (or t_f) factor, the acceleration and beam loading voltages are proportional to $\sqrt{RL}$ and RL (or $\sqrt{Rv_g}$ and Rg_v, $v_g = L/t_f$) respectively. Since v_g has a stronger dependence on the iris radius than R, the rf efficiency is higher in a longer structure.

The group velocity of a traveling wave structure scales approximately as a^3. The structure-to-structure tolerance then scales as

$$y_{tol} \propto \left(\frac{L}{t_f}\right)^{4/3} / L_{acc} = \frac{L^{1/3}}{t_f^{4/3}}\left(\frac{L}{L_{acc}}\right) \tag{5}$$

where L/L_{acc} represents the rf efficiency of the linac. It is clear that the gain in tolerance with a longer structure length comes from the gain in rf efficiency, filling time change due to change in beam loading, and the lengthening of the structure.

The 3- and 4-meter SLAC-type structures (DLWG) were simulated to study the cost and tolerance dependences on the structure length. Results for the two cases are shown in the first two rows in Table 3. It is clear that a longer structure is beneficial for both the rf efficiency and the structure-to-structure tolerance. Fewer modules are needed in the 4-meter design as a result of a better rf efficiency which results in saving about 8% in rf power. The optimal filling time for the 4-meter design is 625 ns, slightly shorter than the 665 ns for the 3-meter design due to a stronger beam loading and the structure-to-structure tolerance is improved by about 30%. Additional increases in the structure length may further improve the efficiency and tolerances, however, such a long structure is thought to be significantly more difficult to manufacture.

2.4 *Cell profile optimization*

In the X-band main linac design, the shunt impedance was optimized to improve the rf efficiency by shaping the cell geometry. A round cell contour (RDS) was obtained as shown in Fig. 1, which gives about 15% better shunt impedance as compared to the standard DLWG. The optimized RDS cell profile can be used in the S-band design for the same purpose. Alternatively, one can use the RDS design to improve the structure tolerance by further opening the iris while maintaining the same rf efficiency. Table 2 shows a comparison between the DLWG and RDS parameters for a S-band cell.

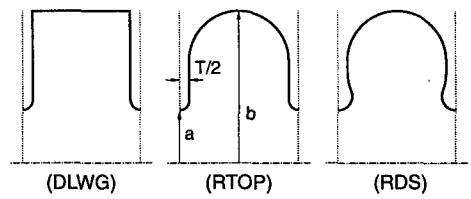

Figure 1: Traveling wave structure cell profiles: DLWG) standard; RTOP) round top; RDS) round contour.

Table 2: A comparison between DLWG and RDS cells

Type	a (mm)	R (MΩ/m)	v_g/c
DLWG	13	54.0	0.0195
RDS	14	54.0	0.0190

For the same R and v_g, the RDS cell yields a much larger iris size. Since the structure tolerance scales as the 4th power of the iris radius, the RDS design will further relax the structure-to-structure tolerance. The third row in Table 3 shows the result for a 4-meter RDS design. The tolerance is about 25% better than the 4-meter DLWG case. The rf efficiencies and costs are comparable.

Table 3: Comparison of the S-band DLWG and RDS structures. *) 4-structure/module; **) 6-structure/module.

Type	L(m)	N_{module}	Cost	a_{av}(mm)	tol
DLWG*	3.0	27	1.0	12.85	1.00
DLWG*	4.0	25	1.0	14.69	1.29
RDS*	4.0	25	1.0	15.40	1.53
RDS**	4.0	22	1.09	15.72	1.43

The results shown in the first three rows of Table 3 are for linacs with a 4-structure per module configuration. The loaded gradient in these cases is about 22 MV/m. A lower gradient design of 17 MV/m has been consider for the NLC S-band linacs. The low gradient design uses the same RDS 4-meter structures but one rf power station will power a module of six structures instead of four. The results of the low gradient design are shown in the last row of Table 3. Due to the longer linac length, the tolerance is slightly tighter and the cost is slightly higher however the overall tolerance improvement is still $> 40\%$ compared to the 3-meter DLWG design.

3 L-BAND LINACS

The beam emittance and energy spread are large in the L-band capture and booster linacs. Strong focusing lattice are required for these linacs to control the beam size. A larger aperture in the structure would allow larger beta functions, which would relax the tolerances on the focusing magnets. The structure alignment tolerances are loose in these linacs and thus the design goal for the L-band structures is simply to maximize the structure aperture.

A length of 5 meters is considered for the L-band structure. There is not a strong argument to use the RDS design in the L-band design. The studies in this paper are based on the RTOP cell profile, shown in Fig. 1, however, the results are applicable to a DLWG design, with minor modifications.

The L-band structure is optimized for the e^+ booster beam current. A booster module consists of six 5-meter structures. Table 4 shows a list of L-band structures with different cell disk thicknesses. The dipole mode detuning ΔF_1, which is determined by the long-range wakefield properties, also impacts the aperture, Because the linac will

Table 4: 5-meter L-band structure with RTOP cell profiles

T (mm)	ΔF_1 (%)	a_{min} (mm)	b_{max} (mm)	G_L (MV/m)
12	3	23.51	89.83	13.1
12	5	22.43	90.29	
15	3	24.37	90.08	12.92
15	5	23.13	90.52	
18	3	25.19	90.40	12.46
18	5	24.24	91.00	

be constructed from an integer number of modules, we actually can reduce the shunt impedance slightly to fully utilize five 6-structure modules. In this case, the loaded gradient in the e^+ booster is 12.4 MV/m to attain the required 1.75 GeV acceleration plus roughly 5% margin.

4 TOLERANCES

Finally, the tolerances for the S-band linacs are listed in Table 5. In the e^- booster and e^+ drive linacs, one-to-one trajectory correction is assumed where the trajectory is corrected to zero the Beam Position Monitors (BPMs) located at the focusing quadrupoles. In the pre-linacs, the trajectory will be corrected using beam-based alignment similar to that used in the main linac [6]. The tolerances in the L-band e^+ booster linac are slightly looser than those in the e^- booster linac.

Table 5: Tolerances for the S-band linacs (rms)

Linac	Quad	BPM to quad	Struct-struct
e^- booster e^+ drive	200 μm	200 μm	500 μm
pre-linac	15 μm	15 μm	40 μm

5 REFERENCES

[1] NLC ZDR Design Group, "Zeroth-Order Design Report for the Next Linear Collider," SLAC Report 474 (1996).

[2] NLC Accelerator Physics Web pages from http://www-project.slac.stanford.edu/lc/nlc-tech.html.

[3] J. C. Sheppard and et. al., "The NLC Injector System," this conference.

[4] Z. Li and et. al., "Beam loading compensation for the Low RF Frequency Linacs of the NLC," this conference.

[5] Z. Li and et. al., "RDDS Cell Design and Optimization for the NLC linac," this conference.

[6] P. Tenenbaum, "Simulation Studies of Main Linac Steering in the Next Linear Collider," this conference.

OPTIMIZATION OF THE LUMINOSITY SPECTRUM IN THE NLC*

K.A. Thompson†, T.L. Barklow, T.W. Markiewicz, T.O.Raubenheimer,
Stanford Linear Accelerator Center, Stanford, CA 94309

Abstract

The energy spectrum of electrons at the interaction point of a linear collider is determined largely by the beamstrahlung spectrum. The beamstrahlung spectrum in turn is sensitive to the design parameters at the interaction point. In this paper we examine the optimization of the luminosity spectrum for discovery and detailed exploration of various physics processes of interest in the NLC, in particular, top and stop pair production, and a class of processes occuring via W-W scattering.

1 INTRODUCTION

The energy spectrum of electrons at the interaction point of a linear collider is determined largely by the beamstrahlung spectrum (emission of photons due to the interaction of an electron with the collective field of the oncoming beam), with additional effects due to initial state radiation and energy spread in the beam coming from upstream. The beamstrahlung spectrum depends on the design parameters at the interaction point. Typically there is roughly half the luminosity very near the nominal center of mass energy, with the remaining luminosity distributed in a tail extending to significantly lower energies. While we realize various processes must be studied individually in greater detail than is presented here, our goal is to examine optimization tradeoffs for some important classes of physics processes in future linear colliders. In this paper, we focus mostly on processes with cross sections increasing with energy over the range of interest.

2 NLC BASELINE DESIGNS

We give some luminosity-related parameters for the basic NLC designs near (but not necessarily exactly at!) 500, 1000, 1500 GeV c.m. energy in Tables 1, 2, and 3[1]. The values shown for the pinch enhancement H_D, number of beamstrahlung photons per incoming particle n_γ, and average beamstrahlung energy loss δ_B are obtained from simulations using the beam-beam code Guineapig[2] and agree to within a few percent with those obtained from analytic formulas in the literature[3].

Note that for a given design, the c.m. energy decreases with higher bunch charge N because of beam loading, which due to costs is not completely compensated. There is also variation in other parameters among different design versions near a given energy. For purposes of understanding the physics tradeoffs, it is also useful to vary only one

Table 1: IP parameters for three ~1/2 TeV c.m. NLC designs

	A-500	B-500	C-500
E_{beam} [GeV]	267.5	257.5	250.
N [10^{10}]	0.75	0.95	1.1
$\gamma\epsilon_x/\gamma\epsilon_y$ [μm-r]	4.0/0.06	4.5/0.1	5.0/0.14
β_x/β_y [mm]	10/0.1	12/0.12	13/0.2
σ_z [μm]	90.	120.	145.
σ_x/σ_y [nm]	276/3.4	327/4.9	365/7.6
Υ_{avg}	0.14	0.11	0.09
H_D	1.36	1.30	1.49
n_γ	1.08	1.18	1.24
δ_B	4.3%	3.9%	3.7%
Bunches/train	95	95	95
Rep. rate	120	120	120
L_D [10^{33} cm^{-2}sec^{-1}]	7.42	6.66	5.94

Table 2: IP parameters for three ~1 TeV c.m. NLC designs

	A-1000	B-1000	C-1000
E_{beam} [GeV]	523.	504.	489.
N [10^{10}]	0.75	0.95	1.1
$\gamma\epsilon_x/\gamma\epsilon_y$ [μm-r]	4.0/0.06	4.5/0.1	5.0/0.14
β_x/β_y [mm]	10/0.125	12/0.15	13/0.2
σ_z [μm]	90.	120.	145.
σ_x/σ_y [nm]	198/2.7	234/3.9	261/5.4
Υ_{avg}	0.39	0.30	0.25
H_D	1.50	1.44	1.50
n_γ (sim)	1.39	1.53	1.62
δ_B (sim)	9.5%	9.2%	8.7%
Bunches/train	95	95	95
Rep. rate	120	120	120
L_D [10^{33} cm^{-2}sec^{-1}]	14.33	12.95	11.67

Table 3: IP parameters for two ~1.5 TeV c.m. NLC designs

	A-1500	B-1500
E_{beam} [GeV]	703	739
N [10^{10}]	1.4	0.95
$\gamma\epsilon_x/\gamma\epsilon_y$ [μm-r]	4.5/0.14	4.5/0.1
β_x/β_y [mm]	15/0.2	13/0.2
σ_z [μm]	130.	150.
σ_x/σ_y [nm]	222/4.5	201/3.7
Υ_{avg}	0.60	0.41
H_D	1.61	1.50
n_γ	2.2	1.7
δ_B	17%	12%
Bunches/train	95	95
Rep. rate	60	90
L_D [10^{33} cm^{-2}sec^{-1}]	14.3	12.3

* Work supported by Department of Energy Contract DE-AC03-76SF00515.

† Email: kthom@SLAC.Stanford.edu

0-7803-5573-3/99/$10.00@1999 IEEE.

Table 4: Fractional luminosities for NLC designs

	500	1000	1500-A	1500-B
beamst. only:				
$L_{99.5\%}$ (sim)	61%	46%	31%	40%
$L_{99\%}$ (sim)	67%	52%	35%	45%
$L_{98\%}$ (sim)	75%	59%	41%	52%
$L_{95\%}$ (sim)	86%	72%	54%	65%
$L_{90\%}$ (sim)	94%	83%	66%	77%
$L_{80\%}$ (sim)	99%	94%	82%	90%
$L_{50\%}$ (sim)	$\sim 100\%$	$\sim 100\%$	99%	$\sim 100\%$
beamst.+ISR:				
$L_{99.5\%}$ (sim)	37%	27%	18%	23%
$L_{99\%}$ (sim)	44%	33%	22%	29%
$L_{98\%}$ (sim)	54%	41%	28%	36%
$L_{95\%}$ (sim)	69%	56%	41%	50%
$L_{90\%}$ (sim)	81%	70%	55%	64%
$L_{80\%}$ (sim)	91%	84%	73%	80%
$L_{50\%}$ (sim)	98%	97%	95%	97%

parameter at a time (for instance, N, σ_z, β_x, β_y, $\gamma\epsilon_y$, or $\gamma\epsilon_x$). In doing such parameter variations, one finds[4] that the best "knobs" for increasing luminosity at the high energy end of the spectrum are $\gamma\epsilon_y$ and N. It is difficult to decrease $\gamma\epsilon_y$ very much, but one may consider increasing N if one is willing either to let the energy drop or compensate for the beam-loading.

We show the luminosity spectra for the nominal designs, with beamstrahlung only and with both beamstrahlung and initial state radiation (ISR) in Table 4. The fractional luminosities are shown, e.g., $L_{99\%}$ denotes the percentage of the luminosity with c.m. energy greater than or equal to 99% of the nominal c.m. energy. (These numbers are not significantly different for the A, B, and C variations of the designs at 500 and 1000 GeV.)

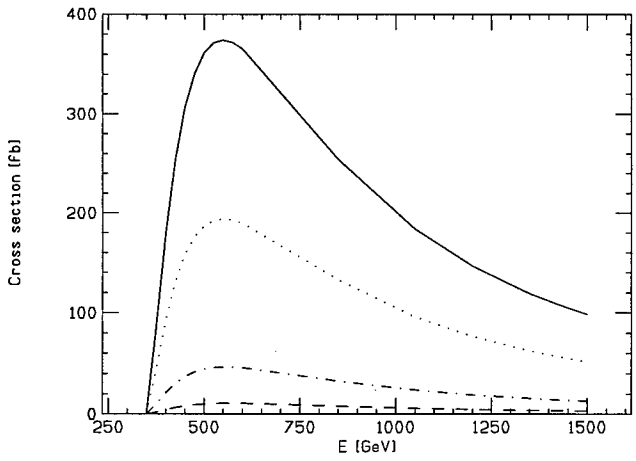

Figure 1: Cross sections for $e_L^- e_R^+ \to \tilde{t}_R \bar{\tilde{t}}_R$ (dot-dashed curve). $e_R^- e_L^+ \to \tilde{t}_R \bar{\tilde{t}}_R$ (dotted curve). $e_L^- e_R^+ \to \tilde{t}_L \bar{\tilde{t}}_L$ (solid curve), $e_R^- e_L^+ \to \tilde{t}_L \bar{\tilde{t}}_L$ (dashed curve).

Table 5: Number of top and stop pair production events in a 10^7 second running year, for nominal designs near 1/2 TeV c.m.

	A-500	B-500	C-500
$e_L^- e_R^+ \to t\bar{t}$	785000	674000	581000
$e_R^- e_L^+ \to t\bar{t}$	357000	305000	262000
$e_L^- e_R^+ \to \tilde{t}_R \bar{\tilde{t}}_R$	22000	17500	14200
$e_R^- e_L^+ \to \tilde{t}_R \bar{\tilde{t}}_R$	92000	74000	60200
$e_L^- e_R^+ \to \tilde{t}_L \bar{\tilde{t}}_L$	178000	143000	116500
$e_R^- e_L^+ \to \tilde{t}_L \bar{\tilde{t}}_L$	4900	3900	3200

Table 6: Number of top and stop pair production events in a 10^7 second running year, for modified B-500 design (varying N and keeping energy fixed).

N [10^{10}]	1.1	1.3	1.5
$e_L^- e_R^+ \to t\bar{t}$	927000	1347000	1856000
$e_R^- e_L^+ \to t\bar{t}$	420000	609000	837700
$e_L^- e_R^+ \to \tilde{t}_R \bar{\tilde{t}}_R$	23900	34000	46000
$e_R^- e_L^+ \to \tilde{t}_R \bar{\tilde{t}}_R$	101000	144000	195000
$e_L^- e_R^+ \to \tilde{t}_L \bar{\tilde{t}}_L$	195000	279000	377000
$e_R^- e_L^+ \to \tilde{t}_L \bar{\tilde{t}}_L$	5300	7600	10200

3 SUSY SCALAR PRODUCTION

We compare the rates of top and stop production in a 500-GeV collider, assuming $m_{\tilde{t}} = m_t$. The total top and stop pair production cross-sections are plotted in Figures 2 and 1 respectively.

The production rates (# events in a running year of 10^7 sec) are shown in Table 5 for the three nominal designs near 1/2 TeV c.m. energy. The rates with bunch charge N pushed up from the nominal B-500 design value are shown in Table 6. Here we assume it is reasonable to compensate the extra beam loading to keep the energy fixed.

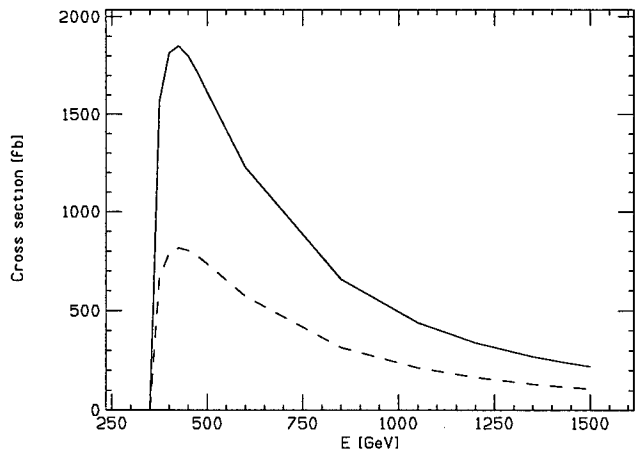

Figure 2: Cross sections for $e_L^- e_R^+ \to t\bar{t}$ (solid curve) and $e_R^- e_L^+ \to t\bar{t}$ (dashed curve).

Table 7: $e^+e^- \to \nu\bar{\nu}t\bar{t}$; M_H = 100 GeV; No polarization

	No. of events	% change B-1000	n_γ
A-1000	2800	+26%	1.4
B-1000	2220	0%	1.5
C-1000	1780	-20%	1.6
B-1000, $\gamma\epsilon_y \downarrow 0.08\mu$m-r	2520	+13%	1.5
B-1000, $\gamma\epsilon_y \downarrow 0.06\mu$m-r	2960	+33%	1.5
B-1000, $\gamma\epsilon_y \downarrow 0.04\mu$m-r	3780	+70%	1.5
B-1000, N $\uparrow 1.1\cdot10^{10}$	2990	+35%	1.8
B-1000, N $\uparrow 1.3\cdot10^{10}$	4200	+89%	2.0
B-1000, N $\uparrow 1.5\cdot10^{10}$	5620	+153%	2.3
B-1000, N $\uparrow 1.1\cdot10^{10}$,E$\downarrow$978	2670	+20%	1.8
B-1000, N $\uparrow 1.3\cdot10^{10}$,E$\downarrow$935	3110	+40%	2.0
B-1000, N $\uparrow 1.5\cdot10^{10}$,E$\downarrow$891	3410	+54%	2.3
B-1000, $\beta_y \uparrow 0.30$ mm	1910	-14%	1.5

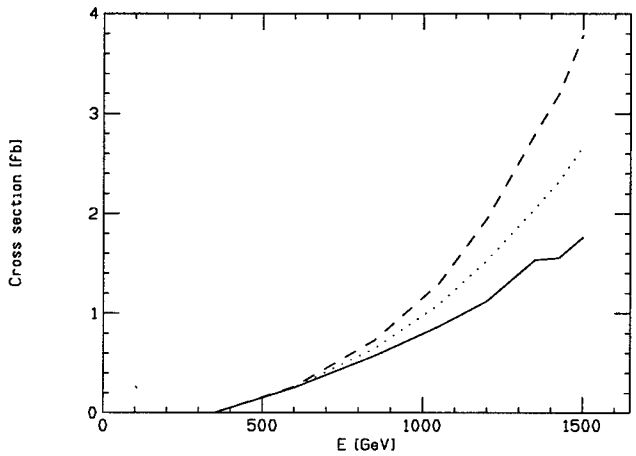

Figure 3: Cross sections for $e^+e^- \to \nu_e\bar{\nu}_e t\bar{t}$ for M_H = 100 GeV (solid curve), M_H = 1000 GeV (dashed curve), $M_H = \infty$ (dotted curve).

4 WW-SCATTERING PROCESSES

The class of processes $e^+e^- \to \ell\ell X$ occurring via WW scattering, where one or both ℓ's is a neutrino and X could be for example $t\bar{t}$, W's and/or Z's, have cross sections which are rising with energy through the TeV energy scale . Taking as a representative example the process $e^+e- \to \nu_e\bar{\nu}_e t\bar{t}$, (see Figure 3) we show the number of events in 10^7 seconds of running for designs near 1 TeV in Table 7. In addition to the nominal A, B, and C designs, we show the increase in luminosity attainable with $\gamma\epsilon_y$ decreased from its nominal value of 0.1μm-r, or with N increased from its nominal value of 0.95×10^{10}, with and without compensation of the extra beam-loading. The biggest gain is to be had by increasing N and keeping the energy fixed; note also that further study is needed to see how high n_γ can be allowd to go. We have also noted[4] that substantially increasing β_y (which relaxes machine tolerances) does not reduce luminosity very much; for our example we see only a 14% reduction in the number of events when β_y is doubled from its nominal value. Similar results for designs near 1.5 TeV are shown in Table 8.

Table 8: $e^+e^- \to \nu\bar{\nu}t\bar{t}$; M_H = 100 GeV; No polarization

	No. of events	% change B-1500	n_γ
A-1500	8610	-9%	2.2
B-1500	9420	0%	1.7
B-1500, N $\uparrow 1.1\cdot10^{10}$	12800	+36%	2.0
B-1500, N $\uparrow 1.3\cdot10^{10}$	18000	+90%	2.3
B-1500, N $\uparrow 1.5\cdot10^{10}$	23900	+154%	2.6
B-1500, $\beta_y \uparrow 0.30$ mm	8700	-8%	1.7

5 DISCUSSION AND CONCLUSIONS

We have not discussed the very important issue of detector backgrounds in this paper – our general philosophy is that when total rate for the various processes considered here is optimized, one will indeed end up with a larger number of useful events even after appropriate cuts are applied to reduce backgrounds. However, we mention some issues that must be kept in mind when designing and optimizing the interaction region and detector. For example, the process $\gamma\gamma \to WW$ (where the γ's are bremsstrahlung photons) is a significant background to $e^+e- \to \nu\bar{\nu}WW$, since the $e^\pm$ that radiate the photons are typically close to the beam axis and may escape tagging. For these electroweak symmetry breaking studies, electron tagging capability down to about 150 mrad is needed[5]. Other processes, for instance some SUSY parameter determinations[6] as well as studies of the perturbative QCD pomeron (BFKL dynamics) in $\gamma^*\gamma^* \to$ hadrons[7, 8] have even more stringent angular coverage requirements, down to about 40 mrad.

We thank Lance Dixon and Michael Peskin for useful discussions and comments.

6 REFERENCES

[1] See http://www-project.slac.stanford.edu/lc/nlc-tech.html under Accelerator Physics parameters.

[2] D.Schulte, Ph.D. thesis, 1996.

[3] Yokoya,K. and Chen,P., in M.Dienes,et.al. (ed.), Frontiers of Particle Beams: Intensity Limitations (Springer-Verlag, 1988).

[4] K.Thompson and T.Raubenheimer, NLC collider note LCC-0014 (1999).

[5] V.Barger, K.Cheung, T.Han, R.Phillips, Phys.Rev.D., **52**, 3815 (1995).

[6] N.Danielson and E.Goodman, COLO-HEP-422, unpublished.

[7] S.Brodsky, F.Hautmann, and D.Soper, 5th International Workshop on Deep Inelastic Scattering and QCD, Chicago, 14-18 April, 1997, hep-ph/9707444.

[8] J.Bartels, A.DeRoeck, and H.Lotter, hep/9710500.

TRAVELING-WAVE ACCELERATING TEST STRUCTURE AT 34.3 GHZ

O. A. Nezhevenko and V. P. Yakovlev
Omega-P Inc., 345 Whitney Avenue, New Haven, CT 06511

Abstract

A future electron-positron linear collider with c.m. energy in the range of 3-5 TeV is understood to require an operating RF frequency in the range of 30-100 GHz. Higher operating frequency can lead to higher acceleration gradient, with a corresponding smaller accelerator length. This paper describes a test structure designed to determine the maximum achievable accelerating gradient for an operating frequency of 34.272 GHz. The ~6-cm long test structure consists of 21 cells operating in the $2\pi/3$ mode. It is to be driven using a magnicon amplifier [1], designed and being built by Omega-P, with a design power of over 40 MW in a 1 μsec pulse. Preliminary calculations indicate that this should make it possible to test the structure to accelerating gradients of over 300 MV/m.

1 INTRODUCTION

Strong motivation for developing high-frequency accelerating structures follows from the scaling of accelerating gradient with frequency, which is approximately linear [2]. Thus ILC, which is to operate at 11.424 GHz, is to achieve an unloaded accelerating gradient of about 77 MeV/m [3], approximately four times greater than the 2.856 GHz SLC. Similarily, at 34 GHz the acceleration gradient could exceed 200 MeV/m. Laboratory tests would allow confirmation (or not) of the widely accepted scaling with frequency of field emission and rf breakdown in high-gradient room-temperature linac structures [4]. Tests has been performed with microsecond-length pulses at S, C and X-band; and at 30 GHz at relatively low power level with 12 nsec pulses on the CLIC structure [5]. But extension upwards in power and pulse length are required to further test the scaling laws at 34.272 GHz in a regime where conventional high-gradient linacs would operate, namely with RF surface electric field gradients greater than 0.5 GeV/m and pulse widths greater than 100 nsec. With a 45 MW magnicon amplifier at 34.272 GHz under development by Omega-P, is it possible to consider such high-power tests of accelerating structures.

Making use of the favorable scaling of accelerating gradient with frequency assumes that RF source and pulse compressor technology will advance sufficiently so as to furnish of the order of 615 MW/m of required RF drive power to achieve 250 MeV/m accelerating gradient [2]. To push the structure up to 250 MeV/m, which corresponds a surface field of ~ 500 MV/m even for the 6-cm long structure described below, would require a peak RF power level of 120 MW. No 34.272 GHz RF source with this power is available. Nor are power enhancement schemes, such as resonant rings or pulse compressors, available for this frequency and power level. Until such RF power enhancement technology becomes available, another approach is required to achieve the surface electric field of more than 500 MV/m in a 34.272 GHz structure. This method is to operate a traveling-wave structure in a standing-wave mode, which can be arranged by placing an RF short circuit at the end of the structure under test. Under this condition, analysis of the energy spectrum of resulting dark current is a common diagnostic used to ascertain the acceleration gradient. Knowledge of the overvoltage factor then allows the maximum surface gradient to be inferred from the acceleration gradient.

2 THE TEST STRUCTURE

Parameters of the accelerating structure are to be chosen so as to achieve an accelerating gradient greater than 250 MeV/m, assuming the necessary RF peak power to be available. Although the design value of peak output power of the Omega-P magnicon is 45 MW in a 1 μsec pulse [1], a more conservative level of 30 MW is chosen for the proposed project.

The customary accelerating structure for linear colliders is a $2\pi/3$ structure with a normalized group velocity v_g/c in the range 0.03 – 0.1. A schematic crossection of the structure is shown in the Fig. 1a. As was discussed in ref.

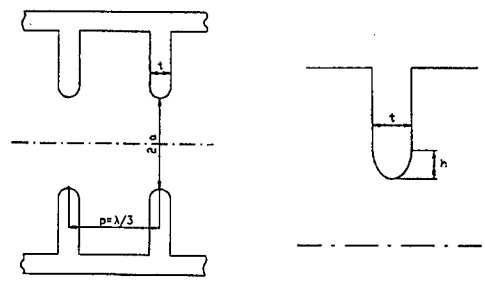

(a) (b)

Fig. 1. A schematic cross section of the $2\pi/3$ structure (a), the disk edge geometry (b).

[4], the maximum accelerating gradient E is determined mainly by the maximum electric field on the cavity surface E_m. Thus, the maximum accelerating gradient for fixed surface field is achieved, if the overvoltage factor

0-7803-5573-3/99/$10.00@1999 IEEE.

$k_m=E_m/E$ is minimized. To minimize k_m, a disk edge geometry was suggested [6] having an elliptical shape, as shown in Fig. 1b. Numerical simulations show, within the range of group velocity $0.01 \le v_g/c \le 0.1$, and for the cavity wall thickness t in the range of 0.056λ to 0.11λ, a reduction in k_m in the range of 5% to 40%. Here λ is the free-space wavelength at the design frequency. The next important issue is the choice of structure length, equivalent to a choice of the number of cells, to investigate effects which may not appear in a single cell. Naturally, the maximum number of cells is limited by the available peak RF power. For the discussion that follows, a structure having 21 cells was chosen. Table I lists results for some parameters of a preliminary design optimization for this structure.

Table I. Preliminary parameters for high-gradient 34 GHz accelerator structure.

Operating frequency	34.272 GHz
Operating mode	$2\pi/3$
Number of cells	21
Structure length	62 mm
Group velocity	0.048 c
Diameter of cell	7.35 mm
Diameter of aperture	3.0 mm
Wall thickness t	0.70 mm
Eccentricity $t/2h$	0.70
Overvoltage factor k_m	2.0
Shunt impedance	130 MOhm/m
Quality factor	3,800

The wall thickness value t that was chosen takes into account mechanical strength and the need for radial cooling. The shape of the disc edge is chosen to minimize k_m [6]. Note that k_m for a round shape disk edge is 2.2, i.e. 10% larger than that found in the preliminary optimization of this structure.

The proposed structure and a corresponding field map in a standing wave mode are shown in Fig. 2. The diameter of the end cell is reduced to 7.26 mm, as compared to 7.35 mm for the intermediate cells in order to compensate effect of a beam tunnel. The dispersion curve for this structure is shown in Fig. 3. These results were found using calculations with the code SLANS [7]. A 30 MW peak power magnicon will allow to test this structure up to

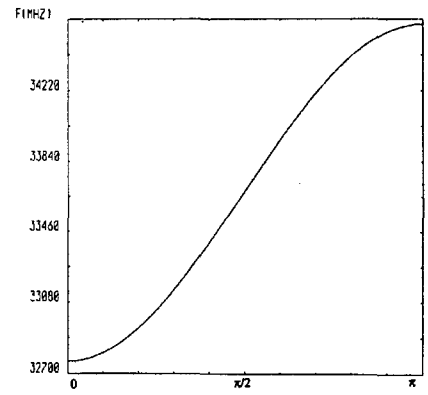

Fig. 3. Dispersion curve for the structure shown in Fig. 2.

maximum surface field of about 700 MV/m. It should be emphasized that, in the case of standing-wave structures, the overvoltage factor k_m is almost twice as high than for the traveling-wave case; in the present instance, $k_m = 3.85$.

3 THE INPUT COUPLERS

Input couplers constitute another important issue. The approach which is taken for the 11.424 GHz structure for NLC [8], and for the 30 GHz structure for CLIC [5], is to use two symmetric input couplers. It has been shown recently [9] that quadrupolar field asymmetries, introduced by input irises having an azimuthal variation, will enhance the surface electric field in the input cell. This enhancement factor in some cases may exceed 25%. To avoid this problem, a so called "racetrack" geometry for the input cavity was introduced [9]. Racetrack geometry allows one to symmetrize the fields; it has been shown to work well at 11.4 GHz and 17 GHz. But at 34.272 GHz, additional problems arise due to the extremely high gradients and microwave power levels in the small size input waveguides. To feed the 34.272 GHz structure described here, four symmetric input couplers will be used. This approach provides the following benefits:

- an increase in the order of perturbation asymmetry from quadrupole to octupole, with a concomitant decrease in the field enhancement factor to below 3%;
- a factor-of-two decrease in power flow through each input waveguide; and

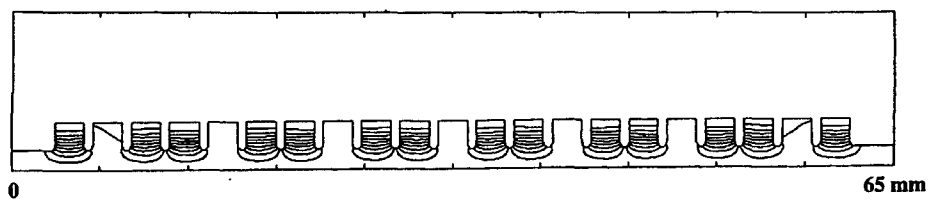

Fig. 2. Field map of $2\pi/3$ standing wave mode in the 21-cell structure.

- a straightforward connection between the magnicon [1] and the accelerator structure input coupler, since the magnicon has four WR-28 output waveguides; thus avoiding need for a complex power divider for input power distribution.

A field map of the input cell with four WR-28 waveguides is shown in Fig. 4. 2-D simulations were carried out for the case of perfect matching, using CLANS code [7]. Width of the coupling irises corresponds to the case of standing-wave operation of the structure. Zoomed picture of this field map is shown in the Fig. 5. One can see that near the structure axis magnetic force lines are practically circular, indicating that only a small field enhancement factor is present.

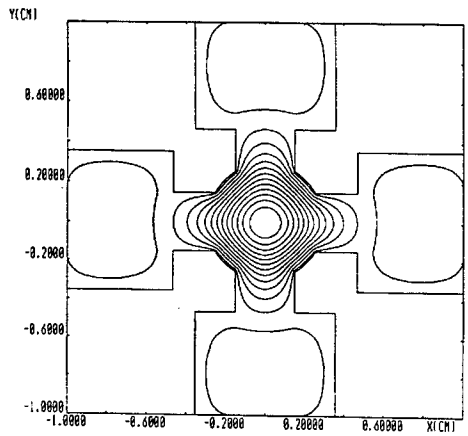

Fig. 4. Field map in the transverse cross section of the input cell.

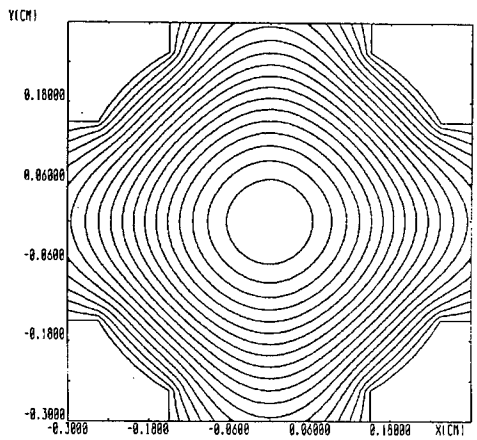

Fig. 5. Zoomed field map, showing good axial symmetry in the center of the input cell.

4 CONCLUSIONS

Continued progress in high energy physics demands a new generation of linear collider, which in turn requires operation at frequencies higher than 11.4 GHz, the frequency chosen for NLC. At 34 GHz, it is expected that an acceleration gradient approximately three times that at 11.4 GHz can be realized. High-power tests on candidate structure are necessary to confirm this hypothesis. These tests on trial accelerator structure at 34 GHz will be possible since a 45 MW, 34 GHz magnicon is being built by Omega-P, Inc. In particular, the tests of this accelerator structure may allow a surface gradient of 700 MV/m, which corresponds to an accelerating gradient of more that 300 MeV/m for a travelling-wave accelerating structure.

5 ACKNOWLEDGMENTS

This research was supported by the US Department of Energy, Division of High Energy Physics. The authors would like to thank Dr. J. L. Hirshfield for careful reading of the manuscript.

REFERENCES

[1] O. A. Nezhevenko, V. P. Yakovlev, A. K. Ganguly, J. L. Hirshfield, "High Power Pulsed Magnicon at 34 GHz ", *RF'98 Workshop*, Pajaro Dunes, CA, October 5-9, 1998 (to be published)

[2] P. B. Wilson, "Scaling Linear Colliders to 5 TeV and Above", SLAC-PUB-7449, April, 1997.

[3] T. O. Raubenheimer, K Yokoya, "Proposed ILC Parameters", SLAC Note 06-05-98.

[4] J. W. Wang, G. A. Loew, "Field Emission and RF Breakdown in High-Gradient – Room-Temperature Structures", SLAC-PUB-7684, October 1997

[5] H. H. Braun, K. Aulenbacher, R. Bosart, F. Cautard, R. Corsini, J. P. Delahaye, J. C. Godot, S. Hutchins, I. Kamber, J.H.B. Madsen, L. Rinolfi, G. Rossat, S. Schreiberg, G. Suberlucq, L. Thorndahl, I. Wilson, W. Wuensch, "Results From the CLIC Test Facility", *Proc. 1996 European Particle Accel. Conf.*, , pp. 42-46.

[6] O. Nezhevenko, D. Myakishev, V. Tarnetsky, V. Yakovlev, "TW Accelerating Structures with Minimal Electric Field", *Proc. 1995 Particle Accelerator Conference and International Conference on High Energy Accelerators*, Dallas, 1995, pp.1076- 1078.

[7] D. Myakishev, V. Yakovlev, "The New Possibilities of SuperLANS Code", *Proc. of 1995 Particle Accelerator Conference and International Conference on High Energy Accelerators,* Dallas, 1995, pp.2348-2350.

[8] K.A. Tomson *et al,* "Design and Simulation of Accelerating Structures for Future Linear Colliders", in *Particle Accelerators,* 1994, vol.47, pp. 65-109.

[9] J. Haimson, B. Mecklenburg and E.L. Wright, "A Racetrack Geometry to Avoid Undesirable Azimuthal Variations of the Electric Field Gradient in High Power Coupling Cavities for TW Structures", *Proc. of 7th AAC Workshop*, Lake Tahoe, October 1996, pp. 898-911.

BROOKHAVEN ACCELERATOR TEST FACILITY ENERGY UPGRADE *

X.J. Wang #, I. Ben-Zvi, J. Sheehan and V. Yakimenko
BNL, Upton, NY 11973

Abstract

Brookhaven Accelerator Test Facility (ATF) is a laser linac complex, with a photocathode RF gun injection system and two sections of travelling wave linac. To satisfy the requirements of short wavelength free electron laser and laser acceleration experiments, ATF started an energy upgrade program with a goal of final energy on the order 100 MeV. Initial stage of the energy upgrade involves replace aged SLAC X-K5 klystron, and upgrade the magnets power supplies for the quadrupole magnets. A SLAC Energy Doubler (SLED) cavity will be installed in the second phase of the energy upgrade. Final stage of the project is to install another modulator and klystron so each section of the linac will be powered individually; which will allows us more flexibility to optimize the electron beam emittance compensation. We will also discuss issue of electron beam dynamics for operating the ATF at the higher energy.

1 INTRODUCTION

Brookhaven accelerator test facility (ATF) is a dedicated user facility for beam physics and radiation source R&D. Though ATF was designed and approved for beam energy up to 120 MeV, funding constrain and resource limited ATF energy below 60 MeV. ATF is the only multi-user facility based on the photocathode RF gun technology in operation in the last decade, it typically delivered more 1000 hours user beam time annually. ATF not only provide service to industry, university and national laboratory to do beam physics research, it also actively involve many user experiments. ATF users and staff have made many significant contributions in many aspects of beam physics research. We have experimentally demonstrated emittance compensation in high field region [1], developed experimental techniques in slice emittance[2], tomography [3] and sub-picosecond timing jitters measurement[4]. We proposed and experimentally demonstrated electron beam micro-bunching in the photoinjector[5]. The photocathode RF injection system developed at ATF now is being used in many laboratories both in abroad and US. ATF users have experimentally demonstrated two laser acceleration techniques, i.e. Inverse Cerenkov Acceleration (ICA) [6] and Inverse Free Electron Laser (IFEL) [7] acceleration; Self Amplified Spontaneous Emission (SASE) was observed at both 1 and 5 μm [8,9]. We have also demonstrated nano-meter resolution beam position monitors [10]and electron beam micro-bunching at optical wavelength [11].

One of the primary missions of the ATF is to explore the new high gradient acceleration techniques, specially various laser acceleration techniques. With new TW CO2 laser system, and the ATF capability of producing Pico-second to femto-second electron beams[6,11], ATF can be the host for many so called second-generation laser acceleration experiments. Pre-bunched, higher energy electron beam injected into the laser accelerators has many advantages, such as better beam quality preservation in plasma laser acceleration schemes and ICA, and longer effective interaction length.

Another type of ATF experiment demanding higher beam energy is SASE FEL and femto-second hard X-ray production by laser Compton scattering. Significant gain was measured in SASE FEL experiments [12] in IR range, but many important issues, such as transverse mode profile, longitudinal mode structure, and saturation remain to be studies if SASE process can be used to produce X-ray for the fourth generation light source. Multi-institute collaboration now is constructing a Visible-Infrared SASE Amplifier (VISA) FEL experiment at the ATF to study those issues. To optimise the SASE FEL gain for the ATF beam parameters of 2.5 mm-mrad normalize rms emittance and 200 A peak current, an undulator of period 1.8 cm and total length of 4 meters is required [13]. It is critical to generate visible radiation so we can take advantage of the sensitive and advanced photon beam diagnostic techniques available in the visible wavelength to study those issues. To generate SASE radiation in the 800-600 nm range with the above undulator, it requires 70 to 85 MeV electron beams. For Compton scattering experiment, 100 MeV electron beam interacts with CO_2 laser (10.6μm) could produce bright sub-picosecond X-ray whose wavelength shorter than 1 Å.

Another important consideration for ATF energy up-grade is to optimise the emittance compensation and produce 100 femto-second or shorter electron beams. For emittance compensation photocathode RF gun injection system, linac plays two important roles. One is to boost the beam energy to reduce the space-charge effect, which decrease rapidly with the beam energy. The second function of the linac is to match the electron beam envelop and minimise the final emittance. Higher energy

*Work supported by U.S D.O.E contract DE-AC02-98CH10886.

Email: xwang@bnl.gov

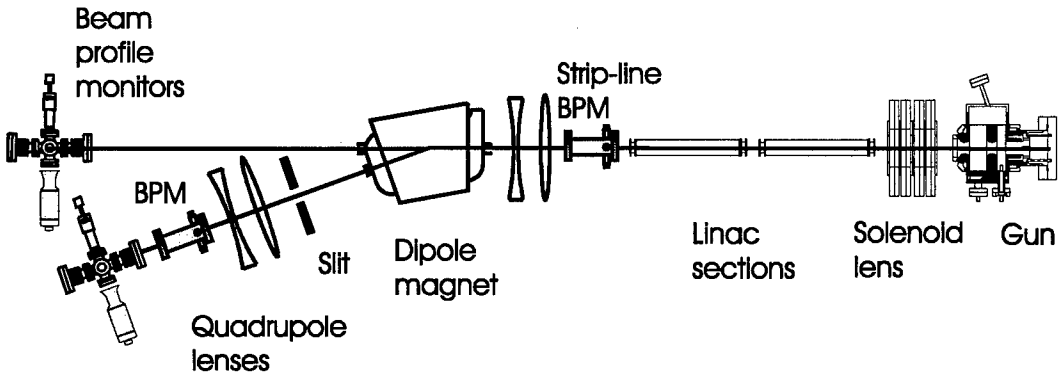

will allow more flexibility to minimise the beam emittance.

We first briefly describe the ATF photocathode RF gun injector and linac, then the strategy of ATF 100 MeV energy up-grade and status of the project is discussed in the following section. The beam dynamic issue involve emittance compensation process will be discussed later.

2 ATF PHOTOCATHODE RF GUN INJECTOR AND LINAC

Fig.1 is the schematic of the ATF photocathode RF gun injection system and linac. The photocathode RF gun injection system consists of a 1.6 cell high brightness photocathode RF gun, single solenoid magnet for emittance compensation, normal incident laser optics station, and photoelectron beam diagnostics station for electron beam charge, energy and RF phase measurements. About one meter downstream of the photocathode RF gun is the linac, which is made up by two 3-meter sections of SLAC-type travelling wave linac. The RF gun and linac were powered separately by two klystrons.

A frequency quadrupled Nd:YAG laser, which synchronised with the ATF linac RF system, is used to drive the photocathode RF gun. It is also used to switch the ATF CO_2 laser system. The CO2 laser system is mainly used as a power source for laser acceleration experiments and study beam photon interaction.

The klystrons used at the ATF are surplus XK-5 klystrons provide by SLAC. After remarkable more 30 years' service, the output of those klystrons now starts to decline. The output of the klystron used to power two sections of the linac was measured to be less than 15 MW. The beam energy of from two sections of the linac can be estimated by:

$$E = 10\sqrt{2P} \qquad (1)$$

Where P is the klystron power in MW, and E is the electron beam energy in MeV. To produce 70 MeV electron beams, we need a 25 MW klystron. The klystron tube we selected is 30 MW Triton klystron 8840, which is compatible with the XK-5 klystron assembly. The second phase of the ATF energy up-grade is to install a SLAC Energy Doubler (SLED) [14] cavity purchased from China IHEP some times ago. SLED cavity give us more energy, but also make ATF linac operation more complex. To take advantage of the SLED cavity, we also installed more capacitors in the linac modulator to increase the RF pulse width. ATF magnets are capable of delivering 100 MeV electron beam with new 30 A power supplies.

The final stage of the ATF energy upgrade involves building a new modulator and installing a new klystron, which allows us more flexibility of to minimise the electron beam emittance.

3 STATUS OF THE ATF 100 MEV ENERGY UPGRADE

The initial stage of the ATF energy upgrade was implemented in the late 1998. The 30 MW Triton klystron 8840 tube was installed and conditioned in the October of 1998. Fig.2 is the maximum electron beam energy as a function of the modulator charging power supply voltage. With beam energy more than 70 MeV, VISA experiment can start the experiment at 800 nm even without the SLED cavity installed.

More capacitors were also installed to achieve the RF pulse width more than 3 μs (Fig.3). The SLED cavity and its water system were tested. From RF measurement data (Fig.4), the Q of the SLED cavity is better than 10^5, which agrees with the design values [14]. From fig.4 of the reference 14 we concluded that, the energy multiple factor of the ATF SLED cavity is about 1.5, which will be able to produce 100 MeV electron beam.

The last stage of the ATF energy upgrade program is to build a new modulator and klystron, so each section of the linac will be powered individually by a single klystron. This will allow us more flexibility in electron beam emittance and bunch length optimisation. If funding

available, we expect the new modulator and klystron come on-line at the end of year 2000.

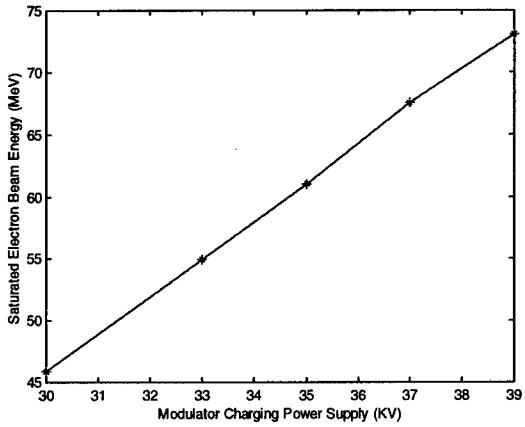

Figure 2: Electron beam energy as function of the linac modulator charging voltage.

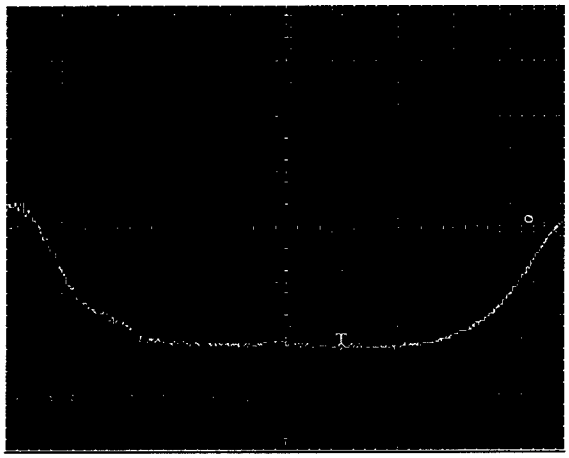

Figure 3: The linac RF pulse width measurement.

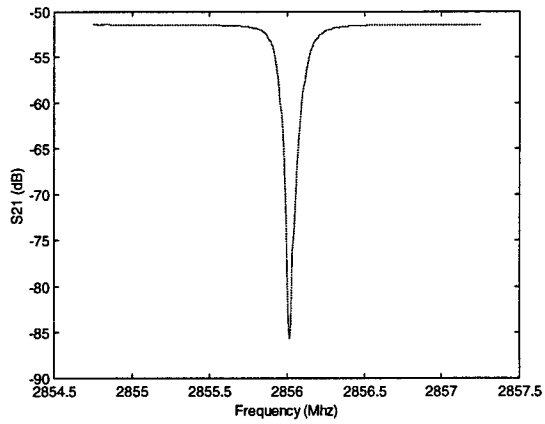

Figure 4: The SLED cavity RF measurement.

4 BEAM MATCHING

For a photocathode RF gun operating at emittance compensation mode [15], the acceleration gradient of the linac and final energy of the beam are critical in minimising the emittance of the photoelectron beam. For normal ATF operation, laser spot size on the cathode, laser pulse length and field gradient on the cathode and electron beam charge are fixed parameters while solenoid magnet strength was adjusted to optimise the beam emittance. With higher accelerating gradient (up to 16 MV/m) in the linac, we will have more freedom to optimise the final beam emittance. The procedure using so called invariant envelop theory [16] proposed by Serafini et al [17] to optimise the ATF type injector can give some guidance in general. But there are two import experimental facts the theory does not considered. We have observed both in simulation[18] and experiment [5] that, significant electron beam micro-bunching occurred for a modest amount charge (< 1 nC) situation. This is crucial for the ATF experiments (such as VISA, high gain harmonic generation FEL) which require high peak current since ATF photocathode RF gun driving laser can only produce 10 ps (FWHM) pulselength. Another important issue was not address in the theory is the coupling we observed between the transverse emittance and electron beam bunch length [18]. Micro-bunched electron will also suffer less emittance growth due to the wakefield.

5 REFERENCES

[1]X.J. Wang *et al*, Proc. Of 1995 Part. Accel. Conf., p.890 –892.

[2] X. Qiu et al, Phys. Rev. Lett. **76,** 3723 (1996).

[3] V. Yakimenko et al, to be published in the Proc. Of EPAC98, BNL-65675 (1998).

[4] X.J. Wang and I. Ben-Zvi, AIP Conf. Proc. 390, p.232 – 239 (1996). [5] X. J. Wang et al, Phys. Rev. E 54, R3121 (1996).

[6] W. D. Kimura et al, Phys. Rev. Lett. **76,** 546 (1995).

[7] A. van Steenbergen at al, Phys. Rev. Lett. **77,** 2690 (1996).

[8] M. Bazien et al, Phys. Rev. E **57,** 6093 (1998).

[9] L.H. Yu et al, these proceeding.

[10] Vladimir Balakin, these proceeding.

[11] Y. Liu et al, Phys. Rev. Lett. **80,** 4418 (1998).

[12] M. Hogan et al, Phys. Rev. Lett. **81,** 4867 (1998).

[13] R. Carr et al, to be published in the Proc. Of FEL 98.

[14] Z.D. Farkas et al, Proc. 9th International Conf. On High Energy Accelerators, p.575 (1974).

[15] B.E. Carlsten, Nucl. Inst. Methods A **285**, 313(1989).

[16] L. Serafini and J.B. Rosenzweig, Phys. Rev. E 54, R3121 (1997).

[17] L. Serafini and J.B. Rosenzweig, Proc. Of PAC 97, p.2876 (1997).

[18] X.J. Wang, UCLA Ph.D thesis, UCLA-CAA0086-2/92 (1992).

[19] X.J Wang and I. Ben-Zvi, Proc. Of PAC 97, p.2793 (1997).

UPGRADE OF THE CEBAF ACCELERATION SYSTEM*

J. R. Delayen# for the Upgrade Cryomodule Development Team,
Thomas Jefferson National Accelerator Facility, Newport News, VA

Abstract

Long-term plans for CEBAF at Jefferson Lab call for providing 12 GeV in the middle of the next decade and 24 GeV after 2010. Such energies can be achieved within the existing footprint by fully populating the accelerator tunnel with cryomodules capable of twice the operating voltage of the existing ones within the same length. In particular, this requires the development of superconducting cavities capable of operating at gradients above 12 MV/m and Q~10^{10}. An R&D program for the development of the cryomodules is under way and will be presented, as well as various options for the upgrade path.

1 CEBAF DESIGN AND STATUS

CEBAF was designed and constructed to accelerate an electron beam to 4 GeV by recirculating five times through two 1497 MHz superconducting linacs, each providing 400 MeV per pass at the accelerating gradient of 5 MV/m. 180-degree isochronous, achromatic recirculating arcs connect the two anti-parallel linacs. The design maximum current is 200 μA cw, corresponding to a beam loading current of 1 mA [1].

From the beginning the performance of the acceleration system exceeded the design goal [2]. Early in 1996 a one-pass energy of 1 GeV was achieved, and in the spring of 1997 a 90 μA beam was accelerated to 1.16 GeV in a single pass (equivalent to a 5.6 GeV, 18 μA 5-pass beam), albeit with stability less than suitable for regular operation.

The average accelerating field in the active cavities was 7.8 MV/m, more than 50% above their design field. In the fall of 1997, the full capacity of CEBAF was demonstrated with the delivery of a 4 GeV, 200 μA beam [3]. The initial performance of the CEBAF cavities corresponded to a reliable 5-pass energy of about 5 GeV. The performance was predominantly limited by electron field emission that can manifest itself in additional cryogenic losses, x-ray production, and periodic arcs at the cold ceramic window which is located close to the beam line [4].

In order to reduce field emission and increase the operational energy of CEBAF, a program to perform *in situ* helium processing of the cavities was initiated in the fall of 1996 and took place during the scheduled machine shutdown periods in 1997, 1998, and 1999 [3]. The *in situ* processing program was nearly completed in February 1999 and has increased the installed voltage by about 200 MV, which corresponds to an added voltage of 1 GeV for a 5-pass beam, and it is expected that the additional gain will allow operation just above 6 GeV.

Some of the arc dipole power supplies have been upgraded in order to deliver high-energy multipass beams, and physics experiments at 5.5 GeV are scheduled to start in April 1999. In order to support high-energy, high-current operation new optimization algorithms and tools have been developed [5].

2 UPGRADE OPTIONS FOR THE ACCELERATION SYSTEM

CEBAF's long-term institutional plan calls for an energy upgrade to 12 GeV in the middle of the next decade, and to 24 GeV after 2010. The short-term goal is to have developed, installed in the accelerator, and demonstrated by 2002 prototypes of the key components of such an upgrade.

While the details of the upgrade path are still being developed, a top-level parameter list has been generated which guides the selection between the various options:

- The highest energy beam of 12 GeV needs to be delivered to only one experimental hall.
- CW operation must be preserved.
- The maximum circulating beam current will be 400 μA (corresponding to an 80 μA beam for a 5-pass design).
- The maximum installed refrigeration capacity will be 8.5 kW at 2 K.
- Cost and impact on accelerator operation during the upgrade must be kept to a minimum.
- Since the purpose of the 12 GeV electron beam is to generate an 8 GeV photon beam, the requirements on the electron beam quality can be relaxed from the existing requirements.
- Since the ultimate goal is an upgrade to 24 GeV, an upgrade path to 12 GeV that could be extended to higher energy would be preferable.

The first upgrade plan for CEBAF called for a maximum energy of about 9 GeV. The most attractive option to achieve this goal called for a systematic "reworking" of the cryomodules. This consisted of removing the cryomodules from the accelerator one at a time, reprocessing the superconducting cavities, and replacing or modifying some of the limiting components (for example relocating the cold windows and shielding them from field-emitted electrons). While this option

*Supported by US DOE Contract No. DE-AC05-84ER40150.
delayen@jlab.org

0-7803-5573-3/99/$10.00@1999 IEEE.

seemed attractive toward obtaining 9 GeV, it could not be easily extended beyond, either because it could not provide enough energy or because the cryogenic consumption would be excessive.

The most attractive option that has emerged from the studies that have been conducted during the last year consists of: (see Figure 1)

- addition of a fourth experimental Hall D at the end of the North Linac (turning CEBAF into a 5-pass machine for Halls A, B, and C, and a 5 1/2-pass machine for Hall D),
- development and construction of high-voltage, high-Q cryomodules to be installed in the 5 empty slots in each of the linacs,
- replacement of a limited number of existing cryomodules by new ones (typically 3 in each of the linacs and 2 in the injector),
- upgrade of the refrigeration capability to 8.5 kW,
- addition of a 10th arc and upgrade of the existing ones.

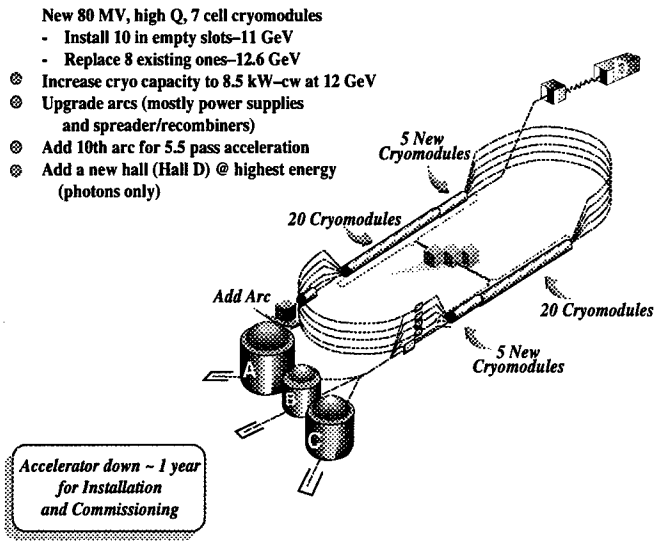

Figure 1: Upgrade path to 12 GeV CEBAF.

3 DESIGN OF THE UPGRADE CRYOMODULE

The Upgrade Cryomodule is clearly the key component of the upgrade of the acceleration system. Its design is also somewhat insensitive to the details of the upgrade option that is ultimately chosen, once the top-level parameters have been defined, and it can be viewed as a building block that can be applied to a large number of upgrade paths. For these reasons, most of the development efforts in support of the upgrade are directed toward the development and demonstration of prototype Upgrade Cryomodules.

3.1 Cavities

In order to increase the voltage that is provided by a cryomodule within a given length, one can either increase the gradient at which the cavities are operating, or increase the effective accelerating length, or both. While it may be argued that maximizing the accelerating length is the approach that presents the least technological risk, for cw accelerators such as CEBAF, maximizing the length instead of the gradient has the added advantage of lowering the dynamic load on the refrigeration system.

For this reason, it was decided early that the Upgrade Cryomodule would still include 8 cavities, but that these would be 7-cell cavities (70 cm) instead of the present 5-cell (50 cm). The option described in Section 2 calls for these cavities to provide a minimum voltage of 8.75 MV with a maximum power dissipation of 17.5 W, *i.e.* their Q must be at least 6.5×10^9 at 12.5 MV/m. Thus the greatest challenge is not so much in achieving a high gradient but in maintaining a high Q at high gradient. Given the constraint imposed by the available refrigeration, cw operation at 15 MV/m would be practical only if the Q at that field were at least 10^{10}.

While the CEBAF cavity cell design could be improved, the potential benefits do not seem critically important, and the first 7-cell cavity prototype has been built using the existing cell design. The first prototype met the requirement of a Q of 6.5×10^9 at 12.5 MV/m [6]. A redesign of the cells is still an option, although a low priority one.

3.2 Cryostat Concept and Cavity String Assembly

The existing CEBAF cryomodule is constructed from 4 cryounits, each containing a sealed cavity pair. These cryounits are then joined with bridging sections. In order to increase the number of cells from 5 to 7 while maintaining the same cryomodule length, this approach had to be abandoned.

Several cryostat concepts were explored:

- Cylindrical cryostat with radial penetrations for the power couplers,
- Cylindrical cryostat with axial (through the end plates) penetrations,
- Bathtub-type cryostat where all the innards are suspended from a top plate.

While all designs had advantages and disadvantages, a cost/benefit analysis did not reveal an obviously preferred option. The overriding consideration was the limited amount of time and resources expected to be available, and the radial design was chosen as it was deemed the one that would require the least amount of development given the on-site experience with the radial design.

The Upgrade Cryomodule will include a continuous 8-cavity string assembly without isolation valves between the cavities. The present design calls for a 30-cm

separation between cavities into which must fit the fundamental power coupler, the higher mode extraction system, the pick-up probe, connecting flanges and connections to the helium tank and mechanical tuners [7]. The design does not include bellows between the cavities.

3.3 Fundamental Power Coupler

Both coaxial and waveguide couplers were explored. The waveguide concept was retained because of its simplicity and flexibility at 1500 MHz. Unlike the present design, though, we have decided to completely separate the functions of fundamental power coupling and higher mode extraction. This produces a coupler design that, unlike the existing CEBAF design, is free of transverse kick imparted to the beam and allows a cryostat design where all the power couplers are on the same side [8,9].

3.4 Higher Order Modes Damping

The requirements for higher-order mode (HOM) damping for the 12 GeV Upgrade have been substantially relaxed from the original CEBAF design. Not only is the energy increased from 4 to 12 GeV but the maximum circulating current is being reduced from 1000 to 400 μA. Additionally, the experience acquired during CEBAF operation has led to a reduction of the "safety factor" for the stability threshold current. As a result an upper limit of 10^6 was adopted for the Q_{ext} of the HOMs.

The design of the HOM couplers is a departure from the existing design: we do not rely on any HOM being extracted from the fundamental power coupler, the 2 HOM couplers will be of a coaxial type as opposed to a waveguide type, the HOM couplers will be located outside the helium tank and the HOM power can be deposited at a temperature other than 2 K.

3.5 Frequency Tuning

The frequency tuners perform several functions: bring the cavities on resonance after installation, detune the cavities that are not operating, and track the changes in frequency due to Lorentz detuning, pressure and temperature fluctuations. For the Upgrade Cryomodule, the bandwidth will be small (~75 Hz), the Lorentz detuning large (~500 Hz), and we want to track the frequency accurately (~2 Hz) in order to minimize the rf power requirements. For this reason the baseline design incorporates two different tuning schemes: a coarse mechanical tuner with 400 kHz range and 100 Hz resolution that will be used infrequently, and a fine piezoelectric tuner with 1 kHz range and 1 Hz resolution that will provide the fine, frequent tracking [10].

3.6 Processes and Procedures

While the gradients required are modest compared to those for proposed linear colliders, a high Q is of primary importance. Furthermore, since rf power will be a hard constraint, "outstanding" cavities cannot operate at higher gradient in order to compensate for "weaker" ones. For these reasons our main goal is to achieve consistent performance as opposed to the less frequent exceptional one. We are engaged in a complete review of all the processes and procedures involved in the fabrication and assembly of cavities and cryomodules. Modifications to the processing and assembly facilities, such as implementation of final chemistry and rinsing in the cleanroom, are under way.

3.7 Microphonics, RF Control, and RF Power

In order to contain the cost of the upgrade we have adopted as a goal only a modest increase of the rf power per cavity from 5.5 to 6 kW. This puts stringent requirements on microphonics and the control system. At 12.5 MV/m and 400 μA circulating current, the maximum allowable amount of detuning (including static and microphonics) is 25 Hz. The optimum Q_{ext} is $2x10^7$, and the Lorentz detuning is much larger than the loaded bandwidth; for this reason a new low-level rf control system will be required. The baseline concept is an agile digital system capable of implementing a self-excited loop on I/Q feedback.

4 ACKNOWLEDGEMENTS

This paper summarizes the work of the Upgrade Cryomodule Development Team which also includes: I. Campisi, L. Doolittle, E. Feldl, J. Hogan, P. Kneisel, J. Mammosser, G. Myneni, V. Nguyen, L. Phillips, J. Preble, C. Reece, W. Schneider, D. X. Wang, M. Wiseman.

REFERENCES

[1] H. Grunder, "CEBAF Commissioning and Future Plans," Proceedings of PAC95, p.1-3.

[2] C. Reece *et al.*, "Performance Experience with the CEBAF SRF Cavities," Proceedings of PAC95, p.1512.

[3] C. Reece, "Achieving 800 kW CW Beam Power and Continuing Energy Improvements at CEBAF," Proceedings of LINAC98.

[4] J. R. Delayen, L. R. Doolittle and C. E. Reece, "Analysis of Performance Limitations for Superconducting Cavities," Proceedings of LINAC98.

[5] J. R. Delayen, L. R. Doolittle, C. E. Reece, "Operational Optimization of Large-Scale SRF Accelerators, these Proceedings

[6] I. E. Campisi *et al.*, "Superconducting Cavity Development for the CEBAF Upgrade", these Proceedings.

[7] J. R. Delayen *et al.*, "Cryomodule Development for the CEBAF Upgrade", these Proceedings.

[8] L. R. Doolittle, "Strategies for Waveguide Coupling for SRF Cavities," Proceedings of LINAC98.

[9] J. R. Delayen *et al.*, "An RF Input Coupler System for the CEBAF Upgrade Cryomodule", these Proceedings.

[10] J. R. Delayen *et al.*, "Frequency Tuning of the CEBAF Upgrade Cavity", these Proceedings.

STUDY OF THE OPERATION OF THE CORNELL LINAC FOR POSITRON PRODUCTION AT HIGH MULTIBUNCH CURRENTS*

V.S. Alexandrov, A.P. Ivanov, N.Yu. Kazarinov, E.A. Perelstein, M.N. Sazonov
JINR, Dubna, Russia, 141980

M.G. Billing
Cornell University, LNS, USA, 14583

Abstract

The Cornell Electron Storage Ring (CESR) operates as an electron-positron collider with 9 trains of 2 to 5 [1] closely spaced bunches per train per beam. The Cornell Linac is the initial component of the injector for CESR and it needs to provide multibunch trains of electrons and positrons at high injection rates for CESR. This paper presents the results of simulations which have studied the effects of operating the Linac at high multibunch currents needed for the production of trains of positron bunches. Results include the effect of longitudinal wakefields induced by the beam in the linac injector prebuncher cavities and a method for the partial compensation of the effect of these wakefields, the effect of transverse wakefields in the linac accelerator sections in the electron linac preceding the positron target and the effect on positron capture of increasing the accelerating gradient in the positron linac. Comparison with some linac measurements is included.

1 WAKEFIELDS IN THE PREBUNCHER CAVITIES OF THE LINAC INJECTOR

The Cornell linac injector creates a beam of 300 MeV electrons or a beam of 200 MeV positrons. The positrons are produced in a tungsten target on the converter installed in the middle of the linac. The linac is modelled with eight SLAC accelerating sections AS#1...AS#8 [2]. The positron conversion efficiency is about 0.1%. Such a small yield requires the highest current of the electron beam during positron production. Thus the largest current is in the initial part of the injector. The first half of the linac consists of the 150 keV electron gun, two identical prebuncher cavities operating at 214 MHz and the first linac sections AS#1...AS#4.

The linac injector provides a high current electron beam with 7 trains of 2 to 5 bunches accordingly to the CESR operation described above. In the case of positron production each bunch is formed from 3 ns gun pulse with $1.4 \cdot 10^{11}$ electrons. These electron pulses excite the wakefields synchronously on the fundamental mode of the prebuncher cavities. The accumulated longitudinal wakefields decelerate the bunches, distort their bunching and reduce the number of particles captured into the linac.

A special method for the partial compensation of these wakefields is used for the CESR injector. The gun introduces an additional delay τ between the electron bunches. As a result the bunches are shifted at the accelerating phase of RF voltages of the prebuncher cavities. Thus the decelerating effect of the wakefields is compensated by the RF field. For example, the simulations of the net voltages (RF bunching voltage and wake potential) for the 14th bunch are shown in Fig. 1 for the gun using compensated and uncompensated timing parameters.

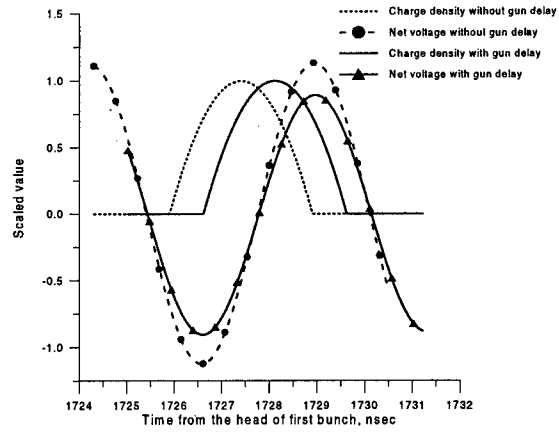

Figure: 1 Net bunching voltage in the first prebuncher.

The wakefields have been simulated for 7 trains of 2 bunches. Two cases of different RF bunching voltages 35kV, 105 kV and 50 kV, 150 kV have been studied for first (PB#1), second (#PB2) prebuncher cavities correspondingly. The wake potentials have been obtained in terms of the cavity mode data calculated by the URMEL code. The quality factor Q at the fundamental mode is high enough to neglect attenuation of the wakefields during the traversal by the entire beam (7 trains by 280 ns). The wakefield amplitudes in the both cavities are proportional to the number of bunches which

* This work has been carried out under NFS contract No. PHY-9310764 SUB U82-8446.

0-7803-5573-3/99/$10.00@1999 IEEE.

passed earlier. The bunching effect in the drift space between the prebuncher cavities squeezes the bunch length. As a result the wakefields have amplitude in 1.2 times higher in the second prebuncher in comparison with the first one. The value of delay τ is chosen from the condition of the wakefield compensation. The result of simulations gives the relative time between the centroids of the bunches [difference in the injection phases of RF linac (1 psec $\leftrightarrow 1^0$) between bunches] are shown in Fig.2.

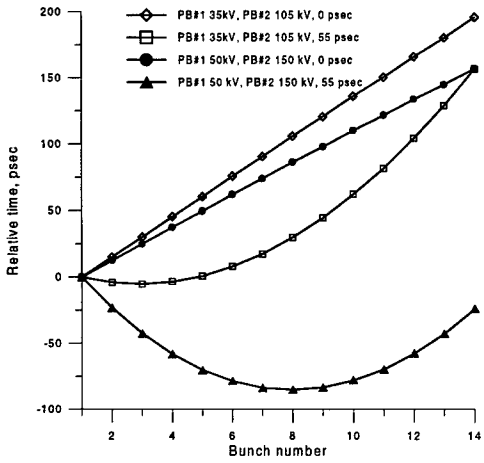

Figure: 2 The relative time between bunches at the linac entrance.

The special gun timing correction provides more successful injection of the high current electron beam into the linac. It is possible to get an optimal case for 14th bunch structure providing 22.5 nC charge per bunch by tuning the RF prebuncher voltages and the gun delay τ. Using the delay τ also provides the maximum current of electron beam for operation with 7 trains per 5 bunches. In this case the optimal charge per bunch is estimated as 11 nC approximately.

2 TRANSVERSE WAKEFIELDS IN THE LINAC

The linac of the CESR injector is modelled to contain SLAC accelerating sections. The experimental measured frequency spectrum of the dangerous dipole modes extends from 4143 to 4350 MHz [3] approximately. The amplitude of the dipole wakefields is proportional to beam displacement away from the electrical center of the linac sections. From estimations of the linac optics we put this displacement to 1 mm at the entrance into the sections. The wakefield model [4] has been developed for constant gradient structures. It assumes the accelerating section consists of a collection (N= 86 cells) of uncoupled oscillators corresponding to the synchronous modes of the periodic structures. Thus the wake potential after the bunch number p is

$$W_p(t) = \frac{1}{N}\sum_{j=1}^{p}\sum_{i=1}^{N} W_{T,i}(k_{T,i}, \omega_i, r_{qi}, Q_i, t + t_{jp}), \quad (1)$$

where k_T[V/C] and r_q are the loss factor and the displacement of an exciting charge, ω and Q are the angular frequency and the quality factor of the dipole mode, i and j are cell and bunch indexes, and t is time between bunches.

There is solenoid focusing in the first accelerating section AS#1 of the linac with the longitudinal magnetic field B = 0.2 T. Simplified assumptions of the bunch motion shows the final beam displacement at the exit of the section should be about 1.1 mm due to solenoid focusing. The wakefields and the bunch motion are calculated in each cell for the second linac section AS#2 which has no solenoid coils.

The bunch to bunch influence depends strongly on the frequency of the dipole modes. In this case it is possible only to determine the worst situation when, due to the wakefields, one of the given bunches gets the maximum displacement after the linac section. We solve the equations of motion changing the frequency of the first cell of the accelerating section and keeping the frequency detuning range up to 5% for the last section cell. The bunch displacements for the "worst" situation are shown in Fig. 3. Time between bunches in the train is 14 ns and time between trains 280 ns. The charge of every bunch is 22.5 nC.

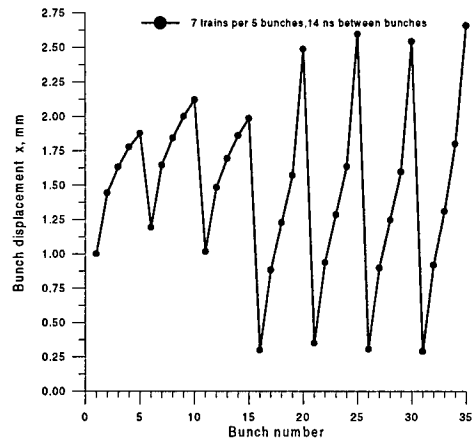

Figure: 3 The bunch displacement after AS#2.

The influence of the wakefields in the next sections is less due to the higher beam energy. It is possible to provide the high multibunch current in each linac sections. However the instability from bunch to bunch coupling should be studied in more details for the whole linac.

3 IMPROVEMENTS IN THE POSITRON LINAC USING HIGHER ACCELERATING GRADIENTS

The simulations of the positron dynamics have been performed assuming the possibility that the input RF power in the accelerating sections #5 and #6 may be increased from 15 MW up to 24 MW to enlarge the positron transfer through the positron linac. The electrons passing through the converter target and secondary

electrons from the conversion process are accelerated in these sections and contribute sufficiently to the net observed charge. The CESR measurements [5] have shown that the total beam charge is negative during acceleration up to the AS#6 where it changes the sign. To have similar results in the simulations we searched for a regime with such effect. In the case of the maximum energy gain for positrons the total beam charge (the difference between the numbers of electrons and positrons) does not change sign during acceleration in the positron linac.

To find out the parameter set which gives this same change in sign of the net accelerated charge, the starting phase (WT0) with the fixed RF field phases of accelerating sections of the positron linac have been variated. Results of the calculations are shown in Fig. 4. The total charge after AS#6 changes sign in a narrow region of the starting phases. Unfortunately the energy gain in this region is very small, i.e. the regime with changing of the charge sign is not optimal to obtain the maximal energy of positrons. To increase the final positron energy to about 200 MeV [6] the appropriate RF phases of AS#6 - AS#8 have been chosen. As result the total charge of the beam becomes near zero after AS#6.

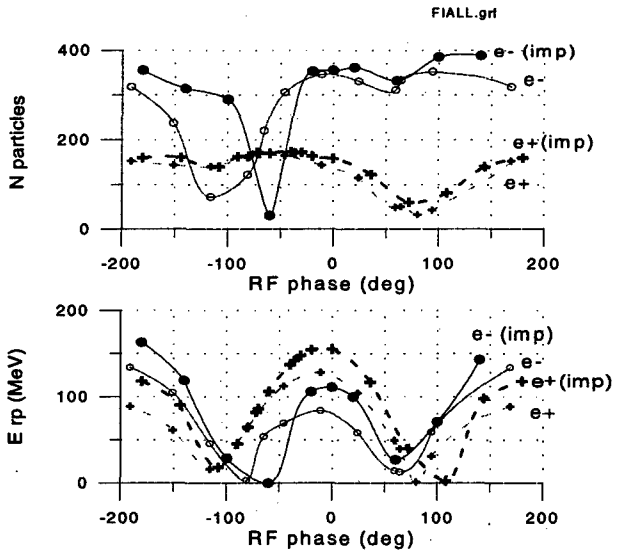

Figure: 4 Number of particles and the reference particle energy at the end of AS#6.

The tuning of the quad gradients was made to maximize the energy spectrum of the beam. Fortunately the gradients in quads between AS#5 - #6 and AS#6 - #7 do not significantly influence on the positron current at the end of AS#8. The gradients of the triplet between AS#7 - #8 noticeably affect the positron transmission.. For example, the changing of the gradients on the value of 100 G/cm remove the positron losses in AS#8.

To estimate the efficiency of the new klystron installation the new (improved) case was simulated. This new variant differs from existing one by improved accelerating gradient in AS#5 and #6, correspondingly tuned lenses gradients and bending magnet field, and decreased on 10% the magnet field of AS#6 solenoid.

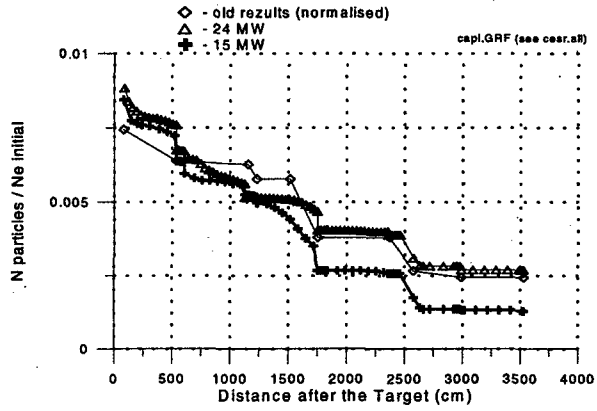

Figure: 5 Positron transmission through the positron linac.

The comparison of the simulation results for the input RF power 15 MW and 24 MW is shown in Fig. 5. It can be seen that the positrons yield at the end of the positron linac has increased about 70%. Additionally the average positron energy gain increases about 20%: from 200 MeV to 235 MeV. The summary plot of the total beam charge transmission through the positron linac and the dipole magnet is shown in Fig. 6.

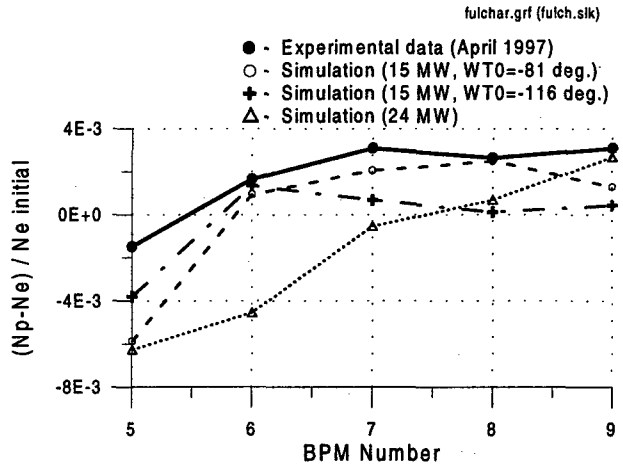

Figure: 6 Total charge transmission through the positron linac.

REFERENCES

[1] D.Rise, Proc. of EPAC96, Barcelona, 1996, p.17.
[2] K.Berkelman et al.,«CESR-B Conceptual design for a B Factory based on CESR», Cornell Univ., CLNS 91-1050.
[3] M.Seidel, et al., SLAC-PUB-7557, May, 1997.
[4] K. A. Tompson, et al, SLAC-PUB-6032.
[5] M.Billing, M.Sazonov, Cornell Univ., LNS, Private communication, April, 1997.
[6] R.Cutler, Cornell Univ., LNS, Private communication, September, 1996.

STATUS OF PLS 2-GEV ELECTRON LINAC

S.H. Nam, Y.J. Han, K.R.Kim, Y.C.Kim
Pohang Accelerator Laboratory, POSTECH
Pohang, 790-784 Republic of Korea

Abstract

The 2 GeV electron linac at the Pohang accelerator laboratory (PAL) has been operated continuously as a full energy injector since its completion on December 1994. The linac system has been continuously upgraded to improve overall system stability and reliability, as well as to increase final injection energy to 2.5 GeV. Eight klystron tubes out of 11 tubes are survived since the beginning of linac operation. The average high voltage operation time of the survived klystrons (E-3712, Toshiba) has been reached near 35,000 hours as of December 1998. Current overall system availability is well over 90%. In this paper, we report the major linac system performance as well as relevant machine statistics, the electron beam parameter measurement, and operational characteristics of cooling water system.

1 INTRODUCTION

PLS linac [1] has been injecting 2-GeV electron beams to Pohang Light Source (PLS) storage ring (SR) since September 1994. The linac klystron modulator system (K&M system) has started its normal operation at the end of 1993, and the total accumulated high voltage run time of the oldest unit has reached beyond 40,000 hours. At the end of 1997 we have installed one more additional K&M module (total 12 modules with 44 accelerating structures) for the higher beam energy margin. The K&M system is normally operating in 70 to 80% of the rated peak power level to avoid the multipactoring phenomena occurring occasionally in random fashion in the waveguide networks and accelerating structures. The sum of all the high voltage run time of the K&M system is approximately 420,000 hours as of December 1998.

In this paper we have reviewed overall system performance statistics of the high power K&M system of the PLS linac for the period of September 1994 to December 1998. In addition, the construction of the MK12 module and the bunch length of electron beam measurement and the cooling water system are reviewed.

2 K&M SYSTEM OVERVIEW

Key features of the K&M system design include 3-phase SCR phase controlled DCHV power supply, resonant charging of the PFN, resistive De-Q'ing, end-of-line clipping with thyrite disks, pulse transformer with 1:17 step-up turns ratio, and high power thyratron switch. The major operational parameters of the K&M system (PLS-200MW modulator) are listed in Table-1.

Table 1: K&M operation parameter summary.

Peak beam power	200MW*max.* (400kV @500A)
Beam vol. pulse width	ESW 7.5μs, 4.4μs flat-top
Pulse rep. rate	120pps *max.* (currently 30pps)
PFN impedance	2.64Ω (5% positive mismatch)
Voltage stabilization	SCR, DC feedback & 5% De-Q'ing
Pulse transformer	1:17(turn ratio), L_L:1.3μH, C_D:69nF
Thyratron switch	heating factor: 46.8x10^9VApps, 8.5kA peak anode current
Klystron tube	drive power:~300W, efficiency.:40%, gain:~53dB, peak power:80/65 MW (currently running at 50 to 65MW)

For the fault free stable operation of the system the thyratron tube is one of the most important active components which require continuous maintenance and adjustment. Performance evaluations of the thyratrons are underway. This effort is initiated to improve the system from the frequent occurring fault caused by the irregular recovery action of the thyratrons, which strongly depends upon the reservoir control.

There are three types of system's interlocks, namely dynamic, static, and personal protection interlocks. All the static fault activation is initiated by the relay logic circuit, and dynamic faults which require fast action response are activated using the electronic comparator circuit. When the system operation is interrupted by the static fault it can be recovered either by the automatic remote control computer or by the manual reset switch.

3 SYSTEM AVAILABILITY STATISTICS

Since the completion of the PLS 2-GeV linac in December 1993 all the K&M systems have been operating continuously except scheduled short term and long term maintenance shut down. Fig. 1 shows the accumulated run times of klystron and thyratron tubes as of December 23, 1998. As one can see in the figure rather shorter bars indicate that corresponding tubes have been replaced at least once or more.

0-7803-5573-3/99/$10.00@1999 IEEE.

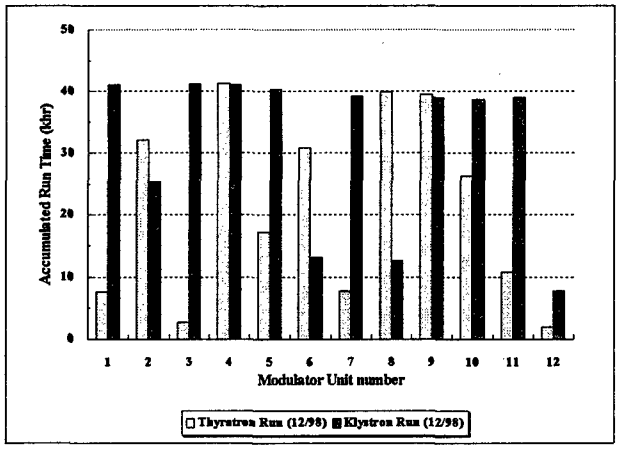

Figure 1: Run time statistics of all klystron and thyratron tubes (as of December 23, 1998). Klystron : M01 : SLAC 5045 tube, M02 : 2nd tube (1995/8/15, magnet coil shorting), M06 : 2nd tube (1997/2/25, gun arcing), M08 : 2nd tube (1997/3/28, heater open), M12 : new module (1997/10/14, system upgrade), Thyratron : ITT F-303 : 8 tube (M01, M04, M07, M08, M09, M10, M11, M12), EEV CX1836A : 2 tube (M03, M05), LITTON L-4888 : 2 tube (M02, M06)

Table 2: K&M system availability of the PLS linac.

Operation period	1994	1995	1996	1997	1998	Total
Total no. of modulators	11	11	11	11	12	11.2
Operation time (hr)	2928	7152	6432	7128	6816	30456
Total failure counts	103	175	131	130	289	828
Total down time (hr)	563	1076	413	529	468	3049
Modulator MTTF (hr)	313	450	540	603	283	412
System MTTF (hr)	28	41	49	55	24	37
MTTR (hr/failure)	5	6	3	4	2	4
Availability (%)	81	85	94	93	93	90

In fact we have replaced total 3 klystrons and 15 thyratrons during the total ~430,000-hr of operation time (run time sum of all 12 K&M modules). Machine availability analysis has been performed based on the data using the techniques described in detail in reference [2]. The results are summarized in Table-2.

During the early phase of the operation, from the late 1993 to early 1995, relatively low machine availability had been obtained. This is due to the maintenance crew training as well as system debugging exercise. Most of time for the repair had been spent for the extensive system diagnostics. The major changes that we implemented at the beginning of 1996 were the computer controlled automatic static fault reset and the modification of the circuit breaker (CB) trip interlock. They greatly contributed to the improved availability reaching over 90% as shown in the Table-2.

It has been observed that the most frequent system fault is the circuit breaker (CB) trip. This is mainly due to the problems in thyratron recovery characteristics which depend on the elaborate reservoir ranging (hydrogen gas pressure control in the tube). Thyratron tubes require ranging adjustment, and according to our experience they are very sensitive to the effects which may cause internal gas pressure change. Once out of normal operating point, self-fire or miss-fire can occur.

Other occasional troubles were corona discharges that are found to occur when there are bad contacts in high voltage components. It has been found also that even a small corona discharge disturbs the ground potential, which are configured to have a single point ground connection inside the modulator, causing noise interference in digital displays as well as SCR phase controls.

4 CONSTRUCTION OF THE MK12 MODULE

The MK12 module of the linac system has been constructed and operated. This contributes to an improvement of the linac energy margin. The installation view of MK12 system in linac tunnel is shown in Fig. 2. The MK12 module consists of two accelerating columns supplied with the rf power by one klystron of 80 MW peak and in-house made modulator of 200 MW peak and one pulse compressor. The auxiliary systems such as vacuum and cooling water were established through extending the existing systems. At commissioning, we obtained the maximum beam energy of about 147 MeV.

Figure 2: Installed view of the MK12 module in linac tunnel.

5 ELECTRON BEAM PARAMETER MEASUREMENT

We are under measurement of electron beam parameters such as the transverse emittance, bunch

lengths and others. In standard injection mode into SR, electron beam current of 1A is transmitted to the end of the linac. The bunch length data are collected by using an optical transition radiation measurement. The bunch lengths as the usual SR injection were measured to be about 12 ps. Fig. 3 shows the streak camera image of the bunch train in one electron beam pulse. Beam parameter measurements at the pre-injector and linac end will be continued. Details of the beam measurement result can be found elsewhere [3].

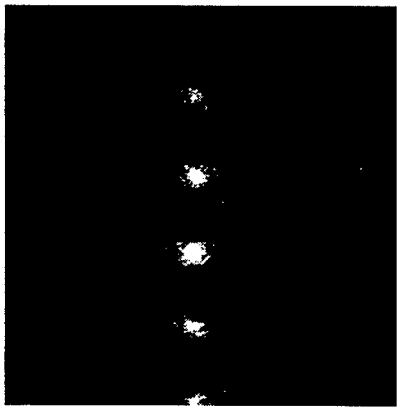

Figure 3: An example of streak camera image of the bunch train in one beam pulse

6 OPERATIONAL CHARACTERISTICS OF COOLING WATER SYSTEM

The total operation time of the PLS linac cooling water system has reached about 38,000 since its normal operation from Dec. 1993. At present, the cooling water system shows 99% availability. The status of system troubles or faults has been daily checked, and maintained during the regular preventive maintenance period. The temperature control within 45±0.2 °C for the rf phase stability of accelerating components has been successfully conducted with precision closed-loop cooling water system temperature controllers.

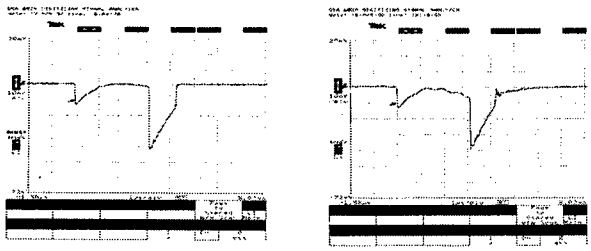

Figure 4: The rf waveform of pulse compressor output power; within temperature control of 45±0.2 °C (left) and beyond temperature control of 45±0.5 °C (right)

An example of the output power waveform of pulse compressor is shown in Fig. 4. Through the periodic tuning test, the system is optimized so that the rf phase of the linac accelerating components including pulse compressors is sustained very stable by adjusting temperature control variation of the structures.

7 SUMMARY

It has been over 5 years since the PLS 2-GeV linac has started its normal operation. We have analyzed the klystron modulator system performance record for the period, which is the major source of the beam injection failure. It is observed that the average lifetime expectancy of the klystron is over 25,000-hr, and it is getting longer. Lifetime of the thyratron tube also appears to be reasonable except the occurrence of the infant failure, however the major improvement is necessary for the reservoir control which is the main source of the system trouble. The machine availability statistics of the K&M system for the beam operation mode is calculated to be over 90%. It appears that there are still lots of rooms for the improvement of the availability more than 95% with a smart design of the protection circuits and control schemes. The MK12 module of the linac system was added, and the additional beam energy of about 147 MeV was acquired. The beam bunch length during normal SR injection was measured to be about 12 ps. To research the characteristics of electron beam of linac, beam parameters measurement at the pre-injector and linac-end will be continued. The cooling water system has performed with 99% availability. Through the temperature control within 45±0.2℃, the rf phase of pulse compressor output power is maintained very stable.

8 ACKNOWLEDGEMENTS

Authors gratefully acknowledge the sincere efforts performed by PAL linac division members to keep the PAL linac system at an excellent condition. This work was supported partly by POSCO and MOST, Korea.

9 REFERENCES

[1] W. Namkung *et. al*, "PLS 2-GeV Linac," Proc. of 17th Int'l Linac Conf., Tsukuba, Japan, Aug. 21-26, pp.14-16 (1994)

[2] A.R. Donaldson and J.R. Ashton, "SLAC Modulator Operation and Reliability in the SLAC Era," IEEE Conf. Proc. 20th Power Modulator Symposium, pp.152-156 (1992)

[3] J.Y. Choi, H.S. Kang, S.H. Nam, S.S. chang, " Measurement of beam characteristics of PLS linac," in these proceedings

STABILITY OF THE RF SYSTEM AT THE SPring-8 LINAC

T. Asaka*, H. Hanaki, T. Hori, T. Kobayashi, A. Mizuno, H. Sakaki,
S. Suzuki, T. Taniuchi, K. Yanagida, H. Yokomizo, H. Yoshikawa
SPring-8, Mihara, Mikazuki, Sayo-gun, Hyogo 678-5198 Japan

Abstract

The stability of the beam energy and energy spread at both the 1-GeV S-band linac and the 8-GeV synchrotron ring are crucial factors for determining the injection time for the storage ring. Since the linac has a lot of high-power RF equipment, any drift of the output power and phase from the various type of RF equipment will affect the beam energy in beam operation. We measured the output power and phase stability for many types of RF equipment.

In order to investigate the drift of the RF parameters in the klystrons, which can be influenced by outside factors, the cooling water temperature and the environmental temperature were also measured. It turns out that the phase of klystrons coincide with the cooling water temperature drift. Although controlled by an air conditioning, the room temperature can vary about 4.0°C in the course of a day, affecting the high-power klystron drive system.

After improvements of the air conditioning control system and the cooling water system for the klystron cavities, a beam current stability was reduced to 0.7% (1σ) from 9.0% (1σ) in beam operation.

1 INTRODUCTION

The 1-GeV linac of SPring-8 consists of a thermionic gun, a bunching system and 26 accelerating structure columns. The linac is able to produce three kinds of the beam pulse widths (1 nsec, 10-40 nsec and 1 μsec) that are requested by the storage ring operation mode; single bunch operation and multi bunch operation. In normal beam operation at two-week or three-week intervals, the beam is injected into the storage ring two times a day. In order to realize uniformity of the bunch train in the storage ring, it has to satisfy the requirements of both the reproduction and stabilization of beam energy at the injector linac, which has a lot of high-power RF equipment. The energy stability as well as the beam change transmission has been a very important issue for stable synchrotron ring injection since the operation of the synchrotron ring began in December 1996. In order to investigate the stability of the beam current and energy at the 1-GeV linac-synchrotron beam transport (LSBT) as illustrated in Fig. 1, the beam current was measured by a wall current monitor placed on the 1-GeV straight line and after the 1-GeV bending magnet while using a beam slit to permit an energy spread of 1.0%. The result of this measurement is shown in Fig. 2. Though there was no change in operating conditions during the measurement, the beam trigger was stopped six times for such reasons as the vacuum deterioration at the RF power line and excessive current of the klystron modulator. It was observed that the drift of the beam current had a period of 25 minutes at the LSBT. In addition, beam drift for the 10 hours was also observed. The following are considered drift factors: change in vacuum pressure, the high-power klystron drive system that depends on the environmental temperature, and the resonant frequency of klystron cavities that depend on the cooling water temperature. Furthermore, the shot-by-shot center energy fluctuation was expected to be caused by PFN voltage fluctuation of the 13-set klystron modulator, along with the jitter of the modulator and thyratron triggers.

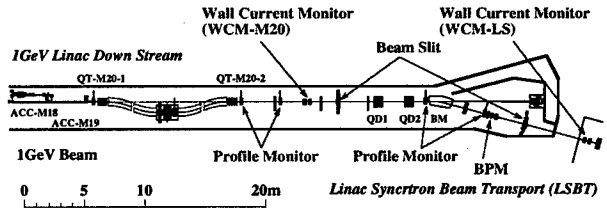

Figure 1: Layout of linac-synchrotron beam transport.

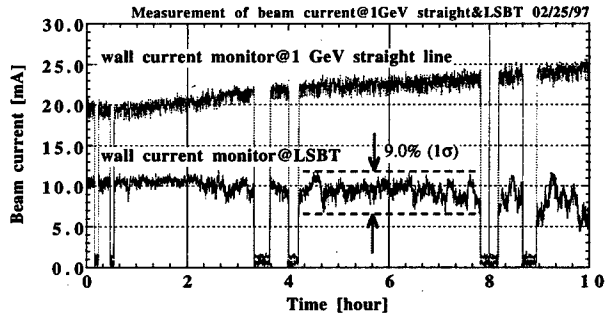

Figure 2: Drift of beam current at 1-GeV straight line and after 1-GeV bending magnet using a beam slit to permit energy spread of 1.0%.

2 MEASUREMENT AND ANALYSIS

2.1 RF system

The schematic of the RF system for the linac is shown in Fig. 3. The RF system consists of a 7 MW booster klystron (MELCO PV2012) drive system, another high-power klystron drive system, and a 13-set 80 MW klystron (TOSHIBA E3712). Each klystron feeds into two 3-m long accelerating structures with the exception of the H0

*Email: asaka@spring8.or.jp

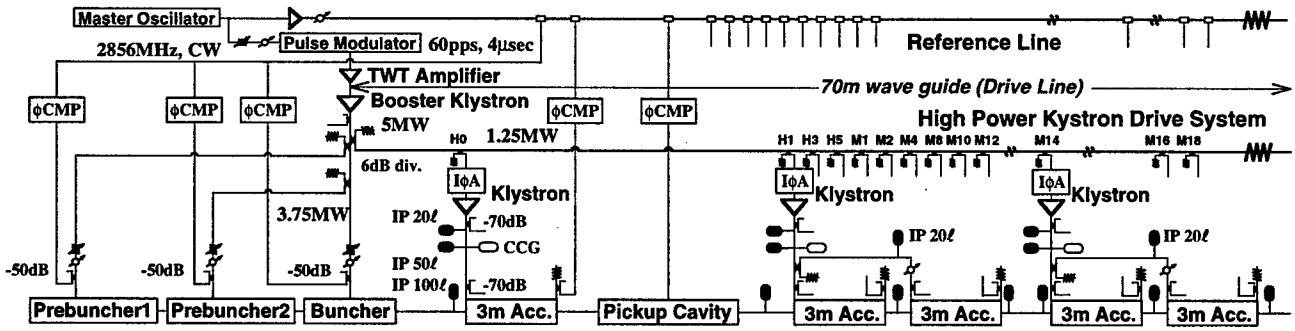

Figure 3: Schematic of RF composition.

klystron, which feeds into a 3-m long accelerating structure at the 60 MeV pre-injector. In addition, a reference line is provided for the phase measurement and feedback system [1].

The 2856 MHz CW output of a master oscillator is divided into two signal lines. One of these lines is modulated by a 1∼4 μsec pulse width and 60 Hz repetition rate by a PIN-diode pulse modulator, and the optimum input power of the booster klystron is fed by a 300 W TWT amplifier. Another line is provided for the reference line through a low-wattage CW amplifier. The output power of the booster klystron is fed into two 2856 MHz prebuncher cavities and a 2856 MHz standing wave 13-cell side couple-type buncher. The klystron drive system has a 70 m waveguide with directional couplers and feeds into the power attenuator/phase shifter (IϕA) placed at each 80 MW klystron. The 13-set klystron is operated in the region from 40 MW to 60 MW in normal operation.

2.2 *Measurement system*

The RF power and phase were measured by using a calibrated crystal detector and a double balanced mixer, respectively. In particular, it was necessary to guarantee the phase stability of the reference line (design value was 0.25 deg./°C at 70 m) with regard to the phase measurement. In order to confirm the high stability at the reference line, the phase was measured by a comparison between the input wave and the reflected wave from the termination of the reference line during one day. This measurement result was 0.8 deg./3.0°C, which was in agreement with the design value.

The following devices were chosen as the RF equipment for the measurement: the master oscillator, the TWT amplifier, the booster klystron, the drive line at the M14 klystron (about 60 m from the booster klystron) and the 80 MW klystron (M14 klystron). In this measurement, the RF pulse width was set at 2.2 μsec. The 2.2 μsec pulsed signal from the crystal detectors and the mixers were measured with oscilloscopes whose triggers were synchronized with the beam trigger. All of the oscilloscopes and the data-taking recorders used for temperature measurement were controlled by a sub-control computer (PC) through the GPIB. The data acquisition program was done for all of the oscilloscopes in the stop condition in order to obtain the simultaneity of each RF equipment state and the beam timing. The data acquisition was completed after compensation of the calibration value and attenuation level for the pulse signal from each piece of equipment. This series of measurements was operated routinely every 15 sec.

2.3 *Measurement and analysis*

This RF measurement was carried out during the period of one month. The power stability of the master oscillator and the TWT amplifier was less than 0.5%, equal to the accuracy of the measurement, and the phase stability was less than 0.2 deg., equal to the accuracy of the measurement. The long term drift was related to the room temperature, which was controlled so as to take priority of the humidity at the klystron gallery. The phase drift of the high-power klystron drive system, which depends on the environmental temperature, was 10.0 deg./4.0°C through one day as shown in Fig. 4.

The high-power RF components including klystron cavities and waveguide had been temperature conditioned within 3.0°C by the cooling water except for the accelerating structure, which was controlled by cooling water regulated within 0.1°C. The power stability for the booster klystron was retained under 0.5%. However, the phase drift that depends on the cooling water temperature was 1.2 deg./3.0°C with a period of 25 minutes. Furthermore, the power and phase drift of the 80MW klystron (M14), which depends on the cooling water temperature, were less than 1.0 MW/3.0°C under 50 MW operation and 2.4 deg./3.0°C with a period of 25 minutes as shown in Fig. 5.

The power and phase drift of klystron were not only affected by the cooling water temperature, which had a period of 25 minutes, but also by an random variation was caused by fluctuation of the PFN voltage at the 80 MW klystron pulse modulator. Although the PFN voltage of all of the pulse modulators had to be regulated with the stability of $\pm$0.5% by the de-Qing system, the PFN voltage fluctuation of the M14 pulse modulator was $\pm$1.0% due to the inadequate adjustment of the de-Qing efficiency. The PFN voltage stability of all the pulse modulators in continuous operation of 12 hours is given in Table 1.

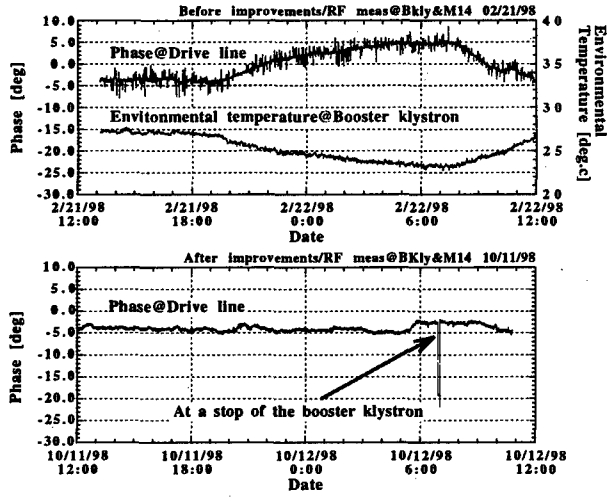

Figure 4: Phase drift for the drive line at M14 IϕA

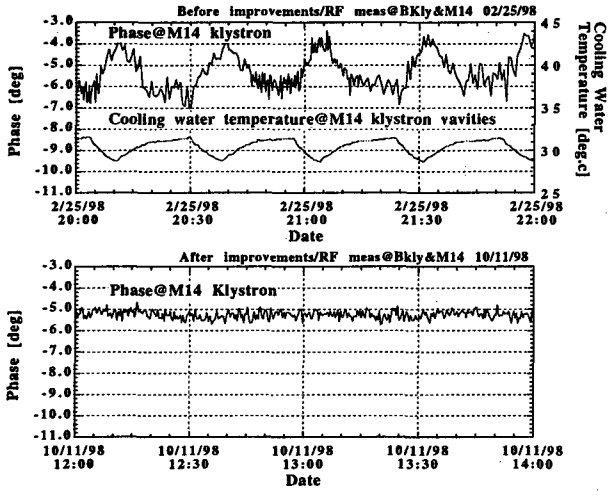

Figure 5: Phase drift for the 80 MW klystron (M14)

2.4 *Results after improvements*

In order to reduce the long term phase drift of the high-power klystron drive system, its 70 m waveguide was covered with a heat insulator. In addition, the priority of humidity control was replaced by the priority of room temperature control in the klystron gallery. After these improvements, the phase drift of the high-power klystron drive system was achieved at levels smaller than 3.0 deg. through one day as shown in Fig. 4. In the cooling water control for klystron cavities, the fan control of the coolant tower had been improved to continuous rotation by using an inverter control from a switching system like an on/off control. After this improvement, the phase stability of the klystrons were reduced to within 0.5 deg. as shown in Fig. 5. Readjustment was made to the specified de-Qing efficiency value of 7.0%, so that the PFN voltage stability achieved 0.2% (1σ) for each klystron as shown in Table 1.

The reproduction and stability of the beam status after the above improvements realized a beam current of 0.7% (1σ) and a center energy of 0.1% (1σ) at the LSBT that was equipped a wall current monitor and a beam position monitor. Figure 6 shows the log data of the beam current and center energy at the LSBT.

Table 1: PFN voltage stability of the pulse modulators (measurement time: 12 hours)

	Klystron Voltage (mean)[kV]	Dispersion (1σ)[%] Before adjustment	Dispersion (1σ)[%] After adjustment
Booster	137.3	0.3	0.16
H0	310.4	1.1	0.25
H1	337.3	0.6	0.21
H3	334.1	0.8	0.22
H5	353.5	0.3	0.22
M2	-	-	-
M4	338.2	0.4	0.20
M6	351.8	0.4	0.21
M8	350.3	0.4	0.20
M10	-	-	-
M12	337.4	0.6	0.22
M14	325.6	1.0	0.22
M16	-	-	-
M18	364.1	0.6	0.19

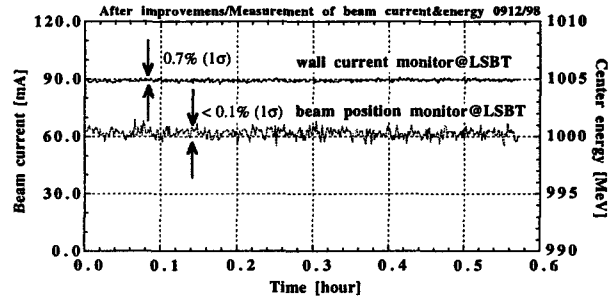

Figure 6: Log data of beam current and center energy

3 CONCLUSION

In order to realize of the high-stability beam injection into the storage ring, we investigated the cause of the drift of the output power and phase for many type of RF equipment. After making improvements in the utility based on the measurement results of these types of RF equipment, the stability of beam current in LSBT could be maintained within 0.7% (1σ) without using a energy feedback system.

4 ACKNOWLEDGEMENTS

The authors wish to thank M. Adachi and T. Ohnishi of SPring-8 service corporation for beam operation, the data recording, and their cooperation and support.

5 REFERENCES

[1] S. Suzuki et al., "Construction of Spring-8 Linac", Proc. of the 4th European Accelerator Conference, London, July 1994

A 100 MEV INJECTOR LINAC FOR THE SWISS LIGHT SOURCE SUPPLIED BY INDUSTRY

M. Peiniger, C. Piel, H. Vogel, P. vom Stein, ACCEL Instruments, Bergisch Gladbach, Germany

Abstract

A 100 MeV 'turn-key' injector electron linac for the Swiss Light Source (SLS) is under construction at ACCEL Instruments. The system will be installed, commissioned and handed over to the SLS in late 1999, after a 18 month design and production period.
This paper will present the special needs of an injector for a third generation synchrotron light source and the two specific modes of operation for this linac. The specification of the system and a description of the design results as well as the planned technical realisation will be given.

1 REQUIREMENTS FOR THE SLS INJECTOR SYSTEM

A third generation synchrotron light source is equipped with several types of insertion devices such as wigglers, undulators and wavelength shifters.
These devices can be driven in several operation modes. To drive a Free Electron Laser for example a single bunch mode operation is required. This results in single and multi bunch operation modes, to fulfil the different needs of the users.

1.1 General specification

The SLS accelerating system will consist of a 100 MeV Linac and a full energy booster. The general parameters [1] of the linac are listed in the following table 1:

Table 1: General Specifications

RF frequency	2.997921 GHz
Max. repetition rate	10 Hz
Energy	100 MeV

1.2 Pulse modes

Two modes of operation are foreseen. One single bunch mode[1] and one variable multi bunch mode. The multi bunch mode will cover the range on 50-500 bunches. To reduce the effect of beam loading the multi bunch mode will carry the same charge as the single bunch mode. The basic parameters of both modes are given in table 2.
In addition the SLS layout foresees a top up injection mode, this mode will deliver a low current to the storage ring, to keep the mean current in the storage ring nearly constant.

Table 2: Operation Modes

	Short Pulse	**Long Pulse**
Pulse length	1 ns	100-1000 ns
Pulse charge	1.5 nC	1.5 nC
Emittance	50 π mm mrad	50 π mm mrad
Energy	100 MeV	100 MeV
ΔE/E	0.5 %	0.5 %

2 LAYOUT OF THE SYSTEM

The main components of the injector system are based on components which were developed for the S-Band Test Facility (SBTF) at DESY 2. Adopting these components for the special needs of the SLS project took place during the design phase.

To fulfil the requirements the system consists of three functional sections:

- The electron source
- The bunching section
- The accelerating structures

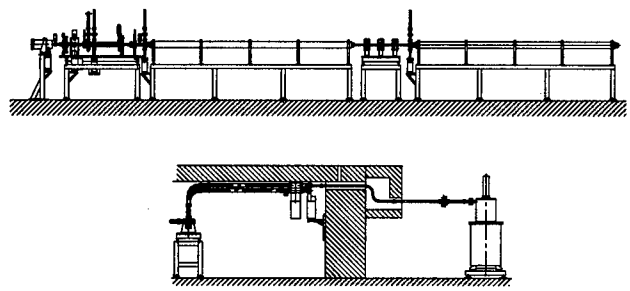

Figure 1: General Layout

2.1 The electron source

The electrons will be provided by a 90 kV DC conventional electron source as shown in Figure 2. The electron emitter is a standard EIMAC cathode YU-171.

The pulser for the electron source comprises two systems, one for the single bunch and one for the multi bunch mode. In the single bunch mode a 1 ns pulse carrying 3 nC will be sufficient to guarantee 1.5 nC at the end of the Linac. The multi bunch mode will be modulated by the 499.652 MHz main ring rf, to insure a high bunch purity.

[1] In this context the bucket length of the ring rf system defines the bunch length of 2 ns

0-7803-5573-3/99/$10.00@1999 IEEE.

The top up injection mode requires, that even the gun is capable of producing a low charge pulse. For that reason the pulse current can be varied by a factor of forty.

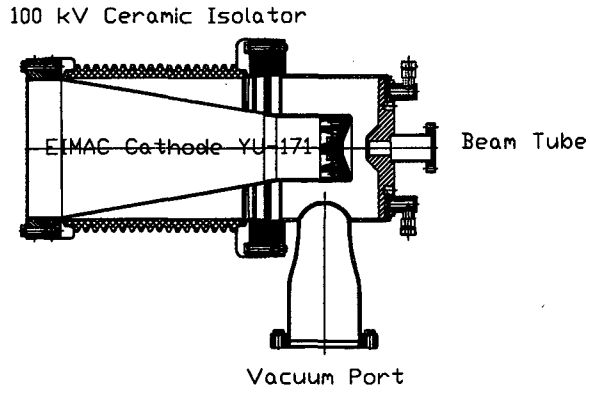

Figure 2: 90 kV Electron Source

The basic parameters of the cathode are listed in the following table:

Cathode YU-171		
Flange	CF	2 ¾
Cathode surface	cm^2	1.0
Emission	A	3
Cathode Radius	mm	5,6
Cathode Typ		Dispenser

2.2 *The bunching section*

The bunching section, as shown below, will consist of a 500 MHz subharmonic prebuncher as shown in Figure 4, a 4 cell travelling wave buncher as sketched in Figure 5 and a 16 cell travelling wave buncher as shown in Figure 6. At the exit of the bunching section the beam will have an Energy of 3 MeV.

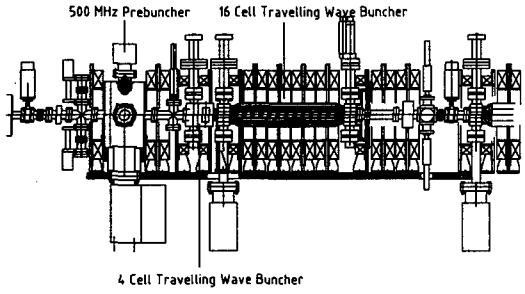

Figure 3: Bunching Section

To compensate space charge effects and rf defocusing the beam is focused by a solenoid magnetic field of up to 0.2 Tesla. This field will be produced by a set of more the 30 pancake coils, which guide the beam until it reaches an energy of 10 MeV.

2.2.1 *The 500 MHz subharmonic Prebuncher*

The subharmonic prebuncher cavity is a standard nose-cone cavity. The needed rf power will be fed into the system by a coaxial line.

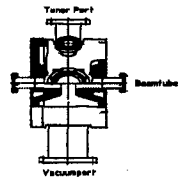

Figure 4: Layout of the 500 MHz Prebuncher

The basic parameters of the buncher are given in the table below:

Table 3: Parameters of the Subharmonic Prebuncher

Frequency	MHz	*500*
Shuntimpedanz	MW/m	37
Q		28000
Amplitude Uo	[kV]	30

2.2.2 *Travelling Wave Buncher System*

Two travelling wave bunchers will be used to insure a sufficient bunching in order to reach a high transmission rate with low energy spread.

The first 2 $\pi/3$ mode buncher consist out of four cells as shown in Figure 5. The layout had been done for β=0.6.

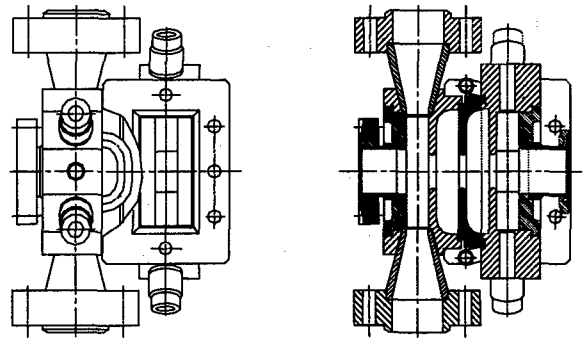

Figure 5: 4 Cell 2 $\pi/3$ mode Buncher

The second buncher, as shown in Figure 6, is optimised for β=0.95, consists of 16 cells and will be operated in the $8\pi/9$ mode.

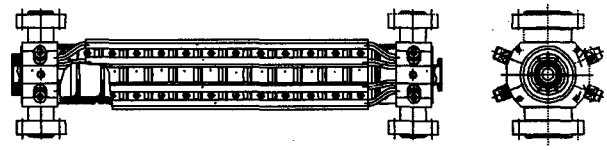

Figure 6: 16 Cell 8 $\pi/9$ Mode Buncher

2.3 Travelling Wave Accelerating Structure

The accelerating structures are of DESY Linac II type.

Table 4: Parameters of the Linac II Structures

length	m	5.2
attenuation	Neper	0.5
group velocity	% of c	3.3-1.2
filling time	ns	750
shunt imped.	MΩ/m	52-62
number of cells		156

3 DESIGN RESULTS

To insure the performance of the system ACCEL carried out simulation calculations for the main components as electron source and bunching system.

The bunching section was optimised for the two different modes mentioned above.

The subharmonic prebuncher will focus more than 80% of the particles into one 3 GHz bucket, for this a gap voltage of 30 kV is needed.
When the beam enters the second travelling wave buncher more than 50% of the particles will populate 20° of the central 3 GHz bucket. The average energy is about 400 keV.

Before entering the first accelerating structure 80% of the particles will be found in 20° of the central bucket at an energy of about 3 MeV.

After passing two accelerating structures of the Linac II DESY type, which will be powered by moderate 18 MW, the beam will have reached 100 MeV. An overall transmission of 96% is designed. The bunching efficiency insures that more then 85% of those particles are within the energy spread acceptance of the booster which will be +/- 1.5%.

4 CONCLUSION

This paper summarises the beam requirements of the injector linac for the 3rd generation light source SLS. It is shown that a Linac with proven and reliable technology can fulfil these needs. The linac components and the design results are presented, showing that the requirements can be reached.

5 ACKNOWLEDGEMENTS

ACCEL Instruments want to use this opportunity to thank DESY for their co-operation in all parts of this project. The DESY experts always helped us with their expertise and discussions.

Beside DESY we also want to thank the SLS staff at PSI for their open and co-operative acting.

6 REFERENCES

[1] Specification for the ELECTRON PRE-INJECTOR LINAC for the SWISS LIGHT SOURCE, SLS SPEC03/RL02
[2] R. Brinkmann, Conceptual Design of a 500 GeV e⁺e⁻ Linear Collider, DESY 1997-048

IMPROVED ETA-II ACCELERATOR PERFORMANCE

J. T. Weir, J. K. Boyd, Y-J Chen, J. C. Clark, D. L. Lager
and A. C. Paul, LLNL*

Abstract

Improvements have been made in the performance of the ETA-II accelerator that allow a nominal 2 kA, 6 MeV beam to be focused to a spot size less that 1 mm in diameter. The improvements include reducing the energy sweep to less than +/- 0.5 % over 40 ns of the pulse using a real time energy diagnostic and improving the magnetic tune of the accelerator to reduce the emittance to 8 cm-mrad. Finally, an automated tuning system (MAESTRO) was run to minimize the time dependent centroid motion (corkscrew) by adjusting the steering dipoles over the focusing solenoids. The corkscrew motion was reduced to less than +/- 0.5 mm at the output of the accelerator.

1 INTRODUCTION

The Lawrence Livermore National Laboratory (LLNL) has begun using the Experimental Test Accelerator (ETA II) to study beam/target interactions at the x-ray converter target for multiple shot, flash radiography experiments. The issues being studied involve the interaction of the electron beam with the plasma that forms on the initial shot and how the plasma affects the focusing and therefore spot size of subsequent shots. Typical multipulse x-ray experiments will use pulse spacings of 200 to 700 nanoseconds. ETA II cannot run at a repetition rate high enough to simulate multiple shots on target so we have used a laser to produce a plasma to simulate the first "shot" and the ETA II electron beam as the next shot in the sequence. To correctly simulate the effects that will occur in DARHT 2 or the proposed Advance Hydrotest Facility (AHF) we needed to achieve a beam spot density 25.5 kA/cm^2. This corresponds to focusing the 2 kA beam into a spot size of less than 1 mm. FWHM. This tight focus was only possible after improvements were made to emittance, energy uniformity, centroid motion of the beam, and shot to shot repeatability.

2 EMITTANCE

Using standard pepper pot techniques the emittance of the ETA II accelerator was measured at 12 cm-mrad when it was first decommissioned. This is real emittance measured in rr' space (un-normalized with no factor of π). Earlier measurements of the cathode brightness suggested the transport of the beam was leading to increased emittance. Modeling the injector and the first 10 cell block of the accelerator with the DPC and ST codes showed that in order to transport the low energy leading and trailing edges of the current pulse we were running the first anode magnet too low. This allowed us to catch the low energy part of the pulse without over focusing but required a mismatched condition on the higher energy center portion of the beam. By relaxing the constraint of maintaining all current through the first cell block, we were able to adjust the magnetic profile to give a smoother match to high energy portion of the beam. Using the improved injector matching and by hand tweaking the rest of the accelerator around the theoretical B_z profile we were able to reduce the emittance to 8 cm. mrad. at the end of the accelerator. Because the final beam spot size is dependent on emittance, this 30% reduction in emittance reduced our spot size by 20%.

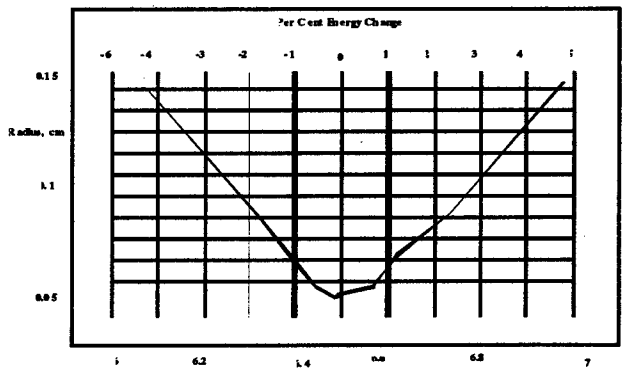

Figure: 1 Energy MeV

3 ENERGY UNIFORMITY

Beam spot size is a strong function of the beam energy. Figure 1 shows the spot size variation as a function of the energy for the final focusing magnet used in our target experiments. ETA II was designed to give an energy flattop of about 40 ns.. Adjustments to the energy uniformity are made by adjusting the timing between the four MAG D1 units that power that injector and the accelerator gaps. Moving the timing of the accelerator pulse power with respect to the injector will change the beam loading and skew the energy flatness. Because the 70 ns. beam pulse needs to fit closely under the 70 ns. accelerating pulse these timing shifts are done in 0.25 ns. steps. Since there are a large number of ways to time the accelerator MAG D1 units with respect to the injector, we wrote a program that displays the reduced data from the energy analyzer system on a real time display in the control room. The data is displayed as a percent diviation from the nominal beam energy. By observing the changes in a real time mode and adjusting the timing of the pulse power units we were able to reduce the energy variation across the flattop portion of the pulse to better than +/- 0.5 %. Figure 2 shows the energy varriation across the center 40 ns. of our beam pulse.

0-7803-5573-3/99/$10.00@1999 IEEE.

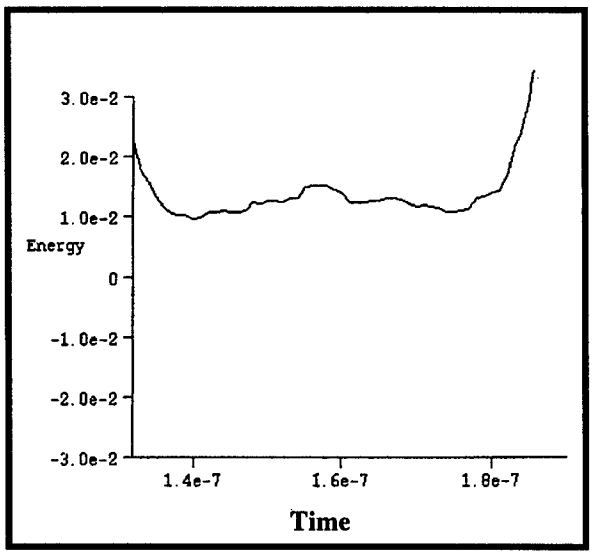

Figure: 2 Energy Variation

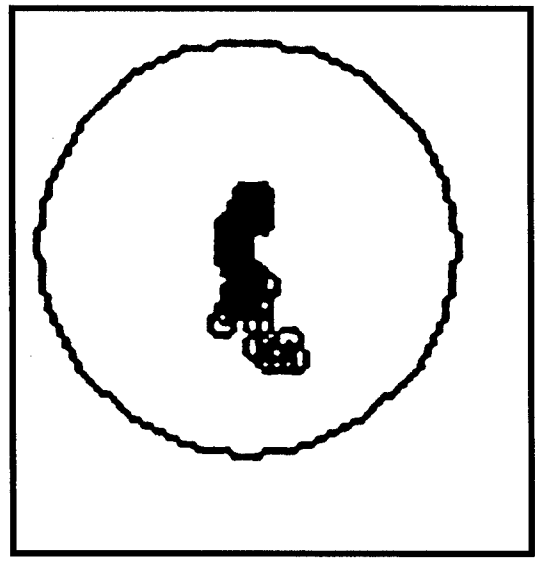

Figure : 3 Centroid Motion Inside a 1mm Radius Circle

4 BEAM CEMTROID MOTION

Beam centroid motion (corkscrew) will also cause an effective growth in the final beam spot size. Corkscrew is caused by a combination of energy variations in the beam and traversing the focusing magnets off the center axis. Minimizing the corkscrew is accomplished by tuning the steering magnets that are wrapped around each of the solenoid magnets in the accelerator. We have developed an automated tuning system, MAESTRO, that can tune the entire accelerator steering system in about one hour. Modeling of our tuning system showed an error in our basic approach to adjusting the steering coils. There are twenty steering coils on each ten cell block (an x and a y coil for each solenoid) but only one pair of resistive wall monitors (beam bugs) after each ten cell block. In our old mode of operation, we would tune each pair of steering coils and work our way through the cell block trying to maintain the beam on center at the end of the cell block. Simulations showed it was very easy to get the beam oscillating through the cell block with larger and larger steering corrections needed to bring the beam back to center. By using only the steering at the first cell to bring the beam through on center and the steering at the last cell to remove the angle we were able to avoid large excursions through the cell block. It can be shown analytically that this is all the steering that is necessary to reduce the corkscrew to a minimum. Figure 3 shows the data from our beam bug at the end of the accelerator. The data is taken from a single shot and is the radial excursion of the beam centroid. The forty data points inside the 1 mm. radius circle are the beam centroid position at 1 ns. intervals through the 40 ns. of beam flattop.

5 SHOT TO SHOT REPEATABILITY

Historically, ETA II was designed to run in a burst mode at 5 KHz. This required large capacitor banks to store the energy and complex charging and switching circuitry to run the MAG 1D units at this repetition rate. We have removed the capacitor banks and the charging and switching circuitry and replaced them with off the shelf, well regulated power supplies. This has eliminated the largest source of shot to shot jitter on the accelerator. In our new configuration we have reduced the timing jitter on the pulse power units to below +/- 0.25 ns. This is below the incremental step size of the timing adjustment and gives the accelerator excellent shot to shot repeatability.

6 CONCLUSIONS

By improving the emittance, energy uniformity, corkscrew motion, and the shot to shot repeatability on ETA II, we have been able to focus a 2 Ka electron beam into a spot with a diameter of less that 1 mm.

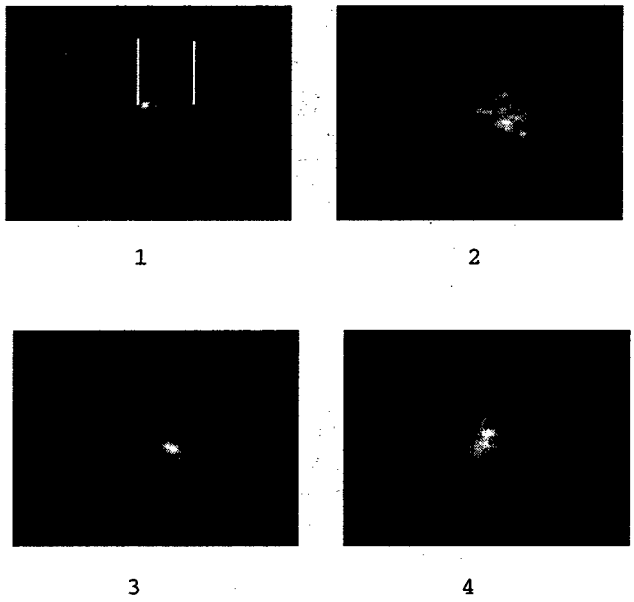

Figure: 4 Time Resolved X-Ray Images, 10 ns. Spacing

Figure 4 shows a time resolved xray image of the beam hitting a 0.005 inch thick Ta. Target. With energy desities produced by such beams we will be able to continue studying beam/target interactions for multipulse radiography.

*This work was performed under the auspices of the U.S. Department of Energy by the Lawrence Livermore National Laboratory underContract No.W-7405-Eng-48.

#Email:weir2@llnl.gov

TEST OF THE REX-RFQ AND STATUS OF THE FRONT PART OF THE REX-ISOLDE LINAC*

H. Bongers, S. Emhofer, D. Habs, O. Kester, K. Rudolph, T. Sieber,
LMU München, Garching, Germany
A. Schempp, C. Welsch, K. U. Kühnel, J.W.Goethe Universität, Frankfurt/Main, Germany

Abstract

For REX-ISOLDE (Radioactive beam EXperiments at ISOLDE / CERN) [1], a test beamline is built up at the Garching Accelerator Lab to perform He^{1+}-experiments with the RFQ [2], the matching (rebunching) section between RFQ and IH-DT-linac, the IH-structure [3] and several electrostatic lenses of the REX-ISOLDE-mass separator [4].
In a first step, the beamline is conceived for tests with the RFQ. This paper presents the parameters and the status of the REX-RFQ, the experimental setup and the particle dynamics simulations with the COSY infinity code for beam injection and beam analysis. Furthermore it shows the design and status of the mass separator, the IH-structure and the buncher section.

1 TEST OF THE REX-RFQ

The REX-ISOLDE Linac consists basically of a 4-Rod-RFQ and an Interdigital-H Drift-Tube-accelerator, followed by three seven-gap resonators for energy variation from 0.8 MeV/u to 2.2 MeV/u [5].

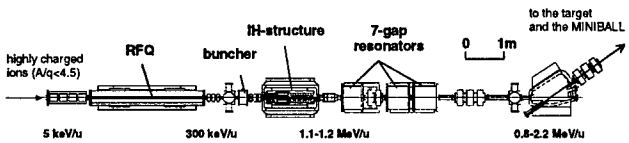

Fig. 1: The REX-ISOLDE Linac

1.1. The RFQ

The REX-RFQ will accelerate the radioactive ions with an A/q 3 - 4.5 from 5 keV/u to 300 keV/u. The according electrode-voltage is 28 - 42 kV, which will require an rf-power of 30 to 40 kW. The accelerator is similar to the GSI HLI-RFQ and to the Heidelberg High current injector RFQ. It has a total length of 3 m (18 stems) and operates at a resonant frequency of 101.28 MHz (duty-cycle: 10%). Low-level measurements of the rf-parameters were in good agreement with the design values. The measurements showed: f=101.18 MHz, Q=3900 and Rp=170 kΩm. The frequency can be shifted with two mounted piston tuners in the range ±200 kHz.

The flatness was tuned from ±20% to ±1%. The distribution of the built in tuning plates has been calculated with the code MAFIA. Fig. 2a shows the voltage distribution of a MAFIA-model with the tuning plate heigths from experimental data and unmodulated electrodes together with the measured voltage distribution of the REX-RFQ *without* tuning plates. The diagram illustrates the compensation of the variable capacitive load (changes in modulation and aperture) in each RFQ-cell by an appropriate variation of its inductance (different heigth of the tuning plates). Figure 2b shows the tuned flatness measured with three different pertubation capacitors. The bars on the bottom of the diagram indicate the heigth of the Tuning-plates.

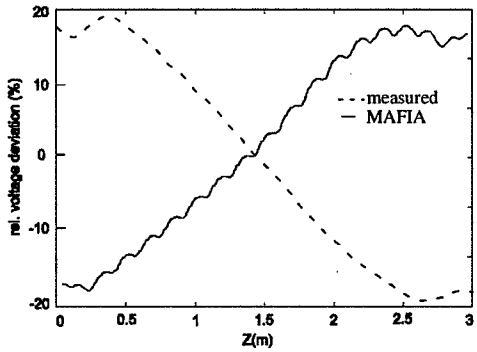

Figure 2a: MAFIA calculated and measured voltage distributions.

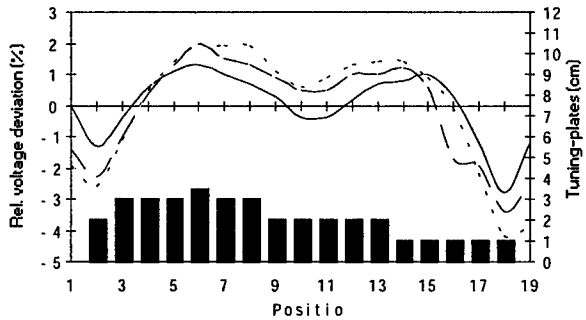

Figure 2b: Tuned voltage distribution of the REX-RFQ measured with 1.2pF (dotted line), 2.2pF (dashed line) and 3.3pF (solid line).

After assembly of the resonator, vacuum- and low-level rf-tests, the RFQ-electrodes are currently aligned with an accuracy of 1/10 mm.

0-7803-5573-3/99/$10.00@1999 IEEE.

1.2. The RFQ-Test Beamline

The test beamline for the RFQ consists of a duoplasmatron ion source, an electrostatic quadrupole quadruplet and a diagnostic box on the injection side, and an electrostatic triplet together with a 90° bending magnet for beam analysis on the high energy side.

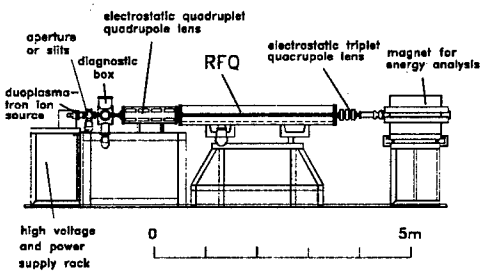

Fig. 3: RFQ test beamline.

The ion source is in operation at the source test stand of the Garching Tandem Lab. It produces a 1 mA, 20 keV He^{1+}-beam with emittances of typically 30-50 π mm mrad. Due to the 0-current design of the REX-ISOLDE accelerators, the current during the tests will be reduced to 1-10 µA. The diagnostic box in the injection system has a Faraday cup and an aperture wheel for measurements of the beam at Munich and the pilot beam at REX-ISOLDE, as well as a low intensity device, which consists of a carbon foil with a secondary electron detection system (phosphor monitor and MSP). The upper beam current limit for this device is a pA. The detection limit is 1 ion/second. The spatial resolution for single particle detection is 0.5 mm.

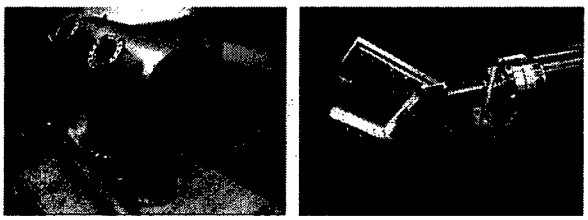

Fig. 4: Emittance measurement device designed by NTG.

The beam quality behind the source, the injection system and behind the RFQ is measured with a slit grid emittance measurement device. It is a new design of the NTG company (Gelnhausen/Germany), which moves in an angle of 45° through the vertical and horizontal plane. The advantage is a measurement of both phase planes at one z-position. The resolution of this device as well as its application for different particle-energies is modified via the length of the beam tube, which connects the chambers for slit and grid. At the beam with the RFQ the angular resolution will be 0.75 (0.2) mrad for an energy of 5keV/u (300 keV/u) the spatial resolution is 0.2 mm.
Beam injection and high energy beam transport have been calculated with the COSY infinity code. In the Figures 5a and 5b the calculated (PARMTEQ) RFQ-acceptances and output emittances are plotted together with the calculated beam envelopes. The calculations show an acceptable matching of the beam with voltages of maximal ±4 kV in the quadrupole quadruplet (maximum voltage: ±6kV).

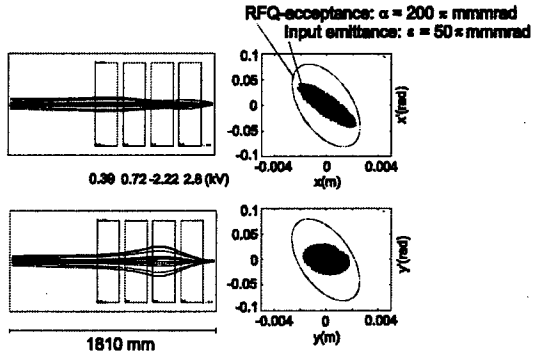

Fig. 5a: Beam injection into the RFQ

The beam transport behind the RFQ can be achieved with voltages of ~±30 kV in the quadrupole triplet (max. voltage: ±50 kV). The required field strength in the 90° bending magnet is 0.9 T (max. field: 1.2 T).

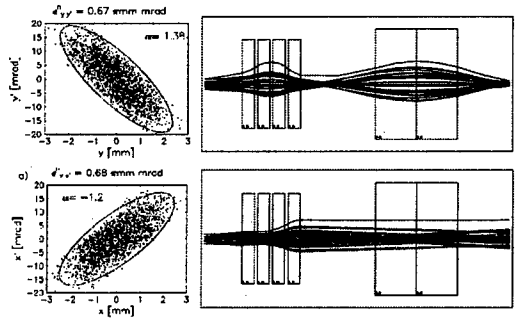

Fig. 5b: Beam transport calculated with COSY.

First beam tests will be done after the electrode alignment and the rf-conditioning of the RFQ. In the next stage, the analyzing magnet will be removed and replaced by the rebunching section and the IH-structure. Fig. 6 shows a Photo of the current setup at Garching.

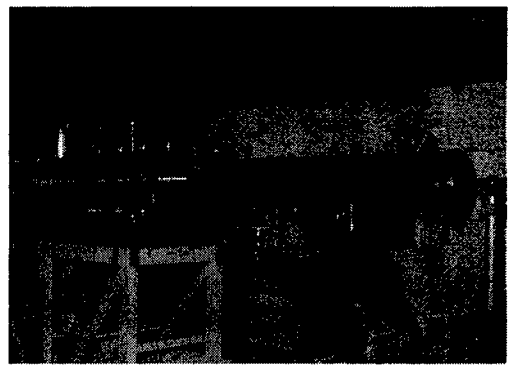

Fig. 6: Injection system (left) and RFQ.

2 STATUS OF THE FRONT PART OF THE REX-ISOLDE LINAC

2.1. The mass separator

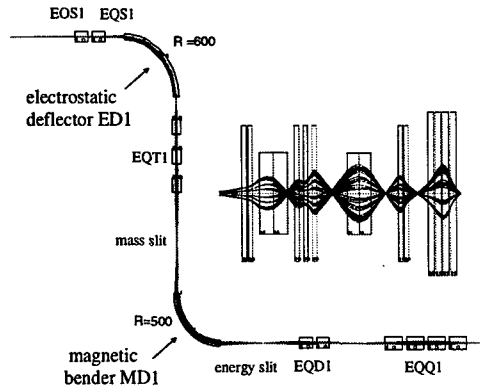

Fig. 7: Beam dynamics simulations for an achromatic system, the final design for the REX-mass separator.

The beam from the EBIS has to be mass separated to reject the ionized buffer gas atoms from the Penning- trap. The REX-ISOLDE mass separator is based on the principle of the Nier-spectrometer. The design shown in Fig. 7 was chosen in the expectation of EBIS emittances of 10 π mm mrad and an energy spread of 0.25%. It has a resolution of 150, which is sufficient to separate most of the radioactive ions from the buffer gas ions (f. ex. not ^{40}Ar from ^{40}Ka).
Currently, the electrostatic octupoles and quadrupoles as well as the electrostatic deflector are in production at our mechanical workshop, while the magnet is manufactured by Sigma Phi (Vannes/France)

2.2. The matching section

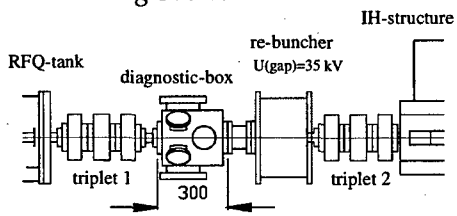

Figure 8: Matching section for the IH-structure.

The Buncher for the matching section is a 3-gap splitring resonator with a gap voltage of 35 kV (A/q=4.5). It was built at the IAP/Frankfurt. The structure is completely assembled and will be delivered to Munich after the rf-power tests. The magnetic lenses are ordered at DANFYSIK (Jyllingen/Denmark) and will be delivered in May. The whole Linac has been calculated with the codes TRANSPORT and COSY for different EBIS emittances. The calculations show required field gradients of the magnetic quadrupoles in the matching section up to 60 T/m.

2.2. The IH-structure

The REX-IH structure is like the CERN lead injector and the GSI HLI IH-Linac a 0-phase synchronous particle structure excited in the H_{110}-Mode. It has a length of 1.5 m and a diameter of 0.6 m. The overall accelerating voltage is 4.2 MV (20 gaps) for ions with A/q=4.5 at a required rf-power of 60 kW.
The end energy can be varied from 1.1 MeV/u to 1.2 MeV/u, whereby this variation is achieved with capacitive plungers, which modify the voltage distribution in the gaps. Fig. 9 shows photos of the IH-structure during manufacturing at NTG. It also shows the measured, MAFIA-calculated and design-voltage distributions of a 1:2 model for two different end energies together with the corresponding positions of the capacitive plungers.

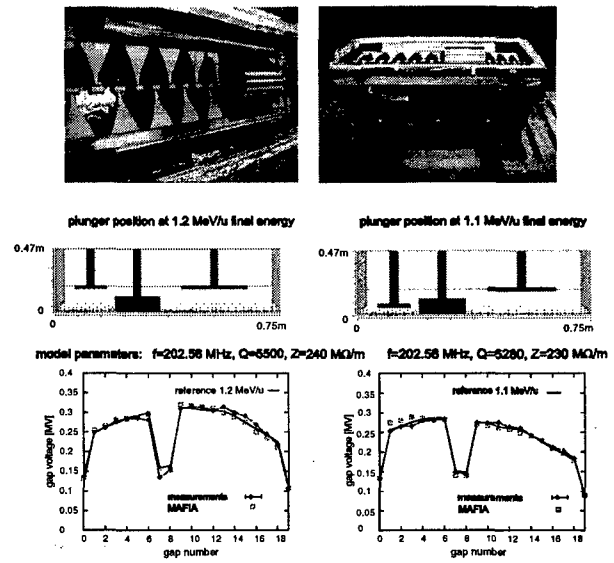

Fig. 9: Drifttube structure and tank of the REX-IH-accelerator (above). Calculated and measured voltage distributions in a 1:2 model.

The IH structure is presently copper plated at GSI and will be integrated in the test beamline after power tests at Munich. The status of the 7-gap resonators is presented at this conference.

3 REFERENCES

[1] D. Habs et al., "The REX-ISOLDE Project", NIM B 139 (1998) 128
[2] T. Sieber et al., „Design and status of the REX-ISOLDE RFQ", Proc. LINAC '98, Aug. 1998 Chicago
[3] O. Kester et al., "The Status of the REX-ISOLDE project", Proc. of the CAARI '98, Denton, Nov. 1998.
[4] R. Rao et al., NIM A 427 (1999) 170.
[5] R. von Hahn., this conference

* work supported by the BMBF under contract 06 LM 868 I/TP:4

BEAM TESTS OF THE VE-RFQ CYCLOTRON INJECTOR*

F. Höllering, O. Engels, A. Schempp, Institut fuer Angewandte Physik,
Johann Wolfgang Goethe-Universität, Frankfurt am Main, Germany
J. Häuser, NTG, Neue Technologien, Gelnhausen-Hailer, Germany
H. Hohmeyer, W. Pelzer, A. Denker, Hahn-Meitner-Institut, Germany

Abstract

The new VE-RFQ-injector for the cyclotron at HMI in Berlin is now being comissioned, The ECR-source together with the RFQs [1, 2] supply heavy ion beams with 90 - 360 keV/u for q/A > 0.15 matched to the isochronous cyclotron. Properties of the new injector and results of first beam tests will be presented.

1 INTRODUCTION

The Ionen-Strahl-Labor (ISL) [3], the former VICKSI-facility, at the Hahn-Meitner-Institut in Berlin has replaced the former Tandem-injector with a combination of an ECR-ion source together with a two stage 4-Rod-Variable Energy-RFQ. Next to the 6 MV Van de Graaff injector, which provides ions at lower intensities but higher final energies out of the cyclotron (32 MeV/n for q/A = 1/2), the ECR-RFQ combination provides beams of higher intensity and final energies between 1.5 and 6 MeV/n. This energy meets the demands of solid state physics. To our knowledge this is the first cyclotron which uses an RFQ as a direct injector. Figure 1 shows an overview of the beamline.

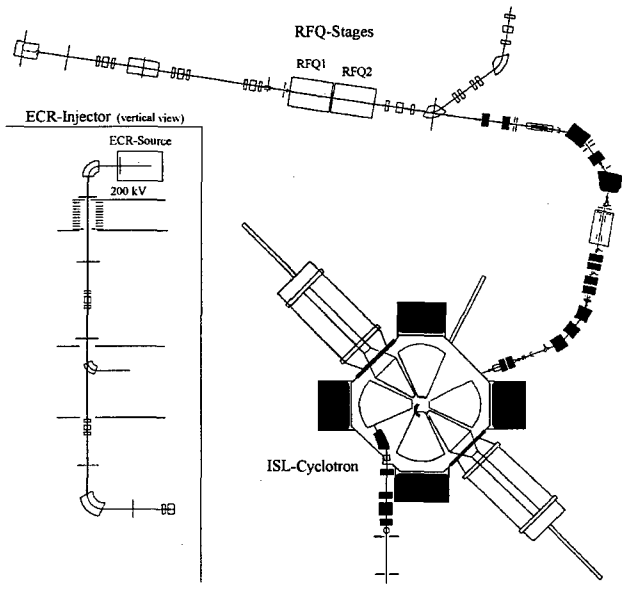

Figure 1: Scheme of the beamline

* Work supported by the BMBF

This VE-RFQ [4, 5] has three special features: First of all it is frequency variable through a moveable tuningplate, which shortens the effective length of the stems. Opposite to single frequency RFQ, where the output energy is fixed by frequency and electrode-shape, the frequency variation leads to a variable output energy proportional to $\sqrt{f}$. The RFQ at ISL covers a frequency-range from 85 to 120 MHz and works on the eighth harmonic of the cyclotron frequency.

Secondly the RFQ is splitted into two stages with the second stage designed to work either in accelerating- or transport-mode. This expands the energy variation of the RFQ from 90 keV/n to 360 keV/n. The concept of an RFQ working as a radial focusing transport channel has not been tested before with a bunched beam [6, 7, 8].

The third point is that this RFQ operates in cw-mode with a maximum power consumption of 20 kW per stage. Therefor the design has been optimized to provide proper cooling of the electrodes, stems and the tuningplate.

Table 1 gives a summary of the ISL-RFQ properties and Figure 2 shows the open RFQ.

Table 1: ISL-VE-RFQ parameters

Length (split into two stages)	3 m
diameter	0.5 m
number of stems per stage	10
minimum aperture	2 mm
min/max E_{in}	15.16/29.72 keV/n
min/max E_{out}	90.98/355.09 keV/n
charge-to-mass-ratio	1/8 - 1/2
frequency-range	85 - 120 MHz
duty factor	100% (cw)
max power consumption p. stage	20 kW

2 CONTROL SYSTEM

2.1 *Frequency-tuner*

Already the first simulations of the frequency-tuner revealed that its design would be difficult, as the simulations showed an eigenmode of tuner near 120 MHz, the highest

0-7803-5573-3/99/$10.00@1999 IEEE.

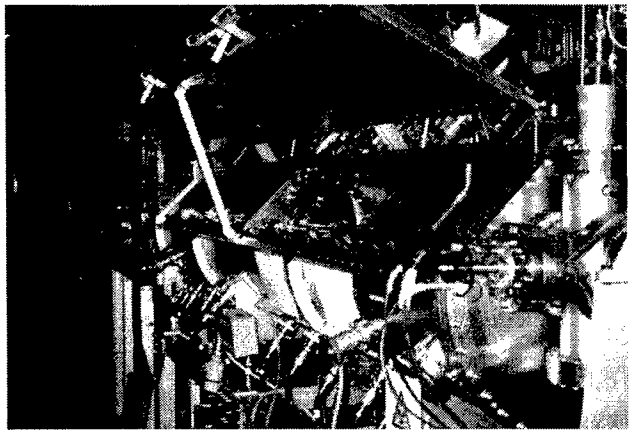

Figure 2: Picture of the open RFQ at HMI

operation frequency of the RFQ. First tests with our standard tuner (a rod with a cup) confirmed the simulations. To raise the eigenmode of the tuner its front part was changed to a small cylinder instead of the cup to decrease the capacitance against the electrodes. The rear part was changed into a large cylinder to decrease the inductivity. This design had the lowest eigenmode at about 135 MHz [9]. Figure 3 shows a picture of this design.

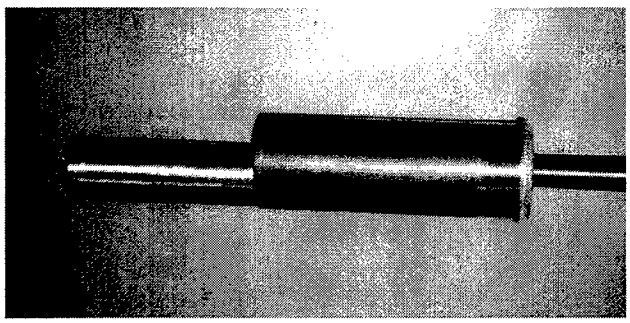

Figure 3: First tuner-redesign

High power tests at NTG in Gelnhausen and after the reinstalation of the RFQ at HMI showed that the frequency-variation of the tuner was not sufficent. Due to thermal expansion of the contacts between stems and tuning-plate during operation the resonance-frequency of the RFQ is shifted to higher frequencies. The range of the tuner was too small to compensate this effect and the normal detuning during operation, so the big tunig-plate had to be moved too to restart the RFQ.

The final shape of the tuner increased the frequency-variation by a factor 2.5 and has no eigenmodes lower than 125 MHz. Figure 4 shows a picture of the final tuner.

2.2 *Automatic Tuning*

To simplify the operation with the RFQs, a computer routine has been developed to perform a self tuning and adjusting sequence by the preset input-parameters rf-frequency and RFQ-electrode-voltage.

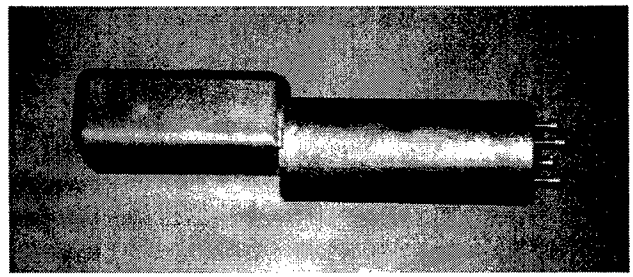

Figure 4: Final tuner-design

In a first step all moveable parts of the RFQ and the rf-power-amplifiers are set to frequency dependent values taken from data-tables. Then the computer performs an optimaziation of the amplifiers to ensure an output of at least 20 kW cw. After this the RFQ is set to the proper resonance-frequency, mainly by moving the tuner. After minimizing the reflected power the correct phase-relation for the resonance-control is set. In contrast to fixed frequency resonators this relation varies because of the changing wavelength and has to be precisely tuned for each frequency.

The second part of the program sets the RFQ to a given electrode voltage. Results from gamma-spectroscopy at a fixed power consumption and various frequencies together with a measured signal from an RFQ-probe provide the necessary information. By an assumed optimal quadratic relationship between power consumption and electrode-voltage resp. probe-signal all parameters are calculated from these measured values. If the calculated value for the probe-signal is reached, the control is given back to the ISL-operators who then can optimize the injector system settings.

3 BEAM MEASUREMENTS

During the last six months a set of beam measurements has been made. It showed that the RFQ successfully reached the design goals and provides the necessary output-energies. The beam has also been injected successfully into the cyclotron.

E.g. a $^{86}Kr^{14+}$ with 300 MeV has been succesfully extracted out of the cyclotron with 2.5 μA before the RFQ and 500 nA after the cyclotron [10].

Even more important is that the transport-mode of the second stage has also been tested succesfully with an $^{129}Xe^{14+}$ beam with 196 MeV and 1.35 μA before the RFQ and 100 nA after the cyclotron. The experiments showed also that a calculated transmission of 2/3 (without a chopper in front of the RFQ) can be reached. Figure 5 shows a result from beam measurments.

4 CONCLUSIONS

The RFQ succesfully reached its design-goals and the new injector for the ISL-cyclotron is now ready for operation.

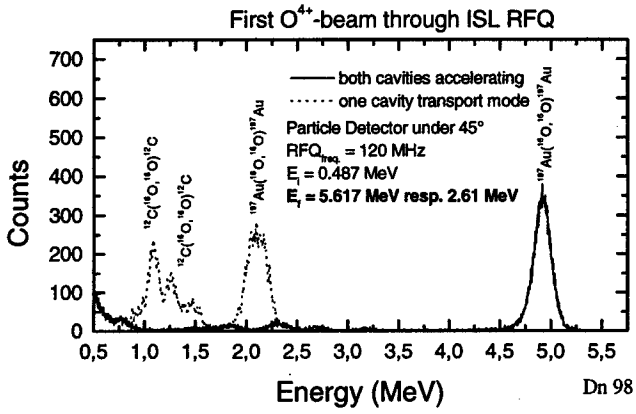

Figure 5: O^{4+}-beam spectroscopy

Training for the operators is scheduled for April. Further work has to be done to improve the contact-rings which connect the moveable tunigplate to the stems. It turned out that after some time of tuning and operation some contact-fingers were broken. This does not affect the operation of the RFQ but a more reliable design has to be found.

5 REFERENCES

[1] I. M. Kapchinsky and V. Teplyakov, Prib. Tekh. Eksp 119, No. 2 (1970) 17

[2] K. R. Crandall, R. H. Stokes, T. P. Wangler, Linac 79, BNL 51134 (1979) 205

[3] H. Hohmeyer, W. Pelzer, "Vorschlag zur Realisierung eines Ionenstrahllabors am HMI (ISL-Berlin)", HMI-Berlin (1992)

[4] A. Schempp, NIM B 40/41 (1989) 937

[5] A. Schempp, Habilitationsschrift, Universitaet Frankfurt am Main (1990)

[6] H. Dehnen, H. Deitinghoff, W. Barth, A. Schempp, "Transport of Ions in a RFQ Accelerator", EPAC 1992, Ed. Frontiers (1002), 967-969

[7] A. Schempp, O. Engels, F. Marhauser, H. Hohmeyer, W. Pelzer, IEEE PAC 1995, Dallas, TX, 914

[8] F. Marhauser, diploma thesis, IAP, Universitt Frankfurt am Main (1996)

[9] O. Engels, thesis, Frankfurt am Main (1998)

[10] W. Pelzer, Internal Report "Zeitablauf beim Aufbau des RFQ-Beschleunigers, IX", HMI-Berlin (1999)

TEST OF A RADIO-FREQUENCY QUADRUPOLE COLD MODEL

G. V. Lamanna#, INFN-Bari, A. Lombardi, A. Pisent, INFN-LNL

Abstract

In the framework of TRASCO Project (the Italian feasibility study for a waste transmutation linac) we have built and tested an aluminium model of a segmented resonantly coupled Radio-Frequency Quadrupole (RFQ), in order to determine the parameters of a 5 MeV and 30 mA proton beam RFQ. Bead perturbation measurements are performed, and the field stabilization respect to small perturbations of quadrupole fundamental mode is studied. A comparison between experimental results and a theoretical model is also reported.

1 INTRODUCTION

The possibility to design an RFQ long respect to the RF wavelength is very important for the feasibility of linacs with different applications, from the high power CW linacs for neutron production to the low power high frequency linacs proposed for hadrotherapy [1]. In particular INFN has been funded for the study of the critical parts of a waste transmutation linac (TRASCO project). In this framework the field stabilization of a 7 m long 352 MHz RFQ has been studied, using the LANL resonant coupling technique.

We looked for an approach able to give a physical insight of the system and fast results to be compared with MAFIA simulations and field measurements; the first results, achieved by an equivalent lumped circuit [2], have been improved by the implementation of a transmission line analysis [3]. Moreover an aluminium model has been built and we are now testing on it the RFQ tuning procedure.

In this paper we describe the aluminium model, we resume the main results of the transmission line analysis and we show the first results of the bead pull measurements.

1 THE MODEL

The aluminium model had to be at the same time similar to the actual Cu construction, flexible, easy to modify and with a reasonable cost. We required very good mechanical tolerances to allow an easy determination of quadrupole and dipole modes. Mechanical errors can be introduced on purpose so to verify RF field tolerances.

The body of each segment has a "sandwich" configuration, with four parts bolted and pined to 20 μm alignment tolerance. The end cells undercuts electrode dimensions were built with some extra material; during tests they were easily dismounted and machined (Fig.1).

Each segment is supported in three points so to permit fine mechanical alignment. Overall mechanical tolerance is about 50 μm. The first and the last segment can slide respect to the central one in order to disassemble the coupling cell and vary its configuration preserving the alignment.

The RFQ consists of three 1m long segments. Vanes are unmodulated with an average aperture radius of 5 mm. The resonant frequency of 352 MHz is provided by 36 tuners, i. e. 12 screws per segment having 20 mm diameter, with a penetration of 13 mm in nominal position. Eight antennas are available in each segment for powering and measuring.

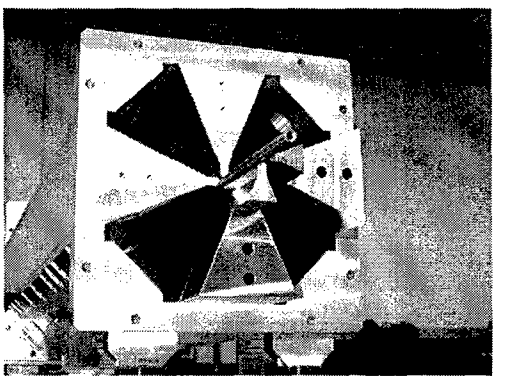

Figure 1 View of coupling cell electrodes

2 RFQ THEORETICAL MODEL

A four vanes RFQ is based on TE_{21} modes, and the vane voltage transformation after a segment of length λ is:

$$\begin{bmatrix} V \\ V' \end{bmatrix}_{\lambda} = \begin{bmatrix} \cos k\lambda & \frac{1}{k}\sin k\lambda \\ -k\sin k\lambda & \cos k\lambda \end{bmatrix} \begin{bmatrix} V \\ V' \end{bmatrix}_{0} = M_{rfq} \begin{bmatrix} V \\ V' \end{bmatrix}_{0}$$

with $k = \frac{2\pi\sqrt{x-1}}{\lambda}$, $x = \frac{\omega^2}{\omega_0^2}$ and $\omega_0 = \frac{2\pi c}{\lambda}$ cut-off frequency. Note that below cut-off frequency k is imaginary, but if we define the trigonometric functions in the complex field the matrix elements are real.

Email: giuseppe.lamanna@ba.infn.it

0-7803-5573-3/99/$10.00@1999 IEEE.

The coupling cell can be modeled by the capacitance C_a in the gap between each couple of electrode terminations, i.e. with the transformation:

$$\begin{bmatrix} V \\ V' \end{bmatrix}_+ = \begin{bmatrix} 1 & -\frac{\lambda\beta}{x} \\ 0 & 1 \end{bmatrix} \begin{bmatrix} V \\ V' \end{bmatrix}_\lambda = M_{gap} \begin{bmatrix} V \\ V' \end{bmatrix}_\lambda ,$$

with: $\beta = \frac{\lambda^2}{4\pi^2} \frac{C}{C_a \lambda}$ and C capacitance per unit length of the quadrupole vane tips per quadrant (approximately 30 pF/m). The Floquet analysis gives the dispersion relation:

$$\cos\alpha = f(x) = \frac{trM_{rfq}M_{gap}}{2} = \cos k\lambda + \frac{k\lambda\beta}{2x}\sin k\lambda$$

with α phase advance per period. For $\beta=0$ the RFQ segments are directly connected and only modes above cut-off frequency exist, while otherwise different bands are present, corresponding to $|f(x)| \le 1$. The fundamental mode $x=1$ of the resonator can be stabilized if around this mode we have the confluence of two bands with lower and higher frequencies; since $f(1)=1$, this happens when $f(x)$ has a maximum at that frequency, i.e. when $f'(1)=0$ or $\beta=1$.

The same dispersion relation can be calculated for TE_{11} modes, normalizing the frequency for the appropriate cut-off frequency ω_d and using the coupling parameter:

$$\beta_d = \beta \frac{1}{2}\left[\frac{\omega_0}{\omega_d}\right]^4 .$$

The results of this model are compared with results in literature in ref [3].

This simple model can be refined introducing the effect of the end cells and by considering the finite number N_{RFQ} of segments that compose our resonator.

Indeed the boundary condition $V'=0$ at the two extremes, that for a TM mode corresponds to a metallic boundary, for a TE mode is obtained by terminating the transmission line on a resonant load, called end-cell (EC), with admittance $1/i\omega L_{EC} + i\omega C_{EC}$. The associated linear transformation is:

$$\begin{bmatrix} V \\ V' \end{bmatrix}_0 = \begin{bmatrix} 1 & 0 \\ \xi(\kappa - x) & 1 \end{bmatrix} \begin{bmatrix} V \\ V' \end{bmatrix}_- = M_{EC} \begin{bmatrix} V \\ V' \end{bmatrix}_-$$

with the parameters: $\xi = \frac{4\pi^2}{\lambda^2} \frac{C_{EC}}{C}$ and $\kappa = (L_{EC}C_{EC}\omega_0^2)^{-1}$.

The array with – subscript corresponds to the ideal termination values. The two parameters κ and ξ correspond respectively to the resonant frequency of the EC and to the relative weight of the EC respect to the RFQ body in terms of stored energy. In a real RFQ ($\xi \neq 0$) the boundary condition $V'=0$ holds only if the ECs are perfectly tuned ($\kappa=1$), while all the other modes see a termination different from the ideal one. In a single RFQ segment, if the EC is tuned too high in frequency, $V'>0$ and the voltage in the EC is lower then in inside the RFQ.

We can therefore calculate the transfer matrix for N_{RFQ} segments:

$$M = (M_{EC}M_{rfq}M_{EC}M_{gap})^{N_{RFQ}-1} M_{EC}M_{rfq}M_{EC}$$

and the modes are defined by the condition

$$\begin{bmatrix} V_{out} \\ 0 \end{bmatrix}_{out} = M \begin{bmatrix} V_{in} \\ 0 \end{bmatrix}_{in} \qquad i.e. \qquad M_{2,1} = 0$$

corresponding to the condition at $V'=0$ the two extremes. In section 3 we shall compare the zeros of M_{21} with the measured mode frequencies.

3 EXPERIMENTAL RESULTS

The experimental apparatus (Fig. 2) consists of the bead pulling system (a dielectric bead of 4 mm radius driven by a cc motor by means of a kevlar thread of 0.25 mm diameter), a Network analyzer (NA) HP 4185A and a trigger unit driving NA and cc motor. The bead touches a couple of electrodes so to have the best reproducibility. Phase measurement is performed with a NA resolution bandwidth RW=300 Hz, resulting in a phase error of 0.14 deg.

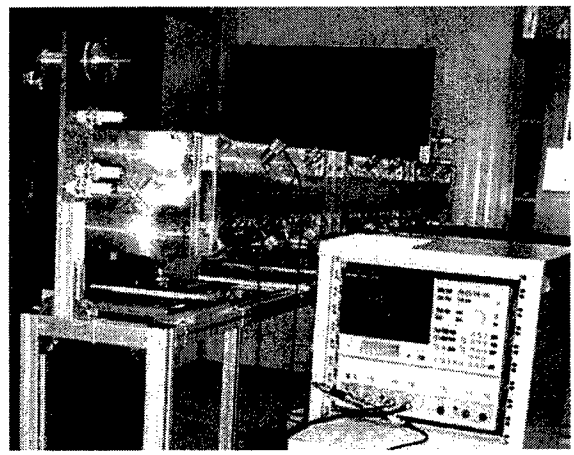

Figure 2 View of the experimental apparatus

For a dielectric bead moving inside the RFQ the electric field $E(z)$ at bead location z and the variation $\Delta\phi(z)$ of the output phase respect to when the bead is outside the RFQ (when exciting the system at the unperturbed resonance frequency) are related (for small $\Delta\phi$) by the equation:

$$\frac{E(z)^2 - E_0^2}{E_0^2} = \frac{\Delta\phi(z) - \Delta\phi_0}{\Delta\phi_0}$$

where $\Delta\phi_0$ is the phase variation corresponding to the maximum field E_0 for a given measurement.

Therefore the phase shift gives a relative measurement of the electric field, with the advantage to be unaffected by temperature variation since a single phase plot is taken in about 30 sec. Moreover no computer control is needed and phase plot, i.e. E-field variation along the structure, is shown on the NA screen. The flatness F (maximum of $\Delta E/E$) is easily evaluated.

Firstly we have tuned end cells by cutting the electrode ends in order to flatten the field (making $\kappa=1$) in each 1 m segment. In Tab 1 the comparison between the frequencies before and after tuning is reported. The frequency is slightly different from ν=350.7 MHz and the tuners insertion turns out to be not exactly 13 mm.

Table 1: Segment frequencies comparison

Segment	Before tuning (MHz)	After tuning (MHz)
1st	350.625	352.046
2nd	350.525	352.040
3rd	350.615	352.045

In Fig.3 phase plots of the tree tuned segments are shown ($F \approx 2.4\%$). If we consider the interval between the two arrows, corresponding to the region between the end cell electrodes, $F \approx 0.55\%$. The tuners are situated in correspondence of the valleys.

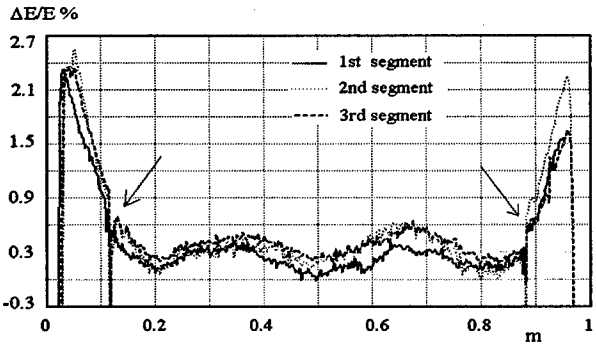

Figure 3: Phase plot of each segments

The phase plot for the three segments connected together and separated by 2 coupling cell is shown in Fig.4. The tuning of the coupling cells have been accomplished by cutting undercuts and working the upper part of coupling cells electrodes. The first action causes a change in the capacitance, so to get $\beta=1$, the second an inductance variation (making $\kappa=1$). The operating frequency is recuperated acting on the tuners; the achieved flatness (end cells excluded) is $F \approx 3.1\%$.

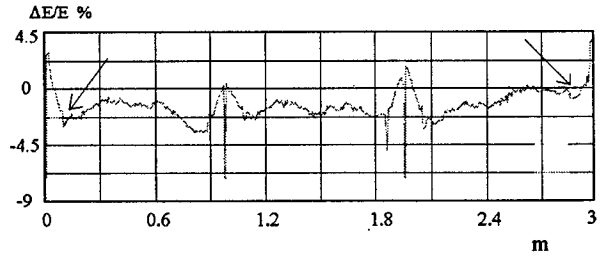

Figure 4: three segments with two coupling cells

The comparison between experimental frequency spectrum and the theoretical one is shown in Fig.5. The spectra are in quite good agreement with the exception of the last two modes, that are close in frequency with a possible mix between dipoles and quadrupoles.

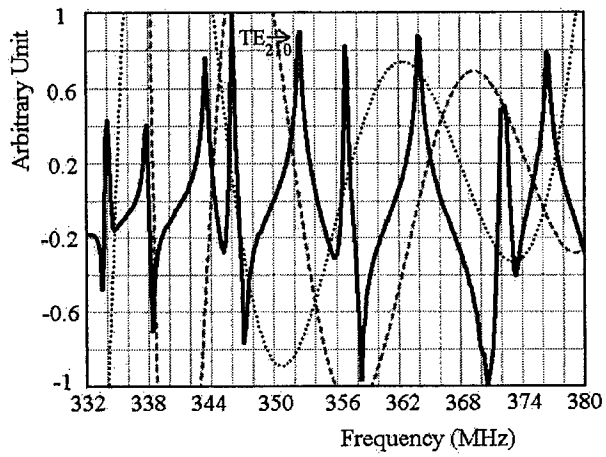

Figure 5: Comparison between experimental (black line) ant theoretical spectra obtained from the zeros of M_{21} of the dipole mode (dotted bleu line) and the quadrupole mode (magenta dashed line)

The future work will be devoted to the modal analysis of the beadpull data in order to set up an automatic procedure to tune the RFQ up to 1-2% E-field error.

4 ACNOWLEDGMENTS

The authors thank S. Marigo, M. Negrato, and V. Valentino for their help in assembling the set-up.

5 REFERENCES

[1]L.M.Young "An 8-meter long coupled cavity RFQ linac" Proceedings of the 1994 International Linac Conference, Tsukuba, Japan, p.178 (1994).

[2]A.Pisent ,R. Celentano, R. Zennaro "Equivalent lumped circuit study for the field stabilization of a long four-vanes RFQ". Presented at 1998 linac conference.

[3] A. Pisent "Transmission line analysis of coupled RFQ's" TRASCO note 01/99 (1999).

DESIGN AND FABRICATION OF THE KOMAC RFQ

J. M. Han, Y. S. Cho, B.J. Yoon and B. H. Choi, KAERI, Korea
Y. S. Bae and I. S. Ko, POSTECH, Korea
B. S. Han, SHI, Korea
Y. Oguri, TIT, Japan

Abstract

A RFQ linac (3MeV, 350MHz, 20mA, CW and 324cm in length) is being built for the Korea Multipurpose Accelerator Complex (KOMAC). The physical and engineering design of the H^+/H^- RFQ linac are described. The fabrication process for the cold model and structure support is described. The current status of the RFQ is reported.

1 INTRODUCTION

The Radio-Frequency Quadrupole (RFQ) linac, which will produce a 20mA beam of H^+/H^- with the energy of 3MeV, was proposed for the Korea Multipurpose Accelerator Complex (KOMAC) [1-4]. This paper presents the physics and engineering design plus the fabrication status of the KOMAC RFQ. The RFQ concept is shown in Fig. 1 with the parameter values given in Table 1.

The main focuses of this physics and engineering design in the RFQ are as follows:

- To understand the transmission of the mixing H^+/H^- beam into the RFQ.
- To obtain the tuning frequency by undercutting the end regions of the vane.
- To determine the locations and shapes of the coolant passages.
- To determine the shape of the brazing surface.

The physics and engineering design study is presented in section 2. Section 3 describes the fabrication status of the KOMAC RFQ.

Table 1. RFQ Linac Parameters.

PARAMETER	VALUE
Operating frequency	350 MHz
Particles	H^+ / H^-
Input / Output Current	21 / 20 mA
Input / Output Energy	0.05 / 3.0 MeV
Input / Output Emittance, Transverse/norm.	0.02 /0.023 π-cm-mrad rms
Output Emittance, Longitudinal	0.246 MeV-deg
Transmission	95 %
RFQ Structure Type	4-vanes
Duty Factor	100 %
Peak Surface Field	1.8 Kilpatrick
Structure Power	350.0 kW
Beam Power	67.9 kW
Total Power	417.9 kw
Length	324.0 cm

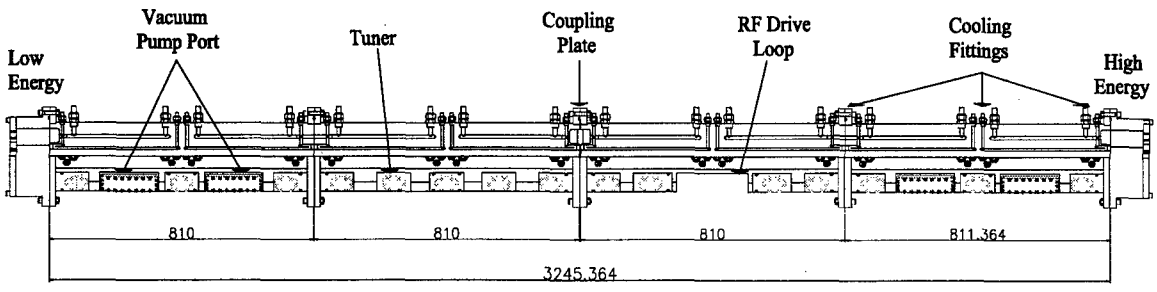

Figure 1. 3MeV, cw KOMAC RFQ Drawing.

2 PHYSICS AND ENGINEERING DESIGN

The motion of the mixing H^+/H^- beam into the RFQ has beeb studied by using a time marching beam dynamics code QLASSI [5]. Fig. 2 shows the dependence of the beam transmission rate and the H^- mixing ratio. The longitudinal beam loss increases with the concentration of negative ions by the bunching process which is distributed by attractive forces. Because of the space charge compensation in the low energy sections, the transverse beam loss decreases with the mixing ratio of H^-. In the KOMAC RFQ, the mixing ratio of H^- is less than 10%.

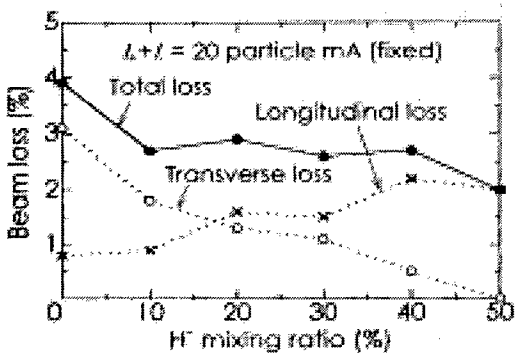

Figure 2. Dependence of Beam Transmission Rate and H^- Mixing Ratio.

In general, most of the RFQ structure can be understood in a two-dimension model. However, the end regions and the joints need full three-dimensional modelling. These regions have been investigated with the three-dimensional electromagnetic code, MAFIA [6]. Fig. 3 shows a three-dimensional simulation model of the end region of the RFQ. The end-gap distance and undercutting depth were varied until the quadrupole mode frequency of the model was tuned to 350.3MHz. In this case, the end-gap distance and undercutting depth are 7.5cm and 2.7cm, respectively. Fig. 4 shows the

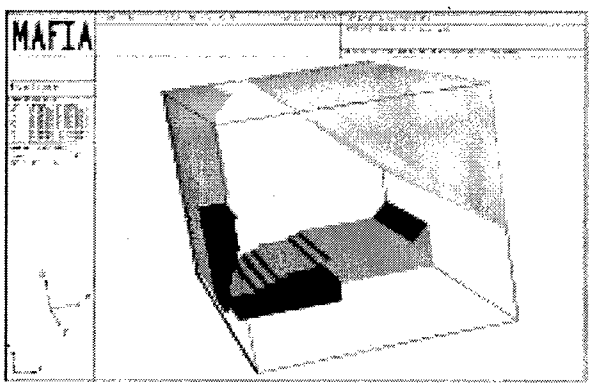

Figure 3. 3D Simulation Model of the End Region.

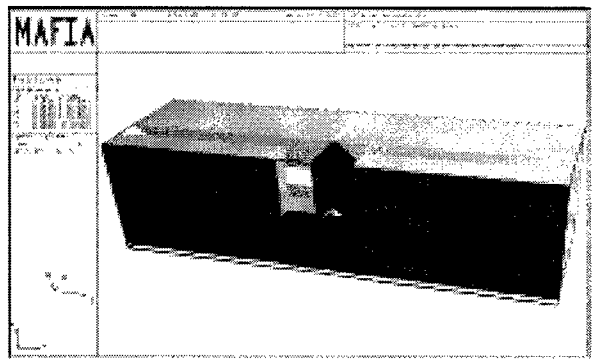

Figure 4. 3D Simulation Model of a Two-Section Coupled RFQ

MAFIA model of a two-section coupled RFQ. The simulation result has shown that a 0.205cm coupling gap-distance, a 2.5cm undercutting depth and 5.2cm coupling plates inner radius results in a near optimum separation between the quadrupole modes. Results simulated by the MAFIA models will be tested on a cold model which has been fabricated with Al6063.

In the design of the coolant passages, we considered the thermal behaviour of the vane during CW operation and manufacturing costs. The thermal and structure analysis is studied with SUPERFISH [7] and ANSYS codes. The average structure power by rf thermal loads is 0.35 MW and the peak surface heat flux on the cavity wall is 0.13 MW/m^2 at the high energy end. In order to remove this heat, we consider 48 longitudinal coolant passages in each of the sections, as shown in Figs. 1 and 5. Fig. 5 shows a thermal distribution of the cavity at the high energy end. The material is oxygen-free high-conductivity copper (OFHC). The thermal loads were given by SUPERFISH analysis. The heat transfer coefficients are between 11kW/m^2-C to 15 kW/m^2-C.

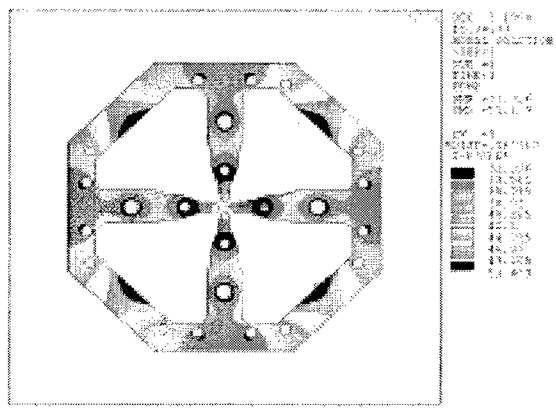

Figure 5. Temperature Distribution of the Cavity at the High Energy End of the KOMAC RFQ.

Because of the flow erosion of the coolant passages, we consider the maximum allowable bulk velocity of the coolant as 4.5m/sec. From the thermal-structural analysis of ANSYS, the peak temperature on the cavity wall is 51.4 °C, the maximum displacement is 42μm and the intensity stress .is 13MPa. We use the cooling tower on the cavity walls and the refrigeration system on the vane area. For rf tuning, the coolant passages on the vane area are operated with 10 °C coolant. However the temperature of the coolant of the passages on the cavity wall is varied to maintain the cavity on resonance frequency. The coolant passages in the cavity wall and vane area are the deep-hole drilled. The entrances of deep holes at the vane end are brazed.

3 FABRICATION STATUS

The RFQ cold model was fabricated with Al6063, as shown in Fig. 6, and the field test with the beadpull perturbation technique will begin next week. A bead is metal and is drawn through the four quadrants of the RFQ near the outer wall.

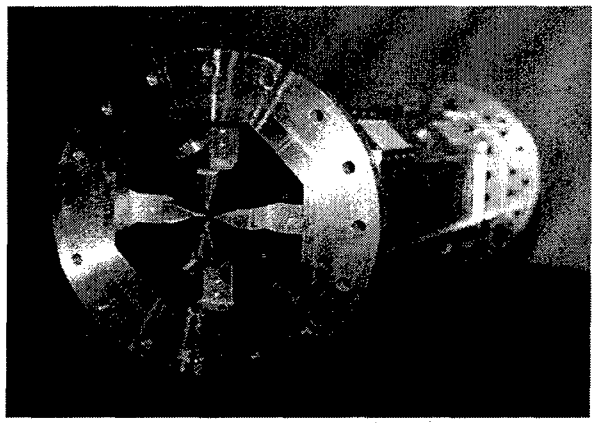

Figure 6. A Section of the KOMAC RFQ Cold Model.

The four quadrants of the RFQ are fabricated separately and brazed. Because of the leak of the brazing surface and the strain of the RFQ structure by furnace heat, it is important to determine the exact shape of brazing area[8]. Fig. 7 shows an 81cm long brazing test unit. The test unit was brazed in a vertical orientation with LUCAS Bag-8, a AgCu alloy with a liquids temperature of 780 °C.

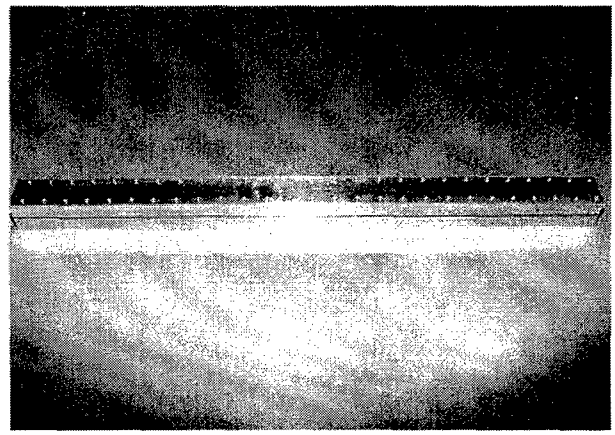

Figure 7. Brazing Test Unit.

At the present time, new brazing test unit is being brazed and one of the four sections is being fabricated.

4 ACKNOWLEDGMENT

We are grateful to Dr. Yanglai Cho at ANL, Y. Y. Lee at BNL, Dr. Kazuo Hasegawa at JAERI and Dr. Lloyd M. Young at LANL. This work has been supported by the Korea Ministry of Science and Technology (MOST).

5 REFERENCES

[1] C. K. Park et al., "The Komac Project: Accelerator and Transmutation Project in Korea", Proceeding of APAC98, Tsukuba, (1998).

[2] Y. S. Cho et al., "Conceptual Design Study of KOMAC DTL", Proceeding of APAC98, Tsukuba, March 23-27 (1998).

[3] J. M. Han et al, "Design of the KOMAC H⁺/H⁻ RFQ Linac", Proceeding of LINAC98, Chicago, (1998)

[4] B. H. Choi, "KOMAC", OECD NEA Workshop, (1998).

[5] Y. Oguri et al., "Beam Tracking in an RFQ Linac with Small Vane-Tip Curvature", Nuclear Sci. Tech., 30, 477 (1993).

[6] R. Klatt et al., "MAFIA-A Three-Dim. Electromagnetic CAD System for Magnets, RF Structures, and Transient Wake-field Calculations", SLAC-303, 276 (1986).

[7] J. H. Billen and L. M. Young, "POISSON SUPERFISH", LA-UR-96-1834 (Revised December, 1997).

[8] D. Schrage et al., "A New RFQ Linac Fabrication Technique", LA-UR-94-2483, (1994).

COMMISSIONING OF THE LOW-ENERGY DEMONSTRATION ACCELERATOR (LEDA) RADIO-FREQUENCY QUADRUPOLE (RFQ)*

K. F. Johnson#, J. D. Gilpatrick, D. Gurd, K. Jones, W. Lysenko, P. McGehee, S. Nath, D. Rees, A. Regan, L. Rybarcyk, J. D. Schneider, J. D. Sherman, H. V. Smith, L. M. Young, Los Alamos National Laboratory, Los Alamos, NM
M. E. Schulze, General Atomics Corporation, San Diego, CA

Abstract

Initial commissioning of a 6.7–MeV 100–mA RFQ is underway. The RFQ is part of LEDA, the H^+ injector for the Accelerator Production of Tritium (APT) project. To benchmark the RFQ performance, beam physics experiments will be done with low and high current beams for both pulsed and cw beam operation. Commissioning efforts thus far have been limited to low–current pulsed–beam LEDA operation. Measurements to fully characterize the RFQ will ultimately include the dependence of RFQ beam transmission on RFQ vane voltage, input beam energy, input match, and input transverse centroids. Other commissioning measurements for the RFQ will include output beam energy, phase, noise, transverse profiles, and transverse rms emittances. This paper contains initial LEDA RFQ commissioning results, including RFQ pulsed output beam currents up to 40 mA.

1 INTRODUCTION

The LEDA RFQ [1] is a 100% duty factor (cw) linac capable of delivering >100–mA of H^+ beam at 6.7–MeV. The 8-m-long, 350-MHz RFQ structure [2] is designed to accelerate the dc 75–keV, 110-mA H^+ beam from the LEDA injector [3,4] with >90% transmission. On March 16, 1999 first beam was accelerated through the LEDA RFQ. The preliminary RFQ commissioning results in this paper are for pulsed beams with low rep-rate and short pulse lengths.

2 LEDA CONFIGURATION

The accelerator configuration for beam commissioning of the LEDA RFQ is shown schematically in Figure 1.

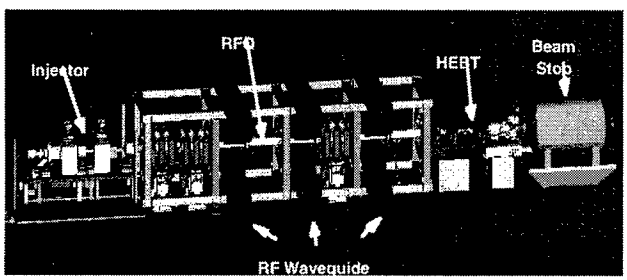

Figure 1: LEDA configuration for RFQ commissioning.

The major accelerator subsystems are the injector [3,4] (source and Low Energy Beam Transport (LEBT)), RFQ [2], High Energy Beam Transport (HEBT) [5], and the beam stop [6].

The layout of LEBT beamline optics and diagnostics is shown in Figure 2. The beamline optics include two solenoids and two steering magnet pairs for proper matching and injection into the RFQ. The suite of diagnostics include two view screens (interceptive diagnostic intended only for low-power density beams), three noninterceptive video profile diagnostics (VD1, VD2, & VD3), three DC current diagnostics (DC1, DC2, & DC3), and two pulsed beam current monitors (not shown in Figure 2). The pulsed beam current monitors are located right after the source and directly before the RFQ.

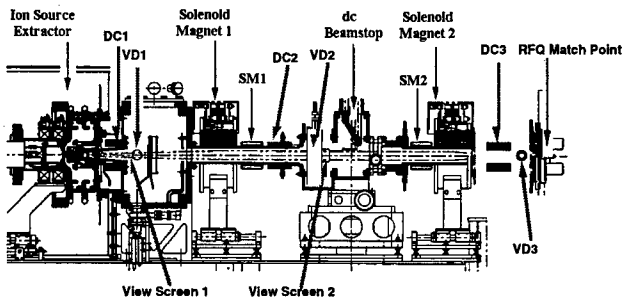

Figure 2: The LEDA LEBT beamline, including optics and diagnostics.

A photograph of the LEDA HEBT showing the location of beamline optics and diagnostics is given in Figure 3. Beam direction is from left to right. The function of the LEDA HEBT is to characterize the properties of the beam and transport the beam with low losses to a shielded beam stop. The beamline optics consists of four quadruples and two X-Y steering magnets. The HEBT beam diagnostics are described in [7]: they include 5 beam position monitors (BPMs), 2 DC and pulsed toroids, 3 capacitive pickoff probes, and 2 profile monitors. This set of diagnostics allow for measurements of beam current (pulsed beam, DC beam, and bunched

*Work supported by the US DOE, Defense Programs.

Email: kfjohnson@bnl.gov

beam), transverse centroids, longitudinal centroids (i.e. beam energy from time–of–flight and beam phase), and transverse beam profiles (wire scanner and video fluorescence).

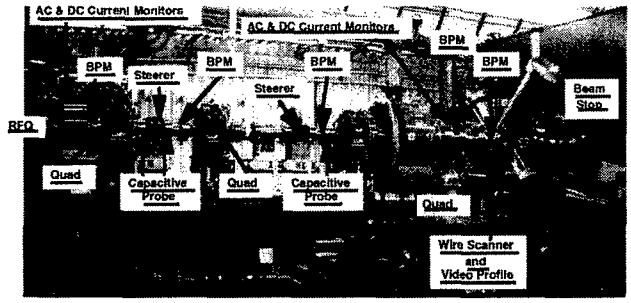

Figure 3: Layout of HEBT beamline optics and diagnostics. Beam direction is from left to right.

3 COMMISSIONING PLAN

Beam commissioning of LEDA will follow a graded approach. Because beam operation will truly be the first fully integrated test of all LEDA systems, commissioning will proceed cautiously. The assumption is that, in all likelihood, subsystems and their interfaces to other subsystems will not operate as expected.

An implication of this approach is that initial beam commissioning of the RFQ is in pulsed rather than cw mode. More specifically, to minimize or even eliminate beam related equipment damage, commissioning began in a pulsed low–power mode defined by short-pulse lengths (i.e. ≤ 500 μs), low-rep rate (i.e. 5 Hz), and low-beam current (i.e. ≤ 10 mA). As the performance of all systems is verified, commissioning will proceed in a stepwise fashion to the full cw high–power mode, 100% duty cycle and full current (100 mA). Pulsed operation is achieved by operating the injector in pulsed mode while operating the RFQ rf system at > 80% duty factor.

Besides protecting equipment (e.g. RFQ, HEBT, and beam stop), beginning beam commissioning with short-pulse lengths, low–rep rate, and low-beam currents has two other advantages. First, it allows for the operation of certain interceptive beam diagnostics that will be unavailable at higher beam-power densities. These diagnostics are for beam profile measurements and include two view screens in the LEBT and a wire scanner in the HEBT. Second, the most complete characterization of the RFQ can occur only when operating in a low-power pulsed mode. For example, measurements of RFQ beam transmission in high-power modes (pulsed or cw) will be considerably restricted due to the risk of beam damage to the RFQ vanes.

A starting pulse length ≤500 μs allows for a variety of transient conditions to stabilize in the first ~100 μs of the beam pulse while providing up to 400 μs in which to sample the time dependence of beam observables. Based on various scenarios of beam loss, especially in the HEBT, the starting beam current of ≤10 mA was considered low risk. A rep-rate of 5 Hz was chosen for initial operation to minimize any potential damage due to beam loss.

Commissioning will proceed in a bootstrap fashion. As systems are commissioned with low-power beam operation, the sequence will be to increase the rep-rate to 10 Hz and to increase both the beam intensity (ultimately to the 100 mA design level) and the pulse length to several 10s of ms. Then LEDA will be switched to a low-power cw mode and, finally, to high-power cw mode.

4 EXPERIMENTAL RESULTS

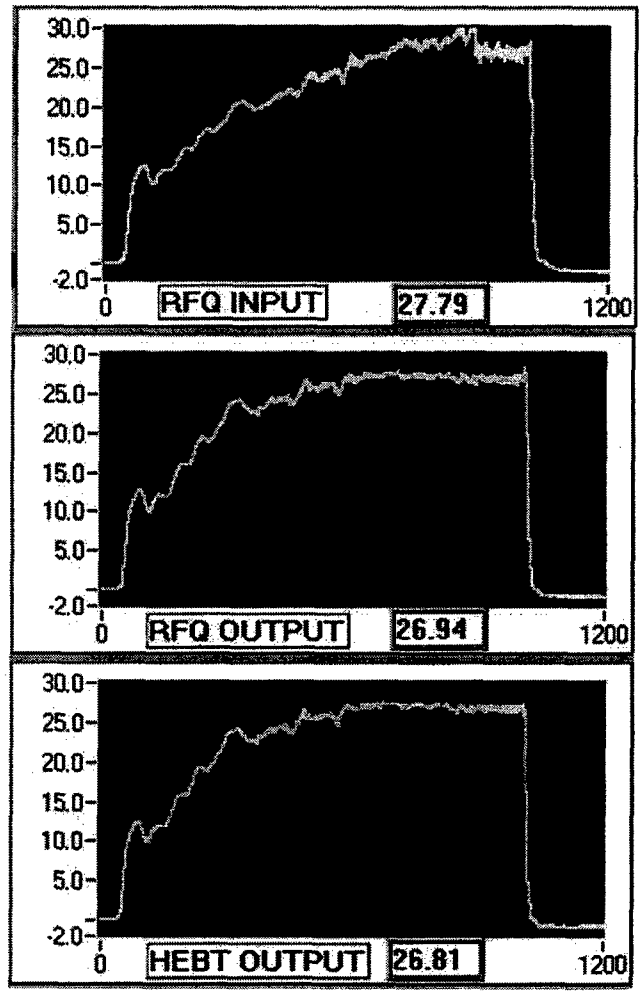

Figure 4: Time dependence of beam current over ~1 ms beam pulse as observed, from top to bottom, at the RFQ entrance, RFQ exit, and HEBT exit. The vertical axis is beam current (mA) and the horizontal is time (μs).

First beam through the RFQ was ~4 mA for a pulse length <500 μs and a rep-rate of 5Hz. As of the writing of this paper, the rep-rate has been increased to 10 Hz, the pulse length to ~2 ms, and the RFQ output current to ~40 mA. Figure 4 shows observed beam currents of >25 mA and ~1 ms pulse lengths at the RFQ entrance, RFQ exit, and HEBT exit.

After optimization of LEBT steering and LEBT match to the RFQ, RFQ transmission >95% and HEBT transmission >98% were obtained. More definitive measurements of transmission will require further tests of the beam current measurement system. Preliminary measurements of RFQ transmission as a function of vane voltage indicate that the RFQ is being operated above the knee in the transmission curve.

Measurements of the RFQ output beam energy, as determined from time-of-flight, and their comparisons to expectations are shown in Figure 5. These first results show that experiment and theory are consistent and that the output beam has the design energy.

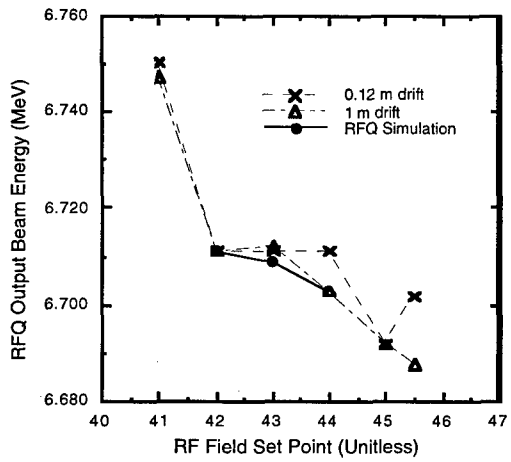

Figure 5: Measured output beam energy from the RFQ as a function of the rf field set point (RFQ design vane voltage corresponds to a set point of ~45).

First measurements of beam profiles using the slow wire scanner have been made and Figure 6 shows a measured horizontal profile. Verification of the BPM system is not complete. However, sufficient data have been taken to demonstrate consistency in beam position determination between BPMs and the wire scanner.

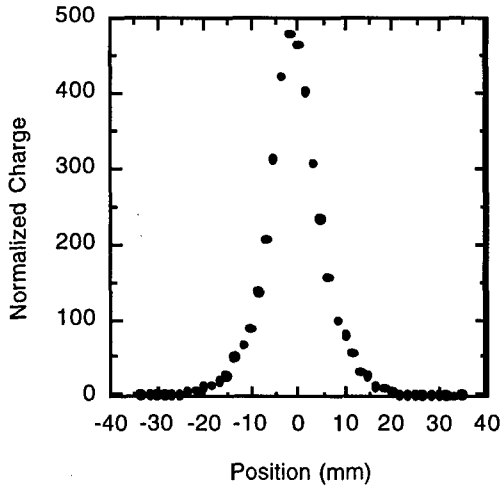

Figure 6: Horizontal beam profile as measured by a wire scanner ~2.8 m downstream from RFQ exit.

5 SUMMARY AND CONCLUSIONS

The initial performance of the LEDA injector, LEBT, RFQ, HEBT, and beamstop is encouraging. Increases in pulse length and current are going well. High RFQ and HEBT beam transmission has been established and the design RFQ output beam energy has been achieved. Observed RFQ transmission, at the present low beam currents, is consistent with PARMTEQM simulations [4] based on modeling of the present injector extraction system.

6 REFERENCES

[1] J.D. Schneider, "Operation of the Low-Energy Demonstration Accelerator: the Proton Injector of APT," this conf.

[2] D. Schrage *et al.*, "CW RFQ Fabrication and Engineering", Proc. LINAC98 (Chicago, 24–28 Aug. 1998) (in press)

[3] J. D. Sherman et al., "Status Report on a dc 130–mA, 75–keV Proton Injector," Rev. Sci. Instrum. 69 (1998) 1003–8

[4] H. V. Smith *et al.*, "Comparison of Simulations with Measurements for the LEDA LEBT H^+ Beam," this conf.

[5] W. P. Lysenko *et al.*, "High Energy Beam Transport Beamline of LEDA," Proc. LINAC98 (Chicago, 24–28 Aug. 1998) (in press)

[6] T. H. Van Hagan and D. W. Doll, "Design of an Ogive-Shaped Beamstop," Proc. LINAC98 (Chicago, 24–28 Aug. 1998) (in press)

[7] J. D. Gilpatrick *et al.*, "Low Energy Demonstration Accelerator (LEDA) Beam Instrumentation: RFQ–Accelerated Beam Results," this conf.

COMMISSIONING THE 2.5-MEV RFD LINAC PROTOTYPE*

D.A. Swenson, F.W. Guy, and W.J. Starling
Linac Systems, 2167 N. Highway 77, Waxahachie, TX 75165

Abstract

The experience of commissioning a 2.5-MeV, "Proof-of-Principle" prototype of the new RFD linac structure will be reported. This structure resembles a drift tube linac (DTL) with radio frequency quadrupole (RFQ) focusing incorporated into each drift tube, hence the name, Rf Focused Drift tube (or RFD) Linac. A prototype of this structure, comprising a 25-keV proton ion source, an Einzel-lens-based LEBT, a 0.65-m-long RFQ linac to 0.8 MeV, and a 0.35-m-long RFD linac to 2.5 MeV, has been designed, fabricated, assembled, and commissioned in our laboratory. Comparisons will be made between the projected and observed performances of this structure. The effect of this new linac structure on the size, cost and complexity of linac-based systems for practical applications will be described. Plans for the use of this new linac structure to satisfy several scientific, industrial and medical applications will be outlined.

1 DESCRIPTION OF THE PROTOTYPE

A 2.5-MeV prototype of a "Compact 12-MeV Proton Linac for PET Isotope Production" is under construction at Linac Systems. This unit will serve as the "proof of principle" for the revolutionary new Rf Focused Drift tube (RFD) linac structure. This structure resembles a drift tube linac (DTL) with radio frequency quadrupole (RFQ) focusing incorporated into each "drift tube". Both the prototype and the production unit will operate at 600 MHz. The prototype comprises a 25-keV proton ion source, an dual einzel-lens-based LEBT, a 0.65-m-long RFQ linac to 0.8 MeV, and a 0.35-m-long RFD linac to 2.5 MeV. The two linac structures will be resonantly coupled and powered by a collection of twelve planar triodes. The extreme simplicity of the interface between the two structures contributes to the practicality of this operational test on a limited budget. The entire length of the two linacs, including their interface, is only one meter. The entire assembly will be evacuated by 2 turbo-molecular pumps and 1 ion pump. The alignment philosophy is based on precision machining and "hard socket" for installation of the drift tubes. We believe that this new structure will become the structure of choice to follow RFQ linacs in many scientific, medical, and industrial applications.

2 ION SOURCE AND RFQ LINAC COMMISSIONING

A prerequisite to testing the performance of the RFD linac structure was the testing of the properties of the 0.8-MeV beam to be injected into the RFD linac structure. This beam originates in the duoplasmatron ion source, passes through the dual Einzel-lens LEBT, and is accelerated to 0.8-MeV by the 600-MHz RFQ linac of the Prototype.

The performance of the Ion source and LEBT was established many months ago by measuring the proton beam current on and through a segmented aperture and falling on a viewing screen. For a 25-kV ion source potential and Einzel-lens potentials near 25 kV, a few milliampere proton beam converged so that most of it went through the segmented aperture and formed a small spot at the center of the viewing screen. Some electrostatic steering was available, but seemed not to be required.

As the RFQ linac gets its rf power from the RFD linac via the resonant coupler, there is no provision for exciting the RFQ linac without also exciting the RFD linac structure. In order to confirm the performance of the RFQ linac, independent of the RFD linac, it was necessary to intercept the beam from the RFQ linac inside the RFD linac and to diagnose its properties while the RFD linac structure was excited with rf power. In order to do this, we removed the RFD drift tubes and insert a single, larger diagnostic drift tube fitted with a 0.5-MeV absorber foil and a Faraday cup. Without the foil, there was a steady increase in beam current with rf power level until some maximum current was reached. With the foil, a definite threshold was observed in the rf power level, below which no beam was accelerated. Based on this threshold, estimates of the design excitation of the RFQ linac were established.

3 RFD LINAC COMMISSIONING

Following the commissioning of the RFQ linac, the RFD drift tubes were reinstalled and the resonant coupler slot dimensions were adjusted to give the desired ratio rf fields in the two linac structures.

For the first few hours of excitation, the RFD linac structure was hung up in a solid multipactor. Although the twin-bladed stems of the RFD drift tubes are prone to

* Supported by the National Institute of Mental Health (NIMH).

0-7803-5573-3/99/$10.00@1999 IEEE.

multipactor, it proved possible to break through that phenomenon. However, once through the multipactor regime , we were unable to get much more power into the combined structures. The following problems were observed and fixed:

1) Discrepancies were found in the phase and amplitude of the drive to each of the 12 final power amplifier (FPA) planar triode tubes. The rf drive configuration involves a three-way power splitter at the IPA amplifier and 3 four-way power splitter near the FPA. The four-way power splitters were replaced with a new and improved design.

2) Standing waves in the rf drive configuration resulted in voltages that exceeded the voltage capabilities of the RG-316 coax and the SMA connectors that were being used. The configuration was changed to use RG-223/U coax and TNC connectors.

3) The length of the 3-1/8 rigid coax line between the FPA and the RFD linac was designed to be one wavelength (0.50 meters). The length of this line is critical to the performance of the rf system. Tests were made with this line both lengthened by 25 mm and shortened by 50 mm. The shorter option seems to be preferred by the rf power protection circuitry.

4) Some of the rf contacts in the sliding tuners of the rf power system were very difficult to operate. These sliding contacts were reworked.

5) Measurements of the Q of the combined structure indicated that the power required for design excitation was more that we could get from the rf power system. SUPERFISH implies that the RFD should have a stored energy of 2.57 J. Early estimates of the Q (or power requirement) for the RFD indicated a Q of about 48,000, implying a power requirement of 200 kW. Improved estimates of the stem losses (two-bladed stems for 12 short cells) and the end wall losses (two end walls for a very short tank) have reduced the expected Q to 37,000, implying a power requirement of 262 kW. The best measured Q of the RFD (isolated from the RFQ) is about 18,000, implying a power requirement of 538 kW.

4 A SEARCH FOR CAVITY Q

At this point, a study was launched to determine why the Q was so low. Under suspicion were the joints between tank ends and the end walls (spring ring under mild compression), the surface conductivity of the copper plating, and the ion pump port. The coupling slot to the RFQ was closed to eliminate the RFQ from suspicion.

Many attempts were made to improve the Q by replacing the original spring ring join with joints based on spring rings under higher compression, copper braid covered spring ring, solid aluminum wire and soft silver wire under very high compression. None of these test resulted in much of an increase in the Q of the structure.

Many attempt were made to test the rf conductivity of the end plates by using an open-sided S-band cavity against the planar copper-plated surfaces of the Prototype. These measurements are difficult to make and were inconclusive.

Finally, we removed the RFD drift tubes, leaving a right circular cylindrical tank 376-mm in diameter and 342.26-mm long. Here we have the possibility to compare our measurements with the well-known properties of the TM_{010} and TE_{011} modes in a right circular cylinder. The TE_{011} mode is of particular interest because it involves only circumferential currents, making the field distribution and Q virtually independent of the quality of the electrical contact between the cylindrical tank and the end plates. This mode primarily tests the conductivity of the copper-plated cavity surfaces. The TM_{010} mode is the drift tube linac mode and is dependent on both the quality of the cavity surfaces and the quality of the joints between the cylindrical tank and the end plates.

The frequency of both modes were within one tenth percent of their theoretical values (610.3 MHz for the TM_{010} mode and 1061.8 MHz for the TE_{011} mode). The Q of the TE_{011} mode (59,489) was 65% of the theoretical value of 91,507. The Q of the TM_{010} mode (16,000) was 35% of the theoretical value of 45,600. This suggests a problem with both the surface conductivity of the copper plating and the conductivity of the end joints.

The RFD linac tank and end plates have been redesigned to utilize copper Helicoflex seals for both the rf and vacuum seal. The design includes an elastomer seal behind the Helicoflex seal for back-up purposes. The linac tank and end plates will be stripped of copper and re-plated. This work should be completed by the second week in April.

5 FINAL COMMISSIONING PLANS

We expect to continue the commissioning of this prototype as soon as the RFD linac structure is re-plated. The challenge then will be to get enough rf power into the structure, to establish that there is an accelerated beam and to measure the properties of it.

6 APPLICATIONS FOR THE RFD LINAC

We expect the RFD linac structure to form the basis of a new family of compact, economical, and reliable linac systems serving a whole host of scientific, medical, and industrial applications. The principal medical applications include the production of short-lived radio-isotopes for the positron-based diagnostic procedures (PET and SPECT), the production of epithermal neutron beams for BNCT,

and accelerated proton beams for injection into proton synchrotrons to produce the energies required for proton therapy. We propose S-Band versions of the structure to serve as 70-MeV injectors to 200-MeV Disk and Washer (DAW) booster linacs for the proton therapy application.

The principal industrial and military applications include the production of intense thermal neutron beams for Thermal Neutron Analysis (TNA), Thermal Neutron Radiography (TNR), and Nondestructive Testing (NDT). High duty factor RFD linac systems could produce nanosecond bursts of fast neutrons to support Pulsed Fast Neutron Analysis (PFNA).

7 REFERENCES

1. D.A. Swenson, "RF-Focused Drift-Tube Linac Structure", 1994 Intern. Linac Conf., Tsukuba, Japan, 1994.
2. D.A. Swenson, "A New Linac Structure for the BNCT Application", Proc. First Intern. Workshop on Accelerator-Based Neutron Sources for BNCT, Jackson Hole, WY, 1994.
3. D.A. Swenson, Crandall, Guy, Lenz, Ringwall, & Walling, "Development of the RFD Linac Structure", Proc. of the 1995 Particle Accelerator Conference, Dallas, TX, 1995.
4. D.A. Swenson, F.W. Guy, K.R. Crandall, "Merits of the RFD Linac Structure for Proton and Light-Ion Acceleration Systems", Proc. of EPAC'96 Conference, Sitges, Spain, 1996.
5. D.A. Swenson, K.R. Crandall, F.W. Guy, J.M. Potter, T.A. Topolski, "Prototype of the RFD Linac Structure", 1996 Linac Conf., CERN, Geneva, Switzerland, 1996.
6. D.A. Swenson, "12-MeV Proton Linac for PET Isotope Production", Institute of Clinical PET Conf., Orlando, FL, 1996.
7. D.A. Swenson, "CW RFD Linacs for the BNCT Application", Fourteenth Intern. Conference on the Applications of Accelerators in Research and Industry, Denton, TX, 1997.
8. D.A. Swenson, K.R. Crandall, F.W. Guy, J.W. Lenz, W.J. Starling, "First Performance of the RFD Linac Structure", Proc of 1998 Linac Conference, Chicago, IL, 1998.
9. D.A. Swenson, "Compact, Inexpensive, Epithermal Neutron Source for BNCT", Proceedings of CAARI'98, Denton, TX, 1998.

BEAM TEST RESULTS WITH THE ISAC 35 MHZ RFQ

R.E. Laxdal, R.A. Baartman, L. Root

Abstract

The ISAC 35 MHz split-ring RFQ is designed to accelerate ions of $A/q \leq 30$ from 2 keV/u to 150 keV/u in cw mode at a constant synchronous phase of $-25°$. Beam tests with 7 of the 19 split rings installed ($E_{\text{fin}} = 0.55$ keV/u) have recently been completed. The tests demonstrated that a constant synchronous phase RFQ with external buncher works splendidly for low beta, low intensity applications. One peculiar aspect of the RFQ is that the longitudinal acceptance is larger for beams injected off-center. The test set-up and results of both the measurements and the simulations are presented and discussed.

1 INTRODUCTION

A radioactive ion beam facility with on-line source and linear post-accelerator is being built at TRIUMF[1]. The accelerator chain includes a 35 MHz split-ring RFQ, operating cw, to accelerate beams of $A/q \leq 30$ from 2 keV/u to 150 keV/u[2]. The final RFQ electrodes will span 7.6 m with 19 modules each consisting of one ring and 40 cm of electrodes. The gross specifications include a bore radius of $r_0 = 7.4$ mm, and a maximum inter-vane voltage of 74 kV. A unique feature of the design is the constant synchronous phase of -25°[3]. The buncher and shaper sections of the RFQ have been eliminated in favour of a four-harmonic sawtooth pre-buncher located ~5 m upstream of the RFQ in the low energy beam transport (LEBT). This shortens the RFQ and yields a smaller longitudinal emittance at the expense of a slightly lower beam capture. The pre-buncher operates at a fundamental frequency of 11.7 MHz, one third the frequency of the RFQ. Presently three harmonics are operational on the pre-buncher resulting in a predicted capture efficiency of 80%.

It was decided to proceed with a two-stage installation. We have installed and tested with beam the first seven rings of the RFQ. Installation of the remaining twelve rings is now in progress.

2 THE TEST SET-UP

A schematic of the test set-up is shown in Fig. 1. An rf short is placed after the seventh module to confine the rf fields. Eight electrostatic quadrupoles are used to transport the beam to a diagnostic station downstream of the RFQ tank. A Faraday cup and profile monitor assembly are placed just after the RFQ short and again in the middle of the electrostatic transport after the fourth quadrupole. The quadrupoles when tuned act as an energy filter; the unaccelerated beam is lost in the first few quadrupoles. Therefore the transmission difference between the first Faraday cup and the second marks the capture efficiency of the RFQ.

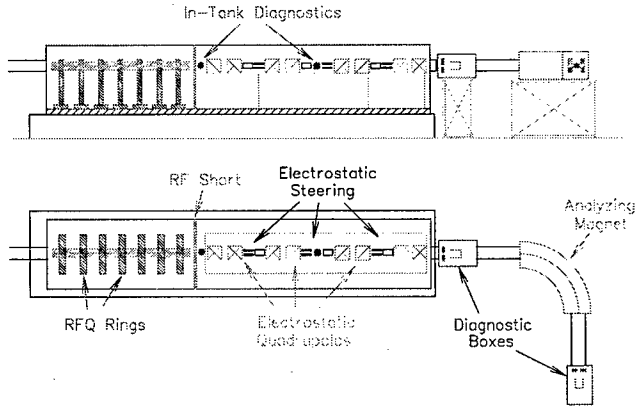

Figure 1: Schematic diagram of the test set-up.

The diagnostic station shown in Fig. 1 includes a Faraday cup, profile monitor and a spectrometer consisting of an object and image slit and a 90 degree bending magnet. A slit and harp transverse emittance rig is positioned upstream of the magnet. An Allison type emittance rig is located in the LEBT to record transverse emittances before acceleration.

3 RESULTS

Both rf and beam tests have been successfully completed. The RFQ was operated in cw mode for all beam tests. The operation of the RFQ at peak voltage (74 kV) is stable[4]. Beams of both N^+ and N_2^+ have been accelerated to test the RFQ at low and high power. Two beam emittances were used: a regular emittance beam of $\beta\epsilon_{x,y} = 0.03\pi$mm-mrad and a collimated 'pencil' beam of $\beta\epsilon_{x,y} = 0.003\pi$mm-mrad.

3.1 Regular Emittance Beam

Beam Capture Beam capture measurements as a function of RFQ vane voltage have been completed for each ion and for both unbunched and bunched input beams. The results are given in Fig. 2 (squares) along with efficiencies predicted by PARMTEQ (dashed lines). The RFQ capture efficiency at the nominal voltage is 80% in the bunched case (three harmonics) and 25% for the unbunched case in reasonable agreement with predictions. The capture efficiencies for one harmonic and two harmonic pre-bunching are 63% and 74% respectively.

Energy and Energy Spread The energy of the beam as measured with the analyzing magnet is 55 keV/u. The energy spread for the bunched and unbunched cases was measured at ±0.4% and ±0.7% respectively and compares well with PARMTEQ predictions (Fig. 3)

Transverse Emittance Transverse emittances were measured before and after the RFQ. The results show that

0-7803-5573-3/99/$10.00@1999 IEEE.

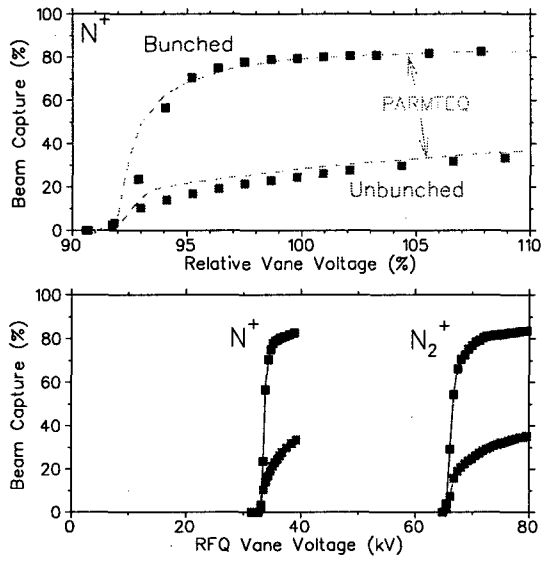

Figure 2: The beam capture (squares) for both bunched and unbunched initial beams of N^+ as a function of relative vane voltage are compared with PARMTEQ calculations (dashed lines). In (b) results for both N_2^+ and N^+ are plotted with respect to absolute vane voltage.

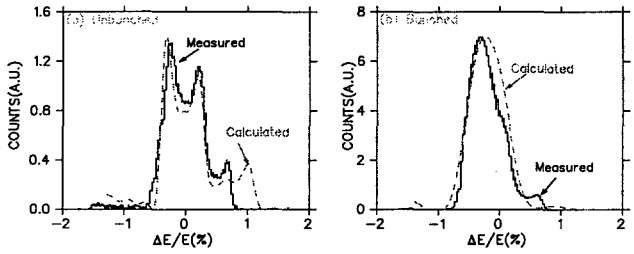

Figure 3: Results of energy spread measurements of accelerated N^+ beams for both (a) unbunched and (b) bunched cases. PARMTEQ simulation results are plotted for comparison.

when the matching is optimized the emittance growth in both planes is less than 10% for an initial beam of 15πmm-mrad. A summary of the results for N^+ is presented in Fig. 4. Space charge forces limit the longitudinal acceptance for currents above ~ 1 μA but do not impact the transverse emittance.

3.2 *Pencil Beam Experiments*

During initial beam commissioning it was observed that when the system was tuned for maximum capture the beams emerged far off-center. There was concern that a dipole component internal to the RFQ was steering the beam. Two circular apertures of 2 mm separated by 0.7 m were placed in the RFQ injection line to create a centered 'pencil beam' to diagnose the problem. A vertical deflecting steerer was available downstream of the collimators to move the beam around the RFQ aperture.

The tests showed that the RFQ dipole component was negligible. However we found that the acceptance of the

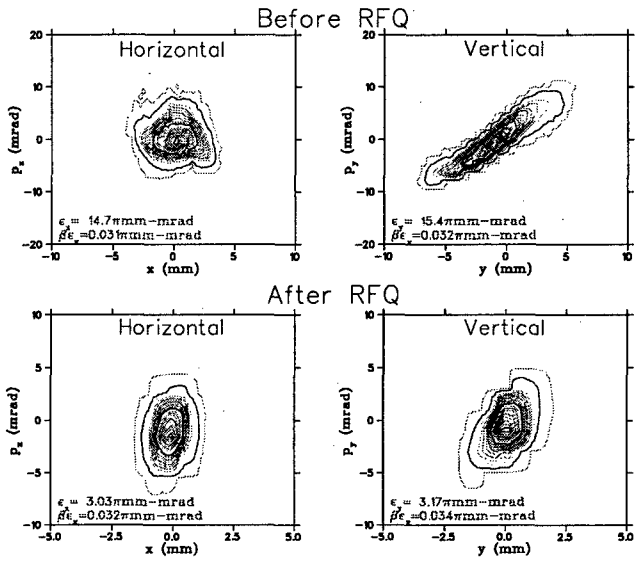

Figure 4: Transverse emittance measurements (4RMS values) for N_{14} before and after the RFQ. The normalized emittance values are also displayed.

RFQ is larger for off-centered beams. The two-term potential function yields the spatial component of the accelerating field as

$$E_z = \frac{kAV}{2} I_o(kr)\sin kz$$

where $k = 2\pi/\beta\lambda$ and β is the relative particle velocity. Hence off-axis particles experience stronger fields than on-axis particles, particularly at injection where β is small. In the ISAC RFQ the design synchronous phase is fixed at $-25°$ at the nominal voltage but for off-axis particles the effective synchronous phase decreases, increasing the acceptance. A typical measure of the synchronous phase is the cut-off voltage, that voltage below which no acceleration can occur. Beam transmission as a function of RFQ voltage measured for a centered beam and two off-centered cases ($A_c = 1.7$ mm and $A_c = 2.7$ mm), plotted in Fig. 5, clearly shows that the cut-off voltage decreases for increasing amounts of off-centering. As the voltage nears cut-off the difference in acceptances between on-axis and off-axis particles is enhanced.

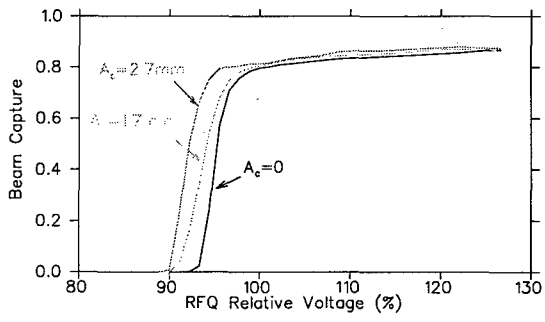

Figure 5: Transmission of 'pencil beam' as a function of RFQ voltage for a centered beam and two cases of off-centered beam.

Transverse Acceptance and Centering Error An off-center small emittance beam passing through the RFQ makes coherent oscillations about the RFQ axis. The transverse phase advance per unit length is dependent on the RFQ voltage. The centering error can be determined by scanning the RFQ voltage to produce a 2π change in the transverse phase advance while recording the final beam position. The rate of phase change with RFQ voltage, when compared with beam simulations, can be used to determine if the centering error was due to a mis-alignment at injection or was developed during acceleration from a dipole error. Beam position as a function of RFQ voltage is given in Fig. 6 for steering plate settings of 0, 400 V and 600 V. The two deflected cases correspond to the transmission data plotted in Fig. 5. Based on the steering/transmission data the transverse acceptance was estimated to be $\geq 140\pi$mm-mrad.

Longitudinal Acceptance The longitudinal acceptance was measured for a centered and an off-centered beam ($A_c = 2.7$ mm) at the nominal RFQ voltage. The energy of the injected beam was varied at the source. For each energy step the phase of the bunched beam was varied with respect to the RFQ phase and the capture efficiency was recorded. Comparison of calculated and measured beam transmission contours for centered and off-centered cases are presented in Fig. 7. The settings where the capture dropped to 50% of peak value is used to define the longitudinal acceptance contour. The measured acceptance is estimated to be 220π%-deg and 460π%-deg at 35 MHz for the centered and off-centered beams repectively (0.35 and 0.73πkeV/u-ns). PARMTEQ simulations predict corresponding acceptances of 310π%-deg and 570π%-deg (0.49 and 0.91πkeV/u-ns).

4 TUNING AND MATCHING

The increase in accelerating field strength for off-axis particles provides a large stable saddle point in the longitudinal motion. One problem however is that the transmission improves (at the expense of beam quality) as the beam moves off-center making tuning difficult. Larger unmatched beams are subject to a spread in the radial tune due to the radial variation in the field strength and produce transverse emittance growth. A larger phase acceptance leads to a higher population of the tails in the accelerated longitudinal emittance. An optimization procedure was developed where the LEBT is tuned at high RFQ voltage for maximum transmission then the last steering plates and matching quadrupoles are re-tuned at an RFQ voltage near cut-off to achieve a local **minimum** in the transmission. The procedure results in both a centered and a matched beam since a matched beam sees more uniform accelerating fields on average.

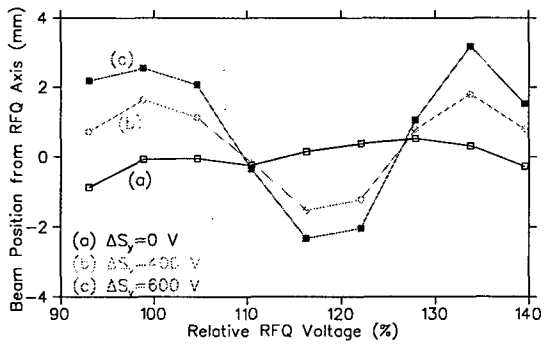

Figure 6: Beam position at RFQ exit as a function of RFQ voltage for steering plate strengths of 0, 400 V and 600 V.

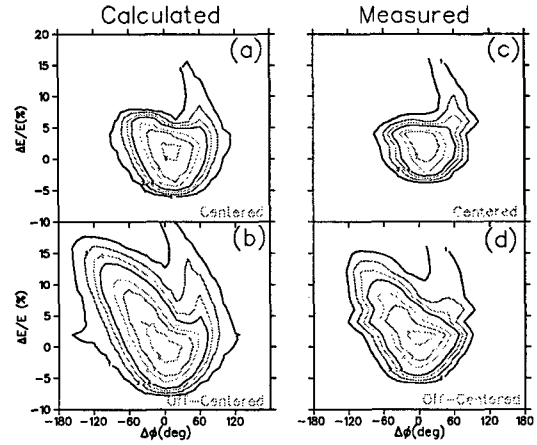

Figure 7: Beam transmission contours (plotted every 10%) for calculated values ((a)centered and (b)off-centered) and measured values ((c)centered and (d)off-centered). Off-centered beams have a coherent amplitude of $A_c = 2.7$ mm.

5 CONCLUSION

The beam test results demonstrate a strong confirmation of both the beam dynamics design and the engineering concept and realization and give us full confidence in proceeding with the installation of the remaining twelve split rings. The 'pencil beam' proved invaluable in diagnosing the effects of off-center beams on beam capture.

6 ACKNOWLEDGMENTS

The tests were made possible by the collaborative effort of many groups; most notably the rf, LEBT, diagnostics and controls groups. Special thanks go to R. Poirier and W. Rawnsley. Thanks also to S. Koscielniak for useful discussions.

7 REFERENCES

[1] P. Schmor, "Initial Commissioning of the ISAC Radioactive Beam Facility", these proceedings.

[2] R. Poirier, "RF Systems of the TRIUMF ISAC Facility", these proceedings.

[3] S. Koscielniak, *et al*, "Beam Dynamics Studies on the ISAC RFQ at TRIUMF", Proceedings of the 1997 Part. Acc. Conf., Vancouver, 1997.

[4] R. Poirier, *et al*, "RF Tests on the Initial 2.8m of the 8m Long ISAC RFQ at TRIUMF", Proceedings of LINAC98.

DESIGN OPTIMIZATION OF THE PROPOSED ISAC-2 PROJECT AT TRIUMF

R.E. Laxdal and R.A. Baartman

Abstract

A radioactive ion beam facility, ISAC, is presently under construction at TRIUMF. The post-accelerator takes ions of $A/q \leq 30$ from 2 keV/u to energies up to 1.5 MeV/u. For the next five year plan, it is intended to increase the final energy above the Coulomb barrier (roughly 6.5 MeV/u) and broaden the mass range up to roughly A=150. The ISAC-2 proposal utilizes the existing RFQ, and a new IH drift tube linac to reach a new stripping energy of 0.4 MeV/u. A post-stripper superconducting linac will accelerate ions with $3 \leq A/q \leq 7$ to 6.5 MeV/u for the heaviest ions and to more than twice this value for the lightest ions. This paper documents the optimization of the ISAC-2 linac design.

1 INTRODUCTION

The ISAC facility now under construction at TRIUMF[1] will provide exotic ions of mass $A \leq 30$ up to energies of 1.5 MeV/u. The post-accelerator (dashed area in Fig. 2) consists of a 35 MHz RFQ to increase the energy of ions with $A/q \leq 30$ from 2 keV/u to the 150 keV/u stripping energy and a post-stripper 105 MHz drift-tube linac (DTL) to accelerate ions with $3 \leq A/q \leq 6$ to a final energy fully variable between 0.15 and 1.5 MeV/u. All linac components operate cw to maintain the intensity of the ions.

For the next five year funding segment beginning April 2000 it is proposed to upgrade the present ISAC facility. The proposed expansion, ISAC-2, would extend the accepted mass range up to 150 and the final energy to above the Coulomb barrier ($E \geq 6.5$ MeV/u) making TRIUMF a unique world class center for exotic beam investigations.

2 OVERVIEW OF SCHEME

The ISAC-2 proposal utilizes the existing ISAC-1 RFQ for low energy acceleration and therefore requires that the ion charge from the source obeys $A/q \leq 30$. Recent advances in charge state booster (CSB) development[3] make this choice feasible. A CSB will be added after the mass-separator to increase the charge state of ions with $A > 30$.

Assuming a single stripping stage the total voltage required to reach 6.5 MeV/u from 2 keV/u is given by

$$V_{tot} = \frac{A}{q_i}(E_s - 0.002) + \frac{A}{q_s}(6.5 - E_s)$$

where q_i is the initial charge injected into the RFQ, q_s is the charge state after stripping and E_s is the stripping energy. The total voltage required for accelerating several different ions to 6.5 MeV/u as a function of stripping energy is given in Fig. 1. The optimum energy for stripping is ~400 keV/u with stripping efficiencies varying from 50% for the lightest ions to 15% for $A = 150$.

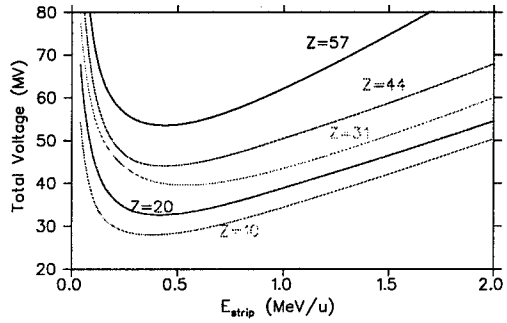

Figure 1: The total voltage required to accelerate various ions from 0.15 to 6.5 MeV/u as a function of stripping energy.

A room-temperature DTL operating in cw mode will be used to accelerate ions of $A/q \leq 30$ from the RFQ from 0.15 – 0.4 MeV/u. The beam then is stripped and the ion charge selected in a new MEBT-2 that bends the beam through 90° to a line parallel to the ISAC-1 DTL line. Ions of mass to charge ratio $3 \leq A/q \leq 7$ are matched into a superconducting DTL on this line and accelerated to at least 6.5 MeV/u and then transported to the experimental stations. A summary of the linac specifications is shown in Table 1. A schematic of the proposed ISAC-2 linear accelerator complex is shown in Fig. 2.

Table 1: Summary of ISAC-2 linac specifications.

Device	E_{in} (MeV/u)	E_{out} (MeV/u)	A/q	ΔV_{max} (MV)
CSB	–	0.002	≤ 30	0.06
RFQ1	0.002	0.15	≤ 30	4.44
IH-DTL2	0.150	0.40	≤ 30	7.50
strip				
SC-DTL	0.40	6.5	$3 \rightarrow 7$	42.7

3 CHARGE STATE BOOSTER

The CSB would take the singly charged radioactive beam from the mass-separator and boost the charge state to be compatible with $A/q \leq 30$ for the RFQ. Both ECR and EBIS sources are being considered. An attractive option is to develop a charge state booster which would give $A/q \leq 7$. This would obviate the need for any stripping and the inherent loss of intensity. Recent results suggest that efficiencies of 2% are possible in this latter mode and from 10-20% in the low-q mode[3]. A budget amount of **2 M$** has been allocated for this project.

0-7803-5573-3/99/$10.00@1999 IEEE.

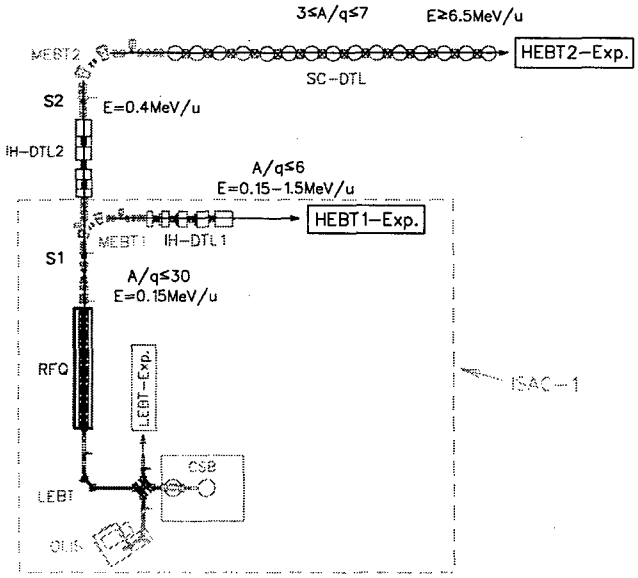

Figure 2: The ISAC-2 linear accelerator complex.

Table 2: Specifications for the pre-stripper IH-DTL.

Parameter	Tank 1	Tank 2
Energy Range	150-250 keV/u	250-400 keV/u
A/q	30	30
V_{eff}	3.0 MV	4.5 MV
No. of cells	13, 21	21, 20
E_g (MV/m)	2.7	2.7
Length (m)	2.2	3.0
Power (kW)	30	45

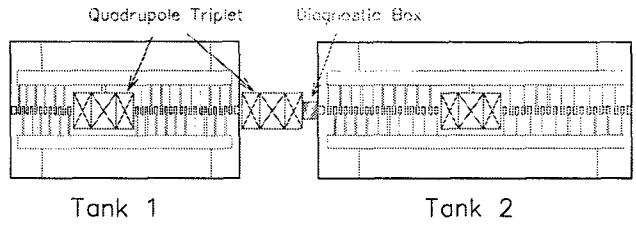

Figure 3: The pre-stripper IH-linac for ISAC-2.

4 PRE-STRIPPER LINAC

The IH linac structure operates at very high shunt impedance values making cw operation at room temperature possible. In ISAC-2 the application is for a fixed final velocity, so long tanks each containing many drift tubes are used to achieve the highest acceleration efficiency. Magnetic quadrupoles are installed both in tanks and between tanks to provide periodic transverse focusing. The small longitudinal and transverse emittances from the RFQ ($\epsilon_z = 0.3\pi$ keV/u ns and $\beta\epsilon_{x,y} = 0.1\pi$mm mrad) allow a frequency of 70 MHz, double that of the RFQ frequency, reducing the size of the DTL tanks and improving the shunt impedance. The shunt impedance for the structure is estimated to be $\sim$ 300 MΩ/m. In a cw DTL the dissipated power is a more limiting factor than the peak surface field in establishing the operating gradient. A power dissipation of 20 kW/m can be safely cooled. The relation $P_l = (\overline{E_oT})^2/Z$, where P_l is the power per unit length and Z is the effective shunt impedance then gives an average effective gradient $\overline{E_oT}$ of 2.4 MV/m.

A schematic diagram of the linac is shown in Fig. 3. In order to reduce the demands on the rf amplifier the DTL is divided into two tanks each with one quadrupole triplet inside roughly midway down the tank and one quadrupole triplet between tanks. Each triplet is $\sim$ 65 cm long with gradients up to 60 T/m. A diagnostic box will also be added to the intertank region. The total length of the linac is 5.8 m. The beam dynamics utilizes the method developed at GSI[2] where a short $-60°$ section is used after each magnet system for rebunching followed by an accelerating section at a synchronous phase of 0°. A summary of the tank specifications is given in Table 2. The acceptance of the linac is $\epsilon_z = 3.6\pi$ keV/u ns and $\beta\epsilon_{x,y} = 0.8\pi$mm mrad. With the expected beams from the RFQ the emittance increase during acceleration is calculated to be less than 5%.

5 POST-STRIPPER LINAC

Recent improvements in accelerating gradient and simplification of fabrication procedures[4] plus flexible operation and high beam quality make a superconducting linac a favourable choice for the ISAC-2 post-stripper accelerator. Superconducting heavy ion linacs are composed of several independently fed cavities arranged in a common cryostat with focusing magnets at periodic intervals down the length. In the ISAC-2 linac we choose a geometry having four resonators in a cylindrical vertically mounted cryostat with room-temperature quadrupoles between cryostats. A two-gap quarter wave structure was chosen for its high velocity acceptance and inherent mechanical stability. The former is useful to efficiently accelerate the wide range of ions with a minimum of cavity types and the latter is essential to produce high accelerating gradients.

For optimization the acceleration efficiency is calculated for both two- and three-gap cavities each using two or three different β regimes. Efficiencies over the whole A/q range are calculated assuming a fixed acceleration gradient. The conclusion is that linac performance even with a two-β, two-gap solution is remarkably good, with an integrated time constant of better than 82% over the whole mass range compared to a theoretical maximum time constant of 90%. The acceleration efficiency for $A/q = 7$ and $A/q = 3$ for two-gap cavities with two β sections (SC-DTL1 and SC-DTL2) corresponding to β_o values of 4.8% and 9.6% and a voltage gain ratio in respective sections of 1:3 are shown in Fig. 4. To reach $V_{\text{eff}} = 42.7$ MV with an integrated time constant of 82% and an average synchronous phase of $-25°$ requires a voltage of 57.5 MV with roughly 14.4 MV and 43.1 MV from the low- and high-β sections respectively.

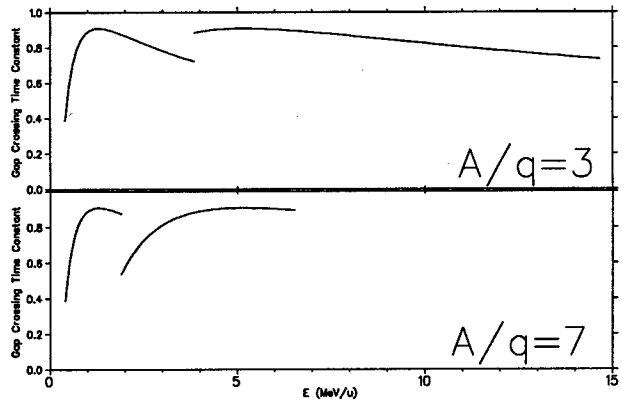

Figure 4: The acceleration efficiency for $A/q = 7$ and $A/q = 3$ for two-gap cavities with low- and high-β sections corresponding to β_o values of 4.8% and 9.6%.

Cavity Dimensions Once the design β_o is established the cavity dimensions are set by the rf frequency choice. The beam is bunched at 11.7 MHz and therefore many harmonics are available. A lower frequency increases the cavity length, hence reduces the required number of cavities but requires a longer inner conductor where mechanical oscillations may be problematic. For the present example we choose frequencies of 70 MHz and 140 MHz, the 6^{th} and 12^{th} harmonics of the bunch frequency, for the low- and high-β linac sections respectively. (The beam emittance is small enough and the inherent acceptance of the SC-linac large enough that higher frequencies are possible if required.) This gives a fixed cavity diameter of 20.5 cm, hence a common cryostat diameter for both sections of about 1 m, and cavity heights of 107 cm and 53.5 cm.

Linac Structure Recent developments at Legnaro[4] have shown that cavities of bulk Niobium or with Niobium films sputtered on a copper substrate can deliver gradients consistently above 5 MV/m and in some cases as high as 8 MV/m with cooling loads of 7 W at 4°K. We have decided to set the number of cavities based on a gradient of 5 MV/m with a lattice that is compatible with gradients up to 10 MV/m. Each cavity is then capable of an accelerating voltage of 1 MV. We opt for 16 low-β cavities (4 cryostats) and 44 high-β cavities (11 cryostats) for 60 MV. (Note that this is somewhat different than the optimum values quoted above since cavities are installed in units of four.) Due to the strength of the accelerating fields and hence the rf defocusing, it is proposed to use quadrupole triplets between cryostats to refocus the beam into the next cryostat. Even in this case accelerating gradients are limited to 5 MV/m and 7.5 MV/m in the first two cryo-stats while 10 MV/m can be tolerated in the remainder of the linac. It is also possible to provide a four-quadrupole transition cell after the low energy section and change the lattice to a triplet every second cryostat at the expense of a larger average beam size. The transverse focusing sections are 50 cm long for the low-β section and 60 cm long in the high-β section with maximum gradients of 70 T/m. A short diagnostic box will be included in each inter-cryostat region. A summary of the specifications for the post-stripper linac is given in Table 3.

Table 3: Specifications for each section of the post-stripper superconducting DTL.

Parameter	SC-DTL1	SC-DTL2
E $(A/q = 7)$	0.4-2 MeV/u	2-7 MeV/u
E $(A/q = 3)$	0.4-4.2 MeV/u	4.2-15 MeV/u
A/q	$3-7$	$3-7$
β_o	4.8	9.6
f (MHz)	70	140
$N_{\rm cav}$	16	44
$N_{\rm cryo}$	4	11
E_g (MV/m)	5	5
V_o,$V_{\rm eff}$ (MV)	16, 11.5	44, 33.1
Length (m)	6.0	18.5

Beam Simulations Beams of initial emittance $\beta\epsilon_{x,y} = 0.2\,\pi$mm-mrad and $1.6\,\pi$keV/u-ns and for $A/q = 3$ and $A/q = 7$ were simulated in the linac code LANA[5] using a triplet every cryostat and a gradient of 5 MV/m. Final beam energies were 14.9 MeV/u and 6.9 MeV/u respectively. Growth in the transverse and longitudinal emittance was less than 5%. The longitudinal acceptance in both cases was 50π keV-ns; 30 times larger than the design input beam.

6 COSTS AND SCHEDULE

The estimated cost of the upgrade, not including internal manpower or building expansion, is 18 M$ (Can). The proposal is now before the funding agency. A decision on the project is expected by Feb. 2000. Assuming the requested funds are obtained, first beams at 5 MV/m and at a limited mass range would be available as early as 2003 with the complete facility operational in April 2005.

7 REFERENCES

[1] P. Schmor, "Initial Commissioning of the ISAC Radioactive Beam Facility", these proceedings.

[2] U. Ratzinger, "A Low Beta RF Linac Structure of the IH type with Improved Radial Acceptance", Proceedings of 1988 Linear Accel. Conf., Newport News Virginia, June 1989.

[3] R. Geller, "Development of ECR Plasmas for Radioactive Ion Beams", Proceedings of HIAT98, Argonne Nat. Lab. 1998, to be published.

[4] A. Facco, et al, "Superconducting Cavity Development at Legnaro", Proceedings of HIAT98, Argonne Nat. Lab. 1998, to be published.

[5] D.V. Gorelov and P.N. Ostroumov, "The LANA Computer Code for the Beam Dynamics Simulation in Multi-Cavity Linacs", INR Internal Report, 1993-1994.

TANK1 OF THE ISAC-DTL LINAC

Pierre Bricault, Roger Poirier, Thomas Ries, Roland Roper and Guy Stanford.
TRIUMF, 4004 Wesbrook Mall, Vancouver, BC, Canada,

Abstract

The first phase of the ISAC radioactive ion beam facility at TRIUMF is now completed. It combines an isotope separator-on-line with a post accelerator. In the second phase a drift-tube LINAC is required to accelerate ions with a charge to mass ratio ≥ 1/6 from E = 0.15 MeV/u to a final energy fully variable up to 1.5 MeV/u. Due to the relatively low intensities of some of the radioactive ion species continuous (cw) operation of the accelerator is preferred. An interdigital H type RF structure is chosen because of its very high shunt impedance. The ISAC-DTL is composed of five IH tanks and three rebunchers, operating at 105 MHz. The basic design of the structure is similar to other IH structures with the exception that the stems are water-cooled. The features of this mechanical design will be discussed and the first results of the RF tests are presented.

1 INTRODUCTION

A radioactive ion beam (RIB) facility has been built at TRIUMF [1-3]. The ISAC facility uses the isotope separation on line (ISOL) technique to produce radioactive ion beams (RIB). The ISOL system consists of a primary production beam, a target/ion source, a mass separator, and a low energy beam transport system. These systems together act as the source of radioactive ion beams to be provided to the accelerator or the low-energy experimental areas.

The accelerator complex comprises an RFQ [4] to accelerate beams of q/A ≥ 1/30 from 2 keV/u to 150 keV/u and a LINAC (DTL) to accelerate ions of q/A ≥ 1/6 to a final energy between 0.15 MeV/u to 1.5 MeV/u. Both LINACs are required to operate cw to preserve beam intensity.

A first proposal, in 1985 envisaged the use of a Wideroe structure for the ISAC DTL LINAC [5]. The idea was quickly abandoned because of the lack of funding and due to the high power consumption of the LINAC. A second study envisaged the use of a superconducting structure [6,7] for the post stripper LINAC. This proposal was also abandoned because the required time to build a superconducting LINAC was incompatible with the scheduled cash flow of the ISAC funding. After approval of the ISAC FIVE-YEAR plan in 1995 we came back to a room temperature solution. The interdigital H type RF structure (IH) was chosen because of its high shunt impedance compared to Alvarez or Wideroe RF structure. Due to the requirement of continuous energy variability and preservation of the time structure the DTL structure has been configured as a *separated function* DTL [8,9]. Five independently phased IH tanks operating at $\phi s = 0°$ provide the main acceleration. Longitudinal focussing is provided by three independently phased, split-ring resonator structures positioned before the second, third and fourth IH tanks. Quadrupole triplets placed after each of the four IH tanks maintain transverse focussing.

2 DTL TANK 1 SPECIFICATION

The code LANA [10] has been used to study the beam dynamics and to set the general specifications for the DTL tanks. At full voltage the beam dynamics are typical for a 0° accelerating structure [11] with the benefits of optimum acceleration efficiency and reduced RF defocusing.

Table 1 gives the basic specifications of the first IH tank for the design particle of q/A ≥ 1/6. The quantity of cells in each tank is chosen to satisfy both transverse beam size requirements and debunching constraints in variable energy mode. Tank apertures are chosen to give sufficient transverse acceptance while maintaining a gap-to- aperture ratio of at least 1.2 for efficient acceleration.

Table 1 : DTL tank1 specifications

NO. Cells	L cm	A mm	β_{IN} %	β_{OUT} %	Q/A	V_{EFF} MV	E_{OUT} MeV/u
9	26	10	1.5	2.2	1/6	0.5	0.23

3 MAFIA SIMULATIONS AND MODEL STUDY

The electromagnetic code MAFIA was used to simulate the DTL tank structure to assist in optimizing the dimensions of the selected configuration. This eliminates construction of a large number of scale models during the optimization process.

The calculations give power density information, which will then be used to determine the cooling requirements of the cw DTL. The electric field distribution inside a cylindrical cavity operating in the H_{111}-mode has a sinusoidal shape. The flatness of the gap voltage distribution along the beam axis is one main problem to solve. This means that we have to make the capacity and inductivity per unit length of the cavity constant. The capacity and/or inductivity per unit length of the cavity have to increase towards the ends. Several MAFIA simulations were performed to obtain the proper flux inducer shape at both ends of the cavity. MAFIA was also used to predict the appropriate g/L dependence to flatten the field distribution. Table 2 gives a summary of the RF characteristics of tank1.

Table 2 : Summary of the RF characteristics of tank1.

Frequency MHz	Q	Z_{eff} MΩ/M	V_{eff} MV	P kW
107.2	11500	356	0.5	2.6

A full-scale model of an 11-gap tank was built to test the tuning of the field distribution and the characteristics of various mechanical tuners. The tank was built from a rolled copper sheet 6 mm thick. The end plates were made from aluminum on which a thin foil of copper was glued. The ridge and the drift tube were made from brass to ease

0-7803-5573-3/99/$10.00@1999 IEEE.

the fabrication. All pieces were bolted together to facilitate changes of the cavity geometry. The coupling loop and the tuner were installed in the median plane, one on each side of the tank. Two types of tuners were evaluated with this IH tank model. The first tuner uses a flat copper plate; 50 mm by 280 mm. Vibrations of that plate make the frequency stabilization extremely difficult. The second tuner uses a half cylinder 50-mm radius. Even if the frequency stabilization is much better the tuner vibration still has some effect. A larger radius of 100 mm does not show any frequency shift due to vibration. Contrary to the flat plate case the capacitance is mainly concentrated on the stem, not on the drift-tube region. Figure 1 shows the result of the frequency and Q value variation as a function of the distance from the stem.

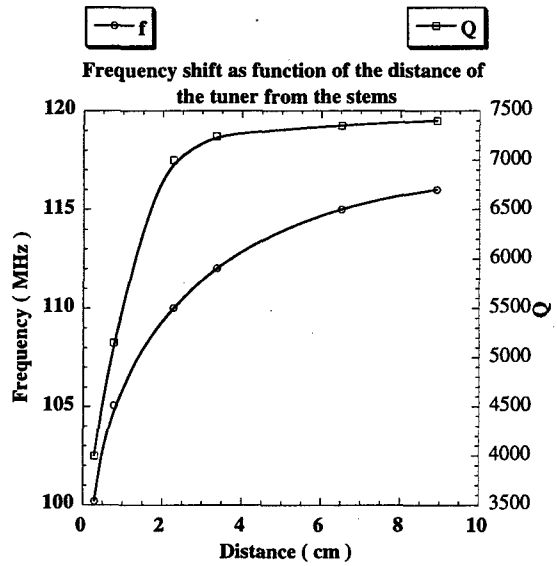

Fig. 1 : The frequency shift as a function of the tuner position from the stems.

Three NC machined models of a stem and drift-tube shown in fig. 2 were made to evaluate the fabrication cost. The first one was made from steel. The inner part was machined such that we obtain a cavity. The water comes in through a stainless steel pipe. The second one is made from a copper block. In that case the stem cooling is done only by heat conduction between the stem and the ridge. In the third case, two cooling channels were drilled at an angle such that they converge close to the drift-tube.

We used them also to measure the temperature of the stem under various heat and water loads. MAFIA simulations tell us that the maximum power loss on the stem is 200 Watts. Assuming only 75% of the calculated Q value input power of 265 Watts was used for temperature measurements.

Four thermocouples were used to measure the temperature on the tip of the drift-tube, at the base of the stem, into the input and output water channels. Figure 2 shows the thermocouples location used to measure the temperature. Table 3 shows the results of the cooling test on the stem models.

The tests show that a water flow of 3 l/min. is sufficient to cool the drift tube to a temperature below 50 °C. The water flow does not produce any measurable mechanical vibrations. From these models we found that the lowest cost stem is the one machined from a copper block.

Stem models for DTL's tank 1

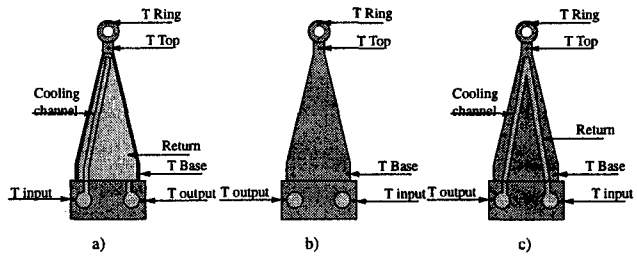

Fig. 2 : Schematic drawing of the three stem models used for the test.

Table 3 : Temperature distribution on the stems. Q = 3 l/min and W = 265 Watts.

	Stem model Temperature in °C		
	a)	b)	c)
T_{in}	10	9.5	9.5
T_{out}	12	11.5	11.5
T_{Base}	21	75	14
T_{Top}	14	108	23
T_{Ring}	47	119	47

4 DTL FABRICATION

The first DTL-IH tank was built from mild steel plate 2.54 cm thick. It is 91.92 cm in diameter by 27.67 cm long. The two lids are 25 mm thick and the maximum deflection is estimated to be less than 0.3 mm. The IH cavity is made in four main components, the cylinder, the ridges, the lids and the stems. The eight drift-tubes and the two ridges are machined from bulk copper blocks. The tank and the two lids are made from mild steel. The interior faces are machined to a surface finish of 16 µinch and then copper plated. The copper plating thickness is larger than the necessary RF required penetration depth to assure a very nice finish.

Several options were investigated for the mounting of the ridges to the tank wall. Ridge made from mild steel welded onto the tank was discarded because of the difficulty of maintaining the proper alignment between the two ridge faces. We finally decided to bolt the ridges onto a flat surface machined on the inner tank wall. Four bolts clamp the ridges in place and the vacuum seal is done using an o-ring. The faces of the ridges and bases are machined and polished to a finish less than 5 µinches to assure a very good rf contact as demonstrated on a test cavity. Provision for alignment was made by allowing an extra 1.5 mm at the base of each stem. At first each stem was installed in the tank and the center of each drift-tube measure with precision. Then the base of each stem was machined to the right height as well as an o-ring groove to seal the vacuum from the cooling line. The stems are bolted down on the ridges at their final location and the alignment was checked to be better than ± 50 µm.

For the first IH tank we made provision for several ports. We have two ports on each lid, one for a turbo pump and the other three for windows if we need to

investigate the inner parts of the cavity. On the side we have four small ports for vacuum gages, two probes and coupling loop. Two larger ports in the median plane will be used for frequency tuners , one fixed and one movable. Figure 3 shows a photograph of the first IH tank. We can see the stems installed on each ridge after proper alignment and the location of the ports.

4.1 Cooling

The ridges are cooled by two channels drilled from the base and two manifolds running inside each ridge delivering cooling water to the stems. The drift tubes are cooled by a water circuit coming up through the ridge and into a drilled out portion of the stem, see fig. 2c. Two channels, 9.5 mm in diameter in each lid provide sufficient cooling. Operation of the LINAC at constant temperature may be required. This will be done by using four 6 mm cooling lines attached on the exterior of the tank.

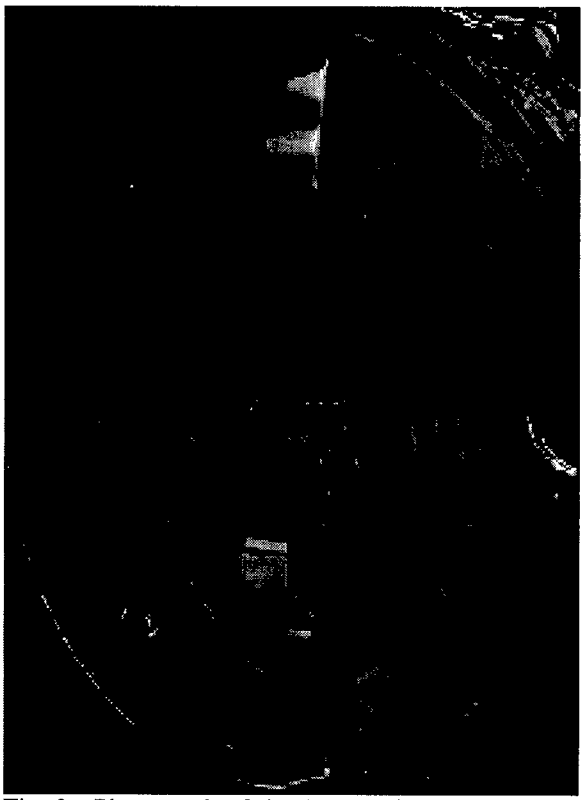

Fig. 3 : Photograph of the DTL tank 1 with the front lid open.

4.2 RF Measurements

The measured frequency of the cavity is 109.7 MHz and the Q value is 9700. The frequency is 2% higher and the Q is about 85 % of the predicted values from MAFIA. The electric field distribution on axis has been measured along the DTL axis. Figure shows a comparison between the measurement and the MAFIA prediction. We obtain a very good agreement between the predicted and the measured field distribution, causing insignificant beam phase error. Figure 4 shows the comparison between the electric field distribution predicted by MAFIA and the measured filed distribution along the tank axis.

4.3 Power test

Full power tests are under way. The RF amplifier was operated in self excited mode delivering 3.6 kW and 87.5 kVolts to the drift tube gap. Stable operation for more than 100 hours was achieved.

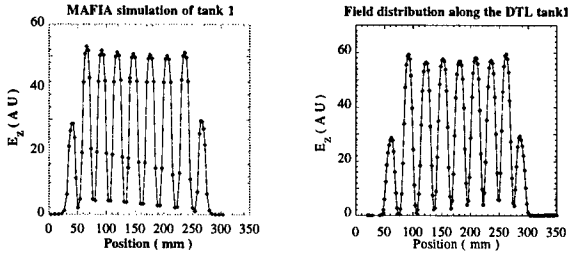

a) b)

Fig. 4 : Electric field distribution along the DTL IH tank. MAFIA field distribution a), measurement using perturbation technique b).

5 ACKNOWLEDGEMENT

The authors would like to thank those who contributed in making the fabrication, assembly and tests a success. In particular we would like to thank MM. E. Knape, B. Gasbarri, P. Harmer, A. Mitra and W. H. Uzat. We appreciated very much discussion with U. Ratzinger, R. Rimmer, Y. Bylinsky, D. Gorelov and R. Laxdal.

6 REFERENCES

[1] Paul Schmor, Initial Commissioning of the ISAC Radioactive Beam Facility, this conference.
[2] Pierre Bricault, M. Dombsky, P. Schmor, G. Stanford, I. Thorson and J. Welz, A 500 MeV 100 μA proton target for ISAC Radioactive Ion Beam Facility, this conference.
[3] P. Bricault, et al., ISAC: Radioactive Ion Beams Facility at TRIUMF, Proc. Of the XVIII International Linear Accelerator Conference, 1996, Genève, Suisse, p. 399.
[4] R. Poirier, et al., The RFQ Prototype for the Radioactive Ion Beams Facility at TRIUMF, Proc. Of the XVIII International Linear Accelerator Conference, 1996, Genève, Suisse.
[5] G. E. McMicheal, B. G. Chidley and R. M. Hutcheon, Conceptual Design Study for the Proposed ISOL Post-Accelerator at TRIUMF, AECL-8960, TRI-DN-85-33.
[6] J. Frazer and H. Schneider, Design of a Superconducting Interdigital Accelerator Structure for Radioactive Ions, Proc. 1990 Linear Accelerator Conf., Los Alamos, p. 88 (1990).
[7] H. R. Schneider, P. Bricault, S. Koscielniak, T. Ries and L. Root, A Post Accelerator for a Radioactive Beam Facility at TRIUMF, Proc. Of the1994 International LINAC Conference, Tsukuba, Japan, p. 752.
[8] R.E. Laxdal and P. Bricault, *Design of a Drift Tube LINAC for the ISAC Project at TRIUMF,* Proc. Of the XVIII Inter. Linear Accelerator Conf. 1996, Genève, Suisse, p. 435
[9] R.E. Laxdal, P.G. Bricault, T. Reis, D.V.Gorelov, *A Separated Function Drift-Tube LINAC for the ISAC Project at TRIUMF,* Proc. Of the 1997 Particle Accelerator Conf. Vancouver, Canada, p. 1195
[10] D.V. Gorelov and P.N. Ostroumov, The LANA Computer Code for the Beam Dynamics Simulation in Multi-Cavity Linacs, INR Internal Report, 1993-1994.
[11] U. Ratzinger, Interdigital IH Structures, Proc. 1990 Linear Accelerator Conf., Los Alamos, p. 525, (1990).

THE 7-GAP-RESONATOR-ACCELERATOR FOR THE REX-ISOLDE-LINAC*

H. Podlech†, M. Grieser, R. von Hahn, R. Repnow, D. Schwalm
Max-Planck-Institut für Kernphysik, Heidelberg, Germany

Abstract

The REX-ISOLDE-Experiment which is presently being under construction at CERN is intended to investigate exotic, very neutron rich, radioactive nuclei. A linear accelerator will deliver radioactive beams which are produced by the isotope separator ISOLDE, with energies between 0.85 and 2.2 MeV/u. The Linac will consist of a RFQ-accelerator, an interdigital H-Structure (IH) and three 7-gap-resonators for variable final energy [1].
Assuming an acceleration voltage of one 7-gap-resonator to be 1.75 MV at 90 kW rf power, the design velocities of the three resonators were chosen to be 5.4%, 6.0% and 6.6% of the velocity of light. Three downscaled models (1:2.5) were built in order to optimize the shuntimpedance and the field-distribution for the operating frequency of the amplifiers of 101.28 MHz.
The development of the resonators was accompanied by extensive MAFIA calculations. It could be demonstrated that spiral-resonators like 7-gap-resonators can be calculated with MAFIA. Important quantities like frequency, shuntimpedance, quality factor and field distribution were compared between simulation and measurement.
The first two power type resonators (5.4% and 6.0%) are finished, frequency tuning and low power measurements were done. The Q-values are about 5560 and 5280, respectively, the shuntimpedance 71 MΩ/m and 68 MΩ/m, respectively, and are in very good agreement with the model measurements. After preparation for high power tests a beam test for the voltage calibration is planned. In this paper the status of the production of the 7-gap-resonators is reported.

1 INTRODUCTION

The high energy section of the REX-ISOLDE Linac (see fig.3) consists of three 7-gap resonators similar to those built for the new high current injector at Heidelberg [2]. Each resonator has a single resonance structure which is shown in fig.1. It consists of a copper half shell to which three copper arms are attached on each side. Each arm consists of two hollow profiles, surrounding the drift tubes and carrying the cooling water. Copper segments on both sides of the half shell allow to tune the resonator to the rf frequency of 101.28 MHz. A tuning plate corrects the detuning effects due to the temperature changes of the tank or half shell during operation. The rf power will coupled into the resonator near one of the three legs, where the magnetic flux is maximum. Assuming a realistic resonator voltage for each resonator of approximately 1.75 MV for 90 kW rf-power (duty cycle 1:10), the design velocities were chosen to 5.4%, 6.0% and 6.6% of the velocity of light [3].

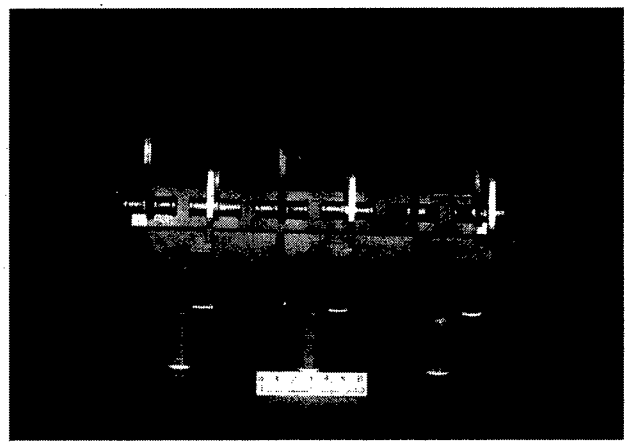

Figure 1: Resonance structure of the 6.0% model (2.5:1)

2 OPTIMIZATION AND TUNING

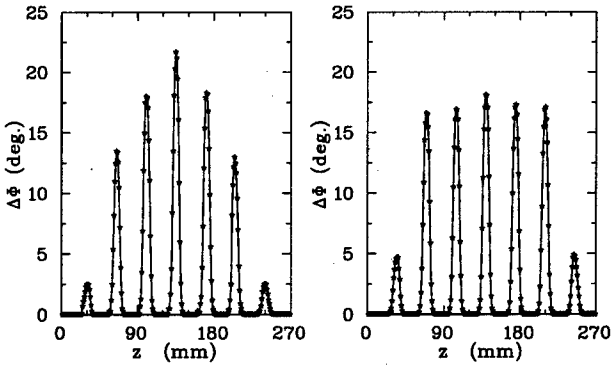

Figure 2: Phase shift distribution (square of the E-field) of the detuned (left) and optimized (right) 6.0% resonator model (push pull mode).

Three down scaled models were built in order to optimize the field distribution of the push pull mode used for acceleration and to tune the eigenfrequency. Therefore the drift tubes and the arms of the models are movable in the half shell. The capacity between the arms is changed by rotation

* Work supported in part by the German Federal Ministery for Education, Science, Research and Technology (BMBF) under contract No. 06HD802I and No. 06LM868I(2).

† Email: hjp@daniel.mpi-hd.mpg.de

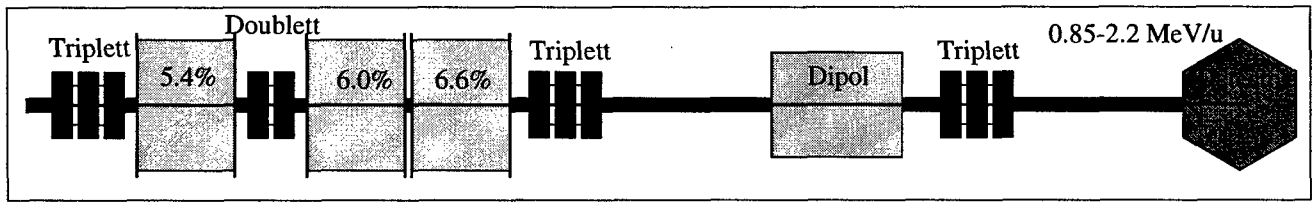

Figure 3: Lay-out of the 7-gap-resonator-accelerator forming the high energy part of the REX-ISOLDE-Linac

of the arms against each other. Fig.2 shows the phase shift distribution along the beam axis before and after optimization. The result of the optimization is a flat field distribution between the inner drift tubes. All field measurements were made with the bead perturbation measurement method. A small perturbation bead influences the electric field of the resonator. This causes a phase shift $\Delta\Phi$ between the signals of the signal generator and the resonator. This phaseshift is proportional to the square of the unperturbed electric field. Fig. 4 (left) shows the frequency of the three models as

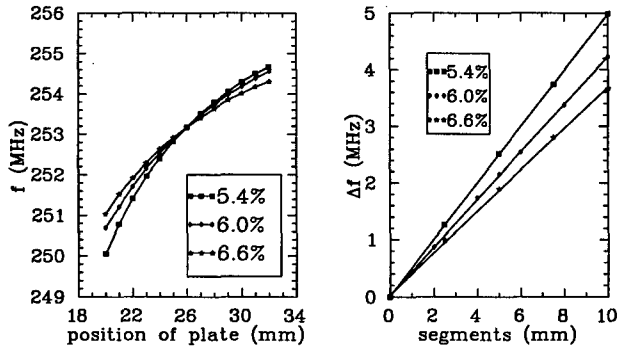

Figure 4: Frequency of the models (2.5:1) as function of the position of the tuning plate (left) and thickness of the segments (right).

function of the position of the tuning plate. Driving the tuning plate results in a variation of the capacity between the resonance structure and the plate and therefore a frequency shift. The copper segments are used to tune the resonators to the frequency of the amplifiers by changing the inductance of the resonance structure. Fig. 4 (right) shows the linear behavior of the frequency as function of the thickness of the segments attached to the ends of the half shell. Table 1 summarizes the measured main parameters of the three model resonators [4].

3 POWER TYPE RESONATORS

Two of the three power type resonators are already finished. Fig. 5 shows the 5.4% power type resonator with resonance structure and plunger prepared for low level rf measuerements. After tuning the eigenfrequency of the push-pull-mode to the operation frequency of the amplifiers (101.28 MHz) the Q-values were determined to 5560 (5.4%) and 5280 (6.0%) respectively. The

Parameter	model resonators		
	5.4%	6.0%	6.6%
f (MHz)	253.2	253.2	253.2
Q-value	3315 ± 30	3340 ± 30	3180 ± 30
Z (MΩ/m)	113 ± 7	105 ± 6	106 ± 8

Table 1: *Measured parameters for the (2.5:1) model resonators, f=frequency, Z=shuntimpedance*

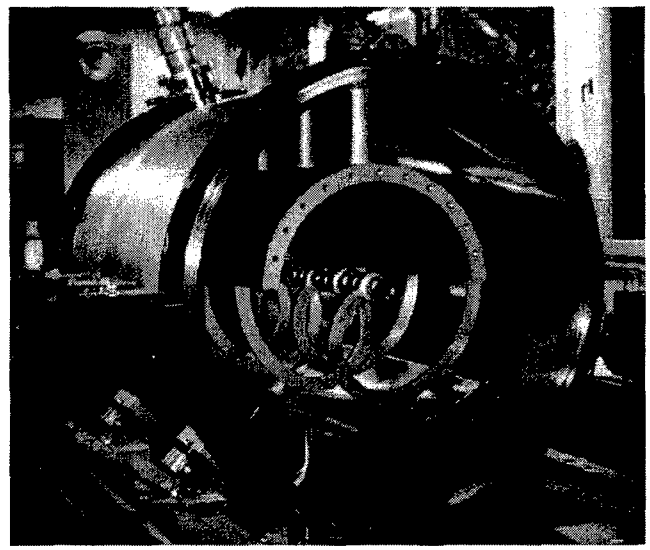

Figure 5: The 5.4% power type resonator prepared for low power rf measurements

shuntimpedances are 71 MΩ/m and 68 MΩ/m. With an rf power of 90 kW we can expect a resonator voltage of 1.9 MV for both resonators. The resonators are now ready for high power and beam tests. Fig. 6 shows the first delivered rf-amplifier which provides an rf power of 100 kW with a duty cycle of 10%. Table 2 summarizes the results of the low level rf measurements of the power type resonators.

4 MAFIA SIMULATIONS

The development of the resonators was accompanied by extensive MAFIA calculations [5]. To investigate the eigenfrequency and voltage distribution in the gaps MAFIA is a

Parameter	power type resonators	
	5.4%	6.0%
f [MHz]	101.28	101.28
Q-value	5560 ± 110	5280 ± 105
Z [MΩ/m]	71 ± 7	66 ± 6
N [kW]	90	90
U_0 [MV]	1.90 ± 0.1	1.90 ± 0.1

Table 2: *Measuered parameters for the power type resonators, f=frequency, Z=shuntimpedance, N=power consumption, U_0=resonator voltage (extrapolated)*

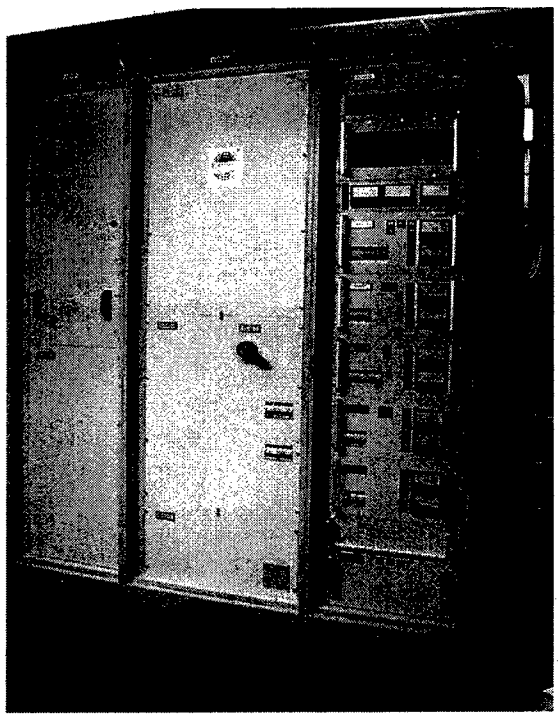

Figure 6: The first of three 100 kW amplifier delivered in December 1998. Left RF part, middle HV rack, right control rack

very powerful calculation code. It could be demonstrated that the frequency of the 7-gap-resonators can be calculated with an accuracy of better than 1% for the push pull mode. The calculated quality factor Q and shuntimpedance Z are always a factor of about two too high [3]. The power losses inside a 7-gap-resonator are also calculated in order to check the cooling water requirements. These investigations have shown that about 75% of the rf power is dissipated at the resonance structure half of which is lost at the arms, which therefore have to be cooled very effectively.

5 BEAM DYNAMICS

Beam dynamic calculations were made to optimize the transmission of the beam to the target [3]. Final energies between 0.85 and 2.2 MeV/u with nearly 100% transmission can be realized. The acceptance of the three resonators in the x-plane is 1.2 π mm mrad (norm.) and in the y-plane 3.0 π mm mrad (norm.). The bunchlength of the fully accelerated beam (2.2 MeV/u) is 2.4 ns at the target, which can be further improved – if necessary – by a rebuncher before the target. Fig. 7 shows the calculated envelope of both transverse directions between the last resonator and the target. Because of the relatively wide transit time factor of the 7-gap-resonators they can be used to vary the output energy of the linac. Even a deceleration of the beam from the IH-structure from 1.1 MeV/u down to 0.85 MeV is feasible.

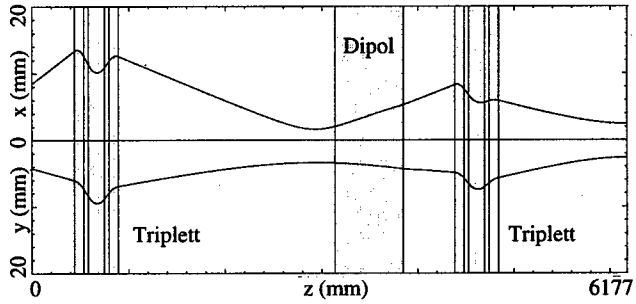

Figure 7: Calculated envelope in x and y direction between the last resonator and the target.

6 REFERENCES

[1] D. Habs et al., The REX-ISOLDE-Project, Nucl. Instr. and Meth. B139 (1998) 28

[2] R. von Hahn et al., Nucl. Instr. and Methods, A328, 270-274 (1993)

[3] H. Podlech, MPI-H–V21–1997, Heidelberg, 1997

[4] H. Podlech et al., The 7-Gap-Resonator-Accelerator for the REX-ISOLDE-Experiment at CERN, Nucl. Instr. and Meth. B139 447-450, 1998

[5] The MAFIA-Collaboration, The Electromagnetic CAD-System, Darmstadt, 1994

DEVELOPMENT OF A PROTON ACCELERATOR FOR THE JAERI NEUTRON SCIENCE PROJECT

N. Akaoka, E. Chishiro, K. Hasegawa#, M. Ichihara, M. Ikegami, T. Ito, M. Kinsho, J. Kusano, E. Minehara, M. Mizumoto, K. Mukugi, F. Noda, H. Oguri, N. Ouchi, J. Sawada, H. Takado, O. Takeda, T. Tomisawa, H. Yokomizo: JAERI, Tokai-mura, Ibaraki, 319-1195, JAPAN

Abstract

The Japan Atomic Energy Research Institute has been proposing the Neutron Science Project (NSP). The joint project of the NSP and the JHF of KEK is under discussion. The new project makes use of the R&D results of the NSP and the JHF. The R&D activities of the proton accelerator at JAERI will be presented in this paper. The development work and characteristics measurements have been made for the low energy components of the linac; performance tests of a negative hydrogen ion source, development of an integrated type RFQ and high duty factor power tests of a DTL model tank. A superconducting linac is a main option for the high energy part of the linac. Vertical tests of a single cell superconducting cavity have been made. The maximum peak surface fields of 44 MV/m and 47 MV/m have been achieved for β=0.5 and 0.89 cavities, respectively. A 600 MHz IOT RF source has been manufactured and dummy load tests at 35 kW CW have been successfully conducted.

1 INTRODUCTION

A high intensity proton linear accelerator with an energy of 1.5 GeV has been proposed for the Neutron Science Project (NSP) at JAERI[1]. The aims of the NSP are to explore basic neutron science and nuclear energy related technologies. We have three stages to upgrade the beam power and duty factor. The operation mode in the first stage is a pulse for the neutron scattering experiments with beam power of 1.5 MW. By increasing a duty factor and peak beam current up to 20 % and 30 mA, respectively, beam power will be upgraded to 5 MW in the second pulse stage. The 8 MW CW beams will be provided for the nuclear waste transmutation experiments in the CW stage.

The joint project of the NSP and the Japan Hadron Facility (JHF) Project of KEK is under discussion to take more effective promotion of the scientific and engineering fields[2]. The new project makes use of the R&D results accomplished for the NSP. Several R&D items have been studied for high intensity accelerator development; 1) beam dynamics design and calculation, 2) a negative hydrogen ion source and fabrication of high power test models of RFQ and DTL, 3) superconducting cavities and 4) high power RF sources.

Email: hasegawa@linac.tokai.jaeri.go.jp

2 LINAC SYSTEM

A schematic drawing of the linac system is shown in Figure 1. The front-end part of the linac, which consists of RFQ, DTL and separated-type DTL (SDTL), uses normal conducting structures and the higher energy part uses superconducting linac (SCL). Basic parameters of the linac components are summarized in Table 1. The linac system design is described in detail in reference 3.

For the pulse mode operation, the intermediate pulsing choppers for the storage ring injection and extraction have to be installed, whereas no choppers are required for the CW operation. To obtain better beam quality by using optimized beam transport systems, injector lines for the pulse and for the CW operations are used. The two lines merge in the DTL section at 7 MeV, where the neutron generation due to the beam loss risks can be avoided.

The SDTL structure[4] is adopted for the higher energy DTL region because of some advantages such as the simpler structures and the smoother matching properties to the following section.

The superconducting linac (SCL) is a main option between 100 and 1500 MeV, because characteristics of the cavities are suitable for the high duty factor operation and less beam loss is expected due to the large bore size.

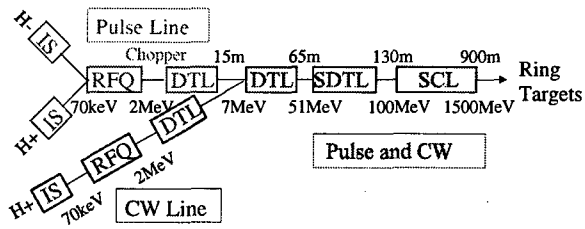

Figure 1. A schematic drawing of the linac system

3 DEVELOPMENT OF ACCELERATOR COMPONENTS

3.1 Negative Hydrogen Ion Source

Negative hydrogen beams are required to inject the beam into a storage ring. The beam extractor of the existing

0-7803-5573-3/99/$10.00@1999 IEEE.

positive ion source has been modified to produce negative ion beams. The characteristics with cesium introduction of the negative ion beam have been examined at the duty factor of 5 %[5]. In the pure volume operation, the ion current has been limited to be 8 mA. In the cesium-seeded operation, the beam current has been enhanced and negative ion current and density of 21 mA and 33 mA/cm^2 have been obtained. An electron to negative ion current ratio is 4 in the cesium seeded, while 34 in the pure volume.

A new negative ion source has been fabricated to accumulate experimental data to fulfil the requirement of the NSP linac. A plasma chamber is installed outside of an insulator to change the configuration of the cusp magnet fields easily. Two differential pumping ports are equipped with the ion source. When the differential pumping system is on, the vacuum pressure in the Low Energy Beam Transport Line is improved from $7.5x10^{-5}$ to $1.0x10^{-5}$ Torr and the negative ion beam current is enhanced by 1.7 times. The experimental data have been obtained to be 11 mA without cesium. The beam test will be continued.

Table 1. Basic parameters of the linac components

Negative Hydrogen Ion Source	
Energy	70 keV
Current	50 mA

CW-RFQ	
Energy	2 MeV
Frequency	200 MHz
Peak field	1.5 Kilpatrick limit
Length	3.57 m
Duty	30 % (Pulse) , 100 % (CW)

CW-DTL/SDTL		
	DTL	SDTL
Energy	51 MeV	100 MeV
Frequency	200 MHz	200 MHz
E_0	1.5 MV/m	1.5 MV/m
Length	58 m	64 m

Superconducting Linac	
Energy	1.5 GeV
Frequency	600 MHz
Maximum Epeak	16 MV/m
No. of Cavities/ Modules	284/142
Length	690 m
Number of Cavity Group	8
Focusing Lattice	Doublet between modules

3.2 CW-RFQ

We have developed a four-vane type 2 MeV RFQ[6] based on the R&D of the OMEGA program. This RFQ has accelerated proton beams at a current of 70 mA with a duty factor of 10 % (a beam pulse length of 1 ms and a repetition of 100 Hz). At a duty factor of 1 % (a beam pulse length of 1 ms and a repetition of 10 Hz), a peak current of 100 mA has been achieved.

A new RFQ for the NSP is designed to operate at much higher duty factor (up to 30 %) pulse and CW modes. The RFQ is designed with lower electric field of 1.5 Kilpatrick limit to keep reliable operations and to reduce an RF wall loss power. The beam simulation results show that more than 95 % beam transmission is expected at the beam current up to 80 mA.

The R&D RFQ has spiral type RF contacts between a tank and vanes. The burnout problem at the contact was one of the most important issues to achieve high duty factor operations. To eliminate this problem, we have been developing an integrated type RFQ without RF contacts. A high power model with 50 cm long has been fabricated by brazing process. The 20 % duty factor operation has been achieved with an RF power of 40 kW, which is approximately 30 % beyond the normal operation power level. The duty factor has been limited by the RF source. An R&D of some metal joint processes such as electron beam welding (EBW) and laser beam welding as well as brazing is now underway.

3.3 CW-DTL and SDTL

The parameters for the CW-DTL are evaluated. Up to 7 MeV, two DTLs are prepared for the pulse and the CW lines. The lower E_0 of 1.5 MV/m is taken to reduce the heat dissipation of the structures and the RF power consumption. An equipartitioned design approach is taken to suppress the emittance growth[3,7]. The rms and the 90 % emittance growth rates are about 7 % and 10 % at the highest, respectively.

An R&D-DTL high power model with 9 cells for mock-up of the first part of the DTL was fabricated to study the RF characteristics and the cooling capabilities[8]. In 1995, the 20 % duty factor operation was achieved with an RF power of 128 kW, which corresponds to E_0=2MV/m. The high power model has been reinstalled and the 50 % duty factor operation with an RF power of 75 kW (E_0=1.5MV/m) has been achieved. The duty factor has been limited by a power supply of the RF source.

3.4 Superconducting linac

In the SC linac part, the proton velocities gradually change from 0.43 to 0.92 corresponding to the energies for 100 MeV and 1.5 GeV. Accordingly, the length of the cavity is also changed. Based on an optimization study, an SC linac with 8 groups has been designed[9]. The

cavities in each group are made with identical 5 cells and two cavities are laid in one doublet focusing period. Q-magnet field gradient is determined by using the equipartitioning scheme. The transverse and the longitudinal rms emittances are nearly constant or only 1 % increase.

For the pulse beam operation, the mechanical resonant frequencies should be higher than the maximum repetition rate of 50 Hz. Analysis for the mechanical resonance has been carried out to evaluate the microphonic vibration[10]. An axial mode of 80 Hz for the β=0.499 cavity with 3 mm thick wall with stiffner is the lowest frequency mode. We have found that the stiffner is effective to increase the structural resonant frequency; in the case without stiffner, the lowest mode is transverse and the frequency is 38 Hz. We are studying better cavity from a practical point of view; stiffner type or thicker wall type.

Two sets of single SC test cavities have been fabricated for β=0.5, which corresponds to the proton energy of 145 MeV. Vertical tests have been conducted to examine the RF and mechanical properties. The maximum surface peak field strengths (E_{peak}) of 32 MV/m at 4.2 K and 44 MV/m at 2.1 K have been successfully obtained[11]. A single-cell cavity of β=0.886 has been also fabricated and tested. The peak fields have been 47 and 36 MV/m at 2 K and 4.2 K, respectively. These test results have satisfied the specification for the conceptual layout of the superconducting linac.

Two 5-cell cavities have been fabricated: one is made of copper and one is niobium. The copper model cavity is used to test a pre-tuning. Maximum deviation of the peak fields on axis at each cell center position is 37.5 % before the pre-tuning. After the pre-tuning, the deviation has improved to be 0.7 %. The pre-tuning, surface treatment and vertical test will be performed for the niobium cavity.

3.5 RF Sources

The RF sources are main components to determine the availability and reliability. They are most costly parts in the accelerator system. Two frequencies, 200 MHz and 600 MHz, have been selected in the low energy and the SC linac part, respectively. Required RF powers are 300 kW for RFQ, 9 MW for DTL/SDTL and 25 (pulse mode) or 7.5 MW (CW mode) for the SC linac, respectively. An RF system design by using a grid tube (tetrode), a Klystron and an IOT (Inductive Output Tube) has been carried out.

In the SC linac RF system, the RF source has to be operated in the high power pulse mode and low power CW mode. Klystrons are to take their maximum efficiency at the full saturation power. To keep higher efficiency in the low power range, the beam voltage reduction is effective[12].

The IOT is one of the favorable RF sources to cover the wide power range without significant degradation of the efficiency. A 600 MHz IOT system (TH760, Thomson) has been manufactured and dummy load tests have been conducted. The gain and the efficiency at 35 kW were 22 dB and 61 %, respectively. The phase and amplitude have kept within +-0.5% and +- 0.5 degree in 270 minutes duration at 35 kW CW.

4 SUMMARY

The linac design and development work has been made for the NSP. The good performances of the components such as an ion source, RFQ, DTL and RF source have been achieved. The vertical SC cavity test has been successfully conducted resulting in the satisfactory maximum surface electric field strength.

The R&D's of the accelerator components will be continued based on the new Joint Project parameters.

5 ACKNOWLEDGEMENT

The authors would like to thank Drs. S. Noguchi, K. Saito, H. Inoue and E. Kako of KEK for discussion and help on the SC cavity development.

6 REFERENCES

[1] M. Mizumoto et al., 'High Intensity Proton Accelerator for Neutron Science Project at JAERI', Proc. of Linac98, Chicago, Aug. 1998

[2] Y. Yamazaki and M. Mizumoto, 'Accelerator Complex for the Joint Project of KEK/JHF and JAERI/NSP', these proceedings

[3] K. Hasegawa et al.,'System Design of a Proton Linac for the Neutron Science Project at JAERI', J. Nucl. Sci. Tech., Vol.36, No.5 (1999)

[4] T. Kato, 'Proposal of a Separated-Type Proton Drift Tube Linac for a Medium-Energy Structure', KEK Report 92-10 (1992)

[5] H. Oguri et al., 'Development of an Injector Section for the High Intensity Proton Accelerator at JAERI', Proc. of EPAC98, p749, Stockholm (1998)

[6] K. Hasegawa et al., 'Development of a High Intensity RFQ at JAERI', Jour. Nucl. Sci. and Tech, Vol. 34, No.7, pp.622-627 (1997)

[7] K. Hasegawa et al., 'Beam Dynamics Design of a Proton Linac for the Neutron Science Project at JAERI', Proc. of EPAC98, p719, Stockholm (1998)

[8] N. Ito et al., 'Fabrication and Tests of the DTL Hot Model in the R&D Works for the Basic Technology Accelerator (BTA) in JAERI', Proc. of 1994 International Linac Conf., p.119, Tsukuba (1994)

[9] Y. Honda et al., 'A Conceptual Design Study of Superconducting Proton Linear Accelerator for Neutron Science Project', Proc. of APAC98, Tsukuba 1998 (1999)

[10] N. Ouchi et al., 'Proton Linac Activities in JAERI', Particle Accelerators, Vol.62, pp.537-554 (1998)

[11] N. Ouchi et al., 'Development of Superconducting Cavities for High Intensity Proton Accelerator at JAERI', Proc. of Applied Superconductivity Conference (ASC-98), Palm Desert, Sep. 1998

[12] E. Chishiro et al.,'A Conceptual Design of RF System in the NSP Superconducting Linac at JAERI', Proc. of Linac98, Chicago, Aug. 1998

DESIGN CONSIDERATIONS FOR A SUPERCONDUCTING LINAC AS AN OPTION FOR THE ESS

W.F. Bräutigam, S.A. Martin, G. Schug, E.N. Zaplatine, FZJ Juelich; P.F. Meads, Oakland;
Y.V. Senichev,University Aarhus

Abstract

An approach for a superconducting high-current proton linac for the ESS has been discussed as an option in the "Proposal for a Next Generation Neutron Source for Europe- the European Spallation Source (ESS)"[1,2]. The following work studies the technical and economic conditions for a superconducting linac at the high-energy end of the proposed accelerator system. The use of superconducting elliptical cavities for the acceleration of high-energetic particles $\beta = v/c \approx 1$ is certainly state of the art. This is documented by many activities (TJNAF, TESLA, LEP, LHC, and KEK). A design study for the cavities is described in another paper on this conference[5]. For low energy particles (β<<1) quarter wave type cavities and spoke-type cavities have been discussed. The main motivation for this study is the expectation of significant cost reduction in terms of operational and possibly investment cost.

1 BASIC PARAMETERS

The basic parameters of the system are given in tables 1,2,3.

Table 1: Basic data of the superconducting ESS linac

Maximum energy	1334	MeV
maximum β=v/c	0.91	
injection energy	70	MeV
injection β	0.4	
average current	3.75	mA
peak current pulse average	63	mA
repetition rate	50	Hz
pulse length	1.2	ms
duty factor	6	%

The high energy linac will transport the beam from 70 MeV up to 1334 MeV. A current of 3.75 mA is necessary for the 5 MW beam power. The pulse length of 1.2 ms is required by the filling mechanism for the 2 accumulator rings. The macro time structure of the beam is 1.2 ms out of 20 ms, result in a duty factor of 6 %. The micro time structure inside the pulse is 360 ns beam-on and 240 ns beam-off. The accumulator uses the beam-off-time for maintaining a beam free section in the circulating beam. The $2*10^9$ particles per bunch are not too critical for the high energy linac. The total number of particles per pulse is $4.7*10^{14}$.

Table 2: Pulse micro structure

revolution frequency accumulator	1.67	MHz
revolution time accumulator	0.6	μs
chopping beam-on time	360	ns
chopping beam-off time	240	ns
intensity		
particles per pulse	$4.7\ 10^{14}$	
particles per RF bunch	$2\ 10^9$	

2 ENERGY GAIN PER CAVITY

The energy gain in cavity is usually given by $\Delta W = eE_0T \cdot l \cdot \cos(\phi)$. Here, T is the transit time-factor and l the length of the cavity. $E_0T = E_{acc}$ is the accelerating field and ϕ is the phase distance of the synchronous particle to the crest at the centre of the cavity. The matched length of one cavity cell is given by $\Lambda = \beta_\Lambda \cdot \lambda/2$ where $\beta_\Lambda = \beta = v/c$ the velocity factor of the synchronous particle. The cell transit-time factor is given by

$$T_\Lambda = \begin{cases} \dfrac{\pi}{2 \cdot \left(1 + \dfrac{2\Lambda}{\beta \cdot \lambda}\right)} & \text{for } \beta \approx \beta_\Lambda (\leq 3\%) \\ \cos\left(\pi \cdot \dfrac{\Lambda}{\beta \cdot \lambda}\right) \cdot \dfrac{1}{1 - \left(\dfrac{2\Lambda}{\beta \cdot \lambda}\right)^2} & \beta \neq \beta_\Lambda \end{cases}$$

These expressions neglect the changes of beam velocities within a cell. Therefore, the lower formula is in accordance with the theory of Wangler [3].We have set up an approximate relation in order to give the validity range of the phase ϕ. The relative T_Λ error holds less than

0.5% (1.5%) for $|\phi| < 76°\ (85°)$.

0-7803-5573-3/99/$10.00@1999 IEEE.

This relation is valid up to the maximally occurring values of velocity mismatch (0.05) and the difference of the beam velocity factors within a cell (0.02).
The energy gain of an N-cell cavity results as addition of gains of N single cells. Thereby, particular synchronous phases of each cell have successively been calculated. This numerical method makes the base of future longitudinal particle tracking of the high-energy part of the linac.

Table 3: Radiofrequency system

frequency	700	MHz
RF wave length	0.428	m
data for a β=0.75 cavity:		
length of a cell Λ	0.182	m
length of a 5-cell cavity	0.91	m
maximum surface electric field E_{peak}	25	MV/m
accelerating field E_{acc}	10	MeV/m
transit time factor per cell T_Λ	0.79	
maximum tension amplitude per cell	2	MV
phase for acceleration in cell #3	-20	degree

The β-dependence of the energy gain of an N-cell cavity can be manifested using Wangler's formalism [3]. Here, the beam velocity along the N cells is set to be constant. The cavity transit-time factor T can then be factorised: $T = T_\Lambda \cdot T_S$. Where the synchronism factor is given by

$$T_S\left(N, \frac{\beta}{\beta_\Lambda}\right) = \begin{cases} (-1)^{\frac{N-1}{2}} \cdot \dfrac{\cos\left(\dfrac{N\pi\beta_\Lambda}{2\beta}\right)}{N \cdot \cos\left(\dfrac{\pi\beta_\Lambda}{2\beta}\right)}, & \text{N - odd} \\ (-1)^{\frac{N}{2}+1} \cdot \dfrac{\sin\left(\dfrac{N\pi\beta_\Lambda}{2\beta}\right)}{N \cdot \cos\left(\dfrac{\pi\beta_\Lambda}{2\beta}\right)}, & \text{N - even} \end{cases}$$

where β is the centre velocity factor being constant over N cells and β_Λ is the cavity geometric velocity

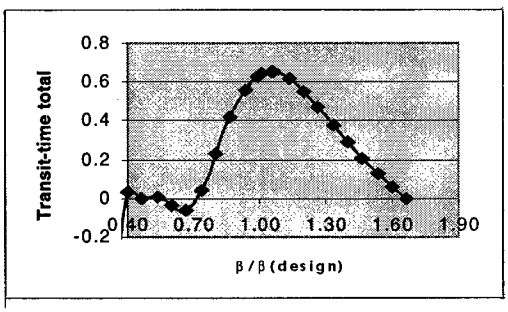

Figure 1: Transit-time factor for a 5-cell cavity vs. the velocity ratio β/β_Λ including β change from cell to cell

factor. The number of cells per cavity has been chosen to be N=5. The transit-time factor for such a 5-cell cavity is shown in the figure 1.

The maximum value occurs at the design velocity factor β_D, which is a little larger than the geometric velocity β_Λ.

3 β-GROUPING

The cell number N=5 have been chosen for ESS because of the smaller influence of the end cells compared to N=4. We have slightly rearranged the high energy linac part by fixing the maximal surface electric field to 25 MV/m. The ratio Epeak/Eacc has been calculated in [4].

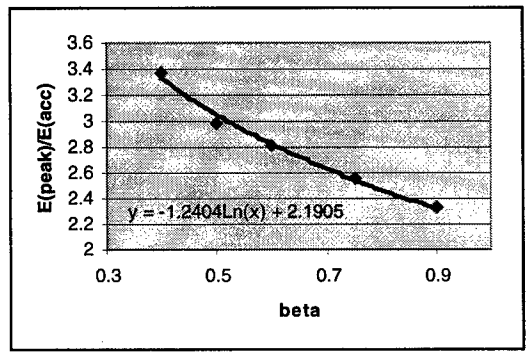

Figure 2: Ratio E_{peak}/E_{acc} as it is calculated by the MAFIA program.

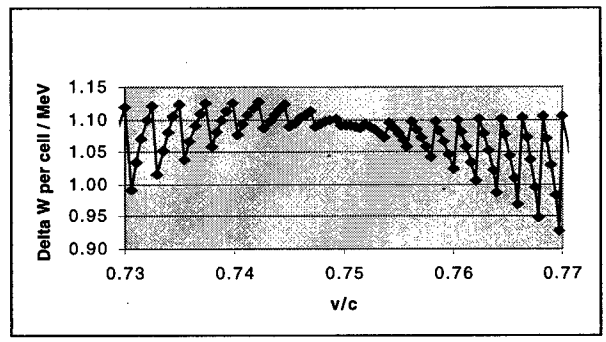

Figure 3: Energy gain per cell β_Λ=0.75 (crp. 480 MeV). The maximum phase ϕ of the centre cell is set to -20°.

The number of groups of identical cavities to be built should be as small as possible for an economic manufacturing. On the other hand, a criterion has been used to tolerate a maximum decrease of the transit-time factor of 5% at the ends of the groups of identical cavities. Hence, 5 different groups of identical cavities will be necessary to accelerate the beam in the linac from 70 MeV up to 1334 MeV. The geometric velocities for the 5 groups are β_Λ=0.353, 0.431, 0.526, 0.641, and 0.782. In a next step the energy gain throughout the

whole family has been optimised by varying the centre velocity factor β_Λ. The result of this optimisation is shown in figure 4.

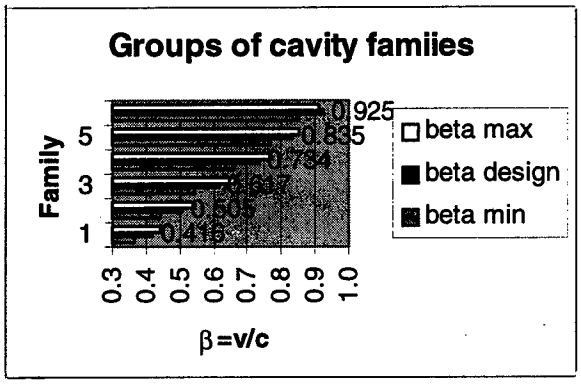

Figure 4: The centre velocity factor β_Λ and the β-range for the cavities of the 6 families. The numbers are given for the centre velocity factor β_Λ

We will create two additional cavity groups at the upper end because most of the energy will be gained at β>0.75 (480 MeV). Figure 3 shows as an example
The energy gain per cell for a group of identical cavities. The single-cell tracking method will be completed to include also power coupler and transverse beam dynamics aspects.

4 TRANSVERSE BEAM DYNAMICS

For the arrangement of the quadrupoles FODO-, doublet-, and triplet-focusing has been studied. The most simple focusing structure the FODO structure. We group 4 cavities between the focusing quadrupole F and the defocusing quadrupole D. The strength of the quadrupoles is constant all along the linac from 70 MeV up to 1333 MeV. The relative focusing force decreases with the increasing energy. The β-functions β_x, β_y increase, the increasing beam diameter is compensated by the adiabatic shrinking of the beam proportional to $1/(\beta\gamma)$. β-functions are shown in figure 5 and the beam radius is seen in Fig. 6.

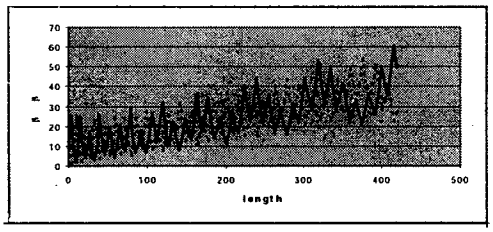

Figure 5: β-functions β_x, β_y for the FODO-focusing in the linac. The quadrupoles are 20 cm long with a gradient of 1.8 T/m at a bore radius of 5 cm.

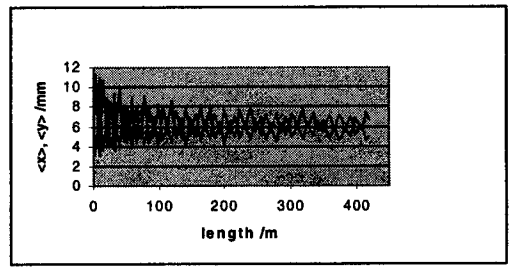

Figure 6: Beam radius for the FODO structure using quadrupoles with identical strength.

5 REQUIREMENTS FOR THE COUPLING COEFFICIENTS

The field flatness in the cells depends on β and the cell-to-cell coupling K_f, it is given in the formula.

$$\frac{\Delta E}{E_{acc}} = e^{\frac{t_{inj}}{\tau}} \sqrt{P \frac{4\beta^2}{(\beta+1)^2} \frac{R_{sh}}{Q} Q_L} \cdot \frac{\pi}{K_f \left[1-\cos\frac{\pi}{N}\right] \cdot Q_L E_{acc}}$$

For a 1% field flatness the K_f is shown in figure 7

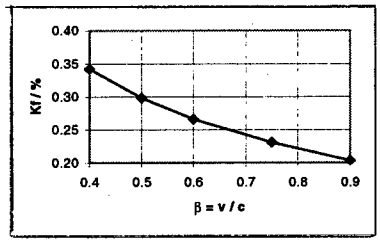

Figure 7: Cell-to-cell coupling factor vs. β. A field flatness of $\Delta E/E_{aac}$=1% has been taken for the N=5 cell cavity.

6 REFERENCES

[1] J.Kjems, A.D.Taylor, J.L.Finney, H.Lengeler, U.Steigenberger (ed.), "ESS - A Next Generation Neutron Source for Europe", Vol III, "The ESS Technical Study", Copyright: ESS Council, March 1997

[2] B.Aminov, A.Gamp, E.Haebel, H.Heinrichs, H.Piel, J.Pouryamout, Th.Schilcher, D.L.Schrage, G.Schulz, S.Simrock, C.H.Rhode, and R.Röth, "Conceptual design of the Superconducting High Energy Linear H⁻-Accelerator for the Future European Spallation Source (ESS)", ESS 96-60-L, December 1996

[3] T.P. Wangler, "Principles of RF Linear Accelerators", Wiley series in beam physics and accelerator technology, 1998

[4] W. Braeutigam, S. Martin, E.Zaplatine, "Design Study for SC Proton Linac Accelerating Cavities", this conference.

[5] W.Diete, B.Griep, M. Peiniger, H. Vogel, P.Vom Stein, W. Braeutigam, "Superconducting Accelerating Test Modulee for the ESS", this conference.

STATUS OF THE 36 MHZ LINAC CAVITIES FOR THE GSI HIGH CURRENT INJECTOR

H. Gaiser, K. Kaspar, U. Ratzinger, GSI, Darmstadt, Germany,
S. Minaev, MEPHI Moscow, B. Krietenstein, TU Darmstadt

Abstract

The new 1.4 MeV/u prestripper linac at GSI will provide intense ion beams to fill the synchrotron SIS to the space charge limit for all elements up to uranium. The design mass to charge ratio A/q is 65, the effective acceleration voltage of the 30 m long LINAC is up to 91 MV. The design beam current in emA is 0.25·A/q, i.e. 15 mA of U^{4+}.

This linac will replace the 27 MHz Unilac Wideröe section which was designed for A/q-values below 24. All cavities of the new linac are operated in the H_{110}-mode. The 9.2 m long IH-RFQ with an energy profile from 2.2 keV/u to 120 keV/u has been completed and rf tuned. RF power tests were performed successfully on 2 out of 10 tank modules. The drift tube linac consists of two 42 MV IH cavities. The 'Combined Zero Degree Structure' KONUS allows to accelerate the beam by a total number of 99 gaps with only 5 quadrupole triplet lenses for transverse focusing.

The experience from the construction and from the rf tuning of all cavities is reported as well as the measured quality and shunt impedance values. The running in of the new prestripper linac is scheduled from April to September 1999.

1 INTRODUCTION

The High Current Linac conceptual design [1] was guided by the aim to fill the synchrotron SIS18 up to the space charge limit. Multi-turn injection during 100 µs has to provide $4 \cdot 10^{11}$ ions for light ions like Ne^{10+} and $4 \cdot 10^{10}$ ions for U^{73+} respectively. Taking into account the beam losses of up to 98.5 % caused by two stripping processes as well as the present state of the art in ion source development, the new 36 MHz front end linac has to provide the beam intensities and an A/q range as mentioned above. Besides the high-current mode (up to 16⅔ Hz, 1 ms pulse train) the new front end linac additionally has to allow the continuation of the original Unilac operation mode (50 Hz, 5 ms at A/q ≤ 26) for experiments in nuclear physics and materials research and with beam energies below or around the Coulomb barrier. The main RFQ [2, 3] as well as the short adapter-RFQ, called Superlens [4], are operated in the H_{110}-mode. The DTL consists of two tanks in the $H_{11(0)}$-mode: There is a gap voltage decrease at all tank end regions to optimize the shunt impedance. Additionally, tank IH1 has a ramped gap voltage distribution due to the pronounced energy increase by a factor of 6.2 along that structure.

Compared to existing ion linacs the A/q design value as well as the beam intensity of the new GSI-injector are outstanding and made a development of efficient cavities for low operating frequencies necessary. The choice of 36 MHz – one third of the succeeding Alvarez section – is a compromise which allows to reach the following aims:

- The RFQ current limit is high enough.
- The DTL tank diameter of around 2 m corresponds to the 108 MHz Alvarez section and can be handled in the GSI galvanic copper plating shop as well as within the Unilac tunnel.
- The frequency can be kept constant along the new linac, which improves the beam quality and beam stability considerably according to LORASR beam dynamics simulations [1].
- The new accelerator is short enough to minimize the costs for a reconstruction of the Unilac tunnel.

The matching between RFQ und DTL is accomplished by a short low aperture quadrupole doublet at the RFQ exit followed by the 11 cell Superlens. The latter is operated at –90° and focuses the beam in 3-dim space into the DTL. This design avoids the local separation between the transverse focusing magnetic lens and a rebuncher.

So far the low level rf measurements and the tuning of all cavities were done successfully. A power test with 2 out of 10 RFQ sections was performed to check the performance of that new structure. The entire linac will be powered after the installation in the Unilac tunnel which is taking place at present.

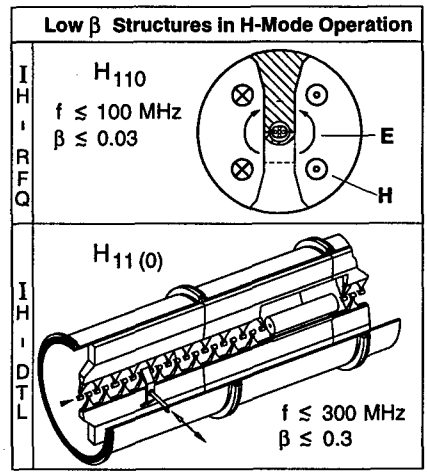

Figure 1: Cross sectional view of the IH-RFQ with electric and magnetic field directions and 3D-plot of the IH2-cavity with the quadrupole triplet lens in the second module.

0-7803-5573-3/99/$10.00@1999 IEEE.

2 RFQ STRUCTURE

The cavity design was developed at GSI during '94 and '95. At the end of '96 the 10 tank modules were ready for in-house copper plating. A first assembly of the whole RFQ with mini vanes took place in July '97 [5]. The resonant frequency was about 1 % higher than predicted by MAFIA calculations [3]. Additionally, it was decided to use inductive tuning by cylindrical plungers instead of capacitive tuning for this cavity. Therefore a total frequency shift of 0.5 MHz (−1.5 %) had to be provided. The IH-RFQ contains 100 mini vane-carrier rings along the 9.2 m long structure. A remake of these rings with modified geometry allowed to distribute the needed capacity increase of 3 % along the whole tank length. At the same time the junction principle was changed (Fig. 2).

In July '98 a RFQ power test was performed: The first and the last of the 10 RFQ modules were assembled to form a short H_{110}-cavity. After a total operation time of about 10 days 4 goals were reached and partly exceeded:

- The vane-vane design voltage of 137 kV was kept stable at duty factors of up to 1 % and pulse lengths up to 1 ms.
- The 40 % design voltage level was held at a duty factor of 30 %.
- The resonant frequency and Q-value returned to their initial values in all cases after switching off the rf power.
- Reliable amplifier operation was proven and all control loops were activated successfully.

The power tests were also used to estimate the temperature increase of the electrode structure with carrier rings (Fig. 2). These parts are made from massive copper and are cooled via heat conduction by the water cooled stems only. As the temperature difference along the electrodes was calculated to remain below 0.4 K [2] it is assumed that the main effect is caused by temperature steps across the two bolted connections stem/carrier ring and carrier ring/electrode with $\Delta T_2 \approx 2 \cdot \Delta T_1$. ΔT_1 and ΔT_2 are the differences relatively to the stem temperature, the latter being approximately independent from the rf power level within the investigated range.

ΔT_2 was derived by measuring the resonance frequency shift and calculating the related capacity change between the electrodes due to heat expansion. The empirical formula from Ref. [6] was used to calculate the quadrupole capacity change caused by expansion of d and h (Fig. 2). This expansion results in a shortening of the RFQ parameters R_o, a and ρ. For the 36 MHz IH-RFQ the electrode capacity C'_Q is 108.5 pF/m while the total capacity is 184.5 pF/m [7].

Summary of Results from the Power Test:

A rf peak power level of 20 kW with 30 % duty cycle into the 1&10-module array causes a resonance shift of 3 kHz. This corresponds to $\Delta C'_Q / C'_Q = 3.5 \cdot 10^{-4}$.

With $\bar{h}$ = 22.2 mm, d = 11 mm and the relations

$$R_o/\rho(\Delta T) = R_o/\rho(\Delta T = 0) \cdot (1 - 1.1 \cdot 10^{-4}\ \Delta T) \quad (1)$$

$$a(\Delta T) = a(\Delta T = 0) \cdot (1 - 0.94 \cdot 10^{-4}\ \Delta T) \quad (2)$$

the temperature difference finally results to

$$\Delta T_2 \approx 3\ \mathbf{K}.$$

As the design power level into the 1&10-module assembly is only 11 kW at 30 % duty cycle this result can be accepted. For ΔT_2-values above 10 K the probability of transverse electrode misalignment in the order of 0.1 mm is estimated to be rather high already.

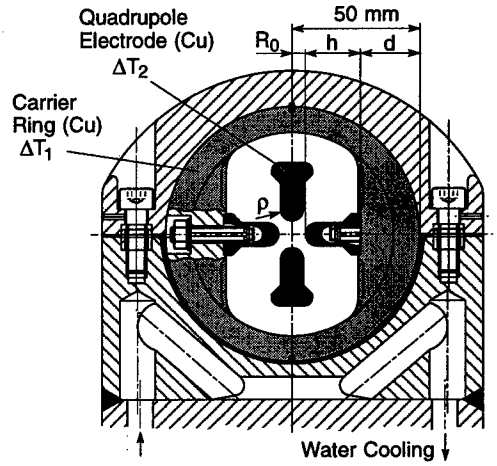

Figure 2: Mini vane electrodes with carrier ring mounted on a stem. The two bolted junctions will cause jumps in the temperature distribution under operation.

The final voltage distribution is flat and constant within ±1 % along the whole electrode length of 9.2 m and is independent of the plungers position which have a tuning range from −0.2 ‰ to +1 ‰ around the operating frequency (Fig. 3). The Q-value is 13000.

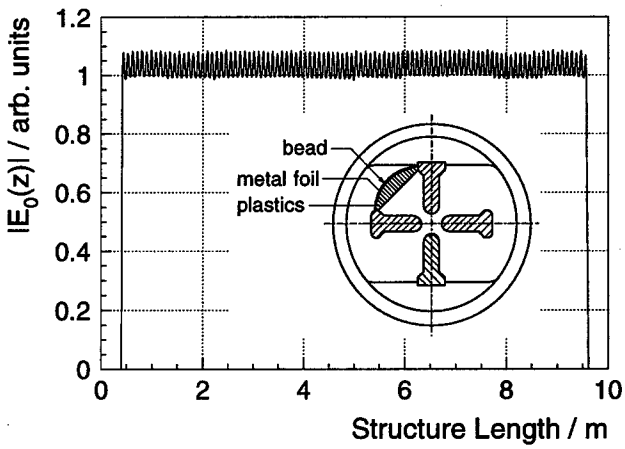

Figure 3: Measured vane-vane voltage along the 36 MHz IH-RFQ. The fast oscillation is caused by field distortions from the mini vane carrier rings along the path of the bead. The small steps between modules are due to small changes in the vane-profile.

At present the RFQ tank is being installed in the Unilac tunnel. Beam tests will be performed early in May '99.

3 IH-DTL

The design of the 83.2 MV DTL is described in ref. [1]. Each of the two IH-tanks consists of 4 modules and two endplates from black steel. The delivery to GSI lasted till to the end of '97. The in house copper plating of these modules with an inner diameter of around 2 m and with the two girder profiles pointing towards the beam axis (Fig. 1) was not trivial. A platinum coated titanium grid was modelled along the inner tank surface in a distance of around 50 mm. Such an electrode generates a homogeneous electric field distribution within the bath during the nickel and copper plating. Good results with that method were obtained when plating smaller components like the RFQ modules. In case of the DTL modules however, the organic bath additives decomposed rapidly during the copper plating process, which takes about 5 hours to get a 100 µm layer. In case of 3 modules a time consuming polishing procedure of the plated surface became necessary because of that unpleasant effect. The DTL plating ended successfully in October '98.

First rf measurements on IH1 were done in September '98. The frequency was 1.1 % higher than expected [8]. Both the resonance frequency and the ramped gap voltage distribution were optimized by means of fixed tuning blocks at foreseen positions (Fig. 4).

It is concluded that the cavity design concept based on MAFIA calculations and on perturbation measurements on a 1:5.88 scaled rf model delivered correct parameters within tolerances of around 1 % for the resonant frequency and of around ±5 % for the sum of gap voltages per drift tube section. After final rf tuning the voltage gain per section deviates by less than ±0.5 % now. This result is important to avoid phase errors of the bunch after passing through each of the long cavity internal triplet lenses. Only one iteration step of the voltage distribution during the rf model measurements was done to get an acceptable agreement between the effective gap voltage distribution as used originally in LORASR beam dynamics simulations and of the according results from tank measurements (Fig. 4). RF tuning of the IH2 cavity happened in March '99. The Q-values are 29000 for IH1 and 34000 for IH2 and do fit to the linac parameter list contained in ref. [1]. Vacuum tests on IH1 and IH2 were successful after repairing module 2 of IH1 and the end plate at the low energy end of tank IH2.

Quadrupole Lenses

The laminated quadrupole cores are based on 1 mm thick sheets of Vacoflux 50 to get pole tip fields of up to 1.3 T. The magnet field levels and tolerances are according to the specifications for the lenses delivered to GSI so far. The production of the magnets is seriously delayed and not all technical problems are solved yet.

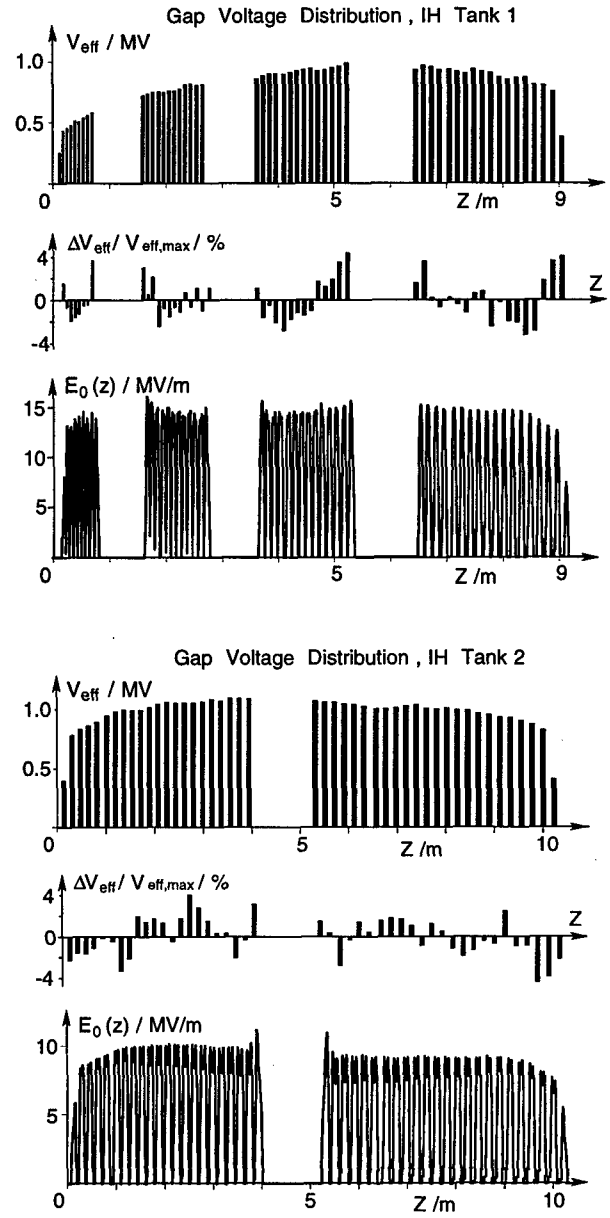

Figure 4: Effective gap voltage distribution as designed by LORASR-simulations, measured deviations of the tuned cavities and electric field distribution along the beam axis.

4 REFERENCES

[1] U. Ratzinger, Proc. LINAC 96, Geneva, CERN 96-07, p. 288.

[2] U. Ratzinger, K. Kaspar, E. Malwitz, R. Tiede, S. Minaev, Proc. EPAC 96, Barcelona, p. 304.

[3] K. Kaspar, U. Ratzinger, Proc. EPAC 96, Barcelona, p. 1973.

[4] U. Ratzinger, R. Tiede, Proc. LINAC 96, p. 128.

[5] U. Ratzinger, K. Kaspar, E. Malwitz, S. Minaev, R. Tiede, Nucl. Instr. and Meth. in Phys. Res., Sect. **A 415**, 281-286 (1998).

[6] I. Ben-Zvi, A. Jain, H. Wang, A. Lombardi, Proc. LINAC 90, Albuquerque, LA-12004-C, p. 73.

[7] U. Ratzinger, Habilitation, submitted at IAP, J.W. Goethe University, Frankfurt.

[8] B. Krietenstein, T. Weiland, U. Ratzinger, R. Tiede, S.A. Minaev, Proc. LINAC 96, Geneva, CERN 96-07, p. 243.

APF OR KONUS DRIFT TUBE STRUCTURES FOR MEDICAL SYNCHROTRON INJECTORS - A COMPARISION

S.Minaev, MEPHI, Moscow, Russia
U.Ratzinger, B.Schlitt, GSI, Darmstadt, Germany

Abstract

Tumor therapy with light ion beams like Carbon out of a synchrotron is a topical accelerator application. In all designs the layout of the injector linac is an important factor with respect to construction and operation costs as well as to the operation performance of such a medical facility. Two alternative linac approaches which keep the number of components and setting parameters as low as possible are discussed. In both cases the Interdigital H-type drift tube structure is used for acceleration of C^{4+} ions from 0.3 MeV/u to 7 MeV/u. The "Combined Zero Degree Structure" KONUS is used in one design; the other approach is "Alternating Phase Focusing" APF without any magnetic quadrupoles for transverse focusing. Both designs were investigated with the LORASR code. As the same linac should also provide protons with beam intensities of a few mA, the comparision was extended towards the capability of accelerating intense ion beams.

1 INTRODUCTION

A "Combined Zero Degree Synchronous Particle Structure" KONUS has been developed for IH structures in order to get an efficient acceleration with a minimum amount of magnetic lenses [1,2]. In case of the injector linac [3] investigated at GSI for a clinical light-ion synchrotron [4] a 216 MHz KONUS structure follows behind of a 0.3 MeV/u RFQ. One IH cavity accelerates the $^{12}C^{4+}$ ions from 0.3 MeV/u to 7 MeV/u and contains three internal quadrupole triplets. The cavity has a length of about 4 m and a diameter of around 0.35 m. However, when such a "small" linac for medical applications is designed, even a few magnetic lenses supplied with electric power and water cooling complicate the machine and contribute to the costs considerably. This is the reason to search for a transverse beam focusing alternative. The requirements of beam quality and intensity are relatively tolerant in this application: $\varepsilon_{n,tr} \leq 0.6\ \pi$ mm mrad, $\Delta W/W \leq \pm 0.2\%$.

The APF idea of beam focusing by a periodically changed synchronous phase is known and developed since the early 50's by many authors, the Ref. [5-13] being only a small part of publications. A general feature (and disadvantage) of APF is the dependence of the rf focusing action on the phase position of the particle. As long as the rf field action is the only mechanism to provide transverse beam stability, the transverse particle oscillations are strongly influenced by the longitudinal motion in contrast to magnetically focusing structures. This is the obvious reason for transverse emittance growth, especially at the low energy end where the bunch phase width is larger. The non-linear transverse rf field components can also reduce the APF beam quality along the low energy range. That is why the favourable region for APF structures is located behind of RFQs where the beam is already bunched and the energy is high enough.

The efficiency of APF depends very much on the correct configuration of each focusing section, but there is no theory which could be applied to the optimization of the drift tube array so far. The stability of small oscillations can be explored with Mathieu-Hill equations, but only for one harmonic or for a step function approximation of the focusing force. On the contrary, one can investigate the large polyharmonic non-linear oscillations by using the smooth approximation method, but only for a small phase advance per focusing period; the complete coupling of longitudinal and transverse motion has not yet been taken into account in both of these methods. Hence, in order to find the best abilities of APF numerical beam dynamics simulations were performed. Finally, a 78 gap APF structure was designed and compared to a 58 gap KONUS structure with identical energy gain (Table 1).

2 BEAM DYNAMICS SIMULATIONS

The same typical RFQ exit beam parameters at the operating frequency of 216.8 MHz have been assumed for the KONUS as well as for the APF structure. Also the typical rf effective gap voltage distribution along the IH cavity with the maximum gap voltage of around 0.45 MV was used in both cases. At the RFQ exit beam energy of 300 keV/u the phase width of the bunch is about 40 degrees. All calculations were carried out by the LORASR code [14], starting with a homogeneous particle distribution in space at the RFQ exit. Each gap transformation is separated in axial direction into 30 steps. The electric field distribution of each gap is defined by 16 parameters. 10 parameter sets for normalized gap geometries with identical outer/inner diameter ratios were calculated by a 2D solver for the electrostatic field distribution. The parameter set for a given gap geometry is then derived from the normalized gap parameter sets by interpolation.

The beam matching after the RFQ is necessary for APF and for KONUS. Both of the matching sections are similar, consisting of a two gap rebuncher and of a quadrupole doublet with the same magnetic gradient [3]. The only

0-7803-5573-3/99/$10.00@1999 IEEE.

difference is that the APF matching doublet contains quadrupoles of different length in order to inject a beam with axial symmetry into the DTL. The total length of the matcher does not exceed 22 cm. The projections of the 6D emittance after that matcher are shown by Fig. 1. A similar particle distribution is injected into the KONUS structure.

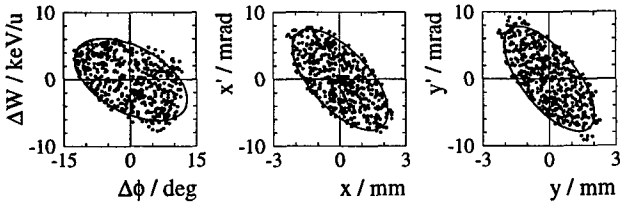

Figure 1: Beam emittance areas at the end of the matcher into the APF structure.

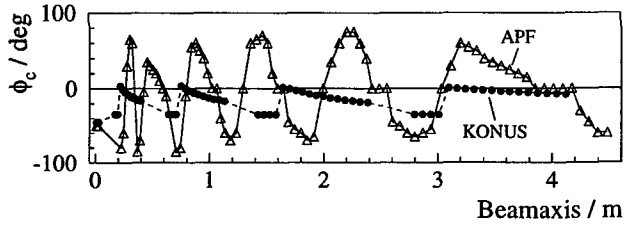

Figure 2: Phase positions of the bunch center along the KONUS and the APF structure, respectively (including two rebuncher gaps for beam matching behind of the RFQ). Note the big phase amplitudes of up to ± 80° in case of APF.

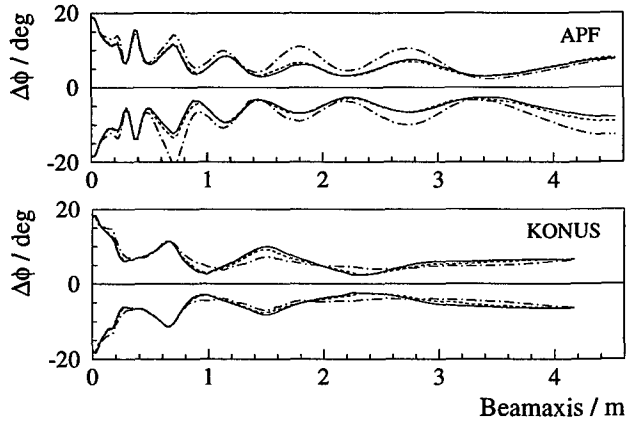

Figure 3: 98% phase envelopes for APF and KONUS structures and different beam currents. Solid line: 0 mA; dashed line: 1 mA; dash-dotted line: 5 mA.

During the optimizing procedure of the APF structure the philosophy was to keep the longitudinal emittance small with accepting a considerable reduction in energy gain. The first and the second APF section each contains one longer $3\beta\lambda/2$-period at the end for shifting the bunch centre to the negative phase in one step. Otherwise the corresponding drift tubes would become too short. The final phase pattern for the APF accelerating channel presented by Fig. 2 consists of 6 sections, each of them being optimized individually. The KONUS design on the other hand contains 4 sections. The resulting phase pattern of the bunch centre is also shown at the same figure. Fig. 3 and 4 show the longitudinal and transverse 98% beam envelopes, respectively (including the matching section behind of the RFQ).

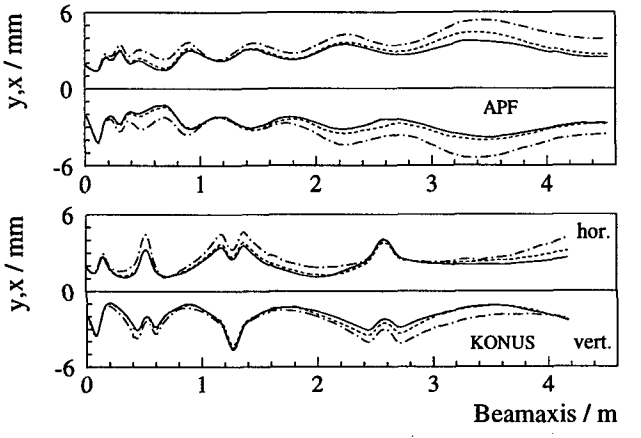

Figure 4: 98% transverse beam envelopes for APF and KONUS structures (for 0 mA, 1 mA and 5 mA).

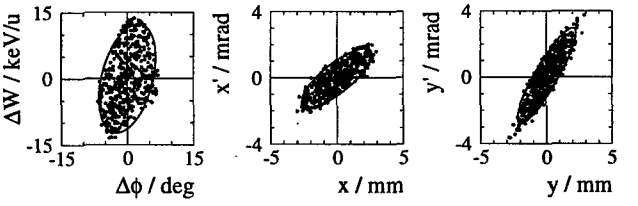

Figure 5: Projections of the exit beam emittance for the KONUS structure. The ellipses contain 90% of the particles.

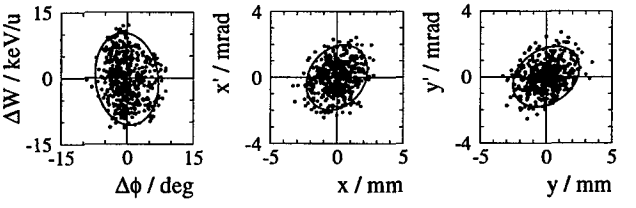

Figure 6: Projections of the exit beam emittance for the APF structure. The ellipses contain 90% of the particles.

The aperture is enlarged from 12 mm to 16 mm at an energy of around 1 MeV/u for APF and at 4.5 MeV/u in case of KONUS. The energy spread is reduced towards the exit considerably for both structures. The exit emittances for zero current are shown by Fig. 5 and 6.

Both structures have been designed for small beam currents. As the calculations show, the space charge influence at 1 mA can be considered as negligibly small while at

5 mA pronounced effects occur in both structures already (see Fig. 3 and 4). The output against the injected beam current is shown at Fig. 7. The KONUS beam transmission is 100% up to about 20 mA. The value of 25 mA is supposed to be the current limit. The 100% beam transmission and current limit for the APF accelerating channel are 10 mA and 16 mA, respectively. Fig. 8 shows the growth factors of the normalized 90% ellipse emittance areas against the injected beam current: For zero current the transverse increase for APF is 70% versus 10% for KONUS. The corresponding rms emittance growth are 44% for APF against 8% in case of KONUS.

Table 1: Main parameters of the investigated KONUS and APF structures.

		KONUS	APF
Operating frequency	MHz	216.8	216.8
Injection energy	MeV/u	0.3	0.3
Exit energy	MeV/u	7.0	7.0
Number of gaps		58	78
Tank length	m	4.0	4.3
Total RF effective voltage	MV	21.2	28.2
Maximum eff. gap voltage	MV	0.45	0.42
Drift tube aperture diam.	mm	12, 16	12, 16
Magn. lens aperture diam.	mm	20	-
RF power loss, peak	kW	1000	1120
Normalized transv. input emittance (90%)	π mm · mrad	0.32	0.32
Long. input emittance (90%)	π ns · keV/u	0.88	0.88
Zero current emittance growth (transv., long.)	%	10, 6	70, 11
Normalized transverse acceptance (100%)	π mm · mrad	0.8	0.8
Exit energy spread	%	±0.17	±0.15
Current limit	mA	25	16

3 CONCLUSION

The absense of magnetic lenses is the most attractive feature of APF which can reduce the costs of a light ion DTL by around 30% at beam energies up to around 7 MeV/u. One main APF disadvantage is a transverse emittance growth caused by the dependence of the transverse focusing action on the particles rf phase position and by nonlinearities in the radial gap field components. Another fact is that an acceptable beam quality in APF structures depends on a very small transversal misalignment along the whole drift tube structure. For these reasons, the KONUS structure was chosen for the therapy injector linac. Nevertheless, the combination of APF beam dynamics with the IH structure seems to be attractive as the second stage of acceleration for inexpensive compact linacs in some cases, when the beam parameter requirements are tolerant enough.

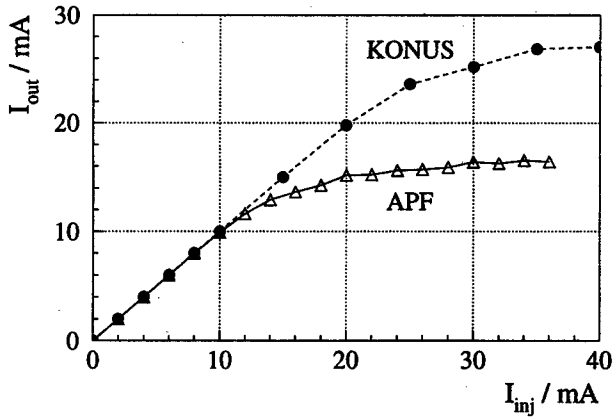

Figure 7: Current transmission for KONUS and APF structures.

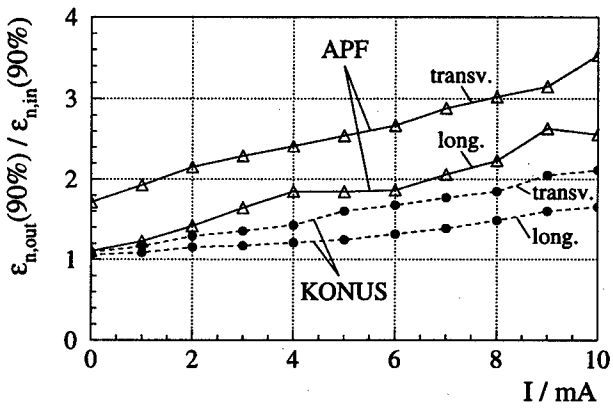

Figure 8: Normalized emittance growth for KONUS and APF structures (90% ellipse areas).

4 REFERENCES

[1] U. Ratzinger, in: *Proc. 1991 IEEE PAC, San Francisco*, p. 567.

[2] U. Ratzinger, in: *Proc. 1996 LINAC Conf., Geneva*, p. 288.

[3] B. Schlitt, U. Ratzinger, in: *Proc. EPAC'98, Stockholm*, p. 2377.

[4] H. Eickhoff, these Proceedings.

[5] M.L. Good, Phys. Rev. **92**, 538 (1953).

[6] J.B. Fainberg, in: *Proc. CERN Symposium on High Energy Accelerators and Pion Physics, Geneva, 1956*, p. 91.

[7] V.V. Kushin, Atomnaya Energiya **29**, 132 (1970).

[8] A.S. Beley, V.S. Kabanov, S.S. Kaplin, N.A. Khizhnyak and N.G. Shulica, Atomnaya Energiya **49**, 294 (1980).

[9] D.A. Swenson, Particle Accelerators **7**, 61 (1976).

[10] W.-H. Cheng, R.L. Gluckstern, S. Nath and T.P. Wangler, in: *Proc. 1992 LINAC Conf., Ottawa*, p.193.

[11] A.N. Antropov, V.K. Baev, N.M. Gavrilov, S.A. Minaev and A.V. Shalnov, Zh. Tekh. Fiz. **59**, 124 (1989).

[12] H. Okamoto, Nucl. Instrum. and Methods Phys. Res., Sect. A **284**, 233-247 (1989).

[13] S. Minaev, in: *Proc. EPAC'90, Nice*, p.1744.

[14] U. Ratzinger, Habilitation, submitted to IAP, J.W. Goethe University, Frankfurt, July 1998.

THE RADIOACTIVE ION BEAM FACILITY PROJECT FOR THE LEGNARO LABORATORIES

L.B. Tecchio on behalf of the SPES Study Group
Laboratori Nazionali di Legnaro, Via Romea 4, 35020 Legnaro (PD), Italy

Abstract

In the frame work of the Italian participation to the project of a high intensity proton facility for the energy amplifier and nuclear waste transmutations, the LNL has been proposed a project for the construction of a second generation facility for the production of radioactive ion beams (RIBs) by using the ISOL method. The final goal consists in the production of neutron rich RIBs with masses ranging from 80 to 160 by using primary beams of protons/ deuterons with energy of 100 MeV/u and 100 kW power. This project is proposed to be developed in about 10 years from now and intermediate milestones and experiments are foreseen and under consideration for the next INFN five year plan (1999-2003). In such period of time is proposed the construction of a deuteron accelerator of 20 MeV energy and 5 mA current, consisting of a RFQ (5 MeV) and a linac (20 MeV), and of a neutron area dedicated to the RIBs production and other applications. Besides the RIBs production, neutron beams for the BNCT applications and neutron physics are also planned.

1 METHODS OF PRODUCTION

Two methods can be used to produce RIBs and are the Projectile Fragmentation (PF) and the post-acceleration of isotopes produced by spallation, fragmentation, or fission reactions with high-intensity proton/light-ion beams in thick targets (ISOL method). The ISOL method takes a complementary approach to the production of RIBs. In the ISOL scheme a primary accelerator (or a nuclear reactor) yields a production beam of charged particles (or neutrons), which is sent on a thick, hot target. The radioactive species thereby produced are transported by a transfer tube to an ion source, then mass separated and breeding to higher charge state; the resulting ions are separated by an isotope/isobar separator, post-accelerated and sent into the experimental area. The comparison and choice between the PF and ISOL methods is strongly dependent on the physics to investigate. One of the relevant parameters for a comparison of the ISOL and the PF production methods is the RIBs production luminosity, which is independent of cross-section. The maximum production luminosity expected for an ISOL facility is three or four order of magnitude higher than in the PF figure. This because the luminosity can be achieved through the combination of a thick production target and a very intense primary beam. The proposed researches which are done at near-Coulomb barrier energies and below, involves studies of nuclear structure, low-energy nuclear reactions, astrophysics, and materials sciences applications and are best served by intense, high-quality, low-energy RIBs provided by the ISOL approach. This because the post-accelerator, optimized for high quality beams, provide the easy energy variability, high-energy precision and small emittances as demanded by the experiments. The main drawback to the ISOL method is that the diffusion/desorption from the production target and ionization of radioactive fragments are strongly element-dependent and slower than in the PF method. However, this feature can be also an advantage of the ISOL method because it give Z selectivity and, consequently, enhance beam purity.

2 THE FACILITY CONCEPT

We propose a two-accelerator ISOL-type facility to provide intense neutron-rich radioactive ion beams of highest quality, in the range of masses between 80 and 160. The proposed production mechanism is the fission induced by fast neutrons in fissile material targets. The fission mechanism has the advantage that very neutron rich radioactive beams can be produced. The conceptual design is based on a high intensity proton/deuteron linac as driver and on the availability of the heavy-ion accelerator ALPI as post accelerator [1]. The main idea is to use the primary beams to produce, by a converting target, an intense flux (~ 3 x 10^{14} cm^{-2} s^{-1}) of neutrons. The use of a converting target partially solves the problems concerning the beam power dissipation and radiation damage in the radioisotope production target/ion source system. The purely nuclear mechanism of energy loss and the long collision length of neutrons allow rather large target thickness to be used for more effective isotope production. The primary accelerator is a sequence of RFQ-DTL linac which can deliver proton/deuteron beams in the energy range of 10 – 100 MeV/u at a beam power of 100 kW. The RFQ accelerates the beam up to 5 MeV while further acceleration up to 100 MeV/u is accomplished by the DTL linac. The facility is planned to be located below ground level to assist in the prompt neutron radiation shielding. The beams delivered by the driver will produce radionuclides by irradiating targets in a well-shielded dedicated area. The radionuclides will be extracted at 20 kV from the target and ionized to the 1+ charge state, charge breeded to obtain a mass over charge ratio of about 10, mass separated, and then sent either directly to an experimental area for research with ion traps, or to the secondary-beam accelerator which will be housed in the existing ALPI building. To fill the ALPI linac with these

0-7803-5573-3/99/$10.00@1999 IEEE.

very low energy beam requires a new accelerating stage (pre-accelerator) up to about 1 MeV/u. The pre-accelerator consists of three low-frequency RFQs similar to the ones of the PIAVE injector [2]. These low-energy secondary beams can be delivered to the experimental area, located in the ALPI building, for low-energy experiments (astrophysics). The further acceleration up to about 5 MeV/u ($^{132}Sn^{13+}$) is accomplished by the ALPI linac and the radioactive beams will be delivered to the existing experimental areas. The capability of the ALPI linac to accelerate stable beams will remain independent of this program, both during construction and operation with radioactive beams.

3 SECONDARY BEAM INTENSITIES

Extensive calculations of production rates of radioisotopes have been performed using Montecarlo codes LAHET [3] and FLUKA [4]. The goal of such a calculations is to provide realistic and accurate estimates of the production yields for secondary ion beams to guide the detailed accelerator design and providing input for the physics program. Since LAHET code does not transport neutrons with energy below 20 MeV, simulations in voluminous thick targets have been performed with the FLUKA code (version '98). In particular, the fission process is computed using ENDF/B-6, JEF2.2 and JENDL3 nuclear data libraries. The most efficient production of neutron-rich isotopes is achieved via neutron induced fission of fissile materials (i.e. uranium and thorium). Neutrons are produced by stopping the primary proton/deuteron beam in a suitable target (stopping target). The stopping target must be chosen according to the primary beam in order to emit secondary neutrons in a forward narrow cone. It is understood that such a two-step device produces its best results when the secondary neutrons production is high. This could be accomplished, for instance, taking advantage of the deuteron stripping in reactions with light elements. The predicted fission fragments spectrum for high energy neutrons has been calculated with the FLUKA code and shown in Fig.1.

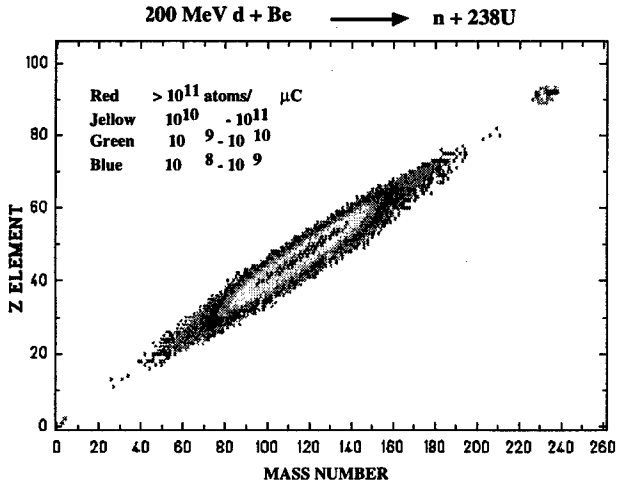

Figure 1: Predicted fission fragments spectrum.

4 THE NEUTRON FACILITY SPES

As an intermediate milestone of the full project the Legnaro Laboratories have been proposed a neutron facility (SPES) to be constructed in the next five years. It will result in a medium intensity neutron facility addressed to the national community and dedicated to the RIBs production as well as to the BNCT applications and to the neutron physics. Because its modularity the primary accelerator is planned to be constructed, at the beginning, in a minimal version and further implemented to accelerate beams up to 100 MeV/u. The primary accelerator consist in the sequence of RFQ-DTL linac limited in energy (10 MeV/u). The beam power to be considered is ranging between 10 and 100 kW. For the remaining part the facility is conceptually planned as described above, thus the secondary beams can be delivered for experiments at low-energy (traps, astrophysics,...) or pre-accelerated and injected in the ALPI linac for a further acceleration to higher energies. The limited energy of the primary accelerator will imply a lower neutron production rate; in any case the estimated neutron yield at the target level is 2×10^{14} n/s (100 kW), high enough to satisfy the demand for an advanced RIBs facility.

5 NEUTRON PRODUCTION RATES AND BEAM INTENSITIES

High energy neutron sources based on high current continuous wave (CW) deuteron or proton accelerators and thick targets of light nuclei provide the most suitable intensities for the aims of the project. The experimental data on deuteron and proton induced neutron source reactions were reviewed by Lone [5] and Barschall [6]. At deuteron energies above a few MeV, the d + Be and d + Li reactions have the highest cross sections for production of neutrons in the forward direction. The high energy neutrons measured from thick beryllium and lithium targets exhibit spectral shapes and angular distributions which are characteristic of the deuteron stripping process. At a comparable projectile energy the intensity and the average energy of neutrons at 0^0 from a thick beryllium target are highest for the deuterons. The dose rates from the d + Be reaction on thick targets are higher than those from the p + Be reaction at the same projectile energy. Also, the angular distributions of neutrons from the deuteron reactions are narrowed than those from the proton reactions at the same projectile energy. The intensity of the neutrons emitted in the forward direction increases rapidly with the deuteron bombarding energy. Independently from the stopping target, the deuterons seems the most appropriate projectiles for the production of neutrons. Stopping targets as beryllium and lithium both present characteristics which are suitable for the task. For some application uranium stopping target is suitable too, even if it shows different angular and energetic distributions. In this contest, for the intermediate milestone of the project, the most suitable driver may

consists of a deuteron accelerator of 20 MeV energy and power up to 100 kW. With minimal changes to the RFQ designed for the high intensity proton driver the same device allows to accelerate also deuterons. The RFQ is followed by a short section of the DTL linac. The expected yield of neutrons with energy above 1 MeV emitted in an angle between 0^0 and 10^0 is 2×10^{14} (n/s), for 100 kW power in the stopping beryllium target. The expected beam intensities for a production deuteron beam of 20 MeV and 100 kW power are shown in Table 1. The stopping target is beryllium and the production target is uranium carbide with a thickness of 100 gcm^{-2}.

Table 1:. Expected beam intensities. The overall efficiency values are taken from Ref. [7]. * Value taken from Ref. [8].

Isotope	Prod.Rate 20 MeV [At./pμC]	Overall Efficiency [%]	Beam Int. 20 MeV [Atoms/s]
Zn^{72}	1.3×10^3	8	5.2×10^5
Zn^{78}	1.2×10^6	0.48	2.9×10^7
Zn^{84}	2.4×10^2	-	-
Kr^{91}	9.4×10^8	29	1.4×10^{12}
Kr^{94}	2.6×10^8	6.4	8.3×10^{10}
Rb^{97}	3.2×10^7	11	1.7×10^{10}
Cd^{131}	10^2	0.25*	10^3
Sn^{132}	6.7×10^8	2.4	8×10^{10}
Sn^{138}	8×10^2	0.37*	1.5×10^4
Xe^{142}	5.5×10^8	26	7×10^{11}
Xe^{144}	4.4×10^7	26	5.7×10^{10}
Cs^{144}	6.3×10^8	38	1.2×10^{12}

6 RESEARCH AND DEVELOPMENT

During the development of the conceptual design for the RIBs facility, numerous areas in which additional research and development seemed appropriated have been identified. These areas are briefly described below, but not in any order of priority.

6.1 Stopping target for neutron production

It was mentioned above that a beryllium or lithium target-converter serves as an efficient neutron source for isotope production by fission in the secondary production target. This solution will allow to solve the technological problems related to the power dissipation (100 kW) from the production target by decoupling the intense particle beam from the secondary target in terms of the energy absorption and consequent target heating. Beryllium and lithium are suitable for such an application, but both kind of targets present design problems that demand a carefully investigation.

6.2 Target/ion source

In order to obtain experimental informations on the neutron-rich nuclei produced by neutron-induced fission of uranium isotopes an experimental program has been approved by INFN and actually in progress at LNL. It foresees the construction of an isotope separator for on-line operation coupled to the 7 MV CN van de Graaff accelerator. The layout of the isotope separator is very similar to presently existing low-current separators and consists of a 60^0 magnet with 1.3 m bending radius, a mass resolving power M/_M ~ 800 and dispersion ~1500/M mm. The idea is to produce neutrons by bombarding thick beryllium targets with deuterons accelerated up to an energy of 7 MeV and current of 3 μA. The expected total neutron yield at 7 MeV deuteron energy is 5×10^9 neutrons/sr/μA at 0^0, with an average energy $\langle E_n \rangle$ = 3.2 MeV. The on-line test stand for study the production yields, the release efficiencies, the delay times in the production targets and for testing the ion source efficiencies and emittances. A high-temperature integrated target-ion-source system has been designed for the on-line mass separator. This system includes, other than the target, a 1+ charge state surface ionization source operating at 20 kV. The targets are composed of uranium carbide (typical thickness 100 g cm^{-2}). In order to have a rapid diffusion and a good selectivity of the fission products the target-ion-source system can be operated up to 2500 ^{0}C. The expected production rates at the target level for several different isotopes is estimate ranging in between $10^4 - 10^6$ atoms/s/grU.

6.3 Production of multiple charged ions

To accelerate radioactive beams efficiently, ions charge greater than +1 may be advantageous. Efficient production of such ions would also reduce the cost of the acceleration stages. A new ion source of the EBIS-type, the Trapped Ion Source (TIS) actually under development is capable, in principle, of producing very highly charged ions [9]. The main new feature of TIS, with respect to an EBIS, is the adding of radial ion confinement of the rf quadrupoles to the potential well of the electron beam space charge, which allow to select the ion type to be contained in the pseudo-potential well (as is done in a common mass spectrometers).

7 REFERENCES

[1]G. Fortuna et al., "Status of ALPI", LINAC'96, CERN 96-07.
[2]A. Lombardi et al.,"PIAVE, the Positive Ion Injector for ALPI", LINAC'96, CERN 96-07.
[3]R.E. Prael and M. Bozoian, LA-UR-88-3238, Los Alamos, 1988.
[4]A. Ferrari and P. Sala, Work. on Nucl. React. Data, Trieste 1996.
[5]M.A. Lone, Symp. On Neutr. Cross Sections 10-40 MeV, BNL- NCS-50681 (1977).
[6]H.H. Barschall, Ann. Rev. Nucl. Part. Sci. 28 (1978) 207.
[7]H.L. Ravn et al., Nucl. Instrum. Meth. B88 (1994) 441.
[8]B. Fogelberg et al., Nucl. Instrum. Meth. B70 (1992) 137.
[9]V. Variale, this conference.

COMMISSIONING OF NEW INJECTION LINE AT INR PROTON LINAC

S. K. Esin, L. V. Kravchuk, A. I. Kvasha, A. N. Mirzojan, P. N. Ostroumov,
O. D. Pronin, V. A. Puntus, G. V. Romanov, S.I. Sharamentov, V. L. Serov, A. A. Stepanov,
A.V. Vasyuchenko, R. M. Vengrov
Institute for Nuclear Research RAS, 117312 Moscow

Abstract

An essential reconstruction of the injection line has been carried out in the INR linac. The original LEBT was designed to inject 750 keV proton and H^- beams simultaneously into the Alvarez tank. It included a section downstream of the merging magnet, where two beams are transported simultaneously. In order to improve reliability of the high voltage transformers as well as to increase average current of the accelerated beam a decision has been taken to insert a booster RFQ downstream of the merging magnet. The 198.2 MHz RFQ has been designed to accelerate hydrogen ions from 400 keV to 750 keV. For the transportation of 400 keV beam from HV injector to the RFQ entrance the old part of the LEBT is used. A 345 mm space between RFQ and DTL contains a buncher with the effective voltage of 110 kV, four electromagnet quadrupole lenses and two boxes for beam diagnostics. The results of the commissioning of the new injection system are reported.

1 INTRODUCTION

The operational experience at the INR linac [1] has shown that the electrical reliability of the 750 kV pulsed transformer and accelerating tube is not sufficient at higher repetition rate (above 50 Hz). Therefore a booster RFQ to upgrade the beam energy from 400 keV to 750 keV has been proposed and developed [2]. The reduction of the pulse transformer voltage allows us to increase the beam pulse duration from 80 μs to 150 μs being operated below the saturation of the core. The duty factor and the average beam current of the linac are increased proportionally.

Historically the injection line (LEBT) of the linac is divided to three sections, the last one is a channel where the hydrogen ions are transported simultaniously. The new RFQ and an additional equipmernt for the beam matching and diagnostics have been designed to install on the third section of the LEBT (see Fig.1). A 45 mm diameter collimator, a wire scanner and a solenoid are placed upstream of the RFQ. Due to the limited space and reletively high energy of the beam being injected the adiabatic capture in the RFQ could not be provided. To improve the longitudinal capture an additional buncher B-400 has been foreseen in front of the RFQ. The matching section between the RFQ and DTL must be designed as short as possible to provide the efficient capture of the RFQ beam with relatively large momentum spread into the DTL. That section length is only 345 mm. A design task to place a large number of the matching and diagnostic equipment in the space between the RFQ and DTL has been successfully solved.

The equipment manufacturing and installation was finished last fall. During the beam production shifts in November-December 1998 the RFQ and matching section were commissioned.

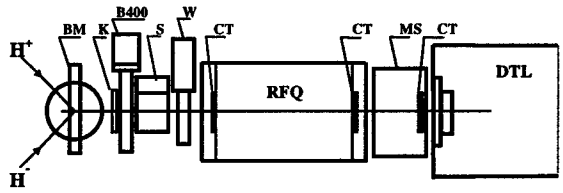

Figure 1: Layout of the LEBT containing the new equipment.

A description of the main equipment, their tuning and first operations with the new LEBT are given below.

2 RFQ CAVITY

The main parameters of the RFQ are shown in Table 1[2].

Table 1: Basic parameters of the RFQ.

Operating frequency	198.2 MHz
Input energy	400 keV
Output energy	750 keV
Energy spread (full width, 100 mA)	4.6%
Phase spread (full width, 100 mA)	70°
Intervane voltage	150 kV
Mean bore radius (r_0)	8 mm
Aperture radius	6.85 mm
Length of the vanes	1199 mm
Cavity length	1300 mm
Inside diameter of the tank	325 mm

A simplified assembly drawing of the RFQ cavity is shown in Fig. 2. The RFQ tank and the end covers are made of stainless steel. The inside surface of the tank is covered by 5 mm layer of oxygen free copper using diffusion welding technique. The tank consists of two sections. Aluminum rings are used as vacuum seals between the sections and end covers. The electrical contact is provided with pressing of inside copper layers. A roughness of the copper surface is ~0.8 μm. The

0-7803-5573-3/99/$10.00@1999 IEEE.

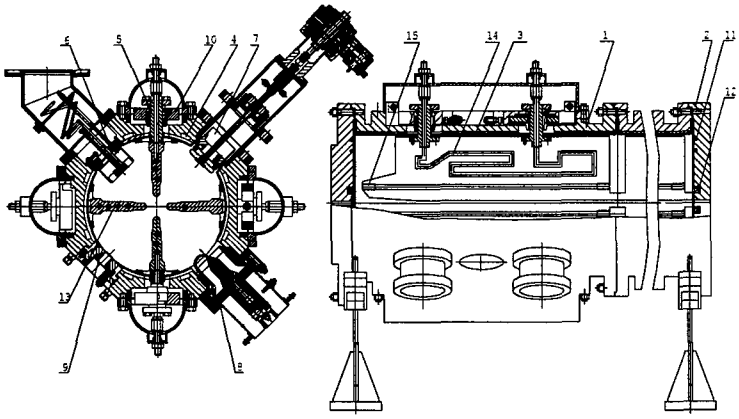

Figure 2: Simplified assembly drawing of the RFQ cavity: 1– tank body; 2– cover; 3– inner lining; 4,11,14 – cooling channel; 5– bellow unit; 6,7- tuning units; 8- rf power loop; 9- peak-up loop port; 10- adjustment plate; 12- beam current transformer; 13- vane; 15- target hub.

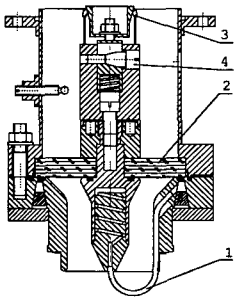

Figure 4: RF power coupling loop: 1- loop; 2- quartz window; 3- collet connector; 4- clamping screw.

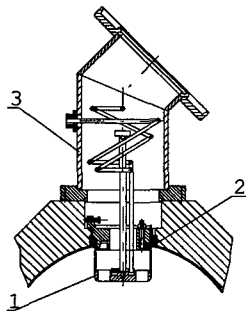

Figure 5: Tuning unit: 1- piston; 2- rf contact; 3- pumping tube.

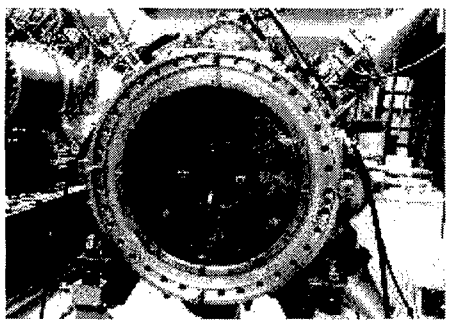

Figure 6: The front end view of the RFQ.

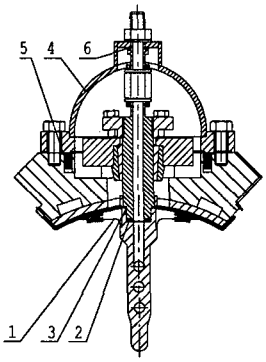

Figure 3: Vane alignment unit.

measured Q-value of the RFQ cavity is 5670. Fig. 3 shows the vane alignment unit covered by vacuum cap (4). The cooling water enters into the vane through the bellow. A RF contact of the vane with the inside copper surface of the tank is provided by copper foil (1). The water seal (2) is made of rubber. For the vacuum sealing of the RFQ cavity several types of material, such as indium (3), aluminum (5) and copper (6) are used. The RFQ cavity is fed by the RF power using four coupling loops (Fig. 4). The RF window (2) is made of quartz. The coupling can be adjusted by the change of the thickness of a copper seal. A VSWR at the frequency of 198.2 MHz has been measured and found to be equal to 1.5. The cavity has eight tuning pistons with a diameter of 75 mm (Fig. 5). The tuning pistons are installed in the vacuum pumping ports. The half of the total number of pistons can be adjusted. Beam current transformers are mounted inside of the end covers. The cavity is equipped with eight 160 l/s titanium pumps. A front view of the RFQ is shown in Fig. 6.

3 RFQ POWER SUPPLY

The four-stage 198.2 MHz power amplifier, similar to the standard DTL tank one, feeds the RFQ cavity. A RF power divider by 4 is installed in the output of 300/130 mm coaxial feeder. The divider is a quarter wavelength transformer with the characteristic resistance of 25 Ω. Four 25 m coaxial cables PK-50-44-17 are connected to the divider. The cable withstands up to 1 MW pulsed power at the average power of 3.5 kW at the frequency of 200 MHz. The divider reliability has been tested by the installation of the similar device in the output of four cables, which has been connected to matched load. Up to 500 kW peak power in 220 μs pulse length at the repetition rate of 100 Hz has been successfully transported into the load. All of four cables have been connected to the RFQ by means of a special angular sockets. An extra attention has been paid to the equalizing of the electrical length of the cables. The cable lengths have been chosen on the basis of capacity measurements with accuracy of 0.3 pF. The final determination of the

cable lengths has been made on the base of low level phase measurements with the precision of ~5°.

The conditioning of the RFQ cavity has been performed at the vacuum pressure of $1 \cdot 10^{-6}$ Torr by smooth rise of average and peak rf power at the pulse duration of 50, 100, 220 μs and repetition rate of 10, 50, 100 Hz. The pulsed power of 280 kW has been gained during 60 hours of conditioning.

The tank, the end covers, coupling loops and tuners are cooled with deionized water from the DTL water-cooling circuit. The resonant frequency is controlled by the water temperature which flows through the vanes. For this purpose a 24 kW electrical heater is used. The heater current is controlled either by temperature gauge or by the phase difference signal taking from the RFQ measuring loop and from capacitor probe installed in one of the RFQ angular sockets. A temperature coefficient is about 50 kHz per 1°C. The operating temperature of the water in the RFQ tank is about 23°C. The water temperature in the vanes is higher by 2.5° C.

4 RFQ-DTL MATCHING SECTION

The matching section (Fig. 7) is designed to match the 6D emittance of the RFQ beam to the DTL acceptance. An effective voltage of 110 kV on the buncher B-750 gap is required to match the beam longitudinal emittance. Four quadrupole lenses Q1...Q4 with maximum gradients of 4.8...3.8 kGs/cm and 8...14 mm radius of aperture are used for the beam transverse matching. The first diagnostic box is located downstream of the lens Q1 (Fig. 7). It contains two slits in X and Y axis and a harp. Another diagnostic box is placed downstream of the lens Q3. It is equipped with multistrip collector, variable collimator, current transformer and a vacuum valve. A general side view of the matching section is shown in Fig. 8.

5 COMMISSIONING RESULTS

The lower beam energy from the injector results in increase of the full unnormalized beam emittance from 10 π·cm·mrad to 15 π·cm·mrad. The transmission of the beam current along the whole LEBT has not optimised yet. Therefore only 28% of the 120 mA total current is transported to the RFQ entrance. The proton beam current at the output of the RFQ is ~25 mA. A 12.5 mA peak current beam has been accelerated along the whole linac without any bunchers. The total particle losses above the 20 MeV part of the linac are eqaul to ~0.1%. For this moment the average current of the beam is sufficient for the users. We believe that the peak current of the accelerated beam can be increased up to 25 mA by the help of careful tuning of the LEBT, bunchers and matching quadrupoles.

6 CONCLUSION

The installation and commissioning of the RFQ has increased the average current and improved the reliability

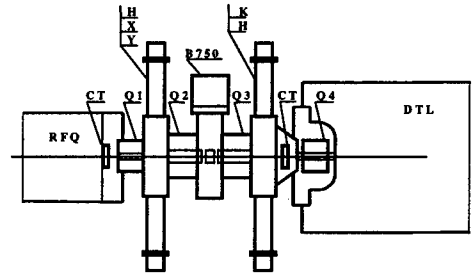

Figure 7: The RFQ-DTL matching section.

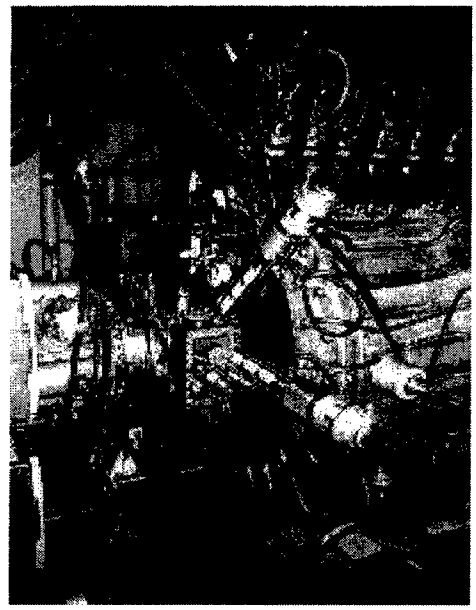

Figure 8: The matching section.

of the linac operation. There are reserves for the further increase of the beam current by the help of careful tuning of the LEBT and matching section.

7 ACKNOWLEDGMENTS

Authors express their gratitude to the linac staff as well as to specialists of ITEP (Moscow), IHEP (Protvino) and Tambov plant "Komsomolets" taking part in development and manufacturing of the new LEBT.

8 REFERENCES

[1] S. K. Esin, et al, "Commissioning/Operation of the Moscow Meson Factory Linac", Proc. of the 1994 Linac Conf., Tsukuba, p. 31.
[2] A. Andreev, et al, "Development of RFQ Accelerator for the MMF Linac", IEEE PAC91, San Francisco, vol. 5, p. 3109.

SPACE LATTICE FOCUSING: ON THE WAY TO EXTREMELY LOW ACCELERATED BEAM DIVERGENCE*

V.V.Kushin and S.V.Plotnikov#, ITEP, Moscow, Russia

Abstract

It is widely known the multiple channel acceleration is the most adequate way to save initial beam parameters due to the possibility of decreasing Coulomb forces in intensive input beams. To keep beam initial emittance and divergence for high enough specific value of the injection ion beam during acceleration the input beam should be split on multiple beams and every the micro beam must be screened from each other as much as possible. On the other hand, it is very much desirable to keep the total macro beam rather compact transversally and try to accelerate all the micro beams within the same accelerator structure at the same RF field. Attempts to use conventional quadruple focusing channels both RF and electrostatic for multiple beam acceleration usually lead to extremely complicate and bulky construction of the structure. We suppose multiple beam linac channels with alternating phase focusing (APF) as more adequate for the purpose while they are limited by less values of beam capture into acceleration process. The original version of the quadruple RF focusing multiple beam system called space lattice focusing (SLF) is supposed for getting intensive ion beam with extremely low divergence. The basic principles of the theoretical approach as well as some possible advances and restrictions for the practical use in RF linac are supposed to be discussed.

1. INTRODUCTION

Requirements of extremely small divergence of intensive accelerated beams may probably be successfully accomplished only by means of multiple beam accelerator systems [1]. The advantage of multiple beam approach takes maximal effect if amount of simultaneously accelerated micro beams is pretty high, i.e. some hundred or even thousands [2]. It follows from that the value of output angular divergence of total beam at given value of its total current is roughly inversely proportional to square root of number of beam channels [3]. The main purpose of multiple channel system designed for small output angular divergence is screening of every the accelerated beam from other micro beams as much as possible to avoid strong space charge forces influence on total beam emittance growth. In searching an adequate accelerating and focusing RF system we have found the principle possibility to screen multiple accelerating from each other by introducing the system of add electrodes of special form in accelerating gaps.

*Work is supported in part by ISTC
#Email: plotnikov@vitep5.itep.ru

2. SPACE LATTICE FOCUSING

Let us consider the multiple beams RFQ system by using a new focusing element called "space lattice" (SL-focusing) [4]. It is well known in drift tube linac (DTL) at the edges of drift tubes particles are exposed to transversal focusing or defocusing pushes from RF field. In particular, in DTL a particle is pushed by defocusing RF field at the input and by focusing field at the output edges of drift tubes while it is roughly free from RF field action within drift tubes and accelerating gaps. We considered a possibility of substantial amplification of focusing action from RF field by increasing a number of appropriate boundary edges. It is acceptable if some additional electrodes are arranged within every accelerating gap.

By executing M horizontal grooves from one flat side of a thin electrode plate to its middle and M vertical grooves from the other side of this electrode again to the middle we get metal space lattice with $M \times M$ rectangular apertures with relatively thin walls in between (fig.1).

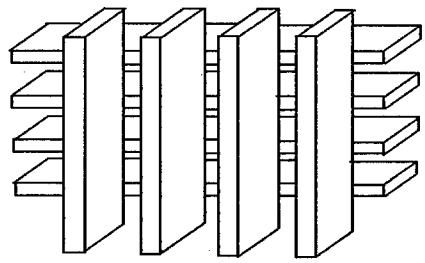

Fig.1. The fragment of Space Lattice electrode.

If several thin SLs are arranged along the common axis at the equal distances between them within accelerating gaps of the multiple channel linac we have a system which can accelerate some hundred and thousands beams simultaneously. In case of circular apertures in thin electrodes focusing and defocusing forces at both edges of thin electrodes are almost mutually compensated while in SL every particle is pushed in vertical direction at the input and in horizontal direction at the output edges even at very thin electrode depth. If we arrange n SLs within an accelerating gap particles will be n times pushed by focusing strength in the vertical plane and n times pushed by defocusing strength in the horizontal plane. When SLs are arranged within every gap particles will be suffered some focusing action in one of transversal direction and defocusing action in other transversal direction. By turning SLs by an angle of 90^0 in every the following gap it is possible to create a sequence of sign-alternating

0-7803-5573-3/99/$10.00@1999 IEEE.

strengths analogous to field strengths at spatially uniform RFQ focusing.

2. TRANSVERSAL STABILITY IN SLF ARRAYS

Let us consider basic aspects of transversal stability of ion motion in SLF arrays. The analysis of the system properties is carried out for a single cell (channel) of SL electrodes according to the approach presented in [5].

RF field potential within the acceleration gap has the planes of symmetry *XOZ* and *YOZ*:

$$U(x,y,z) = U(x,-y,-z) = U(x,-y,z).$$

By introducing the function of $G(x,y,z)$ which defines the level of deviation from axial symmetry in linear approximation and is responsible for quadruple focusing effect

$$G(x,y,z) = \frac{1}{2}\left(\frac{\partial E_x}{\partial x} - \frac{\partial E_y}{\partial y}\right).$$

and taking into account the condition of mutual connection of electric field components $divE=0$, i.e.

$$\frac{\partial E_{x,y}}{\partial x, y} = -\frac{1}{2}\frac{\partial E_z}{\partial z} \pm G,$$

in linear approximation the transversal motion equations may be written in the form:

$$\frac{d^2x}{dt^2} = \frac{ze}{m_0}\frac{\partial E_x(z)}{\partial x}x \cdot \cos\ \omega t(z),$$

$$\frac{d^2y}{dt^2} = \frac{ze}{m_0}\frac{\partial E_y(z)}{\partial y}y \cdot \cos\ \omega t(z),$$

Assuming the conditions of $x=const$, $y=const$ are valid within SL electrodes we can write the expressions for transversal velocity increments in thin lenses approximation:

$$\Delta\frac{dx}{dt} = \frac{zex}{m_0}\int_{-d/2}^{d/2}\frac{\partial E_x(z)}{\partial x}\cdot\frac{dz}{v}\cos\ \omega t(z),$$

$$\Delta\frac{dy}{dt} = \frac{zey}{m_0}\int_{-d/2}^{d/2}\frac{\partial E_y(z)}{\partial y}\cdot\frac{dz}{v}\cos\ \omega t(z),$$

Assuming ion velocity is constant within RF quadruples and going to the independent variable of $\tau = v\,t/S$ (S is the length of focusing period), the expressions for transversal velocity increments may be presented in the form of

$$\Delta\frac{dx}{d\tau} = (b_1 + b_2)x, \qquad \Delta\frac{dy}{d\tau} = (b_1 - b_2)y,$$

$$b_1 = \frac{zeS}{2m_0v^2}\int_{-d/2}^{d/2}\frac{\partial E_z}{\partial z}\cos\ \omega t(z)dz,$$

$$b_2 = \frac{zeS}{2m_0v^2}\int_{-d/2}^{d/2}G(z)\cos\ \omega t(z)dz,$$

Let us consider now the system of SL electrodes arranged according to that presented in Fig.2.

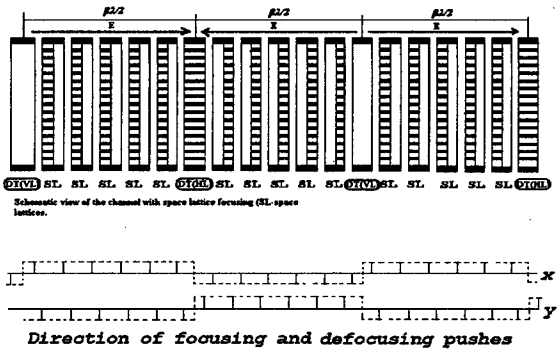

Fig.2. Structure of multiple beam array with $S = \beta\lambda$.

By splitting the focusing period into segments we can get the matrix of the period by means of multiplication matrixes of all the segments.

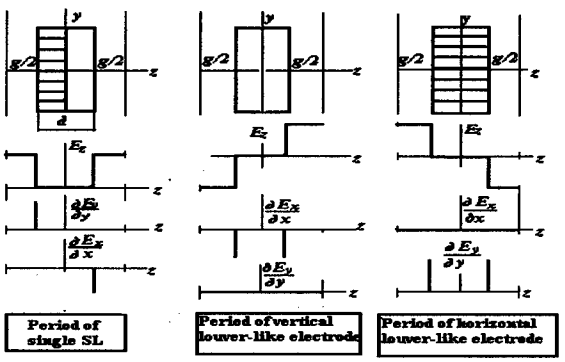

Fig.3. Possible segments of focusing elements (a - space lattice, b - vertical louver, c- horizontal louver).

The segment with a single cell of SL electrode is presented in fig.3a.

The coefficient $G(z)$ changes its sign within this segment.

$$G(z) = \frac{1}{2}\frac{\partial E_z}{\partial z}, z<0, \qquad G(z) = -\frac{1}{2}\frac{\partial E_z}{\partial z}, z>0.$$

As a result of the integrating along the SL electrode length the coefficients b_1 and b_2 may be written as

$$b_1 = p_0\sin\frac{\pi d}{\beta\lambda}\sin\varphi, \qquad b_2 = -p_0\cos\frac{\pi d}{\beta\lambda}\cos\varphi,$$

$$p_0 = \frac{zeS}{2W}E_0.$$

In these expressions p_0 is pick value of RF field focusing. The increments of transversal velocity may be written in the form (d is the length of SL electrode):

$$\Delta\frac{dx}{d\tau} = -p_0\cos(\varphi + \frac{\pi d}{\beta\lambda})x, \qquad \Delta\frac{dy}{d\tau} = p_0\cos(\varphi - \frac{\pi d}{\beta\lambda})y.$$

Coming to the thin lens approximation ($d/\beta\lambda << 1$) the matrixes of focusing element may be written as:

$$p = \begin{bmatrix} 1 & 0 \\ p & 1 \end{bmatrix} \qquad \bar{p} = \begin{bmatrix} 1 & 0 \\ \bar{p} & 1 \end{bmatrix}$$

$$p = -\bar{p} = p_0 \cos\varphi.$$

The matrixes of the segment presented in fig.3a correspond to motions in *XOZ* and *YOZ* planes.

$$T_{nx} = \begin{bmatrix} 1 & \frac{1}{4(N_d+1)} \\ 0 & 1 \end{bmatrix} \begin{bmatrix} 1 & 0 \\ p_0 \cos\varphi_n & 1 \end{bmatrix} \begin{bmatrix} 1 & \frac{1}{4(N_d+1)} \\ 0 & 1 \end{bmatrix}$$

$$T_{ny} = \begin{bmatrix} 1 & \frac{1}{4(N_d+1)} \\ 0 & -1 \end{bmatrix} \begin{bmatrix} 1 & 0 \\ -p_0 \cos\varphi_n & 1 \end{bmatrix} \begin{bmatrix} 1 & \frac{1}{4(N_d+1)} \\ 0 & 1 \end{bmatrix}$$

Here φ_n is a phase of particle in the n^{th} SL of focusing period.

For the segment with vertical orientation of through slots or vertical "louver"(VL) (see fig.3b) the coefficient $G(z)$ does not change its sign):

$$G(z) = -\frac{1}{2} \cdot \frac{\partial E_z}{\partial z}$$

Such electrodes are usually arranged at one of edges of acceleration period. Electrodes with horizontal orientation of through slots (HL) are arranged at the other edge of acceleration period (see fig.3c).

The coefficients of b_1 and b_2 are equal to each other:

$$b_1 = b_2 = b = -p_0 \cos\varphi \cos(\pi d/\beta\lambda).$$

Moving through the electrode with vertical orientation of slots a particle gains double focusing momentum from RF field in *X* direction while is not pushed in *Y* direction

$$\Delta \frac{dx}{d\tau} = -2 p_0 \cos\varphi, \qquad \Delta \frac{dy}{d\tau} = 0.$$

For the edge electrodes arranged $\beta\lambda/2$ apart from these electrodes the through slots are oriented horizontally so particles gain double momentum from RF field in *Y* direction while no pushed in *X* direction.

The analytical calculations have been carried out assuming that focusing effect is proportional to p_0^2; the defocusing effect is proportional to p_0 while higher powers of p_0 were not taken into account.

In fig.4 the results of matrix analysis are plotted for the case of $p_0 = 1$. It is seen that in assumption of zero length of SLs at arrangement of 12 focusing elements within the focusing period all particles are stable in transversal directions independently on their input phase. It is also follows from comparison analytical and matrix calculation results that focusing action of focusing lattices is proportional to the coefficient at p_0^2 with rather high accuracy.

The focusing effect is weakened to some extent with allowance for finite width of SLs. It was found for the case when lattice electrodes occupy one half of focusing period the necessary number of focusing SLs at the period is about 30% more than in case of zero-width SLs to make transversal stability available for any input phase of a particle.

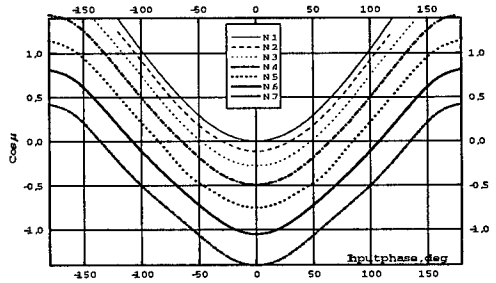

Fig.4. Phase advance vs. input phase of ion (N is amount of space lattices within an acceleration period of $\beta\lambda/2$).

The presence of both grooves and slots distorts to some extent the field structure near the electrode borders. To increase focusing features of the system it is necessary to decrease field penetration into focusing elements by narrowing both grooves and slots. The compromise is probably corresponds to the case of field strength falling to zero in the middle of focusing electrodes.

The preliminary analysis shows that by arranging of appropriate amount of SLs in every the acceleration gap the considering multiple channel focusing acquires features of the spatially uniform RF quadruple focusing. Theoretically any small beam divergence of total accelerated beam may be reached in SLF array while features of practical use of SL focusing in RF linacs seem to be established by adequate ion injectors as well as advanced level of technology and practice.

4. REFERENCES

[1] B.P.Murin, B.I.Bondarev, V.V.Kushin, A.P.Fedotov. Ion Linear Accelerators, Moscow, Atomizdat, p.207 (1978).

[2] A.W.Maschke "MEQALAC: A New Approach to Low Beta RF Acceleration", BNL 51029 (1979).

[3] V.V.Kushin et al, "First Experience of Works With Compact Injectors For Trials and Drills of RF Linac Structures", XIX Intern. Linac Conf. LINAC98, Chicago, (1998), to be published

[4] E.V.Gromov, V.V.Kushin, S.V.Plotnikov, «Multiple Channel Structure For Ion Linac», Inventor's Certificate of USSR № 256492 (1986); and S.V.Plotnikov «Operating variables of RF focusing in linac structures», Thesis, 2 (1986) (in Russian)

[5] I.M.Kapchinsky, "Theory of Linear Resonant Accelerators", Atomizdat, Moscow, (1966), Harwood, 1985.

OVERVIEW OF THE APT ACCELERATOR DESIGN*

J. Tooker†, General Atomics, San Diego, CA
G. Lawrence, LANL, Los Alamos, NM

Abstract

The accelerator for the Accelerator Production of Tritium (APT) Project is a 100-mA continuous-wave (cw) proton linac with an output energy of 1030 or 1700 MeV, depending on the tritium-production capacity that is needed. A high-energy beam transport (HEBT) system conveys the beam to a raster expander, which provides a large-area rectangular power distribution at a target/blanket assembly. Spallation neutrons generated by the beam in the target/blanket are absorbed in Helium-3 to produce tritium. The APT linac has an integrated normal-conducting (NC)/ superconducting (SC) design; the machine architecture, beam dynamics, performance issues, and the supporting engineering-development-and-demonstration program have been discussed elsewhere [1, 2, 3]. The NC linac consists of a 75-keV injector, a 6.7-MeV, 350-MHz radiofrequency quadrupole (RFQ), a 96-MeV, 700-MHz coupled-cavity drift-tube linac (CCDTL), and a 700-MHz coupled-cavity linac (CCL), with an output energy of 211 MeV. This system is followed by a SC linac that employs 700-MHz elliptical-type niobium 5-cell cavities to accelerate the beam to the final energy. The SC linac is built in two sections, using cavities optimised at $\beta = 0.64$ and 0.82. Each section is made up of cryomodules containing two, three, or four five-cell cavities, driven by 1-MW, 700-MHz klystrons. An overview of the current linac design is presented.

1 INTRODUCTION

Figure 1 shows the architecture of the APT plant. The APT linac begins with a normal-conducting low energy (LE) linac, which generates the cw proton beam in a 75-KeV injector and continues the acceleration through a RFQ, a CCDTL, and a CCL to 211 MeV. This is followed by a superconducting high energy (HE) linac that accelerates the beam to full energy. The HE linac is divided into two sections. The first is a medium-β section that has 102 five-cell niobium cavities optimized for $\beta = 0.64$. At the end of this section, the proton beam energy is 471 MeV. The second is a high-β section that has five-cell niobium cavities optimized for $\beta = 0.82$. To attain an output energy of 1030 MeV, 140 cavities are needed; an additional 140 cavities are required to reach 1700 MeV. As shown in Figure 1, the HEBT configuration changes depending on the output energy of the accelerator. The HEBT transports the beam and then expands it to a large-area footprint at the target/blanket or conveys it to a 2% power tuning beam stop.

2 ACCELERATOR DESIGN

The following sections describe the design of the various stages of the APT Linac.

2.1 Normal-Conducting Low Energy Linac

The LE linac consists of the injector, a 350-MHz RFQ, a 700-MHz CCDTL, and a 700-MHz CCL.

2.1.2 Injector

The 2.8-m long injector[4] has a radio frequency (RF)-driven ion source that produces a 110-mA cw proton beam at 75 keV. A low energy beam transport that has two solenoid magnets matches the proton beam into the acceptance of the RFQ.

2.1.2 Radio Frequency Quadrupole

The RFQ[5] is an eight-meter long structure built of four resonantly coupled segments tuned for 350 MHz. The RFQ accepts the 75-keV, 110-mA beam from the injector and produces a 6.7-MeV, 100-mA beam. It is driven by three 1.2-MW klystrons.

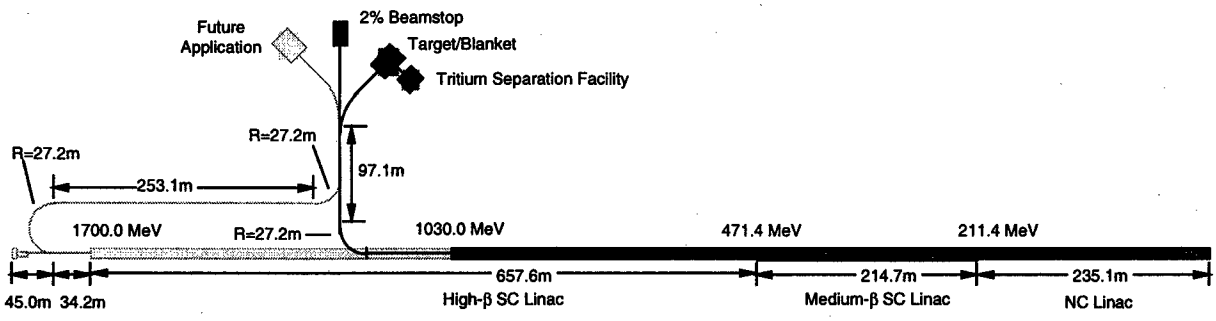

Figure 1: Architecture for APT plant.

*Work supported by DOE DE-AC04-96AL89607
†tooker@gat.com

2.1.3 Coupled Cavity Drift Tube Linac

A 700-MHz CCDTL[6] accepts the 100-mA beam from the RFQ and accelerates it to 96 MeV. The CCDTL cavities are grouped into six resonant structures called supermodules that span a length of 112.8 m. The first supermodule consists of a series of side-coupled 2-gap drift tube linac (DTL) cavities with the quadrupole magnets of the FODO lattice located between them. The focusing lattice begins with a period of 8-$\beta\lambda$ to match the beam from the RFQ and transitions to 9-$\beta\lambda$ at 9 MeV to provide additional space for the quadrupole magnets and beam diagnostics. Module two is made up of DTL cavities with two drift tubes, forming a series of three-gap cavities connected by coupling cells. Modules 3 to 6 consist of two-cavity, two-gap segments. To maintain strong transverse focusing, the quadrupole magnets[7] in the FODO lattice continue with the same 9-$\beta\lambda$ periodicity. The first module is energised by a single 1-MW klystron. The other five supermodules are energised by up to five klystrons.

2.1.4 Coupled Cavity Linac

The CCL is composed of five supermodules spanning a length of 110.4 m. Each is made up of a string of seven-cell segments side-coupled to form a single resonant structure energised by up to seven 1-MW klystrons. The singlet 9-$\beta\lambda$ FODO lattice is continued throughout the CCL.

2.2 Superconducting High Energy Linac

The superconducting cavities of the HE linac are contained in cryomodules that provide the thermal insulation and connection to the cryogenics system to maintain the cavities at their operating temperature of 2.15 K. The FODO lattice of the LE linac transitions to a doublet lattice in the HE linac. The normal-conducting quadrupole magnets[8] are located in the warm regions between the cryomodules. To improve the match from the LE linac, the first six cryomodules in the medium-β section contain two cavities each, providing a relatively short 4.877-m focusing period. The remaining 30 cryomodules in the medium-β section contain three cavities each, with a longer 6.181-m focusing period. Each cryomodule in the medium-β section is powered by a single 1-MW klystron. Each cavity is fed by a pair of RF power couplers, so that the RF power from each klystron is divided by four or six, with up to 210 kW per coupler.

The high-β section is a series of four-cavity cryomodules with the room temperature quadrupole magnets in the warm regions between the cryomodules continuing the doublet lattice with a period of 8.540 m. The quantity of cryomodules in this section is determined by the ultimate proton beam energy needed to achieve the production requirements of the APT plant. This can range from 35 cryomodules at 1030 MeV to 77 at 1700 MeV. Each high-β cryomodule is powered by two 700- MHz klystrons. The power is divided equally between two cavities, and again by two to feed the two power couplers on each cavity. Figure 2 depicts the tunnel in the medium-β section of the high energy linac, showing the RF power splitting to the three-cavity cryomodules and the quadrupole doublets between the cryomodules.

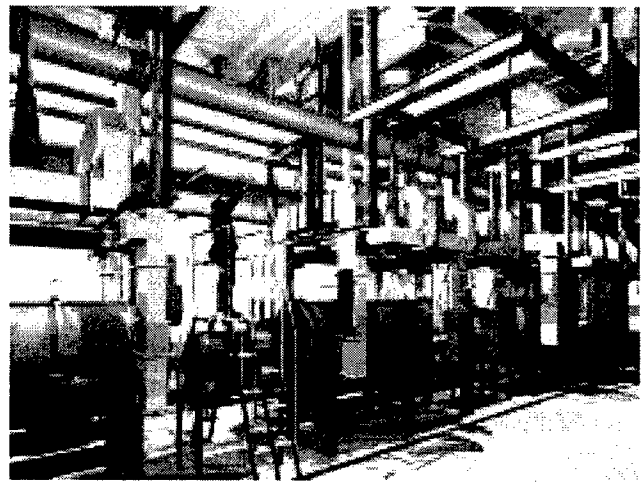

Figure 2: HE linac tunnel section.

2.3 High Energy Beam Transport

The doublet lattice of the HE linac is continued along the transport line of the HEBT. A beam stop capable of handling 2% of the beam power is located at the end of the beam transport line. It is used during commissioning, start up, and tuning of the accelerator. A 45° bend in the switchyard directs the beam from this beam stop to the target/blanket assembly. The beam is expanded onto the target by a beam raster system[9], which sweeps the beam uniformly over the 19-cm wide by 190-cm high tungsten target.

2.4 RF Power Systems

Three 1.2-MW, 350-MHz klystrons are used to energise the RFQ. Only two are required to accelerate the beam in the RFQ; the third is a spare so that the linac can continue to operate if one of the 350-MHz RF power systems fails. The power from each klystron is split by four, feeding twelve iris couplers in the RFQ cavity.

The supermodules in the LE linac and the superconducting cavities in the HE linac are powered by 1-MW, 700-MHz klystrons. There are 52 klystrons in the LE linac, 36 klystrons in the medium-β section of the HE linac, and up to 154 klystrons in the high-β section of the HE linac.

The architecture of the APT linac is configured so that the failure of an RF power system does not result in the loss of production of tritium while it is being repaired.[10] The supermodules in the LE linac, except for the first supermodule of the CCDTL, are fed by one more klystron

than is required to accelerate the beam. Should one of the RF systems that feed these supermodules fail, it is isolated from the supermodule and the RF power output from the remaining operating klystrons is increased to compensate for the RF power lost from the failed klystron. The first supermodule is fed by a single klystron, with a standby unit that can be switched in, if necessary. The RF power systems for the HE linac will normally be operated at a reduced power level, so that if one fails, the affected cavity is detuned and the power from adjacent RF systems is increased to make up for the failed system. The RF power systems in the medium-β section normally operate at 91% of their rated power and 95% in the high-β section. Figure 3 shows a portion of the klystron gallery and tunnel with layouts for the RFQ, the start of the CCDTL, and a two-cavity cryomodule.

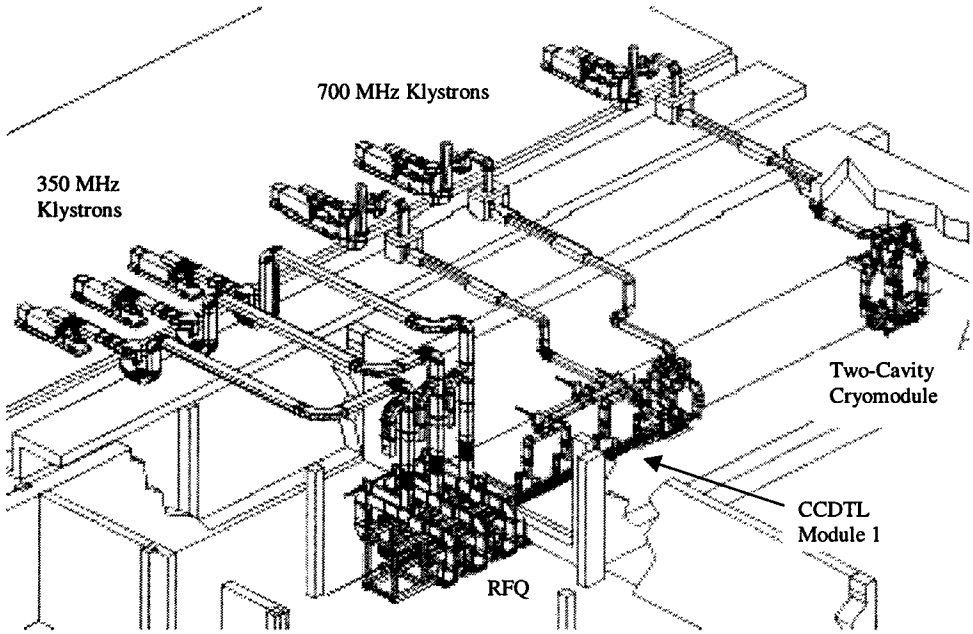

Figure 3: Portion of klystron gallery and tunnel showing various RF layouts along linac.

2.5 *Cryogenic System*

The cryogenic system supplies helium cooling to maintain the niobium cavities at 2.15 K. It will provide approximately 15 kW of refrigeration at 2.15 K for the superconducting RF cavities and approximately 50 kW of refrigeration between 5 K and 30 K for the thermal intercepts on the RF power couplers and thermal shields in the cryomodules and the cryo-distribution system. There is a cryogenic distribution line containing two sets of supply and return lines that runs the length of the HE linac. Sets of four U-tube transfer lines connect each cryomodule to this distribution line. The distribution line is supplied by a cryogenics plant where multiple, semi-independent helium refrigerators provide the closed-loop helium cooling. Each refrigerator contains a 4-K coldbox using gas-bearing turbine expanders, a 2-K coldbox with cold compressors to generate the sub-atmospheric conditions within the cryomodule, warm helium compressors for gas compression, liquid and gas storage, and appropriate instrumentation and controls.

3 REFERENCES

[1] G.P. Lawrence, "High-Power Proton Linac for APT; Status of Design and Development", Proc. 1998 Int. Linac Conf., Chicago, August 1998.

[2] T. P. Wangler, et al., "Basis for Low Beam Loss in the High-Current APT Linac", Proc. 1998 Int. Linac Conf., Chicago, August 1998.

[3] T.P. Wangler, et al., "Beam Dynamics Design and Simulation Studies of the APT Superconducting Linac", these proceedings.

[4] J. Sherman, et. al, "Status Report on a dc 130 mA, 75 keV Proton Injector", Review of Scientific Instruments 69(2), 1003 (1998).

[5] D. Schrage, et. al, "CW RFQ Fabrication and Engineering," Proc. 1998 Int. Linac Conf., Chicago (August 1998).

[6] R. Wood, et. al, "Status of Engineering Development of CCDTL for Accelerator Production of Tritium," Proc. 1998 Int. Linac Conf., Chicago (August 1998).

[7] S. Sheynin, et. al, "Designs of the Low Energy Intertank Quadrupole Magnets for APT," these proceedings.

[8] S. Sheynin, et. al, "APT High Energy Linac Intertank Assembly Design," these proceedings.

[9] S. Chapelle, et. al, "Testing of a Raster Magnet System for Expanding the APT Proton Beam," these proceedings.

[10] M. McCarthy, et. al, "Response of the RF Power System to Off-Normal Conditions on APT," these proceedings

MEASUREMENTS ON THE FREQUENCY EFFECTS AND COUPLING OF SLOTS AND IRISES FOR THE APT CCDTL*

H. Bluem†, M. D. Cole, Advanced Energy Systems, Princeton, NJ
J. H. Billen, L. M. Young, LANL, Los Alamos, NM
P. Greninger, General Atomics, Los Alamos, NM

Abstract

In preparation for the fabrication of the coupled-cavity drift tube linac[1] portion of the Low-Energy Demonstration Accelerator[2] for the Accelerator Production of Tritium[3] project, the effects of coupling slots/irises have been measured and compared to theoretical calculations. A number of multi-cavity cold models have been constructed corresponding to various sections of the coupled-cavity drift tube linac. These models have been used to measure the average cavity to cavity coupling, the frequency effects of the cavity to cavity coupling slots, the coupling into the cavity structures from a waveguide through an iris, and the effect of the iris on the frequency of the cavity being driven. The results of these measurements have been compared to the theoretical values. The effect of a shorting plate placed in one of the feed waveguides was also investigated. This was used to approximate the position of a closed vacuum valve which would be used in the event of a vacuum window failure.

1 INTRODUCTION

In preparation for the fabrication of the coupled-cavity drift tube linac (CCDTL)[1] portion of the Low-Energy Demonstration Accelerator (LEDA)[2] for the Accelerator Production of Tritium (APT)[3] project, the effects of coupling slots/irises have been measured and compared to theoretical calculations. The LEDA CCDTL accelerates a 100 mA CW proton beam from 6.7 MeV to 10.05 MeV. The structure contains 48 two-gap accelerating cavities, two types of coupling cavities, and seven bridge couplers. The power from a single klystron will be split four ways to drive four of the bridge couplers through appropriately sized irises. In later sections of the APT accelerator, the drive irises will be placed in the accelerating cavities.

To efficiently fabricate a large accelerator, it is important that the initial machining of the cavities be as close as possible to the desired final configuration without overshooting. In order to accomplish this, one must be able to predict the frequencies of the individual cells, the cell to cell coupling, and the feed iris coupling. To first order, the frequencies of the cells can be predicted using SUPERFISH[4], but without accounting for the effects of the coupling slots, the resultant fabricated cavity will be too low in frequency. If the coupling can be predicted accurately, then the coupling slots between cavities can be fully cut during the initial machining and will not have to be touched during the tuning procedure. This could potentially save a substantial amount of time. The goal of this work was to develop and verify a method of predicting these effects.

A number of multi-cavity cold models have been constructed corresponding to various sections of the CCDTL. These models have been used to measure the average cavity to cavity coupling using the program DISPER[5], the frequency effects of the cavity to cavity coupling slots, the coupling into the cavity structures from a waveguide through an iris, and the effect of the iris on the frequency of the cavity being driven. The results of these measurements have been compared to formulas for the coupling and frequency effects based upon those derived by J. Gao[6],[7]. The amount of agreement between calculated and measured was mixed, with the largest disagreement occurring in the numbers for the coupling between the waveguide and cavity structure.

The effect of a shorting plate placed in one of the feed waveguides was also investigated. This was used to approximate the position of a closed vacuum valve which would be used in the event of a vacuum window failure. The positions of zero frequency effect on the cavity structure and minimum power loss on the shorting plate were found. Appropriate positioning of the vacuum valve will properly terminate the unusable port from the cavity point of view, thus allowing the accelerator to continue operation even in the event of a vacuum window failure, although driving only three of the four ports.

In the next section, the cavity to cavity coupling measurements will be discussed along with the frequency effects of the cavity to cavity slots. In Section 3, the waveguide to cavity coupling measurements will be discussed and compared to the theory. The shorting plate will be covered in Section 4.

2 CAVITY TO CAVITY COUPLING

The coupling between cavities has been measured for a number of cold models corresponding to different locations in LEDA. These measurements have provided both the cavity to cavity coupling and the frequency effect of the slots.

The frequency effects have been measured by starting with an accelerating cavity which has no coupling slots.

* Work supported by the US DOE under the APT LEDA program.
† Email: bluem@grump.com

0-7803-5573-3/99/$10.00@1999 IEEE.

The slots were then opened in steps until a little past the point where the desired coupling was reached. The coupling at each step was also derived. The average coupling value was arrived at by measuring the frequencies of the structure resonances. These frequencies were used to calculate the nearest neighbor coupling.

The numbers so obtained have been compared to values calculated using the following formulas.

$$k_m = \frac{\pi}{3}\mu_0 e_0^2 L^3 \frac{H_{ac}H_{cc}}{(K(e_0)-E(e_0))}\frac{1}{\sqrt{U_{ac}U_{cc}}}e^{-\alpha_H t} \quad , \qquad (1)$$

$$k_e = -\frac{\pi}{3}\varepsilon_0\left(w/L\right)^2 L^3 \frac{E_{ac}E_{cc}}{(E(e_0))}\frac{1}{\sqrt{U_{ac}U_{cc}}}e^{-\alpha_E t} \quad , \qquad (2)$$

and

$$\delta f_{ac} = \frac{f}{4}\left(k_m \frac{H_{ac}}{H_{cc}} + k_e \frac{E_{ac}}{E_{cc}}\right)\sqrt{\frac{U_{cc}}{U_{ac}}} \quad , \qquad (3)$$

where k_m and k_e are the magnetic and electric coupling respectively, μ_0 and ε_0 are the permeability and permittivity of free space, $e_0 = (1-w^2/L^2)^{1/2}$, 'w' is the slot half-width, 'L' is the slot half-length, H_{ac}, E_{ac}, H_{cc} and E_{cc} are the magnetic and electric fields at the slot position in the accelerating and coupling cavities, $K(e_0)$ and $E(e_0)$ are complete elliptic integrals of the first and second kind, U_{ac} and U_{cc} are the stored energy in the accelerating and coupling cavities, α_H and α_E are the TM and TE cutoff waveguide decay factors of the slot, 't' is the thickness of the slot, δf_{ac} is the frequency change in the accelerating cavity due to the slot and 'f' is the initial frequency of the cavity before slots are introduced. If cc is substituted for ac (and vice verse) in the δf equation, one obtains the frequency change in the coupling cavity. These equations are derived assuming an elliptical slot, and the field values which are intended to be used are at the center of the slot. In the LEDA CCDTL, the slots are not elliptical in shape. They are approximately a semi-ellipse but with very rounded corners at the equator. We have not attempted to fit the actual shape to an equivalent ellipse. As a result of the odd shape, the slot length and field strength to be used in the formulae are somewhat ambiguous. There is insufficient space in the present paper to describe how the slot length is chosen and from which location the field strength is taken.

Figures 1 and 2 show a comparison between the measurements performed on one of the cold models and the anticipated values as calculated from Eqs. 1, 2 and 3. The coupling factor shows very close agreement except for the first point. The first point represents a "knife-edge" slot of zero thickness. In reality, this slot has some finite thickness which was not accounted for in the calculations. The target coupling in the design is 5%. On all of the cold models, the prediction of the coupling factor has been very good. On the other hand, as can be seen in Fig. 2, the prediction of the frequency effect of the slot is not quite as good. The discrepancy is manageable, but it is preferable to have better agreement. A large portion of the discrepancy is probably due to the choice of field strength. With a different choice of field strength, the predicted frequency effect can be brought to within a few percent of the measured values while still keeping the coupling factor values within a percent or two.

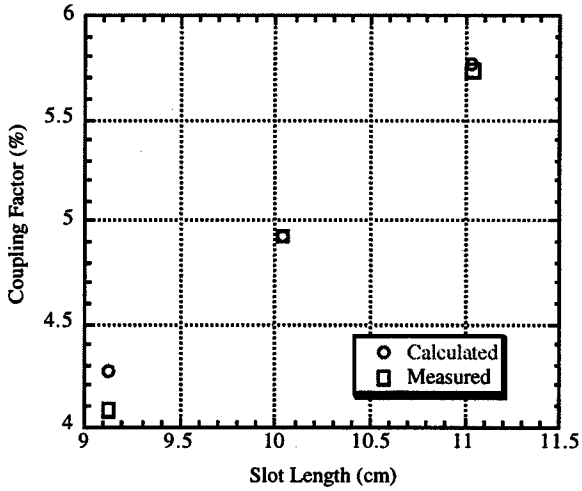

Figure 1. A comparison of the calculated and measured coupling factor as a function of slot length for one of the cold models.

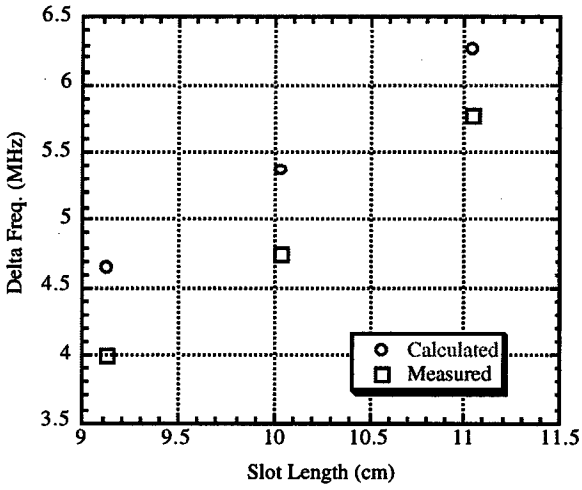

Figure 2. A comparison of the calculated and measured frequency change, in an accelerating cavity, due to the slot as a function of length.

3 WAVEGUIDE TO CAVITY IRIS

The waveguide to cavity coupling has been treated in a manner similar to the cavity to cavity coupling. Except in this case, the coupling factor can be measured directly in an easy and straight forward way. The effects of the waveguide input iris have been measured on three different models. The results between the three models have been similar. The equations used to predict the coupling and frequency effect are:

$$\beta = \frac{120\pi}{9ab}\sqrt{1-\left(\lambda/\lambda_c\right)^2} \times \left[\frac{2\pi}{\lambda}\pi e_o^2 \frac{L^x}{(K(e_o)-E(e_o))} H_{iris}\right]^2 e^{-2\alpha t}\frac{Q_0}{\omega U_{tot}} \quad (4)$$

and

$$\delta f_{cav} = -f\frac{\pi}{12}\mu_0 \frac{L^3 e_0^2}{[K(e_0)-E(e_0)]}\frac{H_{iris}^2}{U_{cav}} \quad , \quad (5)$$

where β is the input coupling factor, 'a' and 'b' are the width and height of the feed waveguide at the iris, λ is the free space wavelength of the input signal, λ_c is the waveguide cutoff wavelength, x is nominally 3, H_{iris} is the field at the iris, Q_0 is the unloaded quality factor for the accelerating structure, U_{tot} is the total stored energy in the accelerating structure, U_{cav} is the stored energy in the cavity containing the iris, and all others are as before.

The measurements and predicted values of the input coupling and the frequency change as a function of iris length are shown together in Figure 3 for one of the cold models. The predicted coupling was adjusted to fit to the experimental data by varying 'x' in Eq. 4. The best fit was given by x=3.115.

Since the iris has a relatively large aspect ratio and is generally rectangular in shape, it was easier in this case to generate an equivalent ellipse for the calculations performed. The equivalent ellipse possessed the same length as the iris. The width was increased in order to achieve equal areas between the equivalent ellipse and the actual slot.

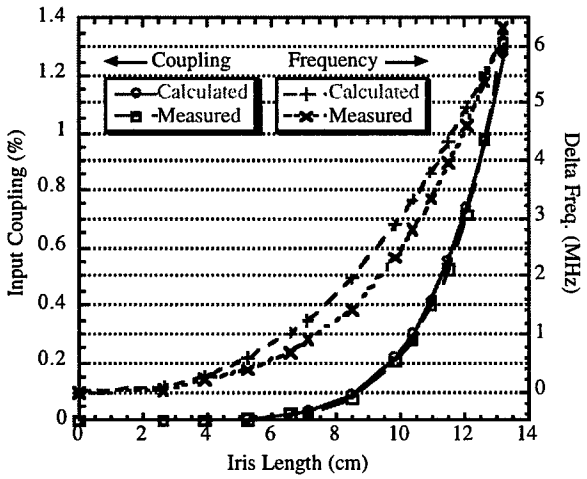

Figure 3. Measured and predicted input coupling and frequency effects as a function of the input iris length.

4 VALVE/SHORT POSITION

Due to the desire to keep operating in the event of an RF vacuum window failure, a vacuum valve needs to be placed between the vacuum window and the input iris. This valve, when closed, will present an RF short circuit in the iris feed arm. If this short circuit is appropriately placed, it will have negligible effect on the structure frequency and will have a minimal amount of dissipated energy on its surface. If it is inappropriately placed, it will have a significant effect on the frequency and will have a substantial power dissipated on its surface.

Conventional impedance matching theory places the short circuit one quarter of a guide wavelength (or an odd multiple thereof) from the cavity's virtual short position. If the short is placed at such a position, the cavity will not 'see' it.

The measurements determined the cavity's virtual short position to be about 2.54 cm inside the waveguide measured from the outer surface of the iris. The position proved to be insensitive to the size of the iris. If the short is placed one quarter of a guide wavelength from this point there will be no stored energy in the waveguide arm and hence the power dissipation will be minimized. However, this is not the point of zero frequency effect. The point of zero frequency effect occurs about 1.25 cm farther back into the waveguide. The position of this point is also insensitive to iris size over a coupling range from about 0.5 to about 2.0.

Since zero frequency effect is most important to proper accelerator operation, the valve will be place at this position. Fortunately, the power dissipation changes very slowly between the minimum power point and this position so that it remains acceptably low. The tolerance on the valve position was found to be plus/minus 2.54 cm in order to keep the resonant frequency within 15 kHz of nominal.

5 SUMMARY

Due to the good agreement between the measured and calculated coupling, the slot sizes can be included in the accelerator design calculations. At this point, accurate incorporation of the frequency effects will require use of an emperically determined factor with the formula.

6 REFERENCES

[1] J.H. Billen, et al, "A New RF Structure for Intermediate-Velocity Particles", Proc. 1994 Int. Linac Conf., Tsukuba, Japan, p341 (1994).

[2] H.V. Smith, "Status Update for the Low-Energy Demonstration Accelerator (LEDA)," Proc. 1998 Int. Linac Conf., Chicago, USA.

[3] G. Lawrence, "High Power Proton Linac for APT; Status of Design and Development", Proc. 1998 Int. Linac Conf., Chicago, USA.

[4] J.H. Billen and L.M. Young, POISSON SUPERFISH, Los Alamos National Lab report LA-UR-1834 (revised November 14, 1998).

[5] DISPER coupled cavity modal analysis program maintained and distributed by Los Alamos Accelerator Code Group.

[6] J. Gao, "Analytical formula for the coupling coefficient β of a cavity-waveguide coupling system", Nucl. Instr. and Meth. A309, (1991) 5.

[7] J. Gao, "Analytical formulas for the resonant frequency changes due to opening apertures on cavity walls," Nucl. Instr. and Meth. A311, (1992) 437.

RF CAVITY DESIGN AUTOMATION FOR THE APT CCDTL AND CCL*

D.W. Christiansen, Paul Greninger, A.W. Magerski, H.J. Rodarte, P. Smith, G. Spalek,
General Atomics, San Diego, CA

Abstract

As part of the APT project, the Coupled-Cavity Drift Tube LINAC (CCDTL) and Coupled-Cavity LINAC (CCL) designs are being developed.[1] These structures contain 341 cavity segments in 11 different modules. This configuration accelerates a proton beam from 6.7 MeV to 211 MeV. Because of the number of individualized cavity arrangements, an automation design process is being developed. This paper discusses the methods of design automation using Pro-Engineer® as well as programs required to feed the Pro-Engineer® drawing generation process. Such programs include SUPERFISH, where cavity parameters are obtained, as well as programmed analytical methods used to define cavity dimensions that produce the desired level of coupling and $\pi/2$ mode frequency. To compute the coupling, a method developed by J. Gao [2] has been used

1 INTRODUCTION

The Los Alamos Nation Laboratory has had good success predicting coupling in the CCDTL using the J. Gao[2] method. Using that as a bases and extending to automate the CCL and later the CCDTL design, significant progress with design automation has been achieved. Automated design methods are being applied to the first half-size CCL cold model. To date, automated CCL coupling slot geometry calculation methods have been verified, CCDTL calculations will start in FY99. The specific computer code developed for automated design is CCT - Coupled-Cavity Tuning code.

2 MECHANICAL DESIGN AUTOMATION

To guarantee success with the APT Low Energy LINAC design, two design approaches have been incorporated into the design process. The first approach is the full automation of the design process by the use of digital computer codes. The other approach, a more traditional approach, uses linear extrapolation from cold model data. The process flow diagram for the design program is shown in Figure 1. In Figure 1, code development is performed and validated by the use of cold models and other analyses. If the validation is successful, design by code is performed. If

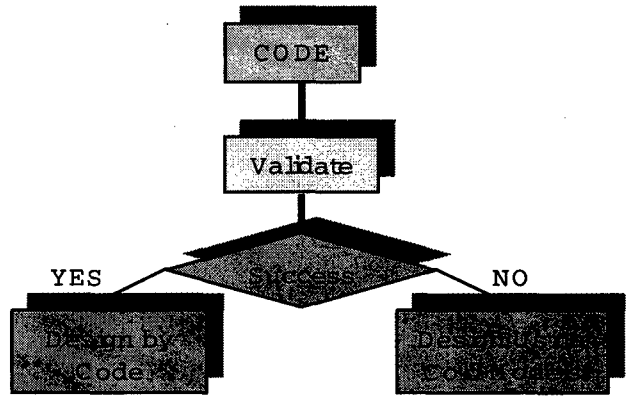

Figure 1. Low Energy LINAC design process flow chart encompassing full automation and use of cold models.

the validation is not successful, schedule and funding are not lost. Since code validation requires the use of cold models, the same cold models would be required for use in the non-fully automated process. Additionally, parts of the automation code that can be validated would still be used. This process, therefore, achieves an effective cost and schedule implementation of the design process.

2.1 Coupling Slot Length, Width and Depth

In order to automate design, an analytic formula for calculating coupling cavity to accelerating cavity slot size is needed. Such a formula has been developed. The equations allow for mechanical manipulation of the coupling cavity relative to the on-axis cavity for digital processing. Solved coupling cavity characteristics are cavity size, coupling-slot size, determination of the coupling coefficients and cavity frequency shifts due to the coupling slots. Once determined, the above parameters are used to iterate coupling and cavity parameters to allow for optimization of the design based on desired coupling and $\pi/2$ mode frequency. An example of a slot formed by the overlap (insertion depth) of the CCL coupling cavity and accelerating cavity is shown in Figure 2. Equations for calculating as a function of insertion depth are shown below.

2.1.1 Coupling Slot Length

From Figure 2, sample equations developed for calculating slot length are shown below. In these equations, slot length is determined by the interaction of two circles (one centered on the coupling cavity centerline and the other centered on the accelerating cavity

* - Work supported by the US DOE under the APT Program.

centerline). The radii of these circles are determined at the insertion height where the coupling cavity and accelerating cavities have zero insertion height, refer to Figure 2

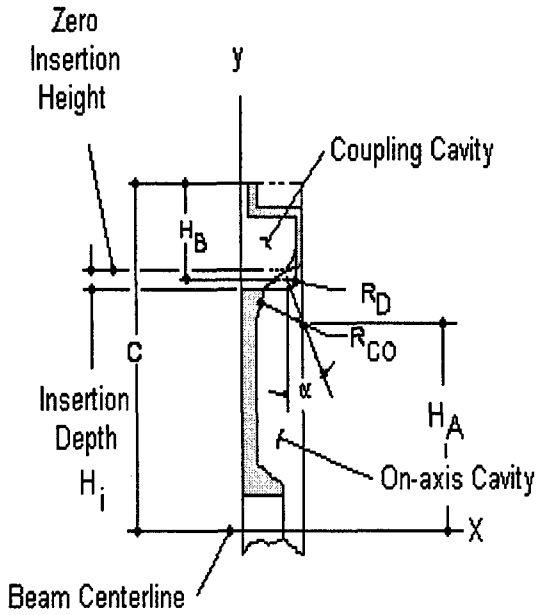

Figure 2. Accelerating cavity to coupling cavity geometry.

$$R_E = H_B + R_D \mathrm{Cos}(\alpha) \quad (1)$$

$$R_F = H_A + R_{CO} \mathrm{Cos}(\alpha) \quad (2)$$

$$C_e = R_F + R_E \quad (3)$$

$$y_i = \frac{-(R_E^2 - R_F^2)}{2(C - H_i)} + \frac{(C - H_i)}{2} \quad (4)$$

$$x_i = 2[(R_F^2 - y_i^2)]^{0.5}] + 2C_H \quad (5)$$

$$C_{a_i} = C_e - H_i \quad (6)$$

Typical slot lengths are shown in Table 1.

Item	H_I (mm)	y_I (mm)	x_I (mm)	C_{ai} (mm)
1	5.08	155.854	55.728	259.893
2	10.16	153.848	76.276	254.813
3	15.24	151.841	91.796	249.733
4	20.32	149.860	104.623	244.653
5	25.40	147.904	115.697	239.573

Table 1. Coupling slot length versus coupling cavity insertion depth.

In Table 1, Item is the case number, H_i is the coupling cavity to accelerating cavity insertion depth, y_i is the height of the slot centerline relative to the beam centerline and C_{ai} is the center to center distance between the coupling cavity and accelerating cavity. C_H in the equations, represents a chamfer around the periphery of the slot, shown in Figure 4.. Results in Table 1 are shown in Figure 3.

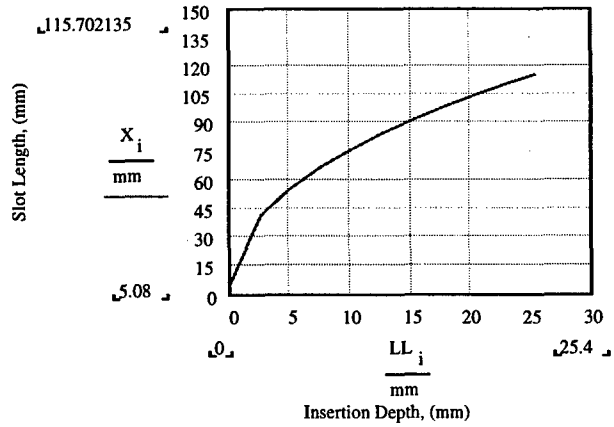

Figure 3. Slot length versus cavity insertion depth.

2.1.2 *Coupling Slot Width and Depth*

Coupling slot width is derived from Figure 4.

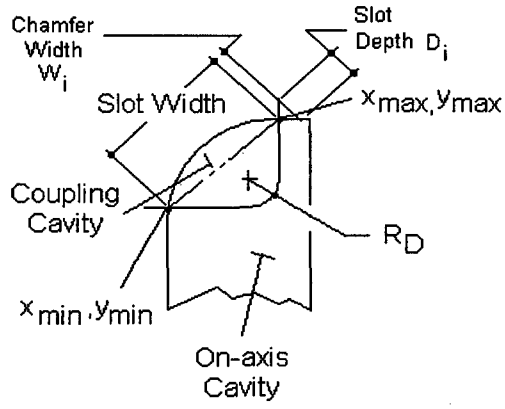

Figure 4. View looking at the center of a typical CCL cloupling slot cross section showing slot width.

In the above, coupling slot width is geometrically defined as the diagonal of two intersecting cavities at the center of the slot in cross section. In equation form, this statement is represented by

$$X_{max_i} = \frac{[-l_i + (l_i^2 - 4m_i n_i)^{0.5}]}{2m_i} \quad (7)$$

$$X_{min\,i} = \frac{[-l_i - (l_i^2 - 4m_i n_i)^{0.5}]}{2m_i} \quad (8)$$

$$Y_{max_i} = [R_D^2 - (X_{max_i} - a)^2]^{0.5} + b_i \quad (9)$$

$$Y_{min_i} = [T_D^2 - (X_{min_i} - a)^2]^{0.5} + b_i \quad (10)$$

$$W_i = [(X_{max_i} - X_{min_i})^2 + (Y_{max_i} - \ldots \quad (11)$$
$$\ldots - Y_{min_i})^2]^{0.5} + 2C_H$$

Slot depth is

$$D_i = (Y_{CC_i} - Y_{OC_i})\mathrm{Cos}(\Theta_i) \quad (12)$$

where

$$\Theta_i = \mathrm{Tan}^{-1}[\frac{(Y_{max_i} - Y_{min_i})}{X_{max_i} - X_{min_i})}] \quad (13)$$

In the solution of these equations, l_i is the second Bernoulli term, m is the first Bernoulli term and n is the third Bernoulli term of a solved set of second order equations. R_D is the coupling cavity radius and b equals C-H_B-H_I from Figure 4. YCC and YOC are vertical distances from the horizontal beam axis to the coupling cavity and on-axis cavity intersection at the extreme end of the slot. A sample of slot size versus insertion depth is shown in Figure 5.

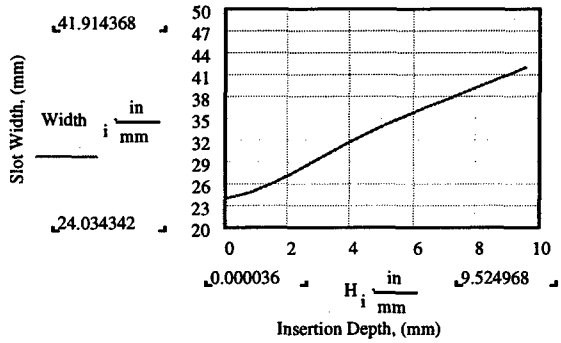

Figure 5. Prototypic CCL coupling slot width..

Determination of cavity geometries with the above equations follows the following general flow of information: SUPERFISH is used to generate initial cavity data. CCT then reads the SUPERFISH input and output files and calculates the slot configuration. If either the final cavity frequency and/or coupling coefficient are off, the cavity geometry is adjusted and the process is repeated. This process continues until cavity frequency and coupling are achieved. Output results are then calculated for ambient 68 °F conditions and fed to automated Pro-Engineer® drafting programs for cavity design.

3 PHYSICS AUTOMATION

There are two areas that deserve mention for the physics automation process. These areas are frequency shift due to coupling and coupling coefficient [1]. To automate the mechanical accelerator design process, the mechanical computer code integrates the physics design calculations. For the frequency shift due to the coupling slots, the frequency shift is

$$\Delta f = k_1 f_0 \frac{[\mu_0 \pi (\frac{x_i}{2})^3 e_0^2 H_1^2]}{[k_2 (K(e_0)_i - E(e_0)_i) U_1]} \quad (14)$$

Where:
- Δf = Change in frequency due to coupling slots
- f_0 = Unperturbed frequency of the cavity
- μ_0 = Permeability of free space
- x_i = Length of the coupling slot
- e_0 = $[1-(x_i/W_i)^2]^{1/2}$
- H_1 = Unperturbed field in on-axis cavity
- $K(e_0)$,$E(e_0)$ = Complete elliptic integral of the first and second kind
- U_1 = Unperturbed stored energy in on-axis cavity
- k1 = Constant determined from cold model testing
- k2 = 12 for cavities with two coupling slots and 6 for one coupling slot

For Coupling

$$k = \frac{\pi \mu_0 e_0^2 (\frac{x_i}{2})^3 H_1 H_c}{3[K(e_0)_i - E(e_0)_i]\sqrt{U_1 U_c}} \} e^{-\varsigma D_i} \quad (15)$$

(16)

and
- H_c = Unperturbed field in the coupling cavity
- U_c = Unperturbed stored energy in the coupling cavity
- ς = Attenuation coefficient of the slot considered as a waveguide.

4 REFERENCES

[1] Thomas Wangler, RF Linear Accelerators, Copyright 1998, John Wiley & Sons, Inc.

[2] J. Gao, "Analytical Formulas for the Resonant Frequency Changes Due to Opening Apertures on Cavity Walls," Nucl. Instr. And Meth in Physics Research. A311 (1992)p. 437-443.

DESIGNS OF THE LOW ENERGY INTERTANK QUADRUPOLE MAGNETS FOR APT*

A. Harvey, E. Hubbard, M. Schulze, S. Sheynin#
General Atomics, San Diego, CA
D. Barlow, and T. Hunter Los Alamos National Laboratory, Los Alamos, NM

Abstract

The 700-MHz room temperature Low Energy (LE) Linac for the Accelerator Production of Tritium (APT) facility employs three different types of Coupled Cavity Drift Tube Linac (CCDTL) structures to accelerate a 100 mA cw proton beam from 6.7 MeV to 96.9 MeV and two different types of side Coupled Cavity Linac (CCL) structures to accelerate the beam from 96.7 MeV to 211 MeV [1,2,3]. Focusing of the beam is done with quadrupole electromagnets located between the segments of the accelerating structures in a FODO lattice. Since the longitudinal space available for the magnets is severely limited, the ratio of the magnet core length to the bore diameter varies over the range from 0.9 to 1.4. The pole tips have been designed with 3-D finite element modeling to keep total field harmonics less than 1% of the quadrupole component within ¾ of the beam tube aperture. In this paper, we present the physics parameters, detailed design, and some magnetic measurements of the prototypes for the two of the quadrupole magnet designs.

1 INTRODUCTION

There are 11 modules in the LE Linac; 6 CCDTL structures and 5 CCL structures. The beam tube diameter increase gradually from 2.0 cm to 6.0 cm in six stages. Four quadrupole magnet designs have been developed for these six beam tube sizes. These magnets are identified as CCDTL-1, CCDTL-2, CCL-1 and CCL-2 although magnet CCDTL-2 is also used in the first sections of the CCL. Table 1 presents the magnet requirements and quantities for the LE Linac.

The quadrupole magnets are located between the segments of the accelerating structures in a FODO lattice. The physical envelope of the quadrupoles and the integrated strength, i.e. the gradient-length product (GL) was determined by the beam optics design and by constrains of available insertion length, interface with vacuum chambers and flanges, and the vertical space envelope defined by the coupling cells between accelerating cavities. The severely limited longitudinal space envelope between the cavities prevents the use of dedicated steering magnets. The apertures of the quadrupoles are designed to allow sufficient radial clearance with respect to the vacuum beam tube to allow translation of the magnets horizontally and vertically which provides beam steering. This approach was chosen both to avoid dipole windings, which introduce significant sextupole fields, and to obtain the maximum cross-sectional area for the quadrupole windings.

Table 1: Magnet Requirements for LE Linac Modules

Module	Magnet	Quantity	GL_{max}(T)	GL_{min}(T)
1	CCDTL-1	49	2.625	2.344
2	CCDTL-1	57	2.332	2.332
3	CCDTL-1	32	2.332	2.063
	CCDTL-2	11	2.055	1.985
4	CCDTL-2	32	1.978	1.795
5	CCDTL-2	34	1.790	1.639
6	CCDTL-2	28	1.635	1.538
7	CCDTL-2	18	1.538	1.538
8	CCDTL-2	19	1.538	1.499
9	CCDTL-2	3	1.496	1.489
	CCL-1	18	1.486	1.434
10	CCL-1	7	1.431	1.413
	CCL-2	14	1.410	1.373
11	CCL-2	20	1.370	1.200

2 DESIGN AND ANALYSIS

The very short length of the iron quadrupole core compared to the required pole tip diameter, especially for the CCL-1 and CCL-2 quadrupoles, where the iron length is less than the aperture size, makes it challenging to meet specified field uniformity requirements. The vertical dimensions are also restricted limiting the flux return yoke area in the middle of vertical plane. The transverse dimensions of all LE intertank magnets are 40 cm wide and 20 cm high with the overall insertion length of the CCDTL-1, CCDTL-2 and CCL1 restricted to 7.0 cm and the CCL-2 restricted to 9.0 cm.

Electromagnetic analyses were performed using Vector Fields [4] and Mermaid [5] 3D finite element software. The pole tip geometry was optimized to minimize the multipole harmonics by gradually flattening a hyperbolic

* Work supported by DOE contract De-AC04-96AL89607
# E-mail: sam.sheynin@gat.com

0-7803-5573-3/99/$10.00@1999 IEEE.

profile. Earlier designs of the CCDTL-1 prototype were developed with a narrow pole tip and correction bumps on the corners to minimize the higher harmonics. A picture of this magnet is shown in Figure 1. The prototype CCL-1 magnet is shown in Figure 2.

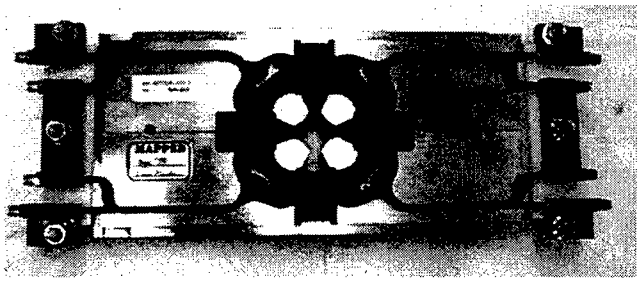

Figure 1: Prototype CCDTL-1 Quadrupole Assembly

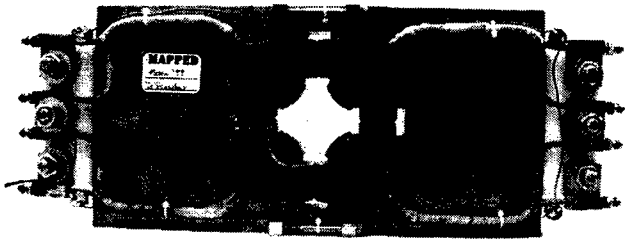

Figure 2: Prototype CCL-1 Quadrupole Assembly

2.1 Field Errors and Harmonics

Field errors are evaluated by obtaining the Fourier series of integrated quadrupole field at a given reference radius R and azimuth angles θ:

$$\int_0^z B_x(R,\theta)\cdot dz \text{ and } \int_0^z B_y(R,\theta)\cdot dz$$

B_x and B_y are horizontal and vertical components of the Field B. The field components B_y and B_x were integrated along the longitudinal axes "z" from the center of magnet out to z = 4 aperture diameters (in air) from the edge of the pole. Thus, values of integrated quadrupole field at the fixed arc of radius R represent a function $F(\theta)$ in the interval $[-\pi < \theta < \pi]$. The azimuth angle $\theta = 0$ lies along the positive "x" axis. Fourier series generated by this function $F(\theta)$ is represented by:

$$F(\theta) = \frac{a_0}{2} + \sum_{k=1}^{\infty}\left(a_k \cdot \cos k\theta + b_k \cdot \sin k\theta\right)$$

The harmonics of B_y are evaluated by the ratios of A_n/A_2, where $A_n = a_{k+1}$, and A_2 is the amplitude of the quadrupole field. Optimization of the pole tip geometry is achieved by minimizing A_6. The calculated 3D harmonics that are allowed by symmetry are presented in Table 2 for each of the four magnet designs. The harmonics are presented a 75% of the beam tube radius. Figure 3 shows a plot of the 2D-field distribution for one quadrant of the CCL-1 magnet. The difference between the vertical and horizontal flux return yokes is evident in this figure.

Table 2: Harmonics of LE Intertank Quadrupoles

	3D HARMONIC CONTENT	
	CCDTL-1	CCDTL-2
A_n/A_2	At R=1cm	At R=1.31cm
A_6/A_2	0.018%	-0.25%
A_{10}/A_2	-0.007%	-0.013%
A_{14}/A_2	-0.008%	0.005%
	CCL-1	CCL-2
	At R = 1.5 cm	At R = 2.25 cm
A_6/A_2	-0.15%	-0.18%
A_{10}/A_2	-0.053%	-0.025%
A_{14}/A_2	-0.006%	-0.008%

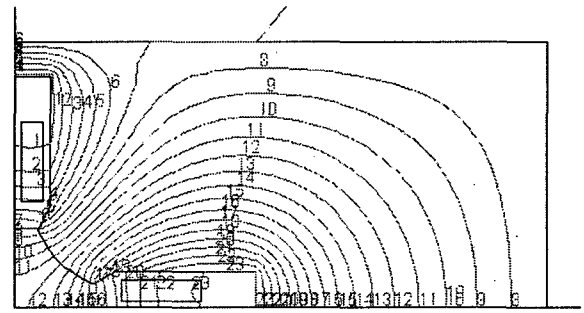

Figure 3: Field Plot of CCL-1 Quadrupole at the Center of the Magnet

The results of magnetic measurements of the CCDTL-1 and CCL-1 prototypes are presented in Table 3. The measurements are presented at an excitation corresponding to the maximum field given in Table 1. The measurements show that these designs will meet the specified requirements. The measurements for CCDTL-1 are for the narrow pole design. A wider pole design is presently in the final stages of assembly. This magnet will be measured and the best magnet will be adopted for the final design.

Table 3: Prototype Measurements

	CCDTL-1	CCL-1
A_n/A_2	At R = 1 cm	At R = 1.5 cm
A_3/A_2	-0.09%	-0.053%
A_4/A_2	-0.05%	-0.02%
A_5/A_2	0.01%	0.018%
A_6/A_2	0.08%	0.135%
A_{10}/A_2	-0.01%	-0.044%

2.2 Magnet Core and Windings

The magnet cores are constructed in quadrants machined from 1006 Low Carbon Steel. The quadrants are keyed and fastened in mid-planes in such a way that each

quadrant is always in the same position with respect to geometrical center after assembly or reassembly. Quadrants are made out of prefabricated blanks, fastened together as a unit, and the pole tip profile is wire EDM machined on all four pole tips. The prefabricated blanks are identical for the CCDTL-1, CCDTL-2 and CCL-1 magnets. Thus, upon disassembly and installation of the vacuum beam pipe or the coil windings, the geometrical and magnetic centers do not move. The keys and fastening components are fiducials, and the four quadrants are kept as a set for a particular magnet. Thus, all assembly tolerances are kept to the minimum.

The magnet and its support stand will be precision aligned and fiducialized with a taught wire system on a bench using an identical mounting system to that used in the beam line. The mounting rails will be pre-aligned to tolerances of better than 0.002".

Magnet windings are epoxy-impregnated structures are tightly fit around each quadrant. Electrical and water cooling connections are connected on both horizontal sides of the core due to the limited space available.

3. POWER SUPPLIES AND CONTROLS

The power supply requirements were based on the following constraints:

- The first four magnets will be independently powered to match the RFQ beam to the CCDTL lattice.
- Power supplies will be sized to energize multiple magnets using shunts to provide adjustment between magnets.
- Power supplies will not power magnets in more than one Linac section.
- The last two magnets will be independently powered to help match the LE Linac beam to the HE Linac lattice.

In addition to the above constraints the following assumptions were made:

- An even number of magnets will be powered by each supply whenever possible.
- In cases where the magnet excitation is the identical for many sequential magnets within a given Linac section, shunts will be provided for tuning an even number of magnets (typically 4).

In general, the quadrupole magnets will be powered in series from a single 40 KW dc supplies. There will typically be eight magnets connected to each supply with a by-pass shunt across each magnet. The shunts will provide a 5% tuning range in the magnet current and minimizes the number of cable runs between the power supply gallery and the tunnel.

4 REFERENCES

[1] P. Lisowski, The Accelerator Production of Tritium Project, Proceedings of the 1997 Particle Accelerator Conference, Vancouver BC, p. 3780 (1997).

[2] G. P. Lawrence and T. P. Wangler, Integrated Normal-Conducting/Superconducting High-Power Proton Linac for the APT Project, Proceedings of the 1997 Particle Accelerator Conference, Vancouver BC, p. 1156 (1997).

[3] J. Tooker & G. Lawrence, Overview of the APT Accelerator Design, these proceedings.

[4] Vector Fields Ltd, Oxford, England, "Software for Electromagnetics", 1997.

[5] Mermaid for DOS, SIM Ltd, 630058 Novosibirsk, Russia.

APT HIGH ENERGY LINAC INTERTANK ASSEMBLY DESIGN*

R. Pearsons, A. Harvey, E. Hubbard, M. Schulze, and S. Sheynin#
General Atomics, San Diego, CA

Abstract

The 700-MHz superconducting High Energy (HE) Linac in the Accelerator for the Production of Tritium (APT) accelerates a 100 mA continuous wave (cw) proton beam from 211 MeV to a final energy of up to 1.79 GeV [1,2,3]. The design of the 700 MHz radio frequency (rf) cavities has been optimized for two beam velocity intervals, β=0.64 and β=0.82. Two intertank designs, medium-β and high-β, have been developed for these two velocity intervals. Three cryomodule designs have been developed corresponding to three different lattice periods in the APT HE Linac. Room temperature quadrupole doublet magnets placed in the intertank assemblies between the cryomodules focus the beam. Each quadrupole magnet contains additional dipole steering windings to correct for small beam misalignments. The intertank assembly between cryomodules also includes beam diagnostic instrumentation, the interconnecting beam pipe, flanges, and the vacuum interface. This paper presents the physics parameters, the results of 3-D magnetic field calculations, and the detailed design of the quadrupoles and the associated intertank assemblies for the medium-β and high-β sections of the HE Linac.

1 INTRODUCTION

The HE intertank focusing (QF) and defocusing (QD) quadrupoles in the high-β and medium-β sections are designed to satisfy the following requirements:

- To fit into the "warm section" between cryomodules with the same beam tube ID as the cryomodules;
- To be mounted as a unit, QF and QD, as a doublet;
- To provide for transverse and longitudinal beam centroid diagnostics (beam position and beam phase monitors);
- To allow space for "special" diagnostics and other instrumentation (e.g. beam profile monitors);
- To have the Steering Dipole Correction Coils in horizontal and vertical planes.

The conceptual design of the APT utilized a FODO lattice throughout the accelerator with superconducting quadrupoles located within the cryomodules [4,5]. The HE Linac was changed to a doublet lattice, and the quadrupoles were moved to the warm sections between cryomodules to streamline the design and minimize alignment problems. The intertank parameters for the four sections of the HE Linac are presented in Tables 1 and 2. The distinction between the two high-β sections is that for a lower production rate facility, Section 4 would not be built. The large aperture of the beam pipe is the same as the cavities and is necessary to keep beam losses to a minimum and permit hands-on maintenance.

Ninety of the high-β magnets are used in the High Energy Beam Transport line to the target/blanket.

Table 1: Medium-β Intertank Parameters

Section	1 (β=0.64)	2 (β=0.64)
Cryomodules	6	30
Period Length (m)	4.876	6.18
Quadrupoles	12	60
Intertank Length (m)	1.606	1.609
Output Energy (MeV)	241.6	471
Quadrupole Effective Length (m)	0.35	0.35
Beam Tube ID (cm)	13	13
Quadrupole Spacing (m)	0.34	0.34
Quadrupole Gradient (T/m)	5.6 – 5.1	5.5 – 6.05

Table 2: High-β Intertank Parameters

Section	3 (β=0.82)	4 (β=0.82)
Cryomodules	35	42
Period Length (m)	8.54	8.54
Quadrupoles	70	84
Intertank Length (m)	1.9	1.9
Output Energy (MeV)	1030	1700
Quadrupole Effective Length (m)	0.45	0.45
Beam Tube ID (cm)	16	16
Quadrupole Spacing (m)	0.34	0.34
Quadrupole Gradient (T/m)	5.0 – 7.25	7.25 – 9.76

2 DESIGN AND ANALYSIS

Electromagnetic simulations of the quadrupole field and steering dipole field were performed using the Vector Fields [6] and Mermaid [7] finite element modeling

* Work supported by DOE contract De-AC04-96AL89607
# E-mail: sam.sheynin@gat.com

software. The ratio of the magnet core length to the bore diameter is 2.26 for the high-β quadrupole and 2 for the medium-β quadrupole. The pole tip profile has been designed to minimize field harmonics of the integrated quadrupole field within ¾ of the aperture. The optimization of pole tip geometry is achieved by gradually flattening the pole tip from a hyperbolic profile and iterating it with radial arcs and corner radii, the so-called "harmonic bump".

2.1 Field Errors and Harmonics

Field errors are evaluated by obtaining the Fourier series of integrated quadrupole field at a given reference radius R and azimuth angle θ:

$$\int_0^z B_x(R,\theta)\cdot dz \text{ and } \int_0^z B_y(R,\theta)\cdot dz$$

B_x and B_y are the horizontal and vertical components of the field B. The azimuth angle θ = 0 on the "x" axis.The field components B_y and B_x were integrated along the longitudinal axis "z" from the center of quadrupole out to 75 cm from the center, which is 3.33 aperture diameters (in air) from the edge of the pole for the high-β quadrupole, and 4.4 aperture diameters for the medium-β quadrupole. Thus, values of integrated quadrupole field at the fixed arc of radius R represent a function $F(\theta)$ in the interval $[-\pi < \theta < \pi]$. The Fourier series generated by this function $F(\theta)$ is represented by:

$$F(\theta) = \frac{a_0}{2} + \sum_{k=1}^{\infty}\left(a_k \cdot \cos k\theta + b_k \cdot \sin k\theta\right)$$

The harmonics of B_y are evaluated by the ratios of A_n/A_2, where $A_n = a_{k+1}$, and A_2 is the amplitude of the quadrupole field. Optimization of the pole tip geometry is achieved by minimizing A_6. The significant harmonics are summarized in Tables 3 and 4.

2.2 Intertank Design

The HE Intertank module consists of the following major components:

- Horizontal focusing quadrupole magnet (QF),
- Vertical focusing quadrupole magnet (QD),
- Diagnostic beam box,
- Beam position and phase detectors,
- Vacuum system,
- Support stand.

The intertank layout and assembly, shown in Figures 1 and 2, is located between gate valves that are part of the adjacent cryomodule assemblies. The intertank is assembled as a unit, and the quadrupole magnets are precision aligned with a taut wire in the lab prior to installation in the tunnel. Each doublet will use quadrupoles with matched excitation functions powered in series by a single power supply. The QF (QD) quadrupoles will be configured for horizontal (vertical) steering fields. All quadrupoles will be constructed with steering windings although only about 40% need be energised based on misalignment and steering simulations.

Table 3: 2-D Harmonic Content of Quadrupole Magnets

	2-D HARMONIC CONTENT	
	Medium-β (r=5 cm)	**High-β (r=6 cm)**
A_6/A_2	0.041 %	0.010 %
A_{10}/A_2	-0.058 %	-0.137 %
A_{14}/A_2	-0.007 %	0.005 %
A_1/A_2*	2.154%	1.579%
A_3/A_2*	0.896%	0.631%

* Calculated for dipole field of 100 Gauss

Table 4: 3-D Harmonic Content of Quadrupole Magnets

	Mermaid 3-D	**Vector Fields 3-D**
	Medium-β (r=5 cm)	
A_6/A_2	-0.260%	-0.255%
A_{10}/A_2	-0.063%	-0.046%
A_{14}/A_2	0.008%	-0.006%
	High-β (r=6 cm)	
A_6/A_2	-0.310%	-0.284%
A_{10}/A_2	-0.120%	-0.193%
A_{14}/A_2	0.004%	0.073%

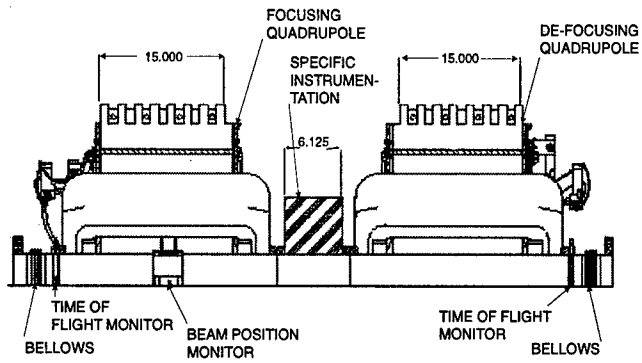

Figure 1: High-β Intertank Layout

The support stand utilizes a modified 6-point support scheme using 3 vertical struts and a floating plate that is positioned with respect to the stand with 2 additional horizontal struts and one axial strut. This allows for accurate, independent positioning of the magnet through all 6 degrees-of-freedom.

2.3 Magnet Electro-Mechanical Design

The electrical and mechanical parameters for the HE intertank quadrupole magnets are summarized in Table 5.

The magnetic circuit consists of four quadrants. Each quadrant is constructed of precision punched laminations (1008 low carbon steel - 1/16" thickness) sandwiched between ½-inch end plates adding to a 15-inch (38.1-cm) core assembly. The end plates will be chamfered as

needed to improve field uniformity on the basis of prototype magnetic measurements.

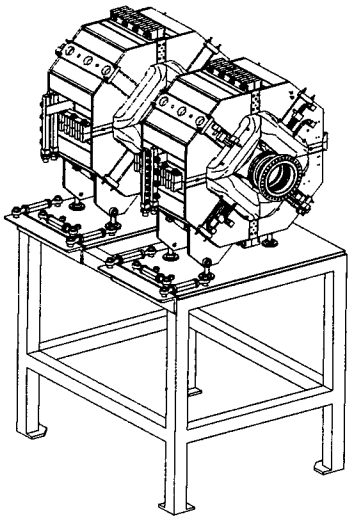

Figure 2: Intertank Assembly

Table 5: Parameters for the HE Intertank Magnets

	Quadrupole Parameters	
PARAMETER	Medium-β	High-β
Integrated Strength	2.12 T	4.39 T
Aperture	13.8 cm	16.8 cm
Effective Length	0.35 m	0.45 m
Core Length	28.1 cm	38.1 cm
Gradient	6.05 T/m	9.76 T/m
Current	290 A	420 A
Conductor	3/8" x 3/16" Ø	3/8" x 3/16" Ø
Turns/Pole	N = 40	N = 66
Resistance	0.037 Ω	0.087 Ω
Voltage	10.7 V	36.6 V
Power	3.11 kW	15.4 kW
Water Flow	2.34 gpm	4.16 gpm
Temperature Rise	5.1°C	14.0°C
	Steering Dipole Parameters	
Dipole Field (Max.)	± 100 Gauss	± 100 Gauss
Current	15.6 A	15.0 A
Conductor	AWG8 wire	AWG8 wire
Turns/Pole	32	40
Resistance	0.038 Ω	0.05 Ω
Voltage	0.6 V	0.75 V
Power	9.25W	11.3 W

The electrical windings for the main quadrupole coil and the dipole steering correction coil are epoxied/potted in one structure as shown in Figure 3. The water-cooled 3/8-inch square hollow copper conductor is used for the main quadrupole coils. The steering dipole correction coils use round AWG8 copper wire and are cooled via conduction from the water-cooled quadrupole coils. Terminals have been provided for the connection of temperature sensors on all cooling water outlets. The high-β coils are constructed with two parallel cooling circuits per pole, and the medium-β has a single cooling circuit per pole.

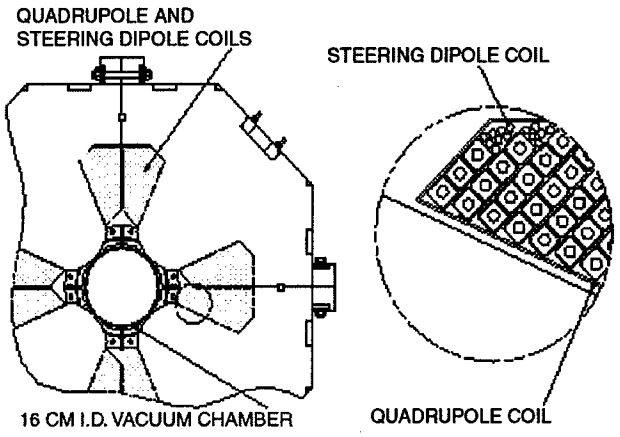

Figure 3: Cross-section, High-β Quadrupole

3 REFERENCES

[1] P. Lisowski, The Accelerator Production of Tritium Project, Proceedings of the 1997 Particle Accelerator Conference, Vancouver BC, p. 3780 (1997).

[2] G. P. Lawrence and T. P. Wangler, Integrated Normal-Conducting/Superconducting High-Power Proton Linac for the APT Project, Proceedings of the 1997 Particle Accelerator Conference, Vancouver BC, p. 1156 (1997).

[3] J. Tooker & G. Lawrence, Overview of the APT Accelerator Design, these proceedings.

[4] Accelerator Production of Tritium Conceptual Design Report, 1997, LA-UR96-4847, APT-Doc-005.

[5] S. Kahn and P. Wanderer, Magnetic Design of Superconducting Quadrupoles for the SC Linac for APT, Proceedings of the 1997 Particle Accelerator Conference, Vancouver BC, p. 3350 (1997).

[6] VECTOR FIELDS Ltd, Oxford, England, "Software for Electromagnetics", 1997.

[7] Mermaid for DOS, SIM Ltd, 630058 Novosibirsk, Russia.

DEVELOPMENT OF A COMMISSIONING PLAN FOR THE APT LINAC*

M.E. Schulze#, General Atomics, San Diego, CA
B. Blind, K.C.D. Chan, J. D. Gilpatrick, G. Lawrence, Sabrata Nath, A. H. Regan, L. J. Rybarcyk, T. P. Wangler and L. Young, Los Alamos National Laboratory, Los Alamos, NM
A. Browman, and K. R. Crandall, TECHSOURCE, Santa Fe, NM
L. W. Funk, Westinghouse Savannah River Company, Aiken, SC

Abstract

The Accelerator Production of Tritium (APT) facility [1,2,3] utilizes a high-intensity CW linear accelerator consisting of both normal-conducting and superconducting (SC) RF structures to accelerate a 100-mA CW proton beam to an energy of between 1030 and 1700 MeV depending upon tritium production needs. The accelerator will be commissioned in stages defined by these different normal and superconducting modules. Different commissioning modes developed to set the transverse and longitudinal beam parameters, require pulsed operation of the accelerator over a wide range of beam currents. These stages and modes and the different techniques utilized to tune the phase and amplitude of the modules are described. Beam-dynamics simulations of the tuning process for the phase and amplitudes of the RF structures in the low energy (LE) Linac will be presented.

1 INTRODUCTION

The major considerations in the commissioning of the APT Linac have been addressed in prior papers [3,4] and this paper will describe the present status of this work. The commissioning plan for the APT Linac describes the process through which the Linac components are operated with beam for the first time and the setpoints for the RF structures and magnet power supplies are determined. Each module of the linac will be commissioned sequentially in order of increasing energy. The LE Linac consists of 13 modules including the RFQ and injector. The present plan is to commission the LE Linac in six stages defined by five beam stop locations. A major objective in commissioning the first few stages is to fully characterize the beam properties. At low energies, it is especially important to understand the beam properties to validate the beam dynamics simulation codes or, if necessary, update the codes. The modules and stages for the LE Linac are presented in Table 1. Beam stop designs are under development to support these commissioning stages. The last commissioning stage of the LE Linac includes the first 4 or 5 cryomodules of the SC Linac. This will allow for testing the match between the FODO lattice in the LE Linac and the doublet lattice in the SC Linac.

*Work supported by DOE contract De-AC04-96AL89607
#E-mail: martin.schulze@gat.com

Table 1: Commissioning Stages of the LE Linac

Stage	Module (s)	Energy Range (MeV)	Beam Power (kW)
1	Injector	.075	8.5
2	RFQ	6.7	50[a]
3	CCDTL1	6.7 - 10.05	50[a]
4	CCDTL2	10.05 – 21.3	50[a]
5	CCDTL3-6	21.3 – 96.7	10
6[b]	CCL7-11	96.7 – 250	25

[a]The same beam stop will be used for these stages
[b]Includes first cryomodules of HE Linac

The SC Linac will accelerate the beam to 1030 MeV with an option to increase the energy to 1700 MeV. The accelerator layout for 1030 MeV is shown in Figure 1. Initially, the SC linac will be commissioned in a single stage with a 0.1% duty factor beam stop located at 1030 MeV and then to a 2% beam stop located after a 90° achromatic bend.

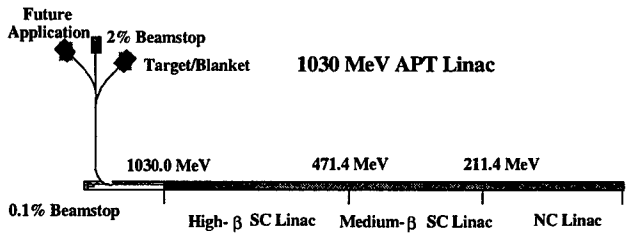

Figure 1: APT Linac Layout for 1030 MeV

There are three cryomodule designs in the SC Linac defined by the velocity interval, β, with the number of cavities and the period length as presented in Table 2. The cryomodules will be commissioned sequentially one module at a time and the high-β cryomodules will be commissioned one klystron at a time.

Table 2: SC Linac Cryomodule and RF Configuration

β	Cavities	Period	Klystrons/ Cryomodule	Cryo-modules
0.64	2	4.88 m	1	6
0.64	3	6.18 m	1	30
0.82	4	8.54 m	2	35

0-7803-5573-3/99/$10.00@1999 IEEE.

2 COMMISSIONING PROCESS

Commissioning will be done with pulsed beams and cw RF power. The pulse length will be at least 200-μs with a repetition rate from 1 to 10 Hz. The injector and RF systems require up to 100 μs to stabilize depending on peak current. The pulsed beam format will depend on the commissioning procedure. The peak current will initially be very small (< 10 mA) consistent with stable beam operation. Commissioning will consist of the following beam operations as each stage and/or module is commissioned:

- Steering and Alignment - low peak current (< 10 mA) and duty factor (1 Hz and 0.2 ms)
- RF phase and Amplitude Scans - low peak current (< 10 mA) and duty factor (10 Hz and 0.2 ms)
- Increase peak current to 100 mA at low duty factor
- Measure beam properties
- Validate beam dynamics codes
- Develop operations database

The quadrupole gradients will be set according to the beam dynamics model based on precise magnetic field measurements prior to turning on the RF. Checking the alignment and setting the steering will then take place and is expected to be straightforward. Determining the proper setpoints for the cavity phase and amplitude will be a major part of the commissioning process and will be described in detail in the next section. Once the cavity phase and amplitude is set the peak current will be slowly increased to full current. As the peak current is increased, the intent will be to eliminate beam losses and understand the transverse beam profile. Beam losses or beam profiles inconsistent with predictions will identify problems, which may include either component errors or physics effects not included in the beam dynamics model. A major consideration will be whether beam halo requires the focusing lattice to be adjusted from the nominal settings, as is the case at LANSCE. The first stages of the LE Linac, where space-charge effects are especially significant, must be understood because discrepancies between measurements and simulation may indicate problems that could lead to beam loss at higher energies. The same beam stop will be used for the RFQ, CCDTL1 and CCDTL2 (2^{nd} to 4^{th} stages of Table 1). This beam stop, designed to be movable with a beam transport line and diagnostics, will operate at duty factors up to 10%.

A commissioning transport line and beam diagnostic package located just upstream of each beam stop will be developed to measure the beam current, beam loss, transverse beam profile, transverse rms emittance, transverse beam halo, final beam energy centroid, and bunch length. This comprehensive set of measurements of the beam properties will be made after each module in the LE Linac is commissioned and periodically in the SC Linac once all components have been set to their nominal values. These measurements will be used to validate the beam dynamics codes as well as to develop an operational database. While there is inadequate space in the beam line to install the beam diagnostics needed to fully characterize the beam except at the two beam stop locations shown in Figure 1 there will be an assortment of beam profile monitors and beam phase probes throughout the linac. Measurements made with these in-line diagnostics will be correlated and calibrated with the detailed measurements made with the commissioning diagnostics package. The objective is to develop an effective and efficient process by which each module may be turned on and performance validated after a shutdown in the absence of a comprehensive diagnostics package. Various failure modes will be simulated and the beam response will be also measured with these in-line diagnostics.

3 RF PHASE AND AMPLITUDE SCANS

The cavity RF amplitude and phase in a given module are optimized by changing the cavity phase and measuring the detected beam signal for different cavity amplitudes. Different phase scan methods are presently under investigation for the different modules. These include:

- Absorber Collector
- Phase Measurement (single phase probe)
- Energy Measurement (two phase probes)

One or more of these techniques will be used to commission the RF structures. Simulations of the commissioning process for the RF structures have been performed for each module of the APT Linac using combinations of these techniques to determine the most effective and efficient approach to commissioning each module. Each of these techniques is described below.

The absorber collector measures the beam transmission through a degrader placed at the end of a module. The thickness is chosen to be the range of a proton a few MeV less than the nominal output energy of the module. The measurement of the transmission as a function of the cavity phase produces a curve as shown in Figure 2. The FWHM and the phase of the 50% transmission are determined from simulation of the ideal module. The RF amplitude and phase are then adjusted to achieve these design values. This technique is very straightforward but is suitable only on the LE Linac at low beam power.

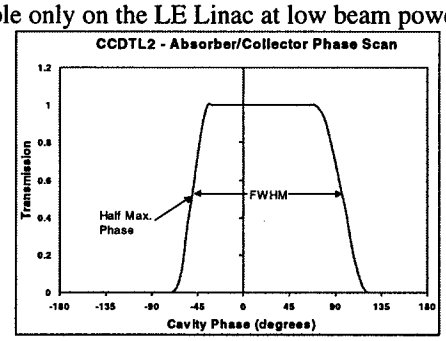

Figure 2: Absorber Collector Phase Scan

Phase scans using a single phase probe measurement result in a curve of the beam phase measured at the phase probe as a function of the cavity phase adjustment. The placement of the probe is at an odd multiple of 90° phase advance in the module. At this location the beam phase is insensitive to small changes in the RF phase resulting in a characteristic curve as shown in Figure 3. This technique appears best suited to the CCDTL structures where the total phase advance ranges between 360 and 1000 degrees and there are many intertank locations where a probe can be located. Figure 3 shows the results after cavity 172 although it is cavity 173 where the phase measurement shows little sensitivity to the cavity phase at the nominal amplitude. The beam phase is insensitive to cavity phase at a unique amplitude of 1.024 nominal as shown and this curve intersects the curve for the nominal amplitude at a phase of –7.66°. This information, obtained from simulations of the ideal machine, is used to define the RF amplitude and phase setpoints for this module. The procedure would be to identify the "signature" curve corresponding to an amplitude of 1.024 nominal, scale the cavity amplitude by this amount and measure the curve at the nominal amplitude to determine the phase and then adjust the phase to –7.66°. A similar phase scan in cavity 173 would result in two curves that are almost parallel where they intersect which would introduce a large uncertainty in setting the cavity phase.

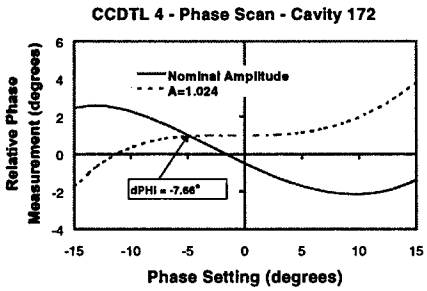

Figure 3: Single Phase Probe Measurement

Perhaps the most versatile and effective type of phase scan measurement is to use two phase probes whereby one can measure the beam time-of-flight (TOF) and infer the beam energy. This measurement appears to be well suited for all modules of the APT Linac. In one application of this measurement, the beam energy is measured as the cavity phase is scanned over a wide range (~ ± 90°). The results are similar to an absorber collector phase scan as seen in Figure 4 except that the width and phase are measured at a specific beam energy.

Another type of phase scan using two phase probes can be performed by measuring the energy as a function of the phase difference between the cavity phase and the phase measured in one of the probes [6] as shown in Figure 5. At a specific amplitude the phase difference remains constant as the energy changes. This is similar to the single phase probe measurement in that the ratio of this amplitude to the nominal amplitude is well known and that the intersection of this curve with that for the nominal amplitude defines the cavity phase setpoint. The spacing between the two phase probes must be chosen carefully so that there is a clear distinction between these two curves.

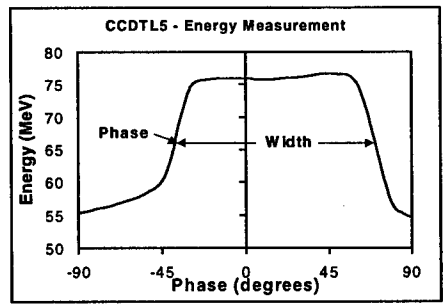

Figure 4: Energy measurement with two phase probes

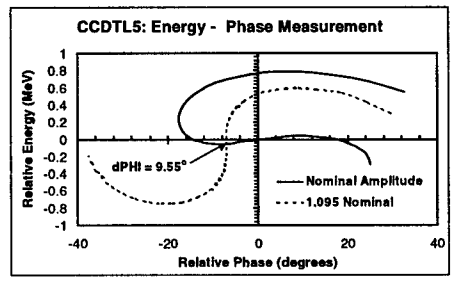

Figure 5: Phase scan of relative energy vs. relative phase

It is anticipated that the RF structures of the SC linac will also be commissioned using two phase probes. In the SC linac, the energy gain in a module is only a small percentage of the total energy and the results of a phase scan similar to that shown in Figure 4 will be a "skewed" sinusoid. The intent is to measure the peak of this curve from which the energy gain and synchronous phase can be determined.

4 REFERENCES

[1] P. Lisowski, The Accelerator Production of Tritium Project, Proceedings of the 1997 Particle Accelerator Conference, Vancouver BC, p. 3780 (1997).

[2] G. P. Lawrence and T. P. Wangler, Integrated Normal-Conducting/Superconducting High-Power Proton Linac for the APT Project, Proceedings of the 1997 Particle Accelerator Conference, Vancouver BC, p. 1156 (1997).

[3] J. Tooker and G. Lawrence, Overview of the APT Accelerator Design, these proceedings.

[4] K. C. D. Chan et al., Commissioning Plan for a High-Current Proton Linac, Proceedings of the 1997 Particle Accelerator Conference, Vancouver BC, p. 1150 (1997).

[5] L. W. Funk et al., Development of a Commissioning Plan for the APT Linac, Proceedings of the 1998 LINAC Conference, Chicago IL.

[6] S. Nath and G. Neuscheafer, Proceedings of the 1991 Particle Accelerator Conference, San Francisco, p. 485 (1991).

LINAC RF STRUCTURES FOR THE SPALLATION NEUTRON SOURCE*

J. H. Billen, H. Takeda, and T. S. Bhatia
Los Alamos National Laboratory, Los Alamos, NM 87545 USA

Abstract

The Spallation Neutron Source (SNS) project is a collaboration among Argonne, Brookhaven, Lawrence Berkeley, Los Alamos, and Oak Ridge National Laboratories. Los Alamos is responsible for the linac that accelerates the H^- beam from 2.5 MeV to 1 GeV. For the baseline design, scheduled for completion in 2005, the linac will deliver to the accumulator ring a beam of 1.1-MW average power. In the SNS linac, a conventional 402.5-MHz drift-tube linac (DTL) accelerates the beam from 2.5 to 20 MeV, at which point 805-MHz structures take over. The 805-MHz linac consists of a coupled-cavity drift-tube linac (CCDTL), followed by a coupled-cavity linac (CCL). The DTL uses permanent magnet quadrupoles inside the drift tubes arranged in a FOFODODO lattice; the focusing period is $4\beta\lambda$ long at 402.5 MHz. The CCDTL and CCL use electromagnetic quadrupole magnets external to the rf structure; the FODO lattice period is $12\beta\lambda$ long at 805 MHz. The cavity field profile maintains smooth longitudinal focusing strength per unit length. High cavity stored energy reduces the effect of beam chopping on the cavity fields. The bore radius is 1.25 cm in the DTL, and increases in the CCDTL and CCL in several steps consistent with adequate shunt impedance, to a final value of 2.0 cm. The rf structures are compatible with a future upgrade to a beam power of 4.4 MW.

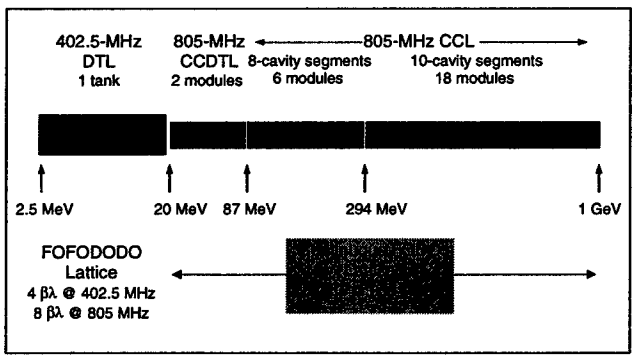

Figure 1. SNS linac layout for 1 MW beam power.

1 INTRODUCTION

Figure 1 shows the major items to be delivered by Los Alamos: the 402.5-MHz drift-tube linac and the 805-MHz coupled-cavity structures. These are room-temperature copper accelerating structures. During operation, the water coolant temperature will control the resonant frequency. Other SNS components appear in papers at this conference. Figure 2 is a plot of the cavity shunt impedance ZT^2 as a function of particle velocity, which is affected strongly by the choice of bore radius. Values of ZT^2 in the figure include all expected losses in the cavities. The SNS linac requires high cavity stored energy in order to reduce the effect of beam chopping on the cavity fields. When designing such cavities, one is usually limited either by the maximum power densities that can be cooled or by the tendency of the cavity to spark at high electric fields. With an rf duty factor of 6.7%, the power density is not the limitation, though water cooling is required. Figure 3 plots the peak surface electric field relative to the Kilpatrick field as a function of particle velocity. The Kilpatrick field is 19.47 MV/m at 402.5 MHz and 26.06 MV/m at 805 MHz. Values below 1.5 Kilpatrick represent a conservative design.

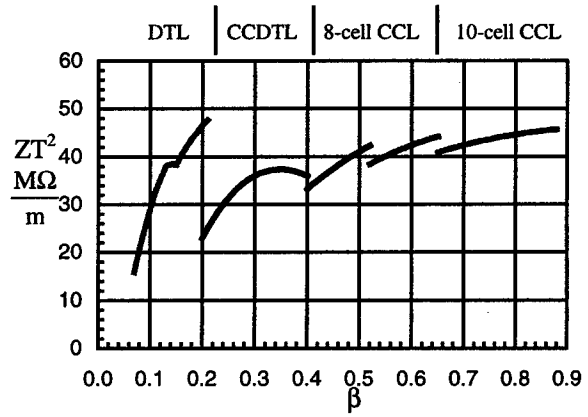

Figure 2. Cavity shunt impedance versus particle velocity.

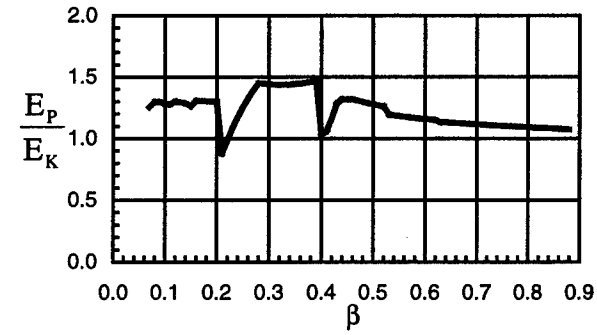

Figure 3. Peak surface electric field in terms of the Kilpatrick field versus particle velocity.

2 DRIFT-TUBE LINAC

Table 1 lists the DTL design parameters. The DTL has a single tank with 84 accelerating gaps. The contour plots in Figure 4 show three representative cells computed by SUPERFISH [1] The lower left corner of each figure of revolution is the center of the gap. The tank diameter D will be slightly larger than 43 cm and the drift-tube

*Work supported by the Office of Energy Research, Basic Energy Science of the US Department of Energy, and by Oak Ridge National Laboratory.

diameter d = 9 cm. The space for post couplers (D – d)/2 is about 91% of λ/4 at 402.5 MHz, an ideal distance for ensuring good stability. A series of 12 static slug tuners along the bottom of the tank will provide several MHz of tuning capability.

Drift tubes have the full 9-cm diameter over a long enough length to house the permanent-magnet quadrupoles. We adjust the face geometry for high shunt impedance constant peak surface electric field of ~1.3 Kilpatrick for an average axial electric field E_0 = 3.0 MV/m. We vary the drift-tube length to tune each cell to 402.5 MHz. Several parameters change with β over part of the DTL. The bore radius increases from 1.25 cm to 1.5 cm over about 11 cells between β = 0.13 and β = 0.15. The face angle varies from 3 degrees to 65 degrees (see Figure 4). The detailed nose shape includes an inner radius R_i in the range 0.16 cm to 0.35 cm, an outer radius $R_o \approx 3R_i$, and a short flat segment between them. This flat segment (in the range 0.05 cm to 0.4 cm) reduces the peak surface electric field at the expense of a small reduction in shunt impedance.

Two values appear in Table 1 for the beam current and total rf power. The lower number is for the baseline 1-MW beam power design and the larger number is for an upgrade to 4 MW discussed below. The power figures include an expected 20% reduction in the SUPERFISH-calculated ZT^2.

Table 1. DTL Design Summary

Frequency	402.5 MHz
Injection/Final Energy	2.5/20.0 MeV
Micropulse Current (1MW/4MW)	28/56 mA
Macropulse Current (1MW/4MW)	18/36 mA
Average Accelerating Field	3.0 MV/m
Quadrupole Focusing Lattice	FOFODODO
Peak Surface Electric Field	1.3 Kilpatrick
Length	8.26 m
Radial Aperture	1.25 and 1.5 cm
Number of Cells	84
Number of Post Couplers	41
Total RF Power (1MW/4MW)	1.6/1.9 MW

3 COUPLED-CAVITY STRUCTURES

After the DTL at 20-MeV beam energy, the linac uses 805-MHz coupled-cavity structures composed of relatively short contiguous sections of a few accelerating cavities called segments. The accelerating cavities within a segment are connected to short, side-mounted coupling cavities in the usual way. Longer side coupling cavities span the drift spaces between segments. The magnetic coupling between cavities is 5%. A transverse focusing period consists of two segments and two drift spaces that contain electromagnetic quadrupole (EMQ) singlets. Diagnostic elements also occupy some of the drift spaces. Table 2 lists the major linac parameters.

In SNS there are three structure sections characterized by the type and number of cavities per segment. In the first part, from 20 MeV to about 87 MeV, a segment contains two CCDTL cavities of total length 3βλ. The drift spaces between segments are also 3 βλ. Segments in the second part to 294 MeV contain 8 CCL cavities of total length 4βλ, but the drift spaces are now 2βλ long. The major part of the linac has 10-cavity CCL segments of total length 5βλ and 1βλ drift spaces. The design has several mechanical, rf, and beam-dynamics advantages:

- There are no transitions in the transverse focusing lattice, which has a constant period of 12βλ at 805 MHz.
- The EMQs are accessible and can be aligned independently from the rf structures.
- Furnace-brazed rf modules eliminate most mechanical rf and vacuum joints.
- The structure contains no bridge couplers.

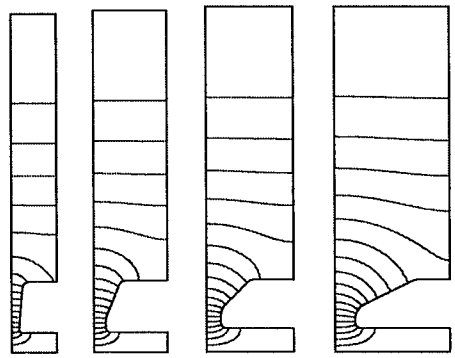

Figure 4. DTL cells for β = 0.08, 0.13, 0.15, and 0.20.

Table 2. CCDTL and CCL Design Summary

Frequency	805 MHz
Injection/Final Energy	20/1000 MeV
Micropulse Current (1MW/4MW)	56/112 mA
Macropulse Current (1MW/4MW)	18/72 mA
Average Accelerating Field	3.7 MV/m
Energy Gain (real-estate average)	2.14 MeV/m
Quadrupole Focusing Lattice	FODO
Transverse Focusing Period	12 βλ
Length	458 m
Radial Aperture	1.5 to 2.0 cm
Peak Surface Electric Field	<1.5 Kilpatrick
Structure Power	80 MW
Beam Power (1MW/4MW)	1.1/4.4 MW
Number of RF Modules	26
Number of Accelerating Cavities	2560
Number of Segments	347
Klystrons/Module (1MW/4MW)	2/3

3.1 Coupled-Cavity Drift-Tube Linac

The first two rf modules have 61 and 30 CCDTL [2] segments. The bore radius R_b = 1.5 cm. Each segment contains two cavities like the one in Figure 5. The CDTFISH code from Ref. 1 helps automate the design and optimization process. At each end of a range of particle velocities β, we first optimize the gap g, drift-tube diameter d, drift-tube face angle α_f, and equator flat length F_{eq}. The optimum has high ZT^2 and is within the acceptable range of power density and peak surface

electric field. We adjust the cavity diameter D for resonance at 805 MHz. If a parameter changes by a substantial amount from its initially chosen value, we repeat the optimization of the parameters studied earlier. After finishing the optimization studies, we design a cavity for every 0.01 step in β, again varying D for resonance at 805 MHz, using linear interpolation for g, d, α_f, and F_{eq}. between the two end-point values. Beam dynamics studies use the transit-time factor data for these representative cavities.

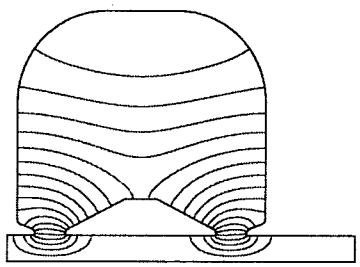

Figure 5. CCDTL cavity for $\beta = 0.24$.

3.2 Coupled-Cavity Linac

Above $\beta \sim 0.4$ the conventional CCL shown in Figure 6 is more efficient than the CCDTL. The exact energy of the transition depends upon other details of the rf partitioning. The first 6 rf modules in the CCL have 8 cavities per segment. At $\beta = 0.65$ a space of length $1\beta\lambda$ is long enough for the EMQ, so later modules have 10 cavities per segment. The CCL has three sections of different bore radius. The smallest radius $R_b = 1.5$ cm occurs at the low β end (modules 3 and 4) and matches R_b at the end of the CCDTL. We increase R_b to 1.75 cm in modules 5, 6, 7, and 8 and to 2.0 cm in modules 9 through 26. The effects of these changes on ZT^2 can be seen in Figure 2. For each bore radius we follow an optimization procedure like that described for the CCDTL. The parameters varied for high ZT^2 are the gap, the cone angle of the nose, and the inner and outer radii of the cavity wall. Again, the cavity diameter varies for tuning to 805 MHz.

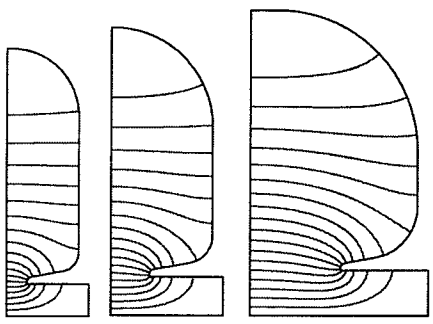

Figure 6. CCL cells for $\beta = 0.43$, 0.60, and 0.87.

3.3 RF Partitioning

The coupled-cavity linac structures will operate in the $\pi/2$ mode, which has remarkably good field stability, low power-flow droop, and negligible power-flow phase shift for a few percent coupling. These structures must be divided into a relatively small number of rf modules whose power requirements are matched to the available power supplies. We plan to use commercial 805-MHz klystrons with a rated output power of 2.5 MW at the SNS duty factor. Of this power, 2.0 MW is available for supplying the cavity fields and accelerating beam. With 300 or fewer cavities (including coupling cells) and 5% coupling between cavities, the mode density near the $\pi/2$ operating mode remains low enough for easy tuning of the structures.

In addition to these power requirements and the limit on the total number of cavities, we have imposed a few other requirements on the partitioning. For thermal management, we allow only one structure type in an rf module. For example, the CCDTL ends at the end of module 2 and the 8-cavity CCL ends at the end of module 7. Also, bore radius changes occur only at ends of modules. Finally, a module can only be lengthened or shortened by adding or subtracting an entire segment. A CCDTL segment has 4 cavities and a CCL segment has either 16 or 20 cavities. The resulting partitioning scheme has 26 rf modules, with each module driven by two klystrons.

4 UPGRADING TO 4 MW

The initial installation of the SNS linac will deliver a 1.1-MW beam to the accumulator ring. One design requirement is the ability to upgrade to four times the initial beam power. The proposed solution is to duplicate the entire 20-MeV, 402.5-MHz front end, double the beam current in each leg, and funnel the two beams together before the beam enters the 805-MHz linac.

Each rf module in the 805-MHz linac has 3 drive irises, placed at the 1/6, 3/6, and 5/6 power points, which is optimum for 4-MW operation. The 1-MW linac, which has lower beam loading, uses the two outside irises. The only major shutdown required is for installation of the duplicate front end and the beam funnel. Upgrading the CCDTL and CCL can be done by installing klystrons during scheduled down times with no impact on the running schedule.

5 CONCLUSION

We have outlined the design of the SNS linac. The design has no transitions in the focusing lattice after the 20-MeV DTL. Magnets are not susceptible to drift-tube vibrations because they mount outside the rf structure where they remain accessible and serviceable. Power densities are manageable and surface electric fields are conservative.

6 REFERENCES

1 J. H. Billen and L. M. Young, POISSON SUPERFISH, Los Alamos National Laboratory report LA-UR-1834 (revised November 14, 1998).

2 J. H. Billen, F. L. Krawczyk, R. L. Wood, and L. M. Young, "A New RF Structure for Intermediate-Velocity Particles," Proceedings of the 1994 International Linac Conference, Vol. 1, p. 341 (August 21-26, 1994).

FUNNEL CAVITIES FOR 4-MW UPGRADE OF SPALLATION NEUTRON SOURCE*

Frank L. Krawczyk and Sergey S. Kurennoy, LANL, Los Alamos, NM 87545, USA

Abstract

The Spallation Neutron Source (SNS) project [1] includes a future upgrade option to 4 MW of beam power. The upgrade scenario stipulates adding a second front end and drift-tube linac, and then merging two 402.5-MHz beams from the parallel legs by interlacing them into a single 805-MHz beam at the entrance to the main linac. The funnel energy is chosen to be 20 MeV. The beam funnel section requires two types of rather special cavities: the two-beam buncher and the RF-deflector. The design options of the funnel cavities and some results of their 3-D electromagnetic modeling with MAFIA are presented. These results show feasibility of the beam funneling for the SNS upgrade.

1 BEAM FUNNELING

The beam funneling combines two beams with frequency f and current I into a single beam of current $2I$ at frequency $2f$, see [2] for references. For the SNS 4-MW upgrade the funneling will provide the 110-mA H^--current in the 1-GeV 805-MHz linac by merging two 402.5-MHz beams at 20 MeV [1]. The main reason for the funneling is that the output current of existing H^--sources is limited. While increasing the effective current, the funneling keeps the charge per bunch the same. The concept of the beam funneling by the longitudinal interlacing of two beams is illustrated in Fig. 1. In the SNS case, two 56-mA beams are delivered by two separate front-end sections (each one includes an ion source, RFQ and DTL) that are phased 180° apart.

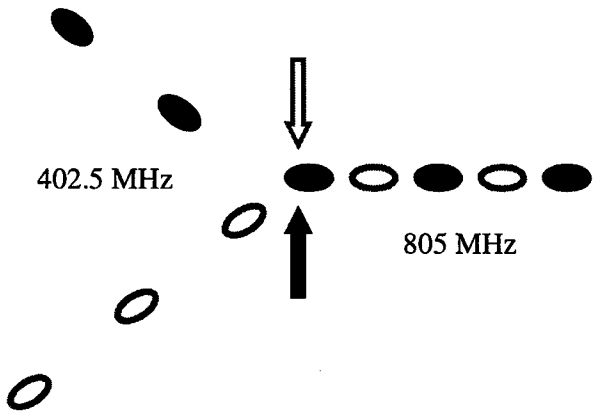

Figure 1: Scheme of beam funnel in SNS. The arrows illustrate the action of an RF deflector.

*Work supported by the U.S. Department of Energy

In addition to two regular beam lines with bending magnets and focusing elements, the SNS funnel section design [1] requires two special cavities. The two-beam buncher provides the longitudinal focusing of the beams when they are close to each other, just before the RF deflector. The RF deflector alternatively kicks the merging beams in the transverse direction to stir them onto a common axis in a matching section

2 TWO-BEAM BUNCHER

The two-beam (or two-channel) buncher cavity contains two DTL-type two-gap segments. Two beam channels are on both side of the cavity axis and have a 1.68° tilt with respect to it. Since the cavity geometry is essentially 3-D, we apply the MAFIA code package [3] to analyze it. A MAFIA model for one-quarter cut of the two-beam buncher cavity is shown in Fig. 2. Symmetry with respect to the two cut planes is assumed. The drift-tubes (DTs, red) of both channels slightly overlap. The central DTs are supported by stems (dark-blue), which also provide water-cooling paths to DTs.

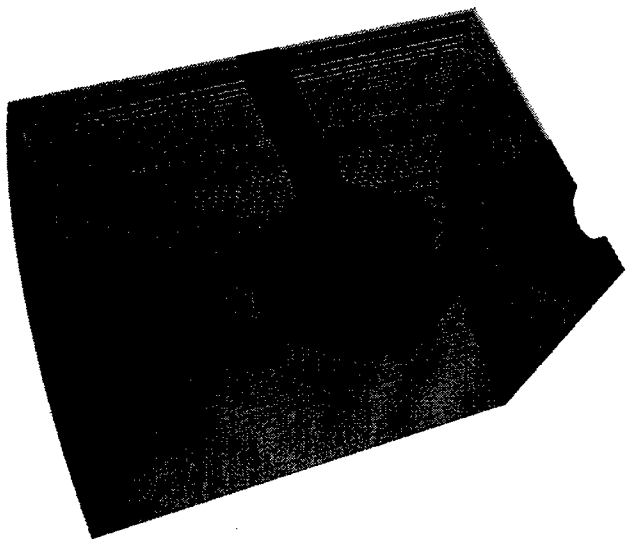

Figure 2: Two-beam buncher cavity (one quarter).

The cavity design frequency is 805 MHz. Its length is chosen to be $2\beta\lambda$=15.14 cm, where β=0.203 for 20 MeV H^--ions, and λ=37.24 cm for 805 MHz. The spacing between the gap centers is $\beta\lambda$ and the gap length is $\beta\lambda/4$. The beam entrance centers are 4.9 cm apart, while the exits are separated by 4 cm. Based on previous experience [4], we choose to model untilted DTs to avoid errors introduced by discretization of slightly tilted shapes.

0-7803-5573-3/99/$10.00@1999 IEEE.

The electric field pattern of the operating 805-MHz mode is shown in Fig. 3. For the preliminary design the mode frequency was adjusted by changing the cavity radius (sensitivity is about -8.5 MHz/mm); the final tuning will be provided by tuning plugs. This mode is well separated from the lower, stem mode (around 500 MHz) and higher modes (>1.3 GHz).

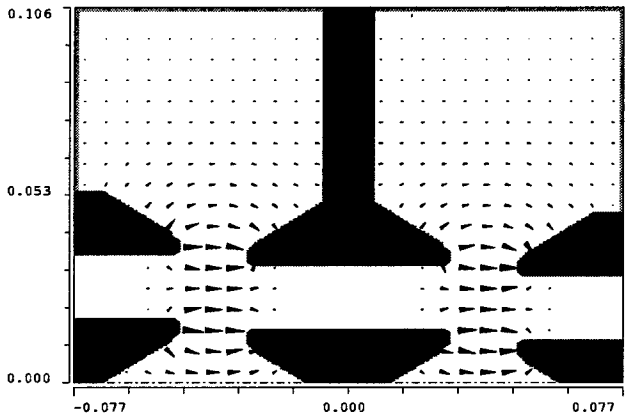

Figure 3: Electric field in the upper half of the buncher cavity cross section. All dimensions are in meters.

Some parameters of the fundamental mode are listed in Table 1. We assume here that the total voltage on the cavity is equal to 625 kV.

Table 1: Buncher 805-MHz Mode Parameters

Parameter	Value
Average longitudinal E field	4.1 MV/m
Maximum E field	29.9 MV/m (1.15 Kp)
Maximum B field	0.033 T
Total stored energy	0.222 J
Total dissipated power*	50.8 kW
Max power loss density*	233 W/cm^2
Q-factor	22725

*CW; for SNS, should be multiplied by the duty factor, about 0.07.

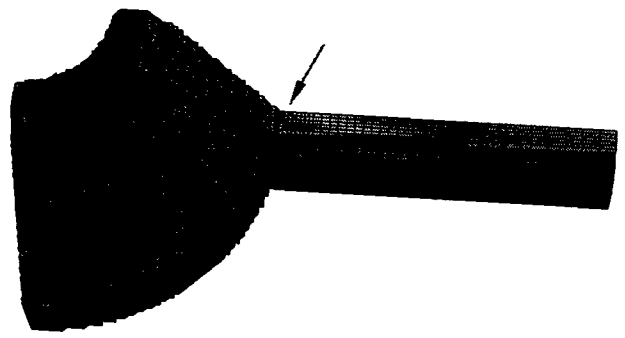

Figure 4: Surface power loss density near the stem-DT connection: the highest density is indicated by red (also by arrow), and the lowest one by dark-blue.

The maximal magnetic field and, correspondingly, the highest surface loss density are near the connection of the stem and DT. The calculated power loss density in this region is shown in Fig. 4, where the red area corresponds to the loss density above 200 W/cm^2 (CW). Making the stem thicker can further reduce the power density.

3 RF DEFLECTOR

The RF deflector provides an alternating 1.28° deflection for two 20-MeV beams entering it, as shown in Fig. 1. The working mode frequency has to be 402.5 MHz, and its transverse electric field between the tips of the cavity deflecting element acts alternatively on one of the two beams. The layout of the RF deflector cavity is illustrated by a 3-D MAFIA model in Fig. 5; it is based on the previous study performed for the ADTT program [5]. The beam path in Fig. 5 is along the upper front edge of the drawn box, and the deflecting element is shown in red.

The total cavity length is about 22 cm, while the distance between the centers of two gaps separating the deflecting element and beam ports is equal to $\beta\lambda/2$=7.57 cm. The gap width between the tips of the deflector is 16 mm, as well as the radii of the beam pipes.

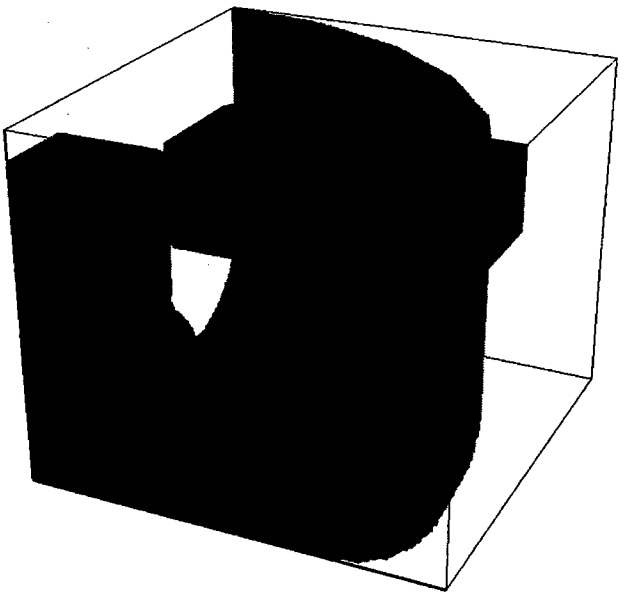

Figure 5: RF deflector cavity (one eighth is shown).

The calculated electric field of the deflecting mode is shown in Fig. 6: the electric field is mostly concentrated in the deflector gap. The magnetic field of the mode is rather low in the gap; it mostly fills the cavity, with the maximum near the side surfaces of the deflecting element. Obviously, the highest surface loss density is also on the sides of the deflector. However, its cooling should not present a problem since the deflecting element is thick enough to allow multiple cooling channels.

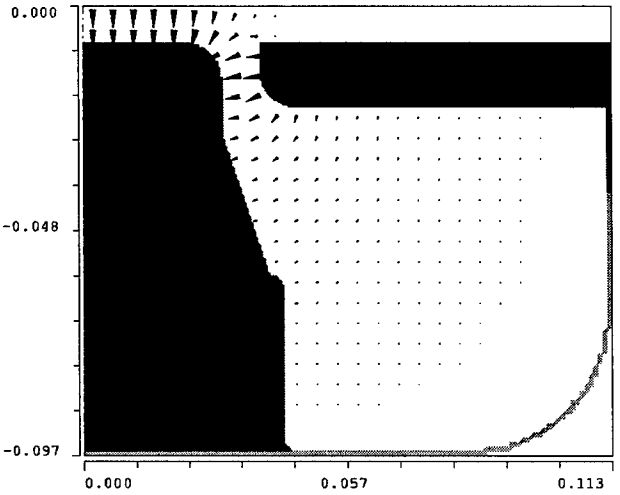

Figure 6: Electric field of the deflecting mode in the right lower quarter of the cavity cross section. The beam path is along the upper side of the drawn box.

A simple way to tune the operating mode frequency in the design is by changing the radius of the deflecting element base, where the magnetic field is rather large. The parameters of the working mode of the RF deflector are collected in Table 2. The cavity voltage is chosen to provide the required deflection of 1.28°.

Table 2: Parameters of Deflecting Mode

Parameter	Value
Deflecting E field: maximum average in the gap	19.7 MV/m 11.6 MV/m
Maximum E field	33.2 MV/m (1.7 Kp)
Maximum B field	0.025 T
Total stored energy	0.213 J
Total dissipated power*	44.5 kW
Max power loss density*	146 W/cm^2
Voltage across the gap	316 kV
Q-factor	12105

*CW; for SNS, should be multiplied by the duty factor, about 0.07.

The cavity parameters are not difficult to achieve. We have also looked at a possibility of an RF deflector cavity, which includes, in addition to the main deflecting mode, also the third harmonic of the deflecting field, at 1207.5 MHz. The cavity design is similar to that shown in Fig. 4. The third harmonic tuning to the required frequency is done by adding a wide circular bulge at the half-height of the deflecting element, see Fig. 7. The tuner's influence on the frequency of the first harmonic is relatively weak. If required, using the third harmonic can further relax the cavity operational parameters; however, the price of that is a more complicated RF system, with two separate RF sources.

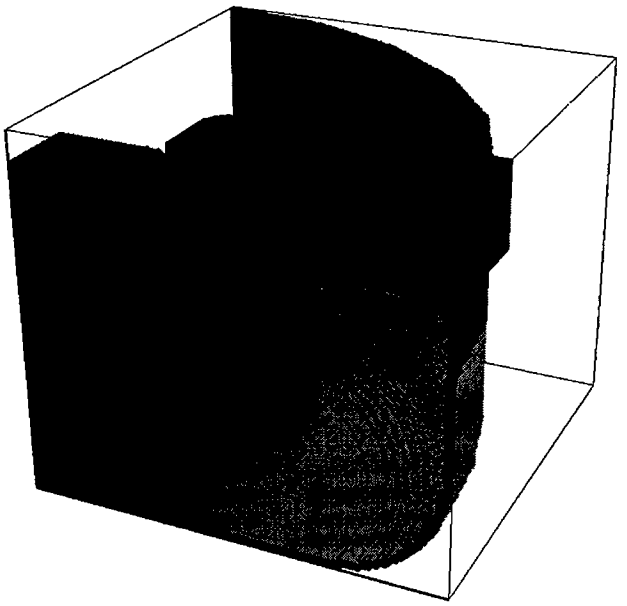

Figure 7: RF deflector cavity with the 3rd harmonic tuned (one eighth).

4 SUMMARY

The preliminary results reported above show that the special cavities for the two-beam funnel in the SNS are feasible. The cavity dimensions will be used in beam dynamics simulations to optimize the funnel section design.

The calculated dissipated power and the density of power loss quoted in Tables 1 and 2 are CW values. They are rather high and would be extremely difficult to achieve for the CW operation. However, the SNS is a pulsed machine. The corresponding power losses in the SNS funnel cavities, obtained by multiplying the CW values in Tables 1 and 2 by the duty factor 0.07, are quite reasonable.

The authors would like to acknowledge useful discussion with James Billen and George Neuschaefer.

5 REFERENCES

[1] NSNS Collaboration, "NSNS Conceptual Design Report", NSNS-CDR-2/V1, Oak Ridge, TN (1997); also available at URL: http://www.ornl.gov/~nsns/nsns.html

[2] T.P. Wangler, "Principles of RF Linear Accelerators" (John Wiley & Sons, NY, 1998). – p.362.

[3] "MAFIA release 4.00" (CST, Darmstadt, 1997).

[4] F.L. Krawczyk et al., in Proceed. ADTT Conf., Las Vegas, NV, 1994; Report LA-UR 94-2733, Los Alamos (1994).

[5] F.L. Krawczyk, in Proceed. PAC95, Dallas, TX, 1995; Report LA-UR 95-1450, Los Alamos (1995).

Thermal/Structural Analysis and Frequency Shift Studies for the Spallation Neutron Source (SNS) Drift Tube Linac

L. Parietti#, N. K. Bultman, and Z. Chen, LANL, Los Alamos, NM

Abstract

The drift tube linac of the Spallation Neutron Source accelerates the beam from 2.5 MeV to 20 MeV at the operating frequency of 402.5 MHz. This pulsed operating linac is about 9 meters long and consists of 84 cells with 83 permanent magnet quadrupole drift tubes. The DTL relies on the cooling system to zero out the frequency shift caused by RF heating on the cavity walls. Thermal expansion and frequency shift studies for three individual cells at a $3x10^6$ V/m accelerating gradient are performed via numerical simulations to help guide the design of the cooling channels.

1 INTRODUCTION

The Spallation Neutron Source (SNS) is an accelerator-based facility that will be built at Oak Ridge National Laboratory by 2005. The SNS will produce pulsed beams of neutrons by bombarding a mercury target with intense beams of 1-Gev protons. This facility is being designed to meet the needs of the neutron scattering community in the United States.

The SNS project is a collaboration of five national laboratories. A full-energy linac injecting into an accumulator ring has been selected among several technology options for the accelerator system. The beam generated by an ion source is accelerated in the linac, accumulated and bunched in the ring structure, then extracted and transported to the target.

Los Alamos National Laboratory is responsible for the linac systems. The linac takes the beam from the front-end system and accelerates it from 2.5 MeV to 1.0 GeV. It consists of a Drift-Tube Linac (DTL) that accelerates the beam to 20 MeV, a Coupled-Cavity Drift Tube Linac (CCDTL) that accelerates the beam to 87 MeV, and a Coupled-Cavity Linac (CCL) that accelerates the beam to 1 GeV. The DTL operates at a Radio Frequency (RF) of 402.5 MHz, while the CCDTL and CCL operate at 805 MHz.

Under normal operation (beam on), about 80% of the RF power is dissipated in the cavity walls. This amounts to 76 kW at a 7% RF duty factor. The power dissipated causes thermal distortions (i. e., shape change) which result in a frequency shift. To maintain the desired resonance frequency, each cavity is cooled by forced water circulation.

This paper summarizes the frequency shift studies conducted for the SNS DTL. This DTL consists of one tank and 83 drift tubes that are cooled on two separate circuits. The thermal deformations resulting from RF heating are evaluated separately for both the tank and three individual drift tubes using finite element models. The frequency shift of these three cells are then computed based on the calculated deformations. Size and location of the cooling channels are designed to provide adequate cooling and resonant frequency control.

2 SNS DRIFT TUBE LINAC DESCRIPTION

The SNS DTL, shown in Fig. 1, is 8.3 m long and accelerates the beam from 2.5 MeV to 20 MeV at a $3x10^6$ V/m accelerating gradient. It consists of one tank, 84 cells and 83 drift tubes.

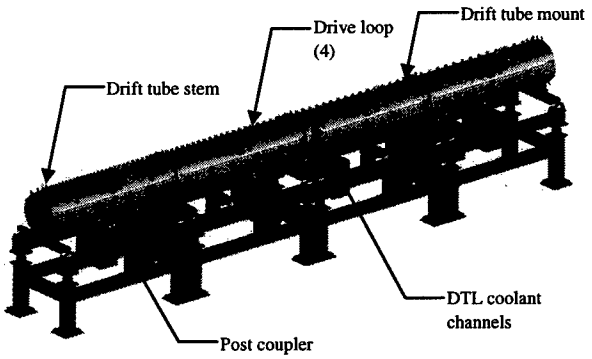

Figure 1: SNS Drift Tube Linac

The DTL tank combines vacuum envelope and RF structure, and provides mechanical rigidity to the assembly. The tank is made of 4 seamless carbon-steel cylinders with a finished wall thickness of about 2.8 inches. The inner diameters are machined and copper-plated to achieve the final dimension and the required surface conductivity. The cylinders are about 2 meters long each and are bolted together with RF and vacuum seals at each joint.

Each of the 83 drift tubes contains a permanent magnet quadrupole. The geometry of the drift tubes (fig. 2) changes with their position along the DTL (since the energy level increases); the face angle increases from 3° to 55°, while the length increases from 4.3 cm at 2.5 MeV to 12.4 cm at 20 MeV. Figure 3 shows a cross-section of the highest energy drift tube. The drift tube body, made of copper, consists of 5 electron-beam (EB) welded parts. The body is brazed to the stainless steel stem before the magnet is inserted. The stem consists of two concentric

0-7803-5573-3/99/$10.00@1999 IEEE.

tubes serving as inlet and outlet ducts for the cooling water.

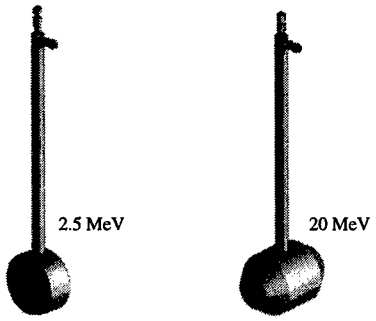

Figure 2: SNS DTL drift tubes at 2.5 and 20 MeV

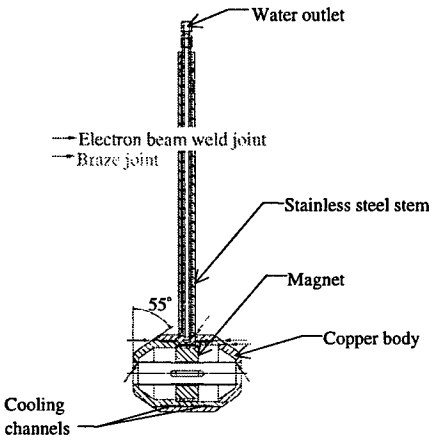

Figure 3: SNS DTL drift tube cross-section at 20 MeV

3 TEMPERATURE DISTRIBUTIONS DUE TO RF HEATING

3.1 Tank Wall

When the RF is turned on, about 32 kW are dissipated into the tank walls. To compensate for the thermal distortions caused by RF heating, the tank is cooled via 12 rectangular stainless-steel cooling channels (1 in wide by 0.5 inches high) that are bonded and clamped in machined groves on the tank walls. The cooling channels are located 1 inch away from the inside wall. An average 30° angle separates two cooling channels. Taking advantage of the problem periodicity, a two-dimensional finite element model of a 15° tank section was created using COSMOS/M. The water velocity is assumed to be 0.5 m/s, which gives a heat transfer coefficient of 2511 W/m^2K for this channel geometry. This heat transfer coefficient is applied on the outer edges of the cooling channels to simulate a forced convection boundary condition. All the other outer surfaces are assumed adiabatic.

Figure 4 shows the tank temperature distribution when the water running through the cooling channels is at 293.2K. The average tank temperature is 297.4K, while the average temperature on the inside wall is 298.5K. These calculated values are used later to evaluate the frequency shift of a DTL cell in the drift tube model (Section 4).

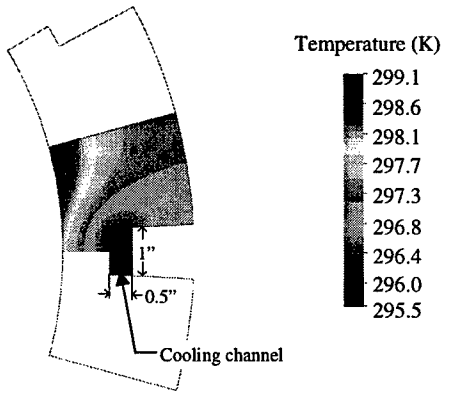

Figure 4: Tank temperature distribution

3.2 Drift Tube

Cooling channels are machined in the drift tube body. The flow of water is fed through the outer tube of the stem, splits in half, circulates around the drift tube body and exits trough the stem inner tube.

Two-dimensional axisymmetric models for three individual drift tubes at 2.5, 10.5 and 20 MeV were built using COSMOS/M. The amount of heat dissipated on the drift tube outside walls is not uniform. The heat fluxes resulting from RF heating are given by the physics code SUPERFISH.

Figure 5 shows the temperature distribution for the high energy drift tube assuming a water temperature of 293.2K.

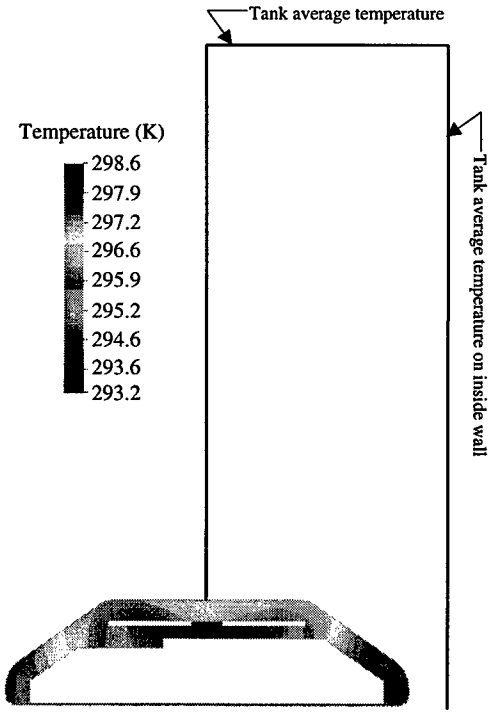

Figure 5: High energy drift tube temperature distribution

The cooling channels are 1 inch wide by 0.06 inch high. They are placed as close as possible from the outer edges to provide maximum cooling. At the interface between parts, the only heat transfer paths are across the EB welds. Small physical gaps are conservatively included in the model when there is only surface contact between two parts. The flow rate through the drift tube stem is limited to 2.19 gpm to avoid having an impingement velocity on the drift tube body greater than 2.5 m/s which would cause material erosion. This flow rate corresponds to a water velocity of 1.7 m/s and gives a heat transfer coefficient of 9607 W/m^2K.

4 FREQUENCY SHIFT STUDIES

Thermal distortions caused by RF heating result in a frequency shift as the shape of the cavity changes. For any given cell, the change in frequency shift can be calculated using the Slater perturbation theory. The change in frequency *df* is a function of the volume change of an infinitesimal volume *dV* laying on the RF surface, as well as the electromagnetic field *H* and the electric field *E* for this volume. The frequency shift is given by:

$$\frac{df}{f} = \frac{\int (\mu H^2 - \varepsilon E^2) dV}{4U},$$

where μ and ε are the free space permeability and permittivity, respectively and *U* is the cavity stored energy.

For a DTL, both the tank deformations (radial and longitudinal) and the drift tube deformations contribute to the frequency shift. To account for the tank deformations, beam elements are added to the drift tube model described in section 3.2. These beam elements, as shown in Fig. 5, are set to a uniform temperature corresponding to the inside tank wall temperature and the average tank wall temperature to simulate the radial and the longitudinal growth of the tank. The thermal deformations corresponding to the drift tube and the tank temperature profile are then solved using the COSMOS/M finite element package. A separate Fortran code reads the displacements output by the finite element package and computes the frequency shift of the cell. The frequency shift for the high energy drift tube for a flow rate of 2.19 gpm is –31 KHz.

The cooling system can be used in several ways to zero out the frequency shift caused by RF heating. The resonant frequency can be controlled by either changing the temperature of the water in the tank circuit or by changing the water temperature in the drift tube circuit. The frequency shift studies can help in the decision making. The sensitivity of the drift tube circuit to water temperature changes was investigated using the model described above. The drift tube circuit frequency shift is 5 to 8 times more sensitive to water temperature changes than the tank circuit (5 times for the low energy drift tube and 8 times for the high energy one). Furthermore, compensating for frequency shift by regulating the tank cooling water would require operating the tank walls at exceedingly high temperatures (300 to 373K). Varying the water in the tank circuit to zero out the cavity frequency shift is therefore not practical. Instead, the cooling water temperature in the drift tube circuit will be dynamically controlled to maintain resonance.

However, the heat dissipated on the drift tube outside walls increases as the energy level increases (0.2 kW for the low energy drift tube compared to 0.5 kW for the high energy drift tube). To avoid field errors and frequency mismatch, the frequency shift needs to be the same for all the DTL cells. This will be achieved by adjusting the flow rate using an orifice plate for each individual drift tube. Figure 6 shows the frequency shift for the cells containing drift tubes #1, #53 and #83 as a function of the flow rate. In addition to balancing the flow rate between the 83 drift tubes, the width of the cooling channels is tailored to keep the flow turbulent.

From a practical standpoint, the structure will be tuned during final assembly to +30 KHz to give a nominal 402.5 MHz resonance during powered operation. The temperature of the flow balanced system can also be adjusted during operation to correct for additional frequency shift. Its sensitivity is about –7.5 KHz/K.

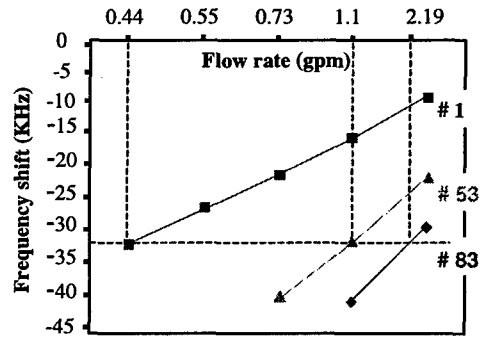

Figure 6: Flow balancing between drift tubes to maintain a uniform frequency shift across the DTL cells

5 CONCLUDING REMARKS

The DTL resonant frequency must be regulated by the cooling system. Frequency shift studies for three DTL cells at 2.5, 10.5 and 20 MeV were performed to help design the cooling channels. Resonance will be maintained by dynamically adjusting the water temperature in the drift tube circuit. A uniform frequency shift for all 84 cells can be obtained by balancing the flow rate and tailoring the cooling channels for each individual drift tube.

This work is supported by the Department of Energy and the Oak Ridge National Laboratory.

E-mail: parietti@lanl.gov

MECHANICAL ENGINEERING OF A LINAC FOR THE SPALLATION NEUTRON SOURCE*

N. K. Bultman, Z. Chen, M. Collier, J. L. Erickson#, A. Guthrie, W. T. Hunter, T. Ilg, R. K. Meyer, N. L. Snodgrass, LANL

Abstract

The linac for the Spallation Neutron Source (SNS) Project will accelerate an average current of 1 mA of H^- ions from 20 MeV to 1 GeV for injection into an accumulator ring. The linac will be an intense source of H^- ions and as such requires advanced design techniques to meet project technical goals as well as to minimize costs. The DTL, CCDTL and CCL are 466m long and operate at 805 MHz with a maximum H^- input current of 28 mA and 7% RF duty factor. The Drift Tube Linac is a copper-plated steel structure using permanent magnet quadrupoles. The Coupled-Cavity portions are brazed copper structures and use electromagnetic quads. RF losses in the copper are 80 MW peak, with RF power supplied by 52 klystrons. Additionally, the linac is to be upgraded to the 2- and 4-MW beam power levels with no increase in duty factor. We give an overview of the linac mechanical engineering effort and discuss the special challenges and status of the effort.

1 INTRODUCTION

Los Alamos will design, build and install the 1-MW H^- linac for the SNS facility. The mechanical engineering responsibility for the linac includes design, analysis, fabrication, assembly, installation & mechanical checkout. The total cost estimate for the mechanical engineering effort is $130 M. The linac accepts a 2.5-MeV H^- beam from the Front-End System being built by Lawrence Berkeley Lab. The Los Alamos linac system is comprised of three major structure types. A Drift Tube Linac (DTL) accelerates the input beam to 20 MeV, a Coupled Cavity Drift Tube Linac (CCDTL) accelerates the beam to 87 MeV, and a Coupled Cavity Linac (CCL) completes the acceleration to 1 GeV and delivers the beam to the Brookhaven-designed High Energy Beam Transport line that leads to the accumulator ring. The CCL is comprised of an 8-cell per segment section and a 10-cell per segment section with the transition point at 295 MeV. The DTL runs at 402.5 MHz while all the coupled cavity structures run at 805 MHz.

2 DESIGN REQUIREMENTS

Selected requirements and overall design parameters are listed in Table 1. The design activity is being completed using the Unigraphics suite of computer-aided design and manufacturing tools. This includes the UG/MGR and IMAN product data management tools. Other engineering software packages being used include ANSYS, COSMOS/M and CFX.

Table 1. Overall linac requirements	
Input H- Energy	2.5 MeV
Output H- Energy	1001 MeV
Average Beam Current	1.04 mA
Average Beam Power	1.04 MW
Macropulse Repetition Rate	60 Hz
Macropulse Length	0.974 ms
Beam Duty Factor	5.84%

Overall, the design of the SNS linac is similar to the LANSCE linac. The primary difference is that the accelerating gradient is twice as high, allowing a much shorter linac with higher RF power. The design must be capable of being upgraded to the 2 MW level by doubling the current and the 4 MW level by funneling at 20 MeV. To prepare the structure for these upgrades, each accelerating module (driven by two 2.5 MW klystrons for the 1 MW linac output level) is designed with a terminated drive port to accept a third klystron.

Table 2 Linac Design Parameters	
Average Accelerating Gradient, E0T	2.7 MV/m
Avg Energy Gain/Real Estate Meter	2.02 MeV/m
Peak Structure Power Losses	80.2 MW
Peak RF Power	97.8 MW
RF Duty Factor	7.02%
Average RF Power to Linac	6.8 MW
No. 1.25 MW 402.5 MHz Klystrons	2
No. of 2.5 MW 805 MHz Klystrons	52
Physical Length of Linac	466 m
Linac Vacuum	$<1\times10^{-7}$ torr
Linac Tunnel, Width x Height	14 x 10 ft
Beam-Floor Distance	5 ft

The linac vacuum requirement of $<1\times10^{-7}$ torr is based on less than 1 nA/m beam loss at 1 GeV. Beam loss also drives the linac aperture, which varies from 2.5 to 4 cm diameter. The aperture is generally set to 10 times the rms beam size at higher energies. The aperture has recently been increased in the upstream structures to provide a negligible probability of beam loss. Additional linac design parameters are listed in Table 2.

* Work supported by the Office of Science, Basic Energy Sciences, of the U.S. Department of Energy; and the Oak Ridge National Laboratory.
# jerickson@lanl.gov

0-7803-5573-3/99/$10.00@1999 IEEE.

3 DRIFT TUBE LINAC

The lattice period for the DTL is 4 $\beta\lambda$ at 402.5 MHz (equivalent to 8 $\beta\lambda$ at 805 MHz). The design has recently been changed to a single tank design rather than a two-tank design. This eliminates the complexity of hardware design in the 1bl intertank region that would have included 2 end walls and beam diagnostics. The single tank shown in Figure 1 will be built up from 4 tank sections bolted together to make the 8.3 m long structure. The tank has 84 cells with 82 drift tubes with permanent magnet quadrupoles. The tanks are copper plated, thick-walled steel tubes in which the drift tube supports are integrated into the walls rather than relying on a separate girder support. The drift tubes are brazed and electron beam welded structures with stainless steel stems, copper bodies and samarium-cobalt permanent magnet quadrupoles. Post couplers are used to stabilize and tune the longitudinal field distribution.

RF power will be coupled to the tank via 4 drive loops. The peak RF structure power loss is 0.994 MW. The DTL will be water cooled and tuned by adjusting the coolant temperature according to feedback from the RF frequency measurement. During initial assembly, and prior to installation on the beamline, the structures will be aligned one tank section at a time using a pulsed taut wire system. Each tank section will be aligned to the next section by aligning the first drift tube only, then removing the upstream tank and aligning the remaining drift tubes in the downstream tank to the first. The DTL is in it's preliminary design phase with the preliminary design review scheduled for the end of FY '99. Prototype tanks sections are being machined and plated, prototype magnets are being built and prototype drift tubes will be built during the summer of '99.

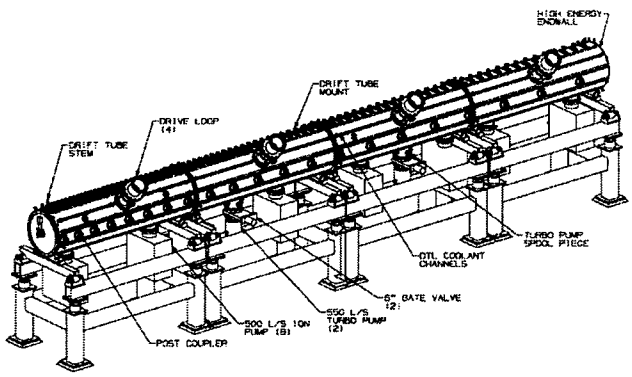

Figure 1: DTL Layout

4 COUPLED CAVITY DRIFT TUBE LINAC

The CCDTL consists of 91 segments and has a total length of 59 m. The segments are arranged into 2 RF modules, which are 33 and 26 m in length. The peak structure power loss is 6.5 MW. Each module is driven by 2 RF klystrons coupled to the structure with waveguide irises. The structure consists of 2 cells per segment, where a segment refers to a continuous brazed section of accelerating cavities between two quadrupole focusing magnets. Each accelerating cavity contains a drift tube. The lattice period for both the CCDTL and the CCL is 12 $\beta\lambda$.

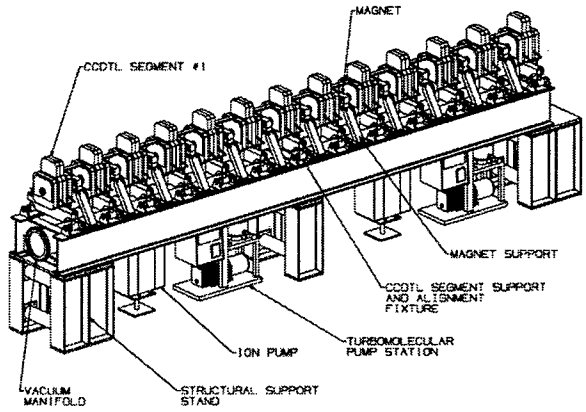

Figure 2: CCDTL Layout – Section 1 of RF Module 1

The CCDTL layout of the upstream end of the first RF module is shown in Figure 2. An electromagnetic quadrupole singlet is located between segments of RF structure. Beam diagnostic elements are also located in these intersegment spaces as necessary. These intersegment spaces are 6 $\beta\lambda/2$ in length and are spanned by long coupling cavities. The long intersegment coupling cells will be fitted with an internal tuning nose to provide for ease of disassembly. Because of the space needed for a magnet, diagnostics and vacuum flanges, special attention has been paid to this area. During the preliminary design, many refinements to the physics design have been made to provide additional spacing between the segments. In addition, special vacuum seals and flanges are being tested to minimize the space occupied by these components.

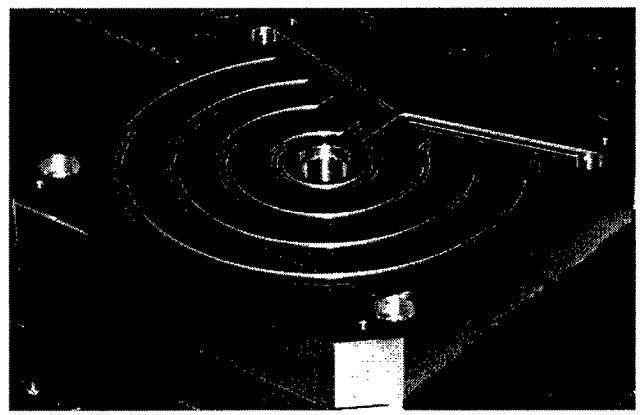

Figure 3: Septum cooling channel configuration

In achieving the desired accelerating gradient (3 MV/m), the copper power density has been pushed to the point that internal cooling of the cavity and drift tubes is

required. The preliminary design has two cooling circuits, one for the bulk copper accelerator cavity and a second for the drift tubes. In order to minimize the temperature differential (and resultant stresses) in the structure, the septum between the accelerator cavities is provided with internal cooling channels. The current configuration for these cooling channels is shown in Figure 3.

5 COUPLED CAVITY LINAC

The bulk of the acceleration, 87 MeV to 1 GeV, takes place in the CCL. The CCL consists of 256 segments and has a total length of 399 m. There are 24 RF modules of which the longest is 19.8 m. The majority of the modules are between 15 and 18 m in length. Peak structure power loss in the CCL is 71.6 MW. The low energy portion has 8 cells per segment while the high-energy portion has 10 cells per segment. The intersegment spaces are 2 $\beta\lambda$ in the 8-cell CCL and 1 $\beta\lambda$ in the 10 cell CCL. This provides sufficient space for electromagnetic quadrupoles and diagnostics at all energies. All the coupled cavity structures use an even number of cells per segment so that the long intersegment coupling cells will be on the same side of the structure in order to simplify the mechanical design. Similarly, all intersegment spacings are even multiples of $\beta\lambda/2$ so that the coupling cavities are oriented parallel to the accelerator axis to simplify the mechanical design.

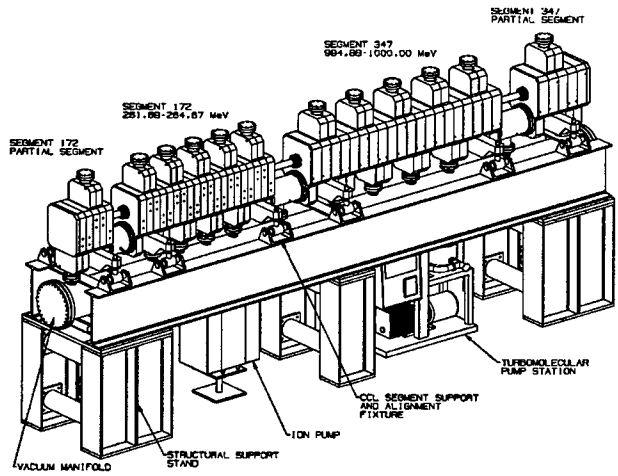

Figure 3: CCL Hot Model Layout

The major effort now is on modeling the structures. Cold models of the low and high-energy ends of the CCL are being fabricated and tested now and will be followed by construction of a hot model which is to be tested early next year. The layout of the hot model for the CCL is shown in Figure 3.

6 COUPLED CAVITY FABRICATION

There are numerous options for fabrication of the coupled cavity structures. One area of review is the extent to which vacuum brazing may be introduced in the plan in place of the historical Los Alamos choice of hydrogen brazing. Another area is the balance between industry fabrication and in-house Los Alamos fabrication. These options are under study with the evaluation parameters being: technical risk, schedule risk, overall cost, quality of the final product and transfer of manufacturing technology to industry.

The current fabrication plan for the structures utilizes capabilities both in industry and at Los Alamos. The material is OFE copper and we are in the process of qualifying material vendors prior to the large procurement of raw material. The key to fabricating these structures is to interleave the brazing processes with the RF tuning processes. Our plan is to machine, measure, and braze half-cells at shops in industry. The septum brazes required to create these half-cells are the critical water-cooling channel to vacuum brazes which will be accomplished using foil braze material. There will be approximately 2000 of these brazed subassemblies required for the CCDTL and CCL, including an allowance for scrap and rework. Once these feeder parts are completed, they will be shipped to Los Alamos for final tuning and stack brazing steps. Once the stacks are completed (2 cells for the CCDTL and 8 or 10 cells for the CCL, the RF structure subassemblies are ready to be assembled into the beam line assembly. Final assembly of the beam line elements will take place at the ORNL site.

The current preferred site for the SNS linac is the Chestnut Ridge site at ORNL. Due to the geology of the area, settlement of the building site has been a concern. This has required additional design effort in providing for the range of alignment features. In addition, the previously envisioned monument system in the building structure is being reviewed to determine if it is practical in this environment.

7 CONCLUSION

The mechanical design of the linac for the Spallation Neutron Source is proceeding into the preliminary design phase. During this fiscal year, numerous test pieces will be fabricated, cold and hot models will be fabricated and the overall manufacturing plan will be further developed.

PROJECT STATUS OF THE 1-GeV SNS LINAC*

R. A. Hardekopf+, D. S. Stout, T. D. Sutton, LANL, Los Alamos, NM

Abstract

The U.S. Department of Energy has initiated construction of a $1.3 B Spallation Neutron Source (SNS) to be located at Oak Ridge, Tennessee. Five national laboratories, ANL, BNL, LANL, LBNL, and ORNL are collaborating in the design and construction of this major new U.S. neutron science facility. The present design is a 60 –Hz, 1-GeV H^- linac injecting into an accumulator ring to produce pulses of <1-μs on the neutron-producing target. The accelerator design has been refined from the CDR concept to provide improvements in assembly and maintainability. A converter-modulator design using IGBT technology replaces the conventional RF system to power the accelerating cavities. Cost estimates for the linac have utilized both accelerator modeling codes and more conventional cost-estimating approaches. Comparison of these two methods has led to increased confidence in the linac cost estimate of about $300 M (including R&D and controls but without contingency). A Monte-Carlo simulation of the project cost using risk-based analysis has further contributed to the estimate and identified critical areas. The project uses Primavera Project Planner as the scheduling software. A linac R&D program to develop key technologies is underway at Los Alamos.

1 LINAC DESIGN

The basic linac architecture has not changed from the CDR in June, 1997 [1]. The energy range from 2.5 to 1000 MeV is achieved with a combination of structures: a Drift Tube Linac (DTL) up to about 20 MeV, a Coupled-Cavity Drift Tube Linac (CCDTL) to about 100 MeV, and a side-Coupled-Cavity Linac (CCL) to the final energy. To accommodate engineering constraints, changes to the lattice structure were made in the spring of 1998 to increase inter-segment spacing and to place all coupling cavities on the same side for ease of assembly and vacuum pumping. In addition to documentation in the SNS Design Manual [1], this architecture was reported at two conferences [2, 3]. Parameters of this scheme and the upgrade path to higher power levels are shown in Table 1.

Table 1: Upgrade path in June 1998.

Number of:	1 MW	2 MW	4 MW
Accelerating Segments	367	367	367
RF Modules	27	28	31
805-MHz klystrons	56	64	80

Although this was an improvement over the CDR design because of a reduction in the number of accelerating modules from 56 (one per klystron) to 27 (most modules with two 2.5-MW peak klystrons), re-modularization of some of the segments was still required for each upgrade.

Therefore, as part of a value-engineering exercise by the entire SNS project we decreased the number of klystrons required at 1 MW and reduced the overall linac length by about 20 meters. We accepted that any upgrade would require increasing RF power directly to the 4-MW level, but this upgrade now requires no re-modularization. The extra beam loading from 1-MW to 4-MW power levels results in almost exactly a 50% increase in overall power (structure plus beam), obtained by adding one klystron to each two-klystron module (see Table 2).

Table 2: Present upgrade path.

Number of:	1 MW	2 MW	4 MW
Accelerating Segments	345	345	345
RF Modules	26	26	26
805-MHz klystrons	52	78	78

2 COST ESTIMATES

Cost estimates are essential to determine the most effective design approach, define the baseline, obtain funding, and manage the project. We recount here a brief history of the SNS linac cost estimates and compare different methods that have contributed to our current projections.

2.1 Engineering Validation Package, 1996

The first official estimate of the SNS linac cost was made in 1996 as part of the Engineering Validation Package (EVP) and led to a cost of $272 M. This was a bottoms-up estimate based on Los Alamos experience with similar linacs and component prices. It was not complete because it did not include several project costs such as management. However, the data were useful in setting the parameters of model-based estimates that followed.

2.2 ASM Model and CDR, 1997

To take advantage of the work that has recently gone into accelerator modeling codes and databases [4], Los Alamos contracted with Northrop-Grumman Corp. (NGC) in January, 1997 to apply their Accelerator Systems

*Work supported by the U.S. Department of Energy.

+Email: hardekopf@lanl.gov

Modeling (ASM) code to the SNS linac. ASM incorporates the experience of multiple projects to increase the validity of the code's design options. NGC has also developed an extensive database of component costs that is used in conjunction with ASM to estimate linac costs. The results of the ASM code and database applied to the SNS linac was initially $456M, but this now included all project costs, including controls, management, and overhead estimates as well as 20% contingency.

We were able to reduce this model-estimated cost to the official CDR number of $319 M by a series of aggressive assumptions that were documented and reviewed. The management challenges included formation of a fully dedicated project team with low overhead and expedited procurement authority. There were also broad discounts taken in materials and installation based on optimization of purchasing through the ORNL construction manager and use of low-cost craft labor for installation at ORNL. CDR numbers in Table 3 have been corrected from the six-year to the seven-year construction schedule recommended by the CDR.

2.3 Independent Cost Estimate, 1997, and DOE Validation, 1998

Subsequent changes to this ASM-based estimate were applied as a result of recommendations by the CDR reviewers and by an Independent Cost Evaluation (ICE) team contracted by DOE. The seven-year project cost (TPC) for the linac subsystem became $330 M, which included 20% contingency as well as the estimated Tennessee tax on purchased components of about $11 M. Changes were made to the Work Breakdown Structure (WBS) including moving all controls to a separate WBS element and moving the bunch rotator (about $4 M) from the ring to the linac costs. A significant amount was added to the R&D budget to do crucial structure modeling and to develop IGBT technology for the RF power system. This was the situation at the time of the June, 1998 DOE validation review, at which time the linac fully-burdened and escalated construction costs were estimated at $260 M with an additional $74.5 M for controls, TN tax, and contingency, for a linac TPC contribution of $334.5 M.

2.4 Bottoms-Up Estimate, 1998-1999

In the summer of 1998 we conducted a new bottoms-up estimate to verify linac costs. At the same time, we incorporated several value-engineering steps to reduce costs, including shortening the linac and implementing the IGBT converter-modulator RF system based on our initial R&D studies. The present cost also reflects a reduced number of klystrons at 1 MW as discussed earlier and the addition of a RF power system for the Front-End RFQ (about $2 M). As a result of these and previous scope changes, it is not appropriate to directly compare bottom-line estimates. Table 3 tracks the cost evolutions for the major categories including the assumptions valid at each major review.

Table 3. Summary of SNS Linac cost estimate ($M),

	EVP (Dec. 96)	CDR, 7 yr. (Jun. 97)	Validation (Jun. 98)	Present (Jan. 99)
Linac	197.6	245.3	260.0	266.6
Controls	19.6	13.8	13.8	19.4
TN tax & CM	*Not Incl.*	14.6	11.2	11.2
Contingency	54.3	46.5	49.5	?
R&D	*Not Incl.*	7.0	16.8	13.6

If one corrects for the major changes in scope (e.g., six to seven years, bunch rotator, 402.5-MHz system for RFQ, increased R&D for hot models and IGBT system), the estimates are not too dissimilar during this two-year period after the CDR, using the different estimating methods. One conclusion that can be drawn is that the linac modeling and cost-estimating tool available with ASM can give a quite dependable first estimate.

3 COST RISK ANALYSIS

Near the completion of the present bottoms-up cost estimate, Los Alamos contracted with Hulett & Associates [5] to complete a cost risk analysis based on the cost data. The purpose of this methodology is to give project managers statistical information gathered from the technical experts in each system as an aid to assessing overall cost risks and which areas are the most vulnerable to cost overruns. The methodology applied was a series of in-depth interviews to obtain a distribution (a triangular distribution was used initially) of best possible, most likely, and worst possible costs at the detailed (WBS level 4 or 5) cost element, as well as obtaining any correlation that might exist between these elements. A standard Monte-Carlo analysis then yielded probable cost distributions at higher WBS levels and probability curves that could help in justifying contingency levels. For the most part, this analysis confirmed that at this stage of the cost estimate a contingency level of 20-25% is appropriate to achieve probabilities in the 80% range. More details of this analysis are available in an internal LANL report.

4 PROJECT SCHEDULING

Following the CDR, we implemented Primavera Project Planner (P3) to schedule and track project performance. A major factor in this choice was the local experience from several accelerator projects, including APT. Initial cost elements (based on the ASM model) from an Excel spreadsheet were transferred to P3, and the unburdened hours and costs were confirmed as identical to those in the ORNL CDR database. Resource tables were then applied in P3 to more precisely define personnel costs, based on standard rate tables published by Los Alamos for the categories. Official burden (G&A) rates, procurement recharge, and other standard factors were applied as part of the resource table, and contingency rates published by

DOE were used. A detailed schedule was produced in P3 that closely matches the project schedule [2] proposed following the CDR. The SNS project has standardized on the use of P3, and processes are in place to exchange files within the collaboration and to generate work packages for the current year. Because changes in schedule impact cost projections in P3, however, we are examining other software to contain the baseline cost estimate.

5 R&D PROGRAM

A vigorous R&D program to prove crucial design concepts is proceeding in parallel with the first two years of construction. The key elements of this program are: completion of the physics design for the cavities [6], cold models and hot models of CCDTL and CCL cavity segments [7], 2.5-MW peak power RF klystrons driven by an IGBT converter-modulator system [8], traveling-wave chopper development [9], and beam dynamics to finalize error tolerances. Cold models have been constructed and measured, and a hot model consisting of two CCL segments will be built this year. Figure 1 shows the envisioned extension of this hot model to include several CCDTL cells next year. Results of the R&D program are reported in other papers at this conference.

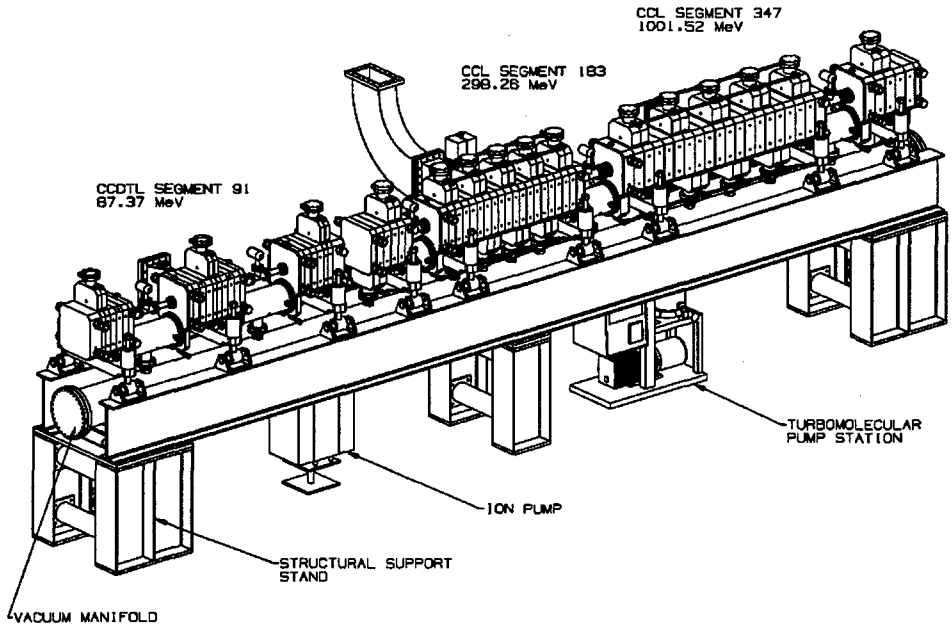

Figure 1. View of the CCDTL and CCL hot-model assembly, to be tested in FY00.

6 ACKNOWLEDGEMENTS

We acknowledge the contributions of Andrew Jason, who provided project leadership through the CDR, and Beverly Hartline, who assumed leadership after November 1998. John Rathke and Tim Myers of NGC (now Advanced Energy Systems, Inc.) applied the ASM code to the SNS linac and contributed greatly to initial cost estimates and transfer of data to P3. Stan Schriber contributed to the most recent bottoms-up cost estimate and supported the project during the value-engineering process. Thanks to David Hulett of Hulett & Associates for the expert advice and assistance on project risk analysis. Finally, the authors acknowledge the expertise and cooperation of the entire SNS linac design team in reaching this stage of the project.

7 REFERENCES

[1] SNS Conceptual Design Review, June, 1997, http://www.ornl.gov/~nsns/
[2] R. Hardekopf et al., "Linac Design for the SNS," Second Intl. Topical Meeting on Nuclear Appl. of Accelerator Technology, Gatlinburg, Sept. 1998, 208.
[3] A. Jason et al., "A Linac for the SNS," Linac98, Chicago, August 1998 (in press).
[4] D. Berwald et al., "Parametric Study of Emerging High Power Accelerator Appl. using Accelerator Systems Model (ASM)" Linac96, August 1996, 456.
[5] D. Hulett, see http://www.projectrisk.com/
[6] J. Billen, H Takeda, T. Bhatia, "Linac RF Structures for the SNS," PAC99, New York, March 1999.
[7] N. Bultman et al., "Mechanical Engineering of the Linac for the SNS," PAC99, New York, March 1999.
[8] M. Lynch, P. Tallerico, W. Reass, SNS RF System Overview," PAC99, New York, March 1999.
[9] S Kurennoy, J. Power, and D. Schrage, "Meander-Line Current Structure for SNS Fast Beam Chopper," PAC99, New York, March 1999.

A COMPARATIVE STUDY OF HIGH POWER, MULTISTAGE, X-BAND TWT AMPLIFIERS*

P. Wang††, Z. XU‡‡, D. Flechtner, Cz. Golkowski, Y. Hayashi, J. D. Ivers, J.A. Nation
Cornell University, Ithaca, NY 14850
S. Banna, and L. Schachter
Technion, Haifa, Israel

Abstract

Our previous work on high-power efficient X-Band TWT amplifiers has used a two stage device with bunching produced in a greater than light phase velocity region, immediately followed by a short low phase velocity output structure. The device is driven by a 7mm diameter 750 kV, 450A pencil electron beam. The structure, which has a 4 GHz bandwidth in the bunching section, produces an amplified output with a power in the range 20-60 MW. At higher output powers pulse shortening develops. A serious candidate for the pulse shortening is excitation of the HEM_{11} mode in the structure. This mode overlaps the frequency domain of the desired TM_{01} mode. We have designed and tested new amplifier structures in which the separation of these modes is substantially increased. The performance of the new amplifier(s) will be compared with that of the older device, and the relevance of the hybrid modes to pulse shortening assessed.

1. INTRODUCTION

In this paper we describe the results from three sets of experiments on the development of High-Power X Band, TWT amplifiers. Two experimental amplifiers have been used in this work, one having a 4 GHz and the other a 2 GHz, passband in the TM_{01} mode in the 'bunching' section. A distinguishing feature of the two amplifiers is the relative location of the lower branch of the HEM_{11} mode therein. In the first device the two modes overlap, whereas in the second there is no frequency overlap. The dispersion relations are shown in figure 1.

The 4 GHz bandwidth amplifier has been studied in 2 modes of operation, namely with an immersed diode and secondly with beam compression. Operation with beam compression limited the useful beam current to about 200 A.

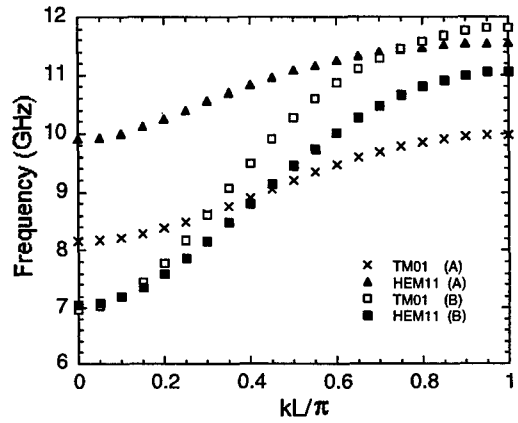

Fig 1 Dispersion relation of the two lowest modes

2. EXPERIMENTAL ARRANGEMENT

We show in figure 2 a schematic of the experimental arrangement. In both cases the rf input is fed into the amplifier via a tuneable sidearm arrangement. The amplifier has two stages, namely a short ~12 cm dielectric (Boron Nitride) stage in which the input power is absorbed, but not amplified. This stage is followed by a non-uniform disk loaded amplifier having two parts [1], a bunching section, in which the cold wave phase velocity may be as high as 1.05 c, followed by a short low phase velocity section used as the 'output'. The dielectric section and the disk loaded regions are separated by a SiC sever. A similar absorber follows the output section, which may or may not use a TM-TEM coaxial mode converter. The converter eliminates re-acceleration of the beam electrons in the amplified rf wave and increases the rf conversion efficiency. It has been described elsewhere [2]. For the experiments in which the beam is compressed during generation an additional SiC absorber was added prior to the dielectric buffer amplifier. This minimised reflections and is important in high gain (~48 dB) operation

* Work supported by the US Department of Energy and by the AFOSR
†† On leave from Tsinghua University, China. E-mail: Pw30@cornell.edu
‡‡ Permanent Address, Institute of Applied Electronics, China

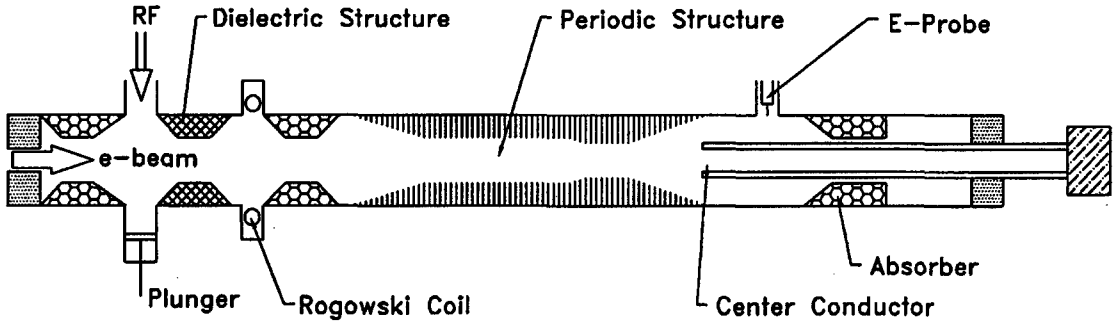

Fig 2. Schematic of experimental arrangement

We show in Table 1, the structure dimensions for the two amplifiers investigated. The buncher and output sections were, in both cases separated from each other by a tapered transition extending over several cells. The cells had a periodic length of 0.75 cm. of which 0.15 cm comprised the disk width. The disk loaded amplifier sections were terminated at each end in gradual tapers to the outside diameter of the cylindrical guide.

	Structure A. Narrow Band	Structure B. Broad Band
Buncher Rin	8 mm	11.75 mm
Rout	14.8 mm	17.13 mm
# Cells	24	45
Output Rin	8.0 mm	10.75 mm
Rout	15.2 mm	17.13 mm
# Cells	7	7

Table 1. Structure dimensions

3 EXPERIMENTAL RESULTS

Experiments were conducted using structure B with the beam generated from a cathode immersed in a 10 kG axial guide magnetic field. The beam amplitude and its profile in time were insensitive to the magnetic field strength. The beam current varied between 450 and 500A. Part way through the work a new gun geometry was employed which required that the beam be radially compressed by a factor of two prior to injection. Both amplifiers were tested in this configuration. In this regime the beam current profile was very sensitive to the magnetic field strength. The experiments were carried out at 5 kG where the beam current was almost constant in time. The beam current in these experiments was about 160-200 A. In both sets of experiments the beam energy was between 700 and 750 keV and the beam diameter was 7 mm.

3.1 Immersed Cathode Experiments: We have separately tested the 'buncher' and the combined 'buncher-output' amplifiers. The output power of the buncher was about 10 MW and continued for the full beam pulse duration. With the complete system we obtained an output peak power of up to 60 MW. At this level pulse shortening of the microwave output developed and the output pulse width decreased until at about 150 MW the microwave pulse width had dropped to about 10 ns. On investigation we found that the process was accompanied by a loss of the electron beam. At microwave peak powers of greater than 60 MW beam current loss occurs even at the input to the amplifier. At this power level the rf conversion efficiency is about 20%. It is clear that beam loss is associated with high power operation.

3.2 Compressed Flow Experiments: We report first results obtained with both of the structures.

In structure A we have obtained rf amplification with no evidence of pulse shortening from 9.03 –9.48 GHz. Output powers of up to 55 MW with a ~1 kW rf input were obtained. A rf power conversion efficiency of up to 45% was obtained. The amplifier gain ranges from 38–48 dB as one sweeps through the frequency range. In these experiments the output mode converter was not used.

Similar experiments were carried out using the broader band structure B. Again the current was limited to about 200 A and with a 5kG axial magnetic field. With this structure the output power ranged from 6 MW at ~9GHz to about ~50 MW at 9.5 GHz. Once again there was no evidence of beam or rf pulse shortening. Since this amplifier has a lower interaction impedance its length was longer and the input power was increased to 13 kW. We have also run this amplifier with the coaxial mode converter obtaining a power output of up to 75 MW at a power conversion efficiency of ~55 %.

We show typical waveforms in figure 3 for the 'broadband' amplifier, and summarize the performance of both of the amplifiers in fig 4. We plot, as a function of the input wave frequency, the gains for both devices. In all cases the amplified output frequency exactly corresponds to the input frequency.

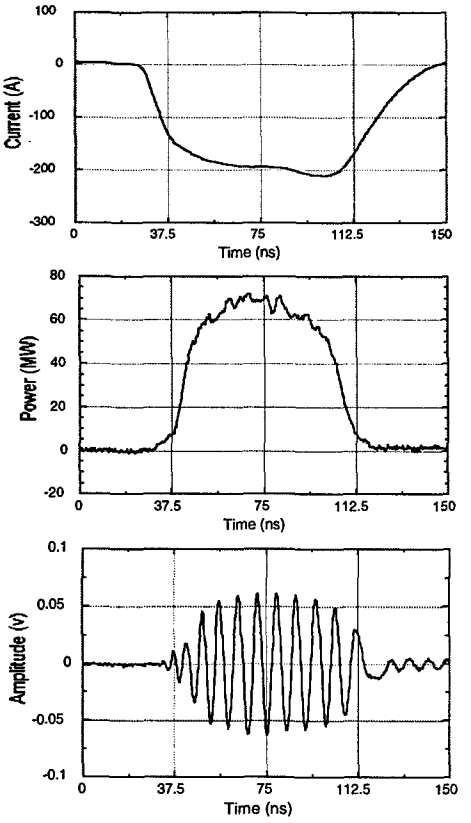

Fig 3. Typical beam current, rf envelop and heterodyne output for amplifier B

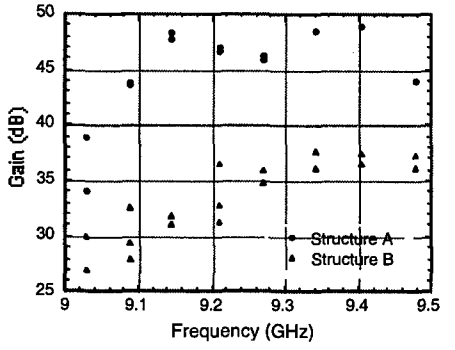

Fig 4. Gain versus frequency for both amplifiers.

4. DISCUSSION OF RESULTS

The results obtained using the immersed cathode configuration strongly suggested that the beam was lost due to the development of the HEM modes in the long uniform amplifier [4]. These results lead to the study reported in reference 3 and the related experimental attempt to suppress these modes using a Shintake cavity [5] to damp the unwanted modes. We have no direct observation of HEM mode interaction at present, and a more detailed search is presently in progress.

The results reported in the compressed flow experiments show no evidence of hybrid mode excitation, nor is there any pulse shortening. At present it is not clear if the difference between the two regimes reported above is due to differences in the beam current levels, or to some other process. The efficiency reported, especially in the experiment using the coaxial output extraction (~55%), is high and comparable to that predicted by PIC codes. The good performance of the larger diameter amplifier B is particularly encouraging for large bore TWT amplifiers, since the HEM_{11} and the TM_{01} modes overlap.

5. CONCLUSIONS

We have investigated microwave amplification in two non-uniform TWT's. In the case of the larger bore structure with high beam currents (Structure B) there was a loss of beam current, which was microwave power level dependent. This limited the amplifier power conversion efficiency to about 20%. In the lower current experiments and with both structures the beam current was limited to ~200 A. Output powers of up to 55MW with a gain of 48 dB were obtained. The efficiency in both structures reached 45% and peaked at 55%, with the higher figure arising from the use of the coaxial mode converter/beam dump.

The high output power full pulse width operation in structure B is interesting as it suggests that high frequency amplifiers (~35 GHz) might be built using large bore structures.

6. Acknowledgment

This work was supported by the Doe and by the AFOSR under the Muri High Power Microwave Program

7. References

[1] S.Naqvi, J.A. Nation, and L. Schachter and Q Wang, "High Efficiency TWT Design Using Traveling Wave Bunch Compression", IEEE Trans on Plasma Science, 26,3, 840-845, (1998)

[2] S.Naqvi, G.S. Kerslick, J.A. Nation, and L. Schachter," Axial Extraction of High Power Microwaves from Relativistic Traveling Wave Amplifiers", Appl. Phys. Letts, 69, 1550,1996.

[3] S. Banna, L. Schachter, J. A. Nation, and P Wang, "Beam Interaction with symmetric and Asymmetric Modes in High-Power, High Efficiency, TW Amplifiers", Proc . this Conference.

[4] J.Haimson and B.Mecklenburg, Suppression of beam induced pulse shortening modes in high power RF generator TW output structures. SPIE vol.1629, Intense microwave and Particle Beams III (1992)/209.

[5] Y. Hayashi, J. D. Ivers, D. Flechtner, J. A. Nation, P. Wang and L. Schachter, "TWT Amplifier using a Ferroelectric Cathode for Electron Beam Generation", Proc. this Conference.

FIRST RESULTS FROM A HIGH POWER Ka BAND TWT *

Cz. Golkowski#, J. D. Ivers, J.A. Nation, and P. Wang.
School of Electrical Engineering, Cornell University, Ithaca, NY 14853,
L. Schächter
Department of Electrical Engineering, Technion, Haifa, Israel

Abstract

In this paper we report first results obtained in a new program to develop high power, high efficiency TWT microwave sources at 35 GHz. In these experiments we use a 30 cm long dielectric (Teflon) amplifier with an 850 kV, 200 A pencil electron beam. The input power is provided from a 250ns long, 10 kW pulse from a magnetron. The experience obtained with this device will guide further development of multistage disk loaded amplifiers. Experimental results indicate output power levels of about 1 MW and a gain of about 18 dB. These results are consistent with expectations from PIC code simulations. Details of the system designs and performance will be presented.

1 INTRODUCTION

Future high gradient accelerators will require the use of high power microwave sources at frequencies in excess of X band. A recent analysis of the requirements of an 5-15TeV accelerator indicates that the operational frequency should probably be in the vicinity of ~35 GHz [1,2]. A source efficiency of order or greater then 40% will be required.

We have initiated a research program to investigate the development of a TWT amplifier at this frequency and we report first results from the program. In other laboratories work is in progress in developing gyroklystron amplifiers at this band [3,4]. In our initial experiments we have used a dielectric amplifier to allow us to obtain experience in the use and measurement of high power Ka band radiation. The dielectric amplifier is probably restricted to output power levels of a few megawatts, but has the advantage of ease of fabrication and matching of the amplifier input and output regions to other waveguide structures. We report a gain of 18 dB from the amplifier and an output power of about 1 MW. A disk loaded amplifier has also been fabricated and initial tests are in progress. This device, which consists of a single stage amplifier, expected to have gain of about 30 dB, an efficiency of close to 15%, and a multimegawatt output power in a 50 ns pulse.

In all of these experiments we use a single shot 900 kV, 200 A, 50 ns electron beam as the primary pulse power source.

In the following sections we describe the dielectric amplifier configuration and show typical data from the amplifier experiments. We also indicate the design of a disk loaded amplifier, which has been constructed and is currently being tested.

2 EXPERIMENTAL CONFIGURATION

The experimental arrangement of the dielectric amplifier is sketched in Figure 1. It uses a Teflon loaded waveguide having a length of 30 cm with 2.5 cm tapers to a uniform cylindrical waveguide at the input end, and to a coaxial guide on the output. The internal diameter of the waveguide is 12.5 mm and the inner diameter of the dielectric is 9.5 mm. The amplifier is terminated with an absorbing load and the output of the amplifier sampled prior to the load. The input rf signal is provided to the amplifier from a Ka band magnetron through pressurized waveguide. Typical input powers injected in the amplifier range from 5-10 kW and the driving beam carries 200-300 A at a beam energy of 850-900 keV. The full width pulse duration is about 50 ns. The electron beam is guided by a 1 Tesla magnetic field, which is carefully aligned with the axis of the experiment. The input coupler design, which is tunable to maximize input to the cylindrical TM_{01} mode, is based on results obtained from the HFSS code. The coupler has two adjustable elements namely an anode stub positioned to suppress coupling to the TE_{11} mode, and the other a rectangular waveguide arm, located directly opposite to the input arm and with a tunable shorting stub which allows us to maximize the deliverable input power from the magnetron. The position of the anode stub is experimentally determined using a network analyzer. A TE_{11} to TE_{10} mode converter and crystal detector is used to minimize the TE_{11} signal. The position of stub in the sidearm is determined by maximizing the power detected by the E field probe located at the output of the amplifier.

We have also assembled a disk loaded amplifier designed to work under identical electron beam and

*Work supported by the US Department of Energy and the AFSOR MURI program
#e-mail cg18@cornell.edu

0-7803-5573-3/99/$10.00@1999 IEEE.

microwave parameters. It has up to 100 uniform cells and employs two 10 cell tapered sections at both ends of the uniform section. The tapered sections are used to minimize the reflections at the transitions between the structure and the uniform waveguide sections. The structure has a phase advance per cell of $\pi/2$ at an operating frequency of 35 GHz for an 850 kV beam. With these parameters each cell has length of 2 mm (a 1mm long iris and a 1mm long cavity). The outer radius of the cavities is R_{ext} = 5.0 mm and the inner radius, R_{int} = 3.5 mm. The input structure and the termination are the same as those used for the dielectric amplifier. Gain has been observed for this structure.

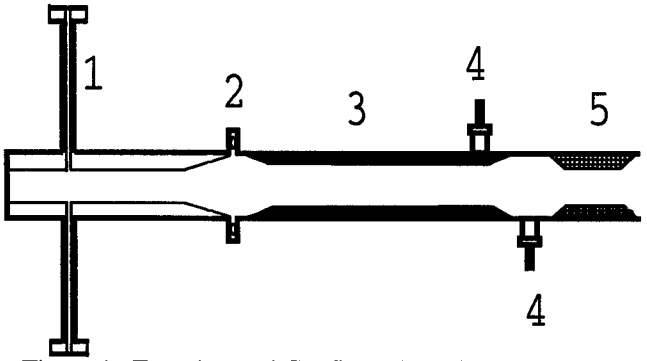

Figure 1. Experimental Configuration. 1) Input structure, 2) Rogowski coil, 3) Dielectric Amplifier 4) Output Wave E Field probes, 5) Microwave absorber

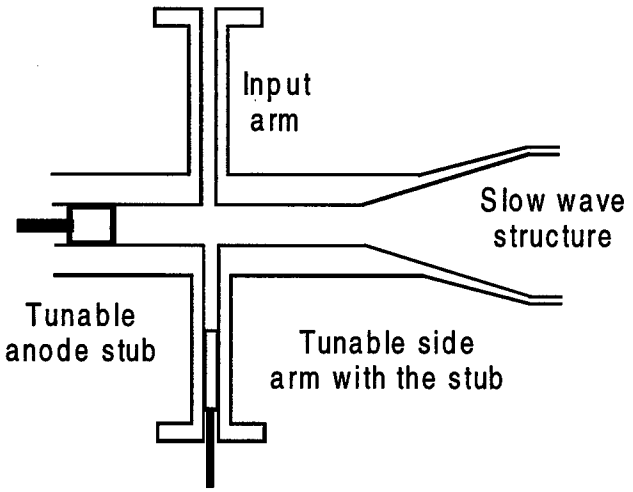

Figure 2. Input coupler.

In typical operation of the amplifier the 250 ns magnetron output pulses are injected via pressurized guide through the input coupler to the amplifier. The coupler tuning elements are adjusted immediately before firing of the beam to maximize the TM_{01} input signal to the amplifier. Although the magnetron source has an output of 40 kW only 10 kW are available at the amplifier input, since the source is kept in the screen room and the waveguide run drops the available power by about 5 dB, limiting the input signal to about 10 kW. The output signal is detected on an electric field probe located in the uniform guide after the output taper. The sampled output is sent to the

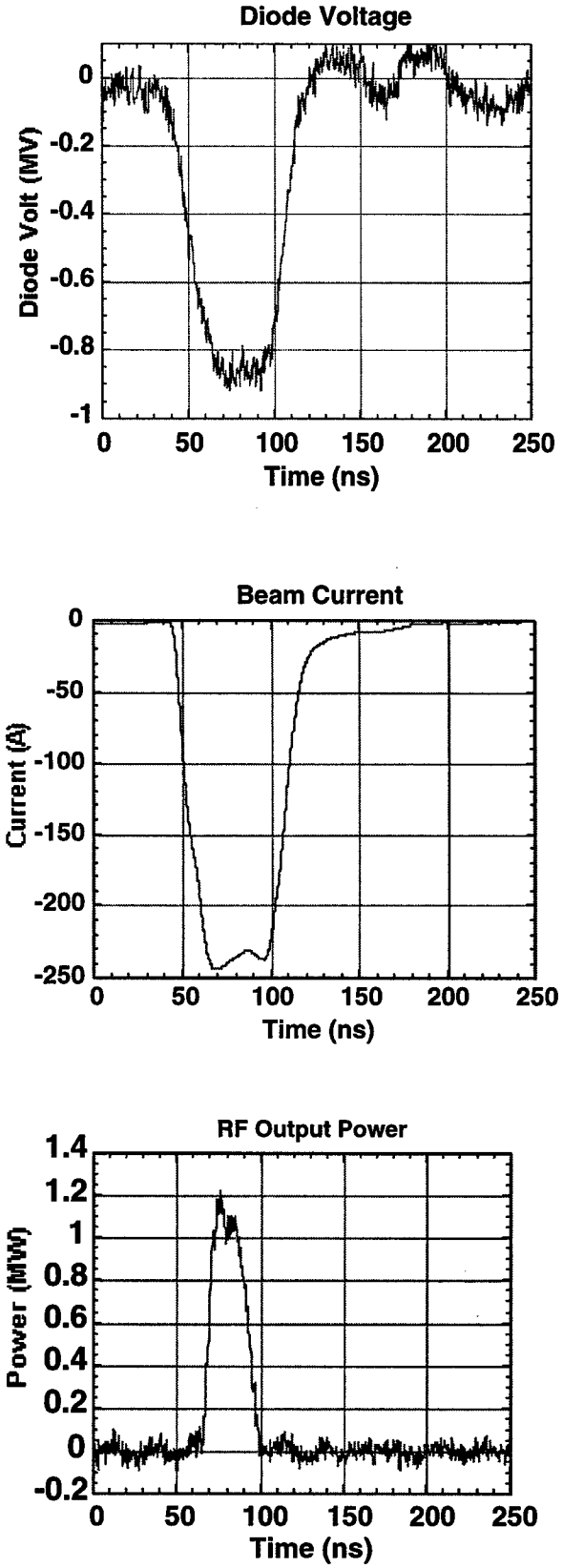

Figure 3. Diode voltage (top trace), Diode current (middle trace), and the RF output signal (bottom)

screen room where the signal is split into two and the envelope detected in one output arm, while the other arm feeds a double balanced mixer with local oscillator input provided by a Gunn diode. The amplifier gain is measured using a substitution technique, comparing the attenuated amplifier signal directly with the input signal measured using the same detector. The attenuation required to reduce the amplifier signal to its input level is a direct measure of the gain.

4 RESULTS

The diode voltage, the diode current and the RF output are shown in Figure 3.

The output signal from the dielectric amplifier as shown in Figure 3 (bottom) has the same length as the "flat" top of the beam current. The output signal is found to track the input frequency and power level for the frequency range available of 34-35.2 GHz and for variations of a factor of 2 in the input power level. Peak output signals of 1.2 MW were obtained with a pulse duration matching that of the pulse power. Typically the data showed a gain of 17.5 ± 2.5 dB.

In Figure 4 we show a heterodyned waveform which illustrates that the amplified output is single frequency. The frequency of the amplified signal matches the frequency of the magnetron input.

We have examined, using a computer calculation the effect of the beam temperature on the gain. For a current of I= 275A at a beam energy of V=0.875MeV, and for an amplifier length of 30cm we find the gain of the

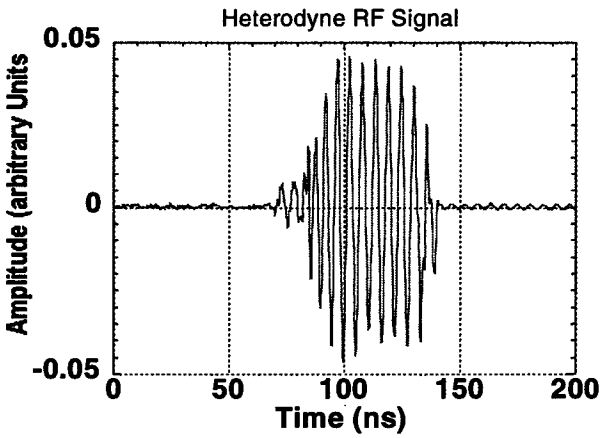

Figure 4. Heterodyne Output Signal. The local Oscillator frequency was 34.6 GHz.

system drops from 22dB to 16dB when the on the energy spread during the 50ns duration of the energy spread at the input increases from 0 to 15%. Based on this calculation we can place an upper limit pulse of 10%. The beam source in these experiments was a field emission tip.

5 CONCLUSIONS

We have successfully tested a 35 GHz dielectric TWT amplifier using a relativistic electron beam as the primary power source. The diode produced an adequate quality electron beam guided by a 1T magnetic field. We have gained experience in using Ka band diagnostics to measure the input and output power from the experiment. The HFSS designed coupler was found to work satisfactory over the frequency (~1 GHz) range available from the magnetron. The full range of the available frequency from the magnetron was amplified by the dielectric amplifier. The output RF power was in the range of one megawatt with a gain of 17.5 ± 2.5 dB in the available frequency range of the magnetron (34-35.2 GHz). The RF output results suggest that the amplifier is sensitive to the current level and its variations. Therefore, special attention will have to be paid to the current beam shape and intensity in the future Ka band experiments

6 ACKNOWLEDGEMENT

This work was supported by the DoE and by the AFOSR under the Muri High Power Microwave Program.

7 REFERENCES

[1] P. Wilson; Proceedings of the Third Workshop on Pulsed RF Sources for Linear Colliders, Editor Shigeki Fukuda, Shonan Village Center, Hayama, Kanagawa, Japan, April 8-12, 1996 p. 9.

[2] P. Wilson, "Scaling Linear Colliders to 5 TeVand Above," SLAC PUB 7449 (1997).

[3] M. R.Arjona, W. Lawson "Design of a High-Efficiency, Broadband, Second Harmonic, 250 kW, Ka-Band Amplifier," IEEE Trans. Plasma Sc. 26, June 1998, p. 461-467.

[4] J. J. Choi, A. H. McCurdy, F. N. Wood, R. H. Kyser, J. P. Calame, K. T. Nguyen, B. G. Danly, T. M. Antonsen, B. Lavush, R. K. Parker, "Experimental Investigation of a High Power Two-Cavity, 35 GHz Gyroklystron Amplifier," IEEE Trans. Plasma Sc. 26, June 1998, p. 416-425.

TWT AMPLIFIER USING A FERROELECTRIC CATHODE FOR ELECTRON BEAM GENERATION*

Y. Hayashi#, J. D. Ivers, D. Flechtner, J. A. Nation, P. Wang, Cornell University, Ithaca, NY
and S.Banna, L. Schächter, Technion, Haifa, Israel

Abstract

We report first experiments on high-power traveling wave amplifiers using an electron beam generated with a ferroelectric cathode. The electron beam, which is driven by a ferrite core transformer-pulse line system, has energy of 440 keV and a beam current of 40-50 Amperes. The beam pulse duration is about 250 ns and the system is operated at 0.07 Hz. The beam is generated from a command switched ferroelectric cathode located in the fringing field of a solenoid. A single stage disk loaded TWT structure is used as the ~9GHz amplifier. A gain of 10 dB is observed over the frequency range from 8.9 to 9.4 GHz. The main purpose of the experiment is to demonstrate that the ferroelectric generated beam is of good enough quality for microwave amplification in X band, and to pave the way for use of this cathode in future high power microwave source experiments. We compare the results obtained using this system with the output from a PIC code simulation.

1 INTRODUCTION

During the last several years, we have investigated the use of ferroelectric cathodes for electron beam generation. Previous experiments have found that diode currents of up to 330 A could be obtained from a cathode of ~1 cm^2 emission area [1]. The beam current in the present design yields 40 A at 440 kV and will, in the next gun design, be increased to 200 A.

2 EXPERIMENTAL ARRANGEMENT

The experimental arrangement is shown schematically in Fig. 1. The cathode gun assembly is connected to the modulator described previously [1]. A more detailed account of the modulator design and the cathode performance in a diode arrangement is to be published shortly [2]. The gun geometry, which was designed using data from the aforementioned diode experiments, uses a planar cathode in a modified Pierce geometry. This geometry produces an approximately uniform cross section beam of 6 mm diameter throughout the 60 cm long experiment. The beam is confined by a ~2000 G magnetic field generated by the field coils. The 3 cm diameter ferroelectric cathode is recessed in order to produce a uniform beam with the existing magnetic field geometry. This limits the beam current to ~40 A at 440 kV in a 250 ns pulse. The ferroelectric cathode is coated with a 0.2 mm silver grid on its front surface and a uniform silver layer on its back.. The trigger pulse is adjusted to start slightly before the maximum of the gun voltage pulse, so that when a ~1.5 kV positive trigger pulse is imposed on the back of the ferroelectric cathode, a beam current pulse is obtained. The rise time of the beam current pulse, under appropriate trigger timing conditions, is much shorter than that for the secondary voltage.

The electron gun is connected to an X-band single stage Traveling Wave Tube (TWT), which has 35 uniform

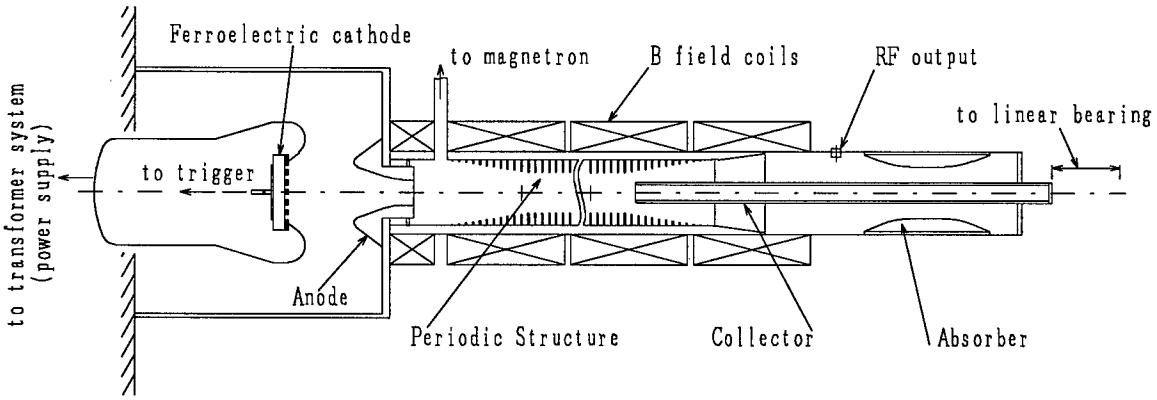

Figure 1: Experimental arrangement for the microwave amplification using a ferroelectric cathode.

*Work supported in by the US Department of Energy and the AFOSR MURI program.

#Email: yh55@cornell.edu

irises and 11 tapered irises on both ends. The inner and outer radii of the iris are 10 mm and 16.4 mm respectively, and the periodic spacing of the irises is 7mm. This corresponds to the $\pi/2$ synchronous mode at the operating voltage and at a wave frequency of 9.0 GHz. The input waveguide at the beginning of the TWT is connected to an X-band magnetron which provides ~10 kW power into the TWT. A reflector mounted on the end of the anode is located at a distance equal to a 3/4 wavelength of the TE_{11} mode, in order to reduce excitation of this mode. At the end of the TWT, a coaxial mode converter/collector is used to separate the beam and amplified RF output [3]. The beam is dumped into the collector, in order to avoid re-acceleration of the beam electrons by the amplified RF. The amplified RF is efficiently mode converted from the TM_{01} mode of the slow wave structure into a TEM mode in the coaxial section. Measurement of the RF output power is made with an E field-probe mounted between the amplifier and the microwave absorber located at the end of the coaxial converter.

3 EXPERIMENTAL RESULTS AND DISCUSSION

Figure 2 shows typical waveforms for the gun voltage, the beam current, and the amplified microwave output pulse. The start of diode voltage is defined as t=0, and the RF power is taken as the relative power with respect to the magnetron output. At t=200 ns, the trigger pulse is applied to the back of the ferroelectric cathode, the current rises to ~40 A with a rise time much shorter than that of the diode voltage pulse. The pulse width of the current is ~265 ns. The RF pulse rises slightly after the current begins, and continues for up to 250 ns, which is comparable in width to the beam current pulse. A series of experiments have been performed at various RF input frequencies. Fig. 3 shows the amplifier gain and the output pulse width as a function of the frequency. The second scale on the abscissa indicates the cold structure wave phase velocity. The TWT is designed for synchronous operation at a beam energy of 430 keV and a wave frequency of 9.0 GHz. In the experiment an RF gain of ~10 dB was obtained over a frequency range from 8.9 to 9.4 GHz. The output gain as predicted by simulation, using the 2D PIC code MAGIC is 16.5 dB at synchronous flow conditions. This value was obtained however with the center conductor mode converter/beam dump optimally located. In the reported experiments it was retracted. The simulated gain curve lies at lower frequencies by about 250 MHz than the experimental observations. The cold wave phase velocity in the TWT structure changes significantly over the frequency range employed in the amplifier ranging from less than 0.7·c to 0.87·c at the lowest frequency. Non-synchronous velocity gain has

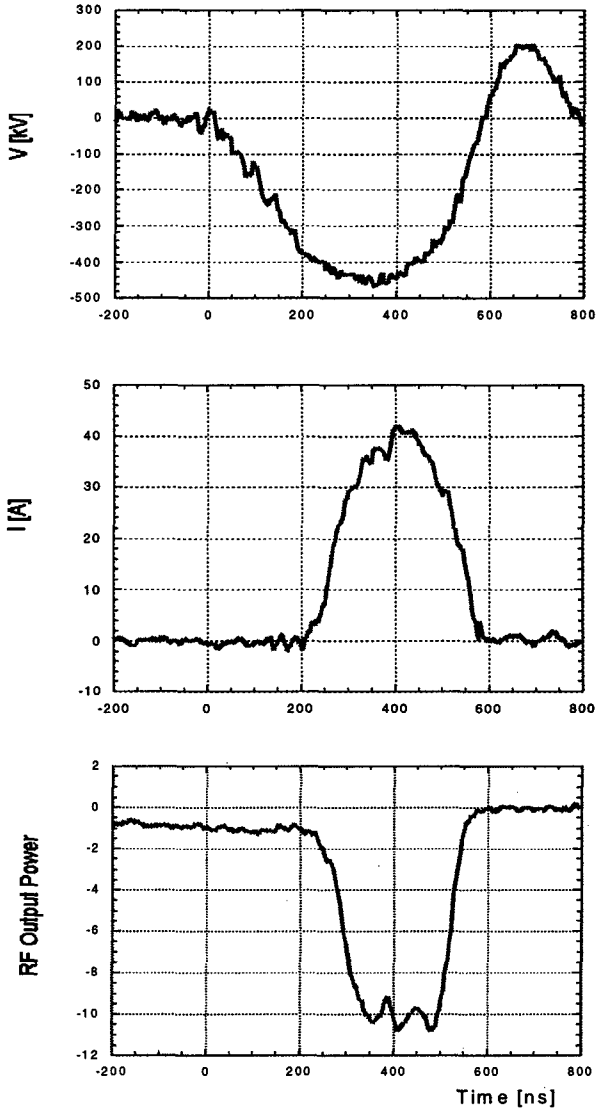

Fig. 2. Waveforms for the electron gun voltage, the beam current, and the microwave output pulse

been previously described and is a relativistic phenomenon [4]. In the simulated data the gain has dropped to zero by 9.2 GHz, but gain is seen experimentally with even higher structure wave phase velocities.

An interesting phenomenon is shown in the second part of figure 3 where we indicate that the RF pulse width increases at the higher end of the frequency band to the full beam pulse width. In long, uniform disk loaded structures there is the expectation that the asymmetric HEM modes may develop [5,6,7]. This is particularly likely when the structure inner radius is relatively large compared to the outer radius and the lower branch of the HEM mode overlaps with the TM01 mode passband. The HEM mode will usually lead to beam loss to the wall. In the present case the mode converter at the end of the output section will also act as a

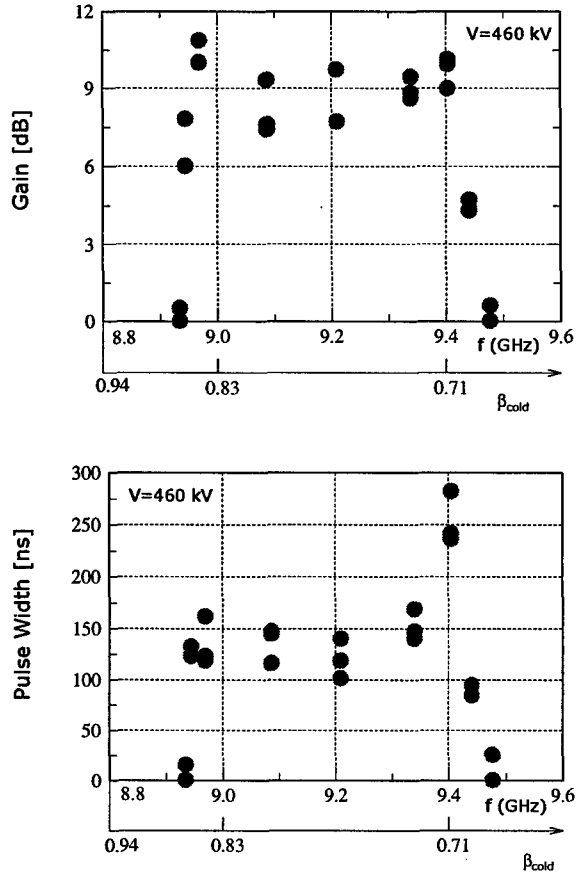

Fig. 3 Characteristics of RF Gain and pulse width vs. frequency.

reflecting boundary for the HEM mode. We have made a preliminary search for the presence of this mode but have not yet identified its presence in these experiments.

In 1992, Shintake [8] proposed the use of choke mode cavities to damp higher-order modes. This approach has also been investigated for use in two beam accelerators [9]. We have performed scalar analyzer measurements of the transmission for a traveling wave structure

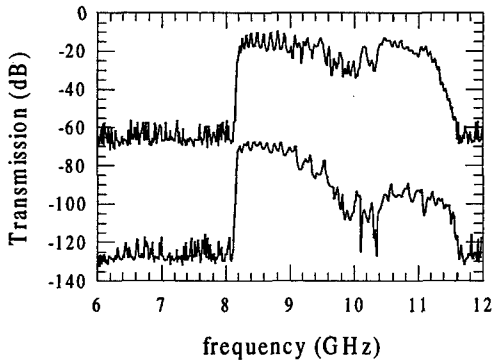

Fig. 4. Comparison of transmission with and without the choke mode cavity. The lower trace is offset by 60 dB.

with and without a choke mode cavity. The inner and outer radii of the traveling wave structure are 8 mm and 14.8 mm respectively, and the periodic spacing of the irises is 7.5 mm. This structure is identical in dimensions to the uniform part of the amplifier designated as Structure A in a companion paper presented at this conference [10]. As shown by Figure 4, the addition of the choke cavity reduced the transmission of the lower HEM_{11} mode by ~20 dB. Further experiments and theory relating to the excitation of the hybrid mode are reported in the companion paper.

4 CONCLUSION

An X-band microwave amplifier using a ferroelectric cathode has been successfully designed and tested. The experimental results mark the first observation of significant microwave amplification from a TWT using a ferroelectric generated electron beam. A 10 dB gain has been measured over the frequency range from 8.9 to 9.4 GHz. The experimental range of frequencies for which gain is observed does not exactly match the simulation result. The reason for this discrepancy is not clear.

A 250 ns wide RF output pulse is obtained at the higher frequencies and some pulse shortening is observed at the lower end of the passband. The pulse shortening might be associated with the onset of excitation of a hybrid mode interaction.

A new electron gun design, which will give the rated beam current of 200 A at 500 kV, is presently under way.

5 REFERENCES

[1] J. D. Ivers, D. Flechtner, Cz. Golkowski, G. S. Kerslick, J. A. Nation "A Ferroelectric Cathode,Electron Gun, for High Power Microwave Research", PAC97, **2**, 1275-1278 , (1998).

[2] J.D. Ivers et al., Accepted for publication in June issue, IEEE Trans on Plasma Physics, (1999).

[3] S.Naqvi, G.S. Kerslick, J.A. Nation, and L. Schachter," Axial Extraction of High Power Microwaves from Relativistic Traveling Wave Amplifiers", Appl. Phys. Letts, **69**, 1550, 1996.

[4] S.Naqvi et al., "Resonance shift in Relativistic Traveling Wave Amplifiers", Phys Rev. E, **53**, 4229-4231, 1996.

[5] S. Banna, L. Schachter, J. A. Nation, and P Wang, "Beam Interaction with symmetric and Asymmetric Modes in High-Power, High Efficiency, TW Amplifiers", Proc . this Conference.

[6] J.W. Wang and G. Loew, "HEM_{11} modes Revisited," LINAC90, LA-12004-C, 135-137, (1990).

[7] J. Haimson and B. Meklenburg, "Suppression of beam induced pulse shortening modes in high power RF generator TW output structures," Intense Microwave and Particle Beams, 209-219, (1992).

[8] T. Shintake, "The Choke Mode Cavity," Jpn. J. Appl. Phys., **31**, p. 1567- 1570, (1992).

[9] J.S. Kim, E. Henesteroza, T. Houck, S. Eylon, B.Kulke, G. Westenskow, S. Yu, "RF structure design for the TBNLC," LINAC 96.

[10] P. Wang, D. Flechtner, Y. Hayashi, J. D. Ivers, J.A. Nation, X. Zhou, S. Banna and L. Schachter, "A comparative Study of High Power, Multi Stage, TWT X-Band Amplifiers", Proc . this Conference.

INTERACTION OF TM_{01} AND HEM_{11} IN A TWT

S. Banna#, L. Schächter, Electrical Engineering Department, Technion-IIT, Haifa 32000, ISRAEL
J. Nation, P. Wang, School of Electrical Engineering, Cornell University, Ithaca, NY 14853, USA

Abstract

We investigate the interaction and the coupling of TM_{01} and HEM_{11L}, with an electron beam in a high-efficiency traveling-wave output structure operating at 9GHz. The coupling between the symmetric and asymmetric mode may be characterized by a single parameter that represents the correlation of the transverse and longitudinal phase-spaces. In order to examine the coupling we consider a pre-bunched beam injected in a uniform structure. For a specific set of parameters simulations indicate that 0.5MW of HEM_{11L} power at the input is sufficient to deflect to the wall a beam of 300A/0.85MV guided by a 0.5T magnetic field.

1 INTRODUCTION

In high-power and high-efficiency traveling-wave amplifiers the electron beam is assumed to interact with the lowest symmetric TM mode. Efficiencies as high as 70% and even higher, may be achieved in coupled cavity TW structures when high order modes do not play a significant role. However, asymmetry may occur either due to the input or output arm or azimuthal electrons' distribution. As a result, asymmetric modes may develop. Such modes are called hybrid electric and magnetic (HEM) modes. The main problem with HEM modes, is their ability to deflect the beam to the wall. Since pulse shortening was observed experimentally, as reported by Wang *et. al.* [1], we investigate in this study, some of the "cold" characteristics of asymmetric modes, and their interaction with the electron beam and the symmetric mode; specifically the beam blow up due to the hybrid mode.

2 DISPERSION RELATION

In the internal region ($r < R_{int}$) of a disk-loaded structure all the components of the electromagnetic field may be derived from the longitudinal components:

$$\begin{pmatrix} E_z \\ H_z \end{pmatrix} = \sum_{n,\nu=-\infty}^{\infty} \begin{pmatrix} \mathsf{E}_{n,\nu} \\ \mathsf{H}_{n,\nu} \end{pmatrix} e^{j\omega t - jk_n z - j\nu\phi} I_\nu(\Gamma_n r) \ , \qquad (1)$$

$k_n = k + 2\pi n / L$, $|k| < \pi / L$, $\Gamma_n \equiv \sqrt{k_n^2 - (\omega/c)^2}$ and $I_\nu(\xi)$ is the modified Bessel function of the first type and order ν. The dispersion relation of a periodic structure may be written in a matrix form as follows:

$$\begin{pmatrix} D^{TM}(\nu) & C_{12}(\nu) \\ C_{21}(\nu) & D^{TE}(\nu) \end{pmatrix} \cdot \begin{pmatrix} \mathsf{E} \\ \mathsf{H} \end{pmatrix} = 0 \qquad (2)$$

where, in principle, the matrices D^{TM}, D^{TE}, C_{12}, C_{21}, are infinite. This notation is convenient since in the case of symmetric modes ($\nu = 0$) the coupling matrices (C_{12}, C_{21}) are identically zero and this equation has two *uncoupled* solutions Det (D^{TM}) = 0 and Det (D^{TE}) = 0 that represent all the symmetric transverse magnetic (TM) and transverse electric (TE) modes, respectively. For any other value of ν the coupling matrices are not zero and as a result, the non-trivial solution of (2) implies that each eigen-mode is a superposition of the two modes (TE & TM). From the perspective of the interaction with the electrons, the main problem with such a mode is that it has a non-zero transverse magnetic field on axis and consequently, electrons may be deflected [2-5].

Similar to the symmetric modes for each radial number ν there are two modes, only that here we can no longer distinguish between TE and TM but rather they are referred to as "lower" and "higher" modes. Figure 1 illustrates the dispersion relation of all the modes up to 20GHz in a structure with internal radius of 8mm. The structure was designed to operate at 9GHz with phase advance per cell of $\pi/2$ and phase velocity of 0.933c; the disk thickness is 1.5mm. In such a relatively small internal radius the TM_{01} and HEM_{11L} modes are well separated and do not intersect. For higher radii the modes get closer to each other.

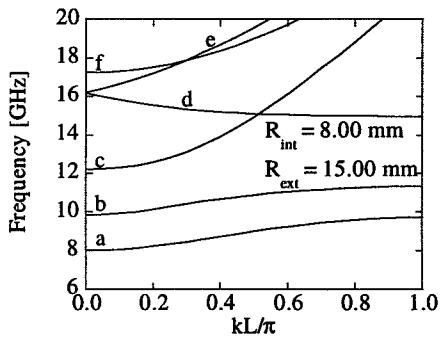

Figure 1: All modes up to 20GHz; a-TM_{01}, b-HEM_{11L}, c-HEM_{11H}, d-HEM_{21L}, e-HEM_{21H}, f-TM_{02}.

Email: Samer@techunix.technion.ac.il

The relative weight of each basic mode (TM and TE) composing the hybrid mode changes at different frequencies. In order to illustrate the "character" of the HEM mode, it is convenient to define the quantity $h_0 = \eta_0 \mid H_{n=0} / E_{n=0} \mid$. When h_0 is smaller than unity, the system behaves as a "TM" mode whereas values larger than unity its behavior resembles the "TE" mode. Figure 2 illustrates the value h_0 for the same structure presented above. The "TE" behavior is primarily in the lower part of the pass band of HEM_{11L} and "TM" behavior in its upper region.

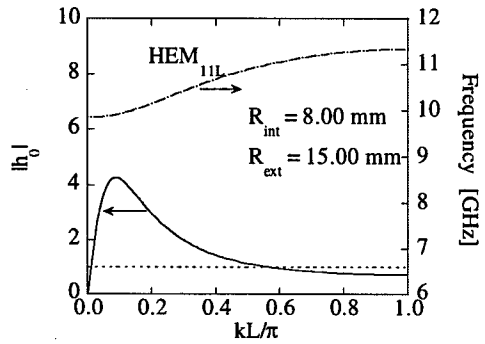

Figure 2: The value h_0 for HEM_{11L} as presented in Figure 1.

Another aspect that is critical in the design of a slow-wave structure is the group velocity of the HEM_{11L} mode. If the latter is negative an inherent positive feedback develops in the system and the system will oscillate. This problem is in particular vital in tapered structures where even if initially the system was designed for a positive group velocity, as the phase velocity of TM_{01} mode is reduced, the group velocity of the HEM_{11L} may become negative. Increasing the internal radius eliminates the positive feedback but it also reduces the interaction impedance; the latter is defined as:

$$Z_{\text{int}}^{(TM_{01})} = \frac{S_W}{2P^{(TM_{01})}} \mid E_{n=0,\nu=0} \mid^2,$$
$$Z_{\text{int}}^{(HEM_{11L})} = \frac{S_W}{2P^{(HEM_{11L})}} \mid E_{n=0,\nu=1} \mid^2 \qquad (3)$$

where S_w is the area the wave propagates and P is the total power which flows in the system in the mode.

3 DYNAMICS OF THE SYSTEM

In order to describe the coupling between TM_{01} and HEM_{11} we developed a quasi-analytic macro-particle model that describes the interaction of a beam of electrons with both TM_{01} and the low branch of the HEM_{11}. In the framework of this approach the dynamics of the particles is fully 3D but the variations effect in the amplitude of the electromagnetic field are assumed to occur only in the longitudinal direction (1D). Additional assumptions of the model include; positive group velocity of both modes, the basic form of both modes is preserved, the energy conversion is controlled by the longitudinal motion and no electrons are reflected. Space limitations will constrain the explicit formulation to the 1D case however subsequently simulation results from a 3D simulations will be presented. In the case of 1D motion the mode coupling is only due to azimuthal asymmetry therefore the governing equations read:

$$\frac{d}{d\xi}\left(\frac{a_1}{\sqrt{\alpha_1}}\right) = \sqrt{\alpha_1}\left\langle e^{-j\chi_{i,1}} I_0(\bar{\Gamma}_1\bar{r}_i)\right\rangle,$$
$$\frac{d}{d\xi}\left(\frac{a_2}{\sqrt{\alpha_2}}\right) = \sqrt{\alpha_2}\left\langle e^{-j\chi_{i,2}} I_1(\bar{\Gamma}_2\bar{r}_i)\right\rangle, \qquad (4)$$
$$\frac{d}{d\xi}\chi_{i,1} = \frac{\Omega_1}{\beta_i} - K_1, \quad \frac{d}{d\xi}\chi_{i,2} = \frac{\Omega_2}{\beta_i} - K_2,$$
$$\frac{d}{d\xi}\gamma_i = -\frac{1}{2}\left[a_1 e^{j\chi_{i,1}} I_0(\bar{\Gamma}_1\bar{r}_i) + a_2 e^{j\chi_{i,2}-j\phi_i} I_1(\bar{\Gamma}_2\bar{r}_i) + c.c\right].$$

The first two are amplitude dynamics equations, followed by the phase dynamics equations and in the last line we have a single particle energy conservation; 1 represents the TM_{01} mode and 2 the HEM_{11L} mode; $\langle ... \rangle$ represents averaging over entire ensemble of particles. The other definitions used here are: $\xi \equiv z/d$, d is the total interaction length, $\Omega \equiv \omega d/c, K \equiv kd, a \equiv eE_{n=0} d/mc^2$, $\gamma_i^{-1} = (1-\beta^2)^{1/2}$, $\chi_{i,1}$ is the phase of the i'th particle relative to the TM_{01} mode whereas $\chi_{i,2}$ is the phase of the same particle relative to the HEM_{11L} mode; ϕ_i is the azimuthal location of the i'th particle; α_1, α_2 are the coupling coefficients defined as $\alpha_\mu \equiv (eIZ_{\text{int}}^\mu / mc^2)(d^2/\pi R_{\text{int}}^2)$, $\mu = 1,2$; $\bar{\Gamma} \equiv \Gamma R_{\text{int}}$ and $\bar{r} \equiv r/R_{\text{int}}$. Based on (4) the spatial growth of the system may be evaluated and the result is:

$$S_\pm^3 = -\frac{1}{2}(S_1^3 + S_2^3) \pm \frac{1}{2}\sqrt{(S_1^3 - S_2^3)^2 + 4S_1^3 S_2^3 \bar{u}^2}\ ; \qquad (5)$$

where $S_\mu^3 = \frac{1}{2} p_\mu \alpha_\mu \Omega_\mu$, $p_1 = \left\langle I_0^2(\bar{\Gamma}_1\bar{r}_i)(\gamma_i\beta_i)^{-3}\right\rangle$, $p_2 = \left\langle I_1^2(\bar{\Gamma}_2\bar{r}_i)(\gamma_i\beta_i)^{-3}\right\rangle$ and the real parameter describing the coupling between the modes $\bar{u}$ is given by:

$$\bar{u} \equiv \frac{\left|\left\langle \frac{e^{-j(\chi_{i,1}-\chi_{i,2}+\phi_i)}}{(\gamma_i\beta_i)^3} I_0(\bar{\Gamma}_1\bar{r}_i) I_1(\bar{\Gamma}_2\bar{r}_i)\right\rangle\right|}{\sqrt{p_1 p_2}} \qquad (6)$$

The solution S_+ corresponds to the "HEM_{11L}"-like solution since at the limit $\bar{u} = 0$, $S_+ = S_2$ whereas S_- corresponds to the "TM_{01}"-like solution. Figure 3 illustrates the

value of $\bar{u}$ as a function of the angular spread of the beam $-\phi_0 < \phi < \phi_0$ with other parameters chosen as follows: $\bar{\Gamma}_1$=3, $\bar{\Gamma}_2$=4.5, $-\pi/2<\chi_{i,1}<\pi/2$, $\chi_{i,2}=1.5\chi_{i,1}$, $0<\bar{r}_i<0.6$ and $2.4<\gamma_i\beta_i<2.5$. It shows that the coupling is maximum when the azimuthal spread of particles is minimal and evidently in the case of a symmetric beam the coupling vanishes.

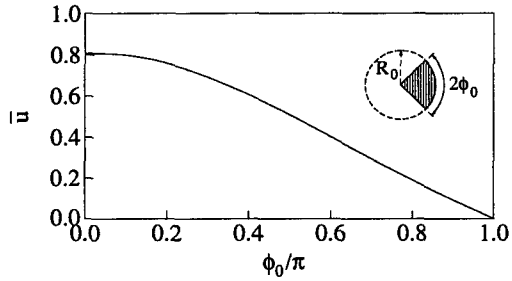

Figure 3: The value of $\bar{u}$ as a function of the angular distribution of the beam.

Finally, the 3D approach that due to space limitations will not be described her, enables to examine the development of the beam expansion. Figure 4 shows the radius of the envelope, $R_e/R_{int} \equiv 2\langle\bar{r}\rangle$, for several initial HEM_{11L} power levels at the input (1,10,100,500,1000kW); the TM_{01} mode is generated by a modulated $|\chi_{i,1}| < \pi/4$ beam. The other parameters of the simulation are as follows: I=300A, V=0.85MV, R_{int}=8mm, R_b=3mm, d=3.11cm, $|h_0|$=0.94, $f_{TM_{01}}=9\text{GHz}, f_{HEM_{11L}}=11\text{GHz}, Z_{int}^{TM_{01}}=1.5\text{k}\Omega, Z_{int}^{HEM_{11L}}=3.8\text{k}\Omega, \chi_{i,2}^{(input)}=\chi_{i,1}^{(input)} f_{TM_{01}}/f_{HEM_{11L}}$.

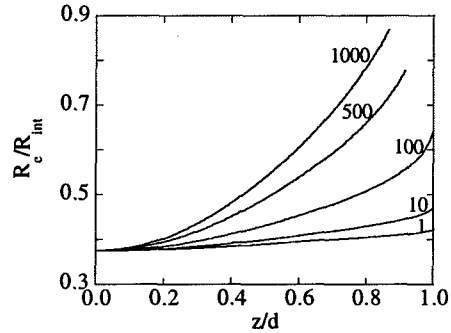

Figure 4: The radius of the envelope for several HEM_{11L} power level at the input (kW).

The increase of beam's envelope is directly correlated with the efficiency of HEM_{11L} mode as illustrated in Figure 5. At the same time, the interaction of the TM_{01} is very efficient reaching the 80% level due to initially bunched beam that drives the system. This efficiency is virtually not affected by the HEM_{11L} mode and all the curves overlap. The efficiencies of the TM_{01} and HEM_{11L} modes are defined as follows:

$$\eta_{TM_{01}}(\%)=\frac{100}{2\alpha_1\left\langle\gamma_i^{in}\right\rangle-1+\frac{1}{2\alpha_1}\left|a_1^{in}\right|^2+\frac{1}{2\alpha_2}\left|a_2^{in}\right|^2}\frac{\left|a_1(\xi)\right|^2-\left|a_1^{in}\right|^2}{};$$
$$\eta_{HEM_{11L}}(\%)=\frac{100}{2\alpha_2\left\langle\gamma_i^{in}\right\rangle-1+\frac{1}{2\alpha_1}\left|a_1^{in}\right|^2+\frac{1}{2\alpha_2}\left|a_2^{in}\right|^2}\frac{\left|a_2(\xi)\right|^2-\left|a_2^{in}\right|^2}{}. \quad (7)$$

For $P_{in}^{(HEM_{11L})}=0.5\text{MW}$ there are particles that hit the structure and for this reason the interaction is terminated.

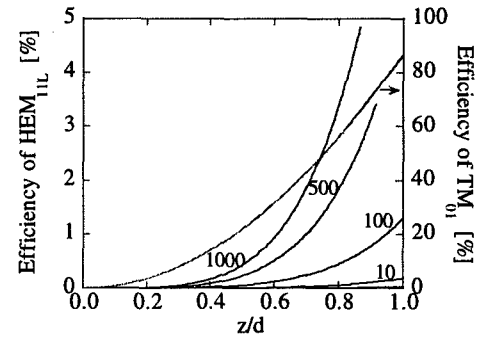

Figure 5: The way the efficiency of both modes develops for several HEM_{11L} power levels at the input (kW).

3 CONCLUSIONS

The design of a slow wave traveling wave structure has to take into consideration the effect of the asymmetric modes that the beam may interact with; the coupling between the symmetric and asymmetric modes was shown to be determined by a single parameter. When substantial power is associated with the HEM_{11L} mode it may cause deflection of the beam to the wall.

4 ACKNOWLEDMENTS

This study was supported by the US DoE and the Bi-National Science Foundation US – Israel.

5 REFERENCES

[1] P. Wang et. al., *A comparative Study of High Power, Multistage TWT Amplifiers;* this Proceedings.

[2] W. K. H. Panofsky and W. A. Wenzel, *Some Considerations Concerning the Transverse Deflection of Charged Particles in Radio-Frequency Fields,* Rev. Sci. Instr. **27**, 967 (1956).

[3] H. Hahn, *Deflection Mode in Circular Iris-Loaded Waveguide,* Rev. Sci. Instr. **34**, 1094 (1963).

[4] H. Deruyter et. al., *Damped Accelerator Structures* SLAC Pub. 5263 (1990).

[5] N.M. Kroll et. al., *Recent Results and Plans for the future on SLAC Damped Detuned Structures (DDS),* in Advanced Accelerator Concepts, Lake Tahoe, CA 1996, Editor Swapan Chattopadhyay AIP Conference, Proceedings 398, Wood-bury, New York p. 455.

PLANAR ACCELERATOR STRUCTURES FOR MILLIMETER WAVELENGTHS*

N.M. KROLL‡, M.E. HILL†*, X.E. LIN†, R.H. SIEMANN†,
D.C. VIER‡, D.H. WHITTUM†, AND D.T. PALMER†
‡*University of California, San Diego, 9500 Gilman Dr., La Jolla, CA 92093*
†*Stanford Linear Accelerator Center, Stanford University, Stanford CA 94309*
**Harvard University, 42 Oxford Street, Cambridge MA 02138*

Abstract

The fabrication of a muffin-tin planar accelerator structure for operation in the 90 GHz range is discussed in Reference. [1]. Fabrication problems subsequently encountered led us to consider an alternative structure, a structure which can be thought of as a muffin-tin with the sides removed and replaced by a pair of side chambers which act as side terminations (Fig. 1). With the side chambers removed, the structure when viewed from the side presents two periodic arrays of vanes facing one another from above and below the beam plane and which extend towards the beam plane from upper and lower plane metallic surfaces. The vane pairs are the analogs of the beam iris in cylindrical structures, and the space between the irises and terminated by the upper and lower plane metallic surfaces correspond to the cavities. Because the general appearance of this view is zipper like, we will refer to the structure as the "zipper" structure. The side chambers are envisaged as extending with uniform cross section from the input to the output cavities.

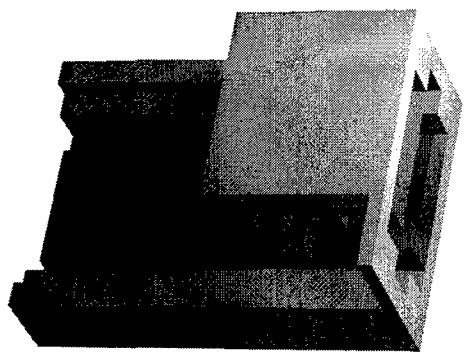

Figure 1:

1 INTRODUCTION

The design and fabrication of a traveling-wave muffin-tin accelerating structure at 90 GHz is presented in Reference. [1]. A prototype seven cell structure was constructed, and because it was to be used only for RF cold tests it was clamped together rather than assembled in a vacuum suitable manner. RF measurements are reported in Reference. [2]. MAFIA simulations indicated that the coupler achieved a fair match and the agreement with S_{11} measurements was reasonably good. Bead pull measurements of accelerating field amplitude and phase were also in reasonable agreement with expectations. On the other hand the transmission (ie S_{12}) achieved was disappointingly low, indicating about one half the power was dissipated within the structure. The electrical contact of the muffin-tin cells' walls with their bases depended upon the effectiveness of the clamping of a copper plate to the back of a row of rectangular holes. Subsequent structures (25 cells) attempted to improve this electrical contact by diffusion bonding the two parts together, but the vane side walls were unable to support the forces involved and no successful structure emerged from this attempt. Material research into a dispersion strengthened copper, Glidcop AL-15, has been conducted to avoid the cell to cell iris distortion reported in Reference [3].

In order to mitigate this problem we imposed on structure design a requirement that there be no brazed or diffusion bonded conducting joints between the vanes (ie the walls which form the cavity cells) and any other part of the structure. An example of such a structure is a muffin-tin with the side walls of the cells omitted. Thus the conducting junction between the vanes and the end walls, required for the muffin-tin, is eliminated. The cells can then be formed by machining grooves into a plate with width equal to that of the structure. Thus the junction between the vanes and the rear surface of the cell cavities is integral to the fabrication procedure and no separate bonding is needed. A generic example of the sort of structure that we have in mind is shown in Fig. 1. The spaces beyond the side ends of the vanes forms a kind of chamber which we refer to as side chambers. Because of the appearance of the structure when viewed from the side with the side chamber exposed, it has been dubbed a zipper structure.

In the following sections we describe some RF properties and constraints which led to the zipper design proposed in this paper (section 2). This is followed by a description of the proposed fabrication procedure (section 3), and a discussion of coupler design where an unanticipated problem was encountered (section 4). We end with concluding comments.

* Work supported by the Department of Energy, contract DE-AC03-76SF00515 and grants DE-FG03-93ER40759 and DE-FG03-93ER40793

0-7803-5573-3/99/$10.00@1999 IEEE.

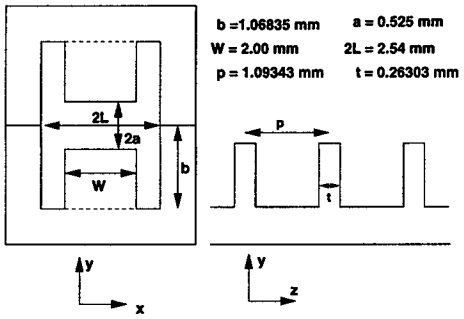

Figure 2: Section views of the zipper structure.

2 RF PROPERTIES OF THE PROPOSED DESIGN

The general configuration and the principal dimensions of the proposed zipper structure are shown by the section through a vane pair and perpendicular to the beam shown in Fig. 2. The structure has reflection symmetry with respect to a centered x-z plane and a centered y-z plane and the couplers are being designed in a manner which preserves this symmetry. Modes are classified by the reflection properties of E_z with respect to these planes, monopole for even-even, quadrupole for odd-odd, dipole-y for odd-even, and dipole-x for even-odd. A MAFIA [4] simulation based Brillouin diagram for the modes within a 50 to 100 GHz range is shown in Fig. 3. The fundamental or accelerating mode is the lowest monopole mode. The light line crosses it at 120 degree phase advance at the design frequency, 91.392 GHz. The lowest dipole mode band is the lowest band and it is noteworthy that it couples strongly to the fundamental TE mode which propagates down the beam tube, a rectangular waveguide like structure, 2.54 by 1.05 mm.

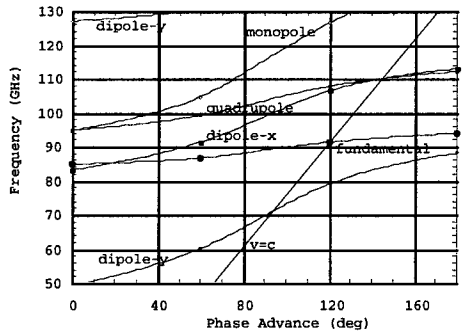

Figure 3: Dispersion diagram of the preferred case zipper structure.

The simulation yields a Q of 1605, R/Q 54.3 ohms per cell, and a group velocity of 0.098 c. The acceleration voltage has a quadrupole like variation characterized by a 1.83% droop 0.2 mm from the center in the x direction. One notes that the band separation is small due to the rather large lateral dimensions and the large end chambers. Careful design is required to avoid overlap of the two monopole bands. The overlap of the dipole-x and fundamental bands appears to be inevitable, but fortunately the coupler structures couple only to monopole bands. We view this mode structure as an undesirable feature but cannot at this stage assess the extent to which it will cause problems.

3 MECHANICAL DESIGN

The present structure we are designing is a symmetrically feed 25 cell constant impedance traveling wave structure. The rf coupling scheme used is a quarter wave transformer. The designed operating mode and frequency of the device is $f_{\frac{2\pi}{3}} = 91.392$ GHz. The cell to cell iris in this novel rf structure do not bear any mechanical loads during a thermal bonding cycle. The mechanical integrity of the structure is also improved by the using a dispersion strengthened material, Glidcop AL-15, as the base material.

The integrated structure is comprised of three layers. As seen in Figure 4 the top and bottom layers are identical and are comprised of the internal 23 cells and the WR-10 waveguide feeds. The two steps located in Figure 4 are used to match the structure with a quarter wave matching transformer that is integrated into the middle interlayer

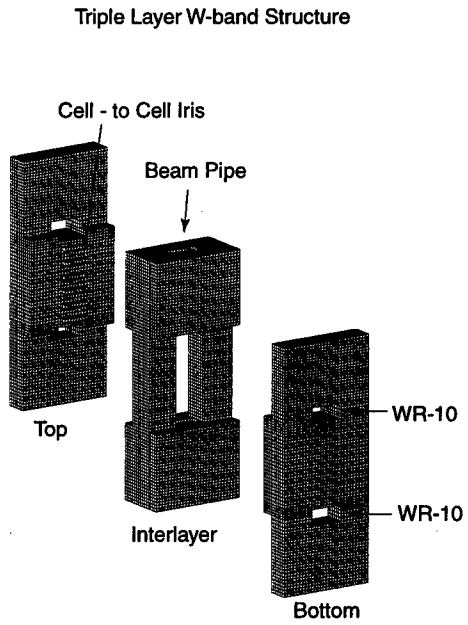

Figure 4: Expanded view of the triple layer stack W-band traveling wave constant impedance structure

The middle layer determines the input and output coupler iris position and transverse size, beam pipe and side chamber, and its termination. The thickness of this layer also determines the cavity iris separation.

When assembled these three layers are self aligning in the longitudinal direction due to the quarter wave matching transformers, which fit into the top and bottom layers and form the matching sections into the traveling wave accelerator. Two alignment pin are used to fix the transverse alignment of the structure, while the vertical alignment is

determined by the the flatness and parallelism of the three components of the triple layer stack. The alignment of the individual cavities that are formed in the top and bottom layers are well aligned since they are machined out of a single base material block during a single wire EDM machining step.

4 COUPLER DESIGN AND BAND INTERFERENCE PROBLEMS

The standard simulation based coupler design procedure is based upon the determination of S matrix parameters of a four cell structure consisting of the input and output cells and two intervening identical structure cells. Coupler match is verified by requiring at the operating frequency first, that $S_{11} = 0$ and second, that the accelerating fields in the two intervening cells have identical amplitudes and phases as functions of z except that the phase in the second cell is shifted by a z independent constant ψ from that in the first cell, where ψ is the phase advance constant associated with the cell Brillouin diagram at the operating frequency. Further confirmation may be obtained by adding a third intervening cell and verifying that the analogous conditions still hold. Many different waveguide to cell coupling iris designs and various modifications in coupler cell dimensions were explored. While we favored a quarter wave transformer design for fabrication simplicity, capacitative and inductive thin irises were also tried. We were, however, never able to come close to satisfying the conditions on the accelerating field.

The procedure described above is based upon the assumption that under steady state excitation at fixed frequency within the pass band of the acceleration mode that the fields in the interior cells can always be represented by some linear combination of the forward and backward propagating wave solutions appropriate to the drive frequency. This is expected to hold for any frequency within the pass band and independently of the S matrix parameters.

A simple test of whether or not this is the case is described below.

Let $F(z_o)$, $B(z_o)$ be the complex forward and backward wave amplitudes of some field component, say E_z at the point z_o along the beam axis. Then

$$E_z(z_o + np) = F(z_o)e^{-jn\psi} + B(z_o)e^{jn\psi} \qquad (1)$$

with $|\frac{B(z_o)}{F(z_o)}|$ independent of z_o, and p the period of the structure. Then by simple algebra

$$\frac{E_z(z_o + p) + E_z(z_o - p)}{E_z(z_o)} = 2\cos(\psi) \qquad (2)$$

This is a very strong constraint because it says that the LHS of Eq.(2) must be the same for all values of z_o for which Eq.(1) holds, must be real and lie on the interval $[-2, 2]$, and indeed must yield a value of $\cos(\psi)$ in agreement with that obtained by, say, a single cell periodic boundary conditions frequency domain simulation. If the test results is affirmative, then a further useful result is

$$|\frac{B(z_o)}{F(z_o)}| = |\frac{2jsin(\psi) + \Delta}{2jsin(\psi) - \Delta}| \qquad (3)$$

where

$$\Delta = \frac{E_z(z_o + p) - E_z(z_o - p)}{E_z(z_o)} \qquad (4)$$

Note that here the RHS of Eq.(3) must be independent of z_o.

This test fails badly for coupler test simulations involving small numbers of interior cavities. We are investigating the presumption that the test fails because of the presence of evanescent higher order modes associated with higher propagation bands. The second monopole band, which is very close to the acceleration band, is considered be a likely candidate, especially since its field configuration is such that its excitation by the coupler geometry is likely to be as large as that of the acceleration mode. If that is the case then the problem should disappear well into the interior of a sufficiently long structure, and simulation, using GdfidL [5], of a structure with 23 interior cells indicates that this is the case. From the behavior of the test with respect to cell position, we conclude that the standard matching procedure should be successful if applied to the interior cells of a structure with at least 15 to 20 cells.

5 CONCLUSION

The upper band contamination problem clearly imposes a computational burden on matched coupler design. We will know how large when we have succeeded in doing it. Fortunately the evanescent modes are non propagating and therefore will have very little interaction with the beam. On the other hand they do contribute to copper losses, reduce R/Q, and may increase peak fields. The design discussed in this paper was selected from a number of similar structures primarily because it had the best shunt impedance. The separation between the upper band and the acceleration frequency was nearly twice as great for one of the alternate designs and the penalty in shunt impedance loss was small. The increased separation should decrease the penetration of the evanescent mode into the structure.

While the RF properties so far determined for zipper type structures are not ideal, it does appear to be able to be fabricated and further investigation aimed at possible construction is planned.

6 REFERENCES

[1] P.J. Chou et al., PAC97, page 464

[2] P.J. Chou et al., PAC97, page 672

[3] D. T. Palmer et al., PAC99 ,THCR3

[4] F. Ebeling et al., MAFIA User Guide, 1992.

[5] W. Bruns, *IEEE Trans. Magn.* 32, pp. 1453-1456, 1996

RESONANCE FAR-FIELD ACCELERATING STRUCTURES AT SHORT WAVELENGTHS

A.V. Smirnov
Russian Research Center «Kurchatov Institute», 123182 Moscow, Russian Federation

Abstract

Resonance far-field structures capable to provide high gradient continuos acceleration at millimeter and micron wavelengths are considered. Among such structures are periodically striped open waveguide and oversized waveguide having periodic small perturbations. Main parameters of the structure composed by flat mirrors are estimated on the base of rigorous analytical solution for the eigenmodes.

Some modifications of diffraction-dominated structures based on open waveguides and resonators are proposed.

1 INTRODUCTION

In the previous paper [1] a concept was proposed for laser resonance acceleration of relativistic charged particles. It is based on a resonance interaction of a straightforward charged particle beam interacting with electromagnetic beam having periodic change of wave vector. Closed waveguide having periodical deformation was considered as the accelerating structure. It was shown earlier, that such an overmoded rectangular [2] or circular [3] waveguide can be excited effectively (with dominant single mode) by a properly focused laser beam having linear polarization. However, the stability of the hybrid EH_{11} mode to the transformation into parasitic higher modes requires further consideration.

In this paper we consider another realization of the principle above based on an open periodic waveguide. It can provide stable propagation of the lowest mode due to diffraction resulting in widely-spaced spectrum of eigenmodes.

2 EIGENMODES OF THE PERIODICAL OPEN MIRROR WAVEGUIDE

The open waveguide (or open periodical resonator) composed by chain of mirrors with period λ_w. For simplicity of consideration we assumed here rectangular flat mirrors with dimensions 2a×2b. The principal scheme is shown in the Fig. 1. To consider the fields of the open mirror waveguide we solve first the problem for the equivalent open resonator with rectangular mirrors having dimensions $2a_1$×2b (see Fig. 2). The e.m. fields of the resonator with rectangular mirrors are found by Vainshtein [4] in terms of eigenmodes for Hertz vector potential $\vec{\Pi}$ at $\lambda_s \ll a,b$, where $\lambda_s=2\pi c/\omega$ is laser wavelength. The vector potential $\vec{\Pi}$ is defined through the potential function Φ, that satisfies to a Helmholtz wave equation: $\Delta\Phi + k^2\Phi = 0$.

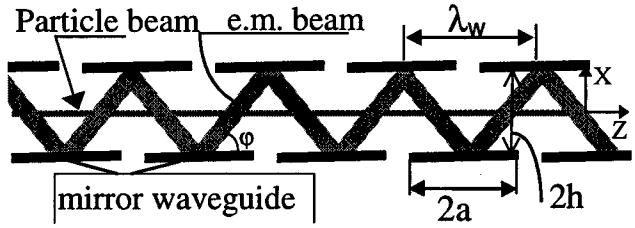

Fig. 1. Schematic drawing of an accelerator with a «wiggling» field propagating in an open mirror waveguide.

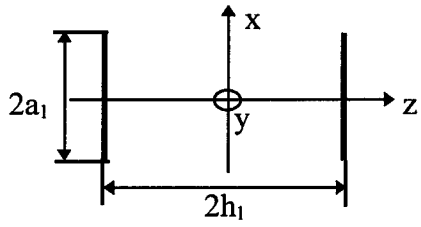

Fig. 2. Equivalent open resonator with rectangular mirrors.

If the fields in the resonator are produced by plain waves propagating with small angles to the axis OZ, the fields of corresponding TE modes can be expressed in the following form:

$$\begin{pmatrix} \vec{E} \\ \vec{H} \end{pmatrix} = \mathrm{Re}\begin{pmatrix} ik\,\mathrm{rot}\vec{\Pi}_{TE} \\ \mathrm{grad}\,\mathrm{div}\vec{\Pi}_{TE} + k^2\vec{\Pi}_{TE} \end{pmatrix} e^{-i\omega t}, \qquad (1)$$

where $\vec{\Pi}_{TE} = \Phi\vec{e}_y$, $k=\omega/c$,

$$\Phi = 2i\sum_{u=0}^{1}\sum_{v=0}^{1}\sum_{q,m,n} e^{i\pi(q(-1)^v z/2h_1 - p)}\, i^{2\{(q-1)/2\}}\Phi_{u,v,n},$$

$$\Phi_{u,v,n} = Ae^{ik_x m(-1)^u x} f_{u,m} f_{v,q} f_n(y),$$

$$f_{u,m} = -(1-u-(-1)^m u)(-1)^{[(n-1)/2]}/2i^{n+1},$$

$$f_n(y) = \begin{cases} \cos(nk_y y), & n = 1,3,5\ldots \\ \sin(nk_y y), & n = 2,4,6\ldots \end{cases}, \qquad M_{a,b} = \sqrt{\frac{2k}{h_1}(a_1^2 b^2)},$$

$$k_{a,b} = \frac{\pi/2}{(a_1,b)(1+\eta(1+i)/M_{a,b})}, \qquad \eta = -\zeta(-0.5)\pi^{-0.5} \approx 0.824,$$

$p_{a,b} = \frac{(\pi/4)(m^2, n^2)}{(M_{a,b} + \eta(1+i))^2}$, $p=p_a+p_b$, $\zeta(z)$ is Riehmann's Zeta function.

To find the potential function for the waveguide it is necessary to make a transition from the standing wave to the traveling one, to make a transformation from local frame xoz (see Fig. 2 corresponding to each half a period) to the waveguide frame XOZ (Fig. 1) and to impose Flouqet condition of periodicity. The transformation is valid under the following conditions:

$\lambda_s << \lambda_w$, $\pi p'' << 1$ and $h_1 = h/\sin\varphi$, $a_1 = a\sin\varphi$, (2)

where $p = p' - ip''$.

After Fourier expanding of the potential function on the period λ_w one can derive:

$$\Phi = Ae^{ik_Z Z}\sum_{q_w} C_{q_w} e^{iq_w k_w Z}, \quad C_q = \sum_{u,m,n} f_n(y) f_{u,m} B^{(q)}_{u,m,n}, \quad (3)$$

where $k_Z = (k - 2k_w p'\cos\varphi)\cos\varphi - ik_w p''$, $q_w = 0,1,2,3...$,

$$B^{(q)}_{u,m,n} = \sum_{\pm} \left\{ e^{i(k_{cu}X - p'3\pi/2)} S\left(\frac{\pi}{2}\left(\frac{k_{su}}{k_w} \mp q_w\right)\right) \times \exp\left[\pm i\left(k'_Z X \mathrm{tg}\varphi + \frac{\pi}{2}\left(p' + \frac{k_{su}}{k_w} \mp q_w\right)\right)\right] \right\},$$

$k_{cu} = k_{am}(-1)^{u+1}\cos\varphi$, $k_{su} = k_{am}(-1)^{u+1}\sin\varphi$,

$S(x) = \sin(x)/x$, $k_w = 2\pi/\lambda_w$.

3 BASIC RELATIONSHIPS

One can see from (3), that the Fourier coefficient C_{q_w} is a function of coordinate X due to wave front inclination. With taking into account condition $\lambda_s << a,b$ the dependency is weak at small glancing angles $\varphi << 1$:

$(k_Z' X \mathrm{tg}\varphi)^2 << 1$, or $(\varphi X k)^2 << 1$ (4)

If the angle φ is small, substantial contribution in Φ give the following terms: $q_w = 0$, $q_w = $ odd. We consider below only resonance acceleration, i.e. $q_w = 1,3,5,...$.

Phase velocity related to the speed of light follows simply from (3):

$$\beta_{ph} = \left(q_w \frac{k_w}{k} + \left(1 - 2\frac{k_w}{k} p'\cos\varphi\right)\cos\varphi\right)^{-1}.$$

Then for $\gamma >> 1$ we have the following condition of resonance:

$$\frac{\lambda_w}{\lambda_s} = \frac{q_w + 4p'}{2\sin^2(\varphi/2) + \gamma^{-2}/2} \quad (5)$$

One can obtain from (5) for $\gamma^2\varphi^2 >> 1$, $\varphi << 1$ and M_a, $M_b >> 1$:

$\lambda_w/\lambda_s \approx 2q_w/\varphi^2$ (6)

Note, that (6) is equivalent to analogous condition (2) in [1] when $\varphi \to \pi r_w\sqrt{2}/\lambda_w << 1$. From (6) one can estimate the tolerance on the most critical parameter φ: $\Delta\varphi/\varphi << 1/2q_w$.

For the practical situation, when $a - \lambda_w/4 << a$, we have from (6) and (2) the following important rule:

$N_{fx} = q_w/2$,

where $N_{fx} = M_a^2/8\pi$ is the Fresnel number for XOZ plane.

If M_a, $M_b >> 1$ and waist of the incident laser beam is matched with the mirror dimensions a_1, b (analogously to [2,3]), we can assume, that the dominant propagating mode is m=1, n=1. Then the power flow through the waveguide is:

$$P = P_0 e^{-2k''_Z Z}, \text{ where} \quad (7)$$

$$P_0 = |A|^2 (k^2 - \frac{k_a^2 + k_b^2}{2}) a_1 b \frac{k^2 - k_b^2}{2Z_0}, \quad k''_Z = k_w p'', \quad Z_o = 120\pi\Omega.$$

For the lowest dominant mode we obtain from (1,3) the following expression for the accelerating field amplitude:

$$E_a = -iAB^{(q)}_{1,1,1} k k'_Z \mathrm{tg}\varphi \cos(k_{s1})\cos(k'_Z \mathrm{tg}\varphi \Delta X), \quad (8)$$

where $\Delta X = X - X_o$, $X_o = \frac{\pi(1-p')}{2k'_Z \mathrm{tg}\varphi} \approx \frac{1}{4}\sqrt{\frac{\lambda_w \lambda_s}{2q_w}}$ defines the optimal transverse position for the particle beam centroid.

In order to remove the details of the specific accelerator mechanism let us define the coupling strength g_c as the ratio between the local acceleration gradient E_a and vacuum electric field $\sqrt{2Z_0 P_0 / S_0}$ of the focused laser beam (here $S_0 \approx 4a_1 b$). Under the conditions above we have from (7,8):

$$g_c \approx 4\varphi / q_w = \sqrt[4]{2\lambda_s / q_w \lambda_w}. \quad (9)$$

Note, for our scheme g_c is equal approximately to E_a/E_e defining the ratio between accelerating field and surface field.

Power attenuation length L_{att} can be defined from (7) provided ohmic losses are negligible:

$$L_{att} = 1/2k_w p'' \approx \frac{\lambda_w}{2\pi^2 \eta} \frac{M_a^3 M_b^3}{M_a^3 + M_b^3}. \quad (10)$$

4 PERFORMANCE ESTIMATIONS

It is seen from (10), that power losses are proportional to $\lambda_w^{-1} q_w^{-3/2}$, whereas the coupling strength scales as $\lambda_w^{-1} q_w^{-1}$. Hence, to use the advantage of long resonance acceleration we should choose higher harmonics. However, as q_w increases tolerances becomes more stringent. Estimated performance parameters of the scheme are presented in the Table 1 for $a_1 \approx b/3$, $a \approx \lambda_w/4$, wavelength $\lambda_s = 10\mu$m and surface field $E_c = 5$ GV/m.

5 DISCUSSION

Since the angle φ is small for short wavelengths, ohmic losses of the TE modes can be considerably reduced with the help of special corrugations made on the mirror surface (having period $\leq \lambda_s/2$ and depth $(0.2 \div 0.5)\lambda_s$) or proper dielectric coating (see [2,5]). Besides, the radiation losses defined in (10) on the basis of diffraction in resonator (Fig. 2) for waveguide are actually less due to interference effect [4]. The diffraction losses can be reduced further by enhancement of both the effect with

proper choose of the relationships between λ_s, λ_w, a,φ and figure of merit Q for single cell due to mirror curvature optimization.

In general case input coupling can give a combination of TE and TM mode [3]. Note, for the TM mode one can derive from (3), that coupling strength is less ($g_c \approx 4\varphi^2/q_w$) and $X_o = 0$. To solve this multi-mode problem further study is necessary.

The main disadvantage of the scheme compared to an Open Iris Loaded Waveguide (OILS, [6]) is dependence of the acceleration rate on the particle transverse coordinate (3). This imposes rather stringent condition for the both particle beam radius and beam alignment tolerance that practically should not exceed several wavelengths (see (4)).

Table 1. Performance parameters for the rectangular mirror waveguide.

q_w	3	5
λ_w, cm	1.2	4
φ, mrad	70	50
2h, mm	0.43	1.0
g_c	0.06	0.025
M_a	6.1	7.9
L_{att}, cm	12.2	80
$I_c=P_0/S_0$, W/cm^2	$4.5\cdot10^{16}$	$1.3\cdot10^{17}$
P_0, W	$2.5\cdot10^{10}$	$4\cdot10^{11}$
R_s, MΩ/m	0.6	0.12
Q	$7.6\cdot10^4$	$5\cdot10^5$
E_a, GeV/m	0.35	0.25

6 SOME VARIANTS

To reduce the diffraction losses limiting the acceleration section length one can use cylindrical or spherical mirrors (see Fig. 3).

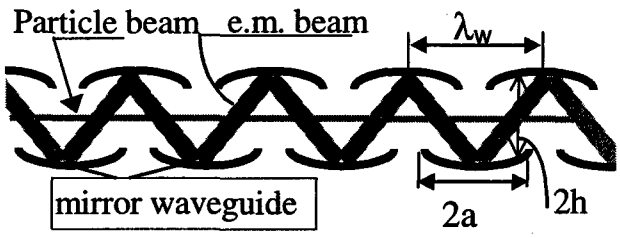

Fig. 3. Accelerating waveguide with reduced losses.

One can provide a resonance mechanism in OILW by means of special sections, where the interaction between particle beam and field is negligible (see Fig. 4). In this sections the propagating mode is converted into A-mode of spheroidal cavity [4]. In the scheme $\lambda_w/2$ lies between $L_s/2$ and L_s (slippage length). An average acceleration rate is less then that local value for OILW (up to twofold).

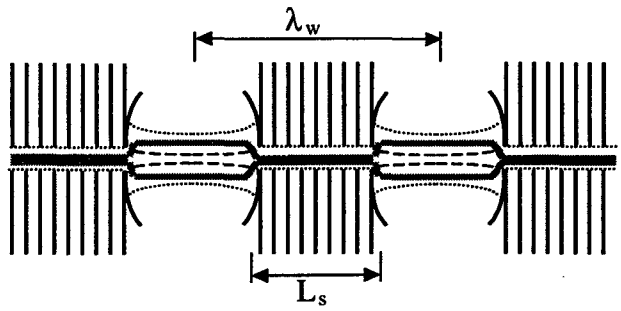

Fig. 4. Modified OILW to provide resonance acceleration. Gray thick lines show flow of primary power. Dotted lines show caustics.

7 CONCLUSION

One can outline the following attractable features of the acceleration scheme considered:

– Relative simplicity for manufacturing of the waveguide composed by flat mirrors and suitability for acceleration of flat beams.

– The final energy gain is limited by attenuation length rather than slippage length, because it is resonance acceleration.

– Tapering is not necessary to provide synchronism between relativistic particles and accelerating harmonic.

– Axicon scheme is not required to couple the laser power in the structure.

– Synchrotron radiation losses are very low due to low equivalent undulator strength $K_w \leq 1$[1].

ACKNOLEDGMENTS

The author would like to thank Dr. David Yu for deep interest and many helpful discussions.

REFERENCES

[1] A.V. Smirnov, Far-Field Acceleration Scheme, Proc. of the 6th European Particle Acceleration Conf., Stockholm, 22-26 June, 1998, p. 824.

[2] W. Zakowicz, J. of Apl. Phys. 55 (1984) 3421.

[3] K.V. Lotov. Driver Channeling in Laser Wakefield Accelerator. Preprint Budker INP 98-40, Budker Inst. Of Nuclear Physics, Novosibirsk, 1998

[4] L.A. Vainshtein, Open resonators and waveguides, 'Sov. Radio', Moscow (1966).

[5] C. Dragone, IEEE Trans. on Microwave theory and and Techniques, V. MTT-28, N7 (1980) 704

[6] M. Xie, Laser Acceleration in Vacuum with an Open Iris-Loaded Waveguide, to be published in the Proceedings of the Particle Acceleration Conf., Vancouver, 12-16 May, 1997, p. 660

CONSTRUCTION AND TESTING OF AN 11.4 GHz DIELECTRIC STRUCTURE BASED TRAVELLING WAVE ACCELERATOR

Peng Zou, Wei Gai, R. Konecny and T. Wong
Argonne National Laboratory, Argonne, IL 6039, USA

Abstract

One major challenge in constructing a dielectric loaded travelling wave accelerator powered by an external rf power source is the difficulty in achieving effcient coupling. In this paper, we report that we have achieved high effiency broadband coupling by using a combination of a tapered dielectric section and a carefully adjusted coupling slot. We are currently constructing an 11.4 GHz accelerator structure loaded with a permitivity=20 dielectric. Bench testing has demonstrated a coupling efficiency in excess of 95% with bandwidth of 600 MHz. The final setup will be tested at high power at SLAC using an X-band klystron rf source.

1 INTRODUCTION

The proposed use of rf driven dielectric based structures for particle acceleration can be traced to the early 50's [1]. Since then, numerous studies have examined the use of dielectric materials in accelerating structures[2,3]. Advantages and potential problems of using dielectric material are discussed in the references. More that recent development of high dielectric constant (ε ~ 20 - 40), low loss materials (Q~ 10,000 - 40,000) warrant a new look at the idea [4, transtech].

One faces a challenging problem when building an actual dielectric accelerator because outer diameter of the dielectric is much smaller than the rectangular waveguide which couples the external rf. Therefore, realising impedance matching becomes a difficult tasks. There is also no technical references treating this subject. We found that by using a combination of side coupled slots and a tapered dielectric near the coupling slots, one can efficiently couple the rf from the rectangular waveguide to the dielectric waveguide. In the prototype 11.4 GHz dielectric loaded accelerator as shown in Figure 1, we have achieved > 95 % power coupling.

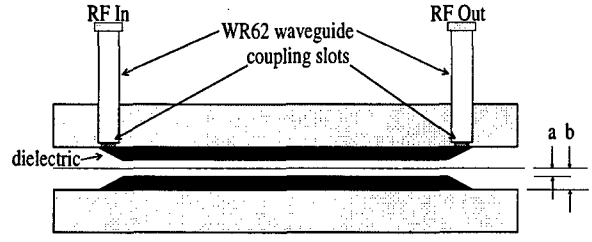

Figure 1. Schematic diagram of a dielelectric loaded travelling wave accelerator.

2 A TRAVELLING WAVE DIELECTRIC LOADED ACCELERATING STRUCTURE BASICS

The dielectric travelling wave accelerator has a simple geometry. Considering a cylindrical structure partially filled with dielectric material (ε) with inner radius a, outer radius b and conducting wall on the outside. There are also two ports on the side for RF coupling purposes, as shown in Figure 1. The axial electric fields inside the structure can be solved for exactly as

$$E_z^{(1)} = E_0 I_0(kr) e^{i(k_z z - \omega t)}$$
$$E_z^{(2)} = [B_1 J_0(s_1 r) + D_1 N(s_1 r)] e^{i(k_z z - \omega t)} \quad (1)$$

Here E_0, B_0 and D_1 are the field amplitudes in the region 0 (vacuum) and 1 (dielectric) respectively and are related by boundary conditions,and

$$k^2 = \frac{\omega^2}{c^2}(1-\beta^2)$$
$$s^2 = \frac{\omega^2}{v^2}(\beta^2\varepsilon - 1) \quad (2)$$

where $\beta c = v = \omega/k$ is phase velocity of the wave travelling inside the tube: β determines the synchronism of the wave and the accelerated particles. By properly choosing *a, b* and ε, one can adjust the phase velocity accordingly. Thus this proposed scheme works not only for acceleration of electrons which typically has phase velocity ~ *c*, but also for low phase velocity particle acceleration, such as heavy ions. The transverse electric field can be written as

$$E_r = \frac{i}{\frac{\omega}{v}(\beta^2\varepsilon - 1)} \frac{\partial E_z}{\partial r} \quad (3)$$

and the magnetic field $H_\phi = \varepsilon E_r$ everywhere inside the tube. By matching the boundary conditions at a and b (E_z and D_r continous), all the field components can be calculated accordingly.

The stored energy per unit length U in the tube is the sum of contributions from both vacuum and dielectric regions, and can be expressed as

$$U = \frac{1}{2}\sum_{0,1}\pi\int(\varepsilon\varepsilon_0 E^2 + \mu_0 B^2)rdr = E_0{}^2 u \quad (4)$$

where u is a geometric factor which depends solely on the structure geometry and dielectric constant. For a given RF power, the axial electric field in the center region of the tube can be expressed as

$$E_0 = [\frac{P}{u\beta_g c}]^{\frac{1}{2}} \quad (5)$$

where β_g is the group velocity. The dielectric loss plus wall loss per unit length is then found from

$$\eta = \frac{2\pi\delta f U_{out}}{v_g(U_{out}+U_{in})} + \frac{R_s \oint_{Wall} ds < H^2 >}{\omega U} \quad (6)$$

The electric fields in the vacuum region described by equation 1 and 3 have very interesting chraracteristics. When $k \to 0$, *i.e.,* the phase velocity of the wave is c, E_z is constant in r. This implies that there are no focusing and de-focusing forces for a relativistics particle travelling inside the vacuum chamber. This is critical for emittance preservation in the linacs, particularly for high brightness electron gun development.

3 CONSTRUCTION AND BENCH TESTING OF THE 11.4 GHZ STRUCTURES

We have developed a design for an X-band structure (11.4 Ghz) using the parameters given in table I. Choice of the dielectric is MgCaTi compound which has dielectric constant of 20. And this material can be readily obtained from commercial vendors. The group velocity for the NLC design is in the 0.03 c ~ 0.05c range [5]. Thus dielectric loaded structure is having a comparable shunt impedence and group velocity to a conventional X-band structure as indicated in the table below. As shown above, one of the interesting characteristics of this structure is that the frequency of the HEM11 mode (first deflection mode) is lower than that of the acceleration mode. Because the deflection force is a function of sin(kz), this implies very different and improved conditions for the single bunch BBU problem compared to conventional structures where the HEM11 is always higher in frequency than the accelerating TM01 mode.

Table : Dimensions and physical properties of the 11.4 GHz dielectric tube

Material	MgCaTi
ε (diele. const.)	20
Tapered Angle	8°
Loss tangent δ	10^{-4}
Inner Radius a	0.3 cm
Outer Radius b	0.456 cm
HEM11	9.96 Hz
group velocity	0.057 c
Attenuation	4 dB/m
Power needed (10MV/m)	2.6 MW

The RF coupling scheme we used here is similiar to the side coupled method used for conventional disk-washer RF cavities. Impedance matching of the coupling slotsis more difficult in the high ε dielectric case because the outer radius of the dielectric tube is much smaller than the waveguide.

Basically speaking, one would like to obtain maximum RF transmission through the two coupling slots. In order to achive high efficiency coupling, the dielectric tube near the coupling slots is tapered. The tapered angle was chosen to be 8° for initial convenience. This tapered section serves as a broad band quarter wave transformer for impedance matching. No other angles were tested, but it is not expected that the taper angle is critical. The detailed configuration of the tapered dielectric structure and coupling slots are shown in Figure 1.

A 25 cm long prototype structure was constructed with the parameters in table 1. The dielectric materials was obtained from Trans Tech. The coupling slot dimensions are 4.7 mm × 5.69 mm. By careful adjustment of the coupling slots and monitoring the S-parameters using an HP8510C network analyzer, we have achieved a reflection coefficeint S11< - 13 dB and transmission S21 > -1.5 dB @ 11.43 GHz as shown in Figures 2 and 3 respectively.

We plan to continue engineering studies of this accelerating structure with improved RF coupling and mechanical fixture to allow operation in vacuum, eventually leading to a high power test at SLAC of a demonstration accelerator section to resolve practical issues such as breakdown voltage, thermal heating etc. With 100 MW power, we can test this structure at a 60 MV/m gradient.

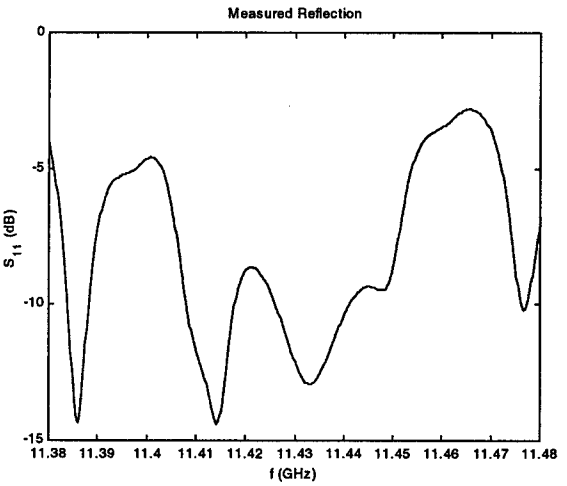

Figure 2. S11 for the optimally coupled waveguide results.

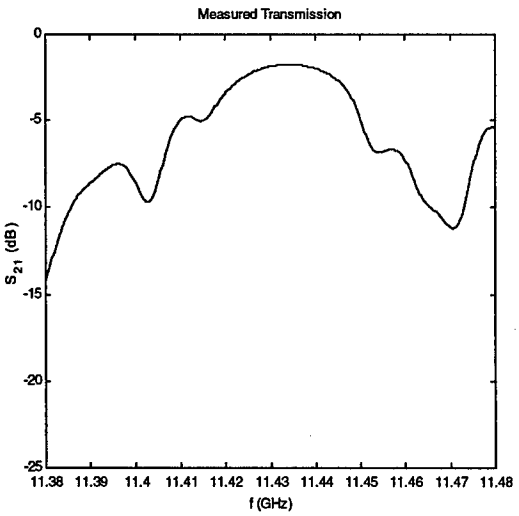

Figure 3. S21 between two optimally coupled 2 ports

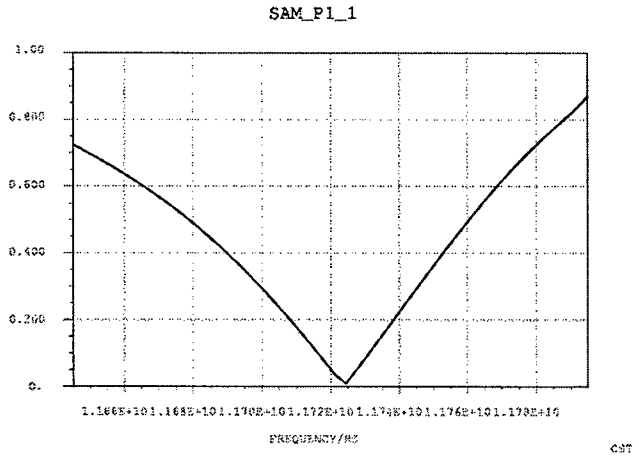

Figure 4. Calculated S11 parameter using MAFIA At 11.7 GHz, the S11 is almost 0.

4 NUMERICAL SIMULATIONS OF THE COUPLING PORT USING MAFIA

In order to verify the coupling method developed experimentally, we have used MAFIA [6] to simulate the parameters described in the last section. As expected, the simulation process was tedious and time consuming. Due to the relatively small size of the coupling slot, special attention has to be given for mesh size in the neighborhood of the slot.

Figure 4 shows the calculated S11, although it is peaked at 11.7 GHz for the given geometry, it does give qualitative agreement with the bench top measurement. In the calculation, with assumption of no dielectric loss and no wall loss, we have achieved S21 of near 1.0 as shown in Figure 5. In comparison with −1.6 dB measurement in Figure 3 where the wall losses dominated.

5 SUMMARY

In summary, we have constructed and studied a prototype 11.4 GHz dielectric loaded waveguide. Careful engineering considerations were implemented. We have achieved efficient coupling from port to port. A demonstration accelerator for high power test has been designed and is under construction. Our goal is to achieve 50 – 100 MV/m so it can be used as a viable alternative for the accelerating structures. Some pratical issues concerning high power breakdown and thermal heating will be answered through careful experimental studies and new materials development.

This work is supported by DOE, High Energy Physics Division under contract No. W-31-109-ENG-38.

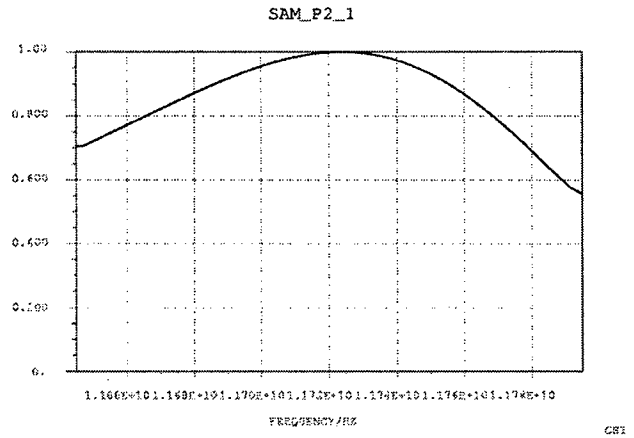

Figure 5. Calculated S21 corresponding to the parameters in the Figure 5. Almost perfect coupling was achieved here.

6 REFERENCES

[1] G. Flesher and G. Cohn, AIEE Transactions, **70,** 887 (1951)
[2] B. Zhang et. al., in Proceedings of 7th Advanced Accelerator Worksop, AIP Proceedings No. 398, p. 618(1996).
[3] W. Gai, R. Konecny and J. Simpson in Proceedings of 1997 Particle Accelerator Conference, p. 636-638, Vancourver, May 1997
[4] Trans-Tech., Catalog, 5520 Adamstown, Adamstow, MD 21710T.
[5] SLAC repor 474, 1996
[6] MAFIA Version 4.0, Gesellschaft fur Computer-Simulationstechnik, Lauteschlagerstrabe 38, D-64289, Darmstadt.

WAKEFIELD EXCITATION IN MULTIMODE STRUCTURES BY A TRAIN OF ELECTRON BUNCHES*

J.G. POWER#, M.E. CONDE, W. GAI, R. KONECNY, and P. SCHOESSOW
Argonne National Laboratory, Argonne, Illinois 60439

Abstract

We discuss wakefield excitation and propagation in dielectric structures, particularly concentrating on the case of multiple drive beam excitation in multimode structures. We emphasize calculations of the energy loss of the drive bunch train, the amplitude of the wakefield, and the relation between power flow and stored energy in the dielectric wakefield device. We show that for a collinear multimode structure the amplitude of the wakefield generated by a bunch train is less than or equal to the wakefield generated by a single bunch of the same total charge. Furthermore, the transformer ratio, R, is shown to be always less than 2, even in the multiple drive beam case. Plans for an experiment to measure wakes in a multimode structure at AWA are presented.

1 INTRODUCTION

The efficiency of a *collinear* wakefield accelerator scheme, *i.e.* one for which the drive and witness beams follow identical trajectories through the accelerator system is limited by the *transformer ratio* R. Under very general assumptions $R < 2$, where R is defined as the ratio of the maximum energy gain behind the drive bunch to the maximum energy loss inside the drive bunch [2]. There have been a number of techniques studied to enhance the transformer ratio by violating one or more assumptions of the wakefield theorem: asymmetric drive beams [3], noncollinear drive/test beams [4] and more [5,6].

A recent article [1] has described a multimode dielectric structure driven by a bunch train. The authors make two claims. One, a small transformer ratio enhancement for the single bunch case is obtained through the use of a superposition of multiple modes. Two, a larger effect (than expected from linear scaling with total drive charge) is predicted in the case of multiple drive bunches and attributed to a process described as "stimulated emission" of Cherenkov radiation. We have reanalyzed the problem of multimode structure wakefields using the same assumptions as the authors of reference [1]. We have concluded that there is no enhancement in the transformer ratio beyond that expected in the linear theory. Multimode dielectric structures, however, are of some scientific interest. We are currently preparing an experiment at the Argonne Wakefield Accelerator [7] to study wakefields produced by a bunch train in one of these devices.*#

2 MULTIPULSE, MULTIMODE DEVICES

2.1 Direct Solution of the Wave Equation

One can determine the wakefield excitation of any cylindrically symmetric structure [9] by first finding the point charged particle (Green Function) solution,

$$G_z(r,z) = \sum_{n=1}^{\infty} G_n(r)\cos(k_n z) \tag{1}$$

For a series of M bunches separated by a distance, λ, (a "bunch train") the charge distribution can be expressed as,

$$f(z) = \sum_{m=1}^{M} f_m(z - m\lambda) \tag{2}$$

The total wakefield excited by a bunch train at any point z (which may be inside a bunch) is obtained by taking the convolution of the Green function [1] over the charge distribution [2],

$$W_z(r,z) = \int_{-\infty}^{z} \sum_{m=1}^{M} f_m(z - m\lambda)\left\{\sum_{n=1}^{\infty} G_n(r)\cos[(k_n z - z')]\right\}dz' \equiv \sum_{m=1}^{M} W_{zm}(r,z) \tag{3}$$

2.2 Conservation of Energy

For the m^{th} bunch in the train, the energy loss per unit distance traveled (U_m) can be expressed as,

$$U_m = \int_{-\infty}^{\infty} dz f_m(z - m\lambda) \int_{-\infty}^{z} dz' f_m(z - m\lambda) G(r, z - z') + \int_{-\infty}^{\infty} dz f_m(z - m\lambda) \sum_{m'=1}^{m-1} W_{zm}(r,z) \tag{4}$$

In (4) the total energy loss is comprised of two terms: that due to the m^{th} bunch (first term) and that due to the previous m-1 bunches (second term). The stored energy per unit length $\left\{\frac{1}{2L}\int_{z}^{z+L} dz \int_{s} ds(\varepsilon \vec{E}^2 + H_\varphi{}^2)\right\}$ is

$$U = K\left(\sum_{m=1}^{M}\sum_{n=1}^{\infty} \eta_{nm} E_n\right)^2 = K\left(\sum_{m=1}^{M} W_m\right)^2 \tag{5}$$

where η_{nm} is a form factor depending on the detailed bunch distribution, W_m is the peak wakefield left behind by the m^{th} bunch and K is a geometric factor that can be determined either through direct integration or by the method shown in the following section.

* This work is supported by DOE contract
# Email: jp@hep.anl.gov

By energy conservation, the stored energy per unit length (5) is equal to the sum of the energy loss by each bunch (4) plus the energy flow (P) of the wave.

$$U = K\left(\sum_{m=1}^{M} W_m\right)^2 = \sum_{m=1}^{M} U_m + \sum_{m=1}^{M} \frac{P_m}{c} = \sum_{m=1}^{M} U_m\left(1+\frac{v_g}{c}\right) \quad (6)$$

where the result $U_m = P_m / v_g$ [10] has been used.

Using (4) to calculate the energy loss of the first bunch, one can use (6) to calculate the wakefield of subsequent bunches (as done in ref. [1]). However, one has to evaluate the right hand side of (6) carefully, because U_m depends not only on the self wakefield, but also on the wakefield generated by previous bunches; more importantly, **it has strong dependence on the detailed distribution of the mth bunch.**

2.3 Gaussian Bunch Train Example

We consider wakefields generated by a train of M gaussian bunches in a perfectly harmonic structure (i.e. where the modes are equally spaced in frequency).

$$f(z) = \frac{N}{(2\pi)^{1/2}\sigma_z}\sum_{m=1}^{M} e^{-\frac{(z-m\lambda)^2}{2\sigma_z^2}} \quad (7)$$

The energy loss by the 1st (m =1) bunch (4) is

$$U_1 = \frac{1}{2}\sum_{n=1}^{\infty} G_n \exp(-(k_n\sigma_z)^2 \quad (8)$$

The wakefield behind this bunch ($z >> \sigma_z$) is then easily obtained (3) as

$$W_1(z) = \sum_{n=1}^{\infty} G_n \exp(-\frac{(k_n\sigma_z)^2}{2})\cos k_n z \quad (9)$$

For a perfectly harmonic structure, at $z=\lambda$, cos ($k_n z$) =1. Therefore, the maximum wakefield left behind at $z=\lambda$ is,

$$W_1 = \sum_{n=1}^{\infty} G_n \exp(-\frac{(k_n\sigma_z)^2}{2}) \quad (10)$$

Using equation 6, we find K as

$$K = \frac{\frac{1}{2}\sum_{n=1}^{\infty} G_n \exp(-(k_n\sigma_z)^2}{\left[\sum_{n=1}^{\infty} G_n \exp(-\frac{(k_n\sigma_z)^2}{2})\right]^2}\left(1+\frac{v_g}{c}\right) \quad (11)$$

Now we calculate the wake amplitude after the 2nd bunch. The energy loss of the second beam, U_2, is

$$U_2 = \frac{1}{2}\sum_{n=1}^{\infty} G_n \exp(-(k_n\sigma_z)^2) + \sum_{n=1}^{\infty} G_n \exp(-(k_n\sigma_z)^2) \quad (12)$$

Solving equation 6 for two bunches we now have $K(W_1+W_2)^2 = (U_1+U_2)(1+v_g/c)$. Using this result and equation 12 we have, $W_1 + W_2 = 2W_1$ and therefore,

$$W_2 = W_1 \quad (13)$$

In the same way, one can prove

$$W_2 = W_3 = \cdots = W_M \quad (14)$$

From above calculation, we conclude that the wakefield can be calculated using linear superposition (convolution of the Green function for a point particle over the charge distribution of the multiple bunches) or by conservation of energy. Both methods yield identical results; there is no transformer ratio enhancement in either the single or multiple bunch multimode devices.

3 DESIGN OF A MULTIMODE DIELECTRIC STRUCTURE

A multiple beam, multimode dielectric wakefield accelerator (M-DWFA) is designed for an experiment at the AWA using the analytic results for dielectric structure derived in reference [9]. The structure is a cylindrical dielectric waveguide (ε = 38.1) with an inner radius 0.5 cm, outer radius 1.44 cm and 60 cm in length. The AWA can transport a 10 nC beam through a 60 cm long tube with a 1 cm diameter hole. For the multiple beam experiment at AWA, the acceleration wavelength is designed to be 23.05 cm since λ_{rf} is 23.05 cm at 1.3 GHz. Successive drive bunches can then be located one fundamental wavelength apart in the M-DWFA.

4 EXPERIMENTAL SETUP

The AWA drive linac is configured to provide a collinear bunch train of 4 bunches, each with charge Q = 10 nC, bunch length, σ_z = 2 mm and energy spread σ_E/E = 1%. Each bunch must be placed so that the individual wakes left by each bunch adds constructively to the wake of the preceding bunch. For our experimental configuration, simulation show that the spacing between bunches must be accurate to within 1 mm out of 230.5 mm for appreciable constructive interference to take place.

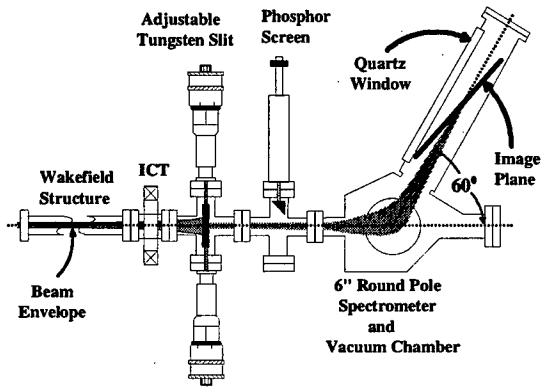

Figure 1: Energy Measurement System. The decelerated drive bunch train passes through a Tungsten slit, which is imaged through a 60^0 bend onto a phosphor screen.

This fact places a high demand on the AWA's energy measurement system. A new imaging spectrometer was developed [Fig. 1] to provide improved momentum

resolution over a wider range while reducing the sensitivity to beam jitter.

5 SIMULATION OF THE EXPERIMENT

Before a witness beam can be accelerated, the 4 drive beams must be properly positioned. To this end, we designed an experiment to accurately measure the energy spectrum of the 4 drive beams. Using the method of [9] and the expression for the wakefield of a bunch train from [8] the computed wake potential as a function of z (the distance behind the first bunch) is shown

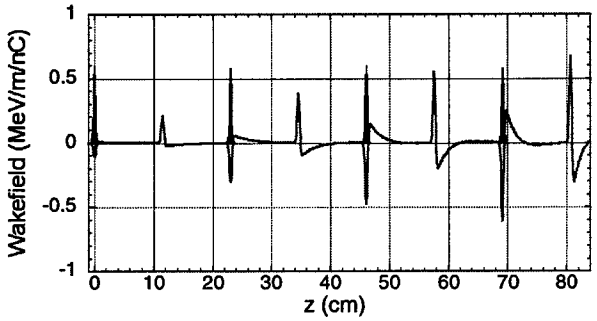

Figure 2: The wake excited by 4 monochromatic drive beams. (Beam moving right to left.)

in Fig. 2. Using the results displayed in Fig. 2 one may easily extract the energy spectrum generated by the 4 monochromatic drive beams. Projecting the wake experienced by each particle within the bunch onto the energy axis and scaling by the appropriate values of L and Q gives this spectrum. The total energy spectrum is then computed by taking the convolution of the monochromatic energy spectrum with the drive bunch's energy distribution function, which is measured to be approximately Gaussian in shape. For tube length L = 59.87 cm, charge Q = 10 nC, energy spread σ_E/E = 1% and initial drive beam energy of 14 MeV we plot the total energy spectrum in Fig. 3.

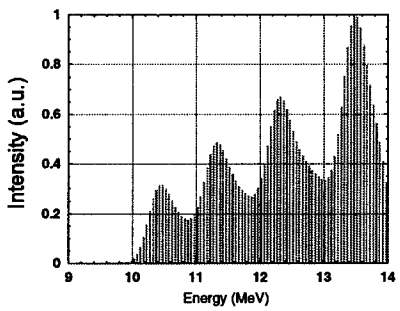

Figure 3: Energy spectrum of bunch train after exiting the multimode structure

The multimode structure may have tighter manufacturing tolerances than the single mode device because of the requirement that the various modes constructively interfere at the appropriate delays corresponding to the spacing of the bunch train. An error in either ε or the geometry leads to a change in the accelerating wavelength. We examine as typical the case of a maximum deviation from the nominal value of the permittivity. Given the vendor's specification of ε = 38.1±2% we calculate the wakefield excited by the same bunch train as above but with ε = 37.34 (38.86) corresponding to -2% (+2%) out of tolerance. This results in a shortening (lengthening) of the acceleration wavelength by 2.5 mm (1.5 mm). The effect of this is that the drive bunches arrive late in the structure causing the wakefields of the individual bunches to begin to destructively interfere with each other. However, the bunch train can easily be adjusted to accommodate the errant wavelength.

A more serious problem is that ε may not be constant over the frequency range excited causing the nearly harmonic spectrum and hence the constructive interference to be disrupted.

6 SUMMARY

We have calculated the wakefields in multimode dielectric structures excited by a bunch train. We found no enhancement to the transformer ratio when a single beam drives this structure. We found no wakefield enhancement for this device over a single beam with the same total charge as the drive train. Our calculations show that the method of linear superposition and the energy conservation method both predict the same wakefields. This type of wakefield device may still have good breakdown properties due to its relatively short rf pulse.

7 REFERENCES

[1] T-B. Zhang, J. L. Hirshfield, T. C. Marshall, B. Hafizi, Phys. Rev. **E56** 4647 (1997)

[2] P. B. Wilson, Proc. of the 13th SLAC Summer Inst. on Particle Physics, SLAC Report No.296, p. 273, E. Brennan ed., (1985)

[3] K.L. Bane, P. Chen, P.B. Wilson, IEEE Trans. Nucl. Sci. **32** 3524 (1985)

[4] P. Schoessow, M. E. Conde, W. Gai, R. Konecny, J. Power, J. Simpson, J. Appl. Phys **84** 663 (1998)

[5] A. G. Ruggiero, P. Schoessow, J. Simpson, Proc. of Symp. on Advanced Accelerator Concepts, Madison, WI, Aug 21-27, 1986, F. Mills ed., AIP Press (1986)

[6] J. Rosenzweig, P. Schoessow, B. Cole, W. Gai, R. Konecny, J. Norem, J. Simpson, Phys. Rev. **A39** 1586 (1989)

[7] URL: http://www.hep.anl.gov/awa/awa/awahome.htm

[8] J.G. Power, W. Gai, P. Schoessow, submitted to Phys. Rev. E. A preprint is also available on the web: http://www.hep.anl.gov/awa/awa/pubs.htm.

[9] M. Rosing, W. Gai, Phys. Rev. **D42** 1829 (1990)

[10]J.D.Jackson, Classical Electrodynamics, J.Wiley 1974

SLAB SYMMETRIC DIELECTRIC MICRON SCALE STRUCTURES FOR HIGH GRADIENT ELECTRON ACCELERATION*

P. V. Schoessow,
Argonne National Laboratory, Argonne, IL 60439
J. B. Rosenzweig,
UCLA Department of Physics and Astronomy,
405 Hilgard Ave., Los Angeles, CA 90095

Abstract

A class of planar microstructures is proposed which provide high accelerating gradients when excited by an infrared laser pulse. These structures consist of parallel dielectric slabs separated by a vacuum gap; the dielectric or the outer surface coating are spatially modulated at the laser wavelength along the beam direction so as to support a standing wave accelerating field. We have developed numerical and analytic models of the accelerating mode fields in the structure. We show an optimized coupling scheme such that this mode is excited resonantly with a large quality factor. The status of planned experiments on fabricating and measuring these planar structures will be described.

1 INTRODUCTION

Advances in the technology of lasers have led to increased interest in their potential applications for accelerating particles. Plasma beat wave[1] and laser wakefield[2] acceleration methods use laser radiation to drive a plasma wave with luminal phase velocity. The longitudinal electric fields in this plasma wave are in turn used to accelerate an electron beam. Inverse Cherenkov[3] and inverse free electron laser [4] acceleration techniques use light optics or magnetic fields respectively to achieve an electric field component parallel to the beam direction from the transverse electric field in the laser pulse. We have proposed a class of resonant dielectric loaded planar structures[5] capable of producing GeV/m accelerating gradients which are driven by laser radiation much as a conventional rf cavity is driven by microwave power from a klystron.

The basic idea is the use of a dielectric microstructure, analogous to a Fabry-Perot resonator, consisting of a two parallel dielectric planes separated by a vacuum gap and with a partially transmissive coating on the exterior (see Figure 1). Some parameters of the structure are assumed to vary periodically in the beam direction at the wavelength of the illuminating laser. A standing wave with an appropriate phase velocity forward component is induced in this periodic structure by the laser pulse, which in turn accelerates the beam. The laser pulse is swept along the surface of the structure such that the cavity is filled only in the neighborhood of the beam. The relatively low Q of these devices (100-1000) and correspondingly short fill times (~0.5 ps) allows gradients of 1 GeV/m to be obtained before breakdown becomes problematic[9]. The beam aspect ratio is highly asymmetric; the ribbon beam-planar structure configuration is advantageous in that dipole deflecting modes are suppressed[6], analogous to the vanishing of the transverse deflection for TM0n modes in conventional structures.

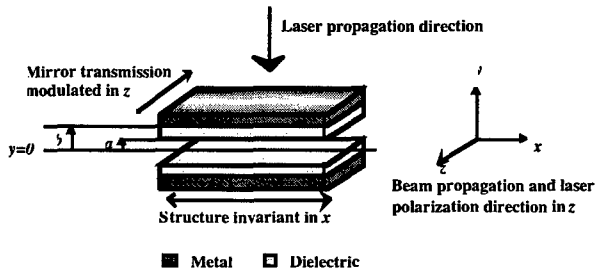

Figure 1. Geometry of slab-symmetric, laser-excited, dielectric-loaded resonant accelerator structure.

A number of different methods have been investigated to introduce the necessary periodic variation in the structure geometry. The original paper in this area[5] suggested the use of a longitudinally modulated permittivity in the dielectric. While this was attractive from the point of view of construction and analysis (one could concievably generate the modulation by "writing" an interference pattern in a photorefractive dielectric with a second laser) it proved to be difficult to obtain good coupling of the laser energy to the accelerating field. More recent analyses have concentrated on using a spatially unvarying dielectric medium and modulating the transmittivity of the coating [7]. This approach was found to improve the laser coupling to the structure significantly but was found to yield uncomfortably large surface fields on the structure.

We discuss here some recent progress in the understanding of slab structure design. We have investigated the use of finite thickness conductive cladding on the structure, with a single coupling slot per period. With this geometry good coupling of laser energy to the accelerating fields can be obtained, while at the same time reducing the surface field/accelerating field ratio significantly over our previous results. The shape of the coupling slot is also seen to be important, in that the

0-7803-5573-3/99/$10.00@1999 IEEE.

introduction of a taper at the slot opening provides improved coupling over the case of a rectangular slot profile.

2 NUMERICAL RESULTS

In the study of these structures we have found it useful to rely on numerical solution of the Maxwell equations in slab geometry. We use a custom finite difference time domain code to inject and propagate the laser fields into the structure geomerty under study. The program implements periodic boundary conditions in z (the beam propagation direction) and absorbing boundary conditions in y (the laser propagation direction) to handle any reflected laser energy from the structure. The structure is assumed to be of infinite extent in the x-view. For a given structure geometry, the integration is continued until a steady state condition is reached. The structure is "tuned" numerically by adjusting one of its parameters (typically the dielectric constant) until the asymptotic stored energy is maximized. (In the laboratory one would tune the structure by changing a geometrical parameter like the vacuum gap size.)

We have analyzed a structure with dielectric thickness (b-a) equal to the vacuum gap (a =1.6 μm), period of 10.6 μm (corresponding to a commone CO_2 laser line), and dielectric constant $\varepsilon \cong 3.7$. The conductive cladding thickness in the simulation is 0.3 μm. The laser coupling and field strengths in the structure were studied as a function of the shape of the coupling slot. While not exhaustive, these calculations indicate a promising approach to the problem of coupling optimization. The following results are normalized to a peak laser electric field of 0.25 Statvolt/cm = 75 kV/m.

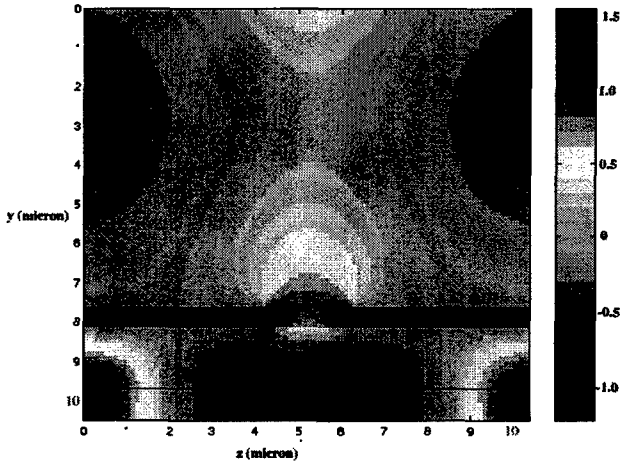

Figure 2. Pseudocolor contour map of E_z in the computational area for the tapered aperture structure. Laser radiation is incident from the top of the figure (y=0). The area depicted in solid black is the conductive cladding, and the thin black line indicates the dielectric-vacuum boundary.

In reference[7], the fields of a similar structure having an infinitesimally thick, sinusoidally modulated transmittivity outer cladding were computed. While reasonable coupling was achieved, it was also pointed out that the surface electric field on the mirror-dielectric interface was undesirably large, roughly twice the maximum field in the vacuum gap. The case of a *finite* thickness mirror with a rectangular aperture was studied for this paper. For a 2 μm slot width the corresponding peak surface field is 2.0 Statvolt/cm for a gap field amplitude of 1.06 Statvolt/cm. The largest surface fields in this device occurred at the exterior corners of the slot; this might be further improved by rounding the corners. (The present version of the simulation code cannot handle curved boundaries except via a stairstep approximation.) An increase in the coupling slot width to 3 μm produced slightly worse results with a surface field/gap field ratio of 1.9/0.87.

The effect of tapering the aperture of the coupling slot is shown in Figure 2. The surface field/gap field ratio is relatively small, 1.56/1.23, while the gap field strength is also a maximum for all similar device geometries. Stored energy and gap field strengths vs time are shown in Figure 3. From the energy history we can read off a fill time of 0.57 ps, corresponding to Q=102. As we have discussed previously[7], the fields in the vacuum gap are a superposition of Fabry-Perot-like (zero phase shift per period, providing no net acceleration) and accelerating (forward wave componet resonant with an ultrarelativistic particle) modes. The Fabry-Perot mode amplitude has been diminished to 20% of the accelerating mode amplitude in the present case, solely through through the periodicity of the coupling. This proportion seems to be about the most favorable we have been able to obtain.

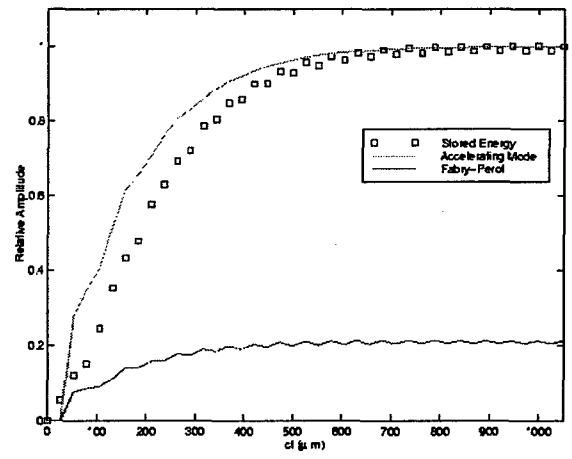

Figure 3. Fill curves for the tapered aperture structure. The fill time is 0.56 ps, corresponding to Q=102. The stored energy is normalized to its maximum value, while the accelerating and Fabry-Perot modes are shown relative to the accelerating field amplitude.

3 CONCLUSIONS

We have studied a class of dielectric loaded structures for laser acceleration which can potentially produce GeV/m gradients. We have given some consideration to questions of structure breakdown and preservation of beam quality. Resonant planar structures showing good coupling of laser radiation to the desired accelerating mode have been demonstrated numerically, with reasonable surface field/vacuum field strengths and quality factors commensurate with the requirements of a practical accelerator. These properties imply that the structure is a good candidate for further development as an accelerator, as it can be coupled well (it can be fully impedance matched upon filling, just as a standing wave linac cavity). This development will probably proceed at 10.6 micron design wavelength. Choice of this wavelengthe is based both on availability (e.g. at the UCLA Neptune laboratory[9]), and on mitigation of the experimental challenges one faces on moving orders of magnitude down in accelerator wavelength.

4 REFERENCES

[1] C. Clayton et al., Phys. Rev. Lett. **70** 37 (1993)
[2] P. Sprangle, E. Esarey, A. Ting and G. Joyce, *Appl. Phys. Lett.* **53**, 2146 (1988).
[3] W.D. Kimura, *et al., Phys. Rev. Lett.*. **74**, (1995).
[4] Y. Liu, *et al., Phys. Rev. Lett.* **80**, 4418 (1998)
[5] J. Rosenzweig, A. Murokh, C. Pellegrini, *Phys. Rev. Lett.* **74** 2467 (1995).
[6] A. Tremaine, J. Rosenzweig, P. Schoessow, *Phys. Rev. E* **56** 7204 (1997).
[7] J. Rosenzweig, P. Schoessow, Proc. 1998 Advanced Accelerator Concepts, (in press)
[8] D. Du et al., Appl. Phys. Lett. **64** 3073 (1994)
[9] C. Clayton, et al., ., *Nucl. Instr. Meth. A* **410**, 235 (1998), J.B. Rosenzweig, *et al., Nucl. Instr. Meth. A* **410**, 437 (1998).

*Work supported by US DoE Contracts W-31-109-ENG-38, DE-FG03-92ER40693 and DE-FG03-98ER45693.

Email: rosenzweig@physics.ucla.edu

AN EXPERIMENTAL TEST OF THE THEORY OF THE STIMULATED DIELECTRIC WAKE-FIELD ACCELERATOR*

J.-M. Fang†, T.C. Marshall, Columbia University, New York, NY
J.L. Hirshfield, M.A. LaPointe, T-B. Zhang, Yale University and Omega-P Inc., New Haven, CT
X.J. Wang, BNL, Upton, NY

Abstract

We have installed a dielectric-lined wakefield accelerator at the Accelerator Test Facility (ATF), Brookhaven National Laboratory. The first experiment, reported here, uses a single 0.2 nC, 10 psec bunch of 40 MeV electrons to excite the multi-mode TM_{0m} wakefields which trail the bunch. The device is configured as a cylindrical waveguide containing an annular alumina liner; the electrons move along the axis of symmetry inside a 3 mm diameter bore hole. The spectrum of modes set up by the electron bunch is picked up by a radial probe and detected by a spectrum analyzer; this is compared with theory. This spectrum can be used to construct the axial wakefield pattern.

1 INTRODUCTION

In a dielectric wakefield accelerator, a dielectric loaded waveguide supports wakefields radiated by the passage of an electron bunch which travels at the speed of light in the structure (Cerenkov Radiation). Our studies here relate to a cylindrical structure, consisting of a thick cylindrical shell of alumina ($\kappa \sim 9.6$) having a small bore hole (3 mm dia.) which permits the electron beam to pass down the axis, and a comparatively large outer radius (R = 2.064 cm), all contained within a close-fitting conducting cylinder which serves as a vacuum wall. In this paper, we describe experimental results including portions of the spectrum of microwave modes excited by the passage of a single 0.2 nC, 10 psec, 40 MeV (ATF diagnostics) bunch of charge provided by the ATF rf linac at Brookhaven National Laboratory. This spectrum compares favorably with the computed spectrum, obtained by solving the dispersion relation of the structure[1].

The particular waveguide used here has two novel properties: First, the dimensions and large κ will favor the coherent superposition of many waveguide modes, travelling with the electron speed, which cause a narrow, highly-defined pulse of axial electric field E_z to repeat periodically along the axis of the device. Factors which favor a sharply-defined high amplitude wakefield pulse are: (1) a small bore hole; (2) a dispersion-free dielectric; (3) a very short bunch containing as much charge as possible. However, these agreeable features do not by themselves advance in a significant way the prospects for using wakefields to achieve high accelerating gradients in future accelerators. Second, we can exploit the nearly-periodic characteristic of these wakefields by locating additional drive bunches in the decelerating field of the previous bunches such that the constructive interference of the fields will build up a truly large accelerating gradient. The strategy of the multiple bunch wakefield accelerator is to use a train of very short (perhaps $\sim$ 1 psec in the future) bunches to build up a larger wakefield than could be obtained from a single bunch of proportionally higher charge. This can occur because shorter bunches are much more effective in setting up strong wakefields than are longer bunches.

The principles of such an accelerator have been set forth[2] in a simplified geometry. The first bunch radiates coherent spontaneous Cerenkov radiation. The next drive bunch in addition radiates stimulated radiation, because it is located in the decelerating field of the first bunches, and so on. This permits a rapid buildup of the wakefields at the position where a test bunch follows in the accelerating phase. The lack of dispersion in alumina[3] means that the waveguide modes can have nearly-constant frequency differences. Thus dispersion does not smear out the pulses of high wakefield intensity. Wakefield devices such as this one are subject to the following problems: (1) dielectric breakdown, at some field; (2) instability (caused principally by the dipole mode); (3) slippage. However, temporarily setting aside these issues (which may be helped by separating the drive beam line from the accelerated beam line and staging), in this paper we are preparing to study the multibunch wakefield acceleration in an experiment which will be run at ATF, starting with a single bunch.

In order to do the multibunch experiment, careful measurements must be made to prepare the device so that the wakefields will have the correct periodicity for the chosen accelerator system. Since the ATF uses a 2.85 GHz power source and a laser rf photocathode gun, the drive bunches are to be separated by 21 cm, and the test bunch will follow at 10.5 cm. These bunches will be obtained by taking one laser pulse and splitting it into three drive bunch pulses and one weak test bunch pulse: the structure is about 54 cm in length. We report our first measurements of the rf spectrum from the passage of a single bunch; this not only permits a check of the accuracy of our calculations, but also a measurement of the wakefield periodicity. Having done this, one can then obtain a very accurate value for the dimensions of the wakefield device which will support a multibunch train that will build up wakefields.

* Work supported by the Department of Energy, Division of High Energy Physics
† Email: fang@beamer8.physics.yale.edu

0-7803-5573-3/99/$10.00@1999 IEEE.

2 APPARATUS

Oversize alumina castings were obtained from LSP Industrial Ceramics (Lambertville, NJ). Since no sample 60 cm in length had the straightness of bore hole that was required, it was decided to use two selected shorter alumina sections smoothly butted together. These samples were placed into a metal-walled cylindrical cavity resonator, and the sequence of TM_{01n} mode frequencies was measured[4]: this yielded a $\kappa = 9.57$. However, this measurement had only so much accuracy — not adequate to get the wakefield period accurate for four bunches (i.e. within 1 mm) — and so it was decided to grind the outer diameter of the alumina slightly oversize, and then determine the correct diameter using the theory from the experimental spectrum of wakefields excited by a single bunch.

The apparatus (Figure 1) is installed on the beamline 3 of the ATF rf linac facility, which is operated so as to produce a single pulse of beam electrons from the irradiation of a rf gun photocathode with a near-UV laser pulse (the fourth harmonic of the Nd:YAG laser). Halo electrons are removed at the input by scrape-off into a tungsten plug. The alumina OD and the stainless steel jacket ID are machined so that a sliding fit is obtained. No problems with pump-

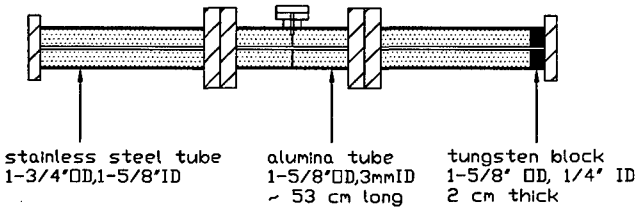

Figure 1: The wakefield device

down were encountered. Halfway along the device, a radial wire probe is inserted into a hole milled along the interface between the two adjacent alumina cylinders. A 3.5 m piece of EZ Flex 402 rf coax (comparable to $MIL - C - 17$ semi-rigid) joins the probe terminal to a terminated crystal detector and the spectrum analyzer (Tektronix 492P); the rf waveform envelope is monitored using a 1 GHz bandwidth oscilloscope. The Cerenkov radiation trails the charge, and is directed downstream; however, it should be reflected by the end walls and contained within the structure. A typical pulse, Fig. 2, shows the radiation set up by the electron bunch lasts $\sim$ 20 nsec, several bounce times; it would appear that cavity modes are not excited, since radiation in these modes should persist much longer ($\sim$ 1 μsec, related to the resonator Q for microwaves).

3 RESULTS

We present two cases of the spectrum scan here. In Fig. 3 which covers 1.7–5.5 GHz band, TM_{01} and TM_{02} modes were detected at near 1.9 and 4.4 GHz respectively. In Fig. 4, TM_{04} and TM_{05} modes were detected near 9.5 and 12.1 GHz. The spectrum analyzer sweep was calibrated us-

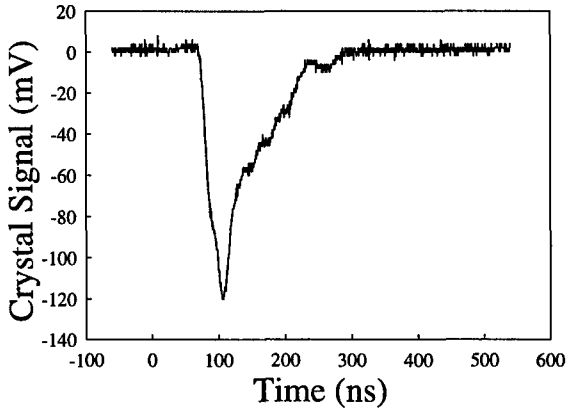

Figure 2: The rectified crystal signal

ing a frequency source and a wavemeter, as it was found to vary somewhat from band-to-band. For these data, a single bunch of charge ($\sim$ 0.2 nC) was passed through the apparatus at 1.5 Hz, while the spectrum analyzer was allowed to accumulate data over many minutes. The spectrum analyzer operates by stepping a fixed bandwidth of frequency along a band, thereby catching radiation which has the correct frequency when that channel is open. There are 1000 frequency bins in a band and it takes 50 seconds to step through the band. We usually accumulate the data over 30–45 minutes. The ordinate is in the logarithmic scale to allow for larger dynamic range.

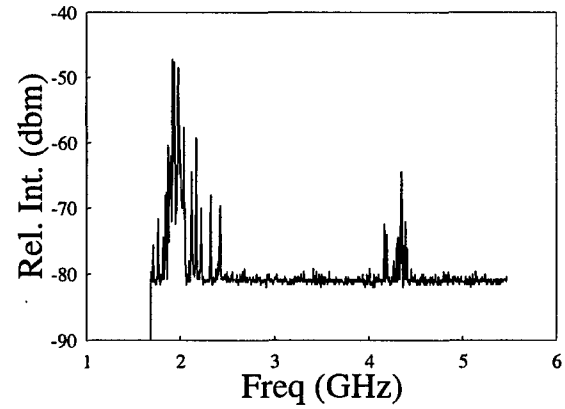

Figure 3: Spectrum between 1.7–5.5 GHz, TM_{01} and TM_{02} are shown.

Table I is a summary of the six frequencies observed. The lowest frequency predicted and observed was 1.9 GHz; the highest frequency detected by the apparatus was about 15 GHz, on the highest band available to us using this spectrum analyzer. Frequencies above 15 GHz would suffer more attenuation from the coaxial cable. Because of the frequency-dependent experimental parameters (e. g, the couplings between the radial wire probe and various modes), the amplitude of the various modes are not known, and so $E_z(t)$ cannot be obtained from the data.

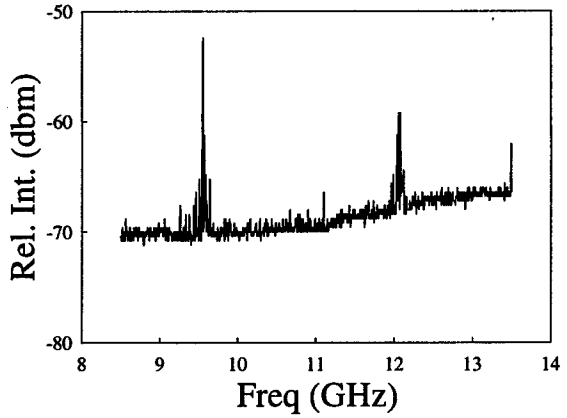

Figure 4: Spectrum between 8.5–13.5 GHz, TM_{04} and TM_{05} are shown.

Table 1: TM_{0m} mode frequency table (GHz)

mode	$Freq_{ex}$	$Freq_{th}$
1	1.920	1.907
2	4.376	4.420
3	6.956	6.983
4	9.545	9.574
5	12.12	12.18
6	14.84	14.80

Column 3 of Table I gives the theoretical prediction of the mode frequencies, using the actual inner and outer radii of the alumina cylinder (with $\kappa = 9.65$ providing the best fit). To analyze this data, we use the dispersion relation[1] for the TM_{0m} modes:

$$\frac{I_1(k_1 a)}{I_0(k_1 a)} = \frac{\kappa k_1}{k_2} \frac{J_0(k_2 R)N_1(k_2 a) - J_1(k_2 a)N_0(k_2 R)}{J_0(k_2 R)N_0(k_2 a) - J_0(k_2 a)N_0(k_2 R)} \quad (1)$$

where a and R are the inner and outer radii of the cylinder, and the mode frequencies are related to the k_1 and k_2 (the transverse wavenumbers in the vacuum and dielectric regions respectively) by

$$k_{1m} = \omega_m / c\beta\gamma = k_{2m}\gamma_\kappa/\gamma \quad (2)$$

where m is the mode index number, γ is the relativistic factor (corresponding to 40 MeV here), and

$$\gamma_\kappa = (\kappa\beta^2 - 1)^{-1/2}. \quad (3)$$

The fit of the dispersion theory for the TM_{0m} series and the data is excellent. Certain spectra also reveal the appearance of additional modes having smaller amplitude. Several of these frequencies correlate well with predicted modes of the HEM_{1n} and HEM_{2n} ("dipole" and "quadrupole") class, which are unstable for finite beam offset from the axis (for example, in Fig. 3, the small peak to the left of TM_{02} is related to HEM_{13}). Indeed, further experimentation has found that the appearance of these modes is favored by deliberate beam misalignment.

4 REFERENCES

[1] T.C. Marshall, T-B. Zhang, and J.L. Hirshfield, "The Stimulated Dielectric Wake-field Accelerator: a Structure with Novel Properties", Advanced Accelerator Concepts review paper, July 1998; AIP conference proceedings, Wes Lawson cd. [1999].

[2] T-B. Zhang, J.L. Hirshfield, T.C. Marshall, and B. Hafizi, Phys. Rev. **E56**, 4647 [1997].

[3] see: A.Ibarra et al, J. Appl. Phys. **80**, 1030 [1996] and references therein.

[4] T-B. Zhang, T.C. Marshall, M.A. LaPointe, J.L. Hirshfield, and A. Ron, Phys. Rev. **E54**, 1918 [1996].

LASER-DRIVEN CYCLOTRON AUTORESONANCE ACCELERATOR*

Changbiao Wang[1] and J. L. Hirshfield[1,2]
[1]Physics Department, Yale University, New Haven, Connecticut 06520-1820
[2]Omega-P, Inc., 202008 Yale Station, New Haven, Connecticut 06520

Abstract

Theory is developed for the cyclotron autoresonance acceleration of electrons in a gently-focused Gaussian laser beam and a gently tapered axial magnetic field. Numerical simulation shows, for example, acceleration from 50 MeV to 178 MeV over a distance of 148 cm, using a 10.6 μm CO_2 laser with a minimum spot size of 0.1 cm.

1 INTRODUCTION

Electron acceleration using intense lasers has engendered significant attention within the accelerator research community. This interest stems from the enormous optical electric field strengths E_0 that can be obtained with a focused laser, i.e. of the order of $E_0 = 3\times10^{-9}\sqrt{I}$ TV/m, where the intensity I is in W/cm^2 [1]. Since compact terawatt focused lasers can have $I > 10^{18}$ W/cm^2, field strengths of the order of teravolts/m are possible. Of course, since this field is transversely polarized, it can not give much net acceleration to a charged particle directly, so a number of indirect means have been devised to achieve net acceleration. For example, in the laser wake field accelerator [2] an intense laser pulse is used to locally polarize a plasma, thus creating a strong longitudinally-polarized plasma wake field for acceleration. In another example, the vacuum beat-wave accelerator [3], two laser pulses of differing frequencies are combined to create a slow optical ponderomotive beat wave that can exert a strong force for acceleration.

Originally a microwave interaction, the cyclotron autoresonance acceleration (CARA) of a low energy electron beam has been studied and demonstrated experimentally to operate with efficiencies exceeding 95% for transforming microwave energy into directed beam energy [4]. For acceleration of a high energy beam, however, the magnetic field required in the microwave CARA becomes so strong that it is not practical.

An alternative CARA is laser-driven cyclotron autoresonance accelerator (LACARA) [5]. The refractive index in LACARA is so close to unity that the upper energy limit for acceleration [6] is removed, and for acceleration of a high energy electron beam the magnetic field required is realizable. Furthermore, the group velocity in LACARA exceeds the axial particle velocity, so operation with strong pump depletion is possible without causing energy spread for the beam. The acceleration gradient in LACARA can be as high as $E_0(v_\perp / v_z)_{\max}$, with $v_\perp$ and v_z the particle transverse and axial velocities respectively.

Recently, by simulation we have studied LACARA for acceleration of electron beams. Here we present the theory and preliminary numerical results.

2 OUTLINE OF LACARA THEORY

The preliminary analysis presented here is for a traveling Gaussian laser beam focused by two spherical mirrors. The laser fields in cylindrical coordinates (r,θ,z) for the lowest-order mode with circular polarization are [7]

$$E_r = cB_\theta = E_0\frac{w_0}{w}\exp\left(-\frac{r^2}{w^2}\right)\cos(\psi-\theta), \quad (1)$$

$$E_\theta = -cB_r = E_0\frac{w_0}{w}\exp\left(-\frac{r^2}{w^2}\right)\sin(\psi-\theta), \quad (2)$$

$$E_z \approx -\frac{2}{kw}\frac{r}{w}\left(E_\theta + \frac{z}{z_R}E_r\right), \quad (3)$$

$$B_z \approx -\frac{2}{kw}\frac{r}{w}\left(B_\theta + \frac{z}{z_R}B_r\right), \quad (4)$$

where c is the vacuum light speed, $w = w_0(1+z^2/z_R^2)^{1/2}$ is the spot size, w_0 is the waist radius (minimum spot size), and z_R is the Rayleigh distance. The waist radius and Rayleigh distance are related by $w_0 = (\lambda z_R/\pi)^{1/2}$, with λ the laser wavelength. The laser phase is $\psi = \omega t - kz + \tan^{-1}(z/z_R) - kr^2/2R$, with ω the laser angular frequency, $k = \omega/c$, and $R = z + z_R^2/z$ the radius of curvature of the ray normals. The axial and radial effective refractive indices (group velocities normalized to c) are given by

$$n = n_z = 1 - \frac{1}{2}\frac{w_0^2}{Rz} + \frac{1}{2}\frac{\left(z_R^2 - z^2\right)r^2}{(Rz)^2} \quad \text{and} \quad n_r = \frac{r}{R}. \quad (5)$$

The non-zero n_r means that there is diffraction loss for the Gaussian beam. The condition for resonance between wave and particles is $\Omega_0 = \gamma\omega(1 - n_z\beta_z - n_r\beta_r)$, where the non-relativistic gyrofrequency is $\Omega_0 = eB_0/m$ with e the electron charge in magnitude and m the rest mass, the relativistic energy factor is $\gamma = (1-\beta_\perp^2-\beta_z^2)^{-1/2}$ with $\beta_\perp = v_\perp/c$ and $\beta_z = v_z/c$, and β_r is the radial velocity normalized to c. Usually, the radial dimension of electron motion in LACARA is much less than the Rayleigh distance. Thus the resonance condition can be written as $\Omega_0 \approx \gamma\omega(1-n\beta_z)$, with $n \approx 1 - w_0^2/(2Rz)$.

The laser power is related to the electric field amplitude by $P_L = 0.5\pi w_0^2 E_0^2/\eta_0$, with $\eta_0 = (\mu_0/\varepsilon_0)^{1/2}$ the wave impedance of a plane wave in free space.

* The work was supported by the U. S. Department of Energy, Divisions of High Energy Physics and Advanced Energy Projects.

0-7803-5573-3/99/$10.00@1999 IEEE.

Eqs. (1)-(4), together with the relativistic equations of motion for the electrons

$$\frac{d}{dt}(\gamma \mathbf{v}) = -\frac{e}{m}(\mathbf{E} + \mathbf{v} \times \mathbf{B}) \qquad (6)$$

allow solutions to be found for single-particle orbits. In the results of computations to be shown below, iterative solutions for the position, velocity and energy of the particles are found at each computational stage by specifying the change in guide magnetic field value necessary to maintain resonance.

3 SIMULATION RESULTS

The simulation results presented below are for three LACARA examples. The laser power is from a CO_2 laser at a wavelength of 10.6 μm. Example 1 is for a 50 MeV cold electron beam driven by a laser power of 4 TW. The interaction length or mirror separation is 148 cm (5 Rayleigh distances). The simulation parameters are given in Table I and the results are shown in Figs. 1-4. In Example 2, the interaction length and the mirror radius are both 59.28 cm (2 Rayleigh distances), and all the other parameters are the same as those in Example 1. The result is shown in Fig. 5. Example 3 is for a 0.5 GeV cold beam driven by a laser power of 4 PW. Simulation parameters are given in Table II and the result is shown in Fig. 6. In all simulations, 8 computational particles initially uniformly distributed over one laser period are taken, and all electrons experience the same acceleration history. Beam loading is neglected.

Table I: Parameters in simulation for Example 1

Input cold beam energy	50 MeV
Laser power P_L	4.0 TW
Waist radius w_0	0.1 cm
Field amplitude E_0	31.0 GV/m
Rayleigh distance z_R	29.64 cm
Mirror radius	85.95 cm
Mirror separation	148 cm

Table II: Parameters in simulation for Example 3

Input cold beam energy	0.5 GeV
Laser power P_L	4.0 PW
Waist radius w_0	0.3 cm
Field amplitude E_0	326.5 GV/m
Rayleigh distance z_R	267 cm
Mirror radius	889 cm
Mirror separation	1600 cm

Fig. 1 shows average axial and transverse normalized velocities versus axial distance. The maximum $<\beta_\perp>$ is 0.0063; the initial $<\beta_z>$ is 0.999949 (minimum) and the final $<\beta_z>$ is 0.999984 (maximum), only 0.0035% change. From this, it is seen that the velocity ratio $\beta_\perp/\beta_z$ is quite small for a high energy beam in the LACARA, compared with a low energy beam in the microwave CARA [8]. This insures that all the electrons have very small transverse displacements, as shown in Fig. 2. The laser waist radius is 0.1 cm; so all the orbits of the 8 particles are within the minimum spot size.

Fig. 3 shows normalized axial group velocity and average axial electron velocity, plotted as $1-n$ and $1-<\beta_z>$, versus axial distance. It can be seen that the group velocity everywhere exceeds the axial particle velocity, allowing for rapid replenishment of laser energy that is given to the beam. This fact bodes well for achievement of an accelerated beam with low energy spread, even with significant beam loading. This allows efficient use of laser power without loss of beam quality.

Fig. 4 shows the dependence of average relativistic energy factor and axial magnetic field on axial distance. It is seen that the beam energy rises monotonically from 50 MeV to 178 MeV in a distance of 148 cm, corresponding to an average acceleration gradient of 86.6 MeV/m. The resonance magnetic field required rises from 52 kG to about 80 kG near the laser focus, and then falls back to about 60 kG. It is the fall in magnetic field that allows continuous acceleration without stalling; the fall in field can be traced to the fall in $(1-n)$ after the focus. This demonstrates that LACARA is not limited to be a $\gamma-$doubler, as in the microwave CARA.

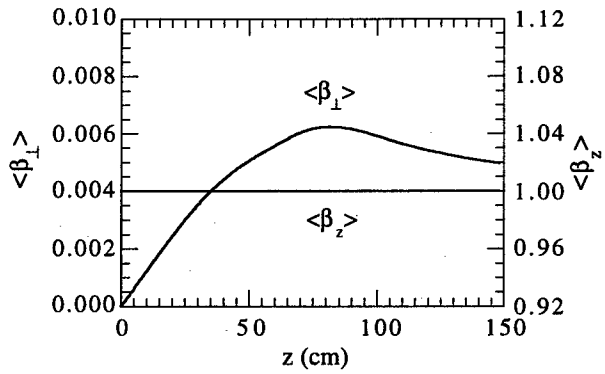

Figure 1: Average axial and transverse normalized velocities for Example 1 with a $5z_R$ interaction length. Initial beam energy is 50 MeV, z_R = 29.64 cm, w_0 = 0.10 cm, and P_L = 4.0 TW.

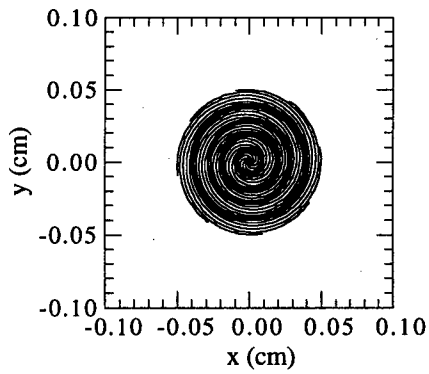

Figure 2: Projection in $x-y$ plane of orbits of 8 computational particles for Example 1. It is seen that the maximum transverse excursion is not greater than $w_0/2$.

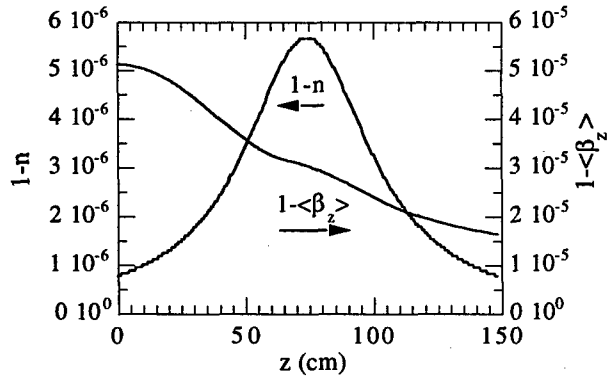

Figure 3: Variation in normalized axial group velocity plotted as $1-n$ (left scale), and normalized average axial velocity plotted as $1-<\beta_z>$ (right scale), for parameters of Example 1. It is seen that n exceeds $<\beta_z>$ throughout the interaction.

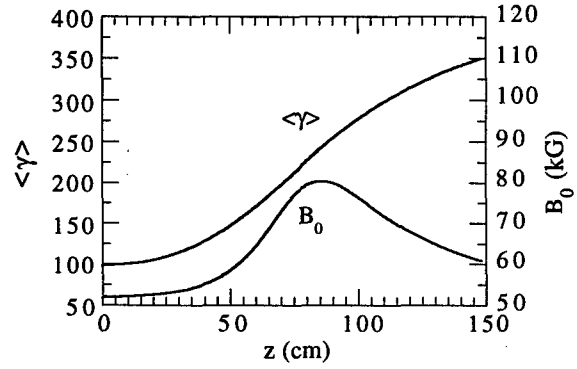

Figure 4: Variation in average relativistic energy factor $<\gamma>$ and axial magnetic field B_0 along LACARA, for parameters of Example 1.

Fig. 5 shows the dependence of average relativistic energy factor and axial magnetic field on axial distance for Example 2. It is seen that the energy rises monotonically from 50 MeV to 110 MeV in a distance of 59.28 cm ($2z_R$), corresponding to an average acceleration gradient of 100 MeV/m. The resonance magnetic field required rises from 54 kG to about 67 kG near the laser focus, and then falls back to about 65 kG. This example shows that a shorter interaction region has a larger average acceleration gradient, since the laser field is weaker in the region far away from the focus.

Fig. 6 shows the dependence of average relativistic energy factor and axial magnetic field on axial distance for Example 3. It is seen that the energy rises from 0.5 GeV to 1.53 GeV in a distance of 16 m ($6z_R$), corresponding to an average acceleration gradient of 64.4 MeV/m. The orbit in this case was seen in the computations to execute only about one full gyration over its 16-m length, with a maximum displacement from the axis of less than 3.0 mm. The magnetic field is seen to vary from 6 kG, up to 24 kG, then down to 13 kG. This example shows that a lower magnetic field is required for a higher energy beam, as expected, in rough proportion to $1/\gamma$.

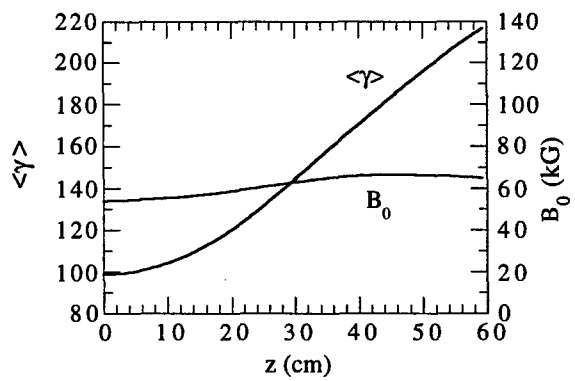

Figure 5: Variation in average relativistic energy factor $<\gamma>$ and axial magnetic field B_0 along LACARA for Example 2. Parameters are the same as Example 1, except for a LACARA of length $2z_R$ with a mirror radius of curvature 59.28 cm.

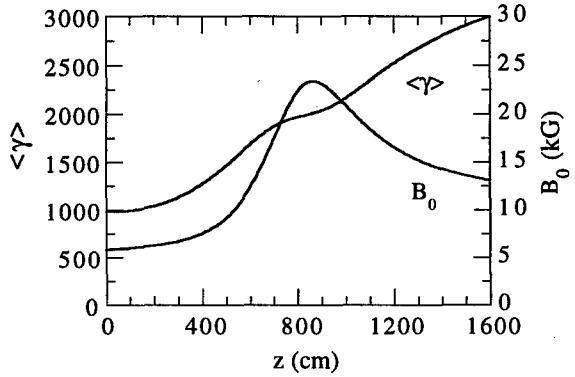

Figure 6: Variation in average relativistic energy factor $<\gamma>$ and axial magnetic field B_0 along LACARA for Example 3. The beam is accelerated from 0.50 GeV to 1.53 GeV within a $6z_R$ interaction length.

4 CONCLUSIONS

It is shown by simulation that in a LACARA driven by a power of 4 TW at 10.6 μm, a 50 MeV electron beam is accelerated to 178 MeV in a distance of 148 cm, corresponding to an average acceleration gradient of 87 MeV/m. The magnetic field varies from 52 kG to 80 kG.

5 REFERENCES

[1] P. Sprangle, et al., *AIP Conf. Proc.* **398**, New York, Amer. Inst. Phys., 96 (1996).

[2] K. Nakajima, et al., *Phys. Rev. Lett.* **74**, 4428 (1995).

[3] E. Esarey, et al., *Phys. Rev.* E **52**, 5443 (1995); P. Sprangle, et al., *Opt. Commun.* **124**, 69 (1996); B. Hafizi, et al., *Phys. Rev.* E **55**, 5924 (1997).

[4] M. A. LaPointe, et al., *Phys. Rev. Lett.* **76**, 2718 (1996).

[5] P. Sprangle, et al., *IEEE Trans.* **NS-30**, 3177 (1983).

[6] J. L. Hirshfield, et al., *Phys. Plasmas* **3**, 2163 (1996).

[7] B. Hafizi (private communication).

[8] C. Wang and J. L. Hirshfield, *Phys. Rev.* E **51**, 2456 (1995).

LASER LINEAR COLLIDER WITH A TRAVELLING LASER FOCUS SUPPLY

A. A. Mikhailichenko*
Wilson Laboratory, Cornell University, Ithaca, NY 14850

Abstract

Requirements considered for 2×1 *km* long linac, driven by a laser radiation distributed within open accelerating structure with special sweeping devices. These devices deflect the laser radiation to the open accelerating structure in accordance with instant position of accelerated particles The power reduction and shortening the time of illumination of every point of the structure is equal to the number of resolved spots, associated with the sweeping device. A 300 J, 100-ps laser flash could provide the energy 30 TeV for $\lambda \cong 1\mu$m and 3 TeV for $\lambda \cong 10\mu$m on 1 km with the method described. For repetition rate 160 Hz the luminosity associated with colliding beams could reach 10^{33} $cm^{-2}s^{-1}$ per bunch. Wall plug power required for operation of LLC is ~ 2 MW.

1 INTRODUCTION

The concept of a Linac, driven by a Traveling Laser Focus (TLF) method was originated in [1-3]. TLF deals with accelerating structure, what scaled down to a laser wavelength. The beam is going *inside* the structure similar to the existing practice. Tiny dimensions of the beam required could be achieved by proper preparation of the beam [4]. For excitation of accelerating cells, each of them has an opening from one side, what gives a possibility for parallel excitation. Laser radiation focused onto these openings. So the cells excited locally. Focusing in transverse direction is more radical, as the focusing lens could be positioned very close to the accelerating structure. Special sweeping (deflecting) device moves this focal spot in *longitudinal* direction in accordance with instant position of the particle. Due to this arrangement, all impulse laser power is acting for generation of accelerating field at the instant particle's location only. These arrangements reduce the power required from the source (laser) and reduce illuminating time. It was shown [2], that the power reduction and shortening of illuminating time of any point on the surface equal numerically to the number of resolved spots (pixels), associated with the sweeping device. One can see that the cells are working with zero phase shift per cell what yields the distance between the cells equal to the laser wavelength. The number of the particles required is about one million only, so the problems with wakes here are not more complicated, than in usual cm-wavelength structure.

2 TLF METHOD

Fig. 1 reminds the idea [1-3]. The laser bunch with longitudinal dimension much bigger, than transverse ones passing trough the sweeping device. This fast sweeping device is driven by electrical pulse synchronously with the particle's passage. It directs the beginning of the laser bunch to the entrance of accelerating structure and the end-to the exit of the structure. So closer to the structure laser bunch has an instant slope of 45 degrees to the direction of sweeping device. The local wave fronts still rectangular to the sweeping device, however. All deflecting elements are synchronized so that the electron bunch has continuous acceleration in all sections. One can see from Fig. 1, that the energy concentrated in the laser's bunch volume delivered here by the source by the time defined by the *length* of the laser bunch what is equal to the length of accelerating structure in Fig.1.

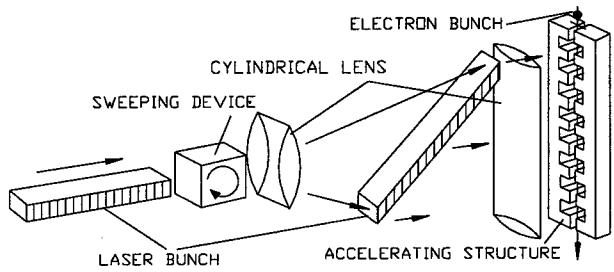

Figure 1: The principle. Lines across the laser bunch indicate the direction of wave fronts.

Optimal laser focus sweep is about 3cm for a practical reasons, so the accelerating device looks like a sequence of 3 cm- long accelerating structures. A short focusing *cylindrical* lens installed close to accelerating structure reduces *the transverse size* of the spot to a minimal one. Each part of the grating structure is illuminated by duration, which is defined by time $\tau \cong L/N_R c \cong 100\,\lambda$, where N_R–is the number of resolved spots, (see lower), L–is the length of the structure. For $\lambda = 1\mu$m, then $\tau \cong 3\cdot 10^{-13}$sec. This time is less than the time between electron-electron collisions, what is $\tau_{coll} \cong 10^{-12}$ sec, still however longer, than the time, corresponding to reaction of electron plasma in a metal, what is $\tau_p \approx 3\cdot 10^{-16}$ s. TLF method does not exclude the problems, associated with a breakdown limit of the structure, but *it allows drastically reduce the laser impulse power, required for excitation the structure* to this level. The latest measurements show a damage threshold increase while the illumination time is shortening. This breaks the $\tau^{1/2}$ low. This was explained by saturation of impact

* Work supported by NSF. Phone: (607) 255-3785, Fax: (607) 255-8062, e-mail "mikhail@lns62.lns.cornell.edu

0-7803-5573-3/99/$10.00@1999 IEEE.

ionization rate per unit distance [5]. Measured threshold for 0.: ps pulse was about 10 J/cm^2. For 1 ps the threshold measure was 6 J/cm^2. In our case we have 10mJ laser pulse distribute over area 3×10^{-3} cm^2 what gives 3 J/cm^2 and acceleratin gradient 3 GeV/m. We believe that these figures could b improved after careful preparation the surface and optimizin the working temperature. Main components of the schem considered below.

3 DEFLECTINGDEVICE

The ratio of deflection angle ϑ to diffraction angle $\vartheta_d \cong \lambda/a$, where a is an aperture of the deflecting device, defines the *number of resolved spots (pixels)*, $N_R = \vartheta/\vartheta_d$. The number of resolved spots N_R is *an invariant* under any optical transformations. As we mentioned above, N_R value gives the number for the lowering the laser power for gradient desired and, also, the number for the duty time reduction.

Electro-optical devices use controllable dependence of refractive index on electrical field strength and direction applied to some crystals (see Ref. To [2-3]). Short laser bunch could be swept with a travelling wave sweeping device [3], Fig. 2 below.

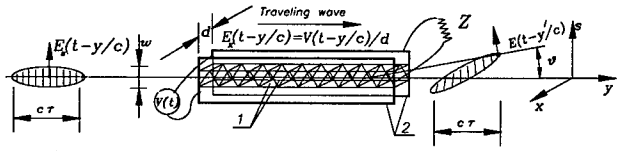

Figure 2: Deflecting device principle. Prisms 1 with *oppositely directed optical axes* installed in series between two parallel strip–line electrodes 2, *d*–is the distance between them. *Z*– is a matching impedance. Lines across the laser bunch schematically show the wave fronts. $E_x(t-y/c)$ –is a driving electrical field.

For the length of deflecting device *L*=50*cm*, one can expect $\Delta\vartheta \cong 10^{-2}$ rad. $N_R \cong 10$ for $\lambda \cong 10\mu$ m and $N_R \cong 100$ for $\lambda \cong 1\mu$ m. *Mechanical deflection system* and *Acousto-optical deflector* could be also used here [3]. Basically they give the same deflecting parameters.

4 ACCELERATING STRUCTURE

We took the foxhole-type structure described in [6] as a basis, Fig. 3. This structure has an advantage in pumping possibilities. The structure gives a good positioning for electrical field map [2,3].

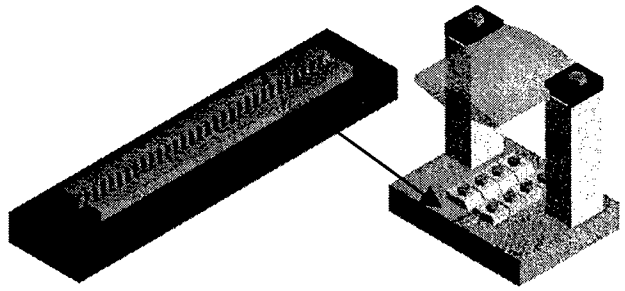

Figure 3: Accelerating structure and cylindrical lens. Structure on the left is scaled. Covers on accelerating structure are not shown.

Covers adjust the coupling between the groove and outer space. With these covers the height of a structure is about half of a laser wavelength and the cells have *inductive* coupling with outer space. The Q_{RF} factor of the order 5-10 could be expected here. Technological possibilities in lithography allow a structure fabrication for a laser with a wavelength $\lambda \cong 1\mu$ m. Each structure installed on a micro-table moved by a piezoelectric. Calculations for this type of structure done with GdfidL code [7]. There were investigated different shapes of cell and transit slit between the cells. Calculation shows that wakes are acceptable here. Despite dimensions are small, the bunch population about 10^6 only drastically rejects the wake problems.

5 DESCRIPTION OF LLC

Parameters of this LLC are represented in Table 1. The beams of electrons and positrons can be polarized what gives the effective gain in luminosity and reduces the background. Details one can find in [2,3].

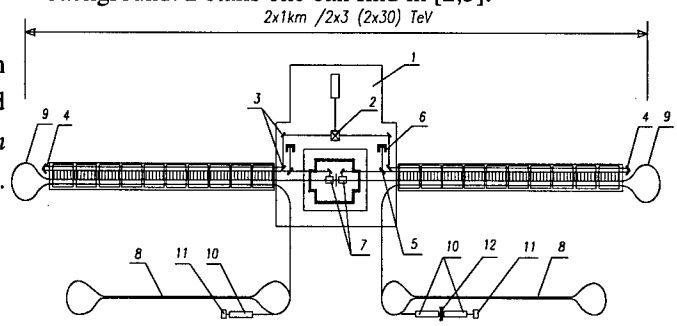

Figure 4: Linear Laser Collider (LLC) complex. 1–is a laser master oscillator platform, 2 –is an optical splitter, 3,4–are the mirrors, 5–is a semi-transparent mirror, 6—is a light absorber. 7–are the Final Focus Systems. 8–are the damping systems for preparing particle's beams with small emittances, 9—are the bends for particle's beam. 10–are the accelerating X-band structures, 11–is electron gun (polarized), 12– is a positron converter.

TABLE 1. Parameters of Laser Linear Collider.

Parameter	$\lambda \cong 10\mu m$	$\lambda \cong 1\mu m$
Energy of $e^{\pm}$ beam	3 × 3 TeV	30 × 30 TeV
Length of section	3cm	3cm
Total length	2 × 1 km	2 × 1 km
Main linac gradient	3 GeV/m	30 GeV/m
Luminosity/bunch	$\leq 1\cdot 10^{33}\,cm^{-2}s^{-1}$	$\leq 1\cdot 10^{33}\,cm^{-2}s^{-1}$
Bunches/pulse	3 (≤ 100)*	10 (≤ 300)*
Laser flash J/Linac	300	300
Repetition rate	160 Hz	160 Hz
Beam power/Linac	2.3 kW	760W
Bunch population	$3\cdot 10^7$	10^6
Bunch length	1μ m	0.1μ m
$\gamma\varepsilon_x$ / $\gamma\varepsilon_y$ cm·rad	$10^{-8}/4\cdot 10^{-10}$	$5\cdot 10^{-9}/1\cdot 10^{-10}$
Damping ring energy	0.7 GeV	0.7 GeV
Wall plug power**	2×0.5 MW	2×0.5 MW

*–Maximal possible number.
**–Laser efficiency ≈ 10%

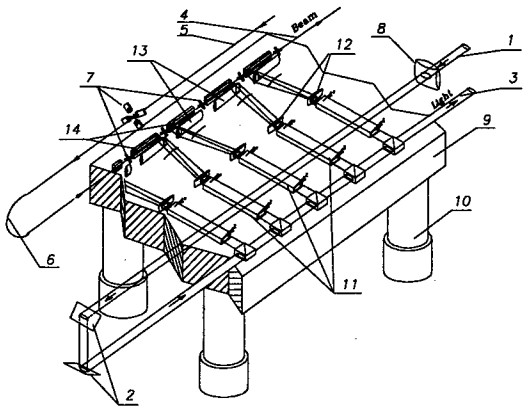

Figure 5: Table with a regular section of accelerator. 1,3–is a laser beam. 4,5–the beam of particles. 7 and 8–are the focusing elements for the particle's and laser beam correspondingly. 9 –is an optical platform. Legs 10 have active damping system to minimize vibrations. 11–are the sweeping devices 12–are the lenses for focusing the laser radiation in longitudinal direction. 13–are short focusing cylindrical lenses. 14–are accelerating structures

After the bend in systems 2,6 on the *back way to IP* necessary voltages applied to correcting elements, distributed along the linac.

A *kayak-paddle cooler* pos. 8, Fig.4 serves as injector [4]. This is basically a racetrack, which has a sequence of wigglers and RF cavities in a straight section. This injector yields the equilibrium emittances

$$(\gamma\varepsilon_x) \cong 1\cdot 10^{-8}\ cm\cdot rad\ , (\gamma\varepsilon_y) \cong 4\cdot 10^{-10}\ cm\cdot rad\ .$$

Scrapping extra particles remains a valid procedure for the emittance lowering. Intra-Beam Scattering is reduced for diluted beam. *The focusing system* includes the quadrupole lenses of appropriate dimensions and a RF focusing. *Accelerating gradient* defined by the laser flash energy Q. A laser flash with $Q \cong 10$ mJ, $\tau \cong 0.1$ ns at $\lambda \cong 1\mu$ m is able to feed the accelerating structure with the length about $c\tau \approx 3$ cm with ≥ 30 GeV/m. Nd-Glass laser can be used here. CO_2 laser based system gives lower final energy. The power required $P_i \cong Q/\tau \approx 10^8\ W$ is within routinely obtained. The laser amplifier could be sectioned with few structures or even each $3cm$ section could has it's own amplifier. For pumping the driving lasers the *diode laser arrays* could be used for the wavelengths indicated.

Bunch population defined by a loading of structure and by wakes. With 5% loading $N \cong 1\cdot 10^6$ for $\lambda \cong 1\mu m$. For $\lambda \cong 10\mu m$ this will be $N \cong 3\cdot 10^7$. *Final focus* made with *a multiplet* of FODO structures having the number of the RF lenses in it of the order of few hundreds. *Luminosity* could reach $L \approx 1\cdot 10^{33}\,cm^{-2}s^{-1}$ for $\lambda \cong 10\mu$ m, $\gamma = 2\cdot 10^6$ (pc=1TeV), $N \cong 2\cdot 10^7$, $f \cong 160$ Hz. For $\lambda \cong 1\mu$ m result will be about the same.

6 CONCLUSION

Reduction of illuminating time and total laser power (or the flash energy) both defined by the number of resolved spots (pixels) associated with a deflecting device. Number of resolved spots $\approx 20-100$ achievable. Lasers for the TLF method need to have more power in intermediate time duration $\tau \approx 100ps$ rather than in a shorter time interval. Equivalent time of illumination of accelerating structure with this pulse is $0.1 \div 1ps$, however. For a 0.5×0.5 TeV Collider the length becomes 2×170 m for $\lambda \cong 10\mu$ m and 2×17 m for $\lambda \cong 1\mu$ m, respectively.

7 REFERENCES

[1] A.A. Mikhailichenko, *The method of acceleration of charged particles*, Author's certificate USSR N° 1609423, Priority May 1989, Bulletin of Inventions (in Russian), N6, p.220, 1994.

[2] A.A. Mikhailichenko, *A concept of a Linac Driven by a Traveling Laser Focus*, 7th Advanced Accelerator oncepts Workshop, AIP 398 Proceedings, p.547.

[3]A.A. Mikhailichenko, *Laser Acceleration: a Practical Approach*, CLNS 97/1529, Cornell, 1997; also a Talk on LASERS'97, Fairmont Hotel, New Orleans LA, December 15-19, 1997.

[4] A.A. Mikhailichenko, *Injector for a Laser Linear Collider*, CLNS 98/1668.

[5] D. Du, X. Lu, G. Korn, J Squuier, G. Mourou, *Optical Breackdown with Femtosecond Laser Pulses*, CLEO94, May 8-13, 1994, Anaheim, California, Vol.8, p.407.

[6] R.C.Fernow, J.Claus, AIP Conference Proceedings, 279, 1992, p.212.

[7] W. Bruns, **GdfidL,** TU Berlin, 1997.

SPACE CHARGE EFFECTS IN DILUTED BEAM*

A. A. Mikhailichenko†
Wilson Laboratory, Cornell University, Ithaca, NY 14850

Abstract

For the particle acceleration with a laser-based source, the beams with particle's population required around one million only. The length of the bunch of the order of a micrometer yields such spacing between the particles, that the pancakes of the electromagnetic fields of individual particles are not overlapped at the cross section of the bunch. The space charge effects in this diluted beam considered. A comparison made with usual formula for betatron tune shift in self-field.

1 INTRODUCTION

The beams with minimal emittances required for successful operation of a laser driven accelerator. This is due to tiny dimensions of accelerating structure. The length of the bunch must be a fraction of the laser wavelength also. So one may expect that the space charge effects can be strong here. From the other hand, the number of the particles required in laser acceleration is about 10^6-10^7 only. This defined by a loading the acceleration structure. So one may hope that space charge effects are not strong enough to destroy the beam emittance.

2 DILUTED BEAM

Average distance between particles in a moving bunch can be defined as l_b / N, where l_b–is the bunch length in Laboratory frame, N–is the number of the particles in the bunch.

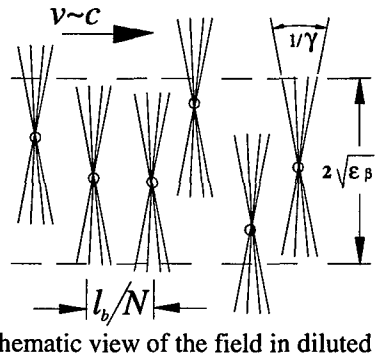

Figure 1: Schematic view of the field in diluted bunch.

We called beam *diluted*, if the particles separated in longitudinal direction so, that the pancakes of its individual fields having an opening angle $1/\gamma$, are not overlapped at the cross section $\sqrt{\varepsilon\beta}$ of the bunch,

$$\frac{l_b}{N} \geq \frac{\sqrt{\varepsilon\beta}}{\gamma}. \qquad (1)$$

Fig. 1 illustrates the condition (1). One can see that this condition is Lorenz-invariant, as the (1) could be rewritten as $\gamma l_b / N \geq \sqrt{\varepsilon\beta}$, where γl_b –is now a bunch length in its rest frame, and transverse size $\sqrt{\varepsilon\beta}$ is an invariant under Lorentz transformations. The last means that the closest particle in rest frame located at the distance of the order of the transverse bunch size.

In [1] there was presented a scheme of a cooler, what is mainly a sequence of wigglers and accelerating structures. The straight sections squeezed together for a compact size, so the back and forward trajectories are congruent. The longer the straight section is–the smaller influence of bends could be made. The bends itself could be made to give a small input into cooling dynamics. Here the particle needs to re-radiate its full energy a few times if the wigglers are dipole type. Let the wigglers have period $2\pi\lambda\!\!\!^{-}$ and the wiggler factor $K_x = eH_\perp \lambda\!\!\!^{-} / mc^2$, $H_\perp$–is a magnetic field value in the wiggler. Then the cooler promises equilibrium emittances as low as

$$(\gamma\varepsilon_x) \cong (1/2)\cdot \lambda\!\!\!^{-}_C \overline{\beta}_x (1 + K_x^2/2) K_x / \lambda\!\!\!^{-}$$

$$(\gamma\varepsilon_y) \cong (1/2)\cdot \lambda\!\!\!^{-}_C \overline{\beta}_y K_x / \lambda\!\!\!^{-},$$

where $\overline{\beta}_{x,y}$ – are averaged envelope functions in the wiggler, $\lambda\!\!\!^{-}_C = r_0/\alpha$ – is the Compton's wavelength, $r_0 = e^2/mc^2$, $\alpha = e^2/\hbar c$. The cooling time is $\tau_{cool} \cong (3/2)\cdot(\lambda\!\!\!^{-2} / c r_0 K_x^2 \gamma)$, $\gamma = E/mc^2$, what is not a function of the wiggler period. Substituting here for estimation $\gamma \cong 2\cdot 10^3$ (1 GeV), $\overline{\beta}_{x,y} \approx 1\,\text{m}$, $\lambda\!\!\!^{-} \cong 5\text{cm}$, $K \cong 5$, one can obtain for *quantum emittances* and for damping time the following estimations

$$(\gamma\varepsilon_x) \cong 2.5\cdot 10^{-8} \text{ cm rad},$$

$$(\gamma\varepsilon_y) \cong 2\cdot 10^{-9} \text{ cm rad},$$

$$\tau_{cool} \cong 8.6\cdot 10^{-3} s, \text{ or } 8.6\, ms.$$

This cooling time obviously does not depend on the length of the straight section, as the influence of the

* Work supported by National Science Foundation
† Phone: (607) 255-3785, Fax: (607) 255-8062, e-mail "mikhail@lns62.lns.cornell.edu

0-7803-5573-3/99/$10.00@1999 IEEE.

bends was neglected: shorter the length, faster the revolution. With such small emittances the beam size is about $\sqrt{\varepsilon\beta} \cong 1.6\cdot 10^{-6}$ cm, $\gamma \cong 10^4$ and this may give a reason for estimation of the transverse effects as a betatron tune shift and longitudinal effects. The length of the bunch required for laser acceleration is a fraction of the laser wavelength. Even suggesting the bunch compression one can have the bunch length in a cooler about 100μm.

For $N \cong 10^7$, the bunch will be diluted if it has the length $l_b \geq N\sqrt{\varepsilon\beta}/\gamma$, what in our case is

$$l_b \geq 10^7 \cdot 1.6\cdot 10^{-6}\cdot 10^{-4} = 1.6\cdot 10^{-3} cm \cong 16\mu m.$$

One can expect that any space charge phenomena can look in diluted beam different from a dense beam. First of all the space charge effects what tolerate to the transverse beam dynamics. The last one includes the betatron tune shift and Intra-Beam Scattering.

One can see also that for diluted beam the effects of radiation at IP of collider may look different also. In this publication we consider the transverse space charge effects.

3 SPACE CHARGE PHENOMENA

The field of the moving charge could be expressed as the following [2]

$$\vec{E} = \frac{e\vec{R}_t}{R_t^3}\frac{1}{\gamma^2(1-\beta^2 Sin^2\vartheta)^{3/2}}, \quad \vec{H} = \vec{\beta}\times\vec{E}, \quad (2)$$

where R_t –is the distance between the observation point and the present instant position of the charge (moment t), ϑ –is an azimuthal angle to the observation point, β –is a speed of the charge normalized to the speed of light. From (2) one can obtain that

$$\vec{E}_\perp = \vec{e}_\perp \gamma\frac{e}{R_t^2}, \qquad \vec{E}_\parallel = \vec{e}_\parallel \frac{e}{\gamma^2 R_t^2}, \quad (3)$$

where first expression corresponds to $\vartheta \cong \pi/2$ and the second one to $\vartheta \cong 0$, $\vec{e}_\perp, \vec{e}_\parallel$ –are unit vectors in rectangular to the trajectory and parallel directions respectively.

Let us calculate the flux of rectangular component $\vec{E}_\perp$ of electrical field over a strip having the width $2R_t/\gamma$ (see Fig.2). As the area of the strip is $2\pi R_t\cdot(2R_t/\gamma)$, from (3) one can obtain estimation as

$$Flux \cong \oint \vec{E}_\perp d\vec{S} \cong \vec{E}_\perp \cdot 2\pi R_t \frac{2R_t}{\gamma} \cong 4\pi e. \quad (4)$$

This is exactly as it must be from the equation $div\vec{E} = 4\pi\rho$, where ρ –is a macroscopic charge density. So for external observer in the laboratory frame at the distances $r \geq l_b\gamma/N$ can use a macroscopic definition of electric field as $E_\perp 2\pi r\cdot l_b = 4\pi eN$. The field at smaller transverse deflections represents much more complicated picture.

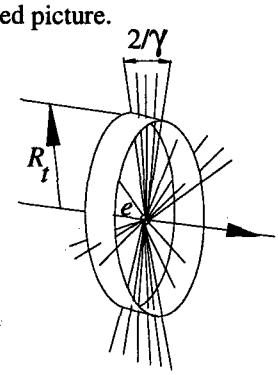

Figure 2. The strip ring around the relativistic charge.

Using (2), (3) one can see that the net force between two charges which longitudinal position is the same (so the fields are overlapping), could be expressed as

$$F_\perp \cong e\vec{E}_\perp - e\vec{\beta}\times\vec{H} = \gamma\frac{e^2}{R_t^2} - \gamma\cdot\beta^2\frac{e^2}{R_t^2} = \gamma\frac{e^2}{R_t^2}(1-\beta^2) \cong \frac{e^2}{\gamma R_t^2}, \quad (5)$$

what is obvious, as the magnetic field is growing proportionally to the electrical field value, so the ratio has the same factor $1/\gamma^2$.

One can see that the interaction between the particles is going more likely as impact, not as a smooth interaction.

To satisfy the condition that the energy of Coulomb interaction between the electrons is small compared with Fermi energy it needs to be $\rho \geq \left(e^2 m/\hbar^2\right)^3$ [3].

Now we consider the namely space charge effect, i.e. self-focusing. Let us, first, consider the *non-coherent tune shift*. This tune shift exists even when the beam is going exactly in the axis of the round chamber.

So let we calculate the tune shift with (2) and suggesting the beam diluted and compare this with calculations for the overlapping field lines.

First let us make a formal estimation with the formula which does not take into account the specific properties of diluted beam. Estimating the electrical field with (4) when the charge density $\rho \cong eN/(a_\perp^2 l_b)$ where $a_\perp^2 \approx (\gamma\varepsilon)\cdot\beta/\gamma$ –is the transverse beam size one can obtain

$$E_\perp \cdot 2\pi R\cdot l_b \cong \rho\cdot\pi R^2 l_b. \quad (6)$$

So the transverse force arising from space charge will be according to (5)

$$F_\perp \cong \frac{e^2 N}{2l_b(\gamma\varepsilon)\beta_x\gamma}\times R\cdot \quad (7)$$

Equation of motion of tested particle will be

$$\ddot{x}+Q^2\omega_0^2 x=\frac{F_\perp}{m\gamma}\cong\frac{e^2}{m}\frac{N}{2l_b(\gamma\varepsilon)\beta_x\gamma^2}x. \qquad (8)$$

So the corresponding tune shift will be

$$\Delta(Q\omega_0)^2_{usual}\cong\frac{e^2}{m}\frac{N}{2l_b(\gamma\varepsilon)\beta_x\gamma^2}. \qquad (9)$$

Now let us make estimations directly with (2). For small oscillation around equilibrium one needs to suggest $\vartheta<<1$ and for electrical field one can take

$$\vec{E}=\frac{e\vec{R}_t}{R_t^3}\frac{1}{\gamma^2(1-\beta^2\vartheta^2)^{3/2}}\to\frac{e}{R^2\gamma^2}\cdot\frac{x}{R}. \qquad (10)$$

For distance between neighboring particles one can suggest estimation in denominator as the following

$$R\cong[(l_b/N)^2+x^2]^{1/2}\approx l_b/N.$$

Now as the beam supposed diluted the only neighboring particle suggested to give an input as the field has a cubic dependence on distance. So for the force one can obtain an estimation

$$F_\perp\cong\frac{e^2}{(l_b/N)^3\gamma^4}\cdot x.$$

For the tune shift one can obtain

$$\Delta(Q\omega_0)^2_{diluted}\cong\frac{e^2}{m}\frac{1}{(l_b/N)^3\gamma^5}. \qquad (11)$$

For comparison (9) and (11) one can make some transformations

$$\frac{\Delta(Q\omega_0)^2_{diluted}}{\Delta(Q\omega_0)^2_{usual}}\cong\frac{l_b(\gamma\varepsilon)\beta_x}{N(l_b/N)^3\gamma^3}\cong\frac{N^2}{l_b{}^2\gamma^2}\frac{(\gamma\varepsilon)\beta_x}{\gamma}\approx 1,$$

where we used condition (1). Of cause exact value of *one* is out of accuracy of our calculations. This result however is a reflection of the fact that from the point of view of the observer in the moving frame there is no *qualitative* difference if the beam is diluted or not. In this system magnetic *focusing magnetic* field of the cooler transferred into electrical field as $E_x'=\gamma B_y$. So the electrical focusing field is horizontal now. Magnetic field $B_y'=\gamma B_y$. So the focusing system in the moving frame looks as incoming electromagnetic wave with a period, which now is γ times higher: $\omega'=\gamma 2\pi\cdot c/\lambda_F$, where λ_F –is a longitudinal period of the focusing system.

So one can use usual formulas for betatron tune shift. Taking into account the ratio between electrical and magnetic field (2) one can obtain the change in local focusing parameter

$$k(z)\cong-\frac{1}{pc}\frac{\partial\Delta F}{\partial r}\cong-\frac{2r_0N}{a^2l_b\gamma^3}\cong-\frac{2r_0N}{\beta_x(s)(\varepsilon\gamma)l_b\gamma^2}.$$

This is a defocusing effect. The corresponding *non-coherent* tune shift is

$$\Delta Q_{NC}\cong-\frac{1}{4\pi}\int_0^C\beta_x(s)k(s)ds\cong-\frac{1}{2\pi}\frac{r_0NC}{l_b\varepsilon\gamma\cdot\gamma^2}$$

where C –is the circumference of the cooler, or the length of the transport line. For the cooler $C\cong 2\pi Q\overline{\beta}$. So, the resulting formula for relative betatron tune shift will be

$$\frac{\Delta Q_{NC}}{Q}\cong-\frac{r_0N\overline{\beta}}{l_b(\varepsilon\gamma)\gamma^2}. \qquad (12)$$

Substitute here for estimation $\overline{\beta}_{x,y}\approx 100$ cm, $\gamma\cong 10^4$, $l_b\cong 100\mu$ m, one can obtain

$$\Delta Q_{NC}/Q\cong-\frac{2.8\cdot10^{-13}10^7100}{10^{-2}2.5\cdot10^{-8}10^8}=-0.011.$$

For vertical relative tune shift one obtains $\Delta Q_{NC}/Q\cong-0.038$.

So one can see, that even for such a tiny emittances (and dimensions) the space charge effects does not look as a drastic ones.

4 REFERENCES

[1] A. A. Mikhailichenko, *Injector for a Laser Linear Collider*, CLNS 98/1568, Cornell, 1998. Presented On 8th AAC Workshop, Renaissance Harborplace Hotel, Baltimore, Maryland, July 5-11, 1998. See also at http:/www.lns.cornell.edu/public/CLNS/.

[2] L.D. Landau, E.M. Lifshitz, *The Field Theory*, Pergamon Press, 1983.

[3] L.D. Landau, E.M. Lifshitz, *Statistical Physics*, Pergamon Press, 1985.

VACUUM LASER ACCELERATION TESTS*

Y. Liu†, P. He, D. Cline, University of California, Los Angeles, CA 90095-1547

Abstract

We propose to test for the possibility of accelerating an electron beam (utilizing the existing high-power CO_2 laser and low emittance electron beam at Brookhaven Accelerator Test Facility) in vacuum to the current CO_2 laser power limit. The latest vacuum laser acceleration results can be verified [1] by the schemes discussed here.

1 INTRODUCTION

Laser acceleration in vacuum has been studied theoretically for many years and several schemes utilizing focused Gaussian laser beam(s) have been proposed [2]–[9]. In most of the schemes, researchers attempt to confine the interaction to a finite length, but none of them has been successful until recently. In 1997, a group of physicists [1] demonstrated direct acceleration of free electrons in vacuum to MeV energies by a linearly polarized and intense subpicosecond laser pulse, appearing directly violate a long-held theorem [10].

A focused, radially polarized, Gaussian laser beam can produce a stronger longitudinal electric field than the linearly polarized one [11]–[14]. The Brookhaven Accelerator Test Facility (ATF) provides a radially polarized, high-power, Gaussian CO_2 laser beam (3-TW, 1-ps) [15, 16] and a high-quality electron beam [17] with which to perform the vacuum laser acceleration test. The electron energy modulation will be ramped up to the current CO_2 laser power limit. Moreover, since the Compton Scattering experiment [18] was recently conducted on the ATF beamline #1 (which is shared by the STELLA experiment), the hardware and optics configurations will require only slight modification since they are quite similar to the requirements for the vacuum acceleration experiment. This similarity provides a great opportunity to utilizing the existing hardware with little additional cost.

2 INTENSITY DISTRIBUTIONS OF A FOCUSED DONUT-SHAPED LASER BEAM

As seen in Figure 1, a parallel or weakly focused Gaussian laser beam passes through an axicon telescope (consisting of two thin axicon lenses) and is focused by a thin lens at distance F. The intensity distribution of the donut-shaped beam transformed from a Gaussian beam is expressed by

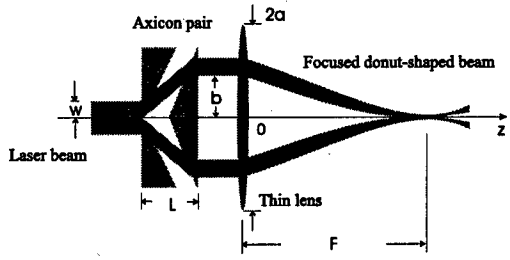

Figure 1: Schematic of generating and focusing a donut-shaped beam at the distance F by a pair of axicon lenses and a thin lens.

$$I(r_0) = \frac{P_0}{\pi w^2}\left(1-\frac{b}{r_0}\right)\exp\left[-2\left(\frac{r_0-b}{w}\right)^2\right], r_0 \geq b, \quad (1)$$

where P_0 is the peak power and $b = L\tan(\theta)$ is the inner radius of the donut-shaped beam, where L is the distance between two axicons and θ is the refraction angle of the axicon, and w is the beam radius at the first axicon surface. By adjusting L, the inner radius, b, is controllable. The maximum intensity, I_m, occurs at r_m where the differential of Eq. (1) is equal to zero. Note that Eq. (1) is derived ideally from the geometrical optics of the axicon telescope. The diffraction of the laser beam in the course of conversion is neglected.

Figure 2 shows the geometric configuration for the usual Fresnel–Kirchhoff diffraction integral formulation with aperture-plane integration. The field amplitude distribution at point $P(r,\theta)$ in the x′–y′ plane is given, up to a constant phase factor, by the Fresnel–Kirchhoff integral for an aperture radius a [19],

$$\Psi_p(r,\theta) = \frac{k}{z}\int \Psi_0(r_0,\theta_0)\exp(-ikR)\Phi_l dS, \quad (2)$$

where k is the wavenumber; $\Psi_0(r_0,\theta_0) \sim \sqrt{I(r_0)}$ is the field amplitude distribution at point $Q(r_0,\theta_0)$ of the lens surface and $I(r_0)$ is given by Eq. (1); Φ_l is the phase retar-

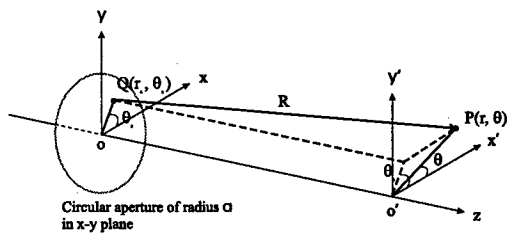

Figure 2: Geometry for Fresnel–Kirchhoff aperture-plane diffraction formulation.

* Work supported by U.S. Department of Energy, Grant No. DE-FG03-92ER40695 with UCLA

† Email: yliu@physics.ucla.edu

dation of the lens expressed as

$$\Phi_l = \exp\left(\frac{ikr_0^2}{2F}\right), \qquad (3)$$

where F is the geometrical focal length; and R is the distance between Q and P,

$$R \approx z + \frac{r_0^2 + r^2 - 2r_0 r\cos(\theta_0 - \theta)}{2z}, \qquad (4)$$

Substituting Eqs. (1), (3), and (4) into Eq. (2)

$$\begin{aligned}\Psi_p(r,\theta) &= E_0 \frac{k}{z}\int_b^a \left(1-\frac{b}{r_0}\right)^{1/2} \exp\left[-\frac{1}{2}\left(\frac{r_0-b}{w}\right)^2\right] \\ &\times \exp\left[ik\left(\frac{r_0^2}{2F} - z - \frac{r_0 2 + r^2}{2z}\right)\right] \\ &\times J_0\left(\frac{kr_0 r}{z}\right) r_0 dr_0 d\theta_0, \end{aligned} \qquad (5)$$

where E_0 is a constant. The relation $\int_0^{2\pi} \exp[ix\cos(\theta_0 - \theta)] = 2\pi J_0(x)$ was used to get Eq. (5), the numerical results of which are shown in Figure 3. Where the lens aperture radius is $a = 2.5$ cm and focal length is $F = 15.0$ cm, the inner radius of the donut-shaped beam is $b = 1.0$ cm and the width is $w = 0.5$ cm at the lens surface. The small peaks at $r = 0$ in Figure 3(a), (b), and (d) are from diffraction effect. The beam width at the focal plane is $w_0 = 31\mu$m [Figure 3(c)] and the donut feature vanishes (w_0 is defined as the beam radius where the intensity drops to e^{-2}). Figure 4 shows the laser intensity distribution on the beam z-axis.

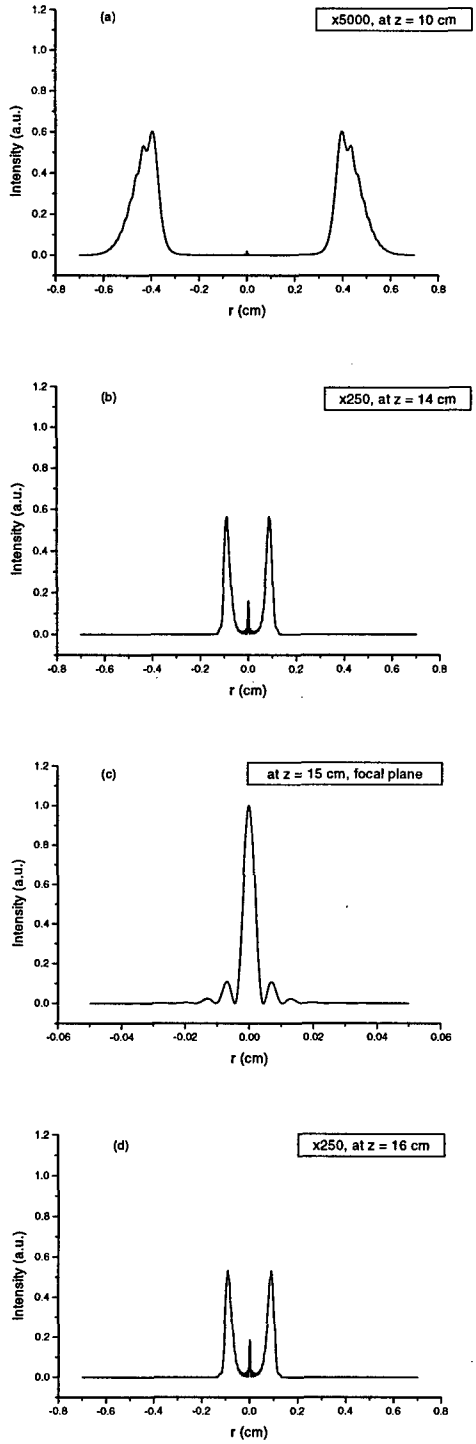

Figure 3: Cross sections of the focused donut beam intensity distributions in different planes. The focal lens position is at z = 0. Note, different scales for r-axes and the intensities in (a), (b) and (d) are normalized by (c).

3 CONCEPTUAL DESIGN OF THE EXPERIMENT

The proposed experiment is to perform four laser–electron beam-interaction processes. The conceptual schematic of the first two test processes is shown in Figure 5. In the first process, a linearly polarized, axisymmetric, annular ("donut-shaped") Gaussian-distributed, CO_2 laser beam is delivered to a vacuum chamber through a ZnSe window. A parabolic mirror with a hole is positioned along the electron beam path (z-axis) in the chamber. The hole is located at the mirror optical center and allows the electron beam to meet with the laser beam in the focal region. A pop-in target, located near the focal point, is able to travel along the beam axis. This diagnostic device is used to align the laser beam with the electron beam in the focal region. The second process will repeat the first one [20], but will utilize a radially polarized beam, which will be delivered by the existing radially polarized converter built for the STELLA experiment. The third process will perform a scheme with two crossed beams, as shown in Figure 6. The two beams are split from a single beam by a beamsplitter and have a phase difference π in the interaction region. The last is a single beam scheme, where one laser beam and the electron beam will cross at the laser focal point with small angle (one of the laser beams having been turned off, see Figure 6).

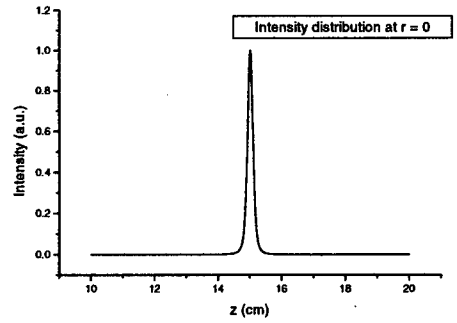

Figure 4: Laser intensity distribution along the beam (z) axis at r = 0.

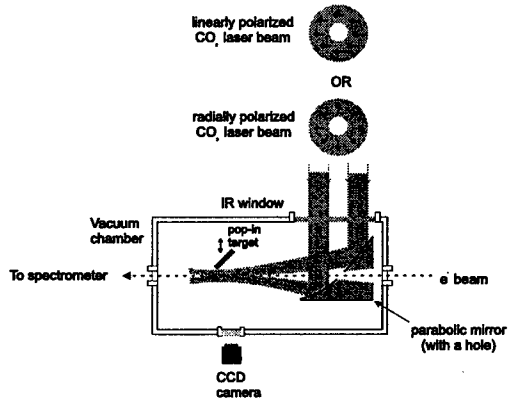

Figure 5: Conceptual layout of vacuum laser acceleration using donut-shaped beam.

4 DISCUSSIONS

The optics configuration, which is fairly simple, can be used to perform all four schemes with only slight changes of the optics setup outside the chamber. The scheme using a donut-shaped beam is able to overcome optical damage difficulty as laser power increases [20]. However, the interaction length is many times more than the Rayleigh length due to diffraction and will degrade or wash out the net energy gain according to the theorem [10]; however, the results reported in Ref. [1] will be verified eventually.

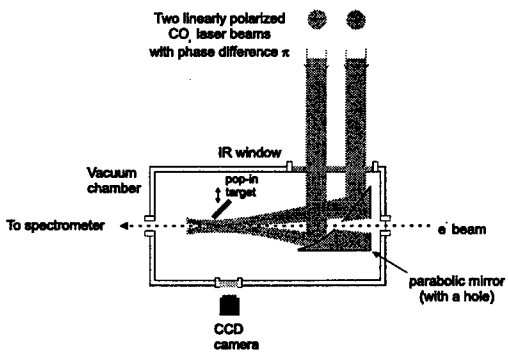

Figure 6: Conceptual layout of vacuum laser acceleration using a two crossed laser-beam scheme. If one of two beams is turned off, it becomes a single beam scheme.

5 REFERENCES

[1] G. Malka, E. Lefebvre, and J.L. Miquel, *Phys. Rev. Letts.*, **78** (17), 3314 (1997).

[2] M. O. Scully, *Appl. Phys. B*, **51**, 238 (1990).

[3] E.J. Bochove, G.T. Moore, and M.O. Scully, *Phys. Rev. A*, **46** (10), 6640 (1992).

[4] S. Takeuchi, R. Sugihara, and K. Shimoda, *J. Phys. Soci. Japan*, **63** (3), 1186 (1994).

[5] T. Hauser, W. Scheid, and H. Hora, *Phys. Lett. A*, **186**, 189 (1994).

[6] E. Esarey, P. Sprangle, and J. Krall, *Phys. Rev. E*, **52** (5), 5443 (1995).

[7] P. Sprangle, E. Esarey, J. Krall, and A. Ting, *Optics Comm.*, **124**, 69 (1996).

[8] B. Hafizi, E. Esarey, and P. Sprangle, *Phys. Rev. E*, **55** (3), 3539 (1997).

[9] B. Hafizi, A Ting, E. Esarey, P. Sprangle, and J. Knall, *Phys. Rev. E*, **55** (5), 5924 (1997).

[10] J.D. Lawson, *IEEE Trans. Nucl. Sic.* **NS-26**, 4217 (1979); P.M. Woodward, *J. Inst. Electr. Eng.* **93**, 1554 (1947); R.B. Palmer, *Lecture Notes in Physics 296, Frontiers of Particle Beams* (Springer, Berlin, 1988) p. 607.

[11] M. Lax, *Phys. Rev. A*, **11** (4), 1365 (1975).

[12] L. Cicchitelli, H. Hora, and R. Postle, *Phys. Rev. A*, **41** (7), 3727 (1990).

[13] K. Shimoda, *J. Phys. Soci. Japan*, **60** (1), 141 (1991).

[14] P.W. Milonni and J.H. Eberly, *Laser* (Wiley, New York, 1988), chap. 14; A. Yariv, *Quantum Electronics*, 3rd ed. (Wiley, New York, 1989), chap. 6.

[15] I. V. Pogorelsky, I. Ben-Zvi, J. Skaritka, et al., *AIP Conference Proceedings* **398** (1997) p. 937.

[16] ATF terawatt CO_2 laser specifications.

[17] D.T. Palmer, X.J. Wang, et al., *AIP Conference Proceedings* **398** (1997) p. 695.

[18] A.Tsunemi, A.Endo, et al., "Ultra-Bright X-ray Generation Using Inverse Compton Scattering of Picosecond CO2 Laser Pulses," in this proceeding.

[19] M. Born and E. Wolf, *Principles of Optics*, 6th ed. (Pergamon Press, Oxford, 1986).

[20] Y. Liu, D. Cline, and P. He, *Nucl. Instr. & Meth. in Phys. Res.* A, 424 (2-3), 296 (1999).

ON THE POSSIBILITY OF CREATION OF ULTRA-HIGH-CURRENT PERIODICAL MICRO-ACCELERATOR OF SUBRELATIVISTIC OSCILLATING ELECTRON BEAM PRODUCED AND CONTROLLED INSIDE ORIENTED CRYSTAL BY POWERFUL SHORT POLARIZED LASER PULSE

Vladimir I. Vysotskii, Kiev Shevchenko University, Radiophysical Faculty
Vladimirskaya St. 64, Kiev, Ukraine, 252033; e-mail viv@vhome.kiev.ua

The paper considers the dynamics and action on the resonant nuclei of fast electrons produced in crystal by short powerful laser pulse[1,2].

The solution of relativistic ponderomotive equation for electron

$$g^{ik}(\partial S/\partial x^i + eA_i/c)(\partial S/\partial x^k + eA_i/c) = m^2c^2$$

in this case has the parametric form

$$x = -g\cos\eta;\ y = 0;\ z = -\Delta z \sin 2\eta;$$
$$p_x=(eE_0/\Omega)\sin\eta,\ p_y=0,\ p_z= -(e^2E_0^2/4\gamma\Omega^2)\cos 2\eta;$$
$$g = eE_0c/\gamma\Omega^2 = 2e(\pi qc)^{1/2}/\gamma\Omega^2;\ \eta = (\Omega t - kz);$$
$$\Delta z = e^2E_0^2c/8\gamma^2\Omega^3 = \pi qe^2/2\gamma^2\Omega^3;$$
$$t= (\eta/\Omega) - (e^2E_0^2/8\gamma^2\Omega^3)\sin 2\eta;$$
$$\gamma^2 = m^2c^2+e^2E_0^2/2\Omega^2 = m^2c^2+2\pi qe^2/c\Omega^2;$$

Here g^{ik} is contravariant metric tensor,

$$\mathbf{A}=\{A_x,0,0\};\ A_x= -(eE_0/\Omega)\sin(\Omega t - kz)$$

is the vector potential of laser field.

If the short (duration $\Delta t \le 10^{-12}$ s) and focused (area of laser beam $\Delta S \le 10^{-4}$ cm^2) optical laser pulse with energy W acts upon the crystal, its electric field with maximal value

$$E_{max}= E_0 \equiv (4\pi W/\Delta Sc\Delta t)^{1/2}$$

can exceed the threshold ionization field $E_i \approx e/r_b^2$ of the atom in the crystal.

For the case of laser field $E_0 << \Omega mc/e$ (e.g., at $\Omega=2.10^{15}$ s^{-1}, λ=1micron and at

$$q \equiv W/\Delta S\,\Delta t << q_0 \equiv \Omega^2m^2c^3/2\pi e^2 \approx 10^{19}\ \mathrm{Wt/cm^2\ s})$$

we have

$$g \equiv \Delta x = eE_0/m\Omega^2 = (4\pi e^2q/m^2c\Omega^4)^{1/2},$$
$$\Delta z = e^2E_0^2/8\Omega^3m^2c = e^2\pi q/2m^2c^2\Omega^3.$$

In this case

$$\Delta z/g = eE_0/8\Omega^2mc << 1.$$

E.g.,at $q = 10^{16}$ Wt/cm^{2}s we have

$$g\equiv\Delta x \approx 100\mathrm{A},\ \Delta z \approx 0{,}7\mathrm{A}.$$

In this case the produced electrons will move synchronously with the laser field **E** , i.e., periodically with subrelativistic velocity

$$v = dx/dt \approx (eE_0/m\Omega)\sin(\Omega t - kz).$$

During the action of short laser pulse the electron system and ion lattise of crystal stays quasi-cold (the electron system thermalizes only at $t \ge \delta t_1 \approx 10^{-11}$ s, while the lattice stays cold until $t \ge \delta t_2 \approx 10^{-8}$ s).

The following items are important for this consideration:.

1) Both free and ionization (ΔZ electrons per atom) atom electrons (with total concentration $n^* \ge 10^{23} - 10^{24}$cm^{-3}) are oscillating. The amplitude of electron oscillations along laser field $\mathbf{E_0}$ polarization equals

$$\Delta x \approx (4\pi e^2W/m^2\Delta Sc\Omega^4\Delta t)^{1/2}.$$

In case of powerful laser pulse ($\lambda\approx$1 mkm, 10^{19} Wt/cm^2 s >> $q \ge 10^{12}$ Wt/cm^2 s) this amplitude reaches the values $\Delta x \approx$ 500 -1000 A and exceeds the interatomic distance d ≈ 2 A by several orders of magnitude.

2) For such regime of coherent electron motion the kinetic energy of periodically moving electron averaged by period of oscillation $2\pi/\Omega$ equals

$$\langle T_{coh}\rangle \approx \pi e^2W/m\Delta Sc\Omega^2\Delta t \ge 50 \div 100\ \mathrm{KeV}.$$

For this case the maximal velocity of electrons equals

$$v_{max} = eE_0/m\omega = (4\pi e^2W/m^2\Delta Sc\Omega^2\Delta t)^{1/2} \approx (0{,}5 - 0{,}8)c.$$

This allows to consider the averaged plane and axis potentials of crystal lattice instead of system of discrete atoms of crystal. Such simplification make it necessary to consider the influence of mutual orientation of laser field $\mathbf{E_0}$ polarisation and crystallographic direction of quasi-cold crystal (at $t \le \Delta t << \delta t_2$) upon the motion of fast electrons and leads to the model (regime) of laser produced electron beam channeling with self-focusing

0-7803-5573-3/99/$10.00@1999 IEEE.

$\phi(\rho)$ of moving electrons to plane (axis) of crystal and increasing of moving electron density (beam density) in the volume of localization of nuclei and inside atomic electrons by $F \approx 3$ - 10 times. If the laser wave polarisation $\mathbf{e}_x=\mathbf{E}_0/E_0$ is parallel to the crystal axes or planes, the density of current of laser generated fast electrons inside atoms equals

$$j_{max} \approx n^* v_{max} F \approx 10^{15} \text{ A/cm}^2.$$

In fact this system can be considered as a unique ultra-high-current subrelativistic periodical micro-accelerator.

3) For this regime of coherent electron motion the average $<T_{coh}>$ and maximal $T_{max}=2<T_{coh}>$ electron energy exceeds the equilibrium plasma electron energy

$$<T_{eq}> = 3KT/2 \approx 0.5 \div 3 \text{ KeV}$$

with the same power $W/\Delta t$ (for longer pulses $\Delta t \gg \delta t_1$) by several orders of magnitude. Also it is possible using this regime to excite nuclear states (direct Coulomb excitation) with superthermal energy

$$\hbar\omega_{sk}^{(max)} \approx <T_{coh}> \gg KT.$$

4) The energy loss of moving electron (accelerated and ruled by laser field **E**) on each spatial period of its oscillation

$$\Delta E = \oint dT(v(x))/dx \approx$$

$$(\pi e^3 n_e / E_0) \, | ln\{1-(eZ^{2/3}m\Omega/16E_0\hbar)^2\}| << 1 \text{ KeV};$$

is small and $<T_{coh}> \gg \Delta E$.

Here for $v \geq e^2Z^{2/3}/\hbar$ (inelastic regime of electron motion)

$$dT/dx = dT_1/dx \equiv -2\pi e^4 n_e\{ ln[(m^2v^2c^2)/(2J^2(1-v^2/c^2)^{3/2})] - ln2(2(1-v^2/c^2)^{1/2}) -1+v^2/c^2+1-v^2/c^2\}/mv^2,$$

and for $v \leq e^2Z^{2/3}/\hbar$ (elastic regime of electron motion)

$$dT/dx << dT_1/dx;$$

J - averaged potential of atom ionization,

$$v(x) = v_{max}\,[1-(x/\Delta x)^2]^{1/2}.$$

The motion of electrons remains quasi-harmonic during $N \approx \Omega\Delta t \approx 10^3$ oscillations with total path

$$x \approx 2N\Delta x \approx 10^6 \text{ Å}$$

5) The angular divergence of the electron beam accelerated by laser equals

$$<\theta^2> = n_0\Delta x \int_{v_{min}}^{v_{max}} f(v)dv \int_0^{\pi} \theta^2 \{d\sigma(v,\theta)/d\theta\} \sin\theta \, d\theta \approx$$

$$(16\, Z^2e^4\, n_0\Delta x/m^2\pi v_{max}) \int_{v_{min}}^{v_{max}} \sqrt{1-(v/v_{max})^2}\; dv/v^4 <$$

$$16\, Z^2e^4\, n_0\Delta x/3m^2\pi v_{max}\, v^3_{min}$$

Here

$$d\sigma(v,\theta)/d\theta =$$

$$(2em/\hbar^2K^2)^2 \Big| \int_0^{\infty} |\sin Kr/Kr|[\rho_n(r) - \rho_e(r)]4\pi r^2 dr\Big|^2 =$$

$$(e^4/4m^2v^2)\{\exp(-3K^2u^2) - (1 - K^2R^2/4)^{-2}\}^2 \operatorname{cosec}^4\theta/2$$

is the differential scattering cross-section for moving electron in crystal lattice[3],

$$K = (2mv/\hbar)\sin\theta/2,\ \rho_n(r) = Ze|\Psi_{n0}|^2,\ |\Psi_{n0}|^2 =$$
$$(2\pi u_0^3)^{-3/2}\exp(-r^2/2u_0^2),\ u_0=\sqrt{3}\,u;$$
$$\rho_e(r) = Ze|\Psi_e|^2 = (Ze/\pi R_0^3)\exp(-2Zr/R_0),$$

u is 1-dimentional averaged amplitude of thermal atom oscillation in lattice in ground state.

According to the result of $<\theta^2>$ calculation

$$[<\theta^2>]^{1/2} \leq \theta_{chan}$$

for a crystal with not very heavy atoms) the motion of fast electrons remains quasi-channeling within each spatial period of laser induced oscillation Δx.

These fast electrons interact with Mossbauer-type nuclei which are non-excited in their initial state. The low energy transitions in nuclei are known to be the result, in most cases, of single-nucleon processes.

Assuming **r** to be the radius of a proton related to Mossbauer transition, one can easily deduce an expression for non-stationary energy of the interaction of a moving electron with a nucleus

$$V(\mathbf{R},t)= \int \rho_e(r)\, \varphi(\mathbf{r},\mathbf{R},t)d\mathbf{r} = -Ze^2 \exp(-R(t)/R_0)/|\mathbf{R(t)} - \mathbf{r}|,$$

where $R_0 = 1{,}4\, \hbar^2/me^2\,(Z - \Delta Z)^{1/3}$ is parameter of electronic shielding,

$$\rho_e(r) = e\sum_{k=1}^{Z} \delta(\mathbf{r} - \mathbf{r_k}),\ \varphi(\mathbf{r},\mathbf{R},t) =$$
$$e\exp(-R(t)/R_o)/\,|\mathbf{R}\,(t)- \mathbf{r}|$$

is Coloumb potential,

$\mathbf{R}=\{vt, \rho, 0\}$, ρ.- targeting distances.

The above interaction can induce excitation of the nucleus. The probability of the excitation can be calculated according to equation

$$P_{sk}= n^* \int_{\rho_{min}}^{\rho_{max}} \int_{v_{min}}^{v_{max}} W_{sk}(\rho,v)\, f(v) v\phi(\rho) 2\pi\rho d\rho dv.$$

Here

$$W_{sk}(\rho,v) = h^{-2} \left| \int_{-\infty}^{\infty} V_{sk}(\rho,v,t) \exp(i\omega_{sk}t)\, dt \right|^2,$$

$$f(v) = [1-(v/g\Omega)^2]^{1/2}/\pi g\Omega \; -$$

the function of velocity distribution for harmonic motion of electron, $g = eE_0/m\Omega^2$.

The motion of fast electrons can be approximated by the laws of classical kinetics.

Expanding now the expression for $V(\mathbf{r},t)$ into a series of the parameter $r/(\rho^2 + v^2t^2)^{1/2}$

$$V(r,t) \approx - Ze^2\{1/R + [\rho y - (x^2+y^2+z^2)/2]/R^3 + 3[(\rho y)^2 + x^2+y^2+z^2)^2/4 - \rho y(x^2+y^2+z^2) + (vtx)^2/2]/2R^5 + 5[(y\rho)^3 \rho^2 y^2 (x^2+y^2+z^2)/2 + 3\rho y(vtx)^2\ 3v^2t^2(x^2+y^2+z^2)^2/2]/2R^7 + 35[(\rho y)^4/2 + (vt)^4 x^4/2 + 3(vt\rho xy)^2]/4R^9\}$$

and calculating the matrix elements of the operator of the nucleon coordinate $\mathbf{r}$ we have

$$W_{sk} \approx (Ze/v\rho\hbar)^2 \left| 2Q^{(1)}_{sk} + Q^{(2)}_{sk}/\rho + 6Q^{(3)}_{sk}/\rho^2 + Q^{(4)}_{sk}/2\rho^3 \right|^2.$$

Here

$$Q^{(1)} \equiv d = ey,\ Q^{(2)} = e(y^2-z^2),\ Q^{(3)} = e(y^3-y^2z/3),$$
$$Q^{(4)} = e(y^4+z^4-6y^2z^2) \; -$$

are correspondingly matrix elements of the dipole moment (l=1), quadrupole one (L=2), octupole moment (L=3) and so on.

The size of direct Coulomb excitation region satisfied the condition for targeting distances

$$\rho_{min} \geq \rho \geq \rho_{max}.$$

Here

$$\rho_{min} \geq R_n = r_n A^{1/3}\ (r_n = 1{,}2 \cdot 10^{-13}\ \text{cm});$$
$$\rho_{min} \geq \rho_{min}^{(1)} = Ze^2/mv^2 \text{ - quasiclassical limit;}$$
$$\rho_{min} \geq \rho_{min}^{(2)} \approx \hbar/mv \text{ - quantum limit}$$

and

$$\rho_{max} \leq R_o = 1{,}4\, \hbar^2/me^2 (Z - \Delta Z)^{1/3};$$
$$\rho_{max} \leq v/\omega_{sk} \text{ - adiabatic limit.}$$

After averaging by v

$$(v_{min} \leq v \leq v_{max},$$
$$v_{min} \approx (2\hbar\omega_{sk}/m)^{1/2},$$
$$v_{max} = 4\pi eW/\Delta Sc\Delta t)^{1/2}/m\Omega)$$

and targeting distances ρ one can derive the result for total probability of direct excitation of the nucleus[1,2].

The total probability of Coulomb excitation of nuclei (or excitation of atomic electron to upper X-level) in dipole approximation equals

$$P_{sk} \approx [3Z^2e^2n^*c^3/2\hbar\omega_{sk}{}^3](m/\hbar\omega_{sk})^{1/2} ln[eE_0/\Omega(m^3/\hbar\omega)^{1/2}]\, FG_\tau.$$

Here

$G_\tau = \Delta t/\tau$ for the case $\tau \geq \Delta t$ and

$G_\tau = 1$ for the other case $\tau \leq \Delta t$,

τ is time of life of excited nucleus state E_k for dipole transition $E_s \rightarrow E_k$ with excitation frequency of nucleus ω_{sk}.

For octupole transitions

$$P_{sk} \approx 9Z^2e^2n^*c^7m^4(eE_0\Omega/m)^3/28\pi\hbar^7\, FG_\tau$$

The probability of Coulomb excitation of nuclei by laser produced subrelativistic oscillating electrons during action of short powerful polarized optical laser pulse on perfect oriented crystal exceeds the probability of Coulomb excitation by thermalized electrons (at same laser power $W/\Delta t$) by the coefficient

$$C \approx (KT/\hbar\omega_{sk})^{1/2} \exp(\hbar\omega_{sk}/KT),$$

which equals several orders of magnitude for case $\hbar\omega_{sk} >> KT$. As a result the probability of Coulomb excitation of lattice nuclei reaches 10-50% (for laser with $q \approx 10^{17}$ Wt/cm^2 and for nuclei with $\tau/\Delta t \approx 10^{-3}$) .

Such nonthermal mechanism of obtaining excited nuclei (or atomic electron) state proves by many orders more effective, than traditional methods of thermal (at $\Delta t >> \delta t_1$) or photo (by equilibrium X-rays) excitation (at $\Delta t >> \delta t_1$) of nuclear or atomic levels for gamma-laser in quasi-equilibrium laser electron or ion plasma.

REFERENCES

1. V.I. Vysotskii., N.V. Maksuta, V.P. Bugrov, A.A. Kornilova, " Channeled motion regime and the peculiarities of interaction with nuclei of the fast ionization electrons produced in crystal matrix under the irradiation by powerful laser pulse", *Surface*, **6**, 20 (1997) (In Russian).

2. V.I. Vysotskii, V.P. Bugrov, A.A. Kornilova, "About the effectiveness of excitation of highly activa nuclear systems at laser pulse heating of the gamma-resonant medium", *Plasma Physics*, **23**, 1127 (1997) (In Russian)

Multi-Harmonic Impulse Cavity*

Y. Iwashita†
Accelerator Laboratory, NSRF, ICR, Kyoto University, Uji, Kyoto 611, Japan

Abstract

A method that may enable very high gradient acceleration is proposed. A short impulse shape wave form can be generated by superposition of many harmonics. It is achieved by a cavity with multi-harmonic resonances, which may have ten or more modes excited simultaneously with proper phases. Such impulse wave form may achieve very high peak accelerating gradient. A preliminary result of a cold model cavity is presented.

1 INTRODUCTION

Acceleration or debunching (a.k.a. phase rotation) of secondary-beams such as pions or muons has to be very quick because of their short life times[1,2]. Because they are supposed to be initially bunched within very narrow time width, duration of the acceleration voltage can be very short (see Fig. 1). This impulse shape wave form can be achieved by a cavity with multi-harmonic resonances, which may have ten or more modes excited simultaneously with proper phases (see Fig. 2). Such impulse wave form may achieve very high peak accelerating gradient, because of the short duration of its peak. One more feature of this scheme may be the power consumption. Assuming that every mode has same order of shunt impedance, the total RF power is proportional to the number of modes that is also proportional to the acceleration gradient, while it is proportional to square of the acceleration gradient for a single mode cavity. This paper explains some ideas for Multi-Harmonic Impulse Cavity (MHIC).

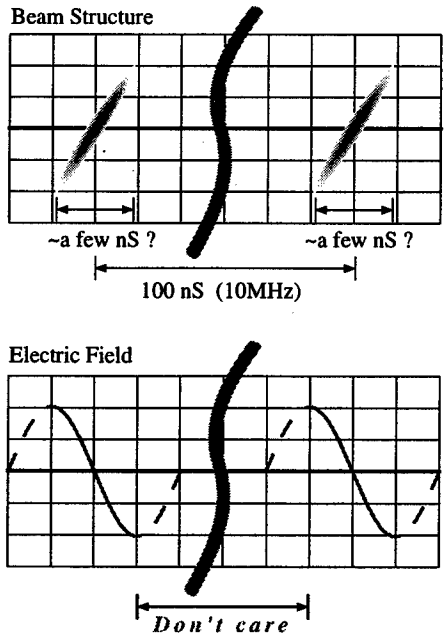

Figure 1: Time structure of a bunched beam and electric field for debunching.

2 COAXIAL CAVITY

A simple example of such a cavity is a λ/2 coaxial resonator, which has harmonic integer resonances (see Fig. 3). Among the resonances, those with even harmonic number cannot be used because they have nodes of electric field distribution at the center. Effects of a beam hole in the conductor should be compensated for a cavity to have right resonant frequencies.

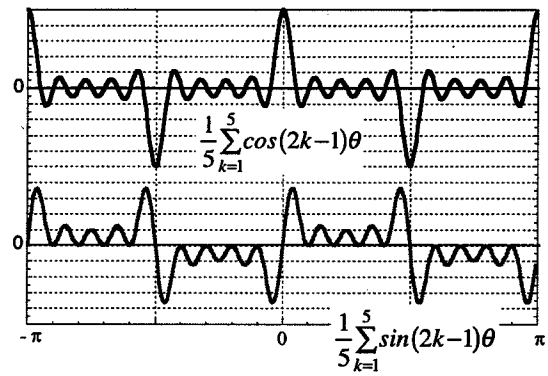

Figure 2: Superposition of harmonics to generate impulse train. Upper one is adequate for acceleration. Lower one is for (de-)bunching.

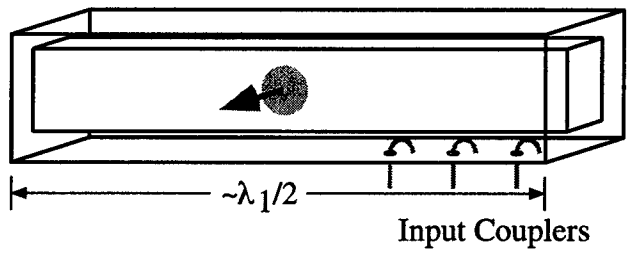

Figure 3: λ/2 coaxial resonator having many input couplers for harmonics.

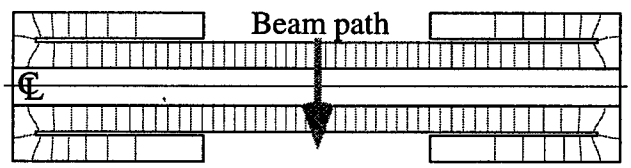

Figure 4: Folded coaxial resonator can reduce the cavity length.

* Work supported in part by Grant-in Aid for Scientific Research from Ministry of Education, Science, Sorts and Culture Government of Japan.

† Email: iwashita@kyticr.kuicr.kyoto-u.ac.jp

Assuming that the fundamental frequency is 10 MHz, a length of a λ/2 coaxial resonator becomes 15 m, which is rather huge for a construction. Folded coaxial configuration (see Fig. 4) can be employed to reduce the cavity length (actually the width in this case). For a real application, these cavities are lined up on a beam axis. The folded coaxial cavities may have cross bar configuration for better space factor. Because there is a vacant space in the inner conductor, this space can be filled with nested cavities for higher harmonics as shown in Fig. 5. On the other hand, this location may be useful for a focusing device such as a Q magnet or a solenoid coil. For a higher order mode, the conductor surface of the peripheral area beyond the first node does nothing but power consume. Choke structures or low pass filters at these points may block power flows to the peripheral area and increase its shunt impedances.

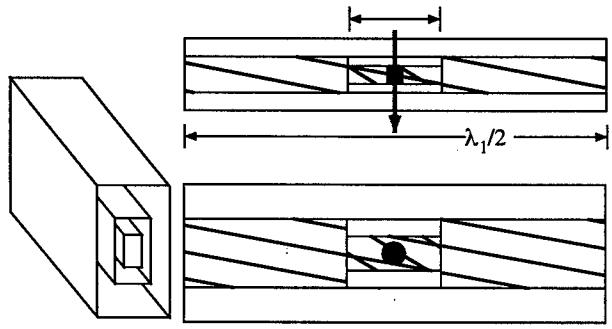

Figure 5: Nested coaxial cavity.

In very rough estimation assuming that shunt impedance of each mode is 4MΩ/m and 40kW/m is available for each mode, we can obtain 1MV/m for 120kW/m. With a naive scaling, operation of thirty modes achieves 10MV/m for 1MW/m. There should be a lot of difficulties achieving this level. One major problem is increase of mode density toward the higher frequency region.

In order to fine-tune the resonant frequencies, many frequency tuners are desired. An RF power feeding scheme should be established. Although a cavity with single RF coupler is simple, the RF circuit may be complicated because many harmonics have to be combined and matched to the cavity. On the other hand, installing multiple couplers on a cavity makes the fabrication complicated. Figure 6 shows a schematic drawing of a proof of principle (POP) model for a coaxial cavity geometry (CoaxPOP). Coupling scheme, frequency tuners and RF characteristics will be investigated. on this cavity. Experiments on the discharge properties are also possible so that it is designed as vacuum tight. Four of frequency tuners and coupling loops are prepared (see Photo 1). One antenna can be installed at the center port for measuring the electric field.

Figure 7 shows a preliminary data from the CoaxPOP, where RF power transmission is measured between a)

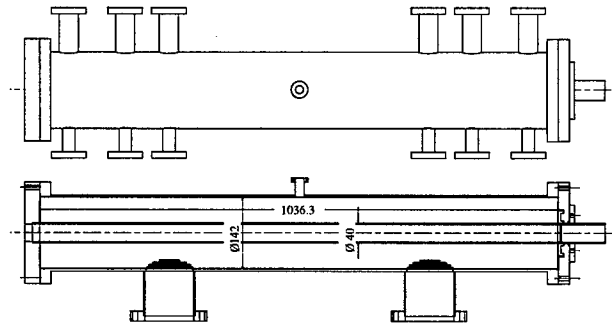

Figure 6: Proof of principle model for coaxial cavity.

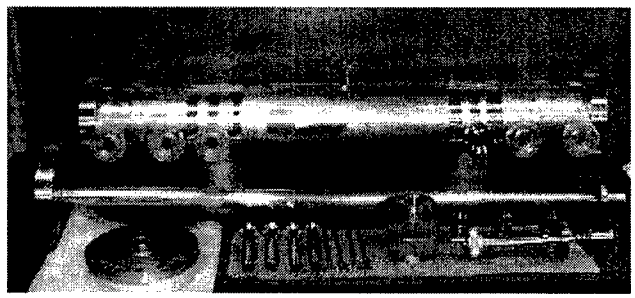

Photo 1: CoaxPOP parts

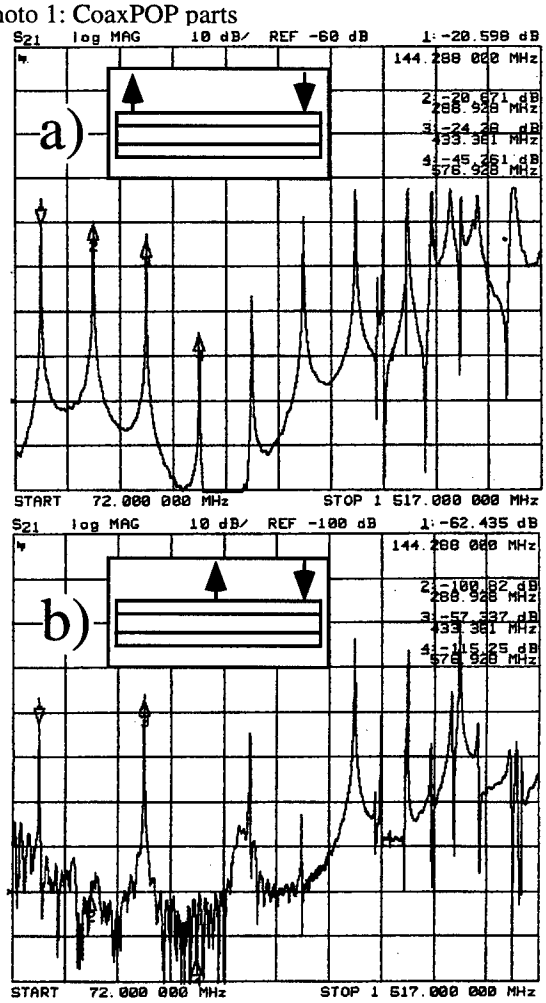

Figure 7: Measured transmissions between a) both end loops and b) from end loop to center antenna.

both end loops and b) from end loop to center antenna. The fundamental frequency agrees with the designed value of 144.5 MHz. Only harmonic modes are observed up to seventh harmonics. Even harmonics are much suppressed at the center antenna as expected. Further measurements are under way.

3 CYLINDRICAL CAVITY

Because a $\lambda/2$ coaxial resonator has two acceleration gaps, it has restrictions on designing a system: the axial length affects transit time factor and a bipolar wave form (single sine wave at least) is required. A single gap cavity using multiple modes such as "signal-cavity with double frequency buncher" [3] is preferred. Figure 8 shows the mode spectra of TMmn0 in a simple cylindrical cavity. Unlike the coaxial cavity, frequencies of higher order modes in a cylindrical cavity are not integral multiple of that of a fundamental mode. Adjustments are needed to satisfy such requirements.

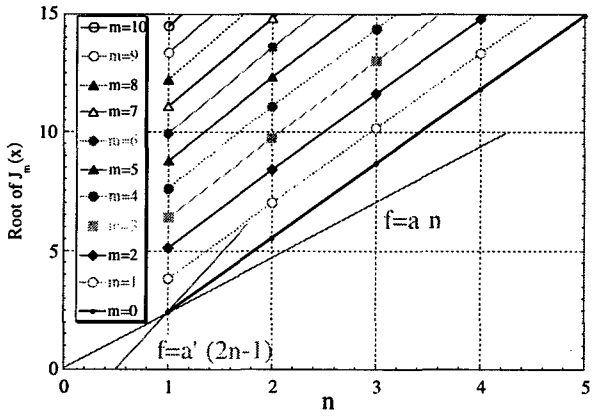

Figure 8: Mode spectra of TMmn0 in a simple cylindrical cavity.

Because the fundamental mode frequency is so low that the cavity diameter becomes too large. It is worse than the coax cavity case because a cylinder with large diameter takes larger volume than a pin point object with the same length. The diameter of a cylindrical cavity can be reduced by folding it radially. Figure 9 compares a size of a simple cylindrical cavity and that of a folded cylindrical cavity with a fundamental mode frequency of 30 MHz. The cavity radius can be reduced less than a half. The frequencies of these cavities are shown in Fig. 10. The lowest three or four frequencies have odd number proportions. The shunt impedance, however, is rather small (~1MΩ/m) and further work may have to be done for a practical use.

4 CONCLUSION

MHIC may enable CW operation of a room temperature cavity with fairly high field gradient because of the superposition of the electric field. It may achieve very high gradient field because of the wave form of the impulse shape (short time duration). Many power amplifiers with different frequency ranges required by this scheme makes the system complicated. Further work has to be done to realize this scheme.

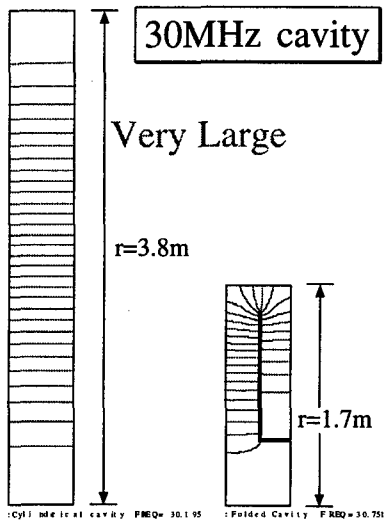

Figure 9: Comparison between a simple cylindrical cavity and folded cylindrical cavity.

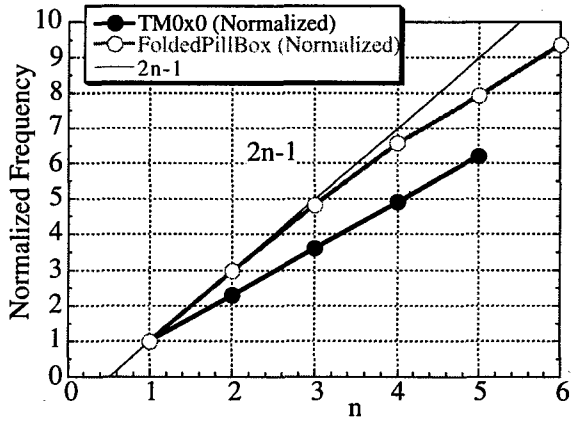

Figure 10: Frequencies in a simple cylindrical cavity and those of a folded cylindrical cavity.

5 ACKNOWLEDGMENT

The author would like to express his thank to Profs. Y. Kuno, N. Sasao, A. Noda and M. Inoue for their continuous encouragement and support. He also thank Mr. Tonguu and Mr. Morita for their technical supports.

6 REFERENCES

[1] S. Sawada, Proc. of the KEK workshop on "Kaon, Muon, Neutrino Physics and Future", Ed. Y. Kuno and T. Shinkawa, Tsukuba, Japan, Oct. 31-Nov. 1, 1997

[2] Y. Kuno, "Lepton Flavor Violating Rare Muon Decays and Future Prospects", Proc. of the workshop on Physics at the First Muon Collider and at the Front End of a Muon Collider", Fermilab, USA, Nov. 6-9, 1997.

[3] S. O. Schriber and D. A. Swenson, "A SINGLE CAVITY DOUBLE-FREQUENCY BUNCHER", IEEE Trans. on Nucl. Sci. NS-26, No. 3, June 1979, pp. 3705-3707.

Short High Charge Bunches in the SLAC Linac for Plasma Experiments

F.-J. Decker, P. Chen, R.H. Iverson, R.H. Siemann
Stanford Linear Accelerator Center, SLAC*, CA 94309, USA

Abstract

The linac at the Stanford Linear Accelerator Center (SLAC) can provide beams to different experiments during PEP-II operations. It is planned to have a 30 GeV beam to the end of the linac into the FFTB (Final Focus Test Beam) area, where there will be two plasma experiments installed, which will demonstrate plasma focussing and plasma acceleration up to 1 GeV/m. The acceleration goes linear with the current and is inversely proportional to the square of the bunch length. These high charge, short bunches will create strong longitudinal wakefields in the linac. They create a strong double-horned energy profile and have different beam dynamics in the linac. Therefore we made a test run in Fall of 1998 to measure and quantify the beam properties, like stability, distributions, tails, and backgrounds, which will be discussed in this paper. The actual plasma experiments are planned for the spring of 1999.

1 INTRODUCTION

The combination of plasma physics and accelerators is studied in two experiments at SLAC. E-150 plans to focus a small high energy beam by a factor of about two (e.g. 5 μm to 3 μm) via a plasma lens, and E-157 plans an acceleration of up to 1 GeV/m over 1 m distance. For these experiments a low emittance, intense beam with short bunch length is required. An SLC-like beam with $4 \cdot 10^{10}$ particles per bunch and an emittance with 5 in x and $0.3 \cdot 10^{-5}$ m-rad in y seems ideal (or $2.5 \cdot 10^{-5}$ m-rad both). The bunch length is a critical factor for the plasma acceleration and 0.6 (or 0.4) mm will give 4-times (9-times) the acceleration than a 1.2 mm long SLC beam. These shorter bunches will generate not only a plasma wakefield, but also a strong longitudinal wakefield in the conventional accelerator giving the beam a large energy spread. This problem is increased since only 2/3 of the linac is accelerating the beam to 30 GeV instead of 45 GeV for power saving reasons. How an initial test run performed, which checked mainly the compatibility with PEP-II is discussed first and then simulations follow, which show how the energy spread develops.

*Work supported by Department of Energy contract DE-AC03-76SF00515.

2 TEST RUN

2.1 Compatibility with PEP-II

A test run together with PEP-II operation [1] showed that several features of running an accelerator had to be separated, or a combined solution found. The timing scheduling and the beam shut off system needed a further separation, and a combined energy profile and betatron lattice made some compromise to the FFTB energy (28.5 instead off 30 GeV).

2.2 Bunch Length and Energy Spread

The bunch length was estimated with a 36 GHz cavity and optimised to about 0.55 mm at 29.5 MeV compressor amplitude. Figure 1 shows the inverted cavity signal after normalising it to a toroid reading (stars:*) and scaling it to the expected curve (solid line, for an $R_{56} = 0.7$ m).

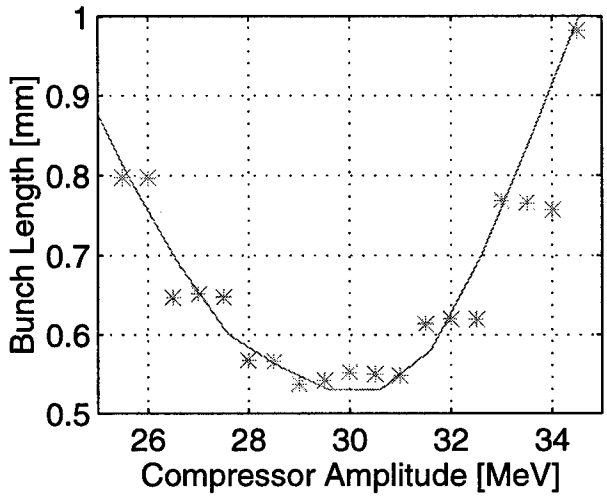

Fig. 1: Linac bunch length versus compressor strength.

Since something was wrong with the beam line (see below) we ran most of the time at 32 MeV compressor strength which lengthens the bunch to about 0.6 mm and gives a very small energy spread of about 0.15 %.

2.3 Emittance Odyssey

After years of watching over the last 10 or 20% emittance growth in the SLC era, it was an eye-opening experience to see emittances changing from roughly 100% to 2000% in a matter of days. This was the initial excuse for a noisy beam in the FFTB tunnel tripping protective ion chambers. After getting different rf phase adjustments working for FFTB and PEP-II [1] and therefore being able

0-7803-5573-3/99/$10.00@1999 IEEE.

to get BNS-damping [2] in place, the emittances came down and the orbits could be steered down to less than 150 μm rms, see Fig. 2.

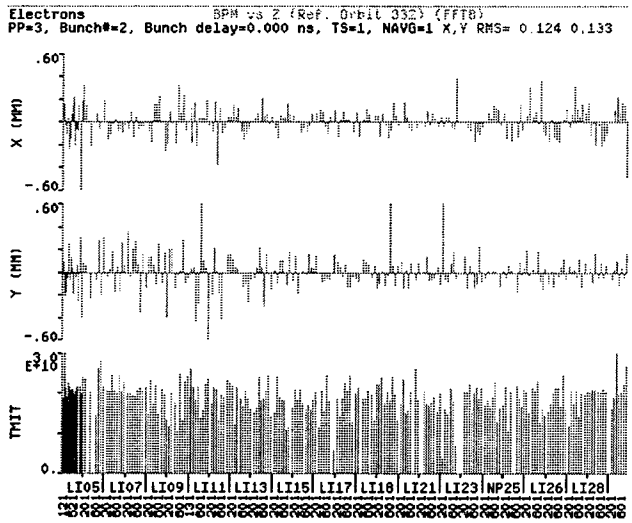

Fig. 2: Well-steered linac orbit.

The beam emittances of $2.2 \cdot 10^{10}$ particles was with $4.7 \cdot 10^{-5}$ m-rad in x and $0.28 \cdot 10^{-5}$ m-rad in y comparable to SLC emittances. This was measured with wire scanners in Sector 28 about 250 m away from the end of the linac. But the beam in the BSY (beam switch yard) looked still fuzzy and bigger than usual. A quadrupole emittance scan revealed a value of $40 \cdot 10^{-5}$ m-rad in y, which is more than 100 times bigger than just 300 m further upstream. This "smelled" like something in the beam line like a profile monitor, a stuck valve with miswired interlocks, or even "ice" built-up in a cooled section between linac and BSY. In a combined effort to solve or localise the problem, everything got adjusted and a not working beam loss monitor system revived, after which the beam was fine and small. Actually it was so "good" that it caused a vacuum to water leak near or at the dump where the beam was parked, before sending it to FFTB. After this odyssey the beam was good enough for some early test in FFTB.

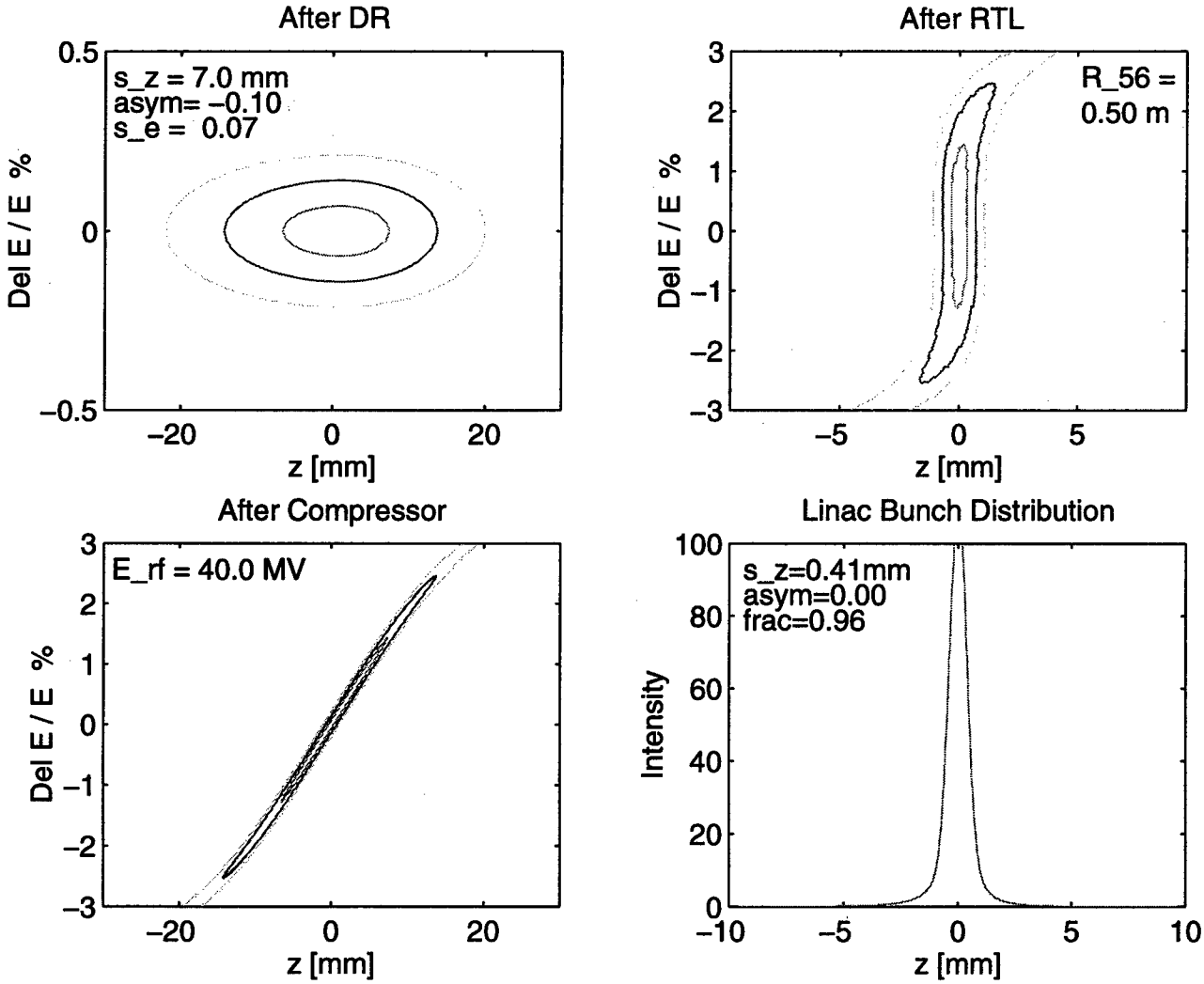

Fig. 3: Bunch length compression in the RTL.

3 SHORT BUNCHES CREATE BIG ENERGY SPREADS

Since the plasma acceleration goes with one over the bunch length squared and only linearly with the current, it is interesting to study the creation and limits of short bunches.

3.1 Creation of Short Bunches

In the ring-to-linac (RTL) section a compressor cavity introduces a correlated energy spread (versus z), which then compresses the bunch length. Different compression strength (R_{56}'s) will end up with different minimum bunch lengths (see Tab. 1).

R_{56}	Compressor optimum	σ_{z_min}
0.7 m	30 MeV	0.55 mm
0.6 m	35 MeV	0.48 mm
0.5 m	40 MeV	0.41 mm

Tab. 1: Lower R_{56}'s reduce the minimum bunch length.

During the last SLC run the R_{56} was raised from 0.6 m to 0.7 m to reduce mainly the beam losses. If the adjustment range in the opposite direction is similar an R_{56} of 0.5 m is possible. This results in a 0.41 mm long bunch with 96 % throughput (see Fig. 3).

A further compression to about 0.3 mm with an inverse "pre-compression" in the damping ring seems possible, but first let's watch the resulting energy spread in the next section.

3.2 Energy Spread due to Longitudinal Wakefields

The longitudinal wakefield of a short, intense bunch will decelerate the bunch core and tail, creating a big correlation and a double-horned energy distribution. At 4 $\cdot 10^{10}$ particles and 0.4 mm bunch length the distance between the two horns is already 6% and cannot be reduced to zero anymore. Even if the beam would sit 90° off the crest, it would be still 1.5% (if the energy itself would not be zero). Being 5 mm (or 17°) off the rf crest, it will be still 4 %, see Fig. 4 and compare Tab. 2 for different currents and end energies.

The end energy of 30 GeV is achieved by not powering 1/3 of the klystrons, but whose accelerating structures will still generate wakefields, making the energy spread of $2 \cdot 10^{10}$ at 30 GeV equal to the one of $3 \cdot 10^{10}$ at 45 GeV. The limit will be set by the energy acceptance of the FFTB line.

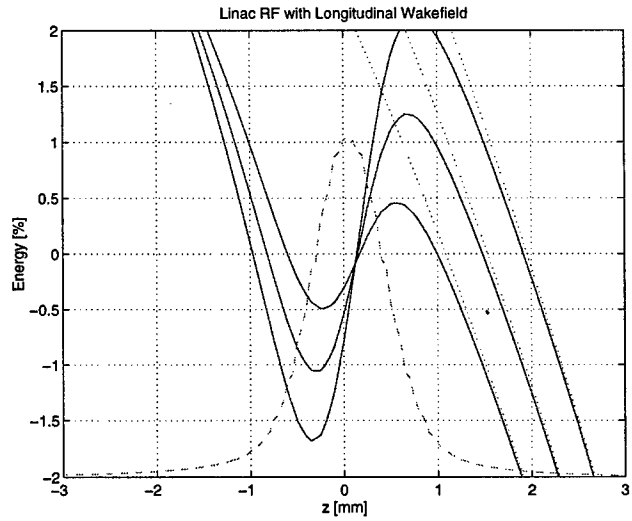

Fig. 4: Linac rf plus wakefield for a 0.41 mm bunch with 2, 3, $4 \cdot 10^{10}$ particles.

N	$\Delta E/E$ at 30 GeV		$\Delta E/E$ at 45 GeV	
	0.41 mm	**0.54 mm**	**0.41 mm**	**0.54 mm**
$4 \cdot 10^{10}$	4.0 %	3.3 %	1.8 %	1.4 %
$3 \cdot 10^{10}$	2.5 %	1.8 %	1.0 %	0.5 %
$2 \cdot 10^{10}$	1.0 %	0.5 %	0.2 %	(-0.1 %)
$1 \cdot 10^{10}$	0.0 %	(-0.5 %)	(-0.5 %)	(-0.8 %)

Tab. 2: Double-horn distance $\Delta E/E$ for different currents at 30 GeV or 45 GeV energy and the two bunch lengths of 0.41 mm and 0.54 mm.

4 CONCLUSION

Pulsed devices in the accelerator make a simultaneous operation of PEP-II and another beam for plasma experiments possible. Initial tests helped to improve this compatibility. Simulations have shown that short bunch lengths are possible, but the resulting energy spread will finally limit the length or the current.

5 REFERENCES

[1] F.-J. Decker, et al., *The SLAC Linac During the PEP-II Era,PAC99, New York, March 1999.*

[2] V.E. Balakin, A.V. Novokhatski, V.P. Smirnov, VLEPP, *Transverse Beam Dynamics,* 12th Int. Conf. On High Energy Accel., FNAL (1983) 119.

LITHIUM PLASMA SOURCES FOR ACCELERATION AND FOCUSING OF ULTRA-RELATIVISTIC ELECTRON BEAMS[i]

P. Muggli,[*,†,ii] J.R. Hoffman,[†] K.A. Marsh,[*] S. Wang,[*] C.E. Clayton,[*] T.C. Katsouleas,[†] and C. Joshi[*]

[*]*Department of Electrical Engineering*
University of California, Los Angeles, CA 90095, USA
[†]*Department of Electrical Engineering-Electrophysics*
University of Southern California, Los Angeles, CA 90089, USA

Abstract

A lithium (Li) plasma source is described that can be used for plasma acceleration as well as for electron beam focusing (plasma lens). The Li vapor with a density in the 2×10^{15} cm^{-3} range is produced in a heat-pipe oven. The Li is ionized to Li^+ through single uv photon absorption. For the plasma wake field acceleration experiment, the plasma density $n_{pe}\approx2\text{-}4\times10^{14}$ cm^{-3} is made uniform over the 1-meter long plasma [1]. A shorter length of uniform plasma density can be used as an underdense plasma lens, or the plasma density can be tapered for an underdense tapered plasma lens.

1 INTRODUCTION

Plasmas can sustain very large amplitude electric fields and are thus very suitable for particle acceleration (longitudinal field) and/or particle focusing (transverse field). In a recently proposed experiment known as E-157 [2], the 30 GeV electron beam of the Stanford Linear Accelerator Center (SLAC) Final Focus Test Beam (FFTB) is sent in a plasma with an electron density n_{pe} in the $2\text{-}4\times10^{14}$ cm^{-3} range. Numerical simulations show that that the electron bunch excites a wake (longitudinal plasma wave) with a maximum amplitude of 1 GV/m, making it possible for the first time to accelerate electrons by 1 GeV over 1 meter. The electrons of the bulk of the electron beam drive the wake and loose about 200 MeV/m, while the trailing electrons of the same bunch experience the acceleration and gain about 1 GeV/m. In previous self-modulated laser wake field acceleration (SM-LWFA) experiments fields in excess of 100 GV/m where excited but only over a few millimeters [3]. In plasma beat wave acceleration (PBWA) experiments a field of 3 GV/m has been excited over 1 cm [4]. the resulting electron energy gains were ≈100 MeV and 30 MeV respectively. The E-157 experiment operates in the "blow-out" regime, and the focusing force exerted by the ion column onto the beam electrons corresponds to a focusing strength in excess of 6×10^5 G/cm. A shorter section of plasma ($L\approx25$ cm) can be used as an effective underdense thick-plasma lens. Alternatively, the ionizing laser beam can be focused into the plasma to produce a tapered plasma density suitable for an underdense plasma lenses. Plasma lenses used at the final focus may significantly improve the beam luminosity and can be used to minimize beamstrahlung. The Li plasma sources combine the ease of ionization and uniformity of the Li vapor (ionization potential 5.3 eV), with the flexibility of a 1-photon laser induced ionization.

2 LI PLASMA SOURCE FOR ELECTRON ACCELERATION

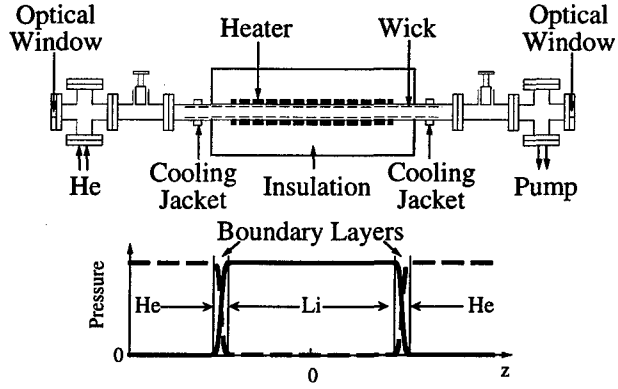

Figure 1: Schematic of the Li vapor/plasma source (not to scale).

Lithium is chosen for the plasma because it has a low ionization potential (5.3 eV) and can thus be ionized over a large volume through a single uv photon absorption process ($\lambda<242$ nm). Li also has a relatively low atomic number ($Z=3$) which minimizes the additional plasma density that is produced through impact ionization by the electrons of the beam to be accelerated. A neutral Li vapor density in the 10^{15} to 10^{16} cm^{-3} range can be obtained by heating the Li to around 750°C. The Li vapor column is produced in a heat-pipe oven [5] (Fig. 1). The hot Li vapor is confined to the heated central part of the heat-pipe by the room temperature He buffer gas located at the ends of the heat-pipe. The vapor temperature is such that the Li vapor pressure is equal to the He pressure (in absence of significant flow). The Li density is thus determined by the adjustable He pressure. The length of the Li column L is approximately equal to the length of the heated section of the pipe, and can be varied around that value by changing the heating power delivered to the oven. A vapor density $n_0=2\times10^{15}$ cm^{-3} was produced over $L=25$ cm in a short oven at a temperature of ≈750°C [6]. The product n_0L was measured using the hook method [7], and by uv and by white light absorption, whereas the column length was deduced from longitudinal temperature profiles measurements.

The vapor was ionized by single photon absorption of a 20 ns, $F_0=145$ mJ/cm^2 (maximum) ArF uv laser pulse

[i] Work supported US DoE under Grants No. DE-FG03-92ER40727 and No. DE-FG03-92ER40745, and by the NSF under Grants No. ECS-9632735 and No. ECS-9617089.

[ii] E-mail: muggli@ee.ucla.edu

0-7803-5573-3/99/$10.00@1999 IEEE.

(λ=193 nm). The line integrated plasma density $n_{pe}L$ was measured by uv absorption, and by CO_2 and visible laser interferometry. The plasma varied linearly with F_0 (Fig. 2) and reached a maximum of 2.96×10^{14} cm^{-3} (limited by F_0) corresponding to a 15% fractional ionization. The time for the plasma density to decrease by a factor of two from its maximum value was 12 μs. The plasma source has reached all the required parameters for the E-157 experiment (Table 1).

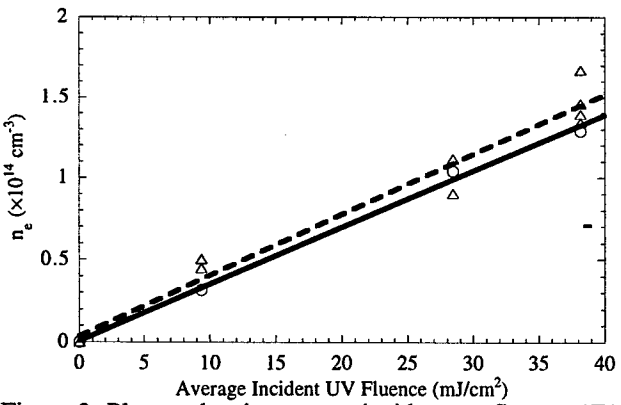

Figure 2: Plasma density versus incident uv fluence (F_0), as measured by CO_2 laser interferometry (triangles), and by uv absorption (circles). The two lines are the best linear fits to the two measurements.

Table 1: Plasma parameters required for the E-157 experiment.

Plasma Density	n_{pe}	2-4 $\times10^{14}$ cm^{-3}
Plasma Length	L	≈1 m
Density Uniformity	$\Delta n_{pe}/n_{pe}$	<25%
Ionization Fraction	n_{pe}/n_0	>15%
Radius	r	>400 μm

For that experiment however, the length of the plasma has to be of the order of one meter for the electrons to gain 1 GeV. More importantly, the product $n_{pe}L$ has to be matched to an integer number of betatron wavelengths of the electron beam envelope in the plasma. The β-function β_b of electron beam is not matched to the plasma β_{pe},: from (Table 2) $\beta_b=\sigma^2/\varepsilon_x$=5.6 m > $\beta_{pe}(n_{pe}=4\times10^{14}\ cm^{-3})$= $(2\gamma)^{1/2}c/\omega_{pe}$=0.09 m, where γ is the relativistic factor of the electron beam and $\omega_{pe}=(n_{pe}e^2/\varepsilon_0 m_e)^{1/2}$ is the plasma frequency. The beam envelope thus experiences betatron oscillations with a wavelength of $\lambda_b/2\approx$29 cm, where $\lambda_b=2\pi c/(2\gamma)^{1/2}\omega_{pe}$ is the betatron wavelength. The beam emerges from the plasma collimated only if $L=m\lambda_b/2$, m=1,2,... The beam size at the pinch is $\sigma_x^*\approx(2\gamma c^2/\omega^2_{pe}\beta_b)^{1/2}\sigma_x\approx$1.73 μm ($n_{pe}=4\times10^{14}$ cm^{-3}), indicating that a shorter plasma could be used as an effective plasma lens.

A 1-meter long source ($\approx3\lambda_b/2$) is presently built for the E-157 experiment, in collaboration with the Laurence Berkeley Laboratory [1], while a 1.5-meter source ($\approx5\lambda_b/2$) is being developed at UCLA for further experiments. In the 1-meter plasma the gradient in n_{pe} resulting from the uv photon absorption can be compensated for by double passing the laser pulse through the Li column. For example the n_{pe} variation is about 30% over L=1 m for $n_0=2\times10^{15}$ cm^{-3} with an average plasma density of $\approx2.9\times10^{14}$ cm^{-3} in the single pass case (incident fluence F_0=100 mJ/cm^2) and is reduced to ≈8% while the plasma density is increased by more than 50% (4.8×10^{14} cm^{-3}) by double passing the oven. Alternatively the plasma density gradient can be minimized by focusing the ionizing laser beam. In a short plasma ($\sigma n_0 L<<1$) the uv photons absorption is linear with distance ($F=F_0exp(-\sigma n_0 L)\approx F_0(1-\sigma n_0 L)$ and can be exactly compensated for by a cylindrical focusing.

Table 2: Electron beam parameters at the interaction point.

Number of Electrons	N_e	3.5-4.0$\times10^{10}$
Initial Energy	E_0	30 GeV
Bunch Length	σ_z	0.6 mm
Bunch Size (@ 1$\times10^{10}$ e$^-$)	σ_x	≈75 μm
	σ_y	≈75 μm
Emittance	$\gamma\varepsilon_x$	60 mm-mrad
	$\gamma\varepsilon_y$	15 mm-mrad

3 BEAM FOCUSING, UNDERDENSE UNIFORM PLASMA LENS

The leading electrons of a long electron bunch ($\sigma_z>c/\omega_{pe}$) expel the plasma electrons in a radius of $\approx c/\omega_{pe}$. In the case where the beam density n_b is larger than the plasma density ($n_b>n_{pe}/2$, the underdense plasma lens case), the core of the electron beam experiences a focusing force originating from the plasma ion column ($n_{pi}=n_{pe}$). The force can be calculated from Poison's equation and varies linearly with radius. Its strength is $W=en_{pe}/2\varepsilon_0 c\approx\ 3n_e[cm^{-3}]/10^{15}$ MG/cm. For comparison, the maximum strength of a typical magnetic quadrupole lenses is ≈10 kG/cm. The plasma acts on the electron beam as a strong, ideal lens. The lens modifies the minimum β-function of the incoming beam according to:

$$\frac{\beta^*}{\beta_0^*}=\frac{1}{1+K(\beta_0-\beta_L)\beta_0^*} \qquad (1)$$

where β_0^* and β^* are the minimum β-functions for the beam without and with the plasma lens respectively, β_0 is the β-function at the lens entrance, and $K=We/\gamma m_e c$. The β-function of the beam at the lens exit β_L is given by:

$$\beta_L=\frac{\beta_0}{2}+\frac{1}{2K\beta_0^*}+\left(\frac{\beta_0}{2}-\frac{1}{2K\beta_0^*}\right)\cos\left(2\sqrt{K}L\right)-\frac{2s_0}{2\sqrt{K}\beta_0^*}\sin\left(2\sqrt{K}L\right) \qquad (2)$$

where $s_0=(\beta_0^*(\beta_0-\beta_0^*))^{1/2}$ is the distance between the lens entrance and the beam focus in absence of the lens. The new beam focus is located a distance $s=(\beta^*(\beta_L-\beta^*))^{1/2}$ away from the lens exit.

The Li plasma source described in the previous section could be used to produce a 10 cm long plasma with a uniform density of $n_{pe}=2\times10^{14}$ cm^{-3} corresponding to c/ω_{pe}=375 μm. The FFTB pulse stretched to σ_z=1.0 mm ($n_b=4.5\times10^{14}$ cm$^{-3}>n_{pe}/2$ with $N_e=4\times10^{10}$ electrons per bunch) would focus to σ_x=2.5 μm (reduction by a factor ≈30) 4.0 cm away from the lens exit.

4 BEAM FOCUSING, UNDERDENSE TAPERED PLASMA LENS

In the uniform plasma lens example described in the previous section, the plasma is underdense at the lens entrance and becomes more and more underdense as the

electron beam focuses. In order to increase the strength of the plasma lens and reduce the final beam spotsize, the plasma density can be increased along the electron beam path while keeping the plasma underdense for the focusing beam.[8] With the plasma source described in Section 2 this can be achieved by sending a de-focusing ionizing laser beam in the opposite direction to that of the electron beam. In this case, the plasma density decreases along the laser beam path (i.e., increases along the electron beam path), because of the depletion of the uv photons and because of the decrease in uv fluence resulting from the beam de-focusing. The uv photons are absorbed following $N(z)=N_0 exp\{-\sigma n_0(L-z)\}$ for $0\le z\le L$, where $N_0=E_0/h\nu$, E_0 is the incident uv energy, and $h\nu$ the energy per photon. The plasma density created by ionization is given by $n_{pe}(z)=(1/A)(-\partial N/\partial z) = (\sigma n_0/h\nu)(N_0/A(z))exp\{-\sigma n_0(L-z)\}$ where A is the laser beam spot size. For a thin plasma ($\sigma n_0 L<<1$), and a beam expanding from an initial radius r_0 to a final radius in the plasma of $r_0+\Delta r$ according to $r(z)=r_0(1+\Delta r(L-z)/L)$, the plasma density is thus:

$$n_{pe}(z)=\frac{\sigma n_0}{h\nu}\frac{E_0}{\pi r_0^2}\frac{\left(1-\sigma n_0(L-z)\right)}{\left(1-\Delta r(L-z)/L\right)^2} \qquad (3)$$

The laser fluence incident upon the Li vapor is $F_0=E_0/\pi r_0^2$ where πr_0^2 is the laser spotsize when entering the plasma. The envelope equation for the beam spot size σ:

$$\sigma''(z)+K(s)\sigma(z)=\frac{\varepsilon^2}{\sigma^3(s)} \qquad (4)$$

can be solved numerically for a plasma density profile given by eq. 4. Figure 3 shows the beam envelope evolution for the case described in the previous section ($n_{pe}=2\times10^{14}$ cm^{-3} over L=10 cm, sharp boundaries). Figure 4 shows the beam envelope evolution in a 10 cm long plasma with a plasma density tapered from 2 to 10×10^{14} cm^{-3} by defocusing the ionizing laser. The initial vapor density is $n_0=2\times10^{15}$ cm^{-3}, and the initial fluence F_0=286 mJ/cm^2. The tapered plasma lens remains underdense over its entire length, and the final spot size is reduced from 2.5 μm (in the constant n_{pe} case) to 1.24 μm. The focal point is now located 5.0 cm away from the plasma exit. Also shown on these figures the same calculations for a plasma density including more realistic continuous vacuum/plasma boundaries. In this case the lens focusing strength is kept approximately the same as in the sharp boundary case by keeping the number of particles in the plasma the same in the sharp and continuous boundaries cases. Note that numerical simulations are required to confirm and optimize the examples presented here.

5 SUMMARY

A lithium plasma source is described that will be used to demonstrate acceleration of ultra-relativistic electrons by ≈1 GeV over ≈1 m. A shorter version (≈10 cm) of the same plasma source could be used as an underdense plasma lens. In the examples described here the SLAC FFTB spot size is reduced from 75 to 2.5 μm in the constant plasma density case, and from 75 μm to 1.25 μm in the case of the plasma density tapered along the electron beam path (2 to 10×10^{14} cm^{-3}). The plasma density taper is obtained by defocusing the ionizing laser pulse.

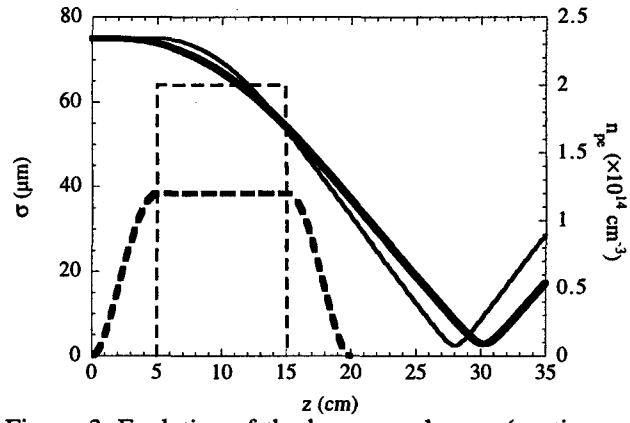

Figure 3: Evolution of the beam envelope σ (continuous lines) when traversing an $n_{pe}=2\times10^{14}$ cm^{-3}, L=10 cm (dashed lines) underdense plasma lens with (thick lines) and without (thin lines) continuous plasma boundaries. The total number of charges in the plasma is the same in both cases. The initial σ is 75 μm, and the minimum σ is 2.5 μm in both cases, 10 respectively 13 cm away from the lens exit.

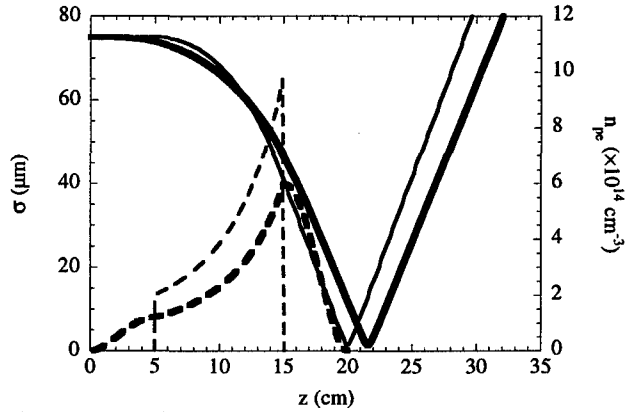

Figure 4: Evolution of the beam envelope σ (continuous lines) when traversing an plasma with a density n_{pe} tapered from 2 to 10×10^{14} cm^{-3} over L=10 cm (dashedlines) with (thick lines) and without (thin lines) continuous plasma boundaries. The plasma remains underdense along the lens. The initial σ is 75 μm, and the minimum σ is 1.24 μm 5 respectively 2.5 cm away from the lens exit.

6 REFERENCES

[1] S. Dimaggio *et al.*, these proceedings.
[2] T. Katsouleas *et al.*, Proceedings of the Particle Accelerator Conference, Vancouver, Canada, May 1997.
[3] D. Gordon *et al.*, Phys. Rev. 80, 2133 (1998), C.I. Moore *et al.*, Phys. Rev. Lett. 79, 3909 (1997).
[4] C.E. Clayton *et al.*, Phys. Rev. Lett. 70, 37 (1993).
[5] C.R. Vidal *et al.*, ," J. Appl. Phys. 40, 3370 (1969).
[6] P. Muggli *et al.*, to be published in IEEE Trans. Plasma Science, June (1999).
[7] W.C. Marlow, Applied Optics 6, 1715 (1967).
[8] T.C. Katsouleas, and C.H. Lai, Proc. Adv. Acc. Conc. Workshop, AIP 279, 551 (1992).

CERENKOV RADIATION FROM A MAGNETIZED PLASMA: A DIAGNOSTIC FOR PBWA EXPERIMENTS[i]

P. Muggli,[ii] J. Yoshii, and T.C. Katsouleas
Department of Electrical Engineering-Electrophysics
University of Southern California, Los Angeles, CA 90089, USA

C.E. Clayton, and C. Joshi
Department of Electrical Engineering
University of California, Los Angeles, CA 90095, USA

Abstract

In the plasma beat wave acceleration scheme, the ponderomotive force of a two-frequency laser pulse resonantly drives a large amplitude ($E^{es}\approx 3$ GV/m) relativistic electrostatic plasma wave. The electro-static (es) wave does not couple to the vacuum modes and its energy is dissipated in the plasma. With a static magnetic field $B_0\mathbf{z}$ applied perpendicularly to the laser beam propagation axis **x**, the two-frequency laser pulse couples to the L branch of the XO mode of the magnetized plasma through Cerenkov radiation. The electromagnetic component (em) of the XO mode couples to the vacuum mode. The plasma wave is not affected by the transverse magnetic field, and measuring the characteristic of the emitted radiation thus provides an in-situ diagnostic for the beat-wave-excited accelerating structure (amplitude, phase, and damping for example). Additionally, the mechanism of interest is a possible source for a gigawatt terahertz radiation source.

1 INTRODUCTION

In the last decade plasmas have entered two fields traditionally reserved to vacuum devices: the microwave sources and the electron accelerators. Self modulated laser wakefield (SM-LWFA) experiments have demonstrated accelerating fields larger than 100 GV/m, resulting in acceleration of electrons by up to 100 MeV in a millimeter [1]. Laser driven plasma beat wave acceleration (PBWA) experiments have shown accelerating fields up to 3 GV/m, resulting in acceleration of electrons by 30 MeV over a 1 cm length [2]. Using laser created, relativistically-propagating ionization fronts in a plasma frequency up-shifting of microwaves from 35 GHz continuously to 170 GHz has been demonstrated [3]. Direct conversion of the static electric field of an array of alternatively biased capacitors using the same ionization front has produced continuously tunable short pulses of radiation between 6 and 93 GHz [4]. Recently a new scheme taking advantage of the large electric field produced in the PBWA experiment has been proposed for generating mega- to gigawatts of THz radiation by applying a static magnetic field perpendicularly to the laser beam path. [5] The radiation is generated by coupling of the two-frequency laser pulse to the left branch of the extraordinary mode of the magnetized plasma through Cherenkov radiation. This scheme can be either used as a THz radiation source, or as a diagnostic for the PBWA experiment itself.

[i]Work supported US DoE under Grants No. DE-FG03-92ER40727 and No. DE-FG03-92ER40745, and by the NSF under Grants No. ECS-9632735 and No. ECS-9617089.

[ii]E-mail: muggli@ee.ucla.edu

2 CHERENKOV RADIATION FROM A MAGNETIZED PLASMA

First consider a two-frequency laser pulse exciting a plasma wave to a large amplitude in an unmagnetized plasma. In the dispersion or (ω,k) diagram the excitation is represented by the intersection between the laser pulse line $\omega=kv_{gl}$, where $v_{gl}=(1-\omega_{12}^2/\omega_{pe}^2)^{1/2}c$ is the laser pulse group velocity in the plasma, and the es plasma wave eigenmode of the cold plasma at $\omega=\omega_{pe}$. At this intersection point the phase velocity of the plasma wave is c but its group velocity is zero. The energy deposited in this mode by the laser pulse does not propagate outside of the plasma and is finally dissipated in the form of plasma heating. The plasma wave is at cut-off in the plasma and only a small volume around the plasma surface about one skin depth deep is expected to radiate in vacuum. Note that the laser pulse line never intersects with the electromagnetic (em) eigenmode of the plasma $(\omega^2=\omega_{pe}^2+k^2c^2)$.

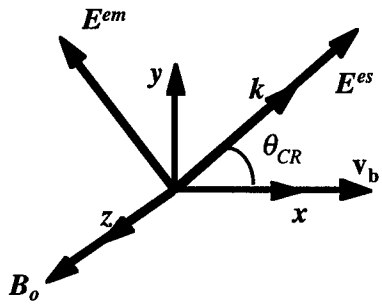

Figure 1: Geometry for the Cherenkov radiation in a magnetized plasma ($\boldsymbol{k}\in(\boldsymbol{x},\boldsymbol{y})$).

Applying a static magnetic field $\boldsymbol{B_0}$ modifies the nature of the plasma eigenmodes. In particular when $\boldsymbol{B_0}$ is perpendicular ($\perp$) to the laser beam path ($\boldsymbol{B_0}=B_0\boldsymbol{z}$, see Fig. 1) and for $\boldsymbol{k}\perp\boldsymbol{B_0}$ ($\boldsymbol{k}=k\boldsymbol{x}$) and $\boldsymbol{E}\perp\boldsymbol{B_0}$ ($\boldsymbol{E}$ the wave electric field), the dispersion relation is:

$$\frac{c^2k^2}{\omega^2}=1-\frac{\omega_{pe}^2}{\omega^2}\frac{\omega^2-\omega_{pe}^2}{\omega^2-\omega_H^2} \qquad (1)$$

where $\Omega_{ce}=eB_0/m_e$ is the electron cyclotron frequency, $\omega_H=(\omega_{pe}^2+\Omega_{ce}^2)^{1/2}$ is the upper hybrid frequency. The eigenmodes of the plasma are the left (L) and right (R) branch of the extraordinary or XO-mode (see Fig. 2) and have cut-off frequencies at $\omega_{R,L}=[\pm\Omega_{ce}+(\Omega_{ce}^2+4\omega_{pe}^2)]^{1/2}$ respectively. These two branches have two components to their electric field; an em component $\boldsymbol{E}^{em}=E^{em}\boldsymbol{y}$, and an es component $\boldsymbol{E}^{es}=E^{es}\boldsymbol{x}$. Their amplitude ratio is obtained from the dielectric tensor for the magnetized plasma: $E^{em}/E^{es}=\Omega_{ce}/\omega_{pe}$. Waves with $\omega<\omega_L$ or $\omega_H<\omega<\omega_R$ are evanescent in the plasma. The laser pulse line intersects

with the L-XO branch of the magnetized plasma. Physically the ponderomotive force of the laser pulses pushes the electrons along the x axis creating E^{es}, they rotate around the B_0 lines in the (x,y) plane and generate E^{em}. Note that the dispersion relation of eq. (1) remains valid for any k in the (x,y) plane. Figure 2 shows that the laser pulse can couple to the L-XO mode through Cherenkov radiation at any angle $\theta_{CR}\leq 90°$, where the velocity of the disturbance (the laser pulse) $v_{gL}\approx c$ is larger than the phase velocity of the L-XO mode. Note that this corresponds to Cherenkov radiation from photon bunches rather than from particles. The Cherenkov condition $cos\theta_{CR}=1/\beta_{gl}n(\omega)$ where $\beta_{gl}=v_{gl}/c$, $v_{gl}=c(1-\omega_{pe}^2/\omega_{12}^2)^{1/2}\approx c$, and $n(\omega)=ck/\omega$ is given by eq. 1. Since the plasma is dispersive different frequencies are emitted at different angles. However, Fig. 2 shows that the group velocity of the L-XO mode decreases with increasing θ_{CR} while the emitted frequency increases from ω_{pe} to ω_H. Cherenkov radiation is thus emitted essentially in the forward direction ($\theta_{CR}=0$) at ω_{pe} since a significant group velocity is necessary for the radiation to exit the plasma.

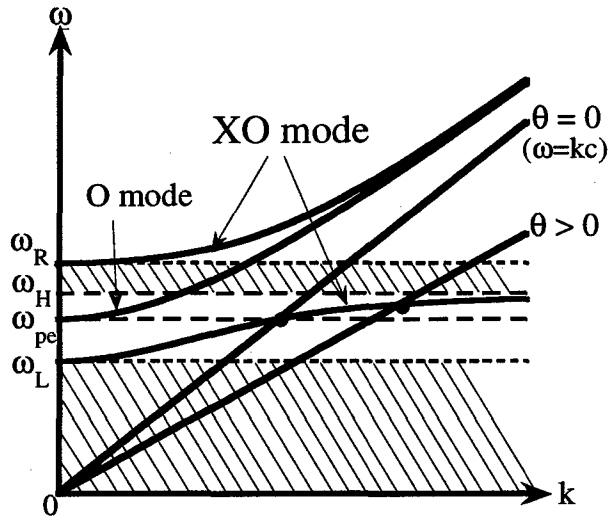

Figure 2: Dispersion relation for the magnetized plasma with $k\perp B_0$, $E\perp B_0$, and k in the (x,y) plane (see Fig. 1). The dashedregion are evanescent regions. The Cherenkov condition is show by the dots at the two angles.

For k in the (z,x) plane, the dispersion relation can be rewritten as a function of θ_{CR} [6], but the major conclusions remain the same as for k in the (x,y) plane: the Cherenkov radiation is emitted essentially in the forward direction ($\theta_{CR}=0$) at ω_{pe}. Figure 3 shows the frequency of the Cherenkov emitted as a function of the Cherenkov angle for the two cases k in the (x,y) plane and k in the (z,x) plane.

The dispersion relation (eq. 1) indicates that at $\theta_{CR}=0$ the index of refraction for the L-XO $n_{L\text{-}XO}$ mode is equal to one. In the case of a step function boundary between the plasma with density n_e and vacuum, the EM component of the L-XO mode couples to vacuum with a transmission coefficient equal to 1 (from $n_{L\text{-}XO}=1$ to $n_{vac}=1$) and thus $E_{vac}^{em}=E^{em}$. The es component of the L-XO mode is confined to the plasma. The power density radiated in vacuum is thus given by the Poynting vector: $S=\varepsilon_0(\Omega_{ce}/\omega_{pe})^2(E^{es})^2c/2$. In the case of a continuous plasma/vacuum boundary, both ω_H and ω_R decrease with the plasma density, and the forward wave at the bulk plasma frequency ω_{pe} has to cross the evanescent region shown on Fig. 2. For the case of a linear plasma density variation over the boundary an analytic expression for the attenuation coefficient can be derived.[5] The electric field is attenuated by a factor ≈ 3 by a linear decrease of the plasma density over three plasma wavelengths. In practice the attenuation can be minimized by abruptly terminating the plasma by, for example, using a gas jet, or by bringing the magnetic field to zero over the smallest possible distance. In the forward direction the group velocity of the L-XO mode is given by $v_{g\text{-}XO}=(\Omega_{ce}/\omega_{pe})^2c$. Once depositedin the plasma by the laser pulse the energy will convect out of the plasma for a time given by the minimum between the transit time for the energy through the plasma of length L_p: $(L_p/v_{gL\text{-}XO})$, and the life time of the plasma wave. This determines the pulse-length of the radiation emitted in vacuum.

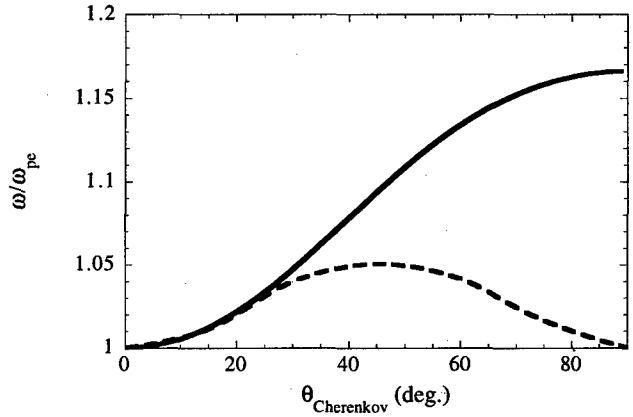

Figure 3: Frequency of the Cherenkov radiation (normalizedto ω_{pe}) as a function of the Cherenkov angle θ_{CR} in the case where k is in the (x,y) plane (solid line), and k is in the (z,x) plane (dashed line), for $E\perp B_0$ and $\Omega_{ce}/\omega_{pe}=0.6$ and $\omega_H\approx 1.17$.

All of the analytical results describedabove have been verified by 2-D particle in cell (PIC) simulations. These simulations also show that the excitation of the plasma wave by the laser pulse is not degraded over the unmagnetized case for B_0 up to values corresponding to $\Omega_{ce}/\omega_{pe}\approx 0.8$. For larger values of B_0 the ratio of E^{em}/E^{es} becomes smaller than the analytical value of Ω_{ce}/ω_{pe}.

3 THE PBWA EXPERIMENT

In the Neptune laboratory PBWA experiment [7] a high power ($\approx$100 J in $\approx$100 ps or $\approx$1 TW), two-frequency CO_2 laser pulse (ω_1, ω_2 corresponding to $\lambda_1=10.592$ μm and $\lambda_2=10.296$ μm) is focusedby an off-axis parabola in a cell containing a static fill of gas (H_2 or D_2) or metallic vapor (Li, Na, or Cs). The spot size of the focused "flat-topped" beam w_0 (radius at 1/e for the fields) at best focus is 280 μm (1.4 times diffraction limited) with an effective Rayleigh range $z_R=2\pi w_0/\lambda_{12}=2.4$ cm where λ_{12} is the average of λ_1 and λ_2. The laser intensity is large enough to strip each atom of the gas/vapor from its first electron through field ionization. The gas/vapor pressure is adjusted so that the electron plasma frequency $\omega_{pe}=(n_e e^2/\varepsilon_0 m_e)^{1/2}$ (n_e is the plasma density $\approx 10^{16}$ cm^{-3}) is exactly equal to the frequency differencebetween the two laser frequencies: $\omega_{pe}=\omega_2-\omega_1$. The ponderomotive force associated with the beat envelope of the two-frequency laser pulse resonantly drives a large amplitude es plasma wave or beat wave $\delta n_e/n_e\approx 0.3$, where δn_e is the plasma density perturbation, which corresponds to $E_x^{es}\approx 3$ GV/m. A 17 MeV electron bunch from a rf-photo-injector with a

radius $\sigma_x \approx \sigma_y \approx 30\text{-}50$ μm is injected into the plasma wave and is accelerated to ≈100 MeV and dispersed in energy by a double-focusing electron magnetic spectrometer. The plasma wave characteristics in time, space, frequency, and wavenumber are measured by Thomson scattering of a 532 nm laser pulse. In the upcoming experiment, the H gas fill is be replaced by a Na or Cs heat-pipe oven. An open oven geometry [8] is chosen to allow for access to the plasma from the side for the different diagnostics. The Na and Cs vapor require a lower laser intensity to be field ionize because their ionization potential (5.1 and 3.9 eV respectively) is lower than that of H (13.6 eV). This allows for ionization and excitation of the plasma wave over a longer length and increases the electrons energy gained. Calculations show that the energy gain increases from 55 MeV over about one z_R in H to about 85 MeV over about $2z_R$ in Li [9]. Their ion mass is larger than that of H which renders the plasma more robust to ion motion and instabilities. A dipole magnet generates the transverse static magnetic field and has an strength of around 6 kG ($\Omega_{ce} << \omega_{pe}$). The field $\boldsymbol{B}_0$ can be applied either over the whole length of the plasma when the electrons are not injected, or only over the last 5 mm when the electrons are injected in the plasma, so that the plasma wave diagnostic and the electron acceleration are obtained at the same time. The plasma frequency is ≈1 THz, and the wavelength of the radiation (≈300 μm) is about equal to the plasma diameter. The radiation will thus strongly diffract from the plasma volume. It is collected by a parabolic mirror and sent out of the vacuum box through a silicon window (see Fig. 4). The temporal shape of the emitted pulse is monitored using a Schotkky-barrier diode. The signal amplitude as a function of time is proportional to the relative plasma wave amplitude as a function of time ($\Omega_{ce} << \omega_{pe}$), while its absolute amplitude is proportional the accelerating field.

The output power expected at 1 THz is 1 MW for B_0=6 kG (for a step plasma/vacuum boundary). This scheme can thus be used to produce powerful THz radiation for remote sensing or for seeding of an FEL. In the Neptune Laboratory experiment neither the plasma boundary, nor the magnetic field are expected to have a sharp boundary. Consequently the power produced in the plasma by Cherenkov radiation is expected to be considerably attenuated at the boundary. However, detecting the emitted radiation will be diagnostically extremely important for the acceleration experiment itself.

4 SUMMARY

A static magnetic field is applied transversely to the laser beam path in the PBWA experiment. The laser pulse emits Cherenkov radiation through coupling to the L branch of the XO mode of the magnetized plasma. The radiation is emitted essentially in the forward direction, at the plasma frequency (≈1 THz). The radiation parameters will be used as a diagnostic for the PBWA experiment. Method to allow for the high power THz radiation generated in the plasma to be transmitted through the plasma/vacuum boundary will also be investigated.

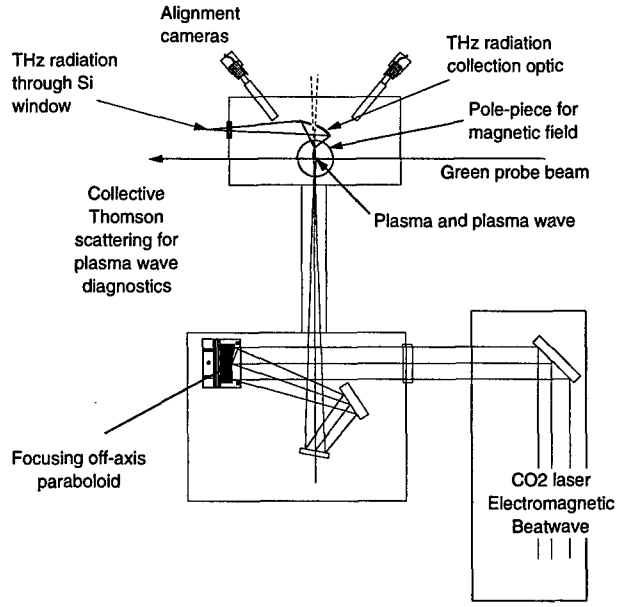

Figure 4: Experimental arrangement for the Cherenkov experiment in the Neptune Laboratory. The THz radiation propagates in the forward direction and is reflected towers the diagnostics, through a silicon window.

5 REFERENCES

[1] D. Gordon *et al.*, Phys. Rev. 80, 2133 (1998), C.I. Moore *et al.*, Phys. Rev. Lett. 79, 3909 (1997).
[2] C.E. Clayton *et al.*, Phys. Rev. Lett. 70, 37 (1993).
[3] R.L. Savage *et al.*, Phys. Rev. Lett. 68, 946 (1992).
[4] C.H. Lai *et al.*, Phys. Rev. Lett. 77, 4764 (1996), P. Muggli *et al.*, Phys. Plasmas, 5(5), 2112 (1998).
[5] J. Yoshii *et al.*, Phys. Rev. Lett. 79, 4194 (1997).
[6] H. Bremmer, in Terrestrial Radio Waves, Elsivier Publishing NY, (1949).
[7] C.E. Clayton *et al.*, Nucl. Instr. and Meth in Phys. Res. A 410, 378 (1998).
[8] M.A. Cappeelli *et al.*, Rev Sci. Instr. 56, 2030 (1985).
[9] P. Muggli, LASERS'98 Conference Proceedings (1998).

POSSIBLE ENERGY INCREASE OF HIGH CURRENT ELECTRON ACCELERATORS

A.Ts. Amatuni, S.G. Arutunian, S.S. Elbakian, M.R. Mailian, M.L. Petrossian
YERPHI, Yerevan, Armenia.

Abstract

Proposal for investigation of the possibility to obtain compact, effective high current electron accelerator for medium energy range using plasma wake field acceleration (PWFA) mechanism is presented. The goal of proposed investigation is not an achivement of highest possible acceleration rate, but effective increase of the energy of high current ($\sim kA$), low energy ($\sim 2MeV$) electron accelerator, due to interaction of electron bunches with plasma wake waves.

1 INTRODUCTION

Plasma based advanced accelerator concepts have been developed mainly in order to obtain high accelerator gradients for furure linear colliders in the TeV energy range. But, simultaneously, the variety of the other possible applications also have been developed. In the recent review [1] some near-term and long-term applications of plasma-based accelerators have been mentioned and discussed.

In the present work the project for investigation of the possibility to obtain compact, effective high current ($\sim kA$) electron accelerators in the medium energy range 20-200 MeV, using plasma wake field acceleration (PWFA) mechanism, is considered. Existing electron accelerators for energy 20-200 MeV have average accelerated current not more than a few milliamper. So the problem of creating the accelerating installation for electrons with energy of order 100 MeV, with pulse current $\sim 100A$, repetition rate $\sim 100Hz$, macropulse duration $\sim 1\mu sec$ and bunch duration $\sim 0.1nsec$ is an actual one.

Up to now the ordinary known accelerator technologies have been unable to create the accelerators with above mentioned parameters. Such kind of accelerators must be of common use and can have wide applications in material science, generation of X-rays and soft gamma rays, possible use in inceneration of some radioactive wastes[2] and others[1].

It seems at the first glance, that an additional acceleration, which can be provided by plasma wake waves, generated by electron bunches from high current ($\sim 1kA$) electron accelerators with energy ($\sim 1MeV$), could be used as a basic physical concept for creating compact, effective, economicaly reliable accelerator installations, with the needed range of the parameters.

The goal of the proposed investigation is not an achivement of highest possible acceleration gradient, but effective increase the energy of high current ($\sim 1kA$), low energy ($\sim 1MeV$) electron beams, due to interaction of electron bunches with plasma wake waves, generated by the beams from the same electron accelerator. The goal is to identify and to develop techniques, which may lead to more efficient, compact and inexpensive high current particle accelerators for medium energy range. Of course the increase in the energy will at the same time reduce subsequently the accelerated current, but it still can be large enough (for example, if initial energy is 1 MeV and initial current 1kA, the final energy could be $\sim 10MeV$ and final accelerated current $\sim 100A$).

The proposed work has some theoretical and experimental foundations, created by previous numerous investigations of PWFA (see, for example, a recent reviews[3], [4], [5]). Proposed work is going further than proof-of-principle experiment, it must be acomplished by the creation of the pilot installation (or test facility) and by the project of high current ($\sim 1kA$) and medium energy ($\sim 100MeV$) electron accelerator. This goal needs some additional physical as well as technological considerations and investigations, which will be briefly described in the following sections.

2 PROBLEMS OF PHYSICAL CONSIDERATIONS

Plasma wake wave acceleration (PWFA) of high current electron beams posed the problems, which are at some extent different from the problems, encountered in the investigations of physical ground of high energy plasma based linear colliders. High luminocity demand, determinating the main features of high energy linear colliders, for its realization needs very narrow bunches, when the transverse dimensions of the bunches are much smaller than plasma wave length. It is not the case for accelerated high current electron beams, where the transverse dimensions of the accelerated beams can be large enough, like in the induction linacs,and if the plasma density is high, in order to obtain high acceleration gradient, the transverse dimensions of the electron beams can be of order or even larger than plasma wave length. The last case opens the possibility to use, as a guiding tool, an one-dimensional approximation in theoretical consideration (see for example exact results, presented in [6]). It means, in particular, that it is possible to obtain high enough accelerating gradient and transformation ratio, when driving bunch parameters (charge density, length, Lorentz factor) are choosen at such a way, that wave breaking phenomenon in plasma wake wave can occure[7], [8]. But, in contrast to narrow bunches case, the blow out regime which is proposed as one of the candidates for nonlinear acceleration mechanisms for future linear colliders[9] is not realized for wide bunches, which will be used in considered case. Hence wave breaking phenomenon originated by wide driving bunches must be the subject of more careful theoretical investigations and for different sets of parameters of plasma- electron bunch sys-

0-7803-5573-3/99/$10.00@1999 IEEE.

tem it must be discovered and investigated experimentaly too.

Plasma wake wave acceleration mechanism can be realized experimentaly by using different driving and witness bunches[10], one long driving bunch or sequence of short driving bunches[11], one bunch with nonuniform charge distribution, when rear part of bunch is selfaccelerated in the field, generated by the bunch head part[12],[13]. The choice of the optimal conditions for investigated PWFA process for high current beams is an another essential physical problem of the proposed work.

Wide bunches with nonuniform tranverse charge distribution, as preliminary nonlinear calculations show, presents the problem of transverse nonlinear instability, connected with plasma wave filamentation. It means that driving bunches must be transversaly uniform at some extend, which must be predicted theoreticaly.

There exist, of course, some problems which are common to that of high energy plasma based linear colliders, e.g. the problem of energy spread and acceleration efficiency, stability of driving and accelerated bunches, value and preservations of the emmitance of accelerated bunches, plasma chamber boundaries, influence on acceleration process and others.

These problems have to be solved at the conditions typical for high current acceleration purposes - i.e. when bunch transverse dimensions are of order or larger than plasma linear wave length.

All these problems must be considered and investigated theoreticaly and experimentaly. For theoretical investigation some approximate methods must be developed as well as a suitable programms for effective computer simulations. For experimental investigations the need for flexible enough (accelerator) test facility, with high current and low energy, long and wide enough plasma chamber with variable plasma electron uniform density are urgent.

3 OUTLINE OF TEST FACILITY

The test facility will be based on high current direct action accelerator fed by Marx generator and with photocathode. The electron energy is 2 MeV and pulse current up to 1kA. The outline of experimental installation is presented on Fig. 1.

The essential part of proposed installation is laser photon bunch shaping device, which allows to change driving electron bunch length, tranverse dimensions, bunch charge value and distribution, witness bunch delay, charge and dimensions, and also allow to originate a sequence of driving bunches.

The fourth harmonic of Nd: YAG laser is used. Pulse power for cooper cathode is 2MW, pulse energy by order of magnitude is $5 \cdot 10^{-4}$J. taking into account the losses, caused by harmonics transformation, the laser must have pulse power $\sim 10MW$ and pulse energy $\sim 1mJ$. On proposed installation it will be possible to investigate different mechanisms of plasma wake wave acceleration and find out

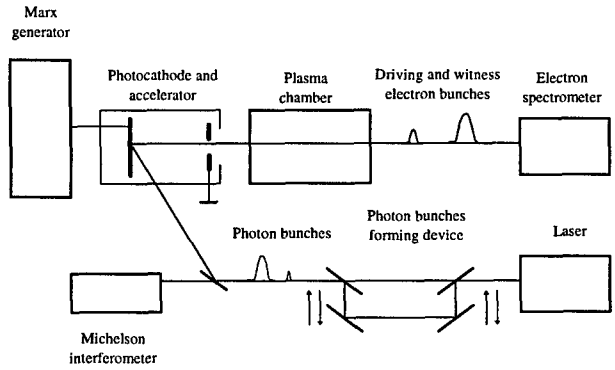

Figure 1:

the optimal one for high current wide electron beams.

Plasma chamber will be constructed using the experience gained at YerPhI during the last years, when different kind of plasma chambers have been constructed, tested and used in experiments. The plasma chamber will be 1m long, 20cm in diameter, with plasma density varied in interval $10^{10} - 10^{13}cm^{-3}$.

The main parameters of proposed test facility are given in Table 1.

Table 1

Initial energy of electrons	1.5-2.0MeV
Energy of accelerated electrons	$\sim 10MeV$
Driving bunch current	1kA
Accelerated electrons current	up to 100A
Electron bunch length	$\geq 3cm$
Electron bunch diameter	$\geq 1.0cm$
Distance between bunches	$\geq 3cm$
Driving bunch density	$2 \cdot 10^{10} - 2 \cdot 10^{11}cm^{-3}$
Plasma electron density	$10^{10} - 10^{13}cm^{-3}$
Plasma chamber length	100cm
Plasma chamber diameter	20cm
Laser pulse power	$\geq 10^{8}W$
Laser wave length	$0.266\mu m$
Laser repetition rate	1-10Hz

4 CONCLUSION

The proposed work pursued the following goals:

1. Theoretical investigation on PWFA mechanisms for high current wide electron bunches, taking into account wave breacking phenomenon, driving bunch

longitudinal and transverse dynamics and stability, focusing, emmitance preservations, energy spread, beam loading and others.

2. Construction and operation of the test facility.

3. Experimental investigation of PWFA mechanisms for high current wide electron bunches and determination of the optimal conditions for high current electron beams acceleration.

4. Research, development and preparation of the project of high current electron accelerator, based on plasma wake field acceleration mechanism, with accelerated electron energy 100MeV and pulse current 100A.

The described proposal will be presented for grant to International Science and Technology Center (ISTC) as a continuation of Project A-013 ISTC, which is realizing now at YerPhI.

5 REFERENCES

[1] T. Tajima, P. Chen NIM, Sec. A, A**410**, 344, (1998).

[2] S. Tõyama, Y.L. Wang et al., PAC'93, May, 1993, Washington D.C, USA.

[3] Ya. B. Fainberg Fizika Plasmi, **23**, 275, (1997).

[4] A. Ogata Beam Dynamics Newsletter, No 12, 34, (1996).

[5] E. Esarey et.al IEEE Trans on Plasma Sc. **24**, 252, (1996).

[6] A.Ts. Amatuni, S.S. Elbakian, E.V. Sekhpossian, R.O. Abramian Part. Acc. **41**, 153, (1993).

[7] A.I. Akhiezer, R.V. Polovin JETP **3**, 696, (1956).

[8] J.M. Dawson Phys. Rev **113**, 383, (1959).

[9] J. Rosenzweig, N. Barov, A. Muroch, E. Colby, P. Colestoek NIM, Sec. A, A**410**, 532, (1998).

[10] J.B. Rozenzweig, D.B. Cline, B.Cole, H.Figeroa, W. Gay, R. Konecny, J. Norem, P. Schoessow, J. Simpson Phys. Rev. Lett. **61**, 98, (1998).

[11] A.M. Kudryavtsev, K.V. Lotov, A.N. Skrinsky NIM, Sec. A A**410**, 388, (1998).

[12] A.Ts. Amatuni Proc. PAC'97, p. 693, (1997).

[13] R. Assman, P. Chen, F.J. Decker, R. Iverson, P.Raimondi, T. Raubenheimer, S. Rokhi, R. Sieman, D. Walt, D. Wittum, S. Chattopadhyay, W. Leemans, T. Katzouleas, S. Lee, C. Clayton, C. Joshi, K. Marsh, W. Mori, G. Wang NIM, Sec. A, A**410**, 396, (1998).

AMPLIFICATION OF EXTERNAL EM-WAVE BY NONLINEAR WAKE WAVES IN COLD PLASMA

A.Ts. Amatuni,YERPHI, Yerevan, Armenia

Abstract

The interaction of external monochromatic, linearly polarized, plane electromagnetic (EM) wave with the nonlinear one-dimensional wake-wave, generated by relativistic electron bunch, moving in cold plasma, is considered. At definite conditions on parameters of plasma and electron bunch, nonlinear plasma electron density wake wave has a pronounced spikes, where density value is nearing the wave breacking limit and plasma electron velocities, being directed along the bunch velocity reach, their maximum. Presented calculations exhibit, that external EM-wave, propagating through plasma at such a conditions normal to the bunch velocity direction and with polarization along the bunch velocity can be amplified inside the spikes. EM-wave, Thomson scattered on the spikes, is also amplified. Amplification factors are obtained for the both cases at different conditions for system plasma-electron bunch - external EM - wave parameters.

It is shown that amplification factor can be larger, especialy at the resonance condition, when frequency of external field is nearing to plasma frequency at spikes.

Presented results are obtained using perturbative approach, when dimensionless externnal EM-wave amplitude is used as a small parameter; the known exact nonlinear one-dimensional solution, obtained previously for cold plasma-relativistic electron bunch system, is taken as a zero order approximation.

Considered amplification process can serve as a physical ground for research and development of powerful klystron type amplifiers for future linear colliders.

1 INTRODUCTION

The problem of interaction of external electromagnetic wave (EM - wave) with electrons, moving in plasma, and plasma wake waves, generated by moving electrons or electron bunches, have been a subject of numerous investigations (see for example[1] and referencies therein).

The goal of the presented investigation is to find out the possibility and conditions, when EM wave inside the plasma with the frequency of external EM - wave and Thomson scattered EM - wave can be amplified, as compared to the external EM - wave. It is shown, that if the nonlinear plasma wake waves spikes, generated by relativistic rigid electron bunch, are taken into account as an active media, where interaction processes take place, the significant field amplification can be achived. Wake wave spikes are occure, when nonlinear waves in plasma are nearing wave breaking limit, described for free plasma waves in[2] - [4] and at some details considered in[5] - [6] for relativistic driving bunches and underdense and overdense plasmas. In[5] - [6], in particular, the connection between wave breaking limits on plasma electron density and velocities and bunch electron parameters are obtained.

Wave breaking has followed so called "blowout" regime, introduced in[7] for PWFA process. In the frame of laser - plasma based acceleration, wave breaking regime is used for generation high current relativistic electron beams[8]. In both cases[7] - [8] the unique features of the nonlinear plasma wake waves near wave breacking limit are used for particle acceleration purposes. Results of present work indicate the possible application of plasma wake wave breaking regime for amplification EM - wave, serving as a physical ground for research and development on powerful EM - wave generators and amplifiers for future colliders and accelerators with a high acceleration gradient.

2 BASIC EQUATIONS AND OUTLINE OF THE FORMALISM

The flat rigid electron bunch, moving in cold plasma with immobile ions along z - direction with velocity v_0 in lab system, is considered. Longitudinal length of the bunch is d, transverse directions of the bunch are taken infinite and problem in zero approximation (in absence of external EM - wave) is treated as one dimensional. This approach is valid for wide enough bunches, when bunch radius $r_0 \gg \frac{c}{\omega_p}$[9], where ω_p is plasma frequency $\omega_p^2 = \frac{4\pi e^2 n_0}{m}$, n_0 is plasma electron density at equilibrium.

This condition could be replaced at some sence more adjustable one, if external constant longitudinal magnetic field H_0 is applied to the system. Then one dimensionality conditions could be $r_0 \gg r_L, \Omega_L \gg \omega_p$, where r_L and Ω_L are subsequently the Larmour radius and frequency for plasma electrons.

The considered cold plasma - relativistic electron bunch system is interacting with the external monochromatic, linearly polarized electromagnetic (EM) wave, propagating through plasma in x - direction and with electric vector directed along z - axis (p -polarization). The external EM-wave inside the plasma is described by:

$$\mathcal{E}_z = \mathcal{E}_{0z} e^{-i\omega_0 t + ik_0 x},$$
$$H_y = -\sqrt{\epsilon}\mathcal{E}_{0z} e^{-i\omega_0 t + ik_0 x},$$
$$k_0 = \sqrt{\epsilon}\frac{\omega_0}{c}, \qquad (1)$$

where ϵ is a dielectric constant for plasma:

$$\epsilon \equiv \epsilon' + i\epsilon'' = 1 - \frac{\varpi_p^2}{\omega_0} + i\frac{\varpi_p^2 \nu_{eff}}{\omega_0^3}; \qquad (2)$$
$$\sqrt{\epsilon} \equiv n + i\eta, n = \frac{1}{\sqrt{2}}(\epsilon' + (\epsilon'^2 + \epsilon''^2)^{1/2})^{1/2},$$

0-7803-5573-3/99/$10.00@1999 IEEE.

$$\eta = \frac{1}{\sqrt{2}}(-\epsilon' + (\epsilon'^2 + \epsilon''^2)^{1/2})^{1/2};$$

$\varpi_p^2 = \frac{4\pi e^2 n^{(0)}(z)}{m}$, ν_{eff} - effective colissions frequency of plasma electron, $n^{(0)}(z)$ - plasma electron density in wake waves in the absence of external EM-wave, $\nu_{eff} \ll \varpi_p < \omega_0$. It is assumed that plasma column has a thickness along the EM- wave propagation direction (0x-axis) equal d_x, which is smaller than coressponding skin depth in plasma.

The considered problem consists in finding out the component of EM-field with frequency ω_0 inside and outside the plasma, induced by the field (1) after interaction with plasma electrons, perturbed by rigid relativistic electron bunch, moving in plasma. The back influence of plasma wake wave on the bunch, considered in[10], as well as interaction of the bunch electrons with external EM-wave (1) are disregarded, according to the assumption that bunch is relativistic.

The considered system cold plasma-rigid relativistic electron bunch- external EM-wave is described by the hydrodinamic equation for the motion of plasma electrons in external $\mathcal{E}, H$) and internal $(\vec{E}, \vec{H})$ electromagnetic fields and Maxwell equations for the EM-fields generated by bunch and plasma electrons.

The dimensionless amplitude of the external EM-wave (1) $a = e\mathcal{E}_0/mc\omega_0$ assumed to be small $a \ll 1$ and external EM- wave considered as perturbation.

In zero order approximation ($a = 0$) the system plasma-electron bunch in steady state regime described by known nonlinear, exact, one dimensional solution, obtained in[5],[6]. In particular the plasma electron density $n^{(0)}(\tilde{z})$ in dimensionless variables is given[6] by:

$$n'^{(0)}_{(\tilde{z})} \equiv \frac{n^{(0)}(\tilde{z})}{n_0} = \frac{\beta_0}{\beta_0 - \beta_z^{(0)}(\tilde{z})} = \tag{3}$$
$$= \frac{\beta_0(1+\rho_z^{(0)2})^{1/2}}{\beta_0(1+\rho_z^{(0)2})^{1/2} - \rho_z^{(0)}(\tilde{z})},$$

where $\beta_0 = v_0/c, \beta_z^{(0)} = \frac{v_e}{c} = \rho_z^0/(1+\rho_z^{(0)2})^{1/2}, \rho_z^{(0)} = \frac{P_{ze}}{mc}$. P_{ze} - is the plasma electron momentum in z-direction, $\tilde{z} = z - \beta_0 t$. Inside the electron bunch $\rho_z^{(0)}(\tilde{z})$ is always negative; behind the bunch in wake waves $\beta_z^{(0)}(\tilde{z})$ is periodic and could be positive. At some places, $\tilde{z} \to \tilde{z}_m$ of wake wave $0 < \beta_z^{(0)}(\tilde{z}) \to \beta_{max} < \beta_0$ tends to it's maximum value $\beta_{max} \equiv \beta_m$ and $n^{(0)}(\tilde{z} \to \tilde{z}_m)$ could be large enough, nearing wave breacking limit. The values of β_m are fixed by plasma and electron bunch parameters $n_0, n_b, d, \gamma_0 = (1-\beta_0^2)^{-1/2}$ and could be estimated, using analytic results of work[6].

Equations for first order approximation ($\sim a$) constitute a set of quasilinear equations, with coeficients known from zero order approximation and depending only on $\tilde{z}$. This last feature of the set permit to search a solution in the form

$$\rho_z^{(1)} = \rho_{z0}^{(1)}(\tilde{z}) e^{-i\omega_0 t + ik_0 x}, etc., \tag{4}$$

which reduces the set of quasilinear differential equation in partial derivatives to the set of quasilinear ordinary differential equations. It is still complicated enough and in order to find an analytic solution in what follows the region of $\tilde{z}$ near to $\tilde{z}_m$ is considered.

In this region, approximately[6]

$$\beta_z^{(0)} \approx \beta_m + \frac{1}{2}\left(\frac{d^2\beta_z^{(0)}}{d\tilde{z}^2}\right)_{z_m} (\tilde{z} - \tilde{z_m})^2 = \tag{5}$$
$$= \beta_m - \frac{n_m(n_m-1)}{2\beta_0(1+\rho_m^2)^{3/2}}(\tilde{z} - \tilde{z}_m)$$

$$|\tilde{z} - \tilde{z}_m| \ll \left(\frac{2\beta_0\rho_m^3}{n_m^2}\right)^{1/2} \sim \frac{\gamma_0^{3/2}}{n_m}, \tag{6}$$

where n_m, ρ_m are the plasma electron density and momenta at wake wave spike region (6) at $\tilde{z} = \tilde{z}_m$. Supposing also that quantities $1-\beta_0^2 = \frac{1}{\gamma_0^2}, 1-\beta_m^2 = \frac{1}{\gamma_m^2}$ are small enough it is possible essentialy simplify the obtained set of equations and then reduce it to one first order equation for $\rho_{z0}^{(1)}$, particular solution of which in the region (6) is not difficult to obtain.

3 ESTIMATES FOR AMPLIFICATION FACTORS

From approximate expression for $\rho_{z0}^{(1)}$, obtained by above mentioned way, it is possible to estimate the amplitudes of internal electric field $E_{x,z,0}^{(1)}$

$$E_{z0}^{(1)} \approx -2\mathcal{E}_{z0}\left(1 - \frac{n_m\omega_p}{\rho_m\omega_0}\right),$$

$$E_{x0}^{(1)} \approx -\frac{\mathcal{E}_{z0}}{2\sqrt{\epsilon}}\frac{\omega_p}{\omega_0}\times$$

$$\times\left[2n_m\left(\frac{\omega_p}{\omega_0}\right)\left(1 - \frac{n_m\omega_p}{\rho_m\omega_0}\right) - \right. \tag{7}$$
$$\left. -\frac{n_m\omega_p}{\rho_m\omega_0}\left(n_m\frac{\omega_p^2}{\omega_0^2} + 2\frac{n_m\omega_p}{\rho_m\omega_0} - 1\right)\right];$$

When $\frac{n_\omega\omega_p}{\rho_m\omega_0} \gg 1, \frac{\omega_p}{\omega_0} \ll 1$ i.e.

$$\beta_0 - \beta_m \ll \frac{\omega_p}{\omega_0}\gamma_0^{-1}, \frac{\omega_0^2}{\omega_p^2} > n_m \gg \frac{\omega_0}{\omega_p}\gamma_0, \gamma_0 \ll \frac{\omega_0}{\omega_p} \tag{8}$$

the field amplification factors

$$K_{x,z} = |E_{x,z0}^{(1)}/\mathcal{E}_{z0}|, K_z \approx 2\frac{n_m\omega_p}{\rho_m\omega_0} \gg 1,$$
$$K_x = \frac{1}{\sqrt{\epsilon}}\left(\frac{n_m\omega_p}{\rho_m\omega_0}\right) n_m\left(\frac{\omega_p}{\omega_0}\right)^2 < \frac{1}{\sqrt{\epsilon}}\times$$
$$\times\left(\frac{n_m\omega_p}{\rho_m\omega_0}\right), K_x \gg 1; \tag{9}$$

The plasma current density, generated by external EM-wave in considered system, in the first approximation is given by

$$j_{x0}^{(1)} = n^{(0)}\beta_{x0}^{(1)}, j_{z0}^{(1)} = n^{(0)}\beta_{z0}^{(1)} + n_0^{(1)}\beta_z^{(0)} \qquad (10)$$

and it can be shown that at the condition (8)

$$j_{x0}^{(1)} \approx \frac{2i}{\sqrt{\epsilon}}\left(\frac{n_m\omega_p}{\rho_m\omega_0}\right)^2 \mathcal{E}_{z0}, j_{z0}^{(1)} \approx -2i\left(\frac{n_m\omega_p}{\rho_m\omega_0}\right)^2 \mathcal{E}_{z0} \qquad (11)$$

and corresponding amplification factors for the intensity of EM wave Thomson scattered from the plasma wake wave spikes are:

$$K_{radx,z} = \frac{1}{W_0}\frac{dW_{x,z}}{d\omega} \sim \frac{|j_{0,x,z}^{(1)}|^2}{|\mathcal{E}_{z0}|^2}, \qquad (12)$$

where $\frac{dW_{x,z}}{d\Omega}$ is radiated energy flux in unit solid angle per second from unit volume of plasma wake wave spike, andW_0 is the incident energy flux of the external EM-wave on unit area of plasma wake wave spike cross section, normal to direction of EM - wave propagation, per second. From (11) and (12) it follows that amplification factors can be large enough at the conditions (8).

$$K_{radx} \sim \frac{4}{|\epsilon|}\left(\frac{n_m\omega_p}{\rho_m\omega_0}\right)^4 \gg 1 \qquad (13)$$

$$K_{radz} \sim 4\left(\frac{n_m\omega_p}{\rho_m\omega_0}\right)^4 \gg 1$$

Further increase of amplification factors K_x and K_{radx} (9, 11, 12) can be realized at resonnance condition $\omega_0 \rightarrow \varpi_p$ when $\epsilon' \rightarrow 0$. Then (see (2))

$$(\sqrt{\epsilon})^{-1} \rightarrow \left(\frac{\omega_0}{\nu_{eff}}\right)^{1/2}, \omega_0 \gg \nu_{eff} \qquad (14)$$

$$|\epsilon|^{-1} \rightarrow \left(\frac{\omega_0}{\nu_{eff}}\right) \gg 1$$

and corresponding increase of K_x and K_{radx} from (9, 12) can be easily noticed. Resonance increase due to factors (14) for K_x, K_{radx} can take place independently from conditions (8).

4 CONCLUSION

The obtained analytical results demonstrate that at certain conditions on cold plasma - relativistic electron driving bunch - external EM wave parameters (8), essentially large amplifications are existed of electric field inside the plasma (9,14) as well as of intensity of Thomson scattered on plasma spikes EM-wave (13,14). Presented results could be used in research and development of powerful klystron type amplifiers and generators of high frequency EM - waves for future linear colliders.

The presented estimates have at some extent qualitative character and must be complemented by more quantative calculations, presumably by computer simulations. May be, more elaborate perturbative approach, for example, based on multiple scales method, could provide the possibility to go further in directions, outlined in the present work.

In order to find out the optimal geometry for experimental deffection of the predicted EM - wave amplification, it is necessary to consider also different directions of propagation and different polarisations of external EM - wave.

5 REFERENCES

[1] E.A. Akopian, G.G. Matevosian in Proc. of Workshop "New Developments in Particle Acceleration Techniques", v.2, p. 476, CERN 87-11, ECFA 87/110, 1987.

[2] A.I. Akhiezer, P.V. Polovin JETP **3**, 696, (1956).

[3] J.M. Dawson Phys. Rev. 113, 383 (1959).

[4] R.C. Davidson "Methods in Nonlinear Plasma Theory", ch. 3, Acad. Press, NY and London, 1972.

[5] A.Ts. Amatuni, M.R. Magomedov, E.V. Sekhpossian, S.S. Elbakian Physica Plasmi **5**, 85, (1979).

[6] A.Ts. Amatuni, S.S. Elbakian, E.V. Sekhpossian, R.O. Abramian Part. Acc. **41**, 153, (1993).

[7] J.B. Rozenzweig, B. Breizman, T. Katzouleas, J.J. Su Phys. Rev. A. **47**, R6189, (1991).

[8] S. Bulanov, F. Pegoraro, J. Sakai NIM Sec. A, A**410**, 477, (1998).

[9] W.B. Mori, T. Katzouleas Proc. EPAC-90, Nice, France, June 1990, v. I, p. 603.

[10] A.Ts. Amatuni Proc. PAC'97, p. 693, Vancouver, Canada, May, 1997.

TWO-DIMENSIONAL NONLINEAR REGIME IN THE PLASMA WAKEFIELD ACCELERATOR*

A. G. Khachatryan#, S. S. Elbakian, Yerevan Physics Institute, Yerevan, Armenia

Abstract

The effect of nonlinearity on plasma wake wave excited by a relativistic cylindrical charged bunch is investigated. It is shown that owing to the nonlinearity the amplitude of wake wave gets modulated in the longitudinal direction. The nonlinear wavelength in the excited field changes in the transverse direction with the result that the phase front is distored and a turbulence developed. The nonlinear phase front distortion may be compensated by radial change of unperturbed plasma density.

1 INTRODUCTION

The plasma-based accelerator concepts are presently actively developed both theoretically and experimentally. This is due to the ability of plasma to support large acceleration rates that will reach tens of GeV/m, far in excess of those attained in conventional accelerators. Charged bunches can be accelerated and focused by the field of relativistic plasma waves that are excited by relativistic charged bunches (Plasma Wakefield Accelerator (PWFA)). Both the linear wakefield and 1D nonlinear theories have been studied in sufficient detail (see e. g. overview in Ref. [1]). The allowance for finite transverse sizes of the drivers (that is more realistic case) and, accordingly, the transverse motion of plasma electrons complicate the treatment of the problem in the nonlinear regime. In the general case the analytical solution of this regime seems impossible and the use of numerical methods are usually required. Here we study the effect of nonlinearity on two-dimensional plasma wake waves as well as discuss the cause of radial steepening of the field shown in Ref. [2].

2 BASIC EQUATIONS

We shall consider nonlinear steady fields excited in plasma by a rigid cylindrical electron bunch in the framework of cold hydrodynamics with immobile ions. Let the bunch travel in Z direction at the velocity v_0 close to that of light, and the distribution of charge in the bunch do not depend on the azimuthal angle θ. Equations for non-zero components of plasma electrons momentum and electromagnetic field that describe the nonlinear wake-fields are (see also Refs. [2,3]):

$$\beta\partial P_z/\partial z-\partial\gamma_e/\partial z-\beta^2 E_z=0, \quad (1)$$

$$\beta\partial P_r/\partial z-\partial\gamma_e/\partial r-\beta^2 E_r=0, \quad (2)$$

$$-\partial H_\theta/\partial z+\beta\partial E_r/\partial z+\beta_r N_e=0, \quad (3)$$

$$\nabla_\perp H_\theta+\beta\partial E_z/\partial z+\beta_z N_e+\beta\alpha=0, \quad (4)$$

$$\beta\partial H_\theta/\partial z-\partial E_r/\partial z+\partial E_z/\partial r=0, \quad (5)$$

$$N_e=N_p(r)-\alpha-\nabla_\perp E_r-\partial E_z/\partial z. \quad (6)$$

As usual, Eqs. (1) and (2) were derived taking into account that the curl of the generalized momentum is zero, $\beta^2\mathbf{H}-rot\mathbf{P}=0$, or in our case

$$\beta^2 H_\theta+\partial P_z/\partial r-\partial P_r/\partial z=0. \quad (7)$$

Also we allow for radial variations of unperturbed plasma density. In Eqs. (1)–(6) $\gamma_e=(1+P_z^2+P_r^2)^{1/2}$ is a relativistic factor, $\beta_{z,r}=P_{z,r}/\gamma_e$ and $N_e=n_e/n_p(0)$ are respectively dimensionless components of velocity and density of plasma electrons, $n_p(r)$ is the unperturbed density of plasma electrons, $N_p=n_p(r)/n_p(0)$, $\alpha=n_b(z,r)/n_p(0)$, n_b is the concentration of bunch electrons, $\beta=v_0/c$, $\nabla_\perp=\partial/\partial r+1/r$. The space variables are normalized to $\lambda_p(r=0)/2\pi=1/k_p(r=0)$, $z=k_p(r=0)(Z-v_0t)$, where λ_p and k_p are the linear wavelength and wavenumber. The momenta and velocities are normalized respectively to m_ec and the velocity of light and the strengths of electric and magnetic fields - to the nonrelativistic wave-breaking field at the axis $E_{WB}(r=0)=m_e\omega_{pe}(r=0)v_0/e$ (E_{WB}[V/cm]$\approx 0.96\times n_p^{1/2}$[cm^{-3}]), $\omega_{pe}=(4\pi n_p e^2/m_e)^{1/2}$ is the electron plasma frequency, m_e and e are the rest mass and absolute value of electron charge. The field of forces acting on relativistic electrons in the excited field is $\mathbf{F}(-eE_z, e(H_\theta-E_r), 0)$.

3 THE CASE OF WIDE BUNCH

Consider the case of wide bunch ($k_pr_b\gg 1$, where r_b is the bunch radius) when the transverse components of an exciting field are small and the longitudinal components close to the bunch axis are approximately equal to those predicted by one-dimensional nonlinear theory. Here one can apply the perturbation method taking the 1D nonlinear mode as the ground state. So, for wide bunches in uniform plasma [$N_p(r)=1$] we shall seek the solution of Eqs. (1)–(6) in the vicinity of bunch axis in the form: $P_z\approx P_0+\rho_z r^2$, $P_r\approx\rho_r r$, $E_z\approx E_0+l_z r^2$, $E_r\approx l_r r$, $H_\theta\approx hr$, $\alpha\approx\alpha_0-\delta r^2$, where $P_0(z)$ and $E_0(z)$ are the values of longitudinal momentum and the strength of electric field at the axis, $\rho_{z,r}(z)$, $l_{z,r}(z)$, $h(z)$, $\delta(z)\ll 1$. In the zero approximation in

*Work supported by the International Science and Technology Center

Email: khachatr@moon.yerphi.am

this values one can obtain the equations for P_0 and E_0 that describe the 1D nonlinear regime that is studied sufficiently well [4]. In the first approximation in the small values we have:

$$d^2\rho_z/dz^2 - Ad\rho_z/dz + B\rho_z = \beta N_0\delta, \quad (8)$$

where $A=(d\beta_0/dz)2N_0/\beta$, $B=(N_0/\beta)(\beta N_0^2/\gamma_0^3-d^2\beta_0/dz^2)$, β_0, N_0 and γ_0 are respectively dimensionless velocity, density and the relativistic factor of plasma electrons in 1D nonlinear regime. The remaining quantities can be expressed through ρ_z. In Fig. 1 we show the focusing gradient $f_r/r=(H_\theta-E_r)/r=-2\rho_z/N_0$, that is excited by d=4.7 long wide bunch with density α_0=0.2.

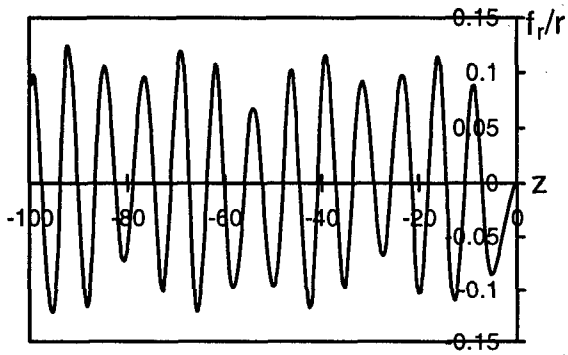

Figure 1: The gradient of dimensionless focusing field as a function of longitudinal coordinate. The bunch is d=4.7 long, and α_0=0.2, δ=0.2α_0, $\gamma=(1-\beta^2)^{-1/2}$=10.

It was shown numerically based on Eq. (8) that although the amplitude of excited transverse components is small, their wavelength is nearly equal to that of one-dimensional nonlinear wave. The amplitude of oscillations periodically changes with z (see Fig. 1). The modulation depth grows and the modulation period decreases as the amplitude of nonlinear longitudinal oscillations increases. These effects take place also for other components of the field.

4 WAKEFIELD IN UNIFORM PLASMA

Eqs. (1)–(6) were solved numerically choosing the Gaussian profile of the bunch both in longitudinal and transverse directions:

$$\alpha = \alpha_0 \exp[-(z-z_0)^2/\sigma_z^2]\exp(-r^2/\sigma_r^2). \quad (9)$$

In case of small amplitudes of the excited wake wave (when α_0<<1) the numerical solutions well agreed with linear theory predictions. Shown in Fig. 2 is the nonlinear 2D plasma wake wave excited in uniform plasma by the relativistic electron bunch with parameters α_0=0.4, σ_z=2, σ_r=5 (for example, in this case $n_{b0}=4\times10^{13}$cm^{-3} and the characteristic longitudinal and transverse sizes of the bunch σ_z/k_p respectively are 1.06mm and 2.65mm when $n_p=10^{14}$cm^{-3}). The main difference here from the linear case is the change of shape and length of the wave with the radial coordinate r, as well as the change of amplitude in the longitudinal

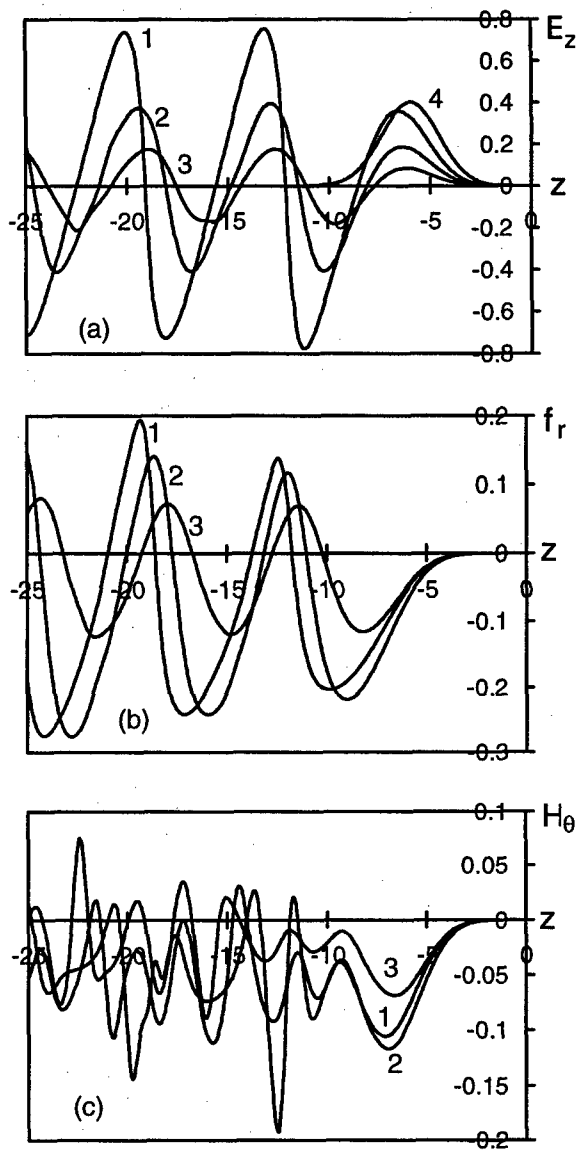

Figure 2: The two-dimensional nonlinear wake wave in uniform plasma. The parameters of the bunch are: α_0=0.4, σ_z=2, σ_r=5, γ=10. (a). The longitudinal electric field. 1–r=0; 2–r=4; 3–r=6; 4–the density of bunch at the axis $\alpha(z, r=0)$. The focusing field $f_r=H_\theta-E_r$ (b) and magnetic field strength (c). 1–r=2; 2–r=4; 3–r=6.

direction. Note also an enlargement of the range of focusing forces (f_r<0) in the nonlinear wake wave.

It is easy to see that due to the dependence of the wavelength on r, the field in the radial direction grows more chaotic as the distance from the bunch increases. In fact, the oscillations of plasma for different r are "started" in the wake wave with nearly equal phases but different wavelengths. As |z| increases, the change of phase in the transverse direction (for fixed z) becomes more and more marked. This leads to a curving of the phase front and to "oscillations" in the transverse direction. Curve 1 in Fig. 3 shows the radial behavior of

the accelerating field E_z in the nonlinear wake wave. Qualitatively, the radial dependence of the field differs from that of the linear case by the change of sign and "steepening" of fields along r (see also Ref. [2]). One can determine the longitudinal space parameter characterizing the wave front curving as follows:

$$\xi = \lambda_p / [2(1 - \lambda_p / \Lambda(0))], \qquad (10)$$

where $\Lambda(r)$ is the nonlinear wavelength. At the distance $|\Delta z| \approx \xi$ from the bunch the oscillation phase at the axis (r=0) is opposite to that on the periphery ($r \geq \sigma_r$) where the wave is nearly linear.

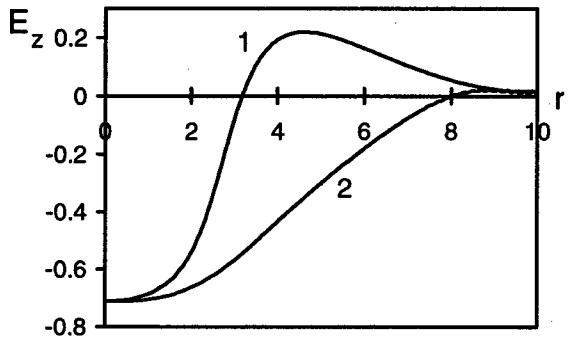

Figure 3: The radial behavior of accelerating electric field strength E_z. 1–$E_z(z=-25, r)$ in the nonlinear wake wave excited in uniform plasma for the case given in Fig.2 ($|\Delta z| \approx \xi$ [see Eq. (10)]); 2–$E_z(z=-25, r)$ in nonuniform plasma for the case given in Fig. 4.

The magnetic field strength in the nonlinear two-dimensional wake wave as shown in Fig. 2(c) is different from zero (note that in the linear case H_θ=0 in the wake, where the wave is potential) due to the fact that the velocities of plasma electrons in the wave are not any more small in comparison with the bunch velocity. The magnitude of higher frequency oscillations (as compared to the plasma frequency) performed by the magnetic field along z grows in proportion to the nonlinearity. Such a behavior of magnetic field is a purely nonlinear effect. The nonlinearity of the wave implies a rise of higher harmonics in P_z and P_r. According to (7), the rise of magnetic field is due to these harmonics and this accounts for frequent oscillations seen in Fig. 2(c). On the other hand, according to (7), the non-zero magnetic field in the wake means that the motion of plasma electrons in the nonlinear wave is turbulent ($rot\mathbf{P} \neq 0$). The degree of turbulence (the measure of which is H_θ) grows as the nonlinearity.

From the viewpoint of acceleration and focusing of charged bunches in the wave, the curvature of the nonlinear wave front is undesired as the quality (emittance, monochromaticity) of the driven bunch worsens. Below we show that in radially-nonuniform plasma one can avoid the curvature of the wave front.

5 RADIALLY-NONUNIFORM PLASMA

Thus, in two-dimensional nonlinear regime the nonlinear wavelength changes with r due to nonlinear increase of the wavelength with wave amplitude. On the other hand, the linear wavelength $\lambda_p \sim n_p^{-1/2}$ decreases with density of plasma. Let us assume that the nonlinear wavelength of the two-dimensional wake wave in the uniform plasma $\Lambda(r)$ is known. Then, one can roughly compensate for the radial variation of the nonlinear wavelength by changing the unperturbed density of plasma in the radial direction according to the relation

$$\Lambda(0) / \Lambda(r) = \lambda_p(r) / \lambda_p(0) = [n_p(0)/n_p(r)]^{1/2}. \qquad (11)$$

If we put the function $\Lambda(r)$ to be Gaussian (according to numerical data for profiles (9), this is approximately the case at least for $r < \sigma_r$), then one can take the transverse profile of the unperturbed plasma density to be also Gaussian: $n_p(r) = n_{p0} \exp(-r^2/\sigma_p^2)$. It follows from Eq. (11) that in this case $\sigma_p = r/[\ln(\Lambda(0)/\Lambda(r))]^{1/2}$. For example, the numerical data for $\Lambda(r)$ in the nonlinear wave shown in Fig. 2 give $\sigma_p \approx 11$. Fig. 4 illustrates the validity of this assertion (see also Fig. 3, curve 2).

Numerical solutions obtained for the case of nonlinear wake wave excitation by a short laser pulse (Laser Wakefield Accelerator, see e. g. Ref. [1]) show that the results given in this work do not change qualitatively.

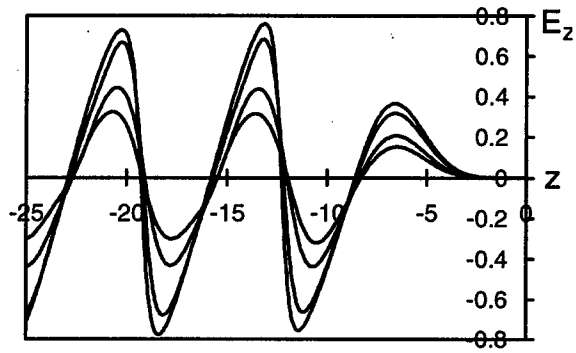

Figure 4: Accelerating electric field of two-dimensional nonlinear wake wave in nonuniform plasma with σ_p=11 for r=0, 2, 4 and 5 in the order of magnitude reduction. The bunch parameters are the same as those in Fig. 2.

6 REFERENCES

[1] E. Esarey, P. Sprangle, J. Krall, and A. Ting, IEEE Trans. Plasma Sci. **24**, 252 (1996).

[2] B. N. Breizman, T. Tajima, D. L. Fisher, and P. Z. Chebotaev, In: *Research Trends in Physics: Coherent Radiation and Particle Acceleration, edited by A. Prokhorov* (American Institute of Physics, New York, 1992), pp. 263-287.

[3] K. V. Lotov, Phys. Plasmas **5**, 785 (1998).

[4] A. Ts. Amatuni, E. V. Sekhpossian, and S. S. Elbakian, Fiz. Plasmy **12**, 1145 (1986); J. B. Rosenzweig, Phys. Rev. Lett. **58**, 555 (1987); A. G. Khachatryan, Phys. Plasmas **4**, 4136 (1997).

CHARACTERISTICS OF ELECTRON ACCELERATION IN A SELF-MODULATED LASER WAKEFIELD*

S.-Y. Chen, M. Krishnan, A. Maksimchuk and D. Umstadter†

Abstract

The electron beam generated in a self-modulated laser wakefield accelerator is characterized. It was observed to have a multi-component beam profile and its energy distribution undergoes discrete transitions as the laser power or plasma density is varied. In addition, dark spots that form regular modes were observed in the electron beam profile.

1 INTRODUCTION

Acceleration of electrons by an electron plasma wave has been of great current interest because of its much larger acceleration gradient than that of conventional rf linacs [1]. Several methods have been proposed for driving a large-amplitude fast-phase-velocity plasma wave [1]. In the Laser Wake-Field Accelerator (LWFA), an electron plasma wave is driven resonantly by a short laser pulse through longitudinal laser ponderomotive force [2]. In the Self-Modulated Laser Wake-Field Accelerator (SMLWFA), an electron plasma wave is excited by a relatively long laser pulse undergoing stimulated Raman forward scattering instability [3, 4, 5]. The injection of electrons can occur by trapping of hot background electrons, which are preheated by other processes such as Raman backscattering and sidescattering instabilities [6, 7, 8], or by wave-breaking (longitudinal [1] or transverse [9]). It can also be achieved by specific injection schemes [10, 11] in order to control the characteristics of the generated electron beam.

Several groups have observed the generation of MeV electrons from the SMLWFA [7, 8, 12, 13, 14, 15]. In this experiment, the electron beam produced from a self-modulated laser wakefield accelerator injected with self-trapping of electrons was characterized in detail. The observations of up-to-three-component electron-beam profiles and up-to-two discrete changes in the slope of electron energy distribution are reported. In addition, dark spots that form regular modes were observed in the first beam-profile component. These new observations provide us important new clues to the underlying dynamics of electron acceleration in a three-dimensional (3-D) plasma wave.

2 EXPERIMENTAL SETUP

The experiment was done by using a Ti:sapphire/Nd:glass laser system that produced 400-fs-duration laser pulses at 1.053-μm wavelength with a maximum peak power of 4 TW. The 50-mm-diameter laser beam was focused with an f/3.3 parabolic mirror onto the front edge of a supersonic helium gas jet. The focal spot in vacuum was a 7-μm-FWHM near-Gaussian spot, which contained 60% of the total pulse energy, and a large dim spot (100 μm FWHM). The helium gas was fully ionized by the foot of the laser pulse. At a laser power of $\geq$ 2 TW and a plasma density of $\geq 2\times10^{19}$ cm^{-3}, the laser pulse underwent relativistic-ponderomotive self-channeling [13, 16], and the laser channel of $<$ 10-μm diameter extended to be 750 μm in length, the length of the gas jet. An electron plasma wave was excited by the laser pulse through stimulated Raman forward scattering instability, as was evident from the observation of Raman satellites in the transmitted light [7]. An electron beam was produced, when the laser power or gas density exceeded a certain threshold, and propagated in the direction of the laser beam. The spatially-averaged time-resolved plasma-wave amplitude was measured using collinear collective Thomson scattering [17]. The peak plasma-wave amplitude was observed to increase with increase of laser power or plasma density, and the maximum observed was about 30% density perturbation.

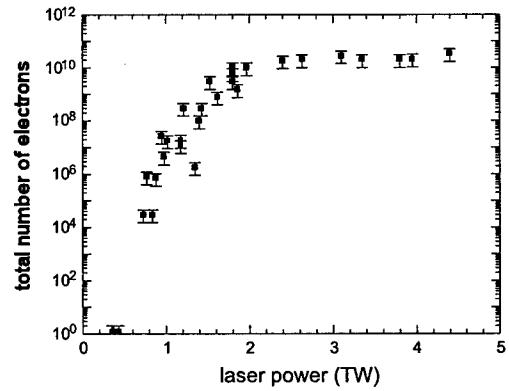

Figure 1: Total number of electrons with energies >60 keV in the generated electron beam as a function of laser power at 3.7 $\times$ 10^{19}-cm^{-3} plasma density.

The electron energy spectrum in the low energy range ($<$ 8 MeV) was measured using a dipole permanent magnet with a LANEX scintillating screen imaged by a CCD camera as the detector. Higher-energy electron energy spectra were obtained by using dipole electro-magnets and a multi-wire proportional chamber (MWPC). The electron-beam spatial profile at 16 cm away from the gas jet was measured using a LANEX scintillating screen imaged by a CCD camera. Because of the aluminum foil in front of the LANEX, which was used for blocking the laser light, only

* Supported by the Division of High Energy Physics, Office of Energy Research, U.S. Department of Energy, award DE-FG02-98ER41071, with facilities supported by the National Science Foundation.

† Center for Ultrafast Optical Science, University of Michigan, Ann Arbor, MI 48109

0-7803-5573-3/99/$10.00@1999 IEEE.

electrons with kinetic energies higher than 100 keV were imaged. Since the source size of the generated electron beam was small, $\sim$ 10 μm in diameter, the electron beam profile on the LANEX was actually a measurement of the angular pattern. The total number of electrons in the beam was measured either by using a Faraday cup to directly collect the entire electron beam or by using a collimator and a calibrated scintillator-PMT (photomultiplier tube).

3 RESULT AND DISCUSSION

3.1 *Number of Electrons*

Figure 1 shows the total number of electrons in the beam as a function of laser power at a fixed plasma density [7]. Below a threshold, no electron is observed. When the laser power exceeds this threshold, the number of electrons increases exponentially with increase of laser power, and then gradually saturates. The variation of the number of electrons with change of plasma density shows the same behavior. The threshold of the electron production is believed to be associated with the electron trapping threshold.

3.2 *Transverse Beam Profile*

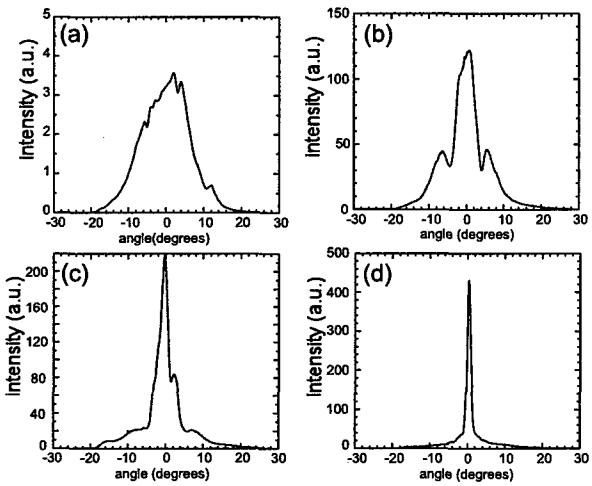

Figure 2: Lineouts of the electron beam profiles for various laser powers at 2.3×10^{19}-cm^{-3} plasma density: (a) 0.6 TW, (b) 1.1 TW, (c) 2.0 TW, and (d) 2.9 TW.

The electron beam profile (angular pattern) was observed to contain several concentric Gaussian-like-profile beams, and the number of beam components depends on laser power and plasma density. For a plasma density of $2.3-6.2 \times 10^{19}$ cm^{-3}, only one beam component ($\sim$ 20° FWHM) exists in the electron beam at 0.6-TW laser power. At a laser power larger than 1 TW, a second beam component grows up on top of the first beam component, with a divergence angle of $5° - 10°$ FWHM. For $2.3-3.4 \times 10^{19}$-cm^{-3} plasma density, a third beam component with a divergence angle of $1° - 3°$ FWHM appears when the laser power is higher than 2 TW. Figure 2 shows the lineouts of the electron beam profiles for various laser powers at 2.3×10^{19}-cm^{-3} plasma density. Basically, the divergence angle of the second beam component increases and that of the third beam component decreases with increase of laser power, while the divergence angle of the first beam component is roughly invariant ($20° - 25°$). The multiple-component electron beam profile is believed to result from the transverse electric field of the plasma wave.

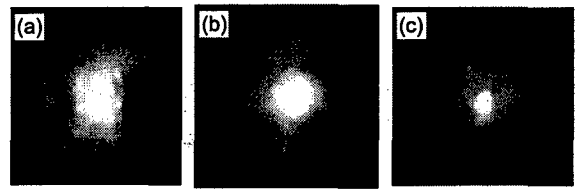

Figure 3: Images of the transverse electron beam profiles at various laser powers and plasma densities: (a) 1.1 TW, 3.4×10^{19} cm^{-3}, (b) 3.5 TW, 6.2×10^{19} cm^{-3}, and (c) 2.0 TW, 2.3×10^{19} cm^{-3}.

The appearance of the second beam component was observed to coincide with the sudden extension of the plasma-wave channel (which is determined by the laser channel) caused by laser self-guiding. In addition, when the second beam component appears, there are usually some holes appearing in the first beam component, as shown in Fig. 3. These holes form regular patterns that are similar to TM_{12}, TM_{22} and TM_{32} electromagnetic modes in a circular waveguide, or to (1,0), (1,1) and (1,2) Hermite-Gaussian modes of a laser beam. Furthermore, under the highest laser power and plasma density in this experiment, a density depression at the center of the accelerated electron beam was observed occasionally, as shown in Fig. 4. The dark modes appearing in the electron beam profile may be caused by the excitation of electron plasma waves with higher-order modes or with density depressions.

3.3 *Electron Energy Spectrum*

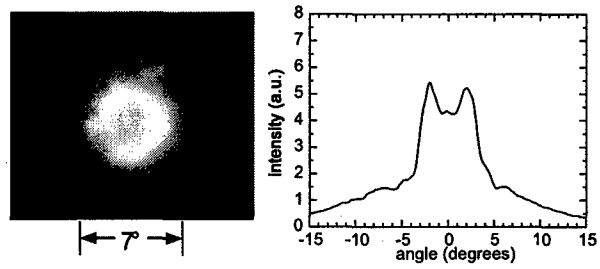

Figure 4: Image and vertical lineout of the transverse electron beam profile at 3.5-TW laser power and 6.2×10^{19}-cm^{-3} plasma density.

Figure 5 shows the normalized electron energy spectra in

the low energy range for various laser powers and plasma densities. The spectra were found to have Maxwellian-like distributions, i.e., exp(-$\alpha\gamma$), where γ is the relativistic factor of electron energy. The slope, α, of the spectrum was found to change discretely with variation of laser power and plasma density. For instance, at a fixed plasma density, the slope remains the same with increasing laser power until a certain threshold is reached. Then the slope α changes to a lower value, and stays the same with further increase of laser power until the next jump. The same behavior occurs for varying plasma density at a fixed laser power. Three α values were observed in this experiment: 1.0, 0.6 and 0.3. The occurrence of the first jump coincides with the extension of the laser channel from < 400 μm to 750 μm; however, when the second jump occurs, there is no change in the laser channel length. The slopes of the electron energy spectra in the low energy range were found to be the same for these three beam components. The transition of the slope may be related to the ratio between the plasma-wave channel length and the electron detuning length.

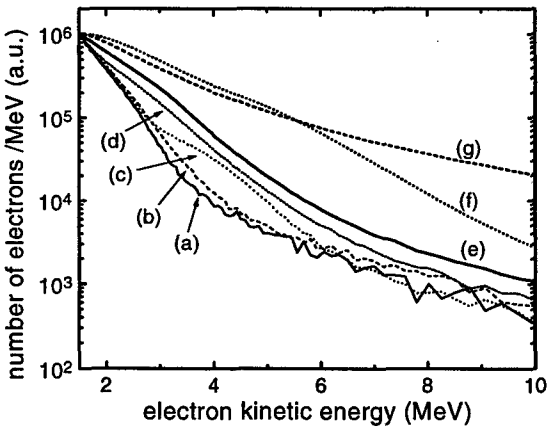

Figure 5: Electron energy spectra for various laser powers and plasma densities: (a) 2.6 TW, 3.4 $\times$ 10^{19} cm^{-3}, (b) 2.9 TW, 3.5 $\times$ 10^{19} cm^{-3}, (c) 3.3 TW, 4.8 $\times$ 10^{19} cm^{-3}, (d) 3.9 TW, 4.8 $\times$ 10^{19} cm^{-3}, (e) 1.7 TW, 6.2 $\times$ 10^{19} cm^{-3}, (f) 2.7 TW, 6.2 $\times$ 10^{19} cm^{-3}, and (g) 3.5 TW, 6.2 $\times$ 10^{19} cm^{-3}.

Another important observation in this experiment is a two-temperature distribution in the electron energy spectrum. As shown in Fig. 6, which was obtained using both the low-energy and high-energy electron spectrometers, the slope of electron energy distribution in the low energy range ($\leq$ 5 MeV) is steep, while the slope in the high energy range is much less steep (almost flat). The two-slope electron energy spectrum is believed to be a result of electron motion inside and outside the separatrix.

3.4 Other Parameters

The temporal duration of the electron pulse should be roughly equal to that of the plasma wave, $\sim$ 2 ps [17], since the former is generated from the latter. The separation between adjacent micro bunches is equal to the plasma-wave period, which is 18 fs for a plasma density of 3.4 $\times$ 10^{19} cm^{-3}. The duration of a micro bunch should be less than that. Therefore, the maximum peak current is estimated to be about 1 kA or higher. The transverse cross section of the electron source should be roughly equal to the cross section of the plasma wave, which roughly equals that of the laser beam, $\sim$ 10 μm. In the best cases, the angular divergence of the electron beam was measured to be $\sim$ 1°, which leads to a normalized transverse emittance of 0.06 π-mm-mrad for 2 MeV electrons.

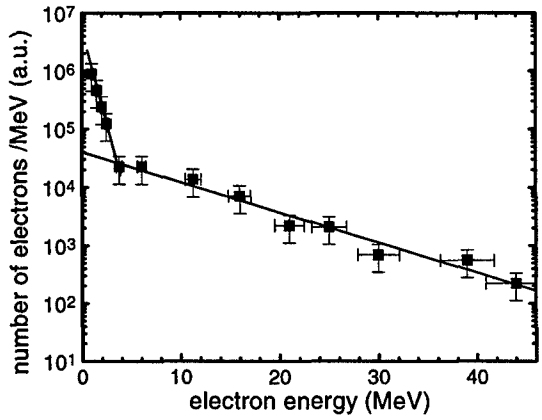

Figure 6: Electron energy spectrum for 3-TW laser power and 3 $\times$ 10^{19}-cm^{-3} plasma density. The solid lines represent exponential fits.

4 REFERENCES

[1] See references in E. Esarey *et al.*, IEEE Trans. Plasma Sci. **PS-24**, 252 (1996).

[2] T. Tajima and J. M. Dawson, Phys. Rev. Lett. **43**, 267 (1979).

[3] P. Sprangle *et al.*, Phys. Rev. Lett. **69**, 2200 (1992).

[4] T. M. Antonsen, Jr. and P. Mora, Phys. Rev. Lett. **69**, 2204 (1992).

[5] N. E. Andreev *et al.*, JETP Lett. **55**, 571 (1992).

[6] P. Bertrand *et al.*, Phys. Rev. E **49**, 5656 (1994).

[7] D. Umstadter *et al.*, Science **273**, 472 (1996).

[8] C. I. Moore *et al.*, Phys. Rev. Lett. **79**, 3909 (1997).

[9] S. V. Bulanov *et al.*, Phys. Rev. Lett. **78**, 4205 (1997).

[10] D. Umstadter, J. K. Kim, and E. Dodd, Phys. Rev. Lett. **76**, 2073 (1996).

[11] E. Esarey *et al.*, Phys. Rev. Lett. **79**, 2682 (1997).

[12] A. Modena *et al.*, Nature **377**, 606 (1995).

[13] R. Wagner *et al.*, Phys. Rev. Lett. **78**, 3125 (1997).

[14] G. Malka *et al.*, Phys. Rev. Lett. **79**, 2053 (1997).

[15] D. Gordon *et al.*, Phys. Rev. Lett. **80**, 2133 (1998).

[16] S.-Y. Chen *et al.*, Phys. Rev. Lett. **80**, 2610 (1998).

[17] S. P. Le Blanc *et al.*, Phys. Rev. Lett. **77**, 5381 (1996).

A VARIATIONAL PRINCIPLE APPROACH TO THE EVOLUTION OF SHORT-PULSE LASER PLASMA DRIVERS*

Brian J. Duda and Warren B. Mori
Departments of Physics and Astronomy, and Electrical Engineering
University of California at Los Angeles

Abstract

The attractiveness of variational principle approaches for obtaining good approximations to complicated problems is well established. Motivated by this fact, we have developed a variational principle approach to the evolution of short-pulse laser-plasma accelerator drivers. We start with an action of the form $\partial_\tau a << k_0 a$ where the Euler-Lagrange equations of L, the Lagrangian density, give the well established coupled equations of short-pulse interactions, in the weakly relativistic regime:

$$(\nabla_\perp^2 - 2\frac{\partial^2}{\partial\psi\partial\tau} - 2ik_0\frac{\partial}{\partial\tau})a = (1-\phi)a$$

$$(\frac{\partial^2}{\partial\psi^2} + 1)\phi = \frac{|a|^2}{4}$$

We substitute appropriate trial functions for a and ϕ into S and carry out the $\int dx_\perp$ integration. The Euler-Lagrange equations of the reduced Lagrangian density provide coupled equations for the trial function parameters, i.e., spot sizes, amplitude, phase, radius of curvature and centroids for both a and ϕ. We present an analysis in the paraxial regime, where the $\partial_\psi\partial_\tau a$ term is neglected.

1 MOTIVATION

Understanding the evolution of short-pulse high-intensity lasers as they propagate through underdense plasmas is essential for the successful development of some plasma accelerator [1] and radiation schemes [2]. Research during the past few years has resulted in the identification of numerous instabilities such as envelope self-modulation [3], where the spot size of the laser becomes unstable, and hosing [4, 5], where the centroid of the laser becomes unstable. To study these instabilities, it is desirable to obtain differential equations for the evolution of the macroscopic quantities that characterize the beam profile, such as the spot size, amplitude, phase, radius of curvature and centroid. There are various methods of obtaining such equations, which include the variational method, as well as moment methods [6, 7], and the Source Dependent Expansion technique [8]. Here, we use a variational approach similar to that used by Anderson and Bonnedal in their study of self-focusing [9], and extend the variational technique to a coupled set of equations so as to include Raman related instabilities.

We start with the two coupled equations for the density perturbation and normalized vector potential, valid in the weakly relativistic regime, $|a|^2<<1$:

$$(\frac{\partial^2}{\partial t^2} - c^2\nabla^2)\vec{a} = 4\pi c\vec{J}_\perp = -\omega_p^2\frac{n}{n_0\gamma}\vec{a}$$

$$= -\omega_p^2(1+\delta n - \frac{|a|^2}{2})\vec{a}$$

$$(\frac{\partial^2}{\partial t^2} + \omega_p^2)\delta n = c^2\nabla^2\frac{|a|^2}{2}$$

where $\delta n \equiv (n-n_0)/n_0$. Then, we normalizing all time dimensions to ω_p^{-1}, space dimensions to $k_p^{-1} \equiv c/\omega_p$, and make a coordinate transformation to the normalized light frame variables ($\psi \equiv t - z$, $\tau \equiv z$). Upon making the substitution $a \rightarrow a\exp[Ik_0\psi]$, switching to the potential $\phi \equiv \delta n - |a|^2/4$, making the envelope approximation $\partial_\tau a << k_0 a$, noting that $\vec{a}$ is unidirectional and describable by a single scalar, and dropping derivatives of $|a|^2$ as slow, we arrive at the well known set of equations:

$$(\nabla_\perp^2 - 2\frac{\partial^2}{\partial\psi\partial\tau} - 2ik_0\frac{\partial}{\partial\tau})a = (1-\phi)a$$

$$(\frac{\partial^2}{\partial\psi^2} + 1)\phi = \frac{|a|^2}{4}$$

2 THE VARIATIONAL APPROACH

Our approach to the analysis of these equations is to first obtain a Lagrangian density for the coupled equations. Then, we choose trial functions for a and ϕ which contain descriptive parameters that depend upon (ψ, τ). We substitute these trial functions into the action, and perform the integration across the transverse coordinates to obtain a reduced Lagrangian density. In this reduced form of the action integral, the parameters

* This work is supported by DOE grants DE-FG03-92ER40727 and DE-FG03-98DP00211, NSF grant DMS-9722121, and LLNL W07405-ENG48

of the trial function represent a new set of dependent variables. In essence, by choosing an approximate form for the transverse beam profile, we replace the infinite degrees of freedom in the transverse directions with a finite number which represent the macroscopic characteristics of the distribution. Then, varying the action with respect to the new dependent variables yields a set of differential equations for the trial parameters.

We now carry out this procedure. We start by noting that the Lagrangian density for this set of equations is:

$$L = \vec{\nabla}_\perp a \cdot \vec{\nabla}_\perp a^* - ik_0(a\,\partial_\tau a^* - a^*\partial_\tau a) - (\partial_\psi a\,\partial_\tau a^* + \partial_\psi a^*\partial_\tau a) - 2(\partial_\psi \phi)^2 + 2\phi^2 - (\phi - 1)|a|^2$$

where the corresponding action is $S = \int dx_\perp d\psi\, d\tau\; L$. It can be readily verified that our starting equations are the result of varying the action with respect to a, a^*, and ϕ. We choose the following trial functions for a, and ϕ:

$$a = A(\psi,\tau)\, e^{i\,k_x(\psi,\tau)\,\tilde{x}_a}\, e^{i\,k_y(\psi,\tau)\,\tilde{y}_a} \times e^{-(1 - i\alpha_x(\psi,\tau))\frac{\tilde{x}_a^2}{w_{xa}(\psi,\tau)^2}}\, e^{-(1 - i\alpha_y(\psi,\tau))\frac{\tilde{y}_a^2}{w_{ya}(\psi,\tau)^2}}$$

$$\phi = \Phi(\psi,\tau)\, e^{-2\left(\frac{\tilde{x}_\phi^2}{w_{x\phi}(\psi,\tau)^2} + \frac{\tilde{y}_\phi^2}{w_{y\phi}(\psi,\tau)^2}\right)}$$

where $\tilde{x}_a \equiv x - x_a(\psi,\tau)$, $\tilde{y}_a \equiv y - y_a(\psi,\tau)$, $\tilde{x}_\phi \equiv x - x_\phi(\psi,\tau)$, $\tilde{y}_\phi \equiv y - y_\phi(\psi,\tau)$, and the amplitude A is a complex amplitude such that $A(\psi,\tau) = \sqrt{\xi(\psi,\tau)}\, e^{i\,\chi(\psi,\tau)}$. Inserting these trial functions into the action and performing the $\int dx_\perp$ integration yields the following reduced action principle:

$$S = \int d\psi\, d\tau \Big[P\Big(\frac{k_x^2}{2} + \frac{k_y^2}{2} + \frac{(1+\alpha_x^2)}{2w_{xa}^2} + \frac{(1+\alpha_y^2)}{2w_{ya}^2} - k_0(\partial_\tau\chi - k_x\,\partial_\tau x_a - k_y\,\partial_\tau y_a)\Big) - P\,k_0\Big(\frac{w_{xa}^2}{4}\partial_\tau\Big(\frac{\alpha_x}{w_{xa}^2}\Big) + \frac{w_{ya}^2}{4}\partial_\tau\Big(\frac{\alpha_y}{w_{ya}^2}\Big)\Big) + \frac{1}{2}(P + w_{x\phi}w_{y\phi}\,\Phi) - \frac{w_{x\phi}w_{y\phi}\,\Phi\,P\; e^{-2\left(\frac{(x_a-x_\phi)^2}{(w_{xa}^2+w_{x\phi}^2)} + \frac{(y_a-y_\phi)^2}{(w_{ya}^2+w_{y\phi}^2)}\right)}}{\sqrt{(w_{xa}^2 + w_{x\phi}^2)(w_{ya}^2 + w_{y\phi}^2)}} + \ldots$$

$$\ldots - \Big(\frac{w_{x\phi}w_{y\phi}}{2}(\partial_\psi\Phi)^2 + \frac{\partial_\psi(\Phi^2)}{4}\partial_\psi(w_{x\phi}w_{y\phi}) + \frac{\Phi^2}{4}(\partial_\psi w_{x\phi})(\partial_\psi w_{y\phi}) + \frac{3}{8}\Phi^2\Big(\frac{w_{y\phi}}{w_{x\phi}}(\partial_\psi w_{x\phi})^2 + \frac{w_{x\phi}}{w_{y\phi}}(\partial_\psi w_{y\phi})^2\Big) + \Phi^2\Big(\frac{w_{y\phi}}{w_{x\phi}}(\partial_\psi x_\phi)^2 + \frac{w_{x\phi}}{w_{y\phi}}(\partial_\psi y_\phi)^2\Big)$$

Varying the action with respect to χ, α_x, α_y, k_x, and k_y yields the equations:

$$\delta\chi: \quad \partial_\tau P = 0 \quad \text{(Power Conservation)},$$

$$\delta\alpha_x: \quad \alpha_x = -\frac{k_0}{4}\partial_\tau(w_{xa}^2),$$

$$\delta\alpha_y: \quad \alpha_y = -\frac{k_0}{4}\partial_\tau(w_{ya}^2),$$

$$\delta k_x: \quad k_x = -k_0\,\partial_\tau x_a,$$

$$\delta k_y: \quad k_y = -k_0\,\partial_\tau y_a$$

We can use these equations to eliminate χ, α_x, α_y, k_x, and k_y from the Lagrangian since χ is an ignorable coordinate, and the other equations are generated by variations of the action with respect to the same variables being solved for. Eliminating these variables yields the following simplified form of the Lagrangian:

$$L = P\Big[\frac{1}{2}\Big(\frac{1}{w_{xa}^2} + \frac{1}{w_{ya}^2}\Big) - \frac{k_0^2}{8}\big((\partial_\tau w_{xa})^2 + (\partial_\tau w_{ya})^2 + 4(\partial_\tau x_a)^2 + 4(\partial_\tau y_a)^2\big)\Big] + \frac{1}{2}(w_{x\phi}w_{y\phi}\,\Phi - \frac{w_{x\phi}w_{y\phi}\,\Phi\,P\; e^{-2\left(\frac{(x_a-x_\phi)^2}{(w_{xa}^2+w_{x\phi}^2)} + \frac{(y_a-y_\phi)^2}{(w_{ya}^2+w_{y\phi}^2)}\right)}}{\sqrt{(w_{xa}^2 + w_{x\phi}^2)(w_{ya}^2 + w_{y\phi}^2)}} - \Big(\frac{w_{x\phi}w_{y\phi}}{2}(\partial_\psi\Phi)^2 + \frac{\partial_\psi(\Phi^2)}{4}\partial_\psi(w_{x\phi}w_{y\phi}) + \frac{\Phi^2}{4}(\partial_\psi w_{x\phi})(\partial_\psi w_{y\phi}) + \frac{3}{8}\Phi^2\Big(\frac{w_{y\phi}}{w_{x\phi}}(\partial_\psi w_{x\phi})^2 + \frac{w_{x\phi}}{w_{y\phi}}(\partial_\psi w_{y\phi})^2\Big) - \frac{\Phi^2}{c^2}\Big(\frac{w_{y\phi}}{w_{x\phi}}(\partial_\psi x_\phi)^2 + \frac{w_{x\phi}}{w_{y\phi}}(\partial_\psi y_\phi)^2\Big)\Big)$$

In this form, P is treated explicitly as a constant.

Variation of this Lagrangian with respect to the remaining parameters yields the desired set of

differential equations for their evolution. These equations can then be used to study the stability of the beam profile.

3 SYMMETRIC ENVELOPE SELF MODULATION AND SELF-FOCUSING

To demonstrate the utility of this approach, we now look at the specific case of the symmetric envelope self modulation instability [3]. Here, we are only interested in the evolution of the spot sizes, with the x and y dimensions identical, i.e. $w_{xa} = w_{ya} \equiv w_a$, $w_{x\phi} = w_{y\phi} \equiv w_\phi$. Making these replacements, setting the centroids to 0, and then varying the resulting action with respect to the remaining parameters - Φ, w_a, w_ϕ - yields:

$$\delta w_a : \frac{k_0^2}{2}\partial_\tau^2 w_a - \frac{2}{w_a^3} + \frac{\Phi w_\phi^2 w_a}{(w_a^2 + w_\phi^2)^2} = 0$$

$$\delta w_\phi : (\partial_\psi \Phi)^2 - \frac{1}{2}\partial_\psi^2(\Phi^2) - 2\partial_\psi(\Phi^2 \partial_\psi w_\phi) + \Phi - \frac{P\Phi w_a^2}{(w_a^2 + w_\phi^2)^2} = 0$$

$$\delta \Phi : 2\partial_\psi(w_\phi^2 \partial_\psi \Phi) + \Phi\partial_\psi^2(w_\phi^2) - 4\Phi(\partial_\psi w_\phi)^2 + w_\phi^2 - \frac{P w_\phi^2}{w_a^2 + w_\phi^2} = 0$$

If we reduce these equations to the limit of no ψ dependence, we obtain the self-focusing equations:

$$w_\phi = w_a, \quad \Phi = \frac{P}{4w_a^2} = \frac{A^2}{4}$$

$$\partial_\tau^2 w_a - \frac{4}{k_o^2 w_a^3}(1 - \frac{P}{32}) = 0$$

From which we obtain the well known critical threshold for self-focusing, $P/P_{crit} = a_0^2 w_a^2/32$ [9, 10]. For $P = P_{crit}$, we have a matched, stationary beam profile, i.e., w_a is a constant.

We now examine the stability of this equilibrium solution. Linearizing the equations using a matched beam as the 0th order solution yields:

$$\partial_\tau^2 w_{a1} + \frac{8}{k_0^2 w_0^4}(3 - \frac{P}{P_{crit}})w_{a1} = -\frac{1}{k_0^2 w_0}\Phi_1$$

$$(\partial_\psi^2 + 1)\Phi_1 = -\frac{16}{w_0^3}\frac{P}{P_{crit}} w_{a1}$$

$$(\partial_\psi^2 + 1)w_{\phi 1} = w_{a1}$$

The first two of these equations show that Φ_1 and w_{a1} behave as coupled harmonic oscillators, which resonantly drive each other, and result in an envelope self-modulation instability.

A more general stability analysis can be done in which the centroids are allowed to evolve, and the spot sizes are allowed to be different in the x and y directions. This more general analysis results in 2 more instabilities: a hosing instability [4, 5, 11], wherein the centroids for a and ϕ resonantly drive each other, and an anti-symmetric envelope self modulation instability, wherein the linearized spot size variables in the x and y directions, for both a and ϕ, are equal and opposite (as opposed to the symmetric case previously analyzed, where the x and y spot sizes are identically equal). A comprehensive analysis of these instabilities has been performed, and will be described in future work.

4 SUMMARY

We have developed a variational principle approach for studying the evolution of short-pulse laser-plasma accelerator drivers. The approach is shown to reproduce previous results, e.g., relativistic self-focusing and spot size self-modulation. It is also useful for describing instabilities such as asymmetric self-focusing, asymmetric spot size self-modulation, as well as new long-wavelength regimes for hosing and spot-size self-modulation. We are currently extending the analysis to fully non-linear driver amplitudes.

REFERENCES

[1] T. Tajima and J.M. Dawson, Phys. Rev. Lett. 43, 267. (1979); E. Esarey et al., IEEE Trans. Plasma Sci. 24, 252 (1996), and references therein.

[2] Special issue, IEEE Trans. Plasma Sci. PS-21(1) (1993), edited by W.B. Mori.

[3] E. Esarey et al., Phys. Rev. Lett. 72, 2887 (1994).

[4] P. Sprangle et al., Phys. Rev. Lett. 73, 3544 (1994).

[5] G. Shvets and J.S. Wurtele, Phys. Rev. Lett. 73, 3540 (1994).

[6] J. F. Lam, et al., Opt. Commun. 15, 419 (1975).

[7] J. F. Lam, et al., Phys. Fluids 20, 1176 (1977).

[8] P. Sprangle et al., Phys. Rev. A, 36, 2773 (1987).

[9] D. Anderson and M. Bonnedal, Physics of Fluids, 22, 105 (1979).

[10] P. Sprangle et al., IEEE Trans. Plasma Sci. vol. PS-15, pp. 145-153, 1987.

[11] B.J. Duda et al., submitted to Phys. Rev. Lett.

DEVELOPMENT OF A PARALLEL CODE FOR MODELING PLASMA BASED ACCELERATORS

R.G.Hemker, F.S.Tsung, V.K.Decyk, W.B.Mori, UCLA, Los Angeles,CA
S.Lee and T.Katsouleas, USC, Los Angeles, CA

Abstract

Advances in computational speed and memory make it now possible to do full scale 2D and 3D PIC simulations of laser and beam plasma interactions. However, the increased complexity of these codes and interactions make it necessary to apply modern programming approaches like object oriented frameworks to the development of these codes. We report here on our progress in developing the object oriented parallel PIC code OSIRIS that is implemented in Fortran 90. In its current state, the code can be used for 1D, 2D, and 3D simulations in Cartesian coordinates and for 2D simulations in cylindrically symmetric coordinates. We will present benchmarks of simulations done with this code for a proposed plasma wake field accelerator experiment [1,2].

1 INTRODUCTION

The introduction of massively parallel computers with hundreds of processors provides now the computational speed and the memory needed to do full scale 2D and 3D simulation of plasma based accelerators and other problems in laser-plasma and beam-plasma physics. In order to take full advantage of the possibilities of this development it has become necessary to use more complex simulation codes. The increased complexity of codes arises for two reasons. One reason is that the realistic simulation of a problem requires a larger number of more complex algorithms interacting with each other than the simulation of a rather simple model system. An example would be that initializing an arbitrary laser or plasma beam in 3D is a much more difficult problem than doing the same in 1D or 2D. The other reason that simulation codes are becoming more complex is that the computer systems are more complex and the performance obtained from them can dramatically differ depending on the code strategy. Parallelized codes that have to handle the problems of parallel communication and parallel IO are an example of this. A way to deal with this increased complexity is to use an object oriented programming style, which divides the code and data structures into independent classes of objects. This programming style maximizes code reusability and reliability.

2 DESCRIPTION OF THE CODE AND CODE DEVELOPMENT

The goal of the code development program was to create a code that breaks up the large problem of a simulation into a set of essentially independent smaller problems that can be solved separately from each other. Object oriented programming achieves this by handling different aspects of the problem in different modules (classes) that communicate through well-defined interfaces. The programming language we chose for this purpose was Fortran 90, mainly because it allow us to more easily integrate already available Fortran algorithms into the new OSIRIS-framework. In its current state, the code contains algorithms for 1D, 2D, and 3D simulations in Cartesian coordinates and for 2D simulations in cylindrically symmetric coordinates. For all of these algorithms the code is fully relativistic and presently uses a charge-conserving current deposition algorithm. It allows for a moving simulation window and arbitrary domain decomposition for any number of dimensions. Benchmarking of the code has so far shown a slowdown of less than 15% compared to other codes using similar algorithms due to the additional overhead that is a side effect of the object oriented implementation.

Figure 1 shows the class hierarchy of OSIRIS. The main physical objects used are particle objects, electromagnetic field objects, and source field objects (for currents and densities). The particle object is an aggregate of an arbitrary number of particle species objects. The most important support classes are the variable-dimensionality-field class, which is used by the electromagnetic and source field class and encapsulates many aspects of the dimensionality of a simulation, and the domain-decomposition class, which handles all communication between nodes. For easy portability of the code to different architectures all code that is machine dependent is encapsulated in the system-, the file-system-, and the utility-module.

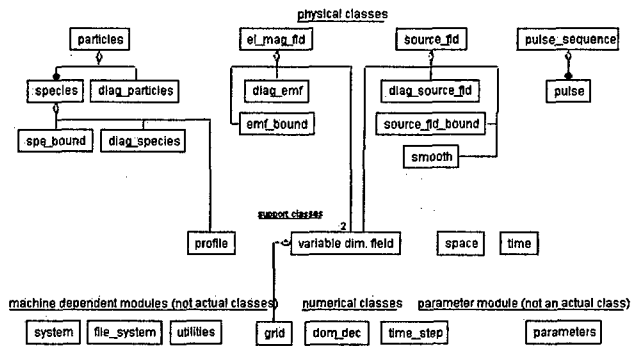

Figure 1: The class hierarchy of OSIRIS

The code was first developed for 1D and 2D simulations in Cartesian coordinates, which took about a year of time.

0-7803-5573-3/99/$10.00@1999 IEEE.

After this fundamental work was completed, extending the code to 2D cylindrically symmetric coordinates took about four weeks and implementation of 3D simulations took about a week. This short time required for the extension to cylindrically symmetric 2D and 3D simulations was possible because the object-oriented style of the code allowed for two specific features. First, most of the code does not make any explicit use of the dimensionality or the coordinate system. Secondly, all communication between the physical domains assigned to the different nodes of a parallel computer is handled as a part of the boundary conditions of the physical domains assigned to each node. This handling of node-to-node communication allows it to consider almost all algorithms as single-node algorithms. Once a single node-algorithm is implemented in OSIRIS, it is automatically already parallelized since it can take advantage of the already existing boundary conditions.

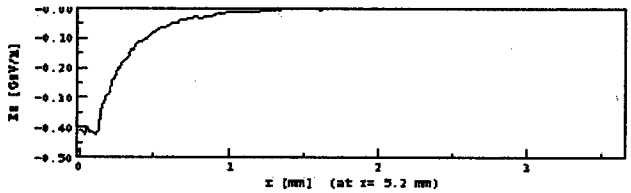

Figure 2: E_z lineout as a function of r at a position of 5.2mm from the back of the simulation box (see figure 4) after a beam propagation of 1m

3 SIMULATION RESULTS

We have benchmarked the 2D cylindrical algorithms of OSIRIS against previously performed simulations [3] of a plasma wakefield accelerator. In this model problem a 30 GeV electron bunch of $4x10^{10}$ electrons with Gaussian profiles (σ_z=0.6mm,σ_r=75μm) and an emittance of ε_N = 15 π mm mrad will propagate through 1m of an underdense plasma with a density of $n=2.1x10^{14}cm^{-3}$. The simulation of the problem was done on a 500x200 grid with 9 particles per cell for the background plasma and 25 particles per cells for the beam. The simulation area, which moved with the beam because of the moving window, had an extension along the axis of 25 c/ω_p and a radial extension of 10 c/ω_p. At the density of $2.1x10^{14}cm^{-3}$ this is 9.2mm x 3.7mm. This grid lead to a grid cell size of $0.05c/\omega_p x 0.05c/\omega_p$ and therefore a time step of $0.02\omega_p^{-1}$ was chosen. The simulation was done on 10 nodes of a Cray T3E and took about 2 1/2 days of turnaround time for the 136000 required time steps. By comparison, another code used before for similar simulations took about 19 days to finish the task[4].

Since the plasma density is less than the beam density a total blowout of the plasma electrons in the wake of the electron bunch, creating a positively charged ion column, is expected. The simulation results clearly support this. Figure 2 shows a lineout of E_z as a function of r. The plot shows the flattening of the accelerating field E_z close to the axis, characteristic of the blowout regime.

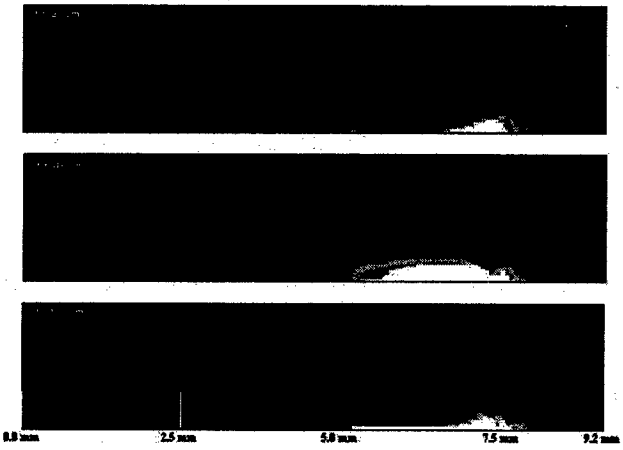

Figure 3: Charge density plot of the beam at three different propagation distances. The betatron oscillations are clearly visible.

The blowout should also lead to betatron oscillations of the middle and tail part of the beam with a wavelength given by

$$\lambda_\beta/2 = \pi\sqrt{\frac{\gamma mc^2}{2\pi n_0 e^2}} \qquad (1)$$

Figure 3 shows a charge density plot of the beam at different times. The upper and middle plot are the minimum and maximum of the oscillation at the propagation distances where they would be expected according to equation (1). The lowest plot shows the beam at the end of the simulation after propagating for 1m.

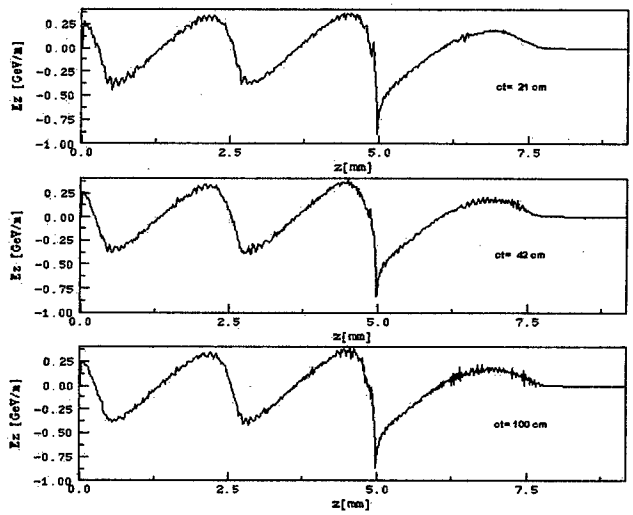

Figure 4: Lineout of the accelerating field along the axis at the first minimum and maximum of the betatron oscillations and at the final propagation distance of 1m

Together the density plots confirm the wavelength of the betatron oscillation given by equation (1) and therefore the underlying ideas about the beam-plasma interactions. It should also be noted that as expected the head of the beam, where the electrons are not fully blown out, oscillates with a longer period that depends on the axial position within the beam.

Figure 4 shows lineouts of the accelerating electric fields along the axis at the same propagation distances as the density plots in figure 2. The simulation results indicate that the magnitude of the peak accelerating field does not vary by more than about 5 -10% during the beam propagation despite of betatron oscillations.

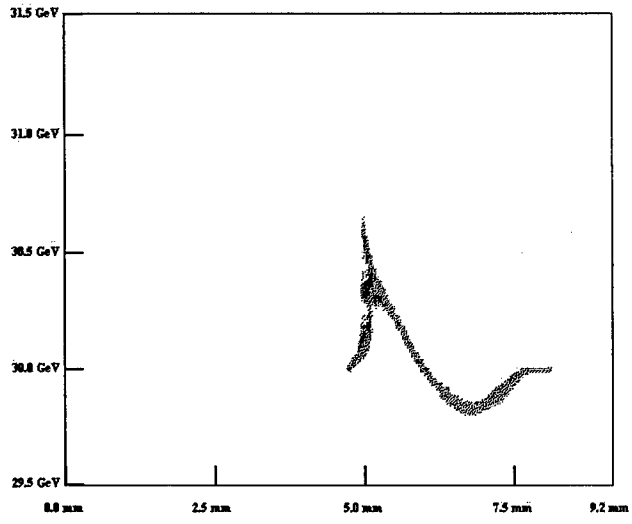

Figure 5: Plot of the energy of the beam particles as a function of position along the axis after 1m of propagation

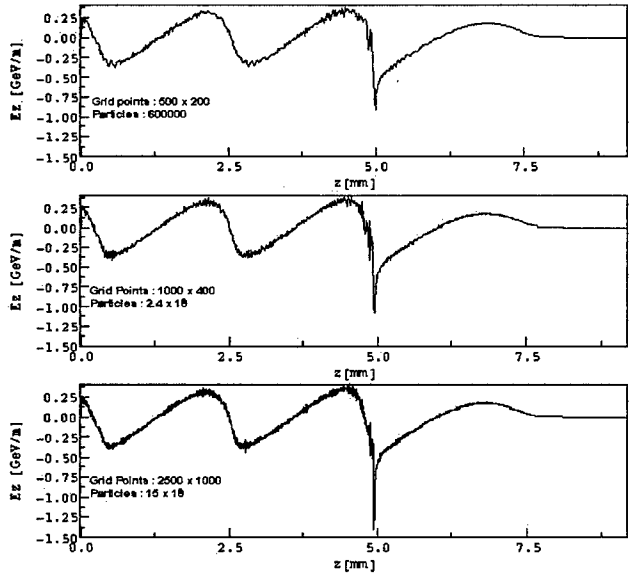

Figure 6: Outline of the accelerating field along the axis after 3 cm of propagation for three simulations with different numbers of grid cells and particles.

Figure 5 shows the energy of the beam particles at the end of the simulation. There are three important features that should be noted in this plot. The front part of the beam did not change energy, the middle part of the beam lost about 200 MeV, and particles in the tail of the beam gained energies up to 700 MeV. These results are mostly consistent with previously presented calculations and simulations of this system [3].

We also did simulations for the same physical setup but with a larger number of grid cells and particles and therefore with a larger numerical accuracy. Figure 6 shows the lineouts of the accelerating electric fields along the axis for the original as well as two higher resolution simulations after 3 cm of propagation. The results differ significantly only in that the peak accelerating field increases with the resolution of the simulation. This leads to the conclusions that the 2D cylindrically symmetric simulations describe most aspects of the PWFA well but that it is hard to get a reliable estimate of the peak field and therefore the maximum obtainable particle energies with this algorithm. Full 3D simulations are probably required to clarify this question [2].

4 CONCLUSIONS

The object oriented framework OSIRIS for laser-plasma and beam-plasma physics has been developed and successfully used for simulations of plasma wake field accelerators. These simulations support previous research results. The code will be used for future research in this area as well as in other areas. New modules adding new physics to the framework will be implemented as our research motivates it. Due to the object oriented programming style these new modules will be able to immediately take full advantage of all the other features already implemented.

Work supported in part by DOE, NSF, and LLNL

5 REFERENCES

[1] R. Assmann et al., paper WEBL6 of these proceedings;

[2] Modeling of E-157 is done in collaboration with E.Esarey at LBNL and C.Schroeder at UC Berkeley;

[3] R.Assmann et al., "Proposal for a GeV Plasma Wakefield Accelerator", SLAC-Pub, 1997;

[4] S.Lee in Proc. AACW, Baltimore (AIP Conf. PROC. 1998);

GENERATION OF PHASE-CONTROLLED ACCELERATING STRUCTURES IN PLASMA*

G. Shvets†, N. J. Fisch, PPPL, Princeton, NJ
A. Pukhov, J. Meyer-ter-Vehn, MPQ, Garching, Germany

Abstract

A novel mechanism for generating large (> 1 GeV/m) accelerating wakes in a plasma is considered. We employ two slightly detuned counter-propagating laser beams, an ultra-short timing pulse and a long pump, which exchange photons and deposit the recoil momentum into the plasma electrons. A rapidly rising electron current is thereby generated, inducing an plasma wake with phase velocity equal to the group velocity of the short pulse, which can be used for particle acceleration. It turns out that, by modulating the amplitude and frequency of the pump, one can generate periodic phase-controlled accelerating structures in the plasma ("plasma linac"). By the judicious choice of the duration of each segment of the pumping beam, acceleration unlimited by the dephasing can be realized. The amount of transverse focusing can be also adjusted. The important advantage of this type of plasma accelerator over the conventional laser wakefield accelerator is that it requires modest laser intensities $I \ll 10^{18}\mathrm{W/cm}^2$.

1 INTRODUCTION

Plasma is an attractive medium for particle acceleration [1] because of the high electric field it can sustain. In a plasma-based accelerator particles gain energy from a longitudinal plasma wave. To accelerate particles to relativistic energies, the plasma wave needs to be sufficiently intense, with a phase velocity close to the speed of light. The longitudinal (accelerating) field of the plasma wave is $E_0 = \hat{n}E_{\mathrm{wb}}$, where $\hat{n} = \delta n/n_0$ is the fractional density perturbation of the plasma by the wave, and $E_{\mathrm{WB}} = mc\omega_p/e$ is the cold wavebreaking field. Here $\omega_p = \sqrt{4\pi e^2 n_0/m}$ is the plasma frequency, n_0 is the plasma density, $-e$ and m are the electron charge and mass. In a laser wakefield accelerator (LWFA) such a plasma wave is excited by an ultra-short pulse of about $1/\omega_p$ duration. Since $\hat{n} \approx a_0^2/2$, where $a_0^2 = 0.37 I_0/10^{18}\mathrm{W/cm}^2$, high laser intensity $I_0 \sim 10^{18}$ W/cm^2 is required.

In this paper we suggest a new approach to generating accelerating wakes in plasma, which we call a colliding-beam accelerator (CBA). This method requires neither ultra-high intensity lasers, nor high-current electron beams. Rather, by colliding two counter-propagating laser beams of sub-relativistic intensities, a short timing beam (TB) a_0 and a long pumping beam (PB) a_1, a plasma wave with phase velocity v_{ph} equal to the group velocity of the short pulse $v_{\mathrm{g}} \approx c$ is generated. This wave induces a fractional density perturbation of the plasma, $\hat{n} \approx \omega_p/\omega_0$, where ω_0 and $\omega_1 \approx \omega_0$ are the laser frequencies. In order to induce a density perturbation of this magnitude, laser intensities should satisfy $a_0 a_1 \geq \omega_p^2/\omega_0^2$. This condition implies non-relativistic laser intensities $I_{0,1} \ll 10^{18}\mathrm{W/cm}^2$, because $\omega_p^2/\omega_0^2 \ll 1$ for tenuous plasmas.

When two laser pulses collide in plasma, they may exchange photons [2]. The direction of the energy flow between the pulses is governed by the Manley-Rowe relation: the higher-frequency photons back-scatter into the lower-frequency photons. The recoil momentum is deposited into the plasma electrons. For example, when the pump frequency is higher, $\Delta\omega = \omega_0 - \omega_1 < 0$, plasma electrons, on average, acquire a negative momentum and produce an electron current. It is essential that this current can generate a plasma wave substantially larger in amplitude (the enhanced wake) than the conventional plasma wake produced by mere forward scattering. Since the sign of the current is controlled by the frequency detuning $\Delta\omega$, so is the phase of the plasma wave $\phi = \omega_p(t - z/v_{ph})$. These two points are illustrated by a numerical simulation, performed using a 1D version of the Particle-in-Cell (PIC) code VLPL [3]. As Fig. 1 indicates, the addition of the counter-propagating laser beam (pump) to the ultra-short pulse increases the magnitude of the wake by order of magnitude. We will, therefore, refer to the wake generated in the presence of the pump as the "enhanced" wake, as opposed to the "regular" wake, produced in the absence of the pump. Moreover, one observes from Fig. 1 that when the frequency of the pump is changed from $\omega_1 = 1.1\omega_0$ to $\omega_1 = 0.9\omega_0$, the phase of the wake is changed by $\Delta\phi = -\pi$.

The remainder of the paper is organized as follows. In Section 2 we consider the basic physics of the enhanced wake excitation: interference of two counter-propagating laser beams generates a spatially periodic (with period $\lambda_0/2$) ponderomotive potential, which can impart an overall momentum to the plasma. Two regimes are considered: when the electron motion in this ponderomotive potential is linear, and when strong electron. In Section 3 we demonstrate how a sequence of acceleration/drift sections can be produced in plasma, mimicking sections of a conventional rf accelerator in the plasma medium.

2 GENERATION OF ENHANCED WAKES

We consider the interaction between the electron plasma and two planar circularly polarized laser pulses $\vec{a}_0$ and $\vec{a}_1$, where $\vec{a}_{0,1} = a_{0,1}(\vec{e}_x \pm i\vec{e}_y)/2$, $\theta_0 = (k_0 z - \omega_0 t)$, and

* Work was supported by the DOE Division of High Energy Physics contract No. DE-AC02-CHO-3073, and the Deutsche Forschungsgemeinschaft.

† Email: gena@pppl.gov

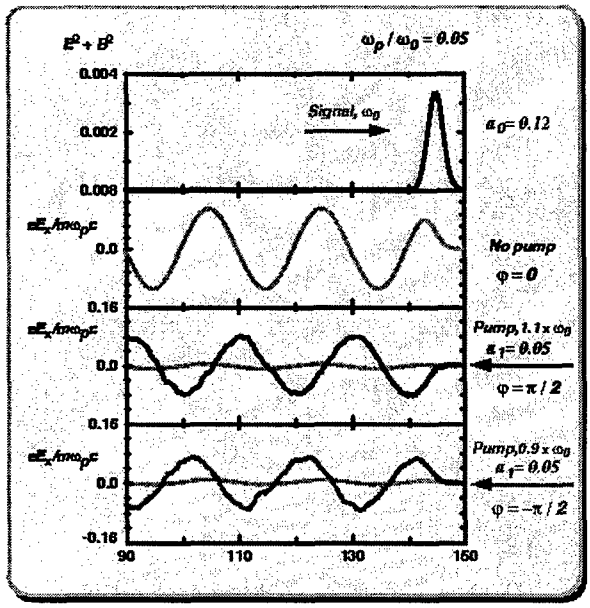

Figure 1: Top to bottom: (i) single short laser pulse with $a_0 = 0.12$ and frequency ω_0 propagates from left to right; (ii) short pulse generates a weak plasma wake E_x; (iii) in the presence of counter-propagating pump with $a_1 = 0.05$ and frequency $\omega_1 = 1.1\omega_0$ the wake is enhanced, and its phase is shifted by $\pi/2$ with respect to the "regular" wake of (ii), which is also shown for comparison; (iv) Same as (iii), only a down-shifted pump with $\omega_1 = 0.9\omega_0$ is used, and the phase shift is $-\pi/2$.

$\theta_1 = (k_1 z + \omega_1 t)$. We assume laser pulses close in frequency $|\Delta\omega| \ll \omega_0$, and tenuous plasma $\omega_p \ll \omega_{0,1}$, so that $k_0 \approx k_1 \approx \omega_0/c$.

Plasma electrons experience the longitudinal ponderomotive force of the laser beatwave $F = -mc^2\partial_z \vec{a}_0 \cdot \vec{a}_1 \approx 2k_0 a_0(\zeta, z)a_1 \cos(2k_0 z - \Delta\omega t)$, where $\zeta = t - z/v_g$. The motion of an arbitrary plasma electron (labeled by index j) is determined by its ponderomotive phase $\psi_j = 2k_0 z_j - \Delta\omega t_j$, where z_j and t_j are the electron position and time, respectively. The equation of motion for the j'th electron can be expressed as

$$\frac{\partial^2\psi_j}{\partial\zeta^2} + \omega_B^2 \sin\psi_j = -\omega_p^2 \sum_{l=1}^{\infty} \hat{n}_l e^{il\psi_j} - \frac{2\omega_0 e E_z}{mc} + \text{c. c.}, \quad (1)$$

where $\omega_B^2(\zeta, z) = 4\omega_0^2 a_0 a_1$ is the bounce frequency of an electron in the ponderomotive potential. It turns out that two plasma waves are excited by the collision of a short pulse with a long pump: a slow wave with the wavelength $\lambda_0/2$, and a fast wave (enhanced wake) with the wavelength λ_p. This is reflected in Eq. (1): $\hat{n}_l = \left\langle e^{-il\psi_j}/l \right\rangle_{\lambda_0/2}$ is the $l-$th harmonic of the slow wave, and E_z, the enhanced wake, is the electric field of the fast wave.

The nonlinear origin of the enhanced wake E_z can be understood as follows. As the photons are exchanged between the counter-propagating beams, electrons, on average, acquire the recoil momentum and produce a current. However, the current in 1-D must be balanced by the displacement current. An electric field E_z is produced, satisfying Faraday's law $\partial E_z/\partial t = -4\pi < J_z >$, where $< J_z >$ is the current averaged over the period of the slow wave. Two flows contribute to $< J_z >$: the linear plasma flow in the field of the enhanced wake $J_f = -en_0 v_f$, and the nonlinear (space-averaged) flow $-e\langle nv\rangle$. Taking the time derivative of Faraday's law, we obtain $\left(\frac{\partial^2}{\partial\zeta^2} + \omega_p^2\right) E_z = -4\pi e \frac{\partial < nv >}{\partial\zeta}$.. Below we consider two regimes: when the slow wave is linear and when electrons are trapped by the ponderomotive potential.

If the slow wave remains linear, its higher harmonics can be neglected, and $\langle nv\rangle = n_0(n_1 v_1^* + n_1^* v_1)$, where, as defined earlier, $\hat{n}_1 = \left\langle e^{-i\psi_j} \right\rangle$ is the plasma density perturbation, and v_1 is the associated velocity perturbation. Using the continuity equation, we find that $\langle nv/c\rangle = (\Delta\omega/\omega_0)|\hat{n}_1|^2$. It can be shown that behind the Gaussian TB $a_0(\zeta) = a_0 \exp(-\zeta^2/2\tau_L^2)$ the accelerating electric field oscillates as $E_z(\zeta) = \tilde{e}(mc\omega_p/e)\sin\omega_p\zeta$, where

$$\tilde{e} = \frac{\pi\Delta\omega}{8\omega_0}\left(4a_1 a_0 \frac{\omega_0^2}{\omega_p^2}\right)^2 \omega_p^2\tau_L^2 e^{-\omega_p^2\tau_L^2/4} \times$$
$$\times \left[e^{-(\omega_p-\Delta\omega)^2\tau_L^2} + e^{-(\omega_p+\Delta\omega)^2\tau_L^2} + \frac{2}{3}e^{-\Delta\omega^2\tau_L^2}\right] \quad (2)$$

The most efficient excitation of the accelerating wake requires $\tau_L \approx 2.0\omega_p^{-1}$ and $\Delta\omega = \pm 1.1\omega_p$. For these parameters $|\tilde{e}| \approx 0.6\omega_p/\omega_0\ (4a_0 a_1\omega_0^2/\omega_p^2)^2$. The enhanced wake exceeds the regular wake from forward scattering whenever $a_1 > (\omega_p/\omega_0)^{3/2}/4$. For $n_0 = 10^{18}\text{cm}^{-3}$, this corresponds to the pump intensity $I_1 > 2\cdot 10^{14}$ W/cm^2.

Equation (2) is valid if the slow plasma wave is linear. To find the maximum magnitude of the enhanced wake, consider the nonlinear regime of Eq. (1) when $\omega_B^2 > \omega_p^2$. In this regime, all the terms in the RHS of Eq. (1) become smaller than the ponderomotive term in the LHS. One may neglect the electrostatic forces acting on plasma electrons during the short time of TB interaction. Hence, the particle motion is qualitatively described by the nonlinear pendulum equation $\ddot{\psi}_j + \omega_B^2(\zeta)\sin\psi_j = 0$.

Plasma electrons, initially stationary in the laboratory frame, enter the time-dependent ponderomotive bucket with the initial "speed" $\dot{\psi} = -\Delta\omega$. If this speed is smaller than the bucket height $\dot{\psi}_{max} = 2\omega_B$, some electrons become trapped and execute a synchrotron oscillation in the bucket. It turns out that, by appropriately choosing the pulse duration and frequency detuning, a substantial average momentum can be imparted to plasma electrons. The largest average momentum gain $P_z \approx mc\Delta\omega/\omega_0$ is realized for $\Delta\omega \approx \omega_B$ and $\tau_L \approx 2/\omega_B$. For these parameters, most of the electrons execute half of a bounce in the ponderomotive bucket. Behind the TB electrons are left with an average momentum P_z, generating an enhanced wake

with the electric field

$$\frac{eE_z}{mc\omega_p} = \frac{\langle P_z \rangle}{mc} \sin\omega_p\zeta \approx \mathrm{sign}(\Delta\omega)\left(\frac{\omega_B}{\omega_0}\right)\sin\omega_p\zeta. \quad (3)$$

Since the bounce frequency $\omega_B \sim I_0^{1/4}$ increases slowly with the intensity of the TB, it is realistic to assume that $\omega_B \sim \omega_p$, so that $\hat{n} \sim \omega_p/\omega_0$. Note that the phase of the enhanced wake is controlled by the sign of the frequency detuning $\Delta\omega$, as observed in the PIC simulation. This is true when the slow plasma wave is either linear, or nonlinear, as predicted by Eqs. (2) and (3), respectively.

3 PLASMA LINAC

The ability to control ϕ is important since it may solve the dephasing problem of wakefield acceleration. Dephasing between the plasma wave and the accelerated relativistic electrons occurs after a distance $L_d = \lambda_p^3/\lambda_0^2$, after which electrons slip into the decelerating phase of the wake. Generating a series of wake sections with tailored relative phases and magnitudes may result in a new type of plasma linac, in which the injected electrons experience acceleration over distances much exceeding L_d. In order to demonstrate the control over the phase and amplitude of the wake in a CBA, we present in Fig. 1(b) the results of a numerical simulation, where two wake sections of 1 mm total length and the relative phase difference of π are shown. The full dephasing distance of $L_d = 1cm$ would involve a considerably more computational effort beyond out present capabilities.

The pump is split into two sections: the leading section of duration $\Delta t_1 = 500 \times 2\pi/\omega_0$, where $\Delta\omega = -1.7\omega_p$, and the trailing section $\Delta t_3 = 250 \times 2\pi/\omega_0$, where $\Delta\omega = 1.7\omega_p$. These two pump beam sections are separated by the middle section of duration $\Delta t_2 = \Delta t_3$, where the pump is switched out.

As Figs. 2(a,b) show, the three pump sections map into three spatial acceleration regions, which are different from each other by the behavior of the TB, as well as the magnitude and *phase* of the plasma wake. In the leading region the pump beam has higher frequency and energy flows into the TB, amplifying it. A strong plasma wake with the peak accelerating gradient of 8 GeV/m is induced. The middle region is void of the pump. Here the TB interacts with the plasma through the usual LWFA mechanism only, producing a weak, < 1GeV/m, accelerating wake. In this region the energy of the injected electrons does not significantly change, as seen from Fig. 2(d). When the trailing (low-frequency) part of the pump collides with the TB, the energy flows from the TB into the PB, Fig. 2(c). Again, a strong plasma wake is induced, Fig. 2(b). This wake, however, is shifted in phase by $\Delta\phi = \pi$ with respect to the leading region. As a result, the particles which gained energy in the leading region are *decelerated* in the trailing region, Fig. 2(d). By repeating the time sequence for the pump, shown in Fig. 2, with the appropriately chosen durations of the pump sections $\Delta t_1 = 2L_d/c$ and $\Delta t_2 = \Delta t_3 = L_d/c$,

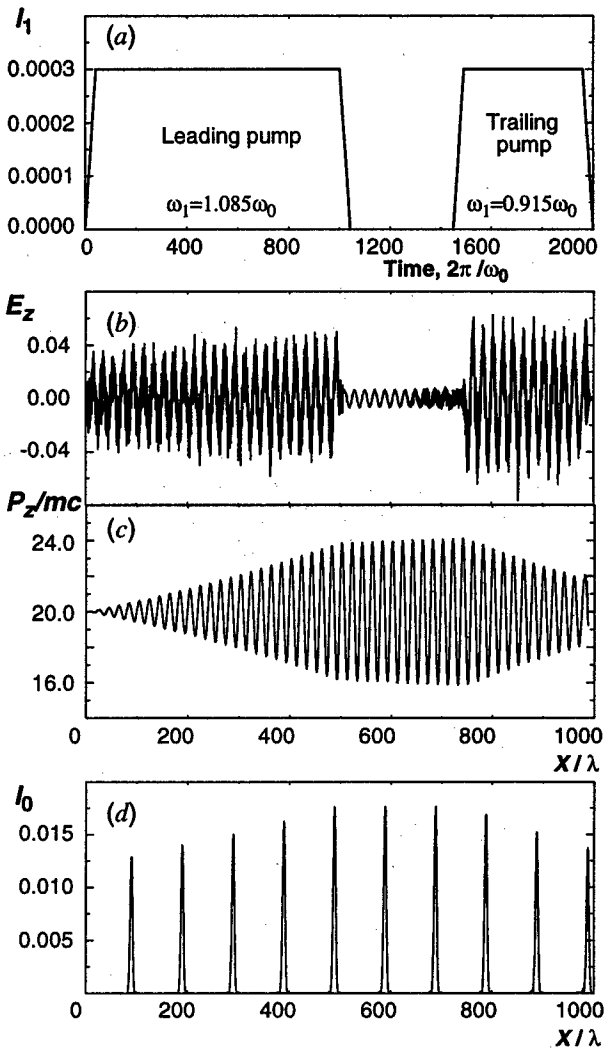

Figure 2: Collision between a short timing beam ($a_0 = 0.08$, $\tau_L = \omega_p^{-1}$) and an intermittent pump ($a_1 = 0.012$) in $n_0 = 2.5\times10^{18}\mathrm{cm}^{-3}$ plasma ($\omega_0/\omega_p = 20$). 10 MeV electrons are continuously injected into the plasma. (a) Time-dependence of the pumping beam intensity $I_1 = 2a_1^2$; (b) longitudinal electric field $eE_z/mc\omega_p$; (c) propagation of the TB through the plasma, $I_0 = 2a_0^2$; (d) phase space of injected electrons.

one can achieve limitless particle acceleration, not encumbered by dephasing. The convenience of this particular sequence is that the particle is accelerated for 3/4 of the time. Also, since $\Delta t_1 > \Delta t_2$, there is a net energy flow from the pump into the beam which can compensate for the diffractive losses.

4 REFERENCES

[1] T. Tajima and J. M. Dawson, Phys. Rev. Lett. **43**, 267 (1979).

[2] G. Shvets *et. al.*, Phys. Rev. Lett. **81**, 4879 (1998).

[3] A. Pukhov and J. Meyer-ter-Vehn, APS Bulletin **41**, 1502 (1996).

LASER ACCELERATION WITH OPEN WAVEGUIDES

Ming Xie, Lawrence Berkeley National Laboratory, Berkeley, USA

Abstract

A unified framework based on solid-state open waveguides is developed to overcome all three major limitations on acceleration distance and hence on the feasibility of two classes of laser acceleration. The three limitations are due to laser diffraction, acceleration phase slippage, and damage of waveguide structure by high power laser. The two classes of laser acceleration are direct-field acceleration and ponderomotive-driven acceleration. Thus the solutions provided here encompass all mainstream approaches for laser acceleration, either in vacuum, gases or plasmas.

1 MODE PROPERTIES

The open waveguides of interest to laser acceleration have the following characteristics in common. First of all, they are over-sized in all dimensions compared to the laser wavelength. As such, field amplitude of a waveguide mode can be much smaller on waveguide surface than in the core. Secondly, they are electromagnetically or even structurally open. As a result, only low order modes are effectively guided. In other words, these waveguides are over-sized but not over-moded for being electromagnetically open. Laser acceleration with two particular types of open waveguides was studied separately in our previous works, one for capillary waveguide (CW) [1] and another for open-iris loaded waveguide (OILW) [2]. In this paper we present a unified framework for laser acceleration in vacuum, gases, and plasmas with both open waveguides. In particular, we propose to use a hybrid of the two to overcome the limitation due to acceleration phase slippage. The notations used here follow that of [1, 2] unless otherwise stated.

Capillary Waveguide The capillary waveguide considered here is made of a hollow core with an index of refraction ν_1 and radius R, embedded in a medium of dielectric or metal with a complex index of refraction ν_2. The eigenmodes of the waveguide can be solved following the same procedure by Marcatili et al.[3] under the conditions $\lambda_1/R \ll 1$ and $|\sqrt{\hat{\nu}^2-1}| \gg \lambda_1/R$, where $\lambda_1 = \lambda/\nu_1$, $\hat{\nu} = \nu_2/\nu_1$, and λ is the wavelength in vacuum. For eigenmodes of the form

$$\begin{Bmatrix} \mathcal{E}(r,\phi,z,t) \\ \mathcal{H}(r,\phi,z,t) \end{Bmatrix} = \begin{Bmatrix} \mathbf{E}_{lm}(r,\phi) \\ \mathbf{H}_{lm}(r,\phi) \end{Bmatrix} e^{i(\beta_{lm}z-\omega t)-\alpha_{lm}z} , \quad (1)$$

the eigenvalues are given by

$$\beta_{lm} = k_1(1-1/2\gamma_g^2) , \quad \alpha_{lm} = \mathrm{Re}(\Lambda)/\gamma_g^2 R , \psi \quad (2)$$

where $k_1 = \nu_1 k$, $k = 2\pi/\lambda$, $\gamma_g = 2\pi R/U_{lm}\lambda_1 \gg 1$, and U_{lm} is the mth root of the equation $J_{l-1}(U_{lm}) = 0$. There are three types of modes, corresponding to

$$\Lambda = \begin{cases} \frac{1}{\sqrt{\hat{\nu}^2-1}} & : \ TE_{0m} \ (l=0) \\ \frac{\hat{\nu}^2}{\sqrt{\hat{\nu}^2-1}} & : \ TM_{0m} \ (l=0) \\ \frac{\hat{\nu}^2+1}{2\sqrt{\hat{\nu}^2-1}} & : \ EH_{lm} \ (l\neq 0) \ . \end{cases} \quad (3)$$

For laser acceleration, we are interested primarily in two low-order modes: TM_{01} mode for direct-field acceleration in vacuum and gases with its on-axis E_z component, and EH_{11} mode for ponderomotive-driven acceleration in plasmas. Accordingly, we consider three cases: $\delta\nu_1 = 0$ when the core is in vacuum, $\delta\nu_1 > 0$ and $\delta\nu_1 < 0$ when the core is filled with uniform gases and plasmas, respectively, where $\delta\nu_1 = \nu_1 - 1$ and $|\delta\nu_1| \ll 1$.

The electric fields within the core $r \leq R$ are given by

$$TM_{01} \ : \ \begin{cases} E_z = E_a J_0(k_{r1}r) \\ E_r = -i(\Gamma/k_{r1})E_a J_1(k_{r1}r) \ , \end{cases} \quad (4)$$

$$EH_{11} \ : \ \begin{cases} E_y = E_0 J_0(k_{r1}r) \\ E_z = -i(k_{r1}/\Gamma)E_0 J_1(k_{r1}r)\sin\phi \ , \end{cases} \quad (5)$$

where E_a is the peak acceleration field for TM_{01} mode, E_0 is the peak transverse field for EH_{11} mode, $\Gamma = \beta_{lm} + i\alpha_{lm}$ and $k_{r1} = (U_{lm} - i\Lambda/\gamma_g)/R$. To leading order, $\Gamma/k_{r1} = \gamma_g$. Given electric field, magnetic field of a mode can be determined by $\mathbf{H}_t = \hat{\mathbf{z}} \times (\Gamma\mathbf{E}_t + i\nabla_t E_z)/kZ_0$, $H_z = (i/\Gamma)\nabla_t \cdot \mathbf{H}_t$, where subscript t denotes transverse component, $\hat{\mathbf{z}}$ is a unit vector in z-direction, and Z_0 is the vacuum impedance. To evaluate surface field E_s at $r = R$, we expand Bessel functions in the transverse fields of Eqs.(4,5) using the expression for k_{r1} and keeping the larger one of the two components

$$\begin{aligned} E_s/E_a &= \max\{1,|\Lambda|\}|J_0(U_{01})| \quad : \ TM_{01} \ , \\ E_s/E_0 &= \max\{1,|\Lambda|\}|J_1(U_{11})|/\gamma_g \quad : \ EH_{11} \ . \end{aligned} \quad (6)$$

Here we come upon one of the most important advantages of the capillary waveguide: for TM_{01} mode, surface field can be smaller than peak acceleration field, superior to other acceleration structures including even microwave linac; and for both modes, surface fields are much smaller than peak transverse fields. Power in each mode can be expressed as $P(z) = P_0 e^{-z/L_{attn}}$, where $L_{attn} = 1/2\alpha_{lm}$ is power attenuation length and to leading order

$$P_0 = \begin{cases} \pi R^2 \gamma_g^2 E_a^2 J_0(U_{01})^2/2Z_0 & : \ TM_{01} \\ \pi R^2 E_0^2 J_1(U_{11})^2/2Z_0 & : \ EH_{11} \ . \end{cases} \quad (7)$$

The on-axis intensity for a free-space TEM_{00} mode falls as $I(z)/I(0) = 1/[1+(z/Z_R)^2]$ away from the waist due to diffraction, and the on-axis longitudinal field for a TEM_{01} mode also falls as $E_z(z)/E_z(0) =$

0-7803-5573-3/99/$10.00@1999 IEEE.

$1/[1+(z/Z_R)^2]$, where $Z_R = \pi w_0^2/\lambda_1$ is the Rayleigh length. Assuming a $TEM_{00}(TEM_{01})$ mode is coupled to a $EH_{11}(TM_{01})$ mode at the optimal condition $w_0/R = 0.64(0.56)$, the effectiveness of guiding can be measured by taking the ratio of the relevant e-folding lengths of the waveguide mode to the free-space mode, yielding $L_{EH11}/L_{TEM00} = L_{TM01}/L_{TEM01} = 2R/\mathrm{Re}(\Lambda)\lambda_1$. Despite the fact that the waveguide modes are leaky, optical guiding can be made quite effective to overcome diffraction for low order modes with sufficiently large R/λ_1. In addition, for waveguide material with anomalous dispersion at certain wavelength, it is possible to have $\mathrm{Re}(\Lambda) \ll 1$. For example, we have $\mathrm{Re}(\Lambda) = 0.1$ for sapphire at $\lambda = 10.6\mu$m with $\nu_2 = 0.67 + i0.04$.

Open-Iris Loaded Waveguide The open iris-loaded waveguide considered here is made of a series of thin screens separated by distance L and each having a circular aperture of radius R. The eigenmodes of such a waveguide are identical to that of a Fabry-Perot resonator. Two distinctively different methods have been used to calculate the transverse field E_t of the modes: the numerical method of Fox and Li [4] and the analytical method of Vainshtein [5]. It is known that the two methods agree well in eigenvalue [6], but differ in detail in mode profile [5, 7]. The fine ripples in Fox-Li's profile are absent from Vainshtein's solution. Based on numerical results, Pantell proposed that advantage may be taken of these ripples of high spacial frequency for direct-field acceleration in vacuum [8], since the longitudinal field E_z is proportional to the transverse gradient of E_t. However, Pantell failed in providing solution to the phase slippage problem. His claim that net energy gain can be achieved by terminating the structure without terminating the interaction is a direct violation of the well-known theorem for laser acceleration in vacuum [9].

On the other hand, we calculated the acceleration mode [2] taking the analytical approach. We argue that the fine ripples, although neglected from Vainshtein approximation, are of less importance for laser acceleration. First, it has been shown [7] that the ripple magnitude is a decreasing function and the frequency of occurrence is an increasing funtion of Fresnel number $N = R^2/\lambda_1 L$. At the large value of N required for low loss mode propagation, the high frequency ripples can become very sensitive to slight variation and fluctuation in system parameters, misalignment, and spread in wavelength. Even the mathematical assumption of infinitely sharp aperture may need to be modified. All these factors tend to smooth out the high frequency ripples and what an electron see on average is the smooth profile predicted by the analytical solution. Last, the validity condition for the numerical method is more restrictive than for the analytical one. In addition to the common conditions $R/\lambda_1 \gg 1$ and $L/\lambda_1 \gg 1$, the Fox-Li method further requires that $L/R \gg 1$ and $(L/R)^2 \gg N$ [4]. In the parameter regime of interest for laser acceleration, these extra conditions are often violated.

Analytical solution for OILW can be obtained by simply taking $\Lambda = \eta_e\sqrt{\pi L/2\lambda_1}\,(1-i)$ in all previous results given for CW, where $\eta_e = 0.824$. Note here we have changed the mode designation, to be consistent with that for CW. In comparison, CW has lower loss and surface field since generally $|\Lambda_{oilw}| > |\Lambda_{cw}|$, whereas OILW is desirable for allowing side access with its open structure. Thus a hybrid waveguide can be conceived in which sections of OILW are inserted in an otherwise uniform CW, wherever necessary. Power coupling coefficient between modes in CW and OILW is given by $\alpha_c = 1 - C_m|\Lambda_{oilw} - \Lambda_{cw}|^2/\gamma_g^2$, where $C_m = 0.33(0.39)$ for $TM_{01}(EH_{11})$ mode. The second term on the right, being $\mathcal{O}(1/N)$, can be made quite small, thus allowing significant reduction in mode coupling loss due to waveguide interruption.

2 DIRECT-FIELD ACCELERATION

Acceleration phase slippage length in vacuum is defined by

$$L_a = \frac{\lambda}{1/\gamma_g^2 + 1/\gamma^2}\,, \tag{8}$$

over which a relativistic electron with energy $W_0 = \gamma mc^2$, while being accelerated, slips π phase with respect to the fast acceleration wave in TM_{01} mode. Energy gain of the electron on the axis is $\Delta W_a = eE_aL_aT_a$, where $T_a = 2/\pi$ is a transit factor. In parallel, a deceleration phase slippage length can be defined over which the electron slips another π phase while losing energy amounted to $\Delta W_d = eE_aL_dT_d$. Average acceleration gradient during a period of 2π phase slippage is then

$$G = \frac{\Delta W_a - \Delta W_d}{L_a + L_d} = \frac{eE_aT_a[1 - L_dT_d/L_aT_a]}{1 + L_d/L_a}\,. \tag{9}$$

To have net acceleration, the ratio L_d/L_a should be made small. This can be done with two methods. The idea is to enhance phase slippage during the half period of deceleration, thus taking a shorter distance L_d. The first method, presented previously [1], works on reducing the longitudinal velocity of an electron by introducing a static transverse magnetic field during deceleration. Instead of tempering electron orbit which could cause significant radiative loss at high energy, the second method works on enhancing phase slippage by increasing phase velocity of the wave during deceleration. This can be done by introducing a plasma layer of thickness

$$L_d = \frac{\lambda}{1/\gamma_g^2 + 1/\gamma^2 + 1/\gamma_p^2}\,, \tag{10}$$

where $\gamma_p = \omega/\omega_p \gg 1$, $\omega_p = c\sqrt{4\pi r_e n_0}$ is the electron plasma frequency and n_0 is the plasma density. In this case, $T_d = T_a$. The dominant energy loss for an ultrarelativistic electron traversing a plasma is due to bremsstrahlung [10]. The rate of energy loss is given by $dW/dz = -W/L_R$, where L_R is the radiation length defined by $1/L_R = 4\alpha r_e^2 n_i Z(Z+1)\ln(233/Z^{1/3})$, n_i is density of ions with atomic number Z, and α is the fine structure constant. For

Hydrogen plasma with density $n_i = n_0 = 10^{17}/\mathrm{cm}^3$, L_R is as long as 4×10^6m. Reflectance of laser power off a sharp interface between vacuum and an underdense plasma at normal incidence is also negligible, according to the Fresnel formula $R_p = (1-\nu_1)^2/(1+\nu_1)^2 = 1/16\gamma_p^4$.

The assumption of a sharp vacuum-plasma interface is not necessary. More rigorous treatment can be obtained with WKB method [11]. For underdense plasma, the only modification required is to replace the factor $\exp(i\beta_{01}z)$ by $\exp[i\int\beta_{01}(z)dz]$. Assuming a density profile $n_e = n_0 f_p(z)$, where $f_p(z) = 1/[1+e^{-(z+L_d/2)/\delta}] - 1/[1+e^{-(z-L_d/2)/\delta}]$, the phase advance for the mode can be calculated by making use of the integral $\int_{-\infty}^{\infty} f_p(z)dz = 2\delta\ln[(1+e^{L_d/2\delta})/(1+e^{-L_d/2\delta})]$. It is seen here that Eq.(10) is accurate enough as long as $L_d/2\delta \gg 1$. In addition, the validity of WKB method requires $|d\nu_1/dz| \ll 2\pi\nu_1^2/\lambda$ [11], which gives $\delta \gg \lambda/16\pi\gamma_p^2$ for $df_p/dz|_{max} = 1/4\delta$, also easily satisfied.

3 PONDEROMOTIVE ACCELERATION

Two methods are presented here to overcome the limit on acceleration distance set by the phase slippage length

$$L_a = \frac{\lambda_p}{1/\gamma_g^2 + 1/\gamma_p^2 - 1/\gamma^2} \tag{11}$$

for laser wakefield acceleration in an open waveguide [1]. The first method requires inserting plasma layers of higher density, each of length L_d, as drift sections in between acceleration sections, each of length L_a. Two conditions need to be satisfied. First, the length of a drift section is given by

$$L_d = \frac{\lambda_p}{1/\gamma_g^2 + 1/\gamma_{pd}^2 - 1/\gamma^2}\ , \tag{12}$$

where $\gamma_{pd} = \lambda_{pd}/\lambda$ and λ_{pd} is the plasma period corresponding to the plasma density in the drift section. This condition guarantees continuous energy gain in each acceleration section, since L_d is the distance for the particle to slip π phase with respect to the acceleration wave of period λ_p. Second, the plasma density in the drift section is set according to $\lambda_p/\lambda_{pd} = 2m$, where m is an integer. This condition ensures that there is no net energy exchange between the particle and the laser wakefield excited in the drift section, since L_d is also the distance over which a particle slips $2m\pi$ phase with respect to the wakefield with period λ_{pd} in the drift section. Thus the average gradient that can be maintained over multiple slippage lengths is $G = \Delta W_a/(L_a+L_d)$, where $\Delta W_a = eE_aL_aT_a$. In a limiting case with $(\gamma/\gamma_p)^2 \gg 1$ and $(\gamma_g/\gamma_p)^2 \gg 1$, we have $L_a/L_d = (\lambda_p/\lambda_{pd})^2$.

The second method utilizes longitudinal modulation in laser intensity due to beating of two waveguide modes. The idea is to choose the beating period same as the distance for a 2π phase slippage, such that the wakefield is stronger when the particle is in accelerating phase, and weaker in decelerating phase, resulting in net energy gain over multiple slippage lengths. When two modes are included, Eq.(24) of [1] is modified to

$$a^2(\rho,\zeta,z) = \frac{a_0^2}{2}|f_b(\rho,z)|^2 e^{-\zeta^2/2\sigma_z^2}\ , \tag{13}$$

where the profile, normalized to $f_b(0,0)=1$, is given by

$$\begin{aligned} f_b(\rho,z) &= \tfrac{1}{1+\eta}\left[E_{11}(\rho,z) + \eta E_{12}(\rho,z)\right]\ , \\ E_{11}(\rho,z) &= J_0(U_{11}\rho)e^{i\beta_{11}z-\alpha_{11}z}\ , \\ E_{12}(\rho,z) &= J_0(U_{12}\rho)e^{i\beta_{12}z-\alpha_{12}z}\ . \end{aligned} \tag{14}$$

Assuming $(\gamma_{g11}/\gamma_p)^2 \gg 1$, $(\gamma_{g12}/\gamma_p)^2 \gg 1$ and $(\gamma/\gamma_p)^2 \gg 1$, where γ_{g11} and γ_{g12} are γ_g factors for EH_{11} and EH_{12} modes, respectively, the group velocity and slippage length then become same for both modes, i.e., $v_g = c(1-1/2\gamma_p^2)$ and $L_a = \gamma_p^2\lambda_p$. There are three characteristic length scales: $l_1 \sim \{1/\alpha_{11}, 1/\alpha_{12}\}$ is due to mode attenuation; $l_2 \sim 1/(\beta_{11}-\beta_{12})$ is due to beating of the two modes; and $l_3 \sim 1/k_p$ is the plasma period. As they satisfy $l_1 \gg l_2 \gg l_3$, we deduce from Eq.(23) of [1] that

$$E_{wz} = E_a|f_b(\rho,z)|^2\cos(k_pz - \omega_pt)\ , \tag{15}$$

and, in particular, for acceleration field on the axis

$$|f_b(0,z)|^2 = \frac{1+\eta^2+2\eta\cos[(\beta_{11}-\beta_{12})z]}{(1+\eta)^2}\ . \tag{16}$$

By requiring $\beta_{11} - \beta_{12} = \pi/L_a$, we have the matching condition $\gamma_{g11}^2/\gamma_p^3 = U_{12}^2/U_{11}^2 - 1$. Energy gain over $2L_a$ distance is then $\Delta W_{2\pi} = eE_a2L_aT_{2\pi}$, where $T_{2\pi} = \eta/(1+\eta)^2$. As expected, $T_{2\pi}$ vanishes when there is only one mode with $\eta = 0$, and it reaches a maximum when the two modes have equal amplitude on the axis with $\eta = 1$. The relative mode amplitude can be adjusted easily by changing TEM_{00} mode waist according to

$$\eta = \frac{J_1^2(U_{11})\int_0^1 J_0(U_{12}\rho)\exp[-\frac{\rho^2}{(w_0/R)^2}]\rho d\rho}{J_1^2(U_{12})\int_0^1 J_0(U_{11}\rho)\exp[-\frac{\rho^2}{(w_0/R)^2}]\rho d\rho}\ . \tag{17}$$

An extended version of this paper will be published elsewhere. This work was supported by the U.S. Department of Energy under contract No.DE-AC03-76SF00098.

4 REFERENCES

[1] M. Xie, *Proc. of 1998 Euro. Part. Accel. Conf.*, 830 (1998).

[2] M. Xie, *Proc. of 1997 Part. Accel. Conf.*, 660 (1997).

[3] E. Marcatili and R. Schmeltzer, *B.S.T.J.*, **43**, 1783 (1964).

[4] A. G. Fox and T. Li, Bell Sys. Tech. J. **40**, 453 (1961).

[5] L. A. Vainshtein, Soviet Physics JETP, **17**, 709(1963).

[6] T. Li, Bell Sys. Tech. J. **44**, 917 (1965).

[7] F. H. Northover, *Applied Diffraction Theory*, Chapter 14 and 15 (American Elsevier, 1971).

[8] R. Pantell, *Nucl. Instr. Meth. in Phys. Res.*, **A393**, 1 (1997).

[9] R. Palmer, *AIP Conf. Proc.* **335**, 90 (1995).

[10] J. D. Jackson, *Classical Electrodynamics*, 2nd edition, Chapter 8 and 15 (John Wiley & Sons, 1975).

[11] V. Ginzburg, *The Propagation of Electromagnetic Waves in Plasmas*, Chapter IV (Pergamon Press, 1964).

STUDIES ON THE INTERACTIONS OF A PROBE ELECTRON BEAM WITH RELATIVISTIC PLASMA WAVES*

R.L. Williams# and K. D. Gebre-Amlak, Department of Physics, Florida A. & M. University, Tallahassee, FL 32307

Abstract

Results of a numerical study which models experiments on a low energy electron beam probe of relativistic plasma waves are discussed. The plasma wave modifies the electron beam cross section and energy distribution. Qualitative results of current experiments on the optical breakdown of Helium and Argon gas by CO_2 laser light in a plasma shutter are presented.

1 INTRODUCTION

Many research groups have demonstrated that the high gradient acceleration of electrons using relativistic plasma waves is possible over short distances. An important parameter for plasma wave acceleration is the amplitude of the accelerating longitudinal electrostatic fields. The results of previous numerical studies suggest that a perpendicularly injected electron beam may be a convenient and sensitive diagnostic of the wave's accelerating fields. The plasma wave's longitudinal fields deflect the electrons, thus distorting the beam's cross section in direct proportion to the magnitude of the longitudinal fields. Those studies focused on using 1.5 MeV [1] and 50 keV [2] electron beams to measure plasma waves having fractional amplitudes, a_w, in the range of 2.5 to 25%. However, in many laboratories performing basic studies on plasma wave acceleration techniques, waves that have fractional amplitudes of 1.0%, or less, are common. A lower energy electron beam probe would be more sensitive and convenient for experiments involving these lower amplitude waves.

In the following are discussed the results of numerical simulations of the interactions of 5 keV to 50 keV electron beams with relativistic plasma waves that have fractional amplitudes in the range of 0.1% to 1.0%. These simulations model an experiment being constructed to compare this electron beam diagnostic with the more commonly used Thomson scattering diagnostic. Part of the experimental effort is to develop a plasma shutter for shortening laser pulses, and qualitative results of recent tests of this device are presented.

2 NUMERICAL SIMULATIONS

The simulations were performed using a 3-D relativistic particle trajectory code which was originally used to model the acceleration of injected electrons by relativistic plasma waves [3], and to model the radiation emitted by an electron beam passing through a plasma wave undulator [4]. For the present simulations, the electron beam energy was varied from 5 keV to 50 keV and the energies were converted to the appropriate relativistic γ. The beam's width and length were approximately 0.5 mm and 10.0 mm, respectively. Uniform and Gaussian random number generators were used to select the electrons' initial positions and momenta in the longitudinal and transverse directions, respectively. The relativistic plasma wave's phase velocity corresponded to a gamma phase, γ_p, of 9.7. In laser plasma beatwave experiments this γ_p could be generated by beating the 10.6 μm and 9.6 μm lines of a CO_2 laser. The amplitude of the plasma wave was varied from $a_w = n_1/n_o = 0.1\%$ to 1.0 %, where n_1 = the density fluctuation and n_o = the background density. The plasma wave propagates in the +z direction and a beam of 5000 electrons is injected transversely through the wave in the +y direction [2]. After the electron beam exits the plasma wave, it drifts approximately 10 cm at which point the positions of the individual electrons are recorded. Figure 1 shows the initial cross section of the electron beam for all simulations. Figure 2 is an example of the cross section of a 5 keV electron beam that has passed through a plasma wave having $a_w = 1\%$. The width of the beam in the z direction, or "spot width", is plotted versus n_1/n_o for various beam energies in figure 3. Figure 3 shows that the lowest energy electron beam is most sensitive to the plasma wave, as expected.

The plasma wave also induces an energy spread in the beam. Figure 4 shows the original energy of the monoenergetic electron beam along with a histogram of the number of electrons in the final energy bins. This shows that electrons gain and lose energy, consistent with the model that electrons sample both accelerating and decelerating fields as it passes through the plasma wave [3]. The final energy spread shown in figure 4 is appoximately 0.03%. Additional sorting of the results was performed to determine the location of the accelerating electrons in the beam and it was found that the electrons that gain and lose the most energy are the ones that are deflected the most. This energy spreading is being analyzed to determine its suitability as an additional diagnostic of the plasma wave.

3 THE PLASMA SHUTTER

The experiment to test this electron beam diagnostic of plasma waves will use CO_2 lasers to create the plasma waves. A plasma shutter will be used to remove the long energetic trailing edge of the CO_2 pulse. The optical breakdown of the CO_2 laser pulse in a gas chamber filled

*Work supported by the Department of Energy: DE-FG02-96ER40998.
Email: williams@cennas.nhmfl.gov

with either Helium or Argon has been studied. The chamber is a ~3.5 cm long, ~3.8 cm diameter, cylinder with windows for transmitting CO_2 and YAG laser light, and with ports for a vacuum pump and a pressure gauge.

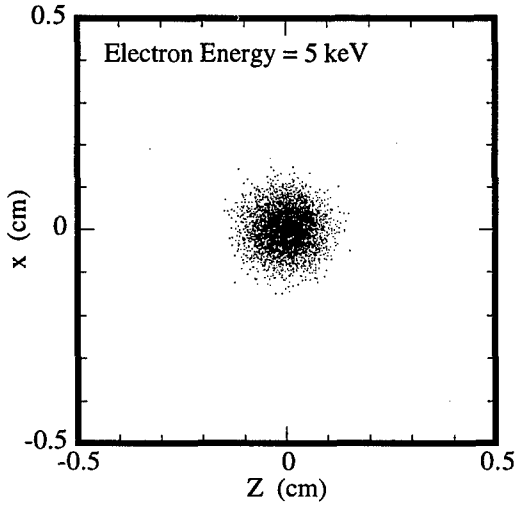

Figure 1: Initial cross section of the electron beam. The beam moves out of the page in the simulation.

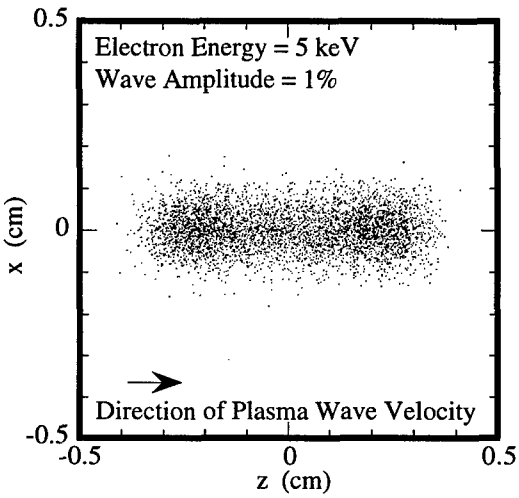

Figure 2: Final cross section of the beam.

The laser (~10^{12} W/cm^2) is focused into the chamber using f/1.7 optics, and the laser energy is measured using a pyroelectric Joulemeter. The pressure is measured using a capacitive manometer and is held steady using a computer controlled leak valve. Figure 5 shows laser energy transmitted versus gas pressure, and indicates the pressure at which breakdown occurs and also the amount of energy transmitted after breakdown. The results suggest that the CO_2 laser breaks down at ~ 30 Torr in Argon and at ~ 105 Torr in Helium, as expected in cascade ionization [5]. The results show, qualitatively, that a larger fraction of the CO_2 laser energy is transmitted when Helium is used as the fill gas in the plasma shutter. Additional tests are underway to use other gases, to study triggering the breakdown using a separate YAG laser and to measure the breakdown time.

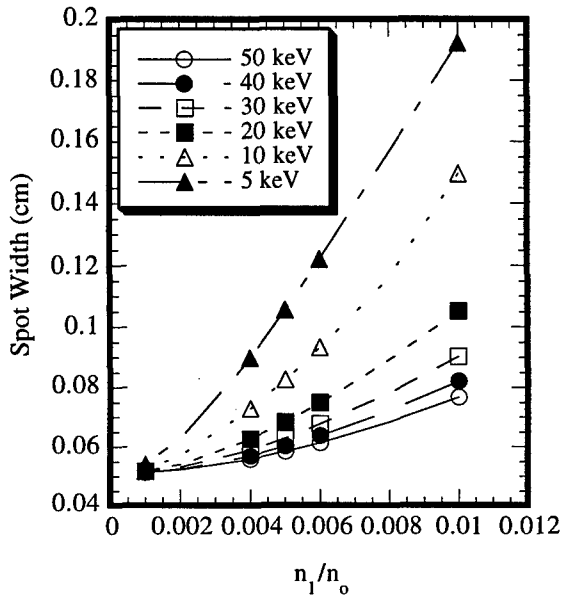

Figure 3: Plot of cross section (spot width) versus fractional plasma wave amplitude for several electron beam energies.

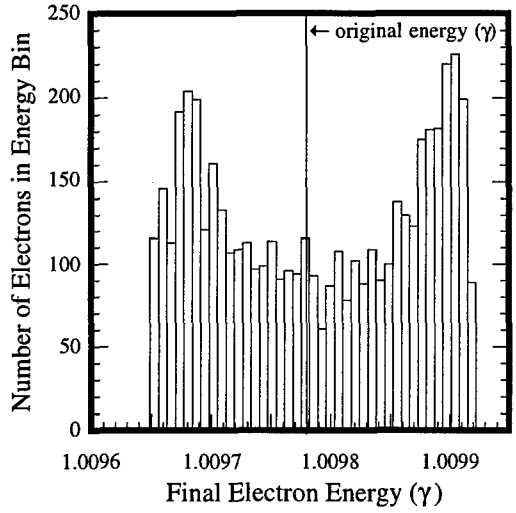

Figure 4: Initial beam energy and histogram of final beam energies.

4 CONCLUSIONS

Recent numerical simulations reveal the relative sensitivity of low energy electron beams to the

electrostatic fields in relativistic plasma waves. These simulations also provide a qualitative picture of the induced energy spreading and the distribution of the accelerated and decelerated electrons within the beam. Initial results indicate that the plasma shutter is capable of controlling a CO_2 laser beam pulse.

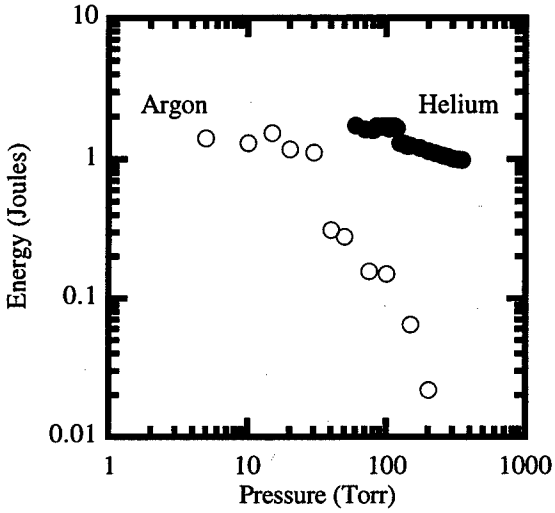

Figure 5: CO_2 laser energy transmitted in the plasma shutter filled with Argon and with Helium, versus pressure.

5 REFERENCES

[1] R. L. Williams, C. E. Clayton, C. Joshi and T. Katsouleas, Rev. Sci, Instrum. **61**, 3037 (1990).
[2] R. L. Williams, Rev. Sci, Instrum. **66**, 468 (1995).
[3] R. L. Williams, C. E. Clayton, C. Joshi, T. Katsouleas and W. B. Mori, Laser and Part. Beams **8**, 427 (1990).
[4] R. L. Williams, C. E. Clayton, C. Joshi and T. Katsouleas, IEEE Trans. Plasma Sci. **21**, 156-166, (1993).
[5] C. G. Morgan, in "Electrical Breakdown in Gases" by J. M. Meek and J. D. Cragg, Wiley & Sons, New York (1978).

Electromagnetically Induced Transparency in a Bounded Plasma and its Relation to Beatwave Physics*

D.F. Gordon, W.B. Mori, and C. Joshi
University of California, Los Angeles, Los Angeles, California 90095

Abstract

The theory of electromagnetically induced transparency (EIT) in a plasma [1] is examined in the context of a bounded system via particle simulations. It is found that when boundaries are introduced into the problem, the requirements of causality preclude the transmission of radiation through an overdense plasma as conceived in the original theory. However, a two-frequency laser, or "beatwave", will cascade into a Stokes satellite with a frequency below the cut-off frequency. This can lead to an *apparent* EIT signature if a specific set of parameters are chosen.

1 INTRODUCTION

In a cold unmagnetized plasma the cut-off frequency for electromagnetic radiation is equal to the plasma frequency, ω_p. It was suggested by S.E. Harris [1] that an electromagnetic wave with a frequency $\omega_- < \omega_p$ will nevertheless propagate in the presence of an intense pump wave with a frequency $\omega_0 \approx \omega_- + \omega_p$. The proposal was based on the fact that a pump wave at ω_0 and a "Stokes" wave at ω_- combine to drive a plasma wave at the beat frequency $\Delta\omega = \omega_0 - \omega_-$. When the plasma wave is driven below resonance ($\Delta\omega < \omega_p$), it is phased such that the beat current associated with the pump wave and the plasma wave tends to cancel the current associated with the Stokes wave. This reduces the amplitude of the current at the Stokes frequency which allows the Stokes wave to propagate despite the relation $\omega_- < \omega_p$. The term "electromagnetically induced transparency" (EIT) was used to describe this process because of its similarity to the analogous process of EIT in a neutral gas which has been studied theoretically and experimentally for some time [2].

Recently, the theory of EIT in a plasma was extended to account for relativistic effects and the presence of the "anti-Stokes" wave with frequency $\omega_+ \approx \omega_0 + \omega_p$ [3]. This was done by considering the relativistic Raman dispersion relation of Ref. [4] in the limit where the density exceeds quarter-critical. It was found once again that an anomalous passband appears when the pump wave is sufficiently intense. It was also found that the system exhibits a Raman-type instability even when the plasma is overdense with respect to the Stokes wave. We note, however, that the dispersion relation used to arrive at these conclusions was derived under the assumption $\omega_0 \gg \omega_p$. We will present a more accurate dispersion relation in a longer paper [5, 6].

* Work supported by DOE grant DE-FG03-92ER40727.

In this paper, we examine the effect of boundaries on the theory of EIT in a plasma. We find that in the case of a bounded system, no dispersion relation is an adequate measure of the transparency or opacity of a plasma. This is because causality plays a fundamental role in the EIT process. In particular, the plasma wave is caused by the Stokes wave, yet the Stokes wave cannot propagate until the plasma wave is present. The result is that the Stokes wave is not transmitted even though the dispersion relation predicts transparency. On the other hand, when the anti-Stokes wave drives the density perturbation, we find that a Stokes wave can be *generated* with a frequency less than ω_p. We equate this process with the cascading of a beatwave (two-frequency laser) into Stokes and anti-Stokes satellites. Particle-in-cell (PIC) simulations are used to verify the findings.

2 UNBOUNDED PLASMA

From the point of view of classical electrodynamics, the transparency or opacity of a medium is related to the magnitude and phasing of the currents driven within it by electromagnetic waves. In one dimension, electromagnetic radiation is described by the wave equation

$$(\partial_{xx} - \partial_{tt})A = -j \tag{1}$$

where A is some transverse component of the vector potential and j is the corresponding component of current density. Here, and in all that follows, velocity is normalized to the speed of light, the electron has unit mass and charge, time is measured in units of ω_p^{-1}, and the vector potential is normalized to mc^2/e. By rewriting the wave equation in frequency space and requiring real wavenumbers, one obtains the inequality

$$\omega^2 > -\frac{\hat{j}}{\hat{A}} \tag{2}$$

where the circumflex denotes a Fourier-transformed quantity.

Now consider a cold unmagnetized plasma consisting of electrons with density $1 + n_1(x,t)$ and an immobile uniform background of neutralizing ions. Conservation of transverse canonical momentum gives the current as

$$j = -\frac{(1+n_1)A}{\gamma} \tag{3}$$

0-7803-5573-3/99/$10.00@1999 IEEE.

where γ is the relativistic Lorentz factor associated with a fluid element. Rewriting this in frequency space and inserting the result into equation (2) one obtains

$$\omega^2 > 1 + \frac{\hat{n_1} * \hat{A}}{2\pi \hat{A}} + R(\hat{A}) \tag{4}$$

where the asterisk denotes convolution and R is some operator that accounts for relativistic effects. We henceforth drop the relativistic term since for the parameters considered it is not important. An algebraic relation can be obtained by considering two discrete electromagnetic modes

$$A = \frac{1}{2} A_- e^{i(\omega_- t - k_- x)} + \frac{1}{2} A_0 e^{i(\omega_0 t - k_0 x)} + cc \tag{5}$$

and one discrete plasma wave mode

$$n_1 = \frac{1}{2} n e^{i(\Delta\omega t - \Delta k x)} + cc \tag{6}$$

If the frequencies and wavenumbers are related by $\Delta\omega = \omega_0 - \omega_-$ and $\Delta k = k_0 - k_-$, then by inserting $\hat{A}$ and $\hat{n_1}$ into equation (4) one obtains

$$\omega_-^2 > 1 + \frac{n^* A_0}{2A_-} \tag{7}$$

The nonlinear term represents current at the frequency ω_- driven by the beating of the pump wave A_0 with the plasma wave n. If the phasing between A_0, A_-, and n is chosen correctly, this term could be negative. In this case the inequality is satisfied for a range of frequencies with $\omega_- < 1$ and anomalous transparency occurs for those frequencies. If the nonlinear term is positive, the inequality is *not* satisfied for a range of frequencies with $\omega_- > 1$ and anomalous opacity occurs for those frequencies.

In order to specify the density n in terms of the electromagnetic field amplitudes, one must self-consistently determine the frequencies and amplitudes of all the waves in the system. The classic Raman dispersion relation for a cold plasma [7] provides an immediate solution to this problem. It is well known that in the context of the Raman dispersion relation, one has

$$n \propto A_0(A_- + A_+) \tag{8}$$

where A_+ is the amplitude of the anti-Stokes wave with frequency $\omega_+ = \omega_0 + \Delta\omega$. It is clear that for EIT applications, one must have $A_- \gg A_+$ since only then will the transparency condition of equation (7) be independent of the probe amplitude A_-.

Also well known is the fact that the Raman dispersion relation generally has four branches when solved for complex wavenumbers and real frequencies. As will be discussed in Ref. [5], and as has been partially addressed before [1, 3], two of the branches indicate EIT passbands in the regime $A_+ \gg A_-$, while the other two branches indicate EIT passbands in the regime $A_- \gg A_+$. We will also show in Ref. [5] that this remains true when the relativistic dispersion relation is used. In the next section, however, we show that these passbands effectively disappear when boundaries are introduced into the problem.

3 BOUNDED PLASMA

The description of EIT in terms of the Raman dispersion relation is limited in that it describes only the normal modes of an infinite plasma. This information is only useful if it can be related to the problem of the transmission of an electromagnetic pulse through a finite plasma. In the nonlinear regime, it is not necessarily the case that a bounded medium will transmit radiation for which the dispersion relation predicts real wavenumbers. Consider first the the case where $A_- \gg A_+$. In this case, the plasma wave is driven mostly by the Stokes wave, yet the Stokes wave cannot propagate until the plasma wave is present. One might conclude therefore that the Stokes wave never penetrates the plasma. This conclusion is supported by one-dimensional PIC simulations, as discussed below.

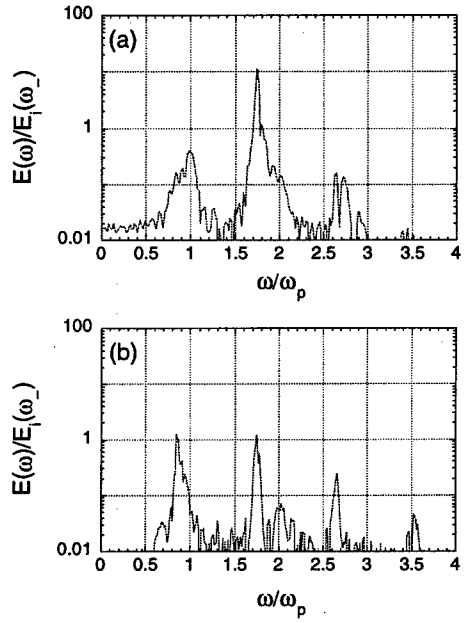

Figure 1: Simulated attempt at EIT with $A_- \gg A_+$ (a) transmitted spectrum of the electric field (b) reflected spectrum of the electric field. Frequencies 1.75 and 0.85 were injected. The data is normalized to the spectral amplitude of the incident wave at $\omega = 0.85$.

In the case where $A_+ \gg A_-$, the plasma wave is driven mostly by the anti-Stokes wave which can enter the plasma unaided. Since the plasma wave is independent of A_-, so is the nonlinear current source at the Stokes frequency, and so too are any waves radiated by this source. In other words, the pump and the anti-Stokes act independently to *generate* a Stokes wave. This suggests that the pump and the anti-Stokes might be regarded as a single two-frequency pump, or "beatwave", which drives a polarization wave at the Stokes frequency. When the polarization wave oscillates at a frequency less than ω_p, it radiates an evanescent wave from every point in the plasma. As will be discussed in detail in another paper [5], the sum of these evanescent waves is a propagating wave. Although within the

plasma this wave propagates only in the direction of the pump, it nevertheless exits the plasma equally in both directions. This is because of the fact that signals due to sources deep within the plasma cannot interfere with signals due to sources near the vacuum. In other words, the normal phase matching conditions do not apply. This will be shown analytically in Ref. [5].

The preceding assertions were tested using one-dimensional PIC simulations. In the two simulations presented here, the Stokes and anti-Stokes amplitudes are ramped linearly for $10\omega_p^{-1}$, and remain constant thereafter. The pump wave is gaussian with a standard deviation of $100\omega_p^{-1}$. The three waves are copropagated into a uniform slab of plasma $30c/\omega_p$ long. The electrons are hot ($v_{th} = 0.1c$) while the ions are held fixed.

Figure 1 shows the results of a simulation in which a pump wave with $A_0 = .3$ and $\omega_0 = .75$ was copropagated with a Stokes wave with $A_- = 0.03$ and $\omega_- = 0.85$. According to the dispersion relation, the plasma is transparent to the Stokes wave for these parameters [5, 6]. However, all the energy in the incident Stokes wave is accounted for by the peak in the reflected spectrum at $\omega = 0.85$. The peak in the transmitted spectrum at $\omega =$ is due to instability. The associated wave emerges from the plasma late and continues long after the pump disappears. Several other simulations were attempted with $A_- \gg A_+$, including cases with longer pulse lengths, gradual plasma-vacuum boundaries, and higher pump intensities. In every case similar results were obtained.

Figure 2 shows the results of a simulation in which a pump wave with $A_0 = .3$ and $\omega_0 = .75$ was copropagated with an anti-Stokes wave with $A_+ = -0.1$ and $\omega_+ = .85$. The data plotted in figures 2(a) and 2(b) was evaluated $10c/\omega_p$ beyond the plasma. The data of figure 2(c) was evaluated $10c/\omega_p$ before the plasma. We see that as stated above, the beatwave generates a Stokes satellite which exits the plasma equally in both directions. We note that the amplitude of the Stokes satellite is consistent with the ratio A_+/A_- given by the Raman dispersion relation.

Note also that an apparent EIT signature can be obtained if in addition to injecting the pump wave and the anti-Stokes wave, one also injects a "probe" wave at the Stokes frequency [5, 6]. When the amplitude and phase of the probe wave are chosen such that the reflected probe wave destructively interferes with the backward propagating Stokes satellite, the probe wave appears to be transmitted with a transmission coefficient proportional to the pump intensity. This is not the same as true EIT, however, since it only works for one particular probe amplitude.

4 CONCLUSIONS

The consideration of boundaries is crucial to a full understanding of EIT in a plasma. The dispersion relation only determines the ability of a particular mode to propagate, not the ability of a pulse to penetrate a bounded medium.

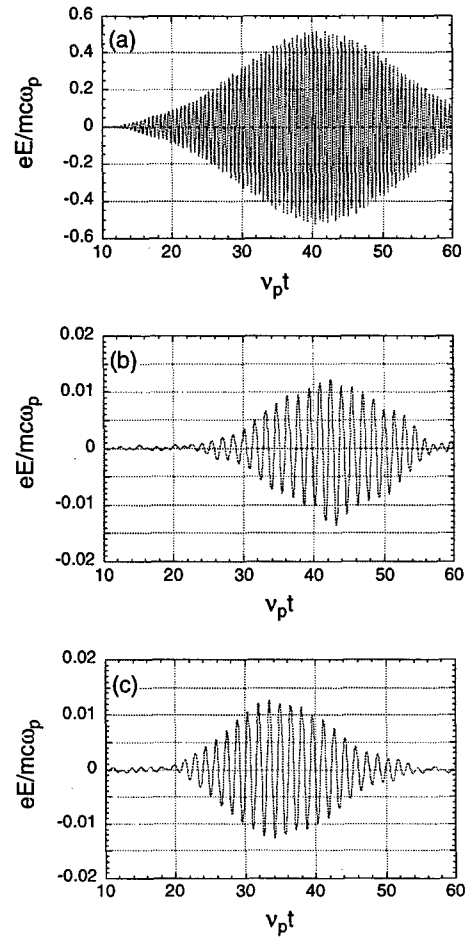

Figure 2: Generation of Stokes radiation in a stopband (a) waveform of the transmitted pump wave (b) waveform of the forward Stokes (c) waveform of the backward Stokes. The injected anti-Stokes wave is not shown.

In the case of a plasma, radiation can be generated in the stopband, but apparently cannot be transmitted through it. A consequence of these findings is that a two-frequency laser will cascade into Stokes satellites not only above the plasma frequency, but also below it.

5 REFERENCES

[1] S.E. Harris, *Phys. Rev. Lett.* **77**, 5357 (1996)

[2] K.-J. Boller, A. Imamoglu, and S.E. Harris, *Phys. Rev. Lett.* **66**, 2593 (1991)

[3] A.B. Matsko and Y.V. Rostovtsev, *Phys. Rev. E* **58**, 7846 (1998)

[4] C.J. McKinstre and R. Bingham, *Phys. Fluids B* **4**, 2626 (1992)

[5] D.F. Gordon *et al.*, to be submitted to *Phys. Plasmas*

[6] D.F. Gordon, Ph.D. dissertation, UCLA Electrical Engineering (1999)

[7] W.L. Kruer, *The Physics of Laser Plasma Interactions*, Addison-Wesley Publishing Co., Redwood City, CA (1988)

LASER DRIVEN ELECTRON ACCELERATION TO GeV ENERGIES IN PLASMA CHANNELS*

P. Sprangle#, B. Hafizi+, A. Ting, C.I. Moore, R. F. Hubbard and A. Zigler♣
Plasma Physics Division, Naval Research Laboratory, Washington, DC 20375

Abstract

This paper presents a brief discussion of ultra-short laser pulse propagation and laser wakefield acceleration in plasma channels. An envelope equation for the perturbed laser beam radius is given, including finite-pulse length and nonlinear effects. Angular distribution of electrons generated by the process of laser ionization and ponderomotive acceleration (LIPA) is also discussed. An example of laser wakefield acceleration to electron energies greater than 1.2 GeV in a preformed plasma channel is described.

1 INTRODUCTION

Electron acceleration in a laser wakefield is limited by a number of processes, including electron slippage and laser beam diffraction. To reduce the effects of diffraction the laser pulse can be propagated in a preformed plasma channel having a suitable (parabolic) radial density profile. In plasma channels propagation distances much longer than a vacuum Rayleigh range, $Z_{R0} = \pi r_0^2/\lambda$, can be achieved [1-3]. Here, r_0 is the laser spot size and λ is the vacuum wavelength. Finite pulse length effects can modify the propagation dynamics in long channels. Short pulse effects lead to envelop modulation, damping due to phase mixing, and group velocity dispersion [3,4]. An envelope equation for the perturbed pulse envelope is presented which includes these effects along with nonlinearity [3]. A second topic discussed is the generation of electrons by laser ionization and ponderomotive acceleration (LIPA) [5]. By means of LIPA electrons can be stripped from atoms in the region of high laser intensity and accelerated by the ponderomotive force. Finally, an example of laser wakefield acceleration of electrons to 1.2 GeV in a 15-cm long plasma channel is described.

2 ENVELOPE EQUATION

An envelope equation for the radius of the laser pulse propagating in a channel can be obtained by assuming the slowly-varying form for the electric field, $\boldsymbol{E} = (E_0/2)\exp[i(kz - \omega t)]\boldsymbol{e}_x$ + c.c., where $E_0(r, t)$ is the amplitude, k is the wavenumber, $\omega = 2\pi c/\lambda$ and c is speed of light *in vacuo*. The amplitude E_0 is assumed to be expressible as $E_0 = b\exp[i\phi - (1 - i\theta)r^2/r_s^2]$, where b is the amplitude, ϕ is the phase, θ is related to the wavefront curvature and r_s is the spot size. The variables b, φ, θ, r_s are taken to be real and slowly varying functions of z and t. The radial dependence of the plasma frequency is given by

$$\omega_p(r) = \left[1 + (\Delta n/n_{po})(r/r_c)^2\right]^{1/2},$$

where n_{po} is the on axis density, $n_{po} + \Delta n$ is the density at the edge of the plasma channel ($r = r_c$), $\omega_{p0} = (4\pi n_{p0}q^2/m)^{1/2}$ is the plasma frequency on axis, q is the charge and m is the mass of an electron. The focusing parameter associated with the channel is $K_c = (\omega_{p0}/c)(\Delta n/n_{p0})^{1/2}$. Making use of the source-dependent expansion approach [6], the equilibrium radius is found to be given by $r_{eq} = r_m(1 - P)^{1/4}$, where $r_m = (2r_c/K_c)^{1/2}$ is the matched beam radius, P is the laser power normalized to the critical power for focusing, r_c is radius of the parabolic channel and K_c is the on axis plasma wavenumber [3]. In the limit $P << 1$ the envelope equation for the perturbed laser pulse radius, normalized to r_0, and is given by

$$\frac{\partial^2\delta R}{\partial Z^2} + \frac{4}{n^2}\delta R - \frac{4\varepsilon}{n^2}\frac{\partial^2\delta R}{\partial Z\partial\zeta} + \frac{32\varepsilon\zeta}{n^2}\frac{\partial\delta R}{\partial Z} = 0,$$

where $Z = z/Z_{R0}$, $\zeta = (z - cnt)/l_0$, $n = ck/\omega$ is the refractive index, an initial axial profile $b(z = 0) \sim \exp(-4\zeta^2/l_0^2)$ has been assumed and $\varepsilon = \lambda/(2\pi l_0) << 1$. The solution to this equation is

$$\delta R = \delta R_0\cos(2Z/n)\exp(-16\varepsilon\zeta Z/n^2 - 16\varepsilon^2Z^2/n^4),$$

where δR_0 is a constant. The first term in the exponential leads to modulation of the pulse, with the back of the pulse ($\zeta < 0$) growing and the front ($\zeta > 0$) damped. The second term in the exponential is due to phase mixing and leads to damping of the perturbation.

The modulation and damping predicted by the envelope equation has been observed in a 2-D simulation of laser

*Work supported by DoE & ONR. The authors acknowledge the assistance of J. Penano in preparing the computer graphics.

Email:sprangle@ppd.nrl.navy.mil

+ Icarus Research, Inc. PO Box 30780, Bethesda, MD 20824-0780

♣ Hebrew University, Jerusalem, Israel

0-7803-5573-3/99/$10.00@1999 IEEE.

propagation in a channel. At early times, δR should exhibit growth or damping at the normalized linear rate $\Gamma(\zeta) = -16\varepsilon\zeta/n^2$. The simulation rate Γ is determined from a semi-logarithmic plot of δR against z, fitting the peaks of the oscillations. The laser parameters were $\lambda = 0.8$ μm, $l_0 = 24$ μm, $r_0 = 14.5$ μm, and $Z_R = 0.083$ cm. Figure 1 is a plot of $\Gamma(\zeta)$ (diamonds) from simulation using the code described in [2]. The straight line is the analytical growth or damping rate. As expected, the front of the beam is damped, while the back exhibits growth in δR. The simulation results consistently lie below the theoretical growth rate. This is due to the phase mix damping contained in the last term in the δR equation. The long time behavior in the simulations is eventually dominated by the phase mixing term and exhibits the expected damping in z^2.

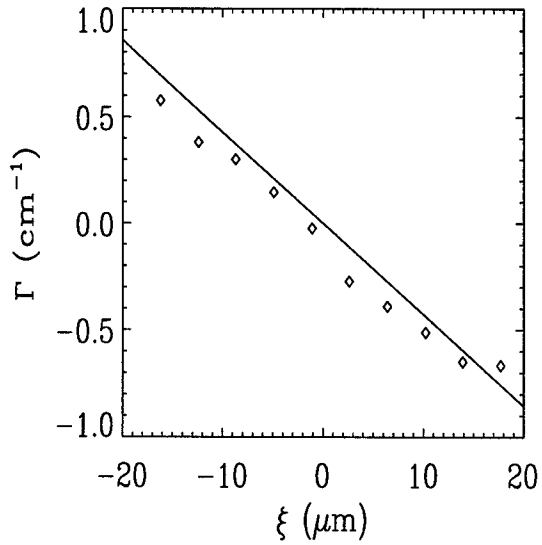

Fig. 1. Linear growth or damping rate Γ versus position ζ within the pulse. The diamonds are from the simulation code, and the solid line is from the analytical solution for δR.

In the high power limit, $P \leq 1$, there are additional contributions to the envelope equation, arising from nonlinearities such as the relativistic focusing effect [3]. Short pulse effects lead to substantial modification of the nonlinear focusing processes. Figure 2 is a surface plot of the spot size R as a function of ζ/λ and Z, with (a) finite pulse length effects ($\varepsilon \neq 0$) and (b) finite pulse length effects neglected ($\varepsilon = 0$). The parameters are $\lambda = 1$ μm, $l_0 = 20$ μm and $P = 0.56$. This plot shows the envelope modulation and significant enhancement of nonlinear focusing.

3 LASER IONIZATION AND PONDEROMOTIVE ACCELERATION

In tunneling ionization the electric field of the laser depresses the Coulomb barrier in the atom allowing an electron to tunnel through. When an electron is released from an atom in the presence of the laser field the ponderomotive force can accelerate it to relatively high energies depending on the laser intensity. Laser acceleration and ponderomotive acceleration (LIPA) [5] can be a source of high brightness electrons for injection into laser driven accelerators. In LIPA, the electrons are ejected from essentially a point source and are highly collimated when the laser beam is linearly polarized [5]. This is borne out by recent experimental results at the Naval Research Laboratory [5]. The electrons are ejected into a forward cone with half angle given by

$$\vartheta = \tan^{-1}\sqrt{2/(\gamma - 1)},$$

where γ is the relativistic factor of the accelerated electrons.

4 ELECTRON ACCELERATION IN A PLASMA CHANNEL

Laser wakefield acceleration in a preformed plasma channel can result in significant energy gain. As an example consider a 1 μm wavelength, $l_0 = 50$ μm, circularly polarized laser pulse with spot size $r_0 = 30$ μm and intensity 2.75×10^{18} W/cm^2 that is matched to a plasma channel with on axis plasma wavelength $2\pi c/\omega_{p0} = 75$ μm (on-axis density 2×10^{17} cm^{-3}). In this case the peak accelerating gradient associated with the wakefield is ~ 24 GV/m and the peak transverse electric focusing field is ~ 5 GV/m. Figure 3 is a plot of energy as a function of propagation distance z for an electron that is injected into the wakefield locally; for example by the LIPA process. For this electron, injected on axis behind the laser pulse with axial momentum 0.3 mc, the plot shows that energies in excess of 1.2 GeV can be reached in a distance ~ 15 cm (~ 54 Z_{R0}). Beyond this length, phase slippage occurs and the energy decreases.

5 CONCLUSIONS

This paper presents highlights of a number of interesting results associated with high intensity short pulse lasers. A brief discussion of ultra-short laser pulse propagation and laser wakefield acceleration in preformed plasma channels is given. In particular, an envelope equation for the perturbed laser beam radius, including finite-pulse length and nonlinear effects, is discussed. Angular distribution of electrons generated by the process of laser ionization and ponderomotive acceleration is also mentioned. An example of laser wakefield acceleration to electron energies greater than 1.2 GeV in a preformed plasma channel is described.

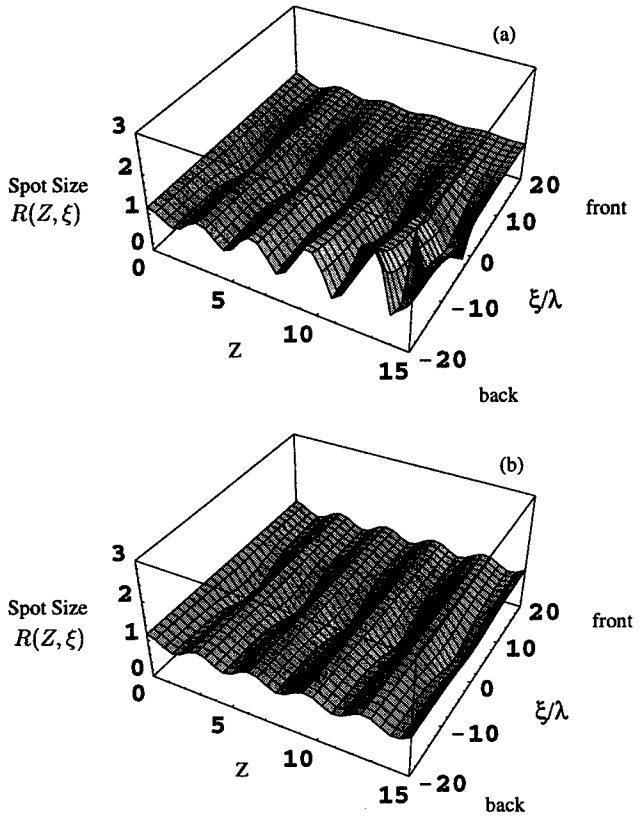

Fig. 2 Surface plot of spot size R as a function of ζ/λ and propagation distance z. In (a) finite pulse length effects are include while in (b) finite pulse length effects are neglected.

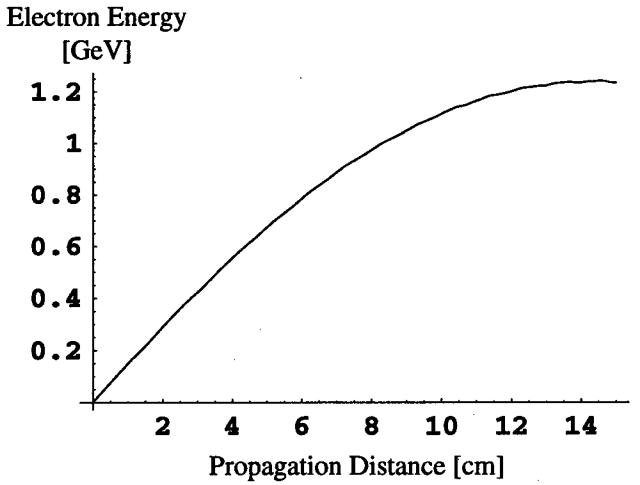

Fig. 3. Plot of electron energy gain due to laser wakefield acceleration versus distance along a preformed plasma channel.

REFERENCES

[1] H.M. Milchberg, T.R. Clark, C.G. Durfee III, T.M. Antonsen and P. Mora, Phys. Plasmas **3**, 2149 (1996)

[2] Y. Ehrlich, C. Cohen, D. Kaganovich, A. Zigler, R.F. Hubbard, P. Sprangle and E. Esarey, J. Opt. Soc. Am. **B15**, 2416 (1998)

[3] P. Sprangle, B. Hafizi and P. Serafim, Phys. Rev. Lett. **82**, 1173 (1999); Phys. Rev. **E59**, 3614 (1999)

[4] E. Esarey and W.P. Leemans, Phys. Rev. **E59**, 1082 (1999)

[5] C.I. Moore, A. Ting, S.J. McNaught, J. Qiu, H.R. Burris and P. Sprangle, Phys. Rev. Lett. **82**, 1688 (1999)

[6] P. Sprangle, A. Ting and C.M. Tang, Phys. Rev. Lett. **59**, 202 (1987); Phys. Rev. **A36**, 2773 (1987).

APPLICATION OF FAST IMPLODING CAPILLARY DISCHARGE FOR LASER WAKEFIELD ACCELERATION

T. Hosokai* , M. Kando, H. Dewa, H. Kotaki, S. Kondo, N. Hasegawa
Advanced Photon Research Center, Kansai Research Establishment
Japan Atomic Energy Research Institute, Tokai-mura Naka-gun Ibaraki-ken 319-1195 Japan
K. Horioka, M. Nakajima, Department of Energy Sciences, Tokyo Institute of Technology
Nagatsuta 4259, Midori-ku Yokohama 226-8502 Japan
K. Nakajima, High Energy Accelerator Research Organization (KEK)
1-1 Oho Tsukuba-shi Ibaraki-ken 305-0801 Japan

Abstract

A new method of optical guiding for the laser wakefield acceleration using an imploding phase of a gas-filled fast capillary discharge has been proposed. An imploding plasma column has a concave electron density profile in the radial direction just before a stagnation phase driven by a converging current sheet and shock wave. The feasibility of optical guiding of high intensity laser pulses using an imploding phase of the fast capillary discharge has been experimentally demonstrated over a distance of 2 cm corresponding to ~12.5 times the Rayleigh length. A high intensity laser pulse ($> 10^{17}$ W/cm^2) focused on the front edge of the capillary has propagated through the center of the column maintaining its spot size. The electron density in the fully ionized channel is estimated to be 6.0 $\times 10^{16}$cm^{-3} on the axis and 1.5 $\times 10^{18}$ cm^{-3} on the peaks with the diameter of 70 μm.

1 INTRODUCTION

In order to increase the energy gain of electrons accelerated by the laser wake-fields, it is a critical issue to propagate a high intensity short laser pulse in a plasma larger than the vacuum Rayleigh length limited by diffraction. [1] Several methods for extending the propagation distances of intense laser pulses have been proposed: relativistic self-guiding in a plasma [2] and guiding in preformed plasma channels generated by a focused laser pulse [3] or by slow discharge through a capillary in vacuum.[4] For the optical guiding of laser pulses, the electron density profile must be symmetric in the radial direction and have a minimum on the axis, causing the wavefront to curve inward and the laser beam to converge. When this focusing force is strong enough to counteract the diffraction of the beam, the laser pulse can propagate over a long distance and maintain a small beam spot size in a plasma. For the guiding of intense ultrashort laser pulses shorter than the plasma wavelength, it is predicted that the relativistic self-channeling is ineffective in preventing diffraction, but the preformed plasma channel can provide a robust optical guiding.[5]

We have presented the first direct observation of optical guiding of high intensity laser pulses over 2 cm through a plasma channel produced by an imploding phase of fast Z-pinch discharge in a gas-filled capillary.

2 FAST CAPILLARY DISCHARGE

A high current fast Z-pinch discharge generates strong azimuthal magnetic field, which contracts the plasma radially inward down to $\sim$ 100 μm in diameter. The imploding current sheet drives the converging shock wave ahead of it, producing a concave electron density profile in the radial direction just before the stagnation phase. The concave profile is approximately parabolic out to a radius of $\sim$ 50 μm, after which the density falls off.

In the research of capillary discharge pumped X-ray laser, it has been shown that stable and reproducible channel can be produced by this scheme, and this scheme can be scalable to form longer and higher density channels by tailoring of the implosion. [6] It was reported that a stable, liner plasma column over the length of 12 cm could be produced at an electron density of more than 10^{19} cm^{-3}. [7]

For the laser wakefield acceleration (LWFA), a plasma channel with a density in the order of 10^{17} cm^{-3} and a length of $\sim$ 10 cm will be required. [1] We have started a study of optical wave-guiding in the density range of 10^{16} - 10^{18} cm^{-3} as the first step for application of the channel guided LWFA. Since the density profile in the capillary depends strongly on the discharge process, we have experimentally investigated the discharge dynamics and plasma channel formation.

3 OPTICAL GUIDING EXPERIMENT

The typical experimental setup is shown in Fig 1. We have used a capillary with an inner diameter of 1 mm and a length of up to 2 cm which was bored at the central axis of an alumina (Al_2O_3) rod of 50 mm in diameter. The capillary load was placed between two electrodes with an in-

*Email:thosokai@hikari.tokai.jaeri.go.jp

0-7803-5573-3/99/$10.00@1999 IEEE.

ner diameter of 400 μm which were made of molybdenum. The electrodes were cylindrically connected to a thyratron (EG&G HY-5) and four ceramic capacitors of 2 nF using four coaxial cables. The capacitor was charged up to 20 kV (1.6 J). With this configuration, the discharge current which was monitored by a Rogowski coil having a peak of 2.4 kA with a rise time of about 20 ns and a duration of 70 ns (FWMH). The capillary was filled with helium, under differential pumping at an initial pressure which was varied from 0.5 to 5 Torr. A DC discharge circuit was used to form an uniformly preionized helium gas.

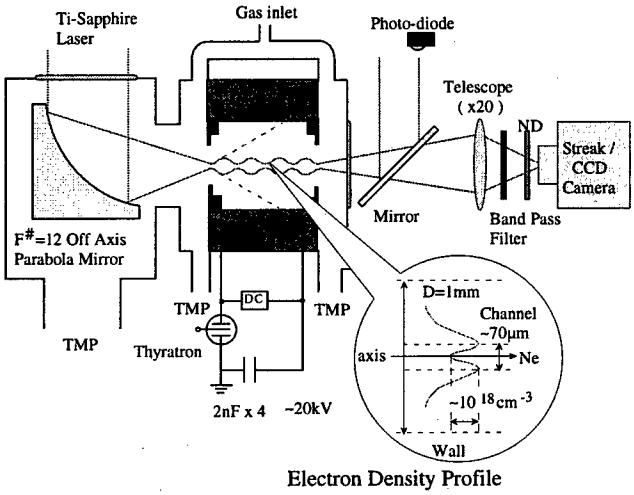

Figure 1: Experimental setup of a fast capillary discharge for a plasma waveguide. A typical electron density profile of the implosion phase of the fast capillary discharge in the radial direction is illustrated in the circle.

The discharge dynamics was observed with a streak camera (HAMAMATSU C-2830) placed on the capillary axis. The visible light emission from the capillary was imaged on the streak-camera slit through a telescope ($\times$ 20). To investigate the guiding channel formation in the capillary, a He-Ne laser beam (λ = 632.8 nm) was focused on the front edge of the capillary to a spot size of 40 μm in diameter by means of a $F^{\#}$ = 20 lens. The transmitted He-Ne laser beam profile at the exit of the capillary was observed through a band pass filter ($\Delta\lambda$ = 1 nm), with the streak camera. As a further investigation, a high intensity Ti-Sapphire laser pulse (λ = 790 nm, 90 fs, $>1 \times 10^{17}$ W/cm^2) was focused on the front edge of the capillary to a spot size of 40 μm in diameter by means of a $F^{\#}$ = 12 off-axis parabolic mirror. The transmitted laser beam profile at the exit of the capillary was observed through a band pass filter ($\Delta\lambda$ = 10 nm), with a CCD camera.

4 RESULTS

Figure.2 shows a typical streak image of the plasma emission for the initial pressure of 0.9 Torr, together with the intensity profile along the radial direction at t = 8.5 ns. The emission from only the central portion of the capillary with a diameter less than 400 μm was imaged on the streak camera. We found that the compression of the column produced a luminous region at t = 2.5 ns, which exhibits good symmetry with respect to the axis. Then, the luminous region on the axis faded out during expansion of the column. Later, the second implosion driven by a larger current produced a brighter luminous region at t = 8.5 ns. It again maintains good symmetry with respect to the axis. In addition, as shown in Fig.2(b), it had a clear dip with a width of 70 μm on the axis. The column oscillated in the radial direction several times while the main power pulse was alive.

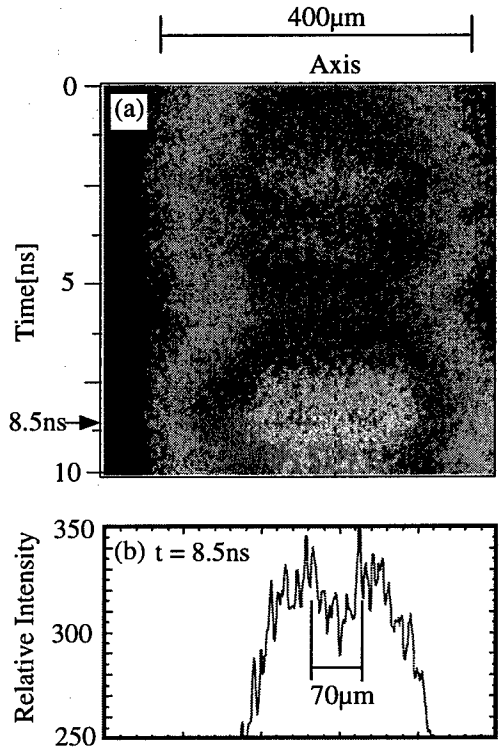

Figure 2: (a) A typical streak image of the capillary discharge at an initial pressure of 0.9 Torr He : t = 0 corresponds to the beginning of the main discharge pulse. (b) The radial intensity profile of the plasma emission was t = 8.5 ns.

We have observed the brightness and the radial profile of the transmitted He-Ne laser beam and high intensity Ti-sapphire laser pulses through the capillary at the exit. A typical streak image of the transmitted He-Ne laser beam profile through the capillary discharge plasma can be seen in Fig.3. Since the observed time window of Fig.3 almost coincided with that of Fig.2(a), the beam profile evolution could be correlated with the discharge dynamics. As shown in Fig.3, the beam radius gradually contracted in the second implosion phase and a brightly enhanced smaller beam spot could be observed at the time (t $\sim$ 8.5 ns) when the luminous profile exhibited double peaks in Fig.2. The observed spot image size (diameter) was $\sim$ 40 μm at the exit of the capillary. These results suggest that the guiding

channel was uniformly formed in the core of the column at the second implosion phase. Figure 4 shows typical CCD images of the transmitted high intensity Ti-sapphire laser pulse profile through the capillary discharge plasma at t = 0 ns (a) and at t $\sim$ 8.5 ns (b). These show clearly that a high intensity laser pulse could be guided through the channel over a distance of 2 cm corresponding to $\sim$ 12.5 Z_{R0}, where $Z_{R0} \sim$ 1.6 mm is the Rayleigh length of the Ti-Sapphire laser system.

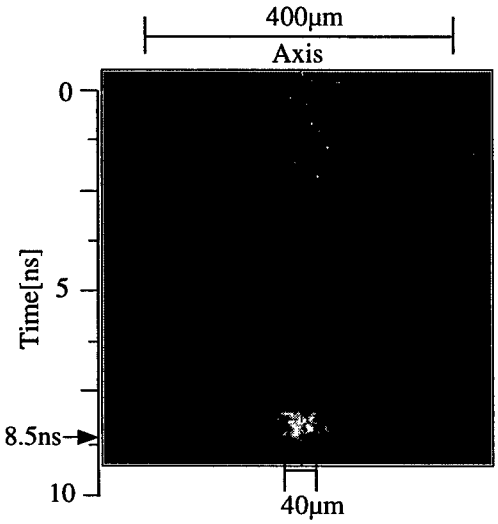

Figure 3: A typical streak image of the transmitted He-Ne laser beam through the capillary at an initial pressure of 0.9 Torr He : t = 0 corresponds to the beginning of the main discharge pulse.

The electron density profile in the channel was estimated by corroborating the transmitted laser images with the results of ray trace calculation [8] . We assumed that the electron density profile of the channel in the radial direction was parabolic and the channel was fully ionized with the electron density on the axis is of 6.0×10^{16}cm^{-3} which was twice the initial gas density. These were based on results of the 1D-MHD simulation using code MULTI-Z. [6, 9, 10] We also assumed that the incident laser had a radial Gaussian profile, the channel was uniform over the channel length and the channel radius r_{ch} was 35 μm according to the observed value. Under these assumptions, we can estimate the electron density on the peaks of the channel to be 1.5×10^{18} cm^{-3} and the density gradient to be $\sim 4 \times 10^{20}$ cm^{-4}. The matched beam radius r_m was given by $r_m = [r_{ch}^2/(\pi r_e \Delta n)]^{1/4}$, where Δn was the channel depth and $r_e = e^2 / mc^2$ was the classical electron radius. [5] With r_{ch} = 35 μm and $\Delta n \sim 1.5 \times 10^{18}$ cm^{-3}, the matched beam radius is $r_m \sim$ 17 μm. The observed spot radius of $\sim$ 20 μm was consistent with this value.

5 SUMMARY

In summary, we have presented the optical guiding of high intensity laser pulse using an imploding phase of a gas-filled capillary discharge and experimentally investigated the guiding channel formation in the capillary. The results indicate that the imploding column could uniformly produce a concave electron density profile in its core over a distance of 2 cm. The electron density in the fully ionized channel was estimated to be 6.0×10^{16} cm^{-3} on the axis and 1.5×10^{18} cm^{-3} on the peaks with a diameter of 70 μm. The optical guiding of high intensity laser pulses (> 1×10^{17} W/cm^2) was experimentally demonstrated in the second imploding phase of the discharge.

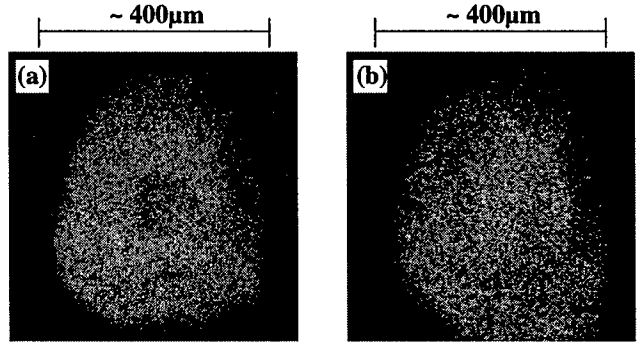

Figure 4: Typical CCD images of the transmitted a high intensity Ti-Sapphire laser pulse ($\sim 1 \times 10^{17}$ W/cm^2) through the capillary at an initial pressure of 0.9 Torr He: The capillary length L = 2cm. (a) t = 0 ns (b) t $\sim$ 8.5 ns.

6 REFERENCES

[1] K. Nakajima, Phys. Plasmas. 3, 2169 (1996)

[2] K. Krushelnick, A. Ting, C. I. Moore, H. R. Burris, E. Esarey, P. Sprangle, and M. Baine, Phys. Rev. Lett. 78, 4047 (1997)

[3] C. G. Durfee III and H. M. Milchberg, Phys. Rev. Lett. 71, 2409 (1993)

[4] Y. Ehrlich, C. Cohen, A. Zigler, J. Krall, P. Sprangle, and E. Esarey, Phys. Rev. Lett. 77, 4186 (1996)

[5] P. Sprangle, E. Esarey, J. Krall, and G. Joyce, Phys. Rev. Lett. 69, 2200 (1992)

[6]] T. Hosokai, M. Nakajima, T. Aoki, M. Ogawa, and K. Horioka, Jpn. J. Appl. Phys. 36, 2327 (1997)

[7] J. J. Rocca, V. N. Shlyaptsev, F. G. Tomasel, O. D. Cortazar, D. Hartshorn, and J. L. A. Chilla, Phys. Rev. Lett. 73, 2192 (1994)

[8] H. Hanajima, M. Nakajima, and K. Horioka, Proc. 6th International Conference on X-ray lasers, Kyoto Japan 1998, to be published

[9] R. Ramis, R. Schmalz, and J. Meyer-Ter-Vehen, Comput. Phys. Commun. 49, 475 (1988)

[10] T. Aoki, K. Horioka, and M. Ogawa, NIFS-Proc-26 Res. Rep. Natl. Inst. Fusion Sci., 179 (1996)

SIMULATION OF DENSITY CHANNEL GUIDING IN CAPILLARY DISCHARGE EXPERIMENTS AND LASER WAKEFIELD ACCELERATORS*

R. F. Hubbard,[a#] C. Moore,[a] P. Sprangle,[a] A. Ting,[a] NRL, D. Kaganovich,[b] A. Zigler[b] and B. Hafizi[c]

Abstract

Laser-driven accelerators require guiding of the laser pulse over many Rayleigh lengths. Plasma channels such as those produced by a capillary discharge have been shown experimentally to be capable of guiding intense laser pulses over distances as long as 6 cm. Simulations of laser propagation in these channels show that the laser pulse radius undergoes oscillations about the matched radius at the expected frequency. The pulse may be distorted by several effects, including laser-generated ionization. Experiments to date have been at relatively high densities (10^{18} - 10^{19} cm^{-3}). For standard laser wakefield accelerator applications, the channel density is likely to be substantially lower. As expected, simulations in this lower density regime show lower accelerating gradients, larger laser spot sizes, and higher wakefield phase velocities and dephasing-limited energy gain.

1 INTRODUCTION

The laser wakefield accelerator (LWFA) [1,2] has emerged as a leading candidate among various advanced accelerator concepts. However, the single-stage energy gain will be severely limited by diffraction of the laser pulse unless the beam is optically guided. Preformed plasma channels offer a promising method for providing such guiding. Channels produced by an axicon-focused laser [3] or capillary discharge [4-7] have successfully guided laser pulses over distances of several cm.

Several LWFA experiments [8,9] have produced very large accelerating gradients (>10 GV/m) and high energies (~100 MeV), but these experiments operate in the highly-unstable self-modulated regime and produce poor beam quality. Experiments in the standard LWFA regime have to date produced moderate energy gain [10].

This paper describes simulations of laser pulses in plasma channels similar to those used in recent capillary discharge guiding experiments. The analysis is extended the lower plasma density regime which will be used in future channel-guided LWFA experiments.

*Work supported by the Dept. of Energy, the Office of Naval Research, and the US-Israeli Binational Science Foundation.

[a]Plasma Physics Division, Naval Research Laboratory, Washington, DC

[b]Racah Institute of Physics, Hebrew University, Jerusalem, Israel

[c]Icarus, Inc., Bethesda, MD

#Email: hubb@ppdu.nrl.navy.mil

2 LASER PROPAGATION IN DENSITY CHANNELS

2.1 Theory for an Ideal Density Channel

Refractive guiding of a laser pulse can occur if the index of refraction peaks on-axis [2-7,11]. A plasma channel with an on-axis density minimum produces the desired effect. For an ideal channel, the plasma density is assumed to be parabolic, with $n = n_0 + \Delta n(r/r_{ch})^2$, where n_0 is the on-axis density, r is the distance from the axis, Δn is the channel depth, and r_{ch} is the channel radius. The laser pulse is assumed to have a Gaussian radial profile, with normalized vector potential $a = a_0 exp(-r^2/r_L^2)$, where r_L is the laser spot size.

The assumptions above lead to an envelope equation for $r_L(z)$ in which the spot size oscillates about the equilibrium or matched radius r_M given by

$$r_M = (r_{ch}^2 / \pi r_e \Delta n)^{1/4}, \qquad (1)$$

where r_e is the classical electron radius. The oscillations have a period given by $\lambda_e = \pi Z_M$, where $Z_M = (\pi r_M)^2/\lambda$ is the Rayleigh length for the matched spot size r_M.

2.2 Laser Guiding Experiments with Capillary Discharges

A capillary discharge provides a simple, controllable method for generating a narrow plasma column suitable for laser guiding [4-7]. The device consists of a thin cylinder of insulating material with high voltage electrodes at the ends. The plasma is generated from material from the inner insulating wall of the capillary. Double capillary designs [12] employ a short higher voltage trigger section preceding the main capillary. Hydrodynamic simulations [12] and Stark broadening measurements [5] indicate a period of time during which the plasma has an off-axis maximum in the density at a distance r_{ch} which is typically 50-70% of the wall radius.

Initial experiments [4,5] utilized a linearly-polarized Ti-sapphire laser with pulse length τ_L = 100 fs, wavelength λ = 0.8 μm, and peak power P_0 up to 0.1 TW. The pulses were focused onto the entrance of the capillary with a focused spot size of 15 μm. Experiments with 1 cm long cylindrical capillaries [4] demonstrated transport efficiencies of up to 85% in both straight and curved configurations. When the discharge was not

0-7803-5573-3/99/$10.00@1999 IEEE.

triggered, transport efficiencies dropped dramatically, and the transported laser spot appeared to fill the capillary. Laser guiding experiments were also performed in 2, 3 and 6.6 cm long capillaries [5]. In the latter case, the pulse radius at capillary exit was <25 μm and did not vary greatly with variations of the discharge parameters. The transport distance was ~30 Z_M. Light transmission was ~10% in comparison to the ~1% without the discharge. Collisional absorption is likely to be the dominant loss mechanism, although ionization-induced losses cannot be discounted [5].

Accelerator applications require substantially higher intensities than are produced by this laser. To investigate the high intensity regime, capillary discharge experiments have recently been carried out using the T^3 laser at the Naval Research Laboratory [6,7]. The laser has a 1.06 μm wavelength, a 400 fs pulse length, and peak power exceeding 2 TW. A 2 cm long double capillary was used. The focused intensities in these experiments exceeded 10^{17} W/cm^2. Transport efficiencies were generally higher than at lower intensities.

2.3 Laser Guiding Simulations

Simulations of laser propagation in plasma channels have been carried out using the LEM 2-D, axisymmetric code developed by Krall, *et al.* [13]. Nonlinear wave equations are solved for the normalized potentials, and the plasma response is treated with a cold fluid model. The evolution of the pulse is followed in a speed-of-light system with coordinates r, $\zeta = ct - z$, and $\tau = t$.

Figure 1 plots the spot size $r_L(z)$ for three simulations in a 2 cm long channel with r_{ch} = 100 μm, similar to that used in the guiding experiments described above [5]. The spot size is calculated at a reference point near the center of the 100 fs long, 0.8 μm wavelength pulse. The entrance to the channel is near the initial focus at z = 0.3 cm, and the pulse exits the channel into vacuum at z = 2.3 cm. The solid curve has $n_0 = 5\text{x}10^{18}$ cm^{-3}, and $\Delta n = 3\text{x}10^{18}$ cm^{-3} and is nearly identical to the dashed curve, which raises n_0 to $1.5\text{x}10^{19}$ cm^{-3}. However, the dotted curve, which has a small reduction in Δn ($2.8\text{x}10^{18}$ cm^{-3}), produces a small but noticeable shift in the spot size oscillation wavelength λ_e, leading to a significant shift in the spot size trajectory after it exits the channel. This is consistent with the predictions of Section 2.1, that r_M and λ_e are independent of n_0 and scale only with Δn. Experimental measurements of post-capillary expansion of the beam show shot-to-shot variations which can be attributed to small changes in Δn.

The pulse may be distorted by a number of effects which are not contained in the simple envelope models. For example, the intense laser pulse may ionize the carbon originating from the polyethylene capillary wall to higher charge states. This will tend to increase the plasma density near the axis, which inhibits the guiding effects and may cause the pulse profile to hollow [4]. Finite pulse length effects [14] may also distort the pulse, causing growth and damping of envelope oscillations.

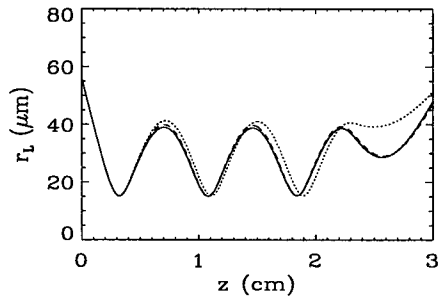

Fig. 1. Simulation results for laser guiding and post-capillary expansion for three cases with different values of n_0 and Δn. Parameters are described in the text.

3 CHANNEL-GUIDED LASER WAKEFIELD ACCELERATORS

3.1 Scaling for LWFA Performance

The channel guiding method described above may be adapted to laser wakefield acceleration. However, to be in the optimal regime for a standard LWFA, the resonance ratio $\alpha_r = c\tau_L/\lambda_p$ should be ~0.5 [1,2]. Here, the nominal plasma wavelength $\lambda_p = 2\pi c/\omega_{p0}$, and $\omega_{p0} = (4\pi n_0 e^2/m)^{1/2}$ is the on-axis plasma frequency. If α_r and τ_L are specified, the on-axis density $n_0 = (\pi m/e^2)(\alpha_r/\tau_L)^2$. For τ_L > 100 fsec, and α_r = 0.5, $n_0 < 3.5\text{x}10^{17}$ cm^{-3}, which is much lower than n_0 values in current experiments [3-7].

Analytical models for predicting LWFA performance are usually based on such physics parameters as a_0, λ, and λ_p. The primary performance quantities are the peak accelerating electric field E_m, the dephasing distance L_d, and the dephasing-limited energy gain $W_d = mc^2\gamma_d$. If the pulse length is optimized, the pulse is linearly-polarized, and $a_0 << 1$, the usual scalings give $E_m = (a_0^2/2)E_0$, $L_d = \lambda_p^3/2\lambda^2$, and $\gamma_d = 2(E_m/E_0)(\lambda_p/\lambda)^2$. Here $E_0 = mc\omega_{p0}/e$ is the 1-D cold fluid wavebreaking field, and the dephasing limits are based on the distance over which a particle moving at c slips by an $\lambda_p/4$ in the wakefield.

Since α_r and τ_L are strongly linked, one may express performance quantities in terms of the following set of laser parameters (λ, P_0, τ_L) and channel parameters (α_r, r_{ch}, and normalized channel depth $\Delta n/n_0$). The spot size in Eq. (1) is given by $r_M^2 = (c/\pi)(r_{ch}\tau_L)/\alpha_r(\Delta n/n_0)^{1/2}$. Thus, longer pulse length lasers tend to have larger spot sizes and thus lower intensities and accelerating fields. If the scaling of E_m with pulse length is assumed to be ~$\sin(\pi\alpha_r)$, then the peak accelerating electric field is

$$E_m = \left(\frac{4e}{mc^5}\right)\frac{\alpha_E\alpha_r^2\lambda^2 P_0(\Delta n/n_0)^{1/2}\sin\pi\alpha_r}{r_{ch}\tau_L^2}, \qquad (2)$$

and the corresponding dephasing-limited energy gain is

$$\gamma_d = \left(\frac{4e^2}{\pi m^2 c^4}\right)\frac{\alpha_E P_0 \tau_L (\Delta n / n_0)^{1/2} \sin \pi\alpha_r}{r_{ch}\alpha_r}. \qquad (3)$$

The scale factor α_E is ~0.8 [1,2]. These simple scalings may be modified for high laser intensity (a_0 ~ 1) and finite spot size.

3.2 LWFA Simulations

The simulation code may be run in the lower density regime and high laser powers appropriate for a LWFA. Fig. 2 gives a surface plot of the axial electric field $E_z(r,\zeta)$ for a prototype channel-guided LWFA with $\lambda = 0.8$ μm, τ_L = 100 fs, P_0 = 25 TW, $n_0 = 2\text{x}10^{17}$ cm^{-3}, $\Delta n/n_0$ = 5, and r_{ch} = 100 μm. The peak field of ~10 GV/m occurs at $\zeta = -80$ μm, and the simulation slippage rate gives an estimated dephasing length L_{ds} = 20.9 cm. The dephasing-limited energy gain for the simulation is $W_{ds} = (2/\pi)E_{ms}L_{ds}$ = 1.36 GeV. This agrees well with the analytical estimate from the previous section when spot size and nonlinear corrections are included. Current LWFA and channel guiding experiments have taken place at much high plasma densities, where L_s ~ 0.1 cm, E_m is substantially higher, but W_d is only ~100 MeV.

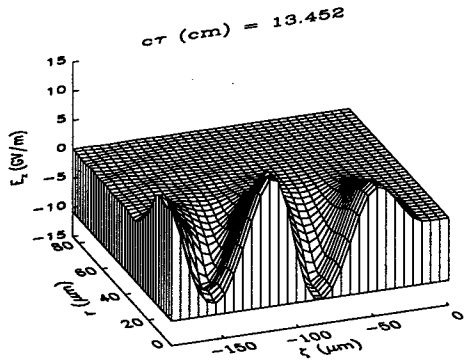

Fig. 2. Axial electric field $E_z(r,\zeta)$ at z = 13.5 cm for the LWFA simulation described above.

Longer pulses require still lower plasma densities but may produce much larger values for L_d and W_d. Simulations with 400 fs long pulses confirm this, but the resulting accelerating gradients are in the 1 GV/m range. Thus, the channels required to take advantage of the higher dephasing limits are probably too long to be practical.

If a long pulse laser is injected into a higher density channel, the pulse will undergo self modulation (SM) as in the SM-LWFA experiments [8,9]. The channel allows the beam to be guided at powers well below the critical power P_c for relativistic self-focusing, and should substantially reduce the highly irregular behavior seen in those experiments. Fig. 3 shows a plot of $E_z(r,\zeta)$ at z = 3.6 cm for a prototype channel-guided SM-LWFA with $\lambda = 1$ μm, τ_L = 400 fs, P_0 = 13 TW, $n_0 = 8\text{x}10^{17}$ cm^{-3}, $\Delta n/n_0$ = 1, and r_{ch} = 150 μm. The simulation produces a well-defined wakefield which peaks at ~35 GV/m.

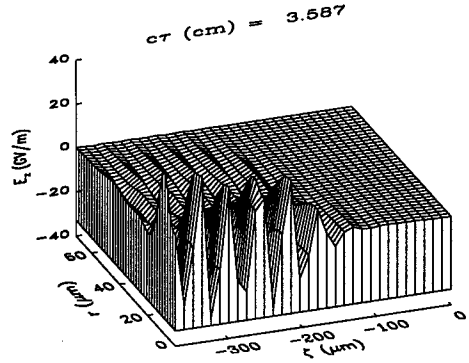

Fig. 3. Axial electric field $E_z(r,\zeta)$ at z = 3.6 cm for the self-modulated LWFA simulation described above

4 SUMMARY

Plasma channels such as those produced by a capillary discharge have guided intense laser pulses over distances of several cm. Simulations have been carried out which reproduce these experiments and illustrate higher order effects which may distort the pulse. For a channel-guided LWFA, the plasma density must be substantially lower that in current experiments. The implications may be seen in simple scaling laws for LWFA performance and in simulations of future LWFA experiments. Simulations of a channel-guided, self-modulated LWFA suggest this approach may be promising.

5 REFERENCES

[1] P. Sprangle, *et al.*, Appl. Phys. Lett. **53**, 2146 (1988).

[2] E. Esarey, *et al.*, IEEE Trans. Plasma Sci. **24**, 252 (1996).

[3] C. G. Durfee, III and H. M. Milchberg, Phys. Rev. Lett. **71**, 2409 (1993);H. M. Milchberg, *et al.*, Phys. Plasmas **3**, 2149 (1996).

[4] Y. Ehrlich, *et al.*, Phys. Rev. Lett. **77**, 4186 (1996).

[5] Y. Ehrlich, *et al.*, J. Opt. Soc. Am. B **15**, 2416 (1998).

[6] D. Kaganovich, *et al.*, to appear in Phys. Rev. E.

[7] R. F. Hubbard, *et al.*, to appear in *Advanced Accelerator Concepts*, AIP Conference Proceedings, 1999.

[8] K. Nakajima, *et al.*, Phys. Rev. Lett. **74**, 4659 (1995); A. Modena, *et al.*, IEEE Trans. Plasma Sci. **PS-24**, 289 (1996); D. Umstadter, *et al.*, Science **273**, 472 (1996).

[9] C. Moore, *et al.*, Phys. Rev. Lett. **79**, 3909 (1997); A. Ting, *et al.*, Phys. Plasmas **4**,1889 (1997).

[10] F. Amiranoff, *et al.*, Phys. Rev. Lett. **81**, 995 (1998).

[11] P. Sprangle and E. Esarey, Phys. Fluids B **4**, 2241 (1992).

[12] D. Kaganovich, *et al.*, Appl. Phys. Lett. **71**, 2295 (1997).

[13] J. Krall, *et al.*, Phys. Rev E **48**, 2157 (1993).

[14] P.Sprangle, B. Hafizi, and P. Serafim, Phys. Rev. Lett. **82,** 1173 (1999); Phys. Rev. E **59**, 3614 (1999); E. Esarey and W. P. Leemans, Phys. Rev. E **59**, 1082 (1999).

LASER WAKEFIELD DIAGNOSTIC USING HOLOGRAPHIC LONGITUDINAL INTERFEROMETRY*

P. Volfbeyn, E. Esarey, and W. P. Leemans, LBNL, Berkeley, CA

Abstract

We propose a diagnostic technique for wakefield measurement in plasma channels. A new technique for plasma channel creation, the Ignitor Heater scheme was proposed and experimentally tested in hydrogen and nitrogen previously [1]. It makes use of two laser pulses. The Ignitor, an ultrashort (sub 100 fs) laser pulse, is brought to a line focus using a cylindrical lens to ionize the gas. The Heater pulse (160 ps long) is used to heat the existing spark via inverse Bremsstrahlung. The hydrodynamic shock expansion creates a partially evacuated plasma channel with a density minimum on axis. Such a channel has properties of an optical waveguide. This technique allows creation of plasma channels in low atomic number gases, such as hydrogen, which is of importance for guiding of highly intense laser pulses. Laser pulses injected into such plasma channels produce a plasma wake that has a phase velocity close to the speed of light. A discussion of plasma wake measurements, using a Longitudinal Interferometry Wakefield Diagnostic Based on Time Domain Rayleigh Refractometry [2] with Holographic Inversion, will be presented.

1 WAKEFIELD EXCITATION IN CHANNELS

Excitation of wakes with intense laser pulses propagating in plasma channels needs to be studied. The goal is to carry out a parametric study of wake characteristics versus plasma channel and laser pulse properties. The longitudinal and transverse plasma density profile in the channel will be measured interferometrically, as discussed previously [1]. Longitudinal femtosecond interferometry [2], [3] will be used to measure the wakefield. The technique measures the phase shift imparted by the plasma wave to an externally injected laser pulse, as a function of delay time behind the driving pulse. In this paper, the focus is on adapting the longitudinal interferometry techniques to the experiments planned at the L'OASIS laboratory and further refining them to provide an accurate and reliable measurement of the wake amplitude.

A description of the principles of the diagnostic is given in Section 3. In Section 4, it is shown that the method can be simply extended to measure a long (multiperiod) temporal record of the plasma wave evolution in a single shot. A holographic inversion technique has been developed and will be applied, that makes the interferometry technique insensitive to the effect of a phase shift common to both pulses. It therefore provides a true measure of the actual phase shift imposed on the laser beam by the plasma wake.

*Work supported by the US Department of Energy, Contract DE-AC03-76SF00098.

2 EXPERIMENTAL PARAMETERS

The planned experimental parameters are: laser pulse duration 50 fs, 1-10 mm long channel, resonant density on axis (assuming Gaussian temporal laser pulse shape) $n_0 = 7 \times 10^{17} cm^{-3}$, with a 1 TW guided beam with guided spotsize of 10 microns. The resultant vector potential is $a_0 = 0.544$, the peak excited axial accelerating field is Ezmax=9.35 GV/m, the plasma wave density perturbation $\delta n/n = 0.112$, and the peak phaseshift accumulated by a probe laser pulse co-propagating with the wake is $\Delta\phi_{max} = 0.182 rad/mm$ for an 800 nm probe pulse, and 91 mrad for a 400 nm probe pulse.

3 OPTICAL WAKEFIELD DIAGNOSTIC

To perform phase shift measurement which are precise and insensitive to noise and fluctuations, Rayleigh's interferometric refractometer technique was applied successfully [3],[2] to measure phase shifts on the order of several mrads. This technique utilizes two laser pulses, propagating down the same path, but separated by a time delay. The leading of the two pulses traverses the plasma before the intense pulse that drives the plasma wake. The trailing pulse propagates through the plasma after the wake was produced. Thus the difference in the phaseshift acquired by the two laser pulses is due to the plasma wave. The interferometric pulses are subsequently combined in an imaging grating spectrometer. After diffracting off the grating the obtained pattern is viewed by a CCD camera at the image plane. Because of the pulse-stretching caused by the diffraction grating, the two laser pulses now overlap in time and a beat pattern is seen on the CCD. The temporal stretching T can be calculated if the resolution of the spectrometer r is known: $T \approx 1/r$. For instance, $\delta\lambda = 0.114$ nm translates into pulse lengthening of $T \approx 1/(\o\delta\lambda/\lambda) = 3$ ps for 800 nm radiation. The spatial periodicity of the beat pattern is directly related to the time separation between the two pulses.

To illustrate it with an example, assume that the two laser pulses are of the form

$$\begin{aligned} E(t) =& e^{(-(t+\Delta)^2/\tau^2)} \cos(\omega_0(t+\Delta)) \\ &+ e^{(-t^2/\tau^2)} \cos(\omega_0 t + \phi) \end{aligned} \tag{1}$$

The effect of the (perfect) grating spectrometer is equivalent to taking one half of the Fourier transform of the pulses (positive or negative frequency):

$$\begin{aligned} E(\omega) = \frac{1}{2}\sqrt{\pi}(& e^{-(\omega-\omega_0)^2\tau^2/4} e^{-(\omega-\omega_0)\Delta} \\ &+ e^{-(\omega-\omega_0)^2\tau^2/4} e^{-i\phi}) \end{aligned} \tag{2}$$

0-7803-5573-3/99/$10.00@1999 IEEE.

The CCD measures the power (proportional to the absolute value of the electric field squared). The CCD pattern, Fig. 1, will contain contributions from DC terms of the individual pulse amplitudes and the beating cross term with frequency domain variation as $\cos(\phi + (\omega - \omega_0)\Delta)$:

$$P(\omega) \propto 2e^{-(\omega-\omega_0)^2\tau^2/2} + 2e^{-(\omega-\omega_0)^2\tau^2/4}\cos(\phi + (\omega - \omega_0)\Delta) \quad (3)$$

The beating contains information about the phase shift

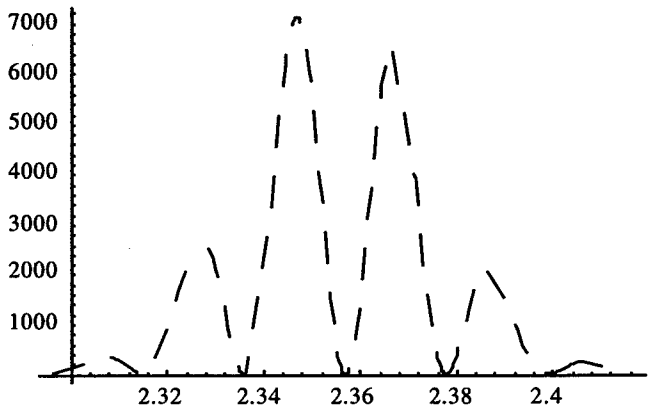

Figure 1: The spectral beat observed after the two interferometer pulses are combined on the spectrometer.

ϕ_{max}. Figure 2 demonstrates the difference between the beating with $\phi = 0$ mrad (solid line), and $\phi = 182$ mrad (dashed line).

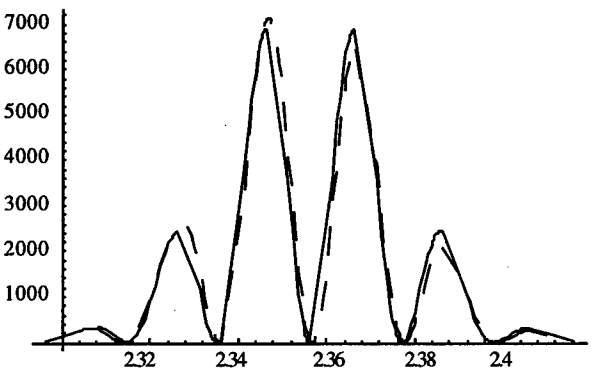

Figure 2: The interference pattern shifts in the spectral domain if the probe pulse has acquired different phaseshift than the reference pulse. $\phi = 0mrad$ (solid line), and $\phi = 182mrad$ (dashed line)

The phaseshift, ϕ, can now be extracted from the beating pattern, by performing a Fourier transform of the spectrum with respect to $(\omega - \omega_0)$. The result of such operation is shown in Fig. 3. The three amplitude peaks correspond to the DC component and two terms at the beat frequency. The phase of the Fourier transform at the two higher frequency peaks is exactly $\pm\phi$.

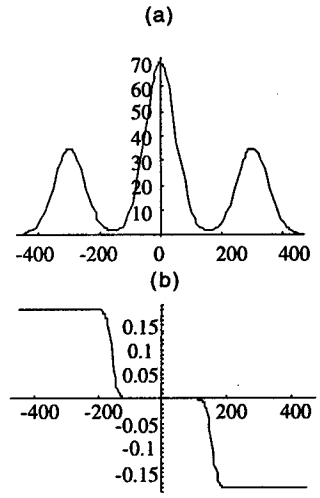

Figure 3: (a) Amplitude and (b) phase of the Fourier transform of the beat pattern of Eq.3 with $\phi = 182$ mrad.

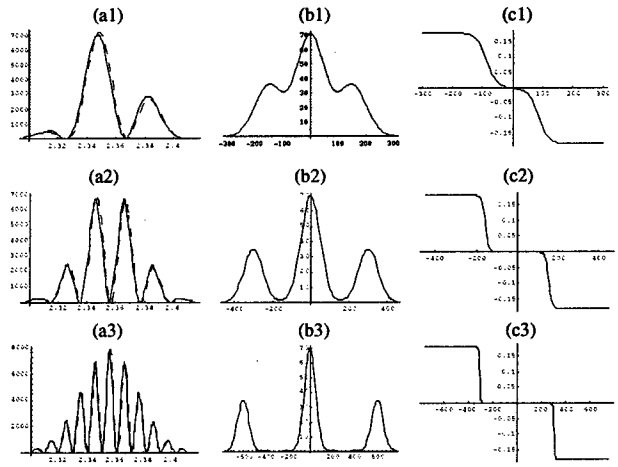

Figure 4: (a1)-(a3) Spectrometer interferometric beat pattern, (b1)-(b3) the amplitude and (c1)-(c3) phase of the Fourier transform of the beat pattern, for Δ = 150 fs, 300 fs and 600 fs, respectively.

The time delay between the two interferometric pulses should be chosen such that the DC peak does not overlap with the two beat frequency peaks. The spectrometer beat patterns and their Fourier transforms are displayed in Figs. 4. From the figures it can be seen that when the time delay between the two pulses is too small (Fig. 4a1,b1,c1), there is considerable overlap between the peaks in the Fourier transform, and that transfers into phase error. On the other hand, if the delay is made too large, the resolution limit of the spectrometer may be reached, and the Nyquist criterion may not be satisfied. We find that the smallest value of Δ for which the peaks no longer overlap is $\Delta = 5 \times t$.

4 TIME VARYING PHASESHIFT RETRIEVAL WITH HOLOGRAPHIC INVERSION

Simple Fourier transformation of the spectral beat provides correct phase shift information only in the case when the phase shift is constant in time. For instance, in the case of a linearly changing (in time) phase shift, the retrieved phase has a slope that's two times smaller than the actual value. The reason for the discrepancy is that instead of taking an inverse Fourier transform of the Fourier transform of the probe pulse, the diagnostic calculates the inverse Fourier transform of the product of the probe and reference pulse transforms.

We have developed a novel theoretical algorithm for time domain Rayleigh refractometry, that relies on holographic inversion of the measured spectra. As mentioned previously, a simple Fourier transformation of the spectral beat provides correct phase shift information only in the case when the phase shift is constant in time. For instance, in the case of a linearly changing (in time) phase shift, the retrieved phase has a slope that is two times smaller than the actual [2]. The reason for the discrepancy is that instead of taking an inverse Fourier transform of the Fourier transform of the probe pulse, the diagnostic calculates the inverse Fourier transform of the product of the probe and reference pulse transforms. If the amplitude of the Fourier transform of the reference pulse is known, and if the only phase difference between the probe and reference pulses is due to the plasma wake (so that any other phase shift that is common to both pulses will cancel when a product with complex conjugate is taken), then by dividing the spectral beat by the amplitude of the reference pulse Fourier transform (square root of the spectrum of the reference pulse alone) before the Fourier transformation is calculated, the true phase shift is found. This procedure is similar to the action of the reference pulse in a hologram.

Figs. 5 presents a numerical simulation of the phaseshift retrieval with and without the holographic correction. The result of numerically calculating the inverse Fourier transform of Eq.3 with $\phi = \phi_{max}\cos(\omega_p t + \Phi_0)$ where $\phi_{max} = 182$ mrad is expected to be close to the experimental values, is shown in Fig. 5 a). Fig. 5 b) presents the result of taking the Fourier transform after the expression of Eq.3 was corrected for the reference pulse Fourier transform amplitude. The phaseshift retrieved without the holographic correction, Fig. 5 a), is drastically different from the actual phaseshift. The corrected retrieval, Fig. 5 b), is shown to extract the prescribed time dependent phaseshift accurately. The holographic inversion technique makes the interferometry technique insensitive to the effect of a phase shift common to both pulses, and therefore provides a true measure of the actual phase shift imposed on the laser beam by the plasma wake. We have also verified that the method can be extended to provide a single shot measurement of multiple periods of the wake pattern. Experimentally, the probe laser pulse will be made temporally longer by spectral filtering.

An important potential source of error is the fact that the diagnostic is unable to distinguish between Fourier limited probe pulses and pulses with a frequency chirp (quadratic phase shift). If both the probe and the reference pulses have similar frequency chirp then, after diffracting off the spectrometer grating, the probe pulse phase shift due to the wake at the front of the pulse will be mixed with that accumulated in the rear of the pulse. In the case of time varying phase shift, the retrieval will be in error. To minimize the contribution of imperfect temporal compression, the production of the blue interferometric pulses will be done in a way that ensures proper compression, provided the driving red pulse in optimally compressed.

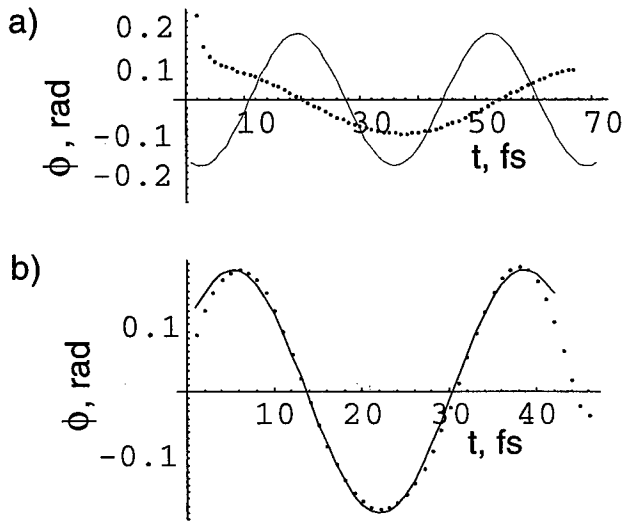

Figure 5: Retrieved phase shift (dots) a) without and b) with reference correction, compared to that prescribed (solid curves).

5 REFERENCES

[1] P. Volfbeyn and W. P. Leemans, "Experimental Studies on Laser Guiding with Plasma Channels," Conf. Proc. E-PAC 98, Stockholm, Sweden, p. 265, (1998)

[2] C.W. Siders et al., Phys. Rev. Lett. **76**, 3570 (1996); C.W. Siders et al., IEEE Trans. Plasma Science **24**, 301-305 (1996).

[3] J.R. Marquès et al., Phys. Rev. Lett. **76**, 3566 (1996); J.R. Marquès et al., Phys. Rev. Lett. **78**, 3463 (1997).

[4] A. Ting et al., Phys. Rev. Lett. **77**, 5377 (1996).

[5] S.P. LeBlanc et al., Phys. Rev. Lett. **77**, 5381 (1996).

[6] C.E. Clayton et al., Phys. Rev. Lett. **81**, 100 (1998).

SCALING LAWS FOR LASER WAKEFIELD ACCELERATORS*

E. Esarey† and W.P. Leemans
Lawrence Berkeley National Laboratory, University of California, Berkeley CA 94720

Abstract

Scaling laws are derived as a function of laser wavelength for various quantities of interest for a single stage of a channel-guided laser wakefield accelerator. Comparisons are made for drive laser pulses of equal energies. Scalings that favor short or long wavelengths depend on the quantity that is to be optimized. For example, holding the number of electrons per bunch constant favors shorter wavelengths, whereas holding the energy gain constant can favor longer wavelengths.

1 INTRODUCTION

Plasma-based accelerators [1] are capable of sustaining ultrahigh electric fields E_z on the order of $E_0 = cm\omega_p/e$, i.e.,

$$E_0[\mathrm{V/m}] \simeq 96 n^{1/2}[\mathrm{cm}^{-3}], \qquad (1)$$

where n is the ambient plasma density and $\omega_p = (4\pi n e^2/m)^{1/2}$ is the plasma frequency. Although the accelerating field is very high, the wavelength of the accelerating structure (i.e., the plasma wave) is very short and on the order of the plasma wavelength $\lambda_p = 2\pi c/\omega_p$, i.e.,

$$\lambda_p[\mu\mathrm{m}] \simeq 3.3 \times 10^{10} n^{-1/2}[\mathrm{cm}^{-3}], \qquad (2)$$

e.g., $E_0 \sim 30$ GV/m and $\lambda_p \simeq 100$ μm for $n \simeq 10^{17}$ cm^{-3}. The shortness of λ_p has important consequences. For example, if an electron bunch is to be injected into the plasma wave such that its initial low energy spread is maintained, then it is desirable for the initial bunch length L_b to be short compared to λ_p. Furthermore, the bunch must be injected at the optimal plasma wave phase with femtosecond timing accuracy. These requirements are beyond the state-of-the-art for conventional injector technology (e.g., photo-injectors). Conversely, the shortness of λ_p and the wide-spread availability of ultrashort high power lasers may allow plasma-based accelerators to be developed as a compact source of ultrashort, high energy electron bunches [2-7].

In the standard laser wakefield accelerator (LWFA) a single, intense, short (a pulse length $L \sim \lambda_p$) is used to drive the wakefield. As the pulse propagates through the plasma, its ponderomotive force $F_p \propto \nabla a^2$ expells plasma electrons, thus exciting a large amplitude plasma wave with phase velocity $v_p \simeq c$ in its wake. Here, a^2 is proportional to the laser intensity I,

$$a^2 \simeq 7.2 \times 10^{-19} \lambda^2[\mu\mathrm{m}] I[\mathrm{W/cm}^2], \qquad (3)$$

* Work supported by the U.S. Department of Energy under contract No. DE-AC-03-76SF0098.

† Email: ehesarey@lbl.gov

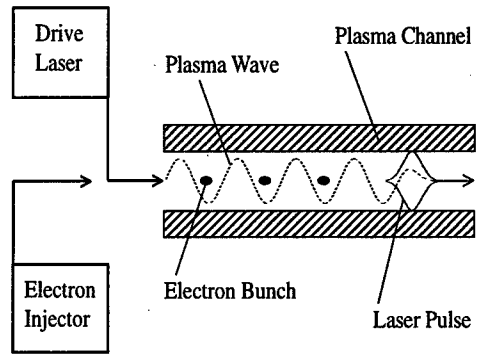

Figure 1: Schematic of a channel-guided LWFA. The plasma channel guides the laser pulse and supports the wakefield, which is generated behind the laser pulse with a phase velocity $v_p \simeq c$. Short electron bunches with length $L_b \ll \lambda_p$ are injected into the wakefield for acceleration to high energy.

and is related to the power P of a Gaussian radial intensity profile $I \propto \exp(-2r^2/r_s^2)$ by $P[\mathrm{GW}] \simeq 21.5 a^2 r_s^2/\lambda^2$, where λ is the laser wavelength, r_s is the spot size, and linear polarization has been assumed.

A practical high-energy LWFA requires the use of a plasma channel to guide the laser pulse (see Fig. 1) . In vacuum, laser propagation is typically limited by diffraction, the characteristic distance of which is the Rayleigh length $Z_R = \pi r_0^2/\lambda$, where r_0 is the laser spot radius at focus (e.g., $Z_R \simeq 3$ mm for $r_0 = 30$ μm and $\lambda = 1$ μm). Extending the single-stage interaction (acceleration) length beyond Z_R requires optical guiding [8]. In the standard LWFA, this can be achieved with a preformed plasma density channel [8-15]. The index of refraction in a plasma is approximately $\eta_R \simeq 1 - \lambda^2/2\lambda_p^2$. As in an optical fiber, a plasma channel can provide optical guiding if the index of refraction peaks on axis, $\partial\eta_R/\partial r < 0$, which can be achieved with a plasma density profile that has a local minimum on axis, $\partial n/\partial r > 0$. Specifically, a channel with a radially parabolic density profile of the form $n(r) = n_0 + \Delta n r^2/r_0^2$ can guide a Gaussian laser pulse with a constant spot size r_0 provided the channel depth Δn satisfies $\Delta n = \Delta n_c$, where $\Delta n_c = 1/\pi r_e r_0^2$ is the crit-

0-7803-5573-3/99/$10.00@1999 IEEE.

ical channel depth [8] and $r_e = e^2/m_e c^2$ is the classical electron radius, i.e.,

$$\Delta n_c[\mathrm{cm}^{-3}] \simeq 1.13 \times 10^{20}/r_0^2[\mu\mathrm{m}]. \quad (4)$$

The following discussion will be restricted to standard LWFAs that utilize channel guiding.

The most common sources of high power, short laser pulses are solid-state systems based on the technique of chirped-pulse amplification (CPA) [16]. Such CPA systems typically have $\lambda \sim 1$ μm and have been used in numerous LWFA and channel-guiding experiments [9-15]. Alternatively, high-power, short-pulse CO_2 laser systems ($\lambda \sim 10$ μm) are being developed and will be available for future LWFA experiments [17]. In this paper, scaling laws with respect to λ for relevant LWFA quantities are derived and discussed.

2 SCALING LAWS

In this section, simple scaling laws for LWFA quantities are presented under idealized assumptions. These idealized scaling laws assume the following:

1. A standard LWFA that is channel guided.
2. The mildly relativistic regime, $a^2 \ll 1$.
3. The acceleration length is limited by electron dephasing.
4. The plasma channel is sufficiently broad such that the formula describing wakefield generation in a uniform plasma apply.
5. The transverse size of the laser pulse is $2c/\omega_p$ and the transverse size of the electron bunch is c/ω_p.
6. The total electrons per bunch is the beam loading limit.

In the following, when equations are presented in practical form (with numerical coefficients), E_z is in V/m, n is in cm^{-3}, λ is in μm, I is in W/cm^2, W_L is in J, L_d is in m, ΔW is in GeV, Lum_s is in cm^{-2}, and a^2 is dimensionless.

In the mildly relativistic limit within a broad channel, the axial electric field of the wake [1] can be written as $E_z = 0.38a^2E_0$, where $E_0 = m_e c\omega_p/e = 96n^{1/2}$, i.e.,

$$\begin{aligned} E_z &= 2.7 \times 10^{-17} I\lambda^2 n^{1/2} \\ &= 3.4 \times 10^{-25} W_L \lambda^2 n^2 \end{aligned} \quad (5)$$

This assumes a linearly polarized laser pulse with Gaussian profiles in the radial and axial directions. This also assumes that the laser pulse length is optimized to maximize the wakefield amplitude, i.e., $L = \lambda_p/\sqrt{2\pi} = 0.4\lambda_p$, where the pulse length L is defined such that $W_L = (1/8\pi)A_L E_L^2 L$ is the pulse energy, $\lambda_p = 2\pi c/\omega_p$ is the plasma wavelength, E_L is the peak laser electric field, $A_L = \pi r_0^2/2$ is the cross-sectional area of the Gaussian pulse, and r_0 is the laser spot size.

The laser spot size is assumed to be $r_0 = 2c/\omega_p$ in order to ensure high efficiency of energy transfer between the wake and the accelerated electrons [18], since electrons loaded near the axis will absorb wake energy out to a radius of approximately c/ω_p. Furthermore,

$$a^2 = 9.4 \times 10^{-27} W_L \lambda^2 n^{3/2} \quad (6)$$

The acceleration length is assumed to be equal to the electron dephasing length $L_D = \lambda_p^2/\lambda^2$,

$$L_d = 3.7 \times 10^{25} \lambda^{-2} n^{-3/2} \quad (7)$$

The ideal maximum energy gain is given by $\Delta W = eE_z L_d$,

$$\Delta W = I/n = 1.3 \times 10^{-8} W_L n^{1/2} \quad (8)$$

The number of electrons accelerated per bunch is assumed to be equal to the beam loading limit [18] $N_b = E_z A_b/4\pi e$, where A_b is the effective cross-sectional area of the beam which is assumed to be $A_b = \pi c^2/\omega_p^2$,

$$N_b = 1.7 \times 10^{-9} W_L \lambda^2 n \quad (9)$$

Another figure of merit is the luminosity $Lum = (k_b f_b/4\pi)N_b^2/\sigma_x\sigma_y$, where k_b is the number of bunches per linac, f_b is the linac rep rate, and $\sigma_{x,y}$ are the transverse rms bunch sizes, which are assumed to be equal to c/ω_p. For scaling purposes, it is convenient to define the "single bunch" luminosity as $Lum_s = N_b^2/\sigma_x\sigma_y$,

$$Lum_s = 9.9 \times 10^{-30} W_L^2 \lambda^4 n^3 \quad (10)$$

3 EXAMPLES

Next, to determine scaling with wavelength, several examples are given. In all these examples, the laser pulse energy W_L is assumed constant.

3.1 Constant E_z

The axial electric field of the wake is held fixed (in addition to the pulse energy). This implies:

$$\begin{aligned} &n \propto \lambda^{-1},\ L_d \propto \lambda^{-1/2},\ \Delta W \propto \lambda^{-1/2}, \\ &N_b \propto \lambda,\ Lum_s \propto \lambda \end{aligned} \quad (11)$$

3.2 Constant L_d

The acceleration length is held fixed (in addition to the pulse energy). This implies:

$$\begin{aligned} &n \propto \lambda^{-4/3},\ E_z \propto \lambda^{-2/3},\ \Delta W \propto \lambda^{-2/3}, \\ &N_b \propto \lambda^{2/3},\ Lum_s \propto constant \end{aligned} \quad (12)$$

3.3 Constant ΔW

The electron energy gain is held fixed (in addition to the pulse energy). This implies:

$$n \propto constant,\ E_z \propto \lambda^2,\ L_d \propto \lambda^{-2},$$
$$N_b \propto \lambda^2,\ Lum_s \propto \lambda^4 \qquad (13)$$

3.4 Constant N_b

The number of electrons per bunch is held fixed (in addition to the pulse energy). This implies:

$$n \propto \lambda^{-2},\ E_z \propto \lambda^{-2},\ L_d \propto \lambda,$$
$$\Delta W \propto \lambda^{-1},\ Lum_s \propto \lambda^{-2} \qquad (14)$$

3.5 Constant Lum_s

The single bunch luminosity is held fixed (in addition to the pulse energy). This implies:

$$n \propto \lambda^{-4/3},\ E_z \propto \lambda^{-2/3},\ L_d \propto constant,$$
$$\Delta W \propto \lambda^{-2/3},\ N_b \propto \lambda^{2/3} \qquad (15)$$

4 DISCUSSION

In making comparisons between $\lambda = 1\ \mu$m and $\lambda = 10\ \mu$m drivers, care must be taken so as not to violate the above assumptions, in particular, $a^2 \ll 1$. Note that $a^2 \propto W_L \lambda^2 n^{2/3}$. Hence, when making comparisons at constant density and pulse energy, as in Case 3.3, the assumption $a^2 \ll 1$ may be violated at long wavelengths. On the other hand, for short wavelengths, operation at high density is valid.

A definitive conclusion regarding an optimum driver wavelength is problematic. For example, at sufficiently low density (such that $a^2 \ll 1$), a design for a fixed energy gain favors longer wavelengths, as implied by Case 3.3. On the other hand, a design for a fixed number of electrons per bunch favors short wavelengths, as implied by Case 3.4. Furthermore, a design for a fixed acceleration distance (and fixed luminosity) allows higher energies to be obtained for short wavelengths, however, a higher bunch number is obtained for long wavelengths. The above scaling laws all assume a fixed laser pulse energy. A rigorous study of a LWFA for various wavelength drivers must also include other properties of the driver, such as repetition rate, pulse stability, and average power. Since laser technology is rapidly progressing, a rigorous design study is premature. In terms of physics experiments, invaluable information can be obtained at both 1 and 10 micron.

5 ACKNOWLEDGMENTS

The authors acknowledge useful conversations with I.V. Pogorelsky, T. Katsouleas, and C. Joshi.

6 REFERENCES

[1] For a review, see E. Esarey, P. Sprangle, J. Krall, and A. Ting, IEEE Trans. Plasma Sci. **24**, 252 (1996).

[2] D. Umstadter, J.K. Kim, and E. Dodd, Phys. Rev. Lett. **76**, 2073 (1996).

[3] R.G. Hemker, K.C. Tzeng, W.B. Mori, C.E. Clayton, and T. Katsouleas, Phys. Rev. E **57**, 5920 (1998).

[4] E. Esarey, R.F. Hubbard, W.P. Leemans, A. Ting, and P. Sprangle, Phys. Rev. Lett. **79**, 2682 (1997).

[5] W.P. Leemans, P. Volfbeyn, K.Z. Guo, S. Chattopadhyay, C.B. Schroeder, B.A. Shadwick, P.B. Lee, J.S. Wurtele, and E. Esarey, Phys. Plasmas **5**, 1615 (1998).

[6] C.B. Schroeder, P.B. Lee, J.S. Wurtele, E. Esarey, and W.P. Leemans, Phys. Rev. E, May (1999).

[7] E. Esarey, C.B. Schroeder, and W.P. Leemans, Phys. Plasmas, May (1999).

[8] For a review, see E. Esarey, P. Sprangle, J. Krall, and A. Ting, IEEE J. Quant. Elect. **33**, 1879 (1997).

[9] H.M. Milchberg, T.R. Clark, C.G. Durfee, T.M. Antonsen, and P. Mora, Phys. Plasmas **3**, 2149 (1996).

[10] V. Malka, E. de Wispelaere, F. Amiranoff, S. Baton, R. Bonadio, C. Coulaud, R. Haroutunian, A. Modena, D. Puissant, C. Stenz, S. Muller, and M. Casanova, Phys. Rev. Lett. **79**, 2979 (1997).

[11] T. Ditmire, R.A. Smith, and M.H.R. Hutchinson, Opt. Lett. **23**, 322 (1998).

[12] P. Volfbeyn and W.P. Leemans, in Proc. 6th European Part. Accel. Conf., Ed. by S. Myers, L. Liljeby, Ch. Petit-Jean-Genaz, J. Poole, and K.G. Rensfelt (Inst. of Phys., Philadelphia, 1998), p. 265; P. Volfbeyn, MIT Ph.D. Thesis, LBNL Report 41892 (1998).

[13] E. Gaul, S.P. Le Blanc, and M.C. Downer, *Advanced Accelerator Concepts*, Edited by W. Lawson, AIP Conf. Proc. (AIP, NY, in press).

[14] P.S. Volfbeyn, E. Esarey, and W.P. Leemans, Phys. Plasmas, May (1999).

[15] Y. Ehrlich, C. Cohen, A. Zigler, J. Krall, P. Sprangle, and E. Esarey, Phys. Rev. Lett. **77**, 4186 (1996); Y. Ehrlich, C. Cohen, D. Kaganovich, A. Zigler, R.F. Hubbard, P. Sprangle, and E. Esarey, J. Opt. Soc. Am. B **15**, 2416 (1998).

[16] G.A. Mourou, C.P.J. Barty, and M.D. Perry, Physics Today **51**, 22 (1998).

[17] I.V. Pogorelsky, Nucl. Instr. Meth. Phys. A **410** 524 (1998); I.V. Pogorelsky et al., in *Advanced Accelerator Concepts*. edited by W. Lawson, AIP Conf. Proc. (Amer. Inst. Phys., NY, in press).

[18] T. Katsouleas, S. Wilks, P. Chen, J.M. Dawson, and J.J. Su, Particle Accelerators **22**, 81 (1987).

DESIGN OF ELECTRON BEAM INJECTION SYSTEM FOR LASER ACCELERATION EXPERIMENTS AT JAERI-KANSAI

M. Kando*, H. Kotaki, H. Dewa, S. Kondo, and T. Hosokai
JAERI, Tokai, Ibaraki 319-1106, Japan
F. Sakai, J. Yang, and T. Hori,SHI, Tanashi, Tokyo 188-8585, Japan
K. Nakajima, KEK, Oho, Tsukuba, Ibaraki 305-0801, Japan

Abstract

We have designed an electron beam injection system for laser wakefield acceleration experiments which will be performed in a new facility of JAERI-Kansai in Kyoto. This system consists of an RF photocathode gun which can produce 5 ps 1 π mm·mrad electron single bunch and race-track microtron (RTM). Here we have estimated an acceptance of laser wakefield in order to achieve more efficient acceleration, and have designed the high quality beam injector.

1 INTRODUCTION

Recent progress of high peak power laser technology enables us to study laser wakefield acceleration (LWFA) experimentally, which is a promising method for a high gradient compact accelerator. Several groups in the world have succeeded in acceleration of electrons by a laser wakefield so far[1]. However, the quality of the accelerated electrons such as energy spread, the number of accelerated particles, and so on, are not satisfied for practical applications as an accelerator. The major reason is because beam matching to the wakefield is not taken into account, or at least not sufficient, in the former experiments. In a typical LWFA experiment, a 100 fs multi-tera watt laser pulse is focused into tens of microns. At a first look, it could be say that the LWFA requires an electron bunch to have the same order of both transverse and temporal sizes as those of the laser pulse.

There seems to be two approaches to accomplish perfect beam matching to the laser wakefield. One is a plasma cathode[2] which has a great potential in producing such high quality beam, because it produces electrons by a similar process of LWFA. However, this technique has not experimentally proved yet and must be tested separately. The other is to use a conventional accelerator for the injection. There exist some difficulties in producing ultra short bunches, but the recent progress of short bunch generation will help it[3].

In order to improve quality of beams accelerated by the wakefield we aim to develop a low emittance short bunch electron injector. For this purpose, a combination of the photocathode RF gun and the 150 MeV race-track microtron (RTM) produces such a high quality beam with an appropriate budget. We have accomplished the photocathode RF gun capable of producing a 5 ps, less than 10 π mm·mrad beam with a charge of 1 nC[4].

In this paper, we present a simple estimation of acceptance of the laser wakefield by a particle tracking code. Then we describe the injection system and improvements in order to make a low emittance beam in transverse direction.

2 ACCEPTANCE OF LASER WAKEFIELD ACCELERATOR

We have developed a particle tracking computer code named *WAKE3D* in order to examine acceptances of the laser wakefield accelerator. This code integrates three dimensional equation of motion where electric fields are given by a linear fluid theory. The integration length is 20 times of the vacuum Rayleigh length. No space-charge effect is included in the code.

Here, we only show typical results of the acceptance for a plasma density of $n_e = 3.48 \times 10^{17}$ cm^{-3}, a laser pulse length of $\tau_L = 100$ fs, a laser pulse energy of $E_p = 500$ mJ, and a spot-size at focus of $\sigma_{r0} = 10$ μm. Figure 1 shows the energy gain versus the initial phase. The initial electrons are injected to the wakefield on axis with energies of 1.3, 15, and 151 MeV. In case of the injected electrons are relativistic ($E > 15$ MeV), no bunching effect is seen in the figure. Our case is 151 MeV, thus, short bunch about 30 degrees (15 fs) is required for an energy gain of 40–60 MeV. Transverse acceptance is shown in Fig. 2. Opposite to the longitudinal, transverse acceptance is wide enough for our system.

Generation of such tens of femtosecond electron pulse has not been achieved. However, we would obtain an improved energy spectrum in Fig. 3 if only the transverse beam matching is achieved. In this case, two side-peaks are seen, which are accelerated or decelerated by the wakefield, while the spectra of the former experiments obeyed power law as a function of an energy gain[1].

3 ELECTRON INJECTION SYSTEM

Figure 4 shows a schematic of the designed electron injection system. The system consists of the RF photocathode

*Email:kando@apr.jaeri.go.jp

0-7803-5573-3/99/$10.00@1999 IEEE.

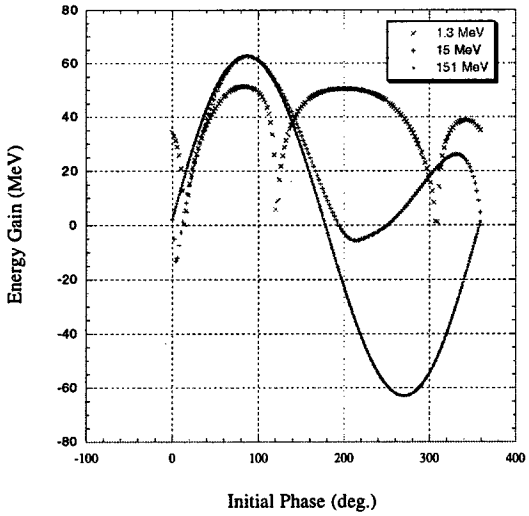

Figure 1: $\Delta E - \phi$ Phase space plot at the exit of the wakefield.

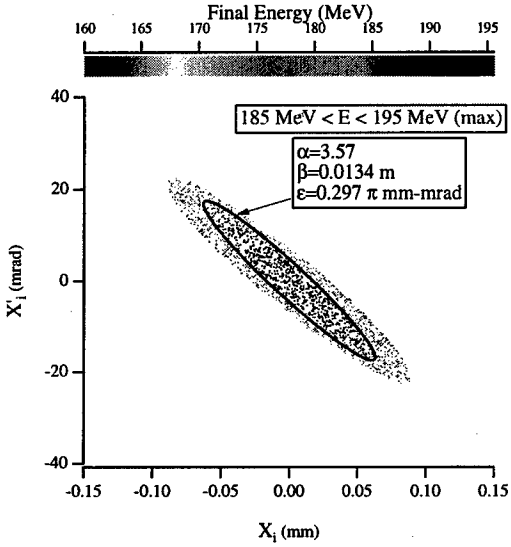

Figure 2: Transverse acceptance of the laser wakefield.

gun, the microtron accelerator and the beam extraction section.

3.1 *Photocathode RF Gun*

We adopted an S-band RF gun developed by the collaboration with BNL, KEK and Sumitomo Heavy Industries, Ltd (SHI). This cavity is based on the gun developed by the BNL / SLAC / UCLA collaboration [5] and is improved for high duty operation (50 Hz). The gun can produce $\sim 1\ \pi$ mm·mrad electron pulses owing to an emittance compensation solenoid magnet. An UV light is introduced to the copper cathode with an incident angle of 68°.

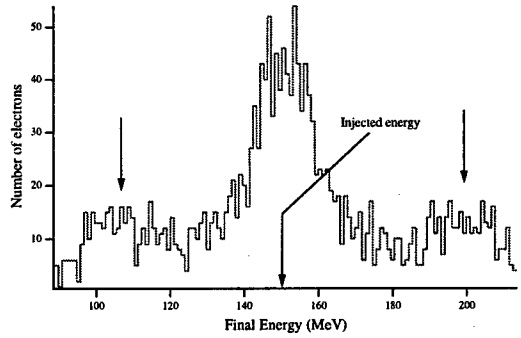

Figure 3: Energy spectrum of the beam matched only in transverse.

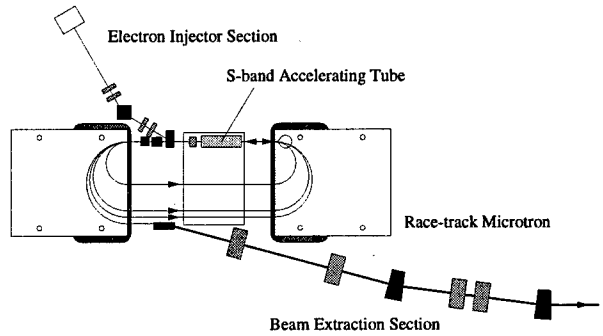

Figure 4: A schematic of the electron injection system.

3.2 *Photocathode Driving Laser*

We use a compact all solid-state Nd:YLF laser system (PULRISE II) developed by SHI as a driving laser for the RF gun. This system consists of three sections; passive mode-locked seed-laser with a repetition rate of 79.3 MHz, laser diode (LD) pumped regenerative amplifier (regen) where a Nd:YLF crystal cut is used as a gain medium and frequency conversion sections.

Seed-laser pulses with a wavelength of 1053 nm are synchronized with an external reference signal (79.3 MHz) by using a phase-locked loop. The regen section captures and amplifies a single seed-laser pulse increasing the pulse energy from the order of sub-nano Joule up to 2 mJ with a maximum repetition rate of 100 Hz. The frequency conversion section generates a green light (527 nm) and an UV (263 nm). The output pulse energy of the UV is 200 μJ at maximum. The energy fluctuation of the UV is 0.5 %. The pulse width of the UV is approximately 6 ps FWHM.

3.3 *Test of Photocathode RF Gun*

We have performed tests of the photocathode RF gun and the driving laser which were installed at the Nuclear Engineering Research Laboratory, the University of Tokyo. The details of the results will be presented in forthcoming publication. As a preliminary result, we measured the electron pulse with a pulse length of 5 ps FWHM, an normalized

emittance of 8 π mm
*cdot*mrad, and an energy of 3.7 MeV.

3.4 *Microtron*

The race-track microtron (RTM) manufactured by SHI is used as a booster accelerator. The original RTM accelerates electrons emitted by a thermionic gun from 120 keV to 150 MeV after 25 turns. We plan to replace the thermionic gun with the photocathode RF gun, thus some improvements should be required.

First, we estimated the acceptance of the RTM for 4.5 MeV injection using a code *MIC* which was developed to design the original RTM[6]. After adjusting the position of the accelerating tube and injection timing, we found that a suitable electron beam is parallel, slightly converging, and 6 ps in horizontal, vertical, and longitudinal direction, respectively (see Fig. 5).

The injection beamline to the RTM is designed to match the acceptance. We designed two bend achromat beamline by employing the transfer matrix, *TRACE-3D*, and *PARMELA* calculations. We obtained beam distributions shown in Fig.6 by the *MIC* code after 25 turns in the RTM. Finally, we found that horizontal and vertical acceptances are 0.33 and 0.13 π mm
*cdot*mrad, respectively. Thus, transverse beam matching will be achieved by an appropriate focusing section, which is under design. The pulse length is 3 ps FWHM for the present design, thus, a longitudinal beam matching to the wakefield requires either to design a bunch compressor or to find a bunch compressed solution through the RTM.

The transmission efficiency of the beam through the RTM has been improved up to 50 %, which was much better than the RTM with the thermionic gun. The expected beam charge is 500 pC/bunch, that is enough for the LWFA experiments.

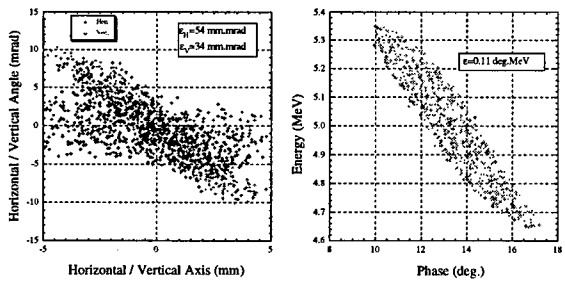

Figure 5: Acceptances of the RTM.

3.5 *Beam Extraction*

The RTM has two straight sections; one is non-dispersive where the accelerating tube is placed, and the other is dispersive due to the 180° bending magnet of the RTM. Because of the space limitation, beam extraction magnet is placed in the dispersive straight section. We designed a dispersion-compensated beam extraction section in order to avoid emittance growth caused by dispersion. The section was designed by employing transfer matrix technique to satisfy doubly achromatic conditions. Finally, we found that three bending magnets and four quadrupole magnets system can efficiently work with transverse focusing.

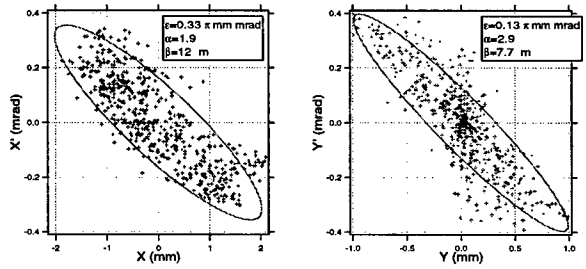

Figure 6: Beam distributions at the exit of the RTM.

4 SUMMARY

We have designed the electron beam injection system oriented to effective electron acceleration by a laser wakefield. The RF photocathode and the race-track microtron are used for a low emittance beam generator and the expected transverse emittance satisfies the required conditions. The design work is still going on, and the left major work is to design short bunch generation and focusing sections.

5 ACKNOWLEDGMENTS

We are grateful to T. Ueda, K. Yoshii, T. Watanabe, and M. Uesaka of the University of Tokyo during the RF gun test.

6 REFERENCES

[1] K. Nakajima *et al.*, Phys. Rev. Lett., **74** (1995) 4428; A. Modena *et al.*, Nature (London) **377** (1995) 606; D. Umstadter *et al.*, Science **273** (1996) 472; H. Dewa *et al.*, Nucl. Instr. and Meth. in Phys. Res. A 410 (1998) 357; F. Amiranoff *et al.*, Phys. Rev. Lett. **81** , (1998) 995.

[2] D. Umstadter *et al.*, Phys. Rev. Lett., **76**, (1996) 2073.

[3] M. Uesaka *et al.*, Nucl. Instr. and Meth. in Phys. Res. A 410 (1998) 424.

[4] F. Sakai *et al.*,Proc. of 11th Symp. on Accel. Sci. and Tech. (1997) 473.

[5] D. T. Palmer *et al.*, Proc. of Part. Accel. Conf. (1995) 982.

[6] M. Sugitani *et al.*, Proc. of 1st Europ. Part. Accel. Conf. (1988) 596.

DEVELOPMENT OF ONE METER-LONG LITHIUM PLASMA SOURCE AND EXCIMER MODE REDUCTION FOR PLASMA WAKEFIELD APPLICATIONS /

S. DiMaggio, L. Archambault, P. Catravas, P. Volfbeyn, and W. P. Leemans,[y] LBNL, Berkeley, CA 94720
K. Marsh, P. Muggli, S. Wang, and C. Joshi, UCLA, Los Angeles, CA 90024

Abstract

A one meter long plasma source has been developed for studies at the Stanford Linear Accelerator Center (SLAC) of plasma wakefield excitation by a 30 GeV electron beam in an extended plasma column. The plasma is formed by ionization of a Li-vapor with an ArF EXCIMER laser (193 nm). The Li-vapor is produced in a heat pipe oven which will be installed in the electron beam transport line. Through control of the oven temperature, neutral vapor densities reaching $2 \pounds 10^{15}cm^{-3}$ are produced. We report the details of the oven construction and temperature profile measurements with and without Lithium vapor. In the experiment, the EXCIMER laser will be located about 15 m away from the plasma source. Beams produced by EXCIMER lasers operating with a stable resonator cavity are unsuitable due to the large number of modes present in such beams. A significant reduction of the modal content has been obtained through the use of an unstable resonator design. Results of the implementation of this cavity configuration on the propagation characteristics of the EXCIMER beam will be presented, including the design of the final telescope for spot size reduction.

1 INTRODUCTION

A one-meter long plasma source has been constructed which will permit the properties of extended plasma columns as optical elements in beamlines to be studied in an operating regime at 30 GeV. The E157 Experiment[1, 2, 3], to take place at the Final Focus Test Beam (FFTB) at the Stanford Linear Accelerator, utilizes a single 30 GeV electron bunch with a bunchlength of $_z \ldots 400¡ 600„m$ and up to $4x10^{10}$ electrons, which will travel through a full meter of plasma. Wakefields excited by the head of the bunch are expected to provide an accelerating gradient to the bunch tail. For efficient wakefield excitation, frequency content at $!_p$ is provided by matching the beam bunchlength to the plasma period, $¿_b \gg 1=!_p$. The wake amplitude expected for the optimal plasma density range of $2x10^{14}cm^{-3}$ is 0.5 GeV/m. Calculations show that the plasma ions will exert focusing forces on the electron beam capable of dramatically changing the bunch transverse size and divergence[2]. Experimental studies of these mechanisms have been performed at lower beam energies (10's of MeV) and wakefield acceleration of the bunch tail has been demonstrated [4]. The two key components for the experiment are the 1 meter plasma source and the beam diagnostics. Here, the practical implementation of the full length source for the E157 experiment is described.

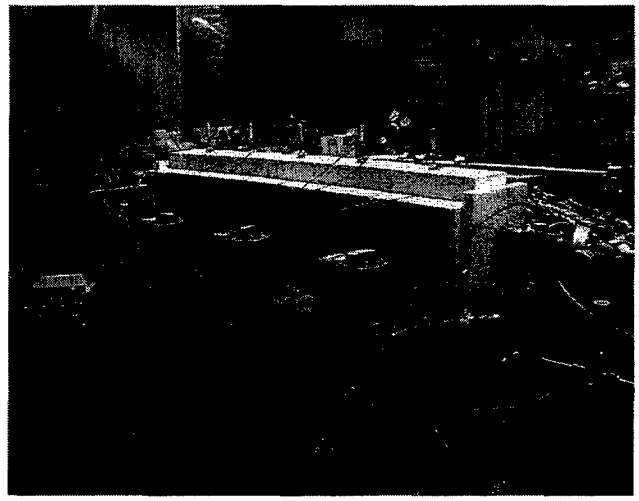

Figure 1: One meter long Lithium heat pipe oven.

The minimum plasma requirements are the following: length of at least 1 meter, density of $2\text{-}5x10^{14}cm^{-3}$ and a transverse dimension on the order of a few mm, large compared with the electron beam spot size of » 50 microns at the plasma entrance. To provide a plasma of the appropriate density and dimensions, while avoiding beam-induced ionization, Lithium was chosen. The ionization potential of Lithium (5.39 eV) is less than the photon energy at 193 nm (5.4 eV) and it can therefore be singly ionized using an ArF based Excimer laser. Typical fluences required are 30-50 mJ/cm^2 to produce a fractional ionization of the neutral vapor by the laser on the order of 10-20%. Beam induced ionization (impact of 30 GeV electrons as well as background electrons) is expected to be less than a percent and its effect should therefore be minimal. In order to obtain a Lithium plasma with the appropriate density, the Lithium vapor temperature must be raised to 750°C. Accordingly, the plasma source is constructed in heat pipe oven configuration[5, 6, 7]. The 1 meter oven built at LBNL and described below is based on the design of a 0.25 meter prototype built at UCLA.[8]

/ Work supported by the U.S. Department of Energy under contract No. DE-AC-03-76SF0098.

[y] Email:wpleemans@lbl.gov

0-7803-5573-3/99/$10.00@1999 IEEE.

2 OVEN DESCRIPTION AND CHARACTERIZATION

The heat pipe oven provides a homogeneous metal vapor over a well defined length. The vapor evaporates from melted metal uniformly distributed by capillary action along a wick lining the pipe interior. Metal vapor pressure is defined by that of an inert gas displaced from the heated length of pipe to cold pipe ends, where it forms a gaseous plug which can be easily monitored[5, 6, 7].

The 1 meter long heat pipe oven shown in Figure 1 was constructed of a 56" long stainless steel tube 1.5 inches in diameter with an inside lining of 3 1/2 turns of fine stainless steel mesh. The pipe exterior is insulated with double layer of oven brick. A total of three independently powered heater tapes are wrapped around the exterior of the oven pipe. The temperature profile is provided by an exterior array of five K-type (Chromel-Alumel) thermocouples evenly spaced along the 1 meter length with spring loading to improve contact with the heat pipe surface. Automatic temperature regulation is performed by monitoring the readouts of three of the exterior thermocouples and adjusting the heater tapes to maintain any input setpoint up to 750°C. Heater tape power is interlocked to the temperature of the water jackets on both ends of the oven.

The temperature profile measured in the oven without Lithium is shown in Figure 2 and was measured by drawing a K type thermocouple braced inside a 3/8 inch stainless steel pipe through the oven. The corresponding exterior thermocouple array profile is shown in Figure 3a, normalized to the oven central temperature. Both measurements provide evidence that the temperature profile taper extends at least 25 cm from the water jackets (circulating at 30°C) into the oven interior when the oven does not contain Lithium.

Lithium (40 g) was then added to the oven and sealed unit was filled with Helium. Raising the oven temperature results in the change in temperature profile shown in Figure 3b. The reduction in boundary effects and flattening of the profile indicates that Lithium vapor extends along a one meter length at the desired density, corresponding to a He pressure of 200 mTorr.

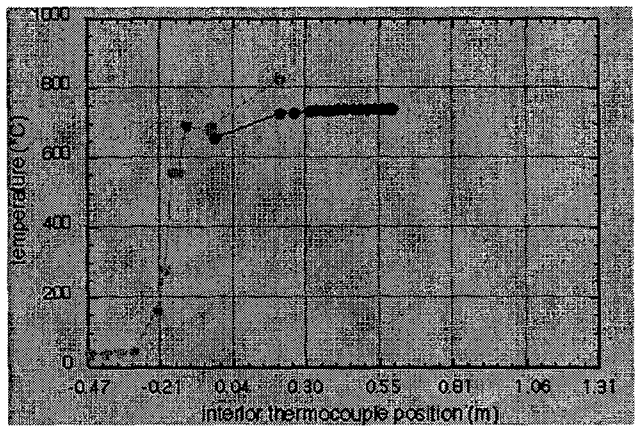

Figure 2: Oven temperature profiles in vacuum (i.e. without Lithium) measured with interior thermocouple for two temperature setpoints reaching or exceeding the desired operating temperature of 750°C.

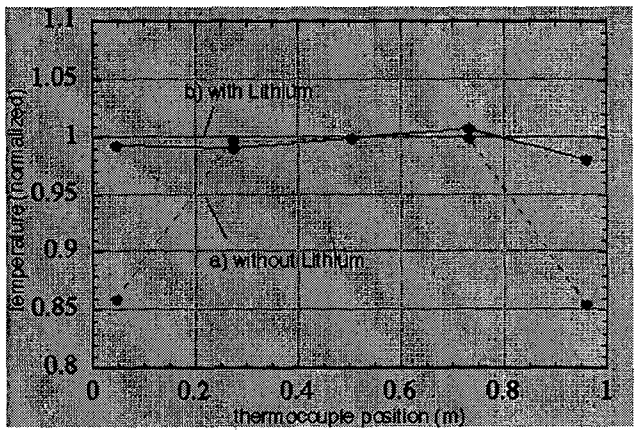

Figure 3: Exterior thermocouple array readouts (normalized to central oven temperature) with and without Lithium as a function of distance along the oven. Note the reduction in edge effects, a signature of the presence of Lithium vapor.

3 EXCIMER MODE CONTENT REDUCTION

While readily available Excimer lasers operating with ArF do provide the necessary photon energy to ionize the plasma, in practice, the use of an Excimer introduces a significant complication. To form a meter-long plasma, the Excimer spot size must be maintained constant over a distance of 1-2 meters, a requirement in conflict with the high mode content typical of Excimers. The original Excimer cavity configuration produced the tophat intensity profile and could not have been coupled into the beamline without significant loss, as the beam diameter, ...w, two meters from a waist of 5 mm was found to be 4 inches. In addition, the high modal content can lead to loss of power in long transport lines if the higher order modes diffract out of the system. For the E-157 Experiment at SLAC, the physical layout of the beamline and surrounding structures requires that the laser and plasma source be separated by a minimum of 15 meters.

We addressed this problem by converting the Excimer cavity from a stable to an unstable resonator design to reduce mode content. The unstable cavity resonator consists of a planar Aluminum coated high reflector and an uncoated meniscus lens as the outcoupler, followed by a collimating lens. The measured mode propagation was consistent with a waist located at the virtual focus of the meniscus lens, as expected from simple ray tracing.

To simulate transport losses for the unstable resonator configuration, power loss as a function of distance was measured using only a single collimating lens positioned

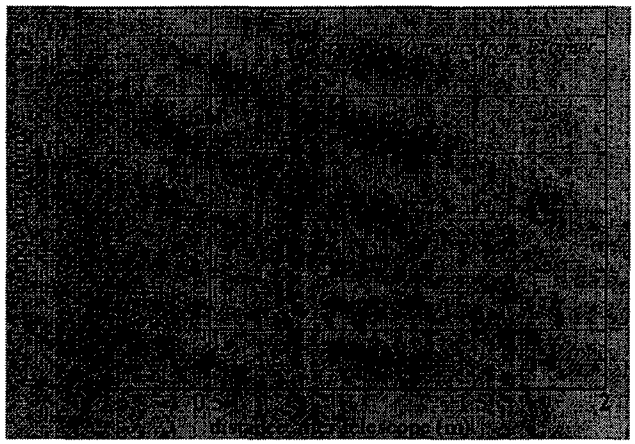

Figure 4: Comparison of mode propagation for 5 mm spot size at 248 nm for stable and unstable resonators shows significant reduction in mode content.

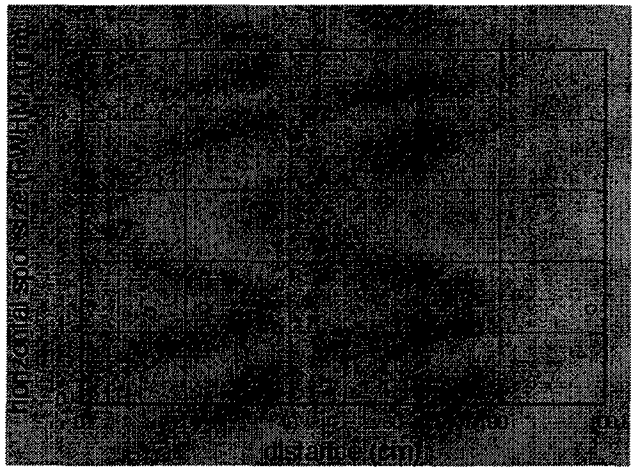

Figure 5: Test of demagnifying telescope for final focus of Excimer at 193 nm into oven: evolution of Excimer mode at 193 nm shows only minor change in spot size over one meter propagation.

about 10 cm from the Excimer output port. 120 mJ at 248 nm propagated for 18 meters without significant loss of power into the 2" aperture, after an initial drop by about a factor of 2 in the first two meters. The initial drop may be reduced through the use of 3" optics.

The mode content figures of merit were quantified by performing systematic scans of the beam profile through a waist. The intensity profile itself was measured by imaging the fluorescence produced by the 193 nm radiation in a BK7 substrate onto a CCD camera. A beamsplitter placed in the Excimer path prevented damage to the substrate from the small spot sizes. The profile corresponding to the stable resonator, which had a mode content, M^2 of 990 at 248 nm; the M^2 figure for the unstable resonator was improved to less than fifty (Figure 4). Mode propagation at 193 nm over a one meter length after demagnification to a spot size between 1 and 2 mm is shown in Figure 5, confirming that the reduced mode content permits the small spot size to be maintained over the full length required for the plasma source.

The final coupling of the Excimer into the beamline will be implemented using thin (150-300 micron) fused silica foils with a high reflecting 193 nm dielectric coating on one side to be located 1-2 meters from the oven center. For the planned wakefield experiments, the Excimer incoupling and outcoupling foils sit directly in the path of the 30 GeV electron beam, which must traverse not only these two foils but two Beryllium foils. The Be foils form the barrier between the heat pipe oven, which operates at a pressure of 200 mTorr, and the ultra-high vacuum of the surrounding beampipe. The potential for scattering and for damage to the foils has been considered. Scattering from a 300 micron fused-silica substrate is expected to be small, increasing an initial beam divergence from 2.5-10 „rad to a little over 20 „rad. The foils have been tested in the beamline without visible signs of damage. As an additional note, the foils are back-coated with an Aluminum substrate and serve a double role as an OTR beam diagnostic as well as Excimer mirrors, taking advantage of their proximity to the oven entrance and exit [3].

In summary, we have developed one-meter long plasma source suitable for experiments to investigate the plasma wakefield excitation of an extended plasma column by a 30 GeV electron beam. The source is designed to provide a plasma density of $10^{14}cm^{-3}$ over dimensions of a few mm^2 by 1 meter. Temperature profiles have been recorded, and the signature of appropriate densities of Lithium vapor has been observed in the temperature profile boundary. In order to provide a Lithium plasma of the required dimensions, the Excimer cavity resonator was reconfigured to solve the problems caused by high mode content. Measurements testing the performance of a demagnifying telescope confirmed that that the Excimer spot could be maintained at 1-2 mm width over extended distances.

4 ACKNOWLEDGMENTS

The authors acknowledge useful conversations with K. Kennedy and the assistance from J. Ayers during the development of the oven and suggestions from Mike Skaggs of Lambda Physik for modification of the Excimer cavity.

5 REFERENCES

[1] R. Assman et al., these Proceedings, WEBL6.

[2] R.G.Hemker et al., these Proceedings, FRA124

[3] P. Catravas et al., these Proceedings, WEA100.

[4] N. Barov et al., Phys. Rev. Lett., 80, 81-4 (1998); *Ibid.*, these Proceedings, WEBL5.

[5] C.R. Vidal and J. Cooper, J. Appl. Phys., 40, 3370-3374 (1969).

[6] G. M. Grover et al., J. Appl. Phys. 35, 1990 (1964)

[7] M. Bacal and W. Reichelt, Rev. Sci. Instrum. 45, 769 (1974).

[8] P. Muggli, these Proceedings, FRA115.

UNDERDENSE PLASMA LENS EXPERIMENT AT THE UCLA NEPTUNE LABORATORY*

H. Suk†, C.E. Clayton, G. Hairapetian‡, C. Joshi, M. Loh, P. Muggli,
R. Narang, C. Pellegrini, J.B. Rosenzweig, UCLA, Los Angeles, CA 90095
T.C. Katsouleas, USC, Los Angeles, CA 90089

Abstract

An underdense plasma-lens experiment is planned at the UCLA Neptune Laboratory. For this experiment, a LaB_6-based discharge plasma source was developed and tested. Test results of the plasma source show that it can provide satisfactory argon plasma parameters for underdense plasma lens experiments, i.e., a density in low 10^{12} cm^{-3} range and a thickness of a few cm. In the plasma chamber a YAG slab and a Cherenkov radiator are placed for electron beam diagnostics so that both time-integrated and time-resolved information will be obtained and compared with the MAGIC code (2 and 1/2 dimensional particle-in-cell) simulations. In this paper, the planned experiment including test results of the plasma source, diagnostics and MAGIC simulation results is presented.

1 INTRODUCTION

The UCLA Neptune beamline was commissioned recently and measurements of basic beam parameters are under way[1]. After initial beam characterizations a series of experiments will be conducted. One of them is the underdense plasma lens experiment, where the beam density is larger than the plasma density. Although some thick plasma lens experiments in underdense and overdense regimes were done before, a thin (in the sense that the plasma thickness is smaller than the focal length) underdense plasma lens has not been explored experimentally yet. Thus, a LaB_6-based plasma source was developed and tested for this experiment at the UCLA Neptune Laboratory. In the ongoing plasma lens experiment, relatively long electron beams will be used so that the head part of the beam is used to produce a nearly uniform ion channel by expelling out the plasma electrons, while the tail part of the beam is focused due to the plasma lens effect of the ion channel.

2 PLANNED EXPERIMENT AND PLASMA SOURCE TEST

The plasma lens experiment will be done in the Neptune Laboratory, which consists of the beamline, drive laser for the photocathode RF gun, RF system, plasma source, etc. Details of each part are shown elsewhere [2, 3] so that only brief descriptions are given here.

2.1 *Neptune Beamline*

The Neptune beamline consists of the new 1.625-cell photocathode RF gun, PWT linac, chicane, focusing and deflection magnets, etc. The photocathode RF gun (f=2.856 GHz) has a copper cathode and it is illuminated by 266-nm UV laser beams for photoelectron generation. In the RF gun, electron beams are accelerated to about 4.5 MeV, and then the beams are injected into the PWT linac with 7 and 2 half cells for further acceleration. In this way, the beams are accelerated up to about 16 MeV.

2.2 *Photocathode Drive Laser*

To generate photoelectrons from the copper cathode of the RF gun, high power UV laser beams are required. As will be shown in Sec. 3, the plasma lens experiment needs electron beams with about 25 ps (FWHM) or longer duration. To generate this kind of relatively long and high power UV laser beams, the 500-m-long optical fiber and the gratings in the present laser system are bypassed [4]. Hence, the photocathode drive laser system for the plasma lens experiment consists of the mode-locked Nd:YAG laser (λ = 1.064 μm, 80 ps FWHM), Nd:glass regenerative amplifier, two BBO crystals for frequency quadrupling, etc. In this way, 266-nm UV beams with 25 to 30 ps duration can be generated.

2.3 *RF System*

The photocathode RF gun and PWT are powered by the same klystron (24 MW SLAC XK-5) and modulator. About 1/3 of the klystron RF power is sent to the gun and about 2/3 of the RF power is fed into the PWT linac. The RF pulse width can be changed in several μs range by the modulator.

2.4 *Underdense Plasma Source*

The plasma source generates argon plasmas resulting from cathode-anode pulse discharges. Figure 1 shows the schematic of the plasma source. It consists of a 7-cm-diameter LaB_6 cathode, tantalum hollow anode, beam-plasma interaction chamber, solenoids for plasma confine-

* Work supported by the U.S. Department of Energy and NSF under contract numbers DE-FG03-92ER40693 and ECS 9617089.

† Email: suk@stout.physics.ucla.edu

‡ Now working at HRL Laboratories

0-7803-5573-3/99/$10.00@1999 IEEE.

ment and guiding, etc. For thermal electron emission the LaB_6 cathode is heated up to over 1300 °C by a 0.1-Ω graphite heater, and a voltage pulse of about 100 V is applied between the cathode and anode for several ms. As a result, a discharge plasma is generated and the plasma is guided to flow towards the beam-plasma interaction chamber with the help of the confining magnetic field. At the entrance of the beam-plasma interaction chamber there is a sliding door to control plasma thickness.

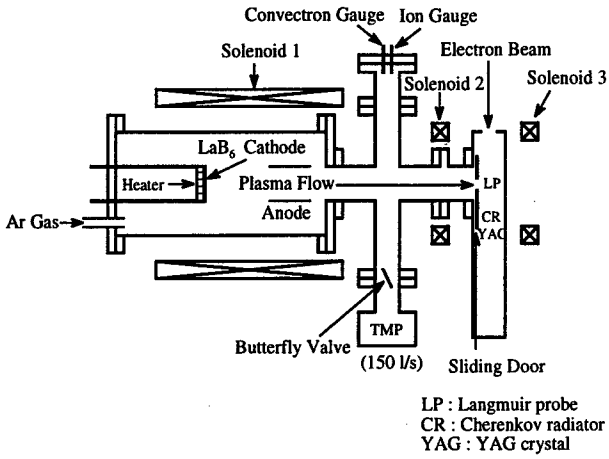

Figure 1: Schematic of the plasma source.

Plasma density in the beam-plasma interaction chamber depends on several parameters such as neutral argon pressure, discharge voltage, magnetic field strength and cathode temperature. To find the optimum condition the parameters were changed one by one and the plasma density was measured in the chamber with a cylindrical Langmuir probe. It turned out that the cathode temperature and magnetic field are two dominant factors. In other words, the plasma density increases significantly when the cathode temperature and magnetic field increases slightly.

Figure 2 shows plasma density profiles measured along the electron beam path for two different conditions. Figure 2(a) was obtained when the sliding door gap was 1.5 cm, while Fig. 2(b) was obtained when the sliding door gap was 1 cm. As expected, Fig. 2(b) profile has a smaller peak plasma density (1.1×10^{12} cm^{-3}) and narrower width (effective width = 2.9 cm) compared to Fig. 2(a).

As shown in Fig. 1, high energy electron beams are designed to propagate in the plasma transversely and the beams will be focused downstream. To take time-integrated beam images resulting from the plasma focusing, an undoped YAG slab with a thickness of 0.5 mm is installed in the beam-plasma interaction chamber. In addition, a Cherenkov radiator is placed in the chamber to obtain time-resolved information of the focused beams. Both the YAG slab and the Cherenkov radiator can be moved longitudinally along the beam path.

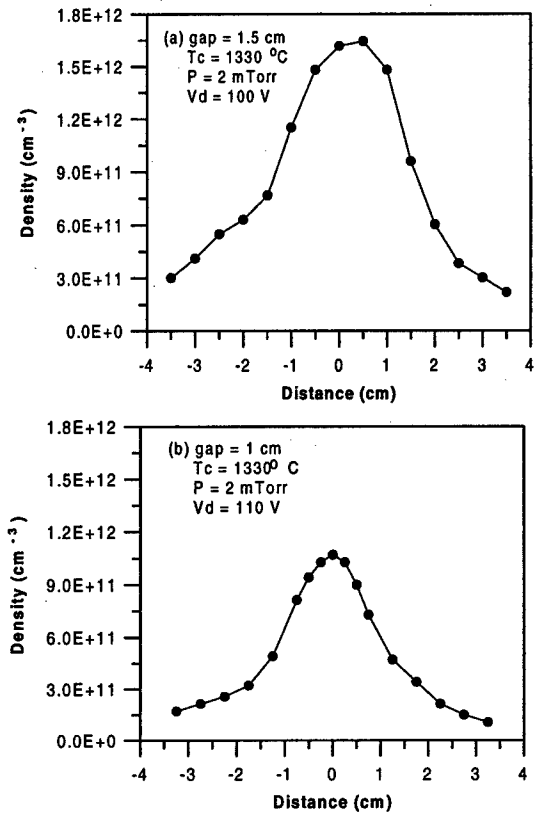

Figure 2: Longitudinal plasma density profiles for two different conditions.

3 PARTICLE-IN-CELL CODE SIMULATION RESULTS

To predict experimental results, computer simulations with a particle-in-cell code (MAGIC) have been performed. For this simulation the beam and plasma parameters in Table 1 were used.

Table 1: Beam and plasma parameters for simulations.

beam energy	16 MeV
charge per bunch	4 nC
beam duration (FWHM)	30 ps
normalized emittance	10 mm-mrad
beam density	2.6×10^{12} cm^{-3}
beam radius at plasma entrance	400 μm
plasma density	1.1×10^{12} cm^{-3}
effective plasma thickness	2.25 cm

Figure 3 shows beam particle trajectories. In this example, the beam density is 2.5 times larger than the plasma density and the beam rise time is also larger than the plasma oscillation time ($1/\omega_p$ = 17 ps) so that the plasma electrons are almost adiabatically expelled from the beam path when the beam propagates in the plasma. Hence, after a couple of plasma oscillations a nearly uniform ion channel

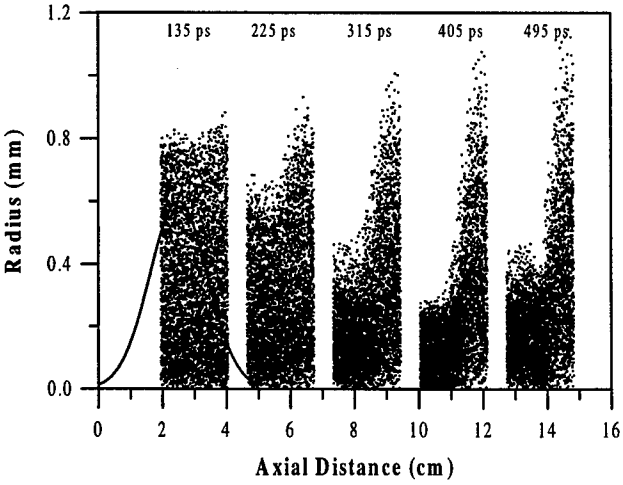

Figure 3: Electron beam trajectory. The solid line shows the plasma density profile with the parameters in Table 1.

is formed and the tail part of the beam is focused by the ion channel. This phenomenon is observed in Fig. 3. As shown in the figure, the head part of the beam is not focused and it continues to expand due to an emittance effect, while the tail part of the beam is tightly focused after about $2/\omega_p$ and then it expands radially. Its focal length is observed to be about 9 cm, which is in good agreement with the impulse focusing approximation [5].

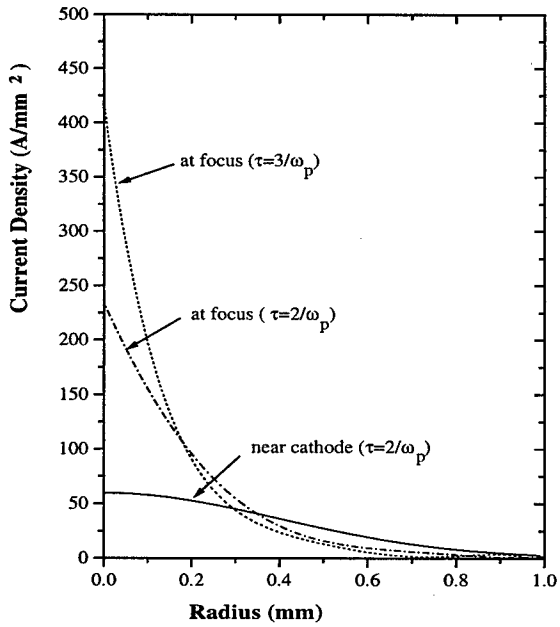

Figure 4: Beam current density profiles near cathode and at focus.

The plasma focusing will change a beam current density profile downstream. This is shown in Fig. 4, where the solid line represents the initial Gaussian density profile near the cathode and the other two dotted lines are profiles at the focus at different instants. It is shown that the beam is radially focused, but its current density profile at the focus is significantly deformed from the initial profile near the cathode. This is related with the highly dynamical process of an ion channel formation in the plasma. To reduce the nonlinear focusing effect the plasma and beam densities can be increased. In this case, the plasma oscillation period is smaller and the ion channel will be formed in a shorter time so that the tail part of the beam will experience a less nonlinear focusing. Then the density profile deformation will be mitigated.

4 PRESENT STATUS AND CONCLUSIONS

Since the test results of the plasma source were reported previously [3], a couple of problems in the plasma source have been improved. For example, some parts of the plasma source were too hot during operation in the past, but this problem was solved by adding an additional cooling structure. In addition, the solenoidal magnetic field for plasma confinement deflects electron beams transversely and this could be a problem for Cherenkov radiator-streak camera measurements. Hence, new solenoids with a smaller diameter and iron shielding were designed and the old solenoids were replaced by the new ones to minimize the beam deflection. Basically the plasma source is ready for experiments. Hence, after the ongoing measurements of basic beam parameters, the plasma source will be assembled with the Neptune beamline for the plasma lens experiment.

5 REFERENCES

[1] S. Aderson et al., "Commissioning of the Neptune Photoinjector", these proceedings.

[2] J.B. Rosenzweig et al., Nucl. Instr. and Meth. A **410**, 437 (1998).

[3] H. Suk et al., "Test Results of the Plasma Source for Underdense Plasma Lens Experiments at the UCLA Neptune laboratory", to appear in Advanced Accelerator Concepts (AIP, New Nork, 1998).

[4] P. Davis, *Plasma Lenses for Relativistic Electron Beams*, Ph. D. Dissertation, Department of Electrical Engineering, UCLA (1996).

[5] J.J. Su et al., Phys. Rev. A **41**, 3321 (1990).

NOVEL SCHEME FOR PROTON AND HEAVY-ION ACCELERATORS

V. V. Gorev

RRC "Kurchatov Institute" and Institute of Physical Ballistics, 123182 Moscow, Russia

1 INTRODUCTION

Proton and heavy ion accelerators of the medial energy are very important in science and technology. First of all in the medicine, in the field of elimination of nuclear waste, for the creation safe subscritical reactors and so on. Their usage will help to cure cancer, to develop safety nuclear energetic, to protect environment and so on. Unfortunately large size of the accelerators that could be about 1 km length and high cost that is about 1 billion and even more gives limitation their wide applications. Right now the society understands the importance of all the problems listed above and we are able to create and develope new solution in the field of these accelerators design.

We have developed a conceptual design for high-gradient linear proton and heavy ion medium energy accelerators, based on the new physical principle.

We are going to discuss only major ideas leaving all the details for the future examine.

2. Accelerator scheme BESTAC (ballistical electrostatical accelerator) has two parts. The main and additional, that are connected in one unit. The main part is responsible for the ion acceleration itself. It has quazispherical shape. The addition part is electron linac for which provides work ability of the main part.

BESTAC operates in impulse regime. The principle of BESTAC performance we can qualitatively explain by dividing the process of the impulse generation into 4 following stages:

1. Vacuum camera ("VC") is made from conductive materials, grounded and put into longitudinal magnetic field. VC has four main and few assisting vacuum windows. The main windows (# 1,2,3,4) are located two perpendicular diameter of the chamber. A small specially shaped and constructed body is injected into VC at the initial moment throughout the window # 1. This body (so called "ballistic anode") freely moves from window # 1 to window # 2 along ballistic trajectory and crosses the central part of VC.

2. Ballistical anode is irradiated by positron beam than it cross the central part of vacuum chamber. We should have such energy current duration and form of the beam impulse to provide accumulation of the positive charge on the ballistical anode, but not the scattering and losses of the positrons on ballistical anode and ballistical anode heating. This is regime exists according to our calculations and is called "change pumping". Quazistatical difference of potential appears between ballistical anode and vacuum chamber wall while ballistical anode moved along ballistic trajectory. The quantity and duration of the potential is determined by competition between the processes of the charge accumulation of positrons and charge losses.

The loss of the charge caused by numerous reasons (cold ion emission from the surface of ballistic anode, cold electron emission from the inner surface of vacuum chamber, photoeffects, electrical break of physical vacuum, generation of electron-positron cascade and so on. The difference of potential between ballistical anode and vacuum chamber could be very high if we can produce sufficient current of positrons, sufficient size of vacuum chamber and sufficiently high vacuum. Current is the most important feature. The potential difference is possible to use for the ions acceleration during the time of its existence.

3. The surface of ballistical anode itself can be the source of the protons and heavy ions, if it is radiated by laser impulse and transformed into plasma. The second way for the protons and heavy ions emission can be the special construction of ballistical anode, when the electric field strength on the small part of ballistical anode surface that is located in front of the window # 2 is enough for cold ion emission. This is very similar to the ion source, based on field evaporation. If our goal is the production of neutral particles we have to put the source of negative ions on the line of windows # 2- # 4 out of vacuum chamber. In this case at first the negative ions are accelerated from the wall of vacuum chamber towards ballistical anode. On ballistical anode they are neutralized and then leave vacuum chamber through the window # 4. They can be transformed into positive ions if the thickness of ballistical anode is large enough and additionally accelerated between ballistical anode and vacuum chamber similar the tandem acceleration scheme.

4. Ballistical anode continues to move uncharged along ballistic trajectory, if the process of ballistical anode

0-7803-5573-3/99/$10.00@1999 IEEE.

charge and discharge occurs during ballistical anode flight time across central part of vacuum chamber. Then it leave vacuum chamber through the window # 3.

It is necessary to repeat all these cycles 1-4 to generate impulse of protons and ions current again.

Addition part of BESTAC is consists of two parts: the accelerator of the positrons (linac) and the source of positrons.

Accelerator shapes the positron beam for the ballistical anode irradiation and charge.

The electric field between ballistical anode and vacuum chamber is the energy source for the ion beam.

This field receives energy from the kinetic energy of the positron beam. We can say that the specially constructed ballistical anode is the transformer of the light positive particles into the heavy ones. Positrons penetrates into ballistical anode substance, and can thermolized and annihilated if their energy is not very high. The part of the electrons disappears and quazineutrality breaks. The major part of electric field is located in the space between ballistical anode and vacuum chamber, and the rest penetrates into ballistical anode substance up to few interatomic distances.

3. The charge pumping regime is not normal for beam-target interaction. As usual the ballistical anode substances is heated and transformed into plasma. In this case it is impossible to have the regime of charge pumping because even cold plasma has practically unlimited emission capability. To realize the maximum charge pumping regime it is necessary to fulfil few conditions.

The major of them are:

1. Ballistical anode has to be positive; In this case the electric field strength on ballistical anode surface can be up to 10^9V/cm and its potential 10^9 r (cm) volts.

2. It is necessary to use the light charged particles because they have the penetration length that is two orders higher than ions have and as a result of the ballistical anode heating will be two orders less.

3. The positrons energy has to grow in time according to the linear law if the beam current is constant ("saw - toothed "voltage). The quantity of electric charge and potential on ballistical anode will have a linear increase also at the constant positrone current. To overcome this potential we should have the linear increase of kinetic energy of the positrones also, according to saw toothlaw and positrones energy should be a little bit higher ($\Delta\varepsilon$) than electrical potential energy of the ballistocal anode surface.

4. The difference between kinetic energy of the particles and the quantity of energetic width $\Delta\varepsilon$ is limited $\Delta\varepsilon$ is determined by the target size, because length of the positrone penertration has to be lower than target size. In this case the positrone penetrates into the substance ballistical anode, thermolized and annihilates approximatly homogeneously in the ballistical anode volume. this reduces the local overheating.

5. Geometrical shape of ballistical anode should provide the maximum cross section of the positrone neglection at the determined value of $\Delta\varepsilon$. We can guarantee almost no loss of positrons through scattering in the the longitudianl magnetic field.

We should have sufficiently high vacuum and large vacuum chamber size to quarantee the regime of charge pumping. The residual gas is going to be tunnel ionized in the vacuum chamber by the strong electric field that leads the electric current formation from vacuum to ballistical anode and ion current formation on the inner surface of vacuum chamber. Definitly this current will be increased with the pressure of residual gas increasee. Gas ionization is going into the sphere with radius equal to few ballistical anode scale during charge pumping.

4. Let us carry out main estimations for the case of 1 GeV proton accelerator by assuming that electrical field strenth is about 5 ·10^8 V/cm, one obtains:

1. Radius of ballistical anode - 2 cm
2. Radius of vacuum chamber - 200 cm
3. Number of positrons ~ 10^15 - 10^16
4. Velocity of ballistical anode - 4 m/sec (min) - 1000 m/sec (max)
5. Linac positron current - (10^-2 - 25) A
6. Saw-tooth low: $\gamma mc^2(Gev) = \frac{t}{\tau} + \Delta\varepsilon$

   τ = 10^-2 (max) - 4.10^-5 (min)
7. $\Delta\varepsilon$ ~ 20 MeV (for light materials),
   ~ 80 MeV (for medial materials)
   ~160 MeV (for heavy materials)
8. $\frac{\Delta\varepsilon}{\gamma mc^2}$ ~ (2-16)%
9. Vacuum ~ 10^(-11-12) torr

5 CONCLUSIONS

We propose new physical principle for the generation of high intensive impulses of electrical fields and for acceleration of protons and ions. The principle involves:

1.Usage of the ballistical anode, as a transformer of charge particles.

2.Usage of the positron beams for the charge pumping of ballistical anode.

3. Usage of the high vacuum and spherical geometry as a high voltage insulator.

4. Usage of the high gradient linac as an energy source for protons and ion beams.

PROTON ACCELERATION IN PLASMA WAVES PRODUCED BY BACKWARD RAMAN SCATTERING

A. Ogata, AdSM, Hiroshima University, Kagamiyama, Higashi-Hiroshima, 739-8526, JAPAN
T. Katsouleas, University of Southern California, Los Angeles, CA 90089-0484 USA

Abstract

This paper proposes a new method of proton acceleration. A slow plasma wave produced by backward Raman scattering captures slow protons injected. A density gradient of a plasma enables the wave phase velocity to increase as the proton test beams are accelerated. A proof-of-principle experiment is proposed using a T^3 laser and test beams from a Van de Graaff accelerator, in which a 500mJ laser will give acceleration gain of $\sim$ 50MeV in a distance of 500μm.

1 INTRODUCTION

This paper proposes a proton acceleration using plasma waves[1], based on the same principle which has successfully accelerated electrons with a large acceleration gradient. It uses the electric field of a plasma wave excited by a laser. The laser is scattered into either forward or backward directions in a plasma. The forward scattering excites a plasma wave whose phase velocity is almost equal to the group velocity of the pump laser. This fast plasma wave has been used in electron acceleration. This method is called self-modulated laser wakefield acceleration, because the laser pulse is modulated at the plasma frequency by the forward instability. To the contrary, the backward scattering excites a slow plasma wave, and it is this slow wave that we are going to use for proton acceleration.

Relativistic electrons have light velocity, so they can be synchronous with the relativistic plasma wave whatever energy they have. Protons below 1GeV, however, increases their velocity as they are accelerated. The technical difficulty of the proton acceleration using a plasma wave is to give it increasing phase velocity synchronous with the accelerated proton velocity. In this proposal, the synchronization is enabled by the density distribution of the plasma.

This paper consists of five sections. Following this introductory section, the second section describes the phase velocity of the plasma wave that can trap the protons. The third section briefly describes backward Raman scattering. The fourth section proposes acceleration in a plasma with tapered density, in which the phase velocity of the plasma wave increases as the test beam is accelerated. A proof-of-principle experiment is also proposed. The last section gives discussion and conclusions.

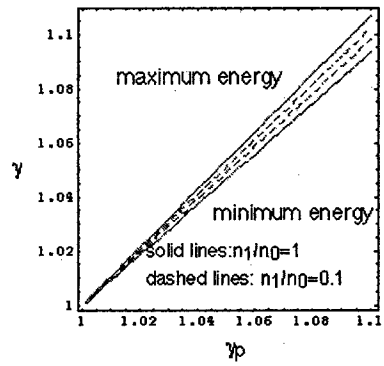

Figure 1: Maximum and minimum proton energies that can be trapped by a plasma wave with γ_p. Solid lines: $n_1/n_0 = 1$, broken lines: $n_1/n_0 = 0.1$.

2 TRAPPING OF PROTONS IN A PLASMA WAVE

The motion of protons in a plasma wave is described by a pair of equations:

$$\begin{aligned} d\gamma/dz &= -(eE/m_pc^2)\sin\phi, \\ d\phi/dz &= k_p(1/\beta_p - 1/\beta), \end{aligned} \tag{1}$$

where E is the field of the plasma wave, m_p is the proton mass, β and γ are those of the protons and β_p is that of the plasma wave. They mean that the wave phase velocity β_p should be equal to the particle velocity β, otherwise the energy gain cannot be constant.

However, the protons can remain to be trapped by the wave even if the condition $\beta_p = \beta$ is not strictly satisfied, as far as $\sin\phi < 0$ in eq. (1). This condition of trapping is equivalent to that the kinetic energy of protons is smaller than the wave potential Φ[2]. We use prime symbols to denote variables in the wave frame. The condition then becomes

$$(\gamma' - 1)m_pc^2 \le e\Phi', \tag{2}$$

so the boundary energy of the protons that can be trapped is $\gamma' m_pc^2 = e\Phi' + m_pc^2$. In the laboratory frame we have two boundary energies,

$$\gamma_\pm = \gamma_p\gamma'(1 \pm \beta_p\beta'). \tag{3}$$

Using $eE = ek_p'\Phi' = ek_p\Phi$ and $eE = (n_1/n_0)m_e\omega_p v_p$, we have $\gamma' = (n_1/n_0)(m_e/m_p)\gamma_p\beta_p^2 + 1$, where n_1 is the electron density in the wave and n_0 is the background

0-7803-5573-3/99/$10.00@1999 IEEE.

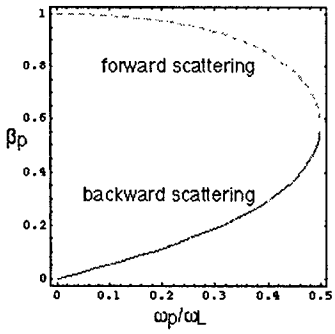

Figure 2: Dependence of phase velocity of the plasma wave produced in the Raman scattering on ω_p/ω_L.

electron density. Inserting this into eq.(3), we have the relation between γ and γ_p, which is depicted in Fig.1. This figure gives the energy range of protons that are trapped by a plasma wave at specific γ_p. This width is $\sim \pm 7\%$ at $\gamma_p = 1.1$ and $n_1/n_0 = 1$, and decreases as γ_p and $n_1/n_0 = 1$ decrease. We have to tune the phase velocity of the plasma wave within this range in order to perform the successful acceleration.

3 BACKWARD RAMAN SCATTERING

In the forward Raman scattering, both the plasma wave (denoted by suffix 'p' hereafter) and the scattered radiation with suffix 'F' propagate in the same direction as the pump radiation (denoted by suffix 'L'). In the backward scattering, the scattered radiation with suffix 'B' propagates in the opposite direction, though the plasma wave has the same direction as the pump radiation. The dispersion relations of the electromagnetic waves in a cold plasma are given by $\omega_x^2 = \omega_p^2 + c^2 k_x^2$, where $x = L, F$ or B. The conditions for resonance are $\omega_L = \omega_p + \omega_x$, $k_L = k_p + k_F$, and $k_L = k_p - k_B$, where $x = F$ or B. They give the phase velocity of the plasma wave $v_p = c\beta_p$, where

$$\beta_p = \frac{\omega_p}{\omega_L} \frac{1}{\sqrt{1-(\omega_p/\omega_L)^2} \mp \sqrt{1-(2\omega_p/\omega_L)}}, \quad (4)$$

with - and + signs corresponding to forward and backward scatterings, respectively. It is shown in Fig.2 as a function of ω_p/ω_L. As is clear in the figure, the phase velocity of the plasma wave produced by the backward scattering is the increasing function of the plasma density. The phase velocity curves of the forward and backward scattering-produced plasmas merge at the point where $\omega_L = 2\omega_p$, at which $\beta_p = 1/\sqrt{3}$.

The backward Raman scattering had been studied vigorously in the 1970's in connection with laser fusion. We summarize here the main features obtained then [3].

Growth rate of the backward Raman scattering is given by $\gamma = (v_q/c)^2(\omega_L\omega_p)^{1/2}$. Landau damping suppresses this scattering, unless [3]

$$\omega_p/\omega_L > 2v_{th}/c, \quad (5)$$

where $v_{th} = (k_B T_e/m_e)^{1/2}$. This requirement is most difficult to fulfill at beam injection. Approximating $k_p = 2k_L$ and $\omega_L = ck_L$, we have $\omega_p/\omega_L = 2\beta_p$. The β value of the injected protons should be equal to the β_p value of the plasma wave. The condition of eq.(5) then becomes $\beta > v_{th}/c$. This restriction limits the lowest-possible injection energy. Electron temperatures 10eV, 100eV, 1keV ... requires the injection β of 0.006, 0.02, 0.06,..., respectively.

The plasma wave decay can be slower than the growth of the backward instability. However, once the pump laser fades out, the plasma wave decays so quickly because of the Landau damping that we cannot expect a short laser pulse to leave a wake which survives until a slow proton beam arrives. In other words, the laser pulsewidth has to be longer than the acceleration time. This situation differs from the case of electron acceleration where "wakefield acceleration" is possible.

The electric field associated with a fast plasma wave is approximately $eE = (n_1/n_0)m_e\omega_p c$. This cannot be applied to our case of a slow plasma wave. We have instead

$$eE = (n_1/n_0)m_e\omega_p v_p. \quad (6)$$

The Manley-Rowe relation gives the maximum-possible n_1/n_0 value as a function of the electron quiver velocity v_q in the laser field[4]:

$$(n_1/n_0)^2 \sim (\omega_L/\omega_p)(2v_q^2/\gamma v_{th}^2), \quad (7)$$

where γ is the specific heat ratio. In one-dimensional model we have $\gamma = 3$.

In this proposal, we use a plasma with tapered density. In such an inhomogeneous plasma, the resonant condition can hold only locally. The propagation of the plasma wave out of this resonant region then provides an additional threshold, which is [3],

$$(v_q/c)^2 k_L L > 1, \quad (2\omega_p < \omega_L), \quad (8)$$

where $L = [(1/n)(dn/ds)]^{-1}$ is a length characterizing the density gradient, with s, the distance along the density gradient.

The laser-driven instability growth has to balance the plasma wave decay. It remains an open question whether such a balance is achievable. One solution to control this instability is the use of a second laser which acts as a seed for the instability[1]. This seed laser should be frequency-shifted by ω_p from the pump laser and injected from the counter direction of the pump laser. In other words, the seed laser should have the same frequency and direction of the backscattered radiation. This is a beatwave acceleration in which the beat frequency of pump and seed lasers is equal to the plasma frequency.

4 TAPERED DENSITY METHOD AND PROOF-OF-PRINCIPLE EXPERIMENT

We now try to carry out a simple calculation, with a proof-of-principle experiment in mind. We assume to

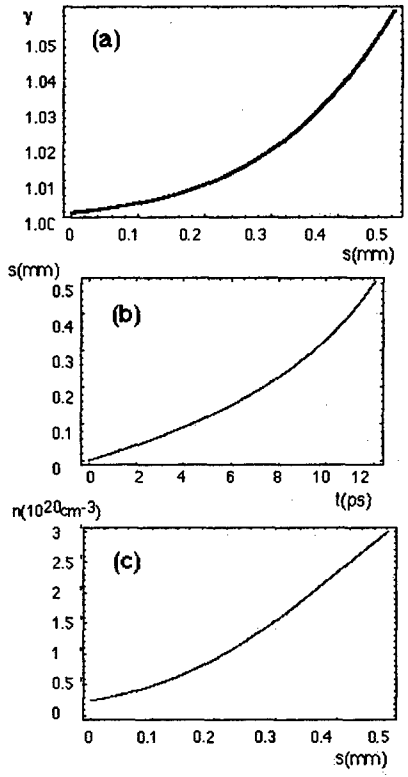

Figure 3: Results of the calculation. (a) beam energy (γ) vs. distance, (b) propagation distance vs time, (c) required plasma density vs distance.

use 2.5MeV proton beams ($\beta = 0.078$, $\gamma = 1.00267$) from a Van de Graaff of Hiroshima University, and a Ti:sapphire laser with λ_L =800nm. We set the final energy as 50MeV ($\beta = 0.314$, $\gamma = 1.0533$). We assume $n_1/n_0 = 1/2$ to have the acceleration gradient as $eE(s) = m_e c\beta_p(s)\omega_p(s)/2$. A more realistic n_1/n_0 value should be determined by PIC simulations.

The calculation is based on eq.(1): The second equation is used to derive the β_p which makes $d\phi/dt = 0$ for given β by the first equation. The plasma density to give this β_p is the solution of eq.(4).

Figure 3 shows results of the calculation. Figure 3 (a) and (b) show that the energy gain of ~50MeV is attained in the acceleration time of $\sim$ 12ps and acceleration distance of $\sim$ 0.5mm. Figure 3 (c) shows that the plasma density has to be tapered from $\sim 2.5 \times 10^{19}\mathrm{cm}^{-3}$ to $\sim 3 \times 10^{20}\mathrm{cm}^{-3}$. Figure 3 (d) shows tha the density-gradient length defined by eq. (8) was larger than 150μm.

The v_q/c value required by eq. (8) is $\sim$ 0.03, or laser intensity $I = 3.90 \times 10^{15}\mathrm{W} \cdot \mathrm{cm}^{-2}$. If we assume the waist size as 15μm, the laser power becomes 27.5GW. The laser pulse width of 15ps requires the laser energy of 413mJ. This laser intensity makes the tunneling ionization possible. Equation 7 tells that the n_1/n_0 value slightly exceeds unity in this laser intensity, though it does not take the spatial inhomogeneity into account.

5 DISCUSSION

There of course exist some problems to be solved in this method. First of all good simulation studies are necessary, which checks the phase continuity of the plasma wave in the density gradient, and estimates exact value of acceleration gradient and its time evolution.

The major technical problem is the creation of the plasma density gradient. A gas flow flux from an orifice limited by a skimmer has the radial distribution similar to that in Fig. 3(c)[5]. Further studies are necessary to apply this method to our experiment. Development of the chirped seed laser may become necessary to control the instability. Even if each technique were independently established, there would remain the problem of synchronization among the acceleration gradient, the plasma-density gradient and the laser-frequency chirping. Some good diagnostics and feedback control are essential to perform the experiment.

In conclusion, a method is proposed to accelerate protons by a slow plasma wave produced in the backward Raman scattering. It adjusts the plasma density to match the phase velocity of the plasma wave to the velocity of the protons accelerated. Energy of a commercially-available laser is large enough to excite such a plasma wave. Physical and technical problems are remain to be studied, which include Raman instability studies and realization of a tapered plasma.

One of the author (A.O.) is grateful to Dr. T. Ishida of Nagoya University for useful discussions on gas dynamics of a gas jet. The present work is supported by the JAERI's Nuclear Research Promotion Program.

6 REFERENCES

[1] A. Ogata and T. Katsouleas, Proc. *1998 Workshop on Advanced Accelerator Concepts*, to be published, and references therein.

[2] T. Katsouleas et al., *AIP Conf. Proc*, **vol.6**, 63 (1985); N. A. Ebrahim and S. R. Douglas, *Laser and Part. Beams*, **13**, 147 (1995).

[3] *Advances in Plasma Physics*, **vol.6**, P. K. Kaw et al., ed., John Wiley and Sons, New York (1976).

[4] J. M. Manley and H. E. Rowe, *Proc. IRE*, **44**, 904 (1956); D. W. Forslund, J. M. Kindel and E. L. Lindman, *Phys. Fluids*,**18**, 1002 (1975)

[5] J. B. Anderson, in *Molecular Beams and Low Density Gas Dynamics*, P.Wegener, ed., Marcel Decker, Ink., New York (1974), p5.

PONDERMOTIVE ACCELERATION OF IONS BY RELATIVISTICALLY SELF-FOCUSED HIGH-INTENSITY SHORT PULSE LASER *

A. Maksimchuk†, S. Gu, K. Flippo, S.-Y. Chen and D. Umstadter ‡,
G. S. Sarkisov§, V. Yu. Bychenkov, V. N. Novikov and V. T. Tichonchuk ¶

Abstract

We report on the observation of high energy ions with energies up to 1 MeV accelerated pondermotively by a relativistically self-focused intense 5 TW, 400 fs laser pulse in a supersonic He gas jet on the distance of a laser spot size. Probing interferometry was used to observe on-axis electron-ion cavitation followed by the plasma expansion with a high radial velocity of $\sim 3.8 \cdot 10^8$ cm/s. Using the nuclear track detector CR-39, we confirmed that the ions are preferentially accelerated in the radial direction and the total energy in high energy ions is about 1% of the laser energy. Developed kinetic modeling provides a reasonable description of a plasma channel formation and ion acceleration.

1 INTRODUCTION

An interaction of ultra-high intensity short laser pulses with underdense plasma is of considerable interest from the standpoint of basic physics and potential application for advanced inertial confinement fusion, x-ray lasers and particle accelerators [1, 2, 3]. The ultra-high electromagnetic fields in the laser focus produce an extremely high pondermotive force that expels free electrons from the laser axis and relativistically modifies the electron mass, plasma frequency and the plasma refractive index so that the plasma acts as a positive lens that further increases the focused intensity . If the laser pulse duration is long enough, the charge separation produces strong electrostatic fields $\sim$ 1 GV/cm which can accelerate ions to MeV energies.

2 EXPERIMENTAL SETUP

The experiment has been performed using the 10 TW Ti:sapphire-Nd:glass CPA laser system at the Center for Ultrafast Optical Science, University of Michigan. The laser operates at the wavelength $\lambda_0 = 1.053\,\mu$m, and produces pulses with the energy up to 4 J in 400 fs (FWHM) with an intensity contrast ratio $\sim 10^5 : 1$. The 50 mm diameter laser beam was focused with an off-axis parabolic mirror ($f/3.3$, $f = 16.5$ cm) to a 10 μm spot with a vacuum intensity of $6 \cdot 10^{18}$ W/cm^2. The radial distribution of laser intensity demonstrates also $\sim 50\ \mu$m in diameter wings that contain approximately 10% of laser energy. The laser beam was focused in a high backing pressure ($\sim$ 7 MPa) He gas jet expanding through a 1 mm diameter nozzle. The optimal conditions for beam guiding correspond to the laser focusing on the jet edge at a distance $x = 0.5 - 0.75$ mm from the nozzle, where the He atom density is $\sim 4 \cdot 10^{19}$ cm^{-3}.

The probe beam with wavelength $\lambda = 1.053\,\mu$m was obtained by splitting $\sim$ 5% of the pump pulse, propagated through an adjustable motorized optical delay, and probed the plasma in the direction perpendicular to the interaction beam. The plasma was imaged by spherical lens with the angular aperture 7° on two 12-bit CCD cameras to produce shadowgram and interferogram. The spatial and temporal resolution was 10 μm and 400 fs, respectively. The air-wedge shearing interferometer has been used for the electron density measurements. To measure ion angular distribution we placed around the gas jet at the distance $\sim$ 16 cm 11 slits with a width $\sim 100\ \mu$m and $\sim$ 10 degrees apart from each other. We positioned nuclear track detectors CR-39 behind the slits at a distance $\sim$ 16 cm. Analysis of ion energy distribution was done by measurements of an individual track size in CR-39 after an etching procedure.

3 RESULTS AND DISCUSSION

We followed the plasma evolution for the time period from -2 to $+55$ ps. We observed a fast gas ionization in the cone angle ($\sim$ 17°) of the laser $\sim$ 2 ps before the pump pulse arrival. The laser intensity in the temporal foot and in the spatial wings of the pulse was above 10^{15} W/cm^2, that was sufficient for the tunneling ionization of He atoms.The transverse size of the formed plasma was about 100 μm in diameter. When the laser power exceeds a critical power $P_c = 17 n_c/n_e$ GW (where n_c is the critical density for the interaction laser pulse) self-focusing and self-channeling can occur as a result of two effects: (i) the relativistic increase of electron mass in the laser field and (ii) the reduction of the electron density on axis due to the expulsion of the electrons by the laser pondermotive force. We observed the first signature of plasma channel formation at $t = 0$ ps. The change in sign of the phase shift derivative in a narrow axial region in the interferogram indicates the decrease of the phase shift and hence the decrease of on-axis electron density Fig. 1.

The two-dimensional reconstruction of the electron density profile has been performed using the Abel inversion procedure with an assumption of the axial symmetry of a

* We acknowledge the support of the Division of High Energy Physics, Office of Energy Research, U. S. Department of Energy, the National Science Foundation and Russian Foundation for Basic Research.

† Email: tolya@umich.edu

‡ Center for Ultrafast Optical Science, University of Michigan, Ann Arbor, MI 48109.

§ Current address Department of Physics, University of Nevada, Reno, NV 89557.

¶ P. N. Lebedev Physics Institute, Russian Academy of Sciences, Moscow.

0-7803-5573-3/99/$10.00@1999 IEEE.

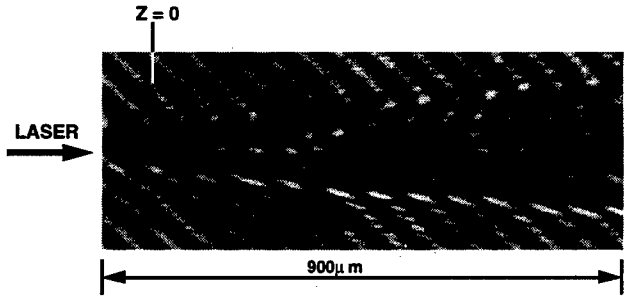

Figure 1: Interferogram taken at time t=5 ps, showing on-axis electron cavitation. Plane $z = 0$ indicates the position of focal plane in vacuum.

plasma and attributing all changes of the refraction index μ to free electrons. The inferred electron density profile for time moment $t = 35$ ps is presented in Fig. 2. The maximum electron density is $\sim 7.6 \cdot 10^{19}$ cm^{-3} at a radius of ~ 20 μm and the estimated depth of the plasma channel is up to $80 - 90\%$. The radius of the plasma channel is less than 10 μm.

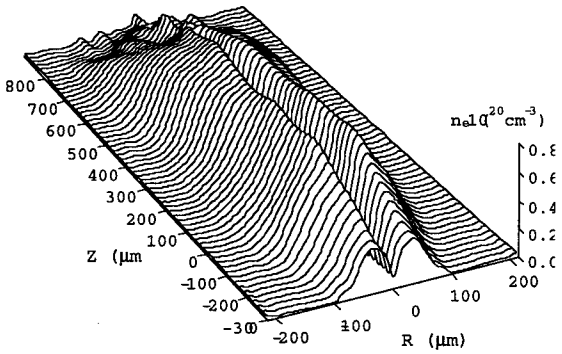

Figure 2: Spatial electron density distribution for time moment of t=35 ps.

We also observed fast ambient gas ionization in the radial direction for probe time delays greater than 10 ps. If we define the plasma edge as a region where the electron density is equal to $5 \cdot 10^{18}$ cm^{-3}, then from $R - t$ diagram of plasma expansion, presented at Fig. 3 one can find, that the radial expansion velocity is equal to $\sim 3.8 \cdot 10^8$ cm/s. Plasma regions with a higher degree of ionization, $1.5 \cdot 10^{19}$ cm^{-3} expand with velocity $\sim 2.5 \cdot 10^8$ cm/s. The channel diameter has even slower velocity $\sim 4 \cdot 10^7$ cm/s.

We attributed an ambient gas ionization to the propagation of fast Helium ions. These ions are accelerated by the electrostatic field of charge separation produced in a plasma when the electrons are expelled from the laser beam channel due to the radial component of the ponderomotive force and have an energy of more than 300 keV. The mean free path of such ions in a normal pressure gas is few millimeters, and they penetrate through a gas as a projectiles, experiencing only small angle elastic scattering and loosing their energy to the neutral atoms via excitation and ionization. The velocity of such fast ions is comparable to the velocities of bound electrons in the Helium atom, and therefore ions efficiently ionize the ambient gas. Their ionization cross-section is about $3 \cdot 10^{-16}$ cm^2 [4], and, therefore, each ion produces approximately one electron-ion pair on a 1 μm path in the Helium gas with a density of $\sim 4 \cdot 10^{19}$ cm^{-3}.

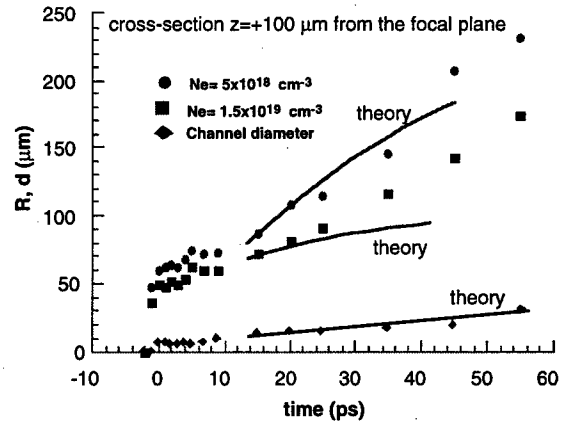

Figure 3: Evolution of the plasma radius for the cross-section $z = 100$ μm. Experimental points show the positions of electron densities $5 \cdot 10^{18}$ cm^{-3} and $1.5 \cdot 10^{19}$ cm^{-3}, and the evolution of the plasma channel diameter. The theoretical curves have been obtained from the developed kinetic model.

To formulate quantitatively the physical model of plasma channel formation we supplement the quasistationary description of the relativistic electrons by the kinetic description of the cold collisionless nonrelativistic ions with the mass m_i and charge Ze. Assuming that ions move only in radial direction, the kinetic equation for the ion distribution function, f_i, reads:

$$\frac{\partial f_i}{\partial t} + v_i \frac{\partial f_i}{\partial r} + \frac{Z}{m_i} F_p \frac{\partial f_i}{\partial v_i} = 0 . \qquad (1)$$

The last term in the left hand side accounts for the ion acceleration due to the electric field produced by the ponderomotive force:

$$\mathbf{F}_p = -m_e c^2 \nabla \sqrt{1 + a^2/2} , \qquad (2)$$

where $a = 0.85 \cdot 10^{-9} \lambda_0[\mu\text{m}] \sqrt{I\,[\text{W/cm}^2]}$ is the normalized slowly varying vector-potential of the laser field and I is the laser pulse intensity. Equation (1) has been solved numerically by the particle-in-cell method. The radial velocity of the ions after the laser pulse ends reads:

$$v_i = -\frac{Z m_e}{m_i} c^2 \frac{\partial}{\partial r} \int dt \sqrt{1 + a^2/2} . \qquad (3)$$

This formula predicts the ion energy spectrum $0 < \epsilon_i \leq \epsilon_{max}$ with the energy cutoff

$$\epsilon_{max} \sim \frac{Z^2 m_e^2 c^4}{16 m_i r_0^2} \frac{a_0^4 \tau^2}{1 + a_0^2/2} \approx 3 \frac{Z^2}{A} \frac{\tau^2}{r_0^2} \frac{a_0^4}{1 + a_0^2/2} \text{MeV} , \qquad (4)$$

where $a_0 \approx 3.6\sqrt{E_0/\tau}\,\lambda_0/r_0$ is the maximum vector-potential of the interaction laser pulse and A is the ion mass number. Here E_0 is measured in Joules, τ in ps, λ_0 and r_0 in microns. According to this formula, in the relativistic limit, $a_0 \geq 1$, the ion energy is approximately proportional to the pulse energy and pulse length, and inversely proportional to the fourth power of the laser beam radius. This high power radius dependence can be used to resolve an inverse problem: to estimate the laser channel radius knowing the ion energy.

The laser channel radius, r_0 has been varied in order to fit the observed rate of secondary plasma production, dN_e/dt, and the velocity of plasma expansion with a given electron density (see Fig. 3). We found also an importance of the He-gas excitation which can contribute as much as 50% to the observed interferometrically change in the plasma refraction index. The comparison of axial velocities of plasma expansion calculated from the model with the measured experimentally allows to deduce an axial dependence of the laser channel radius, $r_0(z)$. Knowing the laser energy in a given cross-section, one finds also the on-axis laser intensity, $I_0(z)$. In this simulation we assume an exponential decrease of E_0 with z that corresponds to 60% laser energy loss on 1 mm length and was measured in other experiment [5]. The results of this reconstruction of the laser channel characteristics in a plasma are shown in Fig. 4. One can see two regions of laser channel compression at $z = 100$ and 600 μm. We infer that the maximum value of laser intensity in the plasma channel exceeds the vacuum intensity by almost 3 times.

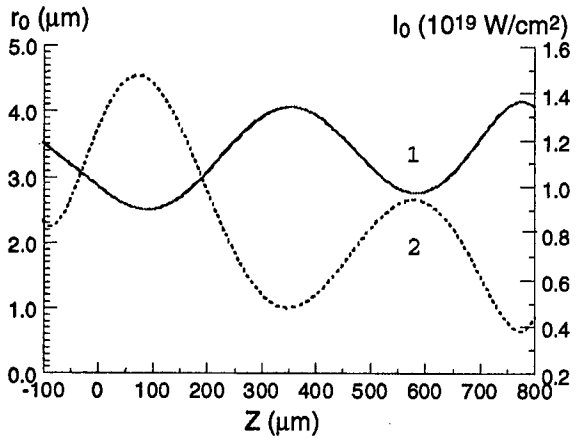

Figure 4: Axial dependence of the laser channel radius (curve 1, solid line) and on-axis laser intensity (curve 2, dashed line) for parameters of the experiment.

Knowing the axial dependence of the laser energy, $E_0(z)$, and the laser channel radius, $r_0(z)$, we can find the axial characteristics of fast ion generation. In Fig. 5a we show the total number of fast ions, with energies above the given energy, ϵ_i, integrated over the laser channel length: $N_{total} = \int dz \int_{\epsilon_i}^{\epsilon_{max}} d\epsilon\, N_i(\epsilon, z)$. We found that the total number of the fast ions with the energy higher than 100 keV is $\sim 10^{12}$ and with the energy higher than 300 keV is $\sim 3 \cdot 10^{11}$. This results were confirmed by the direct observation of high energy ions with the nuclear track detector CR-39. We also found when studying the angular distribution of the emitted ions that they are accelerated preferentially in the direction perpendicular to the channel axis. The FWHM of the ion angular distribution (see Fig. 5b) is $\sim$ 20 degrees which is close to the cone angle of the focused beam. We didn't observed any accelerated ions in a forward direction because of much smaller pondermotive force in this direction.

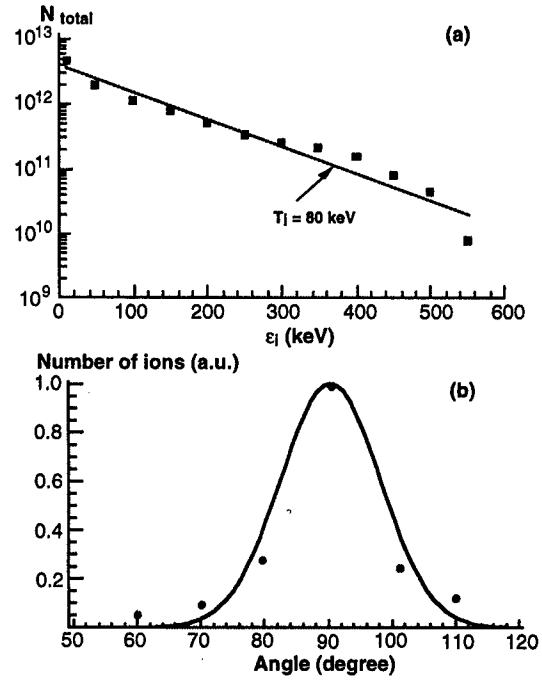

Figure 5: (a) Total number of fast ions with energies exceeded ϵ_i integrated over the laser channel length for parameters of the experiment. Solid line is the Maxwellian function with the temperature of 80 keV. (b) Normalized angular distribution of fast ions emitted from the channel. Solid line is a Gaussian fit to the data.

An estimated total energy in fast ions can be as high as one percent of the laser energy. In spite of predicted by the theory a sharp energy cut-off at about 500 keV we observed α-particles with the energy up to 1 MeV. This result can be explained by the influence of electron pressure due to high-temperature plasma heating which has not been taken into consideration in a theoretical modeling.

4 REFERENCES

[1] M. Tabak *et. al.*, Phys. Plasmas **1**, 1626 (1994).

[2] J. Dunn *et. al.*, Phys. Rev. Lett. **80**, 2825 (1998).

[3] D. Umstadter *et. al.*, Science **273**, 472 (1996).

[4] M. E. Rudd *et. al.*, Phys. Rev. A **32**, 2128 (1985).

[5] S.-Y. Chen *et al.*, Phys. Rev. Lett. **80**, 2910 (1998).

EXPERIMENTAL STUDY OF AN ION CYCLOTRON RESONANCE ACCELERATOR

C.T. Ramsell, T.L. Grimm, and R.C. York
National Superconducting Cyclotron Laboratory
Michigan State University
East Lansing, MI 48824

Abstract

The Ion Cyclotron Resonance Accelerator (ICRA) uses a novel geometry which combines the radial confinement and azimuthal acceleration of cyclotrons together with the axial drift used in gyrotrons. Use of a common NbTi superconducting solenoid and an rf driven magnetron structure lead to a simple, lightweight, and compact machine that could be designed for portability. An ICRA designed to accelerate protons to 10 MeV would be ideal for production of PET isotopes or as an accelerator based neutron source. As a demonstration of the concept, an ICRA has been built that accelerates a proton beam to 50 keV. This paper presents the 50 keV design and gives experimental results.

1 INTRODUCTION

The Ion Cyclotron Resonance Accelerator (ICRA), should provide beam suitable for the production of radioisotopes for positron emission tomography (PET) or neutrons for material research at a fraction of the cost of the cyclotrons or linacs presently used for these applications.

In a cyclotron, the magnetic field confines ions radially and focuses them axially, while the beam is accelerated in the azimuthal direction. In a gyrotron a dc electron beam is radially confined around magnetic field lines but is allowed to drift axially while the energy of the beam is converted into microwaves within a resonant structure. The ICRA is similar to the cyclotron in that ions orbit around magnetic field lines while being accelerated azimuthally. However, the beam is allowed to drift axially, as in a gyrotron. The ICRA differs from the cyclotron primarily in this lack of axial focusing and in the type of rf accelerating structure.

Jory and Trivelpiece demonstrated electron cyclotron resonance acceleration in 1968 [1]. However, until now, this method of acceleration has not been demonstrated for ions. The ICRA extends cyclotron resonance acceleration to ions by using a high field superconducting solenoid together with an rf driven magnetron structure operating at a harmonic of the cyclotron frequency. The resulting high rf frequency together with the fact that the magnetron structure is basically a lumped circuit means that the accelerating structure can be small enough to fit into a solenoid of reasonable diameter [2].

Unlike many accelerators, the beam produced in an ICRA will have a full energy spread ranging from the injected energy to the peak accelerated energy (E_{design}). However, for the applications discussed here a mono-energetic beam is not required, in fact generally all energies above $\frac{1}{2}E_{design}$ will be useful for these applications.

Beam extraction in the ICRA is inherently simple since all beam drifts axially through the solenoid to the target position where it can be isolated from the accelerator mitigating maintenance and radiation shielding issues. Because the compact, superconducting solenoid does not require any steel, the ICRA could be light (<2 tons) and hence portable, making it possible for the radioisotope or neutron source to be shared by several institutions or used in the field.

The main components of an ICRA, shown in figure 1, are the superconducting magnet, ion source, electrostatic bend, accelerating structure, and the target. The ion beam is extracted from the source directly along a field line so that the $\vec{v} \times \vec{B}$ force on the beam is zero. At the electrostatic bend, the dc beam is deflected (into the page in figure 1) so that its momentum perpendicular to the B-field ($p_\perp$) causes ions of charge q to orbit around field lines at radius $r = p_\perp/qB$. The remaining parallel momentum ($p_\parallel$) causes the beam to spiral axially into the high field region. At the acceleration region the B-field is relatively flat and the beam drifts axially through the magnetron structure. While inside the magnetron, the beam is accelerated by rf electric fields which are transverse to the axial B-field. Upon exit from the magnetron, the beam spirals into the lower field of the extraction region until striking a target downstream [3].

Our initial design for a 10 MeV proton model would use an 8 Tesla superconducting magnet and a 488 MHz magnetron. A computer code developed for modeling the ICRA uses many single particle trajectories to model the beam phase space. Modeling of the 10 MeV design predicted that a 2 mA injected beam of 2π mm mrad (unnormalized), would produce 13 μA of beam accelerated to an energy range of 5 to 10 MeV [3]. This current level would be useful for PET isotope or neutron production.

0-7803-5573-3/99/$10.00@1999 IEEE.

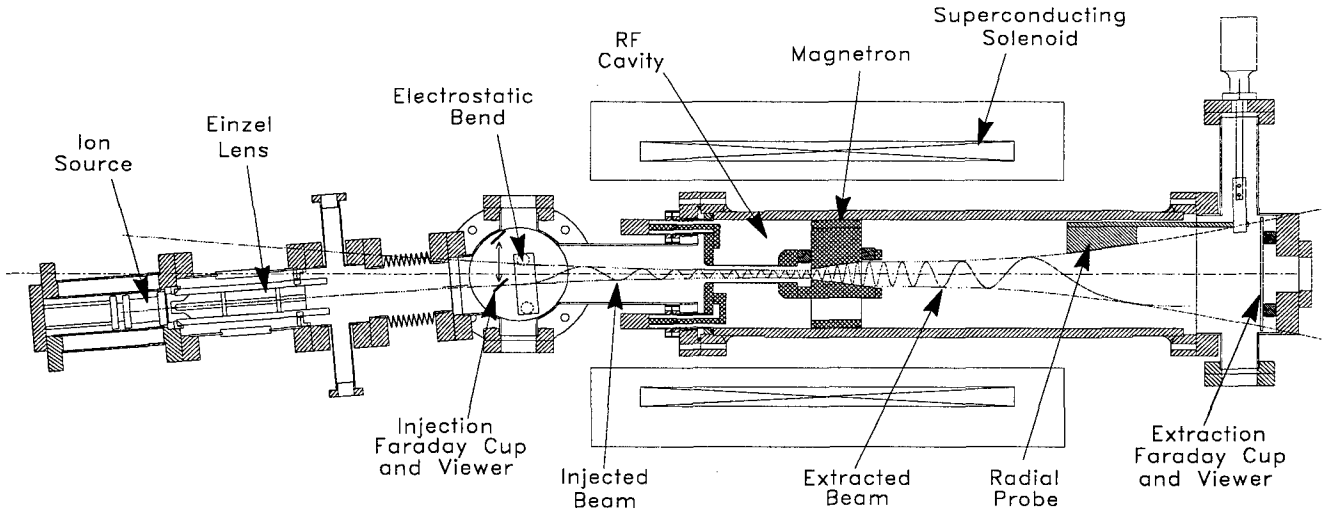

Figure 1: Cutaway view of the 50 keV ICRA experiment

In order to demonstrate the ICRA and benchmark the computer code in a relatively short time and with limited funds, a low energy 50 keV proton ICRA has been designed, built, and tested. The design and experimental results of this proof-of-principle device are presented in the following sections.

2 DESIGN

2.1 Superconducting Magnet

The superconducting solenoid provides a 2.5 Tesla magnetic field in a 20.3 cm warm bore. At this field, the cyclotron frequency for protons is 38 MHz. The resonance requirement over the acceleration region (for about 10 turns), leads to a field flatness criterion of $\Delta B/B_o<0.5\%$. The solenoid used has a field flatness suitable for an acceleration region of 5 cm in axial length.

2.2 Ion Source and Injection

The ion source is a simple electron filament source with a 0.51 mm aperture. H_2 gas is fed into the source along with Argon as a support gas. A 6.4 keV dc beam is extracted along a field line. An Einzel lens provides a wide range of focusing before the beam enters the electrostatic bend. The electrostatic bend consists of two copper plates with an axial length of 2 cm and a gap of 0.8 cm.

2.3 Accelerating Cavity

A classic magnetron structure operating at the 4th harmonic ($\omega_{rf} = 4\omega_c$) would not fit into the 20.3 cm warm bore of the 2.5 Tesla superconducting magnet. The solution was to build a hybrid quarter wave / magnetron cavity. This allowed the inductive component of the resonant structure to be extended in the axial direction rather than radially as in a pure magnetron. The result is a shortened $\lambda/4$ coaxial cavity with magnetron vanes mounted across its open end [4]. Our design operates at the 4th harmonic, thus there are a total of 2n=8 vanes. Of the 8 vanes, every other vane is electrically connected to the outer conductor of the $\lambda/4$ cavity, and the remaining 4 vanes are connected to the inner conductor and interleaved between the first 4 vanes.

The finished rf cavity operates at 152 MHz and generates a gap voltage of 3 kV at 100 watts input power. The inner diameter of the magnetron is tapered for improved acceleration as the beam radius increases. The acceleration region has an entrance diameter of 1.1 cm, an exit diameter of 2.5 cm, and an axial length of 5 cm.

2.4 Beam Diagnostics

The 50 keV ICRA is equipped with three diagnostics for measuring the beam. On the injection side, a Faraday cup with phosphor coating can be moved into the beam at a point immediately upstream from the electrostatic bend. This Faraday cup is used for aligning the ion source on a magnetic field line and for measuring the total injected beam current.

On the extraction end there are two beam diagnostics. The first is a Faraday cup mounted on a motion feedthrough that can be moved radially to intercept the beam. This radial probe is used to measure the beam radius and to obtain the current vs. energy distribution of the accelerated beam. The radial probe has an electron blocker mounted on the upstream edge which prevents secondary electrons from the cavity from reaching the radial probe. The second beam diagnostic on the extraction end is a large Faraday cup with phosphor coating and a glass viewport so that the image of the accelerated and unaccelerated beams can be viewed.

3 EXPERIMENTAL RESULTS

The ion source produces H^+, H_2^+ and Ar^+. However, immediately downstream of the electrostatic bend, ions with greater mass will orbit in the magnetic field with larger radii. Since the size of each gyro radius increases with the bending voltage, each constituent in the beam can be clipped on the aperture at the entrance to the acceleration region until only the innermost ion beam remains. This technique is used to insure that only the H^+ beam is injection into the acceleration region. It can also be used to obtain a mass spectrum of the ion beam and allow measurement of the total H^+ beam current.

Several techniques have been developed for measurement of injected beam parameters such as r, Δr, p_z and Δp_z. These measurements are important for comparison with the full computer model.

Acceleration of the H^+ beam was first obtained in January 1999. The beam orbit was shown to have a large diameter by observing the image of the accelerated beam on the extraction viewer, then moving the radial probe into the beam and observing the shape and location of the shadow cast into the beam image.

Since beam energy is proportional to the square of the radius, a radial scan can be plotted as an energy distribution. Figure 2 shows what fraction of the proton beam is accelerated to above a given energy (rf on) and the 6.4 keV injected beam (rf off). Total beam current was 9.2 nA. Notice that the graph shown is an integrated distribution.

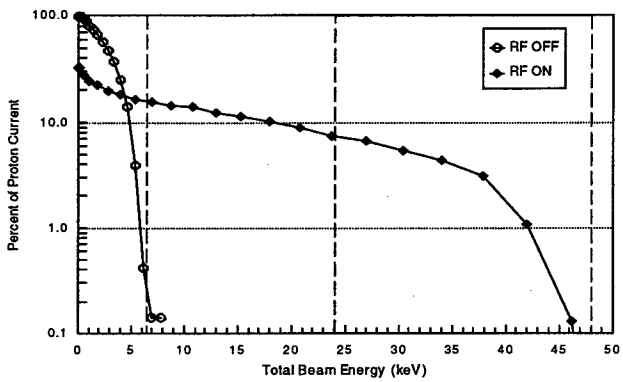

Figure 2: Measured Energy Distribution for the 50 keV ICRA

The measured current requires three corrections due to the geometry of the radial probe. Data in figure 2 has been corrected for beam lost on the electron blocker, and for the fact that the axial length of the probe is insufficient to intercept all of the beam. An additional correction that has not yet been applied to the data is to account for a range of energies included at each data point. This effect is caused by the slope on the radial probe and leads to the roll off seen on the unaccelerated beam in figure 2. However, the magnitude of this correction is small for energies above $\frac{1}{2}E_{design}$ and will only shift current from low energy toward higher energies.

The three vertical dotted lines in figure 2 mark the injected beam energy, $\frac{1}{2}E_{design}$, and E_{design} limited by the exit diameter of the magnetron cavity (E_{design}= 48keV). The figure shows that beam is accelerated up to 46 keV and that more than 7% of the total beam current is above ½ of the design energy.

4 DISCUSSION

The 50 keV ICRA was designed primarily based on analytical calculations, together with experience from previous computer modeling results. Analytical calculations have been shown to be accurate for calculating most aspects of the central ray through the system. However, the computer code is necessary when using many rays to model a finite phase space volume for determination of the accelerated beam current and for calculating the range of magnetic detuning.

Computer modeling is currently underway with the goal of comparing experimental results with the computational predictions and to benchmark the code. Injection beam parameters such as r, Δr, p_z, Δp_z have been measured and should provide the information needed to model the injected beam phase space.

5 CONCLUSION

The 50 keV ICRA experiment has successfully demonstrated ion acceleration using the same axial drift geometry that is characteristic of gyrotrons. A proton beam has been accelerated to the design energy with over 7% of the beam current above ½ of the peak energy. Computer modeling and comparison to measured data is currently underway with the goal being to benchmark the ICRA code. With this tool in hand, it will be possible to design a 10 MeV proton machine that should offer a new low-cost alternative to machines currently being used for applications such as production of medical radioisotopes, accelerator based neutron sources, and for some materials science applications.

6 REFERENCES

[1] H.R. Jory and A.W. Trivelpiece, "Charged Particle Motion in Large-Amplitude Electromagnetic Fields", J. of Applied Physics, **39**, 7, p. 3053-3060 (1968).

[2] R.S.H. Boulding, "The Resonant Cavity Magnetron", D. Van Nostrand Co. Inc., (1952).

[3] T.L. Grimm, C.T. Ramsell, R.C. York, "Ion Cyclotron Resonance Accelerator" Proc. of the 1997 Particle Accelerator Conf., Vancouver (1997).

[4] C.T. Ramsell, T.L. Grimm, R.C. York, S.A. Rice, "Design of an Ion Cyclotron Resonance Accelerator for Experimental Study", Annual Report: National Superconducting Cyclotron Lab, Michigan State University (1998).

PROGRESS ON STELLA EXPERIMENT*

W. D. Kimura,# L. P. Campbell, S. C. Gottschalk, D. C. Quimby, K. E. Robinson, L. C. Steinhauer, STI Optronics, Inc., Bellevue, WA
M. Babzien, I. Ben-Zvi, J. C. Gallardo, K. P. Kusche, I. V. Pogorelsky, J. Skaritka, A. van Steenbergen, V. Yakimenko, BNL, Upton, NY
D. B. Cline, P. He, Y. Liu, UCLA, Los Angeles, CA
R. B. Fiorito, Catholic University of America, Washington, DC
R. H. Pantell, Stanford University, Stanford, CA
D. W. Rule, Naval Surface Warfare Center, West Bethesda, MD
J. Sandweiss, Yale University, New Haven, CT

Abstract

Progress is reported on the Staged Electron Laser Acceleration (STELLA) experiment, which has been assembled on the BNL Accelerator Test Facility (ATF). The primary goal of STELLA is to demonstrate staging of the laser acceleration process by using the BNL inverse free electron laser (IFEL) as a prebuncher, which generates ~1-μm long microbunches, and accelerating these microbunches using an inverse Cerenkov acceleration (ICA) stage. Experimental runs are underway to recommission the IFEL and ICA systems separately, and reestablish the microbunching process. Staging will then be examined by running both the IFEL and ICA systems together.

1 INTRODUCTION

The primary goal of the Staged Electron Laser Acceleration (STELLA) Experiment, located at the BNL Accelerator Test Facility (ATF), is to demonstrate laser acceleration of optically prebunched microbunches [1-2]. Specifically, the BNL inverse free electron laser (IFEL) [3] will be used to prebunch the electrons into a bunch length of ~1 μm. The STI inverse Cerenkov accelerator (ICA) [4] will be used to accelerate these microbunches. Critical issues that will be addressed during this experiment include proper rephasing of the microbunches with the 10-μm laser beam wave inside the ICA gas cell. The basic layout for the experiment is depicted in Fig. 1.

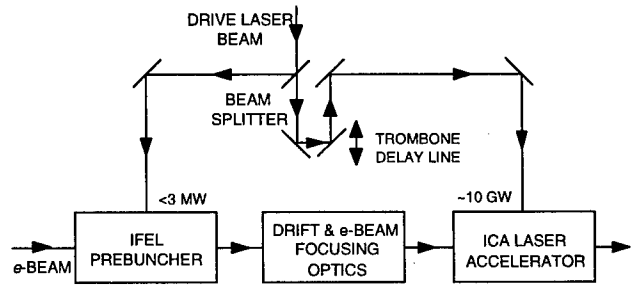

Figure 1: Conceptual layout STELLA experiment.

The experiment is nearly fully assembled at the ATF and is currently undergoing recommissioning of the primary system components. This paper describes the progress to date.

2 DESCRIPTION OF EXPERIMENT

2.1 Electron Beamline

Figure 2 is a drawing of Beamline #1 at the ATF where the STELLA experiment is located. The electrons enter

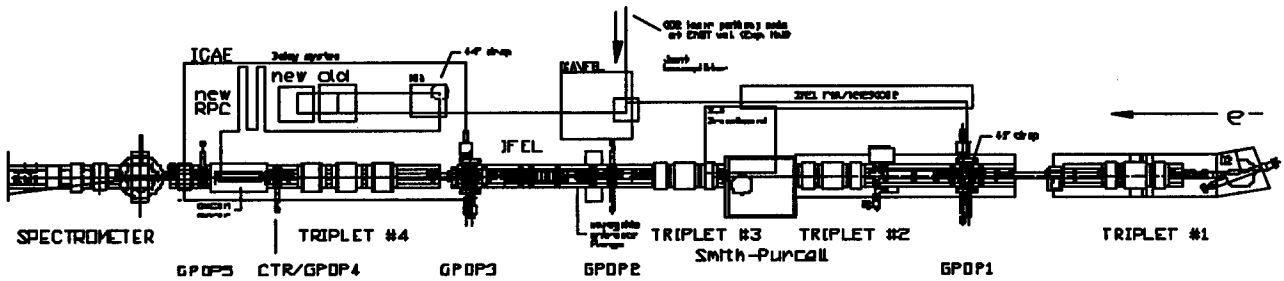

Figure 2: Layout of STELLA beamline.

* Work supported by U.S. Department of Energy, Grant Nos. DE-FG03-98ER41061, DE-AC02-98CH10886, and DE-FG03-92ER40695.
# Email: wkimura@stioptronics.com

from the right. There are three locations along the beamline where the *e*-beam must be focused to small sizes. The first is a turning mirror with a 3-mm dia. central hole located inside the beamline at GPOP1. This mirror is used to direct the ATF psec CO_2 laser beam [5] into the IFEL wiggler. The second constraint is the 60-cm long sapphire waveguide with an internal diameter of 2.8 mm, which is used to channel the laser radiation through the IFEL wiggler [3]. The third constraining location is within the ICA gas cell where the *e*-beam needs to be focused to <100 μm for optimum spatial overlap with the focused laser beam inside the ICA acceleration region. Triplets along the beamline are used to focus the *e*-beam through these various constraint points.

2.2 *Prebuncher (IFEL)*

Details of the IFEL design are in Ref. 3. The wiggler parameter values for STELLA are listed in Table 1.

Table 1: IFEL wiggler parameters for STELLA.

Parameter	Design Value
Wiggler length	47 cm
Wiggler period	3.3 cm (untapered)
Wiggler gap	0.4 cm
K parameter	2.86 for 45 MeV *e*-beam
On axis peak field	0.927 T (based on *K* value)

Unlike the previous IFEL demonstration discussed in Ref. 3, which used a tapered wiggler, the purpose of the IFEL for the STELLA experiment is not to impart large energy gains onto the beam. Rather only a modest amount of energy modulation (±0.55%) is necessary to cause optimum microbunching to occur at the ICA gas cell located 2 m downstream from the IFEL. This implies only relatively low laser power is needed to drive the IFEL. This is one of the reasons for choosing a uniform wiggler. The performance of an untapered wiggler is also more tolerant of variations in the *e*-beam and laser beam parameters.

2.3 *Laser Accelerator (ICA)*

Reference 4 contains more explanation about the ICA system. The gas cell is designed to use a 20 mrad Cerenkov angle. Hydrogen gas is used as the phase matching medium at a pressure of ~2 atm. In order to minimize the effects of gas and window scattering, which can degrade the trapping process, the interaction length inside the cell is 6.5 cm. New, thinner 1-μm thick diamond windows for the *e*-beam will be used at the entrance and exit to the cell.

An important issue during the experiment is spatially overlapping the *e*-beam and laser beam inside the cell. When focused by the axicon [4] onto the *e*-beam, the laser beam focal diameter will be 200 μm FWHM. The central 100 μm of this 200-μm beam is relatively uniform in field. Hence, the *e*-beam, which will be focused to <100 μm, needs to propagate through this central 100-μm width of the focused laser beam over the entire 6.5 cm interaction length.

A new type of beam position monitor (BPM), capable of detecting both the *e*-beam and laser beam with high resolution, will be used inside the gas cell in ensure the spatial overlap of the beams. This BPM consists of a 1-mm thick, 2.54-cm dia. silicon wafer coated with a thin layer of oxidized vanadium (VO_x) [6] that can be inserted perpendicular to the *e*-beam and laser beam propagation. A small mirror held below the centerline of the silicon wafer permits the face of the VO_x-coated side of the wafer to be viewed from above using a camera with a macro-zoom lens.

A photograph of the wafer/mirror system is given in Fig. 3. This BPM is designed to be remotely inserted onto the beam axis using electrical solenoids. Two of these BPMs will be used inside the gas cell near the beginning and end of the interaction region.

The VO_x, when heated to a temperature of ~50°C, changes its reflectivity when the CO_2 laser beam is focused onto it. The extremely fine grain size of the VO_x permits features <1 μm to be resolved. (In this system the resolution is limited to ~10 μm by the camera/lens system.) A Nichrome wire in the shape of a single loop is pressed against the outer edge of the wafer by sandwiching the wafer and wire between two Teflon rings (see Fig. 3). This wire is used to heat the wafer. Another attractive feature of this BPM is that the image on the VO_x remains after exposure to the laser light as long as the wafer is kept heated. This image can be erased by allowing the wafer to cool.

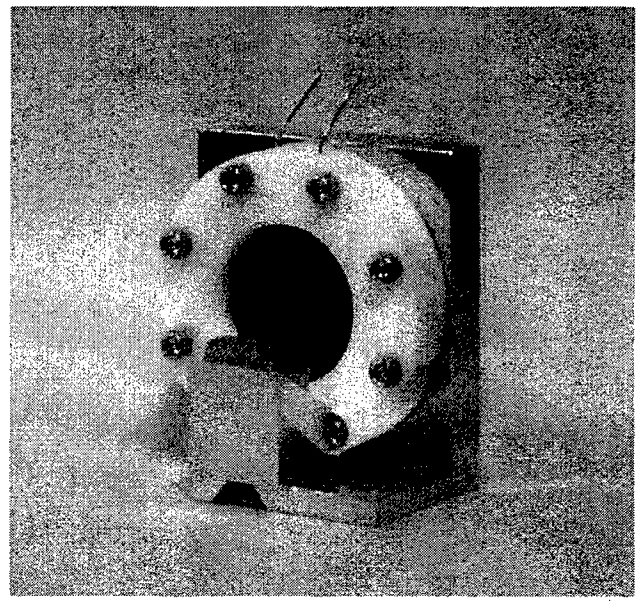

Figure 3: Photograph of oxidized vanadium BPM.

A miniature RTD temperature sensor (not shown in Fig. 3) is attached to the surface of the wafer to permit remote monitoring of the surface temperature.

The *e*-beam position is determined by observing the optical transition radiation (OTR) generated when the *e*-beam passes through the silicon wafer.

2.4 Diagnostics

Two diagnostics are critical for the experiment. The first is a new spectrometer installed at the end of the beamline. Details of this new device can be found in Ref. 7. It features a very broad energy acceptance range (±20%). This is necessary because of the large acceleration/deceleration (~±10 MeV) that can be imparted by the ICA cell. (The first experiments will be intentionally performed at much lower energy gains.) Since initially the accelerated microbunch will be located anywhere within this energy range, it is important to observe the entire energy spectrum at once so that the proper phase adjustment can be made to accelerate the microbunch.

The second important diagnostic is for detecting the presence of the microbunches generated by the IFEL using coherent transition radiation (CTR) [8]. This detector is located just before the ICA cell where maximum bunching is needed. By monitoring the CTR signal, the laser power to the IFEL can be adjusted to obtain optimum bunching at the gas cell. The CTR diagnostic used in STELLA is essentially a stationary position version of the one described in Ref. 8. It also uses a thinner 6.4-μm thick Al foil as the CTR target. This foil together with a tighter *e*-beam focusing capability should significantly increase the CTR signal.

3 RECENT EXPERIMENTAL RESULTS

At the time of the writing of this paper, recommissioning of the IFEL and CTR diagnostic is in progress using the new spectrometer. Table 2 lists the basic parameters for the experiment during the most recent runs.

Table 2: Experimental parameters during recent recommissioning runs.

Parameter	Value during recent runs
Electron beam energy	~45 MeV
Beam charge at end of line	~250 pC
Laser power to IFEL	~200 MW
E-beam focus at CTR	σ ~ 100-200 μm

For a delivered laser power to the IFEL of ~200 MW, a normalized *e*-beam energy modulation of ±0.42% was measured. This value is close to the ±0.55% modulation needed to achieve optimum bunching 2-m downstream from the wiggler. (The higher than expected laser power required to achieve this level of modulation may be due to system inefficiencies, which should be reduced as the system undergoes further fine tuning and testing.)

During these initial CTR tests the IR detector sensed wavelengths shorter than 5 μm. (Recall microbunching should cause enhanced CTR signals at the higher harmonics of the laser beam.) A CTR signal was detected and correlated with the presence of the laser beam in the IFEL. This initial signal was roughly 10 times stronger than those obtained in Ref. 8, which affirms the design improvements made with this new diagnostic.

4 FUTURE PLANS

Recommissioning of the ICA system will occur next where emphasis will be placed on generating a radially polarized laser beam with a minimum of imperfections and minimum beam divergence. It has been shown through modeling investigations that beam imperfections and divergence can degrade the ICA process [9].

After this the IFEL and ICA systems will be operated together and the first staging experiments will commence. Initially only modest acceleration will be attempted as the proper phasing and overlap conditions are found. Later, the laser power to the ICA cell will be increased to demonstrate higher energy gain.

5 REFERENCES

[1] W. D. Kimura, M. Babzien, I. Ben-Zvi, L. P. Campbell, D. B. Cline, R. B. Fiorito, J. C. Gallardo, S. C. Gottschalk, P. He, K. P. Kusche, Y. Liu, R. H. Pantell, I. V. Pogorelsky, D. C. Quimby, K. E. Robinson, D. W. Rule, J. Sandweiss, J. Skaritka, A. van Steenbergen, L.C. Steinhauer, and V. Yakimenko, "STELLA Experiment: Design and Model Predictions," in Proceedings of 8th Workshop on Advanced Accelerator Concepts, Baltimore, MD, Jul. 5-11, 1998.

[2] K. P. Kusche, M. Babzien, I. Ben-Zvi, L. P. Campbell, D. B. Cline, R. B. Fiorito, J. C. Gallardo, S. C. Gottschalk, P. He, W. D. Kimura, Y. Liu, R. H. Pantell, I. V. Pogorelsky, D. C. Quimby, K. E. Robinson, D. W. Rule, J. Sandweiss, J. Skaritka, A. van Steenbergen, L.C. Steinhauer, and V. Yakimenko, "STELLA Experiment: Hardware Issues," in Proceedings of 8th Workshop on Advanced Accelerator Concepts, Baltimore, MD, Jul. 5-11, 1998.

[3] A. van Steenbergen, J. Gallardo, J. Sandweiss, J-M. Fang, M. Babzien, X. Qiu, J. Skaritka, and X-J. Wang, Phys. Rev. Lett., **77**, 2690 (1996).

[4] W. D. Kimura, G. H. Kim, R. D. Romea, L. C. Steinhauer, I. V. Pogorelsky, K. P. Kusche, R. C. Fernow, X. Wang, and Y. Liu, Phys. Rev. Lett. **74**, 546-549 (1995).

[5] I. Pogorelsky, I. Ben-Zvi, W. D. Kimura, N. A. Kurnit, and F. Kannari, Infrared Phys. Tech. **36**, 341 (1995).

[6] Oxidized vanadium coating provided by Optoel Corporation,

[7] http://www.nsls.bnl.gov/AccTest/Beam_Lines/line1spectr.htm

[8] Y. Liu, X-J. Wang, D. B. Cline, M. Babzien, J-M. Fang, J. Gallardo, K. Kusche, I. Pogorelsky, J. Skaritka, and A. van Steenbergen, Phys. Rev. Lett., **80**, 4418 (1998).

[9] L. P. Campbell, W. D. Kimura, and V. Heyfitch, "Inverse Cerenkov Acceleration Modeling Using a Realistic Laser Beam," in preparation.

PHOTON ACCELERATION AS THE LASER WAKEFIELD DIAGNOSTIC FOR FUTURE PLASMA ACCELERATORS

J. M. Dias, N. Lopes, G. Figueira, J. T. Mendonça, GoLP/Instituto Superior Técnico, Lisboa, Portugal
L. Oliveira e Silva, UCLA, Los Angeles, CA

Abstract

In the near future, laser-plasma particle accelerators will be able to sustain electric fields in excess of 100 GeV/m, along plasma channels several Rayleigh lengths long. For these extreme conditions, present day laser wakefield diagnostics such as Frequency Domain Interferometry will not be able to resolve the wake field structure and determine the magnitude of the electric field. In this paper, we present a detailed comparison between frequency-domain interferometry and a photon acceleration based wake field diagnostic. We determine the experimental parameters for which photon acceleration becomes the only viable diagnostic technique. Dispersion effects on the probe beam and the implications of an arbitrary phase velocity of the plasma wave are discussed for both diagnostic techniques. We also propose an experimental set-up for a photon acceleration diagnostic allowing for the simultaneous measurement of the electric field structure and the laser wake field phase velocity. Comparison with results from photon acceleration experiments by ionization fronts will also be presented.

1 INTRODUCTION

One of the most important goals in the plasma particle accelerators research field of is the development of experimental techniques to characterize the electron plasma wave (EPW) generated by intense laser pulses [1, 2].

The first measurements of the temporal and spatial characteristics of the plasma waves generated by an ultrashort laser pulse (laser wakefield) were recently reported [3, 4], using the frequency-domain interferometric technique (FDI) [5]. The purpose of FDI is the measurement of the phase shift experienced by a probe laser pulse travelling through an electron density plasma perturbation. The experimental principle is the following: a double pulse beam (probe and reference pulses) is co-propagating with the EPW (described by the electron density $n_e(z,t)$). The probe pulse will experience an optical phase shift $\Delta\phi$ proportional to $n_e(z,t)$, while the reference pulse, which precedes the laser wakefield, propagates through the interaction region unperturbed. The relative phase shift between these two probing pulses is then measured by the FDI technique. Finally, by sweeping the probe pulse along one or more periods of the plasma wave with a temporal delay line, it is possible to reconstruct the wakefield oscillation. It is important to notice that in experiments [3, 4], the frequency shift and the dependence of the group velocity of the probe pulse on the local plasma density $v_{g_{probe}}(\delta n_e)$ were not taken into account.

Other experiments were performed with the purpose of studying the frequency up-shift resulting from the interaction of short laser pulses with relativistic ionization fronts [6, 7]. An estimate for the velocity of the ionization front and its maximum electron density was obtained, clearly pointing to the feasibility of a new diagnostic tool, the photon acceleration diagnostic (PAD). The frequency shift experienced by a probe laser pulse co-propagating with a relativistic EPW is proportional to the density gradient of the plasma perturbation. Like in the FDI diagnostic technique we can easily map the plasma wave by injecting the probe laser pulse at different positions of the plasma oscillation.

In this work, a detailed comparison of these two diagnostic techniques is carried out. A numerical simulation based on the ray tracing equations for the probe laser pulse is employed to calculate the frequency shift due to photon acceleration and also allows us to determine the phase shift of the laser pulse propagating in the laser wakefield.

2 RAY-TRACING SIMULATIONS

In this ray-tracing simulations the probe pulse length is not considered and the wave packet is only characterized by its central frequency and central wavenumber. When probing is performed by a low-intensity, ultra-short pulse, with a central frequency much higher than the electron plasma frequency we can use the linear dispersion relation in a plasma to describe the probe pulse propagation in the presence of an electron density perturbation. Assuming 1D propagation along the z direction we can then obtain the ray-tracing equations:

$$\frac{dz}{dt} = \frac{\partial\omega}{\partial k} = c\sqrt{1 - \frac{\omega_p^2(z,t)}{\omega^2}} \tag{1}$$

$$\frac{dk}{dt} = -\frac{\partial\omega}{\partial z} = -\frac{1}{2\omega}\frac{\partial\omega_p^2(z,t)}{\partial z} \tag{2}$$

These equations allow us to calculate the frequency shift of the probe laser pulse at any point of its trajectory.

$$\Delta\omega(z,t) = \sqrt{k^2(z,t)c^2 + \omega_p^2(z,t)} - \omega_0 \tag{3}$$

where $k(z,t)$ is the pulse wavenumber and $\omega_p(z,t)$ is the plasma frequency of the wakefield at a point (z,t) along the laser pulse trajectory. ω_0 is the pulse frequency before interacting with the plasma wave. The phase shift ϕ experienced by the laser pulse in the wakefield is determined by

0-7803-5573-3/99/$10.00@1999 IEEE.

using the same ray-tracing trajectories and writing:

$$\phi_{probe}(z,t) = \int_0^z k(z,t)dz - \int_0^t \omega(z,t)dt \qquad (4)$$

where $k(z,t)$ and $\omega(z,t)$ are the wavenumber and frequency along the ray-tracing trajectory. We can then determine the total phase shift relative to a pulse propagating in an unmodulated plasma

$$\Delta\phi(z,t) = \phi_{probe}(z,t) - \phi_{ref}(z,t) \qquad (5)$$

For the laser wakefield scaling, we used the expressions for the laser wakefield excitation in the linear nonrelativistic two-dimensional (2D) limit resonant regime [8, 9, 10]. For simplicity, we have decided to analyze, in all the simulations, only the trajectories along the laser wakefield axis (1D simulations).

Generally, the solution of the ray-tracing equations can only be obtained numerically; however, fully analytical results can be achieved for some electron density perturbation. For instance, we can easily calculate the frequency shift which occurs when a wave packet (classical analog of a photon) crosses over an ionization front without reflection [11]

$$\Delta\omega = \frac{\omega_{p0}^2}{2\omega_0}\frac{\beta}{1 \pm \beta} \qquad (6)$$

where the initial frequency of the photon is much higher than the maximum frequency of the plasma behind the ionization front, i.e., $\omega_0 \gg \omega_{p0}$. The sign + (−) refers to counter-propagation (co-propagation) where $v_p = \beta c$ is the velocity of the ionization front. It is very important to mention that in this new description of the frequency-shift diagnostic technique, the assumption $v_{g_{probe}} = v_p$ is no longer necessary and the limitation to small frequency shifts does not exist.

2.1 *Propagation velocity effects*

It is currently assumed in the FDI diagnostic [3, 4] that the probe laser pulse always stays in phase with the plasma wave, i.e. $v_{g_{probe}} = v_p$. This is not valid for two reasons: i) the probe group velocity depends on the local electron plasma density $v_{g_{probe}}(z,t) = c\sqrt{1-\omega_p^2(z,t)/\omega}$ at each point of the pulse trajectory (see eqs.(1) and (2)); ii) the phase velocity of the wakefield v_p, which is nearly equal to the group velocity of the pump laser pulse, can be considerably different from the velocity given by the linear dispersion relation in a plasma ($v_{g_{pump}} \neq c\sqrt{1-\omega_p^2/\omega}$), due to nonlinear [12] and 3D effects[13].

In our simulations these two aspects of the velocity effects were analyzed for both FDI and PAD diagnostic techniques[10]. For FDI the wakefield oscillation reconstructed from the measured phase shifts is significantly modified in amplitude, if the dispersion effects in the probe beam are included. On the contrary, for the PAD technique, the results are not affected by these dispersion effects, which in fact are fundamental processes in the PAD. When we assume that the phase velocity v_p of the wakefield is no longer equal to the group velocity of the pump, given by the linear dispersion relation in a plasma, both amplitude and wavelength of the phase shift oscillation, as well as the frequency shift oscilation, were modified [10]. To overcome this problem we need an independent measure of the phase velocity of the plasma wakefield, which can be obtained by comparing the frequency shift in co- and counter-propagation, as demonstrated in recent photon acceleration experiments [7].

In these simulations we have considered typical parameters for the pump laser pulse used in recent laser wakefield experiments [3, 4].

2.2 *Large frequency shifts effects*

In the near future it will be possible to excite larger EPW with the help of more powerful lasers, and extend the focal region to longer distances [14]. This will lead to much larger frequency shifts of the probe laser pulse. In order to examine the importance of a large frequency shift in FDI we have changed the pump laser pulse parameters: we have increased the pulse energy to $E_0 = 100mJ$ and decreased the pulse duration to $\tau_{pump} = 30fs$. The new plasma wakefield perturbation obtained from the scaling laws in the 2D resonant regime is $\delta n_e \approx 1.93 \times 10^{18} cm^{-3}$ in the laser focus.

From Fig.1(b) we can see that the frequency shift experienced by the probe pulse is $\Delta\lambda = |\lambda_0 - \lambda| \approx 200nm$ which is of the same order of its initial frequency, $\lambda_0 = 800nm$. But in the present situation the maximum frequency up-shift ($\Delta\lambda_+ \simeq 113nm$) is much smaller than the maximum frequency downshift ($\Delta\lambda_- \simeq 196nm$). This nonlinear effect arises from the fact that the frequency shift at each point of the ray-tracing trajectory of the probe pulse is inversely proportional to its frequency (see eq.(2)).

In Fig.1(a) we can notice that not only the phase shift oscillations become several times larger than π, but a similar nonlinear behavior is also present. This is due to the fact that the final frequency of the probe pulse is very different from the reference pulse frequency (which is constant). Thus the phase difference will depend not only on the plasma length but also on the dispersive optics installed in their optical path before reaching the detector device. This fact, added to the complexity of measuring phase shifts much larger than π and the difficulty of using the FDI of two laser beams with very different frequencies, will be the major drawback of this laser wakefield diagnostic technique. On the other hand, the large frequency shifts play in favor of the PAD technique due to the fact that the extraneous data contributions, such as stray light, pump leakage and detector defects are no longer a technical problem.

3 DISCUSSION

We will now discuss the limits of application for each of the two diagnostic techniques. In order to illustrate these limits

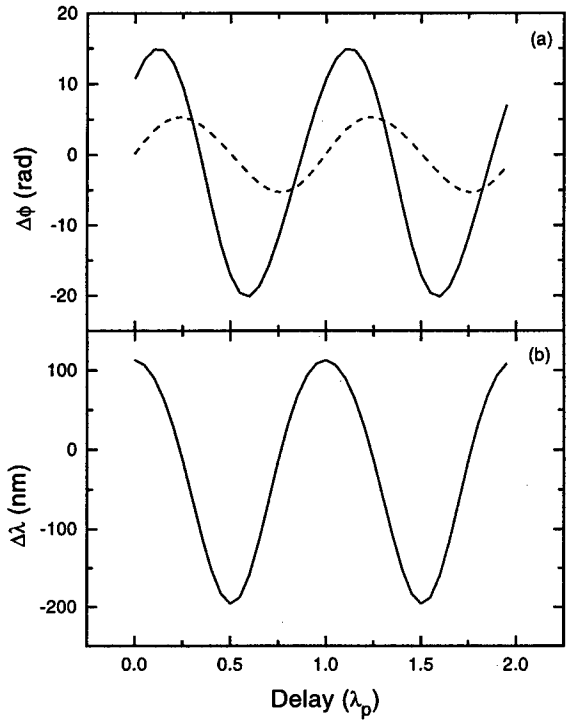

Figure 1: Wakefield oscillation map giving (a) the phase shift and (b) the frequency shift for the laser pulse parameters: $E_0 = 100mJ$, $\tau_{pump} = 30fs$. The calculated phase shifts in (a) are obtained by neglecting the frequency shift of the probe pulse (dashed curve) or by retaining it (solid curve).

we have built up a map representing the pump laser parameters, energy E_p versus pulse length τ_p (see Fig.2). For each set of parameters, the corresponding laser wakefield scaling is obtained for the optimized situation $\delta n_e/n_{e_0} \approx 1$ for the resonant density in the 2D limit. The criteria used to define the limiting curves are as follows. The solid curve is given by the condition of frequency shift $\Delta\omega_{shift}$ measured by the PAD technique equal to the spectral width of the probe pulse $\Delta\omega_{p_{FWHM}}$ The FDI technique is limited by the measured phase shift $\Delta\phi$, which must be lower than 2π. The dotted curve considers the phase shift as given by the refraction index $\Delta\phi_k$, and the dashed curve retains the contribution of the frequency variation $\Delta\phi_{k,\omega}$, eqns. (4)-(5). In this map, we also represent two lines defining the $100GeV/m$ goal for accelerating gradients, already measured by indirect techniques in recent experiments [15]. The lines correspond to the 2D and 1D limits of the resonant density. A close analysis of this map clearly shows that photon acceleration is the most appropriate diagnostic technique for the future laser wakefield accelerators.

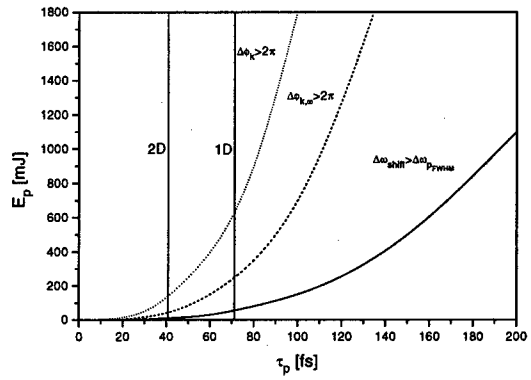

Figure 2: Map of the pump laser pulse parameters. Solid curve defines the limit of applicability of the PAD ($\Delta\omega_{shift} = \Delta\omega_{p_{FWHM}}$). Dashed and dotted curves define the limits of applicability of the FDI. The vertical lines indicate the $100GeV/m$ goal for the 2D and 1D scaling laws.

Recent experimental results [7] have shown a very good agreement with this ray-tracing formalism. The results of the frequency up-shift in the co- and counter-propagation setups of this experiment allow us to determine the electron plasma density and the ionization front velocity, by using the 2D version of eq.(6) [7]. This clearly points to the feasibility of PAD for relativistic coherent structures in laser produced plasmas like that presented in [7]. For all the reasons discussed above PAD is the most promising diagnostic for large amplitude plasma waves in future laser wakefield accelerator experiments.

4 REFERENCES

[1] T. Tajima and J. M. Dawson, Phys. Rev. Lett. **43**, 267 (1979).

[2] J. B. Rosenzweig *et al.*, Phys. Rev. Lett. **61**, 98 (1988).

[3] J. R. Marquès *et al.*, Phys. Rev. Lett. **76**, 3566 (1996).

[4] C. W. Siders *et al.*, Phys. Rev. Lett. **76**, 3570 (1996).

[5] J. P. Geindre *et al.*, Opt. Lett. **19**, 1997 (1994).

[6] W. M. Wood, C. W. Siders, and M. C. Downer, IEEE Trans. Plasma Sci. **21**, 20 (1993).

[7] J. M. Dias *et al.*, Phys. Rev. Lett. **78**, 4773 (1997).

[8] L. M. Gorbunov and V. I. Kirsanov, Sov. Phys. JETP **66**, 290 (1987).

[9] C. W. Siders *et al.*, IEEE Trans. Plasma Sci. **24**, 301 (1996).

[10] J. M. Dias, L. Oliveira e Silva, J. T. Mendonça, Phys. Rev. Special Topics - Accelerators and Beams **1**, 031301 (1998).

[11] J. T. Mendonça and L. O. e Silva, Phys. Rev. E **49**, 3520 (1994).

[12] C. D. Decker and W. B. Mori, Phys. Rev. Lett. **72**, 490 (1994).

[13] E. Esarey, P. Sprangle, M. Pilloff, and J. Krall, J. Opt. Soc. Amer. B **12**, 1695 (1995).

[14] P. Sprangle *et al.*, Phys. Rev. Lett. **69**, 2200 (1992).

[15] A. Modena *et al.*, Nature **377**, 606 (1995).

COMPENSATION OF BEAM-BEAM EFFECTS IN THE TEVATRON COLLIDER WITH ELECTRON BEAMS

V. Shiltsev, D. Finley, A. Sery, FNAL , Batavia, IL
V. Danilov, ORNL, Oak Ridge, TN

Abstract

The beam-beam interaction in the Tevatron collider sets limits on bunch intensity and luminosity. These limits are caused by a tune spread in each bunch which is mostly due to head-on collisions, but there is also a bunch-to-bunch tune spread due to parasitic collisions in multibunch operation. We propose to compensate these effects with use of a countertraveling electron beam, and present general considerations and physics limitations of this technique.

1 INTRODUCTION

The two planned upgrades (Run II and TEV33) of the $p\bar{p}$ Tevatron collider [1] will give higher luminosity and will also have enhanced beam-beam effects. An increase of the betatron tune spread will come not only from head-on collisions of the bunches at the Interaction Points (IP), but also from parasitic long range beam-beam interactions resulting in bunch-to-bunch variation of betatron tunes, the latter being enhanced by the presence of injection gaps in the Tevatron bunch train (Pacman effect).

During Run II with 36 bunches in each beam the bunch-to-bunch spread is expected to be about $\Delta\nu \approx 0.007$, while the single bunch tune spread will be about $\Delta\nu \approx 0.018$. In the TEV33 upgrade the tune spread within each bunch and the bunch-to-bunch tune spread are both about 0.008. These values are about the maximum experimentally achieved value for proton colliders $\Delta\nu \approx 0.025$.

The betatron tune shift and tune spread, if they could be arbitrary controlled, are believed to provide valuable knobs for improving beam lifetime and ultimately for maximizing collider performance. Compensation of the beam-beam effects only for antiprotons is sufficient since the proton bunch population is significantly higher than the antiproton bunch population.

The beam-beam compensation techniques based on the use of intense electron beams have been proposed [2, 3] and are under development now [4, 5, 6, 7]. The present paper reviews the current status of these investigations.

2 LINEAR "ELECTRON LENS"

The tunes of individual bunches in the $\bar{p}$ beam can be corrected if an additional linear focusing is applied to each bunch individually. This focusing can be provided by the field of a wide electron beam ("electron lens", see Figure 1) with the current varying from bunch to bunch [3]. The electron beam must allow a 100% change of current in the 132 ns time between bunches in order to provide independent influence on different bunches.

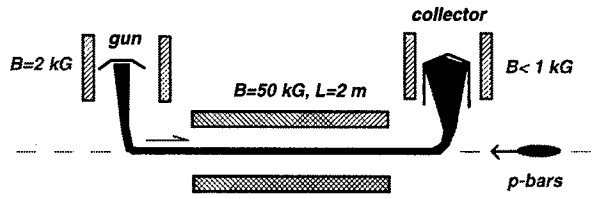

Figure 1: A possible layout of the "electron lens".

For a round, constant density electron beam with total current J_e, radius a, interacting with antiprotons over length L, the tune shifts are

$$\xi^e_\perp = -\frac{\beta_\perp}{2\pi}\frac{(1+\beta_e)Lr_p}{\gamma_{\bar{p}}\, e\,\beta_e\, c}\frac{J_e}{a^2}.$$

For example a beam with $J_e \approx 1.65$ A, $L = 2$ m, $a = 1$ mm, energy 10 kV ($\beta_e = 0.2$) gives $\xi^e_\perp \approx -0.01$ in the Tevatron with $\gamma_{\bar{p}} \approx 1066$ and beta function $\beta_\perp = 100$ m. The electron lens should be installed in a place where a) the electron beam does not interact with the proton beam; b) the beta-functions $\beta_\perp$ are high enough so the electron current density $j_e = J_e/(\pi a^2)$ is reasonable; and c) the dispersion function is small enough. Two electron lenses installed in locations with different β_x/β_y are needed to compensate the x and y bunch-to-bunch tune spreads independently (see Figure 2). An example of linear compensation is shown in Figure 3.

The required tune shift defines the electron beam density while the length L is defined by the space available in the Tevatron. The electron beam radius a is approximately

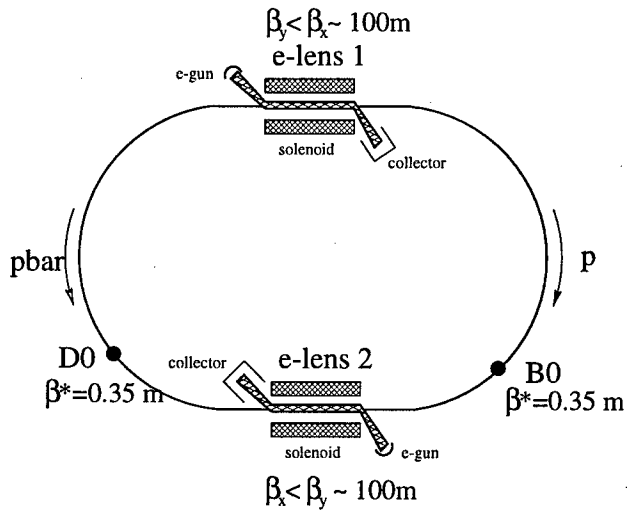

Figure 2: Tevatron layout with two "electron lenses".

0-7803-5573-3/99/$10.00@1999 IEEE.

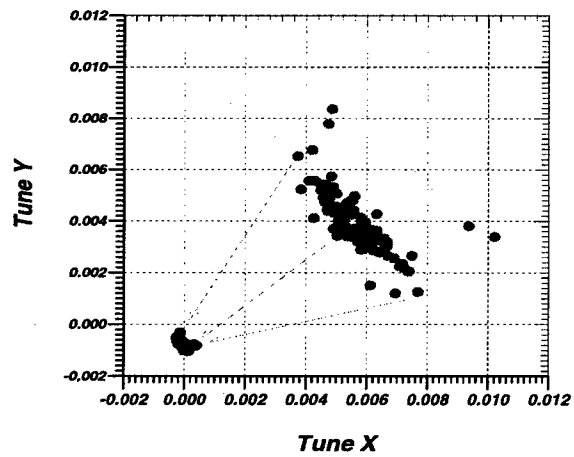

Figure 3: Initial (widely spread points) and resulting $\bar{p}$ bunch tune shifts (core particles only) with 10% error in the compensation.

2–3 times the $\bar{p}$ beam size. For the electron beam energy the lowest possible value should be chosen provided that a) the current production is not limited by a gun; and b) the electron beam can renew faster than the $\bar{p}$-bunch spacing (132 ns).

The gun current is $J_e = \mathcal{P} \cdot U_a^{3/2}$ where U_a is the anode voltage and $\mathcal{P}$ is the perveance that is typically $\approx 2 \cdot 10^{-6}$ A/V$^{3/2}$ for a diode gun. However, it can be made several times higher for a specially designed gun, such as a convex cathode immersed in a magnetic field [9]. Relying on a gun with perveance $(4-5) \cdot 10^{-6}$ A/V$^{3/2}$, the following optimized parameters of the electron beam can be deduced: the energy 10 kV ($\beta_e = 0.2$), $J_e \approx 1.65$ A, $L = 2$ m, radius $a = 1$ mm. Such a beam will achieve a maximum tune shift of $\xi_\perp^e \approx -0.01$ in the Tevatron.

To decrease the current density in the gun to what is achievable for an oxide cathode, one needs to use adiabatic magnetic compression, in which the beam is produced on the cathode with a larger radius a_c in a weak field B_c and then follows the magnetic lines to the region of stronger field B. For an electron lens with cathode current density 2 A/cm^2 and cathode radius $a_c = 5$ mm, one gets the ratio $B/B_c \equiv a_c^2/a^2$ to be about 25.

An experimental installation has demonstrated feasibility of the electron lens. The set-up will serve as a prototype of the device that can later be inserted into the Tevatron ring. The test facility and results of its commissioning are described in detail in [8].

3 NONLINEAR COMPENSATION: "ELECTRON COMPRESSOR"

The head-on collision of proton and antiproton bunches at the interaction point changes the betatron frequency of the on axis $\bar{p}$ by $\Delta\nu_z(0,0) = +\xi^p$ where $\xi^p \equiv N_p r_p/4\pi\varepsilon_n$ is the so called beam-beam parameter. N_p is the proton bunch population, r_p is the proton classical radius and ε_n is the normalized transverse emittance of the proton bunch. Assuming the charge density ρ of the proton bunch is Gaussian-like, the focusing force of the equivalent lens is a nonlinear function of the transverse displacement.

Due to the nonlinear focusing by the p beam the betatron frequencies in the $\bar{p}$ bunch are different for particles with different betatron amplitudes (X, Y) as shown in Figure 4. For the RunII and TEV33 upgrades of the Tevatron the spread of betatron frequencies (so called "footprint") of the $\bar{p}$ beam is $\Delta\nu_{\bar{p}} \approx 0.02$. This is big enough to cause an increase of particle losses due to higher order lattice resonances.

Compensation of this beam-beam induced betatron tune spread within the $\bar{p}$ bunch can be accomplished by an electron beam with an appropriate charge distribution [2]. The nonlinear focusing of antiprotons by the proton beam is compensated if a) the electron transverse charge distribution $\rho_e(r)$ is the same as the proton beam $\rho_p(r)$ (but scaled with r); b) the $\bar{p}$ beam distribution at the "electron compressor" is the same as at the IP (but scaled with r and with zero dispersion); and c) the number of electrons on the path of the $\bar{p}$ beam (for a single IP) is $N_e = N_p/(1+\beta_e)$. For example $N_e \approx 4.5 \cdot 10^{11}$ (or $J_e = 2.2$A) with $\beta_e = 0.2$ and $L = 2$ m for TEV33.

The electron bunch should have a Gaussian transverse distribution in the ideal case, in which the proton bunch has a Gaussian distribution. However, more realistic and practically more easily achievable distributions can give as good a result as the Gaussian case [2]. For example the electron beam density $\propto 1/(1+(r/\sigma)^8)$ was used for the footprint compression simulations presented in Figure 4.

The condition to cancel just the nonlinear tune shift is not the only condition to satisfy for the antiproton dynamics to be improved. An important issue to be considered is a difference of the proton bunch length and the electron beam length expressed in terms of betatron phase advance. Pursuing nonlinear compensation is based on the idea of adding a single thin nonlinear lens to an arbitrary nonlinear lattice in such a way that the particle motion in the modified structure would become resonance-free, though nonlinear, and at the same time the beam of particles would have a zero footprint [7].

Although theoretical studies of both nonlinear and linear compensation are under way, the first stage of experimental activities at Fermilab is devoted to linear compensation studies.

4 PARASITIC EFFECTS

Detailed studies of possible harmful effects produced by the electron lens have shown that all such effects can be made tolerable by a proper choice of the electron beam parameters. The most important issues are briefly described below.

Head tail in the $\bar{p}$ beam due to the electron beam [5]. An off center collision of the $\bar{p}$ bunch with the electron beam results in a drift of the electrons in crossed magnetic and electrical fields, such that, while the head of the $\bar{p}$ bunch sees a vertical field, the tail will also see a horizontal one.

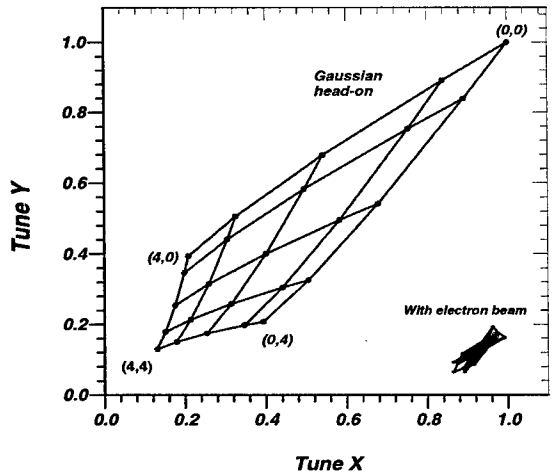

Figure 4: Betatron frequencies (tunes) in the $\bar{p}$ bunch for particles with different betatron amplitudes (X, Y). The head-on collision case (large leaf) and the case with compensation by the electron beam (small leaf, displaced for clarity) [2] are shown. Tune shift is in units of ξ^p, betatron amplitude is in units of the bunch transverse size σ.

Taking into account that the head and the tail exchange their position due to synchrotron motion, one can see that as a result of such a skew interaction the horizontal betatron motion, the vertical betatron motion and the synchrotron motion become coupled resulting in the so called Transverse Mode Coupling Instability (TMCI).

The threshold of this TMCI was found to be inversely proportional to the magnetic field B in the "electron lens". Under the design parameters the minimum magnetic field that will keep the $\bar{p}$ beam stable is $B \gtrsim 17.5$ kG. The instability is additionally suppressed if the electron beam radius is larger than the $\bar{p}$ beam size. The threshold magnetic field scales approximately as $\propto \xi_\perp^e / a^2$.

Electron beam distortion by elliptical $\bar{p}$ beam [4]. If the set-up is located at a place with unequal beta-functions $\beta_x \neq \beta_y$, then axial symmetry is not conserved. The electron beam becomes a rotated ellipse at the moment the tail of the antiproton bunch passes through it, while the head of the bunch sees the original undisturbed round electron beam. The electric fields of the distorted electron beam produce $x - y$ coupling of vertical and horizontal betatron oscillations in the $\bar{p}$ beam.

The choice of magnetic field can decrease the coupling to an acceptable value. If $B = 2$T, the maximum coupling spread is well below the typical residual coupling in the Tevatron (about 0.001). This effect is also additionally suppressed if the electron beam size is larger than the antiproton beam size.

$\bar{p}$ emittance growth due to variations of the electron beam [3]. Fluctuations of the electron current $\Delta J_e / J_e$ from turn to turn cause time variable quadrupole kicks which lead to a transverse emittance growth of the antiproton bunches. The emittance growth time τ (defined as $1/\tau = 1/\epsilon \cdot d\epsilon/dt$) is more than 10 hours (which is assumed to be tolerable) if the peak-to-peak current fluctuations are smaller than $\Delta J_e / J_e \approx 1.8 \cdot 10^{-3}$.

Transverse motion of the electron beam results in dipole kicks and coherent betatron oscillations of the antiprotons. After some decoherence time they will result in emittance growth of the antiprotons. The emittance growth time is more than 10 hours if $\delta X \leq 0.14\,\mu m$.

Deviations of the solenoidal magnetic field $\vec{B}$ from a straight line will cause off-center collisions of the antiproton and electron beams. In the case of the non-linear electron lens this may cause unwanted non-linear components of the space charge forces. The effect is small if $\Delta B_\perp / B \lesssim 10^{-4}$.

All these conditions are believed to be achievable.

Residual ions in the electron beam. Ionization of residual gas by electrons produces ions which could become trapped in the potential well of the electron beam. For typical parameters the "time of neutralization" is a fraction of a second. Nevertheless the ions should be removed because they a) change the charge density, i.e. spoil beam-beam compensation; and b) may result in a two beam drift instability.

The residual ions will be cleaned from the electron beam. Special cleaning electrodes together with a high vacuum (of the order of $3 \cdot 10^{-9}$ Torr), will ensure that the neutralization time is sufficiently longer than the lifetime of ions in the electron beam. An acceptable amount of residual ions in the electron beam is about half a percent.

5 CONCLUSION

Beam-beam compensation with an electron beam looks very promising. It provides additional powerful "knobs" to control beam dynamics in the Tevatron collider. No severe requirements on the electron beam were found for the suggested device. We believe that realization of the idea will give benefits for the Tevatron. Experimental studies of the electron lens prototype are under way.

6 REFERENCES

[1] P.Bagley, *et. al,* FERMILAB-Conf-96/392 (1996).

[2] V.Shiltsev, D.Finley, FERMILAB-TM-2008 (1997).

[3] V.Shiltsev, FERMILAB-TM-2031 (1997).

[4] V.Shiltsev and A.Zinchenko, *Phys. Rev. ST Accel. Beams*, **1**, 064001 (1998); see also in these Proceedings.

[5] A.Burov, V.Danilov, and V.Shiltsev, *Phys. Rev. E*, **59, n.3** (1999); see also in these Proceedings.

[6] V. Shiltsev, V. Danilov, D. Finley, A. Sery, FERMILAB-PUB-98-260 (1998), submitted to *Phys. Rev. ST Accel. Beams.*

[7] V.Danilov, V.Shiltsev, FNAL-FN-671 (1998).

[8] C.Crawford, *et. al,* these Proceedings.

[9] A.Sharapa, A.Grudiev, D.Myakishev, A.Shemyakin, *Nucl. Instr. Meth. A*, **406** (1998), 169.

THE CIRCULAR RFQ STORAGE RING *

A. G. Ruggiero#, Brookhaven National Laboratory, PO BOX 5000, Upton, NY 11973

Abstract

This paper presents a novel idea of storage ring for the accumulation of intense beams of light and heavy ions at low energy. The new concept is a natural development of the combined features of conventional storage rings and ion traps, and is basically a linear RFQ bent on itself. The advantages are: smaller beam dimensions, higher beam intensity, and a more compact storage device.

1 INTRODUCTION

There is need to develop compact storage rings for the accumulation of low-energy beams of ions for a variety of applications: molecular and atomic physics, solid state, chemical-physics, astrophysics, and other more exotic applications like crystalline beams and ion fusion for energy production. Several experiments can be conceived which make use of these compact storage rings: colliding beams circulating in two intersecting storage rings, collision of a stored beam of ions with an internal target, head-on collision with an electron beam or a X-ray beam from a synchrotron radiation source. Relatively high beam intensity is required. Small beam dimensions can be achieved with techniques like electron and laser cooling. In this paper we describe a novel idea of a compact storage ring for the accumulation of intense beams of light and heavy ions. The concept takes advantages of established principles of conventional low-energy storage rings, ion traps, and RFQ's. The proposed new storage ring is basically a circular RFQ bent on itself and closed mechanically. Instead of quadrupole magnets, focusing of the particles is provided by the rf field of the structure. Since electrically the structure is not closed on itself, it is expected that ion beams can be stored at intensities higher than those achieved in conventional storage rings.

2 A CONVENTIONAL STORAGE RING

An example of a low-energy and small storage ring is ASTRID [1], used for the accumulation of light and heavy ions and for the demonstration of Laser Cooling. The ring magnetic rigidity is 1.87 T-m. The circumference is about 40 m. It is made of eight dipole magnets which bend the beam trajectory on a circular and closed orbit and sixteen quadrupole magnets for transverse focusing. There are four periods, each with a straight section about 4 meter long. There is a limit on the intensity that can be stored in a conventional storage ring given by the space-charge tune-depression

$$\Delta\nu = N Q^2 r_0 / 2 A \beta^2 \gamma^3 \varepsilon \qquad (1)$$

where $r_0 = 1.535 \times 10^{-18}$ m is the classical proton radius, Q the ion charge state, A its mass number, β and γ respectively the velocity and energy relativistic factors, N the number of ions stored, and, finally, ε is the beam emittance. The tune-depression $\Delta\nu$ cannot exceed a value of at most 0.5. This limit is understood to be set by the presence of unavoidable random magnet imperfections which cause the creation of stopbands around the half-integral values of the betatron tune. A more relevant parameter is the beam transverse density in the physical space $D = N / S$, where $S = \pi a^2$ is the beam cross-section area. There is a relation between the beam radius a and the emittance ε, so that

$$S = \beta_L \varepsilon \qquad (2)$$

The average value of the amplitude lattice function β_L for ASTRID is about 5 meter. In a conventional storage ring, the amplitude lattice function β_L is a measure of the strength of focusing. The average value of β_L is given roughly by the length of the focusing period. Unfortunately, in a conventional storage ring, the average value of β_L can hardly be less than few meters; in fact, quadrupoles have a significant length, and space between quadrupoles is required to accommodate several devices. In conclusion, the physical density that can be achieved in a conventional low-energy storage ring is limited, first, by the largest amount of space-charge tune-depression according to Eq. 1, and, second, by the strength of focusing according to Eq. 2.

3 THE LINEAR RFQ

Another accelerator device [2] is the Radio-Frequency Quadrupole (RFQ). The device accelerates quickly the beam from an ion source to energies large enough when space-charge effects are considerably reduced, and provides simultaneously focusing of the transverse motion of the particles. The RFQ is not a magnetic device, but employs an alternating rf electric field for both the acceleration and the focusing of the particles. It is a straight waveguide with four internal metallic rods. A rf voltage at the frequency $f = \omega/2\pi$ is applied between diagonally opposite electrodes to generate in the opening a quadrupolar oscillating field of the same frequency. The motion of the particle will modulate the actual field in time, creating the equivalent of an alternating focusing transverse field with periodicity $L = \beta\lambda$, where $\lambda = 2\pi c/\omega$ is the rf wavelength. If acceleration is not required, but only transverse focusing, which is the case of interest here, the electrodes will appear just straight. In this case

* Work performed under the auspices of the US DoE
# Email: agr@bnl.gov

0-7803-5573-3/99/$10.00@1999 IEEE.

the excitation is a rf wave oscillating stationary between the pairs of electrodes.

4 THE ION TRAP

Recently, a quadrupole storage ring [3] has been used for the study of ion crystalline structures. The diameter of the device is of only 12 cm. It is made of four annular electrodes with an internal diameter of only 5 mm. An electrostatic voltage is applied between each pair of diagonally opposing electrodes. This generates a constant radial electric field, which vanishes at the center, and increases about linearly with the distance from the main axis. An atomic gas of the desired ion species is diffused in the region between the electrodes. An electron gun ionizes the atoms, and the resulting ions are trapped transversely in the small storage ring, oscillating around the circular main axis under the effect of the restoring forces of the electrostatic quadrupole. There is no beam in this configuration since the ions do not drift azimuthally along the main axis. The particles adjust their mutual longitudinal distance by Coulomb interaction, whereas the external quadrupolar forces compensate the transverse interaction.

5 THE CRFQ CONCEPT

The Circular Radio-Frequency Quadrupole (CRFQ) is a compact storage ring, which includes features of all the devices described above. It is a storage ring where beams of light and heavy ions (including protons and negative ions) can circulate at constant speed corresponding to energies comparable to those used for ASTRID. Like in the Ion Trap, four annular electrodes provide focussing. Like in the linear RFQ, rf oscillating voltages are applied between the electrodes to provide transverse alternating focusing of motion over a short period of about few centimeters or less. From this point of view, the CRFQ resembles the linear RFQ without acceleration, and without, therefore, corrugated vanes. The CRFQ is actually a linear RFQ curved and closed mechanically on it as shown in Figs. 1 and 2.

6 EQUATIONS OF MOTION

It is required to keep the motion of the ions focused and on a circular orbit, in proximity of the azimuthal axis of the CRFQ. We shall assume that the major radius R of the CRFQ is much larger than the focusing period L, and that this is in turn larger than the internal diameter 2b. The equations of motion are (see Fig. 1 for the orientation of x, y)

$$d^2 y / ds^2 + (B/L^2)\, x \cos(ks) = 0 \qquad (3)$$

$$d^2 x / ds^2 + (B/L^2)\, y \cos(ks) = [1 - B\,(b/L)^2 \cos(ks)] / R \qquad (4)$$

where s is the longitudinal path length, and

$$B = Q e V_0 \lambda^2 / A m c^2 b^2 \qquad (5)$$

It can be seen that the motion is kept on a circular trajectory by the extra term due to the curvature of the restoring forces. All the considerations made for the linear RFQ apply also to the CRFQ. For instance, the B parameter determines the phase advance per period and the amplitude lattice function $\beta_L \sim L$. As an example, the phase advance of 90° requires B = 6.812. Thus, the Circular Radio-Frequency Quadrupole Storage Ring has the advantage to provide a very short focusing alternating period considerably smaller than that can be obtained in a conventional storage ring.

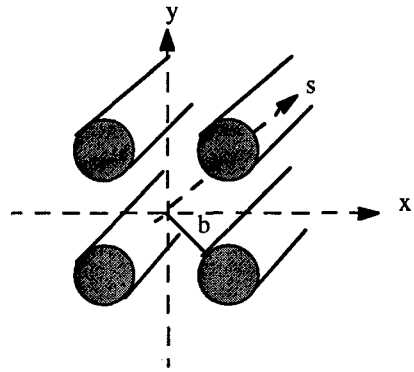

Figure 1. Cross-Section of a CRFQ

7 SPACE-CHARGE LIMIT

The other major advantage for the use of the CRFQ storage ring is the larger beam intensity that can be stored compared to that of a conventional storage ring of the same energy. In the latter there is the limit caused by the Space-Charge Tune-Depression $\Delta\nu$ that cannot exceed a value of at most 0.5. In the CRFQ the situation is different and identical to that encountered in the linear RFQ. First, the focusing periodicity is very high and cannot be broken down by magnetic imperfections that do not exist. Secondly, the structure, though mechanically closed on it, is electrically open. Turn after turn, the CRFQ is just like a long transport. One can then make the analogy with the linear RFQ where the Space-Charge limit is caused by lowering of the phase advance per period from 90° down to 45° (or less), below which the particle motion may become unstable. The equations of motion are then to be modified by adding a space-charge term with the parameter

$$\Delta = Q^2 N r_0 \lambda^2 / A \pi^2 R \qquad (6)$$

The depression of the phase advance of a single period due to space charge forces from 90° down to 45° corresponds to $\Delta \sim 0.044$.

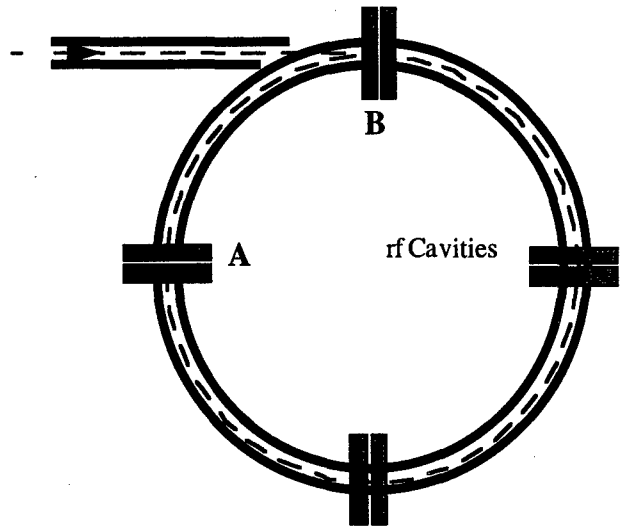

Figure 2. Plan View of a CRFQ

8 RF POWER SOURCE

Powering of a linear four-rod RFQ structure has been discussed by Hutcheon [4]. We follow essentially the same approach, which requires placing a number of cavities around the ring as shown in Fig. 2. These cavities function as rf couplers by providing the needed rf voltage difference between the two pairs of opposite rods. The analysis of Hutcheon had to be extended to include the geometric closure of the CRFQ.

9 INJECTION

Injection of a single beam pulse is possible if the duration is sufficiently shorter than the revolution period in the ring. During injection, the rf is turned off in a section of the CRFQ as shown in Fig. 2, between A and B. This section is mechanically cut out and electrically isolated from the rest of the ring. In the remaining of the ring the rf is kept on. Once the tail of the beam has entered the energized section, then also the isolated section is turned on in a period of time about the duration of the beam gap.

10 AN EXAMPLE

The main purpose of this example is the construction of a prototype to demonstrate the two basic principles: (i) that it is possible to achieve very short alternating focusing periods of few centimeters, and (ii) that it is possible to store ion beams at intensities higher than those that can be achieved in conventional storage rings. We take a proton beam at 100 keV and a rf of 200 MHz. The ring radius is R = 50 cm, the peak rf voltage V_0 = 160 kV, the internal diameter 2b = 15 mm. The density which corresponds to the RFQ space-charge limit is D = 2 x 10^{12} cm^{-2}. With a beam normalized emittance of 1 π cm mrad, the average beam radius at the space-charge limit is a = 5 mm, so that about 2 x 10^{12} protons can be stored in the ring. This is about 10 times larger than the conventional limit given by Eq 1. Thus an experiment can be done to verify that indeed it is possible to store considerable more current in the CRFQ storage ring. The circulating current at the RFQ space-charge limit is 460 mA, and only 50 mA with the conventional limit of Eq 1. An ion source, operating at a very low duty cycle, is certainly capable to produce a beam pulse of about 0.5 μs duration in excess of 100 mA. The pulse duration is shorter than the revolution period so that only one turn need to be injected in the CRFQ. The ion source can be placed on a platform at 35 kVolt. The energy difference to 100 keV can be obtained by accelerating the beam in a short linear RFQ operating also at 200 MHz. At the end of the acceleration, the vanes of the linear RFQ are no longer corrugated, and only focusing is then provided. This linear section would then merge the CRFQ. The experiment can be performed at a very low duty cycle, for example, with a beam pulse injected and stored in the CRFQ every few minutes. There is thus no much beam power involved and the beam itself can directly be disposed by turning off the rf field.

11 CONCLUSIONS

We have described a new concept of Storage Ring for low-energy ion beams. The principle of operation of the new device is similar to that of an ordinary RFQ, except that it is mechanically bent on itself. It is then possible to achieve very short alternating focusing periods, and to store considerable higher beam intensity well beyond the ordinary space-charge limit of conventional storage rings.

12 ACKNOWLEGEMENTS

The author wishes to thank J. Alessi, M. Blaskiewicz and D. Raparia for very useful discussions, and T. Roser for continuous support.

13 REFERENCES

[1] S. P. Møller, IEEE 91CH3038-7, page 2811.
[2] J. W. Staples, AIP Conference Proceedings 249 (1992). Vol. II, page 1483.
[3] H. Walther, Crystalline Beams and Related Issues. Page 149. The Science and Culture Series - Physics 11 (1996). Editors D. M. Maletic and A.G. Ruggiero. World Scientific.
[4] R.M. Hutcheon, Proc. Linac Confer. 1994, page 94.

RHIC INSERTION REGION SHUNT POWER SUPPLY SIMULATION*

D. Bruno#, G. Ganetis, R.F. Lambiase, Brookhaven National Laboratory
Brookhaven Science Associates, Inc., Upton, Long Island, New York 11973

Abstract

A new heavy ion collider called the Relativistic Heavy Ion Collider (RHIC) is now under construction at Brookhaven National Laboratory (BNL) and is scheduled to be completed in June 1999. The collider requires superconducting magnets. Power supplies are required to supply currents to these highly inductive superconducting electromagnet loads. The RHIC Insertion Region contains many shunt power supplies to trim current of different magnet elements in a large superconducting magnet circuit. Shunt power supplies were chosen over all trim magnets or individual power supplies to reduce construction costs. The power supplies in the Insertion Region must be tunable. An understanding of the interaction between these power supplies was critical in determining what type of technology should be chosen in procuring these power supplies. The circuit analysis program MicroCap V by Spectrum Software (TM) was used to simulate the entire RHIC collider ring Insertion Region power supply network. Results of the absolute and dynamic error of the magnet currents are presented over the entire ramping cycle from acceleration to storage. A description of the power supplies regulation loop models is also discussed.

1 INTRODUCTION

The Relativistic Heavy Ion Collider is made up of six sextants. The simulations performed started with a single shunt p.s. model. A single sextant was modeled next. This single sextant was simulated with 4 different variations. These variations included changing the gain and bandwidth of the current loops and also observing the effect of current varying magnet inductances. Finally a simulation of the complete ring was performed. The interaction between the p.s.'s was analyzed by observing the magnet current error during the ramping of the p.s.'s. Each power supply was modeled after a typical 12 pulse SCR p.s. The current loop and voltage loop bandwidths that were used in the model were typical of a 12 pulse SCR p.s. The current loop gain and 3dB bandwidth were adjusted to observe the effect on the magnet current error.

2 SINGLE SHUNT PS MODEL

Figure 1 is a block diagram of the single shunt p.s. model. The nested power supply is p.s. Q7 and the outer p.s. is Main p.s. (p.s. QF). Both p.s.'s had an inner

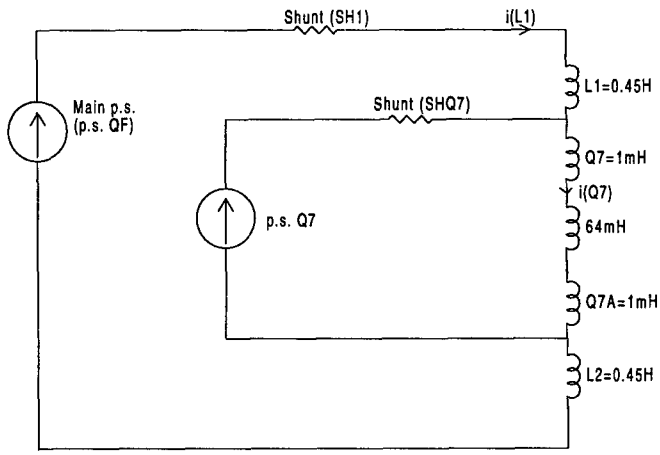

Figure: 1 Single Shunt P.S. Model

voltage loop with a 100Hz bandwidth. Both p.s.'s had an outer current loop. The bandwidth of the current loop for the Main p.s. was 3.5Hz and the DC gain was 104dB. The bandwidth of the current loop for the Q7 p.s. was 5 Hz and the gain was 86dB. The magnet inductances are typical of the magnet inductances for the complete ring.

Figure 2 is a diagram of the different regions in the current waveform as the current ramps up. The waveform is broken up into nine regions. These nine regions are define as follows:

1. Injection
2. Start Acceleration
3. Acceleration
4. Finish Acceleration
5. Acceleration Done
6. Start Beta Squeeze
7. Ramp Squeeze
8. Finish Beta Squeeze
9. Storage

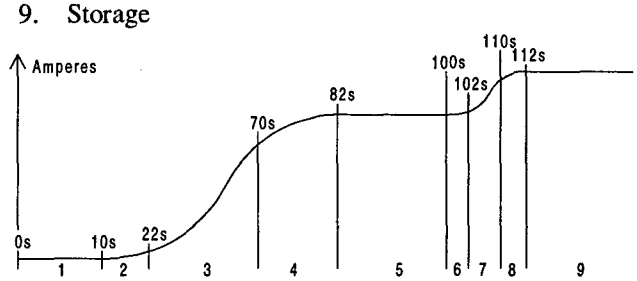

Figure: 2 Current Waveform

The simulation performed on the single shunt p.s. model revealed that the Q7 dynamic magnet current error was greatest in the Region 2. The Q7 maximum dynamic magnet current error in this region was 0.045% of the Q7 magnet current.

* Work performed under Contract No. DE-AC02-76CH00016 with the U.S. Department of Energy.

Email: bruno@bnl.gov

3 SINGLE SEXTANT PS MODEL

The next step in the simulation was to go from a single shunt p.s. model to a single sextant [2] model as shown in the block diagram of Figure 3.

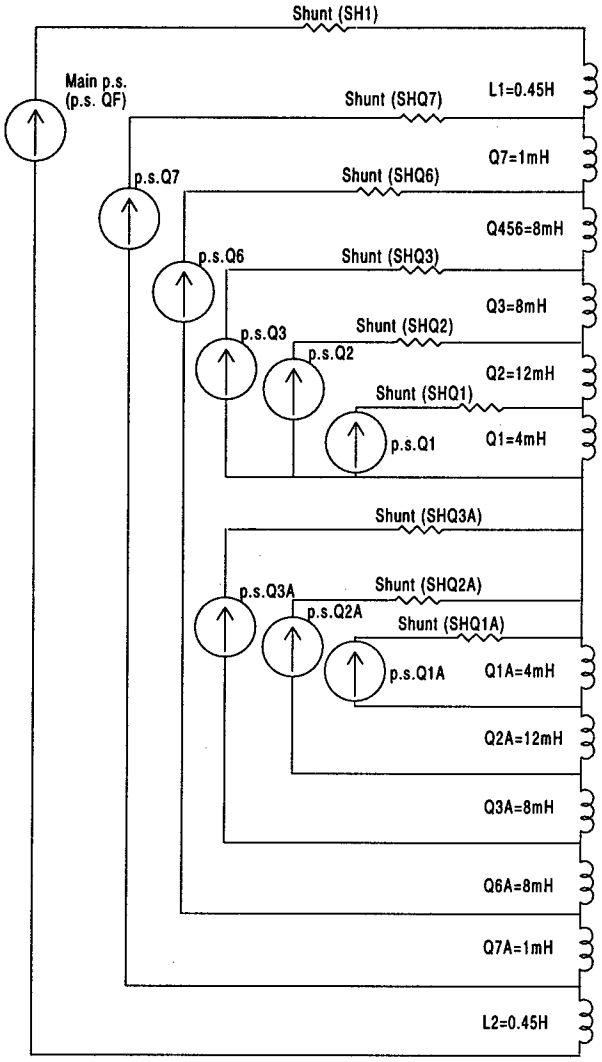

Figure: 3 Single Sextant PS Model

This single sextant model consists of 12 magnets and 9 current regulated p.s.'s. Four Simulations were run on the single sextant model. Once again the magnet inductances are typical of the real magnet inductances. Each one of these p.s.'s were ramped with the true current waveform that was required in the magnets. Table 1 and Table 2 contain data regarding the characteristics of the p.s. regulation loops for this single sextant simulation 1. Table 3 contains data regarding the magnet currents [1] and Table 4 contains magnet current errors (first 3 regions) for this single sextant simulation 1. In simulation 1 all of the p.s.'s (except psMain) have a DC gain of 86dB. PsMain has a DC gain of 104dB. The 3dB bandwidth of all of the p.s.'s was between 2 Hz and 23Hz for Simulation 1. The magnet inductances did not vary with current in this simulation. This simulation also showed that the maximum dynamic magnet current error occurred in Region 2. This agrees with the single shunt p.s. simulation. The maximum dynamic magnet current

Circuits	3dB BW (Hz)	Open Loop DC Gain (dB)	Open Loop 1Hz Gain (dB)
psMain	3.45	104	9.63
psQ7	1.98	86	9.64
psQ456	4.0	86	21.34
psQ3	4.25	86	22.02
psQ2	14.91	86	25.08
psQ1	23.01	86	31
psQ3A	4.25	86	22.02
psQ2A	14.91	86	25.2
psQ1A	23.01	86	31

Table 1. Simulation 1 Regulation Loop Characteristics

Circuits	Open Loop 0dB Crossing (Hz)	Open Loop Phase Margin (degrees)
psMain	3.01	83.57
psQ7	1.94	87.02
psQ456	9.33	110.13
psQ3	4.77	101.61
psQ2	12.83	85.78
psQ1	14.21	69.91
psQ3A	4.77	101.61
psQ2A	12.83	85.73
psQ1A	14.21	69.91

Table 2. Simulation 1 Regulation Loop Characteristics

Circuits	Region 1 (A)	Region 5 (A)	Region 9 (A)
psMain	560	4500	4590
psQ7	68.42	550	110
psQ456	0	0	450
psQ3	-28	-225	-183
psQ2	3	25	-34
psQ1	5.23	42	150
psQ3A	-28	-225	-183
psQ2A	3	25	-34
psQ1A	5.23	42	150

Table 3. Simulation 1 Magnet Currents

Magnets	Absolute Max % Region 1	Dynamic Max % Region 2	Dynamic Max % Region 3
QF	7E-6	0.03	0.025
Q7	7E-6	0.045	0.037
Q456	7E-6	0.047	0.038
Q3	0.174E-3	0.05	0.04
Q2	0.155E-3	0.051	0.042
Q1	0.123E-3	0.051	0.042
Q3A	0.174E-3	0.05	0.04
Q2A	0.155E-3	0.051	0.042
Q1A	0.123E-3	0.051	0.042

Table 4. Simulation 1 Magnet Current Errors

error, in Region 2, varied from 0.03% of magnet current to 0.051% of magnet current.

The single sextant simulation was run a second time, in simulation 2, but this time with current varying magnet inductances to study its effects. The inductances varied by as much as 10% of their nominal value, as a function of current. In this case, the maximum dynamic magnet current error, in Region 2, also varied from 0.03% of magnet current to 0.051% of magnet current.

The single sextant simulation was run a third time, in simulation 3, with the DC gain dropped to 74dB on all p.s.'s except psMain. The gain was dropped to see how much the magnet current error would increase. The maximum dynamic magnet current error, in Region 2, varied from 0.03% of magnet current to 0.14% of magnet current. Here the 12 db decrease in gain caused the dynamic magnet current error to increase by almost 3 times.

The single sextant simulation was run a fourth time, in simulation 4, once again with the 74dB gain and with current varying inductances The current varying inductances do not have much of an effect. The maximum dynamic magnet current error, in Region 2, varied from 0.03% of magnet current to 0.14% of magnet current.

4 COMPLETE RING PS MODEL

The complete ring [2] ps model was made up of six of the single sextant models. The simulation was run on a 150MHZ pentium computer with 32 Mb of RAM. To calculate the magnet current errors of one sextant took approximately 15 hours of run time.

In this simulation all of the p.s.'s (except psMain) have a DC gain of 74dB. PsMain has a DC gain of 104dB. The 3dB bandwidth of all of the p.s.'s was between 0.8 Hz and 25 Hz. The magnet inductances did vary with current in this simulation. This simulation showed that the maximum magnet current error occurred in the Region 2 again. This agrees with the single sextant p.s. simulation. The maximum dynamic magnet current error, in Region 2, varied from 0.04% of magnet current to 0.15% of magnet current. Table 5 and Table 6 contain data regarding the characteristics of the p.s. regulation loops for this complete ring simulation. Table 7 contains magnet current errors (first 3 regions) for this complete ring simulation.

5 CONCLUSIONS

These simulations show that the maximum magnet current error occurs in Region 2, the Start Acceleration region. In the complete ring model the maximum error was found to be near 0.15%. The maximum allowable error is 0.3% of magnet current. Since the magnet current errors from the simulations are less than 0.3%, the p.s.'s which are used in the ring shall have regulation loop characteristics which are close to those in this simulation. PsQ7 shall be a 20V (600A) 12 pulse SCR p.s. PsQ456 shall be a 15V (450A) 12 pulse SCR p.s. PsQ3 shall be a 15V (300A) 12 pulse SCR p.s. PsQ1 shall be a 15V (200A) 12 pulse SCR p.s. PsQ2 shall be a bipolar switchmode ±15V (±150A) p.s.

Circuits	3dB BW (Hz)	Open Loop DC Gain (dB)	Open Loop 1Hz Gain (dB)
psMain	3.57	104	10.76
psQ7	0.8	74	-7.86
psQ456	25.6	74	11.65
psQ3	2.33	74	11.21
psQ2	5.21	74	13.6
psQ1	1.94	74	6.23
psQ3A	2.31	74	10.24
psQ2A	5.2	74	12.85
psQ1A	1.92	74	6.25

Table 5. Complete Ring Regulation Loop Characteristics

Circuits	Open Loop 0dB Crossing (Hz)	Open Loop Phase Margin (degrees)
psMain	3.03	79.76
psQ7	0.69	62.85
psQ456	18.45	70.67
psQ3	3.63	90.49
psQ2	4.1	73.81
psQ1	2.66	99.84
psQ3A	3.62	90.29
psQ2A	4.06	73.81
psQ1A	2.68	99.74

Table 6. Complete Ring Regulation Loop Characteristics

Magnets	Absolute Max % Region 1	Dynamic Max % Region 2	Dynamic Max % Region 3
QF	7E-6	0.041	0.036
Q7H	1.64E-3	0.111	0.094
Q456H	1.64E-3	0.12	0.102
Q3H	0.85E-3	0.13	0.11
Q2H	0.94E-3	0.136	0.114
Q1H	1.1E-3	0.152	0.125
Q3J	0.85E-3	0.13	0.11
Q2J	0.94E-3	0.136	0.114
Q1J	1.1E-3	0.152	0.125

Table 7. Complete Ring Magnet Current Errors

6 REFERENCES

[1] S. Tepikian et al., "Tuning Curves", April 1994, RHIC Application Note, Number 23.

[2] The RHIC Design Manual

PERFORMANCE OF THE RHIC MAIN POWER SUPPLY SYSTEM*

C. Schultheiss#, BNL, Upton, NY

Abstract

Each of the main power supply systems for the Relativistic Heavy Ion Collider (RHIC) consists of a power module, a digital regulator and an output circuit compartment. The sextant test provided an opportunity to test the prototype main power supply system. This test indicated areas where improvements could be made in the system. Changes were incorporated into the design. Testing of the system, using the actual ring as a load, is expected to be complete by March 1999. The performance of this completed system is presented and discussed.

1 INTRODUCTION

The actual ring has not been available for testing; the results presented are from tests of the subsystems that make up the main power supplies.

2 CURRENT SIGNAL CONDITIONER

The Current Signal Conditioner (CSC) printed circuit board develops an error signal based on the difference between the Direct Current Current Transducer (DCCT) and a DAC that receives the commanded current. The error signal is amplified by a factor of 16 and then digitized by a 16 ADC, this provides the equivalent of 20 bits of resolution in the current loop. Figure 1 shows a block diagram of the test configuration of the CSC.

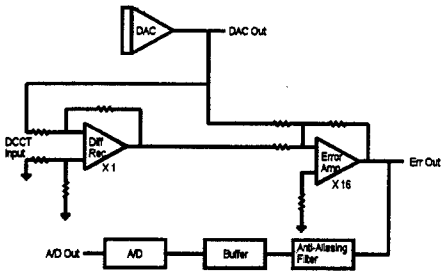

Figure 1 Test Configuration for Current Signal Conditioner

*Work performed under Contract No. DE-AC02-76CH00016 with the U.S. Department of Energy.

Email: carls@bnl.gov

2.1 DAC Linearity

The DAC Out signal was used to measure the linearity of the DAC. Figure 2 presents the results. The numbers at the edge of the graph indicate the extreme values.

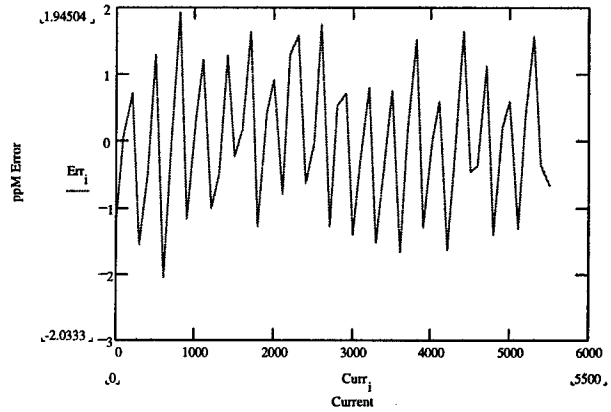

Figure 2 DAC Linearity Error

The linearity error is within the error budget allocated for it. A scheme to improve the linearity is under development; the necessary hardware has been incorporated into the regulator.

2.2 Accuracy and Noise

The Accuracy and Noise was measured at the Err Out signal and at the A/D Out at various currents. Figure 3 shows the typical output at the A/D Out signal in ppM.

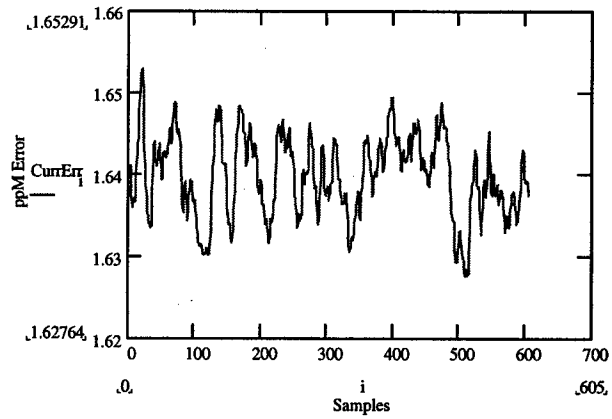

Figure 3 Accuracy and Noise at A/D Out

3 SUB-HARMONIC CORRECTION

The power supply uses digital firing circuits to allow a real-time correction of the sub-harmonic frequencies generated by the phase controlled power converter. [1] The sub-harmonic correction algorithm has been improved since the sextant test. [2] Figure 4 shows the sub-harmonic frequencies without correction and with correction at 1000 amps.

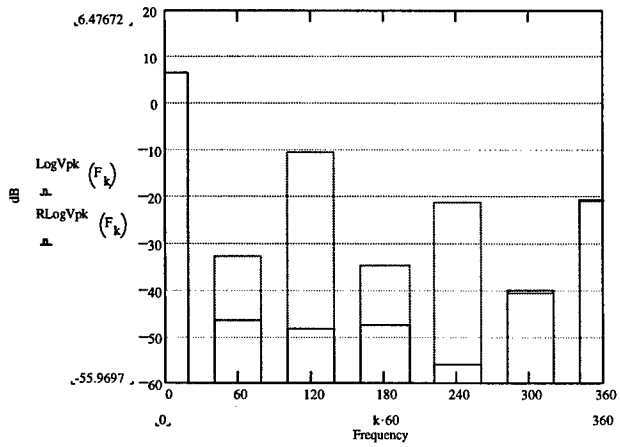

Figure 4 Sub-Harmonic Correction at 1000 Amps

4 QUENCH PROTECTION CIRCUITS

The magnets are super-conducting and require a circuit to extract the energy in the event of a quench. The quench protection circuitry consists of a pair of free-wheeling SCRs that are across the output of the main power supplies. These free-wheeling SCRs will conduct current when the output voltage polarity is the opposite of normal operation. When these SCRs conduct they place energy dump resistors in the circuit as they are triggered. The main SCRs are commutated off by a pulse-forming network (PFN) that back biases them. A quench detection system provides the triggering signal when it detects a quench. The quench protection system also includes self-triggering circuits that will trigger the free-wheeling SCRs if the output voltage rises above the normal operating range.

The quench protection circuits have been tested on a 300 uHenry inductor. The following oscilloscope pictures show the PFN output voltage in the upper trace and the current in the energy dump resistors in the lower trace.

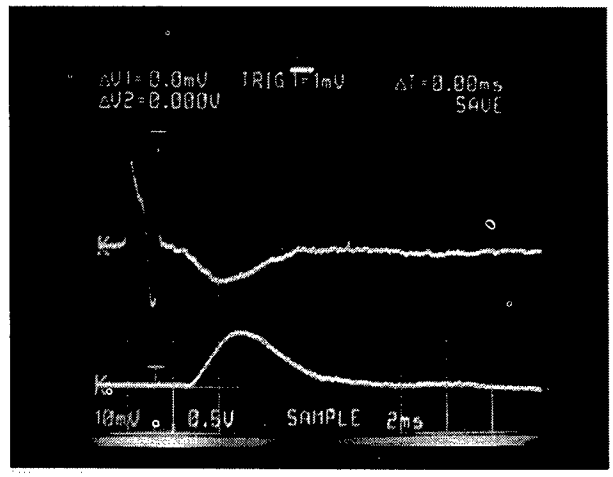

Figure 5 Quench at 500 Amps

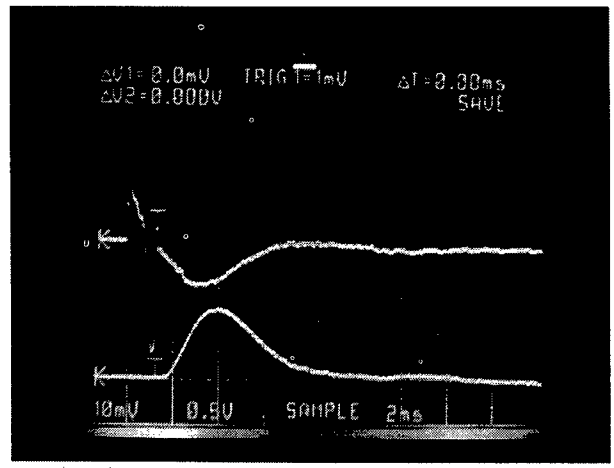

Figure 6 Quench at 3000 Amps

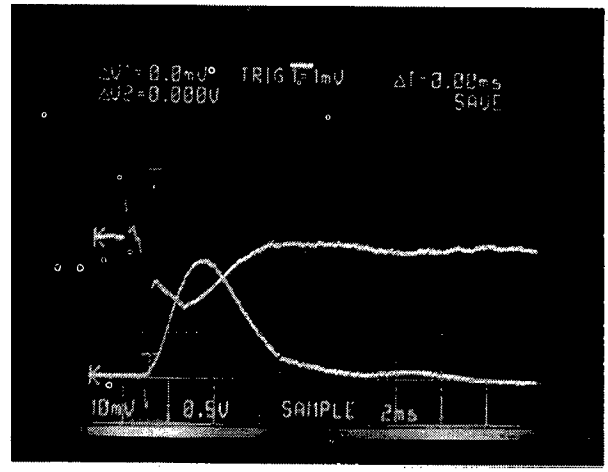

Figure 7 Quench at 5500 Amps

The pictures indicate that the time between the firing of the PFN circuit and the beginning of current flow in the energy dump resistor is dependent on the current in the main circuit. The voltage at the output must reverse polarity before the free-wheeling SCRs can begin to conduct. The output capacitor delays this voltage reversal and is the reason the delay is current dependent. The voltage across the main SCRs is also reduced due to the voltage drop in the resistance of the inductors that form part of the PFN network.

5 CONCLUSIONS

The sub-systems tested in the main power supplies have shown satisfactory performance. When the ring becomes available further testing will be conducted.

6 REFERENCES

[1] C. Schultheiss and T. Haque, "Digital Regulation of a Phase Controlled Power Converter", Nuclear Science Symposium and Medical Imaging Conference, (1994)

[2] C. Schultheiss, D. Bruno, P. K. Feng, T. Haque, and R.F. Lambiase, "Power Systems for the RHIC First Sextant Test", Particle Accelerator Conference , (1997)

FOUR-QUADRANT CONVERTER [±600A, ±12V] PROTOTYPE FOR LHC

G. Kniegl, R. Weber, TRANSTECHNIK, Holzkirchen, Germany
F. Bordry, A. Dupaquier, CERN, Geneva, Switzerland

Abstract

The CERN Large Hadron Collider (LHC) project will make extensive use of true bipolar power converters [±600 A, ±12 V]. The need to install the power converters in excavated caverns underground requires considerably reduced dimensions and high efficiency. Moreover, the LHC machine demands a very high level of performance from the power converters, particularly in terms of DC stability, dynamic response and also with regard to ElectroMagnetic Compatibility (EMC). To meet these requirements, soft-switching techniques are used. The design and the performance (DC stability, bandwidth, efficiency, EMC...) of a compact (6U) and high frequency (30kHz) four-quadrant power converters are presented.

1 INTRODUCTION

The CERN Large Hadron Collider (LHC) machine will make extensive use of true bipolar power converters [±600 A, ±12 V] to correct the multipole errors of the main superconducting magnets [1,2]. These power converters feed sextupole and decapole spool piece circuits as well as octupole magnets. Several trim magnets also require 600A four-quadrant converters. In total there are about 450 converters [±600 A, ±12 V]. The need to install the power converters underground requires considerably reduced dimensions and high efficiency. Moreover, the LHC machine demands a very high level of performance from the power converters, particularly in terms of DC stability, dynamic response and also with regard to Electromagnetic Compatibility (EMC). The outstanding feature of four-quadrant [±600 A, ±12 V] power converter is its high regulation precision. The converter module is 6U high and fits into a 19" rack and is thus very compact.

2 POWER CIRCUIT DESIGN

To meet the LHC requirements, soft-commutation switch-mode techniques will be used [3].

The chosen topology for the [±600A,±12V] converter is described in three parts

- Part 1: Circuit-breaker and contactor together with a soft-start circuit, a three-phase six-pulse diode rectifier on the AC mains (400V) with a damped L-C passive filter having a resonance frequency of about 40 Hz.
- Part 2: Full-bridge Zero Voltage Zero Current Switching Phase Shift Inverter (FB-ZVZCS-PS) at 30kHz, high frequency transformers, rectifier stage and 4th order L-C output filter.
- Part 3: Bipolar Linear Output Stage (BLOS)., Controlled high-current linear amplifier stage with paralleled MOSFETs for realisation of smooth zero crossing of output current.

Figure 1 shows the block diagram of the 4-quadrant converter.

2.1 *Zero Voltage Zero Current Switching Chopper*

The 3-phase mains voltage is rectified and smoothed. The resulting DC intermediate voltage feeds the DC/DC chopper operating at 30 kHz. This stage employs a "phase shifting" switching mode inverter (ZVZCS = Zero Voltage / Zero Current Switching) and provides a

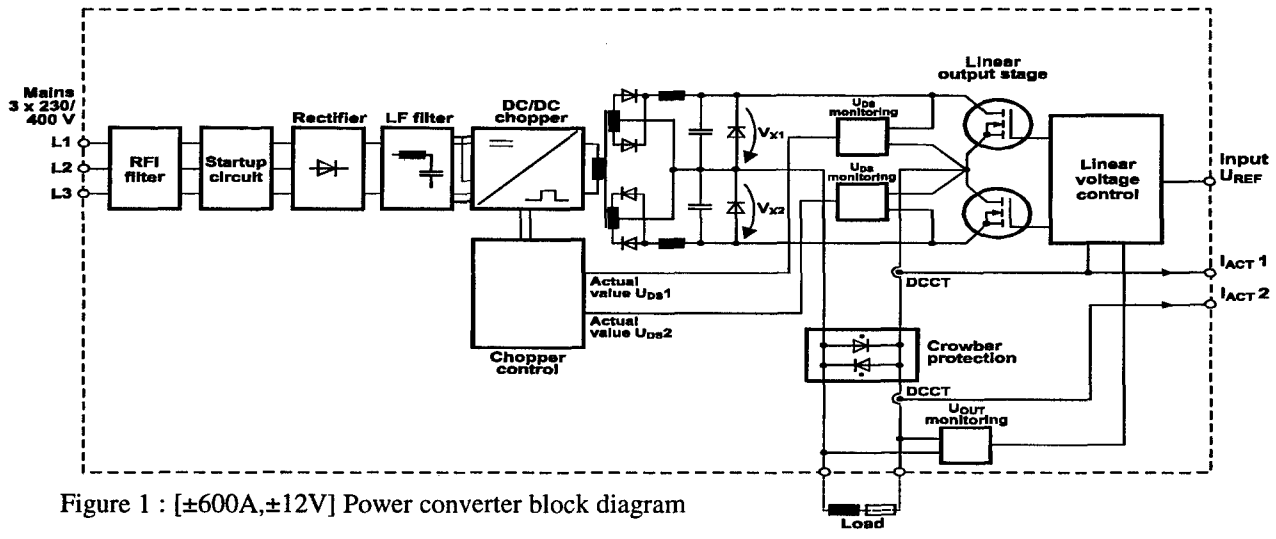

Figure 1 : [±600A,±12V] Power converter block diagram

stabilized, electrically isolated, bipolar, variable output voltage. The control of the power semiconductors (IGBTs) is done, instead of turning off the diagonally opposite switches in the bridge simultaneously as for a classical PWM, by introducing a phase shift between the two legs of the bridge. This phase shift determines the output power whereas the switching frequency is fixed to 30 kHz. The needed energy to achieve soft-commutation conditions for the switching of the leading leg (ZVS) comes from the series inductance, the leakage inductance and the output filter inductance. This means that the energy stored is very large to charge and discharge the parallel switch capacitances (parasitic and snubbers) and the parasitic capacitances of the transformer. By using a dc blocking capacitor and a saturable inductance, the primary current is reset during the freewheeling period, which provides ZCS conditions for the lagging-leg switches.

2.2 Bipolar Linear Output Stage

The chopper's output filter has to filter a 60 kHz square wave to obtain a 4mVrms output voltage ripple and it is designed as a two stage, 4th order filter.

The two choppers' outputs are used as supply voltages for the two halves of the complementary final output stage BLOS (**B**ipolar **L**inear **O**utput **S**tage). The BLOS is used for feeding or discharging the coils of the superconducting correction magnets of the LHC with a high-precision current and a very precise crossing of zero current. In order to keep the losses down in BLOS to a reasonable level during energizing of the superconducting magnet, the drain-source voltage (Vds) of the active MOSFET is monitored and kept constant at about 2 volts. The duty cycle of the inverter is controlled to maintain constant Vds voltage.

The energy stored in the superconducting magnet (maximum inductance is 570mH) is dissipated in the BLOS and in the cable resistance (minimum resistance is 2.8mΩ). The DC/DC chopper is then switched off, the energy discharged through the linear power stage and a free-wheeling diode connected across the output of the DC/DC chopper.

A soft zero-crossing without discontinuity is realised by a regulated constant bias current flowing through both halves of the BLOS.

An electronic device assure a safe path for the magnet current at any fault. The device is constituted of two back-to-back thyristors, called crowbar. One of them turns on if an over-voltage (>20V) appears at the converter output. The triggering of the crowbar is completely autonomous and does not need any auxiliary voltage.

2.3 Control loops

The outstanding feature of the four-quadrant [±600 A, ±12 V] power converter is its high regulation precision. The device provides a DC output voltage which is extremely accurate, follows a predefined reference value without delay and boasts an extremely low output ripple in the mV range.

The converter itself works as a voltage controlled voltage source which is inside CERN's highly accurate current control loop. This loop makes use of precise current transducers (DCCTs), to get a current accuracy in the 100 ppm range.

The DC output voltage is adjusted by the Bipolar Linear Output Stage (BLOS) according to the given reference value by CERN, which is an inner control value of the outer current control loop.

To obtain a smooth zero crossing all MOSFETs, both the active and the passive branch, are held in a conductive state by an additional bias current control loop. This avoids the occurring jump in the gate voltage of the MOSFETs just beginning to conduct current. This loop makes use of two current transducers, which measure the current through each branch. The regulator takes the minimum of both signals as actual value and adjusts the driving voltage for the MOSFETs to maintain a constant circulating bias current of about 10 Amps in the BLOS.

3 MECHANICAL DESIGN

The four-quadrant converter [±600 A, ±12 V] is designed as a 6 U module inserted in a 19"rack and is thus extremely compact. The weight of one power module is 65 kg. To allow easy insertion and extraction, which can be done by one operator, it is placed upon a special drawer system (cf. photo 1). Once withdrawn, it can be carried by two people using the hinged side handles.

Two complete power converters, each including a power module, an output circuit with two DCCT, the crow-bar protection, and two 6U CERN electronics chassis are housed in one 19" rack with a total height of 2 meters.

The water distribution system with valves and flow

Photo 1 : [±600A,±12V] converter; 6U module

meter and an input EMI filter are placed at the bottom of the rack. Each power module is supplied with cooling water independently and are thus fully independent. Before un-plugging a module, only the signal cables to the CERN electronics and the water inlet and outlet have to be removed with self-sealing connectors directly on the front panel. The output bus bars for the connection to the magnets are placed at the rear side of the rack and the connection to the magnet can be made either at the top or at the bottom of the rack.

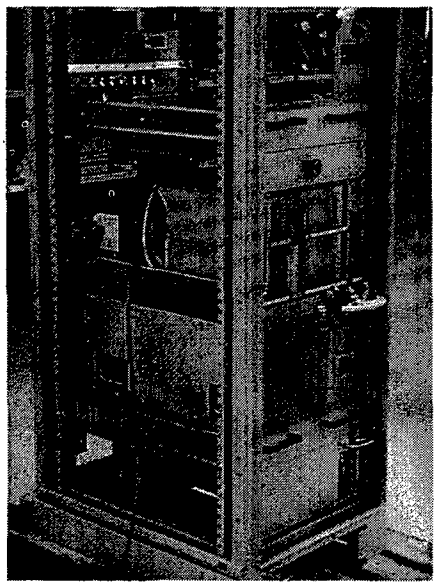

Photo 2 : 6U module inserted in a 19"rack

4 PERFORMANCE

The measured efficiency is 75% at full power and 70% at half power. Most of the main losses are coming from the linear output stage (~65% of the losses).

The measured output voltage ripple is less than 1 mVrms in the 50 - 300Hz frequency band and less than 2mVrms at the switching frequency and its harmonics (Figure 2 and 3).

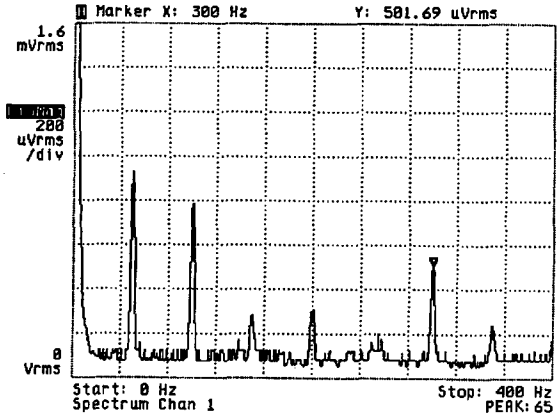

Figure 2: Spectrum Analysis : 0 – 400 Hz

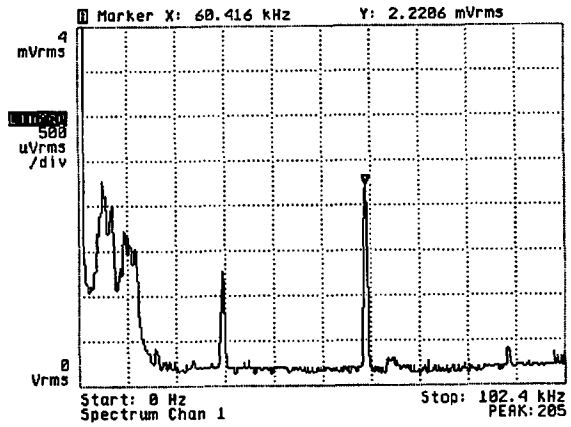

Figure 3: Spectrum Analysis : 0 – 100kHz

The noise emission (EMI) is in compliance with the IEC478-3, curve C (1mV above 0.5 MHz).

Figure 4 presents the zero-crossing of the output voltage with a 0.1Hz sine voltage reference

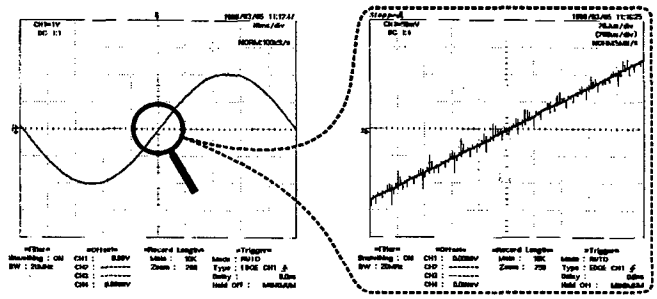

Figure 4: Output-Voltage Zero Crossing

5 CONCLUSION

The performance requirements have been achieved under the severe constraint of small volume. Especially, zero crossings of the output current without discontinuity, i.e. true 4-quadrant operation and extremely low output voltage ripple of lower than 1 mVrms at 300 Hz and of lower than 2 mVrms at the switching frequency of 30 kHz and its harmonics have been realized. This [±600A,±12V] converter can be considered as a full-size LHC prototype. Six converters are built by Transtechnik according to CERN's specification and will be used intensively for the LHC magnet tests.

REFERENCES

[1] "LHC Conceptual Design", CERN/AC/95-05 (LHC)

[2] http://wwwlhc01.cern.ch/lhcpub/Welcome.html

[3] F. Bordry, A. Dupaquier, "High Current, Low Voltage Power Converters for LHC, EPAC'96, Sitges, June 1996.

[4] J.G. Cho, J. Sabate, G. Hua , F.C. Lee, "Zero voltage and zero current switching full bridge PWM converter for high power applications", IEEE PESC Rec., 1994, pp. 102-108

DEVELOPMENTS IN THE HIGH PRECISION CONTROL OF MAGNET CURRENTS FOR LHC

I. Barnett, D. Hundzinger, Q. King, J.G.Pett, CERN, Geneva, Switzerland

Abstract

The LHC will require over 1700 magnet power converters, some of which will need an unprecedented precision of about 1 ppm (of 13 kA). This paper presents the approach taken, prototype methods, initial results and charts future design directions. These results confirm that such performance can be obtained reliably and at a reduced cost compared to conventional methods. Developments of a real-time controls infrastructure needed to support on-line beam feedback are outlined.

1 BACKGROUND

For the LHC machine to achieve its full potential, the power converter system needs to attain a peak performance of about 1 part per million (ppm) in terms of resolution, stability and reproducibility. This represents an improvement over current practice of approximately a factor of ten. In addition, the very large electrical time constants presented by super-conducting magnets, coupled with the need to remove dynamic errors required a new approach. In order to meet this challenge a number of studies and practical tests have taken place over the last few years aimed at proving that such increased performance can be obtained reliably. A strategy for obtaining such improvement was presented in an earlier paper [1]. In brief this strategy was :

- Employ digital regulation methods rather than analogue methods.
- Apply digital corrections of known errors.
- Employ real-time feedback mechanisms (both magnetic and beam related).
- Incorporate in-situ calibration techniques (this subject is not covered further in this paper).

This approach required an extensive revision of present practice for the regulation and remote control. This paper presents the design of the prototype system, the results obtained and outlines future design directions.

2 PROTOTYPE IMPLEMENTATION

The digital regulation hardware, shown in figure 1, has been built using a commercial digital signal processor (DSP) card as the heart of the system. This processor, a Texas TMS320C32, 32 bit floating-point device computes the current reference value every milli-second,

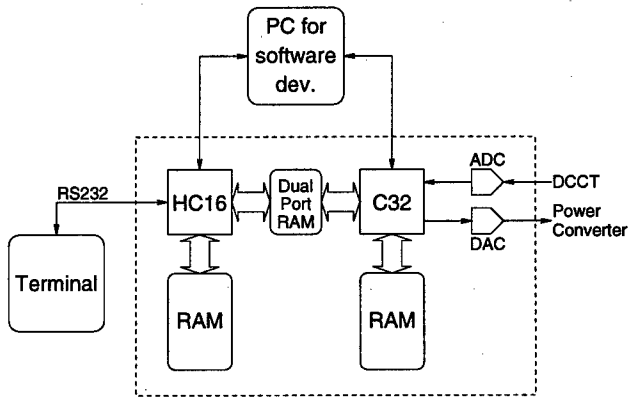

Figure 1: Prototype Hardware.

compares this to the actual measured current and then computes, using a regulation algorithm, the required signal to drive the power converter to the correct value. This signal is converted into analogue form via a digital to analogue converter (DAC). The output current is measured by a purpose designed, Sigma-Delta, analogue to digital converter (ADC), which has better than ±1 ppm performance and is directly interfaced to the DSP. The interface between the DSP, the remote control system and the power converter hardware is provided by a second commercial micro-controller card. This card employs a Motorola MC68HC16Z1 which acts as the 'master' for the DSP.

The software for both processors is written in 'C', using commercial software development tools. Only minor use of assembly language has proven necessary. Both systems employ 'direct to processor' connections to the PC (BDI and JTAG), allowing code down-load and extensive debug capabilities. The reference and regulation algorithms operate as a single repetitive task in the C32 while a simple command monitor running in the HC16 and using a terminal as input, replaces the remote control functionality. For the moment, no real-time operating system is employed but this will be incorporated in the next generation.

In order to evaluate the power converter performance under digital regulation, an independent measurement system has been set up. This uses a high precision HP3458 DVM to measure the current, and also captures data directly from the DSP every millisecond via a FIFO buffer. Display and analysis software is based on MATLAB, which is also used to study and simulate the entire regulation system, allowing theoretical and practical results to be compared.

0-7803-5573-3/99/$10.00@1999 IEEE.

3 CONTROL ALGORITHM DEVELOPMENT

The control algorithm for the power converter regulation is a key element in determining the overall performance. Two methods have been incorporated and are under detailed investigation. They aim to provide the necessary accuracy, resolution and dynamic performance. The first method is a digital realisation of standard analogue techniques employing proportional-integral-integral (PII) plus feed-forward. The second method employs a more modern approach, namely RST. Both methods have been tested in simulation and have proven to give more than adequate performance for LHC. The PII algorithm has been implemented fully and tested extensively with real power converters and magnet loads. A number of practical problems had to be solved, including start-up conditions and loop saturation. Tests have also been successfully conducted on adaptive algorithms but they are probably not necessary. Both algorithms are deceptively simple in code terms, but do require some attention with the mathematical errors due to the single precision maths of the DSP.

4 REFERENCE GENERATION

The generation of an accurate and smooth acceleration waveform is essential for the successful operation of LHC. The preferred form for the main magnetic elements is explained in another contribution to this conference [2]. The control algorithm requires the precise value of this waveform to be evaluated every loop iteration (1ms). A number of possibilities for implementing this complex waveform exist and have been studied in some detail.

Initial tests were performed using a linear ramp function and subsequently the addition of parabolic start and stop regions. This enabled most evaluations of control loop performance to be made easily. More recent work has aimed at numerical methods, employing quadratic or cubic spline fits, and in this area a number studies have indicated the potential of such methods to reduce the amount of data defining the desired waveform. Such reductions are desirable to reduce the network data flow. The direct application of correction multipliers at 100 Hz to the desired reference waveform has been demonstrated successfully in recent tests on the SPS machine

Latterly, a mathematical model of the preferred LHC waveform has been implemented directly in the DSP. This has allowed a number of interesting tests to be performed and will be of value for subsequent magnetic measurements. However, apart from test purposes, such methods are unlikely to be used for the LHC.

5 PROTOTYPE RESULTS

The results which are presented below are only the latest from a long series of measurements. Tests with simulated loads and model power converters have recently been complemented with full-scale tests on power converters up to 20 kA and with a variety of loads with time-constants ranging from 40 ms to 100 s. Final tests can only be made with the 23,000 s load of the actual LHC machine. Figure 2 illustrates low frequency noise and current steps of 1 ppm. Figure 3 shows a 'short' LHC acceleration curve (up to 5 kA). The form of the ramp was computed in real-time from segment equations. The segments were: (i) parabolic acceleration, (ii) exponential acceleration, (iii) linear ramp, (iv) parabolic deceleration. Figure 4 shows the first six seconds of the ramp in more detail, illustrating the excellent resolution and accuracy of the system. Good control at the start of the ramp is particularly important as the beam is then at its most vulnerable to errors. Analysis of the end of the ramp shows equally good behaviour with no overshoot. Finally, the long term stability of the controller is illustrated in figure 5. The linearity of the system is entirely dependent on that of the ADC (±1 ppm) and current transducer (DCCT), both of which are presently undergoing validation tests.

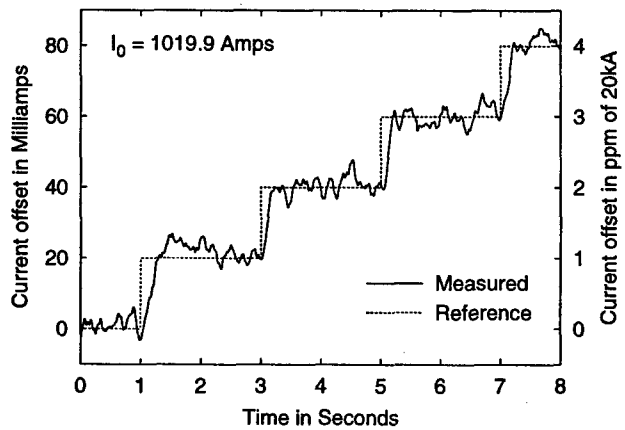

Figure 2: 1 ppm Current Steps.

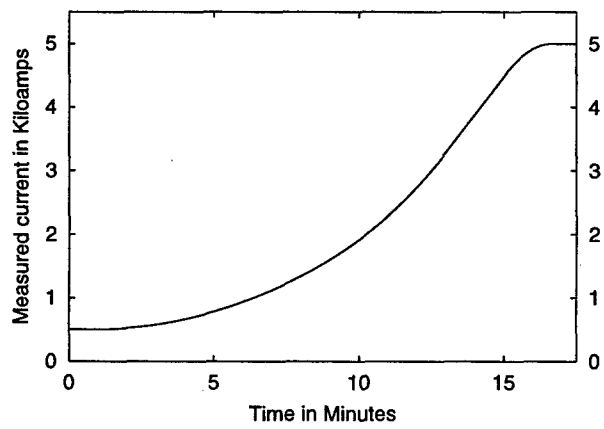

Figure 3: Short LHC Ramp.

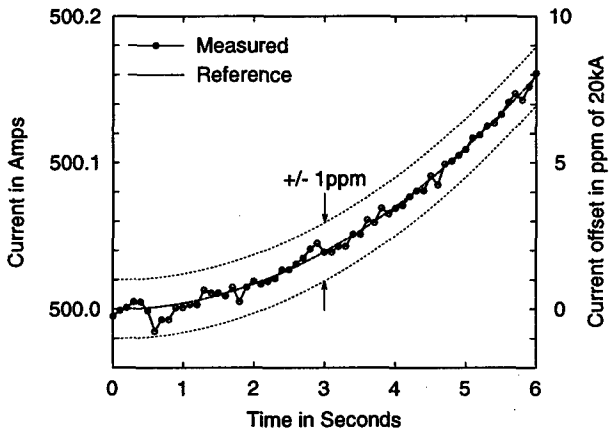

Figure 4: The start of the short LHC ramp.

6 DEVELOPMENT WORK

In order to progress further towards a final system design a number of important steps have been taken recently. The first is the development of a cheaper ADC for the majority of circuits which have less demanding requirements. The second is the completion of a single card design which brings together all of the essential components mentioned earlier. Extensive use has been made of field programmable gate arrays (FPGA's) and a novel serial digital/analogue input system has been developed for power converter surveillance.

A very important third development has occurred recently with the adoption of the WorldFIP field bus as the link between the digital controller card and the LHC accelerator network. This field bus has a number of specific characteristics, among which, its deterministic performance is paramount. This feature enables the WorldFIP to transport reliably the online, 100 Hz, closed-loop correction data around the LHC, while also doubling as a simple transport mechanism for the required machine synchronisation and timing. This results in a considerable cost saving while enhancing reliability due to component reduction. Status and measurement data can equally be up-loaded to the control room at 100 Hz.

Parallel developments in the overall controls network should allow extensive use of real-time control across the entire system. Code down-load and diagnostics up-load also enhances system flexibility and accelerator performance.

7 CONCLUSIONS

The results of the prototype work which have been presented, validate the overall strategy adopted earlier. The performance improvements are such that power converters can now be designed with all major errors reduced to the ppm level. This has been achieved along with an overall reduction in costs. The methods are applicable to a very wide range of power converter loads, ranging from several tens of milliseconds to more than ten thousand seconds. Moreover, on-line feedback can be incorporated at essentially zero cost, while the design realisation allows hardware and software refinement to continue up to and beyond the putting into service of the equipment. Overall system validation remains to be done however, along with an industrialisation process for series manufacture.

8 ACKNOWLEDGEMENTS

The authors wish to thank the many CERN, academic and industrial colleagues without whom this work could not have been made.

9 REFERENCES

[1] . J.G.Pett et al, CERN, "A Strategy for Controlling the LHC Magnet Currents", EPAC'96 p. 2317.

[2] P.Burla et al. CERN, "Optimisation of the Current Ramp for the Main LHC Circuits", PAC'99 NY contribution.

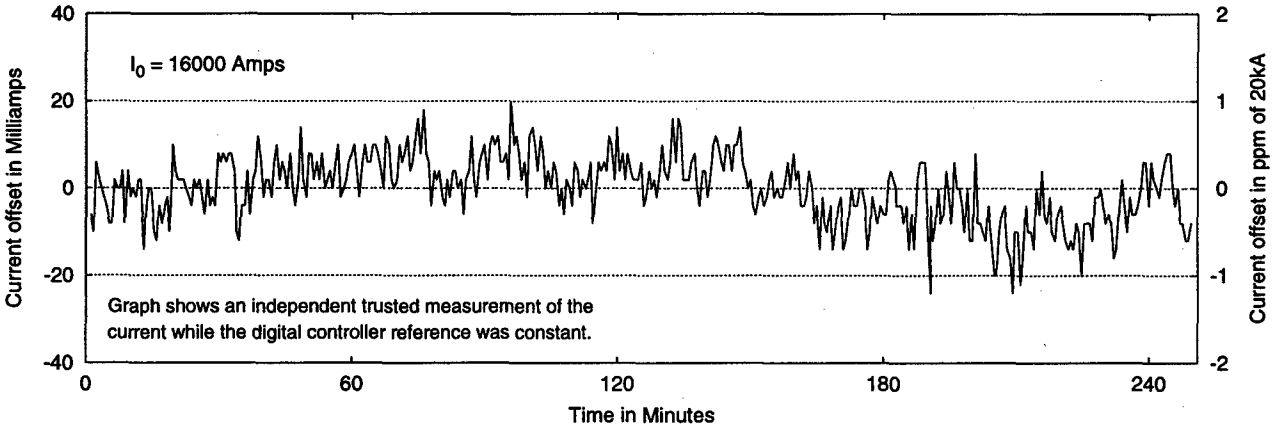

Figure 5: Stability over Time.

UPDATE ON THE POWERING STRATEGY OF LHC

P. Proudlock, on behalf of the LHC Electrical Engineering and Dynamic Effects Working Groups,
CERN, 1211 Geneva 23

Abstract

Over the last two years the powering strategy of the Large Hadron Collider (LHC) has undergone a considerable evolution. This was not only motivated by new requirements but more importantly by a quest to reduce costs and improve operational reliability and flexibility. In order to achieve this, despite an increase in complexity, novel modifications to the strategy and hardware have been proposed both on the warm and cold sides of the machine. During this process the requirements of the accelerator physics have been clarified and met while working within the boundary conditions imposed by the utilisation of the existing CERN infrastructure. After a brief review of the present powering strategy which needs to produce and supply 2MA dc in 1800 circuits, more detailed descriptions will be given of the changes implemented in order to achieve a more rational overall system. Some performance issues of the powering system will also be discussed.

1 INTRODUCTION

The LHC will be installed in an existing underground tunnel of 27km circumference that presently houses the Large Electron Positron machine (LEP). Much of the infrastructure of LEP will be reused, notably the civil engineering and electrical distribution which, while giving substantial economies, will place constraints on the powering equipment which must be designed within certain boundary conditions.

Each of the eight sectors of LHC will be powered individually and, for the main circuits, ring 1 and 2 will be powered in series. However, the main dipoles, focusing quadrupoles and defocusing quadrupoles of the FODO cell structure are separately powered. A continuous cryostat runs along each of the eight sectors with superconducting magnets cooled to < 2K (Fig. 1). This cryostat contains the main lattice circuits as well as the dispersion suppressors and some of the matching section at each end. A large number of superconducting bus-bars run through the cryostats connecting the various circuits which are fed from electrical feed boxes (DFB) located at each end of the sectors. The long straight sections of the interaction regions have several additional magnets that are locally fed. The main lattice circuits are fed from the even points, left and right, while in the odd points the powering is kept to a minimum and is associated with the circuits located at the end of the arcs. This matches the geographic availability of the existing ac power of LEP.

The power converters of LHC must be situated as close as possible to the machine's electrical feed boxes in order to minimize the transport of the high currents required by the machine (up to 13 kA). Therefore, they will be placed underground using, for the most part, the caverns vacated by the Klystrons of LEP (Fig. 2). The LHC has the following superconducting circuits;

- 24 main circuits of 13 kA,
- 8 low beta triplets requiring 8 or 13 kA,
- 212 individually powered quadrupole circuits requiring 6 kA,
- 544 auxiliary circuits of 600 A,
- 956 orbit correctors of 60 to 120 A.

There are also 48 circuits with room temperature magnets.

In all, LHC will require 2000 kA through 1800 circuits.

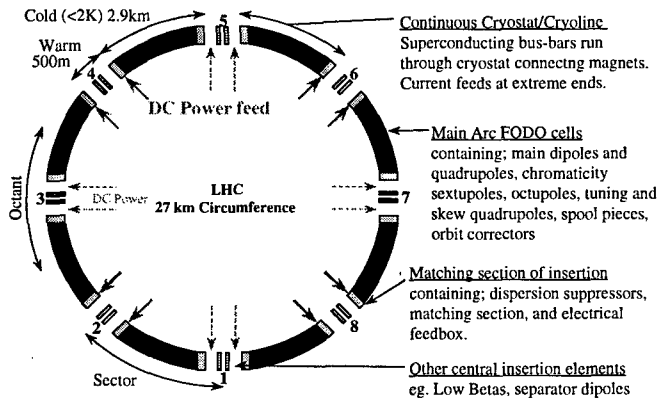

Figure 1: Schematic layout of LHC.

2 MAIN DIPOLES AND THEIR CORRECTORS

Each of the eight main dipole circuits contains 154 dipoles. They have cold bypass diodes and energy extraction to deal with a quench in one or more of the magnets [1]. Half the magnets are placed on the go bus-bar and half on the return so that energy extraction can be performed at the two ends of a sector, thus reducing the voltage withstand requirements. This results in two types of main dipole, at least as far as the connections are concerned. Originally b3 and b5 correctors were placed in all dipole magnets and later the possibility of adding a4

0-7803-5573-3/99/$10.00@1999 IEEE.

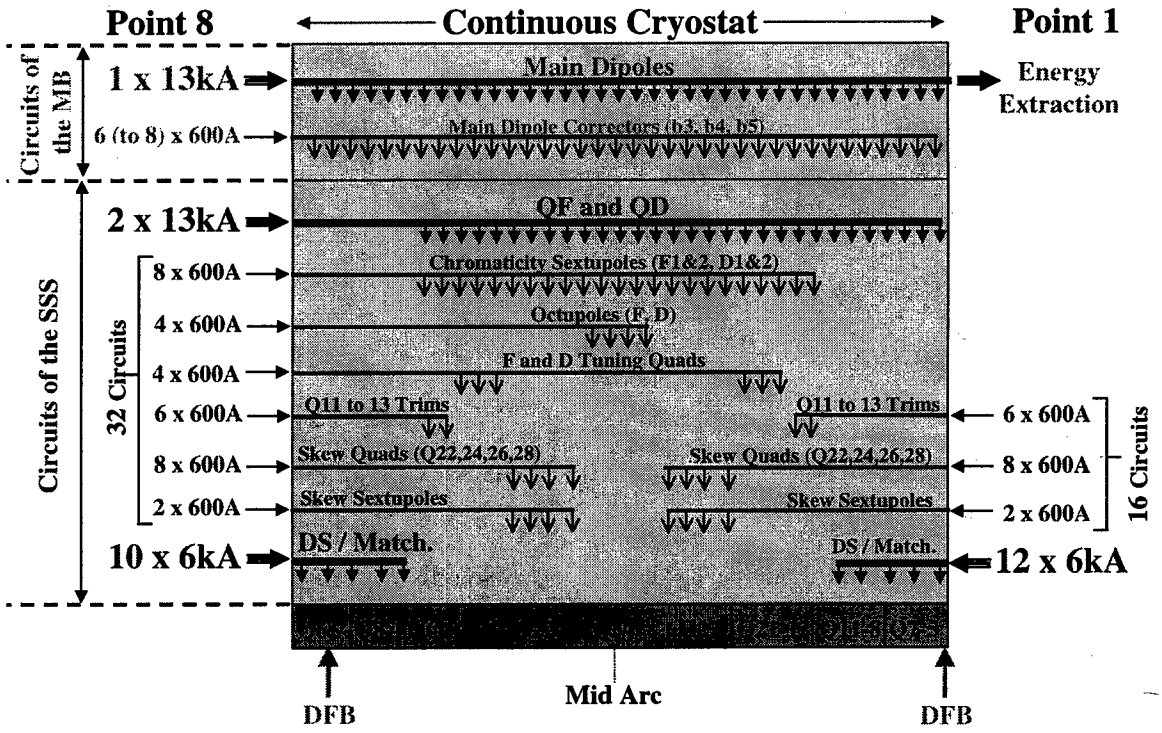

Figure 2: Schematic layout of sector of LHC.

and b4 correctors was considered. However, the exact requirements will not be known until the first pre-series magnets are measured. It has therefore been decided to profit from the existence of two types of dipole. One type will be equipped with a full complement of correctors (nested b4/b5 on one side and b3 on the other) while the other will have only a b3 corrector thus leaving space available if extra correctors are needed following measurements on the first series magnets. Provision for powering these additional circuits will be made.

3 INSERTION QUADRUPOLES

Originally the main arc quadruples were used for the individually powered quadrupoles of the long straight sections. These required 13 kA and, while feasible to power in a chain, were very expensive to power individually. A new magnet has now been designed specifically for such applications, which requires a maximum of 6 kA. Later studies on the dispersion suppressor revealed problems to get an adequate range from the trim system [2]. Therefore, these same magnets are now used in the dispersion suppressor and can be individually powered. Three rather than four bus-bars are used to power the two apertures thus saving on cold bus-bars and space requirements. The trim system is however retained for the dispersion suppressors of the cleaning insertions, but they no longer require the longer version of the main quadrupole. Thus only one length of main quadrupole is now necessary.

4 SUPERCONDUCTING BUS-BARS

The circuits associated with the main dipoles (dipole plus corrector magnets) as well as the two quadrupole circuits are fed through the cold masses of all magnets (Fig. 3). Their bus-bars are installed in slots in the cold masses. The dipoles use two bus-bars of 7.4 mm^2 NbTi with 300 mm^2 of copper stabiliser. Energy is extracted, in case of a quench, at an initial rate of 125 A/s. The quadrupoles use four bus-bars of 7.4 mm^2 NbTi with 180 mm^2 of copper and the initial discharge rate is 320 A/s. The dipole corrector magnets use 20 monolithic rectangular conductors with a cross section of 3 mm^2 and a copper to superconducting ratio of 9:1.

The individually powered quadrupoles and the array of corrector circuits associated with the short straight section (SSS) need to bypass the dipoles and a link is provided along the 53 metres of the half cell. For the 600 A circuits a flexible multi-wire cable is used containing 36 super-conducting wires with a diameter of 1.6 mm and a ratio Cu/SC ratio of 9.5:1. The outer diameter of the complete cable is 15.5 mm. A similar cable is proposed for the 6 kA circuits containing 18 multifilament conductors and having an external diameter of 23 mm. These need to be installed in a tube containing helium II running from SSS to SSS [3]. The number and type of cable varies around the machine according to the local needs for powering. This solution, compared to previous designs, where all routing was done inside the cold masses, reduces the number of electrical interconnections by 48000 and yields

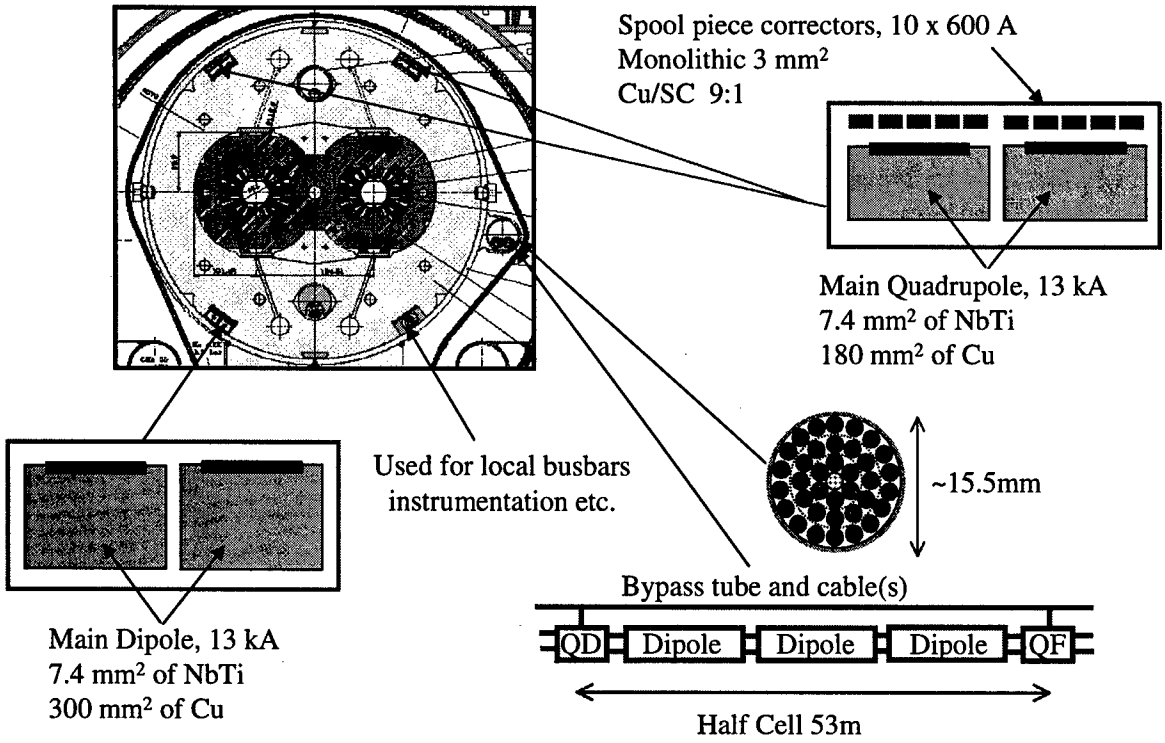

Figure 3: Superconducting busbars.

flexibility and reduction in costs. The 6 kA cable is the most difficult to engineer since the forces acting on it will be appreciable as there is a non-negligible field in the region of the tube. The tube itself needs to be carefully thermalised to the cold mass in order to avoid unacceptable additional cool down times.

5 POWER CONVERTER PERFORMANCE

It has now been established that modular switch-mode power converters with digital current loops will be used for LHC [4]. Some circuits will need a performance of a few parts per million of maximum and resolution of 20 bits. The reference magnets, previously in series with each of the main lattice circuits (24 in all), have now been eliminated. A few remote reference magnets powered by the same current cycle as those in the machine will replace them. They will be used primarily to derive feedback for the dipole correction circuits during persistent current decay and snap-back. Work has continued on beam feedback for orbit, tune and chromaticity [5]. An overall bandwidth of 1 Hz will be necessary and deterministic control will be provided using commercially available field busses

6 CONCLUSIONS

Over the last two years the powering strategy of LHC has undergone a considerable evolution. This was not only motivated by new requirements but more importantly by a quest to reduce costs and improve operational reliability and flexibility. During this process the requirements of the accelerator physics have been clarified and met while working within the boundary conditions imposed by the utilisation of the existing CERN infrastructure.

7 ACKNOWLEDGEMENTS

The members of the Electrical Engineering and Dynamic Effects working groups of the LHC Project carried out much of the work reported above and thanks go to them.

8 REFERENCES

[1] F. Rodriguez-Mateos, The Protection System for the Superconducting Elements of the LHC, this conference.
[2] P. Proudlock, Electrical Powering Strategy of LHC, First design study, P. Proudlock, 5th EPAC, 10-14 June 1996, Sitges, Spain.
[3] A. Poncet, Update of the LHC Arc System Layouts and Integration, this conference.
[4] F. Bordry et al, Four-Quadrant Converter (600 A, 12 V) - LHC Converter Prototype, this conference.
[5] R. Bailey et al., Dynamic Effects and their Control at the LHC, PAC, 12-16 May 1997, Vancoucer, Canada.

POWER COMPENSATION EFFECT OF AN ADJUSTABLE-SPEED ROTARY CONDENSER WITH A FLYWHEEL FOR A LARGE CAPACITY MAGNET POWER SUPPLY

Hirofumi Akagi

Dept. of Electrical Engineering, Okayama University, Okayama, 700-0082, Japan

Hikaru Sato

High Energy Accelerator Research Organization (KEK), Tsukuba, 305-0801, Japan

Abstract

Direct connection of the synchrotron magnet power supply to the utilities causes the effect of pulsed reactive and active power in the ac line. Conventionally, Static Var Control system compensates the reactive power generated by the thyristor converter to reduce the flicker in the power line. However, it is necessary to control not only a reactive power but also an active power for the future large scale synchrotron magnet power supply in order to reduce the dissipation power and to realize the stabilization in the ac line. An adjustable-speed rotary condenser is capable of not only reactive power control but also active power control since it utilize a flywheel effect of the rotor. Research and development on these problems are now under going using a model system of 7.5kW rotary condenser with flywheel (GD^2=3kg-m^2). Control and characteristic of an adjustable-speed rotary condenser and the experiment result will be presented.

1 INTRODUCTION

1.1 Background

The KEK-PS main ring magnet power system works at repetition rate 0.25 - 0.4 Hz for the power to be fed in and fed out from the utility to the magnets by converter and inverter mode operations. The magnet power system, consists of the ring magnet power supply (23.6MVA), the reactive power compensator systems (20 MVar lag for fundamental) and the harmonic filter banks (20 MVar lead) [1].

As a case of the 50 GeV main ring magnet power system of the Japan Hadron Project (JHF), peak power and dissipation power are estimated to be about 120MW and 34.5MW, respectively. For such a large scale magnet power system, the fluctuation of active power produce serious effects on power systems of the installation site of the magnet power supply, even if the reactive power is compensated. Hence, installation of a large-capacity energy storage system to the magnet power supply is now under consideration. For the JHF design, doubly-fed flywheel generating system is under consideration [2]. Attention has been paid to a flywheel energy storage system based on a doubly-fed induction generator-motor for the purpose of power conditioning with aiming at load-leveling over a repetitive period. Figure 1, for example, shows the typical pattern of which active power changes drastically in a range from +55MW to -55MW within 4 sec. It is also referred to as an "adjustable-speed rotary condenser" capable of both active power control and reactive power control, in contrast with a conventional "synchronous-speed rotary condenser" capable of only reactive power control.

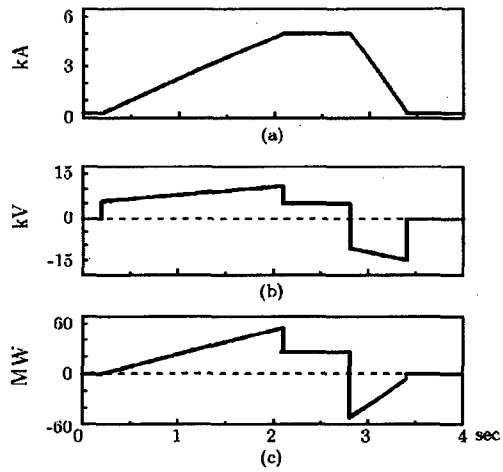

Figure 1 : Typical operating pattern of a magnetic power supply for a proton synchrotron. (a) Magnet current. (b) Magnet voltage. (c) Active power.

1.2 The 200-MJ flywheel energy Storage System

For example, the 200 MJ ROTES (Rotary Energy Storage System) was successfully commissioned at the Chujowan substation on Okinawa island of Japan [3]. The ROTES is an application of adjustable speed pumped

0-7803-5573-3/99/$10.00@1999 IEEE.

storage system technology, and is an excellent system designed to suppress frequency fluctuations caused by sudden and frequent load changes in the power system. With the 200 MJ ROTES, frequency fluctuations have been greatly improved from ± 0.6 Hz to ± 0.3 Hz.

2 SYSTEM CONFIGURATION

A doubly-fed flywheel generator-motor of a wound-rotor induction machine and a cycloconverter or a voltage-source PWM rectifier-inverter which is used as an ac excitor. Adjusting the rotor speed makes the generator-motor either release the kinetic energy to the power system or absorb it from the power system. Thus, the generator-motor has the capability of achieving, not only reactive power control, but also active power control based on a flywheel effect of the rotor.

The control strategy enables the flywheel generator-motor to perform active power control independent of reactive power control even in transient states. The flywheel generator-motor based on leading edge power electronics and electric machine technologies shows promise as a versatile power conditioner, in particular, being capable of repetitively absorbing or releasing electric energy for a periodical operation such as a synchrotron magnet power supply.

The ac excitation on the basis of a rotor-position feedback loop makes it possible to achieve stable variable-speed operation. Adjusting the rotor speed makes the generator-motor either release the electric power to the utility grid or absorb it from the utility grid. Therefore, the flywheel energy storage system is more suitable for repetitively absorbing and releasing electric energy for a short period of time. The required capacity of power electronic equipment for ac excitation is in a range from one-fifth to one-seventh as small as the capacity of the wound-rotor induction machine.

A 40-MJ flywheel energy storage system based on a 70-MVA doubly-fed induction machine should be installed on the ac side of the magnet power supply shown in Fig. 1, in order to achieve perfect load-leveling. Comparison with the 200-MJ system installed for line-frequency regulation leads to the possibility that the 40-MJ system does not need to couple any flywheel with the rotor, because the induction machine rating required to the 40-MJ system is 2.6 times as large as that required to the 200-MJ system. On the contrary, the 40-MJ system needs to achieve much faster charge/discharge of active power than the 200-MJ system.

3 EXPERIMENT SYSTEM AND SIMULATION

3.1 Experiment System

Despite of the 200-MJ successful example, it is necessary to confirm that a new control strategy for a doubly-fed flywheel generator-motor would be effective by an experiment.

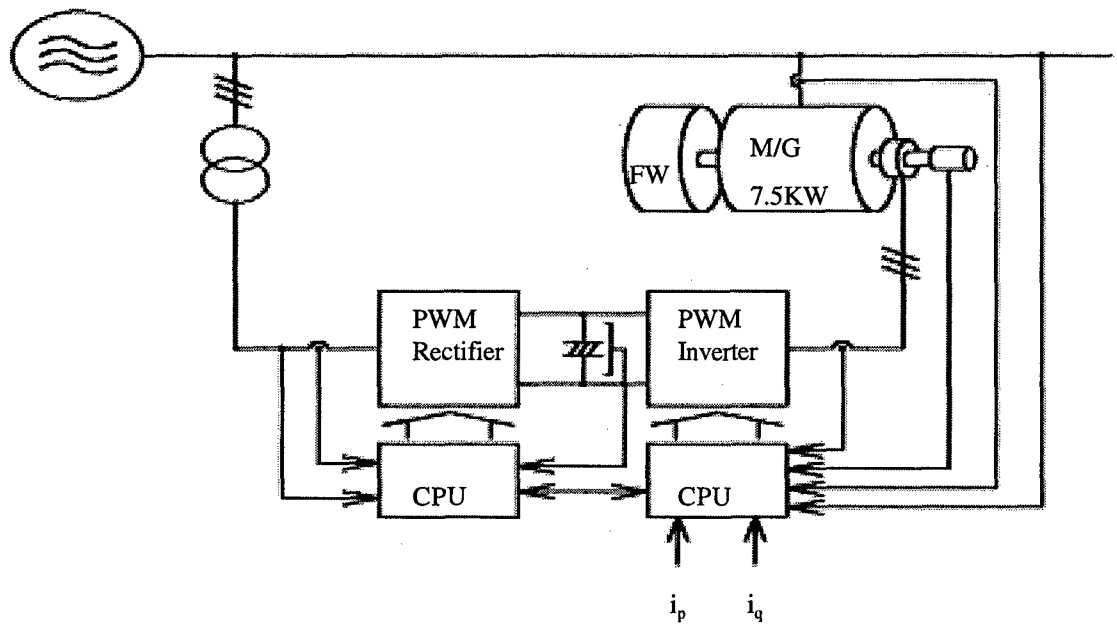

Figure 2 : Experiment system of the 7.5 kW doubly-fed flywheel with IGBT rectifier and inverter

The experiment system consists of a 7.5-kW doubly-fed induction machine equipped with a flywheel of 3 kgm^2, a 2-kVA voltage-source PWM rectifier, a 2-kVA voltage-source PWM inverter, and dual CPUs (Hitachi SH-1). Fig. 2 shows a block diagram of the experiment system. The rectifier and inverter using insulated gate bipolar transistors (IGBTs) rated at 600 V and 30 A, are controlled by the CPUs. Three-phase currents and voltages are detected by CTs or PTs, while the rotor position is detected by a rotary encoder (RE). These signals are sent to the CPUs in order to calculate three-phase inverter output voltages. The inverter excites the secondary winding of the induction machine through slip rings, forcing the active and/or reactive power released to, or absorbed from, the utility to follow its references i_p and i_q. The experiment is now under processing.

3.2 Simulation

Fig. 3 shows simulated waveforms in which the switching operation of the voltage-fed PWM inverter is taken into account [4]. Here, the control system for i_p and i_q has a proportional-plus-integral (PI) controller, the time constant of which is set at 100 ms. The proportional gain is designed to be K = 0.5 [V/A], so that the time constant of i_p and i_q for a step change in i_p^* and i_q^* is T = 2.5 ms. The triangle-carrier frequency of the voltage-fed PWM inverter is 1 kHz, and the dc link voltage is 0.2 pu. The magnitude of the step change in i_p^* and i_q^* is set to be ± 0.25 pu, so that the maximum output voltage of the inverter does not reach the saturation voltage, that is, the dc link voltage of 0.2 pu. If the magnitude of the step change is large enough for the control system to reach saturation, it would be impossible to evaluate the response inherent in the control system from the resulting response to the step change, because the saturation voltage would dominate the resulting response to the step change. Fig. 3 exhibits that the time constant of i_p and i_q is 2.5 ms (ω_c = 400 rad/s) which is equal to its design value, and that no cross-coupling occurs between i_p and i_q. The rotor speed of the induction machine, ω_m varies in Fig. 3 (a), whereas it is held constant at 360 rpm in Fig. 3 (b) because $i_p = 0$. Detailed results of the simulation will be presented in another place [4].

4 CONCLUSION

This paper has described the control strategy and dynamic performance of a flywheel energy storage system based on a doubly-fed induction machine for power conditioning. The validity of the theory developed in this paper is verified by computer simulation.

The flywheel energy storage system based on a doubly-fed induction machine is expected to be used exclusively as a versatile power conditioner, in particular, being capable of repetitively absorbing and releasing electric energy for a short period of time less than a minute. The experiment result of 7.5 kW model should be expected.

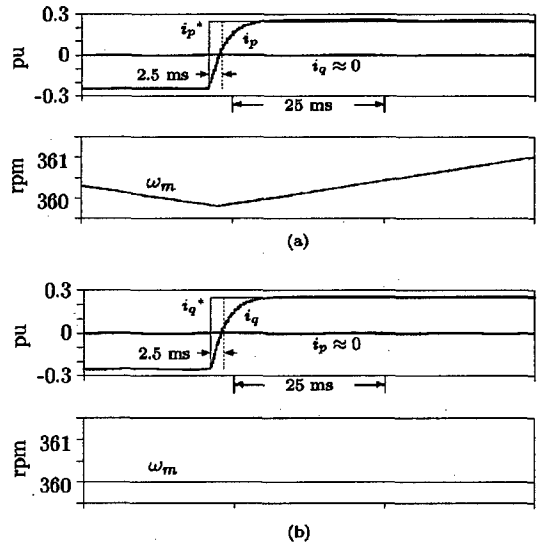

Figure 3 : Simulated waveforms in switching operation of the voltage-fed PWM inverter. (a) Step response of i_p^* under i_q^*=0. (b) Step response of i_q^* under i_p^*=0. ω_m is held constant at 360 rpm in because of $i_p = 0$.

5 ACKNOWLEDGMENTS

The authors would like to express their sincere thanks to M. Kihara, director general of accelerator laboratory, and I. Yamane, director of PS division, for their help. They would like to also thanks to the 50 GeV-PS design group of JHF for there helpful discussion. They are also grateful to Mrs. S. Nohara, chief specialist, power systems division, K. Kudou, senior specialist, hydroelectric power engineering department, T. Sakai, general manager of power electronics department and Y. Hirata, engineer, accelerator technology group of TOSHIBA Corporation, for their help to inspect the ROTES at the Chujowan on Okinawa island.

6 REFERENCES

[1] H. Sato *et al.*,IEEE Transaction on Nuclear Physics, NS39(1992)1490

[2] JHF Accelerator Design Report, KEK Report 97-16, 1997

[3] T. Nohara *et al.*, Proceedings of the CIGRE/IEE Japan Joint Colloquium, No.2-2, 1997

[4] H. Akagi et al., Power Electronics Specialists Conference 1999, Charlston, June 27 - July 2, 1999

PHASE SYNCHRONIZATION OF MULTI-NETWORK SYSTEM FOR RESONANT EXCITATION OF THE JHF 3-GeV BOOSTER MAGNETS

F. Q. Zhang*#, T. Adachi, H. Someya, H. Sato, KEK
1-1 Oho, Tsukuba, Ibaraki, 305-0801 Japan

Abstract

In the Japan Hadron Facility (JHF), the 3-GeV booster is planned to be a 25 Hz rapid cycling separated-function synchrotron. To achieve a stable acceleration, the tune variation due to tracking errors is required to be less than 0.01. Since the White-circuit is adopted with a pulse power supply as its ac source, the relative phase difference of multi-network field becomes one of the main causes of the tune errors and should be minimized. The tolerable phase shift is estimated to be 0.8 mrad. This paper describes a scheme to synchronize the multi-network excitation. A circuit for phase feedback is implemented and experimental results are presented.

1 INTRODUCTION

Rapid cycling synchrotrons of separated function have come into use in several facilities such as ESRF 10 Hz booster [1] and BESSY II 10 Hz booster [2]. In the Japan Hadron Facility (JHF), the 3-GeV booster is designed to be a 25 Hz rapid cycling separated-function synchrotron [3], in which the tune variation due to tracking errors is required to be less than 0.01 to achieve a stable acceleration. Resonant magnet excitation using White circuit powered by biased ac power source is the traditional configuration for rapid cycling synchrotrons. In separated-function machines, tracking errors are caused by high harmonics in resonant magnet current and phase errors between multi-networks. We have built two model networks powered by traditional pulse ac sources to examine the phase synchronization [3]. We designed a phase feedback circuit to achieve the phase synchronization.

2 PHASE ADJUSTMENT SCHEME

A phase adjustment circuit is implemented to synchronize the resonant current in the slave circuit with the master one as shown in Fig.1.

2.1 System Configuration

Two model resonant networks (L_m , C_m) and their pulse ac sources are shown in Fig.1. The upper set is operated as master system while the lower one as slave one.

Half-sine-like current pulses (I_p) are generated by triggering the pulse thyristors (SCR) in the pulse ac sources.

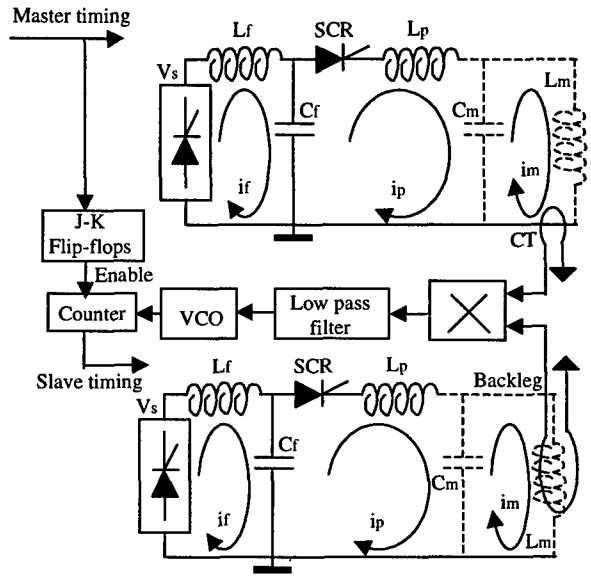

Figure 1: Configuration of multi-network system with a phase synchronizing system.

The phase synchronization of the resonant currents (I_m) is performed by adjusting the slave timing with respect to the master timing for the pulse SCR triggerings. As shown in Fig.1, a mutiplier and low-pass filter detect the phase difference between the master and slave resonant currents. The phase difference is converted to a dynamic dc voltage, and it is used to adjust the frequency of a voltage-controlled oscillator (VCO). Since the slave timing is obtained by counting the VCO pulses, it is regulated automatically by feedback to achieve a close tracking between the resonant currents (I_m) of the two resonant networks.

2.2 Phase Regulating Circuit

The simplified circuit for phase regulation is shown in Fig.2. The master timing is utilized as the synchronization clock for the system operation. The falling edge of the master timing pulse triggers the flip-flop to deliver the enable signal to start the counter. The VCO frequency varies with the changing phase difference around the

*JSPS (Japan Society for the Promotion of Science) Fellow
Email: zhangfq@mail.kek.jp

centre-frequency set by a bias voltage. Counting the VCO pulses regulates the slave timing.

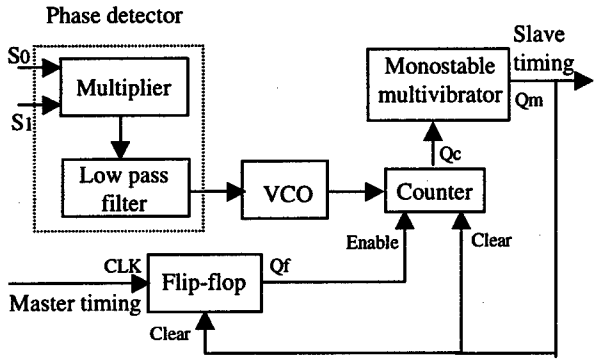

Figure 2: Simplified circuit for the phase regulation.

Since a high tracking accuracy between the master and the slave is required, the phase detector should be sensitive to a very small change of the phase difference ($\Delta\varphi$). The multiplier phase detector is adopted. Taking into account the phase of resonant current with respect to the gating signal of the pulse SCR, we choose S0 the master resonant current picked by a CT (current transformer) but S1 the backleg signal of the slave magnet load. Thus the output signal from the low- pass filter depends on $\sin(\Delta\varphi)$, which is approximated as $\Delta\varphi$.

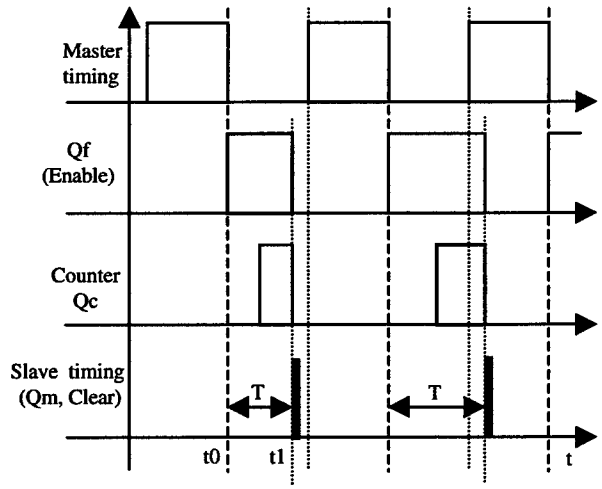

Figure 3: Time diagram of the phase regulation circuit.

As shown in Fig.3, the master timing, with a duty factor of 50%, triggers the negative-edge flip-flop to give the enable signal for the counter to start counting at t0. When the counting ends at t1, the falling edge of Qc produces a one-shot signal Qm that is used as the slave timing and the counting is disabled. As the result, the slave timing (rising edge) is produced either leading or lagging the master timing according to the counting duration T as illustrated in Fig.3.

2.3 *Parameters and Functions*

Basic parameters of the pulse sources and the resonant networks are given below.

Pulse or resonant frequency, f_p : 50 Hz

Energy-storage capacitor, C_f : 23 μF

Filter choke, L_f : 7 H

Pulse choke, L_p : 49 mH

Magnet inductance, L_m : 10 mH

Resonant capacitor, C_m : 1 mF

Quality value of resonant network, Q: 75.

The block diagram shown in Fig. 4 describes the system implementation of the phase adjustment.

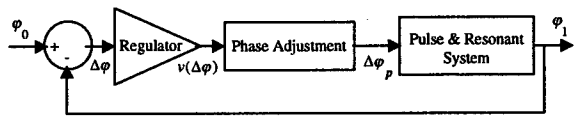

Figure 4: Diagram of the phase adjustment system.

As shown in the figure, $\Delta\varphi$ is the phase difference of the resonant currents (I_m) between the slave and master networks. The phase of the pulse current (I_p) in the slave system is adjusted dynamically according to the variation of $\Delta\varphi$. Since the phase of the resonant current is dependent on triggering timing of the pulse SCR around the resonant frequency, the phase of the resonant current (φ_1) in the slave system is regulated accordingly to be synchronized with the master phase (φ_0).

The phase adjustment is realised by counting the VCO pulses as described above. The VCO centre frequency is given by:

$$f_0 = 2 f_p N ,$$

where f_p is the pulse frequency given by the master timing, $N = 2^{16}$ is the counter length of a 16-bit counter. Both the phase adjustment and the pulse & resonant system can be approximated by simple proportional elements. A PI (Proportional, Integral) regulator can be used to achieve dc stability in φ_1. A simple proportional element is used as the regulator in the experiment.

3 EXPERIMENTAL RESULTS

The system can be operated in free or feedback mode. In free mode, the phase of the slave resonant current can be adjusted freely by changing the VCO bias-voltage. In

feedback mode, phase regulation and synchronization is carried out automatically by the phase feedback. In both modes, reliable operations have been done. With phase feedback, the phase synchronization is performed with a satisfied accuracy in long-term.

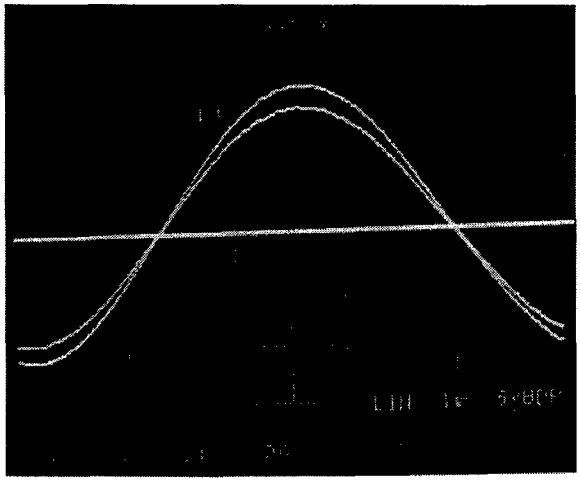

Figure 5(a): Synchronized resonant currents, 2 ms/div.

Figure 5(a) is a photo showing the synchronized resonant currents of the master and slave networks. The phase difference is obtained by comparing their zero-cross signals with a phase-comparator. Figure 5(b) gives the phase-comparator pulse. In Fig. 5(b), we recorded numerous shots, which show that the phases are synchronized within 1 *us* momentarily.

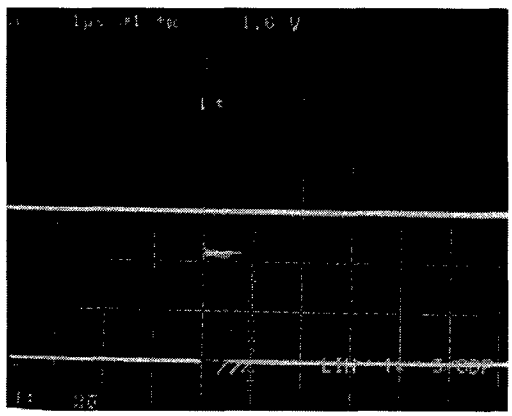

Figure 5(b): Phase difference pulse, 1 *us*/div.

To measure the long term precision of the phase synchronization, the pulse-width of the phase-comparator output is converted to a voltage level by an integrator - holder circuit, which has a conversion ratio of 1*us*/10mV. This voltage is measured with a multimeter (Hp3458) and recorded with Hp-VEE via Hp-IB bus. Figure 6 gives the result measured during 8-hours (1measurement /4second, 7200 measurements in total). In the measurement, the slave timing is shifted about 2 *us* intentionally so that the full variation of the phase difference can be viewed.

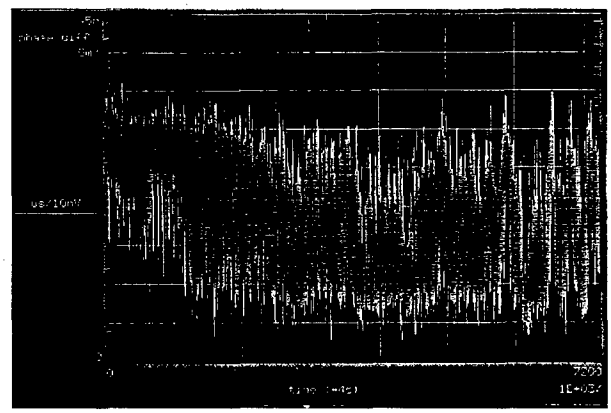

Figure 6: Result of the long-term precision of the phase synchronization, phase difference: 0.5 *us*/div.

The experiment has shown that a high precision of the phase synchronization is achieved and the variation of phase difference is kept within about 3 *us* in the 50 Hz resonant system. If applied to 25 Hz system, a precision less than 6 *us*, which is equivalent to 0.94 mrad, can be expected.

4 CONCLUSIONS

This experimental study shows that using a pulse power supply is still feasible to achieve a high tracking accuracy in rapid-cycling synchrotrons with separated-function. In the experiment, the phase synchronization almost reached the accuracy required by the JHF booster design. In the same time, new concept of ac power sources, e.g. BESSY-II type [2], is also expected to apply in the JHF booster synchrotron to avoid the intrinsic disadvantages of pulse ac sources. An IGBT inverter of the BESSY-II type to power the White circuit is under development.

5 ACKNOWLEDGMENTS

One of the authors, F.Q. Zhang, would like to acknowledge Japan Society for the Promotion of Science for supporting this research program. He also thanks Prof. Y. Irie and Prof. K. Endo at KEK for continuous support.

6 REFERENCES

[1]JM. Filhol, P. Berkvens, et al, "General description of the ESRF injector system", EPAC'88, Rome, pp.332-334.

[2]K. Burkmann, G. Schindhelm, et al, "Performance of the White circuits of the Bessy II booster synchrotron", EPAC'98, Stockholm, pp.2062-2064.

[3]T. Adachi, H. Someya, et al, "Possibility of resonant excitation of the JHF 3-GeV synchrotron magnets using a multi-network", EPAC'98, Stockholm, pp.2053-2055.

ADVANCED BUCK CONVERTER POWER SUPPLY "ABCPS" FOR APT*

E. Bowles, T. Overett, T. Smith, and R. Street#
General Atomics, San Diego, CA 92186-5608 USA

Abstract

To meet the klystron power supply requirements for the Accelerator for the Production of Tritium (APT), a DC power distribution system with a modern DC-DC switching power supply is proposed as one of the options. One power supply is required for each of the approximately 250 continuous wave klystron RF power sources. As the power supplies are one of the largest cost elements in the accelerator, it is desirable to utilize the most economical design. This proposed advanced buck converter high voltage power supply (ABCPS) does not require large transformers to step-up the output voltage and is potentially the lowest cost power supply approach. The power supply must meet the APT requirements for output performance, fault protection for the klystron, high efficiency, high reliability, good maintainability, and be readily manufacturable. A full-scale prototype power supply is being designed and fabricated. The progress of the prototype design, performance validation, and testing follows.

1 INTRODUCTION

The proposed 1700 MeV APT proton accelerator design would utilize three standard 350 megahertz (MHz) klystron RF sources to drive the RF quadrupole. There would be two hundred and forty one 700 MHz klystron RF sources to power the normal temperature low-energy linac and the super-conducting radio frequency cavities in the high energy linac. One high voltage power supply (HVPS) is required for each of the 244-klystron RF power sources. Two megawatt DC power supplies rated for 95 kilovolts (kV) at 21 amperes (A) DC are planned throughout for commonality.

2 ABCPS ADVANTAGE

The DC-DC switch-mode ABCPS is basically a transformer-less power supply design and no large magnetic cores are used. Removing the expensive high voltage step-up rectifier transformer normally present in other designs produces a lower cost approach to satisfy all APT plant requirements. The APT utility distribution system becomes a common DC distribution bus to feed the ABCPS (Figure 1). This design combines the HVPS isolation and rectification, with the utility distribution and eliminates one or more levels of voltage transformation.

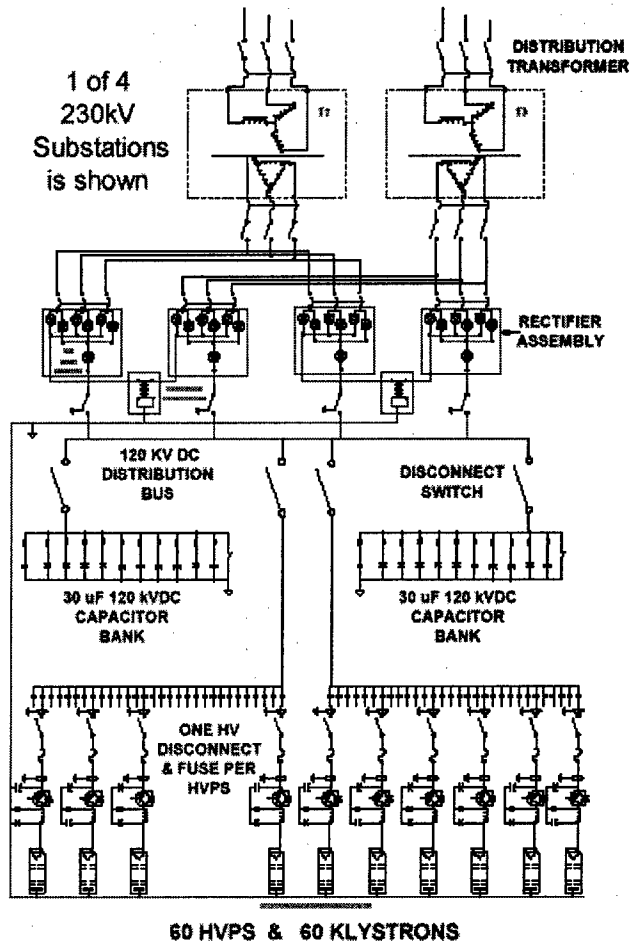

Figure 1: ABCPS DC distribution system for APT

The ABCPS buck-regulator topology is potentially the most efficient because the converter is basically a low loss IGBT switch. A circuit schematic of a single ABCPS is shown in Fig. 2. The raw HVDC input is switched at approximately 18 kilohertz by the HV IGBT switch and charges the output capacitor through a switching inductor. A freewheeling diode (FWD) transfers the inductor energy into the output capacitor (C1) during the IGBT switch off time. The circuit operates in the discontinuous current mode. Almost all the switching circuit energy and the IGBT snubber circuit energy are recovered.

An independent reliability, availability, maintainability, and inspectability (RAMI) analysis has estimated a MTBF of 80,000 hours. With periodic preventive maintenance

* Work supported by DOE under contract DE-AC04-96AL89607
# E-mail: richard.street@gat.com

this can increase to 200,000 hours. The ABCPS high voltage components are modular in design with plug-in circuit cards to produce a highly maintainable system. The majority of the HVPS components are standard off-the-shelf parts. This manufacturing approach reduces cost and procurement lead-time. The entire switch assembly can be bench manufactured without the use of special manufacturing or heavy assembly equipment. This also reduces cost and improves manufacturability. The packaging foot print for this HVPS system is smaller than other power supply designs.

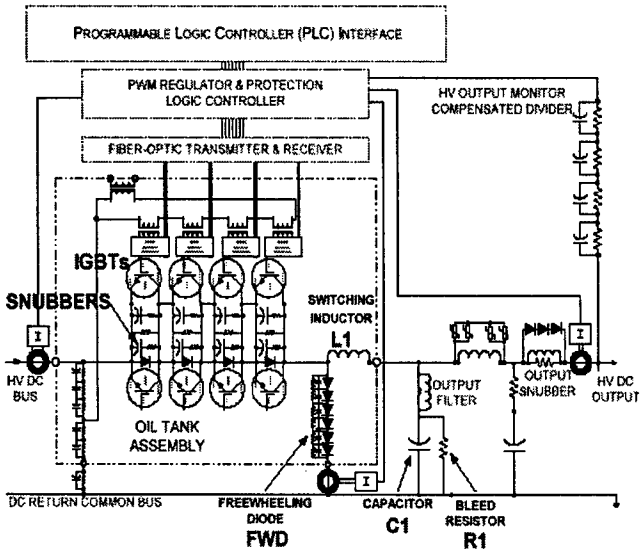

Figure 2: ABCPS schematic

3 ABCPS DESIGN

The topology of this switching power supply is a DC to DC buck converter, which adjusts and regulates the applied voltage to one klystron. There are three major subassemblies in the HVPS enclosure. The first section is a control system that includes a pulse width modulated (PWM) voltage regulator and overload protection circuit card, eight 12-channel fiber-optic gate drive transmitter-receiver circuit cards, and a programmable logic controller (PLC) interface.

The second section contains the high voltage IGBT switch assembly, freewheeling diodes (FWD), switching inductor (L1), and IGBT gate drive power isolation circuitry (Figure 3). All these components are subject to the high frequency chopping waveforms and peak voltage stress. To satisfy thermal cooling needs for continuous operation and assist long term reliability these components are installed in an oil tank filled with Dow Corning®™ silicone fluid 561™. The oil tank has two oil-to-water heat exchangers to transfer the 10 kilowatts of heat dissipation at full load into the APT plant cooling system. All subassembly validation testing was performed in air. The IGBT and FWD circuit cards are plug-in cards and are quickly accessed through a service cover on top of the oil tank. There are 24 IGBT modules and 6 FWD modules (Figures 4 & 5) in the full scale HVPS.

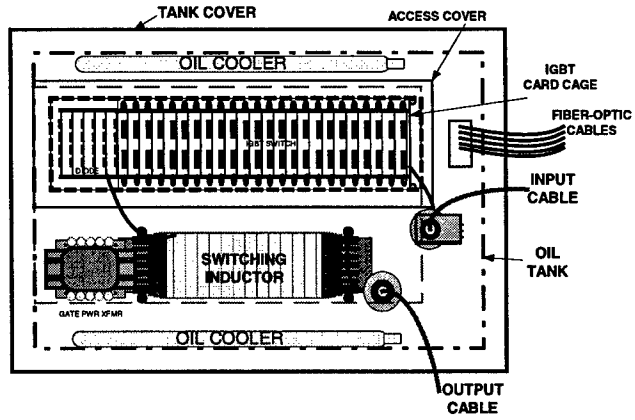

Figure 3: IGBT switch oil tank assembly

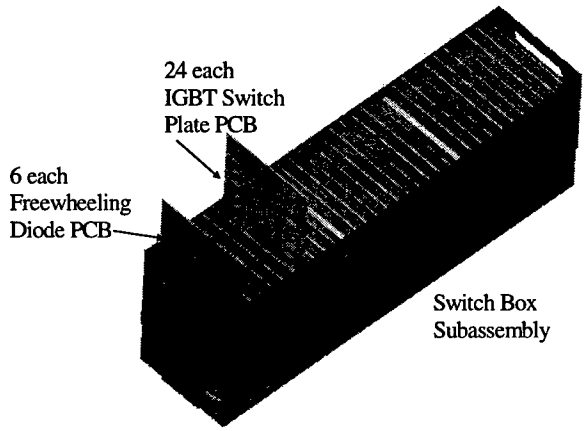

Figure 4: IGBT switch card cage assembly

There are 48 fiber-optic IGBT gate up links, and 48 fiber-optic IGBT data down links. Four fiber-optic cables are needed per IGBT module (Figure 5). The fiber-optic cables provide high voltage signal isolation and connect directly between the IGBT switch modules and transmitter-receiver circuit cards. The fiber-optic cables are color coded for ease of assembly.

The third section is the output ripple filter and fault energy snubber and current bleed resistors. The ripple filter is tuned for optimum ripple reduction while the filter capacitor size is kept to a minimum. All the HVPS inductors are single layer wound air-core coils. Computer PSpice®™ analysis indicates less than 100 volts peak-to-peak output ripple at full load.

The output snubber is designed to limit instantaneous fault energy from being deposited into the klystron load during operation when the klystron arcs internally. Analysis of the output snubber indicates there will be less than 10 joules deposited into the klystron during a tube fault. Once the fault is detected, the IGBT switch can

operate in less than one microsecond to protect the klystron. The high speed IGBT switch will provide fast voltage regulation and control. Individual primary high voltage fast acting fuses will be used for back-up power supply and klystron load protection.

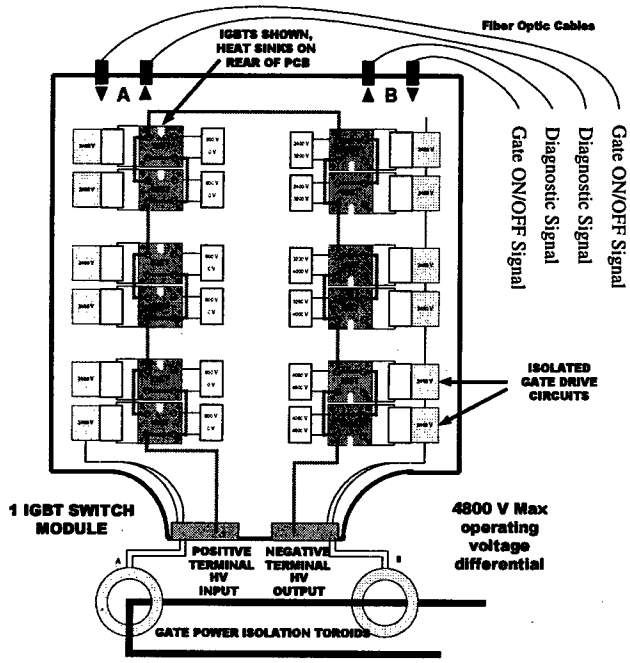

Figure 5: IGBT switch plug-in module

The current bleed resistor (R1, Figure 2) value is directly related to the minimum no load output voltage since it is the lower end resistor in a resistive voltage divider. The upper end resistor being the leakage resistance of the non-conducting IGBT switch.

The 120-kilovolt IGBT switch assembly is a string of 144 series connected IGBTs in parallel with another identical string of 144 IGBTs to provide redundancy. Each IGBT string has independent gate drive power and signals. Because uniform voltage sharing is critical under all operating conditions, each IGBT has forced voltage sharing and transient snubbing. Twelve IGBTs along with their heat sinks, and gate circuits are contained on one plug-in circuit board. Each IGBT module is designed for normal operation at 4,800 volts. The 1,200-volt rated IGBTs operate at 800 volts. Six in series provides 4,800 volts per board. Each board has been tested to a maximum voltage level of 7,000 volts.

4 TESTING AND DESIGN VALIDATIONS

All subassembly testing to date has been in air. Single IGBT module testing at full voltage, full current, and full thermal power were conducted with forced air-cooling. The IGBT module switch design has proved it is capable of handling more than 105 kilowatts. So far four modules have been operated in series. These were connected in a high power pulse mode circuit. They were tested above their design ratings to 7 kilovolts and 50 amperes. All IGBTs uniformly switched on and off. Their turn on time is approximately 150 nanoseconds. The minimum pulse width capability of this IGBT switch module is between 1 and 2 microseconds. To date no problems have been encountered that would require a change in the design. Each circuit board has been tested and the results validate the design goals. The final construction of the full-scale prototype power supply is in progress.

5 APT HVPS OUTPUT CHARACTERISTICS

Output DC voltage: Continuously variable- 4 to - 95 kV
Output DC polarity: Negative with respect to ground
Output voltage set-point accuracy: ± 400 V
Output voltage rate of increase: 10 kV / second max.
Output current rate of increase: 200 A / second max.
Regulation range: 10 – 95 kV
Regulation requirements (line & load): ± 400 V max.
Ripple @ any 60 Hz harmonic: 800 V peak-to-peak max.
Total ripple (all causes): 1100 V peak-to-peak max.
Voltage stability: ± 0.4% max.
Output DC current: 0 - 21 A
Load fault protection: 40 joules max.

6 REFERENCES

[1] Linac98 conference paper No.LA-UR-98-3613 "Advanced Buck Converter Power Supply "ABCPS" for APT", by R. Street, T. Overett, Ed Bowles

[2] Linac98 conference paper No.LA-UR-98-3518 "Overview of the APT RF Power Distribution System", by M. McCarthy , T. Overett, G. Spalek, J. Tooker

TESTING OF A RASTER MAGNET SYSTEM FOR EXPANDING THE APT PROTON BEAM *

S. Chapelle, T. L. Smith, General Atomics, San Diego, CA
D. J. LeBon, M. E. Schulze#, R. E. Shafer, General Atomics, Los Alamos, NM

Abstract

A method of expanding the 1700 MeV, 100 mA proton beam of the APT linear accelerator onto the 19 by 190 cm target has been devised using eight ferrite dipole magnets. These magnets deflect the beam in the x and y-plane, and thereby paint the target area uniformly with a rastered pattern. Insulated Gate Bipolar Transistor (IGBT)-based power modulators drive the raster magnets with triangular current waveforms that are synchronized using voltage controlled crystal oscillators and phase-locked loops (PLLs). Redundant fault detection circuits monitor both the ac magnet currents and magnetic fields to ensure proper operation. This paper presents the test results taken on an integrated prototype system including eight magnets, the associated modulators, the master clock and the fault detection circuitry.

1 BACKGROUND

A raster-type beam expander system, originally described in Ref. [1,2], has been built and the integrated system has been tested. The full prototype system allows evaluation of several aspects of the system-level operation which include interactions between the eight magnets and their power modulators and the ability of the fault detection circuitry to independently detect problems with the raster system. Fig. 1 shows the raster magnets as they fit into the high energy beam transport (HEBT) portion of the APT Linac.

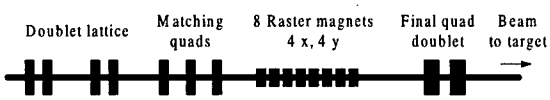

Figure 1: Raster magnets in HEBT

2 SYSTEM DESCRIPTION

The block diagram of the Raster Magnet System shown in Fig. 2 consists of the 1) IGBT modulator, 2) master clock, 3) raster magnet and 4) fault detection circuitry.

2.1 IGBT Modulator

The IGBT modulator consists of an ac/dc converter, a capacitor bank, and an IGBT H-bridge with a gate driver board. The modulator circuit is shown schematically in Fig. 3. Each modulator is powered by uninterruptible

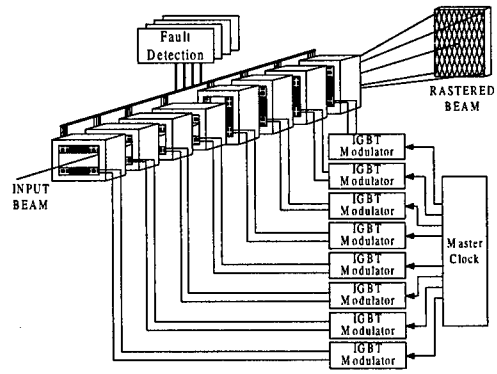

Figure 2: Raster system

power to prevent a common mode failure due to the loss of ac input voltage. The ac/dc converter charges up and maintains a constant voltage on the capacitor bank. The dc output voltage of the ac/dc converter is determined by the rastering frequency and the raster magnet inductance (V = L *dI/dt).

The dc capacitor bank exchanges reactive power with the magnet on a 1 kHz time scale (twice per cycle). The IGBT H-bridge controls the transfer of charge back and forth between the capacitor bank and the magnet. The diodes across each switch, referred to as freewheel diodes, recover the stored magnetic energy.

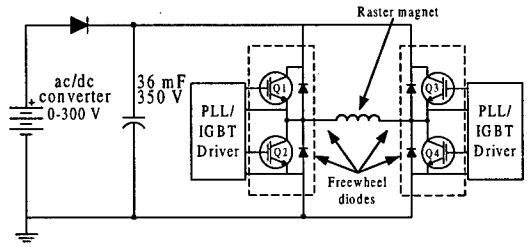

(a)

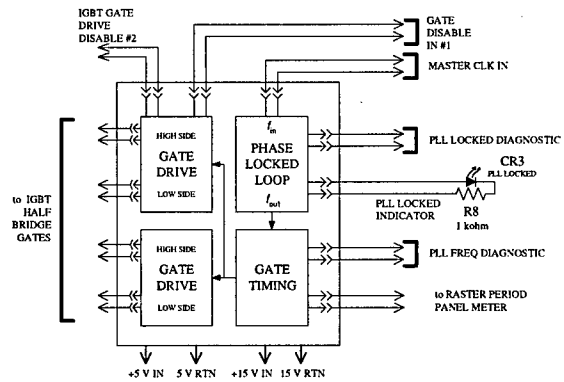

(b)

Figure 3: (a) IGBT modulator schematic and (b) PLL/IGBT gate drive circuitry.

*Work supported by DOE contract DE-AC04-96AL89607
#e-mail: martin.schulze@gat.com

The square wave drive voltage of the modulator's H-bridge and the resulting triangular current waveform in the magnet are shown on the next page. Each modulator is rack mounted with its associated ac/dc power supply as shown in Fig. 4. Verification of rms output current and the output frequency are displayed on digital meters on the front panel.

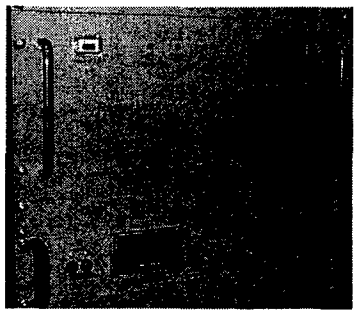

Figure 4: Photo of one modulator and ac/dc converter

Each modulator gets its timing signal from the master clock described in the next section. Each of the modulators has a PLL/IGBT gate driver board that will, using a crystal-controlled phase-locked loop, synchronize itself to the master clock, or else if the master clock fails, is able to produce its own clock so that the beam continues to be rastered onto the target. The phaselock circuit is sequential, rather than an analog type, and the phaselock is accurate to better than ±100 ns. This arrangement is shown in Fig. 3. Such a design approach is used to preclude a common mode failure that might cause damage to the target blanket. The actual hardware consists of a printed circuit card that is mounted inside the modulator enclosure in order to keep the IGBT gate leads as short as possible, and thereby to minimize the drive inductance.

2.2 *Master Clock*

The master clock produces two different frequencies, one for the four x-plane magnets and a second for the four y-plane magnets. The frequency reference is a 1.024 MHz crystal oscillator, identical to those used in each modulator. The choice of x and y rastering frequencies, 508.44 and 573.35 Hz (47/53 ratio) was made to avoid beat patterns and provide uniform beam distribution on the target. The master clock hardware includes on-card fault check circuitry that monitors the clocks to notify the user of a fault. AC power provided to the assembly comes from a UPS, separate from any ac power supplied to the modulators, to preclude a single point failure.

2.3 *Raster Magnet*

The raster magnets are ferrite, 30-cm long with an 8-cm square aperture. The magnets use Ceramic Magnetics CMD5005 Hi-mu, low loss ferrite. This is a nickel-zinc material with a permeability of 4500 * μ_0 H/m at 1500 Gauss. The magnet has an inductance of 1.4 mH and a field of 620 Gauss at 100 A.

A ceramic (alumina) beam tube is required inside the raster magnets in order to eliminate the eddy currents due to rastering. The ceramic tube has a conducting surface, about one skin depth thick, on the inside to shield the rf field of the 350 MHz proton beam and to conduct the liberated charge from residual gas ionization.

The effect of a metallic layer on the magnetic field was tested with a 1-mil (25-micron) SS304 nonmagnetic stainless steel tube (2.75"D), with a resistivity of 77 μohm-cm. The tests were performed with a 620 Gauss peak field at 500 Hz. Test results for the power dissipation and the dB/dt risetime inside the tube agreed with the following equations for power loss and risetime:

$$P = \frac{\pi \ell t a^3}{\rho}\left(\frac{dB}{dt}\right)^2 = 24\,\text{watts, and}$$

$$\tau_{95\%} = 3\tau = 3\frac{\mu_0 a t}{2\rho} = 2\,\mu\text{sec (95\% risetime)},$$

where l is the raster magnet effective length (35 cm), t is the foil thickness (1 mil), a is the beam tube inside radius (1.375"), dB/dt = 124T/s, and ρ = 77 μohm-cm. This verifies that the rf beam shield will not significantly affect the raster magnet dB/dt risetime inside the ceramic tube, and that the eddy current heating can be convection-cooled (does not need active cooling).

2.4 *Fault Detection Circuit*

The beam can not be allowed to stop sweeping across the target. Four independent fault detection circuits, two using dB/dt (B-dot) and two using dI/dT (I-dot) sensors on each magnet monitor proper operation of the raster pattern. If a failure is detected, the fault detection circuit removes the beam enable from the Linac, thus shutting down the beam until repairs can be made.

The 16 B-dot and 16 I-dot signals (square waves) are monitored in four completely independent fault detection circuits. Each of these four circuits removes the beam enable signal from one of the four divisions of the fault detection circuitry if it detects a fault. The beam is shut off if two or more of the four beam enable signals are missing.

3 TEST RESULTS

The primary raster waveforms as measured in an oscilloscope are shown in Fig. 5. Spikes in the modulator voltage are caused by the unavoidable stray inductances being switched by the IGBTs in the modulator. Because of the freewheeling diodes, the modulator efficiently converts dc input power to reactive magnet power as shown in Fig. 6. As an example, at 500 Hz, 32 kVA reactive power requires only 850 W of real input power (100 A peak, 620 Gauss). Power loss contributions come from the modulator, the cabling, and the raster magnet as follows:

Eddy currents in magnet coil	350 W
Resistive loss in magnet coil	180 W
Voltage drop in IGBTs/diodes	175 W
Resistive loss in 50-foot cable	65 W
Other (hysteresis in ferrite, snubber, etc)	80 W

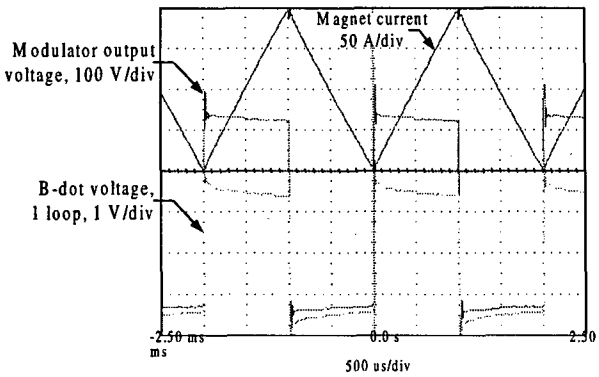

Figure 5: Measured waveform of modulator

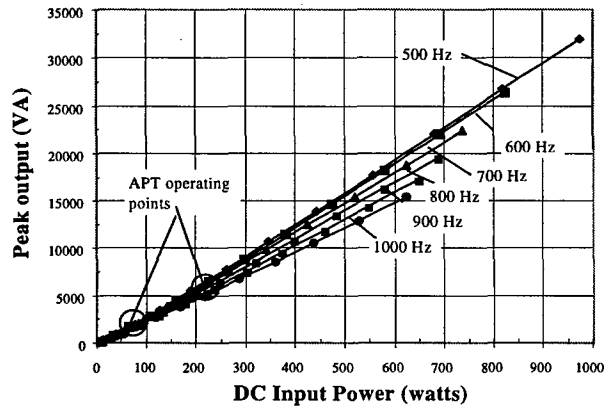

Figure 6: Modulator data of reactive versus real power

As a pair, the magnet and modulator performance test results (Fig. 7) show that the achievable B-field is more than sufficient for the APT requirements of 140-260 G and 500-600 Hz.

Figure 8 shows the x-y raster pattern produced by summing the x and y raster magnet current waveforms. There is good agreement between the simulated pattern and the actual measured pattern. The distortion in the pattern is due to the L/R droop of the magnets causing a slight curvature in the triangular current waveform. Simulations show that the uniformity of the beam distribution in the 19 cm(h) by 190 cm(v) raster pattern is about ±1% with a 1-cm(h) by 2-cm(v) rms beam spot.

The final tests involve the response of the fault detection circuitry to either a loss of a modulator/magnet unit or the loss of the master clock. When a modulator fails, the summed B-dot pattern reduces in amplitude by 25% in either x or y. More interesting is the loss of the master clock, because the square wave slowly evolves into a staircase over many seconds as the voltage controlled crystal oscillators in each modulator drift out of synchronization.

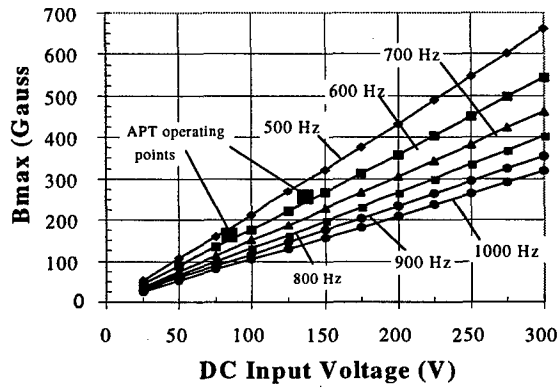

Figure 7: Max B field of magnet vs. modulator dc voltage

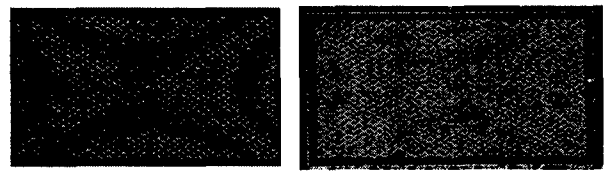

Figure 8: Simulated (l) and real (r) raster patterns

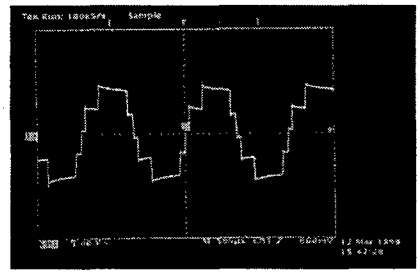

Figure 9: Summed B-dot signal showing loss of PLL synchronization

4 FUTURE WORK

System reliability and power consumption can both be improved by replacing the water-cooled hollow copper magnet coil with a stranded Litz wire coil. This will eliminate the water cooling circuits (and interlocks), and substantially reduce the eddy current power loss.

5 REFERENCES

[1] C.R. Rose and R.E. Shafer, "A 200-A, 500-Hz, Triangular Current Wave Modulator and Magnet Used for Particle Beam Rastering," Proc. 1997 Particle Accel. Conf., #7P089 (Vancouver, 5/97).

[2] S. Chapelle, et. al, "Development of a Raster Electronics System for Expanding the APT Proton Beam," Linac 98 Conference, Aug. 98, Chicago, IL.

FOUR QUADRANT 250KW SWITCHMODE POWER SUPPLY FOR FERMILAB[1] MAIN INJECTOR

Si Fang[2], George Krafczyk, Howie Pfeffer, Dan Wolff
Fermi National Accelerator Laboratory P.O. Box 500 Batavia, Illinois 60510, USA

Abstract

A +/-700 volt,+/-350 amp switchmode power supply has been developed for Fermilab Main Injector Sextupole Correction System. The four quadrant operation is accomplished by using four IGBTs in an H-bridge configuration with a switching frequency of 10 KHz. Current regulation bandwidth of 300 Hz is achieved with stability better than 250 ppm of rated current by using a high precision current transducer. The H-bridge outputs are filtered resulting in a maximum output voltage ripple of 2.5 volts peak to peak. The power supply has power conversion efficiency better than 80% and works at near unity power factor throughout its operation. The critical considerations involved in this power supply are low inductance bus plate and snubber design, selection and thermal management of IGBTs, IGBT gate drive, PWM output filtering, and fiber optic controls. The paper will discuss the design and performance of the power supply.

1 INTRODUCTION

The Fermilab Main Injector Sextupole Correction System consists of a horizontal and a vertical ring for chromaticity compensation[1] [4] to achieve high intensity stable beam during 8.9 *GeV/c* to 150 *GeV/c* proton and anti-proton acceleration and deceleration. Each ring is constructed of 54 sextupole magnets connected in series and powered by a four quadrant 250*KW* switchmode power supply. The Sextupole system requires operating current between -25 amps and 350 amps with a current step as high as 40 amps in 10 ms at 20.5 *GeV* transition (25 amps). The system also requires 8-hour DC current stability at injection level (0-20A) to be better than +/-25mA. Regular thyristor type power supplies are not suitable for this application because of bandwidth and bipolar current operation requirements. The successful development of a four quadrant 2*KW* switchmode power supply using MOSFETs[2] at Fermilab motivated us to investigate the H-bridge switching topology by using IGBTs for much higher power level switching. Recent technology developments in high power and fast switching IGBT technology have made our design become practical. Three units of the four quadrant 250*KW* switching power supplies with voltage output of +/-700 volts and capability of driving +/- 350 amps current have been developed and built for the project.

[1] Operated by the University Research Association Inc., Under contract No. DE-AC02-76CH03000 with the U.S. Department of Energy.
[2] Email: cjf@fnal.gov

2 POWER SUPPLY DESIGN

2.1 Power supply Circuit

Figure 1 shows the circuit diagram for the power supply. The H-bridge is constructed of four IGBT switches *S1*, *S2*, *S3*, and *S4*. The pulse width modulated (PWM) output of the positive half bridge (*S1* and *S2*) is filtered by the top filter and the output of the negative half bridge (*S3* and *S4*) is filtered by the bottom filter. The voltage difference between the two filtered outputs is the voltage output of the power supply.

The switching pattern of the IGBTs is also shown in Fig. 1. The summation of the duty factor of *S1* and *S3* is always unity. For a given S1 duty factor of *DF1* and H-bridge DC input voltage of Vin, the voltage at the top filter output will be *DF1*Vin* and the voltage at the bottom filter output will be *(1-DF1)*Vin*. The power supply output voltage will be *(2*DF1-1)*Vin* with a ripple frequency twice the 10 KHz switching frequency. The power supply will have zero volt output when IGBTs are switching at 50% duty cycle. The power supply output voltage can be controlled by varying the duty factor *DF1*.

The 800 volt H-bridge DC input voltage Vin is derived from a 12-pulse diode rectifier. The rectifier filter is a Praeg filter[3] with the second order roll-off frequency at 60 Hz. The capacitor banks are sized to absorb the energy returned from the inductive load (160 mH and 1.55 ohms) at 350 amps during a trip condition. The 18.2mF total capacitance at the rectifier output limits the transient voltage to 1.2 KV in the worst case. A 9 μH cable inductance was added to limit the amount of high frequency current through the low frequency capacitor banks (4.5mF and 13.5 mF), and thus avoid capacitor over-heating. Most of the high frequency current goes through the 224 μF high frequency capacitor bank.

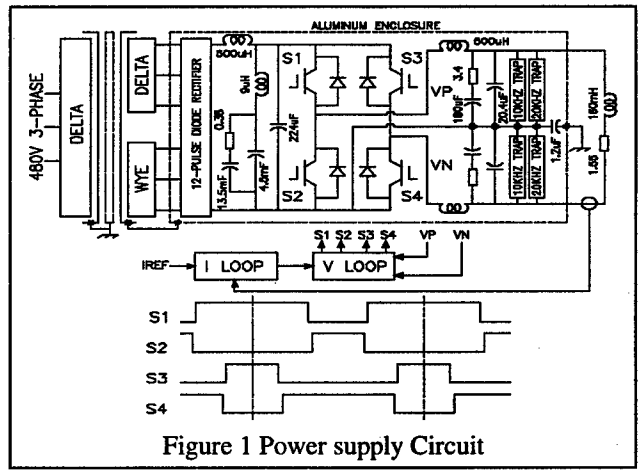

Figure 1 Power supply Circuit

0-7803-5573-3/99/$10.00@1999 IEEE.

2. 2 *Low Inductance Bus Plate and Snubber Design*

The energy stored in the bus parasitic inductance causes transient voltages during IGBTs switching. The 224 μF high frequency capacitor bank consists of 40 capacitors each rated at 5.6μF/1.5KV. Each capacitor has low ESL (23 nH) and is rated 35 amps RMS current at 60 ℃. These capacitors are connected in parallel and distributed around the four IGBTs. The IGBTs, high frequency capacitors, and bus connections are packaged in a laminated bus structure to reduce the bus parasitic inductance. The laminated bus structure is constructed using 1/8" copper plates with 1/8" thick G-10 sheet for insulation layers. The bus equivalent parasitic inductance has been reduced to about 15 nH.

A Snubber circuit (Fig. 2) is used to limit surge voltages during high power and high frequency switching. Snubber capacitor *Cs* is charged to DC bus voltage *Vin* through *Rs*. When IGBT *S1* turns off, parasitic inductance in the DC bus causes a transient voltage across *S1*. The snubber diode *Ds* turns on and diverts the energy stored in the parasitic bus inductance into the snubber capacitor *Cs* as soon as the voltage exceeds the DC bus voltage.

A surge voltage similar to the turn-off surge can occur when the free-wheeling diode recovers. Assume that the lower IGBT *S2* in Fig. 2 is off and the load current I_L is circulating through the free-wheeling diode of the upper IGBT. When the lower device turns on, the current in the free-wheeling diode of the upper IGBT decreases as the load current begins to commutate to the lower IGBT and becomes negative during reverse recovery of the free-wheeling diode. When the free-wheeling diode recovers, the current in the bus quickly decreases to zero resulting in a transient similar to turn-off operation. *Cs* and *Rs* can be calculated using bus parasitic inductance *Ls*, allowable DC bus voltage overshoot ΔV, maximum operating current *I*, and the switching frequency *f* (Fig. 2). By using the low inductance bus plate and snubber design, the IGBT transient voltage overshoot is less than 5% at Vin of 800 volts and *IL* of 350 amps.

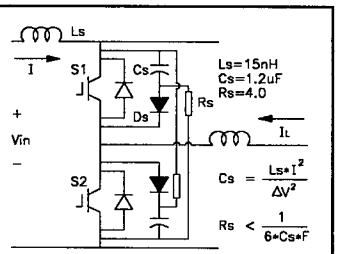

Fig 2 Snubber circuit

2.3 *IGBT Selection and Thermal Management*

We selected the Eupec FZ 1.6KV/1.2KA IGBT for this project because its voltage rating was adequate (more than 75% above the DC supply voltage) and because its switching characteristics allowed us to use it without paralleling devices and to still maintain reasonable junction temperatures. Temperature problems with other devices early in the development led us to carefully evaluate dissipation in the IGBT. Due to the difficulty of measuring currents in our low-inductance structures, we made our dissipation measurements using calorimetry. We determined that the IGBT dissipation was 2.4 *KW* while switching 350 amps at 800 volts at 10 KHz with a 90% *DF*. This compared nicely to the 2.6 *KW* number calculated from the data sheet. We also measured the thermal impedance of the IGBT baseplate with respect to inlet water temperature while mounted on the Eupec heat sink. The result was a rise of 10 °C/*KW*. These results lead to a calculated maximum junction temperature of 98 °C with inlet water of 35 °C.

We normally design systems to maintain junction temperature below 80 °C for optimum reliability. In this case we accepted the slightly elevated levels as a trade-off to developing a circuit with paralleled devices. We had also lowered our switching frequency from 30 KHz to 10 KHz in order to make the single device structure realizable.

2.4 *IGBT Gate Drive*

The IGBT gate drive is built with a Concept drive (IGD-515EI) and is capable of driving IGBT gate with +/– 15 V and a peak current of +/-15 amps. Very low input to output isolation capacitance (< 10 pF) with fiber optic controls are essential for eliminating noise problems caused by ground loops and capacitive coupling in the rapid turn-on and turn-off environment. The gate drive has an IGBT over current protection circuit to turn off the IGBT in less than 8 μs in case of IGBT over current.

2.5 *EMI/RFI Shielding*

A disadvantage of switchmode power supplies is the generation of EMI/RFI noise. In order to control the radiated noise at a minimum acceptable level, a ½" wall aluminum enclosure is used to shield the entire high power and high frequency switching circuits. Primary and secondary shields were installed in the power transformer with the secondary shield tied to the aluminum shielding enclosure. The shielding enclosure is mounted within and isolated from the power supply cabinet. A single point ground is used for safety purpose (Fig. 1). The primary shield in the transformer reduces EMI/RFI from feeding back into the 480 lines. Additional line filtering further attenuates the noise. Fiber optic links are used for control and status read back between control electronics and the shielded high power switching circuits.

2.6 *H-Bridge Output Filtering*

The H-bridge output is filtered by a second order damped filter. The filter has -3dB roll-off frequency at 800 Hz with additional 10 KHz and 20 KHz traps. The filter reduces the peak to peak ripple voltage to 2.5 volts (Fig. 6). This meets our specification for both load ripple and radiated energy from tunnel cables.

3 PERFORMANCE

Preliminary tests were conducted on the power supply with the Main Injector Sextupole ring. The current slew rate of the power supply was limited at 4000 A/Sec. Figure 3 shows the power supply current and voltage during a typical ramp with bipolar current operation (-25 to 350 amps) and 4000A/Sec current step at transition.

The current loop frequency response was tested as indicated in Fig 4. Current regulation bandwidth has been achieved at 300 Hz. The DC current 8-hour stability in injection regions (0 to 25 A) is better than +/-25 mA. Figure 5 shows the current regulation error of +/- 78 mA at 350A (CH1=40A/V, CH3=2A/V). Our first operational problem was excessive ripple due to a bad connector on our current feedback signal. The second problem was also excessive power supply voltage ripple due to noise pickup in the current transducer electronics. This last problem was solved by using a later version of the transducer electronics with improved noise rejection.

Two power supplies were in operation during Main Injector commission between October 98 and January 99. The Main Injector achieved greater than 1E13 protons/6 batch intensity at 150 Gev.

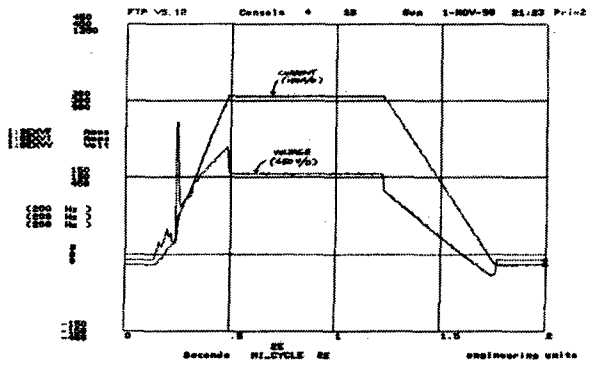

Figure 3 Typical Power supply Voltage and Current

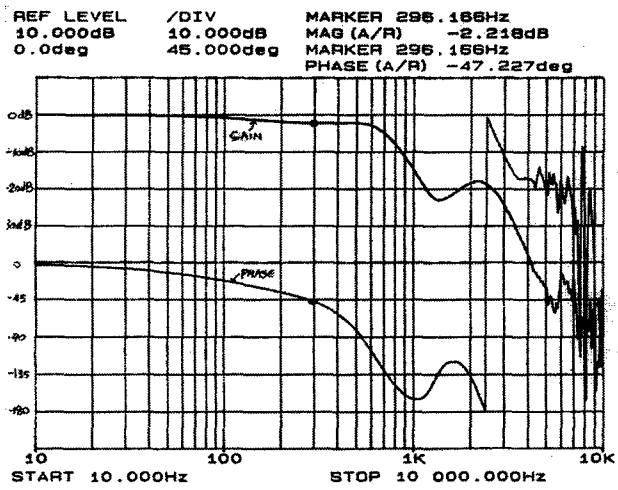

Figure 4 Current Loop Frequency Response

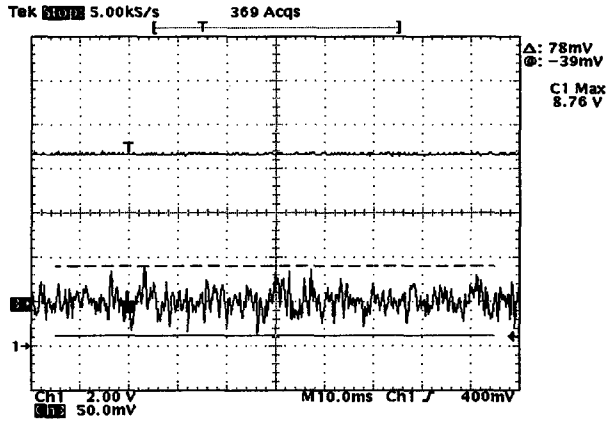

Figure 5 Current Regulation Error of +/- 78mA at 350A

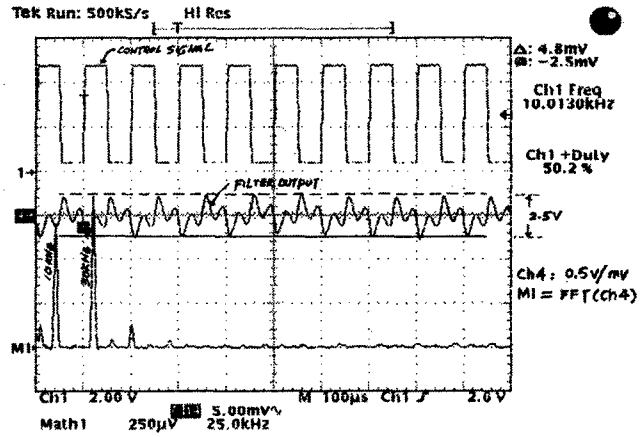

Figure 6 Power Supply Voltage Ripple

4 CONCLUSION

The test results on the four quadrant 250*KW* switchmode power supplies indicate successful application of IGBTs in switchmode power supplies for wide bandwidth and high power operation.

5 ACKNOWLEDGEMENTS

We would like to thank Mike Van Densen, Kevin Roon, Dan Darimont, Olga Glen, and Phil Paul on their work in the development and construction of the project.

6 REFERENCES

[1] C.M. Bhat et al, 'Magnetic Field Measurements of the Main Injector Sextupole Magnets' IEEE Proceedings of the 1997 Particle Accelerator Conference, Vancouver.

[2] L. Bartelson et al, 'Four Quadrant DC to DC Switching Supplies for the Fermilab Main Injector' IEEE proceedings of the 1997 Particle Accelerator Conference, Vancouver.

[3] W. Praeg, 'A High Current Low Pass Filter for Magnet Power Supplies' IEEE Transactions on Industrial Electronics and Control Instrument, February 1970

[4] G. Wu et al, 'Chromaticity Control in the Fermilab Main Injector" This Conference.

RESONANT RAMPING SCHEME FOR CLS BOOSTER DIPOLE MAGNETS

N. G. Johnson*, W. E. Norum, Saskatchewan Accelerator Laboratory, Saskatoon, Saskatchewan

Abstract

The booster for the proposed Canadian Light Source is being designed to ramp the electron beam from 250 MeV to 2.9 GeV in approximately 180 mS, with a repetition frequency of 2.5 Hz. The booster dipole magnets will be connected in series with a capacitor bank and operated as a series resonant circuit. This approach reduces the peak power drawn from the supply and consequent load fluctuations on the incoming AC lines. The series connection ensures that the current through each magnet is identical. The circuit is simple and easy to control, especially when compared to other ramping power supply approaches. An SCR bank, configured as an H-Bridge, controls the orientation of the capacitor bank in the circuit. To initiate a ramp cycle two opposing legs of the bridge are switched on, thereby applying power to the magnets. The magnet current is a half sinusoid; when it drops to zero the SCRs turn off with the capacitors charged to the opposite polarity, ready for the next cycle. The system will apply a peak voltage of approximately 3500 Volts and a peak current of 1550 Amps to the magnet string.

1 CLS BOOSTER

The Canadian Light Source (CLS) [1] will consist of the Saskatchewan Accelerator Laboratory's electron linac operating at 250 MeV, a booster synchrotron to increase the energy to 2.9 GeV, and a 2.9 GeV storage ring. The booster has been designed for an injection frequency of 2.5 Hz. The booster magnet parameters are summarized in Table 1.

Table 1: Booster Dipole Magnet Parameters

Magnet	H-type
Number of Magnets	20 + 1 reference
Core length	2.56 m
Gap	44 mm
Maximum flux density	1.33 T
Peak current	1550 A
Turns per coil	16
Turns per magnet	32
Resistance per magnet	13.2 mΩ
Inductance per magnet	11.4 mH
Interconnection resistance	6.6 mΩ
Dipole string resistance	284 mΩ
Dipole string inductance	239 mH

For very long ramp periods the inductance of the magnets has little effect on the power supply requirements.

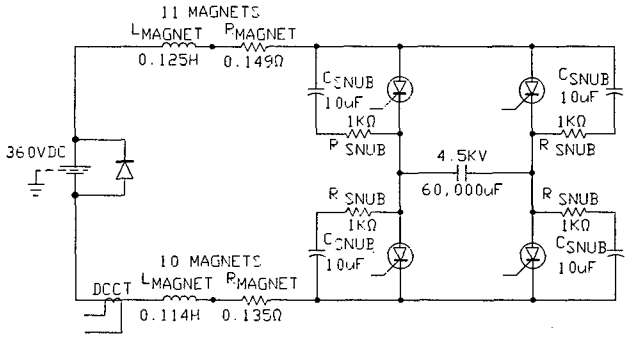

Figure 1: Resonant Ramping Supply Schematic

Varying the current through the magnet coils requires that the power supply voltage be increased to overcome the inductive component of the load. Inductive effects begin to dominate the CLS booster dipole magnet power supply requirements around 1 Hz, which was the initially proposed rate. With an injection rate of 1 Hz, and assuming an equal ramp up/ramp down time, the magnet current must increase 1420 A in 0.5 seconds.

Three power supply designs have been considered: linear ramping; exponential ramping; and series resonant ramping. Comparisons of the designs were made assuming a minimum injection frequency of 1 Hz and equal times for increasing and decreasing the current. The technique referred to as a White circuit seemed overly complicated for this injection frequency, and has not been analyzed.

A linear ramping approach increases the dipole flux at a constant rate, so the waveform of the power supply output voltage is approximately a sawtooth. The proposed CLS booster dipole network has a total resistance of 0.284 ohms, a total inductance of 0.239 Henry, and requires a current of 1550 A at 2.9 GeV (see Table 1). This requires a power supply output voltage of 1120 V just before maximum current is reached, for a peak output of 1.7 MW. The time constant of the circuit is 0.84 seconds so the current will not decay to the level required for 250 MeV injection unless a bipolar supply is used.

A second approach was considered in which the supply would be operated with a stepped output voltage, with the magnet current following exponential curves according to the L/R time constant of the system. The required supply voltage would be 980 V, with a peak output power of 1.5 MW. This supply would also have to be bipolar.

A third approach, and the one chosen for use at the CLS, is to reduce peak power requirements by connecting a capacitor bank in series with the magnets to create a resonant RLC circuit. At resonance the reactive components of the

* Email: neil.johnson@usask.ca

0-7803-5573-3/99/$10.00@1999 IEEE.

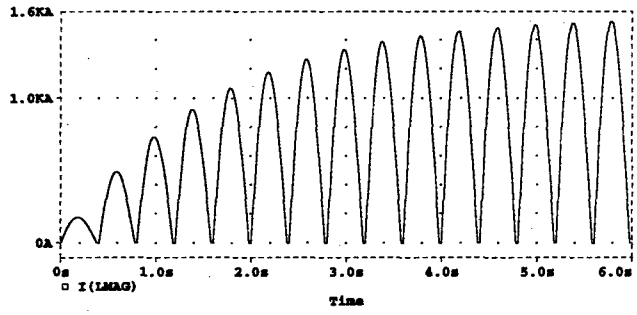

Figure 2: Dipole current as supply switched on

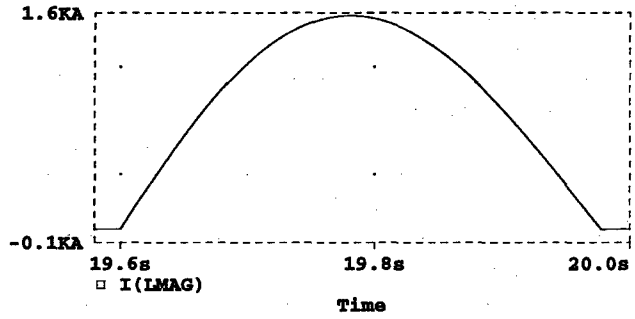

Figure 3: Expanded view of operating state dipole current

capacitance and inductance cancel. This system, and accompanying thyristor switches as shown in Figure 1, can be used with a unipolar, constant output voltage supply. The CLS constant voltage power supply needs to provide only 360 V at 1550 A, for a peak output of 0.56 kW.

The ramp period can be chosen by adjusting the number of turns in the magnet windings to vary the magnet inductance as described below. This has a minimal effect on power consumption. If the overall cross sectional area of the copper is constant there will be no change in the peak power dissipation. The resistance of the winding is proportional to the square of the number of turns. For example doubling the number of turns results in half the conductor area and twice the length, quadrupling the resistance. Since the required field remains the same, the peak current varies inversely with the number of windings so only half the current would be required. Power, which is proportional to I^2R, remains constant. In practice the total cross sectional area of the windings is fixed, so as the number of windings is increased proportionally more area will be occupied by insulation, and resistive losses will increase somewhat.

The magnet load will be split into two sections as shown in Figure 1. This configuration reduces the magnitude of the voltage between the windings and ground since one section is pulsed with a positive voltage while the other is pulsed with a negative voltage. During normal operation the magnets adjacent to the SCR/capacitor section will have to withstand 2 kV between their coils and ground. A fault in either of these locations would impose the full capacitor voltage on the windings of the first coil in the other half of the string of dipoles, so the coil winding insulation must be able to withstand momentary peak voltages of 4 kV. Ground fault detection will be incorporated in the supply to detect these faults and provide protection to the supply and magnets.

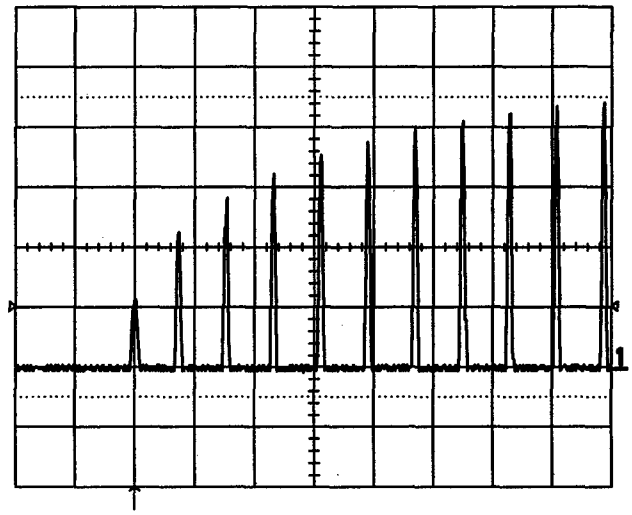

Figure 4: Magnet current in prototype supply as it is switched on. Horizontal scale: 0.5 S/division, Vertical scale 30A/division

A PSpice model of the schematic in Figure 1 was developed by replacing the SCRs with switches in series with diodes. Figure 2 shows the simulation of magnet current I(LMAG) as the power supply ramps up to the operating state. Figure 3 shows an expanded view of the dipole current after it has reached this state.

A low power prototype was designed and tested. The capacitor bank was implemented with twelve 10000 μF electrolytic capacitors. The capacitors were arranged as two sets of 6 capacitors connected back to back. Each set included a bypass diode to protect the capacitors from being charged with the wrong polarity. The magnet string was simulated with an air core coil having a resistance of 110 mΩ and an inductance of 8.1 mH. The capacitors each have an equivalent series resistance of 18 mΩ, resulting in a total resistance of 113 mΩ. A 300 A DCCT, which provides a full scale output of 200 mA, connected to the 50 Ω input of an oscilloscope corresponds to 30 A/V. Figures 4 and 5 show the operation of the prototype as it is switched on and after the current has reached its operating point.

The energy stored in the magnets must be transferred between the magnet flux and the capacitor's electric field. The peak voltage across the capacitors will be inversely proportional to the square root of the capacitance. This voltage will be limited by the voltage rating of available SCRs. The Powerex TC20 SCR which has a rating of 4.5 kV and 2.8 kA_{av}, or the International Rectifier ST1900C52R0 rated at 5.2 kV and 1.6 kA_{av}, are suitable for this design.

Although the resonant supply imposes a smaller tran-

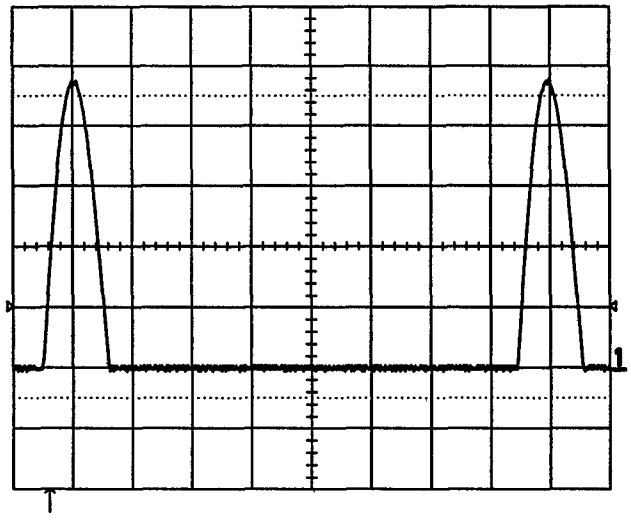

Figure 5: Expanded view of operating state dipole current Horizontal scale: 50 mS/division, Vertical scale 30A/division

sient load on the AC supply lines than do supplies which reverse the power load on the supply lines, the load fluctuation from ramping the booster magnets will induce voltage fluctuations on the 60 Hz voltage distribution throughout the lab. Feeding the ramped supplies from a separate transformer will minimize the effects on other power supplies. This transformer can also function as the transformer in the 360 V DC supply. In this case the transformer would be ordered with both Delta and Wye secondaries, and operated with a twelve phase rectifier. The leakage inductance of this transformer will have a negligible effect on the circuit operation. Assuming a 250 V RMS secondary voltage and a 750 kVA 6 phase transformer with a 10% leakage inductance, each leg would have approximately 70 μH inductance. Two legs would be conducting at a time, so the total inductance seen by the circuit would be 140 μH, which is less than 0.1% of the circuit inductance.

To avoid a large fluctuating dipole effect, the return current path will retrace the outgoing path in close proximity to the outgoing conductors. The booster circumference is 102 m. Allowing 2 m for each dipole connection, the conductor will have a total length of 246 m. Losses in the magnet interconnections should be kept low. Initially the booster was specified for operation at 1 Hz, with the magnets connected in series using water cooled conductors having a copper cross sectional area at least that of a 3" copper pipe with a wall thickness of 0.054". Since the booster's resonant frequency is controlled by varying the number of turns of the booster dipoles, the peak dipole current increases proportionally with this frequency. The current at a ramp rate of 2.5 Hz would result in a peak power dissipation of 90 kW in these conductors. Three 500 MCM conductors will be used instead of the water cooled conductors, reducing the conductor resistance to 6.6 mΩ, the peak power dissipation to 16 kW, and the peak output of the power supply by 74 kW.

With the resonant design the booster ramp period can be reduced with little effect on the dipole power supply's peak output power. Non-resonant supplies, which can be adjusted to match the booster dipole current, will be used for the booster quadrupoles. Shorter periods make the inductive component of the quadrupole magnet load more significant. With the present CLS design the reactive component of the quadrupole load equals the resistive component at 3 Hz. Shorter periods would rapidly increase the quadrupole supply requirements, so 3 Hz was chosen as the maximum booster frequency.

The booster quadrupole supplies and RF have to be regulated to match the dipole current. Either a DCCT or Hall probe could be used as a basis for the control. At the maximum current levels the magnet cores will be somewhat saturated, so flux cannot be assumed to be directly proportional to current. Feedback using a DCCT would require accurate modeling of these saturation effects, based on a complete mapping of the dipole. The Hall probe measures flux directly, so provides a simple feedback system but requires an extra reference dipole. A Hall probe is planned to be used as the main feedback to the magnet control system. A DCCT will be installed for diagnostic purposes.

With the proper number of turns the quadrupole magnets could be connected in series with the dipole magnets and form part of the resonant system. Trim windings on the quadrupoles would allow control over the tune of the booster. This approach was considered, but concerns about the risk of an untested system and limited ability to adjust the tune of the beam resulted in its rejection.

The simplicity of the circuit should result in good reliability for the system. The most common failure will be a shorted capacitor in the 60 mF capacitor bank. The capacitors will be individually fused to limit the energy dissipation during a such a fault. The capacitor bank will be constructed with spare units in place, making it possible to resume operation with a very short down time. A high voltage relay could be used to connect the spare capacitor, reducing down time further. Alternatively, a self healing capacitor construction could be used. These capacitors use a dielectric film with a thin metal coating. The metal in the vicinity of a dielectric fault is unable to carry the fault current, and is blown away, clearing the fault at the expense of reduced capacitance. Banks of electrolytic capacitors could be used to provide a compact design. The reliability of these capacitors would likely be worse than oil filled capacitors, especially since a combination series/parallel bank would be required. Self healing capacitors with manually switchable spares will be used for the CLS.

2 REFERENCES

[1] CANADIAN LIGHT SOURCE, The Proposal for Construction of a National Synchrotron Light Source for Canada, January, 1999.

PULSING A 4.1 MW MOTOR GENERATOR SYSTEM TO 34 MW PEAK POWER UNDER CONSTANT INPUT POWER OPERATION. *

I. Marneris #, V. Badea, M. Bannon, R. Bonati, G. Danowski, J. Sandberg, A. Soukas.
Brookhaven National Laboratory, Upton, New York 11973 USA

Abstract

Brookhaven operates a 9 MW motor generator, made by Siemens, as part of the main magnet power supply of the Alternating Gradient Synchrotron (AGS) accelerator. A cycloconverter power supply system is utilized to ensure that during pulsing the main magnets of the AGS up to 50 MW peak power, the input power of the motor generator remains constant. There is also another motor generator (MG set) at Brookkhaven, a 40 year old system manufactured by Westinghouse. This MG set could be pulsed up to 34 MW peak power while the input average power should not exceed. 4.1 MW. A project is underway to upgrade this MG system and it's controls, so it could be used as a spare while doing maintenance on the Siemens MG and thus not interrupting the RHIC physics program. The purpose of this paper is to show that it is possible to pulse the AGS magnets using the Westinghouse MG system without utilizing a cycloconverter power supply, and still be able to maintain the input power to the motor generator constant. Calculations will be provided to show that we can pulse the position of the liquid rheostat in the motor rotor circuit to support the above, while taking out the power necessary to pulse the AGS magnets. This solution is being implemented due to budget constraints and overall simplicity. The hydraulic system to accomplish this task will also be described.

1 DESCRIPTION/SPECIFICATIONS OF THE MOTOR/GENERATOR

The motor generator is a 40 years old machine manufactured by Westinghouse (WH) with the following ratings. The stator voltage is Vst=13800 Volts 3 phase, stator full-load current is 203 Amps. The motor is an 900 RPM, 6% slip, 5500 horsepower (4.1 MW) wound rotor induction motor. The friction and windage losses are 550 KW. The blocked rotor voltage is 3168 Volts, rotor full-load current is 787 Amps. The moment of inertia of the whole system is 46890 kg*m*m. A liquid rheostat is used for acceleration and speed adjustments. The liquid rheostat consists of the coarse adjustment used during turning on and braking the motor and the fine adjustment used to control the speed during pulsing of the generator. The generator stator voltage generates a maximum of 7500 volts, 3 phase, 2771 Amps, 36000 KVA. It can be pulsed up to 34200 KW, with a power factor of 95%. The continuous rating is 29 MW. The generator rotor is excited by a dc source of 260 Volts at 578 Amps. The 3 phase output is converted to controllable dc by a rectifier (SCR) system and applied to the AGS magnets.

2 THEORY AND CALCULATIONS

Since we can pulse the WH generator to 34MW peak power and assuming a linear change of the magnet current from the front porch to the flat top value and visa versa, we can calculate the optimum magnet current waveform based on the 34MW peak power rating assuming an efficiency of 95% for the rectifiers. The magnet current I(t), magnet voltage V(t) and magnet instantaneous power Pim(t)=I(t)*V(t) are displayed in Fig. 1 and Fig 2, for a typical AGS cycle.

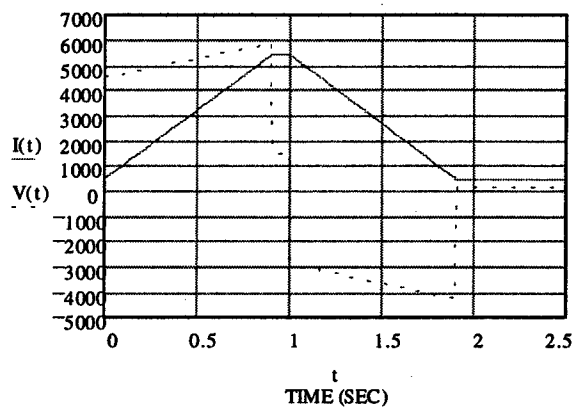

Figure 1: Magnet current (Amps) and voltage (Volts)

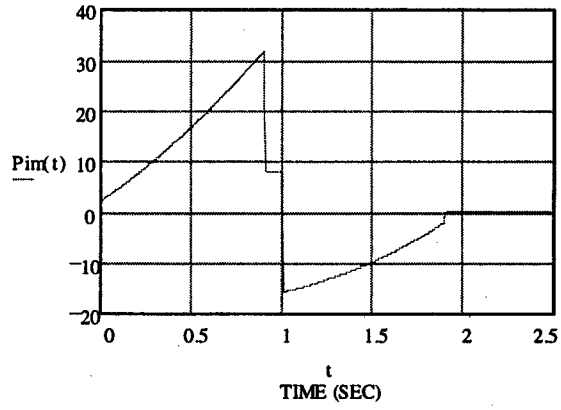

Figure 2: Magnet power (Mwatts)

0-7803-5573-3/99/$10.00@1999 IEEE.

NOTE Pim(t)=I(t)*(L*dI/dt +I(t)*R)
R=0.27 Ohms is the AGS magnet total resistance. L=0.75 Henry is the inductance of the AGS magnets.
The differential equation governing the motor generator power flow is:

$$Pi(t)=J\cdot\Omega(t)\cdot\frac{d^1}{dt^1}\Omega(t)+Pw+Pim(t)+Pscr(t)+Plose(t)$$

Pi(t) is the input power into the motor as function of time. J is the moment of inertia. Ω(t) is the rotational speed of the MG set in rad/sec. Pw=550000 W, is the friction and windage loss. Pim(t) is the instantaneous AGS magnet power. Pscr(t) is the power dissipated on the silicon control rectifiers for the AGSMMPS. Plose(t) represents all other loses measured for a given magnet cycle used in this example. T=2.5 sec, is the period of the AGS magnet cycle. Pi, the average power into the MG set, is equal to the sum of the average power Pam dissipated into the AGS magnets, plus the average power dissipated on the SCR's Pscr, plus the windage loss Pw, plus the all other average losses Plose, for a given magnet cycle. Rlose was measured to be 0.073 Ohms.

$$Pi := Pam + Pw + Pscr + Plose$$

$$Pam := \frac{R}{T}\cdot\int_0^T I(t)^2\,dt \qquad Plose := \frac{Rlose}{T}\cdot\int_0^T I(t)^2\,dt$$

$$Pscr := \frac{1}{T}\cdot\int_0^T I(t)\cdot 32\,dt$$

$$Pi = \frac{R+Rlose}{T}\cdot\left(\int_0^T I(t)^2\,dt\right)+\frac{32}{T}\cdot\left(\int_0^T I(t)\,dt\right)+Pw$$

Pi was calculated to be 3.7 MW for the magnet cycle in Fig. 1. Utilizing Mathcad 5.0 software we solved the differential equation governing the MG set for the rotational speed Ω(t). This is the speed, that the MG set should have for the magnet current in Fig. 1, maintaining the input power Pi=3.7MW constant. Ω0=93.2 rad/sec is the speed of the MG set without a load on the generator. Ωe=94.2 rad/sec is the synchronous speed of the stator magnetic field wich induces EMF on the rotor windings. The result is,

$$\Omega(t)=\sqrt{\Omega 0^2+\frac{2}{J}\cdot(Pi\cdot t-Pw\cdot t-a(t)-b(t)-c(t)-d(t))}$$

Where

$$a(t) := L\cdot\int_{I(0)}^{I(t)} I\,dI \qquad b(t) := R\cdot\int_0^t I(t)^2\,dt$$

$$c(t) := \int_0^t Pscr(t)\,dt \qquad d(t) := Rlose\cdot\int_0^t I(t)^2\,dt$$

S(t) is the slip of the MG set defined as,

$$S(t) := \frac{\Omega e-\Omega(t)}{\Omega e}$$

Fig. 3 is the slip in percent for the magnet current cycle in Fig. 1 while maintaining the motor power Pi constant at 3.7 MW.

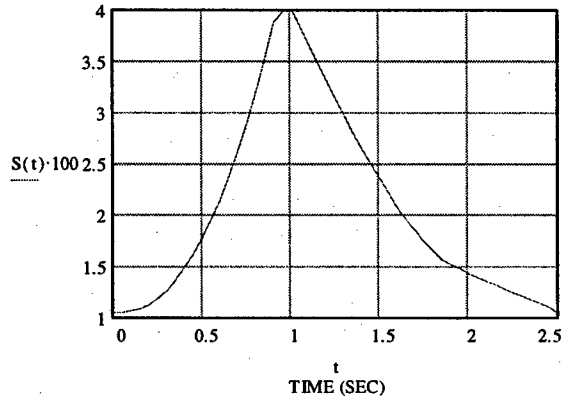

Figure 3: Slip of the MG set in percent

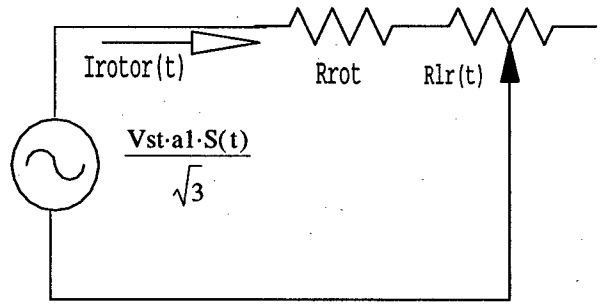

Figure 4: Induction motor rotor equivalent circuit per phase

From induction motor theory we have:

$$a1=\frac{3168}{13800} \qquad \frac{Vroto r(t)}{Vstator(t)}=a1\cdot S(t) \qquad \frac{Irotor(t)}{Istator(t)}=\frac{1}{a1}$$

From the per phase equivalent circuit of the rotor of an induction motor, Fig. 4, assuming the rotor reactance to be 0 we have:

$$Rtot(t)=Rrot+Rlr(t)$$

$$\text{Then } Rtot(t)=\frac{\frac{Vst\cdot a1\cdot S(t)}{\sqrt{3}}}{Irotor(t)}$$

Substituting for Irotor(t) we

$$Rtot(t)=Vst\cdot a1^2\cdot S(t)\cdot\frac{\sqrt{3}}{Istator(t)}$$

$$\text{Since } Istator(t)=\frac{Pi}{\sqrt{3}\cdot Vst\cdot PF(Pi)}$$

$$\text{We finally have } Rtot(t)=Vst^2\cdot a1^2\cdot\frac{S(t)}{Pi}\cdot PF(Pi)$$

From this formula we conclude that to maintain the power into the motor Pi constant, the resistance of the liquid rheostat Rlr(t) should be proportional to the required or desired slip S(t). We measured the power factor versus input power PF(Pi), into the MG and the data are displayed in Fig. 5. Fig. 6 displays the calculated resistance of the liquid rheostat, while pulsing the generator to approximately 34 MW peak power and maintaining the input power to the motor constant at 3.7 MW.

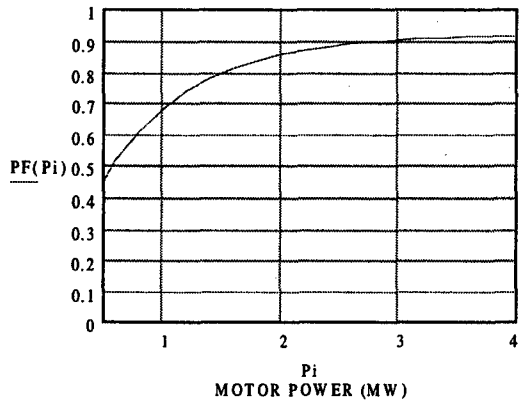

Figure 5: MG set power factor

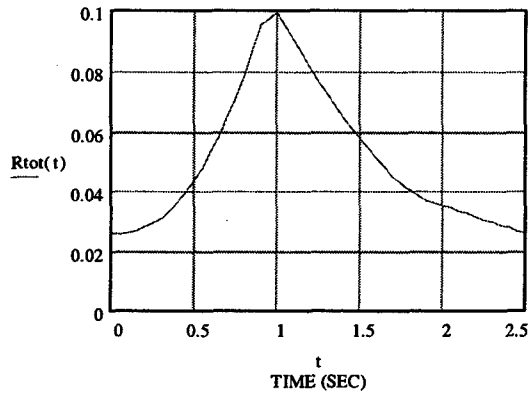

Figure 6: Motor rotor plus liquid rheostat resistance per phase in ohms

Since the resistance of the liquid rheostat is proportional to it's position, if we would pulse the position of the rheostat based on the above calculation subtracting the actual rotor resistance Rrot, which was measured to be 15 mOhm, the input power into the motor should be constant. The actual input power should be constant to +/- 0.5 MW.

3 HYDRAULIC SYSTEM

For pulsing operation of the MG set, a hydraulic system is used. The system consists of a pair of hydraulic pistons capable of moving the liquid rheostat fine adjustment by a maximum of 20 percent of the total liquid rheostat resistance. This corresponds to a maximum fine adjustment of 500 mOms. A 1000 psi pump is used with an electronically controlled Moog valve, to move the position of the fine adjustment. Three different techniques that could be utilized to regulate the motor power, are shown in the block diagram of Fig. 7. When the switch is in position A, a computer generated reference, for a given magnet cycle, will be utilized based on the formula for rotor resistance, calculated above, to drive the Moog valve. If the switch is in position B, the Moog valve will be driven by a computer generated reference based on the formula for the slip. This solution utilizes a feedback loop with reference the slip signal S(t)*100 from Fig. 3, feedback signal the actual slip of the motor in percent, and the error signal driving the position of the fine adjustment of the liquid rheostat. If we choose position C of the switch, then the Moog valve will be driven by a computer generated reference based on the formula for motor power Pi. This solution utilizes a power requlation feedback loop where the error signal drives the position of the fine adjustment of the liquid rheostat, to maintain the input power constant. Sample speed could be used to adjust the power reference.

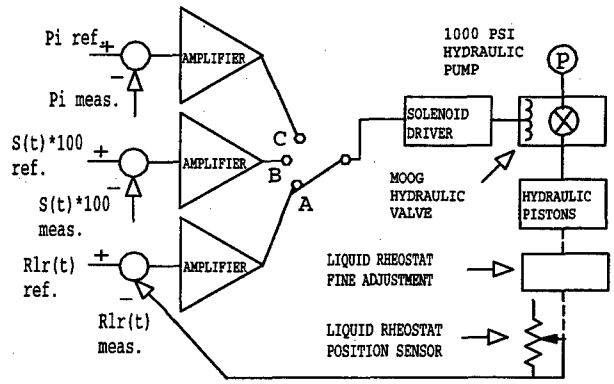

Figure 7: Liquid rheostat hydraulic system block diagram

4 ACKNOWLEDGMENTS

The authors wish to thank M. Meth, J. Spinner, W. Eng, P. Rosas, J. Morris and N. Schumburg, for their engineering support. We also thank S. Savatteri, J. Funaro, J. Lombardo, J. Jimenez, M. Hamilton, W Shaffer and V. Maltese for their technical support of this project.

5 REFERENCES

[1] Power Controller for AGS Main Magnet Power Supply AGS/AD/Tech. Note No. 396, by M. Meth, J. Sandberg and J. Spinner, June 6, 1994.
[2] Electric Machinery Vol. II AC Machines Liwschitz-Garik and Whiple

* Worked performed under the auspices of the U.S.D.O.E.
# Email: marneris@bnl.gov

HIGHLY-PERFORMED POWER SUPPLY USING IGBT FOR SYNCHROTRON MAGNETS

M. Muto#, Y. Mori, K. Niki, KEK, Tsukuba, Japan
S. Koseki, H. Kubo, M. Toriyama, Hitachi Co.Ltd, Hitachi, Japan

Abstract

A new power supply using IGBT is developed in order to investigate the feasibility of use of IGBT to large-scale power supplies for synchrotron magnets. The power supply is constructed with a converter and a chopper blocks, which are made up of IGBT modules. The active peak power and the maximum output current are 1 MW and 3000A. The preliminary tests showed the current ripple is a few x 10^{-6} with only a very small-size passive filter. The paper describes the design parameters of the power supply and the test results in detail.

1 INTRODUCTION

We have developed a new power supply using IGBT to investigate the feasibility of use of IGBT as a power converter element to large-scale power supplies for magnets of synchrotrons such as the JHF main ring [1]. By using IGBT, it becomes possible to construct a power supply basically not generating a reactive power in spite of that the power supply is operated with a trapezoidal output current wave-form. Furthermore, the very high switching frequency makes it easy to control the output current shape with very small tracking error and to regulate the current ripple to be very low level without a large-scale passive filter or an active filter.

The power supply has been designed so as to generate a trapezoidal wave-form output current with the active peak power of 1 MW and the maximum current of 3000 A. Additionally, it is operated as a dc power supply with the peak current of 3000 A. A part of power converter consists of a converter block and a chopper block, which are made up of IGBT modules. The switching frequency of the IGBT module is 8 kHz per each, and the ripple frequency of the output current is 128 kHz.

The preliminary tests with the output current shape based on the JHF excitation-pattern [1] showed that the current ripple at the flat-top of the excitation being a few x 10^{-6} with only a very small-size passive filter, the current stability being less than $5x10^{-5}$ and the tracking error being less than $3x10^{-4}$. The power supply has been operated successfully to study the field quality of the R&D magnet of the JHF 50-GeV main ring [2].

2 CONSTITUTION OF THE POWER SUPPLY

Figure 1 shows the skeleton diagram of the power supply. To realize a very large dynamic range of the output current, the converter-chopper combination method is adopted. The main design parameters of the power supply is summarized

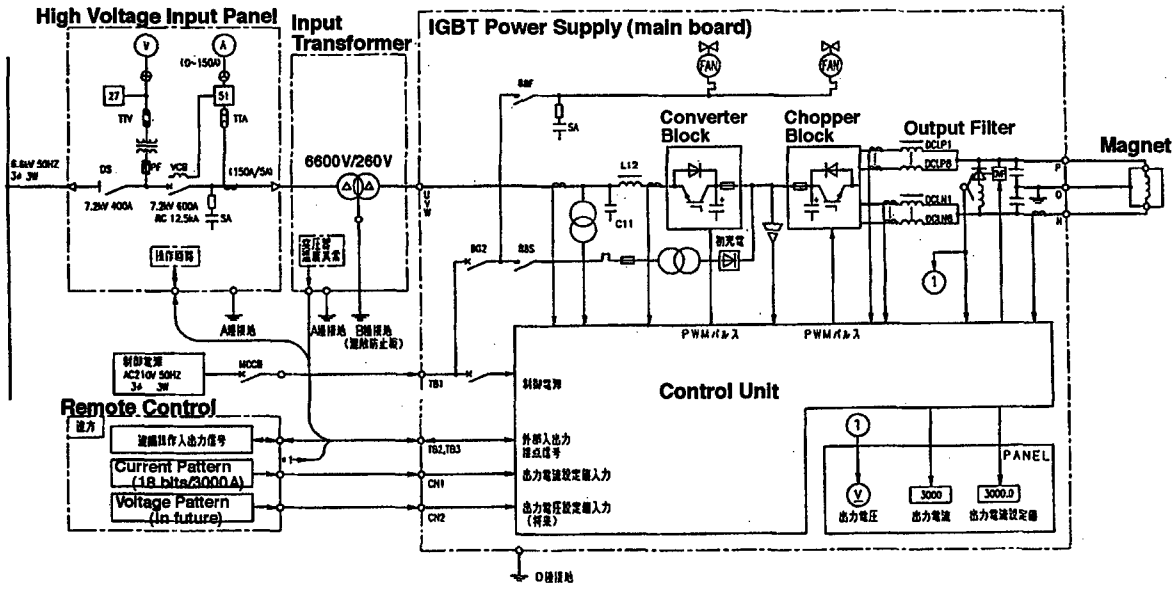

Figure 1: Skeleton diagram of the power supply.

E-mail: masayuki.muto@kek.jp

in Table 1, and the typical output current pattern is shown in Figure 2.

Table 1: Main parameters of the power supply.

input voltage	AC 6600 V (or 3300 V)
converter element	IGBT
method	combination of converter-chopper
operation mode	trapezoidal (peak 1 MW), and DC (max. 3000A)
output current	100 ~ 3000 A
output voltage	0 ~ +- 333V
current ripple	10^{-5} (for H=20 mH) (required) 10^{-6} (expected)
stability	10^{-4}
tracking error*	10^{-3}

* tracking error = (Iactual - Ireference)/Ireference-max

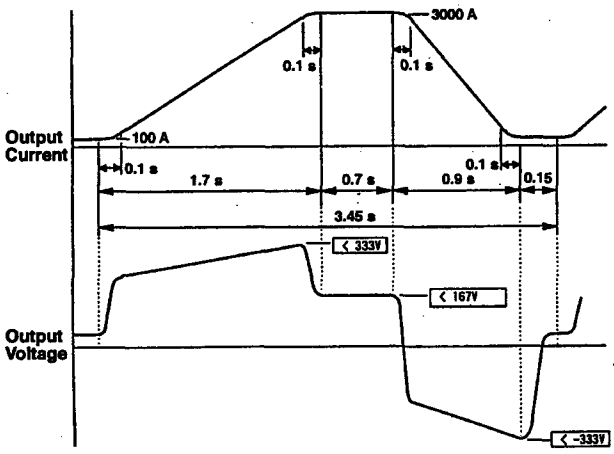

Figure 2: Typical output pattern of the power supply.

2.1 IGBT Module

The converter and chopper blocks are constructed with IGBT modules; 9 modules for the converter and 16 modules for the chopper, and each module is constructed with 5 IGBT packages (2 IGBTs in each package). The maximum rates of voltage and current of the IGBT are 1200 V and 300 A, respectively. Figure 3 shows the circuit diagram of the IGBT module. The specification of the module is the same for the converter and chopper blocks, and it is connected oppositely corresponding to converter or chopper as shown in Figures 1 and 2.

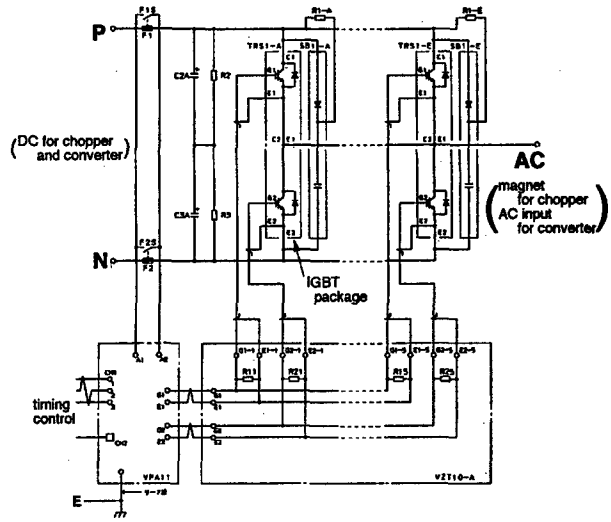

Figure 3: Circuit diagram of the IGBT module

The converter is operated with the switching frequency of 5 kHz for each phase, to convert AC power to DC power with the output voltage of about 410 Vdc (205 Vdc for the case of 3300 V input voltage), and to regulate the input power-factor near unity during operation.

The 16 modules for the chopper block are divided into two groups (P and N), and the 8 modules for each group are connected in parallel, with a small reactor (DCLP or DCLN, shown in Figure 1) for each module. This small reactor forms passive filter with condensers of downstream, whose cut-off frequency is set to be 1.8 kHz. The switching frequency of the chopper module is 8 kHz, then the output ripple frequency becomes 128 kHz (8 x 16 modules). This is enable us to make the control speed fast and the size of output filter very small. Finally, the only passive filter described above is equipped as an output filter and an active filter is not employed.

3 TEST RESULTS

The power supply was tested with the input voltage of only 3300 V, because the 6600 V power line was not available for the R&D facility at present. As a test load, the R&D bending magnet of the JHF 50-GeV main ring (L=8 mH, R=4.3 mΩ) was used.

3.1 Input Characteristics

The power factor and harmonic current of the input power was measured with the condition of trapezoidal output current whose peak current was 3000 A, peak power was 267 kW and ramping up ratio was 9700 A/s. The power factor was nearly unity above the output power level of 150 kW and about 0.87 at the power of 100 kW. The total harmonic current (rms.) was about 4.1%.

3.2 *Output Current Ripple*

A current ripple was calculated from the voltage ripple measured at the output terminal of the power supply.

Figure 4 shows the spectrum pattern of the terminal voltage when the power supply was operated with the output current of DC 3000 A, and Table 2 shows the current ripple calculated from the voltage ripple at the frequency range of 50 ~ 600 Hz.

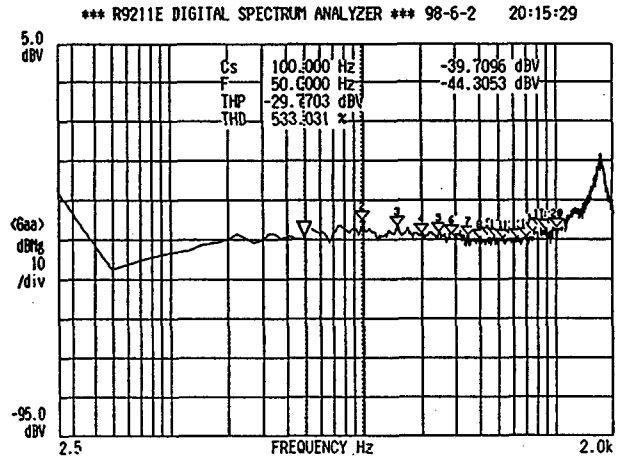

Figure 4: Spectrum distribution of voltage ripple.

Table 2: Current ripple measured with DC 3000 A.

n	f (Hz)	voltage ripple (meas) dBV(0dBV=1Vrms) dBR	dBV	current ripple (cal) (20mH)
1	50	———	-44.3053	9.14069E-07
2	100	4.59569	-39.7096	7.75771E-07
3	150	3.25764	-41.0477	4.43343E-07
4	200	1.35123	-42.9541	2.66981E-07
5	250	1.77125	-42.5341	2.24167E-07
6	300	1.13079	-43.1745	1.73527E-07
7	350	0.90861	-43.3967	1.44981E-07
8	400	0.09316	-44.2121	1.15491E-07
9	450	0.49535	-43.8100	1.07524E-07
10	500	0.15114	-44.1542	9.30113E-08
11	550	0.00755	-44.2978	8.31694E-08
12	600	-0.12508	-44.4304	7.50833E-08

The current ripple at the frequency of 8 kHz and 64 kHz (due to the switching frequency of the chopper module) was 8.28 x 10^{-8} and 1.07 x 10^{-7}, respectively. On the other hand, at the frequency of 1.8 kHz, which was the cut-off frequency of the output filter, was 6.4 x 10^{-7}.

The current ripple when the power supply was operated with the output of trapezoidal wave-form shown in Figure 2 was also measured. Table 3 shows the calculated results of the current ripple. At the frequency range of 50 ~ 300 Hz, it becomes larger than that of DC operation listed in Table 2 by factor 2 ~ 3.

Table 3: Current ripple measured with the output of trapezoidal wave-form.

f(Hz)	dBv	ripple
50	-33.9046	3.027 x10^{-6}
100	-36.3797	1.138
150	-29.2714	1.720
200	-30.5068	1.119
250	-28.3780	1.144
300	-31.6048	6.574 x10^{-7}
350	-35.9082	3.433

3.4 *Tracking Error*

Figure 5 shows the tracking error which defined in Table 1. It was less than 3 x 10^{-4} during ramping-up period of the pattern. The trapezoidal output current wave-form, whose peak current is 3000 A, is also clearly seen.

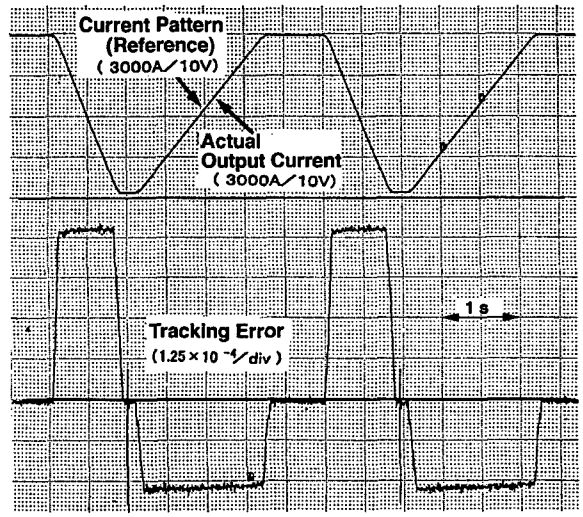

Figure 5: Tracking error and trapezoidal output current wave-form.

4 CONCLUSION

We constructed a new power supply with the output peak power of 1 MW by using IGBT. The test results showed that it might be possible to construct a power supply with the peak power of around 10 MW level with using only IGBT. The power supply developed here has been operated successfully to study the field quality of the R&D magnet of the JHF 50-GeV main ring now, and will be operated for mass field-measurements in future.

5 REFERENCES

[1] JHF Project Office, "JHF ACCELERATOR DESIGN STUDY REPORT", KEK Report 97-16 (JHF-97-10), p2.4-1, (1998)

[2] M.Muto et al., "Magnets and Power Supply System of JHF 50-GeV Main Ring" APAC98, KEK, Tsukuba, (1998)

A GATE DRIVE CIRCUIT FOR GATE-TURN-OFF (GTO) DEVICES IN SERIES STACK*

O. Despe, J. Wang, ANL, Argonne, IL

Abstract

A gate-turn-off (GTO) switch is under development at the Advanced Photon Source as a replacement for a thyratron switch in high power pulsed application [1]. The high voltage in the application requires multiple GTOs connected in series. One component that is critical to the success of GTO operation is the gate drive circuit. The gate drive circuit has to provide fast high-current pulses to the GTO gate for fast turn-on and turn-off. It also has to be able to operate while floating at high voltage. This paper describes a gate drive circuit that meets these requirements.

1 INTRODUCTION

The relatively low voltage ratings of GTO devices compared to thyratrons require the series connection of these devices when used as replacement in certain thyratron applications. For this series configuration, a basic requirement is a gate driver circuit that can be operated at a high floating potential.

The gate current requirement of the GTO used in the study, Westcode WG10040R36, is listed in Table 1. The turn-on gate current has two components, a fast initial pulse and a constant component. The leading edge portion of the current pulse is two to three times the value required to sustain the on state of the device. The high initial current is needed to supply charge quickly into the nonlinear gate capacity of the GTO in order to reduce its turn-on time. The recommended amplitude by Westcode is between 70 and 100 amperes. After the GTO device is turned on, a substantial amount of gate current is still needed to maintain a low on-state resistance and, hence, a low voltage drop across the GTO's anode and cathode.

Table 1: GTO gate current requirement

	Initial Current	Sustained Current
Turn On	70 ~ 100A	20 ~ 50A
Turn Off	> 100A	-

During the turn-off process, a large current is required in the reverse direction to remove charges from the junction and restore the forward-voltage-blocking capability. The amplitude of the turn-off gate current can be much greater than that required for turn-on, depending on the current at which the GTO is trying to turn off. The greater the turn-off current, the greater the amplitude has to be. The speed of the GTO's recovery depends on how fast the charge is removed.

A low-leakage-inductance pulse transformer, which also provides the high voltage isolation, can be used to supply the leading edge portion of the current pulse. The current level needed to keep the on-state resistance low for the duration of the on state, however, will most likely be provided by some other means if this duration is in many microseconds.

2 DIRECT GATE DRIVE CIRCUIT

A direct gate drive circuit has been developed for the GTOs. As shown in Figure 1, the output of the drive circuit is connected directly to the GTO gate without a pulse transformer. The drive circuit is divided into two sections, a low voltage section and a high voltage section. The low voltage section contains a fly-back type DC/DC converter that provides the required power for the high voltage section. The high voltage section has the control

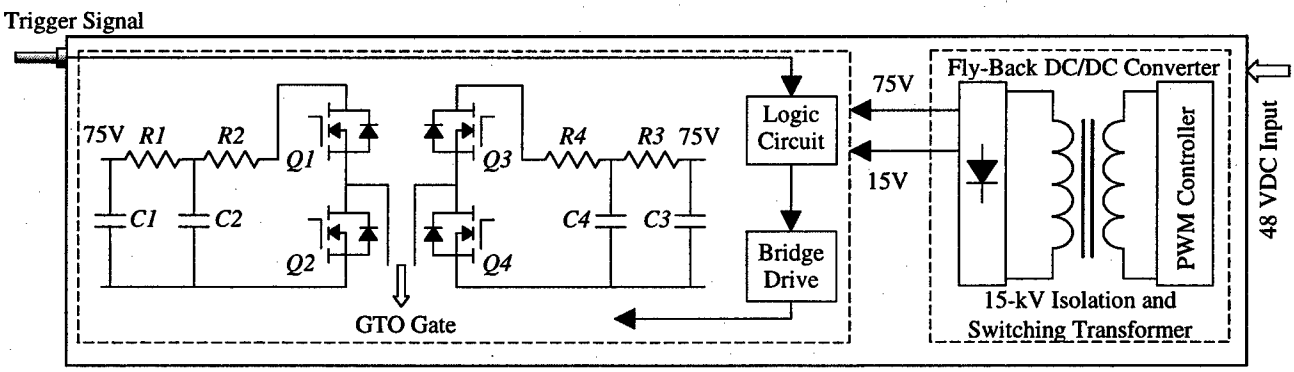

R1 = 1.2Ω, *R2* = 0.5Ω, *C1* = 220μF, *C2* = 4.4μF, *R3* = 30Ω, *R4* = 0.25Ω, *C3* = 220μF, *C4* = 6.6μF

Figure 1: Block diagram of the GTO gate drive circuit

* Work supported by U.S. Department of Energy, Office of Basic Energy Sciences under Contract No. W-31-109-ENG-38.

logic and GTO gate drive circuitry. A high-frequency switching transformer couples the two sections providing the energy transfer and the necessary high voltage isolation.

2.1 DC/DC Converter

The fly-back type DC/DC converter uses a current mode pulse-width modulation (PWM) controller chip, UC2844, with a power MOSFET, IRF640, driving a custom-wound high-frequency and high-voltage isolation (15 kV) transformer. The PWM controller operates at a nominal frequency of 90 kHz. The converter is designed for a 1-A maximum switching current at 50% duty cycle, resulting in a power transfer from the low-voltage section to the high-voltage section of approximately 13 watts maximum. A set of voltage and current switching waveforms is shown in Figure 2.

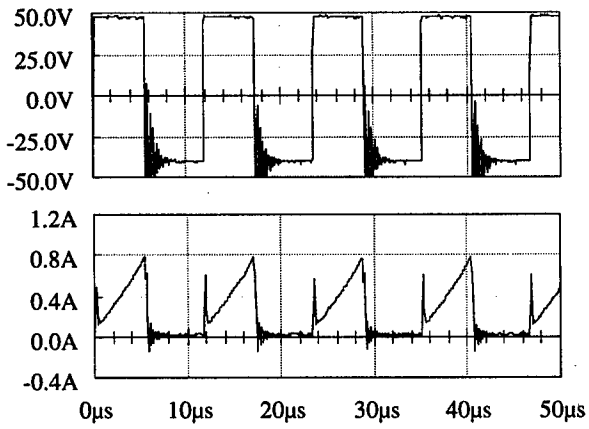

Figure 2: Converter switching voltage and current

Input power to the converter is 48 VDC. The switching transformer has one input winding of ten turns and three output windings of seventeen turns, four turns, and two turns, respectively, all made from #22, 15-kVDC wire. The input winding conducts a ramping current of up to one ampere when the MOSFET turns on. The stored energy in the primary winding is then transferred to the output windings when the MOSFET turns off.

The two-turn output provides a feedback signal to the PWM controller for voltage regulation. A resistor divider reduces the feedback signal before sending it to the voltage feedback input pin of the PWM controller. A variable resistor in the divider is used to adjust the level of the feedback voltage and, in turn, to set the output voltage. The four-turn output is rectified and regulated to supply 15-V power to the logic circuit and the MOSFET drive in the high-voltage section. The seventeen-turn output feeds two rectifiers to charge two dual *RC* circuits to 75 volts.

Taking advantage of the insulation property of ferrite, the switching transformer uses a ferrite toroid, P44914-TC from Magnetics, as the core. The criteria for choosing the type of ferrite core are the need for a large window to accommodate the windings, which are relatively large due to the high-voltage insulation, and low core losses.

2.2 Gate Circuit

The drive circuit is based on power MOSFETs connected in an H-bridge configuration. Figure 1 shows the basic bridge circuits with the *RC* networks that shape and deliver current to the GTO gate. *R1*, *R2*, *C1*, and *C2* are for turn on, while *R3*, *R4*, *C3* and *C4* are for turn off.

During turn on, for a given supply voltage, *R2*, *C2*, the MOSFET bridge on-state resistance, GTO gate resistance, and the stray inductance (which cannot be ignored in this case because of the speed of the pulse) determine the amplitude and duration of the fast component of the current pulse to the GTO gate. The level of the bridge output current after the leading edge portion is mainly determined by resistors *R1* and *R2*. The bridge on-state resistance and the GTO gate resistance are very small compared to the sum of *R1* and *R2* and, therefore, have little effect on the current level after the initial pulse. The relatively large time constant of *R1C1* compared to *R2C2* guarantees that the bridge output current remains essentially constant for the duration of the pulse after the initial high current component dies out.

The requirement for initial GTO device turn-off is similar to the one for turn-on. A large negative short-duration current pulse is produced by the turn-off network, *R3*, *C3*, *R4*, and *C4*, to quickly remove the stored charge in the gate structure of the device. The amplitude of this pulse can be much higher than that required for turn-on, depending on how much current the GTO is forced to turn off. While a substantial amount of current is required to maintain the low on-state resistance of the device, a negative gate voltage of only a few volts is needed to keep it off after the stored gate charge is removed by the initial current pulse. In this case *R3* is much greater than *R1*. The turn-off process continues after the initial pulse terminates. Although the device recovers its reverse blocking capability shortly after this negative current pulse, its forward blocking capability returns much more slowly. This recovery lasts many microseconds after the initial negative pulse.

Both the rise time and the amplitude of the gate current are affected by the stray inductance in the circuit. To achieve a fast gate current pulse, the stray inductance has to be minimized. For this reason, low inductance components are used, short and wide traces are employed on the PC board, and the connection between the gate drive board and the GTO is kept at the minimum length.

Two MOSFETs are connected in parallel to form each switch section of the H-bridge because of the high speed and current demand of the GTO gate. Since the resistance in the *RC* circuit for the initial fast pulse is only a fraction of an ohm, the MOSFETs need to have a low on-state resistance in order not to affect the amplitude of the gate

current. Power MOSFET IRF540N from International Rectifier was chosen for its very low on-state resistance, 0.052Ω, and large drain current rating, 27A.

2.3 Operation

In the normal off state of the H-bridge, *Q1*, *Q3* and *Q4* are off while *Q2* is on. *Q2* provides a return path for a bias circuit (not shown in Figure 1) to provide a negative bias of about -3V to the GTO gate. At the leading edge of the input trigger signal, *Q2* shuts off while *Q1* and *Q4* are driven on and held on for the duration of the trigger signal.

The width of the on pulse is controlled by the trigger signal. Since several GTOs are connected in series and GTOs have different turn-on and turn-off speeds, the leading edge and the trailing edge of each trigger signal are independently controlled in order to turn on or turn off all the GTOs at the same time.

At the termination of the trigger pulse, the GTO turn-off process is started. *Q1* and *Q4* are turned off while *Q2* and *Q3* are turned on. The energy in the turn-off network is discharged into the GTO gate. Ideally *Q3* is turned on only for a duration sufficient to remove the stored gate charge in the GTO. This occurrence is evidenced by the gate voltage going negative and staying negative. Any extra drive is clamped by the zener action of the gate-cathode diode of the GTO device. An *RC* circuit in the logic controls the on duration of *Q3*. It provides easy adjustment for the length of the turn-off pulse. As mentioned earlier, the recovery time for the GTO forward voltage blocking capability is attained many microseconds after the gate voltage goes negative. Therefore *Q2* is held on to maintain a negative gate bias until the next trigger signal arrives. Figure 3 shows a gate current pulse generated by the drive.

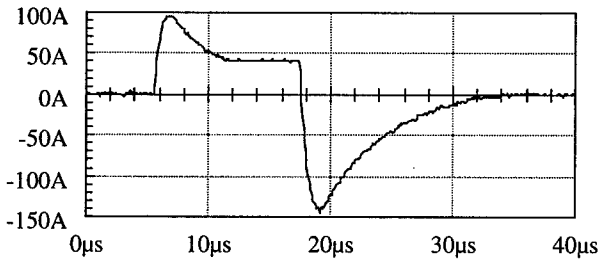

Figure 3: GTO gate current pulse

The trigger signal is transmitted to the card by fiber optics. It provides needed isolation between the high-voltage section and the low-voltage section. An HP HFBR2521 fiber receiver, rated for 5 Mbits/s at 19 meters, is used. Its internal logic operates at 5 volts while its open-collector output is rated for 18 volts. This enables CMOS integrated circuits (ICs) to be used in the logic circuit, thus providing more tolerance for noise produced by switching actions of the power MOSFETs and the GTOs.

Two high voltage half-bridge driver ICs, HIP2500 by Harris, are used to drive the power MOSFET H-bridge. The HIP2500 has current outputs suitable for driving the gates of power MOSFET devices. Its high-voltage section output is also capable of floating up to 500 volts above its ground; thus, it meets the requirements for driving the top switches of an H-bridge configuration.

2.4 Advantages and Disadvantages

A direct gate drive has several advantages compared with conventional single primary and multiple secondary pulsed-transformer-based gate drives. It has very low inductance and, therefore, can supply very fast gate pulses to the GTO gate. It can produce long constant gate current if the GTOs are required to stay on for a long period of time. It also permits adjustment of the turn-on and turn-off timing of each GTO independently to compensate for variations in a GTO's switching speed. The high-frequency switching and high-voltage isolation transformer has a very simple structure and can be constructed easily. Since each GTO/gate drive pair is completely independent, any number of the GTOs can be used in series to accommodate the requirement of the high voltage.

The disadvantage of the direct gate drive is that if one of the drives fails to send the turn-on gate pulse to its GTO, the GTO will be damaged by an over voltage when other GTOs are turned on. A domino effect may follow in which all the GTOs are destroyed. Similarly, if one drive fails to send the turn-off gate pulse, other GTOs may be damaged by excessive voltage in the reverse direction. To improve the reliability of the GTO switch operation, certain voltage redundancy needs to be considered when deciding the number of GTOs to be used in series. Some interlock mechanism may need to be devised to link all of the gate drives together. If a malfunction is detected in one drive, the trigger signals must be stopped for all the drives.

3 CONCLUSION

Seven direct gate drive cards have been built to drive a GTO switch of seven GTOs connected in series. With these cards, the GTO switch has successfully switched a half-sine current pulse of 6000 amperes with a base width of 12 microseconds. Further study will be done on improving the reliability of the drive and finding a suitable interlock mechanism.

4 REFERENCES

[1] O. Despe and J. Wang, "Design of a Gate-Turn-Off (GTO) Switch for Pulsed Power Application," EPAC98, pp. 2281-2283, Stockholm, 1998.

HIGH EFFICIENCY LINEAR POWER SUPPLY WITH A PREREGULATOR CONTROLLED BY KEEPING CONSTANT R_{DS} OF MOSFET

Kuo-Bin Liu, Chen-Yao Liu and Jeng-Tzong Sheu
Synchrotron Radiation Research Center
No. 1 R&D Road VI, Hsinchu Science-based Industrial Park, Hsinchu 30077, Taiwan R.O.C.

Abstract

In Synchrotron Radiation Research Center (SRRC) more than ninety linear power supplies with 100 ppm long-term stability are served for correction magnets. To increase the well-known efficiency problem of linear power supply, inside a customer-made bipolar linear power supply a homemade pre-regulator circuitry is in series in front of power stage. By using constant V_{DS} controlled pre-regulator, the power consumption of linear power supply itself could be reduced and the efficiency changes with respect to the output power. On the other hand, with constant R_{DS} controlled pre-regulator, the efficiency is even higher and is the ratio of load resistance and R_{DS}. Design and performance of the pre-regulator circuitry will be demonstrated.

1 INTRODUCTION

Low efficiency is the drawback of linear mode power supply, most of power is dissipated at power device and transformer. A lot of correction magnet power supplies used at Synchrotron Radiation Research Center (SRRC) are linear mode power supplies. The efficiency of power stage of these power supplies is below 50% and it could be lower than 30% if transformer is included.

A pre-regulator in series in front of power stage of linear mode power supply could keep voltage drop on power device a small value and decrease power dissipation such that the efficiency of power supply is increased. There are different types of pre-regulator, for example, SCR type[1]□variable transformer[2]..... In this experiment a programmable HP6032a DC power supply is used as a pre-regulator for linear mode bipolar correction power supply of SRRC. Two kinds of control strategy will be used to control the output of HP6032a and the efficiency of power stage can be figured out both in calculation and measurement. In the final design, VICOR V375A24C600A[3] programmable DC-DC converter is inserted as a pre-regulator controlled by suitable control strategy and the efficiency will be demonstrated.

2 CONTROL STRATEGY

The main goal of pre-regulator is to decrease the voltage drop on power device and keep power device on normal operation, that needs a good control strategy. Conventionally, the parameter to be controlled is the V_{DS} of MOSFET, the output of pre-regulator will change with respect to the output of power supply and keep V_{DS} of MOSFET a constant value; the power device of correction magnet power supply used at SRRC is IRFH6H250 MOSFET, V_{DS} of this MOSFET should be at least 0.6V to let power supply operate normally at maximum 20 amperes output. V_{DS} is decreased when output current of power supply is increased then the output voltage of pre-regulator should increase to keep V_{DS} constant. If output current of power supply is decreased then the output voltage of pre-regulator should also decrease; under this kind of control strategy there is a minimum value of equivalent resistance R_{DS} of MOSFET when output current of power supply is maximum; that is to say, the efficiency of power stage is dependent on output current of power supply.

If the minimum R_{DS} of MOSFET is the parameter of control strategy, the efficiency of power stage is a ratio of R_{DS} and resistance of load and is independent of output current of power supply. Based on above argument, control strategy of keeping constant R_{DS} is better than keeping constant V_{DS}. The efficiency of power stage in series of pre-regulator with these two kind of control strategy will be discussed, one pre-regulator is called constant V_{DS} pre-regulator and the other is constant R_{DS} pre-regulator.

3 EFFICIENCY OF POWER STAGE WITHOUT A PRE-REGULATOR

If the rectified voltage of linear mode power supply is Vdcbus, Rload is the resistance of magnet load and i_D is the output current, then V_{DS} of MOSFET is :

$$V_{DS} = Vdcbus - i_D * Rload$$

Efficiency of power stage is :

$$i_D^2 * Rload / (i_D * Vdcbus)$$

$$\Rightarrow \quad i_D * Rload / Vdcbus \qquad (1)$$

From (1), the relationship between efficiency of power stage and output current is linear, the more output current the more efficiency; the Vdcbus of correction magnet power supply used at SRRC is 24 volts and Rload is 0.4959Ω, then the relationship becomes:

$$i_D * 0.4959\Omega / 24V \qquad (2)$$

Figure 1 is the plot of efficiency versus output current, efficiency is below 50 % within 0 ~ 20 amperes, it shows more than 50 % of energy is dissipated at MOSFET. The difference between equation (2) and figure1 is because the

0-7803-5573-3/99/$10.00@1999 IEEE.

variation of Vdcbus influenced by output current and resistance of transformer.

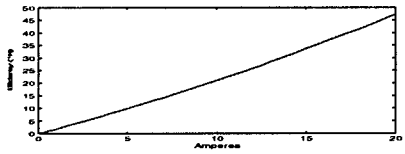

Figure 1

4 EFFICIENCY OF POWER STAGE WITH A PRE-REGULATOR

In the beginning of experiment, there isn't a real pre-regulator in the test setup. HP6032a is an analog programmable power supply, it's function just could be used a pre-regulator and figure 2a is the test setup. The main goal is to know how much efficiency of power stage in series with a pre-regulator controlled by two kind of control strategy could be reached and then to choose a better control strategy, figure 2b is the circuitry of control strategy.

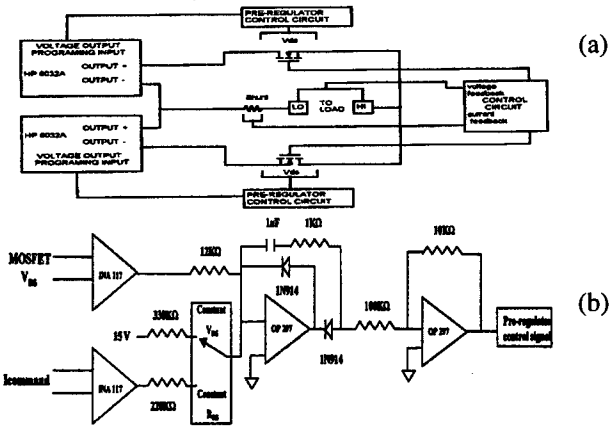

(a)

(b)

Figure 2 (a) test structure setup (b) circuitry of control strategy

4.1 Efficiency of power stage in series with a constant V_{DS} pre-regulator

At this control mode, MOSFET is operated in linear range and the relationship between i_D and v_{DS} is as follow:

$$i_D = K[\, 2(v_{GS} - Vt)\, v_{DS} - v_{DS}^2]$$

because v_{DS} is very small, so v_{DS}^2 is neglected,

$$i_D = 2K(v_{GS} - Vt)\, v_{DS} \quad (3)$$

$$R_{DS} = v_{DS} / i_D = 2K(v_{GS} - Vt) \quad (4)$$

Equation of efficiency is:

$$i_D^2 * Rload / (i_D * Vdcbus)$$

because $Vdcbus = i_D * Rload + v_{DS}$

so equation of efficiency becomes:

$$i_D^2 * Rload / (i_D^2 * Rload + i_D * v_{DS})$$

$$\Rightarrow\ i_D * Rload / (i_D * Rload + v_{DS}) \quad (5)$$

in real design, v_{DS} is set to 0.614 volt, so (5) becomes:

$$i_D*0.4959\Omega/(i_D*0.4959\Omega+0.614V) \quad (6)$$

Figure 3 is the plot of efficiency versus output current, and it follows equation (6) very well. Benefit gained from a constant V_{DS} pre-regulator is obvious, efficiency of power stage is increased very much.

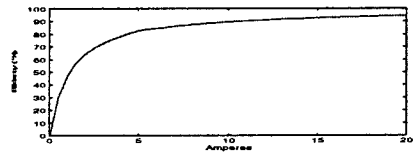

Figure 3

Figure 4 is the plot of variation of v_{DS} within 0 ~ 20 amperes output of power supply, it shows the variation of v_{DS} is very small and the function of control circuit of constant V_{DS} pre-regulator is suitable.

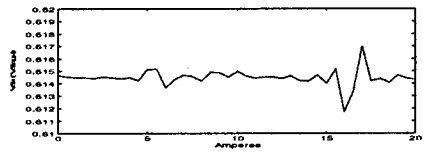

Figure 4

4.2 Efficiency of power stage in series with a constant R_{DS} pre-regulator

Correction magnet power supply used in SRRC is a programmable current mode power supply so that output current i_D is programmed by command $i_{command}$, then

$$i_D \propto i_{command}$$

if v_{DS} is also programmed by $i_{command}$

then $v_{DS} \propto i_{command}$

and $v_{DS} \propto i_D$

let $v_{DS} = R*i_D$

$$R_{DS} = v_{DS} / i_D = R*i_D / i_D = R \quad (7)$$

Based on the control strategy, R_{DS} could be controlled to be a value as wish no matter what output current is; efficiency could be expressed as follow:

$$i_D^2*Rload / (i_D^2*Rload + i_D^2* R)$$

$$\Rightarrow\ Rload / (Rload + R) \quad (8)$$

Under control strategy of constant R_{DS}, efficiency is constant and independent on output current of power supply; the constant value R could be derived from parameter of constant V_{DS} pre-regulator, V_{DS} is set to 0.614 volt so that minimum equivalent R_{DS} is 0.0307Ω (0.614 volt / 20 amperes) and this value is controlled by constant R_{DS} control strategy; efficiency might be calculated as below:

$$0.4959\Omega/(0.4959\Omega + 0.0307\Omega)= 0.942$$

Figure 5 is the plot of efficiency of power stage versus output current of power supply and the efficiency is almost constant.

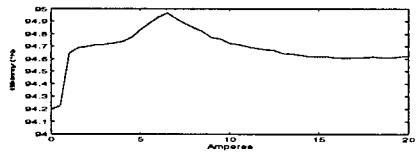

Figure 5

Benefit gained from constant R_{DS} control strategy is more than constant V_{DS} control strategy; figure 6a is the plot of variation of V_{DS} versus output current of power supply, figure 6b is the plot of variation of R_{DS} versus output current of power supply and it is obvious R_{DS} is controlled very well.

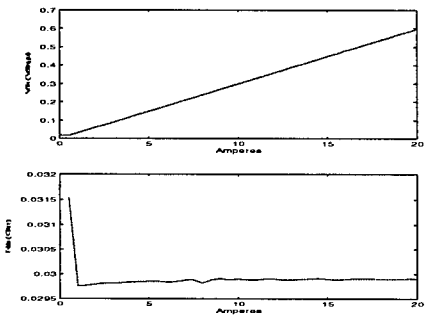

(a)

(b)

Figure 6 (a) V_{DS} vs. output current (b) R_{DS} vs. output current

5 EFFICIENCY OF FINAL DESIGN CIRCUIT

Although HP6032a is used as a pre-regulator to test two kind of control strategy circuits and performance of these two circuits are good, but a real pre-regulator is still needed in real application. VICOR V375A24C600A is a compact and high efficiency 600 watts 2.4 ~ 24 volts output programmable DC-DC converter, it is suitable to be used as a pre-regulator. Control circuit used for this module is constant R_{DS} control strategy because more efficiency could be gained. Figure 7 is the final structure of power supply.

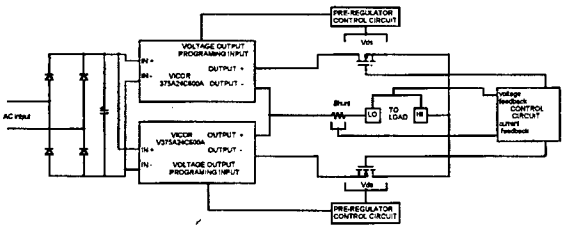

Figure 7

Figure 8 is the plot of efficiency of power stage versus output current of power supply, efficiency is not constant in low output current range because output voltage of VICOR V375A24C600A can not function below 2.4 volts, but normal operation output current of most of correction magnet power supply are larger than 3 amperes so that high efficiency is still gained.

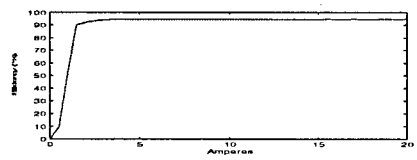

Figure 8

6 CONCLUSION

Efficiency of correction magnet power supply used at SRRC is improved by insertion of a pre-regulator in series in front of power stage, constant R_{DS} control strategy is a better choice for the control of pre-regulator than constant V_{DS} control strategy that could save more power and efficiency is just the ratio of load resistance and R_{DS}. It is not very much suitable for VICOR V375A24C600A to be a pre-regulator because it can't operate below 2.5 volts. But efficiency is higher than 90% in normal operation of correction magnet power supply when output current above 3 amperes.

7 REFERENCES

[1] Operation Manual of BRUKER B-MN 50 / 1500 power supply

[2] Operation Manual of DANFYSIK system 8000 power supply for booster dipole magnet of SRRC

[3] VICOR data sheet: V375A24C600A DC-DC converter

Author Index

Abe, Hiroshi **2015**, **2749**
Aberle, Oliver **949**
Abo-Bakr, Michael **2385**
Acharya, R. **1393**
Adachi, Toshikazu **2271**, **3348**, **3752**
Adamenko, Stanislav V. **3269**, **3271**
Adams, D.J. **2199**
Adderley, P. **1991**
Adolphsen, Christopher D. **253**, **777**, **3411**, **3423**, **3477**
Afonin, A.G. **53**
Agafonov, Alexey V. **1731**, **1734**
Agematsu, Takashi **2259**
Ahle, Larry **1937**, **3248**
Ahn, Hyo-Eun **875**, **1255**
Ahrens, Leif A. **614**, **1276**, **1746**, **2063**, **2286**, **2918**, **3291**, **3294**
Akagi, Hirofumi **3749**
Akai, Kazunori **440**, **1132**, **2731**
Akaoka, Nobuo **3546**
Akasaka, Nobumasa **1132**, **2238**, **2731**, **3411**
Akemoto, Mitsuo **3414**
Akiyama, Atsuyoshi **343**, **3158**
Akre, Ronald A. **2846**
Alai Tafti, A. **2722**
Alba, Rosa **2578**
Aleksandrov, A. **237**, **3321**
Aleksandrov, Aleksander V. **78**, **2948**
Aleksandrov, Vladimir S. **3501**
Alekseev, Nicolay N. **1479**
Aleshaev, Alexander N. **750**
Alessi, James G. **106**, **614**, **1297**, **1902**, **1964**, **3300**
Alexahin, Yuri **1527**
Alford, Owen J. **2590**, **3251**
Alimov, Andrey S. **2301**, **2555**
Alonso, Jose **574**
Alton, Gerald D. **1878**, **1881**
Alton, William J. **845**
Altuna, Xavier **2617**
Amano, Daizo **2403**, **2689**
Amatuni, Andrey Ts. **3657**, **3660**
Ambrosio, G. **174**
Ames, Friedhelm **1955**
Anderegg, Jim **1402**
Anders, W. **197**, **2385**
Anderson, David E. **3390**
Anderson, Edwin B. **1686**
Anderson, James L. **571**
Anderson, Oscar **1908**, **1937**
Anderson, Scott **217**, **2006**, **2039**, **2042**, **2045**
Andersson, Ake **2945**
Andreev, N. **174**, **3194**, **3197**
Andreev, Nikolai **154**
Andreev, V.A. **2256**
Andrianov, Serge N. **1866**, **2701**
Anerella, Michael D. **185**, **3161**, **3170**
Anferov, Vladimir A **392**
Anguelov, Vladimir **2289**
Anthouard, Philippe **3260**
Antoine, Claire **919**
Antonello, M. **1324**
Antonsen Jr., Thomas M. **360**
Aoki, Yasushi **2018**, **2036**
Apel, Ruediger **812**, **818**
Arakawa, Dai **1141**, **1653**, **1821**
Arakawa, Kazuo **2259**
Araki, Sakae **343**
Arapov, L. **237**
Arcan, T. **174**, **3197**
Archambault, L. **325**, **3705**
Arduini, Gianluigi **1282**, **1285**, **2617**, **2996**
Argan, Andrea **1599**
Arimatea, Claudio **2617**
Arkan, T. **3194**
Arkan, Tug T. **3242**
Arnett, Don **1390**
Arnold, Ned D. **2024**
Aronson, A **548**
Artoos, Kurt **154**
Arutunian, Suren G. **1468**, **2105**, **3657**
Arvin, Adrian H. **1444**, **1447**, **1929**, **1946**
Arvin, Andy **349**
Asaka, Takao **2015**, **2749**, **3507**
Asano, K. **777**, **3417**, **3423**
Asaoka, Seiji **667**, **670**
Aspenleiter, Jeffrey **1390**, **2698**
Assadi, Saeed **711**, **720**, **1082**, **1085**, **2719**
Assmann, Ralph **330**, **2996**, **2999**, **3002**
Aston, David **2990**
Atencio, Samuel J. **965**
Aune, Bernard **432**
Autin, Bruno **3071**
Autrey, Daryl **3248**
Avilov, Alexandr M. **2549**
Ayers, James J. **1961**
Baartman, Richard A. **128**, **3534**, **3537**
Babayan, Ruben A. **2424**
Baboi, N. **922**
Babzien, Marcus **2024**, **2158**, **2471**, **2480**, **3722**
Bach, H. **2427**
Backe, H. **165**
Badan, L. **1324**
Badea, V. **3767**
Bae, Young-Soon **3525**
Bai, Mei **387**, **471**, **2725**, **3336**
Bailey, Roger **2617**, **2996**
Bak, J. S. **1384**
Bak, Peter A. **2167**
Bakker, Rene J. **197**, **726**, **2078**, **2379**, **2382**
Baklakov, Boris **1387**
Balakin, Vladimir **461**
Balbekov, Valeri I. **315**, **3062**, **3146**
Baldis, Hector A. **2000**
Ball, M. **498**, **1545**, **1548**
Ball, Millicent J. **3245**
Ballarino, Amalia **1405**
Balleyguier, Pascal P. **1444**, **1447**, **1946**
Baltadoros, D. **1037**
Bane, Karl F. **3432**, **3486**
Bane, Karl L.F. **1725**, **1728**, **2822**, **3423**, **3453**, **3474**, **3477**
Bangerter, Roger O. **3215**
Banks, Thomas I. **1686**
Banna, S. **3600**, **3606**, **3609**
Bannon, M. **3767**
Baptiste, Ken **1471**, **3131**
Baranauskas, V. **2811**
Barber, D. P. **2635**
Bardy, Jacques **3260**
Barklow, Timothy L. **307**, **3489**
Barlow, D. **3576**
Barnard, John J. **1761**, **1803**, **1830**, **3248**
Barnes, C. **321**
Barnes, Michael J. **1509**, **3378**
Barnes, Peter D. **2590**
Barnes, Phil **980**
Barnett, Ian **3743**
Barone Tonghi, L. **2578**
Barov, N. **2027**
Barr, Dean S. **2214**, **2241**
Barraza, Juan **2090**
Barry, Walter C. **636**, **1207**
Barsotti, E.L. **2146**, **2211**
Bartolini, R. **1557**
Barzi, E. **174**, **3330**
Bassalleck, B. **471**
Batchelor, Kenneth **75**
Batskikh, Gennady I. **2564**
Battle, Chris **2936**
Batygin, Yuri K. **1737**, **1740**
Bauda, B. **197**
Bauer, P. **3194**
Baumann, C. A. **2659**
Bayanov, Boris F. **3086**
Bazhan, Anatoli **461**
Bazzani, Armando **1773**
Bechstedt, Ulf **1701**, **2292**
Bechtold, Alexander **530**
Beck, David **1937**, **2849**
Beck, U. **206**
Becker, R. **1899**
Becker, T. **197**
Becker, Ulrich **2951**
Beczek, Kevin J. **1378**
Beebe, E. **1902**
Beebe-Wang, Joanne J. **1743**, **2843**, **3143**, **3185**
Beetham, C.Gary **765**
Behne, Dan **1333**
Beinhauer, Wolfgang **1647**
Bellavia, S. **1902**
Bellomo, Giovanni **1776**
Bellomo, Paul **206**, **3429**
Belomestnykh, Sergey A. **272**, **980**, **1112**
Belousov, Ilja V. **750**
Belov, Victor P. **3086**
Ben-Zvi, Ilan **75**, **2018**, **2158**, **2471**, **2480**, **2552**, **3495**, **3722**
Benabed, Karim **2990**
Benjamin, John **2277**
Benjegerdes, R. **3233**
Benson, S.V. **212**, **2456**
Bent, Bruce **931**
Berg, Georg P. A. **2519**
Berg, J. Scott **3152**
Berg, Jeff **1333**
Berg, William J. **2024**, **2134**
Berger, Christoph **2172**
Bergstrom, Paul M. **1827**
Bernal, Santiago **234**, **1749**, **1758**, **1970**, **2102**, **3372**
Bernard, Michel **922**
Bertolini, Louis R. **2477**, **3251**
Besnier, Gilbert **1192**, **1195**
Besson, Jean-Claude **1569**, **2686**

Bharadwaj, Vinod K. **3429**, **3447**, **3450**
Bhat, Chandra M. **114**, **717**, **3155**
Bhatia, Tarlochan S. **3585**
Biagini, Maria E. **1536**
Biallas, George **2456**, **3306**, **3312**
Bibber, Karl V. **2480**
Bickley, Matthew H. **732**, **735**, **741**
Biedron, Sandra G. **2024**, **2471**, **2483**, **2486**, **2945**
Bieler, Michael **554**
Bielicki, J. **1249**
Bieniosek, F. M. **1249**, **1937**
Bienvenu, Gerard **913**
Billen, James H. **3570**, **3585**
Billen, Ronald **2617**
Billing, Michael G. **410**, **1112**, **1115**, **2975**, **2978**, **3221**, **3501**
Birke, Thomas **197**, **726**, **2382**
Birx, D. **3257**
Biryukov, Valery M. **53**, **1234**, **1237**, **1240**, **3050**
Biscari, Caterina **131**, **1536**
Bish, P. **3233**
Bishofberger, Kip **2006**
Bisoffi, Giovanni **1324**
Blank, M. **1016**
Blas, Alfred **143**
Blasche, K. **527**, **1704**, **1788**
Blaskiewicz, Michael M. **109**, **614**, **857**, **1611**, **2280**, **3185**
Blazhevich, Sergey V. **2584**
Blind, B. **611**, **3582**
Blinov, Boris B. **392**
Bliss, Neil **2656**
Blokland, Wim **1085**, **2211**
Blondel, Alain **2999**
Blosser, H. **1318**
Bluem, Hans **3570**
Blum, Eric B. **2304**
Bocchetta, Carlo J. **2060**, **2313**
Boege, Michael **1129**, **1542**, **2430**
Boehnke, Michael **851**
Bogacz, S. Alex **738**, **2897**
Bogart, S. Locke **603**
Bogdanovitch, Boris Yu. **1291**, **1932**, **2570**, **2573**
Boggia, Antonio **1905**
Bogomolov, Guenrikh. D. **592**
Bohl, Thomas **2617**
Bohlen, Heinz P. **445**
Bohn, Courtlandt L. **2450**, **2456**
Bohne, D. **2513**
Boine-Frankenheim, B. **1788**
Boine-Frankenheim, O. **1785**
Boisvert, Veronique **2217**
Boivinet, Raynald **3260**
Bollen, Georg **1955**
Bolme, Gerald O. **1444**, **1447**, **1946**
Bolotin, Igor M. **1482**
Bolshakov, Timophei **1387**
Bolt, A. Scott **349**, **1444**, **1447**, **1929**, **1946**
Bonati, R. **3767**
Bondarev, Boris I. **1764**, **2808**
Bongardt, Klaus **1767**
Bongers, Henning **3516**
Boni, Roberto **866**
Bonnafond, Christophe **1381**, **3260**
Bonthond, J. **1228**
Booch, Rex **1506**
Bopp, Markus **795**
Borak, Thomas **2990**
Borburgh, Jan C. **2283**
Bordry, Frederick **3203**, **3740**
Boriskin, V.N. **753**
Borland, Michael D. **200**, **1587**, **1644**, **1979**, **2319**, **2939**
Borne, Jean-Luc **919**
Borodich, Andrei, I. **1869**, **1872**
Borovina, Dan L. **786**, **2772**
Borunov, Ivan E. **750**
Bosch, Robert A. **2388**, **2394**, **2397**, **2659**
Boscolo, Ilario **1982**, **1985**
Boscolo, M. **1536**
Bossart, R. **250**
Bosser, Jacques **465**
Bossert, R. **3194**, **3197**
Botman, J.I.M. **759**, **1539**, **2825**, **2864**, **3266**
Bottura, Luca **154**, **3179**
Boucham, Abdel **2990**
Bourdon, Jean-Claude **2012**
Bourque, Robert F. **2954**
Boussard, Daniel **946**, **949**
Bousson, Sebastien **919**
Boutigny, D. **2990**
Bovet, Claude **465**
Bowden, Gordon B. **206**, **824**, **1390**, **3423**, **3426**
Bower, Gary **307**
Bowles, Edward **3755**
Bowling, Bruce A. **732**
Bowman, Jim **1333**
Boyce, Richard M. **206**, **1363**
Boyd, John K. **3513**
Brabson, B. **1548**
Bracco, Roberto **2680**
Bradley III, Joseph T. **1010**
Bradshaw, David J. **2656**
Braeutigam, Werner **957**, **959**, **3549**
Brandt, Daniel **304**, **3005**
Brandt, J. **3194**, **3197**
Braun, Hans H. **250**, **3402**
Brautti, Giulio **1905**
Breese, Mark **53**
Breidenbach, Martin **3384**
Brennan, Joseph M. **614**, **857**, **1746**, **2280**
Brennan, Michale **1258**
Bressanutti, Raffaele **1120**
Bricault, P. **100**, **450**, **3540**
Briggs, R. **3257**
Brinkmann, Reinhard **16**
Bromberek, David J. **3095**
Brooksby, Craig A. **625**
Brouet, Michel **562**
Brovko, Oleg I. **2262**
Browman, Andrew A. **518**, **998**, **2790**, **3582**
Brown, Bruce C. **714**, **717**, **3315**, **3318**
Brown, C.N. **3324**
Brown, Kevin A. **614**, **1258**, **1267**, **1270**, **2123**, **2722**, **2725**, **2728**, **2918**, **3291**
Brown, Terence F. **3381**
Brown, Winthrop J. **81**, **833**
Bruenger, W.H. **2575**
Bruhwiler, David L. **369**
Brumwell, Franklin R. **2274**
Brunelle, Pascale **1569**, **2686**
Brunet, Jean-Claude **1330**, **1339**
Bruning, Oliver **40**, **2629**
Bruno, Donald **3734**
Bruns, Warner **2767**
Bryan, David A. **732**, **735**
Bryant, Phil **2957**
Buckles, Robert **1303**
Budnick, J. **1545**, **1548**
Buerkmann, K. **197**
Buerkmann, Klaus **2385**
Bugrov, Vladimir P. **1312**
Bulfone, Daniele **1120**
Bullard, D. **3309**
Bullard, Donald **3306**
Bultman, Nathan K. **3591**, **3594**
Bulyak, Eugene V. **1770**, **3122**, **3269**, **3271**
Bunce, G. **471**
Burgess, Edward L. **617**, **3257**
Burke, D.L. **3423**
Burke, Jason **1952**
Burkhardt, Helmut **2996**, **3011**
Burla, Paolo A. **762**
Burn, Kenneth W. **2531**
Burns, Michael J. **617**
Burov, Alexey V. **521**, **1088**, **1201**, **1608**, **1707**, **1710**
Bushuev, Alexander A. **2033**
Busse-Grawitz, Max Erick **986**
Butenko, Andrey V. **2262**
Buth, Gernot **2424**
Butterworth, Andy **2996**
Buxton, W. **2128**
Bychenkov, Valery Yu. **3716**
Byer, Robert.L **321**
Byers, B. **2990**
Bylinsky, Yuri V. **450**, **893**
Byrd, John M. **382**, **495**, **1207**, **1806**, **2370**, **3131**
Cai, Y. **296**
Calabretta, Luciano **2578**, **3288**
Calame, J. **1016**
Calatroni, Sergio **949**
Callin, Richard S. **783**
Cameron, Peter R. **2114**, **2117**, **2146**, **2250**, **3185**
Campbell, B. **965**
Campbell, Billy M. **971**, **1327**, **2954**
Campbell, Lora P. **3722**
Campbell, Richard **1515**
Campisi, Isidoro E. **937**, **1177**, **1180**, **2456**
Cao, Jianshe **2140**
Capista, David P. **714**
Caporaso, George J. **617**, **622**, **625**, **1204**, **1303**, **1824**, **1827**, **3254**, **3381**
Carathers, Jeremy R. **1447**
Carlier, Etienne **1509**
Carlson, Charles **2277**
Carlsten, Bruce E. **477**, **617**
Carneiro, Jean-Paul **992**, **2027**
Carr, G. Lawrence **134**
Carr, Roger **1390**, **2477**, **2698**
Carrigan, R.A. **2027**
Carron, Georges **250**
Carter, Anthony **3101**
Carwardine, John A. **2093**
Cary, John R. **369**, **377**, **2784**
Casas-Cubillos, Juan **3203**
Casey, Jeffrey A. **568**, **1491**
Caspers, Fritz **1408**, **2629**
Caspi, Shlomo **174**, **2793**, **3194**, **3197**, **3233**, **3236**
Cassel, Richard L. **1494**, **1500**, **3429**
Cassinari, Lodovico **1168**, **1569**
Castellano, Michele **1985**, **2193**, **2196**, **2695**
Castillo, Vincent **490**
Castle, Mike **1040**, **1046**
Castro, Maurizio **97**
Castro, Pedro **456**
Catani, Luciano **1985**, **2196**
Catravas, Palmyra **325**, **330**, **2111**, **3705**
Caussyn, D.D. **1548**
Celata, Christine M. **1716**, **1803**, **1830**

Celona, Luigi **97, 2578**
Cerny III, Joseph **533**
Chae, Yong-Chul **1644, 2486**
Chai, Jongseo **2265, 3137**
Chai, Xuedong **1453**
Champion, Mark S. **992, 2027**
Chan, C. F. **1937**
Chan, K.C.D. **1327, 2954, 3582**
Chan, Kwok-Chi D. **965, 968, 971**
Chang, Cheng-Hsiang **2671**
Chang, H.P. **2409**
Chang, J. H. **2593**
Chang, Lung Hai **1159**
Chang, Peace **2837**
Chang, S. S. **2009**
Chang, S.S. **679, 2205, 2501**
Chang, Shi-Horng **1375**
Chang, Suk S. **2418**
Channell, Paul J. **1629**
Chao, Yu-Chiu **738**
Chapelle, Sonja **3758**
Chapman-Hatchett, Arthur **2202, 2223**
Chargin, Anthony (Tony) K. **2590**
Charrier, Jean-Pierre **432, 919**
Chattopadhyay, Swapan **330, 2370**
Chavanne, Joel **2662, 2665**
Cheever, Dan **3101**
Chel, Stéphane **916**
Chen Y.-J. **617**
Chen, C.S. **682, 685, 2412**
Chen, Chien-Rong **1150**
Chen, Chiping **1875, 2752**
Chen, H.H. **2671**
Chen, J. **682, 2021**
Chen, J.R. **1605, 2409, 2415**
Chen, J.S. **682, 1450**
Chen, Jenny **685, 2069, 2072, 2412, 2671**
Chen, Jie **741, 747**
Chen, June-Rong **1150, 1375**
Chen, Longkang **2184**
Chen, Pisin **224, 330, 3648**
Chen, Senyu **209**
Chen, Szu-Yuan **3666, 3716**
Chen, W. **3345**
Chen, Y. J. **1824**
Chen, Yu Ju (Judy) **617, 622, 2235, 3254, 3381**
Chen, Yu-Jiuan **1204, 1210, 1303, 1827, 3254, 3257, 3513**
Chen, Zukun **3591, 3594**
Cheng, Daniel W. **1911, 1914, 1958, 1961**
Cheng, Hung-Ming **1150**
Cheng, W.H. **382**
Chepegin, V.N. **53**
Chepurnov, Alexander S. **2584**
Cherbak, Ernest E. **1019**
Cherenshchikov, S. A. **1973, 1976**
Cherepakhin, A. **1249**
Cherix, Jacques **418**
Cherniakin, Alexander D. **3086**
Chernin, David P. **360**
Cherwinka, Jeffrey J. **3221**
Chesnokov, Yury A. **53, 1237**
Chesworth, Andrew A. **2433**
Chiaveri, Enrico **946, 949**
Chichili, Deepak R. **174, 3194, 3197, 3242**
Chin, Y.H. **1058**
Chin, Paul **234, 1970, 2102, 3369, 3372**
Chin, Yongho **633, 3414**
Chines, Franco **97**
Chiou, J.P. **1450, 2009**
Chishiro, Etsuji **3546**
Chitose, Norihisa **2602**
Chiurlotto, F. **1324**
Cho, M.H. **2593**
Cho, Yong-Sub **875, 1255, 3525**
Chohan, Vinod **2202**
Choi, B. H. **206**
Choi, Byung-Ho **875, 1255, 3525**
Choi, J. **1016**
Choi, Jae-Young **2205, 2501, 2593**
Choi, Jinhyuk **2418**
Chojnacki, Eric **845, 980, 2635**
Chong, Henry **2370, 2498**
Chou, Ping-Jung **1159, 2415, 2837**
Chou, W. **565, 3285**
Chow, Ken P. **171, 3233, 3236**
Christiansen, David W **3573**
Christina, Vincent **780, 3306**
Chu, C.M. **392, 1545, 1548, 2286**
Chu, Chunjie **1940**
Chu, W. **2537**
Chung, Kie-Hyung **2558, 2561**
Chung, Sukmin **1357**
Chupyra, Andrei **1387**
Church, Michael D. **56**
Church, Roy A. **1013**
Cianchi, Alessandro **2193, 2196**
Ciavola, Giovanni **97, 2578**
Cimabue, Anthony G. **965**
Cinabro, David **3221**
Citver, G. **1420**
Clark, George S. **3378**
Clark, J. **1991**
Clark, John C. **3513**
Clark, Robert E. **2746**
Clark, William L. **965**
Clarke, James A. **2433, 2653, 2656**
Clauser, Tarcisio **1779**
Claverie, Joseph **2686**
Clayton, Christopher E. **330, 2006, 3651, 3654, 3708**
Clendenin, James E. **1988, 3384, 3447, 3450**
Clifft, Ben E. **524**
Cline, D. B. **2552, 3639, 3722**
Codner, Gerald W. **1115, 1441, 3221, 3224**
Cola, Mark J. **962**
Colby, E. **321**
Cole, M. **780**
Cole, Michael D. **3570**
Colestock, Patrick L. **114, 2027, 2181, 3155**
Collier, Michael **3594**
Collier, Paul **2617, 2996**
Collins, Ian R **2629**
Collins, J.C. **673, 1548**
Comins, J.D. **3257**
Comunian, Michele **1773**
Conde, Manoel E. **2030, 3621**
Conkling Jr., Charles R. **699**
Connolly, Roger C. **2114, 2117, 2250**
Cooke, Simon J. **360**
Coosemans, W. **250**
Corbett, Jeff **206, 2355, 2358, 2364**
Corlett, John N. **296, 800, 896, 1207, 3149, 3429**
Corlier, Muriel **2686**
Cornacchia, Max **267, 2480**
Cornelis, Karel **1189, 2617, 2996**
Cornelius, W. D. **1884, 1887**
Cornuelle, J. **3423**
Corredoura, Paul L. **435, 800, 3429**
Corsini, Roberto **250, 3396**
Corstens, J.M. **2864**
Counsell, Joseph **1025**
Coupal, David **2990**
Cours, Alexander **1022**
Cousin, J.M. **1569**
Coutrakon, George **11**
Cozzolino, John **185, 3230**
Craddock, Michael **2620, 2623**
Craievich, P. **1123**
Craig, George D. **1830, 3248**
Crandall, K.R. **611, 3582**
Crandell, D.A. **392**
Crawford, A.C. **521**
Crawford, Curtis **237, 3321**
Crisp, J. L. **2164**
Crisp, Jim **2146, 2211**
Crist, Charles **1303**
Crockford, Guy **2617**
Crosbie, Edwin A. **1587, 2325**
Cruikshank, Paul **1330, 3203**
Ctcherbakov, Anatoliy M. **1482**
Cullen, J.R. **1267, 1270**
Cummings, Karen A. **881, 1396**
Cundiff, Tim **2090**
Cupola, J. **2117**
Cuttone, Giacomo **2578**
Czarnaski, Mark **360**
d'Amico, Tommaso E. **250, 1638, 2202, 3399**
D'Olando, Stefano **1120**
D'Ottavio, Theodore W. **693**
D'Yachkov, Mikhail **128, 1408**
DaCosta, Tony **1333**
Dahlerup-Petersen, Knud **3200, 3203**
Dai, Jianping **1453**
Dalesio, Leo R. **349, 652, 655**
Daly, E. T. **206, 1363**
Dambach, S. **165**
Danared, Håkan **1698**
Danby, Gordon T. **3185, 3333**
Danilov, Vyacheslav V. **109, 641, 1198, 1201, 1608, 1710, 3140, 3143, 3303, 3728**
Danly, B. **1016**
Danowski, G. **3767**
Darpentigny, Jacques **1168, 1569**
Date, Schin **2346**
Dattoli, Giuseppe **1219**
Datz, Sheldon **1671**
Davidson, Ronald C. **1518, 1623, 1626, 1629, 1875**
Davis, Brent **1506**
Davis, Jerry L. **1001**
Davis, Roger **557**
Day, T. **1991**
de Hoon, Michiel J.L. **1803, 1830**
de Loos, Marieke **2462, 3266**
De Monte, R. **2253**
De Ryck, C. **3212**
De Santis, Stefano **2075, 2873**
De Wit, F.F. **759**
Debeling A. **3248**
Debiak, Ted, W. **587**
Debus, J. **2513**
Decker, Franz-Josef **307, 330, 771, 774, 1252, 1728, 2846, 2987, 3384, 3648**
Decker, Glenn A. **2051, 2093, 3092**
Decking, Winfried **1581**
Decyk, V. K. **3672**
Degasperi, Francisco T. **1366**
Degtyarev, I.I. **1321**
DeHart, Terrance E. **2668**

Dehler, Micha **1129**, **2087**
Dehning, Bernd **2999**
Dejus, Roger J. **2486**, **2489**, **2492**
Dekin, W. D. **2590**
Delahaye, J.P. **250**
DeLamare, Jeffery E. **1494**
Delayen, Jean R. **925**, **928**, **934**, **937**, **940**, **955**, **1462**, **3498**
Dell'Orco, D. **206**, **2355**
Den Hartog, P.K. **1369**, **2483**, **2489**
Deng, Jianjun **3263**
Denker, A. **3519**
Denz, Reiner **3200**
Derbenev, Yaroslav S. **392**
Derenchuk, V. **1548**
Derrick, M. **2635**
Deruyter, H. **590**, **3423**
Deryuga, Vyacheslav A. **2546**, **2549**
DeSantis, Stefano **382**
Desforges, Bernard **2617**
Desmons, Michel **916**
Despas, Claude **2617**
Despe, Oscar **3773**
DeStaebler, Herbert **2990**
Detweiler, Gerald **2468**
DeVan, W.R. **355**
Devin, André **3260**
Devmal, S. **2990**
DeVries, Jan **162**
Dewa, Hideki **3690**, **3702**
Dey, Joseph E. **869**
Di Bartolo, Gaetano **2578**
Diaczenko, Nick **2936**
Dias, Joao M. **3725**
Dickson, R. **646**
Dietderich, D.R. **171**, **3233**, **3236**
Diete, W. **957**
Dietrich, J., **2054**
Dietrich, Jürgen **1701**, **2292**
Dikansky, Nikolay S. **78**, **2167**, **2948**
Dimaggio, S. **325**
DiMaggio, S. **3705**
DiMarco, Joseph **3194**, **3197**, **3318**, **3327**
Ding, Bainan **3263**
Ding, X **2504**
Ding, X. **2003**, **2021**, **2039**, **2042**, **2045**
Ding, Xiaodong **2006**
Dinkel, J. **1249**
Dittmann, B. **197**
Diviacco, Bruno **2680**
Divin, Yuri Y. **2178**
Diwan, Milind V. **3023**
Dix, Brendon **1390**
Dobbing, Gavin S. **2433**, **2653**
Dobrovolski, Nikolaj M. **1468**, **2105**
Dohlus, Martin **1650**
Dolgashev, Valery **2822**
Doll, D.W. **1393**
Dombsky, M. **100**
Dome, George **1408**
Domer, Gregory A. **649**
Donald, Martin H. **296**, **1584**
Dong, Xiaoli **1596**
Donohue, John T. **1797**, **3387**
Dooling, Jeffrey C. **2274**
Doolittle, Lawrence R. **768**, **928**, **934**, **937**, **940**, **1462**
Doose, Charles L. **2024**, **2093**
Dormiani, M. **206**
Dortwegt, Robert J. **1414**, **2024**
Doskow, J. **471**
Doss, J. Daniel **426**
Douglas, David **1177**, **1180**, **2456**, **3306**, **3312**
Douryan, Adnan **2471**
Dovbnya, A. **3122**
Doyle, Stephen **2424**
Doyuran, Adnan **2480**, **2942**
Drago, Alessandro **131**, **636**
Dragt, Alex J. **1551**, **1593**, **2761**
Drees, K. Angelika **2117**
Dressler, Olaf **1279**
Drivotin, Oleg I. **1857**
Drozhdin, Alexandr I. **56**, **1231**, **1234**, **2614**, **3050**
Drury, Michael **931**
Ducimetière, Laurent **1228**, **1509**
Duda, Brian J. **3669**
Duerr, Volker **2385**
Duffau, Michael J. **2096**
Duffy, Patrick **1390**, **2477**
Dugan, Gerald F. **48**, **2057**, **2632**, **3221**, **3224**
Duke, Jonathan P. **2208**
Dunbar, Ann **1100**
Dunham, B. **1991**
Dupaquier, Andre **3740**
Dur, V. **197**
Durkin, Alexander P. **1764**, **2808**
Dutto, Gerardo **106**, **893**
Dykes, Michael D. **1025**, **2096**
Eardley, Matthew **1943**
East, G. **1548**
Ecklund, Stan D. **296**, **3450**
Economou, A. **1037**
Edamenko, N. S. **1866**
Edgell, Dana **1043**, **1890**
Edwards, Helen T. **992**, **2027**
Egawa, Kazumi **3351**, **3354**, **3357**
Egiazarian, Suren L. **1468**
Ehrlich, Richard **980**
Eichhorn, Ralf **2951**
Eichner, John **1512**
Eickhoff, Hartmut **527**, **1704**, **2513**
Eilerts, S. **471**
Einfeld, Dieter **806**, **809**, **1360**, **2424**, **2427**, **3375**
Eisert, D. E. **2659**
El-Shazly, M.N. **1896**
Elbakian, Sergey S. **3657**, **3663**
Elioff, T. **206**
Elleaume, Pascal **2662**, **2665**, **3119**
Elliott, T. **780**
Elliott, Tim **2936**
Ellis, Gretchen G. **965**
Ellison, M. **1548**
Elmer, John **777**
Elzhov, Artem V. **3393**
Emamian, Mark **221**, **2468**
Emery, Louis **200**, **401**, **1644**, **2137**, **2319**, **2939**
Emhofer, Stephan **3516**
Emma, Paul **3429**, **3438**, **3447**, **3456**
Emmerling, M. **1788**
Endo, Akira **2018**, **2036**, **2552**
Endo, M. **600**
Engels, Oliver **3519**
Enomoto, A. **1132**, **2731**
Eppley, Kenneth R. **2778**
Erdmann, M. **1369**, **2489**
Erickson, John L. **3594**
Eriksson, L. **3462**
Eriksson, Mikael **2945**
Ermakov, Dimitry I. **2555**
Erokhin, Alexander **1387**
Esarey, E. **330**, **2111**
Esarey, Eric **325**, **3696**, **3699**
Escallier, John **3161**
Eschenko, Viktor N. **3086**
Esin, Sergei K. **3561**
Etzkorn, Franz-Josef **851**
Evans, I. **206**
Evans, Jr., Kenneth **352**, **744**
Evans, Lyndon R. **21**
Evans, R. **2456**
Eyl, Patrick **3260**
Eylon, Shmuel **1934**, **3248**, **3390**
Eyssa, Y. **3227**
Ezura, Eiji **413**, **440**
Faatz, B. **2486**
Fabris, Alessandro **809**, **1120**, **1123**
Fagan, M.J. **1327**
Fahmie, Michael P. **756**
Falabella, Steve **1303**
Falkenstern, F. **2078**
Fallmann, W. **2575**
Faltens, Andris **1503**, **1830**, **1937**, **2849**, **2852**, **3215**, **3339**
Fan, Kuanjun **1315**, **1596**
Fan, Mingwu **1940**
Fan, T.C. **2671**
Fang, J.M. **3627**
Fang, Lei **2125**
Fang, Shouxian **1695**
Fang, Shuyao **890**
Fang, Si **3761**
Fang, Zhigao **2125**
Fann, C.S. **1450**
Fant, Karen **1435**
Farkas, Zoltan David **771**, **774**, **3423**
Farrell, J. Paul **75**
Fartoukh, Stéphane **922**
Farvacque, Laurent **3119**
Faugier, Andre **2617**, **2996**
Faulbaum, D. **197**
Fawley, William M. **1204**, **1210**, **1934**, **3254**, **3257**
Fedorov, Vacheslav **1479**, **1485**
Fedorov, Vladimir M. **1734**
Fedorova, Antonina **1614**, **1617**, **1620**, **2900**, **2903**, **2906**, **2909**, **2912**
Fedotov, Alexei V. **606**, **1752**, **1755**
Fedotov, M. G. **2167**
Fedotov, Yu.S. **53**
Feher, Sandor **1420**, **1426**, **3191**, **3194**, **3197**
Feigenbaum, Irv **2277**
Feikes, Joerg **197**, **1279**, **2376**
Feldl, Erich **928**, **934**
Fellenz, Brian **2146**, **2211**
Feng, Z.Q. **3345**
Ferianis, Mario **1120**
Fernow, Richard C. **3020**, **3032**
Ferracin, Paolo **3206**
Ferrari, Antoin **2617**
Ferrario, Massimo **1985**, **1997**, **2734**
Fessenden, Tom **2235**
Fieguth, Theodore **296**, **2990**
Field, R. Clive **296**, **307**
Fields, D. **471**
Figueira, Goncalo **3725**
Figueroa, Terry L. **1929**
Filhol, Jean-Marc **2331**, **2334**, **3119**
Filippas, A. V. **1037**
Finkelstein, Ken D. **2217**
Finley, David A. **3728**

Finocchiaro, Paolo **2578**
Fiorito, Ralph B. **487, 3722**
Firebaugh, J. **1246**
Firjahn-Andersch, Arne **530**
Fisch, Nathaniel J. **3675**
Fischer, Claude **465**
Fischer, Wolfram **702, 1261, 2716, 2725, 2921**
Fisher, Alan S. **296**
Fisher, M. V. **2659**
Fitch, Michael J. **2027, 2181**
Fitze, Hansruedi **418, 795**
Fitzgerald, Daniel H. **518, 1198, 1201**
Fitzgerald, Jim **2211**
Flanagan, John W. **1132, 2120, 2731**
Flechtner, D. **3600, 3606**
Fliflet, Arne W. **1049**
Flippo, Kirk **3716**
Floersch, D. **652**
Floersch, Richard H. **649**
Flora, R. H. **714**
Flottman, K. **3450**
Flynn, G. **1533, 1569**
Fong, Ken **450, 890**
Foose, R. **590**
Forest, Etienne **404**
Foster, G. William **182, 3324, 3327, 3330**
Fouaidy, Mohammed **913, 919**
Fournier, P. **103**
Fowkes, W.B. **3423**
Fowkes, William R. **783, 1432, 3426**
Fox, John D. **131, 636, 1207, 1213**
Franchetti, Giuliano **1782, 1785**
Franco, Jose G.S. **2421**
Franczak, B. **527, 1704**
Franks, R. Mark **800, 803**
Franzcak, B. **1788**
Franzke, B. **527, 1704**
Freedman, Stuart J. **1952**
Frei, Hans **418, 795**
Fresquez, M.G. **426**
Freund, Henry P. **2486**
Friedman, Alex **1830, 2758, 3248**
Friedsam, Horst **2051, 2635**
Friesel, Dennis L. **498, 1548**
Frigola, Pedro **217, 2480**
Frisch, Josef C. **253, 3447, 3450**
Fritz, A. **3248**
Frommberger, Frank **3098**
Fromowitz, Daniel B. **1632**
Fuerst, Joel D. **992, 2027**
Fugita, H. **3110**
Fujieda, Miho **413, 798, 857, 860, 863, 1007, 1653, 2271, 2280**
Fujikawa, Brian **1952**
Fujioka, M. **3348**
Fujiwara, Chikara **842**
Fukuda, Mitsuhiro **2259**
Fukuda, Shigeki **3414**
Fukui, Yasuo **3032**
Fukuma, H. **633, 1132, 2731**
Funahashi, Y. **777, 3423**
Funahashi, Yoshisato **2731, 3417**
Funakoshi, Yoshihiro **1132, 2108**
Fung, K.M. **1545, 1548, 2286**
Funk, L.W. **3582**
Furman, Miguel A. **1674, 1791, 1794**
Furst, Mitchell L. **2388**
Furukawa, Kazuro **1132, 2238, 2731**
Furuya, Takaaki **440**
Fuss, Brian **1390**
Futami, Y. **600**
Gaedke, Rudolph **2936**
Gahl, John M. **786, 2772**
Gai, Wei **2030, 3618, 3621**
Gaillard, Michel **2012**
Gaiser, H. **3552**
Galambos, John D. **109, 1198, 1201, 3140, 3143, 3303**
Galayda, John N. **2024, 2471**
Galdi, Vincenzo **2882**
Galimberti, Andrea **2060**
Gallardo, Juan C. **3032, 3722**
Gallo, Alessandro **131, 866, 1147**
Galstjan, Eugene A. **1477**
Galvin, J. **2537**
Gamba, Claudio **1120**
Gambitta, A. **2060**
Gammino, Santo **97, 2578**
Ganetis, George L. **3161, 3170, 3734**
Gao, Jie **1216, 1809, 1812, 1815, 3017**
Gardelle, Jacques **1797, 3387**
Gardner, Christopher J. **614, 1276, 2063, 3182, 3185**
Gardner, K. **2918**
Garnett, Robert **518**
Garren, A. **206**
Garren, Alper A. **2364, 2439, 3050, 3065, 3068, 3152**
Garven, M. **1016**
Garvey, Terrence **916, 2012**
Gassner, D. M. **2123**
Gassot, Huimin **919**
Gaudreau, Marcel P.J. **568, 1491**
Gautier, Cort **977, 1396**
Gavrilov, Nikolay M. **1932**
Gebel, Ralf **2292**
Gebre-Amlak, K. **3681**
Geer, S. **3062**
Geitz, Marc **2172, 2175, 2178, 2507**
Geld, T. **2990**
Gelfand, Norman M. **1677, 2861**
Geller, Joseph M. **2247**
Geng, Rong-Li **429, 980, 983**
Gentzlinger, Robert C. **962, 965, 968**
Georgsson, Mattias **2945**
Gericke, W. **197**
Ghebremedhin, Abiel **11**
Ghigo, Andrea **131, 1536**
Ghiorso, William **2849**
Ghosh, Arup K. **185, 3161, 3188, 3197, 3230**
Ghosh, Subhendu **952**
Giachino, Rossano **2617**
Giannessi, L. **1985**
Gibbins, Peter E. **1025**
Gies, Albert **2424**
Gillespie, George H. **1551, 2805**
Gilpatrick, John D. **2152, 2214, 2241, 3528, 3582**
Ginzburg, Naum S. **1055**
Gioia, Jack G. **977, 1396, 2954**
Giovannozzi, M. **1282**
Girault, F. **1569**
Gladkikh, P. **3122**
Glass, Henry D. **3318**
Glazov, Alim A. **2262**
Glenn, Joseph W. **614, 702, 1258, 1270, 1746, 2918, 3291**
Glover, Ernie **2370, 2498**
Gluckstern, Robert L. **606, 1752, 1755, 2876**
Gluskin, Efim **2489**
Godefroy, Jean-Marie **2686**
Godlove, Terry F. **234, 1758, 1970, 3369**
Godot, J.C. **250**
Goeppner, George A. **2024**
Goergen, R. **2078**
Goerz, D. **625**
Goethe, J.W. **3516**
Gold, Saul **1512**
Gold, Steven H. **1049, 1474**
Goldberg, J. D. **1043**
Goldenberg, Constantin A. **1055**
Golkowski, Cz. **3600, 3603**
Gomez-Costa, Jose Louis **3200**
Gonzalez, Carlota **474, 1408**
Goodenough, C. **2990**
Goodzeit, Carl L. **3245**
Gorbachev, A.M. **1474**
Gorchenko, V.M. **2256**
Gordon, Daniel **3684**
Gorev, V. V. **3711**
Gorski, Anthony J. **1411, 2635, 3342**
Goto, Akira **2268**
Goto, Y. **471**
Gottschalk, Stephen C. **2668, 2674, 2677, 3722**
Gouard, P. **1797**
Gough, Richard A. **884, 1911, 1914, 1917, 1920, 1952, 1958**
Gourlay, S. A. **171, 3236**
Govorov, A.I. **2256**
Graef, Hans-Dieter **2951**
Grafstrom, Per **1671**
Granatstein, Victor **1040, 1046**
Graves, Bill **2471**
Graves, Rossie M. **2388**
Graves, Williams S. **1949**
Green, Michael A. (LBL) **2439, 3149, 3227**
Green, Michael A. (SRC) **2391, 2659**
Greenler, Lee **2388**
Greenwald, Shlomo **3221**
Greenwald, Zipora **1300, 3221**
Greer, James B. **1961**
Gregoire, Guillaume **103**
Grelick, A. **2024**
Greninger, Paul **878, 3570, 3573**
Griep, B. **957**
Grieser, Manfred **1955, 3543**
Griesmayer, Erich **2957**
Griffin, James E. **1201, 3152**
Griffiths, Stephen A. **2960**
Grigorev, Yu. **2927, 3122**
Grimm, Terry L. **3719**
Grippo, A. **2229**
Grishin, Vladislav K. **2581, 2584, 2587**
Grishiu, V.N. **392**
Grobner, Oswald **1339**
Groening, L. **527, 1704**
Gromov, Roman G. **78, 750**
Gross, Dan **2936**
Grossberg, Phyllis **338**
Grote, David P. **1761, 1830, 1833, 1937, 2758, 3248**
Groöbner, Oswald **2629**
Gu, Shaoting **3716**
Gu, Sunhee **1357**
Gubin, Konstantin V. **750, 1456, 2167**
Guerra, Al **3306**
Guharay, S.K. **234, 1306**
Guidi, Vincenzo **2948**
Guiducci, Susanna **277, 1536**
Guignard, Gilbert F. **250, 1635, 1638, 3399**
Guler, Hulya **3026**

Guo, Fanqing **533**
Guo, Zhiyuan **633**
Gupta, Ramesh C. **171, 185, 3161, 3176, 3236, 3239**
Gurd, David P. **355, 3528**
Guthrie, Arthur **3594**
Guy, F.W. **3531**
Göettert, Jost **2424**
Ha, Jangho **2265, 3137**
Haagenstad, Harvey **965**
Haber, Irving **234, 1749, 1758, 1830, 1970**
Haberer, Th. **2513**
Habib, Salman **366, 1845**
Habs, Dietrich **3516**
Haebel, Ernst **946, 949**
Haeuser, Juergen **3519**
Hafizi, Bahman **3687, 3693**
Haga, Kaiichi **2310**
Hagedoorn, H.L. **1539, 2825**
Hagedorn, Dieter **3200**
Hagel, Johannes **250, 1635**
Hagelstein, Michael **2424**
Hagenbuck, F. **165**
Hagestedt, Andre **2424**
Hahn, Alan A. **468, 1085, 2066, 2164**
Hahn, Harald **1100, 1103**
Hahn, Robert von **1955**
Hahn, Ulrich **1369**
Hairapetian, G. **3708**
Halaxa, Ernie **1937, 3248**
Halbach, K. **2301**
Haldemann, Paul **234, 1970**
Hama, Hiroyuki **592**
Hambikov, Valeriy D. **1456**
Hamilton, Andrew **2388**
Hamilton, B. **498, 1545, 1548**
Hammen, A.F.J. **759, 2825, 2864**
Hammon, Duncan L. **965**
Hammonds, J.P. **355**
Han, Bum-Soo **3525**
Han, D. H. **1079**
Han, Jang-Min **875, 3525**
Han, Qian **1228**
Han, Y.J. **3345, 3504**
Hanaki, Hirofumi **2015, 2749, 3507**
Hancock, Steven **143, 2226**
Hanke, K. **2178**
Hanke, Klaus **1282, 1285, 2617**
Hanks, Roy L. **625**
Hanna, S. **3423**
Hanna, Samy M. **2516**
Hannaford, R. **3233**
Hanni, Raymond **949**
Hansborough, Lash D. **1444, 1447, 1929, 1946**
Hansen, Gene **1336**
Hansen, Jan **562**
Hansen, Robert **1049**
Hansknecht, J. **1991**
Hanuska, S. **2635**
Harada, Hisashi **848**
Harada, Kentaro **2436**
Harano, Hideki **2605**
Hardek, Thomas W. **1444, 1447, 1946**
Hardekopf, Robert A. **3597**
Harding, David J. **3318**
Hardy, L. **2331, 2334**
Hargenrater, Thomas **1396**
Harkay, Katherine C. **123, 1641, 1644**
Harnden, W. **171, 3233**
Harper, Mark **1333**
Harrington, Margye P. **349, 1929**
Harriott, Lloyd **595**
Harris, Guy **1342**
Harris, Neville **2656**
Harrison, Michael A. **6, 3176, 3230**
Hartemann, Frederic V. **2000, 2003**
Hartill, Don **980, 2975, 2978**
Hartman, N. **3149**
Hartmann, H. **696**
Hartmann, P. **1991**
Hartouni, Edward P. **2590**
Hartung, Walter H. **992, 2027**
Harvey, A. **3576, 3579**
Harwood, Leigh **3306, 3309**
Hasan, A. **2990**
Hasegawa, Kazuo **3546**
Hasegawa, N. **3690**
Haseroth, Helmut **103**
Hashimoto, Yoshinori **860**
Hassanein, A. **3062**
Haustein, Peter **533**
Hawkey, Timothy P. **568, 1491**
Hawkins, Alonzo **1037, 1515**
Hayano, H. **1994**
Hayano, Hitoshi **256, 2143**
Hayano, Hiyoshi **3432**
Hayashi, K. **3330**
Hayashi, Y. **3600, 3606**
Haynes, W. Brian **965, 977, 1396**
Hayoshi, N. **471**
He, P. **2552, 3639, 3722**
He, Xiaoye **1315**
Heese, Richard H. **2304**
Heidenreich, G. **1360**
Heifets, Samuel **1118, 1665**
Heimann, Philip **2370, 2498**
Helm, D. **259**
Hemker, Roy G. **330, 3672**
Hemmer, Michael **37**
Henchel, Bill **2936**
Henderson L. **296**
Henderson, Stuart D. **410, 1351, 2217, 3221**
Henderson, Tom **803**
Hendrickson, Linda J. **307, 338, 3456**
Henestroza, Enrique **1934, 1937, 2849, 2852, 3390**
Henke, Heino **812, 815, 818, 1034**
Henn, Kurt **1701, 2292**
Henrist, Bernard **2629**
Herbeaux, Christian **2686**
Hermle, Stefan **1360, 2424**
Hernandez, Kenneth **803**
Heron, Mark T. **661**
Herr, Werner F. **304, 3005**
Herrmann, J. **2915**
Herrmannsfeldt, William **1937**
Herrup, David A. **1091**
Hershcovitch, Ady I. **584, 1902**
Hertel, N. **2427**
Hess, Mark **2752**
Hettel, R. **206**
Hezel, T. **165**
Hiatt, Thomas **1462, 3306, 3309**
Hickman, Bradley C. **625**
Hidaka, S. **1821**
Hig **3423**
Higashi, Yasuo **777, 3417, 3423**
Higley, H. **3233**
Higo, Toshiyasu **777, 3417, 3420, 3435, 3468, 3477**
Hilaire, Alain **40**
Hildreth, Mike **2999**
Hill, Barrey W. **1551, 2805**
Hill, Ed **2936**
Hill, Jeremy M. **2480**
Hill, M.E. **3612**
Hill, Marc E. **545**
Hill, R. **2456**
Hilleret, Noel **2629**
Himel, Thomas M. **293, 296, 338**
Hinson, William M. **3212**
Hiramatsu, Shigenori **492, 633, 1132, 2120, 2731**
Hiramoto, Kazuo **2528, 3366**
Hirata, Kohji **1689**
Hiraya, A. **2689**
Hirose, Tachishige **256, 2552**
Hirota, Jun'ichi **3366**
Hirshfield, Jay L. **1049, 1052, 1474, 3627, 3630**
Hitomi, Nobuteru **777, 3417**
Ho, C.H. **1450, 2000, 2009**
Ho, Darwin D.-M. **1827**
Hoag, Harry **777, 3423**
Hoberg, H. G. **197**
Hockman, Jeffrey N. **2590**
Hodgkins, David J. **349, 1444, 1447, 1946**
Hodgkinson, Cheryl L. **2656**
Hoellering, Frank **3519**
Hoeltermann, H. **1899**
Hoff, Lawrence T. **693, 1261**
Hoff, Matthew D. **884, 1958, 1961**
Hoffman, J.R. **3651**
Hoffmann, Markus **3098**
Hoffstaetter, George H. **407**
Hofmann, A. **296**
Hofmann, Ingo **137, 1782, 1785, 1788**
Hogan, Bart **1046**
Hogan, G. E. **579**
Hogan, J. **1462, 1991**
Hogan, John **934**
Hogan, M. **217**
Hogan, Mark J. **330, 1997, 2111**
Holden, Travis **2006**
Holder, David J. **2433**
Holmes, Clifford **2235**
Holmes, Jeffrey A. **109, 1198, 1201, 3140, 3143, 3303**
Holmes, Stephen D. **43**
Holstein, Friedrich **2424**
Holtkamp, Norbert **896, 3062, 3149**
Holtzapple, Robert L. **410, 2057, 2972, 2975, 2978**
Homeyer, H. **3519**
Homeyer, William G. **2954**
Homma, T. **600**
Homscheidt, M. **165**
Honda, Tohru **2310**
Horan, Douglas **1019, 1022**
Hori, H. **3507**
Hori, Toshitada **2298, 2400, 2403, 3702**
Horioka, Kazuhiko **3690**
Horny, M.J. **2000, 2009**
Hosaka, Masahito **592**
Hosokai, Tomonao **3690, 3702**
Hosoyama, Kenji **440, 1132, 2731**
Houck, Timothy L. **1210, 1303, 2755, 3257, 3390**
Hourican, Michael D **2283**
Hovater, Curt **768, 1177**
Howell, Joseph W. **3095**
Hower, Nelson L. **221, 2099, 2468**
Hoyer, Egon H. **162**

Hseuh, Hsiao-Chaun 557, 1345
Hsi, W.C. 1548, 2286
Hsiao, Ko-Ming 1375
Hsiung, Gao-Yu 1375, 1605
Hsu, Ian C. 2220
Hsu, Kuo Tung 682, 685, 1153, 1156, 1159, 1162, 1450, 1605, 2009, 2069, 2072, 2220, 2409, 2412, 2671, 2837
Hsu, S.Y. 1450, 2009, 2072
Hsu, Shen-Nung 1375
Hsu, Yao-Jane 1375
Hu, Hongliang 1596
Hu, Kuo Hwa 2412
Hu, Kwo Hwa 682, 1153, 1156, 2069, 2072
Hu, Shouming 1596
Huan, N. 1132
Huang, H. 471, 1548, 2128
Huang, Hong 633
Huang, Jung-Yun 1076, 2131, 2418
Huang, M.H. 2671
Huang, N. 2731
Huang, Nan 2963
Huang, Yen-Chieh 321
Huang, Zhirong 262, 1644, 2495
Hubbard, E. 3576, 3579
Hubbard, Richard F. 3687, 3693
Huelsmann, Peter 3405
Hughes, Thomas P. 2746
Hughey, Lanny R. 2388
Huhtinen, Mika . 1231
Humpert, Michael 806
Humphries Jr., Stanley 2737, 2772, 2778
Hundzinger, Denis 3743
Hunt, W. A. 676
Hunter, W. Ted 3576, 3594
Hurh, Patrick G. 1423
Husmann, Dirk 3098
Hutchins, S. 250
Huttel, Erhard 1360, 2424
Hwang, C.S. 1450, 2671
Hwang, J.Y. 2000, 2009
Iazzourene, Fatma 2707
Ichihara, Masahiro 3546
Ieiri, Takao 1132, 1135, 2731
Igarashi, Susumu 1141
Igolkin, Alexsandr G. 1456
Iida, Naoko 1132, 2108, 2731
Iino, Youshuke 842
Ikegami, Kiyoshi 1653
Ikegami, Masanori 62, 1818, 1821, 3546
Ikezawa, Mikihiko 2187
Ilg, Thomas 3594
Imai, K. 471
Ingalls, William B. 1917, 1923
Inoue, Makoto 1294, 2528, 3110
Irwin, John 259, 363, 3423, 3453, 3480
Isaev, V.A. 1474
Ishchanov, Boris S. 2584
Ishi, Kimihiro 2187
Ishi, Sadahiro 2271
Ishi, Yoshihi 1653
Ishibori, Ikuo 2259
Ishihara, M. 471
Ishkhanov, Boris S. 2555
Issinsky, Igor B. 2262, 2289
Ito, Takashi 3546
Ivanov, Alexander P. 3501
Ivanov, G. M. 1973, 1976
Ivanov, O.A. 1474
Ivanov, Yu.M. 53
Ivers, J.D. 3600, 3603, 3606
Iverson, R. 2111
Iverson, Richard H. 330, 1252, 2987, 3648
Iwasaki, H. 492
Iwashita, Y. 2280
Iwashita, Yasuhisa 3110
Iwashita, Yoshihisa 857, 1294, 2528, 3645
Izawa, Masaaki 633, 904
Jablonka, Marcel 922
Jackson, Alan 2641
Jackson, G.P. 3324
Jackson, John W. 3185, 3333
Jackson, Leslie T. 3257
Jacob, Jorn 1647
Jacobs, Kenneth D. 3101
Jaekel, Markus 2424
Jaeschke, E. 197
Jagger, Jack M. 1378, 1979, 2635
Jaggi, Andreas 2087
Jahnel, Lucia 2421
Jain, Animesh 185, 3161, 3170, 3173, 3176, 3179, 3188, 3336
Jaitly, Ray 1010
Jakob, Ansgar 1288, 1836
Jander, Donald R. 2668
Janssen, Dietmar 2033
Jansson, Andreas 2223, 2226
Jeanneret, Jean-Bernard 40, 2620, 2623
Jensen, C. 2164
Jensen, Erk 250, 1408
Jeon, D. 1545
Jeon, Dong-o 109, 1198, 1201, 3140, 3143, 3303
Jeong, S. C. 1893
Jeram, B. 658
Jericha, Erwin 2957
Jett, Nelson D. 649
Jia, Qika 2406
Jiang, Daoman 1315
Jin, Yuming 2184, 2406
Job, P.K. 2090
Jobe, R. Keith 253, 3411, 3429, 3447, 3453
Johnson, D. 1318
Johnson, David 518
Johnson, David E. 714, 717, 1243, 2647
Johnson, Erik D. 584, 2471, 2480
Johnson, Kenneth F. 1929, 3528
Johnson, Mark 2936
Johnson, Marty 2468
Johnson, Neil G. 3764
Johnstone, Carol J. 1677, 3050, 3065, 3068, 3071, 3152
Johnstone, John A. 1082
Joly, Jean-marc 922
Jones, Frederick W. 128, 2933
Jones, Justin 2051, 3095
Jones, Kevin H. 518, 3528
Jones, Roger M. 777, 3423, 3468, 3471, 3474, 3477
Jones, W.P. 1548, 2519
Jongewaard, Erik N. 783
Jonker, Michel 2617, 2996
Joosten, Rainer 533
Jordan, Kevin 2229, 2456
Joshi, Chad 931
Joshi, Chan 330, 2006, 3651, 3654, 3684, 3705, 3708
Jowett, John M. 1680
Judkins, J. 206
Juillard, Michel 432
Julian, James 1471, 3131
Julian, R.A. 2394
Jung, Roland 465
Jungmann, K. 1488
Junquera, Tomas 919
Juras, M. 658
Kabel, Andreas 1650, 2507
Kabeya, Zenzaburo 842
Kadantsev, S. 106
Kaganovich, Dmitri 3693
Kageya, Tsuneo 392
Kahn, S. 185
Kahn, Stephen A. 3023, 3026
Kai, Satoru 1309
Kaiser, Hartwig 2385
Kaiser, K.-H. 165, 2915
Kaji, M. 343
Kako, Eiji 432
Kalinichenko, Alexandr I. 2546
Kaltchev, Dobrin 2620, 2623
Kamada, Susumu 256, 2155, 3432
Kaminsky, Alexander A. 1055, 3393
Kaminsky, Alim K. 1055, 3393
Kamitani, T. 1132, 2731
Kamitsubo, Hiromichi 188
Kamiya, Yukihide 904, 1174, 2436, 3363
Kamperschroer, James H. 1444, 1447, 1929, 1946, 2214
Kamps, T. 2075
Kamykowski, Edward 587
Kanai, T. 600
Kanai, Y. 1653
Kanai, Yasumori 3348
Kanaya, Noriichi 664, 667, 670
Kanazawa, Mitsutaka 413, 600, 798, 863, 2271
Kando, Masaki 3690, 3702
Kaneda, T. 592
Kang, H.S. 2205, 2501, 2593
Kang, X. 1545
Kang, Yoon W. 168, 3092
Kaplan, Danniel M. 3032
Kaplan, Roger 980
Karabarbounis, A. 1037
Karantzoulis, Emanuel 1126, 2316
Karasuk, V. 3086
Karliner, Marlen M. 2033
Karn, Jeff 3306, 3309, 3312
Karnaukhov, I.M. 2930, 3122
Karyotakis, Yannis 2990
Kashikhin, Vladimir 174, 182, 3327
Kashiwagi, Shigeru 256, 2143, 3432
Kaspar, Klaus 3552
Kasuga, Toshio 633, 2310
Katane, Mamoru 2528
Katayama, Takeshi 404, 1719, 1722, 1737, 3164
Kato, S. 1132, 2731
Katoh, Masahiro 664, 2307
Katoh, Tdahiko 343
Katonak, David J. 974
Katsouleas, Thomas C. 330, 3651, 3654, 3672, 3708, 3713
Katsumata, Tadasu 1309
Katsumura, Yosuke 2602
Kawachi, K. 600
Kawamoto, Takashi 343, 2108
Kaye, Robert A. 524
Kazacha, Vladimir I. 3393
Kazakov, S. 1058
Kazakov, Serguei 3414
Kazanskiy, Lev N. 1477
Kazarinov, Nikolai Yu. 3501

Kazimi, R. **1991**
Keane, John **1028**
Kedzie, Mark **524, 955**
Keesee, Marie **747**
Keffeler, David R. **1444, 1447**
Kehne, David M. **234, 1970**
Keil, Eberhard **1408**
Keil, J. **2054, 3098**
Keller, L. **2990**
Keller, Roderich **87, 884, 1911, 1914, 1917, 1923, 1926, 1943, 1958**
Kelley, John P. **965**
Kelly, Eugene **185, 3161**
Kempkes, Michael A. **568, 1491**
Kenda, K. **658**
Kennedy, K. **206**
Kennedy, Kurt D. **884**
Kenney, S. **3227**
Kerby, J. **3194, 3197**
Kernel, Philippe **1192, 1195**
Kerner, Thomas M. **696, 699**
Kerstiens, Debora M. **349, 652, 655, 1929, 1946**
Kesselman, Martin **2250**
Kester, Oliver **3516**
Kewisch, Jorg **705, 708**
Kezerashvili, Guram Ya. **2232**
Khachatryan, Arsen G. **3663**
Khan, Sameen A. **2817, 3280**
Khan, Shaukat **197, 1144, 1147, 2831**
Khodyachikh, A. **3122**
Khodzhibagiyan, Gamlet G. **2262**
Khomenko, S. **103**
Kiang, L.L. **1545**
Kikuchi, Mitsuo **1132, 2108, 2731**
Kikutani, Eiji **633, 1132, 1138, 2731**
Kikuzawa, Nobuhiro **2459**
Kim, Eun-San **3053, 3056**
Kim, G.N. **2593**
Kim, Han-Sung **2558, 2561**
Kim, Jin-Soo **1043, 1890**
Kim, Jong-Won **2268**
Kim, K.R. **3504**
Kim, Kwang W. **1384**
Kim, Kwang-Je **2495**
Kim, Mun-Gyung **2418**
Kim, Sang-Ho **2558, 2561**
Kim, Y.C. **3504**
Kim, Yong-Hwan **2558, 2561**
Kim, Young-Hwan **2558, 2561**
Kim, Yujong **1076, 1079**
Kim, Yuseok **3137**
Kimura, Wayne D. **487, 3722**
Kincaid, Brian **152**
Kindermann, Hans-Peter **946**
King, Bruce J. **318, 3035, 3038, 3041**
King, Quentin **762, 3743**
Kinkead, Allen K. **1049**
Kinoshita, Kenichi **2605**
Kinsho, Michikazu **3128, 3546**
Kirbie, Hugh C. **625**
Kirichenko, A.E. **2256**
Kirk, Harold G. **896, 3029, 3032, 3149**
Kishek, Rami A. **234, 1656, 1749, 1758, 1761, 1830, 1970, 3274, 3369, 3372**
Kishiro, Jun'ich **1141**
Kishiyama, Keith **1333, 1336, 1396**
Kitabayashi, Teruyuki **343**
Kitagawa, A. **600**
Kitazawa, Yasuji **592**
Klaffky, Roger **2304**
Klaisner, L. **206**
Kleev, Andrey I. **592**
Kleimenov, Victor **1339**
Klein, Horst **1288, 1836, 3405**
Klein, John **551**
Kleinod, M. **1899**
Klenov, V. **106**
Klette, Hallgeir **562**
Klingmann, Jeffrey **777**
Knapp, Edward A. **2301, 2555**
Kneisel, Peter **937, 943**
Kniegl, Gregor **3740**
Knobloch, Jens **980**
Knoch, Herbert **2424**
Knudsen, Helge **1671**
Knuth, Thomas **197, 1144, 1147**
Ko, In-Soo **1076, 1079, 2131, 2593, 3525**
Ko, Kwok **2822, 3423, 3480**
Koba, Kiyomi **1653, 2271**
Kobayashi, T. **3507**
Kobayashi, Yukinori **633, 2436, 3113, 3363**
Koehler, G. **800**
Koepke, Karl P. **992, 2027**
Koeth, Tim **995**
Koganeya, M. **3330**
Kohaupt, Rolf Dieter **1171**
Koiso, H. **1132, 2731**
Koizumi, Nozomi **343**
Kolbe, J. **197**
Kolysko, A.L. **1474**
Komada, Ichitaka **343**
Kondo, Shuji **3690, 3702**
Kondo, Yasuhiro **2187**
Kondrashev, S. **103**
Kondratenko, Anatoly **2289**
Konecny, Richard **2030, 3618, 3621**
Kononenko, S. **3122**
Konstantinov, Sergey G. **2033**
Koontz, Roland **1512**
Korabelnikov, Maxim B. **2167**
Korenev, Igor L. **1764**
Kornilova, Alla A. **1312**
Korolev, Aleksey **2567**
Koroliov, Alexander N. **2570**
Koscielniak, Shane R. **143, 1839**
Koseki, Shoichiro **3770**
Koseki, Tadashi **592, 2436, 3363**
Koseki, Takashi **904**
Kostas, Chris **360**
Kostial, Stephan **2740, 2951**
Kostin, Denis V. **910, 2301**
Kotaki, Hideyuki **3690, 3702**
Kotov, V.I. **53, 1237**
Kotseroglou, T. **3432, 3447**
Kotseroglou, Theofilos **3450**
Koupsidis, J. **2385**
Kourbanis, Ioanis **2840**
Koutchouk, Jean-Pierre **372**
Koutin, S.V. **392**
Kovalenko, Alexander D. **2256, 2289**
Kowalski, Ludwik **490**
Koyama-Itou, H. **600**
Kozanecki, W. **2990**
Kozanecki, Withold **296**
Kozawa, Takahiro **2018, 2596**
Koziol, Heribert **465**
Kozyrev, Evgeny V. **1049**
Kponou, A. **1902**
Kraemer, Dieter **197, 2379**
Krafczyk, George **3761**
Krafft, Geoffrey A. **1177, 2229, 2448, 2456**
Kraft, G. **2513**
Krakauer, D. **2635**
Kramer, Stephen L. **134, 140**
Krasnopolsky, Vsevolod A. **1479**
Krasnykh, Anatoly **1512**
Kraus, David E. **490**
Krause, Herbert F. **1671**
Kravchuk, Leonid V. **2799, 3282, 3561**
Krawczyk, Frank L. **965, 977, 1396, 3588**
Kreischer, Kenneth E. **81**
Krejcik, Patrick **296, 3429, 3447, 3450**
Kresnin, Yuri A. **2546**
Krienen, Frank **3134**
Krietenstein, Bernd **3552**
Krinsky, Samuel **2304, 2471**
Krisch, Alan D. **392**
Krishnagopal, Srinivas **1674**
Krishnan, Mohan **3666**
Kriznar, I. **658**
Kroc, T. **521**
Krogh, Michael L. **1303, 2611**
Kroll, Norman M. **777, 830, 1432, 1435, 3423, 3468, 3471, 3474, 3477, 3612**
Kruchkov, Jaroslav G. **2033**
Kruessel, Alois **2424, 3375**
Krylov, Stanislav Y. **1479, 1485, 2567**
Krämer, D. **2078**
Kubantseva, Natalia **1423**
Kube, G. **165**
Kubo, Hiroshi **3770**
Kubo, Kiyoshi **256, 2143, 3432, 3435**
Kubo, Ta. **3158**
Kubota, Chikashi **1653**
Kuchnir, Moyses **992, 2027**
Kudinov, Valery V. **1291**
Kudo, Hirofumi **3363**
Kudo, Kikuo **343**
Kugler, Hartmut **103**
Kuhler, S. **197**
Kulikov, Artem V. **3447, 3450**
Kulikov, I.I. **2256**
Kumada, Masayuki **600, 2510**
Kumagai, Keiko **2337, 2343, 2346**
Kumagai, Noritaka **188, 2337, 2340, 2343, 2346, 2349, 2352**
Kuner, B. **197**
Kuno, Kazuo **3363**
Kuo, C.C. **2409, 2412, 2837**
Kuo, Chang Hor **685, 1153, 1156, 1159, 1162, 1165, 2069, 2409, 2412**
Kurennoy, Sergey S. **1399, 2867, 3588**
Kurita, Nadine R. **206, 1363**
Kurnaev, O. **1249**
Kuroda, Ryunosuke **2298**
Kuroda, T. **1306**
Kurokawa, S. **633**
Kurz, Stefan **2796**
Kusano, Joichi **3128, 3546**
Kusche, Karl P. **2552, 3722**
Kushin, Victor V. **3564**
Kusikov, S.V. **1474**
Kuske, Bettina **197, 2379, 2382**
Kuske, Peter **197, 2078, 2379, 2385**
Kustom, Robert L. **168, 518, 998**
Kuszynski, J. **2078**
Kuzay, Tuncer M. **2090**
Kuzminski, Joze **965**
Kuzminski, Jozef **968, 2954**
Kuznetsov, G. **237, 1902**

Kuznetsov, Yu. **106**
Kvasha, Adolf I. **893, 3561**
Kwan, Joe **1937, 1943, 2537**
Kwan, Thomas J.T. **617, 1842**
Kwiatkowski, K. **471**
Kwon, Hyeok-Jung **2558, 2561**
Kwon, Myeun **899, 902, 1076, 1079, 1357**
Kwon, Sung-il **1064, 1067, 1070**
Kwon, Y. K. **1893**
Kühnel, K.U. **3516**
Lach, Joseph **1387**
Laclare, Jean-Louis **1533**
Ladran, A. S. **2590**
Lager, Darrel L. **3513**
Lakatos, Andreas **1288, 1836**
Lalot, Michel **922**
Lamanna, Giuseppe V. **2948, 3522**
Lamarre, J.F. **1569**
Lambertson, Glen R. **1225**
Lambiase, Robert F. **3734**
Lamm, Michael J. **3191, 3194, 3197**
Lamont, Michael **304, 2996, 3008**
Landahl, Eric C. **2000, 2003**
Lange, M. **2424**
Lange, R. **197**
Lange, Ralph **2382**
Lanting, T. **2990**
Lanza, Richard C. **584**
Lapik, Roman M. **2170**
LaPointe, Mike A. **3627**
Lapostolle, Pierre **1860**
Lapshin, V. **3122**
Larbalestier, David C. **177**
Larimer, Ruth-Mary **533**
Larrieu, Christopher A. **741, 747**
Larsen, Ray **636**
Larsen, Richard C. **490**
Latypov, Tomas A. **1485, 2567**
Lau, Wai Keung **1153, 1159, 1162, 1165, 2000, 2837**
Laurent, Jean-Michel **2629**
Lauth, W. **165**
LaVeigne, Joseph **134**
Laverty, Michael **890**
Lawrence, George P. **3567, 3582**
Lawson, Wesley **1040, 1046**
Lawton, Don **234**
Laxdal, Robert E. **893, 3534, 3537**
Lazarus, Donald M. **490**
Laziev, Eduard M. **3393**
Le Duff, Joel **913, 2012**
Le Sage, G.P. **2480**
Lebedev, Pavel **1387**
Lebedev, Valeri A. **646, 738, 1183, 2897**
Leblanc, G. **206**
LeBlanc, Greg **2945**
LeBon, Douglas J. **3758**
Lebrun, Paul **3032, 3062**
LeCocq, C. **1390**
Lee, Y.Y. **1267**
Lee, Bryan S. **625**
Lee, Chun Sik **1893**
Lee, Edward P. **1830, 3254**
Lee, Hyeyoung **3137**
Lee, J.C. **1602, 1605, 2837**
Lee, J.W. **679**
Lee, Jan Fung **1162**
Lee, Jinhyung **2784**
Lee, Kang-ok **2558, 2561**
Lee, P. B. **1716**
Lee, Peter J. **177**
Lee, Roger C. **557, 1348, 2146**
Lee, S. **3672**
Lee, S.H. **682**
Lee, S.Y. **109, 392, 1545, 1548, 1854, 2286**
Lee, Seung **330**
Lee, Seung C. **1384**
Lee, T. **2021**
Lee, Tae-Yeon **679, 1384, 2131, 2418**
Lee, W. Wei-Li **1623, 1626**
Lee, Yong Y. **1297, 1488, 1743, 3182, 3185, 3300**
Lee, Yvette **2540, 2575**
Leemans, Wim P. **325, 330, 2111, 3696, 3699, 3705**
Lefebvre, Daniel **2686**
Lefevre, Thibaud **1797, 3387**
Legan, Al . **56**
Lehrach, A. **1578**
Lehrach, Andreas **1701, 2292**
Lei, Ge **747**
Leissner, Boris **2172**
Leitner, Matthaeus A. **1911, 1914, 1958**
Lekston, J.M. **3387**
Len L. K **70**
Leng, Yongbin **1315, 2125**
Lenkszus, Frank R. **333, 2093**
Leon, Asunción **2531, 2534**
Lepercq, Pierre **916**
Lepeule, Patrick **1339**
Lesjak, B. **658**
Lesrel, Jean **919**
Lessner, Eliane S. **1644, 1967, 2325**
Letchford, Alan P. **1767, 2208**
Lettry, J. **92**
Leung, Ka-Ngo **1911, 1914, 1917, 1920, 1923, 1943, 1958, 2540, 2575**
Leunissen, Leonardus H.A. **1557, 1683**
Level, Marie-Paule **1533**
Levush, Baruch **360, 1016**
Levy, C.D. Philip **106, 1964**
Lewellen, John W. **1979, 2024, 2134, 2483**
Lewis, B. **471**
Lewis, S.A. **355**
Li, C.D. **2671**
Li, Derun **382, 800, 896, 907, 1207, 1548, 3149**
Li, Guangyeng **2125**
Li, Jingyi **2048**
Li, Nanyang **3339**
Li, Rui **118, 2456**
Li, Shaopeng **633**
Li, Weimin **2406**
Li, Yongjun **2406**
Li, Yulin **3221**
Li, Yun **234, 1656, 1758, 1970, 2102, 3369**
Li, Zenghai **2822, 3423, 3447, 3468, 3480, 3483, 3486**
Liaw, Chong-Jer **1345, 3300**
Libkind, Marcus A. **1390, 2477, 2590**
Lidia, Steven M. **1797, 1800, 2698, 2870, 3387, 3390**
Liebermann, Holger **530**
Lietzke, A. **171, 3233**
Likhachev, Sergey P. **2587**
Liljeby, Leif **1955**
Lill, Robert M. **1411**
Lima, Roberto R. **1366**
Limberg, Torsten **1650**
Limborg, Cecile G. **206, 2361, 3104, 3107**
Limon, Peter J. **174, 1420, 2644, 3194, 3197**
Lin, F.Y. **2671**
Lin, Ke Kang **682, 1450, 2009, 2409, 2412, 2415**
Lin, Tsai-Fu **1375**
Lin, Xintian E. **75, 1429, 3612**
Lindgren, Lars-Johan **2945**
Lindroos, Mats **143, 2226**
Linnecar, T. **2617**
Lira, Antonio C. **3125**
Lisi, Nicola **103**
Lisitsyn, A. **461**
Littauer, Raphael M. **410, 2057**
Litvak, A.G. **1474**
Litvinenko, Vladimir N. **221, 2099, 2468**
Liu, Chen-Yao **3776**
Liu, Dekang **633, 2140**
Liu, G. **2337**
Liu, Guangjun **2125**
Liu, H.C. **2671**
Liu, James **3450**
Liu, Jinhong **2048**
Liu, Kuo-Bin **3776**
Liu, Lin **2421, 2891, 2894, 3125**
Liu, Y. **2552, 3639, 3722**
Liu, Yuan **1878, 1881**
Liu, Zuping **2048, 2406**
Lo, C.C. **1471, 3131**
Lobo, Ricardo P.S.M. **134**
Lockey, R. **1902**
Loew, G.A. **3423**
Loewen, Roderick J. **3420, 3423, 3426, 3480**
Logan, B. Grant **3248**
Logatchov, Pavel V. **78, 237, 2167, 2948**
Loh, M. **3708**
Lohrmann, Erich **554**
Lombardi, Alessandra M. **103, 1860**
Lombardi, Augusto **1324, 3522**
Lonza, Marco **1120**
Lopes, Nelson **3725**
Lorenz, Ronald **2075**
Lorenzon, Wolfgan **392**
Loschner, H. **2575**
Losito, Roberto **946, 949**
Lou, G.H. **2220**
Lou, Weiran **1441, 3221, 3224**
Loulergue, Alexandre **1530**
Low, Raymond **1920**
Lozowski, B. **471**
Lu, Chang-guo **3026**
Lu, Ping **2184**
Lucas, Peter W. **1246, 2614**
Luccio, Alfredo U. **1578, 3143**
Ludewig, Hans **548, 3185**
Ludewigt, B. **2537**
Luft, P. A. **1914**
Luhmann, Jr., Neville C. **2000**
Luiten, O.J. **3266**
Lujan, Richard E. **977**
Lumpkin, Alex H. **1644, 2134, 2137, 2161**
Lund, Steven M. **1785, 1788, 3248, 3381**
Lundah, Eric W. **3480**
Lunev, Pavel **461**
Luo, Xiaoan **2963**
Luo, Xuefang **1596**
Luo, Yun **633**
Luong, Michel **250, 821**
Lyles, John T. M. **998, 1001**
Lynch, Don **2244**
Lynch, Michael T. **453, 1061**
Lyneis, Claude M. **533, 1952**
Lyons, Mike B. **962**
Lysenko, Walter P. **3528**

Ma, Li **633, 2140**
Ma, Qing **1342**
Macek, Robert J. **518, 1198, 1201**
MacGill, R.A. **3149**
MacGill, Robert **884**
Machida, Shinji **62, 1653, 1818, 1821, 2271**
Machie, D. **1991**
MacKay, William W. **693, 702**
MacLachlan, J. **521, 1707**
MacLaren, Stephan A. **1937, 2849, 2852**
Madden, Robert P. **2388**
Madrid, Mike **1396**
Maeng, AeHee **1384**
Maerki, Max **418**
Maezawa, Hideki **667, 670**
Magerski, Andy W. **3573**
Magne, Christian **922**
Magurno, Benjamin **490**
Mahler, G. **2128**
Maier, Rudolf **851, 1701, 2292**
Mailian, M.R. **1468, 2105, 3657**
Majka, Richard **1258**
Makarov, A. **3327**
Makarov, K. **103**
Makdisi, Y. **471**
Makhnenko, L. A. **1973, 1976**
Makita, Yo **848**
Mako, Frederick M **70**
Maksimchuk, Anatoly **3666, 3716**
Malamud, E. **3330**
Malchow, Russell **2990**
Malitsky, Nikolay **2713, 3185**
Malone, Robert G. **2158, 2471, 2942**
Mamaev, Gennady L. **1479, 1482, 1485, 2564, 2567**
Mamaev, Sergey L. **1479, 1482, 1485, 2567**
Mamaev, Yuri A. **1988**
Mammosser, John **925, 934, 937, 955, 1462**
Manglunki, D. **1282**
Mangra, Danny **1967, 1979**
Manni, Mario **2277**
Mant, Geoff **3248**
Manwaring, Wm. **498, 673**
Manzo, Mario P. **965**
Mao, Stan **3429**
Mapes, M. **1345**
Marcellini, Fabio **131, 866, 1147**
Marchand, Patrick **986, 989**
Marcouille, Olivier **2686**
Marhauser, Frank **3405**
Marini, J. **919**
Markiewicz, Thomas W. **307, 3462, 3489**
Markovich, G. M. **2024**
Marks, Steve **162, 3429**
Marl, Ron **2656**
Marlats, Jean-Louis **2686**
Marletta, Salvo **97**
Marneris, Ioannis **2543, 3767**
Marone, Andrew **3161, 3170**
Marque, Sébastien **946, 949**
Marriner, John **641, 1707, 2638**
Marsh, Kenneth A. **330, 2006, 3651, 3705**
Marshall, Thomas C. **3627**
Marteau, Fabrice **2686**
Marti, F. **1318**
Martin, D. **206**
Martin, Edward **3309**
Martin, K. S. **714**
Martin, Michael C. **495**
Martin, Philip S. **31, 1082, 3318**
Martin, Siegfried A. **959, 3549**
Martinez, D. **2214**
Martinez, Derwin G. **2241**
Martinez, Felix A. **965**
Martinez, Horace J. **965**
Martini, M. **1282**
Martins, Marcos N. **1366**
Martlew, Brian G. **661**
Martono, Hendy **1551, 2805**
Martyshkin, Pavel V. **1456, 2170**
Marusic, A. **2128**
Marutsuka, Katumi **3360**
Maruyama, T. **3447**
Maruyama, Takahashi **3450**
Maruyama, Takashi **1988**
Marx, Michaela **2385**
Masahiro, Kaji **343**
Masaki, Mitsuhiro **2346**
Masi, M. **1324**
Masullo, Maria R. **1599**
Masunov, E. **2855, 2858**
Masuzawa, Mika **1132, 2731, 3351, 3354, 3357**
Matheisen, A. **2033**
Matheson, John **2999**
Mathis, Yves-Laurent **2424**
Matoba, Suguru **2271**
Matsufuji, N. **600**
Matsumoto, Hiroshi **536, 842, 3411**
Matsumoto, Shuji **3414**
Mattison, Thomas **2990**
Matuk, Charles **1920**
May, Michael P. **1423**
May, T.E. **2394**
Maymon, Jean-Noel **1168**
Mazaheri, G. **296**
Mazur, Peter O. **182, 3318, 3330**
Mazzitelli, Giovanni **1536**
McAllister, Brian **3101**
McAshan, M.S. **182**
McCandless, Brian **3480**
McCarrick, James F. **1303, 1827, 2755**
McCarthy, Michael P. **1061, 1402**
McChesney, David D. **3179, 3188**
McClellan, Jonathan T. **965**
McCormick, Douglas J. **253, 307, 1994, 3411, 3453, 3477**
McDaniel, Boyce **410**
McDonald, Kirk T. **310, 3026**
McGehee, Peregrine M. **652, 3528**
McGehee, Robert **688**
McGinnis, David **59, 854, 1713**
McGuire, David **1402**
McIntosh, Peter A. **1025**
McInturff, Alfred D. **171, 3197, 3233, 3236**
McIntyre, Gary T **3336**
McIntyre, Peter **2936**
McKee, B.D. **3429, 3447**
McKemey, Adrian **2990**
McKinney, W. **495**
McMahan, Margaret A. **533**
McMichael, Gerald E. **2274**
McNerney, A.J. **1267, 1270**
Mead, William C. **2790**
Meadow, B. **2990**
Meads, Phillip, F. **3549**
Meddahi, Malika **304, 2996, 3005**
Meier, Wayne R. **1503**
Meilunas, Ray **2599**
Meinke, Rainer B. **3212, 3215, 3245**
Mele, K. **658**
Melissinos, Adrian C. **2027, 2181**
Meller, Robert E. **1115**
Melnychuk, Stephan T. **587, 2599**
Mendonca, Jose T. **3725**
Menefee, Tina **3306**
Menegat, Al **824, 3420**
Menna, Mariano **2578**
Menshov, Alexander A. **893**
Menzel, Jan **2178**
Meot, Francois **2445**
Merl, Robert **2093**
Merle, Eric **3260**
Merminga, Lia **768, 1177, 1180, 2456**
Merrill, Frank **518**
Merte, Rolf **815, 818**
Mertens, Volker **40**
Meseck, Atoosa **554**
Meth, Marvin **3336**
Metral, G. **1282**
Meurdesoif, Y. **3387**
Meusel, Oliver **1288, 1836**
Mexner, Wolfgang **2424**
Meyer, Christophe **103**
Meyer, Dirk **1917**
Meyer, Earl **1946**
Meyer, H.O. **471**
Meyer, Ross K. **3594**
Meyer-ter-Vehn, Jurgen **3675**
Mezi, Luca **1219**
Mi, J-L. **1488**
Michaut, Jean **2686**
Michelato, P. **2027**
Michizono, Shin-ichiro **1132, 2731, 3414**
Michnoff, Robert J. **693, 2114, 2247**
Michta, Richard J. **2081**
Middendorf, Mark E. **2274**
Miera, D.A. **426**
Miertusova, Jana **2316**
Migliorati, M. **131**
Migliorati, Mauro **1219**
Mikawa, Katsuhiko **3360**
Mikhailichenko, Alexander A. **2814, 3218, 3633, 3636**
Mikhailov, Vladimir A. **2256, 2262, 2289**
Miki, Miyako **2596**
Mikkelsen, Ulrik **1671**
Milardi, Catia **1536**
Milharcic, T. **658**
Millage, Kyle K. **3429, 3447, 3450**
Miller, J.R. **3227**
Miller, Roger H. **777, 3423, 3426, 3468, 3471, 3474, 3477, 3480, 3483, 3486**
Millich, Antonio **250, 1863**
Millo, Daniele **2680**
Millos, Gabriel **171, 3236**
Mills, Frederick E. **3152**
Milton, Bruce **587**
Milton, Stephen V. **1644, 1979, 2024, 2134, 2325, 2483, 2486**
Mimashi, T. **1132, 2731**
Minaev, Sergey A. **1291, 3552**
Minaev, Serguei **3555**
Mincer, Allen **1258**
Minehara, Eisuke J. **2459, 3546**
Minohara, S. **600**
Minty, Michiko G. **256, 296, 307, 338, 771, 800, 1207, 2846, 3384, 3432**
Mirabal, J.S. **426**
Mirochnik, E. **2567**
Mirzojan, Alexandr N. **3561**

Mischenko, Aleksandr V. 2564
Mishin, Andrey V. 590
Mishnev, V. M. 2167
Mishra, C. Shekhar 31, 2641, 2644, 2647, 2719, 3318
Mistry, Nariman B. 3221
Mitchell, John C. 965
Mitchell, Russell R. 965
Mitra, Amiya K. 450, 839, 893
Mitsuhashi, Toshiyuki 492, 2120, 2143, 2307
Mitsumoto, Toshinori 2268
Mitsunobu, Shinji 440
Miyade, Hiroki 2403
Miyahara, N. 600
Miyahara, Tsuneaki 2155
Mizumoto, Motoharu 513, 3128, 3546
Mizuno, Akihiko 2015, 2749, 3507
Mizuno, Hajime 3414
Mizutani, Yasuhiro 2596
Moallem, M. 2099
Mocheshchnikov, N.I. 2924
Mochihashi, Akira 1821
Moeller, Soeren Pape 2295, 2427
Mohos, I., 2054
Moir, David C. 617, 1842
Moir, Ralph W. 1503
Mokhov, Nikolai V. 56, 1231, 1234, 2525, 2614, 3041, 3047, 3050, 3074
Molodkin, V. 3122
Molodozhentsev, Alexander 2522
Molvik, Arthur W. 1503, 3248
Monard, H. 2012
Monchinsky, V.A. 2256
Mondelli, Alfred A. 360
Montag, Christoph 1566
Montoya, Debbie I. 965
Montoya, Dennis R. 965
Moog, Elizabeth R. 2483, 2489
Moore, Christopher I. 3687, 3693
Moore, Craig D. 1246, 2614
Moore, D. 652
Moore, John M. 1551, 2805
Moore, T. L. 2590
Morcombe, Peter H. 221, 688
Moretti, Alfred 896, 3032, 3149, 3152
Morgan, Gerry H. 185, 3161, 3170
Mori, Warren B. 330, 3669, 3672, 3684
Mori, Yoshiharu 106, 413, 565, 798, 857, 860, 863, 1007, 1653, 1821, 1964, 2271, 2280, 3348, 3770
Morita, Akio 1294, 2528
Morpurgo, Giulio 2996
Morrison, L. 171, 3233
Morrison, M. 171, 3233
Morse, W.M. 1488
Mortazavi, Payman 1028
Morvillo, Michele 1408, 2629
Moser, Herbert O. 165, 2424
Moser, S. Scott 3041
Mosnier, Alban 628, 1533, 1662, 2834
Moss, Andrew J. 1025
Moss, James D. 965
Mostacci, Andrea 2873
Mouillet, Marc 3260
Mouton, Bernard 2012
Muchnoi, Nickolay Yu. 2232
Mueller, Roland M. 726, 2078, 2379, 2382, 2385
Mugge, Marshall 777
Muggli, Patrick 330, 2006, 3651, 3654, 3708
Mugnai, G. 2999
Mukherjee, Sam K. 1911, 1914
Mukugi, Ken 3546
Mulhollan, Gregory A. 1988, 3447, 3450
Mullacrane, I. D. 2656
Muller, Anke-Susanne 2885, 3011
Muller, Ralph 197
Mulvaney, J. Michael 568, 1491
Muneyoshi, T. 2689
Munoz, Marc 1542
Munro, Morrison H. 3429, 3447
Munson, D.V. 3257
Murakami,T. 600
Muramatsu, M. 600
Muramatsu, Ryosaku 413, 798, 860, 863, 1007, 2271
Murata, Hirohiko 2403
Muratore, Joseph F. 185, 3161, 3170
Murokh, Alex 217, 2006, 2480
Muroya, Yusa 2602
Murphy, James B. 134, 140, 1106
Musameci, Pietro 2480
Musson, John 768, 1183
Muto, Masayuki 565, 3348, 3770
Myakishev, Dmitry G. 2775
Myers, Stephen 299
Myskin, O. 2033
Mytsykov, A. 3122
Nadji, Amor 1168, 1533, 1569
Nagai, Ryoji 2459
Nagaitsev, Sergei 521, 1088, 1707
Nagaoka, Ryutaro 1192, 1195, 3119
Nagayama, Takahisa 848
Nahon, Laurent 2686
Naito, Takashi 256, 343, 1994, 2143, 2155, 3432
Naitoh, Takashi 492
Nakajima, Kazuhisa 2510, 3690, 3702
Nakajima, Mitsuo 3690
Nakajima, Tsukasa 3360
Nakamura, Eiji 1141
Nakamura, M. 471
Nakamura, Norio 1174, 2436, 3363
Nakamura, Shinsuke 3098
Nakamura, T. 1132, 2731, 3158
Nakamura, Takeshi 2346
Nakamura, Tatsuro 343
Nakamura, Yoshiteru 2259
Nakanishi, T. 3098
Nakayama, Hitoshi 413, 798, 1007
Nam, S.H. 2205, 2501, 3504
Namito, Yoshihito 3450
Namkung, W. 2593
Nantista, Christopher D. 1432
Napoly, Olivier 922
Nara, Takayuki 2259
Narang, R. 3708
Nasonov, Nikolay N. 2584, 2587
Nassiri, Alireza 1073, 1979, 2024, 2483
Nath, Subrata 611, 1929, 3528, 3582
Nation, J.A. 3600, 3603, 3606, 3609
Naumann, Olaf 1647
Navarro, G. 1324
Nawrath, Guenther 554
Nawrocky, Roman J. 2081
Neil, G. R. 2456
Nelson, Eric M. 360, 2778
Nelson, Scott D. 1824, 2235
Nelson, W. Ralph 253, 2990, 3450
Nemoshkalenko, V. 3122
Nesterovitch, Alexandre V. 1291, 1932, 2573
Neuffer, David V. 3062, 3080, 3083, 3152
Neugebauer, F. 2764
Neuman, Charles P. 1949
Neurath, R. 2611
Nevada, Bechtel 1506
Newman, Ernest W. 971
Newsham, D. 2003, 2021
Nezhevenko, Oleg A. 1049, 1052, 1474, 3492
Ng, Cho-Kuen 206, 800, 3423, 3426
Ng, King Y. 872, 1545, 1548, 1854, 3077
Nghiem, Phi 1533
Nguyen, Dinh C. 217, 2480
Nguyen, K. 1016
Nguyen, Minh N. 1494, 1497
Nguyen, Viet 780, 928, 931, 934, 1459
Niederer, James A. 1270, 1578, 2722
Nief, J.-Y. 2990
Niell, Fred M. 237, 1004
Nielsen, B.R. 2427
Niki, Kazuaki 3770
Nikiforov, Alexej A. 750
Nikitine, Iouri 1339
Ninomiya, Shiro 1821
Niquille, C. 2617
Nishi, Masatsugu 2528
Nishimori, Nobuyuki 2459
Nishimura, Hiroshi 203, 234
Nishiura, M. 1306
Nobrega, A. 3194, 3197
Noda, Akira 857, 1294, 2280, 2528, 3110
Noda, Fumiaki 3128, 3546
Noda, Koji 413, 600, 798, 863, 1309, 1821, 2271
Noda, Takashi 2352
Nogiec, Jerzy M. 1426, 3191
Noguchi, Shuichi 432
Nordberg, Emery 980, 3221
Norem, J. 1417, 2635, 3062
Norman, Eric B. 533
Normann, L. 2617
North, William 1037, 1515
Norum, W. Eric 3764
Nosochkov, Yuri 206, 2355, 2358, 2364, 3465
Novikov, Gleb A. 2301
Novikov, Vladimir N. 3716
Novikova, Tat'ana A. 2581
Novitski, I. 3194, 3197
Novokhatski, Alexander 2743, 2879
Nuhn, H. D. 2486
Nurushev, S. 471
Nusinovich, G. 1040
Nyman, M. 3257
O'Hara, James F. 2214
O'Neil, James 533
O'Shea, Patrick G. 234, 1949
Oakeley, Owen 221, 2099
Oakley, Owen 2468
Obina, Takashi 1135, 2310
Oerter, Brian R. 699
Ogata, Atsushi 3713
Ogawa, Y. 2731
Ogawa, Yujiro 1132, 2984
Ogitsu, T. 174, 3158, 3194
Oguri, Hidetomo 3546
Oguri, Yoshiyuki 3525
Oh, Saewoong 2265, 3137
Ohkuma, Haruo 2337, 2340, 2343, 2346, 2349, 2352
Ohmi, Kazuhito 633, 1132, 2731, 3113
Ohmori, Chihiro 413, 798, 857, 860, 863, 1007, 1653, 2271, 2280
Ohnishi, Y. 1132, 2731, 2981

Ohnuma, S. **2590**
Ohsawa, S. **2731**
Ohsawa, Satoshi **1132, 2238**
Ohshima, Takashi **2346**
Ohtomo, Kiyotaka **1722**
Ohuchi, N. **1132, 2731, 3158**
Oide, Katsunobu **288, 1132, 2238, 2731, 3432**
Oishi, Masaya **2352**
Okada, Yasuhiro **2018, 2036**
Okamura, M. **3161**
Okamura, Masahiro **106, 471, 1964, 3164**
Oki, Toshiyuki **1821**
Okita, Shunsuke **2605**
Okugi, Toshiyuki **256, 2143, 2155, 3432**
Okumura, Susumu **2259**
Oliveira e Silva, Luis **3725**
Olsen, David K. **109, 1198, 1201, 3140, 3143, 3303**
Omori, Tsunehiko **2552**
Onda, Takashi **842**
Ongaro, Carla **2531, 2534**
Onillon, Emmanuel **1109**
Ono, Masaaki **432**
Op de Beeck, W.J. **3212**
Opanasenko, Anatoly N. **1976**
Oragiri, Jun-ichi **343**
Oren, Will **3309**
Orlandi, Gianluca **2193, 2196**
Ormond, Kern W. **1354**
Orris, Darryl F. **1420, 1426, 3191, 3194, 3197, 3318**
Orsini, Fabienne **2834**
Ostiguy, Jean-Francois **2710**
Ostojic, R. **1330, 2921**
Ostrikov, Sergey V. **1932**
Ostroumov, Petr N. **103, 893, 3282, 3561**
Otboyev, Alexey **1524**
Ott, Klaus **197, 2385, 2608**
Otting, Donnie **803**
Ouchi, Nobuo **3546**
Overett, Trevor **1061, 3755**
Ovsyannikov, Alexander D. **2808**
Ovsyannikov, Dmitri A. **1857**
Owen, Hywel L. **2433**
Oyaizu, M. **1893**
Ozaki, K. **592**
Ozaki, T. **3158**
Ozelis, J.P. **174, 3194, 3197**
Pabst, Michael **1767**
Padamsee, Hasan S. **429, 980, 983**
Pagani, Carlo **1776, 2027**
Pagano, Oreste **3209**
Pai, Chien-Ih **1100, 1488**
Pakter, Renato **1875, 2752**
Palmer, Dennis T. **545, 1997, 3612**
Palmer, Robert B. **3023, 3032, 3062, 3149, 3152**
Palmieri, Vincenzo **541, 943**
Palumbo, Luigi **1219, 1599, 2873**
Pantell, R. H. **3722**
Panvier, Roger **916**
Paolicelli, Guido **2060**
Paolucci, Giorgio **2060**
Papaleo, R. **2578**
Papanicolas, N. **1037**
Papaphilippou, Yannis **1554, 1557, 1560**
Pappas, Chris **1494, 1500, 3429**
Pappas, G.C. **1488**
Paramonov, Valentin V. **893, 2799**
Pardo, R. C. **1890**
Parietti, L. **3591**
Park, Chongdo **1357**
Park, E.S. **2418**
Park, H. J. **899**
Park, I. S. **899, 902**
Park, S. **206, 2367**
Park, Seong Hee **221, 2468**
Parker, Brett L **3336**
Parkhomchuk, Vasily V. **1387, 1704**
Parodi, Renzo **913**
Parsa, Zohreh **2820, 3044**
Pasky, Stanley J. **1414, 2024**
Pasotti, Cristina **809, 1123**
Pasquinelli, Ralph J. **1094**
Pastrnak, J. W. **2590**
Pate, David **557, 1348**
Paterson, J.M. **3423**
Patterson, Janet L. **2468**
Paul, Arthur C. **1204, 3251, 3254, 3513**
Pavlovic, M. **2513**
Pavlovskii, V. V. **2178**
Payet, Jacques **1530**
Pearce, P. **250**
Pearson, Chris **777, 3423, 3426**
Pearsons, R. **3579**
Peaupardin, Philippe **2686**
Peck, Stuart B. **285, 980**
Pedeau, Dominique **1168**
Pedersen, Flemming **143, 474**
Pedrozzi, Marco **81**
Peggs, Stephen G. **705, 1572, 3176, 3179, 3336**
Pei, A. **1545**
Pei, X. **1548**
Pei, Yuanji **1315, 1596**
Peikert, Martin **815**
Peiniger, M. **957, 3510**
Pekeler, M. **245, 2033**
Pelaia, Thomas A. **1115**
Pellegrin, Eric **2424**
Pellegrini, Claudio **217, 2006, 2021, 2045, 2480, 2504, 3708**
Pellico, William A. **1097**
Pelzer, Wolfgang **3519**
Penn, Gregg **3059**
Peraire, Serge **40**
Perelstein, Elkuno A. **3393, 3501**
Perera, Lalith **3221**
Perevedentsev, Eugene **1521, 1524**
Perez, Francisco **806, 809, 2424**
Perko, M. **658**
Pershing, D. **1016**
Peskov, Nickolay Yu. **1055**
Pestrikov, D. **1132, 2731**
Petelin, M.I. **1474**
Peternel, M. **658**
Peters, Craig **3257**
Peterson, Edward **551**
Peterson, T. **1420, 3194, 3197**
Petillo, John J. **360, 2737, 2778**
Petit, Annie **2686**
Petitpas, Patrick **2990**
Petracca, Stefania **1689, 2882**
Petrak, Sibylle **2990**
Petree, Mark **2990**
Petrichenkov, Michael V. **3086**
Petrossian, Marzik L. **3657**
Petrov, Viktor M. **2033**
Pett, John G. **762, 3743**
Petukhov, Vladimir P. **2584**
Pfeffer, Howie **3761**
Pflüger, Joachim **157, 1369**
Phelps, R.A. **392**
Phillips, H.L. **1459**
Phillips, Lawrence **780, 934, 937, 1462**
Phinney, Nan **307, 338, 3384, 3447, 3456**
Piaszczyk, Christopher **1465**
Pichoff, Nicolas **1860, 3277**
Pickard, D. **1943**
Pico, Randolph E. **2590**
Picon, Jean-Claude **3260**
Pieck, M. **652**
Piekarz, Henryk **182, 3330**
Piel, C. **3510**
Pierini, Paolo **1776**
Pierret, Olivier **3260**
Pikin, A. **1902**
Pilat, Fulvia **37, 2716, 2728, 3179**
Pile, P.H. **1267**
Pile, Geoffery **1022**
Pilipenko, Yuri **2289**
Pillai, Chandra **518**
Piller, C. **955**
Pinayev, Igor V. **221, 2468**
Pincosy, Philip A. **1827**
Pinto, Innocenzo **2882**
Piot, Philip **2229, 2456**
Pipersky, Paul **162**
Piquemal, Alain C. **1851**
Pirkl, Werner **103**
Pirozhenko, A. **2567**
Pirozhenko, Vitaly M. **2564**
Pisent, Andrea **1773, 3522**
Pitts, Cliff **3342**
Pivarc, J. **1896**
Pivarc, J., Jr. **1896**
Pivi, Mauro **2629**
Placidi, Massimo **296, 2999**
Plate, David **162, 803**
Platise, U. **658**
Plawski, Eugeniusz **3408**
Plesko, M. **658, 2424, 2424**
Plettner, Tomas **321**
Plotnikov, Sergey V. **3564**
Plum, Michael A. **518, 1198, 1201**
Podlech, Holger **1955, 3543**
Podlevskih, Vitaly V. **2802**
Podobedov, Boris **146, 1665, 2978**
Poelker, B.M. **1991**
Pogorelsky, Igor V. **2471, 2552, 3722**
Poirier, Roger L. **450, 839, 893, 3540**
Pollet, Patrick **2087**
Polozov, S. **2858**
Pomazan, Yu. V. **1291**
Poncet, A. **1330**
Pont, Montse **2424, 3375**
Poole, Brian R. **1824, 3381**
Poole, Michael W. **2433, 2656**
Pope, Rodd **777**
Popov, Gennadiy F. **2546, 2549**
Poppe, Uli **2178**
Porcellato, A.M. **1324**
Portante, Luciano **1366**
Portmann, Gregory, J **2373**
Potier, J.P. **250**
Potukuchi, Prakash N. **952**
Poutchkov, Sergey N. **1479, 1482, 1485, 2567**
Powell, James **533**
Power, John F. **1399, 2214, 2241**
Power, John G. **1967, 2024, 2030, 3621**
Pozimski, Jürgen **1288, 1836**
Prabhakar, Shayam **131, 636**

Prabhaker, Shyam **1207**
Pradal, Franco **2316**
Praestegaard, L. **2427**
Prange, H. **197**
Prasuhn, Dieter **1701, 2292**
Preble, Joseph P. **780, 931, 934, 1459, 1462, 2456**
Prebys, Eric J. **3026**
Preger, Miro A. **131, 1536**
Prelec, K. **1902**
Prestemon, S. **3227**
Price, J.S. **1991**
Prichard, Benjamin A. **1917, 1923**
Prieto, Peter S. **1246**
Pritzkau, David P. **824**
Prodell, Albert **185, 3161, 3170**
Pronin, Oleg D. **3561**
Prono, Daniel S. **617**
Proudlock, Paul I. **1330, 3200, 3203, 3746**
Pruessner, Marcel **234**
Przeklasa, Roy **1010**
Przewos, B. **471**
Ptitsin, Vadim I. **37, 702, 1575, 2716, 2921**
Puggli, P. **3705**
Pugh, M. J. **2656**
Pukhov, Alexander **3675**
Puntus, Vladimir A. **3561**
Pusterla, Modesto **3280**
Péerez, José **2531**
Qian, Zubao **872**
Qiang, Ji **137, 366, 1845**
Qin, Hong **1623, 1626, 1629**
Qin, Qing **633**
Qinggui, Lai **3263**
Quigley, Peter **980**
Quimby, David C. **2668, 2674, 2677, 3722**
Quintana, Bobby **349**
Quintana, Stephen W. **965**
Rabedeau, T. **206**
Radecke, F. **197**
Radeka, Veljko **2114**
Rago, C. E. **3447**
Raia, Guido **2578**
Raimondi, Pantaleo **307, 338, 2996, 3384**
Raino', Antonio **1905**
Rakowsky, George **1390, 2471, 2477, 2698**
Ramamoorthy, Susila **690**
Ramanathan, Mohan **2051**
Rambo, Peter W. **1827**
Ramos, H.J. **1306**
Ramsell, Christopher T. **3719**
Raparia, Deepak **1297, 1743, 1964, 3185**
Rasson, J. **800**
Rathjen, Eric **2424**
Rathke, J. **780**
Rathke, John **551**
Ratner, Lary G. **392**
Ratschow, S. **2915**
Ratti, Alessandro **884, 1961**
Ratzinger, Ulrich **1788, 1955, 3552, 3555**
Raubenheimer, Tor O. **240, 250, 253, 338, 800, 3423, 3429, 3438, 3441, 3444, 3447, 3453, 3456, 3462, 3465, 3474, 3483, 3486, 3489**
Rauch, Helmut **2957**
Ravello Alberto **2936**
Reass, William A. **426, 453**
Redin, Sergei I. **3167**
Redler, K. **1393**
Reece, C.E. **940**
Reed, C. **3062**
Reed, C.A. **1881**
Rees, Daniel E. **786, 881, 1010, 1061, 1402, 2772, 3528**
Regan, Amy H. **1061, 1064, 1067, 1070, 3528, 3582**
Reginato, Louis L. **2537, 3257**
Regler, Meinhard **2957**
Reiche, S. **2486**
Reichel, I. **296**
Reid, Ron J. **2656**
Reijonen, Jani **1943**
Reilly, John **980**
Reilly, Robert E. **56**
Reiman, Sergei I. **1312**
Reiser, Martin **234, 1040, 1046, 1656, 1659, 1749, 1758, 1970, 2102, 3274, 3369, 3372**
Reitze, David H. **134**
Rendon, Armando M. **965**
Rensfelt, K.G. **1955**
Repnow, Roland **1955, 3543**
Revol, Jean-Luc **1192, 1195**
Reymermier, Christian **1339**
Reyzl, Ingrid **1171**
Riabko, A. **1548**
Ribes, Jean-Bernard **765**
Rice, David H. **410, 2217, 2972, 3221**
Rice, John A. **3242**
Richards, Mitchell C. **349, 655, 1444, 1447, 1929, 1946**
Richardson, Roger A. **1303, 2149**
Riche, A.J. **250, 1863**
Richied, Donald, E. **2954**
Richter, Achim **2740, 2951**
Richter, D. **197**
Riddone, Germana **3203**
Ries, T. **3540**
Rieul, B. **1569**
Rifkin, Jeff **777, 3423**
Rifuggiato, Danilo **2578, 3288**
Rimmer, Robert A. **800, 803, 896, 907, 3131, 3429**
Rindfleisch, Ulrich **851**
Ringwall, A. **3462**
Rinkel, Tomas **392**
Rinolfi, I. **250**
Ristau, U. **2424, 2427**
Ritchie, Gary **2852, 3339**
Rizawa, Takahito **1722**
Roberts, L. **1488**
Roberts, Scott E. **1351, 3221**
Robin, David **203, 1581**
Robin, G. **2617**
Robinson, Kem E. **2668, 2674, 2677, 3722**
Robinson, Theodore G. **702**
Robl, Phil **2388**
Rodarte, Henry J. **3573**
Rode, Claus **3309**
Rodenas, Jose **2534**
Rodier, Jacques **2012**
Rodriguez-Mateos, Felix **154, 3200, 3203**
Roerich, V. **103**
Rogers, G. C. **2659**
Rogers, Joseph T. **1354, 1686**
Rohmig, P. **1330**
Rokni, Sayed **253, 330, 3429**
Romanov, G.V. **2799, 3561**
Romanov, S.V. **2256**
Roncarolo, Frederico **2999**
Root, Larry **3534**
Roper, R. **3540**
Ropert, Annick **2328**
Rosenberg, Richard A. **1641**
Rosenzweig, James B. **217, 2003, 2006, 2021, 2027, 2039, 2042, 2045, 2480, 2504, 3624, 3708**
Roser, Thomas **26, 614, 857, 1267, 1270, 1276, 1578, 1746, 1964, 2128, 2280, 2725, 3291, 3336**
Roshal, A. **2858**
Ross, Marc C. **253, 307, 800, 1994, 3411, 3429, 3432, 3447, 3453, 3477**
Rossmanith, R. **165, 2424, 2427**
Rotela, E. **2635**
Rothemund, Karsten **2787**
Rothman, Jeffrey L. **2081**
Roudskoy, I. **103**
Rovelli, Alberto **482, 2578**
Rowe, Michael **533**
Roy, Ghislain **2617, 2996**
Roybal, William **1396, 1402**
Roódenas, José **2531**
Rubin, David L. **285, 410, 980, 1300, 3221**
Rudiger, H. **197**
Rudolph, Klaus **3516**
Rudychev, Vladimir G. **2549**
Ruegg, Roman **587**
Rueter, M. **1369**
Ruggiero, Alessandro G. **2590, 3731**
Ruggiero, Francesco **1408, 2626, 2629**
Ruland, Robert **1390, 2698**
Rule, Donald W. **487, 3722**
Rullier, Jean-Luc **1797, 3387**
Rusnak, Brian **965, 974, 977, 1396**
Russell, Steven J. **477**
Russenschuck, Stephan **154, 2796**
Ruth, Ronald D. **250, 262, 423, 777, 3423, 3468, 3480**
Rutkowski, Henry L. **617, 3257**
Rutt, P.M. **1991**
Ryan, K. **1991**
Ryan, W. **2114, 2117**
Rybalchenko, G.V. **2689**
Rybarcyk, Lawrence J. **881, 3528, 3582**
Ryne, Robert D. **137, 366, 611, 1845**
Rödel, Volker **946**
Saban, Roberto **3203**
Sabbi, Gianluca **3179, 3194, 3197**
Sabjan, R. **658**
Sachleben, W. **928**
Saeki, Akinori **2596**
Saeki, Hiroshi **2352**
Saethre, Robert B. **625**
Saewert G. **237**
Safa, Henri **432, 919, 1396**
Safranek, James **206, 1584, 2244, 2304, 2364, 3101**
Sagan, David C. **410, 2966, 2969**
Sah, R.C. **2409, 2415**
Saito, Kenji **432**
Sajaev, Vadim V. **2471, 2942**
Saka, K. **592**
Sakai, Fumio **2036, 2298, 3702**
Sakai, I. **2271**
Sakai, Y. **592**
Sakaki, Horonao **3507**
Sakanaka, Shogo **904, 2310**
Sala-Ferrari, Paola **40**
Salakhutdinov, A.S. **2555**
Salazar, Gilbert A. **655**
Sampayan, Stephen E. **617, 1303, 2611**
Sampson, William B. **185, 3230**
Sandberg, J. **3767**
Sander, Oscar R. **518, 1917, 1923**

Sanders, David M. **1303**, **2611**
Sanders, Ralph T. **1100**, **1261**, **1264**, **1488**, **3336**
Sandner, Wolfgang **2033**
Sandweiss, J. **3722**
Sangster, T. Craig **1937**, **3248**
Sannibale, Fernando **131**, **1536**
Santucci, James K. **237**, **2027**
Sapp, W. **590**
Sarkisov, Gennady S. **3716**
Sasao, M. **1306**
Sassowsky, Manfred **3378**
Sato, H. **3098**
Sato, Hikaru **392**, **2650**, **3360**, **3749**, **3752**
Sato, Shigeru **664**
Sato, Yasuo **413**, **600**, **633**, **798**, **857**, **860**, **863**, **1007**, **2271**, **2280**
Satogata, Todd J. **693**, **705**, **2722**, **2728**
Satoh, Kotaro **1132**, **2084**, **2108**, **2731**
Satoh, Masanori **1174**
Satov, Y. **103**
Satpute, Sharad **1402**
Sattarov, Dior **2936**
Savchenko, A.N. **753**
Sawada, Junichi **3546**
Sawamura, Masaru **2459**
Sazonov, Michael N. **3501**
Scandale, Walter **53**, **3206**, **3209**
Scanlan, Ronald M. **171**, **3194**, **3197**, **3233**, **3236**
Schachter, L. **3600**, **3603**, **3606**, **3609**
Schaffner, Sally K. **729**
Scheer, Michael **2385**
Scheidenberger, Christoph **1671**
Schempp, Alwin **530**, **1955**, **3516**, **3519**
Schep, T.J. **1539**
Schieler, H. **658**, **2424**
Schilcher, Thomas **1129**
Schill, J. **75**
Schlabach, Phillip **3194**, **3197**, **3327**
Schlarb, Holger **2879**
Schleuter, Ross **3429**
Schlicher, Thomas **2087**
Schlitt, Bernhard **3555**
Schlott, Volker **1129**, **2087**
Schlueter, Ross **162**
Schmalzle, Jesse D. **3170**
Schmickler, Hermann **465**
Schmidt, C.W. **521**
Schmidt, Frank **1557**, **1560**, **1563**
Schmidt, Gerald **2172**, **2175**, **2507**
Schmidt, Rüdiger **3200**, **3203**
Schmierer, Eric N. **977**, **1396**
Schmolke, Michael **1034**
Schmor, Paul W. **100**, **106**, **508**
Schmueser, Peter **2172**, **2175**, **2178**
Schnase, Alexander **851**, **1701**, **2292**
Schneegans, T. **197**
Schneider, Gerhard **1339**
Schneider, Herbert **1701**
Schneider, J. David **503**, **1946**, **3528**
Schneider, Th. **165**
Schneider, William J. **934**, **1462**, **1991**
Schnuriger, Jean-Claude **103**
Schoenlein, Robert **2370**, **2498**
Schoessow, Paul **1967**, **2030**, **3621**, **3624**
Scholfield, George **1010**
Schonauer, Horst O. **2933**, **2957**
Schonberg, R.G. **590**
Schrage, Dale L. **965**, **1333**, **1399**
Schreiber, Siegfried **84**, **922**
Schröder, Gerhard H. **1228**, **1408**, **1509**
Schuch, Reinhold H. **1671**
Schuett, Petra **2951**
Schug, Gebhard **3549**
Schulte, Daniel **250**, **259**, **1668**, **1863**, **3441**
Schultheiss, Carl M. **3737**
Schultheiss, Thomas **780**, **3306**
Schultz, David C. **1252**, **3447**, **3450**
Schultz, Sheldon **830**
Schulze, Martin E. **3528**, **3576**, **3579**, **3582**, **3758**
Schwalm, Dirk **1955**, **3543**
Schwandt, Peter **392**
Schwartz, Charles **1073**
Schwartzkopf, S. **545**
Schwarz, Heinz **206**, **800**, **3429**
Scorzato, Carlos **2421**
Scott, Benjamin **206**, **1363**
Scott, Mike **1010**
Scott, Paul K. **1911**, **1926**
Scrivens, Richard **103**
Sears, James **980**
Sebek, James J. **206**, **2361**, **3104**, **3107**
Sedlyarov, Igor K. **2033**
Sedykh, Sergey N. **1055**, **3393**
Seeman, John T. **1**, **296**
Seidel, Mike **34**, **554**
Seidl, Peter **1937**, **2849**, **2852**
Selchow, Nicholas **2235**
Seleznev, Igor B. **2567**
Sellyey, W. C. **2152**, **2214**
Semenov, P.A. **392**
Semertzidis, Yannis K. **490**, **1488**
Sen, T. **1677**, **2635**
Senichev, Yurij V. **2442**, **3549**
Senioukov, Victor A. **2570**
Senti, M. **3212**
Seon, Dong K. **2131**
Serafini, Luca **1997**, **2039**, **2734**
Sereno, Nicholas S. **1587**, **1644**, **2322**
Sergeev, Anatoly P. **1055**, **3393**
Serio, Luigi **1405**, **3203**
Serio, Mario **131**, **636**, **1536**
Serov, Valeri L. **3561**
Sertore, D. **2027**
Servranckx, Roger **2620**
Sery, Andrey **237**, **3321**, **3728**
Sessler, Andrew M. **1716**, **3053**, **3056**
Setzer, Stefan **2951**
Shabunov, Alexey V. **2262**
Shadwick, Bradley A. **1716**, **2888**
Shafer, Robert E. **3758**
Shang, Clifford C. **3251**
Shang, Lei **1315**, **1596**
Shank, Charles **2370**
Shapiro, Michael A. **81**, **833**, **836**
Shapiro, Stephen **2990**
Sharamentov, S.I. **3561**
Sharapa, Anatoly **237**
Sharkov, B. **103**
Sharma, Sushil K. **2635**, **3095**, **3342**
Sharonov, S. **3191**
Sharp, William M. **1830**, **1833**, **3248**
Shasharina, Svetlana G. **369**, **377**
Shatilov, Dmitry **1536**
Shchepounov, V. **3288**
Shcherbakov, A. **3122**
Shea, Thomas J. **2114**, **2117**, **2146**, **2250**
Sheehan, J. **3495**
Sheffield, Richard L. **217**
Shemyakin, Alexander **237**, **521**
Shen, Stewart S. **1333**, **1336**, **1372**, **1396**
Shepard, Kenneth W. **524**, **952**, **955**
Sheppard, John C. **3429**, **3447**, **3450**, **3486**
Sherman, Joseph D. **349**, **655**, **1444**, **1447**, **1929**, **1946**, **3528**
Sheu, Jeng-Tzong **1450**, **3776**
Shevchenko, Oleg A. **2492**
Sheynin, S. **3576**, **3579**
Shibata, Yukio **2187**
Shibuya, S. **1653**
Shibuya, Takashi **3363**
Shiltsev, Vladimir **237**, **641**, **1387**, **1608**, **1692**, **2638**, **3321**, **3728**
Shimbo, M. **600**
Shinn, M. **2456**
Shinoe, Kenji **3363**
Shintake, Tsumoru **3411**
Shinto, Katsuhiro **1653**
Shioya, Tatsuro **2683**
Shirai, Toshiyuki **1294**, **2528**, **3110**
Shirakabe, Y. **565**
Shirakata, Masashi **3360**
Shirasawa, K. **2689**
Shirotov, V. V. **2178**
Shishido, Toshio **432**
Shiyankov, Sergei V. **2948**
Shoaee, Hamid **338**
Shoaff, Phillip V. **1336**
Shpak, A. **3122**
Shu, Deming **2051**, **2090**
Shumakov Igor V. **1764**
Shuman, Derek **3339**
Shumshurov, A. **103**
Shurter, Robert B. **2214**, **2241**
Shvedunov, Vasiliy I. **910**, **2301**, **2555**, **2584**, **2915**
Shvets, Gennady **3675**
Sibley, Coles **3101**
Sidorov, Aleksey **1479**, **1485**
Sidorov, Guennady **2522**
Sieber, Thomas **3516**
Siedling, Rolf **2172**
Siegel, Norbert **154**
Siemann, Robert H. **146**, **321**, **330**, **545**, **824**, **3612**, **3648**
Siemko, Andrzej **154**
Sigg, Peter K. **418**
Siggins, T. **2456**
Sikora, John P. **1115**
Sikora, Robert E. **2114**, **2117**
Silbar, Richard R. **2790**
Silvestri, M. **2578**
Silvestrov, Gregory I. **3062**, **3086**, **3089**
Sim, James W. **1426**, **3318**
Simmering, D. **197**
Simon, Rolf **2424**
Simonov, Karlo G. **2567**, **2570**
Simos, Nikolaos **548**
Simrock, Stefan **922**
Sinclair, Charles K. **65**, **1991**
Sinenko, Irina G. **1468**, **2105**
Singatulin, Shavkat **1387**
Singh, Om **2051**, **2093**, **2244**
Sinjavski, A.V. **1468**
Sivers, Dennis W. **392**
Skarbo, Boris **237**, **3321**
Skarita, John **2552**
Skaritka, John **1390**, **2471**, **2477**, **2480**, **3722**
Skarpass, Knut VIII **3384**
Skocic, Ante **2951**
Skoczen, Blazej **1339**

Skowbo, D. 590
Skozen, Blazej 1330
Skrinsky, Alexander N. 3089
Slater, James 11
Slaton, Timothy 3411, 3477
Sloan, T. 498, 1545, 1548
Smart, Loralie A. 557, 1348
Smedley, John 75, 75
Smirnov, Alexei V. 3615
Smith, Brian G. 977, 1396
Smith, David R. 830
Smith, Frank M. 965, 968
Smith, G. 2128, 2286
Smith, H. Vernon 1444, 1447, 1929, 3528
Smith, Howard 2987
Smith, John D. 355, 690, 2713
Smith, Jr., H. Vernon 1946
Smith, Kevin 2280
Smith, Kevin S. 614, 857, 2725
Smith, Peter D. 2954, 3573
Smith, Robert J. 2096
Smith, Susan L. 2433
Smith, Terry L. 3755, 3758
Smith, Todd I. 321
Smithwick, J. 3233
Smolej, M. 658
Smolyakov, M. N. 2692
Smolyakov, N.V. 2689
Snell, Charles M. 1842
Snodgrass, N. Leon 3594
Snyder, Arthur 2990
Sobenin, Nicolay P. 910, 2301
Soga, F. 600
Soika, Rainer 2936
Sokoloff, M. 2990
Solheim, Larry 1515
Solomon, Lorraine 2244, 2471, 2698
Solyak, Nikolay 461
Solyga, Steffen 1034
Someya, Hirohiko 3348, 3752
Sommer, M. 1569, 2686
Song, Jinhu 2229
Song, Joshua J. 168, 789, 3092
Sonnemann, Florian 154, 2999, 3200
Sonnendrucker, Eric 1830, 2758
Soukas, A. 1264, 1267, 1270, 3767
Sourkont, Konstantin V. 392
Soutome, Kouichi 2337, 2340, 2343, 2346, 2349, 2352
Souza, R. J. 2590
Spalek, George 3573
Spataro, Bruno 1147, 2873
Spataro, Charles 3333
Spence, William 1043
Spencer, Cherrill M. 1252, 3429, 3447
Spencer, James E. 321
Spentzouris, Linda K. 114, 2027, 3155
Spentzouris, Panagiotis 3062, 3083
Sperisen, Franz 392
Spiller, P. 1785, 1788
Spinos, Frank 1333
Spitz, Richard 857, 2280
Sprangle, Phillip A. 3687, 3693
Spyropoulos, Basile 2543
Sredniawski, Joseph 587
Srinivasan-Rao, Triveni 75, 490
Staats, Joachim 2740
Stagno, Vincenzo 1779
Stanford, G. 100, 3540
Staples, John W. 884, 1958, 1961
Starling, W.J. 3531
Starostenko, Alexander A. 2167
Stassen, Rolf 1701, 2292
Steck, M. 527, 1704
Stedinger, M. 2978
Stefani, Giovanni 2060
Steier, Christoph 3098
Steigerwald, M. 1991
Steinhauer, Loren C. 3722
Steinhof, A. 165
Steininger, Ralph 2424
Stella, A. 131
Stelzer, James E. 1923
Stengl, G. 2575
Stepanov, A. 103
Stepanov, Anatoli A. 3561
Stepanov, Sergey S. 1932, 2573
Stephani, Dmitri 2114
Steski, Dannie B. 2277
Stettler, Mathew W. 349, 652, 1946, 2214, 2241
Stevens, Alan F. 1013
Stevens, Alan J. 1237
Stevens, Jr., Ralph R. 1444, 1447, 1917, 1923, 1929, 1946
Stiliaris, E. 1037
Stirbet, Mircea 946
Stockhorst, Hans 851, 1701, 2292
Stoner, J. M. 2590
Stout, Daniel S. 3597
Stover, Greg D. 636, 1213
Strait, J. 2921, 3194, 3197
Strasburg, Sean 1518
Stratienko, Vladimir A. 3269, 3271
Street, Richard W. 3755
Streun, Andreas 1542, 2430
Striganov, Sergei I. 2614
Stroman, Charles R. 1115
Stronisch, U. 197
Strubin, Pierre M. 346, 562
Stupakov, Gennady V. 382, 3444, 3453, 3474
Subashiev, Arsen V. 1988
Suberlucq G. 250
Suda, M. 600
Suemine, Shouji 2596
Sueno, Takeshi 3360
Suetake, M. 1132, 2731
Suetsugu, Y. 633, 1132, 2731
Sugahara, Jun 2187, 2602
Sugimoto, Masayoshi 2459
Sugimura, Takashi 1294, 3110
Suk, H. 1659
Suk, Hyyong 2006, 3708
Sukhanova, Asiya K. 2262
Sukhina, Boris 237, 3321
Suller, Victor P. 2433
Sullivan, Kevin 3306, 3309
Sullivan, Michael K. 296, 2990
Summers, Don 3149, 3152
Sun, Baogen 2048, 2184, 2406
Sun, Ding 854
Sun, H. 913
Sun, Yong 3480
Sutton, Terry D. 3597
Suwada, T. 1132
Suwada, Tsuyoshi 2108, 2238, 2731
Suzuki, Shinsuke 2015, 2749, 3507
Suzuki, Shoji 664
Suzuki, Toshikazu 777, 3417
Suzuki, Yasuaki 2352
Svandrlik, Michele 809, 1120, 1123
Sveshnikov, B.N. 2256
Swenson, Donald A. 3531
Swent, Richard L. 321
Swift, Gary 221, 2099, 2468
Sylvester, C. 1420
Sylvestor, C. 3194
Syphers, Michael J. 1578, 2128, 2632
Syphers, Mike 2641
Syratchev, I. 250
Tadokoro, Masahiro 2528, 3366
Taffarello, L. 1324
Tafti, A. Alai 2728
Tagawa, Seiichi 2018, 2596
Tajima, Tsuyoshi 440
Takada, Ei-ichi 600, 1309
Takado, Hiroshi 3546
Takagi, Akira 413, 565, 798, 860, 863, 1007, 1653
Takagi, Makoto 343
Takahashi, Hiroshi 1273
Takahashi, Jiro 1366
Takahashi, Takeshi 904
Takaki, Hiroyuki 592, 2436, 3363
Takanaka, Masao 1719
Takano, M. 256, 3432
Takano, Siro 2346
Takao, Masaru 2337, 2340, 2343, 2346, 2349, 2352
Takata, Koji 3414, 3417
Takatomi, Toshikazu 777, 3417
Takayama, Ken 1141
Takayama, T. 592
Takayama, Takeshi 2403, 2689
Takayama, Yasuhiro 256, 2155
Takeda, Harunori 3585
Takeda, Osamu 3546
Takeda, S. 3447
Takeichi, N. 592
Takeuchi, Takeshi 106, 1964
Takiyama, Youichi 3363
Tallerico, Paul J. 426, 453
Talman, Richard 410, 2713
Tamura, Hiroyuki 2259
Tamura, Kazuhiro 2346
Tanabe, J. 206, 2355
Tanabe, Toshiya 1722
Tanaka, Hitoshi 2337, 2340, 2343, 2346, 2349, 2352
Tang, Ch. 2769
Taniguchi, Yoshiki 1007
Taniuchi, Tsutomu 2015, 2749, 3507
Taniuchi, Yukiko 2352
Tanke, E. 1860
Tanner, David B. 134
Tantawi, S.G. 3423
Tantawi, Sami G. 423, 783, 1432, 1435
Tao, Xiaoping 2125
Tarakanov, Vladimir P. 1734
Tarasov, Sergej G. 2799
Tartaglia, Michael A. 1420, 1426, 3191, 3194, 3197
Tassotto, Gianni 2211
Tatanov, V.I. 753
Tavares, Pedro F. 2421, 2894, 3125
Tavian, L. 1330
Tawada, M. 1132, 2731
Taylor, Brian 1471
Taylor, C. 3233
Tazzari, Sergio 2313
Tazzioli, Franco 1985, 2734

Tecchio, Luigi B. **2948, 3558**
Tecker, Frank A. **711, 720, 1082, 2719**
Tejima, M. **1132, 2731**
Telegin, Yu. **3122**
Telfer, S. **2021**
Temkin, Richard J. **81, 833, 836**
Temnykh, Alexander B. **410, 3221**
Tenenbaum, Peter G. **253, 338, 3453, 3456, 3459, 3462**
Teng, Lee C. **2635**
Tenishev, Vladimir **103**
Tenyakov, Igor E. **1479, 1485, 2567**
Tepes, Frank **3306**
Tepikian, Steven **37, 1575, 2114, 2728**
Terechkine, Iouri **174, 3242**
Terekhov, V.I. **53**
Terunuma, Nobuhiro **2143, 3432**
Teter, Dave F. **962**
Teytelman, Dmitry **131, 636, 1207, 1213**
Theuws, W.H.C. **759, 2825**
Thibus, Jan **530**
Thieberger, Peter **548, 2277**
Thiery, Yves **2012**
Thikim, M. **2659**
Thivent, Michel U. **2283**
Thomae, Rainer **1917, 1920, 1943**
Thomas, Catherine **913**
Thomas, Manfred **1028**
Thomas, Richard A. **3170, 3188**
Thompson, K. **3465**
Thompson, Kathleen A. **259, 307, 3423, 3489**
Thompson, Kenneth **1979, 2635**
Thompson, Pat **185, 3176**
Thorndahl, L. **250**
Thorson, I. **100**
Thuot, Michael E. **349, 1929, 1946**
Tichonchuk, Vladimir T. **3716**
Tiefenback, Michael G. **1183**
Tighe, Richard C. **800, 1438, 3429**
Tilley, K. **2199**
Timm, Martin **2879**
Ting, Antonio C. **3687, 3693**
Tisserand, Vincent **2990**
Tiunov, M. **1902**
Tkacik, G. **658**
Tobiyama, Makoto **633, 1132, 1138, 2731**
Toda, Makoto **413, 1007**
Todd, Robert **557**
Todesco, Ezio **3206, 3209**
Todosow, M. **548**
Toelle, Raimund **2292**
Toge, Nobukazu **777, 2143, 3414, 3417, 3432**
Tohyama, I. **592**
Tojyo, E. **1893**
Toki, Walter **2990**
Tokumoto, Shuichi **3414**
Tollestrup, Alvin V. **3032, 3062**
Tolmachev, Nikolay G. **3269, 3271**
Tolstun, Nickolay **603**
Tominaka, Toshiharu **3164**
Tomisawa, Tetsuo **3546**
Tommasini, Davide **154**
Tompkins, John C. **174, 3191, 3194, 3197, 3318**
Tonguu, Hiromu **1294, 3110**
Tonutti, Manfred **2172, 2178**
Tooker, Joseph F. **1061, 2954, 3567**
Toole, Loren **1402, 2772**
Torikoshi, Masami **600, 1309**
Toriyama, Minoru **3770**
Torrence, Eric **2999**
Tosi, Lidia **1120, 1126, 2316**
Tosin, Giancarlo **3125**
Tovo, E. **1324**
Towne, Nathan A. **1028, 1031, 2828**
Toyama, Takeshi **1141, 1653, 1821, 3098**
Trakhtenberg, Emil **1369, 2489**
Trautwein, T. Ann **206, 1363**
Travier, Christian **916**
Travish, Gil **2024, 2045, 2483**
Trbojevic, Dejan **37, 1237, 2117, 3176, 3336**
Tremaine, Aaron **217, 2006, 2021, 2480**
Tremblay, Kelly **3306, 3312**
Treps **2990**
Tribendis, Alexey G. **2033**
Trines, D. **245**
Trines, R.M.G.M. **1539**
Trofimov, A.V. **2704**
Trofimov, Nikolai **346**
Troha, Anthony L. **2000**
Tromba, G. **2316**
Trombly-Freytag, Kelley **3318**
Tron, Alexander **2190**
Tron, Wolfgang **986**
Tropea, Paola **3206**
Trower, W. Peter **910, 2301, 2555**
Troyanov, E. **53**
True, Richard **1049**
Trujillo, Marcos C. **965**
Trzeciak, Walter S. **2388, 2391, 2659**
Tsai, H.J. **1162, 2409**
Tsai, Y.L. **2000, 2009**
Tsai, Zone-Da **1150**
Tsang, Thomas **490**
Tsarenkov, A.P. **2256**
Tsoupas, Nicholaos **702, 1100, 1267, 1270, 1578, 2114, 2117, 2722, 2725, 2918, 3182, 3185, 3291**
Tsubuku, Hideo **1309**
Tsuchidate, Hiroyuki **848**
Tsuchiya, Kimichika **2683, 3158**
Tsukamoto, K. **633**
Tsukishima, Chihiro **848**
Tsunemi, Akira **2036, 2552**
Tsung, F. S. **3672**
Tsutsui, Hiroshi **1058, 3414**
Tuckmantel, Joachim **949**
Tung, Louann S. **1372**
Tuozzolo, Joseph E. **1100, 1264, 1267, 1270, 3300**
Tupikov, Vitaliy S. **2167**
Turner, James **256, 774, 1252, 3432, 3450**
Turner, William C. **1674, 3149**
Tölle, Reimund **1701**
Ueda, Toru **2187, 2602, 2605**
Ueng, Tzong-Shyan **1375, 1450, 2069, 2072, 2412**
Ueno, Ryuichi **2271**
Uesaka, Mitsuru **2187, 2602, 2605**
Uesugi, Tomonori **62, 413, 798, 860, 863, 1007, 1653, 1818, 1821, 2271**
Umezawa, K. **2271**
Umezawa, Masumi **2528, 3366**
Umstadter, Donald **3666**
Urabe, Osamu **2602**
Urakabe, E. **600**
Urakawa, Junji **256, 2143, 2155, 2552, 3432**
Urbanus, W.H. **2462**
Urita, K.K **471**
Ursic, Rok **1120, 1129, 2087, 2253**
Usack, Victor **490**
Usher, Tracy **307, 3384**
Uythoven, Jan **1228, 2996, 2999**
Uzat, H. W. **450**
Uzunoglou,N. **1037**
v. Drachenfels, Wolther **3098**
Vaccaro, Vittorio G. **1599**
Vahsen, Sven E. **3026**
Vaillancourt, Kurt W. **3423, 3480**
Valdiviez, Robert **1333**
Valentini, Marco **250, 3402**
Valentino, Vincenzo **1905**
Valero, Saby **1860**
Valicenti, Raymond A. **971, 1327**
Valla, Arthur S. **2668**
van Asselt, Willem K. **1746**
van Bibber, Karl A. **777, 3447, 3450**
van der Geer, Bas **2462, 3266**
van der Wiel, M.J. **3266**
van Duppen, Piet **1955**
Van Eijndhoven, S.J.L. **1539**
Van Ginneken, Andy **2525, 3074, 3080**
Van Hagan, T. **1393**
Van Rienen, U. **2764, 2787**
van Steenbergen, Arie **3722**
Van Vaerenbergh, Pierre **2662, 2665**
van Zeijts, Johannes **705, 732, 2146, 2722, 2725, 2728**
VanAsselt, W. **614, 3291**
VanBrocklin, Henry **533**
Vane, C. Randy **1671**
Vanecek, David L. **3390**
Vanenkov, Iouri **154**
Varela-Rodriguez, F. **103**
Variale, Vincenzo **1779, 1905**
Vascotto, Alessandro **2316**
Vasilishin, Bogdan V. **2256, 2262**
Vasiniuk, Ivan E. **1468, 2105**
Vasserman, Isaac B. **2471, 2489**
Vasyuchenko, Alexandr V. **3561**
Vella, Michael C. **3257**
Veness, Raymond J. **1339**
Vengrov, R. M. **3561**
Venturini, Marco **234, 1590, 1593, 1752, 1758, 1970, 3274, 3369, 3372**
Ver Planck, Peter **1491**
Verbeke, Jerome M. **1926, 2540**
Verdier, Andre **304, 398, 1557, 1563, 2623, 3005**
Verdu, Gumersindo **2534**
Verhoeven, A.G.A. **2462**
Vermare, C. **3387**
Vernon, W. **2021**
VerPlanck, Peter **568**
Verstovsek, I. **658**
Verzilov, Viktor A. **2193, 2196**
Veshcherevich, Vadim **980**
Vest, Robert E. **2388**
Veteran, J. **2686**
Vetter, Arthur M. **1186**
Vetter, Paul **1952**
Vier, David C. **830, 3612**
Vignola, Gaetano **131, 866, 1536**
Vikharev, A.L. **1474**
Vilakazi, Zeblon Z. **1671**
Villate, Denis **1381**
Vinciguerra, Domenico **2578**
Vinogradov, N. **2855**
Vinogradov, Stanislav V. **1764**
Vinokurov, Nikolai A. **2492**
Virostek, Steve **884**
Vlieks, Arnold E. **3420, 3423, 3447**
Voevodin, M.A. **2256**

Vogel, Greg **2211**
Vogel, Hans **957, 2033, 3510**
Vogel, Vladimir **461**
Vogt, S. **197**
Voigt, Siegfried **806, 809, 2424**
Volfbeyn, Paul **325, 330, 3696, 3705**
Volk, J.T. **182, 3324**
Volkov, Igor A. **1872**
Volkov, O. Y. **2178**
Volkov, V.I. **2256**
Volkov, Vladimir N. **2033**
vom Stein, Peter **957, 2033, 3510**
von Hahn, R. **3543**
von Hartrott, M. **197**
von Holtey, Georg **3008**
von Przewoski, Barbara **392**
Vondrasek, R. **1890**
Vorobiev, Leonid G. **234, 2781, 3116**
Vos, Lucien **304, 465**
Voss, Gustav A. **2385**
Vossenberg, Eugene B. **1228, 1509**
Vsevolozhskaya, Tatiana A. **3062, 3086, 3089**
Vujic, Jasmina **2540**
Vysotskii, Vladimir I. **1312, 3642**
Wada, M. **1306**
Wagner, Stephen **2990**
Wahl, Dan **2388**
Wait, Gary D. **1509**
Wake, M. **174, 3330**
Walbridge, Dana G.C. **3318**
Walcher, Th **165**
Waldron, William L. **3257**
Walker, J. **548**
Walker, R. **182, 2456**
Walker, Richard P. **2313, 2680**
Wallen,Erik **2945**
Walters, Dean R. **1342, 1378**
Walther, R. **2424**
Walz, Dieter R. **253, 330, 2111, 3453**
Wan, Weishi **395, 1677, 2465, 3065, 3068, 3152**
Wan, Xiang **81**
Wanderer, Peter J. **185, 3161, 3170, 3173, 3176, 3230**
Wang, C.J. **682, 685**
Wang, Ch. **2409, 2671**
Wang, Changbiao **1052, 3630**
Wang, Chunxi **363**
Wang, D. X. **934**
Wang, Fuhua **3101**
Wang, Guicheng **1315, 1596, 2048, 2125, 2184**
Wang, Huacen **3263**
Wang, J.G. **1659, 1970**
Wang, J.M. **1106**
Wang, J.Q. **1058**
Wang, J.W. **3423, 3468**
Wang, Jian-Guang **234, 1656, 2102, 3369, 3372**
Wang, Jihong **2125**
Wang, Jiuqing **633, 3414**
Wang, Ju **3773**
Wang, Junhua **2048, 2184**
Wang, Juwen **777, 3420, 3426, 3477, 3480**
Wang, Lanfa **633**
Wang, Li-Fang **3381**
Wang, Lin **1315, 1596, 2140**
Wang, M.H. **1159, 1602, 1605, 2837**
Wang, P. **3600, 3603, 3606, 3609**
Wang, Ping **221, 2099**
Wang, S. **330, 1695, 3705**
Wang, S.T. **3227**
Wang, Sho Qin **3651**
Wang, Shuhong **633**
Wang, Shumei **2140**
Wang, Tai-Sen F. **1623, 1848, 2876**
Wang, X. **2018**
Wang, X.J. **229, 2024, 3495, 3627**
Wang, Xiangqi **1315, 1596**
Wang, Xijie **2158, 2471, 2480, 2942**
Wang, Yi-Ming **1064, 1067, 1070**
Wangler, Thomas P. **611, 1061, 1848, 3582**
Warburton, D. **1488**
Warner, A. **521**
Warren, David S. **349, 655**
Warsop, C.M. **2199**
Washio, Masakazu **2018, 2298, 2552**
Watanabe, Kowashi **2352**
Watanabe, Takahiro **2187, 2602, 2605**
Watanabe, Tamaki **1653**
Watanabe, Yuichi **777, 3417**
Watson, Scott A. **617**
Waynert, J.A. **977, 1327**
Webber, Robert C. **1097**
Weber, Robert **3740**
Weggel, Robert J. **3041, 3047**
Wei, Jie **548, 1575, 1743, 2713, 2921, 3176, 3179, 3182, 3185**
Wei, Wen-His **1375**
Weihreter, Ernst **197, 2385**
Weijers, S.R. **759**
Weiland, Thomas **2740, 2743, 2879, 2951**
Weindl, A. **658**
Weinrich, U. **2331, 2334**
Weir, John T. **622, 1303, 3513**
Weise, Hans **922, 2507**
Weiss, Daniel **557, 1348**
Weiss, M. **759**
Weisse, Eberhard **40**
Welch, James J. **1441, 3221, 3224**
Welsch, C. **3516**
Welz, J. **100**
Wen, Long **3263**
Weng, Wu-Tsung W. **1297, 3185**
Wenninger, Joerg **2885, 2996, 2999, 3011, 3014**
Werin, Sverker **2945**
Wermelskirchen, C. **206**
Westenskow, Glen A. **617, 1303, 3251, 3254, 3387, 3390**
Westphal, T. **197**
White, Jeff **2217**
White, Karen S. **729, 732, 735**
White, Marion M. **1414, 1967**
Whittum, David H. **330, 2111, 3612**
Wiedemann, Helmut **206, 321**
Wiemerslage, G. **1369**
Wienands, Hans-Ulrich **296, 1252, 2993**
Wieting, James **1923**
Wight, Geoff .W. **106**
Wilcox, Marc **1926**
Wilde, Stephen **1920**
Wildman, David W. **237, 869, 2840**
Will, Ingo **2033**
Wille, K. **206**
Willeke, Ferdinand **407, 554**
Willen, Erich **185, 3161, 3173**
Williams, C. **1881**
Williams, David J. **2223**
Williams, Malcom D. **1911, 1914, 1917, 1920, 1923, 1943, 1958, 2540, 2575**
Williams, Neville W. **2063, 2128, 2286**
Williams, Robert A. **2790**
Williams, Ronald L. **3681**
Wilson, Ian **250, 821**
Wilson, J. H. **2590**
Wilson, P. **2003**
Wilson, Perry B. **423, 3423**
Wind, D. **2936**
Wines, Robin **3309**
Winick, Herman **2385**
Winkler, Martin **2578**
Winkler, T. **527, 1704**
Winschuh, Erich **530**
Winter, W. R. **2659**
Wiseman, Mark **934, 3309**
Wisnivesky, Daniel **792**
Wissmann, Mark **768**
Witherspoon, R. **545**
Witherspoon, Sue D. **732**
Witkover, Richard L. **2128, 2247, 2250**
Wolcott, Chip **1037, 1515**
Wolf, Z. **1390**
Wolff, Dan **3761**
Wolfley, Rick **3306**
Wollnik, Hermann **2578**
Wolski, Andrzej **2433**
Wong, Seung **1043, 1890**
Wong, Tom **3618**
Wong, Victor K. **392**
Woodle, Martin **1028, 2471**
Woodley, Mark D. **256, 307, 3384, 3429, 3432, 3447, 3456**
Woods, Mike **3465**
Woodworth, Lee **2114**
Wright, R. **652**
Wright, Robert **3342**
Wrulich, Albin F. **192**
Wu, G. **714, 717, 1462**
Wu, Guozhong **2602**
Wu, Lydia K. **1926, 2540**
Wu, Xiaoyu **1318, 3116**
Wu, Ying **221, 688, 2099, 2468**
Wu, Yingzhi **282**
Wuensch, Walter **250, 821, 827, 3387**
Wuestefeld, Godehard **197, 2376, 2385**
Wurtele, Jonathan S. **1716, 2888, 3053, 3056, 3059**
Wutte, Daniela **533, 1952**
Wyss, Carlo **149, 3203**
Xavier, Jr., Ademir L. **2891**
Xiao, Meiqin **404**
Xie, Ming **3678**
Xie, Zu Qui **533, 1952**
Xu, Hongjie **209**
Xu, Hongliang **1315**
Xu, Jingwei **633**
Xu, S. **1369**
Xu, X.J. **533**
Xu, Z. **3600**
Xue, K. **2140**
Yadav, S. **174, 3194, 3197**
Yakimenko, Vitaly **461, 2158, 2471, 2552, 2942, 3495, 3722**
Yakovlev, Vyacheslav P. **1049, 2775, 3492**
Yamada, Hironari **592**
Yamada, R. **174**
Yamada, S. **600, 2271**
Yamaguchi, Seiya **1058, 3414**
Yamamoto, Masanobu **413, 798, 860, 863, 1007, 1653**
Yamamoto, N. **2731**
Yamamoto, Nobor **1132**
Yamamoto, Noboru **343**

Yamamoto, Tamotsu **2596**
Yamamoto, Y. **492**, **2271**
Yamashita, H. **600**
Yamauchi, Toshihiko **2459**
Yamazaki, Junichiro **592**
Yamazaki, Yoshishige **513**
Yan, Yiton T. **363**
Yanagida, Kenichi **2015**, **2749**, **3507**
Yanaoka, Eiichi **3348**
Yang, Bingxin **1644**, **2024**, **2134**, **2137**, **2161**
Yang, J. S. **902**
Yang, Jinfeng **2018**, **2036**, **2298**, **3702**
Yang, Ming-Jen **711**, **720**, **723**, **1082**, **1085**, **2719**
Yang, Tz Te **1159**, **2000**
Yang, W.Y. **2265**
Yano, Yasushige **2268**
Yao, Chenggui **1596**
Yarba, V. **174**
Yashin, Yuri P. **1988**
Yazynin, Igor A. **1321**
Ye, Kairong **633**
Yeh, Meng Shu **1153**, **1159**, **1162**, **2000**
Yen, Boris **1506**
Yeremian, A. D. **1994**
Yin, B.G. **3345**
Yin, Yan **2048**
Yip, Harry H. **1402**
Yokoi, Takeichiro **1653**
Yokomizo, Hideaki **3128**, **3507**, **3546**
Yokota, Watalu **2259**
Yokoya, Kaoru **633**, **1725**, **3435**
Yoon, Byung-Ju **3525**
Yoon, J.C. **679**
Yoon, Moohyun **2265**, **3137**
York, Richard C. **234**, **1318**, **2781**, **3116**, **3719**
Yorozu, Masafumi **2018**, **2036**
Yosh **2731**
Yoshida, H. **2689**
Yoshida, Katsuhisa **848**, **848**
Yoshida, Mitsuhiro **3158**, **3411**
Yoshida, Susumu **343**
Yoshida, Yoichi **2596**
Yoshida, Youichi **2018**
Yoshii, Jean **3654**
Yoshii, Kenji **343**
Yoshii, Koji **2187**, **2602**, **2605**
Yoshii, Masahito **413**, **798**, **857**, **860**, **863**, **1007**, **1653**, **2280**
Yoshii, Masato **2271**
Yoshikawa, H. **3507**
Yotam, R. **206**
Young, Andrew **131**, **636**, **1213**
Young, Anthony **162**
Young, Lloyd M. **881**, **1444**, **1447**, **1929**, **1946**, **3528**, **3570**, **3582**
Yourd, Roland **884**
Youssof, S.S. **392**
Yovchev, I. **1040**, **1046**
Yu, D. **2042**
Yu, David **815**, **2003**, **2021**
Yu, H. **2140**
Yu, Li Hua **2471**, **2474**, **2942**
Yu, Simon S. **1800**, **1934**, **2746**, **3257**, **3390**
Yudin, Ivan P. **2704**
Yun, V. **3372**
Yunn, Byung C. **1177**, **1180**, **2453**, **2456**
Zachariadou, Katerina **2990**
Zadorozhny, Vladimir **2820**
Zagar, K. **658**
Zagel, James R. **468**, **2164**, **2211**
Zahir, Nastaran **1926**, **2540**
Zalateu, M. **2680**
Zaltsman, Alexander **857**, **2280**
Zalyubovskiy, Ilya I. **2549**
Zangrando, Dino **2680**
Zanini, Alba **2531**
Zapasek, R. **1488**
Zaplatine, Evguenii N. **887**, **959**, **3549**
Zaugg, Thomas J. **349**, **655**, **1444**, **1447**, **1923**, **1929**, **1946**
Zavialov, V. **592**
Zeitlin, Michael **1614**, **1617**, **1620**, **2900**, **2903**, **2906**, **2909**, **2912**
Zelazny, Michael S. **2987**
Zelenski, Anatoli N. **106**, **1964**
Zelinsky, A.Yu. **2924**, **2927**, **2930**, **3122**
Zeng, J. **2003**, **2021**
Zeno, Keith L. **1276**
Zhabitsky, Vyacheslav M. **1222**
Zhang, Chuang **633**, **1695**
Zhang, F.Q. **3348**, **3752**
Zhang, Jinguo **1315**
Zhang, Jun **1273**
Zhang, Kaizhi **3263**
Zhang, Min **2769**
Zhang, S.Y. **614**, **3185**, **3294**, **3297**
Zhang, T-B. **3627**
Zhang, T. **1881**
Zhang, Tiejue **1940**
Zhang, Wenwei **234**, **1970**, **3263**, **3372**
Zhang, Wu **1261**, **1264**, **2406**
Zhang, Xiaolong **2629**
Zhao, Feng **1315**, **2125**
Zhao, G.Y. **3345**
Zhao, Yongxiang **3149**
Zhao, Zheng **2140**
Zhao, Zhentang **209**, **1453**
Zhogelev, Pavel **461**
Zholents, Alexander A. **1794**, **2370**, **2465**, **2498**
Zhou, Anqi **2406**
Zhou, Feng **633**, **2963**
Zigler, Arie **3687**, **3693**
Zigrosser, Douglas **557**, **1348**
Zimmerman, Robert **1396**
Zimmermann, F. **1560**, **2626**
Zimmermann, Frank **206**, **256**, **307**, **382**, **1728**, **3432**
Zimmermann, Holger **530**
Zinchenko, Alexander **1692**
Ziomek, Chris D. **1064**, **1070**
Zisman, Michael S. **293**, **296**
Zlobin, Alexander V. **174**, **3194**, **3197**
Zobov, Mikhail **131**, **1147**, **1536**
Zolecki, Robert A. **2274**
Zolfaghari, Abbi **1037**, **1515**
Zolotorev, Max S. **2111**, **2370**, **2498**
Zorko, B. **658**
Zotter, Bruno **1118**, **1408**
Zou, Peng **3618**
Zou, Yong **3263**
Zou, Yun **234**, **1659**, **1970**, **2102**, **3369**
Zoubets, V. **106**
Zubovsky, Victor P. **1932**
Zumdieck, John F. **2668**
Zuo, K. **206**
Zvonaryova, O. **2927**

1999 PARTICLE ACCELERATOR CONFERENCE

Brookhaven National Laboratory, Bldg. 911B, P.O.Box 5000, Upton, New York USA 11973-5000 http:/pac99.bnl.gov/

AT THE NEW YORK MARRIOTT MARQUIS
MARCH 29 - APRIL 2, 1999

Conference Chairman
W.T. Weng, BNL
Telephone: 516-344-2135
Fax: 516-344-5954
E-mail: weng@bnl.gov

Program Chairman
I. Ben-Zvi, BNL
Telephone: 516-344-5143
Fax: 516-344-3029
E-mail: ilan@bnl.gov

Organizing Committee
M. Allen, SLAC (NPSS)
J. Ball, ORNL
W. Barletta, LBNL
I. Ben-Zvi, BNL
Y. Cho, ANL
L. Costrell, NIST
M. K. Craddock, UBC & Triumf
W.K. Dawson, TRIUMF (IEEE)
D. Finley, FNAL
D. Friesel, IUCF
D. Hartill, Cornell U.
C. Joshi, UCLA
M. Kihara, KEK (APAC)
S. Krinsky, BNL
C. Leemann, TJNAF
J. Peoples, FNAL (DPB)
M. Reiser, U. Maryland
B. Ripin, APS
C. Roberson, ONR
S. Schriber, LANL
R. Siemann, SLAC
D. Sutter, DOE
S. Tazzari, U. Roma & INFN-LNF (EPAC)
W.T. Weng, BNL, Chairman
G. Westenkow, LLNL
R. York, NSCL

Conference Secretary
M. Campbell, BNL
Telephone: 516-344-5458
Fax: 516-344-5954
E-mail: pac99@bnl.gov

Local Committee, BNL
J. Becker, *Treasurer*
H. Kirk, *Coordinator, Poster & Exhibits*
J. Laurie, *Printing*
E. Lowenstein, *BNL Tour*
P. Lucas, *Publishing (FNAL)*
A. Luccio, *Editor*
W. MacKay, *Editor*
C. Ronick, *Hotel Coordinator*
J. Smith, *Electronic Publishing*
P. Yamin, *Social & Spouse Activities*

February 23, 2000

DTIC
8725 John J Kingman Road
Ste. 0944
Ft. Belvoir, VA 22060-6218

Dear Sir,

The 1999 Particle Accelerator Conference (PAC'99) took place on March 29 - April 2, 1999 at the New York Marriott Marquis. We had approximately 1,195 registrants, 76 invited speakers and 1,528 abstracts covering all aspects of accelerator science, technology and applications. Among the registrants, approximately 2/3 were from the United States, 1/3 from abroad - truly an international conference in its scope and participation. Concurrent with the conference, there were 40 industrial firms participating in the exhibition.

The proceedings of PAC'99 were published and distributed in November 1999. Total published papers are 1,223 which are published in a 5 volume set with the total pages numbering 3,779.

The total amount of the ONR grant of $10,000.00 was all used in the support of the expense of junior staff, graduate students, and scientists from the developing nations and former Soviet Union.

As requested form SF298 is enclosed, and shipped separately is one set of the PAC '99 proceedings.

I would like to express my sincere thanks to ONR for its support to PAC'99 which is a very effective vehicle for the development and communication in the accelerator profession.

Sincerely yours,

Wu-Tsung Weng
Chair, PAC'99

attachment: Form SF298

cc: K. Galuchie, IEEE
Grant Administrator - ONR

WTW:mc

The American Physical Society
IEEE
BROOKHAVEN NATIONAL LABORATORY
BROOKHAVEN SCIENCE ASSOCIATES

A23880 Vol 1 Approved for Public Release, Distribution Unlimited
A23880 Vol 5